CODEN: JASMAN

The Journal of the Acoustical Society of America

ISSN: 0001-4966

Vol. 124, No. 1 July 2008

(Continued)

CONTENTS—*Continued from preceding page*

(Continued)

CONTENTS—*Continued from preceding page*

(Continued)

CONTENTS—*Continued from preceding page*

Method-of-adjustment measures of informational masking between auditory streams

Stanley Sheft
Parmly Hearing Institute, Loyola University Chicago, 6525 North Sheridan Road, Chicago, Illinois 60626
ssheft@luc.edu

William A. Yost
Department of Speech and Hearing Science, Arizona State University, Tempe, Arizona 85287
William.Yost@asu.edu

Abstract: A method-of-adjustment procedure was used to measure thresholds for detecting a continuous sequence of brief 2-kHz tonal pulses in the presence of random-frequency masking sequences. Masker pulses consisted of either one or eight sinusoidal components and were either synchronous or asynchronous with the signal pulses. Effects of pulse rate and asynchronous gating were generally consistent with a reduction in informational masking due to segregation of the signal and masker streams. Despite use of continuous stimulus presentation to encourage stream segregation, masking was still obtained from most listeners in most conditions.

PACS numbers: 43.66.Dc, 43.66.Mk [Q.-J.F.]
Date Received: February 12, 2008 **Date Accepted:** March 28, 2008

1. Introduction

Informational masking refers to difficulty in either signal detection or discrimination beyond that predicted by energetic masking between a signal and masker (for a review, see Kidd *et al.*, 2008). Though initial studies emphasized masker uncertainty as the basis of the interference, more recent considerations have also attributed a role to similarity between the signal and masker (e.g., Durlach *et al.*, 2003; Watson, 2005). Involvement of similarity allows for possible reduction in informational masking by enhancing distinction between the signal and masker. Working with auditory sequences, Kidd *et al.* (1994) demonstrated a release from informational masking through stimulus manipulations intended to promote perceptual segregation of the signal and masker auditory streams. Subsequent work by Durlach *et al.* (2003) confirmed this result with studies by Kidd *et al.* (2003) and Micheyl *et al.* (2007) supporting the interpretation linking the masking release to stream segregation.

As with informational masking, models of auditory streaming invoke involvement of stimulus similarity in the perceptual effect (McNally and Handel, 1977; Moore and Gockel, 2002). For streaming, stimulus-event similarity is seen as the basis of stream coherence, whereas for informational masking, similarity lessens component resolution; with separate streams defined as signal and masker, local similarity encourages stream segregation to enhance signal detection. A common basis for the two effects suggests strong potential for release from informational masking as a result of stream segregation. Though presenting multiple stimulus pulses, overall stimulus duration was relatively brief (roughly 0.5–2.4 s) in the informational-masking studies cited previously. Conversely, studies of the buildup of stream segregation indicate that the effect accumulates over longer time spans (e.g., Anstis and Saida, 1985), especially if attention is not refocused or diverted (Cusack *et al.*, 2004). The present study evaluated signal detection in the presence of random-frequency masker streams, utilizing continuous stimulus presentation intended to fully promote signal stream segregation from a masker of undetermined sequential coherence. Along with overall duration, gating characteristics affect segregation, both in studies of streaming (e.g., Dannenbring and Bregman, 1978; Turgeon *et al.*, 2005) and informational masking (Kidd *et al.*, 1994; Neff, 1991, 1995; Durlach *et al.*, 2003; Leibold

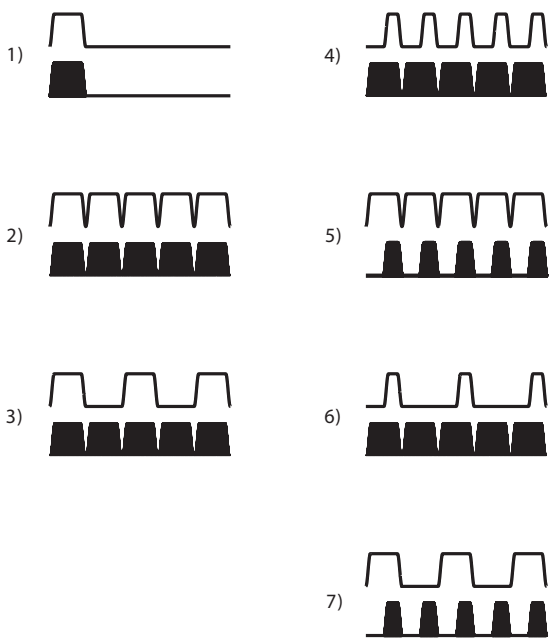

Fig. 1. Schematic illustration of the seven masking conditions. For each condition, the signal stream is illustrated at the top with the open trace and the masker stream below with the filled trace. Signal- and masker-pulse duration was either 40 or 80 ms with concurrent pulses either synchronously or asynchronously gated (see the text for additional details).

and Neff, 2007; Micheyl *et al.*, 2007). Consequently, experimental conditions evaluated the effect of temporal disparities in terms of both asynchronous gating of concurrent signal and masker pulses along with presentation of only alternate signal pulses against the masker stream.

2. Method

Thresholds for detecting a continuous stream of 2-kHz signal pulses were measured for 16 listeners both in quiet and in the presence of a continuous masker stream. Five configurations for the signal sequence were paired with three masker-sequence configurations for a total of seven masking conditions (see Fig. 1). Within the signal and masker sequences, pulse duration was either 40 or 80 ms. When the signal and masker pulses shared a common 80-ms duration, signal and masker pulses were either synchronously gated with an interstimulus interval (ISI) of 420 ms (condition 1) or 0 ms (condition 2), or every other pulse was omitted from the signal stream with the masker ISI maintained at 0 ms (condition 3). In the remaining conditions, signal- and masker-pulse durations differed with the streams aligned so that either signal-pulse onset was delayed by 40 ms relative concurrent masker pulses (conditions 4 and 6), or masker-pulse onset was delayed (conditions 5 and 7). As in condition 3, the signal was presented only during alternate masker pulses in conditions 6 and 7. All signal and masker pulses were shaped with 10-ms cosinusoidal rise/fall times.

Masker pulses consisted of either one or eight sinusoidal components. With a single masker component, masker frequency was either fixed at 1417 Hz, or for each pulse was drawn at random from a uniform distribution evenly spaced on a logarithmic scale ranging from 500 to 7000 Hz, excluding a "protected" region of 1600–2500 Hz about the signal frequency. The component phase was randomly selected from a uniform distribution between 0 and 2π. A similar scheme for random selection was used for each component of the eight-component maskers; in addition, relative component amplitude was randomly drawn from a Rayleigh distribution. With both the one- and eight-component maskers, overall masker level was fixed at 65 dB SPL. Dell PCs with 24-bit Echo Gina 3G soundcards were used for stimulus generation

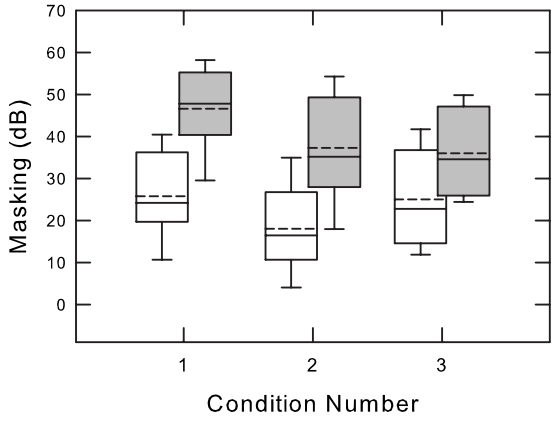

Fig. 2. As a box plot, group masking data from conditions 1–3 in which the common signal- and masker-pulse duration was 80 ms. Masker frequencies were randomly selected with the open boxes for results obtained with the single-component masker, and the gray boxes for the eight-component-masker conditions. Box boundaries indicate the 25th and 75th percentiles, with error bars extending to the 10th and 90th percentiles. Group median and mean threshold values are indicated within each box by horizontal solid and dashed lines, respectively.

and experimental control. Following analog conversion at a 22.05-kHz sampling rate, stimuli were low-pass filtered at 8 kHz and presented diotically through Sennheiser HD 280 Pro headphones with the listeners seated in a double-walled soundproof booth.

To accommodate continuous stimulus presentation, thresholds were measured with a method-of-adjustment procedure. Both Watson *et al.* (2002) and Yost *et al.* (2007) used a method-of-adjustment procedure in investigations of the effects of masker uncertainty, with Watson and his co-workers reporting that in some cases the procedure allowed for listeners to more rapidly adopt a detection strategy that lessened the extent of informational masking. Once a listener initiated a threshold run in the present study, signal level was continuously controlled by the listener via adjustment of a slider on a graphical user interface displayed on a computer monitor. Listeners were instructed to adjust the level so that they could just detect the signal stream. Listeners were encouraged to adopt a bracketing strategy to set threshold levels, and also to allow time between level adjustments for stream formation. In the masking conditions, the procedure began with a 5-s presentation of the signal stream in isolation at 85 dB SPL as a cue. Following a 1.5-s silent pause, the signal and masker streams were presented concurrently with listeners then given control of signal level. In all conditions, a single method-of-adjustment threshold was collected from each of the 16 listeners across two listening sessions. Experimental protocol was approved by the Institutional Review Board of Loyola University Chicago.

3. Results and discussion

As in most studies of informational masking, individual differences characterized results from all conditions. To convey both the distribution of threshold values and data trends, results are displayed as box plots. Figure 2 shows results from conditions 1–3 in which the common signal- and masker-pulse duration was 80 ms. Masking in dB is the threshold difference obtained with and without the masker present. In all conditions, masker frequencies were randomly selected with the open boxes representing conditions with single-component masker pulses, and the gray boxes indicating results obtained with eight-component maskers. Across conditions 1–3, masking was greater in the multi- than single-component conditions. This effect of the number of masker components is consistent with past results from informational-masking studies (e.g., Neff, 1991, 1995; Kidd *et al.*, 1994). With either the single- and eight-component maskers, masking diminished with decreasing ISI from 420 to 0 ms between conditions 1 and 2. In that stream coherence is not expected with the longer ISI (e.g., Bregman *et al.* 2000), a masking

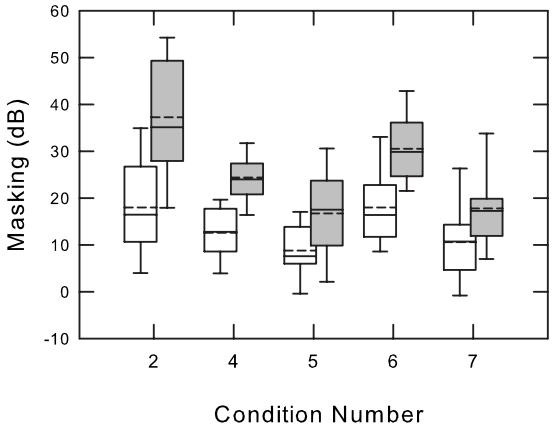

Fig. 3. Same as Fig. 2 for conditions 4–7 in which either the signal- or masker-pulse onset was delayed 40 ms. For comparison, results from condition 2 are replotted from Fig. 2.

release due to segregation of the constant-frequency signal stream from the random-frequency maskers is anticipated only with the 0-ms ISI. An inverse relationship between masking and ISI was a central result used by Kidd *et al.* (2003) to support interpretation of stream segregation as a potential factor in release from informational masking.

In condition 3, presentation of only alternate signal pulses created a temporal disparity between the signal and masker streams. Kidd *et al.* (1994) reported a reduction in masking with signal presentation only during alternate pulses of identical masker samples. The masking release was obtained despite the drop in signal energy due to alternation. With the omission of every other signal pulse and frequency randomization across masker pulses within constrained ranges, Micheyl *et al.* (2007) found that the extent of masking was consistent with change in signal energy. That is, the temporal disparity generated by omitting signal pulses did not aid performance, and in fact led to threshold elevation. In the present conditions in which masker frequency was randomly varied, comparison of results from conditions 2 and 3 indicates that signal alternation either had no effect or led to a slight increase in masking.

These observations were supported by a two-factor repeated-measures analysis of variance (ANOVA), which showed significant main effects of number of masker components $[F(1,15)=59.0; p<0.001]$ and condition $[F(2,30)=5.4; p=0.01]$, along with a significant interaction $[F(2,30)=9.3; p=0.001]$. Tukey's post-hoc pairwise comparisons confirmed a significant effect of ISI, and that only with a single-component masker did omitting signal pulses through alternation significantly affect performance.

Figure 3 shows results from conditions 4–7 in which either the signal- or masker-pulse onset was delayed 40 ms relative to the other. Results from condition 2 in which the signal and masker pulses were synchronously gated are shown on the left for comparison. In all conditions, masker frequencies were randomly selected with box shading again distinguishing the number of masker components. As in the initial data set, increasing the number of masker components from one to eight increased the amount of masking. Comparing group threshold values in conditions 2, 4, and 5 indicates that delay of either the signal or masker onset reduced the amount of masking with a greater masking release observed with delay of the masker rather than the signal. As with condition 3 of the first data set, the stimulus configurations of conditions 6 and 7 presented only alternate signal pulses against the continuous masker stream. Similar to the results from the first data set, temporal disparity due alternation of signal pulses on average had little to no effect.

A two-factor repeated-measures ANOVA supported these observations, showing significant main effects of number of masker components $[F(1,15)=105; p<0.001]$ and condition $[F(4,60)=29.1; p<0.001]$, along with a significant interaction $[F(4,60)=6.7; p<0.001]$.

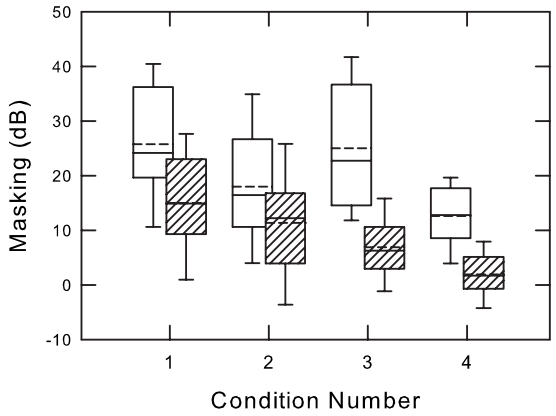

Fig. 4. Same as Fig. 2 for conditions 1–4 with a single-component masker. Right-hatched boxes represent results obtained with the masker frequency fixed at 1417 Hz; the open boxes replot data from Figs. 2 and 3 in which masker frequency was randomized across pulses.

Tukey's post-hoc pairwise comparisons confirmed a significant effect of delaying either the signal- or masker-pulse onset, except in condition 4 with a single-component masker and a 40-ms signal delay. Comparison of performance in conditions 4 and 6 and conditions 5 and 7 indicated a significant effect of omitting signal pulses only with the eight-component masker and the 40-ms signal delay. Among the four reference conditions, this comparison involves the one for which thresholds were, on average, the highest, suggesting that the absence of a release from masking was not due to a ceiling effect.

In conditions with a single 200-ms masker burst, Neff (1991, 1995), and Durlach *et al.* (2003) reported substantial release from informational masking when signal duration was reduced so that it was no longer synchronously gated with the masker. On average, smaller reductions in masking were obtained in the present work with delay of the signal-pulse onset (condition 4), especially in the presence of the single-component masker stream. Differences in stimulus configuration are most likely are the major reason for the distinction (see Sheft, 2008, for a review of influence of configuration on effect of gating asynchrony). In the current study, masker duration was 80 ms to encourage stream segregation with continuous presentation, and signal delay was then limited to 40 ms, half the pulse duration. Though the 40-ms delay is shorter than used in the previous informational-masking studies, results from the streaming studies of Dannenbring and Bregman (1978) and Turgeon *et al.* (2005) demonstrate significant segregation with delay in this range, which in the latter study often approached baseline performance measures. In conditions in which performance may be based on detection of asynchrony rather than signal segregation per se, listeners are sensitive to delays as brief as 1 ms despite masker uncertainty (Huang and Richards, 2006).

In the present work, restriction on masking release due to asynchrony may relate to the suggestion of Dannenbring and Bregman (1978), and one supported by results from Turgeon *et al.* (2005), that in the context of streaming, asynchrony is effective when it leads to presentation of a segment of the signal or target without overlapping masker presentation, a configuration atypical of other informational-masking studies. Although the current results show that this speculation is not exclusively true, group thresholds were lowest in condition 5 in which the signal-pulse onset preceded masker onset by 40 ms. Presumably the relatively small threshold elevations that persist in condition 5 reflect a conventional backward-masking effect.

In the introduction, two factors were discussed as contributing to informational masking, uncertainty and similarity. The final data set compares performance in conditions in which the frequency of the single-component masker was either fixed at 1417 Hz or randomized across pulses. The fixed-masker conditions allow for evaluation of similarity without uncertainty. In Fig. 4, results from conditions 1–4 with the 1417-Hz masker are shown with right-

hatched boxes; thresholds obtained with randomizing masker frequency are replotted from Figs. 2 and 3 with open boxes. In all cases, group thresholds were lower when the masker frequency was fixed rather than randomized across pulses. Two-tailed matched-sample t tests indicated that each difference was statistically significant ($t=2.5, 2.4, 5.8$, and 7.9; $p<0.03$ for conditions 1–4). The trend in which the amount of masking progressively dropped across conditions 1–4 indicates that streaming, augmented by cross-stream temporal disparities, can reduce masking in conditions without frequency uncertainty. Similar results in the context of informational masking have recently been reported by Leibold and Neff (2007) and Buss (2008).

Overall, significant results in the present work, with the number of individual exceptions from the total in parentheses, are as follows: Effects of the number of masker components (2 of 112), pulse ISI (6 of 32), omitting signal pulses (8 of 32), asynchronous gating of the signal and masker (4 of 48), and frequency randomization with a single masker component (10 of 64). In two cases, consideration of exceptions calls for further comment. For omission of signal pulses, the effect itself was obtained with only half of the configurations in which it was used. Regarding the effect of frequency randomization, 6 of the 10 exceptions were from condition 2. As noted earlier, stream segregation tends to become more efficient with introduction of cross-stream temporal disparities as was done in conditions 3 and 4 for which the total number of exceptions dropped to only three.

The motivation of this study was to evaluate the effects of auditory streaming on informational masking. A general criticism of investigations of informational masking is that the effect is often discussed in terms of what it is not, that is, something other than energetic masking. Garner (1974) presented a framework for considering information processing in the context of the perception of structure, arguing that, functionally, information and structure are identical terms. Informational masking can then be viewed as a limitation on information transmission due to poorly defined or insufficient structure. Auditory scene analysis represents perception of structure. By enhancing structure, auditory stream segregation may increase the potential for information transmission with this seen experimentally as a release from informational masking.

Acknowledgments

This research was supported by NIDCD Grant Nos. DC005423 and DC00625.

References and links

Anstis, S., and Saida, S. (**1985**). "Adaptation to auditory streaming of frequency-modulated tones," J. Exp. Psychol. Hum. Percept. Perform. **11**, 257–271.

Bregman, A. S., Ahad, P. A., Crum, P. A. C., and O'Reilly, J. (**2000**). "Effects of time intervals and tone durations on auditory stream segregation," Percept. Psychophys. **62**, 626–636.

Buss, E. (**2008**). "The effect of masker level uncertainty on intensity discrimination," J. Acoust. Soc. Am. **123**, 254–264.

Cusack, R., Deeks, J., Aikman, G., and Carlyon, R. P. (**2004**). "Effects of location, frequency region, and time course of selective attention on auditory scene analysis," J. Exp. Psychol. Hum. Percept. Perform. **30**, 643–656.

Dannenbring, G. L., and Bregman, A. S. (**1978**). "Streaming vs. fusion of sinusoidal components of complex tones," Percept. Psychophys. **24**, 369–376.

Durlach, N. I., Mason, C. R., Shinn-Cunningham, B. G., Arbogast, T. L., Colburn, H. S., and Kidd, G. (**2003**). "Informational masking: Counteracting the effects of stimulus uncertainty by decreasing target-masker similarity," J. Acoust. Soc. Am. **114**, 368–379.

Garner, W. R. (**1974**). *The Processing of Information and Structure* (Lawrence Erlbaum Assoc., Potomac, Maryland).

Huang, R., and Richards, V. M. (**2006**). "Coherence detection: Effects of frequency, frequency uncertainty, and onset/offset delays," J. Acoust. Soc. Am. **119**, 2298–2304.

Kidd, G., Mason, C. R., and Deliwala, P. S. (**1994**). "Reducing informational masking by sound segregation," J. Acoust. Soc. Am. **95**, 3475–3480.

Kidd, G., Mason, C. R., and Richards, V. M. (**2003**). "Multiple bursts, multiple looks, and stream coherence in the release from informational masking," J. Acoust. Soc. Am. **114**, 2835–2845.

Kidd, G., Mason, C. R., Richards, V. M., Gallun, F. J., and Durlach, N. I. (**2008**). "Informational masking," in *Auditory Perception of Sound Sources*, edited by W. A. Yost, A. N. Popper, and R. R. Fay (Springer Science+Business, New York).

Leibold, L. J., and Neff, D. L. (**2007**). "Effects of masker-spectral variability and masker fringes in children and adults," J. Acoust. Soc. Am. **121**, 3666–3676.
Micheyl, C., Shamma, S. A., and Oxenham, A. (**2007**). "Hearing out repeating elements in randomly varying multitone sequences: a case of streaming?" in *Hearing—From Sensory Processing to Perception*, edited by B. Kollmeier, G. Klump, V. Hohmann, U. Langemann, M. Mauermann, S. Uppenkamp, and J. Verhey (Springer, Berlin).
McNally, K. A., and Handel, S. (**1977**). "Effect of element composition on streaming and the ordering of repeating sequences," J. Exp. Psychol. **3**, 451–460.
Moore, B. C. J., and Gockel, H. (**2002**). "Factors influencing sequential stream segregation," Acta. Acust. Acust. **88**, 320–332.
Neff, D. L. (**1991**). "Forward masking by maskers of uncertain frequency content," J. Acoust. Soc. Am. **89**, 1314–1323.
Neff, D. L. (**1995**). "Signal properties that reduce masking by simultaneous, random-frequency maskers," J. Acoust. Soc. Am. **98**, 1909–1920.
Sheft, S. (**2008**). "Envelope processing and sound-source perception," in *Auditory Perception of Sound Sources*, edited by W. A. Yost, A. N. Popper, and R. R. Fay (Springer Science+Business, New York).
Turgeon, M., Bregman, A. S., and Roberts, B. (**2005**). "Rhythmic masking release: Effects of asynchrony, temporal overlap, harmonic relations, and source separation on cross-spectral grouping," J. Exp. Psychol. Hum. Percept. Perform. **31**, 939–953.
Watson, C. S. (**2005**). "Some comments on informational masking," Acta. Acust. Acust. **91**, 502–512.
Watson, C. S., Kidd, G. R., and Pok, S. V. (**2002**). "Attentional focus and the method of adjustment revisited," J. Acoust. Soc. Am. **112**, 2243.
Yost, W. A., Cabel, K., and Sheft, S. (**2007**). "Using method of adjustment to measure informational masking using multitone maskers," J. Acoust. Soc. Am. **121**, 3132.

Suppressing aliasing noise in the speech feature domain for automatic speech recognition

Huiqun Deng and Douglas O'Shaughnessy
Institut National de la Recherche Scientifique, Université du Québec, 800, de la Gauchetière Ouest, Bureau 6900, Montréal, H5A 1K6 Canada
huid@ieee.org, dougo@emt.inrs.ca

Abstract: This letter points out that, although in the audio signal domain low-pass filtering has been used to prevent aliasing noise from entering the baseband of speech signals, an antialias process in the speech feature domain is still needed to prevent high modulation frequency components from entering the baseband of speech features. The existence of aliasing noise in speech features is revealed via spectral analysis of speech feature streams. A method for suppressing such aliasing noise is proposed. Experiments on large vocabulary speech recognition show that antialias processing of speech features can improve speech recognition, especially for noisy speech.

PACS numbers: 43.72.Ne, 43.72.Ar [JH]
Date Received: December 23, 2007 **Date Accepted:** March 25, 2008

1. Introduction

In automatic speech recognition (ASR), multidimensional speech features such as Mel-frequency cepstral coefficients (MFCCs) are estimated via short-time spectral analysis. In this letter, speech features for automatic speech recognition estimated from short-time spectra at a frame rate are viewed as samples of multichannel signals reflecting the movements of articulators in speech production, and the frame rate is viewed as the sampling rate of speech features. This letter considers that speech feature samples should be generated to reflect the physical properties of the targeted speech production and the perceptual importance to the auditory system. One of the properties is that signals reflecting the movements of articulators as well as the importance to auditory perception are limited to low frequencies. Studies in neurophysiology and in psychophysics provide evidence for the existence of temporal integration (i.e., low-pass filtering) mechanisms in the auditory system. It is shown that, in order to preserve speech quality (i.e., for inaudible distortions), the minimum bandwidth of the spectral envelope presented to the auditory channel is considerably smaller than a critical-band bandwidth (roughly one-half of one critical band) (Ghitza, 2001). When speech intelligibility is concerned, it is shown that the time trajectories of spectral envelope coefficients (e.g., LPC cepstrum) of speech signals can be low-pass filtered up to 24 Hz, and the perceived speech intelligibility of the reconstructed signal is not severely impaired (Arai *et al.*, 1996). The present letter samples speech features for ASR by exploiting the property that speech features relevant to speech production and perception are limited to low frequencies. It points out that, before temporal filtering of speech feature streams, speech features should be sampled with an antialias process in the speech feature domain, although antialias low-pass filters have already been used in sampling continuous acoustic speech signals. Spectral analysis of speech feature streams in this letter show that there is significant aliasing noise in speech features sampled at the standard frame rate 100 frames per second (or 100 Hz as the frequency of speech features is also called modulation frequency in Hermansky and Morgan (1994) and Nadeu *et al.* (1997)). The aliasing noise in speech features is attributed to background noise, errors in spectral estimation, and high modulation-frequency components in speech signals irrelevant to phoneme classifications. It is noted that speech features were previously sampled and temporally filtered at 100 frames per second, without suppressing the aliasing noise in the speech feature domain, as shown in the conventional RASTA method (Hermansky and Morgan, 1994; Nadeu *et al.*, 1997;Vicente-Peña *et al.*, c2006). The

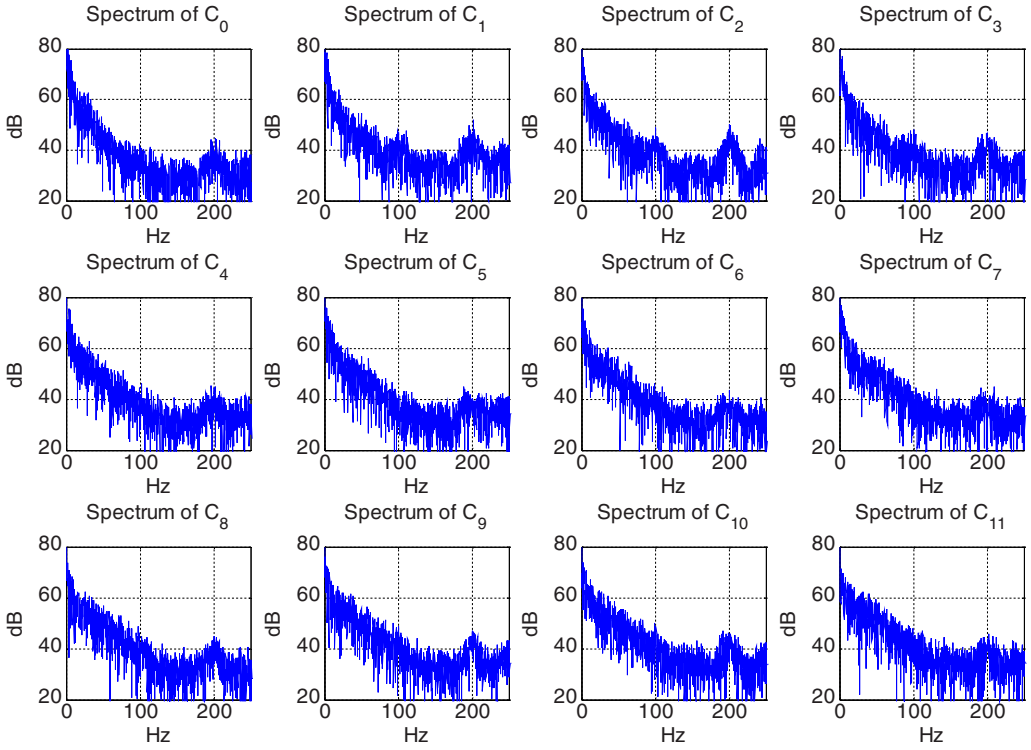

Fig. 1. (Color online) Spectra of 12 MFCCs extracted from a speech signal in a noisy shopping mall.

objective of the present letter is to illustrate the existence of aliasing noise in the speech feature domain and the effect of suppressing such noise on improving automatic speech recognition. In Sec. 2, the existence of aliasing noise in the speech feature domain is discussed. Section 3 presents a method for suppressing aliasing noise in speech features. Section 4 presents the effect of suppressing such aliasing noise on large vocabulary speech recognition. Section 5 concludes the use of the antialias process in obtaining speech features to train acoustic models and recognize speech signals.

2. Aliasing noise in the speech feature domain

Traditionally, speech features for ASR are extracted from short-time spectra at a frame rate of 100 Hz without an antialias process in the speech feature domain, although an antialias filter is used in sampling acoustic speech signals. To reveal the existence of aliasing noise in the speech feature domain, we extract 12 MFCCs at a frame rate of 500 Hz from an utterance recorded in a noisy shopping mall and apply spectral analysis to the MFCC sequences. The spectra of the 12 MFCC sequences are plotted in Fig. 1. As can be seen, there are strong components above 50 Hz. The high modulation frequency components are attributed to background noise, artifacts of short-time spectral estimation, and paralinguistic features. The high-frequency components become aliasing noise in the 0–50 Hz range when the frame rate of speech features is 100 frames per second (Hz), as happens in traditional ASR. For example, the components at 80 Hz are about 30–40 dB, and they can become aliasing noise at 20 Hz if the frame rate is 100 Hz. The baseband components at 20 Hz are merely about 10–20 dB higher than the aliasing noise and can be easily distorted by the aliasing noise. In the next section, we propose a method to prevent high modulation frequency noise from aliasing in the baseband of speech features.

3. Method for suppressing aliasing noise in speech features

We propose a method for suppressing aliasing noise in speech features as shown in Fig. 2. Speech features are sampled at a frame rate F_s higher than the standard frame rate and C_i is the

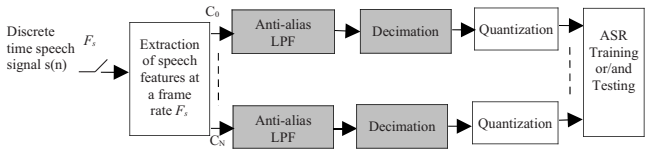

Fig. 2. Proposed antialias process (shaded parts) in extracting speech features for ASR.

stream of the *i*th MFCC. The antialias low-pass filter is designed to have a cutoff frequency F_c at the sampling rate of F_s. The filtered speech features are then decimated to the standard frame rate. The quantization produces finite-length digits at the standard frame rate as required by existing speech recognizers. It should be noted that the antialias process is applied to unquantized MFCCs instead of quantized MFCCs to avoid extra quantization noise. A finite impulse response low-pass filter is employed as the antialias low-pass filter. Let the low-pass filter (LPF) have a unity frequency response from 0 to F_c. Its discrete-time impulse response can be derived from the inverse Fourier transform:

$$h(n) = \frac{1}{2\pi}\int_{-\omega_c}^{\omega_c} e^{j\omega n} d\omega = \frac{\sin(\omega_c n)}{\pi n}, \quad -\infty < n < \infty, \tag{1}$$

where $\omega_c = 2\pi F_c / F_s$. In practice, the length of the ideal impulse response of the LPF is truncated to $2L+1$. To reduce the Gibbs phenomenon due to the truncation, a window weighting function $w(n)$ is applied to $h(n)$. The window function controls the slope of the main lobe and the attenuation of the side lobes of the antialias LPF. Also, to ensure that the dynamics of speech feature streams are preserved after the filtering, the coefficients of the antialias filter are normalized as

$$h'(n) = h(n)w(n) / \sum_{i=-L}^{L} h(i)w(i). \tag{2}$$

A speech feature stream C_i is convolved with the impulse response of the LPF:

$$C_i'(n) = \sum_{\tau=-L}^{L} C_i(n-\tau)h'(\tau). \tag{3}$$

The filtered speech feature streams are then decimated to the standard frame rate of 100 Hz, with components above F_c Hz being suppressed and less aliased in the 0–50 Hz range. The value of the cutoff frequency F_c should be selected to be large enough to cover the maximal changing rate of speech features. Meanwhile, F_c should be also selected to be as small as possible to eliminate high modulation frequency noise. It is known that the maximal rate of phonemes produced by a human is about 12 phonemes per second, and that in a Hidden Markov Model (HMM)-based speech recognizer, each phoneme is represented by a three-state HMM with each state corresponding to one speech frame. Thus, the maximal changing rate of a speech feature stream for HMM-based speech recognition is about 36 frames per second. Therefore, F_c should be selected to be greater than 36 Hz to cover fast-changing speech features. In the next section, given a set of (F_s, F_c), we test the effect of the antialias filtering on speech recognition, and find out the values of F_s and F_c that lead to significant improvements in speech recognition.

4. Effect of antialias filtering of speech feature streams on speech recognition

The proposed antialias process is implemented in the front end of an HMM-based large vocabulary speech recognizer. From the training speech data set, we extract speech features and train an acoustic model from 12-dimensional MFCC streams and their first and second derivatives, with the MFCCs being sampled at F_s frames per second and low-pass filtered up to F_c. For speech features generated with different sets of (F_s, F_c) we train and obtain different acoustic

Table 1. Relative increase in word error rate (%) obtained from spoken speech in noisy shopping malls.

	(F'_s, F'_c) of testing MFCCs													
(F_s, F_c) of training MFCCs	Unprocessed	100 20	100 22.5	100 37	200 20	200 22.5	**200[a] 37[a]**	**200[a] 40[a]**	**200[a] 45[a]**	**500[a] 30[a]**	**500[a] 37[a]**	**500[a] 40[a]**	**500[a] 45[a]**	Avg I
Unprocessed	0.00	−1.59	0.00	−2.79	−0.4	−0.4	−5.58	−2.79	−3.59	−3.59	−3.59	−4.38	−5.58	−3.27
100, 22.5	0.40	1.20	0.80	0.00	0.00	−0.80	−1.59	1.99	−0.40	−2.39	−1.59	−0.80	−1.99	−0.60
200, 20	5.17	0.40	1.20	0.80	−1.20	0.8	1.59	0.40	0.80	1.59	−0.80	1.59	−0.40	0.52
200, 22.5	−0.40	−0.40	−1.99	−1.99	−1.99	−1.59	−6.77	−3.98	−5.58	−4.78	−3.98	−4.38	−4.38	−3.94
200,[b] 37[b]	−0.40	−4.78	−5.18	−4.78	−5.98	−6.37	*−5.18*	*−7.17*	*−5.17*	*−5.98*	*−6.37*	*−5.98*	*−6.77*	−6.00
200,[b] 40[b]	−3.58	−5.58	−5.98	−3.98	−3.19	−5.98	*−3.98*	*−6.37*	*−5.58*	*−6.77*	*−7.17*	*−8.37*	*−8.76*	−6.02
200,[b] 45[b]	−3.18	−2.79	−3.19	−3.98	−3.98	−4.38	*−5.98*	*−6.77*	*−5.98*	*−4.78*	*−9.16*	*−8.77*	*−10.76*	−6.45
500, 37	−0.80	−0.40	0.00	−0.40	−1.59	−0.80	−1.99	−0.80	−1.20	0.00	−1.59	0.40	0.00	−0.80
500, 40	0.00	−3.19	0.40	−1.59	−2.39	−2.39	−5.98	−3.19	−3.19	−6.00	−7.57	−5.98	−8.37	−4.66
500, 45	0.00	−3.19	−3.98	−1.59	−1.99	−1.20	−1.99	−3.19	−3.98	−4.38	−3.98	−6.00	−4.38	−3.27
Avg II	−0.28	−2.03	−1.79	−2.03	−2.27	−2.15	−3.75	−3.19	−3.39	−3.71	−4.58	−4.26	−5.14	

[a]Best (F'_s, F'_c) values for extracting MFCCs for testing.
[b]Best (F_s, F_c) values for extracting MFCCs for training.

models. Given a set of (F'_s, F'_c), we extract 12-dimensional MFCC streams from the testing speech data set at a frame rate F'_s and low-pass filter the feature streams up to F'_c, and test the recognition rate given one of the obtained acoustic models. It should be noted that all training and testing feature streams are decimated to the standard frame rate of 100 frames per second after the low-pass filtering and before deriving the first and second derivatives, as required by standard recognizers. Two test data sets, which are a clean speech data set consisting of 3048 utterances read by 20 speakers in quiet rooms and a noisy speech data set consisting of 256 utterances spoken by 7 speakers in noisy shopping malls, are used in the speech recognition experiments. The effect of the antialias filtering with (F_s, F_c) for training data and (F'_s, F'_c) for test data on speech recognition is measured using relative increase in word error rate (WER):

$$\Delta\text{WER}/\text{WER}_{baseline} = \frac{\text{WER} - \text{WER}_{baseline}}{\text{WER}_{baeseline}} \times 100\,\% \,. \tag{4}$$

The baseline WER is from the acoustic model trained from MFCCs not antialias processed, and the testing MFCCs are not antialias processed either. The results obtained for various settings of (F_s, F_c) applied to testing and training data are listed in Tables 1 and 2 for noisy and clean speech data sets, respectively. The results along a single row are obtained with the same acoustic model, whereas the frame rate F'_s and the cutoff frequency F'_c for sampling and low-pass filtering features for the recognition (test) change. The results along a single column are obtained from the same test feature streams, whereas the acoustic models in the recognizers are trained from features streams sampled and filtered with different sets of (F_s, F_c), respectively. The negative numbers mean relative reduction in WER. As all aspects of the speech recognizers are kept the same except for the processing of training and testing speech feature streams, the reduction in WER can be attributed to the improved discrimination power of the acoustical model or/and the improved SNR of the testing features. The performance of the acoustic model in row (F_s, F_c) is measured by the reduction in WER averaged over this row and is shown by the number in the column Avg I and in the same row. The effect of processing test features with (F'_s, F'_c) is measured by the average reduction in WER in column (F'_s, F'_c) and is shown by the number in the row Avg II and in the same column.

As shown in Table 1, for the noisy speech data set, significant relative reductions in WER (italic numbers) are obtained when the acoustic model is trained from feature streams

Table 2. Relative increase in WER obtained from clean read speech.

(F_s, F_c) of training MFCCs	(F_s', F_c') of testing MFCCs													
	Unprocessed	100 20	100 22.5	100 37	200 20	200 22.5	**200[a] 37[a]**	**200[a] 40[a]**	**200[a] 45[a]**	**500[a] 30[a]**	**500[a] 37[a]**	**500[a] 40[a]**	**500[a] 45[a]**	Avg I
Unprocessed	0.00	2.90	1.45	−1.45	2.90	1.45	1.45	1.45	1.45	1.45	−1.45	0.00	0.00	0.89
100, 22.5	2.90	0	2.90	1.45	1.45	−1.45	1.45	0.00	0.00	0.00	0.00	0.00	0.00	0.67
200, 20	4.35	4.35	4.35	2.90	−1.45	0.00	0.00	0.00	0.00	−1.45	0.00	1.45	0.00	1.11
200, 22.5	7.25	1.45	0.00	4.35	0.00	0.00	0.00	0.00	0.00	0.00	−1.45	0.00	−1.45	0.78
200,[b] 37[b]	2.90	1.45	−1.45	1.45	1.45	0.00	*−1.45*	*0.00*	*0.00*	*−1.45*	*−2.90*	*0.00*	*−1.45*	−0.11
200,[b] 40[b]	1.45	0.00	1.45	1.45	−1.45	−1.45	*0.00*	*−1.45*	*−1.45*	*−2.90*	*−1.45*	*−1.45*	*−1.45*	−0.67
200,[b] 45[b]	2.90	0.00	1.45	1.45	1.45	1.45	*−1.45*	*−1.45*	*0.00*	*−1.45*	*−1.45*	*−1.45*	*0.00*	0.11
500, 37	2.90	2.89	2.90	2.90	2.90	4.35	1.45	1.45	1.45	1.45	−2.90	−1.45	1.45	2.11
500, 40	0.00	1.45	0.00	0.00	1.45	1.45	0.00	0.00	−1.45	−1.45	−2.90	0.00	−2.90	−0.33
500, 45	1.45	0.00	1.45	0.00	0.00	0.00	−1.45	−1.45	−1.45	−1.45	0.00	−1.45	−1.45	−0.45
Avg II	2.61	1.45	1.45	1.45	0.87	0.58	0.00	−0.14	−0.14	−0.72	−1.45	0.14	−0.72	

[a]Best (F_s', F_c') values for extracting MFCCs for testing.
[b]Best (F_s, F_c) values for extracting MFCCs for training.

sampled at $F_s = 200$ frames per second and low-pass filtered with $F_c \geqslant 37$ Hz, and the test features are sampled and low-pass filtered with $F_s \geqslant 200$ frames per second and $F_c \geqslant 37$ Hz.

It is noted that although the testing feature streams in the column (500, 45), which are sampled and low-pass filtered with $F_s = 500$ frames per second and $F_c = 45$ Hz, result in large reductions in WER, such sampling and filtering parameters applied to training features do not result in the best acoustic models. In contrast, the acoustic models in rows (200, 37), (200, 40), and (200, 45), which are trained from features sampled and low-passed filtered with $F_s = 200$ frames per second and $F_c \geqslant 37$ Hz, result in the best recognition rates. The (F_s, F_c) and (F_s', F_c') parameters corresponding to the best acoustic models and the best speech features of noisy speech signals can also retain or improve the recognition of clean speech signals, as shown by italic numbers in Table 2.

The recognition experiments on noisy and clean speech signals show that the proposed method of antialias low-pass filtering of speech features can improve speech recognition. This is explained by that the discrimination power of speech features is concentrated in low modulation frequencies and that reducing aliasing noise in the baseband of speech features increases the SNR of speech features and hence improves the recognition rate. It should be noted that the improvement is obtained by preventing high modulation-frequency components from entering the speech features in the 0–50 Hz modulation frequencies. The noise over the 0–50 Hz modulation frequencies has not been reduced in this letter. The frequency responses of two of the antialias LPFs with $(F_s = 200$ Hz, $F_c = 45$ Hz) and $(F_s = 500$ Hz, $F_c = 37$ Hz) are shown in Fig. 3. The low-pass filtering can suppress high modulation frequency components above 50 Hz by more than 40 dB. The lengths of the LPFs are $2L+1 = 129$ for $(F_s = 200$ Hz) and 321 (for $F_s = 500$ Hz), which impose a $L/F_s = 320$ ms delay, acceptable to human perception. For some applications where long delays may not be allowed, the LPF needs to be designed to have a shorter delay.

5. Conclusion

This letter shows the existence of aliasing noise in the speech feature domain, and suppressing such noise can improve speech recognition. In the proposed method, speech features for training acoustic models and for recognizing speech are extracted at a frame rate of 200 frames per second (or higher for recognizing speech), low-pass filtered, and decimated to the standard

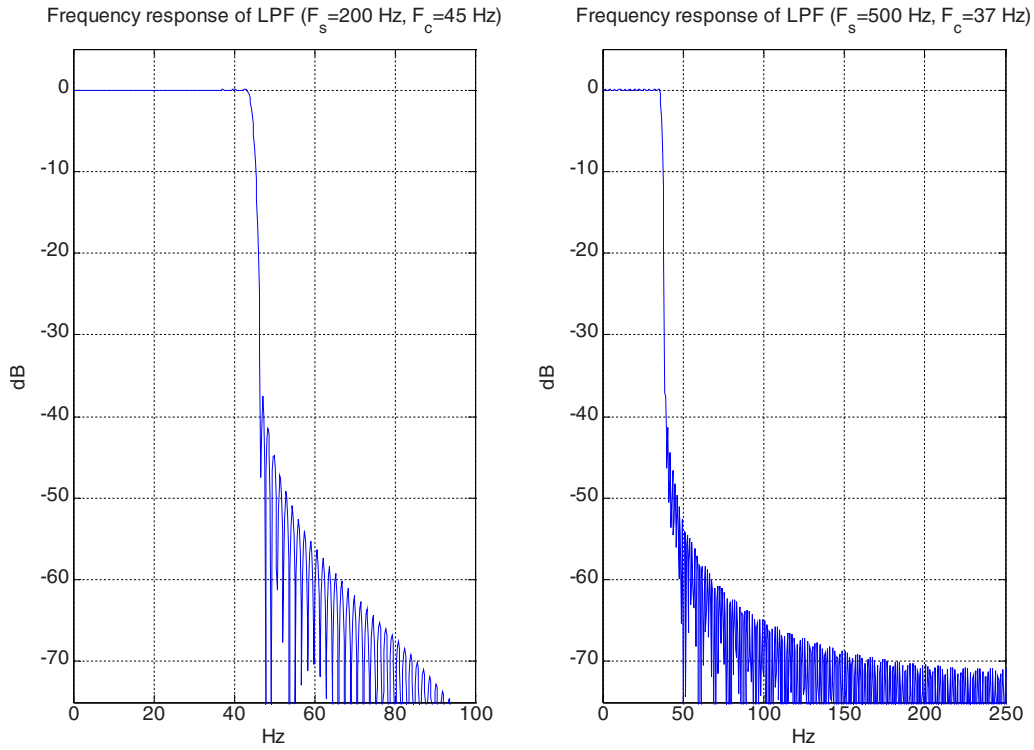

Fig. 3. (Color online) Frequency responses of two antialias LPFs with (F_s=200 Hz, F_c=45 Hz) and (F_s=500 Hz, F_c=37 Hz).

frame rate 100 frames per second. Combining this approach with other noise reduction methods is expected to achieve further improvement for speech recognition. This will be future work.

Acknowledgments

The authors would like to thank Nuance Communications, Inc. for providing the technical supports in testing the method proposed in this letter. Note: The techniques described in this letter are the subject of a pending patent application.

References and links

Arai, T., Pavel, M., Hermansky, H., and Avendano, C. (**1996**). "Intelligibility of speech with filtered time trajectories of spectral envelopes," *Proceedings of the International Conference on Spoken Language Processing'96, Philadelphia*, 2490–2493.
Ghitza, O. (**2001**). "On the upper cutoff frequency of the auditory critical-band envelope detectors in the context of speech perception," J. Acoust. Soc. Am. **110**, 1628–1640.
Hermansky, H., and Morgan, N. (**1994**). "RASTA processing of speech," IEEE Trans. Speech Audio Process. **2**, 578–589.
Nadeu, C., Paches-Leal, P., and Juang, B. (**1997**). "Filtering the time sequence of spectral parameters for speech recognition," Speech Commun. **22**, 315–332.
Vicente-Peña, J., Gallardo-Antolína, A., Peláez-Moreno, C., and Díaz-de-María, F. (**2006**). "Band-pass filtering of the time sequences of spectral parameters for robust wireless speech recognition," Speech Commun. **48**, 1379–1398.

ACOUSTICAL NEWS—USA

Elaine Moran
Acoustical Society of America, Suite 1NO1, 2 Huntington Quadrangle, Melville, NY 11747-4502

Editor's Note: *Readers of this journal are encouraged to submit news items on awards, appointments, and other activities about themselves or their colleagues. Deadline dates for news and notices are 2 months prior to publication.*

USA Meetings Calendar

Listed below is a summary of meetings related to acoustics to be held in the U.S. in the near future. The month/year notation refers to the issue in which a complete meeting announcement appeared.

	2008
28 July–1 Aug	9th International Congress on Noise as a Public Health Problem (Quintennial meeting of ICBEN, the International Commission on Biological Effects of Noise). Foxwoods Resort, Mashantucket, CT [Jerry V. Tobias, ICBEN 9, Post Office Box 1909, Groton, CT 06340-1609; Tel. 860-572-0680; Web: www.icben.org; E-mail: icben2008@att.net]
10–14 Nov	156th Meeting of the Acoustical Society of America, Miami, FL [Acoustical Society of America, Suite 1NO1, 2 Huntington Quadrangle, Melville, NY 11747-4502; Tel.: 516-576-2360; Fax: 516-576-2377; E-mail: asa@aip.org; WWW: http://asa.aip.org].
	2009
18–22 May	157th Meeting of the Acoustical Society of America, Portland, OR [Acoustical Society of America, Suite 1NO1, 2 Huntington Quadrangle, Melville, NY 11747-4502; Tel.: 516-576-2360; Fax: 516-576-2377; E-mail: asa@aip.org; WWW: http://asa.aip.org].
26–30 Oct	158th Meeting of the Acoustical Society of America, San Antonio, TX [Acoustical Society of America, Suite 1NO1, 2 Huntington Quadrangle, Melville, NY 11747-4502; Tel.: 516-576-2360; Fax: 516-576-2377; E-mail: asa@aip.org; WWW: http://asa.aip.org].

Cumulative Indexes to the Journal of the Acoustical Society of America

Ordering information: Orders must be paid by check or money order in U.S. funds drawn on a U.S. bank or by Mastercard, Visa, or American Express credit cards. Send orders to Circulation and Fulfillment Division, American Institute of Physics, Suite 1NO1, 2 Huntington Quadrangle, Melville, NY 11747-4502; Tel.: 516-576-2270. Non-U.S. orders add $11 per index.

Some indexes are out of print as noted below.

Volumes 1–10, 1929–1938: JASA, and Contemporary Literature, 1937–1939. Classified by subject and indexed by author. pp. 131. Price: ASA members $5; Nonmembers $10.

Volumes 11–20, 1939–1948: JASA, Contemporary Literature and Patents. Classified by subject and indexed by author and inventor. pp. 395. Out of Print.

Volumes 21–30, 1949–1958: JASA, Contemporary Literature and Patents. Classified by subject and indexed by author and inventor. pp. 952. Price: ASA members $20; Nonmembers $75.

Volumes 31–35, 1959–1963: JASA, Contemporary Literature and Patents. Classified by subject and indexed by author and inventor. pp. 1140. Price: ASA members $20; Nonmembers $90.

Volumes 36–44, 1964–1968: JASA and Patents. Classified by subject and indexed by author and inventor. pp. 485. Out of Print.

Volumes 36–44, 1964–1968: Contemporary Literature. Classified by subject and indexed by author. pp. 1060. Out of Print.

Volumes 45–54, 1969–1973: JASA and Patents. Classified by subject and indexed by author and inventor. pp. 540. Price: $20 (paperbound); ASA members $25 (clothbound); Nonmembers $60 (clothbound).

Volumes 55–64, 1974–1978: JASA and Patents. Classified by subject and indexed by author and inventor. pp. 816. Price: $20 (paperbound); ASA members $25 (clothbound); Nonmembers $60 (clothbound).

Volumes 65–74, 1979–1983: JASA and Patents. Classified by subject and indexed by author and inventor. pp. 624. Price: ASA members $25 (paperbound); Nonmembers $75 (clothbound).

Volumes 75–84, 1984–1988: JASA and Patents. Classified by subject and indexed by author and inventor. pp. 625. Price: ASA members $30 (paperbound); Nonmembers $80 (clothbound).

Volumes 85–94, 1989–1993: JASA and Patents. Classified by subject and indexed by author and inventor. pp. 736. Price: ASA members $30 (paperbound); Nonmembers $80 (clothbound).

Volumes 95–104, 1994–1998: JASA and Patents. Classified by subject and indexed by author and inventor. pp. 632, Price: ASA members $40 (paperbound); Nonmembers $90 (clothbound).

Volumes 105–114, 1999–2003: JASA and Patents. Classified by subject and indexed by author and inventor. pp. 616. Price: ASA members $50; Nonmembers $90 (paperbound).

 0001-4966/2008/124(1)/1/1/$23.00

ACOUSTICAL STANDARDS NEWS

Susan B. Blaeser, Standards Manager
ASA Standards Secretariat, Acoustical Society of America, 35 Pinelawn Rd., Suite 114E, Melville, NY 11747 [Tel.: (631) 390-0215; Fax: (631) 390-0217; e-mail: asastds@aip.org]

George S. K. Wong
Acoustical Standards, Institute for National Measurement Standards, National Research Council, Ottawa, Ontario K1A 0R6, Canada [Tel.: (613) 993-6159; Fax: (613) 990-8765; e-mail: george.wong@nrc.ca]

American National Standards (ANSI Standards) developed by Accredited Standards Committees S1, S2, S3, and S12 in the areas of acoustics, mechanical vibration and shock, bioacoustics, and noise, respectively, are published by the Acoustical Society of America (ASA). In addition to these standards, ASA publishes catalogs of Acoustical Standards, both National and International. To receive copies of the latest Standards Catalogs, please contact Susan B. Blaeser.

Comments are welcomed on all material in Acoustical Standards News.

This Acoustical Standards News section in JASA, as well as the National and International Catalogs of Acoustical Standards, and other information on the Standards Program of the Acoustical Society of America, are available via the ASA home page: http://asa.aip.org

Standards Meetings Calendar—National

Accredited Standards Committees S1, Acoustics, S2, Mechanical Vibration and Shock, S3, Bioacoustics, S3/SC1, Animal Bioacoustics, and S12, Noise will meet during the week of 10 November 2008 in Miami, FL. The U.S. TAGs to ISO/TC 43, ISO/TC43/SC 1, ISO/TC 108 and its subcommittees, and IEC/TC 29 will also meet during the Standards Plenary meeting. Specific meeting dates and times will be announced soon.

Standards Meetings Calendar—International

8–12 September 2008—Olso, Norway

- ISO/TC 108/SC 4, Human exposure to mechanical vibration and shock

3–7 November 2008—St. Louis, MO, USA

- ISO/TC 108, Mechanical vibration, shock and condition monitoring
- ISO/TC 108/SC 3, Use and calibration of vibration and shock measuring instruments
- ISO/TC 108/SC 6, Vibration and shock generating systems

30 March–3 April 2009—London, UK

- ISO/TC 108/SC 2, Measurement and evaluation of mechanical vibration and shock as applied to machines, vehicles, and structures

Accredited Standards Committee on Acoustics, S1

(P. Battenberg, Chair; R.J. Peppin, Vice Chair)

Scope: Standards, specifications, methods of measurement and test, and terminology in the field of physical acoustics including architectural acoustics, electroacoustics, sonics and ultrasonics, and underwater sound, but excluding those aspects which pertain to biological safety, tolerance and comfort.

S1 WORKING GROUPS

S1/Advisory—Advisory Planning Committee to S1 (P. Battenberg)

S1/WG01—Standard Microphones and their Calibration (V. Nedzelnitsky)

S1/WG04—Measurement of Sound Pressure Levels in Air (Vacant, Chair; E. Dunens, Vice Chair)

S1/WG05—Band Filter Sets (A.H. Marsh)

S1/WG09—Calibration of Underwater Electroacoustic Transducers (R.M. Drake)

S1/WG17—Sound Level Meters and Integrating Sound Level Meters (B.M. Brooks)

S1/WG19—Insertion Loss of Windscreens (A.J. Campanella)

S1/WG20—Ground Impedance (Measurement of Ground Impedance and Attenuation of Sound due to the Ground) (K. Attenborough, Chair; J. Sabatier, Vice Chair)

S1/WG22—Bubble Detection and Cavitation Monitoring (Vacant)

S1/WG26—High Frequency Calibration of the Pressure Sensitivity of Microphones (A.J. Zuckerwar)

S1/WG27—Acoustical Terminology (J.S. Vipperman)

S1 STANDARDS ON ACOUSTICS

ANSI S1.1-1994 (R2004) American National Standard Acoustical Terminology

ANSI S1.4-1983 (R2006) American National Standard Specification for Sound Level Meters. This Standard includes **ANSI S1.4A-1985 (R 2006)** Amendment to ANSI S1.4-1983

ANSI S1.6-1984 (R2006) American National Standard Preferred Frequencies, Frequency Levels, and Band Numbers for Acoustical Measurements

ANSI S1.8-1989 (R2006) American National Standard Reference Quantities for Acoustical Levels

ANSI S1.9-1996 (R2006) American National Standard Instruments for the Measurement of Sound Intensity

ANSI S1.11-2004 American National Standard Specification for Octave-

Band and Fractional-Octave-Band Analog and Digital Filters

ANSI S1.13-2005 American National Standard Measurement of Sound Pressure Levels in Air

ANSI/ASAS1.14-1998 (R2008) American National Standard Recommendations for Specifying and Testing the Susceptibility of Acoustical Instruments to Radiated Radio-Frequency Electromagnetic Fields, 25 MHz to 1 GHz

ANSI S1.15/Part 1-1997 (R2006) American National Standard Measurement Microphones, Part 1: Specifications for Laboratory Standard Microphones

ANSI S1.15/Part 2-2005 American National Standard Measurement Microphones, Part 2: Primary Method for Pressure Calibration of Laboratory Standard Microphones by the Reciprocity Technique

ANSI S1.16-2000 (R2005) American National Standard Method for Measuring the Performance of Noise Discriminating and Noise Canceling Microphones

ANSI S1.17/Part 1-2004 American National Standard Microphone Windscreens—Part 1: Measurements and Specification of Insertion Loss in Still or Slightly Moving Air

ANSI S1.18-1999 (R2004) American National Standard Template Method for Ground Impedance

ANSI S1.20-1988 (R2003) American National Standard Procedures for Calibration of Underwater Electroacoustic Transducers

ANSI S1.22-1992 (R2007) American National Standard Scales and Sizes for Frequency Characteristics and Polar Diagrams in Acoustics

ANSI S1.24 TR-2002 (R2007) ANSI Technical Report Bubble Detection and Cavitation Monitoring

ANSI S1.25-1991 (R2007) American National Standard Specification for Personal Noise Dosimeters

ANSI S1.26-1995 (R2004) American National Standard Method for Calculation of the Absorption of Sound by the Atmosphere

ANSI S1.40-2006 American National Standard Specifications and Verification Procedures for Sound Calibrators

ANSI S1.42-2001 (R2006) American National Standard Design Response of Weighting Networks for Acoustical Measurements

ANSI S1.43-1997 (R2007) American National Standard Specifications for Integrating-Averaging Sound Level Meters

Accredited Standards Committee On Mechanical Vibration and Shock, S2

(A.T. Herfat, Chair; R.L. Eshleman, Vice Chair)

Scope: Standards, specifications, methods of measurement and test, and terminology in the field of mechanical vibration and shock, and condition monitoring and diagnostics of machines, including the effects of exposure to mechanical vibration and shock on humans, including those aspects which pertain to biological safety, tolerance and comfort.

S2 WORKING GROUPS

S2/WG01—S2 Advisory Planning Committee (A.T. Herfat, Chair; R.L. Eshleman, Vice Chair)

S2/WG02—Terminology and Nomenclature in the Field of Mechanical Vibration and Shock and Condition Monitoring and Diagnostics of Machines (D.J. Evans)

S2/WG03—Signal Processing Methods (T.S. Edwards)

S2/WG04—Characterization of the Dynamic Mechanical Properties of Viscoelastic Polymers (W. Madigosky, Chair, J. Niemiec, Vice Chair)

S2/WG05—Use and Calibration of Vibration and Shock Measuring Instruments (D.J. Evans, Chair; B.E. Douglas, Vice Chair)

S2/WG06—Vibration and Shock Actuators (G. Booth)

S2/WG07—Acquisition of Mechanical Vibration and Shock Measurement Data (B.E. Douglas)

S2/WG08—Analysis Methods of Structural Dynamics (M. Mezache)

S2/WG09—Training and Accreditation (R.L. Eshleman, Chair; D. Corelli, Vice Chair)

S2/WG10—Measurement and Evaluation of Machinery for Acceptance and Condition (R.L. Eshleman, Chair; H.C. Pusey, Vice Chair)

S2/WG10/Panel 1—Balancing (R.L. Eshleman)

S2/WG10/Panel 2—Operational Monitoring and Condition Evaluation (R. Bankert)

S2/WG10/Panel 3—Machinery Testing (R.L. Eshleman)

S2/WG10/Panel 4—Prognosis (A.J. Hess)

S2/WG10/Panel 5—Data Processing, Communication, and Presentation (K. Bever)

S2/WG11—Measurement and Evaluation of Mechanical Vibration of Vehicles (A.F. Kilcullen)

S2/WG12—Measurement and Evaluation of Structures and Structural Systems for Assessment and Condition Monitoring (M. Mezache)

S2/WG13—Shock Test Requirements for Shelf-mounted and Other Commercial Electronics Systems (B. Lang)

S2/WG39 (S3)—Human Exposure to Mechanical Vibration and Shock (D.D. Reynolds, Chair; R. Dong, Vice Chair)

S2 STANDARDS ON MECHANICAL VIBRATION AND SHOCK

ANSI S2.1-2000/ISO 2041:1990 American National Standard Vibration and Shock -Vocabulary (a Nationally Adopted International Standard)

ANSI S2.2-1959 (R2006) American National Standard Methods for the Calibration of Shock and Vibration Pickups

ANSI S2.4-1976 (R2004) American National Standard Method for Specifying the Characteristics of Auxiliary Analog Equipment for Shock and Vibration Measurements

ANSI S2.7-1982 (R2004) American National Standard Balancing Terminology

ANSI S2.8-2007 American National Standard Technical Information Used for Resilient Mounting Applications

ANSI S2.9-1976 (R2006) American National Standard Nomenclature for Specifying Damping Properties of Materials

ANSI S2.16-1997 (R2006) American National Standard Vibratory Noise Measurements and Acceptance Criteria of Shipboard Equipment

ANSI S2.17-1980 (R2004) American National Standard Techniques of Machinery Vibration Measurement

ANSI S2.19-1999 (R2004) American National Standard Mechanical Vibration—Balance Quality Requirements of Rigid Rotors, Part 1: Determination of Permissible Residual Unbalance, Including Marine Applications

ANSI S2.20-1983 (R2006) American National Standard Estimating Air Blast Characteristics for Single Point Explosions in Air, with a Guide to Evaluation of Atmospheric Propagation and Effects

ANSI S2.21-1998 (R2007) American National Standard Method for Preparation of a Standard Material for Dynamic Mechanical Measurements

ANSI S2.22-1998 (R2007) American National Standard Resonance Method for Measuring the Dynamic Mechanical Properties of Viscoelastic Materials

ANSI S2.23-1998 (R2007) American National Standard Single Cantilever Beam Method for Measuring the Dynamic Mechanical Properties of Viscoelastic Materials

ANSI S2.24-2001 (R2006) American National Standard Graphical Presentation of the Complex Modulus of Viscoelastic Materials

ANSI S2.25-2004 American National Standard Guide for the Measurement, Reporting, and Evaluation of Hull and Superstructure Vibration in Ships

ANSI S2.26-2001 (R2006) American National Standard Vibration Testing Requirements and Acceptance Criteria for Shipboard Equipment

ANSI S2.27-2002 (R2007) American National Standard Guidelines for the Measurement and Evaluation of Vibration of Ship Propulsion Machinery

ANSI S2.28-2003 American National Standard Guide for the Measurement and Evaluation of Vibration of Shipboard Machinery

ANSI S2.29-2003 American National Standard Guide for the Measurement and Evaluation of Vibration of Machine Shafts on Shipboard Machinery

ANSI S2.31-1979 (R2004) American National Standard Methods for the Experimental Determination of Mechanical Mobility, Part 1: Basic Definitions and Transducers

ANSI S2.32-1982 (R2004) American National Standard Methods for the Experimental Determination of Mechanical Mobility, Part 2: Measurements Using Single-Point Translational Excitation

ANSI S2.34-1984 (R2005) American National Standard Guide to the Experimental Determination of Rotational Mobility Properties and the Complete Mobility Matrix

ANSI S2.42-1982 (R2004) American National Standard Procedures for Balancing Flexible Rotors

ANSI S2.43-1984 (R2005) American National Standard Criteria for Evaluating Flexible Rotor Balance

ANSI S2.46-1989 (R2005) American National Standard Characteristics to be Specified for Seismic Transducers

ANSI S2.48-1993 (R2006) American National Standard Servo-Hydraulic Test Equipment for Generating Vibration—Methods of Describing Characteristics

ANSI S2.60-1987 (R2005) American National Standard Balancing Machines—Enclosures and Other Safety Measures

ANSI S2.61-1989 (R2005) American National Standard Guide to the Mechanical Mounting of Accelerometers

ANSI S2.70-2006 (*Revision of ANSI S3.34-1986*) American National Standard Guide for the Measurement and Evaluation of Human Exposure to Vibration Transmitted to the Hand

ANSI S2.71-1983 (R2006) (*Redesignation of ANSI S3.29-1983*) American National Standard Guide to the Evaluation of Human Exposure to Vibration in Buildings

ANSI S2.72/Part 1-2002 (R2007)/ISO 2631-1:1997 (*Redesignation of ANSI S3.18/Part 1-2002/ISO 2631-1:1997*) American National Standard Mechanical vibration and shock—Evaluation of human exposure to whole-body vibration—Part 1: General requirements (a Nationally Adopted International Standard)

ANSI S2.72/Part 4-2003 (R2007)/ISO 2631-4:2001 (*Redesignation of ANSI S3.18/Part 4 -2003/ISO 2631-4:2001*) American National Standard Mechanical vibration and shock—Evaluation of human exposure to whole-body vibration—Part 4: Guidelines for the evaluation of the effects of vibration and rotational motion on passenger and crew comfort in fixed-guideway transport systems (a Nationally Adopted International Standard)

ANSI S2.73-2002/ISO 10819:1996 (R2007) (*Redesignation of ANSI S3.40-2002/ISO 10819:1996*) American National Standard Mechanical vibration and shock—Hand-arm vibration—Method for the measurement and evaluation of the vibration transmissibility of gloves at the palm of the hand (a Nationally Adopted International Standard)

Accredited Standards Committee on Bioacoustics, S3

(C.A. Champlin, Chair; D.A. Preves, Vice Chair)

Scope: Standards, specifications, methods of measurement and test, and terminology in the fields of psychological and physiological acoustics, including aspects of general acoustics which pertain to biological safety, tolerance, and comfort.

S1 WORKING GROUPS

S3/Advisory—Advisory Planning Committee to S3 (C. Champlin, Chair; D.A. Preves, Vice Chair)

S3/WG35—Audiometers (R.L. Grason)

S3/WG36—Speech Intelligibility (R.S. Schlauch)

S3/WG37—Coupler Calibration of Earphones (B. Kruger)

S3/WG39—Human Exposure to Mechanical Vibration and Shock (parallel to ISO/TC 108/SC 4) (D.D. Reynolds, Chair; R. Dong, Vice Chair)

S3/WG43—Method for Calibration of Bone Conduction Vibrators (J.D. Durrant)

S3/WG48—Hearing Aids (D.A. Preves)

S3/WG51—Auditory Magnitudes (R.P. Hellman)

S3/WG56—Criteria for Background Noise for Audiometric Testing (J. Franks)

S3/WG59—Measurement of Speech Levels (M.C. Killion and L.A. Wilber, Co-Chairs)

S3/WG60—Measurement of Acoustic Impedance and Admittance of the Ear (Vacant)

S3/WG62—Impulse Noise with Respect to Hearing Hazard (J.H. Patterson, Chair; R. Hamernik, Vice Chair)

S3/WG67—Manikins (M.D. Burkhard)

S3/WG72—Measurement of Auditory Evoked Potentials (R.F. Burkard)

S3/WG76—Computerized Audiometry (A.J. Miltich)

S3/WG79—Methods for Calculation of the Speech Intelligibility Index (C.V. Pavlovic)

S3/WG81—Hearing Assistance Technologies (L. Thibodeau and L.A. Wilber, Co-Chairs)

S3/WG82—Basic Vestibular Function Test Battery (C. Wall)

S3/WG83—Sound Field Audiometry (T.R. Letowski)

S3/WG84—Otoacoustic Emissions (G.R. Long)

S3/WG88—Standard Audible Emergency Evacuation and Other Signals (Vacant)

S3/WG89—Spatial Audiometry in Real and Virtual Environments (J. Besing)

S3/WG91—Text-to-Speech Synthesis Systems (C. Bickley and A. Syrdal, Co-Chairs)

S3 Liaison Group

S3/L1 S3 U. S. TAG Liaison to IEC/TC 87 Ultrasonics (W.L. Nyborg)

S3 STANDARDS ON BIOACOUSTICS

ANSI S3.1-1999 (R2003) American National Standard Maximum Permissible Ambient Noise Levels for Audiometric Test Rooms

ANSI S3.2-1989 (R1999) American National Standard Method for Measuring the Intelligibility of Speech over Communication Systems

ANSI S3.4-2007 American National Standard Procedure for the Computation of Loudness of Steady Sounds

ANSI S3.5-1997 (R2007) American National Standard Methods for Calculation of the Speech Intelligibility Index

ANSI S3.6-2004 American National Standard Specification for Audiometers

ANSI S3.7-1995 (R2003) American National Standard Method for Coupler Calibration of Earphones

ANSI S3.13-1987 (R2007) American National Standard Mechanical Coupler for Measurement of Bone Vibrators

ANSI S3.20-1995 (R2003) American National Standard Bioacoustical Terminology

ANSI S3.21-2004 American National Standard Methods for Manual Pure-Tone Threshold Audiometry

ANSI S3.22-2003 American National Standard Specification of Hearing Aid Characteristics

ANSI S3.25-1989 (R2003) American National Standard for an Occluded Ear Simulator

ANSI S3.35-2004 American National Standard Method of Measurement of Performance Characteristics of Hearing Aids under Simulated Real-Ear Working Conditions

ANSI S3.36-1985 (R2006) American National Standard Specification for a Manikin for Simulated in situ Airborne Acoustic Measurements

ANSI S3.37-1987 (R2007) American National Standard Preferred Earhook Nozzle Thread for Postauricular Hearing Aids

ANSI S3.39-1987 (R2007) American National Standard Specifications for Instruments to Measure Aural Acoustic Impedance and Admittance (Aural Acoustic Immittance)

ANSI S3.41-1990 (R2001) American National Standard Audible Emergency Evacuation Signal

ANSI S3.42-1992 (R2007) American National Standard Testing Hearing Aids with a Broad-Band Noise Signal

ANSI S3.44-1996 (R2006) American National Standard Determination of Occupational Noise Exposure and Estimation of Noise-Induced Hearing Impairment

ANSI S3.45-1999 American National Standard Procedures for Testing Basic Vestibular Function

ANSI S3.46-1997 (R2007) American National Standard Methods of Measurement of Real-Ear Performance Characteristics of Hearing Aids

Animal Bioacoustics Subcommittee, S3/SC1

(D.K. Delaney, Chair; W. Au, Vice Chair)

Scope: Standards, specifications, methods of measurement and test, instrumentation and terminology in the field of psychological and physiological acoustics, including aspects of general acoustics which pertain to biological safety, tolerance and comfort of nonhuman animals, including both risk to individual animals and to the long-term viability of populations. Animals to be covered may potentially include commercially grown food animals; animals harvested for food in the wild; pets; laboratory animals; exotic species in zoos, oceanaria or aquariums; or free-ranging wild animals.

S3/SC 1 WORKING GROUPS

S3/SC 1/WG01—Animal Bioacoustics Terminology (A.E. Bowles)

S3/SC 1/WG02—Effects of Sound on Fish and Turtles (R.R. Fay and A.N. Popper, Co-Chairs)

S3/SC 1/WG03—Underwater Passive Acoustic Monitoring for Bioacoustic Applications (A.M. Thode)

Accredited Standards Committee On Noise, S12

(R.D. Hellweg, Chair; W.J. Murphy, Vice Chair)

Scope: Standards, specifications, and terminology in the field of acoustical noise pertaining to methods of measurement, evaluation, and control, including biological safety, tolerance and comfort, and physical acoustics as related to environmental and occupational noise.

S12 WORKING GROUPS

S12/Advisory—Advisory Planning Committee to S12 (R.D. Hellweg)

S12/WG03—Measurement of Noise from Information Technology and Telecommunications Equipment (K.X.C. Man)

S12/WG11—Hearing Protector Attenuation and Performance (E.H. Berger)

S12/WG13—Method for the Selection of Hearing Protectors that Optimize the Ability to Communicate (D. Byrne)

S12/WG14—Measurement of the Noise Attenuation of Active and /or Passive Level Dependent Hearing Protective Devices (W.J. Murphy)

S12/WG15—Measurement and Evaluation of Outdoor Community Noise (P.D. Schomer)

S12/WG18—Criteria for Room Noise (R.J. Peppin)

S12/WG23—Determination of Sound Power (B.M. Brooks and J. Schmitt, Co-Chairs)

S12/WG31—Predicting Sound Pressure Levels Outdoors (L. Pater)

S12/WG32—Revision of ANSI S12.7-1986 Methods for Measurement of Impulse Noise (A.H. Marsh)

S12/WG36—Development of Methods for Using Sound Quality (P. Davies and G.L. Ebbit, Co-Chairs)

S12/WG38—Noise Labeling in Products (R.D. Hellweg)

S12/WG40—Measurement of the Noise Aboard Ships (S. Antonides, Chair; S. Fisher, Vice Chair)

S12/WG41—Model Community Noise Ordinances (L.S. Finegold, Chair; B.M. Brooks, Vice Chair)

S12/WG44—Speech Privacy (G.C. Tocci, Chair; D. Sykes, Vice Chair)

S12/WG45—Measurement of Occupational Noise Exposure from Telephone Equipment (K.A. Woo, Chair; L.A. Wilber, Vice Chair)

S12/WG46—Acoustical Performance Criteria for Relocatable Classrooms (T. Hardiman and P.D. Schomer, Co-Chairs)

S12/WG47—Underwater Noise Measurements of Ships (M. Bahtiarian)

S12/WG48—Railroad Horn Sound Emission Testing (J. Erdreich, Chair; J.J. Earshen, Vice Chair)

S12/WG49—Noise from Hand-operated Power Tools, Excluding Pneumatic Tools (B.M. Brooks)

S12/WG50—Information Technology (IT) Equipment in Classrooms (R.D. Hellweg)

S12 LIAISON GROUPS

S12/L1 IEEE 85 Committee for TAG Liaison—Noise Emitted by Rotating Electrical Machines (Parallel to ISO/TC 43/SC 1/WG 13) (R.G. Bartheld)

S12/L2 Measurement of Noise from Pneumatic Compressors, Tools and Machines (Parallel to ISO/TC 43/SC 1/WG 9) (Vacant)

S12/L3 SAE Committee for TAG Liaison on Measurement and Evaluation of Motor Vehicle Noise (parallel to ISO/TC 43/SC 1/WG 8) (R.F. Schumacher)

S12/L4 SAE Committee A-21 for TAG Liaison on Measurement and Evaluation of Aircraft Noise (J.D. Brooks)

S12/L5 ASTM E-33 on Environmental Acoustics (to include activities of ASTM E33.06 on Building Acoustics, parallel to ISO/TC 43/SC 2 and ASTM E33.09 on Community Noise) (K.P. Roy)

S12/L6 SAE Construction-Agricultural Sound Level Committee (I. Douell)

S12/L7 SAE Specialized Vehicle and Equipment Sound Level Committee (T.M. Disch)

S12/L8 ASTM PTC 36 Measurement of Industrial Sound (R.A. Putnam, Chair; B.M. Brooks, Vice Chair)

S12 STANDARDS ON NOISE

ANSI S12.1-1983 (R2006) American National Standard Guidelines for the Preparation of Standard Procedures to Determine the Noise Emission from Sources

ANSI S12.2-1995 (R1999) American National Standard Criteria for Evaluating Room Noise

ANSI S12.3-1985 (R2006) American National Standard Statistical Methods for Determining and Verifying Stated Noise Emission Values of Machinery and Equipment.

ANSI S12.5-2006/ISO 6926:1999 American National Standard Acoustics—Requirements for the Performance and Calibration of Reference Sound Sources Used for the Determination of Sound Power Levels. (Nationally Adopted International Standard)

ANSI S12.6-1997 (R2002) American National Standard Methods for Measuring the Real-Ear Attenuation of Hearing Protectors

ANSI S12.7-1986 (R2006) American National Standard Methods for Measurements of Impulse Noise

ANSI/ASA S12.8-1998 (R2008) American National Standard Methods for Determining the Insertion Loss of Outdoor Noise Barriers

ANSI S12.9/Part 1-1988 (R2003) American National Standard Quantities and Procedures for Description and Measurement of Environmental Sound, Part 1

ANSI/ASA S12.9/Part 2-1992 (R2008) American National Standard Quantities and Procedures for Description and Measurement of Environmental Sound, Part 2: Measurement of Long-Term, Wide-Area Sound

ANSI/ASA S12.9/Part 3-1993 (R2008) American National Standard Quantities and Procedures for Description and Measurement of Environmental Sound, Part 3: Short-Term Measurements with an Observer Present

ANSI S12.9/Part 4-2005 American National Standard Quantities and Procedures for Description and Measurement of Environmental Sound, Part 4: Noise Assessment and Prediction of Long-Term Community Response

ANSI/ASA S12.9/Part 5-2007 American National Standard Quantities and Procedures for Description and Measurement of Environmental Sound—Part 5: Sound Level Descriptors for Determination of Compatible Land Use

ANSI S12.9/Part 6-2000 (R2005) American National Standard Quantities and Procedures for Description and Measurement of Environmental Sound, Part 6: Methods for Estimation of Awakenings Associated with Aircraft Noise Events Heard in Homes

ANSI/ASA S12.10-2002 (R2007)/ISO 7779:1999 American National Standard Acoustics—Measurement of airborne noise emitted by information technology and telecommunications equipment (a Nationally Adopted International Standard)

ANSI S12.11/Part 1-2003/ISO 10302:1996 (MOD) American National Standard Acoustics—Measurement of noise and vibration of small air-

moving devices—Part 1: Airborne noise emission (a Modified Nationally Adopted International Standard)

ANSI S12.11/Part 2-2003 American National Standard Acoustics—Measurement of Noise and Vibration of Small Air-Moving Devices—Part 2: Structure-Borne Vibration

ANSI/ASA S12.12-1992 (R2007) American National Standard Engineering Method for the Determination of Sound Power Levels of Noise Sources Using Sound Intensity

ANSI S12.13 TR-2002 ANSI Technical Report Evaluating the Effectiveness of Hearing Conservation Programs through Audiometric Data Base Analysis

ANSI/ASA S12.14-1992 (R2007) American National Standard Methods for the Field Measurement of the Sound Output of Audible Public Warning Devices Installed at Fixed Locations Outdoors

ANSI/ASA S12.15-1992 (R2007) American National Standard For Acoustics—Portable Electric Power Tools, Stationary and Fixed Electric Power Tools, and Gardening Appliances—Measurement of Sound Emitted

ANSI/ASA S12.16-1992 (R2007) American National Standard Guidelines for the Specification of Noise of New Machinery

ANSI S12.17-1996 (R2006) American National Standard Impulse Sound Propagation for Environmental Noise Assessment

ANSI S12.18-1994 (R2004) American National Standard Procedures for Outdoor Measurement of Sound Pressure Level

ANSI S12.19-1996 (R2006) American National Standard Measurement of Occupational Noise Exposure

ANSI S12.23-1989 (R2006) American National Standard Method for the Designation of Sound Power Emitted by Machinery and Equipment

ANSI S12.42-1995 (R2004) American National Standard Microphone-in-Real-Ear and Acoustic Test Fixture Methods for the Measurement of Insertion Loss of Circumaural Hearing Protection Devices

ANSI/ASA S12.43-1997 (R2007) American National Standard Methods for Measurement of Sound Emitted by Machinery and Equipment at Workstations and Other Specified Positions

ANSI/ASA S12.44-1997 (R2007) American National Standard Methods for Calculation of Sound Emitted by Machinery and Equipment at Workstations and Other Specified Positions from Sound Power Level

ANSI/ASA S12.50-2002 (R2007)/ISO 3740:2000 American National Standard Acoustics—Determination of sound power levels of noise sources—Guidelines for the use of basic standards. (a Nationally Adopted International Standard)

ANSI/ASA S12.51-2002 (R2007)/ISO 3741:1999 *(Replaces ANSI S12.31-1990 and ANSI S12.32-1990)* American National Standard Acoustics—Determination of sound power levels of noise sources using sound pressure—Precision method for reverberation rooms, including Technical Corrigendum 1-2001 (a Nationally Adopted International Standard)

ANSI S12.53/Part 1-1999 (R2004)/ISO 3743-1:1994 *(Replaces ANSI S12.33-1990 along with ANSI S12.53/Part 2-1999)* American National Standard Acoustics—Determination of sound power levels of noise sources—Engineering methods for small, movable sources in reverberant fields—Part 1: Comparison method for hard-walled test rooms (a Nationally Adopted International Standard)

ANSI S12.53/Part 2-1999 (R2004)/ISO 3743-2:1994 *(Replaces ANSI S12.33-1990, along with ANSI S12.53/Part 1-1999)* American National Standard Acoustics—Determination of sound power levels of noise sources using sound pressure—Engineering methods for small, movable sources in reverberant fields—Part 2: Methods for special reverberation test rooms (a Nationally Adopted International Standard)

ANSI S12.54-1999 (R2004)/ISO 3744:1994 *(Replaces ANSI S12.34-1988)* American National Standard Acoustics—Determination of sound power levels of noise sources using sound pressure—Engineering method in an essentially free field over a reflecting plane (a Nationally Adopted International Standard)

ANSI S12.55-2006/ISO 3745:2003 *(Replaces ANSI S12.35-1990)* American National Standard Acoustics—Determination of sound power levels of noise sources using sound pressure—Precision methods for anechoic and hemi-anechoic rooms (a Nationally Adopted International Standard)

ANSI S12.56-1999 (R2004)/ISO 3746:1995 *(Replaces ANSI S12.36-1990)* American National Standard Acoustics—Determination of sound power levels of noise sources using sound pressure—Survey method using an enveloping measurement surface over a reflecting plane (a Nationally Adopted International Standard)

ANSI/ASA S12.57-2002 (R2007)/ISO 3747:2000 American National Standard Acoustics—Determination of sound power levels of noise sources using sound pressure—Comparison method *in situ* (a Nationally Adopted International Standard)

ANSI S12.60-2002 American National Standard Acoustical Performance Criteria, Design Requirements, and Guidelines for Schools

ANSI S12.65-2006 (*Revision of ANSI S3.14-1977*) American National Standard for Rating Noise with Respect to Speech Interference

ANSI/ASA S12.68-2007 American National Standard Methods of Estimating Effective A-Weighted Sound Pressure Levels When Hearing Protectors are Worn

ASA Committee on Standards (ASACOS)

ASACOS (P.D. Schomer, Chair and ASA Standards Director)

U.S. Technical Advisory Groups (TAGS) for International Standards Committees

ISO/TC 43 Acoustics, **ISO/TC 43/SC 1** Noise (P.D. Schomer, U.S. TAG Chair)

ISO/TC 108 Mechanical Vibration, Shock and Condition Monitoring (D.J. Evans, U.S. TAG Chair)

ISO/TC 108/SC2 Measurement and Evaluation of Mechanical Vibration and Shock as Applied to Machines, Vehicles and Structures (A.F. Kilcullen, and R.F. Taddeo U.S. TAG Co-Chairs)

ISO/TC 108/SC3 Use and Calibration of Vibration and Shock Measuring Instruments (D.J. Evans, U.S. TAG Chair)

ISO/TC 108/SC4 Human Exposure to Mechanical Vibration and Shock (D.D. Reynolds, U.S. TAG Chair)

ISO/TC 108/SC5 Condition Monitoring and Diagnostics of Machines (D.J. Vendittis, U.S. TAG Chair; R. Taddeo, U.S. TAG Vice-Chair)

ISO/TC 108/SC6 Vibration and Shock Generating Systems (C. Peterson, U.S. TAG Chair)

IEC/TC 29 Electroacoustics (V. Nedzelnitsky, U.S. Technical Advisor)

STANDARDS NEWS FROM THE UNITED STATES

(Partially derived from *ANSI Reporter*, and *ANSI Standards Action*, with appreciation)

American National Standards Call for Comment on Proposals Listed

This section solicits comments on proposed new American National Standards and on proposals to revise, reaffirm, or withdrawal approval of existing standards. The dates listed in parentheses are deadlines for submission of comments, and they are for information only.

AHAM (Association of Home Appliance Manufacturers)

Reaffirmations

BSR/AHAM AC-2-2006 (R200x), Method for Sound Testing of Portable Household Electric Room Air Cleaners (reaffirmation of ANSI/AHAM AC-2-2006)

Establishes a method to determine the sound rating of portable household electric room air cleaners. The sound rating is comprised of a set of sound levels that include: (1) Overall A-weighted sound power level (LWA) and (2) Loudness level in SONES. Established in the standard are definitions, tests, calculations, ratings, and minimum data requirements for published ratings and conformance conditions. (June 2, 2008)

ASA (ASC S2) (Acoustical Society of America)

New Standards

BSR/ASA S2.62-200x, Shock Test Requirements for Equipment in a Rugged Shock Environment (new standard)

Defines test requirements and severity thresholds for a large range of shock environments, including but not limited to shipping, transport, and rugged operational environments. This standard shall be used for testing equipment that will be subjected to shock. It will allow vendors to better market, and users to more easily identify, equipment that will operate or simply survive in rugged shock environments. (May 5, 2008)

Revisions

BSR/ASA S2.9-200x, Parameters for Specifying Damping Properties of Materials and System Damping (revision and redesignation of ANSI S2.9-1976 (R2006))

Presents required nomenclature to improve communications among technological fields concerned with material damping used for resilient mountings to enable a clear understanding by both user and manufacturer. Intention is to encourage better communication between manufacturer and user. Should be regarded as nomenclature for specifying damping properties of the resilient materials. Outlines information to enable the experienced designer to select resilient material for machine mountings correctly. (June 2, 2008)

ASA (ASC S12) (Acoustical Society of America)

Revisions

BSR/ASA S12.9-Part 6-200x, Quantities and Procedures for Description and Measurement of Environmental Sound—Part 6: Methods for Estimating of Awakenings Associated with Outdoor Noise Events Heard in Homes (revision and redesignation of ANSI S12.9-Part 6-2000 (R2005))

Provides a method to predict sleep disturbance in terms of percent awakenings or numbers of people awakened associated with noise levels in terms of indoor A-weighted sound exposure level (ASEL). Developed from field studies of behavioral awakening primarily in homes near routine jet aircraft takeoff and landing operations, railroads, roads and highways. Database used to develop the method consists of about 10,000 subject-nights of observations in a variety of communities in the U.S. and the Netherlands. (June 2, 2008)

BSR/ASA S12.6-200x, Methods for Measuring the Real-Ear Attenuation of Hearing Protectors (revision and redesignation of ANSI S12.6-1997 (R2002))

Specifies laboratory-based procedures for measuring, analyzing, and reporting passive noise-reducing capabilities of hearing protection devices. The procedures consist of psychophysical tests conducted on human subjects to determine real-ear attenuation measured at hearing threshold. Two fitting procedures are provided: Method A (trained subject fit) and Method B (inexperienced subject fit), intended to approximate protection that can be attained by groups of informed users in workplace hearing conservation programs. (June 16, 2008)

ASTM (ASTM International)

New Standards

BSR/ASTM WK10107/D7452-200x, Standard Test Method for Evaluation of the Load Carrying Properties of Lubricants Used for Final Drive Axles, Under Conditions of High Speed and Shock Loading. (May 26, 2008)

IEEE (institute of Electrical and Electronics Engineers)

Reaffirmations

BSR/IEEE 260.4-1996 (R200x), Letter Symbols and Abbreviations for Quantities Used in Acoustics (reaffirmation of ANSI/IEEE 260.4-1996 (R2002))

Covers letter symbols for physical quantities used in the science and technology of acoustics. Abbreviations for a number of acoustical levels and related measures that are in common use are also given. The symbols given in this standard are intended for all applications. (June 17, 2008)

TIA (Telecommunications Industry Association)

Reaffirmations

BSR/TIA 631-A-2002 (R200x), Telecommunications—Telephone Terminal Equipment—Radio Frequency Immunity Requirements (reaffirmation of ANSI/TIA 631-A-2002)

Specifies Radio Frequency (RF) immunity performance criteria for two-wire Telephone Terminal Equipment (TTE) having an acoustic output and two-wire TTE adjunct devices with connection port for Telephone Terminal Equipment (TTE) having an acoustic output. (April 28, 2008)

New Standards

BSR/TIA 1005-200x, Telecommunications Infrastructure Standard for Industrial Premises (new standard)

Specifies telecommunications cabling to support industrial premises applications (i.e., voice, data, text, video, industrial and building controls, security, fire alarm and image) while allowing for exposures to wider ranges of temperature, humidity, electrical noise, shock, vibration, corrosive gases, dust, liquids, etc. (May 26, 2008)

Call for Members (ANS Consensus Bodies)

Directly and materially affected parties who are interested in participating as a member of an ANS consensus body for the standards listed below are requested to contact the sponsoring standards developer directly and in a timely manner.

AHAM (Association of Home Appliance Manufacturers)

BSR/AHAM AC-2-2006 (R200x), Method for Sound Testing of Portable Household Electric Room Air Cleaners (reaffirmation of ANSI/AHAM AC-2-2006)

ASA (ASC S1) (Acoustical Society of America)

BSR/ASA S1.20-200x, Procedures for Calibration of Underwater Electroacoustic Transducers (revision and redesignation of ANSI S1.20-1988 (R2003))

ASA (ASC S3) (Acoustical Society of America)

BSR/ASA S3/SC1.1-200x, Animal Bioacoustics Terminology (new standard)

BSR/ASA S3/SC1.2-200x, Underwater Passive Acoustic Monitoring for Bioacoustic Applications (new standard)

Project Initiation Notification System (PINS)

ANSI Procedures require notification of ANSI by ANSI-accredited standards developers of the initiation and scope of activities expected to result in new or revised American National Standards. This information is a key element in planning and coordinating American National Standards.

The following is a list of proposed new American National Standards or revisions to existing American National Standards that have been received from ANSI-accredited standards developers that utilize the periodic maintenance option in connection with their standards. Directly and materially affected interests wishing to receive more information should contact the standards developer directly.

ASA (ASC S1) (Acoustical Society of America)

BSR/ASA S1.20-200x, Procedures for Calibration of Underwater Electroacoustic Transducers (revision and redesignation of ANSI S1.20-1988 (R2003))

Establishes measurement protocols for testing/calibrating underwater electroacoustic transducers and testing for a material's acoustic performance; this standard also describes forms for presenting the resultant data. Project Need: To update the standard in light of new acoustic materials in use and newer data acquisition means that are available. This standard is the guideline in use within the underwater acoustic community. It provides common language and a set of standard procedures for the calibration of underwater acoustic devices. Stakeholders: U.S. Government Agencies, military organizations, DoD, DoD contractors, educational institutions.

ASA (ASC S3/SC1) (Acoustical Society of America)

BSR/ASA S3/SC1.1-200x, Animal Bioacoustics Terminology (new standard)

Provides terms, definitions, and acoustical notation used in animal bioacoustics. Project Need: There is increasing interest in the science of animal bioacoustics among regulatory agencies, industry, and researchers. Researchers come from various areas of science (biology, ecology, acoustics, physics, engineering and others) and do not always share a common scientific language. This document will help unify the language used in their publications. Stakeholders: Scientific researchers in all branches of science concerned with animal bioacoustics.

BSR/ASA S3/SC1.2-200x, Underwater Passive Acoustic Monitoring for Bioacoustic Applications (new standard)

Provides a set of requirements for the information to be documented while recording acoustic data at sea (metadata requirements), the minimum information to be included when reporting the results, and specifies metrics to be used when summarizing the features of an acoustic signal. A set of recommended "best-practice" procedures and equipment capabilities is included as an informative annex. Project Need: To aid the study of the impact of anthropogenic sound on aquatic animals, which is of increasing interest to regulatory agencies and also to industry and the military. Stakeholders: Federal and state regulatory agencies concerned with sound generated in the ocean by human activity.

IEEE (Institute of Electrical and Electronics Engineers)

BSR/IEEE 269-200x, Methods for Measuring Transmission Performance of Analog and Digital Telephone Sets, Handsets, and Headsets (revision of ANSI/IEEE 269-2002)

Provides the techniques for objective measurement of electroacoustic characteristics of analog and digital telephones, handsets and headsets. Application is in the frequency range from 100 to 8,500 Hz. Project Need: To merge IEEE 269-2002 with IEEE 269a-2007. It will also update selected technical subclauses. Stakeholders: Developers, manufacturers and users of analog and digital telephones, handsets and headsets.

Final actions on American National Standards

The standards actions listed below have been approved by the ANSI Board of Standards Review (BSR) or by an ANSI-Audited Designator, as applicable.

AMCA (Air Movement and Control Association)

New Standards

ANSI/AMCA 300-2008, Reverberant Room Method for Sound Testing of Fans (new standard)

ANSI/AMCA 320-2008, Laboratory Method for Sound Testing of Fans Using Sound Intensity (new standard)

ASA (ASC S12) (Acoustical Society of America)

Reaffirmations

ANSI/ASA S12.8-1998 (R2008), Methods for Determining the Insertion Loss of Outdoor Noise Barriers (reaffirmation and redesignation of ANSI S12.8-1998 (R2003))

ANSI/ASA S12.9-Part 2-1992 (R2008), Quantities and Procedures for Description and Measurement of Environmental Sound—Part 2: Measurement of Long-Term, Wide-Area Sound (reaffirmation and redesignation of ANSI S12.9-Part 2-1992 (R2003))

ANSI/ASA S12.9-Part 3-1993 (R2008), Quantities and Procedures for Description and Measurement of Environmental Sound—Part 3: Short-Term Measurements with an Observer Present (reaffirmation and redesignation of ANSI S12.9-Part 3-1993 (R2003))

30-Day Notice of Withdrawal: ANS 5 to 10 years past approval date

In accordance with clause 4.7.1 Periodic Maintenance of American National Standards of the ANSI Essential Requirements, the following American National Standards have not been reaffirmed or revised within the five-year period following approval as an ANS. Thus, they shall be withdrawn at the close of a 30-day public review notice in Standards Action (date in parentheses).

ANSI/SAE J47-JUL98, Maximum Sound Level Potential for Motorcycles. (May 4, 2008)

ANSI/SAE J986-MAY98, Sound Level for Passenger Cars and Light Trucks (May 4, 2008)

ANSI/SAE J1287-JUL98 (RMAY00), Stationary Motorcycles, Measurement of Exhaust Sound Levels of

ANSI/SAE J1470-JUN98, Measurement of Noise Emitted by Accelerating Highway Vehicles (May 4, 2008)

ANSI/SAE J1492-MAY98, Measurement of Light Vehicle Stationary Exhaust System Sound Level Engine Speed Sweep Method

ANSI/SAE J2380-JAN98, Vibration Testing of Electric Vehicle Batteries

ANSI/SAE J2455-JAN98, Drivetrain Systems Vibration Analysis-Data Requirements

ANSI/SAE J/ISO 6394-JUL98, Acoustics—Measurement of Airborne Noise Emitted by Earthmoving Machinery Operator's Position—Stationary Testing Condition (May 4, 2008)

STANDARDS NEWS FROM ABROAD

(Partially derived from *ANSI Reporter* and *ANSI Standards Action*, with appreciation.)

Newly Published ISO and IEC Standards

Listed here are new and revised standards recently approved and promulgated by ISO, the International Standardization Organization.

ISO Standards

BUILDING CONSTRUCTION MACHINERY AND EQUIPMENT (TC 195)

ISO 19433:2008, Building construction machinery and equipment—Pedestrian-controlled vibratory plates—Terminology and commercial specifications

ISO 19452:2008, Building construction machinery and equipment—Pedestrian-controlled vibratory (percussion) rammers—Terminology and commercial specifications

EARTH-MOVING MACHINERY (TC 127)

ISO 6393:2008, Earth-moving machinery—Determination of sound power level—Stationary test conditions

ISO 6394:2008, Earth-moving machinery—Determination of emission sound pressure level at operators position—Stationary test conditions

ISO 6395:2008, Earth-moving machinery—Determination of sound power level—Dynamic test conditions

ISO 6396:2008, Earth-moving machinery—Determination of emission sound pressure level at operators position—Dynamic test conditions

MECHANICAL VIBRATION AND SHOCK (TC 108)

ISO 21289:2008, Mechanical vibration and shock—Parameters to be specified for the acquisition of vibration data

PLASTICS (TC 61)

ISO 6721-4:2008, Plastics—Determination of dynamic mechanical properties—Part 4: Tensile vibration—Non-resonance method

ISO Technical Specifications

ACOUSTICS (TC 43)

ISO/TS 13473-4:2008, Characterization of pavement texture by use of surface profiles—Part 4: Spectral analysis of surface profiles

IEC Standards

PERFORMANCE OF HOUSEHOLD ELECTRICAL APPLIANCES (TC 59)

IEC 60704-2-13 Amd.2 Ed. 1.0 b:2008, Amendment 2—Household and similar electrical appliances—Test code for the determination of airborne acoustical noise—Part 2-13: Particular requirements for range hoods

ISO Draft Standards

COMPRESSORS, PNEUMATIC TOOLS AND PNEUMATIC MACHINES (TC 118)

ISO/DIS 28927-1, Hand-held portable power tools—Test methods for evaluation of vibration emission—Part 1: Angle and vertical grinders (July 12, 2008)

ISO/DIS 28927-2, Hand-held portable power tools—Test methods for evaluation of vibration emission—Part 2: Wrenches, nut runners and screwdrivers (July 12, 2008)

ISO/DIS 28927-3, Hand-held portable power tools—Test methods for evaluation of vibration emission—Part 3: Polishers and rotary, orbital and random orbital sanders (July 12, 2008)

ISO/DIS 28927-5, Hand-held portable power tools—Test methods for evaluation of vibration emission—Part 5: Drills and impact drills (July 12, 2008)

ISO/DIS 28927-6, Hand-held portable power tools—Test methods for evaluation of vibration emission—Part 6: Rammers (July 12, 2008)

ISO/DIS 28927-7, Hand-held portable power tools—Test methods for evaluation of vibration emission—Part 7: Nibblers and shears (July 12, 2008)

ISO/DIS 28927-8, Hand-held portable power tools—Test methods for evaluation of vibration emission-Part 8: Saws, polishing and filing machines with reciprocating action and saws with oscillating or rotating action (July 12, 2008)

ISO/DIS 28927-9, Hand-held portable power tools—Test methods for evaluation of vibration emission-Part 9: Scaling hammers and needle scalers (July 12, 2008)

OPTICS AND OPTICAL INSTRUMENTS (TC 172)

ISO/DIS 11553-3, Safety of machinery—Laser processing machines—Part 3: Safety requirements for noise reduction and noise measurement methods for laser processing machines and hand-held processing devices and associated auxiliary equipment (accuracy grade 2) (June 7, 2008)

BOOK REVIEWS

P. L. Marston
Physics Department, Washington State University, Pullman, Washington 99164

These reviews of books and other forms of information express the opinions of the individual reviewers and are not necessarily endorsed by the Editorial Board of this Journal.

Computational Auditory Scene Analysis: Principles, Algorithms and Applications

Edited by DeLiang Wang and Guy J. Brown

Wiley-IEEE Press, Hoboken, N.J., 2006. xxiii+395 pp. $95.50 (hardcover), ISBN: 0471741094.

This excellent book consists of ten chapters by various authors on the progress that has been made in computationally analyzing sound mixtures into their component sources. This challenging problem is important in speech recognition, psychoacoustics, neuroscience, and hearing aid technology, and both introductory and advanced readers from all these fields will find many of the chapters of this book both comprehensible and enlightening.

A comprehensive and very well-written introductory chapter by the book's editors Wang and Brown whets the reader's appetite. It provides an overview of Computational Auditory Scene Analysis (CASA), reviewing background material from human auditory scene analysis (ASA) and providing a succinct summary of the relatively short history of CASA systems, their goals and their strategies. A recurrent theme at the heart of the book concerns the recognition of speech. Although human listeners are remarkably tolerant of additional sounds being present at the same time as the speech they wish to attend to, machine algorithms for speech recognition are not. Additional sounds corrupt the algorithms' inclusive input data representations and severely degrade performance. As Jon Barker says in his illuminating chapter on Robust Speech Recognition: "speech recognition remains a brittle technology." Many of the authors of the chapters in this book have been at the forefront of work that has attempted a radical solution to this problem. Taking their lead from psychoacoustic work on auditory scene analysis, in particular work covered in Albert Bregman's 1990 book of that title, they have endeavored to use simple properties of sounds, such as harmonicity, onset-time, azimuthal direction, and continuity to perform an allocation of the components in a sound mixture to their respective sources. This "bottom-up" symbolic approach initially met with limited success, at least compared to the best performance of statistical methods such as Independent Components Analysis. However, these statistical methods are themselves brittle, failing badly when the conditions for which they were designed are not met. CASA holds out the promise at least of a more robust, if partial, solution. Although, as Jon Barker points out, there are major problems in interfacing scene analysis modules with existing speech recognition methods, one of the exciting developments that appears in the book is the combination of CASA with the "missing-data" approach to speech recognition (pioneered by Martin Cooke). The issues raised at this interface are important for psychologists interested in the role that ASA plays in speech recognition in humans. Other chapters within this theme provide more technical descriptions of Feature-Based Speech Segregation by Wang and of Model-Based Scene Analysis by Daniel Ellis. These two chapters represent the two opposing approaches to the problem of separation proposed by Bregman, the first using simple properties that the sounds from a particular source share, the second, schema-based, using knowledge about specific sounds to find them in a mixture. The issues addressed here and the proposed solutions should stimulate not only those involved in speech recognition, but also psychoacousticians and other psychologists interested in auditory perception in the presence of competing sounds. The last two decades have seen a flourishing of research addressing the perception of both speech and the basic properties of complex sounds in the context of sound mixtures. There is presently a healthy interchange between this experimental work on auditory scene analysis and the computational work. For example, DeLiang Wang's concept of an ideal binary mask that reveals only those parts of a spectrogram that are dominated by a particular sound source has been a fruitful one not only in CASA but also in experiments on the recognition of speech mixed with that of other talkers. The sparse nature of harmonic sounds such as speech contributes to the success of the binary mask approach.

Another major theme of the chapters in this book is the way that a difference in azimuthal direction is exploited in scene analysis by both human listeners and computer algorithms. Some of the human data are well-reviewed by Richard Stern, Brown, and Wang who rightly raise the question of the relationship between spatial localization and scene analysis. Human listeners certainly use perceived location to help track a particular sound source over time, but how a particular source gets localized at a particular time is something of a puzzle. Do we use location to help simultaneous grouping, or do we group sounds before localizing them? Binaural information about azimuth in any one frequency channel is readily disturbed by, for example, reverberation. So although localization-based grouping works well in acoustically dead environments, as described by Albert Feng and Douglas Jones in their chapter, cues such as interaural time difference (ITD) degrade with reverberation and the grouping suffers. Perhaps as a consequence, human listeners show only weak simultaneous grouping effects with ITD, although it is the dominant cue for azimuthal localization of complex sounds, and also show some evidence for simultaneous grouping preceding localization. The varied effects of reverberation on a range of perceptual abilities and on machine speech recognition are very clearly reviewed in a chapter by Brown and Kalle Palomäki. They argue that in order to successfully combat the effects of reverberation, recognition algorithms need to exploit monaural grouping cues more and reduce their reliance on spatial differences. For example, recent developments in beamforming exploit the sparse nature of harmonic sounds such as speech to identify spectral regions that minimize the adulteration caused by reverberation. Brown and Palomäki also argue that the masking effect of late reflections can be profitably handled within a missing-data/binary mask framework.

A final theme of the book is the application of CASA to problems in music processing. Relevant to this theme as well as to speech is a careful and thorough chapter by Alain de Cheveigné on techniques for the estimation of the pitches of multiple simultaneous sounds; it points out the common principles underlying an apparently wide diversity of methods. Masataka Goto's chapter on the Analysis of Musical Audio Signals primarily reviews in some technical detail his approach to extracting melody and bass lines, beat structure and larger sectional structure from music.

The book's closing chapter by Brown and Wang covers Neural and Perceptual Modelling. It provides a useful review of the use of neural oscillator models to solve the "binding problem" posed by auditory scene analysis, and also covers autocorrelation approaches to vowel separation. It recognizes the somewhat surprising dearth of models for top-down or schema-based grouping and the need to integrate the two approaches, echoing Barker's comments on the challenge of integrating low-level grouping in CASA with model-based recognition algorithms.

In summary, the editors should be congratulated on assembling a well-integrated set of chapters that provide a comprehensive, comprehensible, and astute summary of the state of CASA and its relationship to human auditory scene analysis. As a bonus, the book has an associated website (www.casabook.org) which includes audio demonstrations and software downloads.

CHRIS DARWIN
Department of Psychology
University of Sussex
Brighton, BN1 9QG, U.K.

 0001-4966/2008/124(1)/13/1/$23.00

Wave Scattering by Small Bodies of Arbitrary Shapes

Alexander G. Ramm

World Scientific Publishing, Hackensack, 2005. xviii+293 pp. $66 (hardcover), ISBN: 9812561862.

As a reader of the *Journal of the Acoustical Society of America*, what would you expect this book to contain? The title suggests a coherent survey of the literature on the scattering of sound waves by obstacles that are small compared to the wavelength, the domain of "low frequency scattering." If you want such a survey, consult the fine book with this title by G. Dassios and R. E. Kleinman (Oxford University Press, 2000). Professor Ramm's book is concerned with the same topic, but its aims are quite different. Thus, the "book is based mostly on the author's papers and results" (p. ix). On the back cover, we read "Applications of these results to ultrasound mammography and electrical engineering are considered," but this reviewer could not find such applications in the book.

So, what is in the book? There are 12 chapters: 1. Basic problems (11 pages); 2. Iterative processes for solving Fredholm's integral equations for static problems (11); 3. Calculating electric capacitance (17); 4. Numerical examples (9); 5. Calculating polarizability tensors (15); 6. Iterative methods: Mathematical results (23); 7. Wave scattering by small bodies (31); 8. Fredholm alternative and a characterization of Fredholm operators (12); 9. Boundary-value problems in rough domains (26); 10. Low frequency asymptotics (30); 11. Finding small inhomogeneities from scattering data (7); and 12. Modified Rayleigh conjecture (19). There is a 53-page appendix on quadrature rules for multi-dimensional integrals and a bibliography of 165 items (75 of which are authored or co-authored by Ramm). Chapters 8 and 9 seem to have little to do with the book's title.

The first seven chapters are a re-typed version of Ramm's earlier book, "Iterative Methods for Calculating Static Fields and Wave Scattering by Small Bodies" (Springer, New York, 1982). Everything else is taken almost exactly from his published papers. Indeed, the last five chapters and the appendix all contain statements such as "the presentation follows closely" (p. 138) followed by a citation to Ramm's papers; closer inspection (conveniently, many of his papers are available from his website) suggests that the word "closely" should be replaced by "exactly"! One minor virtue of repackaging a number of papers is that each chapter is self-contained. On the other hand, there is little cross-referencing, no attempt at synthesis of an overview of the subject, and pointless repetition (compare p. 202 and p. 210). In addition, some quantities have several notations. For example, chapter 10 opens with "In this chapter the exterior domain $D'=D_e$ is denoted by Ω": apparently, the author could not be bothered to edit his text so as to use a common notation throughout.

In summary, this is a disappointing book. It contains nothing that is unavailable elsewhere. I cannot recommend it.

P. A. MARTIN
Department of Mathematical and Computer Sciences
Colorado School of Mines
Golden, Colorado 80401-1887

 0001-4966/2008/124(1)/14/1/$23.00

FORUM

Forum is intended for communications that raise acoustical concerns, express acoustical viewpoints, or stimulate acoustical research and applications without necessarily including new findings. Publication will occur on a selective basis when such communications have particular relevance, importance, or interest to the acoustical community or the Society. Submit such items to an appropriate associate editor or to the Editor-in-Chief, labeled FORUM. Condensation or other editorial changes may be requested of the author.

Opinions expressed are those of the individual authors and are not necessarily endorsed by the Acoustical Society of America.

Tent-shaped concert halls, existing and future

David Lloyd (ben Yaacov Yehuda) Klepper
Yeshivat Beit Orot, Shmuel ben Adiya 1, Mt. of Olives, Jerusalem 97400, Israel

(Received 28 November 2007; revised 30 April 2008; accepted 30 April 2008)
[DOI: 10.1121/1.2932342]

I. INTRODUCTION

The success of the Tokyo Opera City Concert Hall[1] indicates that the advantages of the shoebox geometry can be equaled or possibly surpassed in halls with inverted-V cross-section ceilings. Not referenced in the Tokyo Hall paper is the earlier success of The Maltings Concert Hall in Snape, England, nor many North American worship spaces with inverted-V ceilings or entire cross sections that have good reputations for concert hall acoustics, nor the more recent halls for which McKay Conant Brook were consultants. However, from the design of Symphony Hall Boston through such recent halls as Benaroya Hall in Seattle,[2–4] the rectangular shoe box has been considered by many architectural acoustical designers and consultants as an ideal form. The success of concert halls in the round with "vineyards" and/or electroacoustics has not challenged the shoebox's supremacy, but possibly the tent shape will.

Reference 1, concerning the Tokyo hall, shows that reverberation time calculations can be predicted with accuracy in inverted-V designs as well as in rectangular cross-section designs. Beyond concert hall design, the tradition of the rectangular shoebox hall is paralleled by the tradition of North American worship spaces with inverted-V ceilings that have excellent concert hall acoustics, such as the Church of the Advent, Boston,[2] The Bryn Mawr Presbyterian Church, Bryn Mawr, PA, Trinity College Chapel, Hartford, CT, and some with no vertical sidewall surfaces, such as the Air Force Academy Chapel, Colorado Springs, Congregation Beth El, Bloomfield Hills, MI, and the First Presbyterian Church, Stamford, CT, the "Fish Church."[5] The potential advantages of the inverted V as a cross section can include the following: (1) provision of lateral diffusion from smooth surfaces without the need of surface roughness, but only if the apex angle is less than 90°; (2) savings in construction costs, but only if the building or the inverted-V portion of the building is not exceptionally narrow; (3) possibilities for remodeling to increase room volume for increased reverberation time with continuous use of the building during the remodeling. The restraints on the first and second appear contradictory, but there is a range of apex angles where both advantages apply.[9]

In rereading the first reference, I was reminded of a telephone conversation of some 25 years ago. The architect, Yamasaki, called and said: "David, they are opening Beth El with a concert by the Detroit Symphony. I told them the building was designed as a synagogue and not a concert hall, but they are going ahead anyway." I took the number of seconds to mentally review the design, and then replied: "Don't worry, it will be all right. Just be sure to cover the carpet on the Bimah (the front platform) with plywood, especially under the 'cellos and double-bases." And they did so, and the concert was a success, and the acoustics were judged favorably. Refer to Fig. 1, which includes a Congregation Beth El, Bloomfield Hills, Michigan, photograph. The use of reflected light in a small model contributed to the design, and Gerald Marshall worked with me.

However, there is an even earlier worship space demonstrating good concert hall acoustics, the First Presbyterian Church of Stanford, Connecticut, the famous Wallace Harrison "Fish Church."[5] This church's acoustics were changed, unfortunately, by an attempt to correct a noise-produced intelligibility problem by massive sound-absorbing treatment and an underpew sound system without line of sight from the loudspeaker to ear. This situation and the use of an electronic instead of pipe organ prevented the church from serving as a model for good concert hall acoustical design. The installation of a fine Visser–Rowland pipe organ and the restoration of the original acoustics, done under the direction of the music minister, should restore it to that role (Figs. 1 and 2).

II. LATERAL DIFFUSION

The reflections from smooth vertical parallel walls and a flat ceiling are specular and not diffuse, but an inverted-V ceiling with an apex angle less than 90° allows a significant fraction of the energy to be reflected twice off the ceiling before returning to the sound-absorbing audience, and the angles involved can be very different for the double-reflected energy, as compared with the single reflections. This may possibly provide a sense of envelopment and, while not

 0001-4966/2008/124(1)/15/4/$23.00

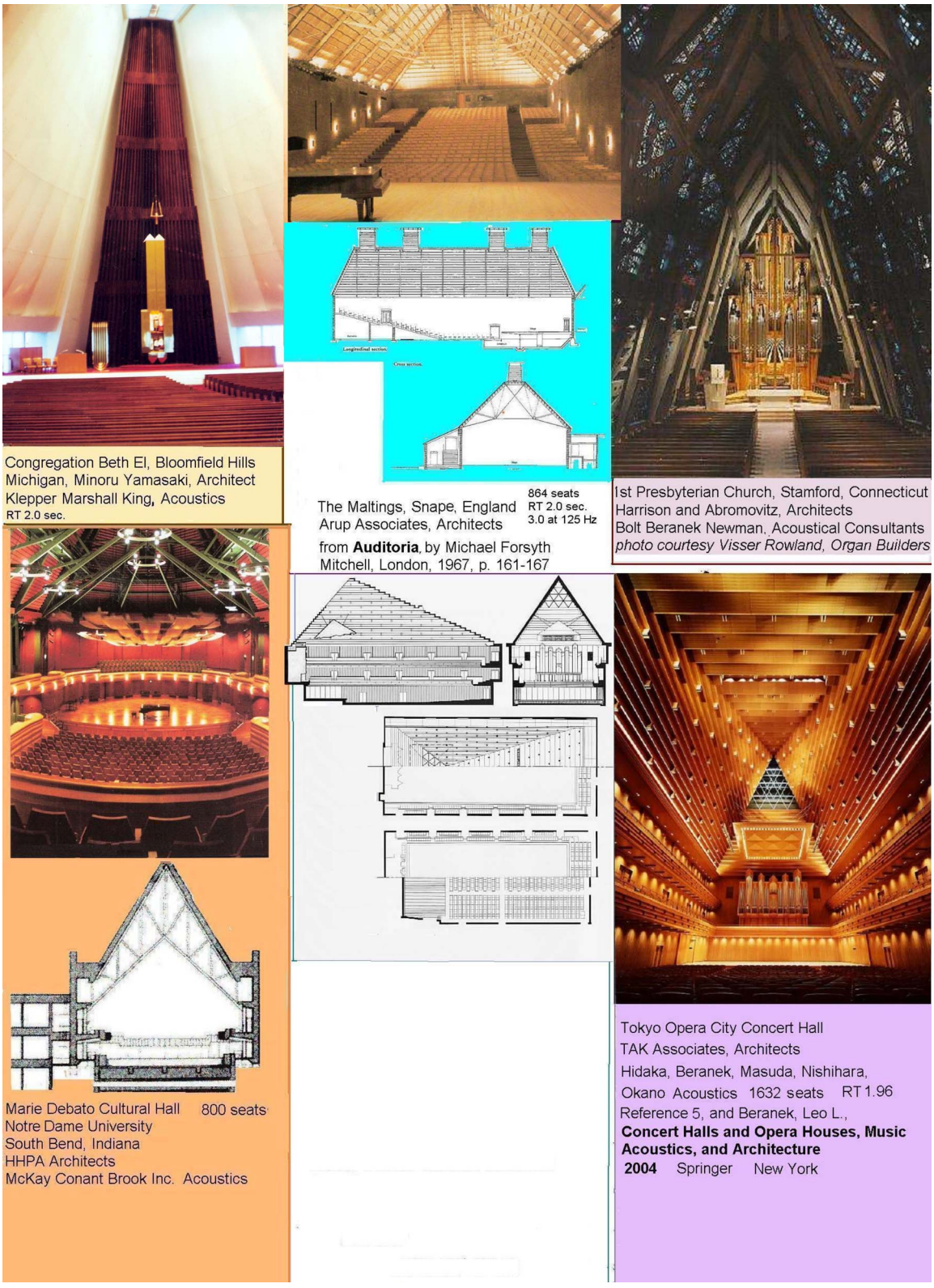

FIG. 1. (Color online) Three concert halls with apex angles at or close to optimum and two worship spaces used as concert halls on occasion.

100% nonspecular, is certainly no longer 100% specular. Figure 3provides a comparison. Very small apex angles can allow multiple ceiling reflections but can also increase construction costs instead of decreasing them.[9]

III. CONSTRUCTION COSTS

Assuming equal interior volume (and end wall areas), a pure inverted-V hall will have twice the height of the comparable rectangular hall, resulting in the same average ceiling

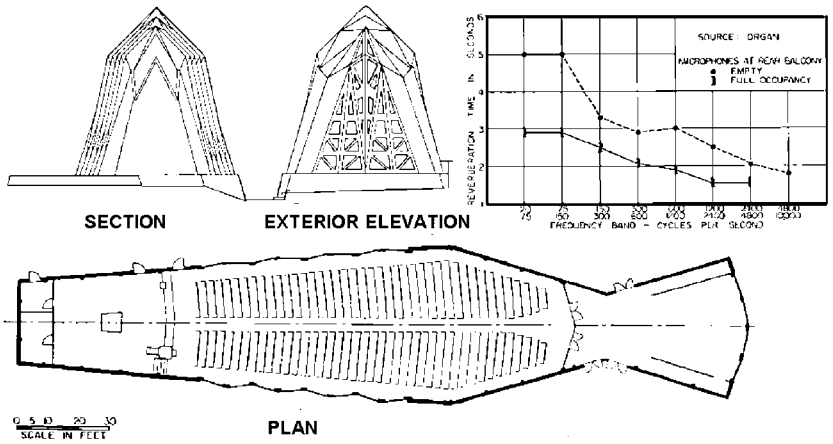

FIG. 2. Design and RT characteristics of the first Presbyterian Church, Stamford, CT (Ref. 5).

height (see Fig. 4). A comparison of the total sidewall and ceiling area of construction and linear length of transverse and vertical steel beams and columns or other frame members may be derived from geometry to be given by the equation:

$$R = 2(4 + r^2/4)^{1/2}/(2 + r) = (16 + r^2)^{1/2}/(2 + r), \quad (1)$$

where r is the width of the hall divided by the height of the rectangular hall, which is average height of the inverted-V hall, and R is the ratio of side and top surface area, which is the inverted-V hall divided by the rectangular hall that is also equal to the ratio of linear distances of side and top framing across the hall.

However, the depth of the steel web required is dependent on the length of the span. As a first approximation, the depth can be considered proportional to the length of the span.[9] This comparison is given by the equation

$$S, \text{ structural depth ratio, } = 2(4 + r^2/4)^{1/2}/2r = (16 + r^2)^{1/2}/2r. \quad (2)$$

Some measure of the total savings in using an inverted V can be obtained by multiplying the results of the two equations. The following table results:

Apex angle	r (width/ average height)	R (V area/ rectangular area)	S (V structure depth/ rectangular structure depth)	RS[10]
180	Inf.	1.00	0.50 (simplification not valid)	0.50
134	10	0.90	0.54	0.47
127	8	0.89	0.56	0.49
113	6	0.90	0.60	0.54
103	5	0.91	0.64	0.58
90	4	0.94	0.71	0.67
73	3	1.00	0.83	0.83
54	2	1.10	1.11	1.22
28	1	1.35	2.24	3.59
Zero	1/Inf.	2.00	Inf. (simplification not valid)	Inf.

Clearly, some recent concert halls have angles that provide both some lateral diffusion and some savings in construction costs, by employing conventional rectangular construction up to a specific height and then transitioning to an inverted V (see Fig. 1and Ref. 4). All credit to their designers.

IV. RENOVATION DURING USEFUL OCCUPANCY

The concept of an inverted-V roof for a concert hall suggests the possibility of remodeling such halls as London's

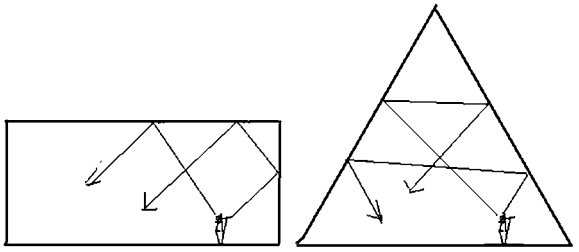

FIG. 3. Lateral section, how the use of an inverted-V ceiling can add lateral diffusion.

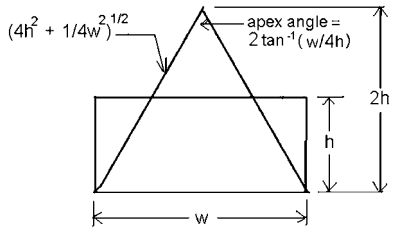

FIG. 4. Height, width, and angle relationships, V ceiling vs rectangular hall.

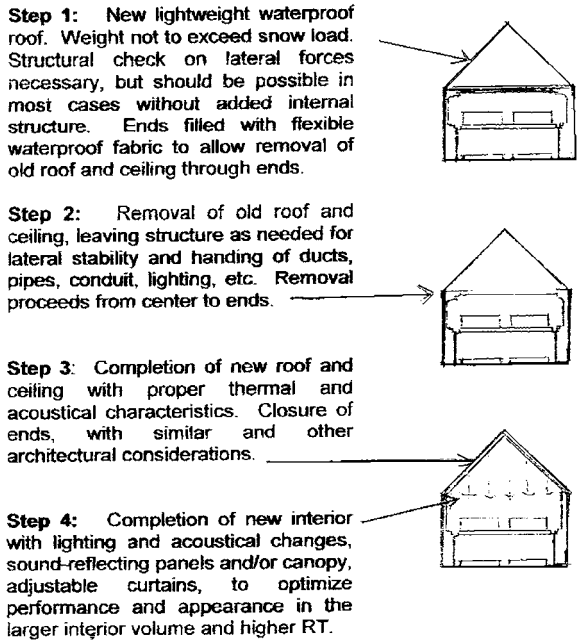

FIG. 5. Use of an inverted-V ceiling for adding volume to a hall for increased RT, lateral section shown.

Royal Festival Hall to have increased volume for increased reverberation time while continuing to use them. Possibly, sidewalls may need some additional structural strength. An initial inverted-V roof within the snow-load or rain-load tolerances of the building is constructed while leaving the original flat roof in place. When the inverted-V roof construction has progressed to the point where the building is weather tight, the flat roof can be removed section by section, opening up the added volume formed by the inverted V. The weight can then be added to the new roof, and the other required acoustical and architectural adjustments can be made to the interior (see Fig. 5).

V. FURTHER WORK

I am hopeful that the future will bring to completion enough halls with the inverted-V cross section to enable objective measurements to show what, if any, differences are there in such measurement tests of concert hall characteristics, including spatial information, variability of levels and directional pattern of received energy at various listening position, early-to-reverberant ratios as a function of frequency, lateral energy fraction as a function of frequency, and directional diffusion, when comparing similar halls in seating capacity and area, cubic volume, reverberation times, and seating and floor plans, differing only in the use of a rectangular cross section on the one hand and an inverted-V cross section on the other.[6] It may be quite a few years before such objective data are available! Until then, the primary values of this brief preliminary analysis may be able to provide a greater degree of freedom for the concert hall designer and a better way to correct existing halls with low volumes and low reverberation times. Essert has done commuter modeling on simple forms, with spaciousness showing up as the only musical subjective quality consistently improved, but this study does not include elements found in real world concert, including side balconies and adjustable suspended canopies.[7] Note that the work of Davies and Cox in reducing seat-dip attenuation still has yet to be applied in a real concert hall.[8]

[1]T. Hidaka, L. L. Beranek., S. Masuda, N. Nishihara, and T. Okano, "Acoustical design of the Tokyo Qpera City concert hall, Japan," J. Acoust. Soc. Am. **107**, 340–367 (2000).
[2]C. M. Harris, "Acoustical design of Benaroya Hall, Seattle," J. Acoust. Soc. Am. **110**, 2841–2844 (2000).
[3]L. L. Beranek, *Music Acoustics, and Architecture* (Acoustical Society of America, New York, 1962).
[4]L. L. Beranek, *Concert Halls and Opera Houses: How they Sound* (Acoustical Society of America, New York, 1996).
[5]D. L. Klepper, "First Presbyterian Church, Stamford, Connecticut," J. Acoust. Soc. Am. **31**, 879–882 (1959). Forty-eight years of hindsight suggests the words "early sound energy" should have been used instead of "direct sound" throughout this paper.
[6]J. S. Bradley and G. A. Soulodre, "The influence of late arriving energy on spatial impression," J. Acoust. Soc. Am. **97**, 2263–2271 (1995); "Objective measures of listener envelopment,"J. Acoust. Soc. Am. **98**, 2950–2957 (1995); A. Abdou and R. W. Guy, "Spatial information of sound fields for room-acoustics evaluation and diagnosis," J. Acoust. Soc. Am. **100**, 3215–3227 (1996); T. Okano, L. Beranek, and T. Hidaka, "Relations among interaural cross-correlation coefficient ($IACC_E$), lateral fraction (LF_E), and apparent source width (ASW) in concert halls," J. Acoust. Soc. Am. **104**, 255–265 (1998).
[7]R. Essert, "Links between concert hall geometry, objective parameters, and sound quality," J. Acoust. Soc. Am. **105**, 985 (1999).
[8]W. J. Davies and T. J. Cox, "Reducing seat dip attenuation," J. Acoust. Soc. Am. **108**, 2211–2218 (2000); D. L. Klepper, "Comment on 'Reducing seat dip attenuation,'" J. Acoust. Soc. Am. **110**, 1260 (2001); W. J. Davies and T. J. Cox, "Response to 'Comments reducing seat dip attenuation,'" J. Acoust. Soc. Am. **110**, 1261–1262 (2001).
[9]I make no claims to be a structural engineer, and obviously many variables will affect the actual cost comparison of a given proposed rectangular and inverted-V hall situation. Materials, required snow and rain loads, nature of joining planes at intersections, even ground conditions, and the required foundations (controlling lateral thrust in addition to providing ordinary support) can affect the comparison. However, the point that costs can be controlled by varying the apex angle remains valid.

REVIEWS OF ACOUSTICAL PATENTS

Sean A. Fulop
Dept. of Linguistics, PB92
California State University Fresno
5245 N. Backer Ave., Fresno, California 93740

Lloyd Rice
11222 Flatiron Drive, Lafayette, Colorado 80026

The purpose of these acoustical patent reviews is to provide enough information for a Journal reader to decide whether to seek more information from the patent itself. Any opinions expressed here are those of reviewers as individuals and are not legal opinions. Printed copies of United States Patents may be ordered at $3.00 each from the Commissioner of Patents and Trademarks, Washington, DC 20231. Patents are available via the internet at http://www.uspto.gov.

Reviewers for this issue:

GEORGE L. AUGSPURGER, *Perception, Incorporated, Box 39536, Los Angeles, California 90039*
ANGELO CAMPANELLA, *3201 Ridgewood Drive, Hilliard, Ohio 43026-2453*
JEROME A. HELFFRICH, *Southwest Research Institute, San Antonio, Texas 78228*
DAVID PREVES, *Starkey Laboratories, 6600 Washington Ave. S., Eden Prairie, Minnesota 55344*
CARL J. ROSENBERG, *Acentech Incorporated, 33 Moulton Street, Cambridge, Massachusetts 02138*
NEIL A. SHAW, *Menlo Scientific Acoustics, Inc., Post Office Box 1610, Topanga, California 90290*
KEVIN P. SHEPHERD, *Mail Stop 463, NASA Langley Research Center, Hampton, Virginia 23681*

7,295,153

43.35.Sx ACOUSTO-RADIO FREQUENCY MODULATOR AND APPLICATIONS THEREFORE

Brett A. Williams, assignor to Lockheed Martin Corporation
13 November 2007 (Class 342/175); filed 29 September 2004

I think I understand how this thing works: An acoustic RF modulator (ARFM) of light beam **306** is claimed where diffraction grating **303** is generated within material **118** by sending 35 GHz ultrasound (arrow) into that material, thereby altering the local refractive index periodically in space **303**. The degree of refractive index perturbation in **118** and **303** caused by

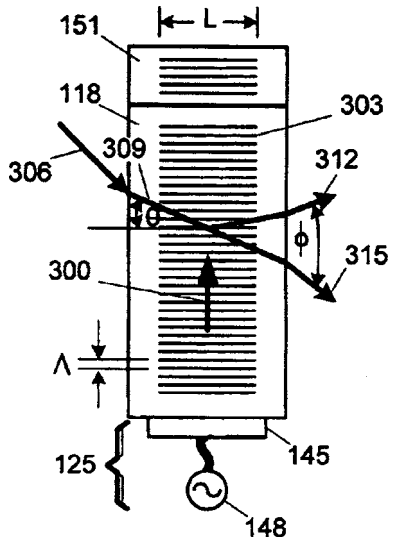

the ultrasound is varied by modulating the amplitude of the 35 GHz drive **148** to transducer **145**. Light **309** passing through **118** encounters Bragg reflection **312** that is in turn modulated via Doppler shifting (hence frequency modulation). Information to be transmitted, occurring as amplitude modulation of the 35 GHz ultrasound, can be in a bandwidth of up to 3 MHz.—AJC

7,328,618

43.35.Yb NON-DESTRUCTIVE TESTING OF PIPES

Osama Hunaidi *et al.*, assignors to National Research Council of Canada
12 February 2008 (Class 73/597); filed 21 June 2005

Water pipes gradually erode. What is needed is a simple method for measuring pipe wall thickness so that pipes can be replaced before they rupture. The patent explains that when a pipe carries water (or any nearly incompressible liquid), the elasticity of the pipe walls affects the velocity of

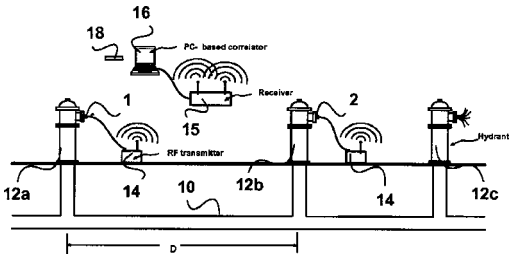

an acoustic disturbance as it travels longitudinally down the pipe. If all other factors can be accounted for, then the measured velocity between two locations—say, two fire hydrants—can be used to estimate the pipe wall thickness.—GLA

7,324,096

43.35.Zc TOUCH PANEL DEVICE

Fumihiko Nakazawa *et al.*, assignors to Fujitsu Limited
29 January 2008 (Class 345/177); filed 23 October 2002

This patent discloses a design for one type of touch panel device of the style that is used in cell phones. There is a lot of information here, from the design of the surface acoustic wave transducers on the perimeter of the display to the signal processing required for contact position detection. It is a lengthy and well-written patent, that has a lot of information for the reader interested in this technology.—JAH

 0001-4966/2008/124(1)/19/13/$23.00

7,325,605

43.35.Zc FLEXIBLE PIEZOELECTRIC FOR DOWNHOLE SENSING, ACTUATION AND HEALTH MONITORING

Michael L. Fripp *et al.*, assignors to Halliburton Energy Services, Incorporated
5 February 2008 (Class 166/250.01); filed 9 May 2007

This patent discloses a method of fabricating piezoceramic transducers for coupling longitudinal vibrations into a pipe. The pipes considered are of 1 to 8 in. diameter, typical of those used in the drilling industry. The technique disclosed herein is to slot one side of the piezoceramic slab, as shown

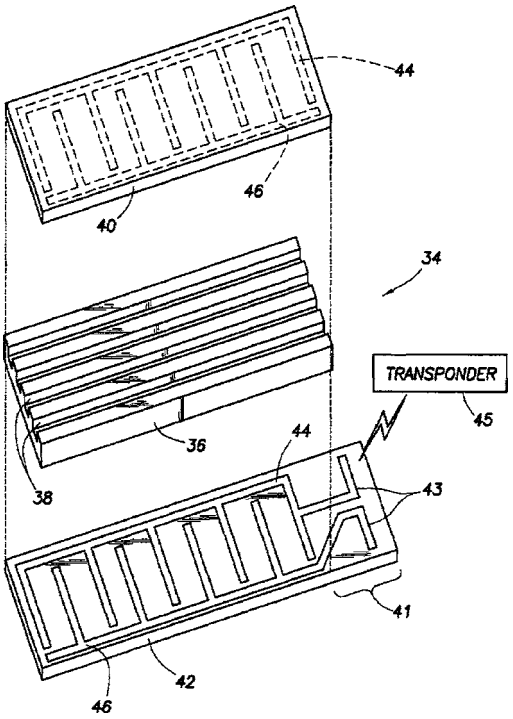

in the figure, thus making the transducer flexible enough to conform to such pipes. The discussion is brief and non-technical, and covers several aspects of transducer placement on pipes as well.—JAH

7,276,839

43.38.Ar BONDABLE FLUOROPOLYMER FILM AS A WATER BLOCK/ACOUSTIC WINDOW FOR ENVIRONMENTALLY ISOLATING ACOUSTIC DEVICES

Patrick J. Monahan, assignor to The United States of America represented by the Secretary of the Navy
2 October 2007 (Class 310/337); filed 30 November 2005

A water blocking film system **10** for underwater transducers **22** is claimed. Fluoropolymer film **12** has an etched surface that is coated on both sides with liquid polyurethane **14**. Polyurethane matrix potting material **30**

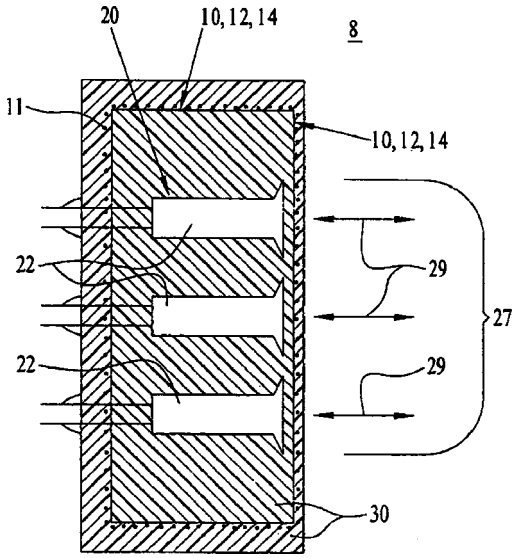

provides acoustical impedance matching to external water medium **8**. Fluoropolymer film system **10** blocks water **8** from permeating through potting material **30** to transducers **22**.—AJC

7,321,181

43.38.Ar CAPACITIVE MEMBRANE ULTRASONIC TRANSDUCERS WITH REDUCED BULK WAVE GENERATION AND METHOD

Butrus T. Khuri-Yakub *et al.*, assignors to The Board of Trustees of the Leland Stanford Junior University
22 January 2008 (Class 310/320); filed 4 April 2005

In this very brief patent, the authors disclose a means for improving upon their previously patented capacitive ultrasonic transducers. Specifically, they describe a way to reduce substrate interactions with the transducers by cutting a series of grooves in them. Referring to the figure, they suggest using a series of grooves **18** that are one-quarter wavelength deep at the resonance frequency. The function of the grooves is to suppress reflections from the substrate layer that is supporting the transducer, and to reduce

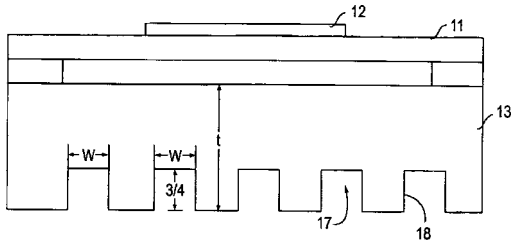

the reflections from the bulk waves introduced in the substrate. In addition, they recommend the use of an impedance mismatching layer of low impedance material below this. These are all useful tactics in general, but the results of doing this on the actual frequency response of one of these transducers is not shown. Note that there appears to be an error in the figure in which one-quarter wavelength is shown as "3/4".—JAH

7,274,798

43.38.Dv SPEAKER DEVICE

Yoshio Ohashi *et al.*, assignors to Sony Corporation
25 September 2007 (Class 381/430); filed in Japan 28 May 2002

A manner and method of joining hemispherical domed diaphragm **11** and edge-like diaphragm **13** to induction ring **3** in an ultra wideband high

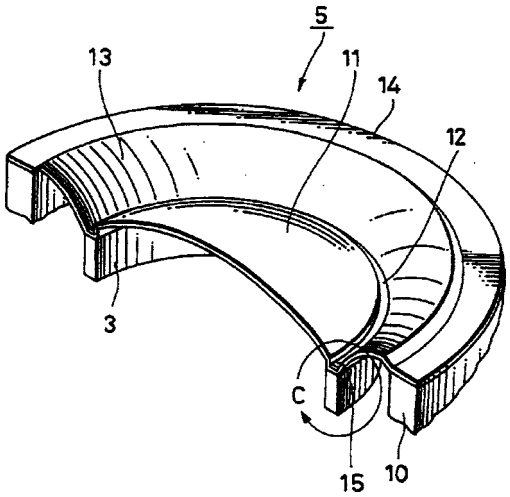

frequency transducer **5** is disclosed so that the dip in frequency response at around 50–60 kHz is reduced by about 3–4 dB.—NAS

7,322,251

43.38.Hz METHOD AND APPARATUS FOR MEASURING A PARAMETER OF A HIGH TEMPERATURE FLUID FLOWING WITHIN A PIPE USING AN ARRAY OF PIEZOELECTRIC BASED FLOW SENSORS

Daniel L. Gysling *et al.*, assignors to CIDRA Corporation
29 January 2008 (Class 73/861.26); filed 2 August 2004

This patent describes the use of PVDF transducers to measure the strains in a pipe with hot liquid flowing in it. The objective of this is to get the speed of sound in and flow velocity of the liquid. The problems addressed are those of keeping the transducers cool, maintaining contact with the pipe during thermal cycling, and arranging the transducers to effectively extract the desired signals passively from the time-dependent power spectrum of strain fluctuations. The patent goes into some detail on all of this, and describes the refrigerated "belt" of transducers used. It is well written and includes data from testing the design.—JAH

6,865,277

43.38.Ja PASSENGER VEHICLE

Graham Bank *et al.*, assignors to New Transducers Limited
8 March 2005 (Class 381/152); filed in United Kingdom 20 July 2001

Another in a long string of patents from New Transducers for so-called distributed mode acoustic radiators (loudspeakers) is aimed at applications within enclosures such as automobile interiors. These fiat panel loudspeakers can be integrated into surfaces of the vehicle such as doors, sun visors, dashboard, etc. so that, for example, the sun visor itself forms the radiating surface, and it is driven by an actuator. A large number of design variations are described which aim to produce a relatively uniform frequency response. One example (Fig. 9) consists of two beams **43**, **51** connected to each other and to a radiating panel **54**. Each beam is a piezoelectric bi-morph. The properties of each beam are chosen so that their individual modal distributions are interleaved, thus enhancing the overall modality of the system. Other design variations include a larger number of beams and the use of disks instead of beams.—KPS

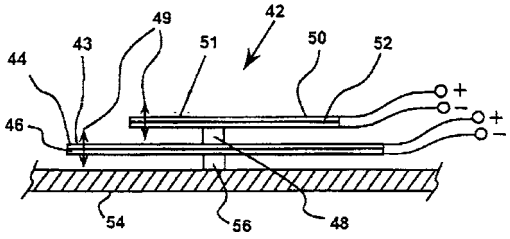

6,868,937

43.38.Ja SUB-WOOFER SYSTEM FOR USE IN VEHICLE

Glenn Cass, assignor to Alpine Electronics, Incorporated
22 March 2005 (Class 181/192); filed 26 March 2002

A subwoofer for use in an automobile consists of a flattened horn. The drive unit is placed under a front seat. The horn has a rectangular cross section, with constant thickness, but increasing width from the drive unit to the horn exit near the front wall of the vehicle interior. This arrangement may be integrated into the floor mat (Fig. 8) and claims a more uniform sound field than other mount locations such as the rear deck.—KPS

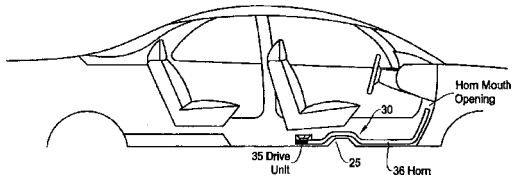

7,278,513

43.38.Ja INTERNAL LENS SYSTEM FOR LOUDSPEAKER WAVEGUIDES

James S. Brawley, Jr., assignor to Harman International Industries, Incorporated
9 October 2007 (Class 181/176); filed 26 June 2002

Lens system **210** comprised of vanes **302**…**322** in slot **114** at the mouth of the horn defined by throat **204** and flare **206**, is said to modify what would be a spherical wavefront emanating from the horn to a cylindrical wavefront. This cylindrical wavefront is said to be better suited for use in loudspeaker assemblies called "line arrays" in the current vernacular. The vanes modify the path length through the horn so that any and all parts of the wavefront developed from driver **202** into throat **204** and the ensuing horn defined by curve **206**, and indicated by **A**…**F**, arrive at the slot at the same time.—NAS

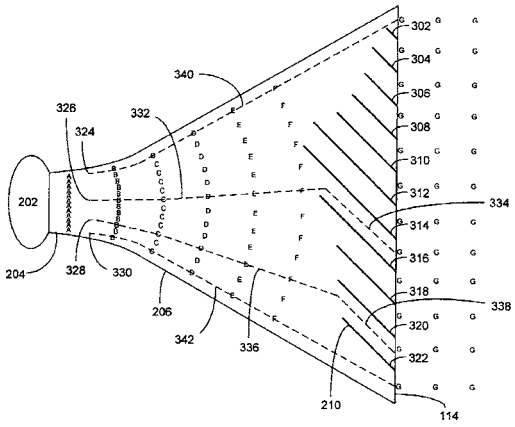

7,299,893

43.38.Ja LOUDSPEAKER HORN AND METHOD FOR CONTROLLING GRATING LOBES IN A LINE ARRAY OF ACOUSTIC SOURCES

John D. Meyer *et al.*, assignors to Meyer Sound Laboratories, Incorporated
27 November 2007 (Class 181/188); filed 20 February 2004

When the distance between drivers in a line array is greater than λ, interference (called *grating* in the patent) lobes occur. Minimizing the interference between the multiple drivers and their associated horns is the object in the instant case. Horn device **11** can accept three acoustic drivers and three subsections that control both pattern and interference between sections. Fins **27**–**29**, horn flared end walls **19**–**21**, and flared side walls **23**–**25**

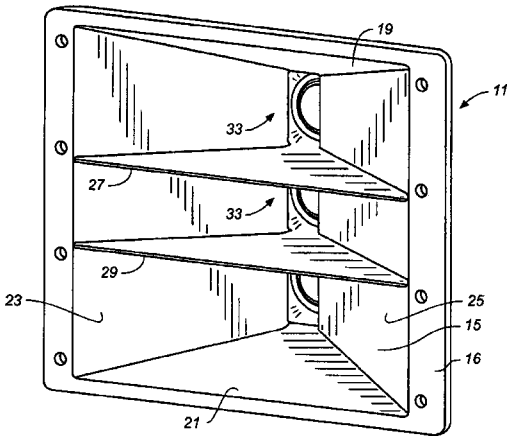

comprise what could be called a 1×3 sectoral horn with three drivers. Fins **27**–**29** are shaped to control the interference and can extend to the horn mouth but do not need to, as determined by the reduction of interference that is needed or desired. The patent is clearly written and straightforward.—NAS

7,274,270

43.38.Rh RESONATOR MATCHING NETWORK

Michael Louis Frank, assignor to Avago Technologies Wireless IP (Singapore) Pte. Limited
25 September 2007 (Class 333/32); filed 13 April 2005

Author claims a surface acoustic wave (SAW) resonator or a film bulk acoustic resonator (FBAR) that will act as the inductance in a tuned RF preamplifier to save manufacturing cost, reduce package size, and to reduce signal loss.—AJC

7,274,358

43.38.Rh FOCUSING-SHAPED REFLECTOR ARRAYS FOR ACOUSTIC TOUCHSCREENS

Joel Christopher Kent, assignor to Tyco Electronics Corporation
25 September 2007 (Class 345/177); filed 6 January 2004

The author claims a touch screen transducer that does not require (but could use) a distributing wave guide. Successive convex faced reflectors

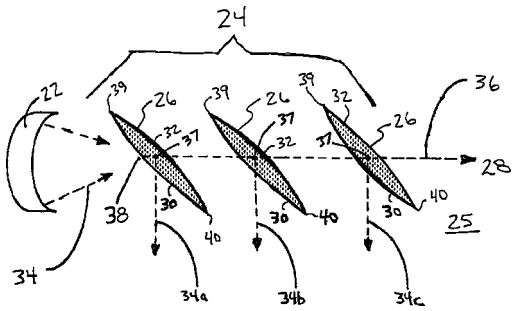

distribute surface waves **34a**, **34b**, **34c**,… over the touch screen to a similar receiver array on the opposite side of the screen.—AJC

7,324,656

43.38.Ja WIDE DISPERSION SPEAKER SYSTEM AND COVER MOUNTING STRUCTURE FOR INSTRUMENT DIRECTLY MOUNTED TO FLAT PORTION

Ken Iwayama and Takashi Nishino, assignors to TOA Corporation
29 January 2008 (Class 381/386); filed in Japan 20 November 2002

This wide dispersion speaker baffle plate has not only a restricted center opening **11** but additional holes or slots **12** and a conical diffuser **4**.

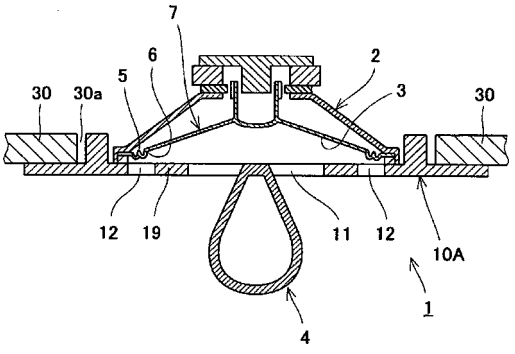

The patent includes response curves and polar plots demonstrating that the peripheral holes can extend high frequency response without substantially changing the directional pattern of the system.—GLA

7,292,822

43.38.Rh WIRELESS COMMUNICATION SYSTEM USING SURFACE ACOUSTIC WAVE (SAW) SECOND HARMONIC TECHNIQUES

Peter J. Edmonson and Colin K. Campbell, assignors to Research In Motion Limited
6 November 2007 (Class 455/41.2); filed 21 September 2004

A low cost SAW device for 2.4 GHz wireless Bluetooth ISM communication is constructed from 1.2 GHz SAW components operating in its second harmonic mode.—AJC

7,324,655

43.38.Si ELECTROACOUSTIC TRANSDUCER

Mamoru Sato, assignor to NEC TOKIN Corporation
29 January 2008 (Class 381/370); filed in Japan 4 July 2002

Cellular phones can produce audible sound and/or tactile vibrations, the vibrations serving as an optional ring signal. At least one multi-purpose cell phone includes a tactile transducer that can generate vibrations in synchronism with music during playback. The next logical step is a vibrating earphone, which is what this patent describes. "Accordingly, the present

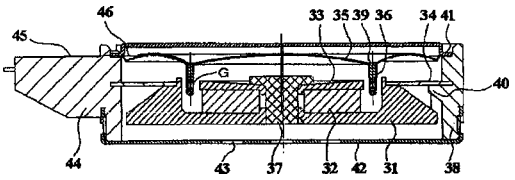

invention provides new media enabling information transmission including representation of emotions by the use of the sound and the body sensible vibration, that is not achieved in the art." A dual-mode transducer has a conventional diaphragm and voice coil, but its magnetic structure is resiliently suspended. Audio frequencies are reproduced normally but infrasonic signals excite the magnetic assembly to produce tactile vibrations.—GLA

7,324,834

43.38.Si SPEAKER SYSTEM

Takuro Yamaguchi *et al.*, assignors to Foster Electric Company, Limited
29 January 2008 (Class 455/556.1); filed 15 August 2005

A stand or docking station for a mobile phone often includes electronic components and transducers to provide speakerphone operation. Add one

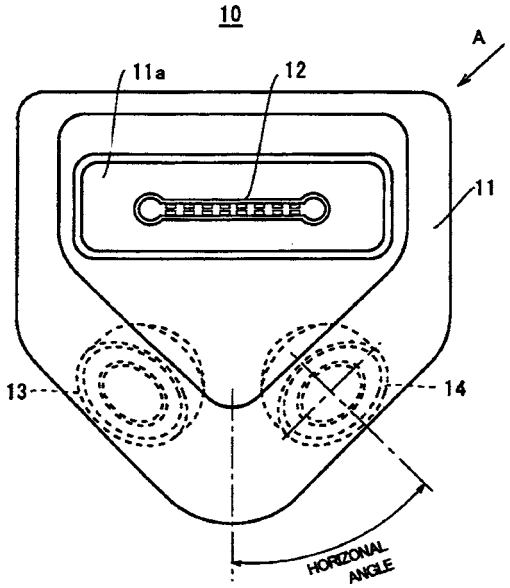

more loudspeaker and, voila, it can provide stereo music reproduction as well. Speakers **13**, **14** may be placed on opposite sides of the enclosure or angled outward as shown.—GLA

7,330,553

43.38.Si AUDIO SIGNAL REPRODUCING APPARATUS

Masayuki Nishiguchi and Yoshihito Fujiwara, assignors to Sony Corporation
12 February 2008 (Class 381/74); filed in Japan 25 October 1989

Believe it or not, the diagram is an accurate depiction of what is covered by the patent claims. (Another embodiment omits recording capabilities.) The only physical requirements are that the device be portable and

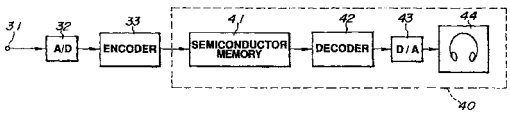

that audio playback be heard through headphones. Has Sony actually managed to retroactively patent the iPod? The plot is thickened by the time span involved: this patent is a division of a division of an earlier patent, and the original filing date in Japan goes back to 1989.—GLA

7,327,330

43.38.Vk ELECTRONIC DEVICE HAVING STEREO SPEAKERS

Kenji Kawai and Shigenobu Chichimatsu, assignors to Canon Kabushiki Kaisha
5 February 2008 (Class 345/6); filed in Japan 15 February 2000

The 21 claims of this patent are so broadly written as to cover any camera, DVD player, or personal computer having a pair of loudspeakers and a pivoting screen. Or maybe a pair of loudspeakers and a pivoting

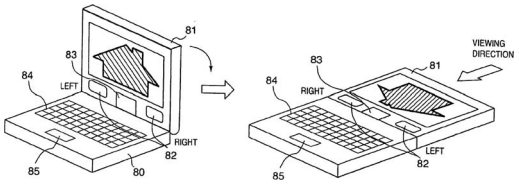

screen on which the image can be reversed to correspond with the viewing direction. And if you are still concerned about prior art, how about automatically switching the left/right channels to correspond with the image?—GLA

7,330,552

43.38.Vk MULTIPLE POSITIONAL CHANNELS FROM A CONVENTIONAL STEREO SIGNAL PAIR

Andrew LaMance, East Ridge Tennessee
12 February 2008 (Class 381/18); filed 19 December 2003

Fourier transforms are performed on left and right stereo signals and individual frequency bands are then processed by reverse-pan algorithms to derive original source locations. The information can be used to control a visual display (color organ) that accurately tracks phantom acoustic images.

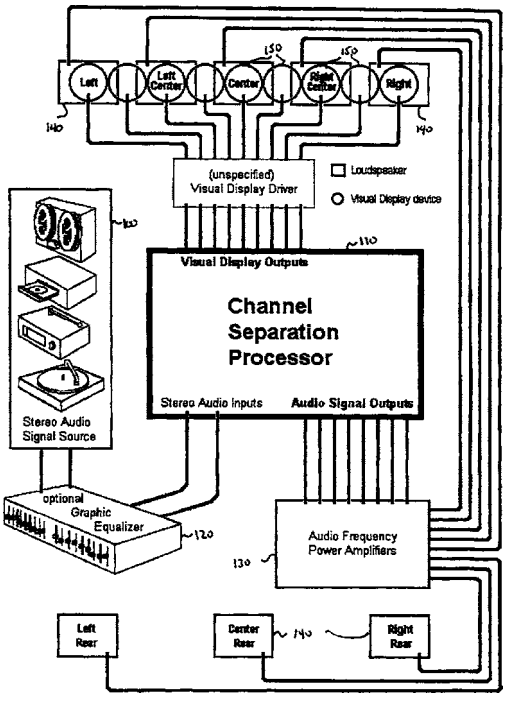

The method can also be used to expand the number of audio playback channels. "The result is not exact, but if the number of frequency bands is high, their width is sufficiently narrow to produce acceptable results."—GLA

7,273,423

43.40.Ey GOLF CLUB HEAD

Yasunori Imamoto, assignor to Bridgestone Sport Corporation
25 September 2007 (Class 473/332); filed in Japan 5 December 2003

The trend to larger volumes for golf club driver heads means that the thickness of the crown **5** and sole **3** of the club head have become thinner in order for the club head weight to remain more or less the same. To mitigate the increased vibration in the sole **3**, stiffening ribs **10** and weight **7**, which

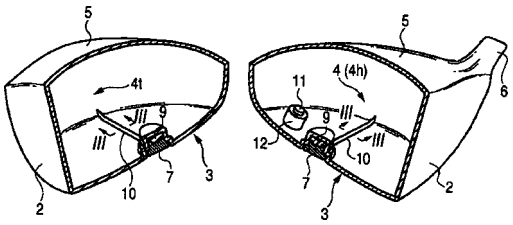

takes the form of a threaded insert, are proposed. The stiffening ribs **10** can run in the transverse direction as shown, and also in the longitudinal direction. Additional weight **11** may also be utilized.—NAS

7,281,994

43.40.Ey GOLF CLUB HEAD

Drew T. De Shiell *et al.*, assignors to Taylor Made Golf Company, Incorporated
16 October 2007 (Class 473/345); filed 2 June 2005

The size and shape of ledge **40** and shoulder **42** of rim **38** of front **18**,

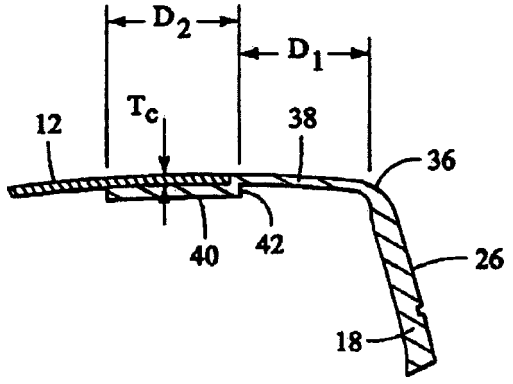

which attaches to crown **12**, are chosen to improve the durability and acoustic qualities of a wood type golf club head.—NAS

7,281,417

43.40.Le METHOD FOR EVALUATING QUALITY OF GOLF CLUB HEAD, METHOD FOR CONDUCTING QUALITY CONTROL OF GOLF CLUB HEAD, METHOD FOR MANUFACTURING GOLF CLUB HEAD AND GOLF CLUB, GOLF CLUB HEAD, AND GOLF CLUB

Hiroshi Saegusa and Kazunori Ono, assignors to The Yokohama Rubber Company, Limited
16 October 2007 (Class 73/65.03); filed in Japan 11 April 2002

The title says it all. Details in text discuss the coefficient of restitution, club face fatigue, the useful life of a club head, the resonant frequency of

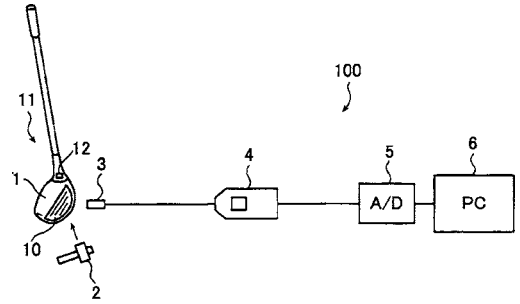

vibration of club head, and much more. Duffers will find the text informative.—NAS

7,284,434

43.40.Le RIGID-CONTACT DRIPLESS BUBBLER (RCDB) APPARATUS FOR ACOUSTIC INSPECTION OF A WORKPIECE IN ARBITRARY SCANNING ORIENTATIONS

Marvin F. Fleming, Sammamish, Washington
23 October 2007 (Class 73/644); filed 2 November 2004

Drip-less contact of ultrasonic inspection tool **1** to work piece **101** is achieved by vacuum contact **110**–**112** for the couplant (a sound purveying fluid) in coupler chamber **102**. Inspecting ultrasound travels from transducer **100** through channel **102** to membrane **107** that has a small perforation that

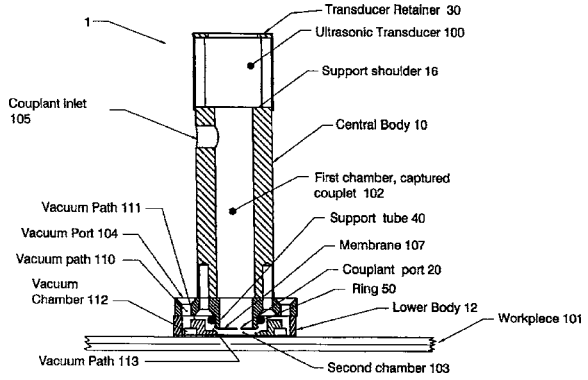

allows some coupling fluid to seep into a second chamber **103**, via a vacuum applied through path **104**–**110**–**111**, to flush clear remaining debris and bubbles on work piece surface **101**, thus assuring a continuous ultrasound propagation path to and from the work piece.—AJC

7,288,861

43.40.Tm INERTIAL ACTUATOR WITH MULTIPLE FLEXURE STACKS

Charles L. Willard *et al.*, assignors to Motran Industries Incorporated
30 October 2007 (Class 310/15); filed 19 October 2004

An inertial force actuator for helicopter active vibration control, having a large force amplitude at low frequencies, is claimed where control current through a coil wound on bobbin **38** creates an electromotive force on a permanent magnet in a coaxial core moving inside bobbin **38** (all inside

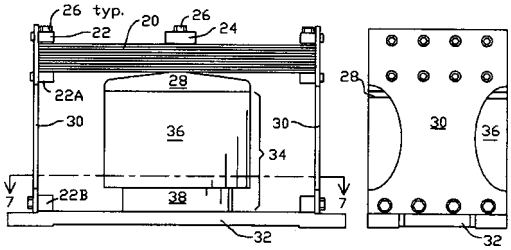

cover **36**) and attached to mass **28** by bolt **26**, and thence to leaf spring stack **20** whose ends are connected by side leaves **30** to coil base **32**. The spring rates of **20**+**30** combine with masses **36**+**28**+**24** and the mass of the permanent magnet to determine the resonance frequency of this actuator.—AJC

7,276,823

43.40.Vn ACTIVE VIBRATION DAMPING DEVICE

Hiroyuki Ichikawa and Yoshinori Watanabe, assignors to Tokai Rubber Industries, Limited
2 October 2007 (Class 310/23); filed in Japan 11 November 2004

A semiconductor exposure apparatus vibration stabilizing system is claimed. One embodiment has the etch beam source platform **6** carrying

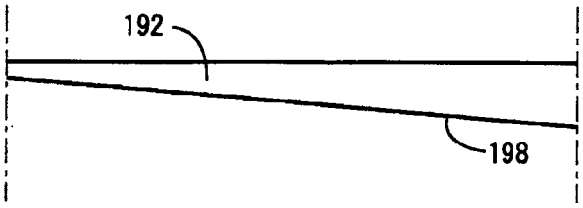

rotation detector **3C** which sends a signal to computer **4C** to drive a countering flywheel in **60**.—AJC

7,286,776

43.40.Vn COLOR IMAGE FORMING APPARATUS WITH VIBRATION CONTROL METHOD FOR CONTROLLING THE SAME AND CONTROL PROGRAM FOR IMPLEMENTING THE METHOD

Kenji Morita *et al.*, assignors to Canon Kabushiki Kaisha
23 October 2007 (Class 399/36); filed in Japan 1 October 2004

In a dry color laser printer, vibrations of the assembly carrying toner cartridge **23Y**, **23C**, **23M**, and **23K** can blur the developed image. The vibration that occurs when carrier rotation starts and stops is sensed by vibration sensor **21**. When excess vibration is sensed, the increase of the

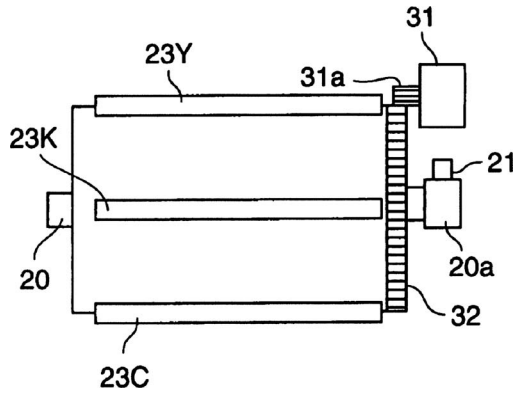

speed of motor **31** is reduced to where such vibrations fall below a predetermined level. This fact is held in a memory for successive print jobs. Control logic is also claimed.—AJC

7,282,697

43.40.Yq HIGH SENSITIVITY FIBRE OPTIC VIBRATION SENSING DEVICE

Sean Dormer Thomas *et al.*, assignors to Qinetiq Limited
16 October 2007 (Class 250/227.14); filed in United Kingdom 25 January 2002

A sensitive single axis accelerometer is claimed for use in seismic exploration. Disk **11** is held only by cones **15** secured by bolt **16**. Mass **12** acts to deflect the perimeter of **11** when accelerated along the axis of **16**, for instance stretching member **13** while compressing **17**. Members **13** and **17**

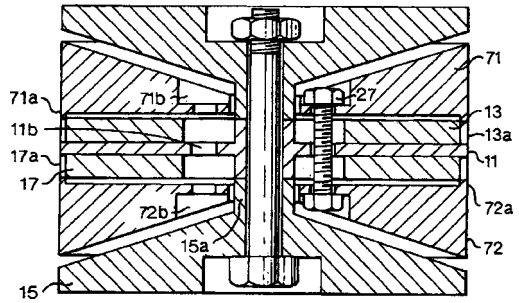

each include a coil of optical fiber which is elongated or shortened. Acceleration detection proceeds by counting interference fringes that occur when light beams from the same source are recombined after passing through each coil separately.—AJC

7,282,822

43.40.Yq SENSOR

Tord Cedell, assignor to Covial De vice AB
16 October 2007 (Class 310/26); filed in Sweden 20 June 2002

A strain sensor with wide bandwidth and high sensitivity is claimed. A band or tape of amorphous ferromagnetic material, having a permeability from 5,000 to 200,000 and having high magnetostriction, is anchored at its ends to a substrate that may be strained. When the substrate is strained, the voltage induced in a coil wound on the tape serves as a signal proportional

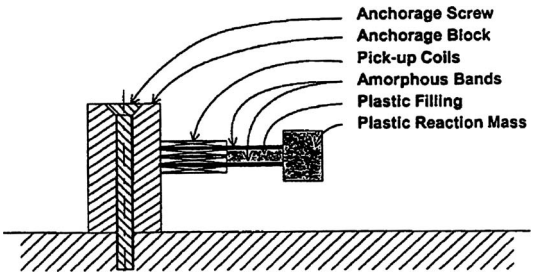

to the strain rate. A single axis accelerometer may be formed by mounting such amorphous bands on the surfaces of a plastic beam which is deflected by a plastic reaction mass. The beam anchor block is attached to a surface that may vibrate.—AJC

7,284,408

43.40.Yq SENSOR SYSTEM

Kenji Kato, assignor to DENSO CORPORATION
23 October 2007 (Class 73/1.37); filed in Japan 25 March 2004

A turning and forward acceleration sensor **100** for the automatic driving of vehicles is claimed using only variable capacitors. Plates **41a** and **41b**, suspended on beams **42i** and **43i**, are caused to vibrate in the X-direction by alternating electrostatic force drive voltages **D1** and **D2** to be applied between fingers **56a** and **66a**, and respectively **56b** and **66b**. During a turn, both + and −Y vibration results from the coriolis force on vibrating plates **41a** and **41b**. During forward Y acceleration a displacement of both

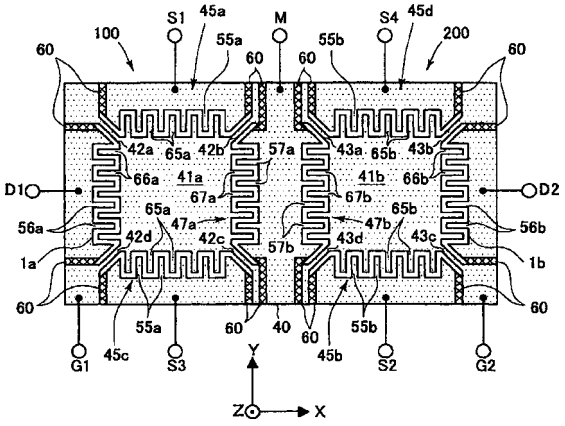

41a and **41b** only in the −Y direction occurs, increasing the amplitude of only **S1** and **S2** for instance. Signals **S1**, **S2**, **S3**, and **S4**, transferred through the capacitance between fingers **65a** and **55a**, and **65b** and **55b**, are processed as $(S1+S2)-(S3+S4)$ for angular velocity and $(S2+S3)-(S1+S4)$ for acceleration. This acceleration signal is also compared to that from a separate transducer to provide an angular velocity reliability indication. Claims include the electronic logic to compute and condition these signals.—AJC

6,868,939

43.50.Gf EXHAUST SILENCER SYSTEM

John C. Ziehl, assignor to Vicious Cycle Performance Incorporated
22 March 2005 (Class 181/256); filed 25 February 2003

A motorcycle muffler is described that consists of concentric perforated shells with sound absorbing material sandwiched between them. Much is made of the geometry of the inlet and exhaust "flow diverters," **40** and **50**.

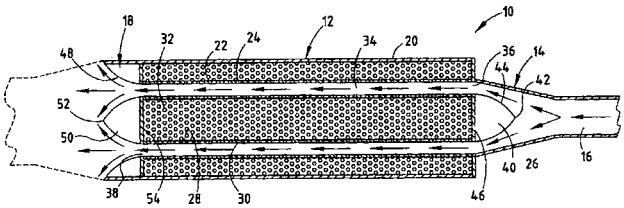

Both increases in power and reductions in noise levels relative to a standard muffler are claimed in this patent from Vicious Cycle Performance Inc.—KPS

7,279,857

43.50.Gf SYSTEM, METHOD, AND COMPUTER-READABLE MEDIUM FOR REDUCTION OF COMMUTATION-RELATED ACOUSTIC NOISE IN A FAN SYSTEM

Samuel M. Babb *et al.*, assignors to Hewlett-Packard Development Company, L.P.
9 October 2007 (Class 318/254); filed 27 August 2003

A brushless DC fan motor drive circuit is claimed where stator winding switch current transients and the subsequent magnetostriction sound emission are reduced by computer-shaping of pulses to increase current rise time.—AJC

7,281,878

43.50.Gf ROAD SURFACE SOUND REDUCTION SYSTEM

Gary Schulz, Cary Illinois
16 October 2007 (Class 404/17); filed 3 May 2006

A means of scoring road surfaces with a maximum linear sequence (MLS) random pattern **25** in the direction of travel is claimed. This pattern

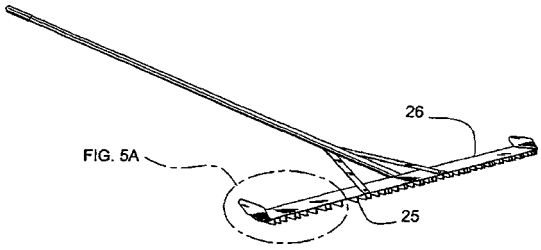

of grooves is created during the initial phase of concrete curing by means of a rake **25**-**26**, or an embossing tool or a cutting tool.—AJC

7,282,873

43.50.Gf MUTUAL ACTIVE CANCELLATION OF FAN NOISE AND VIBRATION

Bulent Abali *et al.*, assignors to Lenovo (Singapore) Pte. Limited
16 October 2007 (Class 318/41); filed 16 November 2004

A CPU fan noise (blade tone and a few harmonics) cancellation scheme is claimed where fan **620** (similar to fan **630**) is caused to rotate at

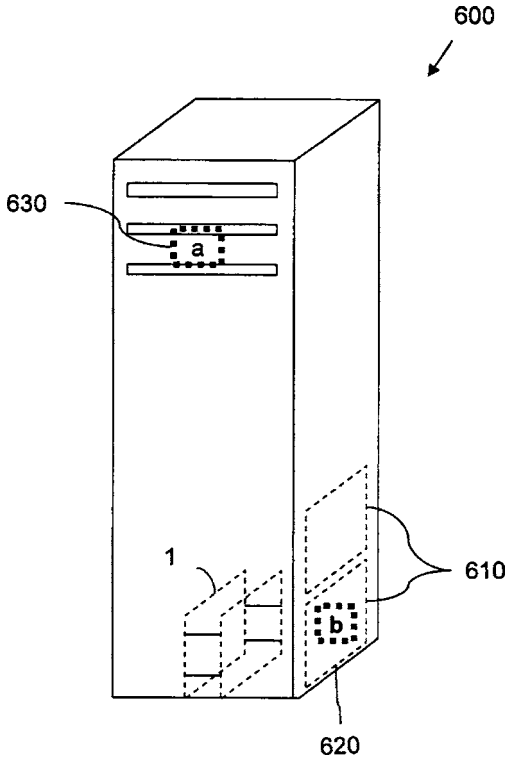

the same RPM as fan **630** by a controller that also can adjust the rotational phase between the two fans. This phase is adjusted to minimize the sound level at a bystander location (not shown).—AJC

7,286,348

43.50.Gf HOUSING ASSEMBLY FOR A COMPUTER

Wade D. Vinson *et al.*, assignors to Hewlett-Packard Development Company, L.P.
23 October 2007 (Class 361/695); filed 16 November 2004

A computer cooling fan noise reducing assembly is claimed where fan **107**, driven by motor **106**, is mounted inside computer housing **102** so that passageways for air entering **103**, **104** and exhausting are along a path that

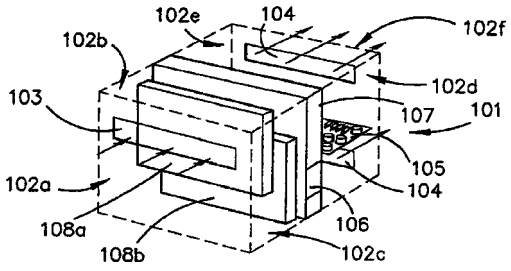

is sufficiently convoluted that "sound that is emitted from the fan and enters into the tortuous passageway is dissipated therein so as to minimize the level of sound emanating from the passageway."—AJC

6,885,295

43.50.Lj REVERSING ALARM

Christopher Hanson-Abbott and Masato Yamashita, assignors to Brigade Electronics Plc
26 April 2005 (Class 340/474); filed in United Kingdom 28 March 2000

Reversing (back-up) warning signals emitted by vehicles typically consist of single or multiple tones. Since the human hearing system is able to localize sources of broadband sound more precisely than tonal ones, this patent simply proposes that a zener diode be used to produce a broadband signal along with a circuit to enable the signal to be intermittently pulsed.—KPS

7,322,440

43.55.Ti ULTRALIGHT TRIM COMPOSITE

Hameed S. Khan *et al.*, assignors to Rieter Technologies AG
29 January 2008 (Class 181/286); filed in the European Patent Office 9 December 2002

This composite panel combines a sound blocking underlayment with a sound absorbing flow resistant layer. The two layers are separated by a sound transparent film (only 0.01 mm thick) that allows the different layers to be kept separate. This reduces production costs, improves performance reliability, and allows the separate absorption and transmission loss attributes of the composite to be tuned or balanced. The composite is suitable for reducing noise in a vehicle.—CJR

7,277,358

43.60.Qv APPARATUS, METHOD AND SYSTEM FOR DIGITALLY TRANSMITTING ACOUSTIC PULSE GUN SIGNALS

Dean Finnestad and Scott Finnestad, both of Red Deer, Alberta, Canada
2 October 2007 (Class 367/82); filed in Canada 7 June 2004

Reflection of a sound pulse (shot gun blank, etc,) from the liquid surface of petroleum deep in a borehole is used to measure the distance to that surface. The number of pulse reflections from successive casing junctions provides a measure of that distance. Transducer assembly **30** comprising a stainless steel 3 in. $D \times 8$ in. cylinder **32** withstanding pressures up to

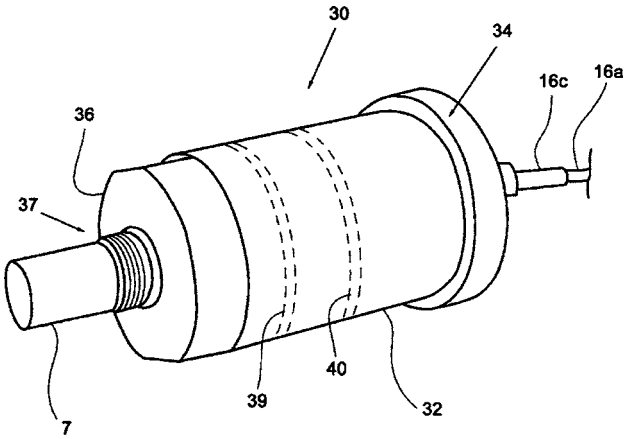

3,000 psi with end caps **34**, **36**. Cabling **16a**, **16c** provide communication and conveying means. Threaded section **37** interfaces with the pulse gun (not shown). D/A circuitry boards **39**, **40** contain signal processing claimed to have superior signal to noise ratio for distinguishing successive casing reflection pulses. The pulse gun, D/A conversion circuitry and Wireless (Bluetooth etc.) means (not shown) are also claimed.—AJC

7,321,662

43.66.Ts HEARING AID FITTING

Peter Lundh and Don Schum, assignors to Oticon A/S
22 January 2008 (Class 381/314); filed in Denmark 28 June 2001

Computer-controlled hearing aid fitting software has two variant settings of automatic gain control (AGC) gain for soft sounds and release time

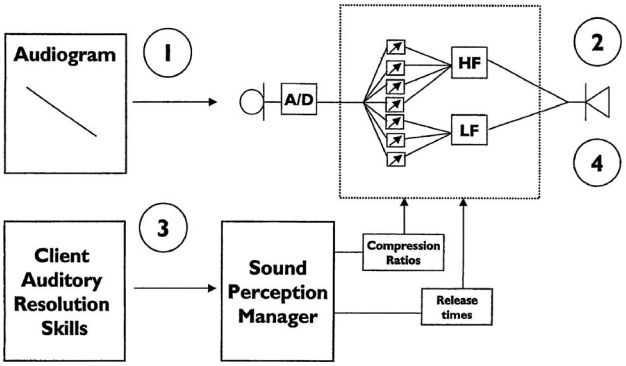

in both a low frequency channel having fast-acting AGC and a high frequency channel having slow-acting AGC. The settings are adaptively offset in relation to a default AGC gain and release time setting. In one variant, for both channels release times are lengthened and gain for soft sounds is reduced. For the other variant, release time is shortened only in the high frequency channel and gain for soft sounds is increased in both channels.—DAP

7,321,663

43.66.Ts COMPACT MODULAR IN-THE-EAR HEARING AID

Jorgen Mejner Olsen, assignor to Widex A/S
22 January 2008 (Class 381/322); filed in Denmark 15 April 1997

A socket mounted on an electronics module retains a microphone and is fastened to the faceplate on several sides with a notch, two grooves, and

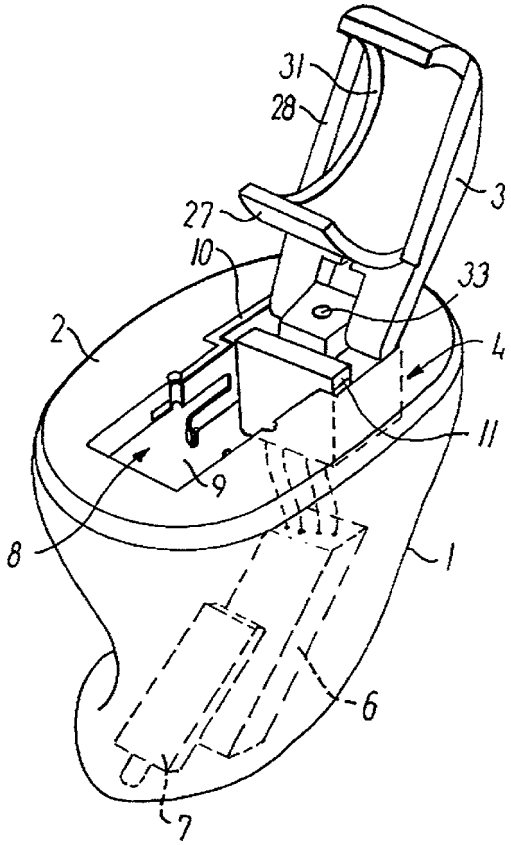

a pair of tracks. The socket has projecting resilient lugs that allow nondestructive removal of the module with a suitable tool.—DAP

7,321,797

43.66.Ts INCREMENTAL STIMULATION SOUND PROCESSOR

Peter J. Blamey *et al.*, assignors to Cochlear Limited
22 January 2008 (Class 607/57); filed 28 February 2005

A modeler for a cochlear implant first calculates an excitation pattern present on the unaided auditory nerve. An increment generator determines

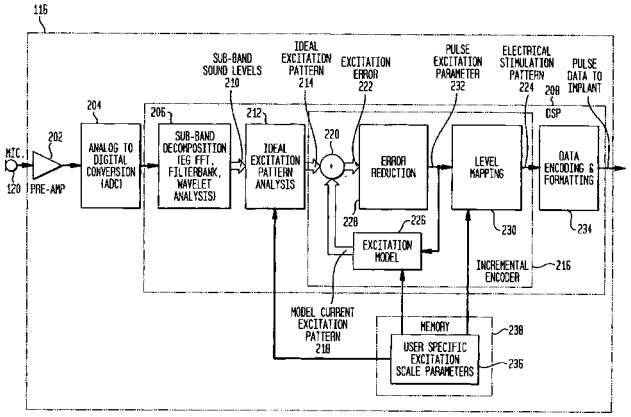

the difference between an ideal and the existing excitation patterns and produces, in concert with an error reducer, modified stimulation signals accordingly.—DAP

7,322,930

43.66.Ts IMPLANTABLE MICROPHONE HAVING SENSITIVITY AND FREQUENCY RESPONSE

Eric M. Jaeger *et al.*, assignors to Vibrant Med-El Hearing Technology, GmbH
29 January 2008 (Class 600/25); filed 5 August 2003

A membrane over an implantable microphone housing defines a sealed primary air cavity that is coupled through an aperture-controlled acoustic resistance to a secondary air cavity. The sensitivity and resonant peak frequency of the microphone are raised by making the membrane very thin to

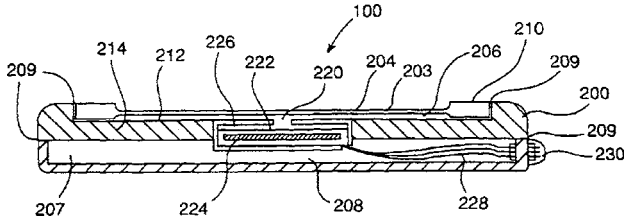

increase its flexibility and by reducing the primary air cavity volume and acoustic compliance. A biodegradable material is positioned on the membrane outside of the primary air cavity to prevent tissue growth on the membrane.—DAP

7,324,649

43.66.Ts HEARING AID DEVICE, COMPRISING A DIRECTIONAL MICROPHONE SYSTEM AND A METHOD FOR OPERATING A HEARING AID DEVICE

Benno Knapp and Hartmut Ritter, assignors to Siemens Audiologische Technik GmbH
29 January 2008 (Class 381/313); filed in Germany 2 June 1999

The outputs of at least two microphones are combined to form a multichannel directional microphone system simultaneously of first order and

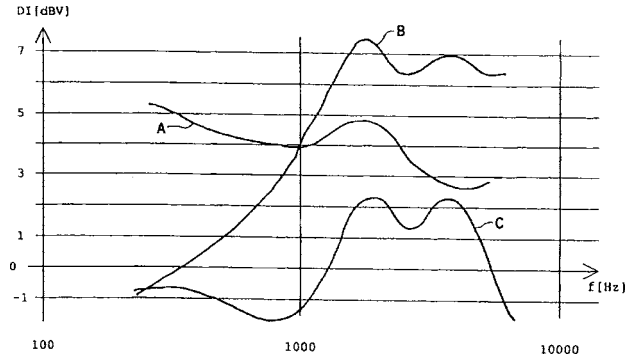

higher order. First order directivity patterns are generally applied to lower frequencies and second order patterns to higher frequencies.—DAP

7,324,650

43.66.Ts HEARING AID DEVICE WITH AUTOMATIC SITUATION RECOGNITION

Eghart Fischer *et al.*, assignors to Siemens Audiologische Technik GmbH
29 January 2008 (Class 381/314); filed in Germany 7 August 2002

A hearing aid that produces an acoustic or mechanical output senses the presence of a television by detecting the line signal that deflects an electron beam generated in a conventional image tube output and radiates

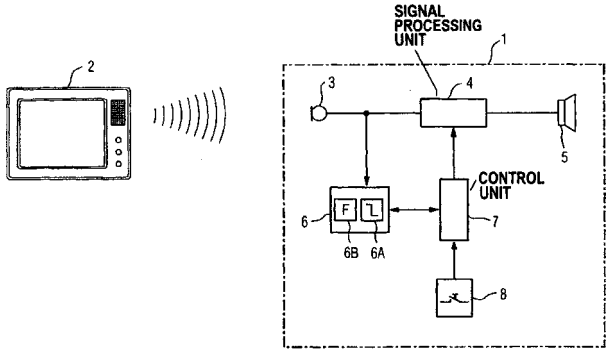

from the television at the screen's refresh rate. When the television is detected, the hearing aid adjusts its signal processing parameters automatically to improve wearer benefit.—DAP

7,324,652

43.66.Ts HEARING AID HAVING A SUPPLY SOURCE PROVIDING MULTIPLE SUPPLY VOLTAGES

David A. Preves and Mike Sacha, assignors to Starkey Laboratories, Incorporated
29 January 2008 (Class 381/323); filed 30 December 2003

Different supply voltages are provided from a single, flexible battery having a common substrate with a number of voltage taps. The different

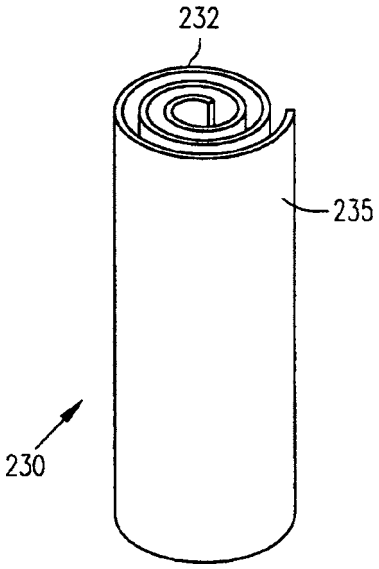

voltages supply several electronic devices within a hearing aid that operate from different supply voltages without up-converting or down-converting voltage levels.—DAP

7,330,558

43.66.Ts REMOTE CONTROL FOR HEARING AID DEVICES

Winfried Arz and Torsten Niederdränk, assignors to Siemens Audiologische Technik GmbH
12 February 2008 (Class 381/315); filed in Germany 29 September 2003

To increase ease of use and to prevent incorrect operation, operating elements for remote-to-hearing aid control function transmissions are located on one side of a remote control, and operating elements for hearing

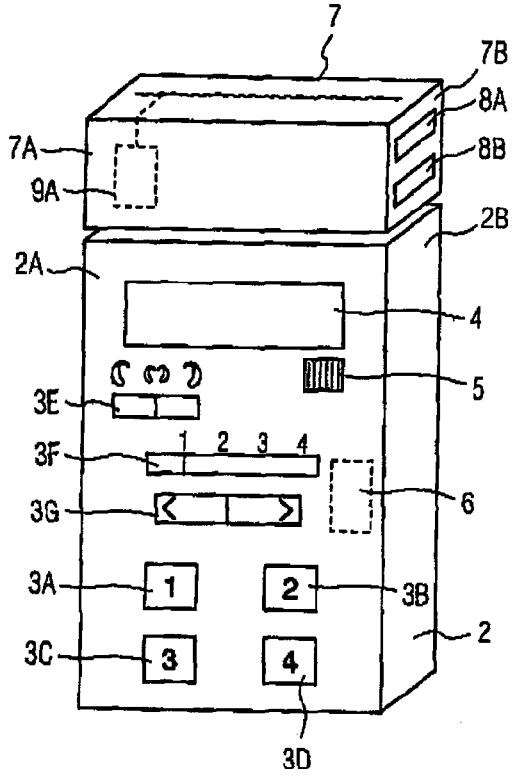

aid-to-remote transmissions and indicators such as a visual display or acoustic generator are placed orthogonally on another side of the remote control.—DAP

7,324,653

43.66.Ts SUSPENSION MEANS FOR TRANSDUCER

Ulrik Mehr, assignor to Oticon A/S
29 January 2008 (Class 381/324); filed in Denmark 12 July 2002

To minimize mechanical feedback from the earphone to the microphone, hearing aids employ some kind of resilient mounting for both

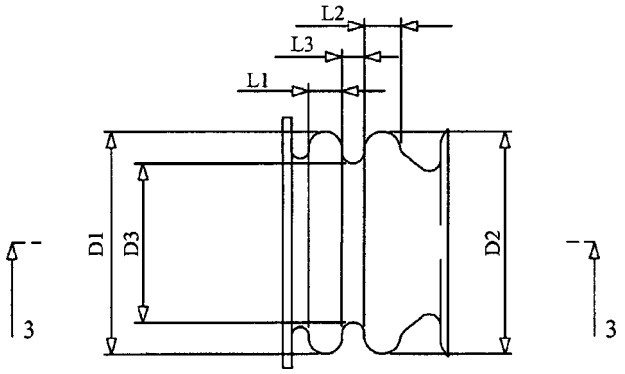

transducers. This patent describes a bellows-shaped microphone suspension that also functions as an acoustical waveguide.—GLA

7,326,171

43.66.Ts ADJUSTABLE BONE BRACKET

James Frank Kasic II *et al.*, assignors to Otologics, LLC
5 February 2008 (Class 600/25); filed 12 September 2005

A mounting support for an implantable hearing aid device, conforming to and attaching to the surface of a bone in the patient's skull, consists of a support member, one or more mounting legs connected to the support member and having apertures for bone attachment devices, and one or more

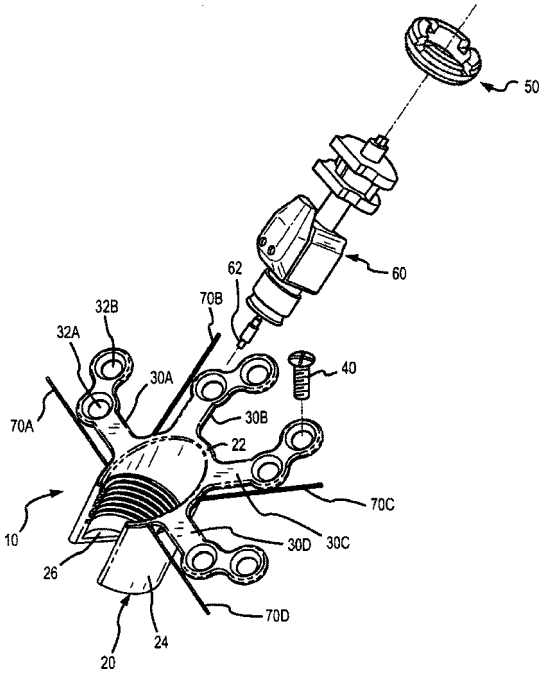

guide legs connected to the support member. The guide legs have less average cross-sectional size and less minimum yield strength along their lengths than those of the mounting legs.—DAP

7,330,556

43.66.Ts BINAURAL SIGNAL ENHANCEMENT SYSTEM

James M. Kates, assignor to GN ReSound A/S
12 February 2008 (Class 381/312); filed 3 April 2003

Wiener filtering in prior art binaural hearing systems is performed frequently with the assumptions that noise at the two ears is uncorrelated and the desired signal source is in front-center of the listener. This patent

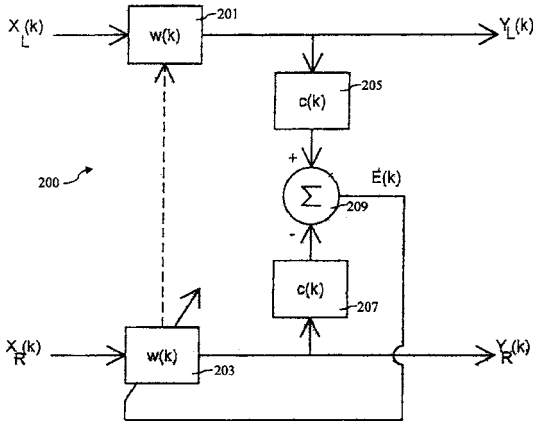

states that these assumptions are invalid and recommends binaural processing so that filter coefficients of the filters for the left and right ear processing channels are adjusted to minimize the difference between the left and right channel outputs.—DAP

7,330,557

43.66.Ts HEARING AID, METHOD, AND PROGRAMMER FOR ADJUSTING THE DIRECTIONAL CHARACTERISTIC DEPENDENT ON THE REST HEARING THRESHOLD OR MASKING THRESHOLD

Eghart Fischer and Volkmar Hamacher, assignors to Siemens Audiologische Technik GmbH
12 February 2008 (Class 381/313); filed in Germany 20 June 2003

A hearing aid, having a directional system with two or more microphones, generates test signals to determine the wearer's hearing thresholds and masking thresholds for the microphone noise. Then the directional characteristic is adjusted over frequency adaptively to produce the greatest

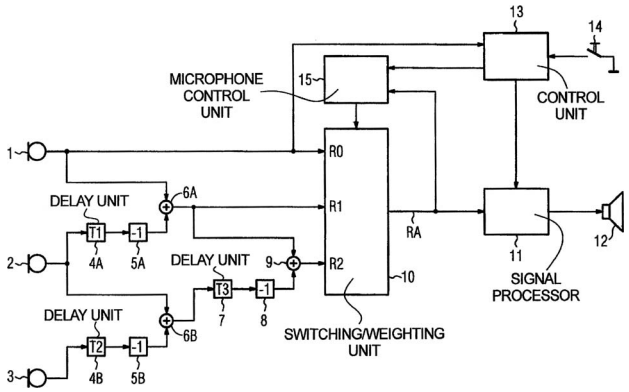

amount of directionality while preventing the noise of the directional microphone system from disturbing the wearer.—DAP

7,321,855

43.70.Gr METHOD FOR QUANTIFYING PSYCHOLOGICAL STRESS LEVELS USING VOICE PATTERN SAMPLES

Charles Humble, West Palm Beach, Florida
22 January 2008 (Class 704/270); filed 15 December 2003

Voice stress analysis is a patented method of detecting tremor, that is, low-frequency variations of a speaker's fundamental frequency, in order to detect a condition of stress and, ultimately, to determine whether the speaker is lying. The exact nature of the indicative tremor signal seems to have changed slightly since the original patent, United States Patent 3,971,034, issued in 1976. The original version simply detected the presence of tremor

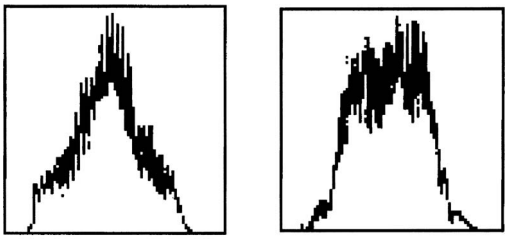

as an indication of stress. According to this patent, "In moments of stress, the body prepares for fight or flight by increasing the readiness of its muscles to spring into action. Their vibration increases from the relaxed 8 to 9 Hz to the stressful 11 to 12 Hz range." The emphasis of the present patent is a computer algorithm for evaluation of the detected tremor signal. The exact details of the algorithm are not disclosed, other than the above quotation.—DLR

7,326,057

43.70.Kv LANGUAGE LEARNING COMPUTER SYSTEM

Kenichiro Nakano, Uji-shi, Kyoto, Japan
5 February 2008 (Class 434/176); filed 17 May 2004

The patent describes a computer system for language learning. A simple animated figure moves, first in step with foreign language sounds played over the loudspeaker, then according to the learner's responses spoken into the microphone. Details of the acoustic signal analysis are not provided. Exactly what happens if the language phrase does not involve walking, running, jumping, raising an arm, sitting, or standing up is not discussed.—DLR

7,321,850

43.72.Ne LANGUAGE TRANSFERENCE RULE PRODUCING APPARATUS, LANGUAGE TRANSFERRING APPARATUS METHOD, AND PROGRAM RECORDING MEDIUM

Yumi Wakita, assignor to Matsushita Electric Industrial Company, Limited
22 January 2008 (Class 704/10); filed in Japan 4 June 1998

This system for live, simultaneous translation operates by performing a full syntactic and semantic analysis of the input and re-expressing the message content of the input speech to an expression in the desired target language. A feature of the system is its ability to perform at least a partial translation when less than a full sentence of input material is available. Certain of the translation rules are shown here in example forms, although it is not at all clear that the entire system could be constructed so as to perform

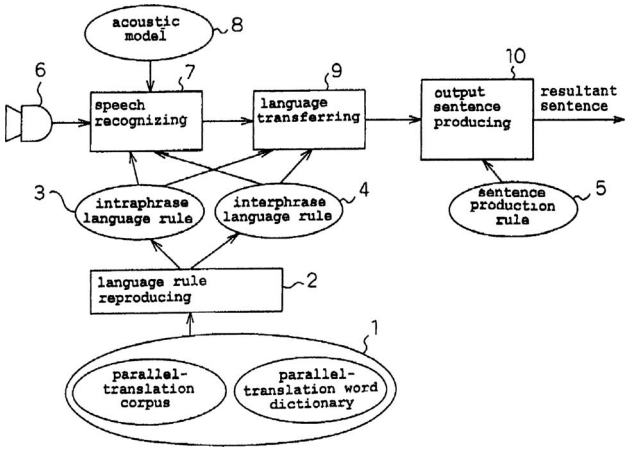

as described. The figure shows one version of a number of different system configurations.—DLR

7,328,269

43.72.Ne APPARATUS AND METHOD FOR PROVIDING SERVER STATE AND ATTRIBUTE MANAGEMENT FOR VOICE ENABLED WEB APPLICATIONS

Ryan Alan Danner and Steven J. Martin, assignors to Cisco Technology, Incorporated
5 February 2008 (Class 709/228); filed 15 March 2004

Web-enabled voice messaging sessions are enabled using an IP packet-switched network with HTTP and HTML open standards. A first and second markup language page containing first and second voice web application parameters, respectively, are generated and sent to the user with corresponding session identifiers in response to first and second markup language requests by executing first and second web application instances. Data records of application states and session identifiers that also contain user attribute information are stored and accessed.—DAP

7,330,536

43.72.Ne MESSAGE INDEXING AND ARCHIVING

Christopher Hercules Claudatos *et al.*, assignors to EMC Corporation
12 February 2008 (Class 379/68); filed 1 July 2004

Intended primarily for financial corporations, such as banks, credit card companies, brokers, etc., this patented device would be attached to the company telephone system to monitor incoming phone calls. In addition to recording the conversation, the time, and any related information, such as from a caller ID system, a speech recognition system would search the audio signal for any of a list of predetermined keywords. Keyword text would be used to generate retrieval keys, using a hash coding system, for example, by which recording of phone conversations could be stored and cross-referenced for later access. A system of rules or company policies could be used to determine actions to be taken by the system, such as the activation of additional keywords or the activation of call quarantine procedures in compliance with government or company regulations or policies.—DLR

7,330,815

43.72.Ne METHOD AND SYSTEM FOR NETWORK-BASED SPEECH RECOGNITION

Christopher S. Jochumson, assignor to GlobalEnglish Corporation
12 February 2008 (Class 704/231); filed 24 August 2004

In a system with two or more clients and a server, speech recognition in approximate real time is supported over the Internet. Compressed audio speech and information about pronunciation accuracy is transmitted in packets from each client to the server where it is decoded and stored. After speech recognition is performed, a text response is returned from the server to each client.—DAP

LETTERS TO THE EDITOR

This Letters section is for publishing (a) brief acoustical research or applied acoustical reports, (b) comments on articles or letters previously published in this Journal, and (c) a reply by the article author to criticism by the Letter author in (b). Extensive reports should be submitted as articles, not in a letter series. Letters are peer-reviewed on the same basis as articles, but usually require less review time before acceptance. Letters cannot exceed four printed pages (approximately 3000–4000 words) including figures, tables, references, and a required abstract of about 100 words.

Monitoring thickness deviations in planar multi-layer elastic structures using impedance signatures (L)

Karl A. Fisher[a)]
Lawrence Livermore National Laboratory, L-333, 7000 East Avenue, Livermore, California 94566

(Received 20 February 2007; revised 6 July 2007; accepted 18 July 2007)

In this letter, a low frequency ultrasonic resonance technique that operates in the 20–80-kHz regime is presented that demonstrates detection of thickness changes on the order of ± 10 μm. This measurement capability is a result of the direct correlation between the electrical impedance of an electro-acoustic transducer and the mechanical loading it experiences when placed in contact with a layered elastic structure. The *relative* frequency shifts of the resonances peaks can be estimated through a simple one-dimensional transmission model. Separate experimental measurements confirm this technique to be sensitive to subtle changes in the underlying layered elastic structure. [DOI: 10.1121/1.2770542]

PACS number(s): 43.35.Zc, 43.60.Ac, 43.40.Le [EJS] Pages: 32–35

I. INTRODUCTION

The motivation for this letter is to report on a resonance technique that is useful for detecting material and geometrical variations in high contrast, lossy multilayered planar elastic structures. With this technique, subtle changes in the underlying structure can be monitored quantitatively with a single transducer by tracking the frequency shifts of the resonance peaks of the electrical impedance. A significant amount of research has been done in the area of electrical-mechanical impedance monitoring of elastic structures. The technique utilizes piezoelectric transducers that are physically attached to the elastic structure. Park *et al.*[1] has assembled an excellent overview and literature survey of the current state of impedance based health monitoring. In most cases these techniques rely on a comparison between an initial (pristine) state of the structure and corresponding measurements taken throughout the lifetime of the structure. The resulting differences are then used to infer qualitative states of damage or change in the health of the structure. Because the total electrical response (impedance) of the transducer is determined, in part, from the mechanical drive point impedance of the structure, changes in the underlying mechanical structure will alter the electrical impedance of the transducer. Thus, electrical impedance spectrograms can be utilized to infer changes in structural quantities, either geometrical or material provided a suitable model for the structure is developed.

II. THEORETICAL FORMULATION

The solution method approaches the problem by modeling the impedance response of the PZT transducer and the corresponding structure using a transmission matrix.[2–7] Arbitrary backing and the load impedances can be applied at the mechanical terminals of the three-port network.

A. Total system impedance model

Following the convention presented in Ref. 6, (Eqs. 5.50 and 5.51), a generalized representation of a planar one-dimensional transducer model with arbitrary mechanical loading is given as

$$Z_{\text{total}} = \frac{V}{I} = \frac{\left[Z_{31} - \frac{Z_{32}Z_{21}}{Z_{\text{back}} + Z_{22}}\right] - Z_{13} - \frac{Z_{13}Z_{21}}{Z_{\text{back}} + Z_{22}}}{\left[Z_{\text{load}} + Z_{11} - \frac{Z_{12}Z_{21}}{Z_{\text{back}} + Z_{22}}\right]} + \left[Z_{33} - \frac{Z_{32}Z_{23}}{Z_{\text{back}} + Z_{22}}\right]. \quad (1)$$

Here, Z_{total} is the impedance of the *entire* system, comprising the transducer and the planar multilayered elastic structure. The net effect of structure is represented by Z_{load}. Mechanical transducer characteristics are represented by Z_{back}, and the coefficients from the transmission matrix are

$$Z_{11} = Z_{22} = A\sqrt{\rho_e c^D}\cot\left(\omega\sqrt{\frac{\rho_e}{c^D}}L\right),$$

[a)]Electronic mail: fisher34@llnl.gov

$$Z_{12} = Z_{21} = A\sqrt{\rho_e c^D}\csc\left(\omega\sqrt{\frac{\rho_e}{c^D}}L\right),$$

$$Z_{13} = Z_{31} = Z_{23} = Z_{32} = \frac{e}{\omega\varepsilon^S}, \tag{2}$$

$$Z_{33} = L/\omega\varepsilon^S A_o,$$

where the density of the piezoelectric is ρ_e, and the elastic and piezoelectric stiffness coefficients are c^E and c^D, respectively. The piezoelectric field coefficient is e and the clamped (open circuit) dielectric constant is ε^S. The cross-sectional area of the transducer is A, L is the thickness, and ω is the frequency. The mechanical input impedance, Z_{load}, is calculated from the impedance translation kernal[8] of Z_i^{local}, shown in Fig. 1. Each layer is represented by a known thickness, L_n, and an intrinsic specific impedance $\rho_n c_n$ based on layer density, ρ, and longitudinal sound speed, c. The load impedance is determined by starting with a known local impedance, Z^{known} at $x=N$, and successively *translating* the calculated mechanical impedance through the entire structure to the $x=L$ interface where the transducer layer is located. Thus, the total mechanical input impedance for the planar multilayered structure, Z_L^{local}, is equivalently the load impedance, Z_{load}. Equation (1) provides a concise method to estimate the impedance signature of a piezoelectric transducer mounted on a planar multilayered structure.

III. MODELING RESULTS

A numerical simulation was performed on the physical system described in Fig. 2. Impedance signatures were generated at discrete frequencies from 10 through 100 kHz. As a test to determine the sensitivity of the model to changes in layer thickness, five different impedance signatures were calculated for a range of thickness variations about a nominal acrylic layer thickness of $L_{\text{nom}}=23$ mm. The variations are

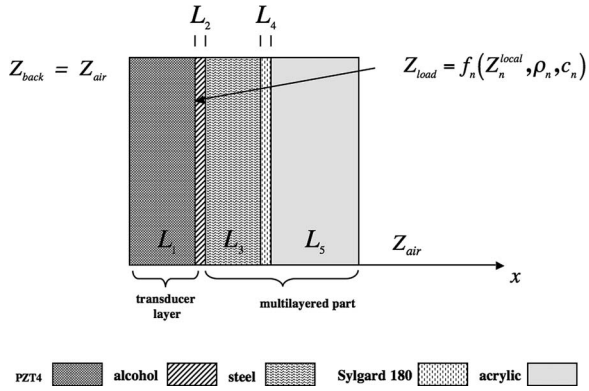

FIG. 2. The numerical model for the impedance study. The transducer is modeled as a single air backed layer of PZT4 coupled to the upper surface of the elastic structure by a thin layer of alcohol. Here, Z_{load} is the *translated* input impedance beginning on the rhs at $x=L_5$ and stepping through each layer to the transducer to $x=L_1$. Materials are listed in Table I and Refs. 9 and 10.

defined as $L_{\text{acrylic}}=L_o+\delta$, where $\delta_{1,\ldots,N}=-0.051$ to 0.051 mm in steps of 0.025 mm. The intent is to investigate the sensitivity of the total impedance model to variations in the thickness of individual layers. The range of frequencies investigated spans several resonances of the transducer layer. It is near these resonant peaks of the transducer that the impedance signatures are sensitive to subtle changes in the underlying planar structure. Figure 3 shows the magnitude of the *total* impedance Z_{total} as calculated from Eq. (1). Resonances of the coupled transducer structure are notated with Roman numerals. For each of the three boxed regions, an expanded view has been provided to illustrate the frequency shifts that occur as the thickness of the lower acrylic layer is varied. These regions were selected at the point of steepest ascent [i.e., $\max(dZ_{\text{total}}(\omega)/df)$], which defines locations along $|Z_{\text{total}}(\omega)|$ where the frequency shifts are most sensitive to structural variations. These regions also correspond to locations in the phase space where the phase changes sign,

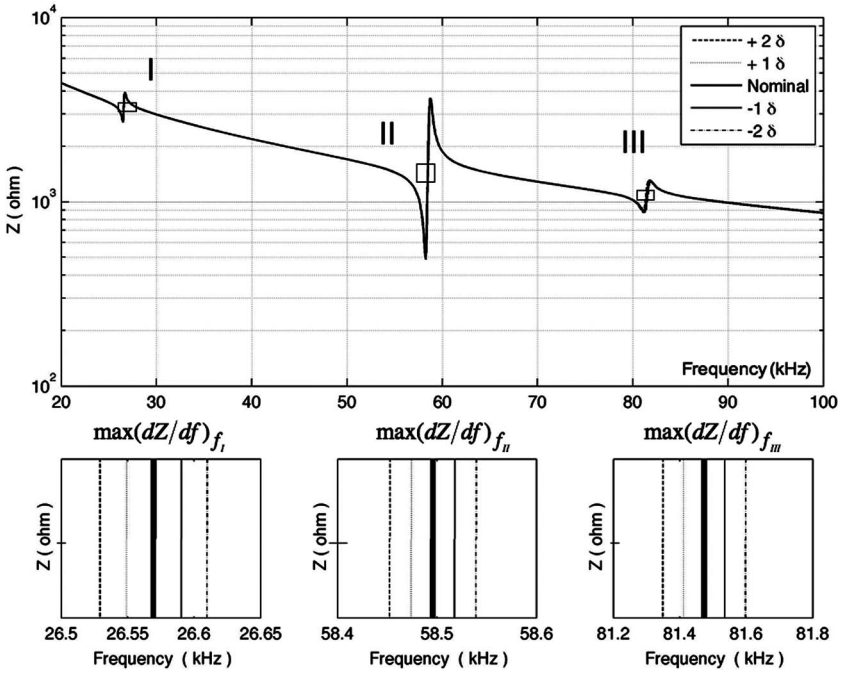

FIG. 3. Frequency shifts of the *total* input impedance $Z_{\text{total}}(\omega)$ due to changes in the thickness of the lower acrylic layer. Five different impedance signatures were calculated based on a range of thicknesses for the acrylic layer ($L_{\text{acry}}=L_o+\delta$), where $\delta=-0.051$ to 0.051 mm in steps of 0.025 mm. The nominal impedance signature ($L_o=23$ mm, see Table I) is denoted with a heavy black line. The three resonances, notated by Roman numerals and zoom boxes, indicate the regions where max (dZ/df) and are therefore sensitive to structural variation.

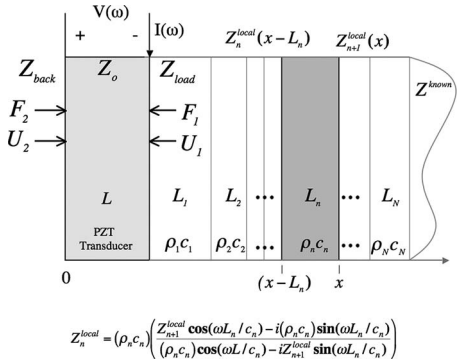

FIG. 1. Basic one-dimensional geometry and transducer orientation for the interrogation of a planar multilayered elastic structure. Each layer is described by a thickness, L, a density, ρ, and a longitudinal sound speed, c. The current into the transducer is I, and the drive voltage is V. The impedances, Z_{back} and Z_{load}, represent either known impedances on the boundary or an intrinsic specific impedance for an unbounded region. At each interface, Z_n^{local} and Z_{n+1}^{local} denote the translated impedances through a given layer. The mathematical kernel for the nth layer is also shown.[8] The total mechanical input impedance for the multilayered elastic structure is Z_{load} and Z_o is the intrinsic impedance of the transducer.

$\text{sgn}(d\phi/df) = \pm 1$, also indicating a resonance condition. The expanded regions clearly illustrate measurable shifts in the frequency of the transducers' impedance due to small changes in the acrylic layer thickness. Table I summarizes a parametric study of the geometrical sensitivities by varying each elastic layer separately by $\delta_{1,\ldots,N}$. The corresponding frequency shift at each resonance for a given layer change will be different, owing to the dynamic interaction between the different layers. This frequency selectivity provides a method to target individual layers by monitoring the resonance peaks with the greatest sensitivity to those layers.

IV. EXPERIMENTAL RESULTS

An experimental assessment of the detection sensitivity was conducted on two planar multilayered structures identical in diameter (30 cm) and material composition to the previous numerical study with a slight thickness variation in two of the layers. Metrological differences between the disks A and B are listed in Table II. The transducer is a simple PZT disk 30 mm diam. $\times$ 2.76 mm thick. The fundamental resonance mode for this thickness poled transducer is estimated at 58 kHz, which represents a radial mode with uniform bowing through the thickness of the transducer.[10] A thin (0.25 mm) layer of alcohol is used as a mechanical coupling layer between the transducer and the disks. The thickness of the coupling layer is maintained by a small plastic shim (0.25 mm thick $\times$ 30 mm diam. $\times$ 2 mm wide) that is attached to the PZT disk. An Agilent 4294 precision impedance analyzer is used to measure the electrical impedance signature from the PZT4 disk mounted in the center of the multilayered disks. The analyzer captured impedance measurements at 4000 discrete frequencies between 40 and 80 kHz using a 1-Volt drive signal.

TABLE II. Measurements and model estimates of relative frequency shifts of resonance II, due to thickness differences.

Layer	Thickness[a] disk A	Thickness[a] disk B	Model Δf (Hz)	Measured[b] Δf (Hz)
Steel	2.760	2.760	0	
Sylgard	0.203	0.153	−46.29	
Acrylic	23.724	23.770	38.95	
Total frequency shift Δf of Resonance II due to changes in sylgard and acrylic layers			3.69	3.28

[a]All measurements in mm ($\pm$0.001 mm).
[b]Repeatability of 10 separate measurements ($\pm$0.65 Hz).

A large planar geometry relative to the transducers size is chosen to minimize edge effects from the test object throughout the frequency band of operation and to emphasize quasi-one-dimensional behavior through the thickness of the disks. The objective is to compare the *relative* frequency shifts at $\max(dZ_{\text{total}}(\omega)/df)$ estimated by the model and measured experimentally. The results for the experimental measurements and the one-dimensional planar predictions, in each layer and the total, are given in Table I. The sign of the frequency shift indicates an increase or decrease in a layer's thickness. For each experimental measurement, the transducer was removed and reattached to the center of the disk. Ten separate measurements were recorded on each disk, from the ten measurements on each disk; an average frequency shift was measured. In this case, the predicted frequency shift (Δf_{mod}) from the model is 3.69 Hz and the experimental frequency shift (Δf_{exp}) is 3.28 ± 0.65 Hz. Variations in the mechanical coupling (bond) between the PZT disk and the structure for the measurements are the limiting factor for the determination of the smallest displacement, which, in terms of experimental measurements, is on the order of 10 μm.

The actual response (impedance signature) of the transducer used in the experiments will be different from the modeled impedance signatures. This is expected due to the fact that the PZT transducer used in the experiments is not a one-dimensional layer, but a three-dimensional disk operating in a thickness mode resonance. However, the mechanical responses (Z_{load}) of the planar disks are accurately represented using a one-dimensional approximation. Since the re-

TABLE I. Predicted displacement sensitivities (mm/Hz) in each layer and for each resonance.

Layer	L (mm)	ρ (g/cm)	c (mm/μS)	Resonance I (mm/Hz)	Resonance II (mm/Hz)	Resonance III (mm/Hz)
PZT	5.76	4.32	4.50			
Alcohol	0.25	0.78	1.15			
Steel	2.76	7.70	5.90	9.34×10^{-3}	2.29×10^{-4}	2.42×10^{-4}
Sylgard	0.23	1.12	1.03	2.10×10^{-4}	1.08×10^{-3}	6.63×10^{-5}
Acrylic	23.0	1.11	2.5	1.38×10^{-3}	1.08×10^{-3}	4.11×10^{-4}

gions under investigation (e.g., multilayered planar disks) are effectively one-dimensional in thickness, the relative shifts in the model and the experiment will be in good agreement. Further refinements might include numerically fitting the model estimate of the transducer impedance to experimental measurements when the transducer is off the structure. A constrained optimization procedure could be used to adjust material parameters and loss coefficients and essentially calibrate the transducer model against experimental impedance measurements, thus removing them as unknowns. Alternatively, the three-dimensional complexities of the transducer could easily be included in the modeled estimates by incorporating finite elements. In either case, the transducer is simply a method to relate electrical quantities (frequency, voltage, and current) to mechanical quantities (Z_{load}). Absolute comparisons between the model and experimental impedance signatures are not necessary.

Accurate interpretation of the frequency shifts of the resonance peaks will require prior knowledge about the multilayered system as found in design documents or manufacturing specifications; these in turn are incorporated into the one-dimensional model to guide the selection of an optimal transducer with impedance characteristics tuned for the particular layer under investigation. Because simultaneous variation of the layers in the structure can and will affect the resonant frequency shift in a complicated manner, this simple one-dimensional model can also be implemented in a Bayesian approach with measured impedance signatures to infer quantitative results regarding changes in the layers.

V. CONCLUSIONS

An approach has been developed for estimating the impedance shifts associated with changes in the geometry and elastic properties of a multilayered elastic structure. The simple examples have shown that resonances in the total system impedance are sensitive to small variations in layer thicknesses in the multilayered structure. The current one-dimensional model is sufficient for accurately predicting *relative* resonant frequency shifts of a piezoelectric transducer on planar structures.

ACKNOWLEDGMENTS

The author would like to thank Steve "Maddog" Benson for instrumentation and system development. This work was performed under the auspices of the U. S. Department of Energy by the University of California, Lawrence Livermore National Laboratory under Contract No. W-7405-48.

[1]G. Park, H. Sohn, C. R. Farrar, and D. J. Inman, "Overview of piezoelectric impedance-based health monitoring and path forward," Shock Vib. Dig. **35**(6), 415–463 (2003).
[2]F. P. Sun, Z. Chaudhry, C. Liang, and C. A. Rogers, "Truss structure integrity identification using PZT sensor-actuators," J. Intell. Mater. Syst. Struct. **6**, 314–319 (1995).
[3]V. Girugiutiu and A. N. Zagrai, "Embedded self-sensing piezoelectric active sensors for online structural identification," J. Vibr. Acoust. **124**, 116–125 (2002).
[4]R. Krimholtz, D. A. Leedholm, and G. L. Ma'itaei, "New equivalent circuit for elementary piezoelectric transducers," Electron. Lett. **6**, 398–399 (1970).
[5]L. P. Tran-Huu-Hue, R. Desmare, F. Levassort, and M. Lethiec, "A KLM circuit-based method for modeling multilayered piezoelectric structures," *IEEE Ultrasonics Symposium Proceedings* (IEEE, New York, 1998), pp. 995–998.
[6]V. Ristic, *Principles of Acoustic Devices* (Wiley-Interscience, New York, 1983).
[7]J. Hossack and B. A. Auld, "Improving the characteristics of a transducer using multiple piezoelectric layers," IEEE Trans. Ultrason. Ferroelectr. Freq. Control **38**(6), 618–629 (1991).
[8]A. Pierce, *Acoustics, An Introduction to Its Physical Principles and Applications* (AIP, Woodbury, NY, 1989).
[9]R. Holland, "Representation of dielectric elastic, and piezoelectric losses by complex coefficients," IEEE Trans. Sonics Ultrason. **SU14**(1), 18–20 (1966).
[10]*Piezoelectric Design Manual*, Morgan Metroc Electro-ceramics Division, Newark, NJ (1995).

Effect of spatial uncertainty of masker on masked detection for nonspeech stimuli (L)

Wei Li Fan,[a] Timothy M. Streeter,[b] and Nathaniel I. Durlach[c]
Hearing Research Center, Boston University, Boston, Massachusetts 02215

(Received 1 June 2007; revised 25 April 2008; accepted 30 April 2008)

Research on informational masking for nonspeech stimuli has focused on the effects of spectral uncertainty in the masker. In this letter, results are presented from some preliminary probe experiments in which the spectrum of the masker is held fixed but the spatial properties of the masker are randomized. In addition, in some tests, the overall level of the stimulus is randomized. These experiments differ from previous experiments that have measured the effect of spatial uncertainty on masking in that the only attributes (aside from level) that distinguish the target from the masker are the spatial attributes; in all of the tests, the target and masker were statistically identical, statistically independent, narrowband noise signals. In general, the results indicate that detection performance is degraded by spatial uncertainty in the masker but that compared both to the effects of spectral uncertainty and to the effects of overall-level uncertainty, the effects of spatial uncertainty are relatively small. © *2008 Acoustical Society of America.* [DOI: 10.1121/1.2932257]

PACS number(s): 43.66.Dc [RAL] Pages: 36–39

I. INTRODUCTION AND BACKGROUND

The idea that spatial uncertainty in the masker might degrade detection of a target signal arises naturally from previous results obtained in two areas: informational masking and binaural unmasking. In the first area, it has been shown that the threshold for a tonal target in a multitone masker with most of its energy outside a protected zone around the target tone can be raised 20–40 dB by randomly varying the masker spectrum (see references in Durlach *et al.*, 2005). Also, it has been shown in studies of speech intelligibility that uncertainty about the spatial properties of the masker degrades the intelligibility of the speech target (Kidd *et al.*, 2007). Although theoretical efforts have been made to explain these and other informational masking results (e.g., see Watson, 1987, 2005; Lutfi, 1993; Oh and Lutfi, 1998; Durlach, 2006; Durlach *et al.*, 2003, 2005; Shinn-Cunningham, 2005; Kidd *et al.*, 2007), no satisfactory theory is yet available. Furthermore, there are currently no data available for simple nonspeech stimuli on the effects of spatial uncertainty of the masker for cases in which target and masker have the same spectrum.

In the second area, it has been shown that binaural detection thresholds are decreased when the interaural relations of the masker differ from those of the target. In particular, for a diotic target signal, performance is better when the masker is dichotic than when it is diotic. Moreover, this improvement occurs both when the interaural relations are determined by the locations of loudspeakers in field listening or by the values of interaural time delays (ITDs) or interaural level differences (ILDs) in earphone listening. Relevant data and theory in this area can be found in Durlach and Colburn (1978), Colburn and Durlach (1978), and Stern and Trahiotis (1995). Of particular interest here is the idea that the binaural processing effectively creates binaural spatial channels (like the peripheral processing creates frequency channels) with different channels corresponding to different source angles or, more generally, different interaural configurations (i.e., different pairs of ITDs and ILDs). If one further assumes that rather than focusing on the target the listener attempts to reduce the effects of masking by nulling out the masker (see discussion in Durlach *et al.*, 2003; Durlach, 1972; and de Cheveigne and McAdams, 1995), then it is reasonable to expect that masked detection performance will be especially vulnerable to randomization of the spatial properties of the masker.

Past work of particular relevance to our experiments is that of Bernstein and Trahiotis (1997) in which they measured the effect of roving interaural differences (imposed on both masker and masker plus target) on the detection of a 500 Hz tone in the presence of masking noise. Although the effects of this roving were found to be small (and to be consistent with a version of the equalization and cancellation model), these experiments differed from those reported here in that (among other things) the target and masker had distinguishable spectra.

In this letter, we report results of three preliminary, relatively independent, probe experiments concerned with the effects on target detection of uncertainty in the spatial properties of the masker for cases in which the target and masker are simple nonspeech stimuli that differ only in spatial properties. Although these experiments were limited both in the types of tests performed and the manner in which procedures and parameter values varied across experiments, we believe that they are well worth reporting.

II. EXPERIMENTS

All signals were presented through earphones; targets and maskers were statistically identical, statistically indepen-

[a]Electronic mail: wei.l.fan@gmail.com
[b]Electronic mail: timstr@cns.bu.edu
[c]Author to whom correspondence should be addressed. Tel.: 617 253 2534. FAX: 617 258 7003. Electronic mail: durlach@mit.edu

 0001-4966/2008/124(1)/36/4/$23.00

dent random noise signals with identical spectra; the spectrum of these signals was flat in the region 300–800 Hz and fell off rapidly outside this region; the signal durations were 250 ms in experiment 1 and 500 ms in experiments 2 and 3, with target and masker gated on and off together; and the experimental paradigm was a one-interval 2AFC (respond "target present" or "target absent") detection paradigm with trial-by-trial feedback and equal a priori probabilities for target present and target absent. The target was always diotic and the masker (with only one exception in experiment 3) always lay outside a spatially protected zone around the target. In some cases, the spatial properties of the masker were held fixed, and in other cases they varied randomly from trial to trial. The spatially fixed case is denoted SF, and the spatially random case SR. Finally, in some of the tests the overall stimulus level (masker or masker plus target) was roved randomly to reduce loudness cues. When the overall level is fixed, it is denoted LF, when random, LR. Thus, for example, LRSF denotes "level random, space fixed." Because the roving level applied to the whole stimulus and not just the masker, it never affected the target-to-masker ratio (TMR). In all experiments, subjects were between the ages of 18 and 30, had normal hearing, and participated in training sessions (1 h long) prior to and identical to the test sessions.

In experiment 1, the maskers consisted of triplets (three simultaneous noise samples) with each component of the triplet having zero ILD and an ITD selected randomly without replacement from the set $\{\pm 600, \pm 400, \pm 300, \pm 200\ \mu s\}$. The protected zone around the diotic target (ITD=0 μs) was thus -200 to 200 μs. The masker was selected randomly from a fixed set of ten such triplets. The level was always roved randomly over the range 50–70 dB SPL and the TMR was always computed using the energy in the whole masker triplet. In experiment 2, the ITDs of the maskers were replaced by virtual azimuth angles using HRTFs based on recordings made with the KEMAR mannequin in anechoic space (Gardner and Martin, 1995). The ten triplets used were drawn from the azimuth set $\{\pm 70°, \pm 45°, \pm 30°, \pm 20°, \pm 15°\}$ and the protected zone was $-15°$ to $+15°$. Again, the masking triplets were chosen randomly and the masking level includes all three components of the triplet. The base level was 54 dB SPL and, when the level was roved, the range was 54–64 dB SPL. In experiment 3, the ten triplets of angles used for the maskers were replaced by six unitary angles. These angles were drawn from the set $\{\pm 75°, \pm 40°, \pm 20°\}$, thus providing a protected zone of $-20°$ to $+20°$. In addition, LF tests were performed in which the masker, like the target, was diotic (so that the only detection cue was stimulus energy). The base level in this experiment was 58 dB SPL, and in those tests where the overall level was roved, the range was 58–68 dB SPL. In the SF tests, all angles in the above set of angles were used. Also, the TMR for a given masker was defined as the average TMR across the two ears. In all experiments, for each TMR, condition, and subject, the stimulus-response matrix obtained was processed to obtain estimates of sensitivity d' and response bias β in the usual fashion (e.g., Durlach *et al.*, 2005). Further comments on experimental procedures and data-analysis procedures are presented below.

III. EXPERIMENTAL RESULTS

The d' vs TMR curves obtained in experiment 1, as well as threshold and slope estimates based on linear fits, are shown in the top row of Fig. 1. In graphs for individual subjects, and for both LRSF and LRSR, each point is based on 1000 trials (100 per triplet). For the LRSF case, the points were obtained by computing d' for each fixed case and then averaging over these values of d' (the error bars giving the standard deviations across this set of d''s). The ordering of the tests was random, except that the LRSF tests were conducted before the LRSR tests and, for each of these cases, the value of TMR was held constant during each 100-trial run, with different values of TMR being tested in descending order. In the graph showing the results averaged over subjects, the error bars show the standard error in the mean.

The d' curves, together with the threshold and slope estimates, obtained in experiment 2 are shown in the middle row of Fig. 1. In the graphs for individual subjects, the points for the spatially fixed cases (LFSF and LRSF) are based on 2000 trials (200 per case) and for the spatially random cases (LFSR and LRSR) on 400 trials. For the spatially fixed cases, the values of d' were again obtained by averaging across the d' values obtained with the individual fixed constituents (the error bars again showing the standard deviations across these values of d'). The various conditions in this experiment were tested in the order LFSF, LFSR, LRSF, LRSR and the various TMRs in descending order.

The d' results obtained in experiment 3 are shown in the bottom row of Fig. 1. The number of trials per point and the ordering of the tests were similar to those in experiment 2 with the following exceptions: (a) the number of trials per point for the fixed cases was 1200 rather than 2000 (corresponding to the reduction in the number of maskers from 10 to 6) and (b) the case in which the masker, like the target, was diotic was tested at the end of the experiment (with 400 trials per TMR value).

In all experiments, informational masking in the spatial domain occurs to the extent that the SR curves are on the right of (or lower than) the SF curves (compare LFSR to LFSF and LRSR to LRSF). Such results are clearly apparent in experiments 2 and 3 (where the roving-level range was less than or equal to 10 dB) but not in experiment 1 (where the roving-level range was always 20 dB). In terms of estimated thresholds, the shifts between the SR cases and the SF cases (examined over both the LR and LF conditions in both experiments 2 and 3) are of the order of 2–4 dB. The consistency of these results, combined with the small standard error in the estimates of threshold across subjects (less than 1 dB for all test conditions in both experiments 2 and 3), is a strong indication of the degrading effect of spatial uncertainty.

The tendency for roving level to play a dominant role in these experiments is evidenced not only by the results of experiment 1 (where any effect of spatial uncertainty has

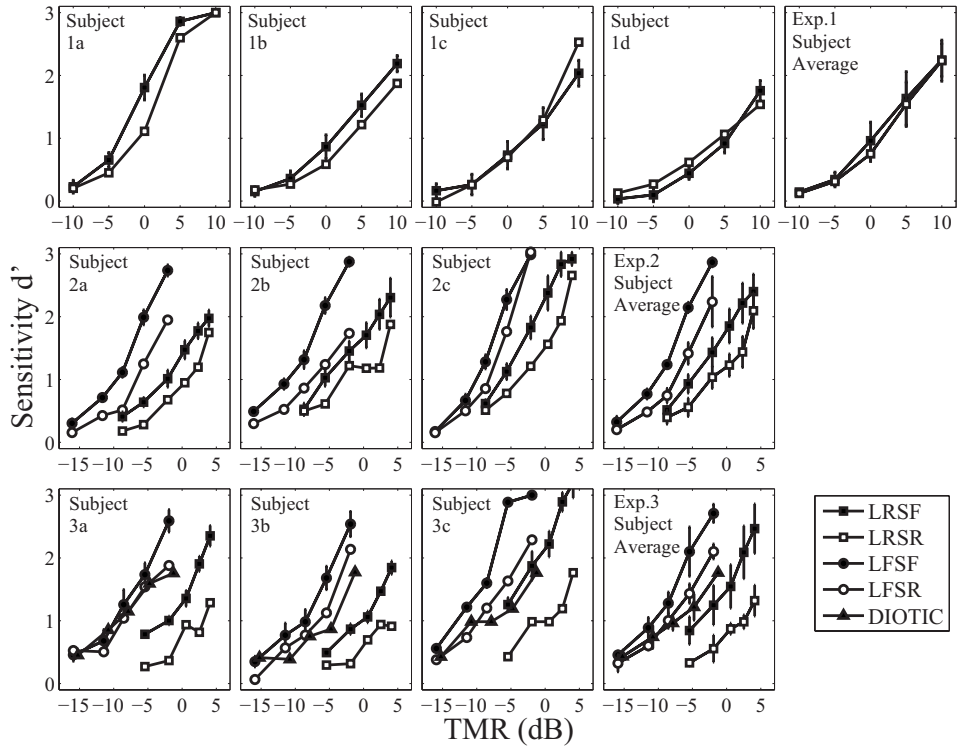

Exp.1	Slope	Threshold (dB) (where d' = 1)
LRSF	0.11 ± 0.01	0.15 ± 0.90
LRSR	0.11 ± 0.01	0.81 ± 0.73
LFSF	—	—
LFSR	—	—
DIOTIC	—	—

Exp.2	Slope	Threshold (dB) (where d' = 1)
LRSF	0.11 ± 0.03	-3.81 ± 0.96
LRSR	0.09 ± 0.02	-1.83 ± 0.71
LFSF	0.18 ± 0.01	-11.34 ± 0.20
LFSR	0.15 ± 0.02	-8.67 ± 0.42
DIOTIC	—	—

Exp.3	Slope	Threshold (dB) (where d' = 1)
LRSF	0.13 ± 0.03	-2.60 ± 0.92
LRSR	0.07 ± 0.02	1.66 ± 0.82
LFSF	0.17 ± 0.01	-11.44 ± 0.49
LFSR	0.13 ± 0.01	-9.38 ± 0.38
DIOTIC	0.09 ± 0.00	-8.21 ± 0.59

FIG. 1. Experimental results on sensitivity d'. Rows 1, 2, and 3 give results for experiments 1, 2, and 3, respectively. LFSF means level fixed, spatial structure fixed; LFSR means level fixed, spatial structure random; LRSF means level random, spatial structure fixed; LRSR means level random, spatial structure random; and diotic means that the masker signal (like the target signal) is the same in both ears. Results for LFSF and LRSF show averages over results for the various fixed maskers with any $d' > 3$ being given the value 3 and with error bars indicating standard deviations across fixed spatial conditions. Graphs in the rightmost box in each row give averages over subjects, with error bars indicating standard errors over subjects. In some cases, the error bars are hidden behind the symbols used for marking the average data points. Estimates of threshold values (in dB and defined by the condition $d' = 1$), as well as estimates of the slopes, for all the average-subject d' curves, are shown (along with the standard error of these estimates) at the right edge of each row.

been overwhelmed by level uncertainty) but also by the results of experiments 2 and 3. Compared with the threshold shifts of 2–4 dB associated with spatial uncertainty, threshold shifts associated with level uncertainty are 7–10 dB.

The importance of roving level is also evident in comparisons of thresholds (defined by $d' = 1$) across experiments. Whereas the thresholds in experiment 1 (where there was a rove of 20 dB) are roughly 0 dB, the thresholds in experiments 2 and 3 for cases in which there was no level rove are roughly −10 dB. (That this difference in thresholds is due primarily to the roving-level factor and not other differences between the experiments is indicated by the similarities in the thresholds when one compares the results of experiment 1 to those of experiments 2 and 3 when the level is roved in experiments 2 and 3). In addition, roving level appears to affect the slope of the d' curves: when the rove was increased from 0 to 10 dB in experiments 2 and 3, the slope always decreased (for both the SF cases and the SR cases).

Differences among the d' values across individual maskers for the LFSF and LRSF cases (see the error bars associated with the filled symbols for individual subjects) generally appear modest. Differences across subjects shown by the error bars in the average-subject graphs vary from very small (see filled circles for experiment 2) to very large (e.g., see top open circle in experiment 2 and filled circle at TMR = −5 dB in experiment 3).

The results for the diotic tests in experiment 3 are roughly consistent with what one would expect from previous results on intensity JNDs. According to the data in Fig. 1, the threshold for the diotic case is roughly −8 dB, which corresponds to a Weber fraction of approximately 0.5 dB. Note also that the difference in performance for this case and the LFSF case in experiment 3 indicates that the detection cue for the LFSF case cannot be merely the total energy level in the whole stimulus.

Overall, the results on β showed little response bias. Pooling the data across subjects, test conditions, and values of TMR, we found the mean and standard error for each experiment to be −0.22 and 0.15 (experiment 1), 0.03 and 0.09 (experiment 2), and −0.02 and 0.07 (experiment 3). Further analysis of the data for experiment 1 in which trials for the top half and bottom half of the 20 dB roving-level range were kept separate showed that the negative mean bias for this experiment (−0.22) was due entirely to the existence of a negative bias in the top half of the range: whereas the mean bias for the bottom half was 0.07, the mean bias for the top half was −0.57. Inasmuch as a negative value of β corresponds to a bias to say target present, this result is consistent with the notion that the overall stimulus level served as at least one component of the detection cue used in experiment 1. (An equivalent analysis of the d' data in experiment 1 showed a slight tendency for d' to be larger at the higher levels).

IV. DISCUSSION

In general, the results indicate that sensitivity d' tends to be reduced by spatial randomization of maskers with little energy at the target location, but that the magnitude of this "spatial informational masking" is small compared both to the effect of randomizing the level of the stimulus or, as documented in the literature (e.g., Durlach *et al.*, 2005), to the effect of "spectral informational masking."

Some of the factors that might be related to our results are the following. First, in experiments 2 and 3, the use of HRTFs necessarily involved the introduction of some spectral differences among the various maskers (and between target and masker). Thus, our explanation of the difference between the results of experiments 2 and 3 and those of experiment 1 solely in terms of the much larger roving-level range in experiment 1 may be incomplete. Second, the number of JNDs in the spatial domain is relatively small compared to that in the spectral domain. Thus, perceptual randomization in the spatial domain might be more difficult to achieve than in the spectral domain. Third, a change in spatial location might be less likely to induce the perception of a change in auditory source ("auditory object") than a change in spectrum. Thus, spatial randomization might be less distracting (attention grabbing) than a change in spectrum. Fourth, susceptibility to informational masking may decrease as the domain of masker randomization becomes more central. It would be interesting to compare spatial to spectral informational masking in a system where spatial processing precedes spectral processing.

Further issues of interest in connection with our results focus on the effects of level randomization. For example, to what extent does the strong effect of level randomization that is seen in our experiments on spatial informational masking also occur in spectral informational masking? Currently available information relevant to this question is rather meager. On the one hand, to the extent that the model considered in Durlach *et al.* (2005) is correct (a model in which the reduction in sensitivity d' caused by spectral randomization of the masker is interpreted in terms of level randomization at the output of a spectral filter), one would predict a strong effect in the spectral domain as well as the spatial domain. On the other hand, there exist at least some data that suggest that the level randomization effect is very weak in the spectral domain (e.g., Mason *et al.*, 1984; Richards and Neff, 2004). In the authors' opinion, further experimental work is needed on the effect of level randomization in both the spatial domain and the spectral domain.

ACKNOWLEDGMENTS

The authors are indebted to Chris Mason for many useful comments on drafts of this material and to the following grants for supporting this work: NIH RO1 DC00100, NIH/NIDCD P30 DC004663, and AFOSR FA9950-05-01-2005.

Bernstein, L. R., and Trahiotis, C. (**1997**). "The effects of randomizing values of interaural disparities on binaural detection and on discrimination of interaural correlation," J. Acoust. Soc. Am. **102**, 1113–1120.

Colburn, H. S., and Durlach, N. I. (**1978**). "Models of binaural interaction," in *Handbook of Perception*, edited by E. C. Carterette and M. P. Friedman (Academic, New York), Vol. IV.

de Cheveigne, A., and McAdams, S. (**1995**). "Identification of concurrent harmonic and inharmonic vowels: A test of the theory of harmonic cancellation and enhancement," J. Acoust. Soc. Am. **97**, 3736–3748.

Durlach, N. I. (**2006**). "Auditory masking: Need for improved conceptual structure," J. Acoust. Soc. Am. **120**, 1787–1780.

Durlach, N. I. (**1972**). "Binaural signal detection: Equalization and cancellation theory," in *Foundations of Modern Auditory Theory*, edited by J. V. Tobias (Academic, New York).

Durlach, N. I., and Colburn, H. S. (**1978**). "Binaural Phenomena," in *Handbook of Perception*, edited by E. C. Carterette and M. P. Friedman (Academic, New York), Vol. **IV**.

Durlach, N. I., Mason, C. R., Kidd, G., Jr., Arbogast, T. L., Colburn, H. S., and Shinn-Cunningham, B. G. (**2003**). "Note on informational masking," J. Acoust. Soc. Am. **113**, 2984–2987.

Durlach, N. I., Mason, C. R., Gallun, F. J., Shinn-Cunningham, B. G., Colburn, H. S., and Kidd, G., Jr. (**2005**). "Informational masking for simultaneous nonspeech stimuli: Psychoacoustic functions for fixed and randomly mixed maskers," J. Acoust. Soc. Am. **118**, 2482–2497.

Gardner, W. G., and Martin, K. D. (**1995**). "HRTF measurements of a KEMAR," J. Acoust. Soc. Am. **97**, 3907–3908.

Kidd, G. I., Jr., Mason, C. R., Richard, V. M., Gallun, F. J., and Durlach, N. I. (**2007**). "Informational masking," in *Auditory Perception of Sound Sources*, Springer Handbook of Auditory Research Vol. **29**, edited by W. Yost (Springer, New York).

Lutfi, R. A. (**1993**). "A model of auditory pattern analysis based on component-relative-entropy," J. Acoust. Soc. Am. **94**, 748–758.

Mason, C. R., Kidd, G., Jr., Hanna, T. E., and Green, D. M. (**1984**). "Profile analysis and level variation," Hear. Res. **13**, 269–275.

Oh, E. L., and Lutfi, R. A. (**1998**). "Nonmonotonicity of informational masking," J. Acoust. Soc. Am. **104**, 3488–3499.

Richards, V. M., and Neff, D. L. (**2004**). "Cuing effects for informational masking," J. Acoust. Soc. Am. **115**, 289–300.

Shinn-Cunningham, B. G. (**2005**). "Influences of spatial cues on grouping and understanding sound," Proceedings of the Forum Acusticum, 29 August–2 September.

Stern, R. M., and Trahiotis, C. (**1995**). "Models of binaural interaction," in *Handbook of Perception and Cognition*, edited by B. C. J. Moore (Academic, New York), Vol. 6.

Watson, C. S. (**1987**). "Uncertainty, informational masking, and the capacity of immediate auditory memory," in *Auditory Processing of Complex Sounds*, edited by W. A. Yost and C. S. Watson (Erlbaum, Hillsdale, NJ).

Watson, C. S. (**2005**). "Some comments on informational masking," Acta Acust. **91**, 502–512.

Number and duration of echolocation click trains produced by a harbor porpoise (*Phocoena phocoena*) in relation to target and performance (L)

Ronald A. Kastelein[a] and Mariska Verlaan
Sea Mammal Research Company (SEAMARCO), Julianalaan 46, 3843 CC Harderwijk, The Netherlands

Nancy Jennings
Dotmoth, 1 Mendip Villas, Crabtree Lane, Dundry, Bristol BS41 8LN, United Kingdom

(Received 16 October 2007; revised 30 March 2008; accepted 16 April 2008)

Echolocation effort (number and duration of echolocation click trains produced) by a harbor porpoise is described in relation to target presence, strength and distance, and performance of the detection task. The porpoise was presented with two target sizes at five distances (12–20 m), or no target, and had to indicate whether it could detect the target. Small, distant targets required long and multiple click trains. Multiple click trains mostly occurred when the small target was far away and not detected, and during target-absent trials in which the animal correctly responded. In target-absent trials, an incorrect response was linked to short click trains. Click train duration probably increased until the animal's certainty about the target's presence or absence exceeded a certain level, after which the porpoise responded. © *2008 Acoustical Society of America.*
[DOI: 10.1121/1.2924132]

PACS number(s): 43.80.Ev, 43.80.Jz, 43.80.Lb, 43.80.Ka [WWA] Pages: 40–43

I. INTRODUCTION

Although some information exists about the echolocation ability of harbor porpoises (*Phocoena Phocoena*; Busnel and Dziedzic, 1967; Kastelein *et al.*, 1997; Kastelein *et al.*, 1999; Verfuß *et al.*, 2005), less is known about their echolocation effort (as studied in bottlenose dolphins, *Tursiops truncatus*; Murchison, 1980; Nachtigall, 1980; Au *et al.*, 1982; Penner, 1988).

In the echolocation ability experiment by Kastelein *et al.* (1999), a porpoise's echolocation signals were recorded. Teilmann *et al.* (2002) analyzed recordings from 126 of the 772 trials, and showed that click intervals are independent of target range (at 12–20 m) and that detection of a small target requires significantly more clicks than detection of a larger target.

The echolocation recordings from all 772 trials form the basis of the present study. The porpoise produced click trains of various duration and sometimes used multiple click trains; we aimed to test the hypothesis that the number and duration of echolocation click trains produced, or the effort expended in echolocation, was related to the context of the trials. Therefore the aim of the present study was to investigate the echolocation strategy of the harbor porpoise by quantifying the click train duration and number of click trains used in relation to target presence, strength, and distance, and the animal's performance.

II. MATERIALS AND METHODS

The data used in the present study were collected as part of an echolocation ability study in which full methodological details are given (Kastelein *et al.*, 1999). The study animal was a 4-year-old male harbor porpoise (body weight 35 kg; body length 133 cm).

The experiment was conducted in a floating pen (34 m × 20 m; water depth: 2.4–2.8 m; Fig. 1) at Neeltje Jans, The Netherlands. The small and large targets were water-filled stainless-steel spheres of 5.08 and 7.62 cm diameter with peak-to-peak target strengths of −38 and −27 dB, respectively. The porpoise was trained to indicate that it had detected a target by leaving its hoop station. If it did not detect the target it was trained to remain in the hoop until the trainer blew a whistle.

Each session consisted of 50% target-present trials (25% with the large target and 25% with the small target) and 50% target-absent trials, in pseudo-random order. Targets were offered in random order (between sessions) at 12, 14, 16, 18, and 20 m from the hoop. No sessions were carried out when it rained, or when wind speed was over Beaufort 5. Sessions were conducted on 51 days between June and September 1997.

Echolocation clicks were recorded by means of a hydrophone (Bruel & Kjaer, model 8103) 1 m in front of the porpoise, on the axis between the porpoise and the target (Fig. 1). The hydrophone was connected to a charge amplifier (Bruel & Kjaer, model 2635) and a bat detector (Pettersson Elektronik AB, Sweden, model D230), which made the echolocation signals audible by frequency division (:10). The modified echolocation signals and the video images were recorded by a video recorder (Sharp, VCH91). The sounds were stored on the hard disk of a computer, which contained a sound card (Creative, Soundblaster PCI 128). Click trains were visualized in the time domain by using a sound analysis program (Magix, Music Studio, 2.01). The click trains were counted, and their duration and intervals were digitally mea-

[a]Author to whom correspondence should be addressed. Electronic mail: researchteam@zonnet.nl

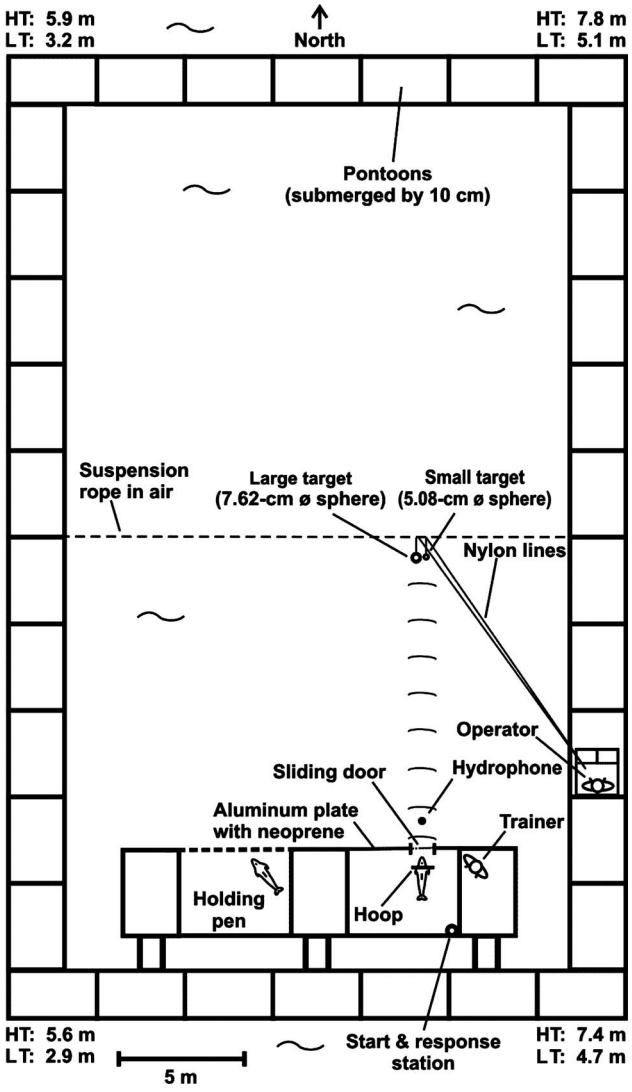

FIG. 1. The study area, showing the floating pen, the holding and research pens, the start and response station, the hoop, the targets, and the operator's cabin. Note that the trainer is facing away from the targets. The water depths at high tide (HT) and low tide (LT) are also shown. From Kastelein *et al.* (1999).

sured with an accuracy of 1 ms. The number of clicks per train and the intervals between clicks within trains were also determined.

A total of 772 trials were available for analysis. The parameters: duration of each of the up to four click trains and the total number of clicks per click train were highly correlated with one another (Pearson's correlations, $P<0.0001$ in all cases). The total duration of the first click train was used in quantitative analysis as a measure of the total energy, or effort, spent by the animal on echolocation.

For target-absent trials, an analysis of variance (ANOVA) was carried out on the relationship between the duration of the first click train and the distance to the target (above the water in target-absent trials) and response (correct or false alarm). To investigate the effect of target size and distance, an ANOVA on duration was carried out for target-present trials in which the response was correct (hits). In trials with the large target, only two incorrect responses (misses) occurred, so the effect of response could only be investigated for the small target. Therefore, only for the small target size, an ANOVA on duration with the factors distance and response was carried out. In all three ANOVAs, factors were crossed and fixed, and transformed values for duration (duration$^{0.25}$) were used, since these conformed to the assumptions of ANOVA (Zar, 1999). Interaction terms were omitted from the final model if not significant. Analysis was carried out on Minitab 13 with a significance level of 5% (Zar, 1999).

III. RESULTS

The mean interval between click trains was 800 ms (range 200–5300 ms). The mean click interval, within click trains, was 48 ms (range 20–120 ms). Based on this natural division, a click train was defined as a series of clicks separated from another series of clicks by at least 200 ms. Click trains were numbered in the order in which they occurred in a trial. The mean click repetition rate was 21 Hz. The rate was fairly constant: only the first and last three click intervals in a train were usually two to four times longer than the mean.

Analysis of data from target-present trials showed that the duration of the first click train was dependent on the difficulty of the task (ANOVA for target-present, correct detection trials: Factor "distance" $F_4=10.22$, $P<0.001$; factor "target size" $F_1=214.64$, $P<0.001$, interaction "distance $\times$ target size" $F_4=3.15$, $P<0.05$. For all small target present trials: Factor distance $F_4=3.83$, $P=0.005$; factor response $F_1=6.48$, $P=0.012$). The small target required on average longer click trains (1.3–2.3 s depending on the target distance) than the large target [~1 s; Figs. 2(a) and 2(c)]. The relationship between the animal's response and the duration of its click train differed for target-present and target-absent trials: in target-present trials the animal used longer and often multiple click trains when the target could not be detected [Fig. 2(d)]. This applied to the small target; only two responses to the large target were incorrect [Fig. 2(b)]. In contrast, in target-absent trials an incorrect response was linked to a short single click train [Fig. 2(f)]. In general, longer (~2.3 s) and more click trains were produced during target-absent trials [Fig. 2(e)] than during target-present trials in which the animal correctly responded [Figs. 2(a) and 2(c)].

In target-absent trials the click train duration was not related to distance (factor distance $F_4=1.77$, not significant, factor response $F_1=20.93$, $P<0.001$). This was as expected since the target was not in the water. However, the animal's response was related to the duration of the first click train: correct responses were based on longer click trains [Fig. 2(e)] than were incorrect responses [false alarms; Fig. 2(f)].

IV. DISCUSSION AND CONCLUSIONS

All echolocation clicks produced were probably recorded, despite the lateral head movements the porpoise made to increase its field of detection, because the hydrophone was very close to the porpoise's head, the signal-to-noise ratio was high, and the projecting echolocation beam of the harbor porpoise is wide (Au *et al.*, 1999). The video

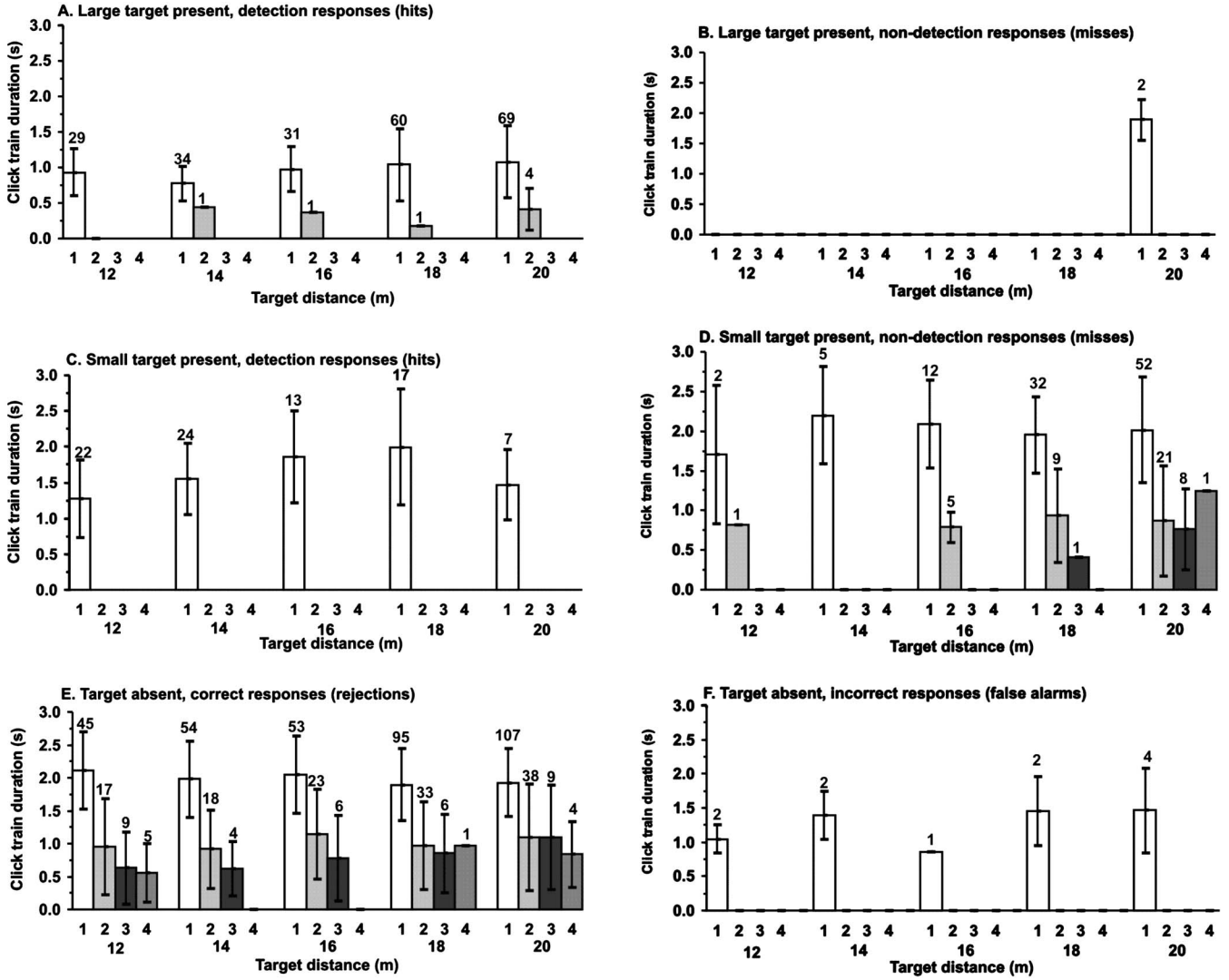

FIG. 2. Mean click train duration and standard deviations (bars) in relation to target distance for: A. Large target present, detection responses (hits), B. Large target present, nondetection responses (misses; NB there were no misses for targets at 12–18 m, as all large targets at this distance were detected), C. Small target present, detection responses (hits), D. Small target present, nondetection responses (misses), E. Target absent, correct responses (rejections), F. Target absent, incorrect responses (false alarms). The numbers 1–4 along the *x* axis indicate the successive click trains. Small numbers above bars are sample sizes (No. of trials). For example in D, when the target was at a distance of 12 m, the animal missed the target in two trials. In one trial the animal produced one click train, in the other two click trains.

images showed that the porpoise usually stopped making lateral head movements during the 0.2–5.3 s intervals between click trains, so the intervals were not artifacts due to head movements.

The porpoise used multiple click trains, rather than single longer click trains, when detection was difficult (or impossible in target-absent trials). The second, third, and fourth click trains were always much shorter than the first. These phenomena may be characteristic of the click generating mechanism or the echolocation strategy of the animal.

The animal stopped echolocating when it detected a target, or after a click train duration of about 2.5 s. Therefore, below that maximum, the click train duration is not fixed, but is determined by the animal; porpoises may abort a click train when they have received sufficient information. Teilmann *et al.* (2002) analyzed a subset of the data from the present study and concluded the same based on the mean number of clicks used before the animal made a decision (13 clicks for the large target, 34 clicks for the small target, and 37 clicks in target-absent trials). Bottlenose dolphins also exert control over their click train duration (Au *et al.*, 1982; Moore and Pawloski, 1990; Roitblat *et al.*, 1991).

The study animal stopped echolocating after roughly 2.5 s, perhaps because it learned that increasing the duration beyond 2.5 s did not provide additional information or improve performance. Assuming all noise is random (noncoherent), the target echo-to-noise ratio can be improved at best by the root of the number of repetitions or $\sqrt{N}$ (Green and Swets, 1988; Carr and Brown, 2001). Because of the $\sqrt{N}$ relationship, the information added by using 50 instead of 40 clicks is much less than that added by using 20 instead of 10 clicks. At some point as the number of clicks increases, it becomes impossible to integrate information over all clicks without loss, and performance levels out. As a result, there is an optimal number of repeats (N) for a particular test environment beyond which performance no longer improves. The

maximum duration of click trains observed during the present study was around 2.5 s (N=approximately 50 clicks). The associated predicted maximum improvement in target echo-to-noise ratio is 20 log ($\sqrt{N}$)=17 dB.

The mean 48 ms click interval seen in the present study allows a maximum range of roughly 30 m to a target, before pulse-echo overlap occurs. This time interval may be a further optimization based on the task. In wild porpoises, click intervals of 30–200 ms (mean 60 ms) have been measured (Villadsgaard *et al.*, 2007); the wild porpoises were probably searching for more distant objects than our study animal.

It is not clear how representative the study animal is of its species. In bottlenose dolphins, different click train lengths and numbers of click types are used by different individuals for the same target detection task (Au, 1980; Houser *et al.*, 1999). More studies of this kind are needed to determine if the results from the present study are indicative of the species. However, for this individual in the specific context of this study, echolocation is highly flexible, and the effort expended is related to the difficulty of the task.

ACKNOWLEDGMENTS

We thank Tineke Rippe and Muriël Drenthe for help with data collection, and Dick de Haan (IMARES) and Rob Triesscheijn for technical assistance. We also thank Peter van der Sman, Willem Verboom, Alexander Supin (Institute of Ecology and Evolution, Moscow, Russia), Jacob Tougaard (National Environmental Research Institute, Roskilde, Denmark), and Ursula Verfuß (German Oceanographic Museum) for their comments. Funding was obtained from The North Sea Directorate, The Netherlands (Wanda Zevenboom; Contract No. 76/315725; 1055; 1997). Work was conducted under authorization of the Netherlands Ministry of Agriculture, Nature Management and Fisheries (Endangered Species Permit FEF27 06/2/98/0184).

Au, W. W. L. (**1980**). "Echolocation signals of the Atlantic bottlenose dolphin (*Tursiops truncatus*) in open water," in *Animal Sonar Systems*, edited by R. G. Busnel and J. F. Fish (Plenum, New York), pp. 251–282.

Au, W. W. L., Kastelein, R. A., Rippe, T., and Schooneman, N. M. (**1999**). "Transmission beam pattern and echolocation signals of a Harbor Porpoise (*Phocoena phocoena*)," J. Acoust. Soc. Am. **196**, 3699–3705.

Au, W. W. L., Penner, R. H., and Kadane, J. (**1982**). "Acoustic behavior of echolocating Atlantic Bottlenose Dolphins," J. Acoust. Soc. Am. **71**, 1269–1275.

Busnel, R. G., and Dziedzic, A. (**1967**). "Résultats Métrologiques Expérimentaux de l'écholocation chez le *Phocaena phocaena* et leur Comparaison avec Cuex de Certaines Chauves-souris (Experimental measurements of echolocation in the *Phocoena phocoena* and comparison with those in certain bats)," in *Animal Sonar System, Biology and Bionics*, edited by R. G. Busnel (Lab. Physiol. Acoust. Jouey-en-Josas, France), pp. 307–356.

Carr, J. J., and Brown, J. M. (**2001**). "Noise Reduction." Introduction to *Biomedical Equipment Technology*, 3rd ed. (Prentice–Hall, Englewood cliffs, NJ).

Green, D. M., and Swets, J. A. (**1988**). *Signal Detection Theory and Psychophysics* (Peninsula, Los Altos, CA).

Houser, D. S., Helweg, D. A., and Moore, P. W. (**1999**). "Classification of dolphin echolocation clicks by energy and frequency distribution," J. Acoust. Soc. Am. **106**, 1579–1585.

Kastelein, R. A., Au, W. W. L., Rippe, H. T., and Schooneman, N. M. (**1999**). "Target detection by an echolocating harbor porpoise (*Phocoena phocoena*)," J. Acoust. Soc. Am. **105**, 2493–2498.

Kastelein, R. A., Schooneman, N. M., Verboom, W. C., and Vaughan, N. (**1997**). "The ability of a harbour porpoise (*Phocoena phocoena*) to discriminate between objects buried in sand," in *The Biology of the Harbour Porpoise*, edited by A. J. Read, P. R. Wiepkema, and P. E. Nachtigall (De Spil, Woerden, The Netherlands), pp. 329–342.

Moore, P. W. B., and Pawloski, D. A. (**1990**). "Investigations on the control of echolocation pulses in the dolphin (*Tursiops truncatus*)," in *Sensory Abilities of Cetaceans*, edited by J. Thomas and R. Kastelein (Plenum, New York), pp. 305–316.

Murchison, A. E. (**1980**). "Detection range and range resolution in echolocating Bottlenose Porpoise (*Tursiops truncatus*)," in *Animal Sonar Systems*, edited by R. G. Busnel and J. F. Fish (Plenum, New York), pp. 43–70.

Nachtigall, P. E. (**1980**). "Odontocete echolocation performance on object size, shape and material," in *Animal Sonar Systems*, edited by R. G. Busnel and J. F. Fish (Plenum, New York), pp. 71–95.

Penner, R. H. (**1988**). "Attention and detection in dolphin echolocation," in *Animal Sonar*, edited by P. E. Nachtigall and P. W. B. Moore (Plenum, New York), pp. 707–713.

Roitblat, H. L., Moore, P. W. B., Nachtigall, P. E., and Penner, R. H. (**1991**). "Natural dolphin echo recognition using an integrator gateway network," in *Advances in Neural Information Processing Systems*, edited by D. S. Touretsky, J. E. Moody, and R. Lippman (Morgan Kaufmann, San Mateo, CA), Vol. **3**, pp. 273–281.

Teilmann, J., Miller, L. A., Kirketerp, T., Kastelein, R. A., Madsen, P. T., Nielsen, B. K., and Au, W. W. L. (**2002**). "Characteristics of echolocation signals used by a harbour porpoise (*Phocoena phocoena*) in a target detection experiment," Aquat. Mamm. **28**, 275–284.

Verfuß, U. K., Miller, L. A., and Schnitzler, H.-U. (**2005**). "Spatial orientation in echolocating harbour porpoises (*Phocoena phocoena*)," J. Exp. Biol. **208**, 3385–3394.

Villadsgaard, A., Wahlberg, M., and Tougaard, J. (**2007**). "Echolocation signals of wild harbour porpoises, *Phocoena phocoena*," J. Exp. Biol. **210**, 56–64.

Zar, J. H. (**1999**). *Biostatistical Analysis*. Prentice Hall, Upper Saddle River, NJ.

Click-evoked potentials in a large marine mammal, the adult male northern elephant seal (*Mirounga angustirostris*) (L)

Dorian S. Houser
BIOMIMETICA, 7951 Shantung Drive, La Mesa, California 92071

Daniel E. Crocker
Department of Biology, Sonoma State University, 1801 East Cotati Avenue, Rohnert Park, California 94928

James J. Finneran
U.S. Navy Marine Mammal Program, Space and Naval Warfare Systems Center, San Diego, Code 7150, 53560 Hull St., San Diego, California 92152

(Received 31 December 2007; revised 18 April 2008; accepted 25 April 2008)

Auditory evoked potential (AEP) hearing studies in marine mammals should consider an expected size-dependent reduction in AEP amplitude. This study is the first to measure the click-evoked response in a large marine mammal, the adult male elephant seal (*Mirounga angustirostris*). Click stimuli were presented at peak-peak equivalent sound pressure levels of 117–118 dB re: 20 μPa. Three positive peaks (P1–P3) and two negative peaks (N4 and N5) were observed in the AEP. Response latencies were longer than previously observed in a 1.8 yr old seal and the maximum peak-peak amplitude was comparatively reduced by more than 60%. The inverse relationship between size and AEP amplitude will likely require increased averaging with larger subjects and possibly modifications to electrode placement and design in order to increase the quality of recorded evoked responses. © *2008 Acoustical Society of America.* [DOI: 10.1121/1.2932063]

PACS number(s): 43.80.Lb, 43.80.Ev [WWA] Pages: 44–47

I. INTRODUCTION

Auditory evoked potentials (AEPs) are commonly used in humans and terrestrial mammals for both clinical and research purposes. AEP methods have also enjoyed considerable success in the study of hearing in small odontocetes (dolphins and porpoises), primarily because of the large brain and robust auditory evoked responses observed in these animals (Supin *et al.*, 2001). The application of AEP methods to other marine mammals is promising but must overcome several challenges before being broadly applied. For example, in pinnipeds, the amplitude of evoked responses from comparable stimuli (e.g., clicks) is attenuated relative to that observed in small odontocetes (Houser *et al.*, 2007; Reichmuth *et al.*, 2007), in part due to the anatomy and physiology of the auditory pathway and the increased thickness of the skull. Larger marine mammals, both cetacean and pinniped, are also expected to have diminished surface-recorded evoked responses because of an increase in head size and a decreased brain-to-body mass ratio (Szymanski *et al.*, 1999). Such relationships may pose a significant obstacle to the goals of measuring the auditory function of mysticete whales, which have large body masses (tens of thousands of kilograms) and relatively small brains (Ridgway and Carder, 2001).

The research described here attempts to measure click-evoked responses in the largest of the pinnipeds, the elephant seal (genus *Mirounga*). Adult male northern elephant seals can exceed 2500 kg (Deutsch *et al.*, 1994) and have thick, ossified skulls. Measuring evoked potentials in these large, nonodontocete marine mammals was sought as a step toward addressing the impact of the brain-to-body mass ratio on evoked response recordings. The large size and structure of the skull were anticipated to substantially reduce or obliterate the ability to record evoked responses. Successful recording of the click-evoked response demonstrates that AEP methods are possible in large marine mammals but will likely require adaptations to methods that are typically applied to smaller odontocetes.

II. METHODS

A. Subjects

Recordings of click-evoked responses were attempted on three adult (M1, M2, and M3) and one subadult (SA) male elephant seal at the Año Nuevo State Reserve, CA, USA during March and August of 2006. Adult elephant seals were selected based upon complete maturation as determined from physical characteristics (e.g., size and development of the neck shield and nose). The SA was similarly categorized based on its intermediate level of development of secondary sexual characteristics. Seals were immobilized with a tiletamine HCl/zolazepam HCl mixture (0.4–1.0 mg/kg) administered intramuscularly. Subsequent intravenous injections of ketamine HCl were administered to maintain immobilization, as necessary (Briggs *et al.*, 1975). Procedures ranged in time from 1.5 to 4 h; however, additional audiometric testing was conducted beyond that which is described here.

 0001-4966/2008/124(1)/44/4/$23.00

FIG. 1. (Color online) Application of AEP methods to a chemically immobilized northern elephant seal.

B. Stimuli

A rugged notebook computer with a multifunction data acquisition card (National Instruments PCI-6251) was used to generate stimuli at a 2 MHz update rate and with 16-bit resolution. Sounds were lowpass filtered (20 kHz, Krohn-Hite 3C module) and passed through a custom attenuator before delivery to TDH-39 headphones (Telephonics Corp.) placed over the acoustic meatus of the seal (Fig. 1). Stimuli consisted of 200 μs rectangular waveforms, with no rise or fall time, presented at a rate of approximately 33–42 Hz. The polarity of the clicks was sequentially alternated to cancel any stimulus artifact introduced into the AEP recordings. Clicks presented to the subjects were calibrated by using an Etymotic probe microphone (sensitivity of 50 mV/Pa). Click peak-peak equivalent sound pressure levels (ppeSPLs) for all presentations were between 117 and 118 dB re: 20 μPa. The ppeSPL of a transient is defined as the (rms) sound pressure level of a continuous sine wave having the same peak-peak amplitude as the measured transient.

C. AEP recordings

Subcutaneous stainless steel needle electrodes (Neuroline, 1.7 cm needle, 100 cm lead wires) were used for the detection of evoked potentials. The noninverting (+) electrode was inserted between 5 cm anterior and 10 cm posterior of the vertex of the skull, equidistant from the left and right external ears. The inverting electrode (−) was placed 7 cm below and 11 cm behind either the right or the left external meatus. The ground was placed on the midline neck of the seal, approximately 1 m behind the insertion of the noninverting electrode (more information on the placement of the electrodes may be found in Houser *et al.* 2007). Prior to testing, the impedance difference across the electrodes was checked to ensure that it was less than 5kΩ.

Electrode signals were differentially amplified and filtered by using a biopotential amplifier (Grass ICP-511). The biopotential amplifier gain was fixed at 100 000. High and lowpass filters were set at 100 Hz and 1 or 3 kHz, respectively. The resulting signal was digitized by using the PCI-6251 at a rate of 10 or 20 kHz and the evoked response recording window varied from 15 to 20 ms. The artifact rejection level, the voltage above which signals were rejected from analysis, was set at either 6 or 8 μV. Either 2000 or 4000 evoked responses were averaged for each stimulus presentation trial.

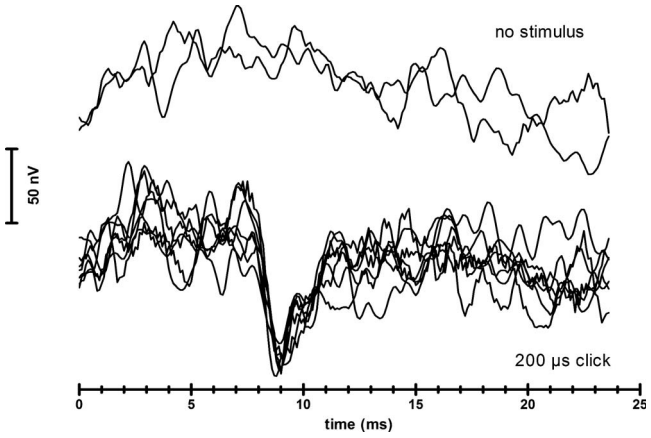

FIG. 2. The click-evoked response from seven click presentation trials made to subject M2. Each trace is the average resulting from 4000 click-stimulus presentations. Two "no-stimulus" recordings are provided for comparison.

III. RESULTS

Quality click-evoked response records were obtained for a single adult male (M2) and for the SA. No evoked responses were detected in one adult male (M3) and usable but lower quality recordings were obtained on the remaining adult male (M1). Physiological background noise varied from individual to individual. Background noise was dependent on the degree of immobilization that could be obtained and whether the animals developed tremors in response to ketamine immobilization. Of the two highest quality records, the physiological noise was greatest in SA. Figure 2 shows individual evoked responses (thin lines) for seven different click-stimulus presentation trials and two no-stimulus presentation trials made to M2 on 10 March 2006. The grand average of all of the evoked responses from this animal is shown in Fig. 3. Dominant peaks were identified in order of occurrence and polarity and consistent with prior designation (Houser *et al.*, 2007), as P1, P2, P3, and N4 (Fig. 3). The final negative peak was designated as N5; although not designated previously by Houser *et al.* (2007), this negative peak was observed in the recording of click-evoked responses of a 1.8 yr old elephant seal and appears to be a consistent feature of the click-evoked response.

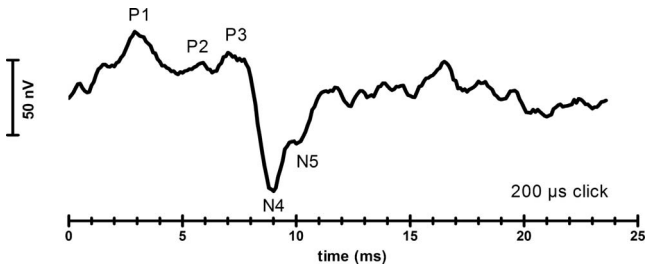

FIG. 3. The grand average of the seven trials presented in Fig. 2 (i.e., 28 000 click-stimulus presentations). Peaks in the evoked response are designated above (positive) and below (negative) the waveform.

The dominant feature of the click-evoked response of the adult and SA male elephant seal was the presence of N4. The N4 peak was easily observed in the individual waveforms and was the only feature that was observable in the recordings of both M1 and M2. In both animals, N4 occurred at 9 ms after the stimulus onset. In M2, the subsequent N5 occurred at 10 ms after the stimulus onset. The corresponding peaks occurred 1 ms earlier in the click-evoked response recorded from SA (N4=8 ms and N5=9 ms). The average peak-peak amplitude of N4 in M2 was 96 nV and was 117 nV in SA. The earlier positive peaks (P1–P3) occurred at 3, 5.9, and 7 ms after the stimulus onset in M2, respectively. As with the N4 and N5 peaks, these peaks appeared earlier in the click-evoked response of SA (P1=2.7 ms, P2 =5.2 ms, and P3=6.8 ms).

IV. DISCUSSION

Within humans, head size appears to moderately impact evoked response latencies and amplitude, although the strength of the relationship depends on the metrics for head size that are employed (Dempsey *et al.*, 1986; Chambers *et al.*, 1989; Yamaguchi *et al.*, 1991). A similar trend might be expected to occur as head size (and thus, overall mass) increases within and between other animal species, although results from tests of this assumption in different dog breeds are equivocal (Pook and Steiss, 1990; Meij *et al.*, 1992; Munro *et al.*, 1997). Considering prior measurements made on a 1.8 year old northern elephant seal (Houser *et al.*, 2007), the latencies and amplitude of the evoked responses increased and decreased, respectively, with increasing size of this species of seal. The masses of the elephant seals in this study and in the prior study of Houser *et al.* (2007) were not measured; however, considerable prior work with elephant seals suggests that there is nearly an order of magnitude difference in the masses of a 1.8 year old seal and an adult male seal (approximate masses would be 200 and 2000 kg, respectively). Figure 4(a) demonstrates the increase in measured latency that occurs with the increase in the age (and mass) of the animal. The pattern holds for all comparisons except for N5, where the latency is slightly longer for the 1.8 yr old than was measured in the SA. Similarly, Fig. 4(b) demonstrates a more than 60% reduction in the peak-peak amplitude of the obtained evoked response over an expected order of magnitude difference in mass. The peak of N4 measured in the M2 was 168 nV less than the average of 264 nV amplitude recorded for the same peak in a 1.8 yr old seal (Houser *et al.* 2007). Considering all age (size) classes, the results are consistent with a size-dependent effect on evoked response latency and amplitude.

This is the first study to record evoked potentials in an adult male elephant seal. It demonstrated that evoked responses can be obtained from a large marine mammal and one which has a much diminished click-evoked response compared to that observed in dolphins and porpoises. The results highlight the challenges that lay ahead for the measurement of auditory evoked responses in similar sized and larger marine mammals; specifically, with increasing mass, the amplitude of the evoked signals will diminish and the

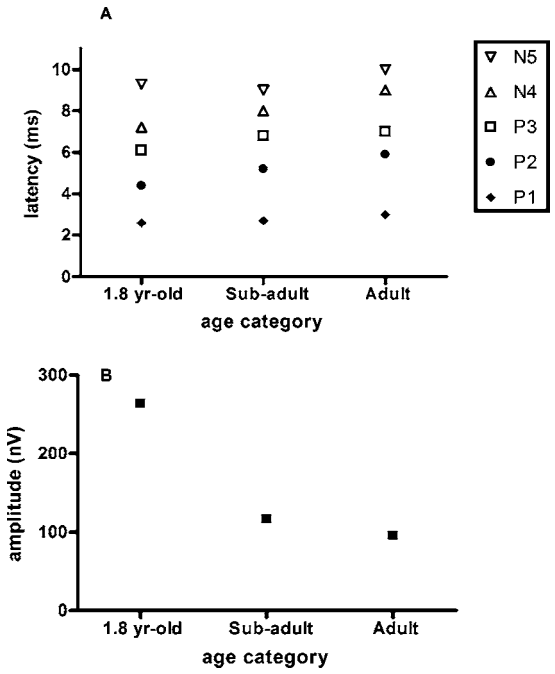

FIG. 4. (A) Variation in the latency of click-evoked response peaks as a function of animal age category (and size). (Note that the number of averages is different for each animal: 1.8 yr old=8000 averages; SA=12 000 averages; adult=28 000 averages.) Latencies for the individual peaks are designated by the symbols presented in the legend. (B) Reduction in the peak-peak amplitude of the N4 peak as a function of animal age category (and size). For both graphs, values for the 1.8 yr old seal are taken from the data collected and reported as part of Houser *et al.* (2007).

impact of physiological noise will increase. Although the direct relationship between AEP latency and subject mass is likely not a major hindrance to the eventual goal of obtaining AEP audiograms in large nonodontocete marine mammals, the negative relationship between the amplitude of the evoked response and animal size is problematic. It is immediately obvious from this study that the collection of quality evoked response records on large marine mammals, particularly if they are obtained in the wild, will require an increase in the number of epochs collected per average. The number of epochs averaged to observe the click-evoked response in a 1.8 yr old elephant seal was 4000. A similar number of epochs were averaged for each of the stimulus presentation trials made for M2 in this study, but the detail of the click-evoked response was not comparable to that of the 1.8 yr old until multiple trials were averaged (i.e., 8000+ averages). Increasing the number of averages directly impacts the time required to collect data, which is a point of concern when working with chemically immobilized wild marine mammals or those which are stranded. In the former scenario, chemical immobilization cannot be maintained indefinitely; in the latter, issues of animal welfare and distress will need to be balanced against the time allotted for data collection.

Future efforts to acquire auditory evoked potential recordings in large nonodontocete marine mammals will have to give consideration to the time available for data collection because of the inverse relationship between AEP amplitude and body size. New methods of enhancing signal strength or obtaining recordings closer to the brain with minimal invasiveness should be pursued. Such options may include alter-

native electrode placements (e.g., pharyngeal electrodes) or, particularly in the case of mysticete whales, the design of signal amplifiers that are integrated with and located at the tip of the long needle electrodes. It is only through methodological advancements that reductions in the time required for AEP testing are likely to be minimized while preserving or improving the quality of the data collected.

ACKNOWLEDGMENTS

The authors would like to thank B. Wenzel, G. McDonald, P. Robinson, J. Mulsow, and C. Reichmuth for assistance in the field. The authors would also like to thank G. Strachan and the rangers and staff of Año Nuevo State Reserve. This work was performed under Permit No. 87-1743-03 from the National Marine Fisheries Service and was funded by the Office of Naval Research (ONR N00014-04-1-0455). All research procedures approved by the Institutional Animal Care and Utilization Committee of Sonoma State University are in accordance with the *Ethical Principles of the Acoustical Society of America for Research Involving Human and Non-Human Animals in Research and Publishing and Presentations*, as established by the Acoustical Society of America.

Briggs, G. D., Henrickson, R. V., and Le Boeuf, B. J. (**1975**). "Ketamine immobilization of northern elephant seals," J. Am. Vet. Med. Assoc. **167**, 546–548.

Chambers, R. D., Matthies, M. L., and Griffiths, S. K. (**1989**). "Correlations between various measures of head size and auditory brainstem response latencies," Hear. Res. **41**, 179–187.

Dempsey, J. J., Censoprano, E., and Mazor, M. (**1986**). "Relationship between head size and latency of the auditory brainstem response," Audiology **25**, 258–262.

Deutsch, C., Costa, D. P., and Le Boeuf, B. J. (**1994**). "Sex differences in reproductive effort in northern elephant seals," in *Elephant Seals: Population Ecology, Behavior, and Physiology*, edited by B. J. Le Boeuf and R. M. Laws (University of California Press, Berkeley, CA), pp. 169–210.

Houser, D. S., Crocker, D. E., Kastak, C., Mulsow, J., and Finneran, J. J. (**2007**). "Auditory evoked potentials in northern elephant seals (*Mirounga angustirostris*)," Aquat. Mamm. **33**, 110–121.

Meij, B. P., Venker-van Haagen, A. J., and van den Brom, W. E. (**1992**). "Relationship between latency of brainstem auditory-evoked potentials and head size in dogs," Vet. Q. **14**, 121–126.

Munro, K. J., Shiu, J. N., and Cox, C. L. (**1997**). "The effect of head size on the auditory brainstem response for two breeds of dog," Br. J. Audiol. **31**, 309–314.

Pook, H. A., and Steiss, J. E. (**1990**). "Correlation of brain stem auditory-evoked responses with cranium size and body weight of dogs," Am. J. Vet. Res. **51**, 1779–1783.

Reichmuth, C., Mulsow, J., Finneran, J. J., Houser, D. S., and Supin, A. Y. (**2007**). "Measurement and response characteristics of auditory brainstem responses in pinnipeds," Aquat. Mamm. **33**, 132–150.

Ridgway, S. H., and Carder, D. A. (**2001**). "Assessing hearing and sound production in cetaceans not available for behavioral audiograms: Experiences with sperm, pygmy sperm, and gray whales," Aquat. Mamm. **27**, 267–276.

Supin, A. J., Popov, V. V., and Mass, A. M. (**2001**). *The Sensory Physiology of Aquatic Mammals* (Kluwer Academic, Boston).

Szymanski, M. D., Bain, D. E., Kiehl, K., Pennington, S., Wong, S., and Henry, K. R. (**1999**). "Killer whale (*Orcinus orca*) hearing: Auditory brainstem response and behavioral audiograms," J. Acoust. Soc. Am. **106**, 1134–1141.

Yamaguchi, J., Yagi, T., Baba, S., Aoki, H., and Yamanobe, S. (**1991**). "Relationship between auditory brainstem response waveform and head size," ORL **53**, 94–99.

Using streamlines to visualize acoustic energy flow across boundaries[a)]

David M. F. Chapman[b)]
Defence Research and Development Canada-Atlantic, P.O. Box 1012, Dartmouth, Nova Scotia B2Y 3Z7, Canada

(Received 3 December 2007; revised 15 April 2008; accepted 23 April 2008)

For spherical waves that radiate from a point source in a homogeneous fluid and propagate across a plane boundary into a dissimilar homogeneous fluid, the acoustic field may differ significantly from the geometric acoustic approximation if either the source or receiver is near the interface (in acoustic wavelengths) or if the stationary phase path is near the critical angle. In such cases, the entire acoustic field must be considered, including inhomogeneous waves associated with diffraction (i.e., those components that vanish with increasing frequency). The energy flow from a continuous-wave monopole point source across the boundary is visualized by tracing acoustic streamlines: those curves whose tangent at every point is parallel to the local acoustic intensity vector, averaged over a wave cycle. It is seen that the acoustic energy flow is not always in line with the "Snell's law" or stationary phase path. Also, plots of acoustic energy streamlines do not display unusual behavior in the vicinity of the critical angle. Finally, it is shown that there exists a law of refraction of acoustic energy streamlines at boundaries with density discontinuities analogous to Snell's law of refraction of ray paths across sound speed discontinuities. Examples include water-to-seabed transmission and water-to-air transmission.
 [DOI: 10.1121/1.2931956]

PACS number(s): 43.20.El, 43.20.Dk, 43.30.Cq, 43.30.Ma [RAS] Pages: 48–56

I. INTRODUCTION

Geometric ray tracing, which is based on an approximation to solutions of the acoustic wave equation, provides an intuitive visualization of propagation of an acoustic field from source to receiver,[1] but has limitations. Being the high-frequency limit of the solution, geometric ray theory does not include diffracted components of the field. Also, geometric rays only coincide with the direction of energy flow when the medium has slowly varying properties and negligible reflection and diffraction. To correctly determine energy flow, the full wave-theory solution to the acoustic wave equation (with appropriate boundary conditions) is required, including reflected and diffracted components of the field. However, it would be instructive to have a raylike visualization of the acoustic field that portrays the propagation of energy from source to receiver, especially in cases where diffraction and/or reflection significantly alter the field. Such a visualization is provided by the acoustic energy streamline (also called the acoustic streamline or the intensity streamline). The acoustic energy streamline is the curve which at every point is tangent to the direction of the local average acoustic intensity vector, that is, the product of acoustic pressure and acoustic particle velocity averaged over one wave cycle.[2]

The acoustic streamline is not a new concept, having previously been applied to homogeneous media with multiple coherent sources and nearby boundaries. Waterhouse *et al.*[3,4] introduced continuous streamlines as an alternative to grids of intensity vectors. Skelton and Waterhouse[5] and Zhang and Zhang[6] applied the method of Ref. 3 to radiation from a spherical shell. These papers established not only that sound energy from cw sources propagates along streamlines but also that adjacent streamlines constitute a streamline tube of energy flow, as there is no energy flow across streamlines. In this way, the magnitude of acoustic intensity varies inversely as the cross-sectional area of the streamline tube, a property already employed in ray acoustics.[7]

In this paper, the acoustic streamline concept is applied to problems involving propagation of acoustic waves across fluid-fluid boundaries, that is, propagation from a continuous-wave (cw) monopole source in a semi-infinite homogeneous fluid medium having a plane boundary with a second semi-infinite homogenous fluid medium with different density and sound speed. Specifically, two examples are considered: water-to-seabed transmission and water-to-air transmission. The acoustic fields and streamlines in these relatively simple environments provide a variety of sometimes surprising physical results.

At the outset it should be emphasized that, unlike rays, streamlines do not represent alternate solutions or approximations to the acoustic field. The acoustic field must be known for streamlines to be traced. Thus, there are no savings in computational time or efficiency; there is only the benefit of an improved visualization of the average energy flow in the acoustic field.

The current analysis is restricted to cw fields. In the case of time-dependent fields (pulse propagation, for example) involving multipaths with different times of flight, geometric

[a)]Portions of this material have been presented orally at the Seventh International Conference on Theoretical and Computational Acoustics, Heraklion, Greece, July 2007.
[b)]Electronic mail: dave.chapman@ns.sympatico.sa

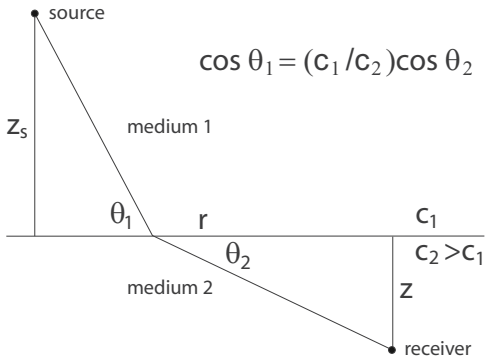

FIG. 1. Geometry of transmission from a point source in one homogeneous medium to a receiver in another, separated by a plane boundary, the case $c_2 > c_1$.

ray paths and acoustic streamlines are more likely to coincide as the pulse components propagating via the multipaths may not overlap at the receiver; however, diffraction may still have a role to play in time-dependent fields. Even for cw fields, streamlines and rays can be practically the same particularly in slowly varying media away from reflectors and diffractors.

The analysis below is limited to fluid media. Although it would be more realistic (and likely interesting) to include the elastic properties of the lower medium in the water-to-seabed case, these properties are assumed to be not important for the purpose at hand. This is a common approximation made when the seabed is unconsolidated sediment.[8]

II. THEORY

A. Integral representation of acoustic fields

Referring to Fig. 1, consider a homogeneous fluid half-space of density ρ_1 and sound speed c_1 in contact with a second (lower) homogeneous fluid half-space of density, $\rho_2 = g\rho_1$, and sound speed, $c_2 = c_1/n$, separated by the plane boundary, $z=0$. (That is, the lower:upper density ratio is g and the upper:lower speed ratio, or index of refraction, is n.) A monopole cw source of angular frequency ω is placed in the upper medium at height $z=z_s$, and the receiver could either be in the upper medium ($z>0$) or the lower medium ($z<0$) at horizontal range r. The exact wave-theory solution for the acoustic potential is well-known;[9] however, there is no straightforward functional form, only a representation based on expanding the spherical waves into an integral over plane waves traveling in all directions. Taking advantage of the cylindrical symmetry, the incident acoustic velocity potential reduces to the single integral

$$\Psi_{\text{inc}} = \frac{e^{ik_1\sqrt{r^2+|z_s-z|^2}}}{\sqrt{r^2+|z_s-z|^2}} = \frac{ik_1}{2\pi}\int_{i\infty}^{\pi/2} J_0(k_1 r\cos\theta)e^{ik_1|z_s-z|\sin\theta}\cos\theta d\theta \quad (z>0), \tag{1}$$

in which J_0 is the Bessel function of zero order, $k_1 = \omega/c_1$ is the wavenumber in medium 1, and θ is the integration variable. (There is an implied time factor $e^{-i\omega t}$.) Note that the incident potential has a source singularity at $(r,z)=(0,z_s)$, a fact which has computational consequences.

The integration contour runs from $+i\infty$ in the θ-plane along the positive imaginary axis to the origin and then along the real axis to $\pi/2$. Equation (1) represents an integral over cylindrical waves with horizontal wavenumber $k_1\cos\theta$ and vertical wavenumber $k_1\sin\theta$, so θ represents the grazing angle of the wave relative to the boundary plane. Waves associated with real θ are the familiar homogeneous waves (constant amplitude along constant phase fronts), while waves associated with imaginary θ are inhomogeneous waves[10] (evanescent amplitude along constant phase fronts).[11] Inhomogeneous waves are necessary to represent the near field of the point source and diffracted components of the reflected and transmitted fields. There exists an alternate—yet mathematically equivalent—formulation that uses wavenumber integration, a basis for several computational wave propagation codes.[12–14]

The reflected potential (which must be added to the incident potential to represent the entire field in the upper medium) is

$$\Psi_{\text{refl}} = \frac{ik_1}{2\pi}\int_{i\infty}^{\pi/2} J_0(k_1 r\cos\theta)e^{ik_1(z_s+z)\sin\theta}R(\theta)\cos\theta d\theta \quad (z>0) \tag{2a}$$

and the transmitted potential (the entire field in the lower medium) is

$$\Psi_{\text{trans}} = \frac{ik_1}{2\pi g}\int_{i\infty}^{\pi/2} J_0(k_1 r\cos\theta)e^{ik_1(z_s\sin\theta - z\sqrt{n^2-\cos^2\theta})} \times T(\theta)\cos\theta d\theta \quad (z<0), \tag{2b}$$

in which z is positive upward and $R(\theta)$ and $T(\theta)$ are the familiar plane-wave reflection and transmission coefficients for pressure, respectively,

$$R(\theta) = \frac{g\sin\theta - \sqrt{n^2-\cos^2\theta}}{g\sin\theta + \sqrt{n^2-\cos^2\theta}} \tag{3a}$$

and

$$T(\theta) = \frac{2g\sin\theta}{g\sin\theta + \sqrt{n^2-\cos^2\theta}}. \tag{3b}$$

The acoustic pressure and two components of particle velocity in either medium are given by

$$p = \rho\frac{\partial\Psi}{\partial t} = -i\omega\rho\Psi, \tag{4a}$$

$$v_r = -\frac{\partial\Psi}{\partial r}, \tag{4b}$$

$$v_z = -\frac{\partial\Psi}{\partial z}. \tag{4c}$$

In this paper, the integrals in Eqs. (2a) and (2b) will be evaluated numerically, so the derivatives in Eqs. (4a)–(4c) need to be applied before the integration. Note the factor g in the denominator of Eq. (2b); this is needed to ensure that

both the pressure and the vertical component of the particle velocity are continuous at the boundary, and it also governs the ratio of the horizontal components of particle velocity on either side of the boundary, as will be seen in Sec. V.

B. Asymptotic evaluation, phase functions, and Snell's law

Brekhovskikh[9] and Brekhovskikh and Godin[12] derive the geometric acoustics limit of the reflected and transmitted fields, using Eqs. (2a) and (2b) as starting points, applying the method of steepest descent. These results are not necessary for the streamline calculations below, but the stationary phase paths are of interest, as they are the geometric ray paths. Because the media are homogeneous, the ray paths in both media are straight line segments with associated grazing angles.

For a receiver in the upper medium, the rays are simply straight lines: (a) for the direct path, a straight line from the source at height z_s above the boundary to the receiver at horizontal distance r and height z, and (b) for the reflected path, a straight line from the image source at depth z_s below the boundary to the same receiver in the upper medium straightforward. This image construction ensures that the angle of incidence equals the angle of reflection for the reflected ray, a straightforward consequence of the stationary phase condition applied to the reflected field.

For a receiver in the lower medium, the phase of the transmitted field is

$$\Phi_{\text{trans}} = k_1 r \cos\theta + k_1(z_s \sin\theta - z\sqrt{n^2 - \cos^2\theta}) \quad (z < 0). \tag{5}$$

The geometric ray angles follow from the stationary phase condition, that is, $\partial\Phi/\partial\theta = 0$. In this case, the stationary phase path is given by

$$\begin{aligned} r &= z_s \cot\theta_1 - z\cos\theta_1/\sqrt{n^2 - \cos^2\theta_1} \\ &= z_s \cot\theta_1 - z\cot\theta_2, \end{aligned} \tag{6}$$

in which θ_1 is the ray angle in the upper medium and θ_2 is the ray angle in the lower medium, given by

$$\cos\theta_1 = n\cos\theta_2, \tag{7}$$

which is Snell's law of refraction.[15] For a given source-receiver geometry, Eq. (6) is numerically solved for θ_1 and then Eq. (7) gives θ_2. In the geometric acoustic approximation, the wavefront is perpendicular to the ray, and the particle velocity is parallel to the ray. Later, these geometric ray propagation angles will be compared to the direction of energy flow.

C. Critical angle

Note that for $n < 1$ there is a critical angle $\theta_c = \cos^{-1} n$ dividing the range of θ into two regions: $\theta > \theta_c$ and $\theta < \theta_c$. In the absence of absorption, for $\theta > \theta_c$, the vertical wavenumber in the lower medium is real, and the reflection and transmission coefficients are real. In this domain of angles, the reflected and transmitted plane waves are homogeneous, and the reflected wave has reduced amplitude. For $\theta < \theta_c$, the vertical wavenumber in the lower medium is imaginary, and the reflection and transmission coefficients are complex. The reflected plane wave is homogeneous (with a phase shift and unreduced amplitude) and the transmitted plane wave is inhomogeneous. The presence of these inhomogeneous transmitted waves just beneath the boundary has significant influence on the energy flow there and have, in fact, been observed in nature[16] and in propagation models.[17–19]

Conventionally, absorption in either medium is introduced by adding a small negative imaginary component to the corresponding sound speed. [If $c \to c(1 - i\varepsilon)$, the attenuation in dB/wavelength becomes $(40\pi \log_{10} e)\varepsilon \approx 54.6\varepsilon$.] The index of refraction, reflection coefficient, and transmission coefficient become generally complex. Waves that are purely homogeneous or purely inhomogeneous retain their principle characteristics but acquire a small dose of the opposite characteristics.

III. METHOD OF COMPUTATION

All computations are performed in MATHEMATICA 6 (Ref. 20) on a typical laptop computer with an Intel Pentium 2 GHz processor.

A. Calculating acoustic field variables

The computation of the acoustic field necessarily depends on whether the field point is on the same side of the boundary as the source or the other side of the boundary. Assuming the source is in the upper medium, if the receiver is also in the upper medium, the total field is the sum of the incident field and the reflected field; if the receiver is in the lower medium, the total field is simply the transmitted field.

When needed, the field values for pressure and particle velocity are computed from Eqs. (1), (2a), and (2b). In the upper medium, $\Psi_1 = \Psi_{\text{inc}} + \Psi_{\text{ref}}$. The incident field Ψ_{inc} has analytic form, so no integration is needed, as Eqs. (4a)–(4c) can be applied directly and the result can be evaluated. (In principle, the integral for the incident field could be combined with the integral for the reflected field, but this introduces instabilities in the numerical integral in the vicinity of the source singularity.) For the reflected field Ψ_{refl}, the integral in Eq. (2a) is numerically calculated, applying Eqs. (4a)–(4c) to the integrand first. In the lower medium, $\Psi_2 = \Psi_{\text{trans}}$, and again Eqs. (4a)–(4c) must be applied to the integrand of Eq. (2b) first. The calculation uses the MATHEMATICA function NIntegrate, an adaptive algorithm that subdivides the range and chooses the appropriate method according to the nature of the integral. Integration over real-valued angles and imaginary-valued angles must be performed separately, and the latter integral must be truncated at a finite value (of the order 100 divided by the source frequency in kilohertz, enough to span significant contributions from inhomogeneous waves). Although the integrands are naturally oscillatory, this poses no difficulty for MATHEMATICA at the low frequencies where diffraction effects are significant. (Poor convergence is flagged by MATHEMATICA, which also suggests remedies.) Including realistic values of acoustical absorption dampens the oscillations somewhat and aids convergence. For a given environ-

ment, all three acoustic field variables at a point are calculated in about a second.

B. Acoustic intensity of a continuous-wave field

The instantaneous acoustic intensity (the vector of acoustic energy flux) is the product of pressure and velocity.[21] For a cw field, writing the acoustic potential in terms of real-valued amplitude and phase functions,

$$\Psi(\mathbf{x},t) = A(\mathbf{x})e^{i[\Phi(\mathbf{x})-\omega t]}, \tag{8}$$

the instantaneous intensity is, from Eqs. (4a)–(4c)

$$\mathbf{j} = \mathrm{Re}\, p\ \mathrm{Re}\, \mathbf{v} = \rho\omega A^2 \nabla\Phi \sin^2[\Phi - \omega t] - \rho\omega A \nabla A \sin[\Phi - \omega t]\cos[\Phi - \omega t]. \tag{9}$$

Note that the instantaneous intensity is the sum of a pulsating (nonreversing) component in the direction of the gradient of phase and an oscillatory (zero-average) component in the direction of the gradient of amplitude. Averaging over one cycle of time, the average intensity is[22]

$$\langle\mathbf{j}\rangle = \tfrac{1}{2}\rho\omega A^2 \nabla\Phi \equiv \tfrac{1}{2}\mathrm{Re}\, p^*\mathbf{v}. \tag{10}$$

The average intensity governs the net transport of energy, which is in the direction of the gradient of phase. The instantaneous intensity is always in the direction of the particle velocity, which may not be the same as the direction of net energy flow. This is discussed by D'Spain *et al.* in detail.[23] For visualizing net energy flow, it is the average intensity that is relevant.[24]

C. Tracing acoustic streamlines

Acoustic streamlines are tangent everywhere to the direction of the local average intensity vector, so the first step in tracing streamlines is to calculate the acoustic intensity and determine its orientation. For monopole sources in layered media, we can restrict our view to the single plane containing source and receiver. The grazing angle of the average intensity vector is (after Ref. 3)

$$\varphi = \tan^{-1}(\langle j_z\rangle/\langle j_r\rangle), \tag{11}$$

and the differential equation of the streamline in parametric form is

$$dz/ds = \sin\varphi(r,z), \tag{12a}$$

$$dr/ds = \cos\varphi(r,z), \tag{12b}$$

in which ds is the element of arc length along the streamline. The streamline is traced in a simple two-stage marching-style solution based on algorithm with stepsize Δs

$$\hat{z}_i = z_i + \tfrac{1}{2}\Delta s \sin\varphi(r_i,z_i), \tag{13a}$$

$$\hat{r}_i = r_i + \tfrac{1}{2}\Delta s \cos\varphi(r_i,z_i), \tag{13b}$$

$$z_{i+1} = z_i + \Delta s \sin\varphi(\hat{r}_i,\hat{z}_i), \tag{13c}$$

$$r_{i+1} = r_i + \Delta s \cos\varphi(\hat{r}_i,\hat{z}_i). \tag{13d}$$

In words: From a given point (r_i,z_i), the direction $\varphi(r_i,z_i)$ of the intensity vector is determined, and a half step $\Delta s/2$ is taken in that direction to a provisional point $(\hat{r}_i,\hat{z}_i)$. At this provisional point, a revised direction $\varphi(\hat{r}_i,\hat{z}_i)$ of the intensity vector is determined. Finally, a full step Δs is taken from the original point (r_i,z_i) in the direction $\varphi(\hat{r}_i,\hat{z}_i)$. The final position (r_{i+1},z_{i+1}) is the estimated next point on the streamline. Without the half step, this would be the Euler method; the modification using the half step has lower error. Overall error is minimized by making the step size sufficiently small.

In practice, a variable step size Δs is used that adapts to the local curvature of the streamline. The distance between the provisional point $(\hat{r}_i,\hat{z}_i)$ and the point halfway between the original point (r_i,z_i) and the final point (r_{i+1},z_{i+1}) is compared to two threshold values, t_1 and t_2, with $t_1 < t_2$. As long as

$$t_1 < |(r_{i+1}-r_i, z_{i+1}-z_i)/2 - (\hat{r}_i - r_i, \hat{z}_i - z_i)| < t_2, \tag{14}$$

the step size is maintained; should the difference drop below t_1, the step size is increased to speed up the streamline tracing; should the difference exceed t_2 the step size is reduced to improve accuracy. In this paper, in which the source-receiver distance is only a few meters, the starting step size is typically 0.05 m, the error thresholds are of the order 10^{-4} m, and $t_2 = 2t_1$. When needed, the step size is altered up or down by the factor of $\sqrt{2}$. The number of steps required to trace a streamline can vary between around 10 to several hundred, depending on the geometry, source frequency, and complexity of the field.

When the streamline crosses a density discontinuity, care must be taken to account for the discontinuous change of direction that occurs. (The law of streamline refraction at boundaries will be discussed in Sec. V.) If the new point lies across the boundary from the previous point, the crossing position is interpolated and that becomes the new point. The step size is reduced and the calculation resumes in the new medium.

In the case of multipath interference, the structure of the acoustic field becomes finer as frequency increases and wavelength decreases. The steps of a streamline trace become smaller and smaller. This makes streamline tracing in such cases more expensive, computationally speaking, as frequency increases. On the other hand, when there are no multipaths, the amplitude of any diffracted field component decreases with increasing frequency, so convergence to the high-frequency limit is more rapid in this case.

The above streamline tracing method is elementary, and without a doubt it could be improved upon for speed while maintaining accuracy; however, it is adequate for the purpose at hand, and is validated by tracing streamlines in both directions, discussed below.

1. Streamline between source and receiver

To trace a streamline between source and a receiver at a specified location, the initial field point is chosen to be the receiver location, the direction of travel is deemed to be the opposite of the intensity vector, and the streamline tracing

procedure outlined above (presumably) finds its way back to the source. As the source is approached, the incident spherical-wave field dominates, becoming a "sink" for the streamline. The calculation is terminated at a point suitably close to the source. To check the calculation, the streamline is relaunched at the terminal point, with the direction of travel the same as the intensity vector. If the initial step size and error tolerances are chosen well, the return streamline will pass the receiver at an acceptably small distance. Some tuning of the numerical parameters is needed to achieve convergence, which is judged by eye. This procedure is a necessary check if streamline fans are to be computed.

2. Tracing of streamline fans

A streamline fan is a group of streamlines launched from the source, usually at equally spaced angles around a central streamline. According to the development in this paper, sound energy from cw sources propagates along streamlines; therefore streamlines in a streamline fan can be viewed as cross sections of streamline tubes of equal energy flow, as there is no energy flow across the tube wall. In this way, the downstream spacing of streamlines provides an indication of the relative intensity (see Ref. 4). To ensure this interpretation, the launch radius must be sufficiently small that any reflected field is insignificant at the launch point; for the computations in this paper, a launch radius of about 1/20 of the source-boundary distance is used and the ratio of reflected to incident field is verified to be less than 1/100 before proceeding. Highly dissimilar media demand a smaller launch radius, owing to the strong reflection from the boundary.

IV. COMPUTED EXAMPLES

Two examples of cross-boundary acoustic transmission are provided: one water-to-sediment and the other water-to-air. In each case, 31 streamlines or rays are launched into 180°, 6° apart.

A. Water-to-sediment transmission

For the water-to-sediment example, inspired by the SAX04 experiment,[25,26] the environment used is $c_1=1531$ m/s, $c_2=1687$ m/s, sediment attenuation $=0.23$ dB/wavelength, and $g=2.02$. (That is, $c_2=1687-7.1i$ m/s or $n=0.9075+0.0038i$.) The critical angle ($\mathrm{Re}[\cos^{-1} n]$) for this environment is $\theta_c=24.8°$. The source is at height $z_s=2.58$ m. (In the experiment, the sensors were between 7 and 9 m from the source at less than 1 m depth.) Figures 2(a)–2(c) show the streamline fans at frequencies of 150, 500, and 1500 Hz. Figure 2(d) shows the corresponding ray fan.

Whereas the geometric ray paths are straight lines, the streamlines are, in general, curved, owing to constructive interference between waves. Note that the streamlines may cross the critical ray (heavy dashed line), that is, the ray incident at the critical angle. Also note the discontinuous change in streamline direction at the boundary. (This is discussed in Sec. V in detail.)

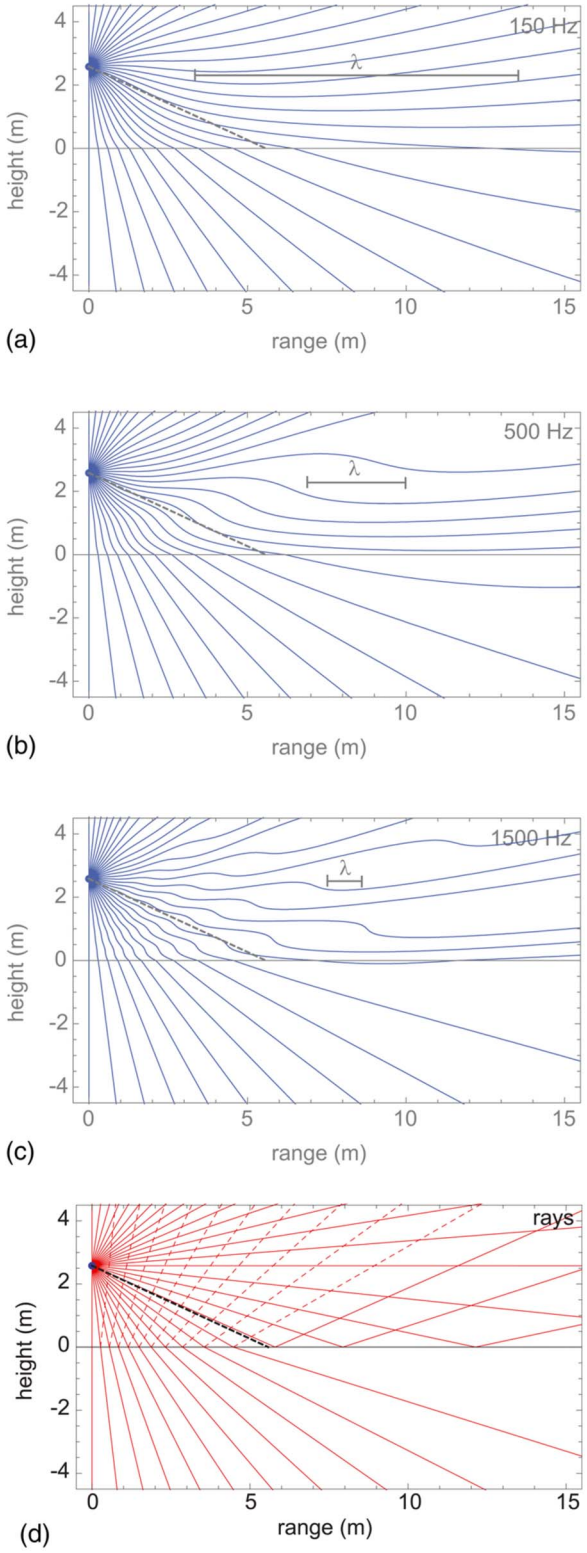

FIG. 2. (Color online) Streamlines of energy flow for water-to-sediment transmission: (a) 150 Hz, (b) 500 Hz, (c) 1500 Hz, and (d) the corresponding ray paths. Solid lines: streamlines [(a)–(c)] or incident, transmitted, and totally reflected rays (d). Dashed lines: partially reflected rays. Heavy dashed line: critical ray. Associated acoustic wavelengths in water: (a) 10.2 m, (b) 3.1 m, (c) 1.0 m.

The structure of the field in the upper medium becomes increasingly complicated as frequency increases, owing to the interference of the incident and reflected fields at shorter

wavelengths. As frequency increases in a cw multipath environment, a streamline will not converge to a ray, unless all other paths are increasingly attenuated; however, the streamline should converge to a limiting trajectory around which the streamline weaves with fine scale structure. There is evidence of this in Fig. 2(c), particularly for those streamlines that enter the sediment.

In regions where streamlines have significant curvature, linear extrapolation of the local intensity vector would not be a good indicator of the path of energy transport to that point. One even sees streamlines enter the lower medium and then turn back and return to the upper medium well downstream. This return of energy to the upper medium is reminiscent of "head waves" or "lateral waves" that travel substantially at the speed of the lower medium but are sensed in the upper medium, and which have practical application in seismoacoustic inversion.[26]

Beyond the point at which the critical ray ends, just under the boundary, ray theory predicts a "shadow zone" of low intensity. Diffractive wave corrections to ray theory[27] in this region can be interpreted as a vertically inhomogeneous wave traveling horizontally in the lower medium, associated with a perfectly reflected ray striking the boundary. This inhomogeneous wave is strongest at the boundary, penetrates deeply at lower frequencies and vanishes in the limit of infinite frequency. The streamline visualization of this phenomenon in Figs. 2(a)–2(c) shows that the energy in this region actually enters the lower medium considerably upstream of the measurement point, resolving the apparent contradiction that a ray could be perfectly reflected yet still transmit a sensible signal.

In the lower medium, there are only transmitted waves, both refracted and diffracted, without the complication of reflected waves. At all frequencies shown, in the region beneath the source, the streamlines are nearly straight, owing to the dominance of the geometrically refracted field there. Further downstream, the stronger influence of the inhomogeneous waves of the diffracted component causes the streamlines to curve more upward as the boundary is approached. The transition between the refracted-dominated field and the diffraction-dominated field is gradual at the lowest frequency shown [Fig. 2(c)]. At the highest frequency shown [Fig. 2(c)], there is a more obvious demarcation between these extremes, as one would expect as the geometric acoustic limit is approached [compare to Fig. 2(d)].

Detailed directional differences between geometric rays and intensity vectors are difficult to see by simply comparing streamline fans with ray fans. To more clearly demonstrate the difference between the direction of the geometric ray through a point and the direction of the acoustic intensity at that point, their differences (ray minus intensity) at three frequencies are plotted in Figs. 3(a)–3(c) as two-dimensional contour plots spanning the lower medium. Positive values indicate where the ray direction is steeper than the associated streamline and vice versa. Note that there is an island of negative values (streamlines steeper than rays) just beneath the point where the critical ray joins the boundary; this island shrinks with increasing frequency. Further downstream, there is generally a region of positive values (rays steeper than

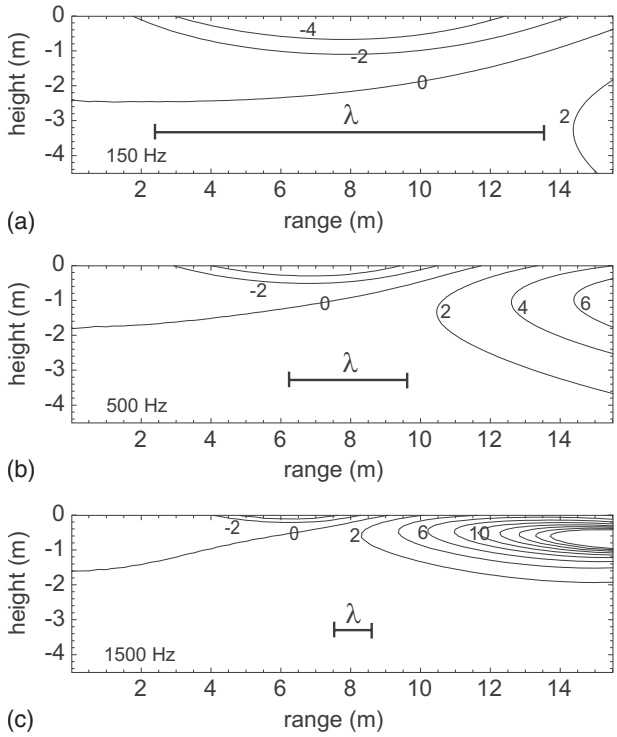

FIG. 3. Contour plots of ray direction minus intensity vector direction (in degrees) in the lower medium for water-to-sediment transmission. (a) 150 Hz, (b) 500 Hz, and (c) 1500 Hz. Positive values: rays steeper than streamlines. Negative values: streamlines steeper than rays. Associated acoustic wavelengths in sediment: (a) 11.2 m, (b) 3.4 m, and (c) 1.1 m.

streamlines). The directional differences in this region grow remarkably large in this region as frequency increases, yet it should be recalled from Figs. 2(a)–2(c) that the magnitude of the intensity is quite small there. This feature disappears as frequency is increased to 5000 Hz (not illustrated). Overall, for the transmitted wave, one can see that the direction of the intensity tends to coincide more with the direction of the geometric ray path as frequency increases. Even so, directional measurements with intensity probes should be interpreted with caution with respect to the path along which the signal arrived.

B. Water-to-air transmission

For the water-to-air example, inspired by recent interest in anomalous acoustic transparency of the water/air boundary,[28] the environment used is $c_1=1500$ m/s, $c_2=330$ m/s, and $g=0.001\,25$. (That is, $c_2=330-0.06i$ m/s or $n=4.5454+0.0008i$.) A very mild absorption coefficient of 0.01 dB/wavelength is included to stabilize the calculation. The source is at height $z_s=0.5$ m in water. (The air layer is placed below to aid comparison with the previous water-to-sediment case.) Figures 4(a)–4(c) show the streamline fans at frequencies of 15, 150, and 1500 Hz. Figure 4(d) shows the corresponding ray fan.

This sequence of streamline fans shows the strong frequency sensitivity of anomalous transmission of sound from water to air. Godin *et al.*[26] explains how incident inhomogeneous waves in the near field of the source interfere with inhomogeneous waves reflected by the boundary with the result that significant energy can be transmitted across the

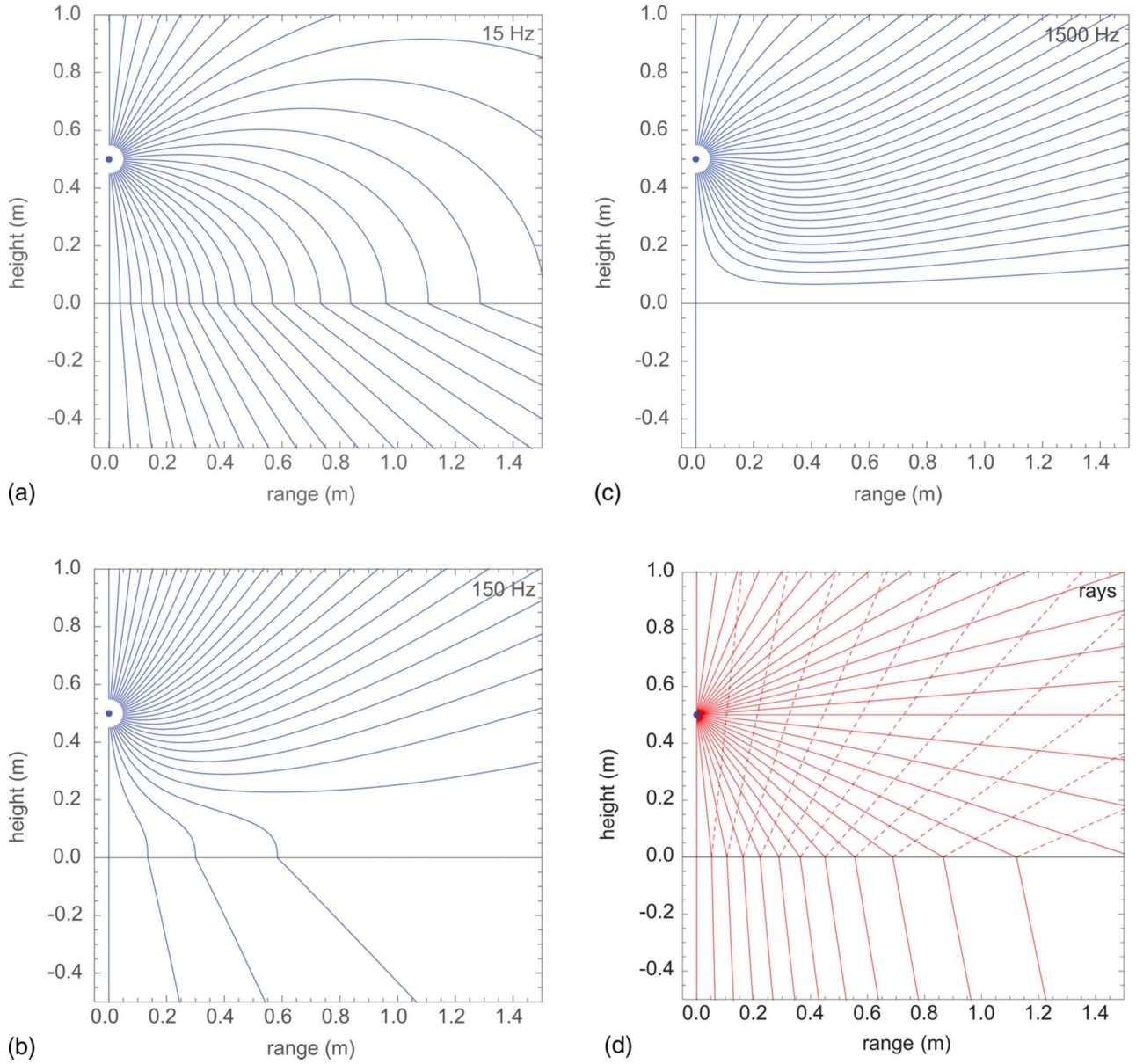

FIG. 4. (Color online) Streamlines of energy flow for water-to-air transmission (note that the water is *above* the air): (a) 15 Hz, (b) 150 Hz, and (c) 1500 Hz. Solid lines in (a)–(c): streamlines. Solid lines in (d): incident and transmitted rays. Dashed lines in (d): partially reflected rays. Associated acoustic wavelengths in water: (a) 100 m, (b) 10 m, and (c) 1 m.

boundary at very low frequencies. This is considered anomalous because this high impedance contrast (mostly due to the 800-fold density ratio) conventionally implies that the boundary would act as an acoustic mirror. As frequency increases, more and more streamlines are turned back from the boundary until at the highest frequency shown the conventional mirrorlike nature of the boundary is restored.

In this example, the ray fan bears little resemblance to any of the three streamline fans, and hence provides little insight to the energy flow from the source. Considering the streamline trajectories, note the very large direction change at the boundary associated with the large density contrast, which will shortly be explained analytically. Also note that the transmitted streamlines, when traced back linearly, appear to emanate from the true source position, a peculiarity that is not fully understood at this time.

V. REFRACTION OF STREAMLINES AT A BOUNDARY WITH A DENSITY DISCONTINUITY

From the computed examples, it is evident that acoustic streamlines are generally curved (even in homogeneous media) according to the structure of the acoustic fields that governs them. Additionally, there appears to be discontinuous refraction of streamlines at the boundary between dissimilar fluids. In fact, this discontinuous refraction only occurs when the density changes abruptly across the boundary and this fact can be stated in the form of a refraction law analogous to Snell's law.

Since both the acoustic pressure and vertical component of particle velocity are continuous across a horizontal boundary between two fluids, it follows from Eq. (10) that the vertical component of average intensity is also continuous at the boundary:

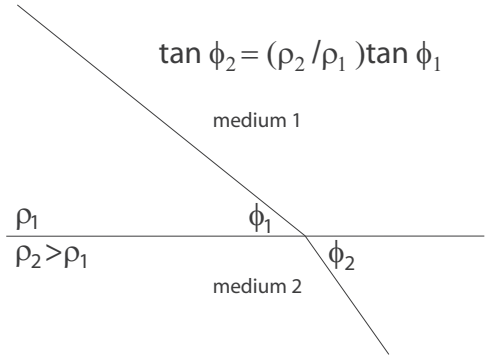

FIG. 5. Acoustic streamline refraction by a density discontinuity, for the case $\rho_2 > \rho_1$.

$$\langle j_{z1} \rangle = \langle j_{z2} \rangle. \tag{15}$$

The horizontal intensity components are related as well: From the integrands in Eqs. (1), (2a), and (2b), consider the acoustic field at an individual incident angle θ. From Eqs. (3a), (3b), and (4a)–(4c), the ratio of the horizontal components of particle velocity at the boundary is

$$\frac{v_{r1}(\theta)}{v_{r2}(\theta)} = \frac{1 + R(\theta)}{g^{-1} T(\theta)} = g, \tag{16}$$

Since this ratio turns out to be independent of angle, it applies equally well to the entire field (i.e., the entire integral). That is (at the boundary),

$$v_{r1} = g v_{r2}. \tag{17}$$

Again, pressure is continuous at the boundary, so the horizontal components of average intensity have the same ratio as those of the particle velocity:

$$\langle j_{r1} \rangle = g \langle j_{r2} \rangle. \tag{18}$$

Since the vertical component of average intensity is always continuous and the horizontal component of average intensity changes according to the density contrast, it follows that the streamlines must change direction at a density discontinuity. In fact, from Eq. (8),

$$\frac{\tan \varphi_2}{\tan \varphi_1} = \frac{\langle j_{z2} \rangle / \langle j_{r2} \rangle}{\langle j_{z1} \rangle / \langle j_{r1} \rangle} = g, \tag{19}$$

that is,

$$\tan \varphi_2 = g \tan \varphi_1, \tag{20}$$

as illustrated in Fig. 5. This law of streamline refraction at a boundary is comparable to Snell's law of ray refraction in Eq. (7), with the interesting difference that the streamline bends toward the denser medium, whereas the ray bends away from the faster medium. Although derived for the restricted cases considered in this paper, it is believed that the law of streamline refraction at a boundary is more generally true. (The identical argument also applies to instantaneous intensity, which is not considered in this paper.)

VI. CONCLUSIONS

An acoustic streamline is a curve whose tangent everywhere along its path is parallel to the the average local intensity vector. The acoustic streamline thus represents the path of mean energy flow. This concept was applied to visualize energy flow from a monopole cw source across boundaries between dissimilar fluids. Streamline fans were calculated and shown for two examples: (1) water-to-sediment transmission, typical of sediment acoustic experimentation, and (2) anomalous water-to-air transmission at infrasonic frequencies. It was observed that significant levels of diffracted waves (inhomogeneous waves) alter the energy flow significantly from what would be expected from geometrically traced rays. It was also observed that the critical angle (when one can be defined) is less relevant to energy flow as frequency decreases. A material density contrast across a boundary leads to the discontinuous bending of acoustic streamlines, governed by a law of streamline refraction at a boundary analogous to Snell's law for ray refraction, but involving the cross-boundary ratio of densities rather than the ratio of sound speeds. Potential for further work includes (1) investigating streamlines based on instantaneous intensity, leading to realistic tracing of energy propagation in pulses when interference and diffraction are significant, (2) consideration of the role of elastic properties of seabed media, and (3) consideration of the role of acoustic absorption on streamline trajectories and energy loss along their arcs.

ACKNOWLEDGMENTS

The author thanks John Osler of DRDC Atlantic for encouraging this line of investigation and Oleg Godin of NOAA for several stimulating discussions on this work. The Associate Editor and reviewers contributed insightful comments. This work was supported, in part, by ONR under Grant No. N000140310883 (Code 32).

[1] A. D. Pierce, *Acoustics: An Introduction to Its Physical Principles and Applications* (Acoustical Society of America, Melville, New York, 1989), Chap. 8, pp. 371–419.
[2] The term "streamline" is borrowed from the field of hydrodynamics, in which the streamline is the curve everywhere tangent to the direction of the local fluid velocity.
[3] R. V. Waterhouse, T. W. Yates, D. Feit, and Y. N. Liu, "Energy streamlines of a sound source," J. Acoust. Soc. Am. **78**, 758–762 (1985).
[4] R. V. Waterhouse and D. Feit, "Equal-energy streamlines," J. Acoust. Soc. Am. **80**, 681–684 (1986).
[5] E. A. Skelton and R. V. Waterhouse, "Energy streamlines for a spherical shell scattering plane waves," J. Acoust. Soc. Am. **80**, 1473–1478 (1986).
[6] J. Zhang and G. Zhang, "Analysis of acoustic radiation and scattering from a submerged spherical shell by energy streamlines," J. Acoust. Soc. Am. **88**, 1981–1985 (1990).
[7] A. D. Pierce, *Acoustics: An Introduction to Its Physical Principles and Applications* (Acoustical Society of America, Melville, New York, 1989), Chap. 8–5: pp. 396–400.
[8] K. L. Williams, D. R. Jackson, E. I. Thorsos, D. Tang, and S. G. Schock, "Comparison of sound speed and attenuation measured in a sandy sediment to predictions based on the Biot theory of porous media," IEEE J. Ocean. Eng. **27**, 413–427 (2002).
[9] L. M. Brekhovskikh, *Waves in Layered Media, Second Edition* (Academic, Orlando, 1980), Chap. IV (translated by R. T. Beyer).
[10] L. M. Brekhovskikh and O. A. Godin, *Acoustics of Layered Media I: Plane and Quasi-Plane Waves* (Springer-Verlag, Berlin, 1990), Chap. 2, p. 17.
[11] That is, $\cos(i|\theta|) = \cosh(|\theta|)$, while $\sin(i|\theta|) = i \sinh(|\theta|)$, so the oscillatory exponential in the integrand becomes an evanescent exponential.
[12] L. M. Brekhovskikh and O. A. Godin, *Acoustics of Layered Media II: Point Sources and Bounded Beams*, 2nd ed. (Springer-Verlag, Berlin, 1999), Chap. 1, pp. 1–16.

[13]F. B. Jensen, W. A. Kuperman, M. B. Porter, and H. Schmidt, *Computational Ocean Acoustics* (American Institute of Physics, New York, 1994), Chap. 4.
[14]C. H. Chapman, "A new method for computing synthetic seismograms," Geophys. J. R. Astron. Soc. **54**, 481–518 (1978).
[15]Equation (6) and (7) demonstrate that Snell's law is consistent with a stationary phase or minimum time condition, that is, Fermat's principle (see Ref. 1, p. 375.)
[16]R. A. Stephen and S. T. Bolmer, "The direct wave root in marine seismology," Bull. Seismol. Soc. Am. **75**, 57–67 (1985).
[17]R. A. Stephen and S. A. Swift, "Modeling seafloor geoacoustic interaction with a numerical scattering chamber," J. Acoust. Soc. Am. **96**, 973–990 (1994) (Fig. 5).
[18]J. N. Tjotta and S. Tjotta, "Theoretical study of the penetration of highly directional acoustic beams into sediments," J. Acoust. Soc. Am. **69**, 998–1008 (1981).
[19]F. B. Jensen and H. Schmidt, "Subcritical penetration of narrow Gaussian beams into sediments," J. Acoust. Soc. Am. **82**, 574–579 (1987).
[20]Wolfram Research, Inc., MATHEMATICA, Version 6.0, Champaign, IL, 2007.
[21]A. D. Pierce, *Acoustics: An Introduction to Its Physical Principles and Applications* (Acoustical Society of America, Melville, New York, 1989), p. 37.
[22]A. D. Pierce, *Acoustics: An Introduction to Its Physical Principles and Applications* (Acoustical Society of America, Melville, New York, 1989), p. 26.
[23]G. L. D'Spain, W. S. Hodgkiss, and G. L. Edmonds, "Energetics of the deep ocean's infrasonic sound field," J. Acoust. Soc. Am. **89**, 1134–1158 (1991).
[24]This has been questioned. See J. A. Mann III and J. Tichi, "Acoustic intensity analysis: Distinguishing energy propagation and wave-front propagation," J. Acoust. Soc. Am. **90**, 20–25 (1991); C. F. Chien and R. V. Waterhouse, "Singular points of intensity streamlines in two-dimensional sound fields," *ibid.* **101**, 705–712 (1997); however, away from singular points, it is a reasonable approximation [J. Adin Mann III, personal communication (March 14, 2005)].
[25]J. C. Osler, A. P. Lyons, P. C. Hines, J. Scrutton, E. Pouliquen, D. Jones, D. M. F. Chapman, M. O'Connor, D. Caldwell, M. MacKenzie, I. B. Haya, and D. Nesbitt, "Measuring sound speed dispersion at mid to low frequency in sandy sediments: An overview of complementary experimental techniques developed for SAX04," in Underwater Acoustic Measurements: Technologies & Results, Heraklion, Crete, Greece, Edited by J. S. Papadakis and L. Bjorno, 28 June – 1 July, 277–284 (2005).
[26]L. M. Brekhovskikh and O. A. Godin, *Acoustics of Layered Media II: Point Sources and Bounded Beams*, 2nd ed. (Springer-Verlag, Berlin, 1999) Chap. 3; O. A. Godin, N. R. Chapman, M. C. A. Laidlaw, and D. E. Hannay, "Head wave data inversion for geoacoustic parameters of the ocean bottom off Vancouver Island," J. Acoust. Soc. Am. **106**, 2540–2551 (1999).
[27]L. M. Brekhovskikh, *Waves in Layered Media, Second Edition* (Academic, Orlando, 1980), p. 281 (translated by Robert T. Beyer); L. M. Brekhovskikh and O. A. Godin, *Acoustics of Layered Media II: Point Sources and Bounded Beams*, 2nd Ed. (Springer-Verlag, Berlin, 1999), p. 19.
[28]O. A. Godin, "Transmission of low-frequency sound through the water-to-air interface," Acoust. Phys. **53**, 1063–7710 (2007).

Evidence of wave front folding of sonic booms by a laboratory-scale deterministic experiment of shock waves in a heterogeneous medium

Lili Ganjehi, Régis Marchiano, and François Coulouvrat
Institut Jean Le Rond d'Alembert, Université Pierre et Marie Curie, Paris 6, UMR CNRS 7190, Paris 75005, France

Jean-Louis Thomas
Institut des NanoSciences de Paris, Université Pierre et Marie Curie, Paris 6, UMR CNRS 7588, 4 Place Jussieu, 75252 Paris, Cedex 05, France

(Received 6 March 2007; revised 26 November 2007; accepted 17 December 2007)

The influence of the planetary boundary layer on the sonic boom received at the ground level is known since the 1960s to be of major importance. Sonic boom propagation in a turbulent medium is characterized by an increase of the mean rise time and a huge variability. An experiment is conducted at a 1:100 000 scale in water to investigate ultrasonic shock wave interaction with a single heterogeneity. The experiment shows a very good scaling with sonic boom, concerning the size of the heterogeneities, the wave amplitude, and the rise time of the incident wave. The wave front folding associated with local focusing, and its link to the increase of the rise time, are evidenced by the experiment. The observed amplification of the peak pressure (by a factor up to 2), and increase of the rise time (by up to about one magnitude order), are in qualitative agreement with sonic boom observations. A nonlinear parabolic model is compared favorably to the experiment on axis, though the paraxial approximation turns out less precise off axis. Simulations are finally used to discriminate between nonlinear and linear propagations, showing nonlinearities affect mostly the higher harmonics that are in the audible range for sonic booms.
 [DOI: 10.1121/1.2832621]

PACS number(s): 43.25.Cb, 43.25.Jh, 43.28.Gq [MFH] Pages: 57–71

I. INTRODUCTION

Classical sonic boom theory (Whitham, 1956; Hayes *et al.*, 1969) predicts perfect shock waves (typically *N*-wave) for the far-field pressure signature of supersonic aircrafts. However, it is known since the first measurements of sonic booms in the 1960s (Maglieri, 1966; Garrick, 1968) that this theory is insufficient to predict (i) the measured sonic boom rise times at the ground level, (ii) the changes in the wave form, which may show large deviations from the ideal *N*-wave and in some cases significant amplification, and finally (iii) the fast spatial variations of the sonic boom field. Sonic boom rise time is a parameter measuring the sharpness of shocks, and is usually defined as the time necessary for the front shock to jump from 10% to 90% of the peak overpressure. Absorption due to the molecular relaxation of nitrogen and molecular diatomic molecules has been identified as partly responsible for the observed rise times (Bass *et al.*, 1983) but remains insufficient to explain all these characteristics, and it is now widely accepted that the sonic boom distortion, and the variability in rise time and peak pressure, are caused by atmospheric turbulence (Pierce and Maglieri, 1972). Note that such highly variable parameters as the peak pressure, the rise time, and the wave form are the main parameters that determine the loudness of the sonic boom (Zepler *et al.*, 1965) for outdoor perception.

Two main theories have been proposed to explain the sonic boom distortion and anomalous rise times. The first one (Crow, 1969) treats the effect of turbulence as a first-order scattering effect by modifying the wave equation to include inertial and thermal perturbations terms. An averaging process then leads to a relation between the rise time and the spectrum of the turbulence. This scattering approach has been refined by Boulanger *et al.* (1995) who simulated the variability of sonic boom through a first-order Born approximation of the scattering due to randomly distributed Gaussian "turbules" chosen by a Monte Carlo method realizing an atmosphere with a given temperature spectrum. This physical model is based on an earlier work developed by McBride *et al.* (1992) for scattering of sound by turbulence in a refractive shadow zone. Note that this model neglects nonlinear effects and is valid only for thermal turbulence. The model has been extended (Kelly *et al.*, 2000) for more realistic turbulent conditions by introducing elliptic turbules. The model qualitatively reproduces some features of the statistical variability of the sonic boom characteristics but *cannot* accurately predict the statistics of sonic boom propagation through the turbulent planetary boundary layer. It is assumed that some effects are not taken properly into account such as multiple scattering, changes in the time of flight within turbules, turbulence anisotropy, nonlinearities, and, most important, inertial effects. The second model (Pierce, 1968) suggests by a geometrical interpretation in terms of wave front folding and caustics formation that the augmentation of the rise time and the sonic boom distortion are due to focusing and defocusing induced by atmospheric inhomogeneities. The amplified booms with a spiky wave form are those ob-

TABLE I. Comparison of different laboratory-scale sonic boom experiments.

	Sonic boom	Davy and Blackstock (1971)	Lipkens and Blackstock (1998)	Blanc-Benon *et al.* (2002)	Present study
T signal duration/period	0.15 s	10 μs	15 μs	40 μs	1 μs
A amplitude	100 Pa	245 Pa	650 Pa	100 Pa	5 bars
τ rise time	1 ms	1 μs	0.5 μs	3 μs	24 ns
d size of heterogeneity/outer length scale of turbulence	100 m	3.8 cm	1 cm	10 cm	3 mm
$\Delta c/c_0$ relative sound speed heterogeneity (T) or u/c_0 flow to sound speed ratio (u)	0.03	−0.07 (Ar) (T) +1.92 (He) (T)	6.7×10^{-3} (u)	2.4×10^{-3} (T) 7×10^{-3} (u)	−0.27 (T)
βM nonlinear parameter	8.6×10^{-4}	2×10^{-3}	5.6×10^{-3}	8.6×10^{-4}	8×10^{-4}
c_0T/d geometrical parameter	2	0.09	2	0.14	2
T/τ rise time parameter	150	10	30	13	42
Type of wave	Cylindrical	Spherical	Plane	Spherical	Plane
Type of heterogeneity	Random	Deterministic	Random	Random	Deterministic

served in the immediate vicinity of caustics. In this case, the increase of the rise time is associated with the change of the wave form from an N-wave to a U-wave. On the contrary, the rounded wave forms with long rise times would correspond to the multifolding of the wave front after propagation through heterogeneities, the different folds giving rise to a small amplitude wave whose arrivals at slightly different times build up a rounded shock (Pierce and Maglieri, 1972). This model remains, however, mostly qualitative. A quantitative numerical approach of this viewpoint is provided with the help of the parabolic approximation combined with nonlinear effects through the Khokhlov-Zabolotskaya (KZ) equation (Zabolotskaya and Khokhlov, 1969). The numerical simulation allows us to observe the wave front folding after inertial rippling, and the spiky distortion of an initial step shock (Piacsek, 2002). In the case of an ideal curved wave front corresponding to a perfect cusp caustic, this distortion has been confirmed experimentally and the key role of nonlinearities has been emphasized (Marchiano *et al.*, 2005). That approach has been generalized (Blanc-Benon *et al.*, 2002) to describe numerically the propagation of the sonic boom through turbulence by coupling the geometrical and the nonlinear parabolic approximations with a Fourier mode representation of a two-dimensional (2D) isotropic turbulent field (Blanc-Benon *et al.*, 1991). These simulations outline the statistical variability of the sonic boom parameters (note that no quantitative comparison with sonic boom recordings is performed) and the correlation of the increase of rise time with the occurrence of caustics. This may also explain some discrepancy between the scattering model and the sonic boom recordings, as the inertial turbulence due to atmospheric flow is known to modify the probability of occurrence of caustics (Blanc-Benon *et al.*, 2002). The parabolic approximation has been recently extended to include flow vectorial inhomogeneities (Aver'yanov *et al.*, 2006).

Given the difficulty to perform and analyze flight test recordings, laboratory-scale experiments in a controlled environment are a useful alternative to provide information about the process of shock wave propagation in a heterogeneous or turbulent medium. However, it is of course difficult to reproduce at the laboratory scale all the features of sonic boom propagation with the proper similitude. A few experiments of this kind have been realized. Their characteristics scaled to sonic boom typical values are summarized in Table I. The sonic boom values have been chosen for a small size aircraft (military fighter or business jet about 50 m long) producing at the ground level a sonic boom of conventional level such as Concorde (100 Pa) with a rise time of about 1 ms corresponding to a calm atmosphere with little turbulence. The size of the heterogeneities has been chosen to be smaller than 100 m, which is a typical value for the outer scale of the turbulent planetary boundary layer. The relative fluctuation of sound speed has been chosen around 0.03, which corresponds to a turbulence with a wind speed about 10 m/s. The first one (Davy and Blackstock, 1971) produced N-waves by an electric spark, refracted and diffracted by a gas-filled soap bubble (helium and argon). It was found that the converging lens (Ar) caused peaking of the N-wave, while the diverging lens (He) caused its rounding. However, the relative sound speed heterogeneity in the case of the diverging lens (He) is very strong in comparison to sonic boom ($\times64$), while the size of the heterogeneity is much too large ($\times22$). Another experimental model (Lipkens and Blackstock, 1998) produced N-waves by electric sparks reflected by a parabolic mirror into a nonlinear plane wave propagating through a turbulent velocity field established by a plane jet. The experiments are performed in a rather strong nonlinear regime. They show a wave form distortion, a mean increase of the rise time, and a mean decrease of the peak amplitude similar to the sonic boom, but the detailed statistics do not fit exactly (compare their Figs. 4 and 16). The experimental setup of Blanc-Benon *et al.* (2005) is similar but produces a spherical wave with a better amplitude scaling to sonic boom; as the counterpart, the size of the outer length scale is quite small compared to the planetary turbulence. Their main result is to show the increase of the rise time with the propagation distance and its correlation with the probability of occurrence of caustics.

The aim of the present work is to study in detail the respective roles of focusing, size of heterogeneity and nonlinearity on the increase of rise time, pressure amplification, and wave form distortion. So, we performed an experimental study, in a water tank containing semicylindrical heterogeneities in silicon. These heterogeneities act like an acoustical lens. The experiment is fully deterministic. The parameters have been chosen to reach the best possible scaling with sonic boom (Table I), and the obtained values are exactly those hoped, for nonlinear effects and heterogeneity size. The sound speed contrast is about one magnitude order larger than sonic boom, but this compensates the fact that we have yet only a single heterogeneity and thus enables us to observe significant effects similar to those for sonic boom. This experiment in water, for which sound attenuation is much smaller than in air, also enables us to have the best ratio of rise time (without heterogeneities) to signal duration compared to the other experiments, even though we are working at much higher frequency. Here, since the signal is a periodic shock wave instead of a transient "*N*-wave" for sonic booms, the definition of the rise time has been adapted to take into account the fact that the shock is preceded by an expansion phase. Omitting that expansion phase in the definition of the rise time might strongly underestimate it. Hence, we define here and in all the present study the rise time as the time necessary for the shock to vary between 90% of the minimum pressure to 90% of the maximum pressure. Note also that, for all of the above experiments, the rise time is governed by the limited bandwidth of the recording system (microphones or hydrophones) rather than by the physical attenuation. Also, the present experiment is the only one that is directly and quantitatively compared to a numerical model, a clear advantage provided by the fact that the experiment is deterministic. Though we do not pretend to fully reproduce in a water tank the full physics of sonic boom propagation in turbulence, we will (1) demonstrate the reality of the wave front folding effect and its link with pressure amplification and increase of the rise time; (2) analyze for the first time experimentally the influence of the heterogeneity size; and (3) investigate precisely the influence of nonlinearities.

II. EXPERIMENT

A. Experimental setup

The experimental setup is depicted in Fig. 1. The acoustical source is a 2D array of 128 piezoelectric transducers (Imasonic, France), each with individual electronic control (Lecoeur Electronique, France). Each transducer can emit a wave up to a 5×10^5 Pa amplitude at a 1 MHz frequency in water (of density ρ_0 and sound speed c_0). This leads to a shock formation distance $L_s=1/(k\beta M)\approx30$ cm, where $\beta=1+B/2A=3.5$ in water and B/A is the nonlinearity parameter, $M=P_0/\rho_0c_0^2$ is the acoustical Mach number with P_0 the pressure wave amplitude, and $k=2\pi/\lambda$ the wave number. The heterogeneities are (sub)wavelength cylinders (the wavelength λ is equal to 1.5 mm in water), embedded in the middle of a planar plate about 1.3 mm thick, 10 cm long (in the direction parallel to x-axis), and 20 cm wide (in the direction parallel to the cylinder y-axis, Fig. 1).

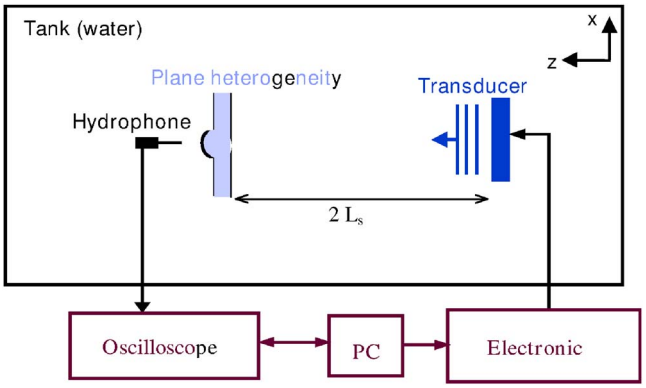

FIG. 1. (Color online) The experimental setup. A 1 MHz, 5 bar plane wave is emitted by an array of 256 transducers (right) so as to create a well-formed sawtooth shock wave at twice the shock formation distance L_s. Plane wave front is achieved, thanks to the inverse filter technique and programmable electronic control (128 independent channels). The plane shock wave impinges a heterogeneity (center) made of a semicylinder of silicone playing the role of an acoustical lens with a diameter comparable to the acoustical wavelength (1.5 mm) and supported by a silicone plate. The scattered pressure field is scanned behind the heterogeneity by a movable, wide-band, calibrated hydrophone.

They are located in the water tank at twice the shock distance, in order to get a well formed incident shock. The parallelism of the heterogeneity plate with the emitting surface of the array of transducers is checked experimentally. The heterogeneities are made of silicon rubber. The cylinder diameters ($d=0.4$, 0.7, 1.1, and 3 mm) are accurately known. The speed of sound of silicon rubber (c_h) has been determined with a time of flight measurement through a planar silicon plate. The resulting value is $c_h=1083$ m s^{-1}, which amounts to a contrast of speed of sound between water and silicon around 27%. The coefficient of attenuation of silicon rubber was determined using the following procedure: A nonlinear periodic shock wave with 1 MHz frequency and 5×10^5 pa amplitude was measured before and after propagating through a 1.3 mm thick planar plate of silicon. Using the frequency spectrum of the shock wave up to 35 harmonics, the ratio of these two signals in the frequency domain yields the coefficient of attenuation in silicon (noting that nonlinear propagation over 1.3 mm inside the silicon is negligible). Measurements were made using two types of instruments (described more precisely below) and giving the same law of attenuation with a linear dependence of the attenuation coefficient α with frequency f (Fig. 2).

B. Hydrophone phase calibration

A hydrophone with a bandwidth as large as possible—here 40 MHz bandwidth—is necessary, because the theoretical rise time of a 1 MHz frequency planar shock wave at 5×10^5 Pa in water is around 5 ns at twice the shock distance (Rudenko and Soluyan, 1977). The small active surface of the hydrophone ($\varnothing=0.2$ mm) is required to scan the pressure field with a good lateral resolution. As a counterpart, it results also into a relatively poor sensitivity of the detector, which nevertheless enables us to get a good signal-to-noise

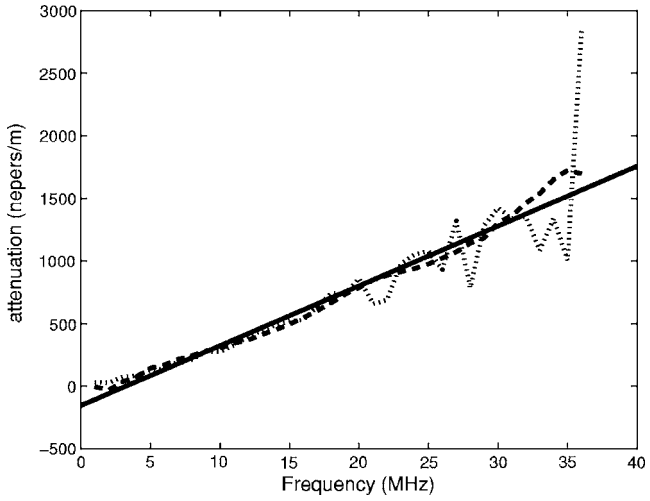

FIG. 2. Measurement of the coefficient of attenuation with the membrane hydrophone (dashed line), with the optical interferometer (dotted line) and the theoretical fit (solid line).

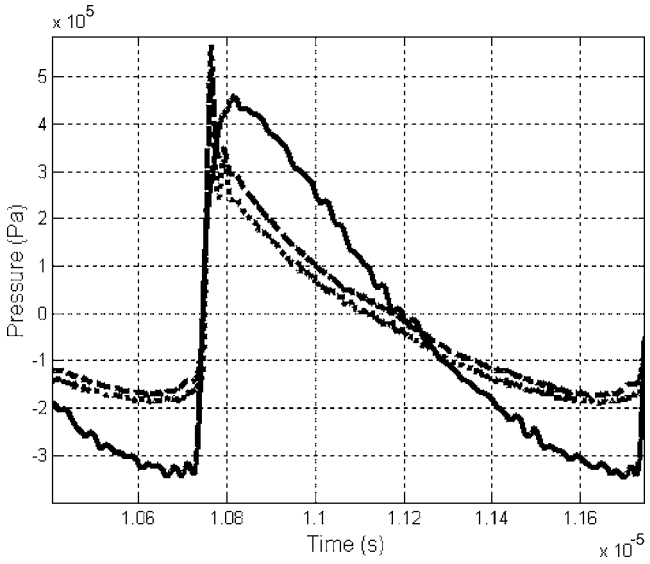

FIG. 3. Calibration of the membrane hydrophone: incident pressure measured with the uncalibrated membrane hydrophone (dashed line), with the constructor's calibration (dotted line) and with the optical interferometer (solid line).

ratio because of the high amplitudes of the present experiment. Because the membrane hydrophone (Precision Acoustics) cannot be ensured to be perfectly parallel to the emitter and because the pressure field displays fast spatial variations, this good lateral resolution is required; otherwise, the very short wavelengths contained in the shock wave (due to high order harmonics) would be spatially averaged. For shock waves, this kind of hydrophone is also known to produce a signal called "overshoot" just behind the shock and related to a 30 MHz resonance of the two planar membranes, having a 15 μm thickness and constituting the hydrophone. To reduce this overshoot, the constructor provides the amplitude of the hydrophone frequency response, hence its calibration in amplitude but not in phase. As the wave form of a shock wave is very sensitive to the relative phases of the harmonics, this calibration is not sufficient to fully suppress the overshoot. To obtain this phase calibration, we used an optical interferometer coupled to a 3-μm-thick metalized Mylar membrane immersed in water, to calibrate all pressure fields in the 1–40 MHz bandwidth, using the fact that the optical interferometer provides an absolute measurement (Barrière and Royer, 2001). Note that the optical interferometer could not be used directly for the present experiment, as it is not easily movable so that it cannot scan the pressure field in a large volume.

Figure 3 shows the incident shock wave profile measured (1) directly with the membrane hydrophone and (2) with the optical interferometer calibration. The phase calibration clearly suppresses the overshoot and the measured signal looks much closer to a typical saw tooth wave, while the amplitude calibration only reduces the amplitude of the overshoot. Starting from this point, all displayed measurements will use the phase and amplitude calibration of the membrane hydrophone.

Figure 4 shows the incident shock wave at $z=3$ mm before the heterogeneity. The maximum amplitude of the incident shock wave is $P_{\max}=4.3\times10^5$ Pa and the measured rise time of the shock is $\tau=24$ ns. Note that there is a factor of 5 between the theoretical (5 ns) and experimental rise times. This difference comes mostly from the limited bandwidth of the hydrophone but also from approximate parallelism between the array of transducers and the hydrophone, and from the electronic jitter.

C. The plane wave and the inverse filter

In order to examine only the effect of the heterogeneity, the shock wave has to be as plane as possible in front of the heterogeneity. This is obtained by using the inverse filter technique, which enables us to determine the signals to be emitted by each element of the array in order to minimize linear diffraction effects induced by the finite size of the transducer (Tanter *et al.*, 2000). This technique consists in measuring the propagation operator h between the area of emission and a set of control points, where the target field (here a plane wave) must be synthesized. The acquisition of h consists in the measurement of the impulse response be-

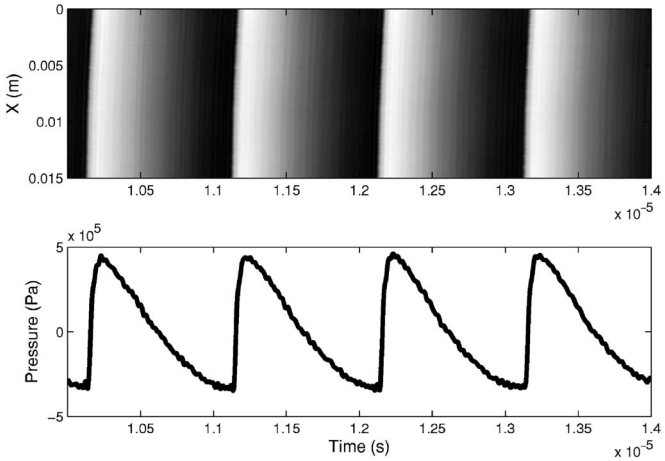

FIG. 4. The spatiotemporal representation of the incident shock wave (top) and the temporal signal of the incident shock wave (bottom) measured just before the heterogeneity.

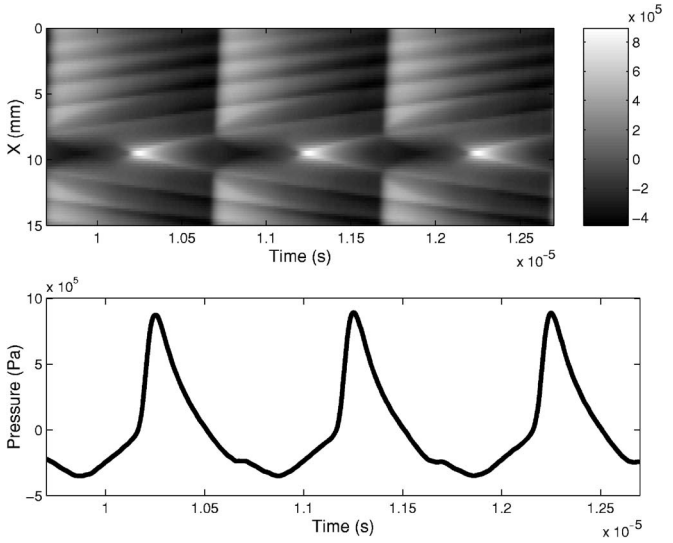

FIG. 5. The spatiotemporal representation of the pressure field measured at the focus of a $d=3$ mm heterogeneity (up) and pressure measured at the center of the focusing (bottom).

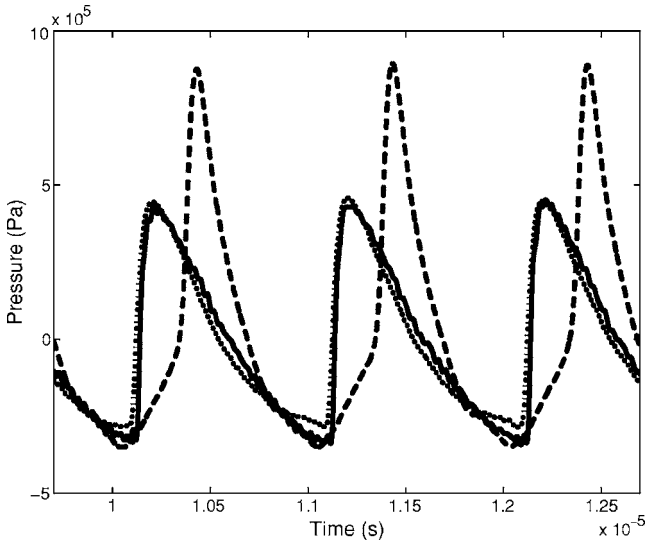

FIG. 6. Time dependence of the pressure measured before the heterogeneity (solid line), behind a plane silicon plate (dotted line) and at the focus (dashed line).

tween each transducer and each control point. Formally, a field sampled at the control points can be written as $r_m(t) = \Sigma_{j=1}^{128} h_{mj}(t) * e_j(t)$, where $r_m(t)$ is the set of temporal signals received at the control points m, h_{mj} is the measured impulse response between the transducer j and the control point m, and $e_j(t)$ is the signal emitted by the transducer j. In the frequency domain, we obtain $R(\omega)=H(\omega)\cdot E(\omega)$ where R, H, and E, are, respectively, the Fourier transforms of r, h, and e. To determine E, the matrix H is regularized and inversed using singular value decomposition. Then, the computed signals $e_j(t)$ are simultaneously emitted in order to synthesize experimentally the objective $r_m(t)$ (here a plane wave). This last operation is achieved thanks to a fully programmable electronic control which imposes on each transducer j of the piezoelectric array the required time dependence of the signal $e_j(t)$.

As our objective is to obtain a collimated plane wave in front of the heterogeneity, the inverse filter technique is very constrained. After many tests to avoid the focusing of the emitted wave, the best target turned out to be a uniform plane wave over a *plateau* 6 cm parallel to the *Ox*-axis with a Gaussian amplitude distribution 1.5 cm wide at half-height parallel to the *Oy*-axis. This technique is valid in the linear regime and in a nonmoving medium, but it has already been employed successfully in the nonlinear regime to reach various target wave fields (Marchiano *et al.*, 2003b, 2005). In the nonlinear regime, the signals calculated by the inverse filter technique in linear regime are simply amplified by a factor of 10. The efficiency of the method is illustrated in Fig. 4, which shows that the incident wave front (top of Fig. 4) is almost perfectly plane even though we are far beyond the shock formation (bottom of Fig. 4).

III. EXPERIMENTAL RESULTS

A. Focusing effect

The first feature that is observed experimentally is the focusing due to the heterogeneity. Figure 5 shows the spatiotemporal pressure field measured at $z=z_{foc}=2$ mm (the theoretical value of the focus position is 1.5 mm) behind a $d=3$ mm heterogeneity (twice the wavelength). The amplification factor is almost equal to 2 (the focused peak pressure is about 9 bars compared to 4.5 bars for the incident wave). This focusing is due to the acoustical lens effect of the semicylindrical heterogeneity, which curves the incident wave front as its central part propagates over a larger thickness inside the slow silicon medium. Note that the amplification is significant, even though the heterogeneity radius is equal to only one wavelength of the incident wave. This results in a typical "U-shape" focused waveform, which is characteristic of the focusing of shock waves (Guiraud, 1965; Wanner *et al.*, 1972). Note, however, that this wave focusing does not correspond to caustics as described by the high-frequency asymptotic theory of catastrophes (Thom, 1972; Berry, 1976). Indeed, that theory is valid only if the curved wave front aperture is large compared to the wavelength (the difference between ideal infinite incident wave front satisfying catastrophe theory and a finite one has been outlined by Marchiano *et al.*, 2005), an assumption that is obviously not satisfied here because of the small size of the heterogeneity. Moreover, if the incoming wave presents shocks, the analytical solutions of the linear problem at the fold (Guiraud, 1965) or the cusp caustics (Coulouvrat, 2000) lead to an unphysical infinite amplitude that can only be reduced by introducing local nonlinear effects. An important observation of this work is the increase of the rise time at the focus. Figure 6 shows (1) the incident pressure, and the pressure measured (2) behind a plane silicon plate and (3) at the center of the focus of the semicylindrical heterogeneity. While in the two first cases the rise time keeps almost unchanged ($\tau=24$ ns) despite the strong absorption in the silicon, the rise time increases one order of magnitude in the case of focusing ($\tau=230$ ns). So, the present experiment demonstrates that a single wavelength-size heterogeneity is sufficient (i) to sig-

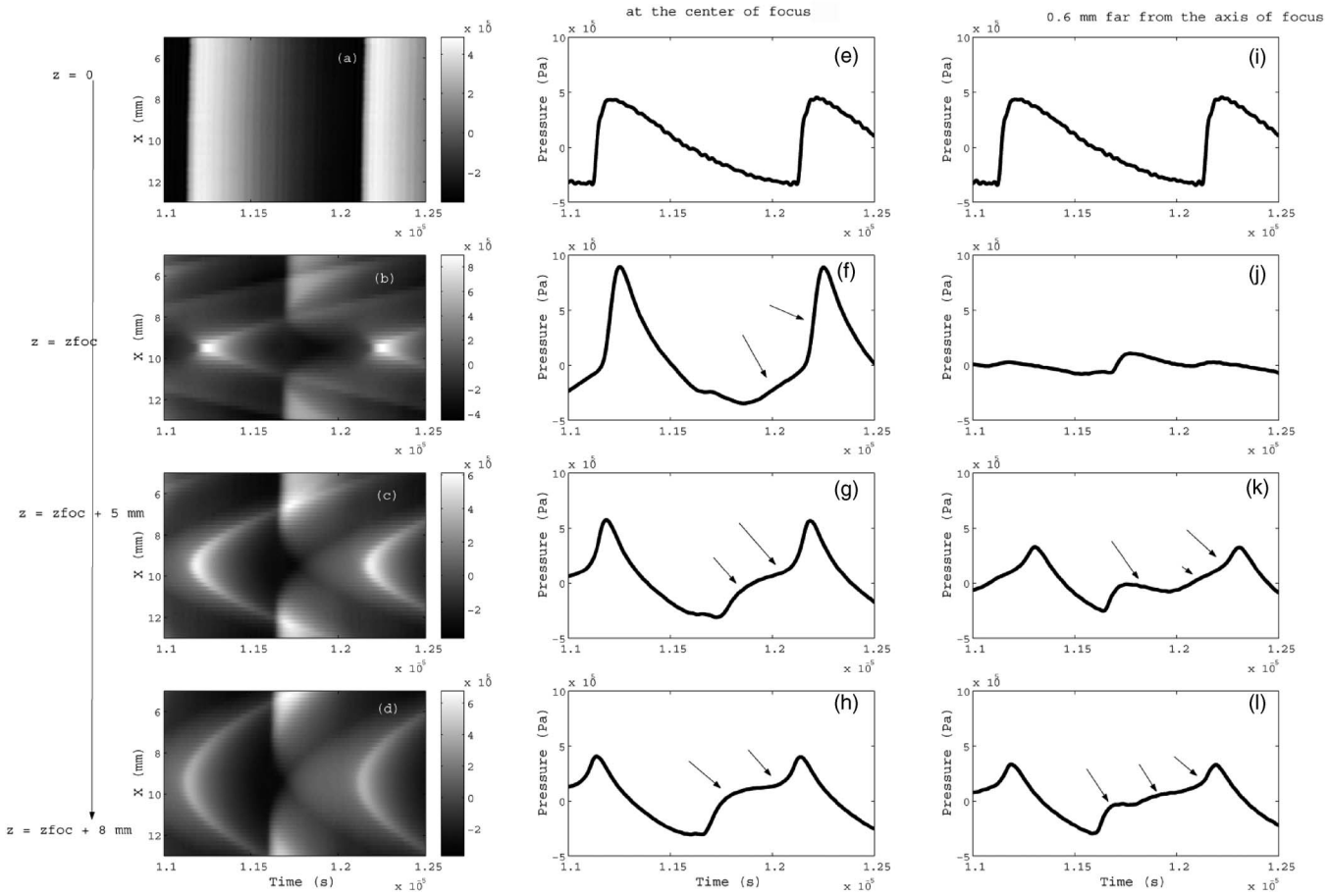

FIG. 7. The spatiotemporal representation of the pressure field (a) before a $d=3$ mm heterogeneity, (b) at the focus, (c) at $z=z_{foc}+5$mm, and (d) at $z=z_{foc}+8$mm. [(e)–(h)] Time dependence of the pressure on the axis at the same distances. [(i)–(l)] Time dependence of the pressure off axis at the same distances.

nificantly amplify a shock wave, (ii) to modify the waveform into a characteristic U-shape, and (iii) to dramatically increase the rise time.

B. Wave front folding

Figures 7(a)–7(d) represent the pressure field measured respectively, (a) before the heterogeneity (incident field), (b) in the focal plane $z=z_{foc}=2$ mm, and at two positions beyond the focus at (c) $z=z_{foc}+5$ mm and (d) $z=z_{foc}+8$ mm in the case of the $d=3$ mm heterogeneity. The figure shows the wave front evolution, from the incident plane wave (a) to the focusing (b) to the wave front folding (c) and (d) where the swallow-tail pattern of a cusp caustic (Marston, 1992) is very obvious (here, as a jump between the white and dark pressure levels). So, the present deterministic experiment enables us to observe the wave front folding effect of a shock wave after propagation through a wavelength-size heterogeneity according to the theory of Pierce and Maglieri (1972, their Fig. 12), which explains the increase of the sonic boom rise time. This is presently confirmed by the waveforms at different distances, along (Fig. 7, second column) and off ($x=0.6$ mm away from the axis, Fig. 7, third column) the axis. Figures 7(e)–7(h) present the pressure time dependence on the axis at the same distances as Figs. 7(a)–7(d). These signals display an evolving structure, from the incident sawtooth wave [Fig. 7(e)] to the focused U-wave [Fig. 7(f)] to the two-shock waveform sufficiently far beyond the focus [Figs. 7(g) and 7(h)], each shock associated with one fold of the wave front. As one goes away from the focus, the size of the swallow tail increases and the two shocks gets more separated as visible by comparing Figs. 7(g) and 7(h). Off axis, the same two shocks are more separated in time as expected (Piacsek, 2002) and a third intermediate one, associated with the folded sheet of the swallow tail, is also visible, though of smaller amplitude.

These observations prove that the waveform distortions are associated with geometric wave front folding. Note that the variations of these waveforms are fast in the transverse direction and are significant over distances less than one wavelength (here 0.6 mm) in agreement with sonic boom observations.

The wave front folding is observable also for smaller size heterogeneities. Figure 8 displays the same pressure B-scans at the same distance $z=7$ mm behind the heterogeneity but for a smaller one here $d=\lambda=1.5$ mm [Figs. 8(a) and 8(b)] and $d\sim 0.3\ \lambda=0.4$ mm [Figs. 8(c) and 8(d)]. Though the heterogeneity is now smaller, the wave front folding into the characteristic swallow-tail shape is still visible at $d=\lambda$ though the different folds of the wave front are less separated in time. For the smallest heterogeneity, however, the folding is less obvious: The heterogeneity is now too small, and the

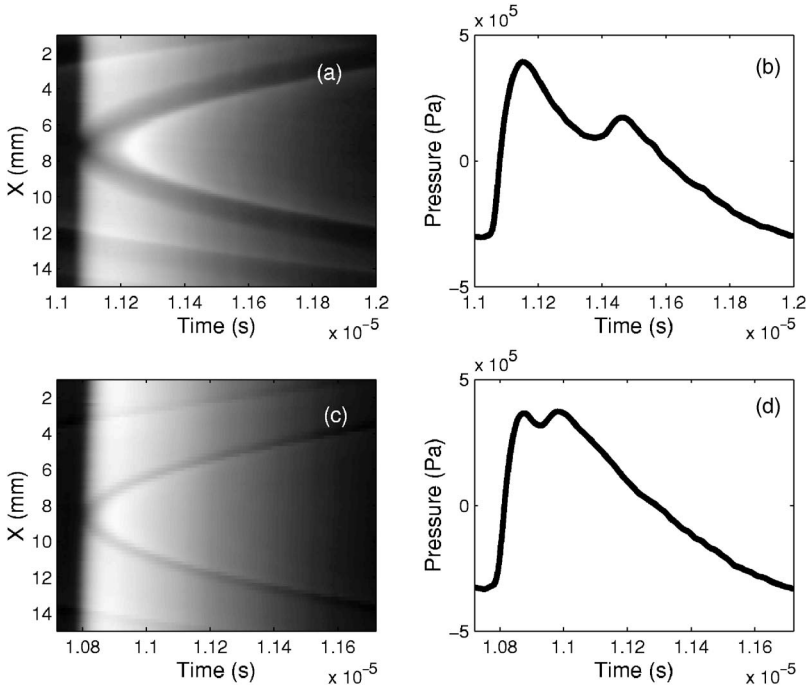

FIG. 8. Spatiotemporal representation of the pressure field measured behind ($z=7$ mm) (a) $d=1.1$ mm and (c) $d=0.4$ mm heterogeneities. Corresponding time dependence of pressure off axis ($x=1.2$ mm) behind (b) $d=1.1$ mm and (d) $d=0.4$ mm heterogeneities.

time delay between the different sheets of the wave front is very small so that the wave front looks more slightly dislocated than folded.

C. Consequences on the variability of the waveform

According to the experimental results, the wave front folding explains two phenomena observed both for sonic boom and for the present experiment: the increase of the rise time and the distortion of the wave profile.

(a) *The augmentation of the rise time.* Indeed, the occurrence of focusing has been shown above to be responsible for the increase in rise time due to the change of the waveform from an *N*- to a *U*-wave. Now the question is about the evolution of this rise time beyond the focal point after propagating a certain distance through a homogenous medium. To explore this, Fig. 9 compares the time waveforms of the pressure measured on the axis behind the three heterogeneities $d=2\lambda$, $d=0.7\lambda$, and $d\sim0.3\lambda$ at the same distance $z=14$ mm, i.e., about 10 λ, which, at the sonic boom scale, is around the thickness of the planetary boundary layer. For the largest heterogeneity, the waveform distortion is clearly associated with geometric wave front folding (Sec. III B) and the rise time is equal to 380 ns: It is larger than the rise time measured at the focusing of the same heterogeneity (230 ns). For the medium-size case, the wave front folding into the swallow-tail characteristic is still visible (Sec. III B) and the rise time is now equal to 130 ns. Finally, in the small-size third case, the wave front looks

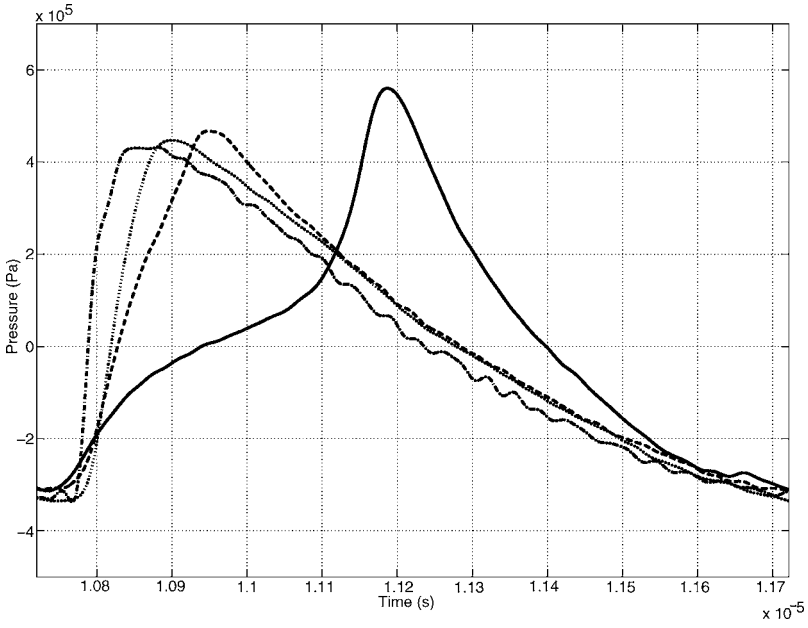

FIG. 9. Time dependence of pressure measured before (dash-dotted line) and behind ($z=14$ mm) a $d=3$ mm (solid line), $d=1.1$ mm (dashed line), or $d=0.4$ mm (dotted line) heterogeneity.

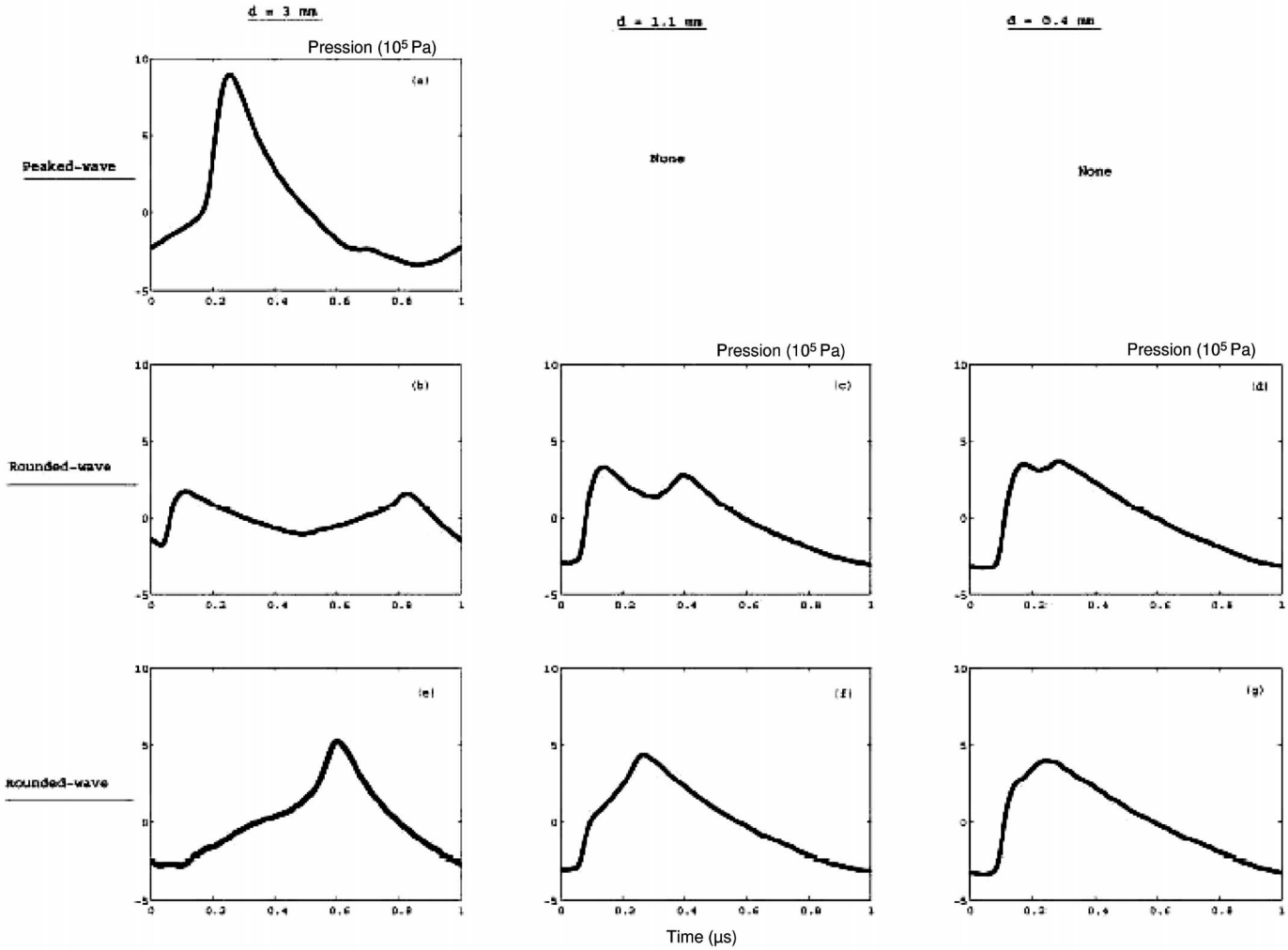

FIG. 10. Different waveforms measured with a single heterogeneity of different sizes ($d=2\lambda$—first column, $d=0.7\lambda$—second column, and $d=0.3\lambda$—third column). The measurement points are located on the axis and at the focus ($z=2$ mm) of the largest heterogeneity (first row), 5 mm beyond the focus and 1.2 mm off axis (second row) and 15 mm beyond the focus and 1.2 mm off axis (third row).

more slightly dislocated than folded (Sec. III B) and the rise time at the center of the heterogeneity is equal to 65 ns. Anyway, in all cases, the rise times are significantly larger than the incident one, by a factor between 3 and 16. So, in agreement with the model of Pierce and Maglieri (1972), the increase of the rise time after focusing is due to the breaking up of the incident shock wave into two shocks, each one associated with one fold of the wave front. This breaking is obvious on the strongly heterogeneous case $d=2\lambda$, but remains visible for the medium case $d=0.7\lambda$ though the two folds are less clearly separated in time. So clearly the augmentation of the rise time depends on the size of the heterogeneity, the influence of wave front folding being strongest for the largest heterogeneities.

(b) *The waveform distortion*. According to Raspet *et al.* (1994), the sonic wave shapes are classified into three main groups of waveforms: *N*-wave, peaked wave, and rounded wave (their Fig. 2). Here, Fig. 10 shows different waveforms measured with a single heterogeneity of different sizes ($d=2\lambda$—first column, $d=0.7\lambda$—second column, and $d=0.3\lambda$—third column). The measurement points are located on the axis and at the focus of the largest heterogeneity (first row), 5 mm beyond the focus, respectively, at 1.8, 2, and 1.6 mm off axis (second row) and 15 mm beyond the focus, respectively, at 0.4, 0.9, and 1.2 mm off axis (third row). The peaked wave with a characteristic U-shape associated with strong focusing is observed behind the $d=3$ mm heterogeneity, while such a peaked wave cannot be observed behind the $d=1.1$ mm and $d=0.4$ mm heterogeneities. It is certainly related to the intensity of the focusing, which is stronger in the case of $d=2\lambda$.

The rounded-wave type is observed in our experiment for each case of diameter. The first type is observed near the axis and the focus [second row, Figs. 10(b)–10(d)], and is characterized by two successive shocks, a first one of large amplitude, corresponding to the first fold of the wave front, and a second one of smaller amplitude, corresponding to the second and third folds of the wave front. This second shock is smaller because the observation point is relatively close to the focus. It is more and more separated from the first one, as the heterogeneity size is larger. For the two smallest heterogeneities, this produces some "plateau" behind the main shock with a "ripple" associated with the wave front folding.

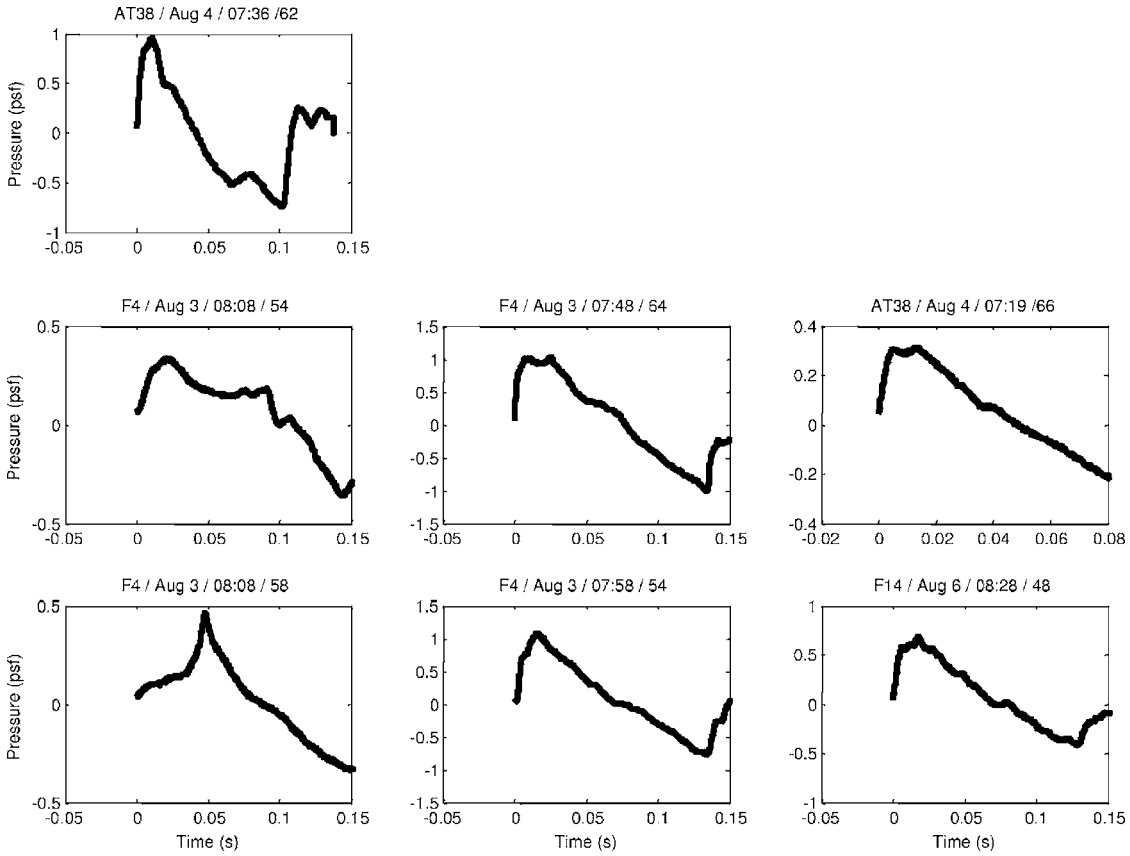

FIG. 11. Example of sonic boom time waveforms from the BoomFile database (Lee and Downing, 1991).

The third type is characterized by two shocks of more similar amplitudes, as the observation point is now farther from the focus and the wave front folding is now well developed.

Figure 11 shows several measured sonic booms from the Boom File tests (Lee and Downing, 1991) performed in 1987 with different supersonic aircrafts flying at different Mach numbers. Among the more than 450 recorded waveforms, we have selected a few ones displaying the characteristic features observed in our experiment, for a qualitative comparison with the present study. Of course, the present experiment with a single heterogeneity does not pretend at all to reproduce the whole complexity associated with propagation through the turbulent multiscale, inhomogeneous, anisotropic, thermal and inertial, planetary boundary layer. Nevertheless, it is quite striking that the present, very simple case, is sufficient to reproduce several of the sonic boom waveforms as illustrated by comparing Figs. 10 and 11. Let us recall that the only objective here is to investigate in the laboratory the detailed physical effects associated with the interaction of a shock wave with a heterogeneity, and to profit from the opportunity offered by the deterministic aspect of the experiment. In particular, this deterministic aspect will now allow us to make a detailed comparison with a numerical model, including a waveform to waveform comparison at the same point in the same propagation conditions, something that is impossible to perform in a statistical propagation case, either during flight tests or even in a laboratory turbulence experiment (such as Lipkens and Blackstock, 1998 or Blanc-Benon *et al.* 2002).

IV. THE PHYSICAL MODEL

A. KZ equation in heterogeneous medium

We have derived a generalization of the KZ equation (Zabolotskaya and Khokhlov, 1969) to model the sonic boom propagation through heterogeneous media. This equation describes the one-way nonlinear propagation along the axial direction z (longitudinal variable) taking into account the diffraction in (x,y) directions (transverse variables) through a weakly heterogeneous medium [heterogeneities can depend on (x,y,z)]. Performing the paraxial approximation, the conservation and state equations lead to the nonlinear parabolic wave equation in a heterogeneous medium as follows:

$$\frac{\partial^2 \bar{P}}{\partial\tau\partial\sigma} - \frac{\partial}{\partial\tau}\left(\bar{P}\frac{\partial\bar{P}}{\partial\tau}\right) - \frac{\eta^2}{2\beta M}\Delta_\perp P = H_c\frac{\partial^2\bar{P}}{\partial\tau^2} + O(\varepsilon). \qquad (1)$$

The dimensionless variables in the generalized KZ equation are the pressure $\bar{P}(X,Y,\sigma,\tau)=P/P_0$, the retarded time $\tau=\omega t-kx$, the longitudinal variable $\sigma=z/L_s$, and the transverse variables $X=x/a$ and $Y=y/a$ with ω the fundamental angular frequency, $k=\omega/c_0$ the wave number based on the mean sound speed c_0, and a the characteristic size of the acoustical source. The coefficient $\eta^2/2\beta M$ compares the diffraction to nonlinear effects, with $\eta=1/ka$ is the small parameter associated with diffraction. The function

$$H_c = \frac{c_h(x,y,z) - c_0}{c_h(x,y,z)\beta M} \tag{2}$$

compares heterogeneity to nonlinear effects. Heterogeneity is of the order $\varepsilon = \max(|c_h - c_0|/c_0)$, and nonlinearities are measured by the acoustical Mach number M. Equation (1) is identical to the one used by Blanc-Benon *et al.* (2002), except the fact that the heterogeneous sound speed c_h here appears at the denominator of H_c, instead of the mean sound speed c_0. Both equations are consistent with one another at the precision $O(\varepsilon)$, but Eq. (1) has the advantage to provide the exact travel time of a plane wave in a medium with heterogeneity varying along the axis $c_h(z)$. In the present case, it will not introduce artificial phase mismatch in our reference case of a plane wave propagating through the silicon plate. To derive this equation, it is necessary to assume that the medium is weakly heterogeneous, nonmoving, and steady. The derivation of the equation takes into account in a consistent way heterogeneities of pressure, density, entropy, and speed of sound (all supposed to be of the same order ε), though finally only the sound speed heterogeneity appears in the equation at the main order. The degree of heterogeneity is supposed to be of the same order than the nonlinear effects, while it is proportional to the square root of the diffraction effect: $\varepsilon \approx M \approx \eta^2$, so that the coefficients of Eq. (1) are all supposed to be of order 1.

B. Numerical simulation

On the above theoretical basis, a numerical simulation of the 2D KZ equation developed for homogeneous medium has been extended to the simulation of the propagation of acoustic shock waves in heterogeneous medium. The simulation is based on a potential formulation of the generalized KZ equation. This formulation improves the treatment of the shock waves (Marchiano *et al.*, 2003a). The numerical algorithm is inspired from the "BERGEN code" (Ginsberg and Hamilton, 1998): A split step procedure is employed to treat separately on one hand diffraction and heterogeneities in the frequency domain, and on the other hand nonlinearities in the time domain. Diffraction and heterogeneity are taken into account by finite differences through an implicit scheme. Thus, all the linear effects are treated together. Moreover, this treatment in the spectral domain allows us to add absorption, by adding the absorption decay over one propagation step. For propagation in water absorption is neglected, while for the propagation in silicon the absorption coefficient satisfies the law of attenuation measured in Sec. II A. As mentioned in this section, attenuation in silicon is important. The nonlinear part is solved with an algorithm based on the "Hayes" method in the time domain (Hayes *et al.*, 1969; Marchiano *et al.*, 2003a), which is well adapted to weak shock theory. Given the problem geometry, only 2D simulations are performed. The imposed "input" boundary condition corresponds to the plane wave measured just before the heterogeneity (Fig. 4). The lateral extent $x = x_{\max}$ of the numerical domain is chosen sufficiently large so that the wave scattered by the heterogeneity does not reach it at the most far away propagation distance z. Consequently, on this boundary, the imposed pressure field is the plane wave that has propagated through water and the silicone plane [solution of Eq. (1) with diffraction term omitted]. For simulations, the map of heterogeneity is with the geometry of the experiment depicted in Fig. 1, with $c_{water} = c_0 = 1500$ m s^{-1} and $\rho_0 = 1000$ kg/m^3.

V. NUMERICAL RESULTS

A. Comparisons between numerical and experimental results

Figure 12 shows the spatiotemporal representation of the pressure field measured (up) and simulated (bottom) at the focal point of a $d = 3$ mm heterogeneity. The agreement between numerical and experimental results is very good in the neighborhood of the axis of propagation. Figure 13 shows the comparison of the measured (solid line) and the simulated (dashed line) pressure versus time exactly on the axis of propagation. The U-shape, the augmentation of amplitude, and the augmentation of rise time are very well reproduced by the simulation. So, the main characteristics of the shock waves focusing are well simulated with the generalized KZ equation. However, away from the axis of propagation, numerical and experimental results are not as good as on the axis. The interferences between the incident plane wave and the diffracted cylindrical ones are not much visible on the numerical results. Figure 14 shows the pressure measured (up) and simulated (bottom) behind a $d = 3$ mm heterogeneity at $z = 8.5$ mm for several x (1.2, 1.4, and 1.6 mm off axis). Two shocks are visible in each case. This is due to the wave front folding as explained in Sec. III B. Nevertheless, there are differences between measured and simulated pressures. All these differences are due to the adopted model. Indeed, the generalized KZ equation is a paraxial approximation of the nonlinear wave equation, which introduces a phase error that is the large of as the wave direction deviates from the axis. This equation is generally considered valid only under a 15° approximation (Claerbourt, 1976). This means that the model ensures a correct description of the physical effects within a cone of 15°, which is confirmed by our simulations: Agreement is good within this cone, but significant deviations appear out of it. Thus, the simulated results turn out to be in very good agreement in the domain of validity of the paraxial equation. However, scattering of waves far off axis would require to using a less restrictive approximation such as a wide angle equation (Claerbourt, 1976) in the nonlinear regime and in a heterogeneous medium.

B. Nonlinear effects

The numerical modeling can be used to study the physical mechanisms separately. In particular, it is interesting to investigate the role of the nonlinearity as its influence on sonic boom in turbulence is not clearly established (see Introduction). Figure 15 shows the difference between the frequency spectrum of the pressure measured at the focus of the $d = 3$ mm heterogeneity (normalized by the incident pressure) in nonlinear and linear propagation from 1 to 8 MHz. As the objective here is to investigate the importance of nonlinearities by comparing a nonlinear simulation with a linear one, these simulations have been performed here *without* the high

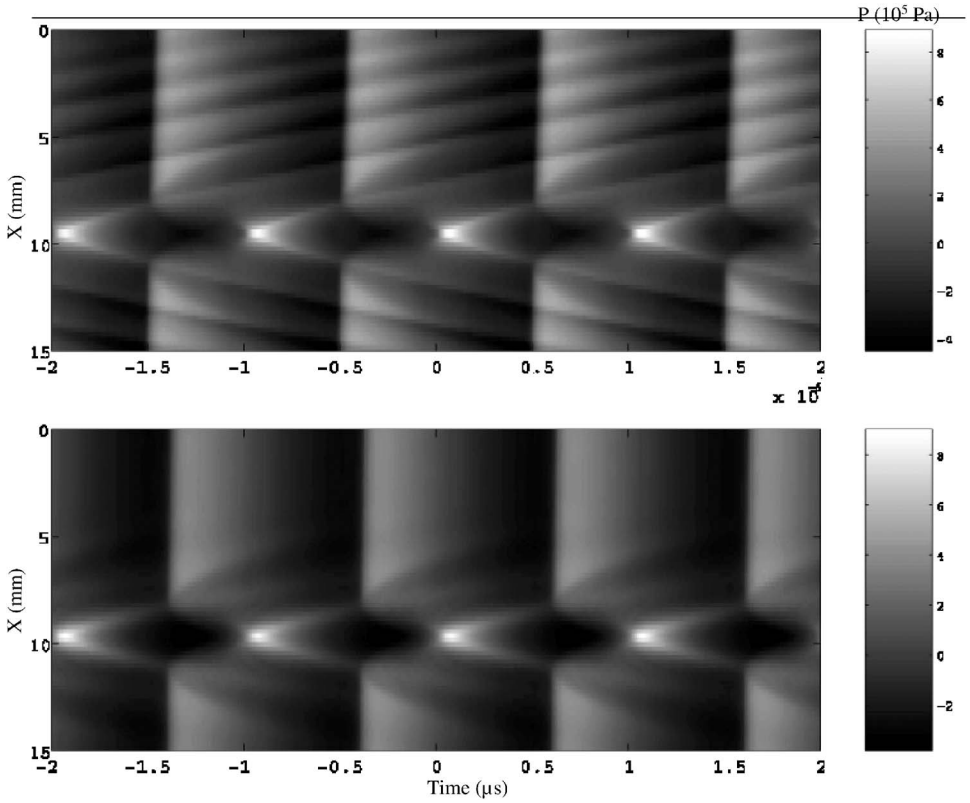

FIG. 12. The spatiotemporal representation of the pressure field measured (up) and simulated (bottom) at the focus (z=2 mm) of a d=3 mm heterogeneity.

attenuation due to silicon that might artificially (at least for sonic booms) overcome nonlinear effects. *No* difference is visible (not shown here) on the *time waveform* and peak pressure between linear and nonlinear simulations. This clearly indicates that nonlinear effects are *not* the dominant mechanism. However, in the *frequency domain*, the pressure amplitude at 1 MHz is slightly weaker if nonlinearity is included, whereas at higher frequencies this effect is inverted. This effect can be interpreted as a classical nonlinear effect. In nonlinear regime, energy is pumped from the fundamental to the higher harmonics. So, the energy of the fundamental is lower in nonlinear regime than in linear one, while this is the contrary for the higher harmonics. Thus, nonlinear effects affect mainly the higher harmonics. Consequently, even if the distance of propagation is short, it may nevertheless be important to take into account the nonlinear effects for sonic boom. Indeed, using the *A*-frequency weighting of most noise metrics, the audio perception of the *outdoor* sonic boom is very sensitive to the higher harmonics, which can go up to 100 times the fundamental. Figure 16 investigates the importance of nonlinearities for different harmonics as a function of the heterogeneity size. With this in view, the amplitudes of the harmonics (from the first to the eighth ones) of the pressure wave spectrum at the focus (axial point where the peak overpressure reaches its maximum) are plotted as a function of the heterogeneity size. For comparison, all quantities are without dimensions. Amplitudes are normalized by the amplitude of the fundamental of the incident wave, and diameters are normalized by the fundamental wavelength (1.5 mm). Nonlinear simulations (dashed lines) are compared to linear ones (solid lines). Previously, it is clear that nonlinear effects are not dominant, even for the largest heterogeneity, and affect only the highest harmonics. The global increase of the harmonic amplitudes at the focus with the size is also logical: The largest the heterogeneity, the most efficient is its role as an acoustic lens. The differences in the slopes are nevertheless noticeable. They can be explained as follows. On the one hand, the increase of the heterogeneity diameter tends to focus more the harmonics, as the relative size of the heterogeneity considered as an acoustical lens compared to the wavelength increases. On the other hand, high frequencies will focus very close to the geometrical focus, whose position is different from the actual focal

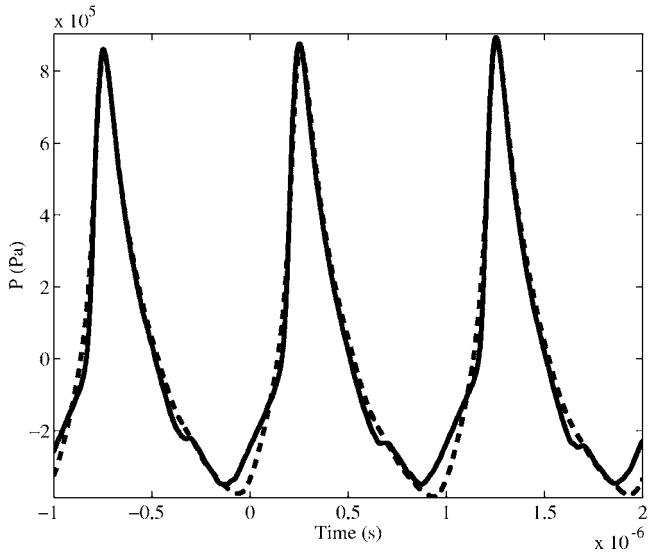

FIG. 13. Time dependence of pressure measured (dashed line) and simulated (solid line) on the axis of propagation at the focus (z=2 mm) behind a d=3 mm heterogeneity.

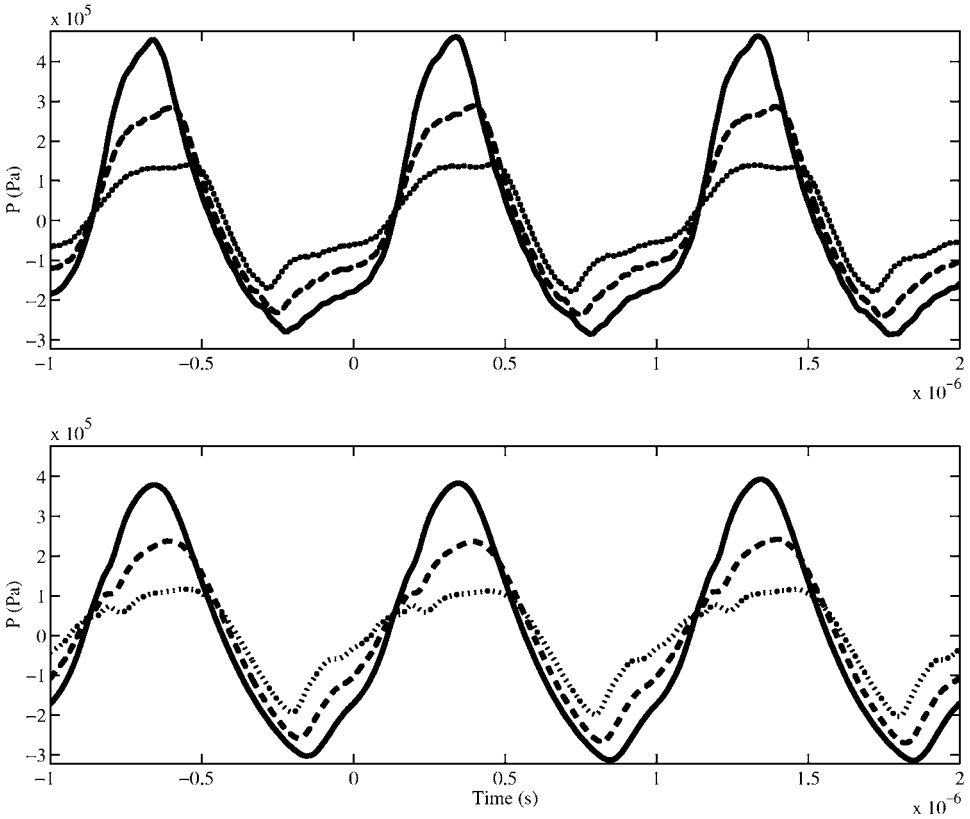

FIG. 14. Pressure measured (up) and simulated (bottom) behind a $d=3$ mm heterogeneity at $z=8.5$ mm for several off axis distances (solid line: $x=1.2$ mm, dashed line: $x=1.4$ mm, and dotted line: $x=1.6$ mm).

point because this last one is mostly governed by the lower fundamental frequency (which carries most of the signal energy). Hence, when increasing the diameter, there is a competition in terms of the efficiency of the amplification of the harmonics between these two effects. The role of the size is prevalent for the lowest harmonics, while the role of the focus shift is prevalent for the highest ones. It is only for very large heterogeneities (note shown here and not realistic for sonic booms) that all frequencies, including the fundamental, would focus almost at the same point. In this case, the high-frequency assumption becomes valid and it is possible to use the asymptotic theory of catastrophes. Then, local nonlinear effects play a dominant role near the caustic (Marchiano *et al.*, 2005), at the difference of the present situation.

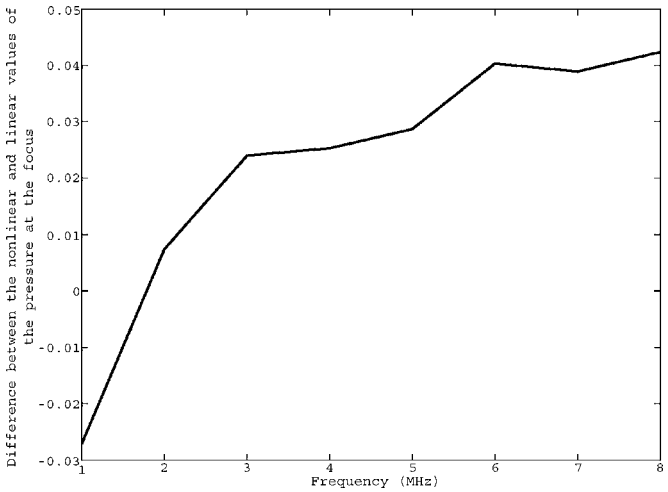

FIG. 15. Difference between the pressure frequency spectrum, measured at the focus of a $d=3$ mm heterogeneity (normalized by the incident pressure) in nonlinear and linear propagations, from 1 to 8 MHz.

C. The evolution of rise time

The amplification factor induced by the focusing depends on the size of the heterogeneity (Fig. 16). In the experimental part, we have shown that the rise time is related to the focusing, and its increase depends on the wave front folding. In this part, the numerical simulation investigates the evolution of the rise time with, on the one hand, the distance of propagation, and, on the other hand, the size of the heterogeneity. Once again, as for nonlinear effects (Sec. V B), simulations are performed through a lossless silicon layer, in order to quantify the evolution of the rise time due to the scattering by heterogeneity, and not the one due to silicone absorption. Figure 17 represents the rise time (normalized by the rise time of the incident shock wave) as a function of the distance of propagation for $d=3$ mm, $d=2$ mm, $d=1.1$ mm, and $d=0.7$ mm. The rise time clearly increases from the occurrence of the focus, until it reaches some stabilization. This observation is in agreement with laboratory-scale statistic experiments of Blanc-Benon *et al.* (2002, 2005) in a turbulent jet, showing a correlation between the increase of rise time and the occurrence of the first caustic. The stabilized value is equal to $d=3$ mm and $d=2$ mm. These values are large, but not as much as when taking into effect absorption in silicon (Sec. III B). This shows the usefulness to have simultaneously a deterministic experiment and a numerical model, this last ones being able to correct the unavoidable biases introduced by the scaling of

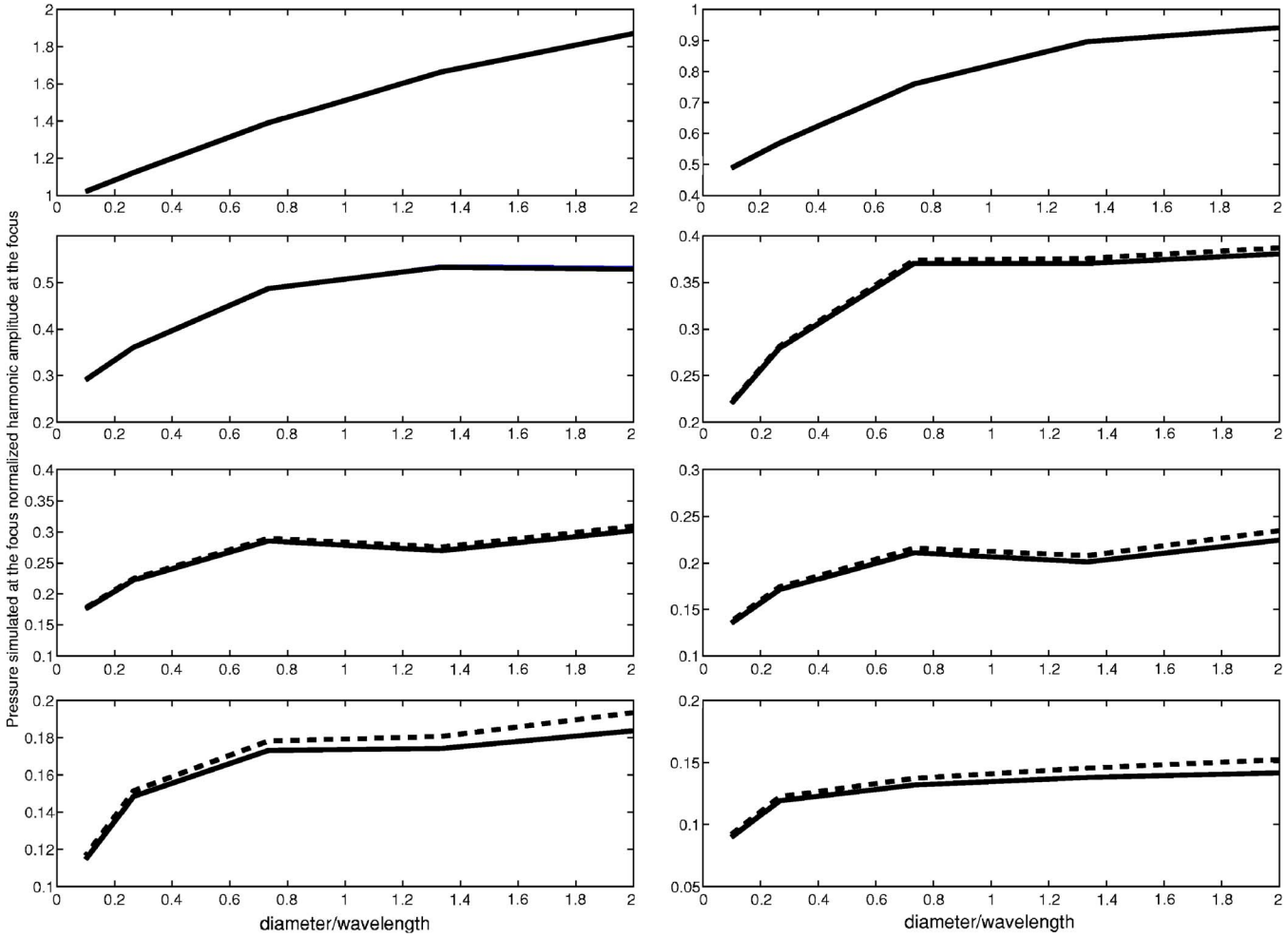

FIG. 16. (Color online) Simulated amplitude of the harmonics of the pressure frequency spectrum at the focus (axial point of maximum peak overpressure) vs the diameter of the heterogeneity. Comparisons between linear (solid lines) and nonlinear (dashed lines) numerical simulations. Harmonic amplitudes are normalized by the amplitude of the fundamental of the incident pressure field. Heterogeneity diameter is normalized by the fundamental wavelength (1.5 mm). From left to right and top to bottom: first to eighth harmonics.

the experiment at the laboratory size (such as enhanced absorption here). Also noticeable is the saturation value that decreases with the size of the heterogeneity. Finally, at least over a propagation distance of about 10 λ, the nonlinear effects once again seem to have little importance because no decrease of the rise time is observed, as one would have expected if nonlinearities would have begun to sharpen the wave profiles.

The present experiment is far from a full scale model of sonic boom in turbulence. However, its deterministic aspect and its laboratory dimensions make it a useful tool for a better understanding of the physics of the shock waves in heterogeneous media and for the validation of the numerical models. Moreover, the present analysis on a very simple case (a single heterogeneity with a rather strong sound speed contrast) nevertheless provides some quantitative indications that are comparable to sonic boom data. We find the largest heterogeneities (those who would be the less probable in the atmosphere) amplify by a factor about 2 the pressure. This is not contradictory with the statistical data on sonic booms (Maglieri, 1966, Fig. 9), which show amplifications by a factor more than 2 would be quite rare. Also, we find that the increase of the rise time is up to about one magnitude order

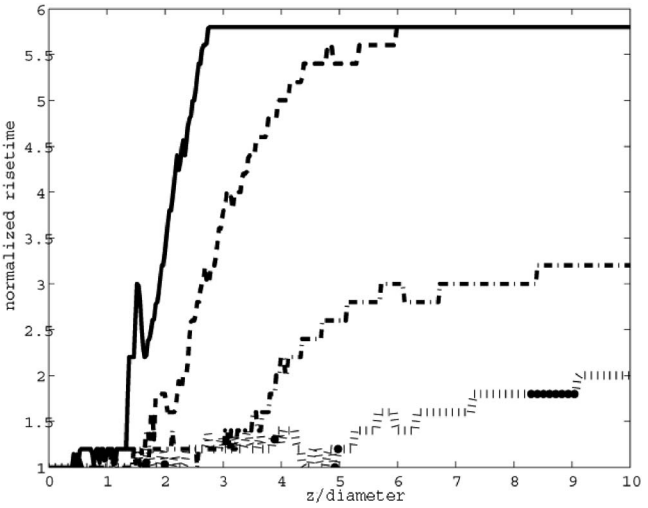

FIG. 17. Numerical simulation of the axial ($x=0$) waveform rise time vs the axial distance z. Rise time is defined as the time interval separating the two times at which pressure time waveform at a given point is equal to 90% of, respectively, the minimum and the maximum pressure values. Rise time is normalized by the rise time of the incident shock wave (equal to 24 ns). Distance is normalized by the diameter d of the heterogeneity. Simulations are shown for a heterogeneity with diameter $d=3$ mm (solid line), $d=2$ mm (dashed line), $d=1.1$ mm (dash-dotted line), or $d=0.7$ mm (dotted line).

(the largest value being observed at the focus of the largest heterogeneities). This is also in agreement with data collected by Pierce and Kang (1990), or Concorde recordings (Parmentier *et al.*, 1973) showing rise time fluctuates by about one magnitude order.

VI. CONCLUSION

The first part of the present work studied experimentally the wave front folding and its consequences on the rise time and the waveform distortion. The second part developed a physical model, which allows us to study exactly the influence of nonlinearities and remove the influence of the additional absorption introduced by the experimental scaling.

First, our deterministic experiment with a single heterogeneity allows us to investigate the wave front folding. We have shown experimentally that the increase of the rise time depends on the occurrence of the focusing. Then, its increase is due to the breaking up of the incident shock wave into two shocks, each one associated with one fold of the wave front. This physical effect explains also the variability of the wave front (U-shape and rounded wave) and its fast spatial variations. Of course, the present experiment is not sufficient to reproduce several of the sonic boom waveforms. However, the deterministic nature of the experiment enabled us to investigate the dependence of the wave front folding with the size of heterogeneity. Thus, we have shown that this effect exists only for the biggest heterogeneities and consequently this result provides a lower bound for eddies in the meteorological model used to predict the shape of sonic boom: The influence of structures smaller than 0.3 wavelength may be small. Moreover, this deterministic experiment aspect is adapted to make a quantitative comparison with a theoretical and numerical model. We performed an exact derivation of the generalized KZ equation that models the nonlinear propagation through a weakly heterogeneous medium. The numerical simulation is then used to discriminate between nonlinear and linear propagations. Even if the nonlinear effect can be neglected if one is only interested in overall pressure time dependence, the audible higher harmonics amplitude may be significantly increased by the nonlinear propagation in the case of the biggest heterogeneities. Moreover, we also confirmed that the increase of the rise time occurs at the focus, whatever the size of heterogeneities, and we showed that this increase remains stable up to a distance corresponding to the ground level.

A perspective of this work is to carry out deterministic experiments with a set of heterogeneities arranged in 2D or three-dimensional configurations, more realistic from a sonic boom point of view. However, we have also shown that the classical parabolic approximation is not sufficient to model accurately the waveforms off axis. So, for comparison with a numerical model, such experiments would require the derivation of a wide angle approximation of the KZ equation in heterogeneous medium.

ACKNOWLEDGMENTS

The present work has benefited from a Research Contract between Airbus France and Université Pierre et Marie Curie—Paris 6.

Aver'yanov, M. V., Khokhlova, V. A., Sapozhnikov, O. A., Blanc-Benon, Ph., Cleveland, R. O. (**2006**). "Parabolic equation for nonlinear acoustic wave propagation in inhomogeneous moving media," Acoust. Phys. **52**, 623–632.

Barrière, C., and Royer, D. (**2001**). "Optical measurement of large transient mechanical displacements," Appl. Phys. Lett. **79**, 878–880.

Bass, H. E., Ezell, J., and Raspet, R. (**1983**). "Effect of vibrational relaxation on rise times of shock waves in the atmosphere," J. Acoust. Soc. Am. **74**, 1514–1517.

Berry, M. V. (**1976**). "Waves and Thom's theorem," Adv. Phys. **25**, 1–26.

Blanc-Benon, Ph., Juvé, D., and Comte-Bellot, G. (**1991**). "Occurrence of caustics for high-frequency acoustic waves propagating through turbulent fields," Theor. Comput. Fluid Dyn. **2**, 271–278.

Blanc-Benon, Ph., Lipkens, B., Dallois, L., Hamilton, M. F., and Blackstock, D. T. (**2002**). "Propagation of finite amplitude sound through turbulence: Modeling with geometrical acoustics and the parabolic approximation," J. Acoust. Soc. Am. **111**, 487–498.

Blanc-Benon, Ph., Ollivier, S., Attenborough, K., and Qin, Q. (**2005**). "Laboratory experiments to study N-waves propagation: Effects of turbulence and/or ground roughness," *17th International Symposium on Nonlinear Acoustics*, July 18–22 (State College, Pennsylvania, PA).

Boulanger, P., Raspet, R., and Bass, H. E. (**1995**). "Sonic boom propagation through realistic turbulent atmosphere," J. Acoust. Soc. Am. **98**, 3412–3417.

Claerbourt, J. F. (**1976**). *Fundamentals of Geophysical Data Processing: With Applications to Petroleum Prospecting* (McGraw-Hill, New York).

Coulouvrat, F. (**2000**). "Focusing of weak acoustic shock waves at a caustic cusp," Wave Motion **32**, 233–245.

Crow, S. C. (**1969**). "Distortion of sonic bangs by atmospheric turbulences," J. Fluid Mech. **37**, 529–563.

Davy, B. A., and Blackstock, D. T. (**1971**). "Measurements of the refraction and diffraction of a short N wave by a gas-filled soap bubble," J. Acoust. Soc. Am. **49**, 732–737.

Garrick, I. E. (**1968**). "Atmospheric effects on the sonic boom," in Second Conference on Sonic Boom Research, edited by I. R. Schwartz, pp. 3–17, NASA SP-180.

Ginsberg, J. H., and Hamilton, M. F. (**1998**). "Computational methods," in *Nonlinear Acoustics*, edited by M. F. Hamilton and D. T. Blackstock (Academic, San Diego, CA), pp. 309–341.

Guiraud, J.-P. (**1965**). "Acoustique géométrique, bruit balistique des avions supersoniques et focalisation," J. Mec. **4**, 215–267.

Hayes, W. D., Haefeli, R. C., and Kulsrud, H. E. (**1969**). "Sonic boom propagation in a stratified atmosphere with computer program," NASA CR-1299.

Kelly, M., Raspet, R., and Bass, H. E. (**2000**). "Scattering of sonic booms by anisotropic turbulence in the atmosphere," J. Acoust. Soc. Am. **107**, 3059–3064.

Lee, R. A., and Downing, J. M. (**1991**). "Sonic booms produced by United States Air Force and United Stated Navy Aircraft: Measured data," Report No. AL-TR-1991-009, Armstrong Laboratory, Wright-Patterson Air Force Base, Brodes, Texas.

Lipkens, B., and Blackstock, D. T. (**1998**). "Model experiment to study sonic boom propagation through turbulence. Part 1: General results," J. Acoust. Soc. Am. **103**, 148–158.

Maglieri, D. J. (**1966**). "Some effects of airplane operations and the atmosphere on sonic boom signatures," J. Acoust. Soc. Am. **39**, S36–S42.

Marchiano, R., Coulouvrat, F., and Grenon, R. (**2003a**). "Numerical simulation of shock wave focusing at fold causics, with application to sonic boom," J. Acoust. Soc. Am. **114**, 1758–1771.

Marchiano, R., Thomas, J.-L., and Coulouvrat, F. (**2003b**). "Experimental simulation of supersonic superboom in a water tank: Nonlinear focusing of weak shock waves at a fold caustic," Phys. Rev. Lett. **91**, 184301.

Marchiano, R., Coulouvrat, F., and Thomas, J.-L. (**2005**). "Nonlinear focusing of acoustic shock waves at a caustic cusp," J. Acoust. Soc. Am. **117**, 566–577.

Marston, P. L. (**1992**). "Geometrical and catastrophe optics method in scattering," in *High Frequency and Pulse Scattering*, Physical Acoustics Vol. **XXI**, edited by A. D. Pierce and R. N. Thurston (Academic, San Diego,

CA), pp. 1–234.
McBride, W. E., Bass, H. E., Raspet, R., and Gilbert, K. E. (**1992**). "Scattering of sound by atmospheric turbulence: Predictions in a refractive shadow zone," J. Acoust. Soc. Am. **91**, 1336–1340.
Parmentier, G., Mathieu, G., Schaffar, M., and Johe, Ch. (**1973**). "Bang sonique de Concorde: Enregistrement hors trace des variations de pression au sol. Centre d'Essais des Landes; 13 au 15 juin 1973," Institut Franco-Allemand de Recherches de Saint-Louis, Rapport Technique RT19/73 (in French).
Piacsek, A. A. (**2002**). "Atmospheric turbulence conditions leading to focused and folded sonic boom wave fronts," J. Acoust. Soc. Am. **111**, 520–529.
Pierce, A. D. (**1968**). "Spikes on sonic-boom pressure waveforms," J. Acoust. Soc. Am. **44**, 1052–1061.
Pierce, A. D., and Kang, J. (**1990**). "Molecular relaxation effects on sonic boom waveforms," in *Frontiers of Nonlinear Acoustics, Proceedings of the 12th International Symposium on Nonlinear Acoustics*, edited by M. F. Hamilton and D. T. Blackstock (Elsevier, London), pp. 165–170.
Pierce, A. D., and Maglieri, D. J. (**1972**). "Effects of atmospheric irregularities on sonic boom propagation," J. Acoust. Soc. Am. **51**, 702–721.
Raspet, R., Bass, H. E., Yao, L., Boulanger, P., and McBride, W. E. (**1994**). "Statistical and numerical study of the relationship between turbulence and sonic boom characteristics," J. Acoust. Soc. Am. **96**, 3621–3626.
Rudenko, O. V., and Soluyan, S. I. (**1977**). *Theoretical Foundations of Nonlinear Acoustics*, Studies in Soviet Science (Consultants Bureau, New York/Plenum, New York).
Tanter, M., Thomas, J.-L., and Fink, M. (**2000**). "Time reversal and the inverse filter," J. Acoust. Soc. Am. **108**, 223–234.
Thom, R. (**1972**). *Stabilité Structurelle et Morphogenèse* (Benjamin, Reading, MA), pp. 72–107.
Wanner, J. C., Vallée, J., Vivier, C., and Théry, C. (**1972**). "Theoretical and experimental studies of the focus of sonic booms," J. Acoust. Soc. Am. **52**, 13–32.
Whitham, G. B. (**1956**). "On the propagation of weak shock waves," J. Fluid Mech. **1**, 290–318.
Zabolotskaya, E. A., and Khokhlov, R. V. (**1969**). "Quasi-plane waves in the nonlinear acoustics of confined beams," Sov. Phys. Acoust. **15**, 35–40.
Zepler, E. E., and Harel, F. R. P. (**1965**). "The loudness of sonic booms and other impulsive sounds," J. Sound Vib. **2**, 249–256.

Aerodynamic sound generation of flapping wing

Youngmin Bae and Young J. Moon[a)]
Department of Mechanical Engineering, Korea University, Seoul 136-701, South Korea

(Received 21 November 2007; revised 29 April 2008; accepted 30 April 2008)

The unsteady flow and acoustic characteristics of the flapping wing are numerically investigated for a two-dimensional model of *Bombus terrestris* bumblebee at hovering and forward flight conditions. The Reynolds number Re, based on the maximum translational velocity of the wing and the chord length, is 8800 and the Mach number M is 0.0485. The computational results show that the flapping wing sound is generated by two different sound generation mechanisms. A primary dipole tone is generated at wing beat frequency by the transverse motion of the wing, while other higher frequency dipole tones are produced via vortex edge scattering during a tangential motion. It is also found that the primary tone is directional because of the torsional angle in wing motion. These features are only distinct for hovering, while in forward flight condition, the wing-vortex interaction becomes more prominent due to the free stream effect. Thereby, the sound pressure level spectrum is more broadband at higher frequencies and the frequency compositions become similar in all directions.
 [DOI: 10.1121/1.2932340]

PACS number(s): 43.28.Ra, 43.80.Ka, 43.50.Nm [AH] Pages: 72–81

I. INTRODUCTION

A flapping motion of the insect wing has many intriguing features for biologists, physicists, and engineers. For example, highly efficient flight performance of insects has fascinated engineers who are interested in developing a micromechanical flying insect (MFI) based on biomimetic principles. With this respect, a great deal of experimental[1–3] and numerical[4–6] studies have been conducted to understand the high-lift mechanism of the insect flight. On the contrary, the aerodynamic sound of flying insects has received less attention, although its acoustic characteristics and the associated generation mechanisms are important not only for the fundamental studies of insect physiology and evolution but also for their biomimetic applications.

The sound of a flying insect could be used for various biological functions such as sexual communication, territory defense, echolocation, etc. Earlier observation of Bennet-Clark and Ewing[7] showed that the sound from a flapping wing is often directional, i.e., dominant frequency changes around a flying insect. Sueur *et al.*[8] also analyzed both the radiation pattern and the frequency composition of the sound using a tethered flying *Lucilia sericata*, showing that the wing beat frequency is dominant in front of the fly, while its second harmonic is dominant at sides.

The frequency characteristics of the flapping wing sound also play an important role in the survival and courtship of the insects. In the study of Robert and Göpfert,[9] it was shown that the antennae of *D. melanogaster* respond to the sound physically similar to their own species. These observations afford a definite proof that, by analyzing the frequency characteristics as well as the sound directivity, insects are able to distinguish their own species from a comimic, or to detect and evade pursuers. Birds sometimes can perceive the signals emanated from their favorite preys.[10]

A biomimetic principle can be applied to the sound of a flying insect; for example, an engineering challenge to develop a MFI, which can maneuver within a confined space with other MFIs', via echolocation of the sound generated by their flapping wings. For the research of this kind, one should understand first how the flapping wing sound or the so-called "buzz" sound is generated during the flight.

The objective of this study is to provide more comprehensive explanations on the radiation pattern and sound generation mechanisms associated with the flapping wing sound. With this aim, the unsteady flow and acoustic characteristics of the flapping wing are numerically investigated for a two-dimensional model of *Bombus terrestris* bumblebee, even though three-dimensional (3D) flow physics and turbulence, 3D acoustical radiation, as well as the wing flexibility may be considered as effects something that can be added to the basic features studied in the present work. Furthermore, an effect of mean flow during the forward flight on flow and acoustic fields is investigated here, along with discussion on the effects of stroke plane angle of the flapping wing.

II. COMPUTATIONAL METHODOLOGIES

The sound from a flying insect is, in general, generated by a weak compressibility effect at very low Mach number, and its direct computation becomes problematic because the scale disparity between flow and acoustics grows inversely proportional to the Mach number. Thereby, a hydrodynamic/acoustic splitting method[11,12] is considered, in which flow and acoustic fields are computed separately with two different grid systems but coupled through an acoustic source term (DP/Dt). In this section, computational methods are described in detail and both the computational accuracy and efficiency of the present method are evaluated for a benchmark problem.

[a)]Author to whom correspondence should be addressed: electronic mail: yjmoon@korea.ac.kr.

A. Hydrodynamic/acoustic splitting method

In the hydrodynamic/acoustic splitting method, the total flow variables are decomposed into the incompressible and perturbed compressible variables as

$$\rho(\vec{x},t) = \rho_0 + \rho'(\vec{x},t), \tag{1}$$

$$\vec{u}(\vec{x},t) = \vec{U}(\vec{x},t) + \vec{u}'(\vec{x},t), \tag{2}$$

$$p(\vec{x},t) = P(\vec{x},t) + p'(\vec{x},t). \tag{3}$$

The incompressible variables of $\vec{U}$ and P represent hydrodynamic flow field, while acoustic fluctuations and other compressibility effects are resolved by perturbed quantities denoted by ($'$).

In the present study, the hydrodynamic flow field around the flapping wing is computationally modeled as a two-dimensional, incompressible, and laminar flow and computed by solving the incompressible Navier–Stokes equations (INS),

$$\nabla \cdot \vec{U} = 0, \tag{4}$$

$$\frac{\partial \vec{U}}{\partial t} + (\vec{U}\cdot\nabla)\vec{U} = -\frac{1}{\rho_0}\nabla P + \frac{\mu_0}{\rho_0}\nabla^2\vec{U}, \tag{5}$$

where ρ_0 and μ_0 are constant values of density and dynamic viscosity of a fluid, respectively.

The corresponding sound field is then calculated by the linearized perturbed compressible equations (LPCEs),

$$\frac{\partial \rho'}{\partial t} + (\vec{U}\cdot\nabla)\rho' + \rho_0(\nabla\cdot\vec{u}') = 0, \tag{6}$$

$$\frac{\partial \vec{u}'}{\partial t} + \nabla(\vec{u}'\cdot\vec{U}) + \frac{1}{\rho_0}\nabla p' = 0, \tag{7}$$

$$\frac{\partial p'}{\partial t} + (\vec{U}\cdot\nabla)p' + \gamma P(\nabla\cdot\vec{u}') + (\vec{u}'\cdot\nabla)P = -\frac{DP}{Dt}, \tag{8}$$

where $DP/Dt = \partial P/\partial t + (\vec{U}\cdot\nabla)P$ and γ is the specific heat ratio.

The left hand sides of LPCE represent the effects of acoustic wave propagation and refraction in the unsteady, inhomogeneous flows, while the right hand side only contains the acoustic source term, which will be projected from the hydrodynamic solution. For very low Mach number flows, it is interesting to note that the total change in hydrodynamic pressure DP/Dt is considered as the only explicit noise source term. The details of LPCE can be found in Ref. 12.

In order to include the effects of periodic wall motion, the governing equations are solved in a moving coordinate system. The components of the transformation matrix between the physical space (x,y,t) and computational space (ξ,η,τ) are defined by

$$\xi_x = \frac{y_\eta}{J}, \quad \xi_y = -\frac{x_\eta}{J}, \quad \eta_x = -\frac{y_\xi}{J}, \quad \eta_y = \frac{x_\xi}{J}, \tag{9}$$

$$\xi_t = \frac{(-x_\tau y_\eta + x_\eta y_\tau)}{J}, \quad \eta_t = \frac{(x_\tau y_\xi - x_\xi y_\tau)}{J}, \quad \tau = t, \tag{10}$$

where a Jacobian of the coordinate transformation $J = x_\xi y_\eta - x_\eta y_\xi$, and x_τ and y_τ represent moving velocities at each control surface which are determined using a second-order central difference. The moving wall boundary conditions, when used in the splitting method, can approximately be decomposed into the incompressible and perturbed variables as

$$\vec{U}_w = \frac{\partial \vec{x}_w}{\partial \tau}, \qquad \left.\frac{\partial P}{\partial n}\right|_w = 0 \tag{11}$$

and

$$\vec{u}_w'\cdot n = 0, \qquad \left.\frac{\partial \rho'}{\partial n}\right|_w = 0, \qquad \left.\frac{\partial p'}{\partial n}\right|_w = 0, \tag{12}$$

where n denotes a unit normal vector.

The LPCE is computed in a standard time-marching fashion, whereas the INS is solved by an iterative fractional step method (Poisson's equation for the hydrodynamic pressure). Both the INS and LPCE are solved in a body fitted moving grid system and integrated in time by a four-stage Runge–Kutta method and spatially discretized with a sixth-order compact finite difference scheme.[13] A tenth-order spatial filtering[14] is also applied every iteration in order to suppress high frequency errors that might be caused by grid nonuniformity. Since the INS and LPCE computations are conducted with different grids for computational efficiency,[11,12] a bilinear shape function is used in space to interpolate the source term DP/Dt and hydrodynamic variables onto the acoustic grid. This method maintains sufficient accuracy when interpolation is conducted from fine grid to coarse grid and this is always the case in the present study (hydrodynamic grid, fine; acoustic grid, coarse). For acoustic calculation, an energy transfer and annihilation boundary condition[15] with buffer zone is used for eliminating any reflections of out-going waves at the far-field boundaries.

B. Validation

In order to validate the aforementioned numerical methods applied with moving coordinates, a dipole sound generation from an oscillating cylinder is considered. As depicted in Fig. 1, a circular cylinder initially located in the middle of the computational domain periodically oscillates with the prescribed center position, $O(x,y) = (0, dh\sin(2\pi ft))$. A computational domain is set to $r = 500D$ and an O-type grid is used with 301×181 grid points distributed in the radial and circumferential directions, respectively. An unsteady laminar flow around the circular cylinder is calculated with the sound field. A quiescent air is used as an initial condition and Reynolds number Re_D, based on the maximum translational velocity and the cylinder diameter, is set to 1780. A characteristic Mach number (maximum translational velocity of the oscillating cylinder) is 0.03. The sound field is predicted by both direct numerical simulation (DNS) and INS/LPCE, and numerical results are compared with an analytical solution of Morse and Ingard[16]

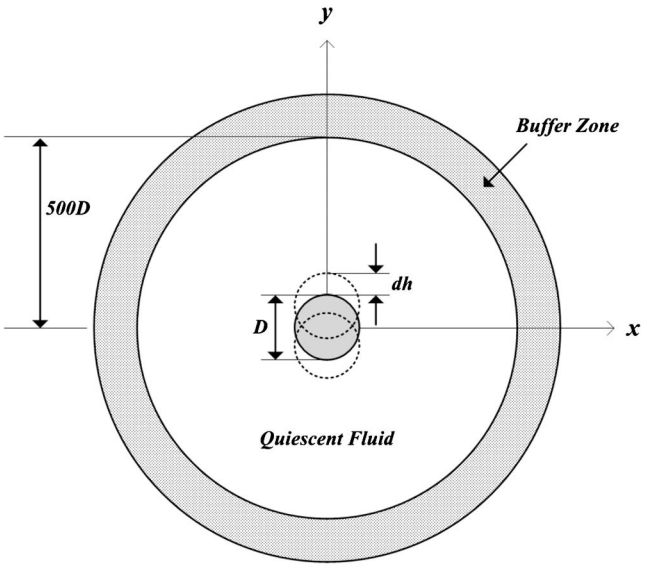

FIG. 1. Dipole sound by a vertically oscillating circular cylinder.

$$p(s,t) = \frac{\pi^3 f^2 \rho_0 D^2 U_0}{2c_0} \cos\varphi \left[J_1\left(\frac{2\pi fs}{c_0}\right) + iN_1\left(\frac{2\pi fs}{c_0}\right)\right] e^{-2\pi ift}, \quad (13)$$

where ρ_0 is the density, c_0 is the speed of sound, f is the oscillation frequency, D is the cylinder diameter, and $U_0(=2\pi f \times dh)$ is the maximum velocity at the cylinder surface. In Eq. (13), s denotes a radial distance from the cylinder center, φ is defined as an angle measured from the plane of vibration, and J_1 and N_1 indicate the first-order Bessel function and the Neumann functions, respectively.

Figure 2(a) shows the instantaneous pressure fluctuations, $\Delta p' = p - \bar{p}$ along the $x=0$ line for $f=0.05$, $dh=0.1$, with all the variables nondimensionalized by ρ_0, c_0, and D. First, the INS/LPCE result is in excellent agreement with the DNS solution. It also agrees well with the analytical solution except at y/D close to 0, in which any viscous effects were not taken into account. Furthermore, the directivity patterns at $r=50D$ shown in Fig. 2(b) are very well met. Thus, it is expected that the present INS/LPCE method has comparable accuracy to the DNS solution.

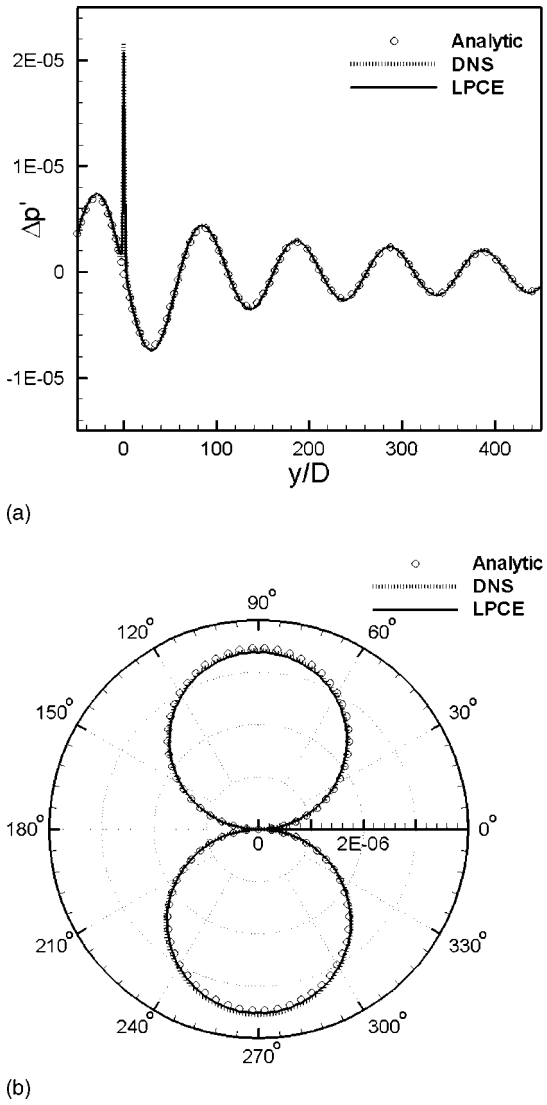

FIG. 2. (a) Instantaneous pressure fluctuation $\Delta p'$ distributions along the $x=0$ line and (b) directivity patterns of $\Delta p'$ at $r=50D$.

C. Computational efficiency

The computational efficiency of the present INS/LPCE method can be approximately estimated by simply comparing the time step of each method. According to the numerical stability condition, a time step is normally restricted by the characteristic speed as well as the minimum grid spacing. The time steps for DNS (or LPCE) and INS can be written as $\Delta t_{\mathrm{DNS}} = \mathrm{CFL} \times \Delta x_{\min}/(U_0 + c_0)$ and $\Delta t_{\mathrm{INS}} = \mathrm{CFL} \times \Delta x_{\min}/U_0$, respectively. For low Mach number flows ($M_0 < 0.1$), the time step allowed for DNS can be approximated as $\Delta t_{\mathrm{DNS}} = M_0 \times \Delta t_{\mathrm{INS}}$, if the same grid size and CFL number are used for DNS and INS. On the other hand, if the minimal grid spacing for LPCE is enlarged $1/M_0$ times that for INS, then the time step for LPCE could become comparable to that of INS. Thus, computational efficiency of the splitting method is proportional to the ratio, $\Theta = \Delta x_{\min,A}/\Delta x_{\min,H}$ (A, acoustics; II, hydrodynamics). For considering the spatial accuracy of LPCE, Θ is usually set to 5 and the required computational time for the present benchmark problem ($M=0.03$) is approximately six to nine times less than that for the DNS. The details on computational efficiency of the splitting method can be found in Ref. 11.

III. WING MODEL

In this study, the time-dependent flow and acoustic fields are computed for the prescribed flapping wing motions which mimic the real wing kinematics employed by superposition of the pitching and heaving motions, sometimes referred to as a figure-eight motion.[4] Figure 3 illustrates the flapping motion of a two-dimensional elliptic wing (chord length c and thickness $d=0.1c$). The unsteady motion is replicated by a wing motion of two strokes (down and up), and

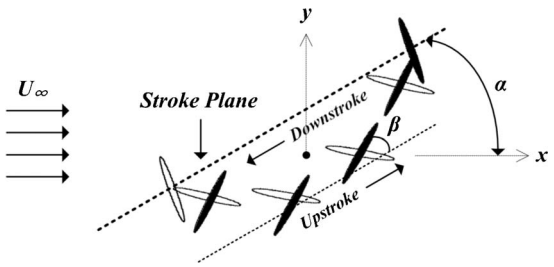

FIG. 3. Flapping motion of an elliptic wing. The downstroke is indicated by the hollow ellipses and the upstroke by the filled ellipses.

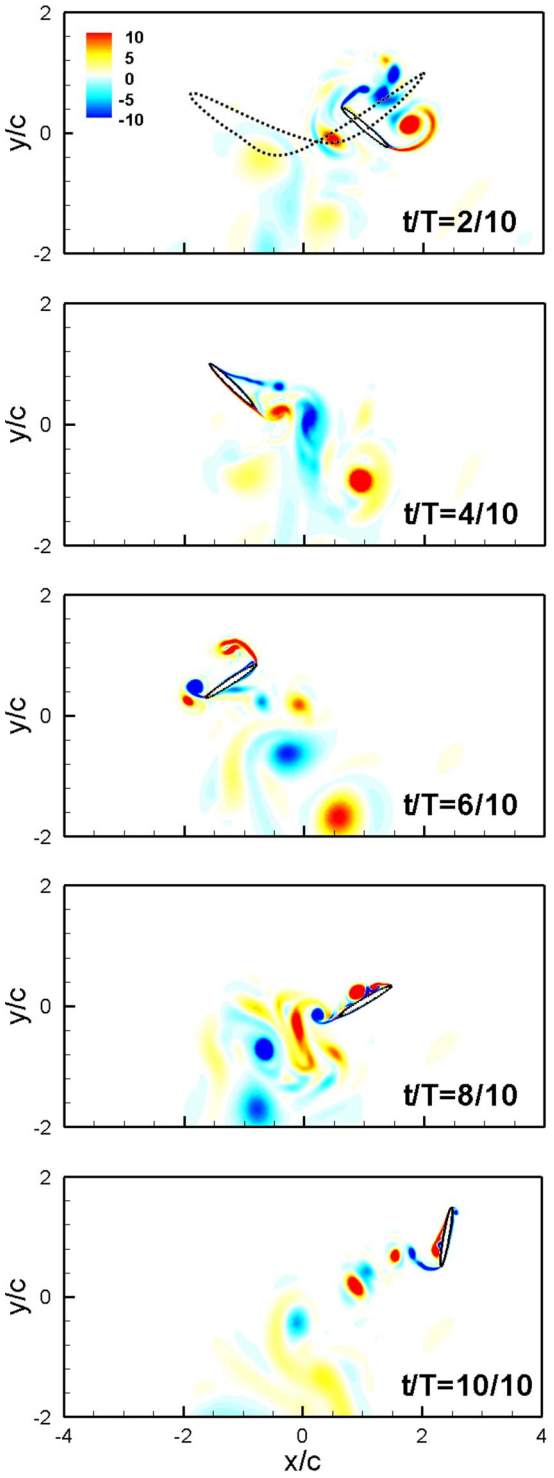

FIG. 4. (Color online) Time evolution of vorticity fields around the flapping wing in one period at $\alpha=0$, $U_\infty=0$ (hovering). $T=1/f$ denotes a period and the black dotted line indicates the stroke path tracing the center of the wing.

each stroke consists of three stages (transverse, tangential, and rotational motions). The stroke plane is set to an inclined angle of α (or called stroke plane angle), while the wing motion at the center is described by

$$x(t)/c = 0.4 + 2\cos(2\pi ft),$$

$$y(t)/c = 0.5 + 0.5\cos(4\pi ft) - 0.2\exp\left[-200\left(\frac{t}{T} - \frac{2}{3}\right)^2\right], \tag{14}$$

where f is the wing beat frequency and $T(=1/f)$ denotes a period. A torsional angle β, the angle between the stroke plane and the line that connects the wing head and the tip, is determined by

$$\beta(t) = 80 + 60\tanh(1.6/|4tf-1| - 1.6|4tf-1|) \quad \text{for} \quad 0 \leqslant t < \frac{T}{2},$$

$$\beta(t) = 80 - 50\tanh(1.6/|4tf-3| - 1.6|4tf-3|) \quad \text{for} \quad \frac{T}{2} \leqslant t < T. \tag{15}$$

Here, all the specific parameters of the flapping wing are based on a *Bombus terrestris* bumblebee.[17,18] Chord length (c) is 0.8 cm, wing span (R) which is the distance from base of the wing to tip is 1.7 cm, beat frequency (f) is 170 Hz, and stroke amplitude (Φ) is 150°, defined as the angle swept out by the leading edge from dorsal reversal (start of downstroke) to ventral reversal (start of upstroke) in the mean stroke plane.

IV. RESULTS AND DISCUSSION

This study investigates the flow and acoustic characteristics of the flapping wing at hovering and forward flight conditions. A computational domain of circle is extended to $r=500c$, and the nondimensional beat frequency $St=fc/c_0$ is set to 0.004. The INS calculation is conducted with moving hydrodynamic grid (401×181) in order to compute the flow field around the flapping wing. The sound field is then com-

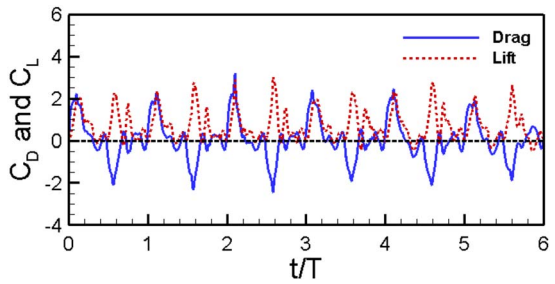

FIG. 5. (Color online) Time history of drag and lift coefficients during hovering.

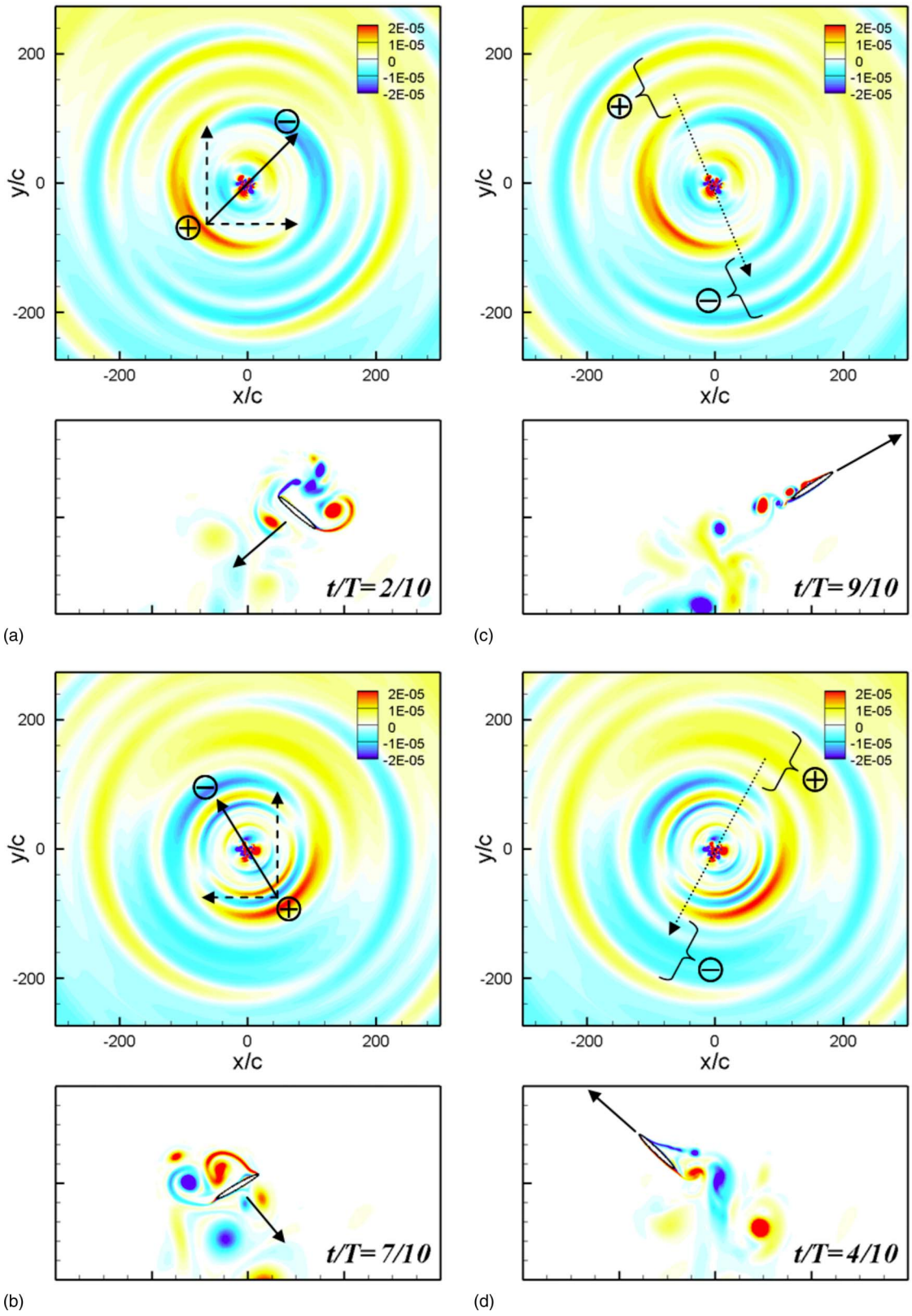

FIG. 6. (Color online) Top: instantaneous pressure fluctuation $\Delta p' = (P+p') - (\overline{P+p'})$ contours around the wing in hovering motion at $t/T=0.5$ for (a) and (c) and at $t/T=1$ for (b) and (d). The pressure fluctuations are normalized by ρc_0^2, where c_0 is the speed of sound. Bottom: hydrodynamic flow fields representing the associated sound sources: [(a) and (b)] wing loading by transverse motion and [(c) and (d)] vortex edge-scattering during tangential motion.

puted by LPCE on the moving acoustic grid (251×91), with minimum grid spacing five times that of the hydrodynamic grid. Both the INS and LPCE are coupled through an acoustic source term, DP/Dt and solved with the same time step so that a time interpolation between INS and LPCE is avoided. Also note that all the variables investigated here are nondimensionalized by the speed of sound c_0, chord length c, and air density ρ_0.

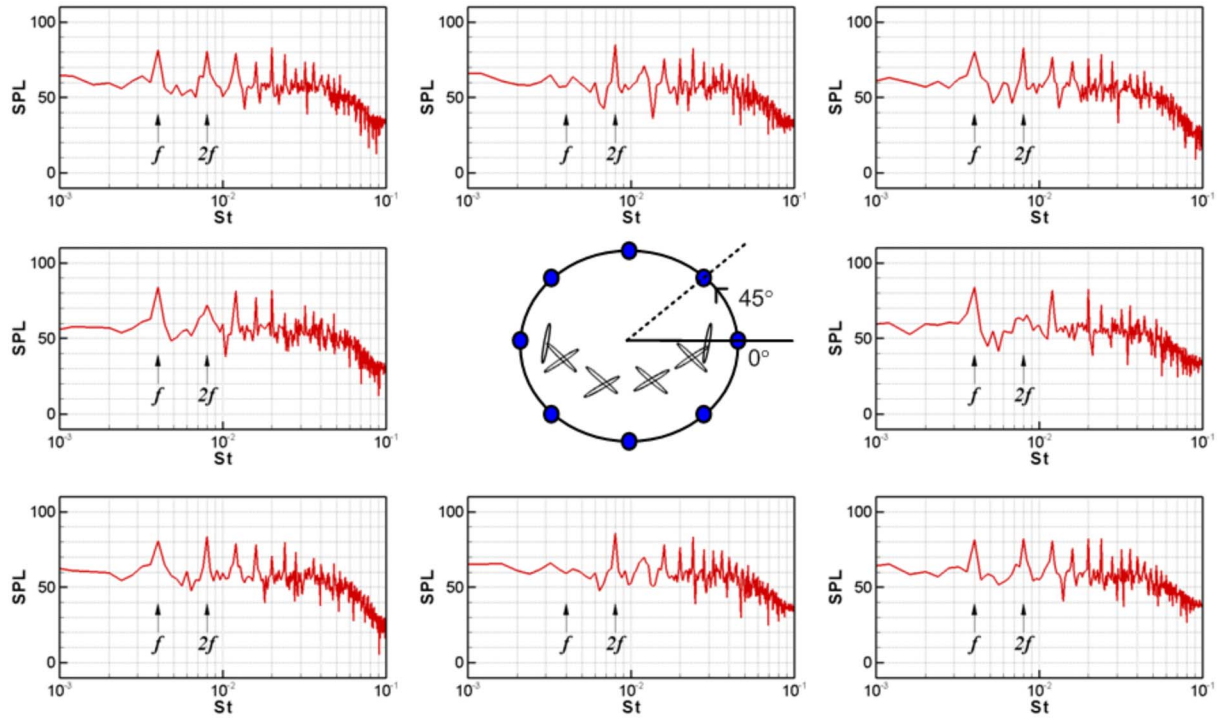

FIG. 7. (Color online) Sound pressure level (SPL) spectra around a hovering insect ($\alpha=0°$ and $\Psi=0$; $U_\infty=0$ m/s) at $r=100c$ and every 45° position.

A. Hovering

First, the flow and sound fields are computed for the flapping wing in hovering motion. For hovering, the flapping angle α is set to 0 and the advance ratio defined by the ratio of the flight speed to the mean flapping velocity of the wing $\Psi=U_\infty/(2\Phi fR)$ [18] is also set to 0. The Reynolds number based on the maximum translational velocity, $\mathrm{Re}_c=U_{\max}c/\nu_{\mathrm{air}}$ is 8800 and the Mach number $M=U_{\max}/c_0$ is 0.0485, where c_0 is the speed of sound.

Figure 4 shows the time evolution of the computed vorticity field around the wing for one cycle of the hovering motion. In the transverse motion ($t/T=1/10\sim2/10$), the leading and trailing-edge vortices are generated in large scale. During tangential motion ($t/T=3/10\sim4/10$), the eddies shed from the leading-edge scatter at the trailing-edge, and at the end of the downstroke ($t/T=5/10$), the rotational motion lets the leading-edge vortex be swept away from the wing so that the dipole vortices move downward by themselves due to their induced velocity fields. This process is repeated in another half cycle. It is interesting to note that the commoving vortices created in the previous downstroke (or upstroke) do not interfere with the formation of the vortices during another half cycle because they have been already out of the stroke path through a self-propelled motion.

The time variations of the drag and lift coefficients of the flapping wing are also presented in Fig. 5, which are constructed from the vertical and horizontal forces, respectively. It is indicated that the mean drag coefficient (averaged over ten periods) is nearly 0, while the mean lift coefficient is about 0.66. From the definition of $C_L=F_L/0.5\rho_0U_{\max}cR$, one can calculate the lift force on a 3D wing, employing the properties of the bumblebee.[17] In this study, the maximum translational velocity $U_{\max}$ of the bumblebee is 17 m/s so that the lift force generated by a pair of 3D wing is about 3.11×10^{-2} N. This value is large enough to support the weight of bumblebee, 8.63×10^{-3} N, although the 3D effects neglected in this study could partially reduce the lift force.

The computed sound fields of the flapping wing in hovering motion are presented in Fig. 6. The result indicates that the flapping wing sound is generated by two different basic mechanisms. First, a dipole sound is generated by a transverse motion of the wing [Figs. 6(a) and 6(b)]. Due to the fact that the dipole axis changes its direction from downstroke to upstroke, a drag dipole is generated at wing beat frequency ($St=fc/c_0=0.004$), while the lift dipole is produced at $2f$ (i.e., $St=0.008$), similar to the drag and lift coefficients. Hence, the flapping wing sound is directional, as shown in Fig. 7. The sound pressure level (SPL) peak corresponding to the lift dipole ($St=0.008$) is not present or weak at 0° and 180°, while the wing beat frequency (drag dipole) is also not present at 90° and 270°. At other angles, both the drag and lift dipoles clearly exhibit their peaks. This result is similar to the previous observation by Sueur *et al.*,[8] indicating that the wing beat frequency is most dominant in front, whereas the second harmonic is most appreciable at sides.

Another sound source is associated with the vortex edge scattering during tangential motion of the wing. In Figs. 6(c) and 6(d), one can identify the sound waves (bracketed) at $150c\sim175c$ from the center with wavelengths (λ) observed as $41c$ and $48c$ at $t/T=0.5$ and 1, respectively. Considering the wave speed c_0(=340 m/s=$250c/T$), the travel time of the waves is estimated as $0.6\sim0.7$ (i.e., $\Delta t/T=150/250\sim175/250$). So, it is figured that these waves were generated during $t/T=8/10\sim9/10$ and $3/10\sim4/10$ at each stroke. Now, one can note that the flow fields at $t/T=9/10$ and $4/10$ clearly exhibit the vortical structures that are responsible for

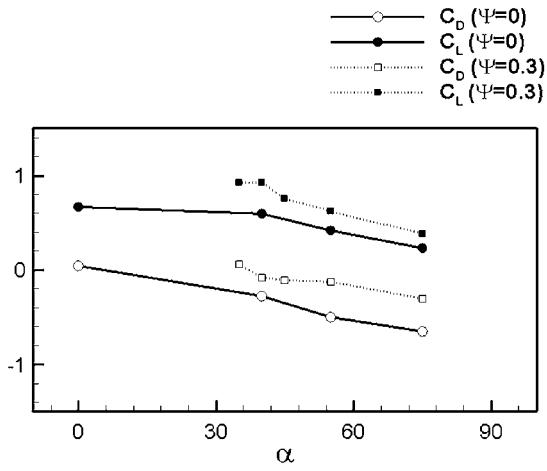

FIG. 8. Mean drag and lift coefficients versus stroke plane angle α for hovering ($\Psi=0$) and forward flight ($\Psi=0.3$).

producing the dipole sound during tangential motion of the wing. The vortices in the shear layer emanated from the leading-edge scatter at the trailing-edge of the wing and generate waves radiating perpendicularly to the wing. It is also found that the frequencies of these waves are close to $St(=fc/c_0=c/\lambda)=1/48\simeq 0.02$ and $1/41\simeq 0.024$. These frequencies of dipole tones generated at the trailing-edge agree fairly well with the theory of shear layer instability:[19] the frequency of the shear layer breaking-off is calculated as 0.021 with $St=0.017M_L/\theta$, where $M_L=0.044$ is a local free stream Mach number and $\theta=0.035$ is the momentum thickness normalized by the chord length at $t/T=9/10$, for example. Finally, one can note in the spectrum that the SPL peaks are multiples of the wing beat frequency with comparable amplitudes (see Fig. 7). This frequency composition closely resembles the buzz sound of fly measured by Sueur *et al.*[8]

B. Forward flight

In order to mimic the forward flight of bumblebee, the wing motion and its related parameters must be selected properly. In the previous studies,[18,20] it was shown that the wing beat frequency and stroke amplitude of the bumblebee are not significantly different, as compared to the hovering motion. So, all the properties are kept constant, except the advance ratio Ψ and stroke plane angle α.

The advance ratio is generally used to determine the free stream velocity U_∞. It ranges from 0 (hovering) to 0.6 (fast flight),[21,22] and an intermediate value of $\Psi=0.3$ corresponding to $U_\infty=4.5$ m/s is considered in this study. The stroke plane angle is then determined by the force balance condition;[21] the mean thrust must be equal to the mean drag for a flight at constant speed. Figure 8 presents the computed mean drag and lift coefficients associated with the advance ratio and the stroke plane angle. In the presence of free stream velocity ($\Psi=0.3$), it is found that the mean drag coefficient is nearly 0 at $\alpha=40°$. At this angle, the thrust force generated by the flapping wing is almost the same as the drag force caused by the forward flight of bumblebee. So, the

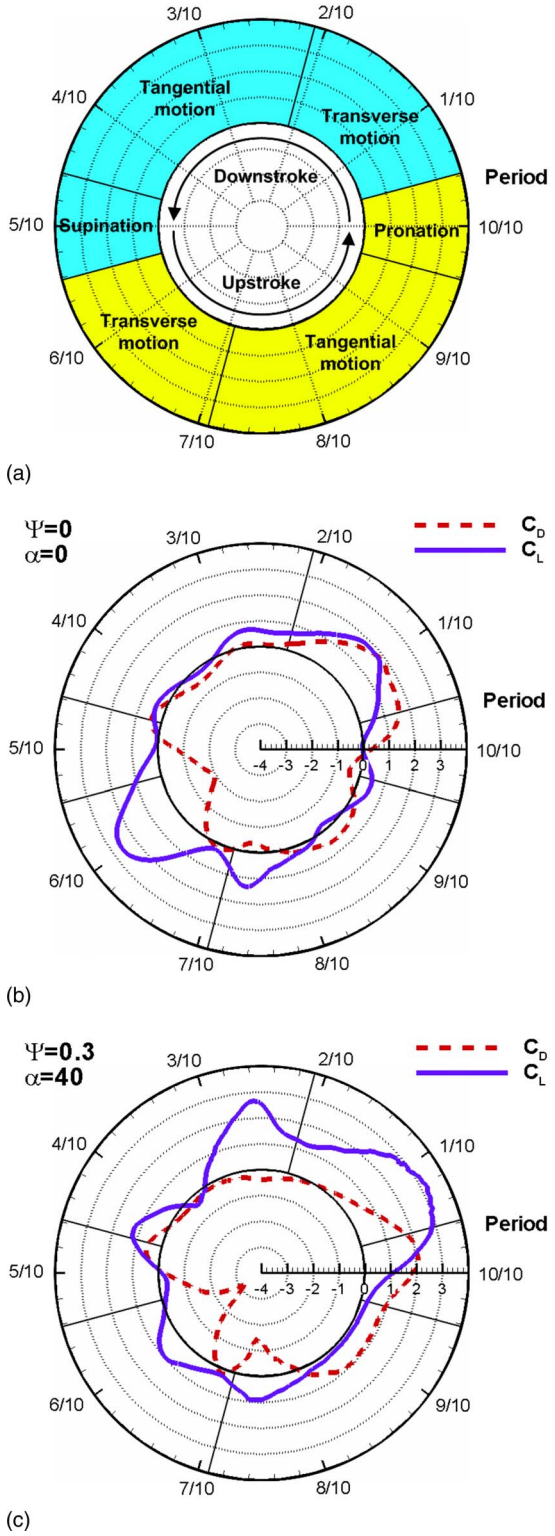

FIG. 9. (Color online) (a) Wing drag and lift coefficients averaged over ten periods during one cycle for (b) $\alpha=0°$ and $\Psi=0$ at hovering, and (c) $\alpha=40°$ and $\Psi=0.3$ at forward flight.

stroke plane angle is determined as $\alpha=40°$, which is very similar to the real bumblebee[18] for the flight speed at $U_\infty=4.5$ m/s.

To describe the effects of stroke plane angle and flight speed, the flapping wing motion is investigated in Fig. 9, where their aerodynamic roles are examined with the drag and lift coefficients (averaged over ten periods). At hovering

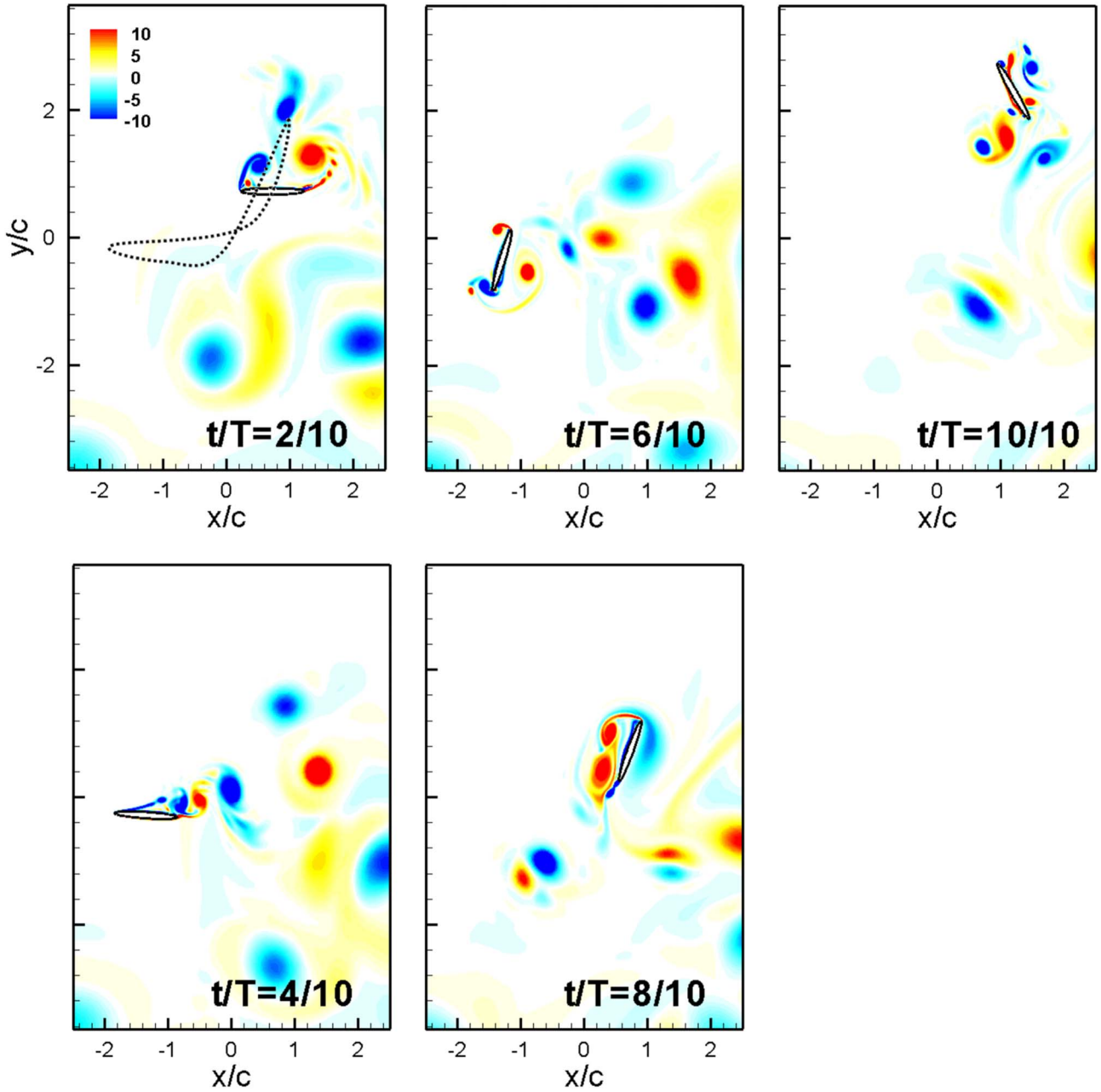

FIG. 10. (Color online) Time evolution of vorticity fields around the flapping wing at $\alpha=40°$ and $\Psi=0.3$ (forward flight). The black dotted line indicates the stroke path of the forward flight.

($\alpha=0°$ and $\Psi=0$), a positive lift is contributed by the transverse motions in both down- and upstroke. The same wing motions also create positive and negative drags (or negative and positive thrust) so that the mean drag is equal to 0, satisfying the force balance condition. Here, the tangential motion at hovering is nearly not related to any generation of lift or drag in down- or upstroke. On the other hand, if the flapping wing is imposed with the given free stream velocity ($\alpha=40°$ and $\Psi=0.3$), lift and thrust are generated by the downstroke and upstroke motions of the wing, respectively. During downstroke, the transverse motion as well as the tangential motion of the wing play a noticeable role in lift generation. The lift peak during tangential motion in downstroke may be due to the interaction between the wing and the vortices, which is called a "wake capture."[3,23] The wake capture will be discussed later in association with the sound generation. In this case, the mean drag is also nearly 0, satisfying the force balance condition because the tangential motion in upstroke and pronation produces a positive drag to compensate the negative drag generated by the transverse motion in upstroke. These aerodynamic roles in forward flight agree well with the previous studies on bumblebees[18,24] and fruit flies.[21]

Now, Fig. 10 shows the vortical structure around the wing at forward flight with $\alpha=40°$ and $U_\infty=4.5$ m/s. Due to the free stream effect, the vortices shed from the leading and trailing edge of the wing during transverse motion do not develop as symmetric as for the hovering case and so are the induced velocity fields. Therefore, these vortices cannot self-propel away from the wing but rather remain in the stroke

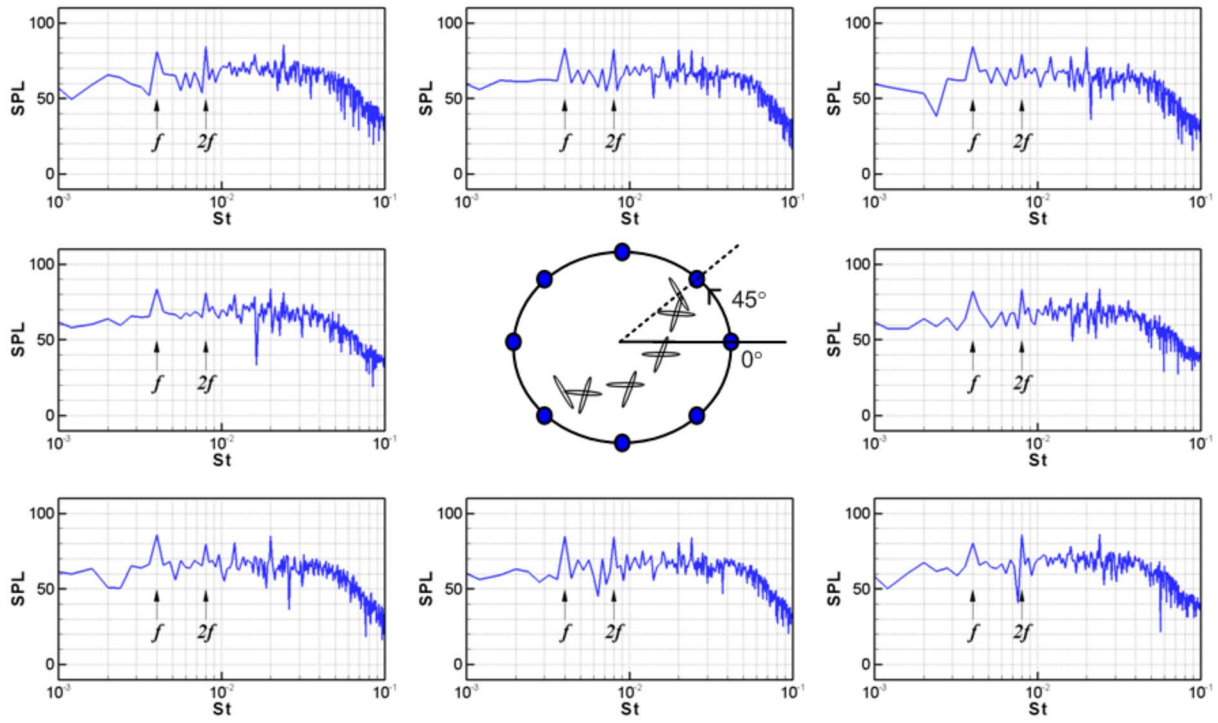

FIG. 11. (Color online) SPL spectra around the flapping wing in forward flight (α=40° and Ψ=0.3; U_∞=4.5 m/s) at r=100c and every 45° position.

paths. Besides, the ratio between the free stream velocity and the maximum translational velocity of the wing is close to 0.26 and so the convection effect is quite weak. As a result, the vortices drifting around the flapping wing encounter complex wing-vortex interactions (t/T=8/10). When compared with the hovering case, this clear distinction in vortical flow structure is expected to change the aerodynamic sound characteristics for the forward flight case.

The sound fields for the flapping wing in forward flight are investigated by comparing the sound spectra in Fig. 11. Similar to the hovering case, the transverse motion of the dipolar axis results in drag (St=0.004) and lift dipoles (St=0.008). It is, however, important to note that the directivity change is not as clear as that at hovering. The dominant frequency does not vary significantly and both the drag and lift dipoles exhibit their peaks with comparable amplitudes, regardless of directions. One may also note that the dipole tones generated at the trailing edge (St=0.02 and 0.024) are not as distinct as for the hovering case (Fig. 7). These are largely due to the prominent interactions between the wing and the vortices being considered as a discernible difference in acoustic feature between hovering and forward flight. This indicates that the radiation pattern and frequency composition can change with flight conditions and it is expected that these could be used as some biological functions such as communication, territory defense, and echolocation.

V. CONCLUSIONS

This study investigates the flow and acoustic characteristics of the bumblebee at hovering (α=0° and Ψ=0) and forward flight (α=40° and Ψ=0.3) conditions. The computed results show that, within the limits of two-dimensional computation and rigid wing assumption, the flapping wing sound is mainly generated by the transverse and tangential motions of the wing with different sound generation mechanisms. A primary dipole tone at wing beat frequency is generated by the transverse motion, while other dipole tones at higher frequencies are produced during tangential motion via scattering of the vortex at the trailing edge of the wing. It is also found that the frequency composition of the primary tone changes with the angle (drag and lift dipoles) because of the torsional angle of the wing motion. This feature is only distinct for hovering, while at forward flight condition, the dipole tone at wing beat frequency is generated not only by the transverse motion but also by the wing-vortex interactions during upstroke. This wing-vortex interaction at forward flight also makes the SPL spectrum more broadband. This is a quite discernible acoustic feature between the hovering and forward flight conditions, which may be used to elucidate a certain biological function. In the future, a more comprehensive investigation will be conducted, considering the effects of 3D flow physics and turbulences as well as the wing flexibility.

[1]C. P. Ellington, C. van den Berg, A. P. Willmott, and A. L. R. Thomas, "Leading-edge vortices in insect flight," Nature (London) **384**, 626–630 (1996).
[2]J. M. Birch and M. H. Dickinson, "Spanwise flow and the attachment of the leading-edge vortex on insect wings," Nature (London) **412**, 729–733 (2001).
[3]M. H. Dickinson, F. O. Lehmann, and S. P. Sane, "Wing rotation and the aerodynamic basis of insect flight," Science **284**, 1954–1961 (1999).
[4]Z. J. Wang, "Two dimensional mechanism for insect hovering," Phys. Rev. Lett. **85**, 2216–2219 (2000).
[5]M. Sun and J. Tang, "Unsteady aerodynamic force generation by a model fruit fly wing in flapping motion," J. Exp. Biol. **205**, 55–70 (2002).
[6]M. Sun and J. Tang, "Lift and power requirements of hovering flight in *drosophila*," J. Exp. Biol. **205**, 2413–2427 (2002).
[7]H. C. Bennet-Clark and A. Ewing, "The wing mechanism involved in the courtship of *drosophila*," J. Exp. Biol. **49**, 117–128 (1968).

[8]J. Sueur, E. J. Tuck, and D. Robert, "Sound radiation around a flying fly," J. Acoust. Soc. Am. **118**, 530–538 (2005).
[9]D. Robert and M. C. Göpfert, "Acoustic sensitivity of fly antennae," J. Insect Physiol. **48**, 189–196 (2002).
[10]R. B. Srygley, "Evolution of the wave: aerodynamic and aposematic functions of butterfly wing motion," Proc. R. Soc. London, Ser. B **274**, 913–917 (2007).
[11]J. H. Seo and Y. J. Moon, "Perturbed compressible equations for aeroacoustic noise prediction at low mach numbers," AIAA J. **43**, 1716–1724 (2005).
[12]J. H. Seo and Y. J. Moon, "Linearized perturbed compressible equations for low mach number aeroacoustics," J. Comput. Phys. **218**, 702–719 (2006).
[13]S. K. Lele, "Compact finite difference schemes with spectral-like resolution," J. Comput. Phys. **103**, 16–42 (1992).
[14]D. Gaitonde, J. S. Shang, and J. L. Young, "Practical aspects of higher-order numerical schemes for wave propagation phenomena," Int. J. Numer. Methods Eng. **45**, 1849–1869 (1999).
[15]N. B. Edgar and M. R. Visbal, "A general buffer zone-type non-reflecting boundary condition for computational aeroacoustics," Proceedings of the 9th AIAA/CEAS Aeroacoustics Conference, 2003, AIAA Paper No. 2003–3300.
[16]P. M. Morse and K. U. Ingard, *Theoretical Acoustics* (McGraw-Hill, New Jersey, 1968).
[17]T. Weig-Fogh, "Quick estimates of flight fitness in hovering animals, including novel mechanism for lift production," J. Exp. Biol. **59**, 169–230 (1973).
[18]R. Dudley and C. P. Ellington, "Mechanics of forward flight in bumblebees. i. kinematics and morphology," J. Exp. Biol. **148**, 19–52 (1990).
[19]W. K. Blake, *Mechanics of Flow-Induced Sound and Vibration* (Academic, Orlando, 1986), Vol. 4.
[20]A. P. Willmott and C. P. Ellington, "The mechanics of flight in the hawkmoth *manduca sexta.* i. kinematics of hovering and forward flight," J. Exp. Biol. **200**, 2705–2722 (1997).
[21]M. Sun and J. H. Wu, "Aerodynamic force generation and power requirements in forward flight in a fruit fly with modeled wing motion," J. Exp. Biol. **206**, 3065–3083 (2003).
[22]A. R. Ennos, "The kinematics of aerodynamics of the free flight of some diptera," J. Exp. Biol. **142**, 49–85 (2002).
[23]M. H. Dickinson, "The effects of wing rotation on unsteady aerodynamic performance at low Reynolds numbers," J. Exp. Biol. **192**, 179–206 (1994).
[24]R. Dudley and C. P. Ellington, "Mechanics of forward flight in bumblebees. ii. quasisteady lift and power requirements," J. Exp. Biol. **148**, 53–88 (1990).

Uncertainty estimation in simultaneous Bayesian tracking and environmental inversion

Stan E. Dosso[a] and Michael J. Wilmut
School of Earth and Ocean Sciences, University of Victoria, Victoria, British Columbia, Canada V8W 3P6

(Received 19 February 2008; revised 7 April 2008; accepted 9 April 2008)

This paper develops a Bayesian approach for two related inverse problems: tracking an acoustic source when ocean environmental parameters are unknown, and determining environmental parameters using acoustic data from an unknown (moving) source. The formulation considers source and environmental parameters as unknown random variables constrained by noisy acoustic data and by prior information on parameter values (e.g., physical limits for environmental properties) and on inter-parameter relationships (limits on radial and vertical source speed). The goal is not simply to estimate parameter values, but to rigorously determine parameter uncertainty distributions, thereby quantifying the information content of the data/prior to resolve source and environmental parameters. Results are presented as marginal posterior probability densities (PPDs) for environmental parameters and joint marginal PPDs for source ranges and depths. Given the numerically intensive inversion, an efficient Markov-chain Monte Carlo importance-sampling approach is developed which combines Metropolis and heat-bath Gibbs' sampling, employs efficient proposal distributions based on a linearized PPD approximation, and considers nonunity sampling temperatures to ensure a complete parameter search. The approach is illustrated with two simulated examples representing tracking a quiet submerged source and geoacoustic inversion using noise from an unknown ship of opportunity. In both cases, source, seabed, and water-column parameters are unknown. © *2008 Acoustical Society of America.* [DOI: 10.1121/1.2918244]

PACS number(s): 43.30.Pc, 43.30.Wi, 43.60.Pt [AIT] Pages: 82–97

I. INTRODUCTION

Matched-field methods have been applied extensively to the problems of source localization/tracking[1–7] and geoacoustic inversion[8–16] based on matching (correlating) acoustic fields measured at a sensor array with replica fields computed using a numerical propagation model. In matched-field processing (MFP) for localization, replica fields are computed for a grid of trial source locations. The computed matches are displayed as a function of range and depth (referred to as an ambiguity surface), and the source location is estimated as the position of maximum match, with the ambiguity surface providing a qualitative indication of the uncertainty of this estimate. In matched-field inversion (MFI), the matching procedure is carried out over unknown seabed parameters. Due to the high dimensionality and nonlinearity of the parameter space, global search methods are generally used to estimate the optimal geoacoustic model.[8–11] More recently, Bayesian methods have been applied to MFI to estimate quantitative geoacoustic parameter uncertainties from the posterior probability density (PPD), which combines data and prior information.[12–16]

Matched-field localization and geoacoustic inversion problems are related, since MFP requires an estimate of geoacoustic parameters and MFI requires an estimate of source locations; in both cases errors in these estimates degrade solutions. In MFI of controlled-source data, source locations are often included as unknown parameters with small search bounds to account for experimental uncertainty. However, if source locations are unknown over a wide region (e.g., ship-noise inversion employing an unknown ship of opportunity), expanding the source search region beyond a small correction can admit a large number of local optima to the parameter space and greatly increase the complexity of the inverse problem.[17,18]

In MFP, errors in geoacoustic parameters result in biased localization errors, referred to as environmental mismatch,[19–21] which often represents the limiting factor for localization. The method of focalization[22–24] addresses environmental uncertainty in MFP by including environmental parameters as additional unknowns in an augmented localization problem. This problem is solved using a global search which provides the optimal source location, but no indication of localization uncertainty (e.g., no ambiguity surface).

The optimum uncertain field processor[25–27] (OUFP) represents a Bayesian approach to MFP with environmental uncertainty, based on integrating the PPD over uncertain environmental parameters to produce a joint marginal probability distribution over source range and depth, referred to as a probability ambiguity surface (PAS). The peak of the PAS represents the most probable source location, and the distribution itself provides a quantitative measure of localization uncertainty. In OUFP, approximate integration is carried out by drawing a fixed number of Monte Carlo samples from the prior distribution for environmental parameters. A similar method, referred to as Bayesian focalization,[18] computes PASs by applying Markov-chain Monte Carlo importance-sampling methods which draw samples directly from the PPD (rather than the prior) with a rigorous convergence cri-

[a]Author to whom correspondence should be addressed. Electronic mail: sdosso@uvic.ca

 0001-4966/2008/124(1)/82/16/$23.00

terion. This approach was applied to shallow-water Mediterranean Sea data to investigate which combinations of data information (i.e., signal-to-noise ratio, SNR, and number of frequencies) and prior environmental information (i.e., uncertainties on water-column and seabed parameters) allowed successful localization.[18]

The OUFP approach has been extended to source tracking in an uncertain environment to produce the optimum uncertain field tracking algorithm[28] (OUFTA). OUFTA is a sequential algorithm that, in addition to Monte Carlo sampling over environmental priors, builds ambiguity surfaces of track probabilities incorporating constraints on allowable source motion. Hence, the track ambiguity surface for a given data observation is influenced by previous observations but is independent of later observations, and the surfaces tend to become more focused along the track. The goal is to obtain the most probable source track. OUFTA has been successfully applied to shallow-water Pacific data.[29]

Including environmental parameters in MFP or including source parameters in MFI can both be accommodated within a general Bayesian formulation in which source and environmental parameters are treated as unknowns, with the goal of estimating uncertainty distributions for all parameters from the multidimensional PPD. This goal is pursued here for the general case of multiple acoustic observations of a moving source. The localization/tracking aspect of this inversion has some conceptual similarities to OUFTA, but with several important differences. The Bayesian algorithm developed here treats acoustic data from a series of observations together in a simultaneous inversion. This provides the most informative solution, since data from multiple source locations are brought to bear simultaneously on the environmental unknowns, which in turn better constrain source locations. Further, by applying track constraints as interparameter prior information in simultaneous inversion, the PAS for each location of the source is influenced by all acoustic data (e.g., PASs for early source locations along a track are constrained by later data), treating all source locations in an equivalent manner. Probability distributions for source and environmental parameters computed in this manner quantify the total information content of acoustic data from multiple source locations (together with prior information). Rigorous computation of these probability distributions, rather than parameter estimation, represents the primary goal of this paper, although optimal parameter estimates (with uncertainties) are easily extracted from the distributions. Finally, although the algorithm inverts all data simultaneously, if additional observations become available after an inversion is carried out, they can be incorporated efficiently into an augmented model using sequential Bayesian methods (i.e., applying the PPD from one inversion as prior in a subsequent inversion), although this extension is not considered here.

While simultaneous inversion captures the full information content of moving-source acoustic data, it can substantially increase the dimensionality and complexity of the problem, particularly when track constraints are imposed. Given this numerically challenging inversion, an efficient Markov-chain Monte Carlo importance-sampling approach is applied which combines Metropolis and heat-bath Gibbs' sampling (GS) to sample from the PPD,[18] and several innovations are introduced to Bayesian ocean acoustic inversion. These include drawing parameter perturbations in Metropolis GS from a proposal distribution[30,31] based on a linearized approximation to the PPD to improve sampling efficiency, and employing nonunity sampling temperatures[32] to ensure complete sampling of the parameter space.

The remainder of this paper is organized as follows. Section II describes the theoretical basis for the new inversion algorithm, including the Bayesian formulation, GS, proposal distributions, and sampling temperatures. Section III illustrates the approach with synthetic examples representing tracking a quiet submerged source and environmental inversion using noise from a ship of opportunity. Finally, Sec. IV summarizes and discusses this work.

II. THEORY AND ALGORITHM

A. Bayesian matched-field formulation

This section summarizes the Bayesian approach to source localization/tracking and geoacoustic inversion; more complete treatments of Bayesian theory can be found elsewhere.[31,33,34] Let $\mathbf{d}$ represent the acoustic data from a source at one or more locations and $\mathbf{m}$ represent the model comprised of the unknown source locations and environmental parameters, with elements of both vectors considered to be random variables. Bayes' rule may be written

$$P(\mathbf{m}|\mathbf{d}) \propto P(\mathbf{d}|\mathbf{m})P(\mathbf{m}), \tag{1}$$

where the PPD, $P(\mathbf{m}|\mathbf{d})$, represents the state of information for the model incorporating both data information, $P(\mathbf{d}|\mathbf{m})$, and prior information, $P(\mathbf{m})$. Interpreting the conditional probability $P(\mathbf{d}|\mathbf{m})$ as a function of $\mathbf{m}$ for the (fixed) measured data defines the likelihood function, $L(\mathbf{m}) \propto \exp[-E(\mathbf{m})]$, where E is the data misfit function (considered below). Combining data and prior as a generalized misfit

$$\phi(\mathbf{m}) \equiv E(\mathbf{m}) - \log_e P(\mathbf{m}), \tag{2}$$

the PPD can be written

$$P(\mathbf{m}|\mathbf{d}) = \frac{e^{-\phi(\mathbf{m})}}{\int e^{-\phi(\mathbf{m}',\mathbf{d})} d\mathbf{m}'}, \tag{3}$$

where the domain of integration spans the M-dimensional parameter space.

In the Bayesian formulation, the PPD represents the general solution to the inverse problem. However, since high-dimensional distributions cannot be easily understood, the PPD is typically interpreted by computing properties defining parameter estimates, parameter uncertainties, and interparameter relationships. Parameter estimates include the maximum *a posteriori* (MAP) estimate (i.e., the most-probable model) and the posterior mean model, defined

$$\hat{\mathbf{m}} = \mathrm{Arg}_{\max}\{P(\mathbf{m}|\mathbf{d})\}, \tag{4}$$

$$\bar{\mathbf{m}} = \int \mathbf{m}' P(\mathbf{m}'|\mathbf{d}) d\mathbf{m}'. \tag{5}$$

Parameter uncertainties can be quantified by the model covariance matrix

$$\mathbf{C_m} = \int (\mathbf{m}' - \bar{\mathbf{m}})(\mathbf{m}' - \bar{\mathbf{m}})^T P(\mathbf{m}'|\mathbf{d}) d\mathbf{m}', \tag{6}$$

with diagonal elements representing parameter variances and off-diagonal elements representing covariances. Marginal probability distributions are particularly useful for understanding parameter uncertainties by reducing the multidimensional PPD to representative one-dimensional (1D) or two-dimensional (2D) probability distributions according to

$$P(m_i|\mathbf{d}) = \int \delta(m_i' - m_i) P(\mathbf{m}'|\mathbf{d}) d\mathbf{m}', \tag{7}$$

$$P(m_i, m_j|\mathbf{d}) = \int \delta(m_i' - m_i)\delta(m_j' - m_j) P(\mathbf{m}'|\mathbf{d}) d\mathbf{m}', \tag{8}$$

where δ is the Dirac delta function; 2D marginals also illustrate relationships between pairs of parameters. Inter-parameter relationships are quantified by normalizing the covariance to produce the correlation matrix

$$R_{ij} = C_{m_{ij}} / [C_{m_{ii}} C_{m_{jj}}]^{1/2}. \tag{9}$$

Correlation values vary between ± 1, with +1 indicating perfect correlation, −1 indicating perfect anti-correlation, and 0 indicating uncorrelated parameters.

Analytic solutions to Eqs. (4)–(9) exist for linear inverse problems with Gaussian-distributed errors and Gaussian prior distributions.[33,34] However, numerical solutions are required for strongly nonlinear problems, at increased computational effort. In this paper, MAP estimates $\hat{\mathbf{m}}$ are determined by minimizing $\phi(\mathbf{m})$ using adaptive simplex simulated annealing, a hybrid optimization algorithm that combines the downhill simplex method with very fast simulated annealing.[11] The integrals of Eqs. (5)–(8) are evaluated using GS methods, including new developments for sampling efficiency and completeness, described in Secs. II B–II D.

To define the data misfit, $E(\mathbf{m})$, consider complex acoustic-field data due to a (moving) source at S locations as measured at an array of N sensors at F frequencies, i.e., $\mathbf{d} = \{\mathbf{d}_{jk},\ j=1,S,\ k=1,F\}$. Assuming the data errors are complex, circularly symmetric, Gaussian-distributed random variables uncorrelated over space and frequency with variance ν, the likelihood function is given by

$$L(\mathbf{m}) = \prod_{j=1}^{S} \prod_{k=1}^{F} \frac{1}{(\pi \nu_{jk})^N} e^{-|\mathbf{d}_{jk} - A_{jk} e^{i\theta_{jk}} \mathbf{d}_{jk}(\mathbf{m})|^2 / \nu_{jk}}, \tag{10}$$

where $\mathbf{d}_{jk}(\mathbf{m})$ is the replica acoustic field computed for model $\mathbf{m}$, and A and θ represent source amplitude and phase. An unknown source can be treated by maximizing the likelihood over A, θ, and ν (i.e., setting $\partial L/\partial A = \partial L/\partial \theta = \partial L/\partial \nu = 0$) yielding[35,36]

$$E(\mathbf{m}) = N \sum_{j=1}^{S} \sum_{k=1}^{F} \log_e B_{jk}(\mathbf{m}), \tag{11}$$

where $B_{jk}(\mathbf{m})$, represents the Bartlett mismatch

$$B_{jk}(\mathbf{m}) = |\mathbf{d}_{jk}|^2 - \frac{|\mathbf{d}_{jk}(\mathbf{m})^\dagger \mathbf{d}_{jk}|^2}{|\mathbf{d}_{jk}(\mathbf{m})|^2}. \tag{12}$$

Prior information considered in this paper consists of uniform distributions for each parameter on bounded intervals $m_i^- \leq m_i \leq m_i^+$, i.e.,

$$P(\mathbf{m}) = \begin{cases} \prod_{i=1}^{M} (m_i^+ - m_i^-)^{-1} & \text{if } m_i^- \leq m_i \leq m_i^+,\ i = 1, M, \\ 0 & \text{otherwise.} \end{cases} \tag{13}$$

In addition, prior constraints can be applied on inter-parameter relationships in the form of realistic limits on radial and vertical source velocity (described below).

B. Gibbs' sampling and track constraints

This section considers numerical evaluation of integral properties of the PPD, such as Eqs. (5)–(8), which can be written in the general form

$$I = \int f(\mathbf{m}) P(\mathbf{m}|\mathbf{d}) d\mathbf{m}. \tag{14}$$

Standard Monte Carlo integration[37] is based on drawing models at random from a uniform distribution over the integration domain. By drawing Q models and calculating the posterior probability for each according to

$$P(\mathbf{m}_k|\mathbf{d}) = \frac{e^{-\phi(\mathbf{m}_k)}}{\sum_{j=1}^{Q} e^{-\phi(\mathbf{m}_j)}}, \tag{15}$$

the integral can be estimated as

$$I \approx \frac{V}{Q} \sum_{k=1}^{Q} f(\mathbf{m}_k) P(\mathbf{m}_k|\mathbf{d}), \tag{16}$$

where V represents the M-dimensional volume of integration. However, drawing models from a uniform distribution is inefficient if the integrand is concentrated in localized regions of the space. The method of importance sampling[37] is based on preferentially drawing samples from regions that contribute significantly to the integral. Let $g(\mathbf{m})$ denote the sampling distribution from which Q models are drawn, with the normalization condition

$$\int g(\mathbf{m}) d\mathbf{m} = 1. \tag{17}$$

Equation (14) can then be written

$$I = \int \left[\frac{f(\mathbf{m}) P(\mathbf{m}|\mathbf{d})}{g(\mathbf{m})} \right] g(\mathbf{m}) d\mathbf{m} \approx \frac{1}{Q} \sum_{k=1}^{Q} \frac{f(\mathbf{m}_k) P(\mathbf{m}_k|\mathbf{d})}{g(\mathbf{m}_k)}. \tag{18}$$

Note that the standard Monte Carlo integration, Eq. (16), represents the special case of importance sampling, Eq. (18),

with a uniform sampling function $g(\mathbf{m})=1/V$.

GS provides an effective sampling function, based on an analogy with statistical thermodynamics according to which the probability that a system of many atoms is in a state $\mathbf{m}_k$ with free energy $\phi(\mathbf{m}_k)$ is given by the Gibbs distribution[34]

$$P_G(\mathbf{m}_k,T)=\frac{e^{-\phi(\mathbf{m}_k)/T}}{\sum_j e^{-\phi(\mathbf{m}_j)/T}}, \tag{19}$$

where T represents absolute temperature and the normalization term, known as the partition function, involves summation over all possible states. Metropolis GS simulates equilibrium behavior by repeatedly perturbing system parameters and accepting perturbations for which a random number ξ drawn from a uniform distribution on $[0,1]$ satisfies the Metropolis criterion

$$\xi \leqslant e^{-\Delta\phi/T}. \tag{20}$$

In heat-bath GS, a discrete conditional probability distribution is formed for each parameter m_i in turn by sampling $\exp[-\phi(\mathbf{m})/T]$ across the parameter's limits while holding other parameters fixed. A new value for m_i is drawn at random from this distribution and accepted unconditionally. Markov-chain analysis verifies that, in the limit of a large number of perturbations at constant temperature, both Metropolis and heat-bath GS provide an unbiased sampling of the Gibbs' PDF, Eq. (19).[31,34]

Comparison of the Gibbs PDF, Eq. (19), with the PPD, Eq. (3), indicates the two are of identical form at temperature $T=1$. Hence, GS at $T=1$ provides an unbiased sampling of the PPD.[33,34] Employing GS at $T=1$ as the importance sampling function, i.e., $g(\mathbf{m})=P(\mathbf{m}|\mathbf{d})$ in Eq. (18), the integral estimate becomes

$$I \approx \frac{1}{Q}\sum_{k=1}^{Q} f(\mathbf{m}_k). \tag{21}$$

Thus, integral estimates are computed as the average of $f(\mathbf{m})$ over the set of models drawn via GS.

Although GS results are independent of the starting point, the sampling typically converges faster by initiating from a good (i.e., high-probability) starting model, such the as the MAP estimate as determined by nonlinear optimization.[12,13] Convergence can be monitored by comparing integral estimates from two or more independent samples collected in parallel: when the difference is suitably small, the procedure is considered to have converged and the final sample is taken as the union of the two samples.

Metropolis GS has proved effective for sampling geoacoustic parameters, and new developments for improved efficiency are presented in Sec. II C. However, 2D heat-bath GS is superior for sampling source-location parameters due to the potentially large number of isolated local optima in the $r-z$ plane without dominant correlation patterns.[18] For range-independent problems, $r-z$ conditional probability surfaces can be computed efficiently using normal-mode methods, since modal properties are defined by the environment not source locations. Hence, the tracking/inversion algorithm developed here employs a hybrid scheme of Metropolis GS over environmental parameters and heat-bath GS over source locations.[18]

To impose track constraints limiting radial and vertical source velocities to less than v_r^+ and v_z^+, respectively, the $r-z$ values for heat-bath GS for a source at time t are restricted to be within $v_r^+\Delta t$ in range and $v_z^+\Delta t$ in depth of the model values for neighboring source positions at times $t\pm\Delta t$ (one-sided constraints are applied at the track endpoints). While track constraints can greatly reduce uncertainties in source locations, they can also make GS much more challenging. If, for example, two or more distinct source tracks exist that fit the data and satisfy the track constraints but are separated from each other by more than the allowable perturbation in source range or depth, the model cannot make the transition between tracks in a single step. Rather, the range and depth parameters comprising the track must accept a series of high-misfit (low-probability) states to transit between tracks. To ensure that relatively improbable transitions such as these can occur in finite sampling, nonunity sampling temperatures can be applied in GS, as described in Sec. II D. First, however, new methods to improve the efficiency of Metropolis GS are described in the following section.

C. Proposal distributions

In Metropolis GS, parameter perturbations can be drawn from any (stationary) distribution, known as the proposal distribution.[30,31] The choice of proposal distribution does not effect the integral estimates at convergence, but can strongly effect the sampling efficiency (i.e., convergence rate). The goal is to achieve a well-mixed Markov chain that efficiently samples important regions of the space, avoiding both small, ineffectual perturbations and high rejection rates.

To date, proposal distributions applied in geoacoustic inversion have been limited to parameter rotation and uniform distributions.[12–16] Parameter rotation is designed to overcome ineffectual sampling due to correlated parameters which result in narrow, oblique valleys in misfit. Perturbations are applied in a principal-component parameter space where the axes align with the dominant correlation directions. The orthogonal transformation between physical parameters $\mathbf{m}$ and rotated parameters $\mathbf{m}'$ is given by

$$\mathbf{m}'=\mathbf{U}^T\mathbf{m}, \quad \mathbf{m}=\mathbf{U}\mathbf{m}', \tag{22}$$

where $\mathbf{U}$ is the column-eigenvector matrix of the model covariance matrix $\mathbf{C}_\mathbf{m}$,

$$\mathbf{C}_\mathbf{m}=\mathbf{U}\mathbf{W}\mathbf{U}^T, \tag{23}$$

and $\mathbf{W}=\mathrm{diag}[w_1,\ldots,w_M]$ is the eigenvalue matrix, with w_i representing the variance projected along eigenvector $\mathbf{u}_i$. Once the rotation matrix is obtained, rotated parameters are perturbed individually, with the perturbed models rotated back to the physical space for misfit evaluation. Parameter rotation has been shown to increase sampling efficiency by orders of magnitude in geoacoustic inversion problems.[12]

Rotation matrices are typically obtained by applying initial unrotated sampling to estimate $\mathbf{C}_\mathbf{m}$.[12–14,16] Alternatively, Battle *et al.*[15] based parameter rotations on the Cramer–Rao

lower bound matrix evaluated at an initial maximum-likelihood model estimate, and reported a factor of 2 improvement in efficiency. A similar initiation scheme is one component of the sampling approach developed in this work.

The approach developed here is based on the idea that the linearized approximation to a nonlinear inverse problem can provide information to be exploited for a more efficient nonlinear sampling algorithm. In particular, the optimal choice of proposal distribution is given by the PPD itself, but this is obviously not available during sampling in practical problems. However, a local linear approximation to the PPD can be estimated and applied during sampling. According to standard linearized inverse theory, the PPD for a reference solution $\mathbf{m_0}$ is given by an M-dimensional (real) Gaussian distribution[33,34]

$$P(\mathbf{m}|\mathbf{d}) = \frac{1}{(2\pi)^{M/2}|\mathbf{C_m}|^{1/2}} e^{-(\mathbf{m}-\mathbf{m_0})^T \mathbf{C_m}^{-1}(\mathbf{m}-\mathbf{m_0})/2}. \tag{24}$$

In Eq. (24), the model covariance matrix for the linearized problem is given by

$$\mathbf{C_m} = [\mathbf{J}^T \mathbf{C_d}^{-1} \mathbf{J} + \mathbf{C_{m_0}}^{-1}]^{-1}, \tag{25}$$

where $\mathbf{J}$ represents the Jacobian matrix of partial derivatives evaluated at $\mathbf{m_0}$,

$$J_{ij} = \frac{\partial d_i(\mathbf{m_0})}{\partial m_j}, \tag{26}$$

$\mathbf{C_d}$ is the data covariance matrix, and $\mathbf{C_{m_0}}$ is the covariance matrix of an assumed Gaussian prior distribution about $\mathbf{m_0}$.

To apply these concepts to Metropolis GS, rotated sampling is initiated using the linearized covariance matrix estimate, Eq. (25), evaluated at the MAP starting model determined by optimization. This avoids the need for (inefficient) unrotated sampling to build up initial covariance information, and should provide a reasonable local approximation near the starting point. Further, the linearized PPD can be applied as proposal distribution for parameter perturbations: to do so, the ith rotated parameter can be perturbed using a Gaussian distribution with variance w_i from Eq. (23). However, for strongly nonlinear problems, Gaussian perturbations may not be large enough to transit between potentially disjoint regions of high probability. This can be addressed by employing a Cauchy proposal distribution (in rotated space), scaled according to the estimated (rotated) variances. Figure 1 shows that the Cauchy distribution is similar to the Gaussian near the mode (producing similar local sampling), but has heavier tails (producing much wider sampling). As sampling progresses, the initial linearized estimate for $\mathbf{C_m}$ is adaptively replaced with the nonlinear estimate based on the GS solution to Eq. (6) to that point, which better represents the overall covariance of the parameter space and the actual prior distribution. This procedure applies the directional information inherent in parameter rotations together with a perturbation distribution and length scale for each parameter based on the linearized approximation to the PPD.

To implement the algorithm, the partial derivatives of Eq. (26) can be evaluated numerically using a central difference scheme. Under the assumption of uncorrelated errors,

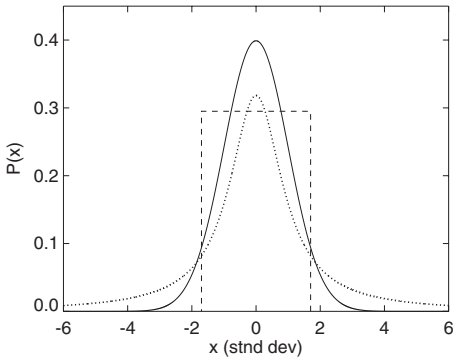

FIG. 1. Comparison of Gaussian (solid line), Cauchy (dotted), and bounded-uniform (dashed) probability distributions. Gaussian and bounded-uniform distributions have unit standard deviation; Cauchy distribution has unit width parameter.

$\mathbf{C_d}$ in Eq. (25) is taken to be a diagonal matrix with representative variances for data at the jth frequency and kth source location estimated from the residuals evaluated at the MAP starting model[36]

$$\nu_{jk} = B_{jk}(\hat{\mathbf{m}}, \mathbf{d})/N. \tag{27}$$

In the common case where the parameter priors consist of bounded uniform distributions, $\mathbf{C_{m_0}}$ is taken to be a diagonal matrix with variances equal to those of the uniform distributions, i.e., $(m_i^+ - m_i^-)^2/12$ (see Fig. 1). For numerical stability, covariance estimation, rotation, and perturbations are carried out for nondimensionalized parameters scaled to vary over $[0,1]$. The new approach of linearized proposal distributions in GS has been tested extensively on synthetic geoacoustic inversion problems, and produces identical results to those obtained using an earlier implementation based on parameter rotations and adaptive uniform sampling, but is typically three to ten (or more) times faster. The basic algorithm employed here to estimate PASs and other integral quantities using GS is summarized in Table I.

D. Sampling temperature

As discussed previously, integral properties of the PPD can be evaluated by applying GS at $T=1$. However, to verify completeness of the sampling, it can be useful to consider sampling at $T>1$ to more widely wander the parameter space, then correct the results to $T=1$. Following Brooks and Frazer,[32] write integral Eq. (14) as

$$I = \int f(\mathbf{m}) \frac{e^{-\phi(\mathbf{m})}}{Z_1} d\mathbf{m}$$
$$= \frac{Z_T}{Z_1} \int f(\mathbf{m}) e^{-\phi(\mathbf{m})(1-1/T)} \frac{e^{-\phi(\mathbf{m})/T}}{Z_T} d\mathbf{m}, \tag{28}$$

where

$$Z_1 = \int e^{-\phi(\mathbf{m})} d\mathbf{m}, \tag{29}$$

TABLE I. Basic outline of GS algorithm for computing PASs and other integral quantities used here.

1. Estimate MAP model $\hat{\mathbf{m}}$ via numerical optimization.
2. Compute approximate model covariance matrix $\mathbf{C_m}(\hat{\mathbf{m}})$ by linearization.
3. Choose sampling temperature T.
4. Burn-in. Starting with $\hat{\mathbf{m}}$ and $\mathbf{C_m}(\hat{\mathbf{m}})$, generate two independent samples of models by:
(a) Metropolis GS over environmental parameters, employing linearized PPD as proposal distribution. Adaptively update linearized $\mathbf{C_m}(\hat{\mathbf{m}})$ to sampled estimate $\mathbf{C_m}$ as sampling proceeds.
(b) Heat-bath GS over source ranges and depths.
(c) Burn-in is complete when the difference between model correlation matrices for the two samples is less than a preset tolerance. Discard burn-in samples.
5. Sampling. Starting with final models and sampled $\mathbf{C_m}$ from burn-in, generate two independent samples of models by:
(a) Metropolis GS over environmental parameters, employing linearized PPD based on sampled $\mathbf{C_m}$ as proposal distribution. Adaptively update $\mathbf{C_m}$ as sampling proceeds.
(b) Heat-bath GS over source ranges and depths.
(c) Sampling is complete when the difference between PASs for the two samples is less than a preset tolerance. Final PASs and other integral quantities arecomputed from the union of the two samples.

$$Z_T = \int e^{-\phi(\mathbf{m})/T} d\mathbf{m} \tag{30}$$

represent the partition functions for sampling temperatures of 1 and T, respectively. Drawing a sample of Q models from $e^{-\phi(\mathbf{m})/T}/Z_T$ using GS at temperature T, Eq. (28) can be approximated

$$I \approx \frac{Z_T}{Z_1}\frac{1}{Q}\sum_{k=1}^{Q} f(\mathbf{m}_k) e^{-\phi(\mathbf{m}_k)(1-1/T)}. \tag{31}$$

To write the factor Z_T/Z_1 in a more convenient form, note that

$$\frac{Z_1}{Z_T} = \int e^{-\phi(\mathbf{m})(1-1/T)} \frac{e^{-\phi(\mathbf{m})/T}}{Z_T} d\mathbf{m} \approx \frac{1}{Q}\sum_{k=1}^{Q} e^{-\phi(\mathbf{m_k})(1-1/T)}, \tag{32}$$

where $\{\mathbf{m}_k,\ k=1,Q\}$ represent samples drawn from $e^{-\phi(\mathbf{m})/T}/Z_T$. Equation (31) thus becomes

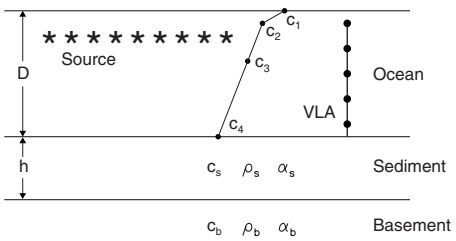

FIG. 2. Schematic diagram of model parameterization including source positions and geoacoustic and SSP parameters.

TABLE II. True values and uniform prior bounds for the environmental parameters used in the inversion examples.

Parameter and units	True value	Lower bound	Upper bound
h (m)	9	0	30
c_s (m/s)	1495	1450	1600
c_b (m/s)	1530	1500	1650
ρ_s (g/cm^3)	1.4	1.0	1.7
ρ_b (g/cm^3)	1.6	1.5	2.2
α_s (dB/λ)	0.2	0	1.0
α_b (dB/λ)	0.2	0	1.0
D (m)	130	128	132
c_1 (m/s)	1520	1515	1525
c_2 (m/s)	1517	1510	1520
c_3 (m/s)	1515	1510	1520
c_4(m/s)	1510	1505	1515

$$I \approx \frac{1}{\sum_{k=1}^{Q} e^{-\phi(\mathbf{m}_k)(1-1/T)}} \sum_{k=1}^{Q} f(\mathbf{m}_k) e^{-\phi(\mathbf{m}_k)(1-1/T)}. \tag{33}$$

Hence, the integral can be estimated from GS at arbitrary sampling temperature T by weighting each model in the sample by a factor that depends on its misfit ϕ and on T, and appropriate normalization. Note that for $T=1$, Eq. (33) simplifies to standard GS, Eq. (21). Further, for $T\to\infty$, this approach simplifies to standard Monte Carlo integration. To see this, note that as $T\to\infty$ every perturbed model is accepted, $Z_T \to V$ according to Eq. (30), and Eq. (31) approaches Eq. (16). This represents the widest sampling, with no preference for important regions of the space, but can be impractically slow for realistic problems.

The approach adopted here to ensure complete sampling is to repeat the GS inversion at a sequence of sampling temperatures, say, $T=1,2,3,5$. A change in-the PASs for the source track due to an increase in sampling temperature in-

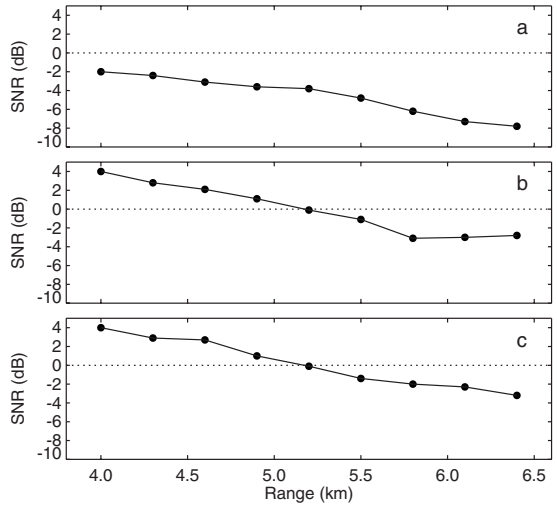

FIG. 3. SNR as a function of source range for: (a) source-tracking example at frequency 300 Hz; (b) and (c) ship-noise geoacoustic inversion example at 300 and 350 Hz, respectively.

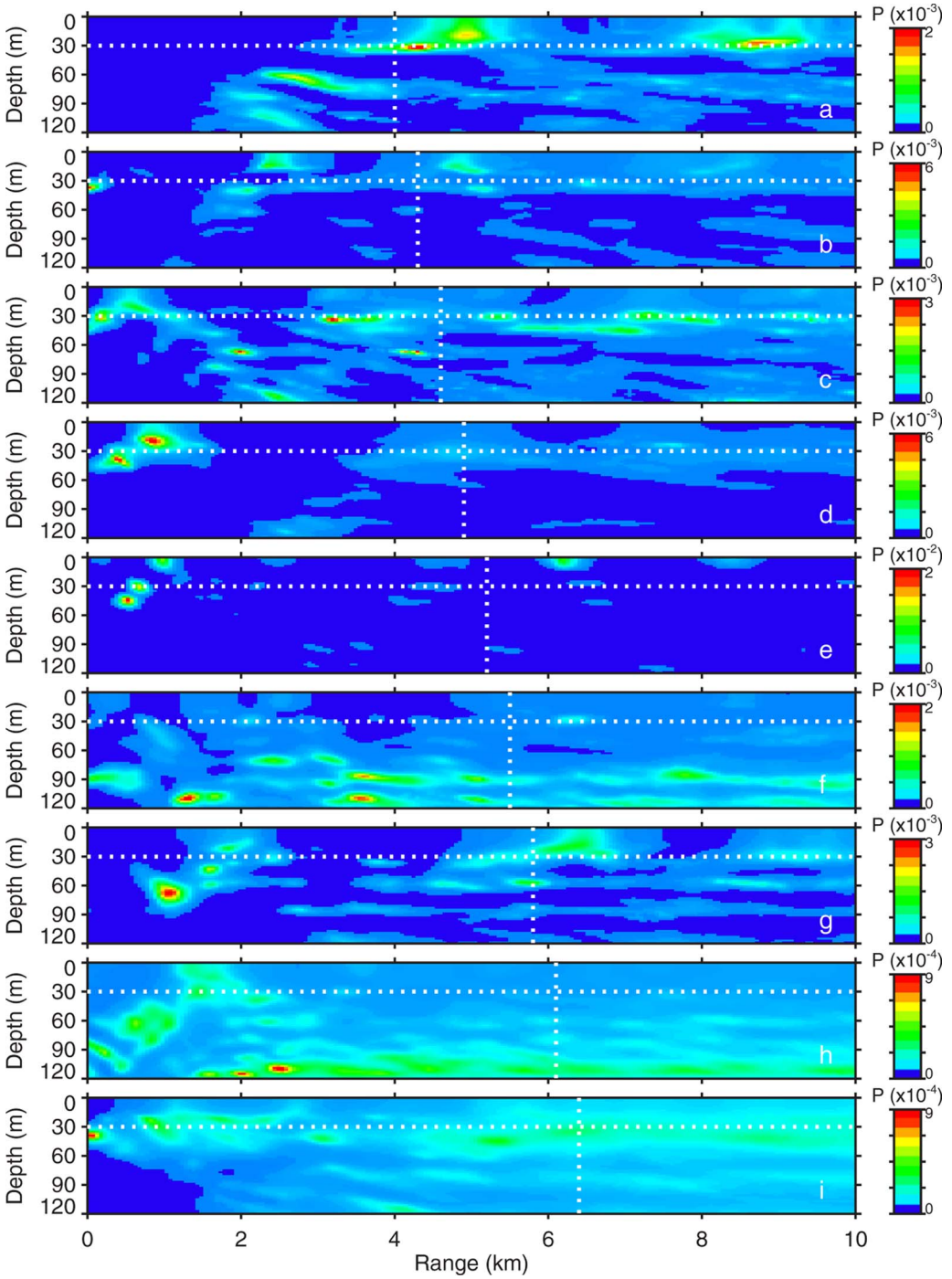

FIG. 4. (Color online) PASs computed via independent inversions for nine positions of a moving source (tracking example). True source ranges and depths are indicated by dotted lines.

dicates incomplete sampling. No change in PASs with a significant increase in temperature suggests complete sampling and satisfactory integral estimation.

III. EXAMPLES

A. Tracking in an unknown environment

The first example illustrates localizing and tracking a quiet submerged source in shallow water with little knowledge of environmental parameters (seabed and water column). The environment and source parameters are illustrated in Fig. 2. Seabed geoacoustic parameters include the thickness h of an upper sediment layer with sound speed c_s, density ρ_s, and attenuation α_s, overlying a semi-infinite basement with sound speed c_b, density ρ_b, and attenuation α_b. The water depth is D, and the water-column sound-speed profile (SSP) is represented by four parameters c_1-c_4 at depths of 0, 10, 50, and D m. Table II gives the true values for the environmental parameters together with the limits for the wide uniform prior distributions (search intervals) assumed for all parameters.

Acoustic data are simulated at a frequency of 300 Hz at a vertical array consisting of 24 sensors at 4 m spacing from

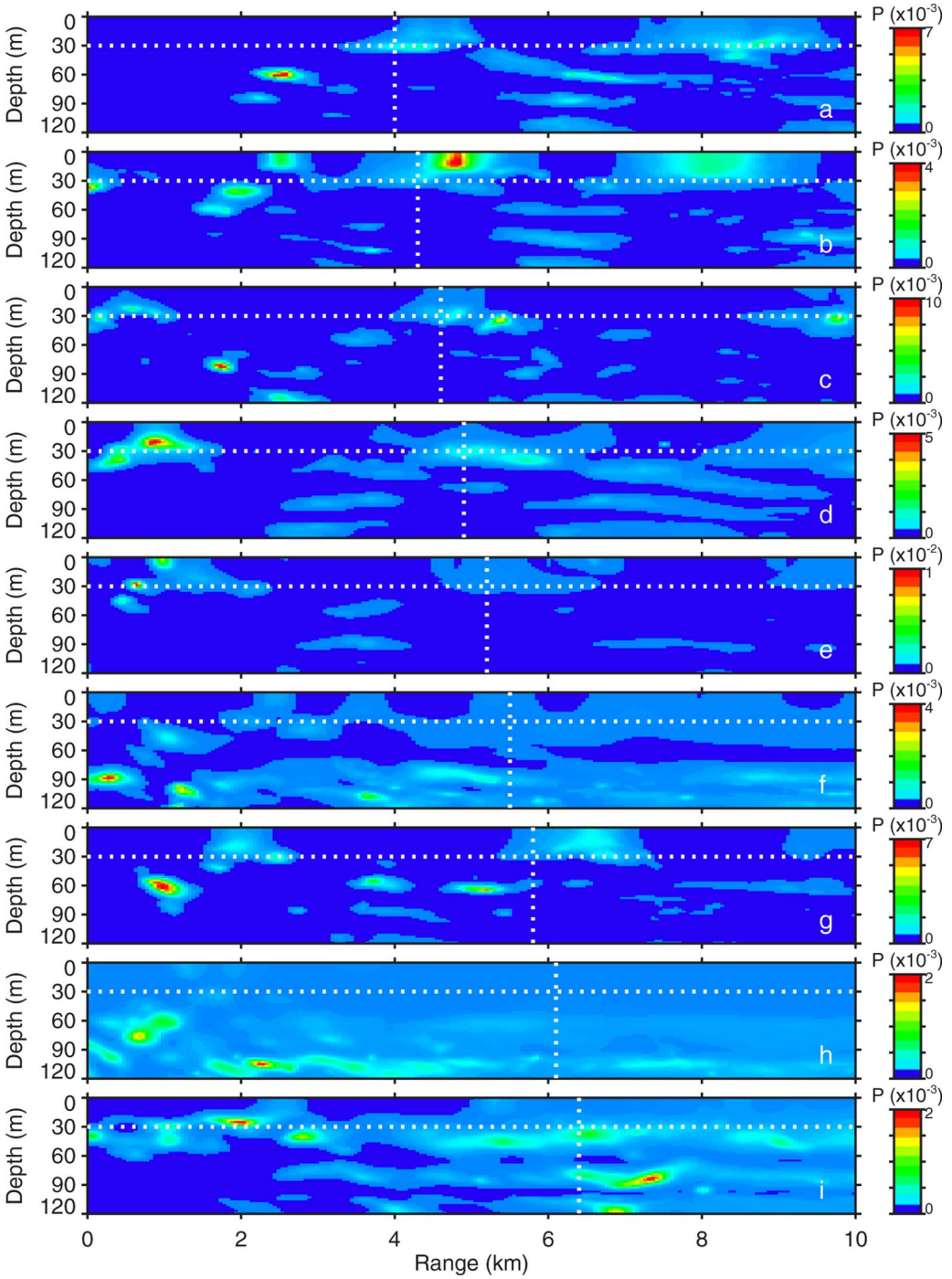

FIG. 5. (Color online) PASs computed via simultaneous inversion for nine positions of a moving source (tracking example). True source ranges and depths are indicated by dotted lines.

26 to 118 m depth (acoustic fields are computed using the normal-mode model ORCA[38]). The track consists of an acoustic source at 30 m depth moving away from the array at a constant radial speed of 5 m/s (~10 kts). Acoustic data are collected at the array once per minute for 9 min, corresponding to source-receiver ranges of $4.0, 4.3, \ldots, 6.4$ km. Prior bounds for the source location at all times are 0–10 km range and 0–120 m depth (numerical grids with 50 m spacing in range and 2 m spacing in depth are applied for the heat-bath GS in source location). Complex Gaussian-distributed random errors of constant variance are added to the acoustic data to achieve a signal-to-noise ratio (SNR) of −2 dB for the shortest source range, with SNR decreasing as the signal strength decreases with range to approximately −8 dB at the longest range, as shown in Fig. 3(a). (SNR is defined here as $\mathrm{SNR} = 10 \log |\mathbf{s}|^2 / |\mathbf{n}|^2$, where $\mathbf{s}$ and $\mathbf{n}$ represent the signal and noise vectors over the array, respectively.)

PASs from three approaches to Bayesian tracking of increasing complexity and information content are shown in Figs. 4–6. In each case, 9 PASs are computed (one for each acoustic measurement of the moving source) by numerically integrating over the unknown geoacoustic and SSP parameters to produce joint marginal PPDs in source range and depth, as described in Sec. II. Figure 4 shows results for the

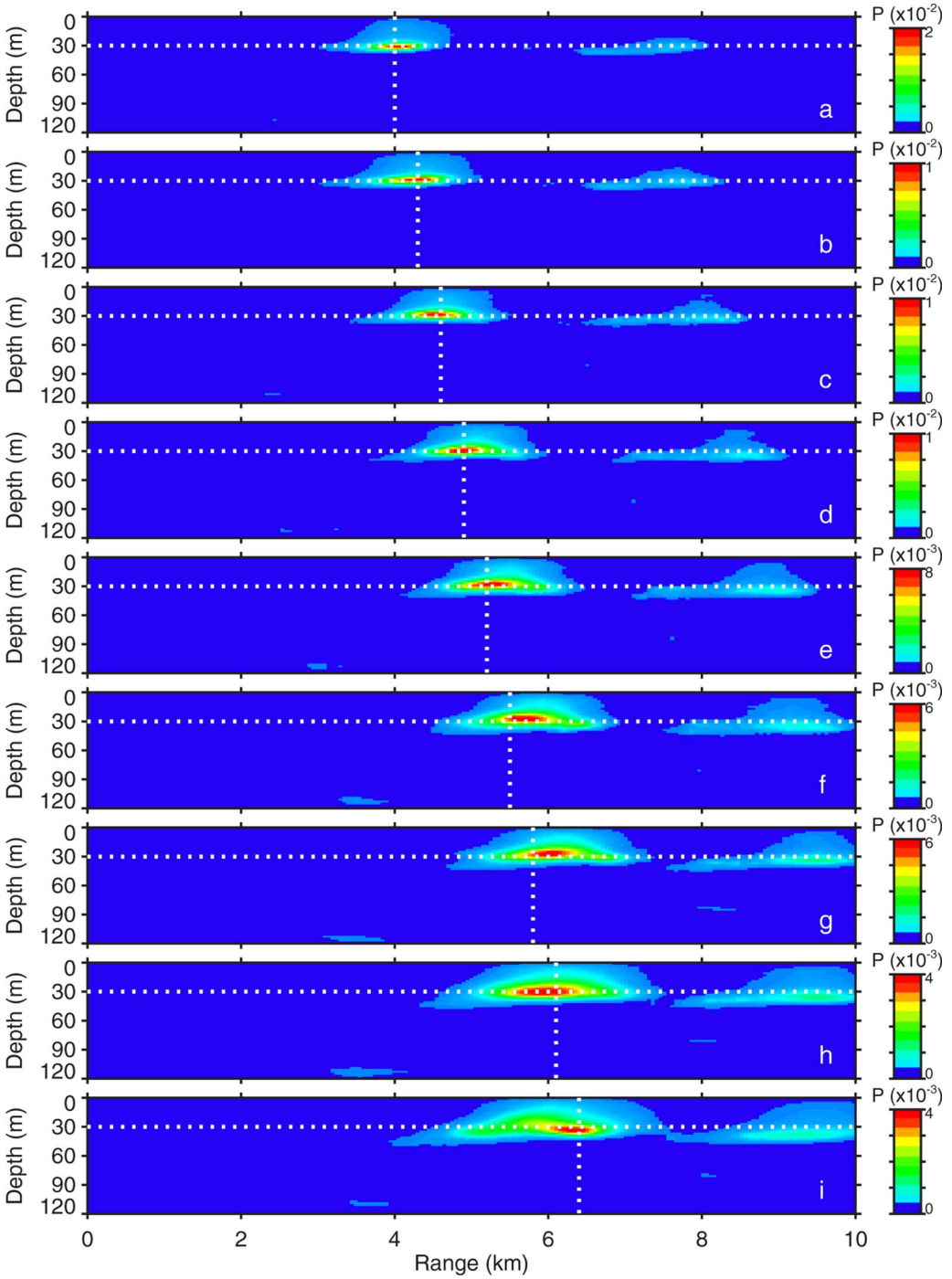

FIG. 6. (Color online) PASs computed via track-constrained inversion for nine positions of a moving source (tracking example). True source ranges and depths are indicated by dotted lines.

simplest approach: treating each source localization separately and solving nine independent inversions for the 9 PASs. This is the least computationally demanding approach, since each individual inversion involves only 14 unknowns consisting of the 12 environmental parameters plus one source range and depth. However, it is also the least informative approach, since the acoustic data for only one source location constrain the environmental parameters in each inversion, which in turn leads to greater uncertainty in source locations. The PASs in Fig. 4 show little ability to localize/track the source given the low SNR and large environmental uncertainties. At the shortest source range, Fig. 4(a) indicates a peak in the PAS near the correct source location; however, another similar peak occurs near 9 km range and other local maxima are scattered throughout the search region. For the next four source ranges, Figs. 4(b)–4(e) indicate generally higher probabilities near the correct source depth, but little or no ability to localize in range. The longer-range PASs in Figs. 4(f)–4(i) show no particular concentration of probability near the correct depth or range, and become increasingly flat for the longest source ranges.

Figure 5 shows the PASs computed from simultaneous inversion of all nine acoustic data sets for the moving source. This constitutes a more informative formulation than inde-

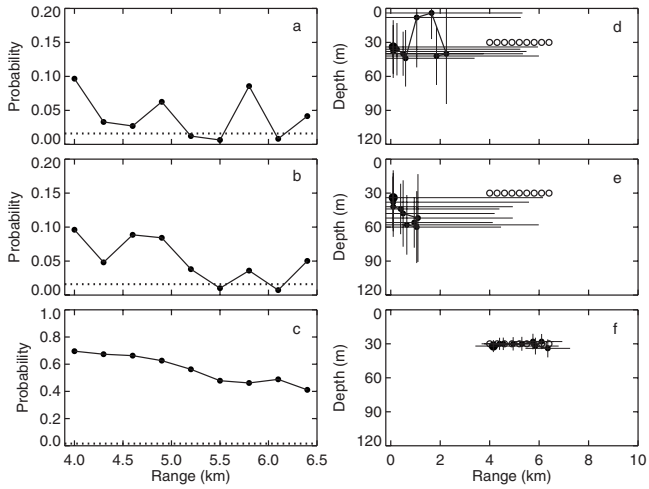

FIG. 7. Integrated probability within 10 m depth and 500 m range of the true source locations are shown for independent, simultaneous, and track-constrained inversions in (a)–(c), respectively, with dotted lines indicating IP value of a flat distribution. Optimal source tracks are shown as filled circles with mean absolute-deviation uncertainties in (d)–(f) for the corresponding cases. Larger filled circles indicate track start points, and open circles indicate the true track.

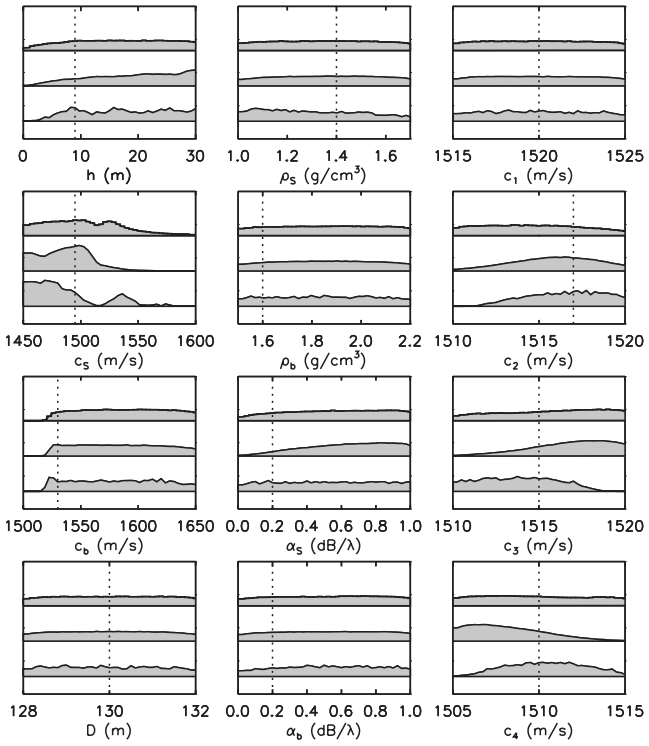

FIG. 8. Marginal PPDs for environmental parameters from source-tracking inversions. Upper, middle, and lower distributions in each panel correspond to independent, simultaneous, and track-constrained inversions, respectively.

pendent inversions, since all nine data sets constrain a single set of environmental parameters, which should in turn better constrain source locations. However, it is also much more computationally demanding, since it involves 30 unknown parameters including nine source ranges and depths. Figure 5 shows PASs tend to be generally less diffuse than those for independent inversions in Fig. 4, with some concentration of probability near the correct source depth for PASs. However, overall, Fig. 5 indicates that the information content of the noisy data and wide environmental priors is not sufficient to localize or track the source with any certainty.

Figure 6 shows the PASs computed from simultaneous inversion of all acoustic data, together with additional prior information in the form of track constraints that the radial and vertical speeds of the source are limited to less than $v_r^+ = 10$ m/s and $v_z^+ = 0.06$ m/s, respectively (i.e., the source moves less than 600 m radially and 4 m vertically in the minute between data observations). No constraints are placed on the direction of motion or on changes in direction in this example (although such constraints are straightforward). Figure 6 shows that the PASs computed with track constraints have a strong global maximum near the true source location for all source ranges. The maxima are most tightly focused for the shorter source ranges (with higher SNRs), and spread out (particularly in the radial) as range increases. A significantly weaker secondary maximum occurs at approximately 30 m depth and roughly 3 km beyond the true source range in each PAS, and other very weak local maxima are also evident in some cases.

Figure 6 indicates that, with the additional prior information provided by track constraints, the source can be localized and tracked with a high degree of certainty despite the poor environmental knowledge and low SNR. Track constraints greatly reduce the parameter search space, but also make GS more challenging, as discussed in Sec. II. To verify completeness of the sampling, the inversion was run with sampling temperatures of $T = 1, 2, 3, 5$. The results shown in Fig. 6 correspond to sampling at $T = 2$, with essentially identical results obtained for the higher temperatures. However, the PASs obtained for $T = 1$ (standard GS) differed from those for $T > 1$ in that the local maxima were not well represented, indicating the sampling did not transit freely between maxima. Hence, GS at $T > 1$ appears to be required to properly evaluate the marginal integrals for this case. Several sampling temperatures $T \geqslant 1$ were also applied in computing the PASs without track constraints in Figs. 4 and 5; however, identical results were obtained for all temperatures, and the $T = 1$ results are shown here.

The probabilistic tracking results can be considered further in terms of the integrated probability (IP) for an acceptable localization, defined to be the integral of the PAS over an acceptable region, taken for this example to be within 10 m depth and 500 m range of the true source location. Figures 7(a)–7(c) show IP values for the PASs in Figs. 4–6, respectively. In each case, the IP for a completely flat PAS (0.017) is also included, representing a noninformative reference level. Figures 7(a) and 7(b) show that IP values for the inversions without track constraints are low ($\sim 0.005 - 0.1$), but are above the reference level in most cases, particularly at shorter ranges. IP values for the track-constrained inversion, shown in Fig. 7(c), are much higher (0.4–0.7) and decrease almost monotonically with range.

While the primary goal of this example is to quantify the information content of data and priors for source tracking in terms of PASs, it is also interesting to consider optimal tracks which are easily extracted from a set of PASs using the Viterbi algorithm[28,39] to compute the most probable sequence of

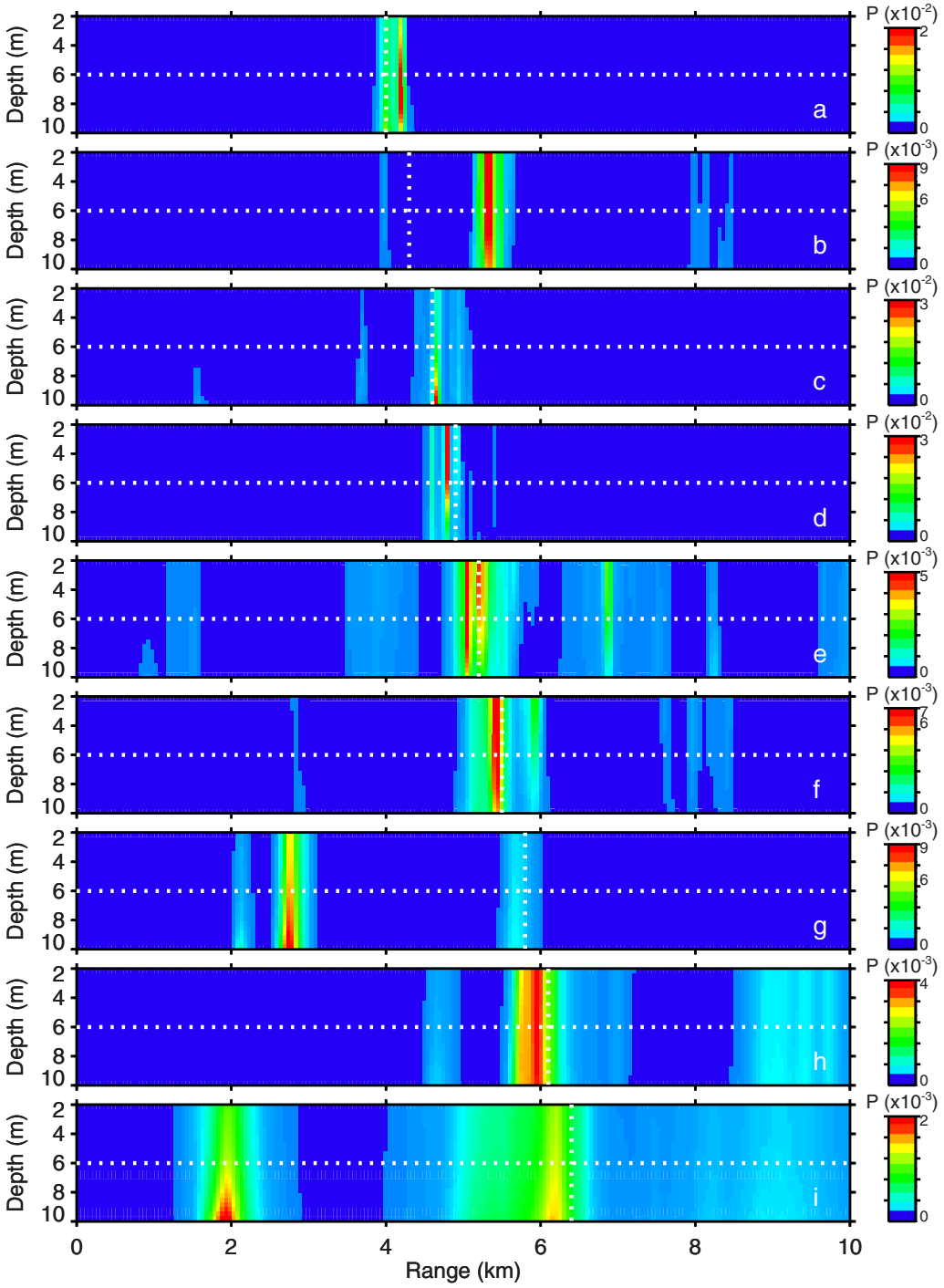

FIG. 9. (Color online) PASs computed via independent inversions for nine positions of a moving source (ship-noise geoacoustic inversion example). True source ranges and depths are indicated by dotted lines.

source locations that satisfy given bounds on radial and vertical motion. Figures 7(d)–7(f) show the optimal tracks computed from the PASs in Figs. 4–6, respectively, using the Viterbi algorithm with $v_r^+ = 10$ m/s and $v_z^+ = 0.06$ m/s. Mean absolute-deviation uncertainties in range and depth computed from the PASs are also included. Figures 7(d) and 7(e) show that the optimal tracks from the inversions without track constraints do not agree with the true track: source ranges are much too short in both cases, although there is some correspondence in depth and the tracks generally run in the right direction (i.e., range increases). In contrast, Fig. 7(f) shows excellent agreement in both range and depth between the optimal track from the track-constrained PASs and the true track.

Finally, Fig. 8 shows marginal PPDs computed for the environmental parameters as part of the three approaches to tracking inversion considered here. Given the low-SNR data and the fact that both the seabed and water column are unknown, it is not surprising that environmental parameters are not well resolved, although some sensitivity to sound-speed parameters is evident. It is important to note that the wide marginal distributions do not indicate that any and all envi-

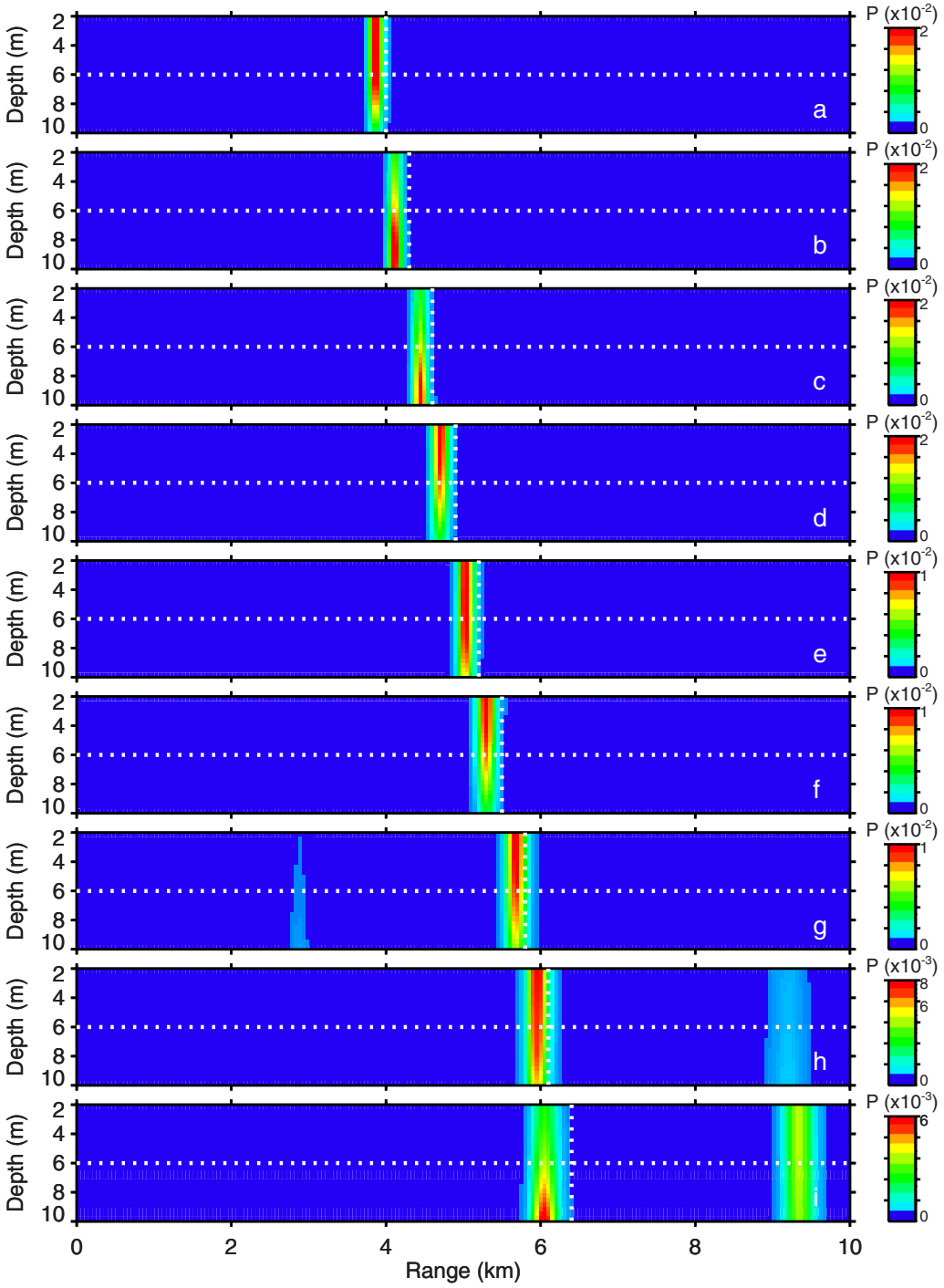

FIG. 10. (Color online) PASs computed via simultaneous inversion for nine positions of a moving source (ship-noise geoacoustic inversion example). True source ranges and depths are indicated by dotted lines.

ronmental models within the prior bounds suffice for localization and tracking. Rather, the Bayesian inversion samples parameter combinations that are consistent with the acoustic data (within uncertainties) in integrating over environmental parameters.

B. Ship-noise geoacoustic inversion

The second example simulates geoacoustic inversion using noise lines emanating from a moving ship of opportunity of unknown location. The environmental parameters, sensor array, and source track are identical to those in Sec. III A, except that the source depth is 6 m with prior bounds of 2–10 m (i.e., prior knowledge that the source is a surface ship). Acoustic data are considered at two frequencies of 300 and 350 Hz, with SNR of 4 dB at the shortest source range and SNR decreasing with range to approximately −3 dB, as shown in Figs. 3(b) and 3(c).

PASs for the source track are shown in Figs. 9–11 for the three inversion approaches considered in the previous section. Figure 9 shows that independent inversions do not reliably track the ship, given the environmental uncertainties, with global maxima that differ significantly from the true

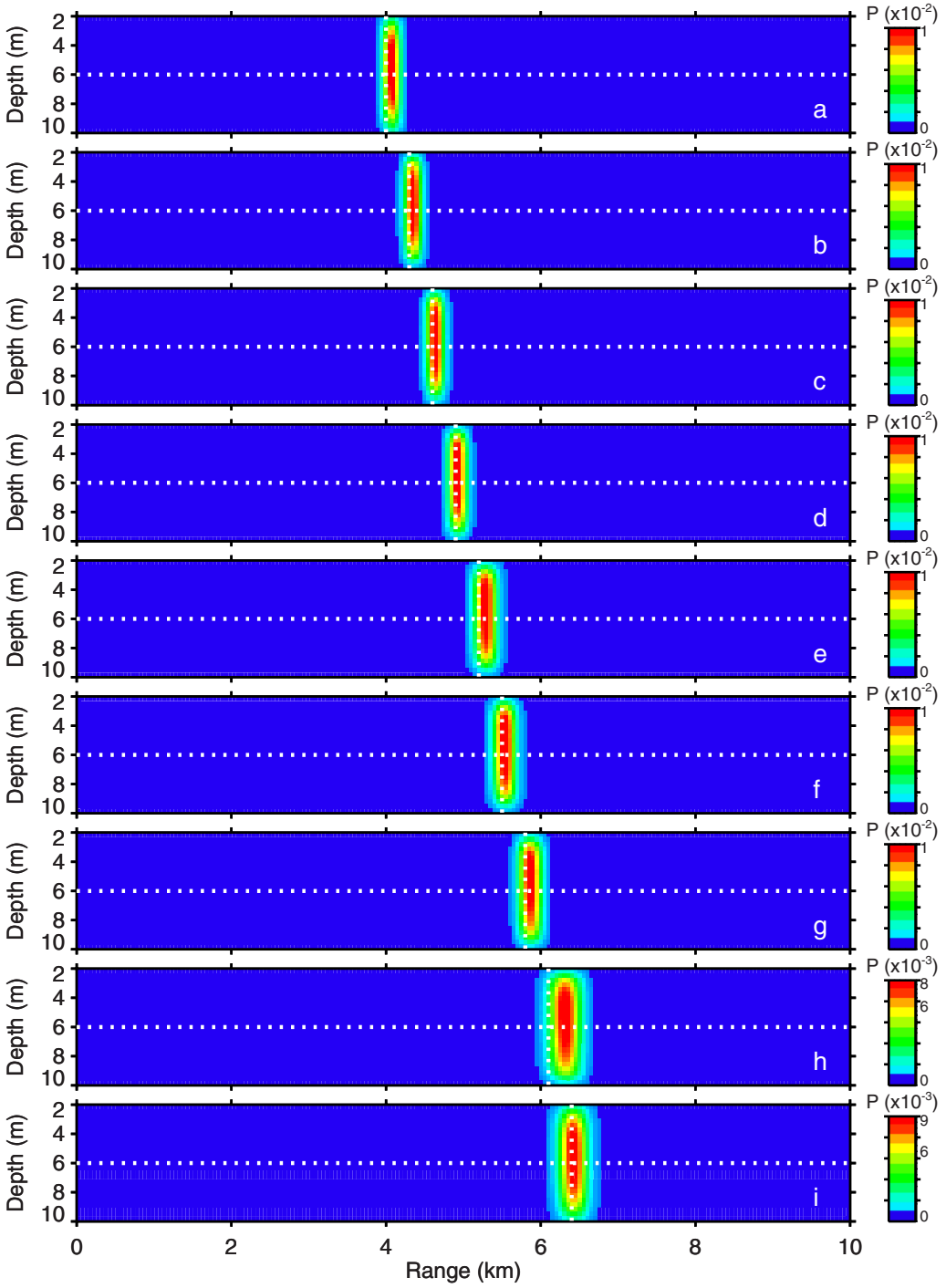

FIG. 11. (Color online) PASs computed via track-constrained inversion for nine positions of a moving source (ship-noise geoacoustic inversion example). True source ranges and depths are indicated by dotted lines.

source location in range in three PASs, and no ability to discern source depth within the prior bounds. Figure 10 shows substantially improved tracking results for simultaneous inversion, with the global maximum near the true range in all cases, although secondary maxima occur in PASs at the longer source ranges and there is little ability to discern source depth. The PASs shown in Fig. 11 track-constrained inversion ($v_r^+ = 10$ m/s, $v_z^+ = 0.06$ m/s) provide unambiguous tracking with a high level of certainty, as indicated by well-focused global maxima near the true source range and depth and no secondary local maxima. The inversion approaches were run at several sampling temperatures $T \geqslant 1$, with identical results for all temperatures; the results shown here are for $T = 1$.

Figures 12(a)–12(c) show IP values for the three inversion approaches, with acceptable regions defined to be within 2 m depth and 500 m range of the true source locations. The highest values (IP ~ 0.7) are obtained for track-constrained inversion, with somewhat lower values for simultaneous inversion (IP ~ 0.5) and for independent inversions (IP $\sim 0.4 - 0.5$ when the global maximum is near the true source location and much smaller otherwise, see Fig. 9). Optimal source

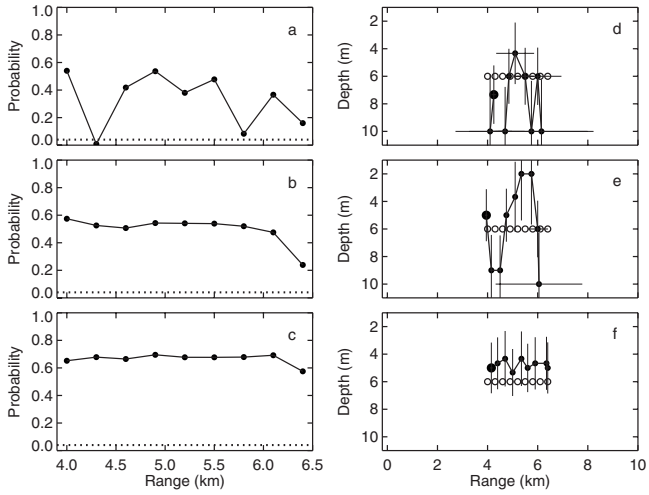

FIG. 12. Integrated probability within 2 m depth and 500 m range of the true source locations are shown for independent, simultaneous, and track-constrained inversions of ship-noise data in (a)–(c), respectively, with dotted lines indicating IP value of a flat distribution. Optimal source tracks are shown as filled circles with mean absolute-deviation uncertainties in (d)–(f) for the corresponding cases. Larger filled circles indicate track start points, and open circles indicate the true track.

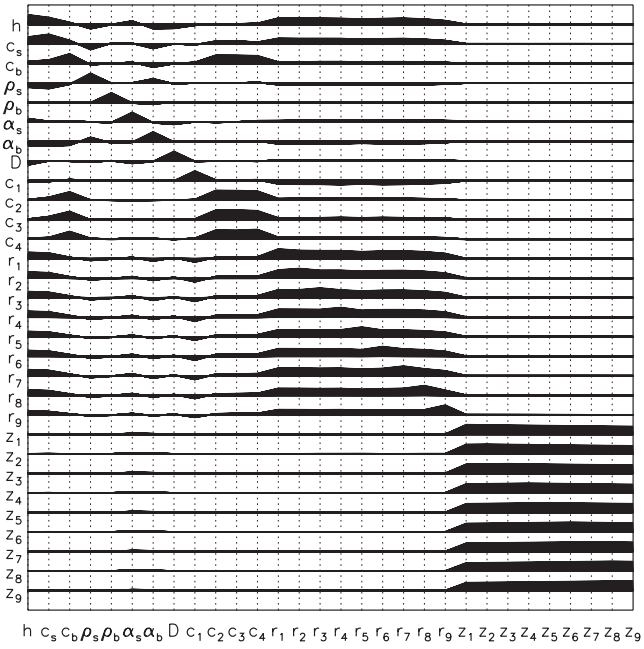

FIG. 14. Correlation matrix for track-constrained ship-noise inversion.

tracks (computed via the Viterbi algorithm) and mean absolute deviation uncertainties are shown in Fig. 12(d)–12(f), with notably better results for the track-constrained inversion.

The goal of this example is to quantify the information content for geoacoustic parameters given no knowledge of the ship track and limited SSP knowledge. Figure 13 shows marginal PPDs for the environmental parameters computed from the track-constrained inversion (results from the simultaneous inversion are essentially identical). For comparison, Fig. 13 also includes marginals computed from two other simulations of interest: (i) an identical case but with exact knowledge of all ship locations, and (ii) a typical controlled-source geoacoustic experiment. The controlled-source experiment is based on a single source location of 4 km range and 6 m depth, with tight prior bounds of $[3.9,4.1]$ km and $[4,8]$ m representing experimental uncertainty. The data are at the same frequencies as the ship noise (300 and 350 Hz) but with a higher SNR of 10 dB. Further, the prior uncertainties on the SSP parameters are reduced from 10 m/s bounds (Table II) to ± 1 m/s about the true values, representing good-quality measurements made during the experiment. Figure 13 shows that the marginal PPDs for the seabed parameters are generally similar for the three inversions, with some minor exceptions: h, c_s, and α_b are slightly better resolved with exact ship locations, and c_b is better resolved with the simulated geoacoustic-experiment data. In all three cases, parameters defining the seabed sound-speed structure (h,c_s,c_b) are well resolved, the basement attenuation (α_b) is reasonably well resolved, the sediment attenuation and density (α_s and ρ_s) are poorly resolved, and the basement density (ρ_b) is unresolved. The water-column SSP parameters (c_1-c_4) are poorly resolved for the two ship-noise inversions. The narrower SSP marginals for the geoacoustic experiment result largely from the tighter prior bounds: repeating the inversion with wider priors gave correspondingly wider marginals (not shown). Figure 13 indicates that lack of knowledge of ship locations need not adversely affect ship-noise geoacoustic inversion: the acoustic data contain sufficient information to resolve both seabed parameters and ship tracks. In principle, ship-noise inversion can produce results

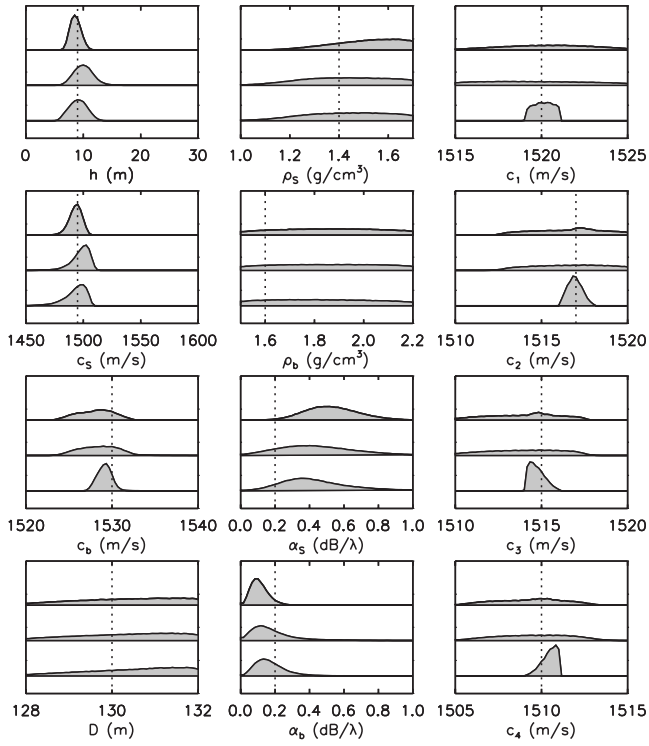

FIG. 13. Marginal PPDs for environmental parameters for ship-noise inversion example. Upper distributions in each panel are from inversion in which the ship locations are known exactly. Middle distributions are from ship-noise inversion with unknown source locations and track constraints. Lower distributions are from simulated controlled-source geoacoustic experiment.

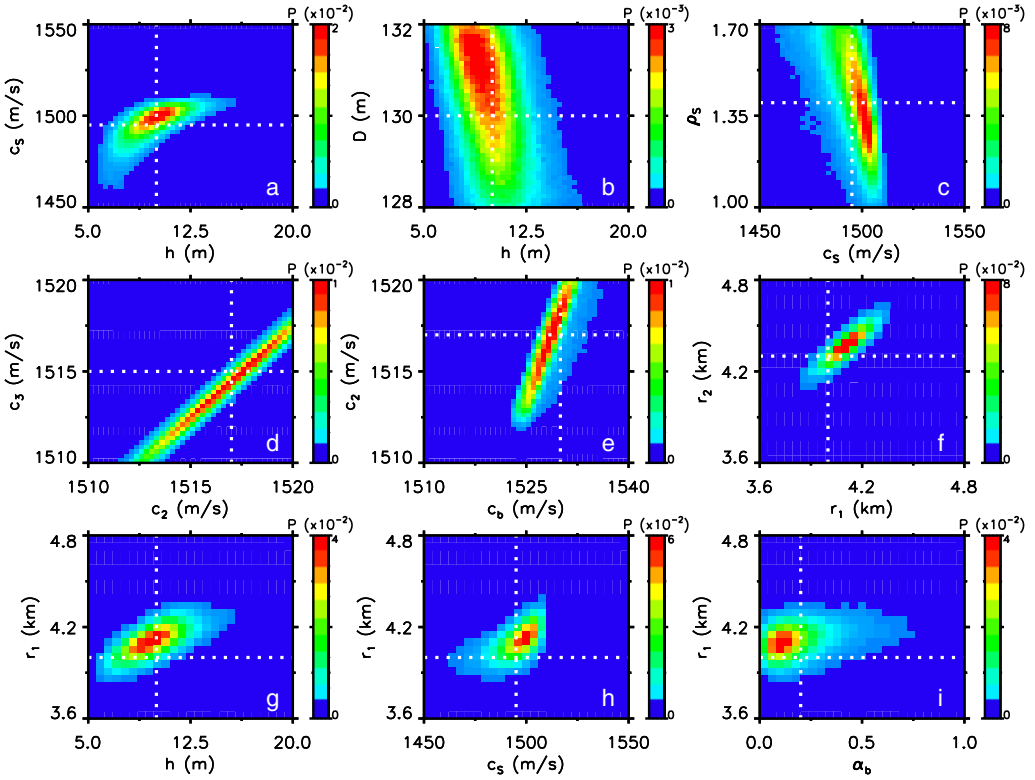

FIG. 15. (Color online) Selected joint marginal PPDs for track-constrained ship-noise inversion, illustrating important inter-parameter correlations.

similar to geoacoustic experiments based on a higher-SNR source at a well-known location with good knowledge of the water-column SSP.

To consider inter-parameter relationships in ship-noise inversion, Fig. 14 shows the correlation matrix for the track-constrained inversion. Correlations between environmental parameters such as between sediment thickness h and sound speed c_s, between h and water depth D, between c_s and density ρ_s, and between SSP parameters c_1-c_4 have been discussed elsewhere.[13,18] The strong positive correlations between the various source range parameters r_1-r_9 and between the source depth parameters z_1-z_9 result from the track constraints. Of particular interest here are correlations which are relevant to the marginal PPD comparisons in Fig. 13. For instance, the strong positive correlations between c_b and c_2-c_4 in Fig. 14 explain the improved resolution for c_b in the geoacoustic-experiment case (Fig. 13) where SSP parameters have much tighter priors. Further, the positive correlations between$h$ and r_1-r_9 and between c_s and r_1-r_9 explain the improved resolution for the sediment thickness and sound speed with exact knowledge of ship locations. The weaker but nonzero correlations between α_b and both r_1-r_9 and z_1-z_9 also account for the better resolution of α_b with exact source locations. The correlations described above are illustrated in Fig. 15 in terms of terms of joint marginal PPDs for the track-constrained inversion, showing how these inter-parameter relationships serve to increase parameter uncertainties.

IV. SUMMARY AND DISCUSSION

This paper develops and illustrates a Bayesian approach to the general problem of determining source and environmental parameters in ocean acoustic inversion, with specific applications to tracking a quiet acoustic source in an unknown environment and geoacoustic inversion using an unknown moving source (e.g., noise from a ship of opportunity). The goal in all cases is to quantify the information content of the data and prior in terms of marginal probability distributions for the unknown parameters, with source-tracking results represented as a series of joint marginal distributions over source range and depth (probability ambiguity surfaces). Analytic results are applied for unknown source amplitude/phase and data variances resulting in an efficient implicit formulation that does not require additional parameters to represent these quantities. Constraints on physically realistic source motion are applied as inter-parameter prior information in the inversion.

Given the numerically intensive inversion, an efficient Markov-chain Monte Carlo importance-sampling approach is developed which combines Metropolis Gibbs' sampling (for environmental parameters) and a 2D variant of heat-bath GS (for $r-z$ surfaces with many local optima). The efficiency of Metropolis GS is improved significantly by drawing parameter perturbations from a proposal distribution based on a linearized approximation to the PPD, initiated from an optimal model. This incorporates rotation to a principal-component parameter space (with no need for a preliminary sampling stage), as well as providing a characteristic perturbation length scale and distribution for each (rotated) parameter. To ensure complete sampling of the parameter space, GS at nonunity sampling temperatures (with subsequent correction of the samples) is considered and found to be necessary in some cases when track constraints are applied.

In terms of source tracking, results of the simulated examples indicate that simultaneous inversion of multiple acoustic observations for a moving source provides a more informative solution (more focused PASs) than sequential independent inversions, and that applying track constraints can provide a further (sometimes profound) improvement. Track-constrained inversion for a quiet submerged source (single-frequency data with SNR of −2 to −8 dB along the track) and large uncertainties in seabed and water-column properties provided PASs indicating an almost-unambiguous track, while inversions without track constraints failed. Environmental parameters were poorly determined for this case due to the low SNR and lack of prior knowledge of source location; however, the goal of source tracking was achieved.

The geoacoustic inversion example indicated that the seabed information content of data from an unknown moving near-surface source (two frequencies with SNR of +4 to −2 dB along the track) with a poorly known sound-speed profile was similar to that of a controlled-source experiment with a higher SNR (10 dB) and well-known SSP and source location. Further, inverting the moving-source data with exact knowledge of source locations provided only a small improvement, indicating the acoustic data contain sufficient information to resolve both seabed and ship-track parameters in an appropriate inversion.

[1]H. P. Bucker, "Use of calculated sound fields and matched field detection to locate sound sources in shallow water," J. Acoust. Soc. Am. **59**, 368–373 (1976).

[2]J. M. Ozard, "Matched field processing in shallow water for range, depth, and bearing determination: Results of experiment and simulation," J. Acoust. Soc. Am. **86**, 744–753 (1989).

[3]A. Tolstoy, *Matched Field Processing for Underwater Acoustics* (World Scientific, Singapore, 1993).

[4]A. B. Baggeroer, W. A. Kuperman, and P. N. Mikhalevsky, "An overview of matched field methods in ocean acoustics," IEEE J. Ocean. Eng. **18**, 401–424 (1993).

[5]H. Bucker, "Matched-field tracking in shallow water," J. Acoust. Soc. Am. **96**, 3809–3811 (1994).

[6]M. J. Wilmut and J. M. Ozard, "Detection performance of two efficient source tracking algorithms for matched-field processing," J. Acoust. Soc. Am. **104**, 3351–3355 (1998).

[7]L. T. Fialkowski, J. S. Perkins, M. D. Collins, M. Nicholas, J. A. Fawcett, and W. A. Kuperman, "Matched-field source tracking by ambiguity surface averaging," J. Acoust. Soc. Am. **110**, 739–746 (2001).

[8]M. D. Collins, W. A. Kuperman, and H. Schmidt, "Nonlinear inversion for ocean-bottom properties," J. Acoust. Soc. Am. **92**, 2770–2783 (1992).

[9]S. E. Dosso, M. L. Yeremey, J. M. Ozard, and N. R. Chapman, "Estimation of ocean-bottom properties by matched-field inversion of acoustic field data," IEEE J. Ocean. Eng. **18**, 232–239 (1993).

[10]P. Gerstoft, "Inversion of seismoacoustic data using genetic algorithms and *a posteriori* probability distributions," J. Acoust. Soc. Am. **95**, 770–782 (1994).

[11]S. E. Dosso, M. J. Wilmut, and A. L. Lapinski, "An adaptive hybrid algorithm for geoacoustic inversion," IEEE J. Ocean. Eng. **26**, 324–336 (2001).

[12]S. E. Dosso, "Quantifying uncertainty in geoacoustic inversion I: A fast Gibbs sampler approach," J. Acoust. Soc. Am. **111**, 129–142 (2002).

[13]S. E. Dosso and P. L. Nielsen, "Quantifying uncertainty in geoacoustic inversion II: Application to broadband, shallow-water data," J. Acoust. Soc. Am. **111**, 143–159 (2002).

[14]C. A. Gillard, D. J. Thomson, and G. J. Heard, "Estimating geoacoustic parameters using matched-field inversion methods," IEEE J. Ocean. Eng. **28**, 394–413 (2003).

[15]D. J. Battle, P. Gerstoft, W. S. Hodgkiss, W. A. Kuperman, and P. L. Nielsen, "Bayesian model selection applied to self-noise geoacoustic inversion," J. Acoust. Soc. Am. **116**, 2043–2056 (2004).

[16]S. E. Dosso, P. L. Nielsen, and M. J. Wilmut, "Data error covariance in matched-field geoacoustic inversion," J. Acoust. Soc. Am. **119**, 208–219 (2006).

[17]S. E. Dosso, "Environmental uncertainty in ocean acoustic inversion," Inverse Probl. **19**, 419–431 (2003).

[18]S. E. Dosso and M. J. Wilmut, "Bayesian focalization: Quantifying source localization with environmental uncertainty," J. Acoust. Soc. Am. **121**, 2567–2574 (2007).

[19]D. R. Del Balzo, C. Feuillade, and M. R. Rowe, "Effects of water-depth mismatch on matched-field localization in shallow water," J. Acoust. Soc. Am. **83**, 2180–2185 (1988).

[20]A. Tolstoy, "Sensitivity of matched field processing to sound-speed prone mismatch for vertical arrays in a deep water Pacific environment," J. Acoust. Soc. Am. **85**, 2394–2404 (1989).

[21]E. C. Shang and Y. Y. Wang, "Environmental mismatching effects on source localization processing in mode space," J. Acoust. Soc. Am. **89**, 2285–2290 (1991).

[22]M. D. Collins and W. A. Kuperman, "Focalization: Environmental focusing and source localization," J. Acoust. Soc. Am. **90**, 1410–1422 (1991).

[23]S. E. Dosso, "Matched-field inversion for source localization with uncertain bathymetry," J. Acoust. Soc. Am. **94**, 1160–1163 (1993).

[24]R. N. Baer and M. D. Collins, "Source localization in the presence of gross sediment uncertainties," J. Acoust. Soc. Am. **120**, 870–874 (2006).

[25]A. M. Richardson and L. W. Nolte, "*A posteriori* probability source localization in an uncertain sound speed, deep ocean," J. Acoust. Soc. Am. **89**, 2280–2284 (1991).

[26]J. A. Shorey, L. W. Nolte, and J. L. Krolik, "Computationally efficient Monte Carlo estimation algorithms for matched field processing in uncertain ocean environments," J. Comput. Acoust. **2**, 285–314 (1994).

[27]J. A. Shorey and L. W. Nolte, "Wideband optimal *a posteriori*, probability source localization in an uncertain shallow ocean environment," J. Acoust. Soc. Am. **103**, 355–361 (1998).

[28]S. L. Tantum and L. W. Nolte, "Tracking and localizing a moving source in an uncertain shallow water environment," J. Acoust. Soc. Am. **103**, 362–373 (1998).

[29]S. L. Tantum, L. W. Nolte, J. L. Krolik, and K. Haramci, "The performance of matched-field track-before-detect methods using shallow-water Pacific data," J. Acoust. Soc. Am. **112**, 119–127 (2002).

[30]W. R. Gilks, S. Richardson, and G. J. Spiegelhalter, *Markov Chain Monte Carlo in Practice* (Chapman and Hall, London, 1996).

[31]J. J. K. O. Ruanaidh and W. J. Fitzgerald, *Numerical Bayesian Methods Applied to Signal Processing* (Springer-Verlag, New York, 1996).

[32]B. F. Brooks and L. N. Frazer, "Importance reweighting reduces dependence on temperature in Gibbs samplers: An application to the inverse coseismic geodetic problem," Geophys. J. Int. **161**, 12–20 (2005).

[33]A. Tarantola, *Inverse Problem Theory: Methods for Data Fitting and Model Parameter Estimation* (Elsevier, Amsterdam, 1987).

[34]M. K. Sen and P. L. Stoffa, *Global Optimization Methods in Geophysical Inversion* (Elsevier, Amsterdam, 1995).

[35]C. F. Mecklenbräuker and P. Gerstoft, "Objective functions for ocean acoustic inversion derived by likelihood methods," J. Comput. Acoust. **6** 1–28 (2000).

[36]S. E. Dosso and M. J. Wilmut, "Estimating data uncertainty in matched-field geoacoustic inversion," IEEE J. Ocean. Eng. **31**, 470–479 (2006).

[37]W. H. Press, S. A. Teukolsky, W. T. Vetterling, and B. P. Flannery, *Numerical Recipes in FORTRAN* (Cambridge U.P., Cambridge, 1992).

[38]E. K. Westwood, C. T. Tindle, and N. R. Chapman, "A normal mode model for acousto-elastic ocean environments," J. Acoust. Soc. Am. **100**, 3631–3645 (1996).

[39]A. J. Viterbi, "Error bounds on convolutional codes and an asymptotically optimal decoding algorithm," Proc. IEEE **61**, 268–278 (1973).

Pressure sensitivity kernels applied to time-reversal acoustics

Kaustubha Raghukumar,[a] Bruce D. Cornuelle,
William S. Hodgkiss, and William A. Kuperman
Marine Physical Laboratory, Scripps Institution of Oceanography, University of California, San Diego 9500 Gilman Drive, La Jolla, California, 92093-0238

(Received 30 June 2007; revised 9 April 2008; accepted 15 April 2008)

Sensitivity kernels for receptions of broadband sound transmissions are used to study the effect of the transmitted signal on the sensitivity of the reception to environmental perturbations. A first-order Born approximation is used to obtain the pressure sensitivity of the received signal to small changes in medium sound speed. The pressure perturbation to the received signal caused by medium sound speed changes is expressed as a linear combination of single-frequency sensitivity kernels weighted by the signal in the frequency domain. This formulation can be used to predict the response of a source transmission to sound speed perturbations. The stability of time-reversal is studied and compared to that of a one-way transmission using sensitivity kernels. In the absence of multipath, a reduction in pressure sensitivity using time reversal is only obtained with multiple sources. This can be attributed both to the presence of independent paths and to cancellations that occur due to the overlap of sensitivity kernels for different source-receiver paths. The sensitivity kernel is then optimized to give a new source transmission scheme that takes into account knowledge of the medium statistics and is related to the regularized inverse filter. © *2008 Acoustical Society of America.* [DOI: 10.1121/1.2924130]

PACS number(s): 43.30.Re, 43.30.Pc [DRD] Pages: 98–112

I. INTRODUCTION

Time-reversed acoustics, due to its ability to focus energy in space and time, has found numerous applications ranging from underwater and wireless communications to medical ultrasound therapy.[1–3] Time reversal works by transmitting a signal which is a time-reversed version of the observed Green's function between a source and receiver. This scheme assumes that the Green's function has not significantly changed between its acquisition and time-reversed retransmission. Despite this assumption, the ability of time reversal to produce a focal spot has been found to be remarkably robust to environmental changes. In the ocean, the focal spot has been shown to persist for a week at 445 Hz (50 ms pulse),[4] and close to 1 hour at 3.5 kHz (10 ms pulse).[5]

Various explanations have been offered to understand the reason for the robustness of time reversal to environmental perturbations. Kim *et al.*,[5] using the theory of waveguide invariants for an oceanic waveguide, showed that while there is little degradation in the intensity of the focal spot, it is seen to shift back and forth in range as a result of internal wave induced sound speed fluctuations. While any one realization of the focal spot may or may not be stable, an ensemble average of focal spots tends to have high stability.[6] The presence of spatial diversity (large arrays) has the same effect as an ensemble average and results in stability of the focal spot. In random media,[7] the probability of a realization of the focal spot significantly differing from its expected value is small. This feature was referred to as the self-averaging property of the focal spot which leads to the statistical stability of time reversal for broadband signals. The self-averaging property is based on specific asymptotic limits more suited to optical and infrared time reversal than sonar or ultrasound.

The above contributions suggest the use of a formal sensitivity analysis to analyze the stability of the time-reversal focal spot with respect to sound speed perturbations. Sensitivity, when defined as the derivative of the received pressure signal with respect to medium sound speed fluctuations, provides a way to compare time-reversal transmissions to one-way transmissions. Sensitivity kernels can be a useful tool for analyzing various transmission schemes that have been proposed that seek to provide an even more stable focal spot,[5] or a focal spot with reduced spatio-temporal sidelobes.[8,9] The present work develops a pressure sensitivity kernel that can be used with a variety of source transmissions. The sensitivity kernels obtained for different source transmissions can be used as a performance measure to study the effect of medium sound speed fluctuations on the received signal. As an example, time reversal is compared to a one-way transmission, and an explanation is provided for the lower sensitivity of time reversal. The ability to express the received pressure perturbation as a function of the sensitivity kernel allows for the development of a regularized version of the inverse filter,[10] with a physically relevant regularization. In this paper, source transmissions may sometimes be referred to as source functions, or source shading functions (for an array of sources) in order to explicitly denote the time, frequency, or spatial dependence of the source transmission. This paper can be seen as primarily providing a theoretical framework, which is then visualized using a simple acoustic

[a]Author to whom correspondence should be addressed. Electronic mail: kaus@mpl.ucsd.edu

 0001-4966/2008/124(1)/98/15/$23.00

propagation scenario. Free space acoustic propagation, followed by a Pekeris waveguide, is used to visualize various sensitivity kernels.

Wave-theoretic sensitivity kernels were first proposed in seismology as a finite-frequency tomography alternative to the more commonly used time-of-arrival tomography.[11–13] A key contribution was in revealing that it is possible to have zero sensitivity to sound speed perturbations along a ray path, while having nonzero sensitivities in the region surrounding a ray path. More recently, travel-time sensitivity kernels for ocean-acoustic tomography were developed and were shown to exhibit similar properties to those developed in seismology.[14] These kernels are currently being employed to invert for sound speed perturbations in a shallow water waveguide using broadband acoustic signals.[15] All of these kernels make use of a first-order Born approximation, which results in a linear relation between the sound speed perturbation and either the induced pressure perturbation in the Green's function or a travel-time perturbation. The first Born approximation restricts the use of these sensitivity kernels to linear regimes where the sound speed perturbation is small compared to the background sound speed profile. For larger perturbations, nonlinearities result, which can, to an extent, be handled by iterative adjoint methods.[16] As a result of the first-order Born approximation, it is assumed that the Green's function used as a source transmission in time reversal represents an unperturbed medium, and that medium perturbations are restricted to a linear regime.

The contents of this work are organized as follows. In Sec. II, pressure sensitivity kernels are developed for the general case of an array of hydrophones transmitting to a single receiver (broadside transmission). The theory can be easily extended to a multiple-input multiple-output scenario. Sections III and IV show examples of sensitivity kernels in free space and for a Pekeris waveguide, respectively. The goal is to examine the sensitivity of time reversal versus that of a one-way transmission. In a dispersionless propagation environment, and in the absence of a transmit array, there is no difference in sensitivity between time-reversal and a one-way transmission. As suggested in Roux and Fink,[17] a reduction in sensitivity through time reversal is only made in the presence of multiple sources, or multipath propagation. Sensitivity kernels for a source-receiver path have a Fresnel zone-like interference pattern, and a reduction in sensitivity for a finite-frequency, finite-bandwidth case is caused by an averaging of several kernels that correspond to multiple sources or multiple paths. Time reversal results in each of the multiple paths arriving at the same time, as a consequence of which the sensitivity kernels for each of the paths add coherently to give an overall reduction in sensitivity. This holds true not just for time reversal, but also for inverse filters, or any transmission that results in the simultaneous arrival of different paths. In addition to the coherent cancellation of sensitivities, there is also an incoherent reduction in sensitivity that comes from independent paths having uncorrelated sound speed perturbations. The incoherent reduction, however, is not addressed in this paper.

In Sec. V, the sensitivity kernels are examined from an optimization point of view, the goal being to design source functions that offer the flexibility of trading mainlobe width for increased robustness. Semianalytic expressions for the optimized signals are offered, which result from a minimization of pressure perturbations together with a constraint on the focusing capabilities of the source function. This approach leads to an expression for the optimized source function which is an enhancement to the inverse filter.[18] Section VI presents the results of simulations in a Pekeris waveguide, where the optimized source function is compared to time reversal and the inverse filter. Sensitivity kernels for the optimized source functions are presented, which explicitly use knowledge of fluctuation statistics to lower sensitivity to medium perturbations. Finally, Sec. VII contains a discussion of the results and draws conclusions from this work.

II. PRESSURE SENSITIVITY KERNELS

The Green's function $G(\boldsymbol{r}|\boldsymbol{r}_s)$ describes the acoustic field of a harmonic point source of unit strength and satisfies the following inhomogeneous Helmholtz equation

$$\left[\nabla^2 + \frac{\omega^2}{c^2(\boldsymbol{r})}\right] G(\boldsymbol{r}|\boldsymbol{r}_s) = -\delta(\boldsymbol{r}-\boldsymbol{r}_s), \tag{1}$$

where $\boldsymbol{r}$ is the space vector, ω the circular frequency of the source, and $\boldsymbol{r}_s$ its location, $c(\boldsymbol{r})$ the sound speed distribution, and δ the Dirac δ function.

Following the same approach as Skarsoulis and Cornuelle,[14] a perturbation to the sound speed is introduced in Eq. (1) along with the resulting perturbation to the Green's function. Expanding the resulting equation and retaining only the first order terms will yield an expression that relates medium sound speed fluctuations to the change in the Green's function

$$\Delta G(\boldsymbol{r}|\boldsymbol{r}_s) = -2\omega^2 \int_V G(\boldsymbol{r}|\boldsymbol{r}')G(\boldsymbol{r}'|\boldsymbol{r}_s)\frac{\Delta c(\boldsymbol{r}')}{c^3(\boldsymbol{r}')}d\boldsymbol{r}'. \tag{2}$$

This is called the first Born approximation.[19] It is also called the single- or weak-scattering approximation, or wave-field linearization, and is widely used in connection with scattering problems.[20] It is a linear relation between the perturbation in the sound speed distribution and the induced perturbation in the Green's function. The integration volume in Eq. (2) is all space or the region encompassing the source and receiver over which sound speed perturbations result in perturbations to the Green's function.

A key assumption upon which the validity of the first order Born approximation rests is that $\Delta c/c$, integrated over the volume, be small. A consequence of the volume integration in Eq. (2) is that the validity of the first Born approximation in a waveguide will depend on the path length. Longer path lengths will result in the linear approximation breaking down at smaller sound speed perturbations than for shorter path lengths. The effect of nonlinearities was seen to start to creep in for a Δc of 4 ms^{-1} with a background sound speed of around 1500 ms^{-1}.[21]

The Green's function above is defined in the frequency domain—the circular frequency ω enters the Helmholtz equation as a parameter. Further, the Green's function depends on the sound speed distribution which also enters the

Helmholtz equation. In order to explicitly note these dependencies, G is written in the following as $G(\boldsymbol{r}|\boldsymbol{r}_s;\omega;c)$.

For a single point source the resultant pressure field can be written as

$$P(\boldsymbol{r}_r;\omega) = G(\boldsymbol{r}_r|\boldsymbol{r}_s;\omega;c)S(\boldsymbol{r}_s;\omega), \tag{3}$$

where $P(\boldsymbol{r}_r;\omega)$ is the frequency-domain pressure at receiver location $\boldsymbol{r}_r$, from a source located at $\boldsymbol{r}_s$. $G(\boldsymbol{r}_r|\boldsymbol{r}_s;\omega;c)$ is the frequency-domain Green's function that turns pressure at the source at frequency ω to pressure at the receiver. $S(\boldsymbol{r}_s;\omega)$ is the signal at source $\boldsymbol{r}_s$ at frequency ω. For an array transmitting to a single receiver, the received signal is given by adding up all source contributions:

$$P(\boldsymbol{r}_r;\omega) = \sum_{i=1}^{N_s} G(\boldsymbol{r}_r|\boldsymbol{r}_{si};\omega;c)S(\boldsymbol{r}_{si};\omega), \tag{4}$$

where $\boldsymbol{r}_{si}$ is the location of the ith source element, and N_s is the number of source elements.

In the time domain, the received signal is then given by

$$P(\boldsymbol{r}_r;t) = \sum_{i=1}^{N_s} \int_{-\infty}^{\infty} G(\boldsymbol{r}_r|\boldsymbol{r}_{si};t-t';c)S(\boldsymbol{r}_{si};t')dt'. \tag{5}$$

It is seen from Eq. (5) that, in the case of an array-to-a-point transmission, the time-domain Green's function has been accumulated over source and time, weighted by S, as opposed to a point-to-point transmission where the Green's function is only accumulated over time. For now, a heuristic argument can be made that this additional spatial averaging could make the received signal more stable. This will be shown more rigorously in Sec. VI.

In a perturbed propagation environment, the frequency domain perturbation to the received pressure can be approximated by substituting the perturbed Green's function into Eq. (4)

$$\Delta P(\boldsymbol{r}_r;\omega) = \sum_{i=1}^{N_s} \Delta G(\boldsymbol{r}_r|\boldsymbol{r}_{si};\omega;c)S(\boldsymbol{r}_{si};\omega). \tag{6}$$

Using Eq. (2) for the perturbed Green's function

$$\Delta P(\boldsymbol{r}_r;\omega) = \sum_{i=1}^{N_s} \left(-2\omega^2 \int_V G(\boldsymbol{r}_r|\boldsymbol{r};\omega;c)G(\boldsymbol{r}|\boldsymbol{r}_{si};\omega;c)\frac{\Delta c(\boldsymbol{r})}{c^3(\boldsymbol{r})}d\boldsymbol{r} \right) \times S(\boldsymbol{r}_{si};\omega). \tag{7}$$

Exchanging the order of integration and summation will yield the effective pressure sensitivity kernel

$$\begin{aligned}\Delta P(\boldsymbol{r}_r;\omega) &= -2\omega^2 \int_V \left(\sum_{i=1}^{N_s} G(\boldsymbol{r}_r|\boldsymbol{r};\omega;c)G(\boldsymbol{r}|\boldsymbol{r}_{si};\omega;c) \times \frac{\Delta c(\boldsymbol{r})}{c^3(\boldsymbol{r})}S(\boldsymbol{r}_{si};\omega) \right) d\boldsymbol{r} \\ &= \int_V \left(\sum_{i=1}^{N_s} K_{pp}^i(\boldsymbol{r};\omega;c) \right) \Delta c(\boldsymbol{r})d\boldsymbol{r} \\ &= \int_V K_{ap}(\boldsymbol{r};\omega;c)\Delta c(\boldsymbol{r})d\boldsymbol{r}, \end{aligned} \tag{8}$$

where $K_{pp}^i(\boldsymbol{r};\omega;c)$ is the sensitivity of the received pressure for a receiver located at $\boldsymbol{r}_r$ to a sound speed perturbation at location $\boldsymbol{r}$, for the single source with index i located at $\boldsymbol{r}_{si}$

$$\begin{aligned} K_{pp}^i(\boldsymbol{r};\omega;c) &= -2\omega^2 G(\boldsymbol{r}_r|\boldsymbol{r};\omega;c)G(\boldsymbol{r}|\boldsymbol{r}_{si};\omega;c)\frac{1}{c^3(\boldsymbol{r})}S(\boldsymbol{r}_{si};\omega) \\ &\equiv M_{pp}^i(\boldsymbol{r};\omega;c)S(\boldsymbol{r}_{si};\omega) \end{aligned} \tag{9}$$

and $K_{ap}(\boldsymbol{r};\omega;c)$ is the sensitivity of the received pressure to a sound speed perturbation at location $\boldsymbol{r}$, for an array of sources transmitting to a single receiver. M_{pp}^i can be recognized as part of the integrand in Eq. (2), i.e., integrating M_{pp}^i times the sound speed perturbation over the region between source and receiver will give the Born approximation to the perturbed Green's function.

Equation (8) is a linear relation between the pressure perturbation at the receiver and sound speed perturbations in the medium, valid when $\Delta c/c$ is sufficiently small.

Equations (8) and (9) provide the framework for studying the effect of source transmission schemes on the received pressure perturbation. Replacing $S(\boldsymbol{r}_s;\omega)$ by $G^*(\boldsymbol{r}_r|\boldsymbol{r}_s;\omega;c)$, will result in an expression for the pressure perturbation for a time-reversal scheme. Replacing $S(\boldsymbol{r}_s;\omega)$ by $1/G(\boldsymbol{r}_r|\boldsymbol{r}_s;\omega;c)$ will result in an expression for the pressure perturbation for a scheme involving inverse filters.[18]

Finally, an additional way of looking at Eq. (8) is in terms of an optimization problem where the goal is to obtain a set of source transmissions that will minimize the pressure perturbations at the receiver. This is more fully explored in Sec. V.

III. FREE SPACE SENSITIVITY KERNELS

As a first step towards visualizing pressure sensitivity kernels, the analytical framework developed in Sec. II is applied to acoustic propagation in free space. The analytical framework for free space closely follows that of Skarsoulis.[14]

A. Analytical results

The complex amplitude of the three-dimensional (3D) Green's function between a point source located at $\boldsymbol{r}_s$ and receiver at $\boldsymbol{r}_r$ in a medium with uniform background sound speed c has the form,

$$G_s(\omega) = \frac{e^{ikR}}{4\pi R}, \tag{10}$$

where $R=|\boldsymbol{r}_s-\boldsymbol{r}_r|$ is the source-receiver distance, $k=\omega/c$.

Scatterers in the medium between source and receiver, each of which contribute a sound-speed perturbation $\Delta c(x,y,z)$, will cause a perturbation to the Green's function [Eq. (2)]. Denoting the distance from the source to a scatterer (sound speed anomaly) by R_1 and from the scatterer to the receiver by R_2, the perturbation to the received pressure will be

$$\Delta P(\omega) = \frac{-2\omega^2}{(4\pi)^2 c^3} \int\int\int \frac{e^{ik[R_1(x,y,z)+R_2(x,y,z)]}}{R_1(x,y,z)R_2(x,y,z)} \times S(\omega)\Delta c(x,y,z)dxdydz. \tag{11}$$

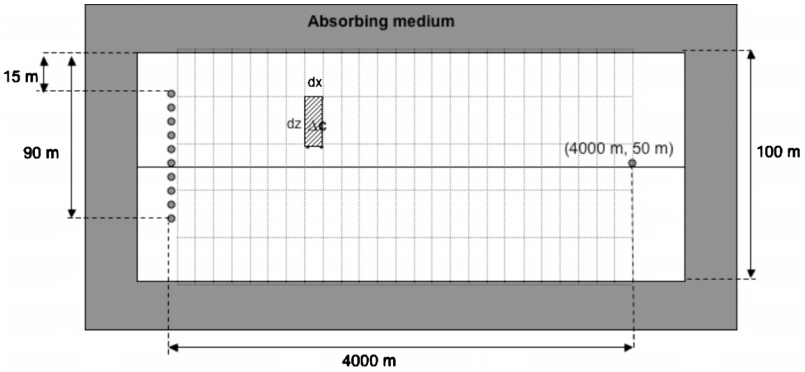

FIG. 1. (Color online) Computational geometry for free space sensitivity kernels.

From Eqs. (11) and (9), the free space sensitivity kernel for a single source-receiver pair is

$$K_{pp}(x,y,z;\omega) = \frac{-2\omega^2}{(4\pi)^2 c^3} \frac{e^{ik[R_1(x,y,z)+R_2(x,y,z)]}}{R_1(x,y,z)R_2(x,y,z)} S(\omega). \quad (12)$$

The three-dimensional pressure sensitivity kernel can be reduced to two dimensions by integrating Eq. (12) over the horizontal cross-range dimension. This assumes that the sound speed anomalies between source and receiver do not vary in the horizontal cross-range direction. Next, the continuous-valued kernel in Eq. (12) can be discretized by integrating Eq. (12) without the source term over grid cells (Fig. 1), with the sound-speed anomaly assumed to be constant over each cell. These two operations yield the integrated pressure sensitivity for each grid cell [Eq. (9)],

$$M^i_{pp}(x_n,z_m;\omega) = \frac{-2\omega^2}{(4\pi)^2 c^3} \int_{-y_0}^{y_0} \int_{x_n-dx/2}^{x_n+dx/2} \int_{z_m-dz/2}^{z_m+dz/2} \times \frac{e^{ik[R_1(x_n,y,z_m)+R_2(x_n,y,z_m)]}}{R_1(x_n,y,z_m)R_2(x_n,y,z_m)} dz dx dy. \quad (13)$$

Equation (13) is numerically evaluated in Sec. V.

Equation (13), multiplied by a source function, will yield the point-to-point sensitivity kernel [Eq. (12)], following which the pressure perturbation can be calculated using Eq. (11).

It is helpful to look at the time-domain pressure sensitivity equations for the simple case of free space propagation using both a unity frequency domain source function and the phase conjugated Green's function as source functions.

For a one-way transmission, $S(\omega)=1$ (delta function in time, centered at $t=0$). This will result in a single arrival at time $t=R/c=T$. Hence, the time-domain sensitivity kernel for pressure at the time of the peak arrival is evaluated at time $t=R/c$. For time reversal, the shape of the spectrum stays the same, but the signal is phased and shaded in such a way that the source function $S(\omega) \sim e^{-ikr}/R$. This phasing will result in the single arrival occurring at time $t=0$, as opposed to the one-way transmission where the arrival occurs at $t=R/c=T$. Hence, for time reversal, the sensitivity kernel for pressure at the time of the peak arrival is evaluated at time $t=0$. The sensitivity kernel at the time of an arrival provides quantitative information about the sensitivity of the pressure amplitude of the peak of the arrival to sound speed perturbations at any point in the medium. Henceforth, the term time-domain sensitivity kernel is used to denote time-domain pressure sensitivity for a particular time, usually the peak of an arrival, to sound-speed perturbations.

Using the appropriate source function $S(\omega)$, and applying the inverse Fourier transform to Eq. (12) will give the time-domain sensitivity kernels for point-to-point and time-reversal transmissions,

$$K_{pp}(t) = \frac{2}{(4\pi)^2 c^3 R_1 R_2} \int_{\infty}^{\infty} -\omega^2 e^{i\omega(T_1+T_2-t)} d\omega$$

$$= \frac{1}{(4\pi)^2 c^3 R_1 R_2} \delta''(T_1+T_2-t)$$

$$K_{tr}(t) = \frac{2}{(4\pi)^2 c^3 R_1 R_2} \int_{\infty}^{\infty} -\omega^2 e^{i\omega(T_1+T_2-T-t)} d\omega$$

$$= \frac{1}{(4\pi)^2 c^3 R_1 R_2} \delta''(T_1+T_2-T-t), \quad (14)$$

where $\delta(.)$ is the Dirac delta function and $'$ denotes its time derivative, $T_1=R_1/c$ and $T_2=R_2/C$. The notation has been simplified to drop the explicit dependence of R_1, R_2, T_1 and T_2 on x, y, z. Equation (14) for the time-domain pressure sensitivity kernels is similar to what was derived with respect to travel-time sensitivity kernels.[14]

Evaluating the sensitivity kernels at the respective arrival times will result in

$$K_{pp}(t=T) = \frac{2}{(4\pi)^2 c^3 R_1 R_2} \delta''(T_1+T_2-T)$$

$$K_{tr}(t=0) = \frac{2}{(4\pi)^2 c^3 R_1 R_2} \delta''(T_1+T_2-T). \quad (15)$$

Thus, in the trivial case of a point-to-point transmission in free space, both time-reversal and a one-way transmission have identical pressure sensitivities.

In a finite frequency, finite bandwidth case, the infinite bandwidth Dirac delta function is replaced by a $\sin(x)/x$ (sinc) form where the argument of the sinc function is given by T_1+T_2-T. As a result, the sensitivity kernel in Eq. (15) can be approximated by the second derivative of the sinc function. This gives rise to a pattern in the range-depth space marked by lines over which T_1+T_2 is constant, which is the broadband equivalent of the lines of constant phase in a single-frequency Fresnel interference pattern.

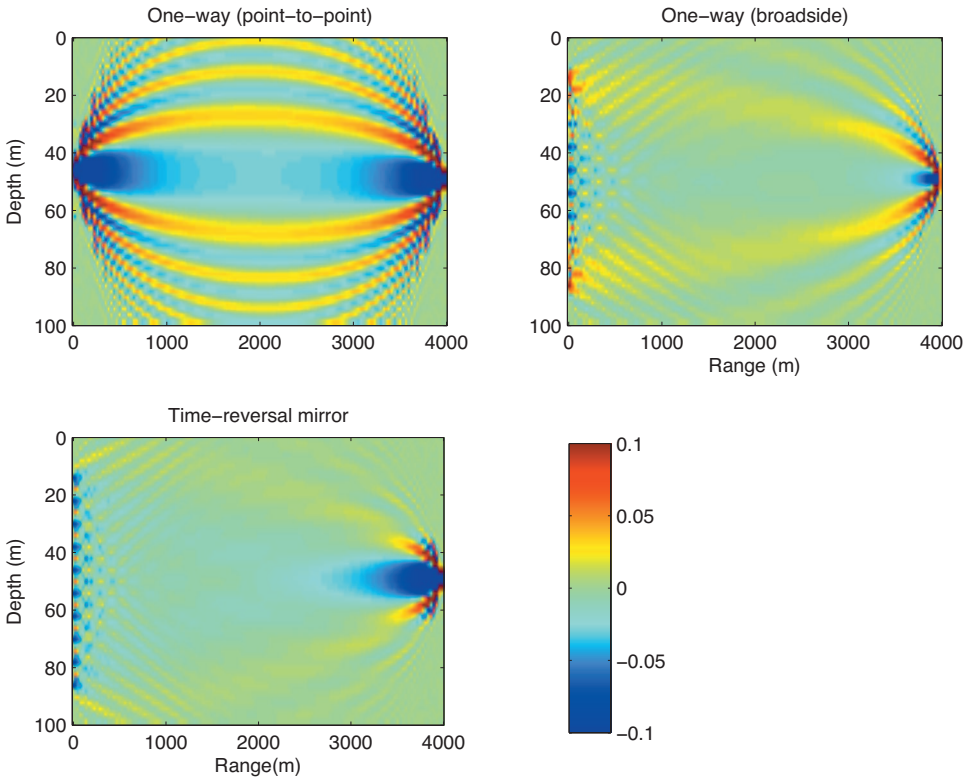

FIG. 2. Time domain sensitivity kernels (10^{-5} μPa s m^{-4}) evaluated at the peak of the arrival for: **Top left:** Point-point one-way, **top right:** Array-to-point one way (broadside), **bottom left:** Array-to-point time reversal (time-reversal mirror). Receiver is on the right hand side of each plot, at a depth of 50 m.

B. Numerical results

A simple way to test the sensitivity kernels [Eq. (9)] from previous sections is to conduct numerical simulations involving acoustic propagation in free space where there are sound speed anomalies $\delta c(x,z)$ in the medium between source and receiver.[14]

The scenario studied involves a two-dimensional (2D) area, 4000 m in length and 100 m in depth. While the theory developed here applies to 3D geometries, the results are more easily visualized by integrating the 3D pressure sensitivity kernel along the horizontal cross-range dimension [Eq. (13)]. It was shown[22] that three-dimensional scattering effects become important only when the Fresnel width approaches and exceeds the cross-range coherence length of the sound speed perturbations. This is because, under such a scenario, out-of-plane scattering becomes important, which cannot be accounted for by 2D models. As shown in the next section, the Fresnel width for pressure sensitivity kernels in the free space scenario considered is approximately 20 m. The cross-range scale for sound speed perturbations was assumed to be larger than 30 m, thus satisfying the criterion under which a two-dimensional example is sufficient to yield realistic results. As a result, it is possible to work in two dimensions by using sensitivity kernels that are integrated in the horizontal cross-range dimension. There are ten transmit transducers spanning depths 15–90 m. The receive transducer is at a range of 4000 m and at a depth of 50 m. The background sound speed is assumed to be 1500 ms^{-1}. The transducers operate at a central frequency of 3.5 kHz (λ_C =0.4 m) with a bandwidth of 128 Hz. These values are chosen to roughly reflect those used in recent ocean acoustics experiments. Figure 1 shows the computational geometry employed to illustrate sensitivity kernels in free space. The size of each grid cell is dx=30 m by dz=2 m. Sensitivity kernels are numerically integrated over three dimensions for each grid cell. The size of the grid cell is representative of spatial coherence scales of sound speed perturbations in the ocean.[23]

Broadband Green's functions were calculated from each source to the domain and from the receiver to the domain (a finely sampled three-dimensional grid cell), over the 128 Hz bandwidth centered around 3.5 kHz, using a frequency step of 1 Hz. The product of the two Green's functions is then numerically integrated over each grid cell. This allows for the calculation of the frequency-domain sensitivity kernel according to Eq. (13). A fast Fourier transform (FFT) is then applied to the frequency-domain sensitivity kernels at each grid point, which results in a time series of sensitivity for each cell. For each cell, the value of the sensitivity time series at the time of an unperturbed arrival is the time-domain pressure sensitivity for the arrival. This may be expressed as

$$K(t) = \int_{-\infty}^{\infty} M(\omega)S(\omega)e^{-i\omega t}d\omega. \tag{16}$$

For a one-way point-to-point transmission, $M(\omega)=M^i_{pp}(\omega)$, $S(\omega)=1$, and $t=R/c$. For a broadside transmission, $M(\omega)=\Sigma_{i=1}^{N}M^i_{pp}(\omega)$, $S(\omega)=1$, and $t=R/c$. For a time-reversal mirror, $M(\omega)=\Sigma_{i=1}^{N}M^i_{pp}(\omega)$, $S(\omega)=G^*_{si}(\omega)$, and $t=0$. The top left panel in Fig. 2 shows the time-domain pressure sensitivity kernels for the main (only) arrival, for one-way point-to-point transmissions between a source at 50 m and a receive element at 50 m depth, at a range of 4 km. The structure of the sensitivity map shows an approximate Fresnel-zone behavior with an oscillatory structure.[14] The significance of the

Fresnel zones is that within each zone, the phase difference between the interfering Green's functions is less than π. While the Fresnel zone is a single-frequency concept, the time-domain analogue, called the "zone of influence"[24] is a weighted average of many single-frequency Fresnel interference patterns. As the central frequency increases, the width of the zone of influence becomes smaller as the propagation becomes more ray like. As the bandwidth increases, the higher order Fresnel zones of different frequencies begin to destructively interfere, and only the first zone of influence is discernible. The width of the central lobe of the kernel is approximately the same as that of the first Fresnel zone at the central frequency, given by[25]

$$R_F(r) = \sqrt{\frac{r(R-r)c}{fR}}, \tag{17}$$

where R is the source-receiver distance, f is the central frequency of the signal, and c is the sound speed. Taking $R=4000$ m, $r=2000$ m, $c=1500$ m/s, and $f=3500$ Hz gives $R_F=20.7$ m, which is consistent with the observed value of approximately 20 m in Fig. 2. As $\omega \to \infty$, $R_F(r) \to 0$, and the wave-theoretic sensitivity kernel becomes the ray-theoretic kernel. The sensitivity on the source-receiver path is nonzero, which is different from 3D travel-time sensitivity kernels which have zero sensitivity along the ray path. In seismic literature,[11] 3D travel-time sensitivity kernels are often referred to as "banana-doughnut" kernels with the "banana" shape arising from the shape of the kernel as a result of refraction of the ray path, and the "doughnut" referring to the region of zero sensitivity along the ray path. The nonzero sensitivity along the ray path has also been observed for 2D travel-time kernels.[26] Because the 2D kernel is obtained from the cross-range averaging of the 3D kernel, the 2D kernel has nonzero sensitivity along the ray path.

With an understanding of the pressure sensitivity kernels in place, it is now possible to study the effect of time reversal on the sensitivity kernel. Any reduction in sensitivity obtained through time reversal[27] may be thought of as a two-part process. First, there is the reduction in sensitivity, if any, obtained through the use of a time-reversed Green's function as a source function. Second, there is the effect of using an array of sources, which involves a phased sum of several one-way point-to-point kernels such as shown in Fig. 2. Thus, when studying the effect of time reversal on sensitivity, it is helpful to break up the problem into a time-reversal part followed by an array gain part, or vice versa.

The top right, and bottom panels in Fig. 2 show sensitivity, in the time domain, for one-way and time-reversal transmissions involving an array transmitting to a single receiver. In the case of time reversal, the power of the time-reversed Green's function has been normalized to have the same total power as the uniform source function used in a one-way transmission. Since the sensitivity kernels for the array-to-point kernels are a sum of individual point-to-point kernels, the array-to-point kernels have been divided by the number of sources. The broadside sensitivity kernel is computed by first summing the individual frequency-domain sensitivity kernels for each source, followed by evaluating the broadside time-domain sensitivity kernel at the time of arrival of a pulse from a source at 50 m depth. This is because the received signal for a broadside transmission consists of just a single arrival corresponding to a source at 50 m depth since the difference in range between the various sources and the receiver is insufficient to produce several distinct direct arrivals. If there were indeed distinct arrivals, the broadside time-domain sensitivity kernel would have to be evaluated at each of the arrival times.

TABLE I. The rms values for one-way and time-reversal free space sensitivity kernels, normalized to the sensitivity for a one-way transmission.

One way (point-to-point)	Time reversal (point-to-point)	Broadside (array-to-point)	Time-reversal mirror (array-to-point)
1	1	0.48	0.33

The rms values of sensitivities for the various schemes are listed in Table I, divided by the rms value for a one-way transmission. The rms values are divided by the peak amplitude of the arrival for the one-way transmissions, or the peak amplitude of the focal spot for time reversal. The statistical significance of using the rms of the sensitivity kernel follows from Eq. (8). For uncorrelated perturbations, the rms of the sensitivity map is shorthand for the rms of the expected pressure perturbation.

Point-to-point time reversal is identical to a one-way transmission in terms of sensitivity [Eq. (15)]. The use of time reversal shows a reduction in sensitivity in free space only when used along with an array. For an array in free space, time reversal results in a phasing of transmissions from different sources such that the peak of all arrivals occurs at the same time. The phased addition of several point-to-point sensitivity kernels results in a net cancellation of the oscillating Fresnel-like zones of influence. A given sound speed perturbation will be in the zone of influence of sensitivity kernels for multiple paths. When these paths are phased such that they all arrive at the same time, then evaluating the sensitivity at that time corresponds to an average of all the sensitivity kernels. Due to overlapping positive and negative regions of sensitivity, there is an overall reduction in sensitivity. As frequencies get larger, there are two effects that need to be considered. First, increasing the bandwidth results in the addition of kernels for each frequency, and this smears out the higher order zones of influence which reduces the overall rms sensitivity. At the same time, there is less overlap of sensitivity kernels for the multiple paths. Second, increasing the central frequency results in a larger pressure sensitivity due to larger phase shifts. The combined effect is that time reversal involving higher frequencies has a greater sensitivity to sound speed perturbations, as has been experimentally observed.[5]

In the example shown, the time-reversal mirror reduces the sensitivity of the peak magnitude to about two thirds that of a broadside transmission. While the broadside transmission in this example also results in a single arrival, the alignment of the different peaks is not perfect, and the sensitivity of the peak of the arrival is larger than that for time reversal.

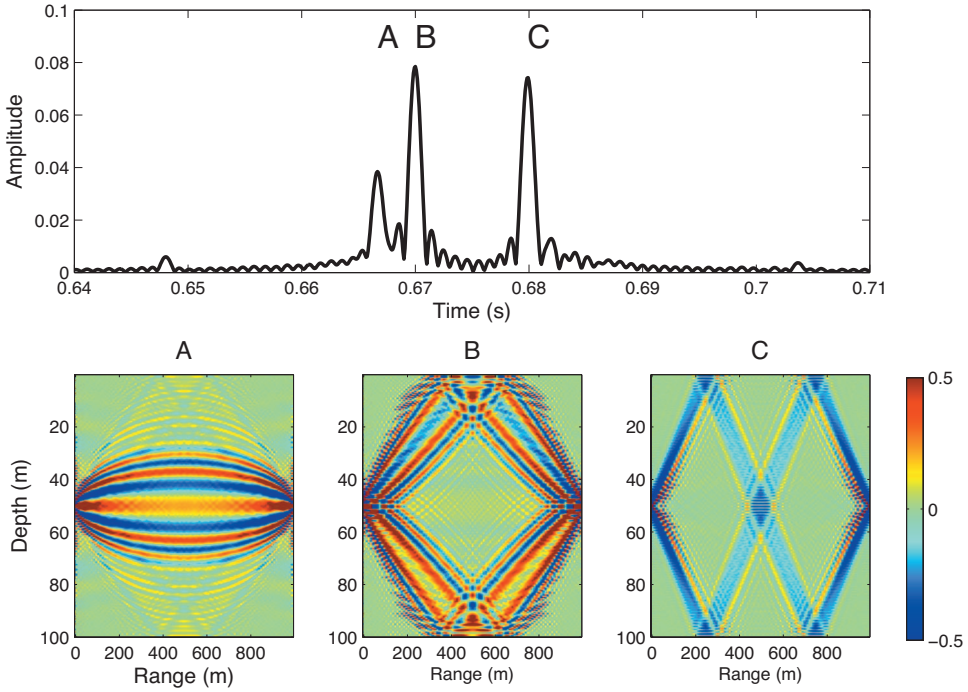

FIG. 3. Time domain sensitivity kernels (10^{-10} μPa s m^{-4}) for one-way transmission, for a source at 50 m and receiver 1000 m away at a depth of 50 m. **Top:** Envelope of Green's function. A,B,C are the individual multipaths corresponding to direct path, single surface/bottom bounce, double bounce off the surface and bottom. **Bottom:** Time-domain sensitivity kernel for each arrival.

IV. PEKERIS WAVEGUIDE SENSITIVITY KERNELS

The complex amplitude Green's function in a two-dimensional Pekeris waveguide for a source located at (r_s, z_s) and a receiver at (r, z) is given by[28]

$$G(r,z) = \frac{i}{4\rho(z_s)} \sum_{m=1}^{M} \psi_m(z_s)\psi_m(z) H_0^{(1)}(k_{rm} r). \tag{18}$$

For mode m, k_{rm} is the horizontal wave number, ψ_m is the vertical mode shape, and $H_0^{(1)}(k_{rm}r)$ is the Hankel function of the first kind. Equation (18), along with Eq. (9), will give the frequency-domain pressure sensitivity kernel for a Pekeris waveguide. The waveguide geometry for which the Pekeris sensitivity kernels are computed has dimensions identical to Fig. 1, with the surrounding absorbing medium replaced by a pressure release surface and an absorbing bottom. The density and sound speed in the bottom are 1800 kg/m^3 and 1800 m/s, respectively. While it was relatively straightforward to compute closed form sensitivity kernels for free space propagation, the same is not true for the Pekeris waveguide. However, it can now be expected that multipath propagation will result in differences between time-reversal and one-way transmissions, as opposed to free space propagation where the two are identical for a point-to-point application.

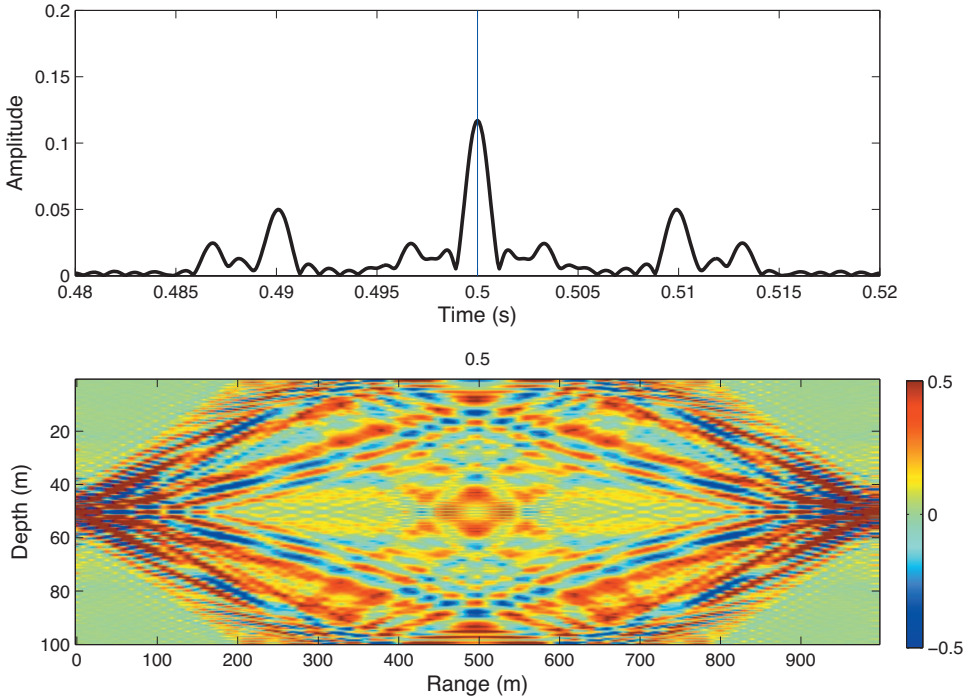

FIG. 4. Time domain sensitivity kernels (10^{-10} μPa s m^{-4}) for the peak of a point-to-point time-reversal focal spot, for a source at 50 m and receiver 1000 m away at a depth of 50 m. **Top:** Pressure envelope of the focal spot. **Bottom:** Time-domain sensitivity kernel for the focal spot, with the time of arrival in seconds.

TABLE II. The rms sensitivities for one-way, time reversal, and a time-reversal mirror in a Pekeris waveguide, normalized to pressure sensitivity on the direct path.

	One way (point-to-point)	Time reversal (point-to-point)	Time-reversal mirror (array-to-point)
Direct path	1		
One bounce	0.69	0.71	0.37
Two bounces	0.52		

Frequency-domain pressure sensitivity kernels are computed every 1 Hz over a bandwidth of 1 kHz with, a central frequency of 3.5 kHz. The two-dimensional grid over which the sensitivity kernels are computed is sampled well above the spatial Nyquist frequency in order to avoid spatial aliasing, with a depth step of $dz=0.1$ m and a range step of $dr=10$ m. Unlike the 3D free space sensitivity kernels, which were averaged over the cross-range dimension, no averaging is needed for the 2D Pekeris waveguide example, since the Green's function in Eq. (18) is specifically defined for a 2D geometry. Green's functions for this example are on the order of 10^{-5}, as a result of which sensitivity kernels will be on the order of 10^{-10}. In order to avoid plotting these extremely small values. Green's functions are scaled up by 10^5.

An inverse FFT of the frequency-domain sensitivity kernels in Eq. (9) will result in a time series for each grid point. This time series is then sampled at times corresponding to the time of arrival of the various multipaths for a pulse propagating in the unperturbed medium. This will result in a number of sensitivity kernels, each of which corresponds to a particular multipath arrival. The resulting sensitivity kernels are broadband, and centered around the carrier frequency.

Figure 3 shows the time-domain sensitivity kernels for a source located at a depth of 50 m and a receiver located at the same depth, but 1000 m away in range. The same Fresnel-like interference pattern as free space propagation is seen, centered around each ray path. The sensitivity kernel for the bottom bounce is seen to have the opposite polarity compared to the sensitivity kernel for the surface bounce. This is a result of a negative reflection coefficient associated with the surface bounce. Another feature of the sensitivity kernels in Fig. 3 is the reduction in sensitivity as the launch angle gets steeper. This is a direct consequence of Snell's law $(\cos\theta/c=\text{const},\ \cos\theta=k_r/k,\ d\theta/dc\to 0\ \text{as}\ \theta\to\pi/2)$, where θ is the angle of incidence with respect to the horizontal. As $d\theta/dc$ gets smaller with an increasing angle of incidence (θ), a reduction in sensitivity (dP/dc) follows.

Figure 4 shows the time-domain sensitivity kernel for the time-reversal focal spot, obtained using the time-reversed Green's function in Fig. 3 as a source transmission. The time-reversed Green's function is normalized to have unit power. Time reversal leads to the different multipath arrivals being phased in a way such that they all arrive at the same time, resulting in a focal spot. Similarly, time-reversal results in the sensitivity kernel for the focal spot being a phased sum of the sensitivity kernels for the peak of each arrival. Table II lists rms sensitivities normalized by the rms sensitivity of the direct path. The peak amplitude of the focal spot is different from the peak amplitude of the multipath arrivals. In order to compare the sensitivity of the focal spot versus that of the individual arrivals, the different sensitivity kernels are first divided by the peak pressure of the respective arrival.

Next, the use of an array (time-reversal mirror) is investigated, and the resulting sensitivity map is shown in Fig. 5. Ten sources are employed in the same configuration as shown in Fig. 1. The resulting sensitivity kernels are divided by the number of sources, in order to make a comparison with Figs. 3 and 4. It is seen that the sensitivity kernel for a time-reversal mirror is a superposition of sensitivity kernels corresponding to different sources, each of which transmits a time-reversed Green's function.

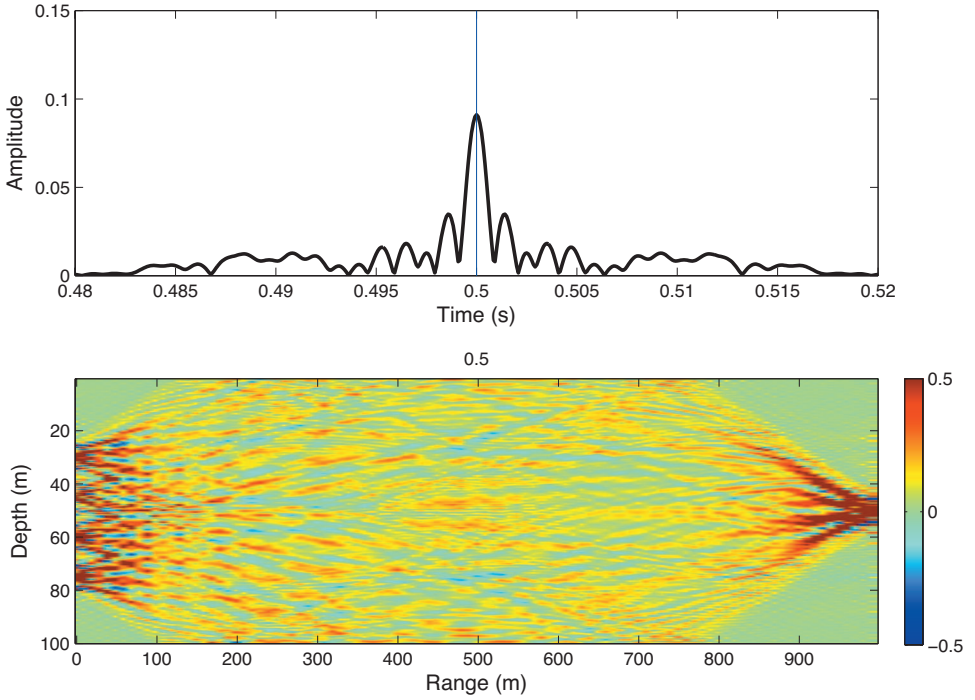

FIG. 5. Time domain sensitivity kernels (10^{-10} μPa s m^{-4}) for the peak of the focal spot for a time-reversal mirror. There are ten sources located between 30 and 75 m and receiver 1000 m away at a depth of 50 m. **Top:** Pressure envelope of focal spot. **Bottom:** Time-domain sensitivity kernel for the focal spot, with the time of arrival in seconds.

As seen in Table II, the use of a time-reversal mirror results in a reduction by 0.34 in sensitivity compared to a single-source time-reversed transmission (point-to-point time reversal). This is caused by the averaging of the sensitivity kernels corresponding to the different sources in a manner similar to that of the free space example in Sec. III, in addition to averaging over the multipath arrivals.

V. SOURCE FUNCTION OPTIMIZATION

As mentioned in Sec. II, expressing the array-to-point sensitivity kernel with the source transmissions as adjustable parameters allows for optimization of the source signal with regard to the sensitivity of the received signal to sound speed perturbations. Other constraints on the source signal can be added, resulting in a joint optimization problem. In this section, the optimization problem is posed in terms of obtaining a spatio-temporal (depth and time) focal spot, while at the same time minimizing the effect of fluctuations. The optimization is applied in the frequency domain since the pressure perturbations caused by sound speed fluctuations [Eq. (8)] are more simply expressed in the frequency domain. As a result of the optimization, the quality of the focal spot (mainlobe intensity, width, mainlobe to sidelobe ratio) may be traded off for increased stability.[5]

A. Minimizing pressure perturbations

In order to state the optimization problem in matrix form, the frequency domain, time domain, and medium are discretized. To be conceptually simple, the medium is parameterized by a two-dimensional grid in range and depth. Thus, sound speed perturbations of the medium can be specified by the matrix $\Delta\mathbf{c}$, where the rows correspond to depth and columns to range. Similarly, the frequency-domain point-to-point sensitivity kernel [Eq. (8)] over the medium can be expressed as a matrix $\mathbf{K}(\omega)$. Next, in order to express the integral in Eq. (8) as the dot product of two vectors, the $N_z \times N_x$ two-dimensional matrices $\Delta\mathbf{c}$ and $\mathbf{K}(\omega)$ are written as $(N_z N_x)\times 1$ vectors after stacking the columns. Using the $vec\{\cdot\}$ notation to denote a vectorized (stacked columns) matrix, Eq. (8) may be written as

$$\Delta P(x_r,z_r;\omega) = vec\{\mathbf{K}_{ap}(\omega)\}^T vec\{\Delta\mathbf{c}\}\Delta x\Delta z, \tag{19}$$

where the superscript $(\cdot)^T$ denotes matrix transpose. The area element (volume element for 3D) $\Delta x\Delta z$ may be absorbed into $\Delta\mathbf{c}$ or $\mathbf{K}_{ap}(\omega)$ so the integral becomes a dot product. The two-dimensional $(N_z\times N_x)$ matrix $\mathbf{K}_{ap}$ is obtained by the multiplication of the three-dimensional $(N_z\times N_x\times N_s)$ matrix $\mathbf{M}_{pp}$ and the $N_s\times 1$ source vector $\mathbf{S}(\omega)$. The multiplication can also be presented in stacked form,

$$vec\{\mathbf{K}_{ap}(\omega)\} = vec\{\mathbf{M}_{pp}(\omega)\}\mathbf{S}(\omega), \tag{20}$$

where $vec\{\mathbf{M}_{pp}(\omega)\}$ is the $(N_z N_x)\times N_s$ matrix obtained from stacking the first and second dimension of $\mathbf{M}_{pp}$. Equation (20) will yield the $(N_z N_x)\times 1$ vector $vec\{\mathbf{K}_{ap}\}$ which expresses how the arrival at the receiver is sensitive to medium perturbations.

The received pressure perturbation [Eq. (19)] can now be expressed as

$$\Delta P(\omega) = \mathbf{S}(\omega)^T vec\{\mathbf{M}_{pp}(\omega)\}^T vec\{\Delta\mathbf{c}\}. \tag{21}$$

The portion of the optimization problem involving the minimization of the received pressure perturbation can now be conveniently stated in terms of a cost function component

$$\begin{aligned} J_1(\omega) &= \langle|\Delta P|^2\rangle \\ &= \mathbf{S}(\omega)^H vec\{\mathbf{M}_{pp}(\omega)\}^H vec\{\Delta\mathbf{c}\}vec\{\Delta\mathbf{c}\}vec\{\mathbf{M}_{pp}(\omega)\} \\ &\quad\times\mathbf{S}(\omega) \\ &= \mathbf{S}(\omega)^H vec\{\mathbf{M}_{pp}(\omega)\}^H\mathbf{C}_{dc}vec\{\mathbf{M}_{pp}(\omega)\}\mathbf{S}(\omega) \\ &= \mathbf{S}(\omega)^H\mathbf{C}_{\mathrm{mdc}}\mathbf{S}(\omega), \end{aligned} \tag{22}$$

where $\mathbf{C}_{dc}$ is the sound speed perturbation covariance matrix. The superscript $(\cdot)^H$ denotes matrix complex conjugate transpose (Hermitian). $\mathbf{C}_{\mathrm{mdc}}$ is the $N_s\times N_s$ covariance matrix of the Born-approximation perturbed Green's functions at frequency ω between an array of sources and a single receiver. So element ij of $\mathbf{C}_{\mathrm{mdc}}$ is the covariance between the pressure perturbation at the receiver from a transmission from source i and the pressure perturbation at the receiver from a transmission from source j. J_1 is not minimized separately, but is done so as part of the joint optimization in order to avoid the trivial case of $S(\omega)=0$.

The cost function component [Eq. (22)] does not take into account time and range shifts in the focal spot that may occur, caused, for example, by internal wave induced sound speed fluctuations.[5] It also requires each realization of the focal spot to be stable, without addressing the ensemble average of focal spots, which was found to have a high stability.[6]

The cost function is computed independently for each frequency in the bandwidth of interest. This has been done in order to be consistent with the formulation of the inverse filter[18] which is more conveniently described on a single frequency basis. While the optimization can be done across all frequencies simultaneously, doing it on a frequency-by-frequency basis is a stronger constraint.

B. Obtaining a focal spot

The other part of the optimization is the choice of source function that will yield a focal spot. It was shown by Tanter *et al.*[18] that while time reversal only optimizes the pressure amplitude at the focus, the inverse filter adds constraints on the field around the focus, and is thus able to impose a desired sidelobe level or mainlobe width. Since this is a more general optimization problem, it is clearer to develop the optimized source function as a robust version of the inverse filter rather than as a robust version of time reversal.

The ideal focal spot is defined as a delta function in depth and time at the range of the receiver

$$u(t,z) = \delta(z-z_r)\,\delta(t-t_0). \tag{23}$$

In the frequency domain, $u(t,z)$ is written as the $N_p\times 1$ vector $\mathbf{U}(\omega)$, which is the desired focal spot, defined over N_p depths. The problem now becomes one of choosing $\mathbf{S}(\omega)$ to produce a received pressure field at a set of N_p depths that is as close to a delta function as possible, given a finite bandwidth. This may be stated in the frequency domain as

TABLE III. Peak-to-sidelobe ratio (PSR), sensitivity cost function (J_1), and focal spot cost function (J_2) for time reversal (TR), inverse filter (IF), and the optimized source function (opt.). Cost functions are % reduction with respect to time reversal, averaged over 1 kHz. "No structure" corresponds to uncorrelated random Gaussian sound speed perturbations. "Channel" denotes a channel of zero variance in sound speed perturbations at a constant depth of 52 m. "Structure" denotes a long depth and range decorrelation scale for sound speed perturbations.

	PSR (dB)			J_1		J_2	
	TR	IF	Opt.	IF	Opt.	IF	Opt.
No structure	31.17	32.95	32.14	−2.5%	34.15%	99.9%	99.8%
Channel	31.17	32.95	33.33	−26.58%	19.9%	99.9%	99.8%
Structure	31.17	32.95	32.77	52.73%	98.2%	99.9%	99.8%

$$\mathbf{U}(\omega) = \mathbf{G}(\omega)\mathbf{S}(\omega) + \Delta\mathbf{G}(\omega)\mathbf{S}(\omega) + \mathbf{r}. \tag{24}$$

$\mathbf{G}$ is a $N_p \times N_s$ matrix of unperturbed Green's functions from each source to each of the N_p depths at the range of the receiver. $\Delta\mathbf{G}$ is the (unknown) perturbation to the Green's function due to the perturbed sound speed field. In the absence of knowledge about $\Delta\mathbf{G}$, it is assumed that $\Delta\mathbf{GS}$ is a random variable, which can be included as part of the error term, $\mathbf{r}$. The misfit vector $\mathbf{r}$ is a $N_z \times 1$ random vector which is assumed to be jointly normally (Gaussian) distributed with prior joint probability density function (PDF) $\mathcal{N}(0, \mathbf{C_r})$. Equation (24) then reduces to a linear model

$$\mathbf{U}(\omega) = \mathbf{G}(\omega)\mathbf{S}(\omega) + \mathbf{r}. \tag{25}$$

While a full-depth representation is needed in Eq. (25) in order to obtain a spatio-temporal focal spot, such a representation is not needed in the first cost function [Eq. (22)] where the emphasis is on minimizing received pressure sensitivity to fluctuations only at the receiver depth. Multiple receiver depths can be treated by adding terms to the cost function corresponding to other depths.

A Bayesian approach is now adopted to find the optimum estimator for $\mathbf{S}(\omega)$ that will satisfy Eq. (25). The $N_s \times 1$ vector of source excitations $\mathbf{S}(\omega)$ is treated as an unknown random variable to be estimated. It is assumed to be jointly normally distributed with PDF $\mathcal{N}(0, \mathbf{C_S})$. $\mathbf{C_S}$ expresses constraints on the size of $\mathbf{S}$ and the correlation between the signals from different sources. For example, assuming $\mathbf{C_S} = \beta\mathbf{I}$ means that the signals from different sources can be chosen independently, but the power of each source is constrained to be usually less than 2β. Assuming $\mathbf{C_r} = \alpha\mathbf{I}$ means a uniformly distributed independent Gaussian misfit at each depth, with variance α. This is a convenient assumption, but it may not be accurate, since the minimum width of the focal spot is determined by the multipaths available for focusing.

Solving Eq. (25) is equivalent to minimizing the penalty function (where the penalty is the difference between the delta function and the focal spot at the receiver),

$$J_2 = \mathbf{r}^H\mathbf{C_r}^{-1}\mathbf{r} + \mathbf{S}^H\mathbf{C_S}^{-1}\mathbf{S}. \tag{26}$$

J_2 may be recognized as the negative of log likelihood function for $\mathbf{S}$ given $\mathbf{U}$. The penalty function is affected by the number of depths at which the misfit vector is enforced, where a large number of closely spaced depths results in a larger penalty function. Minimizing J_2 with respect to $\mathbf{S}$ will give the maximum *a posteriori* estimator, which for the Gaussian-distributed case considered is equivalent to the minimum mean square estimator,[29]

$$\hat{\mathbf{S}}(\omega) = (\mathbf{C_S}^{-1} + \mathbf{G}^H\mathbf{C_r}^{-1}\mathbf{G})^{-1}\mathbf{G}^H\mathbf{C_r}^{-1}\mathbf{U}. \tag{27}$$

The above estimator, with $\mathbf{C_r} = \alpha\mathbf{I}$ and $\mathbf{C_S} = \beta\mathbf{I}$ gives a generalized inverse filter[10,30] which does not require $\mathbf{G}$ to be full rank,

$$\hat{\mathbf{S}}(\omega) = \left(\mathbf{G}^H\mathbf{G} + \frac{\alpha}{\beta}\mathbf{I}\right)^{-1}\mathbf{G}^H\mathbf{U}. \tag{28}$$

If the only concern is to obtain a temporal focal spot at a single depth (in which case $\mathbf{U}$, $\mathbf{r}$, and $\mathbf{GG}^H$ are scalars), it is simpler to solve Eq. (27) in its equivalent form of

$$\hat{\mathbf{S}}(\omega) = \mathbf{C_S}\mathbf{G}^H(\mathbf{G}\mathbf{C_S}\mathbf{G}^H + \mathbf{C_r})^{-1}\mathbf{U}. \tag{29}$$

If $\mathbf{C_S} = \beta\mathbf{I}$, Eq. (29) reduces to scalar times $\mathbf{G}^H\mathbf{U}$ (phase conjugation). This shows that for purely temporal focusing, time reversal and the inverse filter are the same.

C. Joint optimization

Adding the minimum sensitivity cost function in Eq. (22) to the inverse filter cost function in Eq. (26) gives

$$J_3 = \mathbf{S}^H\mathbf{C}_{\mathrm{mdc}}\mathbf{S} + \mathbf{S}^H\mathbf{C_S}^{-1}\mathbf{S} + \mathbf{r}^H\mathbf{C_r}^{-1}\mathbf{r}. \tag{30}$$

The source function that will minimize J_3 with respect to $\mathbf{S}$ has a form similar to Eq. (27) except for the added sensitivity terms, and is given by,

$$\hat{\mathbf{S}}(\omega) = (\mathbf{C_S}^{-1} + \mathbf{C}_{\mathrm{mdc}} + \mathbf{G}^H\mathbf{C_r}^{-1}\mathbf{G})^{-1}\mathbf{G}^H\mathbf{C_r}^{-1}\mathbf{U}. \tag{31}$$

If $\mathbf{C_r} = \alpha\mathbf{I}$ and $\mathbf{C_S} = \beta\mathbf{I}$, then Eq. (31) yields

$$\hat{\mathbf{S}}(\omega) = \left(\frac{\alpha}{\beta}\mathbf{I} + \alpha\mathbf{C}_{\mathrm{mdc}} + \mathbf{G}^H\mathbf{G}\right)^{-1}\mathbf{G}^H\mathbf{U}. \tag{32}$$

A few observations may be made regarding the optimized source function obtained in Eq. (32). The ratio α/β is misfit to transmit power ratio. Setting $\alpha = 0$ (no error tolerated in the focal spot criterion) yields the inverse filter. Thus, Eq. (32) is a modification of the generalized inverse filter, with a stability term ($\alpha\mathbf{C}_{\mathrm{mdc}}$) that takes into account knowledge of the medium statistics and the sensitivity of the Green's function to sound speed perturbations ($\mathbf{C}_{\mathrm{mdc}} = vec\{\mathbf{M}\}^T\mathbf{C}_{\mathrm{dc}}vec\{\mathbf{M}\}$). In a medium with uncorrelated perturbations or extremely short scale inhomogeneities, pressure

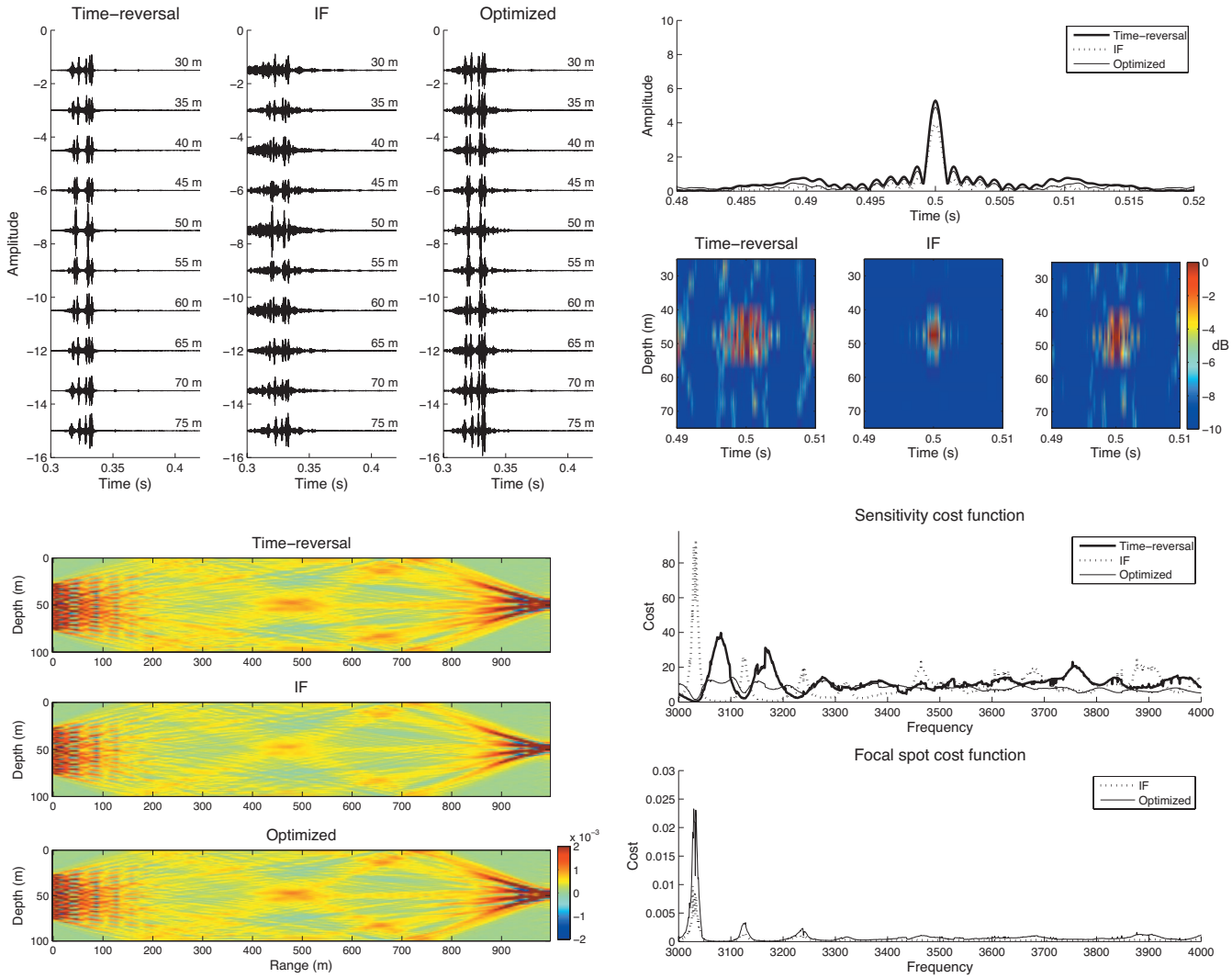

FIG. 6. Performance of time reversal, the inverse filter, and the optimized source function. Sound speed perturbations are homogeneous, isotropic and uncorrelated on a 10 m × 1 m scale. **Top left:** Transmit signals across depth, **top right:** Received signals, in time and depth, at the focal spot. **Bottom left:** Pressure sensitivity kernels (10^{-4} μPa s m^{-4}) for time reversal, the inverse filter, and the optimized source function. **Bottom right:** Cost functions. The focal spot cost function for time reversal is fixed to be a constant value of 1.

perturbations will tend to be uncorrelated between sources, so $\mathbf{C}_{\mathrm{mdc}}$ will tend to be an identity matrix, and Eq. (32) tends to the regularized inverse filter. Letting $\beta \to \infty$ (no constraint on transmit power) will yield an alternatively regularized inverse filter. Finally, setting α to large values will result in increased stability at the cost of degradation of the focal spot because α reflects the allowed difference between the observed focal spot and the desired delta-function like focal spot.

It is useful to look at the form of Eq. (32) when only a temporal focus is desired (no focusing in depth). In such a case, $\mathbf{G}\mathbf{C}_{\mathbf{r}}^{-1}\mathbf{G}^{H}$ is a scalar, and an equivalent form of Eq. (32), similar to Eq. (29), may be obtained by writing $\mathbf{P}^{-1} \equiv (\alpha/\beta)\mathbf{I} + \alpha\mathbf{C}_{\mathrm{mdc}}$. The optimized source functions are then given by

$$\hat{\mathbf{S}}(\omega) = \mathbf{P}\mathbf{G}^{H}(\mathbf{G}\mathbf{P}\mathbf{G}^{H} + \mathbf{C}_{r})^{-1}\mathbf{U} = \lambda\mathbf{P}\mathbf{G}^{H}\mathbf{U}. \tag{33}$$

It is thus seen that the optimized solution for purely temporal focusing reduces to the matrix $\mathbf{P}$ times the phase conjugated Green's function. If $\mathbf{P}$ is a scaled identity matrix, then this is again time reversal.

As seen in Eq. (32), the optimized source function requires rather complete knowledge of the medium in order to compute the sensitivity kernels, in addition to knowledge of statistics of sound speed perturbations. If these were available, then the optimized source function can be expected to perform better than time reversal but it must be kept in mind that an attractive feature of time reversal is that only the Green's function between source and receiver need be known.

VI. OPTIMIZATION APPLIED TO A PEKERIS WAVEGUIDE

Studies of the optimized source function with focusing in both time and depth are conducted for three scenarios involving different spatial structures of sound speed perturbations in a Pekeris waveguide. For each case, three transmission schemes are considered: time-reversal, the inverse filter [Eq. (28)], and optimized source function [Eq. (32)].

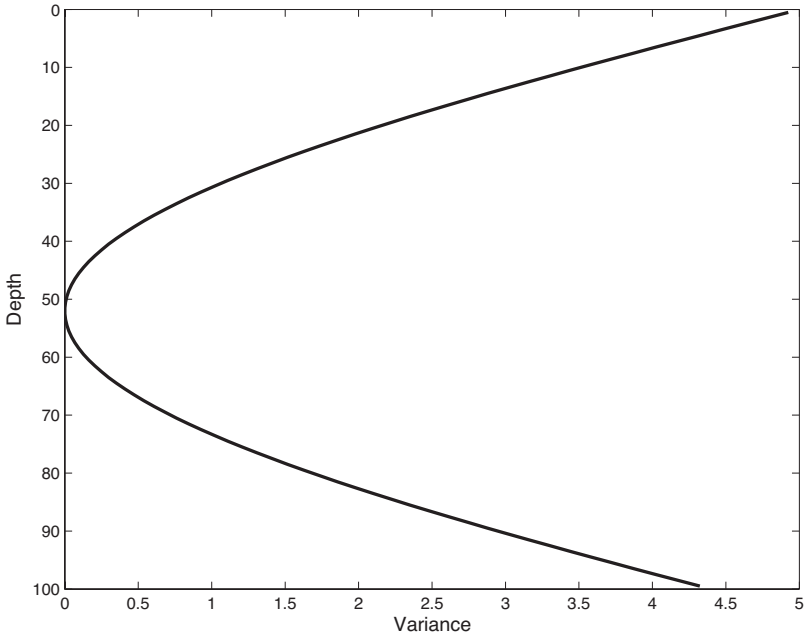

FIG. 7. Shape of depth-dependent variance of sound speed perturbations. The sound speed perturbations obtained were used to generate Fig. 8.

The dimensions of the waveguide and number of sources are the same as in Sec. IV. Sound speed perturbations are assumed to be constant over a cell size of 10 m in range, 1 m in depth, and a long distance in the horizontal cross-range dimension. The sound speed perturbation in each cell is modeled as a Gaussian-distributed random variable. Changes in the perturbation variance with depth and horizontal correlation scales of different lengths are introduced while comparing time reversal with the optimized source shading function. In the first case, there is no correlation between perturbations in different cells. The second case involves a channel of zero variance in sound speed perturbations between source and receiver, while the third case has a long decorrelation scale in both range and depth for sound speed perturbations.

For the given medium. Green's functions were on the order of 10^{-4}, resulting in sensitivities on the order of 10^{-8}. In order to avoid plotting these extremely low values, the Green's functions were scaled up by 10^4, resulting in sensitivities on the order of 1. The scaling used here is different from that in Sec. IV due to the fact that the sensitivity kernels in this section have been summed over 10 m $\times$ 1 m cells in depth in order to deal with more manageable matrices.

Cost functions are calculated for the various perturbation scenarios, where the cost function for sensitivity, $J_1(\omega)$, is computed using Eq. (22), and the cost function for the sharpness of the focal spot, $J_2(\omega)$, is computed according to Eq. (26), with the ideal focal spot specified at 11 equally spaced depths from 25 to 75 m. Recognizing that the inverse filter produces the best achievable focal spot for a given medium, the ideal focal spot [$\mathbf{U}(\omega)$ in Eq. (25)] is chosen such that the focal spot cost function $J_2^{IF}(\omega)=0$ for the unregularized inverse filter. The value of α is now chosen such that the focal spot cost function for time-reversal $J_2^{TR}(\omega)=1$, for all frequencies. A value of 1 is chosen for the convenience of plotting, and can be set to a different value in a practical problem. Next, β can be varied to yield a focal spot cost function that varies between 0 and 1, depending on the amount of trade-off desired between quality of focal spot and sensitivity to medium perturbations. For all case studies in this section, $\beta=50$. The values of α and β will depend on the specific scaling used for the Green's function.

Sensitivity kernels and source shading functions will be the same for time-reversal and the inverse filter for all three cases since they are ignorant of the presence or absence of structure in the sound speed perturbations. As a result, source shading functions and sensitivity kernels for time-reversal and the inverse filter are only shown for the first case where there is no structure in sound speed perturbations. The received signals for time-reversal and the inverse filter are also the same for different cases and hence are only shown for the first case. Finally, as seen in Table III, since the focal spot cost function is very similar for the inverse filter and the optimized source function, this is also not shown for the last two case studies. Sensitivity cost functions for the three transmission schemes (time-reversal, inverse filter, and optimized source function), however, will be different for each case considered due to differences in the $\mathbf{C}_{\text{mdc}}$ term for each case [Eq. (22)]. The range of values for the sensitivity cost function depends on the specific Green's functions considered and the statistics of the medium. The value of the sensitivity cost function also depends on the number of points (and spacing) at which the sensitivity kernel is evaluated.

The performance of time-reversal, the inverse filter [Eq. (28)] and the optimized source function under various sound speed perturbation scenarios is summarized in Table III. The use of an inverse filter imposes explicit constraints on sidelobe levels in both time and depth.[18] Since the optimized solution is similar to the inverse filter, in the absence of noise, the focal spot obtained will have lower sidelobe levels, and hence, a smaller focal spot cost function [Eq. (26)] than time reversal. The peak-to-sidelobe ratios for the inverse filter and optimized source function is about 2 dB greater than that of time reversal. The focal spot cost function (Table III) for the inverse filter and the optimized source function is always about 90% less than that of time reversal. However, although all three source functions are normalized to have

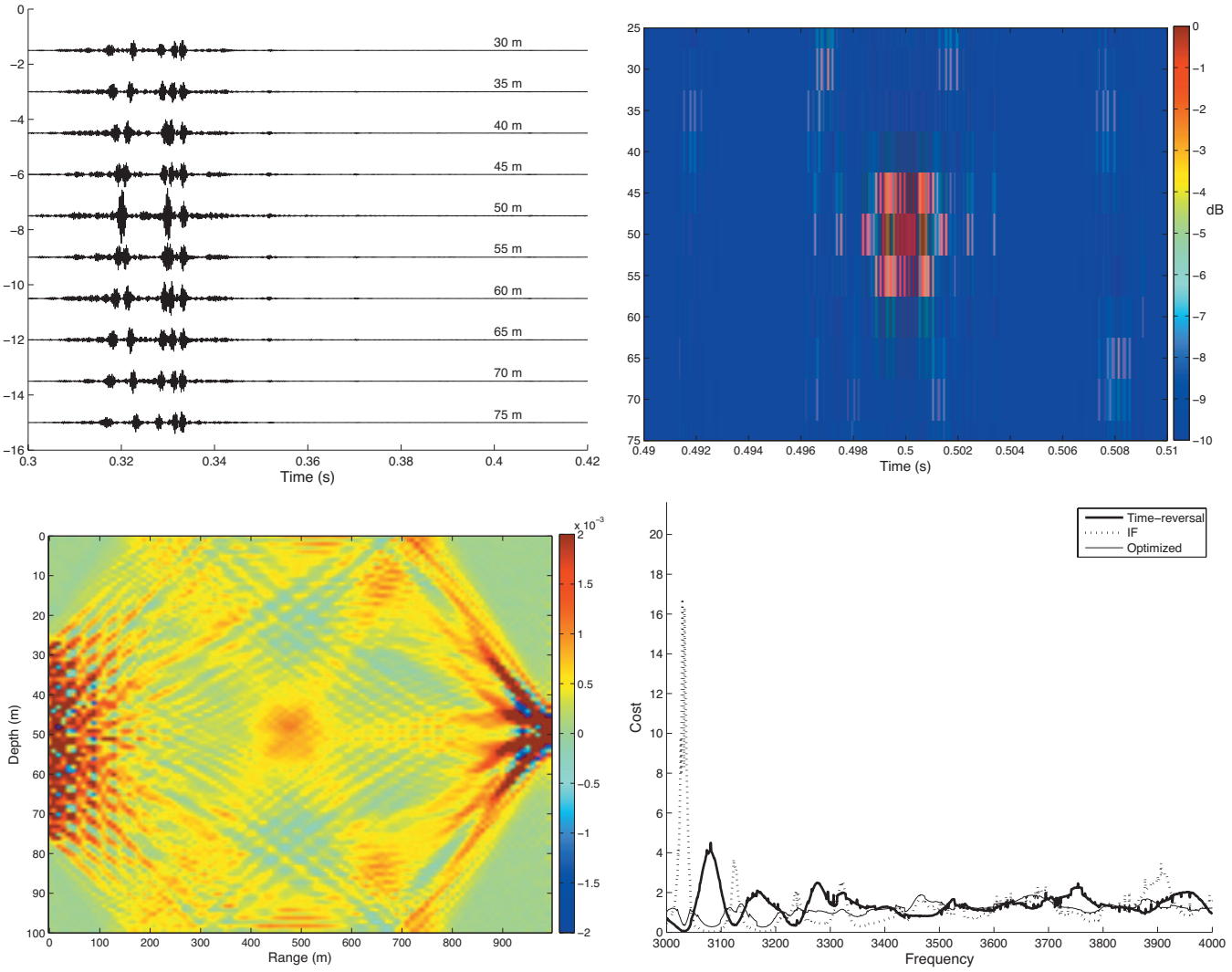

FIG. 8. Performance of time reversal, the inverse filter and the optimized source function. Sound speed perturbations are homogeneous, isotropic, and uncorrelated on a 10 m × 1 m scale. The variance of sound speed perturbations reduces to zero at 52 m as shown in Fig. 7. The source shading function and sensitivity kernel for time reversal and the inverse filter are identical to those in Fig. 6, and have been omitted. **Top left:** Optimized transmit signals across depth. **Top right:** Received signal in time and depth, near the focal spot, for the optimized source function. **Bottom left:** Optimized pressure sensitivity kernel (10^{-4} μPa s m^{-4}). **Bottom right:** Sensitivity cost function. The focal spot cost function is almost identical to the case in Fig. 6.

the same source power, time reversal has a higher peak received power. This is because time reversal is a matched filter, which is the optimal solution for maximizing received power, without other constraints.

Figure 6 shows the results of the numerical simulation involving the first scenario where the sound speed perturbations have the same variance and are uncorrelated between grid points in both dimensions. The top panels of Fig. 6 show the transmit and receive signals for time reversal and the optimized source shading functions. The bottom left panel shows the sensitivity kernels for each scheme while the bottom right panel shows the cost function metrics over a 1 kHz bandwidth for time reversal and the optimized source function. The focal spot cost function for time reversal is fixed to be 1, and is not shown in order to show more clearly the cost functions for the inverse filter and the optimized source function which are on the order of 0.01. The lack of structure in the sound speed perturbation results in only a 2.5% difference in sensitivity between the inverse filter and time reversal (Table III). However, despite the lack of structure, the sensitivity cost function for the optimized source function is about 35% less than that of time reversal, while the focal spot cost function for both the inverse filter and optimized source function is about 90% less than that of time reversal.

Next, structure in the sound speed perturbations is introduced by means of a region where the variance of the sound speed perturbations drops to zero. The depth of zero variance is placed at a constant depth of 52 m. The shape of the depth-dependent variance is shown in Fig. 7. The sound speed perturbations, however, are still uncorrelated between cells. The ratio of transmit power for the source at 50 m to the average power at other depths for the optimized scheme is about 100% higher than that for time reversal, indicating a concentration of power in the unperturbed region. For this case, the inverse filter is 26% more sensitive to sound speed perturbations (see Fig. 8) than time reversal, while the optimized source function is about 20% less sensitive compared to time reversal. The focal spot cost functions are similar to the previous case.

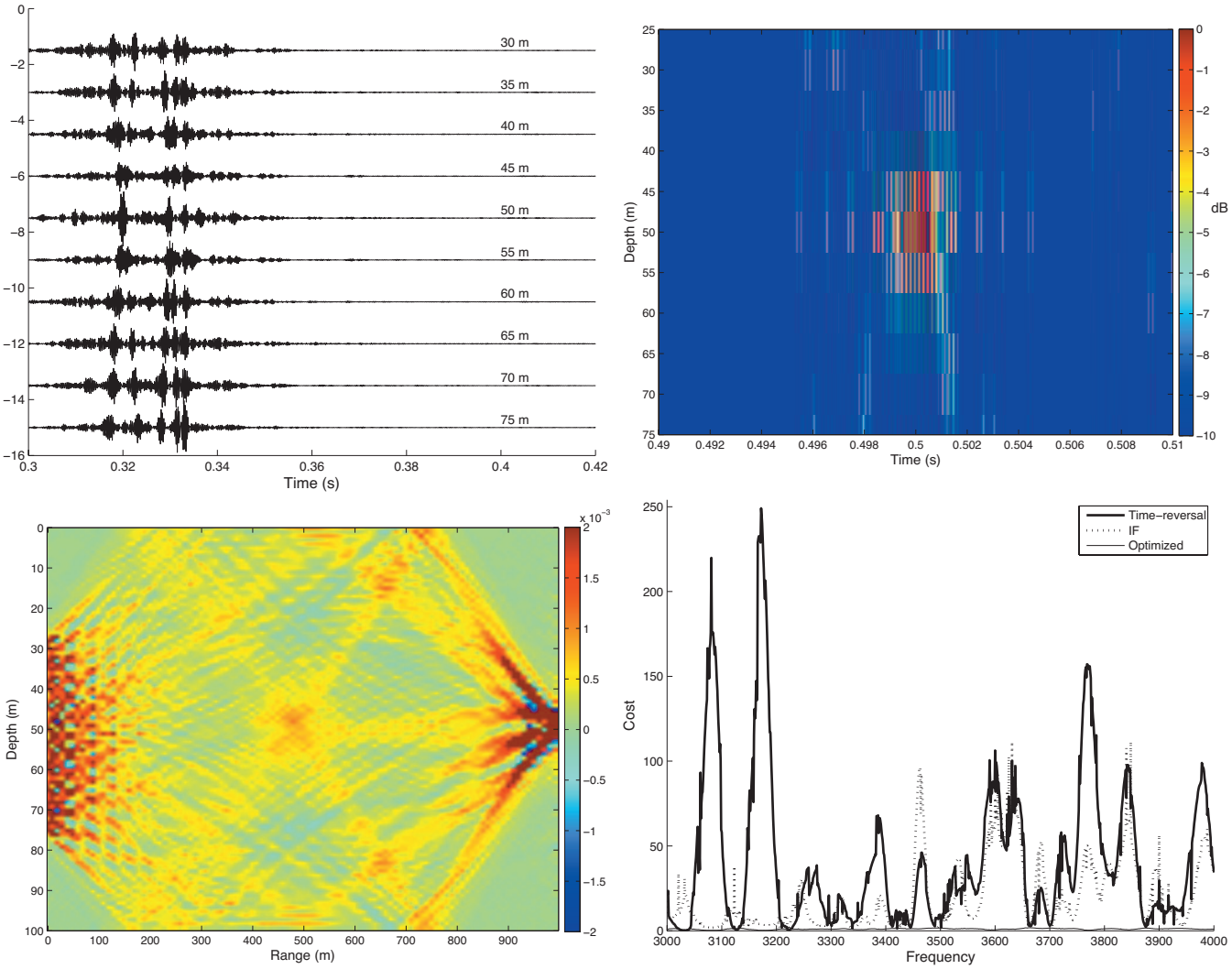

FIG. 9. Performance of timer reversal, the inverse filter, and the optimized source function. Sound speed perturbations have a long decorrelation scale in range (100 m) and depth (100 m). The source shading function and sensitivity kernel for time reversal and the inverse filter are identical to those in Fig. 6, and have been omitted. **Top left:** Optimized transmit signals across depth. **Top right:** Received signal, in time and depth, near the focal spot, for the optimized source function. **Bottom left:** Optimized pressure sensitivity kernels (10^{-4} μPa s m^{-4}). **Bottom right:** Sensitivity cost function. The focal spot cost function is almost identical to the case in Fig. 6.

The third study (Fig. 9) involves the use of a long (100 m in range, 100 m in depth) spatial decorrelation scale for the sound speed perturbations. The correlation decays exponentially over 100 m in range and 100 m in depth. The perturbations are still isotropic and homogeneous. This is meant to represent low-mode internal waves in the ocean. The optimized source function shows significantly lower sensitivity, with a 98% reduction (Table III) compared to time reversal, while the inverse filter shows a 52% reduction with respect to time reversal. At the same time, the quality of the focal spot is similar to that of the inverse filter in terms of peak-to-sidelobe ratio, although the peak amplitude has been reduced. Thus, the presence of structure allows the optimized source function to exploit the knowledge of sound speed perturbations to produce a focal spot that is very similar to that of the inverse filter, but at the same time considerably less sensitive to sound speed perturbations than time reversal (Table III).

VII. CONCLUSIONS

A pressure sensitivity kernel was developed for the case where an array of sources transmits to a single receiver. This kernel is extendable to multiple-input multiple-output scenarios. The Born-approximated sensitivity kernel for the received pressure was used to provide an explanation for why time reversal and the inverse filter are more stable compared to a one-way transmission. In the absence of multipath, the sensitivity of a time-reversed transmission for a single source-receiver pair was shown to be identical to a one-way transmission. A reduction in pressure sensitivity is only obtained through the use of a time-reversal mirror which results in the coherent addition of the kernels from different sources as opposed to an incoherent addition in the case of a broadside transmission. Time reversal allows for the coherent addition of the kernels corresponding to different paths arriving at the same time. The presence of multipath has an effect similar to a time-reversal mirror, with a lowering of sensitivity resulting from the superposition of the multipath kernels.

The linear (first Born) approximation is only valid when sound speed perturbations are very small compared to the background sound speed. Ongoing simulations, beyond the scope of this paper, show that the Born approximation for a 1 km by 100 m waveguide is valid for sound speed perturbations up to about 0.2 m/s, for a background sound speed of 1500 m/s. If only the envelope of the Green's function is of interest, the range of validity is extended until about 5 m/s. This is within the range of most internal wave induced sound speed fluctuations in the ocean. Further, as a result of the volume integral expression for the perturbed Green's function, the effect of longer path lengths is to lower the range of sound speed perturbations for which the linear approximation is valid.

The pressure sensitivity kernel was used to obtain an optimized source shading function that can be considered an environmentally adaptive version of time reversal and the inverse filter. While this optimized source function was almost identical to the inverse filter when there is no structure in the sound speed perturbation field, the gains are significant in the presence of structure, such as a depth of zero variance, or a long decorrelation length in the sound speed perturbations.

ACKNOWLEDGMENT

This work was supported by the Office of Naval Research under Grant Nos. N00014-04-1-0360, N00014-05-1-0263 and N00014-07-l-0739.

[1]M. Fink, D. Cassereau, A. Derode, C. Prada, P. Roux, M. Tanter, J.-L. Thomas, and F. Wu, "Time-reversed acoustics," Rep. Prog. Phys. **63**, 1933–1965 (2000).
[2]G. F. Edelmann, T. Akal, W. S. Hodgkiss, S. Kim, W. A. Kuperman, and H. C. Song, "An initial demonstration of underwater acoustic communication using time-reversal," IEEE J. Ocean. Eng. **27**, 602–608 (2002).
[3]H. Nguyen, J. Andersen, and G. Pederson, "The potential use of time-reversal techniques in multiple element antenna systems," IEEE Commun. Lett. **9**, 40–42 (2005).
[4]W. S. Hodgkiss, H. C. Song, W. A. Kuperman, T. Akal, C. Ferla, and D. R. Jackson, "A long-range and variable focus phase-conjugation experiment in shallow water," J. Acoust. Soc. Am. **105**, 1597–1604 (1999).
[5]S. Kim, W. A. Kuperman, W. S. Hodgkiss, H. C. Song, and G. F. Edelmann, "Robust time-reversal focusing in the ocean," J. Acoust. Soc. Am. **114**, 145–157 (2001).
[6]D. R. Dowling and Darrel R. Jackson, "Narrow-band performance of phase-conjugate arrays in dynamic random media," J. Acoust. Soc. Am. **91**, 3257–3277 (1992).
[7]G. Papanicolaou, L. Rhyzhik, and K. Solna, "Statistical stability in time reversal," SIAM J. Appl. Math. **64**, 1133–1155 (2004).
[8]G. Montaldo, G. Lerosey, A. Derode, A. Tourin, J. de Rosny, and M. Fink, "Telecommunication in a disordered environment with iterative time reversal," Waves Random Media **14**, 287–302 (2004).
[9]M. Stojanovic, "Retrofocussing techniques for high rate acoustic communications," J. Acoust. Soc. Am. **117**, 1173–1185 (2005).
[10]M. Tanter, J.-F. Aubry, J. Gerber, J.-L. Thomas, and M. Fink, "Optimal focussing by spatio-temporal inverse filter. I. Basic principles," J. Acoust. Soc. Am. **110**, 37–47 (2001).
[11]H. Marquering, G. Nolet, and F. A. Dahlen, "Three-dimensional waveform sensitivity kernels," Geophys. J. Int. **132**, 521–534 (1998).
[12]F. A. Dahlen, S. H. Hung, and G. Nolet, "Frechét kernels for finite-frequency travel times-I. Theory," Geophys. J. Int. **141**, 157–174 (2000).
[13]F. A. Dahlen, S. H. Hung, and G. Nolet, "Frechét kernels for finite-frequency travel times-II. Examples," Geophys. J. Int. **141**, 175–1203 (2000).
[14]E. K. Skarsoulis and B. D. Cornuelle, "Travel-time sensitivity kernels in ocean acoustic tomography," J. Acoust. Soc. Am. **116**, 227–238 (2004).
[15]J. Sarkar, B. Cornuelle, and W. A. Kuperman, "Estimating sound-speed perturbations with full-wave environmental sensitivity kernels," J. Acoust. Soc. Am. **119**, 3246 (2006).
[16]P. Hursky, M. B. Porter, B. D. Cornuelle, W. S. Hodgkiss, and W. A. Kuperman, "Adjoint modeling for acoustic inversion," J. Acoust. Soc. Am. **115**, 607–619 (2004).
[17]P. Roux and M. Fink, "Time reversal in a waveguide: Study of the temporal and spatial focussing," J. Acoust. Soc. Am. **107**, 2418–2429 (2000).
[18]M. Tanter, J.-L. Thomas, and M. Fink, "Time-reversal and the inverse filter," J. Acoust. Soc. Am. **108**, 223–234 (2000).
[19]M. Born, "Quantum mechanics of impact processes," Z. Phys. **38**, 803–827 (1926).
[20]J. R. Taylor, *Scattering Theory* (Wiley, New York, 1972).
[21]E. K. Skarsoulis, G. A. Athanassoulis, and U. Send, "Ocean acoustic tomography based on peak arrivals," J. Acoust. Soc. Am. **100**, 797–813 (1996).
[22]T. Chen, P. Ratilal, and N. C. Makris, "Mean and variance of the forward field propagated through three-dimensional random internal waves in a continental-shelf waveguide," J. Acoust. Soc. Am. **118**, 3560–3574 (2005).
[23]C. Garret and W. Munk, "Space-time scales of internal waves," Geophys. Fluid Dyn. **2**, 225–264 (1972).
[24]M. Bruhl, G. J. O. Vermeer, and M. Kiehn, "Fresnel zones for broadband data," Geophysics **61**, 600–604 (1999).
[25]J. Pearce and D. Mittleman, "Defining the fresnel zone for broadband radiation," Phys. Rev. E **66**, 056602/1-4 (2002).
[26]B. Cornuelle, M. Dzieciuch, and E. Skarsoulis, "Wave-theoretic kernels for long-range ocean travel-time measurement," J. Acoust. Soc. Am. **119**, 3248 (2006).
[27]W. A. Kuperman, W. S. Hodgkiss, H. C. Song, T. Akal, C. Ferla, and D. R. Jackson, "Phase conjugation in the ocean: Experimental demonstration of an acoustic time-reversal mirror," J. Acoust. Soc. Am. **103**, 25–40 (1998).
[28]F. B. Jensen, W. A. Kuperman, M. B. Porter, and H. Schmidt, *Computational Ocean Acoustics* (American Institute of Physics, Woodbury, NY, 1994).
[29]S. M. Kay, *Fundamentals of Statistical Signal Processing—Estimation Theory* (Prentice–Hall, Englewood Cliffs, NJ, 1993), Chap. 10.
[30]W. J. Higley, P. Roux, and W. A. Kuperman, "Relationship between time-reversal and linear equalization in digital communications," J. Acoust. Soc. Am. **120**, 35–37 (2006).

Temporal coherence of sound transmissions in deep water revisited

T. C. Yang[a)]
Naval Research Laboratory, 4555 Overlook Avenue. S.W., Washington, DC 20375

(Received 28 February 2007; revised 29 April 2008; accepted 30 April 2008)

This paper examines the signal coherence loss due to internal waves in deep water in terms of the signal coherence time and compare to data reported in the literature over the past 35 years. The coherence time of the early raylike arrivals was previously modeled by Munk and Zachariasen ["Sound propagation through a fluctuating stratified ocean: Theory and observation," J. Acoust. Soc. Am. **59**, 818–838 (1976)] using the supereikonal approximation and by Dashen *et al.* ["Path-integral treatment of acoustic mutual coherence functions for arrays in a sound channel," J. Acoust. Soc. Am. **77**, 1716–1722 (1985)] using the path integral approach; a $-\frac{1}{2}$ power frequency dependence and a $-\frac{3}{2}$ power range dependence were predicted. Recent data in shallow water in downward refractive environments with internal waves suggested that the signal coherence time of the mode arrivals follows a $-\frac{3}{2}$ power frequency dependence and a $-\frac{1}{2}$ power range dependence. Since the temporal coherence of the acoustic signal is related to the temporal coherence of the internal waves, based on the observation that the (linear) internal waves in deep and shallow waters have a similar frequency spectrum, it is argued that the modelike arrivals in deep water should exhibit a similar frequency dependence in deep and shallow waters. This argument is supported by a brute-force application of the path integral to mode arrivals based on the WKB relation between the ray and mode. It is found that the data are consistent with the $-\frac{3}{2}$ power frequency dependence but more data are needed to further test the hypothesis. [DOI: 10.1121/1.2932337]

PACS number(s): 43.30.Re, 43.30.Zk [WMC] Pages: 113–127

I. INTRODUCTION

Acoustic signals propagating through a dynamic (time-varying) ocean fluctuate with time. The rate of the signal fluctuation can be characterized in terms of the temporal coherence length of the signal, known as the signal coherence time, which reveals the time scale by which the signal becomes uncorrelated (as when the temporal coherence drops to $1/e$).

The rate of temporal fluctuation or the (temporal) coherence time has implications for many practical applications. For example, for detection and localization of an acoustic signal, one often needs to integrate the signal over a period of time to achieve the temporal processing gain, i.e., the gain due to coherent addition of the signal. The achievable processing gain is determined by how long the signal remains coherent. Signal processing issues related to the temporal coherence (for detection) and time-delay estimation (for localization) were extensively studied in the 1980s, see, for example, the collection of papers edited by Carter.[1] Second, matched field processing correlates a replica field with the data field for source localization. If the data field is stable only for a short period of time, then the replica can only be good for that period of time. How long a replica field can be used to localize the source is determined by the signal coherence time. For matched-field processing or model-based signal processing,[2] the temporal coherence supported by the physical medium (ocean) influences the model design and performance.[3] Third, for adaptive signal processing, as in the case of underwater acoustic communications, the rate of signal adaptation is controlled by the temporal stability of the signal. The performance of the adaptive equalizer depends on how well it adapts itself to the changing channel within the signal coherence time. If the signal is stable for a short period of time, and the adaptive equalizer fails to update (converge) within that time window, the processor will most likely fail. The performance of an equalizer in time-varying environments is a subject of active research.

For the various applications mentioned above, the performance depends on the temporal coherence of the acoustic signals. This requires an ability to model the temporal coherence for sound propagation through a random medium either empirically or theoretically. To develop a theory, the cause for the coherence loss (due to the various oceanographic processes in the ocean) needs to be analyzed. Toward this goal, many experiments have been conducted over the past 40 years to measure the signal temporal coherence and the associated processing gain. Most of the earlier work in the literature were concerned with low (<1 kHz) frequency, long range propagation in deep oceans, where the dominant cause for the coherence loss is internal waves. Dyson *et al.*[4] and Dahl *et al.*[5] provided a general formulation of the temporal coherence and the associated data analysis. Spindel *et al.*[6] and Clark and Kronengold[7] conducted experimental studies of 406 Hz signal propagation to and from Eleuthera in 1974. Williams[8] and Williams and Battestin[9] studied 400 Hz signal propagation around Bermuda in 1976. Fitzgerald *et al.*[10] focused on 10 Hz signal propagation in the Hatteras Abyssal Plain in 1976. Georges *et al.*[11] and Birdsall *et*

[a)]Electronic mail: yang@wave.nrl.navy.mil

al.[12] investigated 57 Hz signal propagation to thousands of kilometers from the Heart Island in 1994. Parvulescu[13] reported his earlier work on matched-signal processing in 1995. Recently, Spiesberger *et al.* analyzed the data from the acoustic thermometry experiment in 1983.[14] Wage *et al.*[15] and Colosi *et al.*[16] analyzed long signal propagation near 100 Hz between Hawaii and Northern California in the Acoustic Thermometry of Ocean Climate (ATOC) related experiments. To extend the measurements over a larger depth span, two vertical arrays were deployed in 2006 to double the vertical aperture of the receivers.[17,18] The Long-range Ocean Acoustic Propagation Experiment (LOAPEX) deployed the sources at various ranges from the receiver arrays with a stated purpose that includes, among other things, the measurement of the temporal coherence as a function of range and frequency.[17]

In contrast to the experimental effort, there has been very limited progress in theoretical understanding and modeling of the temporal coherence. The theory of temporal coherence is very complicated and no simple closed form solution has been derived for the temporal coherence, except under special circumstances. No theory, to the author's knowledge, has been able to successfully predict temporal coherence with any useful accuracy (given the measured internal-wave magnitude). Early work by Munk and Zachariasen calculated the phase rate (the inverse of signal coherence time) in a canonical sound channel by using the supereikonal (a generalization of the Rytov) approximation.[19] Dashen *et al.* provided a path integral formulation for the signal coherence in both the temporal and spatial domains.[20] They assumed that all multipath arrivals are uncorrelated and have an identical phase rate. A review of the early theoretical work can be found in the monograph by Flatte *et al.*[21] and recent update by Flatte and Rover.[22] Recent experimental results have shown that the model predictions are inadequate in many respects (see below). In particular, one notes that the late (*finale*) arrivals are modelike (not raylike); significant mode couplings are indicated by the data. Acoustic scattering from the internal waves is responsible for the coherence loss (as well as the mode coupling).

The lack of a useful theoretical model has prompted an empirical analysis of the temporal coherence[23] similar to what has been done for the spatial coherence[24] in shallow and deep waters. While an empirical model may not reveal the physics of the coherence loss, it is useful for performance assessment in practical applications. In this regard, one notes that the relationship between temporal coherence and processing gain is identical to that between spatial coherence and signal (beam forming) gain. In the spatial domain, the signal horizontal coherence, in a first order approximation, seems to scale according to the receiver separation divided by the acoustic wavelength[24] and can be modeled by an exponential function of this ratio or ratio squared. This empirical function allows one to predict the signal gain as a function of frequency and conversely estimate the horizontal coherence length based on the measured signal gain. Other empirical models have served useful purposes, such as the Lambert model for backscattering from the bottom,[25] and the Wenz ambient noise curves,[25] which have not been replaced by theoretical models, despite tens of years of research. An empirical approach for the temporal coherence is attempted in this paper, based on the same motivations as mentioned above.

This paper examines the range and frequency dependence of the signal coherence time. Published literature (over the past 35 years) on theory and experimental measurements of temporal coherence in the deep ocean are first reviewed in Sec. II. The previous predicted relationship of the phase rate as a function of frequency is tested against recent experimental results in shallow water; the analysis is given in Sec. III. Due to the inadequacy of the path integral (or the Munk–Zachariasen) model in explaining many of the recent experimental results, a generalized model is proposed for the frequency dependence of the signal coherence time to comply with that found in shallow water. The specific assumptions for the proposed model are spelled out in Sec. IV followed by experimental analysis. The model predictions can be tested by using Monte Carlo simulations of signal propagation through a random medium, which is the last resort when no theoretical prediction is available. This is discussed in Sec. V. Section VI is a short summary.

II. REVIEW OF TEMPORAL COHERENCE IN DEEP WATER

Temporal coherence can be measured by using either narrow band or broadband signals. Most of the experimental measurements in deep water use a narrow band signal.[4–13] Note that a true continuous wave (cw) signal has a constant phase in the base band. In a time-varying medium, the phase of the cw signal (for a single path arrival) in the base band changes with time, causing an increase in the signal bandwidth (Doppler spread). The increase in bandwidth is related to the signal phase rate (see below). The coherence time is the inverse of the Doppler spread or the phase rate.

A (pulse) cw signal centered at frequency f can be represented in the base band as

$$p(t) = R(t)e^{i\phi(t)}, \tag{1}$$

where $R(t)$ is the amplitude and $\phi(t)$ is the phase. For single path propagation, one may assume that the amplitude variation is smaller than the phase variation $[\mathrm{var}(\dot{\phi}) > \mathrm{var}(\dot{R})/\mathrm{var}(R)]$ and can thus be neglected, i.e., $R(t+\tau) \approx R(t)$. Taking the Taylor expansion for small τ, one finds that the autocorrelation of the pressure field can be approximated by

$$\langle p^*(t)p(t+\tau)\rangle \simeq \mu^2\langle e^{-i\phi(t)}e^{i\dot{\phi}(t+\tau)}\rangle \simeq \mu^2 e^{-(1/2)\dot{\phi}^2\tau^2} \tag{2}$$

for $\dot{\phi}\tau < 1$, where τ is the delay time (the time separation between the signals), $\langle\ \rangle$ denotes the ensemble average, μ^2 denotes the mean intensity $\langle R(t)R(t+\tau)\rangle = \mu^2$, and $\dot{\phi}^2$ is a shorthand for $\langle\dot{\phi}^2\rangle$, where $\dot{\phi} = \sqrt{\dot{\phi}^2}$ denotes the time derivative of the signal (phase rate). For multipath propagation, many investigators have shown that the same result [Eq. (2)] can be derived by assuming that the phase and phase rate are Gaussian random variables and have the same distributions for all the paths.[4,5]

TABLE I. Summary of phase rate measurements in deep water. Earlier data until 1995 were analyzed in Ref. 26.

Authors	Frequency (Hz)	Range (km)	v/f ($\times 10^{-6}$)	Location
Spindel *et al.* (1974)	406	210	1.71–3.42	Eleuthera Shelf
Clark *et al.* (1974)	406	550–1250	6.9–9.9	Eleuthera-Bermuda (Project MIMI)
Williams (1976)	400	107–495	0.76–2.3	Bermuda Plateau
Williams *et al.* (1976)	400	270–1200	1.3–5.21	Bermuda-Eleuthera
Fitzgerald *et al.* (1976)	10	65–71	4.15	Hatteras Abyssal Plain
Georges *et al.* (1994)	57	9100	2.3–7.0	Heart Island to Ascension Island
Birdsall *et al.* (1994)	57	5510	$\leqslant 35$	Heart Island to Kiritimati Island
Parvulescu (1995)	420	36.5	0.63	Tongue of the Ocean
Speisberger (2004)	133	3709	4.1	Kaneohe Island to Northern California
Calosi and the ATOC group (2005)	84	3502 5158	10.5 14	Pioneer Seamount to Hawaii and Kiritimati

The temporal coherence defined by

$$\rho(\tau) \equiv \frac{\langle p^*(t)p(t+\tau)\rangle}{\sqrt{\langle p^*(t)p(t)\rangle\langle p^*(t+\tau)p(t+\tau)\rangle}} \tag{3}$$

can then be expressed as

$$\rho(\tau) = e^{-1/2\dot{\phi}^2\tau^2} \tag{4}$$

Expressing the phase rate by $\dot{\phi}=2\pi\nu$, one finds that the signal coherence time, defined as (or extrapolated to) the delay time at which $\rho(\tau)=1/e$, is given by

$$\tau_{1/e} = (\sqrt{2}\pi\nu)^{-1}. \tag{5}$$

Both $\dot{\phi}$ and ν have been referred to as the phase rate (expressed in different units) and will be used interchangeably. The same parametrization, Eq. (4), is also used for temporal coherence of broadband signals.

In the above derivation, a small τ is assumed, i.e., $\tau < 1/\dot{\phi}$, or $\rho > 0.6$. On the other hand, $\tau_{1/e}$ is normally not small, but it should be noted that $\tau_{1/e}$ is a (theoretical) parameter used in Eq. (4) to model the rate of coherence decrease for $\rho > 0.6$. Coherence time is in practice measured at $\rho > 0.6$, say, $\rho=0.8$, from which one can estimate the parameter $\tau_{1/e}$ and determine the corresponding phase rate (see below).

A. Experimental results

Early experimental measurements of the phase rate were summarized in Table I below (see Ref. 26). Table I also includes some recent measurements. They are briefly described below.

Spindel *et al.*[6] (1974) measured the phase rate from cw signals transmitted from a fixed source to a drifting receiver. The signal frequency is 406 Hz. The source-receiver range is approximately 210 km. After correcting for motion-induced phase change, they found ν/f to lie between 1.71×10^{-6} and 3.42×10^{-6}. Clark and Kronengold (1974) measured the phase rate on a propagation path from Eleuthera to Bermuda (project MIMI) at the same frequency.[7] They found ν/f to be 6.9×10^{-6}–9.9×10^{-6} at ranges from 550 to 1250 km. Williams (1976) measured the phase rate on the Bermuda Plateau at 400 Hz.[8] He found ν/f to be 0.76×10^{-6}–2.3×10^{-6} at ranges from 107 to 495 km. William and Battestin measured the phase rate of refraction-surface-refract rays on a propagation path from Bermuda to Eleuthera at the same frequency.[9] They found ν/f to be 1.3×10^{-6}–5.21×10^{-6} at ranges from 270 to 1200 km. Fitzgerald *et al.* measured the phase rate on the Hatteras Abyssal Plain at 10 Hz.[10] They found ν/f to be 4.15×10^{-6} at a range between 65 and 71 km. Georges *et al.* (1994) measured the phase rate on a propagation path from Heard Island to Ascension Island.[11] At a frequency of 57 Hz and source-receiver range of 9100 km, they found ν/f to lie between 2.3×10^{-6} and 7.0×10^{-6}. Birdsall *et al.* (1994) measured the phase rate of the same signal from Heard Island to Kiritimati (Christmas) Island[12] and found ν/f to not exceed 35×10^{-6} at a range of 5510 km. Parvulescu (1995) inferred a value of 0.63×10^{-6} for ν/f at $f=420$ Hz and range of 36.5 km from his earlier experimental data.[13] As illustrated by Dyson *et al.*,[4] phase rate measurement was based on the phase difference over a period of time after removing the carrier phase. These were snapshot measurements and a statistical analysis of the uncertainty in the measurement was not possible.

Recently, Speisberger *et al.* (2003) reported measurements of the temporal coherence based on broadband signal data transmitted from a bottom mounted source near Kaneohe Island to a receiver near the coast of northern California,[14] from which one estimated a coherence time, $\tau_{1/e}\sim 8$ min. The signal has a bandwidth of 16 Hz, centered at 133 Hz. The source-receiver range is 3709 km. Using Eq.

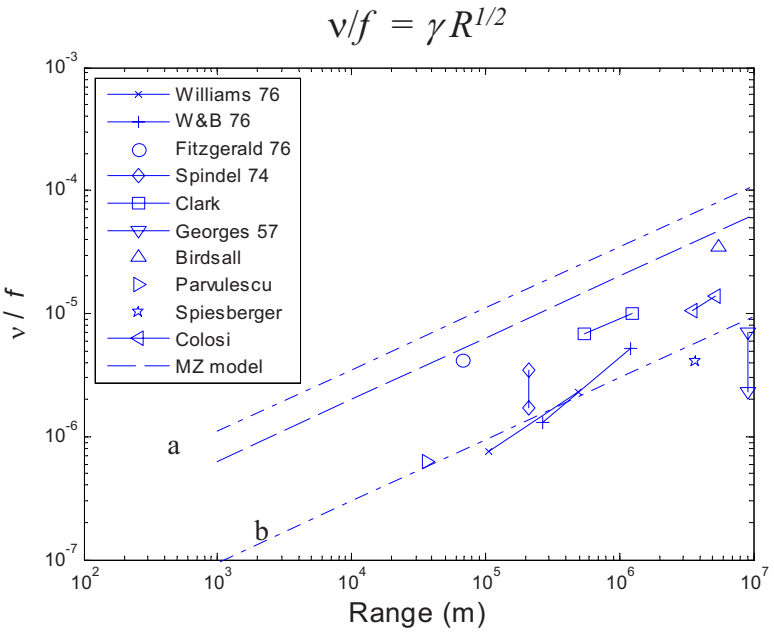

FIG. 1. (Color online) Deep-water data: ν/f vs range. The three lines are the Garret–Munk model predictions for different magnitudes of internal waves, displaying a $\frac{1}{2}$ power range dependence.

(5), one finds $\nu/f \sim 4.1 \times 10^{-6}$. Wage *et al.* measured the coherence time of first order mode from two long range sources received on a vertical line array.[15] Coherence times for mode 1 at 75 Hz are on the order of 8 min for the 2515 km range and 6 min for the 5171 km range. Colosi *et al.* measured the temporal coherence of signals propagated from Pioneer Seamount to Hawaii and Kritimati Island.[16] Data were collected at 24, 75, and 84 Hz using two different periods (20 and 40 min) of transmission. The temporal coherence measurements (for coherence above ~0.6) at 84 Hz are reasonably consistent between data with two different periods of transmissions. At a coherence value of 0.8, it reveals approximately 2 and 1.5 min of coherence times at ranges of 3502 and 5158 km, respectively.[16] Using Eq. (4), one finds the equivalent $\tau_{1/e}$ to be 254 and 191 s, respectively. The 75 Hz data were collected by using 40 min transmissions (no 20 min transmissions). The coherence time at a range of 3515 is approximately the same as that measured at 84 Hz at a range of 3502 km, whereas the coherence time at a range of 5171 is about twice longer than that measured from the 84 Hz signal at a range of 5158 km. For frequency dependence study on a log scale, the 75 Hz data do not add useful information and will not be explicitly included in the analysis below. The temporal coherence data at 24 Hz had a high uncertainty; temporal resolution is poor due to the limited bandwidth at (very) low frequencies. The measured numbers differ significantly depending on the periods of the transmissions. At the range of 3502 km, the coherence time at a coherence value of 0.8 ranges from 2 to 18 min; the differences between data of different transmissions are significantly larger at the range of 5158 km. These results will not be used here due to large uncertainties.

The above data (expressed in ν/f) are plotted as a function of source-receiver range in Fig. 1. (The mode coherence time is not used because it is not a full field measurement.) This is called a scattered plot, where data from different environments with different magnitudes of internal waves are plotted collectively to determine their behavior. The data are compared to a square root of range dependence represented by the dashed lines (as suggested by the Munk–Zachariasen[19] and the path integral[20] models discussed below). If this range dependence is correct, the data should congregate along the predicted curves. One finds that the square-root range dependence is indeed supported by the data. Ideally, one would test the range dependence by using data under the same environmental condition, but this is difficult to achieve in practice.

B. Theoretical expectation

In deep water, the loss of temporal coherence of acoustic signals is predominantly due to scattering from internal waves at low frequencies.[21] Using the path integral approach,[20] the temporal coherence function can be expressed in terms of the phase structure function $D(\tau)$:

$$\rho(\tau) = \exp[-D(\tau)/2], \tag{6}$$

where $D(\tau)$, using the Markov approximation, is given by

$$D(\tau) = f^2 \int_0^R \langle \mu^2 \rangle L_p \langle \omega^2 \rangle \tau^2 dx \equiv \langle \dot{\phi}^2 \rangle \tau^2, \tag{7}$$

where $\langle \mu^2 \rangle$ is in the fractional sound-speed variance for the internal waves, $\langle \omega^2 \rangle$ is the spectrum averaged value of the square of the internal-wave frequency, L_p is an effective internal-wave correlation length along a ray, and ω^2 is the internal-wave frequency. Munk and Zachariasen[19] obtained, using the supereikonal approximation for acoustic rays,

$$\langle \dot{\phi}^2 \rangle = \frac{2f^2}{\pi C^2} n_0 B \int_0^R dx \sec^2 \theta \sum_j j^{-1} \int_{\omega_{\text{in}}}^{n_0} d\omega \frac{\omega^2 F(\omega, j; z)}{\sqrt{\omega^2 - \omega_{\text{in}}^2}}, \tag{8}$$

where

$$F(\omega, j; z) = \langle \dot{\zeta}^2(z) \rangle G(\omega) H(j),$$

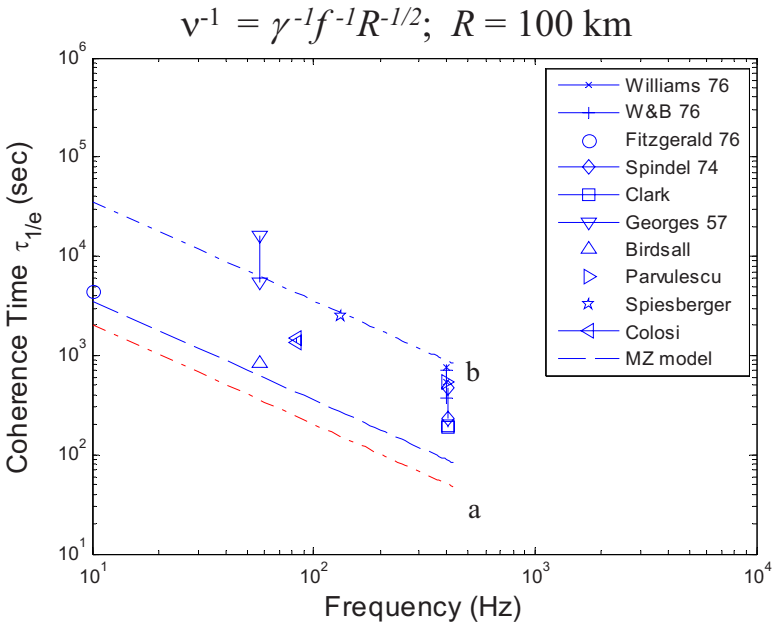

FIG. 2. (Color online) Coherence time $\tau_{1/e}$ vs frequency at a reference range of 100 km. The three lines are the Garret–Munk model predictions for different magnitudes of internal waves, displaying a −1 power frequency dependence.

$$G(\omega) = \frac{4}{\pi} \frac{\omega_{\text{in}} \sqrt{\omega^2 - \omega_{\text{in}}^2}}{\omega^3}, \tag{9}$$

where $\langle \zeta^2(z) \rangle$ is the mean-square internal-wave displacement, ω_{in} is the initial frequency, n_0 is the buoyancy frequency, and $G(\omega)$ is the frequency spectrum and $H(j)$ is the mode spectrum of the internal waves. Note that the buoyancy frequency is depth dependent and the integral in Eq. (6) is to be carried out for all multipaths. The above equations can be used to estimate the phase rate for a Garrett–Munk internal-wave model. For example, it was found[19] that

$$\langle \dot{\phi}^2 \rangle = \langle (\delta C/C)^2 \rangle \langle j^{-1} \rangle (f^2/C^2) BR \omega_{\text{in}} n_0 F_2, \tag{10}$$

where the first factor is the mean-square percentage variation in the sound speed at the sound axis, the second factor is the internal-wave mode spectrum, $B=1$ km, and F_2 is an integral over the internal-wave spectrum. In the deep ocean, one finds typically $\text{rms}(\delta C/C) = 4.9 \times 10^{-4}$, $\langle j^{-1} \rangle = 0.435$, $\omega_{\text{in}} = 7.3 \times 10^{-5}$ s^{-1}, and $n_0 = 5.2 \times 10^{-3}$ s^{-1}.

We shall take an empirical approach. Taking the square root of Eq. (10), one has

$$\nu/f = \gamma \sqrt{R}, \tag{11}$$

where f is frequency in Hz, and R is range given in meter. Using the phase rate measured from the MIMI experiment as analyzed by Dyson *et al.*,[4] it was found that $\nu = 2.8 \times 10^{-3}$ s^{-1} for a signal of 406 Hz at a range of 550 km, from which one finds $\gamma = 9.3 \times 10^{-9}$. For the data in Fig. 1, one finds a range of γ falling between 3.0×10^{-9} and 3.5×10^{-8} as shown by the two dash-dotted lines, labeled by b and a, respectively in Fig. 1. The lower value of γ corresponds to a half-scale Garrett–Munk internal-wave model as suggested by Spiesberger *et al.*[14] We also show a "full-scale" Garrett–Munk internal-wave model with $\gamma = 2 \times 10^{-8}$, as shown by the dashed line in Fig. 1.

Equation (11) can be converted into an expression for the coherence time using Eq. (5). One has

$$\tau_{1/e} = \delta f^{-1} R^{-1/2}, \tag{12}$$

where $\delta = (\gamma \sqrt{2} \pi)^{-1}$.

C. Frequency dependence

To study the frequency dependence using the Munk–Zachariasen model, one needs to examine the temporal coherence at the same range. To accomplish this, the data in Fig. 1 are converted to a reference range of 100 km based on the square-root range dependence as predicted by the model [Eq. (10) or (11)]. The data (at a range of 100 km) are then expressed in terms of the coherence time $\tau_{1/e}$ [the inverse of ν as given in Eq. (5)] and plotted in Fig. 2 as a function of frequency. The data are compared to the Munk–Zachariasen model which predicts an f^{-1} frequency dependence for the coherence time $\tau_{1/e}$ [Eq. (12)]. The coherence time for a full-scale Garrett–Munk model, expressed in terms of Eq. (11) with $\gamma = 2 \times 10^{-8}$, is shown in Fig. 2 as the dashed line. Also shown are two (dash-dotted) curves labeled as b and a for $\gamma = 3.0 \times 10^{-9}$ and 3.5×10^{-8}, respectively.

D. The status of the path integral predictions

The path integral approach assumed that the multipaths are uncorrelated ray arrivals. This assumption leads to a simple prediction for the phase structure function which is a quadratic function of frequency:[27]

$$D(\Delta) \simeq 2f^2(\tau_w^2 - \tau_1 \tau_2) \tag{13}$$

where τ_w^2 is the mean-squared travel time fluctuation (pulse wander) and $\tau_1 \tau_2$ is the travel time fluctuation covariance. Consequently, the phase rate is a linear function of frequency.

For the high-frequency (3500 Hz) short range (35 km) pulse propagation as part of the Azores Fixed Acoustic Range experiment, the observed pulse wander and pulse spread τ_0 were both about 2 ms as predicted by the theory.[22] However for the low-frequency (75 Hz) long range (3200)

signals in the Acoustic Engineering Test (AET), the observed pulse spread and that predicted by the path integral were 3 and 300 ms, respectively, differing by a factor of 100.[27,28] The observed pulse spread τ_0 is much smaller than the travel time variance (wander),[27,28] which is between 11 and 19 ms. The observed intensity probability density function, the intensity variance, and the fact that $\tau_0 \ll \tau_w$ suggest that the acoustic fluctuations are consistent with unsaturated or nearly partially saturated statistics, whereas the predictions of the wave propagation based on the path integral approach indicate strong saturated behavior in contradiction to the observations.[27,28]

Earlier work by Munk–Zachariasen assumed the supereikonal approximation to simplify the calculation (of the phase structure function) along a ray. Recently, Colosi *et al.* calculated the phase structure function exactly by numerically evaluating the ray weighting function $\langle \mu^2 \rangle L_p / c^2$ along the ray.[28] The disagreement between the model predictions and data still exist.

The most noticeable shortcoming of the ray approach has to do with its inability to model the late (finale) arrivals.[27] A series of North Pacific Acoustic Laboratory (NPAL) experiments were initiated to study this issue, among other things.[29] Existing data showed that the finale arrivals are dispersive and characteristic of normal modes. To model the internal-wave effect on the finale arrivals, a normal mode theory would be required.[27] However, noting that internal waves are often anisotropic and range dependent, one needs a coupled mode analysis which has not been done to our knowledge.

In view of the disagreements between the theory and data, investigators have resorted to numerical models, e.g., the parabolic equation (PE) model, for explanation of the data. Often, the calculations have been done over a range of two convergence zones, e.g., 50 km (and extend to long ranges by assuming range independence) rather than the range of the experiment (several thousand kilometers). A recent study[28] showed that the PE model and the path integral predictions differ by a factor of 2. The specifics are as follows: For the SLICE89 experiment, the PE predictions for the travel time variance as a function of the ray upper turning point in depth between 100 and 300 m are in good agreement with data whereas the path integral predictions are about twice the data. For the same quantity, the path integral predictions are 1.5 times smaller than the data for the AET experiment. The travel time bias for the pulse arrival calculated by the path integral method is a factor of 2 smaller than PE calculations. One thus concludes that the ray based theory (path integral) is inadequate for many aspects of the data. One finds that numerical (PE) models yield a diffused late arrival structure which agrees qualitatively with data.[27] The extended arrival structure can be (qualitatively) explained by internal-waves-induced mode coupling.[27]

III. TEST OF THE ν/f DEPENDENCE IN SHALLOW WATER

Shallow-water propagation, particularly at low frequencies, exhibits dispersive arrivals which are characteristic of normal modes. Does the coherence time of the normal modes follow the ν/f dependence as predicted by the path integral model assuming uncorrelated rays? To address this question, we briefly review the experimental results in shallow water.

A comprehensive study of the temporal coherence of acoustic signal propagation in shallow water has been conduced recently by Yang using data collected from four experiments covering a wide range of frequencies.[30] Broadband acoustic data were analyzed from the Assessment of Skill for Coastal Ocean Transients (ASCOT) experiment,[31,32] the Shallow-Water Acoustics in a Random Medium (SWARM) experiment,[33] and the first part of the Relationship of Array Gain to Shelf Processes (RAGS) experiment.[30] Multitone data were analyzed earlier using data from the Adventure Bank (ADVENT) experiment.[34] All data have a high signal-to-noise ratio (>20 dB) so that noise is not the contributing factor for the coherence loss.

The 2001 ASCOT experiment was conducted on New England Shelf at a water depth of 100 m. The data covered three frequency bands with center frequencies at 450, 1200, and 3550 Hz. Both the 1995 SWARM and 2003 RAGS experiments were conducted on New Jersey Shelf. The data analyzed from the 1995 SWARM experiment were *m*-sequence data received on the NRL vertical array, located at a distance of 42 km from the source. It contained two bands of data at center frequencies of 224 and 400 Hz. The data analyzed from the 2003 RAGS experiment were broadband signals at a center frequency of 20 kHz. The source-receiver range was 6 km. All these three experiments as well as the 1999 ADVENT experiment had downward refractive (summer) sound-speed profiles.

Given the measurements of the signal temporal coherence as a function of the delay time, one can estimate the signal coherence time. Theoretical discussions generally use a coherence time defined as the delay time $\tau_{1/e}$, the time when the signal coherence drops to a value of $1/e=0.37$, as discussed above. Experimentally, it is often necessary to use a different coherence time, e.g., $\tau_{0.8}$, which is defined as the delay time τ when the signal coherence $\rho(\tau)$ drops to a value of 0.8. The reason for using $\tau_{0.8}$ is due to the increasing variance in the measurements at lower coherence values. (The variance in the coherence time increases significantly as the coherence value decreases, making measurements of the coherence time at lower coherence values difficult and sometimes meaningless. For details, see Ref. 30.) Note that the theoretical expression for the coherence, Eq. (4), derived under the assumption of a small delay time (when the coherence value is close to 1) may or may not hold for a large delay time depending on the channel conditions.

Experimental measurement, $\tau_{0.8}$, can be used to estimate $\tau_{1/e}$ by assuming Eq. (4),

$$\tau_{1/e} = 2.12\tau_{0.8}. \tag{14}$$

This relation will be used later for comparison of shallow-water data with deep-water data. The measured coherence time $\tau_{0.8}$ from the four experiments (from Ref. 27) are plotted in Fig. 3 as a function of frequency. For the 1999 ADVENT and 2001 ASCOT experiments, the data were obtained at a range of 10 km. For studying the frequency

$$\nu^{-1} = \alpha^{-1} f^{-3/2} R^{-1/2}$$

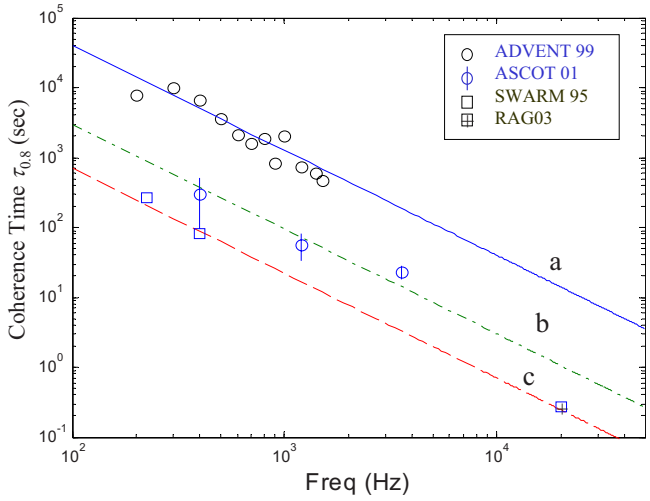

FIG. 3. (Color online) Coherence time $\tau_{0.8}$ vs frequency at a range of 10 km based on shallow-water data. Three lines labeled a, b, and c are fits to the data showing a $-\frac{3}{2}$ power frequency dependence. SWARM95 and RAG03 data were from the same general area with a similar sound-speed profile.

dependence, the data from the 1995 SWARM and 2003 RAGS experiments have been converted to the same (reference) range of 10 km by assuming an inverse-square-root range dependence. One finds that the data in Fig. 3 can be fitted with an inverse $\frac{3}{2}$ power frequency dependence as shown by the three different lines over a frequency range of 200 Hz to 20 kHz, reflecting a different magnitude of internal waves.

Figure 4 shows the signal coherence time as a function of range as reported in Ref. 30. The data were obtained from the 2001 ASCOT experiment conducted at two different ranges: 5 and 10 km, and three different frequencies: 450, 1200, and 3550 Hz. The data are consistent with an inverse-square-root range dependence as shown by the dashed curve.

Figure 5 displays the same data in terms of phase rate over frequency (ν/f) following the convention for plotting the deep-water data. Assuming Eq. (4), the phase rate is obtained using

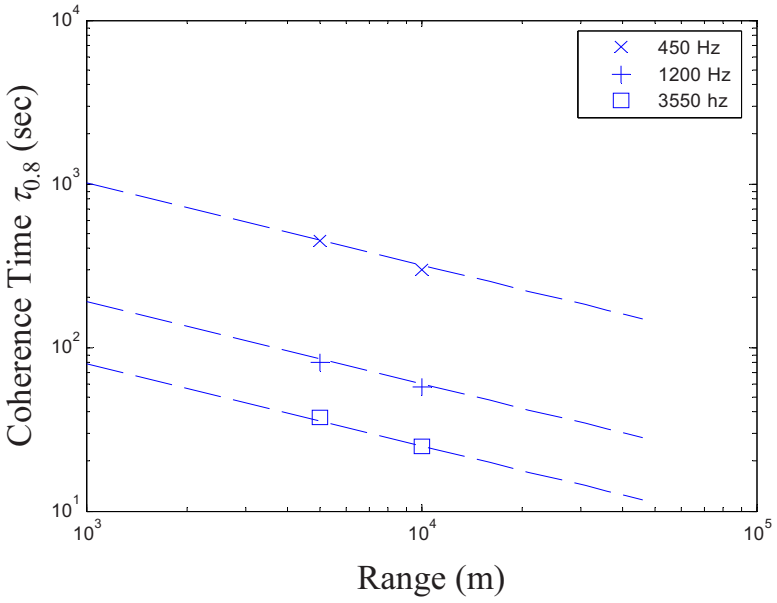

FIG. 4. (Color online) Coherence time $\tau_{0.8}$ measured at 5 and 10 km for three frequencies as shown in the legend (ASCOT01data). The three lines are fits to the data assuming a $-\frac{1}{2}$ power range dependence.

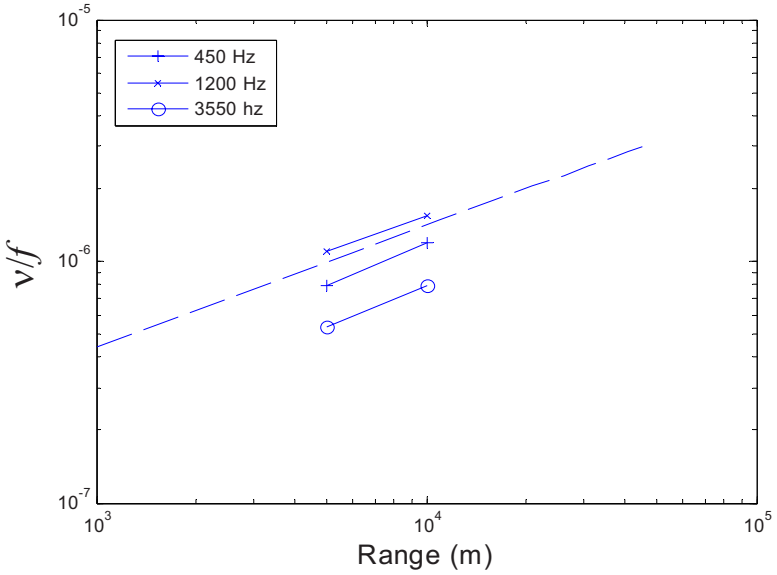

FIG. 5. (Color online) Data of Fig. 4 displayed in terms of ν/f vs range.

$$\nu = \sqrt{-\ln(0.8)/2\pi^2}\,\tau_{0.8}^{-1} \simeq 0.11\,\tau_{0.8}^{-1}. \tag{15}$$

Note that according to the path integral or the Munk–Zachariasen model, assuming uncorrelated ray arrivals having the same phase rate, the ν/f data at three different frequencies would fall on top of each other since it is supposed to be frequency independent. Figure 5 indicates this is not the case. It is a clear indication that the uncorrelated ray model does not fit the shallow-water data. This should not be a surprise since an acoustic signal in shallow water is well described by normal modes. Each normal mode is consisted of an up going ray and a down traveling ray, which are coherent with each other.

Fitting the coherence time data with

$$\tau_{0.8} = \beta_S f^{-3/2} R^{-1/2}, \tag{16}$$

one finds that $\beta_S = 4\times10^9$, 3×10^8, and 7×10^7 $(\mathrm{m/s})^{1/2}$ for the 1999 ADVENT, 2001 ASCOT, and the combination of 1995 SWARM and 2003 RAGS data, respectively, as labeled by curves a, b, and c in Fig. 3. Using Eq. (15), the above results can be converted into

$$\nu = \alpha_S f^{3/2} R^{1/2}, \tag{17}$$

where $\alpha_S = 0.11/\beta$. One thus finds $\alpha_S = 0.28\times10^{-10}$, 3.6×10^{-10}, and 1.6×10^{-9} $(\mathrm{m/s})^{-1/2}$ for the above mentioned experiments, respectively.

The different values of α are related to the different strengths of internal waves as measured by the sound-speed standard deviation (SD) near the bottom of the pycnocline where internal waves are most intense.[30] The 1999 ADVENT environment generally has weak internal-wave activities (sound-speed SD ~0.3 m/s), the 2001 ASCOT experimental area (New England Shelf) has medium internal-wave activities (sound-speed SD ~2–3 m/s), and the 1995 SWARM site (New Jersey Shelf) has the highest internal-wave activities (sound-speed SD ~5 m/s). One finds that α is proportional to the second power of the sound-speed SD.[30]

IV. AN EMPIRICAL MODEL FOR THE COHERENCE TIME IN DEEP OCEAN

The Munk–Zachariasen and path integral models assume that the multipath rays are uncorrelated and have an identical phase rate; coherence time is basically described by that of a single path. We take the point of view that the uncorrelated rays are inconsistent with normal modes since each mode requires two (up and down traveling) rays having the same phase. Thus, a different model will be needed to describe the temporal coherence of the finale arrivals which are modelike. Lacking a theoretical normal mode model for the temporal coherence time, the following expression is proposed for the coherence time (for normal modes):

$$\tau_{1/e} = (\sqrt{2}\pi\alpha)^{-1} f^{-\kappa} R^{-1/2}, \tag{18}$$

which yields a phase rate

$$\nu = \alpha f^{\kappa} R^{1/2}, \tag{19}$$

where κ is a free parameter to be determined from the data. We shall provide the reason why the range dependence of the phase rate should follow the square-root power dependence and argue below that $\kappa \simeq \frac{3}{2}$ for deep water, as is (found) in shallow water. Why should the coherence time of the mode arrivals in deep water and shallow water have the same frequency dependence? The physical explanation is that the linear internal waves in deep and shallow waters have a similar spectrum with comparable spatial and temporal correlation lengths.[35,36] Note that the temporal coherence of the acoustic field is directly related to the temporal coherence of the internal waves. Acoustic signals at different frequencies can then be used to inversely study the temporal (and spatial) coherence of the internal waves in terms of the frequency response of the signal coherence. The fact that internal waves have a similar spectrum and comparable correlation lengths suggests that the frequency response should be similar between the deep and shallow water.

The technical reasons for the above model are discussed next. One notes that the range dependence of the signal coherence time reflects the rate of the signal temporal coherence loss due to the internal waves as range increases. The argument that the range dependence follows a square-root power law is as follows. For propagation through a random medium, assuming the sound-speed perturbation is randomly distributed over range, the change in a narrow band acoustic field is, to the first order of the sound-speed perturbation δC, described by scattering of the acoustic field with the sound-speed perturbation $\delta C(r,z)$. The perturbation can be expressed as the product of the Green function from the source to $\delta C(r,z)$, the source term associated with $\delta C(r,z)$, and the Green function from $\delta C(r,z)$ to the receiver, integrated over (r,z). The coherence function is a second moment of the acoustic field. Dashen *et al.* gave a path integral formulation of the coherence function which shows that ν^2 is proportional to range R for an individual path due to integration along the range. A similar formulation for the interference between multipaths would suggest that the interference follows the same range dependence. Consequently, the phase rate for a normal mode, which is consisted of two rays, will exhibit the same square root of range dependence as for a single ray. As shown above, the data in both shallow and deep waters are consistent with an inverse-square-root dependence on range.

Next, we discuss the frequency dependence. The phase rate squared, $\langle\dot{\phi}^2\rangle$, for uncorrelated multipaths, is given by Eq. (7):

$$\langle\dot{\phi}^2\rangle = f^2 \int_0^R \langle\mu^2\rangle L_p \langle\omega^2\rangle dx, \tag{20}$$

which is linear in fR, fL_p, and $\langle\omega^2\rangle$. Hence, one can argue, based on the dimensional argument, that the phase rate should scale with the acoustic frequency. One notes that the integral in Eq. (20) integrates along a single ray path. It is a one-dimensional integration (in a rotated coordinate) along the ray path, where the effective correlation length L_p is approximately the horizontal correlation length L_x of the internal waves. For normal modes consisting of up and down traveling rays which are coherent with each other, one needs to include the interference between the rays. This requires a

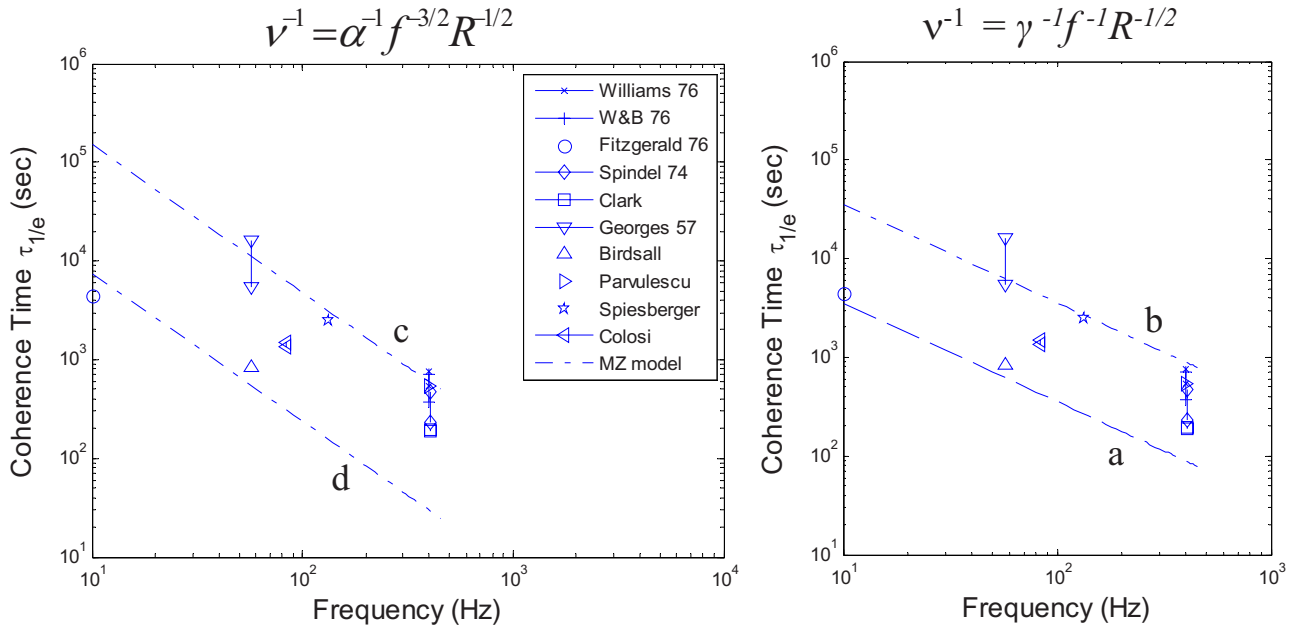

FIG. 6. (Color online) Deep-water data compared to $-\frac{3}{2}$ and -1 power frequency dependence models. Lines c and d in the left panel are model predictions for two values of α. The right panel is a repeat of Fig. 2. Range=100 km.

two dimensional integration. In that case, Eq. (20) is modified by[37]

$$\langle \dot{\phi}^2 \rangle = f^2 \int_0^R \left[\int \langle \mu^2(x,z) \rangle U_m^2(z) dz \right] L_p \langle \omega^2 \rangle dx \tag{21}$$

for an mth normal mode, where $U_m(z)$ is the mode depth function. Note that the sound-speed change due to the internal wave is proportional to the internal-wave mode function, which spans a depth of the order of the vertical coherence length of the internal waves L_z. In other words, $\langle \mu^2(x,z) \rangle \simeq 0$ for $z > L_z$. One can then make the following approximations,

$$\left\langle \int \mu^2(x,z) U_m^2(z) dz \right\rangle \simeq \langle \mu^2(x) \rangle \int_0^{L_z} U_m^2(z) dz$$
$$\sim k_m L_z \langle \mu^2(x) \rangle, \tag{22}$$

where k_m is the acoustic mode wave number. Equation (22) is linear in L_z since $U_m^2(z)$ has the dimension of inverse meter, i.e., $\int U_m^2(z) dz = 1$. In deep water, the mode depth function is a function of the mode wave number (only) as the water depth has negligible influence on the internal waves.[38] As noted above, internal waves are confined to the upper water column.

Noting that the wave number of an acoustic normal mode is proportional to the acoustic frequency, one finds $\langle \dot{\phi}^2 \rangle \sim f^3$ based on Eq. (22). Consequently, one expects the phase rate to exhibit a $\frac{3}{2}$ power dependence on the acoustic frequency. In the above discussions, although we have not explicitly related the coherence time (or the phase rate) of an acoustic signal to the coherence time of the internal waves, one notes that the relationship is implicitly there since the spatial coherence lengths of the internal waves are related to the temporal coherence length (coherence time) of the internals through the internal-wave dispersion relation.

A. Deep-water data revisited

Given sufficient measurements, one could check the range and frequency dependence [Eqs. (18) and (19)] and estimate the value of the parameter κ. Unfortunately, the available data are limited; thus, we shall simply test if $\kappa = \frac{3}{2}$ is supported by the data. In other words, we assume

$$\tau_{1/e} = (\sqrt{2} \pi \alpha_D)^{-1} f^{-3/2} R^{-1/2},$$

$$\nu = \alpha_D f^{3/2} R^{1/2}. \tag{23}$$

To compare to the data in Fig. 2, the signal coherence times calculated using Eq. (23) are plotted in Fig. 6, left panel, for two values of α_D: $\alpha_D = 1.5 \times 10^{-10}$ and 3×10^{-9} $(\mathrm{m/s})^{-1/2}$ as labeled by c and d respectively; $R = 100$ km. Figure 2 is repeated as shown in the right panel for γ between 3.0×10^{-9} and 3.5×10^{-8} as labeled by b and a, respectively.

To compare how well the new model, Eq. (23), and the path integral prediction, Eq. (12), fit the data, we conduct an error analysis. For each value of α and γ, the coherence time is calculated for each frequency. We then calculate the mean normalized squared error, defined by the error between the data and model squared, normalized by the model prediction squared, and averaged over the data points. The resulting normalized error is plotted as a function of α and γ and superimposed in Fig. 7 for comparison. One finds that the best fit normalized error for the -1 power frequency dependence is about 50% higher than the best fit normalized error assuming the $-\frac{3}{2}$ power frequency dependence. This analysis shows that the $-\frac{3}{2}$ frequency dependence is slightly favored by the data reported above. While the difference in the rms error may not be significant, it is fair to conclude that the $-\frac{3}{2}$ power frequency dependence model is, at least, as consistent with the data as the -1 power frequency dependence model. The result argues for the need for more experimental mea-

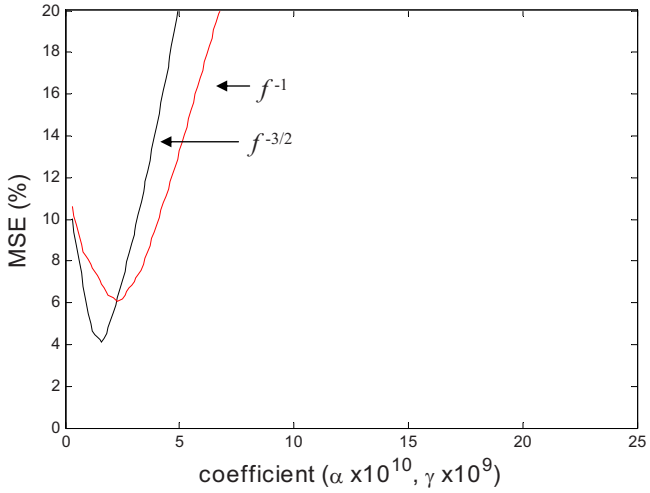

FIG. 7. (Color online) Normalized mean-square error as a function of the model parameters (α and γ) for the two models of frequency dependence.

surements. At this stage, a full statistical analysis is not warranted as the result does not carry much weight due to the small number of data samples.

Continuing the analysis, one notes that according to Eq. (23), the quantity $\nu/f^{3/2}$ (for a given α) should be independent of frequency and be a function of range only. In Fig. 8, the experimental data are displayed in terms of $\nu/f^{3/2}$ versus range using the values given in Table I. Also shown are two curves using Eq. (23) for two values of α_D, $\alpha_D=1.5\times10^{-10}$ and 3×10^{-9} as labeled by c and d, respectively. One finds that the data cluster around and lie within the two curves. The data plotted in this format also show a square-root power dependence on range.

Since the convention has been to plot the data in terms of ν/f versus range (as shown in Fig. 1), the (new) model predictions are plotted in this format in Fig. 9, left panel. Note that ν/f is now a function of frequency and range ($\nu/f=\alpha_D\sqrt{Rf}$). To compare with data, the curves in Fig. 9 (for each value of α_D) use the range and frequency of the

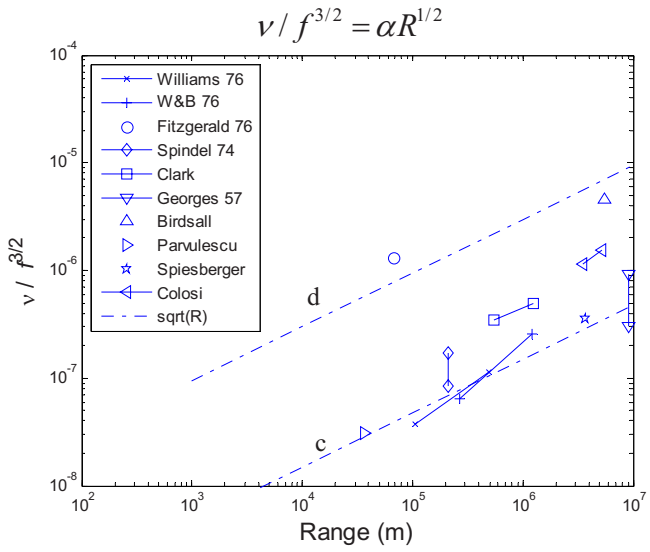

FIG. 8. (Color online) Deep-water data displayed in terms of $\nu/f^{3/2}$ vs range. Lines c and d are model predictions for two values of α.

nearest adjacent data points. The model-prediction points are connected by dashed lines as shown in Fig. 9 for display purposes and labeled as c and d as before. Compared with Fig. 1 (repeated in the right panel), where one observes that some data points (inverted triangles and stars) are outside the model predictions of Eq. (9), one finds that the new model predictions based on Eq. (12) actually follow the data trend as displayed by the inverted triangles and stars. In other words, the dotted lines in Fig. 9, left panel, seem to fit the data better than the dash-dotted lines in Fig. 11, right panel.

B. Discussions

1. Temporal coherence: Early versus finale arrivals

Assume that a signal consists of two components, $p=s_1+s_2$, which are uncorrelated. For example, s_1 denotes the early arrivals which exhibit ray characteristics and s_2 denotes the late arrivals which exhibit characteristics like normal modes. If both the early and later arrivals have approximately the same coherence time, so will the total signal. The following analysis will consider the possibility that the early and later arrivals have a different coherence time. This possibility is prompted by the fact that the early (ray) arrivals exhibit a statistical (amplitude) distribution which is close to unsaturated or partially saturated statistics, i.e., log-normal distribution, whereas the late arrivals exhibit a statistical distribution closer to fully saturated distribution.[27] A fully saturated distribution implies more randomness; hence the late arrivals are expected to have a shorter coherence time than the early arrivals.

The temporal coherence $\rho(\tau)$ of the total signal can be expressed as

$$\rho(\tau)=\rho_1(\tau)\frac{S_1^2}{S^2}+\rho_2(\tau)\frac{S_2^2}{S^2}, \tag{24}$$

where S_i^2 and $\rho_i(\tau)$ are the intensity and temporal coherence of the signal s_i, respectively; $i=1,2$, and $S^2=S_1^2+S_2^2$. Assume $\rho_i(\tau)=\exp(-\tau^2/\tau_i^2)$, and that the coherence time τ_1 of the signal s_1 is shorter than the coherence time τ_2 of the signal s_2, i.e., $\tau_1<\tau_2$. One finds that $\rho(\tau)\simeq\rho_1(\tau)(S_1^2/S^2)+$ a near constant at a short delay time, $\tau<\tau_1$. In other words, the short delay-time coherence is predominantly controlled by the signal component that has the shortest coherence time. For the deep-water signal, this is assumed to be the later arrivals. Thus the coherence time of the total signal is expected to follow a frequency dependence close to $-\frac{3}{2}$ power as analyzed above.

At a longer delay time, $\tau_2>\tau>\tau_1$, one finds $\rho(\tau)\simeq\rho_2(\tau)(S_2^2/S^2)+$ residual term, where the residual term from S_1 is near zero based on the simplified model; in reality it may not be negligible. The model suggests that it may be possible to see two stages of coherence decay (with possibly two different slopes) in real data; detailed phenomenon will depend on how close the two coherence times τ_2 and τ_1 are. Assuming that the coherence time of the early arrivals has a -1 power frequency dependence and the late arrivals have a $-\frac{3}{2}$ power dependence, one notes that the coherence time at a time scale between τ_1 and τ_2 could have a frequency dependence somewhere in between -1 and $-\frac{3}{2}$ power.

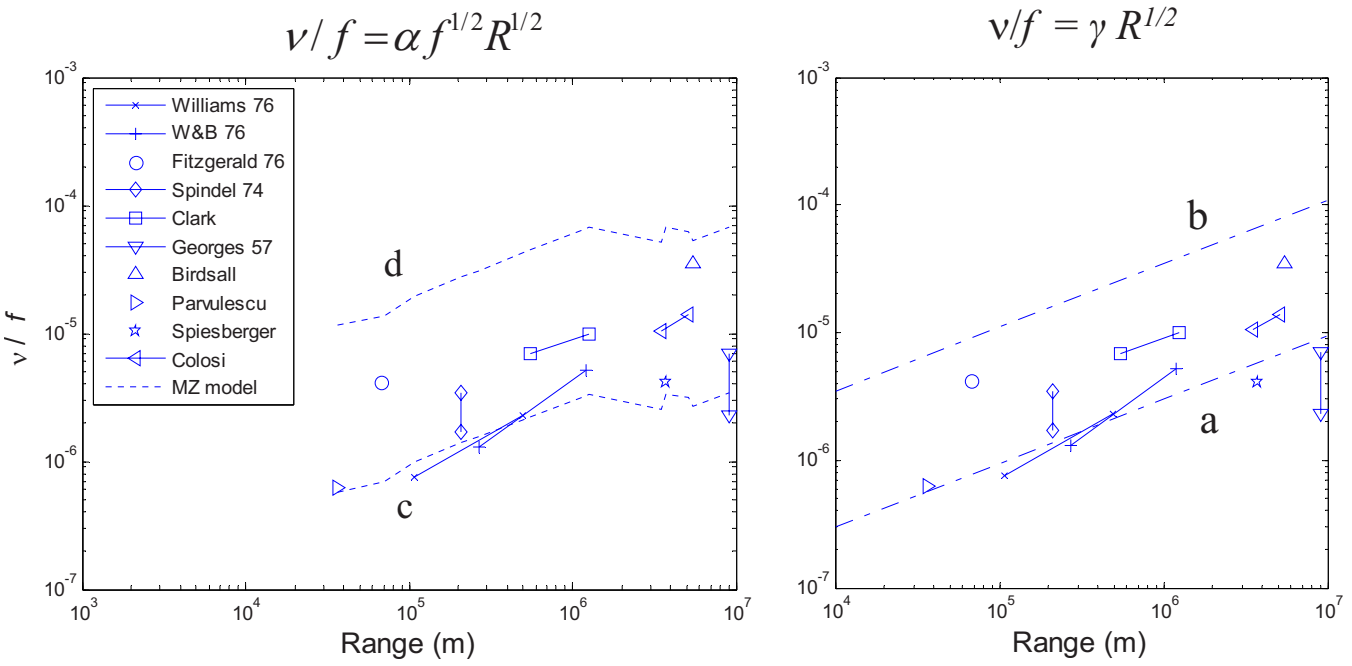

FIG. 9. (Color online) Deep-water data displayed in the conventional format (ν/f) compared to the model predictions. The right panel is a repeat of Fig. 1. Wiggled lines in the left panel are envelope to the data using the two values of α and using the frequency of the neighboring data points.

To test the above model, it is suggested that the deep-water data be reanalyzed by dividing the signal into two groups (early and late arrivals) and analyzing the temporal coherence of individual groups separately. Another method is to divide the data into two groups according to the source/receiver depth. For source-receiver depths near the surface, the signal will be dominated by deep traveling rays (high depression and elevation angle) with shallow turning points. These rays spend a small percentage of time interacting with the internal waves. For source-receiver depths near the sound axis, the signal consists, mainly, of rays with a shallow depression and elevation angle; they travel through a water column dominated by internal waves. One expects that the two groups of signals will exhibit a different rate of temporal coherence loss. The signal coherence times will have different frequency dependences.

2. Magnitude of the internal waves: Deep versus shallow water

One notes that α_S and α_D are proportional to the SD of the sound-speed variation, Eq. (10), which is in turn proportional to the internal-wave amplitude. From Sec. III, one finds that α_S lies between 0.28×10^{-10} and 1.6×10^{-9} $(\mathrm{m/s})^{-1/2}$ for shallow water. It is noted that α_S is about two to five times smaller than α_D in deep water [$\alpha_D = 1.5\times10^{-10}$ and 3×10^{-9} $(\mathrm{m/s})^{-1/2}$]. This suggests that the signal coherence time in shallow water is about two to five times longer than that in deep water at the same frequency and range. Note that at the same range, the signal would have had many more bottom bounces in shallow water than in deep water. Since the bottom has the effect of stripping the higher order modes, and the low order modes are generally more coherent than the high order modes, the signal in shallow water could be more coherent than that in deep water.

A more appropriate way to compare the deep and shallow-water data will be in terms of the range to the (maximum) ray depth-span ratio. (The ray depth span in shallow water is normally the water depth and the ray depth-span in deep water is the smaller of the water depth and the sound-speed conjugation depth. For our discussions, one can use the range-to-depth ratio as a good approximation.) The motivation is that the acoustic rays would have traveled approximately the same number of ray cycles for the same range-to-depth ratio. Comparing Fig. 3 with Fig. 6, one finds that the coherence time as a function of frequency has roughly the same order of magnitude in shallow and deep waters. (Assuming that the shallow-water depth is one-tenth of that in deep water, then one has the same R/D for Figs. 3 and 6. Changing (the ratio of) the water depths would affect the comparison somewhat.) Expressing the coherence time as $\tau/\tau_0 = \zeta(f/f_0)^{-3/2}(R/R_0)^{-1/2}$, where, τ_0, f_0, and R_0 denote the time, frequency, and range scales of an ocean (for simplicity, we have dropped the subscript $1/e$ from τ), the above analysis suggests that the range scale R_0 is proportional to the water depth—a geometrical influence. For this discussion, we assumed that τ_0 and f_0 are approximately the same in shallow and deep waters, since the (linear) internal waves have the same time and frequency scales in shallow and deep waters.

V. NUMERICAL TESTING

In the absence of a theoretical derivation of the temporal coherence, one can use numerical models to evaluate the range and frequency dependences of the signal coherence time.[36] These Monte Carlo calculations are computationally intensive. The first step of the numerical modeling is to calculate the sound-speed variation/perturbation given a model of internal waves. A discrete-time realization of the ocean

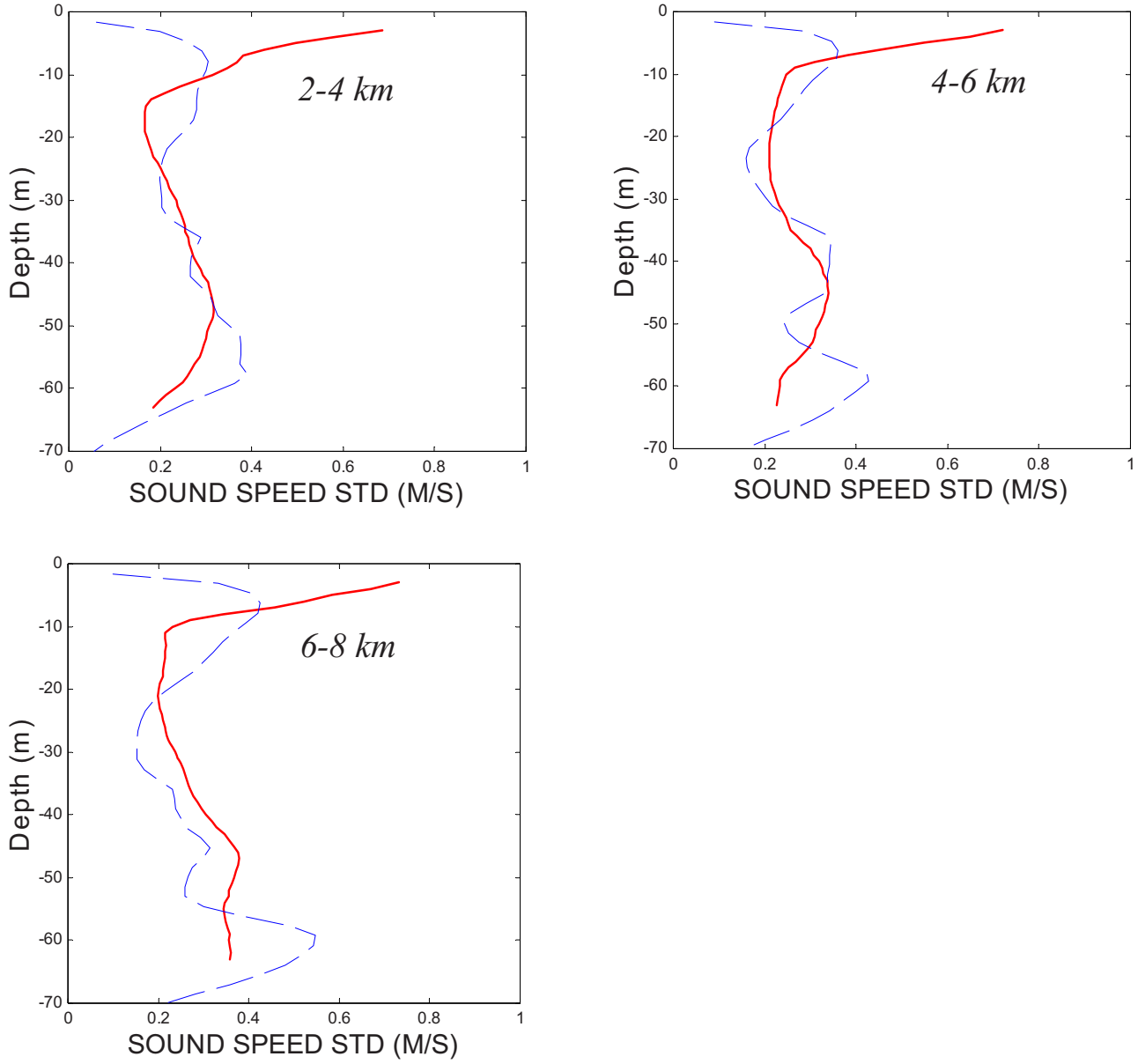

FIG. 10. (Color online) Sound-speed SDs computed from an internal-wave model (dashed lines) compared to that measured from the ADVENT99 experiment (solid lines).

sound-speed profile (as a function of range and depth) is generated and treated as frozen for the purpose of sound propagation. Given an (arbitrary) initialization, the internal-wave theory also predicts how the sound-speed variation (as a function of range and depth) will evolve with time. Most of the numerical models assume random realization of the sound-speed profiles and calculate the statistical mean and variance of the signal propagation through these realizations of sound-speed profiles. For temporal coherence modeling, each random realization provides an initial condition of the sound-speed profile. This sound-speed profile (as a function of range and depth) will evolve with time according to the dynamic equations of the internal waves. By propagating sound through each numerically generated time-varying, range-dependent sound-speed field, one can simulate the acoustic field variation with time at the receivers. Temporal coherence can then be measured from this simulated data the same way it is applied to real data. In other words, a signal transmitted at geotime t is correlated with the signal transmitted at a delay time $t+\tau$. The signal temporal correlation is then averaged over data generated with different initial sound-speed profiles (generate with different, random initial conditions). The coherence time of the signal could then be estimated from the signal coherence curve for a given coherence value.

A PE model has been implemented to model the coherence time of narrow band signals propagating through shallow water. The results agree reasonably well with the measured data and show a $-\frac{3}{2}$ power dependence as a function of frequency. The numerical modeling is done for the 1999 ADVENT experiment in the Strait of Sicily.[36] A vertical line array of conductivity-temperature-depth (CTD) sensors were deployed and towed between the source and receivers. The CTD data were taken during the same time when acoustic transmissions were taking place. From the CTD data, the

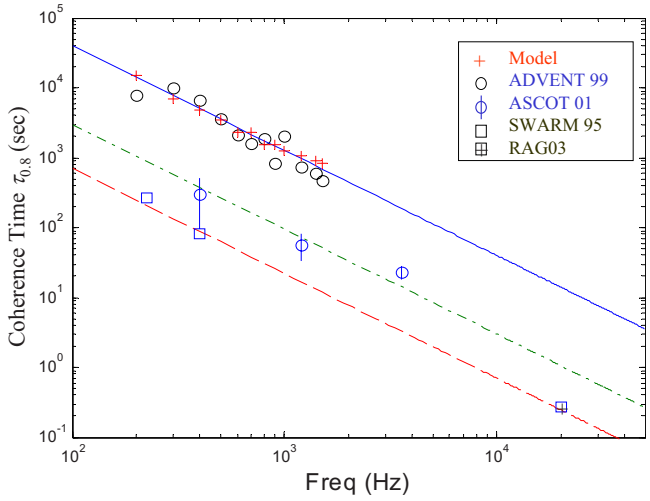

FIG. 11. (Color online) Comparison of the modeled coherence time $\tau_{0.8}$ (denoted by +) with the ADVENT99 data as displayed in Fig. 3.

buoyancy profile was obtained as a function of depth to determine the frequency–wave number dispersion relation. The buoyancy profile indicated a bimodel structure of internal waves near the surface and near the bottom. There might be some elevation nonlinear internal waves, but their presence is weak. The internal-wave mode depth functions $W(k_h j, z)$ and mode spectrum parameters (j_* and p) were measured for the low order modes using the eigenvector decomposition method.[36] The deduced mode depth functions compared favorably to those calculated from theory based on the measured buoyancy profile.[36] The internal-wave spectra are also determined from the internal-wave mode amplitudes. Armed with these measurements, random realizations of the sound-speed profiles were generated. From that, the sound-speed SD was calculated. To show the quality of the model predictions, the calculated sound-speed SD is plotted in Fig. 10 and compared to measured sound-speed SD. The agreement between model and data is good except near the surface. The reason is that the internal-wave model does not include near-surface sound-speed perturbations due to, for example, bubbles. Fortunately, the near-surface sound-speed perturbations have little effect on sound propagation from a bottom moored source to receivers in the lower half of the water column. The reason is that the mean sound-speed profile is downward reflective. As a result, the high angle rays from a bottom mounted source are quickly attenuated by bottom interactions. The acoustic field at the receiver consists of primarily shallow angle rays which do not touch the surface.

For each random initialization of the internal-wave field, the time-evolving acoustic field was correlated with the field at time zero over an array of receivers to produce the "matched field" temporal coherence of the signals the same way as the data were processed.[36] The temporal coherence calculations are then averaged over different initial conditions (of the internal-wave fields). The results for 12 frequencies in Fig. 11 and compared with 1999 ADVENT data. Good agreement is observed. The significance of this numerical simulation work is that all (critical) parameters of the internal-wave model have been determined from the CTD data. There is no free parameter left to make adjustments.

The above study shows that the frequency dependence can be checked using numerical Monte Carlo calculations. It is recommended that a similar calculation needs to be done for propagation in deep water. The practical difficulty is that each propagation can take a long time to complete because of the long ranges (thousands of kilometers). To reduce the computation time, many numerical simulations in deep water have used a coarse grid (tens of meters in range and meters in depth) which may be reasonable at low frequencies, e.g., 75 Hz. To determine the frequency dependence, the calculation needs to be done at various frequencies, as high as 1–3 kHz. At, say, above 1 kHz, the high wave number spectral components of the internal waves (extending to and covering the turbulence generated by the internal waves) may influence (reduce) the coherence time of the acoustic signal and need to be incorporated into the numerical model. A fine grid size may be required. Neglecting the high-frequency spectrum of the internal waves could result in an overestimate of the signal coherence time at high (>1 kHz) frequencies.

Since the coherence time as discussed in this paper is based on the geotime variation of the broadband signal, it is natural to check the quality of the numerical model by asking how well the modeled impulse response agrees with the measured impulse response in terms of intensity as well as delay time. Often one finds that the modeled impulse response incorporating the Garrett–Munk internal waves do not quite match the measured impulse response.[16] Part of the disagreement between the model and data is lack of environmental data, as environmental sampling is coarse in deep water; hence one is forced to make assumptions about the environments which may not be correct. For studying the frequency dependence of the signal coherence time, one may argue that while the numerical value of the signal coherence time will likely depend on the detail of the internal-wave model, the frequency dependence of the coherence time is perhaps a fundamental property related to the time scale of the internal wave and thus could be tested with a generic internal-wave model.

VI. SUMMARY

In this paper, the coherence time of acoustic signals propagating to long ranges in deep water are reviewed, representing 35 years of research work. At low frequencies, the loss of temporal coherence is attributed predominantly to internal waves. The coherence time provides a measure of the rate of temporal coherence loss. In theory, the coherence time of the acoustic signal is directly related to the coherence time of the internal waves. But such a relationship has not been derived, nor does one have knowledge of the relationship on an empirical basis.

The theme of this paper is the range and frequency dependences of the signal coherence time in deep water. The range dependence of the coherence time in the presence of internal waves should reflect the rate of temporal coherence loss due to the internal waves as range increases. The frequency dependence of the coherence time shall reveal the rate of coherence loss as a function of the acoustic frequency.

Based on the observation that the (linear) internal waves in deep and shallow water have a similar frequency spectrum, it is argued that the modelike finale arrivals should exhibit similar frequency dependence in deep as in shallow water. The measured coherence time in shallow water indicates a $-\frac{1}{2}$ power range dependence and $-\frac{3}{2}$ power frequency dependence.

Previously, the path integral theory or the supereikonal model predicts a -1 power frequency dependence for the coherence time of uncorrelated ray arrivals. It is suggested in this paper that the inclusion of the mode functions into the path integral should yield a $-\frac{3}{2}$ power frequency dependence for the coherence time of the finale arrivals; this prediction still needs to be verified by rigorous theoretical development. Assuming that the finale arrivals have a shorter coherence time, it is expected that the coherence time of the entire signal also follows a $-\frac{3}{2}$ power frequency dependence. The $-\frac{1}{2}$ power range dependence is expected by the theory for both the ray and mode arrivals.

The above predictions are examined with respect to existing experimental data in deep water. It is found that the measured signal coherence times are consistent with a $-\frac{1}{2}$ power range dependence and $-\frac{3}{2}$ power frequency dependence. Due to the scarcity of the data, the frequency dependence is consistent with a power law between -1 and $-\frac{3}{2}$, favoring the $-\frac{3}{2}$ power slightly. This argues for more temporal coherence-time measurements in deep water, particularly at different frequencies. Note that most of the coherence time measurements are based on the signal phase rate, which does not say anything about the coherence times of individual path arrivals. The question whether the coherence times of the raylike early arrivals and the modelike finale arrivals have a different frequency dependence is an important one, and needs to be checked against data specifically. To do so, it is proposed that the existing data be reanalyzed by evaluating the temporal coherence of the early and finale arrivals separately. The analysis should include data from the more recent series of NPAL experiments, for example, the LOAPEx which includes, among its objectives, the measurement of the temporal coherence as a function of range and frequency.[17]

ACKNOWLEDGMENT

The work is supported by the Office of Naval Research.

[1]G. C. Carter, *Coherence and Time Delay Estimation: An Applied Tutorial for Research, Development, Test, and Evaluation Engineers* (IEEE, 1993).
[2]J. V. Candy, *Signal Processing: The Model-Based Approach* (McGraw-Hill, New York, 1968).
[3]Most work on matched field processing assumed a stationary ocean. The importance of temporal coherence for matched field localization was addressed in K. Yoo and T. C. Yang, "Broadband source localization in shallow water in the presence of internal waves," J. Acoust. Soc. Am. **106**, 3255–3269 (1999).
[4]F. Dyson, W. Munk, and B. Zetler, "Interpretation of multipath scintillations Eleuthera to Bermuda in terms of internal waves and tides," J. Acoust. Soc. Am. **59**, 1121–1133 (1976).
[5]P. H. Dahl, A. B. Baggeroer, P. Mikhalesky, and I. Dyer, "Measurement of the temporal fluctuations of CW tones propagated in the marginal ice zone," J. Acoust. Soc. Am. **83**, 2175–2179 (1988).
[6]R. C. Spindel, R. P. Porter, and R. J. Jaffee, "Long-range sound fluctuations with drifting hydrophones," J. Acoust. Soc. Am. **56**, 440–446 (1974).
[7]J. G. Clark and M. Kronengold, "Long period fluctuations of CW signals in deep and shallow water," J. Acoust. Soc. Am. **56**, 1071–1083 (1974).
[8]R. E. Williams, "Creating an acoustic synthetic aperture in the ocean," J. Acoust. Soc. Am. **60**, 60–73 (1976).
[9]R. E. Williams and H. F. Battestin, "Time coherence of acoustic signals transmitted over resolved paths in the deep ocean," J. Acoust. Soc. Am. **59**, 312–328 (1976).
[10]R. M. Fitzgerald, A. N. Guthrie, and J. D. Shaffer, "Low-frequency coherence transverse to the direction of propagation," J. Acoust. Soc. Am. **60**, 752–753 (1976).
[11]T. M. Georges, L. R. Boden, and D. R. Palmer, "Features of the Heard Island signals received at Ascension," J. Acoust. Soc. Am. **96**, 2441–2447 (1994).
[12]T. G. Birdsall, K. Metzger, M. A. Dzieciuch, and J. Spiesberger, "Integrated autocorrelation phase at one period lag," J. Acoust. Soc. Am. **96**, 2353–2356 (1994).
[13]A. Parvulescu, "Matched-signal ("MESS") processing by the ocean," J. Acoust. Soc. Am. **98**, 943–960 (1995).
[14]J. L. Spiesberger, F. Tappert, and A. R. Jacobson, "Blind prediction of broadband coherence time at basin scales," J. Acoust. Soc. Am. **114**, 3147–3154 (2003).
[15]K. E. Wage, M. A. Dzieciuch, P. F. Worcester, B. M. Howe, and J. A. Mercer, "Mode coherence at megameter ranges in the North Pacific Ocean," J. Acoust. Soc. Am. **117**, 1565–1581 (2005).
[16]J. A. Colosi, A. Baggeroer, B. Cornuelle, M. Dzieciuch, W. Munk, P. Worcester, B. Dushaw, B. Howe, J. Mercer, R. Spindel, T. Birdsall, K. Metzger, and A. Forbes, "Analysis of multipath acoustic field variability and coherence in the finale of broadband basin-scale transmissions in the North Pacific Ocean," J. Acoust. Soc. Am. **117**, 1538–1564 (2005).
[17]J. A. Mercer, B. M. Howe, R. K. Andrew, M. A. Wolfson, P. F. Worcester, M. A. Dzieciuch, and J. A. Colosi, "The Long-range Ocean Acoustic Propagation Experiment (LOAPEX): An overview," J. Acoust. Soc. Am. **120**, 3020 (2006).
[18]B. D. Dushaw, R. Andrew, B. Howe, J. Mercer, B. Cornuelle, M. Dzieciuch, W. Munk, P. Worcester, T. Birdsall, K. D. Menemenlis, and R. Spindel, "Ocean acoustic thermometry and the seasonal cycle of temperature in the North Pacific Ocean," J. Acoust. Soc. Am. **120**, 3020 (2006).
[19]W. H. Munk and F. Zachariasen, "Sound propagation through a fluctuating stratified ocean: Theory and observation," J. Acoust. Soc. Am. **59**, 818–838 (1976).
[20]R. Dashen, S. Flatté, and S. Reynolds, "Path-integral treatment of acoustic mutual coherence functions for rays in a sound channel," J. Acoust. Soc. Am. **77**, 1716–1722 (1985).
[21]S. M. Flatte, R. Dashen, W. Munk, K. Watson, and F. Zachariasen, *Sound Transmission Through a Fluctuating Ocean*, edited by S. M. Flatte (Cambridge University Press, Cambridge, 1979).
[22]S. M. Flatte and G. Rovner, "Calculations of internal-wave-induced fluctuations in ocean-acoustic propagation," J. Acoust. Soc. Am. **108**, 526–534 (2000).
[23]T. C. Yang, "Comparison of temporal coherence of signal propagation in shallow and deep water," Proceedings of the Eighth European Conference on Underwater Acoustics, edited by S. M. Jesus and O. C. Rodrigues2006, pp. 169–174.
[24]W. M. Carey, "The determination of signal coherence length based on signal coherence and gain measurements in deep and shallow water," J. Acoust. Soc. Am. **104**, 831–837 (1998) and references therein.
[25]See, for example, R. Urick, *Principle of underwater sound for engineers* (McGraw-Hill, New York, 1983).
[26]K. D. Rolt and P. A. Abbot, "Littoral coherence limitations on acoustic arrays," in *Acoustic Imaging*, edited by S. Lees and L. A. Ferrari (Plenum, New York, 1997), Vol. **23** and references therein.
[27]J. A. Colosi and the ATOC Group, "A review of recent results on ocean acoustic wave propagation in random media: Basin scales," IEEE J. Ocean. Eng. **24**, 138–155 (1999).
[28]J. Colosi, E. Scheer, S. Flatté, B. Cornuelle, M. Dzieciuch, W. Munk, P. Worcester, B. Howe, J. Mercer, R. Spindel, K. Metzger, T. Birdsall, and A. Baggeroer, "Comparisons of measured and predicted acoustic fluctuations for a 3250-km propagation experiment in the eastern North Pacific Ocean," J. Acoust. Soc. Am. **105**, 3202–3218 (1999).
[29]B. D. Dushaw, B. M. Howe, J. A. Mercer, R. C. Spindel, J. A. Colosi, B. D. Cornuelle, M. A. Dzieciuch, and P. F. Worcester, "The North Pacific Acoustic Laboratory (NPAL) Experiment," J. Acoust. Soc. Am. **107**, 2829–2829 (2000).
[30]T. C. Yang, "Measurements of temporal coherence of sound transmissions

through shallow water," J. Acoust. Soc. Am. **120**, 2595–2614 (2006).
[31]J. Sellschopp, P. Nielsen, and M. Siderius, "Combination of acoustics with high-resolution oceanography," in *Impact of Littoral Environmental Variability on Acoustic Prediction and Sonar Performance*, edited by N. G. Pace and F. B. Jensen (Kluwer, The Netherlands, 2002), pp. 19–26.
[32]J. Sellschopp, "High resolution measurements of the ocean fine structure and their relation to sound transmission," Proceedings of the Internal Conference on Underwater Acoustic Measurements: Technologies and Results, edited by J. S. Papadakis and L. BjornoHeraklion, Greece, June 2005.
[33]J. R. Apel, and the SWARM group, "An overview of the 1995 swarm shallow water internal wave acoustic scattering experiment," IEEE J. Ocean. Eng. **22**, 465–500 (1997).
[34]T. C. Yang and M. Siderius, "Temporal coherence and fluctuation of acoustic signals in shallow water," Proceedings of the Fifth European Conference on Underwater Acoustics, edited by M. E. Zakharia, P. Chervet and P. Dubail, Lyon, France, 11–14 July 2000, pp. 63–68.
[35]T. C. Yang and K. Yoo, "Internal waves spectrum in shallow water: Measurement and comparison with the Garrett-Munk model," IEEE J. Ocean. Eng. **24**, 333–345 (1999).
[36]T. C. Yang, K. Yoo, and M. Siderius, "Internal waves and its effect on signal propagation in the Adventure Bank," Proceedings of the Eighth International Congress on Sound and Vibration, Hong Kong, 2–6 July 2001, pp. 3001–3008.
[37]A geometric ray has a phase $k_z z$, where z is the depth of the ray. The WKB approximation of a normal mode depth function has a phase $\pm\int_{z'}^{z} k_z(z,k_m)dz$ for upward and downward traveling waves where $k_z = \sqrt{k^2(z)-k_m^2}; z'$ is a constant. See, for example, L. Tolstoy, "The W.K.W. Approximation, turning points and the measurement of phase velocities," J. Acoust. Soc. Am. **52**, 356–363 (1972). Hence for the path integral, $e^{ik_z z}$ is replaced by the mode depth function, and for the second moment, one inserts the mode depth-function squared, integrated over depth.
[38]In shallow water, the mode depth function is often expressed in terms of the water depth, which can be re-expressed in terms of the mode wave number by using the mode dispersion relation. In other words, the intrinsic parameter is the mode wave number, not the water depth.

Calibration of broadband active acoustic systems using a single standard spherical target

Timothy K. Stanton[a] and Dezhang Chu
Department of Applied Ocean Physics and Engineering, Woods Hole Oceanographic Institution, Woods Hole, Massachusetts 02543-1053

(Received 26 September 2007; revised 27 March 2008; accepted 8 April 2008)

When calibrating a broadband active acoustic system with a single standard target such as a sphere, the inherent resonances associated with the scattering by the sphere pose a significant challenge. In this paper, a method is developed which completely eliminates the source of resonances through isolating and exploiting the echo from the front interface of a sphere. This echo is relatively insensitive to frequency over a wide range of frequencies, lacking resonances, and is relatively insensitive to small changes in material properties and, in the case of spherical shells, shell thickness. The research builds upon the concept of using this echo for calibration in the work of Dragonette *et al.* [J. Acoust. Soc. Am. **69**, 1186–1189 (1981)]. This current work generalizes that of Dragonette by (1) incorporating a pulse compression technique to significantly improve the ability to resolve the echo, and (2) rigorously accounting for the scattering physics of the echo so that the technique is applicable over a wide range of frequencies and material properties of the sphere. The utility of the new approach is illustrated through application to data collected at sea with an air-filled aluminum spherical shell and long broadband chirp signals (30–105 kHz).
 [DOI: 10.1121/1.2917387]

PACS number(s): 43.30.Yj, 43.58.Vb, 43.20.Fn, 43.30.Vh [AJZ] Pages: 128–136

I. INTRODUCTION

There is a wide variety of methods to calibrate active acoustic systems. In some cases, it is not essential to know both the source level and receive sensitivity separately and determining the combination of the two, i.e., the system response, would suffice. The standard calibration target has been used commonly as it can determine system response and is frequently convenient to deploy. For example, in the field of fisheries acoustics, solid elastic spheres are considered a standard by which ship-mounted echosounders are calibrated (as reviewed in Simmonds and MacLennan, 2005). In these and other applications, the measured echo from the sphere is normalized by the predicted echo of the sphere (based on known size and material properties) which allows the system response to be calculated.

One major challenge in using targets for calibration involves the resonances of the target [see, for example, thin line in Fig. 1(a)]. The frequencies at which the resonances occur strongly depend on the size and material properties of the target. Minute changes in the resonance frequency, such as due to changes or uncertainties in those physical parameters, can cause significant errors in the calibration at frequencies near the resonance. For narrowband systems, the size and material properties of the sphere can be chosen so that the center frequency of the system occurs between the resonances. This portion of the scattering response is much less sensitive to frequency and material properties and provides a reliable means of calibrating the system. However, for broadband systems, the frequency range may span multiple resonances of the sphere and another method must be used. One solution has been suggested which involves use of multiple spheres of various sizes and used one at a time, to connect subbands of near-stationary response of the spheres (Foote *et al.*, 1999; Foote, 2006). Collectively, the spheres could calibrate the system over its entire band. However, for systems of large bandwidth, use of multiple spheres could pose significant logistical constraints. It would be ideal to use a single sphere in a single measurement involving the entire band of the system, without errors associated with the resonances. This paper presents a general approach for the use of a single sphere for the entire frequency band by completely removing the source of the resonances in the time domain.

The resonances are due to interference between the echo from the front interface of the sphere, internally refracted and reflected waves, and various circumferential waves (see, for example, reviews in Hackman, 1993; Marston, 1992; and Numrich and Überall, 1992). These echoes, or "partial waves," can be investigated through use of the exact solution to the sphere in the far field limit and in the backscattering direction. This modal or partial wave series applies to a variety of spherically symmetric profiles of material properties, including solid elastic spheres and liquid- or gas-filled elastic spherical shells. Examples of predictions over a wide range of properties are given in Stanton (1990). Equation (6) in that paper is the modal series solution used in this paper.

Although the modal series solution contains all information regarding the various partial waves, they are inseparable in this current form of the equation. As a result, the equation is normally used to predict the total scattering by the sphere due to all effects, i.e., a "full-wave" prediction, resulting in complex scattering characteristics with many resonances for

[a]Author to whom correspondence should be addressed. Electronic mail: tstanton@whoi.edu

 0001-4966/2008/124(1)/128/9/$23.00

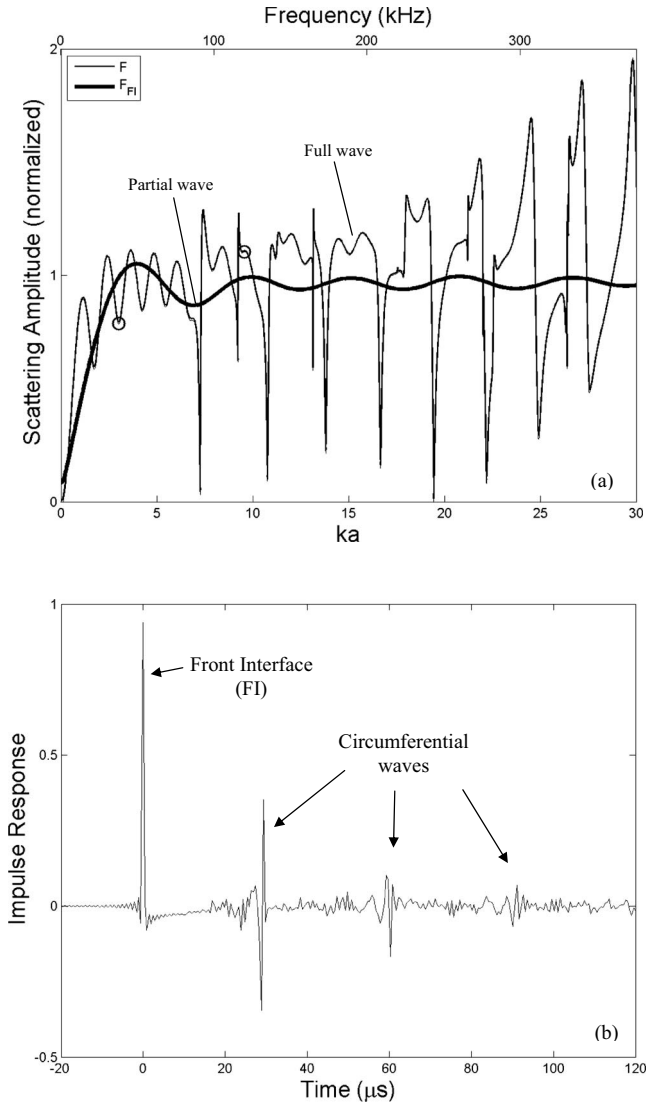

FIG. 1. Acoustic backscattering by a dense solid elastic sphere. (a) The full-wave solution to the sphere (scattering amplitude, F; thin curve) which involves a summation of all partial waves and is shown to be strongly dependent upon frequency, containing numerous strong and narrow resonances. The partial-wave solution (scattering amplitude, F_{FI}; thick curve) for the echo from the front interface of the sphere which is calculated from the first arrival of the impulse response in Fig. 1(b) and is shown to be weakly dependent upon frequency for higher frequencies. Both solutions for the scattering amplitude are normalized by $a/2$. In this example, a tungsten carbide sphere of 38.1 mm diameter was used. The circles correspond to two standard frequencies (38 and 120 kHz) used in fisheries acoustics. (b) Impulse response of scattering.

values of ka greater than unity [thin line in Fig. 1(a), where k is the acoustic wave number of the surrounding fluid ($=2\pi/\lambda$, where λ is the acoustic wavelength] and a is the radius of the sphere. It is this full-wave analysis that is the basis of the commonly used calibration methods as described in Foote (1982, 2006); Foote *et al.* (1999, 2007); Feuillade *et al.* (2002); Simmonds and MacLennan (2005), and others.

The partial waves are inseparable in the modal series solution principally due to the fact that the equation is in the frequency domain. In this "continuous wave" formulation, echoes arriving at different times are not resolved. The waves can be resolved through calculating the impulse response of the sphere, which can be determined by calculating the inverse Fourier transform of the modal series solution (see, for example, Sun *et al.*, 1991; Kaduchak *et al.*, 1995). The resulting time-domain expression is composed of the partial waves arriving at different times [Fig. 1(b)]. The first echo to arrive is from the front interface ("FI"), while all other echoes, such as due to internally refracted and reflected waves and circumferential waves, arrive at later times.

Through various methods, and as given below, the scattering by the front interface has been shown to vary weakly with frequency (at fixed radius) over a wide range of frequencies for $ka>1$ [thick line in Fig. 1(a)] (see, for example, Marston, 1992). The sum of all of the remaining partial waves is strongly dependent upon frequency. The predictions in Fig. 1(a) show that in the limit of high frequencies (high ka at fixed a), the echo from the front interface is independent of frequency. This has also been shown analytically:

$$F_{\mathrm{FI}} \simeq \frac{1}{2} aRe^{-i2ka}, \quad ka \gg 1, \tag{1}$$

where $R=(gh-1)/(gh+1)$

$$g \equiv \rho_2/\rho_1; \quad h \equiv c_2/c_1.$$

Here, F_{FI} is the scattering amplitude in the backscattering direction of the echo from the front interface; R is the plane-wave, plane-interface reflection coefficient for the front interface; $i=\sqrt{-1}$, g and h are the density and sound speed contrasts, respectively, of the sphere; and ρ and c are density and sound speed, respectively. Medium "1" is the surrounding water and medium "2" is the sphere. Here, the upper case notation for F_{FI} and other terms throughout this paper refers to the frequency domain while the lower case notation (for example, f_{FI}) refers to the time domain. Also, the partial wave target strength TS_{PW} for the echo from the front interface, as defined by Chu and Stanton (1998), is $TS_{\mathrm{PW}} = 10\log|F_{\mathrm{FI}}|^2$.

Given the fact that the echo from the front interface is relatively insensitive to frequency, it is desirable to use this echo from a standard target for calibrating a system. This fact was recognized by Dragonette *et al.* (1981) who used the echo in a partial-wave analysis to calibrate a broadband system. In that study, they achieved the resolution needed through use of a short high frequency signal. The analysis showed excellent agreement between the predicted and measured form function (which is related to scattering amplitude).

Part of the success of their results was attributed to the fact that the experiments were at very high frequencies—values of ka ranging from 14 to 70. In that region, the echo from the interface can be assumed, to first order, to be independent of frequency, as shown in Eq. (1). The analysis also benefited by the use of a dense solid calibration sphere, as the amplitude of the echo from the front interface was assumed to be due to a rigid sphere [i.e., $R=1$ in Eq. (1)]. Also, since the system used very short pulses, then the first echo could be resolved simply through analyzing the raw, unprocessed, echo. The pulses were made short through limiting the transmit signal to just a small number of cycles of high frequency sound. The assumptions that the first echo is independent of frequency and due to a rigid sphere, as well as the

use of the raw echo, limits the calibration with this approach to high values of *ka*, dense solid spheres, and short transmit signals. Because of these limitations, the calibration method is not practical for calibration spheres of less dense materials and systems that operate at lower frequencies and/or with long transmission signals.

In this paper, the partial-wave analysis of Dragonette *et al.* (1981) is generalized to cover a much wider range of frequencies, transmit signals with long durations, and calibration spheres with a wide range of materials. The generalization involves a combination of applying a signal processing technique to the echo and accounting rigorously for the scattering physics associated with the first echo:

(1) Signal processing. Rather than using the raw echo, whose range resolution is limited by the duration of the transmitted signal, the broadband echo is processed through cross correlating it with a replica signal. This signal processing significantly reduces the duration of the echo (similar to matched filter processing) and the duration of the compressed echo is now related to the inverse bandwidth of the system, which can be much shorter than the duration of the original raw signal.
(2) Scattering physics. Rather than assuming that the echo from the front interface is independent of frequency and due to a rigid sphere, the characteristics of the echo are exactly calculated. This is obtained through calculating the impulse response (time domain) of the exact solution (frequency domain) of the scattering function and temporally isolating the first echo in the impulse response for analysis. The exact solution can be applied to a wide range of material properties of spheres including solid elastic (any material) and elastic spherical shell (any material and shell thickness) filled with gas or liquid. Furthermore, the equation is exact for all frequencies.

The paper is organized as follows: In Sec. II, the raw, unprocessed echo voltage received in an experiment due to a target is expressed in the frequency domain in terms of the applied voltage, system response, and scattering amplitude of the target. In Sec. III, pulse compression processing is incorporated into those equations, resulting in an equation for system response in terms of the pulse-compressed signals associated with the calibration sphere. In Sec. IV, the results from Sec. III are applied to data collected in an at-sea calibration where the duration of the raw broadband signal corresponds to a distance of more than three times the diameter of the calibration sphere. Finally, in Sec. V, recommendations are made for the design of spheres for broadband calibrations. Here, a sensitivity analysis is conducted demonstrating how use of the echo from the front interface is relatively insensitive to small changes in material properties and thickness of shell. Also, design curves are given for recommended diameter for a range of bandwidths and several types of spheres.

II. GENERAL EQUATIONS FOR SYSTEM RESPONSE

The voltage, $V_r(\omega)$, of the received echo due to the scattering by a target located arbitrarily in the acoustic beam can be written as:

$$\underbrace{V_r(\omega)}_{\substack{\text{received}\\ \text{voltage}}} = \underbrace{V_t(\omega)}_{\substack{\text{applied}\\ \text{voltage}}} \underbrace{H_0(\omega)B_r(\omega)B_t(\omega)}_{\substack{\text{system response}\\ H(\omega)}} \underbrace{\frac{r_{\text{ref}}}{r^2} e^{i(2\omega/c)r} e^{-2\alpha(\omega)r}}_{\substack{\text{transmission loss}\\ L(\omega)}} \underbrace{F_{\text{bs}}(\omega)}_{\substack{\text{scatterer}\\ \text{response}}}, \tag{2}$$

where ω is the angular frequency, $V_t(\omega)$ is the voltage applied to the transmitter transducer, $H_0(\omega)$ is the system response of the combination of transmitter and receiver transducers evaluated in the center of the main lobe of the beam pattern (i.e., the product of the voltage-to-pressure and pressure-to-voltage ratios of the transducers), $B_r(\omega)$ and $B_t(\omega)$ are the beam patterns (normalized to unity in the center of each main lobe) of the receiver and transmitter transducers, respectively, r_{ref} is the reference distance at which the voltage-to-pressure ratio is measured for the transmitter transducer, r is the distance between the transceiver and the target, c and $\alpha(\omega)$ are the sound speed and absorption coefficient, respectively, of the water, and $F_{\text{bs}}(\omega)$ is the backscattering amplitude of the target.

This equation is written in general form and can be applied to both the calibration target as well as targets of interest in a field application. Furthermore, it can be used for either the commonly used full-wave calibration in which the exact modal series solution is used to include all of the scattering components or the partial-wave calibration, which is the focus of this paper, in which a subset of the scattering components, such as only the echo from the front interface, is used. For the "steady state" solution in which all partial waves contribute to $F_{\text{bs}}(\omega)$, then the traditional definition of target strength applies: $TS=10\log|F_{\text{bs}}(\omega)|^2$. However, if this equation is applied to partial waves, such as in subsequent sections, the partial-wave target strength applies, as discussed earlier as well as in detail in Chu and Stanton (1998).

For the calibration, the above equation is written in more compact form, with the superscript "(cal)" assigned to quantities corresponding to the calibration measurement:

$$V_r^{(\text{cal})}(\omega) = V_t^{(\text{cal})}(\omega)H(\omega)L^{(\text{cal})}(\omega)F_{\text{bs}}^{(\text{cal})}(\omega). \tag{3}$$

At this point, Eq. (3) is one equation with two unknowns, the system response and backscattering amplitude of the target. The essence of using a standard target for calibration is that the scattering by the target can be accurately predicted, which normally requires an accurate scattering model and an accurate measure of the material properties and dimensions of the target. With this accurate knowledge, then the measured scattering by the target can be replaced by the predicted scattering:

$$F_{\text{bs}}^{(\text{pred})}(\omega) = F_{\text{bs}}^{(\text{cal})}(\omega). \tag{4}$$

Substituting this expression into Eq. (3) and rearranging terms gives an expression for the system response:

$$H(\omega) = \frac{V_r^{(\text{cal})}(\omega)}{V_t^{(\text{cal})}(\omega)L^{(\text{cal})}(\omega)F_{\text{bs}}^{(\text{pred})}(\omega)}. \tag{5}$$

This is a general expression for the system response for both the full-wave and partial-wave calibration methods. For the full-wave case, the predicted scattering amplitude is simply

the modal series solution to the scattering function where none of the various components of the scattering from the target are resolved. For narrowband systems this equation can be used directly in the calibration. However, for broadband systems, as discussed above, resolving the echo from the front interface can greatly facilitate the calibration. There are conditions under which the center frequency is high enough and the calibration sphere is large enough so that the raw, unprocessed echo from the front interface can be resolved and Eq. (5) can be used directly. However, for other cases when it cannot be resolved, the received signal needs to be processed so that the resolution approaches the theoretical limit, which is approximately equal to the inverse bandwidth of the system. In the next section, pulse compression processing is applied to the signal to improve the temporal resolution and Eq. (5) is expressed in terms of the processed signal.

III. DETERMINING SYSTEM RESPONSE THROUGH PULSE COMPRESSION PROCESSING

In order to resolve the echo from the front interface, pulse compression processing may need to be performed to improve the temporal resolution. A method similar to matched filter processing is used, which involves cross correlating the received signal with a "replica" signal (Chu and Stanton, 1998; Turin, 1960). Generally, a true replica would account for the system response. However, since it is the system response that is being determined, such a replica cannot be used. Furthermore, it is important that the replica match or come close to matching the echo from a single partial wave. If, in contrast, the replica fully accounted for all partial waves, then the compressed signal would resemble a sinc function with a single main lobe, with none of the partial waves resolved. By treating each of the partial waves as being due to a scattering center with a phase specific to its respective scattering process, then a replica chosen to match a single scattering center will tend to resolve the partial waves. For this purpose using the applied transmitter signal or one similar to it can be used as an approximation. Although use of these signals is not optimum, as they do not account for system response or perfectly match each partial wave, their use in pulse compression processing still significantly improves the temporal resolution toward the theoretical limit of the inverse bandwidth. Furthermore, another benefit of using a pulse-compression method (optimum or not) is that the signal-to-noise ratio significantly increases. Development and application of pulse compression techniques to scattering by marine organisms is described in Chu and Stanton (1998), including illustrations of treating each organism as a distributed target with different scattering centers.

Another issue concerns the need for enough separation between the echo from the front interface and subsequent echoes. With large enough separation, then the time "gate" or "window" used to process the echo from the front interface can be large enough to provide satisfactory spectral resolution on that echo for calculation of the system response. Having a sufficiently large separation also simultaneously satisfies the criterion of the temporal or "range" processing sidelobes of sequential echoes not overlapping, which otherwise would be a source of error. However, in a practical application, since the transducer response is nonuniform, the signal becomes temporally shaded, thus these sidelobes tend to be significantly reduced and are much less of a problem (Chu and Stanton, 1998). A detailed description of the gating process and associated spectral resolution is given in Sec. IV. Choice of diameter of sphere for a range of material properties and bandwidths that provides for a sufficiently long separation between the first and second echoes is described in Sec. V. The calculations given below associated with a partial wave analysis are based on the assumption of a sufficiently long separation.

The compressed pulse signal, $\mathrm{cp}_1(t)$, associated with the signal of interest, $v_1(t)$, is given by the following general expression:

$$\mathrm{cp}_1(t) \equiv k_{\mathrm{cp}} v_1(t) \otimes v_2(t), \tag{6}$$

where the normalization factor, k_{cp}, is defined by

$$k_{\mathrm{cp}} \equiv R_2^{-1}(0),$$

$$\text{where } R_2(t) \equiv v_2(t) \otimes v_2(t). \tag{7}$$

The term $\otimes$ denotes the correlation operation, and the signal $v_2(t)$ is either the replica (for matched filter processing) or a similar signal, such as the signal applied to the transmitter as discussed above.

As a result of this processing, the duration of $\mathrm{cp}_1(t)$ can be as short as (approximately) inverse bandwidth of the $v_1(t)$, regardless of the duration of $v_1(t)$. Thus, in the calibration experiment, for a sufficiently large bandwidth of the transmitter signal, it is possible that the desired partial waves (such as the echo from the front interface) can be resolved, even when those features are not resolved in the raw signal before processing.

Since it is desirable to determine the system response in the frequency domain, the Fourier transform of the compressed pulse signal given by Eq. (6) is first taken:

$$\mathrm{CP}_1(\omega) = k_{\mathrm{cp}} V_1^*(\omega) V_2(\omega), \tag{8}$$

where the superscript * symbol denotes the complex conjugate.

Multiplying the numerator and denominator of Eq. (5) by the complex conjugate of the replica $V_{\mathrm{rep}}^{(\mathrm{cal})*}(\omega)$ and using Eq. (8) gives an expression for the system response in terms of the Fourier transforms of two compressed pulse signals:

$$H(\omega) = \frac{\mathrm{CP}_r^{(\mathrm{cal})*}(\omega)}{L^{(\mathrm{cal})}(\omega) CP_{\mathrm{pred}}^{(\mathrm{conv})*}(\omega)}, \tag{9}$$

where $\mathrm{CP}_r^{(\mathrm{cal})}(\omega)$ and $CP_{\mathrm{pred}}^{(\mathrm{conv})}(\omega)$ are the Fourier transforms of the compressed pulse signals, $\mathrm{cp}_r^{(\mathrm{cal})}(t)$ and $\mathrm{cp}_{\mathrm{pred}}^{(\mathrm{conv})}(t)$, respectively, as defined below:

$$\mathrm{cp}_r^{(\mathrm{cal})}(t) \equiv k_{\mathrm{cp}}^{(\mathrm{cal})} v_r^{(\mathrm{cal})}(t) \otimes v_{\mathrm{rep}}^{(\mathrm{cal})}(t) \tag{10}$$

and

$$\mathrm{cp}_{\mathrm{pred}}^{(\mathrm{conv})}(t) \equiv k_{\mathrm{cp}}^{(\mathrm{cal})} \left\{ f_{\mathrm{bs}}^{(\mathrm{pred})}(t) * v_t^{(\mathrm{cal})}(t) \right\} \otimes v_{\mathrm{rep}}^{(\mathrm{cal})}(t). \tag{11}$$

Here, $\mathrm{cp}_r^{(\mathrm{cal})}(t)$ is the compressed pulse associated with the calibration measurement in which the received voltage due

to the backscattering by the standard target is cross correlated with the replica signal, $v_{\mathrm{rep}}^{(\mathrm{cal})}(t)$. Again, as stated above, this does not need to be a true replica. The second term, $\mathrm{cp}_{\mathrm{pred}}^{(\mathrm{conv})}(t)$, is more complex. First, the impulse response $f_{\mathrm{bs}}^{(\mathrm{pred})}(t)$ of the backscattering amplitude of the standard target is predicted through calculating the inverse Fourier transform of the modal series solution and convolved (*) with the voltage signal $v_t^{(\mathrm{cal})}(t)$ applied to the transmitting transducer in the calibration measurement (here, the convolution operator, *, appears as a product-like operator, not a superscript). This convolution product is then cross correlated with the replica signal, which results in the compressed pulse signal. The normalization constant, $k_{\mathrm{cp}}^{(\mathrm{cal})}$, which is defined in Eq. (7) [where $v_2(t)=v_{\mathrm{rep}}^{(\mathrm{cal})}(t)$], is the same for each compressed pulse signal in Eq. (9) and cancels out (implicitly) as it appears as a factor to both the numerator and denominator. The derivation of Eq. (9) makes use of the fact that the product $F_{\mathrm{bs}}^{(\mathrm{pred})}(\omega)V_t^{(\mathrm{cal})}(\omega)$ in the frequency domain is the Fourier transform of the convolution product $f_{\mathrm{bs}}^{(\mathrm{pred})}(t)*v_t^{(\mathrm{cal})}(t)$ in the time domain.

Equation (9) is a general equation that can be used for either a full-wave analysis or partial-wave analysis. That is, once the measured signal of interest is compressed through the processing, the time gate can be chosen to either include just one partial wave (such as the echo from the front interface of the sphere) or all partial waves. Given the generality, it is important that the same time gate is used in both the calibration measurement and the predictions. Specifically, if a particular partial wave is selected in the calibration measurement to give $\mathrm{cp}_r^{(\mathrm{cal})}(t)$, then that same corresponding wave must be selected in the impulse response, $f_{\mathrm{bs}}^{(\mathrm{pred})}(t)$.

IV. AT-SEA CALIBRATION OF BROADBAND SYSTEM

The above formulation is applied to an experiment at sea in which a broadband system was calibrated. The calibrations took place near Provincetown, MA (tip of Cape Cod) in 50-m-deep water using the R/V Tioga on September 11, 2006. The system, made by Edgetech, consisted of three broadband transducers, including a Reson transducer (Model TC2138), which is the subject of this study (Stanton *et al.*, 2007). The Reson transducer was sensitive over a band of approximately 30–105 kHz and a linear frequency modulated signal ("chirp") was applied to that transducer (Fig. 2). This range is not the bandwidth as conventionally defined relative to the −3 dB points of the spectrum but the range over which the system has usable energy.

The echoes were digitized at a sampling rate of 260 kHz and processed at that same rate without downsampling. The chirp signal was chosen as it is a commonly used signal and it provided the necessary resolution in this experiment, although it is not necessarily the optimal signal. As a result of pulse-compression processing, the original 2 ms pulse (which corresponds to a range resolution of 1.5 m) is compressed to a signal with a duration of about 35 μs (which corresponds to a range resolution of 3 cm). This value of 35 μs is greater than the ideal value of 11.4 μs shown in

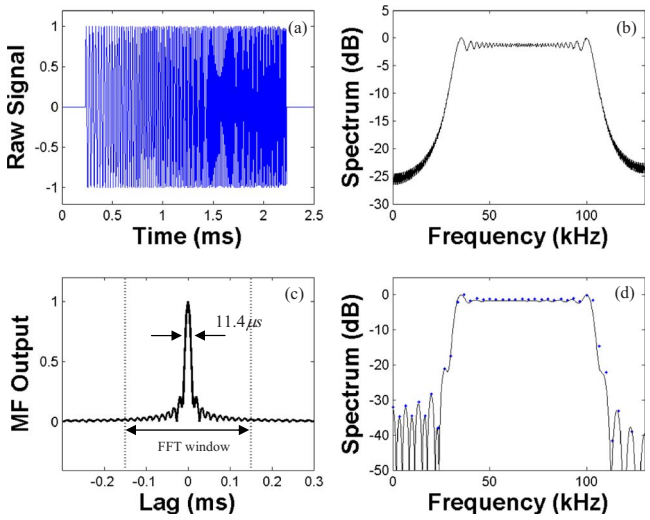

FIG. 2. (Color online) Effects of pulse-compression processing of a broadband signal. (a) A 2-ms-long (raw) chirp signal applied to Reson transducer, (b) frequency spectrum of signal from (a), (c) envelope of pulse-compressed signal in which autocorrelation function of signal shown in (a) is calculated, (d) frequency spectrum of pulse-compressed signal (before envelope was calculated) from (c). Dots: Spectrum calculated using 300-μs-long window shown in (c). Solid: spectrum calculated using 10-ms-long window, which involves beginning with the signal within the 300-μs-long window and zero padding each side.

Fig. 2 due to a combination of factors: the transducer response is not uniform over the band and a true replica was not used in the processing.

The system, which is normally towed in surveys with its acoustic beams aimed downward, was suspended 10 m directly below the vessel, which was anchored. The system was tethered so that the acoustic beams would still be aimed generally in the downward direction. Several calibration spheres were used, one at a time, suspended 30 m below the towbody. For the 41.5-cm-diam air-filled spherical aluminum shell discussed in this paper (4.1 mm average wall thickness), a 110 lb weight was tethered with a 5-m-long line to the bottom of the sphere since the sphere was positively buoyant by approximately 95 lbs.

The towbody, sphere, and weight were all free to move, which caused significant variability in the echo level which needed to be accounted for. The most significant movement was the pitch and roll of the towbody due to the up and down motion of the vessel in the waves. The pitch and roll angles were sampled at a high rate relative to the motion. In plotting echo amplitude versus pitch and roll angle (not shown) the highest amplitude echoes were tightly clustered around a value near pitch=roll=0°. These are assumed to be the echoes from very close to or at the center of the acoustic beam and are the ones analyzed in this paper. Although this was not an ideal approach toward determining the location of the target in the beam, it was satisfactory for the purpose of this study. Use of an acoustic imaging system, such as a multibeam, split beam, or lens system, outside of the band of interest and used simultaneously, could have directly provided the information. Or, had the broadband system itself been an imaging system, it could have directly provided that information as well.

The replica signal used in the pulse-compression processing was based on a separate experiment conducted in a laboratory tank in which the system was aimed upward at the smooth air-water interface. The echo from the interface was used as the replica signal in the at-sea calibration. Since the echo from the interface was so strong, and to prevent saturation, the transmission power in the laboratory measurement was significantly reduced resulting in significant distortion in the spectrum of the echo. The distortion is presumably due to nonlinearities in the transmission/reception isolation electronics which operate on the assumption of a strong transmission signal. Because of this nonlinearity, the laboratory echo is not a true replica. In spite of the fact that the signal was not a true replica, it still significantly improved the resolution of the calibration echoes through pulse-compression processing. This particular waveform was used because of its availability. As discussed earlier, and for practical reasons, other waveforms such as the signal applied to the transmitter could have been used as well, providing the desired improvement in resolution.

Another issue involves the fact that a gate of finite duration was used in the analysis. The gate needed to be small enough to adequately resolve the echo from the front interface, but not so small so as to compromise the spectral resolution of the measurement. A gate of 300 μs was used which resolved the echo from the front interface and provided a spectral resolution of 3.3 kHz. Effects of different gate durations on the calculated spectrum of the compressed pulse are shown in Fig. 2. Zero padding values of the signal before and after the window are shown to create a finer spectral grid, although the inherent resolution is not improved beyond the value of the inverse gate duration.

Once the echoes in the at-sea calibration were temporally compressed through pulse-compression processing, the various scattering features from the sphere were resolved (top panel of Fig. 3; envelope of processed signal). The envelope of the compressed-pulse signal shows a strong initial return which corresponds to the echo from the front interface. At approximately 0.6 ms after that first echo is another strong echo associated with a circumferential wave. The impulse response of the exact solution for the scattering amplitude gives qualitatively similar results in that there is a strong initial echo and a strong secondary echo at about 0.6 ms later (middle panel of Fig. 3). In addition, both the data and the impulse response show small echoes between the two much stronger echoes. Part of the calibration formulation involves convolving the applied transmit signal with the impulse response. This convolution process broadens the echoes in the impulse response (bottom panel of Fig. 3; the envelope of the convolved signal is illustrated). Also, calculation of the impulse response involves an inverse Fourier transform over a finite range of frequencies. Artifacts of truncating the spectrum were suppressed through use of an amplitude weighting function.

The spectrum of the compressed-pulse echo from the calibration sphere was calculated using the data in the top panel of Fig. 3 over two different time gates; a short, 300-μs-long gate including only the echo from the front interface (with that echo centered in the gate) and a longer gate

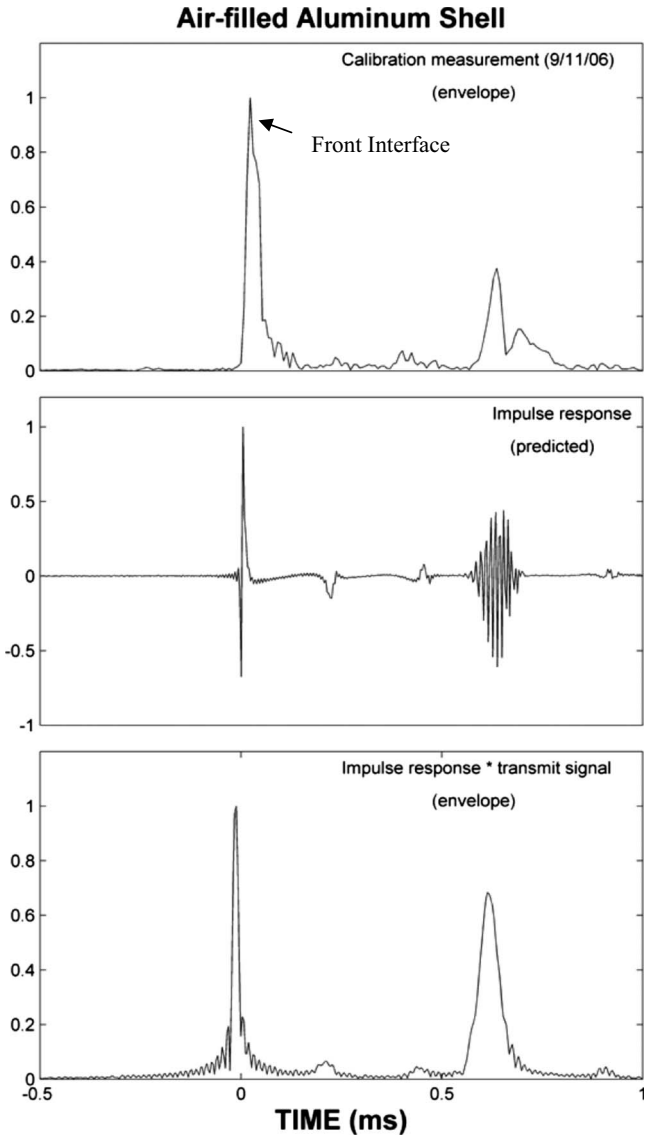

FIG. 3. Time-domain analysis of calibration signal. Top panel: Envelope of pulse-compressed echo from air-filled aluminum spherical shell in at-sea measurement. The echo was cross correlated with echo measured in a tank experiment with the system aimed up at the smooth air-water interface. Middle panel: Impulse response of predicted echo from spherical shell through calculating inverse Fourier transform of exact modal series solution. Bottom panel: Envelope of the convolution of the impulse response from middle panel and the applied transmitter signal. Each plot is normalized to unity. The data were collected on September 11, 2006 with the 41.5-cm-diam sphere suspended 30 m below the towbody.

(3 ms) that includes the entire series of partial wave echoes. Once gated, each signal was "zero padded" to form a 4-ms-long signal for Fourier analysis. The results illustrate the significant differences in spectra of the different components of the echo [Fig. 4(a)]. The spectrum of the echo from the front interface alone is smoothly varying over the entire band while the spectrum of the entire echo (i.e., front interface and circumferential waves), is rapidly oscillating over the band. This observation is consistent with the theoretical predictions discussed in Sec. I where the scattering amplitude of the echo from the front interface alone (i.e., partial wave) is weakly dependent upon frequency and the scattering amplitude from all echoes from the sphere (i.e., full wave) is

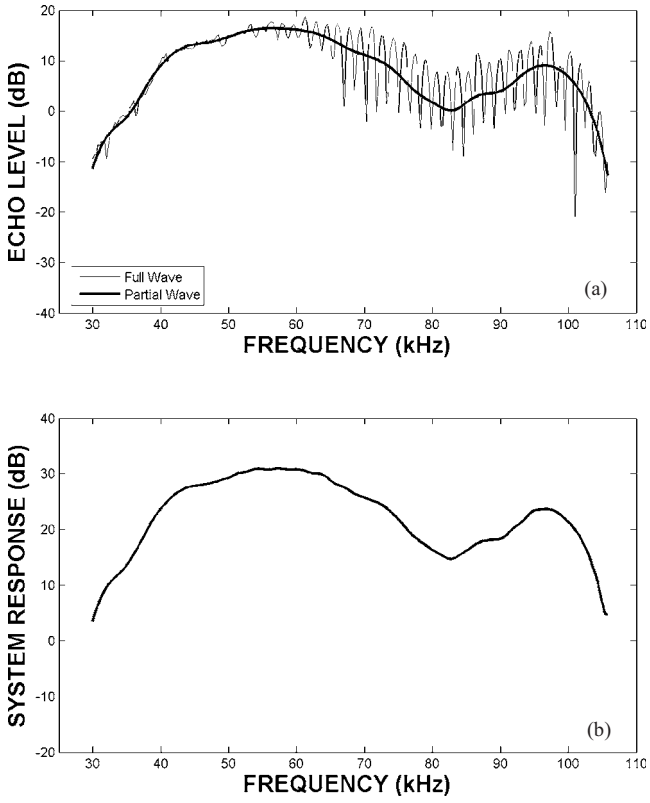

FIG. 4. Spectra of signals and system response associated with calibration measurement with air-filled spherical shell. Upper panel: Spectrum of (partial wave) echo from front interface (thick line) compared with spectrum of (full wave) echo from all partial waves (thin line). The spectra were calculated using the pulse-compressed signal illustrated in the top panel of Fig. 3. Lower panel: System response of broadband transducer as derived through partial-wave analysis using echo from front interface.

strongly dependent upon frequency due to the frequency-dependent interference between the various partial waves.

Using the equations described in Sec. III, the system response is determined through the partial-wave analysis [Fig. 4(b)]. Here, the measured echo from the front interface (top panel of Fig. 3) is used in combination with the corresponding echo in the predicted impulse response convolved with the signal applied to the transmitter (bottom panel of Fig. 3) to produce the system response. As with Fig. 4(a), the echo from the front interface was obtained through a 300-μs-long gate, zero padded to 4 ms long. This response is shown to be quite similar to the spectrum of the pulse-compressed echo of the front interface [Fig. 4(a)]. The similarity is due to the fact that the scattering amplitude of that partial wave depends weakly upon frequency, resulting in the majority of the frequency dependence of that echo being due to the system response.

The partial-wave-based response shown in Fig. 4(b) has also been compared with the response determined by a full-wave analysis from data involving a smaller (20 cm diameter) solid aluminum sphere where there are fewer resonances (not shown). Although the overall levels and trends of the two results were quite similar, there were significant differences at resonance frequencies where the full-wave solution is prone to error. An attempt was made to reduce the errors in the full-wave analysis by smoothing the calculated

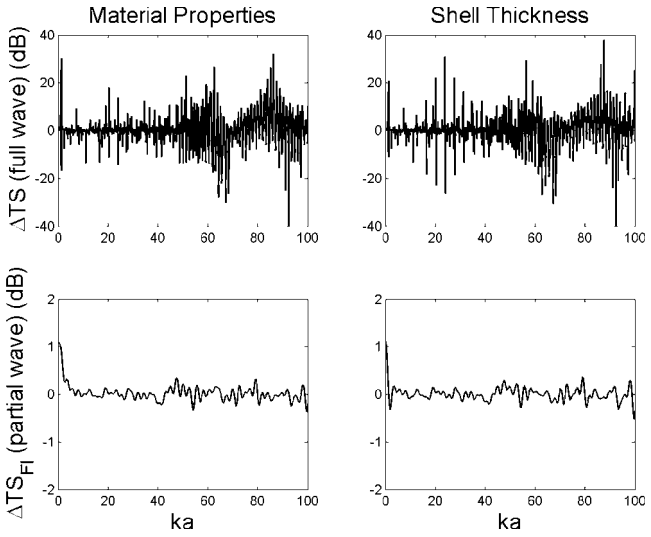

FIG. 5. Sensitivity analysis of full-wave (upper panels) and partial-wave (lower panels) echoes for aluminum spherical shell, whose shell thickness is about 1% of the diameter. Material properties (density, compressional sound speed, and shear sound speed) of spherical shell are varied by about 1% between two sets of predictions in the left panels. Shell thickness is varied by 7% between two sets of predictions in the right panels.

response. Even after the smoothing, there were errors in the full-wave analysis of up to 3 dB due to the uncertainties associated with the nulls.

V. DESIGNING A CALIBRATION SPHERE AND SIGNAL PROCESSING APPROACH

Choice of the sphere and signal processing approach depends strongly upon the center frequency and bandwidth of the acoustic signal. For a narrowband system, the previously published methods cited above can be used which involve choosing the diameter and material properties of the sphere so that the center frequency does not involve a resonance of the sphere. Specifically, the frequency of the acoustic system is in a section of the curve illustrating scattering amplitude versus frequency that is relatively insensitive to frequency and a full-wave analysis is performed. However, as discussed above, once the bandwidth of the system spans multiple resonances, then a partial wave analysis should be considered in order to eliminate the sensitivity of the calibration to the resonances. These design criteria are elaborated upon below.

A. Sensitivities of partial-wave and full-wave analysis with respect to uncertainties in material properties and shell thickness

A calibration involving a partial-wave analysis which makes use of the echo from the front interface of the sphere is relatively insensitive to changes in material properties and, in the case of spherical shells, the thickness of the shell (Fig. 5). This insensitivity is due to the fact that the echo from the interface does not contain any resonances, as shown in Eq. (1) and Fig. 1(a). However, if a full wave analysis were to be applied to a broadband system in which the spectrum of the signal spanned many resonances, the calibration would be extremely sensitive to changes in material properties and

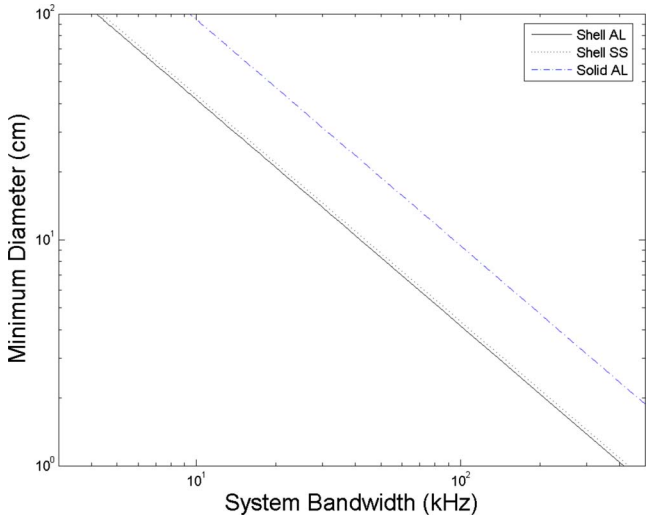

FIG. 6. (Color online) Design curves for minimum diameter of calibration sphere that can be used in partial-wave analysis. Combinations of solid elastic and air-filled elastic shell for aluminum ("AL") and stainless steel ("SS") are given. A separation between the echo from the front interface and the next major partial wave is assumed to be two times the inherent temporal resolution of the system (i.e., two times the inverse bandwidth). A larger than minimum diameter will allow for a longer processing gate and corresponding improved spectral resolution.

thickness of shell. Since the resonances are very narrow, then it only takes a slight change in those parameters to shift the resonance an amount comparable to its width. Since the resonance gives rise to variations in scattering amplitude of up to 10–20 dB, and since the calibration involves dividing by the predicted scattering amplitude, then a slight shift in resonance due to uncertainties in the properties can cause errors near those frequencies of up to 10–20 dB (Fig. 5). Thus, it is clear that in order to avoid such strong sensitivities, a partial-wave analysis should be considered.

B. Diameter of sphere

A partial-wave analysis can be used only when the echo from the front interface is resolved from the other echoes from the sphere. The resolution requirement is a function of diameter of the sphere, bandwidth of the system, frequencies involved, material properties, and whether or not the sphere is a solid or shell. The combination of material properties, type of sphere (solid or shell), diameter, and frequencies involved will determine the speed of the circumferential waves. Knowledge of the speed of those waves (especially the speed of the first arrival after the echo from the front interface), in combination with the bandwidth of the system, will dictate the smallest diameter of sphere to use. Given the complexity of this problem, the diameter should be determined through simulations of the scattering. At sufficiently high values of *ka* and for fixed material properties and type of sphere, the minimum diameter of sphere to be used in the calibration varies inversely with bandwidth (Fig. 6). In addition, our simulations show that the minimum diameter depends strongly upon whether or not the sphere is solid or an air-filled thin-walled spherical shell. In our particular case of spherical shells, the minimum diameter does not depend strongly upon material type (e.g., aluminum vs. stainless steel) (Fig. 6).

VI. SUMMARY AND CONCLUSIONS

An approach has been developed for calibrating broadband active acoustic systems with a single standard spherical target. The approach involves a partial-wave analysis which uses the echo from the front interface of a calibration sphere. This echo is relatively insensitive to acoustic frequency, in contrast to the full-wave signal that contains significant narrow resonances. Furthermore, the echo is relatively insensitive to uncertainties in material properties and sphere dimensions. Isolating this echo for analysis requires resolving it from the subsequent echoes, such as circumferential waves. Pulse-compression processing was incorporated into the approach, resulting in significantly improved temporal resolution. The calibration equations were written in terms of the pulse-compressed echoes. Also, design curves were presented for the recommended minimum diameter of the sphere as a function of system bandwidth and material properties of the sphere.

This partial-wave analysis is an attractive alternative to the traditional full-wave analysis for the calibration of broadband systems. As a result of the complete elimination of the source of resonances, this approach significantly reduces errors in the calibration associated with uncertainties or errors in values of material properties and sphere dimensions. Furthermore, through use of pulse-compression processing, the diameter of the sphere used in the calibration can be minimized.

ACKNOWLEDGMENTS

The authors are grateful to the following people from the Woods Hole Oceanographic Institution (WHOI), Woods Hole, MA, for their assistance on this project: Ken Houtler (captain of the R/V Tioga), Jeff Lord, Don Peters, and Shirley Barkley. This work was supported by the U.S. Office of Naval Research Grant Nos. N00014-04-1-0475 and N00014-04-1-0440 and the J. Seward Johnson Chair at WHOI.

Chu, D., and Stanton, T. K. (**1998**). "Application of pulse compression techniques to broadband acoustic scattering by live individual zooplankton," J. Acoust. Soc. Am. **104**, 39–55.

Dragonette, L. R., Numrich, S. K., and Frank, L. J. (**1981**). "Calibration technique for acoustic scattering measurements," J. Acoust. Soc. Am. **69**, 1186–1189.

Feuillade, C., Meredith, R. W., Chotiros, N. P., and Clay, C. S. (**2002**). "Time domain investigation of transceiver functions using a known reference target," J. Acoust. Soc. Am. **112**, 2702–2712.

Foote, K. G. (**1982**). "Optimizing copper spheres for precision calibration of hydroacoustic equipment," J. Acoust. Soc. Am. **71**, 742–747.

Foote, K. G. (**2006**). "Optimizing two targets for calibrating a broadband multibeam sonar," *Proc. Oceans 2006 MTS/IEEE*, (Boston).

Foote, K. G., Atkins, P. R., Bongiovanni, C. C., Francis, D. T. I., Eriksen, P. K., Larsen, M., and Mortensen, T. (**1999**). "Measuring the frequency response function of a seven-octave bandwidth echo sounder," *Proc. I.O.A.*, Vol. **21**(1), pp. 88–95.

Foote, K. G., Francis, D. T. I., and Atkins, P. R. (**2007**). "Calibration sphere for low-frequency parametric sonars," J. Acoust. Soc. Am. **121**, 1482–1490.

Hackman, R. H. (**1993**). "Acoustic scattering from elastic solids," in *Physical Acoustics*, edited by A. D. Pierce and R. N. Thurston (Academic, San Diego) Vol. **XXII**, Chap. 1, pp. 1–194.

Kaduchak, G., Kwiatkowski, C. S., and Martson, P. L. (**1995**). "Measurement and interpretation of the impulse response for backscattering by a thin spherical shell using a broad-bandwidth source that is nearly acoustically transparent," J. Acoust. Soc. Am. **97**, 2699–2708.

Marston, P. L. (**1992**). "Geometrical and catastrophe optics methods in scattering," in *Physical Acoustics*, edited by A. D. Pierce and R. N. Thurston (Academic, San Diego), Vol. **XXI**, Chap. 1, pp. 2–234.

Numrich, S. K., and Überall, H. (**1992**). "Scattering of sound pulses and the ringing of target resonances," in *Physical Acoustics*, edited by A. D. Pierce and R. N. Thurston (Academic, San Diego), Vol. **XXI**, Chap. 2, pp. 235–318.

Simmonds, J., and MacLennan, D. (**2005**). *Fisheries Acoustics: Theory and Practice*, 2nd ed. (Blackwell, Oxford, UK).

Stanton, T. K. (**1990**). "Sound scattering by spherical and elongated shelled bodies," J. Acoust. Soc. Am. **88**, 1619–1633.

Stanton, T. K., Chu, D., Jech, J. M., and Irish, J. D. (**2007**). "A broadband echosounder for resonance classification of swimbladder-bearing fish," *Proc. Oceans 2007 IEEE* (Aberdeen).

Sun, Z., Gimenez, G., Vray, D., and Denis, F. (**1991**). "Calculation of the impulse response of a rigid sphere using the physical optic method and modal method jointly," J. Acoust. Soc. Am. **89**, 10–18.

Turin, G. L. (**1960**). "An introduction to matched filters," IRE Trans. Inf. Theory **IT-6**, 311–329.

Modeling broadband ocean acoustic transmissions with time-varying sea surfaces

Martin Siderius and Michael B. Porter
HLS Research Inc., 3366 N. Torrey Pines Ct., Suite 310, La Jolla, California 92037

(Received 2 October 2007; revised 11 April 2008; accepted 15 April 2008)

Solutions to ocean acoustic scattering problems are often formulated in the frequency domain, which implies that the surface is "frozen" in time. This may be reasonable for short duration signals but breaks down if the surface changes appreciably over the transmission time. Frequency domain solutions are also impractical for source-receiver ranges and frequency bands typical for applications such as acoustic communications (e.g. hundreds to thousands of meters, 1–50 kHz band). In addition, a driving factor in the performance of certain acoustic systems is the Doppler spread, which is often introduced from sea-surface movement. The time-varying nature of the sea surface adds complexity and often leads to a statistical description for the variations in received signals. A purely statistical description likely limits the insight that modeling generally provides. In this paper, time-domain modeling approaches to the sea-surface scattering problem are described. As a benchmark for comparison, the Helmholtz integral equation is used for solutions to static, time-harmonic rough surface problems. The integral equation approach is not practical for time-evolving rough surfaces and two alternatives are formulated. The first approach is relatively simple using ray theory. This is followed with a ray-based formulation of the Helmholtz integral equation with a time-domain Kirchhoff approximation.
 [DOI: 10.1121/1.2920959]

PACS number(s): 43.30.Zk, 43.30.Cq, 43.30.Hw, 43.30.Re [SLB] Pages: 137–150

I. INTRODUCTION

For many sonar applications, scattering is treated as an effective loss mechanism and Doppler shifts are often ignored. This may be reasonable for certain types of sonar systems, particularly the low frequency ones. However, new underwater acoustic systems, including those for underwater acoustic communications, are sensitive to both scattering losses and Doppler. In particular, channel equalizers used with bandwidth-efficient, phase-coherent communications methods can be extremely sensitive to Doppler spread. Designing these equalizers to compensate for Doppler often presents a substantial challenge. Significant Doppler spread can be introduced simply from the sound interacting with the moving sea surface; however, the effects are much greater when the source and receiver are also in motion. Simulating signals using a physics-based model can greatly aid in the development of new algorithms and provide valuable performance predictions. Two simulation methods for signals that interact with a time-varying, rough sea surface will be described in this paper. First, a simple technique is proposed that includes Doppler effects due to source/receiver and sea-surface motion. This is an extension of an earlier work that was developed to simulate active sonar receptions on moving marine mammals.[1] The need for comparisons as well as determining the limitations of this approach led to the second technique, which uses an implementation of the time-domain Kirchhoff approximation.

This paper is organized as follows. In Sec. II, the Makai experiment is described, which is useful in motivating the problem by presenting measurements of Doppler-sensitive signals that have interacted with the moving sea surface. In Secs. III and IV, a ray-based approach is used to model moving sources/receivers as well as a slowly varying sea surface. To model interactions from finer scale sea-surface roughness, Sec. V describes the time-harmonic approach using the Helmholtz–Kirchhoff integral equation. This approach is exact for two dimensional problems with a line source. This section also provides an implementation of the Kirchhoff approximation, which is numerically much less demanding than the integral equation. The described methods are developed for line sources but the applications of interest are better modeled with point sources. Therefore, in Sec. VI, the conversion of line source solutions to point source solutions is described. Finally, in Sec. VII, the time-domain solution is developed for rough surfaces that move in time by using the time-domain Kirchhoff approximation.

II. THE MAKAI EXPERIMENT

The motivation for the modeling techniques developed here can be illustrated with data collected during the Makai experiment which took place from September 15 to October 1, 2005 near the coast of Kauai, HI.[2] The site has a coral sand bottom with a fairly flat bathymetry that was nominally 100 m. The water column was variable but typically had a mixed layer depth of 40–60 m and was downward refracting below. The data were measured on September 24th using both stationary and towed sources (from R/V Kilo Moana). The sources were programmable, underwater acoustic modems developed at SPAWAR Systems Center (referred to as the Telesonar Testbeds, T1 and T2).[3] Signals were received on the AOB array, which is an autonomous system developed at the University of Algarve, Portugal. The AOB is a drifting

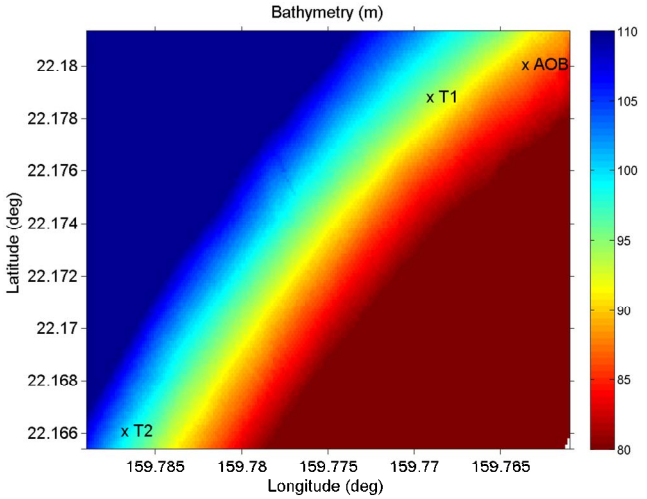

FIG. 1. (Color online) Bathymetry near Kauai with the positions of the AOB vertical array and the Telesonar Testbeds T1 and T2 at 01:00 on JD 268. T1 was about 600 m away from AOB and being towed while T2 is about 2.8 km away and is stationary.

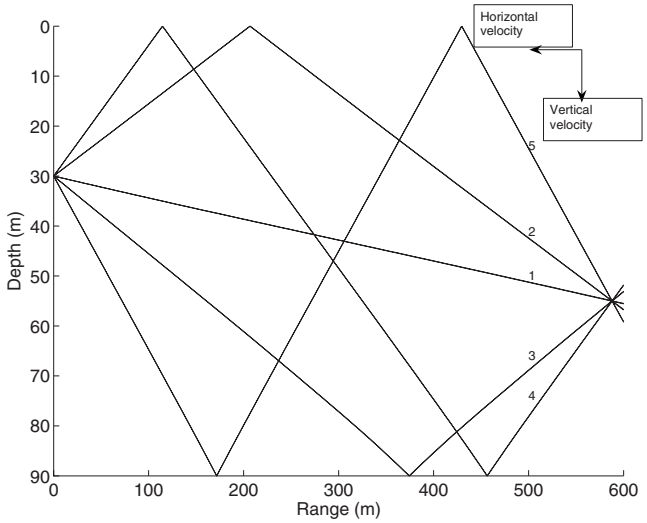

FIG. 2. Ray trace between testbed T1 and the AOB array. The various paths are labeled (1) direct, (2) surface bounce, (3) bottom bounce, (4) surface-bottom bounce, and (5) bottom-surface bounce.

eight-element self-recording array that resembles the size and weight of a standard sonobuoy.[4] The experiment geometry and bathymetry are shown in Fig. 1. Figure 2 shows a ray trace of the T1-AOB acoustic paths. The paths are numbered on the figure and correspond to (1) direct bounce, (2) surface bounce, (3) bottom bounce, (4) surface-bottom bounce, and (5) bottom-surface bounce. The different path directions have sensitivity to different velocity components. The higher numbered paths are more Doppler sensitive to the vertical velocity components (e.g., from the moving sea surface) and the lower numbered paths (e.g., direct path) are more sensitive to the horizontal velocity components (e.g., from the source or receiver motion).

A binary-phase-shift-keying (BPSK) transmission was used to analyze the channel.[5] This waveform is commonly used for communication transmissions but for this analysis, it is simply a highly Doppler-sensitive signal that can separate the multipath in time and Doppler spaces. The transmission used cycles of a 9.5 kHz sinusoid with phase shifts introduced to represent a string of 1's and 0's defined by an m sequence.[5] This signal uses an m sequence (size 1024) with 1500 chips/s. The total length of the sequence was 0.682 s. In a static situation, using a matched filter on this waveform produces an estimate of the channel impulse response. However, in situations with source/receiver and/or sea-surface motion, each path can have a different Doppler shift (due to the angle-dependent propagation paths). A single Doppler shift can be applied to the BPSK signal before the matched-filter process. By sweeping over a variety of shifts, the Doppler for each received arrival can be estimated. The resulting picture provides an estimate of the so-called channel scattering function.[5] This is referred to as an estimate since a true scattering function requires knowing the continuous time evolution of the impulse response. This is a difficult measurement to make since, in practice, the estimate of the impulse response requires time. The described method to estimate the scattering function does, however, provide the essential information about the relative arrival times of the multipath and how each is Doppler shifted.

Examples of the processed scattering functions at two ranges from the Makai experiment are shown in Fig. 3. Each horizontal trace in the figure results from a matched-filter process using different Doppler-shifted replicas denoted $\tilde{s}_j(t)$. The index j corresponds to applied Doppler shifts according to the shift factor $1-v_j/c$, where v_j is the assumed speed and c is the reference sound speed. The Doppler replicas, $\tilde{s}_j(t)$, are matched filtered against the received time series.[6] That is,

$$r_j(t) = \int_{+\infty}^{\infty} p(\tau)\tilde{s}_j(\tau - t)d\tau, \tag{1}$$

where $p(\tau)$ is the received time series and $r_j(\tau)$ is the matched-filter output. In this way, $r_j(t)$ is indexed over time and Doppler and each multipath arrival produces a peak

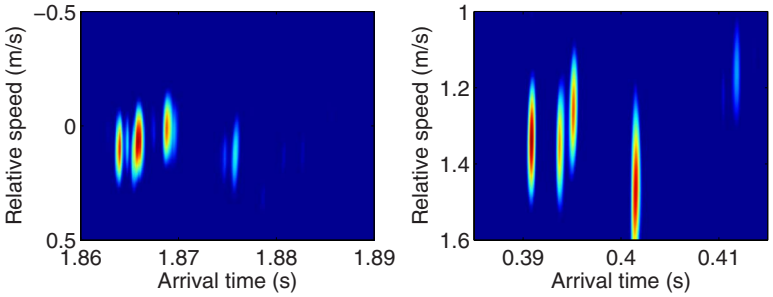

FIG. 3. (Color online) Left panel shows the measured impulse response (or scattering function) for various Doppler shifts indicated on the y axis (as relative speed in m/s) between the drifting AOB and the stationary T2 at 01:04 on JD 268. Each bright spot corresponds to an arrival with delay time shown along the x axis. Right panel is for a reception from the towed source T1 at 01:02 on JD 268.

when the Doppler shift of the replica is matched with that arrival.

In the left panel of Fig. 3, the measured scattering function is shown for a 2.8 km range separation between the fixed Testbed T2 and the drifting AOB. The second measured scattering function is shown in the right panel and is from the towed Testbed T1 and received on the AOB about 600 m away. The bright spots indicate an arrival in time (i.e., delay time) along the x axis. Note that only the relative time is known so the time series are aligned based on the first arrival and the known distance between the source and receiver. The y axis shows the relative speed (i.e., Doppler) that corresponds to the peaks. The left panel had the stationary source and the Doppler indicates that the AOB was drifting at about 0.1–0.2 m/s. The estimate from GPS positions indicated about 0.12 m/s. The first arrivals show decreasing Doppler followed by the last visible arrival having an increased Doppler shift. For horizontal velocity one expects the later arrivals to have decreasing Doppler shifts due to higher propagation angles relative to the direction of motion. The high Doppler on the last arrival implies a component in the vertical which would introduce larger shifts for late arrivals. The right panel of Fig. 3 shows the reception from T1 which was being towed with relative speed between T1 and the AOB of about 1.2–1.4 m/s. The estimate from GPS positions is 1.24 m/s. Like the stationary case, Doppler shifts do not decrease monotonically on the steeper paths but, in some cases, increase. The paths can be identified using the ray trace in Fig. 1. The second and fourth arrivals both have *increased* Doppler shifts relative to the direct path while the third arrival has a slightly *decreased* Doppler. Paths 2 and 4 correspond to the surface and surface-bottom bounce paths while the third arrival is the bottom bounce. Note that in both figures, only the first few paths are visible; the later arrivals are more attenuated due to surface/bottom interactions.

In the context of acoustic communications, the spread factor is often used to determine the type of channel and therefore the signaling waveforms. The spread factor is defined as $T_m B_d$ where T_m is the multipath time duration (s) and B_d is the Doppler spread (Hz). If the spread factor is less than 1, the channel is said to be underspread, and if it is greater than 1 it is overspread. It can be highly useful to model the effects that influence the channel spread as this can lead to acoustic communication improvements as well as performance prediction. While the spread factor is a simple metric, it does not give a complete description. For example, does the multipath consist of many arrivals or just a few? The information given in Fig. 3 show not only the multipath delay and Doppler spread but also show the total number and strength of the arrivals. In this example, the spread factor is relatively large but the total number of arrivals is small (i.e., sparse channel). All of these factors are important for communications and correct modeling of these is the primary goal of this work. Modeling techniques that can be applied in estimating the multipath delay and Doppler spread are the topic of the next sections.

III. MODELING SOURCE AND RECEIVER MOTION WITH RAYS

In this section, a relatively simple implementation of two dimensional ray methods is extended to treat moving receivers and a moving sea surface. The goals are somewhat similar to the work of Keiffer *et al.*[7] but the approach is different, and the emphasis is on broadband signals for application to underwater communications, for example. In a ray formulation, the complex pressure field, $P(\omega)$, can be represented as a sum of N arrival amplitudes $A_n(\omega)$ and delays $\tau_n(\omega)$ according to

$$P(\omega) = S(\omega)\sum_{n=1}^{N} A_n e^{i\omega\tau_n}, \tag{2}$$

where $S(\omega)$ is the spectrum of the source. The specifics of the ray trace algorithm are not critical and there are a number of ray trace models that could have been used here. A summary of most of these type of models can be found from Etter[8] and Jensen *et al.*[9] In the cases considered here, an azimuthally symmetric geometry is assumed and the arrival amplitudes and delays are computed using the two dimensional Gaussian beam implementation in the Bellhop package.[10,11]

According to the convolution theorem, a product of two spectra is a convolution in the time domain. This leads to the corresponding time-domain representation for the received waveform, $p(t)$, which is often written as

$$p(t) = \sum_{n=1}^{N} A_n(t) s[t - \tau_n(t)], \tag{3}$$

where $s(t)$ is the source waveform. This expression shows how the sound is represented as a sum of echoes of the transmission with associated amplitudes and delays. A time dependency has been introduced in the amplitudes and delays to allow the channel to be time varying. The time variations can be caused by many factors including source/receiver motion or sea-surface changes.

The situation is a bit more complicated because the amplitudes in Eq. (3) are actually complex numbers. This is due, for example, to bottom reflections that introduce a phase shift (e.g., a $\pi/2$ phase shift). Since this is a constant phase shift over frequency, it does not simply introduce an additional time delay. Therefore, a more careful application of the convolution theorem is required:

$$p(t) = \sum_{n=1}^{N} \mathrm{Re}[A_n(t)] s[t - \tau_n(t)] - \mathrm{Im}[A_n(t)] s^{+}[t - \tau_n(t)], \tag{4}$$

where $s^{+} = \mathcal{H}(s)$ is the Hilbert transform of $s(t)$. The Hilbert transform is a 90° phase shift of $s(t)$ and accounts for the imaginary part of A_n. An interpretation of Eq. (4) is that any arbitrary phase change is treated as a weighted sum of the original waveform and its 90° phase-shifted version. The weighting controls the effective phase shift.

One of the goals of this work is to simulate the received field in cases where the receiver and/or sea surface is in

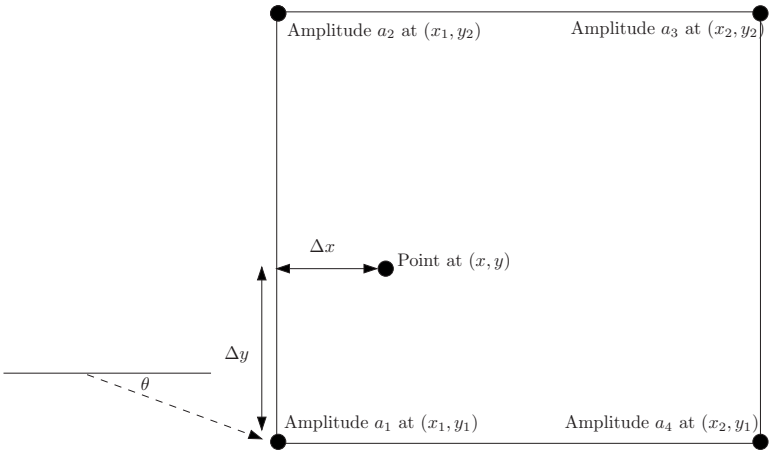

FIG. 4. Four points of the computational grid for a ray trace. The actual arrivals are computed at the four corners and any point in the interior computed through interpolation of the amplitudes and extrapolation of the delays. A sample arrival is shown traveling at angle θ.

motion. In those cases, the arrival amplitudes and delays in Eq. (3) change continuously in time. Therefore, new values for A_n and τ_n are required at each time step of the signal transmission. In theory, at each time step, a new set of arrival amplitudes and delays could be computed with an entirely new ray trace from the source to the exact receiver location at that particular time step. However, this would be computationally expensive and mostly unnecessary since the changes (in amplitude and delay) are likely to be very small between time steps. Alternatively, the ray amplitudes and delays are computed on a relatively sparse grid of points in range and depth. The ray information at any given location and time is computed through interpolation. The interpolation scheme is critical to avoid glitches in the final time series that might be caused by jumping too suddenly between points in the computational grid.

The interpolation of ray amplitudes and delays may appear simple enough but there are some subtleties which can cause difficulties. Consider four neighboring grid points as shown in Fig. 4 where at some particular time step, the receiver is located somewhere inside those points. The most straightforward way one might think to calculate the field at this interior point is to identify the same arrival on each of the four corners and then interpolate that arrival amplitude and delay from the four grid points to the receiver location. A problem with that approach occurs when arrival patterns on one grid point do not correspond to those at another. That is, reflections and refraction effects can cause a different number of rays and different ray types on each of the grid points. For example, consider a direct arrival on one corner of the grid that is refracted away from another grid point. In this case, interpolating between these grid points for that arrival number may involve interpolation of a direct path with a bottom bounce path and this will produce incorrect results.

One could keep careful track of all rays and ray types to ensure proper interpolation but that can lead to excessive bookkeeping and storage. Instead, a different interpolation approach is used here. The amplitudes at the four grid points are maintained as separate quantities and their corresponding delays are adjusted by the ray path travel time differences between the corners of the computational grid and the point of the receiver (x,y). The geometry is shown in Fig. 4 with an arrival indicated as a dashed line traveling at angle θ at the lower left grid point. The delay time for that arrival is adjusted from position (x_1,y_1) to position (x,y) by the distance divided by sound speed,

$$\Delta_{\text{delay}} = (\Delta x \cos\theta + \Delta y \sin\theta)/c, \tag{5}$$

where, for example, $\Delta x = x - x_1$ is positive (increased delay) for position 1.

The contribution of the arrivals from each of the grid points is weighted according to

$$\begin{aligned} &(1-w_1)\times(1-w_2)\times a_1,\\ &(1-w_1)\times w_2 \times a_2,\\ &w_1 \times w_2 \times a_3,\\ &w_1 \times (1-w_2)\times a_4, \end{aligned} \tag{6}$$

where a_1, a_2, a_3, and a_4 represent the arrival amplitudes at each corner and the weights are

$$\begin{aligned} w_1 &= (x-x_1)/(x_2-x_1),\\ w_2 &= (y-y_1)/(y_2-y_1). \end{aligned} \tag{7}$$

Thus, w_1 represents a proportional distance in the x direction and w_2 represents a proportional distance in the y direction. To summarize, the received field is constructed using Eq. (4) with an additional sum over each of the four corners (weighted amplitudes).

A. Test cases for source/receiver motion

The previous section presented the method and here, a few examples are given to illustrate the model at low and high frequencies. The first example will illustrate the quality of the ray interpolation. A tone is transmitted at 350 Hz from a source at a depth of 30 m [i.e., continuous wave or (cw)]. The environment has a linearly decreasing sound speed that is 1500 m/s at the surface and 1490 m/s at the seabed at 100 m depth. The seabed has a compressional sound speed of 1600 m/s, density of 1.5 g/cm^3, and attenuation of 0.1 dB/λ (decibels per wavelength). In Fig. 5 is a static frequency domain solution for the transmission loss (TL) out to

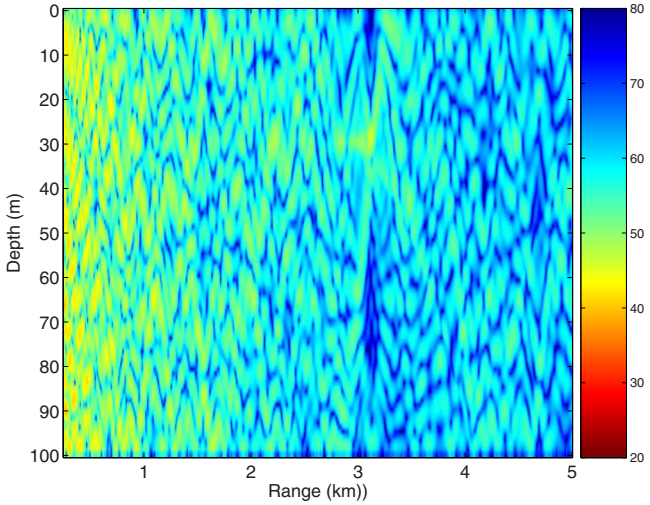

FIG. 5. (Color online) Frequency domain (350 Hz) TL calculation (dB) over range and depth with the source at a depth of 30 m.

5 km in range (i.e., a standard TL calculation).[9] Next, the time-series simulator records the pressure field on a receiver that sweeps out the same 5 km range in time. By using 100 of these receivers placed at 1 m increments in depth, the entire range-depth volume is swept out over 100 s (each receiver moves from 0 to 5 km over 100 s). The amplitude of these time-series data are plotted on a decibel scale in Fig. 6. For this simulation, a single ray trace computed the arrival amplitudes and delays at each point in a grid of 1 m in depth and 100 m in range. Each moving receiver was placed at depths in between these grid points to ensure all computed values were from interpolation rather than exactly falling on grid points. Even for the relatively large grid spacing, the technique produces a good result when compared to the cw TL in Fig. 5.

The second example is for a higher frequency transmission at 10 kHz and illustrates the interpolation as well as the Doppler effects. The environment is the same as for the first

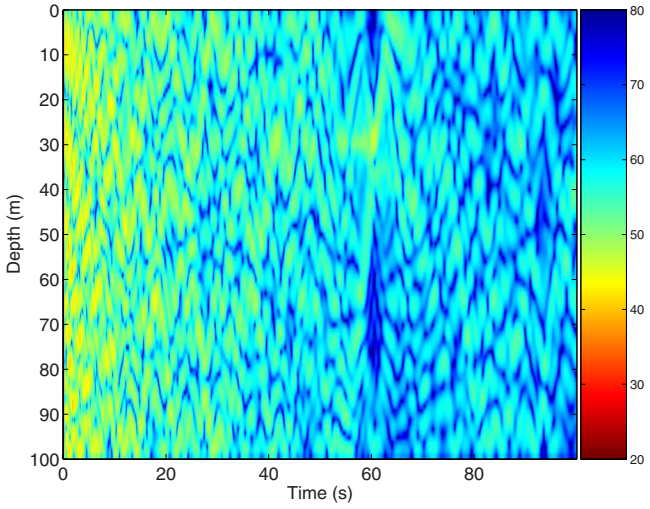

FIG. 6. (Color online) Same as Fig. 5 except calculated using the time-domain approach. That is, a set of moving receivers sweep out (in time) the acoustic TL. Note the different x axes between this figure and Fig. 5. At this low frequency, the Doppler shift is not significant enough to noticeably change the TL.

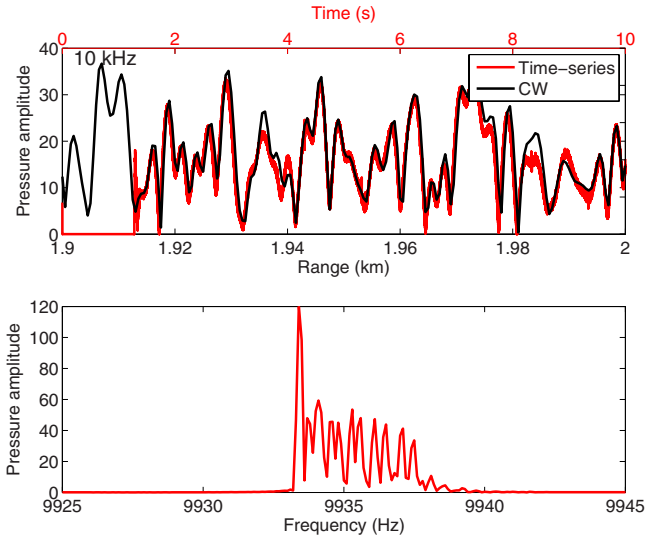

FIG. 7. (Color online) Top panel shows the cw solution vs range and the time-series solution vs time as the receiver moves out in range. The corresponding range and time x axes are indicated. The lower panel shows the spectrum of the time-series solution with the Doppler shifts which differ for the various paths.

example, but a slightly denser grid is used for the ray calculation due to the higher frequency (0.5 m depth spacing and 50 m range spacing). This is still around three wavelengths in depth and several hundred wavelengths in range between grid points. A single line of pressure amplitude is shown in the upper panel of Fig. 7 at a receiver depth of 50.25 m (between grid points) and is compared to the cw calculation. The moving receiver speed is 10 m/s and this introduces a Doppler shift of around 67 Hz (moving away from the source horizontally). From the agreement in the pressure amplitudes (between static and moving), one might incorrectly assume that the Doppler effects are of little importance. However, various acoustic systems may be significantly impacted by Doppler. For example, the spectrum of the received time series is shown in the lower panel of Fig. 7. The spectrum shows the direct path shifted by the expected 67 Hz as well as a set of less Doppler-shifted peaks due to the multipath that travels more vertically than the direct path. This type of Doppler spread is one of the primary mechanism that cause channel equalizers to fail in coherent communication schemes (i.e., coherent acoustic modems).

IV. MODELING TIME-VARYING SEA SURFACES

The previous section only considered the motion of the receiver. This could also approximate the solution for the case when both source and receiver are moving horizontally (possibly at different speeds) in a range independent environment. A time-varying sea surface can be added to the model (with receiver motion only) with slight modifications. In this case, the sea surface is assumed to vary slowly in range as might be the case for swell, ignoring small scale roughness. This limitation will be explored further in the next sections when the rough, time-varying surfaces are considered. To modify the previously described algorithm, additional ray traces are computed to sample the time-evolving sea surface. Figure 8 diagrams the required interpolation scheme to in-

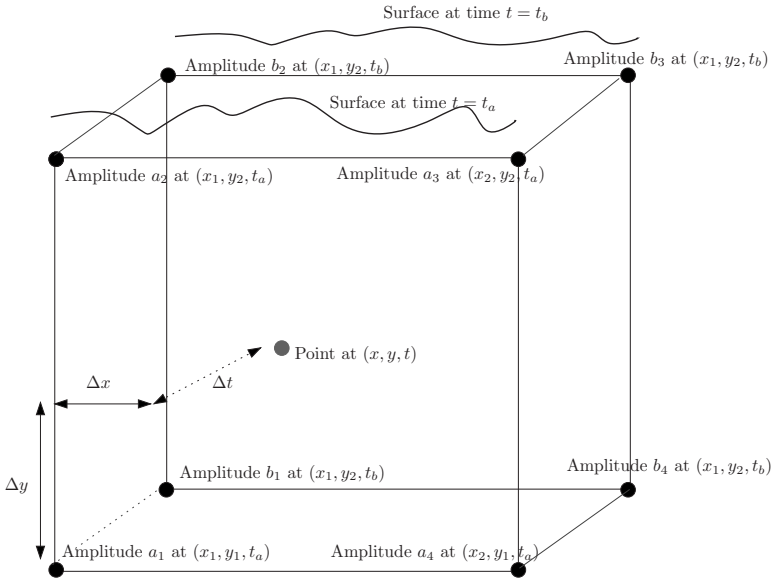

FIG. 8. Same as Fig. 4 except with the added dimension to allow for time changing surface.

clude surface motion. At an initial time, $t=t_a$, the surface can have an arbitrary shape and this evolves in time to produce a surface shape defined at time $t=t_b$. The time interval to sample the surface adequately is on the order of the time interval of the swell being modeled. This is typically much less than the sampling interval for the acoustic transmission. Therefore, ray arrival amplitudes and delays are computed for surfaces at $t=t_a$ and $t=t_b$ and trilinear interpolation is used in much the same way as described previously with bilinear interpolation. One difference is that the delays are not extrapolated for this third dimension. The proper arrival amplitudes and delays are simply determined through the weights applied to the eight corners of the computation grid. As with the previous two dimensions, the arrivals are kept as separate quantities on each of the eight corners of the cube depicted in Fig. 8. The delays at each corner of the cube are advanced or retarded according to distance and the weight given to each corner is determined by

$$
\begin{aligned}
&(1-w_1)\times(1-w_2)\times(1-w_3)\times a_1,\\
&(1-w_1)\times w_2\times(1-w_3)\times a_2,\\
&w_1\times w_2\times(1-w_3)\times a_3,\\
&w_1\times(1-w_2)\times(1-w_3)\times a_4,\\
&(1-w_1)\times(1-w_2)\times w_3\times b_1,\\
&(1-w_1)\times w_2\times w_3\times b_2,\\
&w_1\times w_2\times w_3\times b_3,\\
&w_1\times(1-w_2)\times w_3\times b_4,
\end{aligned}
\tag{8}
$$

where a_1, a_2, a_3, and a_4 represent the arrival amplitudes at each corner at $t=t_a$ and b_1, b_2, b_3, and b_4 represent the arrival amplitudes at each corner at $t=t_b$. The weights are

$$
\begin{aligned}
w_1 &= (x-x_1)/(x_2-x_1),\\
w_2 &= (y-y_1)/(y_2-y_1),\\
w_3 &= (t-t_a)/(t_b-t_a).
\end{aligned}
\tag{9}
$$

The time steps, t_a and t_b, where the ray traces are computed, are typically at time intervals much greater than the acoustic sampling time interval. Therefore, many of the time steps rely on interpolated arrival information.

A. Test cases for source/receiver motion with a time-varying sea surface

To check the developed algorithm, a comparison can be made between results using the approach outlined in the previous sections with an exact solution. The exact solution requires the water column to be isospeed and the sea surface to be flat but can vary in height over time (i.e., a flat surface that can move up and down). This is a reasonable comparison since the approach outlined using a ray tracing algorithm is the same whether the sound speed is depth dependent (or not) and regardless of the shape of the surface.

The exact solution is developed based on the method of images[9] and the geometry is given in Fig. 9. The pressure field is constructed using Eq. (4) with a set of amplitudes A_{mn} and corresponding delays τ_{mn} with $n=1,2,3,4$ and $m=0\rightarrow\infty$. The amplitudes and delays are as follows:

$$
\begin{aligned}
A_{mn} &= \frac{1}{R_{mn}},\\
R_{mn} &= \sqrt{r^2+z_{mn}^2},\\
\tau_{mn} &= \frac{R_{mn}}{c},\\
z_{m1} &= 2Dmz_s + z_r,\\
z_{m2} &= 2D(m+1) - z_s - z_r,\\
z_{m3} &= 2Dm + z_s + z_r,
\end{aligned}
\tag{10}
$$

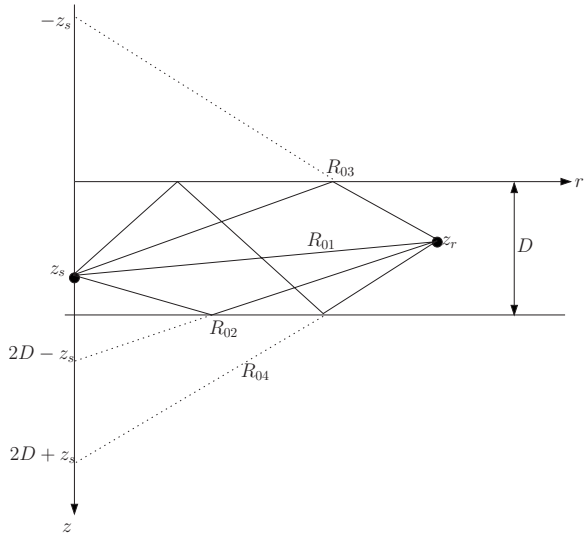

FIG. 9. Geometry showing the location and ranges of the source, receiver, and corresponding images.

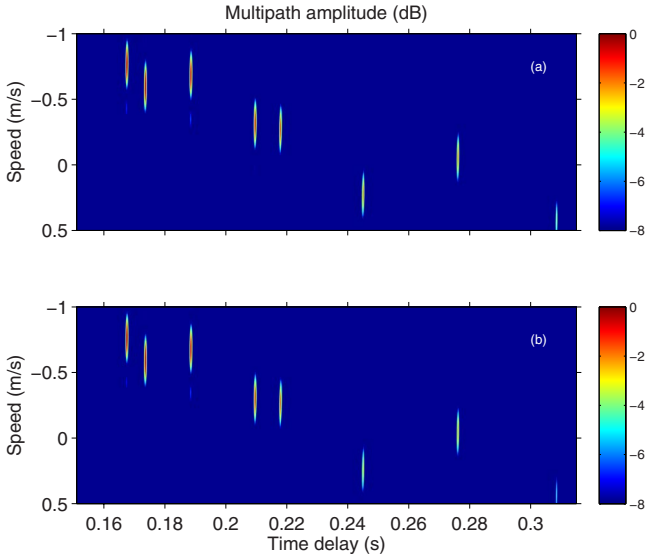

FIG. 10. (Color online) In panel (a), the exact impulse response (normalized) is computed using the method of images and in (b), it is computed using the time-dependent ray interpolation method described. The first arrival in time is from the direct path and shows only a Doppler shift due to the receiver horizontal motion of −0.75 m/s. The next two paths that follow are from the surface and bottom bounces. The additional multipaths are due to multiple interactions with the sea surface and the bottom.

$$z_{m4} = 2D(m+1) + z_s - z_r,$$

where z_s is the source depth, z_r is the receiver depth, r is the receiver range, D is the water depth, and c is the water sound speed (isospeed at 1500 m/s). The one twist in this standard formulation is that the surface is moving in time, which causes the amplitudes and delays to vary in time. The variations in the surface are incorporated into the terms of Eq. (10) through adding a time dependence to D, z_s, and z_r since the effective water depth and the source and receiver depths change with time. By making use of Eq. (4) with these time-dependent amplitudes and delays, the exact received time series can be determined.

To illustrate the comparison, consider an example with D=100 m, z_s=30 m, z_r=40 m, and r=250 m. The receiver is moving toward the source at 0.75 m/s. The sea surface is moving away from the seabed at a speed of 0.25 m/s. In this way, the Doppler shifts for surface interacting paths will be reduced from 0.75 m/s. The waveform chosen for this example is extremely Doppler sensitive such that the multipath (each having distinct Doppler shifts) can be separated in both delay time and Doppler space. The transmission waveform used is the BPSK signal that was used in the Makai experiment. The separation between grid points (as in the cube shown in Fig. 8) are as follows: the depth spacing was 1 m, the range spacing was 5 m, and the distance between surfaces was 0.0125 m; this implies a new surface every 12.5 ms (i.e., 40 ray traces were computed for surface perturbations between 0 and 0.5 m).

The results are shown in Fig. 10. In panel (a) of the figure is the exact impulse response shown in delay and Doppler space (i.e., the "scattering function"). In panel (b) of Fig. 10 is the arrival structure using the time-dependent ray interpolation algorithm previously described. In (a) and (b), the first path is the direct one and has a Doppler shift corresponding to −0.75 m/s due to the horizontal receiver motion (directly toward the source). The next path is due to the surface bounce and is less Doppler shifted due to the sea-surface motion acting to Doppler shift in the opposite direction. The next path is the bottom bounce and this path is unaffected by the surface motion and is Doppler shifted less than the direct path due to the more vertical directionality of the ray path. The next arrivals are due to multiple bottom-surface bounces.

V. MODELING STATIC, ROUGH SEA SURFACES

The previous section developed a method for modeling time series with gently varying sea surfaces like that from swell and the next sections provide an alternative formulation which is more appropriate for finer scale roughness. Rough surface scattering has been extensively studied and there is a huge amount of literature on the subject (see, for example, the text by Ogilvy).[12] To begin, exact solutions for one-dimensional static rough surfaces are described by using the Helmholtz integral equation. This will be compared to solutions found with a ray trace solution (e.g., Bellhop) with surface roughness. This will be further developed with the use of the Kirchhoff approximation to yield a time-domain version for scattering from rough, time-evolving surfaces.

A. Helmholtz integral equation

The description in this section will follow the notation and derivation from Thorsos.[13] Those results are presented for completeness and to establish the notation being used. The exact solution to the time-harmonic ($e^{-i\omega t}$) one-dimensional sea surface (free surface boundary) is given by the Helmholtz integral equation,

$$p(\vec{r}) = p_{\text{inc}}(\vec{r}) - \frac{1}{4i}\int_S H_0^{(1)}(k|\vec{r} - \vec{r}'|)\frac{\partial p(\vec{r}')}{\partial n'}ds'. \tag{11}$$

That is, the total field is a sum of the incident and scattered fields, $p(\vec{r}) = p_{\text{inc}}(\vec{r}) + p_{\text{scat}}(\vec{r})$. In Eq. (11), the acoustic wave

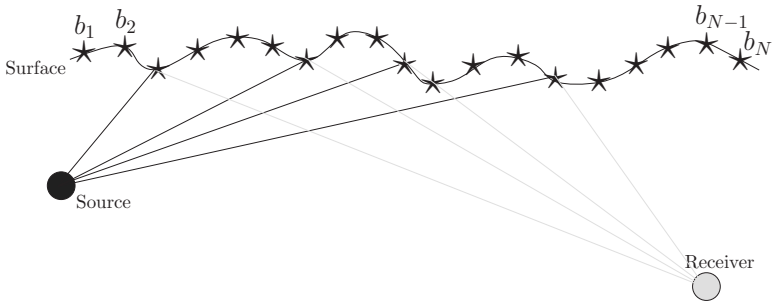

FIG. 11. Diagram illustrating the surface is replaced by a set of Huygens sources.

number is given by $k=\omega/c$, the quantity $\partial p(\bar{r}')/\partial n'$ is the normal derivative of the pressure field on the surface, and $H_0^{(1)}$ is the zero-order Hankel function of the first kind. On the surface the pressure field is zero, such that

$$p_{\text{inc}}(\bar{r}) = \frac{1}{4i}\int_S H_0^{(1)}(k|\bar{r}-\bar{r}'|)\frac{\partial p(\bar{r}')}{\partial n'}ds'. \tag{12}$$

The quantity of interest is the total pressure field $p(\bar{r})$ which requires first solving Eq. (12) for $\partial p(\bar{r}')/\partial n'$.

Equation (12) can be approximately solved by using numerical integration,

$$a_m = \sum_{n=1}^{N} A_{mn}b_n, \quad m=1,\ldots,N, \tag{13}$$

where a_m is the incident field, and A_{mn} are the Hankel functions,

$$a_m = p_{\text{inc}}(\bar{r}_m),$$
$$A_{mn} = \begin{cases} H_0^{(1)}(k|\bar{r}_m-\bar{r}_n|) & \text{if } m\neq n \\ H_0^{(1)}[(k\Delta x/2e)\gamma_m] & \text{if } m=n, \end{cases} \tag{14}$$

and

$$b_n = \left.\frac{\Delta x}{4i}\gamma_n\frac{\partial p(\bar{r}')}{\partial n'}\right|^{\bar{r}_n}. \tag{15}$$

The surface height function is defined as $f(x)$ with $\gamma^2(x') = 1+[df(x')/dx']^2$ and $ds'=\gamma(x')dx'$. Using unit vectors $\hat{x}$ and $\hat{z}$, the vector $\bar{r}$ is defined as $\bar{r}_m=x_m\hat{x}+f(x_m)\hat{z}$ and $x_m = (m-1)\Delta x - L/2$, with $\gamma_m=\gamma(x_m)$ and L being the total length of the surface.

By using matrix notation, Eq. (13) can be written as

$$\mathbf{a} = \mathbf{A}\mathbf{b}, \tag{16}$$

with solution for $\mathbf{b}$ determined through inversion of $\mathbf{A}$,

$$\mathbf{b} = \mathbf{A}^{-1}\mathbf{a}. \tag{17}$$

Once this equation is solved for $\mathbf{b}$, the scattered field is obtained by using

$$p_{\text{scat}}(\bar{r}) = \sum_{n=1}^{N} H_0^{(1)}(k|\bar{r}_m-\bar{r}_n|)b_n. \tag{18}$$

The practical limitations of numerically solving these equations is the inversion of matrix $\mathbf{A}$. In practice, the sampling of the surface requires approximately five points per wavelength. To keep from introducing artifacts, the computational domain has to be even larger than the region of interest (here, it was extended by 250 m). If the objective is to solve a problem with a 1 km surface at 10 kHz (for example, for an acoustic communication simulation), the number of discrete points is over 30 000, which requires inversion of a $30\,000\times 30\,000$ matrix for each frequency. This increases to $300\,000\times 300\,000$ for a 10 km simulation. Add to this the requirement that this be done over a broad band of frequencies for many practical problems, and it becomes even more difficult. To make matters worse, if the objective is to determine the time-evolving nature of the scattering, this must be done at many time steps. The size of the problem by using exact solutions becomes apparent and leads to the approximations used in the next sections. The exact approach outlined here is valuable, however, to provide ground-truth comparison with the approximate methods.

B. Ray approach with the Kirchhoff approximation

The Kirchhoff approximation is as follows:

$$\frac{\partial p(\bar{r})}{\partial n} \cong 2\frac{\partial p_{\text{inc}}(\bar{r})}{\partial n}. \tag{19}$$

The value of this approximation is that the elements of b_n required for the scattered field are no longer dependent on the total field but only on the incident field. This removes the need to store and invert the matrix $\mathbf{A}$. Another way to think about the solution for the scattered field is that the surface is removed and replaced by point sources at each discrete location x_n. The weight of each point source is determined by the coefficients b_n. This is basically a statement of the Huygens principle[14] and is depicted in Fig. 11. For the exact solution, each point source amplitude b_n depends on each of the others, while for the Kirchhoff approximation, it is only a local reflection. However, the Huygens sources can reradiate in all directions and the dense sampling allows for a more complicated scattered field than that from a specularly reflected ray trace.

The incident field can be written in terms of a ray amplitude and delay (far field approximation for the Hankel Function) from the source to each of the Huygens secondary sources,

$$p_{\text{inc}}(\bar{r}_n) \cong \frac{1}{\sqrt{kR_{1n}}}e^{i\omega\tau_{1n}}, \tag{20}$$

where R_{1n} and τ_{1n} are computed similarly to Eq. (10) for the 01 path for the surface bounce (suppressing the first index which is unnecessary here since there are no higher order images). Since the Huygens reconstruction removes the sur-

face boundary and replaces it with secondary sources, the only other path to arrive in the incident field is from the bottom bounce path 02. The total incident field at each Huygens secondary source has two terms,

$$p_{\text{inc}}(\bar{r}_n) = \frac{e^{i\omega\tau_{1n}}}{\sqrt{kR_{1n}}} + \frac{V_n e^{i\omega\tau_{2n}}}{\sqrt{kR_{2n}}}, \tag{21}$$

where the second term has been modified to include the bottom loss V_n that occurs for a nonpressure release bottom. This term will generally be a function of the angle incident on the bottom and is therefore indexed to each point on the surface. Further, this assumes a plane wave reflection loss which is a slight approximation. The expression for the incident field has been written out for this isospeed case for clarity; however, these two terms can be easily taken from a ray trace algorithm that would include refraction for more realistic cases. The weights for the Huygens secondary sources are computed using Eq. (15) and taking the derivative of $p_{\text{inc}}(\bar{r}_n)$,

$$b_n \cong k\tilde{N}_n\left(\frac{e^{i\omega\tau_{1n}}}{\sqrt{kR_{1n}}} + \frac{V_n e^{i\omega\tau_{2n}}}{\sqrt{kR_{2n}}}\right), \tag{22}$$

where

$$\tilde{N}_n = \frac{e^{-i\pi/4}\Delta x \gamma_n}{\sqrt{2\pi}}(\hat{s}_{r,n}\cos\theta_n + \hat{s}_{z,n}\sin\theta_n), \tag{23}$$

with $\hat{s}_{r,n}$ $\hat{s}_{z,n}$ the unit vector components for the normal to the surface at r_n and θ the direction of propagation of p_{inc}. The $\tilde{N}$ and k in Eq. (22) appear due to the derivative in the direction normal to the surface. The value of b_n is an approximation to the derivative since the higher order terms of the derivative are neglected (i.e., the terms with $R^{-3/2}$).

For the general cases considered here, there is a seabed boundary so the free-space Hankel function is replaced in Eq. (11) with the Green's function $G(k|\bar{r}-\bar{r}'|)$ representing the point source response between $\bar{r}$ and $\bar{r}'$.

$$p(\bar{r}) = p_{\text{inc}}(\bar{r}) - \frac{1}{4i}\int_S G(k|\bar{r}-\bar{r}'|)\frac{\partial p(\bar{r}')}{\partial n'}ds'. \tag{24}$$

For the numerical implementation, the Green's function has a similar form as the incident field,

$$G(|\bar{r}-\bar{r}_n|) = \frac{e^{i\omega\tilde{\tau}_{1n}}}{\sqrt{k\tilde{R}_{1n}}} + \frac{V_n e^{i\omega\tilde{\tau}_{2n}}}{\sqrt{k\tilde{R}_{2n}}}, \tag{25}$$

where in this case, $\tilde{R}_{1n}$ represents the distance for the direct path between the Huygens secondary source (at r_n) and the field point (at $\bar{r}$) and $\tilde{R}_{2n}$, represents the distance for the bottom bounce path.

The scattered field is then constructed as

$$p_{\text{scat}}(\bar{r}) = \sum_{n=1}^{N} G(k|\bar{r}-\bar{r}_n|)b_n, \tag{26}$$

where the total scattered field is a sum of four components for each Huygens source,

$$p_{\text{scat}}(\bar{r}) = \sum_{n=1}^{N}\sum_{m=1}^{4}\tilde{N}_n\{A_m e^{i\omega T_m}\}, \tag{27}$$

with the amplitudes

$$\begin{aligned} A_1 &= \frac{1}{\tilde{R}_{1n}R_{1n}}, \\ A_2 &= \frac{V_n}{\tilde{R}_{2n}R_{1n}}, \\ A_3 &= \frac{V_n}{\tilde{R}_{1n}R_{2n}}, \\ A_4 &= \frac{V_n^2}{\tilde{R}_{2n}R_{2n}}, \end{aligned} \tag{28}$$

and the delays

$$\begin{aligned} T_1 &= \tilde{\tau}_{1n} + \tau_{1n}, \\ T_2 &= \tilde{\tau}_{2n} + \tau_{1n}, \\ T_3 &= \tilde{\tau}_{1n} + \tau_{2n}, \\ T_4 &= \tilde{\tau}_{2n} + \tau_{2n}. \end{aligned} \tag{29}$$

The frequency dependent k term conveniently cancels out. However, this is a line source formulation and this frequency dependence will become necessary when extending to a point source, which is required for typical applications. This issue will be discussed further in Sec. VI. It is also worth noting that this formulation includes one surface bounce path. That is, the total field will consist of a direct path, bottom-bounce, bottom-surface-bounce, surface-bottom-bounce, and bottom-surface-bottom-bounce paths. For many applications, these six paths will provide a sufficient impulse response representation. However, paths with multiple surface bounces could be included in an approximate way by modifying the amplitude of the first surface bounce by taking only the specular path and then include the scattering in the second interaction with the surface.

C. Examples of scattering approaches for static surfaces

Static surfaces at a single frequency are useful for checking the approximate solutions since the exact Helmholtz–Kirchhoff integral equation can be used as the ground truth. The time-domain Kirchhoff approach will not immediately show its utility for these time-harmonic examples. However, that formulation will be critical when extending to the time-varying surfaces in Sec. VII.

1. Surface scattering without a seabed

In the first example, the field interactions with the rough sea surface is determined without a seabed. Using an isospeed water column allows the exact Hankel functions to be

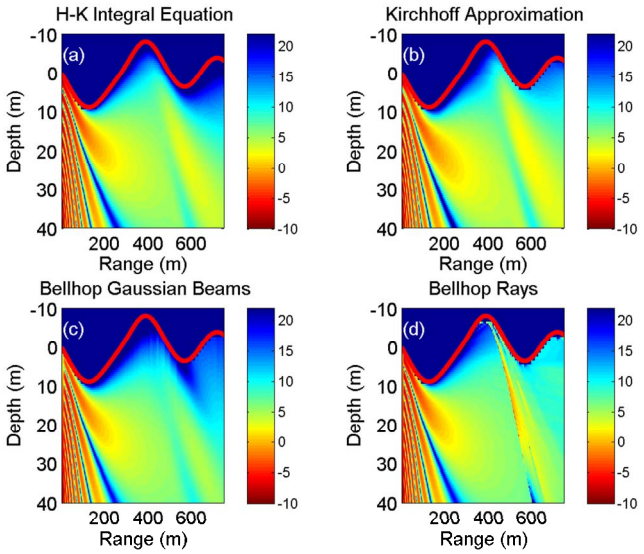

FIG. 12. (Color online) TL (referenced to 1 μPa at 1 m) for different numerical methods with a rough surface and no seabed. The source depth was 40 m from the surface and the frequency was 200 Hz, the surface height standard deviation is 0.5λ and the correlation length is 50λ. Panel (a) is the exact solution using the Helmholtz-Kirchhoff integral equation, in (b) the solution shown is for the time-domain Kirchhoff approximation and in (c) is the output from the Bellhop ray/beam trace using Gaussian beams and (d) for geometric rays.

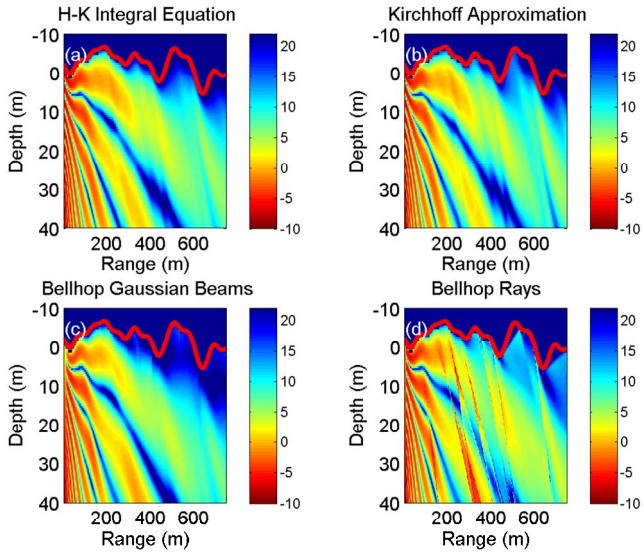

FIG. 13. (Color online) Same as Fig. 12 except with surface roughness correlation is 20λ.

included in the Helmholtz–Kirchhoff integral equation. The source depth was 40 m from the surface and the frequency was 200 Hz.

To generate the random surface shape, a spectral method was used similar to that by Thorsos.[13] That is, white noise is filtered with a Gaussian spectrum to provide a one-dimensional random sequence with height and correlation distance governed by the parameters of the Gaussian density, its mean, and correlation. For the first example, the surface height standard deviation is 0.5λ and the correlation length is 50λ.

The results are shown in the four panels in Fig. 12. The field is displayed as TL (TL is referenced to 1 μPa at 1 m) with the line near depth 0 being the shape of the sea surface. Panel (a) is the exact solution using the Helmholtz–Kirchhoff integral equation. In (b), the solution shown is for the time-domain Kirchhoff approximation. In (c) is the output from the Bellhop ray/beam trace using Gaussian beams and (d) is the same using geometric rays. The results show nearly perfect agreement between (a), (b), and (c) while the geometric rays in (d) show indications of typical ray artifacts. These types of artifacts are the motivation for improved methods such as Gaussian beams.

In Fig. 13, the correlation length is reduced to 20λ. In this case, the geometric rays in panel (d) are clearly showing artifacts while the Kirchhoff method (b) is still in reasonable agreement with the exact solution in (a) and to some degree also the Gaussian beam solution in (c). Although these are just samples, the results for other cases were similar. That is, as the roughness increased (either by reducing the correlation length or the height) the geometric beams appeared to produce erroneous results first, followed by the Gaussian beams, and then the Kirchhoff approach.

2. Surface scattering with a seabed

As a second example, the seabed was included in the calculation. As before, the surface had 20λ correlation length, surface height standard deviation of 0.5λ, and the source was at 40 m depth. The water column was 100 m with a homogeneous (in depth) seabed with a sound speed of 1600 m/s, density of 1.5 g/cm^3, and attenuation factor of 0.75 dB/λ. Since the Kirchhoff approximation method includes only a single surface bounce path, the figure that it is compared against was computed with the same paths. In Fig. 14, results from a single realization are shown comparing the Helmholtz–Kirchhoff integral equation result with the Kirchhoff approximation.

The results shown are for just single realizations of the random rough surface; however, these were typical and showing results for many realizations is not possible here. Results for many more realizations are summarized by the plots in Fig. 15. In this figure, there are three panels showing TL at 200, 400, and 600 Hz for the same conditions as the previous case (i.e., source depth of 40 m and 100 m water column). In each panel, 50 realizations of rough surfaces are averaged. This is similar to the comparisons made by Thorsos[13] but those were for a scattering cross section and here the results are for a receiver at a fixed depth of 25 m.

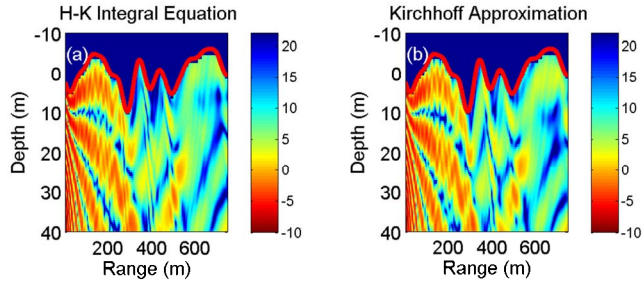

FIG. 14. (Color online) Same as Fig. 13 except with the inclusion of a smooth seabed at 100 m depth. Panel (a) is the exact solution using the Helmholtz–Kirchhoff integral equation. In (b), the solution shown is for the time-domain Kirchhoff approximation.

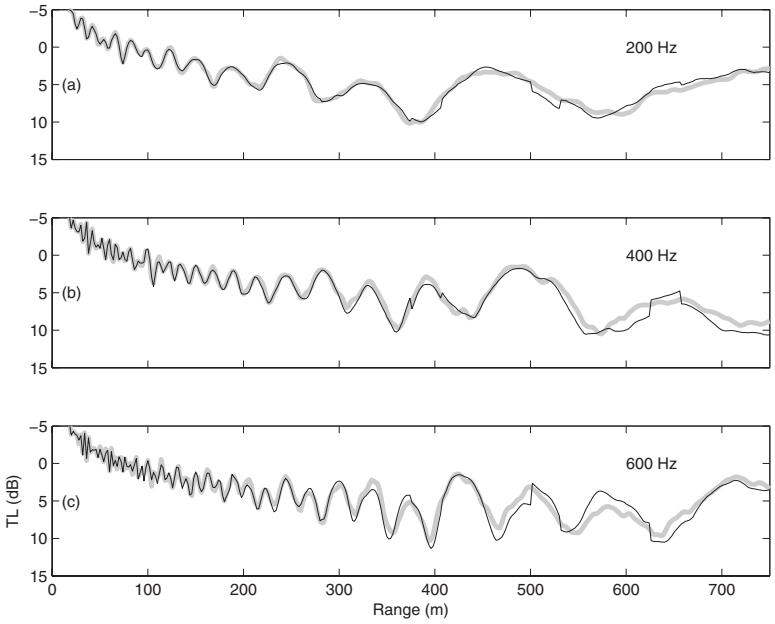

FIG. 15. Averaged TL for 50 realizations at frequencies of 200 Hz in (a), 400 Hz in (b), and 600 Hz in (c). The heavy gray line is the Helmholtz–Kirchhoff result and the thin black line is the Kirchhoff approximation.

The heavier gray line indicates the Helmholtz–Kirchhoff integral equation results and the thin black line is for the Kirchhoff approximation. In general, not only the average levels are in good agreement, but also the details of the finer structure.

VI. APPROXIMATING POINT SOURCE SOLUTIONS FROM LINE SOURCES

The previous solutions using the Helmholtz–Kirchhoff integral equation as well the Kirchhoff approximation assumed line sources for the excitation field. This is convenient for the derivations but is not particularly good for simulating the types of sound sources used in underwater acoustic systems. These are much more accurately modeled using point sources. The line source solutions can be converted to point source solutions in a fairly simple way.

Consider the field from a line source in free space,

$$p_L(R) = \frac{i}{4} H_0^{(1)}(kR) \simeq \sqrt{\frac{i}{8\pi kR}} e^{ikR}, \tag{30}$$

where, as before, k is the acoustic wave number and $R = |\bar{r} - \bar{r}'|$ is the distance between the source and receiver. The point source field is

$$p_P(R) = \frac{e^{ikR}}{4\pi R}. \tag{31}$$

The line source field is converted to an equivalent point source field by multiplying by the factor $\sqrt{k/i2\pi R}$,

$$p_P(R) = \sqrt{\frac{k}{i2\pi R}} p_L(R). \tag{32}$$

An additional complication arises since the line source solution is determined in an x-z plane geometry coordinate system. Therefore, the true range R from the source to receiver is related to the plane geometry distance x according to $x = R\cos\alpha$, where α is the angle from the horizontal line between the source and the receiver. The conversion from a plane-geometry line source solution to an equivalent axisymmetric, cylindrical geometry, point source solution is then

$$p_P(r,z) = \sqrt{\frac{k\cos\alpha}{i2\pi|x|}} p_L(x,z), \tag{33}$$

where, for the cylindrical coordinate system, $r = |x|$. The $\sqrt{\cos\alpha}$ term is generally small except at short ranges where there can be strong arrivals propagating at steep angles. The main amplitude contribution to the conversion factor is from the $\sqrt{x}$ term in the denominator. It will be seen in the next section that the $\sqrt{k}$ term is also important in forming the time-domain solution.

As an example of the correction from a line source solution to a point source solution, the exact field was computed for a point source using two reflecting boundaries separated by 100 m and the point source at 40 m depth. This was computed using the method of images. This result is compared to the described Kirchhoff approximation for a line source with the conversion factor applied. Since the boundaries are flat, the Kirchhoff approximation is exact for the line source. Note that the $\sqrt{\cos\alpha}$ term is applied to just the incident field in Eq. (21) according to the source launch angle. The full solution includes an infinite number of reflections. However, as previously mentioned, the Kirchhoff formulation only includes paths with a single surface reflection so the image solution is computed and limited to the same number of paths. In Fig. 16, the exact solution and the line source converted solution are shown for three receiver depths. The lines are nearly on top of each other so the exact solution is shown as a slightly thicker light gray line and the converted line source result is in black.

The conversion of line source results to an equivalent point source result comes about in various propagation solutions. For example, the Gaussian beam formulation also has this same factor which is derived more formally by Porter and Bucker.[11] Another version of this conversion can be il-

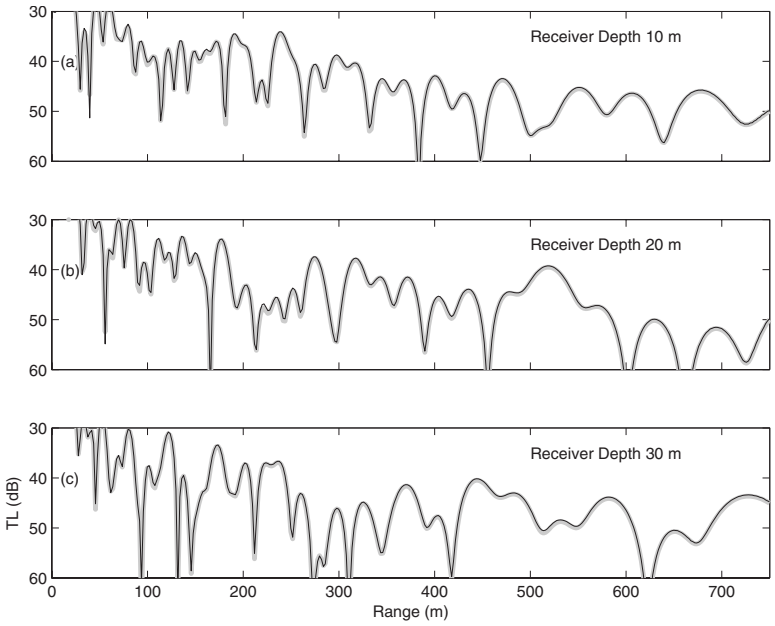

FIG. 16. TL at 200 Hz for an exact (light gray line) point source and a conversion factor applied to the line source solution (black line). The three panels are for different receiver depths, 10 m in (a), 20 m in (b), and 30 m in (c) for a source at 40 m.

lustrated for waveguide propagation using normal modes. The pressure field for a line source is derived by Jensen *et al.*[9] as

$$p_L(x,z) = \sum_{m=1}^{\infty} \frac{i}{2\rho(z_s)} \Psi_m(z_s)\Psi_m(z) \frac{e^{ik_m|x|}}{k_m}, \tag{34}$$

where the depth dependent mode functions are Ψ, the source depth is z_s, the receiver depth is z, the density is ρ, and the horizontal wave number that corresponds to the mode is k_m. The corresponding modal sum for the axial symmetric point source in cylindrical coordinates (r,z) is

$$p_P(r,z) = \sum_{m=1}^{\infty} \frac{1}{\rho(z_s)} \sqrt{\frac{i}{8\pi r}} \Psi_m(z_s)\Psi_m(z) \frac{e^{ik_m r}}{\sqrt{k_m}}, \tag{35}$$

where $|x|=r$. To obtain the point source solution from the line source solution requires multiplying $p_L(x,z)$ by $\sqrt{k_m/i2\pi|x|}$, that is,

$$p_P(r,z) = \sqrt{\frac{k_m}{i2\pi|x|}} p_L(x,z). \tag{36}$$

Representing the horizontal wave numbers in terms of the corresponding angle, $k_m = k\cos\alpha$, results in the conversion factor $\sqrt{k\cos\alpha/i2\pi|x|}$, which is exactly the same as shown previously for free space. The weighting of the rays by $\sqrt{\cos\alpha}$ according to their launch angle would be equivalent to weighting the mode function source excitation by this factor, that is, $\Psi_m(z_s)\sqrt{\cos\alpha}$. As mentioned, the greatest influence is due to the $\sqrt{|x|}$ term in the denominator and, for the time-domain solution, the $\sqrt{k}$ factor.

VII. TIME-DOMAIN KIRCHHOFF APPROXIMATION FOR TIME-VARYING SURFACES

The approach outlined in Sec. V with the Kirchhoff approximation can be applied to time-varying sea surfaces. The surface shape varies at each time step and the Kirchhoff solution is recomputed. This is possible since the Kirchhoff approximation is numerically efficient and does not require the matrix inversion needed for the integral equation. There is one subtle point to obtain a time series that resembles measurements. In Sec. VI, it was pointed out that to obtain the field from a point source, the line source solution required multiplying by $\sqrt{k\cos\alpha/i2\pi|x|}$. The $\sqrt{1/|x|}$ term is easy enough to include at each receiver position after the simulation. The $\sqrt{\cos\alpha}$ factor is applied to each of the rays launched from the source according to their angle. The $\sqrt{k}$ factor depends on each frequency component but is also simple to include through the source function. The Fourier transform of the transmit waveform, $S(\omega)$, is multiplied by the $\sqrt{k}$ factor and inverse Fourier transformed back to the time domain as the new transmit waveform used in the convolution sum.

Three examples will be given using this approach. In the first case a flat sea surface moves uniformly. The second example uses a rough, moving sea surface at a single point at a relatively high frequency. The third case is a lower frequency example showing a pulse propagating and reflecting off the rough surface.

A. Modeling a flat, time-varying surface

This example for a flat but moving surface is similar to that shown previously in Sec. III and is a convenient check since the image method can be used for comparison. Here, the source is at 30 m depth and the receiver is at 250 m range from the source at 40 m depth. The sea surface is moving at 0.25 m/s. The same Doppler-sensitive BPSK signal (centered at 9500 Hz) as used previously (in Secs. II and III) was the source transmission and the received time series was matched filtered with Doppler adjustments as before. The results for the Kirchhoff time-domain model and the image method are shown in Fig. 17. Note, that this approach does not currently treat receiver motion so the receiver is at a fixed location.

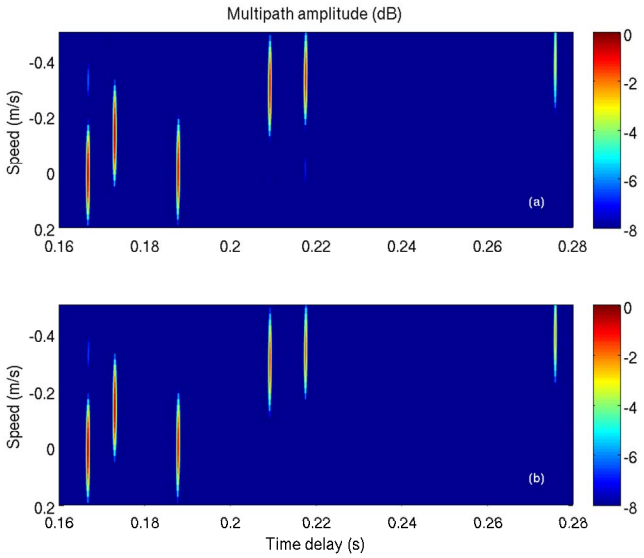

FIG. 17. (Color online) In panel (a), the impulse response (or scattering functions) is computed using the method of images and in (b), it is computed using the time-dependent Kirchhoff approximation method described. The first arrival in time is from the direct path and the third arrival from the bottom bounce both show no Doppler shift. The other paths that follow are from the surface and surface/bottom bounces and are Doppler shifted.

B. Modeling a rough, time-varying surface

In this example, the sea surface is generated using the Gaussian filtered white noise method and the entire surface is moving at 0.25 m/s. The standard deviation of the surface is 1.6 m and the correlation length is 8 m. The surface shape is shown in panel (a) of Fig. 18 and the received time series after applying the Doppler adjusted matched filter to approximate the scattering function in panel (b).

C. Pulse propagation with a rough surface

A pulse was transmitted from a source at 40 m depth using the band from 50 to 600 Hz. The time evolution of this pulse is shown in Fig. 19. This example helps illustrate that

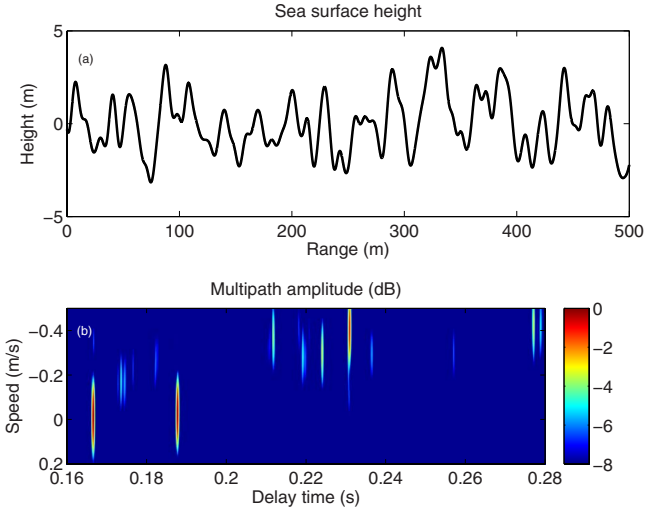

FIG. 18. (Color online) In panel (a), the rough surface is shown for the simulation. This surface moves with a uniform speed of 0.25 m/s. Shown in (b) is the received time series after applying the Doppler adjusted matched filter to approximate the scattering function.

the model produces the correct pulse shape as well as the reflections from the rough boundary.

VIII. CONCLUSION

Correct scattering and Doppler modeling is important for a variety of underwater acoustic systems such as acoustic modems for communications. The type of communication modulation schemes and data rates depend on the channel spread factor, which is determined by the multipath duration and the Doppler spread. Estimating these quantities is useful for both system design and performance prediction. A binary phase-shift keying communication signal was shown from the Makai experiment, which is typical for that type of ocean environment. The first few arrivals are generally the strongest with the surface interacting paths having Doppler shifts that depend on the surface motion.

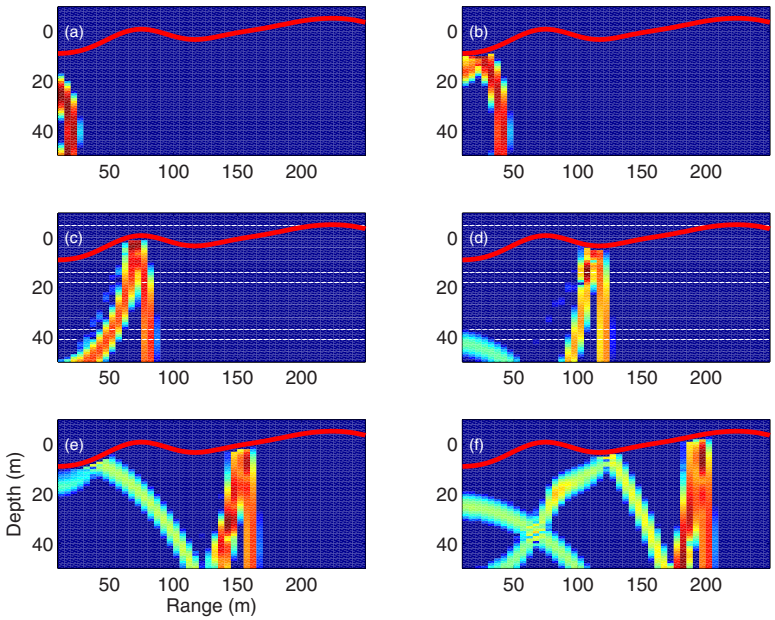

FIG. 19. (Color online) Time evolution of pulse with a rough surface. Times correspond to the following: (a) 0.013 s, (b) 0.026 s, (c) 0.053 s, (d) 0.079 s, (e) 0.11 s, and (f) 0.13 s.

Two simulation methods have been developed for acoustic propagation in the ocean with a time-evolving, rough sea surface. The first method is relatively easy to implement and conveniently allows for receiver motion as well as a changing sea surface. A second method uses the Kirchhoff approximation and was shown to compare well against the exact solutions. There are a number of approximations within this approach including the limitation to six arrivals. However, the approach produces results that are useful for determining how each path is modified by interaction with the rough, time-evolving sea surface.

ACKNOWLEDGMENTS

The authors are grateful for the support provided for this work by the Office of Naval Research. The authors would like to thank Keyko McDonald (SPAWAR) for the development and deployment of the Telesonar Testbeds used for the experimental data. The authors would also like to thank Sergio Jesus, Antonio da Silva, and Friedrich Zabel at the Signal Processing Laboratory at the University of Algarve, Portugal for their support and cooperation with the received AOB data used for this analysis. The authors would also like to acknowledge their colleagues: Katherine Kim for her help during the Makai experiment, Paul Hursky for his advice on communication topics and his assistance during the Makai experiment, and Ahmad Abawi for many valuable discussions.

[1]M. Siderius and M. B. Porter, "Modeling techniques for marine mammal risk assessment," IEEE J. Ocean. Eng. **31**, 49–60 (2006).
[2]M. B. Porter, "The Makai experiment: High-frequency acoustics," in *Proceedings of the Eighth European Conference on Underwater Acoustics* (Tipografia Uniao, Algarve, Portugal, 2006), pp. 9–18.
[3]V. K. McDonald, P. Hursky, and the KauaiEx Group, "Telesonar testbed instrument provides a flexible platform for acoustic propagation and communication research in the 8–50 kHz band," in *Proceedings of the High-Frequency Ocean Acoustics Conference* (AIP, Melville, NY, 2004), pp. 336–349.
[4]A. Silva, F. Zabel, and C. Martins, "The acoustic oceanographic buoy telemetry system—A modular equipment that meets acoustic rapid environmental assessment requirements," Sea Technol. **47**(9), pp. 15-20 (2006).
[5]J. G. Proakis, *Digital Communications*, 3rd ed. (McGraw-Hill, New York, NY, 1995).
[6]W. S. Burdic, *Underwater Acoustic System Analysis* (Prentice-Hall, Englewood Cliffs, NJ, 1991).
[7]R. S. Keiffer, J. C. Novarini, and R. W. Scharstein, "A time-varient impulse response method for acoustic scattering from moving two-dimensional surfaces," J. Acoust. Soc. Am. **118**, 1283–1299 (2005).
[8]P. C. Etter, *Underwater Acoustic Modeling*, 2nd ed. (EFN Spon, London, UK, 1996).
[9]F. B. Jensen, W. A. Kuperman, M. B. Porter, and H. Schmidt, *Computational Ocean Acoustics* (AIP, New York, 1994).
[10]M. B. Porter, Ocean Acoustics Library, Bellhop (http://oalib.hlsresearch.com/, viewed April 10, 2008).
[11]M. B. Porter and H. P. Bucker, "Gaussian beam tracing for computing ocean acoustic fields," J. Acoust. Soc. Am. **82**, 1349–1359 (1987).
[12]J. A. Ogilvy, *Theory of Wave Scattering from Random Rough Surfaces* (IOP, London, UK, 1991).
[13]E. I. Thorsos, "The validity of the Kirchhoff approximation for rough surface scattering using a Gaussian roughness spectrum," J. Acoust. Soc. Am. **83**, 78–92 (1988).
[14]E. Hecht and A. Zajac, *Optics* (Addison-Wesley, Reading, MA, 1979).

Uniformly valid solution for acoustic propagation in weakly tapered circular waveguides: Liquid jet example

Joel B. Lonzaga,[a] David B. Thiessen, and Philip L. Marston
Department of Physics and Astronomy, Washington State University, Pullman, Washington 99164-2814

(Received 28 January 2008; revised 26 April 2008; accepted 30 March 2008)

The propagation of ultrasound down laminar liquid jets has potential applications to the stimulation of liquid drop production [J. B. Lonzaga, C. F. Osterhoudt, D. B. Thiessen, and P. L. Marston, J. Acoust. Soc. Am. **121**, 3323–3330 (2007)] as well as to the coupling of ultrasound to objects through contact with a jet. In normal gravity, a jet issuing from a nozzle becomes tapered as the jet accelerates downward. A uniformly valid solution for the acoustic propagation in a weakly tapered, liquid jet waveguide in air with a turning point is derived using Langer's transformation and the method of multiple scales. The loss of energy from transmission into the air and from thermal viscous absorption is neglected. A solvability condition is used to obtain the leading-order correction due to the taper of the waveguide. This asymptotic solution is validated using finite-element numerical calculations. The ultrasonic wave amplitude is enhanced in the region of the jet close to the cutoff of the excited mode. © *2008 Acoustical Society of America.* [DOI: 10.1121/1.2932348]

PACS number(s): 43.35.Zc, 43.25.Qp, 43.20.Bi, 43.20.Mv [TDM] Pages: 151–160

I. INTRODUCTION

This paper extends previous research[1] on the propagation of ultrasound down laminar liquid jets issuing from a nozzle to allow for the jet to be tapered. While the emphasis of the prior research was on the response of the jet to modulated radiation pressure, it is anticipated that understanding the propagation of ultrasound in jets may also be applicable to ultrasonic nondestructive testing in situations where jets are used to couple ultrasound to tested objects. The goal of this paper is to present the derivation of a uniformly valid approximation of the sound field internally applied on a weakly tapered liquid jet waveguide with a turning point using Langer's transformation.[2,3] In this case, the more commonly used elementary form of the WKB method cannot be employed as it leads to undefined sound field properties at the turning point where the wave is cut off. The analytical approximation derived is validated using finite-element numerical calculations. The analytical derivation follows from that of Nayfeh and Telionis[4] who considered uniformly valid approximations for the acoustic propagation in hard-walled ducts with slowly varying cross sections.

Acoustic or electromagnetic wave propagation in circular waveguides with slowly varying radius has been an important subject of many research efforts. Mode coupling in weakly tapered acoustic waveguides has been investigated using the "method of cross section."[5,6] In this method, the solution at a given cross section is expressed as an expansion of the eigenmodes of a uniform (cylindrical) waveguide having the same cross section. It has been found that mode coupling is a second order effect. Neglecting mode coupling, Temkin[7] derived an analytic theory for the transverse electric TE modes of a cylindrical cavity consisting of a straight section joined onto a slowly tapered section. At the tapered section, he reasonably assumed that the radial and axial components of the solution are separable. His treatment of the axial distribution uses a technique first introduced by Langer[2,3] that treats a class of second order differential equations with a simple turning point. This approximate solution is a powerful tool when the WKB method fails. The analytical approximation of Temkin, however, is not accurate since it neglects the fact that the varying waveguide radius would give rise to a slowly varying amplitude coefficient similar to one found by Nayfeh and Telionis.[4]

In this paper, we formulate the problem associated with the acoustic propagation in a tapered liquid jet waveguide in Sec. II. A uniformly valid approximation using multiple-scale analysis, power series expansion, and a solvability condition is given in Sec. III. A validation of the analytical solution will be presented in Sec. IV by comparing the analytical solution with finite-element numerical calculations. Throughout the analysis, the Doppler shift associated with flow within the waveguide is neglected since the jet velocity is taken to be much less than the speed of sound, which is typically the case for laminar liquid jets.[1,8]

II. FORMULATION OF THE PROBLEM

If the mean-flow velocity of a liquid jet waveguide is negligible compared to the sound speed in the waveguide, the acoustic velocity potential Φ is governed by the wave equation

$$\bar{\nabla}^2\Phi - \frac{1}{c^2}\frac{\partial^2\Phi}{\partial \bar{t}^2} = 0$$

and must satisfy the Dirichlet boundary condition

$$\Phi|_{\bar{r}=\bar{a}} = 0, \tag{1}$$

where $\bar{a}$ is the waveguide radius and c is the speed of sound. Let $r \equiv \bar{r}/R_o$, $z \equiv \bar{z}/R_o$, and θ be the radial, axial, and azimuthal cylindrical coordinates, respectively (see Fig. 1),

[a]Present address: US Naval Research Laboratory, 4555 Overlook Ave., SW Code 7123, Washington, DC 20375.

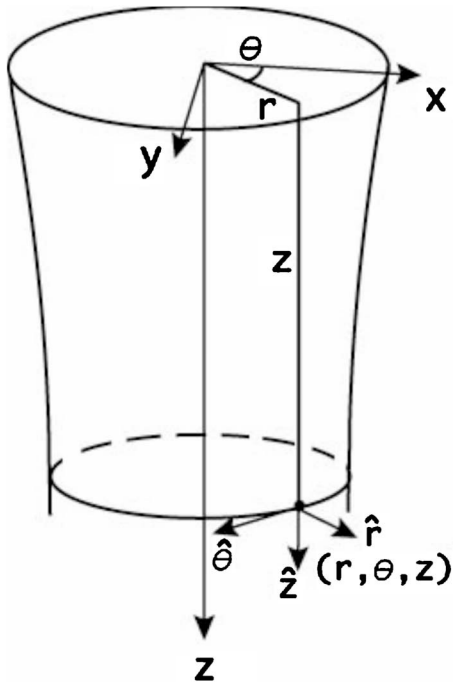

FIG. 1. A cylindrical coordinate system.

where R_o is a length scale which will be taken as the nozzle radius. Furthermore, let $a \equiv \bar{a}/R_o$ be the nondimensionalized waveguide radius. Assume that the wave field has the form $\Phi \equiv \phi(r,z)\cos(m\theta)e^{-i\omega t}$, so that the wave equation is reduced to the two-dimensional Helmholtz equation in cylindrical coordinate system:

$$\frac{1}{r}\frac{\partial}{\partial r}r\frac{\partial \phi}{\partial r} + \frac{\partial^2 \phi}{\partial z^2} + \left(\omega^2 - \frac{m^2}{r^2}\right)\phi = 0, \tag{2}$$

where $\omega \equiv \bar{\omega}R_o/c$, $\bar{\omega}$ is the angular frequency, and m is the azimuthal index. Imposing $\omega t = \bar{\omega}\bar{t}$, we find that $\bar{t} = tR_o/c$. The above equation can be solved by separation of variables, i.e., $\phi \equiv R(qr)Z(z)$, where q, a radial wave number, is determined by applying the boundary condition at $r=a$. Due to the taper of the waveguide typified by Fig. 1, q depends weakly on the axial coordinate which then constrains R to also depend weakly on the axial coordinate.

III. APPROXIMATE SOLUTION

The problem stated above can be partly solved using the method of multiple scales. This method presupposes that there exists ε such that a new variable can be defined as $\eta \equiv \varepsilon z$ and the radius behaves as $a=a(\eta)$. η and z are the so-called slow and fast (axial) variables. The literature definition of the parameter ε varies according to the nature of the problem being dealt with.[9–11] Following the definition used by Huerre and Monkewitz,[11] the parameter ε can be defined as

$$\varepsilon \equiv \left\| \frac{\lambda}{\bar{a}}\frac{d\bar{a}}{d\bar{z}} \right\| \ll 1, \tag{3}$$

where λ is a wavelength and $\|\,\|$ denotes magnitude. This criterion is equivalent to saying that the wavelength is much less than the length scale over which the radius changes significantly. The velocity potential is expected to depend on the fast and slow axial coordinates in addition to the radial coordinate, i.e., $\phi = \phi(r,z,\eta)$. In situations where Eq. (3) holds, the following transformations:

$$\frac{\partial}{\partial z} \to \frac{\partial}{\partial z} + \varepsilon\frac{\partial}{\partial \eta},$$

$$\frac{\partial^2}{\partial z^2} \to \frac{\partial^2}{\partial z^2} + \varepsilon\left(\frac{\partial}{\partial z}\frac{\partial}{\partial \eta} + \frac{\partial}{\partial \eta}\frac{\partial}{\partial z}\right) + \mathcal{O}(\varepsilon^2), \tag{4}$$

must be applied to the governing equation[4,12,13] which, for the problem at hand, is Eq. (2). This is needed to incorporate into Eq. (2) the leading-order dependence on the slow variable η.

In the WKB framework, it is possible to have operators $\partial/\partial z$ and $\partial/\partial \eta$ that do not commute[12] because z and η are not truly independent of each other. To illustrate this, let

$$f(z,\eta) \equiv g(\eta)e^{i\int_0^z k(\eta)dz}.$$

Twice differentiating f, first with respect to z, then with respect to η, yields

$$\frac{\partial}{\partial \eta}\frac{\partial f}{\partial z} = [kg'(\eta) + gk'(\eta)]e^{i\int_0^z k(\eta)dz}.$$

Interchanging the order of differentiation yields

$$\frac{\partial}{\partial z}\frac{\partial f}{\partial \eta} = kg'(\eta)e^{i\int_0^z k(\eta)dz}.$$

Furthermore, the transformation in Eq. (4) becomes

$$\frac{\partial^2}{\partial z^2} \to -k^2 + i\varepsilon\left(2k\frac{\partial}{\partial \eta} + k'(\eta)\right) + \mathcal{O}(\varepsilon^2),$$

a transformation used by Rienstra[13] except for the opposite algebraic sign in the second term due to his choice of a negative sign in the exponential part of f. This noncommutativity between $\partial/\partial z$ and $\partial/\partial \eta$ also applies to Langer's transformation employed in this paper. Langer's transformation is employed here due to the existence of a turning point where the elementary WKB method cannot be used. A turning point is a location in the waveguide where k becomes zero. At this location, an excited mode is cut off and thus turns around. Beyond the turning point, the mode becomes evanescent.

Applying the transformation prescribed by Eq. (4) in Eq. (2) yields

$$\tilde{L}\phi + \varepsilon\left(\frac{\partial}{\partial z}\frac{\partial}{\partial \eta} + \frac{\partial}{\partial \eta}\frac{\partial}{\partial z}\right)\phi + \mathcal{O}(\varepsilon^2) = 0, \tag{5}$$

where

$$\tilde{L} \equiv \frac{1}{r}\frac{\partial}{\partial r}r\frac{\partial}{\partial r} + \frac{\partial^2}{\partial z^2} + \left(\omega^2 - \frac{m^2}{r^2}\right).$$

We now put forward the following ansatz:

$$\phi(r,z,\eta) \equiv Z(z,\eta)(R^{(0)}(r,\eta) + \varepsilon R^{(1)}(r,\eta) + \cdots). \tag{6}$$

Z is not expanded in a power series of ε because an approximation of Z already exists in the literature.[2,3] Using this form of the wave field in Eq. (5) yields

$$\mathcal{O}(\varepsilon^0): \tilde{L}(R^{(0)}Z) = 0, \tag{7}$$

$$\mathcal{O}(\varepsilon^1): \tilde{L}(R^{(1)}Z) = -\left(\frac{\partial}{\partial z}\frac{\partial}{\partial \eta} + \frac{\partial}{\partial \eta}\frac{\partial}{\partial z}\right)(R^{(0)}Z). \tag{8}$$

The boundary condition, Eq. (1), becomes

$$R^{(\beta)}|_{r=a} = 0 \quad \text{for } \beta = 0,1,2,\ldots . \tag{9}$$

We use the method of separation of variables to decouple $R(r,\eta)$ and $Z(z,\eta)$. Let

$$\frac{1}{Z}\frac{\partial^2 Z}{\partial z^2} \equiv -k^2(\eta), \tag{10}$$

where $k(\eta)$ is a function of η or a slowly varying function of z. It can be seen that k is nothing but a dimensionless local wave number to be determined from a dispersion relation. That k depends on the slow variable η is the only condition that makes this approach different from the usual separation of variables. Equation (10) can be rewritten as

$$\varepsilon^2\frac{d^2Z}{d\eta^2} + k^2(\eta)Z = 0. \tag{11}$$

It is previously mentioned that the assumption of a slowly varying radius implies that $\varepsilon \ll 1$. The solution to Eq. (11) is accessible by the WKB method if there is no turning point or k never goes to zero, and by Langer's transformation if a turning point exists. We consider here the second case and a uniformly valid solution to Eq. (11) derived in Appendix A using Langer's transformation is given by Eq. (A7).

$$Z(z,\eta) = \frac{\left[\frac{3}{2}G(z,\eta)\right]^{1/6}}{[-H(z-z_{co})k^2(\eta)]^{1/4}}\mathrm{Ai}\left[H(z-z_{co}) \times \left(\frac{3}{2}G(z,\eta)\right)^{2/3}\right], \tag{12}$$

where the constant C has been set to unity. Ai is the Airy function and z_{co} denotes the cutoff location. $G(z,\eta)$ and $H(z-z_{co})$ are given by Eqs. (A8) and (A9), respectively.

We now derive the radial part R of ϕ. Using Eq. (10), Eqs. (7) and (8) are reduced to

$$\mathcal{O}(\varepsilon^0): LR^{(0)} = 0, \tag{13}$$

$$\mathcal{O}(\varepsilon^1): LR^{(1)} = -\frac{1}{Z}\left(\frac{\partial}{\partial z}\frac{\partial}{\partial \eta} + \frac{\partial}{\partial \eta}\frac{\partial}{\partial z}\right)(R^{(0)}Z), \tag{14}$$

where

$$L \equiv \frac{1}{r}\frac{\partial}{\partial r}r\frac{\partial}{\partial r} + \left(q^2 - \frac{m^2}{r^2}\right) \tag{15}$$

and

$$q^2(\eta) \equiv \omega^2 - k^2(\eta). \tag{16}$$

A solution to Eq. (13) that is finite at $r=0$ is

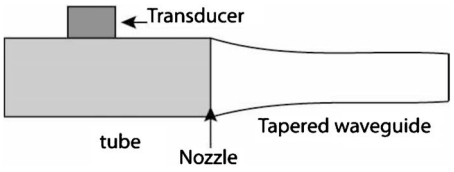

FIG. 2. A tapered ultrasonic waveguide.

$$R_{mn}^{(0)}(r,\eta) = A_{mn}(\eta)J_m(qr), \tag{17}$$

where J_m is the mth order Bessel function of the first kind, and the amplitude coefficient $A_{mn}(\eta)$ is a constant of integration that depends on η since the latter is held constant when Eq. (13) is integrated. From Eq. (9), the radial wave number is given by

$$q = \frac{\alpha_{mn}}{a(\eta)}, \tag{18}$$

where α_{mn} satisfies $J_m(\alpha_{mn})=0$. The A_{mn} are determined in Appendix B from the solvability condition of Eq. (14), given by $A_{mn}(\eta)=A_{mn}(\eta_{co})/a(\eta)$. Hence the velocity potential becomes

$$\Phi_{mn}(r,z,\eta) = \frac{A_{mn}(\eta_{co})}{a(\eta)}J_m\left(\frac{\alpha_{mn}}{a}r\right)Z(z,\eta)\cos(m\theta)e^{-i\omega t} + \mathcal{O}(\varepsilon^1), \tag{19}$$

where $Z(z,\eta)$ is given by Eq. (12).

IV. COMPARISON BETWEEN THE ANALYTICAL SOLUTION AND FINITE-ELEMENT METHOD CALCULATIONS

This section demonstrates the validity of the analytical solution derived above for the Dirichlet boundary-value problem in predicting the field distribution by comparing it with finite-element method numerical calculations. We consider a tapered cylindrical acoustic waveguide formed by a vertical water jet exiting from a circular nozzle and subsequently acted upon by gravity, as shown in Fig. 2. The effect on the sound field of the mean-flow velocity of the water jet is ignored since the Mach number is very small (typically less than 0.1%). The domain of interest is from the nozzle whose radius R_o is 0.11 cm to where the sound field is cut off in the tapered water jet waveguide. The entire length of the jet is considered as the $+z$ axis with $z=0$ at the nozzle (see Fig. 1). The expression below is used for the water jet waveguide profile.

$$a = \frac{1}{(1+\epsilon z)^{1/4}}, \tag{20}$$

obtained using conservations of mass and energy and neglecting surface tension.[14] In Eq. (20), $a \equiv \bar{a}/R_o$, $\epsilon \equiv 2gR_o/u_o^2$, and $z=\bar{z}/R_o$. $\bar{a}$ is the jet radius, g is the gravitational acceleration, R_o and u_o are the nozzle jet radius and velocity, respectively, and $\bar{z}$ is the axial coordinate.

The response to the steady ultrasonic radiation pressure is neglected in this analysis. It is anticipated, however, that the response to *modulated* ultrasound will be greatest in the region of the jet below the cutoff of the ultrasonic mode. For

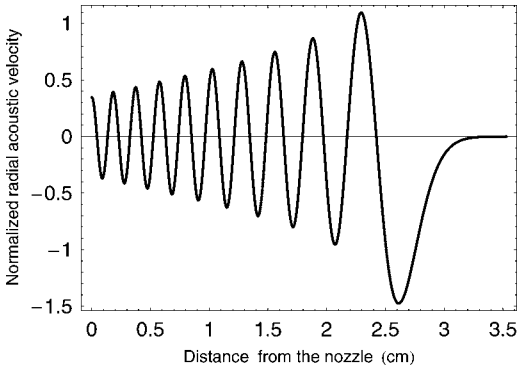

FIG. 3. Plots of the radial acoustic velocity at the surface of the waveguide. The radial acoustic velocity is calculated using Eq. (24) for $r=a$ and $\theta=0$ with $u_o=41.6$ cm/s in (a) and $u_o=49.5$ cm/s in (b).

that reason, it is especially important to understand the ultrasonic fields near the cutoff region of the jet. It was previously shown in the Appendix of Lonzaga *et al.*[1] that for an untapered jet having pressure release boundary condition, the outward radiation pressure on the interface is proportional to $|u_r|^2$, where u_r is the first-order radial acoustic velocity evaluated at the free surface of the jet. For weakly tapered jets in which the outward normal to the jet is nearly horizontal, this proportionality will not be significantly altered. (The first-order pressure vanishes at the free surface so that the local acoustic pressure does not enter into the calculation of the local radiation pressure.) As shown in the present investigation, $|u_r|^2$ is maximized in the region just above the cutoff location. Lonzaga *et al.*[1] demonstrated that surface perturbations induced by modulated ultrasound can significantly grow as they travel downstream.

We first discuss the analytical calculation of the field distribution in the liquid jet. At the surface of the liquid jet, the pressure is approximately zero (pressure release condition). In Appendix C, it is found that there are no modes propagating in the water jet waveguide except mode (1,1) for $R_o=0.11$ cm and frequency $f=1169$ kHz (the significance of this frequency is noted in that appendix). Thus the appropriate dispersion relation given by Eq. (16) with the aid of Eq. (18) can be written as

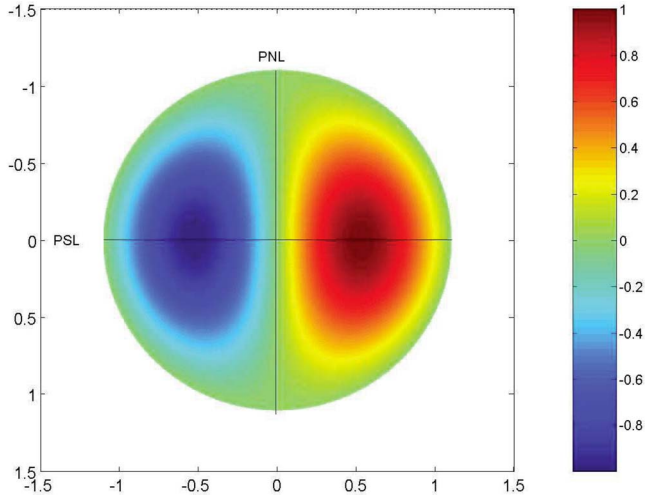

FIG. 4. (Color online) A typical (normalized) pressure field distribution in the jet waveguide showing the pressure nodal line (PNL) and pressure symmetry line (PSL). Both the horizontal and vertical axes of the plot are in mm.

$$k_{11}^2 = \omega^2 - \frac{\alpha_{11}^2}{a^2}, \tag{21}$$

where $k_{11} \equiv \bar{k}_{11} R_o$ is the dimensionless wave number. Equation (21) allows for the calculation of the local wave number k_{11} as a function of the axial coordinate. The pressure, $p = \rho \partial \Phi / \partial t$ (ρ is the density of water), of this mode can be calculated using Eq. (19). The boundary condition on the jet pressure amplitude (the pressure at the nozzle) should be approximated as $-i\omega\rho c_{11} J_1(\alpha_{11} r)\cos(\theta) e^{-i\omega t}$, as discussed in Appendix C. Thus

$$c_{11} J_1(\alpha_{11} r)\cos(\theta) e^{-i\omega t} = A_{11}(\eta_{\mathrm{co}}) J_1(\alpha_{11} r) Z(0,0)\cos(\theta) e^{-i\omega t}, \tag{22}$$

where from Eq. (12),

$$Z(0,0) = \frac{\left(\frac{3}{2}\int_0^{z_{\mathrm{co}}} k_{11} dz\right)^{1/6}}{\sqrt{k_{11}(0)}} \mathrm{Ai}\left[-\left(\frac{3}{2}\int_0^{z_{\mathrm{co}}} k_{11} dz\right)^{2/3} \right].$$

Since the turning point is far away from the origin, then $k_{11}(0) \gg 0$. Thus $Z(0,0)$ can be expressed asymptotically as

$$Z(0,0) = \frac{\sin\left(\int_0^{z_{\mathrm{co}}} k_{11} dz + \pi/4\right)}{\sqrt{\pi k_{11}(0)}}$$

and Eq. (22) becomes

$$c_{11} = A_{11}(\eta_{\mathrm{co}}) \sin\left(\int_0^{z_{\mathrm{co}}} k_{11} dz + \pi/4\right) \Big/ \sqrt{\pi k_{11}(0)}.$$

The pressure in the jet at the nozzle is approximated as a local extremum so that

$$\sin\left(\int_0^{z_{\mathrm{co}}} k_{11} dz + \pi/4\right) = \pm 1$$

or equivalently,

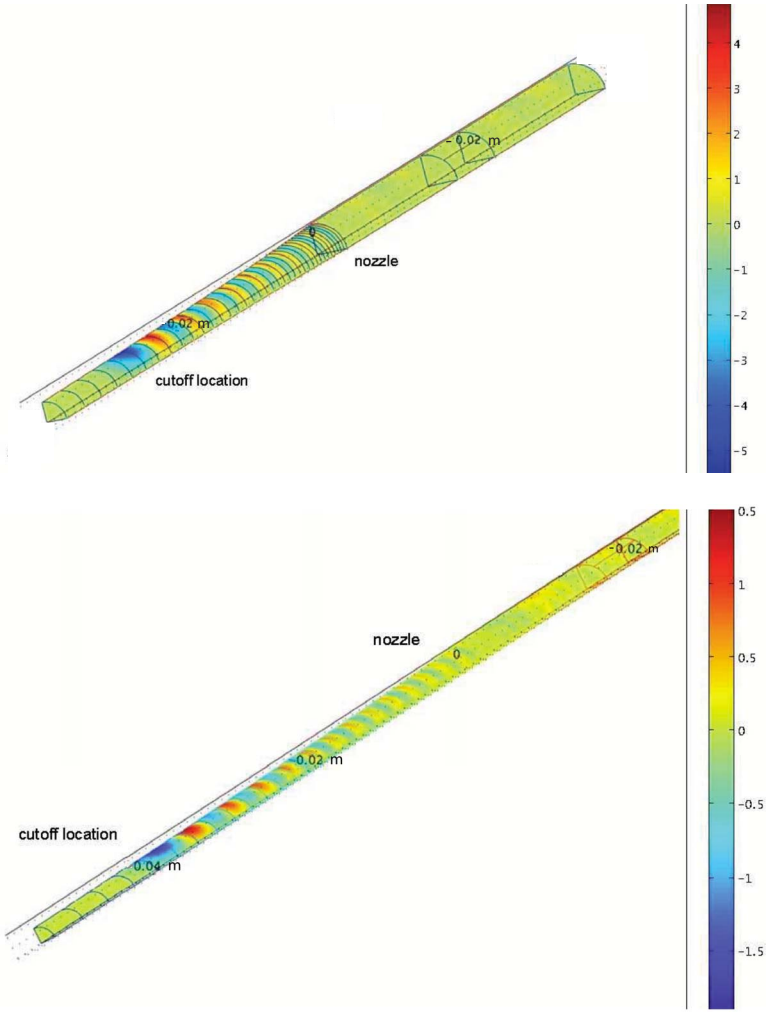

FIG. 5. (Color online) Finite-element domain and calculation. The top and bottom frames showing the (normalized) radial acoustic velocity at the waveguide surface are for nozzle jet velocities of 41.6 and 49.5 cm/s, respectively. The finite-element numerical calculation is implemented by using COMSOL MULTIPHYSICS. The jet profile is calculated by using Eq. (20).

$$\int_0^{z_{\rm co}} k_{11} dz = \frac{\pi}{4}(2l-1), \tag{23}$$

where $l=1,3,5,\ldots$. This relation should be enforced. Otherwise, the analytical solution would not account for the boundary at the nozzle and would be expected to not agree with the finite-element numerical calculations. This was verified with the finite-element procedure that will be discussed subsequently by adjusting the value of u_o and consequently the shape of the jet.

Because sound can couple from the water in the tube into the jet, it also follows that upward propagating acoustic modes of the jet will only be partially reflected at $z=0$. It follows that taking $z=0$ to be the antinode, used in Eq. (23), is only an approximation. It is not unreasonable to expect that modes in the jet propagating upstream will show significant reflection at the nozzle where the lateral boundary condition changes from pressure release to hard wall. Because of this, a resonance condition should exist in the tapered jet as sound is reflected back and forth between the nozzle and cutoff location. For a fixed jet taper that corresponds to a particular jet velocity, there will be resonant frequencies. On the other hand, if the wall of the waveguide is modifiable such as the case of the waveguide considered here and by Lonzaga *et al.*,[1] by changing the nozzle velocity u_o, the frequency can be kept at a fixed value while properly selecting u_o dictated by Eq. (23).

Evaluate the radial acoustic velocity u_{r11} of mode (1,1) at the surface along the line with azimuthal angle $\theta=0$. Since $\mathbf{v}\equiv-\nabla\Phi$, then

$$u_{r11} \approx -\frac{A_{11}(\eta_{\rm co})\alpha_{11}J_1'(\alpha_{11})}{a^2}\frac{\left[\frac{3}{2}G(z,\eta)\right]^{1/6}}{[-H(z-z_{\rm co})k_{11}^2]^{1/4}} \times {\rm Ai}\left[H(z-z_{\rm co})\left(\frac{3}{2}G(z,\eta)\right)^{2/3}\right]e^{-i\omega t}. \tag{24}$$

The radial acoustic velocity for $f=1169$ kHz at the surface of the waveguide is calculated using Eq. (24) and is plotted in Fig. 3 for the cases with $u_o=41.6$ and 49.5 cm/s. These nozzle velocities satisfy Eq. (23) for this value of f. Since the jet radius far from the nozzle increases with increasing u_o, the cutoff length for a given mode also increases, a result demonstrated in these plots. The cutoff location in the first case is 2.76 cm and that in the second is 3.90 cm, which can be verified by using the following equation for the dimensional cutoff length $\bar{z}_{\rm co}$:

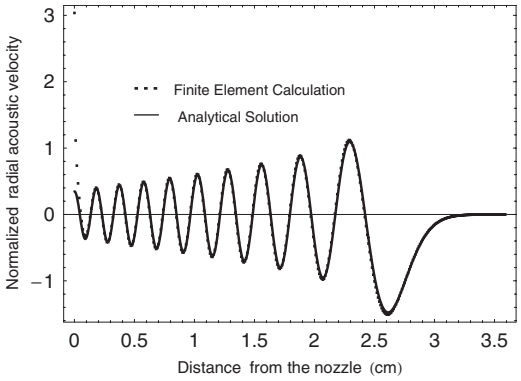

FIG. 6. Comparison between an analytical solution and a finite-element calculation of the radial acoustic velocity at the waveguide surface. The waveguide profile is given by Eq. (20) where the nozzle velocity u_o of 41.6 cm/s is chosen satisfying Eq. (23). The nozzle is designated as $z=0$.

$$\bar{z}_{\mathrm{co}} = \frac{u_o^2}{2g}\left(\left[\frac{2\pi f R_o}{c\alpha_{11}}\right]^4 - 1\right),$$

with $f=1169.2$ kHz, $R_o=0.11$ cm, $c=148\,000$ cm/s, and $\alpha_{11}=3.832$. The foregoing equation is obtained by substituting the liquid jet profile given by Eq. (20) into Eq. (21), setting $k_{11}=0$, and solving for $\bar{z}_{\mathrm{co}}$. The cutoff length for mode (1, 2) is obtained by replacing α_{11} by α_{12}, which is 7.016.

Let us determine if the "slowness" criterion, Eq. (3), is satisfied. Since

$$\left\|\frac{1}{\bar{a}}\frac{d\bar{a}}{d\bar{z}}\right\| \equiv \left\|\frac{1}{R_o}\frac{da}{dz}\right\| = \frac{\epsilon}{4R_o(1+\epsilon z)},$$

then

$$\varepsilon = \frac{\pi}{2k_{11\mathrm{typ}}}\frac{\epsilon}{1+\epsilon z},$$

where $k_{11\mathrm{typ}}$ is the typical (dimensionless) wave number of mode (1, 1). If $u_o=41.6$ cm/s or equivalently, $\epsilon=0.12$, then at the nozzle, $\varepsilon_{\mathrm{noz}}=0.05$. On the other hand, if $u_o=49.5$ cm/s, then $\varepsilon_{\mathrm{noz}}=0.04$. Thus, for the two nozzle velocities considered here, $\varepsilon \ll 1$.

Consider now the finite-element numerical calculation using a commercial package called COMSOL MULTIPHYSICS. The computational domain includes the tube and the entire length of the water jet waveguide typified by Fig. 2 but using only a quarter of the cross section. The reduction in the computational domain is justified by symmetry arguments. The existence of a pressure nodal plane affords the use of the pressure release condition at this plane. Because the nodal plane is perpendicular to the plane of the plot shown in Fig. 4, the nodal plane can only be seen as a nodal line labeled PNL in this figure. There is also a pressure symmetry plane (labeled PSL in the figure) that cuts the pressure nodal plane perpendicularly. The acoustic velocity across this symmetry plane vanishes because the pressure is at its extremum value. This pressure symmetry plane is therefore equivalent to a hard-wall condition at this plane, hence, the reduction in the computational domain into a quadrant. To further reduce the computational domain, the inner wall of the tube is assumed to be rigid except at a tiny patch that simulates a transducer imparting a unit normal acceleration. The boundary condition at the surface of the water jet waveguide in air is pressure release.

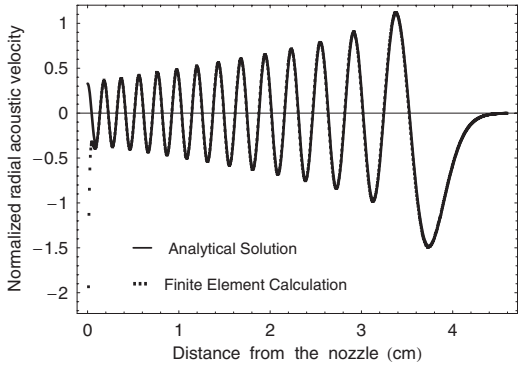

FIG. 7. Plot similar to that in Fig. 6 but with a nozzle jet velocity of 49.5 cm/s.

Finite-element domains and calculations are displayed in Fig. 5 for the two different nozzle velocities. While the domain of interest is the tapered liquid jet waveguide only, the tube domain is also shown for better illustration. To properly compare the finite-element and analytical calculations, finite-element data are processed further and a line at the surface of the waveguide is selected. The analytical solution and numerical calculation using finite element of the radial acoustic velocity are shown in Fig. 6 for the case with a nozzle velocity of 41.6 cm/s and in Fig. 7 for the case with a nozzle velocity of 49.5 cm/s. In both cases, the radial acoustic velocity is evaluated at the surface of the waveguide and the azimuthal coordinate $\theta=0$ is chosen. (The line with $\theta=0$ cuts the transducer lengthwise into two equal parts.) The analytical calculation agrees well with the finite-element calculation in both cases showing the validity of the analytical solution. The analytical solution is obtained using the lone propagating mode, mode (1, 1), beyond the nozzle. Consequently it does not account for the higher order $(1,n)$ modes (see discussion in Appendix C) that are cut off close to or at the nozzle, which give rise to the enhanced acoustic field at $z=0$ (see Figs. 6 and 7).

ACKNOWLEDGMENT

This work was supported by NASA.

APPENDIX A: APPLICATION OF LANGER'S TRANSFORMATION

If the radius of a sufficiently long waveguide is decreasing in the direction of propagation, the propagating mode is eventually cut off somewhere in the waveguide at z_{co}. The location in the waveguide where this takes place is called the cutoff location. It is also called a turning point because the wave turns around at this point. A WKB solution breaks down because $k \to 0$. However, Langer's transformation[2,3] provides a suitable, uniformly valid approximation which will be utilized in seeking a solution to Eq. (11). Though the derivation here closely follows from that of Nayfeh,[15] there are subtle aspects that are emphasized here and made clearer.

Let the radius of the tapered waveguide decrease with increasing z, as shown in Fig. 1. Let us introduce variable transformations of the form[15]

$$s \equiv f(\eta) \text{ and } y[f(\eta)] \equiv g(\eta)Z(\eta),$$

which transforms Eq. (11) into

$$\frac{d^2y}{ds^2} + \frac{1}{f'^2}\left(f'' - \frac{2f'g'}{g}\right)\frac{dy}{ds} + \frac{1}{f'^2}\left[\frac{1}{\varepsilon^2}k^2 - g\left(\frac{g'}{g^2}\right)'\right]y = 0,$$

where the prime denotes derivative with respect to η. In his derivation, Nayfeh used v for our y, x for η, and ϕ for f. The assumption that y indirectly depends on η through f is implicitly made in his derivation where he equivalently wrote $y \equiv g(\eta)Z(\eta)$. In this form, one would believe at the outset that $y=y(\eta)$ instead of the intended form $y=y[f(\eta)]$.

The middle term vanishes if $g=\sqrt{f'}$, leaving

$$\frac{d^2y}{ds^2} + \frac{k^2}{\varepsilon^2 f'^2}y = \delta y, \tag{A1}$$

where

$$\delta = -\frac{3}{4}\frac{f''^2}{f'^4} + \frac{1}{2}\frac{f'''}{f'^3}.$$

Since $\delta=\mathcal{O}(1)$ and $1/\varepsilon \gg 1$, Eq. (A1) can be approximately expressed as

$$\frac{d^2y}{ds^2} + \frac{k^2}{\varepsilon^2 f'^2}y \approx 0. \tag{A2}$$

We follow Nayfeh by choosing

$$\frac{k^2}{\varepsilon^2 f'^2} = f \tag{A3}$$

and Eq. (A2) becomes

$$\frac{d^2y}{ds^2} + sy \approx 0. \tag{A4}$$

The solution to Eq. (A3) is

$$\frac{2f^{3/2}}{3} = \frac{1}{\varepsilon}\int_{\eta}^{\eta_{co}} k(\eta)d\eta \tag{A5}$$

for $\eta \leqslant \eta_{co}$ and

$$\frac{2(-f)^{3/2}}{3} = \frac{1}{\varepsilon}\int_{\eta_{co}}^{\eta} \sqrt{-k^2(\eta)}d\eta \tag{A6}$$

for $\eta \geqslant \eta_{co}$, where $\eta_{co} \equiv \varepsilon z_{co}$. Equations (A5) and (A6) can be put into one single expression for f as

$$f(\eta) = -h(z - z_{co})\left(\frac{3}{2\varepsilon}F(\eta)\right)^{2/3},$$

where

$$F(\eta) \equiv h(\eta - \eta_{co})\int_{\eta_{co}}^{\eta} \sqrt{-h(\eta - \eta_{co})k^2(\eta)}d\eta$$

and

$$h(\eta - \eta_{co}) \equiv \begin{cases} 1, & \eta > \eta_{co} \\ -1, & \eta \leq \eta_{co}. \end{cases}$$

The solution to Eq. (A4) is

$$y(s) = C_1\,\mathrm{Ai}(-s) + C_2\,\mathrm{Bi}(-s).$$

Hence, to first approximation,

$$Z(\eta) = \frac{1}{\sqrt{f'(\eta)}}\{C_1\,\mathrm{Ai}[-f(\eta)] + C_2\,\mathrm{Bi}[-f(\eta)]\},$$

where C_1 and C_2 are constants of integration and Ai and Bi are the Airy functions. For a bounded system everywhere, C_2 must be set to zero since $\mathrm{Bi}(s) \to \infty$ as $s \to \infty$. Using this condition and Eq. (A3), we finally have

$$Z(\eta) = \frac{C_1\sqrt{\varepsilon}[(3/2\varepsilon)F(\eta)]^{1/6}}{[-h(\eta - \eta_{co})k^2(\eta)]^{1/4}}\mathrm{Ai}\left[h(\eta - \eta_{co}) \times \left(\frac{3}{2\varepsilon}F(\eta)\right)^{2/3}\right].$$

In keeping with the idea of multiple scales, the last equation can be rewritten as

$$Z(z,\eta) = C\frac{\left[\frac{3}{2}G(z,\eta)\right]^{1/6}}{[-H(z - z_{co})k^2(\eta)]^{1/4}}\mathrm{Ai}\left[H(z - z_{co}) \times \left(\frac{3}{2}G(z,\eta)\right)^{2/3}\right], \tag{A7}$$

where $C \equiv C_1\sqrt{\varepsilon}$,

$$G(z,\eta) \equiv H(z - z_{co})\int_{z_{co}}^{z} \sqrt{-H(z - z_{co})k^2(\eta)}dz \tag{A8}$$

and

$$H(z - z_{co}) \equiv \begin{cases} 1, & z > z_{co} \\ -1, & z \leq z_{co}. \end{cases} \tag{A9}$$

APPENDIX B: SOLVABILITY CONDITION

We now determine A_{mn} in Eq. (17) by using a solvability condition for Eq. (14). If we let $L^\dagger$ be the adjoint of L, then[16]

$$L^\dagger = r\frac{\partial}{\partial r}\frac{1}{r}\frac{\partial}{\partial r} + \left(q^2 + (1 - m^2)\frac{1}{r^2}\right).$$

Let $R^{(0)\dagger}$ satisfy

$$L^\dagger R^{(0)\dagger} = 0 \tag{B1}$$

and the specified boundary condition for $R^{(0)}$. The bounded solution to Eq. (B1) is

$$R_{mn}^{(0)\dagger} = C_{mn}(\eta)rJ_m(qr), \tag{B2}$$

where $C_{mn}(\eta)$ is an integration constant that depends on η for the same reason as that of A_{mn}. The inner product between $R_{mn}^{(0)\dagger}$ and Eq. (14) yields

$$\langle R_{mn}^{(0)\dagger}|LR^{(1)}\rangle = -\frac{1}{Z}\left\langle R_{mn}^{(0)\dagger}\left|\left(\frac{\partial}{\partial z}\frac{\partial}{\partial \eta}+\frac{\partial}{\partial \eta}\frac{\partial}{\partial z}\right)(R_{mn}^{(0)}Z)\right\rangle\right. . \tag{B3}$$

For any functions $\mathfrak{F}(r)$ and $\mathfrak{G}(r)$, the inner product is denoted by the (Dirac) bra-ket notation:

$$\langle \mathfrak{F}|\mathfrak{G}\rangle \equiv \int_0^a \mathfrak{F}\mathfrak{G}dr.$$

Since $L^\dagger$ is the adjoint of L, then

$$\langle R_{mn}^{(0)\dagger}|LR_1\rangle = \langle L^\dagger R_{mn}^{(0)\dagger}|R^{(1)}\rangle + R_{mn}^{(0)\dagger}\left.\frac{\partial R^{(1)}}{\partial r}\right|_{r=0}^{a} - R^{(1)}r\left.\frac{\partial}{\partial r}\left(\frac{R_{mn}^{(0)\dagger}}{r}\right)\right|_{r=0}^{r=a}. \tag{B4}$$

The second and third terms of the right-hand side of Eq. (B4), the boundary terms, vanish by virtue of Eq. (9). The first term also vanishes by virtue of Eq. (B1). Equation (B3) thus yields

$$0 = \left\langle R_{mn}^{(0)\dagger}\left|\left(\frac{\partial^2}{\partial z\partial \eta}+\frac{\partial^2}{\partial \eta\partial z}\right)(R_{mn}^{(0)}Z)\right\rangle\right. . \tag{B5}$$

To remind ourselves, $R_{mn}^{(0)}=R_{mn}^{(0)}(r,\eta)$ and $Z=Z(z,\eta)$. The first term in the ket of the above equation can be written as

$$\frac{\partial^2(R_{mn}^{(0)}Z)}{\partial z\partial \eta} = \frac{\partial R_{mn}^{(0)}}{\partial \eta}\frac{\partial Z}{\partial z}+R_{mn}^{(0)}\frac{\partial^2 Z}{\partial z\partial \eta}. \tag{B6}$$

Similarly, the second term can be shown to be given by

$$\frac{\partial^2(R_{mn}^{(0)}Z)}{\partial \eta\partial z} = \frac{\partial R_{mn}^{(0)}}{\partial \eta}\frac{\partial Z}{\partial z}+R_{mn}^{(0)}\frac{\partial^2 Z}{\partial \eta\partial z}. \tag{B7}$$

Let us calculate $\partial^2 Z/\partial z\partial\eta$ and focus on the region $z<z_{co}$. Since Z is given by Eq. (12), differentiating with respect to η and then z:

$$\frac{\partial^2 Z}{\partial z\partial \eta} = -\frac{1}{2\sqrt{k}}\left(\frac{1}{4}Q^{-5/6}\,\mathrm{Ai}(-Q^{2/3})-Q^{-1/6}\,\mathrm{Ai}'(-Q^{2/3})\right), \tag{B8}$$

where

$$Q \equiv \frac{3}{2}\int_z^{z_{co}} k dz$$

and $\mathrm{Ai}'(Q)\equiv d\,\mathrm{Ai}(Q)/dQ$. Interchanging the order of integration yields the following:

$$\frac{\partial^2 Z}{\partial \eta\partial z} = \frac{1}{2\sqrt{k}}\left(\frac{1}{4}Q^{-5/6}\,\mathrm{Ai}(-Q^{2/3})-Q^{-1/6}\,\mathrm{Ai}'(-Q^{2/3})\right). \tag{B9}$$

Comparing Eqs. (B8) and (B9) yields

$$\frac{\partial^2 Z}{\partial z\partial \eta}+\frac{\partial^2 Z}{\partial \eta\partial z} = 0, \tag{B10}$$

illustrating that $\partial/\partial z$ and $\partial/\partial\eta$ do not commute with the technique used here for a nontrivial solution. The same result is obtained for the region $z>z_{co}$.

Using Eqs. (B6), (B7), and (B10), Eq. (B5) can be reduced to

$$0 = \left\langle R_{mn}^{(0)\dagger}\left|\frac{\partial R_{mn}^{(0)}}{\partial \eta}\right\rangle\right. . \tag{B11}$$

Using Eqs. (17) and (B2) in Eq. (B11) yields

$$0 = \frac{\partial A_{mn}}{\partial \eta}\int_0^a rJ_m^2(qr)dr + A_{mn}\int_0^a rJ_m(qr)\frac{\partial J_m(qr)}{\partial \eta}dr. \tag{B12}$$

Letting $y\equiv qr$ and the second term of Eq. (B12) denoted by $\mathcal{T}_2$ yields

$$\mathcal{T}_2 = A_{mn}\frac{1}{q^3}\frac{dq}{d\eta}\int_0^{qa} y^2 J_m(y)\frac{dJ_m(y)}{dy}dy.$$

Using the identity

$$y^2 J_m(y)\frac{dJ_m(y)}{dy} = \frac{d}{dy}\left[\frac{y^2 J_m^2(y)}{2}\right]-yJ_m^2(y)$$

in $\mathcal{T}_2$ yields

$$\mathcal{T}_2 = A_{mn}\left[\frac{a^2 J_m^2(qa)}{2}-\int_0^a rJ_m^2(qr)dr\right]\frac{1}{q}\frac{dq}{d\eta}.$$

Substituting this result back to Eq. (B12) and simplifying, we obtain

$$\frac{1}{A_{mn}}\frac{dA_{mn}}{d\eta} = \left[1-\frac{a^2 J_m^2(qa)}{2\int_0^a rJ_m^2(qr)dr}\right]\frac{1}{q}\frac{dq}{d\eta}.$$

Since $q=\alpha_{mn}/a$ and $J_m(\alpha_{mn})=0$, then

$$A_{mn}(\eta) = \frac{A_{mn}(\eta_{co})}{a(\eta)}, \tag{B13}$$

where $A_{mn}(\eta_{co})$ is a constant and η_{co} is the cutoff location.

APPENDIX C: COUPLING OF ULTRASOUND INTO THE WATER JET

The sound field is generated by a broadband transducer glued to the outer wall of a 22 cm long glass tube with a geometry like that discussed by Goddard and Kaduchak.[17] It is then coupled to the water inside the tube and then to the tapered water jet exiting at the nozzle, as shown in Fig. 2. Here we assume that the liquid jet velocity is negligible compared to the sound speed. Before we can validate the approximate solution of the sound field in a tapered waveguide derived in Sec. III, it is crucial to identify the different modes propagating in the tapered water jet. For a given acoustic mode frequency of the tube, we will determine the mode coupling at the nozzle and identify the acoustic modes that are not cut off at the vicinity of the nozzle.

To determine the resonant frequency in the tube, we consider only the radial and azimuthal dependence of the acoustic fields. This is justified because the piezoelectric transducer and the tube length are both long in comparison with the inner radius of the tube. This assumption reasonably predicts the resonant frequencies of a liquid-loaded tube.[8,17] In this framework, the resonant frequency is given by

$$f_{1\ell} = \frac{\alpha'_{1\ell} c}{2\pi R_o}, \tag{C1}$$

where c is the sound speed in water, R_o is the tube's inner radius, and α'_{1n} is given by $J'_1(\alpha'_{1\ell}) = D(\alpha'_{1\ell})$. The quantity $D(\alpha'_{1\ell})$ is a frequency-dependent parameter. Since the acoustic impedance of the glass tube is much larger than that of water, it is expected that $D \ll 1$. In the limit that the tube's inner wall acts as a rigid wall, the radial acoustic velocity vanishes there and $D=0$.[18] For the purpose of demonstrating mode coupling at the nozzle, the rigid-wall model is a reasonable approximation. Thus, the first two $\alpha'_{1\ell}$ are 1.83 and 5.32. With $R_o = 0.001\,08$ m and $c = 1487$ m/s, the resonant frequency of mode (1, 2) is approximately 1166 kHz, calculated by using Eq. (C1). This is very close to the experimentally determined resonant frequency of 1168 kHz.[8]

The pressure distribution in the tube very close to the nozzle, p^-, is proportional to $-i\omega\rho J_1(\alpha'_{12} r/a)\cos\theta$, as shown in Fig. 8(a). When coupled to the water jet at the nozzle, the sound field experiences a transition of the boundary condition from hard wall to pressure release. This gives rise to the radial redistribution of the acoustic pressure in the water jet waveguide while preserving the azimuthal symmetry. Thus in the water jet waveguide, the eigenfunctions are $J_1(\alpha_{1n} r/a)\cos\theta$, where α_{1n} is a root of $J_1(\alpha_{1n}) = 0$. The waveguide pressure field in the immediate vicinity of the nozzle can then be expressed as

$$p^+ = -i\omega\rho \sum_n c_{1n} J_1\left(\frac{\alpha_{1n}}{a} r\right)\cos\theta.$$

This should be equal to p^-. Thus,

$$B J_1\left(\frac{\alpha'_{12}}{a} r\right)\cos\theta = \sum_n c_{1n} J_1\left(\frac{\alpha_{1n}}{a} r\right)\cos\theta,$$

where B is the amplitude coefficient associated with the pressure in the tube. The coefficient c_{1n} is given by (see Ref. 16, p. 689)

$$c_{1n} = \frac{2B}{a^2 J_2^2(\alpha_{1n})} \int_0^a J_1\left(\alpha'_{12}\frac{r}{a}\right) J_1\left(\alpha_{1n}\frac{r}{a}\right) r dr. \tag{C2}$$

Using the result of Example 11.2.1 of Ref. 16 (p. 691), the coefficient c_{1n} is finally given by

$$c_{1n} = \frac{2B\alpha_{1n}}{\alpha'^2_{12} - \alpha^2_{1n}} \frac{J_0(\alpha_{1n}) J_1(\alpha'_{12})}{J_2^2(\alpha_{1n})}.$$

With $\alpha'_{12} = 5.32$ and the first three α_{1n}, namely: $\alpha_{11} = 3.832$, $\alpha_{12} = 7.016$, and $\alpha_{13} = 10.174$, the first three c_{1n} can be calculated as $c_{11} \approx 0.4838B$, $c_{12} \approx 0.7736B$, and $c_{13} \approx -0.3751B$. It can be verified that

$$\sum_n^\infty c_{1n} = B,$$

as it should be.

Just because the pressure amplitude coefficients of modes $(1,n)$ are nonzero does not mean that they can propagate beyond the nozzle. They are also affected by the properties of the waveguide. A dispersion relation analogous to Eq. (21) should be considered to calculate the complex k_{1n}. With $f = 1169$ kHz (which is close to the experimental resonant frequency of the water-filled tube[8]), $R_o = 0.108$ cm, and $c = 148\,700$ cm/s, this relation yields k_{1n} that are all imaginary except that of mode (1, 1). Hence only mode (1, 1) can propagate beyond the nozzle having a pressure distribution as shown in Fig. 8(b). All the other modes having a $\cos\theta$ angular dependence are evanescent beyond the nozzle and are associated with a localized acoustic field in the jet near the nozzle.

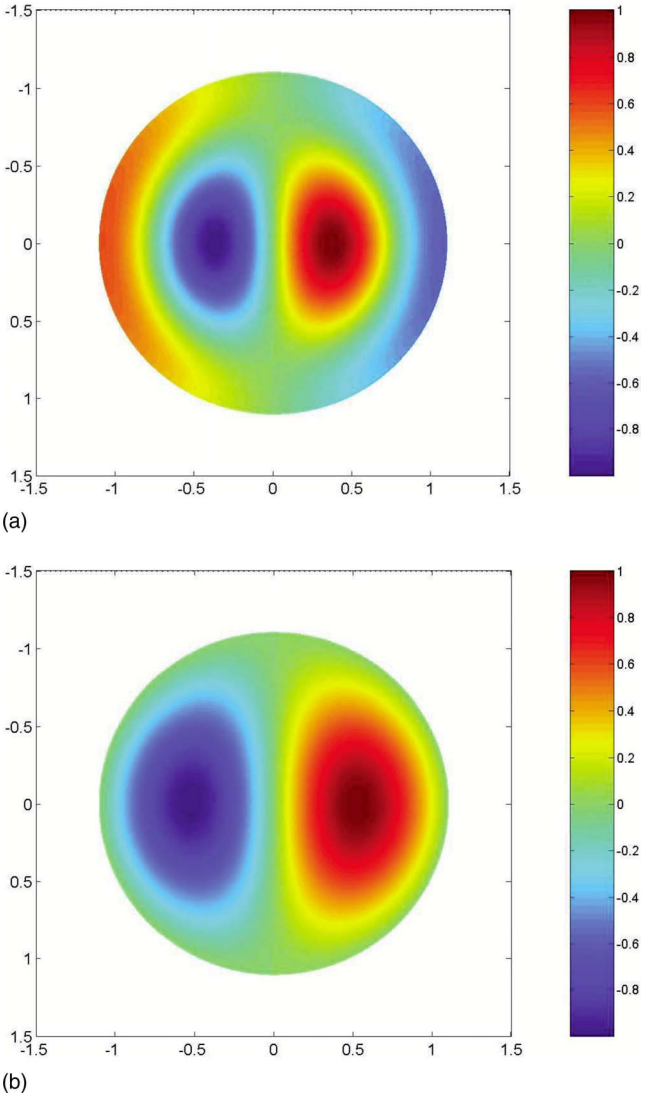

FIG. 8. (Color online) Pressure field distribution (normalized). (a) shows the pressure field distribution of mode (1, 2) within the tube. As the acoustic energy is coupled to the water jet waveguide at the nozzle, the pressure is radially redistributed to accommodate for the new wall condition from elastic hard wall to pressure release. (b) shows the pressure field distribution of mode (1, 1) in the water jet waveguide. The horizontal and vertical axes in both plots are in mm.

[1] J. B. Lonzaga, C. F. Osterhoudt, D. B. Thiessen, and P. L. Marston, "Liquid jet response to internal modulated ultrasonic radiation pressure and stimulated drop production," J. Acoust. Soc. Am. **121**, 3323–3330 (2007).
[2] R. E. Langer, "On the asymptotic solutions of ordinary differential equations, with an application to the Bessel functions of large order," Trans. Am. Math. Soc. **33**, 23–64 (1931).
[3] R. E. Langer, "On the connection formulas and the solutions of the wave equation," Phys. Rev. **51**, 669–676 (1937).

[4]A. H. Nayfeh and D. P. Telionis, "Acoustic propagation in ducts with varying cross sections," J. Acoust. Soc. Am. **54**, 1654–1661 (1973).
[5]A. F. Stevenson, "Exact and approximate equations for wave propagation in acoustic horns," J. Appl. Phys. **22**, 1461–1463 (1951).
[6]B. Z. Katsenelenbaum, "On the theory of irregular acoustic waveguides," Sov. Phys. Acoust. **7**, 159–164 (1961).
[7]R. J. Temkin, "Analytic theory of a tapered gyrotron resonator," Int. J. Infrared Millim. Waves **2**, 629–650 (1981).
[8]J. B. Lonzaga, "Capillary jets in normal gravity: asymptotic stability analysis and excitation using Maxwell and ultrasonic radiation stresses," Ph.D. thesis, Washington State University, 2007.
[9]P. M. Morse and H. Feshbach, *Methods of Theoretical Physics* (McGraw-Hill, New York, 1953), pp. 1092–1105.
[10]L. I. Schiff, *Quantum Mechanics* (McGraw-Hill, New York, 1948), pp. 180–181.
[11]P. Huerre and P. A. Monkewitz, "Local and global instabilities in spatially developing flows," Annu. Rev. Fluid Mech. **22**, 473–537 (1990).
[12]P. A. Monkewitz, P. Huerre, and J. M. Chomaz, "Global linear stability analysis of weakly non-parallel shear flows," J. Fluid Mech. **251**, 1–20 (1993).
[13]S. W. Rienstra, "Sound transmission in slowly varying circular and annular lined ducts with flow," J. Fluid Mech. **380**, 279–296 (1999).
[14]M. J. Hancock and J. W. M. Bush, "Fluid pipes," J. Fluid Mech. **466**, 285–304 (2002).
[15]A. Nayfeh, *Perturbation Methods* (Wiley, New York, 1973), pp. 340–341.
[16]G. B. Arfken and H. J. Weber, *Mathematical Methods for Physicists* (Harcourt Academic, San Diego, 2001), pp. 575–577.
[17]G. Goddard and G. Kaduchak, "Ultrasonic particle concentration in a line-driven cylindrical tube," J. Acoust. Soc. Am. **117**, 3440–3447 (2005).
[18]W. Wei, D. B. Thiessen, and P. L. Marston, "Acoustic radiation force on a compressible cylinder in a standing wave," J. Acoust. Soc. Am. **116**, 201–208 (2004).

Temperature effects in ultrasonic Lamb wave structural health monitoring systems

Francesco Lanza di Scalea[a] and Salvatore Salamone[b]
NDE and Structural Health Monitoring Laboratory, Department of Structural Engineering, University of California, 9500 Gilman Drive, M.C. 0085, La Jolla, San Diego, California 92093-0085

(Received 19 February 2008; revised 24 April 2008; accepted 27 April 2008)

There is a need to better understand the effect of temperature changes on the response of ultrasonic guided-wave pitch-catch systems used for structural health monitoring. A model is proposed to account for all relevant temperature-dependent parameters of a pitch-catch system on an isotropic plate, including the actuator-plate and plate-sensor interactions through shear-lag behavior, the piezoelectric and dielectric permittivity properties of the transducers, and the Lamb wave dispersion properties of the substrate plate. The model is used to predict the S_0 and A_0 response spectra in aluminum plates for the temperature range of −40–+60 °C, which accounts for normal aircraft operations. The transducers examined are monolithic PZT-5A [PZT denotes Pb(Zr–Ti)O_3] patches and flexible macrofiber composite type P1 patches. The study shows substantial changes in Lamb wave amplitude response caused solely by temperature excursions. It is also shown that, for the transducers considered, the response amplitude changes follow two opposite trends below and above ambient temperature (20 °C), respectively. These results can provide a basis for the compensation of temperature effects in guided-wave damage detection systems.
 [DOI: 10.1121/1.2932071]

PACS number(s): 43.35.Zc, 43.35.Yb, 43.40.Le, 43.38.Fx [YHB] Pages: 161–174

I. INTRODUCTION

With the advent of condition-based maintenance of structures, structural health monitoring (SHM) systems using permanently attached piezoelectric patches [often Pb(Zr–Ti)O_3 (PZT)] for ultrasonic guided-wave testing are becoming increasingly popular. While the wave actuation and sensing properties of PZT elements have been studied extensively, the effect of temperature variation is much less understood. However, temperature effects are critical in structures such as aircraft which can experience changes from −40 °C (during high altitude flights) to +60 °C (during storage in closed hangers). What is missing is a model that includes the cumulative role of transducer elements (actuator and sensor), substrate structure, and transducer/structure interaction to predict the full pitch-catch guided-wave response under changing temperature.

One of the earliest works on the temperature effects on Lamb wave signals was performed by Blaise and Chang (2001) who considered a pitch-catch arrangement between 50 and 150 kHz on sandwich panels at low temperatures (−90 °C). The authors observed a decrease in wave amplitude and time of flight from ambient temperature to −90 °C, and they developed an empirical model to fit the experimental data. Lee *et al.* (2003) examined experimentally the effect of high temperature values (35–70 °C) on the response of PZT patches in an S_0 pitch-catch configuration on an aluminum plate. They measured a decrease in S_0 amplitude with increasing temperature, and they suggested different feature extraction strategies to detect damage in a changing temperature environment. Chambers *et al.* (2006) acquired pulse-echo measurements in aluminum plates by using Lamb wave transducers by Metis Design Corporation at high temperature (85 °C). A drop in wave amplitude from room temperature was observed, and it was justified by a degradation of the couplant between the plate and the clamp used to produce a wave reflection. Extremely high temperatures, up to 230 °C, were considered by Schulz *et al.* (2003) who used PZT-5A patches as free vibration sensors bonded on aluminum beams by using various adhesives. It was experimentally observed that the sensing performance of the patches degraded with increasing temperature. This was attributed to the loss of piezoelectric properties through depoling and to the increased compliance of the patch-beam adhesive layer.

Additional work on temperature effects on guided-wave SHM systems was performed in the area of reverberating signals. Konstantinidis *et al.* (2006) isolated the variation in wave amplitude between 22 and 32 °C for various portions of Lamb wave measurements in aluminum plates, specifically coherent noise, first arrivals of S_0 and A_0 modes, and their edge reflections. They experimentally observed that temperature changes result in shifts in wave arrival times and in center frequency of the received waves under constant excitation frequency. These effects were explained by shifts in the wave dispersion curves due to thermal expansion and elastic properties of the plate. Lu and Michaels (2005) and Michaels and Michaels (2005) examined the difference in various damage-sensitive features of diffuse Lamb wave signals at temperatures varying between 5 and 40 °C. Their main experimental observation was a changing time of flight, which was attributed to thermal expansion and Young's modulus of the substrate. They recommended adopting a

[a]Electronic mail: flanza@ucsd.edu
[b]Electronic mail: ssalamone@ucsd.edu

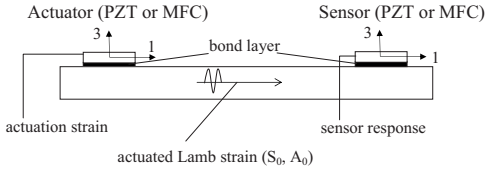

FIG. 1. Problem statement: pitch-catch Lamb wave monitoring by piezoelectric patches.

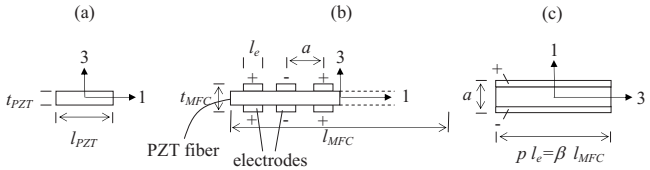

FIG. 2. Schematics for (a) monolithic PZT patch, (b) composite MFC type P1 patch, and (c) equivalent model for MFC type P1 sensor patch.

"bank" of baseline signals acquired at the various temperatures to discriminate the effects of damage from those of environmental changes.

Among the most comprehensive studies on temperature effects on guided-wave signals from PZT patches is the work by Raghavan and Cesnik (2007). This paper examined the pitch-catch response of PZT-5A patches for temperature range internal to spacecraft structures (20–150 °C), limited to the S_0 mode at the specific frequency of 120 kHz. Pitch-catch measurements were taken on an aluminum plate in an autoclave showing an increase in S_0 time of flight with increasing temperature and a nonmonotonic amplitude change (increasing amplitude from 20 to 90 °C and decreasing amplitude from 90 to 150 °C). A theoretical model was developed to corroborate the experiment. The temperature dependence of several parameters was included in the model. The PZT/structure interaction was modeled by perfect-bond conditions, i.e., the classical pin-force model with two Dirac functions for the shear stress at the PZT actuator ends (Raghavan and Cesnik 2005). The properties of the bond layer were considered to be constant with temperature, and shear-lag effects were approximated by the reduction in PZT length ("effective length"). While the agreement between model and experiment was found to be satisfactory for the wave time-of-flight results, the discrepancies found for the wave amplitude results were attributed by the authors to the assumption of perfect bond and constant adhesive layer properties through the temperature range.

The present study continues the work on the temperature effects in Lamb-wave SHM systems. The full temperature range typical of aircraft operations (−40–+60 °C) is considered in a large Lamb frequency range of ~100–500 kHz. The proposed temperature-dependent model combines the steps of (a) wave generation by the actuator patch, (b) wave propagation in the substrate plate, and (c) wave detection by the sensor patch. Actuator-plate and sensor-plate interactions are modeled by shear-lag theories. The study considers monolithic PZT patches and macrofiber composite (MFC) patches. MFC patches, originally developed at NASA Langley Research Center for low-frequency structural control (Wilkie *et al.* 2000, Sodano *et al.* 2004), are recently being used for guided-wave transduction owing to their superior flexibility and durability compared to monolithic PZTs (Thien *et al.* 2005, Lanza di Scalea *et al.* 2007b, Matt and Lanza di Scalea 2007).

II. PROBLEM STATEMENT

The problem examined (Fig. 1) is that of a piezoelectric patch actuator on an isotropic (aluminum) plate exciting the fundamental Lamb modes which are detected by a similar piezoelectric patch sensor (pitch catch). The cases of monolithic PZT patches and MFC patches are considered. The problem is studied in two dimensions and assuming plane waves.

III. ACTUATION STRAIN

A. Monolithic PZT actuator

The strain generated by an excitation voltage in a monolithic PZT actuator is governed by the converse piezoelectric effect (IEEE 1978),

$$\boldsymbol{\varepsilon} = -\boldsymbol{dE} + \boldsymbol{S\sigma}, \tag{1}$$

where ε is the strain vector (6×1), $\boldsymbol{d}$ is the piezoelectric coefficient matrix (6×3), $\boldsymbol{E}$ is the electric field vector (3×1), $\boldsymbol{S}$ is the elastic compliance matrix (6×6), and $\boldsymbol{\sigma}$ is the stress vector (6×1).

Assuming in-plane axes (1, 2) and out-of-plane axis 3 for the PZT actuator [Fig. 2(a)], the actuated normal strains from Eq. (1) are given by

$$\begin{bmatrix} \varepsilon_{11} \\ \varepsilon_{22} \\ \varepsilon_{33} \end{bmatrix} = \begin{bmatrix} 0 & 0 & d_{31} \\ 0 & 0 & d_{32} \\ 0 & 0 & d_{33} \end{bmatrix} \begin{bmatrix} E_1 \\ E_2 \\ E_3 \end{bmatrix}. \tag{2}$$

For monolithic PZTs ($d_{31}=d_{32}$), poled along the thickness direction 3 ($E_1=E_2=0$), the actuation strain $\varepsilon_{\mathrm{PZT}}$ simplifies to

$$\varepsilon_{\mathrm{PZT}} = \varepsilon_{11} = d_{31}E_3 = -d_{31}\frac{V_{\mathrm{appl}}}{t_{\mathrm{PZT}}}, \tag{3}$$

where V_{appl} is the applied voltage and t_{PZT} is the thickness of the actuator.

B. Composite MFC actuator

MFC type P1 transducers are composed of PZT fibers that are unidirectionally aligned, embedded into an epoxy matrix, and sandwiched between two sets of interdigitated electrode patterns (Smart Material Corporation, Saratoga, FL). Because of their polymer-based composite design, MFC transducers are more flexible and durable than monolithic PZT transducers. The model in Fig. 2(b) shows the in-plane axes (1, 2), out-of-plane axis 3, interelectrode spacing a, and electrode length l_e. The actuated normal strain for the MFC is given by

$$\begin{bmatrix} \varepsilon_{11} \\ \varepsilon_{22} \\ \varepsilon_{33} \end{bmatrix} = \begin{bmatrix} d_{11} & 0 & 0 \\ d_{12} & 0 & 0 \\ d_{13} & 0 & 0 \end{bmatrix} \begin{bmatrix} E_1 \\ E_2 \\ E_3 \end{bmatrix}. \tag{4}$$

Poling is now along the in-plane (fiber) direction 1 ($E_2=E_3=0$), and the actuation strain $\varepsilon_{\mathrm{MFC}}$ is given by

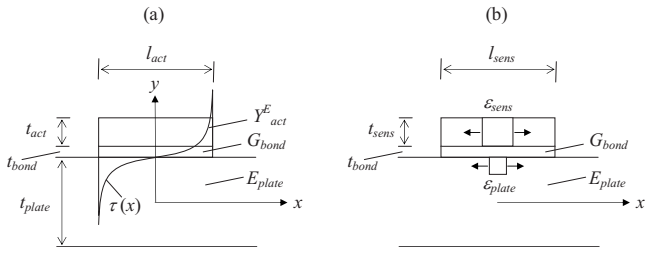

FIG. 3. (a) Shear-lag actuator model and (b) shear-lag sensor model.

$$\varepsilon_{\mathrm{MFC}} = \varepsilon_{11} = d_{11}E_1 = -d_{11}\frac{V_{\mathrm{appl}}}{a}. \tag{5}$$

The equivalence between a monolithic PZT actuator and a type P1 MFC actuator is, thus, readily obtained by considering the appropriate piezoelectric coefficient (d_{11} versus d_{31}) and replacing the PZT thickness t_{PZT} with the MFC interelectrode spacing a.

IV. ACTUATED STRAIN IN THE PLATE

A. Actuated shear stress

The strain generated in the plate by the actuator is here modeled by coupling the shear-lag theory of Crawley and de Luis (1987) with the Lamb wave generation model by Giurgiutiu (2005). The present model is, therefore, complementary to these previous studies because the former work was not concerned with wave generation or detection, and the latter work did not consider shear-lag phenomena.

Assuming the surface-bonded actuator system in Fig. 3(a), the nondimensional shear-lag parameter Γ from Crawley and de Luis (1987) is given by

$$\Gamma^2 = \frac{G_{\mathrm{bond}}}{Y^E_{\mathrm{act}}}\frac{l^2_{\mathrm{act}}}{t_{\mathrm{bond}}t_{\mathrm{act}}}\frac{\Psi+\alpha}{\Psi}, \tag{6}$$

where G_{bond} and t_{bond} are the shear modulus and thickness of the adhesive layer, Y^E_{act}, l_{act}, and t_{act} are the in-plane Young's modulus, length, and thickness of the PZT or MFC actuator, the factor α is 1 or 3 for extensional or bending actuation, respectively, and Ψ is the plate-actuator stiffness ratio given by

$$\Psi = \frac{E_{\mathrm{plate}}t_{\mathrm{plate}}}{Y^E_{\mathrm{act}}t_{\mathrm{act}}}. \tag{7}$$

It should be said that the above values of α rely on low-frequency plate theory and are not necessarily applicable to high frequency times plate thickness products. Substitution of Eq. (7) into Eq. (6) yields

$$\Gamma^2 = \frac{G_{\mathrm{bond}}l^2_{\mathrm{act}}}{t_{\mathrm{bond}}}\left(\frac{1}{Y^E_{\mathrm{act}}t_{\mathrm{act}}} + \frac{\alpha}{E_{\mathrm{plate}}t_{\mathrm{plate}}}\right). \tag{8}$$

It is well-known that the shear-lag effect increases with increasing compliance and thickness of the bond layer. Perfect bonding (no shear lag) is achieved for a thin and stiff bond layer where $\Gamma \to \infty$.

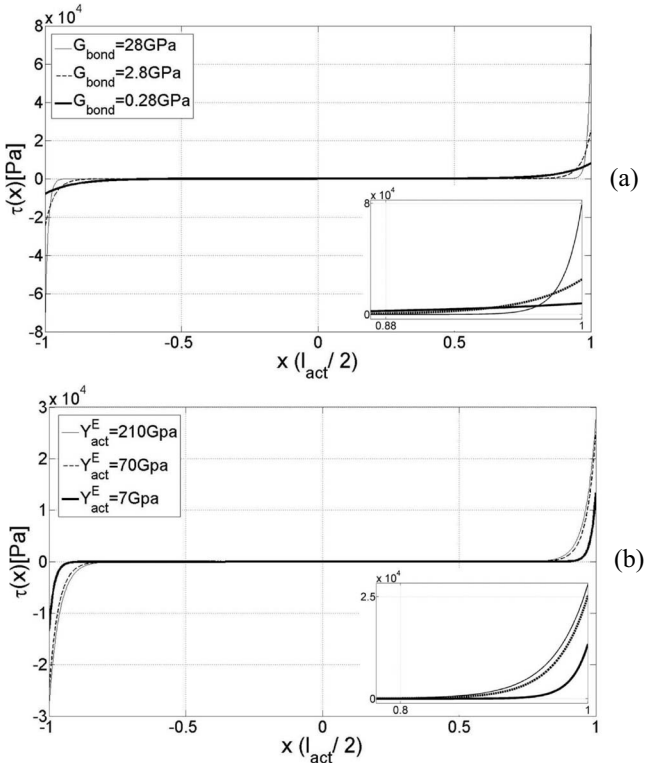

FIG. 4. In-plane shear stress at the actuator/plate interface under shear-lag conditions: (a) changing bond layer stiffness and (b) changing actuator stiffness. Insets zoom near the end of the actuator.

In a general shear-lag condition, Crawley and de Louis' (1987) distribution of in-plane shear stresses applied by the actuator to the bond layer into the plate, $\tau(x)$, can be rewritten as

$$\tau(x) = -\frac{G_{\mathrm{bond}}l_{\mathrm{act}}\varepsilon_{\mathrm{act}}}{t_{\mathrm{bond}}\Gamma\cosh\Gamma}\sinh\left[\Gamma\left(\frac{2x}{l_{\mathrm{act}}}\right)\right] = A\sinh(Bx), \tag{9}$$

where the actuation strain is $\varepsilon_{\mathrm{act}}=\varepsilon_{\mathrm{PZT}}$ in Eq. (3) for a monolithic PZT and $\varepsilon_{\mathrm{act}}=\varepsilon_{\mathrm{MFC}}$ in Eq. (5) for a MFC. The variables A and B are

$$A = -\frac{G_{\mathrm{bond}}l_{\mathrm{act}}\varepsilon_{\mathrm{act}}}{t_{\mathrm{bond}}\Gamma\cosh\Gamma}, \quad B = \frac{2\Gamma}{l_{\mathrm{act}}}. \tag{10}$$

Figure 4(a) shows the effect of changing bond layer stiffness on the generated shear stress. Figure 4(b) shows, instead, the effect of changing plate/actuator stiffness ratio. Both cases consider a baseline PZT-5A actuator (Y^E_{act}=70 GPa, l_{act}=10 mm, t_{act}=0.63 mm, $d_{31}=-168\times10^{-12}$ m/V), excited by a unity voltage (V_{appl}=1 V), bonded by an adhesive layer (t_{bond}=0.01 mm) on an aluminum plate (E_{plate}=70 GPa, G_{plate}=27 GPa, t_{plate}=1.58 mm). Extensional actuation is considered (α=1).

In Fig. 4(a), $\tau(x)$ from Eq. (9) is plotted for a nominal bond layer stiffness of G_{bond}=2.8 GPa (corresponding to a shear-lag parameter Γ=68.4) and for two extreme cases of a very stiff adhesive (G_{bond}=28 GPa or Γ=216.4) and a very compliant adhesive (G_{bond}=0.28 GPa or Γ=21.6). The PZT actuator stiffness is maintained constant at Y^E_{act}=70 GPa. This figure shows the known result that a stiffer adhesive increasingly confines the shear stress transfer toward the ac-

tuator's ends. However, the different adhesive stiffnesses maintain a roughly constant area under the $\tau(x)$ curve [see inset of Fig. 4(a)], indicating little change in the net force transferred to the plate.

In Fig. 4(b), $\tau(x)$ is plotted for a constant $G_{\text{bond}}=2.8$ GPa and with changing actuator stiffness from a nominal $Y^E_{\text{act}}=70$ GPa ($E_{\text{plate}}/Y^E_{\text{act}}=1$) to a very stiff actuator ($Y^E_{\text{act}}=210$ GPa or $E_{\text{plate}}/Y^E_{\text{act}}=0.33$) and a very compliant actuator ($Y^E_{\text{act}}=7$ GPa or $E_{\text{plate}}/Y^E_{\text{act}}=10$). The most relevant effect in this case is the change in the area under the $\tau(x)$ curve [see inset of Fig. 4(b)], indicating a smaller force transfer with decreasing stiffness of the actuator.

The shear stress distribution of Eq. (9) provides the excitation of the Lamb waves generated in the plate. This problem was studied by Giurgiutiu (2005) by taking a spatial Fourier transform on the excitation to move to the wave number domain k. The perfect-bond condition assumed by Giurgiutiu (2005), i.e., two Dirac functions for $\tau(x)$ at the actuator's ends, readily admits a closed-form spatial Fourier transform. It is here shown that a closed-form Fourier transform $\tilde{\tau}(k)$ can also be obtained in the more general shear-lag case, where $\tau(x)$ is a hyperbolic sine function [Eq. (9)], once the finite length of the actuator is taken into account. The Fourier transform linearity property ($\widetilde{Zf(x)}|_k=Z\widetilde{f(x)}|_k$) and scaling property ($\widetilde{f(Zx)}|_k=1/|Z|\,\widetilde{f(x)}|_{k/Z}$) are first invoked. Considering that the shear stress $\tau(x)$ is bounded by the actuator length in $-l_{\text{act}}/2\leqslant x\leqslant l_{\text{act}}/2$, applying the scaling property also requires changing the integration limits of the Fourier transform to the new variable $-Zl_{\text{act}}/2\leqslant Zx\leqslant Zl_{\text{act}}/2$,

$$\begin{aligned}\tilde{\tau}(k)&=A\,\widetilde{\sinh(Bx)}|_k=\frac{A}{|B|}\int_{-Bl_{\text{act}}/2}^{Bl_{\text{act}}/2}\left(\frac{e^x-e^{-x}}{2}\right)e^{-i(k/B)x}dx\\&=\frac{A}{|B|}\left[\frac{e^{(Bl_{\text{act}}/2)(1-ik/B)}-e^{(-Bl_{\text{act}}/2)(1-ik/B)}}{2\left(1-\frac{ik}{B}\right)}\right.\\&\left.+\frac{e^{(-Bl_{\text{act}}/2)(1+ik/B)}-e^{(Bl_{\text{act}}/2)(1+ik/B)}}{2\left(1+\frac{ik}{B}\right)}\right].\end{aligned}\tag{11}$$

By substituting A and B from Eq. (10), using the properties of hyperbolic functions [$\cosh(ix)=\cos x$; $\sinh(ix)=i\sin x$], Eq. (11) can be simplified to

$$\begin{aligned}\tilde{\tau}(k)=&-2i\frac{G_{\text{bond}}l^2_{\text{act}}}{t_{\text{bond}}(4\Gamma^2+k^2l^2_{\text{act}})}\varepsilon_{\text{act}}\\&\times\left[kl_{\text{act}}\frac{\tanh(\Gamma)}{\Gamma}\cos\left(\frac{kl_{\text{act}}}{2}\right)-2\sin\left(\frac{kl_{\text{act}}}{2}\right)\right].\end{aligned}\tag{12}$$

Points of zero actuation are found by setting Eq. (12) to 0, which yields

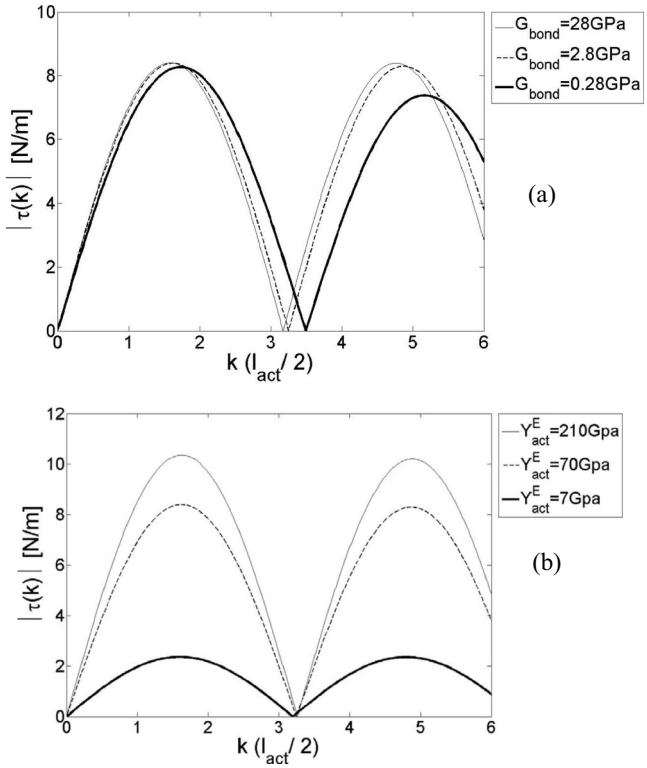

FIG. 5. Magnitude of spatial Fourier transform of in-plane shear stress at the actuator/plate interface under shear-lag conditions: (a) changing bond layer stiffness and (b) changing actuator stiffness.

$$|\tilde{\tau}(k)|=0\quad\text{(zero actuation)}\quad\text{when}\quad\frac{\tan\left(k\frac{l_{\text{act}}}{2}\right)}{k\frac{l_{\text{act}}}{2}}=\frac{\tanh(\Gamma)}{\Gamma}.\tag{13}$$

This equation can be solved numerically. For the perfect-bond case ($\Gamma\to\infty$), since $\lim_{\Gamma\to\infty}\tanh(\Gamma)/\Gamma=0$, points of zero actuation are found when $\tan(kl_{\text{act}}/2)=0$ or $kl_{\text{act}}/2=n\pi$ for $n=0,1,2\ldots$ (i.e., actuator length equals an integer multiple of the wavelength λ). This coincides with the known "wavelength tuning" result by Giurgiutiu (2005) under perfect-bond assumptions. Points of maximum actuation are, instead, found by setting $\partial|\tilde{\tau}(k)|/\partial k=0$ in Eq. (12). This equation can also be solved numerically. For perfect bond ($\Gamma\to\infty$), one can demonstrate that the maximum actuation occurs for $kl_{\text{act}}/2=\pi(2n-1)/2$ (i.e., actuator length equals an odd multiple of the half wavelength $\lambda/2$), which also retrieves Giurgiutiu's (2005) perfect-bond model.

The shear stress Fourier transform $|\tilde{\tau}(k)|$ from Eq. (12) is plotted versus the nondimensional wave number ($kl_{\text{act}}/2$), for the same cases previously presented in Fig. 4. Changing bond layer stiffness is shown in Fig. 5(a), and changing plate-actuator stiffness is shown in Fig. 5(b). In both graphs, the wavelength tuning conditions are evident. From Fig. 5(a), the predominant effect of a changing adhesive stiffness is a slight shift in zeroes and maxima of the $|\tilde{\tau}(k)|$ curve, with little effect on the magnitude of $|\tilde{\tau}(k)|$. As discussed in the previous Fig. 4(a), a stiffer adhesive layer approaches perfect bond where the ideal wavelength tuning conditions above

apply. A decreasing G_{bond} moves the shear stress transfer away from the actuator's ends. This decreases the "effective length" of the actuator l_{eff}, which shifts the $|\tilde{\tau}(k)|$ curve toward increasing l_{act} (hence, $k \times l_{\text{act}}$) to compensate for the shorter l_{eff}, hence, the shifts in Fig. 5(a). However, these shifts are not expected to be substantial for realistic ranges of adhesive properties. It is the actuator stiffness Y^E_{act} that influences highly the magnitude of the stress transfer, as shown in Fig. 5(b). Clearly, $|\tilde{\tau}(k)|$ substantially decreases with degrading actuator stiffness.

Under temperature variations, both G_{bond} and Y^E_{act} will vary. As will be shown later, the temperature range of interest in this study (−40–+60 °C) will have a substantial influence on the actuation magnitude, with little change in the wavelength tuning points.

B. Generated Lamb strain

The Lamb strain generated by the actuator is found from the mode expansion formulation by Giurgiutiu (2005) coupled with the Fourier transform of the shear stress excitation in the shear-lag case derived in Eq. (12). Damping in the plate is neglected.

The time-domain in-plane strain at the surface of the plate and in the direction of wave propagation x is given using the residue theorem by

$$\varepsilon_x(x,t)\big|_{y=t_{\text{plate}}/2} = \frac{1}{2G_{\text{plate}}}\left[\sum_{k^S} \tilde{\tau}(k^S)\underbrace{\frac{N_S(k^S)}{\partial D_S(k^S)/\partial k}}_{\text{Symmetric modes}} e^{i(k^S x-\omega t)} + \sum_{k^A} \tilde{\tau}(k^A)\underbrace{\frac{N_A(k^A)}{\partial D_A(k^A)/\partial k}}_{\text{Antisymmetric modes}} e^{i(k^A x-\omega t)}\right], \tag{14}$$

where $k^S_i(\omega)$ are the eigenvalues for the Lamb symmetric modes (solutions of $D_S=0$), $k^A_i(\omega)$ are the eigenvalues for the Lamb antisymmetric modes (solutions of $D_A=0$), and the remaining terms are the following well-known Rayleigh–Lamb expressions (Rose 1999):

$$\begin{aligned} N_S(k) &= kq(k^2+q^2)\cos\left(p\frac{t_{\text{plate}}}{2}\right)\cos\left(q\frac{t_{\text{plate}}}{2}\right), \\ D_S(k) &= (k^2-q^2)^2\cos\left(p\frac{t_{\text{plate}}}{2}\right)\sin\left(q\frac{t_{\text{plate}}}{2}\right) + 4k^2pq\sin\left(p\frac{t_{\text{plate}}}{2}\right)\cos\left(q\frac{t_{\text{plate}}}{2}\right), \\ N_A(k) &= kq(k^2+q^2)\sin\left(p\frac{t_{\text{plate}}}{2}\right)\sin\left(q\frac{t_{\text{plate}}}{2}\right), \\ D_A(k) &= (k^2-q^2)^2\sin\left(p\frac{t_{\text{plate}}}{2}\right)\cos\left(q\frac{t_{\text{plate}}}{2}\right) + 4k^2pq\cos\left(p\frac{t_{\text{plate}}}{2}\right)\sin\left(q\frac{t_{\text{plate}}}{2}\right), \end{aligned} \tag{15}$$

$$p^2 = \left(\frac{\omega^2}{c_L^2}-k^2\right), \quad q^2 = \left(\frac{\omega^2}{c_T^2}-k^2\right),$$

with c_L and c_T as the bulk longitudinal and shear velocities, respectively.

By substituting $\tilde{\tau}(k)$ from Eq. (12) into Eq. (14) and rearranging, the actuated surface strain in the plate can be written as

$$\varepsilon_x(x,t)\big|_{y=t_{\text{plate}}/2} = i\varepsilon_x e^{i(kx-\omega t)}, \tag{16}$$

where the actuated wave amplitude is

$$\varepsilon_x = \frac{\tau_1}{2G_{\text{plate}}}\left[\sum_{k^S} \tau_2(k^S)\underbrace{\frac{N_S(k^S)}{\partial D_S(k^S)/\partial k}}_{\text{Symmetric modes}} + \sum_{k^A} \tau_2(k^A)\underbrace{\frac{N_A(k^A)}{\partial D_A(k^A)/\partial k}}_{\text{Antisymmetric modes}}\right]. \tag{17}$$

In Eq. (17), the shear stress expression is decomposed into the following constant term, τ_1, and k-dependent term, $\tau_2(k)$:

$$\begin{aligned} \tau_1 &= \frac{-2G_{\text{bond}}l^2_{\text{act}}\varepsilon_{\text{act}}}{t_{\text{bond}}}, \\ \tau_2(k) &= \frac{kl_{\text{act}}\dfrac{\tanh(\Gamma)}{\Gamma}\cos\left(\dfrac{kl_{\text{act}}}{2}\right)-2\sin\left(\dfrac{kl_{\text{act}}}{2}\right)}{4\Gamma^2+k^2l^2_{\text{act}}}. \end{aligned} \tag{18}$$

Figure 6 shows the actuated strain amplitude in the plate from Eq. (17) for the fundamental Lamb modes S_0 and A_0 as a function of the nondimensional wave number $(kl_{\text{act}}/2)$. The case of a monolithic PZT actuator in Fig. 6(a) is compared to that of a MFC type P1 actuator in Fig. 6(b). The graphs assume the properties of actuators, adhesive layer, and plate listed in Table I at ambient temperature. The excitation voltage is unity ($V_{\text{appl}}=1$ V). In both graphs, the wavelength tuning conditions are evident. The amplitude of the actuated wave changes depending on the particular distribution of surface strain for S_0 and A_0. The PZT actuator [Fig. 6(a)] generates S_0 more efficiently than A_0 at low kl values. The MFC actuator [Fig. 6(b)] generates A_0 more efficiently than S_0 throughout the kl range. Also noticeable is that the wave amplitude generated by the MFC actuator is one order of magnitude larger than that generated by the PZT actuator of the same length and for the same (unity) excitation voltage. This is primarily due to the actuator's geometrical properties (MFC interelectrode spacing a smaller than PZT thickness t_{act}) and piezoelectric properties (MFC constant d_{11} larger than PZT constant d_{31}), which both influence the actuation strains in Eqs. (3) and (5). Interestingly, it will be shown later that the geometrical parameters of interelectrode spacing for the MFC and actuator thickness for the PZT, which are relevant to the actuator generation efficiency, do not influence the actuator-sensor pitch-catch response.

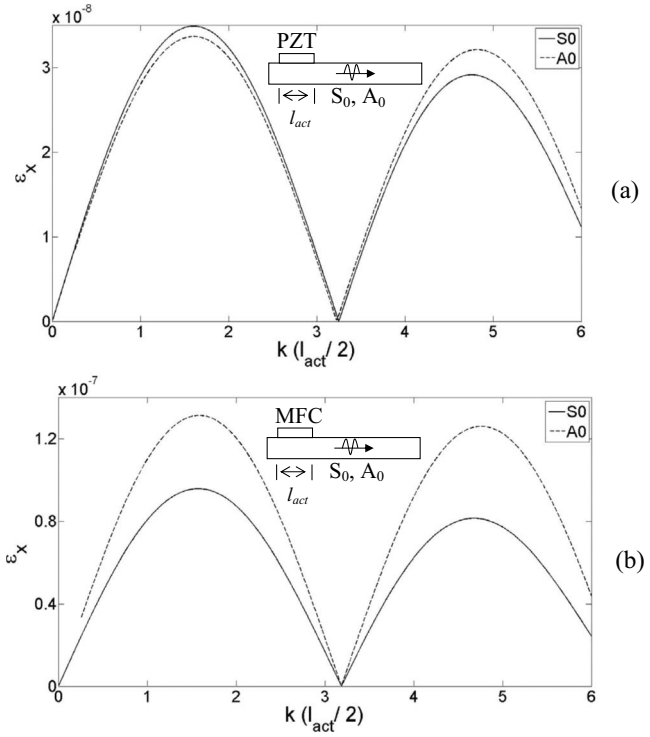

FIG. 6. Actuated strain amplitude of the fundamental S_0 and A_0 modes in a 1.58-mm-thick aluminum plate: (a) monolithic PZT actuator and (b) composite MFC-P1 actuator.

V. SENSOR RESPONSE

A. Shear-lag model for sensor

The shear-lag behavior considered for the actuator-plate interaction must now be extended to the plate-sensor interaction Fig. 3(b). To model the plate-*sensor* interaction, the equilibrium and compatibility conditions considered by Crawley and de Luis (1987) for their study of the *actuator*-plate system can be applied. However, different boundary conditions must be considered in the case of the sensor, which lead to a different expression for the strain transferred to the sensor.

The shear-lag model by Crawley and de Luis (1987) leads to a pair of uncoupled fourth-order differential equations. As general solutions of these equations, the strain at the surface of the plate $\varepsilon_{\text{plate}}$, and the strain transferred to the sensor $\varepsilon_{\text{sens}}$ are

$$\varepsilon_{\text{plate}} = B_1 + B_2\frac{2x}{l_{\text{sens}}} + B_3\sinh\left(\Gamma\frac{2x}{l_{\text{sens}}}\right) + B_4\cosh\left(\Gamma\frac{2x}{l_{\text{sens}}}\right), \tag{19}$$

$$\varepsilon_{\text{sens}} = B_1 + B_2\frac{2x}{l_{\text{sens}}} + \frac{\Psi}{\alpha}B_3\sinh\left(\Gamma\frac{2x}{l_{\text{sens}}}\right) - \frac{\Psi}{\alpha}B_4\cosh\left(\Gamma\frac{2x}{l_{\text{sens}}}\right),$$

where l_{sens} is the sensor length in the wave propagation direction, and Ψ and Γ are the shear-lag terms given in Eqs. (7) and (8) with the substitution of the actuator properties with the sensor properties. The four integration constants B_i are found by applying the following boundary conditions at the ends of the sensor:

$$\varepsilon_{\text{plate}} = \varepsilon_x(\text{Lamb strain}) \quad \text{and } \varepsilon_{\text{sens}} = 0 \quad \text{at } x = \pm\, l_{\text{sens}}/2. \tag{20}$$

These assume that the strain in the plate is due to the Lamb waves and the sensor ends are free from normal stresses. These yield the following constants:

$$B_1 = \varepsilon_x\Psi/(\alpha+\Psi), \quad B_2 = B_3 = 0, \qquad B_4 = \varepsilon_x\alpha\,\text{sech}(\Gamma)/(\alpha+\Psi). \tag{21}$$

Notice that the integration constants for the sensor case are different from those derived by Crawley and de Luis (1987)for the actuator case. Substitution of Eq. (21) into Eq. (19) provides the following solution:

$$\varepsilon_{\text{sens}} = \varepsilon_x\left(\frac{\Psi}{\alpha+\Psi}\right)\left[1 - \frac{\cosh\left(\Gamma\frac{2x}{l_{\text{sens}}}\right)}{\cosh\Gamma}\right], \tag{22}$$

which is the final expression of the strain transferred to the sensor $\varepsilon_{\text{sens}}$ as a function of the incoming Lamb strain in the plate ε_x and the shear-lag parameters Ψ, Γ, and α.

TABLE I. Ambient temperature properties of aluminum plate, adhesive layer, monolithic PZT patch, and composite MFC patch.

Aluminum plate					
E_{plate}=70 GPa		G_{plate}=27 GPa		t_{plate}=1.58 mm	
Transducer-plate adhesive layer					
	G_{bond}=2.8 GPa			t_{bond}=0.01 mm	
Monolithic PZT patch					
Y^E=70 GPa	ν=0.3	$d_{31}=-168\times10^{-12}$ m/V	$e_{33}=15\times10^{-9}$ F/m	l_{act}=10 mm	t_{act}=0.63 mm
Composite MFC-P1 patch					
Y_1^E=30 GPa	Y_2^E=7.65 GPa	ν_{12}=0.31		$d_{11}=404\times10^{-12}$ m/V	$d_{12}=-168\times10^{-12}$ m/V
$e_{11}=15\times10^{-9}$ F/m	β=0.5	a=0.1 mm		l_{act}=10 mm	t_{act}=0.2 mm

B. Sensor output

This subsection will derive the voltage output generated by the sensor as a result of the strain in Eq. (22). The direct piezoelectric effect can be written as (IEEE 1978)

$$\boldsymbol{D} = \boldsymbol{eE} + \boldsymbol{d\sigma}, \tag{23}$$

where $\boldsymbol{D}$ is the electric displacement vector (3×1), $\boldsymbol{e}$ is the dielectric permittivity matrix (3×3), and $\boldsymbol{E}$, $\boldsymbol{d}$, and $\boldsymbol{\sigma}$ represent the electric field, piezoelectric coefficient, and stress components.

1. Monolithic PZT sensor

The voltage response of a surface-mounted PZT sensor subjected to ultrasonic waves was derived in a recent work (Lanza di Scalea *et al.* 2007a). This work considered a monolithic PZT patch ($d_{31}=d_{32}$) poled along the thickness direction 3 ($E_1=E_2=0$), under plane stress conditions (thin sensor, $\sigma_{33}=\sigma_{13}=\sigma_{23}=0$), and modeled as an open circuit ($\int D_3 dA=0$). This previous work neglected shear-lag effects; hence, the strain in the sensor $\varepsilon_{\text{sens}}$ was considered to be equal to the Lamb strain in the substrate plate ε_x of Eq. (17). The work is here extended to account for shear lag, therefore, using Eq. (22) for the strain transferred to the sensor. The voltage output V_{PZT} is found by integrating the in-plane strain $\varepsilon_{\text{sens}}$ along the sensor length,

$$V_{\text{PZT}} = S_{\text{PZT}} \int_{-l_{\text{PZT}}/2}^{l_{\text{PZT}}/2} \varepsilon_{\text{sens}} dx, \tag{24}$$

where the sensitivity term (Lanza di Scalea *et al.* 2007a) is

$$S_{\text{PZT}} = \frac{t_{\text{PZT}}}{l_{\text{PZT}}} \frac{d_{31} Y^E}{[e_{33}(1-\nu) - 2d_{31}^2 Y^E]}. \tag{25}$$

In this expression, Y^E and ν are Young's modulus and Poisson's ratio, respectively, of the PZT material; l_{PZT} and t_{PZT} are the sensor length and thickness.

2. Composite MFC sensor

Referring to Fig. 2(b), the MFC poling is along the fiber direction 1 ($E_2=E_3=0$, the nonzero piezoelectric coefficients are d_{11} and d_{12}, and the nonzero dielectric permittivity coefficient is e_{11}. The nonzero charge density term D_1 can, thus, be written as

$$D_1 = [d_{11}\ d_{12}\ 0] \times \begin{bmatrix} Y_1^E/(1-\nu_{12}\nu_{21}) & \nu_{12}Y_2^E/(1-\nu_{12}\nu_{21}) & 0 \\ \nu_{12}Y_2^E/(1-\nu_{12}\nu_{21}) & Y_2^E/(1-\nu_{12}\nu_{21}) & 0 \\ 0 & 0 & G_{12} \end{bmatrix} \times \begin{bmatrix} \varepsilon_{\text{sens}} - E_1 d_{11} \\ -E_1 d_{12} \\ 0 \end{bmatrix} + e_{11}E_1, \tag{26}$$

where $\varepsilon_{\text{sens}}$ is the in-plane strain in the MFC patch assumed along the fiber direction 1, and Y_i^E, ν_{ij}, and G_{12} are the in-plane orthotropic elastic constants of the MFC patch.

To derive the voltage response, the equivalent model shown in Fig. 2(c) is considered. Here, the MFC is reduced to an equivalent PZT with thickness equal to the MFC electrode spacing a and length equal to the MFC net electrode length (pl_e), where p is the number of electrodes on a single face of the MFC. The net electrode length is, thus, a fraction of the full MFC length, $pl_e=\beta l_{\text{MFC}}$, where β is a reduction factor depending on the design of the MFC. The equivalent model also requires a rotation of the sensor axes (1,3), as shown in Fig. 2(c).

Considering the equivalent model as an open circuit,

$$\int\int D_1 dxdy = 0, \tag{27}$$

and the resulting generated voltage V_{MFC} is given by the integral of the electric field divided by the sensor area,

$$V_{\text{MFC}} = -\frac{\int\int\int E_1 dxdydz}{\beta l_{\text{MFC}} b_{\text{MFC}}}, \tag{28}$$

where b_{MFC} is the width of the patch. Solving Eq. (26) for E_1, and substituting into Eq. (28), yields the voltage generated by the P1-type MFC sensor V_{MFC} as a function of the in-plane strain in the sensor $\varepsilon_{\text{sens}}$,

$$V_{\text{MFC}} = S_{\text{MFC}} \int_{-l_{\text{MFC}}/2}^{l_{\text{MFC}}/2} \varepsilon_{\text{sens}} dx, \tag{29}$$

where the sensitivity term is

$$S_{\text{MFC}} = \frac{a}{\beta l_{\text{MFC}}} \frac{(d_{11}Y_1^E + d_{12}\nu_{12}Y_2^E)}{[e_{11}(1-\nu_{12}\nu_{21}) - (d_{11}^2 Y_1^E + 2d_{11}d_{12}\nu_{12}Y_2^E + d_{12}^2 Y_2^E)]}. \tag{30}$$

This result is similar to that derived previously for a P2-type MFC sensor (Matt and Lanza di Scalea 2007) with the substitutions of the P1-sensor equivalent thickness $t_{\text{MFC}} \rightarrow a$ and P1-sensor equivalent length $l_{\text{MFC}} \rightarrow \beta l_{\text{MFC}}$.

VI. COMPLETE ACTUATOR-SENSOR RESPONSE

The complete pitch-catch solution for a pair of PZT or MFC transducer patches (Fig. 1) can now be found by substituting the strain expression of Eq. (22) into the sensor response of Eqs. (24) and (29). Indicating by $V_{\text{PZT}\rightarrow\text{PZT}}$ the

voltage generated by a PZT actuator-sensor pair and by $V_{\mathrm{MFC}\to\mathrm{MFC}}$ the voltage generated by a MFC actuator-sensor pair, the following result is obtained:

$$V_{\mathrm{PZT}\to\mathrm{PZT,MFC}\to\mathrm{MFC}} = S_{\mathrm{PZT,MFC}} \int_{-l_{\mathrm{sens}}/2}^{l_{\mathrm{sens}}/2} \varepsilon_{\mathrm{sens}} dx = iS_{\mathrm{PZT,MFC}} \varepsilon_x \left(\frac{\Psi}{\alpha + \Psi} \right) \int_{-l_{\mathrm{sens}}/2}^{l_{\mathrm{sens}}/2} \left[1 - \frac{\cosh(2\Gamma x / l_{\mathrm{sens}})}{\cosh \Gamma} \right] \times e^{i(kx - \omega t)} dx, \quad (31)$$

where the sensor sensitivities, S_{PZT} or S_{MFC}, are given in Eqs. (25) or (30), and the actuated Lamb wave amplitude ε_x is given in Eq. (17). The shear-lag parameter Γ and the plate/sensor stiffness ratio Ψ are given in Eqs. (6) and (7) with the substitution of the actuator properties (Y^E_{act}, l_{act}, t_{act}) with the corresponding sensor properties (Y^E_{sens}, l_{sens}, t_{sens}). The integral in Eq. (31) can be solved in closed form, similar to what was done in Eq. (11) for the Fourier transform of the actuation shear stress. This requires making a variable substitution $x \to 2\Gamma x / l_{\mathrm{sens}}$, which yields the following final voltage expression:

$$V_{\mathrm{PZT}\to\mathrm{PZT,MFC}\to\mathrm{MFC}} = iS_{\mathrm{PZT,MFC}} \varepsilon_x \left(\frac{\Psi}{\alpha + \Psi} \right) (R_{\text{perf-bond}} - R_{\text{shear-lag}}) e^{-i\omega t}, \quad (32)$$

where it was possible to isolate the two terms responsible for the perfect-bond response $R_{\text{perf-bond}}$ and for the shear-lag response $R_{\text{shear-lag}}$ given by

$$R_{\text{perf-bond}} = \frac{2 \sin(k l_{\mathrm{sens}}/2)}{k}, \quad (33)$$

$$R_{\text{shear-lag}} = \frac{4 l_{\mathrm{sens}} \Gamma}{(k^2 l_{\mathrm{sens}}^2 + 4\Gamma^2)} [\tanh(\Gamma) \cos(k l_{\mathrm{sens}}/2) + (k l_{\mathrm{sens}}/2\Gamma) \sin(k l_{\mathrm{sens}}/2)]. \quad (34)$$

From Eq. (32), the general pitch-catch response emerges as a combination of the perfect-bond response and the shear-lag response whose effect is to decrease the overall signal amplitude (notice the minus sign for $R_{\text{shear-lag}}$).

The case of perfect strain transfer between the plate and the sensor is retrieved by letting $\Gamma \to \infty$ (the shear-lag term disappears as $\lim_{\Gamma\to\infty} R_{\text{shear-lag}} = 0$) and by assuming an ideal sensor [thin and compliant sensor such that $E_{\mathrm{plate}} t_{\mathrm{plate}} >> E_{\mathrm{sens}} t_{\mathrm{sens}}$ or $\Psi >> 1$, hence, $\Psi/(\alpha+\Psi) \simeq 1$]. Under these perfect-sensor conditions, Eq. (32) simplifies to

$$V_{\text{perf-bond}} = iS\varepsilon_x \frac{2 \sin(k l_{\mathrm{sens}}/2)}{k} e^{-i\omega t}, \quad (35)$$

which is equivalent to the result obtained previously for piezoelectric wave sensors under perfect strain-transfer assumptions (Lanza di Scalea *et al.* 2007a; Matt and Lanza di Scalea 2007).

The pitch-catch response magnitude from Eq. (32) is plotted in Fig. 7(a) for a PZT pair and in Fig. 7(b) for a MFC pair as a function of the nondimensional wave number

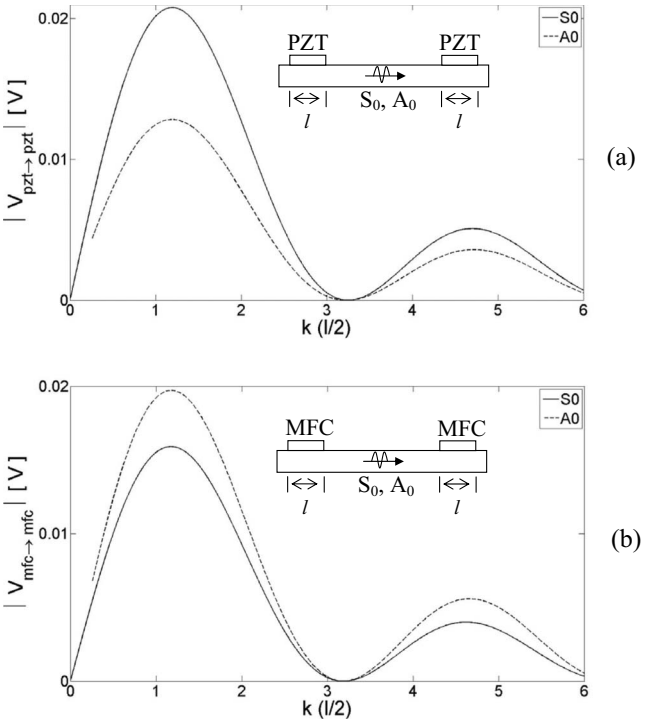

FIG. 7. Pitch-catch response to the fundamental S_0 and A_0 modes in a 1.58-mm-thick aluminum plate and (a) monolithic PZT actuator-sensor pair and (b) composite MFC-P1 actuator-sensor pair.

$(kl/2)$. The lengths of actuators and sensors are assumed to be equal ($l = l_{\mathrm{act}} = l_{\mathrm{sens}} = 10$ mm). The thicknesses are $t_{\mathrm{act}} = t_{\mathrm{sens}} = 0.63$ mm for the PZTs and $t_{\mathrm{act}} = t_{\mathrm{sens}} = 0.2$ mm for the MFCs. The excitation voltage is 1 V. All other properties are listed in Table I. Notice that the PZT pair is more sensitive to S_0 than to A_0, and the opposite is true for the MFC pair. This result is similar to what seen in Fig. 6 which only considered actuation. Wavelength tuning conditions are still evident at points of zero and maximum response. However, the pitch-catch model predicts a drop in the response with increasing kl values, as a result of the decreasing S_0 and A_0 strain amplitudes at the surface of the plate with increasing frequency. Finally, it is interesting to note that the response of the PZT pair is similar in magnitude to that of the MFC pair. Thus, the effect of the one order of magnitude stronger MFC actuation seen in the previous Fig. 6 is compensated by the smaller MFC sensing ability. This is partly due to the disappearance of the MFC interelectrode spacing a and PZT thickness t from the pitch-catch response in Eq. (32) (these terms are at the denominator of the actuation strains [Eqs. (3) and (5)] and at the numerator of the sensitivity terms [Eqs. (25) and (30)]).

VII. TEMPERATURE EFFECTS

The expression in Eq. (32) allows isolating the temperature dependence of the properties of actuator, sensor, bond layers, and plate substrate. These properties are examined in the following subsections considering the typical aircraft range of −40–+60 °C. Unless otherwise specified, a linear dependence of each property on temperature is assumed,

$$P(T) = P(T_0) + \frac{\partial P(T)}{\partial T}\Delta T, \tag{36}$$

where P represents one of the properties, T is the generic temperature, T_0 is the ambient temperature 20 °C, and $\partial P/\partial T$ is the sensitivity to temperature.

A. Temperature effects on actuator and sensor properties

The temperature-dependent properties of the PZT or MFC actuator and sensor patches influencing the response in Eq. (32) are the following: Young's moduli Y^E(PZT), Y_1^E, Y_2^E(MFC) from Eqs. (6), (7), (25), and (30); Poisson's ratios ν(PZT), ν_{12}, ν_{21}(MFC) from Eqs. (25) and (30); piezoelectric coefficients d_{31}(PZT), d_{11}, d_{12}(MFC) from Eqs. (3), (5), (25), and (30); dielectric permittivity terms e_{33}(PZT), e_{11}(MFC) from Eqs. (25) and (30); and length and thickness dimensions. All of these terms are considered in the following.

1. Monolithic PZT patch

Type 5A PZT material is considered. Young's modulus and Poisson's ratios were modeled according to Eq. (36) by using $Y^E(T_0)=70$ GPa, $\nu(T_0)=0.31$, and temperature sensitivities of $\partial Y^E/\partial T=0.16$ GPa/ °C and $\partial \nu/\partial T=-0.013$/ °C (Sherrit *et al.* 1999).

The piezoelectric coefficient was also modeled linearly assuming $d_{31}(T_0)=-168\times10^{-12}$ m/V and sensitivity $\partial d_{31}/\partial T=-0.5$ m/V °C (Lee and Saravanos 1998). The dielectric permittivity term was considered to be bilinear to best fit the data by Lee and Saravanos (1998) will be also discussed later and shown in Fig. 11. The ambient value was $e_{33}(T_0)=15\times10^{-9}$ F/m, with sensitivities $\partial e_{33}/\partial T=0.043\times10^{-9}$ F/m °C below ambient temperature and $\partial e_{33}/\partial T=0.14\times10^{-9}$ F/m °C above ambient temperature. Patch length and thickness changes were modeled assuming a thermal expansion coefficient for PZT 5A of 3×10^{-6} m/m °C (Lee and Saravanos 1998).

2. Composite MFC patch

Conventional rules of mixture were used to calculate the effective Young's moduli and Poisson's ratios of the MFC patches from the constituent properties of fibers (E_f,υ_f) and matrix (E_m,υ_m) through the fiber volume fraction V_f (Jones 1975),

$$Y_1^E = E_f V_f + E_m(1-V_f), \quad Y_2^E = \frac{E_f E_m}{(1-V_f)E_f + V_f E_m},$$
$$\upsilon_{12} = (1-V_f)\upsilon_m + V_f \upsilon_f, \quad \upsilon_{21} = \upsilon_{12}\frac{Y_2^E}{Y_1^E}. \tag{37}$$

The temperature dependence of E_m and υ_m for the PZT-5A fibers was modeled as in the previous Sec. VII A 1. The matrix properties were obtained experimentally from longitudinal and shear ultrasonic time-of-flight measurements conducted on epoxy coupons in an environmental chamber with temperature control between −40 and +60 °C. The measurements were averaged over two separate coupons and three temperature cycles. The following matrix properties were obtained: $E_m(T_0)=4.7$ GPa and $\upsilon_m(T_0)=0.45$, with sensitivities of $\partial E_m/\partial T=-0.028$ GPa/ °C and $\partial \upsilon_m/\partial T=0.009$/ °C. A constant volume fraction $V_f=0.4$ was assumed. The temperature sensitivity of the MFC properties Y_1^E, Y_2^E, υ_{12}, and υ_{21} was then calculated from Eq. (37).

Regarding the piezoelectric coefficients, the following values were used: $d_{11}(T_0)=404\times10^{-12}$ m/V, $d_{12}(T_0)=-167\times10^{-12}$ m/V, as obtained from manufacturer's data; sensitivities $\partial_{d_{11}}/\partial T=1$ m/V °C from Hooker (1998); $\partial d_{12}/\partial T$ was assumed equal to $\partial d_{31}/\partial T$ of the previous Sec. VII A 1 (as d_{12} of the MFC fibers is equivalent to d_{31} of the monolithic PZT). The dielectric permittivity trend for $e_{11}(T)$ was also set equal to the trend $e_{33}(T)$ of the previous section, with $e_{11}(T_0)=15\times10^{-9}$ F/m (e_{11} of the MFC fibers is equivalent to e_{33} of the monolithic PZT). Patch length and thickness changes were modeled assuming a coefficient of thermal expansion of 5×10^{-6} m/m °C along the fibers and 15×10^{-6} m/m °C across the fibers (Williams *et al.* 2004).

B. Temperature effects on transducer/plate bond layer properties

The bond layer enters the final Eq. (32) through its shear modulus G_{bond} and thickness t_{bond}, both present in Eqs. (6) and (18). Ambient-cure epoxy adhesive (Loctite from Henkel Corporation, Rocky Hill, CT) was used in this study. The temperature dependence of G_{bond} was measured by ultrasonic shear-wave velocity measurements on epoxy coupons tested in the autoclave between −40 and +60 °C. By averaging the measurements over two separate coupons and three temperature cycles, the following regression line was obtained with a 0.96 regression coefficient:

$$G_{\text{bond}}(T)\ (GPa) = 3.2 - 0.013T\ (°\text{C}) \tag{38}$$

Changes in thickness of the bond due to thermal expansion were considered negligible and ignored.

C. Temperature effects on substrate plate properties

Properties of the substrate plate affecting the pitch-catch response include Young's modulus E_{plate}, thickness t_{plate} from Eq. (7), and shear modulus G_{plate} from Eq. (17). In addition, G_{plate} and density ρ_{plate} will affect the bulk longitudinal wave velocities, hence, the Lamb dispersion relations $k(\omega)$. The following values were considered for aluminum 2024: $E_{\text{plate}}(T_0)=70$ GPa, $G_{\text{plate}}(T_0)=27$ GPa, $\rho_{\text{plate}}(T_0)=2700$ kg/m^3, and temperature sensitivities of $\partial E_{\text{plate}}/\partial T=-0.04$ GPa/ °C and $\partial G_{\text{plate}}/\partial T=-0.015$ GPa/ °C. The nominal coefficient of thermal expansion for aluminum of 2.31×10^{-5} m/m °C was assumed for the t_{plate} changes.

Figure 8 shows the dispersion curves $k(\omega)$ for S_0 and A_0 in a 1.58-mm-thick aluminum plate at the different temperatures of −40, +20, and +60 °C. As expected, the temperature increase causes a decrease in phase velocities ω/k for both modes. It can also be seen that, for the temperature range of interest, the shifts in $k(\omega)$ are quite small. Hence, little change should be expected on the wavelength tuning points of the pitch-catch response spectrum.

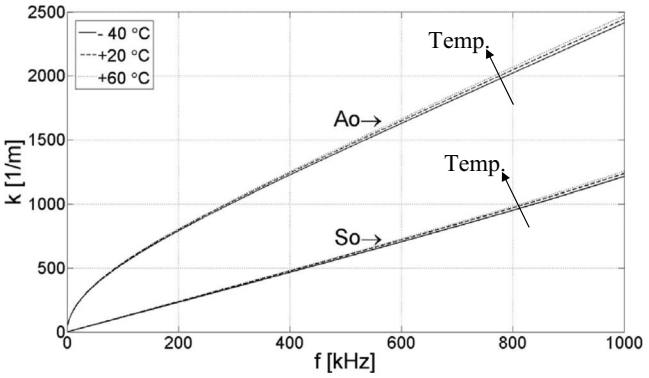

FIG. 8. Dispersion curves for the fundamental Lamb modes in a 1.58-mm-thick aluminum plate at the temperatures of −40, +20, and +60 °C.

D. Results

Results from the pitch-catch model of Eq. (32), with the temperature dependences discussed in Secs. VII A–VII C, are shown in Fig. 9 for the S_0 mode and in Fig. 10 for the A_0 mode. The amplitude of the PZT-PZT response $V_{PZT\to PZT}$ and the MFC-MFC response $V_{MFC\to MFC}$ is plotted against the nondimensional wave number $(kl/2)$ as a function of temperature (below ambient, $-40\ ^\circ\mathrm{C} \leqslant T \leqslant +20\ ^\circ\mathrm{C}$, or above ambient, $+20\ ^\circ\mathrm{C} \leqslant T \leqslant +60\ ^\circ\mathrm{C}$, every 10 °C). It is assumed that $l = l_{act} = l_{sens}$ and a unity voltage is applied to the actuator, $V_{appl} = 1$ V. The plots show that the main effect of temperature is a change in the response amplitude, caused by both actuator/plate and plate/sensor systems. The shifts in wavelength tuning points (zeroes and maxima of the response spectra), due to shear lag and to the $k(\omega)$ shifts of Fig. 8, are negligible. The changes in response amplitude between the highest (+60 °C) or the lowest (−40 °C) temperature and ambient temperature are on the order of 20% in the first response peak (at $kl/2 \simeq 1.2$). With increasing kl values, the temperature-induced amplitude variations decrease as a result of the drop in the overall response caused by the decreasing S_0 and A_0 strain amplitudes with increasing frequency.

Most interestingly, the response amplitude follows two opposite trends at opposite sides of the ambient temperature: decreasing response with increasing temperature in $+20\ ^\circ\mathrm{C} \leqslant T \leqslant +60\ ^\circ\mathrm{C}$ and increasing response with increasing temperature in $-40\ ^\circ\mathrm{C} \leqslant T \leqslant +20\ ^\circ\mathrm{C}$. These trends are consistent for both PZT and MFC pairs and for S_0 and A_0 modes. The reason for the opposite trends should be attributed to the competing roles of the piezoelectric coefficients and the dielectric permittivity terms. By isolating the effect of these two parameters and considering the PZT-PZT case, the pitch-catch response amplitude of Eq. (32) is proportional to the following expression:

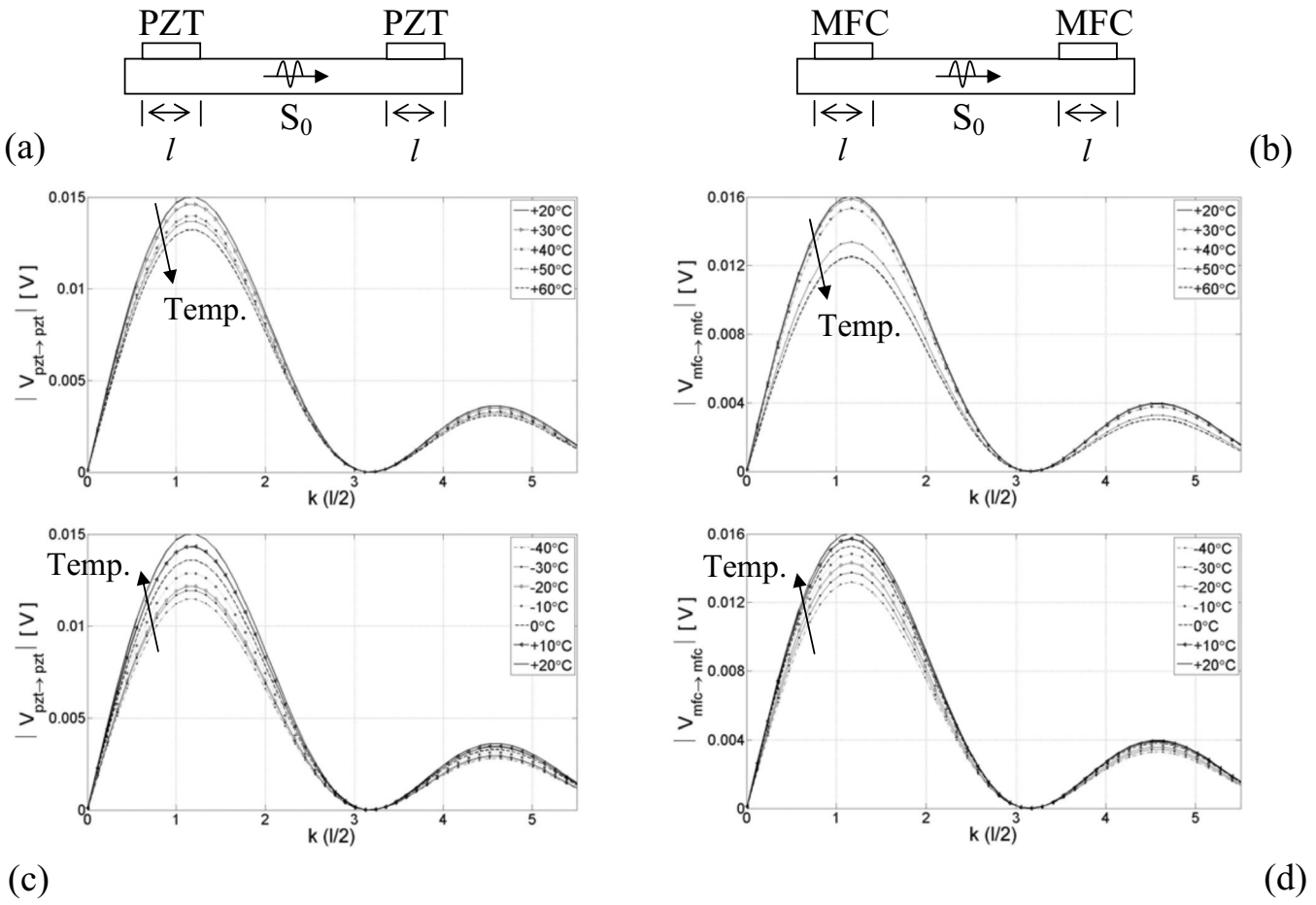

FIG. 9. Pitch-catch response to S_0 Lamb mode in a 1.58-mm-thick aluminum plate for [(a) and (c)] PZT actuator-sensor pair and [(b) and (d)] MFC actuator-sensor pair, under changing temperature in the ranges [(a) and (b)] above ambient (+20–+60 °C), and [(c) and (d)] below ambient (−40–+20 °C).

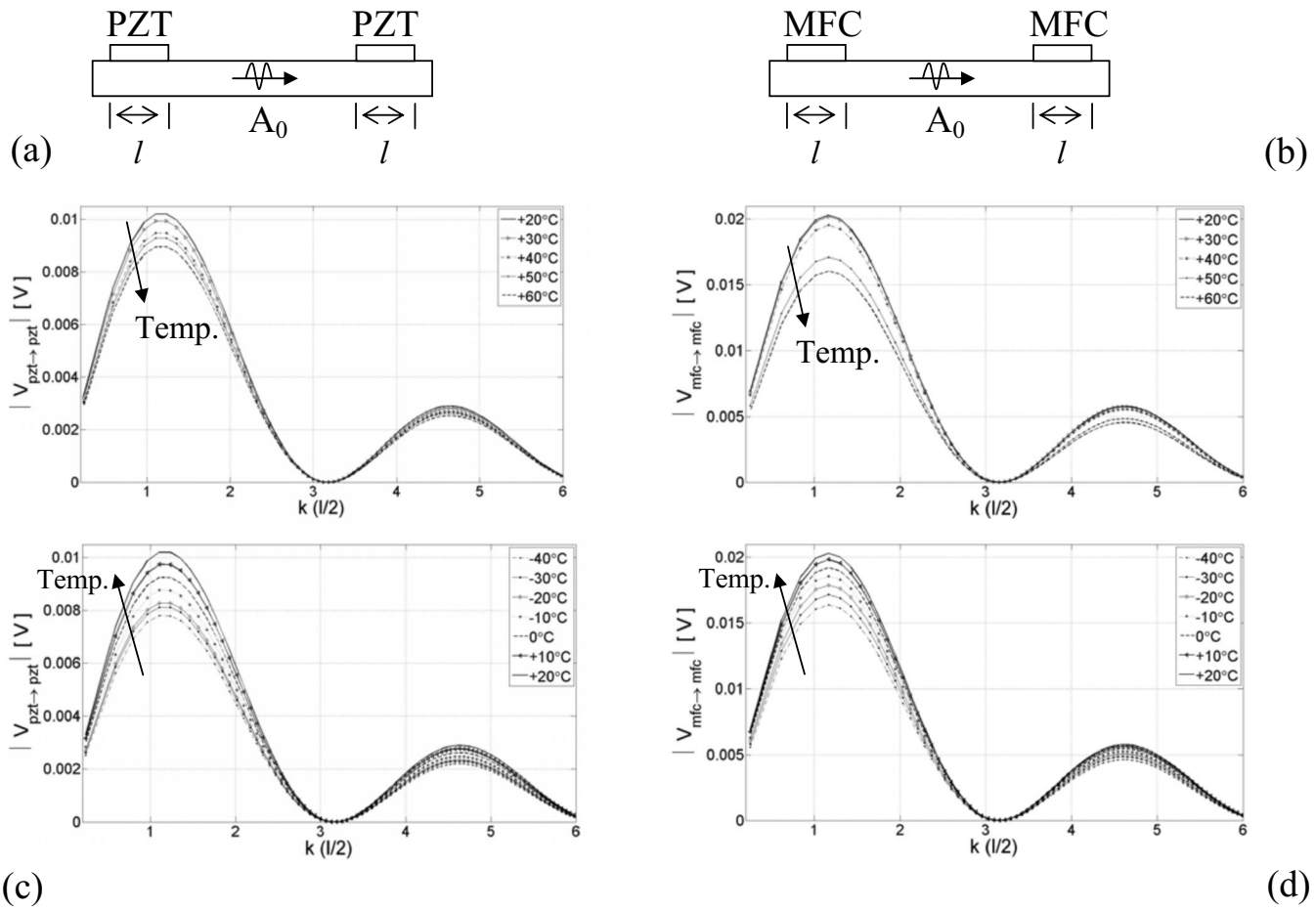

FIG. 10. Pitch-catch response to A_0 Lamb mode in a 1.58-mm-thick aluminum plate for [(a) and (c)] PZT actuator-sensor pair and [(b) and (d)] MFC actuator-sensor pair, under changing temperature in the ranges [(a) and (b)] above ambient (+20–+60 °C) and [(c) and (d)] below ambient (−40–+20 °C).

$$|V_{\mathrm{PZT}\to\mathrm{PZT}}| \propto \frac{d_{31}^2}{e_{33}(1-\nu)-2d_{31}^2 Y_E}, \tag{39}$$

where d_{31}^2 at the numerator results from the product of d_{31} in the actuator's strain expression of Eq. (3) and d_{31} in the sensor's strain expression of Eq. (25). From Eq. (39), the competing roles are now clear, since a larger d_{31} generates a stronger $|V_{\mathrm{PZT}\to\mathrm{PZT}}|$ response, whereas a larger e_{33} generates a weaker $|V_{\mathrm{PZT}\to\mathrm{PZT}}|$ response. The trends of d_{31} and e_{33} as a function of temperature for PZT-5A are shown in Fig. 11 (Lee and Saravanos 1998). Both parameters, in absolute values, increase with increasing temperature. However, while the rates of change for d_{31} and e_{33} are comparable below ~20 °C, the rate of change for e_{33} substantially increases above ~20 °C. Consistently with the results of Figs. 9 and 10, for the given PZT material, the role of d_{31} on $|V_{\mathrm{PZT}\to\mathrm{PZT}}|$ is dominant below 20 °C (i.e., stronger response with increasing temperature); the role of e_{33} becomes, instead, dominant above 20 °C (i.e., weaker response with increasing temperature). Similar arguments hold for the MFC-MFC pair, which uses the same PZT-5A fibers.

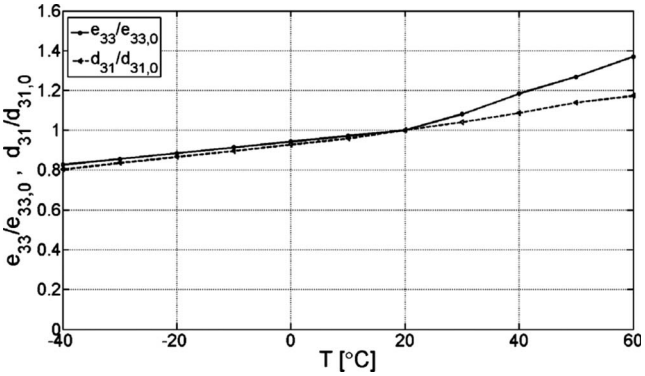

FIG. 11. Piezoelectric coefficient d_{31} and dielectric permittivity e_{33} relative to ambient temperature (+20 °C) values, as a function of temperature for PZT-5A.

E. Experiment

The theory was compared to pitch-catch measurements taken on 1.58-mm-thick aluminum plates [Fig. 12(a)]. The

FIG. 12. Experimental tests: (a) aluminum plate with MFC actuator-sensor pair and (b) environmental chamber with temperature control.

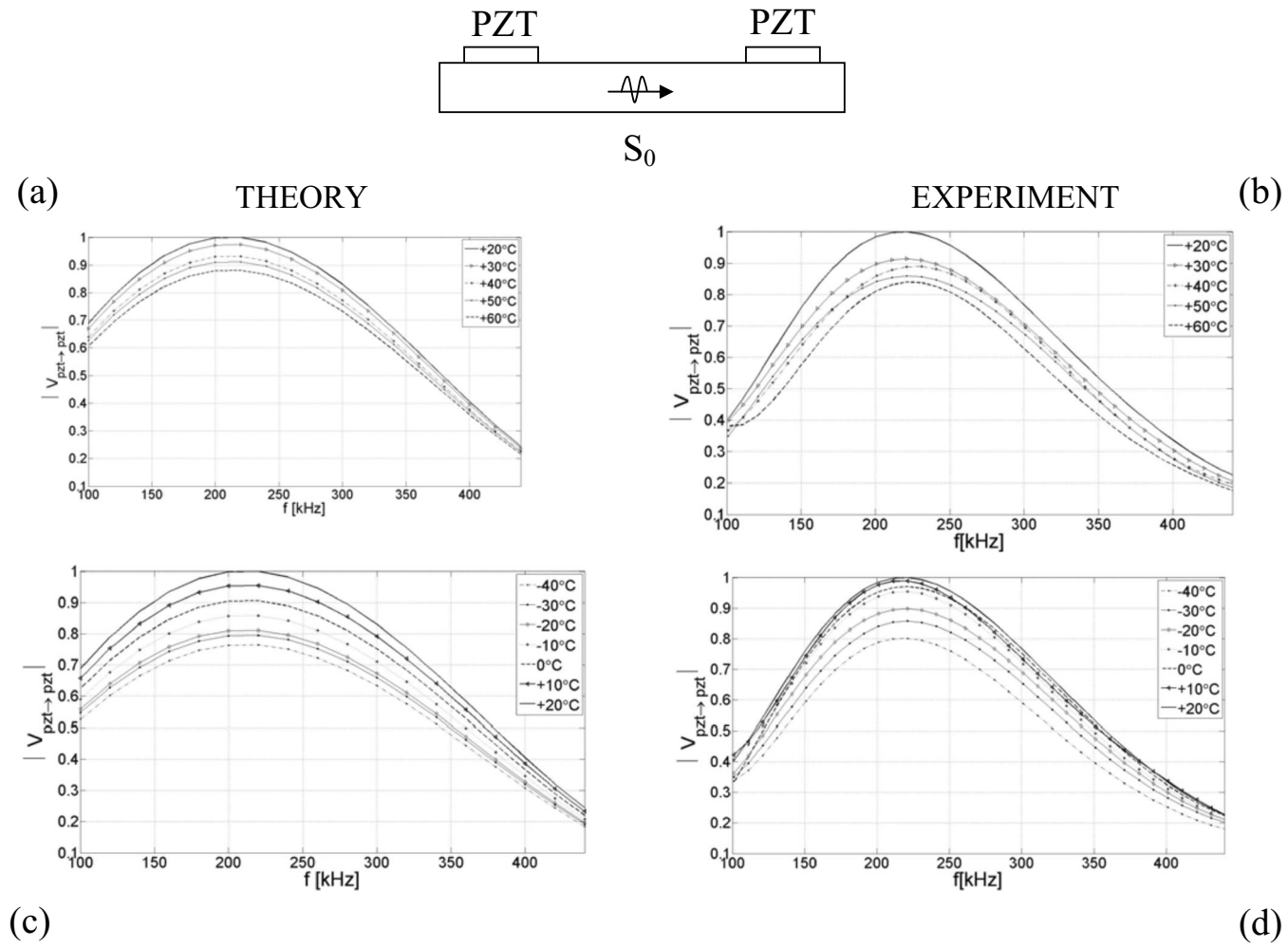

FIG. 13. Pitch-catch response to S_0 Lamb mode in a 1.58-mm-thick aluminum plate for the PZT actuator-sensor pair under changing temperature in the ranges [(a) and (b)] above ambient (+20–+60 °C) and [(c) and (d)] below ambient (−40–+20 °C). Comparison between [(a) and (c)] model and [(b) and (d)] experiment.

PZT patches used for the tests (American Piezo Corporation, Mackeyville, PA) were type 5A disks with a diameter of 10 mm and other properties listed in Table I. The MFC patches were type P1 rectangular transducers (Smart Materials Corporation, Saratoga, FL) with an active length of 28 mm and other properties also listed in Table I. The transducers were bonded to the plates by using the ambient-cure epoxy adhesive from Loctite, which was characterized in Sec. VII B. The actuator-sensor distance was kept at 100 mm for both PZT pair and MFC pair. The measurements were taken in an environmental chamber [Fig. 12(b)] between −40 and +60 °C at 10 °C intervals. Thermocouples were attached to the plates to verify that thermal equilibrium was achieved at each temperature step. A 3.5-cycle, Hanning-modulated toneburst was used as the actuating signal. The excitation was swept between 100 and 500 kHz. The dominant S_0 mode was received and analyzed. The root-mean square of the detected S_0 was computed at each excitation frequency to quantify signal strength.

The results are plotted in Fig. 13 for the PZT pair and in Fig. 14 for the MFC pair. The corresponding results from the model in Eq. (32) are also shown for comparison. The data are plotted separately for the above ambient temperatures (+20 °C$\leqslant T\leqslant$+60 °C) and the below ambient temperatures (−40 °C$\leqslant T\leqslant$+20 °C). The plots are normalized to the relative maxima; since the model neglected wave damping in the plate, measured and predicted absolute amplitudes cannot be compared.

The plots show the expected trends seen in the previous figures of decreasing response with increasing temperature above 20 °C and increasing response with increasing temperature below 20 °C. As discussed in the previous section, the competing roles of piezoelectric coefficients and dielectric permittivity terms are responsible for the opposite trends in the two ranges. The agreement between model and experiment is quite satisfactory for both the PZT-PZT pair (Fig. 13) and the MFC-MFC pair (Fig. 14). The wavelength tuning points match to within a few percent. The model for the PZT pair overestimates the response amplitude at the lower frequencies of 100–200 kHz. At the points of peak responses, the discrepancy between model and experiment is within 5% for the PZT pair and within 10% for the MFC pair. Overall, the results demonstrate that the proposed model captures well the general trend of a pitch-catch measurement under changing temperature within the −40–+60 °C range of interest.

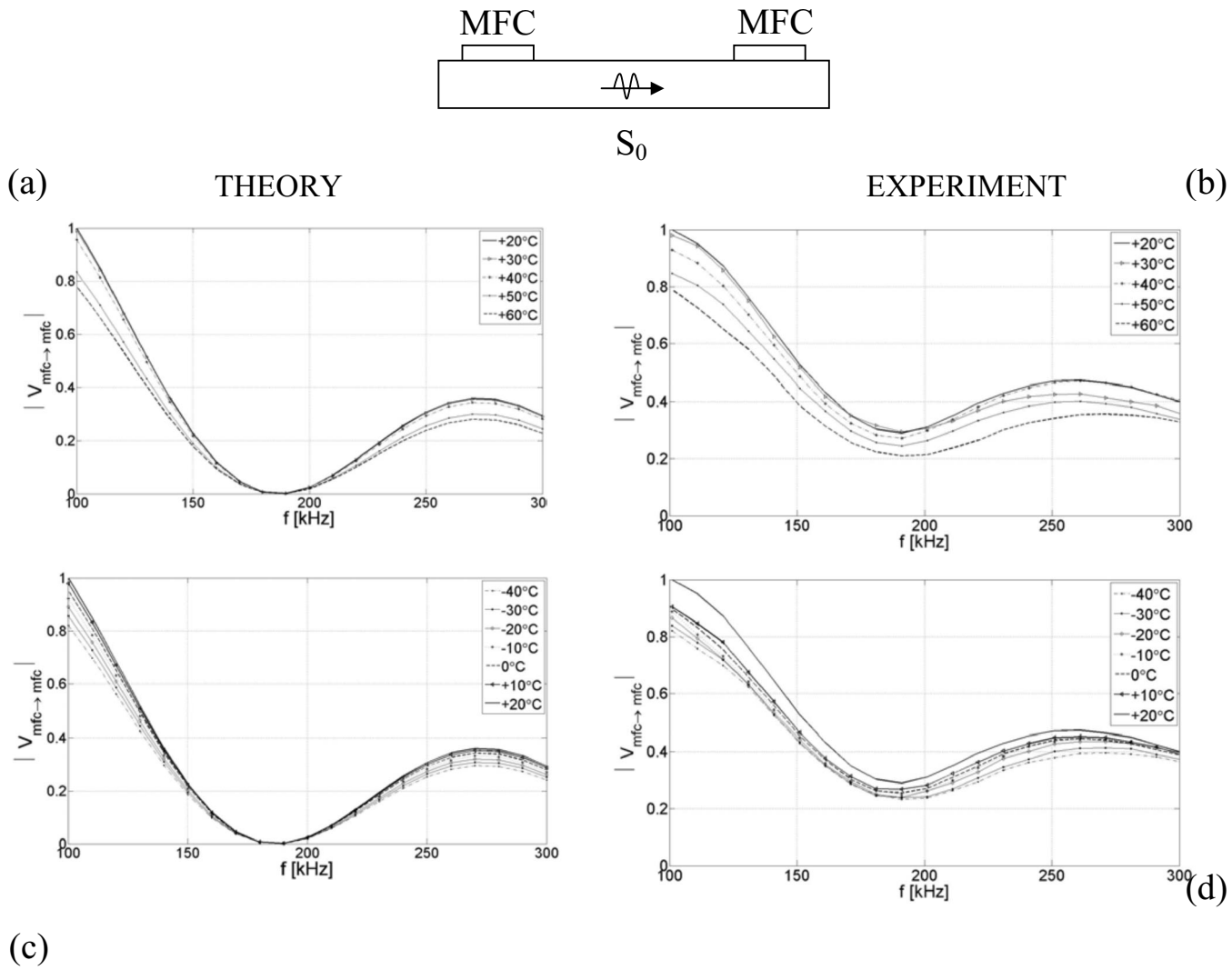

FIG. 14. Pitch-catch response to S_0 Lamb mode in a 1.58-mm-thick aluminum plate for the MFC actuator-sensor pair under changing temperature in the ranges [(a) and (b)] above ambient (+20–+60 °C), and [(c) and (d)] below ambient (−40–+20 °C). Comparison between [(a) and (c)] model and [(b) and (d)] experiment.

VIII. CONCLUSIONS

A model for predicting the response of Lamb wave pitch-catch SHM systems has been developed. The model combines the piezomechanical properties of the actuator and the sensor patches, the interaction between the actuator and sensor with the substrate plate, and the Lamb wave dispersion in the plate. The formulation explicitly accounts for the relevant temperature-dependent parameters of the system, including the transducer piezoelectric and dielectric permittivity properties, the transducer-to-plate adhesive bond properties in a shear-lag framework, and the dispersion curves of the plate. One of the key steps has been deriving a closed-form solution for the spatial Fourier transform of the shear stress transferred from the actuator into the plate under shear lag. The Fourier transform expression enables the use of mode expansion to predict the Lamb waves generated in the plate. The output voltage from the sensor has been derived by accounting for the actual strain transferred from the plate, again under shear lag. The cases of monolithic PZT patches and composite MFC patches on aluminum plates have been considered. The focus of the study has been the temperature range of −40–+60 °C, which is typical of aircraft operations.

On the wave actuator side, the shear-lag results indicate that changing bond layer stiffness has a small effect on the wavelength tuning points and a similarly small effect on the net shear force transferred to the plate. Changing actuator stiffness, instead, has a marked effect on the net shear force transferred to the plate, with stiffer actuators producing larger forces. Comparing PZT-5A and MFC type P1 actuator patches of the same length and under the same excitation voltage, the latter produces S_0 and A_0 Lamb wave strain amplitudes, which are one order of magnitude larger than the former. This is due to the small interelectrode spacing of the MFC, coupled with the MFC's larger piezoelectric constant d_{11} compared to the PZT's d_{31}. However, once the transducers are used in a pitch-catch actuator-sensor pair, the S_0 and A_0 responses of the PZT pair become comparable in magnitude to those of the MFC pair. This is partly due to the disappearance of the MFC interelectrode spacing term.

By letting all relevant parameters in the model change with temperature, the pitch-catch S_0 and A_0 response spectra for PZT and MFC pairs on an aluminum plate were calculated between −40 and +60 °C. It was found that the changing temperature has a negligible effect on the wavelength tuning points and a marked effect on the response amplitude. The changes in response amplitude, relative to the ambient temperature value, were predicted as high as 20% at the extreme temperatures of −40 and +60 °C. These changes affect mainly the primary response peak (first wavelength tuning point near $kl=\pi$) and become less relevant as kl (i.e., frequency) increases. Experimental measurements followed the same behavior. Limited discrepancies were found between theory and experiment, more markedly so for the MFC case. It was also consistently observed that the trend in response amplitude switches at the ambient temperature, with stronger responses with increasing temperature for $-40\ ^\circ\mathrm{C} \leqslant T \leqslant +20\ ^\circ\mathrm{C}$ and weaker responses with increasing temperature for $+20\ ^\circ\mathrm{C} \leqslant T \leqslant +60\ ^\circ\mathrm{C}$. This is the result of the competing roles of the piezoelectric coefficients and the dielectric permittivity terms (larger d result in stronger response; larger e result in weaker response). For the PZT-5A material examined, the temperature sensitivity of the dielectric permittivity increases above ambient temperature, causing the weakening of the overall response.

This study can be used to develop strategies for compensation of the temperature effects in guided-wave damage detection systems. The results shown apply to PZT-5A and MFC type P1 transducers bonded on aluminum plates with ambient-cure epoxy. However, the model can be easily extended to other systems by inputting the appropriate piezoelectric, dielectric, and mechanical properties of transducers, adhesives, and plates. The limiting requirements of the formulation are those of thin transducer patches (plane stress in the plate's surface), undamped isotropic plates (Lamb modes), straight-crested wave fronts (plane strain in the plate's cross section), and low frequency times plate thickness values (shear-lag theory). The extension of this study to include damping in the plate and circularly crested waves is an ongoing work.

ACKNOWLEDGMENTS

Dr. Ivan Bartoli at UC San Diego is acknowledged for obtaining the results shown in Fig. 8. Dr. Howard Matt, formerly at UC San Diego and currently at ATA Engineering in San Diego, CA is acknowledged for the helpful discussions on Lamb wave actuator and sensor models.

Blaise, E., and Chang, F.-K. (**2001**). "Built-in diagnostics for debonding in sandwich structures under extreme temperatures," in *Proceedings of the Third International Workshop on Structural Health Monitoring*, Stanford University, CA, 154–163.

Chambers, J. T., Wardle, B. L., and Kessler, S. S. (**2006**). "Durability assessment of Lamb wave-based structural health monitoring nodes," in *Proceedings of the 47th AIAA/ASME/ASCE/AHS/ASC Structures, Structural Dynamics, and Materials Conference, Newport, RI*, Paper No. AIAA-2006–2263.

Crawley, E. F., and de Luis, J. (**1987**). "Use of piezoelectric actuators as elements of intelligent structures," AIAA J. **25**, 1373–1385.

Giutgiutiu, V. (**2005**). "Tuned Lamb wave excitation and detection with piezoelectric wafer active sensors for structural health monitoring," J. Intell. Mater. Syst. Struct. **16**, 291–305.

Hooker, M. W. (**1998**). "Properties of PZT-based piezoelectric ceramics between −150 and 250 °C," Technical Report No. NASA/CR-208708.

IEEE (**1978**). *Piezoelectricity IEEE Standard 176* (IEEE, New York).

Jones, R. M. (**1975**). *Mechanics of Composite Materials* (Hemisphere, New York).

Konstantinidis, G., Drinkwater, B. W., and Wilcox, P. D. (**2006**). "The temperature stability of guided wave structural health monitoring systems," Smart Mater. Struct. **15**, 967–976.

Lanza di Scalea, F., Matt, H., and Bartoli, I. (**2007a**). "The response of rectangular piezoelectric sensors to Rayleigh and Lamb ultrasonic waves," J. Acoust. Soc. Am. **121**, 175–187.

Lanza di Scalea, F., Matt, H., Bartoli, I., Coccia, S., Park, G., and Farrar, C. (**2007b**). "Health monitoring of UAV wing skin-to-spar joints using guided waves and macro fiber composite transducers," J. Intell. Mater. Syst. Struct. **18**, 373–388.

Lee, B. C., Manson, G., and Staszewski, W. J. (**2003**). "Environmental effects on Lamb wave responses from piezoceramic sensors," Mater. Sci. Forum **440–441**, 195–202.

Lee, H.-L., and Saravanos, D. A. (**1998**). "The effect of temperature dependent material properties on the response of piezoelectric composite materials," J. Intell. Mater. Syst. Struct. **9**, 503–508.

Lu, Y., and Michaels, J. E. (**2005**). "A methodology for structural health monitoring with diffuse ultrasonic waves in the presence of temperature variations," Ultrasonics **43**, 717–731.

Matt, H., and Lanza di Scalea, F. (**2007**). "Macro-fiber composite piezoelectric rosettes for acoustic source location in complex structures," Smart Mater. Struct. **16**, 1489–1499.

Michaels, J. E., and Michaels, T. E. (**2005**). "Detection of structural damage from the local temporal coherence of diffuse ultrasonic signals," IEEE Trans. Ultrason. Ferroelectr. Freq. Control **52**, 1769–1782.

Raghavan, A., and Cesnik, C. E. S. (**2005**). "Finite-dimensional piezoelectric transducer modeling for guided wave based structural health monitoring," Smart Mater. Struct. **14**, 1448–1461.

Raghavan, A., and Cesnik, C. E. S. (**2007**). "Studies on effects of elevated temperature for guided-wave structural health monitoring," Proc. SPIE **6529**, 65290A1–65290A12.

Rose, J. L. (**1999**). *Ultrasonic Waves in Solid Media* (Cambridge University Press, Cambridge).

Schulz, M. J., Sundaresan, M. J., Mcmichael, J., Clayton, D., Sadler, R., and Nagel, B. (**2003**). "Piezoelectric materials at elevated temperature," J. Intell. Mater. Syst. Struct. **14**, 693–705.

Sherrit, S., Yang, G., Wiederick, H. D., and Mukherjee, B. K. (**1999**). "Temperature dependence of the dielectric, elastic, and piezoelectric material constants of lead zirconate titanate (PZT) ceramics," in *Proceedings of the Smart Material Structures and Systems*, Bangalore, India, 121–126.

Sodano, H. A., Park, G., and Inman, D. J. (**2004**). "An investigation into the performance of macro fiber composites for sensing and structural vibration applications," Mech. Syst. Signal Process. **18**, 683–697.

Thien, A. B., Chiamori, H. C., Ching, J. T., Wait, J. R., and Park, G. (**2005**). "Piezoelectric active sensing for damage detection in pipeline structures," in *Proceedings of the 23rd International Modal Analysis Conference*, Orlando, FL, 323–336.

Wilkie, W. K., Bryant, R. G., High, J. W., Fox, R. L., Hellbaum, R. F., Jalink, A., Little, B. D., and Mirick, P. H. (**2000**). "Low-cost piezocomposite actuator for structural control applications," Proc. SPIE **3991**, 323–334.

Williams, R. B., Inman, D. J., and Wilkie, W. K. (**2004**). "Temperature-dependent thermoelastic properties for Macro Fiber Composite actuators," J. Therm. Stresses **27**, 903–915.

Analytical model for viscous damping and the spring force for perforated planar microstructures acting at both audible and ultrasonic frequencies

Dorel Homentcovschi[a] and Ronald N. Miles
Department of Mechanical Engineering, SUNY Binghamton, Binghamton, NY 13902-6000

(Received 27 September 2007; revised 10 April 2008; accepted 10 April 2008)

The paper presents a model for the squeezed film damping, the resistance of the holes, and the corresponding spring forces for a periodic perforated microstructure including the effects of compressibility, inertia, and rarefied gas. The viscous damping and spring forces are obtained by using the continuity equation. The analytical formula for the squeezed film damping is applied to analyze the response of an ultrasonic transducer. The inclusion of these effects in a model significantly improves the agreement with measured results. Finally, it is shown that the frequency dependence of the total damping and total spring force for a cell are very similar to those corresponding to a rectangular open microstructure without holes. A separate analysis reveals the importance of each particular correction. The most important is the compressibility correction; the inertia has to be considered only for determining the spring force and the damping force for sufficiently high frequencies. © *2008 Acoustical Society of America.* [DOI: 10.1121/1.2918542]

PACS number(s): 43.38.Bs, 43.35.Ae [AJZ] Pages: 175–181

I. INTRODUCTION

Recent progress in micromachining technology has enabled the fabrication of microelectro-mechanical systems (MEMS), such as microphones, microaccelerometers, pressure sensors, switches, mirrors, tunable interferometers, ultrasonic motors, resonators, etc. MEMS devices often use parallel plate electrodes as the capacitive sensing and electrostatic actuation mechanisms. In order to increase sensitivity for sensing and to increase force for actuation, designers try to increase the electrode area and decrease the gap between plates. This type of device typically requires etch holes to reduce the time required to release the micromechanical structure during the etching of sacrificial materials. Therefore, the study of a thin air layer being squeezed between a moving plate and a perforated backplate, referred to as a perforated planar microstructure, is important in many MEMS.

As the movable electrode displaces sinusoidally, the sinusoidal backforce on the plate due to the air separating it from the backplate has two components:[1] The viscous damping force, which is in phase with velocity, and the spring force, which is in phase with the plate displacement.

Viscous damping is a critical factor for many MEMS transducers and actuators. In many applications sensors require low damping in order to achieve sufficient sensitivity of the system under a given driving force. In the case of microphones, the mechanical-thermal noise is often one of the limiting noise components. The magnitude of thermal noise depends only on temperature and the magnitude of mechanical damping.[2] Consequently, high viscous damping is also associated with large mechanical-thermal noise. Many devices need to be damped for stable operation. Therefore, in designing a MEMS device, the effects of viscous damping must be taken into account at the earliest stage.[3] The efficient etching, the proper value of the viscous damping, the control of the structure stiffness, and the electrical sensitivity are all directly influenced by the holes on the backplate. Consequently, MEMS design requires a comprehensive understanding of the micromachined perforated systems and their dynamic behavior.

While viscous forces dominate the mechanical behavior of planar microstructures at small velocities, the compressibility of the gas and inertial forces become important factors in determining the spring force at higher frequencies. The dynamic stiffness, the damping coefficients, and the transitional frequencies in compressible viscous thin films have been analyzed previously for the case of infinite strips, thin annuli, and circular plates. A detailed review was given by Andrews, Harris, and Turner.[4] In the case of perforated planar microstructures a similar analysis can be performed for mechanical structures containing a periodic system of holes. While the periodic hypothesis proves valid only in the case of infinite plates, the edge correction introduced in Ref. 5 permits one to assume periodicity (with a certain precision) for the inner cells of a finite domain containing a square web of aligned holes. Therefore, the theory developed in this paper can be applied to analyze real structures of a general shape.

In Sec. II the squeezed film damping is analyzed by taking into consideration the inertia, compressibility, and rarefaction effects. In the case where the basic domain is approximated by an annulus, the solution is obtained analytically. In Sec. III B the formulas obtained are applied to the analysis of the ultrasonic transducer developed by Oppen-

[a]Author to whom correspondence should be addressed. Permanent address: University Politechnica of Bucharest, Applied Science Department and Institute of Mathematical Statistics and Applied Mathematics of Romanian Academy, Calea 13 Septembrie #13, RO-76100, Bucharest, Romania. Electronic mail: homentco@binghamton.edu

heim, Jain, and Greve in Ref. 6. Consideration of compressibility, inertia, and rarefied gas effects reduced the error in predicting the quality factor of the damping of the diaphragm of the transducer from 48% to 14% as compared with the measured value.

In Sec. IV we first obtain a model for the direct resistance of a hole. The determination of the rim pressure p_1 is complicated by the compressibility of the gas and requires the consideration of the equation of continuity. Once the rim pressure is obtained, the total damping (and correspondingly the spring force) can be obtained by adding the squeezed film damping and the hole resistance under their complex form.[7] The example considered in Sec. IV C shows that the frequency dependence of the damping force and spring force for a cell are very similar to the corresponding elements determined by Veijola[8] for the case of rectangular plates without holes. Separate analysis of each special effect (compressibility, inertia, and rarefaction) shows that the most important is the compressibility factor. The inertia modifies the spring force and the damping coefficient only at high frequencies while the rarefaction correction has to be considered for gaps significantly thinner than 2 μm.

II. SQUEEZED FILM DAMPING

The complex three-dimensional (3D) motion of the air in a perforated planar microstructure can be decomposed in two simpler flows: a quasi-horizontal flow in the gap of the microstructure and a vertical (Poiseuille type) flow in the cylindrical holes. The presence of the holes implies two effects: a "*direct*" resistance of the holes obtained by adding the shear stress effect on the wall of the pipe (hole) and "*an indirect resistance of holes*" which changes the rim pressure (in the quasi-horizontal flow) from the value zero (corresponding to the external pressure) to a certain value "p_1" determined again by the resistance of the holes (see Ref. 5). The quasi-horizontal flow includes the squeeze film flow, corresponding to the zero pressure condition on the rim of the holes, and also the indirect hole resistance contribution due to the change of the pressure boundary condition to p_1. In this section both components are determined simultaneously.

A. Equations of the problem

In order to study the viscous damping in the gap of a planar microstructure we consider the continuity and the momentum equations for a viscous compressible gas.[7] The system has to be completed by a state equation. The relationship between the pressure and density at any point in the gas is assumed as described by a polytropic process with exponent n_γ

$$p\rho^{-n_\gamma} = const.$$

In the case where the plates are metal having a high conductivity or the relative velocity of the plates is relatively low, the film will be isothermal and $n_\gamma \cong 1$. If the relative velocities are very high the process will approach an adiabatic condition and n_γ equals the ratio of the specific heats ($n_\gamma = 1.4$ for an adiabatic process at ambient conditions).

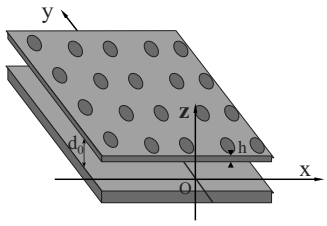

FIG. 1. A periodic perforated planar microstructure.

It is helpful to recast the equations using dimensionless variables. As the domain is the narrow air gap between the two plates (Fig. 1), we will use different scales in the x, y directions (parallel to the plane of the microstructure) and the z direction. Thus, d_0, the distance between the plates at equilibrium, will be used as a scale for the z-axis and L_0, a characteristic length connected to the planar domain for the other directions. We suppose that $\epsilon = d_0/L_0$ is a small parameter. To the lower order in ϵ and for harmonic oscillations (of frequency $\omega/2\pi$) the system describing the motion of the gas can be written as in Ref. 7

$$\frac{\partial^2 v_x}{\partial z^2} + iK^2 v_x = \frac{\partial p}{\partial x}, \tag{1}$$

$$\frac{\partial^2 v_y}{\partial z^2} + iK^2 v_y = \frac{\partial p}{\partial y}, \tag{2}$$

$$\frac{\partial p}{\partial z} = 0, \tag{3}$$

$$\nabla \cdot \mathbf{v} - i\frac{\sigma}{12 n_\gamma} p = 0, \tag{4}$$

where

$$\sigma = 12\frac{\omega \mu L_0^2}{P^a d_0^2} K = d_0 \sqrt{\frac{\rho\omega}{\mu}},$$

ρ is the equilibrium density of the gas, μ the viscosity, and P^a is the ambient pressure (atm). If V_0 is a characteristic velocity of the microstructure plane, the characteristic pressure is $P_0 = \mu V_0 L_0/d_0^2$. Hence, the total physical pressure is

$$P^{\text{phys}} = P^a + P_0 p(x,y) e^{-i\omega t}.$$

The squeeze number σ measures the degree of compression of the fluid in the gap. If σ is close to 0 (low frequency) the air film obeys nearly incompressible viscous flow; at very high frequencies the fluid is essentially trapped in the gap and behaves like a spring.

B. Boundary conditions for gas velocity and pressure

If the gap thickness is comparable to the mean free path of the gas molecules or the pressure is lower than the ambient pressure, the tangential velocity of the fluid at the boundary is no longer strictly zero, which is called the slip-flow effect (gas rarefaction). The slip velocity on the boundary gives rise to a decrease of the viscous forces in the squeezed air film.

For including the gas rarefaction in this analysis we consider the slip velocity conditions at solid boundaries

$$v_x\left(x,y,\pm\frac{1}{2}\right) = \mp K_{\mathrm{ch}}\frac{\partial v_x}{\partial z}\left(x,y,\pm\frac{1}{2}\right),$$
$$v_y\left(x,y,\pm\frac{1}{2}\right) = \mp K_{\mathrm{ch}}\frac{\partial v_y}{\partial z}\left(x,y,\pm\frac{1}{2}\right), \tag{5}$$

Here K_{ch} is the Knudsen number introduced by Veijola in Ref. 8 as a measure of the rarefaction

$$K_{\mathrm{ch}} = \sigma_P\frac{\lambda}{d_0},$$

λ is the mean free path of the gas molecules ($\lambda = 0.068 \times 10^6/P^a$ at ambient temperature and pressure P^a). The slip coefficient σ_P, for the diffuse specular scattering model,[9] can be written as

$$\sigma_P = \frac{2-\alpha}{\alpha}[1.016 - 0.1211(1-\alpha)],$$

where α is the momentum accommodation coefficient. For diffuse scattering, $\alpha = 1$ and $\alpha_P = 1.016$. Also, in the direction normal to the plates the impenetrability condition yields

$$v_z\left(x,y,-\frac{1}{2}\right) = 0, \quad v_z\left(x,y,\frac{1}{2}\right) = w. \tag{6}$$

By w we denote the dimensionless Oz component of the velocity of the mobile surface, assumed a known quantity ($v_z^{\mathrm{phys}} = \epsilon V_0 w$). The classical nonslip condition can still be obtained for $K_{\mathrm{ch}} = 0$. Therefore, the present analysis proves true in the continuum flow regime and in the slip flow domain as well.

In the case where the viscous loss through holes is not neglected, the pressure at the rim of the holes is assumed to be equal to a constant unknown value p_1. This gives the condition

$$p = p_1 \text{ on the rim } \partial D_D. \tag{7}$$

The pressure gradient is zero in a direction that is normal to any line of symmetry of the planar microstructure. On all symmetry lines, (denoted by δD_N) we can then write a new boundary condition as

$$\frac{\partial p}{\partial n} = 0 \text{ on } \partial D_N. \tag{8}$$

We suppose that the holes (of circular form of r_1-radius) are located at the vertices of a regular system of equilateral triangles of side length l_3(in the case of a staggered system of holes) or in the vertices of a regular system of squares, of side length l_4 for the case of aligned holes (Fig. 2). We take advantage of the repetitive pattern of the perforated plate and define a "*cell*" as the space occupied by a hole and its surrounding web space (the plane region where the hole is collecting the flow). The *basic domain D* is defined as the plane region obtained from a cell excluding the hole. The external boundary of the basic domain is a regular hexagon or a square and the inner boundary is the rim of the hole.

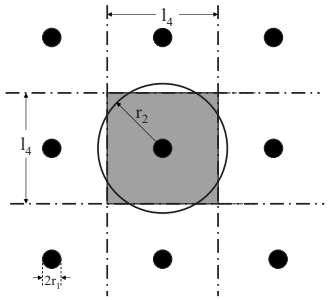

FIG. 2. The cell, the influence domain of a hole, and its circular approximation.

C. Reynolds' equation including inertia and rarefied gas effect

Since the pressure $p(x,y)$ does not depend upon z [Eq. (3)] the differential Eqs. (1)–(4) can be integrated giving the solution

$$v_x(x,y,z) = \frac{i}{K^2}\frac{\partial p}{\partial x}\left(\frac{\cos(\sqrt{i}Kz)/\cos(\sqrt{i}K/2)}{1-\sqrt{i}K_{\mathrm{ch}}K\tan(\sqrt{i}K/2)} - 1\right), \tag{9}$$

$$v_y(x,y,z) = \frac{i}{K^2}\frac{\partial p}{\partial y}\left(\frac{\cos(\sqrt{i}Kz)/\cos(\sqrt{i}K/2)}{1-\sqrt{i}K_{\mathrm{ch}}K\tan(\sqrt{i}K/2)} - 1\right), \tag{10}$$

$$v_z(x,y,z) = i\frac{\sigma}{12n_\gamma}p\left(z+\frac{1}{2}\right) + \frac{i}{K^2}\left(\frac{\partial^2 p}{\partial x^2}+\frac{\partial^2 p}{\partial y^2}\right)\times\left\{z+\frac{1}{2}\right.$$
$$\left. - \frac{\sin(\sqrt{i}Kz)/\cos(\sqrt{i}K/2)+\tan(\sqrt{i}K/2)}{(\sqrt{i}K/2)[1-\sqrt{i}K_{\mathrm{ch}}K\tan(\sqrt{i}K/2)]}\right\}. \tag{11}$$

Here $\sqrt{i} = (1+i)/\sqrt{2}$. The second condition (6) yields the equation for the pressure

$$\frac{\partial^2 p}{\partial x^2} + \frac{\partial^2 p}{\partial y^2} + \alpha^2 p = 12Mw. \tag{12}$$

Here we have used the notations

$$\alpha^2 = iM\sigma/n_\gamma,$$
$$M = \frac{i}{12}K^2\left(\frac{\tan(\sqrt{i}K/2)}{\sqrt{i}K/2[1-\sqrt{i}K_{\mathrm{ch}}K\tan(\sqrt{i}K/2)]} - 1\right)^{-1}. \tag{13}$$

Equation (12) is the Reynolds' equation for solving the squeezing film problem in the case of a compressible gas accounting also for the influence of inertia and gas slip on the plates.

Simple numerical calculations show that $M = 1$ is a good approximation for frequencies less than 100 kHz, while the expression $M = 1 - iK^2/10$ can be used for frequencies less than 10 MHz.

III. ANNULAR APPROXIMATION OF BASIC REGION

A. Determination of squeeze-film damping and hole indirect resistance

We consider an approximation of the outer boundary of the basic domain by an equivalent circle having the same

area (Fig. 2). In this case the domain D is an annulus of $r_1 < r_2$ radii. The radius of the outer circle r_2 is connected with the distance l between the holes by

$$r_2 = 0.525 l_3 \text{ or } r_2 = l_4/\sqrt{\pi},$$

due to the equality of areas. This approximation works well only in the case of small inner radius r_1 as compared with the linear dimension of the cell.[7] We take as a reference length $L_0 = r_2$ and denote $r_0 = r_1/r_2$. In polar coordinates Eq. (12) then becomes

$$\frac{1}{r}\frac{\partial}{\partial r}\left(r\frac{\partial p}{\partial r}\right) + \alpha^2 p = 12Mw, \quad for \quad r_0 < r < 1. \tag{14}$$

The boundary conditions for the function $p(r)$ are

$$p(r_0) = p_1, \quad \frac{\partial p}{\partial r}(1) = 0. \tag{15}$$

The solution of Eq. (14) satisfying the conditions (15) can be written as

$$p(r) = \frac{12 n_\gamma w}{i\sigma}\left[1 - \left(1 - i\frac{\sigma}{12 n_\gamma}p_1^0\right) \times \frac{Y_1(\alpha)J_0(\alpha r) - J_1(\alpha)Y_0(\alpha r)}{Y_1(\alpha)J_0(\alpha r_0) - J_1(\alpha)Y_0(\alpha r_0)}\right], \tag{16}$$

where $p_1 = p_1^0 w$ and J_0, J_1, Y_0, Y_1 are the Bessel functions of the first and second kind.

We have also

$$\int\int_{D_1'} p(r)dxdy = -12\pi M C(\alpha, r_0)w, \tag{17}$$

where

$$C(\alpha, r_0) = C^{(0)}(\alpha, r_0) - \frac{p_1^0}{12M}C^{(1)}(\alpha, r_0),$$

$$C^{(0)}(\alpha, r_0) = \frac{1}{\alpha^2}\left(\frac{2r_0}{\alpha}\frac{J_1(\alpha)Y_1(\alpha r_0) - Y_1(\alpha)J_1(\alpha r_0)}{Y_1(\alpha)J_0(\alpha r_0) - J_1(\alpha)Y_0(\alpha r_0)} - 1 + r_0^2\right),$$

$$C^{(1)}(\alpha, r_0) = \frac{2r_0}{\alpha}\frac{J_1(\alpha)Y_1(\alpha r_0) - Y_1(\alpha)J_1(\alpha r_0)}{Y_1(\alpha)J_0(\alpha r_0) - J_1(\alpha)Y_0(\alpha r_0)}. \tag{18}$$

The total pressure on the domain D_1' in Eq. (17) contains two terms: the first term corresponding to $C^{(0)}(\alpha, r_0)$ is the squeezed film damping and the second one, involving the function $C^{(1)}(\alpha, r_0)$, is the indirect resistance of the holes.

In the case $|\alpha^2| \ll 1$, which corresponds to a weak compressible fluid and low to moderate frequencies, where the power series expansion can be used

$$\frac{2r_0}{\alpha}\frac{J_1(\alpha)Y_1(\alpha r_0) - Y_1(\alpha)J_1(\alpha r_0)}{Y_1(\alpha)J_0(\alpha r_0) - J_1(\alpha)Y_0(\alpha r_0)} = 1 - r_0^2 + c_0\alpha^2 + c_1\alpha^4 + O(\alpha^6),$$

where

$$c_0(r_0) = \frac{r_0^2}{2} - \frac{3}{8} - \frac{r_0^4}{8} - \frac{1}{2}\ln r_0,$$

$$c_1(r_0) = \frac{11}{64} - \frac{5r_0^2}{16} + \frac{11r_0^4}{64} - \frac{r_0^6}{32} + \frac{3}{8}\ln r_0 + \frac{1}{4}(\ln r_0)^2 - \frac{r_0^2}{4}\ln r_0.$$

Therefore,

$$C^{(0)}(\alpha, r_0) = c_0(r_0) + c_1(r_0)\alpha^2 + O(\alpha^4),$$
$$C^{(1)}(\alpha, r_0) = 1 - r_0^2 + c_0(r_0)\alpha^2 + c_1(r_0)\alpha^4 + O(\alpha^6). \tag{19}$$

The total force on the domain D due to the squeeze-film damping and indirect hole resistance can be written as

$$F^s = 12\frac{\pi\mu r_2^4}{d_0^3}MC(\alpha, r_0)w^{\text{phys}}. \tag{20}$$

If the first boundary condition (15) is changed to $p(r_0) = 0$, Eq. (20) gives only the squeeze-film damping.

For an incompressible fluid ($\alpha = 0$) and for small or moderate frequencies, the resulting expression for the squeeze-film damping reduces to

$$F^{\text{inc}} = \frac{12\pi\mu r_2^4}{d_0^3}\left(\frac{1}{2}r_0^2 - \frac{1}{8}r_0^4 - \frac{1}{2}\ln r_0 - \frac{3}{8}\right)w^{\text{phys}}, \tag{21}$$

which coincides with Škvor's formula.[10,11]

B. Application to analysis of an ultrasonic transducer

The ultrasonic transducer developed in Ref. 6 consists of an array of diaphragms connected in parallel. The capacitive diaphragm has a hexagonal shape (of 45 μm side length) and contains 5 μm square holes spaced on a square 30 μm grid. The gap between upper and lower polysilicon electrodes is 2.0 μm and the upper polysilicon electrode thickness is 2.0 μm. The measured resonant frequency is 3.47 MHz.

In order to estimate parameters for a single degree of freedom (SDOF) dynamic model, the hexagonal diaphragm was replaced with a simply supported circular diaphragm having the same resonant frequency. The equivalent SDOF mass is $m^* = 4.87 \times 10^{-12}$ kg, the SDOF spring constant $k^* = 2.33 \times 10^3$ N/m, and the equivalent area is $S^* = 1.06 \times 10^{-9}$ m^2 for a single diaphragm.

The damping is characterized by two terms. The first term describes the contribution of the radiation of ultrasonic energy. The radiation of acoustic energy across the equivalent SDOF area S^* yields a quality factor given by

$$Q_{\text{radiation}} = \frac{\sqrt{m^* k^*}}{Z_{\text{air}} S^*} = 233,$$

where the acoustic impedance of air $Z_{\text{air}} = 430$ N$-$s/m^2 and where m^*, K^*, and S^* from the SDOF model have been used.

The other contribution to the damping comes from the squeeze-film damping. In Ref. 6 the squeeze-film damping was calculated by using the lubrication approximation for an incompressible fluid. In the model, each grid square was re-

placed with a circular piston traveling within a cylinder, having outer radius $r_1=16.9$ μm and a central circular vent hole of inner radius $r_2=2.82$ μm, preserving the area in one grid square. The analysis, similar to Škvor's approach, yields the total force acting against the face of the piston as $F=3.65\times10^{-6}$ w^{phys}, describing an equivalent viscous damper with dashpot constant $c=3.65\times10^{-6}$ N−s/m.

In the model, the authors consider the five etch holes nearest the center to represent the location of discrete dashpots that are transformed into one equivalent SDOF dashpot by summing the product of each dashpot constant by the square of the mode shape at each etch hole location. In this geometry, the equivalent SDOF dashpot constant is $c^*=4.15\times10^{-6}$ N−s/m. The one vent hole at the center, where the mode shape amplitude is 1.0, is the dominant contributor to the equivalent dashpot constant, because the diaphragm velocity at the four next nearest dashpots, each 30 μm away from the center, is very low. The quality Q factor associated with the squeeze film damping effect for the SDOF is then obtained as

$$Q_{\text{squeeze-film}}=\omega_0\frac{m^*}{c^*}=29.1, \tag{22}$$

leading to a predicted combined Q value calculated as

$$Q=\left[\frac{1}{Q_{\text{radiation}}}+\frac{1}{Q_{\text{squeeze-film}}}\right]^{-1}=25.9. \tag{23}$$

The measured value of the quality factor is $Q_{\text{mes}}=49.6$ at atmospheric pressure.

By taking into consideration the compressibility of the air, the inertia effect and the rare gas effect formula (20) (corresponding to the case $p_1=0$) yields the total force acting against the face of the piston as $F=2.6\times10^{-6}$ w^{phys}. In the given geometry the equivalent SDOF dashpot constant is $c^*=2.96\times10^{-6}$ N−s/m. Correspondingly, $Q_{\text{squeeze-film}}$ determined by formula (22) has the value 35.9, which introduced in formula (23) gives the predicted combined quality factor $Q=42.44$.

Thus the consideration of compressibility, inertia, and rare gas effects reduced the difference between the predicted and measured quality factor of the damping of the diaphragm of the transducer from 48% to 14%.

IV. TOTAL VISCOUS DAMPING AND SPRING FORCE

A. Direct hole resistance

In this section, we extend the results presented above by determining the direct resistance of the flow through holes. As in the above formulation, the effects of compressibility, inertia, and gas rarefaction will be accounted for. The last effect is determined by the breakdown of the continuum behavior of the gas determined by the narrowness of the holes or by the drop of the pressure under the ambient pressure. In order to determine the "*resistance of the holes*" we assume a pressure p_1 along the upper edge of a perforation and model a plate hole as a pipe of diameter $2r_1$ and of length h equal to the plate thickness. In this case the only nonvanishing component of velocity in the hole is v_z (fully developed *Poiseuille flow*).[12] We can then write the equation

$$\Delta v_z+\frac{i\omega}{\nu}v_z=\frac{1}{\mu}\frac{\partial p}{\partial z},$$

$\nu=\mu/\rho$ being the dynamic viscosity. In polar coordinates this becomes

$$\frac{1}{r}\frac{\partial}{\partial r}\left(r\frac{\partial v_z}{\partial r}\right)+\frac{i\omega}{\nu}v_z=\frac{p_1}{\mu h}, \tag{24}$$

an equation similar to Eq. (14). Its solution, finite in the domain $r<r_1$, also has to satisfy the following boundary condition on the pipe wall $r=r_1$:

$$v_z(r_1)=-K_{\text{tb}}r_1\frac{\partial v_z(r_1)}{\partial r}, \tag{25}$$

where

$$K_{\text{tb}}=\sigma_P\frac{\lambda}{r_1}$$

is the other Knudsen number introduced in Ref. 13 as a measure of the rarefaction in a pipe.

The solution of Eq. (24) satisfying the condition (25) is

$$v_z=\frac{p_1}{i\omega\rho h}\left[1-\frac{J_0(\beta r)}{J_0(\beta r_1)-K_{\text{tb}}\beta r_1 J_1(\beta r_1)}\right], \tag{26}$$

where $\beta^2=i\omega/\nu$. The total volume rate of flow results by integration in the form

$$Q^h=-\frac{\pi p_1 r_1^4}{8\mu h}H(\beta r_1), \tag{27}$$

where

$$H(\beta r_1)=\frac{8}{(\beta r_1)^2}(G(\beta r_1)-1),$$

$$G(\beta r_1)=\frac{2}{\beta r_1}\frac{J_1(\beta r_1)}{J_0(\beta r_1)-K_{tb}\beta r_1 J_1(\beta r_1)}.$$

The wall shear stress can be shown to be

$$\tau=-\mu\frac{dv_z}{dr}(r_1).$$

By using Eq. (26) for the velocity this becomes

$$\tau=-\frac{p_1 r_1}{2h}G(\beta r_1). \tag{28}$$

The direct resistance of the holes F_d^h is obtained by integrating the wall shear stress (28) along the boundary of the pipe. There results

$$F_d^h=-\pi r_1^2 p_1 G(\beta r_1). \tag{29}$$

Remark 1 *In the case where the thickness of the plate h and the radius r_1 are of comparable dimensions a correction has to be made for the effect of the end of the hole. Sharipov and Seleznev, in Ref. 9, have shown that this effect can be included in Eq. (29) by replacing the length h of the hole with*

$$h_{\text{eff}}=h+3\pi r_1/8.$$

Finally, the total viscous damping on a cell is obtained by adding the two viscous forces given by formulas (20) and (29)

$$F^T = F^s = \left[12\frac{\pi\mu r_2^4}{d_0^3} MC(\alpha, r_0) - \pi r_1^2 p_1^0 G(\beta r_1) \right] w^{\text{phys}}. \tag{30}$$

B. Determination of rim pressure p_1

The compressibility of the gas makes the determination of the rim pressure p_1 more difficult. Thus, the linearized continuity Eq. (4) can be written in dimensional variables as

$$\nabla \cdot \mathbf{v} = \frac{i\omega}{n_\gamma P^a} p. \tag{31}$$

The integration of Eq. (31) over the 3D space D_3 between the microstructure plates corresponding to a cell (in its cylindrical approximation) yields

$$\int\int_{\partial D_3} \mathbf{v} \cdot \mathbf{n} dS = \frac{i\omega d_0}{n_\gamma P^a} \int\int_{D \cup D_1} p dS.$$

Here D is the basic 2D domain (considered on the lower plate) and the plane domain D_1 corresponds to the holes' entrance. Hence,

$$\pi r_2^2 w^{\text{phys}} - \int\int_{D_1} v_z(x,y,0) dx dy = \frac{i\omega d_0}{n_\gamma P^a} \left\{ \int\int_D p dS + \pi r_1^2 p_1 \right\}. \tag{32}$$

Now, defining $p_1 = p_1^0 w^{\text{phys}}$, and noting that the integral in left-hand side of Eq. (32) is given by formula (27) and the integral in the right-hand side by formula (20), we obtain

$$r_2^2 + \frac{r_1^4}{8\mu h} H(\beta r_1) p_1^0 = \frac{i\omega d_0}{n_\gamma P^a} \left\{ -\frac{12\mu r_2^4}{d_0^3} MC^{(0)} + \frac{\mu r_2^4}{d_0^3} C^{(1)} p_1^0 + r_1^2 p_1^0 \right\}.$$

Finally, the rim pressure is given by

$$p_1 = -\frac{r_2^2 + 12i\mu r_2^4 \Omega MC^{(0)}}{r_1^4 H(\beta r_1)/(8\mu h) - i\Omega[\mu r_2^4 C^{(1)} + d_0^3 r_1^2]} w^{\text{phys}},$$

where

$$\Omega = \frac{\omega}{n_\gamma P^a d_0^2}.$$

C. Example

As an example we consider a capacitive diaphragm (having the velocity 1 m/s) of thickness 2.0 μm having a regular pattern of holes of radius $r_2 = 2.82$ μm and having the equivalent radius of the external circle $r_1 = 16.9$ μm. The gap equals 2 μm. The calculation of the total force on a cell was performed in the range of frequencies from 100 Hz to 1 MHz. In order to clarify which of the effects studied in this paper are of most importance to designers, some of the results are shown in Fig. 3, where the continuous line represents the damping force and the dotted line the spring force in the case where all the effects (inertia, compressibility, and slip on the boundary due to rarefaction) are included. The case of the no-slip boundary condition (without the rarefaction correction) is also presented in Fig. 3 as (– · –) for the damping force and (– · · –) for the spring force. In this case the differences are very small. In the case of smaller gaps this correction could be more important. The damping force dominates at low frequencies. The cutoff frequency is slightly lower than 3 kHz. For higher frequencies the spring force dominates. The graph is very similar to Fig. 2 in Veijola's paper,[8] where the author has considered a modified Reynolds equation including the effect of inertial forces and rare gas in the relative flow-rate coefficient and has applied this equation to a squeezed-film damper model for a rectangular geometry. This shows that a cell of a regular perforated microstructure has the same mechanical behavior as a function of frequency as an open rectangular (unperforated) plate. To investigate the influence of compressibility we plotted in Fig. 4 the same elements as in Fig. 3 in the case of incompressible fluid. The damping force is in this case independent of frequency while the spring force is increasing linearly with frequency. For all the frequencies between 100 Hz and 1 MHz the spring force is much smaller than the damping force. There is a small increase in damping force due to the rarefaction effect but, practically, the spring force is not affected by the slip condition on solid boundaries. The effect of inertia can be also seen in Figs. 3 and 4 as a dependence on frequency. In the case of incompressible fluids and also for small frequencies in the compressible case, the damping force is independent of inertia.

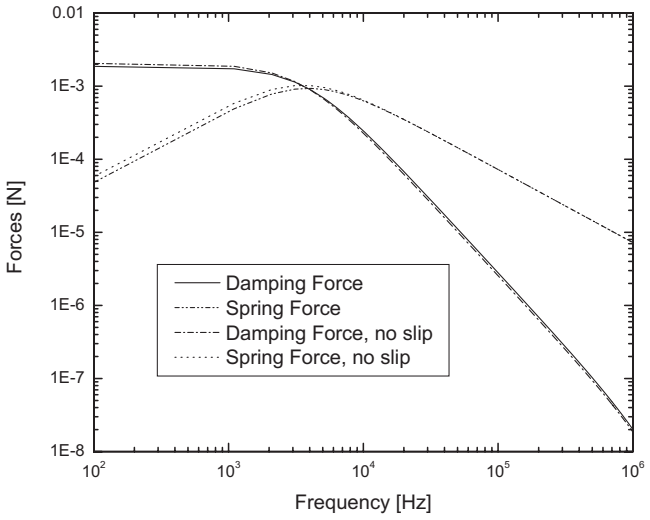

FIG. 3. The variation of the total damping and spring forces for a cell with frequency in the case of slip and no-slip boundary conditions.

V. CONCLUSIONS

This paper provides analytical formulas for the squeeze film damping, the direct and indirect resistances due to holes,

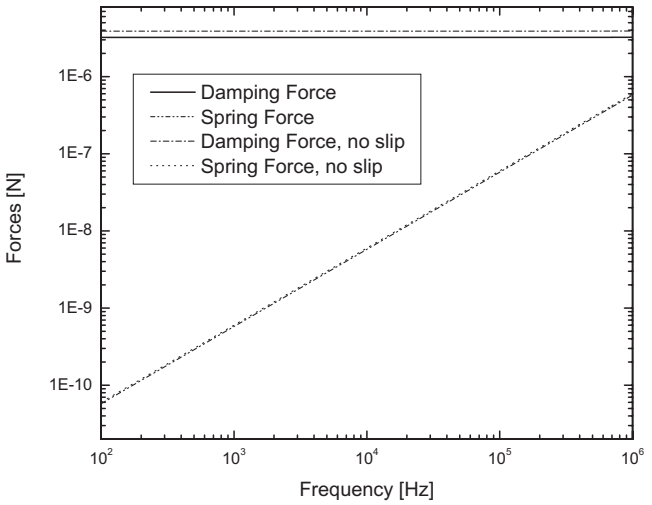

FIG. 4. The variation of the total damping force and spring force for a cell with frequency for incompressible fluids in the case of slip and no-slip boundary conditions.

and the corresponding spring forces for a periodic perforated microstructure including the effects of compressibility, inertia, and rarefied gas.

The total damping and spring forces are obtained by using the continuity equation.

Consideration of compressibility, inertia, and rarefied gas effects have reduced the error in predicting the quality factor of the damping of the diaphragm of the ultrasonic transducer analyzed in Sec. III B from 48% to 14% as compared with the measured value.

The total damping and spring forces for a cell are very similar to those corresponding to a rectangular open microstructure without holes. The separate analysis of each special correction shows that the largest correction is given by accounting for compressibility. The effect of inertia can be considered as important for the spring force and for the damping for sufficiently high frequencies. The rarefaction correction for the gaps larger than 2 μm is very small.

ACKNOWLEDGMENT

This work has been supported through NIH Grant No. R01 DC05762-1A1 to R.N.M.

[1] J. J. Blech, "On isothermal squeeze films," J. Lubr. Technol. **105**, 615–620 (1983).
[2] T. B. Gabrielson, "Mechanical-thermal noise in micromachined acoustic and vibration sensors," IEEE Trans. Electron Devices **40**, 903–909 (1993).
[3] M. Gad-el-Hak, editor, *MEMS Applications* (CRC Press, Taylor & Francis Group, Boca Raton, FL, 2006).
[4] M. Andrews, I. Harris, and G. Turner, "Compařison of squeeze-film theory with measurements on a microstructure," Sens. Actuators, A **36**, 79–87 (1993).
[5] D. Homentcovschi and R. N. Miles, "Viscous microstructural dampers with aligned holes: Design procedure including the edge correction," J. Acoust. Soc. Am. **122**, 1556–1567 (2007).
[6] I. J. Oppenheim, A. Jain, and D. W. Greve, "Electrical characterization of coupled and uncoupled MEMS ultrasonic transducers," IEEE Trans. Ultrason. Ferroelectr. Freq. Control **50**, 297–304 (2003).
[7] D. Homentcovschi and R. N. Miles, "Viscous damping of perforated planar micromechanical structures," Sens. Actuators, A **119**, 544–552 (2005).
[8] T. Veijola, "Compact models for squeezed-film dampers with inertial and rarefied gas effects," J. Micromech. Microeng. **14**, 1109–1118 (2004).
[9] M. H. Shapirov and V. Seleznev, "Data on internal rarefied gas flows," J. Phys. Chem. Ref. Data **27**, 657–706 (1997).
[10] Z. Škvor, "On acoustical resistance due to viscous losses in the air gap of electrostatic transducers," Acustica **19**, 295–297 (1967–1968).
[11] D. Homentcovschi and R. N. Miles, "Modelling of viscous damping of perforated planar micro-mechanical structures. Applications in acoustics," J. Acoust. Soc. Am. **116**, 2939–2947 (2004).
[12] F. M. White, *Viscous Fluid Flow* (McGraw–Hill, New York, 1992).
[13] T. Veijola, "Analytic damping model for an MEM perforation cell," Microfluid. Nanofluid. **2**, 249–260 (2006).

Beamforming correction for dipole measurement using two-dimensional microphone arrays

Yu Liu,[a] Alexander R. Quayle, and Ann P. Dowling
Department of Engineering, University of Cambridge, Cambridge CB2 1PZ, United Kingdom

Pieter Sijtsma
Department of Helicopters and Aeroacoustics, National Aerospace Laboratory NLR, 8300 AD Emmeloord, The Netherlands

(Received 8 October 2007; revised 18 April 2008; accepted 19 April 2008)

In this paper, a beamforming correction for identifying dipole sources by means of phased microphone array measurements is presented and implemented numerically and experimentally. Conventional beamforming techniques, which are developed for monopole sources, can lead to significant errors when applied to reconstruct dipole sources. A previous correction technique to microphone signals is extended to account for both source location and source power for two-dimensional microphone arrays. The new dipole-beamforming algorithm is developed by modifying the basic source definition used for beamforming. This technique improves the previous signal correction method and yields a beamformer applicable to sources which are suspected to be dipole in nature. Numerical simulations are performed, which validate the capability of this beamformer to recover ideal dipole sources. The beamforming correction is applied to the identification of realistic aeolian-tone dipoles and shows an improvement of array performance on estimating dipole source powers.
 [DOI: 10.1121/1.2931950]

PACS number(s): 43.38.Hz, 43.28.Tc, 43.25.Zx, 43.28.Ra [AJZ] Pages: 182–191

I. INTRODUCTION

Over the past decade, an increasing need has emerged for noise source localization in acoustic measurement. Phased microphone arrays, based on the technique of acoustic beamforming,[1,2] have been widely applied to experimental acoustics and numerous engineering fields. The theoretical foundation of microphone array was established by Billingsley and Kinns,[3] who constructed a one-dimensional linear microphone array for real-time jet-noise source location on full-size jet engines. Fisher *et al.*[4] also measured jet noise with two microphones using a polar correlation technique. More recent applications of microphone arrays in aeroacoustics include airframe noise,[5–7] aircraft flyover noise,[8–10] and ground vehicle noise.[11,12]

The principle idea for microphone array processing techniques is to sum the signals coherently at different microphones to enhance the signal emanating from a focal position while minimizing the contribution from out-of-focus locations.[1] A crucial step for this technique is to specify a rule, which is referred to as "beamforming," for appropriate summation of the microphone signals to reconstruct the spatial distribution of noise sources.[13] For the simplest delay-and-sum beamformer, the outputs of time-delayed signals are summed, with the delays as a function of focus position and microphone location, to estimate the source distribution.[1] When a source is at the focus position, the signals add to produce an enhanced signal, whereas for out-of-focus positions, the signals cancel.

The conventional beamforming algorithm normally assumes monopole propagation characteristics to steer the focus of the array. Although such beamforming techniques work well in locating monopolelike sources with uniform directivities, they can perform poorly when used to reconstruct directional noise sources, such as dipoles. In fact, for many aeroacoustic systems, the noise sources arise from fluctuating loading forces and these are principally of dipole type. Therefore, array measurements can be misinterpreted if applied directly to aeroacoustic sources without considering the source mechanism, particularly if the axes of the dominant dipoles are not in line with the receiver.

Jordan *et al.*[14] demonstrated how the monopole assumption can be problematic for a dipole source. They developed a correction for the phase difference in microphone signals to be compatible with a dipole source, and applied it to measurements of a 30 channel linear array for an aeolian-tone dipole produced by cross flow over a cylinder. The true source location and source energy of the dipole was then retrieved. Liu *et al.*[15] pointed out the inability of conventional beamforming to directly validate theoretical predictions for dipole-type surface roughness noise. Instead of altering the beamforming algorithm, they processed numerical simulation through the same algorithm as the experiment and compared the simulated and measured source maps. Quayle *et al.*[16] have also suggested that a similar mismatch could help explain differences in estimates of source power from two nested arrays. More accurate estimates of aeroacoustic dipoles through array measurements are therefore useful as they can provide insight into the noise generation mecha-

[a]Electronic mail: yl275@cam.ac.uk

nism, enable the validation of theoretical and numerical models, and assist the development of noise reduction technologies.

The analysis made by Jordan *et al.*[14] suggests a technique for dipole correction of microphone array systems which extend the conventional delay-and-sum procedure to a process of delay-analyze-and-sum. The analysis stage adds an examination of the phase characteristics of microphone signals for each focus position and so is recognized as a "signal correction." The examination process is not very time consuming for a linear focus region, but it will increase the CPU time quadratically in the case of a two-dimensional (2D) focus region, typically with many more grid points. Furthermore, modeling the exact phase alignment of a real acoustic source is difficult due to the inherent nonideal nature of propagation characteristics. A significant drawback of the signal correction is that when extended to a 2D microphone array it is only applicable to one single dipole with position and direction known. This technique therefore limits the main objective of a phased array, which is to localize noise sources.

In this paper, a beamforming correction to array processing techniques is presented for identifying dipole sources. The main idea is to modify the conventional beamforming algorithm source description to account for the dipole propagation characteristics. This improves the ability of conventional beamforming for estimating dipole sources and extends the technique of Jordan *et al.*,[14] yielding a new beamforming algorithm capable of evaluating the true source location and source power of multiple dipoles with known orientation. This dipole-beamforming algorithm is then applied to numerical simulations and experiments for validation.

The paper commences with a theoretical formulation for the far-field sound field of aeroacoustic sources in Sec. II. The monopole description is based on Sijtsma[17] to be consistent with the array software used in this work, and the dipole characteristic term is derived. In Sec. III, two approaches for dipole correction to conventional beamforming techniques, i.e., through microphone signals and beamforming algorithm, are described and compared. A dipole-beamforming algorithm is presented by applying the dipole characteristic term to the source definition for correction. Section IV validates these two approaches through numerical simulations and demonstrates the advantages of the beamforming correction. Following the validation, some results from the application of the beamforming correction to dipole source localization of aeolian tones are presented and discussed in Sec. V.

II. THEORETICAL FORMULATION

A. The monopole source

An ideal point source with uniform directivity (monopole) is assumed to be located at $\boldsymbol{\xi}$ in a medium with a uniform flow $\boldsymbol{U}$. The acoustic pressure $p(\boldsymbol{x},t)$ at the receiver $\boldsymbol{x}$ satisfies the following convective wave equation:[17]

$$\frac{1}{c^2}\left(\frac{\partial}{\partial t}+\boldsymbol{U}\cdot\nabla\right)^2 p(\boldsymbol{x},t)-\nabla^2 p(\boldsymbol{x},t)=-Q(t)\delta(\boldsymbol{x}-\boldsymbol{\xi}), \quad (1)$$

where c is the speed of sound in free field, $Q(t)$ is the monopole strength, and $\delta(\boldsymbol{x}-\boldsymbol{\xi})$ is the Dirac delta function. In the frequency domain, Eq. (1) transforms into the convective Helmholtz equation,

$$\frac{1}{c^2}(i\omega+\boldsymbol{U}\cdot\nabla)^2 p(\boldsymbol{x},\omega)-\nabla^2 p(\boldsymbol{x},\omega)=-a(\omega)\delta(\boldsymbol{x}-\boldsymbol{\xi}), \quad (2)$$

where $a(\omega)$ is the Fourier transform of $Q(t)$.

The solution to Eq. (1) is

$$p(\boldsymbol{x},t)=\frac{-Q(t-\Delta t_e)}{4\pi\sqrt{(\boldsymbol{M}\cdot\boldsymbol{r})^2+\beta^2|\boldsymbol{r}|^2}}, \quad (3)$$

where $\boldsymbol{M}=\boldsymbol{U}/c$ is a vector of mean flow Mach number, $\boldsymbol{r}=\boldsymbol{x}-\boldsymbol{\xi}$ is the propagation vector from source to receiver, Δt_e is the emission time delay,

$$\Delta t_e=\frac{1}{c\beta^2}(-\boldsymbol{M}\cdot\boldsymbol{r}+\sqrt{(\boldsymbol{M}\cdot\boldsymbol{r})^2+\beta^2|\boldsymbol{r}|^2}), \quad (4)$$

and $\beta^2=1-|\boldsymbol{M}|^2$.

The frequency-domain form of Eq. (3), i.e., the solution of Eq. (2), can be expressed as

$$p(\boldsymbol{x},\omega)=\frac{-a(\omega)e^{-i\omega\Delta t_e}}{4\pi\sqrt{(\boldsymbol{M}\cdot\boldsymbol{r})^2+\beta^2|\boldsymbol{r}|^2}} \quad (5)$$

because

$$\int_{-\infty}^{\infty} p(\boldsymbol{x},t)e^{-i\omega t}\mathrm{d}t = \frac{e^{-i\omega\Delta t_e}\int_{-\infty}^{\infty}-Q(t-\Delta t_e)e^{-i\omega(t-\Delta t_e)}\mathrm{d}(t-\Delta t_e)}{4\pi\sqrt{(\boldsymbol{M}\cdot\boldsymbol{r})^2+\beta^2|\boldsymbol{r}|^2}}. \quad (6)$$

B. The dipole source

A dipole source can be modeled as a coherent pair of closely placed monopoles $Q(t)$ with opposite phase at a distance $\boldsymbol{l}$ apart. The total source strength is

$$\boldsymbol{F}_{\mathrm{tot}}=-Q(t)[\delta(\boldsymbol{\xi})-\delta(\boldsymbol{\xi}-\boldsymbol{l})]. \quad (7)$$

If the distance $l=|\boldsymbol{l}|$ is small (i.e., $kl<1$), the total source strength simplifies to

$$\boldsymbol{F}_{\mathrm{tot}}=-\nabla\cdot[\boldsymbol{F}(t)\delta(\boldsymbol{\xi})] \quad (8)$$

by the Taylor expansion, where $\boldsymbol{F}(t)=Q(t)\boldsymbol{l}$ is the dipole strength vector. Hence, for a dipole located in a medium with a uniform flow, the convective wave equation [Eq. (1)] is

$$\frac{1}{c^2}\left(\frac{\partial}{\partial t}+\boldsymbol{U}\cdot\nabla\right)^2 p(\boldsymbol{x},t)-\nabla^2 p(\boldsymbol{x},t)=-\nabla\cdot[\boldsymbol{F}(t)\delta(\boldsymbol{r})], \quad (9)$$

and the convective Helmholtz equation in the frequency domain is

$$\frac{1}{c^2}(i\omega + \boldsymbol{U}\cdot\nabla)^2 p(\boldsymbol{x},\omega) - \nabla^2 p(\boldsymbol{x},\omega) = -a(\omega)\boldsymbol{l}\delta(\boldsymbol{r}). \quad (10)$$

Similar to the solution to Eq. (1) for a monopole, the solution of Eq. (9) for source $-\nabla\cdot[\boldsymbol{F}(t)\delta(\boldsymbol{r})]$ is

$$p(\boldsymbol{x},t) = -\nabla\cdot\left[\frac{\boldsymbol{F}(t-\Delta t_e)}{4\pi\sqrt{(\boldsymbol{M}\cdot\boldsymbol{r})^2+\beta^2|\boldsymbol{r}|^2}}\right]. \quad (11)$$

For a given Mach number vector $\boldsymbol{M}$ and dipole source vector $\boldsymbol{F}$, we can express the solution to Eq. (9) as

$$p(\boldsymbol{x},t) = -\nabla\cdot\left[\frac{\boldsymbol{F}(t-\Delta t_e)}{4\pi r\alpha}\right] = \frac{1}{4\pi\alpha}\left[\frac{\nabla(r\alpha)}{r^2\alpha} + \frac{\nabla(\Delta t_e)}{r}\frac{\partial}{\partial t}\right]\cdot\boldsymbol{F}(t-\Delta t_e), \quad (12)$$

where

$$\alpha = \sqrt{(\boldsymbol{M}\cdot\boldsymbol{r}/r)^2+\beta^2}, \quad (13)$$

$$\nabla(r\alpha) = \frac{(\boldsymbol{M}\cdot\boldsymbol{r})\boldsymbol{M}+\beta^2\boldsymbol{r}}{r\alpha}, \quad (14)$$

$$\nabla(\Delta t_e) = \frac{-\boldsymbol{M}+\nabla(r\alpha)}{c\beta^2}. \quad (15)$$

As we are only interested in the far-field sound, we discard the first term in the bracket, $\nabla(r\alpha)/r^2\alpha$, and obtain the far-field acoustic pressure as

$$p(\boldsymbol{x},t) = \frac{\nabla(\Delta t_e)}{4\pi r\alpha}\cdot\frac{\partial}{\partial t}\boldsymbol{F}(t-\Delta t_e). \quad (16)$$

The Fourier transform of Eq. (16) is

$$p(\boldsymbol{x},\omega) = \frac{\nabla(\Delta t_e)}{4\pi r\alpha}\cdot i\omega a(\omega)\boldsymbol{l}e^{-i\omega\Delta t_e} = \frac{a(\omega)e^{-i\omega\Delta t_e}}{4\pi r\alpha}[i\omega\boldsymbol{l}\cdot\nabla(\Delta t_e)]. \quad (17)$$

Comparing the above expression with the pressure spectrum of a monopole in Eq. (5), we obtain the dipole characteristic term representing the ratio between dipole and monopole fields, as indicated

$$\mathrm{DPL} = -i\omega\boldsymbol{l}\cdot\nabla(\Delta t_e). \quad (18)$$

III. BEAMFORMING ALGORITHM

A. Conventional beamforming

Following the work of Sijtsma,[17] the array processing software stores the measured pressure amplitude in frequency domain in an N-dimensional vector,

$$\mathbf{p} = [p_1(f), \ldots, p_N(f)], \quad (19)$$

where N is the number of array microphones. The cross-power matrix $\mathbf{C}$ is introduced by

$$\mathbf{C} = \tfrac{1}{2}\overline{\mathbf{p}\mathbf{p}^*}, \quad (20)$$

where the asterisk denotes a complex conjugate and the overbar denotes an ensemble the average or, in practice, average over the Fourier transforms obtained from discrete time blocks. The assumed source description is put in the "transfer vector" $\mathbf{g}$, i.e., its components g_n are the pressure amplitudes at the microphone location of an ideal source with unit strength. For the case of a monopole in a medium with uniform flow, $\mathbf{g}$ can be obtained from Eq. (5) by setting the source strength $a(\omega)=1$, namely,

$$g_n = \frac{-e^{-i\omega\Delta t_e}}{4\pi\sqrt{(\boldsymbol{M}\cdot\boldsymbol{r})^2+\beta^2|\boldsymbol{r}|^2}}. \quad (21)$$

The purpose of beamforming is to determine the amplitude a of sources at grid points $\boldsymbol{\xi}$. This is done by comparing the measured pressure vector $\mathbf{p}$ with the transfer vector $\mathbf{g}$, for instance, through minimization of

$$J = \overline{|\mathbf{p}-a\mathbf{g}|^2}. \quad (22)$$

The solution of this minimization problem is

$$a = \frac{\mathbf{g}^*\mathbf{p}}{|\mathbf{g}|^2}, \quad (23)$$

and the source autopower is

$$A = \frac{1}{2}\overline{|a|^2} = \frac{1}{2}\overline{\frac{\mathbf{g}^*\mathbf{p}}{|\mathbf{g}|^2}\left(\frac{\mathbf{g}^*\mathbf{p}}{|\mathbf{g}|^2}\right)^*} = \frac{\mathbf{g}^*\mathbf{C}\mathbf{g}}{|\mathbf{g}|^4}. \quad (24)$$

Expression (24) is known as "conventional beamforming."[17]

B. Signal correction

As mentioned earlier, conventional beamforming usually assumes monopole sources to enable the minimization solution. Here, it is referred to as the monopole-beamforming (M-Beam) algorithm. There are two approaches to correct conventional beamforming techniques for dipole source identification. The first approach is to correct the array microphone signals stored in the cross-power matrix $\mathbf{C}$ before the beamforming procedure, as proposed by Jordan *et al.*[14] This is essentially a "signal correction" rather than a correction to the beamforming algorithm. The application of this correction is limited for a 2D microphone array because it is time consuming, not easily processed by computer (due to nonideal phase alignment) and restricted to one single fixed dipole source. Nevertheless, the signal correction method provides a useful validation for the dipole characteristic term which will be used in a corrected beamforming algorithm for dipoles.

If the source strength of a monopole is $a(\omega)=1$, we can model a dipole with two coherent monopoles with the same strength but opposite phase. In this case, the signal correction for the cross-power matrix $\mathbf{C}$ would be

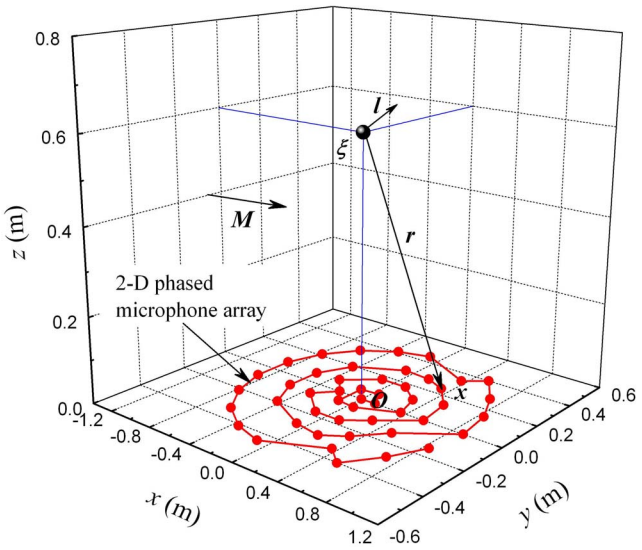

FIG. 1. (Color online) Schematic of the simulation for a dipole source.

$$C_{mn} = \frac{\frac{1}{2}\overline{p_m p_n^*}}{\mathrm{DPL}_m \mathrm{DPL}_n^*}, \tag{25}$$

where the dipole correction term DPL is an N-dimensional vector containing the information of both amplitude and phase for all array microphones, and the suffix denotes the mth or nth microphone. If the corrected dipole simulation gives the same source location and source power as the reference monopole simulation, the correction of Eq. (25) is validated.

C. Beamforming correction

The second approach for estimating dipole source power is to correct the beamforming algorithm itself to account for a dipole source. It is therefore recognized as the "beamforming correction," and the corrected algorithm is referred to here as the dipole-beamforming (D-Beam) algorithm. To implement the beamforming correction, the transfer vector $\mathbf{g}$ for a dipole should be defined by setting the dipole strength $a(\omega)l=1$ in Eq. (17),

$$g_n = \frac{-e^{-i\omega\Delta t_e}\mathrm{DPL}}{4\pi r \alpha l}, \tag{26}$$

and then the beamforming procedure should proceed as normal to represent the true source location and source power for a dipole. With the dipole signature imprinted in the source description, the beamforming correction allows the user to find the true amplitude and location of a suspected dipole.

In principle, it would be possible to determine the most likely orientation and amplitude of dipoles anywhere on the scanning grid. However, for complex source patterns, which might be encountered on an aeroacoustic model, iterations through amplitude and orientation of potential dipoles for each grid point would be computationally expensive. Such a method might also lead to inaccuracies due to insufficient signal-to-noise ratio. For the present method, we assume that the user has some information about likely source orientation and is interested in determining a more accurate estimate of source location and amplitude. A reference dipole direction is therefore required as an input parameter when the D-Beam algorithm is applied. The software divides the region of interest into a number of grid points, and then scans this region point by point for dipoles in the reference direction, estimating the source autopower using Eq. (24).

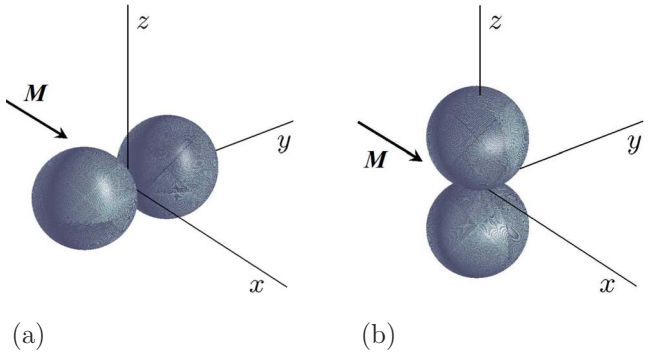

FIG. 2. (Color online) Dipole directivities for (a) case 1 and (b) case 2.

IV. NUMERICAL SIMULATION

A. Simulation setup

In this section, numerical simulations are performed to validate the two approaches mentioned previously. Figure 1 shows a candidate dipole source located in a uniform flow, $\boldsymbol{M}=(0.1,0.0,0.0)$, with the dipole distance vector $\boldsymbol{l}$ at arbitrary directions. In Fig. 2, two cases are examined with the dipole aligned parallel to the y or z axis, referred to as the Y or Z dipole, respectively. The y-z axes are parallel and normal to the array plane, respectively. The source location $\boldsymbol{\xi}$ and dipole vector $\boldsymbol{l}$ for these two test cases are listed in Table I and Figs. 2(a) and 2(b) show the respective dipole directivity patterns. In each test case, an ideal monopole at the same location with source strength $a(\omega)=1$ is also simulated for comparison. As shown in Table I, the dipole size is chosen to be small, $l=0.002$ m, to ensure a compact source. Since there is no sound radiation (DPL=0) in the plane normal to a dipole, an offset of source location $\Delta\xi=0.005$ m is included in case 1 to avoid divide-by-zero errors when applying the dipole correction of Eq. (25).

The simulation array geometry is identical to the nested microphone arrays installed in the Cambridge Markham wind tunnel.[16,18] The use of both a high-frequency (HF) array and a low-frequency (LF) array allows estimates over large frequency ranges. However, differences in estimates of source power for the same model at common frequencies can be a problem if the sources are not well modeled. Hence, for

TABLE I. Source location $\boldsymbol{\xi}$ and dipole vector $\boldsymbol{l}$ for test cases 1 and 2.

Case No.	Dipole	$\boldsymbol{\xi}$ (m)[a]	$\boldsymbol{l}$ (m)[b]
1	Y	(0.0, $\Delta\xi$, 0.6)	(0.0, Δl, 0.0)
2	Z	(0.0, 0.0, 0.6)	(0.0, 0.0, Δl)

[a] $\Delta\xi=0.005$ m.
[b] $\Delta l=0.002$ m.

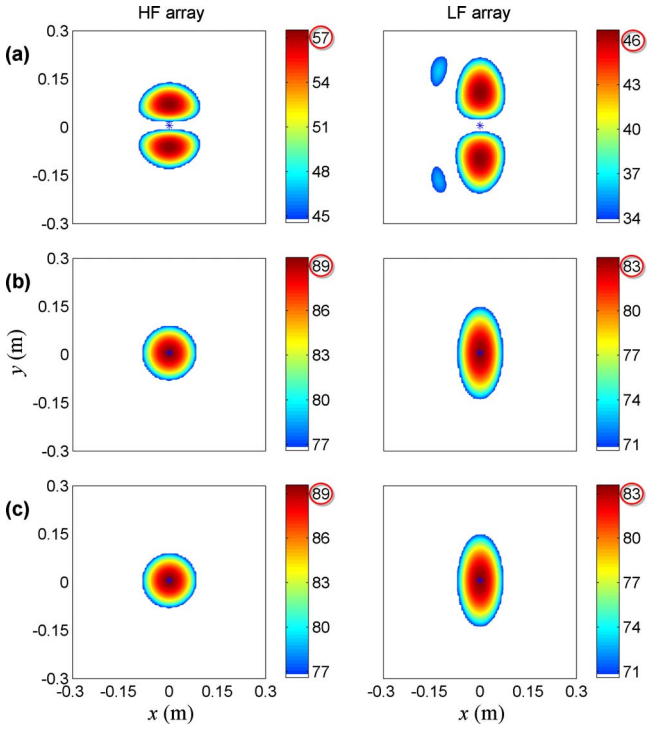

FIG. 3. (Color online) Simulated source maps for case 1: (a) dipole without correction, (b) dipole with signal correction, and (c) reference monopole. HF array, $f=8000$ Hz; LF array, $f=2000$ Hz.

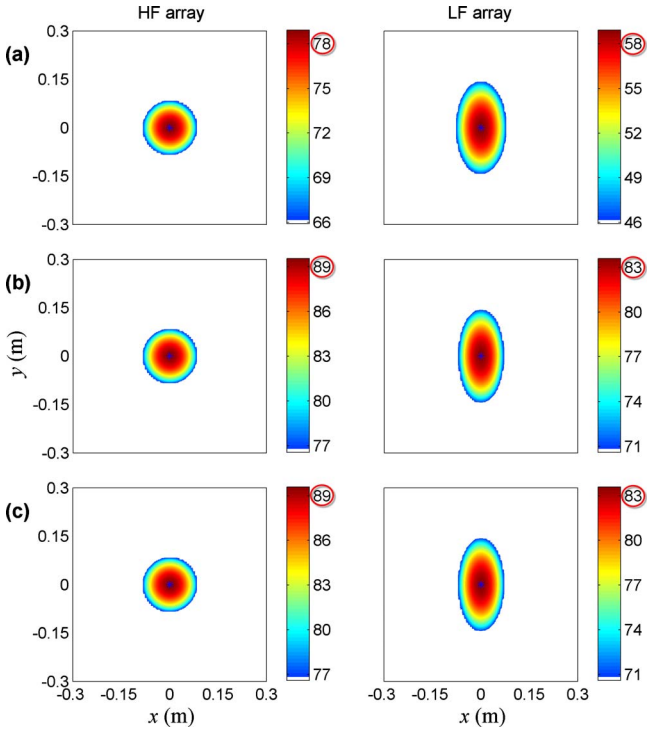

FIG. 4. (Color online) Simulated source maps for case 2: (a) dipole without correction, (b) dipole with signal correction, and (c) reference monopole. HF array, $f=8000$ Hz; LF array, $f=2000$ Hz.

both simulation and experiment, we look at information from both arrays. The beamforming source maps are generated in 1/3 octave-band frequencies, and the source autopowers have been converted to sound pressure levels [SPL in dB $=20\log_{10}(p/p_{\text{ref}})$, $p_{\text{ref}}=2\times10^{-5}$ Pa] at a reference distance of $1/\sqrt{4\pi}$ m from the source[17] and in the dipole direction if the D-Beam algorithm is applied.

B. Signal correction

Figures 3 and 4 show the simulated source maps for cases 1 and 2 using the signal correction technique. The top row of the figures shows the dipole as interpreted by conventional beamforming (M-Beam algorithm), the middle row is the dipole after signal correction, and the bottom row gives the reference monopole with conventional beamforming. For brevity, only the results of 8000 and 2000 Hz are shown for the HF and LF arrays, respectively.

For the Y dipole, Fig. 3 shows that the dipole source is missed at the true location (marked by an asterisk) by the conventional beamforming because the phase variation in the radiated sound is entirely different from a monopole in directions close to the normal of the dipole vector $\boldsymbol{l}$, i.e., the sign of the acoustic pressure changes across this normal plane. Instead, the sound is interpreted as coming from elsewhere on the scan grid. More striking are the dipole source powers that are significantly underestimated compared to the reference monopole simulations. As can be found from the color bars in Fig. 3, without correction, the detected peak source powers are 57.6 and 46.7 dB for the HF and LF arrays, respectively, which are about 32 and 37 dB lower than those of the reference monopoles used to construct the dipoles.

Conventional beamforming is able to better detect the source at the original dipole location for case 2 (Fig. 4), where the radiation of the Z dipole has a phase variation similar to that of a monopole over the area of the arrays. However, the source powers before correction are still much lower than those of the reference monopole, which can be largely accounted for by the relatively small value of the term DPL in the dipole pressure spectrum [Eq. (17)]. The frequency-dependent DPL also explains the 20 dB difference between the source powers (without correction) detected by the HF and LF arrays because of the different chosen frequencies, 8000 and 2000 Hz, respectively.

With the signal correction applied, however, the true source maps for a dipole are recovered for both cases 1 and 2, and they agree with those of the reference monopole in both source pattern and source power, as shown clearly in the middle rows and bottom rows of Figs. 3 and 4. This provides confirmation for the validity of the dipole correction form [Eq. (25)].

Figure 5 shows the variation of the peak source power S with 1/3 octave-band center frequency f for cases 1 and 2 with both arrays. For a monopole with $a(\omega)$ independent of frequency, S scales on f because the 1/3-octave bandwidth B varies linearly with f. Actually, S should increase by 1 dB between two adjacent 1/3 octave-band center frequencies f_1 and f_2 because

$$\Delta S = 10\log_{10}(B_2/B_1) = 10\log_{10}(f_2/f_1)$$
$$= 10\log_{10}2^{1/3} = 1\ \text{dB}, \tag{27}$$

and the corrected estimates (solid lines) show this tendency. However, without correction, estimates of S (solid squares and circles) vary with f^3 in each case because the sound

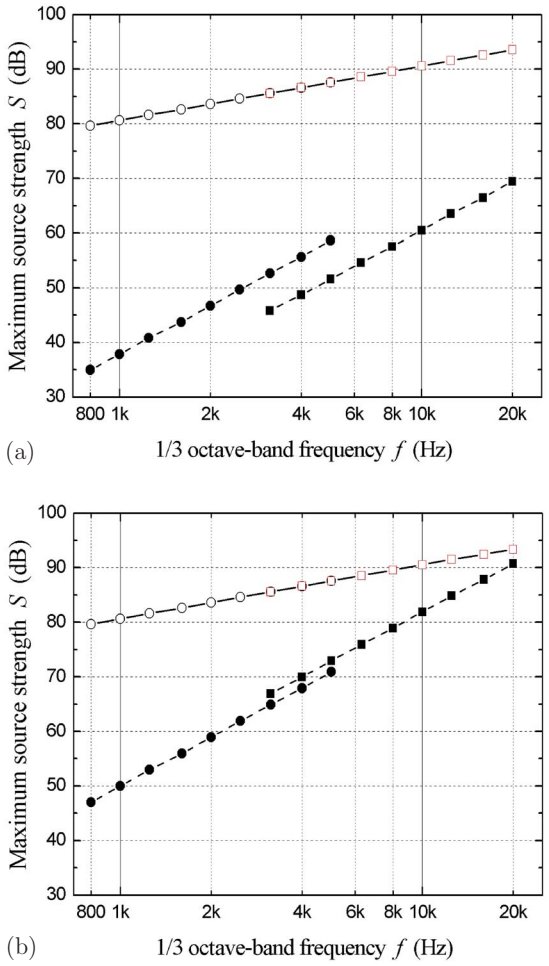

FIG. 5. (Color online) Variation of peak source power S with 1/3 octave-band center frequency f for (a) case 1 and (b) case 2. Dipole without correction: (■) HF array, (●) LF array; dipole with signal correction: (□) HF array, (○) LF array; --- $S \sim f^3$, — $S \sim f$.

power of a dipole scales on ω^2 as well as the frequency-dependent 1/3-octave bandwidth B, so that

$$\Delta S = 10 \log_{10}(f_2^2 B_2 / f_1^2 B_1) = 10 \log_{10}(f_2^3 / f_1^3)$$
$$= 10 \log_{10} 2 = 3 \text{ dB}. \quad (28)$$

After correction, estimates of S (open squares and circles) vary with frequency as $S \sim f$, which is simply a 1/3-octave bandwidth dependence. The same relationship is seen for estimates of a monopole with uniform strength. The signal correction also presents the same values of S at a fixed frequency for the HF and LF arrays, which is in line with the expectation that the algorithm should be independent of the array geometry.

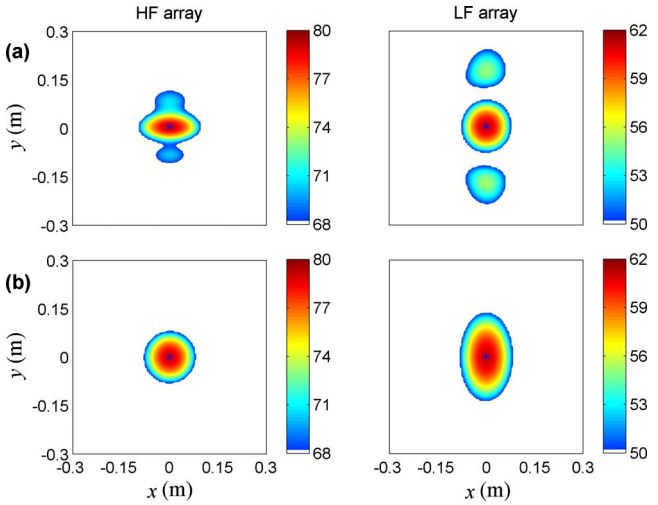

FIG. 6. (Color online) Simulated source maps by the D-Beam algorithm for (a) case 1 and (b) case 2. HF array, f=8000 Hz; LF array, f=2000 Hz.

C. Beamforming correction

With the dipole correction term DPL validated by the signal correction method, we apply the D-Beam algorithm to identify the original dipole source instead of the corrected monopole source as in the middle rows of Figs. 3 and 4. The effect of the beamforming correction on the source maps of cases 1 and 2 is shown in Fig. 6. We can see from the corrected algorithm that the main source is correctly placed at the true source location, although low-level side lobes occur away from the main source. Note that the microphone arrays now detect very similar peak source powers S for both dipole orientations (see Table II).

Comparing the source maps of the signal correction (Figs. 3 and 4) and beamforming correction (Fig. 6), we see that both techniques are able to recover the true location of a single dipole. However, the signal correction gives the amplitude of the constituent monopoles of the dipole, whereas the beamforming correction directly identifies the amplitude of the dipole. Table III shows the elapsed CPU time of the two techniques for cases 1 and 2 on a personal computer with an Intel Pentium 4 processor of 3.4 GHz clock speed and a 1 Gbyte random access memory. The CPU time is very close in each column of Table III and it is evident that the signal correction uses much longer CPU time than the beamforming correction, i.e., $t_s \sim 7t_b$, because the signal correction includes a process of delay-analyze-and-sum while the beamforming correction processes the data directly using the D-Beam algorithm. The CPU time varies significantly between the HF and LF arrays due to the different frequencies

TABLE II. Simulated peak source powers S (dB) by the M-Beam and D-Beam algorithms for cases 1 and 2. HF array, f=8000 Hz; LF array, f=2000 Hz.

		HF array		LF array	
Case no.	Dipole	M-Beam	D-Beam	M-Beam	D-Beam
1	Y	57.55	79.11	46.71	61.10
2	Z	78.92	79.12	58.93	61.12

TABLE III. Comparison of elapsed CPU time (s) between the signal correction (t_s) and beamforming correction (t_b). HF array, f=8000 Hz; LF array, f=2000 Hz.

		HF array		LF array	
Case no.	Dipole	t_s	t_b	t_s	t_b
1	Y	141.7	21.4	41.6	6.8
2	Z	141.8	21.4	41.4	6.7

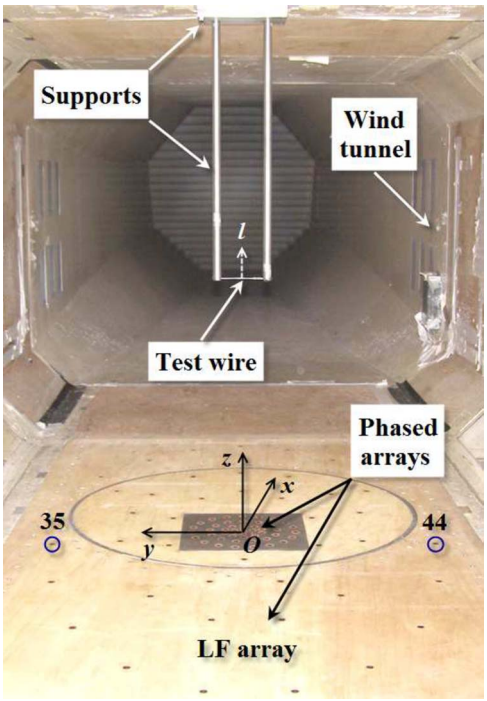

(a)

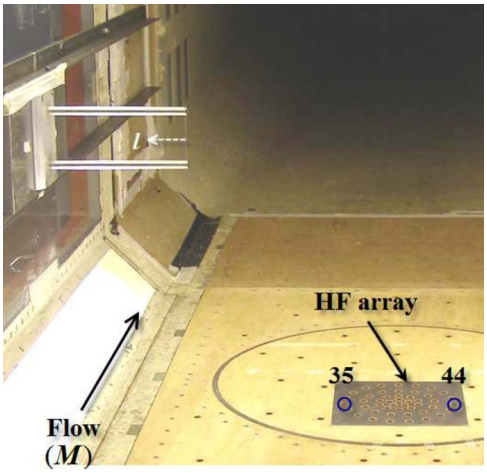

(b)

FIG. 7. (Color online) Experimental setup for aeolian-tone dipoles in two different directions: (a) Z (0, 0, 1) and (b) Y (0, 1, 0).

used. With an identical frequency bandwidth for both arrays ($\Delta f = 117.2$ Hz, see Sec. V A), the higher center frequency of 1/3 octave-band contains more frequency bands and thus takes longer CPU time to process. In addition, the beamforming correction has the advantage over the signal correction in that it can be used in the case of multiple dipoles, as we show in Sec. V.

V. EXPERIMENT

A. Experimental setup

A series of experiments were conducted in the low-speed Markham wind tunnel at the Department of Engineering, University of Cambridge, to test the performance of the D-Beam algorithm. Figure 7 illustrates the experimental setup of the wind tunnel, the phased microphone arrays, and a test wire with supports. The test wire was 1.5 mm in diameter and aligned perpendicular to the flow in order to generate an aeolian tone, representing a realistic aeroacoustic dipole source. Acoustic measurements were performed at free stream flow velocities, $U = 20$, 40 m/s, to obtain aeolian-tone dipole sound at different peak frequencies. The wire was orientated to hopefully obtain dipoles in the Z and Y directions, as shown in Table IV. The "Y dipole" configuration was moved to the side to provide a better view for the microphone arrays. The support structure included two support rods 10 cm apart and one or two support plates, and was mounted to the tunnel ceiling or side wall.

TABLE IV. Dipoles in two different directions.

Dipole	Direction	Coordinates of wire center (m)		
		x	y	z
Z	(0, 0, 1)	0.075	0.003	0.60
Y	(0, 1, 0)	−0.005	0.465	0.60

Measurements were made with both the HF and LF arrays at sampling frequency of 120 or 30 kHz, respectively. Both arrays contain 48 microphones and are flush mounted into the rigid tunnel floor. In the post processing, the time-domain signals were broken down into 1024 (HF array) or 256 (LF array) data blocks, and each block Fourier transformed, resulting in frequency-domain signals with bandwidth $\Delta f = 117.2$ Hz for each array. Narrow-band acoustic beamforming scans were performed to determine source autopowers, as described in Sec. III. Both monopole (M-Beam) and dipole (D-Beam) source descriptions were examined in each case. For each experiment, a horizontal scan plane was used which intersected the test wire at the midpoint. Finally, source maps were generated by summing the narrow-band data to 1/3 octave-band data, with source auto-powers shown as SPL (dB), at a reference distance of $1/\sqrt{4\pi}$ m and a reference dipole direction if applicable.

B. Noise spectra

Cross spectra between a pair of microphones are shown in Fig. 8 for each experimental case together with the noise generated by the support (without the wire) for comparison. Microphones used for the cross spectra are marked by circles in Figs. 7(a) and 7(b) for each array. The aeolian tones are clearly audible around 6000 Hz for the HF array ($U = 40$ m/s) and 3000 Hz for the LF array ($U = 20$ m/s), corresponding to a Strouhal number of ~0.225. As the spectral peaks span a range of frequencies, 1/3-octave frequency bands were used for beamforming source maps to capture the total acoustic energy of the aeolian tone. In this case, the center frequencies of 6300 Hz (HF array) and 3150 Hz (LF array) were selected because they cover the frequency bands of 5613–7072 and 2806–3536 Hz, respectively, which are sufficiently large for the spectral peaks of interest.

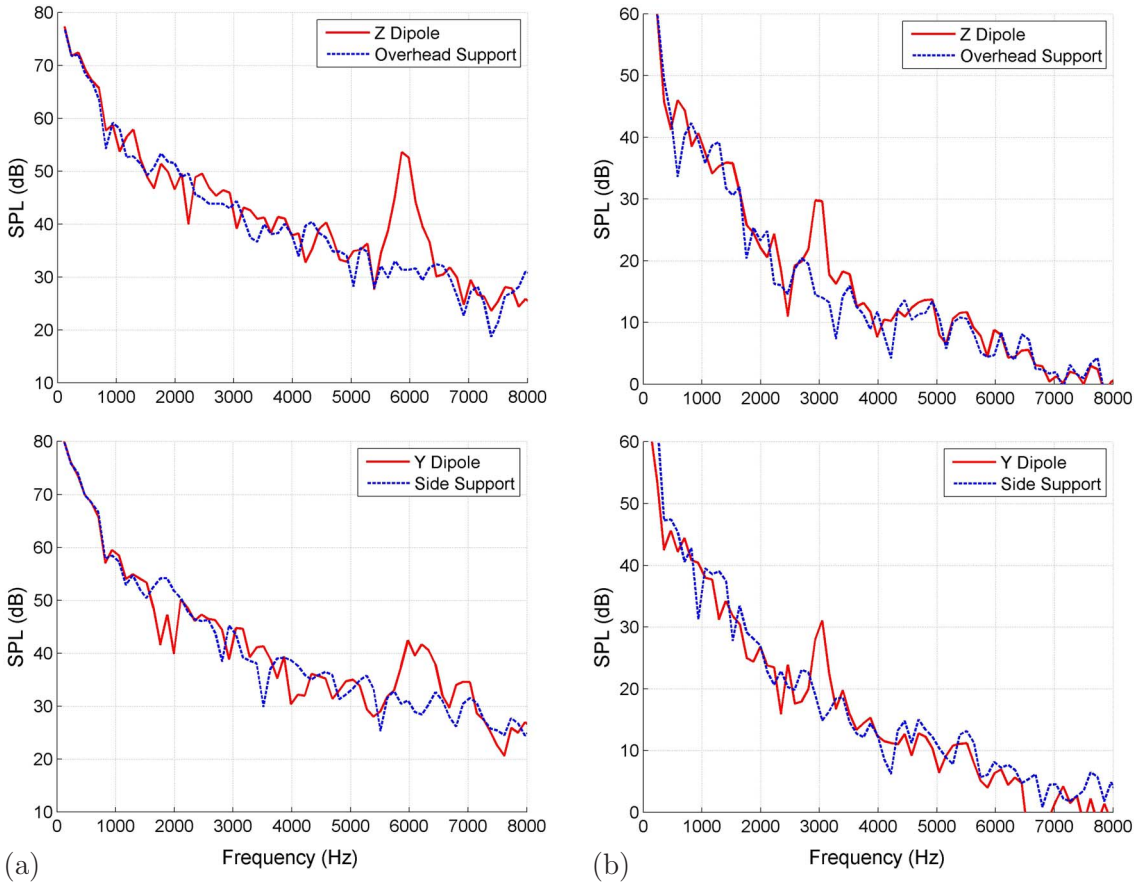

FIG. 8. (Color online) Measured cross spectra for dipoles in two different directions: Z (0, 0, 1) and Y (0, 1, 0) with cross spectra of overhead and side supports for comparison. (a) HF array, U=40 m/s; (b) LF array, U=20 m/s; Δf=117.2 Hz.

C. Beamforming correction

1. Simulation

Theoretical simulations were first carried out to examine the performance of the proposed beamforming correction on identifying distributed aeolian-tone dipoles, and to provide a baseline for comparison with experimental results. Liu *et al.*[15] used this method to validate their prediction model for surface roughness noise by comparing the measured and simulated source powers. In this work, however, we are not concerned about the source power itself. Instead, we compare the increase (ΔS_s) in the estimated peak source power S from the M-Beam algorithm to the D-Beam algorithm. To implement the simulation for the Z and Y dipoles, we assume that 11 identical incoherent dipoles are uniformly distributed in the direction of the wire, and the same value of $a(\omega)$ is used as the input source strength for both algorithms and both arrays.

Figure 9 illustrates the simulated source maps at 6300 Hz by the HF array for the Z and Y dipoles, and the comparison between the M-Beam and D-Beam algorithms. The color bar on the right restricts the SPL data within the range of 0–15 dB, and the source maps of different dipoles and algorithms are shown on identical scales for comparison. Support structures are also sketched on the source maps. Note that since $a(\omega)$ has been set equal to some value, these simulated SPL data do not represent the true source powers of the aeolian-tone dipoles and are merely meaningful as relative levels to show the effect of the beamforming correction. In fact, both the M-Beam and D-Beam algorithms detect the true location of the main source for the distributed dipoles. However, only the D-Beam algorithm correctly identifies strength of the Z and Y dipoles, as both dipoles have the similar source powers. The M-Beam algorithm ap-

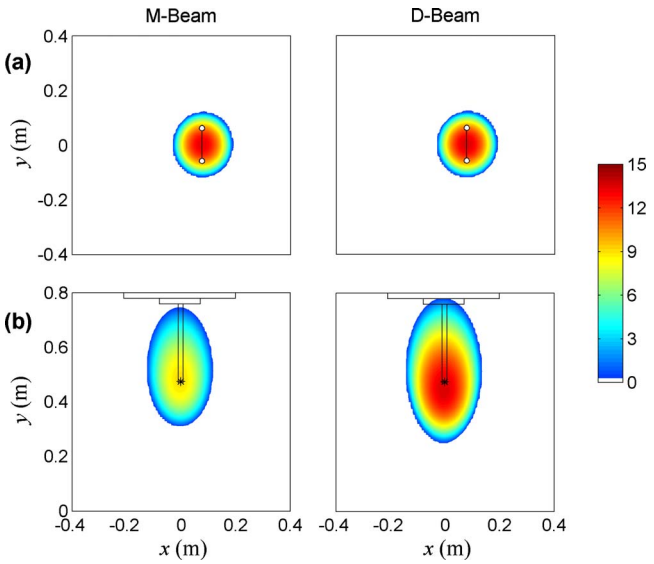

FIG. 9. (Color online) Comparison of simulated source maps by the M-Beam and D-Beam algorithms for dipoles in two different directions: (a) Z (0, 0, 1) and (b) Y (0, 1, 0). HF array, f=6300 Hz.

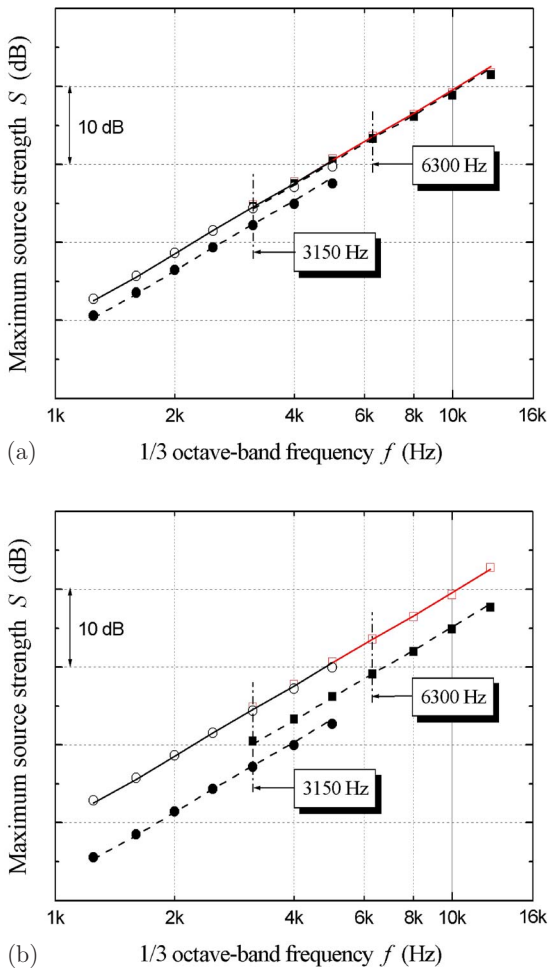

FIG. 10. (Color online) Variation of simulated peak source power S with 1/3 octave-band center frequency f for (a) Z dipole and (b) Y dipole. M-Beam algorithm: (■) HF array, (●) LF array; D-Beam algorithm: (□) HF array, (○) LF array; ---, — $S \sim f^3$.

pears to substantially underestimate source strength of the Y dipoles, as anticipated by earlier simulation (Fig. 3).

Figures 10(a) and 10(b) show the variation of S with 1/3 octave-band center frequency f. As expected from Eq. (28), the simulated S of the Z and Y dipoles varies as f^3, independently of the different arrays and algorithms used. After applying the beamforming correction, the estimated peak source powers S by the HF and LF arrays almost coincide with one another, consistent with the tendency of the ideal individual sources as in Fig. 5. For the Z dipole, the effect of

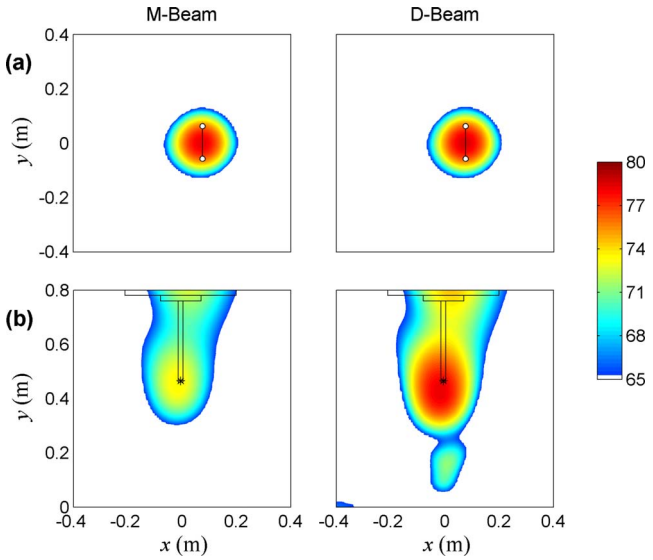

FIG. 11. (Color online) Comparison of measured source maps by the M-Beam and D-Beam algorithms for dipoles in two different directions: (a) Z (0, 0, 1) and (b) Y (0, 1, 0). HF array, f=6300 Hz.

the beamforming correction is generally small, i.e., $\Delta S_s \approx 2.2$ dB for the LF array and nearly negligible for the HF array (see Table V). However for the Y dipole, the values of S increase significantly from the M-Beam algorithm to the D-Beam algorithm by about 7.2 dB (LF array) and 4.6 dB (HF array). This is because for the Z dipole the variation of phase over the microphones is just due to propagation distance and is correctly captured by the M-Beam algorithm. However, for the Y dipole, there is an additional phase change due to the dipole directivity.

2. Measurement

Figure 11 illustrates the measured source maps at 6300 Hz by the HF array for the Z and Y dipoles. The source powers of the aeolian-tone dipoles identified by the M-Beam and D-Beam algorithms are shown in the SPL range of 65–80 dB. Comparing Figs. 9 and 11, we see that the simulated and measured source maps show very similar source patterns and similar effects of the beamforming correction.

Table V compares the estimated peak source power S of the two dipoles, as recorded by both of the nested arrays at 6300 and 3150 Hz. For each dipole orientation, the value of S is given for both the M-Beam and D-Beam algorithms. In

TABLE V. Peak source powers S (dB) of measurement and simulation for the Z and Y dipoles. (a) HF array, U=40 m/s, f=6300 Hz; (b) LF array, U=20 m/s, f=3150 Hz.

	Measurement		Simulation		
Dipole	M-Beam	D-Beam	ΔS_m	ΔS_s	$\lvert\Delta S_m - \Delta S_s\rvert$
(a)					
Z	78.31	78.57	0.26	0.24	0.02
Y	73.59	78.32	4.73	4.57	0.16
(b)					
Z	51.73	53.92	2.19	2.16	0.03
Y	48.01	55.18	7.17	7.22	0.05

each case, the M-Beam algorithm shows a lower estimate of source power. The differences between the M-Beam and D-Beam algorithm are also much greater for the *Y* dipole, as seen in simulation. In addition, the D-Beam algorithm correctly identifies the wire as producing very similar sound power in both orientations. Corrected source maps are also shown in the right column of Fig. 11.

The difference in the measured peak source powers between the M-Beam and D-Beam algorithms is shown in Table V as ΔS_m. Due to the source directivity, the *Y* dipole shows larger ΔS_m because much of its sound radiation is missed without the beamforming correction. The corresponding values of ΔS_s obtained from a simplified simulation of the experimental setup are shown in Table V. This enables the evaluation of the difference $|\Delta S_m - \Delta S_s|$. It indicates that ΔS_m agrees with ΔS_s fairly well for all cases with the largest discrepancy of 0.16 dB, occurring at the *Y* dipole by the HF array. This suggests that the modeling of the aeolian tones from the wire as a series of incoherent dipoles is realistic and provides a preliminary validation of the D-Beam algorithm for an experimental dipole source.

VI. CONCLUSIONS

It has been shown that conventional beamforming techniques can misinterpret the microphone array measurement for a simple dipole due to the inherent monopole assumption. A correction for the phase differences in microphone signals was presented by Jordan *et al.*[14] and it displayed the capability to recover the source location of a single dipole in the resulting source map. In this paper, we present a method of modifying the source transfer vector to search the scanning plane for dipole sources. The resulting algorithm is able to identify the source location and amplitude of dipoles with a suspected orientation. This method extends the capability of the signal correction by Jordan *et al.*[14] to deal with multiple dipoles.

In simulations of dipoles normal to the flow, the dipole-beamforming (D-Beam) algorithm recovered the true source location and amplitude. For a point dipole, the use of a dedicated dipole-beamforming algorithm can lead to large increases in source estimates. For simulations with distributed dipole sources and comparable measurements of aeolian tones, the improvement in estimates of source power with the D-Beam algorithm was less marked. However, the implementation of the new algorithm did allow recovery of the same source strength from different orientations of the same aeolian tone.

While both simulations and measurements have validated the capability of the D-Beam algorithm to improve conventional techniques for identifying dipole sources, the present implementation requires specification of the dipole direction. A potential improvement would be to iterate through different dipole orientations at each point on the scanning grid. However, in many aeroacoustic experiments, it may be possible to readily identify the likely dipole orientations by using knowledge of the source mechanisms. In such cases, it is hoped that more accurate estimates of source amplitude can be determined with this method.

ACKNOWLEDGMENTS

Financial support from the Cambridge-MIT Institute is gratefully acknowledged. The authors would like to thank the National Aerospace Laboratory (NLR), The Netherlands, for assisting in the design and manufacture of the microphone array system and providing the analysis software (Ref. 18). Y. Liu acknowledges the Overseas Research Students Awards Scheme (ORSAS) and the Gates Cambridge Scholarships and A. R. Quayle is grateful to the Engineering and Physical Science Research Council (EPSRC), U.K. for doctoral research funding.

[1] D. H. Johnson and D. E. Dudgeon, *Array Signal Processing: Concepts and Techniques* (Prentice-Hall, London, 1993).
[2] R. P. Dougherty, "Beamforming in acoustic testing," in *Aeroacoustic Measurements*, edited by T. J. Mueller (Springer-Verlag, Berlin, 2002).
[3] J. Billingsley and R. Kinns, "The acoustic telescope," J. Sound Vib. **48**, 485–510 (1976).
[4] M. J. Fisher, M. Harper-Bourne, and S. A. L. Glegg, "Jet engine noise source location: The polar correlation technique," J. Sound Vib. **51**, 23–54 (1977).
[5] J. F. Piet and G. Elias, "Airframe noise source localization using a microphone array," AIAA Paper No. 97-1643, May 1997.
[6] J. A. Hayes, W. C. Horne, P. T. Soderman, and P. H. Brent, "Airframe noise characteristics of a 4.7% scale DC-10 model," AIAA Paper No. 97-1594, May 1997.
[7] W. H. Herkes and R. W. Stoker, "Wind tunnel measurements of the airframe noise of a high-speed civil transport," AIAA Paper No. 98-0472, January 1998.
[8] U. Michel, B. Barsikow, J. Helbig, M. Hellmig, and M. Schuttpelz, "Flyover noise measurements on landing aircraft with a microphone array," AIAA Paper No. 98-2336, June 1998.
[9] U. Michel and W. Qiao, "Directivity of landing gear noise based on flyover measurements," AIAA Paper No. 99-1956, May 1999.
[10] J. F. Piet, G. Elias, and P. Lebigot, "Localization of acoustic source from a landing aircraft with a microphone array," AIAA Paper No. 99-1811, May 1999.
[11] B. Barsikow, W. F. King, and E. Pfizenmaier, "Wheel/rail noise generated by a high-speed train investigated with a line array of microphones," J. Sound Vib. **118**, 99–122 (1987).
[12] H. Kook, G. B. Moebs, P. Davies, and J. S. Bolton, "An efficient procedure for visualizing the sound field radiated by vehicles during standardized passby tests," J. Sound Vib. **233**, 137–156 (2000).
[13] S. R. Venkatesh, D. R. Polak, and S. Narayanan, "Beamforming algorithm for distributed source localization and its application to jet noise," AIAA J. **41**, 1238–1246 (2003).
[14] P. Jordan, J. A. Fitzpatrick, and J.-C. Valière, "Measurement of an aeroacoustic dipole using a linear microphone array," J. Acoust. Soc. Am. **111**, 1267–1273 (2002).
[15] Y. Liu, A. P. Dowling, and H.-C. Shin, "Measurement and simulation of surface roughness noise using phased microphone arrays," J. Sound Vib. **314**, 95–112 (2008).
[16] A. R. Quayle, A. P. Dowling, H. Babinsky, W. R. Graham, and Y. Liu, "Phased array measurements from landing gear models," AIAA Paper No. 2007-3463, May 2007.
[17] P. Sijtsma, "Experimental techniques for identification and characterisation of noise sources," in *Advances in Aeroacoustics and Applications*, VKI Lecture Series 2004–05, edited by J. Anthoine and A. Hirschberg (von Kármán Inst. for Fluid Dynamics, Rhode-Saint-Genèse, Belgium, 2004).
[18] H.-C. Shin, W. R. Graham, P. Sijtsma, C. Andreou, and A. C. Faszer, "Implementation of a phased microphone array in a closed-section wind tunnel," AIAA J. **45**, 2897–2909 (2007).

Simple vibration modeling of structural fuzzy with continuous boundary by including two-dimensional spatial memory

Lars Friis[a)]
Acoustic Technology, Ørsted·DTU, Technical University of Denmark, Building 352, DK-2800 Kgs. Lyngby, Denmark and Widex A/S, Ny Vestergaardsvej 25, DK-3500 Vaerloese, Denmark

Mogens Ohlrich[b)]
Acoustic Technology, Ørsted·DTU, Technical University of Denmark, Building 352, DK-2800 Kgs. Lyngby, Denmark

(Received 6 November 2007; revised 8 April 2008; accepted 28 April 2008)

Many complicated systems of practical interest consist basically of a well-defined outer shell-like *master* structure and a complicated internal structure with uncertain dynamic properties. Using the "fuzzy structure theory" for predicting audible frequency vibration, the internal structure is considered as one or more *fuzzy substructures* that are known in some statistical sense only. Experiments have shown that such fuzzy substructures often introduce a damping in the master which is much higher than the structural losses account for. A special method for modeling fuzzy substructures with a one-dimensional continuous boundary was examined in a companion paper [L. Friis and M. Ohlrich, "Vibration modeling of structural fuzzy with continuous boundary," J. Acoust. Soc. Am. **123**, 718–728 (2008)]. In the present paper, this method is extended, such that it allows modeling of fuzzy substructures with a two-dimensional continuous boundary. Additionally, a simple method for determining the so-called equivalent coupling factor is presented. The validity of this method is demonstrated by numerical simulations of the vibration response of a master plate structure with fuzzy attachments. It is revealed that the method performs very well above a nondimensional frequency of 500 of the master, and it is shown that errors below this frequency are caused mainly by simplifying assumptions concerning the shape of the master vibration displacement. © *2008 Acoustical Society of America.* [DOI: 10.1121/1.2932077]

PACS number(s): 43.40.At, 43.40.Tm [DF] Pages: 192–202

I. INTRODUCTION

For about 20 years, the "theory of fuzzy structures"[1–3] has been known as a suggested alternative method for predicting the vibration of complex systems having many degrees of freedom and uncertain properties. By using this theory, a system is divided into a well-defined *master* structure and one or more complex parts termed as *fuzzy substructures*. It is assumed that the deterministic master, which is typically a shell-like structure, can be modeled by using traditional methods, whereas the fuzzy has imprecisely known properties that are known only in some statistical sense. Examples of real-life fuzzy systems varying from small size to large size are electro-mechanical hearing aids, machines, aircraft, and ship hulls.

Experiments have shown that such fuzzy attachments seemingly introduce high damping in the master structure, due to the dissipation of energy into the many degrees of freedom. The theory of fuzzy structures explains this damping effect, caused by multiple reflections rather than actual damping, by regarding the dynamic behavior of the fuzzy similar to that of a multitude of dynamic neutralizers or absorbers.[4–6] Despite of this relatively simple hypothesis, publications on experimental investigations and practical use of the theory of fuzzy structures have so far been very limited in open literature. This is not only partly due to difficulties in determining the fuzzy parameters but also because of complicating issues such as the incorporation of different motion coordinates and modeling of fuzzy structures connected to the master through a continuous boundary.

The present paper examines and extends a special method of modeling structural fuzzy with a continuous boundary. This method was originally formulated by Soize and briefly presented in a paper from 1993.[3] A successful modeling of structural fuzzy with continuous boundary requires that its stiffness must be taken into account. Soize achieved this by introducing spatial memory in the fuzzy boundary impedance. However, such boundary impedance is nonlocal and, therefore, laborious to implement in numerical methods. A full implementation is, therefore, circumvented by introducing an equivalent coupling factor that converts the distributed impedance to a local form. Soize's method of including spatial memory is clearly innovative; however, in the author's opinion, the main ideas of the method need clarification and physical interpretation.

In a companion paper,[7] Soize's method was thoroughly examined and physical interpretations were offered. Furthermore, the smoothed fuzzy boundary impedance was formulated from simple mathematics without the use of probabilistic concepts. The present paper contributes with an extension of the method to two dimensions and with a simple and

[a)]Electronic mail: lf@oersted.dtu.dk
[b)]Electronic mail: mo@oersted.dtu.dk

 0001-4966/2008/124(1)/192/11/$23.00

general method for determining the equivalent coupling factor. This method is examined through numerical simulations and its limitations are discussed. The companion paper and the present paper represent a continuation of the papers by Pierce *et al.*[8] and Strasberg and Feit[9] but for structural fuzzy with *continuous boundary*.

The theory of fuzzy structures was originally developed by Soize and presented in a series of papers[1–3] from 1986 to 1993. During the last 20 years, the literature has partly focused on interpretation and simplification of Soize's theory that involves probabilistic concepts in order to account for model uncertainties. One milestone was the publications of simple and deterministic methods by Pierce *et al.*[8] and Strasberg and Feit.[9] These papers clarified the main concepts of the theory of fuzzy structures and have provided simple procedures for predicting the smoothed average response of complex systems. Furthermore, it was revealed that the damping induced in the master was governed mainly by the frequency-dependent *resonating mass per unit frequency* of the fuzzy. Several authors have examined the fuzzy damping effect in great detail. This includes Maidanik and Becker[10–12] who unambiguously demonstrated the nature of the damping and set up design rules for complex attachments. The damping caused by different local oscillators was likewise investigated by Maidanik and Becker.[13,14] Moreover, Weaver[15] and Carcaterra and Akay[16] revealed that the fuzzy damping is a transient phenomenon in the case of a finite number of complex attachments. It was shown that the energy returns to the master at later times when excited by a transient. One of the most difficult challenges in applying the theory of fuzzy structures is the determination of the resonating mass per unit frequency. During the last ten years, both Soize[17,18] and Pierce[19] addressed this problem. Another important highlight was the development of a method[3] for including spatial memory in the modeling of structural fuzzy with continuous boundaries. With the exception of a few publications,[7,17,18] succeeding literature has mainly focused on developing methods that regard the structural fuzzy as local fuzzy substructures. Many real-life structures, however, involve fuzzy structures with continuous boundaries, and the authors of the present paper believe that further study in this area is strongly needed in order to clarify some of the main ideas.

In favor of the reader, the method of including spatial memory in structural fuzzy will be briefly outlined in Sec. II below. Hereafter, a general method of determining the equivalent coupling factor is presented for a master structure with one-dimensional wave motion. Next, in Sec. IV, the fuzzy boundary impedance will be derived for structural fuzzy attached to the master through an area. After this, the method of finding the equivalent coupling factor is extended to two-dimensional wave motion in the master structure. Finally, in Sec. V, the method will be validated through numerical simulations and its usability and limitations will be discussed in Section VI.

II. STRUCTURAL FUZZY WITH CONTINUOUS BOUNDARY

A. Introduction

Fuzzy structure theory is intended for predicting the vibration and damping induced in a master structure due to one or more fuzzy substructures. The method is applicable mainly in the midfrequency range, where the master structure has well separated modes and where the fuzzy is highly resonant. Since the fuzzy is more or less compliantly attached to the master, the fuzzy behaves predominantly similar to a large number of "sprung masses" or "dynamic neutralizers" resonating at different frequencies. If these resonance frequencies of the fuzzy are closely spaced, then the fuzzy substructure will minimize and absorb vibration energy from the master over a considerable frequency band. Consequently, by considering the vibration response of the master, it appears as if the master is highly damped.

In the theory of fuzzy structures, each fuzzy substructure is modeled as infinitely many dynamic neutralizers attached to the connection surface. These neutralizers have different masses and their resonance frequencies are closely spaced, and altogether they, therefore, introduce a frequency-dependent damping in the master. Further, it is assumed that the total mass of all the oscillators is equal to the mass of the fuzzy substructure that is to be modeled. A fuzzy substructure is typically separated from the master and conveniently modeled in terms of its boundary impedance $\underline{z}_{\text{fuzzy},\varepsilon}(x_0,y_0;x_1,y_1)$. This boundary impedance expresses the relationship between the force per unit area $\underline{F}''(x_0,y_0)$ induced at (x_0,y_0) due to the velocity $\underline{v}(x_1,y_1)$ of an infinitesimal area element dA at (x_1,y_1), while all other positions are locked, that is,

$$\underline{F}''(x_0,y_0) = \underline{z}_{\text{fuzzy},\varepsilon}(x_0,y_0;x_1,y_1)\underline{v}(x_1,y_1)dA|_{\underline{v}[(x,y)\neq(x_1,y_1)]=0}. \quad (1)$$

B. The spatial oscillator

In many cases, the fuzzy substructure is attached to the master through a continuous boundary. This also implies that the stiffness distribution of the fuzzy has to be taken into account and that the associated transfer terms of the impedance in Eq. (1) can only be neglected in special cases.[7] Consider a fuzzy substructure connected to the master structure through a continuous boundary. Generally, this continuous boundary will be a surface, but for the sake of simplicity, we shall here consider a fuzzy attached to the master through a one-dimensional boundary of length L_{fuzzy}. Soize[3] incorporates the stiffness of such a fuzzy substructure by including a spatial memory in the fuzzy boundary impedance. This is accomplished by introducing a spatial oscillator as sketched in Fig. 1(a). The oscillator is defined by its stiffness width or spatial memory 2ε, the point mass M, the lossfactor η, and the resonance frequency f_r. Furthermore, it has a stiffness density distribution $\underline{s}_\varepsilon(x'-x_1)$ that only depends on $(x'-x_1)$ and which is defined as

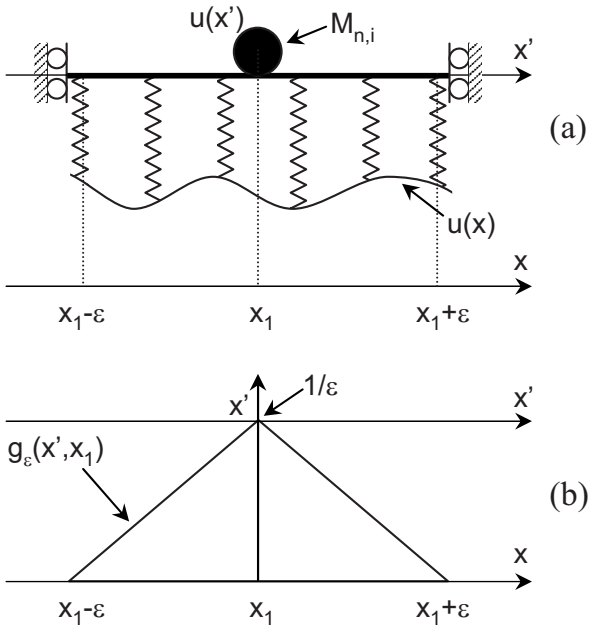

FIG. 1. Fuzzy oscillator with spatial memory. (a) Oscillator attached to a boundary of motion $u(x)$ and (b) stiffness distribution function of the oscillator springs $g_\varepsilon(x'-x_1)$.

$$\underline{s}_\varepsilon(x'-x_1)=\underline{s}g_\varepsilon(x'-x_1)=(M\omega_r^2)(1+i\eta)g_\varepsilon(x'-x_1), \tag{2}$$

where $\omega_r=2\pi f_r$ is the angular resonance frequency and $\underline{s}$ is the complex total stiffness of the oscillator. The distribution function $g_\varepsilon(x'-x_1)$ is an even function with an area of 1. As a one-dimensional spatial memory, Soize suggests[3] that $g_\varepsilon(x'-x_1)$ is a triangular distribution, as shown in Fig. 1(b). This distribution is given as

$$g_\varepsilon(x'-x_1)=g_\varepsilon(x_1-x')=\frac{\varepsilon-|x'-x_1|}{\varepsilon^2}1_{[x_1\in(x'-\varepsilon,x'+\varepsilon)]}, \tag{3}$$

where $1_{[x_1\in(x'-\varepsilon,x'+\varepsilon)]}$ is a function, which is equal to 1 when $x_1\in[x'-\varepsilon,x'+\varepsilon]$ and 0 elsewhere. The spatial oscillator is discussed in more detail in Ref. 7.

C. Sets of infinitely many identical oscillators

Let us consider a fuzzy substructure with spatial memory connected to the master over a length L_{fuzzy}. Such a substructure comprises a *double infinity* of spatial oscillators, as sketched in Fig. 2, where each oscillator is depicted as a point mass and the triangular stiffness distribution shown in Fig. 1(b). First, the oscillators are grouped into sets of infinitely many *identical* oscillators overlapping one another such that each position on L_{fuzzy} is associated with a point mass. Second, the structural fuzzy consists of infinitely many *different* sets, each with its *individual resonance frequency, mass, and spatial memory*.

Now, the nth set $(n\in[1,\infty[)$ of spatial oscillators is shown in Fig. 3(a). This set has a resonance frequency $f_{r,n}$, a total mass of M_n, and a spatial memory of $2\varepsilon_n$. Further, the ith spatial oscillator $(i\in[1,\infty[)$ of this nth set has the natural frequency $f_{r,n,i}=f_{r,n}$, a mass $M_{n,i}=M_n/L_{\text{fuzzy}}$, and a total stiffness $\underline{s}_{n,i}$. The relationship between the force per unit length $F'_{\varepsilon,n}(x_0)$ at x_0 and the velocity $v(x_1)$ at x_1, that is, the boundary impedance of the nth set $\underline{z}_{\varepsilon,n}(x_0-x_1,f_{r,n})$, was derived in Ref. 1. When multiplied by dx_1, this is given as

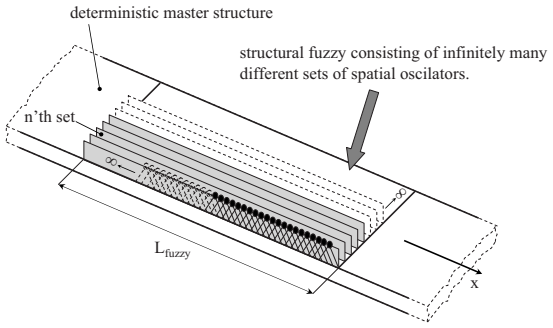

FIG. 2. Master structure undergoing one-dimensional wave motion with a fuzzy substructure attached through a one-dimensional continuous boundary in the x direction. The fuzzy substructure has infinitely many sets of spatial oscillators and the nth set consists of infinitely many identical oscillators with resonance frequency $f_{r,n,i}$, mass $M_{n,i}$, and spatial memory ε_n.

$$\begin{aligned}\underline{z}_{\varepsilon,n}(x_0-x_1,f_{r,n})dx_1=&\frac{\underline{s}_{n,i}}{i\omega}\left[\delta_{x_0,x_1}-\frac{\underline{s}_{n,i}}{\underline{s}_{n,i}-\omega^2M_{n,i}}(g_{\varepsilon_n}*g_{\varepsilon_n})\right.\\&\left.\times(x_0-x_1)dx_1\right]\\=&-i\omega\left(\frac{f_{r,n}^2}{f^2}\right)(1+i\eta)M_{n,i}\\&\times\left[\delta_{x_0,x_1}\right.\\&-\frac{f_{r,n}^2(1+i\eta)}{f_{r,n}^2(1+i\eta)-f^2}(g_{\varepsilon_n}*g_{\varepsilon_n})\\&\left.\times(x_0-x_1)dx_1\right],\end{aligned} \tag{4}$$

where δ_{x_0,x_1} is the Kronecker delta and $*$ means convolution with the argument (x_0-x_1). It is seen that the transfer terms of the boundary impedance in Eq. (4) are proportional to $(g_{\varepsilon_n}*g_{\varepsilon_n})(x_0-x_1)$. This function has been plotted in Fig. 4, and it can be observed that these transfer terms are largest close to x_1 and that the spatial memory in effect reaches $2\varepsilon_n$ on either side of the response point x_1.

The total boundary impedance of the fuzzy substructure can be determined as the sum of all the impedances of all the sets, which yields

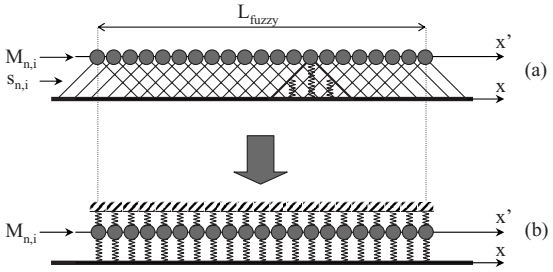

FIG. 3. A set of infinitely many identical oscillators attached to the master: (a) spatial oscillators and (b) equivalent local oscillators.

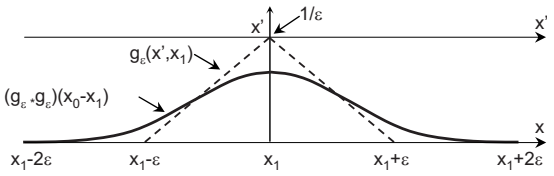

FIG. 4. Fuzzy oscillator with spatial coupling: ---, stiffness distribution function $g_\varepsilon(x'-x_1)$ of the oscillator springs and —, convolution of the stiffness distribution with itself $(g_\varepsilon * g_\varepsilon)(x_0-x_1)$.

$$\underline{z}_{\text{fuzzy},\varepsilon}(x_0-x_1)dx_1=\sum_{n=1}^{\infty}z_{\varepsilon,n}(x_0-x_1,f_{r,n})dx_1. \tag{5}$$

This discrete sum can be replaced by an integral if there is sufficient modal overlap.[20] This is done by replacing $z_{\varepsilon,n}(x_0-x_1,f_{r,n})dx_1$ from Eq. (4) with a continuous distribution denoted by $z_\varepsilon(x_0-x_1,f_r)dx_1df_r$, where f_r is a continuous frequency variable $(f_{r,n}\to f_r)$, and further by assuming that the sets resonate between bounding frequencies $f_{r,\text{lower}}$ and $f_{r,\text{upper}}$. This gives

$$\underline{z}_{\text{fuzzy},\varepsilon}(x_0-x_1)dx_1=\int_{f_{r,\text{lower}}}^{f_{r,\text{upper}}}z_\varepsilon(x_0-x_1,f_r)dx_1df_r. \tag{6}$$

By substituting herein the detailed expression of a continuous version of Eq. (4), the fuzzy boundary impedance becomes

$$\begin{aligned}\underline{z}_{\text{fuzzy},\varepsilon}(x_0-x_1)dx_1&=-\frac{i2\pi f}{L_{\text{fuzzy}}}\int_{f_{r,\text{lower}}}^{f_{r,\text{upper}}}\left(\frac{f_r^2}{f^2}\right)(1+i\eta)m_{\text{fuzzy}}(f_r)\\&\times\left[\delta_{x_0x_1}-\frac{f_r^2(1+i\eta)}{f_r^2(1+i\eta)-f^2}(g_\varepsilon*g_\varepsilon)(x_0-x_1)dx_1\right]df_r,\end{aligned} \tag{7}$$

where $M_{n,i}$ has been replaced by $m_{\text{fuzzy}}(f_r)df_r$ that corresponds to the total mass of the fuzzy substructure resonating in the infinitesimal frequency band between f_r and f_r+df_r.

D. Equivalent local modeling method

A numerical implementation of the boundary impedance given in Eq. (7) is rather complicated due to its *nonlocal* nature and requires, for instance, the use of a finite element model with special fuzzy elements. Unfortunately, this is in contradiction with the idea of the theory of fuzzy structures being a simple modeling tool. However, as indicated in Fig. 3(b), Soize[3] solved this problem by introducing a set of *equivalent local oscillators* that can imitate the boundary forces induced by a set of spatial oscillators. This means that the boundary impedance $\underline{z}_{\text{fuzzy},\varepsilon}$ in Eq. (7) can be replaced with an equivalent boundary impedance $\underline{z}_{\text{fuzzy,equ}}$ that has direct terms only. Figure 3(b) shows that the equivalent local oscillator corresponds to a modified simple oscillator with a spring stiffness $\underline{s}_{1,n,i}$, but where the point mass is grounded via a second spring with stiffness $\underline{s}_{2,n,i}$, such that $\underline{s}_{n,i}=\underline{s}_{1,n,i}+\underline{s}_{2,n,i}$. This means that the equivalent oscillator is springlike at low frequencies because the massless bar that supports the point mass in Fig. 1(a) is unable to rotate; the spatial oscillators, therefore, impose springlike properties on the master at low frequencies.

The relationship between the stiffnesses of the springs for the nth set of equivalent oscillators shown in Fig. 3(b) is given in terms of the *equivalent coupling factor* $\alpha_{n,i}$ and can be expressed as[7]

$$\alpha_{n,i}=\underline{s}_{1,n,i}/(\underline{s}_{1,n,i}+\underline{s}_{2,n,i})=\underline{s}_{1,n,i}/\underline{s}_{n,i}, \tag{8}$$

where $\alpha_{n,i}\in]0,1]$. This parameter $\alpha_{n,i}$ must be determined as a function of the characteristic dimension ε_n of the spatial oscillators, and such a derivation is presented in Sec. III. By introducing $\alpha_{n,i}$, the boundary impedance $\underline{z}_{\text{equ},n}(x_0,f_{r,n})$ of the nth set of equivalent local oscillators becomes[3]

$$\begin{aligned}\underline{z}_{\text{equ},n}(x_0,f_{r,n})&=\frac{\underline{s}_{n,i}}{i\omega}\left(1-\frac{\underline{s}_{n,i}}{\underline{s}_{n,i}-\omega^2M_{n,i}}\alpha_{n,i}\right)\\&=-i\omega\left(\frac{f_{r,n}^2}{f^2}\right)(1+i\eta)M_{n,i}\\&\times\left[1-\frac{f_{r,n}^2(1+i\eta)}{f_{r,n}^2(1+i\eta)-f^2}\alpha_{n,i}\right].\end{aligned} \tag{9}$$

Note that $\alpha_{n,i}\to 1$ when $\underline{s}_{2,n,i}\to 0$ and $\underline{z}_{\text{equ},n}$ will then approach the impedance of a simple oscillator. Further, when $\alpha_{n,i}\to 0$, then $\underline{s}_{1,n,i}\to 0$, which indicates that the structural fuzzy has no effect on the master. Inserting a continuous version of Eq. (9) into Eq. (6) yields the boundary impedance $\underline{z}_{\text{fuzzy,equ}}(x_0)$ of the equivalent fuzzy,

$$\begin{aligned}\underline{z}_{\text{fuzzy,equ}}(x_0)&=-\frac{i2\pi f}{L_{\text{fuzzy}}}\int_{f_{r,\text{lower}}}^{f_{r,\text{upper}}}\left(\frac{f_r^2}{f^2}\right)(1+i\eta)m_{\text{fuzzy}}(f_r)\\&\times\left[1-\frac{f_r^2(1+i\eta)}{f_r^2(1+i\eta)-f^2}\alpha\right]df_r.\end{aligned} \tag{10}$$

This expression also applies for two-dimensional structural fuzzy when the connection *length* L_{fuzzy} is replaced by the connection area A_{fuzzy}. It should be noted that the equivalent coupling factor α generally is a function of frequency. In a companion paper,[7] it was suggested that α can be determined as a function of the ratio ε/λ, where λ is the wavelength of vibration in the master structure, which has one-dimensional wave motion only.

III. METHOD OF DETERMINING THE EQUIVALENT COUPLING FACTOR

A. Matching of boundary forces

Before the suggested equivalent modeling method can be utilized, it is necessary to establish a relationship between the parameters ε and α. This requires that the boundary forces induced by the set of spatial oscillators are matched with the forces induced by the equivalent local oscillators. Results for the equivalent coupling factor α determined in this way were published by Soize[3] but only for a very specific case of a simply supported beam with an attached fuzzy substructure with continuous boundary. His results show the mean value of α as a function of the spatial width ε for only

three coarse frequency bands with a width of 100 Hz going from 350 to 650 Hz. The authors of the present paper, however, seek a simple and general method for finding α. Accordingly, a method for determining α will be presented in the following, again as a function of the ratio $c=\varepsilon/\lambda$. For simple master structures with sinusoidal vibration, the wavelength λ is equal to the free wavelength. For master structures with more complicated eigenfunctions, it is suggested that the term wavelength is replaced by twice the distance between adjacent nodes.

Next, the matching of the boundary forces induced by the nth set of spatial and equivalent oscillators can be expressed as

$$\underline{F}_{\mathrm{equ},n}'(x_0) = \underline{F}_{\varepsilon,n}'(x_0). \tag{11}$$

In terms of velocities and impedances, this becomes

$$\underline{z}_{\mathrm{equ},n}(x_0)\underline{v}(x_0) = \int_{L_{\mathrm{fuzzy}}} \underline{z}_{\varepsilon,n}(x_0 - x_1)\underline{v}(x_1)dx_1. \tag{12}$$

Inserting herein the expressions for the impedances $\underline{z}_{\varepsilon,n}(x_0 - x_1)$ and $\underline{z}_{\mathrm{equ},n}(x_0)$ from Eqs. (4) and (9), respectively, yields

$$\begin{aligned}\underline{s}_{n,i}&\left(1 - \frac{\underline{s}_{n,i}}{\underline{s}_{n,i} - \omega^2 M_{n,i}}\alpha\right)\underline{u}(x_0) \\ &= \underline{s}_{n,i}\left[\underline{u}(x_0) - \int_{L_{\mathrm{fuzzy}}} \frac{\underline{s}_{n,i}}{\underline{s}_{n,i} - \omega^2 M_{n,i}}(g_\varepsilon * g_\varepsilon)\right. \\ &\left.\times(x_0 - x_1)\underline{u}(x_1)dx_1\right].\end{aligned} \tag{13}$$

Next, by rearranging, we obtain an equation that has similar terms on each side of the equality sign,

$$\begin{aligned}\underline{s}_{n,i}&\left[\underline{u}(x_0) - \frac{\underline{s}_{n,i}}{\underline{s}_{n,i} - \omega^2 M_{n,i}}\alpha\underline{u}(x_0)\right] \\ &= \underline{s}_{n,i}\left[\underline{u}(x_0) - \frac{\underline{s}_{n,i}}{\underline{s}_{n,i} - \omega^2 M_{n,i}}\right. \\ &\left.\times\int_{L_{\mathrm{fuzzy}}} (g_\varepsilon * g_\varepsilon)(x_0 - x_1)\underline{u}(x_1)dx_1\right].\end{aligned} \tag{14}$$

By eliminating these terms, Eq. (14) is reduced to

$$\alpha\underline{u}(x_0) = \int_{L_{\mathrm{fuzzy}}} (g_\varepsilon * g_\varepsilon)(x_0 - x_1)\underline{u}(x_1)dx_1, \tag{15}$$

from which an expression for α is obtained,

$$\alpha(x_0) = \frac{\displaystyle\int_{L_{\mathrm{fuzzy}}} (g_\varepsilon * g_\varepsilon)(x_0 - x_1)\underline{u}(x_1)dx_1}{u(x_0)}. \tag{16}$$

B. Approximate expressions for the master's equivalent coupling factor

Determining α from Eq. (16) requires a detailed knowledge about the form of the motion displacement $\underline{u}(x_1)$ of the master. At this point in the analysis, this form has not been identified and it is, therefore, preliminarily approximated by a suitably simple function of x. Moreover, since we are mostly concerned with prediction in the midfrequency range, it is assumed that the wavelength of the master vibration is shorter than the length L of the structure. This also implies that the wave motion in the master is relatively independent of its boundary conditions. Therefore, a sinusoidal function is a good approximation for the one-dimensional vibration of the master, with the exception of the regions very close to the edges. Thus, it is assumed that the displacement $u(x_1)$ of the master can be described as

$$\underline{u}(x_1) = \sin\left(\frac{2\pi}{\lambda}x_1\right), \tag{17}$$

where λ is the free wavelength.[21] Inserting this in Eq. (16) yields α as a function of x_0 and c,

$$\alpha(x_0,c) = \frac{\displaystyle\int_{L_{\mathrm{fuzzy}}} (g_\varepsilon * g_\varepsilon)(x_0 - x_1)\sin\left(\frac{2\pi}{\lambda}x_1\right)dx_1}{\sin\left(\dfrac{2\pi}{\lambda}x_0\right)}. \tag{18}$$

Now, the convolution product inherent in Eq. (18) has only nonzero values when $x_1 \in [(x_0-2\varepsilon),(x_0+2\varepsilon)]$ and it is, therefore, sufficient to solve the integral in this interval provided that x_1 is at least 2ε from the edge of the fuzzy. If this is fulfilled, no truncation errors occur and an analytical solution of Eq. (18) is found by using the symbolic mathematics software MAPLE® (version 10),

$$\alpha(x_0,c) = \alpha(c) = \left[\frac{\sin(\pi c)}{\pi c}\right]^4. \tag{19}$$

This is a surprisingly simple result, which is *independent* of the position x_0 on the master structure because of the homogeneity of the fuzzy. The function $\sin(\pi c)/(\pi c)$ in Eq. (19) is recognized as the sink function. Figure 5 shows α as a function of $c=\varepsilon/\lambda$ for two different regions. In Fig. 5(a), it is seen that $\alpha=1$ when $\varepsilon=0$, which is the case of no spatial memory. Up to about $c=0.8$, α appears to be a uniformly descending function. For values higher than $c=0.8$, α becomes very small and the ordinate is, therefore, extended in Fig. 5(b). Here, the behavior of the sink function is easily recognized, showing soft minima and maxima, and it is revealed that α becomes zero when $c=1,2,3,\ldots$.

For the remaining part of the fuzzy where x_1 is closer than 2ε from the edge of the fuzzy, it is not possible to integrate with respect to x_1 in the whole interval $[(x_0-2\varepsilon),(x_0+2\varepsilon)]$ and the solution for α becomes quite complicated. The simplest way to overcome this problem is to *assume* that α takes on a constant value that can be calculated from Eq. (19). The truncation error introduced because of this assumption naturally depends on the length 2ε. Hence, the larger the values of ε are, the larger the introduced truncation error is.

At this point, two assumptions have been made: First, the vibration of the master is approximated by a sinusoidal function. Errors due to this assumption will only be significant at low frequencies where the free wavelength[21] in the master is large. Second, α is considered to be constant with position. As mentioned, this assumption depends on the

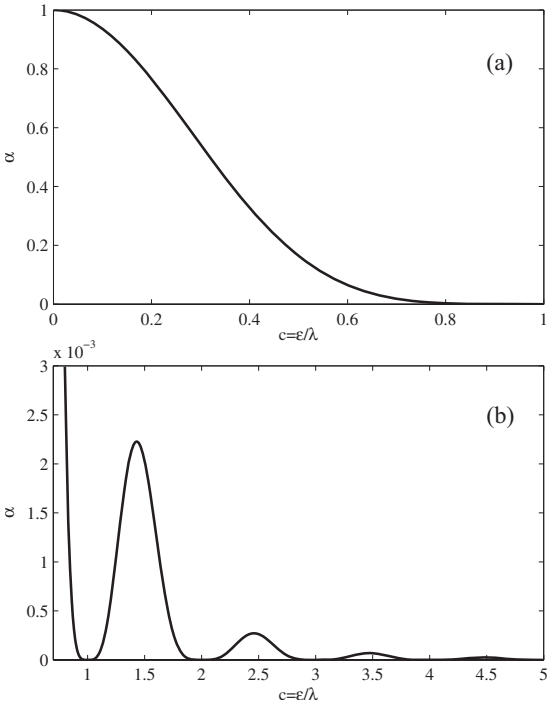

FIG. 5. Variation of the equivalent coupling factor α as a function of the ratio $c=\varepsilon/\lambda$. (a) Values of c from 0 to 1 and (b) from 0.8 to 5.

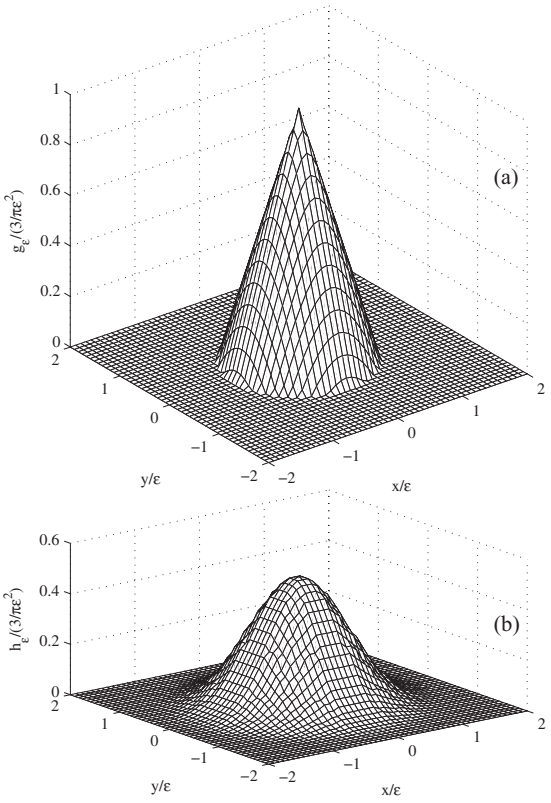

FIG. 6. (a) Normalized stiffness density distribution g_ε of the oscillator springs. (b) Variation of the function h_ε with x and y.

variation of ε with frequency. The significance of these errors in the prediction of α will be examined in Sec. V, where numerical simulations will be presented for a plate master structure with an attached fuzzy substructure with spatial memory.

IV. STRUCTURAL FUZZY WITH TWO-DIMENSIONAL SPATIAL MEMORY

A. Determination of the two-dimensional fuzzy boundary impedance

So far, the method of including spatial memory has been restricted to fuzzy substructures attached to the master structure through a one-dimensional boundary. Most real-life fuzzy structures, however, are attached to their master through a surface that also undergoes two-dimensional vibration. Therefore, the method of including spatial memory in this modeling of fuzzy structures is required and it is, therefore, extended to two dimensions in the following.

To accomplish this, the stiffness distribution function $g_\varepsilon(x'-x_1)$ in Eq. (3) for the spatial oscillator is initially replaced by a two-dimensional version $g_\varepsilon(|r',\theta';r_1,\theta_1|)$, which is a function of the distance $|r',\theta';r_1,\theta_1|$ between two surface points (r',θ') and (r_1,θ_1) described in polar coordinates; it should be noted that the point mass of the spatial oscillator is located at (r',θ'). This two-dimensional stiffness distribution that is shown in Fig. 6(a) in a Cartesian coordinate system represents a cone with a *radius* of ε at its base and a *volume* of 1. Based on these requirements, the distribution can be expressed mathematically as

$$g_\varepsilon(|r',\theta';r_1,\theta_1|) = \frac{\varepsilon - |r',\theta';r_1,\theta_1|}{\frac{1}{3}\pi\varepsilon^3} 1_{[|r',\theta';r_1,\theta_1|\le\varepsilon]}$$

$$= \frac{\varepsilon - \sqrt{r'^2 + r_1^2 - 2r'r_1\cos(\theta'-\theta_1)}}{\frac{1}{3}\pi\varepsilon^3} \times 1_{[|r',\theta';r_1,\theta_1|\le\varepsilon]}, \quad (20)$$

where $1_{[|r',\theta';r_1,\theta_1|\le\varepsilon]}$ is a function that is unity when $|r',\theta';r_1,\theta_1|\le\varepsilon$, and 0 elsewhere. The corresponding stiffness distribution of a two-dimensional spatial oscillator $\underline{s}_{\varepsilon,n,i}(|r',\theta';r_1,\theta_1|)$, thus, becomes

$$\underline{s}_{\varepsilon,n,i}(|r',\theta';r_1,\theta_1|) = \underline{s}_{n,i} g_\varepsilon(|r',\theta';r_1,\theta_1|)$$

$$= (M_{n,i}\omega_{r,n}^2)(1+i\eta) g_\varepsilon(|r',\theta';r_1,\theta_1|), \quad (21)$$

where it applies that $M_{n,i}=M_n/A_{\text{fuzzy}}$ and A_{fuzzy} is the area of the fuzzy connection surface. In the case of a one-dimensional connection boundary, Ref. 7 gives an expression for the force per unit length $\underline{F}_{n,i}'(x_0)$ at x_0 due to the displacement $\underline{u}(x_1)$ at x_1 caused by *only one* spatial oscillator. By replacing this one-dimensional version of g_ε by the new two-dimensional version, we obtain an expression for the relationship between the force per unit area $\underline{F}_{n,i}''(r_0,\theta_0)$ and the displacement $u(r_1,\theta_1)$ that reads

$$\underline{F}_{n,i}''(r_0,\theta_0) = \underline{s}_{\varepsilon,n,i}(|r',\theta';r_1,\theta_1|)\left[\delta_{(r',\theta'),(r_1,\theta_1)} - \frac{\underline{s}_{\varepsilon,n,i}(|r',\theta';r_1,\theta_1|)r_1 dr_1 d\theta_1}{-\omega^2 M_{n,i}+\underline{s}_{n,i}}\right]\underline{u}(r_1,\theta_1), \tag{22}$$

where the infinitesimal area dA_1 is given as $dA_1 = r_1 dr_1 d\theta_1$. Next, to find the force per unit area $\underline{F}_n''(r_0,\theta_0)$ due to a set of infinitely many *identical* spatial oscillators with the base displacement $\underline{u}(r_1,\theta_1)$, Eq. (22) is integrated with respect to (r',θ') over the fuzzy connection surface as

$$\underline{F}_n''(r_0,\theta_0) = \int_{A_{\text{fuzzy}}} \underline{s}_{\varepsilon,n,i}(|r',\theta';r_1,\theta_1|)\left[\delta_{(r',\theta'),(r_1,\theta_1)} - \frac{\underline{s}_{\varepsilon,n,i}(|r',\theta';r_1,\theta_1|)dA_1}{-\omega^2 M_{n,i}+\underline{s}_{n,i}}\right]\underline{u}(r_1,\theta_1)dA'. \tag{23}$$

Finally, this expression can be reduced to

$$\underline{F}_n''(r_0,\theta_0) = \left[\underline{s}_{n,i}\delta_{(r',\theta'),(r_1,\theta_1)} - \frac{\underline{s}_{n,i}^2}{-\omega^2 M_{n,i}+\underline{s}_{n,i}} \times h_\varepsilon(|r_1,\theta_1;r_0,\theta_0|)dA_1\right]\underline{u}(r_1,\theta_1), \tag{24}$$

where the function $h_\varepsilon(|r_1,\theta_1;r_0,\theta_0|)$ is given by

$$\begin{aligned} &h_\varepsilon(|r_1,\theta_1;r_0,\theta_0|) \\ &= \int_{A_{\text{fuzzy}}} g_\varepsilon(|r',\theta';r_1,\theta_1|)g_\varepsilon(|r',\theta';r_0,\theta_0|)dA' \\ &= \int_0^{2\pi}\int_0^{2\varepsilon} g_\varepsilon(|r',\theta';r_1,\theta_1|)g_\varepsilon(|r',\theta';r_0,\theta_0|)r'dr'd\theta'. \end{aligned} \tag{25}$$

It follows that the boundary impedance of the nth set multiplied by dA_1 is given as

$$\begin{aligned} &\underline{z}_{\varepsilon,n}(|r_0,\theta_0;r_1,\theta_1|)dA_1 \\ &= \frac{\underline{s}_{n,i}}{i\omega}\left[\delta_{(r',\theta'),(r_1,\theta_1)} - \frac{\underline{s}_{n,i}}{-\omega^2 M_{n,i}+\underline{s}_{n,i}} \times h_\varepsilon(|r_1,\theta_1;r_0,\theta_0|)dA_1\right], \end{aligned} \tag{26}$$

and by analogy to Eq. (7), the fuzzy boundary impedance becomes

$$\begin{aligned} &\underline{z}_{\text{fuzzy},\varepsilon}(|r_0,\theta_0;r_1,\theta_1|)dA_1 \\ &= -\frac{i2\pi f}{A_{\text{fuzzy}}}\int_{f_{r,\text{lower}}}^{f_{r,\text{upper}}}\left(\frac{f_r^2}{f^2}\right)(1+i\eta)m_{\text{fuzzy}}(f_r) \\ &\quad\times\left[\delta_{(r',\theta'),(r_1,\theta_1)} - \frac{f_r^2(1+i\eta)}{f_r^2(1+i\eta)-f^2} \times h_\varepsilon(|r_1,\theta_1;r_0,\theta_0|)dA_1\right]df_r. \end{aligned} \tag{27}$$

From Eq. (27), it is seen that transfer impedance terms of the fuzzy substructure are proportional to the function $h_\varepsilon(|r_1,\theta_1;r_0,\theta_0|)$. This function can be calculated numerically and the result is shown in Fig. 6(b) for the case $(r_1,\theta_1)=(0,0)$. It is clearly observed that h_ε looks similar to a two-dimensional version of the convolution shown in Fig. 4. Also, it can be seen that h_ε extends to a radius of 2ε relative to (r_1,θ_1) and that the volume under the surface is unity.

B. Determination of the equivalent coupling factor

By analogy to the method in Sec. III, the equivalent coupling factor will now be determined as a function of $c=\varepsilon/\lambda_b$, where λ_b is the vibration wavelength for bending waves. Again, λ_b is suggested to be the free wavelength for simple master structures and twice the distance between adjacent nodes for more complicated master structures. An expression for the equivalent coupling factor is found by extending the expression in Eq. (16) to two dimensions yielding

$$\begin{aligned} \alpha(r_0,\theta_0;c) &= \frac{\int_{A_{\text{fuzzy}}} h_\varepsilon(|r_1,\theta_1;r_0,\theta_0|)\underline{u}(r_1,\theta_1)dA_1}{\underline{u}(r_0,\theta_0)} \\ &= \frac{\int_0^{2\pi}\int_0^{2\varepsilon} h_\varepsilon(|r_1,\theta_1;r_0,\theta_0|)\underline{u}(r_1,\theta_1)r_1 dr_1 d\theta_1}{\underline{u}(r_0,\theta_0)}. \end{aligned} \tag{28}$$

As for the one-dimensional case, the determination of α requires prior knowledge of the vibration displacements of the master structure. Again this problem is overcome by approximating the displacements by a product of two sinusoidals as

$$\underline{u}(x_1,y_1) = \sin\left(\frac{2\pi}{\lambda_x}x_1\right)\sin\left(\frac{2\pi}{\lambda_y}y_1\right), \tag{29}$$

where λ_x and λ_y are the vibration wavelengths for bending motion in the x and y directions, respectively. By substituting $x_1=r_1\cos(\theta_1)$ and $y_1=r_1\sin(\theta_1)$ in Eq. (29), the displacement is transformed to polar coordinates, giving

$$\underline{u}(r_1,\theta_1) = \sin\left[\frac{2\pi}{\lambda_x}r_1\cos(\theta_1)\right]\sin\left[\frac{2\pi}{\lambda_y}r_1\sin(\theta_1)\right]. \tag{30}$$

Further, the bending wavelength λ_b can be found from the relation between the wave numbers,[21]

$$k_b^2 = k_x^2 + k_y^2 \Leftrightarrow \left(\frac{2\pi}{\lambda_b}\right)^2 = \left(\frac{2\pi}{\lambda_x}\right)^2 + \left(\frac{2\pi}{\lambda_y}\right)^2, \tag{31}$$

which by rearranging becomes

$$\lambda_b = \sqrt{\frac{\lambda_x^2\lambda_y^2}{\lambda_x^2+\lambda_y^2}}. \tag{32}$$

As for the one-dimensional case, it is suggested that λ_b is replaced by the free wavelength for simple master structures and by twice the distance between adjacent nodes for master structures with more complicated eigenfunctions. Again, by only considering positions on the fuzzy connection surface that are at least a distance of 2ε from the edges of the fuzzy,

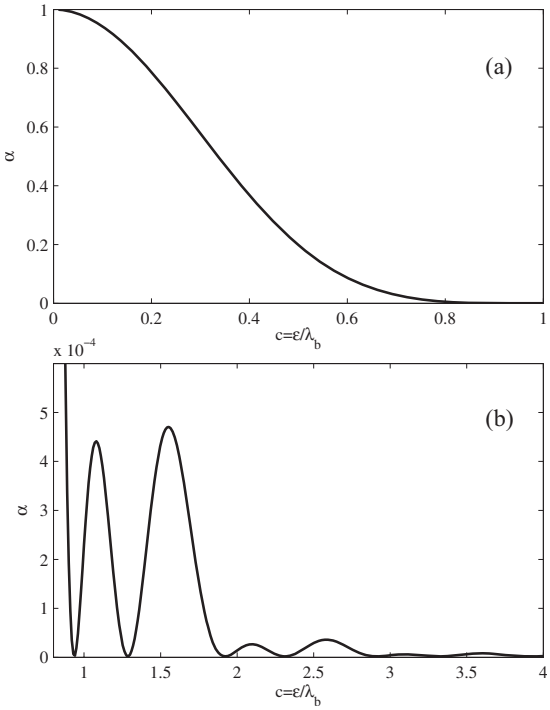

FIG. 7. Variation of the equivalent coupling factor α as a function of $c=\varepsilon/\lambda_b$. (a) Values of c from 0 to 1 and (b) from 0.8 to 4.

an expression for α is found by substituting Eqs. (25) and (30) into Eq. (28). This expression becomes quite complicated and the integrals cannot be solved analytically. Nevertheless, by using numerical integration, α has been determined as a function of $c=\varepsilon/\lambda_b$ and the results are shown in Fig. 7.

First, it should be noted that α does not depend on the forcing position (r_0,θ_0) as long as the response position (r_1,θ_1) is at least a distance of 2ε from the edges of the fuzzy connection surface. Second, it is found that α is insensitive to the specific values of λ_x and λ_y and only depends on λ_b. Figure 7(a) shows that the variation of α resembles the uniformly descending function seen in Fig. 5(a) for values up to $c=0.8$. Again, for values above $c=0.8$, the equivalent coupling factor takes on very small values. Closer inspection of this low value region [see Fig. 7(b)] reveals a different pattern of smooth minima and maxima from that observed in Fig. 5(b). Nevertheless, the equivalent coupling factor still becomes 0 for certain values of c.

V. NUMERCIAL VALIDATION OF EQUIVALENT MODELING METHOD

In a companion paper,[7] it was shown that the spatial memory in the structural fuzzy significantly reduces its damping effect. This finding was achieved by using the equivalent modeling method just described in Sec. II. In the following, the equivalent modeling method will be validated for certain two-dimensional problems by numerical simulations. The finite element method[22] has been used to solve the flexural vibration response of a rectangular plate that is considered as the master; the plate undergoes two-dimensional bending vibration and is assumed to be simply supported along all four edges that have side lengths L_x and L_y, with an

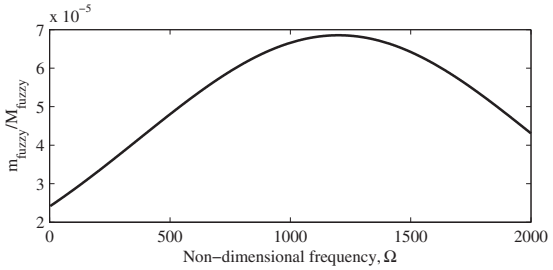

FIG. 8. Normalized resonating mass per unit frequency described by a normal distribution with a centre frequency f_{r0} corresponding to $\Omega=1200$ and a standard deviation std$=0.7f_{r0}$.

aspect ratio given by $L_y=1.3L_x$. A fuzzy substructure is attached to the plate on the whole surface area $A=L_xL_y$, so that $A_{\text{fuzzy}}=A$. The loss factor of the plate is set to 0.005, whereas the loss factor of the fuzzy oscillator springs has been chosen to be 0.03. The resonating mass per unit frequency $m_{\text{fuzzy}}(f_r)$ is a normal distribution given as

$$m_{\text{fuzzy}}(f_r)=\frac{M_{\text{fuzzy}}}{\text{std}\cdot\sqrt{2\pi}}e^{-(f_{r0}-f_r)^2/(2\cdot\text{std}^2)}, \tag{33}$$

where f_{r0} is the center frequency and std is the standard deviation. For this distribution, the bounding frequencies $f_{r,\text{lower}}$ and $f_{r,\text{upper}}$ corresponds to $\Omega=0$ and ∞, respectively. The chosen mass distribution is shown in Fig. 8 as a function of the plate's nondimensional frequency Ω defined as

$$\Omega=\omega\sqrt{\frac{12\rho(1-\nu^2)}{E}}\frac{\sqrt{L_x^2+L_y^2}}{h}, \tag{34}$$

where h is the plate thickness, and ρ, E, and ν are the density, Young's modulus, and Poisson's ratio of the plate, respectively. The center frequency f_{r0} corresponds to $\Omega=1200$ and the standard deviation std$=0.7f_{r0}$. The total mass of the attached fuzzy M_{fuzzy} is one-twentieth of the plate mass, ρAh. Also, the free bending wavelength λ_b in the master plate is found[21]

$$\lambda_b=2\pi\sqrt{\frac{L_x^2+L_y^2}{\Omega}}. \tag{35}$$

For the following response prediction, the boundary impedance of the fuzzy is computed by numerical integration of the integrals in Eqs. (27) and (10), where L_{fuzzy} is replaced by A_{fuzzy} in the latter. Further, $\varepsilon=c\lambda_b$ is assumed to be constant with frequency implying that c and α, respectively, increases and decreases with frequency.

First examined is the effect of a simple fuzzy without spatial memory that is modeled by using Eq. (27) with $\varepsilon=0$. Figure 9 shows results for the vibration velocity response per unit harmonic force of the simply supported master plate, with and without such a fuzzy substructure. Here, the response location (x,y) and excitation position (x_0,y_0) coincide, so the results represent the direct mobility of the system. Since the fuzzy has no spatial memory, it is clearly seen that it has a strong damping effect on the vibration response of the master. This effect mainly occurs from $\Omega=500$ and upwards, where the resonating mass per unit frequency has an appreciable value; that is, it is approximately

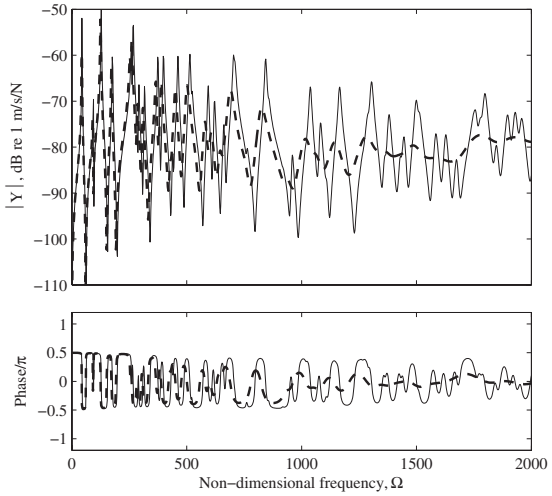

FIG. 9. Vibration velocity response per unit harmonic force of a simply supported plate, $\underline{Y}(x,y;x_0,y_0)=\underline{v}(x,y)/\underline{F}(x_0,y_0)$, at $(x,y)=(x_0,y_0)=(0.175L_x,0.5525L_x)$. Curves: —, without structural fuzzy and ---, with structural fuzzy without spatial memory using Eq. (27) with $\varepsilon=0$.

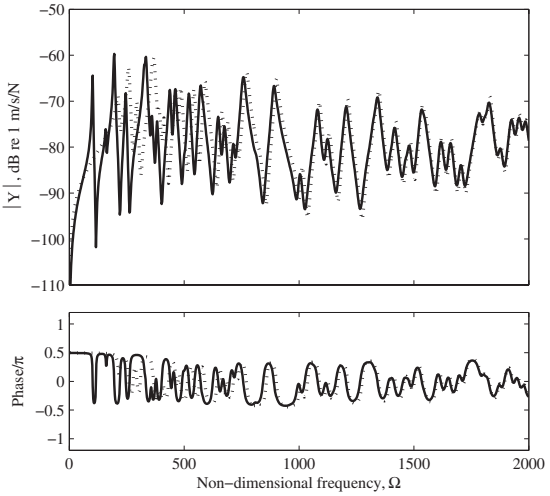

FIG. 11. Vibration velocity response per unit harmonic force of a simply supported plate, $\underline{Y}(x,y;x_0,y_0)=\underline{v}(x,y)/\underline{F}(x_0,y_0)$, at $(x,y)=(x_0,y_0)=(0.175L_x,0.5525L_x)$. Conditions: Structural fuzzy with $\varepsilon=0.2L_x$ and modeled by —, spatial oscillators using Eq. (27) and ⋯·⋯·⋯, equivalent local oscillators using Eq. (10).

half or more of its maximum value according to the results in Fig. 8. At frequencies above $\Omega=1000$, it is furthermore seen that the direct mobility closely approaches the asymptote of −80 dB for a master plate of infinite size. It should be noted that such high damping effect only occurs at early and moderate times for fuzzy substructures consisting of a finite number of oscillators, which are excited by an impulse, since the "absorbed" energy returns from the fuzzy to the master at later times.[15,16] Drexel and Ginsberg[23] also investigated this damping effect for a master cantilever beam with a finite number of spatially distributed discrete oscillators.

An example of the *transfer* mobility of the plate with and without structural fuzzy is shown in Fig. 10. As in Fig. 9, the vibration velocity response of the master is reduced significantly due to the fuzzy from about $\Omega=500$ and upwards. Also, at high frequencies, the response is strongly reduced and is even less than the transfer mobility of a corresponding infinitely large plate which has a low value of −94 dB at $\Omega=2000$.

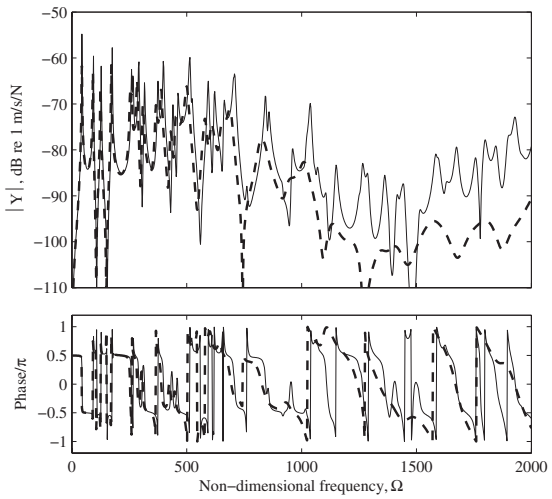

FIG. 10. As in Fig. 9, but for response at $(x,y)=(0.575L_x,1.1375L_x)$ and excitation at $(x_0,y_0)=(0.175L_x,0.5525L_x)$.

Next presented is the validation of the equivalent prediction method. This validation consists in a comparison of simulated responses based on the prediction method using the equivalent local oscillators [Eq. (10)] and the reference method based on spatial oscillators [Eq. (27)]. Consider the simply supported master plate with an attached structural fuzzy that has a constant and *high* spatial memory $\varepsilon=0.2L_x$. By using this value of ε in Eq. (28), the corresponding equivalent coupling factor is found as a function of frequency and substituted in Eq. (10). A comparison of the two predictions is shown in Fig. 11 that displays the vibration responses in terms of the direct mobility. This reveals that there is a very good agreement between the two prediction methods from about $\Omega=500$ and upwards. Significant deviations occur only at low frequencies because of the assumed sinusoidal vibration [Eq. (29)]. Since the plate's edges are simply supported, the sinusoidals are only a really good approximation around the plate's natural frequencies; that is, the frequencies where the conditions $2L/\lambda_x=1,2,3,\ldots$, and $2L/\lambda_y=1,2,3,\ldots$, are both fulfilled. Nevertheless, this error in the estimation of α rapidly reduces with increasing frequency. Evidently, truncation errors that occur at all frequencies due to the constant value of ε do not have a large influence on the prediction based on equivalent oscillators. Moreover, compared to the previous case of no spatial memory (Fig. 9), it is also observed that the spatial memory drastically reduces the damping effect of the fuzzy. In the companion paper,[7] it was shown how the damping effect decreases when α is reduced. The reason for this is that a reduction in α corresponds to an increase in ε. Thus, due to the local angular motion in the master structure, the spring elements in the spatial oscillators counteract one another when $\varepsilon>0$.

The corresponding transfer mobility of the master plate with structural fuzzy of high spatial memory is shown in Fig. 12. Again, the two predictions are seen to be in good agree-

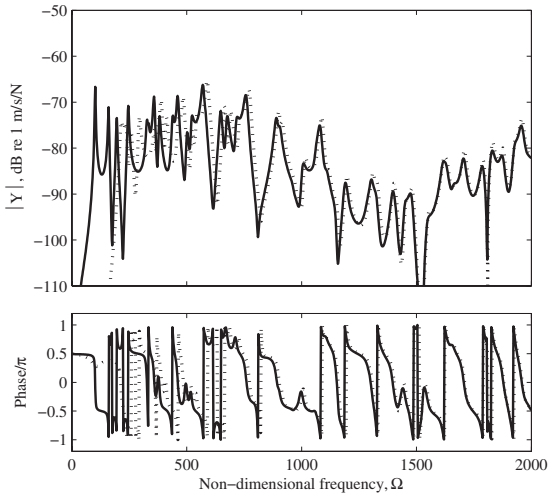

FIG. 12. As in Fig. 11, but for response at $(x,y)=(0.575L_x,1.1375L_x)$ and excitation at $(x_0,y_0)=(0.175L_x,0.5525L_x)$.

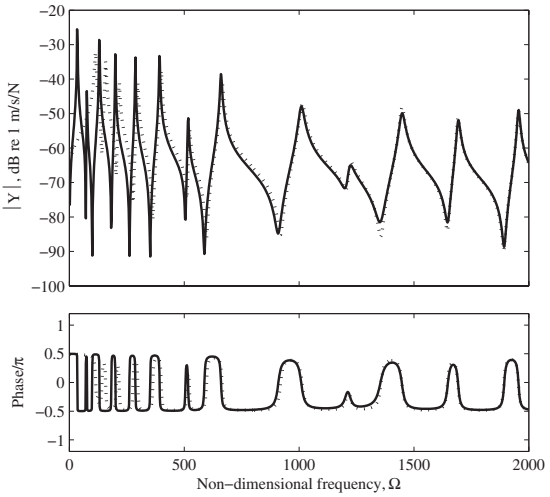

FIG. 13. Vibration velocity response per unit harmonic force of a simply supported beam, $\underline{Y}(x,x_0)=\underline{v}(x)/\underline{F}(x_0)$, at $x=x_0=0.445L$. Conditions: Structural fuzzy with $\varepsilon=0.1L$ modelled by —, spatial oscillators using Eq. (7) and ⋯⋯, equivalent local oscillators using Eq. (10).

ment at frequencies from $\Omega=500$ and upwards. Furthermore, the spatial memory in the fuzzy here is also seen to radically reduce the damping effect.

The equivalent method of prediction performs poorly at low frequencies, say, below $\Omega=500$, because the sine-function approximations of the master vibration pattern have to hold for two dimensions. For a one-dimensional master structure, however, this approximation only involves one direction, and the equivalent method is, therefore, expected to perform well also at lower frequencies. To demonstrate this, a beam with one-dimensional wave motion is considered as the master. A fuzzy substructure is attached on the whole length L of the beam, so that $L_{\text{fuzzy}}=L$. The loss factor of the beam is set to 0.005, whereas the loss factor of the fuzzy oscillator springs has been chosen to be 0.03. The resonating mass per unit frequency is again a normal distribution where the center frequency f_{r0} corresponds to $\Omega=1200$ and std $=0.27f_{r0}$. The nondimensional frequency Ω for the beam is defined as

$$\Omega=\omega\sqrt{\frac{12\rho}{E}}\frac{L^2}{h}. \tag{36}$$

In this example, the spatial memory $\varepsilon=0.1L$ and the total mass of the fuzzy M_{fuzzy} is one-twentieth of the beam mass, ρSL, where S is its cross-sectional area. The vibration velocity of the beam in terms of the input mobility is shown in Fig. 13. It is seen that the results of the two types of predictions given by Eqs. (7) and (10) are almost coinciding from $\Omega=250$ and upwards. Thus, as was anticipated, the equivalent method is found to apply at lower frequencies in the one-dimensional case. The results show that the prediction is reliable at least one octave lower in frequency for the two-dimensional case.

VI. SUMMARY AND DISCUSSION

In 1993, Soize[3] introduced a method for modeling structural fuzzy with a continuous boundary. This method was later extended[17] and validated.[18] Moreover, a part of this method was systematically examined and *reformulated* in a more simple form in a companion paper.[7] The main objective of the present paper is to extend the method to two dimensions and to improve its usability.

Structural fuzzy with a continuous boundary can be modeled by including the stiffness of the fuzzy in terms of a spatial memory. Soize implemented such spatial memory by introducing the so-called spatial oscillators. However, to make the implementation of the fuzzy boundary impedance viable, he replaced these nonlocal spatial oscillators with *local equivalent oscillators* that can imitate boundary forces imposed on the master. This approximation required the introduction of the *equivalent coupling factor* that describes the relationship between the width of the spatial oscillators and the stiffness of the local equivalent oscillators. The current paper has presented a simple and general method for determining this factor as a function of a practical parameter given by the ratio between the width of the spatial oscillators and the free structural wavelength in the master structure. By assuming that the vibration pattern of the master structure can be approximated by one or more sinusoidals and that truncation effects at the end of the fuzzy connection boundary can be ignored, an expression for the equivalent coupling factor has been derived. This expression was evaluated analytically for one-dimensional wave motion in the master structure, and it is revealed that the solution is a very simple expression in the form of a sink function to the power of 4.

For instructive reasons, the method of including memory in the structural fuzzy was originally formulated for a structural fuzzy attached to the master through a one-dimensional boundary. In the present paper, this formulation has been extended to two dimensions, so that it applies for structural fuzzy attached to the master through an area. This is achieved by introducing a two-dimensional stiffness distribution for the spatial oscillator. Additionally, an expression for the equivalent coupling factor is derived and computed numerically as a function of a practical parameter, that is, the ratio between spatial memory and the free wavelength of the

vibration in the master. This solution proved to be closely related to the solution for one-dimensional wave motion in the master.

A validation of the equivalent method by using local equivalent oscillators as a replacement for the spatial oscillators has not previously been published in open literature. In the present paper, the validity of the method has, therefore, been tested by comparing numerical simulations of the response of a master plate with attached structural fuzzy. Results, based on the use of spatial oscillators and equivalent oscillators show a very good agreement for frequencies above $\Omega=500$, where Ω is the nondimensional frequency of the master structure. Below this frequency, errors are mainly caused by the assumption of sinusoidal vibration displacement. For a master beam with one-dimensional wave motion and a fuzzy substructure attached on the whole length, it is revealed that good agreement between predictions is already achieved from about $\Omega=250$. The reason is that the assumption of sinusoidal vibration displacement only has to be fulfilled for one dimension.

The present paper has made various assumptions in order to develop a viable method for modelling structural fuzzy with a continuous boundary. First of all, it has been assumed that the size of the spatial memory in the fuzzy is known beforehand. In real-life engineering structures, the spatial memory is often unknown and relatively difficult to measure. Further, the method of determining the equivalent coupling factor only applies for fairly simple master structures, where its vibration pattern can be approximated as one or more sinusoidals in the midfrequency range. Also important is the estimation of the distribution of resonating mass per unit frequency. It is clear that practical methods for determining these fuzzy parameters are still needed.

[1]C. Soize, "Probabilistic structural modeling in linear dynamic analysis of complex mechanical systems, part I," (English edition), Rech. Aerosp. **5**, 23–48 (1986).

[2]F. Chabas, A. Desanti, and C. Soize, "Probabilistic structural modelling in linear dynamic analysis of complex mechanical systems, part II," (English edition), Rech. Aerosp. **5**, 49–67 (1986).

[3]C. Soize, "A model and numerical method in the medium frequency range for vibroacoustic predictions using the theory of structural fuzzy," J. Acoust. Soc. Am. **94**, 849–865 (1993).

[4]J. Ormondroyd and J. P. Den Hartog, "Theory of dynamic vibration absorber," Trans. ASME **50**, APM-241 (1928).

[5]*Noise and Vibration*, edited by R. G. White and J. G. Walker (Ellis Horwood, Chichester, England, 1982), Chap. 25.

[6]D. F. Mead, *Passive Vibration Control* (Wiley, Chichester, England, 1999), Chap. 8.

[7]L. Friis and M. Ohlrich, "Vibration modelling of structural fuzzy with continuous boundary," J. Acoust. Soc. Am. **123**, 718–728 (2008).

[8]A. D. Pierce, V. W. Sparrow, and D. A. Russell, "Fundamental structural-acoustic idealizations for structures with fuzzy internals," J. Vibr. Acoust. **117**, 339–348 (1995).

[9]M. Strasberg and D. Feit, "Vibration damping of large structures induced by attached small resonant structures," J. Acoust. Soc. Am. **99**, 335–344 (1996).

[10]G. Maidanik and K. J. Becker, "Various loss factors of a master harmonic oscillator coupled to a number of satellite harmonic oscillators," J. Acoust. Soc. Am. **103**, 3184–3194 (1998).

[11]G. Maidanik and K. J. Becker, "Characterization of multiple-sprung masses for wideband noise control," J. Acoust. Soc. Am. **106**, 3109–3118 (1999).

[12]G. Maidanik and K. J. Becker, "Criteria for designing multiple-sprung masses for wideband noise control," J. Acoust. Soc. Am. **106**, 3119–3127 (1999).

[13]G. Maidanik and K. J. Becker, "Dependence of the induced loss factor on the coupling forms and coupling strengths: linear analysis," J. Sound Vib. **266**, 15–32 (2003).

[14]G. Maidanik and K. J. Becker, "Induced noise control," J. Sound Vib. **277**, 1041–1058 (2004).

[15]R. L. Weaver, "The effect of an undamped finite degree of freedom "fuzzy" substructure: Numerical solutions and theoretical discussion," J. Acoust. Soc. Am. **100**, 3159–3164 (1996).

[16]A. Carcaterra and A. Akay, "Transient energy exchange between a primary structure and a set of oscillators: Return time and apparent damping," J. Acoust. Soc. Am. **115**, 683–696 (2004).

[17]C. Soize, "Estimation of fuzzy substructure model parameters using the mean power flow equation of the fuzzy structure," J. Vibr. Acoust. **120**, 279–286 (1998).

[18]C. Soize, "Estimation of fuzzy structure parameters for continuous junctions," J. Acoust. Soc. Am. **107**, 2011–2020 (2000).

[19]A. D. Pierce, "Resonant-frequency-distribution of internal mass inferred from mechanical impedance matrices, with application to fuzzy structure theory," J. Vibr. Acoust. **119**, 324–333 (1997).

[20]G. Maidanik, K. J. Becker, and L. J. Maga, "Replacement of a summation by an integration in structural acoustics," J. Sound Vib. **291**, 323–348 (2006).

[21]L. Cremer, M. Heckl, and E. E. Ungar, *Structure-Borne Sound* (Springer-Verlag, Berlin, 1988).

[22]R. Cook, D. S. Malkus, M. F. Plesha, and R. J. Witt, *Concepts and Applications of Finite Element Analysis* (Wiley, New York, 2002).

[23]M. V. Drexel and J. H. Ginsberg, "Modal overlap and dissipation effects of a cantilever beam with multiple attached oscillators," J. Vibr. Acoust. **123**, 181–187 (2001).

Local vibration of an elastic plate and zero-group velocity Lamb modes

Claire Prada,[a] Dominique Clorennec, and Daniel Royer
Laboratoire Ondes et Acoustique, ESPCI-Université Paris 7-CNRS UMR 7587, 10 rue Vauquelin, 75231 Paris Cedex 05- France

(Received 26 October 2007; revised 6 March 2008; accepted 10 April 2008)

Elastic plates or cylinders can support guided modes with zero group velocity (ZGV) at a nonzero value of the wave number. Using laser-based ultrasonic techniques, we experimentally investigate some fascinating properties of these ZGV modes: resonance and ringing effects, backward wave propagation, interference between backward and forward modes. Then, the conditions required for the existence of ZGV Lamb modes in isotropic plates are discussed. It is shown that these modes appear in a range of Poisson's ratio about the value for which the cutoff frequency curves of modes belonging to the same family intercept, i.e., for a bulk wave velocity ratio equal to a rational number. An interpretation of this phenomenon in terms of a strong repulsion between a pair of modes having a different parity in the vicinity of the cutoff frequencies is given. Experiments performed with materials of various Poisson's ratio demonstrate that the resonance spectrum of an unloaded elastic plate, locally excited by a laser pulse, is dominated by the ZGV Lamb modes.
 [DOI: 10.1121/1.2918543]

PACS number(s): 43.40.Dx, 43.20.Mv, 43.35.Yb [RLW] Pages: 203–212

I. INTRODUCTION

Material characterization using elastic waves is an active domain of applied research. Ultrasonic thickness gauges, which operate by measuring the round-trip interval for a longitudinal wave pulse to traverse the plate or wall under inspection, are routinely used for industrial process control.[1] To be accurate, this pulse echo method requires the use of high frequency piezoelectric transducers for launching bulk waves having wavelength much smaller than the plate thickness. It suffers limitations on rough or curved surfaces and also due to the significant increase of attenuation with frequency. Guided waves emerged as an alternative to this conventional point-by-point nondestructive evaluation for fast inspection of large structures.[2] In a specific approach, developed simultaneously with noncontact laser ultrasonics techniques, the dispersion characteristics of some Lamb modes are exploited for extracting the mechanical properties or the thickness of a given plate. It needs lower frequency waves but requires many local measurements of the normal displacement along several wavelengths on the surface of the plate.[3] Consequently, this method is slow and limited to homogenous plates.

Resonance techniques have the advantage to operate at lower frequencies (bulk wavelength of the order of plate thickness). Among them, the "impact echo" method has been developed for civil engineering applications.[4] The vibration excited by a point-like shock is detected close to the impact. This local investigation technique is, however, limited to thick structures. For ultrasonic applications, the use of electro-magneto-acoustic transducers allows noncontact evaluation of metal sheets.[5] Like in the pulse echo technique, the sheet is assumed to be uniform over a large number of thicknesses leading to a poor spatial resolution. For a long time, engineers considered only bulk wave propagation in the direction normal to the plate and did not pay much attention to the guided nature of elastic waves propagating in the plate. In many cases, the role of Lamb modes is not significant because the lateral dimensions of the source are larger than the Lamb mode wavelength. However, in the case of sources having dimensions of the order of the plate thickness, Lamb modes are generated and must be considered.

The propagation of elastic waves in a plate or in a cylindrical shell has been extensively investigated during the last century. The dispersive properties of guided modes in a free standing plate are well understood.[6,7] Fifty years ago, Tolstoy and Usdin pointed out that for the S_1 Lamb mode, group velocity vanishes at a particular point of the dispersion curve.[8] They also predicted that this zero group velocity (ZGV) point "must be associated with a sharp continuous wave resonance and ringing effects." However, they did not discuss the manner to generate such a resonance. Although the derivation of the transient response of a plate to a point source was achieved by Weaver and Pao in 1982,[9] it is only recently that the importance of zero group velocity Lamb modes in the measurements with short distances between excitation and detection points has been pointed out through some numerical studies[10] and experimental works.[11–16]

Since at a ZGV points the phase velocity and then the wavelength remains finite, the energy can be locally trapped in the source area without any transfer to the adjacent medium. In a narrow range of frequency above this ZGV point and for a given energy propagation direction (from the source to the observation point), two waves can propagate spatially with opposite phase velocities and wave vectors. This backward propagation has been experimentally ob-

[a]Author to whom correspondence should be addressed. Electronic mail: claire.prada-julia@espci.fr.

served in elastic cylinders or plates immersed in water.[17,18] In these conditions, the surrounding fluid causes a large damping of the ZGV resonance.

Using broadband, focusing air-coupled transducers, Holland and Chimenti[11] found that the mechanical softening due to this resonance allows efficient transmission of airborne sound waves through a thick plate. However, laser based ultrasonic techniques, developed for noncontact evaluation of materials, provide an invaluable tool for investigating these ZGV resonances. Direct evidence of this phenomenon was observed by Prada, Balogun, and Murray, with an amplitude modulated laser diode and a Michelson interferometer.[13,14] By scanning the modulation frequency, they show that the thermoelastic source is efficiently coupled to the first symmetric (S_1) Lamb mode at the ZGV point and that the same effect can be observed for the second antisymmetric (A_2) Lamb mode. Recently, the "ringing effect," predicted by Tolstoy and Usdin, has been excited by a laser pulse and optically detected in the time domain.[15] With the same experimental setup, we demonstrated that these resonances can be used for locally measuring the mechanical properties of isotropic materials.[16]

This paper is organized as the following: The nature of ZGV Lamb modes is investigated through laser based ultrasonic (LBU) measurements in Sec. II. These experiments, performed on the S_1-Lamb mode, give a clear evidence of the propagation of a backward wave. The conditions of existence of ZGV-Lamb modes versus Poisson's ratio are established in Sec. III. An interpretation, valid for all ZGV modes in terms of a strong repulsion between a pair of modes in the vicinity of the cutoff frequencies is given. In Sec. IV, it is shown that the local vibration spectrum of an elastic plate is dominated by the ZGV resonances and that these resonances can be exploited for locally measuring the mechanical properties of isotropic materials in plates and hollow cylinders.

II. EXPERIMENTAL EVIDENCE OF S1 ZGV LAMB MODE RESONANCE AND BACKWARD WAVE

Before discussing the whole set of ZGV Lamb modes, we investigate the fascinating behavior of these particular modes through measurements and analysis of the S_1 ZGV mode generated and detected on a Duralumin plate.

Lamb modes (frequency f, wavelength λ) are represented by a set of curves giving the angular frequency ω of each symmetric (S) and antisymmetric (A) mode versus the wave number k. Figure 1 shows the dispersion curve of the lower order modes for a Duralumin plate of thickness d (longitudinal wave velocity V_L=6.34 km/s and transverse velocity V_T=3.14 km/s). We have plotted the variations of the frequency thickness product $fd=\omega d/2\pi$ versus the thickness to wavelength ratio $d/\lambda=kd/2\pi$. The A_0 and S_0 modes exhibit free propagation to zero frequency, whereas higher order modes admit a cutoff frequency f_c when the wave number k approaches zero. Conversely to other modes, the first order symmetric (S_1) mode exists for small wave numbers at values of fd below the cutoff frequency ($f_c d=V_T$ =3.14 MHz mm). The slope of the dispersion curve is negative and the frequency begins to increase at a point ($k_0 d$ =1.58, $f_0 d$=2.866 MHz mm) where the frequency undergoes a minimum and then the group velocity $d\omega/dk$ vanishes. In contrast with the cutoff modes, at this ZGV point, the S_1-mode phase velocity remains finite (V_0=11.25 km/s). In a narrow range between this minimum frequency f_0 and the cutoff frequency f_c, the dispersion curve is double valued. For wave numbers $k<k_0$, phase and group velocities are of opposite signs: backward propagation occurs. In the literature,[17,19,20] the negative slope branch is classified as part of the S_2 mode and is labeled S_{2b}, where b stands for "backward wave." As shown in Kaduchak *et al.*,[19] the distinction between S_1 and S_{2b} modes appears clearly by solving the Rayleigh Lamb equation for a complex wave number. Indeed, the S_{2b} branch is connected to the S_2 branch by a purely imaginary branch. Furthermore, for a water loaded plate, due to leakage, the two branches S_1 and S_{2b} are separate.

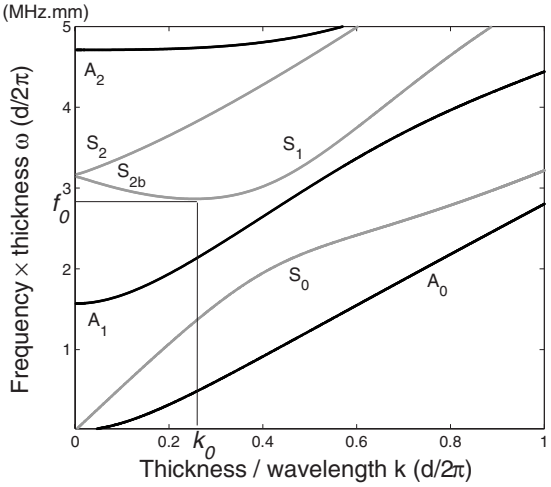

FIG. 1. Dispersion curves for a Duralumin plate of thickness d and bulk wave velocities equal to V_L=6.34 km/s and V_T=3.14 km/s. Vertical scale: $fd=\omega d/2\pi$, horizontal scale: $d/\lambda=kd/2\pi$.

For nondissipation, both in the material and across the waveguide boundaries, it has been shown that the energy velocity is equal to the group velocity.[21] At the frequency f_0, the energy of the S_1-Lamb mode is trapped under the source resulting in ringing and resonance phenomena. This behavior is observed in solids having a Poisson's ratio $\nu<0.45$, i.e., for most usual materials.

Since any mechanical contact with the plate is responsible for an energy leakage, these effects are not easily observed with standard piezoelectric transducers. On the contrary, laser-based ultrasonic (LBU) techniques are appropriate for investigating ZGV modes. They eliminate coupling issues in the generation and detection of the waves, and their high temporal resolution enables studying the resonance spectrum of the plate over a large frequency range.

A. Experimental setup

As shown in Fig. 2, Lamb waves were generated by a Q-switched Nd:YAG (yttrium aluminium garnet) laser providing pulses having a 20 ns duration and 4 mJ of energy. The spot diameter of the unfocused beam is equal to 1 mm.

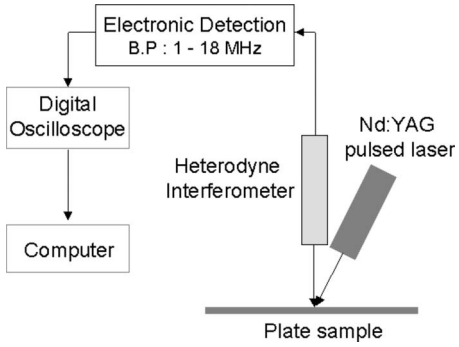

FIG. 2. Experimental setup.

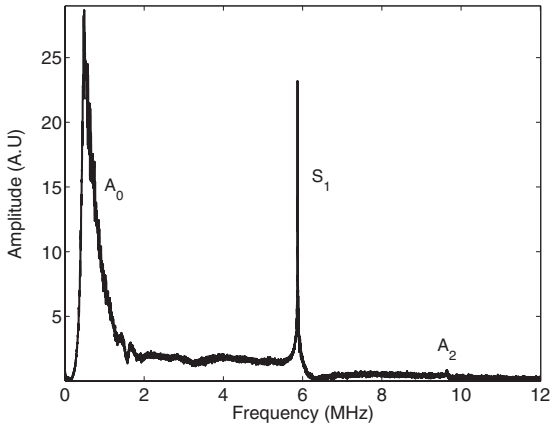

FIG. 3. Spectrum of the signal measured on a 0.49-mm-thick Duralumin plate.

Local vibrations were measured by a heterodyne interferometer equipped with a 100 mW frequency doubled Nd:YAG laser (optical wavelength $\Lambda=532$ nm). This interferometer is sensitive to any phase shift $\Delta\phi$ along the path of the optical probe beam, and then to the mechanical displacement u normal to the surface. As previously shown,[22] the calibration factor (10 nm/V), deduced from the phase modulation $\Delta\phi=4\pi u/\Lambda$ of the reflected beam, was constant over the detection bandwidth (50 kHz–20 MHz). Signals detected by the optical probe were fed into a digital sampling oscilloscope and transferred to a computer.

As discussed in Balogun *et al.*,[14] for a laser spot diameter equal to half the ZGV mode wavelength λ, the efficiency of the thermoelastic generation of this mode is much larger than for other Lamb modes. Numerical simulations show that the wavelength to thickness ratio (λ_0/d) does not vary much with Poisson's ratio ν. For the S_1-Lamb mode: λ_0/d varies from 3.4 to 5 as ν varies from 0 to 0.4. Except for ν values close to the limits where the ZGV resonance disappears, the optimal conditions are approximately fulfilled when the spot diameter is of the order of twice the plate thickness. So, for a 0.5-mm-thick Duralumin plate ($\nu=0.34$), there is no need to focus the Nd:YAG laser beam.

B. S1 mode ZGV resonance

Since the acoustic energy of ZGV modes does not propagate, it is judicious to use superimposed source and detection points. However, the laser energy absorption heats the air in the vicinity of the surface and produces a variation of the optical index along the path of the probe beam. The resulting phase shift induces a very large low frequency voltage, which saturates the electronic detection circuit of the optical probe. This spurious thermal effect is eliminated by interposing a high-pass filter before the amplifying stage. The cutoff frequency of this filter was chosen equal to 1 MHz.

Experiments were carried out on a commercially available Duralumin plate of average thickness $d=0.49$ mm and lateral dimensions equal to 100 and 150 mm. Figure 3 shows the fast Fourier transform of the first 300 μs of the signal measured by the optical probe. The spread spectrum corresponds to the A_0 Lamb mode. In the low frequency range, this flexural mode gives rise to large displacement amplitudes for the out-of-plane component. However, the prominent feature is a sharp peak at 5.86 MHz. From the theoretical dispersion curve of the S_1 mode ($f_0d=2.866$ MHz mm) and taking account of the average plate thickness, the resonance is expected to occur at a frequency $f_0=5.85$ MHz, very close to the experimental value. The relative difference, smaller than 0.2%, can be ascribed to the uncertainty range in the material parameters and in the plate thickness. The small peak at 9.6 MHz corresponds to the thickness resonance at $fd=4.71$ MHz mm of the A_2 Lamb mode in Fig. 1.

C. Backward-wave propagation and dispersion curves

As discussed in several papers,[17,18] at the ZGV frequency the S_1 and S_{2b} modes interfere, having opposite wave vectors. In order to confirm the origin of this resonance, we have measured, with the aid of LBU techniques, the distribution of temporal and spatial frequencies of the out-of-plane displacement. The interference phenomena and the backward S_{2b} branch can be clearly identified by investigating the wave propagation along the Duralumin plate.

The laser source to probe distance r was varied from 0 to 10 mm in 10 μm steps. At each source to receiver distance, the normal displacement $u(r,t)$ was recorded during 300 μs with a 50 MHz sampling frequency. The measured signals are time Fourier transformed into $U(r,f)$. In Fig. 4, the amplitude $|U(r,f)|$ plotted for f varying from 5.85 to 5.93 MHz, reveals a standing mode due to the interference of two waves propagating in opposite directions, and generated with comparable amplitudes. The distance between adjacent nodes is equal to about half a wavelength of the S_1 and S_{2b} modes ($\lambda=V_0/f_0=1.92$ mm). It can be observed that the resonance frequency slightly increases with the distance to the source. At the ZGV resonance frequency f_0 the acoustic energy does not propagate, and as Lamb modes at frequencies lower than f_0 are evanescent, only propagative Lamb waves at frequencies higher than f_0 contribute at distances from the source larger than λ_0.

This existence of counter propagative modes is confirmed by calculating the spatial Fourier transform $\bar{U}(k,f)=\int U(r,f)e^{ikr}dr$. The power spectrum is computed at a frequency (5.89 MHz) slightly higher than the ZGV resonance frequency, for which the modes are propagative. The spec-

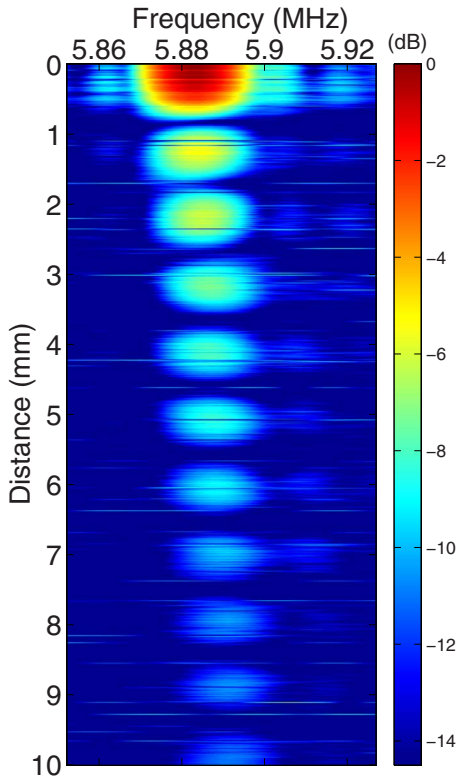

FIG. 4. (Color online) Spatial distribution of the displacement amplitude resulting from the interferences of the two counter-propagating waves S_1 and S_{2b}.

trum, plotted in Fig. 5, is composed of two main peaks. The peak at a negative value of k, similar to the larger one in the positive wave number domain, clearly demonstrates the backward propagation. Due to the up-shift of the operating frequency, the positive and negative k values are not exactly opposite. The wave numbers (-2.95 mm^{-1} and 3.77 mm^{-1}) correspond to the expected ones for the S_1 and S_{2b} modes around the ZGV point ($k_0d=1.58$ and $d=0.49$ mm$\rightarrow k_0=3.22$ mm^{-1}). The other two peaks in Fig. 5 can be ascribed to the S_0 and A_0 Lamb modes.

Applying this signal processing in a large range of frequencies allows us to plot the dispersion curves. As previ-

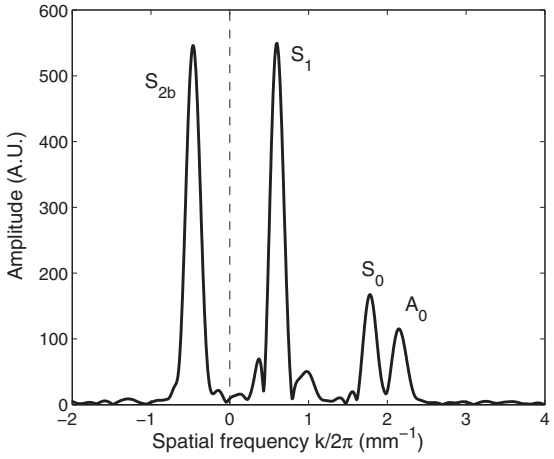

FIG. 5. Spatial Fourier transform of the normal displacement at 5.894 MHz. The negative wave number is clearly put in evidence.

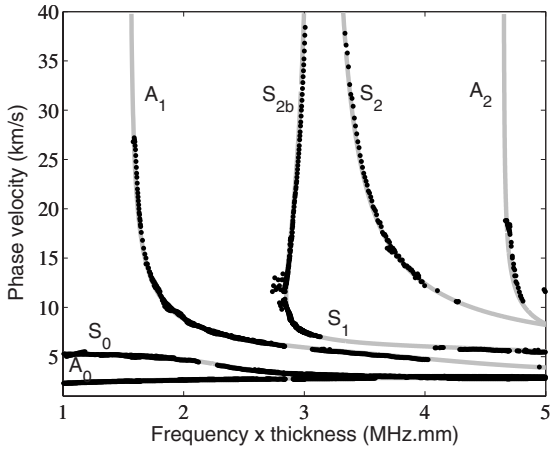

FIG. 6. Measured (dots) and predicted (continuous lines) dispersion curves for the 0.49-mm-thick Duralumin. The high velocity branches are obtained with the unfocused laser source, while the low phase velocity branches are obtained by focusing the laser beam.

ously indicated, the laser source beam was unfocused, providing a 1 mm spot size, approximately equal to half the S_1 ZGV wavelength λ_0. This allows an efficient generation of this mode and of most modes of wavelength larger than 2 mm. In order to complete the dispersion curves with the modes of smaller wavelength, a second set of measurements was performed using a 50 μm source diameter. At each temporal frequency, spatial Fourier transform was applied to the data taken over all spatial steps. The spatial frequencies of the laser generated acoustic modes were then determined by identifying the peaks in the power spectrum. The obtained dispersion curves are plotted in Fig. 6.

These experimental results highlight the main features of the S_1-ZGV Lamb mode, such as resonance effect, backward wave propagation, interference between backward and forward modes. Such an unusual behavior is often qualified as "anomalous."[23] In fact, the occurrence of a ZGV mode is not a unique phenomenon. For an isotropic plate of any Poisson's ratio, it exists in a large range of frequencies, involving nearly all the Lamb modes. In the next section, the conditions required for the existence of ZGV Lamb modes are investigated and an interpretation in terms of a strong repulsion between a pair of modes in the vicinity of the cutoff frequencies is proposed.

III. EXISTENCE OF ZGV LAMB MODES

Elastic properties of an isotropic material are characterized by two constants c_{11} and c_{12}. However, Lamb wave propagation can be expressed in terms of only one dimensionless parameter, the bulk wave velocity ratio $\kappa=V_L/V_T$ or the Poisson's ratio ν.

$$\nu=\frac{\kappa^2-2}{2(\kappa^2-1)}, \quad \text{with } \kappa=\sqrt{\frac{2(1-\nu)}{1-2\nu}}. \tag{1}$$

An important distinction in the behavior of plate modes occurs for small k values ($kd\ll 1$). As shown in Fig. 1, only the fundamental modes A_0 and S_0 exhibit free propagation to zero frequency. The higher modes admit a cutoff frequency f_c for $k=0$ and the dispersion curves start from the frequency

axis with a zero group velocity. However, these cutoff modes do not correspond to ZGV modes like the one discussed in the previous section for which $k \neq 0$.

At cutoff frequencies, multiple reflections of longitudinal or shear waves between the top and bottom faces of the plate give rise to a thickness shear resonance (modes S_{2n} or A_{2m+1}) or to a thickness stretch resonance (modes S_{2m+1} or A_{2n}). For symmetric modes, the even solutions are such that

$$f_c d = nV_T, \quad \text{mode } S_{2n} \ (n \geqslant 1) \tag{2}$$

and the odd solutions are such that

$$f_c d = (2m+1)\frac{V_L}{2}, \quad \text{mode } S_{2m+1} \ (m \geqslant 0), \tag{3}$$

where n and m are integers. For antisymmetric modes, the even solutions are such that

$$f_c d = nV_L, \quad \text{mode } A_{2n} \ (n \geqslant 1) \tag{4}$$

and the odd solutions are such that

$$f_c d = (2m+1)\frac{V_T}{2}, \quad \text{mode } A_{2m+1} \ (m \geqslant 0). \tag{5}$$

For example, in Fig. 1, the cutoff frequency of mode S_1 occurs at $V_L/2d$ and that of mode S_2 at V_T/d. Following Ref. 24, the index of each Lamb mode in the previous classification and in Fig. 7 is equal to the number of nodes in the plate thickness both for shear (in-plane) displacements (modes S_{2n} and A_{2m+1}) and normal (out-of-plane) displacements (modes S_{2m+1} and A_{2n}). This numbering, different from that found in many textbooks, is fundamental for understanding the conditions of occurrence of the ZGV modes.

In the same family and for modes of different parity, the order of cutoff frequencies and then of dispersion curves depends on the bulk wave velocity ratio $\kappa = V_L/V_T$, i.e., on the Poisson's ratio ν. For example, the curves for mode S_1 and S_2 interchange their relative positions for the critical values $\kappa = 2$ and $\nu = 1/3$. This exceptional case, when two branches of the dispersion curves of the same symmetry intersect at cutoff, was first pointed out by Mindlin.[25] For ν equal to $1/3$, the S_1 and S_2 branches intersect the frequency axis at the same point with nonzero slopes, of equal magnitude and opposite signs.[17]

In the following, we show that such coincidence of two cutoff frequencies plays a fundamental role in the existence of a ZGV mode corresponding to a minimum frequency f_0 for a nonzero wave number k_0. Extensive numerical calculations have been performed in order to determine the ZGV modes versus Poisson's ratio ν. For a shear wave velocity, arbitrarily chosen as $V_T = 3.0$ km/s, and a given Poisson's ratio varying by 0.001 step from 0 to 0.5, the longitudinal wave velocity V_L is computed. Using well-known Rayleigh–Lamb equations, the group velocity is calculated by numerical differentiation and the minimum frequencies f_0 corresponding to ZGV points are determined by the zero crossings of the group velocity. Results are presented in Fig. 8 as a universal plot, first used by Meitzler[17] for the S_1 and S_2

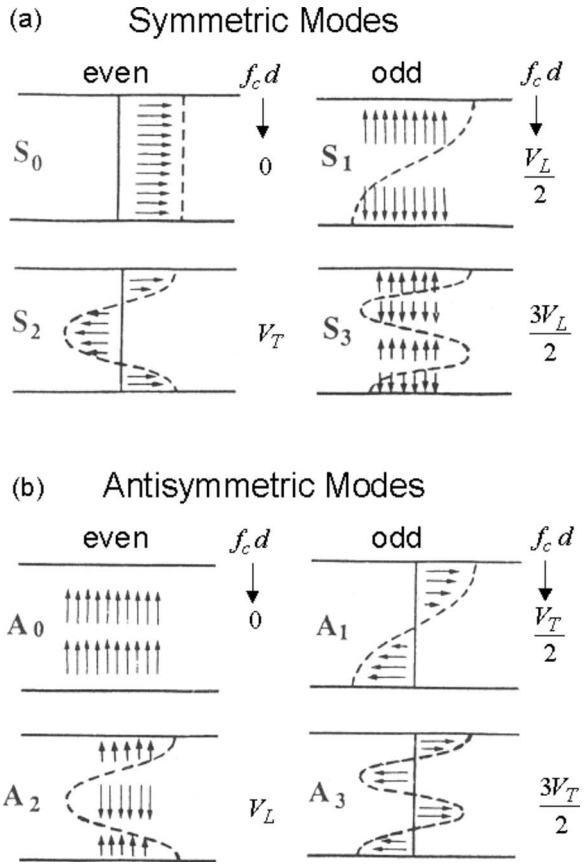

FIG. 7. Mechanical displacements and cutoff frequencies for the first few symmetric (a) and antisymmetric (b) Lamb modes in an isotropic plate of thickness d, for $k=0$ (from Fig. 5.38, Ref. 24).

modes, of the dimensionless quantity $F = fd/V_T$ (with $f = f_0$ or f_c) varying in the range $0 \leqslant F \leqslant 5$, versus Poisson's ratio in the usual range $0 \leqslant \nu < 0.5$.

According to Eqs. (2)–(5), horizontal lines at levels $0.5, 1, 1.5, 2, \ldots$, correspond alternatively to cutoff frequencies of A_{2m+1} and S_{2n} Lamb modes and dashed curves labeled $0.5V_L/V_T, V_L/V_T, 1.5V_L/V_T, \ldots$, correspond alternatively to cutoff frequencies of S_{2m+1} and A_{2n} Lamb modes. From the minimum frequency curves (thick lines) it appears that ZGV modes exist only in the vicinity of crossing points of cutoff frequency curves for modes belonging to the same family: symmetric or antisymmetric. The difference between the minimum frequency and the nearest cutoff frequency is the largest at the coincidence points. These observations lead to explain the ZGV phenomenon as resulting from a strong repulsion between a pair of modes in the vicinity $k=0$. The smaller the frequency gap at $k=0$, the stronger the repulsion.

For example, let us consider a pair of symmetric modes of different parity like S_5 and S_8. As shown in Fig. 9, the difference between their cutoff frequencies, respectively $2.5V_L/d$ and $4V_T/d$, depends on the Poisson's ratio ν. For $\nu = 0.13$, this difference is relatively large and the modes are weakly interacting [Fig. 9(a)]. For $\nu = 0.155$, a stronger interaction leads to a nearly flat lower branch [Fig. 9(b)]. Since the wave velocity ratio is equal to the critical value $\kappa = 1.6$ for $\nu = 0.179$, the cutoff modes are degenerated and the very strong repulsion creates a zero group velocity mode in the lower branch at $k = k_0$ [Fig. 9(c)], similar to the one observed

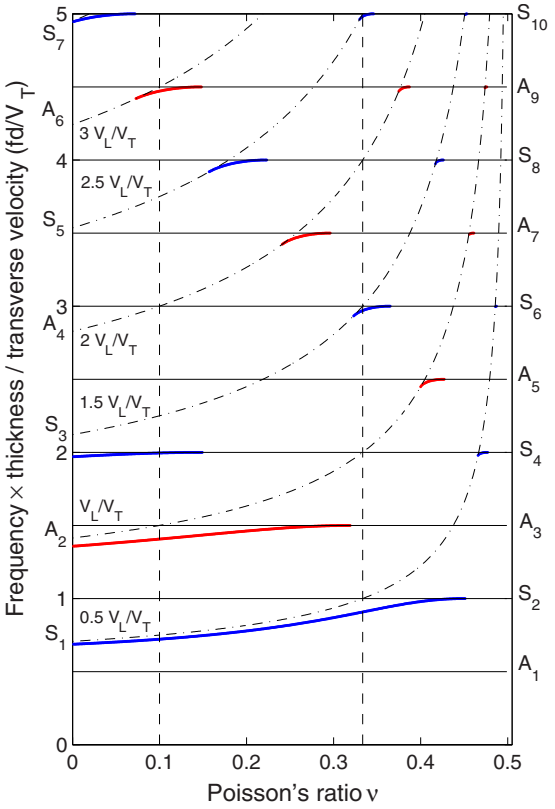

FIG. 8. (Color online) Dimensionless cutoff frequencies $f_c d/V_T$ (horizontal lines) and $f_c d/V_L$ (dashed curves) and minimum frequency $f_0 d/V_T$ versus the Poisson's ratio in the range $0 \leqslant \nu \leqslant 0.5$. The ZGV branches (thick lines) appear about crossing points of cutoff frequency curves for modes belonging to the same family: symmetric or antisymmetric. Vertical dashed lines correspond to the critical values $\nu_1 = 1/3$ and $\nu_2 = 1/10$.

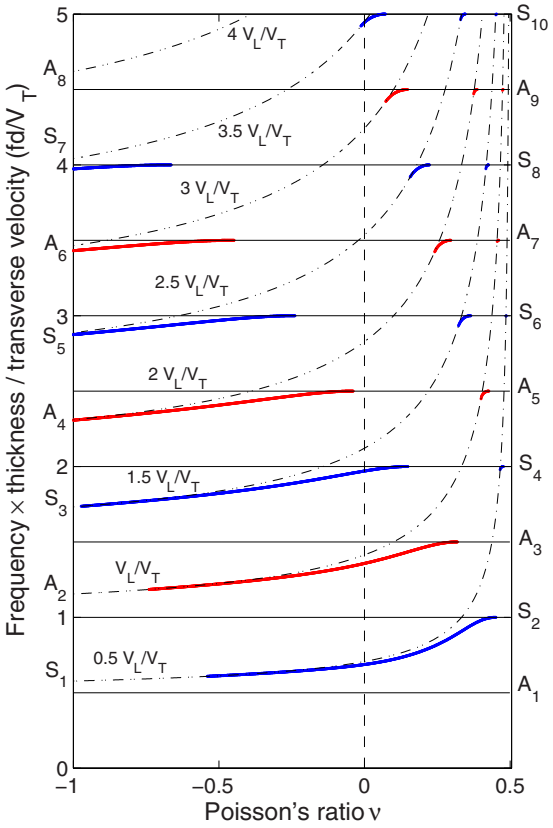

FIG. 10. (Color online) Dimensionless cutoff frequencies and minimum frequency of Lamb modes versus the Poisson's ratio in the physical range $-1 \leqslant \nu \leqslant 0.5$. The third ZGV branch results from the coupling between S_3 and S_4 Lamb modes for a negative Poisson's ratio $\nu = -1/7$.

in Fig. 1. For $\nu = 0.20$, the S_5-mode cutoff frequency passes beyond the S_8-mode ones and the weaker coupling gives rise to a less pronounced trough [Fig. 9(d)].

Due to the symmetry through the median xy plane of the plate, symmetric and antisymmetric Lamb modes are uncoupled for any k. A dispersion curve for a symmetric (antisymmetric) mode may cross a curve for an antisymmetric (symmetric) mode. It is not the case for modes belonging to the same family.[26] However, in Fig. 7 it can be observed that

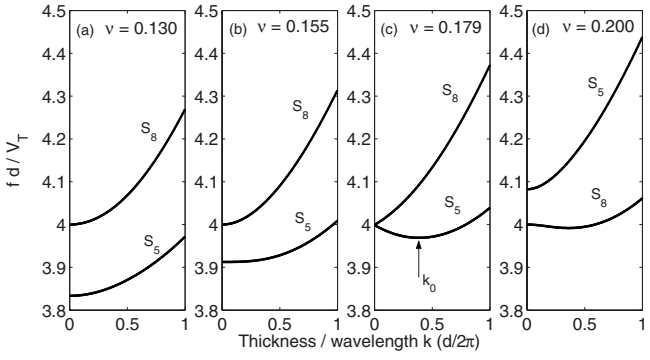

FIG. 9. Dispersion curves of S_5 and S_8 modes for selected Poisson's ratio ν. (a) Weakly interacting modes. (b) Stronger interaction leading to a nearly flat lower branch. (c) Poisson's ratio such as the cutoff modes degenerate ($\kappa = 1.6$): the very strong repulsion creates a zero group velocity mode at $k = k_0$. (d) S_5 and S_8 cutoff frequencies separate: The weaker repulsion gives rise to a less pronounced trough.

for $k = 0$ even and odd modes of the same family are also uncoupled. This property is general because it has its origin in the reflection symmetry through the transverse yz plane, shared for $k = 0$ by any waveguide uniform along the x-propagation direction.[27] Then the difference between cutoff frequencies of a pair of symmetric (antisymmetric) Lamb modes can be made arbitrarily small. For a nonzero wave number, the propagation along the $+x$ or $-x$ direction breaks this symmetry. Odd and even modes belonging to the same family are not yet orthogonally polarized. Both longitudinal and transverse components are involved in the mechanical displacement of each mode, introducing a wave coupling. This phenomenon leads to a strong repulsion between the dispersion curves of the two neighboring modes, responsible of the negative-slope region and zero group velocity point of the lower branch in Figs. 9(c) and 9(d).

From these considerations, the following rules for selecting ZGV modes can be stated:

1- since symmetric and antisymmetric modes are uncoupled for any wave number, the ZGV phenomenon occurs only between modes of the same family,
2- in the same family no coincidence exists between cutoff frequencies of modes having the same parity, then ZGV modes results only from the repulsion between S_{2m+1} and S_{2n} Lamb modes or A_{2n} and A_{2m+1} Lamb modes,
3- for symmetric ZGV modes, the repulsion, i.e., the difference $f_0 - f_c$, is maximum for the critical Poisson's ratio ν given by Eq. (1) with:

TABLE I. Symmetric Lamb modes (frequency thickness product $fd<5V_T$). Critical bulk wave velocity ratio V_L/V_T and Poisson's ratio ν for the 12 ZGV modes plotted in Fig. 8.

Symmetric ZGV modes	S_3/S_4	S_7/S_{10}	S_5/S_8	S_5/S_{10} S_3/S_6 S_1/S_2	S_3/S_8	S_3/S_{10}	S_1/S_4	S_1/S_6	S_1/S_8	S_1/S_{10}
V_L/V_T	4/3	10/7	8/5	2	8/3	10/3	4	6	8	10
ν	−0.1429	0.0196	0.1795	0.3333	0.4182	0.4505	0.4667	0.4857	0.4921	0.4949

$$\kappa_S = \left(\frac{V_L}{V_T}\right)_S = \frac{2n}{2m+1}, \tag{6}$$

4- for antisymmetric ZGV modes, the repulsion is maximum for the critical bulk wave velocity ratio:

$$\kappa_A = \left(\frac{V_L}{V_T}\right)_A = \frac{2m+1}{2n}. \tag{7}$$

κ_A and κ_B are rational numbers, that is, ratios of even integers to odd integers.

For the first symmetric ZGV mode ($m=0, n=1 \rightarrow \kappa_{S1}=2$) the repulsion between the S_1 and S_2 Lamb modes is maximum for $\nu_1=1/3$. For the first antisymmetric ZGV mode ($m=1, n=1 \rightarrow \kappa_{A2}=3/2$) the repulsion between the A_2 and A_3 Lamb modes is maximum for $\nu_2=1/10$. As pointed out by Negishi,[28] the existence range of these so-called S_1 and A_2-ZGV modes are relatively wide with extinction points of $\nu=0.45$ and 0.32, respectively. As shown in Fig. 8, higher order ZGV modes exist over narrower ranges of Poisson's ratio ν and frequency × thickness product fd. It should be noted that symmetric (S_3/S_6 or S_5/S_{10}) and antisymmetric (A_6/A_9)-ZGV modes correspond to the same values ν_1 and ν_2 than fundamental (S_1/S_2) and (A_2/A_3)-ZGV modes, respectively. The reason is that the indices of the pair of modes are multiplied by an odd number, 3 or 5, leading to unchanged bulk wave velocity ratio: $\kappa_{S1}=2$ and $\kappa_{A2}=3/2$. Such high order ZGV modes can be considered as harmonics of the fundamental ones S_1/S_2 and A_2/A_3.

For $\nu<0.14$, a minimum frequency is exhibited in Fig. 8, just below the cutoff frequency ($fd=2V_T$) of the S_4 mode. It can be predicted that this branch corresponds to the coupling with the S_3 mode. According to Eq. (1), the bulk wave velocity ratio $\kappa=4/3$ leads to a negative Poisson's ratio $\nu=-1/7$. As shown in Fig. 10, where the minimum frequencies are plotted in the whole physical range of Poisson's ratio from $-1 \leqslant \nu < 0.5$, other ZGV modes with cutoff frequency coincidences for negative ν values have no extension in the usual material range from $0 \leqslant \nu < 0.5$.

Limiting the frequency thickness product fd to $5V_T$ and for $0 \leqslant \nu < 0.5$, 12 symmetric ZGV modes can be found in Fig. 8. The critical values of the bulk wave velocity ratio and of the Poisson's ratio are given in Table I. The ranges of existence [$\nu_{\min}$ $\nu_{\max}$] of these modes are gathered in Table II. In the same domain of variations for fd and ν, only seven antisymmetric ZGV modes exist. Their characteristics are given in Tables III and IV.

It should be noted that Eq. (6) was given by Werby and Überall for symmetric Lamb modes.[23] However, these authors developed only the simplest case $V_L=2V_T$, reported earlier,[25] and many of their conclusions concerning the existence and the extinction points of ZGV Lamb modes are in contradiction with results of the present work.

Then, in an isotropic plate, the existence of zero group velocity modes is not a rare phenomenon. All Lamb modes, except the first three S_0, A_0, and A_1, exhibit such a behavior. This effect, which cannot be qualified as "anomalous" as it is often the case in the literature, is predicted by using simple rules. Since the negative slope branches in the dispersion curves result from a strong repulsion, in the vicinity of the cutoff frequencies, between two modes having the same symmetry, the frequency minima always occur for small wave numbers. According to this physical meaning, ZGV modes should be labeled with the name of the two coupled Lamb modes: S_{2m+1}/S_{2n} for the symmetric ones and A_{2n}/A_{2m+1} for the antisymmetric ones.

In the next section, using LBU techniques, we investigate the local vibrations of an elastic plate of uniform thickness and we establish a link between the experimental resonance spectrum and the predicted ZGV Lamb modes.

IV. LOCAL RESONANCE SPECTRUM OF A PLATE AND MATERIAL CHARACTERIZATION

Local resonance techniques, such as the "Impact Echo" method developed for concrete applications, are of a great interest for nondestructive evaluation of materials. Therefore it is important to understand the transient response of a slab-like structure to a mechanical or a laser impact. The term "local resonance" means that the distance between the source and the detector is less than the wavelength. At higher frequencies and in our experiments using LBU techniques, the lateral extension of the source is of the order of the plate thickness and the point-like detection is localized in the source area.

TABLE II. Range of existence versus Poisson's ratio [$\nu_{\min}$ $\nu_{\max}$] for the first ten symmetric ZGV Lamb modes.

ZGV mode	S_3/S_4	S_7/S_{10}	S_5/S_8	S_1/S_2	S_3/S_6	S_5/S_{10}	S_3/S_8	S_3/S_{10}	S_1/S_4	S_1/S_6
$\nu_{\min}$	−0.973	−0.012	0.156	−0.540	0.323	0.330	0.417	0.451	0.466	0.485
$\nu_{\max}$	0.149	0.072	0.223	0.451	0.365	0.346	0.426	0.453	0.477	0.487

TABLE III. Antisymmetric Lamb modes (frequency thickness product $fd<5V_T$). Critical bulk wave velocity ratio V_L/V_T and Poisson's ratio ν for the seven ZGV Lamb modes plotted in Fig. 8.

Antisymmetric ZGV modes	A_6/A_9 A_2/A_3	A_4/A_7	A_4/A_9	A_2/A_5	A_2/A_7	A_2/A_9
V_L/V_T	3/2	7/4	9/4	5/2	7/2	9/2
ν	0.1000	0.2576	0.3769	0.4048	0.4556	0.4740

Experiments have been performed according to the procedure described in Sec. II A on plates of thickness d in the millimeter range, made of various materials (steel, nickel, zinc, fused silica and Duralumin). The time Fourier transform was computed with the first 60 μs of the signals measured by the optical probe at the same point. Figure 11 shows the relative magnitude of the frequency spectrum (in dB) versus the frequency normalized to the shear wave velocity (vertical scale: $F=fd/V_T$) for two of them: fused silica and Duralumin. The central part in Fig. 11 reproduces the theoretical ZGV branches in the range $0 \leqslant F \leqslant 5$. The upper limit corresponds to the higher frequencies in the laser pulse spectrum ($f_{\max} \cong 15$ MHz), the plate thickness ($d \cong 1$ mm) and the transverse wave velocity ($V_T \cong 3$ km/s). Vertical dotted lines are drawn for the Poisson's ratio of fused silica (on the left) and Duralumin (on the right). In both cases, each intersection of these lines with a ZGV branch corresponds to a clear resonance peak. Taking into account that for Duralumin the Poisson's ratio $\nu=0.338$ is very close to the critical value $\nu_1=1/3$, the first, third, and fourth peaks correspond to the fundamental (S_1/S_2)-ZGV mode and to its harmonics S_3/S_6 and S_5/S_{10} (see Table I). The second one at $F=1.5$, for which the intersection is close to the extinction point of the (A_2/A_3)-ZGV mode, is less intense than the other peaks for which the intersection nearly coincides with the maximum repulsion between the coupled modes. For fused silica ($\nu=0.172$) the first and second peaks are of the same order of magnitude. The third one, at $F=2$, is weak since the intersection lies outside the zone of existence of the (S_3/S_4)-ZGV mode.

Similar results obtained with other materials lead to the conclusion that *the local resonance spectrum of a plate is entirely governed by the zero-group-velocity Lamb modes*. This conclusion is based on two points: first, the high excitability of such ZGV modes by a laser source of lateral dimensions of the order of the plate thickness. Second, the energy of other laser-excited Lamb modes flows outside the source area, at their nonzero group velocity, in less than 1 μs. Then, only ZGV modes, trapped under the source, give rise to a local vibration of the plate detectable over a long time.

For a given pair of Lamb modes, the ZGV resonance frequency f_0 is slightly smaller than the cutoff frequency f_c:

$$f_0 = \beta f_c \quad \text{with} \quad f_c = p\frac{V}{2d}, \tag{8}$$

where p is an integer and V is equal to V_L or V_T, according to Eqs. (2)–(5). The dimensionless parameter β was first incorporated as a "shape factor" in the American Society for Testing and Materials standards in order to correct the wall thickness measured by the impact echo method.[4] Its value, less than unity, depends only on the Poisson's ratio ν.[12]

For a given homogeneous material, the resonance frequency is sensitive to the plate thickness d. We have shown that relative variations as small as 0.02% can be measured, without any mechanical contact, from the shift of the resonance frequency of the S_1 ZGV mode.[15] The lateral resolution, in the millimeter range, is one order of magnitude better than the one obtained with electromagnetic acoustic transducers.[5] Moreover, the ZGV resonance method is not limited to metallic materials.

The material damping can be also estimated from the half-power bandwidth Δf_0 of the resonance peak and from the phase velocity V_0 at the ZGV point. Assuming a viscoelastic mechanism, the attenuation coefficient α (m^{-1}) is related to the acoustic quality factor $Q=f_0/\Delta f_0$:

$$\alpha = \frac{k_0}{2Q} = \pi\frac{\Delta f_0}{V_0}. \tag{9}$$

For an accurate determination of the attenuation coefficient, the signal acquisition time window must be larger than the inverse of the bandwidth. This method, first applied with the S_1 mode,[15] can be extended to other ZGV modes, providing the attenuation coefficient at higher frequencies.

Figure 11 and experiments performed on other materials show that many ZGV resonances can be excited in a single shot and detected locally on a plate. The ratio of two resonance frequencies is independent of the plate thickness d. It depends only on the Poisson's ratio ν, the value of which can be determined accurately from frequency measurements. Using LBU techniques, this method has been tested on a large number of isotropic materials. The Poisson's ratio and the bulk wave velocities were determined locally in thin plates or shells.[16] In these experiments, only the first two resonances at the minimum frequencies of S_1 and A_2 Lamb

TABLE IV. Antisymmetric ZGV Lamb modes. Range of existence versus Poisson's ratio $[\nu_{\min}\ \nu_{\max}]$.

ZGV mode	A_2/A_3	A_6/A_9	A_4/A_7	A_4/A_9	A_2/A_5	A_2/A_7	A_2/A_9
$\nu_{\min}$	–0.740	0.073	0.241	0.375	0.400	0.455	0.474
$\nu_{\max}$	0.319	0.148	0.296	0.387	0.427	0.461	0.476

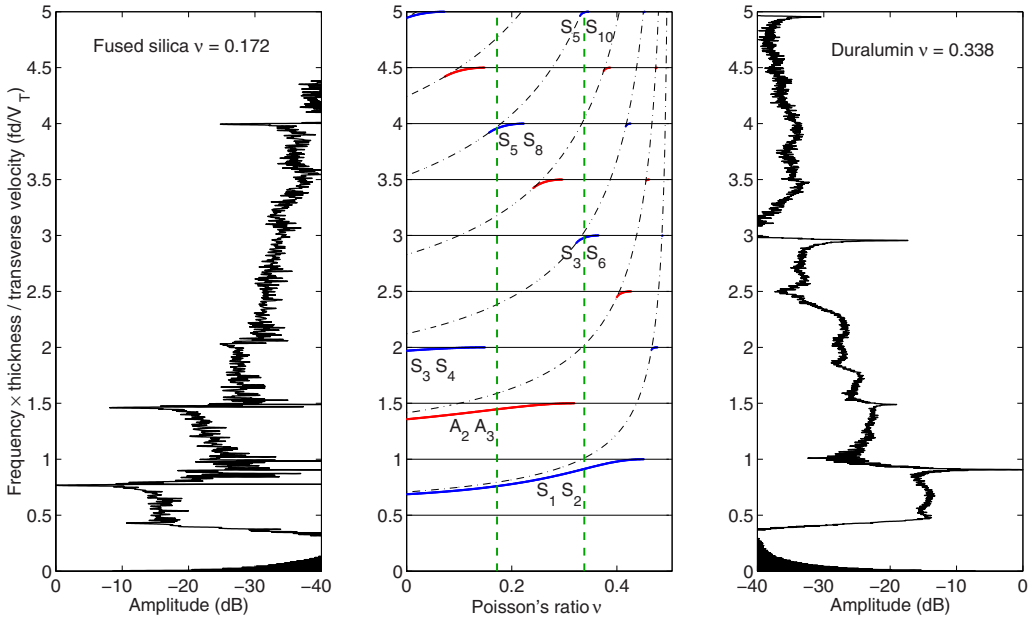

FIG. 11. (Color online) Local vibration spectrum of a fused silica plate of thickness $d=1.1$ mm (on the left) and of a Duralumin plate of thickness $d=1.0$ mm (on the right). Resonance peaks occur at the intersection of the minimum frequency curves of Lamb modes, plotted in the central part. The vertical dotted lines correspond to the Poisson's ratio of fused silica ($\upsilon=0.172$) and of Duralumin ($\upsilon=0.338$).

modes are used. From the previous analysis, it is clear that this characterization method can be generalized to higher order ZGV modes. Taking into account these modes having a narrow range of existence (see Tables II and IV) for the correlation between the experimental and theoretical local resonance spectra would dramatically improve the determination of the elastic parameters.

It should be recalled that in all experiments, the vibrations are excited locally in the thermoelastic regime and that the measurements are performed on the same face of the sample, without any mechanical contact.

V. CONCLUSION

Using laser-based ultrasonic techniques, we have experimentally investigated the resonance and ringing effects associated with the S_1 ZGV Lamb mode in an isotropic plate. The spatial distribution of the mechanical displacement has been optically measured on the surface of the plate. The spatial Fourier transform, computed at the ZGV resonance frequency, exhibits two peaks for opposite wave numbers. Backward and forward wave propagation, clearly revealed in these experiments, explained the observed standing wave pattern.

We developed a simple analysis based on the coincidences of Lamb modes cutoff frequencies, which demonstrates that the occurrence of zero group velocity (ZGV) Lamb modes is not a rare phenomenon. Numerical calculations show that the frequency × thickness product undergoes a minimum in a range of Poisson's ratio about the critical value for which the cutoff frequency curves of modes of similar symmetry intercept. An interpretation of this phenomenon in terms of mode coupling has been given. Using a classification where the index of each mode is equal to the number of nodes at the cutoff frequency in the plate thickness, ZGV Lamb modes result from the coupling of a pair of modes having a different parity, such as S_{2m+1} and S_{2n} or A_{2n} and A_{2m+1}.

Vibrational spectra measured on plates made of various materials lead to the conclusion that the local resonance spectrum of an unloaded elastic plate is entirely governed by the zero-group-velocity Lamb modes. We indicate how these ZGV resonances can be exploited for measuring the plate thickness, the attenuation coefficient, the Poisson's ratio, and the bulk wave velocities of thin plates. Since the vibrations are excited in the thermoelastic regime by a laser pulse and detected at the same point by an optical interferometer, these measurements are local and performed in a single shot on the same face of the plate, without any mechanical contact. Moreover, this ZGV resonance method, based on frequency measurements, is very accurate. ZGV modes have also been observed in anisotropic or multilayered plates and in cylindrical shells. We expect that most results presented in this paper can be generalized to these various structures.

[1]L. C. Lynnworth, *Ultrasonic Measurements for Process Control: Theory, Techniques Applications* (Academic, Boston, 1989).
[2]P. Cawley, M. J. S. Lowe, D. N. Alleyne, B. Pavlakovic, and P. Wilcox, "Practical long range guided wave testing: Applications to pipes and rail," Mater. Eval. **61**, 66–74 (2003).
[3]W. Gao, C. Glorieux, and J. Thoen, "Laser ultrasonic study of Lamb waves: Determination of the thickness and velocities of a thin plate," Int. J. Eng. Sci. **41**, 219–228 (2003).
[4]M. Sansalone and N. J. Carino, "Impact echo: A method for flaw detection in concrete using transient stress waves," Report No. NBSIR86-3452, National Bureau of Standards, Gaithersburg, MD (1986).
[5]S. Dixon, C. Edwards, and S. B. Palmer, "High accuracy non-contact ultrasonic thickness gauging of aluminium sheet using electromagnetic acoustic transducers," Ultrasonics **39**, 445–453 (2001).
[6]I. A. Viktorov, *Rayleigh and Lamb Waves* (Plenum, New York, 1967).
[7]J. D. Achenbach, *Wave Propagation in Elastic Solids* (North-Holland, Amsterdam, 1980).
[8]I. Tolstoy and E. Usdin, "Wave propagation in elastic plates: Low and high mode dispersion," J. Acoust. Soc. Am. **29**, 37–42 (1957).

[9]R. L. Weaver and Y.-H. Pao, "Spectra of transient waves in elastic plates," J. Acoust. Soc. Am. **72**, 1933–1941 (1982).
[10]T. Liu, W. Karunasena, S. Kitipornchai, and M. Veidt, "The influence of backward wave transmission on quantitative ultrasonic evaluation using Lamb wave propagation," J. Acoust. Soc. Am. **107**, 306–314 (2000).
[11]D. Holland and D. E. Chimenti, "High contrast air-coupled acoustic imaging with zero group velocity Lamb modes," Appl. Phys. Lett. **83**, 2704–2706 (2003).
[12]A. Gibson and J. S. Popovics, "Lamb wave basis for impact-echo method analysis," J. Eng. Mech. **131**, 438–443 (2005).
[13]C. Prada, O. Balogun, and T. W. Murray, "Laser based ultrasonic generation and detection of zero-group velocity Lamb waves in thin plates," Appl. Phys. Lett. **87**, 194109 (2005).
[14]O. Balogun, T. Murray, and C. Prada, "Simulation and measurement of the optical excitation of the S1 zero group velocity Lamb wave resonance in plate," J. Appl. Phys. **102**, 064914 (2007).
[15]D. Clorennec, C. Prada, D. Royer, and T. W. Murray, "Laser impulse generation and interferometer detection of zero-group velocity Lamb modes," Appl. Phys. Lett. **89**, 024101 (2006).
[16]D. Clorennec, C. Prada, and D. Royer, "Local and noncontact measurement of bulk acoustic wave velocities in thin isotropic plates and shells using zero-group velocity Lamb modes," J. Appl. Phys. **101**, 034908 (2007).
[17]A. H. Meitzler, "Backward-wave transmission of stress pulses in elastic cylinders and plates," J. Acoust. Soc. Am. **38**, 835–840 (1965).
[18]J. Wolf, T. D. K. Ngoc, R. Kille, and W. G. Mayer, "Investigation of Lamb waves having negative group velocity," J. Acoust. Soc. Am. **83**, 122–126 (1988).
[19]G. Kaduchak, D. H. Hughes, and P. L. Marston, "Enhancement of the backscattering of high-frequency tone bursts by thin spherical shells associated with a backwards wave: Observations and ray approximation," J. Acoust. Soc. Am. **96**, 3704–3714 (1994)
[20]P. L. Marston, "Negative group velocity Lamb waves on plates and applications to the scattering of sound by shells," J. Acoust. Soc. Am. **113**, 2659–2662 (2003).
[21]M. A. Biot, "General theorems on the equivalence of group velocity and energy transport," Phys. Rev. **105**, 1129–1137 (1957).
[22]D. Royer and E. Dieulesaint, *Proceedings of the 1986 IEEE Ultrasonics Symp.* (IEEE, New York, 1986), p. 527.
[23]M. F. Werby and H. Überall, "The analysis and interpretation of some special properties of higher order symmetric Lamb waves: The case for plates," J. Acoust. Soc. Am. **111**, 2686–2691 (2002).
[24]D. Royer and E. Dieulesaint, *Elastic Waves in Solids 1: Free and Guided Propagation* (Springer, Berlin, 1999), p. 317.
[25]R. D. Mindlin, *An Introduction to the Mathematical Theory of Vibrations of Elastic Plates*, U.S. army Signal Corps Eng. Lab., Ft Monmouth, N. J., Monograph. Sec. 2.11 (1955). Edited by, J. Yang (World Scientific, Singapore, 2006).
[26]B. Auld, *Acoustic Fields and Waves in Solids* (Wiley Interscience, New York, 1973), Vol. **II**, p. 81.
[27]M. Ibanescu, S. G. Johnson, D. Roundy, C. Luo, Y. Fink, and J. D. Joannopoulos, "Anomalous dispersion relations by symmetry breaking in axially uniform waveguides," Phys. Rev. Lett. **92**, 063903 (2004).
[28]K. Negishi, "Existence of negative group velocity in Lamb wave," Jpn. J. Appl. Phys., Part 1 **26**, Supplement 26-1, 171–173 (1987).

Analysis of noncircular fluid-filled boreholes in elastic formations using a perturbation model

Ergün Şimşek and Bikash K. Sinha[a)]
Schlumberger-Doll Research, 1 Hampshire Street, Cambridge, Massachusetts 02139

(Received 16 November 2007; revised 11 March 2008; accepted 23 April 2008)

This paper presents a perturbation model to obtain flexural mode dispersions of noncircular fluid-filled boreholes in homogeneous elastic formations. The perturbation model is based on Hamilton's principle with a modified procedure for the reference state selection in order to handle the directional sensitivity of the flexural modes. The accuracy of the perturbation model has been confirmed by comparison to boundary integral solutions. Numerical results confirm that for a fast formation, even modes, and for a slow formation, odd modes are more sensitive to changes in the borehole elongation and azimuth. Even though the focus of this work is on elliptical boreholes and breakouts, the formulation is valid for any kind of noncircular borehole.
 [DOI: 10.1121/1.2931954]

PACS number(s): 43.40.Ph, 43.20.Bi, 43.20.Ks, 43.20.Mv [RAS] Pages: 213–217

I. INTRODUCTION

Borehole cross section affects the propagation of guided modes, such as the lowest-order axisymmetric Stoneley, flexural, and quadrupole modes. Breakouts, which are commonly encountered during underbalance drilling in the presence of large tectonic stresses, can cause complex perturbations to the borehole cross section. The influence of breakouts on the borehole Stoneley, flexural, and quadrupole dispersions has been studied by using finite-difference time domain (FDTD),[1] finite element,[2] and boundary integral equations (BIEs).[3] Since the breakout azimuth coincides with the minimum horizontal stress direction, the distorted borehole cross section can be used to estimate the maximum horizontal stress magnitude.[4–7] Ellefsen *et al.*[8] have also presented a perturbation model (PM) for analyzing modes in noncircular boreholes in anisotropic formations. However, computational results for noncircular boreholes are described only for axisymmetric tube waves.

It has been indicated that the presence of a symmetric breakout causes the flexural wave splittings in the intermediate frequency band similar to the case of an elliptical hole. The two canonical dispersions in a fast formation approximately correspond to the largest and smallest diameters of the distorted borehole cross section.[1] When the influence of breakouts on borehole dispersions is obtained by using FDTD formulation, small changes in the borehole elongation or angular spread are not distinguished very easily. However, such small changes in the borehole cross section can be identified by monitoring perturbations in the guided mode dispersions from a reference circular borehole case. Hence, to understand the effect of breakouts on borehole dispersions, we develop a PM based on Hamilton's principle, which is more sensitive than FDTD. A PM relates fractional changes in the harmonic frequency to fractional changes in the model parameters for a fixed propagation constant. In addition, we analyze the effects of noncircular boreholes on flexural dispersions by using a BIE solver. In other words, we use two different approaches (PM and BIE) to analyze elliptical boreholes and symmetric breakouts that lead to splitting of flexural waves into two canonical waves which are largely sensitive to the long and short diameters of the distorted borehole.

We describe an appropriate method for the selection of reference state for the PM to minimize the difference between perturbed and reference states. We compare results obtained from these two different approaches for both fast and slow formations. Both methods confirm that flexural modes split into two distinct branches (odd and even modes) according to radial polarization parallel to the minor and major axes of the borehole.

The organization of this paper is as follows. In the first section, we briefly describe the implementation of variational principle to the case of a noncircular borehole and a selection procedure for a reference state for even and odd modes. We review a boundary integral formulation and present some illustrative examples. In the second section, we present numerical results obtained from these two different approaches and compare their sensitivity to borehole elongation/breakout azimuth to show the accuracy of the model. Finally, some conclusions are provided.

II. THEORY

In this work, we use two different numerical techniques to analyze noncircular boreholes: a PM and a BIE solver.

Different ways of deriving PMs for elastodynamic problems have been reported.[8–11] In this work, we follow a PM developed by Sinha[12] based on Hamilton's principle that conveniently predicts changes in dispersion curves due to small alterations in either borehole cross section or any of the six fundamental material parameters of the borehole model (borehole fluid mass density ρ_f, fluid compression modulus λ_f, formation mass density ρ, formation elastic moduli λ and μ, and borehole radius a).

[a)]Electronic mail: sinha1@slb.com

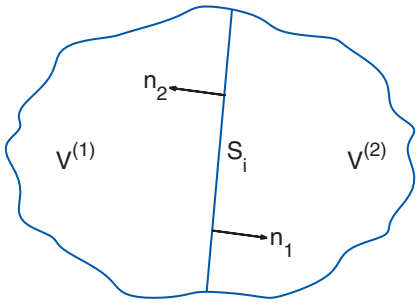

FIG. 1. Outward surface normal n_i is defined on internal surface of discontinuity S_i which is a fluid-solid boundary.

To deal with noncircular boreholes or effects of altered borehole diameter on modal propagation, we express perturbations in the harmonic frequency $\Delta\omega$ and wavenumber Δk_z in terms of the following integrals:[12]

$$\Delta k_z \int_V dV e_{ij} c_{ijkl} e_{kl} - \Delta\omega \int_V dV \rho\omega u_j u_j = \frac{1}{2}\int_V dV(\omega^2 u_j u_j \Delta\rho - e_{ij}\Delta c_{ijkl} e_{kl}) + \int_{S_i} dS[n_i \tau_{ij} \Delta u_j]_{(1)}^{(2)}, \quad (1)$$

where the surface normal is n_i and the Lagrangian energy density in a volume V is expressed as a functional of displacements associated with the wave solution u_j, harmonic frequency ω, wavenumber k_z, elastic moduli c_{ijkl}, mass density ρ, stress tensor elements $\tau_{ij}=c_{ijkl}u_{l,k}$, associated strains $e_{ij}=0.5(u_{i,j}+u_{j,i})$, and locations of interfaces or internal surfaces of discontinuity S_i. We have used a Cartesian tensor notation, and the convention that a comma followed by an index j denotes differentiation with respect to x_j. The summation convention for repeated tensor indices is also implied. The integral on an internal surface of discontinuity S_i between $V^{(1)}$ and $V^{(2)}$ is calculated in terms of outward surface normal n_i, as shown in Fig. 1. Note that the unperturbed cross section corresponds to a circular borehole whose solution is known.

Since the displacement and traction are continuous at a solid-solid interface, and only normal components of the displacements and traction are continuous at a fluid-solid interface, the resulting perturbation in the harmonic frequency ω can be calculated for a fixed wavenumber k_z as follows:

$$\Delta\omega \int_V dV \rho\omega u_j u_j = \frac{1}{2}\int_V dV(\Delta c_{ijkl} e_{kl} e_{ij} - \omega^2 \Delta\rho u_i u_i) + \int_{S_i} dS[h n_i \tau_{ij} n_k u_{j,k}]_{(1)}^{(2)} - \int_{S_i} dS(h_{,j} - n_j n_l h_{,l})[u_j n_k n_i \tau_{ki}]_{(1)}^{(2)}, \quad (2)$$

where h is the radial displacement along n_i and $h_{,i}$ denotes change in the normal between the perturbed and unperturbed interfaces.

For each value of the axial wavenumber k_z, the unperturbed modal eigenfunction is first obtained. Then the integrals in Eq. (2) are performed to obtain the frequency perturbation $\Delta\omega$. These are added to the eigenfrequency ω for various values of k_z to obtain the final dispersion curves for the perturbed case.

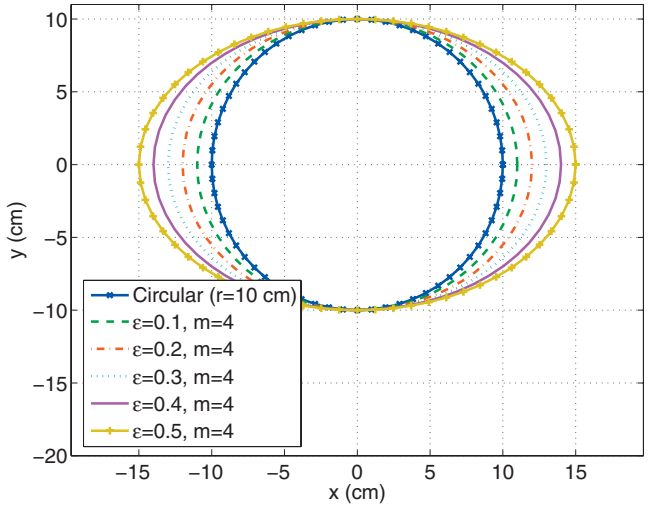

FIG. 2. Noncircular borehole examples for fixed m and changing ϵ.

Phase slowness dispersions can be readily obtained by expressing the slowness perturbation in terms of the frequency perturbation at a given wavenumber. Let the unperturbed modal phase slowness be S_0 and the actual phase slowness be $S=(S_0+\varepsilon\Delta S)$ at a given wavenumber k_z. Then

$$k_z = \omega S = (\omega + \varepsilon\Delta\omega)(S_0 + \varepsilon\Delta S), \quad (3)$$

which yields the following relationship between the slowness and frequency perturbations at a given wavenumber:

$$\Delta S = -\frac{S}{\omega}\Delta\omega, \quad (4)$$

where terms of order higher than ϵ are neglected.

Closed form expressions for the integrals in the denominator are given in Appendix B of Ref. 11, and closed form expressions are given for the ϕ integration of the flexural wave solution in cylindrical coordinates in Sec. B of Ref. 12.

A major contribution of this work is in modeling of modal dispersions for noncircular boreholes and an optimal selection of reference state. We use the following equation to define elliptical boreholes and breakouts:

$$r_{\rm nc}(\theta) = r_{\rm circ}(1 + \epsilon\cos^m\theta), \quad (5)$$

where $r_{\rm nc}(\theta)$ is the radial distance at an angle θ, $r_{\rm circ}$ is the radius of the circular borehole, ϵ is the borehole elongation, and different angular spreads can be obtained by using different m values. For example, $m=4$ provides a good approximation of an elliptical case as shown in Fig. 2 which depicts five different geometries obtained by using $\epsilon=\{0.1,0.2,0.3,0.4,0.5\}$, $m=4$, and $r_{\rm circ}=10$ cm. Figure 3 shows four different geometries obtained by using $m=\{4,12,24,48\}$ and $\epsilon=0.5$; clearly increasing m decreases the angular spread.

To minimize the difference between the reference and perturbed states, we use a circular borehole with a radius $r_{\rm ref}$ that depends on the shape of noncircular borehole as follows:

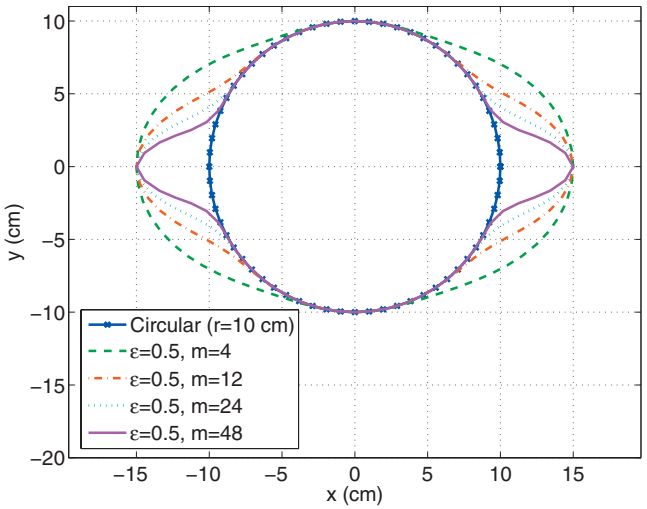

FIG. 3. Noncircular borehole examples for fixed ϵ and changing m.

$$r_{\text{ref}}^{\text{fast,even}} = r_{\text{ref}}^{\text{slow,odd}} = \frac{\int r_{\text{nc}}(\theta)\cos^n \theta d\theta}{\int \cos^n \theta d\theta},$$

$$r_{\text{ref}}^{\text{fast,odd}} = r_{\text{ref}}^{\text{slow,even}} = \frac{\int r_{\text{nc}}(\theta)\sin^n \theta d\theta}{\int \sin^n \theta d\theta}, \tag{6}$$

where n is a parameter appropriately selected for even and odd modes. Equation (6) clearly indicates that borehole radius in the reference state is sensitive to radial polarization direction. Based on our simulation results, we obtain optimum values for n, which are $n=6$ for even modes and $n=2$ for odd modes for a fast formation, and $n=2$ for even modes and $n=6$ for odd modes for a slow formaiton. Figure 4 shows the radius of the reference state for different m values for $\epsilon=0.5$.

Another approach for obtaining modal dispersions of noncircular boreholes is to solve a BIE.[3] In this method, the displacement and stresses on the borehole wall are expressed as integrals over a surface distribution of effective sources, in the frequency-axial wave number (ω-k_z) domain. The unknown sources are approximated by sums of finite basis functions, which are then determined by enforcing boundary

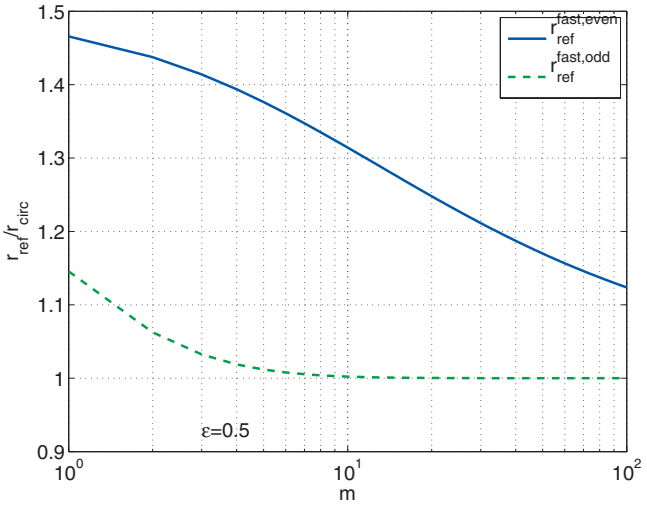

FIG. 4. The radius of the reference state vs m for even and odd modes.

TABLE I. Formation and borehole fluid properties.

Formation	V_P (km/s)	V_S (km/s)	ρ (g/cm^3)
Fast	4.848	2.601	2.16
Slow	2.545	1.018	2.00
Fluid	1.5	⋯	1.0

conditions. The discretized equations form a homogeneous system whose determinant vanishes when (ω-k_z) correspond to a nontrivial solution for the mode of interest.

Again, we have four boundary conditions: the continuity of normal displacement, the continuity of normal stress, the vanishment of the radial-axial stress, and the vanishment of the radial-hoop stress at the solid/liquid boundary. These conditions can be written as

$$\int_C [\hat{\mathbf{n}}(s)\cdot G_u^l(s,s')\mathbf{f}^l(s') - \hat{\mathbf{n}}(s)\cdot G_{uf}^l(s,s')Q(s')]ds' = 0, \tag{7}$$

$$\int_C [\hat{\mathbf{n}}(s)\cdot G_\tau^l(s,s')\mathbf{f}^l(s') - G_{\tau f}^l(s,s')Q(s')]ds' = 0, \tag{8}$$

$$\int_C \hat{\mathbf{s}}(s)\cdot G_\tau^l(s,s')\mathbf{f}^l(s')ds' = 0, \tag{9}$$

$$\int_C \hat{\mathbf{z}}(s)\cdot G_\tau^l(s,s')\mathbf{f}^l(s')ds' = 0, \tag{10}$$

where $\mathbf{f}$ and Q are the distribution of forces and sources, respectively, over the borehole surface S and $G_\eta^l(s,s')$'s are transformed Green's tensors.[3] To solve above equations numerically, we approximate the unknowns ($\mathbf{f}^l$ and Q) by sums of triangular basis functions, remove the integrable singularities, and calculate their contribution analytically. The remaining smooth functions are integrated by a third-order Gaussian quadrature.

Note that a typical "mode-search" routine requires evaluation of the above integrals for $N_f \times N_V$ times, where N_f is the number of the frequency samples of interest and N_V is the number of the velocity samples to calculate the determinants. By analyzing the sign changes in these determinant values, we roughly know where the root is. A simple interpolation technique can provide us more accurate estimate of the root location. Higher N_V value gives more accurate and more smoother results but it requires more computation time. The interpolation and low N_V might create some oscillations in the final result.

III. NUMERICAL RESULTS

To check the accuracy of our PM, we conduct two sets of numerical experiments: one with a fast formation and one with a slow formation. The properties of these formations are presented in Table I.

For each numerical experiment, we first analyze elliptical boreholes, then borehole breakouts for even and odd modes separately. The radius of the circular borehole in Eq.

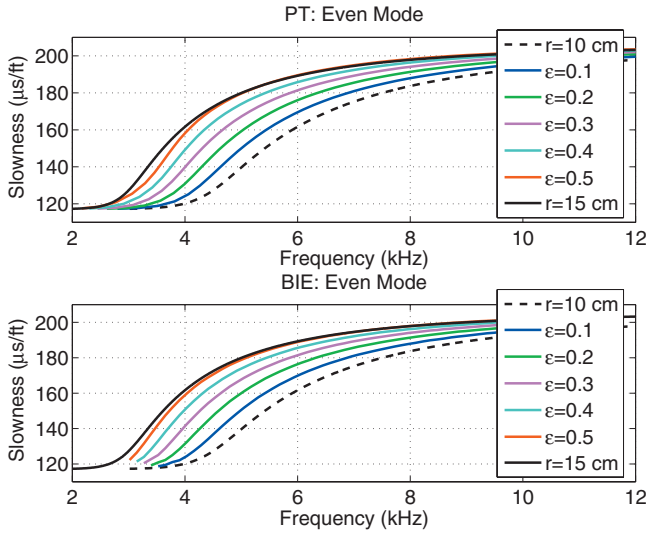

FIG. 5. *Fast formation, even modes, fixed m, and changing* ϵ: Dispersion curves obtained by two different approaches: PT (top) and BIE (bottom), $r_{\text{circle}}=10$ cm, $m=4$, $\epsilon=\{0.1,0.2,0.3,0.4,0.5\}$.

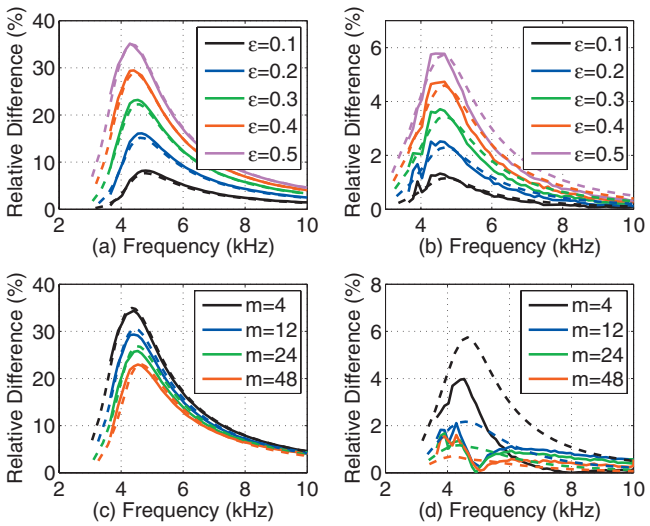

FIG. 6. *Fast formation: sensitivity analysis using two different approaches: PT (lines) and BIE (dashed lines).* (a) Even mode for $m=4$ and changing ϵ, (b) odd mode for $m=4$ and changing ϵ, (c) even mode for $\epsilon=0.5$ and changing m, and (d) odd mode for $\epsilon=0.5$ and changing m.

(5) is 10 cm, and then we generate five different elliptical boreholes using $\epsilon=\{0.1,0.2,0.3,0.4,0.5\}$ for $m=4$, shown in Fig. 2. To mimic breakouts, we use $m=\{4,12,24,48\}$ for $\epsilon=0.5$, shown in Fig. 3. We obtain dispersion curves for each case separately. For example, Fig. 5 shows even mode dispersions obtained by a perturbation theory (PT) and BIE for five different elliptical boreholes. Clearly, the dispersion curves obtained from the PT and BIE methods agree well with each other.

However, sometimes it is not easy to distinguish differences between dispersions due to small changes in the borehole elongation or angular spread. To make the comparison easier, we plot relative slowness difference (ΔS) between the dispersion curve of a noncircular borehole (S_{nc}) and a corresponding reference dispersion of a circular borehole (S_{c}) with $r=r_{\text{minor}}$, such as

$$\Delta S = \left| \frac{S_{\text{c}} - S_{\text{nc}}}{S_{\text{c}}} \right|. \tag{11}$$

Figure 6 shows sensitivity analyses for a fast formation using two different techniques: PT (regular lines) and BIE (dashed lines). In the top row, we plot the sensitivity of even (a) and odd (b) modes to changes in borehole elongation, whereas the bottom row depicts the sensitivity of even (c) and odd (d) modes to changes in breakout azimuth. Notice that the sensitivity of the odd mode to breakout azimuth could not be evaluated smoothly using BIE due to the interpolation scheme used for the calculation of the modal dispersion. However, the main conclusions of these comparisons are (i) the results obtained with PM agree well with BIE solver results confirming the accuracy of our PM, (ii) even modes are more sensitive than odd modes to changes in borehole elongation/breakout azimuth for a fast formation.

Figure 7 follows the same notation and results for a slow formation (see Table I for the formation properties). Even though the difference between the results of PT and BIE is more significant than the fast formation case, we can still conclude that for a slow formation odd mode is more sensitive to borehole elongation/breakout azimuth than the even mode.

We also analyze the influence of the breakout parameters on the maximum perturbations in slowness dispersions. Figure 8 shows ϵ versus ΔS_{max} in *linear-linear* scale (top row) and m versus ΔS_{max} in *log-linear* scale (bottom row) for the fast and slow formations in the left and right columns, respectively. We can conclude that the maximum perturbation changes linearly with the change in the borehole elongation, whereas there is a logarithmic relationship between m and the maximum perturbation. Again, from Fig. 8 we can conclude that even modes are more sensitive to breakout elongation/azimuth than odd modes in fast formations; in contrast, odd modes are more sensitive to breakout elongation/azimuth than even modes in slow formations.

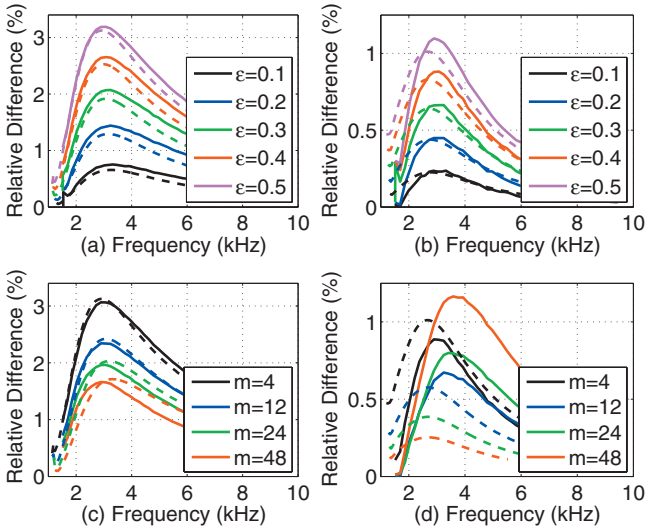

FIG. 7. *Slow formation: sensitivity analysis using two different approaches: PT (lines) and BIE (dashed lines).* (a) Odd mode for $m=4$ and changing ϵ, (b) even mode for $m=4$ and changing ϵ, (c) odd mode for $\epsilon=0.5$ and changing m, and (d) even mode for $\epsilon=0.5$ and changing m.

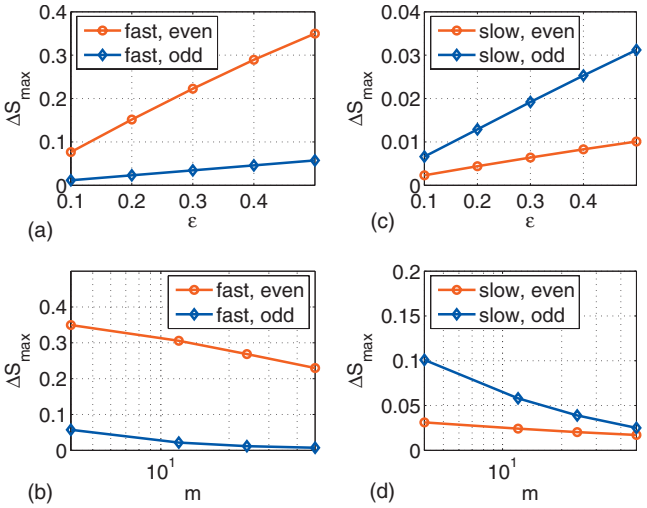

FIG. 8. The influence of the geometry parameters on the maximum perturbations: left column for the fast formation and right column for the slow formation; top row ϵ vs $\Delta S_{\max}$ in *linear-linear* and bottom row m vs $\Delta S_{\max}$ in *log-linear* scale.

We observe that evaluation of boundary integrals at high frequencies becomes less accurate because of a need for an increasingly finer discretization of the geometry. In contrast, a PM is likely to become less accurate with an increasing amount of perturbation from a chosen reference state. We are able to maintain a high degree of accuracy with the PM because of a new technique used for calculating the circular borehole reference state for both the fast and slow formations. Consequently, we find that the PM results are more sensitive to small perturbations in borehole shape than the BIE results.

IV. CONCLUSION

A PM based on Hamilton principle enables us to obtain flexural dispersions of noncircular boreholes in homogeneous elastic formations. We use different reference states depending on borehole elongation and its angular spread for even and odd modes. The accuracy of the method has been validated with a BIE solver. It has been observed that even modes are more sensitive to breakout elongation/azimuth than odd modes in fast formations; whereas odd modes are more sensitive to breakout elongation/azimuth than even modes in slow formations. We have observed that the maximum slowness perturbation from a reference circular borehole exhibits a linear dependence on breakout elongation ϵ and a logarithmic dependence on breakout width parameter m. These can be used for inversion of formation parameters and also as indicators of the presence of breakouts. The results of sensitivity of flexural dispersions to changes in borehole breakout parameters are very similar using either PM or BIE technique. However, numerical results show that our PM is even more sensitive than BIE solution, since in a BIE approach, the modes are obtained via an interpolation technique. Even though we have analyzed elliptical boreholes and breakouts, the formulation is valid for any kind of noncircular borehole.

[1]E. Simsek, B. K. Sinha, S. Zeroug, and N. Bounoua, "Influence of breakouts on borehole sonic dispersions," SEG Technical Program Expanded Abstracts **26**, 313–317 (2007).

[2]L. Nicoletis, A. Bamberger, J. Quiblier, P. Joly, and M. Kern, "Hole geometry and anisotropic effects on tube-wave propagation: A quasi-static study," Geophysics **55**, 167–175 (1990).

[3]C. Randall, "Modes of noncircular fluid-filled boreholes in elastic formations," J. Acoust. Soc. Am. **89**, 1002–1016 (1991).

[4]J. Bell and D. Gough, "The use of borehole breakout in the study of crustal stress," in *Hydraulic Fracturing Stress Measurements*, edited by M. Zoback and B. Haimson (National Academic, Washington, D.C., 1983), pp. 201–209.

[5]M. Zoback, D. Moos, L. Mastin, and R. Anderson, "Wellbore breakouts and in-situ stress," J. Geophys. Res. **90**, 5523–5530 (1985).

[6]L. Vernik and M. Zoback, "Estimation of maximum horizontal principal stress magnitude from stress-induced wellbore breakouts in the cajon pass scientific research borehole," J. Geophys. Res. **97**, 5109–5119 (1992).

[7]S. K. Grandi, R. Rao, X. Huang, and M. N. Toksoz, "In situ stress modelling at a borehole—a case study," SEG Technical Program Expanded Abstracts **22**, 297–300 (2003).

[8]K. Ellefsen, C. Cheng, and M. Toksöz, "Applications of perturbation theory to acoustic logging," J. Geophys. Res. **96**, 537–549 (1991).

[9]B. A. Auld, *Acoustic Fields and Waves in Solids* (Wiley, New York, 1973), vols. 1 and 2.

[10]H. Tiersten and B. Sinha, "A perturbation analysis of the attenuation and dispersion of surface waves," J. Appl. Phys. **49**, 87–95 (1979).

[11]B. Sinha, A. Norris, and S. Chang, "Borehole flexural modes in anisotropic formations," Geophysics **59**, 1037–1052 (1994).

[12]B. Sinha, "Sensitivity and inversion of borehole flexural dispersions for formation parameters," Geophys. J. Int. **128**, 84–96 (1997).

Implications of human performance and perception under tonal noise conditions on indoor noise criteria

Erica E. Ryherd[a] and Lily M. Wang
Architectural Engineering Program, University of Nebraska-Lincoln, 101A Peter Kiewit Institute, 1110 S. 67th St., Omaha, Nebraska 68182-0681

(Received 17 September 2007; revised 7 April 2008; accepted 27 April 2008)

This research investigated differences in task performance and perception under six non-time-varying ventilation-type background noise spectra with differing tonality. The results were related to five indoor noise criteria systems: noise criteria, balanced noise criteria, room criteria, room criteria mark II, and the *A*-weighted equivalent sound pressure level (L_{Aeq}). These criteria systems are commonly used in the U.S. building industry, but concerns exist over whether they are appropriate for all noise situations. Thirty test subjects completed three types of performance tasks (typing, reasoning, and math) and answered questions about their perception of the indoor environment under each noise condition. Results showed that performance scores did not change significantly across the six noise conditions, but there were differences in subjective perception. For example, perception trends for tonality, annoyance, and distraction changed based on the frequency and prominence of discrete tones in noise. However, these perceptual changes were not fully reflected in the criteria level or spectral quality ratings. Additionally, task performance was related to subjective perception but not to criteria level predictions. As a result, the authors suggest that the current criteria should be modified to account for the frequency and prominence of tones in background noise. © *2008 Acoustical Society of America.* [DOI: 10.1121/1.2932075]

PACS number(s): 43.50.Ba, 43.50.Jh, 43.50.Qp [BSF] Pages: 218–226

I. INTRODUCTION

An important design consideration of any space is that of background noise, as ambient sound is something building occupants readily encounter in their everyday environments. Heating, ventilating, and air-conditioning (HVAC) systems constitute a primary source of noise and subsequent complaints. Several indoor noise criteria systems are currently used to quantify the background noise in buildings resulting from HVAC systems. Some of the more popular methods are noise criteria (NC),[1] balanced noise criteria (NCB),[2] room criteria (RC),[3] room criteria mark II (RC mark II),[4] and *A*-weighted equivalent sound pressure level (L_{Aeq}).[5] These criteria are used by acoustical consultants, noise control engineers, mechanical system designers, architects, and others.

Detailed descriptions and comparisons of these five criteria are available in several sources, i.e., Refs. 6–12. As a brief overview, these systems provide an evaluation of the overall level of noise, given as a single number rating. The rating is found by comparison of the measured background noise to a defined set of sound pressure level versus frequency curves. NCB, RC, and RC mark II also include quality descriptors that give an indication of the spectral character of the sound. NCB and RC indicate the presence of rumble (excessive low frequency energy) and hiss (excessive high frequency energy), as well as noise induced vibration. RC mark II also indicates the presence of roar (excessive midfrequency energy) and evaluates occupant acceptance through a calculation of the quality assessment index (QAI). The QAI is found based on the range of energy-averaged spectral deviations between the measured noise and the RC contour levels.

The criteria are commonly used to set background noise goals and diagnose noise problems in buildings. However, the appropriate applications of these criteria have been called into question due to several factors. Previous studies have shown that there can be large differences among indoor noise criteria predictions for the same spectrum, [8,9,13] leaving the end user unsure as to which system to rely on. As a result, preferences among building designers and standards as to which criterion to use varies greatly. This is immediately apparent from a review of the criteria guidelines set by several sources.[12,14,15]

Several limitations also exist in the current criteria. A primary shortcoming is insufficient characterization of discrete tones[16] and variance over time, which are commonly found in building HVAC noise. A project is underway which investigates these limitations in the criteria and evaluates the general ability of these systems to relate to occupant perception and performance under a variety of HVAC noise conditions. This paper discusses one study in the overall project that focused on tonality in background noise.

II. PREVIOUS RESEARCH

Several recent studies have investigated the relationship between subjective impression of ambient noise and measured sound spectra, with some evaluation of indoor noise criteria.[17–24] Ayr *et al.* examined the effectiveness of several criteria methodologies using questionnaires and *in situ* office

[a]Present address: Woodruff School of Mechanical Engineering, Georgia Institute of Technology, Atlanta, GA 30332-0405. Electronic mail: eryherd@hotmail.com

 0001-4966/2008/124(1)/218/9/$23.00

noise measurements. They found that L_{Aeq} generally performed well in evaluating occupation response to ventilation noise.[22,23] The studies by Tang *et al.* also found L_{Aeq} to be generally well correlated with subjective auditory sensation, with other metrics performing well in certain circumstances.[18–21] Tang and Wang noted that many of their measured spectra contained some degree of tonality, but a detailed investigation of such was not the focus of their work.[21]

Despite these previous studies generally supporting L_{Aeq}, other studies have demonstrated limitations in the metric.[17,25] Persson *et al.* demonstrated that annoyance perception differed for ventilation noises with similar L_{Aeq} ratings but differing low frequency content,[17] supporting the concept that L_{Aeq} is less suited for spectra having strong low frequency components.[26] Ayr *et al.* noted that the good performance of L_{Aeq} in their previously described studies may be in part due to the large number of hissy spectra included.[23] In addition to the types of noise conditions examined, the differences in comparing previous work can also be partially attributed to the testing methodologies. Regardless, a clear consensus on the performance of the various criteria has not been reached, and additional investigations of their limitations are warranted.

Much work has been conducted on loudness and annoyance of tones in noise,[27–32] but little has been done to correlate these with commonly used indoor noise criteria systems. Modern HVAC systems are replete with examples of pure tones. Certain types of mechanical equipment, such as motors and fans, can emit lower frequency tones. Research indicates that higher frequency pure tones may also be disturbing.[31,32]

Other research has examined how background noise impacts task performance. Although a lot of work has been done on how high levels of noise affect productivity,[33–35] the pool of research examining how typical office background noise affects worker performance is more limited. The effect of excessive low frequency background noise on task performance has been the topic of several projects.[30,36–43] Some of the conclusions from these studies are that task performance can be affected by background noise and the frequency character of the noise is an important consideration. These studies provide important information about the relationship between noise and performance but generally do not relate the results to indoor noise criteria.

The current research expands upon previous work by evaluating the ability of five criteria methods to relate to task performance and subjective perception under ventilation systems-induced background noise. The goal of the research was to investigate whether significant changes in subjective response existed when comparing six noise conditions with differing tonality yet similar criteria rating. The results are used to provide insight into future criteria modifications with regards to tonality.

III. METHODOLOGY

A. Testing chamber

A floor plan of the experimental test chamber is shown in Fig. 1. The room is 26.5 m^3 and furnished as a typical office with carpet, gypsum board wall construction, and acoustical ceiling tiles. It exhibits a reverberation time of 0.25 s at 500 Hz. The sound field can be controlled in the test chamber, which has a low naturally occurring L_{Aeq} of 35 dB. The surrounding structure of the test chamber achieves STC 47 to minimize noise intrusions. To ensure maximum isolation, the spaces immediately surrounding the test chamber were unoccupied during testing, with the exception of a researcher sitting quietly in an adjacent room. The chamber was maintained at comfortable working conditions of approximately 20 °C and 764 lx at the work plane.

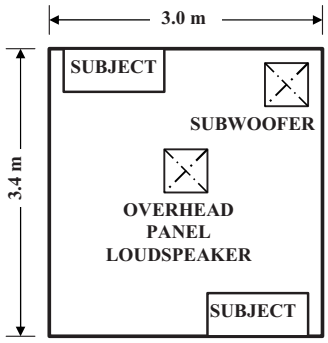

FIG. 1. Plan view of the test chamber setup (not to scale). Floor to ceiling height is 2.6 m.

The intent was to present the noise in such a manner that it would be perceived as similar to typical ventilation systems sound. Noise conditions were presented with an Armstrong iceiling™ overhead panel loudspeaker that supplied the primary mid- to high frequency energy and a JBL Northridge™ E250P subwoofer that supplied the primary low frequency energy. Neither loudspeaker was immediately identifiable as audio equipment. The iceiling™ loudspeakers look like acoustical lay-in ceiling tiles and the subwoofer was covered in acoustically transparent fabric and placed in the corner of the room to resemble an end table. An Armstrong iceiling™ D2001 digital processor and an Armstrong D4100 amplifier were used for mixing and amplification. At the conclusion of the study, subjects reported that they thought that the noise sounded like mechanical systems, and that it was coming from the ventilation, pipes, or the ductwork.

B. Noise conditions

The effects of six different background noise conditions were examined. Under each noise condition, subjects completed three types of tests and a subjective perception questionnaire. The noise conditions were presented in random order for each subject. The spectra of the six noise conditions are shown in Figs. 2–5:

(1) *Midlevel neutral condition* (see Fig. 2): broadband noise, simulated with −5 dB/octave band slope, intersecting 40 dB at 1000 Hz.
(2) 120 *Hz tonal condition*, *PR=5* (see Fig. 3): broadband noise with a tonal component at 120 Hz, measured from an existing facility, with the overall L_{Aeq} equalized to 47 dB. The prominence ratio (PR) of the tone is 5.[44] The source was a wall mounted heat pump in cooling mode.

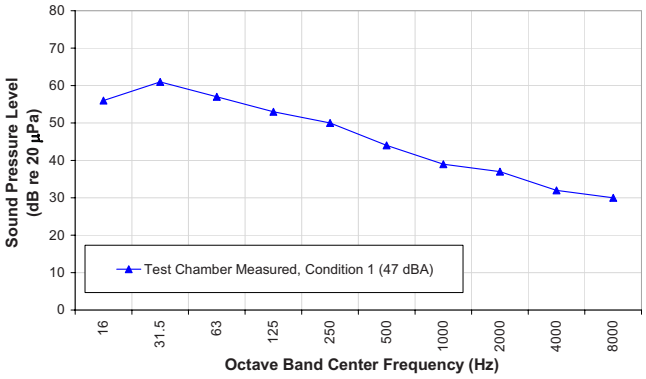

FIG. 2. (Color online) Octave band spectrum of midlevel neutral noise condition (1), as measured in the test chamber.

(3) 120 *Hz tonal condition*, *PR=9* (see Fig. 3): similar to signal 2, with the PR of the tone increased to 9.
(4) 235 *Hz tonal condition*, *PR=5* (see Fig. 4): broadband noise with a tonal component at 235 *Hz*, measured from an existing facility, with the overall L_{Aeq} equalized to 46 dB. The PR of the tone is 5. The source was a laboratory fume hood.[45]
(5) 235 *Hz tonal condition*, *PR=9* (see Fig. 4): similar to signal 4, with PR of the tone increased to 9.
(6) 595 Hz *tonal condition*, *PR=9* (see Fig. 5): broadband noise with a tonal component at 595 Hz, measured from an existing facility, with the overall L_{Aeq} equalized to 47 dB. The PR of the tone is 9. The source was a screw compressor.

Previous research demonstrates that the sound level affects performance and perception, so to highlight differences due to tones rather than level, all noise conditions in this study were set to a similar overall L_{Aeq}.[10,11] An important difference between noise condition (2) versus (3) and condition (4) versus (5) is the tonal PR. The PR is a ratio of the power of the critical band centered on a tone compared to the mean power of the two adjacent critical bands.[44] The 1995 version of the ANSI S1.13 standard states that tones were considered prominent or clearly audible if the PR is greater than or equal to 7. The noise conditions in this study were selected based on this standard to fall both below and above

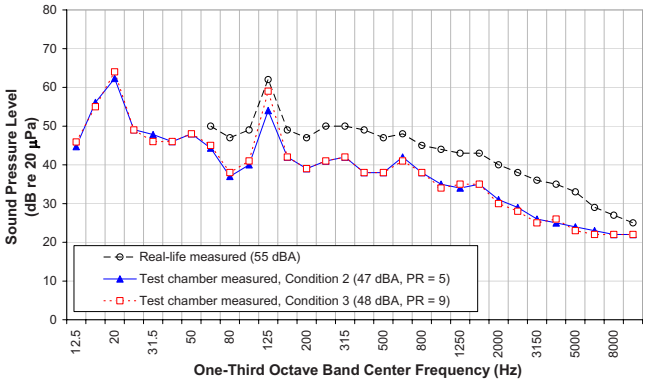

FIG. 3. (Color online) One-third octave band spectrum of 120 Hz tonal noise conditions (2) (PR=5) and (3) (PR=9), as measured in the real installation and the test chamber.

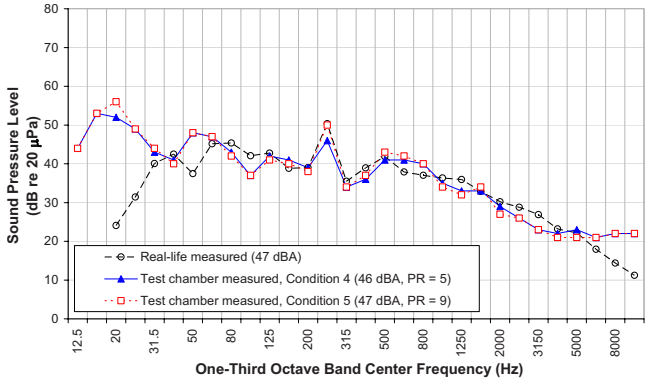

FIG. 4. (Color online) One-third octave band spectrum of 235 Hz tonal noise conditions (4) (PR=5) and (5) (PR=9), as measured in the real installation and in the test chamber.

the prominence limit at PR=5 and PR=9. However, more recent research indicates that even higher PR values may be required for a tone to be considered prominent, particularly for lower frequencies.[46]

The measurements shown in Figs. 2–5 were made at the test subject's location using a Larson Davis 824 sound level meter. The values shown represent an average of measurements taken at the two work stations over several measurement trials on multiple days. The difference between stations was no greater than 3 dB L_{Aeq} on average and the sound field surrounding each subject was relatively uniform (to within 3 dB L_{Aeq}).

Noise condition (1) was simulated in previous work.[10,47] Conditions (2)–(6) were recordings. Some manipulation of these recorded signals was necessary, primarily because the equalization of the system had to remain preset at certain levels across frequency to facilitate automated playback. The noise conditions were calibrated by digitally filtering the raw recorded audio files by using COOL EDIT 2000 software until the one-third octave band equivalent sound pressure levels measured in the test chamber closely matched those recorded in the real-life spaces, as shown in Figs. 3–5.

The indoor noise criteria ratings calculated for the six noise conditions are provided in Table I. Although the tonal frequency and prominence differed between the noise conditions, there was little difference in the noise criteria ratings due to the overall sound levels being similar.

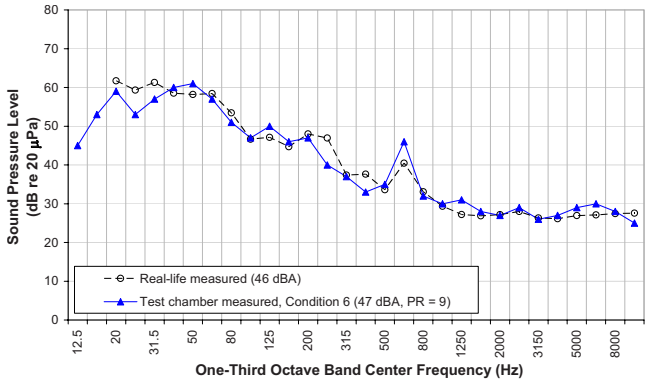

FIG. 5. (Color online) One-third octave band spectrum of 595 Hz tonal noise condition (6) (PR=9), as measured in the real installation and in the test chamber.

TABLE I. Indoor noise criteria ratings of the six noise conditions used. N=neutral, R=rumbly, H=hissy, V=vibrational, LF=excessive low frequency, MF=excessive midfrequency, HF=excessive high frequency.

Noise condition	Indoor noise Criteria rating				
	NC	NCB	RC	RC mark II	L_{Aeq}
(1) *Midlevel neutral*	40	38 N	40 N	40 HF, marginal	47
(2) 120 Hz *tonal*, *PR*=5	40	38 N	41 N	41 HF, marginal	47
(3) 120 Hz *tonal*, *PR*=9	44	38 R	41 N	41 HF, marginal	48
(4) 235 Hz *tonal*, *PR*=5	41	37 H	40 N	40 HF, objectionable	46
(5) 235 Hz *tonal*, *PR*=9	42	37 R,H	41 N	41 HF, marginal	47
(6) 595 Hz *tonal*, *PR*=9	43	37 R,H	39 H	39 N, acceptable	47

C. Subjects

Thirty subjects (15 male and 15 female) participated in this study. The subjects were prescreened in accordance with methods previously used by the authors.[47] A GSI 17 audiometer was used to verify that all the subjects had hearing thresholds below 25 dB hearing level from 125 Hz to 8 kHz. A Keystone ophthalmic telebinocular was used to evaluate visual function. All subjects were found to have a minimum typing ability of 20/min words by using SKILLCHECK software.

D. Experimental procedure

Each subject attended six 55 min sessions on six separate days, with each subject scheduled at approximately the same time on all days when possible. The session length was selected based on previous research by the authors that examined the influence of exposure time on task performance and questionnaire results.[47] Results from the previous study indicated that performance did not change significantly over testing sessions ranging from 20 min to 4 h, but shorter noise exposures (20 min) may have allowed for more comparison between sequential noise conditions. Therefore, in this study, subjects were only exposed to a single noise condition per testing day to minimize biasing effects.

A flowchart of the experimental procedure for a single testing session is shown in Fig. 6. Subjects completed paper-based tasks for the first 25 min. These tasks were developed from the verbal portion of the Graduate Record Examination (GRE) test. To limit the total amount of data collected, these tests were not scored, although subjects were operating under the assumption that they would be. The intent was to allow subjects to adjust to the background noise while staying mentally active. Two sequences of task performance tests and a subjective rating portion followed the paper-based task. Two subjects completed testing at the same time whenever possible and were not allowed to communicate with each other during testing.

E. Performance tasks

Task performance was evaluated under each noise condition using three types of computer-based tests developed in previous work by the authors.[47] Participants in the previous study were excluded from participating in the current study. The testing software was developed by the SKILLCHECK company.[48] Multiple versions of each task were developed and all subjects completed all versions of the tests with the order of presentation randomized for each subject. The multiple versions were carefully developed to be approximately equal in length and difficulty based on standardized testing metrics.[47]

The typing test required the subjects to retype printed paragraphs. Analysis of these tasks was based on the net typing speed, which accounted for the typing speed and the number of errors made. The grammatical reasoning task required the subjects to determine if a given statement correctly described the order of a letter sequence.[40,42,49] For example, the subject may have been presented with the following: CA—C is before A (true or false). The answer is "true" because the sentence correctly describes the letter combination. The math task consisted of math statements and short word problems. Subjects were allowed to use paper and pencil, but no calculators.

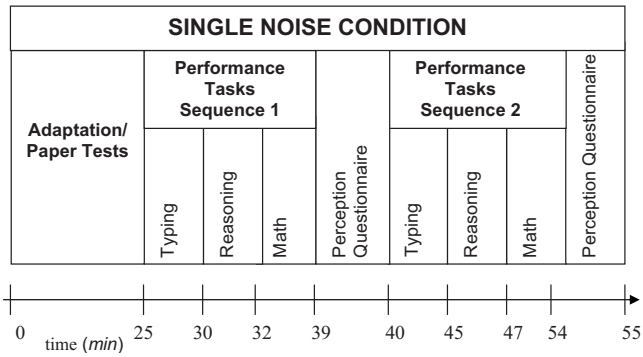

FIG. 6. The experimental sequence in time for a single noise condition. 25 min of adaptation were followed by 30 min of performance testing and perception rating questionnaires, for a total time of 55 min.

F. Subjective perception questionnaire

After each set of computer tasks, subjects completed a questionnaire about their perception of the testing environment. The questionnaires were developed in previous research by the authors.[47] Eight noise questions asked specifically about loudness, rumble, roar, hiss, tonality, fluctuations over time, distraction, and annoyance. Subjects were also asked five questions about air freshness, temperature comfort, air movement, lighting, and work station comfort. The only factor changing in the room was the noise; temperature, lighting, etc., were all controlled to be relatively constant, although subjects did not know what specifically was changing in the room. The additional questions on the non-noise conditions were included to divert attention somewhat away from the acoustics. Estimations were based on a seven-point discrete scale.

Prior to the testing session, subjects completed a training module in which they were exposed to several of the questionnaire terms. The module described "rumbly," "roaring," and "hissy" noise as containing excessive low, mid-, and high frequencies, respectively. They listened to corresponding audio samples of band-limited white noise covering the 16–63 Hz, 125–500 Hz, and 1–8 kHz octave bands. They also listened to a "tonal" broadband noise with a tone at 500 Hz. No specific instructions were given on any other descriptors included in the questionnaire.

IV. RESULTS

Linear mixed models, analysis of variance (ANOVA), and Pearson product moment correlations (r) were used to assess the differences in performance task scores, subjective ratings, and noise criteria predictions using SPSS software.[50,51]

A. Subjective perception questionnaires versus criteria level ratings

Subjective perception of loudness, annoyance, distraction, rumble, roar, hiss, fluctuations, and tonality were compared to the criteria level ratings. Very few statistically significant relationships were found, in part because the criteria level ratings were not changing markedly, as shown in Table I. Conditions with higher L_{Aeq} were perceived as louder ($F=4.96$, $p<0.05$), more annoying ($F=3.83$, $p<0.05$), and more rumbly ($F=8.69$, $p<0.01$). These results agree with a previous study by the authors.[10]

Conditions with higher RC and RC mark II level ratings were perceived as more roaring ($F=4.86$, $p<0.05$) and less hissy ($F=39.97$, $p<0.01$). It might be expected that some of the conditions with the highest RC mark II level ratings would be rated as roaring based on the perception rating, but this was not the case. RC does not provide a roaring descriptor. Based on the perception results, it might also be expected that some of the conditions with the lowest RC and RC mark II level ratings would be rated as hissy. Interestingly, the condition with the lowest RC and RC Mark II level rating [condition (6): high frequency tonal, 595 Hz, PR=9] was rated hissy by RC but not by RC mark II.

Conditions with higher NC level ratings were perceived as more tonal ($F=7.46$, $p<0.01$) and fluctuating ($F=9.56$, $p<0.01$) by subjects. Possibly there is some link between perception of fluctuation and tones or the spectral quality of these conditions. The tonal finding makes sense based on the NC level ratings shown in Table I. NC levels were slightly higher for tonal conditions (3)–(6) as compared to the nontonal condition (1). The NC rating also increases slightly as the PR increases from condition (2) (120 Hz tonal, PR=5) to condition (3) (120 Hz tonal, PR=9) and from condition (4) (235 Hz tonal, PR=5) to condition (5) (235 Hz tonal, PR=9). Although the NC rating appears to be sensitive to tonality in this study, it still may not be an ideal choice of descriptors for all tonal environments. A tonal component in an octave band can dictate the overall rating due to the tangential nature of the NC methodology. In background noise scenarios where the tones are even more prominent than those presented in this study, the NC level rating may shift to a level rating that is not representative of the perceived overall loudness of the background noise. Also, as will be shown later in Sec. IV C 2, condition (1) (NC 40) was perceived as significantly louder than two other conditions with similar criteria ratings [condition (2), NC 40 and condition (4), NC 41].

B. Task performance results

1. Task performance versus criteria level ratings

No significant relationships were found between typing, reasoning, and math scores and individual criterion predictions of level. This result is in agreement with previous research by the authors which used 12 nontonal conditions and different types of performance tasks.[10,11] In previous work, it was hypothesized that the fact that performance scores were not significantly related to the criteria ratings may indicate that these criteria do not fully reflect occupant response to background noise. In this study, however, caution must be used in interpreting results due to the small change in the criteria level ratings as previously mentioned.

2. Task performance versus subjective perception

Previous research by the authors indicated that performance and perception were related to each other.[10,11,47] Example significant results from current study are depicted in Figs. 7 and 8 and summarized below:

- *Typing* performance *decreased* as subjects perceived the noise to be more distracting ($F=18.75$, $p<0.01$), more annoying ($F=14.19$, $p<0.01$), more rumbly ($F=13.52$, $p<0.01$), more roaring ($F=5.21$, $p<0.05$), or more fluctuating ($F=3.81$, $p<0.05$). These trends are in the expected direction.
- *Reasoning* task performance *decreased* as subjects perceived the noise to be more rumbly ($F=4.81$, $p<0.05$). This trend is in the expected direction. However, performance improved as subjects perceived noise as more roaring ($F=7.19$, $p<0.01$) or more hissy ($F=25.86$, $p<0.01$).
- *Math* task performance *improved* as subjects perceived the noise to be more roaring ($F=9.45$, $p<0.01$) or more hissy ($F=8.91$, $p<0.01$).

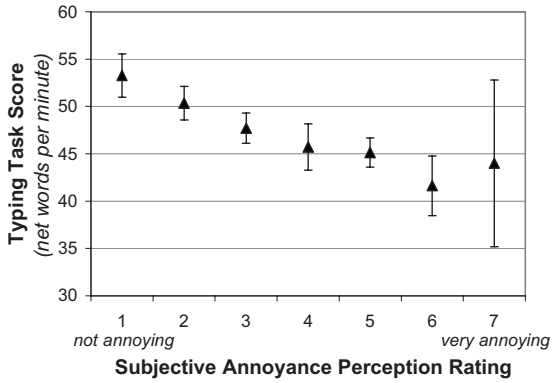

FIG. 7. Subjective annoyance perception ratings, averaged across all subjects and conditions vs typing task score. Net typing speed decreased as subjects perceived noise as more annoying ($p<0.01$). Standard error of the mean bars are shown. The larger error bars indicate more variability in the data at these points; nonetheless, the overall trends were significant.

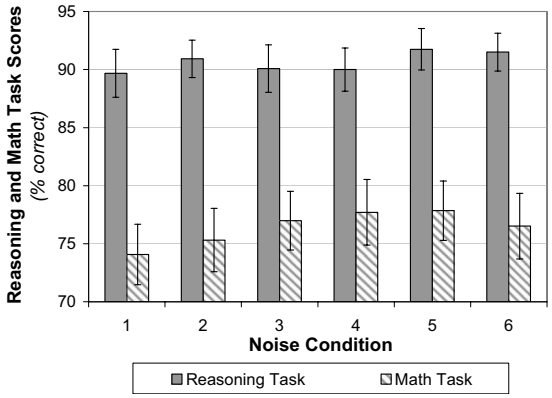

FIG. 9. Mean reasoning and math task scores, averaged across all subjects for each noise condition. The difference in performance scores across noise conditions was not statistically significant. Similarly, differences in typing task scores were nonsignificant. Standard error of the mean bars are shown.

As shown in Fig. 7, typing speed slowed down as subjects perceived noise as more annoying. This result is in agreement with previous research by the authors which used 12 nontonal conditions and different types of performance tasks.[10,11]

Figure 8 shows the reasoning task scores improving as subjects perceived the noise as more roaring. This result is quite interesting when compared to previous research by the authors that examined primarily nontonal background noises.[47] In both the current study and the previous one, math and reasoning performance improved with perception of increasing roar, while typing performance decreased. Given the repeatability of these results, it is possible that performance was negatively impacted by midfrequency noise perception on the more routine task (i.e., typing), whereas subjects were forced to concentrate on the more difficult tasks (i.e., reasoning and math) and therefore performed better. However, as stated in an earlier publication, one should not conclude that more roaring spectra necessarily produce better performance on certain tasks.[10] Instead, one may conclude that the test subjects participating in this laboratory study wished to perform well on their tasks and may have produced better test scores by concentrating harder on specific tasks in the roaring scenarios presented in these studies.

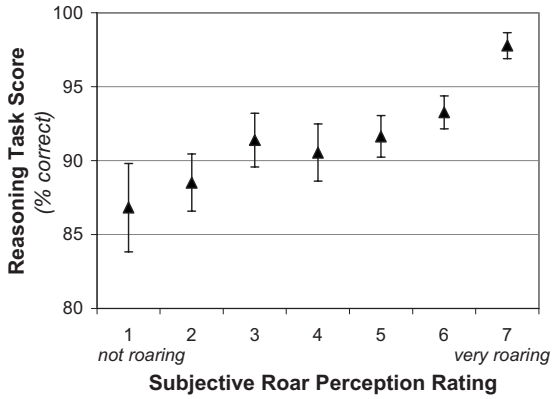

FIG. 8. Subjective roar perception ratings, averaged across all subjects and conditions vs reasoning task score. Reasoning performance scores increased as subjects perceived noise as more roaring ($p<0.01$). Standard error of the mean bars are shown.

C. Influence of noise condition

Also of interest was whether significant differences in task performance scores and subjective perception ratings existed between the various noise conditions despite their similar criteria ratings. This section contains results of ANOVA, Mauchly's sphericity, and Bonferroni *post hoc* tests.[50,51]

1. Noise condition vesus task performance

Results showed no significant effect of noise condition on task performance scores. Figure 9 shows the reasoning and math task scores averaged across all subjects for each of the six noise conditions. The change in scores between different noise conditions is not statistically significant. Similar nonsignificant results were obtained for the typing task. It might be expected that subjects would perform worse when comparing any of tonal conditions (2)–(6) to nontonal condition (1), when comparing a less prominent tonal condition to a more prominent tonal condition [such as from conditions (2) and (3) or from conditions (4) and (5)]. Trend directions were as expected in some instances and not in others.

Previous work has demonstrated that the types of noises being compared can largely influence results. Landström *et al.* found no significant difference in performance on a figure identification test when comparing a broadband ventilation noise to a second broadband ventilation noise with a tone added at 100 Hz (both at L_{Aeq}=40 dBA).[30] However, when comparing the tonal noise to the same noise with a masking pink noise (41 dBA) added in the frequency range of 50–200 Hz, they found a tendency toward better performance, higher wakefulness, higher annoyance, and lower tolerated levels under the pink noise added exposure.[30] The fact that differences were seen when comparing the tonal noise to the masked noise but not when comparing the tonal noise to the broadband noise indicates that the types of noise conditions used play a strong role. In the current research project, more obvious differences in task performance across the

TABLE II. Example statistically significant differences in perception between the six noise conditions used, $^{*}p<0.05$.

Subjective perception descriptor	Statistically significant perception differences between noise conditions	
Annoyance	(1) Midlevel neutral was more annoying than→	Condition (4) (235 Hz tonal, PR=5)
Loudness	(1) Midlevel neutral was louder than→ and→	Condition (2) (120 Hz tonal, PR=5) Condition (4) (235 Hz tonal, PR=5)
Tonality	(3) 120 Hz tonal, PR=9 was more tonal than→ (5) 235 Hz tonal, PR=9 was more tonal than→ and→	Condition (4) (235 Hz tonal, PR=5) Condition (1) (midlevel neutral) Condition (4) (235 Hz tonal, PR=5)

various noise conditions may have been observed with greater differences in the PR between the paired signals.

It is also apparent in examining Fig. 9 that the subjects scored higher overall on the reasoning task. This result is in agreement with previous research by the authors.[47] A more difficult administration of this task or the others may have resulted in greater variance in scores under the different noise conditions.

2. Noise condition versus subjective perception

An analysis was conducted to determine whether subjective perception of tonality, loudness, annoyance, and distraction differed from one noise condition to another. Example significant results are provided in Table II and are described below.

Figure 10 shows the mean subjective tonality and loudness perception ratings for the six noise conditions. Results showed a main effect of signal on subjective tonality perception ratings ($F=4.84$, $p<0.01$). Although a significant difference in tonality was perceived between the paired 235 Hz tonal conditions [(4) and (5)], a difference was not significantly perceived between PRs for the lower frequency 120 Hz tonal conditions [(2) and (3)]. This falls in line with

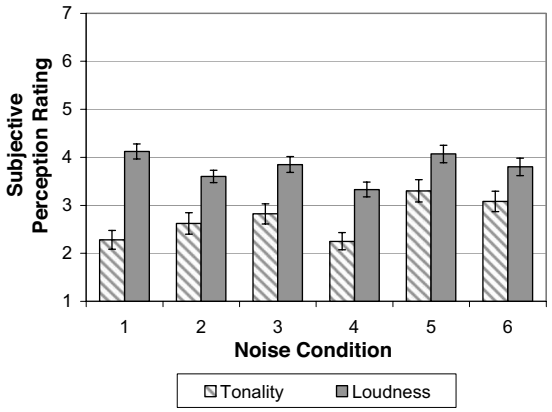

FIG. 10. Mean subjective tonality and loudness perception ratings, averaged across all subjects for each noise condition. The tonality scale ranges from 1=no tones to 7=very noticeable tones, and the loudness scale ranges from 1=very quiet to 7=very loud. Standard error of the mean bars are shown.

Hellweg, Jr. and Nobile's study which determined that low frequencies require a higher PR for the tone to be considered prominent (around 18 dB for 120 Hz).[46] As shown in Fig. 10, the general trend direction was for condition (3) to be perceived as more tonal than condition (2).

Tonality perception results also indicated that condition (5) (235 Hz tonal) with a higher PR was more tonal than the neutral noise [condition (1)]. Not all of the tonal conditions were perceived as significantly more tonal than condition (1), though, which again supports the higher PR values recommended for tonal prominence by Hellweg, Jr. and Nobile.[46] As shown in Fig. 10, the general trend direction was for the tonal conditions to be perceived as more tonal than condition (1), with the exception of condition (4) (midfrequency tonal noise, 235 Hz, PR=5).

Results showed a main effect of signal on subjective *loudness* perception ratings ($F=3.40$, $p<0.05$). The neutral noise [condition (1)] was perceived as louder than the two PR=5 tonal conditions [conditions (2) and (4)]. This indicates that the overall level of the broadband frequency component had to be louder to compensate for the tonal contribution. Thus it makes sense that the PR of 5 for conditions (2) and (4) was not enough to "match" the loudness of condition (1), but with the PR of 9 [as seen in conditions (3), (5), and (6)], the loudness is perceived as approximately equal to broadband condition (1).

Results also showed a main effect of signal on subjective *annoyance* ($F=2.57$, $p<0.05$) and *distraction* perception ratings ($F=2.32$, $p<0.05$). The trends for the mean subjective annoyance and distraction perception ratings were similar to the loudness trend shown in Fig. 10. Although statistically significant relationships were not observed, the general trends were for the mean annoyance and distraction perception ratings to be higher for the PR=9 exposures as compared to their PR=5 counterparts. However, the trend showed that tonal conditions (2)–(6) were not perceived as generally more annoying or distracting than condition (1). Previous studies have shown that a pure tone in noise can make the noise more annoying.[27,31] For example, Landström *et al.* found that annoyance increased when comparing a broadband noise to a tonal noise.[31] The effect was more prominent with a high frequency (1000 Hz) tone, whereas the effects of a low frequency (100 Hz) tone were more unclear. It is possible that in this study, because subjects perceived condition (1) as being approximately as loud or louder than conditions (3), (5), and (6) (as shown in Fig. 10), they also perceived condition (1) as being equally or more annoying and distracting than the nontonal conditions.

Differences in annoyance may have also been expected when comparing the tonal frequencies (120, 235, 595 Hz). Landström *et al.* investigated which tonal frequencies in ventilation noise were found to be the least and most annoying.[32] Subjects listened to a ventilation noise and were told to adjust a tone frequency at 40 dBA to the lowest and highest annoyance within the frequency range of 35–500 Hz. Subjects found 58 Hz to be the least annoying and 380 Hz to be the most annoying. The higher frequency was also correlated to higher discomfort and lower performance. Despite the lack of significant findings, the trend in the current study was

for condition (5) (235 Hz tonal, PR=9) to be perceived as slightly more annoying and distracting than the other tonal noise conditions (120 and 595 Hz).

V. CONCLUSIONS

The influence of tones in background noise on human task performance and subjective perception and the relationship to noise criteria was analyzed in this study. As in previous research, clear relationships between performance and criteria level predictions were not observed.[10,11] In addition, few statistically significant relationships existed between subjective perception and criteria level ratings. The lack of significant relationships may have been due in part to the fact that there was very little difference in the criteria level ratings of the signals. Subjective perception of noise was significantly related to task performance scores, though.

Although significant differences in performance were not observed between the noise conditions, there were some differences in perception. Statistically significant relationships were not observed in all the expected cases, but the perception trends were generally as expected with higher PR (PR=9) conditions perceived as more tonal, louder, more annoying, and more distracting than their counterpart PR =5 conditions. It appeared that the perceived loudness of the nontonal condition may have contributed to perceived annoyance and distraction of this condition. Therefore, a tradeoff between loudness and tonality perception is required to fully match perception of adverse response.

This study provided insight into how the tonality of background noise can impact task performance and perception. Overall, the indication is that although there were no significant differences in performance between the various noise conditions, there were differences in perception. These differences in perception are not adequately reflected in the criteria methods analyzed. Although the six noise conditions used in this study contained different tonal qualities, and were thus perceived as significantly different in some cases, there was essentially no change in the criteria level ratings across the noise conditions. Although there were minor changes in the criteria spectral quality descriptors across the noise conditions, it is difficult to relate these easily or accurately to tonality.

Putting performance aside for a time, if a primary goal of a criterion is to relate to occupant perception, the existing criteria should be modified to account for tonality, including frequency and prominence. However, more research is needed before specific modification recommendations can be made, using different noise scenarios, types of tasks, and noise metrics. Due to the few statistically significant tonality perception findings in this study, it would be advantageous to develop a criterion from a set of data that has a greater range of subjective response. Future work could include a greater variety of noise conditions that include changes in both level and tonality in addition to a wider range of tonal frequency and prominence.

Existing tonal metrics can be tested against the data, such as the PR, tone-to-noise ratio,[44] the Joint Nordic method,[52] or Aures' model of tonalness, all of which are detailed by Hastings *et al.*,[53] are also recommended. Depending on how well the tonal metrics are correlated with subjective response, it may then be possible to develop a combined criterion which accounts for both level and tonality. Another option would be to incorporate the tonal recommendation given by ANSI.[14] This suggests that if a pure tone is detected in noise, then the tone level should be at least 5 dB less than the level in the octave band of the NCB or RC criterion curve in which it falls. However, this guideline has not been widely adopted or incorporated into design standards. Perhaps a numerical penalty could be applied to a criterion when this recommended guideline is not met.

The process of improving the noise criteria should continue as more information becomes available on how occupants respond to indoor noise. Ultimately, the goal of any background noise criterion is to accurately reflect occupant response to noise to ensure that acoustical problems in buildings are correctly diagnosed, abated, or prevented. Additional consideration of tonality and other acoustical factors not yet fully accounted for (such as variance over time) will improve the performance of these commonly used tools.

ACKNOWLEDGMENTS

This work has been supported by the American Society of Heating, Refrigerating, and Air-Conditioning Engineers (ASHRAE) RP-1322, the Institute of Noise Control Engineering (INCE) Martin Hirschorn IAC Prize, the University of Nebraska-Lincoln (UNL) Center for Building Integration, and a UNL Research Council Faculty Seed Grant. The authors are grateful for the assistance of Cathy Novak and Marc Choiniere in administering the subjective tests, and for the recording contributions of Warren Blazier, Norman Broner, Mark Fly, Jerry Lilly, and Mark Schaffer.

[1]L. Beranek, "Revised criteria for noise in buildings," Noise Control **3**, 19–27 (1957).
[2]L. Beranek, "Balanced noise-criterion (NCB) curves," J. Acoust. Soc. Am. **86**, 650–664 (1989).
[3]W. Blazier, "Revised noise criteria for application in the acoustical design and rating of HVAC systems," Noise Control Eng. **16**, 64–73 (1981).
[4]W. Blazier, "RC Mark II: A refined procedure for rating the noise of heating, ventilating, and air-conditioning (HVAC) systems in buildings," Noise Control Eng. J. **45**, 243–250 (1997).
[5]American National Standards Institute, *Design Response of Weighting Networks for Acoustical Measurements: S 1.42-2001* (Acoustical Society of America, Melville, New York, 2001).
[6]L. Beranek, "Applications of NCB and RC noise criterion curves for specification and evaluation of noise in buildings," Noise Control Eng. J. **45**, 209–216 (1997).
[7]W. Blazier, "Noise control criteria for heating, ventilating, and air-conditioning systems," in *Handbook of Acoustical Measurements and Noise Control*, edited by C. Harris (Acoustical Society of America, Melville, NY, 1998), Chap. 43, pp. 43.1–43.18.
[8]G. Tocci, "Room noise criteria—State of the art in the year 2000," Noise News Int. **8**, 106–119 (2000).
[9]L. Wang and E. Bowden, "Performance review of indoor noise criteria," Architectural Engineering Institute 2003 Proceedings, Austin, TX, 2003, Vol. **116**, No. 2.
[10]E. Bowden and L. Wang, "Relating human productivity and annoyance to indoor noise criteria systems: A low frequency analysis," ASHRAE Winter Meeting Transactions, Orlando, FL, 2005, Vol. **111**, Issue 1, pp. 684–692.
[11]E. Bowden, "Investigations of indoor noise criteria systems based on human perception and task performance," Ph.D. thesis, University Nebraska, 2006.
[12]American Society of Heating, Refrigerating and Air-Conditioning Engi-

neers, Inc., "Sound and vibration control," *2007 ASHRAE HVAC Applications Handbook* (American Society of Heating, Refrigerating and Air-Conditioning Engineers, Atlanta, GA, 2003), Chap. 47, pp. 47.30–47.35.
[13]L. Goodfriend, *RP-126: A Study to Update Indoor Sound Criteria for Air Conditioning Systems* (American Society of Heating, Refrigerating and Air-Conditioning Engineers, Atlanta, GA, 1975).
[14]American National Standards Institute, *Criteria for Evaluating Room Noise: S 12.2-1995* (Acoustical Society of America, Melville, NY, 1995).
[15]American National Standards Institute, *Acoustical Performance Criteria, Design Requirements, and Guidelines for Schools: S 12.60-2002* (Acoustical Society of America, Melville, NY, 2002).
[16]ISO-DIS 12001, "Draft glossary of terms used in noise control engineering," Noise News Int. **3**, 161–168 (1995).
[17]K. Persson, M. Bjorkman, and R. Rylander, "An experimental evaluation of annoyance due to low frequency noise," Low Freq. Noise, Vib., Act. Control **4**, 145–153 (1985).
[18]S. Tang, J. Burnett, and C. Poon, "Aural environment survey in air-conditioned open-plan offices," Build. Services Eng. Res. Technol. **17**, 97–100 (1996).
[19]S. Tang, "Performance of noise indices in air-conditioned landscaped office buildings," J. Acoust. Soc. Am. **102**, 1657–1663 (1997).
[20]S. Tang and C. Wong, "Performance of noise indices in office environment dominated by noise from human speech," Appl. Acoust. **55**, 293–305 (1998).
[21]S. Tang and M. Wong, "On noise indices for domestic air conditioners," J. Sound Vib. **274**, 1–12 (2004).
[22]U. Ayr, E. Cirillo, and F. Martellotta, "An experimental study on noise indices in air conditioned offices," Appl. Acoust. **62**, 633–643 (2001).
[23]U. Ayr, E. Cirillo, I. Fato, and F. Martellotta, "A new approach to assessing the performance of noise indices in buildings," Appl. Acoust. **64**, 129–145 (2003).
[24]P. Susini, S. McAdams, S. Winsberg, I. Perry, S. Vieillard, and X. Rodet, "Characterizing the sound quality of air-conditioning noise," Appl. Acoust. **65**, 763–790 (2004).
[25]K. Persson Waye and R. Rylander, "The prevalence of annoyance and effects after long-term exposure to low-frequency noise," J. Sound Vib. **240**, 483–487 (2001).
[26]N. Broner, "Considerations in the rating and assessment of low-frequency noise," ASHRAE Annual Meeting Transactions, Denver, CO, Vol. **99**, Issue 2, pp. 1025–1030 (1993).
[27]K. Kryter and K. Pearsons, "Judged noisiness of a band of random noise containing an audible pure tone," J. Acoust. Soc. Am. **38**, 106–112 (1965).
[28]R. Hellman, "Loudness, annoyance, and noisiness produced by single-tone-noise complexes," J. Acoust. Soc. Am. **72**, 62–73 (1982).
[29]R. Hellman, "Perceived magnitude of two-tone complexes: Loudness, annoyance, and noisiness," J. Acoust. Soc. Am. **77**, 1497–1504 (1985).
[30]U. Landström, A. Kjellberg, L. Söderberg, and B. Nordström, "The effects of broadband, tonal, and masked ventilation noise on performance, wakefulness and annoyance," Low Freq. Noise, Vib., Act. Control **10**, 112–122 (1991).
[31]U. Landström, A. Kjellberg, and M. Byström, "Acceptable levels of sounds with different spectral characteristics during the performance of a simple and complex nonauditory task," J. Sound Vib. **160**, 533–542 (1993).
[32]U. Landström, A. Kjellberg, L. Söderberg, and B. Nordström, "Measures against ventilation noise—which tone frequencies are least and most annoying?," Low Freq. Noise, Vib., Act. Control **13**, 81–88 (1994).
[33]K. Kryter, "Mental and psychomotor task performance in noise," *The Effects of Noise on Man* (Academic, New York, NY, 1985), Chap. 9, pp. 343–387.
[34]D. Jones and D. Broadbent, "Human performance and noise," in *Handbook of Acoustical Measurements and Noise Control*, edited by C. Harris (Acoustical Society of America, Melville, NY, 1998), Chap. 24, pp. 24.1–24.24.
[35]M. Muzammil and F. Hasan, "Human performance under the impact of continuous and intermittent noise in a manual machining task," Noise Vib. Control Worldw. **35**(7), 10–15 (2004).
[36]K. Kyriakides and H. G. Leventhall, "Some effects of infrasound on task performance," J. Sound Vib. **50**, 369–388 (1977).
[37]S. Benton and H. G. Leventhall, "Experiments into the impact of low level, low frequency noise upon human behaviour," Low Freq. Noise, Vib., Act. Control **5**, 143–162 (1986).
[38]S. Benton and G. Robinson, "The effects of noise on text problem solving for the word processor user (WPU)," Proceedings of the Sixth International Congress: Noise as a Public Health Problem, Nice, France, 1993, pp. 539–541.
[39]K. Holmberg, U. Landström, and A. Kjellberg, "Effects of ventilation noise due to frequency characteristic and sound level," Low Freq. Noise, Vib., Act. Control **16**, 115–122 (1993).
[40]K. Persson Waye, R. Rylander, S. Benton, and H. G. Leventhall, "Effects on performance and work quality due to low frequency ventilation noise," J. Sound Vib. **205**, 467–474 (1997).
[41]K. Persson Waye, R. Rylander, J. Bengtsson, A. Clow, F. Hucklebridge, and P. Evans, "Does low frequency noise induce stress?," Proceedings of the Ninth International Low Frequency Noise and Vibration Meeting, Aalborg, Denmark, pp. 203–209 (2000).
[42]K. Persson Waye, J. Bengtsson, A. Kjellberg, and S. Benton, "Low frequency noise "pollution" interferes with performance," Noise Health **4**, 33–49 (2001).
[43]J. Bengtsson, K. Persson Waye, A. Kjellberg, and S. Benton, "Low frequency noise "pollution" interferes with performance," Proceedings of the Ninth International Low Frequency Noise and Vibration Meeting, Aalborg, Denmark, pp. 15–21 (2000).
[44]American National Standards Institute, *Measurement of Sound Pressure Levels in Air: S 1.13-1995* (Acoustical Society of America, Melville, NY, 1995).
[45]National Aeronautics and Space Administration, *Auditory Demonstrations in Acoustics and Hearing Conservation CD* (NASA Glenn Research Center, Cleveland, OH, 2004).
[46]R. D. Hellweg, Jr. and M. Nobile, "Modification to procedures for determining prominent discrete tones," Proceedings of Internoise, Dearborn, MI, 2002, Vol. **111**, Issue 1, pp. 1707–1714.
[47]E. Ryherd and L. Wang, "Effects of exposure duration and type of task on subjective performance and perception in noise," Noise Control Eng. **55**, 334–347 (2007).
[48]SkillCheck™ Corporation, 2007 (http://www.skillcheck.com).
[49]A. Baddeley, "A 3 min reasoning test based on grammatical transformation," Psychonomic Sci. **10**, 341–342 (1968).
[50]SPSS™ Corporation, 2007 (http://www.spss.com).
[51]A. Field and G. Hole, *How to Design and Report Experiments* (Sage, London, 2003).
[52]"Objective method of assessing the audibility of tones in noise," Delta report AV on the Joint Nordic method, Version 2, 1952/99.
[53]A. Hastings, K. Lee, P. Davies, and A. Surprenant, "Measurement of the attributes of complex tonal components commonly found in product sound," Noise Control Eng. J. **51**, 195–209 (2003).

A straightforward method for wall impedance eduction in a flow duct

Xiaodong Jing,[a] Sen Peng, and Xiaofeng Sun
Fluid and Acoustic Engineering Laboratory, School of Jet Propulsion, Beijing University of Aeronautics and Astronautics, Beijing 100083, People's Republic of China

(Received 16 December 2007; revised 27 April 2008; accepted 30 April 2008)

The development of the advanced liner technology for aeroengine noise control necessitates the impedance measurement method under realistic flow conditions. Currently, the methods for this need are mainly based on the inverse impedance eduction principle, confronting with the problems of initial guess, high computation cost, and low convergence. In view of this, a new strategy is developed that straightforwardly educes the impedance from the sound pressure information measured on the duct wall opposing to the test acoustic liner embedded in a flow duct. Here, the key insight is that the modal nature of the duct acoustic field renders a summed-exponential representation of the measured sound pressure; thus, the characterizing axial wave number can be readily extracted by means of Prony's method, and further the unknown impedance is calculated from the eigenvalue and dispersion relations based on the classical mode-decomposition analysis. This straightforward method is simple in its basic principle but remarkably has the advantages of ultimately overcoming the drawbacks inherent to the inverse methods, incorporating the realistic multimode nonprogressive wave effects, high computational efficiency, possibly reducing the measurement points, and even avoiding the necessity of the duct exit impedance that bothers perhaps all the existing waveguide methods.
[DOI: 10.1121/1.2932256]

PACS number(s): 43.50.Gf, 43.20.Mv, 43.58.Bh [AH] Pages: 227–234

I. INTRODUCTION

Acoustic treatments in the form of various liner structures have been demonstrated as the most effective means to control the noise of an aircraft engine over the past five decades and will continually play an important role in achieving the aggressive noise reduction goal of the next-generation quiet aeroengines. The new trend of higher bypass ratio turbofan design raises the formidable demand of greatly increasing noise attenuation with effectively diminished acoustically treated surface.[1] This is such a challenge that the current knowledge and techniques are inadequate; thus, major advancements are highly expected in future study.

To this end, the development of advanced liner technology fundamentally necessitates the progress in the impedance measurement method for nearly all the aspects, from improving the physical insights into the liner absorption mechanism to exploring the novel liner concepts such as the bias flow liner[2] and the active/passive hybrid types.[2] Moreover, more especially, driven by the need for increasing suppression efficiency, the acoustic liner optimization must be greatly enhanced over the current level. For this objective, a prediction model is essentially needed to determine the liner impedance as the crucial boundary condition for a propagation model to simulate the noise attenuation in the lined duct. The impedance model for such purpose not only depends on the experiment for validation but also must be highly empirical in its development process since a pure theory for practical impedance prediction would be a remote possibility.

However, subjected to the complicated high-speed flow condition in an aeroengine nacelle, reliable impedance measurement has long been proved a very difficult problem confronting the research community. Yet, it is well known that the grazing flow has considerable influence on the performance of an acoustic liner and, thus, its effect must be taken into account.[3] The enthusiasm and also the difficulty with this research topic can be evaluated from the numerous related papers and the various ideas being attempted over the past decades. A brief review of the representative inventions can be found in Ref. 4. Unfortunately, most of these have eventually been abandoned due to their limitations. Dean[4] made a successful improvement leading to the two-microphone *in situ* method that has gained wide application up to now. However, several problems have been reported with the use of this method. The *in situ* method requires the destructive installation of the microphones into the test liner, only provides the point-to-point measurement rather than the global impedance information that is more pertinent for the liner design purpose, and even fails when measuring the liners of multilayer structure or with the porous materials that have been extensively applied to meet the recent need for broadband noise control.[1]

To overcome the shortcomings of the *in situ* method, the inverse impedance eduction methods (also referred to as "inverse method" for brevity) have been developed and attracted wide research attention in recent years. This category of methods is based on the principle that the impedance of an acoustic liner strategically placed in a flow duct can be in-

[a]Electronic mail: jingxd@buaa.edu.cn

versely educed from minimizing the difference between the measured acoustic information at some characteristic points and the prediction of a forward propagation model. This concept, first put forward by Watson in the 1980s,[5,6] has recently evolved into many practical forms, in which the forward computation is done by the finite element[7–9] or mode-matching method,[10,11] and the measured acoustic information can be the sound pressure,[7–9] the reflection and transmission coefficients,[10,11] or the insertion loss.[12] However, all these methods are subjected to the general disadvantages. First, being relied on and sensitive to the initial guess, the convergence of the targeted searching is probably slow and even fails in the worse cases. Furthermore, since unique solution cannot be mathematically guaranteed except for very simple cases, the reliability of the inverse methods is compromised by the uncertainty whether the numerical searching converges to the true physical value or just a false result. Also, the computation cost is a major concern due to the repeated running of the numerical code in the iteration process, especially when the forward model is computationally intensive.

As for the inverse impedance eduction methods or perhaps all the existing waveguide methods in general, an inherent but not well-addressed weakness is the dependence of the methods on the duct exit reflective condition. Theoretically, the nonreflection condition is desired for these methods, but in practice this can only be nearly realized by employing a cumbersome anechoic duct termination, which is particularly inconvenient or even impractical for low-frequency measurement. Alternatively, the duct exit impedance is measured by the two-microphone method or similar techniques, but inevitably at the expense of bringing an additional source of error to the impedance eduction. It was found that in some situation, the inverse method is very sensitive to the duct exit condition and that a little variation in it causes a marked change of the educed impedance.[13] However, as far as we know, this negative influence on the impedance measurement accuracy has not been further analyzed in the previous investigations.

The limitations of the existing methods motivate the innovative research of impedance measurement methods under flow condition. It is the objective of this paper to develop a new method that straightforwardly educes the impedance of an acoustic liner strategically placed in a flow duct. In fact, the first attempt of straightforward impedance eduction in a flow duct is made by Armstrong *et al.*[14] even before the advent of the inverse methods. However, the so-called infinite waveguide method is based on the assumption of a single unidirectional propagating mode, too ideal to be satisfied in a physical experimental facility. Since then, confronted with the problem of how to consider the realistic acoustic environment containing multimode nonprogressive sound waves, little effort has been attempted along the direction of straightforward impedance eduction. Here, it is demonstrated that this tricky problem can be tackled by a methodology that takes full advantage of the modal nature of the duct acoustic field and draws inspiration from the application of the well-known Prony's method. Although extensively used to extract the wave numbers or propagation constants that are closely related to the absorption of various waves,[15,16] the potential value of Prony's method in impedance measurement has received little attention so far in the field of acoustics. The present method is simple in its basic principle but has several striking advantages, for which the details are presented in the following context.

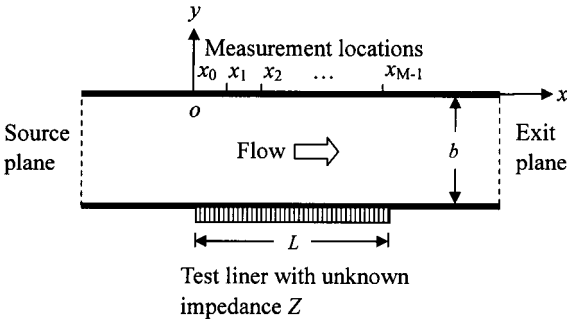

FIG. 1. Illustration of the straightforward impedance eduction in a flow duct.

II. DESCRIPTION OF THE STRAIGHTFORWRD IMPEDANCE EDUCTION METHOD

As depicted in Fig. 1, a grazing flow environment is formed in a rectangular duct whose height is b. An acoustic liner of length L is placed in the lower central portion of the otherwise rigid duct wall. The test liner is treated as locally reacting with the unknown uniform impedance Z to be determined. It is reasonable to assume that the subsonic flow is uniform, with the Mach number being M_0. In the flow duct, when the time-harmonic plane sound wave generated in the hard wall section is incident upon the acoustic liner, multimode reflected and transmitted sound waves are excited. To collect the acoustic field information for the impedance eduction, the axial sound pressure distribution $p_u(x)$ is measured at a sequence of equally spaced locations on the upper-wall region directly over the acoustic liner. It can be seen that both the experimental facility and the implementation of the measurements are very similar to, but no more complicated than, the conventional inverse impedance eduction method.[7]

To facilitate the theoretical development, a coordinate system is introduced with x being along the duct axis and originated from the liner leading edge and putting $y=0$ on the upper duct wall. The harmonic sound propagation in the flow duct is governed by the convective Helmholtz equation for the sound pressure p,

$$\nabla^2 p - M_0^2 \frac{\partial^2 p}{\partial x^2} - 2ikM_0 \frac{\partial p}{\partial x} + k^2 p = 0, \tag{1}$$

where $i=\sqrt{-1}$, k is the free-space wave number, $k=2\pi f/c$, f is the frequency, and c is the sound speed. The boundary conditions at the rigid walls are that the normal particle velocity vanishes or, equivalently,

$$\frac{\partial p}{\partial y} = 0. \tag{2}$$

On the lined duct wall, the following impedance boundary condition is imposed,[17]

$$\frac{\partial p}{\partial y} = \frac{1}{Z}\left(ikp + 2M_0 \frac{\partial p}{\partial x} + \frac{M_0^2}{ik}\frac{\partial^2 p}{\partial x^2} \right). \quad (3)$$

It can be intuitively deduced and mathematically proved that the uniformity of both the wall impedance and the incident sound pressure in the z direction renders an essentially two-dimensional sound field in the flow duct. A further analysis based on the classical mode-decomposition theory indicates that the sound pressure p inside the lined segment can be expressed in the following form:[10]

$$p(x,y) = \sum_{n=1}^{\infty} A_n^+ \cos(\beta_n^+ y) e^{-i\mu_n^+ x} + A_n^- \cos(\beta_n^- y) e^{-i\mu_n^- x}, \quad (4)$$

where $A_n^{\pm}$ are the complex modal amplitudes, and $\mu_n^{\pm}$ and $\beta_n^{\pm}$ are the complex axial and transverse wave numbers, respectively, which are related to each other through the dispersion relation

$$\mu_n^{\pm} = \frac{-M_0 k \pm \sqrt{k^2 - (1-M_0^2)(\beta_n^{\pm})^2}}{1-M_0^2}. \quad (5)$$

Moreover, the transverse wave numbers are determined from the eigenvalue equation as

$$\frac{ik}{Z}\left\{ \frac{1}{1-M_0^2}\left[1 \mp M_0 \sqrt{1 - \frac{1-M_0^2}{k^2}(\beta_n^{\pm})^2} \right] \right\}^2 = \beta_n^{\pm} \tan(\beta_n^{\pm} b). \quad (6)$$

Conversely, Eq. (6) provides a key relation to explicitly determine the unknown impedance from the transverse wave number and, thus, the axial wave number when combined with the dispersion relation.

It is obvious from Eq. (4) that on the upper duct wall where $y=0$, the sound pressure distribution $p_u(x)$ can be represented by a sum of complex exponentials,

$$p_u(x) = \sum_{n=1}^{N} A_n e^{-i\mu_n x}. \quad (7)$$

Note that the superscript "±" is omitted from the variables for simplicity, and for practical reason, the infinite summation has been truncated at the maximum mode number of N. A key insight of the present work is that, constrained by the measured data, the summed-exponential representation of $p_u(x)$ or Eq. (7) is deterministic, and the characterizing parameters μ_n and A_n can be identified by means of Prony's method. With the axial wave numbers being obtained, the impedance eduction is straightforwardly achieved by the simple algebraic manipulation of the dispersion relation (5) for transverse wave numbers and then the eigenvalue equation (6) for the unknown impedance.

Prony's method has extensively been used to extract the crucial parameters from both real-valued and complex-valued functions consisting of complex exponentials. For ease of reference, this method is outlined here. When the values of $p_u(x)$ are specified by the data measured at the M equal-spaced points, Eq. (7) turns to be

$$p_j = \sum_{n=1}^{N} A_n w_n^j \quad \text{for } j = 0,1,\ldots,M-1, \quad (8)$$

where $p_j = p_u(j\Delta x)$, $w_n = e^{-i\mu_n \Delta x}$, and Δx is the distance interval of the measurement points. Equation (8) can be further organized into $(M-N)$ consecutive sets of equations as

$$p_{s+r} = \sum_{n=1}^{N} A_n w_n^{s+r} \quad \text{for } s = 0,1,\ldots,N \text{ and } r = 0,1,\ldots,M-N-1. \quad (9)$$

It has been recognized that w_n is given by the roots of the Nth order polynomial equation

$$\sum_{s=0}^{N} C_s w^s = 0 \quad \text{with } C_N = 1. \quad (10)$$

Then, multiplying both sides of Eq. (9) by C_s and carrying out the summation over s, we get a set of linear algebraic equations for the coefficients of Eq. (10),

$$\sum_{s=0}^{N} p_{r+s} C_s = 0 \quad \text{for } r = 0,1,\ldots,M-N-1. \quad (11)$$

For solving Eq. (11), it is required that $M \geqslant 2N$ and the equal relation is used to keep M minimum for a fixed N in this paper. The pseudoinverse matrix method based on the singular value decomposition is employed to solve the involved linear equation sets, which is advantageous in handling the possible ill-condition issue of the matrix manipulation.

In principle, we can use any of the identified axial wave numbers to determine the unknown impedance. However, limited by the numerical accuracy of Prony's method, it is very important to choose the most appropriate wave number in practice. For this consideration, a simple and convenient selection criterion is proposed that the reliable wave numbers must be associated with the dominant modes with considerably larger amplitudes. Also, a systematic approach has been devised to differentiate the physical wave numbers from the spurious ones in Ref. 18. It is a big advantage of the present method that only one reliable axial wave number is sufficient to educe the unknown impedance, and it is readily found through the above identification and selection process. As expected, the picked-up wave number usually corresponds to the first-order forward traveling mode, in consistency with the way of introducing the sound wave into the flow duct.

It is worth noticing that, except for the algebraic dispersion relation (5) and eigenvalue equation (6), the present method is not burdened with the need for solving a complete duct propagation model, thus is computationally far more efficient than the inverse impedance eduction methods.

III. THE RESULTS AND DISCUSSIONS

In the present study, in order to validate the straightforward impedance eduction method (also referred to as "straightforward method" for brevity) via the widely accepted benchmark results, the experimental setup illustrated in Fig. 1 is taken to have the geometry identical to the NASA Langley Flow Impedance Test Facility[13] with the basic pa-

rameters being the duct height, 0.051 m, and the length of the test liner, 0.406 m. Some other conditions are that the sound speed is 344.3 m/s and the sound pressure level (SPL) at the source plane is kept to be 130 dB.

A. Straightforward impedance eduction from the FEM simulation of the flow duct experiment

For the initial validation purpose, a finite element model (FEM) duct propagation model is set up to simulate the acoustic experiment in the flow duct. To numerically solve the governing equation (1), two additional boundary conditions must be specified, i.e., at the duct inlet,

$$p = p_s, \tag{12}$$

where p_s is the sound pressure at the source plane, and at the duct exit,

$$\frac{\partial p}{\partial x} = -\frac{ikp}{M_0 + Z_e}, \tag{13}$$

where Z_e is the normalized specific acoustic impedance of the imaginary exit plane. In this paper, Z_e is either taken to be unity in a pure simulation or given by the NASA benchmark experiment when the test cases in Ref. 13 are considered. The present Galerkin FEM is similar to that of Ref. 7, but there is a major difference in the treatment of the impedance boundary condition at the acoustic liner. To incorporate into the FEM the second-order derivative term in Eq. (3), according to Ref. 7, cubic or higher-order basis function is necessarily used. Here, an alternative approach is adopted which reduces the derivative order of this term by the partial integration rule when the weak formulation of the FEM is written as follows:

$$\int_0^L \frac{M_0^2}{ikZ}\frac{\partial^2 p}{\partial x^2}N_m dx = \frac{M_0^2}{ikZ}\left(-\int_0^L \frac{\partial N_m}{\partial x}\frac{\partial p}{\partial x}dx + \left. N_m \frac{\partial p}{\partial x}\right|_0^L\right), \tag{14}$$

where N_m is the basis function. In Ref. 19, similar BC treatment method has already been proposed for the more general three-dimensional situation while discarding the term evaluated at the boundary of the lined area on the assumption of rapid but continuous impedance variation. However, the boundary evaluation term at $x=0$ and L is retained here, as shown by Eq. (14). So, based on Eq. (14), the linear basis function is employed to construct the FEM in this paper.

In Fig. 2, when $M_0=0.3$, $f=1.5$ kHz, $Z=2.0+i1.0$, and the duct exit is nonreflective, the FEM is compared to the mode-matching method that has been well established to represent the standard exact solution of the acoustic simulation.[10] The excellent agreement, as shown by the nearly overlapped solid and dash lines, readily lends the FEM being used to provide the simulation input for the present straightforward method. To best mimic the measurements, a random perturbation error is added to the FEM computation of the upper wall sound pressure as

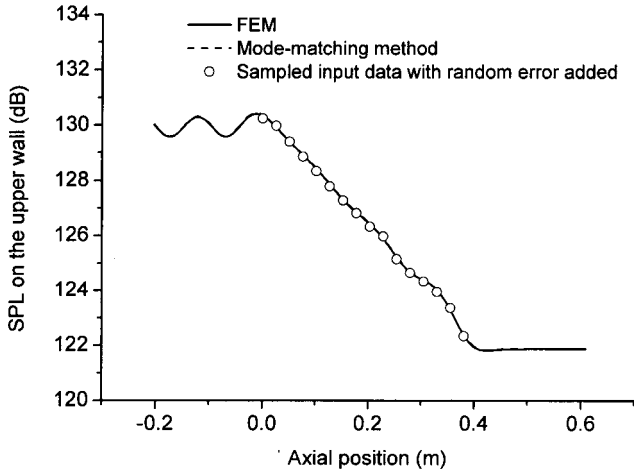

FIG. 2. FEM simulation of the upper-wall sound pressure compared to the standard mode-matching method. $M_0=0.3$, $f=1.5$ kHz, $Z=2.0+i1.0$, and $Z_e=1.0+i0.0$.

$$\hat{p}_u(x_k) = 10^{\Delta dB/20} p_u(x_k), \tag{15}$$

where $\Delta dB=(2N_R-1)\delta$, N_R is a random number between 0 and 1, and δ is set to the level of 0.1 dB typically experienced in the benchmark experiment.[8]

As the crucial step of the present method, Prony's method is employed to extract the axial wave numbers from the simulated upper-wall sound pressure that is uniformly sampled at a spacing of 0.0254 m over the x range from 0.0 to 0.381 m, as shown by the symbols in Fig. 2. The data sample range does not necessarily cover the whole length of the test liner. Actually, to avoid the contamination of the trivial evanescent modes due to the impedance discontinuities, the sound pressure data near the leading and trailing edges of the liner can be deliberately excluded from those used for the identification purpose.

For comparison purpose, the exact axial wave numbers are solved from the combination of Eqs. (5) and (6), and the corresponding modal amplitudes are computed from the mode-matching method of Ref. 10. Several approaches can be applied to solving the transcendental equation (6), such as the well-known Newton–Raphson, Eversman's integration,[20] and the newly homotopy methods,[21] but special care must be taken on the unfavorable possibilities of wrong initial guess, eigenvalue missing, etc. Because of this concern, the winding-number integral method[22] is recommended for the reliable calculation of transverse wave numbers in this paper.

In Table I, for the first two acoustic modes, the extracted axial wave numbers and the corresponding modal amplitudes show very good agreement with the exact results. So, as expected, the liner impedance eduction can be successfully accomplished by substituting either of the extracted μ_n into Eq. (5) for β_n and then using Eq. (6) to calculate Z. Relating to the dominant mode and thus being more reliable, $\mu_1 = 19.85 - i2.299$ gives the result of $Z=1.993+i1.016$ that excellently reproduces the target value of $2.0+i1.0$.

B. Straightforward impedance eduction from the experimental data

With the success of the initial validation, it is very attractive to apply the present method to the situation of a real

TABLE I. Comparison between the exact and the extracted modal parameters from the FEM simulation shown in Fig. 2.

Mode number	Exact		Presently extracted	
	μ_n	A_n	μ_n	A_n
1^+	$19.87-i2.310$	$-31.06+i58.74$	$19.85-i2.299$	$-30.67+i58.35$
1^-	$-34.23+i5.276$	$-0.144-i0.013$	$-34.53+i4.886$	$-0.168+i0.018$

experiment. For years, the NASA Langley Flow Impedance Test Facility has provided benchmark data for the verification of various duct aeroacoustic simulation and measurements, particularly the inverse impedance eduction techniques. So, this experimental platform is also regarded as the touchstone of the present straightforward impedance eduction method. For this purpose, Ref. 13 is very helpful in publishing a comprehensive set of tabulated experimental data conveniently to be used by the present study. Although the sound pressure data given in the reference are distributed at almost evenly spaced measurement locations, this data format does not completely meet the requirement of using Prony's method. Hence, to prepare the input for the present method, a data preprocessing is performed with an interpolation scheme to create the equal-distance data sequence over the x coordinate range from 0.0003 to 0.3813 m. In this paper, if no specification is given, the data point number $M=16$ or, correspondingly, the spacing of 0.0254 m is chosen so that most of the sample points coincide with the original measurement locations, thus minimizing the interpolation error.

When there is no flow and the test frequency is 1.5 kHz, the measured sound pressure on the upper duct wall and the sampled input data are presented in Fig. 3. The effect of the higher-order modes can be assessed from the phenomenon that the sound pressure generally decays along the duct but with oscillations, which can hardly be treated by the infinite waveguide method requiring a perfect linear region on the SPL curve,[14] but brings little difficulty to the present method. From the input data, both the axial wave numbers and the modal amplitudes are extracted by Prony's method, as given in Table II. Note that the wave numbers are listed according to the magnitude of the modal amplitudes, so their sequences do not necessarily correspond to the orders of the real acoustic modes except for the most important situation that μ_1 is physically attributed to the 1^+ mode. It is also worth mentioning that in the experimental validation cases, the extracted wave numbers tend to be unreliable or even spurious as n increases due to their negligible influence and the numerical accuracy of Prony's method. So, evidently, the first extracted wave number is the correct choice for the impedance eduction purpose. In this case, with $\mu_1=22.88-i2.789$, we obtain $Z=0.98+i1.28$ from the simple calculation of Eqs. (5) and (6). This result is in very good agreement with that of the conventional two-dimensional (2D) inverse method,[13] $Z=1.02+i1.30$.

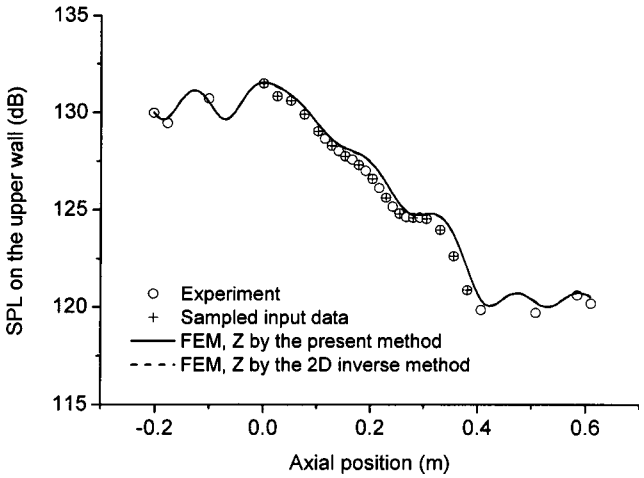

FIG. 3. The upper-wall sound pressure distribution presented by the experiment, the sampled input data, and the FEM simulations based on Z educed by the present method and the 2D inverse method of Ref. 13. $M_0=0.0$, $f=1.5$ kHz, and $Z_e=1.03+i0.08$.

Furthermore, the present method is applied to the situation when flow is present. For $M=0.255$ and $f=1.5$ kHz, the measured SPL and the sampled input data are depicted in Fig. 4. Similarly, the axial wave numbers and the modal amplitudes are extracted and presented in Table II. From $\mu_1=19.06-i2.204$, the impedance is readily calculated to be $Z=1.12+i1.32$, showing good agreement with the previous result,[13] $Z=1.26+i1.26$. Another case is considered when the Mach number is up to 0.4 and the frequency is changed to 2.5 kHz. Although the experimental data exhibit larger oscillations at the liner edges due to the influence of higher speed flow, as shown in Fig. 5, the present method successfully extracts the key modal parameters (see Table II), and thus obtaining the liner impedance, $Z=0.89-i1.30$, that is quite near to $Z=0.75-i1.29$ from the 2D inverse method.[13] A thorough comparison between the present straightforward

TABLE II. The extracted axial wave numbers and the modal amplitudes for the first four significant modes at different Mach numbers.

M	f (kHz)	μ_n	A_n
0.000	1.5	$22.88-i2.789$	$55.14+i50.23$
		$6.723-i8.306$	$2.914-i0.600$
		$70.12-i29.57$	$0.918-i2.038$
		$-54.10-i32.15$	$-1.402-i1.576$
0.255	1.5	$19.06-i2.204$	$-18.31+i68.30$
		$4.794-i14.01$	$5.517+i3.735$
		$-87.74-i23.50$	$-0.755-i1.911$
		$-28.76+i4.140$	$0.975-i0.475$
0.400	2.5	$35.39-i2.173$	$54.71-i13.71$
		$-8.782-i28.49$	$27.10-i15.74$
		$-67.50-i20.20$	$-2.661+i3.766$
		$114.1-i2.059$	$0.053+i0.571$

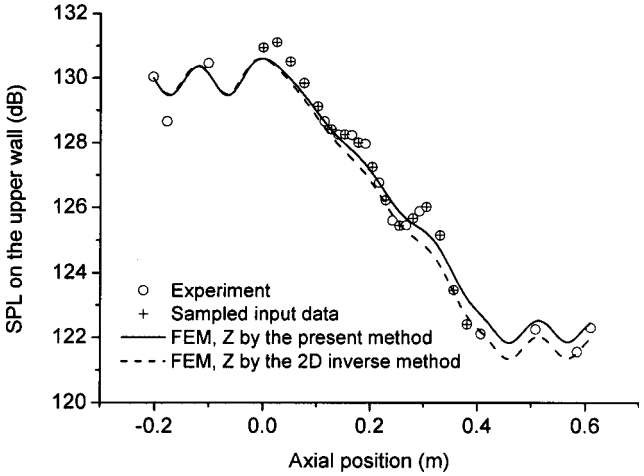

FIG. 4. The upper-wall sound pressure distribution presented by the experiment, the sampled input data, and the FEM simulations based on Z educed by the present method and the 2D inverse method of Ref. 13. $M_0=0.255$, $f=1.5$ kHz, and $Z_e=1.10-i0.09$.

method and the 2D inverse method of Ref. 13 is made for a variety of flow Mach numbers from 0 to 0.4 at two test frequencies, 1.5 and 2.5 kHz, respectively. As seen from Table III, the impedances educed by both methods agree well with each other. The occurrence of some discrepancies is understandable and can be explained in the way that the two educed impedances afford almost equally good FEM predictions of duct sound attenuation when compared to the measured data, as shown in Figs. 3–5 for the three typical flow speeds. Thus, the present straightforward method is satisfactorily validated for impedance measurement under practical flow condition.

The present method also reveals that although expected to be complicated in its spatial variations due to the presence of wall impedance discontinuities, the duct acoustic field can be adequately described with only a few predominant modes. Figure 6 shows that for the case of Fig. 4, the measured upper-wall sound pressure can be well reconstructed from summing the first four modal terms according to Eq. (7) with A_n and μ_n given in Table II. This simple truncated modal

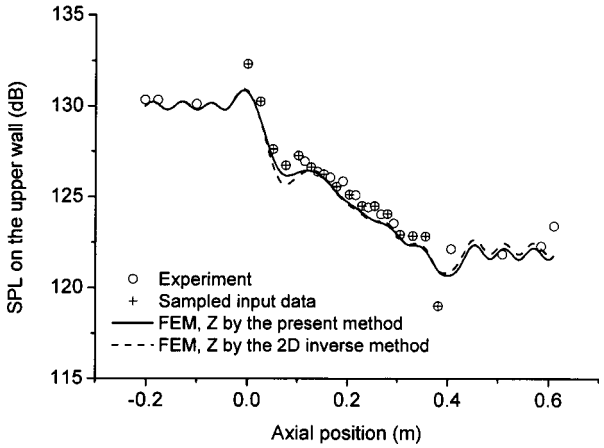

FIG. 5. The upper-wall sound pressure distribution presented by the experiment, the sampled input data, and the FEM simulations based on Z educed by the present method and the 2D inverse method of Ref. 13. $M_0=0.4$, $f=2.5$ kHz, and $Z_e=0.92-i0.14$.

TABLE III. Comparison between the present method and the previous 2D inverse method (Ref. 13) for the educed impedance at different Mach numbers when $f=1.5$ and 2.5 kHz, respectively.

	1.5 kHz		2.5 kHz	
M_0	Present	2D inverse	Present	2D inverse
0.000	$0.98+i1.28$	$1.02+i1.30$	$1.43-i1.65$	$1.54-i1.60$
0.079	$1.00+i1.22$	$1.01+i1.25$	$1.37-i1.57$	$1.42-i1.39$
0.172	$1.07+i1.22$	$1.25+i1.18$	$1.17-i1.47$	$1.19-i1.55$
0.255	$1.12+i1.32$	$1.26+i1.26$	$1.04-i1.43$	$1.02-i1.46$
0.335	$1.05+i1.23$	$1.18+i1.27$	$0.98-i1.36$	$0.93-i1.43$
0.400	$1.07+i1.22$	$1.21+i1.08$	$0.89-i1.30$	$0.75-i1.29$

representation not only forms the basis for the present straightforward method but also provides valuable insights into the physical nature of the sound field under concern, and thus possibly leading to better understanding of the interaction between the acoustic liner and the duct sound waves in future study.

C. The influence of the number of the measurement points

As demonstrated in the previous subsections, the unknown impedance can be straightforwardly educed using 16 input data points, nearly as half as that used by the inverse method of Ref. 13. In this subsection, we will further explore the possibility of educing the impedance with a relatively small number of measurement points. This is very important since the reduction of measurement points not only means increasing the measurement efficiency but also reducing the sources of error and thus improving the reliability. For the acoustic phenomenon under consideration, the simplicity of the incident sound wave renders that there are only one or a few dominant propagating modes in the flow duct. In this situation, Prony's method can be very effective and the crucial wave numbers can be precisely extracted but not necessarily using densely distributed data points.

Here, the case shown in Fig. 4 is re-examined. When reducing the measurement points, the input data of the sound

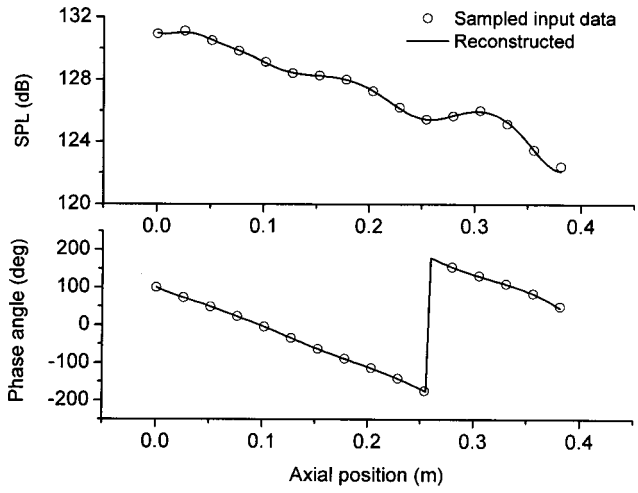

FIG. 6. The upper-wall sound pressure reconstructed from Eq. (7) with μ_n and A_n given in Table II. $M_0=0.255$, $f=1.5$ kHz, and $Z_e=1.10-i0.09$.

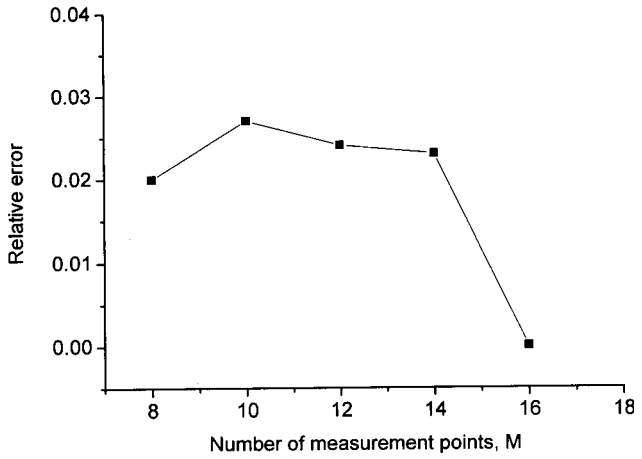

FIG. 7. The influence of the number of the measurement points on the educed impedance. $M_0=0.255$ and $f=1.5$ kHz.

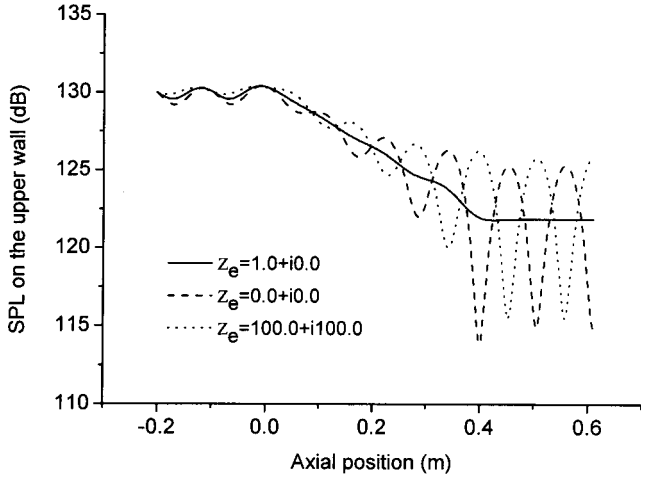

FIG. 8. The variation of the upper-wall sound pressure distribution subjected to different duct exit impedances. $M_0=0.3$ and $f=1.5$ kHz.

pressure are obtained by means of the interpolation method described in Sec. II B. Figure 7 shows that we can use as few as eight measurement points to satisfactorily educe the liner impedance with a relative error of less than 3% defined by $|Z-Z_0|/|Z_0|$, where Z_0 is the result for $M=16$. On the other hand, the reduction of the measurement points is limited by the aliasing effect in Prony's method. In order to avoid the multivalue problem when determining μ_1 from the relation $w_1=e^{-i\mu_1\Delta x}$, the distance interval must meet the requirement

$$\Delta x < \frac{2\pi}{\mathrm{Re}(\mu_1)}. \tag{16}$$

The above relation is derived using the condition that $\mathrm{Re}(\mu_1)$ is always positive. So, if $\mathrm{Re}(\mu_1)$ is approximately taken to be $k/(1+M_0)$ with $M_0=-0.4$ and $f=3400$ Hz given by the cutoff frequency of the rectangular duct, we can estimate that the smallest distance interval is 0.06 mm or, correspondingly, the minimum number of the measurement points is 8. A common principle for choosing M and N would be very difficult and beyond the scope of the present work. However, a numerical survey over the experimental cases in Ref. 13 indicates that the modal expansion can be effectively truncated at $N=2$ or 3 and generally using eight measurement points is sufficient to satisfactorily educe the unknown impedance.

It is further discussed that, as for the issue of reducing the measurement points, the difference between the conventional inverse impedance eduction methods and the present method lies in whether a direct or a parametric fitting is adopted. The direct fitting of the inverse methods is based on a sort of black box approach and thus necessitates dense data points to follow the variation of sound pressure curve as exactly as possible in order to minimize the residual error. By comparison, best using the modal representation of duct sound propagation as prior knowledge, the present straightforward method fits a model equation to the measured data and therefore is able to extract the crucial parameters by means of fewer measurement points.

D. The influence of the duct exit reflective condition

It is a striking feature that the present method is independent of the duct exit reflective condition, as inferred from its basic principle. In contrast, whether the previous infinite waveguide method or inverse methods, they are based on a full duct propagation model, thus requiring the complete avoidance or the accurate determination of the duct exit reflection. However, this is by no means an easily treated problem when there is flow present, as discussed in the Introduction.

The benchmark experiment on the NASA Langley Flow Impedance Test Facility[13] is conducted only on the nearly anechoic duct exit condition. Because of lacking experimental data, the FEM simulation is used to provide the input data for the validation purpose in this subsection. For the case of $M_0=0.3$ and $f=1.5$ kHz, as plotted in Fig. 8, when the duct exit impedance varies within a wide range, the upper-wall sound pressure level exhibits a marked change in its distribution along the duct, showing strong standing wave pattern under the highly reflective exit conditions. Regardless of the changes in Z_e, the present method can educe the unknown impedance in the same accuracy, as indicated by the results in Table IV. Actually, the present straightforward method essentially has no need for the information of the duct exit reflection.

IV. SUMMARY

In this paper, to overcome the limitations of existing methods for impedance measurement under practical flow

TABLE IV. The extracted axial wave numbers and educed impedance when the duct exit impedance has different values.

	Exit impedance Z_e		
Results	$1.0+i0.0$	$0.0+i0.0$	$100.0+i100.0$
μ_n	$19.85-i2.299$ $-34.53+i4.886$	$19.86-i2.300$ $-34.06+i5.166$	$19.87-i2.337$ $-35.19+i5.442$
Z	$1.993+i1.016$	$1.997+i1.013$	$1.989+i0.981$

condition, a new straightforward strategy is developed to educe the impedance of an acoustic liner embedded in a flow duct. Here, the basic principle is that the modal nature of the duct acoustic field renders a summed-exponential representation of the sound pressure measured on the duct wall; thus, the characterizing axial wave number can be readily extracted by means of Prony's method, and further the unknown impedance is straightforwardly calculated from the combination of the eigenvalue equation and the dispersion relation. At current stage, an assumption of uniform flow remains made but it is reasonable for most of the practical applications.

The present method is simple but remarkably has the following advantages.

(1) Being a straightforward method, it ultimately avoids the various problems of initial guess dependence and low or even wrong convergence that are inherent to the inverse methods.
(2) Except for the algebraic manipulation of the dispersion relation and the eigenvalue equation, it needs neither the complete solution of a duct propagation model nor any iteration computations; thus is numerically very efficient.
(3) Based on the parametric rather than the direct fitting approach, it shows the possibility of educing the liner impedance with considerably reduced number of measurement points compared to the inverse impedance eduction methods.
(4) Different from the early attempt of the straightforward impedance eduction or the so-called infinite waveguide method, it considers the realistic acoustic environment containing the multi-mode nonprogressive sound waves in the flow duct, without making any assumption on the modal contents of the acoustic field.
(5) It unexpectedly circumvents the necessity of the duct exit boundary condition that causes trouble to the existing waveguide methods for either using a cumbersome anechoic termination or accuracy degeneration due to the errors in the exit impedance measurement.

It is well anticipated that, having been validated by the well-accepted benchmark experiment, this novel method will demonstrate its potential benefits in the future study and applications.

ACKNOWLEDGMENTS

The authors gratefully acknowledge the financial support for this work from the NSFC (10302003 and 50736007), the FANEDD (200249), the NCET (05-0188), and the NSFC (50736007).

[1]G. Bielak, J. Gallman, R. Kunze, P. Murray, J. Premo, M. Kosanchick, A. Hersh, J. Celano, B. Walker, J. Yu, H. Kwan, S. Chiou, J. Kelly, J. Betts, J. Follet, and R. Thomas, "Advanced nacelle acoustic lining concepts development," NASA Report No. CR-2002-211672, 2002.
[2]R. H. Thomas, M. M. Choudhari, and R. D. Joslin, "Flow and noise control: Review and assessment of future directions," NASA Report No. TM-2002-211631, 2002.
[3]X. Jing, X. Sun, J. Wu, and K. Meng, "Effect of grazing flow on the acoustic impedance of an orifice," AIAA J. **39**, 1478–1484 (2001).
[4]P. D. Dean, "An in situ method of wall acoustic impedance measurement in flow ducts," J. Sound Vib. **34**, 97–130 (1974).
[5]W. R. Watson, "A method for determining acoustic-liner admittance in a rectangular duct with grazing flow from experimental data," NASA Report No. TP-2310, 1984.
[6]W. R. Watson, "A new method for determining acoustic-liner admittance in ducts with sheared flow in two cross-sectional directions," NASA Report No. TP-2518, 1985.
[7]W. R. Watson, M. G. Jones, and T. L. Parrott, "Validation of an impedance eduction method in flow," AIAA Paper No. 98-2279 (1998).
[8]W. R. Watson, M. G. Jones, S. E. Tanner, and T. L. Parrott, "A finite element propagation model for extracting normal incidence impedance in nonprogressive acoustic wave fields," J. Comput. Phys. **125**, 177–186 (1996).
[9]W. R. Watson, M. B. Tracy, M. G. Jones, and T. L. Parrott, "Impedance eduction in the presence of shear flow," AIAA Paper No. 2001-2263 (2001).
[10]T. Elnady and H. Bodén, "An inverse analytical method for extracting liner impedance from pressure measurements," AIAA Paper No. 2004-2836 (2004).
[11]Y. Aurégan, M. Leroux, and V. Pagneux, "Measurement of liner impedance with flow by an inverse method," AIAA Paper No. 2004-2838 (2004).
[12]A. A. Syed, J. Yu, H. W. Kwan, and E. Chien, "The steady flow resistance of perforated sheet materials in high speed grazing flows," NASA Report No. CR-2002-211749 (2002).
[13]M. G. Jones, W. R. Watson, and T. L. Parrot, "Benchmark data for evaluation of aeroacoustic propagation codes with grazing flow," AIAA Paper No. 2005-2853 (2005).
[14]D. L. Armstrong, R. J. Beckemeyer, and R. F. Olsen, "Impedance measurements of acoustic duct liners with grazing flow," 87th Meeting of the Acoustical Society of America, New York, NY, 1974.
[15]K. Naishadham and X. P. Lin, "Application of spectral domain Prony's method to the FDTD analysis of planar microstrip circuits," IEEE Trans. Microwave Theory Tech. **42**, 2391–2398 (1994).
[16]C. J. Wisse, D. M. J. Smeulders, M. E. H. van Dongen, and G. Chao, "Guided wave modes in porous cylinders: Experimental results," J. Acoust. Soc. Am. **113**, pp. 890–895 (2002).
[17]M. K. Myers, "On the acoustic boundary condition in the presence of flow," J. Sound Vib. **71**, 429–434 (1980).
[18]S. Braun and Y. M. Ram, "Determination of structural modes via the Prony model: System order and noise induced poles," J. Acoust. Soc. Am. **81**, 1447–1459 (1987).
[19]W. Eversman, "The boundary condition at an impedance wall in a non-uniform duct with potential mean flow," J. Sound Vib. **246**, 63–69 (2001).
[20]W. Eversman, "Computation of axial and transverse wave numbers for uniform two-dimensional ducts with flow using a numerical integration scheme," J. Sound Vib. **41**, 252–255 (1975).
[21]X. Sun, L. Du, and V. Yang, "A homotopy method for determining the eigenvalues of locally or non-locally reacting acoustic liners in flow ducts," J. Sound Vib. **303**, 277–286 (2007).
[22]S. Ivansson and I. Karasalo, "Computation of modal wavenumber using an adaptive winding-number integral method with error control," J. Sound Vib. **161**, 173–180 (1993).

Active cancellation of occlusion: An electronic vent for hearing aids and hearing protectors

Jorge Mejia,[a] Harvey Dillon, and Michael Fisher
National Acoustic Laboratories and CRC Hear Pty Ltd., 126 Greville Street, Chatswood New South Wales 2067, Australia

(Received 13 September 2007; revised 4 February 2008; accepted 17 March 2008)

The occlusion effect is commonly described as an unnatural and mostly annoying quality of the voice of a person wearing hearing aids or hearing protectors. As a result, it is often reported by hearing aid users as a deterrent to wearing hearing aids. This paper presents an investigation into active occlusion cancellation. Measured transducer responses combined with models of an active feedback scheme are first examined in order to predict the effectiveness of occlusion reduction. The simulations predict 18 dB of occlusion reduction in completely blocked ear canals. Simulations incorporating a 1 mm vent (providing passive occlusion reduction) predict a combined active and passive occlusion reduction of 20 dB. A prototype occlusion canceling system was constructed. Averaged across 12 listeners with normal hearing, it provided 15 dB of occlusion reduction. Ten of the subjects reported a more natural own voice quality and an appreciable increase in comfort with the cancellation active, and 11 out of the 12 preferred the active system over the passive system.
 [DOI: 10.1121/1.2908279]

PACS number(s): 43.50.Hg, 43.60.Ac [BSF] Pages: 235–240

I. INTRODUCTION

In completely blocked or partially blocked ears, one's own voice is perceived as echoing or hollow, and hence in most cases, subjectively rated as annoying and unnatural. This is the result of own voice sound level amplification at predominantly low frequencies, arising from bone transmission to the ear canal [Carle *et al.* (2002); Pirzanski (1998); Mueller (1996); and Mackenzie *et al.* (1989)]. This phenomenon is referred to as "the occlusion effect." To solve this problem, hearing aid providers may attempt to fit adequately vented ear-molds. The mean increase in sound pressure level (SPL) for blocked (occluded) and vented ears is shown in Fig. 1 [May and Dillon (1992)]. This figure indicates that vents of 3.5 mm in diameter or larger are necessary so that most of the sound vibration escapes through the relatively lower impedance posed by the vent path. Unfortunately, hearing aid amplified sounds also leak out through the vent path, potentially resulting in positive feedback-induced oscillation [MacKenzie *et al.* (1989); Dillon (2001)]. Current commercial hearing aids fitted with feedback management techniques address this problem by limiting the hearing aid gain or by using feedback path cancellation techniques. In many cases, however, hearing aids are still not able to provide adequate amplification to the hearing aid wearer [Dillon (2001)]. A second solution consists of a deep ear-mold insertion into the bony part of the ear canal. The aim is to stop the soft tissue from radiating sound vibrations into the ear canal. However, this latter solution tends to produce discomfort and/or irritation inside the ear canal walls. In addition, deep ear mold insertions are not always possible due to the small sizes of some ear canals. Prior to the introduction of open-fitting hearing aids incorporating feedback path cancellation, 28% of hearing aid wearers were reported to not like the quality of their own voice while wearing hearing aids [Dillon *et al.* (1999)]. Open-fitting hearing aids have presumably improved this situation, but anecdotal information indicates that a considerable problem remains in simultaneously avoiding occlusion and avoiding feedback oscillation, while simultaneously achieving an optimal high-frequency gain in the hearing aid.

This article investigates the principles behind an acoustic active feedback cancellation strategy initially proposed by Olson (1961), and recently adapted to, and optimized for, hearing aids by Mejia *et al.* (2004). This occlusion management strategy aims to reduce the level of own voice amplification in minimally vented devices, thus avoiding feedback oscillation, and at the same time allowing optimally high-frequency gain in hearing aids. In order to examine the scheme, in a first experiment, the effectiveness of occlusion reduction is predicted by combining mathematical models based on feedback cancellation theory with transducer measures in the Zwislocki ear simulator. In addition, potential benefits such as active vent effect cancellation are also examined. A second experiment examines the benefits and limitations of an active occlusion reduction strategy. In order to do so, 12 normal hearing listeners were fitted with a hearing aid prototype, which further included an active occlusion reduction system, thus the objective measures of occlusion reduction and subjective responses are also presented in this document.

II. EXPERIMENT 1: ACTIVE OCCLUSION REDUCTION MODEL

A. Method

The aim of this first experiment was to investigate the theoretical sound level reduction produced by an active oc-

[a]Electronic mail: jorge.mejia@nal.gov.au

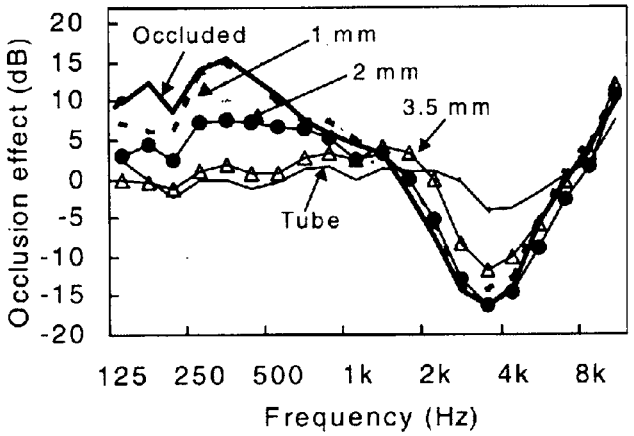

FIG. 1. The mean increase in SPL (relative to no ear mold) in the ear canal for ten subjects, as they talked while wearing ear molds with vents of different sizes [May and Dillon (1992)].

clusion cancellation device, based on a configuration suited for an unvented in-the-ear (ITE) hearing aid, as illustrated in Fig. 2. The figure depicts the external microphone, hearing aid amplifier H, precompensation filter C, feedback loop filters A and B, receiver and internal microphone, and the tubes that couple them to the ear canal. The temporal bone is illustrated in very close proximity to the bony portion of the ear canal, whereas cartilaginous tissue is shown to transmit vibrations from the mandible to the outer portion canal wall.

A transducer transfer response measure T from the receiver input to internal microphone output is shown in Fig. 3, where the ear shell was acoustically coupled to a Zwislocki ear simulator. The receiver was driven with a voltage-controlled voltage source, and the amplitude and phase response of the transducer arrangement were measured with a two channel network signal analyzer (Standford Research System model SR780). The electrical input applied to the receiver R generated 80 dB SPL at 1 kHz inside the ear

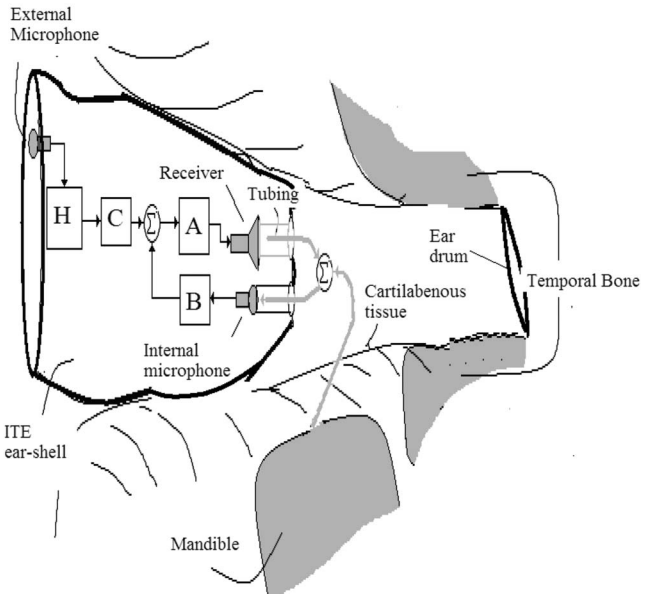

FIG. 2. Illustration of the active occlusion canceling system incorporated in an un-vented ITE hearing aid.

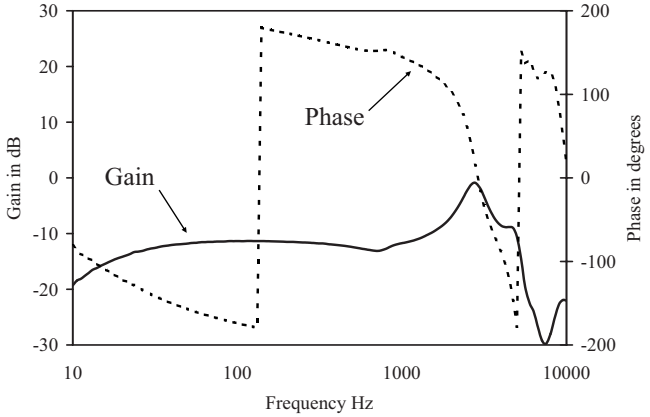

FIG. 3. Transducer transfer response, gain (faded line), and phase (solid line) measures recorded in the Zwislocki coupler.

simulator. A frequency sweep started at 10 Hz and stepped up every 1/12 octave band, with a stop frequency of 10 000 Hz.

B. Active occlusion cancellation models

The predicted effect of this feedback loop on bone-conducted sound pressure in the ear canal is shown in Eq. (1). The equations presented here were derived from well known principle of feedback control theory [Hitay (1999); Benjamin (1982)].

$$E = \frac{1}{1 + |TAB|\cos(\theta^\circ)}, \tag{1}$$

where for a given frequency, E is the effective sound pressure reduction inside the ear canal, T is the transducer gain response from the receiver input to the internal microphone output, which is affected by the ear canal and middle-ear impedance, A is the gain in the forward path within the loop, B is the gain in the feedback path within the loop, and θ is the phase of the open loop

The feedback loop will reduce the signal and sound levels that enter the loop at any point. As a result, it will reduce the level of hearing aid amplified sounds. However, this effect can be corrected by a precompensation filter. The combination of ideal precompensation denoted by C as shown in Eq. (2) yields a forward transfer response F, from the input of block C to the ear canal, as shown in Eq. (3).

$$C = \frac{1}{A}[1 + |TAB|\cos(\theta)], \tag{2}$$

$$F = \frac{CA}{1 + |TAB|\cos(\theta)} R = R. \tag{3}$$

The ideal Eq. (3) yields a theoretically transparent forward response F, whereby the total response is equal to the receiver response R as shown in Eq. (3). The predicted real-ear aided gain is therefore as shown in Eq. (4),

$$G = M_{\text{ext}} \cdot H \cdot R, \tag{4}$$

where for a given frequency H is the hearing aid amplifier gain, M_{ext} is the *in situ* response of the external microphone,

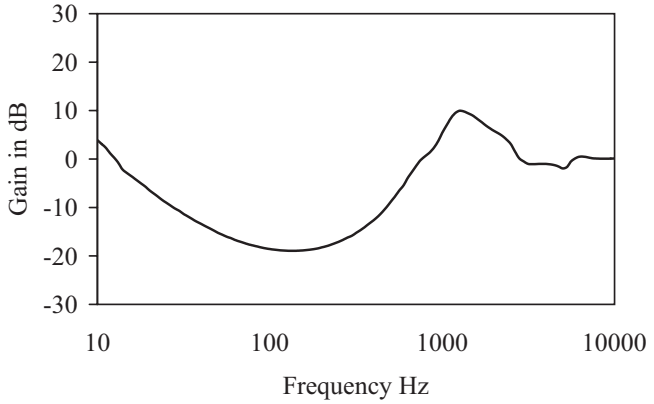

FIG. 4. Predicted effective sound pressure reduction in the ear canal $|E|$, derived from Eq. (3).

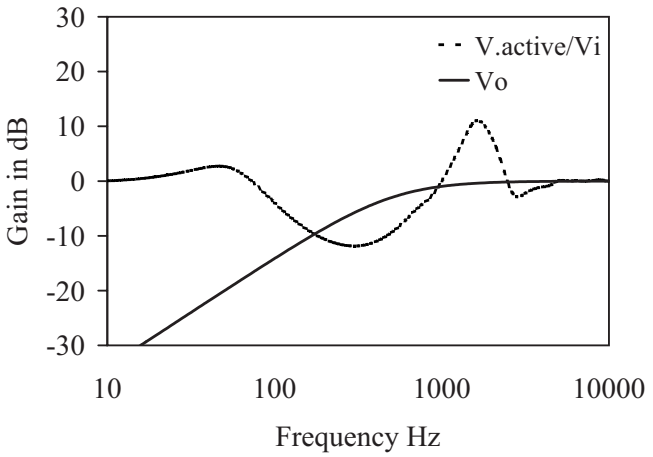

FIG. 5. Active occlusion reduction $|V_{active}|/|V_i|$ (solid line) with corresponding simulated vent high-pass filtering effect $|V_0|$ (faded line).

and R is the receiver response in the ear canal. A second interesting property relates to vented devices. Adding a vent to an ear mold produces two acoustic effects. First, low-frequency sounds in the ear canal escape through the low impedance posed by the vent path, producing a high-pass filtering V_0 of the amplified sound pressure within the ear canal. Second, low-frequency sounds enter the ear canal through the vent, producing a low-pass transmission path, denoted as V_i. With loop active, the predicted effective inward vent response V_{active} is shown in Eq. (5),

$$V_{active} = \frac{V_i}{1 + |TABV_0|\cos(\theta^\circ)}. \quad (5)$$

This inward-transmission vent response can then be combined with the hearing aid amplified path to calculate the total real-ear aided gain, as shown in Eq. (6),

$$G_{vented} = \frac{V_i + M_{ext}HCARV_0}{1 + |TABV_0|\cos(\theta^\circ)}. \quad (6)$$

For the precompensation response shown in Eq. (2), this reduces to

$$G_{vented} = \frac{V_i}{1 + |TAB|\cos(\theta^\circ)} + M_{ext}HRV_0. \quad (7)$$

That is, the level of the vent-transmitted sound in Eq. (7) (shown in the first term) is less compared to the level of the amplified sound (shown in the second term) than would be the case for a conventional hearing aid without occlusion canceling. Cascaded quadratic filters A and B were combined with the measured transducer responses T and R in order to predict feedback loop responses following the mathematical equations presented earlier. Then, an optimally cascaded quadric filter design was produced but adjusting filters A and B with the goal of achieving maximum occlusion reduction while maintaining stability around the negative feedback loop. Similarly, the precompensation filter C was optimized to produce a transparent predicted forward response F.

C. Results and discussions

1. Sealed ear-shell fittings

The predicted occlusion reduction for the completely sealed ear shell is shown in Fig. 4, following Eq. (1). For this simulation, the occlusion reduction is predicted to be −18 dB at 200 Hz, and to extend over a range of low frequencies, including the frequency range in which the fundamental frequencies and first formant frequencies of closed vowels usually lie (from 80 to 400 Hz).

In contrast to the occlusion reduction achieved in the low frequencies, amplification is observed at very low and high frequencies, in the regions of 10 Hz and 1.3 kHz, respectively. This amplification occurs because the phase shift around the loop causes positive feedback to occur at these frequencies. A greater degree of occlusion reduction could be achieved by increasing the gain at any point within the loop. However, significantly increased gain will eventually produce an instability (i.e., oscillation), in one or both of the 10 Hz or 1.3 kHz regions.

Fortunately, although occlusion reduction appears to be achievable over only a restricted range of frequencies, the range achieved is well matched to the range of frequencies over which occlusion occurs, as shown by comparing Fig. 4 to the occluded response in Fig. 1. Furthermore, across this frequency range, the degree of occlusion reduction achievable is well matched to the degree of occlusion that typically occurs in unvented hearing aids.

The predicted ear-simulator aided response following Eq. (4) suggests that it is possible to produce occlusion cancellation without adversely affecting the ear-simulator aided response. However, the real filters needed to generate the frequency responses idealized in Eqs. (1) and (2) are typically extremely complex to formulate and implement. Fortunately, Mejia *et al.*, (2004) proposed a simplified and practical closed loop and precompensating biquadratic filter structures that produces an aided response that does not significantly differ from that of the natural receiver response shown in Fig. 3(b), while effectively producing adequate closed loop reductions, idealiszd in Fig. 4.

2. Vented ear-mold fittings

Figure 5 shows the predicted reduction in the ear canal SPL caused by a 1 mm vent and by the feedback loop relative to the SPL present for the 1 mm vent. The latter shows less reduction than that indicated in Fig. 4 because of the

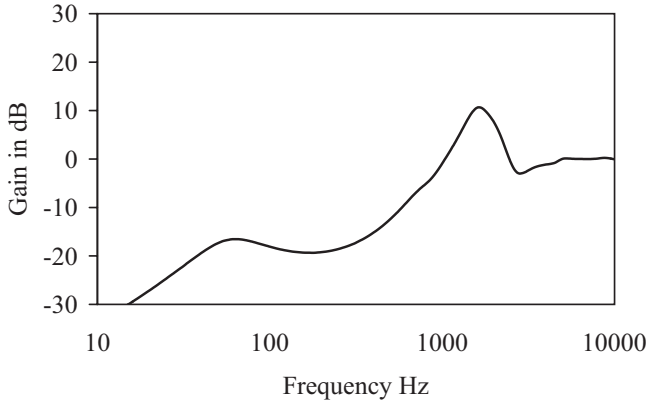

FIG. 6. Predicted occlusion reduction for the combined effects of venting and active occlusion canceling.

effect of the vent on the gain and phase of the open loop responses. The combination of both vent and occlusion canceling produces an occlusion reduction of more than 20 dB at 200 Hz, as shown in Fig. 6. As an analogy, a reduction of 20 dB at 200 Hz is equivalent to that of a substantially larger vent size, greater than or equal to 3.5 mm in diameter, as shown in Fig. 1. However, as in the completely sealed ear canal simulations, there is a significant increase in amplification above 1 kHz and below 80 Hz. Fortunately, the very low-frequency amplification caused by positive feedback is more than offset by the overall high-pass filtering provided by the vent response $|V_0|$, as shown in Fig. 6.

Figure 7(a) shows the predicted ear-simulator gain of the vent-transmitted path and the amplified path with no occlusion canceling. The graph indicates that, for this particular receiver response and flat hearing aid amplifier response, the amount of sound transmitted through the vent dominates the hearing aid response for frequencies below 300 Hz. The combined gain response is shown in Fig. 7(b). This figure also shows the simulated real-ear aided gain with occlusion canceling. As before, there are differences in the high-frequency response arising from limitations in the precompensation filter. Although the low frequency response of the active and passive systems is very similar, there is an important difference in the origin of those responses. Whereas the passive system is vent dominated below 300 Hz, the active system is vent dominated only up to 50 Hz. In many conventional hearing aids, vent dominance extends up to 1000 Hz or more, so the increased range of amplification dominance offered by occlusion cancellation will be even greater in these cases.

The active cancellation of vent-transmitted sounds produces a secondary effect, whereby negative amplification of low-frequency sounds is possible, as illustrated by the ear-simulator aided gains shown in Fig. 8. As the hearing aid gain, block H in Fig. 2, is decreased, the device produces negative gain in the low frequencies, where the vent-transmitted path would otherwise dominate and provide 0 dB gain. This secondary vent-canceling effect will allow directional microphones and noise reduction strategies to operate down to lower frequencies.

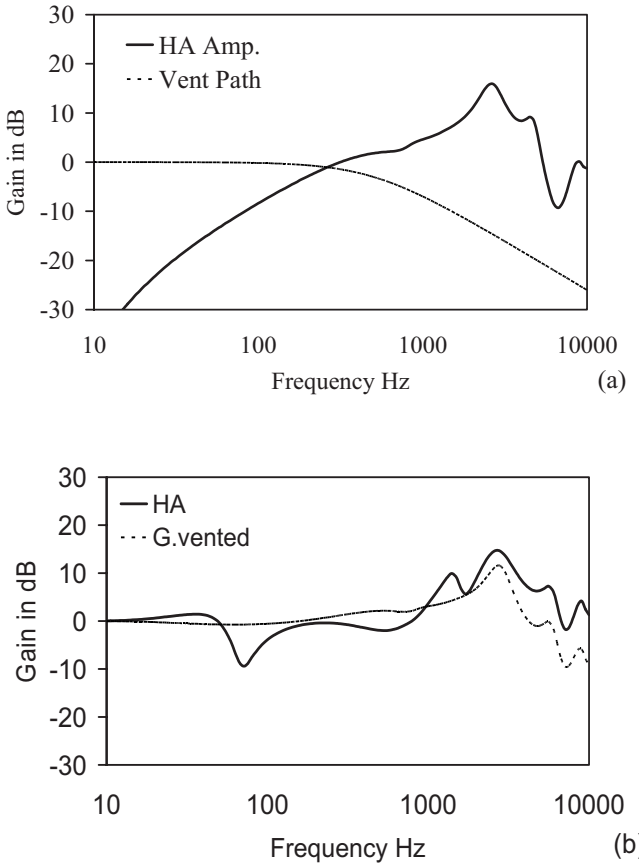

FIG. 7. (a) Ear-simulator gain of the vent-transmitted path (dotted line) and the amplified path (dashed line). (b) Predicted ear-simulator aided gain with occlusion canceling $|G_{\text{vented}}|$ (solid line) and the combined vent-transmitted and amplified path for a conventional hearing aid (shaded line).

III. EXPERIMENT 2: ANALOG ACTIVE OCCLUSION CANCELER

This experiment investigated the actual performance of a prototype active occlusion cancellation system.

A. Method

12 normal hearing subjects were bilaterally fitted with specially designed ITE unvented ear shells. All subjects had anatomically normal ear canals. The ITE shells were constructed with identical external and internal microphones and

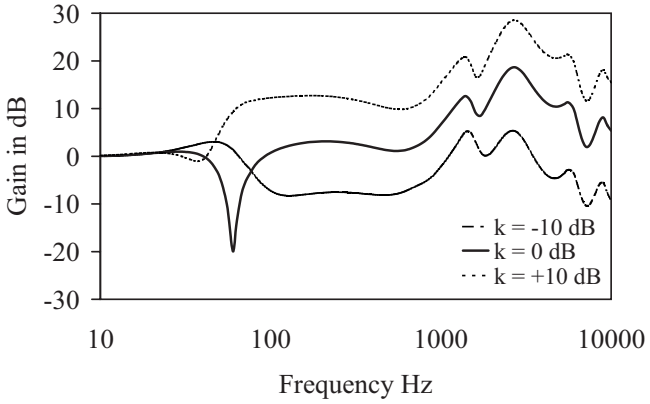

FIG. 8. Predicted ear-simulator aided gain, for three levels of amplification in block H.

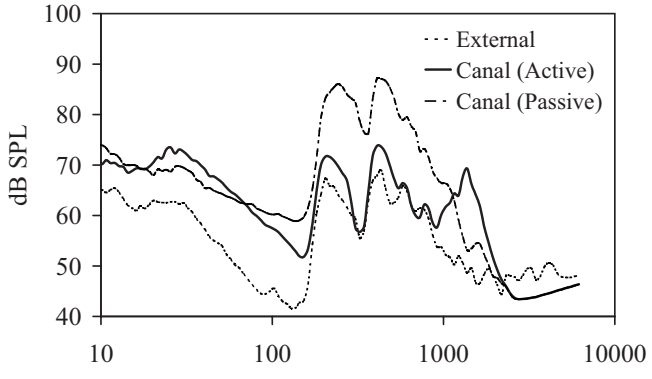

FIG. 9. Sound pressure level measured in the occluded ear canal, recorded during the active and passive modes of operation. The external pressure was measured immediately outside the entrance of the ear canal in the blocked ear.

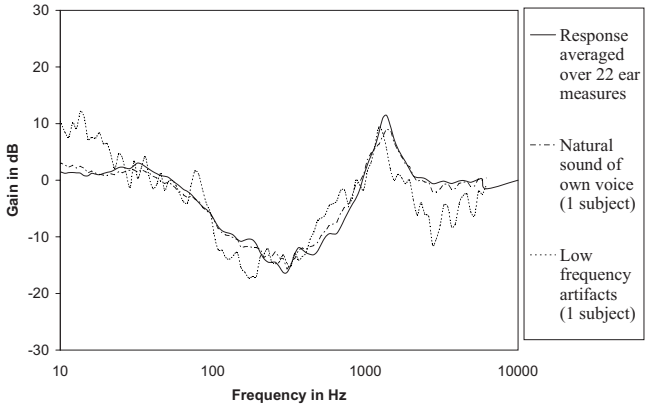

FIG. 10. Measure occlusion reduction responses including the averaged reductions based on sample populations of 22 ears (solid line), the occlusion reduction from one subject reporting a more natural perception of own-voice sound quality (dot-dash line), and the occlusion reduction recorded from a subject reporting adverse sensations during jaw movements (dotted line).

a low-power receiver. The receiver and internal microphone were coupled to the ear canal by a tube and wax protection device. The transducers were connected with a 1 m cable to external electronic circuitry. The electronic circuitry comprised of a hearing aid amplifier and a custom-designed analog active occlusion canceling system. The circuit could be switched between active (feedback loop operating) and passive (feedback loop disabled) modes of operation. A volume control and feedback overall gain control were also available. It was also possible to probe the voltage signal from the external and ITE microphone outputs and connect them to a two channel network signal analyzer (Standford Research System model SR780) which was programmed to perform 1/12 octave linear spectral averaging of the recorded signals. The third microphone was directly connected to a sound level meter and positioned directly in front of the participant.

During the sound recordings, each subject was asked to read an arbitrary sentence paragraph at a normal vocal effort which resulted in a 55–70 dB SPL, recorded approximately 30 cm away from the mouth, for at least 5 min. Both external and ITE canal microphones were simultaneously recorded. Throughout the recordings, the hearing aid amplifier was muted.

Following the recording, the subjects were asked about their subjective reaction to the sound of their own voices. In order to do so, the subjects were allow to freely switch between the active and passive modes of operation. Subjects were not aware of the mode of operation corresponding to a given location of the control switch. Throughout the subjective assessments, the hearing aid amplifier was adjusted to yield 0 dB ear-simulator gain.

The measured and subjective responses were digitally stored on the hard disk of a Toshiba Tecra S1 computer. All tests were conducted in a test booth. Ethical aspects for the experiment were approved by the Australian Hearing Ethics Human Research Ethics Committee.

B. Results and discussion

1. Objective measures in real ears

Figure 9 shows the 1/12-octave long-term sound pressure level recorded inside the ear canal of a subject, as illustrated in Fig. 2. The occluded ear pressure refers to the sound level recorded inside the blocked ear canal in the passive mode of operation. The graph shows the increase in pressure levels of up to 18 dB in the low frequencies relative to the SPL present immediately outside the ear, caused by the occlusion effect. This result of the occlusion effect is comparable to the results reported in the literature, as shown in Fig. 1. The residual ear pressure refers to the sound level recorded inside the blocked ear canal in the active mode of operation. The graph shows lower levels of pressure in the low frequencies caused by the active occlusion cancellation. The open ear pressure refers to a free field measurement from a microphone located just outside the blocked ear canal (i.e., ITE faceplate microphone).

The effective occlusion reduction based on the difference between the passive and active sound level measures, averaged across 22 ears, is shown in Fig. 10 (solid line). The average reduction recorded at 300 Hz is 15 dB, with 9 dB amplification at 1.3 kHz, and 3 dB amplification at 10 Hz. The very high frequencies were not affected by the occlusion canceling system, producing on average of 0 dB of amplification at frequencies above 2 kHz.

2. Subjective ratings of own voice

Ten out of 12 subjects indicated that their own voices were perceived as more natural or gave a more open sound sensation in the active mode of operation and preferred the active mode. A typical response is shown in Fig. 10 (dot-dash line). One subject described the sounds as unnatural or electronically filtered in both conditions but more so with active occlusion cancellation. This subject nonetheless preferred the active mode of operation and made this choice on the basis of the lower, more comfortable own voice sound levels in the active system. The final subject preferred the passive mode of operation. The measured response, as shown in Fig. 10 (dot line), indicates excessive amplification in the low frequencies, consistent with his reported annoyance from moving the jaw. This latter result suggests limitations in the fixed analog design, as the feedback filters were not individualized to limit the sound amplifications in the low frequencies. In future hearing aid implementations, individual-

ized transducer responses could be combined with closed loop predictions to generate a set of feedback filters yielding maximum occlusion reduction with minimum amplification of very low and high frequencies, thus reducing the likelihood of artifacts that may result from either jaw movements or instability of the closed loop.

IV. CONCLUSIONS

In conclusion, the experiments present here demonstrated that the active occlusion cancellation strategy reduces the bulk of own voice amplification due to occlusion. It was also shown that the simulation of the active cancellation combined with 1 mm vented ear-shell fittings predicted an active vent effect, yielding more occlusion reduction than either the passive vent or the active occlusion reduction system alone. Normal hearing subjects indicated a noticeable reduction of blocked ear effects, without needing a large opening in the hearing aid.

In addition, the occlusion canceling system greatly reduces the level of sounds traveling into the ear via any vent or leakage paths. This canceling enables the sounds received by the hearing aid wearer to be electronically controlled over a much lower frequency range than is currently possible in hearing aids, where vent-transmitted sounds would otherwise dominate. Greater electronic control of sound should increase the effectiveness of directional microphones and adaptive noise suppression systems by widening the frequency range over which they operate.

ACKNOWLEDGMENTS

This paper is dedicated to John Coelho, who worked on the early stages of this project, until his untimely death in 2001.

Benjamin, C. K. (**1982**). *Automatic Control System: Fourth Edition* (Prentice-Hall, Englewoods Cliffs).

Carle, R., Laugesen, S., and Nielsen, C. (**2002**). "Observations on the relations among occlusion effect, compliance, and vent size," J. Am. Acad. Audiol **13**, 25–37.

Dillon, H. (**2001**). *Hearing Aids* (Boomerang, Sydney).

Dillon, H., Birtles, G., and Lovegrove, R. (**1999**). "Measuring the outcomes of a national rehabilitation program: Normative data for client oriented scale of improvement (COSI) and the hearing aid user's questionnaire (HAUQ)," J. Am. Acad. Audiol **10**, 67–79.

Hitay, O. (**1999**). *Introduction to Feedback Control Theory* (CRC, Boca Raton, PL).

MacKenzie, K., Browning, G. G., and McClymont, L. G. (**1989**). "Relationship between earmould venting, comfort and feedback," Br. J. Audiol. **23**, 335–337.

May, A. E., and Dillon, H. (**1992**). "A comparison of physical measurements of the hearing aid occlusion effect with subjective reports," The Australian Journal of Audiology, Supplement 5, May 12.

Mejia, J., Dillon, H., and Fisher, M. (**2006**). "Acoustically transparent occlusion reduction system and method," WIPO Pub. No. WO/2006/037156 A1, April.

Mueller, H. G., Bright, K. E., and Northern, J. L. (**1996**). "Studies of the hearing aid occlusion effect," Semin. Hear. **17**, 21–32.

Olson, H. F. (**1961**). U.S. Patent No. 2,983,790.

Pirzanski, C. Z. (**1998**). "Diminishing the occlusion effect: clinician/manufacturer-related factors." Hear. J. **51**, 66–78.

Model independent control of lightly damped noise/vibration systems

Jing Yuan[a)]
Department of Mechanical Engineering, The Hong Kong Polytechnic University, Hunghom, Kowloon, Hong Kong

(Received 21 March 2007; revised 28 April 2008; accepted 3 May 2008)

Feedforward control is a popular strategy of active noise/vibration control. In well-damped noise/vibration systems, path transfer functions from actuators to sensors can be modeled by finite impulse response (FIR) filters with negligible errors. It is possible to implement noninvasive model independent feedforward control by a recently proposed method called orthogonal adaptation. In lightly damped noise/vibration systems, however, path transfer functions have infinite impulse responses (IIRs) that cause difficulties in design and implementation of broadband feedforward controllers. A major source of difficulties is model error if IIR path transfer functions are approximated by FIR filters. In general, active control performance deteriorates as model error increases. In this study, a new method is proposed to design and implement model independent feedforward controllers for broadband in lightly damped noise/vibration systems. It is shown analytically that the proposed method is able to drive the convergence of a noninvasive model independent feedforward controller to improve broadband control in lightly damped noise/vibration systems. The controller is optimized in the minimum H_2 norm sense. Experiment results are presented to verify the analytical results. © *2008 Acoustical Society of America.*
[DOI: 10.1121/1.2936365]

PACS number(s): 43.50.Ki, 43.40.Vn, 43.40.Tm, 43.50.Gf [KA] Pages: 241–246

I. INTRODUCTION

Feedforward control is a popular strategy of active noise/vibration control[1,2] (ANVC) if the primary source is either available or recoverable as the reference signal. In many ANVC systems, path transfer functions from actuators to sensors are minimum required information. Parameters of a feedforward ANVC may be adaptive to generate destructive interference at sensed locations. The filtered-x least mean squares (FxLMS) algorithm is very popular for such a purpose. Stability of FxLMS depends on the accuracy of secondary path models. A FxLMS system may be unstable if phase errors in the secondary path model exceed 90°.[3–5] Since transfer functions in noise/vibration systems may change due to variation of boundary or environmental conditions, many ANVC systems adopt online modeling to keep path models as accurate as possible. These are called model independent feedforward controllers (MIFCs) for ease of reference.

Noise/vibration systems have different degrees of damping. In this study, a system is considered well damped if its path transfer functions can be modeled by finite impulse response (FIR) filters with negligible errors. Otherwise, the system is considered lightly damped. For well-damped noise/vibration systems, there are many MIFCs in the literature. Most of the available MIFCs require "persistent excitations"[6]—the invasive injection of probing signals[7] to ensure accurate online path modeling. Some researchers propose to avoid the probing signals by controller perturbation.[8–10] A noninvasive MIFC that abandons persistent excitations completely is possible by a method called orthogonal adaptation.[11]

For broadband control in lightly damped noise/vibration systems, it is difficult to implement noninvasive MIFC systems, since most noninvasive MIFC systems use FIR filters to approximate path transfer functions. Mismatches between FIR filters and infinite impulse response (IIR) path transfer functions degrade control performance. Although the performance difference between FIR and IIR models can be made arbitrarily small by increasing FIR filter taps, many researchers still propose ANVC systems with IIR path models or IIR controllers.[12–14] The main reason is to reduce coefficients, which means lower implementation costs, faster convergence rates, and better estimation accuracy. Adaptation of an IIR filter is a nonlinear process with multiple stationary points. There is no guarantee that an adaptive IIR filter will converge to its global optimal.[14] An adaptive ANVC, with FIR or IIR path models, has the same problem of either being model dependent or requiring invasive persistent excitations.

In this study, a modified MIFC system is proposed. It is a stable and noninvasive system for broadband control in lightly damped noise/vibration systems. It is also optimized in the minimum H_2 norm sense. These are significant differences between the modified MIFC and available ANVC systems with either FIR or IIR path models. Experimental results are presented to verify the modified MIFC when it is applied to lightly damped noise/vibration systems.

II. PROBLEM STATEMENT

In a noise/vibration system, the primary and secondary transfer functions are denoted by $P(z)$ and $S(z)$, respectively.

a)Electronic mail: mmjyuan@polyu.edu.hk

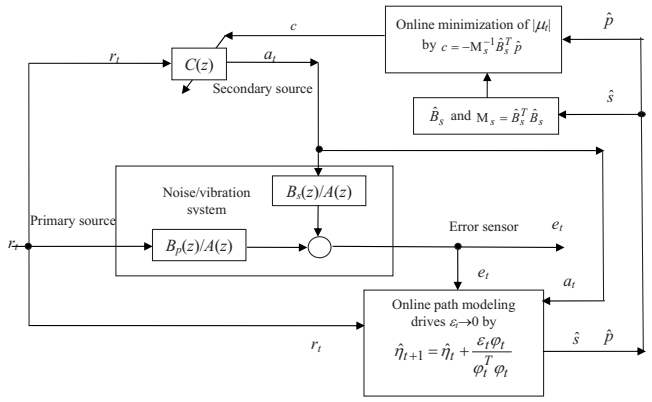

FIG. 1. Block diagram of the modified MIFC system.

If the primary source signal is either available or recoverable as the reference $r(z)$, the actuation signal $a(z)=C(z)r(z)$ may be synthesized by a controller whose transfer function is $C(z)$. The objective is destructive interference of the error signal modeled by

$$e(z)=P(z)r(z)+S(z)a(z)=[P(z)+S(z)C(z)]r(z). \quad (1)$$

In a lightly damped noise/vibration system, path models, $P(z)=B_p(z)/A(z)$ and $S(z)=B_s(z)/A(z)$ are IIR filters with a common denominator polynomial $A(z)$.[15] Equation (1) is equivalent to a discrete-time regression

$$e_t=-\sum_{k=1}^{m_r}\alpha_k e_{t-k}+\sum_{k=0}^{m}p_k r_{t-k}+\sum_{k=0}^{m}s_k a_{t-k}, \quad (2)$$

where $\{\alpha_k\}$, $\{p_k\}$, and $\{s_k\}$ are coefficients of polynomials $A(z)$, $B_p(z)$, and $B_s(z)$. Introducing coefficient vector $\eta^T=[-\alpha^T,p^T,s^T]$ and regression vector $\varphi_t=[e_{t-1},e_{t-2},\ldots,e_{t-m_r},r_t,r_{t-1},\ldots,r_{t-m},a_t,a_{t-1},\ldots,a_{t-m}]^T$, one may express Eq. (2) as

$$e_t=\eta^T\varphi_t=-\alpha^T x_t+p^T\upsilon_t+s^T\phi_t, \quad (3)$$

where $x_t=[e_{t-1},e_{t-2},\ldots,e_{t-m_r}]^T$, $\upsilon_t=[r_t,r_{t-1},\ldots,r_{t-m}]^T$, and $\phi_t=[a_t,a_{t-1},\ldots,a_{t-m}]^T$. Since the regression vector φ_t and its subvector ϕ_t contain actuation signal a_t, different controllers are designed to regulate ϕ_t and minimize $|e_t|=|\eta^T\varphi_t|$.

In this study, a noninvasive MIFC is proposed for broadband control in lightly damped noise/vibration systems. It is described by the block diagram in Fig. 1. A recursive least squares (RLS) algorithm is applied for online path modeling. Estimates of $A(z)$, $B_p(z)$, and $B_s(z)$ are denoted by $\hat{A}(z)$, $\hat{B}_p(z)$, and $\hat{B}_s(z)$, respectively. The estimated parameter vector is denoted by $\hat{\eta}^T=[\hat{\alpha}^T,\hat{p}^T,\hat{s}]$, where $\hat{\alpha}$, $\hat{p}$, and $\hat{s}$ consist of coefficients of $\hat{A}(z)$, $\hat{B}_p(z)$, and $\hat{B}_s(z)$, respectively. Estimation residue is calculated as

$$\varepsilon_t=e_t-\hat{\eta}^T\varphi_t=\Delta\eta^T\varphi_t=-\Delta\alpha^T x_t+\Delta p^T\upsilon_t+\Delta s^T\phi_t, \quad (4)$$

where $\Delta\eta=\eta-\hat{\eta}$, $\Delta\alpha=\alpha-\hat{\alpha}$, $\Delta p=p-\hat{p}$, and $\Delta s=s-\hat{s}$. The objective of online modeling is to drive $\varepsilon_t\to 0$. This task is represented by a block below the noise/vibration system in Fig. 1, with inputs r_t, a_t, and e_t for construction of φ_t.

Part of the online estimates, $\hat{p}$ and $\hat{s}$, are used in Fig. 1 to solve optimal controller $C(z)$ and minimize $\|\hat{B}_p(z)+\hat{B}_s(z)C(z)\|_2$. In broadband noise control, power spectral density of $r(z)$ is nearly constant in the entire frequency range. Minimizing $\|\hat{B}_p(z)+\hat{B}_s(z)C(z)\|_2$ is equivalent to minimizing magnitude of

$$\mu_t=\sum_{k=0}^{m}\hat{p}_k r_{t-k}+\sum_{k=0}^{m}\hat{s}_k a_{t-k}=\hat{p}^T\upsilon_t+\hat{s}^T\phi_t. \quad (5)$$

One may study the joint effects of the two online tasks by using $\mu_t=\hat{p}^T\upsilon_t+\hat{s}^T\phi_t$, Eqs. (3) and (4) to derive

$$|e_t+\hat{\alpha}^T x_t|=|\varepsilon_t+\mu_t|\leqslant|\varepsilon_t|+|\mu_t|. \quad (6)$$

In the rest of this paper, it will be shown that (i) the RLS algorithm will drive the convergence of $\varepsilon_t\to 0$, and the online optimization task will force $\mu_t\approx 0$; (ii) $e_t+\hat{\alpha}^T x_t\approx 0$ is implied by (i) and is equivalent to $\hat{A}(z)e(z)\approx 0$; (iii) in broadband control, $\varepsilon_t\to 0$ implies $\hat{A}(z)\to A(z)$ and therefore $\hat{A}(z)e(z)\approx 0$ will be equivalent to $A(z)e_t\approx 0$; (iv) the modified MIFC is noninvasive and optimal and it minimizes $\|\hat{B}_p(z)+\hat{B}_s(z)C(z)\|_2$ without persistent excitations.

III. ONLINE MODELING

A simple RLS algorithm is applied to drive $\varepsilon_t=\Delta\eta^T\varphi_t\to 0$ in this section. The estimated parameter vector is updated by

$$\hat{\eta}_{t+1}=\hat{\eta}_t+\frac{\varepsilon_t\varphi_t}{\varphi_t^T\varphi_t}. \quad (7)$$

A positive definite function $V(t)=\Delta\eta_t^T\Delta\eta_t$ is introduced here to analyze the convergence of Eq. (7). Similar to identity $a^2-b^2=(a-b)(a+b)$, it can be shown that

$$V(t+1)-V(t)=(\Delta\eta_{t+1}-\Delta\eta_t)^T(\Delta\eta_{t+1}+\Delta\eta_t). \quad (8)$$

With the help of Eq. (7) and $\Delta\eta=\eta-\hat{\eta}$, one can see that

$$\Delta\eta_{t+1}-\Delta\eta_t=\hat{\eta}_t-\hat{\eta}_{t+1}=\frac{-\varepsilon_t\varphi_t}{\varphi_t^T\varphi_t} \quad (9)$$

and

$$\Delta\eta_{t+1}+\Delta\eta_t=2\eta-\hat{\eta}_t-\hat{\eta}_{t+1}=2\Delta\eta_t-\frac{\varepsilon_t\varphi_t}{\varphi_t^T\varphi_t}. \quad (10)$$

By substituting Eqs. (9) and (10) into Eq. (8), one can derive

$$V(t+1)-V(\mathrm{t})=\frac{-\varepsilon_t\varphi_t^T}{\varphi_t^T\varphi_t}\left(2\Delta\eta_t-\frac{\varepsilon_t\varphi_t}{\varphi_t^T\varphi_t}\right). \quad (11)$$

Since $\varepsilon_t\varphi_t^T\Delta\eta_t=\varepsilon_t^2$, the above equation is equivalent to

$$V(t+1)-V(t)=-\frac{\varepsilon_t^2}{\phi^T\phi}\leqslant 0. \quad (12)$$

This indicates monotonous decrease of $V(t)=\Delta\eta_t^T\Delta\eta_t$ until $\varepsilon_t\to 0$.

IV. ONLINE OPTIMIZATION

If $\hat{B}_s(z)$ is minimum phase, an IIR filter $C(z)=-\hat{B}_s^{-1}(z)\hat{B}_p(z)$ will achieve $\mu_t=0$. In case $\hat{B}_s(z)$ is nonmini-

mum phase, $\hat{B}_s^{-1}(z)$ is unstable and a different $C(z)$ must be sought. Although it takes an IIR $C(z)$ to minimize $\|\hat{B}_p(z)+\hat{B}_s(z)C(z)\|_2$ to the best extent,[11] a FIR $C(z)$ is sought here to minimize

$$\|\hat{B}_p(z)+\hat{B}_s(z)C(z)\|_2=\|\hat{B}(z)\|_2 \tag{13}$$

while reducing online computations.

Let n denote the degree of $C(z)$. The impulse response of Eq. (13) is given by

$$\hat{b}=\begin{bmatrix}\hat{b}_0\\ \hat{b}_1\\ \vdots\\ \\ \vdots\\ \hat{b}_{m+n}\end{bmatrix}=\begin{bmatrix}\hat{p}_0\\ \hat{p}_1\\ \vdots\\ \hat{p}_m\end{bmatrix}+\begin{bmatrix}\hat{s}_0 & & & \\ \hat{s}_1 & \hat{s}_0 & & \\ \vdots & \hat{s}_1 & \ddots & \\ \hat{s}_m & \vdots & \ddots & \hat{s}_0\\ & \hat{s}_m & \vdots & \hat{s}_1\\ & & \ddots & \vdots\\ & & & \hat{s}_m\end{bmatrix}\begin{bmatrix}c_0\\ c_1\\ \vdots\\ c_n\end{bmatrix}$$

$$=\hat{b}_p+\hat{B}_s c, \tag{14}$$

where $\hat{b}=[\hat{b}_0,\ldots,\hat{b}_{m+n}]^T$ and $c=[c_0,\ldots,c_n]^T$ are coefficient vectors of $\hat{B}(z)$ and $C(z)$. Coefficients of $\hat{B}_s(z)$ are used to construct an n-column matrix

$$\hat{B}_s=\begin{bmatrix}\hat{s}_0 & & & \\ \hat{s}_1 & \hat{s}_0 & & \\ \vdots & \hat{s}_1 & \ddots & \\ \hat{s}_m & \vdots & \ddots & \hat{s}_0\\ & \hat{s}_m & \vdots & \hat{s}_1\\ & & \ddots & \vdots\\ & & & \hat{s}_m\end{bmatrix}. \tag{15}$$

The rank of $\hat{B}_s$ is n if $\hat{B}_s(z)\neq 0$, since $\hat{B}_s$ contains an $n\times n$ triangular submatrix.

According to Parserval's theorem, minimizing $\|\hat{b}\|^2$ is equivalent to minimizing Eq. (13). Equation (14) is equivalent to

$$\hat{b}^T\hat{b}=(\hat{p}+\hat{B}_s c)^T(\hat{p}+\hat{B}_s c)$$

$$=\hat{p}^T\hat{p}+\hat{p}^T\hat{B}_s c+c^T\hat{B}_s^T\hat{p}+c^T M_s c, \tag{16}$$

where $M_s=\hat{B}_s^T\hat{B}_s$ is the autocorrelation matrix of $\hat{B}_s(z)$. Let $\zeta=\hat{B}_s^T\hat{p}$, then one can use $c^T\hat{B}_s^T\hat{p}=c^T M_s M_s^{-1}\zeta$ to rewrite Eq. (16) as

$$\hat{b}^T\hat{b}=\hat{p}^T\hat{p}-\zeta^T M_s^{-1}\zeta+(M_s c+\zeta)^T M_s^{-1}(M_s c+\zeta). \tag{17}$$

In Eq. (17), vector c only affects $(M_s c+\zeta)^T M_s^{-1}(M_s c+\zeta)$. Therefore it is possible to force $(M_s c+\zeta)^T M_s^{-1}(M_s c+\zeta)=0$ and minimize $\|\hat{b}\|^2$ by

$$c=-M_s^{-1}\zeta=-M_s^{-1}\hat{B}_s^T\hat{p}. \tag{18}$$

This equation is used to obtain parameters of suboptimal FIR filter $C(z)$ in Fig. 1.

V. PARAMETER CONVERGENCE

With online tasks driving $\varepsilon_t\to 0$ and $\mu_t\approx 0$, one can see $e_t+\hat{\alpha}^T x_t\approx 0$ in Eq. (6). Since $\hat{A}(z)=1+\sum_{k=1}^{m_r}\hat{\alpha}_k z^{-k}$ and $x_t=[e_{t-1},e_{t-2},\ldots,e_{t-m_r}]^T$, it follows that $e_t+\hat{\alpha}^T x_t\approx 0$ is equivalent to $\hat{A}(z)e(z)\approx 0$. However, this does not indicate the minimization of $|e_t|$ until it is proven that $\hat{A}(z)\to A(z)$.

Let $B(z)=B_p(z)+B_s(z)C(z)$, then one can obtain an equivalent expression of Eq. (3) as

$$e_t=-\sum_{k=1}^{m_r}\alpha_k e_{t-k}+\sum_{k=0}^{2m}b_k r_{t-k}, \tag{19}$$

where $\{b_k\}$ are coefficients of $B(z)=B_p(z)+B_s(z)C(z)$. Estimate of $B(z)$ is denoted by $\hat{B}(z)$ and defined in Eq. (13). Similar to the derivation of Eq. (4), one can obtain

$$\varepsilon_t=-\sum_{k=1}^{m_r}\Delta\alpha_k e_{t-k}+\sum_{k=0}^{2m}\Delta b_k r_{t-k}, \tag{20}$$

where $\{\Delta\alpha_k=\alpha_k-\hat{\alpha}_k\}$ and $\{\Delta b_k=b_k-\hat{b}_k\}$ are estimation errors of $A(z)$ and $B(z)$, respectively. In Ref. 6, it is shown that convergence of $\varepsilon_t=\varphi_t^T\Delta\eta\to 0$ implies

$$\begin{bmatrix} e_{t-l} & e_{t-l-1} & \cdots & e_{t-m_r-l+1} & r_{t-l-1} & r_{t-l-2} & \cdots & r_{t-m-n-l}\\ e_{t-l+1} & e_{t-l} & \cdots & e_{t-m_r-l+2} & r_{t-l} & r_{t-l-1} & \cdots & r_{t-m-n-l+1}\\ \vdots & \vdots & \cdots & \vdots & \vdots & \vdots & \cdots & \vdots\\ e_{t-2} & e_{t-3} & \cdots & e_{t-m_r-1} & r_{t-1} & r_{t-2} & \cdots & r_{t-m-n-1}\\ e_{t-1} & e_{t-2} & \cdots & e_{t-m_r} & r_t & r_{t-1} & \cdots & r_{t-m-n}\end{bmatrix}\begin{bmatrix}\Delta\alpha_1\\ \Delta\alpha_2\\ \vdots\\ \Delta\alpha_{m_r}\\ -\Delta b_0\\ -\Delta b_1\\ \vdots\\ -\Delta b_{m+n}\end{bmatrix}\to 0. \tag{21}$$

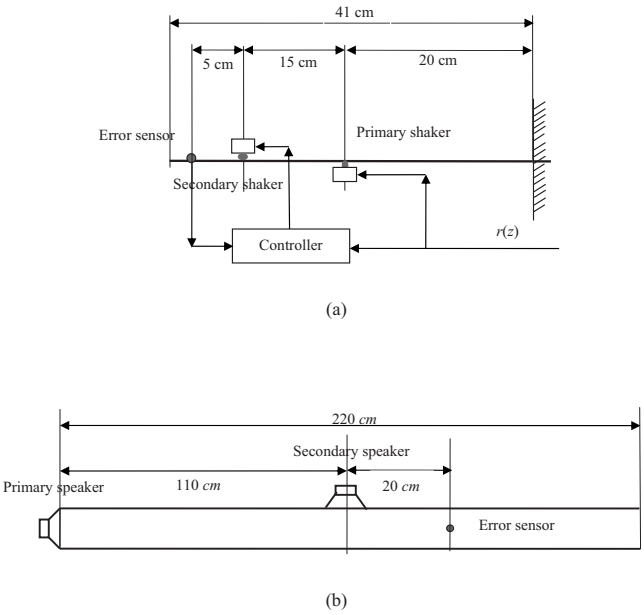

FIG. 2. Experiment setup: (a) top view of vibration system and (b) noise system.

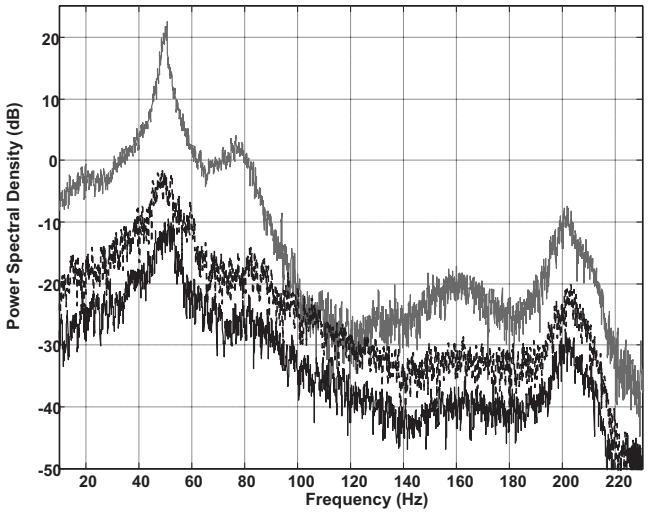

FIG. 3. Normalized PSD of error signal in experiment 1: uncontrolled (gray), controlled by an ordinary MIFC (dashed black), and controlled by the modified MIFC (solid black).

Here $t>l\geqslant m_r+m+n+1$. If r_t contains more than $0.5(m_r+m+n+1)$ frequency components, then the above data matrix is full rank[6] and $\varepsilon_t\rightarrow 0$ implies $\{\Delta\alpha_k\rightarrow 0\}$ and $\{\Delta b_k\rightarrow 0\}$. As a result, $\hat{A}(z)e(z)\approx 0$ converges to $A(z)e(z)\approx 0$ in broadband control operations and stability of $|e_t|$ is ensured by the modified MIFC.

The z-transform domain version of Eq. (19) is $A(z)e(z)=B(z)r(z)$, where $A(z)$ and $B(z)$ are, respectively, the autoregressive and moving-average parts. A feedforward controller can only minimize the moving-average part $\|B(z)\|_2$. After the convergence of $\hat{B}(z)\rightarrow B(z)$, there are infinitely many pairs of $\hat{B}_p(z)$ and $\hat{B}_s(z)$ satisfying $\hat{B}_p(z)+\hat{B}_s(z)C(z)=B(z)$, from which only one pair matches $B_p(z)$ and $B_s(z)$ exactly. When an accurate $\hat{B}_s(z)$ is required to ensure stable adaptation of FxLMS, the only available way to drive $\hat{B}_s(z)\rightarrow B_s(z)$ is persistent excitation in the actuation signal.

A significant feature of the modified MIFC is online optimization instead of FxLMS. Analytically, one may write

$$\|B(z)\|_2=\|\Delta B(z)+\hat{B}_p(z)+\hat{B}_s(z)C(z)\|_2$$
$$\leqslant\|\Delta B(z)\|_2+\|\hat{B}_p(z)+\hat{B}_s(z)C(z)\|_2. \quad (22)$$

Since $\varepsilon_t\rightarrow 0$ implies $\|\Delta B(z)\|_2\rightarrow 0$ and $\mu_t\approx 0$ is the result of minimizing $\|\hat{B}_p(z)+\hat{B}_s(z)C(z)\|_2$, the modified MIFC minimizes $\|B(z)\|_2$ by the joint effects of online tasks. The objective is achieved without persistent excitation.

VI. EXPERIMENTS

In this study, three experiments were conducted to demonstrate advantages of the modified MIFC. The experiment setups are shown in Figs. 2(a) and 2(b), respectively. In the experiments, the controllers were implemented in a dSPACE 1103 board, and the primary source $r(z)$ was a broadband pseudorandom signal. While it is possible to recover $r(z)$ from a measured signal, it would require additional online modeling of feedback path and cancelation of actuation feedback. To simplify programming, $r(z)$ was directly available to the controller in all experiments.

A. A well-damped vibration system

The first experiment was conducted to test an ordinary MIFC in a well-damped vibration system. Major dimensional information is given in Fig. 2(a). Cross-sectional area of the steel beam was 50×1.5 mm^2. The error sensor was a B&K 4382 accelerometer. The system sampling rate was 500 Hz. All signals were low-pass filtered with cutoff frequency of 200 Hz. Both actuators were shakers with shafts connected to the beam and solenoids attached to fixed bases. Damping coefficients of the shakers were different since the shakers were made by different manufacturers. The primary shaker was one with weak damping and the secondary shaker was one with strong damping.

The controllers were turned off first to collect the error signal $e(z)$. Power spectral densities (PSDs) of $e(z)$ and $r(z)$ were computed with the MATLAB command "pmtm( )" and denoted as P_e=pmtm(e) and P_r=pmtm(r), respectively. Here e and r are vectors containing data of $e(z)$ and $r(z)$. The normalize PSD of $e(z)$ is calculated as $P_{ne}=10\log(P_e/P_r)$ and plotted as the gray curve in Fig. 3. It is the reference for comparison. The PSD indicates a well-damped vibration system with fat resonant peaks.

An ordinary MIFC, proposed in Ref. 11, was tested first. The degrees of $C(z)$, $\hat{P}(z)$, and $\hat{S}(z)$ were $n=m=300$. The total number of adaptive coefficients was 900. The dashed-black curve in Fig. 3 represents the normalized PSD of the error signal collected after the convergence of the ordinary MIFC. Since the system was well damped, the ordinary MIFC was able to suppress vibration with reasonably good control performance.

The modified MIFC system was then tested under the same experimental conditions. The degrees of $\hat{A}(z)$, $C(z)$, and $\hat{B}_p(z)$ and $\hat{B}_s(z)$ were $m_r=100$, $n=300$, and $m=200$. The

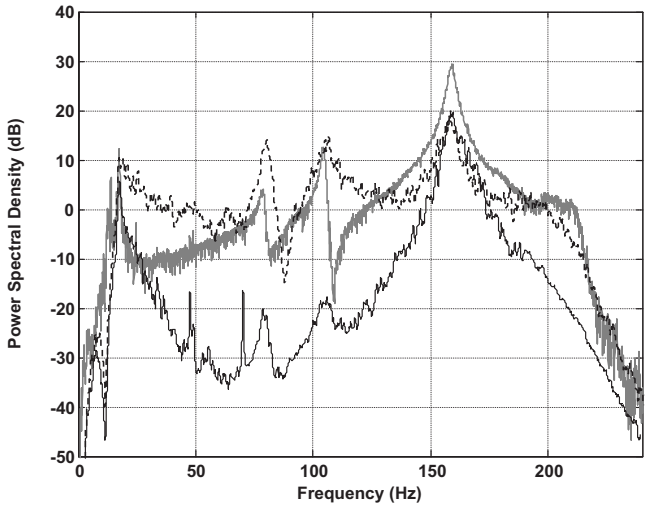

FIG. 4. Normalized PSD of error signal in experiment 2: uncontrolled (gray), controlled by an ordinary MIFC (dashed black), and controlled by the modified MIFC (solid black).

total number of adaptive coefficients was 800, which was almost the same as the ordinary MIFC system. Normalized PSD of the error signal was obtained after the convergence of the modified MIFC system. It is plotted as the solid-black curve in Fig. 3. The modified MIFC system improved control performance in the entire frequency range of interests. The improvement was not very significant since this was a well-damped system with negligible errors between transfer functions and FIR path models.

B. A lightly damped vibration system

In the second experiment, the setup was almost the same as in the first case. Only the secondary shaker was replaced by an inertial actuator with very weak damping. The inertial actuator was attached to the beam without other support. Its mass caused significant loading effect and reduced the fundamental frequency of the vibration system. The system sampling rate was still 500 samples/s and all signals were low-pass filtered with cutoff frequency of 200 Hz.

Again, the controllers were turned off first to collect the error signal $e(z)$. The normalized PSD of $e(z)$ is shown as the gray curve in Fig. 4. With very weak damping in both primary and secondary actuators, the system became lightly damped. In particular, the low-frequency resonant peaks of the PSD are very narrow, which implies IIR path transfer functions.

The ordinary MIFC was implemented and tested. The degrees of $C(z)$, $\hat{P}(z)$, and $\hat{S}(z)$ were $n=m=300$. The dashed-black curve in Fig. 4 represents the normalized PSD of the error signal collected after the convergence of the ordinary MIFC. Although the ordinary MIFC suppressed vibration, the effect was not significant. The controller even enhanced vibration in some frequencies. An important reason for the poor performance is the model error in approximating IIR path transfer functions with FIR filters.

The modified MIFC was then implemented and the degrees of $\hat{A}(z)$, $C(z)$, and $\hat{B}_p(z)$ and $\hat{B}_s(z)$ were $m_r=100$, $n=300$, and $m=200$. The solid-black curve in Fig. 4 represents the normalized PSD of the error signal collected after the convergence of the modified MIFC. Comparing all curves in Fig. 4, one can see that the modified MIFC suppressed vibration much more significantly. The complexity of the ordinary MIFC was 300 coefficients for $P(z)$, $S(z)$, and $C(z)$, respectively, with a total number of 900 coefficients. The complexity of the modified MIFC was 100 coefficients for $A(z)$, 200 coefficients for $B_p(z)$, $B_s(z)$, and 300 coefficients for $C(z)$, with a total number of 800 coefficients. The modified MIFC system improved control performance significantly with almost the same complexity in terms of adaptive coefficients.

In experiment 2, the beam was so lightly damped that its vibration, if caused by an impulsive impact, would last for at least 6 s. The long-lasting impulse response must be modeled by a FIR filter with at least $m=3000$ taps when the sampling rate was 500 Hz. The author did not have the fast hardware to test a MIFC with so many adaptive coefficients. Increasing FIR filter taps has other negative effects because convergence rate and estimation accuracy of system identification algorithms are related to rank and condition number of the data matrix in Eq. (21).[6] Here the matrix had $l=m_r+m+n+1=601$ columns for the modified MIFC, but at least $l=m+n+1=3301$ columns for the ordinary MIFC if the FIR path model had been increased to $m=3000$ taps while $n=300$ unchanged. More than five times of columns in the data matrix of Eq. (21) would have required more than five times longer t to meet the necessary full rank condition. It means a much slower convergence rate. Besides, condition number of a large matrix is sensitive to quantization errors, finite word-length effects, etc. With a large size, the data matrix of Eq. (21) may have been analytically full rank, but numerically ill conditioned to degrade estimate accuracy. The modified MIFC is preferred with lower implementation cost, faster convergence rate, and better estimation accuracy due to a much smaller data matrix in Eq. (21).

C. A noise control system

The third experiment was conducted to test the modified MIFC for noise control. Major dimensional information is given in Fig. 2(b). Cross-sectional area of the duct was 11×14.5 cm^2. The system sampling rate was 2.7 kHz samples/s and all signals were low-pass filtered with cutoff frequency of 1.2 kHz. Similar to the previous two experiments, the controllers were turned off first to collect the error signal $e(z)$. The normalized PSD of $e(z)$ is represented by the gray curve in Fig. 5. The experimental duct is not very lightly damped since resonant peaks of the PSD are not as narrow as those in Fig. 4.

The ordinary MIFC was tested. The degrees of $C(z)$, $\hat{P}(z)$, and $\hat{S}(z)$ were $n=m=300$. The dashed-black curve in Fig. 5 represents the normalized PSD of the error signal obtained after the convergence of the ordinary MIFC. The ordinary MIFC suppressed noise better than it did in vibration control. In all experiments, the ordinary MIFC had the same complexity but the control performances were different. An important reason is model error in approximating IIR path transfer functions with FIR models.

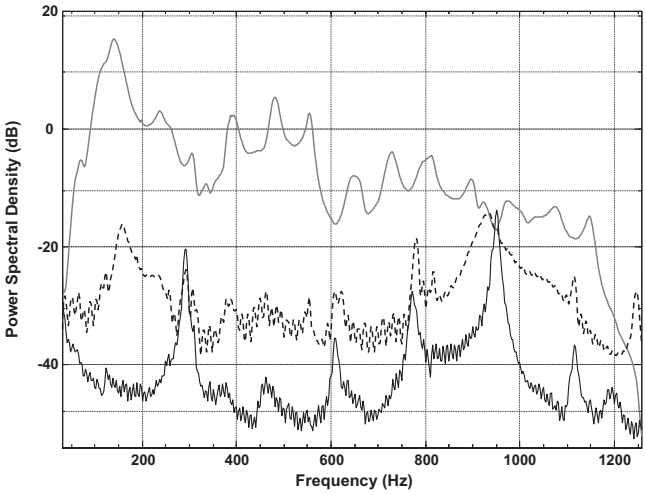

FIG. 5. Normalized PSD of error signal in experiment 3: uncontrolled (gray), controlled by an ordinary MIFC (dashed black), and controlled by the modified MIFC (solid black).

The modified MIFC was also tested in case 3. The degrees of $\hat{A}(z)$, $C(z)$, and $\hat{B}_p(z)$ and $\hat{B}_s(z)$ were $m_r=100$, $n=300$, and $m=200$. The solid-black curve in Fig. 5 represents the normalized PSD of the error signal collected after the convergence of the modified MIFC. Comparing all curves in Fig. 5, one can see that the modified MIFC improved noise control significantly in the entire frequency range of interest. Similar to case 2, the complexity of the ordinary MIFC was 300 coefficients for $P(z)$, $S(z)$, and $C(z)$, respectively, with a total number of 900 coefficients. The complexity of the modified MIFC was 100 coefficients for $A(z)$, 200 coefficients for $B_p(z)$ and $B_s(z)$, and 300 coefficients for $C(z)$, with a total number of 800 coefficients. Again, the modified MIFC system improved performance significantly with almost the same complexity in terms of adaptive coefficients.

Similar to experiment 2, the ordinary MIFC system may improve its performance by increasing FIR filter taps. That means higher implementation cost, slower convergence rate, and potentially worse estimation accuracy.

VII. CONCLUSION

It is more difficult to design and implement MIFC for lightly damped noise/vibration systems. The difficulty becomes worse as the degree of damping reduces. A modified MIFC is proposed here to improve broadband control in such systems, with modified online modeling to identify IIR path models. The controller is optimized by an online algorithm that only uses the numerators of IIR path estimates. It is shown analytically that the modified MIFC is noninvasive, stable, and able to improve broadband control in lightly damped noise/vibration systems. Experimental results are presented to verify the analytical results.

[1]C. H. Hansen and S. D. Snyder, *Active Control of Noise and Vibration* (E and FN Spon, London, 1997).
[2]P. A. Nelson and S. J. Elliott, *Active Control of Sound* (Academic, London, 1992).
[3]M. A. Vaudrey, W. T. Baumann, and W. R. Saunders, "Stability and operation constraints of adaptive LMS-based feedback control," Automatica **39**, 595–605 (2003).
[4]E. Bjarnason, "Analysis of the filtered-x LMS algorithm," IEEE Trans. Speech Audio Process. **3**, 504–514 (1995).
[5]S. D. Snyder and C. H. Hansen, "The influence of transducer transfer functions and acoustic time delay on the LMS algorithm in active noise control systems," J. Sound Vib. **140**, 409–424 (1990).
[6]G. C. Goodwin and K. S. Sin, *Adaptive Filtering, Prediction and Control* (Prentice-Hall, Englwood Cliffs, NJ, 1984).
[7]L. J. Eriksson and M. C. Allie, "Use of random noise for on-line transducer modeling in an adaptive active attenuation system," J. Acoust. Soc. Am. **85**, 797–802 (1989).
[8]W. C. Nowlin, G. S. Guthart, and G. K. Toth, "Noninvasive system identification for multichannel broadband active noise control," J. Acoust. Soc. Am. **107**, 2049–2060 (2000).
[9]X. Qiu and C. H. Hansen, "An algorithm for active control of transformer noise with on-line cancellation path modelling based on the perturbation method," J. Sound Vib. **240**, 647–665 (2001).
[10]B. J. Kim and D. C. Swanson, "Linear independence method for system identification/secondary path modeling for active control," J. Acoust. Soc. Am. **118**, 1452–1468 (2005).
[11]J. Yuan, "Orthogonal adaptation for active noise control," J. Acoust. Soc. Am. **120**, 204–210 (2006).
[12]L. J. Eriksson, "Development of the filtered-u algorithm for active noise control," J. Acoust. Soc. Am. **89**, 257–265 (1991).
[13]J. Lu, C. Shen, X. Qiu, and B. Xu, "Lattice form adaptive infinite impulse response filtering algorithm for active noise control," J. Acoust. Soc. Am. **113**, 327–335 (2003).
[14]P. A. Regalia, *Adaptive IIR Filtering in Signal Processing and Control* (Dekker, New York, 1995).
[15]J. S. Vipperman and R. A. Burdisso, "Adaptive feedforward control of non-minimum phase structural systems," J. Sound Vib. **183**, 369–382 (1995).

Numerical inverse method predicting acoustic spinning modes radiated by a ducted fan from free-field test data[a)]

Serge Lewy[b)]
CFD and Aeroacoustics Department, ONERA (National Aerospace Research Agency), MB 72, 92322 Chatillon, France

(Received 7 September 2007; revised 5 February 2008; accepted 21 April 2008)

Spinning modes generated by a ducted turbofan at a given frequency determine the acoustic free-field directivity. An inverse method starting from measured directivity patterns is interesting in providing information on the noise sources without requiring tedious spinning-mode experimental analyses. According to a previous article, equations are based on analytical modal splitting inside a cylindrical duct and on a Rayleigh or a Kirchhoff integral on the duct exit cross section to get far-field directivity. Equations are equal in number to free-field measurement locations and the unknowns are the propagating mode amplitudes (there are generally more unknowns than equations). A MATLAB procedure has been implemented by using either the pseudoinverse function or the backslash operator. A constraint comes from the fact that squared modal amplitudes must be positive which involves an iterative least squares fitting. Numerical simulations are discussed along with several examples based on tests performed by Rolls–Royce in the framework of a European project. It is assessed that computation is very fast and it well fits the measured directivities, but the solution depends on the method and is not unique. This means that the initial set of modes should be chosen according to any known physical property of the acoustic sources.
 [DOI: 10.1121/1.2931952]

PACS number(s): 43.50.Lj, 43.20.Mv, 43.60.Pt [KA] Pages: 247–256

I. INTRODUCTION

The modal structure of the acoustic field generated by a ducted fan is directly linked to the sources and is a key information for noise reduction. Experimental techniques of modal analysis have become common since the article of Tyler and Sofrin,[1] but they remain tedious and expensive, requiring a rotating microphone or an array of fixed microphones. Moreover, they generally need some probes inside the duct which can disturb the generated acoustic field. It is thus an attractive challenge to deduce the modal structure at a given frequency by using only conventional free-field measurements.

Several laboratories have recently tackled such inverse problems mainly for source reconstruction or for near-field acoustical holography.[2–4] Configurations that are more or less similar to the present one have been addressed, but each work has its own characteristics.[5–10] For instance, Luo and Li reconstructed the pressure fluctuations along the chord of a stator vane (in the case of a two-dimensional cascade) from (simulated) acoustic measurements.[5] Kim and Nelson determined locations and strengths of sources in a cross section of a cylindrical duct.[6] Acoustic field inside the duct is modeled on the basis of Green's function, which gives a frequency response function matrix but this still requires a special experimental arrangement consisting in rings of microphones on the duct wall. Gerard *et al.* considered a low speed automotive cooling fan and very few spinning modes may propagate.[7] The transfer function matrix must be well conditioned to avoid unstable solutions dominated by errors in sound pressure measurements. This is done through the Tikhonov regularization parameter chosen according to the *L*-curve criterion.[11] Venditti *et al.* are involved in the same issue as is dealt with here.[8] They placed forward two mode identification methods, one based on a gradient algorithm and the other on a least squares optimizer. Castres and Joseph also studied a turbofan model and they took the opportunity of an upstream turbulence control screen to fasten a large number of microphones to it.[9,10] They get an overdetermined system of linear equations, and they optimize the sensor locations on the screen such that the condition number of the radiation matrix is low.

The practical objective of the present work is to identify the generated spinning modes and their amplitudes in order to use them as input data for acoustic computations of nontested configurations, e.g., optimization of duct lining. An original inverse method is suggested in this article. It only relies on conventional directivity patterns of sound pressure levels (SPLs). No phase information is needed and measurements can be made with several microphones or a moving microphone as well. Results would surely be more accurate by using a special array of microphones but the present data processing is very fast and seems to be valid enough to reach the above objective.

It has been shown in a previous paper how the sound field can be described on the basis of an analytical equation governing acoustic propagation in a hard-walled cylindrical duct and of a Rayleigh or a Kirchhoff integral to deduce the directivity of sound radiation in the far field.[12] The inverse

[a)]Portions of this work were presented at Inter-noise 2006, Honolulu, Hawaii, 3-6 December 2006.
[b)]Electronic mail: serge.lewy@onera.fr

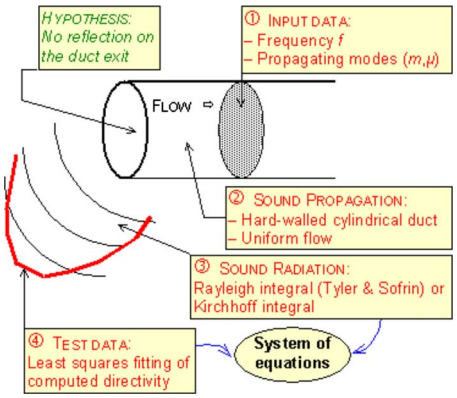

FIG. 1. (Color online) General diagram of the inverse method.

problem is however ill posed because there are generally much more possible propagating modes than the experimental data (as soon as frequency is not very low). The next section reminds the equations involved in a least squares fitting and suggests an inverse method based on MATLAB programming. Solutions are checked on numerical simulations in Sec. III and some examples of application on actual tests made by Rolls–Royce in a European project are discussed in Sec. IV.

II. LEAST SQUARES FITTING

Figure 1 presents the general diagram of the proposed inverse method.

A. Computed data

The computational model has been detailed in a previous article.[12] Only useful equations are reminded here. Steps 1–3 of Fig. 1 lead to the sound pressure P (normalized to a reference pressure p_{re}), radiated from a cylindrical duct into the far field at a given frequency f at a distance d to the duct exit center, and at an angle φ ($\varphi=0$ on the nacelle centerline). Pressure P is split into spinning modes (m,μ), where m is the circumferential mode and μ is the radial mode ($\mu \geqslant 1$),

$$P(d,\varphi)=\sum_m \sum_\mu P_{m\mu}(d,\varphi), \tag{1}$$

and sums on m and μ are limited to propagating modes. The $P_{m\mu}$ are written as

$$P_{m\mu}(d,\varphi)=A_{m\mu}e^{i\psi_{m\mu}}F_{m\mu}(d,\varphi), \tag{2}$$

with $A_{m\mu}$ and $\psi_{m\mu}$ being the amplitude and phase factors, respectively, and the $F_{m\mu}(d,\varphi)$ are the eigenfunctions of the wave equation. They can be given by a Rayleigh integral (Tyler and Sofrin model)[1]

$$F^{(R)}_{m\mu}(d,\varphi)=i^{m+1}\frac{Rk_z}{2d/R}e^{i(\omega t-Kd)}J_m(k_tR) \times\left[\frac{(2KR\sin\varphi)J'_m(KR\sin\varphi)}{(k_tR)^2-(KR\sin\varphi)^2}\right]. \tag{3}$$

In this equation, R is the duct radius, $\omega=2\pi f$ is the angular frequency, $K=\omega/a$ and k_t are the total and transverse wave numbers, respectively (where $a=340$ m/s is the speed of sound), and J_m is the Bessel function of first kind and of order m. The last term in square brackets is the directivity factor. Superscript (R) is added to $F_{m\mu}$ in Eq. (3) to remind us that it comes from a Rayleigh integral.

A Kirchhoff integral, however, better simulates actual configurations mainly for lateral radiation because there is no hypothesis of flanged inlet. In this case, labeled with a superscript (K),

$$F^{(K)}_{m\mu}(d,\varphi)=\left(\frac{1}{2}+\frac{K\cos\varphi}{2k_z}\right)F^{(R)}_{m\mu}(d,\varphi). \tag{4}$$

The Kirchhoff method is selected in this paper. This allows us to take advantage of the measurements at angles φ that are slightly larger than 90°. Moreover, Eq. (4) can be extended to a uniform flow in the free space (simulation of flight conditions). A simple means of taking into account the flow velocity in the duct has been suggested[12] but the mean speed is neglected here because the main objective is to check the validity of the method and its robustness.

Finally, the root mean square value of sound pressure in Eq. (1) P_{rms} is

$$P^2_{\mathrm{rms}}(d,\varphi)=\sum_m \sum_\mu \frac{A^2_{m\mu}}{2}|F_{m\mu}(d,\varphi)|^2, \tag{5}$$

where the cross terms have been dropped. Indeed, it is assumed that the spinning modes are incoherent, which was assessed experimentally for the circumferential modes m in a low speed fan.[13] This can be supported by the fact that each mode m at an acoustic frequency f is generated by a different loading harmonic. These harmonics are orthogonal (see Parseval's theorem) and it can be expected that Eq. (5) is split on spinning modes in the same way. There is no similar argument for radial modes μ but it has been experimentally demonstrated by Castres and Joseph that they are incoherent.[10] Moreover, they are much less numerous to propagate and the first radial modes often dominate in a hard-wall duct. It seems sufficient for the present purpose to make the same approximation on μ as is done for m.

Equation (5) has also been justified in Ref. 8 by averaging the phase cross product in $\cos(\psi_{m\mu}-\psi_{m'\mu'})$ over 2π. In summary, Eq. (5) is widely admitted and its unknowns are the amplitudes $A_{m\mu}$ to be determined.

B. Least squares fitting on measured data

SPLs are measured in the far free field at a given distance d of the duct exit for J radiation angles φ_j (step 4 in Fig. 1). Of course, it would be easy to correct to a fixed distance if d was not constant. Parameter d will thus be dropped from the arguments of the various functions. Experimental values of the squared rms sound pressure (normalized to the reference pressure p_{re}) are

$$Z_j=10^{\mathrm{SPL}_{\mathrm{test}}(\varphi_j)/10} \quad \text{for } j=1 \text{ to } J. \tag{6}$$

These data should be equal to the computed squared pressures from Eq. (5)

$$Y_j \equiv P_{\text{rms}}^2(\varphi_j) \quad \text{for } j=1 \text{ to } J, \tag{7}$$

where the Y_j are a sum on N propagating modes $n \equiv (|m|,\mu)$. In fact, terms Z_j include some errors due to extraneous noise at the microphones such that $Z_j = Y_j + e_j$.

Let us set $\Phi_{nj} = |F_{m\mu}(\varphi_j)|^2$ for the known eigenfunctions and $\alpha_n \equiv A_{m\mu}^2/2$ for the unknown amplitudes (α_n must not be negative). The Φ_{nj} are the directivities of $P_{\text{rms}}^2(\varphi)$ computed from φ_1 to φ_J for a single mode n with a unit amplitude $\alpha_n = 1$. Using Eqs. (5)–(7) gives a system of J equations with N unknowns

$$Y_j + e_j = Z_j \text{ or } \sum_{n=1}^{N} \Phi_{nj}\alpha_n + e_j = Z_j \quad \text{for } j=1 \text{ to } J. \tag{8}$$

Due to the error terms e_j, a least squares fitting is the best way to solve the system of Eq. (8) (also see Sec. IV B). This consists in searching the coefficients α_n minimizing the standard deviation between test and computed data, i.e., minimizing the function Ψ

$$\Psi = \sum_{j=1}^{J} e_j^2 = \sum_{j=1}^{J} (Y_j - Z_j)^2. \tag{9}$$

This leads to

$$\forall \nu \in \{1,N\}, \quad \sum_{n=1}^{N} \left(\sum_{j=1}^{J} \Phi_{nj}\Phi_{\nu j} \right) \alpha_n = \sum_{j=1}^{J} (\Phi_{\nu j} Z_j). \tag{10}$$

It is a system of N equations with N unknowns α_n. The number of measurement locations J must be at least equal to the number of modes N, i.e., $J \geqslant N$. However, this is generally not true in this study because there are more propagating modes than test data as soon as frequency is not very low. It is the reason why the MATLAB library is used.

C. Numerical procedure using MATLAB

Let us write the system of Eq. (8) in a matrix form: $\Phi\alpha = Z$ (the e_j being now implicit inside Z). Matrix Φ has J lines and N columns, vector α has N lines, and vector Z has J lines. Contrary to the assumption at the end of the preceding subsection, this system is generally underdetermined. Indeed, there are usually more propagating modes N or unknowns α_n than measurement locations or equations J. This system can be solved through two rather similar ways available in MATLAB but they do not give the same results because the solution is never unique if $N > J$.

(a) As matrix Φ is not square, its Moore–Penrose pseudoinverse Φ^+ (unique matrix of N lines and J columns) is computed by using the "pinv" function of MATLAB and

$$\alpha = \Phi^+ Z \text{ or } \alpha = \text{pinv}(\Phi) * Z. \tag{11}$$

(b) A QR decomposition is performed on Φ (Q is an orthogonal matrix of size J by J and R is an upper triangular matrix of size J by N) to minimize the norm $\|\Phi\alpha - Z\|$ in a least squares sense, and this is done by using the MATLAB backslash operator "\"

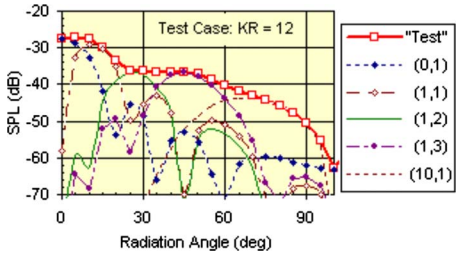

FIG. 2. (Color online) Numerical simulation of the test data.

$$\alpha \text{ such that } \|\Phi\alpha - Z\| = \text{minimum or } \alpha = \Phi \backslash Z, \tag{12}$$

which returns a vector α with at most J nonzero components.

Finally, data processing is performed in two main steps.

(i) The eigenfunctions $|F_{m\mu}|$ in Eq. (5) are computed for the propagating modes at the measurement angles φ_j according to Eq. (3) or (4).

(ii) Operation pinv or \ in Eq. (11) or (12) is repeated in an iterative process because of the constraint that $\alpha_n \equiv A_{m\mu}^2/2$ may not be negative.[14] The modes $n = (|m|,\mu)$ that give a negative α_n are removed from the following iteration. The system of J equations has $N_1 = N$ unknowns in the first iteration, N_2 ($< N_1$) unknowns in the second iteration, and so on. The procedure is stopped at iteration I_f when all the unknowns get positive values (i.e., N_{I_f+1} would be equal to N_{I_f}). If a valid final result was not found, this would mean that the initial choice of the N modes misses some modes that are actually generated.

In fact, the system of equations is different at each iteration and the solutions α_n are also different. A negative α_n in a system with N_I unknowns should be deleted from iteration $I+1$ but it could retrieve a positive value if it were kept in that iteration, i.e., in a system with $N_{I+1}+1$ ($< N_I$) unknowns. It thus seems better to place a slightly negative threshold instead of zero but it must be very small because negative α_n may not remain at the end (say, absolute value of the threshold of the order of 10^{-3}–10^{-4} times the maximum amplitude of the α_n at each iteration).

III. NUMERICAL SIMULATIONS

A. Simulated test case

The method is tested in a case similar to the experiments analyzed in Sec. IV.[15] The duct diameter is $2R = 0.864$ m, free-field radiation is available at a distance $d = 18.5$ m from the duct exit every $\Delta\varphi = 5°$ from $\varphi = 0$ (on the duct centerline) to $\varphi = 100°$. There is thus a system of $J = 21$ equations to be solved. The frequency is $f = 1500$ Hz, i.e., the reduced frequency is $KR = 2\pi Rf/a = 12$. There are 24 propagating modes $(|m|,\mu)$ in these conditions: (0,1)–(10,1), (0,2)–(6,2), (0,3)–(3,3), and (0,4) and (1,4). It is assumed in the simulated test that only 5 modes out of the 24 are generated: (0,1), (1,1), (10,1), (1,2), and (1,3) with amplitudes $A_{m\mu} = 0.3$, 1, 8, 1, and 2, respectively (Fig. 2). There is about 30 dB difference be-

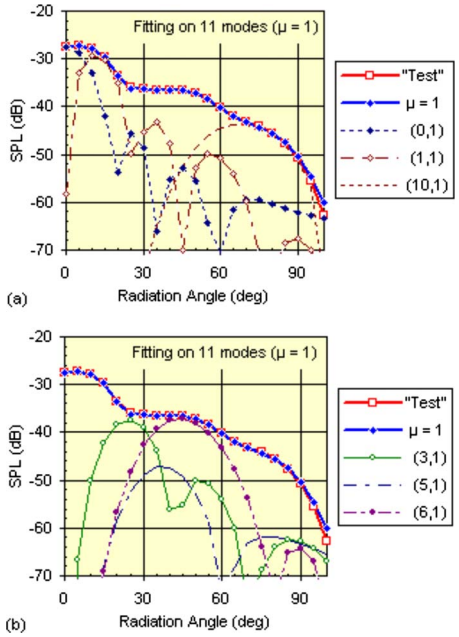

FIG. 3. (Color online) Iterative fitting on simulated test data from Fig. 2, starting from the first radial mode (11 propagating modes): (a) with directivities of the generated modes and (b) with directivities of other predicted modes.

tween radiations on the centerline (0°) and around the duct exit plane (90°).

It is checked in this section if these data can be retrieved. The main question is that the initial system of equations in underdetermined and the solution is not unique. It is also shown in Sec. IV that the reconstructed directivity can be of poor quality if all of the propagating modes are taken (e.g., see Fig. 8). The objective of these numerical simulations is to assess how the result depends on the initial set of modes. The SPLs in Eq. (6) are thus the exact levels to avoid any effect of possible experimental errors (this issue will be discussed in Sec. IV C).

A first fitting uses only the 11 modes $\mu=1$ [Figs. 3(a) and 3(b)]. The two upper curves are the given "test" data (open square symbols) and the calculation (solid diamonds). The overall directivity is well retrieved and is due to six modes whose directivities are also plotted. They are ordered in the legends on the right according to the angle of maximum radiation. The three modes with $\mu=1$, (0,1), (1,1), and (10,1) are predicted as expected [Fig. 3(a)]. Mode (1,2) is replaced by (3,1) and (1,3) by (6,1), which nearly have the same directivities [Fig. 3(b)]. Mode (5,1) of low level is also predicted and it improves the accuracy around 35° [Fig. 3(b)]. It has already been pointed out that the solution is not unique because several modes may generate the same directivity pattern. The second fitting (not shown) starts from the 18 modes $\mu=1$ and 2. The overall directivity is again very well retrieved, along with modes (0,1), (1,1), (10,1), and (1,2). Mode (6,1) replaces (1,3) as before. Two more modes of low levels are also found, (2,1) and (8,1).

The system of equations is overdetermined in these two cases and the two methods pinv or \ give the same results. This is no longer true at the beginning of the iterations in the

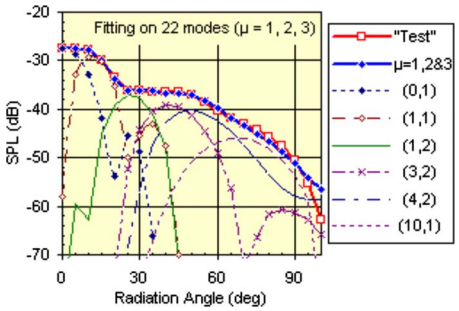

FIG. 4. (Color online) Iterative backslash fitting on simulated test data from Fig. 2, starting from radial modes $\mu=1$, 2, and 3 (22 propagating modes).

following cases. The pseudoinverse function leads to the exact solution. Only inversion using the backslash operator is thus discussed below.

The third fitting uses the 22 modes $\mu=1$, 2, and 3 (Fig. 4). There are now more unknowns ($N=22$) than equations ($J=21$) for the first iteration. The result looks like the previous one with the modes (0,1), (1,1), (10,1), and (1,2). There is no mode $\mu=3$, mode (1,3) is not predicted and is replaced by (3,2) instead of (6,1). Modes (2,1) and (8,1) are changed into (4,2) which is high between 45° and 70° (only the main lobe from each mode is plotted in the figures for clarity). The fourth fitting uses the 24 propagating modes (Fig. 5). The result is nearly the same as above, again without mode (1,3). There is only another extra mode (0,2) but its amplitude is very small, which is more than 10 dB below the overall level.

The last fitting based on all of the propagating modes ($N=24$) is replayed assuming now that the spatial resolution of the measurements is $\Delta\varphi=2.5°$ (Fig. 6), i.e., the number of test data is doubled ($J=41$). The system of equations is overdetermined like in the first two previous cases but the two methods do not give the same solution. The result using the backslash operator, plotted in Fig. 6, is not improved compared to Fig. 5. It could be expected that the pseudoinverse function would give a similar result, but this is false, and prediction (not shown) is rather poor above 70°.

B. Consequences of the numerical simulations

Table I summarizes the modal amplitudes for the simulated test and for the four fittings with $\Delta\varphi=5°$ described above. The second line is the cut-on ratio k_t/K. It increases from left to right and gives an idea of the angle of maximum

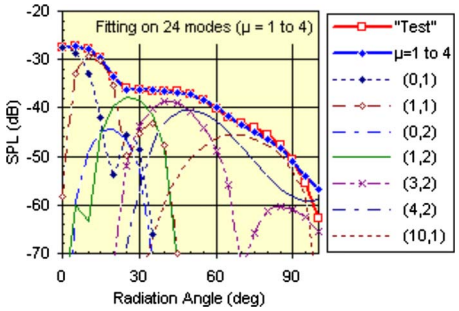

FIG. 5. (Color online) Iterative backslash fitting on simulated test data from Fig. 2, starting from all the 24 propagating modes.

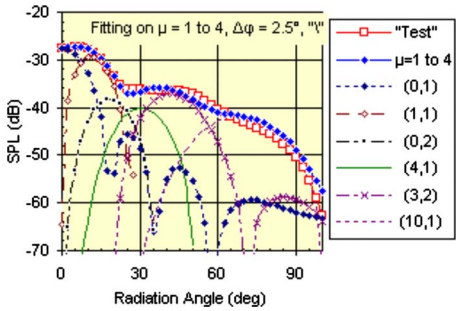

FIG. 6. (Color online) Iterative backslash fitting starting from all the propagating modes, $\Delta\varphi=2.5°$.

radiation $\varphi_{\max}$ for each mode:[16] $\sin\varphi_{\max}\approx k_t/K$. Initial modes or those replacing them are in bold. Amplitudes in brackets refer to non-useful modes, i.e., their maximum is about 10 dB lower than the overall computed level at the same angle.

The accuracy of the solution of the system of equations is related to the condition number C of the matrix Φ.[17] That number is defined for square matrices as the product of norms $C=\|\Phi\|\|\Phi^{-1}\|$ and Φ^{-1} is replaced by the pseudoinverse if Φ is not square. It is shown that[17]

$$\frac{\|\delta\alpha\|}{\|\alpha\|}\leqslant C\frac{\|\delta Z\|}{\|Z\|}, \tag{13}$$

where δZ and $\delta\alpha$ are the deviations of Z and α in Eq. (8). It means that small perturbations in test data Z can have a very large effect on the solution α if the matrix Φ is badly conditioned (large values of C).

The condition number of the initial matrix Φ is given in Table II for the predictions of the preceding subsection. Matrix Φ is very badly conditioned if there are several radial modes μ. This is physically explained in Fig. 7, which shows that some modes m for different values of μ have similar Φ_{nj} elements ($j=1$ to J). For instance, the main directivity lobes of modes (1,3), (6,1), and (3,2) are very close together as it has been noted in the comments of the various simulations (see Table I). It can be noted that Venditti *et al.* chose modes according to measured far-field directivity to get an overdetermined system of equations in their second identification method.[8] This does not prevent ambiguity in the solution because several propagating modes can be selected for a given angle of measured maximum according to Fig. 7. Anyway, it does not seem to be harmful to change a mode into another one of similar directivity in the input of a computation for a nontested case. Again, Venditti *et al.* checked that this is true in reconstructing the directivity curve of a lined duct from that of a hard-wall duct.[8]

TABLE II. Condition number of the initial matrix Φ and number of iterations for the backslash operator.

Modes	Number of modes	Condition number of initial matrix Φ	Number of iterations for \ operator
$\mu=1$	11	5.6×10^5	3
$\mu=1$ and 2	18	2.2×10^{12}	4
$\mu=1$, 2, and 3	22	8.9×10^{15}	4
$\mu=1-4$	24	7.2×10^{15}	4
$\mu=1-4$, $\Delta\varphi=2.5°$	24	3.5×10^{16}	5

The condition number decreases during the iterative process because there are less and less unknowns, as is shown in Table III, in the case $\mu=1$ to 3 (Fig. 4). It is only 5.3×10^6 in the second iteration by using the backslash operator (on 13 modes instead of 22) and its final value is 2.4×10^4, which is nearly equal to the value found in the pseudoinverse method. It can be noted that Castres and Joseph achieved condition numbers as low as 200 but with a number of microphones larger than the number of propagating modes and a proper choice of their locations.[10]

Some comments can be drawn from these numerical simulations.

(a) It was not sure that all of the fittings would lead to a valid set of modes with positive squared amplitudes. It can also be expected that the strategy eliminating modes, whose squared amplitude is negative, is not always valid. A mode could recover a positive squared amplitude in a following iteration.
(b) Two methods have been tested to solve the system of equations. They do not give the same result as it was known but it cannot be said that one is better than the other. A refinement could consist in implementing both methods, one for the underdetermined system at the beginning of the iterations, the other when the system becomes overdetermined after the removal of some modes due to the constraint on positive squared amplitudes.
(c) Several modes can have similar free-field directivities and the prediction depends on the initial set of selected modes. However, most of the modes actually generated are generally retrieved and with the right amplitude. More test data may slightly improve the fitting but the condition number of the system matrix can become worse.

TABLE I. Amplitudes $A_{m\mu}$ for the simulated test (backslash operator).

Mode	**(0,1)**	**(1,1)**	**(2,1)**	(0,2)	(3,1)	(1,2)	(5,1)	(6,1)	(3,2)	**(1,3)**	(4,2)	(8,1)	**(10,1)**
k_t/K	0.000	0.154	0.255	0.320	0.351	0.445	0.536	0.626	0.669	0.713	0.775	0.806	0.983
Test	**0.30**	**1.00**				**1.00**				**2.00**			**8.00**
$\mu=1$	**0.30**	**0.99**			**1.03**		(0.63)	**2.62**					**7.81**
$\mu=1,2$	**0.30**	**0.99**	(0.34)			**0.88**		**2.64**				(1.20)	**6.88**
1, 2, 3	**0.30**	**1.00**				**0.97**			**1.47**		1.81		**6.03**
1–4	**0.30**	**0.99**		(0.29)		**0.91**			**1.54**		1.72		**6.36**

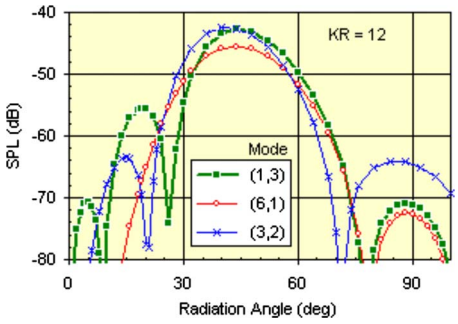

FIG. 7. (Color online) Comparison of directivity patterns radiated by the modes (1,3), (6,1), and (3,2), the three amplitudes $A_{m\mu}$ being equal to 1.

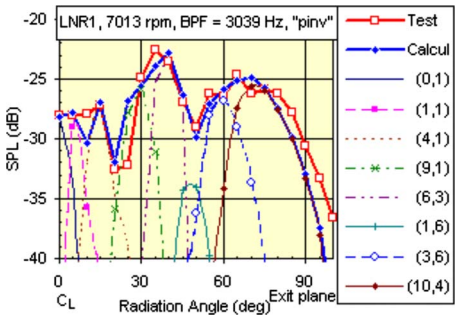

FIG. 8. (Color online) Prediction of modes generating the measured directivity at BPF, starting from all the propagating modes.

(d) Final result is not improved (and can even be worse) if a very large number of propagating modes is taken to start the iterative process. This means that a limited choice of the possible generated modes based on known physical properties helps us to get valid predictions.

IV. APPLICATION TO SOME EUROPEAN TESTS

A. First test case

Let us consider a Rolls–Royce test from European project RESOUND on a low noise rotor called LNR1 (diameter $2R=0.864$ m, 26 blades) at 7013 rpm. Blade passing frequency (BPF) is 3039 Hz (reduce frequency $KR=24.26$) and there is no rotor-stator interaction mode propagating on this tone. Far-field measurements consist in $J=21$ SPLs at a distance $d=18.5$ m from 0° to 100° every 5°. In fact, there is no measurement on the centerline and the same value as the 5° data is taken at 0° to have realistic smooth curves (this means that the plane wave must be generated). Also note that the reference of decibels p_{re} is arbitrary but is the same in all of the following figures.

There are $N=83$ propagating modes, from $\mu=1$ ($|m|=0$ to 21) to $\mu=8$ ($m=0$). There are thus $N=83$ unknown mode levels, much more than the $J=21$ equations. The system is thus underdetermined but the constraint that α_n may not be negative is fulfilled by iterations which remove several unknowns at each step. Prediction by using the pinv function is displayed in Fig. 8. Five iterations are required and eight modes are found. It must be noted that the plane wave (0,1) for instance would be deleted if the negative amplitudes were removed and no level would be found on the centerline. A slightly negative threshold is thus preferred (here, −0.0001 times the maximum amplitude of the α_n found at each iteration). However, the result is not very good, the standard deviation is $\sigma=2.2$ dB, which is defined by the following mean value over the radiation angle φ:

$$10^{\sigma/10}=\frac{1}{J}\sum_{j=1}^{j=J}10^{|\mathrm{SPL}_{\mathrm{calc}}(\varphi_j)-\mathrm{SPL}_{\mathrm{test}}(\varphi_j)|/10}. \tag{14}$$

It has been checked in numerical simulations that several modes can have a very similar free-field directivity (Fig. 7) and the prediction depends on the initial set of selected modes. It is thus suspected that there are too many useless modes. Mode (1,6) in Fig. 8 has a very low level and mode (10,4) does not well fit the test data at large angles. As a consequence, computation is run again with $N=53$ propagating modes from $\mu=1$ to $\mu=3$. The two methods pinv and \ are shown in Figs. 9 and 10, respectively. Bottom graphs are the differences between computation and test data, ΔSPL, with an enlarged vertical scale.

Both results are now in close agreement with test data, standard deviation is around 0.5 dB, which is within the experimental errors. It is however noticed that the predicted modes are not the same but there are many similarities. There are 9 modes in the second case and 11 modes in the first case but mode (2,1) is below the scale of Fig. 9 and mode (14,1) is very low. Mode (9,3) in Fig. 10 could also be deleted. Six modes are the same in the two computations and directivities of modes (11,1) and (12,1) are close together.

These comments are better evidenced in Fig. 11, which summarizes the SPL of each mode on the duct wall and the sound power levels (PWLs) computed inside the duct (label "in") or integrated in the free field (label "out"). It is checked that the two sound powers are equal (some slight differences are due to the rather large step of 5° for the integration in the free field). This is a basic validation of the calculation.

TABLE III. Change in the condition number of Φ during the iterations: case $\mu=1-3$.

Pseudoinverse method pinv			Backslash operator \		
Iteration	Number of modes	Condition number	Iteration	Number of modes	Condition number
1	22	8.9×10^{15}	1	22	8.9×10^{15}
2	15	4.8×10^{9}	2	13	5.3×10^{6}
3	8	4.2×10^{4}	3	8	2.5×10^{5}
4	5	1.8×10^{4}	4	6	2.4×10^{4}

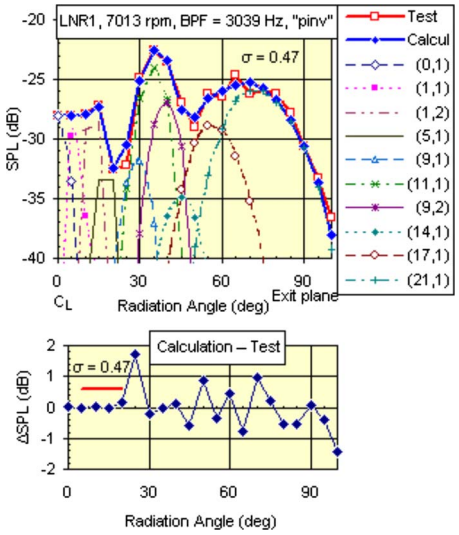

FIG. 9. (Color online) Prediction of modes generating the measured directivity at BPF, starting from propagating modes $\mu=1$ to 3 (pinv function).

It must be noted that the levels of low-order modes are rather small because they radiate efficiently around the centerline. For instance, the ratio of the squared amplitudes $\alpha_{(21,1)}/\alpha_{(0,1)}$ is about 2×10^5. It is why the threshold to remove modes from the following iteration is slightly negative. As it was suspected before, a mode with a negative squared amplitude α_n can recover a positive value of α_n in a following iteration with a reduced set of modes.

Evolutions of the number of modes N and of the condition number C of matrix Φ during the iterations are shown in Fig. 12 for the two above computations. It is seen that the matrix is badly conditioned at the beginning but C sharply decreases when the system of equations becomes overdetermined (as it has been observed in other papers).[6] The backslash operator returns J nonzero values at the most (positive or negative) but the modes with $\alpha_n=0$ are not removed from the following iteration because the threshold is slightly negative. This explains why convergence is a little longer using that operator. However, the full calculations remain very fast.

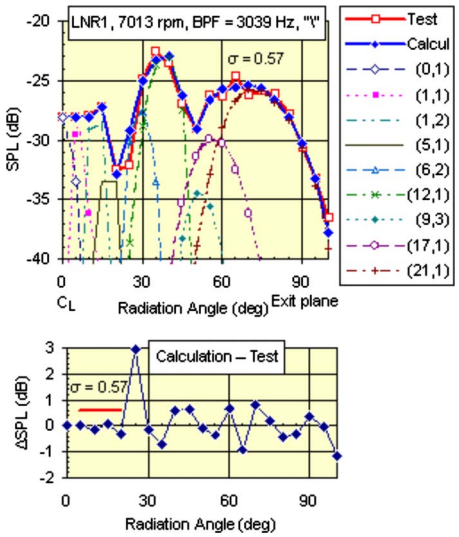

FIG. 10. (Color online) Prediction of modes generating the measured directivity at BPF, starting from propagating modes $\mu=1-3$ (\ operator).

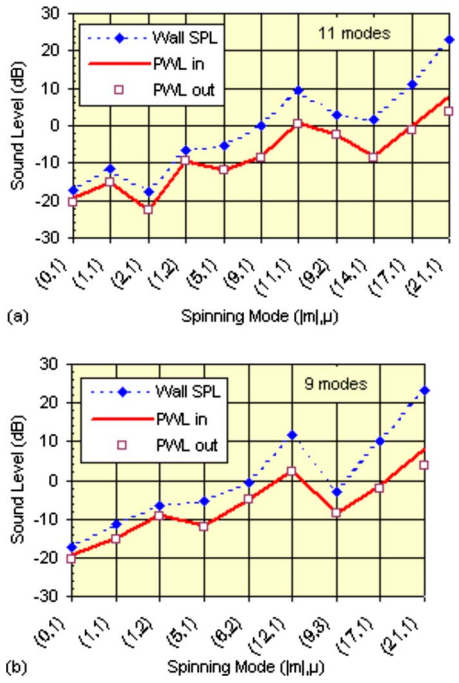

FIG. 11. (Color online) Duct-wall SPL and PWLs of the modes predicted in: (a) case of Fig. 9 (pinv function) and (b) case of Fig. 10 (\ operator).

B. Comments on the transfer matrix

It could seem easier to directly solve the system of Eq. (8). It is a system of J equations with N unknowns α_n. If $N=J$, the transfer matrix Φ can be inverted to get the α_n but this is quite different from the least squares fitting. It is in

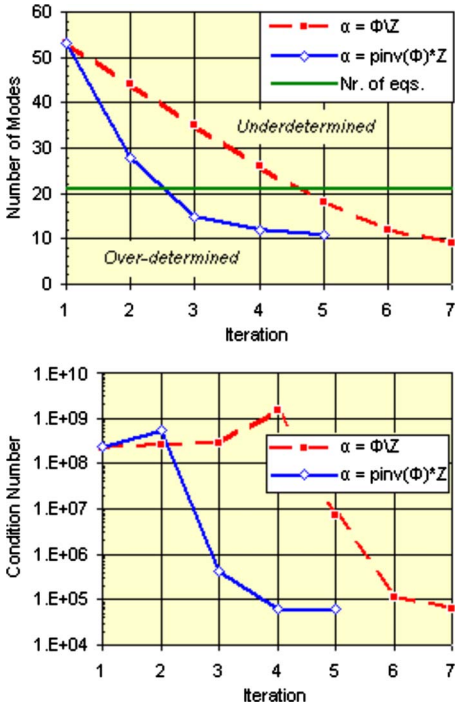

FIG. 12. (Color online) Evolution of the number of modes and of the matrix condition number during the iterations in the case of Figs. 9 and 10.

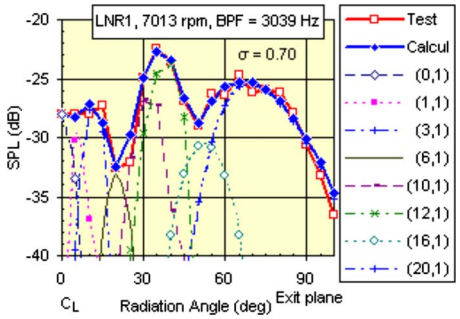

FIG. 13. (Color online) Prediction of modes generating the measured directivity at blade passing frequency, starting from 21 propagating modes $\mu=1$.

fact admitted that the method is unusable in actual applications.[18] The main problem is that it can become unstable and unreliable for two reasons. (i) If two measurements Z_j are not rigorously independent, determinant $|\Phi|$ tends to zero which may lead to unstable results. This does not happen in the least squares fitting because the second member of Eq. (10) depends on a function Φ with a different index ν. (ii) If there is an error on one measurement Z_j, the transfer matrix returns coefficients α_n such that the result perfectly duplicates all the test data from $j=1$ to J. The solution thus strongly depends on the experimental errors. Again, this does not happen in the least squares fitting because all of the test data are mixed at the right hand side of Eq. (10) and one wrong measurement only slightly shifts the solution.

Moreover, the signs of the squared amplitudes α_n are arbitrary and the iterative procedure remains compulsory. An example is displayed in Fig. 13 for $N=J=21$ modes, i.e., all of the modes $\mu=1$ except (4,1). The pseudoinverse function and the backslash operator give the same result. The first iteration is the exact solution of the system of the equations but 11 α_n out of 21 are negative, and three iterations are required to lead to 8 positive α_n.

The comparison of the three results in Figs. 9, 10, and 13 shows that there are several differences but they are without great consequence for practical applications, e.g., using the modes for prediction of radiation in other conditions. The large hump around 70° can be generated either by mode (20,1) or (21,1), which have close directivities. In the same way, the peak around 35° can be due to mode (11,1) plus a small contribution of (9,2) or to mode (12,1) plus a small contribution of (6,2) or (10,1).

C. Effect of signal-to-noise ratio

It has been claimed above that the transfer matrix method exactly retrieves the test data but is very sensitive to any inaccuracy. On the contrary, a least squares fitting smoothes the errors and is much more recommended to get valid physical results.

This is analyzed in Table IV where the two columns named "Test" summarize the modes found in Figs. 9 and 10. In the other columns, the $\mathrm{SPL}_{\mathrm{test}}(\varphi_j)$ in Eq. (6) are replaced by $\mathrm{SPL}_{\mathrm{test}}(\varphi_j)+\Delta(\varphi_j)$, where the $\Delta(\varphi_j)$ are random numbers. Using the notations of Eq. (8), the relative errors on the rms pressures are

$$\frac{\Delta P_{\mathrm{rms}}(\varphi_j)}{P_{\mathrm{rms}}(\varphi_j)} = -\frac{1}{2}\frac{e_j}{Z_j} = \frac{1}{2}[10^{\Delta(\varphi_j)/10} - 1]. \tag{15}$$

The heads of columns "±0.5 dB" mean that all of the $\Delta(\varphi_j)$ are drawn between −0.5 and +0.5 ($\Delta P_{\mathrm{rms}}/P_{\mathrm{rms}} \approx \pm 5\%$). This was repeated three times (1–3). Two examples with $|\Delta(\varphi_j)| \leqslant 1$ dB ($\Delta P_{\mathrm{rms}}/P_{\mathrm{rms}} \approx \pm 10\%$) and one with $|\Delta(\varphi_j)| \leqslant 1.5$ dB ($\Delta P_{\mathrm{rms}}/P_{\mathrm{rms}} \approx \pm 15\% - 20\%$) are also recorded in Table IV. Each case was computed by using the two methods. Modes grouped together on one line have close cutoff frequencies. It appears that results are not identical from one column to another but are rather similar.

The standard deviation σ defined in Eq. (14) remains of the order of 1 dB (last line of Table IV). More precisely, Fig. 14 details the differences between the computed and input SPL versus the radiation angle (like in bottom graphs of Figs. 9 and 10). It can be deduced that the solution remains rather stable and signal processing is robust in presence of a signal-to-noise ratio. It is also seen that the smallest standard devia-

TABLE IV. Effect of random errors in the test of Figs. 9 and 10 on the predicted modes and the standard deviation (last line): BPF=3039 Hz, $\mu=1-3$ (53 propagating modes).

Modes (m,μ) and σ, pinv function							Modes (m,μ) and σ, \ operator						
Test	±0.5 dB No. 1	±0.5 dB No. 2	±0.5 dB No. 3	±1 dB No. 1	±1 dB No. 2	±1.5dB	Test	±0.5 dB No. 1	±0.5 dB No. 2	±0.5 dB No. 3	±1 dB No. 1	±1 dB No. 2	±1.5dB
(0,1)	(0,1)	(0,1)	(0,1)	(0,1)	(0,1)	(0,1)	(0,1)	(0,1)	(0,1)	(0,1)	(0,1)	(0,1)	(0,1)
(1,1)		(1,1)	(1,1)	(1,1)			(1,1)	(1,1)	(1,1)	(1,1)	(1,1)	(1,1)	
(2,1)	(2,1)	(3,1)		(3,1)	(2,1)								(4,1)
(1,2)	(1,2)		(1,2)		(1,2)	(0,2)	(1,2)	(1,2)	(1,2)	(1,2)	(1,2)	(1,2)	(0,2)
(5,1)	(5,1)	(5,1)	(3,2)	(5,1)	(5,1)	(2,2)	(5,1)	(6,1)	(6,1)	(6,1)	(6,1)	(6,1)	(0,3)
(9,1)	(9,1)	(9,1)	(9,1)				(6,2)				(5,2)		
(11,1)	(11,1)	(11,1)	(11,1)	(11,1)	(11,1)	(10,1)	(12,1)	(7,2)	(7,2)	(7,2)	(11,1)	(7,2)	(10,1)
(9,2)	(9,2)	(9,2)	(9,2)			(6,3)	(9,3)	(16,2)	(16,2)	(16,2)	(10,2)	(9,2)	(9,2)
(14,1)	(14,1)	(14,1)	(14,1)	(14,1)	(14,1)			(14,1)	(14,1)	(14,1)			
(17,1)	(17,1)	(17,1)	(17,1)	(17,1)	(17,1)	(19,1)	(17,1)	(16,1)	(16,1)	(16,1)	(17,1)	(17,1)	(19,1)
(21,1)	(21,1)	(21,1)	(21,1)	(21,1)	(21,1)		(21,1)				(21,1)	(21,1)	
0.47	0.79	0.56	0.55	0.74	1.05	1.35	0.57	1.24	1.19	1.27	0.72	0.88	1.27

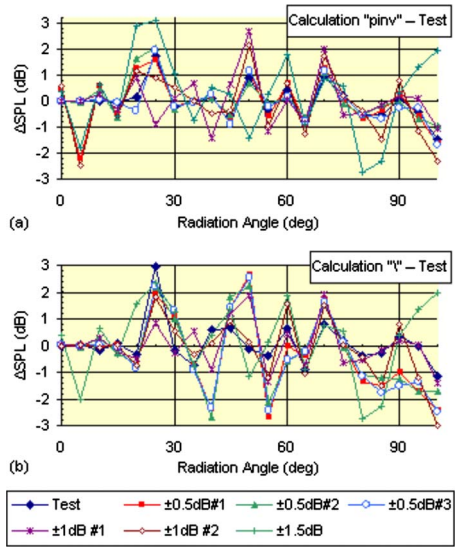

FIG. 14. (Color online) Effect of random errors on test data from Figs. 8 and 9.

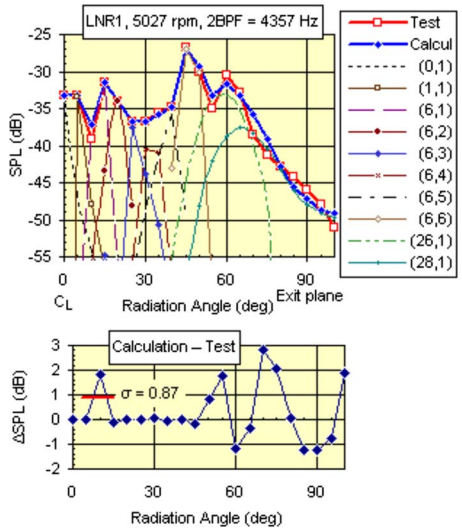

FIG. 16. (Color online) Final prediction of modes generating the measured directivity on the first harmonic of BPF.

tions are reached for the actual test data which surely means that measurement errors are less than ±0.5 dB.

D. Second test case

Let us now consider another test of RESOUND fan LNR1 at 5027 rpm and the first harmonic of BPF (2BPF) at 4357 Hz ($KR=34.78$). There is a low-order interaction mode between the 26-bladed rotor and the 58 outlet guide vanes in the bypass duct: $|m|=6$. Modes (6,1)–(6,8) may propagate in the duct. The system of equations is overdetermined by using only these eight modes. This is a conventional least squares fitting and the two methods [Eqs. (11) and (12)] give the same result. Squared amplitudes of the eight modes already are positive in the first iteration. It is seen in Fig. 15 that prediction is very accurate between 10° and 60° but some other modes are required to explain the sound levels at small and large angles.

As it was done in a previous paper,[12] modes (0,1)–(5,1) are also taken for radiation around the duct centerline, along with the last modes with $\mu=1$, i.e., (26,1)–(32,1) for lateral radiation. Computation is thus made on $N=21$ modes, again for the $J=21$ test data. Prediction (not shown) is of very poor quality around 25° and at 40°. Standard deviation is $\sigma=3.6$ dB. Since it is known that modes $|m|=6$ are theoretically present, they are maintained for the second iteration in another run. Result is then in good agreement with the test data (Fig. 16). Ten modes instead of eight are found. Modal sound levels are summarized in Fig. 17 (like Fig. 11). It is again assessed that the two computed PWLs are equal.

This second test case appears to be very interesting because it is proven that the strategy eliminating modes whose squared amplitude is negative is not always valid. Moreover, it is shown that the initial selection of modes must take into account the known physical properties of the acoustic field.

V. CONCLUSIONS

The present work follows a previous article to estimate the acoustic modes and their amplitudes generating a measured free-field directivity, without requiring expensive experimental modal analyses. The proposed model is based on analytical equations describing ducted propagation, and on a Kirchhoff (or a Rayleigh) integral for far-field radiation. Calculations are split into two steps. First, sound pressures of all the propagating modes at the frequency under study are computed at the measurement locations, assuming a unit amplitude for each mode. Second, the system of equations with the measured data in the second member has to be solved to find the unknown actual modal amplitudes.

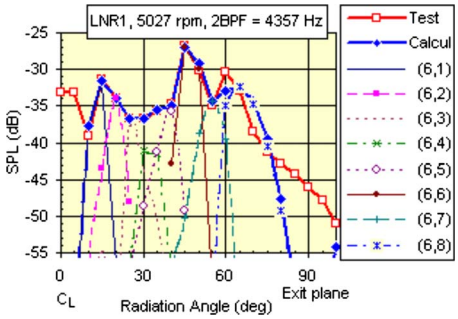

FIG. 15. (Color online) Prediction of modes $|m|=6$ generating the measured directivity on the first harmonic of BPF.

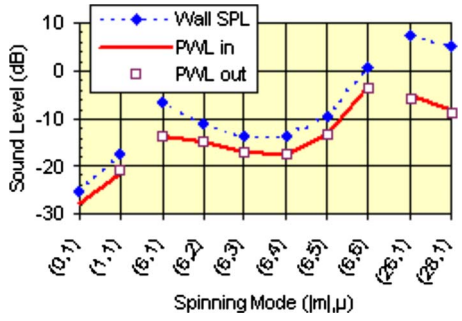

FIG. 17. (Color online) Duct-wall SPL and sound PWLs for the prediction in Fig. 16.

It has been outlined that a least squares fitting is the best way to get the expected result because a method based on transfer matrix would be very sensitive to measurement errors. There is however a difficulty because the number of unknowns is generally higher than the number of experimental data. Two methods have thus been tested, by using either the pseudoinverse function or the backslash operator of MATLAB. An iterative process is required to fulfill the constraint that the squared modal amplitudes must be positive. The system of equations, which usually is underdetermined (more unknowns than measurements) at the beginning, becomes overdetermined during the iterations because the modes, which do not fulfill the constraint, are deleted.

Numerical simulations and analyses of some RESOUND tests have proven that several solutions can well fit the test data. This means that the initial set of modes used in the calculations must be carefully chosen, according to any *a priori* knowledge of the physical mechanisms generating the acoustic sources, e.g., rotor-stator interactions.

The most interesting result is that only a few iterations are necessary, such that computation is very fast and can be made online. Predictions accurately fit the test directivities, standard deviations are less than 1 dB.

Future improvements should solve two issues. First, it has been outlined that the strategy consisting eliminating the modes whose squared amplitude is negative is not always valid because some of them could recover a positive squared amplitude in following iterations. Second, the two methods from MATLAB do not give the same results (as expected), but it is not clear which is better, and they could be mixed during the iterations.

ACKNOWLEDGMENTS

This work has been done within the framework of the European integrated project SILENCE®. The author would like to thank Helene Gounet for her valuable contribution to numerical simulations.

[1]J. M. Tyler and T. G. Sofrin, "Axial flow compressor noise studies," SAE Trans. **70**, 309–332 (1962).
[2]P. A. Nelson, "A review of some inverse problems in acoustics," Int. J. Acoust. Vib. **6**, 118–134 (2001).
[3]M. B. S. Magalhães and R. A. Tenenbaum, "Sound sources reconstruction techniques: A review of their evolution and new trends," Acta. Acust. Acust. **90**, 199–220 (2004).
[4]E. G. Williams, "Regularization methods for near-field acoustical holography," J. Acoust. Soc. Am. **110**, 1976–1988 (2001).
[5]J. Luo and X. D. Li, "An inverse aeroacoustic problem on rotor wake/stator interaction," J. Sound Vib. **254**, 219–229 (2002).
[6]Y. Kim and P. A. Nelson, "Estimation of acoustic source strength within a cylindrical duct by inverse methods," J. Sound Vib. **275**, 391–413 (2004).
[7]A. Gerard, A. Berry, and P. Masson, "Control of tonal noise from subsonic axial fan. Part 1: reconstruction of aeroacoustic sources from far-field sound pressure," J. Sound Vib. **288**, 1049–1075 (2005).
[8]D. A. Venditti, O. Mehdizadeh, N. Joshi, and A. A. Ali, "Turbofan duct-mode identification using farfield noise measurements and numerical predictions," 12th AIAA/CEAS Aeroacoustics Conference, Cambridge, MA (2006), AIAA Paper No. 2006-2641.
[9]F. O. Castres and P. F. Joseph, "Mode detection in turbofan inlets from near field sensor arrays," J. Acoust. Soc. Am. **121**, 796–807 (2007).
[10]F. O. Castres and P. F. Joseph, "Experimental investigation of an inversion technique for the determination of broadband duct mode amplitudes by the use of near-field sensor arrays," J. Acoust. Soc. Am. **122**, 848–859 (2007).
[11]A. Schuhmacher, J. Hald, K. B. Rasmussen, and C. Hansen, "Sound source reconstruction using inverse boundary element calculations," J. Acoust. Soc. Am. **113**, 114–127 (2003).
[12]S. Lewy, "Inverse method predicting spinning modes radiated by a ducted fan from free-field measurements," J. Acoust. Soc. Am. **117**, 744–750 (2005).
[13]S. Lewy, J. Lambourion, C. Malarmey, M. Perulli, and B. Rafine, "Direct experimental verification of the theoretical model predicting rotor noise generation," AIAA 5th Aeroacoustics Conference, Seattle, WA (1979), AIAA Paper No. 79-0658.
[14]R. W. Schaffer, R. M. Mersereau, and M. A. Richards, "Constrained iterative restoration algorithm," Proc. IEEE **69**, 432–450 (1981).
[15]S. Lewy and H. Gounet, "Numerical inverse method predicting acoustic spinning modes radiated by a ducted fan from free-field simulated test data," 13th International Congress on Sound and Vibration, Vienna, Austria (2006).
[16]E. J. Rice, "Multimodal far field acoustic radiation pattern using mode cutoff ratio," AIAA J. **16**, 906–911 (1978).
[17]P. A. Nelson and S. H. Yoon, "Estimation of acoustic source strength by inverse methods: Part I, conditioning of the inverse problem," J. Sound Vib. **233**, 643–668 (2000).
[18]C. J. Moore, "Measurement of radial and circumferential modes in annular and circular fan ducts," J. Sound Vib. **62**, 235–256 (1979).

Self-reported sleep disturbances due to railway noise: Exposure-response relationships for nighttime equivalent and maximum noise levels

Gunn Marit Aasvang[a)]
Department of Air Pollution and Noise, Division of Environmental Medicine, Norwegian Institute of Public Health, P.O. Box 4404 Nydalen, N-0403 Oslo, Norway

Torbjørn Moum
Department of Medical Behaviour, University of Oslo, P.O. Box 1111 Blindern, N-0316 Oslo, Norway

Bo Engdahl
Division of Mental Health, Norwegian Institute of Public Health, P.O. Box 4404 Nydalen, N-0403 Oslo, Norway

(Received 21 November 2007; revised 8 April 2008; accepted 27 April 2008)

The objective of the present survey was to study self-reported sleep disturbances due to railway noise with respect to nighttime equivalent noise level ($L_{p,A,\mathrm{eq,night}}$) and maximum noise level ($L_{p,A,\mathrm{max}}$). A sample of 1349 people in and around Oslo in Norway exposed to railway noise was studied in a cross-sectional survey to obtain data on sleep disturbances, sleep problems due to noise, and personal characteristics including noise sensitivity. Individual noise exposure levels were determined outside of the bedroom facade, the most-exposed facade, and inside the respondents' bedrooms. The exposure-response relationships were analyzed by using logistic regression models, controlling for possible modifying factors including the number of noise events (train pass-by frequency). $L_{p,A,\mathrm{eq,night}}$ and $L_{p,A,\mathrm{max}}$ were significantly correlated, and the proportion of reported noise-induced sleep problems increased as both $L_{p,A,\mathrm{eq,night}}$ and $L_{p,A,\mathrm{max}}$ increased. Noise sensitivity, type of bedroom window, and pass-by frequency were significant factors affecting noise-induced sleep disturbances, in addition to the noise exposure level. Because about half of the study population did not use a bedroom at the most-exposed side of the house, the exposure-response curve obtained by using noise levels for the most-exposed facade underestimated noise-induced sleep disturbance for those who actually have their bedroom at the most-exposed facade.
 [DOI: 10.1121/1.2932074]

PACS number(s): 43.50.Qp, 43.50.Lj [BSF] Pages: 257–268

I. INTRODUCTION

Sleep disturbances are regarded as being among the most serious effects of environmental noise (Berglund *et al.*, 2000) and one of the most common reasons for noise complaints (Guski, 1977). Experimental studies have found that partial sleep deprivation has negative effects on sleepiness, performance, and mood (Dinges *et al.*, 1997), as well as on some metabolic, hormonal, and immunological variables (Irwin *et al.*, 1996; Spiegel *et al.*, 1999); thus, it may have serious long-term health effects (Ferrara and Gennaro, 2001). Field surveys have shown that transportation noise disturbs sleep (Horne *et al.*, 1994; Fidell *et al.*, 1995; Passchier-Vermeer *et al.*, 2002; Basner *et al.*, 2006), as have laboratory studies (Griefahn, 1986; Thiessen, 1988; Öhrström and Rylander, 1990; Öhrström, 1995). A number of different methods have been used to assess noise effects on sleep quality, such as questionnaires to determine self-reported sleep disturbances, behaviorally confirmed awakenings, motility recordings (actimetry), and physiologically recorded responses obtained by polysomnography, the latter of which is most often done in laboratory settings. A comprehensive review (Pearson *et al.*, 1995) revealed substantial and systematic differences in noise-induced sleep disturbance between the findings of studies conducted in the laboratory and those in the home environment. This discrepancy has been attributed both to methodological differences among studies and to a higher sensitivity to noise in the laboratory setting. More naturalistic field studies with high-quality noise exposure characterization have therefore been in great demand.

Railway noise can disturb daily activities and generate annoyance, and interference with communication is the most frequent problem associated with noise from railways (Moehler, 1988). Nevertheless, the effects of noise and the kinds of disturbances it generates depend on the time of day the noise occurs. With increasing railway traffic during nighttime hours, railway noise can also significantly interfere with sleep. Railway noise is characterized by isolated events with high maximum noise levels ($L_{p,A,\mathrm{max}}$).

Studies on the effects of noise on humans, including noise-induced sleep disturbances, have primarily focused on aircraft and road traffic noise. Fewer studies have targeted the possible harmful effects of nighttime noise from railways

[a)]Author to whom correspondence should be addressed. Tel.: 47-21-07-65-38. FAX: 47-21-07-66-86. Electronic mail: gunn.marit.aasvang@fhi.no

(e.g., Vernet, 1979, 1983; Griefahn *et al.*, 2000; Bluhm and Nordling, 2005; Griefahn *et al.*, 2006). Most of these studies compared the effects on sleep from different noise sources (railway, aircraft, and road traffic) and were not specifically aimed at quantifying exposure-response relationships. One exception is a recent meta-analysis reported by Miedema and Vos (2007), in which the main objective was to establish the exposure-response relationship between average nighttime noise exposure and self-reported sleep disturbances.

The Directive on Environmental Noise proposed by the EU (European Commission, 2002) specifies the indicator L_{night}, which is the annual-average equivalent noise level during (an 8 hour) nighttime to predict noise-induced sleep disturbances. L_{night} is a cumulative noise metric intended for regulatory use in preventing the possible harmful effects of long-term exposure to nocturnal noise. Scientific knowledge about how such an average equivalent noise metric relates to noise-induced sleep disturbances remains limited. It has been argued that a cumulative noise exposure metric ($L_{p,\text{eq},T}$) is inappropriate for predicting human responses to noise, especially sleep disturbances (Fidell *et al.*, 1995). Some authors have suggested that a noise metric that reflects the peak level of single noise events, such as $L_{p,A,\max}$ or L_E, and the number of noise events is a better predictor of noise-induced sleep disturbances when the noise is not of a continuous nature (Rylander and Björkman, 1988; Griefahn *et al.*, 2000).

In field studies on the health impact of community noise, noise exposure is commonly assessed for the most-exposed facade of the dwelling (e.g., Miedema and Vos, 2007). Not all people have their bedroom facing the side of the house with the highest noise exposure. Exposure-response relationships developed from studies by using noise exposure calculated at the most-exposed facade may therefore be biased because a proportion of the study population will actually be exposed to a lower noise level outside their bedroom. Further, there is a need for more knowledge about noise-induced sleep disturbances in relation to indoor noise levels from outdoor sources at home under real-life conditions.

The main objective of the present study was to obtain data on exposure-response relationships between railway noise and self-reported sleep disturbances. We specifically studied equivalent noise level ($L_{p,A,\text{eq,night}}$) and maximum noise level ($L_{p,A,\max}$) during nighttime both indoors and outdoors to compare their predictive power for self-reported difficulty falling asleep and awakenings. The exposure-response relationships were further studied in light of possible modifying factors such as the duration of residence and noise sensitivity, as well as train pass-by frequency. We also addressed the possible difference in exposure-response relationships when noise is assessed for the most-exposed facade compared to noise exposure calculated for the bedroom facade.

II. METHODS

A. Sample and survey

In the autumn of 2000, a questionnaire together with an introductory letter was administered to a population sample exposed to railway noise in and around Oslo ($n=2193$). The geographical areas chosen were not highly exposed to other types of transportation noise. Addresses were obtained from the Norwegian National Rail Administration in connection with its ongoing work on railway noise mapping. From the addresses, an age- and gender-stratified sample of participants was selected by using the central Norwegian person registry (49% female and 51% male >18 yr). The questionnaire consisted of items concerning perceived sleep quality and sleep disturbances, sleep problems because of noise, noise annoyance, properties of the dwelling, and personal characteristics such as year of birth, gender, total income, education, and noise sensitivity. A reminder letter was sent to subjects who did not answer within 2–3 weeks. To avoid a possible influence on responses to the noise questions, we presented the study in the introductory letter to the respondents as a general investigation of health and quality of life, with no specific focus on noise.

B. Noise exposure assessment

The Nordic Prediction Model for railway traffic noise (Nordic Council of Ministers, 1996) and Cadna A (DataKustik, 2004) were used for assessment of noise exposure based on the geographical coordinates of the address of each respondent. The respondents' houses were located along the railway line between 10 and 160 m from the track. Digital maps and data on railway traffic frequency were used as the basis for the noise calculations. Traffic data were obtained from the Norwegian National Rail Administration for a representative weekday for the relevant time period (autumn 2000) at the different railway stretches. The effects of distance from receiver to railway line, air absorption, ground properties, topography, and screens were included as major sound propagation effects. The noise metrics $L_{p,A,\text{eq,night}}$ and $L_{p,A,\max}$ were chosen for the characterization of nocturnal noise exposure. These parameters were calculated at two different locations outside each respondent's dwelling: at the most-exposed facade and at the bedroom facade. For each address, we used information provided on the questionnaire about which side of the dwelling the bedroom faced and the elevation of the bedroom. $L_{p,A,\text{eq,night}}$ was calculated by integrating the sound energy from all noise events over an 8 h nighttime. The 8 h nighttime is defined here as the period from 2300 to 0700. The maximum noise level for a train pass-by ($L_{p,A,\max\,M}$) was calculated as an energy average for the time it took for the train to pass. Thus, the $L_{p,A,\max}$ used for individual noise exposure assessment in this study was the highest value of $L_{p,A,\max\,M}$ obtained from all train passbys during nighttime for the actual railway stretch for each respondent. Compared to the more common parameter $L_{p,A,F\,\max}$ with time weighting, "fast" measurements suggest that the difference between $L_{p,A,\max\,M}$ and $L_{p,A,F\,\max}$ depends on two main factors: distance from the train and whether the train is diesel powered or electrically driven. If the distance from the train is more than 100 m, $L_{p,A,\max\,M}$ is assumed to be equal to $L_{p,A,F\,\max}$ (for more details, see Nordic Council of Ministers, 1996). Diesel-powered trains are seldom used at the routes included in this study. The outdoor noise levels are all given as free-field values.

The noise metrics $L_{p,A,\mathrm{eq,night}}$ and $L_{p,A,\mathrm{max}}$ were also calculated inside the respondents' bedroom. For each address, we used additional information provided on the questionnaire about the type of bedroom window and type of facade. The calculation of noise levels inside the bedroom was based on the noise exposure levels determined outside the bedroom facade and the estimation of facade sound insulation. Assessment of the facade sound insulation was conducted according to Handbook 47 (Norwegian Building Institute, 1999). No exact information regarding ventilation, size of windows, walls, or room volume was available in this study. The indoor noise exposure levels were therefore calculated for an "average" sized bedroom of 15 m^2, 36 m^3, facade wall of 10 m^2, window size of 1.5 m^2, and reverberation time of 0.5 s, and with the assumption that windows and ventilation inlets were kept shut.

C. Assessment of sleep quality and sleep disturbances due to traffic noise

Some of the questions on sleep quality and sleep disturbances were asked in general terms without any reference to noise. The general sleep questions were adopted from the Basic Nordic Sleep Questionnaire (Partinen and Gislason,1995), e.g., how well have you been sleeping? The response scale is as follows:

(1) well,
(2) rather well,
(3) neither well nor badly,
(4) rather badly, or
(5) badly.

For all questions regarding sleep, the time frame employed was the last three months prior to the time of responding to the questionnaire. In addition, the following questions were included among the questions on sleep disturbances.

(1) If you have difficulty falling asleep, what might the reasons be?
(2) If you wake up during the night or too early in the morning, what might the reasons be?

Following each of these two questions, a list of several possible reasons for sleep interference was presented. The respondents were asked to tick off one or more of the listed reasons for sleep problems. Embedded among the possible reasons for sleep problems were "I get disturbed by traffic noise" [question No. (1)] and "I wake up by traffic noise [question No. (2)]." The responses to these two questions formed the numerical values that were used as dependent variables (response/yes=1; no response=0) in the logistic regression analyses. The other possible reasons for sleep problems that were listed were "I ruminate about things," "I drink too much coffee during late evening," "I am stressed," "I get disturbed by neighborhood noise," "I wake up by own children," "I wake up because of pain," and "I wake up because of bad dreams/nightmare." By listing other possible reasons for sleep problems in the questionnaire, we reduced the attention toward noise, and at the same time, we obtained data on the relative proportions of different self-reported reasons for sleep disturbances.

D. Covariates

In the multivariate analyses, the following covariates were included:

- Age (year).
- Gender (F/M).
- Total income of the household (five categories recoded into two categories: $<$400 000 NOK/$\geqslant$400 000 NOK)
- Education, four categories recoded into two categories: basic education up to 10 yr (completed primary or secondary school)/completed high school ($\geqslant$12 yr).
- Noise sensitivity: The last question of Weinstein's noise sensitivity scale was used (Weinstein, 1978) (six-point ordinal variable recoded into three categories: not sensitive/somewhat sensitive/rather to very sensitive).
- Type of bedroom windows (three categories: single-glazed or two single windows with separate frames/double-glazed or insulated single-glazed/triple-glazed or riaphon windows).
- Duration of residence (3 months–1 yr/1–5 yr/$>$5 yr).
- Pass-by frequency of trains [number of pass-bys per night (2300-0700)] (four categories: $<$30/30–40/80–100/$>$100).

Two-way statistical interactions between the exposure variables and the other variables were tested for significance. The possibility of nonlinear associations was tested statistically by the addition of a quadratic term into the logistic regression analyses.

E. Statistical analyses

The relationship between noise-induced sleep disturbances and the different noise metrics ($L_{pA,\mathrm{eq,night}}$ and $L_{p,A,\mathrm{max}}$) was explored by multivariate logistic regression analyses by using self-reported difficulty falling asleep and awakenings due to traffic noise as dependent variables and railway noise exposure as an independent variable. The potential confounders or effect modifiers, described in Sec. II D, were included as covariates in the regression models. For each independent variable, a slope value (beta) was estimated. The level of significance and 95% confidence interval (CI) for the parameters were tested with Wald statistics. The significance of the whole model was tested with Hosmer–Lemeshow goodness-of-fit statistics to test the adequacy of each model in predicting the empirically obtained data. The greater the P value (the smaller the chi-square value), the better the model fits the data. CIs for proportions of subjects that reported sleep disturbances were calculated according to Wilson (Wilson, 1927; Altman *et al.*, 2001). The data were analyzed by using SPSS version 14.00 and Excel 2003 for Windows.

TABLE I. Number and percentage of respondents exposed to railway noise assessed outdoors.

$L_{p,A,\mathrm{eq,night}}$ bedroom facade			$L_{p,A,\max}$ bedroom facade			$L_{p,A,\mathrm{eq,night}}$ most-exposed facade		
dB	N	%	dB	N	%	dB	N	%
<40	50	3.7	<65	168	12.5			
40–44	233	17.3	65–69	248	18.4	<45	27	2.0
45–49	248	18.4	70–74	179	13.3	45–49	39	2.9
50–54	202	15.0	75–79	227	16.8	50–54	175	13.0
55–59	241	17.9	80–84	231	17.1	55–59	405	30.0
60–64	269	19.9	85–89	219	16.2	60–64	508	37.7
⩾65	106	7.9	>90	77	5.7	⩾65	195	14.5
Total	1349	100		1349	100		1349	100

III. RESULTS

A. Sample

A total of 1395 respondents (63.7% of those approached) answered and returned the questionnaire. Forty-six people who had either moved or whose home address was not verifiable were excluded from the analyses. A total of 1349 respondents ranging in age from 18 to 96 (51.3% female and 48.7% male) were used for the further analyses. The mean age of the respondents was 49 yr (±15.9 yr).

Differences between respondents and nonrespondents were analyzed based on variables that were available for the nonrespondents: gender, age, and noise exposure data based on crude characteristics (<42 dB or ⩾42 dB $L_{p,A,\mathrm{eq,24\ h}}$ inside the house). No significant differences between the respondents and the nonrespondents were found in the proportion of subjects exposed to noise below or above 42 dB. Slight differences in age and gender distribution were found, however. Compared to the total sample approached, a somewhat higher response rate for females than for males was obtained, and the younger (<37 yr) and the elderly (>78 yr) were slightly under-represented compared to the total survey sample.

B. Descriptive results

1. Noise exposure

Noise exposure outside of the most-exposed facade of the house and outside of the bedroom was calculated for all respondents included in the analyses (n=1349). Because of missing information in the questionnaires on the type of bedroom window and/or facade for some of the addresses (n =202), calculation of the noise level inside of the bedroom was possible for 1147 respondents only. Tables I and II summarize the number and percentage of respondents exposed to nighttime noise categorized into 5 dB interval groups (except from the first and last categories). The difference between outdoor and indoor (bedroom) noise levels, i.e., the facade insulation, ranged from 30 to 42 dB; the mean value of facade insulation was 36 dB. The total number of train passbys during the night (2300-0700) varied between 11 and 136 for the different railway stretches. The number of pass-bys of freight trains during the night varied between 3 and 19, and the proportion of freight trains ranged from 4% to 51%. As could be expected, there were strong correlations between the outdoor and indoor noise levels (Table III). $L_{p,A,\max}$ and $L_{p,A,\mathrm{eq,night}}$ were also highly correlated ($r>0.9$, $P<0.01$). The total number of train pass-bys during the night showed a weak negative correlation with $L_{p,A,\max}$ but did not correlate with $L_{p,A,\mathrm{eq,night}}$.

2. Sleep quality and sleep disturbances

Responses to the question on sleep quality showed that 74% of respondents had slept well or rather well during the last three months. Sleeping rather badly or badly was reported by 8.8%. The mean total sleep time was about 7 h (419 min ± 60 min). The number and percentage of the respondents that reported various reasons for experiencing difficulty falling asleep and awakenings are presented in Table IV. Noise from traffic was given as the reason for difficulty falling asleep and awakenings by 82 (6.1%) and 111 respon-

TABLE II. Number and percentage of respondents exposed to railway noise assessed inside of the bedroom.

$L_{p,A,\mathrm{eq,night}}$ inside the bedroom			$L_{p,A,\max}$ inside the bedroom		
dB	N	%	dB	N	%
<10	147	12.8	<30	81	7.1
10–14	215	18.7	30–34	195	17.0
15–19	182	15.9	35–39	161	14.0
20–24	185	16.1	40–44	167	14.6
25–29	224	19.5	45–49	198	17.3
⩾30	194	16.9	50–54	204	17.8
			>55	141	12.3
Total	1147	100		1147	100

TABLE III. Correlation matrix for the different noise metrics determined outside the bedroom facade, inside of the bedroom, and train pass-by frequency.

	$L_{p,A,\mathrm{eq,night}}$ outside	$L_{p,A,\mathrm{eq,night}}$ inside	$L_{p,A,\mathrm{max}}$ outside	$L_{p,A,\mathrm{max}}$ inside	Pass-by frequency
$L_{p,A,\mathrm{eq,night}}$ outside	1				
$L_{p,A,\mathrm{eq,night}}$ inside	0.97[a]	1			
$L_{p,A,\mathrm{max}}$ outside	0.95[a]	0.92[a]	1		
$L_{p,A,\mathrm{max}}$ inside	0.93[a]	0.95[a]	0.97[a]	1	
Pass-by frequency	−0.03	−0.02	−0.12[a]	−0.11[a]	1

[a]Correlation is significant at the 0.01 level (two tailed).

dents (8.2%), respectively. There was a substantial degree of overlap between the responses to these two questions. Among those who reported awakenings because of transportation noise, 62% also claimed to have difficulty falling asleep because of noise. 68% of respondents reported sleeping with their bedroom windows open at night, and 12% reported sleeping with the bedroom windows closed because of nocturnal traffic noise.

3. Exposure-response relationships

Results from the logistic regression analyses (Tables V and VI) confirmed the simple exposure-response curves (no adjustment for covariates), which are depicted in Figs. 1 and 2 for $L_{p,A,\mathrm{eq,night}}$ and $L_{p,A,\mathrm{max}}$ outside the bedroom facade. Similar trends in the exposure-response relationships were found for the indoor parameters (Tables VII and VIII) because of a high correlation between outdoor and indoor noise levels (Table III). The nonsignificant covariates showed similar patterns in all models and therefore are shown only in the analyses of the outdoor noise metrics (Tables V and VI). All models, except the model including $L_{p,A,\mathrm{max}}$ inside the bedroom versus noise-induced awakenings, indicate a good overall fit ($P>0.05$, Hosmer–Lemeshow goodness-of-fit test).

(*a*) $L_{p,A,\mathrm{eq,night}}$ *and reported sleep disturbances due to noise*. Exposure-response relationships were analyzed between $L_{p,A,\mathrm{eq,night}}$ and reported difficulty falling asleep and awakenings, respectively. A significant odds ratio (OR) for difficulty falling asleep was found for $L_{p,A,\mathrm{eq,night}}>65$ dB at the bedroom facade (Table V) and $L_{p,A,\mathrm{eq,night}}\geqslant 25-29$ dB inside of the bedroom (Table VII), when controlled for possible modifying factors. A significant OR for the noise-induced awakenings was found at $L_{p,A,\mathrm{eq,night}}\geqslant 60-64$ dB outside of the bedroom and at $L_{p,A,\mathrm{eq,night}}\geqslant 25-29$ dB inside the bedroom (Tables V and VII, respectively). The simple exposure-response relationships for $L_{p,A,\mathrm{eq,night}}$ at the bedroom facade and self-reported noise-induced sleep disturbances are depicted in Fig. 1.

None of the sociodemographic variables included in the analyses—age, gender, basic education, or total income—showed a significant impact on self-reported sleep disturbances. Neither the duration of residence nor the number of train pass-bys during the night affected the noise-induced sleep problems significantly in the regression model. On the other hand, self-reported noise sensitivity was a strong and significant predictor. In the present study, 29% were categorized as rather or very sensitive to noise, 38% were somewhat sensitive, and 33% were not sensitive. No significant association between noise sensitivity and noise level was found ($r_s=-0.004$, $P=0.88$).

The degree of insulation of the bedroom window showed a significant effect only on reported difficulty falling asleep (Table V). Those who had single-glazed windows or two single windows with separate frames (older windows) reported significantly more often having difficulty falling

TABLE IV. Reported reasons for difficulty falling asleep and awakenings (total number of affected respondents, *N*, and percentage, %).

	Difficulty falling asleep		Awakenings	
	N	%	*N*	%
Ruminate about things	447	33.1	⋯	⋯
Do not know	248	18.4	454	33.6
Stress	237	17.6	⋯	⋯
Other	224	16.6	406	30.1
Too much coffee	149	11.0	⋯	⋯
Awakened by own children	⋯	⋯	238	17.6
Pain	⋯	⋯	142	10.5
Bad dreams/nightmare	⋯	⋯	81	6.0
Traffic noise	82	6.1	111	8.2
Neighborhood noise	24	1.8	24	1.8

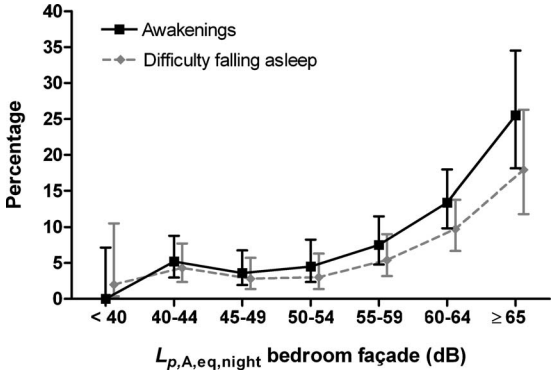

FIG. 1. Self-reported sleep disturbances due to noise as a function of outdoor nighttime $L_{p,A,\mathrm{eq,night}}$ (bedroom facade): proportions with 95% CIs.

TABLE V. Associations between $L_{p,A,\mathrm{eq,night}}$ outdoor (bedroom facade) and reported sleep problems due to noise (OR with 95% CI and significance level P).

Variable	Difficulty falling asleep		Awakenings	
	OR[a] (95% CI)	P	OR[a] (95% CI)	P
$L_{p,A,\mathrm{eq,night}}$ bedroom facade	(reference: 0=<40 dB)		(reference: 0=40–44 dB)[b]	
40–44 dB	2.21 (0.25–19.37)	0.47	1.00	
45–49 dB	1.22 (0.13–11.49)	0.86	0.72 (0.28–1.90)	0.51
50–54 dB	1.73 (0.19–15.67)	0.63	0.89 (0.34–2.35)	0.81
55–59 dB	2.77 (0.32–23.74)	0.35	1.67 (0.73–3.84)	0.23
60–64 dB	6.40 (0.78–52.62)	0.08	3.60 (1.69–7.63)	0.01
≥65 dB	13.75 (1.60–118.10)	0.02	7.13 (3.10–16.37)	0.00
Age	0.99 (0.97–1.01)	0.19	0.99 (0.98–1.01)	0.51
Gender (0=female/1=male)	1.35 (0.80–2.28)	0.26	0.95 (0.61–1.48)	0.83
Total income (0=<400 000 NOK/1=≥ 400 000 NOK)	1.17 (0.67–2.02)	0.59	1.01 (0.67–1.71)	0.78
Education (0=up to junior secondary school (≤10 yr)/1=high school (≥12 yr))	0.84 (0.47–1.52)	0.57	0.90 (0.54–1.48)	0.67
Duration of residence (reference: 0=<1 yr)				
1–5 yr	1.54 (0.47–5.02)	0.47	1.01 (0.40–2.99)	0.86
>5 yr	1.23 (0.37–4.03)	0.73	1.06 (0.39–2.88)	0.91
Noise sensitivity (reference: 0=not sensitive)				
Somewhat sensitive	1.66 (0.72–3.84)	0.24	1.66 (0.87–3.14)	0.12
"Rather to very" noise sensitive	7.72 (3.61–16.48)	0.00	4.52 (2.47–8.26)	0.00
Type of bedroom window [reference: 0=sound-insulated windows (triple glazed or riaphon)]				
Single-glazed or two single windows with separate frames	2.32 (1.04–5.15)	0.04	1.04 (0.48–2.24)	0.92
Double-glazed or insulated single-glazed window	0.95 (0.46–1.92)	0.88	1.30 (0.71–2.40)	0.40
Pass-by frequency during the night (reference: 0=<30)				
30–40	1.34 (0.37–4.86)	0.66	0.78 (0.28–2.16)	0.64
80–100	1.70 (0.47–6.15)	0.42	1.61 (0.59–4.40)	0.35
>100	3.63 (0.63–20.94)	0.15	1.03 (0.17–6.31)	0.97

[a]Multivariate model; adjusted for all other variables in the table.
[b]In the analysis of awakenings, the category $L_{p,A,\mathrm{eq,night}}$=40–44 dB was chosen as the reference due to no reported awakenings and a small number of respondents in the lowest noise level category (<40 dB). Hosmer–Lemeshow goodness-of-fit test for difficulty falling asleep: chi square=8.23, df=8, and P=0.41. Hosmer–Lemeshow goodness-of-fit test for awakenings: chi square=11.71, df=8, and P=0.17.

asleep because of noise (OR=2.32, 95% CI=1.04–5.15) compared to those who had bedroom windows with better sound insulation (triple-glazed or riaphon) (Table V).

(*b*) $L_{p,A,\max}$ *and reported sleep disturbances due to noise*. $L_{p,A,\max}$ also showed an exposure-response relationship with both reported difficulty falling asleep and awakenings due to noise. In Tables VI and VIII, results are presented from the logistic regression analyses for $L_{p,A,\max}$ at the bedroom facade and inside of the bedroom as major exposure variables, respectively. A significant OR for difficulty falling asleep was found for $L_{p,A,\max} \geqslant 85-89$ dB at the bedroom facade and $L_{p,A,\max} \geqslant 50-54$ dB inside the bedroom when adjusted for possible modifying factors. A significant OR for noise-induced awakenings was found at $L_{p,A,\max} \geqslant 80-84$ dB at the bedroom facade and $L_{p,A,\max} \geqslant 50-54$ dB inside the bedroom. The simple exposure-response relationships for $L_{p,A,\max}$ at the bedroom facade and self-reported noise-induced sleep disturbances are depicted in Fig. 2.

Neither the sociodemographic variables included in the analyses nor the duration of residence showed a significant impact on self-reported sleep disturbances (Table VI). The pass-by frequency of trains during the nighttime showed an effect on reported sleep disturbances, but it was different for difficulty falling asleep and for awakenings. With respect to difficulty falling asleep, there was a steady increase in ORs with increasing number of train pass-bys during the night. This relationship was not found for the self-reported awakenings, in which a significantly higher OR was found only for the intermediate category (80–100 pass-bys) and not for the highest number of train pass-bys (>100 pass-bys) (Tables VI and VIII). This pattern was most pronounced in

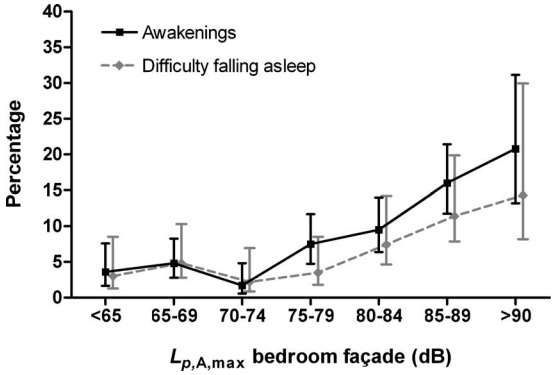

FIG. 2. Self-reported sleep disturbances due to noise as a function of outdoor nighttime $L_{p,A,\max}$ (bedroom facade): proportions with 95% CIS.

TABLE VI. Associations between $L_{p,A,\max}$ outdoor (bedroom facade) and reported sleep problems due to noise (OR with 95% CI and significance level P).

Variable	Difficulty falling asleep		Awakenings	
	OR[a] (95% CI)	P	OR[a] (95% CI)	P
$L_{p,A,\max}$, bedroom facade (reference: 0=<65dB)				
65–69 dB	1.01 (0.31–3.28)	0.98	1.04 (0.36–3.06)	0.94
70–74 dB	0.71 (0.18–2.79)	0.71	0.46 (0.11–1.90)	0.28
75–79 dB	0.91 (0.26–3.15)	0.88	2.01 (0,74–5.48)	0.17
80–84 dB	2.23 (0.77–6.53)	0.14	2.91 (1.12–7.58)	0.03
85–89 dB	4.35 (1.54–12.27)	0.01	5.36 (2.11–13.65)	0.00
>90 dB	7.48 (2.23–25.03)	0.00	9.81 (3.42–28.18)	0.00
Age	0.99 (0.97–1.01)	0.25	1.0 (0.98–1.01)	0.62
Gender (0, female/1, male)	1.40 (0.83–2.34)	0.21	0.98 (0.63–1.52)	0.93
Total income (0=<400 000 NOK/1=≥ 400 000 NOK)	1.20 (0.69–2.09)	0.51	1.08 (0.68–1.73)	0.74
Education (0=up to junior secondary school (≤10 yr)/1=high school (≥12 yr).	0.80 (0.45–1.45)	0.48	0.88 (0.53–1.44)	0.60
Duration of residence (reference: 0=<1 yr)				
1–5 yr	1.32 (0.40–4.34)	0.64	1.03 (0.38–2.80)	0.96
>5 yr	1.04 (0.32–3.44)	0.94	0.96 (0.35–2.58)	0.93
Noise sensitivity (reference: 0=not sensitive)				
Somewhat sensitive	1.60 (0.69–3.72)	0.271.65 (0.87–3.12)	0.13	
"Rather to very" noise sensitive	7.98 (3.73–17.05)	0.00	4.75 (2.60–8.71)	0.00
Type of bedroom window (reference: 0=sound-insulated windows (triple glazed or riaphon)				
Single-glazed or two single windows with separate frames	2.34 (1.05–5.24)	0.04	1.06 (0.49–2.29)	0.88
Double-glazed or insulated single-glazed window	0.95 (0.47–1.93)	0.86	1.32 (0.72–2.43)	0.38
Pass-by frequency during the night (reference: 0=<30) (n)				
30–40	2.49 (0.71–8.80)	0.16	1.66 (0.61–4.51)	0.32
80–100	3.25 (0.91–11.62)	0.07	3.49 (1.28–9.48)	0.01
>100	7.95 (1.41–45.02)	0.02	2.50 (0.41–15.23)	0.32

[a]Multivariate model, adjusted for all other variables in the table. Hosmer-Lemeshow goodness-of-fit test for difficulty falling asleep: chi square=7.40, df =8, and P=0.50. Hosmer-Lemeshow goodness-of-fit test for awakenings: Chi square=7.56, df=8, and P=0.47.

the model of $L_{p,A,\max}$ at the bedroom facade (Table VI), but the same tendency was also shown for indoor $L_{p,A,\max}$ (Table VIII).

As in the models including $L_{p,A,\mathrm{eq,night}}$, the degree of insulation of the bedroom window showed a significant effect only for reported difficulty falling asleep. Those who had single-glazed windows or two single windows with separate frames (older windows) reported significantly more often having difficulty falling asleep due to noise (OR =2.34, 95% CI=1.05–5.24) compared to those who had bedroom windows with better sound insulation (triple-glazed or riaphon) (Table VI).

A systematic search for statistical interactions between the noise exposure variables and the other independent variables, performed by adding multiplicative terms to the regression equations, revealed no cases of effect modification.

(*c*) *Exposure-response relationship for the most-exposed facade versus bedroom facade*. 45% of the sample reported using a bedroom located inside of the facade toward the railway line. 50% used a bedroom located toward a garden or a backyard. Figure 3 demonstrates the difference in exposure-response relationship when the noise level was calculated outside of the most-exposed facade and when noise was assessed outside the bedroom facade. In this figure, the number of respondents either reporting difficulty falling asleep and/or awakenings due to noise were pooled together to give the percentage of noise-induced sleep-disturbed respondents. For the two lowest categories of noise level at the most-exposed facade (<40 and 40–44 dB), there were too few exposed respondents, so no data representing these noise levels are shown in the figure. When relating percentage of sleep-disturbed subjects to noise levels determined for a

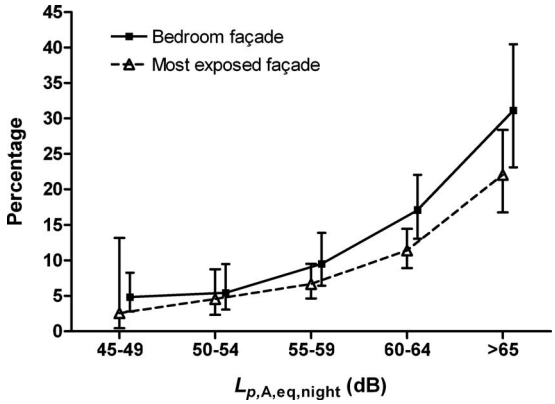

FIG. 3. Proportion of self-reported sleep disturbances (difficulty falling asleep and/or awakenings) due to noise as a function of outdoor nighttime $L_{p,A,\mathrm{eq,night}}$ calculated for the most-exposed facade and for the bedroom facade: proportions with 95% CIs.

TABLE VII. Associations between $L_{p,A,\mathrm{eq,night}}$ inside the bedroom and reported sleep problems due to noise (OR with 95% CI and significance level P). Only the variables with significant effects are shown in this table.

Variable	Difficulty falling asleep		Awakenings	
	OR[a] (95% CI)	P	OR[a] (95% CI)	P
$L_{p,A,\mathrm{eq,night}}$ bedroom (reference: 0=<10 dB)				
10–14 dB	0.67 (0.16-2.80)	0.58	1.05 (0.33–3.35)	0.94
15–19 dB	1.24 (0.33–4.63)	0.75	1.13 (0.34–3.73)	0.84
20–24 dB	1.56 (0.43–5.61)	0.50	1.77 (0.58–5.42)	0.32
25–29 dB	3.49 (1.11–11.00)	0.03	3.68 (1.32–10.24)	0.01
⩾30 dB	5.79 (1.87–17.92)	0.00	7.50 (2.75–20.48)	0.00
Noise sensitivity (reference: 0=not sensitive)				
Somewhat sensitive	1.52 (0.66–3.54)	0.33	1.54 (0.79–2.99)	0.21
"Rather to very" noise sensitive	6.41 (3.00–13.68)	0.00	4.41 (2.37–8.22)	0.00

[a]Multivariate model, adjusted for the other variables in the table and age, gender, education, total income, train pass-by frequency, and duration of residence. Hosmer–Lemeshow goodness-of-fit test for difficulty falling asleep: chi square=12.88, df=8, and P=0.12. Hosmer–Lemeshow goodness-of-fit test for awakenings: chi square=8.88, df=8, and P=0.35.

point outside of the most-exposed facade, the percentage of noise-induced sleep-disturbed respondents is 1%–10% lower at the same level of noise exposure calculated for the bedroom facade. The exposure-response relationships indicate that the difference becomes greater with increasing noise levels (Fig. 3).

IV. DISCUSSION

A. Summary of findings

10% of the total sample reported sleep disturbances because of traffic noise. The proportion of reported difficulty falling asleep as well as awakenings due to noise increased as both nighttime $L_{p,A,\mathrm{eq,night}}$ and $L_{p,A,\mathrm{max}}$ from railway increased. The simple exposure-response curves presented in Figs. 1 and 2 were confirmed by the logistic regression analyses controlling for possible modifying factors and taking the number of nocturnal noise events into account. Our results showed that noise-induced difficulty falling asleep was reported significantly more often when $L_{p,A,\mathrm{eq,night}} \geqslant 65$ dB and $L_{p,A,\mathrm{max}} \geqslant 85-89$ dB outside of the bedroom facade compared to the reference values of $L_{p,A,\mathrm{eq,night}} < 40$ dB and $L_{p,A,\mathrm{max}} < 65$ dB, respectively. Awakenings were reported significantly more often when $L_{p,A,\mathrm{eq,night}} \geqslant 60-64$ dB and $L_{p,A,\mathrm{max}} \geqslant 80-84$ dB outside of the bedroom facade compared to the reference values of $L_{p,A,\mathrm{eq,night}} = 40-44$ dB and $L_{p,A,\mathrm{max}} < 65$ dB, respectively. With respect to indoor noise levels, problems falling asleep as well as awakenings due to noise were reported significantly more often when $L_{p,A,\mathrm{eq,night}} \geqslant 25-29$ dB and $L_{p,A,\mathrm{max}} \geqslant 50-54$ dB inside the bedroom compared to the reference values of $L_{p,A,\mathrm{eq,night}} < 10$ dB and $L_{p,A,\mathrm{max}} < 30$ dB, respectively. These noise levels are not to be interpreted as representing any threshold values for noise-induced sleep disturbance; rather,

TABLE VIII. Associations between $L_{p,A,\mathrm{max}}$ inside the bedroom and reported sleep problems due to noise (OR with 95% CI and significance level P). Only the variables with significant effects are shown in this table.

Variable	Difficulty falling asleep		Awakenings	
	OR[a] (95% CI)	P	OR[a] (95% CI)	P
$L_{p,A,\mathrm{max}}$ bedroom (reference: 0=<30 dB)				
30–34 dB	2.02 (0.23–17.59)	0.53	3.41 (0.42–27.58)	0.25
35–39 dB	2.51 (0.29–21.94)	0.41	2.04 (0.23–18.15)	0.52
40–44 dB	1.78 (0.19–16.61)	0.62	2.75 (0.32–23.64)	0.36
45–49 dB	3.56 (0.43–29.60)	0.24	6.82 (0.87–53.28)	0.07
50–54 dB	9.82 (1.27–76.16)	0.03	14.08 (1.85–106.96)	0.01
>55 dB	9.53 (1.19–76.41)	0.03	14.97 (1.93–116.04)	0.01
Noise sensitivity (reference: 0=not sensitive)				
Somewhat sensitive	1.50 (0.64–3.48)	0.35	1.54 (0.79–2.99)	0.20
"Rather to very" noise sensitive	6.55 (3.07–13.96)	0.00	4.64 (2.49–8.64)	0.00
Pass-by frequency during the night (reference: 0=<30 events)				
30–40	1.76 (0.50–6.19)	0.38	1.64 (0.55–4.91)	0.38
80–100	2.57 (0.73–9.07)	0.14	3.46 (1.16–10.35)	0.03
>100	5.25 (0.92–29.88)	0.06	1.60 (0.25—10.42)	0.62

[a]Multivariate model, adjusted for the other variables in the table and age, gender, education, total income, and duration of residence. Hosmer–Lemeshow goodness-of-fit test for difficulty falling asleep: chi square=10.19, df=8, and P=0.25. Hosmer–Lemeshow goodness-of-fit test for Awakenings: chi square=15.84, df=8, and P=0.045.

these noise levels yield a statistically significant increase in the probability of reporting noise-induced sleep problems compared to the reference level (the lowest noise level category).

Noise sensitivity, type of bedroom window, and train pass-by frequency were the only significant factors affecting noise-induced sleep disturbances in our analyses, in addition to the noise exposure level. Because about half of the study population did not use a bedroom at the most-exposed side of the house, the exposure-response curve obtained by using noise levels for the most-exposed facade underestimated noise-induced sleep disturbance for those who actually have their bedroom at the most-exposed façade.

Although the response rate in this study was fairly good ($>60\%$), nonresponse may lead to bias if respondents and nonrespondents differ systematically. No differences in noise exposure (crude characteristics) between the respondents and nonrespondents were found. There were slight differences in the distribution of gender and age between the respondents and the nonrespondents. Since neither gender nor age was significant covariates in the regression analyses, we assume that this sampling has not biased the results to a considerable degree. However, a sampling bias might have occurred based on other characteristics, about which we have no information regarding if or how much the nonrespondents may have differed from the respondents.

B. Assessment of individual noise exposure

A considerable advantage of the present study was the information available on bedroom position, type of bedroom window, and facade insulation properties for the assessment of individual nocturnal noise exposure inside as well as outside of the bedroom facade. Such information is rarely available or has not been used in large field surveys on self-reported noise-induced sleep disturbances, in which noise levels commonly are assessed for the most-exposed facade. It should be stressed, however, that despite the available information in this study, the calculation of indoor noise level based on noise level assessed outdoors, as well as the determination of facade insulation, are subject to inaccuracy. The actual dampening properties of a given type of window will depend on how old the windows are and how well they are maintained. Exact information on this, as well as on room dimensions, requires visual inspection at each respondent's dwelling, which was not possible in the present project. Assessment of the actual indoor noise level from railway noise is further complicated by differences in window opening and closing behaviors and the fact that this, to a certain extent, depends on the noise level. Therefore, the noise level inside the bedroom was calculated by assuming closed windows and ventilation inlets are kept shut. In spite of this limitation, this assumption can be justified because this method is the most common practice in indoor noise mapping for regulative purposes in Norway. The railway noise level to which the respondents were actually exposed during sleep in their bedroom may therefore be somewhat higher than in our calculations because many respondents slept with their bedroom windows open during the night.

C. Measures on noise-induced sleep disturbances

Two measures on sleep disturbance due to noise were used as dependent variables in our analyses: whether or not the respondents had difficulty falling asleep or experienced awakenings due to traffic noise during the last three months. These variables do not contain any information on the severity of sleep problems experienced by each respondent, and none represents threshold values for noise-induced sleep disturbances but rather are indicators of the extent of self-reported sleep disturbances due to noise. The longer the involuntary periods of lying awake and the more difficult it is to fall asleep or to return to sleep, the more likely will these states be recalled in the morning, thus determining the subjectively experienced sleep quality (Griefahn *et al.*, 2000). Retrospective self-reports of sleep problems provide valuable information about the subjects' global impressions and attributions of their own sleep. Such measures may, however, yield different data compared to those obtained using sleep diaries for single nights, as well as to those obtained with more objective assessment (Baker *et al.*, 1999; Griefahn *et al.*, 1999). Some self-reported sleep parameters have been shown to correlate poorly with physiological recordings of sleep. In general, for single nights, subjects tend to overestimate the time it takes to fall asleep compared to polysomnograhical recordings, whereas the number of recalled awakenings is underestimated relative to the objective assessments (Baker *et al.*, 1999; Carskadon *et al.*, 1976). However, a more recent study of self-reported sleep measures indicates that some quantitative estimates of habitual sleep behavior are highly reliable (Gerhrman *et al.*, 2002).

In the questions on noise-induced problems with falling asleep and awakenings, we did not specify the noise type but asked about sleep disturbances arising from traffic noise. It is possible, therefore, that sleep disturbances attributable to other types of transportation noise may have influenced the responses, especially at lower levels of railway noise exposure. The geographical areas chosen for the railway noise survey were not highly exposed to other types of transportation noise, although some exposure to road traffic noise is unavoidable. However, none of the addresses included in this study were simultaneously included in the noise mapping program of the Norwegian Public Roads Administration. Therefore, dwellings with exposure to road traffic noise exceeding $L_{p,A,\mathrm{eq},24\ \mathrm{h}}=35$ dB indoors were not included in the study sample. The possible influence of nocturnal exposure to aircraft noise is considered negligible since the nearest airport (Oslo Airport, Gardermoen) is located 47 km north of Oslo. The gradual increase in OR for noise-induced sleep disturbance with increasing railway noise exposure (for bedroom facade levels from $L_{p,A,\mathrm{eq,night}} \geqslant 45-49$ and $L_{p,A,\max} \geqslant 70-74$) also indicates that the reported sleep disturbances due to noise are indeed mainly attributable to railway noise and not to other types of transportation noise. In addition, there is no reason to assume a correlation between railway noise and noise from other traffic sources.

D. Exposure-response relationship

Compared to other studies on sleep disturbances due to railway noise, the exposure-response relationship obtained in

our survey indicates a lower percentage of sleep-disturbed respondents at a given level of noise exposure. In a Swedish study (Bluhm and Nordling, 2005), an exposure-response relationship between railway noise level and sleep disturbances was found for both $L_{p,A,\max}$ and $L_{p,A,\mathrm{eq},T}$, as in the present study. However, compared to the present study, the Swedish study indicated a higher level of both difficulty falling asleep and awakenings at a given noise level calculated at the most-exposed facade. Thus, at $L_{p,A,\mathrm{eq},24\ \mathrm{h}}$ of 55–59 dB in the Swedish study, 18% reported difficulty falling asleep "once a week or more often" and 16% reported awakenings "once a week or more often." In the present study, the percentages were 3.5% and 6%, respectively, in the interval of $L_{p,A,\mathrm{eq,night}}$=55–59 dB. These results are not directly comparable, however, because of differences in the definition of sleep disturbance and the use of different noise descriptors: $L_{p,A,\mathrm{eq},24\ \mathrm{h}}$ in the Swedish study and $L_{p,A,\mathrm{eq,night}}$ in the present study. The difference in these two descriptors depends on the diurnal distribution of train pass-bys and types of trains. $L_{p,A,\mathrm{eq},24\ \mathrm{h}}$ will most probably be higher than $L_{p,A,\mathrm{eq,night}}$. Some studies have found only a small difference (0–4 dB) between $L_{p,A,\mathrm{eq,day}}$ and nighttime $L_{p,A,\mathrm{eq,night}}$ (Fields and Walker, 1982; Griefahn *et al.*, 2000; Moehler, 1988), although this may not be applicable to other railway routes. One important contribution to the higher proportion of self-reported sleep problems reported in the Swedish study (Bluhm and Nordling, 2005) may be that the respondents were living in an area in which, according to the authors, there "recently has been a major extension of railway traffic" because of a new Express line and an increase in speed limit up to 200 km/h. Some authors have reported higher subjective responses to noise after a change (increase) in noise exposure compared to what could be estimated from an exposure-response relationship obtained for a steady-state situation (Langdon and Griffiths, 1982; Fidell *et al.*, 2002). Other possible factors that may contribute to the lower degree of noise-induced sleep disturbances in the present study are a possible higher proportion of the sample with a bedroom located toward a garden or backyard (50% in our study) and better insulation of bedroom windows. Differences in personal factors such as noise sensitivity might also have contributed to the difference between the studies.

Results from our study are more in line with the results shown in a recent meta-analysis (Miedema and Vos, 2007). In the range of 45–65 dB, $L_{p,A,\mathrm{eq,night}}$ outside of the most-exposed facade, the percentage of railway noise-induced sleep-disturbed respondents increased steadily from around 7% up to 20%. In the present study, the percentage of sleep-disturbed respondents (those who reported either difficulty falling asleep and/or awakenings due to traffic noise) increased steadily from about 3% up to 22% in the same range of noise levels outside of the most-exposed facade (Fig. 3).

E. Noise metrics

The present findings suggest that both nighttime $L_{p,A,\mathrm{eq,night}}$ and $L_{p,A,\max}$ predict self-reported sleep disturbances due to railway noise. It is important to stress, however, that the two noise metrics were highly correlated in this study. This result is expected when the type of train that gives the highest maximum noise level is frequently traveling the railway line for which the noise level is calculated. A Swedish study reported a higher correlation between self-reported sleep disturbances due to road traffic and $L_{p,A,\mathrm{eq,night}}$ than between the disturbances and $L_{p,A,\max}$ (Öhrström *et al.*, 2006). Because of acoustical and temporal differences between road traffic and railway noise, the results obtained from studies of road traffic noise may not be applicable to effects of railway noise and vice versa. In another Swedish study (Bluhm and Nordling, 2005) of self-reported sleep disturbances due to railway noise, exposure-response relationships for both equivalent and maximum noise levels were reported, as in the present study. However, these relationships were not quantified. A recent publication by Griefahn *et al.* (2006) concluded from their findings that the equivalent noise level seems to be a suitable predictor for subjective evaluation of sleep but not for the physiological effects of noise on sleep. Neither of the papers referred to in this section reported any results regarding the relationship between the two noise metrics, $L_{p,A,\mathrm{eq},T}$ and $L_{p,A,\max}$.

F. Number of noise events

The number of nocturnal railway noise events affected both the probability of self-reported difficulty falling asleep and awakenings but in different ways and significantly only in the analyses including $L_{p,A,\max}$. This outcome is not surprising because the number of noise events to a certain degree is included in the $L_{p,A,\mathrm{eq},T}$ metrics but not in $L_{p,A,\max}$. $L_{p,A,\mathrm{eq},T}$ is calculated by integrating the sound energy from all noise events over a given time T. The same number of noise events, though, can give very different values of $L_{p,A,\mathrm{eq},T}$ depending on the sound energy of each noise event. In this study, the number of train pass-bys during the nighttime ranged from 11 to 136 but did not vary in a homogeneous fashion because the study population was located only along six different railway routes. This implied that large groups were exposed to almost the same number of nocturnal noise events.

An increasing OR for difficulty falling asleep was found with increasing pass-by frequency of trains during the nighttime. With respect to noise-induced awakenings, a significant probability (OR) was found only for the intermediate category of pass-by frequency (80-100 train pass-bys). When the number of train pass-bys per night was above 100, no significant increase in OR for noise-induced awakenings was found. A possible interpretation of these results is that above a certain number of train pass-bys, there will be a reduced probability in awakenings for each pass-by due to habituation (a decrease in behavioral response to a repeated nonnoxious stimulus). Results from other studies have shown that the frequency of noise-induced awakenings and body movements increases with the number of noises (partly at the expense of spontaneous awakenings and movements), but the relationships are not linear because the risk of reacting to an individual stimulus decreases with the total number of stimuli (Öhrström, 1995). Our results suggest that at a high pass-by frequency (>100/night), beyond what can be ex-

plained by the $L_{p,A,\max}$ (or $L_{p,A,\mathrm{eq,night}}$), no further increase in self-reported noise-induced awakenings occurs, even though such results must be interpreted cautiously. In our study, we did not record the number of noise-induced awakenings per night, although the number of awakenings perceived by the respondents would clearly have affected the probability of remembering the awakening episode(s) the day after, thus increasing the probability of reporting noise-induced awakenings in the survey.

G. The effect of nonacoustic factors

None of the sociodemographic variables included in the analyses—age, gender, basic education, or total income—showed a significant impact on the probability of noise-induced self-reported sleep disturbances in this study. Although these factors have not been systematically studied with respect to self-reported noise-induced sleep disturbances in previous studies, our findings are in agreement with several studies of personal factors affecting noise annoyance (Fields, 1993). Some contradictory results have been reported, however, especially with respect to gender (Kageyama *et al.*, 1997) and age (Miedema and Vos, 1999), and a curvilinear relationship between age and noise annoyance has been suggested (Fields, 1993). In our model, we used and presented age as a continuous variable. Another model, in which age was categorized into four groups, was also explored and revealed a statistically nonsignificant decrease in self-reported sleep disturbances with age group. In a previous study by the same author, younger people were found to be more annoyed than older people by structurally radiated noise from railway tunnels (Aasvang *et al.*, 2007).

The duration of residence was chosen as a covariate in the regression model based on findings from earlier studies that some responses to noise, especially awakenings during sleep, may habituate or adapt over time (Pearsons *et al.*, 1995). No effect of length of residence was found in the present study, suggesting no habituation to noise with respect to its effect on perceived sleep quality over time. The length of residence has also not proved to be an important factor affecting noise annoyance (Fields, 1993). Measuring a possible habituation to noise is complicated by the fact that some of those who have lived in noise-exposed areas for some time may subjectively habituate while others may be more sensitized; thus, these effects may cancel each other out. Habituation may also take place shortly after initial exposure (within days), as suggested from results obtained in laboratory experiments (Xin *et al.*, 2000), and no further diminishing of responses to noise may appear thereafter.

Noise sensitivity, assessed by the response to a single-item rating scale, proved to be a strong and highly significant personal predictor of noise-induced self-reported sleep disturbances. Sensitivity toward noise has been shown to affect subjective reactions to noise in several previous studies of noise annoyance (Weinstein, 1978; Fields, 1993; Miedema and Vos, 2003), as well as in studies of sleep disturbances due to noise (Öhrström and Rylander, 1990; Belocevic *et al.*, 1997). In accordance with the results of several other studies (e.g., Job, 1988, Miedema and Vos, 2003), our study demonstrated no correlation between noise sensitivity and noise level. Little is known about the underlying mechanism, but earlier findings suggest that noise sensitivity pose an effect of noise exposure on noise annoyance (and maybe other reactions to noise as well) and does not (only) have an additive effect (Miedema and Vos, 2003). Noise sensitivity is regarded as a personality trait covering attitudes toward a wide range of environmental sounds, and earlier findings suggest that self-reported noise sensitivity captures evaluative rather than sensory aspects of auditory processing (Ellermeier *et al.*, 2001).

V. CONCLUDING REMARKS

In the present study, both $L_{p,A,\mathrm{eq,night}}$ and $L_{p,A,\max}$ were significantly related to self-reported sleep disturbances due to railway noise. The results of the regression analyses confirmed the importance of taking the number of nocturnal noise events into account when using $L_{p,A,\max}$ as a predictor. A high correlation between the two noise exposure metrics, $L_{p,A,\mathrm{eq,night}}$ and $L_{p,A,\max}$, was found in this study. Except for the noise exposure and the pass-by frequency, only the noise sensitivity and type of insulation of bedroom windows affected the self-reported noise-induced sleep disturbances in the present study. The authors emphasize that the exposure-response curves were obtained from a steady state situation and that the results may not be applicable in predicting responses shortly after immediate changes in noise exposure, e.g., reactions following noise-abatement measures or the opening of new railway lines. Because a certain proportion of the population uses a bedroom facing a garden or backyard, an exposure-response relationship developed by using a noise-exposure level outside of the most-exposed facade of the house may underestimate the effect on those using a bedroom facing the noise source. In line with previous findings, the present results suggest that a cumulative noise metric such as $L_{p,A,\mathrm{eq,night}}$ is a good predictor of noise-induced self-reported sleep disturbances. It must be emphasized that self reported sleep disturbances are not necessarily substantiated by objective sleep abnormalities. How a cumulative noise metric, such as $L_{p,A,\mathrm{eq,night}}$, is related to physiological measures of a whole night's sleep structure should be studied in more detail. In future studies on how noise-induced sleep disturbances relate to different noise metrics, the relationship between the noise metrics should also be analyzed and reported.

ACKNOWLEDGMENTS

The authors thank Eyjolf Osmundsen and Gaute Birkeli (Miljøakustikk as, Norway) for the thorough work on the assessment of railway noise exposure. We are also grateful to Evy Öhrstöm, University of Gothenburg, Sweden and Reidun Ursin at the University Of Bergen, Norway for valuable advice and ideas during the planning phase of the study. Professor Reidun Ursin also provided valuable comments to the manuscript. This study was funded by the Norwegian Research Council and the Norwegian National Rail Administration.

Aasvang, G. M., Engdahl, B., and Rothschild, K. (**2007**). "Annoyance and self-reported sleep disturbances due to structurally radiated noise from railway tunnels," Appl. Acoust. **68**, 970–981.
Altman, G. A., Machin, D., Bryant, T. N., and Gardner, M. J. (**2000**). *Statistics with Confidence*, 2nd ed. (BMJ Books, London).
Baker, F. C., Maloney, S., and Driver, H. S. (**1999**). "A comparison of subjective estimates of sleep with objective polysomnographic data in healthy men and women," J. Psychosom. Res. **47**, 335–341.
Basner, M. F., Samel, A. F., and Isermann, U. (**2006**). "Aircraft noise effects on sleep: Application of the results of a large polysomnographic field study," J. Acoust. Soc. Am. **119**, 2772–2784.
Belojevic, G., Jakovljevic, B., and Aleksic, O. (**1997**). "Subjective reactions to traffic noise with regard to some personality traits," Environ. Int. **23**, 221–226.
Berglund, B., Lindvall, T., Schwela, D., and Kee-Tai, G. (**2000**). Guidelines for Community Noise, published on behalf of World Health Organization.
Bluhm, G., and Nordling, E. (**2005**). "Health effects of noise from railway traffic: The heat study," Internoise, Rio de Janeiro, Brazil, 7–10 August.
Carskadon, M. A., Dement, W. C., Mitler, M. M., Guilleminault, C., Zarcone, V. P., and Spiegel, R. (**1976**). "Self-reports versus sleep laboratory findings in 122 drug-free subjects with complaints of chronic insomnia," Am. J. Psychiatry **133**, 1382–1388.
DataKustik. (**2004**). CADNAA Computer program, computer aided noise abatement, manual, ver. 3.4.
Dinges, D. F., Pack, F., Williams, K., Gillen, K. A., Powell, J. W., Ott, G. E., Aptowicz, C., and Pack, A. I. (**1997**). "Cumulative sleepiness, mood disturbance, and psychomotor vigilance performance decrements during a week of sleep restricted to 4–5 hours per night," Stud. Cercet Inframicrobiol **20**, 267–277.
Ellermeier, W., Eigenstetter, M., and Zimmer, K. (**2001**). "Psychoacoustic correlates of individual noise sensitivity," J. Acoust. Soc. Am. **109**, 1464–1473.
European Commission (**2002**). European Parliament and Council Directive 2002/49/EC of 25.
Ferrara, M., and De Gennaro, L. (**2001**). "How much sleep do we need?" Sleep Med. Rev. **5**, 155–579.
Fidell, S., Pearsons, K., Tabachnick, B., Howe, R., Silvati, L., and Barber, D. S. (**1995**). "Field study of noise-induced sleep disturbance," J. Acoust. Soc. Am. **98**, 1025–1033.
Fidell, S., Silvati, L., and Haboly, E. (**2002**). "Social survey of community response to a step change in aircraft noise exposure," J. Acoust. Soc. Am. **111**, 200–209.
Fields, J. M. (**1993**). "Effects of personal and situational variables on noise annoyance in residential areas," J. Acoust. Soc. Am. **93**, 2753–2763.
Fields, J. M., and Walker, J. G. (**1982**). "The response to railway noise in residential areas in Great Britain," J. Sound Vib. **85**, 177–255.
Gehrman, P., Matt, G. E., Turingan, M., Dinh, Q., and Ancoli-Israel, S. (**2002**). "Towards an understanding of self-reports of sleep," J. Sleep Res. **11**, 229–236.
Griefahn, B. (**1986**). "A critical load for nocturnal high-density road traffic noise," Am. J. Ind. Med. **9**, 261–269.
Griefahn, B., Marks, A., and Robens, S., (**2006**). "Noise emitted from road, rail and air traffic and their effects on sleep," J. Sound Vib. **295**, 129–140.
Griefahn, B., Möhler, U., and Schuemer, R. (**1999**). *Vergleichende Untersuchung über die Lärmwirkung bei Straßen—und Schienenverkehr (Comparative investigation of the effects of noise from traffic and railway)* (SGS, München).
Griefahn, B., Schuemer-Kohrs, A., Schuemer, R., Moehler, U., and Mehnert, P. (**2000**). "Physiological, subjective, and behavioural responses during sleep to noise from rail and road traffic," Noise Health **3**, 59–71.
Guski, R. (**1977**). "An analysis of spontaneous noise complaints," Environ. Res. **13**, 229–236.
Horne, J. A., Pankhurst, F. L., Reyner, L. A., Hume, K., and Diamond, I. D. (**1994**). "A field study of sleep disturbance: Effects of aircraft noise and other factors on 5,742 nights of actimetrically monitored sleep in a large subject sample," Sleep **17**, 146–159.
Irwin, M., McClintick, J., Costlow, C., Fortner, M., White, J., and Gillin, J. C. (**1996**). "Partial night sleep deprivation reduces natural killer and cellular immune responses in humans," FASEB J. **10**, 643–653.
Job, R. F. S. (**1988**). "A review of factors influencing the relationship between noise exposure and reaction," J. Acoust. Soc. Am. **83**, 991–1001.
Kageyama, T., Kabuto, M., Nitta, H., Kurokawa, Y., Taira, K., Suzuki, S., and Takemoto, T. (**1997**). "A population study on risk factors for insomnia among adult Japanese women: A possible effect of road traffic volume," Sleep **20**, 963–971.
Langdon, F. J., and Griffiths, I. D. (**1982**). "Subjective effects of traffic noise exposure. II. Comparisons of noise indices, response scales, and effects of changes in noise exposure," J. Sound Vib. **83**, 171–182.
Miedema, H. M. E., and Vos, H. (**1999**). "Demographic and attitudinal factors that modify annoyance from transportation noise," J. Acoust. Soc. Am. **105**, 3336–3344.
Miedema, H. M. E., and Vos, H. (**2003**). "Noise sensitivity and reactions to noise and other environmental conditions," J. Acoust. Soc. Am. **113**, 1492–1504.
Miedema, H. M. E., and Vos, H. (**2007**). "Associations between self-reported sleep disturbance and environmental noise based on reanalyses of pooled data from 24 studies," Behav. Sleep Med. **5**, 1–20.
Moehler, U. (**1988**). "Community response to railway noise: A review of social surveys," J. Sound Vib. **120**, 321–332.
Nordic Council of Ministers (**1996**). *Railway noise—the Nordic Prediction Model* (TemaNord environment, Aarhus), pp. 524.
Norwegian Building Institute (**1999**). Insulation against external noise. NBI Handbook 47.
Öhrström, E. (**1995**). "Effects of low levels of road traffic noise during the night: a laboratory study on number of events, maximum noise levels and noise sensitivity," J. Sound Vib. **179**, 603–615.
Öhrström, E., and Rylander, R. (**1990**). "Sleep disturbance by road traffic noise—a laboratory study on number of noise events," J. Sound Vib. **143**, 93–101.
Öhrström, E., Skånberg, A.-B., Svensson, H., and Gidlof-Gunnarsson, A. (**2006**). "Effects of road traffic noise and the benefit of access to quietness," J. Sound Vib. **295**, 40–59.
Partinen, M., and Gislason, T. (**1995**). "Basic Nordic sleep questionnaire (BNSQ): A quantitated measure of subjective sleep complaints," J. Sleep Res. **4**, 150–155.
Passchier-Vermeer, W., Vos, H., Steenbekkers, J., van der Ploeg, F., and Groothuis-Oudshoorn, K. (**2002**). "Sleep disturbance and aircraft noise exposure: Exposure-effect relationships," TNO Inro Report No. 027, pp. 1–245.
Pearsons, K. S., Barber, D. S., Tabachnick, B., and Fidell, S. (**1995**). "Predicting noise-induced sleep disturbance," J. Acoust. Soc. Am. **971**, 331–338.
Rylander, R., and Björkman, M. (**1988**). "Maximum noise levels as indicators of biological effects," J. Sound Vib. **127**, 555–163.
Spiegel, K., Leproult, R., and Van Cauter, E. (**1999**). "Impact of sleep debt on metabolic and endocrine function," Lancet **354**, 1435–1439.
Thiessen, G. J. (**1988**). "Effect of traffic noise on the cyclical nature of sleep," J. Acoust. Soc. Am. **84**, 1741–1743.
Vernet, M. (**1979**). "Effects of train noise on sleep for people living in houses bordering the railway line," J. Sound Vib. **66**, 483–492.
Vernet, M. (**1983**). "Comparison between train noise and road noise annoyance during sleep," J. Sound Vib. **87**, 331–335.
Weinstein, N. D. (**1978**). "Individual differences in reactions to noise: A longitudinal study in a college dormitory," J. Appl. Psychol. **63**, 458–466.
Wilson, E. B. (**1927**). "Probable inference, the law of succession, and statistical inference," J. Am. Stat. Assoc. **22**, 209–212.
Xin, P., Kawada, T., Sasawa, Y., and Suzuki, S. (**2000**). "Habituation of sleep to road traffic noise assessed by polygraphy and rating scale," J. Occup. Health Psychol. **42**, 20–26.

Prediction of energy decay in room impulse responses simulated with an image-source model

Eric A. Lehmann[a] and Anders M. Johansson
Western Australian Telecommunications Research Institute, 35 Stirling Highway, Crawley WA 6009 Australia

(Received 21 January 2007; revised 25 February 2008; accepted 4 May 2008)

A method is proposed that provides an approximation of the acoustic energy decay (energy–time curve) in room impulse responses generated using the image-source technique. A geometrical analysis of the image-source principle leads to a closed-form expression describing the energy decay curve, with the resulting formula being valid for a uniform as well as nonuniform definition of the enclosure's six absorption coefficients. The accuracy of the proposed approximation is demonstrated on the basis of impulse-response simulations involving various room sizes and reverberation levels, with uniform and nonuniform sound absorption coefficients. An application example for the proposed method is illustrated by considering the task of predicting an enclosure's reflection coefficients in order to achieve a specific reverberation level. The technique presented in this work enables designers to undertake a preliminary analysis of a simulated reverberant environment without the need for time-consuming image-method simulations.
 [DOI: 10.1121/1.2936367]

PACS number(s): 43.55.Ka, 43.55.Br, 43.60.−c [WMC] Pages: 269–277

I. INTRODUCTION

The image-source model (ISM) has become an ubiquitous tool in many fields of acoustical and engineering research over the past few decades. Its success relies mainly on its conceptual simplicity, which makes ISM-based algorithms relatively straightforward to implement. As a result, the ISM approach has been used as a basis principle for a wide range of purposes including, for instance, prediction of sound propagation in enclosed environments[1,2] and long tunnels,[3] architectural modeling and design,[4,5] noise control in large spaces,[6] and analysis of perceptual properties such as speech intelligibility and speech transmission index in various enclosures.[7] In recent times, the image-source model has also been implemented for the purpose of binaural auralization,[8] spatialized sound rendering in virtual environments[9] and interactive systems,[10] and augmented-reality applications such as video games.[11]

Another important domain of application of the image-source technique is in order to assess the performance of various signal processing algorithms operating in reverberant environments. Some application examples include algorithms for blind source separation,[12] channel identification and equalization,[13,14] acoustic source localization and tracking,[15] speech recognition,[16] and speech enhancement.[17] In this context, the image model is generally used to determine the algorithm's robustness against increasing levels of environmental reverberation. Although not usually addressed in literature, a significant issue during this process is related to predicting the reverberation time in the resulting room impulse responses generated with the ISM. Well established formulas, such as Sabine or Eyring's reverberation time, do not provide accurate results when used to determine the enclosure's sound absorption in order to achieve a desired reverberation level.[18,19] This discrepancy between predicted and actual reverberation time, which is highlighted in this paper, is especially pronounced with a nonuniform definition of the sound reflection coefficients in the considered ISM room setup. As a result, a risk exists that the algorithm under test may be ultimately simulated with a reverberation level different from what is assumed during the experiment, leading to a potentially significant bias in the performance results. Finding an efficient solution to this specific issue was the original motivation behind the research presented in this work.

This paper describes a method for predicting the energy decay in a room impulse response (RIR) simulated with the ISM. The proposed approximation method is based on a geometrical consideration of the ISM principle: the acoustic power in the transfer function at a specific time lag can be seen as the addition of the contributions from the image sources located on a sphere centered around the receiver. This approach leads to a closed-form expression which then allows a numerical prediction of the energy decay curve (EDC); this alleviates the need to practically simulate the RIR of interest, which represents a computational advantage, for instance, during the process of adjusting the RIR's reverberation time. Furthermore, this method efficiently deals with situations where current reverberation-time prediction techniques experience significant inaccuracies, such as in the case of nonuniform absorption coefficients. The ability to accurately predict the acoustic energy decay in a given enclosure hence provides a computationally efficient solution to the above mentioned problem of predicting the RIR's reverberation level, and also represents a general development tool providing some preliminary insight into the acoustical characteristics of the simulated environment.

[a]Tel.: +61 (0)8 6488 4642. FAX: +61 (0)8 6488 7254. Electronic mail: eric.lehmann@watri.org.au

In the following, the basic principles underlying the image-source method are first briefly reviewed in Sec. II, which also presents a modification of the original ISM algorithm leading to more practically accurate impulse responses. This modified ISM technique is used as a basis for the proposed EDC approximation method, the details of which are then presented in Sec. III. The accuracy and practical relevance of this approximation method are then demonstrated using a series of numerical evaluations in Sec. IV, which considers a typical application example and provides a computational efficiency assessment. Finally, Sec. V concludes with a discussion of the main concepts presented in this work.

II. IMAGE-SOURCE METHOD

This section briefly reviews the basic principles of the image-source technique and establishes the notation used throughout the rest of the paper.

A. Original approach

The conventional image-source method, as presented originally in a landmark paper by Allen and Berkley,[20] is a well established algorithm for generating simulated RIRs in a given room. Assume that a Cartesian coordinate system with coordinates (x,y,z) is defined in the considered enclosure, with its origin corresponding to one of the room corners. Let $\boldsymbol{p}_s$ and $\boldsymbol{p}_r$ denote the position vectors of a source and a receiver, respectively, in this setting:

$$\boldsymbol{p}_s = [x_s, y_s, z_s]^{\mathrm{T}}, \tag{1}$$

$$\boldsymbol{p}_r = [x_r, y_r, z_r]^{\mathrm{T}}, \tag{2}$$

where $[\cdot]^{\mathrm{T}}$ denotes the matrix transpose operator. Similarly, let

$$\boldsymbol{r} = [L_x, L_y, L_z]^{\mathrm{T}} \tag{3}$$

represent the vector of room dimensions, with length L_x, width L_y, and height L_z. It is assumed that the acoustical property of each surface in the enclosure is characterized by means of a sound reflection coefficient β, related to the absorption coefficient α according to

$$\alpha = 1 - \beta^2. \tag{4}$$

The reflection coefficients for each surface are denoted as $\beta_{x,i}$, $\beta_{y,i}$, and $\beta_{z,i}$, with $i=1,2$, where the subindex 1 refers to the wall closest to the origin. As commonly assumed, this work is based on geometrical room-acoustics principles and assumes that the reflection coefficients are frequency independent as well as angle independent.[21]

The room impulse response from the source to the receiver can be determined by considering image sources on an infinite grid of mirror rooms expanding in all three dimensions. The contribution of each image source to the receiver signal is a replica of the source signal delayed by a lag τ and attenuated by an amplitude factor A. The RIR $h(\cdot)$ hence follows as[20]

$$h(t) = \sum_{\boldsymbol{u}=0}^{1} \sum_{\boldsymbol{l}=-\infty}^{\infty} A(\boldsymbol{u},\boldsymbol{l}) \cdot \delta[t - \tau(\boldsymbol{u},\boldsymbol{l})], \tag{5}$$

where t denotes time, $\delta(\cdot)$ is the Dirac impulse function, and the triplets $\boldsymbol{u}=(u,v,w)$ and $\boldsymbol{l}=(l,m,n)$ are parameters controlling the indexing of the image sources in all dimensions. For conciseness, the sum over $\boldsymbol{u}$ or $\boldsymbol{l}$ in Eq. (5) is used to represent a triple sum over each of the triplet's internal indices. The attenuation factor $A(\cdot)$ and time delay $\tau(\cdot)$ in Eq. (5) are defined as follows:

$$A(\boldsymbol{u},\boldsymbol{l}) = \frac{\beta_{x,1}^{|l-u|}\beta_{x,2}^{|l|}\beta_{y,1}^{|m-v|}\beta_{y,2}^{|m|}\beta_{z,1}^{|n-w|}\beta_{z,2}^{|n|}}{4\pi \cdot d(\boldsymbol{u},\boldsymbol{l})}, \tag{6}$$

$$\tau(\boldsymbol{u},\boldsymbol{l}) = d(\boldsymbol{u},\boldsymbol{l})/c, \tag{7}$$

where c is the sound propagation velocity and $d(\cdot)$ represents the distance from the image source to the receiver,

$$d(\boldsymbol{u},\boldsymbol{l}) = \|\mathrm{diag}(2u-1, 2v-1, 2w-1) \cdot \boldsymbol{p}_s + \boldsymbol{p}_r - \mathrm{diag}(2l, 2m, 2n) \cdot \boldsymbol{r}\|, \tag{8}$$

with $\|\cdot\|$ as the Euclidean norm and $\mathrm{diag}(\cdot)$ denoting a diagonal matrix with the arguments as diagonal elements.

Finally, note that the number of image sources to include in the summation of Eq. (5) grows exponentially with the considered order of reflections. The simulation of a full-length RIR using an image-source approach can thus lead to a considerable computational load in practice.

B. Modified ISM technique

The basic image-source simulation method can be improved in a number of different ways. This section presents two such modifications, which lead to more efficient simulations and better practical results. The resulting algorithm will be used as a basis for the simulations presented at the end of this paper.

1. Frequency-domain computations

The ISM implementation presented in Sec. II A typically needs to be updated in practice when dealing with discrete-time signals since the time delay $\tau(\cdot)$ does not usually correspond to an integer multiple of the sampling period. In the approach of Allen and Berkley,[20] this problem is dealt with by using nearest-integer rounding of each image source's propagation time, resulting in a shift of the corresponding impulse in the RIR. This approach thus leads to a coarse histogramlike representation of the desired RIR, which subsequently requires high-pass filtering in order to remove the nonphysical defect of this model resulting at zero frequency.

A more accurate solution to this problem is to carry out the ISM computations in the frequency domain, which allows the representation of delays that are not necessarily integer multiples of the sampling period. In the frequency domain, a time shift τ is represented as $\exp(-j\omega\tau)$, with $j=\sqrt{-1}$ and ω denoting the frequency variable. The frequency-domain RIR $H(\cdot)$ hence results from Eq. (5) as

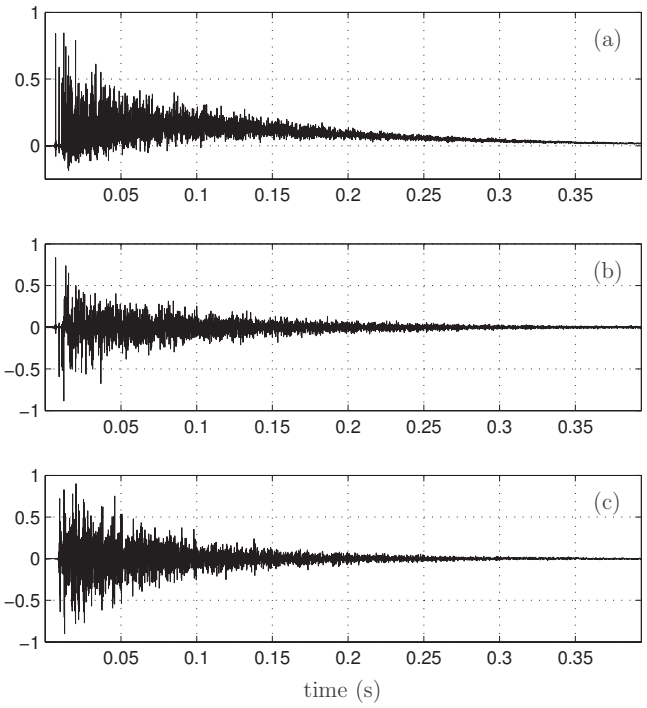

FIG. 1. (a) Typical RIR obtained using frequency-domain ISM (equivalent to Peterson's method) with positive reflection coefficients, $\boldsymbol{r}=[3.2\ \mathrm{m}, 4\ \mathrm{m}, 2.7\ \mathrm{m}]^{\mathrm{T}}$, $\boldsymbol{p}_r=[1.1\ \mathrm{m}, 1\ \mathrm{m}, 1.2\ \mathrm{m}]^{\mathrm{T}}$, $\boldsymbol{p}_s=[2\ \mathrm{m}, 3\ \mathrm{m}, 2\ \mathrm{m}]^{\mathrm{T}}$, sampling frequency $F_s=16$ kHz, and uniform reflection coefficients $\beta=0.92$. (b) Typical RIR obtained with the same environmental setup but using negative reflection coefficients. (c) Typical measurement of a real RIR recorded in a room with reverberation time $T_{60}\approx 0.6$ s.

$$H(\omega)=\sum_{u=0}^{1}\sum_{l=-\infty}^{\infty}A(\boldsymbol{u},\boldsymbol{l})e^{-j\omega\tau(\boldsymbol{u},\boldsymbol{l})}, \tag{9}$$

where $A(\cdot)$ and $\tau(\cdot)$ are computed according to Eqs. (6) and (7), respectively. The time-domain RIR follows as the inverse Fourier transform of $H(\cdot)$, i.e.,

$$h(t)=\mathcal{F}^{-1}\{H(\omega)\}. \tag{10}$$

Note that for time-sampled, and hence band-limited signals, the contribution of each image source in the time domain then results as a (truncated) sinc-like fractional-delay filter that accounts for noninteger propagation times. This approach, which was previously used by various authors,[13,18] essentially represents the frequency-domain equivalent to the low-pass impulse method (with infinite window duration) proposed by Peterson.[22]

2. Negative reflection coefficients

Given a specific absorption coefficient α characterizing any room surface, the corresponding reflection coefficient β follows from Eq. (4) as

$$\beta=\pm\sqrt{1-\alpha}. \tag{11}$$

The original ISM implementation makes use of the positive definition of the β parameter. However, when used in conjunction with a frequency-domain implementation (or equivalently, Peterson's method), this approach generates anomalous RIRs showing a distinctively nonphysical tail decay, as depicted in Fig. 1(a).

An alternative approach is to use the negative definition of the parameter β in Eq. (11). This can be explained by considering the angle-dependent formula[23] for the reflection coefficient of a boundary with impedance ζ,

$$\beta=\frac{\zeta\cos(\psi)-1}{\zeta\cos(\psi)+1}, \tag{12}$$

which can become negative for a certain range of incidence angle ψ.[24] As shown in Fig. 1(b), and contrary to Fig. 1(a), this alternative approach results in RIRs whose shape compares well to that of practical RIR measurements, an example of which is displayed in Fig. 1(c). Thus, because this model can be seen as being more accurate in replicating the effects of a real acoustic environment, the ISM algorithm used in the remainder of this work will be based on Eqs. (9) and (10) with the following definition of each image source's amplitude factor:

$$A(\boldsymbol{u},\boldsymbol{l})=\frac{1}{4\pi d(\boldsymbol{u},\boldsymbol{l})}(-\beta_{x,1})^{|l-u|}(-\beta_{x,2})^{|l|}(-\beta_{y,1})^{|m-v|}\times(-\beta_{y,2})^{|m|}(-\beta_{z,1})^{|n-w|}(-\beta_{z,2})^{|n|}, \tag{13}$$

where $d(\cdot)$ is computed according to Eq. (8), and with the β parameters corresponding to the usual definition of sound reflection coefficients.[25] Finally, it must be noted that this "negative-coefficient approach" was previously studied and used by António *et al.*[18]

C. Energy decay

Given a RIR $h(t)$ computed for a specific environment according to Eq. (10), the energy decay envelope $E(t)$, known in literature as energy–time curve or energy decay curve (EDC), can be computed using a normalized version of the Schroeder integration method,[7,26]

$$E(t)=10\log_{10}\left[\frac{\int_t^\infty h^2(\xi)\mathrm{d}\xi}{\int_0^\infty h^2(\xi)\mathrm{d}\xi}\right], \tag{14}$$

where $E(\cdot)$ is expressed in dB. The result from Eq. (14) can then be used as a basis for deriving an estimate of the reverberation time, such as T_{20} or T_{60}.

III. PROPOSED ENERGY DECAY APPROXIMATION

This section presents the developments leading to the proposed method for EDC approximation. For clarity, the derivations are first carried out in a two-dimensional (2D) (x,y)-plane, and the results are then extended to the three-dimensional (3D) case.

A. Two-dimensional case

With the ISM technique, each image source can be seen as releasing a single sound "particle" (impulse) traveling in the direction of the receiver at the speed of sound. Each particle carries a unit amount of acoustic power, which decreases upon each reflection on a boundary surface according to its absorption coefficient, and as a function of the distance

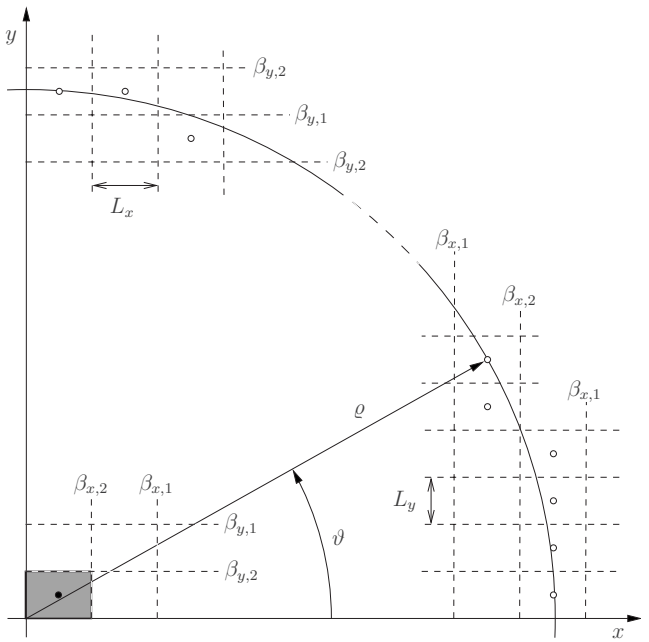

FIG. 2. Two-dimensional representation of the ISM principle. Dashed lines represent the grid of images of the original room, which is displayed as a shaded rectangle. The β parameters indicate the reflection coefficients of the corresponding boundaries, and circles (∘) represent the considered image sources.

traveled to the receiver. At the receiver, these sound particles are then added together at the corresponding time lags to create the impulse response.

Based on this principle, the value of the impulse response $h(t)$ for a given time t corresponds to the addition of the sound amplitude contributions from all the image sources located on, or very close to a circle of radius ϱ around the receiver, with $\varrho \triangleq \varrho(t) = ct$. This principle is demonstrated in Fig. 2 for one quadrant of the (x,y)-plane. Dashed rectangles represent images of the considered room, and circles denote the image sources of interest for the given radius ϱ. The original source has been placed at the center of the room for illustration purposes. The analysis presented in this section is based on the assumption of a large radius, that is,

$$\varrho \gg \max\{L_x, L_y, L_z\}. \tag{15}$$

For simplicity of the following derivations, it is also assumed that the receiver is located at the center of the coordinate system, as depicted in Fig. 2. This assumption, together with the fact that some image sources do not lie perfectly on the considered circle, typically leads to approximation errors that become negligible as the radius ϱ of the considered circle increases.

Let us now consider an image source located at an angle ϑ along the considered circle, see Fig. 2. Prior to reaching the receiver, its sound impulse traverses a number $W_x \triangleq W_x(\varrho, \vartheta)$ of walls in the x direction, and $W_y \triangleq W_y(\varrho, \vartheta)$ walls in the y direction, which can be determined in a straightforward manner on the basis of the known position of the image source. Consequently, the power contribution $P(\cdot)$ made by this source to the transfer function can be expressed as

$$P(\varrho, \vartheta) = \frac{(\beta_{x,1}^2)^{W_x/2}(\beta_{x,2}^2)^{W_x/2}(\beta_{y,1}^2)^{W_y/2}(\beta_{y,2}^2)^{W_y/2}}{(4\pi\varrho)^2}. \tag{16}$$

Note that in contrast to Eq. (13), this expression effectively corresponds to a squared amplitude coefficient since the current developments are based on acoustic power rather than amplitude.[5] Equation (16) makes use of the assumption that along the path to the receiver, the number of walls with coefficient $\beta_{x,1}$ ($\beta_{y,1}$) is approximately equal to the number of walls with coefficient $\beta_{x,2}$ ($\beta_{y,2}$), that is, approximately equal to half the number of walls $W_x/2$ ($W_y/2$). Once again, this condition essentially becomes valid as the radius ϱ becomes large. In order to ultimately achieve a closed-form expression of the desired EDC approximation, the number of boundaries between the source and the receiver, in both dimensions, is determined according to a first-order approximation based on Fig. 2 (for $\vartheta \in [0, \pi/2]$),

$$W_x = \frac{\varrho}{L_x}\left(1 - \frac{2\vartheta}{\pi}\right), \tag{17}$$

$$W_y = \frac{\varrho}{L_y}\frac{2\vartheta}{\pi}. \tag{18}$$

Using the approach described so far, it follows that the value of the power impulse response $h_P(t)$ at time t, where the subscript in $h_P(\cdot)$ emphasizes the fact that the RIR is here power-based, can be determined as

$$h_P(t) = \sum_{i \in \mathcal{I}_c} P(\varrho, \vartheta_i), \tag{19}$$

with $\varrho = ct$, the variable ϑ_i denoting the angle of the ith image source, and $\mathcal{I}_c$ representing the index set of the sources located on the considered circle. The basis of the proposed approximation is then to consider Eq. (19) as a Riemann sum, which can be represented as the integral of a continuous function over the angle ϑ,

$$h_P(t) \cdot \Delta\vartheta = \sum_{i \in \mathcal{I}_c} P(\varrho, \vartheta_i) \cdot \Delta\vartheta \tag{20}$$

$$\approx \int_0^{2\pi} P(\varrho, \vartheta)\mathrm{d}\vartheta. \tag{21}$$

As a result of the symmetry in the problem definition, the analysis can be restricted to a quarter of the circle, i.e., for $\vartheta \in [0, \pi/2]$. An estimate $\hat{h}_P(\cdot)$ of the power transfer function then follows from Eq. (21) as

$$h_P(t) \approx \hat{h}_P(t) = \frac{4}{\Delta\vartheta}\int_0^{\pi/2} P(\varrho, \vartheta)\mathrm{d}\vartheta. \tag{22}$$

The angular variable $\Delta\vartheta$ can be determined as

$$\Delta\vartheta = \frac{2\pi}{N_s}, \tag{23}$$

where N_s corresponds to the total number of image sources considered on the circle, or located very close to it. From Fig. 2, it can be seen that for $\vartheta \to 0$, the average distance between the image sources on the circle approaches L_y; simi-

larly, it approaches L_x for $\vartheta \to \pi/2$. Consequently, the parameter N_s is defined here as the circle's circumference divided by the average room dimension, i.e.,

$$N_s = \frac{2\pi\varrho}{\bar{r}}, \tag{24}$$

with $\bar{r}=(L_x+L_y)/2$. The value of $\Delta\vartheta$ then follows as $\Delta\vartheta = \bar{r}/\varrho$, which, together with Eq. (22), leads to the following approximation of the power RIR for the 2D setting:

$$\hat{h}_P(t) = \frac{4\varrho}{\bar{r}} \int_0^{\pi/2} P(\varrho, \vartheta) \mathrm{d}\vartheta. \tag{25}$$

B. Extension to three dimensions

An extension to the 3D case is obtained via a generalization of the above developments and the introduction of the polar angle $\varphi \in [0, \pi]$, as depicted in Fig. 3. Limiting here again the analysis to one eighth of the sphere, this results in Eq. (25) then becoming

$$\hat{h}_P(t) = \frac{8\varrho}{\bar{r}} \int_0^{\pi/2} \int_0^{\pi/2} P(\varrho, \vartheta, \varphi) \mathrm{d}\vartheta \mathrm{d}\varphi, \tag{26}$$

where $\bar{r}$ now includes the third room dimension,

$$\bar{r} = \frac{L_x + L_y + L_z}{3}, \tag{27}$$

and with the 3D extension of the power coefficient and number of walls,

$$P(\varrho, \vartheta, \varphi) = \frac{(\beta_{x,1}\beta_{x,2})^{W_x}(\beta_{y,1}\beta_{y,2})^{W_y}(\beta_{z,1}\beta_{z,2})^{W_z}}{(4\pi\varrho)^2}, \tag{28}$$

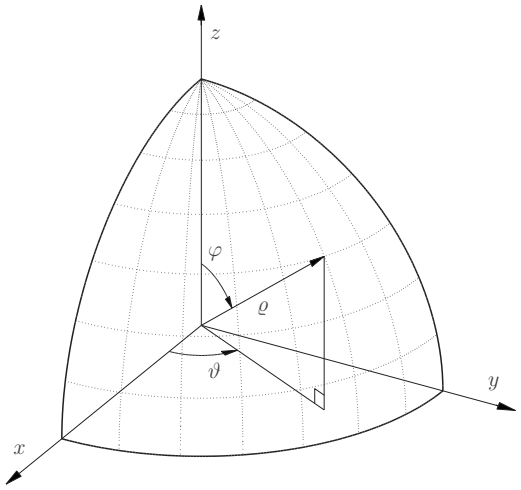

FIG. 3. Definition of the spherical coordinate system.

$$W_x = \frac{\varrho}{L_x}\left(1 - \frac{2\vartheta}{\pi}\right)\frac{2\varphi}{\pi}, \tag{29}$$

$$W_y = \frac{\varrho}{L_y}\frac{2\vartheta}{\pi}\frac{2\varphi}{\pi}, \tag{30}$$

$$W_z = \frac{\varrho}{L_z}\left(1 - \frac{2\varphi}{\pi}\right). \tag{31}$$

Inserting Eqs. (28)–(31) into Eq. (26) and analytically solving the double integral finally leads to the following estimate $\hat{h}_P(\cdot) \approx h_P(\cdot)$ of the power transfer function:

$$\hat{h}_P(t) = \frac{1}{8\varrho\bar{r}} \begin{cases} \dfrac{B_z}{\log\left(\frac{B_y}{B_x}\right)} \left\{ \mathrm{Ei}\left[\log\left(\frac{B_z}{B_x}\right)\right] + \log\left[\log\left(\frac{B_z}{B_x}\right)\right] - \mathrm{Ei}\left[\log\left(\frac{B_z}{B_y}\right)\right] - \log\left[\log\left(\frac{B_z}{B_y}\right)\right] \right\} & \text{if } B_x \neq B_y \neq B_z \\ \dfrac{B_z}{\log\left(\frac{B_z}{B}\right)} \left\{ \mathrm{Ei}\left[\log\left(\frac{B_z}{B}\right)\right] + \log\left[\log\left(\frac{B_z}{B}\right)\right] + \gamma \right\} & \text{if } B_z = B_y \neq B_x \triangleq B \text{ or } B_z = B_x \neq B_y \triangleq B \\ \dfrac{B - B_z}{\log\left(\frac{B}{B_z}\right)} & \text{if } B_z \neq B_x = B_y \triangleq B \\ B, & \text{if } B_x = B_y = B_z \triangleq B. \end{cases} \tag{32}$$

with $\gamma = 0.577\,215\,7\cdots$ the Euler–Mascheroni constant, $\mathrm{Ei}(\cdot)$ denoting the first-order exponential integral,[27] $\varrho \triangleq \varrho(t) = ct$ as defined earlier, and with the following definitions:

$$B_x = (\beta_{x,1}\beta_{x,2})^{\varrho/L_x}, \tag{33}$$

$$B_y = (\beta_{y,1}\beta_{y,2})^{\varrho/L_y}, \tag{34}$$

$$B_z = (\beta_{z,1}\beta_{z,2})^{\varrho/L_z}. \tag{35}$$

In Eq. (32), rotation of the coordinates x, y and z can be applied in order to avoid cases that would otherwise lead to negative arguments for the logarithm function or the exponential integral.

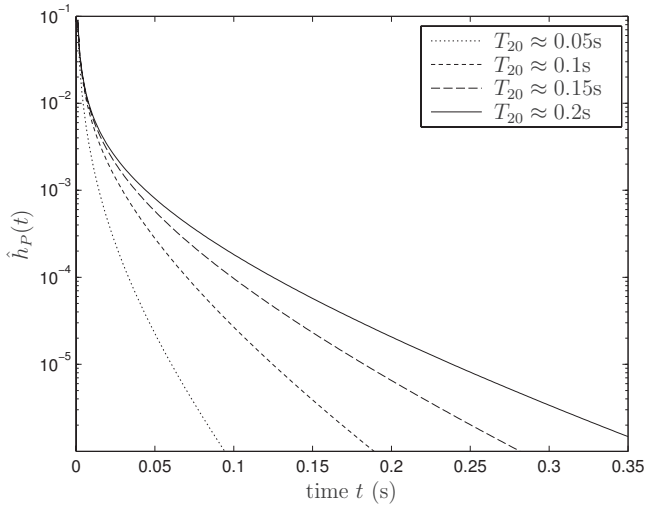

FIG. 4. Numerical evaluation of the approximate power transfer function $\hat{h}_P(\cdot)$, for various levels of reverberation, i.e., various values of β coefficients, and simulated with $\boldsymbol{r}=[4\text{ m}, 5\text{ m}, 2.9\text{ m}]^{\mathrm{T}}$.

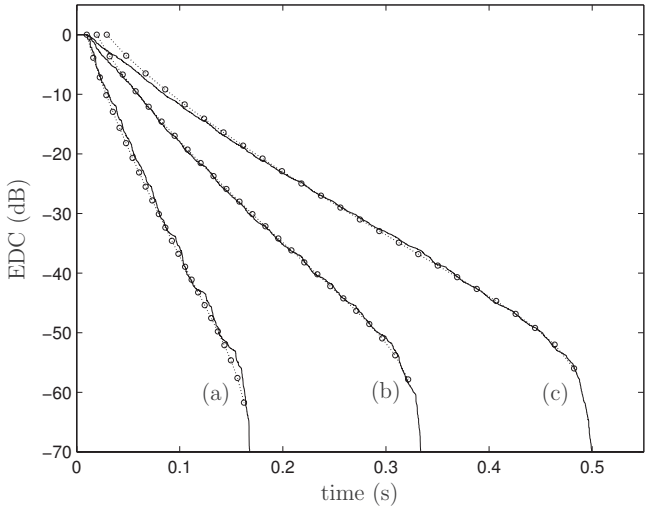

FIG. 5. Examples of energy decay curves with uniform reflection coefficients. (a) $\beta=0.669$ ($T_{20}\approx 0.05$ s), (b) $\beta=0.831$ ($T_{20}\approx 0.1$ s), and (c) $\beta=0.889$ ($T_{20}\approx 0.15$ s). Solid lines represent $E(t)$ obtained from ISM computations, circles (○) indicate values obtained with the proposed approximation $\hat{E}(t)$.

C. Approximation of energy decay

On the basis of Eq. (14), an estimate of the energy decay curve can be computed as

$$\hat{E}(t) = 10\log_{10}\left[\frac{\int_t^\infty \hat{h}_P(\xi)\mathrm{d}\xi}{\int_0^\infty \hat{h}_P(\xi)\mathrm{d}\xi}\right]. \tag{36}$$

In practice, the integrals in Eq. (36) can be replaced with Riemann sums as follows:

$$\int_t^\infty \hat{h}_P(\xi)\mathrm{d}\xi \approx T\cdot\sum_{i=0}^{\infty}\hat{h}_P(t+iT), \tag{37}$$

with an appropriate discretization step T. The validity of this approximation depends on the function $\hat{h}_P(\cdot)$ being smooth and bounded in the considered interval, which is supported by the plots in Fig. 4; it is also shown in the next section that Eq. (37) indeed holds true for the type of function defined in Eq. (32). Thus, the estimated energy–time curve can be finally computed according to Eqs. (36) and (37), and for $t > t_0$, as

$$\hat{E}(t) \approx 10\log_{10}\left[\frac{\sum_{i=0}^{\infty}\hat{h}_P(t+iT)}{\sum_{i=0}^{\infty}\hat{h}_P(t_0+iT)}\right], \quad t > t_0. \tag{38}$$

The introduction of the parameter t_0 in Eq. (38) can be explained as follows. According to the assumptions made in this work, the EDC approximation is expected to be inaccurate for small ϱ values, that is, for $t\to 0$. Therefore, the approximation formula in Eq. (38) can be considered as relevant only for values of t greater than a specific threshold, denoted here as t_0. Section IV will provide more detail regarding an appropriate setting of the t_0 parameter for numerical simulation purposes.

D. Discussion

Two distinct sources of error can be identified in relation to the expression proposed in Eq. (38). As mentioned above, the assumption of a large radius ϱ will typically lead to a poor approximation of the true EDC as $t\to 0$. In addition, the parameter t_0 effectively introduces an additive error term related to $\int_0^{t_0} h^2(\xi)\mathrm{d}\xi$ in the denominator of Eq. (38). This error term is, however, independent of the time variable t, and thus potentially creates a constant offset in the EDC approximation curve $\hat{E}(\cdot)$. These two distinct effects will be illustrated more specifically in the following section.

Finally, the infinite sums in Eq. (38) have to be truncated to a finite set of indices in practice. As shown in Fig. 4, the function $\hat{h}_P(t)$ tends toward 0 very quickly as t increases, and as a result, the summation can be terminated relatively early while still providing a good approximation for practical purposes.

IV. EXPERIMENTAL RESULTS

A. Numerical evaluations

This section provides some examples of the results obtained with the proposed EDC approximation method. Figure 5 considers a typical enclosure setup, the details of which are provided in Table I, for three different levels of reverberation and assuming uniform reflection coefficients β for all enclosure surfaces. The solid lines represent the energy decay lines computed via Eq. (14) on the basis of the impulse responses simulated with the ISM technique of Sec. II B. Circle markers (○) indicate the values obtained via Eqs. (32) and (38) computed at several discrete values of time. Figure 6 shows similar results, obtained using a different room setup

TABLE I. Parameter setup for the results presented in Figs. 5–7. F_s denotes the sampling frequency.

	Figure 5	Figures 6 and 7
$\boldsymbol{r}$ (m)	$[4.0, 5.0, 2.9]^{\mathrm{T}}$	$[3.2, 4.0, 2.7]^{\mathrm{T}}$
$\boldsymbol{p}_s$ (m)	$[1.5, 1.0, 1.0]^{\mathrm{T}}$	$[1.1, 1.0, 1.2]^{\mathrm{T}}$
$\boldsymbol{p}_r$ (m)	$[3.5, 3.8, 1.9]^{\mathrm{T}}$	$[2.0, 3.0, 2.0]^{\mathrm{T}}$
F_s (Hz)	16000	16000

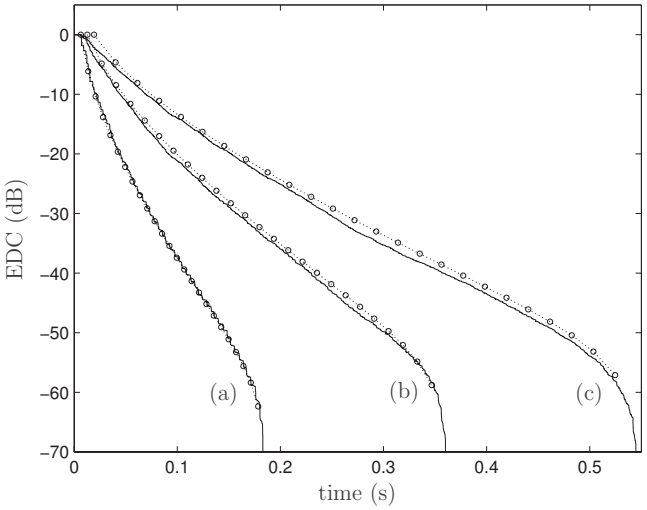

FIG. 6. Examples of energy decay curves with nonuniform reflection coefficients, for (a) $T_{20} \approx 0.05$ s, (b) $T_{20} \approx 0.1$ s, and (c) $T_{20} \approx 0.15$ s. See Table II for the corresponding β values. Solid lines represent $E(t)$ obtained from ISM computations, circles (∘) are values from the proposed approximation $\hat{E}(t)$.

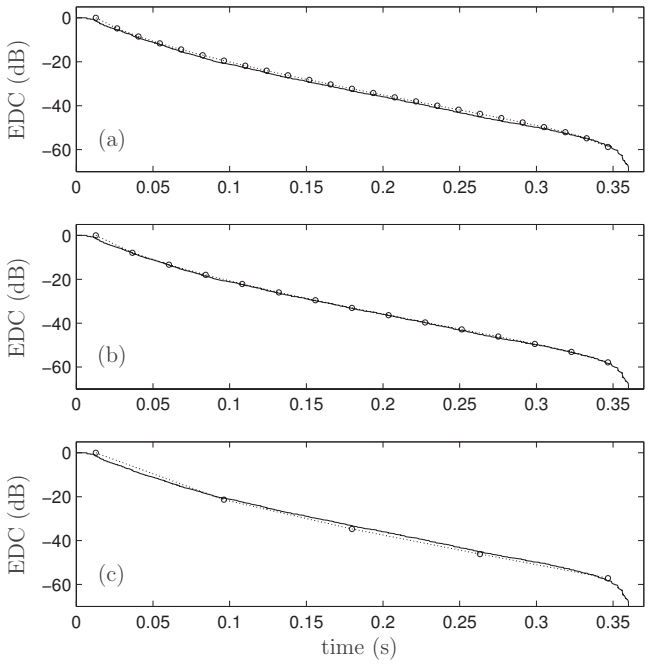

FIG. 7. EDC approximation results with varying interval lengths, for $T_{20} \approx 0.1$ s (see Table I for setup parameters). The discretization interval is defined as (a) $T=0.014$ s, (b) $T=0.024$ s, and (c) $T=0.083$ s.

(see Table I) in the case of nonuniform wall reflection coefficients, the values of which are given in Table II. Note that the curves in Fig. 6 correspond to a scenario where a pair of opposing walls is significantly different in reflectivity compared to other surfaces; this specific case was found to lead to discrepancies between the estimated and measured reverberation times in the publication of Allen and Berkley.[20]

Despite several simplifying assumptions made in this work, Figs. 5 and 6 demonstrate that the proposed EDC approximation technique is quite accurate when estimating the energy decay in RIRs produced with the image-source method. The overall decay rate, as well as the shape (curvature) of the decay lines for nonuniform β coefficients, match the practical results relatively well. With respect to the effects of the large-radius assumption mentioned previously, these numerical results also illustrate the discrepancy between the approximated and the practical results at low t values, which appears as a slight upward bias at the beginning of the approximation curves. This effect becomes more pronounced for larger reverberation times but remains nonetheless relatively negligible for most practical purposes.

It must be noted here that the results in Figs. 5 and 6 have been obtained with an optimal setting of the variable t_0 (i.e., the time lag of the first value on the approximation curves). This effectively compensates for the constant error term discussed in Sec. III D, and thus enables a better visual comparison of the displayed results. In practice, a nonoptimal setting of t_0 would hence result in a slight offset in the corresponding EDC approximation curve. It was found empirically that choosing $t_0 = 1.5 \cdot \|\boldsymbol{p}_s - \boldsymbol{p}_r\|/c$ or $t_0 = 1.5 \cdot \bar{r}/c$ achieves a relatively good match for a large array of enclosure sizes and reflection coefficients. Note also that this offset only has a marginal effect when assessing the overall energy decay of the considered RIR or when measuring quantities such as the reverberation time. Reference 19 further demonstrates the practical accuracy of the proposed method by providing more results from extensive numerical simulations.

Finally, the different plots in Fig. 7 provide an insight into the influence of the discretization interval T in Eq. (38). This figure displays the approximation results for three different time lengths, computed with $T_{20} \approx 0.1$ s and for an environmental setup as described in Table I. These results clearly demonstrate the fact that the accuracy of the approximation remains very good regardless of the number of points considered along the curve, which corroborates the validity of the approximation in Eq. (37). If necessary, the calculations can hence be made more computationally efficient by reducing the number of points on the approximation curve, with only a marginal reduction of the representation accuracy.

In addition to the practical results presented in this section, the accuracy of the proposed technique has been further tested and confirmed for a wide range of scenarios involving different enclosure volumes, various source and sensor positions, as well as uniform and nonuniform reflection coefficients.

TABLE II. Values of reflection coefficients for each boundary surface, for the curves displayed in Fig. 6.

Curve	$\beta_{x,1}$	$\beta_{x,2}$	$\beta_{y,1}$	$\beta_{y,2}$	$\beta_{z,1}$	$\beta_{z,2}$
(a) $T_{20} \approx 0.05$ s	0.032	0.032	0.548	0.548	0.837	0.837
(b) $T_{20} \approx 0.1$ s	0.675	0.675	0.787	0.787	0.915	0.915
(c) $T_{20} \approx 0.15$ s	0.802	0.802	0.866	0.866	0.945	0.945

TABLE III. Desired vs measured reverberation times with nonuniform sound absorption coefficients. The relative error percentage is displayed in brackets.

	Measured T_{20} (s)		
Desired T_{20} (s)	Proposed	Sabine	Eyring
0.05	0.045 (10%)	0.048 (4%)	0.074 (48%)
0.10	0.092 (8%)	0.131 (31%)	0.161 (61%)
0.15	0.144 (4%)	0.212 (41%)	0.238 (59%)
0.20	0.201 (1%)	0.284 (42%)	0.311 (56%)
0.25	0.255 (2%)	0.352 (41%)	0.371 (48%)
0.30	0.318 (6%)	0.416 (39%)	0.438 (46%)

TABLE IV. Average CPU times required for EDC computations at various reverberation times T_{60}, for ISM-based simulations and the proposed EDC approximation method.

	CPU time (s)	
T_{60} (s)	Proposed	ISM-based
0.1	0.0082	2.72
0.2	0.015	7.75
0.3	0.022	32.96
0.4	0.029	101.18
0.5	0.036	236.17
0.6	0.042	466.92

B. Application example

As discussed in Sec. I, the proposed EDC approximation method can be used to efficiently determine which values of reflection coefficients must be chosen to achieve a desired reverberation level T_{20} in a given environment. This is illustrated here with the typical example of a $4\times5\times2.9$ m^3 room with nonuniform wall absorption coefficients defined by the following ratios:

$$(\alpha_{x,1}:\alpha_{x,2}:\alpha_{y,1}:\alpha_{y,2}:\alpha_{z,1}:\alpha_{z,2}) = (1.0:0.9:0.7:0.6:0.4:0.3), \tag{39}$$

where the notation $(\mu_1:\mu_2:\mu_3:\cdots)$ is used to describe a series of ratios between multiple variables, i.e., $\mu_1:\mu_2,\mu_2:\mu_3$, etc. Using the method proposed in Sec. III, the approximate EDC can be computed with varying values of absorption coefficients [while ensuring that the ratios in Eq. (39) remain satisfied], until α parameters are found that yield the correct reverberation time, i.e., the correct slope in the predicted energy–time curve. Note that this optimization process is very fast since each iteration consists only of a few numerical evaluations of the expressions in Eqs. (32) and (38). The frequency-domain ISM computation is then carried out according to Sec. II B with the resulting α values, and the "true" reverberation time is measured directly from the computed RIR. For comparison, the same process is carried out with two commonly used formulas for predicting the reverberation time, namely, Sabine's equation,[28]

$$T_{20,\mathrm{Sab}} = \frac{1}{3}\frac{0.161V}{\sum_{i=1}^{6} S_i\alpha_i}, \tag{40}$$

and Eyring's equation,[29]

$$T_{20,\mathrm{Eyr}} = \frac{1}{3}\frac{0.161V}{-S\log(1-\sum_{i=1}^{6} S_i\alpha_i/S)}, \tag{41}$$

where V is the room volume, S is the total surface area of the enclosure, and S_i and α_i, $i=1,\ldots,6$, represent the surface areas and absorption coefficients of each individual wall, respectively. In the simulations, Eqs. (40) and (41) are used in conjunction with Peterson's ISM implementation[22] with positive reflection coefficients, as this represents the approach chosen by many authors in order to assess the performance of various signal processing algorithms.

Table III presents the assessment results, which correspond to an average over 20 randomly selected source–receiver configurations in the considered environment. These results are shown for various desired values of the reverberation time T_{20}, which is defined here as the time required by the acoustic energy $E(t)$ in the RIR to decrease from -5 to -25 dB. Note that any other quantity could have been chosen as a measure of reverberation: the developments presented in this paper are valid for any parameter of interest defined on the basis of the EDC, such as T_{60}, T_{30}, early decay time, etc.

As mentioned in Sec. I, Table III highlights the significant discrepancies existing between the desired reverberation level and that predicted with Sabine or Eyring's formulas; these expressions severely underestimate the value of the α parameters, leading to reverberation times that are significantly higher than targeted. On the other hand, because the proposed method is based on a relatively accurate prediction of the resulting acoustic energy decay, its reverberation time estimates remain within a small percentage of the desired T_{20} values, even when the sound reflection coefficients are not defined uniformly in the environment. In the specific context of testing signal processing algorithms using ISM simulations, this consequently minimizes the discrepancy between the assumed and actual reverberation times and ensures a minimal bias in the resulting performance assessment.

C. Computational requirements

As mentioned earlier, the computation of energy–time curves by means of ISM-based simulations can be computationally very demanding. The EDC approximation method proposed in this work alleviates this heavy computational burden by providing a closed-form expression allowing the quasi-instantaneous computation of a room's EDC curve.

To highlight the computational advantages of the proposed approach, Table IV presents the average CPU (central processing unit) time required by each method for the computation of an energy decay curve, as a function of the reverberation time T_{60}. These results represent the average over 80 EDC simulations carried out for various enclosures with randomly generated dimensions and source–sensor configurations. For the proposed approach, all EDCs were approximated with a constant discretization step $T=0.005$ s. Both methods were implemented in the MATLAB programing language with a sampling frequency $F_s=8$ kHz, and the computations were carried out on a modern 2.0 GHz computer. For both methods, the computation of each separate

EDC was terminated once the energy level in the RIR had decreased by approximately 60 dB.

As demonstrated by the results in Table IV, the proposed technique considerably reduces the computational requirements compared to ISM simulations. This computational advantage is even more significant with the multiple computation of one RIR, for instance, in the process of adjusting sound reflection coefficients to achieve a desired reverberation time (as in the example of Sec. IV B). Note also that the computational requirements of the ISM-based simulations further increase dramatically as the sampling frequency F_s is increased.

V. CONCLUSIONS

This paper proposes a method for approximation of the acoustic energy decay in simulated room impulse responses, and demonstrates that this technique provides an accurate prediction of the energy–time function generated on the basis of a modified version of the widely used image-source model. This method thus enables designers to efficiently investigate some of the acoustical characteristics of a simulated room without the need to generate the impulse responses of interest. Due to the considerable computational demands usually associated with the image-source model, this consequently represents a substantial reduction in the resulting computational burden. Furthermore, the developments presented here explicitly establish an unequivocal connection between environmental factors such as the walls' absorption coefficients and the level of reverberation resulting in the considered enclosure. As shown in this work, this relation is not currently well modeled by classical reverberation-time formulas, especially with a nonuniform definition of the sound absorption coefficients. In order to test audio processing algorithms, the proposed method hence provides engineers with a valuable tool to generate realistic impulse responses, whose main parameter of interest, namely the reverberation level, can be effortlessly and accurately tuned. The technique described in this paper can also be of potential interest in other application fields such as virtual auditory environments, perceptual acoustics, architectural design, sound field modeling, etc.

ACKNOWLEDGMENTS

This work was supported by National ICT Australia (NICTA). NICTA is funded through the Australian Government's *Backing Australia's Ability* initiative, in part through the Australian Research Council.

[1]S. Dance, J. Roberts, and B. Shield, "Computer prediction of sound distribution in enclosed spaces using an interference pressure model," Appl. Acoust. **44**, 53–65 (1995).
[2]M. Hodgson, "On the accuracy of models for predicting sound propagation in fitted rooms," J. Acoust. Soc. Am. **88**, 871–878 (1990).
[3]K. Li and K. Iu, "Full-scale measurements for noise transmission in tunnels," J. Acoust. Soc. Am. **117**, 1138–1145 (2005).
[4]Y. Lam, "Issues for computer modelling of room acoustics in non-concert hall settings," Acoust. Sci. & Tech. **26**, 145–155 (2005).
[5]J. Suh and P. Nelson, "Measurement of transient response of rooms and comparison with geometrical acoustic models," J. Acoust. Soc. Am. **105**, 2304–2317 (1999).
[6]S. Dance and B. Shield, "The complete image-source method for the prediction of sound distribution in non-diffuse enclosed spaces," J. Sound Vib. **201**, 473–489 (1997).
[7]K. Li and P. Lam, "Prediction of reverberation time and speech transmission index in long enclosures," J. Acoust. Soc. Am. **117**, 3716–3726 (2005).
[8]L. Savioja, T. Lokki, and J. Huopaniemi, "Auralization applying the parametric room acoustic modeling technique—the DIVA auralization system," Proceedings of the International Conference on Auditory Display, Kyoto, Japan, 2002, pp. 219–224.
[9]J. Miller and E. Wenzel, "Recent developments in SLAB: a software-based system for interactive spatial sound synthesis," Proceedings of the International Conference on Auditory Display, Kyoto, Japan, 2002, pp. 403–408.
[10]T. Lokki, L. Savioja, R. Väänänen, J. Huopaniemi, and T. Takala, "Creating interactive virtual auditory environments," IEEE Comput. Graphics Appl. **22**, 49–57 (2002).
[11]D. Zotkin, R. Duraiswami, and L. Davis, "Rendering localized spatial audio in a virtual auditory space," IEEE Trans. Multimedia **6**, 553–564 (2004).
[12]M. Ikram and D. Morgan, "A multiresolution approach to blind separation of speech signals in a reverberant environment," Proceedings of the IEEE International Conference on Acoustics, Speech, and Signal Processing, Salt Lake City, UT, 2001, pp. 2757–2760.
[13]B. Radlović, R. Williamson, and R. Kennedy, "Equalization in an acoustic reverberant environment: robustness results," IEEE Trans. Speech Audio Process. **8**, 311–319 (2000).
[14]F. Talantzis and D. Ward, "Robustness of multichannel equalization in an acoustic reverberant environment," J. Acoust. Soc. Am. **114**, 833–841 (2003).
[15]E. Lehmann and A. Johansson, "Particle filter with integrated voice activity detection for acoustic source tracking," EURASIP Journal on Advances in Signal Processing **2007**, Article ID 50870, 11 pages (2007).
[16]K. Palomäki, G. Brown, and D. Wang, "A binaural processor for missing data speech recognition in the presence of noise and small-room reverberation," Speech Commun. **43**, 361–378 (2004).
[17]S. Doclo and M. Moonen, "GSVD-based optimal filtering for single and multimicrophone speech enhancement," IEEE Trans. Signal Process. **50**, 2230–2244 (2002).
[18]J. António, L. Godinho, and A. Tadeu, "Reverberation times obtained using a numerical model versus those given by simplified formulas and measurements," Acust. Acta Acust. **88**, 252–261 (2002).
[19]E. Lehmann, A. Johansson, and S. Nordholm, "Reverberation-time prediction method for room impulse responses simulated with the image-source model," Proceedings of the IEEE Workshop on Applications of Signal Processing to Audio and Acoustics, New Paltz, NY, 2007, pp. 159–162.
[20]J. Allen and D. Berkley, "Image method for efficiently simulating small-room acoustics," J. Acoust. Soc. Am. **65**, 943–950 (1979).
[21]This assumption is mainly for conciseness reasons. Both the angle and frequency dependence could be included in the acoustic model, but only at the expense of significantly complicating the derivations presented in this work.
[22]P. Peterson, "Simulating the response of multiple microphones to a single acoustic source in a reverberant room," J. Acoust. Soc. Am. **80**, 1527–1529 (1986).
[23]H. Kuttruff, *Room Acoustics*, 4th ed. (Spon, London, 2000).
[24]Please note that Eq. (12) is only provided here in order to provide some insight into the physical meaning of using negative β coefficients. As mentioned in Sec. II A, the derivations in this work assume angle-independent reflection coefficients.
[25]Note further that the use of negative β coefficients in Eq. (13) when computing simulated RIRs does not impact on the subsequent developments since this work focuses on acoustic energy which, in turn, relies on squared amplitude coefficients (i.e., acoustic power).
[26]M. Schroeder, "New method of measuring reverberation time," J. Acoust. Soc. Am. **37**, 409–412 (1965).
[27]The exponential integral Ei(·) is a standard function built into several mathematical packages such as MATLAB, MAPLE, and MATHEMATICA.
[28]W. Sabine, *Collected Papers on Acoustics* (Dover, New York, 1964).
[29]C. Eyring, "Reverberation time in "dead" rooms," J. Acoust. Soc. Am. **1**, 217–241 (1930).

Monaural room acoustic parameters from music and speech

Paul Kendrick, Trevor J. Cox, and Francis F. Li
Acoustic Research Centre, University of Salford, Salford M5 4WT, United Kingdom

Yonggang Zhang and Jonathon A. Chambers
Advanced Signal Processing Group, Department of Electronic and Electrical Engineering, Loughborough University, Leicestershire LE11 3TU, United Kingdom

(Received 12 October 2007; revised 21 April 2008; accepted 23 April 2008)

This paper compares two methods for extracting room acoustic parameters from reverberated speech and music. An approach which uses statistical machine learning, previously developed for speech, is extended to work with music. For speech, reverberation time estimations are within a perceptual difference limen of the true value. For music, virtually all early decay time estimations are within a difference limen of the true value. The estimation accuracy is not good enough in other cases due to differences between the simulated data set used to develop the empirical model and real rooms. The second method carries out a maximum likelihood estimation on decay phases at the end of notes or speech utterances. This paper extends the method to estimate parameters relating to the balance of early and late energies in the impulse response. For reverberation time and speech, the method provides estimations which are within the perceptual difference limen of the true value. For other parameters such as clarity, the estimations are not sufficiently accurate due to the natural reverberance of the excitation signals. Speech is a better test signal than music because of the greater periods of silence in the signal, although music is needed for low frequency measurement.
 [DOI: 10.1121/1.2931960]

PACS number(s): 43.55.Mc, 43.60.Np, 43.60.Cg [NX] Pages: 278–287

I. INTRODUCTION

Room acoustic parameters, such as reverberation time, are routinely used in the design and evaluation of enclosed and semienclosed spaces such as concert halls, classrooms, and stadia. Normally, these parameters are measured by with artificial test stimuli, such as gun shots, pseudorandom noise, or sine sweeps, because this yields accurate and reliable results. The interest in this paper, however, lies in trying to measure the parameters using the natural sounds occurring in rooms; of particular interest is the use of speech or music as a test signal. Measuring by using natural sounds should make occupied measurement easier because the signals will not disturb the room occupants. Consequently, it should facilitate the monitoring of in-use conditions; this is what motivates the work presented.

Li and Cox[1] developed a machine learning method to determine the speech transmission index from received running speech. This method is quasiblind: source signals do not need to be monitored during measurements but they are required during the training phases of the machine learning algorithm. A key limitation of this method is that it is an empirical approach which requires extensive training before use. Even so, it can be shown that with about a minute of speech, high accuracy can be obtained. With slightly compromised accuracy, the method can be made completely blind because the low frequency statistical properties of speech are not very different from speaker to speaker.[2] This method is termed the "envelope spectrum method" because of the preprocessor used.

The envelope spectrum method was originally developed to be used with narrated speech. For parameters used in the evaluation of concert halls, however, it is natural to examine the use of music as an excitation signal, and this has not been considered with the method before. In comparison to speech, music offers a larger bandwidth of excitation and so enables acoustic parameters to be measured over a wider range of frequencies. In particular, in comparison to speech, music has more sound power in the lower octave bands that are considered in room design. Music, however, is a rather imperfect test signal, as shall be shown later. To work with music, the envelope spectrum method needed to be adapted to deal with the inherent statistical differences between speech and music, and these adaptations are outlined in this paper. Since the development of the envelope spectrum method, the data set of room impulse responses used to train the machine learning algorithm has been improved, and this affects the accuracy of the method. Details of this are also provided in the paper.

An alternative to the envelope spectrum method is one using a maximum likelihood estimation (MLE). This approach was originally developed by Ratman *et al.*[3] The concept is to use decay phases following speech utterances or music notes to estimate the reverberation time. The method is inherently blind because it works off sound decays and uses the shortest decay as the one where the excitation is most impulsive and the decay is least corrupted by noise. The accuracy demonstrated by Ratman *et al.*, however, was insufficient for parameter evaluation. Kendrick *et al.*[4] improved the method by using a more realistic model for the envelope of room impulse responses, one that allowed for nondiffuse spaces, and they demonstrated good accuracy with reverberation time and early decay time (EDT). As de-

tailed below, a further extension is needed to extract other monaural parameters[5] because an accurate estimation of the decay curve energy is needed.

When designing a room for music production, a measure of clarity, such as clarity, center time, or an early to late energy ratio, is usually used alongside reverberation parameters to evaluate the acoustic quality. For speech, the Deutlichkeit serves a similar purpose. This paper examines how the two methods, envelope spectrum and MLE, can be used to estimate parameters which examine the relative balance of the early and late energies. Finally, the paper compares and contrasts the two methods for both speech and music examining, which is the best method and which is the best test signal.

II. METHOD

A. Parameters

This paper considers the following monaural parameters: reverberation time (T_{60}), EDT, clarity (C_{80}), and center time (T_s), which are well established and defined in an international standard.[6] In this paper, the reverberation time is calculated from 25 dB of decay. In typical speech and music, it is difficult to measure the end of reverberant tails because of masking from other utterances and notes, and this often makes the estimation of the more normal T_{30} inaccurate. Unless otherwise stated, the results are shown for the 1 kHz octave band.

Many of the results in this paper are presented in terms of how many of the estimations fall within one perceptual difference limen of the true value. The difference limen is a measure of the smallest perceivable difference in a stimulus. The difference limen for reverberation time with music signals is around 5% for reverberation times above 0.6 s, and increases to about 12% for shorter reverberation times.[7] There is limited information concerning the EDT difference limen so the criterion for the required accuracy is set at $\pm 5\%$ but with a minimum error of ± 0.1 s, as having accuracy better than this is not usually required.[8] The difference limen for clarity and center time were taken from Cox *et al.*[9]

B. Data sets

To test and develop the methods, a data set of room impulse responses is needed. For the envelope spectrum method, this data set has to include many thousand examples; too many to be obtained from real room measurements. Previously,[1] stochastically generated impulse responses were used. However, in recent years, there have been significant advances in the modeling of rooms by using geometric algorithms. Consequently, a commercial package[10] with a proven track record that utilizes randomized tail-corrected cone tracing was used to generate a training set of examples for teaching the machine learning algorithm used in the envelope spectrum method. The geometric model was also used to generate the first validation set used to examine the performance of both the envelope spectrum and MLE methods.

Rooms with randomized geometries, surface treatments, source, and receiver positions were generated, and the impulse response then calculated by using the geometric room acoustic model. Two room types were used: a box shaped room and a fan shaped design. Each model had a variable source position on stage and an audience area with a variable population density. The receiver grid was spread over the audience area. The algorithm that generated the random rooms was given limits for overall room dimensions, aspect ratios, and material properties to ensure the generated impulse responses were realistic. Room volumes ranged from 75 to 30 000 m^3. Material properties were randomly selected so that the reverberation time of the spaces (calculated by using Sabine's formulation) was set to be less than 4 s; longer reverberation times are seen in the results below because of the nondiffuse nature of many of the spaces. The idea is to generate a wide variety of spaces to allow the machine learning algorithm to learn all possible cases which might occur in reality, and also to rigorously examine the robustness of both methods by testing with a wide range of cases. In addition, a second validation set containing 20 real room impulse responses[11] were used to evaluate performance.

One problem with the use of the geometric room acoustic model was the fact that the calculation was done in octave bands and the results then recombined into an impulse response. This can result in significant discontinuities in parameter values at the edges of octave bands; something which will not arise in real rooms. As shall be shown later, such differences between the simulated and real room responses affect the performance of the methods to extract the parameters.

Music[12] and speech[13] recorded in anechoic conditions were convolved with the room impulse responses to produce the test signals.

C. Envelope spectrum

Figure 1 shows a schematic of the envelope spectrum method used to estimate an acoustic parameter in a single octave band from music. (Li and Cox[1] contains a more detailed description of this approach applied to speech, together with justifications for the technique). An anechoic signal is convolved with a room impulse response to provide an example of a transmitted signal. This is then passed through the low frequency envelope spectrum preprocessor, shown by the dashed box in Fig. 1, and from there to the artificial neural network (ANN). The ANN outputs an estimate of an acoustic parameter. The correct value for the acoustic parameter is calculated from the impulse response by using standard definitions.[6] The difference, or error, between the true and estimated parameters is used to update the internal weights and biases within the ANN. This process is repeated for thousands of different example impulse responses and, gradually, the ANN learns to produce more accurate estimations of the parameter for a wide variety of rooms.

After training, the weights and biases of the ANN are fixed and the performance of the ANN is tested by using impulse responses not previously used in training; these data sets are referred to as validation sets. Approximately 6500 artificially generated impulse responses were used for train-

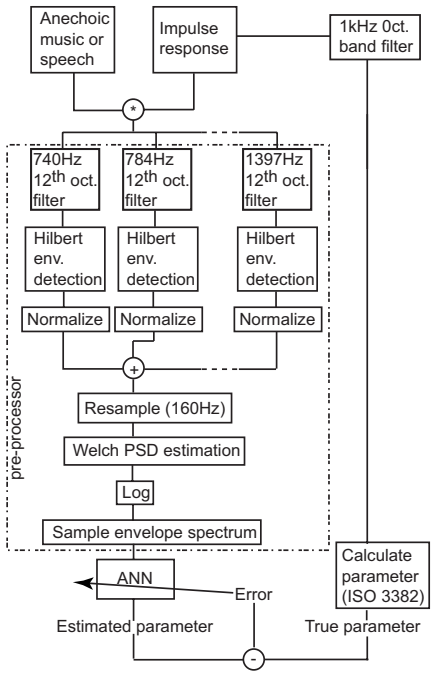

FIG. 1. Schematic of envelope spectrum method for estimating room acoustic parameters from music.

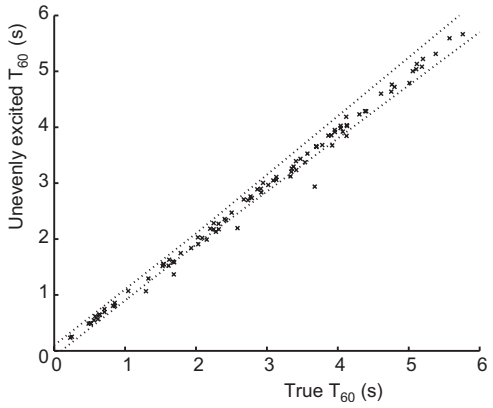

FIG. 2. Unevenly excited reverberation time compared to the true, evenly excited value. The unevenly excited reverberation time has the same octave band frequency response as a typical piece of music. The dashed lines indicate limits derived from the perceptual difference limen.

ing and about 700 examples for validation. These were generated by using the geometric room acoustic model described previously. A second validation set was based on the measured impulse responses.

The ANN is being used to carry out a mapping from the sampled envelope spectrum outputted from the preprocessor, to the desired acoustic parameter; it is essentially learning an unknown nonlinear relationship. An ANN is well suited to this task because of its inherent ability to deal with nonlinear mappings in an efficient manner. A multilayer perceptron with 40 input neurons, 30 and 10 neurons on the first and second hidden layers, respectively, and 1 output neuron was used. The network size was determined by trial and error. A bipolar sigmoid activation function was used. The Levenberg–Marquardt method was used, which offers an order of magnitude decrease in learning time over the back propagation rule.[14] To prevent overfitting, training was stopped when the validation error increased for a number of iterations.

The key stage in the development of this machine learning regime is the development of a suitable preprocessor. The primary role of the preprocessor is to greatly reduce the amount of data so that it can be effectively processed by the ANN. A few minutes worth of audio has to be reduced to a few tens of pieces of data. Finding a preprocessor that can do this while retaining meaningful information regarding the room acoustic parameters is a significant challenge. Reverberation is known to act as a low frequency filter on the envelope of signals. Houtgast and Steeneken[15] showed that the low frequency envelope spectrum can be used as an indicator of the level of reverberation added to speech. It is suggested that the low frequency envelope spectrum also contains information about other decay curve characteristics such as clarity—this hypothesis will be explored below.

As shown in Fig. 1, the first stage of the preprocessor is to break the signal down into one-twelfth octaves across the octave band being considered, where each one-twelfth octave corresponds to a note within an even-tempered chromatic scale. Previous work[1] with speech did not have to do this because it has a flatter frequency response than music across each octave band. Without individually processing each one-twelfth octave, the estimations using music were found to be quite poor.

Excitation within an octave band is uneven with respect to frequency for music signals. This unevenness in the excitation signal must be compensated for by the parameter extraction system. Consider comparing an acoustic parameter calculated from a standard impulse response with even excitation, and the same parameter calculated by using an impulse response filtered to have a frequency response corresponding to the average power spectrum of a piece of music, i.e., an uneven frequency response.

To get the latter impulse response, first, the frequency content of the music extract was estimated by using the Welch power spectrum method using 0.5 s windows and 50% overlap Hanning windows. This frequency response is used to design a linear phase finite impulse response (FIR) filter with the same frequency response as the average spectrum of the music signal. Linear phase is used so that the time response of the impulse response is least distorted, only delayed. This delay is removed after the filtering process (equivalent to zero phase filtering). A short tap length of 301 is used for the FIR filter. The "reverberation time" of the weighing filter was checked to make sure that it did not ring for too long and generally, it was 0.07 ± 0.01 s. The impulse response is passed through this filter and the delay compensated for.

Figure 2 shows the reverberation time for an uneven excitation (excitation with similar spectrum to a music signal) plotted against the reverberation time with even excitation (broadband excitation) for the impulse responses simulated by using the geometric room acoustic model. The dotted lines indicate the required accuracy for parameter estimation and is based on the perceptual difference limen. The result shown is for the 1 kHz octave band. The error intro-

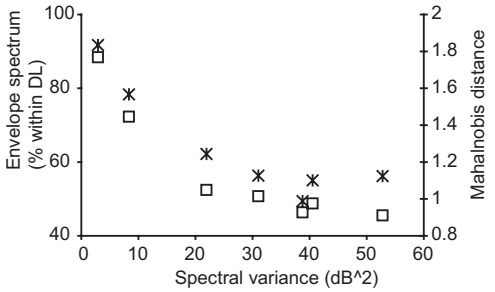

FIG. 3. Variation of the □ Mahalnobis distance and * envelope spectrum method accuracy with the variance of the music spectrum. Six pieces of music and one piece of speech.

duced by the uneven excitation is the same order of magnitude as the difference limen. For the validation set using the 20 real room measurements, the error is somewhat less, being approximately halved. This might be due to the restricted range of reverberation times in the real room dataset, or that the real room impulse responses have less variation in the acoustic parameters across the octave band. For all the other acoustic parameters, EDT, clarity, and center time, the error is larger, at worse being about twice the difference limen.

The one-twelfth octave filtering used in the preprocessor helps to compensate for the uneven excitation. After the one-twelfth octave filters, the envelope of each of the twelve signals is detected by using the Hilbert transform[16] and a normalization to the root mean square in each one-twelfth octave carried out. This normalization reduces the effect of uneven excitation with respect to frequency. The objective is to get a result closer to the one which would be obtained from an artificial test signal with even excitation with respect to frequency. Even with this normalization, however, the unevenness of the power spectrum of the music across the octave band has a significant effect on the accuracy of the parameter estimations. Figure 3 illustrates this for reverberation time. Seven source signals are used comprising six pieces of music and one piece of speech. For each source signal, the ANN within the envelope spectrum method is trained. The validation set, simulated by using the geometric room acoustic model, is used, with the percentage of estimations within one difference limen of the true result being used as a measure of success. This success rate is plotted against the spectral variance calculated across the octave band. The results show that as the excitation becomes more even across the octave band, as the spectral variance decreases, the envelope spectrum method becomes more successful at estimating reverberation time.

For each ANN, the same piece of music or speech is used in both training and validation phases. Li *et al.*[1] presented a method that enabled almost any speech source to be used once the ANN is trained. This facilitated "source independent" estimation of the parameters. Source independence is successful with speech, as the low frequency envelope spectra between talkers are similar. However, due to the highly diverse range of music signals, the low frequency envelope spectrum for a piece of music is quite unique and source independence in the presented framework is not feasible.

Producing each of the envelope spectrum results in Fig. 3 requires training an ANN. Because there is always uncertainty about certain aspects such as ANN size and update rate, a measure to assess the quality of the input data was sought, which is more mathematically rigorous. The Mahalnobis distance[17] is a measure of data separability applied to the input data of the ANN. The measure gives a statistically weighted Euclidian distance between two sets of data. If the distance between the data are large, the data are well separated, and this makes it much more likely that the ANN will be able to carry out the mapping to the acoustic parameters. If the distance is small, however, this indicates ambiguity in the input data set which will make it difficult for the ANN to be successfully trained.

To calculate the Mahalnobis distance, the data are split into groups whose sizes are determined by the difference limen. For example, the difference limen for clarity is known to be about 1 dB, therefore, the range of possible clarity values is quantized into 1 dB steps, and all input data relating to a clarity value within ± 0.5 dB of the center value are assigned to that group. The Mahalnobis distance is calculated between each adjacent group which gives a useful indicator of how separability varies with the parameter. The overall separability of the data set, as shown in Fig. 3, is calculated by averaging the Mahalnobis distances for all clarity groups. (Incidentally, the spectral variance used is not simply a variance of the power spectral density values across the octave band of the signal. To be consistent with the ANN input, it is necessary to first split the data into one-twelfth octave bands and to normalize these as was done in the preprocessor, before recombining the results and calculating the variance.)

As Fig. 3 confirms, pieces of music with more even excitation produce more accurate results with the envelope spectrum method. An alternative way of improving accuracy is to use multiple pieces of music and average the results for the acoustic parameters.

Returning to the preprocessor, the one-twelfth octave normalized envelopes are then recombined, down sampled, and the power spectral density estimated. This is done by using a Welsh algorithm using 50% overlap and 3.5 s Hanning windows (the best window size was determined empirically). After taking a log of the envelope spectrum, the spectrum is converted into a constant percentage bandwidth spectrum. To get 40 bandwidths and hence, 40 spectral samples from 0.2 to 25 Hz, required a bandwidth of $\approx 9/50^{\text{ths}}$ of an octave to be used. These data then form the input data for the ANN.

D. Maximum likelihood estimation

This method has recently been detailed in another paper[4] so only an outline is provided here with the adaptations necessary to obtain other monaural acoustic parameters. The signal is filtered into the octave band being considered. The envelope of the received reverberated music or speech is detected by using the Hilbert transform.[16] A signal segmentation and selection process is undertaken to find parts of the signal that contain free decay—the reverberant tail at the ends of words or notes (decay phases). Decay phases with

sufficient dynamic range for parameter estimation are sought (>25 dB). A MLE is undertaken on these decay segments providing a robust estimation of the envelope of the room impulse response. The estimated impulse response h_e is modeled as a noise signal modulated by an envelope with a double exponential decay

$$h_e(n) = [\alpha a_1^n + (1-\alpha)a_2^n]s(n), \tag{1}$$

where n is the time index, s is the Gaussian noise signal, a_1 and a_2 determine the decay rate of the two exponential functions, and α gives the relative importance of the two exponential decays. A double decay is used to better model the nondiffuse spaces. The fine details (individual reflections) of the impulse response are represented by the zero mean Gaussian noise signal. The MLE is essentially an efficient and robust method of fitting this estimated impulse response to the measured free decay at the end of words or notes. a_1, a_2, α, and the variance of the Gaussian noise are determined via numerical optimization; this is done by forming a likelihood function[18] and maximizing it.

Any piece of music or speech will yield a number of free decay segments from which a number of impulse response envelopes can be found. Previously,[3] the envelope equating to the shortest reverberation time was chosen as the best estimated because this has least contamination from noise. This selection method, however, is not appropriate when trying to estimate other acoustic parameters. For this, a new approach was developed which builds up a best estimate of the decay curve in sections, by considering the energy along the decay phase.

Consider a single measured decay phase x; this can be split into a number of components,

$$x(n) = h(n) \otimes [\delta(n) + d(n)] + r(n), \tag{2}$$

where $\delta+d$ represent the direct sound, h is the room impulse response, and r are the reflections excited by signals occurring before the start of the selected decay phase or other unwanted noise. The direct sound is split into two components, δ representing ideal impulsive excitement at the start of the frame and a competing noise term d representing the subsequent decay of the musical note or speech utterance.

Calculating the signal energy based on Eq. (2) yields a number of squared and cross terms. However, provided that the energy is estimated over a sufficiently long time window, it may be assumed that the cross terms reduce to zero as variables within these cross terms are uncorrelated and have a zero mean value. Therefore, the signal energy is approximately given by

$$\sum x^2 \approx \sum h^2 + \sum (d \otimes h)^2 + \sum r^2. \tag{3}$$

The first term on the right hand side of Eq. (3) is constant so the energy in a decay phase only changes with d and r. Therefore, by finding the decay phase with the smallest energy for a given time period, the cleanest region of free decay is being found—freest from additional notes masking the decay phase, reverberance of the notes or speech utterances, and the region most like the room impulse response. This preference toward the minimum energy favors the most impulsive musical notes or speech utterances, which is assumed to also tend to reduce the unwanted effects of uneven excitation.

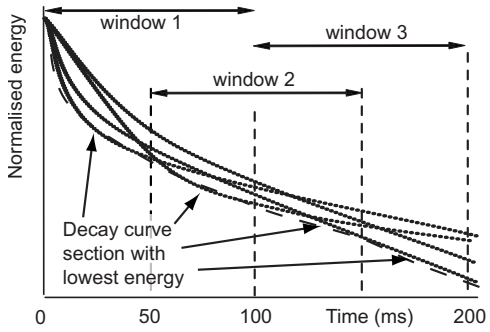

FIG. 4. Illustration of method for reconstructing (– – – – –) best decay curve estimate from (————) four decay curve estimates. In each of the three windows, four decay curves with least energy are chosen. Triangular windowing is used to smooth the response between windows.

Experience has shown that there may be no single decay phase that is "cleanest" for the full length of the impulse response and, consequently, the following process is used, as illustrated in Fig. 4. The decay phase estimates are windowed by using a 0.1 s rectangular window using 50% overlap and the energy is calculated for each window. Figure 4 shows four such estimates. The decay curve with the least energy in each 0.1 s window is selected as the cleanest portion for that range. The final decay curve estimate is constructed from these cleanest portions, using triangular windows to smooth discontinuities in the decay curve. This is then the best estimate of the impulse response envelope which is shown as the dashed line.

Rather than taking a single best estimate of the impulse response envelope from a long piece of speech or music, an average across several best estimates is taken to improve accuracy. With speech, an 8 min recording is split into eight blocks each 1 min long. Within each of these 1 min blocks, the above procedure is undertaken to get a best estimate of the impulse response envelope, yielding eight estimates in total. These estimates are then "averaged" to get the final form of the impulse response envelope. The presence of background noise causes outlying estimates due to overestimation of the rate of decay. Outliers of this nature are common and, therefore, the median is used rather than taking an average using the mean. This operation is illustrated in Fig. 5, illustrating, among others, an outlying decay curve and showing that by using the median, the final estimation has not been overly biased by the outlier. This averaging across eight-estimates helps overcome stochastic variability in the frequency content of single decay phases.

Incidentally, the impulse response should be time invariant, but in many rooms, this is not true. However, as the estimation is over the smoothed envelope of the impulse response, the effect of time variance is probably not going to be a great problem; although this has yet to be formally tested. Once the optimal envelope of the impulse response has been estimated, standard definitions are used to obtain the room acoustic parameters.

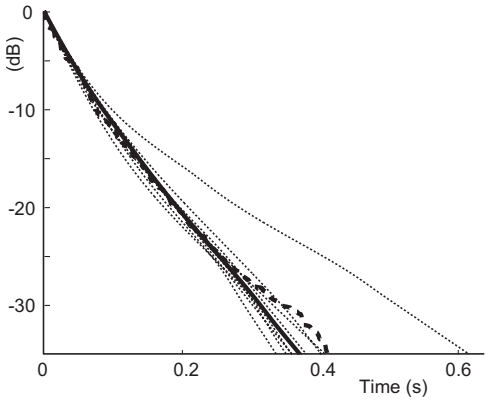

FIG. 5. Impulse response envelopes (……) individual estimates including one outlier shown to right, (————) best estimate formed by taking median of individual estimates, and (– – – – –) true envelope.

III. RESULTS

A. Speech

In this section, performance of the envelope spectrum and MLE methods are compared by using speech excitation. About 9 s of anechoic, male, narrated running speech[13] is used in both cases. By narrated speech, it is meant that the speaker is given a passage of text to be read aloud. This technique tends to slow down the rate at which the narrator speaks and so gives more gaps between utterances where decays can be seen.

Two data sets are used to examine the success of the methods, one based on speech convolved with simulated impulse responses generated by the geometric room acoustic model and the second, a set based on speech convolved with real measured room impulse responses. The performance of the parameter estimation methods vary between these two data sets and comparing the two sheds light on the robustness of the methodologies.

Consider first the results for the data set based on the simulated impulse responses from the geometric room acoustic model. The envelope spectrum method produces as good or better parameter estimation accuracy than the MLE method for these data. In general, the MLE method finds it harder to accurately estimate the early parts of the impulse response because it cannot separate the decay due to the room reflections from the decay of the speech utterances. Because the envelope spectrum method is based on an experiential method, the ANN learns to compensate for the overestimation of the early reverberation that occurs due to the inherent reverberance of the speech utterances. Consequently, the envelope spectrum method is more accurate than the MLE method for parameters such as clarity, center time, and EDT, but for reverberation time, there is little difference in the accuracy of the two methods.

Figure 6(a) shows the results for reverberation time, showing similar accuracy for both methods. To improve the accuracy of the methods further, especially at middling reverberation times, a longer section of speech can be used, or further averaging of the estimated parameters across many lengths of recorded speech can be done.

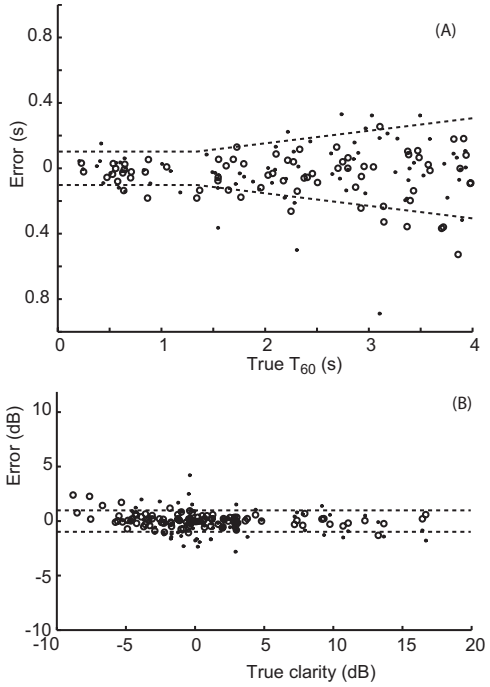

FIG. 6. Error in parameter estimation verses the true value: (A) reverberation time and (B) clarity. The dotted lines indicates the difference limens. (●) MLE and (○) envelope spectrum method. Validation set using simulated impulse responses. Speech excitation.

Figure 6(b) shows the results for clarity, as an example of one of the other parameters where estimation is more difficult. Clarity requires the accurate estimation of the energy arriving in the first 80 ms after the direct sound, and the MLE method finds it difficult to precisely obtain this value because of the natural reverberance of many speech utterances. In contrast, a method based on machine learning, such as the envelope spectrum method, can learn to compensate for errors in the estimation. Hence, for medium and large clarity values, the envelope spectrum method is more accurate than the MLE method. For very low clarity values, there are no results for the MLE method because the segmentation method failed to find any decay phases with sufficient dynamic range; these are very reverberant rooms where the start of the current utterance significantly masks the end of the decay of the previous utterance. To obtain a MLE estimation at such low clarity values requires larger time gaps between the utterances. As the clarity increases, the accuracy of the MLE estimations increases. While the envelope spectrum method does provide an estimation at these low clarity values, the accuracy of the estimation suffers because there is an insufficient information about the late part of the decay which is masked by subsequent utterances.

Tests on real room measurements, however, yield a slightly different story to that found with the simulated impulse responses. This validation set uses impulse responses measured in real rooms convolved with anechoic speech. Both the envelope spectrum and the MLE methods provide roughly the same accuracy for all the parameters. Figure 7 shows the results for reverberation time and clarity for the real room measurements, which can be compared to those shown in Fig. 6 for the validation set using simulated im-

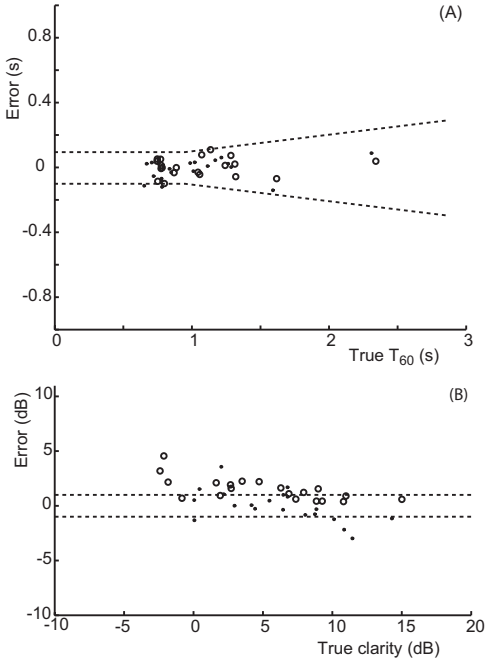

FIG. 7. Error in parameter estimation verses the true value: (A) reverberation time and (B) clarity. (●) MLE and (○) envelope spectrum method. Validation set using real room measurements. Speech excitation.

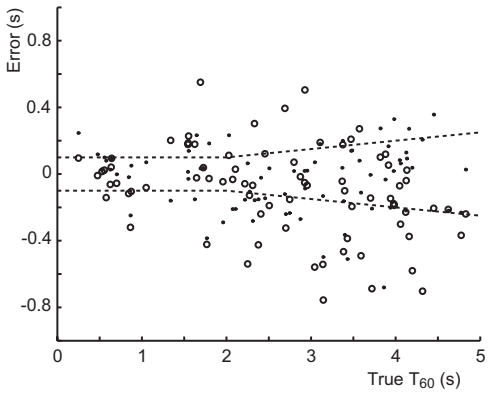

FIG. 8. Error in reverberation time estimation verses the true value. The dotted lines indicates the difference limen. (●) MLE and (○) envelope spectrum method. Validation set using simulated impulse responses. Music excitation.

pulse responses. For reverberation time, the MLE method becomes more accurate for the real room measurements in comparison to the validation set using simulated impulse responses. (Note that although the graphs imply this is also true for the envelope spectrum method, the difference is not statistically significant). For EDT, the envelope spectrum method is slightly more inaccurate and the MLE method is slightly more accurate when using the real measurements in comparison to the simulated ones. For clarity and center time, the MLE method gives similar accuracy for the real and simulated validation datasets, but the envelope spectrum becomes less accurate and furthermore, a bias error is introduced.

The loss in accuracy with the envelope spectrum method when estimating some parameters probably occurs because the simulated room impulse responses used to generate reverberated speech for training the ANN are not completely representative of real room impulse responses. Consequently, the data used for training and validation have some significant statistical differences. The introduction of a bias, as shown with some parameters and illustrated in Fig. 7(b), is good evidence for this. As an ANN works to minimize the mean square error, a well trained ANN should not generate a bias error, unless something is wrong, such as differences between the validation and training sets. It might be anticipated that as the accuracy of the geometric room acoustic models improves, then this problem should disappear because the training set will better match reality.

The MLE performs better with real room measurements when compared to the results for the reverberated speech by using simulated impulse responses. The real impulse responses have a greater reflection density than the simulated ones and, consequently, there is a smoother transition from the early to the reverberant sound field. It is suggested that this might improve the fitting of the simple model of envelope-shaped Gaussian noise [Eq. (1)] to the real room data, and this could therefore explain the improved accuracy in the parameter estimation.

B. Music

1. Envelope spectrum versus MLE

In this section, the performance of the envelope spectrum and MLE methods are compared using music. Six different pieces of music[12] are used, 2–4 min in length. As noted above, the accuracy of the estimation changes from piece to piece, for instance, the spectral variance affects the accuracy of the envelope spectrum method estimation (Fig. 2). Consequently, the results from the parameter estimations are averaged across all six pieces of music to improve accuracy and to reveal underlying trends.

Consider first the validation set generated by using simulated impulse responses from the geometric room acoustic model. For reverberation time, the MLE and envelope spectrum methods produce similar accuracy, as shown in Fig. 8, although the MLE is marginally more accurate. However, for the other parameters—EDT, clarity, and center time—the envelope spectrum method is more accurate than the MLE method. Again, the MLE method finds it difficult to accurately estimate the early parts of the impulse response due to the presence of the reverberance of the musical notes themselves. Figure 9 shows the results for these three parameters. For the envelope spectrum method, most of the parameter estimations are within the difference limen. For the EDT and center time, there is a tendency for the MLE method to overestimate the value by an amount larger than the difference limen. For clarity, there is a tendency for the MLE to overestimate low values of clarity and underestimate large values, in other words, the range of clarity estimated by the MLE is smaller than the true range.

With real room measurements, the results are again somewhat different. Figures 10 and 11 show the error in the four parameters as a function of their true value. In comparison to the use of the simulated validation set, the estimation of reverberation time and EDT has become more accurate with real room measurements for the MLE, while the enve-

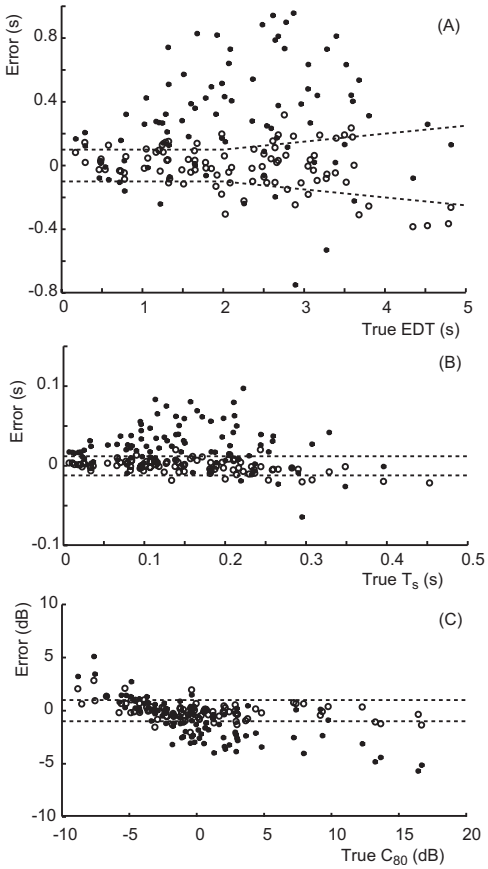

FIG. 9. Error in parameter estimation verses the true value: (A) EDT, (B) center time, and (C) clarity. The dotted lines indicate the difference limens. (●) MLE and (○) envelope spectrum method. Validation set using simulated impulse responses. Music excitation.

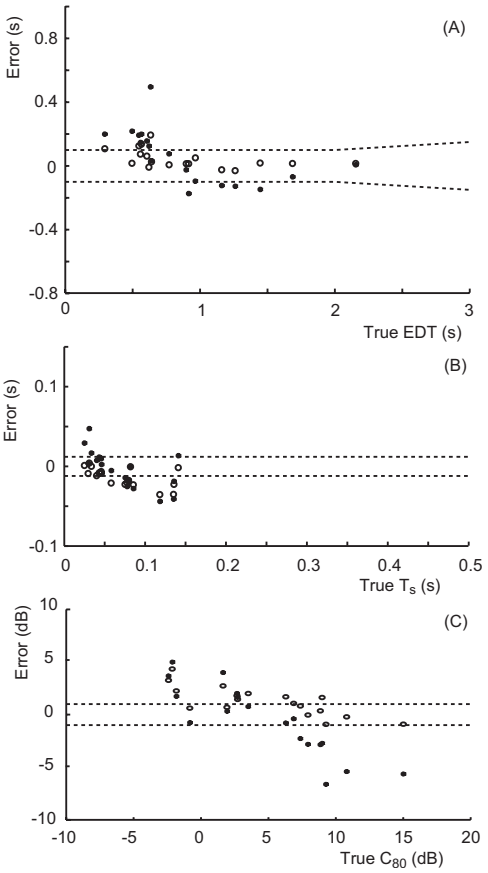

FIG. 11. Error in parameter estimation verses the true value: (A) EDT, (B) center time, and (C) clarity. The dotted lines indicate the difference limens. (●) MLE and (○) envelope spectrum method. Validation set using real room measurements. Music excitation.

lope spectrum method gives similar accuracy. The estimation of clarity is still problematic with the MLE method; there is a tendency for overestimation of low clarity values for the envelope spectrum method. For center time, the MLE method gets somewhat more accurate with real room measurements, but for the envelope spectrum method, a bias error is introduced with the parameter values being underestimated.

The introduction of a bias within the envelope spectrum results is probably again indicative of differences between the training data set which used simulated room impulses responses and the real room measurements (see discussions on speech above). The envelope spectrum method has problems estimating reverberation times. It is suggested that this arises because of the masking of the later parts of the impulse response by subsequent notes. The envelope spectrum method carries out an evaluation on the whole music passage, and in a piece of reverberated music, the early decay of notes is going to be more prominent than later decay portions. Consequently, the envelope spectrum method struggles to accurately estimate reverberation times because the information about late decay are lost in the vast amount of data from the whole music passage. (To explore this further, companding was carried out on the signal before it was fed to the envelope spectrum preprocessor. Companding biases the signal toward late decay and, as expected, this improved the reverberation time estimation, but at the expense of accurate EDT estimation). This was not such a problem with speech because this has more periods of silence. The MLE deliberately pulls out free decay sections and selects those with sufficient decay, therefore, it does not suffer from the same problem. It is suggested that by applying a similar signal segmentation process to the envelope spectrum method, the accuracy of reverberation time estimation might be improved.

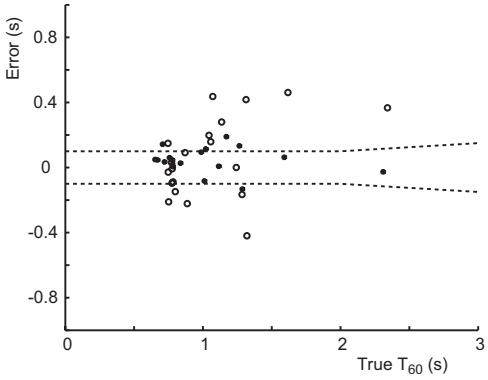

FIG. 10. Error in reverberation time estimation verses the true value. The dotted lines indicates the difference limen. (●) MLE and (○) envelope spectrum method. Validation set using real room measurements. Music excitation.

TABLE I. Standard errors for parameters when estimated using the maximum likelihood and envelope spectrum method. Standard errors calculated using responses where $T_{60}<2.3$s to allow comparison of real and simulated.

Room impulses	Method	Source signal	Standard error RT (s)	EDT (s)	C80 (dB)	T_s (ms)
Simulated	MLE	Music	0.15	0.20	2.8	13
		Speech	0.14	0.25	1.5	8
	Envelope spectrum	Music	0.19	0.07	0.79	3
		Speech	0.09	0.06	0.56	3
Real	MLE	Music	0.08	0.14	2.5	15
		Speech	0.06	0.12	1.5	10
	Envelope spectrum	Music	0.18	0.10	1.5	12
		Speech	0.06	0.08	1.05	12

For the MLE method, the improvement in estimation of reverberation time parameters when using real measurements is again thought to be due to the real room impulse responses having greater reflection density than the simulated ones, and so it is easier to fit the simplified room model to the data. For high clarity values, where underestimation occurs, then, the reverberance of the notes is causing an overestimation of both the early and late sound energies, hence, resulting in a lower clarity than expected. For low clarity values, the MLE method struggles to fit the detailed effects of strong reflections in the early sound field, and so produces a consistent overestimation.

IV. DISCUSSIONS

Music and speech are obvious choices for measurement using naturalistic signals in performance spaces, and each has their own particular advantages and disadvantages.

Narrated speech has the advantage of containing plenty of gaps between the signal excitations, and so is rich in clean decay phases. This offers many opportunities for averaging estimations when using the MLE method and more accurate estimation with the envelope spectrum method, as there will be many decay phases where late reflections are not masked by subsequent utterances. However, speech excitation has limited bandwidth and lacks energy in low frequencies, say, for the 250 Hz octave band and below, and consequently, estimations are less accurate in lower octave bands,[4] and consequently, music is needed for these bandwidths. The music tracks used in this study lacked high frequency excitation above 2 kHz, which means that estimation accuracy is affected there also.

Table I compares the standard error of each parameter estimate for speech and music by using both the MLE and envelope spectrum methods. Table I indicates that the MLE method more accurately predicts the late decay properties than the envelope spectrum method, while the envelope spectrum method more accurately predicts the early decay behavior than the MLE method.

The ideal music signal is one that has plenty of short transient sounds, and whose excitation is even across the octave band, in other words, a piece of music which breaks traditional rules of western harmony and gives the same weight to all notes in the chromatic scale. Alternatively, averaging over different pieces of music can be effective, especially if the pieces are in a variety of musical keys. Another approach is to use pieces with lots of untuned percussion. The best music also has large gaps between the notes so the decay phrases are prominent.

Table II indicates how many regions of decay with at least 25 dB of dynamic range each of the anechoic signals contain. This can indicate how accurate the ML estimates are using a particular signal. Table II also indicates the percentage of silence within each signal; this combined with the spectral variance previously detailed in Fig. 3 is a good indicator as to the suitability of the signal for parameter estimation using the envelope spectrum method.

Neither the envelope spectrum method nor the MLE technique offers a single foolproof method for estimating room acoustic parameters from naturalistic signals. The MLE technique is appealing because it is not empirical and so is potentially more robust. Furthermore, it is truly blind and does not require explicit knowledge of the anechoic excita-

TABLE II. Average number of decay phases per minute exhibiting at least 25 dB of decay, and percentage of relative quiet in each anechoic signal. Percentage of relative quiet is calculated by computing the percentage of (non-overlapping) 0.05s length windows in each signal with energy 40 dB less than the maximum energy.

Signal	Average number of decay phases/minute	Amount of relative quiet in signal (%)
Music track 1	4.2	0.19
Music track 2	4.3	2.2
Music track 3	4.8	0.86
Music track 4	12	6.4
Music track 5	3.2	0.53
Music track 6	5.0	0.17
Speech	37	25

tion signal. However, the MLE method has problems accurately estimating the early sound field because it cannot compensate for the inherent reverberance of music notes and speech utterances. As the calculation of reverberation time by definition avoids this problematic region of decay, the MLE method is most successful in estimating reverberation times.

Currently, the inaccuracies of geometric room acoustic models used to provide training data for the envelope spectrum method limit the accuracy that can be obtained. Hopefully, as geometric room acoustic models improve, this problem will be resolved. The envelope spectrum method is not blind but requires knowledge of the test signal during training. This limits the applicability of the method. For example, with live orchestras, the accuracy will be compromised.

V. CONCLUSIONS

This paper has examined two methods for extracting room acoustic parameters from music and speech. The motivation is to enable in-use measurements of spaces without using artificial test signals. The first method uses a machine learning approach combined with a envelope spectrum preprocessor. Previously, this method had been used for speech; this paper details adaptations necessary to make this method work for music. The second method uses a MLE applied to decay phases at the end of speech utterances or musical notes. The two methods are compared and contrasted for common monaural measures used in performance space design. The MLE method is best for estimating reverberation time. For center time, clarity, and EDT, neither method is better. The indications are that when geometric room acoustic models become more accurate, enabling better quality training data for the machine learning algorithm, then the envelope spectrum method will be most successful for parameters needing accurate estimation of early decays. Both speech and music have a role in enabling naturalistic measurement. Speech is a better signal at mid- and high frequencies because it naturally has more pauses and has more predictable low frequency statistics. However, music is needed to gain parameters at lower frequency bands, where speech has insufficient power for excitation.

ACKNOWLEDGMENTS

Thanks go to Henrik Möller for supplying the real room impulse responses. The authors would like to acknowledge the support of the Engineering and Physical Sciences Research Council, UK for funding this project.

[1]F. F. Li and T. J. Cox, "Speech transmission index from running speech: A neural network approach," J. Acoust. Soc. Am. **113**, 1999–2008 (2003).
[2]F. F. Li and T. J. Cox, "A neural network for blind identification of speech transmission index," Proc. IEEE **2**, 757–760 (2003).
[3]R. Ratnam, D. L. Jones, B. C. Wheeler, W. D. O'Brien, Jr., C. R. Lansing, and A. S. Feng, "Blind estimation of reverberation time," J. Acoust. Soc. Am. **114**, 2877–2892 (2003).
[4]P. Kendrick, F. F. Li, T. J. Cox, Y. Zhang, and J. A. Chambers, "Blind Estimation of Reverberation Parameters for Non-Diffuse Rooms," Acta. Acust. Acust. **93**, 760–770 (2007).
[5]P. Kendrick, T. J. Cox, F. F. Li, Y. Zhang, and J. A. Chambers, "Blind estimation of clarity, centre time and deutlichkeit from speech and music signals," Proceedings of the 19th ICA, Madrid (2007), Paper No. RBA-07-013.
[6]International Standard, "Acoustic—Measurement of the reverberation time of rooms with reference to other acoustical parameters," Report No. EN ISO 3382:2000.
[7]H. P. Seraphim, "Investigations on the difference limen of exponentially decaying bandlimited noise pulses," Acustica **8**, 280–284 (1958).
[8]L. Cremer and H. A. Müller, *Principles and Applications of Room Acoustics*, translated by T. Schultz (Applied Science, London/New York, 1982), Vol. **1**.
[9]T. J. Cox, W. J. Davies, and Y. W. Lam, "The sensitivity of listeners to early sound field changes in auditoria," Acustica **79**, 27–41 (1993).
[10]CATT-ACOUSTIC v8.0c, room acoustic modeling software, http://www.catt.se/ Last viewed 21/04/2008
[11]T. Lahti, A. Ruusuvuori, and H. Moller, "The acoustic conditions in Finnish concert spaces-Preliminary results," Proceedings of the Audio Engineering Society 110th convention (2001), p. 5356.
[12]Denon Anechoic Orchestral Music Recording, CD PG-6006, 1995.
[13]Music for Archimedes. CD B&O 101, 1992.
[14]M. T. Hagan and M. Menhaj, "Training feedforward networks with the Marquardt algorithm," IEEE Trans. Neural Netw. **5**, 989–993 (1994).
[15]T. Houtgast and H. J. M. Steeneken, "Envelope spectrum and intelligibility of speech in enclosures," Proceedings of the IEEE-AFCRL Speech Conference (1972), pp. 392–95.
[16]H. Kuttuff Kuttruff, *Room Acoustics*, (Spon, London, 2000).
[17]P. C. Mahalanobis, "On the generalized distance in statistics," Proc. Nat. Inst. Sri. India A **2**, 49–55 (1936).
[18]J. Aldrich, "R.A. Fisher and the making of maximum likelihood 1912-1922," Stat. Sci. **12**, 162–176 (1997).

Influence of *in situ*, sound-level calibration on distortion-product otoacoustic emission variability

Rachel A. Scheperle,[a] Stephen T. Neely, Judy G. Kopun, and Michael P. Gorga
Boys Town National Research Hospital, 555 North 30th Street, Omaha, Nebraska 68131

(Received 25 January 2008; revised 19 April 2008; accepted 22 April 2008)

Standing waves can cause errors during in-the-ear calibration of sound pressure level (SPL), affecting both stimulus magnitude and distortion-product otoacoustic emission (DPOAE) level. Sound intensity level (SIL) and forward pressure level (FPL) are two measurements theoretically unaffected by standing waves. SPL, SIL, and FPL *in situ* calibrations were compared by determining sensitivity of DPOAE level to probe-insertion depth (deep and "shallow") for a range of stimulus frequencies (1–8 kHz) and levels (20–60 dB). Probe-insertion depth was manipulated with the intent to shift the frequencies with standing-wave minima at the emission probe, introducing variability during SPL calibration. The absolute difference in DPOAE level between insertions was evaluated after correcting for an incidental change caused by the effect of ear-canal impedance on the emission traveling from the cochlea. A three-way analysis of variance found significant main effects for stimulus level, stimulus frequency, and calibration method, as well as significant interactions involving calibration method. All calibration methods exhibited changes in DPOAE level due to the insertion depth, especially above 4 kHz. However, SPL demonstrated the greatest changes across all stimulus levels for frequencies above 2 kHz, suggesting that SIL and FPL provide more consistent measurements of DPOAEs for frequencies susceptible to standing-wave calibration errors. © *2008 Acoustical Society of America.* [DOI: 10.1121/1.2931953]

PACS number(s): 43.58.Vb, 43.25.Gf, 43.64.Jb [BLM] Pages: 288–300

I. INTRODUCTION

Concern exists regarding measurement variability of distortion-product otoacoustic emissions (DPOAEs). Many of the sources of variability are extrinsic and potentially correctable (Mills *et al.*, 2007). One example is the method for calibrating stimulus level. Current DPOAE systems use the emission probe to calibrate sound pressure in the ear canal. *In situ* calibration is performed in an effort to equalize stimulus level across frequencies and subjects by compensating for individual differences in ear-canal acoustics. However, standing waves in the ear canal cause a partial cancellation of sound pressure near the emission probe around quarter-wave frequencies (e.g., Stinson, 1985; Gilman and Dirks, 1986; Dirks and Kincaid, 1987; Chan and Geisler, 1990; Siegel, 1994), resulting in inaccurate stimulus-level estimates, especially for frequencies above 2 kHz. These errors have the potential to impact both stimulus magnitude and DPOAE levels by as much as 20 dB in individual subjects (Siegel, 1994; Siegel and Hirohata, 1994; Dreisbach and Siegel, 2001). Proposed solutions are limited in terms of practicality of implementation and accuracy of estimate (Dirks and Kincaid, 1987; Siegel, 1994; Siegel and Hirohata, 1994; Whitehead *et al.*, 1995; Dreisbach and Siegel, 2001) and, consequently, none are being routinely used in the clinic.

The purpose of this study was to determine whether alternative measures of stimulus level in the ear canal provide practical solutions to calibration problems associated with standing waves and, as a consequence, decrease DPOAE variability. Sound intensity level (SIL) is one measure unaffected by standing waves and, thus, intensity measured at the emission probe is expected to be a good estimate of intensity at the eardrum at all frequencies (Neely and Gorga, 1998). In fact, Neely and Gorga demonstrated that behavioral thresholds were more consistent following *in situ* calibration using SIL compared to SPL, indicating that SIL was a more reliable measure of ear-canal stimulus level. SIL calibration, however, has not been extended to DPOAE measurements. A second alternative method for measuring level in the ear canal is forward pressure level (FPL). Ear-canal pressure can be separated into incident and reflected components (e.g., Farmer-Fedor and Rabbitt, 2002). Isolation of the incident pressure wave (i.e., FPL) eliminates the problem of standing waves and offers a theoretically stable *in situ* calibration that is equal to SPL when standing waves are not present.

Estimating the SIL or FPL of a stimulus with a microphone that directly measures only SPL is possible after performing a calibration procedure that estimates ear-canal load impedance. This calibration procedure requires known acoustic loads (i.e., a set of acoustic cavities) to determine the Thevenin-equivalent characteristics (impedance and pressure) of the sound source (Møeller, 1960; Rabinowitz, 1981; Allen, 1986; Keefe *et al.*, 1992). The specific procedure used in this study was based on the approach described by Neely and Gorga (1998).

In the present study, SPL, SIL, and FPL calibration methods were compared by focusing on the influence of calibration variability (errors) on measured DPOAEs using a within-subject design modeled after Neely and Gorga (1998). Repeated measurements of DPOAE levels were made for two ear-canal probe-insertion depths (deep and "shallow")

[a]Electronic mail: r.scheperle@gmail.com

 0001-4966/2008/124(1)/288/13/$23.00

for each subject, which changed the frequencies with standing-wave minima at the emission probe and, thus, intentionally introduced variability into the SPL calibration. Because middle ear and cochlear status is assumed to remain constant within a test session, changes in DPOAE level with changes in probe placement were taken as an indication of errors in the stimulus calibration.

Another concern with any *in situ* calibration is the consistency of observed errors. While all errors are undesirable, consistent errors are preferred to inconsistent errors because they can be predicted. Therefore, the effect of frequency and stimulus level was also of interest to further assess and compare calibration procedures. It is assumed that frequencies with standing-wave minima at the emission probe are most susceptible to calibration errors and, as a consequence, changes in DPOAE level following calibration methods affected by standing waves (i.e., SPL) are expected to be frequency dependent. There is evidence that the effect of calibration errors on DPOAE level is also dependent on stimulus level (Whitehead *et al.*, 1995; Dreisbach and Siegel, 2001). Errors in calibration are more likely to influence measured DPOAE levels on the steeply rising portion of the DPOAE input/output (I/O) function (where DPOAE level is dependent on stimulus level) and less likely to affect DPOAE levels on the asymptotic or saturating part of the I/O function (where DPOAE level is less dependent on stimulus level) (e.g., Lonsbury-Martin *et al.*, 1990; Nelson and Kimberley, 1992; Popelka *et al.*, 1993; Gorga *et al.*, 1994, 2000; Dorn *et al.*, 2001; Neely *et al.*, 2003). Therefore, changes in DPOAE level caused by calibration errors are expected to be larger at low stimulus levels.

The results of this study describe the influence of calibration procedure on the outcome measure of interest (change in DPOAE level). Depending on the outcome, the results may help determine whether SIL and/or FPL is preferable to SPL for *in situ* calibration both in experimental work and in the clinic.

II. METHODS

An ER-10C probe microphone (Etymōtic Research) was used to deliver stimuli generated with a 24 bit sound card (CardDeluxe, Digital Audio Labs) and to record responses. A locally developed software (EMAV Version 2.88; Neely and Liu, 1994) was used to perform (1) probe-source calibrations, (2) calculations of Thevenin equivalents, (3) SIL and FPL conversions, and (4) DPOAE measurements.

A. Calibration

The first step in estimating the Thevenin-equivalent source characteristics of the probe is to measure wideband pressure responses in known acoustic loads. For tubes of known lengths, an ideal expression for cavity impedance is

$$Z_c = -iZ_0 \cot(kL), \tag{1}$$

where Z_0 is the acoustic impedance of a plane wave propagating in the tube, L is the cavity length, and k is the wave number (Keefe *et al.*, 1992). The cavity set used for this study consisted of five brass tubes (11/32 in. o.d., 8 mm i.d.) that were 83, 54.3, 40, 25.6, and 18.5 mm in length. Tube lengths were selected so that, with the coupler and probe in place, resonant peaks would occur at approximately 2, 3, 4, 6, and 8 kHz. A wideband chirp stimulus with a sampling rate of 32 kHz was presented to each tube of the cavity set, and the pressure response was measured with the probe microphone. Total averaging time was approximately 4 s per source channel per cavity, resulting in a total of 160 averaged chirps. Ideal cavity impedance (Z_c) and measured cavity pressure (P_c) are related to source pressure (P_s) and source impedance (Z_s) by the following equation:

$$\frac{P_s}{Z_s + Z_c} = \frac{P_c}{Z_c}. \tag{2}$$

An improved set of cavity lengths and corresponding Thevenin-equivalent source characteristics (P_s and Z_s) was obtained by iterative solution of a set of five linear equations that minimized deviation between measured and expected pressure responses based on Eq. (2) (Allen, 1986). Cavity calibration to determine P_s and Z_s was performed daily. Figure 1 shows the agreement typically observed between empirical and ideal cavity impedances. The separation between empirical and ideal data sets (error) increases with frequency and is the greatest at the pressure nulls, where the measured pressure is higher than what would have been ideal. These trends are consistent with the effects of cross-talk described by Siegel (1995) for the ER-10C probe; however, the implications on the calculation of P_s and Z_s are small. The error calculation weights the peaks and, consequently, estimated Thevenin-equivalent characteristics should have little dependence on whether the nulls are inaccurate.

Prior to initiating DPOAE measurements, a preliminary investigation demonstrated that air temperature within the calibration cavities significantly affects the estimated source characteristics (see Appendix A). In light of this result and

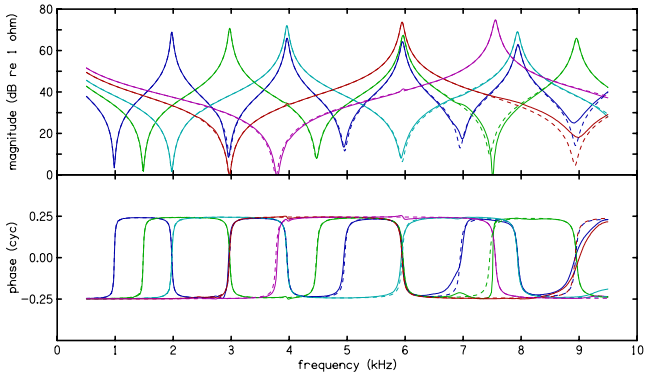

FIG. 1. (Color online) Ideal and empirical impedance of a calibration cavity set with error values of <1.0. The top panel displays the magnitude and the bottom panel displays phase, both as a function of frequency. Each tube (with lengths L_1–L_5) is represented by a pair of lines. Dotted lines represent ideal values based on equations from Keefe (1984) and solid lines represent the empirical values for one sound-source channel. The lines are nearly superimposed, indicating close agreement between ideal and empirical values. Tube length can be identified by the corresponding resonant frequency (e.g., the solid and dotted lines with the first maximum at ~2 kHz correspond with the longest tube in the set). The phase of the bottom panel does not exceed $\frac{1}{4}$ cycle in either the positive or negative direction, signifying that the real part of the impedance value is positive, which is a physical requirement for a passive system.

the absence of a procedure to adjust for temperature, the cavities were warmed to approximate body temperature (95–105 °F) during each daily probe calibration.

In situ calibration was performed on each subject with the same DPOAE probe and chirp stimulus that was used for the source calibration. Load pressure (P_ℓ) was measured by the probe microphone and ear-canal load impedance (Z_ℓ) was calculated,

$$Z_\ell = \frac{Z_s P_\ell}{P_s - P_\ell}. \tag{3}$$

Load impedance provides the information necessary to convert load pressure, which is measured as SPL, into the corresponding SIL and FPL.

B. SIL and FPL conversion

When Z_ℓ is known, sound intensity (I_ℓ) is determined by

$$\mathcal{I}_\ell = \tfrac{1}{2}|P_\ell|^2 \cdot G_\ell, \tag{4}$$

where $G_\ell = \Re(1/Z_\ell)$ is the load conductance, which is defined as the real part ($\Re$) of the load admittance. SIL does not include the reactive/imaginary components of impedance, which store (but do not consume) energy. Consequently, SIL is unaffected by reflected waves.

Forward pressure (P_+) is determined by

$$P_+ = \frac{1}{2} P_\ell \left(1 + \frac{Z_0}{Z_\ell}\right), \tag{5}$$

where Z_0 is the characteristic impedance of the calibration cavities. FPL calibration is based on the forward-traveling component of the sound wave, thereby avoiding interactions with reflected waves and eliminating the potential for standing-wave calibration errors. A derivation of FPL is provided in Appendix B.

C. Subjects

Data collection was completed on 21 subjects, ranging in age from 14 to 49 years. Inclusion criteria included (1) normal audiometric thresholds (≤15 dB HL re: ANSI, 1996, for octave and interoctave audiometric frequencies from 0.25 to 8 kHz) and (2) normal 226 Hz immittance test results (peak compensated, static acoustic admittance of 0.3–1.8 mmho and tympanometric peak pressure (TPP) of −50 to 25 daPa) just prior to DPOAE measurements. In addition, otoscopic examinations revealed no contraindications to making DPOAE measurements (i.e., excessive cerumen or scarring of the eardrum). If both ears met the inclusion criteria, then the ear with better behavioral thresholds, TPP closest to 0 daPa, and/or easiest probe insertion was chosen. If there were no differences between ears, then the test ear was chosen randomly. Subjects were seated in a comfortable reclining chair situated in a sound-attenuating booth during data collection, which lasted approximately 2–3 h. Subjects were paid an hourly rate for participation.

D. Procedures

Measurements were obtained with the probe at two different insertion depths in the selected ear canal. For the first probe position, effort was made to insert the probe as deeply as possible so that calibration of the wideband chirp stimulus would show an ear-canal pressure spectrum with a "notch" at the highest possible frequency (i.e., between 4 and 8 kHz), indicating a standing-wave minimum. After measurements were obtained for all three calibration methods (SPL, SIL, and FPL) with the probe placed deeply, the probe was removed, the ear tip was replaced, the probe was reinserted approximately 2–3 mm less deep than the first insertion (i.e., shallow), and the measurements were repeated. While the deep insertion was always performed first, the order of calibration methods was counterbalanced. Adhesive tape secured the probe to prevent movement during measurements. Subjects were not excluded based on the absence of a notch or lack of downward shift in the notch frequency during the shallow insertion.

DPOAEs were elicited by pairs of primary tones (f_1 and f_2) with a fixed frequency ratio ($f_2/f_1 = 1.22$) and with levels set according to $L_1 = 0.4L_2 + 39$ (Kummer *et al.*, 1998). For each probe-insertion depth and for each calibration method, DPOAE levels were elicited across $f_2 = 1–8$ kHz (four points per octave) at $L_2 = 20$, 30, 40, 50, and 60 dB. *In situ* calibrations were repeated prior to each L_2.

Ear-canal wave forms were placed in alternate buffers during DPOAE measurements. After performing Fourier transforms on each buffer, DPOAE level was determined at $2f_1 - f_2$ by summing the bins (width=4 Hz) containing this frequency. Noise level was estimated by combining the four adjacent frequency bins on each side of $2f_1 - f_2$ in addition to the bin containing $2f_1 - f_2$. For each stimulus condition, averaging continued until one of three stopping criteria was met: (1) noise was ≤−25 dB SPL, (2) artifact-free averaging time reached 32 s, or (3) signal-to-noise ratio (SNR) was ≥60 dB. The SNR criterion was selected so that it was never invoked, resulting in a situation in which the measurements stopped mainly on the noise criterion and seldom on test time.

E. Estimation of expected, incidental changes in emission level

The study was designed to produce DPOAE level changes when the calibration method was unreliable in controlling *stimulus level* in the ear canal (i.e., when standing-wave minima were present at the emission probe). Unfortunately, DPOAEs are doubly affected by insertion depth. Even if the input level is controlled at the eardrum and the response from the cochlea is the same, the *measured* response in the ear canal will depend on the insertion depth because DPOAE level measured with the ER-10C probe some distance from the eardrum depends on the impedance of the volume of air in the ear canal, which acts as an acoustic load for the emitted sound. Increasing the volume by moving the probe to a more shallow insertion decreases ear-canal impedance. Assuming that the volume velocity of the eardrum (due to the DPOAE traveling out of the cochlea) remains constant

for an ideally calibrated stimulus, a shallower insertion will cause pressure of the DPOAE to decrease at the emission probe. Consequently, a cochlear response (DPOAE level) measured with a deep probe placement will be larger than a response of the same size measured with a shallow probe placement. This level difference (i.e., incidental change) will occur in conjunction with any changes in emission level caused by calibration errors. Since the study design introduced the additional, incidental change in DPOAE level unrelated to stimulus level, it was important to try to eliminate this variable prior to analysis. Isolating the effects of calibration errors on DPOAE level allows a more accurate comparison among calibration methods. It is acknowledged that predicting the incidental effect of ear-canal impedance on measured emission level is more complicated than addressed in our estimate (described below), which reflects the gross effects on emission level and is more accurate for low frequencies.[1]

Because ear-canal impedance is similar to the impedance of a tube, the incidental change in DPOAE level can be estimated using the relationship between length and impedance in Eq. (1). When kL is small, $\cot(kL) \approx 1/kL$. The wave number (k) is small at low frequencies because $k \approx \omega/c$ (Beranek, 1954). Accordingly, low-frequency impedance approximates inverse proportionality to length of the ear canal between the probe and the eardrum,

$$Z_c \approx \frac{-iZ_0}{kL}. \tag{6}$$

Impedance of the ear canal was calculated from 4 to 15 996 Hz (in 4 Hz increments) during each of the *in situ* SIL and FPL calibrations. For each subject, four of the calibrations were used to assess changes in probe-insertion depth during data collection: two representing deep probe placement and two representing shallow placement. Each of the four representative load estimates was reduced to a single value by averaging impedance magnitude across 250 to 500 Hz.[2] This frequency range is both high enough to have a good SNR and low enough to have the expected proportional relationship between impedance and length. The resulting mean impedance values for the two deep-insertion and the two shallow-insertion calibrations were averaged. The incidental change in DPOAE level due to changes in the probe-insertion depth was assumed to be equal to the decibel difference in impedance magnitude between the two depths over the selected low-frequency range.

Figure 2 shows low-frequency impedance magnitudes used to estimate the incidental change in DPOAE level for three subjects. The top panel represents a favorable case in which the estimate appeared ideal. Note the consistency in the decibel difference (the estimated, incidental change due to changes in volume) for both sets of measurements. The middle panel illustrates a less favorable case in which the two deep-insertion impedance levels are separated, indicating an *unintentional* change in insertion depth over time within the same probe placement. Furthermore, the decibel differences between insertion depths for the lowest frequencies are larger than the decibel differences at the highest frequencies, indicating a change in estimated impedance difference between insertions over the frequency range for which the impedance difference was assumed to be constant. The bottom panel shows the worst case from the subject in which the largest volume change with (supposedly) the same probe placement occurred. Results from this subject were atypical but were not excluded from the analysis.

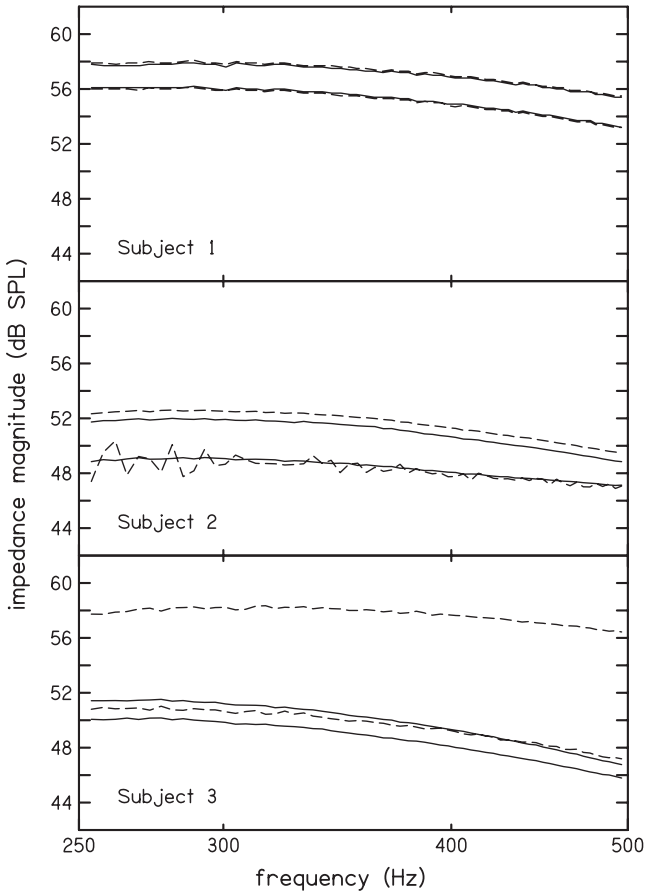

FIG. 2. Four sets of ear-canal impedance magnitudes from 250 to 500 Hz for three subjects. In each panel, the solid and dotted lines closer to the top are impedance values obtained with the deep probe insertion, and the solid and dotted lines lower in the panel are impedance values obtained with the probe inserted less deeply (shallow). The differences between the two solid lines and the two dotted lines were averaged to provide the estimate of intentional probe movement (the incidental change in DPOAE level introduced by the study design) for each subject. The differences between the top-solid and top-dotted lines and the lower-solid and lower-dotted lines provided estimates of unintentional probe movement for each insertion. The top two panels are representative of the types of impedance values obtained for the majority of subjects. The bottom panel is from the subject with the greatest estimated volume change for a single insertion (notice the difference between the top-dotted and top-solid lines).

F. Estimation of unintentional changes in emission level

Differences in impedance estimates for the *same* insertion raised concern about unintentional changes in ear-canal volume within a given probe placement, for which impedance magnitude was expected to be stable. While efforts were made to secure the probe in the ear canal, and *in situ* calibrations were examined for spectral changes that would indicate probe movement, empirical data reveal differences in impedance magnitude for a single insertion depth, suggesting that it was not always possible to maintain constant

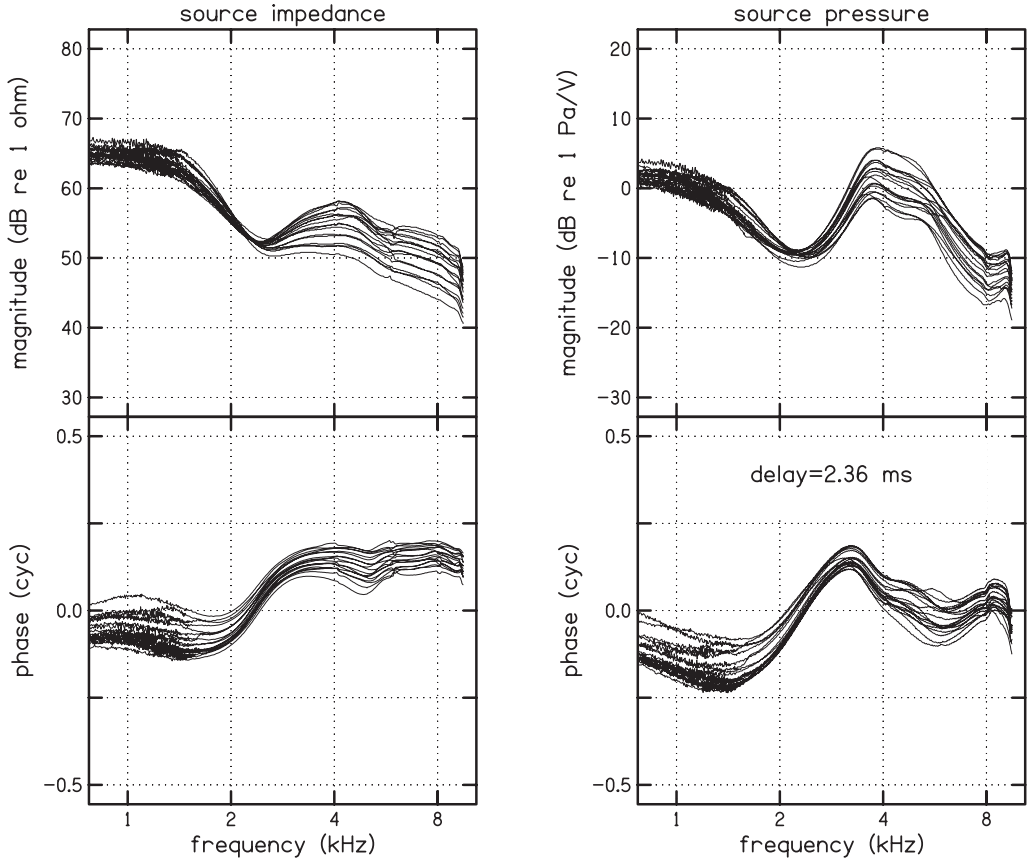

FIG. 3. Eighteen calculations of Thevenin-source (ER10-C probe) characteristics from the daily acceptable (error of <1.0) cavity calibrations. The characteristics for only one sound-source channel are plotted. The delay value in the fourth panel refers to the measurement-system delay between stimulus generation and response recording by the sound card, a small portion of which is due to the internal travel time of the acoustic signal through the ER-10C probe. The number of cycles that occur during this time was subtracted from the phase value on a frequency basis, resulting in the values plotted in panel four.

probe position during the entire set of measurements for a given placement. These differences may be viewed as estimates of within-subject measurement error. The effect of unintentional probe movement on DPOAE level was estimated using the same impedance values described above and taking the difference between values for a single insertion depth. Ideally, these differences would be zero, but as shown in Fig. 2, this was not always the case.

III. RESULTS

A. Daily cavity calibrations

The consistency of the Thevenin-equivalent source characteristics calculated during daily probe calibrations was examined by plotting the magnitude and phase of source impedance and pressure (see Fig. 3). The range of values (variability) suggests that the calibration procedure is a potential source of error when converting to SIL and FPL. While cross-talk is recognized as an error that may have influenced the Thevenin-equivalent source characteristics, it is expected that the effects would be the same upon repeated measurements and therefore would not be a source of variability. Additionally, while variability indicates error in the calibration procedure used to determine SIL and FPL, observed variability in probe characteristics does not necessarily indicate the same variability in load-impedance estimates because the relationship between probe characteristics and load impedance is not simply proportional.

B. Estimation of incidental changes in DPOAE level

Incidental DPOAE level changes unrelated to calibration errors were anticipated as a result of the study design, for which probe movement was intentional. Unintentional movement of the probe, however, was unavoidable. Figure 4 describes the distributions of the estimated impact of intentional and unintentional probe movement on DPOAE responses. The distributions are displayed in the form of box-and-whisker plots, in which average absolute changes in decibel are plotted. Absolute changes were preferred in case unintentional movement of the probe was in the direction opposite of what would be expected.

Intentionally moving the probe from a deep to a shallow insertion resulted in a larger decibel change than unintentional probe movement during either the deep or shallow insertions. The distribution when intentionally moving the probe is large, indicating that the estimated, incidental change observed across subjects varied widely. In two subjects, the decibel difference is <1.0 dB, which might imply that the insertion depth was not altered in these cases. For the majority of subjects (19 of 21), the estimated, incidental

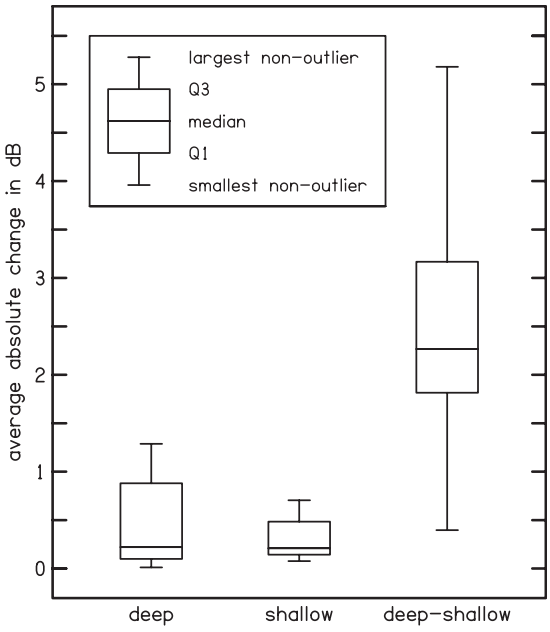

FIG. 4. Distributions of estimated, incidental changes in DPOAE level in response to changes in the ear-canal volume. The first two plots (deep and shallow) are estimates of unintentional volume changes due to slipping of the probe during a single insertion depth. The third plot (deep-shallow) represents estimates of the incidental change in DPOAE level that can be expected based on intentionally changing ear-canal volume by moving the probe. Outliers are not plotted in this figure. The largest unintentional change was 8 dB for one subject, which could not be explained based on review of the *in situ* calibration spectra. While excluded from the figure, this subject's data were included in the analyses.

change in emission level was >1.0 dB, indicating that manipulating probe placement had the intended effect.

Prior to data collection, there was greater concern about unintentional probe movement during the shallow insertion, on the assumption that less deep insertions would be less stable; however, Fig. 4 shows a larger decibel change for the deep insertion. For the deep insertion, a smaller shift in probe position has a greater impact on the decibel value due to a greater proportional change in volume. In other words, the larger decibel change during the deep insertion does not necessarily indicate greater probe movement. Rather, the same absolute movement for deep and shallow insertions produces a larger relative change for the deep insertions. More importantly, the unintentional changes for both deep and shallow insertions are small compared to the decibel change produced by intentionally moving the probe.

C. DPOAE level

The mean DPOAE and noise levels across subjects for deep and shallow insertions are plotted for all three calibration methods as a function of frequency (DPgrams) in Fig. 5 and as a function of level (I/O functions) in Fig. 6. Positive SNRs, even at 20 dB, indicate that reliable DPOAE measurements were possible (except, perhaps, at the lowest stimulus levels when f_2=8 kHz). Averaging across subjects could reduce or eliminate some of the changes in emission level that exist for individual subjects, especially for the SPL calibration, where standing waves introduce greater errors in estimates of stimulus level on an individual basis. However, while the specific effects of standing-wave minima are idiosyncratic and likely to be underestimated when averaging across subjects, they are not random and should be evident to some degree.

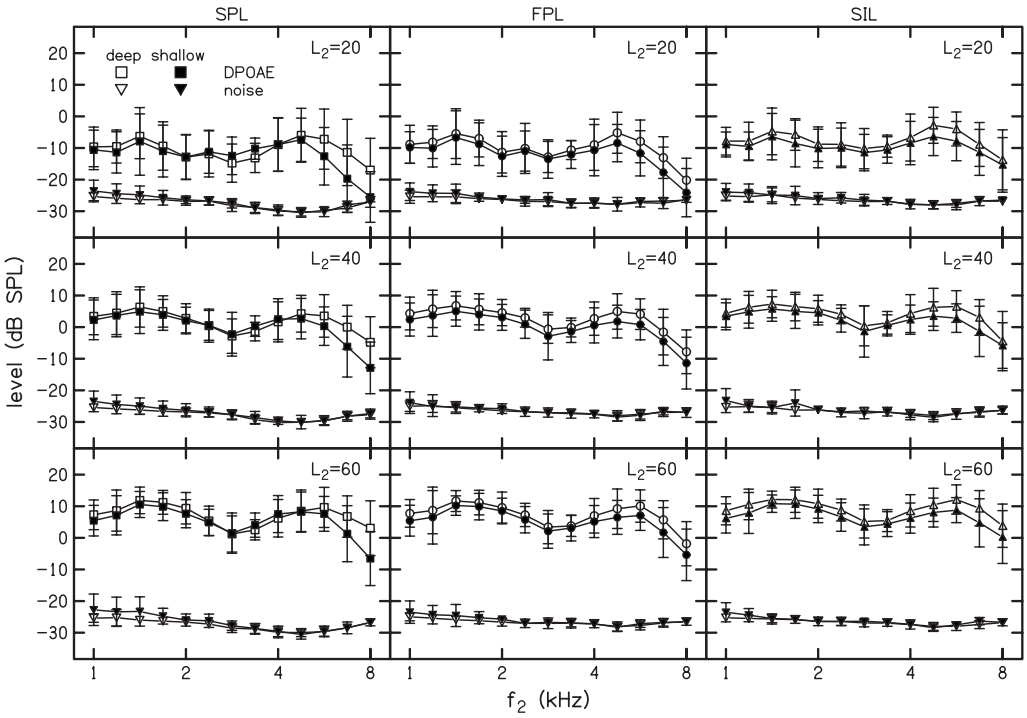

FIG. 5. DPgrams of subject means and standard deviations of noise and DPOAE levels for three calibration methods (SPL, FPL, and SIL) and three stimulus levels (20, 40, and 60 dB). Open symbols represent values obtained during deep insertion and closed symbols represent values obtained during shallow insertion.

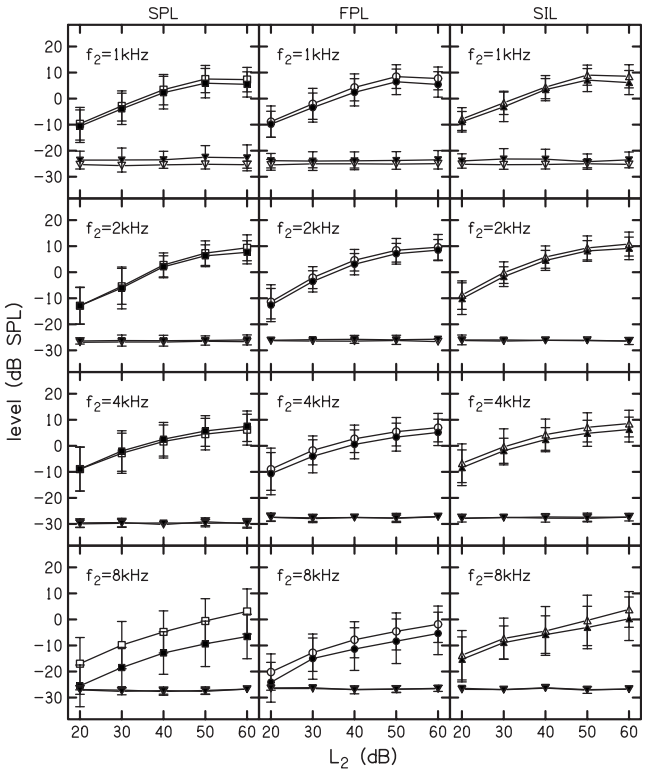

FIG. 6. Input/output functions of subject means and standard deviations of noise and DPOAE levels for the three calibration methods (SPL, FPL, and SIL) and four frequencies (1, 2, 4, and 8 kHz). Open symbols represent values obtained during the deep insertion and closed symbols represent values obtained during the shallow insertion.

The difference in DPOAE levels between insertion depths is the measurement of interest. Although difference values are not plotted in Figs. 5 and 6, the relationship between DPOAE levels obtained with the deep and shallow insertions can be observed. The summaries provided in Figs. 5 and 6 indicate that probe placement had a greater effect on DPOAE level for the SPL calibration compared to either FPL or SIL. Because the data have not been corrected, a uniform decrease in DPOAE level for the shallow insertion is expected based on the inverse relationship between pressure and volume (i.e., the incidental change introduced by the study design). For SIL and FPL calibrations, the deep insertion always resulted in higher DPOAE levels than the shallow insertion. Additionally, the change in DPOAE level is relatively uniform across frequency and intensity for SIL and FPL, especially for the 40 and 60 dB stimulus-level conditions (Fig. 5). A similar uniformity is noted for SPL at frequencies below 2 kHz (where standing-wave errors are less of a concern); however, at higher frequencies, more variability is evident, with DPOAEs measured for the deep insertion lower than, equal to, or higher than the emissions measured during the shallow insertion, with the greatest difference at 8 kHz. The presence of smaller DPOAEs for the deep insertion is opposite of what would be predicted if the effect of ear-canal impedance on the *measured* response was the sole determinant of changes in emission level. The greater variability with the SPL calibration in how DPOAE levels for the two insertion depths are related across frequency suggests calibration errors. Figure 5 shows systematic decreases in DPOAE level for the deep insertion, for frequencies between 2 and 4 kHz, and increases at higher frequencies (relative to DPOAE level during the shallow insertion), which is what would be predicted as a result of the effects of ear-canal length on frequencies affected by standing-wave calibration errors.

For SPL calibration, variability of DPOAE level changes across stimulus level is also noted. In Fig. 6, SPL calibrations for 2 and 4 kHz reveal increasing differences between the two insertions as the stimulus level increases. Not only is the relationship nonuniform across level, but it is also opposite of the prediction based on the growth rate of DPOAEs, which is linear at low levels, and becomes increasingly compressive (e.g., Dorn *et al.*, 2001; Neely *et al.*, 2003). It was expected that at high-stimulus levels, where the I/O function exhibits the most compression, a calibration error would result in little or no change in measured DPOAE level. Larger changes were predicted for responses on the steeper portion of the DPOAE I/O function (lower stimulus levels). The possibility that standing waves affected the calibration of the two primary levels (L_1 and L_2) differently (Whitehead *et al.*, 1995) may account for the unexpected outcome. DPOAE level is not only dependent on the absolute stimulus level but also on the difference between L_1 and L_2. Standing-wave errors have the greatest impact on a narrow frequency range, so when a calibration error affects the level of one primary, the level difference between primaries will also be affected. This may result in either a more or less optimal stimulus for eliciting a DPOAE, making the change in DPOAE level less predictable. A second explanation is that zero difference in uncorrected data does not necessarily mean that DPOAE level was not affected, as an incidental change was introduced by the study design. This same reasoning may also explain the apparent difference at higher intensities. This finding demonstrates a situation where it is more appropriate to base interpretations on corrected values, which allows for changes caused by calibration procedure to be isolated.

Figure 7 displays the mean absolute differences between deep and shallow insertions after applying the individual corrections that remove the incidental effect of volume change on DPOAE level, while leaving intact the differences due to calibration procedure. *Absolute* changes in DPOAE level for each subject were used to avoid averaging out differences in sign that may have occurred if the direction of the difference was not removed. The rationale for evaluating absolute values is that all changes, whether in the positive or negative direction between insertion depths, were considered to reflect calibration errors. Note that the *y* axis covers a 10 dB range in Fig. 7 compared to the 50 dB ranges used in Figs. 5 and 6, making the differences among calibration procedures more apparent. The smallest corrected differences in DPOAE level between deep and shallow insertions were observed mainly for frequencies below 2 kHz for all three calibration methods. The largest differences in DPOAE level were observed at the highest frequencies regardless of the calibration procedure. This effect indicates that controlling stimulus level with *in situ* calibrations is more difficult at higher frequencies for all three methods. While the change in DPOAE level varies as a function of stimulus frequency for all calibration

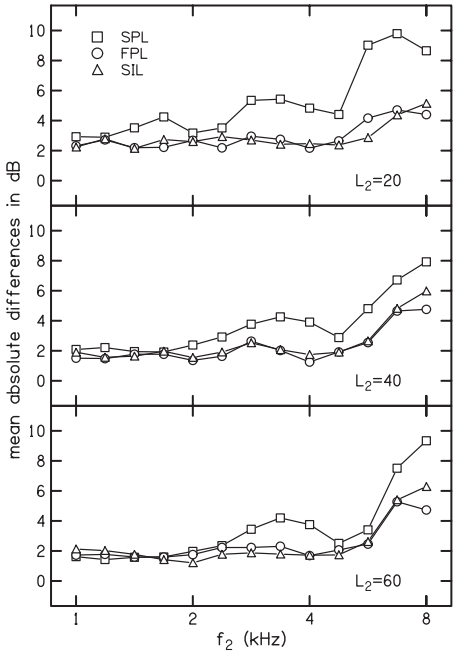

FIG. 7. DPgrams of the mean absolute changes in DPOAE levels due to changes in insertion depth after individually correcting for the expected change in emission level introduced by the study design. The three calibration methods (SPL, FPL, and SIL) are compared for three stimulus levels (20, 40, and 60 dB). The *y* axis differs in this figure from Figs. 5 and 6 by a factor of 5, making the differences between calibration methods more apparent.

methods, SPL, as expected, produced more variable measurements.

A three-way analysis of variance (ANOVA) was performed on the absolute differences in DPOAE levels with the following factors: calibration method (3 levels), L_2 (5 levels), and f_2 (13 levels). Because incidental changes were estimated and not always ideal (see footnote 1 and Fig. 2), adding a correction to the measured values introduces another potential source of error into the calculation. Therefore, both uncorrected and corrected data were analyzed. The significance observed in both sets of data is similar, indicating that correcting for the incidental changes in DPOAE level did not confound the results. Moreover, the *F* ratio was almost four times larger for the measurement effect when the correction was applied, which is evidence that removing the estimated, incidental change in DPOAE level positively influenced the analysis and subsequent interpretation. Due to these findings, only the results of the ANOVA on the corrected values are described (Table I).

The effects of stimulus level, stimulus frequency, calibration method, and interactions involving calibration method on changes in DPOAE level were significant ($p < 0.05$). While the ANOVA does not specify which calibration method had the greatest impact on the significance, Figs. 5–7 demonstrate that DPOAE level differences for SIL and FPL are similar and that data based on SPL calibrations are more variable across frequency and intensity. These findings suggest that SPL calibration is responsible for both the significant main effects and the interactions. None of the calibration methods resulted in zero change in DPOAE level after correcting for the expected, incidental change (Fig. 7), which indicates that none of them are completely insensitive to probe-insertion depth.

The observations thus far demonstrate that both SIL and FPL calibrations result in smaller changes in DPOAE level when the insertion depth is varied compared to SPL calibration. However, the least variable calibration method may depend on stimulus frequency or stimulus level. It is not practical to customize calibration depending on the frequency and/or level of a specific stimulus. Therefore, to provide a more general assessment of the calibration methods, the changes in DPOAE level were averaged across stimulus frequency and eventually level for each calibration method (Table II).

At each stimulus level, probe-insertion depth had a greater impact for measurements based on SPL calibrations, as expected, with the mean differences in DPOAE level about 1–2 dB greater than the differences obtained with SIL and FPL calibrations. In contrast, the greatest difference in mean emission levels between SIL and FPL calibrations is about 0.2 dB. SPL calibration also resulted in the largest standard deviations at each stimulus level due to individual variability of the frequencies at which standing-wave errors occur. Another noteworthy observation is that mean differences in DPOAE level decrease as the intensity increases for SPL calibration, which was the expected trend and is oppo-

TABLE I. The main effects for and interactions between calibration method, stimulus level, and frequency on the absolute change in DPOAE level between deep and shallow insertions after correcting for the incidental difference due to a change in ear-canal volume. The asterisk (*) denotes statistical significance for $p < 0.05$.

Source	Sum Sq.	df	Mean Sq.	*F* ratio	*p* value
		Main effects			
*Stimulus level (L_2)	525.9	4	131.48	15.40	<0.0001
*Calibration method	2 195.1	2	1 097.55	128.58	<0.0001
*Frequency (F_2)	8099.8	12	674.98	79.08	<0.0001
		Interactions			
*L_2 and method	213.4	8	26.68	3.13	0.0016
L_2 and F_2	291.8	48	6.08	0.71	0.9329
*Method and F_2	1 168.6	24	48.69	5.70	<0.0001
Error	34 108.6	3 996	8.54		
Total	46 603.3	4094			

TABLE II. Means and standard deviations of the absolute change in DPOAE level between insertions after correcting for the expected, incidental change. The first five rows are averaged across frequency for each calibration method and the sixth row is also averaged across level..

	Calibration method					
	SPL		SIL		FPL	
L_2	Mean	SD	Mean	SD	Mean	SD
20	5.21	2.41	2.91	0.87	2.93	0.90
30	4.41	2.21	2.49	1.20	2.50	1.02
40	3.67	1.88	2.48	1.36	2.26	1.16
50	3.56	2.12	2.40	1.49	2.26	1.16
60	3.44	2.42	2.44	1.56	2.42	1.19
Average	4.06	0.75	2.54	0.21	2.47	0.28

site of the trend observed in Fig. 6. The most probable reason for the apparent disagreement between Fig. 6 and Table II is that the summary provided in Table II removes the estimated, incidental change in DPOAE level and is based on absolute values, whereas Fig. 6 plots the uncorrected raw data. When averaged across levels, SPL calibration differs from SIL and FPL by approximately 1.5 dB, whereas SIL and FPL differ from each other by about 0.07 dB, which is less than half the standard deviation for either calibration method. All of the changes in DPOAE level are small in the aggregate; yet, the effects of calibration method and interactions of calibration method with stimulus frequency and level are statistically significant (Table I).

IV. DISCUSSION

The results from this study are summarized by the following observations.

(1) DPOAEs measured after SPL calibration demonstrated greater changes and greater variability of changes across frequency and stimulus level than DPOAEs following SIL or FPL calibrations when the probe-insertion depth was manipulated.
(2) All calibration methods were sensitive to probe placement, especially above 4 kHz.
(3) Temperature significantly affected estimates of source impedance and, therefore, SIL and FPL calibration procedures.

A. Temperature effects

A significant effect of temperature on the calculation of ear-canal impedance was observed, similar to results reported by Neely and Gorga (1998). A summary of the temperature effect is provided in Appendix A. Since estimates of ear-canal impedance are essential for conversion of SPL into SIL and FPL, the cavities were warmed to approximate body temperature during daily calibrations. However, cavity temperatures across the daily calibrations varied over a 10° range due to imprecision in the method used to warm the cavities, and this could have affected the accuracy of SIL and FPL calibrations. Additionally, it may be clinically impractical to warm test cavities to approximate body temperature as part of daily calibrations. A frequency-specific correction factor might reduce the influence of temperature on SIL and FPL calibrations; however, current methods do not offer a simple correction factor. Furthermore, the differences between the mean Thevenin-equivalent source characteristics calculated at room and body temperatures (Fig. 8) were similar to the differences between repeated measurements at a single temperature (Fig. 3), which complicates understanding the temperature effect. Until the effect of temperature is better understood and/or a method of temperature compensation becomes available, it is recommended, based on observations from Neely and Gorga (1998) and the present study, that consideration be given to cavity temperature for sound-source calibrations.

B. Incidental changes in DPOAE level

If the ear-canal volume had no effect on stimulus level but only affected DPOAE level measured at the emission probe, then applying the individualized correction would have eliminated any gross changes in DPOAE level, but this was not seen for any of the calibration methods. Mills *et al.* (2007) made repeated measurements of DPOAE level with the probe in a constant position and found variations of 1–2 dB, which were attributed to intrinsic variability. While intrinsic variability could account for most of the changes that were observed with SIL and FPL calibrations (and SPL at frequencies below 2 kHz), changes in DPOAE level greater than 2 dB were observed at frequencies above 4 kHz (Fig. 7). Although this is the frequency range where standing-wave problems are expected, SIL and FPL calibrations are, in principle, unaffected by standing waves, and the source of additional variability in DPOAE level remains unknown at this time.

C. Unintentional change in DPOAE level

The impedance values used to determine unintentional probe movement represent repeated measurements for the same condition (deep or shallow insertion), for which the measured responses were not expected to vary. While the impedance change from unintentional probe movement was estimated to be <0.2 dB for more than half of the subjects, it was $\geqslant 1$ dB for four subjects. This was unexpected because calibrations (performed prior to each DPgram for a single insertion) were monitored for probe stability. If pressure-

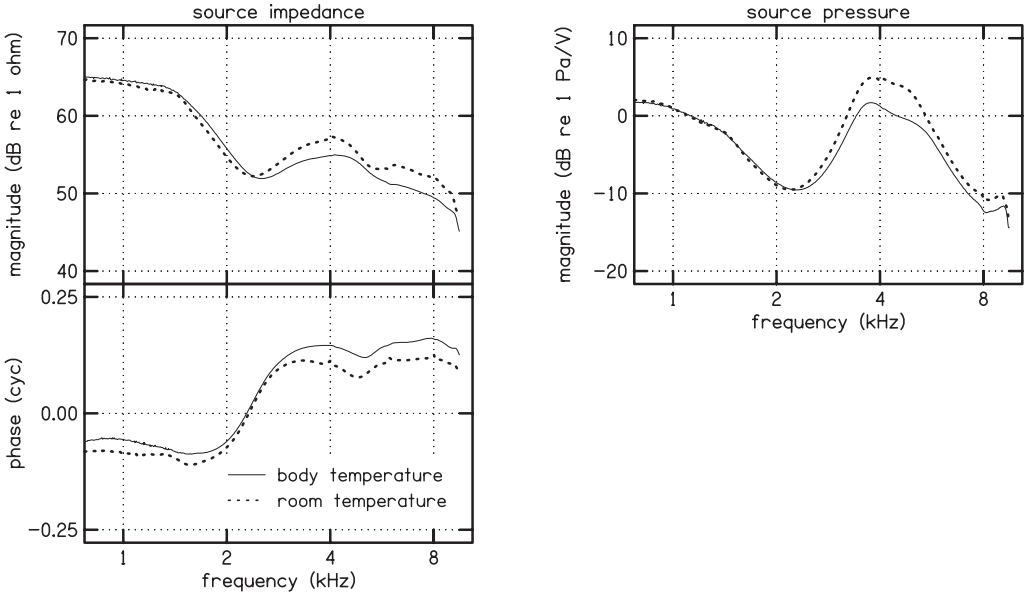

FIG. 8. Means for 18 repeated cavity calibrations at both room and body temperatures as a function of frequency. Phase of source pressure was not plotted as subtracting the delay complicated averaging. The delay values were within 0.01 ms of each other.

spectrum changes were detected from one calibration to the next (i.e., the notch became shallower or shifted to a lower frequency), then the affected conditions were repeated. However, Mills *et al.* (2007) reported an informal observation that even slight probe movement could affect DPOAE level by several decibels. More formal assessment by Kalluri and Shera (2007) suggested that apparent calibration stability might still allow slight changes in stimulus pressure, which can significantly affect DPOAE level.

For this investigation, unintentional movement compromised the study design; however, as shown in Fig. 4, the effects of intentional probe movement were larger than those due to unintentional movement. As a result, while errors (unintentional effects) are evident in the present data, the effects are small relative to the effects resulting from intentional changes in probe placement, which were the main focus of this study. While unintentional movement does not invalidate our findings, it may have reduced the observed differences among the calibration methods, even though counterbalancing the order of the calibration methods reduced possible bias due to probe shift over time. Aside from the potential effects on the present study, the findings indicate that it may be important to consider the impact of unintentional probe movement in all DPOAE studies.

D. Clinical implications

The present study suggests that both FPL and SIL are more reliable calibration methods compared to SPL, even with our conservative study design, which (1) did not attempt to maximize the emission changes caused by standing-wave errors by comparing DPOAE level when calibrating the stimulus at the tympanic membrane and at the emission probe, (2) did not exclude subjects even if a null was not observed in the pressure spectrum of the *in situ* calibration, and (3) averaged across subjects and eventually frequencies and stimulus levels, even though the frequencies at which standing-wave errors occur are idiosyncratic. Our method of manipulating the probe-insertion depth within the ear canal was expected to result in SPL calibration differences of 5–6 dB for individual subjects, depending on frequency (Dirks and Kincaid, 1987). Thus, the potential changes in DPOAE level were also expected to be smaller than the 10–20 dB changes noted in other studies (Dreisbach and Siegel, 2001; Siegel and Hirohata, 1994), which more accurately quantify the errors that are currently occurring when controlling the SPL of the stimulus. While it may have been beneficial to create an experimental design to maximize calibration errors and, consequently, to maximize differences among the calibration methods, the design is reflective of clinical measurement reliability. Our method underestimates the magnitude of calibration errors but is similar to potential test/retest situations that are encountered clinically, where a calibration microphone near the eardrum is not used. Additionally, probe-insertion depth during clinical measurements is not exact but dependent on many factors including probe design, physical properties of the ear canal, skill/experience of the clinician (especially if there are multiple testers for the same patient), and patient comfort. Given these factors, it is likely that probe placement will be different from trial to trial. In this study, the probe was intentionally moved approximately 2–3 mm, which is within a range that could feasibly occur during clinical test/retest DPOAE measurements.

Restricting the analysis to data at frequencies relative to pressure minima during SPL calibrations may also have been beneficial in order to make the differences between calibration methods more evident; however, nulls were not present in all subjects. A criterion requiring evidence of a standing-wave minimum at the emission probe during *in situ* SPL calibration was not included, in part, based on the knowledge that test-performance data are best around the same frequencies most susceptible to standing-wave errors (e.g., Gorga

et al., 1993, 1997, 2005; Kim *et al.*, 1996), which implies that standing-wave errors may not cause diagnostic errors when DPOAEs are used clinically. While this study does not assess test performance, the results are meant to relate to clinical issues.

Even though the differences between calibration methods were underestimated, the fact that effects were present and statistically significant indicates that the differences among calibration methods were substantial enough to withstand the conservative study design. The present results demonstrate that measurement reliability was the worst following SPL calibration, which further supports the need for an alternative calibration method.

E. Comparison of SIL and FPL

SIL and FPL *in situ* calibrations are both unaffected by standing waves and resulted in similar changes in DPOAE level between insertions. One concern with a power measurement (such as SIL) is the relationship between power and hearing thresholds (Hudde *et al.*, 1999). While Rosowski *et al.* (1986) demonstrated similarity between the SPL required to maintain a constant power at the cochlea and the SPL-referenced behavioral thresholds across frequency, Puria *et al.* (1997) subsequently demonstrated, across a broader frequency range, that pressure in the cochlea related more closely to behavioral thresholds than power. Although DPOAEs are not directly proportional to behavioral thresholds, the two measurements are often compared during clinical evaluations. A potential advantage to using FPL (instead of SIL) is that this method uses the same sound reference as SPL (i.e., 20 μPa rms). The relationship between hearing thresholds and SPL is well known across frequency (e.g., Sivian and White, 1933; Dadson and King, 1952; Robinson and Dadson, 1957; Killion, 1978), while the relationship between hearing thresholds and SIL is not well known. Therefore, using FPL to measure stimulus level may facilitate comparisons between hearing thresholds and DPOAE levels.

A more practical reason for selecting FPL over SIL stems from experience with implementing these two calibration methods. Initially, the protocol included a 70 dB stimulus-level condition; however, the relationship between SIL and SPL is frequency dependent. Subject discomfort due to excessively loud stimuli became a concern, especially at high frequencies, resulting in the decision to eliminate the 70 dB condition. FPL calibration did not raise concerns about subject comfort because the relationship between FPL and SPL is closer.

V. CONCLUSIONS

Our results indicate that both SIL and FPL calibrations are less susceptible than SPL to standing waves; however, further research is needed to determine whether these calibration methods improve test performance clinically. Although implementation of either of these two methods may be easier than the alternative procedure of placing a microphone close to the eardrum, the possible need to control the temperature of the calibration cavities may reduce the clinical practicability of both SIL and FPL. Further study of the impact temperature has on test performance is needed to determine whether heating the cavities is warranted in clinical implementation. The present results indicate that SIL and FPL calibrations lead to measured DPOAE responses that are less variable than those obtained with SPL calibration. FPL may be of particular interest because it simplifies comparisons with behavioral thresholds based on SPL calibration and reduces concerns about subject comfort when presenting high stimulus levels at high frequencies. Errors due to standing waves that are known to occur during *in situ* SPL calibration may be avoided by switching to either SIL or FPL calibration.

ACKNOWLEDGMENTS

This study was supported by the NIH (R01 DC2251, R01 DC8318, and P30 DC4662). The work was performed while the first author was supported by a training grant (T35 DC8757-01). The authors thank Hongyang Tan for valuable assistance during data analyses and Sarah Michael, Wafaa Kaf, Jonathan Siegel, and an anonymous reviewer for their suggestions.

APPENDIX A: TEMPERATURE EFFECTS

Neely and Gorga (1998) noted that calibrating the probe at body temperature resulted in fewer negative conductance values (a physically unrealistic occurrence) than when calibrating at room temperature. Because of this observation, the impact of cavity temperature on Thevenin-equivalent source and load characteristics was evaluated prior to initiating DPOAE measurements. Due to unknown measurement errors, repeated cavity calibrations are typically variable even when temperature is constant. Therefore, a preliminary study was undertaken with the objective of determining whether there are significant differences in source and load values between cavities at room temperature and body temperature (beyond typical repeated-measurement variability).

Five cavity calibrations were performed at both room and body temperatures. Body temperature was produced with an inexpensive heating pad that raised the internal temperature of the cavities to the range from 94.5 to 100.1 °F, as measured by a digital, oral thermometer placed inside each tube. Although these temperatures are closer to body temperature than they are to room temperature, which was about 70 °F, ear-canal temperatures in humans are more stable and closer to 98 °F. The implications of differences between body and cavity temperatures will be discussed below. Ten load-impedance estimates were obtained for one subject by repeated in-the-ear calibrations, which, by definition, were made at body temperature. Five of these estimates used the Thevenin-equivalent source characteristics calculated at room temperature and five used the source characteristics at body temperature.

Magnitude and phase values based on the cavity and *in situ* calibrations of one sound source were analyzed for 4, 4.758, 5.656, 6.727, and 8 kHz. ANOVAs were performed with the following factors: temperature (two levels), frequency (five levels), and repetitions (five levels). Both impedance and pressure measurements were analyzed for the

cavity calibrations, but for the *in situ* calibrations, only impedance measurements were analyzed as load pressure is not dependent on the calculation of source characteristics.

For the purposes of these analyses, a p value <0.05 was considered significant. Source pressure magnitude was significantly affected both by temperature and an interaction between temperature and frequency ($p<0.0498$ and $p<0.0411$, respectively). For calibrations in the ear canal, main effects of temperature and frequency, along with temperature and frequency interactions, were found on both impedance magnitude and phase ($p<0.0001$).

Based on these results, the decision was made to warm the cavities to approximate body temperature for the daily calibrations required for this study. However, while the effect of temperature was significant, it remains unknown how temperature affects the calculation of source-pressure magnitude and, subsequently, load-impedance magnitude and phase. The procedure used in this study to heat the cavities was imprecise, resulting in temperatures ranging from 95 to 105 °F for the calibrations used during DPOAE data collection. Additionally, while controlling temperature may be feasible in the research setting, heating the cavities is time consuming and may be impractical for clinics. Therefore, additional effort was made to further describe the effects of temperature.

The magnitudes and phases of source impedance and the magnitudes of source pressure from the 18 daily cavity calibrations at body temperature were averaged for frequencies from 4 to 15 996 Hz (in 4 Hz increments). The same averages were obtained for 18 repeated cavity calibrations at room temperature. Both sets of averages are plotted in Fig. 8. Recall that pressure magnitude was the only Thevenin-equivalent source characteristic significantly affected by temperature, most probably due to the differences observed around 4 kHz. However, it should also be noted that, for all panels, the mean data sets for both temperatures fall within the range of daily variability (Fig. 3), which may have a greater effect on the accuracy of SIL and FPL calibration methods than temperature. Since we do not have a way to determine the accuracy of the Thevenin-equivalent source calculations at this point, effort should be placed on reducing variability. A calibration procedure that compensates for differences in temperature between the calibration cavities and ear canals and reduces variability could improve the estimation of load impedance for SIL and FPL calibrations.

APPENDIX B: FORWARD PRESSURE LEVEL

A solution of the wave equation for a one-dimensional wave with harmonic time dependence is

$$P(x,t) = A_+ e^{i(\omega t - kx)} + A_- e^{i(\omega t + kx)}, \tag{B1}$$

where $\omega = 2\pi f$ is the frequency in radians per unit time and k is the wave number in radians per unit distance. One-dimensional wave propagation is often analyzed in terms of a wave traveling along a transmission line. In a uniform transmission line, Z_t (series impedance per unit length) and Y_t (shunt admittance per unit length) do not vary with x, and the relation between $P(x)$ (pressure) and $V(x)$ (volume velocity) is described by the following differential equations:

$$\frac{\partial}{\partial x} P(x) = -Z_t V(x), \tag{B2}$$

$$\frac{\partial}{\partial x} V(x) = -Y_t P(x). \tag{B3}$$

When $k^2 = -Z_t Y_t$, the expression for $P(x,t)$ in Eq. (B1) satisfies Eqs. (B2) and (B3) and may be interpreted as the sum of forward and reverse propagating waves, $P_+ = A_+ e^{i(\omega t - kx)}$ and $P_- = A_- e^{i(\omega t + kx)}$, respectively.

The impedance of an acoustic load is defined as $Z_\ell = P/V$ and can be expressed in terms of P_+ and P_-,

$$Z_\ell = Z_0 \frac{P_+ + P_-}{P_+ - P_-}, \tag{B4}$$

where $Z_0 = \sqrt{Z_t / Y_t}$ is the characteristic impedance of the transmission line. For acoustic plane waves in a cylindrical cavity, $Z_0 = \rho c / A$, where ρ is the air density, c is the sound speed in air, and A is the cross-sectional area of the cavity. Rearranging Eq. (B4) allows for the expression of forward pressure P_+ in terms of Z_0 and Z_ℓ,

$$P_+ = \frac{1}{2} P_\ell \left(1 + \frac{Z_0}{Z_\ell} \right). \tag{B5}$$

In this equation, $P = P_\ell$ represents the cavity load pressure. Note that $|P_+|$ can be much larger than $|P_\ell|$ when $|Z_\ell|$ is small and that $|P_+|$ approaches $\frac{1}{2}|P_\ell|$ when $|Z_\ell|$ is large. Note also that there is no reverse wave when $Z_\ell = Z_0$.

[1]Ideally, surge impedance would have been used for frequencies above 1 kHz, where the ear canal is more accurately represented as a transmission line instead of a lumped volume. However, doing so would have had a small impact on the estimated correction. A more complicated issue with the correction is that, at high frequencies, standing waves can create problems when measuring emission level the same as when measuring stimulus level. At this time, it is complicated, and perhaps impossible, to account for all of the factors influencing measured emission level, which is why the estimate was general. The fact that the statistical analysis was stronger (see Sec. III) when the corrections were applied is evidence of a positive influence and convinced us to incorporate the corrections in our analyses and subsequent interpretations.

[2]In one subject, the frequency range was relocated to 750–1500 Hz to avoid a poor impedance magnitude estimate at lower frequencies, which was probably due to an air leak caused by an improper probe fit.

Allen, J. B. (**1986**). "Measurement of eardrum acoustic impedance," in *Peripheral Auditory Mechanisms*, edited by J. B. Allen, J. L. Hall, A. Hubbard, S. T. Neely, and A. Tubis (Springer-Verlag, New York), pp. 44–51.

ANSI (**1996**). "Specifications for audiometers," ANSI Report No. S3.6-1996, American National Standards Institute, New York.

Beranek, L. L. (**1954**). "The wave equation and solutions," in *Acoustics* (MIT, Cambridge, MA), pp. 16–46.

Chan, J. K., and Geisler, C. D. (**1990**). "Estimation of eardrum acoustic pressure and of ear canal length from remote points in the canal," J. Acoust. Soc. Am. **87**, 1237–1247.

Dadson, R. S., and King, J. H. (**1952**). "A determination of the normal threshold of hearing and its relation to the standardization of audiometers." J. Laryngol. Otol. **66**, 366–378.

Dirks, D. D., and Kincaid, G. E. (**1987**). "Basic acoustic considerations of ear canal probe measurements," Ear Hear. **8**, 60S–67S.

Dorn, P. A., Konrad-Martin, D., Neely, S. T., Keefe, D. H., Cyr, E., and Gorga, M. P. (**2001**). "Distortion product otoacoustic emission input/output functions in normal-hearing and hearing-impaired human ears," J. Acoust. Soc. Am. **110**, 3119–3131.

Dreisbach, L. E., and Siegel, J. H. (**2001**). "Distortion-product otoacoustic emissions measured at high frequencies in humans," J. Acoust. Soc. Am. **110**, 2456–2469.
Farmer-Fedor, B. L., and Rabbitt, R. D. (**2002**). "Acoustic intensity, impedance and reflection coefficient in the human ear canal," J. Acoust. Soc. Am. **112**, 600–620.
Gilman, S., and Dirks, D. D. (**1986**). "Acoustics of ear canal measurement of eardrum SPL in simulators," J. Acoust. Soc. Am. **80**, 783–793.
Gorga, M. P., Neely, S. T., Bergman, B., Beauchaine, K., Kaminski, J. R., Peters, J., and Jesteadt, W. (**1993**). "Otoacoustic emissions from normal-hearing and hearing-impaired subjects: Distortion product responses," J. Acoust. Soc. Am. **93**, 2050–2060.
Gorga, M. P., Neely, S. T., Bergman, B. M., Beauchaine, K. L., Kaminski, J. R., and Liu, Z. (**1994**). "Towards understanding the limits of distortion product otoacoustic emission measurements," J. Acoust. Soc. Am. **96**, 1494–1500.
Gorga, M. P., Neely, S. T., Ohlrich, B., Hoover, B., Redner, J., and Peters, J. (**1997**). "From laboratory to clinic: A large scale study of distortion product otoacoustic emissions in ears with normal hearing and ears with hearing loss," Ear Hear. **18**, 440–455.
Gorga, M. P., Nelson, K., Davis, T., Dorn, P. A., and Neely, S. T. (**2000**). "Distortion product otoacoustic emission test performance when both $2f_1-f_2$ and $2f_2-f_1$ are used to predict auditory status," J. Acoust. Soc. Am. **107**, 2128–2135.
Gorga, M. P., Dierking, D. M., Johnson, T. A., Beauchaine, K. L., Garner, C. A., and Neely, S. T. (**2005**). "A validation and potential clinical application of multivariate analyses of distortion-product otoacoustic emission data," Ear Hear. **26**, 593–607.
Hudde, H., Engel, A., and Lodwig, A. (**1999**). "Methods for estimating the sound pressure at the eardrum," J. Acoust. Soc. Am. **106**, 1977–1992.
Kalluri, R., and Shera, C. A. (**2007**). "Comparing stimulus-frequency otoacoustic emissions measured by compression, suppression, and spectral smoothing," J. Acoust. Soc. Am. **122**, 3562–3575.
Keefe, D. H. (**1984**). "Acoustical wave propagation in cylindrical ducts: Transmission line parameter approximations for isothermal and nonisothermal boundary conditions," J. Acoust. Soc. Am. **75**, 58–62.
Keefe, D. H., Ling, R., and Bulen, J. C. (**1992**). "Method to measure acoustic impedance and reflection coefficient," J. Acoust. Soc. Am. **91**, 470–485.
Killion, M. C. (**1978**). "Revised estimate of minimum audible pressure: Where is the "missing 6 dB?" " J. Acoust. Soc. Am. **63**, 1501–1508.
Kim, D. O., Paparello, J., Jung, M. D., Smurzynski, J., and Sun, X. (**1996**). "Distortion product otoacoustic emission test of sensorineural hearing loss: Performance regarding sensitivity, specificity and receiver operating characteristics," Acta Oto-Laryngol. **116**, 3–11.
Kummer, P., Janssen, T., and Arnold, W. (**1998**). "The level and growth behavior of the 2f1-f2 distortion product otoacoustic emission and its relationship to auditory sensitivity in normal hearing and cochlear hearing loss," J. Acoust. Soc. Am. **103**, 3431–3444.
Lonsbury-Martin, B. L., Harris, F. P., Stagner, B. B., Hawkins, M. D., and Martin, G. K. (**1990**). "Distortion product emissions in humans I. Basic properties in normally hearing subjects," Ann. Otol. Rhinol. Laryngol. **99**, 3–14.
Mills, D. M., Feeney, M. P., Drake, E. J., Folsom, R. C., Sheppard, L., and Seixas, N. S. (**2007**). "Developing standards for distortion product otoacoustic emission measurements," J. Acoust. Soc. Am. **122**, 2203–2214.
Møeller, A. R. (**1960**). "Improved technique for detailed measurements of the middle ear impedance," J. Acoust. Soc. Am. **32**, 250–257.
Neely, S. T., and Liu, Z. (**1994**). "EMAV: Otoacoustic emission averager," Technical Memo No. 17 Boys Town National Research Hospital, Omaha, NE.
Neely, S. T., and Gorga, M. P. (**1998**). "Comparison between intensity and pressure as measures of sound level in the ear canal," J. Acoust. Soc. Am. **104**, 2925–2934.
Neely, S. T., Gorga, M. P., and Dorn, P. A. (**2003**). "Cochlear compression estimates from measurements of distortion-product otoacoustic emissions," J. Acoust. Soc. Am. **114**, 1499–1507.
Nelson, D. A., and Kimberley, B. P. (**1992**). "Distortion-product emissions and auditory sensitivity in human ears with normal hearing and cochlear hearing loss," J. Speech Hear. Res. **35**, 1142–1159.
Popelka, G. R., Osterhammel, P. A., Nielsen, L. H., and Rasmussen, A. N. (**1993**). "Growth of distortion product otoacoustic emissions with primary-tone level in humans," Hear. Res. **71**, 12–22.
Puria, S., Peake, W. T., and Rosowski, J. J. (**1997**). "Sound-pressure measurements in the cochlear vestibule of human-cadaver ears," J. Acoust. Soc. Am. **101**, 2754–2770.
Rabinowitz, W. M. (**1981**). "Measurement of the acoustic input immittance of the human ear," J. Acoust. Soc. Am. **70**, 1025–1035.
Robinson, D. W., and Dadson, R. S. (**1957**). "Threshold of hearing and equal-loudness relations for pure tones, and the loudness function," J. Acoust. Soc. Am. **29**, 1284–1288.
Rosowski, J. J., Carney, L. H., Lynch, T. J., III, and Peake, W. T. (**1986**). "The effectiveness of external and middle ears in coupling acoustic power into the cochlea," in *Peripheral Auditory Mechanisms*, edited by J. B. Allen, J. L. Hall, A. Hubbard, S. T. Neely, and A. Tubis (Springer-Verlag, New York), pp. 3–12.
Siegel, J. H. (**1994**). "Ear-canal standing waves and high-frequency sound calibration using otoacoustic emission probes," J. Acoust. Soc. Am. **95**, 2589–2597.
Siegel, J. H. (**1995**). "Cross-talk in otoacoustic emission probes," Ear Hear. **16**, 150–158.
Siegel, J. H., and Hirohata, E. T. (**1994**). "Sound calibration and distortion product otoacoustic emissions at high frequencies," Hear. Res. **80**, 146–152.
Sivian, L. J., and White, S. D. (**1933**). "On minimum audible sound fields," J. Acoust. Soc. Am. **4**, 288–321.
Stinson, M. R. (**1985**). "The spatial distribution of sound pressure within scaled replicas of the human ear canal," J. Acoust. Soc. Am. **78**, 1596–1602.
Whitehead, M. L., Stagner, B. B., Lonsbury-Martin, B. L., and Martin, G. K. (**1995**). "Effects of ear-canal standing waves on measurements of distortion-product otoacoustic emissions," J. Acoust. Soc. Am. **98**, 3200–3214.

Beamforming synthesis of binaural responses from computer simulations of acoustic spaces

Mark A. Poletti
Industrial Research Limited, P.O. Box 31-310, Lower Hutt, Wellington 5040, New Zealand

U. Peter Svensson
Centre for Quantifiable Quality of Service in Communication Systems, Norwegian University of Science and Technology, NO-7491 Trondheim, Norway

(Received 14 November 2007; revised 7 April 2008; accepted 17 April 2008)

Auditorium designs can be evaluated prior to construction by numerical modeling of the design. High-accuracy numerical modeling produces the sound pressure on a rectangular grid, and subjective assessment of the design requires auralization of the sampled sound field at a desired listener position. This paper investigates the production of binaural outputs from the sound pressure at a selected number of grid points by using a least squares beam forming approach. Low-frequency axisymmetric emulations are derived by assuming a solid sphere model of the head, and a spherical array of 640 microphones is used to emulate ten measured head-related transfer function (HRTF) data sets from the CIPIC database for half the audio bandwidth. The spherical array can produce high-accuracy band-limited emulation of any human subject's measured HRTFs for a fixed listener position by using individual sets of beam forming impulse responses.
 [DOI: 10.1121/1.2924206]

PACS number(s): 43.60.Fg, 43.55.Ka, 43.55.Fw, 43.66.Pn [TDM] Pages: 301–315

I. INTRODUCTION

Computer simulation of acoustic spaces is becoming increasingly feasible as processing power increases and algorithms for simulation become more efficient. These simulations use either efficient but approximate algorithms based on geometrical acoustics or accurate but computationally demanding numerical solutions to the wave equation. For the former methods, auralization using binaural synthesis is straightforward, but for the latter methods, it is less so. The methods for numerically solving the wave equation include volume-element based ones, such as the finite element method, finite difference in the time domain (FDTD), digital wave guides (DWGs), and transmission-line modeling (TLM), as well as the boundary element method which subdivides the surrounding surfaces into elements. All of these methods produce pressure calculations at discrete points and often on a regular three dimensional (3D) grid (FDTD, DWG, and TLM). Due to the considerable processing involved, simulations often have low bandwidths. Accurate results require at least four to ten samples per wavelength.[1–3] However, as computer resources increase, such simulations will become increasingly practical.

In order to auralize—that is, listen to—the output of these simulations, binaural signals must be generated. Earlier, simplified approaches used two points of the grid that approximately corresponded to the distance between the two ears.[4] Such a simple approach is limited to very low frequencies.

A more accurate method is to undertake a plane wave decomposition of the sound field in a region around the intended listener position.[5] Each plane wave signal is filtered with a measured head-related transfer function (HRTF) for each angle of arrival and for each ear. The combined ear signals for all plane waves then constitute the binaural signal for auralization. In practice, a 3D plane wave decomposition would be carried out by treating a selected set of pressure responses from numerical simulations as a sensor array and using beam forming techniques to select plane waves from the angle of arrival corresponding to each measured HRTF. A spherical array would, for example, provide consistent beam widths for all angles of arrival. A beam former could be designed by using a least squares approach or by carrying out a spherical harmonic decomposition of the sound field[6–8] and synthesizing a beam former for each direction of arrival for which an HRTF is available.[9] The HRTF could also be synthesized from the spherical harmonic decomposition of a HRTF set,[10] allowing binaural synthesis for a set of incident plane wave angles independent of the measured HRTF angles (governed, for example, by the beamwidth of the plane wave decomposition beam former).

A third approach to auralization is to directly synthesize a binaural response from the computed pressure samples by using beam forming techniques. This approach combines the decomposition and synthesis steps and therefore should be more efficient than other methods since it does not require a spherical harmonic decomposition of the HRTFs or a plane wave decomposition of the sound field (which requires a beam former for each measured HRTF angle). The technique would less easily allow the rotation of the head position; nevertheless since simple auralization does not require head rotation, it is of interest to develop a direct synthesis method.

[a]Electronic mail: m.poletti@irl.cri.nz.
[b]Electronic mail: svensson@iet.ntnu.no.

Similar approaches have been suggested earlier. A trilinear microphone array was used to represent a full 3D set of HRTFs in a compact way,[11] but the interaural time delay was stored and separately processed, and the linear array was used for generating a minimum phase response. Such an implementation works well for binaural synthesis of individual plane waves but does not work for a complex sound field which is not decomposed into plane waves. In a different approach, a microphone array was used to detect the direction of arrival of a dominating sound wave, followed by a filtering with appropriate HRTFs.[12] Again, this is unsuitable for use in complex sound fields. Earlier work has suggested the use of a beam forming microphone array to represent the outer-ear transfer functions of a cat. An L-shaped array was used to represent the azimuthal (horizontal plane) variation of the HRTFs, again by using minimum phase modeling.[13]

This paper applies the least squares beam forming approach to emulating HRTFs, or low-frequency approximations to HRTFs, by using free field pressure samples obtained on a rectangular grid. The work aims to exactly emulate HRTFs without minimum phase simplifications and over all angles.

Section II presents the theory of least squares beam forming and investigates the robustness of the technique by comparison to a modal beam forming approach. Section III presents the results for HRTF emulation by using low-frequency simplified models and full 3D emulations of HRTFs. At low frequencies, the head is small compared to the wavelength and HRTFs predominantly show phase variations with angle of azimuthal incidence and little magnitude variation. At frequencies below 1 kHz, the effects of the torso are small[14] and the HRTFs become approximately constant with elevation. Hence, for low bandwidth computer simulations of rooms, a solid sphere model of HRTFs that emulates azimuthal interaural time delay and level difference will be sufficient.[15] This model will be symmetric about a line through the two ears and can be emulated by using line arrays.

At frequencies above 1 kHz, the torso contributes to the HRTF, and at frequencies above 3 kHz, pinna effects allow further perception of elevation effects.[14] Therefore, for higher bandwidth simulations, it is necessary to emulate the more complicated directionality of a dummy head or measured human subject.[16,17] This is achieved here by using a spherical array and deriving the beam forming filters for emulation of human subjects. The 3D array is also used to emulate the known responses of the sphere and to allow comparison to the line array case.

II. THEORETICAL DEVELOPMENT

A. Least squares beam forming

Consider a general 3D array of omnidirectional "microphone" elements with coordinates (x_l, y_l, z_l), $l=1,2,\ldots,L$ which is required to emulate an arbitrary HRTF $H(\theta,\phi,k)$, where θ and ϕ are the spherical coordinate elevation and azimuth angles, respectively, and k is the wave number. We assume that the HRTF is measured for sources sufficiently far away from the head so that the head receives plane wave fronts.

For an incident plane wave with vector wave number $\vec{k}$, the microphone outputs are weighted and summed to form a "beam former" output

$$\hat{H}(\theta,\phi,k) = \sum_{l=0}^{L-1} w_l(k) e^{i\vec{k}\cdot\vec{r}_l}. \tag{1}$$

This is required to match the desired subject HRTF for one ear, $H(\theta,\phi,k)$.

If Eq. (1) is written for Q angles $(\theta_q,\phi_q), q=1,2,\ldots,Q$, then it can be expressed in matrix form at each frequency

$$\mathbf{P}w = H, \tag{2}$$

where $\mathbf{P}$ is a $Q\times L$ matrix of plane wave terms $\exp(i\vec{k}_q\cdot\vec{r}_l)$, w is an $L\times 1$ vector of weights, and H the desired $Q\times 1$ vector of HRTF values.

The weights may be found by minimizing the mean squared error $\|\mathbf{P}w-H\|^2$. To regularize the solution, the power in the weights $\|w\|^2$ may be included as a constraint. The solution has the form[5,8,18]

$$w = [\mathbf{P}^H\mathbf{P} + \lambda\mathbf{I}]^{-1}\mathbf{P}^H H, \tag{3}$$

where λ is the regularization parameter. This may be termed the pressure matching solution.

To produce a set of beam former filters, the solution in Eq. (3) is calculated at a uniformly spaced set of positive frequencies and the inverse Fast Fourier Transform (FFT) is used to produce beam former impulse responses. The weights for each filter are stored in the positive frequency bins and their conjugate in the corresponding negative frequency bin, so that the resulting filter is real. The dc term is set to zero, and for even FFT sizes, the Nyquist frequency term is also set to zero.

B. Robustness analysis

The robustness of the least squares beam former is governed by the singular values of the matrix $\mathbf{P}$. These are in turn governed by the assumed angles of incidence and the array geometry. We demonstrate this by using the spherical harmonic decomposition.

The spherical harmonic decomposition of the desired HRTF for incidence angles (θ_q,ϕ_q) can be written as[19]

$$H(\theta_q,\phi_q,k) = \sum_{n=0}^{\infty}\sum_{m=-n}^{n} A_n^m(k) Y_n^m(\theta_q,\phi_q)^*. \tag{4}$$

Similarly, the decomposition of the beamformer output is, using the expansion of the plane wave,[19]

$$\hat{H}(\theta_q,\phi_q,k) = \sum_{l=1}^{L} w_l(k) 4\pi \sum_{n=0}^{\infty}\sum_{m=-n}^{n} i^n j_n(kr_l) \times Y_n^m(\theta_q,\phi_q)^* Y_n^m(\theta_l,\phi_l). \tag{5}$$

We assume that the HRTF and beam former responses can be

accurately represented by limiting the expansion to a maximum order $n=N$.

The pressure matching Eqs. (1) and (2) may be written in matrix form as

$$\mathbf{\Psi\Phi}w = \mathbf{\Psi}A, \tag{6}$$

where $\Psi(q,v)=Y_n^m(\theta_q,\phi_q)^*$ is a frequency-independent Q by $(N+1)^2$ matrix containing the spherical harmonic terms associated with the qth incoming plane wave angle, $v=n^2+n+m+1$ is the spherical harmonic index from 1 to $(N+1)^2$, $\Phi(v,l)=4\pi i^n j_n(kr_l)Y_n^m(\theta_l,\phi_l)$ is a frequency-dependent $(N+1)^2$ by L matrix containing the array plane wave terms, and $A(v)=A_n^m$ is the vector of desired HRTF coefficients.

It may now be seen that for least squares beam forming, the effectiveness of an array depends both on the range of expected input directions and on the array geometry. The matrix $\mathbf{\Psi}$ has a small effect on the solution if it contains a range of input angles uniformly spread, in which case $\mathbf{\Psi}^H\mathbf{\Psi}$ is approximately equal to the identity matrix. In practice, however, it has some influence on the least squares solution. For example, the matrix is not an exact identity for the set of angles used in the CIPIC database.[16,17]

The mode-matching solution to the HRTF emulation problem is obtained by directly comparing the elements of Eqs. (4) and (5). The elements in $\mathbf{\Psi}$ may be canceled from both equations [Eq. (6)], and the mode-matching equation

$$\mathbf{\Phi}w = A \tag{7}$$

is obtained. The least squares solution for the beam former weights for the overdetermined case $(N+1)^2>L$ is then

$$w = [\mathbf{\Phi}^H\mathbf{\Phi} + \gamma I]^{-1}\mathbf{\Phi}^H A, \tag{8}$$

where γ is a regularization parameter. This solution is dependent only on the array geometry and not on the set of arrival angles. However, it requires knowledge of the vector A of spherical harmonic coefficients of the HRTF (which allow interpolation between the measured angles). By assuming a sufficiently uniform range of input angles, the pressure matching solution will produce similar accuracy to the mode-matching solution without requiring the spherical harmonic decomposition. Furthermore, the conditioning of the least squares pressure matching will be at best equal to that of the mode-matching solution.

For many 3D audio applications, a spherical array of microphones is used.[6–8] We consider the conditioning of the mode matrix $\mathbf{\Phi}$ for this case.

For a spherical array with radius R, $\mathbf{\Phi}$ can be written as the product of a $(N+1)^2\times(N+1)^2$ diagonal matrix $\mathbf{J}$ with entries $i^n j_n(kR)$ and an $(N+1)^2\times L$ array of spherical harmonic terms $\mathbf{Y}$. Thus, the Bessel function amplitudes scale the rows of $\mathbf{Y}$.

At low frequencies, only the zeroth Bessel function is significant and the mode matrix $\mathbf{\Phi}$ condition number is high due to the small amplitudes of the higher order functions. At higher frequencies, the higher order Bessel functions become significant and the mode matrix becomes better conditioned, except at the zeroes of the Bessel functions. The frequencies at which these zeros occur are the eigenfrequencies of the spherical array.[6] At these zeros, there are $2n+1$ zeros in $\mathbf{J}$ and $2n+1$ zero rows in $\mathbf{\Phi}$. For an ideal spherical array with radius of 87.5 mm, these zeros are given in Table I, sorted by frequency.

TABLE I. Bessel function zeros for spherical array of radius $R=87.5$ mm.

Bessel function order	Frequency (Hz)
0	1954
1	2795
2	3585
0	3908
3	4347
1	4806
4	5090

For $(N+1)^2=L$, the mode-matching solution can be obtained from the matrix inversion

$$w = \mathbf{Y}^{-1}\mathbf{J}^{-1}A. \tag{9}$$

The matrix $\mathbf{J}$ is singular at the zeros of each spherical Bessel function and so there is no solution at these frequencies. These singular values occur because the array uses omnidirectional microphones (i.e., the pressure calculations from computer simulations). The zeros can be removed by using directional microphones,[8] but this is not practical for computer simulations.

For the overdetermined case $(N+1)^2>L$ (required for the least squares solution), the mode matrix is "tall." Consider a zero of the nth Bessel function. For $(N+1)^2>L+2n+1$, the rank of the mode matrix remains greater than L. In this case, the least squares solution is well conditioned. However, it cannot produce the $2n+1$ spherical harmonic coefficients of order n. The least squares estimate $\hat{A}=\mathbf{\Phi}w$ has zeros at $2n+1$ positions, and therefore produces a larger error.

The problems caused by the use of pressure microphone elements in a spherical array may be reduced by ensuring that the microphone radii are not all the same. A method for doing this is discussed in the following section, and the effects of the variable radii on the error are presented.

Finally, for completeness, we consider the calculation of the spherical harmonic coefficients. While in practice, the pressure matching solution [Eq. (3)] was used to derive the final beam former filters the spherical harmonic decomposition can offer a useful analysis of measured HRTFs and was used in the initial assessment of the CIPIC data in this paper.

In principle, the coefficients $A_n^m(k)$ in Eq. (4) can be determined by using the orthogonality of the harmonics as

$$A_n^m(k) = \int_\Omega H(\theta_i,\phi_i)Y_n^m(\theta_i,\phi_i)d\Omega. \tag{10}$$

However, this must be implemented in practice using a finite sum with a set of angles specified by the measurements. Evans *et al.* used uniform angles in azimuth, and a product Gaussian quadrature was used to select the elevation angles.[10] In the application here, we use the measurement angles specified in the CIPIC database and cannot apply this technique. Instead, the spherical harmonic coefficients may be determined by expressing the measured HRTFs [Eq. (4)]

in matrix form $\mathbf{H}=\mathbf{\Psi}A$ and determining the coefficients by using the least squares solution

$$A=[\mathbf{\Psi}^H\mathbf{\Psi}+\beta\mathbf{I}]^{-1}\mathbf{\Psi}^H H, \tag{11}$$

where β is a regularization parameter.

III. RESULTS

In this section, we apply line array beam forming to the emulation of low-frequency, axisymmetric HRTFs and then apply spherical arrays to 3D HRTF emulation over wider frequency ranges.

At low frequencies, human HRTFs become reasonably invariant to elevation and may be approximated by the azimuthal response in the horizontal plane. The responses become rotationally invariant about the line through the two ears. Such responses can be emulated by line arrays. We first consider a low-frequency approximation to the HRTF that only requires two elements, as mentioned in the Introduction, and then consider the wider bandwidth axisymmetric case.

A. The acoustic center low-frequency approximation

The HRTF for a sphere is defined as the pressure on the sphere divided by the pressure that would exist at the sphere center in the absence of the sphere. For a plane wave arriving from spherical coordinate angle θ from the z-axis, and for a sphere radius R, the low-frequency approximation to the HRTF can be shown to be[20]

$$\mathrm{HRTF}(\theta,k)\rightarrow 1-i\tfrac{3}{2}kR\cos(\theta). \tag{12}$$

Assuming the ear is on the z-axis at $\theta=0$, the low-frequency delay as a function of the incidence angle relative to $\theta=\pi/2$, for which $\cos(\theta)=\sin(\theta_{\mathrm{inc}})$, is

$$\tau(\theta)=-\frac{3R}{2c}\sin(\theta_{\mathrm{inc}}). \tag{13}$$

The left ear HRTF produces the same delay with opposite sign, and hence the low-frequency interaural time delay (ITD) is

$$\mathrm{ITD}=\frac{3R}{c}\sin(\theta_{\mathrm{inc}}), \tag{14}$$

which is the same as previously shown by Kuhn.[21]

This result may be compared to a simple free field model. Consider the sound pressure produced at points $z=\pm a$, $x=y=0$ due to a plane wave. The relative delay between these two points is

$$\mathrm{ITD}=\frac{2a\sin(\theta_{\mathrm{inc}})}{c}. \tag{15}$$

Hence, the low-frequency ITD for the sphere is the same as that for the free space case with $a=3R/2$.

For the acoustic-reciprocal case, it can be shown that at low frequencies, the acoustic center[22] of a point source at $z=R$ on a sphere of radius R is at $z=3R/2$. Specifically, the sound field due to a point source on a sphere of radius R at $z_s=R$ is

$$p_t(r,\theta,k)=-\frac{1}{4\pi kR^2}\sum_{n=0}^{\infty}[2n+1]\frac{h_n(kr)}{h_n'(kR)}P_n(\cos\theta), \tag{16}$$

which has the far-field, low-frequency approximation

$$p_t(r,\theta,k)\approx\frac{e^{ikr}}{4\pi r}\left[1-i\frac{3}{2}kR\cos\theta\right]. \tag{17}$$

Comparing this to the far-field response due to a point source at $z=z_s$ in the absence of the sphere

$$p(r,\theta,k)\approx\frac{e^{ikr}}{4\pi r}[1-ikz_s\cos\theta] \tag{18}$$

shows that the acoustic center of the source is at $z_s=3R/2$.

Hence, at low frequencies, the simplest binaural output may be obtained by using the calculated free-field sound pressure at two points on a line through the two ears positioned at the acoustic centers $y_0=\pm 3R/2$. An important consequence of this is that for very low-frequency computer simulations using a regular grid, a head should be represented by two points of 263 mm apart rather than the standard head size of 175 mm. Furthermore, for higher bandwidth emulations, the low-frequency performance will improve if the array has elements in the vicinity of the acoustic centers.

B. Axisymmetric approximation using line arrays

At higher frequencies, sphere HRTF responses begin to display amplitude variations. If only azimuthal variations are simulated, then, the sphere approximation to a HRTF may be emulated by using a line array.

The sphere HRTF may be obtained from the pressure response on a sphere due to a negative frequency plane wave incident along the z axis, normalized by the free field response at the origin[19,20]

$$\mathrm{HRTF}(\theta,k)=\frac{i}{(kR)^2}\sum_{n=0}^{\infty}(-i)^n\frac{[2n+1]}{h_n'(kR)}P_n(\cos\theta). \tag{19}$$

This axisymmetric response can be produced by using an infinite, continuous line array which produces the beam former response,

$$b(\theta,k)=\int_{-\infty}^{\infty}w(z)e^{-ikz\cos\theta}dz. \tag{20}$$

The required weighting function to produce $b(\theta,k)=\mathrm{HRTF}(\theta,k)$ is (see Appendix)

$$w(z)=\frac{i}{\pi kR^2}\sum_{n=0}^{\infty}(2n+1)\frac{j_n(kz)}{h_n'(kR)}. \tag{21}$$

Approximating the theoretical solution $w(z)$ using a finite discrete array and truncated sum produces poor results for angles of incidence near 0° and 180°. A more accurate solution is obtained by using a least squares approach. The desired HRTF is calculated from the order N truncated form of Eq. (19) and used to derive the least squares beam former weights. The least squares solution weights approach the the-

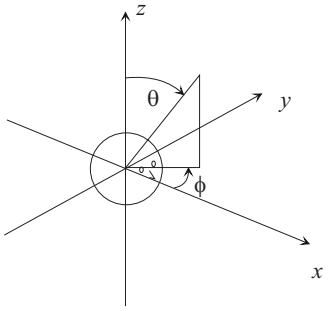

FIG. 1. Spherical coordinates and head orientation.

oretical solution in Eq. (21) for large apertures and small sensor spacings.

The head alignment in spherical coordinates is shown in Fig. 1. The y-axis is chosen as the axis through the two ears, and the ear angles are at elevation of 90° and azimuths ±90°. A line array along the y-axis will produce azimuthal responses which are symmetric about the y-axis and which will be sufficient for emulation of low-frequency ITD and interaural level difference (ILD). Therefore, for determining the beam former coefficients, the incident plane waves are restricted to azimuthal variations only, with $\theta=\pi/2$.

A uniform line array with element spacings Δ will allow beam formed polar responses up to the spatial Nyquist frequency $f_{\mathrm{Nyq}}=c/(2\Delta)$. A good design may therefore be achieved by requiring that the spatial Nyquist frequency of the array equals the temporal Nyquist sample frequency $f_s/2$, for which $\Delta=c/f_s$. For a sample rate of $f_s=44.1$ kHz, this yields a spacing of 7.75 mm. Better performance near the Nyquist limit will occur for spacings slightly less than this limit.

Simulations were run for a number of array lengths by using 512 frequency samples, producing 512 tap beam former filters. The relative mean squared error over all M angles was determined as[13]

$$\varepsilon(f)=\frac{\sum_{m=1}^{M}|H(f,\phi_m)-\hat{H}(f,\phi_m)|^2}{\sum_{m=1}^{M}|H(f,\phi_m)|^2}. \tag{22}$$

The regularized least squares solutions provide a trade-off between the error and the weight amplitudes. A value of $\lambda=0.01$ in Eq. (3) was empirically found to produce reasonable accuracy and beam former filter amplitudes.

The mean relative error obtained by using a linearly spaced line array is shown in Fig. 2 for L values from 5 to 50. The error increases with frequency for all values of L, and there is a peak in error at or above 10 kHz for array sizes greater than 20.

For array sizes less than 25, the low-frequency performance is poor because the array width is smaller than the sphere diameter. To improve these cases, a quadratic spacing was used for the K positive array positions, $K=(L-1)/2$ for L odd and $K=L/2$ for L even, of the form $y_l=\alpha l+\beta l^2$, $l=1:K$ with the constraints $y_1=\Delta$ for L odd and $y_1=\Delta/2$ for L even, and $y_K=R$. The resulting positions were requantized to integer multiples of Δ for L odd and integer and a half values for L even and adjusted to ensure that all sample positions were monotonically increasing. The error with the quadratic variation for array sizes less than 25 is shown in Fig. 3. The low-frequency performance is significantly improved, although the small arrays still fail at high frequencies because the element spacings do not all meet the Nyquist requirement and because the aperture width is limited to $2R$. For array sizes greater than 35, the array has elements beyond the acoustic center.

We have used a symmetric two-sided array above to allow the emulation of left and right ear responses. The error using a one-sided array is uniformly worse than the two-sided results due to the reduced aperture width.

The beam formed head-related impulse response (HRIR) can be obtained for a given angle of incidence by calculating the relative delay for each element in the array, delaying the

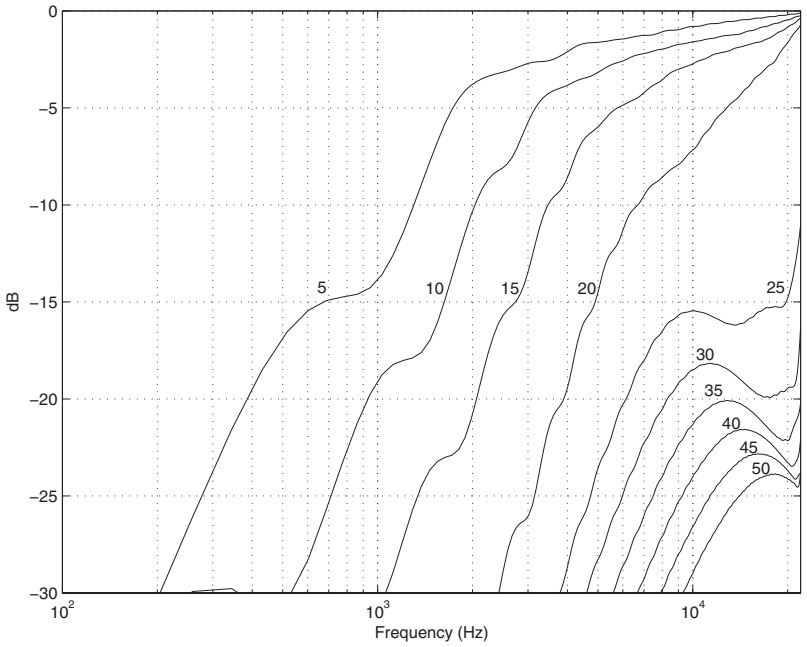

FIG. 2. Line array emulation of sphere, error in decibels for $L=5-50$ array elements, element spacing of 7.5 mm, sphere radius $R=87.5$ mm, with 512 tap beam former filters.

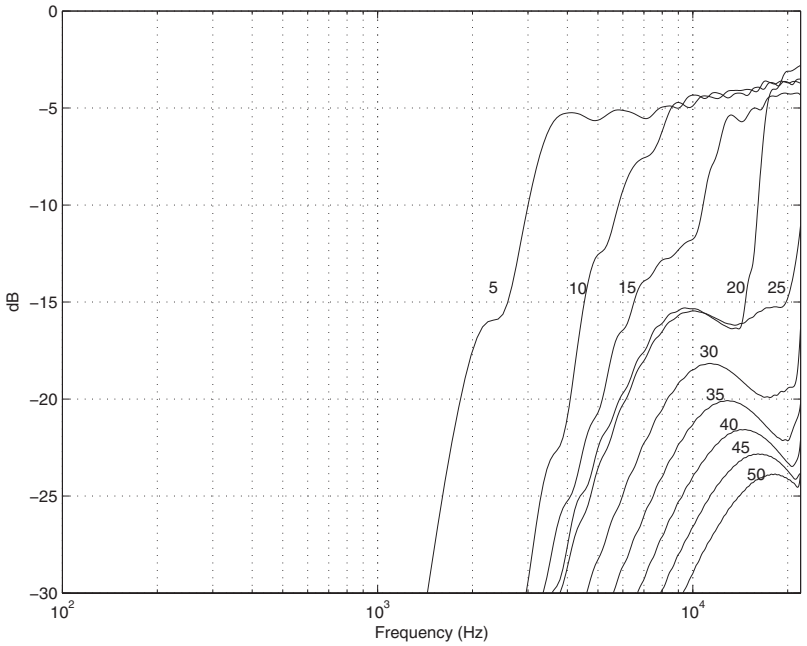

FIG. 3. Line array emulation of sphere, error in decibels for $L=5-50$ array elements, element spacing of 7.5 mm with quadratic variations for $L<25$, sphere radius $R=87.5$ mm, 512 tap beam former filters.

associated beam former filter, and adding the responses. This was carried out in the frequency domain where the (fractional) delays are most simply implemented. The impulse responses and transfer function magnitudes in decibels are shown in Figs. 4 and 5 for incidence angles of 90° and −45°, using 75 elements, for which the least squares error is minimal. The responses are good approximations to the theoretical sphere responses, although there are some high frequency oscillations due to the truncation of the approximate theoretical response at the Nyquist frequency. The tail in the 45° impulse response is caused by surface waves travelling by various paths around the sphere to the ear position.

C. 3D emulation of HRTFs

For the complete emulation of HRTFs, we use a spherical array, which as discussed produces reasonably well-conditioned solutions provided there is some variation of the radius. We first determine the frequency range over which the emulation of measured HRTFs is possible. The sphere and selected CIPIC subject HRTFs are then emulated.

The approximate Nyquist frequency of a spherical array may be determined by requiring average interelement spacings of half a wavelength over the surface area of the sphere.[8] For an array radius R, this produces a required number of array elements $L=(kR+1)^2$. A more accurate value is obtained from the fact that the field over a radius R can be represented by a spherical harmonic decomposition, and the number of terms required for wave number k and radius R can be determined by bounds on the radial Bessel functions.[23] This yields the slightly larger value $L=(ekR/2+1)^2$, where $e=\exp(1)\approx 2.7183$.

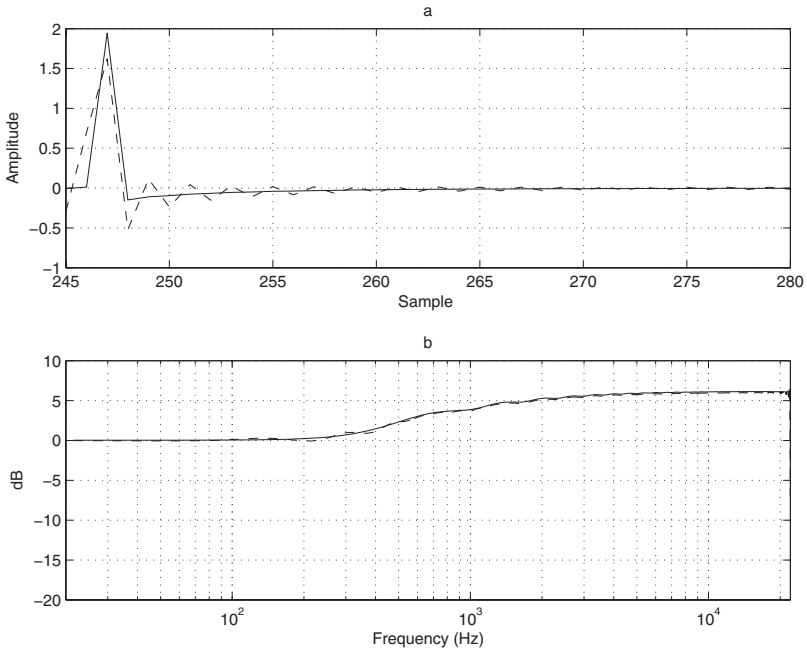

FIG. 4. (a) Approximated theoretical sphere HRIR (-) and line array emulated HRIR (--) for azimuth of 90° (0° to right ear) using 75 array elements. (b) Transfer function magnitudes.

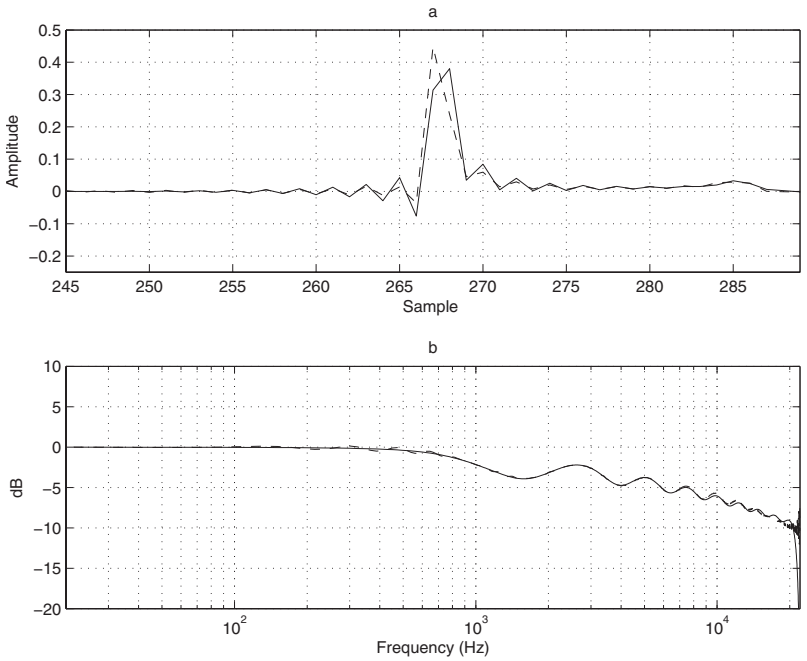

FIG. 5. (a) Approximated theoretical sphere HRIR (-) and line array emulated HRIR (--) for azimuth of 45° degrees (135° to right ear) using 75 array elements. (b) Transfer function magnitudes.

The Nyquist frequency of a sphere of radius R with L regularly arranged elements is thus

$$f_{\mathrm{Nyq}} \approx \frac{c}{e\pi R}[\sqrt{L}-1]. \tag{23}$$

For operation up to the Nyquist sampling frequency $f=f_s/2$, the required radius is

$$R_{\mathrm{Nyq}} \approx \frac{2c}{e\pi f_s}[\sqrt{L}-1]. \tag{24}$$

Hence, the array radius increases with L, and large array sizes are required to produce large aperture widths and the emulation of fine structure in the HRTFs. Alternatively, for a given sphere radius R, the number of array elements required to operate up to the Nyquist sampling frequency is

$$L_{\mathrm{Nyq}} \approx \left\lceil \left(\frac{e\pi R f_s}{2c} + 1 \right)^2 \right\rceil, \tag{25}$$

where $\lceil\cdot\rceil$ denotes the next highest integer. Empirically, using an array radius similar to the size of the diffracting object produces the lowest errors. For array dimensions smaller than that of the diffracting object, the array is unable to match the directivity of the scattered field, whereas for larger arrays, the responses can produce large lobes in the responses, particularly for smaller numbers of matching points. While we might expect better low-frequency emulation if the array radius is equal to that of the low-frequency acoustic center, the required number of array elements would be larger. We therefore use an array of radius of 87.5 mm (the typical radius of a human head).

The Nyquist frequencies for several values of L are shown in Table II. Very large arrays are required for full bandwidth emulation. For example, an array size of 2560 allows a Nyquist frequency of 22.7 kHz and a sample rate just exceeding 44.1 kHz. With array sizes greater than the number of HRTF measurements, the least squares beamformer cannot be determined. More fundamentally, the number of measurements required for emulation of a measured HRTF has a similar form to Eq. (25). This may be demonstrated from a consideration of the diffraction of a plane wave around the head. The analysis of diffraction expresses the total field as the incoming plane wave field and an outgoing scattered field.[19] The spherical harmonic expansion of both fields must be accurate at the radius of the head, where the boundary condition is applied. This argument leads to the same dimensionality as above. Hence, the number of HRTF measurements required for emulation of diffraction over a radius R at frequency f is

$$M = \left\lceil \left(\frac{e\pi R f}{c} + 1 \right)^2 \right\rceil. \tag{26}$$

For example, 20 kHz bandwidth requires 1988 HRTF measurements, which exceeds the number in the CIPIC database (1250). Hence, while the HRTFs can be emulated to any accuracy at the measurement angles, the accuracy between measurement angles will be poor at high frequencies.

The subjective impression of room acoustics is primarily obtained over the lower half of the audio bandwidth.[24] Therefore, the emulation of HRTFs at frequencies less than 20 kHz can still produce useful subjective assessments of

TABLE II. Spherical array Nyquist frequencies for array radius R =87.5 mm.

L	Nyquist frequency (kHz)
40	2.4
80	3.6
160	5.3
320	7.7
640	11.1
1280	15.9
2560	22.7

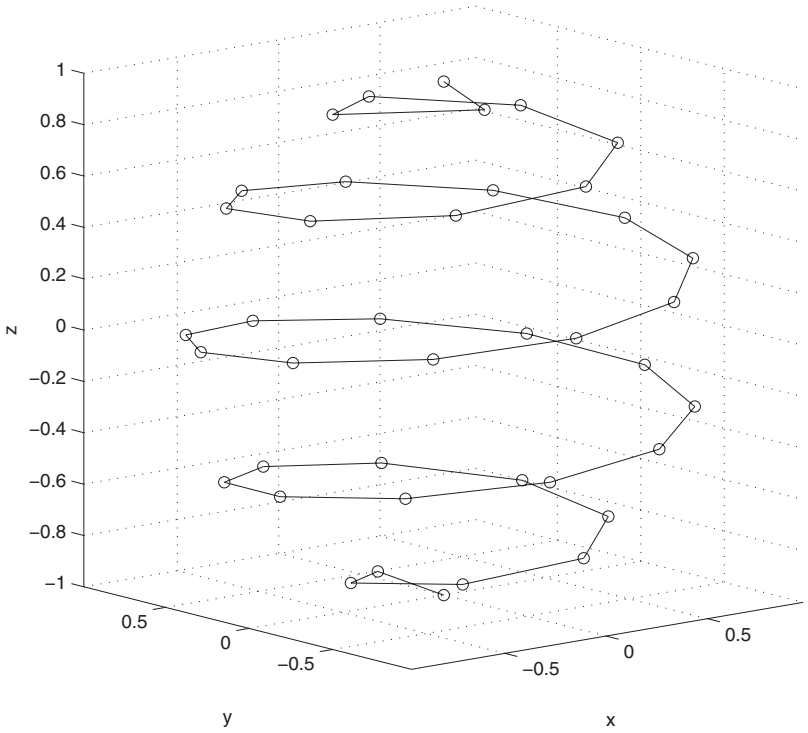

FIG. 6. Spiral spherical array with unit radius and 40 elements.

room acoustics. For example, at half the audio bandwidth the processing can be reduced by downsampling the head related impulse responses by two and using 640 array elements. We will use this approach and a range of array sizes for the sphere emulations to examine the error above the Nyquist frequency and then investigate the accuracy of the HRTF emulation for some representative CIPIC subjects.

The spherical array is generated from angular coordinates (θ_l, ϕ_l) obtained from a spiral sampling scheme developed by Rakhmanov *et al.*.[25] For the fractional array index

$$h_l = -1 + 2\frac{(l-1)}{L-1}, \quad l = 1,2,\ldots,L, \tag{27}$$

the array angles are given by

$$\theta_l = \cos^{-1}(h_l), \tag{28}$$

$$\phi_1 = \phi_L = 0, \tag{29}$$

and

$$\phi_l = \left(\phi_{l-1} + \frac{3.6}{\sqrt{L}}\frac{1}{\sqrt{1-h_l^2}}\right) \bmod 2\pi. \tag{30}$$

For example, the sample points for 40 elements are shown in Fig. 6. This sampling scheme produces close to equiangle sampling and approximates a minimum power law potential energy between sample points.[25]

To moderate the effect of the spherical array eigenfrequencies, mentioned in Sec. II, the array positions are generated for a mean radius R, and then the array radius is varied over a range approaching $\pm\Delta_R$ as a function of the index l by

$$R_l = R + \Delta_R \cos(2\pi l/N_c), \tag{31}$$

where N_c is the number of samples per cycle. The array coordinates are then quantized to the nearest grid point with quantization $\Delta = 0.0075$.

The CIPIC coordinate system is shown in Fig. 7. The subject looks along the positive x axis (as in Fig. 1). Elevation ε is measured from the x-axis and azimuth α is measured clockwise in the elevation plane. For a 3D array with coordinates (x_l, y_l, z_l), the beam former output for a plane wave incident from angle (α, ε) and time dependency $\exp(i\omega t)$ is

$$\hat{H}(\alpha,\varepsilon,k) = \sum_{l=0}^{L-1} w_l(k) e^{ik[x_l \cos\alpha \cos\varepsilon - y_l \sin\alpha + z_l \cos\alpha \sin\varepsilon]}. \tag{32}$$

This output is required to match the desired HRTF polar response at each frequency $H(\alpha, \varepsilon, k)$. The least squares so-

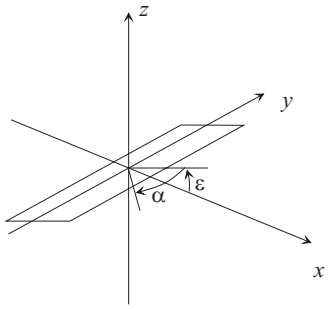

FIG. 7. CIPIC coordinates, elevation ε and azimuth α.

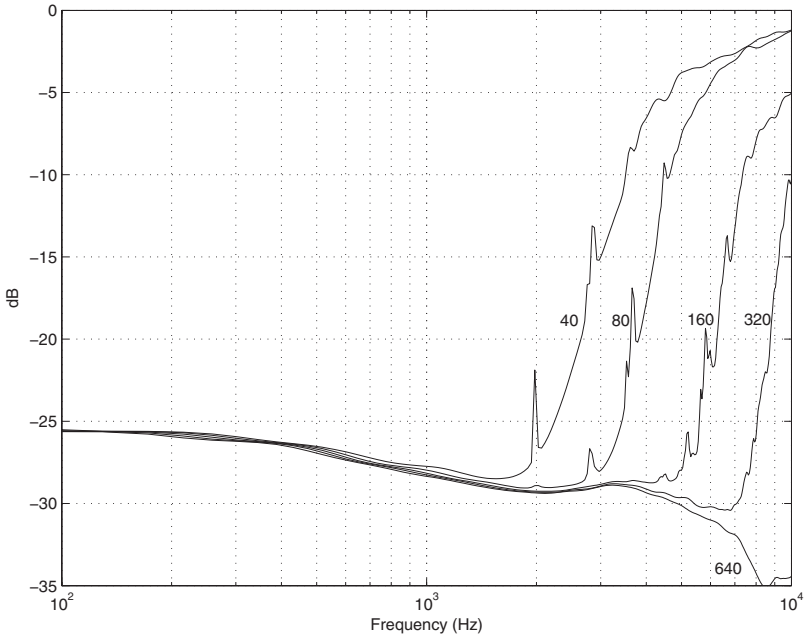

FIG. 8. Error for 3D emulation of solid sphere HRTFs, with ears at ±100° azimuth, for $L=40-640$, sphere radius $R=87.5$ mm, coordinates quantized to 7.5 mm. HRIRs downsampled by 2.

lution in Eq. (3) is then applied and a set of beam forming filters derived from the solutions at all frequencies.

At high frequencies, the number of HRTF measurements is typically insufficient to meet the requirement of Eq. (26), and large sidelobes can occur in the beam former responses for angles between the measured HRTF angles. These do not affect the least squared error over the HRTF angles and are not seen in the beam formed polar response unless it is calculated over a finer resolution than the original HRTF angles. The sidelobe levels are governed by the number of measurements made for each subject HRTF relative to Eq. (26) and by how uniformly spaced they are, as discussed in Sec. II.

The sidelobes may be reduced by increasing the regularization parameter. They can be further reduced by generating interpolated HRTF data. This was done for the CIPIC data as follows. First, for each azimuth, a linear interpolation was carried out for eight elevation angles linearly spaced between 230.625° and −45°. This prevents the production of downward-facing lobes in the beam formed solutions at high frequencies. Second, values were generated for azimuths of −85° and +85° for all elevations, with values equal to the −80° and +80° values, which reduced the occurrence of large high frequency lateral sidelobes. There are 1250 angles in the CIPIC measurements, and an additional 300 interpolation angles were used, so the data matrix dimension for an L-element array is $1550\times L$. The number of rows is sufficient to ensure that the matrix is well conditioned for the maximum array size of 640.

As a first example, we emulate the response of a sphere of radius of 87.5 mm with ear position at elevation 0° and azimuth 100°.[26] The sphere emulation is a useful test of the spherical array since the analytic solution is known and there is no risk of measurement errors affecting the results.

For 3D emulation, the sphere HRTF was generated by using the axisymmetric expression for the pressure on a sphere due to a source on the z axis at $z=r_s$,[20]

$$\mathrm{HRTF}(r_s,\theta,k) \approx -\frac{r_s}{kR^2}e^{-ikr_s} \times\sum_{n=0}^{N}[2n+1]\frac{h_n(kr_s)}{h_n'(kR)}P_n(\cos\theta). \quad (33)$$

To improve the high frequency behavior of the HRTF and reduce oscillations in the impulse response, the HRTF was calculated over twice the required frequency range. The impulse response was obtained from an inverse FFT and the result was downsampled by 2. The low-frequency response was normalized to one to avoid small variations in dc response due to the downsampling operation. The HRIR data were generated in the same format as the CIPIC data files, for a source distance of $r_s=5$ m, and the same interpolation described above was applied before calculation of the least squares beam formers.

The error for an emulation array of radius $R=87.5$ mm and a radial variation of $0.1R$ (8.75 mm) with $N_c=6$ is shown in Fig. 8 for 40–640 elements. The error is below −25 dB up to the region of the Nyquist frequency of the array. The Nyquist frequencies predicted by Eq. (23) and given in Table II are good predictors of the frequencies above which the error significantly rises. The error also slightly rises at low frequencies. This is believed to be due to the increased low-frequency condition number of the data matrix.

Despite the radial variation in the beam forming array, small spikes in error still occur at frequencies where the zeros of the Bessel functions occur (Table I). Figure 9 shows a closeup of the sphere emulation error on a linear frequency scale for the 640 element spherical array with no variation of radius through to 0.3 times the mean radius. The error peaks for no variation occur at the zeros of the Bessel functions as in Table I. The effect of the variable radius is to reduce the error peaks which occur for the perfectly spherical case and to distribute the error over a wider frequency range.

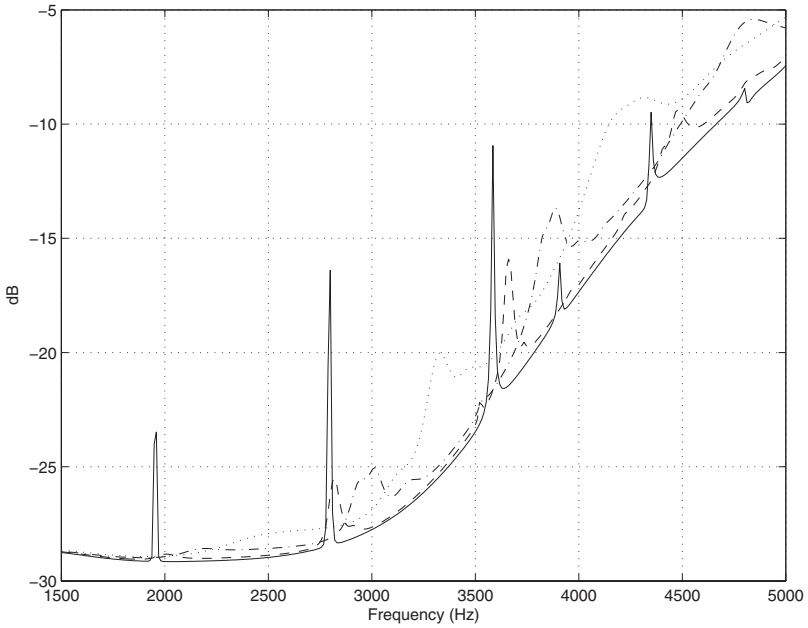

FIG. 9. Error for 3D emulation of solid sphere HRTFs, with ears at $\pm 100°$, for sphere radius $R=87.5$ mm, and radius variations of 0 (solid), $0.1R$ (dashed), $0.2R$ (dash dot), and $0.3R$ (dotted) without coordinate quantization, for $L=80$, 2048 frequency samples and downsampled by 2.

The beam formed HRIRS were calculated in the frequency domain by applying the required spatial delays to each beam former filter and adding them. The original and emulated HRIRs and HRTF magnitudes using a 640 element array are shown in Fig. 10 for 0° elevation and azimuth angles of −80 (nearly on axis to the ear) and in Fig. 11 for +40° azimuth. The emulated responses closely match the band-limited sphere responses in both cases.

The emulation of measured human subjects or manikins is more problematic than that of theoretical models due to the possibility of measurement errors. This is most likely to occur for measured human subjects where the movement of the subject between measurements can lead to inconsistencies in the polar responses. For example, Algazi *et al.* eliminated measurements for which abrupt changes in interaural time differences were apparent.[17] Therefore, before emulating the CIPIC subject data, an analysis was carried out of the consistency of the polar responses, based on the fact that at low frequencies, HRTFs do not rapidly vary with small changes in angle. The (zero-padded) 2048-point FFT of each HRIR was taken to form the set of HRTFs. For eight frequencies ranging from 100 to 250 Hz, the complex polar response at each angle was compared to the eight adjacent values by calculating the mean squared difference and the square root taken to obtain a rms deviation. The mean of these values over the frequency range was then calculated. The ten subjects with the lowest deviations were subjects 3, 9, 27, 48, 51, 58, 153, 154, 155, and 163, with subjects 51 and 154 having the highest rms deviations of 10 (Table III).

It was found that for other subjects with larger measurement variations, the spherical harmonic spectrum [found by

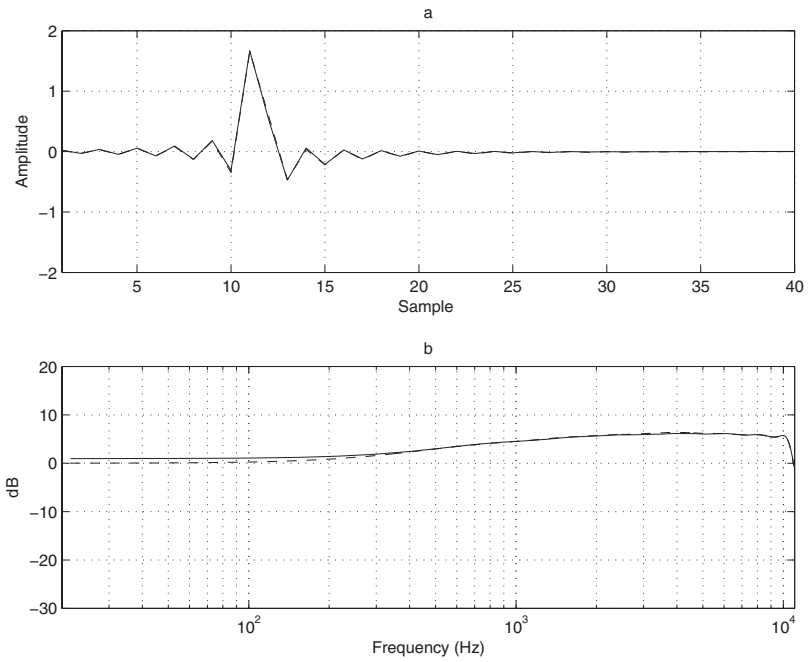

FIG. 10. (a) Original (-) and emulated (--) HRIRs for a solid sphere at elevation 0 and azimuth −80° using an array of 640 elements. (b) Transfer function magnitudes.

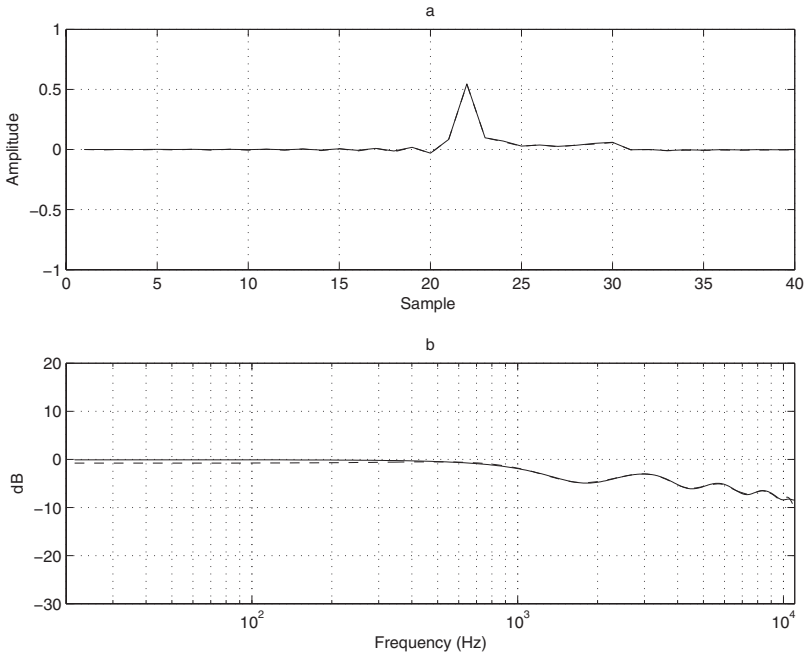

FIG. 11. (a) Original (-) and emulated (--) HRIRs for a solid sphere at elevation 0 and azimuth of +40° using an array of 640 elements. (b) Transfer function magnitudes.

using Eq. (11)] had large high-order terms, and the array was unable to accurately match the polar responses and produced oscillatory lobing due to aliasing effects.

The emulation error for the ten CIPIC subjects using a 640-element array with radius of 87.5 mm and radial variation of 8.75 mm with $N_c=6$ are shown in Fig. 12. The error is similar to that of the sphere at low frequencies, but rises with frequency, whereas the sphere error tends to reduce with frequency up to the Nyquist frequency of the array. At 1 kHz, the error is −28 dB for the sphere but is around -16 ± 5 dB for the CIPIC subjects. The lowest error occurs for subject 3. (Subject 3 does not have the lowest rms deviation in Table III, but this value is only relevant at low frequencies.) The highest error at high frequencies occurs for subjects 51 and 154, which have the highest rms deviation. It is clear that human subjects are harder to emulate than spheres and that the subject movement further affects the accuracy of the emulation.

The synthesized HRIRs and HRTF magnitudes for subject 3 are shown in Figs. 13 and 14 for elevation 0 and for azimuths of −80° and 40°. The emulated responses reproduce the main features of the measured HRTFs, such as the notch at 7 kHz in the −80° response and the notch above 1 kHz in the 40° response.

Figures 15 and 16 show the polar response magnitudes for subject 3 at 2 and 4 kHz. The emulated polar responses are smoothed forms of the measured responses and the match is reasonably accurate, although there is some slight lobing at 4 kHz. The response at 8 kHz is close to the Nyquist frequency and reveals a greater degree of lobing (Fig. 17), but is still a reasonable emulation of the desired response.

Finally, the HRIR and HRTF are shown in Fig. 18 for elevation 0 and azimuth 40° for subject 58, which had the lowest rms variation from Table III but a higher emulation error. The high frequency HRTF is less well matched by the emulation in the region of 6–10 kHz compared to Fig. 14 but is still reasonable.

IV. CONCLUSIONS

This paper has derived methods for the auralization of computer simulations of acoustic environments, with an emphasis on high-accuracy emulations based on numerical solution of the wave equation, which produce the calculated sound pressure on a rectangular grid.

A low-complexity implementation using a line array has been developed for the axisymmetric spherical head which will produce a reasonable binaural impression, particularly below 1 kHz. For full 3D emulation, a spherical array is used for which the required number of elements is a quadratic function of frequency. Accurate full bandwidth emulation is not possible with the angular resolution of the HRTF measurements. Examples have been given by using half the audio sample rate and 640 pressure samples, which is sufficient to convey the majority of subjective cues for the evaluation of room acoustics.

A limitation of the emulated responses is the occurrence of sidelobes that occur at high frequencies for angles where

TABLE III. Mean CIPIC subject rms deviation from nearest neighbor angles from 100 to 250 Hz.

Subject	3	9	27	48	51	58	153	154	155	163
rms deviation	0.041	0.043	0.045	0.039	0.050	0.036	0.040	0.050	0.038	0.047

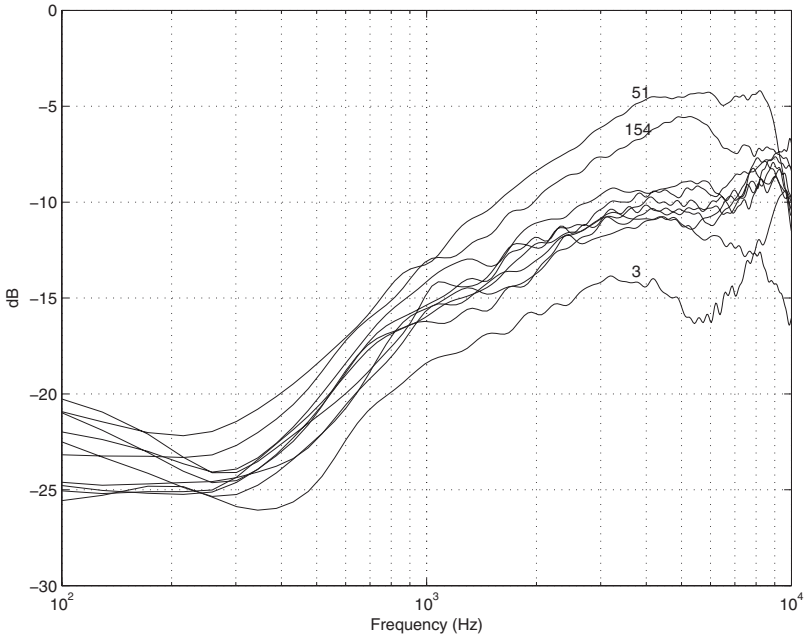

FIG. 12. Emulation errors for CIPIC subjects 3, 9, 27, 48, 51, 58, 153, 154, 155, and 163, with $L=640$ element array.

there are no HRTF measurements. In the CIPIC dataset, these are particularly large for directions below the subject, where no measurements are available, but they also occur at other directions at high frequencies. The sidelobes are reduced by using interpolation of the HRTF data and least squares regularization. For angles below the subject, the emulated HRTF is likely to be different from the actual HRTF, which will, for example, depend on whether the subject is sitting or standing. However, the main reason for the interpolation is to control excessive sidelobes rather than to offer an accurate response at these angles.

A limitation specific to the emulation of human subject HRTFs is that measurement errors due to subject movement or loudspeaker radial variation can produce complex polar responses with sharp transitions, and this causes aliasing effects in the emulated responses. Dummy heads eliminate subject movement but do not allow accurate emulation of all human subjects. Using acoustic reciprocity to measure multiple HRTFs at a time would reduce movement-related errors.[27]

The pressure matching approach allows fixed-subject emulations with high accuracy, and this is the primary aim of the paper. The technique is less well suited to allowing rapid rotation of the listener. However, if a spherical coordinate grid was used in which N uniformly spaced azimuth angles were the same for each elevation angle,[10] then the array could be rotated by discrete angles $2\pi/N$. Alternatively, if the spherical harmonic responses were determined from the measured data, then these could be relatively easily rotated in azimuth. More complicated rotations using spherical harmonic expansions can, in principle, be carried out as discussed Ref. 28.

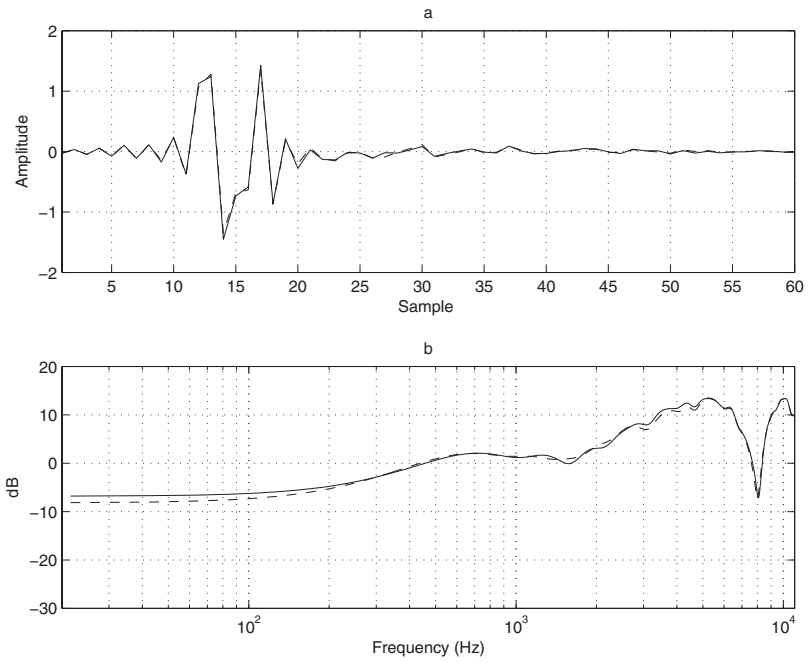

FIG. 13. Original (-) and emulated (--) HRIRs for CIPIC subject 3 at elevation 0 and azimuth of −80° using an array of 640 elements. (b) Transfer function magnitudes.

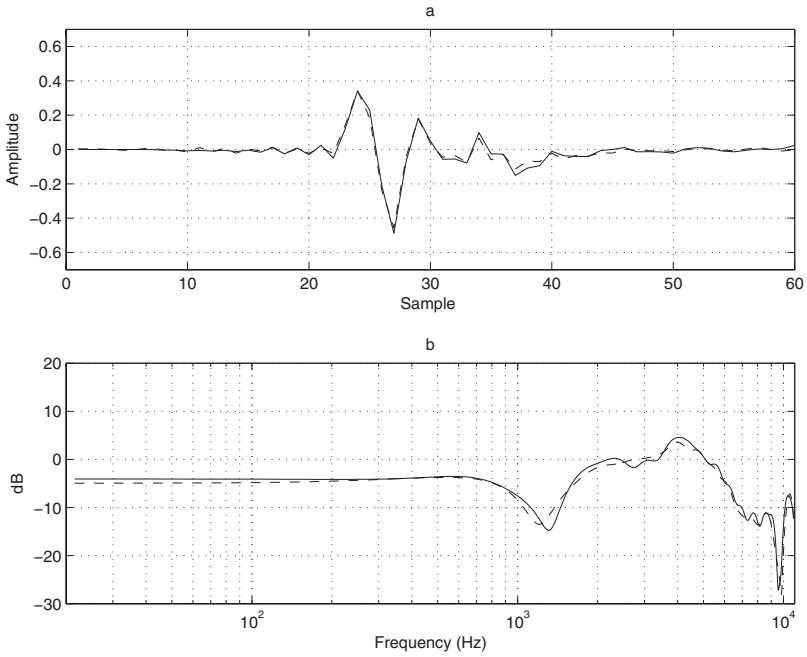

FIG. 14. (a) Original (-) and emulated (--) HRIRs for CIPIC subject 3 at elevation 0 and azimuth of 40° using an array of 640 elements. (b) Transfer function magnitudes.

The presented approach uses a set of HRTFs for plane wave incidence which means that the sound sources, or objects causing scattering, very near to the head would be inaccurately modeled. Such sources or objects would, however, need to be closer than 1 m for this effect to be significant. Also, for reflecting surfaces very close to the head, a real person's head could give rise to reflections that are audible via such close reflecting surfaces. The results in this paper are thus applicable for listener positions sufficiently far from sound sources and reflecting surfaces.

The effectiveness of the beam forming–based binaural synthesis has been evaluated here purely in terms of estimation error, and formal subjective comparisons have not been undertaken. Preliminary subjective evaluations carried out using the beam former filters, by synthesizing the left and right HRIRs for CIPIC measured angles of incidence, convolving these with low-pass filtered white noise signal and comparing with the results by using the CIPIC HRIR, indicated that azimuthal localization is good, but that some slight differences occurred in creating elevation cues for a fixed azimuth. For these "cones of confusion," the HRTFs have minimal variation in interaural time delay and level difference, and localization is governed by subtle pinnae responses and shoulder reflections which will be more susceptible to errors in the beam forming responses. Further work would be required to subjectively quantify these errors.

The auralization of computer models of auditoria by using the approach described here allows efficient subjective assessment of designs before construction but will not allow a detailed examination of angles of arrival, as would be possible by using a plane wave decomposition. However, the technique will allow the generation of binaural subjective

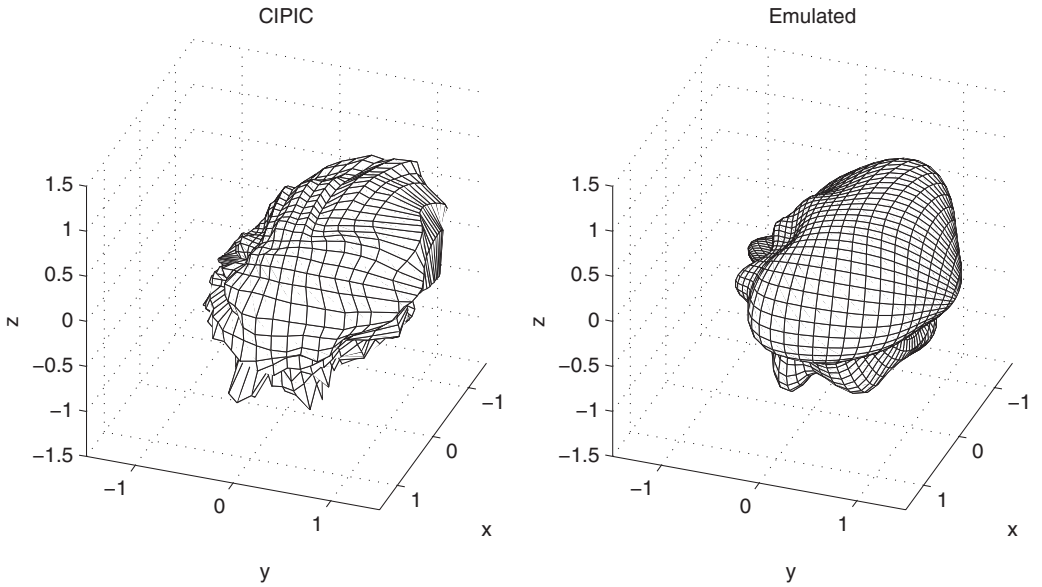

FIG. 15. CIPIC subject 3 polar response at 2 kHz and emulation using 640 element array.

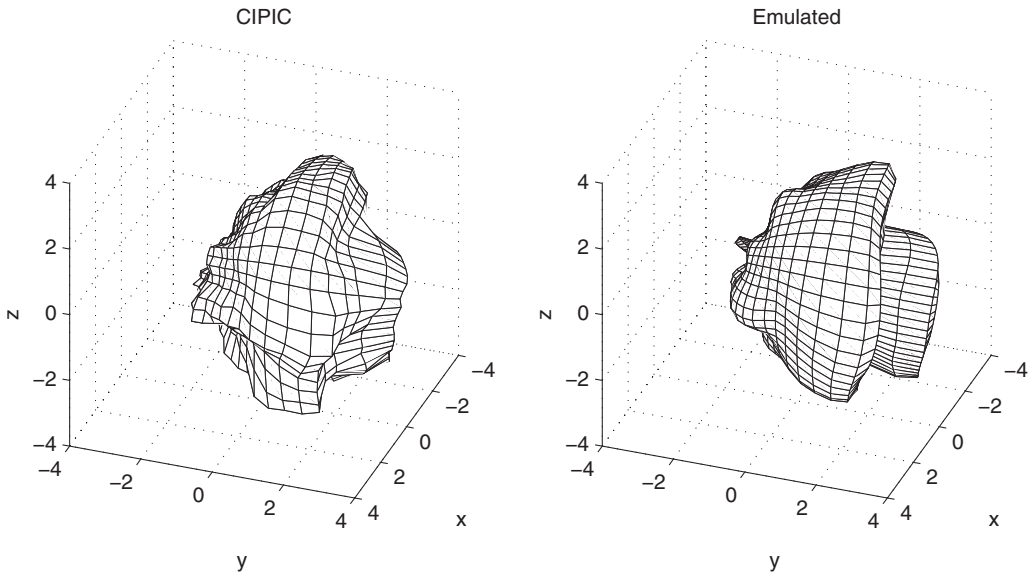

FIG. 16. CIPIC subject 3 polar response at 4 kHz and emulation using 640 element array.

parameters such as the early and late interaural cross correlation functions,[24] which describe apparent source width and envelopment and which will assist in the design process.

APPENDIX: EMULATION OF SPHERE HRTFS USING A CONTINUOUS, INFINITE LINE ARRAY

We require the function $w(z)$ such that the beam former response in Eq. (20) produces the plane wave HRTF in Eq. (19).

Substituting the spherical Bessel expansion for the plane wave

$$e^{-ikz\cos\theta} = \sum_{n=0}^{\infty} (-i)^n (2n+1) j_n(kz) P_n(\cos\theta) \tag{A1}$$

into Eq. (20) and comparing term by term show that we require, for each n,

$$\int_{-\infty}^{\infty} w(z) j_n(kz)\, dz = \frac{i}{(kR)^2} \frac{1}{h_n'(kR)}. \tag{A2}$$

We make use of the orthogonality of the spherical Bessel functions[29]

$$\int_{-\infty}^{\infty} j_n(kz) j_m(kz)\, dz = \begin{cases} 0, & m \neq n \\ \dfrac{\pi}{k(2n+1)}, & m = n \end{cases} \tag{A3}$$

and assume that $w(z)$ has the expansion

$$w(z) = \sum_{n=0}^{\infty} \alpha_n j_n(kz). \tag{A4}$$

Substituting this into Eq. (A2) and using Eq. (A3) yield the coefficients

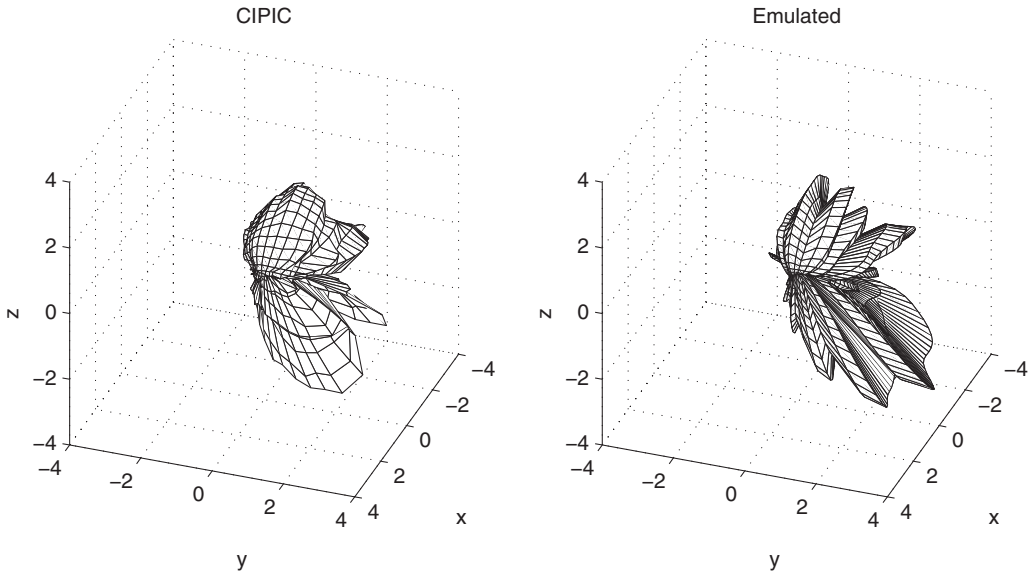

FIG. 17. CIPIC subject 3 polar response at 8 kHz and emulation using 640 element array.

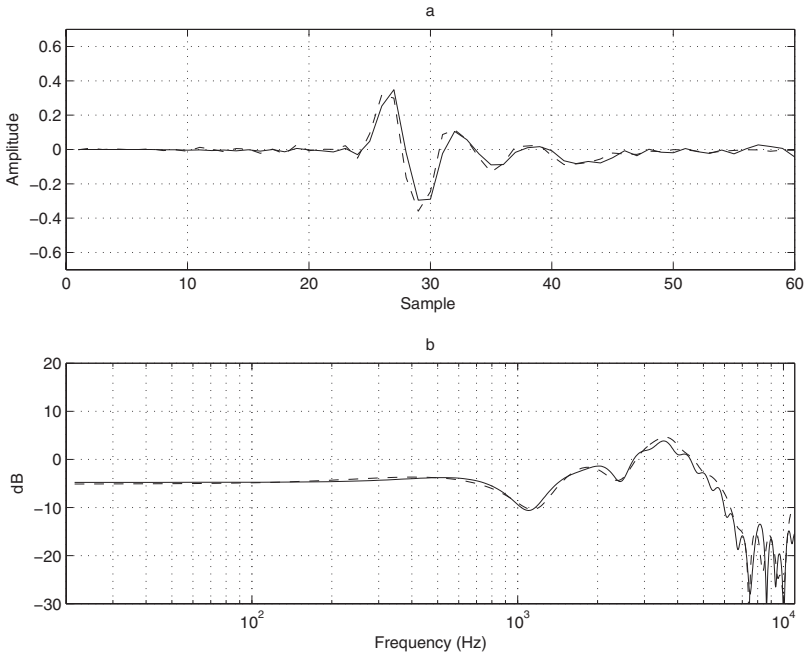

FIG. 18. (a) Original (-) and emulated (--) HRIRs for CIPIC subject 58 at elevation 0 and azimuth of 40° using an array of 640 elements. (b) Transfer function magnitude.

$$\alpha_n = \frac{i(2n+1)}{\pi k R^2} \frac{1}{h_n'(kR)}, \tag{A5}$$

yielding Eq. (21).

[1]D. Botteldooren, "Finite-difference time-domain simulation of low-frequency room acoustic problems," J. Acoust. Soc. Am. **98**, 3302–3308 (1995).
[2]J. LoVetri, D. Mardare, and G. Soulodre, "Modeling of the seat dip effect using the finite-difference time-domain method," J. Acoust. Soc. Am. **100**, 2204–2212 (1996).
[3]L. Savioja and V. Välimäki, "Interpolated 3-D digital waveguide mesh with frequency warping," in Proceedings of the IEEE International Conference on Acoustics Speech, Signal Processing (ICASSP'01), 2001, pp. 3345–3348.
[4]E. Granier, M. Kleiner, B.-I. Dalenbäck, and P. Svensson, "Experimental auralization of car audio installations," J. Audio Eng. Soc. **44**, 835–849 (1996).
[5]B. Støfringsdal and U. P. Svensson, "Conversion of discretely sampled sound field data to auralization formats," J. Audio Eng. Soc. **54**, 380–400 (2006).
[6]T. D. Abhayapala and D. B. Ward, "Theory and design of high order sound field microphones using spherical microphone array," IEEE International Conference on Acoustics, Speech, and Signal Processing, 2002, Vol. 2, pp. 1949–1952.
[7]B. N. Gover, J. G. Ryan, and M. R. Stinson, "Microphone array measurement system for analysis of directional and spatial variations of sound fields," J. Acoust. Soc. Am. **112**, 1980–1991 (2002).
[8]M. A. Poletti, "Three dimensional surround sound systems based on spherical harmonics," J. Audio Eng. Soc. **53**, 1004–1025 (2005).
[9]R. Duraiswami, D. N. Zotkin, Z. Li, E. Grassi, N. A. Gumerov, and L. S. Davis, "High order spatial audio capture and its binaural head-tracked playback over headphones with HRTF cues," 119th AES Convention, 7–10 October 2005, New York.
[10]M. Evans, J. Angus, and A. Tew, "Analyzing head-related transfer function measurements using surface spherical harmonics," J. Acoust. Soc. Am. **104**, 2400–2411 (1998).
[11]M. Bai and K. Ou, "Head-related transfer function(HRTF) synthesis based on a three-dimensional array model and singular value decomposition," J. Sound Vib. **281**, 1093–1115 (2005).
[12]M. Bai and C. Lin, "Microphone array signal processing with application in three-dimensional spatial hearing," J. Acoust. Soc. Am. **117**, 2112–2121 (2005).
[13]J. Chen, B. Van Veen, and K. Hecox, "External ear transfer function modeling: A beamforming approach," J. Acoust. Soc. Am. **92**, 1933–1944 (1992).
[14]V. R. Algazi, C. Avendano, and R. O. Duda, "Elevation localization and head-related transfer function analysis at low frequencies," J. Acoust. Soc. Am. **109**, 1110–11122 (2001).
[15]P. M. Morse and K. U. Ingard, *Theoretical Acoustics* (McGraw-Hill, New York, 1968).
[16]http://interface.cipic.ucdavis.edu/CIL_html/CI_HRTF_database.htm, last accessed 19th June 2007, Copyright (c) 2001 The Regents of the University of California. All Rights Reserved.
[17]V. R. Algazi, R. O. Duda, D. M. Thompson, and C. Avendano, "The CIPIC HRTF Database," Proceedings of the 2001 IEEE Workshop on Applications of Signal Processing to Audio and Acoustics, Mohonk Mountain House, New Paltz, New York, 21–24 October 2001, pp. 91–102.
[18]C. W. Therrien, *Discrete Random Signals and Statistical Signal Processing*, Signal Processing Series (Prentice Hall, Englewood Cliffs, NJ, 1992).
[19]E. G. Williams, *Fourier Acoustics* (Academic, New York, 1999).
[20]R. O. Duda and W. Martens, "Range dependence of the response of a spherical head model," J. Acoust. Soc. Am. **104**, 3048–3058 (1998).
[21]G. F. Kuhn, "Model for the interaural time differences in the azimuthal plane," J. Acoust. Soc. Am. **62**, 157–167 (1977).
[22]J. Vanderkooy, "The acoustic center: A new concept for loudspeakers at low frequencies," 121st AES Convention, 5–8 October 2006, San Francisco, CA, USA.
[23]R. Kennedy, P. Sadeghi, T. D. Abhayapala, and H. Jones, "Intrinsic limits of dimensionality and richness in random multipath fields," IEEE Trans. Signal Process. **55**, 2542–2556 (2007).
[24]L. Beranek, *Concert and Opera Halls, How They Sound* (American Institute of Physics, New York, 1996) [an updated version of *Music, Acoustics and Architecture* (Wiley, New York, 1962)].
[25]E. A. Rakhmanov, E. B. Saff, and Y. M. Zhou, "Minimal discrete energy on the sphere," Math. Res. Lett. **1**, 647–662 (1994).
[26]C. P. Brown and R. O. Duda, "A structural model for binaural sound synthesis," IEEE Trans. Speech Audio Process. **6**, 476–488 (1998).
[27]D. N. Zotkin, R. Duraiswami, E. Grassi, and N. A. Gumerov, "Fast head-related transfer function measurement via reciprocity," J. Acoust. Soc. Am. **120**, 2202–2215 (2006).
[28]N. A. Gumerov and R. Duraiswami, *Fast Multipole Methods for the Helmholtz Equations in Three Dimensions*, Elsevier Series in Electromagnetism (Elsevier, Amsterdam, 2004).
[29]H.-P. Chang, T. K. Sarkar, and O. M. C. Pereira-Filho, "Antenna Pattern Synthesis Utilizing Spherical Bessel Functions," IEEE Trans. Antennas Propag. **48**, 853–859 (2000).

Perceptually motivated wavelet packet transform for bioacoustic signal enhancement

Yao Ren,[a] Michael T. Johnson, and Jidong Tao
Speech and Signal Processing Laboratory, Marquette University, P.O. Box 1881, Milwaukee, Wisconsin 53233-1881

(Received 14 December 2007; revised 18 April 2008; accepted 25 April 2008)

A significant and often unavoidable problem in bioacoustic signal processing is the presence of background noise due to an adverse recording environment. This paper proposes a new bioacoustic signal enhancement technique which can be used on a wide range of species. The technique is based on a perceptually scaled wavelet packet decomposition using a species-specific Greenwood scale function. Spectral estimation techniques, similar to those used for human speech enhancement, are used for estimation of clean signal wavelet coefficients under an additive noise model. The new approach is compared to several other techniques, including basic bandpass filtering as well as classical speech enhancement methods such as spectral subtraction, Wiener filtering, and Ephraim–Malah filtering. Vocalizations recorded from several species are used for evaluation, including the ortolan bunting (*Emberiza hortulana*), rhesus monkey (*Macaca mulatta*), and humpback whale (*Megaptera novaeanglia*), with both additive white Gaussian noise and environment recording noise added across a range of signal-to-noise ratios (SNRs). Results, measured by both SNR and segmental SNR of the enhanced wave forms, indicate that the proposed method outperforms other approaches for a wide range of noise conditions.
 [DOI: 10.1121/1.2932070]

PACS number(s): 43.60.Hj, 43.50.Rq, 43.80.Nd [WWA] Pages: 316–327

I. INTRODUCTION

The presence of background noise and interfering signals is a fundamental problem in the collection and analysis of bioacoustic data, regardless of the specific species under study or the type of environment. This noise takes a variety of forms, including ambient background noise due to weather conditions, continuous interference from nearby vehicular or boat traffic, or the presence of numerous nontarget vocalizations from other species and individuals. Since the distance from the acoustic recording device to the individuals under study can be quite large leading to significant signal attenuation, interfering noise can create a substantial obstacle to analysis and understanding of the desired vocalization patterns.

Common techniques to reduce noise artifacts in bioacoustic signals include basic bandpass filters and related frequency-based methods for spectrogram filtering and equalization, often incorporated directly into acquisition and analysis tools (Mellinger, 2002). Other approaches in recent years have included spectral subtraction (Liu *et al.*, 2003), minimum mean-squared error (MMSE) estimation (Álvarez and García, 2004), adaptive line enhancement (Yan *et al.*, 2005; Yan *et al.*, 2006), and denoising using wavelets (Gur and Niezrecki, 2007).

In comparison, there are a wide variety of advanced techniques used for human speech enhancement, some of which form the basis for the more recent bioacoustic enhancement methods cited above. Historically the most common approaches for speech enhancement have focused on spectral subtraction (Boll, 1979), Wiener filtering (Lim and Oppenheim, 1978), and MMSE and log-MMSE estimations using Ephraim–Malah (EM) filtering (Ephraim and Malah, 1984; 1985). Added to this in recent years are newer methods based on subspace estimation and filtering (Ephraim and Trees, 1995) and wavelet decomposition (Johnson *et al.*, 2007).

In this paper, we introduce a new bioacoustic signal enhancement technique which is based on a perceptually scaled wavelet packet decomposition, using spectral estimation methods similar to those used for human speech enhancement. The underlying goal is to obtain higher quality and more intelligible enhanced signals through the use of more perceptually meaningful frequency representations. This method is robust across a wide range of species, needing only $f_{\min}$ and $f_{\max}$ frequency boundary parameters to generalize for application to a new species of interest.

The new method is compared to a variety of other enhancement and denoising techniques, including simple bandpass filtering, spectral subtraction, Wiener filtering, and the EM log-MMSE estimation. To evaluate and compare its applicability across a variety of species, the method is applied to the animals of the order Passeriformes (ortolan bunting), Primates (rhesus monkey), and Cetaceans (humpback whale). Evaluation is done by using both signal-to-noise ratio (SNR) and segmental SNR (SSNR), which is known to be a more perceptually relevant quality measure for human speech (Deller *et al.*, 2000).

[a]Electronic mail: yao.ren@marquette.edu

II. CURRENT ENHANCEMENT METHODS

A. Bandpass filtering

Bandpass filtering removes signal energy outside of a specified frequency range. This can be applied in either the time domain or the frequency domain (e.g., applied to a spectrogram) and is effective primarily in cases where signals are predominately narrow band and are well separated from the noise spectrum.

B. Spectral subtraction

Spectral subtraction (Boll, 1979) was one of the first algorithms applied to the problem of speech enhancement. It is based directly on the additive noise model:

$$y(n) = x(n) + d(n), \tag{1}$$

where $y(n)$, $x(n)$, and $d(n)$ denote the noise-corrupted input signal, clean signal, and additive noise signal, respectively. The noise spectrum is estimated from the Fourier transform magnitude of a silence region in the wave form, so that for each frame of the signal, an estimate for the clean signal in the frequency domain can be given directly as

$$\hat{X}(\omega) = [|Y(\omega)| - |\hat{D}(\omega)|]e^{j\phi_y(\omega)}, \tag{2}$$

where $\phi_y(\omega)$ is the phase component of the noisy signal, used under the assumption that the spectral phase is much less important than the spectral magnitude for reconstruction.

Note that application of Eq. (2) may result in negative magnitude values, which are typically set to zero. This often results in some processing artifacts that are usually described by listeners as "musical tones." The presence of such artifacts is one disadvantage of the spectral subtraction approach.

C. Wiener filtering

Wiener filtering is conceptually similar to spectral subtraction but replaces the direct subtraction with a mathematically optimal estimate for the signal spectrum in a MMSE sense (Lim and Oppenheim, 1978).

The frequency domain formulation of the Wiener filter is given as

$$H(\omega) = \frac{S_{xx}(\omega)}{S_{xx}(\omega) + S_{dd}(\omega)}, \tag{3}$$

where $H(\omega)$ is the desired filter response and $S_{xx}(\omega)$ and $S_{dd}(\omega)$ are power spectral densities (PSDs) of the desired clean signal and noise. Since these two PSDs are unknown, this filter cannot be determined directly and instead needs to be realized in an iterative fashion. In particular, $S_{dd}(\omega)$ is estimated from a silence region and $S_{xx}(\omega)$ is initialized from the noisy wave form and then updated from the output of the filter after each iteration. This process is repeated either a fixed number of times or until a convergence criterion is reached.

D. Ephraim–Malah filtering

The Wiener filter is an optimal linear estimator of the clean signal spectrum in a MMSE sense. Ephraim and Malah extended this idea by deriving an optimal nonlinear estimator of the clean spectral amplitude. This estimator assumes that the real and imaginary parts of the spectral magnitude have a zero-mean Gaussian probability density distribution and are statistically independent. Under this statistical model, a short time spectral amplitude estimator was derived by using the MMSE optimization criteria (Ephraim and Malah, 1984). This work was then modified to use log spectral amplitude (LSA) rather than spectra as an optimization criterion (Ephraim and Malah, 1985) since the log spectral distance is a more perceptually relevant distortion criteria, resulting in improved overall enhancement results. This estimator, known as the EM filter, can be summarized by using the following estimation formula for the clean signal Fourier transform coefficient $\hat{A}_k$ in each frequency bin:

$$\hat{A}_k = \frac{\xi_k}{1+\xi_k} e^{(1/2)\int_{\upsilon_k}^{\infty}(e^{-t}/t)dt} R_k, \tag{4}$$

In this equation, $\xi_k = \lambda_x(k)/\lambda_d(k)$, $\upsilon_k = [\xi_k/(1+\xi_k)]\gamma_k$, and $\gamma_k = R_k^2/\lambda_d(k)$, where R_k is the noisy speech Fourier transform magnitude in the kth frequency bin, and $\lambda_d(k)$ and $\lambda_x(k)$ are the average noise and signal powers in each bin. Similar to the spectral subtraction method, the noise power is estimated from silence regions in the wave form, while $\lambda_x(k)$ is a moving average of spectrally subtracted noisy spectra $[R_k^2 - \lambda_d(k)]$. The *a priori* SNR ξ_k is estimated via the EM well-known "decision-directed method," which is updated from the previous amplitude estimate using a forgetting factor α as follows:

$$\hat{\xi}_k(n) = \alpha \frac{\hat{A}_k^2(n-1)}{\lambda_d(k,n-1)} + (1-\alpha)P[\gamma_k(n)-1], \tag{5}$$

where the indicator function P is given by

$$P[\gamma_k(n)-1] \triangleq \begin{cases} \gamma_k(n)-1, & \gamma_k(n)-1 \geqslant 0 \\ 0 \text{ otherwise}. \end{cases} \tag{6}$$

The key characteristics of this estimator are that it tends to do less enhancement (i.e., less change to the noisy signal spectrum) when the SNR is high, and that musical noise artifacts are significantly reduced.

E. Wavelet denoising

Spectral subtraction, Wiener filtering, and EM filtering are all based on the same mathematical tool, the short time Fourier transform (STFT), with the waveform divided into short frames during which the signal is assumed to be stationary. The STFT is a compromise between time resolution and frequency resolution: a shorter frame length results in a better time resolution but poorer frequency resolution. The wavelet transform (WT) by comparison has the advantage of implicitly using a variable window size for different frequency components. This often results in better handling of broadband nonstationary signals, including speech and bioacoustic data.

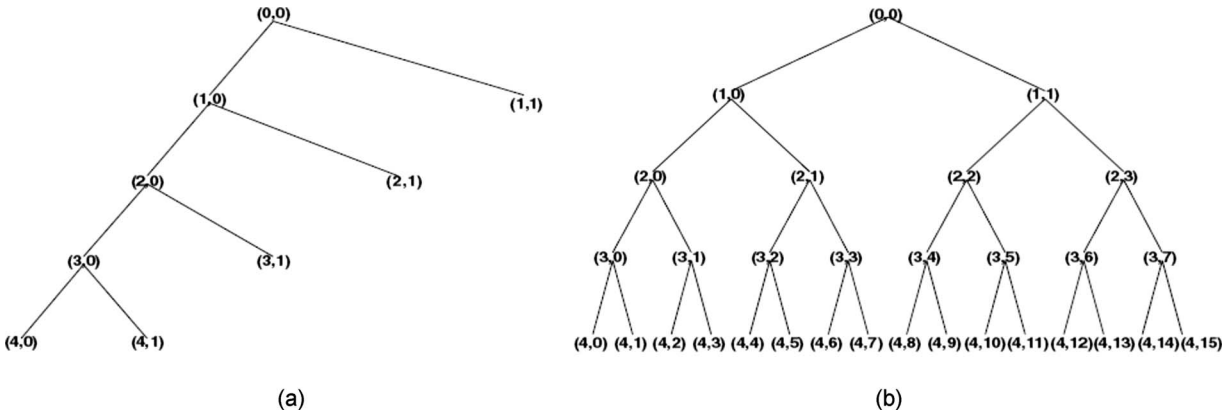

FIG. 1. (a) Discrete WT. (b) Wavelet packet decomposition tree.

Whereas the STFT is a function of frequency for each individual signal frame, the WT is a function of two variables, time and scale. Scale is used rather than frequency because depending on the wavelet basis being used, each scale may actually represent information across a range of frequencies. Like the Fourier transform, the WT has both continuous WT and discrete WT (DWT) implementations. A DWT can be efficiently implemented by using a quadrature mirror filter decomposition, resulting in scales that are powers of 2, called a dyadic transform. A further generalization of the DWT is the wavelet packet transform (WPT). In the WPT, the filtering process is iterated on both the low frequency and high frequency components, whereas the DWT iterates only on the low frequency components. Filter decomposition structures for the DWT and WPT are shown in Fig. 1. In the decomposition tree, each node is labeled (l,n), where l is the decomposition level and n represents a subband node index. The root of the tree, $(l,n)=(0,0)$, refers to the entire signal space. The left and right branches denote low-pass and high-pass filterings followed by 2:1 downsampling, respectively.

The application of wavelets for signal enhancement, sometimes referred to as denoising, is a three step procedure involving wavelet decomposition, wavelet coefficient thresholding, and wavelet reconstruction. Given an appropriate choice of the wavelet basis function, the signal energy will be concentrated in a small number of relatively large coefficients while ambient noise will be spread out, allowing coefficients to be thresholded.

Threshold selection and implementation are two factors which significantly impact wavelet denoising methods. Common methods include hard, soft, and nonlinear thresholding approaches. Hard thresholding sets all coefficient values beneath the threshold to zero, leaving the others unchanged (Jansen, 2001); soft thresholding additionally reduces all coefficient values to maintain continuity; while nonlinear thresholding typically enforces a smoothness constraint on the coefficient mapping function as well. Typical threshold selection methods include universal thresholding and the Stein unbiased risk estimator (Donoho, 1995), both implemented by using soft thresholding.

Recently, the EM suppression rule (Ephraim and Malah, 1984) for speech enhancement has been applied to the wavelet domain as a more advanced time-varying thresholding approach (Cohen, 2001). This method helps reduce the "musical noise" artifacts caused by uniformly applied thresholds.

III. PROPOSED METHOD

The method introduced here is based on a modified wavelet packet decomposition using a MMSE coefficient estimation for thresholding. The key element of the technique is the use of the Greenwood warping function to determine the WPT decomposition structure based on a perceptually motivated frequency axis.

Greenwood (1961) has shown that many land and aquatic mammals perceived frequency on a logarithmic scale along the cochlea, which corresponds to a nonuniform frequency resolution. This relationship can be modeled by the equation

$$A(10^{\alpha x}-k), \tag{7}$$

where α, A, and k are species-specific constants and x is the cochlea position. Transformation between true frequency f and perceived frequency f_p can be obtained through the following equation pair:

$$F_p(f)=(1/\alpha)\log_{10}(f/A+k), \tag{8}$$

$$F_p^{-1}(f_p)=A(10^{\alpha f_p}-k). \tag{9}$$

The constants α, A, and k can be found if frequency-cochlear position data are available. However, since cochlear information has never been measured for many species, an approximate solution is needed. Lepage (2003) has shown that k can be estimated as 0.88 based on both theoretical justification and experimental data acquired on a number of mammalian species. By assuming this value for k, α and A can be solved for a given approximate hearing range, $f_{\min}$–$f_{\max}$, of the species (Clemins, 2005; Clemins and Johnson, 2006; Clemins *et al.*, 2006):

$$A=\frac{f_{\min}}{1-k}, \tag{10}$$

$$\alpha=\log_{10}\left(\frac{f_{\max}}{A}+k\right). \tag{11}$$

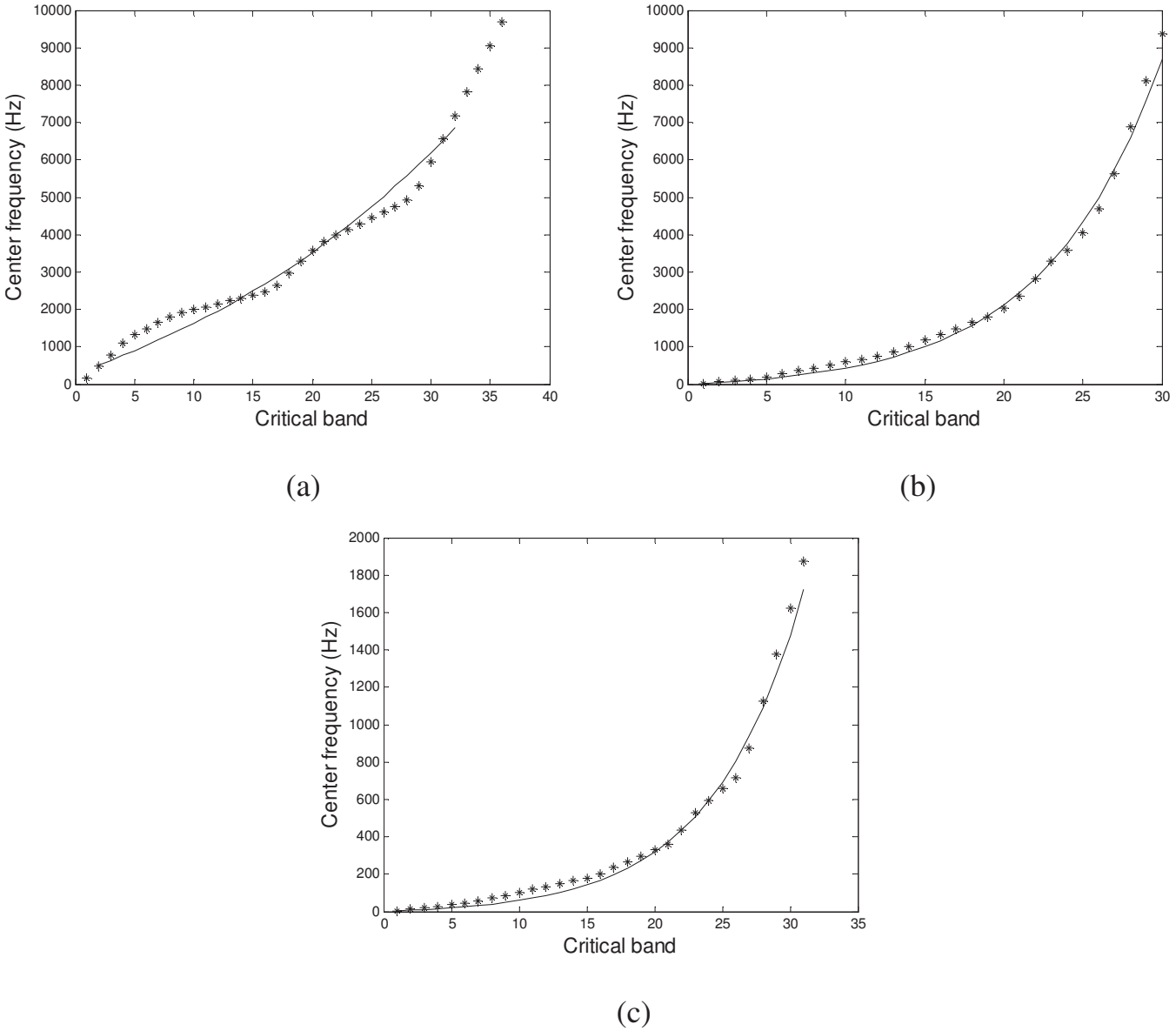

FIG. 2. Center frequencies of the Greenwood scale (solid line) and WPD critical bands. (a) Ortolan bunting. (b) Rhesus monkey. (c) Humpback whale.

Thus, a frequency warping function can be constructed by using the species-specific values of $f_{\min}$ and $f_{\max}$.

A perceptually motivated WT can be designed to mimic the auditory frequency scale by using decomposition critical bands. This implementation was originally proposed by Black for coding (Black and Zeytinoglu, 1995) and has been widely used for perceptual speech enhancement (Cohen, 2001; Fu and Wan, 2003; Shao and Chang, 2006). To generalize this technique to bioacoustic signal enhancement, we propose to decompose a wavelet packet tree into the critical bands with respect to the species-specific Greenwood frequency warping curve.

Figure 2 shows an approximation of the Greenwood scale by critical-band WPD for three distinct species: ortolan bunting (*Emberiza hortulana*) downsampled to 20 kHz, rhesus monkey (*Macaca mulatta*) downsampled to 20 kHz, and the humpback whale (*Megaptera novaeanglia*) sampled at 4 kHz. The corresponding decomposition trees are illustrated in Fig. 3. The perceptual WPD splits the frequency range corresponding to different species data into critical bands: ortolan bunting, 0 Hz–10 kHz, 36 critical bands; rhesus monkey, 0 Hz–10 kHz, 30 critical bands; humpback whale, 0 Hz–2 kHz, 31 critical bands. The bands are established automatically by optimally matching the subband center frequencies to the perceptual scale curve in the mean error sense. For the Greenwood scale calculation, the $f_{\min}$ and $f_{\max}$ used in Eqs. (10) and (11) are 400 and 7200 Hz for the ortolan bunting (Edward, 1943), 20 and 42 000 Hz for the rhesus monkey (Heffner, 2004), and 2 and 6000 Hz for the humpback whale (Helweg, 2000).

Given this perceptual decomposition structure, a MMSE estimator for performing thresholding can be derived in the wavelet domain (Cohen, 2001; Cohen and Berdugo, 2001). Using an additive time-domain model, the resulting wavelet domain model is

$$Y_{l,n}(k) = X_{l,n}(k) + D_{l,n}(k), \tag{12}$$

where $Y_{l,n}=\langle y, \varphi_{l,n,k}\rangle$, $X_{l,n}(k)=\langle x, \varphi_{l,n,k}\rangle$, $D_{l,n}(k)=\langle d, \varphi_{l,n,k}\rangle$, k is the index of the coefficients in each subband, l is the

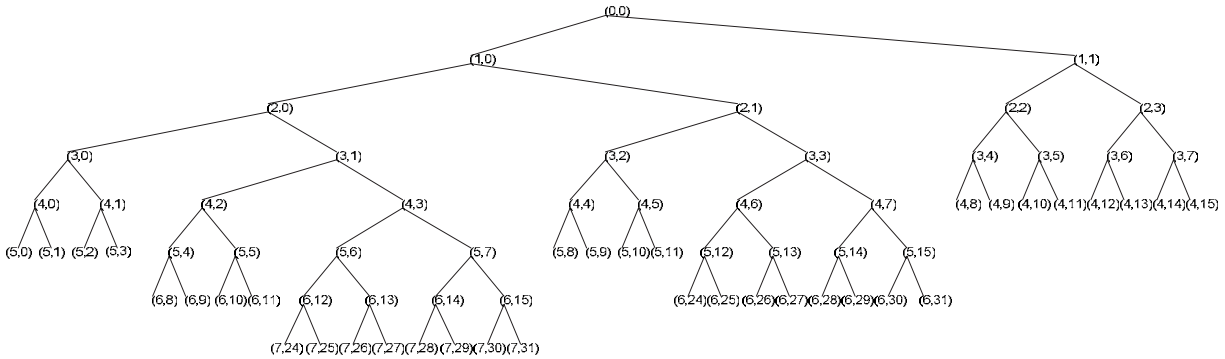

(a)

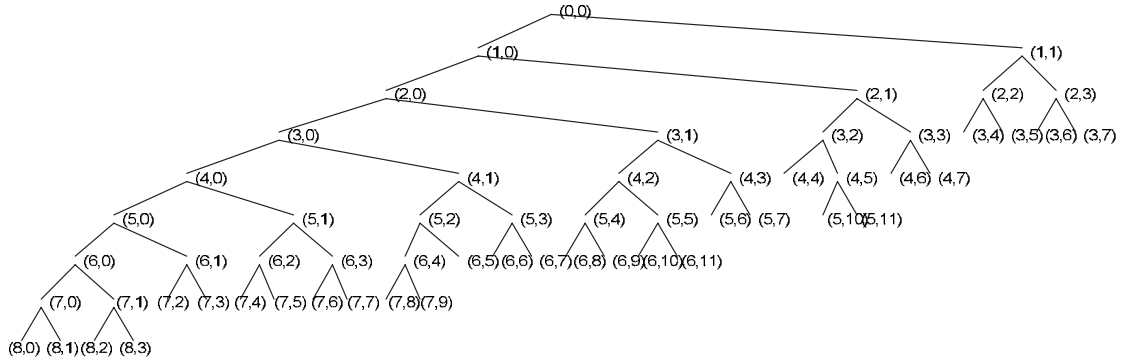

(b)

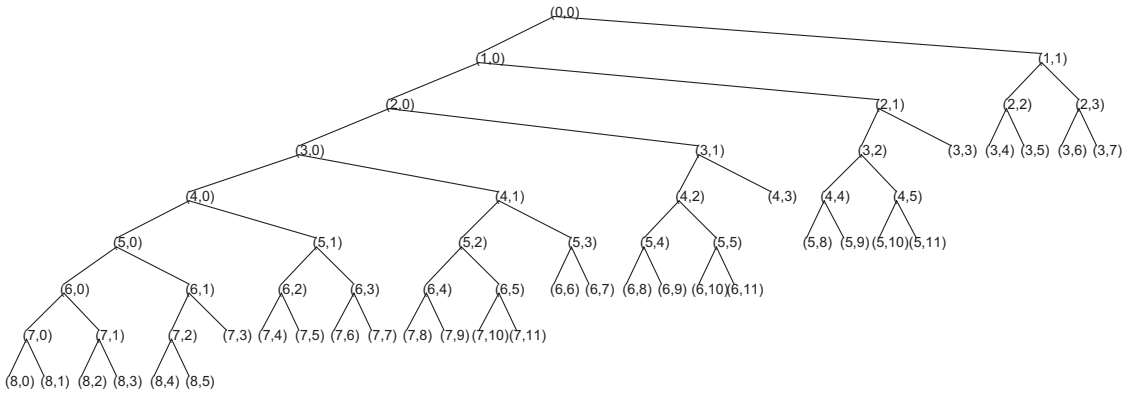

(c)

FIG. 3. Perceptual wavelet decomposition tree. (a) Ortolan bunting. (b) Rhesus monkey. (c) Humpback whale.

decomposition level, n is the node index, and $\varphi_{l,n,k}$ is the scaled and shifted mother wavelet. The notation $\langle x, \varphi \rangle$ represents the WT of signal x by using φ as the mother wavelet.

The optimally modified LSA estimator (Cohen and Berdugo, 2001) is used to perform wavelet denoising. Under this approach, the clean speech wavelet packet coefficients are estimated by using a MMSE criterion under the assumptions that both speech and noise are complex Gaussian variables. Speech presence uncertainty is also incorporated by using the hypothesis testing framework given by

$$H_0 = D_{l,n}(k), \tag{13}$$

$$H_1 = X_{l,n}(k) + D_{l,n}(k). \tag{14}$$

Under this framework, a parameter of signal presence uncertainty is calculated through the equation (Cohen and Berdugo, 2001)

$$p_{l,n}(k) = \left\{ 1 + \frac{1 + \xi_{l,n}(k)}{q_{l,n}^{-1}(k) - 1} \exp[-\upsilon_{l,n}(k)/2] \right\}^{-1}, \tag{15}$$

where $\xi_{l,n}(k)$ is the *a priori* SNR, $\upsilon_{l,n}(k)$ is from Eq. (4), and $q_{l,n}(k)$ is the *a priori* probability for signal absence, which is estimated by

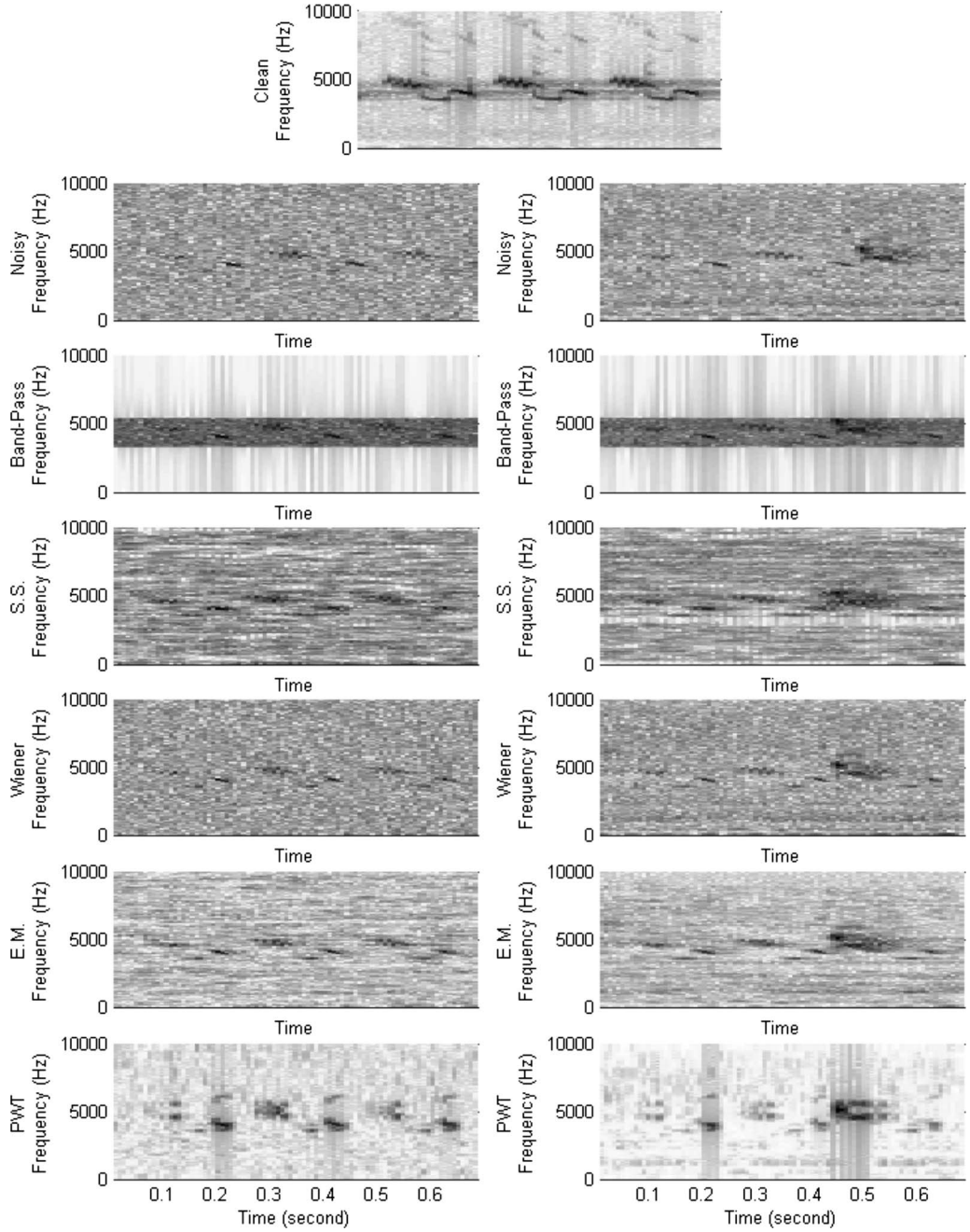

FIG. 4. Spectrograms of ortolan bunting signals: Clean signal, −10 dB SNR noisy signals, and signals enhanced by bandpass filtering, spectral subtraction, Wiener filtering, EM log-MMSE filtering, and perceptual WPT filtering (the left column is for white noise and the right is for environment noise).

$$\hat{q}_{l,n}(k) = 1 - \begin{cases} \dfrac{\log[\xi_{l,n}(k)/\xi_{\min}]}{\log(\xi_{\max}/\xi_{\min})} & \text{if } \xi_{\min} \leqslant \xi_{l,n}(k) \leqslant \xi_{\max} \\ 0 \text{ if } \xi_{l,n}(k) \leqslant \xi_{\min} \\ 1 \text{ otherwise,} \end{cases} \tag{16}$$

where $\xi_{\min}$ and $\xi_{\max}$ are empirical constants, $\xi_{\min}=-10$ dB, and $\xi_{\max}=-5$ dB.

An estimate for the clean speech, which minimizes the mean-square error, results in

$$\hat{X}_{l,n}(k) = \frac{\lambda_{l,n}(k)p_{l,n}(k)}{\lambda_{l,n}(k) + \sigma_{l,n}^2(k)} Y_{l,n}(k), \tag{17}$$

where the signal variance is given by using the decision-directed method of Ephraim and Malah:

$$\hat{\lambda}_{l,n}(k) = \alpha|\hat{X}_{l,n}(k-1)| + (1-\alpha)\max[|Y_{l,n}(k)| - \sigma_{l,n}(k), 0]. \tag{18}$$

IV. EXPERIMENTAL SETUP AND RESULTS

The proposed method and comparative baseline approaches were applied to ortolan bunting (*Emberiza hortu-*

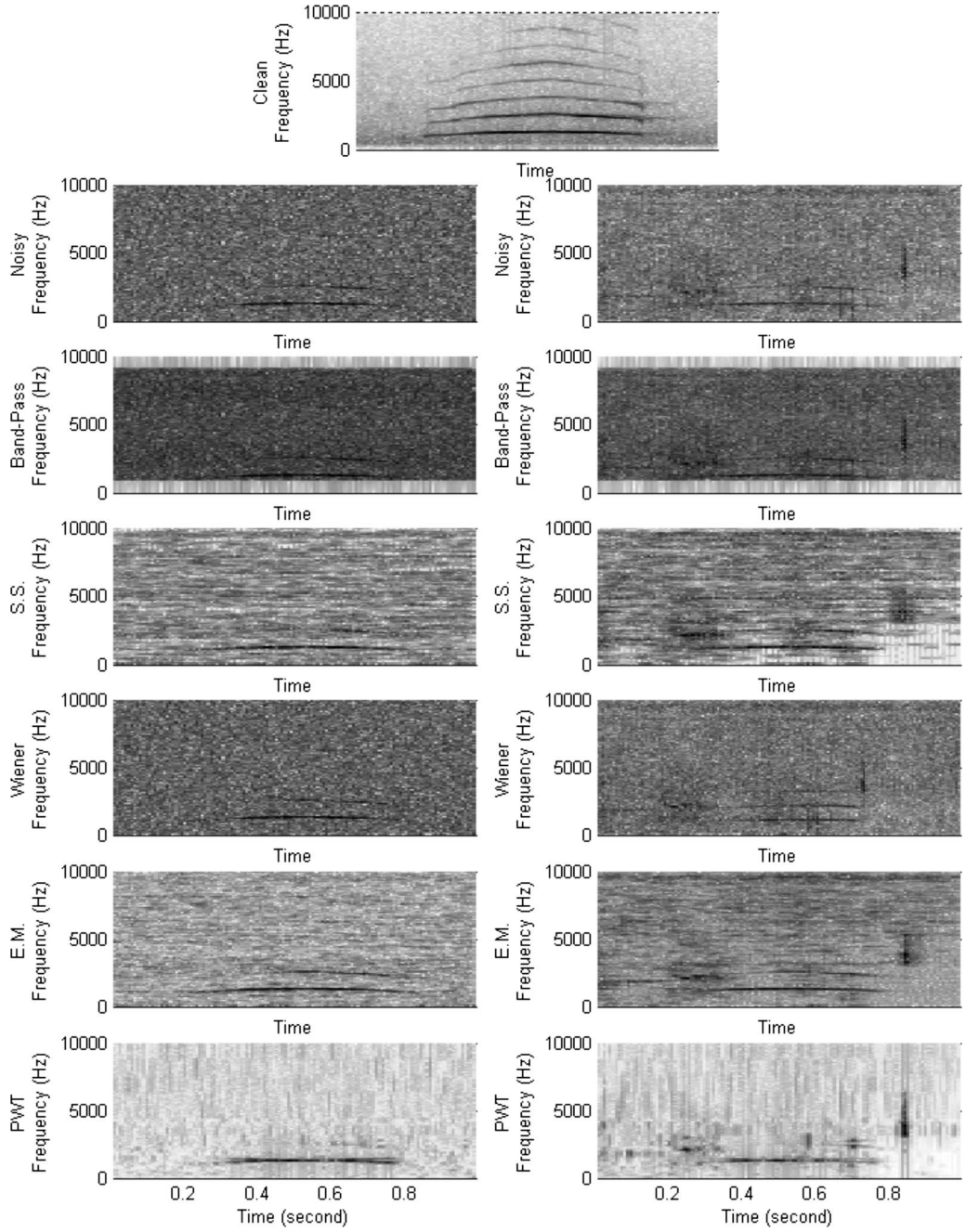

FIG. 5. Spectrograms of rhesus monkey signals: Clean signal, −10 dB SNR noisy signals, and signals enhanced by bandpass filtering, spectral subtraction, Wiener filtering, EM log-MMSE filtering, and perceptual WPT filtering (the left column is for white noise and the right is for environment noise).

lana), rhesus monkey (*Macaca mulatta*) and humpback whale (*Megaptera novaeanglia*). Norwegian ortolan bunting vocalization data were collected from County Hedmark, Norway in May of 2001 and 2002 (Osiejuk *et al.*, 2003). Rhesus data were recorded on the island of Cayo Santiago, Puerto Rico by Joseph Solitis and John D. Newman (Li *et al.*, 2007). Humpback whale data (Payne and McVay, 1971) was provided by MobySound (Mellinger and Clark, 2006), a database for research in automatic recognition of marine animal calls. These data were collected in March 1994 off the north coast of the island of Kauai, HI. Ten clean vocalizations from each species were segmented from the original recording data.

Both white noise and true environment noise were added to the clean data at SNR levels of −15, −10, −5, 0, +5, and +10 dB. The environment noise came from ambient noise regions of appropriate domain recordings for each species, spectrally flattened with a low order filter to preserve the basic noise characteristics while ensuring that the energy is spread through the entire frequency band. For the rhesus monkey vocalizations, background noise was taken from a Vervet monkey data set (Seyfarth and Cheney, 2004). For the ortolan bunting vocalizations, background noise came directly from the data set. For the humpback whale, marine noise was taken from a Beluga whale vocalization data set (Scheifele *et al.*, 2005), downsampled to 4000 Hz.

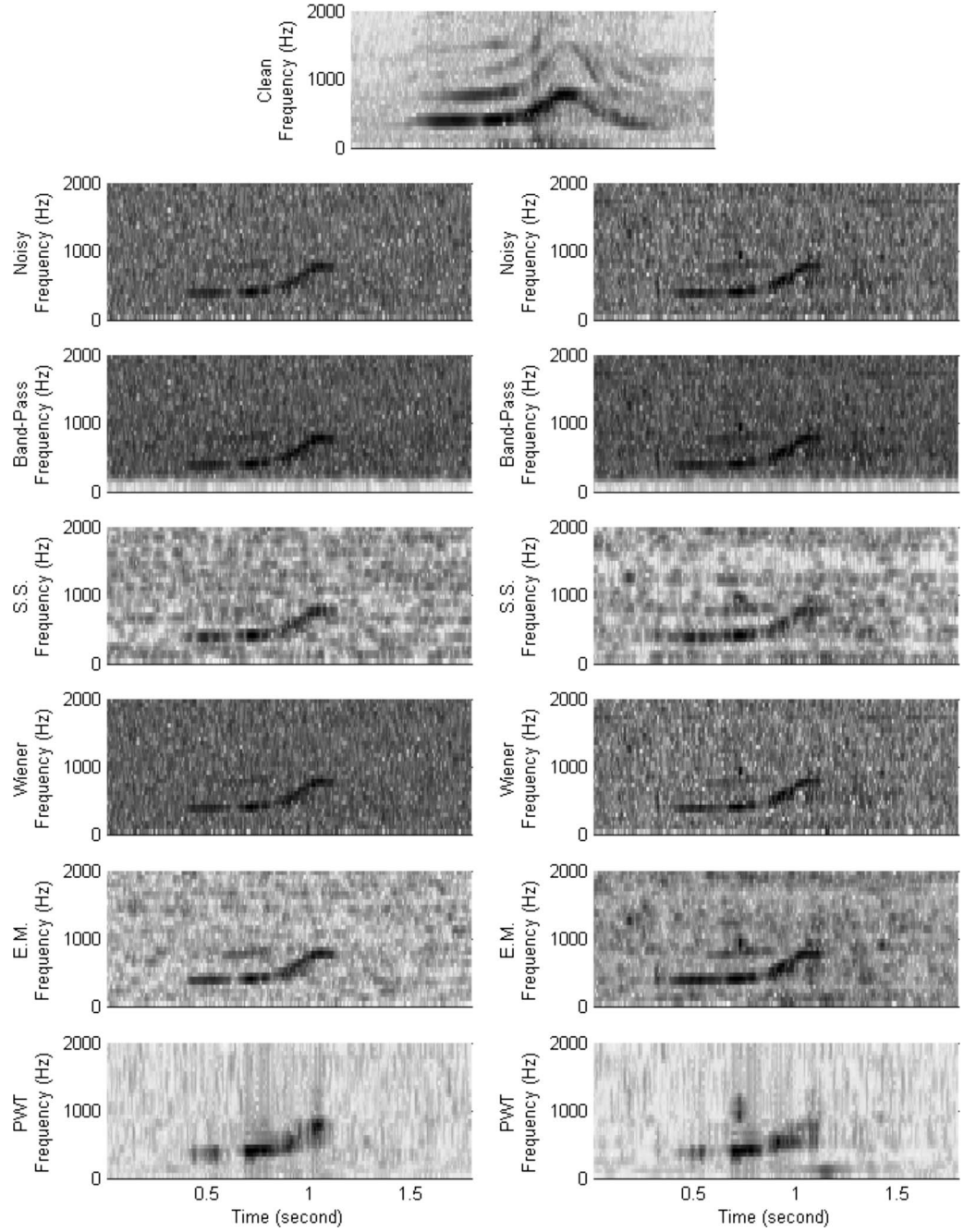

FIG. 6. Spectrograms of humpback whale: Clean signal, −10 dB SNR noisy signals, and signals enhanced by bandpass filtering, spectral subtraction, Wiener filtering, EM log-MMSE filtering, and perceptual WPT Filtering (the left column is for white noise and the right is for environment noise).

Based on visual examination of the clean data from Figs. 4–6, tight passbands are chosen around the vocalizations. Selected ranges are 2600–5600, 1000–10 000, and 200–2000 Hz for the ortolan bunting, rhesus monkey, and humpback whale data, respectively. For the spectral subtraction, Wiener filter, and EM filter approaches, the signal is divided into 32 ms windows with 75% overlap between frames. This frame length was chosen empirically, as it is sufficiently long for good spectral estimation in each frame but not so long as to affect temporal change in the signals, and adjustments to this value cause only minor changes to the overall enhancement results. Frequency analysis is done using a Hanning window and noise estimation is accomplished using the first three frames of the signal. For wavelet analysis, the discrete Meyer wavelet is used as the mother wavelet, which was chosen to provide good separation of subbands due to their regularity property (Cohen, 2001). The decomposition was done as illustrated in Fig. 3. The forgetting factor α used in Eqs. (5) and (18) is set to 0.98 for the EM filter and 0.92 for the wavelet denoising.

SNR and SSNR are used as objective measurement criteria for all sets of experiments. SSNR is computed by calculating the SNR on a frame-by-frame basis over the signal and averaging these values. This permits the measure to assign equal weights to the loud and soft portions of the signal,

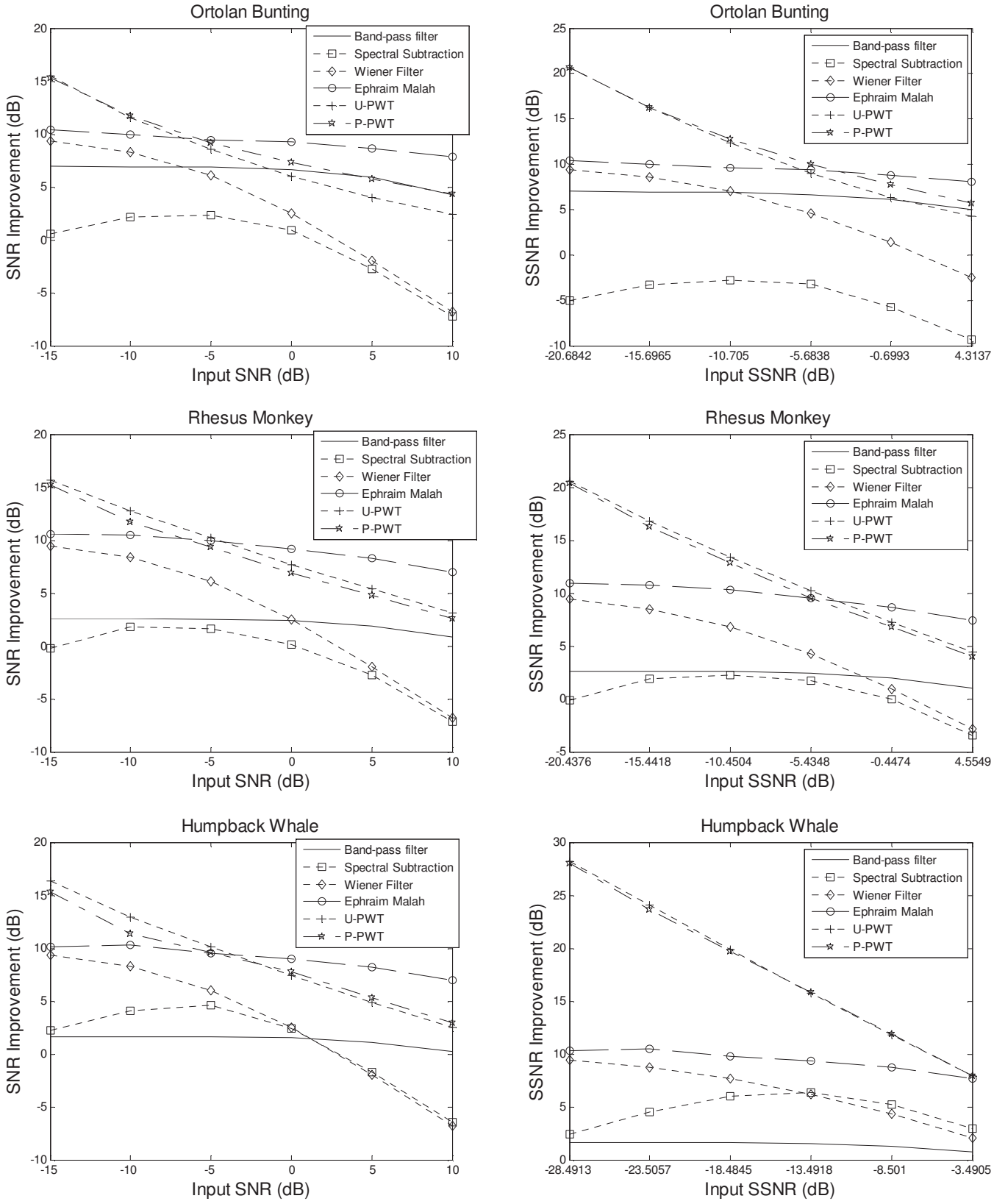

FIG. 7. SNR and SSNR results for white noise at −15, −10, −5, 0, +5, and +10 dB SNR levels.

which has been shown to have a higher correlation with perceived quality in human speech evaluation (Deller *et al.*, 2000). The formulas for SNR and SSNR are

$$\mathrm{SNR} = 10 \log_{10} \frac{\Sigma_n x^2(n)}{\Sigma_n [x(n) - \hat{x}(n)]^2}, \tag{19}$$

$$\mathrm{SSNR} = \frac{1}{M} \sum_{j=0}^{M-1} 10 \log_{10} \left[\sum_{n=Nj+1}^{N(j+1)} \frac{x^2(n)}{[x(n) - \hat{x}(n)]^2} \right], \tag{20}$$

where M is the number of frames, each of length N, and $x(n)$ and $\hat{x}(n)$ are the original and enhanced signals, respectively.

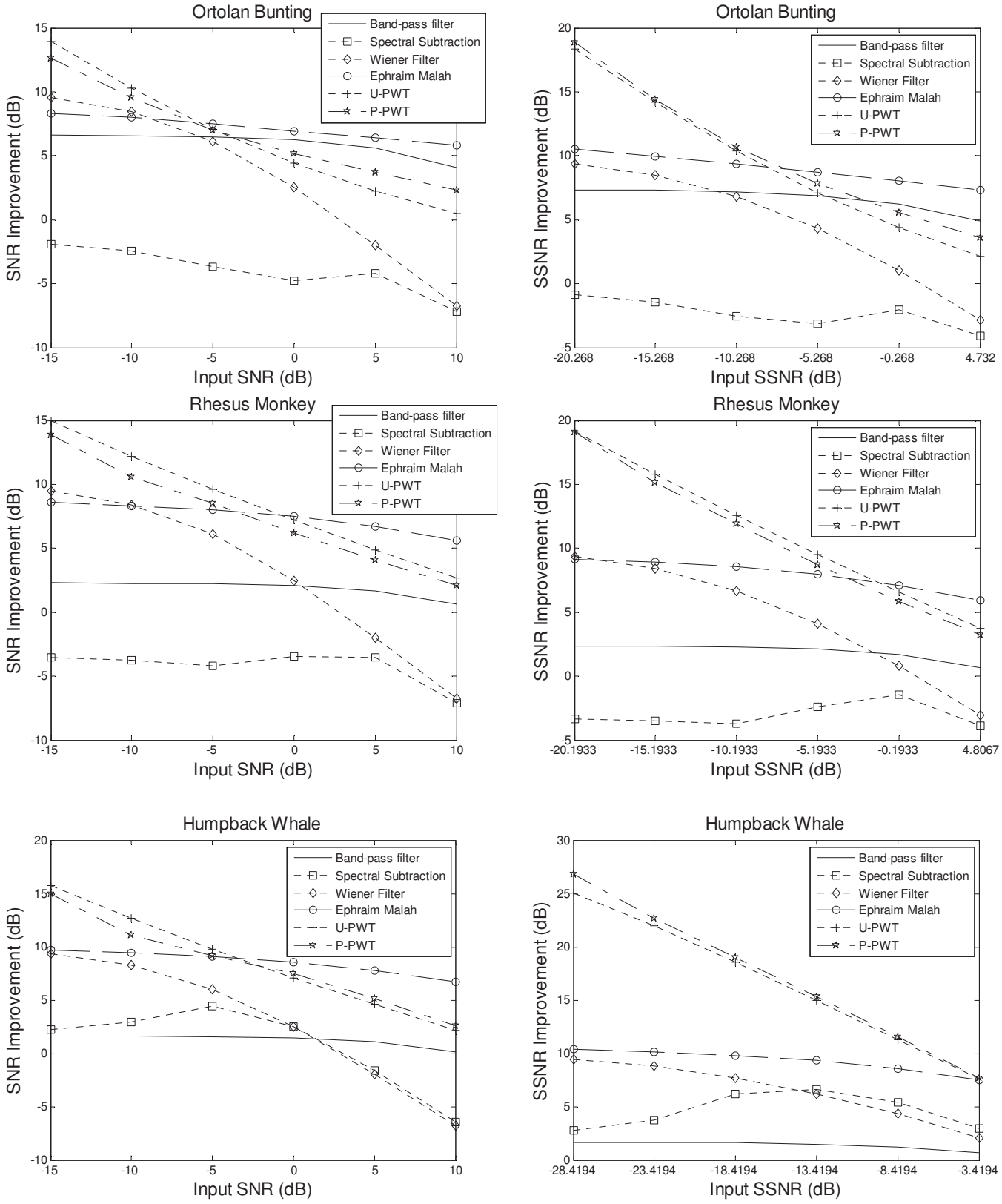

FIG. 8. SNR and SSNR results for environment noise at −15, −10, −5, 0, +5, and +10 dB SNR levels.

For visualization, spectrograms of the enhanced signals for the white noise and environment noise conditions at −10 dB SNR can be seen in Figs. 4–6.

SNR and SSNR results for the white noise and environment noise are shown in Figs. 7 and 8. The SNR and SSNR values are given as amount of improvement over the original input noisy values. The methods shown in these figures include bandpass filtering, spectral subtraction, Wiener filtering, EM filtering, the proposed perceptual wavelet packet transform (P-WPT), as well as a uniform band wavelet

packet transform (U-WPT), which is identical to the proposed method except that it utilizes uniformly spaced frequency bands rather than the perceptual scaling.

From reviewing the spectrograms and the SNR and SSNR plots, several conclusions can be drawn. It is clear that the proposed perceptual wavelet denoising method and the EM filtering method have the best overall performance in both the white noise and the environment noise conditions. The proposed method shows better enhancement performance for the higher noise (lower original SNR) cases, in particular. By comparing the SNR improvement to the SSNR improvement in Figs. 7 and 8, it can be seen that the SSNR, which is generally considered to be a more perceptually meaningful metric, shows greater superiority for the proposed method over the other methods than does SNR. Wiener filtering and spectral subtraction have moderate enhancement performance overall, while bandpass filtering results are a little sporadic, giving generally moderate results with good results in a few specific environment cases. Specifically, as expected, bandpass filtering works relatively well in the ortolan case where the vocalization frequency range is narrow and has limited overlap with the environment noise spectrum. By comparing the P-WPT and U-WPT results, it can be seen that the use of the perceptual scale has little overall impact. In the white noise case, the SNR is slightly higher for the uniform scaling, and SSNR measures show little difference. For environmental noise, the SNR is again slightly higher for the uniform scaling, and SSNR is again similar, showing a slight benefit for the perceptual scaling in two of the three examples. Under the noisiest conditions, the two wavelet-based enhancement techniques significantly outperform all of the baseline methods.

One interesting thing to note is that each of the different enhancement methods has unique characteristics, as seen in the spectrograms of Figs. 4–6. Bandpass filtering has the expected look, keeping all noise in the target range and eliminating nearly everything out of band. Spectral subtraction shows some temporal streaking due to the fact that the noise spectrum being removed is fixed. Wiener filtering and EM filtering have similar looks, except that the EM provides better overall results. The proposed method has the best noise removal but can also be seen to possess an artifact (most noticeable in Fig. 5), seen as a faint reflection of the primary signal. This artifact, which is not audible and does not contain enough energy to significantly impact the SNR or SSNR metrics, illustrates some of the processing differences between a frequency domain approach such as the EM and a wavelet domain approach such as the proposed method. Because the mother wavelet used for analysis is somewhat broadband, each of the nodes in the decomposition trees shown in Fig. 3 contains more than a single frequency component. Thus the nodes that are given primary emphasis for reconstruction have energy at more than one frequency. However, since the nature of this wavelet representation is also more compact, coefficients not given primary emphasis can be more strongly thresholded, yielding less energy throughout the entire background frequency range, as can also be seen in the spectrograms. The selection of the mother wavelet also impacts the degree of this artifact. The overall effect is that while the residual noise for the EM and perceptual wavelet approaches have similar total energy (with the perceptual wavelet having a little less in high noise situations), this residual noise in the EM approach is spread more evenly across the frequency range, while in the perceptual wavelet approach, it is more concentrated.

V. CONCLUSIONS

Enhancement techniques taken from the field of speech processing have been generalized and applied to noise reduction of bioacoustic vocalizations. Four baseline methods, including spectral subtraction, Wiener filtering, and EM filtering, as well as simple bandpass filtering, were compared to a new technique based on perceptual wavelet decomposition. Results indicate improved performance of the new method, particularly for the most noisy conditions. The new approach can be easily applied to any species, requiring only upper and lower frequency limits for the species to create the appropriate Greenwood function frequency warping curve.

ACKNOWLEDGMENTS

This material is based on work supported by National Science Foundation under Grant No. IIS-0326395. The authors also want to express their thanks to Joseph Solitis and John D. Newman for providing the rhesus monkey vocalizations, T. S. Osiejuk for providing the ortolan bunting vocalizations, and Mobysound for providing the humpback whale vocalizations.

Álvarez, B. D., and García, C. F. (**2004**). "System architecture for pattern recognition in eco systems," ESA Special Publication No. 553, Madrid, Spain.

Black, M., and Zeytinoglu, M. (**1995**). "Computationally efficient wavelet packet coding of wide-band stereo audio signals," in Proceedings of the IEEE International Conference on Acoustics, Speech, and Signal Processing, Detroit, MI, Vol. **5**, pp. 3075–3078.

Boll, S. F. (**1979**). "Suppression of acoustic noise in speech using spectral subtraction," IEEE Trans. Acoust., Speech, Signal Process. **ASSP-27**, 113–120.

Clemins, P., and Johnson, M. T. (**2006**). "Generalized perceptual linear prediction (gPLP) features for animal vocalization analysis," J. Acoust. Soc. Am. **120**, 527–534.

Clemins, P. J. (**2005**). "Automatic speaker identification and classification of animal vocalizations," Ph.D. thesis, Marquette University.

Clemins, P. J., Trawicki, M. B., Adi, K., Tao, J., and Johnson, M. T. (**2006**). "Generalized perceptual feature for vocalization analysis across multiple species," in Proceedings of the IEEE International Conference on Acoustics, Speech, and Signal Processing, Paris, France, Vol. **1**, pp. 253–256.

Cohen, I. (**2001**). "Enhancement of speech using bark-scaled wavelet packet decomposition," in Proceedings of Eurospeech, Aalborg, Denmark, pp. 1933–1936.

Cohen, I., and Berdugo, B. (**2001**). "Speech enhancement for non-stationary noise environments," Signal Process. **81**, 2403–2418.

Deller, J. R., Hansen, J. H. L., and Proakis, J. G. (**2000**). "Speech quality assessment," in *Discrete-Time Processing of Speech Signals* (IEEE, Piscataway, NJ), Chap. 9, pp. 584–587.

Donoho, D. L. (**1995**). "De-noising by soft-thesholding," IEEE Trans. Inf. Theory **41**, 613–627.

Edward, E. P. (**1943**). "Hearing ranges of four species of birds," Auk **60**, 239–241.

Ephraim, Y., and Malah, D. (**1984**). "Speech enhancement using a minimum mean-square error short-time spectral amplitude estimator," IEEE Trans. Acoust., Speech, Signal Process. **ASSP-32**, 1109–1121.

Ephraim, Y., and Malah, D. (**1985**). "Speech enhancement using a minimum mean-square error log-spectral amplitude estimator," IEEE Trans. Acoust., Speech, Signal Process. **ASSP-33**, 443–445.

Ephraim, Y., and Trees, H. L. V. (**1995**). "A signal subspace approach for speech enhancement," IEEE Trans. Speech Audio Process. **3**, 251–266.
Fu, Q., and Wan, E. A. (**2003**). "Perceptual wavelet adaptive denoising of speech," in Proceedings of EuroSpeech, Geneva, Switzerland, pp. 577–580.
Greenwood, D. D. (**1961**). "Critical bandwidth and the frequency coordinates of the basilar membrane," J. Acoust. Soc. Am. **33**, 1344–1356.
Gur, B. M., and Niezrecki, C. (**2007**). "Autocorrelation based denoising of manatee vocalizations using the undecimated discrete wavelet transform," J. Acoust. Soc. Am. **122**, 188–199.
Heffner, R. S. (**2004**). "Primate hearing from a mammalian perspective," Anat. Rec. **281A**, 1111–1122.
Helweg, D. A. (**2000**). "An integrated approach to the creation of a humpback whale hearing model," Technical Report No. 1835, San Diego, CA.
Jansen, M. (**2001**). *Noise Reduction by Wavelet Thresholding* (Springer, New York).
Johnson, M. T., Yuan, X., and Ren, Y. (**2007**). "Speech signal enhancement through adaptive wavelet thresholding," Speech Commun. **49**, 123–133.
Lepage, E. L. (**2003**). "The mammalian cochlear map is optimally warped," J. Acoust. Soc. Am. **114**, 896–906.
Li, X., Tao, J., Johnson, M. T., Solitis, J., Savage, A., Leong, K. M., and Newman, J. D. (**2007**). "Stress and emotion classification using jitter and shimmer features," in Proceedings of the IEEE International Conference on Acoustics, Speech, and Signal Processing, Honolulu, HI, Vol. **IV**, pp. 1081–1084.
Lim, J., and Oppenheim, A. V. (**1978**). "All-pole modeling of degraded speech," IEEE Trans. Acoust., Speech, Signal Process. **26**, 197–210.
Liu, R. C., Miller, K. D., Merzenich, M. N., and Schreiner, C. E. (**2003**). "Acoustic variability and distinguishability among mouse ultrasound vocalizations," J. Acoust. Soc. Am. **114**, 3412–3422.
Mellinger, D. K. (**2002**). Ishmael 1.0 User's Guide, Pacific Marine Enviromental Laboratory, Seattle, WA.
Mellinger, D. K., and Clark, C. W. (**2006**). "MobySound: A reference archive for studying automatic recognition of marine mammal sounds," Appl. Acoust. **67**, 1226–1242.
Osiejuk, T. S., Ratynska, K., Cygan, J. P., and Svein, D. (**2003**). "Song structure and repertoire variation in ortolan bunting (Emberiza hortulana L.) from isolated Norwegian population," Ann. Zool. Fenn. **40**, 3–19.
Payne, R. S., and McVay, S. (**1971**). "Songs of humpback whales," Science **173**, 585–597.
Scheifele, P. M., Andrew, S., Cooper, R. A., and Darre, M. (**2005**). "Indication of a Lombard vocal response in the St. Lawrence River beluga," J. Acoust. Soc. Am. **117**, 1486–1492.
Seyfarth, R. M., and Cheney, D. L. (**2004**). *TalkBank Ethology Data: Field Recordings of Vervet Monkey Calls* (Linguistic Data Consortium, Philadelphia).
Shao, Y., and Chang, C.-H. (**2006**). "A generalized perceptual time-frequency subtraction method for speech enhancement," in Proceedings of ISCAS 2006, pp. 2537–2540.
Yan, Z., Niezrecki, C., and Beusse, D. O. (**2005**). "Background noise cancellation for improved acoustic detection of manatee vocalizations," J. Acoust. Soc. Am. **117**, 3566–3573.
Yan, Z., Niezrecki, C., Cattafesta, L.N., III, and Beusse, O. D. (**2006**). "Background noise cancellation of manatee vocalizations using an adaptive line enhancer," J. Acoust. Soc. Am. **120**, 145–152.

Model-based automated detection of echolocation calls using the link detector

Mark D. Skowronski[a] and M. Brock Fenton[b]
Department of Biology, University of Western Ontario, London, Ontario, Canada N6A 5B7

(Received 1 November 2007; revised 11 April 2008; accepted 15 April 2008)

The link detector combines a model-based spectral peak tracker with an echo filter to detect echolocation calls of bats. By processing calls in the spectrogram domain, the links detector separates calls that overlap in time, including call harmonics and echoes. The links detector was validated by using an artificial recording environment, including synthetic calls, atmospheric absorption, and echoes, which provided control of signal-to-noise ratio and an absolute ground truth. Maximum hit rate (2% false positive rate) for the links detector was 87% compared to 1.5% for a spectral peak detector. The difference in performance was due to the ability of the links detector to filter out echoes. Detection range varied across species from 13 to more than 20 m due to call bandwidth and frequency range. Global features of calls detected by the links detector were compared to those of synthetic calls. The error in all estimates increased as the range increased, and estimates of minimum frequency and frequency of most energy were more accurate compared to maximum frequency. The links detector combines local and global features to automatically detect calls within the machine learning paradigm and detects overlapping calls and call harmonics in a unified framework. © *2008 Acoustical Society of America.* [DOI: 10.1121/1.2924122]

PACS number(s): 43.60.Uv, 43.80.Ev [JAS] Pages: 328–336

I. INTRODUCTION

Acoustic analysis of echolocation calls from bats typically requires hand labeling of call end points before estimating global call features (i.e., duration, bandwidth, and frequency of most energy), a time-consuming process susceptible to errors due to human expert subjectivity and bias, fatigue, and lack of repeatability. Automated methods have been introduced for call detection, including energy thresholds,[1,2] spectrogram thresholds,[3,4] rule-based detectors,[5] and model-based methods.[6] For all of these methods, calls are analyzed by using a data window typically much shorter than the duration of a call, and the methods explicitly assume that each window contains at most a single echolocation call. Therefore, these methods cannot handle calls that overlap in time with other calls, harmonics, or echoes.

To increase the reliability of automated call detection algorithms, a method is required that handles overlapping calls. Calls that overlap in time but not time and frequency simultaneously can be separated in the spectrogram domain. Echolocation calls are characterized as harmonic sinusoids with smoothly varying frequency and amplitude modulation and are represented in the time-frequency domain as spectrogram ridges. One way to detect overlapping calls in the spectrogram domain is to highlight spectrogram ridges and filter out those that are not echolocation calls. We have developed a ridge-finding method, the links algorithm, using principles from the machine learning paradigm of detection[6] and combined the links algorithm with filters to form the links detector for echolocation calls, described in the next section. We validated detector performance using synthetic echolocation calls embedded in white noise[7] and constructed passes of calls in an artificial recording environment (1) to provide an absolute ground truth for the detection experiments, (2) to account for atmospheric absorption and spherical spreading which produced a natural distribution of signal-to-noise ratios, and (3) to assess call detectability and extracted global call feature accuracy in terms of distance between bat and microphone. We added artificial echoes and quantized the recorded data to 16 bits to mimic characteristics of real recordings.

II. METHODS

A. Links algorithm

The links algorithm is designed to connect local spectrogram peaks along the ridges of echolocation calls. The first step of the links algorithm is to form the spectrogram of a signal and find the local peaks. The log-compressed magnitude spectrum of each frame of the spectrogram is computed by using a fast Fourier transform (FFT),

$$X_i(k) = 20 \log_{10} \left| \sum_{n=0}^{N-1} x_i(n) w(n) e^{-j(2\pi/N)kn} \right|,$$

where $x_i(n)$ is the ith frame of data of length N, $w(n)$ is a windowing function, and $X_i(k)$ is the spectrum of $x_i(n)$ at discrete frequency index (FFT bin) $k \in [0, \ldots, N_{\mathrm{FFT}}/2]$ constructed with an N_{FFT}-point FFT. The analysis frame should be much shorter than the expected duration of the echolocation call. In most cases, a Blackman window should be used in the analysis of echolocation recordings because it has a lower side lobe suppression (−57 dB) than the Hamming (−41 dB) or Hanning (−31 dB) windows.[8] Higher side lobes

[a]Electronic mail: mskowro2@uwo.ca.
[b]Electronic mail: bfenton@uwo.ca.

 0001-4966/2008/124(1)/328/9/$23.00

lead to higher spectral leakage levels that can mask fainter call characteristics (i.e., harmonics) for calls with sufficiently high signal-to-noise ratios (SNRs). A limitation of the Blackman window for the analysis of echolocation calls is that calls and overlapping echoes are more likely to blur together because of the wider main lobe width of the Blackman window. However, the main lobe width can be decreased by using longer analysis windows at the loss of temporal resolution (side lobe suppression is independent of window length). The spectrogram is normalized by placing the noise floor at 0 dB, which is estimated as the median value of all spectrogram pixels.

A *local peak* of a spectrogram is defined as any spectrogram pixel with a magnitude larger than the neighboring pixels in the same analysis frame,

$$\lambda_i = [k{:}X_i(k-1) < X_i(k) \geq X_i(k+1)], \tag{1}$$

where λ_i is a vector of discrete frequencies $k \in [1,\ldots,N_{\mathrm{FFT}}/2-1]$ that are local peaks of frame i. Each frame has M_i local peaks.

Once local peaks λ_i are determined for all analysis frames, the links algorithm connects local peaks to those in the adjacent left- and right-hand analysis windows that are *most likely* to be part of an echolocation call. For each local peak $\lambda_i(m_i)$, $m_i \in [1,\ldots,M_i]$ in frame i, all combinations of $\lambda_i(m_i)$ with all M_{i-1} local peaks in frame $i-1$ and all M_{i+1} local peaks in frame $i+1$ are constructed and used to calculate the feature vector ϕ_i for input into the likelihood function,

$$\phi_i(m_{i-1},m_i,m_{i+1}) = [E,F,dE,dF,sE,sF],$$

$$E = X_i(\lambda_i(m_i)),$$

$$F = \lambda_i(m_i)\frac{f_s}{N_{\mathrm{FFT}}},$$

$$dE = \bar{E}' \cdot A,$$

$$dF = \bar{F}' \cdot A,$$

$$sE = 10\log_{10}(\bar{E}' \cdot B \cdot \bar{E}),$$

$$sF = 10\log_{10}(\bar{F}' \cdot B \cdot \bar{F}), \tag{2}$$

where

$$\bar{E} = [X_{i-1}(\lambda_{i-1}(m_{i-1})),X_i(\lambda_i(m_i)),X_{i+1}(\lambda_{i+1}(m_{i+1}))]',$$

$$\bar{F} = [\lambda_{i-1}(m_{i-1}),\lambda_i(m_i),\lambda_{i+1}(m_{i+1})]'\frac{f_s}{N_{\mathrm{FFT}}}$$

are vectors of spectral peaks and frequencies, respectively, f_s is the sampling rate, and

$$A = [-1,0,1]'\frac{f_s}{2},$$

$$B = \frac{1}{6}\begin{vmatrix} 1 & -2 & 1 \\ -2 & 4 & -2 \\ 1 & -2 & 1 \end{vmatrix}$$

are the linear regression terms for calculating the slope (delta features dE and dF) and residual squared error (smoothness features sE and sF), respectively. If a local peak has no neighboring local peak to one side, then slope features are calculated between the two remaining local peaks, and smoothness features are not included in the likelihood model. The combination of local peaks yielding the maximum likelihood are connected together,

$$[\alpha_i(m_i),\beta_i(m_i)] = \underset{\forall m_{i-1},\forall m_{i+1}}{\arg\max}\ p(\phi_i(m_{i-1},m_i,m_{i+1})|\Theta_l), \tag{3}$$

where $\alpha_i(m_i)$ is the index m_{i-1} of the most likely left-hand local peak, $\beta_i(m_i)$ is the index m_{i+1} of the right-hand local peak, and Θ_l is the set of parameters for the links model. If a local peak has no left- or right-hand neighboring local peaks, then the value for α_i or β_i for that local peak, respectively, is set to $\{\varnothing\}$. A likelihood threshold may be used to remove highly unlikely connections.

Local peaks that connect to each other reciprocally are said to be *linked* together, and a set of local peaks linked together is called a *link chain*. Let Λ_p be a vector of discrete frequencies of local peaks for the pth link chain, Γ_p be a corresponding vector of spectral peak values, and τ_p be a corresponding vector of analysis frame indices. A link chain starts with a local peak that has no left-hand connection,

$$\Lambda_p(1) = \lambda_i(m_i) \quad \text{if } \alpha_i(m_i) = \{\varnothing\},$$

$$\Gamma_p(1) = X_i(\lambda_i(m_i)),$$

$$\tau_p(1) = i. \tag{4}$$

The link chain is constructed iteratively between reciprocal connections,

$$\Lambda_p(1+l) = \lambda_{i+l}(m_{i+l}) \quad \text{if } \beta_{i+l-1}(m_{i+l-1}) = m_{i+l} \quad \text{and } \alpha_{i+l}(m_{i+l}) = m_{i+l-1},$$

$$\Gamma_p(1+l) = X_{i+1}(\lambda_{i+l}(m_{i+l})),$$

$$\tau_p(1+l) = i+l, \tag{5}$$

for $l \in [1,\ldots,L_p-1]$, where L_p is the number of local peaks in the completed chain. The construction terminates when $\beta_{i+l-1}(m_{i+l-1})=\{\varnothing\}$ or when the condition in Eq. (5) is not met. In summary, the vectors Λ_p, Γ_p, and τ_p constitute the frequency, energy, and time, respectively, of the pth link chain. The top panel in Fig. 1 shows all link chains generated by the links algorithm for an echolocation call of *Eptesicus fuscus*. Most of the link chains highlight the echoes and background noise, and a method is needed to filter out such links.

B. Links filtering

Link chains have both local features (i.e., energy, slope, and smoothness) and global features (i.e., peak energy, dura-

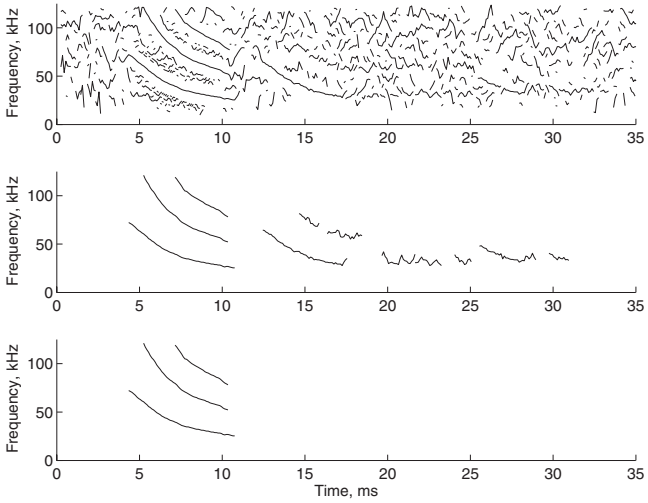

FIG. 1. Output of links algorithm for an echolocation call of *Eptesicus fuscus*. The top panel shows traces of all link chains, Λ_p vs τ_p. The middle panel shows link chains when the thresholds $\theta_E=10$ dB and $\theta_L=1$ ms are used to remove noncall link chains. The bottom panel shows link chains when the echo filter, $\theta_F=0$ dB, is applied to the results in the middle panel.

tion, bandwidth, and frequency of most energy), which can be used to filter out noncall link chains from the output of the links algorithm. Link chains of background noise are typically shorter than call link chains, have less energy, and are not as smooth in terms of energy and frequency. Link chains of echoes are also typically shorter than link chains of calls, are not as smooth, and closely follow a preceding call of higher energy. These observations may be leveraged to design methods that discriminate between call link chains and noncall link chains. We employed two thresholds and an echo filter to remove noncall link chains from the output of the links algorithm.

1. Energy and length thresholds

The middle panel in Fig. 1 shows the output of the links algorithm when two thresholds were applied: (1) the minimum local peak energy threshold θ_E and (2) the minimum link length threshold θ_L. The minimum peak energy threshold is applied to the links algorithm by adding θ_E to the conditional statement in Eq. (1),

$$\lambda_i = [k: X_i(k-1) < X_i(k) \geq X_i(k+1), X_i(k) \geq \theta_E]. \quad (6)$$

The energy threshold affects the links algorithm in several ways. First, removing local peaks below θ_E inhibits the formation of low-energy background link chains. Second, removing local peaks below θ_E reduces the number of local peaks in each analysis window, which reduces computational costs because the algorithm is $O(M^3)$, where M is the number of local peaks per analysis window. Third, θ_E sets the minimum end point energy of link chains. The beginning and end of the first and second harmonics in the top panel of Fig. 1 were trimmed off in the middle panel by θ_E.

The minimum length threshold θ_L is applied to the output of the links algorithm. Link chains with fewer than θ_L elements are discarded from the output. Let $\mathbf{\Lambda}$ be the set of link chains with at least θ_L local peaks,

$$\mathbf{\Lambda} = \{\Lambda_p, \Gamma_p, \tau_p: L_p \geq \theta_L\}, \quad (7)$$

where $p \in [1, \ldots, P]$ over all P link chains. Several of the tightly clustered link chains in between call harmonics in the top panel of Fig. 1 had energies above the background noise link chains due to spectral leakage and were not removed by θ_E unless the energy threshold was prohibitively high. Those links were removed by θ_L. A fourth harmonic of the call, ending near the 10 ms mark in the top panel of Fig. 1, was removed by θ_E and θ_L and demonstrates that a tradeoff exists between removing noncall link chains and preserving link chains of calls when applying the thresholds.

2. Echo filter

The middle panel of Fig. 1 contains link chains for an echolocation call and several link chains for echoes following the call. Echoes can have high SNRs and long link chains, so θ_E and θ_L cannot be used to remove echo link chains without also removing link chains of calls of comparable length and energy. Because echoes differ from calls in many characteristics, we designed statistical models of call link chains and echo link chains to use in an echo filter. Unlike the model used in the links algorithm, the echo filter models operate on link chains with access to both local and global features. The feature vector ψ_p is constructed for each link chain for input into the echo filter models,

$$\psi_p = [L_p, \max(\Gamma_p), \text{med}(dE), \text{med}(dF), \text{med}(sE), \text{med}(sF), \text{med}(\xi_p)] \quad (8)$$

where the slope and smoothness features are the same as those in Eq. (2) and ξ_p is a vector of masking energy for each local peak in Λ_p:

$$\xi_p(l) = \max([X_{\tau_p(l)-W}(\Lambda_p(l)), \ldots, X_{\tau_p(l)}(\Lambda_p(l))]) - X_{\tau_p(l)}(\Lambda_p(l)), \quad (9)$$

where W is the length of the masking window in frames. Equation (9) calculates the maximum spectrogram value in a row spanning back in time W frames from each local peak in a link chain and subtracts from the maximum the local peak spectral value. For local peaks $\Lambda_p(l)$ that are part of a call, $\xi_p(l)=0$ because no spectral peaks preceding $\Lambda_p(l)$ in the same row exceed $\Gamma_p(l)$. However, for local peaks $\Lambda_p(l)$ that are part of an echo, $\xi_p(l)>0$ because echoes are typically fainter than the calls that generated them (the exception is due to the directionality of the source and microphone, but such cases can be avoided with proper microphone placement).

The set of link chains of calls $\mathbf{\Lambda}$ from Eq. (7) is modified to include the echo filter,

$$\mathbf{\Lambda} = \{\Lambda_p, \Gamma_p, \tau_p: L_p \geq \theta_L, \log(p(\psi_p|\Theta_c)) - \log(p(\psi_p|\Theta_e)) \geq \theta_F\}, \quad (10)$$

where Θ_c and Θ_e are the model parameters for the distribution functions of call and echo link chains, respectively, and θ_F is the echo filter likelihood threshold in decibels. As θ_F increases, more link chains are labeled as echo link chains. The bottom panel in Fig. 1 shows the output of the echo filter

for equal *a priori* probabilities between calls and echoes ($\theta_F=0$).

The links algorithm, with links model parameters Θ_l and energy threshold θ_E, combined with the echo filter, with model parameters Θ_c and Θ_e, link length threshold θ_L, and echo filter threshold θ_F, constitute the links detector. Each detected link contains the time, frequency, and energy for all analysis frames of a detected call which are useful for further call analysis (e.g., species identification).

To quantify the accuracy of the links detector and compare it to a conventional detection algorithm, we designed automated detection experiments by using synthetic calls in an artificial recording environment. Using synthetic calls provided the detection experiment with an absolute ground truth and also allowed us to quantify the accuracy of global call estimates from detected link chains. The artificial recording environment provided a realistic distribution of call SNRs for the detection experiment and degraded calls in a realistic manner which affected detection and call feature estimates.

C. Synthetic calls

A limitation of previous automated detection experiments is the lack of an absolute ground truth for call end points and global call features. Typically, a human expert hand labels a sequence of echolocation calls recorded in field or laboratory settings and uses hand labels as a ground truth to judge the quality of an autodetection algorithm. This approach has two problems. First, expert subjectivity influences labeling, primarily for low-intensity calls perceived as "useless" to varying degrees by different experts. An unlabeled low-intensity call my be detected by an automated algorithm, only to be scored as a false positive. Second, global call features (i.e., duration, bandwidth, and frequency of maximum energy) extracted from hand-labeled calls represents what is *recorded* and not what is *broadcast*. Without knowing what signal was broadcast, determining the error in global call feature estimates, due to atmospheric propagation effects, directionality of the bat and microphone, and recording equipment noise, is impossible.

To circumvent the problems of using a hand-labeled ground truth, we began to use synthetic bat calls in autodetection experiments.[7] Synthetic calls were constructed by using a piecewise-exponential model with five parameters: call duration, start frequency, end frequency, and two parameters (the turning point) that control the curvature of the call. The model parameters were used to create a frequency modulation curve of a sinusoid for each call, and a Hanning window was used to amplitude modulate the sinusoid. Synthetic calls of five species common to North America were used in the current experiments (fundamental frequencies only). Table I lists the synthetic call parameters.

D. Artificial recording environment

To increase the realism of the synthetic calls, we created an artificial recording environment. Synthetic calls were emitted from points in space along an artificial flight path, and atmospheric propagation effects between the emission points and the microphone (spherical spreading and atmospheric absorption losses) were included. We also included echoes from a diffuse reflecting ground surface.

TABLE I. Synthetic species call parameters. Parameters selected from uniform distribution over the litsted range of values. The turning point parameters, t_0 and g_0, are normalized time and frequency, respectively.

Species	F_{start} (kHz)	F_{end} (kHz)	Duration (ms)	t_0	g_0
Eptesicus fuscus	70–80	26–30	7–11	0.35–0.45	0.24–0.34
Lasiurus cinereus	35–45	20–24	12–18	0.16–0.26	0.33–0.43
Myotis lucifugus	85–95	35–40	5–7	0.32–0.42	0.28–0.38
M. septentrionalis	110–120	39–49	3–4	0.43–0.53	0.25–0.35
Pipistrellus subflavus	85–95	39–41	9–13	0.16–0.20	0.18–0.22

1. Flight paths

Calls were recorded in the artificial environment by bats flying past a microphone along an artificial flight path, creating a realistic distribution of call SNRs. One call was emitted at each point along the flight path. The microphone and bats were assumed to be omnidirectional, and the microphone had a fixed detection radius (defined as the distance at which a reference call from the synthetic *E. fuscus* had a SNR of −10 dB). For all experiments, the detection radius was 20 m. The microphone was 2 m off the ground (the *xy* plane) on the *z* axis, creating a spherical detection space cut by the ground plane.

An artificial flight path was constructed by first randomly selecting a point on the surface of the spherical detection space then drawing a unit vector from the point toward the *z* axis, parallel to the ground. This ensured that the path started out heading toward the midline of the detection space and aided in creating relatively long passes with a wide range of call SNRs. The next point on the path was determined by the previous point, the direction of the unit vector, the flight speed of the bat (5 m/s, fixed), and the intercall interval (ICI, 150 ± 25 ms, uniform distribution), measured from the start of one call to the start of the next. Selected values for flight speed[9] and ICI (Ref. 10) are typical for a wide range of bat species. Each unit vector after the initial vector was determined by adding to the previous unit vector a random offset ($\sigma=0.05$, zero-mean normal distribution). If a point on the path was less than 1 m off the ground, the unit vector of the next point was pointed upward to ensure that the path remained above ground. The path terminated when a point was constructed outside the detection sphere. Paths were typically 8 s in duration and contained approximately 50 calls.

A synthetic call was emitted from each point on a flight path (assumed to be omnidirectional) and propagated through the air to the microphone and ground. The energy of the call decreased as it propagated due to spherical spreading and atmospheric absorption.[11] For atmospheric absorption, the air properties were 20 °C, 50% relative humidity, and 1 atm pressure. Absorption increased roughly linearly with frequency from 0.9 dB/m at 30 kHz to 3.3 dB/m at 100 kHz.

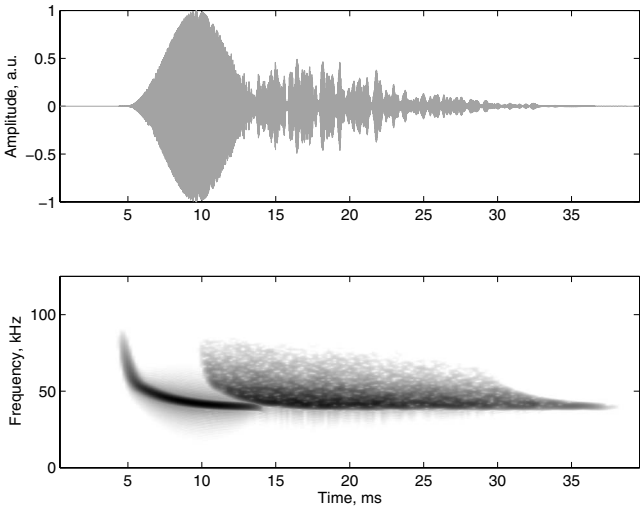

FIG. 2. Noise-free synthetic call and echo. The upper panel shows the time domain signal, while the lower panel shows the spectrogram (250-point Blackman window, zero padded to 1024-point FFT, 200-point overlap between adjacent windows, and 250 kHz sampling rate).

2. Ground echoes

Echoes are common in field recordings. They may be specular (e.g., from a building side or lake surface) or diffuse (e.g., from a grassy field or dense canopy), depending on the characteristics of the surrounding reflective surfaces. Echoes reflecting off the ground were included in the artificial recording environment using a stochastic ray approach.[12] Uniformly distributed random points on the lower half surface of a unit sphere around each point on a flight path were selected, and the emitted call propagated along a ray from the center of the sphere through each point on the surface toward the ground. Each stochastic ray hit the ground at a reflection point and produced a specular reflection ray. If the angle ϕ_r between a stochastic specular reflection ray and a line between the corresponding reflection point and the microphone was less than a threshold (100°), then a scaled and delayed version of the emitted call was added to the recorded microphone signal. The scale factor included spherical spreading and atmospheric absorption along the path of the stochastic ray and a constant ground absorption factor (25 dB), and the delay was due to the increased path length of the reflected ray compared to the direct propagation path from the call emission point to the microphone. Propagation delays were rounded to the nearest sample for simplicity (4 μs resolution at 250 kHz sampling rate). Frequency-dependent atmospheric absorption was created using finite impulse response (FIR) filters designed in MATLAB (The Mathworks, Natick, MA) and the absorption formulas from Bass *et al.*[11] Figure 2 shows an example of a synthetic call and echo in the time domain and as a spectrogram.

Once a pass of synthetic calls and echoes was constructed, white noise was added to the signal. The noise power was constant for calls from all species. The noisy signal was written to a WAV file at 16 bit resolution to mimic quantization effects of typical recorded signals.

E. Detection experiments

For each synthetic species, 200 artificial passes of calls were synthesized and written to individual WAV files. Files contained a mean ± standard deviation of 52 ± 4 calls. Emission points were 12 ± 5 m from the microphone, and the 10th and 90th percentiles for distances were 5.4 and 18.7 m, respectively. For each pass of calls, the WAV file was read into MATLAB and converted to a spectrogram by using 0.3 ms Blackman analysis windows (75 samples), zero padded to 512 points for FFT analysis, at a frame rate of 10 000 frames/s. The spectrogram was normalized by subtracting the median value of all log-compressed spectrogram values from the spectrogram. This placed the median value of the noise in the spectrogram at 0 dB, and negative spectrogram values were truncated at 0 dB to reduce the number of local peaks to be considered by the links algorithm.

The spectrogram was processed by the links detector, using thresholds θ_E, θ_L, and θ_F, and produced a set $\mathbf{\Lambda}$ of link chains. The set of link chains was compared to the ground truth for a WAV file and scored for hits, misses, and false positives. If the frame of peak energy of a link chain was within the end points of a synthetic call, the link chain was scored as a hit (multiple hits for the same call were ignored); otherwise, the link chain was scored as a false positive. Each labeled call that was not hit by any link chain was scored as a miss.

A spectral peak detector was used in the experiments as a base line detector. The maximum spectral value in each spectrogram analysis window was compared to a threshold, θ_S. Consecutive analysis windows above θ_S were grouped together as a single detected entity. If the frame of peak energy for each group was within the end points of a synthetic call, the group was scored as a hit (as with the links detector, multiple hits for the same call were ignored); otherwise, the group was scored as a false positive. A miss was scored for each labeled call not hit by any group.

F. Global feature estimates

Echolocation calls are usually detected so that call features may be extracted for further analysis. The use of synthetic calls in the detection experiments allowed for extracted call features to be compared to features of *emitted* calls. The following global call features were extracted from the output of the links detector: $F_{\min}$, $F_{\max}$, FME, and duration, where $F_{\min}$ is the minimum frequency of a detected call, $F_{\max}$ is the maximum frequency, FME is the frequency of most energy, and duration is the difference between the start point and end point of a detected call. The exact values were tabulated from parameters used to synthesize each call.

III. RESULTS

All detectors were characterized by their *receiver operator characteristic* (ROC) curve showing the tradeoff between hit rate (HR) and false positive rate (FPR) as the detector threshold changed. Hit rate and false positive rate are defined as follows:

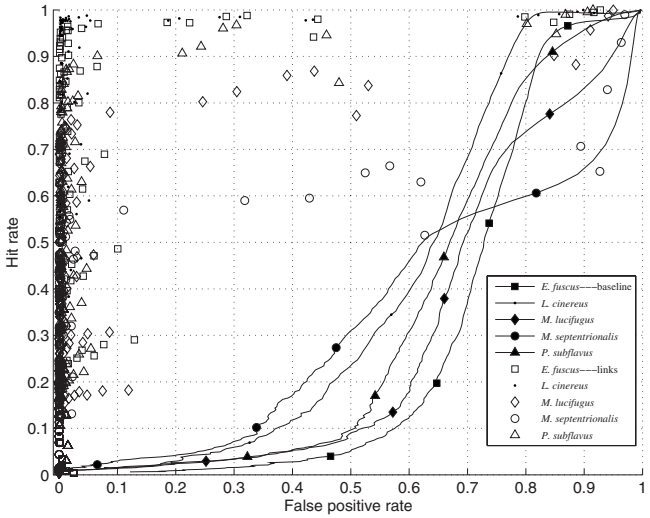

FIG. 3. ROC curves for each species.

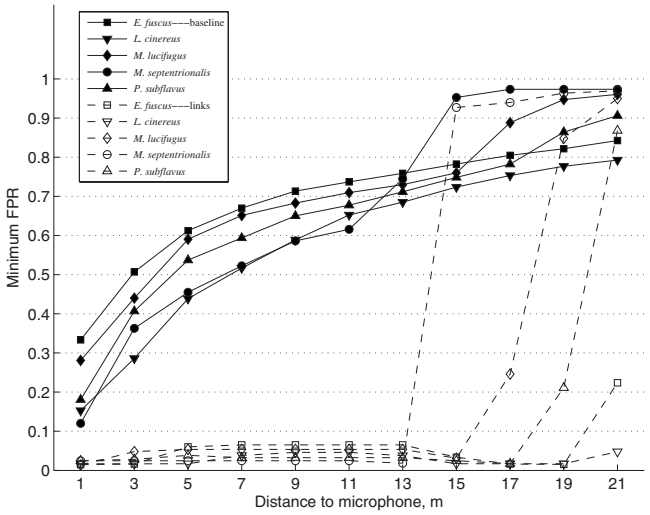

FIG. 4. Minimum FPR vs distance to microphone for each species. Each data point is the median value of minimum FPR for emission locations grouped into bins for every 2 m distance.

$$\mathrm{HR} = \frac{\text{hits}}{\text{hits} + \text{misses}},$$

$$\mathrm{FPR} = \frac{\text{false positives}}{\text{false positives} + \text{hits}}, \tag{11}$$

where hits is the number of labeled calls detected, misses is the number of labeled calls not detected, and false positives is the number detector outputs that were not labeled calls. Note that hits+misses is the total number of labeled calls and that false positives+hits is the total number of detector outputs. An ideal detector has HR=1 and FPR=0 (no misses and no false positives).

The ROC curve for the base line detector was generated by sweeping the threshold for the spectral peak energy between 0 and 50 dB in 0.25 dB increments. The ROC curve for the links detector is the set of points generated by each triplet of thresholds $[\theta_E, \theta_L, \theta_F]$ for all combinations of $\theta_E = [5, 10, 15, 20, 25, 30]$ dB, $\theta_L = [0, 4, 8, 12, 16, 20]$ frames, and $\theta_F = [-10, -5, 0, 5, 10]$ dB. The total number of thresholds used for the base line detector was 201, and the total number of threshold triplets used for the links detector was 180.

Results varied for each species since the frequency range of each species was affected by atmospheric absorption differently (Fig. 3). The ROC curves for the base line were affected by echoes at low hit rates and false positives from the background noise at higher hit rates. The ROC curves for the links detector were affected much less by echoes but varied across species. The species with the highest frequency calls, *M. septentrionalis*, had a maximum hit rate of 55.7% for detectors with FPR $<2\%$ compared to (in order of decreasing frequency range) 74.8% for *M. lucifugus*, 87.3% for *P. subflavus*, 96.4% for *E. fuscus*, and 98.6% for *L. cinereus*. Lower call frequency range and bandwidth led to higher detection accuracy. The maximum hit rate for all calls from all species was 87.0%.

Since the position of each call was known, we quantified detector accuracy as a function of distance to the microphone. For each call, we tabulated the minimum FPR for all detector thresholds that detected the call. Calls that were easy to detect (presumably ones that were close to the microphone) had minimum FPRs near zero, while calls that were more difficult to detect (farther from the microphone) had larger minimum FPRs. Figure 4 shows minimum FPR versus distance to microphone for each species.

For the base line detector, minimum FPR steadily increased as the distance to the microphone increased. For small distances, false positives were dominated by echoes, while for larger distances, false positives were dominated by peaks in the background noise. The links detector showed variation in performance according to species. All species were detectable up to 14 m from the microphone with less than 10% FPR. Between 14 and 16 m, the calls of *M. septentrionalis* became much more difficult to accurately detect, while the calls of the other species were still detectable with less than 10% FPR. Performance diminished for each species as the distance to the microphone increased according to the frequency range and bandwidth of each species.

The thresholds that attained the minimum FPR varied with distance for the base line detector (Fig. 5) and links detector (Fig. 6). The base line detector threshold that produced the minimum FPR decreased as the distance to the microphone increased, as expected. To detect calls close to the microphone, a relatively high threshold was sufficient to detect the calls and reject false positives. As the distance between the emission point of a call and the microphone increased, call intensity decreased due to spherical spreading and atmospheric absorption, necessitating a lower spectral peak threshold to successfully detect the call. Lower thresholds, however, increased false positives from echoes and background noise.

The parameters that produced the minimum FPR for the links detector showed interesting trends as a function of distance to the microphone. The number of link chains output by the links detector generally increased as any of the three thresholds decreased, but the results in Fig. 6 show that the minimum FPR was achieved by increasing and decreasing

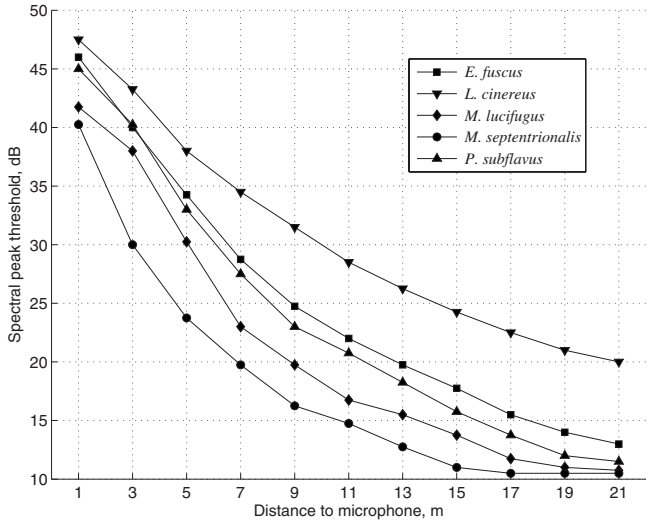

FIG. 5. Base line detector threshold for minimum FPR vs distance to microphone.

the parameters in combination for different distances. For distances less than 10 m, the minimum local peak threshold decreased from 22 to 18 dB as the minimum link chain length also decreased from 7 frames to 3 frames. For distances greater than 10 m, the minimum local peak energy continued to decrease, while the minimum length increased in a species-specific trend (species with calls in the highest frequency range increased starting at a lower distance). The echo filter threshold remained near the minimum of the range of tested values for short distances but increased by 5–6 dB for each species at the point where minimum FPR increased sharply as the distance increased.

The previous results demonstrated the accuracy of the links detector but did not quantify the *quality* of detected calls. A call may be detectable at 20 m distance to the microphone with a low FPR but may be a poor representation of what was actually emitted by the bat. In many applications, call features of detected calls are extracted and further analyzed. Since the actual global call parameters (i.e., duration and frequency range) of the synthetic calls were known, we measured the accuracy of global feature estimates from calls detected by the links detector. We did not use the base line detector in these experiments because relevant global features were not readily obtainable from the base line measure (i.e., spectral peak energy), whereas all the global call features of interest were easily determined from the link chains. Figure 7 shows the rms error for each species for the global features $F_{\min}$, $F_{\max}$, FME, and duration.

rms error in $F_{\min}$ and FME for all species increased almost linearly between 1 m distance and the distance at which the minimum FPR for each species increased sharply. For calls of *M. septentrionalis*, $F_{\min}$ and FME rms error were 9.5 and 7.4 kHz, respectively, at 11 m, and for the calls of *L. cinereus*, $F_{\min}$ and FME rms error were 1.2 and 0.65 kHz, respectively, at 17 m. rms error in $F_{\max}$ was much larger than the errors in $F_{\min}$ and FME for two reasons: (1) higher atmospheric absorption at higher frequencies and (2) steep downward frequency modulation from $F_{\max}$ for all species in combination with the Hanning amplitude modulation window. The species with calls with the steepest initial slope (*P. subflavus*) had the highest $F_{\max}$ rms error at short distances, while the species with calls with the shallowest initial slope (*L. cinereus*) had the lowest $F_{\max}$ rms error at short distances. rms error in duration increased roughly linearly at different rates for each species. The order of species at the farthest distance for duration rms error (small to large) was the same order for average call duration for each species (Table I).

IV. DISCUSSION

Previous experiments with synthetic calls showed that a model-based detector increased the detection range by about 1 m compared to a spectral peak detector,[7] and the current experiments showed that the difference was significantly larger when including propagation losses and echoes in the synthetic recordings. The base line detector was not

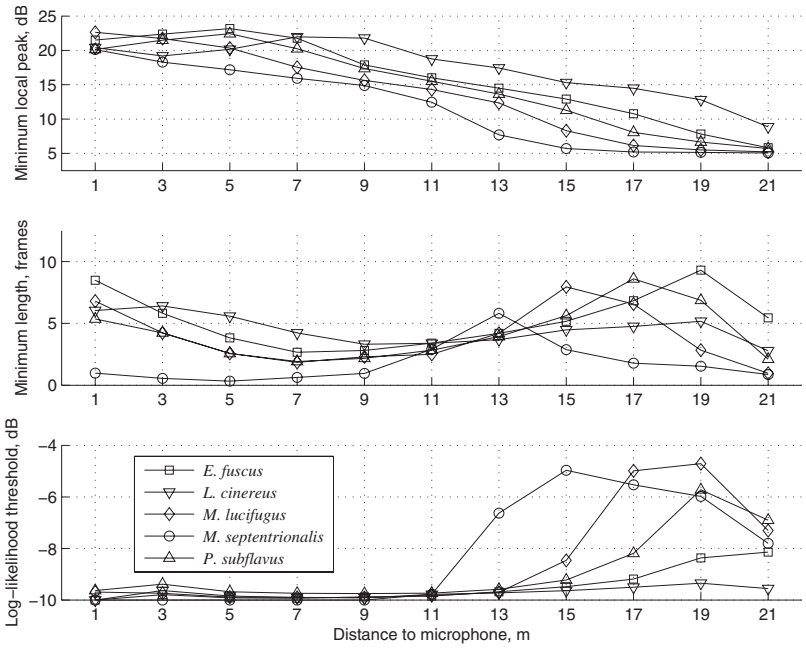

FIG. 6. Links detector parameter values for minimum FPR vs distance to microphone.

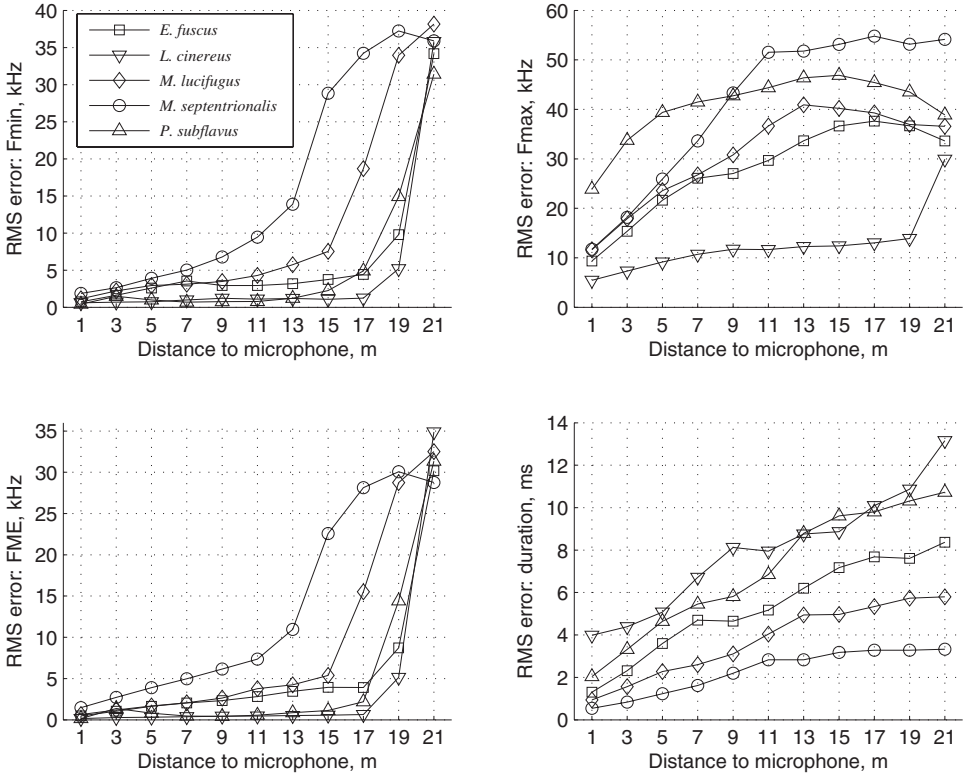

FIG. 7. RMS error for global call features detected by links detector at minimum FPR.

equipped to handle echoes and tended to produce several false positives as spectral peaks of echoes fluctuated above and below the detector threshold. The links detector was trained to discriminate between link chains from calls and from echoes, resulting in much lower FPRs. The models in the links algorithm and the echo filter were trained with calls from ten passes from each species by using bootstrapping.

The feature vectors used in the links algorithm [ϕ_i, Eq. (2)] and echo filter [ψ_p, Eq. (8)] use local and global call features, but both vectors could be augmented with other measures. Concavity could be included in both feature vectors to add more local shape information, and intercall interval could be added to ψ_p if consecutive calls in a pass could be reliably identified. Other statistics besides the median value of each local feature could be added to ψ_p. If more than one microphone is used to record bats, intermicrophone information (i.e., timing differences, intensity differences, and source location estimates) could be added to ψ_p so that calls and echoes could be separated spatially.

The artificial recording environment lacked several characteristics of real-world environments. Perhaps, the most important characteristics not included in the current experiments are the directionality of the source and microphone. Our synthetic passes contained about 50 calls per pass, which is larger than what is observed with field recordings of real bats. A directional source and microphone would affect the intensity of echoes recorded by the microphone as well as the amplitude modulation of the call. Off-axis spectral characteristics of calls may drop by 100 dB compared to on-axis characteristics because of morphological characteristics of a bat's face, and the "notch" level and spatial location vary by frequency.[13] Spectral notches are observed in otherwise intense echolocation calls recorded in the field and violate the assumption made by the links algorithm that echolocation calls vary smoothly in frequency and amplitude. For such calls, the links algorithm produces "broken" links.

Broken links may be mended by using a larger local neighborhood at the cost of an exponential increase in computation cost or by computing N-best link chains similar to N-best paths in models of continuous speech.[14] Broken links may also be mended by replacing the links model in Eq. (3) with a state machine that tracks the progression of local peaks throughout a call.[15] The state machine, a hidden Markov model,[16] combines the statistical model used by the links algorithm with a probabilistic mechanism for transition between the states "call" and "no call," adding context to the detection decision process. The call state may be split into states that specialize on search-phase calls and feeding buzzes or on calls of specific species. The state model may also be expanded to model overlapping passes of calls which would improve performance because of the added information available for the detector.

V. CONCLUSIONS

We introduced the links algorithm for finding spectrogram ridges and also the links detector for automatically detecting echolocation calls from field recordings. To quantify the performance of the links detector, we created a synthetic recording environment, including synthetic piecewise-exponential search-phase echolocation calls, synthetic echoes reflected from a diffuse surface, and acoustic propagation losses due to atmospheric absorption and spherical spreading. We compared the links algorithm to a popular automatic detection algorithm, a spectral peak detector, as a base line, and we found that echoes and atmospheric absorption sig-

nificantly degraded base line detector performance compared to the links detector. The base line detector produced more than 10% false positives for even the closest bats (less than 2 m from the microphone), while the links detector detected calls of all species used in the experiments with less than 10% false positives for bats up to 14 m away from the microphone and at least 22 m away from the microphone for the species with the lowest frequency range and bandwidth of calls. For calls detected with the links detector, global call feature estimates degraded with increased distance to the microphone for all species. The features $F_{\min}$ and FME were the most robust, varying less than 6 kHz in rms error up to 14 m distance to the microphone for all but the highest frequency-range species. Estimate errors in call duration steadily increased as the distance increased, up to the duration of the emitted call, indicating that the link chain output by the links detector only highlighted the spectral peaks of the call above the noise level.

ACKNOWLEDGMENTS

The current work was funded by the International Fellowship Research Program from the National Science Foundation and the Natural Sciences and Engineering Research Council of Canada.

[1]S. Parsons and G. Jones, "Acoustic identification of twelve species of echolocating bat by discriminant function analysis and artificial neural networks," J. Exp. Biol. **203**, 2641–2656 (2000).
[2]M. K. Obrist, R. Boesch, and P. F. Fluckiger, "Variability in echolocation call design of 26 Swiss bat species: Consequences, limits and options for automated field identification with a synergetic pattern recognition approach," Mammalia **68**, 307–322 (2004).
[3]L. Pettersson, "Bat specific signal analysis software—BatSound," in *Bat Echolocation Research: Tools, Techniques and Analysis*, edited by R. M. Brigham, E. K. V. Kalko, G. Jones, S. Parsons, and H. J. G. A. Limpens (Bat Conservation International, Austin, TX, 2004), pp. 130–133.
[4]W. M. Masters, S. C. Jacobs, and J. A. Simmons, "The structure of echolocation sounds used by the big brown bat *Eptesicus fuscus*: Some consequences for echo processing," J. Acoust. Soc. Am. **89**, 1402–1413 (1991).
[5]S. Bayefsky-Anand, M. D. Skowronski, M. B. Fenton, C. Korine, and M. W. Holderied, "Variations in the echolocation calls of the European free-tailed bat," J. Zool. **275**(2), 115–123 (2008).
[6]M. D. Skowronski and J. G. Harris, "Acoustic microchiroptera detection and classification using machine learning: Lessons learned from automatic speech recognition," J. Acoust. Soc. Am. **119**, 1817–1833 (2006).
[7]M. D. Skowronski and M. B. Fenton, "Model-based detection of synthetic bat echolocation calls using an energy threshold detector for initialization," J. Acoust. Soc. Am. **123**(5), 2643–2650 (2008).
[8]A. V. Oppenheim and R. W. Schafer, *Discrete-Time Signal Processing* (Prentice-Hall, Englewood Cliffs, NJ, 1989).
[9]U. M. Norberg, in *Recent Advances in the Study of Bats*, edited by M. B. Fenton, P. Racey, and J. M. V. Rayner (Cambridge University Press, Cambridge, 1987), pp. 43–56.
[10]N. V. Jennings, S. Parsons, K. E. Barlow, and M. R. Gannon, "Echolocation calls and wing morphology of bats from the West Indies," Acta Chiropterologica **6**, 75–90 (2004).
[11]H. E. Bass, L. C. Sutherland, and A. J. Zuckerwar, "Atmospheric absorption of sound: Update," J. Acoust. Soc. Am. **88**, 2019–2021 (1990).
[12]B. L. Dalenback, "Room acoustic prediction based on unified treatment of diffuse and specular reflection," J. Acoust. Soc. Am. **100**, 899–909 (1996).
[13]Q. Zhuang and R. Muller, "Noseleaf furrows in a horseshoe bat act as resonance cavities shaping the biosonar beam," Phys. Rev. Lett. **97**, 218701 (2006).
[14]J. R. Deller, J. H. L. Hansen, and J. G. Proakis, *Discrete-Time Processing of Speech Signals* (Macmillan, New York, 1993).
[15]R. E. Bethel and R. G. Rahikka, "Optimum time delay detection and tracking," IEEE Trans. Aerosp. Electron. Syst. **26**, 700–712 (1990).
[16]L. R. Rabiner, "A tutorial on hidden Markov models and selected applications in speech recognition," Proc. IEEE **77**, 257–286 (1989).

A nonlinear finite-element model of the newborn middle ear

Li Qi
Department of BioMedical Engineering, McGill University, Montréal H3A 2B4, Canada

W. Robert J. Funnell[a)]
Departments of BioMedical Engineering and Otolaryngology, McGill University, Montréal H3A 2B4, Canada

Sam J. Daniel
Department of Otolaryngology, McGill University, Montréal H3H 1P3, Canada

(Received 27 December 2007; revised 10 April 2008; accepted 12 April 2008)

A three-dimensional static nonlinear finite-element model of a 22-day-old newborn middle ear is presented. The model includes the tympanic membrane (TM), malleus, incus, and two ligaments. The effects of the middle-ear cavity are taken into account indirectly. The geometry is based on a computed-tomography scan and on the published literature, supplemented by histology. A nonlinear hyperelastic constitutive law is applied to model large deformations. The middle-ear cavity and the Young's modulus of the TM have significant effects on TM volume displacements. The TM volume displacement and its nonlinearity and asymmetry increase as the middle-ear cavity volume increases. The effects of the Young's moduli of the ligaments and ossicles are found to be small. The simulated TM volume changes do not reach a plateau when the pressure is varied to either −3 kPa or +3 kPa, which is consistent with the nonflat tails often found in tympanograms in newborns. The simulated TM volume displacements, by themselves and also together with previous ear-canal model results, are compared with equivalent-volume differences derived from tympanometric measurements in newborns. The results suggest that the canal-wall volume displacement makes a major contribution to the total canal volume change, and may be larger than the TM volume displacement. [DOI: 10.1121/1.2920956]

PACS number(s): 43.64.Bt, 43.64.Ha [BLM] Pages: 337–347

I. INTRODUCTION

High static pressures are used in several types of hearing examination, including admittance tympanometry (e.g., Shanks and Lilly, 1981; Margolis and Shanks, 1991; Keefe *et al.*, 1993), reflectance tympanometry (e.g., Keefe and Levi, 1996; Margolis *et al.*, 2001; Sanford and Feeney, 2007), pressure-volume measurement (e.g., Elner *et al.*, 1971; Gaihede, 1999), and pressurized acoustical transfer function measurement (Keefe and Simmons, 2003). Understanding the mechanical response of the middle ear to high static pressures is important for understanding the results of such measurements.

The mechanical deformations of the tympanic membrane (TM) in response to high static pressures have been experimentally studied in human adult (Elner *et al.*, 1971; Dirckx and Decraemer 1991; Dirckx and Decraemer 1992; Vorwerk *et al.*, 1999; Gaihede, 1999) and in animals (von Unge *et al.*, 1993; Dirckx *et al.*, 1997; Dirckx *et al.*, 1998; Dirckx and Decraemer, 2001; Larsson *et al.*, 2001; Lee and Rosowski, 2001; Rosowski and Lee, 2002; Ladak *et al.*, 2004; Larsson *et al.*, 2005; Dirckx *et al.*, 2006). The TM in response to high static pressures has also been studied by the nonlinear finite-element method (Ladak *et al.*, 2006; Cheng *et al.*, 2007). To date, neither mechanical measurements nor modeling studies have been reported for the newborn middle ear.

Understanding the volume displacement of the newborn TM in response to high static pressures is important for interpreting pressurized measurements in newborn hearing screening and diagnosis. As we have discussed in more detail in a previous paper (Qi *et al.*, 2006), it is important to be able to distinguish conductive hearing loss from sensorineural hearing loss soon after birth but the usual clinical test, tympanometry, gives quite different results in newborns than it does in adults. For example, some newborns with confirmed middle-ear effusion exhibit normal-appearing single-peak tympanograms (e.g., Paradise *et al.*, 1976; Meyer *et al.*, 1997). This is because the external ear and middle ear in newborns differ significantly from those in adults. For one thing, unlike the adult ear canal, of which the inner two thirds are bone, the entire newborn ear canal is composed of soft tissue. It is thus difficult to differentiate the clinically interesting TM volume displacement from the associated canal-wall volume displacement in response to high static pressures (as used in tympanometry). Holte *et al.* (1990) first measured newborn canal-wall displacement in response to static tympanometric pressures (±2.5 to ±3 kPa) using video otoscopy. They found, with considerable variability, that the diameter of the ear canal can change by up to 70% in newborns at birth. We recently presented a nonlinear newborn ear-canal model, which for the first time simulated the

[a)]Author to whom correspondence should be addressed. Electronic mail: robert.funnell@mcgill.ca

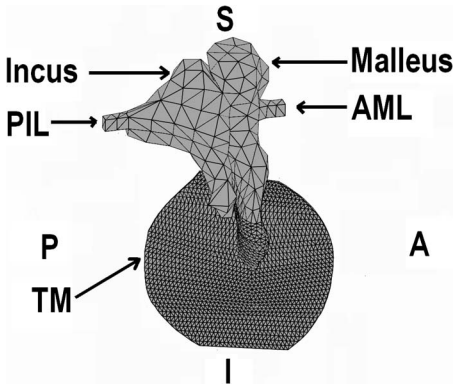

FIG. 1. Medial view of the middle-ear model. S is superior, I is inferior, P is posterior, A is anterior. AML is the anterior mallear ligament, PIL is the posterior incudal ligament.

newborn canal-wall displacement (Qi *et al.*, 2006). Our results indicated that the volume changed by between 27 and 75% in response to static pressures of ±3 kPa. The purpose of the present study is to extend our earlier work by including the middle ear, in order to investigate newborn TM volume displacements under tympanometric pressures.

In this study, we present a three-dimensional nonlinear finite-element model of a 22-day-old newborn middle ear. The geometry is based on a clinical x-ray computed tomography (CT) scan and the published literature. A polynomial hyperelastic constitutive law is applied to model large deformations of the TM. Plausible ranges of material properties of the newborn middle ear are explored. The volume displacement of the TM under high static pressures is estimated in both open-cavity and closed-cavity conditions. The simulated TM volume displacement is compared with equivalent-volume differences calculated from measurements in both healthy full-term newborns (Margolis *et al.*, 2003; Shahnaz *et al.*, 2008) and neonatal intensive care unit (NICU) newborns (Margolis *et al.*, 2003).

II. MATERIALS AND METHODS

A. 3D reconstruction

The geometry of the model is based on the same data as our ear-canal model (Qi *et al.*, 2006), namely, a clinical CT scan of a 22-day-old newborn. The CT scan contained 47 horizontal slices. Two local programs, Fie and Tr3 (http://audilab.bmed.mcgill.ca/sw/), were used to generate a surface model. A solid model with tetrahedral elements was then generated using Gmsh (http://www.geuz.org/gmsh/) and imported into COMSOL version 3.3 (http://www.comsol.com) for finite-element analysis. Figure 1 shows a medial view of the TM, ossicles, and ligaments.

The TM, malleus, incus, anterior mallear ligament, and posterior incudal ligament were modeled using second-order ten-node tetrahedral elements. Second-order tetrahedral elements can model complex structures more accurately with fewer elements. This leads to more accurate simulation results and saves computation time.

The pars flaccida is not included in this study for two reasons. First, the area of the pars flaccida is much smaller than that of the pars tensa (e.g., Anson and Donaldson, 1981). Second, even in the gerbil, with a much larger pars flaccida, the volume displacement of the TM is caused mainly by the deformation of the pars tensa when the static pressures are varied from 0.4 to 2 kPa. The volume displacements of the pars flaccida remain nearly unchanged for pressures above 0.4 kPa (Dirckx *et al.*, 1998).

Dirckx and Decraemer (2001) studied gerbil eardrum deformations under quasi-static pressures of ±2 kPa. They found that the cochlea, tensor tympani, and stapes had little influence on eardrum deformations. Thus, in this model, we do not take into account the tensor tympani, the stapes, or the cochlear load.

There are two synovial joints linking the ossicles together. The incustapedial joint was not included here because the stapes was not included. Studies have shown that the incudomallear joint is somewhat flexible (e.g., Decraemer and Khanna, 1995; Nakajima *et al.* 2005) but it has for simplicity been assumed to be rigid in this study The effect on TM volume displacement is probably small.

B. Material properties and hyperelastic models

1. Thickness of TM

The thickness distribution of the human adult TM has been measured by several investigators (e.g., Lim, 1970; Schmidt and Hellstrom, 1991). It has been found that there is significant variation in the thickness across the surface of the TM and large intersubject differences. Recently, Kuypers *et al.* (2006) measured three human adult TM thicknesses using confocal microscopy. They found that the pars tensa has a rather constant thickness in a central region, ranging from 0.040 to 0.12 mm across three subjects. The study of newborn TM thickness is sparse. To the best of our knowledge, the only study was conducted by Ruah *et al.* (1991). They investigated the thickness distribution for different ages of human TMs using histological images with the help of both light and electron microscopy. They measured the thicknesses of TMs from 54 temporal bones, aged from newborn to adult. They found that from newborn to adult the thickness of the TM decreases significantly. Thicknesses of the pars tensa were measured in four different quadrants. They found in newborns that the thickness of the posterior-superior region ranged from 0.4 to 0.7 mm; the thicknesses of the posterior-inferior, anterior-superior and anterior-inferior regions were similar, ranging from 0.1 to 0.25 mm; and the thickness of the umbo area ranged from 0.7 to 1.5 mm.

In this study, a nonuniform thickness for the TM model was developed based on the measurements of Ruah *et al.* (1991), supplemented by thickness measurements on histological images from two one-month-old ears. The thicknesses of the posterior-inferior, anterior-superior, and anterior-inferior quadrants are all 0.1 mm in our model. The thickness of the posterior-superior quadrant is 0.5 mm. In the vicinity of the umbo the TM thickness (excluding the manubrium) is 0.75 mm.

2. Young's modulus of TM

The TM consists of three layers: the epidermis, the outer layer, whose ultrastructure is similar to the epidermis of skin;

the lamina propria, the middle layer, which contains loose ground matrix and two layers of densely packed collagen fibers arranged in radial and circular patterns, respectively; and the lamina mucosa, the thin inner layer, which contains a large number of columnar cells (Lim, 1970). The overall mechanical properties of the TM depend mainly on the lamina propria, which is characterized by the presence of type II collagen fibers.

The Young's modulus of the human adult TM has been investigated by both experimental and modeling studies. Békésy (1960) first measured Young's modulus of TM using a beam-bending test on a strip of cadaver TM. He reported a Young's modulus of 20 MPa. Kirikae (1960) measured the Young's modulus of a strip of TM using a longitudinal vibration. He reported a Young's modulus of about 40 MPa. Decraemer *et al.* (1980) used a quasi-static uniaxial tensile test on strips of TM. They found that the incremental Young's modulus was shown to vary with the stress level, from almost zero up to a value of approximately 23 MPa. Cheng *et al.* (2007) also used uniaxial tensile tests and combined the experimental results with an Ogden hyperelastic model. They estimated that the Y.m of the TM is between 0.4 and 22 MPa, again depending on the stress level. Fay *et al.* (2005) proposed three approaches to estimate the Young's modulus of the TM in adult human and cats. They concluded that the Young's modulus of the adult human TM is between 30 and 90 MPa for an isotropic model and 100–400 MPa for an orthotropic TM model. Their values are much higher than those of other investigators at least in part because they are calculated based on the thicknesses of the dense fibrous layers of the TM rather than on the overall thickness.

To date, the Young's modulus of the newborn TM has not been investigated. Ruah *et al.* (1991) examined the ultrastructure of the TM from newborns to adults using electron microscopy. They observed that with age the TM becomes less vascular and less cellular, and has more collagen fibers and elastins. They concluded that age-related changes occurring in the lamina propria of the TM are very similar to changes observed in the human skin. Although no direct measurements of the mechanical properties of the TM in newborns are available, the age-related mechanical properties of various other collagenous tissues have been studied. The mechanical properties of collagen are mainly decided by its density, length, and cross-linking, and by the diameters and orientations of the collagen fibrils and fibers. The lengths of collagen fibers also increase with age. It has been reported that fibers in rat tail tendon increased from 20–100 nm at four weeks old to 30–200 nm by 1 year old (e.g., Schwarz, 1957). It has also been found that collagen density and cross-links increase with age and that collagen becomes more aligned with age (e.g., Hall, 1976; Stoltz, 2006). Age-related Young's modulus changes of human skin have also been reported. Rollhauser (1950) studied the age-related Young's modulus of skin from 3-month-old infants to adults. He found that the Young's modulus of skin in adults is approximately 7–8 times as large as that in infants. Similar results were reported by Yamada (1970). They found that the Young's modulus of skin in adults is about six times as large as the Young's modulus of infant skin. Grahame and Holt (1969) found that the Young's modulus of skin increased by a factor of 2 from 19 years old to 80 years old. Histological examination of the skin also shows that as the age of the skin increases the collagen density becomes higher and the collagen fibers become less extensible (Agache *et al.*, 1980).

In this study, three Young's moduli are used for the TM: 0.6, 1.2 and 2.4 MPa. Consistent with the adult/infant ratios of 6 to 8 found by Rollhauser (1950) and Yamada (1970), the 0.6 MPa value is several times smaller than a typical small-strain Young's modulus from Decraemer *et al.* (1980); and 2.4 MPa is approximately 8–10 times smaller than the measurement of Békésy (1960) and the large-strain value of Decraemer *et al.* (1980).

3. Young's moduli of ossicles and ligaments

Studies have shown that development of the ossicles continues after birth. Ossicular weight and size are smaller in newborns (Olszewski, 1990). It has been reported that a long, narrow anterior mallear process exists in at least some newborns (Anson and Donaldson, 1981; Unur *et al.*, 2002). We observed a long process in our 1-month-old histological images. We do not see a long process in our 22-day-old newborn CT scan, probably due to the limited resolution of the scan.

Yokoyama *et al.* (1999) studied the postnatal development of the ossicles in 32 infants and children, aged from one day to nine years. They found that the newborn malleus and incus contain much bone marrow, which is gradually replaced by bone. They concluded that ossification of the ossicles takes place after birth until about 25 months.

In this study, the Young's modulus of the ossicles is assumed to be 1, 3, or 5 GPa. The value of 5 GPa is at the low end of the range of the Young's modulus of bone given by Nigg and Herzog (1999), and it is approximately 2.5 times smaller than the values used in adult middle-ear models (e.g., Koike *et al.*, 2002). Similarly, the Young's modulus of the ligaments is assumed to be 1, 3, or 5 MPa, which is approximately 2 to 10 times smaller than typical values used in human adult middle-ear models (e.g., Koike *et al.*, 2002). Ligaments were assumed to be hyperelastic. Ossicles were assumed to have linear material properties due to the high Young's modulus.

4. Hyperelastic model

The method is only briefly described here, since a detailed report has been published elsewhere (Qi *et al.*, 2006). A polynomial hyperelastic constitutive law was applied, which allows us to simulate nearly incompressible biological materials with large deformations. The strain energy is given by

$$W = C_{10}(I_1 - 3) + C_{01}(I_2 - 3) + \frac{\kappa}{2}(J-1)^2, \quad (1)$$

where I_1 and I_2 are the first and second strain invariants; J is the volume-change ratio; and κ is the bulk modulus. C_{10} and C_{01} are material constants. Under small strains the Young's modulus of the material, E, may be written as

$$E = 6(C_{10} + C_{01}) \tag{2}$$

and the bulk modulus may be written as

$$\kappa = \frac{3}{3(1-2\nu)}, \tag{3}$$

where ν is Poisson's ratio. We assume that the Poisson's ratios of the TM and ligaments are 0.48, which is a typical value used for nearly incompressible soft tissue (e.g., Qi *et al.*, 2006); and that the Poisson's ratio of the ossicles is 0.3, a widely used value for bone (e.g. Funnell and Laszlo, 1982). The ratio $C_{10}:C_{01}$ is taken to be 1:1, which has been widely used for biological soft tissue (e.g., Mendis *et al.*, 1995; Samani and Plewes, 2004; Qi *et al.*, 2006); from Eq. (2), therefore, $C_{10}=C_{01}=E/12$.

The TM volume displacement was calculated by the integration of the nodal displacements over the entire TM surface using COMSOL.

5. Boundary conditions

The boundary of the TM and the ends of the anterior mallear and posterior incudal ligaments are taken to be fixed. The positive and negative static pressures are uniformly applied to the lateral surface of the TM.

C. Middle-ear cavity

The middle-ear cavity is an irregular, air-filled space within the temporal bone, and is mainly comprised of four parts: tympanic cavity, aditus ad antrum, mastoid antrum, and mastoid air cells (e.g. Anson and Donaldson, 1981). In the human adult, the middle-ear cavity volume is between 2000 and 22 000 mm^3 (e.g., Molvær *et al.*, 1978). The air enclosed in the middle-ear cavity has a compliance that is proportional to its volume, so the larger the volume of the trapped air, the larger the compliance. Studies have shown that the middle-ear cavity may exert significant effects on middle-ear admittance (e.g., Zwislocki, 1962; Guinan and Peake, 1967; Funnell and Laszlo, 1982; Ravicz and Rosowski, 1997; Stepp and Voss, 2005). Ravicz *et al.* (1992), for example, estimated that reducing the air volume of the gerbil middle-ear cavity by 75% would approximately triple the effective middle-ear input impedance.

The compliance at the TM (C_{TM}) can be written as

$$1/C_{TM} = 1/C_{TOC} + 1/C_{CAV}, \tag{4}$$

where C_{TOC} is the compliance of the TM, ossicles and cochlea; and C_{CAV} is the compliance of the middle-ear air cavity [cf. Stepp and Voss, 2005, Eq. (2)]. In our case C_{TOC} represents the compliance of the TM, malleus, and incus, since the stapes and cochlea are not included in our model. [Note that the compliances C_{TM}, C_{TOC}, and C_{CAV} are not related to the material constants C_{10} and C_{01} in Eq. (1)].

Previous studies have shown that the mastoid grows in all three dimensions, length, width, and depth, from birth to adulthood (Eby and Nadol, 1986). However, the volume of the mastoid in infants has not been quantitatively measured so far. To the best of our knowledge, only the tympanic cavity has been quantitatively measured in infants. Ikui *et al.* (2000) reconstructed 14 normal human temporal bones aged from 3 months old to adulthood. They reported that the tympanic cavity is about 1.5 times as large in adults (about 640 mm^3) as in infants (about 450 mm^3).

One factor affecting the volume of the middle-ear cavity in newborns and infants is the presence of residual mesenchyme (embryonic tissue of mesodermal origin). It has been reported that most of the mesenchyme is found in the aditus ad antrum, the round-window niche and the oval-window niche (Takahara *et al.*, 1986; Northrop *et al.*, 1986). Northrop *et al.* (1986) found that the volume of mesenchyme remained constant at approximately 72 mm^3 in newborns from 20 to 36 days old. They estimated that mesenchyme probably occupies less than one-tenth of the entire middle-ear cavity.

In this study, the middle-ear cavity volume was estimated based on our CT-scan reconstruction. The mesenchyme was excluded from the calculation. The tympanic cavity alone is approximately 330 mm^3, which is smaller than the reports from Ikui *et al.* (2000). This is consistent with the fact that our subject was a 22-day-old while their subjects were about 3 months old. It is very difficult to accurately estimate the entire middle-ear cavity volume because the mastoid antrum and some air-cell spaces have very complicated shapes that are difficult to delineate accurately in the CT images. Based on an approximate segmentation of all but the smallest spaces, the combined volume of the aditus ad antrum, the mastoid antrum, and the mastoid air cells in our scan was estimated to be between 400 and 600 mm^3. The total middle-ear cavity volume is thus between 730 and 930 mm^3. For the model we have thus used minimum and maximum middle-ear cavity-volume parameter values of 700 mm^3 and 1000 mm^3, respectively.

D. Tympanometry measurements

The multifrequency tympanometry data for well babies presented here are based on measurements from Shahnaz *et al.* (2008). Sixteen full-term healthy 3-week-olds participated in the study. All infants passed a hearing screening at birth and again at 3 weeks of age. Multifrequency tympanometry was done in both ears of 15 out of 16 subjects, and in the right ear of the remaining subject. Tympanograms were recorded in the 31 ears using the Virtual 310 system with the extended high-frequency option. The admittance magnitude and phase were recorded at nine frequencies (226, 355, 450, 560, 630, 710, 800, 900 and 1000 Hz). The susceptance and conductance were derived from the measured magnitude and phase. The pump rate was 125 daPa/s and the pressure was varied from +250 to −300 daPa (1 daPa = 10 Pa). For a more detailed description see Shahnaz *et al.* (2008).

We use the following equations to calculate equivalent volumes (Shanks *et al.*, 1993) from the susceptance tails [Eq. (5)] and from the admittance tails [Eq. (6)] respectively:

$$V_{ea}^{B\pm} = B^{\pm}\frac{1000}{f/226}, \tag{5}$$

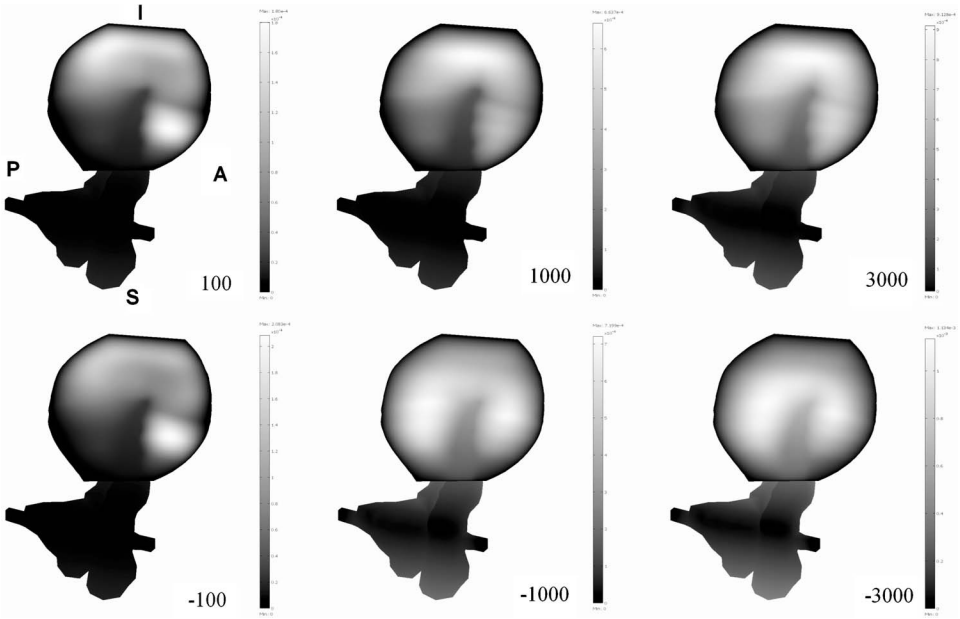

FIG. 2. Simulated displacement patterns for static pressures of ±100, ±1000 and ±3000 Pa. Lighter colors represent larger values.

$$V_{ea}^{Y\pm} = Y^{\pm}\frac{1000}{f/226}, \tag{6}$$

where $V_{ea}^{B\pm}$ and $V_{ea}^{Y\pm}$ represent the equivalent volume (mm^3) calculated from the positive or negative susceptance or admittance tail; $B^{\pm}$ and $Y^{\pm}$ are the susceptance and the admittance magnitude at the positive (+) or negative (−) tail, respectively; and f is frequency (Hz). It should be noted that Eq. (6) is valid only when the conductance (the real part of the admittance) is zero. For newborns, the equivalent volume calculated from Eq. (6) may include significant errors due to nonzero conductance at the tails. In this study, however, the model results are compared with the difference between the equivalent volumes at the two tails ($\Delta V_{ea}^{B}, \Delta\ V_{ea}^{Y}$), calculated as

$$\Delta V_{ea}^{B} = V_{ea}^{B+} - V_{ea}^{B-}, \tag{7}$$

$$\Delta V_{ea}^{Y} = V_{ea}^{Y+} - V_{ea}^{Y-}. \tag{8}$$

As discussed in Sec. IV below, in newborns the conductances at the two tails are almost equal and therefore almost cancel each other.

III. RESULTS

A. Model displacements

Convergence tests were conducted to investigate how many elements should be used in the model. A nonuniform mesh was created. Four different resolutions were compared. The TM has nominal numbers of elements per diameter of 80, 120, 160, and 200, respectively. The ossicles and ligaments have nominal numbers of elements per diameter of 20, 40, 60, and 90, respectively. We found that the difference in TM volume displacement is less than 1.7% between the model with 160 elements/diameter for the TM and 40 elements/diameter for the ossicles and ligaments and the model with 200 elements/diameter for the TM and 90 elements/diameter for the ossicles and ligaments. Thus, the former model (160 and 40 elements/diameter) was selected for further simulations. The model has a total of 12 815 elements, 9250 of which belong to the TM.

Our simulations show that varying the Young's modulus of the ossicles and ligaments has little effect on the TM volume displacements. The changes of the TM volume displacements are less than 3% when the Young's modulus of the ossicles increases from 1 to 6 GPa. The changes of the TM volume displacements are less than 6% when the Young's modulus of the ligaments increases from 0.6 to 6 MPa.

Figure 2 shows the model displacement patterns corresponding to different static pressures under open-cavity conditions. The location of the maximum displacement moves when the pressures are changed, which agrees with observations in human adult middle-ear measurements (Dirckx and Decraemer, 1991). At low pressures (±100 Pa), the negative and positive displacement patterns are similar, with the maximum displacements in the antero-superior quadrant. When pressures are increased, the negative and positive displacement patterns become significantly different from each other. At the extreme positive pressure, the maximum displacement occurs inferiorly. At the extreme negative pressure, however, the maximum displacements occur anteriorly and posteriorly.

B. Middle-ear cavity effects on TM volume displacement

Our finite-element model does not explicitly include the middle-ear cavity. We use Boyle's Law to estimate the effects of the cavity volume on TM volume displacements. Details are given in the Appendix.

Figure 3 compares the model TM volume displacements corresponding to different Young's moduli of the TM under open and closed-cavity conditions (700 mm^3), and the TM volume displacement measured in adults (Elner *et al.*, 1971; Dirckx and Decraemer, 1991). The TM volume-displacement curves are nonlinear, with larger slopes for low pressures than for high pressures; and asymmetrical, with larger dis-

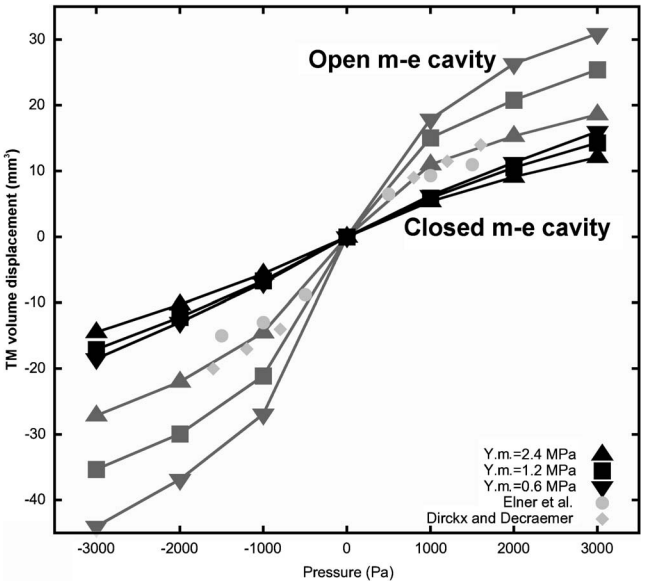

FIG. 3. Simulated TM volume displacements as functions of pressure, for different TM Young's moduli, for both open middle-ear cavity and closed middle-ear cavity (700 mm^3), and experimental volume displacements measured in human adults from Dirckx and Decraemer (1992), Table VI and Elner *et al.* (1971), Table III, respectively. Dirckx and Decraemer (1992) gave middle-ear cavity pressures rather than canal pressures, so their curve has been reversed.

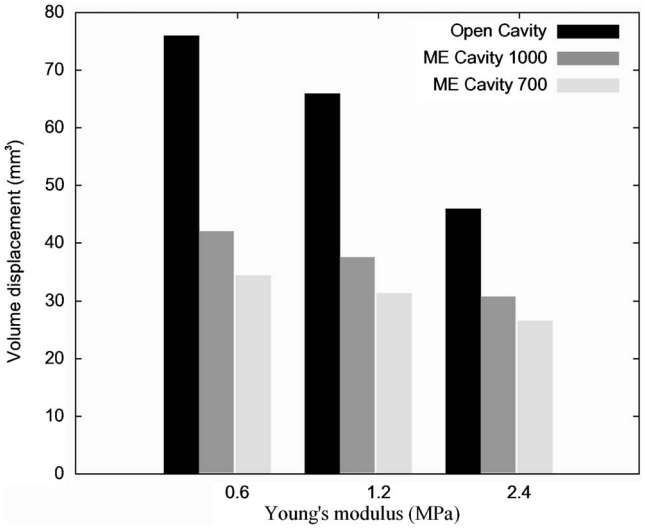

FIG. 4. Simulated TM volume displacements between −3 and +3 kPa, for different middle-ear cavity volumes (700, 1000 mm^3 and open cavity).

placements for negative pressures, which agrees with adult TM measurements (Dirckx and Decraemer, 1991; Elner *et al.*, 1971). The form of the observed nonlinearity is determined by a combination of the material nonlinearity [expressed by Eq. (1)] and geometric nonlinearities resulting from the large deformations.

Our simulation results indicate that, from −3 to +3 kPa, the TM volume displacements are approximately 27, 32, and 35 mm^3 when the middle-ear cavity volume is 700 mm^3; and approximately 46, 60, and 75 mm^3 under open-cavity conditions, corresponding to Young's moduli of the TM of 2.4, 1.2, and 0.6 MPa. The closed middle-ear cavity significantly reduces the TM volume displacements, and also reduces the degree of non1inearity and asymmetry of the TM volume displacement. The TM volume displacements under open-cavity conditions are about 1.7–2.2 times as large as those under closed-cavity conditions with a volume of 700 mm^3. The simulated TM volume displacements under open-cavity conditions show an asymmetry similar to that of the volume displacements measured in adults, with larger volume displacements at negative pressures.

Figure 4 compares the TM volume displacements between −3 and +3 kPa when the middle-ear cavity is 700 mm^3, 1000 mm^3, and open. When the middle-ear cavity volume increases, the TM volume displacement increases, and the nonlinearity and asymmetry of the TM volume displacement increase as well. When the cavity volume increases from 700 to 1000 mm^3 (an increase of about 43%), the TM volume displacements increase by approximately 16%, 20%, and 22% for TM Young's moduli of 2.4, 1.2, and 0.6 MPa, respectively. When the cavity volume increases from 1000 mm^3 to the open situation (infinitely large), the TM volume displacements increase by 50%, 81%, and 88% for TM Young's moduli of 2.4, 1.2, and 0.6 MPa, respectively.

C. Comparisons with tympanometric data

To date, no direct measurements of newborn TM displacements have been made. Thus, in this section we shall compare our simulation results with two sets of tympanometric equivalent-volume differences, one calculated from 3-week-olds (Shahnaz *et al.*, 2008) and the other calculated from healthy infants and NICU infants aged from 1 day to 2 months old (Margolis *et al.*, 2003).

1. Equivalent-volume differences from Shahnaz et al.

The equivalent-volume difference (ΔV_{ea}^{B}) between the positive tail (+2.5 kPa) and the negative tail (−2.75 kPa) was derived from susceptances using Eq. (7) in 16 3-week-olds (Shahnaz *et al.*, 2008). Figure 5 shows the ΔV_{ea}^{B} (median and 25th and 75th percentiles) for left and right ears combined. As shown in the figure, the medians of ΔV_{ea}^{B} in newborns

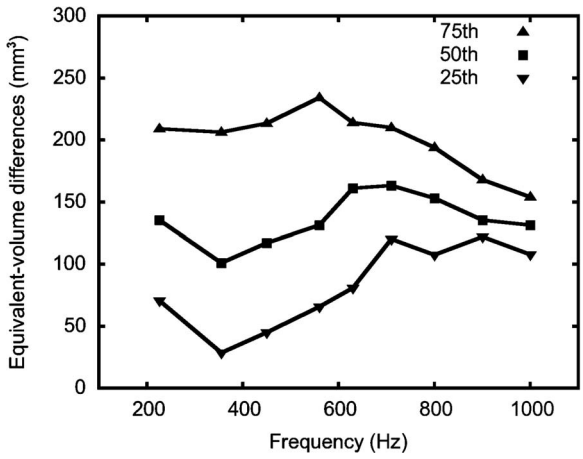

FIG. 5. Equivalent-volume differences (median and 25th and 75th percentiles) between susceptance tails from study of Shahnaz *et al.* (2008).

stay almost constant over the entire frequency range. The median ΔV_{ea}^{B} across frequencies is about 132 mm^3.

Our simulation results indicate that from −2.75 to +2.5 kPa the TM volume displacements, corresponding to a Young's modulus of the TM of 2.4, 1.2 or 0.6 MPa, were approximately 24, 28, and 31 mm^3 for a middle-ear cavity volume of 700 mm^3, and 28, 34, and 38 mm^3 for a cavity volume of 1000 mm^3.

2. Equivalent-volume differences from Margolis et al.

Margolis *et al.* (2003) investigated the 1 kHz admittance both in 46 ears of 30 full-term healthy newborns (aged 2–4 weeks) and in 105 ears of 65 NICU newborns (aged 3.9 ± 3.8 weeks, mean ± SD). The equivalent-volume difference (ΔV_{ea}^{Y}) between the positive tail (+2 kPa) and the negative tail (−4 kPa) was derived from the admittance using Eq. (8). The median ΔV_{ea}^{Y} at 1000 Hz is 158 and 136 mm^3 for NICU newborns and healthy full-term newborns, respectively.

Our simulation results indicate that from −4 to +2 kPa the TM volume displacements, corresponding to a Young's modulus of the TM of 2.4, 1.2 or 0.6 MPa, were approximately 28, 33, and 36 mm^3 for a middle-ear cavity volume of 700 mm^3, and 33, 39, and 44 mm^3 for a cavity volume of 1000 mm^3.

The predicted TM volume displacements calculated for the NICU newborns are larger than those calculated for the healthy newborns. This may be caused by the age difference between the two groups. The healthy-newborn ages were from 2 to 4 weeks, while the NICU-newborn age distribution was 3.9 ± 3.8 weeks (mean ± SD). A larger number of very young infants in the NICU group might account for the larger median ΔV_{ea} in that group.

3. Comparison

In both cases the simulation results are lower than the median equivalent-volume differences calculated from tympanometric measurements. This is consistent with the fact that the experimental equivalent-volume changes include contributions from the movements of the ear-canal wall, probe tip, and tympanic ring as well as the TM. This will be further discussed below.

IV. DISCUSSION AND CONCLUSIONS

A nonlinear hyperelastic model of the newborn middle ear is presented and compared with tympanometric data. For static pressures from −3 kPa to +3 kPa, the simulated TM displacements and volume displacements are nonlinear.

In our simulations, the TM volume displacements show considerable asymmetry under open-cavity conditions, with larger displacements for negative pressures. Adult human TM volume displacements also displayed asymmetry in the measurements of Dirckx and Decraemer (1992), which were conducted under open-cavity conditions, and in the measurements of Elner *et al.* (1971), which were conducted under closed-cavity conditions. The similarity between the measurements of Dirckx and Decraemer and those of Elner *et al.* suggests that in adults the middle-ear cavity volume generally has little effect on the TM volume displacement. This does not appear to be true for newborns.

Our simulated TM volume displacements are nearly symmetrical under closed-cavity conditions, as shown in Fig. 3. The reason for the near symmetry under closed-cavity conditions is that the newborn cavity is relatively small, so C_{CAV} is relatively low, which leads to smaller displacements. This means that the TM is not driven into its nonlinear range. This is similar to the way that the nonlinearities decrease when Young's modulus increases: The system is still intrinsically nonlinear but it is not pushed so far into the nonlinear range.

The effects of cavity volume on TM volume displacements increase as the Young's modulus of the TM decreases. As shown in Fig. 4, when the volume of the middle-ear cavity increases from 700 to 1000 mm^3, the TM volume displacements increase by 16%, 20%, and 22% when the Young's modulus of the TM is 2.4, 1.2, and 0.6 MPa, respectively. Similarly, when the volume of the middle-ear cavity increases from 700 mm^3 to infinitely large (the open-cavity condition), the TM volume displacements increase by 70%, 91%, and 117% when the Young's modulus of the TM is 2.4, 1.2, and 0.6 MPa, respectively. This is to be expected because when the Young's modulus of the TM decreases, $1/C_{TOC}$ decreases and the ratio of $1/C_{CAV}$ to $1/C_{TOC}$ increases.

Our simulations show that the Young's modulus of the TM has a significant effect on the TM volume displacement, as shown in Figs. 3–5. The effect is more pronounced for a larger middle-ear cavity. As the Young's modulus of the TM decreases from 2.4 to 1.2 MPa and then to 0.6 MPa, the TM volume displacements increase by approximately 19% and 10% when the middle-ear cavity is 700 mm^3; by approximately 23% and 12% when the middle-ear cavity is 1000 mm^3; and by approximately 44% and 15% when the middle-ear cavity is open.

The simulated TM volume changes do not reach a plateau when the pressure is varied to either −3 kPa or +3 kPa, which is consistent with the nonflat tails often found in susceptance tympanograms in newborns (e.g., Paradise *et al.*, 1976; Holte *et al.*, 1990). The failure of the model to reach a plateau is also consistent with the report by Shanks and Lilly (1981) that even at pressures of +2 and −4 kPa the adult middle ear is not rigid.

The tail-to-tail equivalent-volume differences shown in Fig. 5 consist of two components: (1) the actual air-volume change in response to the static pressure, corresponding to the static displacement of the ear-canal wall, the TM and the probe tip; and (2) a component due to the vibration of the canal wall and TM in response to the probe tone. The actual air-volume change should be independent of frequency, while the vibration-related component is presumably dependent on frequency. Both our previous newborn ear-canal model (Qi *et al.*, 2006) and the current middle-ear model under closed-cavity conditions predict nearly symmetrical nonlinear responses, which suggests that the vibrations at the extreme positive and negative pressures are similar. In that case, their effects will tend to cancel when subtracting either

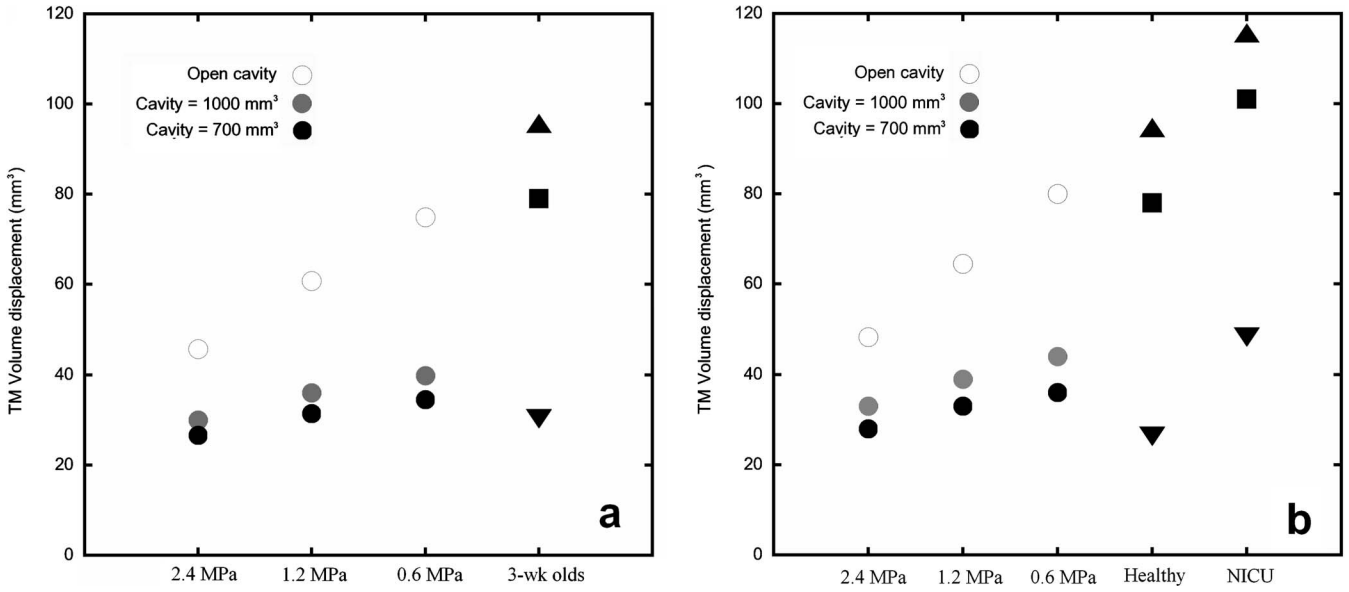

FIG. 6. Comparison of simulated TM volume displacements, for different cavity volumes, with the equivalent-volume differences in 3-week-old newborns (a), and with the equivalent-volume differences in NICU and healthy newborns (b).

admittances or susceptances and the ΔV_{ea} will be mainly determined by the actual volume change (Qi *et al.*, 2006). In our analysis of the data of Shahnaz *et al.* (2008), shown in Fig. 5, the median ΔV_{ea} varies little across the entire frequency range, which is consistent with interpreting the equivalent-volume difference as the actual volume change. (It should be mentioned, however, that tail-to-tail equivalent-volume differences calculated for human adults may have a significant vibration-related component, given the asymmetrical TM volume displacement in adults.)

Based on our previous ear-canal model (Qi *et al.*, 2006), when the Young's modulus of the ear-canal wall is 30, 60, and 90 kPa, the simulated canal-wall volume displacement is 101, 53, and 37 mm^3, respectively, from −2.75 to +2.5 kPa. Subtracting these canal-wall volume displacements from the median equivalent-volume change of 132 mm^3 obtained from the tympanometric data of Shahnaz *et al.* (Sec. III C 1) yields predicted TM volume displacements of about 31, 79, and 95 mm^3, respectively.

For use with the data of Margolis *et al.* (2003), the pressure response of our canal model has been extended from −3 to −4 kPa. The resulting simulated canal-wall volume displacements, for Young's moduli of 30, 60, and 90 kPa, are 109, 56, and 42 mm^3, respectively. Again subtracting the simulated canal-wall volume displacements from the median tympanometric equivalent-volume differences (Sec. III C 2), we obtain predicted TM volume displacements of 48, 101, and 115 mm^3 for NICU newborns and 27, 77, and 94 mm^3 for healthy full-term babies.

In Fig. 6, parts *a* and *b* compare the TM-model volume displacements under closed-cavity (700 and 1000 mm^3) and open-cavity conditions with the TM volume displacements predicted by combining our canal-model results with the measurements of Shahnaz *et al.* (2008) and Margolis *et al.* (2003), respectively.

In an attempt to obtain an estimate of canal-wall displacement separate from that of the TM, we note that Margolis *et al.* (2003) recommended using the peak-to-negative-tail difference of admittance at the 5th percentile as a pass-fail criterion for conductive hearing loss. Since middle-ear effusion (MEE) is the most common cause of conductive hearing loss in newborns, we suppose that the pass-fail criterion can be used as a criterion for MEE. For newborns with MEE, the TM cannot move as freely as usual and the admittance of the middle ear may be nearly zero. As a result, the equivalent-volume difference (ΔV_{ea}) between the two tails would be mainly due to the canal-wall, tympanic-ring and probe-tip movement. The ΔV_{ea} at the 5th percentile of Margolis *et al.* is 113 mm^3. This is close to the maximum canal-wall volume displacement of 109 mm^3 predicted by our canal model, when the Young's modulus of the ear-canal wall is 30 MPa. In that case, the closed-cavity TM-model volume displacements are close to the minimum TM volume displacements predicted from the canal model. Note that the TM volume displacement predicted from our canal model actually also includes any volume displacements due to tympanic-ring and probe-tip movement. Thus, on the one hand, if we adopt the lowest Young's modulus (30 MPa) for the canal-wall model then the predicted canal-wall and TM volume displacements match the total volume displacements obtained from the tympanometric data. On the other hand, if the canal wall is stiffer, then we would predict some additional volume displacement due to the tympanic ring and probe tip. The fact that 113 mm^3 is a large fraction of their median ΔV_{ea}^{Y} values of 136 mm^3 and 158 mm^3 is consistent

TABLE I. Three sets of answers for initial cavity volume=700 mm^3 and canal pressure=1 kPa.

	V_1	P_1	ΔP	ΔV
Answer 1	720.554	97147.5	3852.52	20.5539
Answer 2	15.7314	0.444972	0.455072E7	715.731
Answer 3	694.647	100771.0	229.475	5.35243

TABLE II. TM volume displacements for initial cavity volume=700 mm^3.

Young's modulus (MPa)	Pressure (Pa)					
	−3000	−2000	−1000	1000	2000	3000
2.4	−14.44	−10.26	−5.55	5.35	9.07	12.09
1.2	−17.04	−12.16	−6.61	5.93	10.46	14.26
0.6	−18.86	−12.97	−6.90	6.23	11.26	15.60

with our model-based prediction that the canal-wall volume displacement makes a major contribution to the total canal volume change. The relative contributions of these different components clearly depend strongly on the corresponding material properties, especially stiffnesses and TM thicknesses. Further work is required in order to further constrain estimates of the Young's moduli, and the effects of current simplifications such as the rigidity of the incudomallear joint and the uniform TM thickness in each quadrant should be explored.

As a first step in modeling the newborn middle ear, our results show that the volume of the middle-ear cavity and the Young's modulus of the TM have significant effects on the TM volume displacement. It is not clear whether the volume displacement of the probe tip and tympanic ring make significant contributions to the total volume change. It will be necessary to combine the ear-canal and middle-ear models and to incorporate the tympanic ring and the probe tip. Modeling the small-amplitude dynamic response of the ear canal and middle ear to the probe tone, and then combining that with the nonlinear static response modeled here, will permit a complete model of tympanometry in newborns.

ACKNOWLEDGMENTS

This work was supported by the Canadian Institutes of Health Research and the Natural Sciences and Engineering Research Council (Canada), the Fonds de recherche en santé du Québec, the Montréal Children's Hospital Research Institute, the McGill University Health Centre Research Institute, and the Hearing Foundation of Canada. The authors thank C. Northrop (Temporal Bone Foundation, Boston) for the histological images used to supplement and help interpret our CT scan, C. B. Ruah for helpful discussion of his TM thickness data, and J. Lufty for his work on the initial segmentation of the CT scan.

APPENDIX: CALCULATION OF EFFECTS OF MIDDLE-EAR CAVITY ON TM VOLUME DISPLACEMENT

Our finite-element model does not include the effects of the middle-ear cavity. In order to estimate the effects of the cavity on TM volume displacement, we start with Boyle's law, assuming that temperature is constant because the pressure changes are slow (cf. Elner *et al.*, 1971):

$$P_0V_0 = P_1V_1, \tag{A1}$$

where P_0 (in Pa) is the initial pressure in the middle ear (atmospheric pressure, 10^5 Pa); V_0 (in mm^3) is the initial middle-ear cavity volume, before the TM is displaced; and P_1 and V_1 are the final pressure and volume in the middle ear. Suppose that overpressure p is applied in the ear canal. The pressure difference across the TM is then

$$\Delta P = P_0 + p - P_1, \tag{A2}$$

and the TM volume displacement is

$$\Delta V = V_0 - V_1. \tag{A3}$$

The relationship between ΔP and ΔV is defined by our finite-element model, as shown in Fig. 3. The relationship is strongly asymmetrical, but on each side of the origin it can be approximated by using a second-order polynomial equation. Therefore, for the purpose of calculating the effect of the closed middle-ear cavity, we represent the relationship by

$$\Delta P = a\Delta V^2 + b\Delta V, \tag{A4}$$

where a and b are fitted coefficients. The coefficients a and b in Eq. (A4) were estimated using the least-squares method (Gnuplot version 4.0, http://www.gnuplot.info). The coefficients were estimated separately for the positive-pressure and negative-pressure parts and for each of the three TM Young's modulus values. Therefore, six sets of a and b were estimated.

Given P_0, V_0, p, a and b, we have four simultaneous equations (A1)–(A4) and four unknowns (P_1, V_1, ΔP and

TABLE III. TM volume displacements for initial cavity volume=1000 mm^3.

Young's modulus (MPa)	Pressure (Pa)					
	−3000	−2000	−1000	1000	2000	3000
2.4	−17.14	−12.49	−7.01	6.50	10.53	13.72
1.2	−20.81	−15.31	−8.74	7.52	12.65	16.81
0.6	−23.40	−16.82	−9.37	8.11	14.02	18.90

ΔV). The computer-algebra system Axiom (http://axiom-wiki.newsynthesis.org) is used to solve the system of equations either symbolically or numerically.

If we adopt some specific values for the given parameters, e.g., $P_0=10^5$, $V_0=700$, $p=1000$, $a=8.89$, and $b=-4.7$, then we can solve the set of Eqs. (A1)–(A4) numerically using the Axiom *solve* command. Since the solution to the set of equations involves a cubic equation, we obtain three sets of answers, as shown in Table I. Since we know that $\Delta V>0$ and $\Delta V<V_0$, only one answer is physically reasonable. Thus we see that, for these particular values for P_0, V_0, a and b, the TM volume displacement is approximately 5.35 mm^3 when the canal pressure p is 1 kPa.

The results for two different initial middle-ear volumes (700 and 1000 mm^3) are given in Tables II and III for six different pressures (± 1000, ± 2000 and ± 3000 Pa) and three different values of TM Young's modulus (0.6, 1.2 and 2.4 MPa). Only the physically reasonable solutions are shown in Tables II and III.

Agache, P. G., Monneur, C., Leveque, J. L., and De Rigal, J. (**1980**). "Mechanical properties and Young's modulus of human skin in vivo," Arch. Dermatol. Res. **269**, 221–232.

Anson, B. J., and Donaldson, J. A. (**1981**). "The temporal bone," in *Surgical Anatomy of the Temporal Bone*, edited by B. J. Anson and J. A. Donaldson (Saunders, Philadelphia).

Békésy, G. V. (**1960**). *Experiments in Hearing* (AIP Press, New York).

Cheng, T., Dai, C., and Gan, R. Z. (**2007**). "Viscoelastic properties of human tympanic membrane," Ann. Biomed. Eng. **35**, 305–314.

Decraemer, W. F., and Khanna, S. M. (**1995**). "Malleus vibration modeled as rigid body motion," Acta Otorhinolaryngol. Belg. **49**, 139–145.

Decraemer, W. F., Maes, M. A., and Vanhuyse, V. J. (**1980**). "An elastic stress–strain relation for soft biological tissues based on a structural model," J. Biomech. **13**, 463–468.

Dirckx, J. J. J., Buytaert, J. A. N., and Decraemer, W. F. (**2006**). "Quasi-static transfer function of the rabbit middle ear measured with a heterodyne interferometer with high-resolution position decoder," J. Assoc. Res. Otolaryngol. **7**, 339–551.

Dirckx, J. J. J., and Decraemer, W. F. (**1991**). "Human tympanic membrane deformation under static pressure," Hear. Res. **51**, 93–106.

Dirckx, J. J. J., and Decraemer, W. F. (**1992**). "Area change and volume displacement of the human tympanic membrane under static pressure," Hear. Res. **62**, 99–104.

Dirckx, J. J. J., Decraemer, W. F., von Unge, M., and Larsson, C. (**1997**). "Measurement and modeling of boundary shape and surface deformation of the Mongolian gerbil pars flaccida," Hear. Res. **111**, 153–164.

Dirckx, J. J. J., Decraemer, W. F., von Unge, M., and Larsson, C. (**1998**). "Volume displacement of the gerbil eardrum pars flaccida as a function of middle ear pressure," Hear. Res. **118**, 35–46.

Dirckx, J. J. J., and Decraemer, W. F. (**2001**). "Effect of middle ear components on eardrum quasistatic deformation," Hear. Res. **157**, 124–137.

Eby, T. L., and Nadol, J. B., Jr. (**1986**). "Postnatal growth of the human temporal bone. Implications for cochlear implants in children," Ann. Otol. Rhinol. Laryngol. **95**, 356–364.

Elner, A., Ingelstedt, S., and Ivarson, A. (**1971**). "The elastic properties of the tympanic membrane system," Acta Oto-Laryngol. **72**, 397–403.

Fay, J. Puria, S., Decraemer, W. F., and Steele, C. (**2005**). "Three approaches for estimating the elastic modulus of the tympanic membrane," J. Biomech. **38**, 1807–1815.

Funnell, W. R. J., and Laszlo, C. A. (**1982**). "A critical review of experimental observations on eardrum structure and function," ORL **44**, 181–205.

Gaihede, M. (**1999**). "Mechanics of the middle ear system: Computerized measurements of its pressure-volume relationship," Auris Nasus Larynx **26**, 383–399.

Grahame, R., and Holt, P. J. (**1969**). "The influence of ageing on the in vivo elasticity of human skin," Gerontologia **15**, 121–319.

Guinan, J. J., Jr. and Peake, W. T. (**1967**). "Middle-ear characteristics of anesthetized cats," J. Acoust. Soc. Am. **41**, 1237–1261.

Hall, D. A. (**1976**). *The Aging of Connective Tissue* (Academic, London).

Holte, L., Cavanaugh, R. M., Jr., and Margolis, R. H. (**1990**). "Ear canal wall mobility and tympanometric shape in young infants," J. Pediatr. (St. Louis) **117**, 77–80.

Ikui, A., Sando, I., Haginomori, S., and Sudo, M. (**2000**). "Postnatal development of the tympanic cavity: A computer-aided reconstruction and measurement study," Acta Oto-Laryngol. **120**, 375–379.

Keefe, D. H., Bulen, J. C., Arehart, K. H., and Burns, E. M. (**1993**). "Ear-canal impedance and reflectance coefficient in human infants and adults," J. Acoust. Soc. Am. **94**, 2617–2637.

Keefe, D. H., and Levi, E. (**1996**). "Maturation of the middle and external ears: Acoustic power-based responses and reflectance tympanometry," Ear Hear. **17**, 361–372.

Keefe, D. H., and Simmons, J. L. (**2003**). "Energy transmittance predicts conductive hearing loss in older children and adults," J. Acoust. Soc. Am. **114**, 3217–3238.

Kirikae, I. (**1960**). *The Structure and Function of the Middle Ear* (University of Tokyo, Tokyo).

Koike, T., Wada, H., and Kobayashi, T. (**2002**). "Modeling of the human middle ear using the finite-element method," J. Acoust. Soc. Am. **111**, 1306–1317.

Kuypers, L. C., Decraemer, W. F., and Dirckx, J. J. J. (**2006**). "Thickness distribution of fresh and preserved human eardrums measured with confocal microscopy," Otol. Neurotol. **27**, 256–264.

Ladak, H. M., Decraemer, W. F., Dirckx, J. J. J., and Funnell, W. R. J. (**2004**). "Response of the cat eardrum to static pressures: Mobile versus immobile malleus," J. Acoust. Soc. Am. **116**, 3008–3021.

Ladak, H. M., Funnell, W. R. J., Decraemer, W. F., and Dirckx, J. J. J. (**2006**). "A geometrically nonlinear finite-element model of the cat eardrum," J. Acoust. Soc. Am. **119**, 2859–2868.

Larsson, C., Dirckx, J. J. J., Bagger-Sjöbäck, D., and von Unge, M. (**2005**). "Pars flaccida displacement pattern in otitis media with effusion in the gerbil," Otol. Neurotol. **26**, 337–343.

Larsson, C., von Unge, M., Dirckx, J. J. J., Decraemer, W. F., and Bagger-Sjöbäck, D. (**2001**). "Displacement pattern of the normal pars flaccida in the gerbil," Otol. Neurotol. **22**, 558–566.

Lee, C. Y., and Rosowski, J. J. (**2001**). "Effects of middle-ear static pressure on pars tensa and pars flaccida of gerbil ears," Hear. Res. **153**, 146–163.

Lim, D. J. (**1970**). "Human tympanic membrane. An ultrastructural observation," Acta Oto-Laryngol. **70**, 176–186.

Margolis, R. H., Bass-Ringdahl, S., Hanks, W. D., Holte, L., and Zapala, D. A. (**2003**). "Tympanometry in newborn infants–1 kHz norms," J. Am. Acad. Audiol **14**, 383–392.

Margolis, R. H., Paul, S., Saly, G. L., Schachern, P. A., and Keefe, D. H. (**2001**). "Wideband reflectance tympanometry in chinchillas and human," J. Acoust. Soc. Am. **110**, 1453–1464.

Margolis, R. H., and Shanks, J. E. (**1991**). "Tympanometry: Principles and procedures," in *Hearing Assessment*, edited by W. F. Rintelmann (Pro-Ed., Austin, Texas), pp. 179–246.

Mendis, K. K., Stalnaker, R. L., and Advani, S. H. (**1995**). "A constitutive relationship for large deformation finite element modeling of brain tissue," J. Biomech. Eng. **117**, 279–285.

Meyer, S. E., Jardine, C. A., and Deverson, W. (**1997**). "Developmental changes in tympanometry: A case study," Br. J. Audiol. **31**, 189–195.

Molvær, O., Vallersnes, F., and Kringlebotn, M. (**1978**). "The size of the middle ear and the mastoid air cell," Acta Oto-Laryngol. **85**, 24–32.

Nakajima, H. H., Ravicz, M. E., Merchant, S. N., Peake, W. T., and Rosowski, J. J. (**2005**). "Experimental ossicular fixations and the middle ear's response to sound: Evidence for a flexible ossicular chain," Hear. Res. **204**, 60–77.

Nigg, B. M., and Herzog, W. (**1999**). *Biomechanics of the Musculo-Skeletal System*, 2nd ed. (Wiley, New York).

Northrop, C., Piza, J., and Eavey, R. D. (**1986**). "Histological observations of amniotic fluid cellular content in the ear of neonates and infants," Int. J. Pediatr. Otorhinolaryngol. **11**, 113–127.

Olszewski, J. (**1990**). "Zur Morphometrie der Gehöknöchelchen beim Menschen im Rahmen der Entwicklung" ("The morphometry of the ear ossicles in humans during development"), Anat. Anz **171**, 187–191.

Paradise, J. L., Smith, C. G., and Bluestone, C. D. (**1976**). "Tympanometric detection of middle ear effusion in infants and young children," Pediatrics **58**, 198–210.

Qi, L., Liu, H., Lutfy, J., Funnell, W. R. J., and Daniel, S. J. (**2006**). "A non-linear finite-element model of the newborn ear canal," J. Acoust. Soc. Am. **120**, 3789–3798.

Ravicz, M. E., and Rosowski, J. J. (**1997**). "Sound-power collection by the auditory periphery of the Mongolian gerbil Meriones unguiculatus: III. Effect of variations in middle-ear volume," J. Acoust. Soc. Am. **101**, 2135–2147.

Ravicz, M. E., Rosowski, J. J., and Voigt, H. F. (**1992**). "Sound-power collection by the auditory periphery of the Mongolian gerbil Meriones unguiculatus. I: Middle-ear input impedance," J. Acoust. Soc. Am. **92**, 157–177.

Rollhauser, H. (**1950**). "Die Zugfestigkeit der Menschlichen Haut" ("The tensile strength of human skin"), Gegenbaurs Morphol. Jahrb **90**, 249–261.

Rosowski, J. J., and Lee, C. Y. (**2002**). "The effect of immobilizing the gerbil's pars flaccida on the middle-ear's response to static pressure," Hear. Res. **174**, 183–195.

Ruah, C. B., Schachern, P. A., Zelterman, D., Paparella, M. M., and Yoon, T. H. (**1991**). "Age-related morphologic changes in the human tympanic membrane. A light and electron microscopic study," Arch. Otolaryngol. Head Neck Surg. **117**, 627–634.

Samani, A., and Plewes, D. (**2004**). "A method to measure the hyperelastic parameters of ex vivo breast tissue sample," Phys. Med. Biol. **49**, 4395–4405.

Sanford, C. A., and Feeney, M. P. (**2007**). "Energy reflectance tympanometry in infants," *30th Midwinter Res. Mtg., Assoc. Res. Otolaryngol.*, Denver.

Schmidt, S. H., and Hellstrom, S. (**1991**). "Tympanic-membrane structure – new views. A comparative study," ORL **53**, 32–36.

Schwarz, W. (**1957**). *Connective Tissue* (Blackwells, Oxford).

Shahnaz, N., Miranda, T., and Polka, L. (**2008**). "Multi-frequency tympanometry in neonatal intensive care unit and well babies," J. Am. Acad. Audiol, in press.

Shanks, J. E., and Lilly, D. J. (**1981**). "An evaluation of tympanometric estimates of ear canal volume," J. Speech Hear. Res. **24**, 557–566.

Shanks, J. E., Wilson, R. H., and Cambron, N. K. (**1993**). "Multiple frequency tympanometry: Effects of ear canal volume compensation on static acoustic admittance and estimates of middle ear resonance," J. Speech Hear. Res. **36**, 178–185.

Stepp, C. E., and Voss, S. E. (**2005**). "Acoustics of the human middle-ear air space," J. Acoust. Soc. Am. **118**, 861–871.

Stoltz, J. F. (**2006**). *Mechanobiology: Cartilage and Chondrocytes* (IOS, Washington, DC), Vol. 4.

Takahara, T., Sando, I., Hashida, Y., and Shibahara, Y. (**1986**). "Mesenchyme remaining in human temporal bones," Otolaryngol.-Head Neck Surg. **95**, 349–357.

Unur, E., Ülger, H., and Ekinci, N. (**2002**). "Morphometrical and morphological variations of middle ear ossicles in the newborn," Erciyes Med. J. **24**, 57–63 (http://tipdergisi.erciyes.edu.tr/project6/112.pdf, last viewed 2007 Dec 22).

von Unge, M., Decraemer, W. F., Bagger-Sjöbäck, D., and Dirckx, J. J. J. (**1993**). "Displacement of the gerbil tympanic membrane under static pressure variations measured with a real-time differential moire interferometer," Hear. Res. **70**, 229–242.

Vorwerk, U., Steinicke, G., and Begall, K. (**1999**). "Observation of eardrum movements during quasi-static pressure changes by high-speed digital imaging," Audiol. Neuro-Otol. **4**, 150–155.

Yamada, H. (**1970**). *Strength of Biological Materials* (Williams and Wilkins, Baltimore).

Yokoyama, T., Iino, Y., Kakizaki, K., and Murakami, Y. (**1999**). "Human temporal bone study on the postnatal ossification process of auditory ossicles," Laryngoscope **109**, 927–930.

Zwislocki, J. (**1962**). "Analysis of the middle-ear function. 1. Input impedance," J. Acoust. Soc. Am. **34**, 1514–1523.

Finite element modeling of acousto-mechanical coupling in the cat middle ear

James P. Tuck-Lee, Peter M. Pinsky, Charles R. Steele, and Sunil Puria[a)]
Department of Mechanical Engineering, Stanford University Stanford, California 94305, USA

(Received 16 August 2007; revised 28 March 2008; accepted 29 March 2008)

The function of the middle ear is to transfer acoustic energy from the ear canal to the cochlea. An essential component of this system is the tympanic membrane. In this paper, a new finite element model of the middle ear of the domestic cat is presented, generated in part from cadaver anatomy via microcomputed tomographic imaging. This model includes a layered composite model of the eardrum, fully coupled with the acoustics in the ear canal and middle-ear cavities. Obtaining the frequency response from 100 Hz to 20 kHz is a computationally challenging task, which has been accomplished by using a new adaptive implementation of the reduced-order matrix Padé-via-Lanczos algorithm. The results are compared to established physiological data. The fully coupled model is applied to study the role of the collagen fiber sublayers of the eardrum and to investigate the relationship between the structure of the middle-ear cavities and its function. Three applications of this model are presented, demonstrating the shift in the middle-ear resonance due to the presence of the septum that divides the middle-ear cavity space, the significance of the radial fiber layer on high frequency transmission, and the importance of the transverse shear modulus in the eardrum microstructure. © *2008 Acoustical Society of America.* [DOI: 10.1121/1.2912438]

PACS number(s): 43.64.Bt, 43.64.Ha, 43.20.Tb, 43.40.Ey [BLM] Pages: 348–362

I. INTRODUCTION

In mammals, the peripheral ear consists of six primary structures: the pinna, the ear canal, the tympanic membrane (commonly called the eardrum), the ossicles, the middle-ear cavities (MEC), and the cochlea (Fig. 1). The function of the middle ear, consisting of the eardrum, ossicles, and MEC, is to transform acoustic pressures in the ear canal to hydrodynamic pressures in the cochlea. The first pressure-to-mechanical transduction takes place at the eardrum, where sound in the form of vibrations in the air is transformed into mechanical vibrations in the ossicles, which in turn transfer these vibrations to the cochlea. Recent computational models have been used to simulate the behavior of the middle ear in order to understand the relationship between its structure and function. Such an understanding could help improve the design and function of prosthetics and improve methodologies and planning of surgical procedures in the middle ear. Modern medical imaging technologies such as microcomputed tomography (μCT) aid in these goals, allowing realistic anatomical geometries to be used with physics-based modeling to simulate the middle ear, instead of fitting model parameters to measurements from average ears. As *in vivo* imaging techniques improve, this would allow current *in vitro* biomechanics modeling to be applied to patient-specific anatomies.

The eardrum has been the focus of previous studies aimed at explicating the possible relationships between the behavior of the ear and its morphological structure. Notable works include Funnell (1983), Rabbitt and Holmes (1986), Wada *et al.* (1992), Gan *et al.* (2002), and Fay *et al.* (2006). Of these models, only Fay *et al.* (2006) explored the consequences of the tympanic membrane microstructure by incorporating a model for a multilayered orthotropic composite. This detailed model of the eardrum has been shown to be important in understanding the effect of the microstructural properties on middle-ear sound transmission. The acoustic spaces of the ear canal and the middle-ear cavity have also been modeled in conjunction with these eardrum models recently in Gan *et al.* (2006) and Fay *et al.* (2006) to simulate the interaction between the acoustic spaces and the movement of the eardrum. This interaction is crucial in understanding the function the eardrum plays in the hearing process as it responds to acoustic input, and the relationship of this function to its structure. However, Fay *et al.* (2006) was limited to one-dimensional and lumped models for the acoustic spaces. Due to the computational difficulties that arise in coupling the three-dimensional (3D) acoustics to the tympanic membrane, Gan *et al.* (2006) used a reduced spatial resolution of the acoustic spaces in computing the coupled frequency response. These inherent limitations potentially inhibit the validity of the coupled models at higher frequencies.

A new multilayered finite element model of the eardrum of the domestic cat, coupled to 3D models of the middle-ear cavities and a portion of the ear canal, is described in this paper based on μCT imaging of cadaver specimens and recent anatomical observations. The domestic cat is chosen for this model because of the availability of physiological measurements for frequencies up to 20 kHz and with various middle-ear manipulations. A fully coupled finite element model is used to simulate the response across the frequency range from 100 Hz to 20 kHz, applying a new adaptive reduced-order modeling procedure based on the matrix Padé-via-Lanczos (MPVL) algorithm. This new computational technique allows for an increased spatial resolution for the

[a)]Also at Otolaryngology-HNS, Stanford University Stanford, CA 94305; electronic mail: puria@stanford.edu.

 0001-4966/2008/124(1)/348/15/$23.00

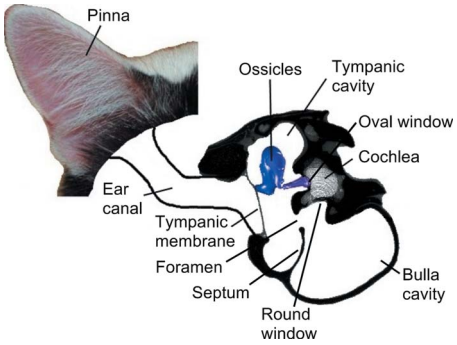

FIG. 1. (Color online) A composite schematic for the domestic cat auditory periphery. For visualization purposes only, as components are misaligned and of different scales from various sources, including visual photography, μCT imaging, and 3D reconstructions.

acoustical domains compared to previous models, which allow higher frequency acoustic modes to be resolved in the simulation. Testing of the model is done by comparison to existing measurements for both the intact ("closed") middle-ear cavity and for the case where the tympanic and bulla cavities have been surgically opened widely to the environment ("open"). Finally, the model is used to examine three questions regarding the structure and function of the middle ear: the purpose of the bony septum partitioning the cat middle-ear cavities, the consequences of disrupting the radial fibers in the eardrum and of patching perforations, and the effect of the shear modulus in material models of the eardrum.

II. ANATOMICAL MODEL

A. Model geometry

The middle-ear anatomy was determined by using μCT imaging of frozen cadaver specimens acquired from Carolina Biological Supply. Temporal bone sections were isolated, removing the pinna while keeping the eardrum and middle-ear cavities intact [Fig. 2(a)]. A Scanco vivaCT 40 machine at the VA Palo Alto Health Care System (VAPAHCS) Bone and Joint Center was used to image the specimens with a voxel (both in plane and out of plane) resolution of 10 μm. The frozen samples were initially wrapped in plastic wrap to preserve moisture, and the scans proceeded over an 8–10 h time period per specimen. However, for the single sample that was finally used, a small hole in the bulla cavity was made to vent condensed moisture from the middle-ear cavities that had been found to interfere with identification of the cavity boundaries. Segmentation was done manually by using the vivaCT software to extract the geometry of the acoustic spaces of the ear canal and middle-ear cavities, as well as the ossicle geometries, using visual identification of contrast differences together with automatic edge detection [Fig. 2(b)]. The ear canal was artificially truncated 5 mm from the eardrum to represent the acoustic space typically remaining in the ear canal during impedance measurements. A surface description of these spaces was exported by using standard tessellation language (STL), which was manipulated by using Raindrop GEOMAGIC and MSC PATRAN to generate a 3D mesh of the ear canal and middle-ear cavities.

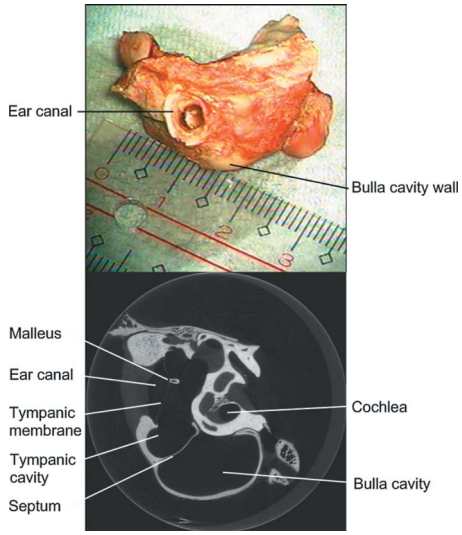

FIG. 2. (Color online) (a) Isolated temporal bone from a domestic cat cadaver with centimeter scale. (b) μCT image of the isolated temporal bone from a domestic cat, showing (roughly from left to right) a portion of the ear canal, eardrum, cross section of the malleus, tympanic and bulla cavities, and portion of the cochlea. The scan diameter is 21.5 mm.

B. Eardrum microstructure

To construct a finite element mesh of the eardrum, a quadrilateral surface mesh was created on the surface of the ear canal bordering the eardrum, aligned in its observed radial and circumferential layer directions [Fig. 3(a)]. Radial splines were constructed from this surface mesh and fit to conical and toroidal regions to remove small variations in the geometries as in Fay *et al.* (2006). The thickness of the tympanic membrane was determined by using recently published physiological measurements by Kuypers *et al.* (2005) from confocal microscopic observations, projected onto the radial spline geometries [Fig. 3(b)]. These measurements were used because of the limited μCT resolution of 10 μm, which was not capable of accurately resolving the minimum thickness of 13 μm in the cat eardrum.

Microstructural observations by Lim (1968) were used to construct radial and circumferential fibrous layers within the lamina propria of the eardrum. However, the fiber layers themselves are not visible to μCT imaging, due to contrast and scale, nor are they visible with confocal imaging. Further, fiber density variations are also unknown throughout the eardrum. With the lack of fiber density and thickness information except at a few locations within the eardrum, a thickness distribution for the fibrous layers similar to that assumed by Fay *et al.* (2005, 2006) was chosen for all radial sections. A smooth polynomial was chosen to gradually increase the thickness of each layer (a departure from the model of Fay *et al.*), as shown in Fig. 3(d), from reported observations at the manubrium and tympanic annulus. A hexahedral mesh was then constructed for each of the sublayers from the radial splines and layer thicknesses, creating distinct models for the radial and circumferential fibrous layers, as well as two layers corresponding to the combined epidermal and subepidermal layers and the mucosal and submucosal layers.

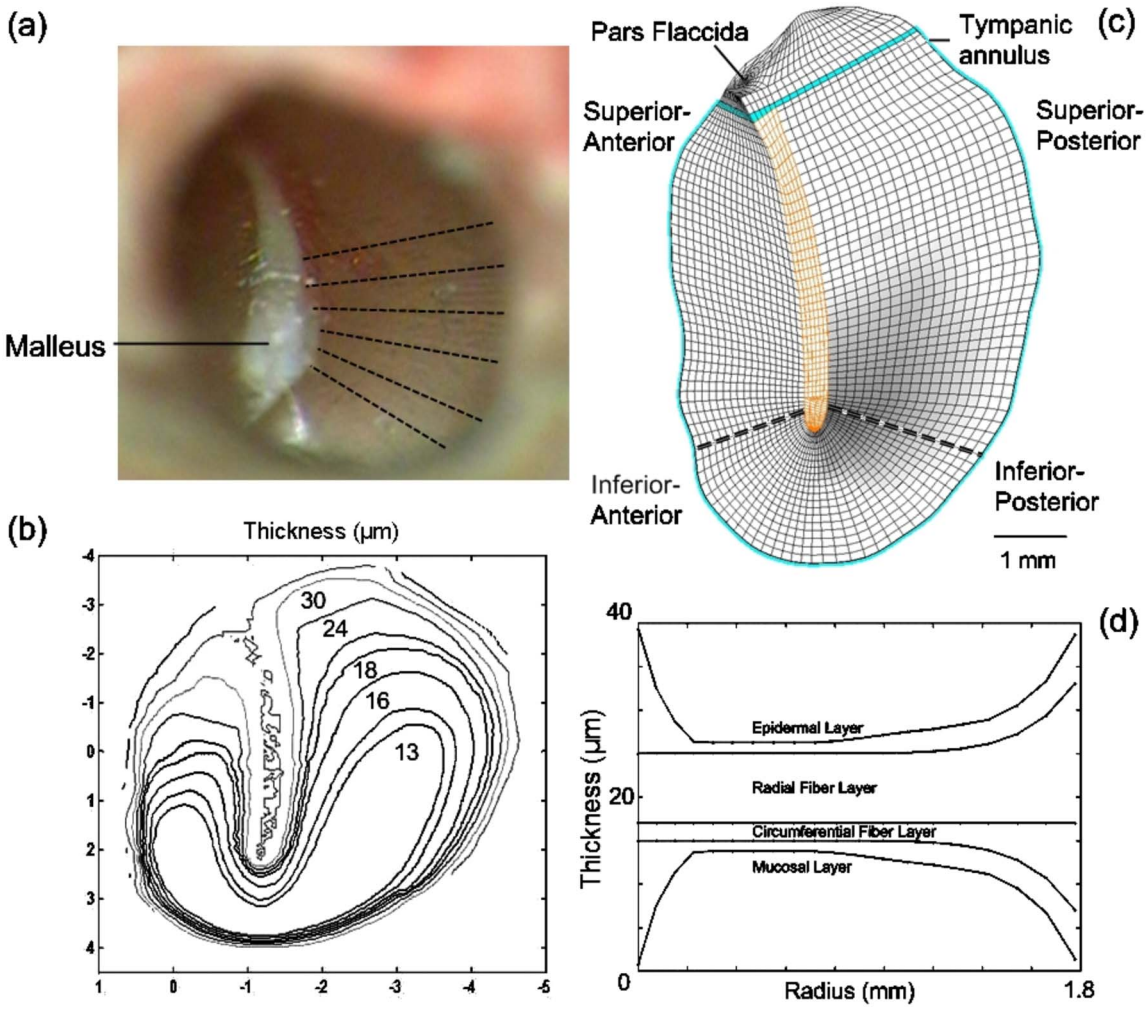

FIG. 3. (Color online) (a) View of the eardrum through the ear canal, showing the manubrium and radial fiber directions (dashed lines). (b) Thickness contours from Kuypers *et al.* (2005) projected onto the eardrum model. (c) Finite element mesh for the eardrum, dashed lines separating labeled quadrants. (d) Microstructural model of the eardrum, showing the radial thickness profile of the four layers of a representative radial slice from the malleus (0 mm) to the tympanic annulus (1.8 mm).

C. Eardrum constitutive model

As Lim (1968) observed using scanning electron microscopy, the fibrous layers of the eardrum are made up principally of ordered collagen fibers within a matrix material. These collagen fibers are known to be much stiffer than the surrounding soft tissue matrix, which includes short elastin fibers. The fibrous layers are thus modeled as transversely isotropic materials, oriented with the observed fiber directions. The outer layers without the collagen fibers are modeled by using only the isotropic matrix material. As soft tissues, all layers are treated as being composed primarily of water, leading to a density of $\rho=1100\ \mathrm{kg/m^3}$ and Poisson's ratio of $\nu=0.45$ (nearly incompressible).

To implement the fiber directions in the model, the mesh of the eardrum was aligned such that the local coordinate systems match the observed fiber orientations [Fig. 3(a)]. Based on visual observations, the radial fibers in the inferior portion of the eardrum seem to converge to the umbo, while the remainder connect to the manubrium. Thus, the radial fibers in the model are partitioned into those in the inferior region that converge to the umbo and those that do not [as shown by the dashed lines in Fig. 3(c)]. The converging (radial) fiber layer moduli increase asymptotically as $1/r$ to model the increasing fiber density, while the moduli of other layers are unchanged. The pars flaccida lacks the ordered collagen fiber layers in the pars tensa and is thus modeled as an isotropic material.

Finally, the radial fiber moduli are normalized by the layer thickness due to the observation that the fibers span the distance between the manubrium and the annulus and do not seem to start in the middle of the eardrum. Thus, it is logical to expect the number of fibers, and the area and stiffness of each fiber, to remain constant along its length, with the collagen fibers anchored on either end to act as load-bearing structures. Alternatively, having incomplete fibers within the tympanic membrane would require the load to be transmitted through fiber cross-linking or the soft tissue matrix, neither being strong load-bearing materials given the current understanding of the microstructure. The consequence of this assumption is that the resultant stiffness of the fibers should remain constant, regardless of the thickness of the fiber layer. Therefore, a thicker radial layer would automatically suggest

TABLE I. Material properties of the eardrum model.

Parameter	Value	Units	Comments
E_r (posterior)	0.1	GPa	
E_r (anterior)	0.1	GPa	
E_r (inferior)	0.1	GPa	(Normalized by radius from umbo in mm)
E_θ	0.1	GPa	
E_{matrix}	1	MPa	
$E_{\text{pars flacida}}$	1	MPa	
$E_{\text{manubrium}}$	1000	GPa	(Approximately rigid)
$G_{\text{pars tensa}}$	35	MPa	
ν	0.45		(Nearly incompressible)
ρ_e	1100	kg/m^3	

a lower fiber density to maintain the same total fiber count, area, and stiffness. To model this, Young's modulus of the radial fibers are normalized by the local thickness in order to compute a local equivalent modulus for the layer. This assumption could be tested for future development by investigation of the variation in fiber layer thickness and fiber densities throughout the eardrum, which could then be added to this computational model. The circumferential fibers are also assumed to be continuous following the circumference of the eardrum. However, as the thickness for the fibrous sublayers are assumed to be constant between radial slices, the circumferential modulus is not normalized by thickness but is instead assumed to have a constant volume fraction.

Table I summarizes the material properties used for the tympanic membrane model. In this model, a nominal Young's modulus of 0.1 GPa is assigned to both the radial and circumferential fibers, with the radial fibers normalized by thickness with a reference of 17 μm. In the inferior quadrant, the radial fiber moduli increase by $1/r$ relative to the umbo location, with a value of 0.1 GPa at 1 mm distance from the umbo. The matrix material and outer layers are assumed to have an isotropic Young's modulus of 1 MPa, corresponding to a soft tissue reinforced with elastin. The pars flaccida has an isotropic Young's modulus of 1 MPa due to the nonoriented collagen and elastin fibers in the matrix. To model material damping effects, a complex elastic modulus is used for each component. This simple viscoelastic model adds an imaginary component to the stiffness (20% of Young's modulus in the present model) that does not increase with frequency. Viscous damping was not chosen for this model because at high frequencies viscous effects would likely overdamp the structure and suppress higher order modes of vibration as in Gan *et al.* (2002). For example, the 20% imaginary stiffness in the current model has the same effect as 0.003% viscous damping when compared at a frequency of 1 kHz and 0.0003% at 10 kHz.

D. Ossicular model and cochlear load

A simplified ossicular model is used for the current middle-ear simulations. First, the ossicles are assumed to act rigidly such that they do not bend under acoustic loads. Second, a fused incudomalleolar joint is used, preventing relative motion of the malleus and incus. Both of these assumptions have been observed to be accurate below 3 kHz by Guinan and Peake (1967) and greatly simplify the model. Finally, the suspensory ligaments are modeled to act with resultant forces and moments on the center of gravity (CG) of the malleus-incus complex, which would thus create a hinging axis through the CG at low frequencies. As the CG lies close to the axis running from the anterior process of the malleus to the short process of the incus, this matches experimental observations of the ossicles at low frequencies by Guinan and Peake (1967). Furthermore, rotation about the CG is justified from kinematics, as a fixed center of gravity would allow the best transfer of energy through the ossicles to the cochlea since translational motion of the CG would require additional kinetic energy over simple rotation.

TABLE II. Mass and principle moments of inertia of the malleus-incus complex.

Parameter	Value	Units
m_{oss}	1.54×10^{-5}	kg
I^{I}_{CG}	1.04368×10^{-11}	kg m^2
$I^{\text{II}}_{\text{CG}}$	3.59162×10^{-11}	kg m^2
$I^{\text{III}}_{\text{CG}}$	4.12912×10^{-11}	kg m^2

Based on the μCT imaging, the mass distribution of the ossicles was computed (Table II), including the location of the center of gravity (Fig. 4), the principal axis directions, and the moments of inertia for the combined malleus-incus complex (Puria *et al.*, 2006). A circuit model representation of the incudostapedial joint (ISJ), the stapes, and the cochlea used in Puria and Allen (1998) was chosen. As the motion of the stapes has been observed to be pistonlike at low frequencies, the displacement of the stapes normal to the stapes footplate is taken as the input to the cochlea. Additional translational (perpendicular to the stapes normal) and rotational stiffnesses are added at the ISJ to represent the effects of the

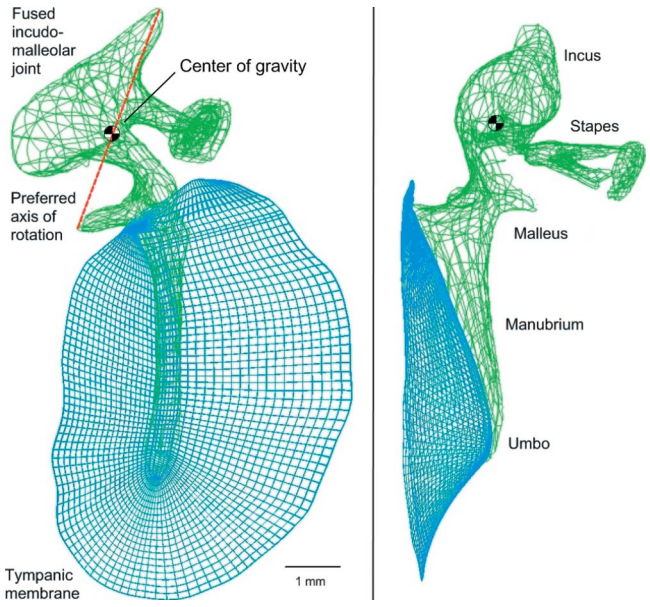

FIG. 4. (Color online) Ossicular geometry used in the computational model. Computed center of gravity is indicated, as is the classical axis of rotation (dashed line).

annular ligament and joint, respectively, that would not be captured in the 1D circuit model. For modeling the drained cochlea, the cochlear impedance is removed from the circuit model. Disarticulating the stapes removes the entire impedance of the stapes and cochlea, leaving only the inertial properties of the malleus-incus complex and the suspensory ligaments modeled at the CG as the load to the eardrum.

III. COMPUTATIONAL MODEL

A. Finite element formulation

The interaction between the eardrum and adjacent acoustic spaces is modeled by using a coupled structural acoustics formulation, solving simultaneously for the displacement of the eardrum $\mathbf{u}$ and acoustic pressure P in the ear canal and middle-ear cavities. The finite element method is chosen in order to represent accurately the effects of changes in the anatomy in the fully coupled system. This coupled model allows the direct simulation of various changes to the coupled system, including modifications of the middle-ear cavity structures and perforations of the eardrum.

For the current model, acoustic behavior is assumed to be small perturbations of pressure with negligible viscosity, governed by the Helmholtz equation for acoustic pressure P, with density ρ_a and wave speed c. Small strains are assumed for the eardrum, allowing the usage of 3D linear time-periodic elastodynamics for the displacements $\mathbf{u}$ (e.g., Hughes, 2000). For this model, ρ_e will denote the density of the solid (elastic) domain, and the generalized Hooke's law, $\sigma=\mathbb{C}:\nabla^S\mathbf{u}$, are used to relate linearized stress σ and strain $\nabla^S\mathbf{u}$ by the elasticity tensor $\mathbb{C}$. Coupling on the structural acoustic interface is governed by enforcement of continuity of momentum and displacements. Using a standard $(\mathbf{u},p)$ formulation (that is, solving for displacements in the solid and pressures in the fluid) leads to a matrix equation for discrete degrees of freedom $\mathbf{d}_P$ and $\mathbf{d}_\mathbf{u}$ for the acoustic and structural domains, resulting in the asymmetrical matrix system (e.g., Morand and Ohayon, 1995),

$$\left(\begin{bmatrix}\mathbf{K}_a & \mathbf{0}\\ \mathbf{K}_c^T & \mathbf{K}_e\end{bmatrix}-\omega^2\begin{bmatrix}\frac{1}{c^2}\mathbf{M}_a & -\rho_a\mathbf{K}_c\\ \mathbf{0} & \mathbf{M}_e\end{bmatrix}\right)\begin{bmatrix}\mathbf{d}_P\\ \mathbf{d}_\mathbf{u}\end{bmatrix}=\begin{bmatrix}\mathbf{F}_P\\ \mathbf{F}_u\end{bmatrix}, \quad (1)$$

where $\mathbf{K}_a$ and $\mathbf{M}_a$ relate to the acoustic domain, $\mathbf{K}_e$ and $\mathbf{M}_e$ to the structural domain, and $\mathbf{K}_c$ to the coupling conditions (e.g., Tuck-Lee and Pinsky, 2008).

The acoustic medium is modeled by using linear tetrahedral elements due to the difficulty in constructing a hexahedral mesh on arbitrary 3D geometries. A hexahedral solid shell element is used for the eardrum, using modern element technology developed by Vu-Quoc and Tan (2003). A solid shell element offers several distinct advantages for the eardrum model. First, it simplifies the usage of fully 3D constitutive relations for the eardrum material. Second, the element simplifies modeling of thickness variations. Third, it forms distinct coupling surfaces for both sides of the shell to interface separately to the ear canal and MEC. Fourth, the elements can be used within a multilayered composite, in addition to just a single layer. The element has been formulated by using a combination of assumed natural strains (Dvorkin and Bathe, 1984) and enhancing strains (Simo and Rifai, 1990) to avoid locking. The element is also formulated for nonlinear elasticity, which is needed for the future addition of prestress in the eardrum due to a static pressure input. The structural acoustic interface is modeled by using node-on-node coupling, integrating over quadrilateral faces of the shell, although the coupling of tetrahedral and hexahedral elements introduces an interpolation error on the interface. The mesh for the cat middle ear contains 100 000 degrees of freedom for displacements and pressures, corresponding to 23 000 acoustic tetrahedra and 2500 shell elements [Fig. 5(a)].

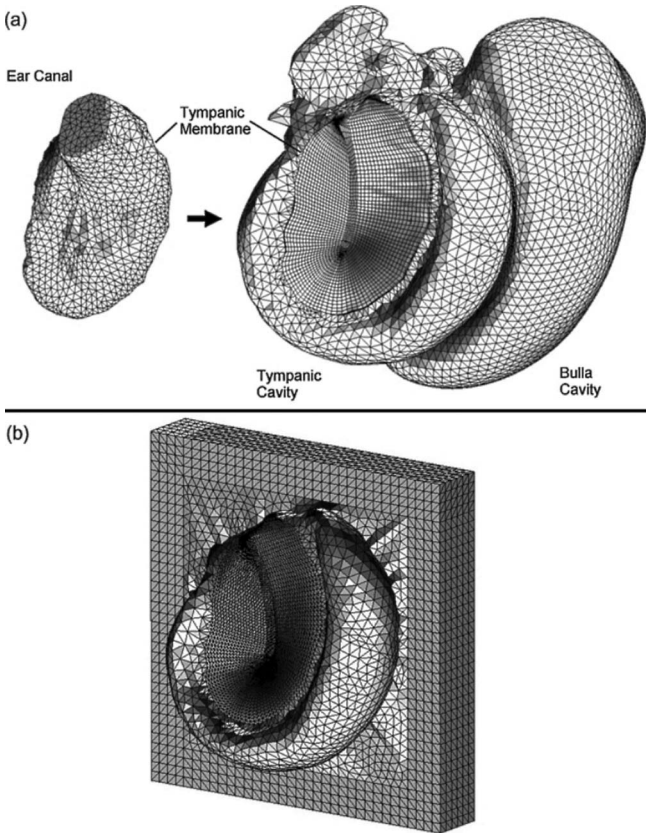

FIG. 5. (a) Finite element model of the intact middle ear. (b) Finite element mesh for the middle ear with open middle-ear cavities and absorbing PML boundary conditions.

The rigid ossicular model is added directly into the finite element formulation. The eardrum is constrained along the manubrium by using very stiff massless elements to represent the presence of the malleus [shown in Fig. 3(c)]. However, the motions of the ossicles as a rigid body (its mass and the stiffness of the attached ligaments and cochlea) are defined solely by local displacements near the umbo location, using the eight nodes of a local hexahedral element. The advantage of this approach is that it requires no additional degrees of freedom while accurately representing the observed mass distribution and rigid body behavior. Instead of using a mesh of the ossicles, the contributions of linear and angular inertia of the malleus-incus complex are added to the kinetic energy in the variational equation, leading to a modification of the mass matrix. Likewise, an associated strain

energy is applied to represent the translational and rotational stiffness from ligaments and tendons acting on the center of gravity and the incudostapedial joint. The observed transfer function for the stapes and cochlea by Puria and Allen (1998) is added by using the related work quantity for the motion at the incudostapedial joint. The mathematical details and implementation of this model may be found in the Appendix.

The walls of the ear canal and middle-ear cavities are modeled by using an elastic boundary condition to simulate the epithelial and mucosal linings. This appears as a mixed boundary condition to the acoustic domain parameterized by the thickness of the layer t, Young's modulus E, and Poisson's ratio ν. A thin layer of $t=0.1$ mm, with $E=1$ MPa and $\nu=0.45$, is used to model the incompressibility of the soft tissue. The viscoelastic properties are modeled by using a complex stiffness of 20%. This gives a mixed boundary condition for the acoustic field of

$$\nabla P \cdot \mathbf{n} = \omega^2 \rho_a t \frac{(1+\nu)(1-2\nu)}{E(1-\nu)} P. \quad (2)$$

The effect of this damping condition, combined with the material damping of the eardrum, is to prevent unbounded acoustic resonances without changing the overall acoustic response and to be consistent with earlier uncoupled acoustic models of the middle-ear cavities, which would otherwise be undamped.

B. Solution methodology

A uniform pressure flux, representing a volume velocity input, is applied across the truncated ear canal entrance to stimulate the acoustic response. A reduced-order approach based on MPVL with an adaptive frequency windowing algorithm (Tuck-Lee and Pinsky, 2008) is used in order to compute efficiently the response across the entire frequency range of interest. The reduced-order model provides the opportunity to compute, in a time span of hours instead of days, the effect of changes to the morphological properties and structure on the response of the middle ear while maintaining a resolved mesh for the entire system in order to capture high frequency behavior. The damping from the complex stapes and cochlear impedance is added via a low-rank update formulation. The points of interest for this simulation are the umbo, several locations on the eardrum corresponding to measurements by Decraemer *et al.* (1989), pressure in the center of the ear canal corresponding to measurements by Lynch *et al.* (1994), Puria and Allen (1998), Huang *et al.* (2000), and Rosowski *et al.* (2000), and pressures at the oval and round windows of the cochlea.

C. Mesh refinement study

Numerical experiments were conducted on the chosen mesh size on sample problems of similar dimensions. For the frequency range in question, the mesh size chosen, $h=0.4$ mm, was adequate for this problem up to 20 kHz, giving a 0.2% error for a model problem of similar dimensions (but much simpler geometry). A mesh bisection on the uncoupled eardrum also confirmed that the given mesh was adequate, although with a much larger error than the simpler coupled example. Higher mesh resolutions proved to not be feasible for the coupled problem, requiring excessive amounts of memory even on a parallel computing cluster. Thus, the given mesh is used for practical purposes, noting that it may introduce some small discretization errors at higher frequencies in resolving the higher order modes. This may result in a stiffer response at higher frequencies than a truly resolved solution. The size of the uncoupled eardrum model allows for simulation on a laptop for parameter verification, and the coupled problem for the given mesh density was run on six processors in a cluster.

D. Open cavity modifications

To simulate the response with open middle-ear cavities, a common experimental situation, the MEC model was truncated in the tympanic cavity [Fig. 5(b)]. In place of the remaining volume, an absorbing perfectly matched layer (PML) was added to model the radiation condition due to the open cavity walls (Turkel and Yefet, 1998). A new formulation by Bermúdez *et al.* (2006) was chosen due to better performance at low wave numbers. Unlike traditional PML, this method uses an asymptotic absorption parameter automatically tuned by the wave speed of the medium but is not perfectly matched at the interface, which is beyond the scope of this paper. Unfortunately, the form of the PML absorbing layers prohibit the practical usage of the reduced-order MPVL algorithm, in which these introduce complicated frequency dependencies. Thus, the open cavity response is computed sequentially over the frequency range at a reduced frequency resolution.

E. Removal of the septum

In many small mammals, the middle-ear cavity is physically subdivided by a thin bony wall called the septum. Some have a single septum (e.g., cat), while others have multiple septa (e.g., chinchilla). Acoustic energy is coupled between the cavities via small irregularly shaped openings called foramina. What role this specialized structure has on hearing is not well understood. One hypothesis relates the interaction of the cavity resonances with spatially dependent pinna diffraction cues (Puria, 1991).

To gain insight into the role of the septum in the functioning of the middle ear, a model was created without this bony partition. In the finite element mesh, the boundary between the tympanic cavity and the bulla cavity was removed, and the resulting combined space remeshed with acoustic tetrahedra. This changes the geometry of the middle-ear cavities but has no effect on the eardrum or ear canal mesh.

F. Perforation and repair of the tympanic membrane

In order to simulate the effect of eardrum perforations and subsequent patching, a recent experiment made in human cadavers by O'Connor *et al.* (2008) was simulated (in the cat model), in which four cuts were made in the tympanic membrane and repaired using paper patches. These experiments were conducted to illustrate the effect of collagen fibers on sound transmission at high frequencies. Two cases

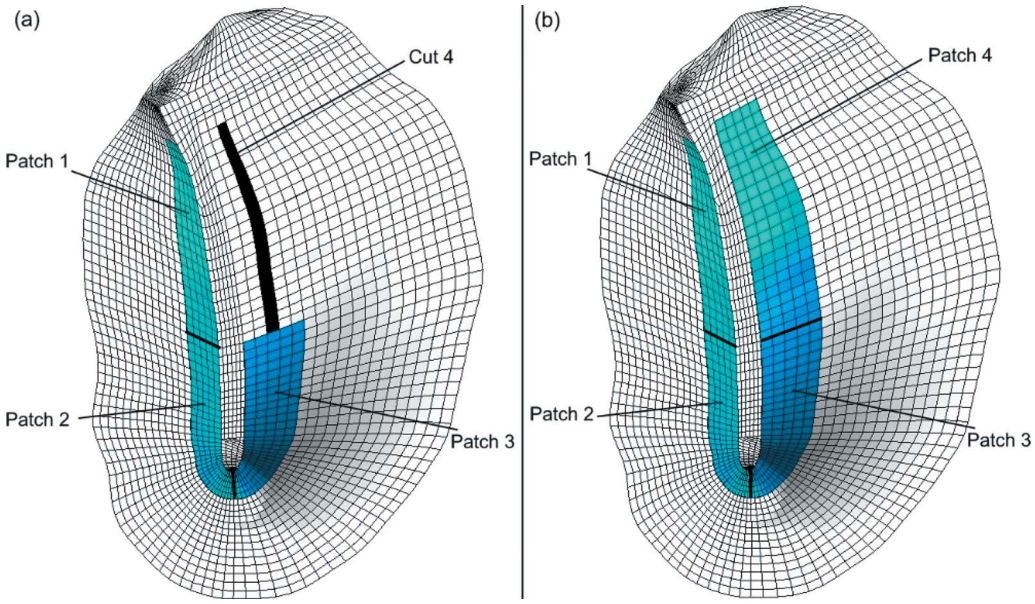

FIG. 6. (Color online) Perforation with cuts and repair with patches of the tympanic membrane along the manubrium: (a) with incomplete patching and (b) with complete patching.

are presented here. The first consists of four circumferential cuts made in the tympanic membrane, with three of the four cuts sealed by paper patches. The second refers to the same four cuts but with all four sealed with patches. To model these cases, a single 0.2 mm wide cut was made around the manubrium, in the direction of the circumferential fibers, representing all four cuts in the experiment (each approximately 2–3 mm in length). A 65 μm thick patch was firmly attached over the cuts, corresponding to either three or four patches in the experiment. The patch extended over several elements around the perforation but was not kept to constant width in order to simplify the creation of the model, as shown in Fig. 6. For the first case, the acoustic cavities were joined through the remaining perforation (2.5 mm long) and meshed as a single acoustic space. In the second case, the middle-ear cavities remained distinct from the ear canal. To remove the effect of the middle-ear cavity resonances, the open cavity modifications were also applied. The patch is assigned an isotropic Young's modulus of 1 MPa, with an equal density to the eardrum. To study the possible influence of patch materials, three additional variations are studied. First, the density is decreased by an order of magnitude and compared to the normal response. Second, the stiffness of the patch is increased instead. Lastly, both the stiffness and the mass of the patch are increased to simulate heavier and stiffer materials.

IV. MODEL TESTING AND RESULTS

To study the behavior of the middle-ear model, three primary measurements are considered. Functionally, the most significant measurement of the middle-ear function is the middle-ear transfer function, which is the ratio of pressure in the cochlear vestibule to ear canal pressure (Dallos, 1970; Puria *et al.*, 1997). For the cat, this has been measured for opened middle-ear cavities (Nedzelnitsky, 1980; Decory, 1989) and for intact cavities (Decory *et al.*, 1990). Another relevant measurement is the middle-ear input impedance, which is the pressure normalized by volume velocity in the ear canal. This has been measured for intact and opened cavities by Lynch *et al.* (1994), as well as in measurements reported by Puria and Allen (1998) for opened cavities with intact and disarticulated stapes and for cases with a drained cochlea. Finally, the displacements of the tympanic membrane for a given pressure in the ear canal have been measured by Tonndorf and Khanna (1967) using holography and more recently by Decraemer *et al.* (1989) using laser vibrometry. The main result from these measurements is the displacement at the umbo as a function of frequency but also of interest are the displacements of other locations of the eardrum relative to the umbo displacement. It is this last measurement condition that is not matched well with many current finite element models, as it is the most sensitive to the orthotropic material properties and applied damping values.

The ossicular ligament parameters (Table III) were determined by comparing normal and disarticulated stapes measurements with model predictions, as well as against circuit model results in Puria and Allen (1998). The eardrum elastic moduli were primarily constrained by the off-umbo displacements measured by Decraemer *et al.* (1989) and the placement of the primary resonance in the disarticulated stapes measurements. The mass properties were determined from known properties of biological materials and the total

TABLE III. Parameter values for the suspensory ligaments, as applied to the center of gravity and the incudostapedial joint.

Parameter	Value	Units
$K_{\mathrm{CG}}^{\mathrm{trans}}$	$(1+0.1i)\times 10^{4}$	N/m
$K_{\mathrm{CG},\parallel}^{\mathrm{rot}}$	$(1+0.1i)\times 10^{-3}$	N m
$K_{\mathrm{CG},\perp}^{\mathrm{ort}}$	$(1+0.1i)$	N m
$K_{isj,\perp}^{\mathrm{trans}}$	10^{6}	N/m
K_{isj}^{rot}	$(1+i)\times 10^{-3}$	N m

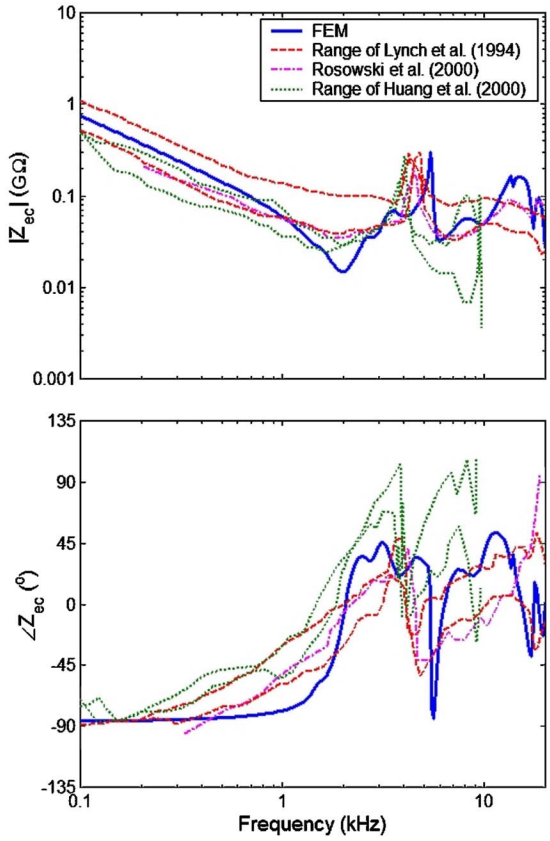

FIG. 7. (Color online) Middle-ear impedance, defined as the pressure normalized by the volume velocity in the ear canal ($Z_{ec}=P_{ec}/V_{ec}$), in units of SI acoustic GΩ. Finite element simulation compared against measurements by Lynch *et al.* (1994), Rosowski *et al.* (2000), and Huang *et al.* (2000) for the closed middle-ear cavity condition.

mass and computed mass distribution of the ossicles. It should be noted that in using a rigid joint model for the ossicles, the final model is expected to be valid principally below 3 kHz. The eardrum model should be valid to a much higher frequency, but without a more detailed ossicular model, this becomes difficult to justify against experimental measurements. However, comparisons between different physiological conditions should nevertheless be useful even above 3 kHz, as these all use the same ossicle model (which means that observed changes should be primarily independent of the ossicle model). Furthermore, the goal of this present research was to combine a multilayered orthotropic model of the tympanic membrane with 3D acoustic simulation. Thus, the simple ossicle model is used for the present in order to concentrate principally on the mechanics of the eardrum and surrounding acoustic spaces. However, in formulating the ossicular model using an energy-based formulation, it is possible to use any 3D ossicular model, as desired in future calculations.

A. Middle-ear impedance

Figure 7 shows the middle-ear impedance, $Z_{ec}=P_{ec}/V_{ec}$, for the fully coupled intact ear with closed cavities. The impedance is approximated by the computed pressure in the center of the truncated ear canal model (analogous to a probe tube measurement) and normalized by the applied uniform volume velocity on the same truncated surface. With a few exceptions, the impedance matches very well with the measurements by Lynch *et al.* (1994), Huang *et al.* (2000), and Rosowski *et al.* (2000) in both magnitude and phase. The resonance at 5 kHz occurs at a slightly higher frequency than the measurements, but it is observed that the volume of the bulla cavity in the cat specimen was much smaller than those reported by Lynch: 380 mm^3 compared to 615–865 mm^3. Thus, a shift in the cavity resonance is expected due to the difference in the specific geometry. In addition, a small peak at 3 kHz is also apparent, which is attributed to a slight resonance in the ossicle model that either does not appear in the physical measurements or normally coincides with the acoustic resonance.

B. Stepwise modifications with open cavities

Figure 8 shows the comparison of normal, drained cochlea, and disarticulated stapes middle-ear impedances for the case of widely opened cavities. The effect of cochlear damping on the 1–2 kHz resonance is observed, as well as the stiffness effect of the annular ligament at lower frequencies. The model does appear to be slightly stiffer than most measurements, but less stiff than one measurement set by Lynch *et al.* (1994), and generally agrees very well. In addition, the primary resonance between 1 and 2 kHz is not as damped as was observed in measurements.

C. Umbo displacements

The umbo displacements, normalized by the computed ear canal pressures (again measured at the center of the ear canal), are compared against measurements by Decraemer *et al.* (1989) and Khanna and Tonndorf (1972) in Fig. 9. At low frequencies, the eardrum model is stiffer by a factor of 2–3, showing a resonance at 2 kHz. Following this resonance, the displacements decay at a similar slope to the measurement data. However, above the resonance at 5 kHz, the computed displacements become much smaller than those measured by Decraemer *et al.* The model results also show a steeper phase roll-off than the measurement data.

D. Eardrum displacements

Figure 10 compares the displacements at various points on the eardrum to the umbo displacement. As can be seen, the displacements show a volumetric (fundamental mode) response of the eardrum below about 2 kHz and then quickly breaks up into higher order modes. This behavior has been discussed as spatial integration in Funnell *et al.* (1987) and recently in Fay *et al.* (2006) as the discordant eardrum, with the hypothesis that multiple vibratory modes present in the eardrum are averaged at the manubrium, which may serve to transmit the most sound pressure to the cochlea. In comparison to the velocity measurements of Decramer *et al.*, it should be noted that as the eardrum starts vibrating in higher modes, the measured velocities or displacements become more sensitive to the exact measurement location. One major discrepancy is the presence of a resonance at 2 kHz, which is not seen in the measurement data. Another discrepancy is the calculated anterior displacement. Decraemer *et al.* observed

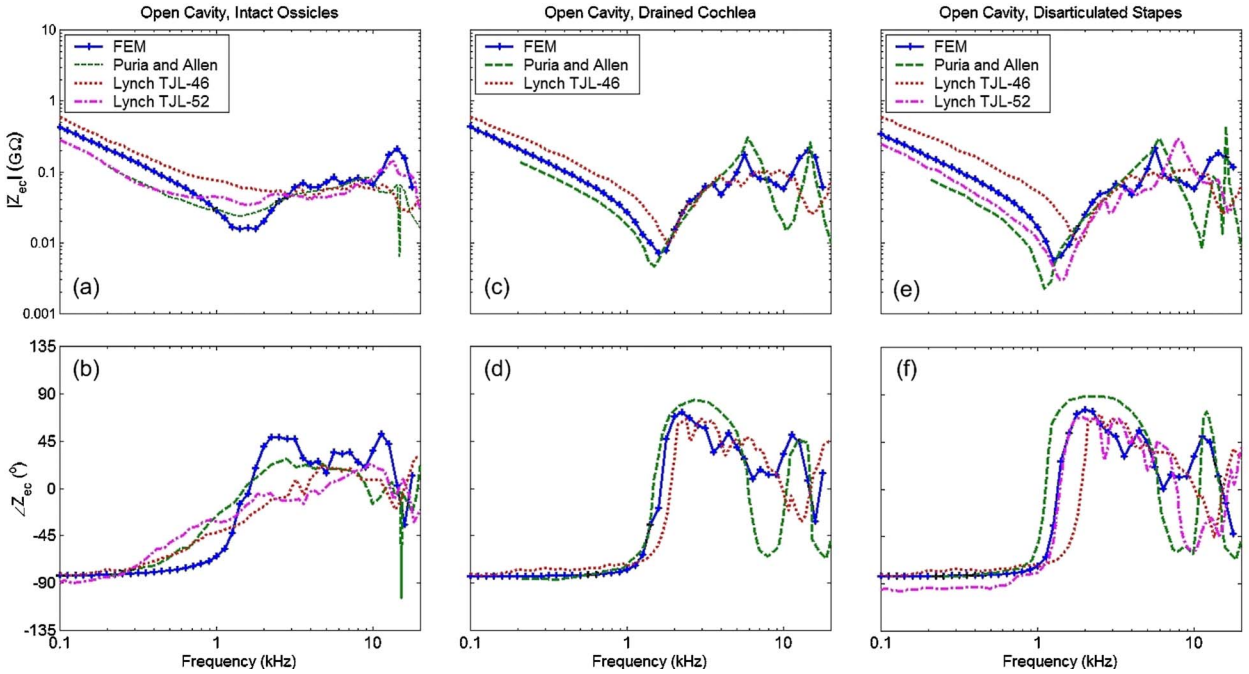

FIG. 8. (Color online) Middle-ear impedance (magnitude and phase) for open cavities. Three conditions considered: [(a) and (b)] intact ossicular chain [(c) and (d)], drained cochlea, and [(e) and (f)] disarticulated stapes. Finite element simulation compared against measurements by Puria and Allen (1998) and Lynch *et al.* (1994).

a lower displacement in points on the anterior side of the manubrium compared to the umbo at low frequencies. The current model, however, shows a small increase in displacement. Additionally, at lower frequencies, an increase in the off-umbo displacements by a factor of 3 is computed on the posterior side compared to the factor of 2 shown in Decraemer *et al.* However, Khanna and Tonndorf (1972) also showed an increase in displacements on the posterior side by a factor of 3 and near unity on the anterior side. Thus, although there are discrepancies between the model results and the measurements by Decraemer *et al.*, the membrane displacements remain consistent with those measured by Khanna and Tonndorf.

E. Middle-ear pressure gain

The middle-ear transfer function is calculated from the computed displacements at the umbo. Translations and rotations at the umbo are transformed into the equivalent motion at the incudostapedial joint through the assumption of rigid body dynamics for the ossicles. The ISJ motion is then projected onto the normal of the stapes footplate and used as the input into the stapes-cochlear transfer function, Z_{sc}, to calculate the pressure inside the vestibule of the cochlea. This is then normalized by the computed ear canal pressure to give the middle-ear pressure gain. Figure 11 shows the computed transfer function compared to measurements by Decory *et al.* (1990) for closed cavities and by Nedzelnitsky (1980) for open cavities. Below 1 kHz, the model results seem to match the Nedzelnitsky slope, which is known to be −6 dB/octave regardless of the state of the middle-ear cavity (Guinan and Peake, 1967). The current model matches the decrease in the Decory measurements at about 3 kHz (as observed in the impedance) but also sees an additional notch at 5 kHz corre-

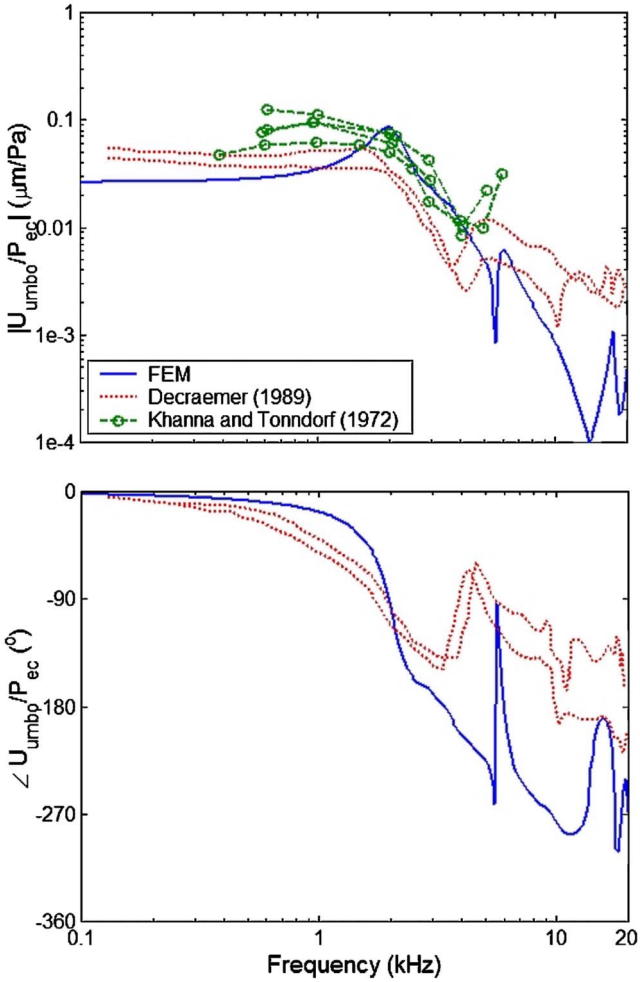

FIG. 9. (Color online) Displacement of the umbo (magnitude and phase). Finite element simulation compared against measurements by Decraemer *et al.* (1989) and Khanna and Tonndorf (1972).

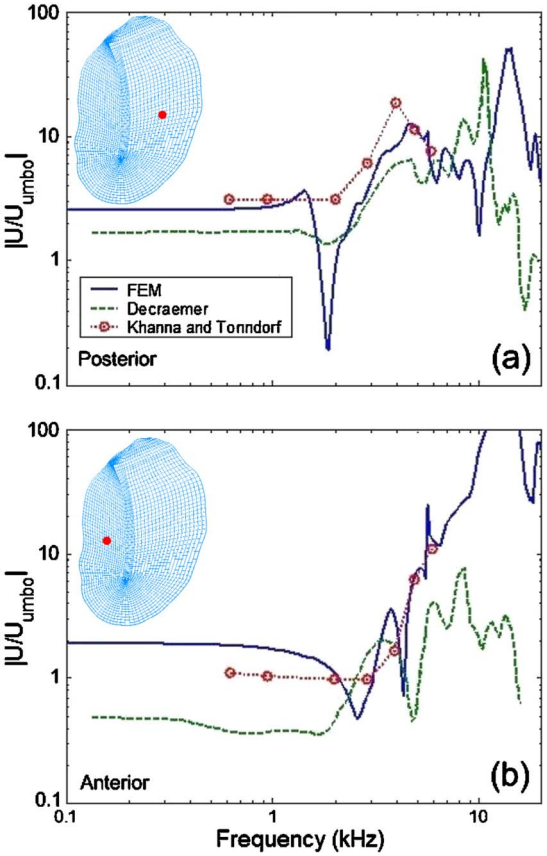

FIG. 10. (Color online) Relative displacement of (a) posterior and (b) anterior regions of tympanic membrane to the displacement at the umbo. Finite element simulation compared against corresponding measurements by Decraemer *et al.* (1989) and Khanna and Tonndorf (1972).

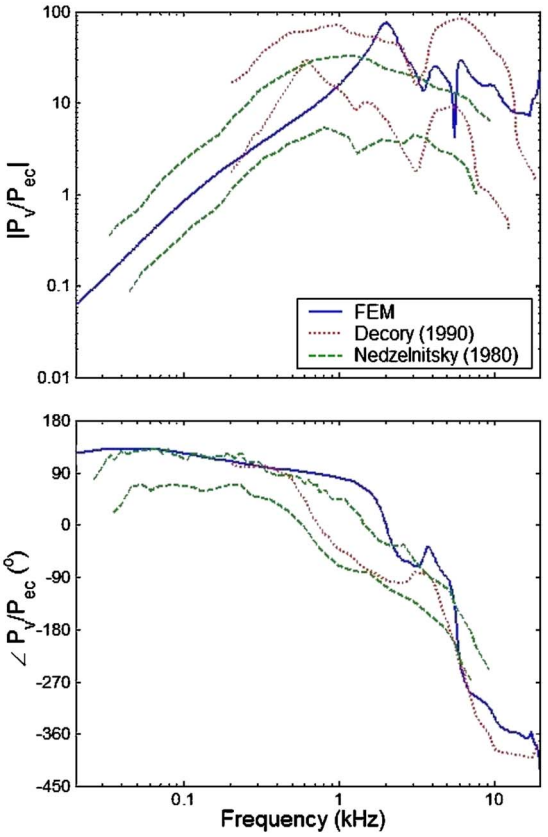

FIG. 11. (Color online) Middle-ear pressure gain, defined as the pressure in cochlea vestibule normalized by pressure in the ear canal. Closed middle-ear cavity finite element simulation compared against open cavity measurements by Nedzelnitsky (1980) and closed cavity measurements by Decory *et al.* (1990).

sponding more closely to the observed cavity resonance. In addition, there is less phase roll-off in the model results from 1 to 2 kHz, although good agreement at low frequencies and a similar phase roll-off at high frequencies.

F. Role of the septum

In the middle-ear impedance measurements by Rosowski *et al.* (2000), the presence of the septum was shown to cause a shift in the middle-ear resonance ("notch") from near 10 to 4–5 kHz [Fig. 12(a)]. This shift in resonance due to the septum was previously tested and confirmed by using a one-dimensional lossy cylindrical tube model for the MEC by Puria (1991). The present results show that the MEC resonance shift hypothesis is consistent even when realistic anatomy is incorporated in the computational framework. In the intact case, a resonance in the 4–5 kHz range is shown. However, when the septum is removed, this resonance shifts to above 10 kHz, as seen in Fig. 12(b). Thus, the computational model is consistent with the measurement findings regarding the shift in the middle-ear cavity resonance as a function of the cavity geometry.

As suggested by Peake *et al.* (1992), a consequence of the placement of the septum between the oval and round windows is a functional advantage in cases where the eardrum or ossicles are missing or damaged. To analyze this condition, the computed 3D structural model was used to compute the pressure difference between the oval and round windows in the cat MEC, both for an intact middle-ear cavity and for the removed septum (Fig. 13). As expected, there is a decrease in the effective volume between the two coupled cavity conditions (intact case) versus the single cavity condition (no septum). At low frequencies, this results in an increase in the pressure difference magnitude, $|P_{ow}-P_{rw}|$, by the bony septum between the two windows. There is a greater difference between pressures at the oval and round windows with an intact septum, and thus $|P_{ow}-P_{rw}|$ is closer to unity. A similar response at the resonant frequencies of the cavities at the round and oval window pressure differences can be observed in both cases. Comparing the response of the normal cavities to those with the septum removed, a similar frequency shift to the impedance at the eardrum is observed.

G. Slit experiment

Recent measurements by O'Connor *et al.* (2008) showed that cutting and then patching of the eardrum has an insignificant effect at low frequencies but has a larger effect on high frequency sensitivity than what was previously measured. Figure 14 predicts the ratio of stapes velocity to the ear canal pressure for three conditions: an intact tympanic membrane, four cuts with three patches, and four cuts with four patches. All simulations were done for open cavities,

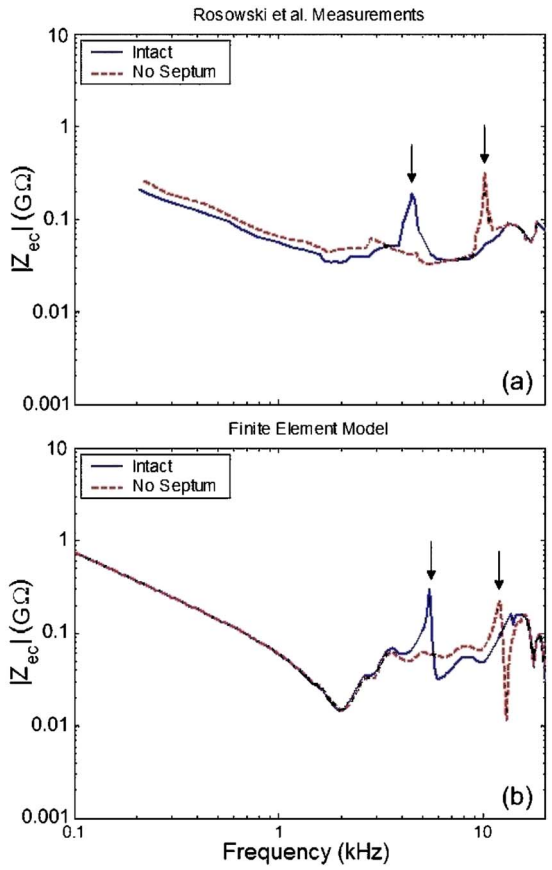

FIG. 12. (Color online) Middle-ear impedance for normal cavities and removal septum. (a) Measurements by Rosowski *et al.* (2000) and (b) finite element simulation results.

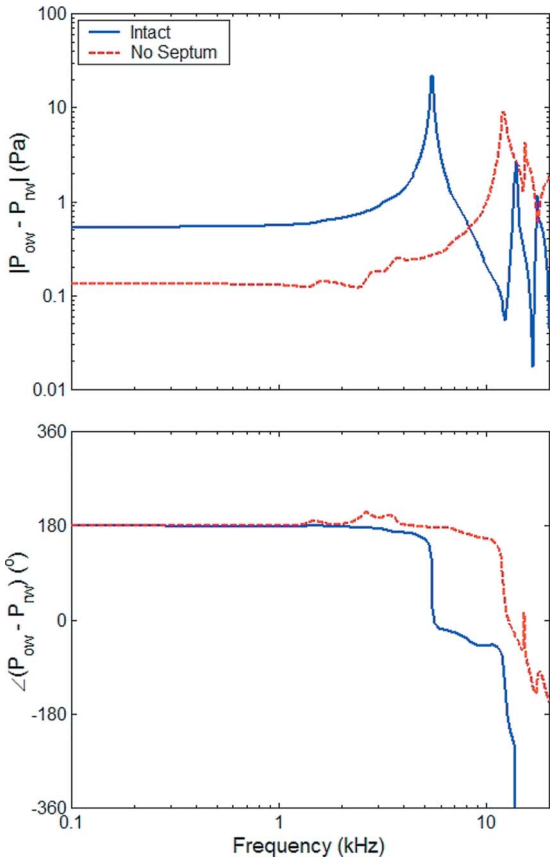

FIG. 13. (Color online) Pressure difference at oval and round windows computed by using the coupled model with and without the septum.

apparent from the lack of middle-ear resonances. Consistent with measurements, the finite element model results clearly show a loss in stapes velocity at low frequencies when the cuts are not fully patched and a loss above 4 kHz for both cases. Variations on patch material properties predict a stronger sensitivity to the elastic modulus of the patch compared to the density, as shown in Fig. 15.

V. DISCUSSION

A. Properties of the tympanic membrane

The comparisons between the current model and eardrum measurements of Decraemer *et al.* are perhaps the most intriguing of the validation comparisons. These comparisons illustrate the advantages over current finite element models of using a multilayered composite model for the eardrum to better represent the physical microstructure, as in Fay *et al.* (2006). Previous finite element models (Gan *et al.*, 2006, e.g.) have yet to reproduce the tympanic membrane response pattern where there are multiple modes. As medical imaging technology improves, such models will be able to capture these anatomical features, which the current isotropic and orthotropic single layer models cannot.

Young's moduli similar to Fay *et al.* (2006) are used, which are much larger than those in other finite element models such as those of Funnell and Decraemer (1996). However, the thickness of the fiber layers play a crucial role in the resultant transverse and bending stiffnesses such that using a multiple layered representation with much smaller thicknesses for the individual layers has a very large impact on the observed stiffness of the composite material. It should also be noted that comparing the fiber moduli with the observed volume fraction of collagen fibers from scanning electron microscopy imaging leads to Young's moduli for the collagen fibers to be about 1 GPa, which is consistent with the "linear" regime of the measured stress-strain behavior of individual collagen fibers under pretension (Sasaki and Odajima, 1996). This consistency illustrates an advantage of the composite model, in which it can provide a closer physical link between chosen material properties and observable microstructure, and paves the path toward future multiscale modeling using results from molecular simulations. However, the persistent anomalous 2 kHz peak in the model results may indicate a stronger coupling of the eardrum modes in the present model compared to the previously described "discordant" eardrum in Fay *et al.* (2006), although this may also be a function of the simple ossicular model presently used.

One key related observation is the issue of the shear modulus, which only appears explicitly in orthotropic models where the shear modulus is independent of transverse Young's moduli. This presents an anatomical puzzle, which needs future consideration. Parameter estimation for this model revealed that a high shear modulus on the order of the in-plane moduli was necessary to match experimental obser-

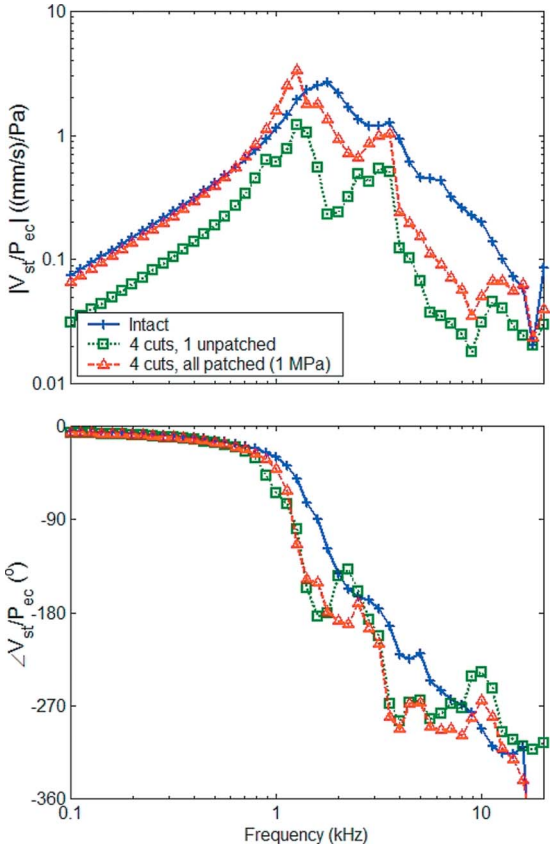

FIG. 14. (Color online) Stapes velocity, normalized by the ear canal pressure, for three simulated conditions with open cavities: intact tympanic membrane, four circumferential cuts with one left unpatched, and four cuts all patched.

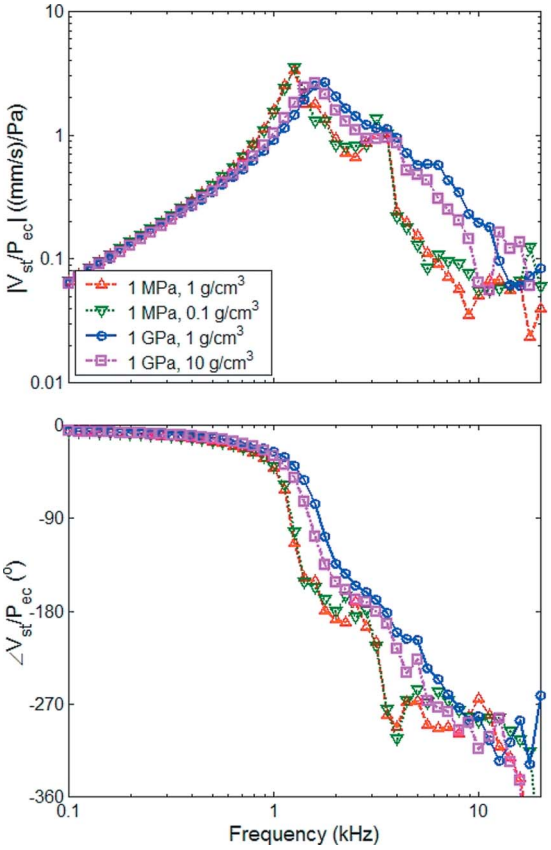

FIG. 15. (Color online) Same as Fig. 14 except with four cuts all patched using (1) a low stiffness (1 MPa) and normal density material, (2) a low stiffness and low density (0.1 g/cm^3) material, (3) a high stiffness (1 GPa) and normal density material, and (4) a high stiffness and high density (10 g/cm^3) material.

vations on the order of 35 MPa. This is seen mostly in the comparisons to eardrum displacements, where a low shear modulus resulted in much higher relative displacements away from the umbo than those observed by Decraemer *et al.* (1989) and at earlier frequencies. Figure 16 shows an example of this behavior, if the shear modulus was decreased to 10% of the original value. A higher relative magnitude is observable at low frequencies (starting at almost eight times the umbo displacement, as opposed to three times) and an earlier onset of higher order resonances (1 kHz instead of 2–3 kHz). There does not appear to be a strong effect on the impedance, particularly at low frequencies (not shown), but this might become important when considering the mistuned eardrum resonances at higher frequencies. This sensitivity is perhaps not apparent in earlier models due to the increased resultant bending and shear stiffness from using only a single layer, which could obscure the effects of the shear modulus on eardrum displacements seen in the current multilayer composite model.

This observation seems to contradict what is known regarding the microstructure of the eardrum. The high shear modulus is also apparent in Fay *et al.* (2006) using an asymptotic shell model and is implicit in isotropic models where the shear modulus is a function of the resultant Young's modulus and Poisson's ratio. The inconsistency in this observation is that the shear modulus is thought to correspond to cross-linking between the fibrous microstructure, and shear is interpreted as a relative slip between the collagen fibers. The ordered collagen fibers contribute to in-plane Young's moduli, but only the matrix material and superstructure connecting the collagen fibers together contribute to the shear moduli. However, microstructural observations (Lim, 1968, 1970) have previously concluded that there was minimal cross-linking between fibers in the ear-

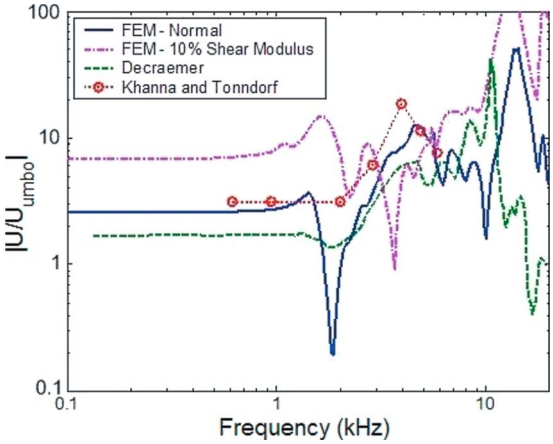

FIG. 16. (Color online) Relative displacement of the posterior region of the tympanic membrane to the displacement at the umbo. Finite element simulation compared to similar simulation with 10% shear modulus and against relevant measurements.

drum. This suggests that either the existing cross-linking is exceptionally strong or that there is some additional mechanism to prevent the eardrum from deforming via shear, such as interweaving of the collagen fibers. These unknown microstructural details, as illustrated by the computational model, may have implications on the behavior of the eardrum or selection of materials for myringoplasty.

B. Role of the septum

It has been shown that the cat uses vertical localization cues in the 8–16 kHz range (Musicant *et al.*, 1990; Rice *et al.*, 1992). According to the current hypothesis, the function of the septum is to shift the middle-ear resonance away from this useful frequency range, so as not to interfere with sound localization (Puria, 1991). The model results, as shown in Figs. 12 and 13, support the earlier experimental measurements in predicting the migration of the middle-ear resonance away from this range. The pressure difference predicted between the round window and oval window would also seem to indicate that even without the direct input from the eardrum to the cochlea, as transmitted by the ossicles in the middle ear, the cat would be able to detect and respond to acoustic input (Wever and Lawrence, 1950; Peake and Rosowski, 1996; Voss *et al.*, 1996). This may indicate that the septum could also play a role in increasing the pressure differences at the oval and round window, which would increase the input to the cochlea in cases where the eardrum is missing or there is a disruption of the ossicular chain.

C. Slit experiment

An important prediction from this experiment is that the patched condition does not show any decrease in stapes velocity until about 2–4 kHz (Fig. 14), after which it shows a loss of up to 15 dB. Thus, the numerical simulations agree qualitatively with the measurements done in human cadaver temporal bones, predicting that although a paper patch may restore low frequency hearing, it may not function as well at frequencies above 3–4 kHz. As the principle difference between the intact and patched condition is the interruption of the radial fibers, this illustrates the importance of these fibers to the function of the eardrum, even in the absence of pretension. An alternative explanation is the increased mass due to the patches. This possibility is explored by decreasing the mass of the patch by a factor of 10 and comparing those results to the original condition. As shown in Fig. 15, decreasing the mass of the patch does not predict a decrease in transmission loss, indicating that this is a stiffness-related effect rather than mass driven. It also should be noted that Young's modulus used for the patch was several orders of magnitude below the normal modulus for dry paper. However, in the experiment in question, the paper was heavily moistened, which is known to greatly reduce the elastic modulus (Alava and Niskanen, 2006). This makes the material much closer to the properties of biological soft tissue (which is normally used for as the graft material). As seen in Fig. 15, increasing the stiffness of the patch to a high stiffness (1 GPa) predicts a lower high frequency loss, assuming that the patch is firmly attached to the tympanic membrane. This has some important possible clinical implications, as the stiffer patch model predicts better high frequency behavior, which is not indicated from the normal low frequency testing. However, a stiffer patch may require a higher density material. As can be seen in the figure, an increase in patch density may add to the loss of high frequency transmission. Thus, a balance must be made between patch stiffness and density, suggesting the usage of reinforced composite materials in cases where the hole sizes are much bigger than the small slits simulated here.

VI. SUMMARY

In this paper, a new finite element model for the middle ear has been developed for the domestic cat. This fully coupled model combines realistic anatomical geometries from medical imaging with a multilayered composite model for the tympanic membrane. The model has been tested against physiological measurements under a wide variety of conditions, and numerical experiments have been conducted to gain insight on the middle-ear structure and function. Three observations are reported here: the role of the septum in avoiding a middle-ear resonance around 10 kHz, the high frequency loss in transmission capability due to the radial collagen fibers, simulated by replacing portions of the eardrum with paper patches, and the unusually high shear modulus required for the model to successfully replicate experimental data.

The finite element model results give generally good agreement with the experimental measurements. In most of the comparisons, however, there are deviations in the 2–3 kHz range, a consistent difference in phase with lower roll-off at low frequencies and higher phase roll-off above 2 kHz. The phase differences seem to be related to the ossicle and cochlea models, as seen in Fig. 8 where the phase in the drained cochlea conditions is in better agreement to the measurements than the intact model. This indicates that a more realistic ossicular model, such as the one recently developed by Sim and Puria (2008), and an improved cochlear model may improve the coupled model and correspond better with experimental measurements. The anomalous 2 kHz peak, on the other hand, seems to indicate an increased "tuning" of the eardrum model over the actual discordant eardrum. In addition, a nonlinear model for the tympanic membrane is currently being developed for simulation of the hearing response at elevated static pressures. The application of the modeling formulation to the human middle ear using medical imaging data is also an obvious next step, now that the approach has been demonstrated by using the domestic cat. Finally, accurate ultrastructural information is needed to construct the fibrous sublayers of the tympanic membrane. If these become available using modern advances in medical imaging technology, layer thickness and fiber density data can be incorporated directly into the model.

ACKNOWLEDGMENTS

The authors wish to acknowledge the assistance of Dr. Richard Goode and the VA Palo Alto Health Care System. The authors would also like to thank Dr. Donna Bouley for

her assistance in dissecting and preparing the cadaver samples and Derek Lindsey for assistance on the μCT machine. This work has been sponsored in part by a Stanford Graduate Fellowship, NIH:NIDCD Ruth L. Kirschstein Predoctoral Fellowship (F31DC6327), and an NIH:NIDCD R01 Grant (DC05960).

APPENDIX: ADDITION OF OSSICLES AND COCHLEA TO MODEL

A Hamiltonian approach is used to add the effects of the ossicles onto the coupled structural acoustic model. The ossicles, suspensory ligaments, and cochlea add both potential and inertial energies to the total energy of the dynamical system. The umbo is used as the reference location for determining the motions about the center of gravity for the malleus-incus complex, and the displacement and rotation about this point are computed by using local displacements around the umbo.

Given a mass and moment of inertia, the rotations of the malleus-incus complex, θ, are defined by the displacements $\mathbf{u}_a$ at the local nodes of a hexahedral element centered at the umbo,

$$\theta(\mathbf{u}) = \frac{1}{2}\nabla \times \mathbf{u}, \tag{A1}$$

$$= \frac{1}{2}\begin{bmatrix} u_{3,2} - u_{2,3} \\ u_{1,3} - u_{3,1} \\ u_{2,1} - u_{1,2} \end{bmatrix}, \tag{A2}$$

$$= \sum_a \mathbf{B}_a \mathbf{u}_a, \tag{A3}$$

$$\mathbf{B}_a = \frac{1}{2}\begin{bmatrix} 0 & -N_{a,3} & N_{a,2} \\ N_{a,3} & 0 & -N_{a,1} \\ -N_{a,2} & N_{a,1} & 0 \end{bmatrix}, \tag{A4}$$

where the displacements within the element are defined by using the standard interpolation functions N_a.

The motion of the center of gravity for the malleus-incus complex is then written as

$$\mathbf{x}_{\mathrm{CG}} = \mathbf{x}_{\mathrm{umbo}} + \mathbf{r}, \tag{A5}$$

$$\mathbf{u}_{\mathrm{CG}} = \mathbf{u}_{\mathrm{umbo}} + \theta \times \mathbf{r}. \tag{A6}$$

The kinetic energy contribution for a rigid body with respect to the center of mass is

$$T = \frac{1}{2}M\mathbf{v}_{\mathrm{CG}} \cdot \mathbf{v}_{\mathrm{CG}} + \frac{1}{2}\dot{\theta} \cdot \mathbf{I}_{\mathrm{CG}}\dot{\theta}, \tag{A7}$$

with total mass M and moment of inertia $\mathbf{I}$. For an arbitrary reference (in this case, the umbo location), this is rewritten as

$$T = \frac{1}{2}M\mathbf{v} \cdot \mathbf{v} + M\mathbf{v} \cdot (\dot{\theta} \times \mathbf{r}) + \frac{1}{2}\dot{\theta} \cdot \mathbf{I}\dot{\theta}. \tag{A8}$$

Finding the minimum energy, this gives the variational form (in the frequency domain)

$$\delta T = -\omega^2 \left\{ M\delta\mathbf{u} \cdot \mathbf{u} + \frac{1}{4}(\nabla \times \delta\mathbf{u}) \cdot \mathbf{I}(\nabla \times \mathbf{u}) \cdots + \frac{1}{2}M[(\nabla \times \delta\mathbf{u}) \cdot (\mathbf{r} \times \mathbf{u}) + (\mathbf{r} \times \delta\mathbf{u}) \cdot (\nabla \times \mathbf{u})] \right\}. \tag{A9}$$

This in turn adds to the mass matrix of the system (using moment of inertia $\mathbf{I}$ related to the umbo),

$$\mathbf{m}^e = \mathbf{N}^T M\mathbf{N} + \mathbf{B}^T M[\mathbf{r} \times]\mathbf{N} + \mathbf{N}^T[\mathbf{r} \times]^T M\mathbf{B} + \mathbf{B}^T\mathbf{I}\mathbf{B}, \tag{A10}$$

where

$$[\mathbf{r} \times] = \begin{bmatrix} 0 & -r_3 & r_2 \\ r_3 & 0 & -r_1 \\ -r_2 & r_1 & 0 \end{bmatrix}, \tag{A11}$$

and $\mathbf{N}$ and $\mathbf{B}$ are the assembled matrices of N_a and $\mathbf{B}_a$, respectively.

Similarly, the effects of the suspensory ligaments are represented by six spring parameters, representing the resultant translational and rotational stiffnesses. These springs are added to the potential energy given the displacement and rotation at the umbo,

$$\Pi = \frac{1}{2}\sum_i k_i^{\mathrm{trans}}(\mathbf{u}_{\mathrm{CG}} \cdot \mathbf{e}_i)^2 + \frac{1}{8}\sum_i k_i^{\mathrm{rot}}((\nabla \times \mathbf{u}_{\mathrm{CG}}) \cdot \mathbf{e}_i)^2, \tag{A12}$$

where $\mathbf{e}_i$ define the local basis oriented with the observed rotational axis. Taking the variation, and keeping the same finite element approximation as before, gives an addition to the stiffness matrix of the system,

$$\mathbf{k}^e = \sum_i k_i^{\mathrm{trans}}\mathbf{V}_i^T\mathbf{V}_i + \sum_i k_i^{\mathrm{rot}}\mathbf{B}^T\mathbf{e}_i^T\mathbf{e}_i\mathbf{B}, \tag{A13}$$

$$\mathbf{V}^i = \mathbf{e}_i^T\{\mathbf{N} - [\mathbf{r} \times]\mathbf{B}\}. \tag{A14}$$

The 1D transfer function relating force and displacements at the stapes head, as in Puria and Allen (1998), can be written as

$$F_{isj} = i\omega Z_{isj}u_{isj}. \tag{A15}$$

For this model, both u_{isj} and F_{isj} act only in a direction normal ($\mathbf{n}_{\mathrm{fp}}$) to the stapes footplate (assuming pistonlike motion). In particular, for $s = i\omega$,

$$Z_{\mathrm{sc}}(s) = \frac{K_{\mathrm{al}}}{s} + sM_s + R_{\mathrm{al}} + sM_v + \frac{1}{sC_{\mathrm{rw}}} + \cdots (R_0 + sM_0)R_c/(R_0 + sM_0 + R_c), \tag{A16}$$

$$Z_{isj}(s) = (sR_{isj} + K_{isj})A_{\mathrm{fp}}^2 Z_{\mathrm{sc}}/(sR_{isj} + K_{isj} + A_{\mathrm{fp}}^2 sZ_{\mathrm{sc}}), \tag{A17}$$

where the numerical parameters are defined in Puria and Allen (1998). The potential energy associated with this transfer function can be written as

$$\Pi = \frac{1}{2} s Z_{isj}(s)(\mathbf{u}_{isj} \cdot \mathbf{n}_{\mathrm{jp}})^2, \tag{A18}$$

and the corresponding matrix form,

$$\mathbf{k}_e(s) = s Z_{isj}(s) \mathbf{V}_{isj}^T \mathbf{V}_{isj}, \tag{A19}$$

$$\mathbf{V}_{isj} = \mathbf{n}_{\mathrm{fp}}^T \{\mathbf{N} - [r_{isj} \times]\mathbf{B}\}, \tag{A20}$$

is added to the finite element model.

Alava, M., and Niskanen, K. (**2006**). "The physics of paper," Rep. Prog. Phys. **69**, 669–723.

Bermúdez, A., Hervella-Nieto, L., Prieto, A., and Rodríguez, R. (**2006**). "An optimal perfectly matched layer with unbounded absorbing function for time-harmonic acoustic scattering problems," J. Comput. Phys. **223**, 469–488.

Dallos, P. (**1970**). "Low-frequency auditory characteristics: Species dependence," J. Acoust. Soc. Am. **48**, 489–499.

Decory, L. (**1989**). "Origines des differences interspecifiques de susceptibilite au bruit (origins of interspecies differences of susceptibility to noise)," Ph.D. thesis, University of Bordeaux II.

Decory, L., Franke, R. B., and Dancer, A. L. (**1990**). "Measurements of the middle ear transfer function in cat, chinchilla, and guinea pig," in *The Mechanics and Biophysics of Hearing*, edited by P. Dallos, C. Geisler, J. Matthews, M. Ruggero, and C. Steele (Springer-Verlag, New York), pp. 270–277.

Decraemer, W. F., Khanna, S. M., and Funnell, W. R. J. (**1989**). "Interferometric measurements of the amplitude and phase of tympanic membrane vibrations in cat," Hear. Res. **38**, 1–18.

Dvorkin, E. N., and Bathe, K.-J. (**1984**). "Continuum mechanics based four-node shell element for general non-linear analysis," Eng. Comput. **1**, 77–88.

Fay, J. P., Puria, S., Decraemer, W. F., and Steele, C. R. (**2005**). "Three approaches for estimating the elastic modulus of the tympanic membrane," J. Biomech. **38**, 1807–1815.

Fay, J. P., Puria, S., and Steele, C. R. (**2006**). "The discordant eardrum," Proc. Natl. Acad. Sci. U.S.A. **103**, 19743–19748.

Funnell, W. R. J. (**1983**). "On the undamped natural frequencies and mode shapes of a finite-element model of the cat eardrum," J. Acoust. Soc. Am. **73**, 1657–1661.

Funnell, W. R. J., Decraemer, W. F., and Khanna, S. M. (**1987**). "On the damped frequency response of a finite-element model of the cat eardrum," J. Acoust. Soc. Am. **81**, 1851–1859.

Funnell, W. R. J., and Decraemer, W. R. (**1996**). "On the incorporation of moire shape measurements in finite element models of the cat eardrum," J. Acoust. Soc. Am. **100**, 925–932.

Gan, R. Z., Sun, Q., Dyer, Jr., R. K., Chang, K.-H., and Dormer, K. J. (**2002**). "Three-dimensional modeling of middle ear biomechanics and its applications," Otol. Neurotol. **23**, 271–280.

Gan, R. Z., Sun, Q., Feng, B., and Wood, M. W. (**2006**). "Acoustic-structural coupled finite element analysis for sound transmission in human ear-pressure distributions," Med. Eng. Phys. **28**, 395–404.

Guinan, Jr., J. J., and Peake, W. T. (**1967**). "Middle-ear characteristics of anesthetized cats," J. Acoust. Soc. Am. **41**, 1237–1261.

Huang, G. T., Rosowski, J. J., and Peake, W. T. (**2000**). "Relating middle-ear acoustic performance to body size in the cat family: Measurements and models," J. Comp. Physiol. [A] **186**, 447–465.

Hughes, T. J. R. (**2000**). *The Finite Element Method: Linear Static and Dynamic Finite Element Analysis* (Dover, Mineola, NY).

Khanna, S. M., and Tonndorf, J. (**1972**). "Tympanic membrane vibrations in cats studied by time-averaged holography," J. Acoust. Soc. Am. **51**, 1904–1920.

Kuypers, L. C., Decraemer, W. F., Dirckx, J. J. J., and Timmermans, J.-P. (**2005**). "Thickness distribution of fresh eardrums of cat obtained with confocal microscopy," J. Assoc. Res. Otolaryngol. **6**, 223–233.

Lim, D. J. (**1968**). "Electron microscopic observation, part I: Pars tensa," Acta Oto-Laryngol. **66**, 181–198.

Lim, D. J. (**1970**). "Human tympanic membrane: An ultrastructural observation," Acta Oto-Laryngol. **70**, 176–186.

Lynch, III, T. J., Peake, W. T., and Rosowski, J. J. (**1994**). "Measurements of the acoustic input impedance of cat ears: 10 Hz to 20 kHz," J. Acoust. Soc. Am. **96**, 2184–2209.

Morand, H. J.-P., and Ohayon, R. (**1995**). *Fluid Structure Interaction* (Wiley, West Sussex).

Musicant, A. D., Chan, J. C., and Hind, J. E. (**1990**). "Direction-dependent spectral properties of cat external ear: New data and cross-species comparisons," J. Acoust. Soc. Am. **87**, 757–781.

Nedzelnitsky, V. (**1980**). "Sound pressures in the basal turn of the cat cochlea," J. Acoust. Soc. Am. **68**, 7676–7689.

O'Connor, K. N., Tam, M., Blevins, N. H., and Puria, S. (**2008**). "Tympanic membrane collagen fibers: A key to high frequency sound conduction," Laryngoscope **118**, 483–490.

Peake, W. T., and Rosowski, J. J. (**1996**). "Middle-ear structural and functional dependence on animal size," in *Diversity in Auditory Mechanics*, edited by E. R. Lewis, G. R. Long, R. F. Lyon, P. M. Narris, C. R. Steele, and E. Hecht-Poinar (World Scientific, Singapore).

Peake, W. T., Rosowski, J. J., and Lynch, III, T. J. (**1992**). "Middle-ear transmission: Acoustic vs. ossicular coupling in cat and human," Hear. Res. **57**, 245–268.

Puria, S. (**1991**). "A theory of cochlear input impedance and middle ear parameter estimation," Ph.D. thesis, The City College, CUNY.

Puria, S., and Allen, J. B. (**1998**). "Measurement and model of the cat middle ear: Evidence of tympanic membrane acoustic delay," J. Acoust. Soc. Am. **104**, 3463–3481.

Puria, S., Peake, W. T., and Rosowski, J. J. (**1997**). "Sound-pressure measurements in the cochlear vestibule of human-cadaver ears," J. Acoust. Soc. Am. **101**, 2754–2770.

Puria, S., Sim, J. H., and Shin, M., Tuck-Lee, J., and Steele, C. R. (**2006**). "Middle Ear Morphometry from Cadaveric temporal bone microCT imaging," Middle Ear Mechanics in Research and Otology — IV., edited by A. Eiber and A. Huber, World Scientific, Singapore.

Rabbitt, R. D., and Holmes, M. H. (**1986**). "A fibrous dynamic continuum model of the tympanic membrane," J. Acoust. Soc. Am. **80**, 1716–1728.

Rice, J. J., May, B. J., Spirou, G. A., and Young, E. D. (**1992**). "Pinna-based spectral cues for sound localization in cat," Hear. Res. **58**, 132–152.

Rosowski, J. J., Huang, G. T., Atencio, C. A., and Peake, W. T. (**2000**). "Acoustic effects of multiple middle-ear air spaces: Measurements in cats," in *Recent Developments in Auditory Mechanics*, edited by H. Wada, T. Takasaka, K. Ikeda, K. Ohyama, and T. Koike (World Scientific, Singapore), pp. 15–21.

Sasaki, N., and Odajima, S. (**1996**). "Stress-strain curve and young's modulus of a collagen molecule as determined by the x-ray diffraction technique," J. Biomech. **29**, 655–658.

Sim, J. H., and Puria, S. (**2008**). "Soft tissue morphometry of the malleus-incus complex from micro-ct imaging," J. Assoc. Res. Otolaryngol. **9**, 5–21.

Simo, J. C., and Rifai, M. S. (**1990**). "A class of mixed assumed strain methods and the method of incompatible modes," Int. J. Numer. Methods Eng. **29**, 1595–1638.

Tonndorf, J., and Khanna, S. M. (**1967**). "Some properties of sound transmission in the middle and outer ears of cats," J. Acoust. Soc. Am. **41**, 513–521.

Tuck-Lee, J. P., and Pinsky, P. M. (**2008**). "Adaptive frequency windowing for multifrequency solutions in structural acoustics based on the matrix Padé-via-Lanczos algorithm," Int. J. Numer. Methods Eng. **73**, 728–746.

Turkel, E., and Yefet, A. (**1998**). "Absorbing PML boundary layers for wave-like equations," Appl. Numer. Math. **27**, 533–557.

Voss, S. E., Rosowski, J. J., and Peake, W. T. (**1996**). "Is the pressure difference between the oval and round windows the effective acoustic stimulus for the cochlea?," J. Acoust. Soc. Am. **100**, 1602–1616.

Vu-Quoc, L., and Tan, X. G. (**2003**). "Optimal solid shells for non-linear analyses of multilayer composites," Comput. Methods Appl. Mech. Eng. **192**, 975–1059.

Wada, H., Metoki, T., and Kobayashi, T. (**1992**). "Analysis of dynamic behavior of human middle ear using a finite element model," J. Acoust. Soc. Am. **92**, 3157–3168.

Wever, E. G., and Lawrence, M. (**1950**). "The acoustic pathways to the cochlea," J. Acoust. Soc. Am. **22**, 460–467.

Gerbil middle-ear sound transmission from 100 Hz to 60 kHz[a)]

Michael E. Ravicz[b)]
Eaton-Peabody Laboratory, Massachusetts Eye and Ear Infirmary, 243 Charles Street, Boston, Massachusetts 02114 and Research Laboratory of Electronics, Massachusetts Institute of Technology, 77 Massachusetts Avenue, Cambridge, Massachusetts 02139

Nigel P. Cooper
School of Life Sciences, Keele University, Keele, Staffordshire ST5 5BG, United Kingdom

John J. Rosowski
Eaton-Peabody Laboratory, Massachusetts Eye and Ear Infirmary, 243 Charles Street, Boston, Massachusetts 02114; Department of Otology and Laryngology, Harvard Medical School, Boston, Massachusetts 02115; and Harvard-MIT Division of Health Science and Technology, Massachusetts Institute of Technology, 77 Massachusetts Avenue, Cambridge, Massachusetts 02139

(Received 25 February 2008; revised 25 April 2008; accepted 25 April 2008)

Middle-ear sound transmission was evaluated as the middle-ear transfer admittance $\mathbf{H_{MY}}$ (the ratio of stapes velocity to ear-canal sound pressure near the umbo) in gerbils during closed-field sound stimulation at frequencies from 0.1 to 60 kHz, a range that spans the gerbil's audiometric range. Similar measurements were performed in two laboratories. The $\mathbf{H_{MY}}$ magnitude (a) increased with frequency below 1 kHz, (b) remained approximately constant with frequency from 5 to 35 kHz, and (c) decreased substantially from 35 to 50 kHz. The $\mathbf{H_{MY}}$ phase increased linearly with frequency from 5 to 35 kHz, consistent with a 20–29 μs delay, and flattened at higher frequencies. Measurements from different directions showed that stapes motion is predominantly pistonlike except in a narrow frequency band around 10 kHz. Cochlear input impedance was estimated from $\mathbf{H_{MY}}$ and previously-measured cochlear sound pressure. Results do not support the idea that the middle ear is a lossless matched transmission line. Results support the ideas that (1) middle-ear transmission is consistent with a mechanical transmission line or multiresonant network between 5 and 35 kHz and decreases at higher frequencies, (2) stapes motion is pistonlike over most of the gerbil auditory range, and (3) middle-ear transmission properties are a determinant of the audiogram. © *2008 Acoustical Society of America.* [DOI: 10.1121/1.2932061]

PACS number(s): 43.64.Ha, 43.64.Kc, 43.64.Yp, 43.64.Tk [BLM] Pages: 363–380

I. INTRODUCTION

This paper continues an inquiry into high-frequency sound transmission through the external and middle ear (ME) of the Mongolian gerbil *Meriones unguiculatus* that began with a study of the distribution of ear canal (EC) sound pressure (Ravicz *et al.*, 2007). In that study, we established that sound pressure could be measured in the EC over the tympanic membrane (TM) near the umbo over a broad frequency range and that sound pressure at that point provided an adequate characterization of ME input up to 60 kHz. In this paper, we use similar EC sound measurements to characterize the ME input and measurements of stapes velocity to characterize the ME output. The transfer function computed as the ratio of these two variables describes sound transmission through the ME over a frequency range that spans the range of gerbil hearing.

The nature of high-frequency ME sound transmission has recently been a matter of considerable debate. Though simple models suggest that ME sound transmission should be bandpass in nature and limited at high frequencies by the mass of the ossicles and the cochlear fluids (see, e.g., Zwislocki, 1962; Hemilä *et al.*, 1995), most data suggest that sound transmission is broadband (see, e.g., Johnstone and Sellick, 1972; Ruggero and Temchin, 2002). A pertinent question is whether sound transmission is maintained at high levels at high sound frequencies, as in lossless transmission through a matched transmission line (Puria and Allen, 1998; Ruggero and Temchin, 2002), or decreases at some high-frequency limit. Published data in gerbil do not resolve this debate: Some measurements of the stapes velocity (normalized by EC sound pressure) show a bandpass characteristic (Rosowski *et al.*, 1999), while others show scala vestibuli sound pressure or stapes velocity (normalized as above) that remains roughly constant to the highest frequency of measurement (e.g., Olson, 1998; Overstreet and Ruggero, 2002).

A complication in nearly all of these previous studies of ME sound transmission is adequate characterization of the ME input, sound pressure stimulus in the EC, at high frequencies (Rosowski *et al.* 1999; Overstreet and Ruggero, 2002; Dong and Olson, 2006). The similarity between the wavelength λ of sound in air at high frequencies and the dimensions of the gerbil EC and TM ($\lambda/10$ is less than the length of even a surgically shortened EC (~4 mm) above

[a)]Portions of this work were presented by Olson and Cooper (2000) and Ravicz and Rosowski (2004).
[b)]Author to whom correspondence should be addressed. Electronic mail: mike_ravicz@meei.harvard.edu

8 kHz) suggests that the sound pressure produced by stimuli at higher frequencies will vary substantially along the EC and, to a lesser extent, over the surface of the TM (Ravicz *et al.*, 2007). In the earlier study, we explored possible causes of error in estimating ME input (Ravicz *et al.*, 2007) and concluded that sound pressure measurements made within 1 mm of the umbo were a good estimate of the sound pressure at the TM over the umbo and therefore of ME input at frequencies up to at least 60 kHz. In this study, we use such sound pressure measurements as the normalization for stapes velocity to evaluate ME sound transmission.

Another complication in using stapes velocity to evaluate ME sound transmission is that the ME output, stapes velocity, has components in all three dimensions, especially at high frequencies (Decraemer *et al.*, 2000; Decraemer *et al.*, 2006b, 2007). Though evidence suggests that stapes motion in the piston direction is the effective stimulus to the cochlea (Decraemer *et al.*, 2006a, 2007) and therefore the effective ME output, the three dimensionality of stapes motion means that the velocity of a single point may not be a good descriptor of stapes piston motion. In this study, we compute the motion of a measured point on the stapes posterior crus in three dimensions and estimate the accuracy of this motion in describing piston stapes motion.

Determining ME sound transmission helps address another question: whether the frequency range of hearing is determined primarily by cochlear limitations or whether ME limitations could also play a role. Several investigators (e.g., Khanna and Tonndorf, 1969; Khanna and Sherrick, 1981; Rosowski *et al.*, 1986, 1988; Rosowski, 1991a, 1991b) have postulated that cochlear sensitivity is approximately constant across frequency and that the audiogram is determined by the sound transmission properties of the ME. Other investigators (e.g., Overstreet and Ruggero, 2002; Ruggero and Temchin, 2002) have pointed out that the frequency sensitivity of the ensemble of cochlear sensory cells spans only the auditory range and claim that (1) efficient ME sound transmission spans a wider frequency range than cochlear sensitivity and hence (2) the audiogram is determined only by cochlear sensitivity. A weakness of all previous studies is that the highest frequency examined is still within the gerbil auditory range.

In this paper, we evaluate ME transmission by a transfer function between stapes velocity and EC sound pressure from 100 to 60 kHz. This frequency range spans the gerbil's range of hearing.[1] We define the ME transfer admittance $\mathbf{H_{MY}}(f)$ as the ratio of the stapes velocity spectrum $\mathbf{V_S}(f)$ (the ME output) to the spectrum of sound pressure $\mathbf{P_U}(f)$ near the umbo (the ME input) by

$$\mathbf{H_{MY}}(f) = \mathbf{V_S}(f)/\mathbf{P_U}(f), \tag{1}$$

where $\mathbf{V_S}(f)$, $\mathbf{P_U}(f)$, and $\mathbf{H_{MY}}(f)$ are functions of frequency f.[2] Stapes velocity is described by the velocity of a point on the stapes posterior crus measured in a direction as close to the piston direction as practicable. (Henceforth, velocities, sound pressures, and admittances will be understood to be functions of f unless otherwise noted.)

We present measurements from two laboratories in which somewhat different techniques were used: the Eaton-Peabody Laboratory at MEEI (Ravicz and Rosowski) and an auditory physiology laboratory at the University of Bristol (where Cooper was at the time). We show that the ME transfer admittance has features of a simple resonant system at low frequencies, is representative of a multiresonant network or a transmission line below about 35 kHz, and decreases rapidly with frequency above that, consistent with a multiresonant network. These results confirm and extend conclusions of other recent studies of stapes motion and ME transmission (Decraemer *et al.*, 2007; de la Rochfoucauld *et al.*, 2008). We present evidence that errors in specifying cochlear input from single-point stapes velocity measurements versus whole-stapes measurements are small below 50 kHz. We compute cochlear input impedance from $\mathbf{H_{MY}}$ and previous measurements of scala vestibuli sound pressure measured in a similar fashion (Olson, 2001) and show that cochlear input, as evaluated by $\mathbf{V_S}$ or by cochlear sound power transmission, is a fairly good predictor of the entire gerbil audiogram.

II. METHODS

A. Animal preparation

The preparation and use of the experimental animals were approved by the Institutional Animal Care and Use Committees at MEEI and Bristol as applicable and have been described in detail previously (Ravicz *et al.*, 2007). Briefly, 19 young adult Mongolian gerbils (13 at MEEI, the same as those used in the 2007 study; 6 at Bristol) were anesthetized, the pinna flange and cartilaginous EC were removed, and the soft tissue was removed from the surface of the skull around the opening of the bony EC and for some distance posteriorly. One or more holes were made in the exposed wall of the auditory bulla to preclude a buildup of static pressure within the ME air spaces and to provide visual access to the stapes. A coupling tube was cemented around the bony EC opening with dental cement or cyanoacrylate glue to permit a high-frequency sound source to be coupled and recoupled reliably to the ear.

B. Experimental methods

The experiments were conducted in a sound-isolation booth. Heart rate was monitored throughout the experiment, and body temperature was maintained at (37 ± 1) °C with a heating pad. Anesthesia boosters at half the initial surgical dose were provided as necessary to suppress the pedal withdrawal reflex. The animal's head was clamped securely in a custom holder. At Bristol, the animal and holder were mounted in nested goniometers such that the axis of the outer goniometer was parallel to the interaural axis (transverse), the axis of the inner goniometer was approximately anterior-posterior (longitudinal), and the intersection of the goniometer axes was at the stapes of the measured ear (cf., Decraemer *et al.*, 1994, 2007). At the conclusion of the live experiment, the animal was euthanized with a fatal dose of anesthesia.

1. Stapes velocity

To assess stapes velocity, a small target comprising four to six retroreflective balls was placed on the posterior crus of

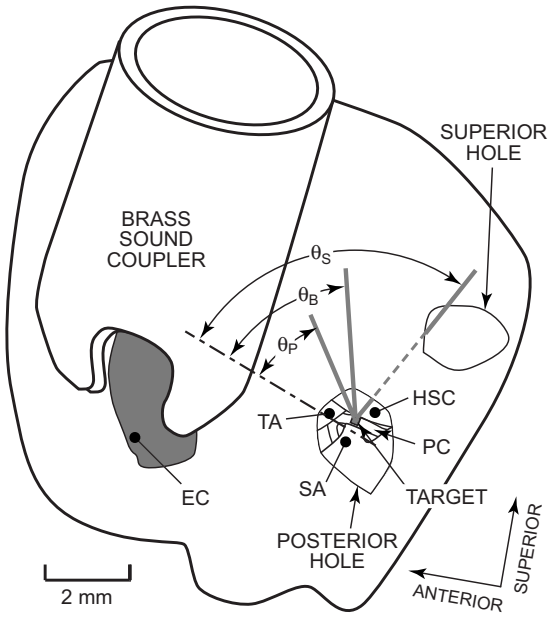

FIG. 1. View of the left side of a gerbil head showing the locations of measurement access holes and the view of the stapes through the posterior hole used for most stapes velocity measurements. The skin and soft tissue were removed from the superior and lateral aspects of the auditory bulla. A brass sound coupler was cemented about the opening of the bony ear canal (EC). A hole was made in the bulla wall posterior to the bony EC ("posterior hole"). A retroreflective target (gray square) was placed on the stapes posterior crus (PC). The view of the stapes was limited by the tympanic annulus (TA), the horizontal semicircular canal (HSC), and the stapedial artery (SA). At MEEI, stapes velocity was measured from a direction as close to the piston direction (dot-dashed line) as possible. The angle θ between the measurement direction (the baseline direction, thick gray line) and the piston direction (labeled θ_P) was 27°–37°. (Note that angles are foreshortened in this view and appear larger or smaller than they actually were.) At Bristol, this hole was larger, and θ between this baseline measurement direction and the piston direction (labeled θ_B) was approximately 47°. Another hole ("superior hole") was made in the bulla superior to the posterior hole to vent the ME and (in some bones) to provide an alternate view of the posterior crus target for stapes velocity measurements: θ for this measurement direction (solid and dashed gray line, labeled θ_S) was 61°–65°.

the stapes, and the velocity $\mathbf{V_S}$ of this stapes target in response to chirp or tone sound stimuli presented in the EC was measured with a laser-Doppler vibrometer [MEEI: OPV 501/2600, Polytec PI, Waldbronn, Germany; Bristol: custom (Cooper, 1999)]. Both velocity magnitude $|\mathbf{V_S}|$ and phase $\angle\mathbf{V_S}$ relative to the stimulus were measured. Visual access to the stapes was through the small hole(s) in the bulla wall posterior to the EC opening (Fig. 1; see also Rosowski *et al.*, 1999). At MEEI, most measurements were made through an ~2 mm diameter hole located approximately in the same horizontal plane as the EC opening—the "posterior hole" (Fig. 1). The vibrometer laser beam (thick gray line in Fig. 1) was oriented in a direction as close to the direction of pistonlike stapes motion (dot-dashed line) as permitted by the edge of the hole and the anatomical structures within the ME: the angle θ between this "baseline" measurement direction and the piston direction (θ_P in Fig. 1) was 27°–37°. At Bristol, the access hole was larger (4–5 mm diameter), and the vibrometer laser was oriented in a baseline direction somewhat further from the direction of pistonlike stapes motion than the MEEI measurements: $\theta \approx 47°$ (θ_B in Fig. 1). Each vibrometer measured velocity only in the direction of its line of sight.

To estimate $\mathbf{V_S}$ in three-dimensional (3D) space, additional velocity measurements were made as the direction of the line of sight was changed. At MEEI, $\mathbf{V_S}$ was also measured in three ears in another direction through a second similar-size hole superior to the original hole (the "superior hole"), θ_S in Fig. 1. Components of stapes motion could then be computed within a plane defined by the two measurement directions (see the Appendix). At Bristol, $\mathbf{V_S}$ was also measured in three ears from a range of directions permitted by the edges of the wider access hole. Velocities measured from five to six different directions were used to compute components of stapes motion in three dimensions (as in Decraemer *et al.*, 1994, 2007; see the Appendix).

The measurement directions were determined differently at MEEI and Bristol, with differing degrees of precision. At MEEI, directions were estimated postmortem by separating the head from the body and orienting it so the stapes footplate was nearly horizontal. An operating microscope was oriented along each measurement direction (as determined by the hole and anatomical limits described above), and the angles from the measurement direction to the horizontal plane and the plane defined by the stapes crura were measured with a protractor. Repeatability was within 5°. At Bristol, the goniometers enabled the measurement direction to be changed in 0.1° increments. Determination of the orientation of the stapes relative to the measurement direction was estimated visually and so was less precise (±20°) than at MEEI.

2. Ear-canal sound pressure

EC sound pressure $\mathbf{P_{EC}}$ was measured simultaneous to stapes target velocity: Both magnitude $|\mathbf{P_{EC}}|$ and phase $\angle\mathbf{P_{EC}}$ relative to the stimulus were measured. At MEEI, $\mathbf{P_{EC}}$ was measured at various locations within the bony EC remnant with a custom probe tube microphone (based on a Larson–Davis 2520 1/4–in. condenser microphone, Provo, UT—see Ravicz *et al.*, 2007; 1.27 mm outer diameter) that was advanced ~0.5–1 mm down the bony EC toward the TM along an approximately longitudinal trajectory [see Ravicz *et al.*, 2007, Fig. 2(b)]. In the last four ears measured at MEEI, EC sound pressure was also measured over the TM at a point near the umbo $\mathbf{P_U}$ (Ravicz *et al.*, 2007). At Bristol, $\mathbf{P_{EC}}$ was measured with a probe tube microphone (based on a Brüel+Kjær 4134 1/4-in. condenser microphone, Denmark) near the border of *pars tensa* and *pars flaccida*, within 1 mm of the EC remnant opening and 2.5–3 mm from the umbo.

3. Stimulus generation and response measurement

Computer-controlled experimental systems at MEEI and Bristol were used for stimulus generation and measurement of sound pressure and velocity responses. The system used at MEEI is described in Ravicz *et al.* (2007). Stimuli were broadband chirps 0.05–99 kHz, and vibrometer and microphone responses were digitized at 225 kHz. Some stimuli were deemphasized by 20 dB below 5 kHz to allow higher stimulus levels to be used to deliver more high-frequency sound energy into the EC. Broadband sound levels (summed across frequency) were 90–95 dB sound pressure level

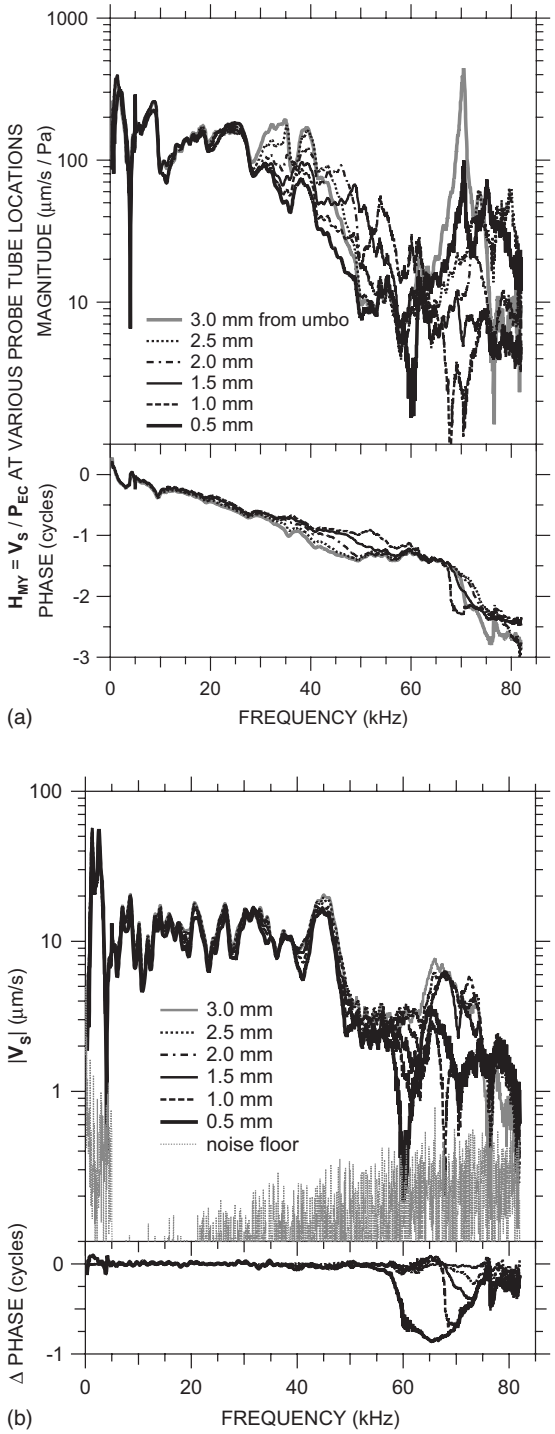

FIG. 2. (a) Transfer admittance $\mathbf{H_{MY}}=\mathbf{V_S}/\mathbf{P_{EC}}$ with the probe tube at various locations along an approximately longitudinal trajectory. Legend indicates the approximate distance from the probe tube tip to a point on the TM over the umbo. Top: magnitude; bottom: phase. (b) $\mathbf{V_S}$ with the probe tube at the various locations. The relative invariance of $\mathbf{V_S}$ with probe tube location below 58 kHz shows that variations in $\mathbf{H_{MY}}$ with probe tube location are due primarily to variations in $\mathbf{P_{EC}}$ among those locations. Also shown is a typical $\mathbf{V_S}$ measurement noise floor (gray dots). Top: magnitude; bottom: phase relative to $\angle\mathbf{V_S}$ with the probe tube approximately 3.0 mm from the umbo.

(SPL). The system used at Bristol is described in Cooper and Rhode (1992) and comprised a Tucker–Davis Technologies (Alachua, FL) System II digital to analog converter and attenuators and a fast (1 MHz) Analogic (Peabody, MA) analog to digital converter to digitize vibrometer and microphone responses. The system presented tones in the EC at 80 dB SPL with a logarithmic frequency spacing of eight points per octave.

C. Computation of transfer admittance from stapes velocity and ear canal sound pressure

Because the transfer admittance used to describe ME function and facilitate comparisons among ears in this study and to other studies depends on both stapes velocity and EC sound pressure, the accuracy of EC sound pressure measurement is important. We have shown in a previous paper that, even with the EC shortened by removing the cartilaginous EC (leaving only the bony EC), EC sound pressure $\mathbf{P_{EC}}$ varies substantially between the opening of the bony EC and the TM over the umbo at frequencies above 30 kHz (Ravicz *et al.*, 2007).

The effect of this variation in $\mathbf{P_{EC}}$ on the transfer admittance is shown for one ear (0402R) in Fig. 2(a). The curves show $\mathbf{H_{MY}}$ computed from $\mathbf{V_S}$ and $\mathbf{P_{EC}}$ measured with the probe tube at various positions between the EC entrance and the umbo. Though there are small variations in $\mathbf{H_{MY}}$ between probe tube positions at sound frequencies less than 30 kHz, above that frequency, $|\mathbf{H_{MY}}|$ varies by a factor of 3 or more depending on the probe tube position. A plot of the stapes velocity (not normalized by $\mathbf{P_{EC}}$) measured with the probe tube at these various positions [Fig. 2(b)] demonstrates that $\mathbf{V_S}$ is nearly invariant with probe tube position below 58 kHz; hence, the $\mathbf{H_{MY}}$ variations below 58 kHz in Fig. 2(a) are almost entirely attributable to variations in $\mathbf{P_{EC}}$. Consequently, we will use $\mathbf{P_U}$ for $\mathbf{H_{MY}}$ computations in those ears in which $\mathbf{P_U}$ measurements are available. The technique for computing $\mathbf{H_{MY}}$ in other ears is described below.

Figure 2(b) also shows that there are variations in $\mathbf{V_S}$ with probe tube position at higher frequencies. Below 58 kHz, $\mathbf{V_S}$ varied by less than a factor of 1.2 when the probe tube position was varied. Above 58 kHz $\mathbf{V_S}$ varied substantially ($|\mathbf{V_S}|$ decreased by a factor of 3, $\angle\mathbf{V_S}$ decreased by almost 0.5 cycles) when the probe tube approached to within 0.5 mm of the umbo, which suggests that the presence of the probe tube affected the sound field at the umbo at higher frequencies.[3] To minimize the effects of the probe tube on $\mathbf{H_{MY}}$ computations, we use $\mathbf{V_S}$ measured with the probe tube near the EC entrance, where there was minimal effect on $\mathbf{V_S}$.

Both $\mathbf{V_S}$ and $\mathbf{P_{EC}}$ were measured at frequencies up to 99 kHz at MEEI, but sound pressure measurements were valid only up to 82 kHz, and sound pressure variations in the microphone calibration setup limited accurate $\mathbf{P_{EC}}$ measurements to 60 kHz and below (Ravicz *et al.*, 2007; see Sec. I). For these reasons and because of the probe-tube-induced variation in $\mathbf{V_S}$ near 60 kHz described above, we limit our presentation of $\mathbf{V_S}$, $\mathbf{P_{EC}}$, and $\mathbf{H_{MY}}$ to frequencies below 60 kHz.

In the four later MEEI ears (including the one shown in Fig. 2), measurements of EC sound pressure within 0.5 mm of the umbo (and throughout the EC) were available, and $\mathbf{H_{MY}}$ in those ears was computed from $\mathbf{V_S}$ normalized by $\mathbf{P_U}$ as described above. In the nine early MEEI ears and the six

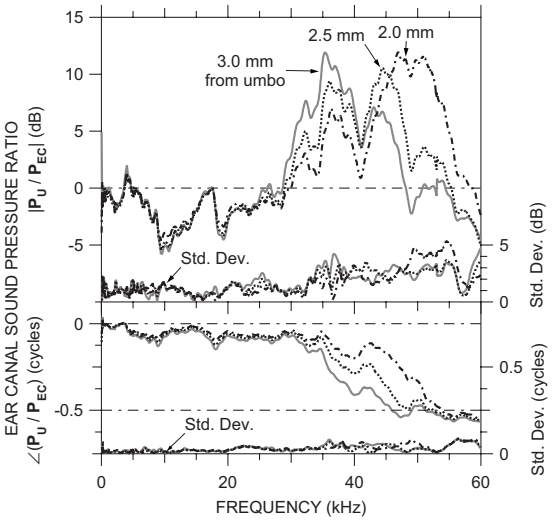

FIG. 3. Ratios of sound pressure near the umbo $\mathbf{P_U}$ to sound pressure in the bony EC $\mathbf{P_{EC}}$ at various distances from the umbo. Each curve is the mean (in dB) of measurements in four ears. Top: magnitude ratio in dB; bottom: phase difference. At the bottom of each panel is the s.d. (right-hand vertical scale). $\mathbf{V_S}/\mathbf{P_{EC}}$ in the other 15 ears (see Figs. 5 and 6) was corrected by the mean $\mathbf{P_U}/\mathbf{P_{EC}}$ curve corresponding to the $\mathbf{P_{EC}}$ measurement location in that ear.

Bristol ears, the only $\mathbf{P_{EC}}$ data available were measured closer to the bony EC canal entrance, 2–3 mm from the umbo. For these 15 ears, we correct $\mathbf{H_{MY}}$ computed from $\mathbf{V_S}$ and $\mathbf{P_{EC}}$ in each ear by an appropriate sound pressure transformation $\mathbf{P_U}/\mathbf{P_{EC}}$ between the umbo and the $\mathbf{P_{EC}}$ measurement location, computed from measurements in the four later MEEI ears mentioned above.

Figure 3 shows the mean $\mathbf{P_U}/\mathbf{P_{EC}}$ ratio for the four later MEEI ears at three EC locations that span the range of $\mathbf{P_{EC}}$ measurement locations in the other ears: approximately 3.0 mm from the umbo, near the bony EC entrance; and approximately 2.5 and 2.0 mm from the umbo. $\mathbf{P_U}/\mathbf{P_{EC}}$ at each of these three locations was remarkably similar among ears [as revealed by the small standard deviations (s.d.)—right axis], consistent with previous acoustical measurements in gerbil (see, for example, Ravicz *et al.*, 1992, 1996; Teoh *et al.*, 1997). The variance in $|\mathbf{P_U}/\mathbf{P_{EC}}|$ at each location was due primarily to broadband differences—the overall frequency dependence and the frequencies of magnitude peaks and notches varied little among ears. The magnitude ratio was significantly[4] greater than 0 dB between 30 and 45–55 kHz (depending on location) and differed significantly between the three locations from 28 to 35 kHz and from 48 to 52 kHz. ($|\mathbf{P_U}/\mathbf{P_{EC}}|$ was also significantly less than 0 dB from 8 to 17 kHz at all three locations, perhaps due to effects of the opening in the EC wall). The phase difference decreased to −0.5 cycles between 30 and 50 kHz (depending on location) and differed significantly between the three locations over this frequency range. In the 30–55 kHz range where $|\mathbf{P_U}/\mathbf{P_{EC}}|$ was significantly different from unity, differences in $\mathbf{P_U}/\mathbf{P_{EC}}$ between locations were greater than the $\mathbf{P_U}/\mathbf{P_{EC}}$ differences between ears.

For each of the other ears, the particular $\mathbf{P_U}/\mathbf{P_{EC}}$ for the correction was chosen as the curve for which the frequency of the $|\mathbf{P_U}/\mathbf{P_{EC}}|$ peak (35, 44, or 47–51 kHz) was closest to the frequency of the first $|\mathbf{P_{EC}}|$ minimum in that ear (29–50 kHz). Except for a minor mismatch near the frequency of the first $|\mathbf{P_{EC}}|$ minimum, $\mathbf{H_{MY}}$ in the other ears was quite similar to $\mathbf{H_{MY}}$ in the four later ears.

III. RESULTS

In this paper, we present results from independent experiments in two laboratories. The results from the two laboratories (MEEI and Bristol) have complementary strengths and considerable similarities. Stapes velocity was measured to higher frequencies at MEEI than at Bristol. At MEEI, $\mathbf{V_S}$ and $\mathbf{P_{EC}}$ were measured with a broadband chirp stimulus; at Bristol, pure-tone stimuli were used. The baseline measurement direction for $\mathbf{V_S}$ at MEEI was generally closer to the direction of piston stapes motion than that at Bristol, and $\mathbf{P_{EC}}$ was measured closer to the umbo at MEEI than at Bristol. For investigations of the 3D motion of the stapes posterior crus, $\mathbf{V_S}$ was measured from five or six directions at Bristol but at most two directions at MEEI.

The $\mathbf{H_{MY}}$ data shown in Figs. 4–7 were computed from $\mathbf{V_S}$ measured in the baseline direction normalized by sound pressure near the umbo $\mathbf{P_U}$ (directly or indirectly) as described in Sec. II C. As such, they show $\mathbf{H_{MY}}$ in an "experimental" reference frame (along the line of sight of the laser vibrometer) rather than in a direction defined by the stapes orientation (an "intrinsic" reference frame; Decraemer *et al.*, 2007). Later (in Sec. IV A), we will discuss the extent to which $\mathbf{H_{MY}}$ estimates the ME transfer admittance in the piston direction in the intrinsic reference frame.

A. Middle-ear transfer admittance at MEEI

The stapes velocity transfer function $\mathbf{H_{MY}}$ is shown for four ears in Fig. 4: against a logarithmic frequency scale (to show low-frequency data more clearly) in panel (a) and against a linear frequency scale (to show high-frequency data more clearly) in panel (b). The $\mathbf{H_{MY}}$ curve for each ear is the logarithmic mean[5] of several $\mathbf{V_S}$ measurements normalized by $\mathbf{P_U}$. $\mathbf{H_{MY}}$ is shown for frequencies at which $|\mathbf{V_S}|$ was above the measurement noise and motion artifact estimated from measurements of the sound-induced motion of the bone of the cochlear promontory [see Fig. 2(b)].[6] The s.d. of measurements in each ear is plotted against the right-hand axis: as a magnitude ratio and as a phase addend. Both $\mathbf{V_S}$ and $\mathbf{P_U}$ were linear with stimulus level over at least a 40 dB range in these ears and those shown in Fig. 5.

In all ears, $\mathbf{H_{MY}}$ shows a magnitude slope with frequency ($d|\mathbf{H_{MY}}|/df$) of ~+1 (on a log-log scale) and phase angle near +0.25 cycles at frequencies below 0.5–1 kHz, consistent with a compliance-dominated admittance [Fig. 4(a)]. The value of this compliance varies considerably (a factor of 10) among ears. The magnitude of $\mathbf{H_{MY}}$ in all ears has a peak in the 0.5–2 kHz range and $\angle\mathbf{H_{MY}}$ crosses zero at about the same frequency, consistent with a ME resonance. The relatively flat $|\mathbf{H_{MY}}|$ peak and shallow $\angle\mathbf{H_{MY}}$ slope indicate that the resonance is highly damped. Above the resonance, $|\mathbf{H_{MY}}|$ decreases sharply to a notch near 3 kHz, and there is a positive $\angle\mathbf{H_{MY}}$ ripple at the notch frequency. This $|\mathbf{H_{MY}}|$ notch and $\angle\mathbf{H_{MY}}$ ripple pair is con-

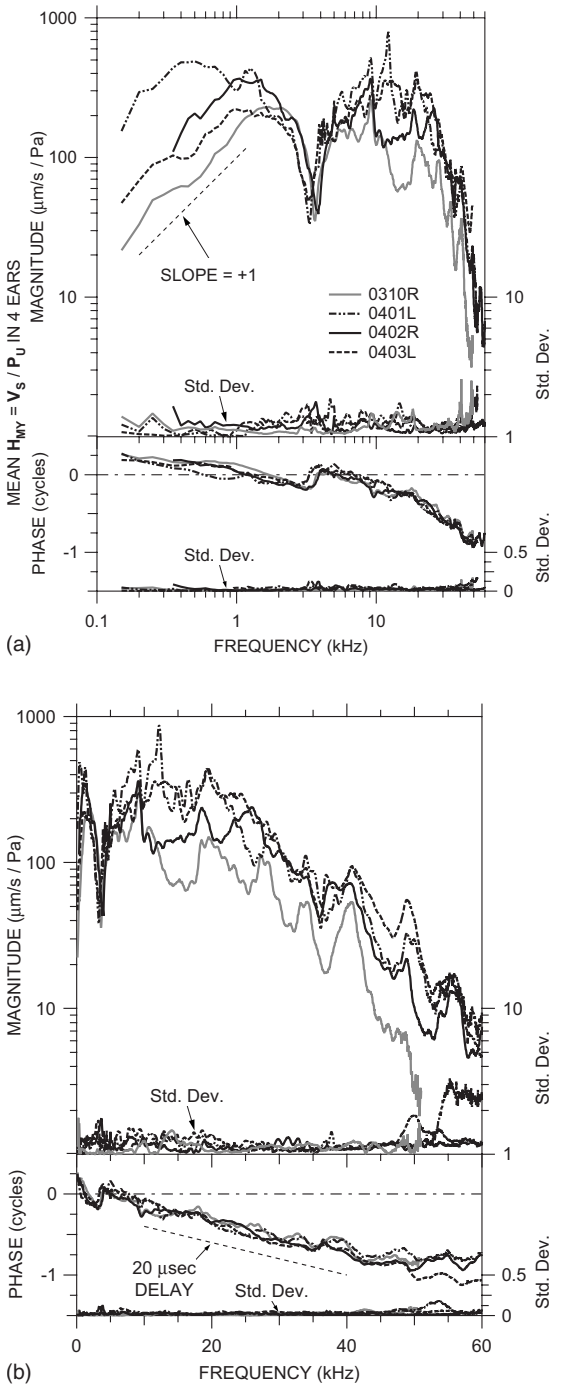

FIG. 4. Mean $\mathbf{H_{MY}}=\mathbf{V_S}/\mathbf{P_U}$ in four ears at MEEI in which $\mathbf{P_U}$ was measured, shown in the experimental reference frame of the vibrometer. Each curve is the logarithmic mean of 11–22 $\mathbf{V_S}$ measurements normalized by $\mathbf{P_U}$. Top: magnitude; bottom: phase. At the bottom of each panel is the s.d. (right-hand vertical scale). The $|\mathbf{H_{MY}}|$ dip and $\angle\mathbf{H_{MY}}$ ripple near 3–4 kHz are due to a resonance between the compliance of the air in the bulla and the mass of the bulla hole. (a) Logarithmic frequency scale; (b) linear frequency scale. The thin dashed line in panel (a) shows a log-log slope of +1. The thin dashed line in panel (b) indicates the phase slope corresponding to a 20–μs delay.

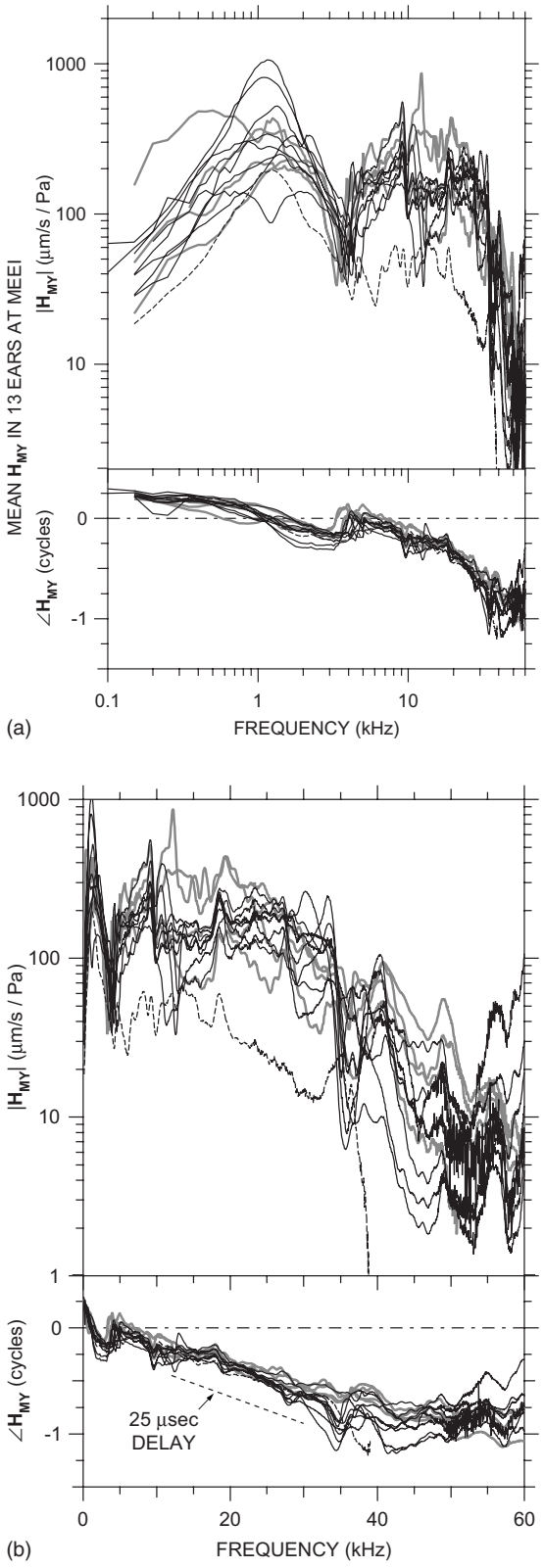

FIG. 5. Mean $\mathbf{H_{MY}}=\mathbf{V_S}/\mathbf{P_U}$ in nine ears at MEEI in which $\mathbf{P_{EC}}$ was measured 2–3 mm from the umbo (black lines), corrected by a $\mathbf{P_U}/\mathbf{P_{EC}}$ curve from Fig. 3. Each curve is the logarithmic mean of two to six measurements. $\mathbf{H_{MY}}$ in the four ears in Fig. 4 is shown by gray lines. An outlier (0309L) is shown by a dashed line. Top: magnitude; bottom: phase. (a) Logarithmic frequency scale; (b) linear frequency scale. The thin dashed line in panel (b) indicates the phase slope corresponding to a 25–μs delay.

sistent with a resonance between the compliance of the air in the ME and the mass of the air in the bulla hole (see, e.g., Ravicz *et al.*, 1992; also Sec. III C below). Above the notch frequency, $|\mathbf{H_{MY}}|$ increases to a peak near 10 kHz (ear 0401L has a second peak at a slightly higher frequency), and $\angle\mathbf{H_{MY}}$ has a small ripple at the frequency of the peak.

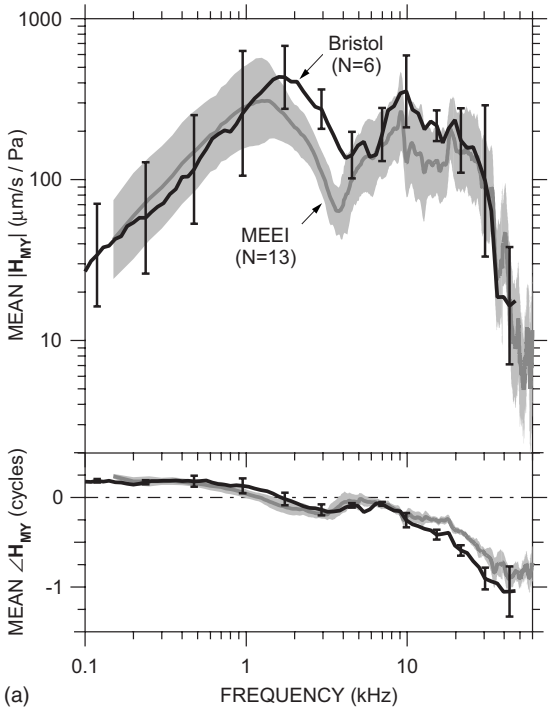

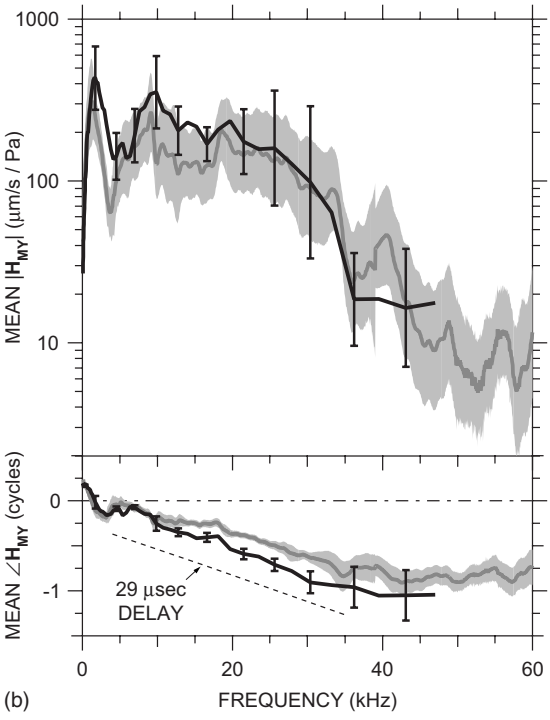

FIG. 6. Means ± s.d. of $\mathbf{H_{MY}}$ in 6 ears at Bristol (black line, error bars) and 13 ears at MEEI (gray line, shading). Top: magnitude; bottom: phase. (a) Logarithmic frequency scale; (b) linear frequency scale. The dashed line indicates the phase slope corresponding to a 29 μs delay.

At frequencies above the peak(s), $|\mathbf{H_{MY}}|$ is approximately constant with frequency (±a factor of 2) up to 30–35 kHz. $\angle\mathbf{H_{MY}}$ continues to accumulate approximately linearly with frequency above the ripple [Fig. 4(b)], consistent with a delay. Below 35 kHz, the slope of $\angle\mathbf{H_{MY}}$ with frequency ($d\angle\mathbf{H_{MY}}/df$) suggests a delay of 20 μs. At higher frequencies, $|\mathbf{H_{MY}}|$ decreases sharply, and the rate of $\angle\mathbf{H_{MY}}$ accumulation slows. Between about 40 and 60 kHz, $d\angle\mathbf{H_{MY}}/df$ suggests a group delay of zero.

In addition to the four ears shown in Fig. 4, $\mathbf{H_{MY}}$ was computed from $\mathbf{V_S}/\mathbf{P_{EC}}$ in nine earlier MEEI ears and corrected by an appropriate mean $\mathbf{P_U}/\mathbf{P_{EC}}$ as described in Sec. II C. Logarithmic means of multiple estimates of $\mathbf{H_{MY}}$ (computed from two to six $\mathbf{V_S}$ and $\mathbf{P_{EC}}$ measurement pairs) in each of these nine ears are shown as black lines in Fig. 5; $\mathbf{H_{MY}}$ in the four ears in Fig. 4 is shown by gray lines. $\mathbf{H_{MY}}$ in the earlier ears shows nearly all of the same features as $\mathbf{H_{MY}}$ in the later ears. In all ears at low frequencies $d|\mathbf{H_{MY}}|/df$ is near +1 and $\angle\mathbf{H_{MY}}$ is near +0.25 cycles; there is a broad $|\mathbf{H_{MY}}|$ peak near 1–1.5 kHz (except in ear 0301L) and a shallow $\angle\mathbf{H_{MY}}$ zero crossing at the same frequency; there is a $|\mathbf{H_{MY}}|$ notch and $\angle\mathbf{H_{MY}}$ ripple near 3 kHz, and there is a $|\mathbf{H_{MY}}|$ peak and $\angle\mathbf{H_{MY}}$ ripple near 10 kHz.[7] At higher frequencies, up to 30–35 kHz, $|\mathbf{H_{MY}}|$ is approximately constant (±a factor of 2 as above) in all ears (except 0309L, dashed line), and $\angle\mathbf{H_{MY}}$ accumulates with frequency with a slope that implies a delay of about 25 μs. At still higher frequencies, above 35 kHz, $|\mathbf{H_{MY}}|$ decreases sharply and $\angle\mathbf{H_{MY}}$ flattens. (The magnitude and phase ripples near 35–40 kHz may be artifacts of the $\mathbf{P_U}/\mathbf{P_{EC}}$ correction; see Sec. II C.) Except for the outliers above, $|\mathbf{H_{MY}}|$ and $\angle\mathbf{H_{MY}}$ have the same spectral shape among ears, and $\mathbf{H_{MY}}$ in these earlier ears generally falls within the range of the $\mathbf{H_{MY}}$ measured in the four ears of Fig. 4.

B. Middle-ear transfer admittance at Bristol

At Bristol, stapes velocity was measured on the posterior crus and $\mathbf{P_{EC}}$ was measured near the EC entrance in a manner similar to that described above for measurements in the earlier nine ears at MEEI. Figure 6 shows the logarithmic mean of $\mathbf{H_{MY}}$ in six ears, computed from $\mathbf{V_S}$ and $\mathbf{P_{EC}}$ measurements and the $\mathbf{P_U}/\mathbf{P_{EC}}$ correction for a probe tube location 2.5–3 mm from the umbo as described above and in Sec. II C. The mean $\mathbf{H_{MY}}$ (black line) is plotted against a logarithmic frequency scale in panel (a) and against a linear frequency scale in panel (b); the s.d. is shown at representative points by error bars. These data are compared to the mean $\mathbf{H_{MY}}$ ± s.d. in all MEEI ears (gray line and shading).

There is a marked similarity among the mean $\mathbf{H_{MY}}$ measured at Bristol and MEEI: Both show a $|\mathbf{H_{MY}}|$ slope of approximately +1 and $\angle\mathbf{H_{MY}}$ near +0.25 cycles below 1 kHz [Fig. 6(a)], a broad $|\mathbf{H_{MY}}|$ peak near 1–1.5 kHz, a $|\mathbf{H_{MY}}|$ notch and $\angle\mathbf{H_{MY}}$ ripple near 3–5 kHz, a $|\mathbf{H_{MY}}|$ peak and $\angle\mathbf{H_{MY}}$ ripple near 10 kHz, approximately constant $|\mathbf{H_{MY}}|$ and linearly accumulating $\angle\mathbf{H_{MY}}$ up to 30 kHz [Fig. 6(b)], and a fairly sharp rolloff in $|\mathbf{H_{MY}}|$ and a flattening of $\angle\mathbf{H_{MY}}$ above 35 kHz. There were some minor differences, but these differences were not statistically significant except in narrow frequency ranges: $\angle\mathbf{H_{MY}}$ between 1 and 2 kHz, due to $\angle\mathbf{H_{MY}} > 0.25$ cycles in two Bristol ears; $|\mathbf{H_{MY}}|$ between 2 and 4 kHz, around the $|\mathbf{H_{MY}}|$ dip due to the bulla hole resonance in MEEI measurements described above; $\angle\mathbf{H_{MY}}$ around 5 kHz from a local $\angle\mathbf{H_{MY}}$ dip probably due to a bulla hole resonance in Bristol measurements; and $\angle\mathbf{H_{MY}}$ between 15 and 30 kHz, due to more delay in the Bristol ears (29 μs) than the MEEI ears (20–25 μs). The

results from the two laboratories are sufficiently similar that conclusions about stapes motion from results in one laboratory should apply to all measurements.

C. Effect of middle-ear air spaces on middle-ear transfer admittance

The $\mathbf{H_{MY}}$ measurements shown in Figs. 4–6 include two assumptions (one stated explicitly, one implied) about the effect of opening the ME on $\mathbf{H_{MY}}$: (1) the dip in $|\mathbf{H_{MY}}|$ near 3–5 kHz was due to a resonance between the compliance of the ME air space and the mass of the air in the bulla hole, and (2) the open ME had no other effect on $\mathbf{H_{MY}}$. We tested these assumptions in three ears by measuring $\mathbf{V_S}$ and $\mathbf{P_{EC}}$ while the posterior hole was sealed with a small transparent window (piece of polycarbonate cover slip) and the ME was vented with a long thin polyethylene tube in the superior bulla hole (Ravicz *et al.*, 1992; see Fig. 1). Only a few measurements could be taken, as the window quickly became fogged with condensation. Consistent effects were seen in two ears: the $|\mathbf{H_{MY}}|$ notch and $\angle\mathbf{H_{MY}}$ ripple at 3–4 kHz disappeared when the posterior hole was sealed, but the $|\mathbf{H_{MY}}|$ notch and $\angle\mathbf{H_{MY}}$ ripple at ~10 kHz remained. The change was in stapes velocity; $\mathbf{P_{EC}}$ did not vary. This result verifies that the $|\mathbf{H_{MY}}|$ dips and $\angle\mathbf{H_{MY}}$ ripples near 3 kHz in the MEEI data set were produced by the bulla opening and that the open bulla holes did not affect $\mathbf{H_{MY}}$ at higher frequencies. Differences between Bristol and MEEI data in the 2–6 kHz range can be explained by the difference in the size of the bulla hole in the two preparations: The smaller acoustic mass associated with the larger bulla hole used in Bristol measurements would be expected to resonate with the ME air space compliance at a higher frequency (Ravicz *et al.*, 1992).

D. Effect of removing inner-ear load on middle-ear transfer admittance

The extent to which cochlear load influences $\mathbf{H_{MY}}$ was examined by measuring $\mathbf{V_S}$ and $\mathbf{P_{EC}}$ in three ears after the cochlear load was irreversibly removed by puncturing the round window and suctioning the cochlear fluids. Results from a representative ear are shown in Fig. 7; results from the other two ears were similar. Removing the cochlear load had several effects on $\mathbf{H_{MY}}$ that were consistent among the three ears: (1) The $|\mathbf{H_{MY}}|$ peak near 1 kHz was much greater (by a factor of 3–5) and sharper. $|\mathbf{H_{MY}}|$ was elevated over the intact case between 800 Hz and 10 kHz. The sharper $|\mathbf{H_{MY}}|$ peak was accompanied by an abrupt $\angle\mathbf{H_{MY}}$ transition from about +0.2 to −0.2 cycles at the frequency of the $|\mathbf{H_{MY}}|$ peak. This peak was unrelated to the $|\mathbf{H_{MY}}|$ notch and $\angle\mathbf{H_{MY}}$ peak near 3 kHz associated with the bulla hole. (2) Another comparable-size $|\mathbf{H_{MY}}|$ peak and smaller $\angle\mathbf{H_{MY}}$ transition were observed at 15–20 kHz. (3) In two of the three ears, a third $|\mathbf{H_{MY}}|$ peak and $\angle\mathbf{H_{MY}}$ transition were observed at a frequency approximately twice the frequency of the second $|\mathbf{H_{MY}}|$ peak. These $|\mathbf{H_{MY}}|$ peaks and $\angle\mathbf{H_{MY}}$ transitions are consistent with removal of damping from a multiresonant network. These results show that the cochlear load is a significant influence on $\mathbf{H_{MY}}$ at frequencies up to at least 40 kHz.

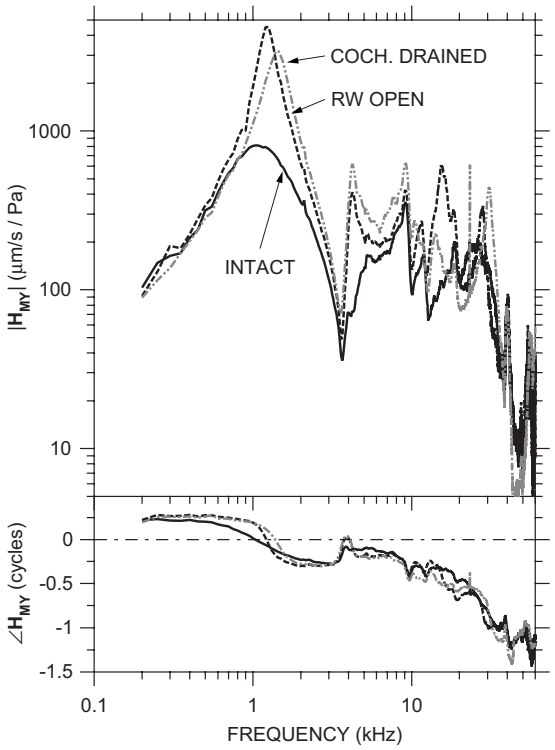

FIG. 7. $\mathbf{H_{MY}}$ in a representative ear (0306L) at MEEI with the inner ear intact (solid line), with the round window punctured and open (dashed line), and with the inner ear drained (dot-dashed gray line). Results in two other MEEI ears were similar. Top: magnitude; bottom: phase.

The observations of increased $|\mathbf{H_{MY}}|$ excursion and less-damped $\mathbf{H_{MY}}$ behavior after draining the cochlear fluids are consistent with measurements of cochlear input impedance in cat and human with the inner ear open (Lynch *et al.*, 1982; Merchant *et al.*, 1996) and ME input admittance or impedance in cat with the inner-ear lymphs drained (Lynch, 1981; Allen, 1986). The similarity of these observations to the accentuation of multiple admittance maxima and minima seen in cat (Puria and Allen, 1998) suggests that the gerbil ME also can be described as a multiresonant network or distributed system at frequencies up to 40 kHz.

E. Stapes velocity measured from other directions

The unidirectional stapes velocity measurements used in the computed $\mathbf{H_{MY}}$ shown in Figs. 4–7 describe the motion of the stapes target only along the line of measurement. Additional measurements are needed to determine stapes motion in the piston direction. Besides the baseline $\mathbf{V_S}$ measurements described above, all of which were made from approximately the same direction (the angle θ between the baseline direction and the piston direction was 28°–47°; see Sec. II B 1), additional measurements were made from different directions for the purpose of describing the motion of the stapes target in 3D space.

At Bristol, stapes velocity was measured in three ears from several well-controlled directions within 28° of the baseline direction. The measurement direction was varied

from the baseline by rotating the animal with one or both of the goniometers: Moving the animal approximately about the longitudinal axis through an angle L from its baseline position varied θ substantially, while moving the animal about the transverse axis through an angle T from its baseline position had little effect on θ. At MEEI, stapes velocity was measured in three ears through a superiorly-located bulla hole (θ=61°–65°) in addition to the posterior bulla hole used for baseline measurements (θ=27°–37°; see Sec. II B 1 and Fig. 1).

Figure 8(a) shows the ratio of $\mathbf{V_S}$ measured from five other directions in one ear (ugb15) at Bristol to the mean of three $\mathbf{V_S}$ measurements from the baseline direction. Below 7 kHz, changing the measurement direction through an angle L caused regular variations in $|\mathbf{V_S}|$: for negative L that decreased θ (closer to the piston direction, solid line), $|\mathbf{V_S}|$ increased, and for positive L that increased θ (long-dashed lines), $|\mathbf{V_S}|$ decreased. These variations were larger than the range of variation among baseline measurements (about ±10% for $|\mathbf{V_S}|$, shading). Changes through an angle T (dotted lines) had virtually no effect on $|\mathbf{V_S}|$ in this frequency range. No values of L or T caused any substantive change in $\angle\mathbf{V_S}$ below 7 kHz. These trends were common to variations in L and T in the two other ears.

Near 10 kHz, both $|\mathbf{V_S}|$ and $\angle\mathbf{V_S}$ in all three ears varied with changes in L or T. The variations in $|\mathbf{V_S}|$ with changes in L described above were larger, and $\angle\mathbf{V_S}$ varied as well. Changes in T caused a change in $|\mathbf{V_S}|$ just below 10 kHz and a change in the opposite direction in $|\mathbf{V_S}|$ just above. $\angle\mathbf{V_S}$ was also more variable with changes in T just above the frequency of maximum $|\mathbf{V_S}|$ variability. Between 15 and 36 kHz (the highest frequency in this series), changes in $|\mathbf{V_S}|$ were similar to those described above at low frequencies but smaller, and $\angle\mathbf{V_S}$ varied very little with changes in L or T.

Figure 8(b) shows the ratio of stapes velocity measured through the superior bulla hole to the mean of baseline measurements in each of the three ears at MEEI. Similar to Fig. 8(a), $|\mathbf{V_S}|$ measured from a direction further from the piston direction was smaller than $|\mathbf{V_S}|$ measured from a direction closer to the piston direction (the ratio was <1), and the difference was greater at low frequencies (below 7–10 kHz) than at frequencies above 15 kHz (except above 50 kHz). Both $|\mathbf{V_S}|$ and $\angle\mathbf{V_S}$ varied with measurement direction near 10 kHz. The variations with direction were larger than those in Fig. 8(a), perhaps because θ for superior hole measurements was larger, the angle between measurement directions was greater (39°–78° at MEEI versus 23°–28° at Bristol), or the frequency resolution was finer.

The changes in $|\mathbf{V_S}|$ and $\angle\mathbf{V_S}$ as θ varied are similar to those seen in human temporal bones but occur at higher frequencies. As in gerbil, increasing θ in human caused a monotonic decrease in $|\mathbf{V_S}|$ and no change in $\angle\mathbf{V_S}$ at low frequencies below a critical frequency, a decrease in $|\mathbf{V_S}|$ variation and increase in $\angle\mathbf{V_S}$ variation near the critical frequency, and a smaller dependence of $|\mathbf{V_S}|$ on θ above the critical frequency (Chien *et al.*, 2006), but the break frequency was higher in gerbil (~10 kHz) than that in human (~1.5 kHz). The higher critical frequency in gerbil might be related to the smaller size of the gerbil TM and ossicular chain, but the common frequency dependence suggests that similar mechanisms influence stapes motion.

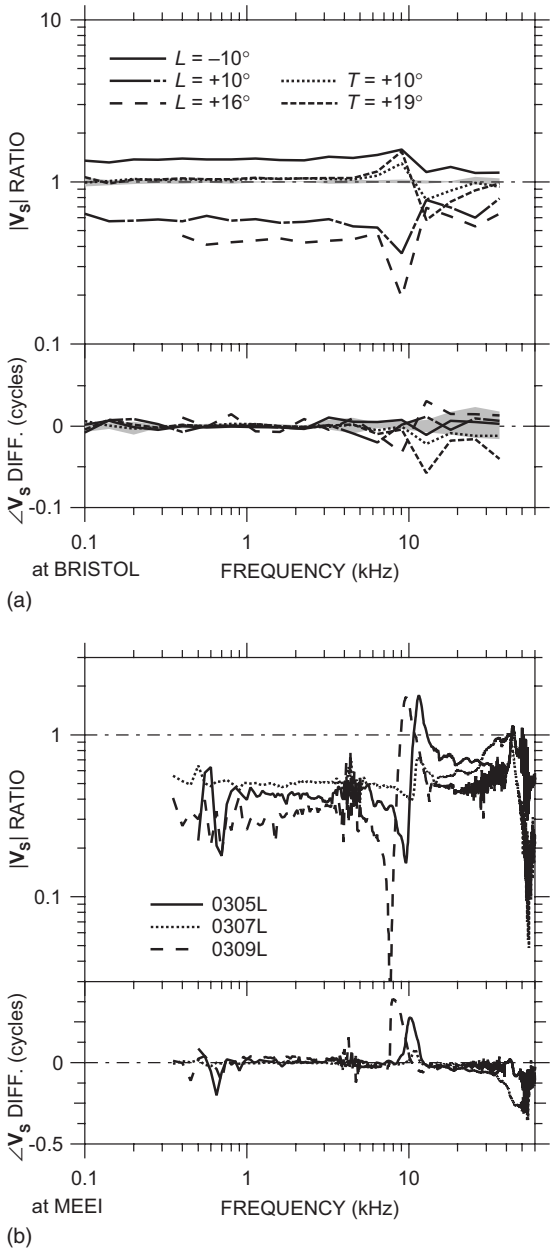

FIG. 8. Variations in $\mathbf{V_S}$ with measurement direction. (a) Magnitude ratios (top) and phase differences (bottom) for a typical ear at Bristol as the measurement direction was varied from the baseline direction through goniometer angles L and T about longitudinal and transverse axes, respectively (see Sec. II B). Effects of various L (which correspond approximately to changes in the angle θ between the measurement direction and the piston direction) are shown as solid and long-dashed lines; effects of various T (which had little effect on θ) are shown by dotted lines. The range of measurements from the baseline direction is shown by the shading. (b) Ratio of $\mathbf{V_S}$ measured through the superior vs posterior bulla holes in three ears at MEEI. Top: magnitude ratio; bottom: phase difference.

IV. DISCUSSION

A. Estimates of piston stapes motion from measurements

The ME transfer admittance estimates of Figs. 4–6 were computed from the motion of the stapes target along the line

of measurement in the baseline direction (the experimental reference frame). To relate any single-point stapes motion measurements (such as ours) to stapes piston motion (the assumed input to the cochlea; Decraemer *et al.* 2007), two fundamental assumptions must be made: (1) the motion in the baseline measurement direction is proportional to piston motion and (2) the motion of the posterior crus is representative of the motion of the stapes footplate; i.e., the stapes acts as a rigid body without bending. By using measurements from various directions in addition to the baseline direction (see Fig. 8), we compute the motion in three dimensions (Bristol data) and estimate the relative importance of transverse motion components relative to the baseline direction (MEEI and Bristol data). We use the geometric relationship between the baseline direction and the direction of stapes piston motion to express the motion of the stapes target in an intrinsic (stapes-centered) reference frame, $\hat{\mathbf{V}}_S = \hat{V}_{S,x}\hat{\mathbf{i}} + \hat{V}_{S,y}\hat{\mathbf{j}} + \hat{V}_{S,z}\hat{\mathbf{k}}$, by using the transformations described in the Appendix. We use a rigid-body assumption to predict footplate piston motion from target piston motion, and we show that the difference between our measured $\mathbf{V_S}$ and this footplate motion is sufficiently small that $\mathbf{H_{MY}}$ computed from $\mathbf{V_S}$ is a good estimate of the effective cochlear input.

We define the intrinsic coordinate system with its origin at the center of the stapes footplate; x is defined by the long footplate axis, z is defined by the short footplate axis, and y is in the direction of piston motion, orthogonal to the plane defined by the x and z axes (Decraemer *et al.*, 2007). For consistency with Decraemer *et al.* (2007), we define $+x$ as the posterior direction and $+z$ as the inferior direction; so, for a right-hand coordinate system, $+y$ is into the cochlea in the right ear. For ease of comparison of results in the left and right ears, we use a left-hand coordinate system for left ears, so $+y$ is into the cochlea in the left ear also. We use stapes dimensions from Decraemer *et al.*, 2007 (one ear). The target was located ~0.9 mm from the footplate and ~0.3 mm from the y axis in the $+x$ direction. Translational velocities are unchanged by a translation of the reference frame; so (assuming that contributions of stapes rotations to y-direction motion are negligible, see the Appendix), for rigid-body motion, $\hat{\mathbf{V}}_{S,y}$ at the target is equal to $\hat{\mathbf{V}}_{S,y}$ at the footplate.

The computed 3D motion of the stapes target in one ear at Bristol in the intrinsic reference frame is shown in Fig. 9 as Lissajous figures of target *displacement* in time at several frequencies. The motion is viewed along the three principal directions: Panels (a) and (c) are side views to compare the relative amplitude and phase of transverse to piston components, and panel (b) is a "top" view looking along the y axis toward the stapes footplate showing the relative amplitudes and phases of the two transverse components. The displacement amplitude is multiplied by the stimulus frequency for easier comparison at different frequencies.[8] Several points are evident: (1) At low frequencies below 9 kHz, stapes motion is consistent with simple translation in the piston direction—the deviation of the motion from the y direction is within the 20° measurement error of the baseline measurement direction in the y-z plane [Fig. 9(a)] and nearly within the measurement error in the x-y plane [Fig. 9(c)]. Nonpiston

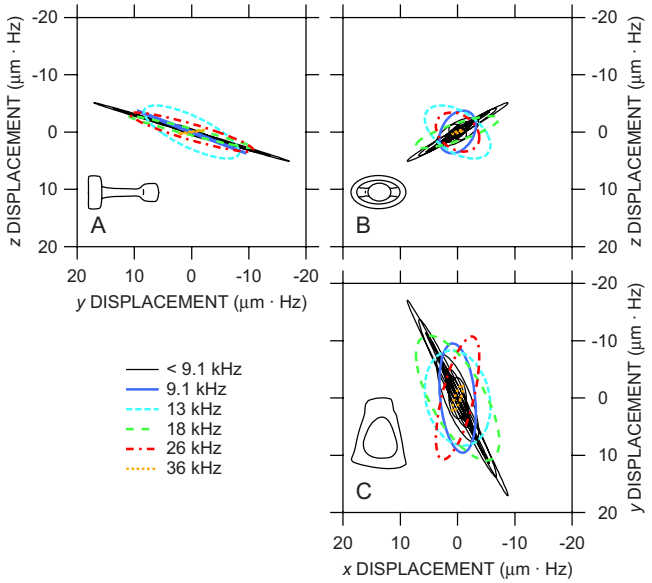

FIG. 9. (Color online) Reconstructed Lissajous figures of the displacement of the stapes posterior crus target (normalized by frequency) at several frequencies in three dimensions in an intrinsic reference frame aligned with the stapes (insets) from one right ear (ubg17) at Bristol; two other ears (one left, one right) were similar. (a) Looking in the $-x$ direction (approximately anterior); (b) looking in the $+y$ direction (from the stapes head into the cochlea); (c) looking in the $-z$ direction (approximately superior).

components are small and in phase with piston motion—the Lissajous figures resemble straight lines, so quadrature components are insignificant—and are largest in the direction of the long footplate axis [x; Fig. 9(b)]. (2) At 9 and 13 kHz, transverse components become more significant, and substantial phase differences occur between the different components—the Lissajous figures in Figs. 9(a) and (especially) 9(c) open up into ellipses. (3) At higher frequencies (18, 26, and 36 kHz), stapes motion is again generally consistent with piston-direction translation, as at low frequencies, but the primary direction of motion (ellipse major axis) is different than that at low frequencies. Transverse components are out of phase with piston motion (ellipses are open) and are approximately equal [Fig. 9(b)]. Similar results were obtained from the two other ears.

These results and the results from the two other ears are presented in a different way in Fig. 10(a): Each curve in Fig. 10(a) is the ratio of stapes target motion in a transverse direction $\hat{\mathbf{V}}_{S,x}$ (black curves) or $\hat{\mathbf{V}}_{S,z}$ (gray curves) to piston motion $\hat{\mathbf{V}}_{S,y}$. Below 9 kHz, transverse components in all ears were generally between $0.1\times$ and $0.5\times|\hat{\mathbf{V}}_{S,y}|$ and were 0.5 cycle out of phase with inward stapes motion: Inward stapes piston motion was accompanied by transverse motion anteriorly and superiorly. In two of the ears, the magnitude ratios and phase differences were approximately constant across frequency; in the third, the ratios and x-direction phase were more variable. Between 9 and 13 kHz, transverse components in each ear were larger than those at other frequencies (in one ear, larger than the piston motion), and phase differences were more variable. At higher frequencies, the transverse component ratios were similar to their low-frequency values, though phase differences remained vari-

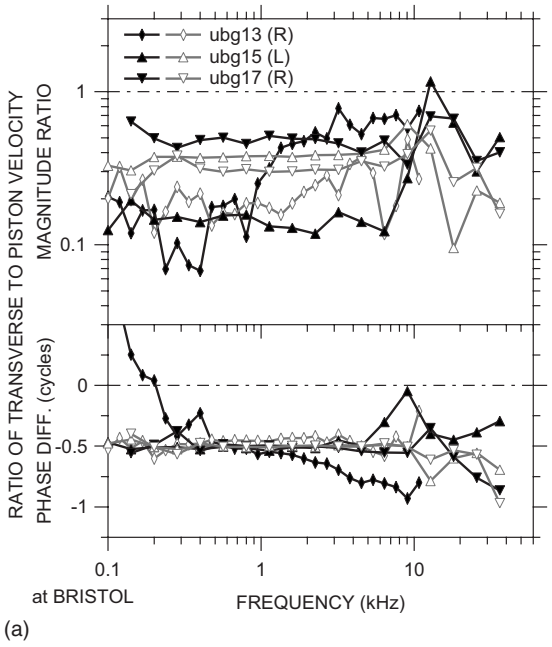

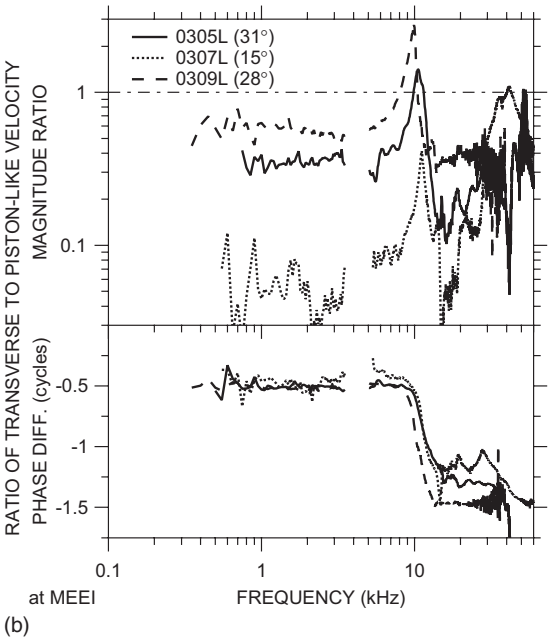

FIG. 10. Ratio of transverse to pistonlike stapes motion. (a) $\hat{\mathbf{V}}_{\mathbf{S},x}/\hat{\mathbf{V}}_{\mathbf{S},y}$ (black lines and filled symbols) and $\hat{\mathbf{V}}_{\mathbf{S},z}/\hat{\mathbf{V}}_{\mathbf{S},y}$ (gray lines and open symbols) in three ears at Bristol (in the intrinsic reference frame), where $\hat{\mathbf{V}}_{\mathbf{S},y}$ is the motion in the piston direction. (b) $\mathbf{V}_{\mathbf{S,t}}/\mathbf{V}_{\mathbf{S,p}}$ in three ears at MEEI, where $\mathbf{V}_{\mathbf{S,p}}$ is the direction in the measurement plane (defined by the two measurement directions) closest to the piston direction and $\mathbf{V}_{\mathbf{S,t}}$ is in the orthogonal direction. The legend indicates the angle between $\mathbf{V}_{\mathbf{S,p}}$ and $\hat{\mathbf{V}}_{\mathbf{S},y}$. Noisy data at 3.5–5.5 kHz are omitted. Top: magnitude ratio; bottom: phase difference.

able. Except in a fairly narrow frequency range around 10 kHz, stapes motion is mostly pistonlike in the range 0.1–36 kHz.

Because we measured $\mathbf{V}_\mathbf{S}$ at only a single point, we can draw only limited conclusions about the nature of transverse stapes motion: we cannot distinguish transverse stapes translation from rocking about a footplate axis, and we cannot distinguish rotation about the piston axis. It seems reasonable to assume, based on ME geometry and observations in other species (von Békésy, 1960; Guinan and Peake, 1967; Decraemer *et al.*, 2000), that most of the transverse target motion is due to stapes rocking about the footplate axes.[9] If we assume that all transverse motion at the target 0.9 mm from the stapes footplate is due to rocking, we compute an angular footplate displacement considerably less than that observed by Decraemer *et al.* (2007). In general, the transverse motion we observed was lower and more uniform among ears than that observed by Decraemer *et al.* (2007).

A different estimate of transverse stapes target motion in ears at MEEI is presented in Fig. 10(b): In these experiments, target velocity was measured in only two directions, so we are limited to computing motion in the plane defined by the measurement directions. We computed in-plane velocity components in the direction closest to the piston direction, $\mathbf{V}_{\mathbf{S,p}}$, and transverse to that direction, $\mathbf{V}_{\mathbf{S,t}}$. Figure 10(b) shows the relative amplitude and phase of transverse motion in three left ears. (Data are omitted between 3.5 and 5.5 kHz where low stimulus levels caused computed $\mathbf{V}_{\mathbf{S,t}}$ to be noisy.) In all three ears, $|\mathbf{V}_{\mathbf{S,t}}|$ is lower than $|\mathbf{V}_{\mathbf{S,p}}|$ (by a factor of 0.05–0.5) below 7–8 kHz and 0.5 cycles out of phase with inward stapes motion as in Fig. 10(a). $|\mathbf{V}_{\mathbf{S,t}}|$ peaks near 10–12 kHz, higher than $|\mathbf{V}_{\mathbf{S,p}}|$ in two of the three ears, and $\angle\mathbf{V}_{\mathbf{S,t}}$ accumulates approximately 1 cycle relative to $\angle\mathbf{V}_{\mathbf{S,p}}$. [The frequency spacing in Figs. 9 and 10(a) is sufficiently large that a phase cycle could have been missed.] At higher frequencies, transverse motion is generally lower again and the phase is near −1.5 cycle, though motion becomes more complex above 40 kHz. These results are consistent with Fig. 10(a), and together, these data indicate that gerbil stapes motion is primarily pistonlike to high frequencies except for a narrow frequency band near 10 kHz.

It is also interesting to note in Fig. 10(b) that the lowest transverse components were observed in ear 0307L, in which the measurement direction was closest to the piston direction (15°). The highest transverse components were observed in ear 0309L, which had the lowest $|\mathbf{V}_\mathbf{S}|$ among the 19 ears measured (dashed curve in Fig. 5). Perhaps the low $|\mathbf{V}_\mathbf{S}|$ in this ear was due to some anomaly in the ossicular chain that allowed higher transverse motion.

The aspect of 3D stapes motion of most practical interest to us is the degree to which our measured $\mathbf{V}_\mathbf{S}$ estimates the piston stapes velocity $\hat{\mathbf{V}}_{\mathbf{S},y}$. Figure 11 compares $\mathbf{V}_\mathbf{S}$ to $\hat{\mathbf{V}}_{\mathbf{S},y}$ in the three Bristol ears of Fig. 10(a). The difference between $\mathbf{V}_\mathbf{S}$ and $\hat{\mathbf{V}}_{\mathbf{S},y}$, denoted as $\Delta\mathbf{V}_{\mathbf{S},y}=\mathbf{V}_\mathbf{S}/\hat{\mathbf{V}}_{\mathbf{S},y}$, is mostly in magnitude and relatively small: $|\Delta\mathbf{V}_{\mathbf{S},y}|$ is approximately constant with frequency up to 8–10 kHz at about a factor of 0.5–0.6, slightly lower than what might be expected from a simple cosine correction (dividing by the cosine of the angle between the measurement direction and the *y* axis, namely, 47°; dot-dashed line) but within the range expected from the ±20° error in baseline direction (shading). This value of $|\Delta\mathbf{V}_{\mathbf{S},y}|$ is also consistent with the observation in Fig. 9 that the primary direction of stapes motion is consistent with piston motion. $|\Delta\mathbf{V}_{\mathbf{S},y}|$ is more variable between 8 and 13 kHz and then gradually increases toward 1 as frequency increases further. Differences in phase are extremely small (generally <0.02 cycle) except in the 8–13 kHz range; the largest val-

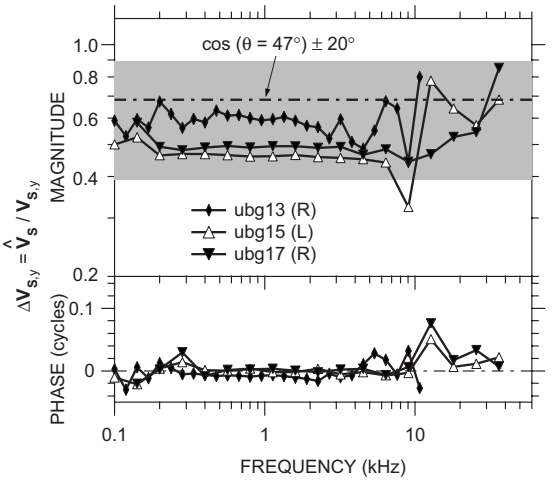

FIG. 11. $\Delta\mathbf{V}_{\mathbf{S},y}$, the ratio of measured $\mathbf{V}_\mathbf{S}$ to the piston component $\hat{\mathbf{V}}_{\mathbf{S},y}$, in three ears at Bristol in the intrinsic reference frame. The dot-dashed line is the cosine of the angle (~47° ± 20°, shading) between the measurement direction and the *y* axis. Top: magnitude; bottom: phase.

ues of $\angle\Delta\mathbf{V}_{\mathbf{S},y}$ occur in two of the three ears near the frequency of the maximum $|\Delta\mathbf{V}_{\mathbf{S},y}|$. Results were similar among the three ears. This result suggests that $\mathbf{V}_\mathbf{S}$ measured within 47° of the piston direction is a good estimate of $\hat{\mathbf{V}}_{\mathbf{S},y}$ at nearly all frequencies from 100 Hz to 36 kHz.

A recent study has shown that scala vestibuli pressure in gerbil tracks $\hat{\mathbf{V}}_{\mathbf{S},y}$ very closely from 0.2 to 50 kHz (de la Rochefoucauld *et al.*, 2008), even though transverse stapes velocity can be significant at those frequencies (Decraemer *et al.*, 2007). This close tracking with $\hat{\mathbf{V}}_{\mathbf{S},y}$ is further support for the idea that transverse components do not affect cochlear input and $\mathbf{V}_\mathbf{S}$ should be an adequate estimate of cochlear input. A more cautionary note was sounded by Decraemer *et al.* (2006a, Fig. 11), but even they show (from reconstructions) that (1) the velocity of a point on the anterior aspect of the stapes head along a direction within 20° of the piston direction differs from piston stapes motion by less than a factor of 2 in magnitude and ~0.1 cycle at any frequency between 0.1 and 40 kHz and (2) stapes velocity measured within 40° of the piston direction differs by more than a factor of 2 in magnitude at only a few frequencies (~3, 7–10, and ~30 kHz) over the same range.[10] Because $\mathbf{V}_\mathbf{S}$ is not much different from $\hat{\mathbf{V}}_{\mathbf{S},y}$, we will continue to use $\mathbf{V}_\mathbf{S}$ in subsequent $\mathbf{H}_\mathbf{MY}$ calculations and comparisons.

B. Comparison of middle-ear transfer admittance to earlier measurements

Our $\mathbf{H}_\mathbf{MY}$ measurements are summarized in Fig. 12. The thick black line is the mean of the MEEI and Bristol measurements weighted by the number of ears measured at each laboratory; the shaded area is the s.d. in $\mathbf{H}_\mathbf{MY}$ at MEEI from Fig. 6. The small jump in $\angle\mathbf{H}_\mathbf{MY}$ near 47 kHz is due to the differing delays in the MEEI and Bristol measurements (20–25 versus 29 μs). As mentioned in the previous section, the $|\mathbf{H}_\mathbf{MY}|$ shown (computed from $\mathbf{V}_\mathbf{S}$) probably underestimates $|\hat{\mathbf{H}}_\mathbf{MY}|$ in the piston direction (computed from $\hat{\mathbf{V}}_{\mathbf{S},y}$) by

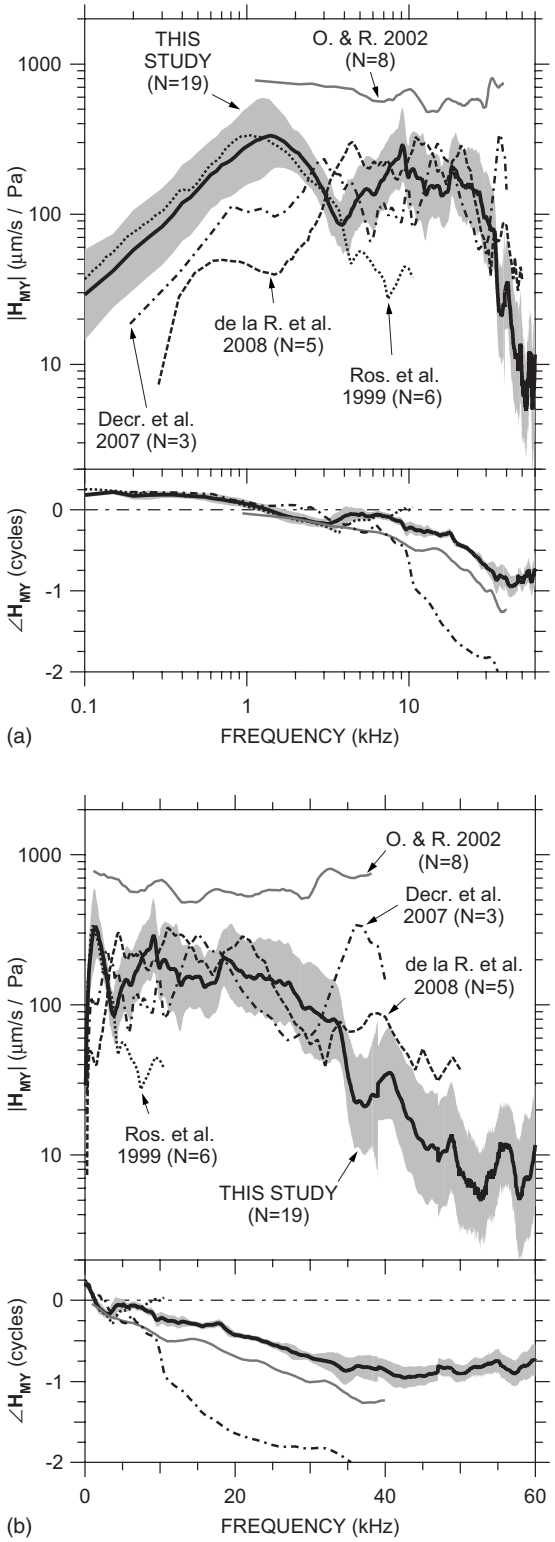

FIG. 12. Comparison of our mean $\mathbf{H}_\mathbf{MY}$ (thick black line) ± s.d. (shaded area) to previously published measurements: Rosowski *et al.* (1999) (logarithmic mean; "Ros. *et al.*;" dotted); Overstreet and Ruggero (2002) (median; "O. & R.;" gray line), de la Rochefoucauld *et al.*, 2008 (in piston direction; linear mean; "de la R. *et al.*;" dashed), and Decraemer *et al.*, (2007) (piston, computed in an intrinsic reference frame; logarithmic mean; "Decr. *et al.*;" dot-dashed). Top: magnitude; bottom: phase. (a) Logarithmic frequency scale; (b) linear frequency scale.

no more than a factor of 2 below 10 kHz, less at higher frequencies, and $\angle\mathbf{H}_\mathbf{MY}$ should provide a close estimate of $\angle\hat{\mathbf{H}}_\mathbf{MY}$.

Figure 12 also includes data from four previous studies in gerbil: the mean $\mathbf{H_{MY}}$ in six ears measured by Rosowski *et al.* (1999; dotted line), the *median* $\mathbf{H_{MY}}$ of eight ears measured by Overstreet and Ruggero (2002; gray line), the mean $\hat{\mathbf{H}}_{\mathbf{MY}}$ computed from three ears measured by Decraemer *et al.* (2007; dot-dashed line), and the mean $|\mathbf{H_{MY}}|$ in five ears in the piston direction by de la Rochefoucauld *et al.* (2008); magnitude only; dashed line). The data of Decraemer *et al.* were computed from whole-stapes rigid-body motion calculated for the piston direction from measurements in other directions (as in Figs. 8 and 9); the data of de la Rochefoucauld *et al.* were computed from $\mathbf{V}_{S,y}$ measured on the incus long process above the incudostapedial joint through a hole in the *pars flaccida*; and the data from the other studies were measured on a single point on the stapes posterior crus from a direction similar to ours.

Our data show similarities to most previous measurements, but the similarities are to different measurements over different frequency ranges. Our mean $\mathbf{H_{MY}}$ is similar to that of Rosowski *et al.* (1999) below 4 kHz, but at higher frequencies, our $|\mathbf{H_{MY}}|$ remains roughly constant and our $\angle\mathbf{H_{MY}}$ continues to decrease. Our mean $\angle\mathbf{H_{MY}}$ has a slope similar to that of Overstreet and Ruggero (2002) up to 40 kHz, but their $\angle\mathbf{H_{MY}}$ is ~0.25 periods lower than ours and their $|\mathbf{H_{MY}}|$ is considerably higher than ours and those of other studies. Our $|\mathbf{H_{MY}}|$ shows rough similarities to that of Decraemer *et al.* up to 30 kHz, but their $\angle\hat{\mathbf{H}}_{\mathbf{MY}}$ accumulation is much greater. Our $|\mathbf{H_{MY}}|$ is most similar to that of de la Rochefoucauld *et al.* (2008) above 5 kHz. (Below 5 kHz, the open *pars flaccida* hole in the experiments of de la Rochefoucauld *et al.* influenced their measured $\mathbf{H_{MY}}$.) In general, most studies (including this one) are consistent with the idea that $|\mathbf{H_{MY}}|$ and phase delay remain roughly constant as frequency increases above 2–3 kHz. This study shows that the range of roughly constant $|\mathbf{H_{MY}}|$ and phase delay extends up to about 35 kHz, above which $|\mathbf{H_{MY}}|$ decreases rapidly with frequency.

C. The middle ear as a mechanical transmission line?

Several investigators have suggested that the ME acts as a lossless mechanical transmission line matched to its terminating impedance, in that the magnitude of sound transmission is fairly constant at low and high frequencies but a delay is introduced (Wilson and Bruns, 1983; Olson, 1998; Puria and Allen, 1998; Overstreet and Ruggero, 2002). Others (e.g., Zwislocki, 1962; Hemilä *et al.*, 1995) have suggested that the ME acts as a second- (or higher-) order resonant system in which high-frequency sound transmission is limited by the mass of the system, though little evidence has been offered in support (see Rosowski, 1994; Overstreet and Ruggero, 2002). A matched lossless transmission line would produce constant $|\mathbf{H_{MY}}|$ and a constant delay (constant negative $\angle\mathbf{H_{MY}}$ slope with frequency) at all frequencies, while a simple second-order resonant system would show stiffness-domination characteristics ($|\mathbf{H_{MY}}|$ slope=+1 on a log-log plot, $\angle\mathbf{H_{MY}}$=+0.25 cycle) at low frequencies, a resonant $|\mathbf{H_{MY}}|$ peak with a $\angle\mathbf{H_{MY}}$ zero crossing, and mass-domination characteristics ($|\mathbf{H_{MY}}|$ slope=−1, $\angle\mathbf{H_{MY}}$=−0.25 cycle) at higher frequencies.

Our measurements and most previous measurements of gerbil ME sound transmission (Fig. 12) suggest that the behavior of the gerbil ossicular system cannot be described as either a matched lossless transmission line or a simple resonant system but includes aspects of both. Our $\mathbf{H_{MY}}$ clearly shows low-frequency stiffness dominance, a rather broad resonant $|\mathbf{H_{MY}}|$ peak with $\angle\mathbf{H_{MY}}$ zero crossing, and a continued decrease in $|\mathbf{H_{MY}}|$ and $\angle\mathbf{H_{MY}}$ as frequency increases to about 3 kHz [as does $\mathbf{H_{MY}}$ measured by Rosowski *et al.* (1999) and, to a lesser extent, Decraemer *et al.* (2007)], but our $|\mathbf{H_{MY}}|$ also shows approximately constant $|\mathbf{H_{MY}}|$ and approximately linear $\angle\mathbf{H_{MY}}$ decrease with frequency from 5 to 35 kHz [as does $\mathbf{H_{MY}}$ measured by Overstreet and Ruggero (2002), Decraemer *et al.* (2007; to 10 kHz only), and de la Rochefoucauld *et al.* (2008); $|\mathbf{H_{MY}}|$ only)] consistent with a transmission line. This behavior in the 5–35 kHz range is also consistent with a multiresonant network whose resonances are distributed in frequency (see, e.g., Decraemer *et al.*, 1990).[11] Above 35 kHz, our data show a definite change in behavior: $|\mathbf{H_{MY}}|$ decreases sharply [also seen in some ears by de la Rochefoucauld *et al.* (2008)] and $\angle\mathbf{H_{MY}}$ levels off [as does $\angle\mathbf{H_{MY}}$ of Overstreet and Ruggero (2002)], consistent with a multiresonant network but inconsistent with a transmission line. These results indicate that the gerbil ME behaves as a simple resonant system at low frequencies and as a distributed multiresonant network at higher frequencies. ME behavior is consistent with a transmission line from 5 to 35 kHz but not at higher frequencies.

D. Estimates of gerbil cochlear input impedance

Our ME transfer admittance data ($=\mathbf{V_S}/\mathbf{P_U}$) are used with measurements of the ME-to-scala-vestibuli sound pressure gain $\mathbf{G_{MP}}=\mathbf{P_{SV}}/\mathbf{P_U}$ (where $\mathbf{P_{SV}}$ is the sound pressure in scala vestibuli) and the stapes footplate area A_{fp} to compute the cochlear acoustic input impedance $\mathbf{Z_C}$ (the ratio of $\mathbf{P_{SV}}$ to stapes volume velocity $\mathbf{U_S}=A_{fp}\cdot\mathbf{V_S}$) by

$$\mathbf{Z_C}=\frac{\mathbf{P_{SV}}}{\mathbf{U_S}}=\frac{\mathbf{P_{SV}}}{A_{fp}\cdot\mathbf{V_S}}=\frac{\mathbf{G_{MP}}}{A_{fp}\cdot\mathbf{H_{MY}}}. \quad (2)$$

We use the mean scala vestibuli sound pressure from Olson (2001) (Fig. 2, in 14 ears, normalized by $\mathbf{P_U}$) rather than more recent measurements because they were taken in a similar fashion to our $\mathbf{V_S}$ data: closed-field sound stimulus, with $\mathbf{P_U}$ measured concurrently very near the umbo. The mean $|\mathbf{G_{MP}}|$ (Olson, 2001) and $\angle\mathbf{G_{MP}}\pm1$ s.d. (not presented in that paper)[12] are compared to our mean $\mathbf{H_{MY}}$ in Fig. 13. There is a marked similarity in the frequency dependence of $\mathbf{G_{MP}}$ and $\mathbf{H_{MY}}$ below 30 kHz: Both $|\mathbf{G_{MP}}|$ and $|\mathbf{H_{MY}}|$ are roughly constant with frequency and $\angle\mathbf{G_{MP}}$ and $\angle\mathbf{H_{MY}}$ are similar. [A comparable relationship was observed below 30 kHz by de la Rochefoucauld *et al.* (2008).] Above 30 kHz, $|\mathbf{G_{MP}}|$ increases while $|\mathbf{H_{MY}}|$ decreases, and $\angle\mathbf{G_{MP}}$ continues to accumulate while $\angle\mathbf{H_{MY}}$ becomes roughly constant.

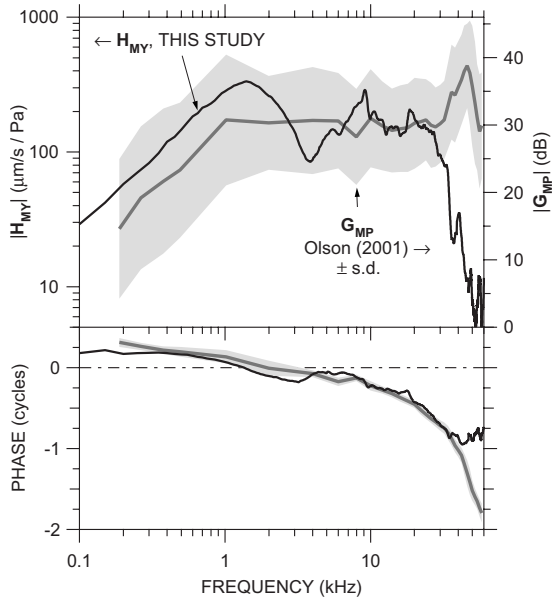

FIG. 13. Comparison of our mean $\mathbf{H_{MY}}$ (thick black line; left axis) to the mean scala vestibuli pressure gain $\mathbf{G_{MP}}$ described by Olson (2001) ($N=15$; gray line) ± s.d. (shading; right axis). Top: magnitude; bottom: phase. The relative positions of the left and right magnitude axes were chosen for the closest alignment of midfrequency $|\mathbf{H_{MY}}|$ and $|\mathbf{G_{MP}}|$.

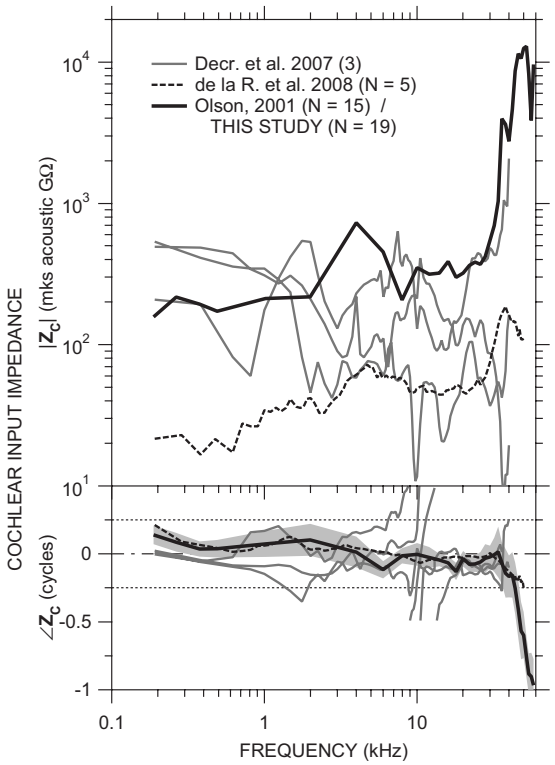

FIG. 14. Cochlear input impedance $\mathbf{Z_C}$ (thick black line) computed from the mean $\mathbf{H_{MY}}$ and $\mathbf{G_{MP}}$ in Fig. 13. Top: magnitude; bottom: phase angle. Dotted lines indicate ±0.25 cycle limits of $\angle\mathbf{Z_C}$ for a passive system. S.d of $|\mathbf{Z_C}|$ (not shown) is about a factor of 12; s.d. of $\angle\mathbf{Z_C}$ is shown by shading. Also shown are $\mathbf{Z_C}$ in three ears by Decraemer *et al.* (2007, gray lines, phase-wrapped as suggested in that publication) and the mean $\mathbf{Z_C}$ in five ears by de la Rochefoucauld *et al.*, 2008, dashed line).

The s.d. of $|\mathbf{G_{MP}}|$ is high, but the spectral shape of $|\mathbf{G_{MP}}|$ is nearly constant among the ears: in all ears, $|\mathbf{G_{MP}}|$ was roughly constant at frequencies between 1 and 30 kHz but increased by a factor of 2-3 between about 30 and 50 kHz. Most of the variance in $|\mathbf{G_{MP}}|$ may be due to frequency-independent changes in the sensitivity of the fiber-optic pressure sensor used for $\mathbf{G_{MP}}$ measurements (Dong and Olson, 2005; de la Rochefoucauld *et al.*, 2008). The fact that most of the $|\mathbf{G_{MP}}|$ variance is frequency independent allows us to draw conclusions about the frequency dependence of quantities computed from $\mathbf{G_{MP}}$.

The cochlear input impedance computed by Eq. (2) from the mean $\mathbf{G_{MP}}$ and $\mathbf{H_{MY}}$ in Fig. 13 and $A_{fp}=0.62$ mm^2 (Lay, 1972) is shown in Fig. 14. The magnitude and phase of $\mathbf{Z_C}$ (black line) are consistent with a resistance over most of the frequency range: $|\mathbf{Z_C}|$ is roughly constant with frequency and $\angle\mathbf{Z_C}$ is approximately zero below 30 kHz. Above 30 kHz $|\mathbf{Z_C}|$ increases, and above 35 kHz, $\angle\mathbf{Z_C}$ decreases sharply. Above 43 kHz, $\angle\mathbf{Z_C}$ is less than −0.25 cycle, which results from the flattening of $\angle\mathbf{H_{MY}}$ with frequency (Fig. 13).

There are some similarities among our computed $\mathbf{Z_C}$ and $\mathbf{Z_C}$ computed for gerbil by de la Rochefoucauld *et al.*, 2008; dashed line) and by Decraemer *et al.* (2007; gray lines): Our $|\mathbf{Z_C}|$ is similar to $|\mathbf{Z_C}|$ in one of the ears of Decraemer *et al.*, and our $\angle\mathbf{Z_C}$ is similar to $\angle\mathbf{Z_C}$ in another of the ears of Decraemer *et al.* The high-frequency increase in $|\mathbf{Z_C}|$ and decrease in $\angle\mathbf{Z_C}$ computed from our $\mathbf{V_S}$ measurements are hinted at by the $\mathbf{Z_C}$ of de la Rochefoucauld *et al.* but our higher-frequency data suggest that the $|\mathbf{Z_C}|$ increase and $\angle\mathbf{Z_C}$ decrease continue at frequencies above the limit of the measurements of de la Rochefoucauld *et al.* The frequency dependence of our $\mathbf{Z_C}$ below 30 kHz is similar to $\mathbf{Z_C}$ measured in other species (reviewed by de la Rochefoucauld *et al.*, 2008).

The s.d. in $|\mathbf{Z_C}|$ is rather high (about a factor of 12 across frequency) due mostly to the high variance in $|\mathbf{G_{MP}}|$. However, as mentioned above, even though the $|\mathbf{G_{MP}}|$ variance is high, the spectral dependence of $|\mathbf{G_{MP}}|$ is fairly uniform among those ears; so even though the $|\mathbf{Z_C}|$ variance is high, most of the variance can be explained by a frequency-independent variability in sensitivity.

The decrease in $\angle\mathbf{Z_C}$ above 35 kHz suggests that the cochlear input impedance becomes more reactive at high frequencies, i.e., less input power is absorbed by the cochlea and more is reflected. This increased power reflectance is consistent with (a) the idea by Lighthill (1981)[13] that reactance and reflectance increase above the maximum frequency where a cochlear traveling wave can form and (b) the increase in EC sound power reflectance $\mathfrak{R}_{EC}$ above 50 kHz observed by Ravicz *et al.* (2007).

Some features of our computed $\mathbf{Z_C}$ above 35 kHz are inconsistent with a driving-point impedance: The decrease in $\angle\mathbf{Z_C}$ associated with the increase in $|\mathbf{Z_C}|$ above 35 kHz is inconsistent with a minimum-phase driving-point impedance, and the continued decrease in $\angle\mathbf{Z_C}$ to <-0.25 cycle above 43 kHz implies a negative resistance inconsistent with a passive system (see, e.g., Oppenheim and Schafer, 1989). Possible explanations for these inconsistencies include (a) a significant phase delay in $\mathbf{P_{SV}}$ between the stapes and the $\mathbf{P_{SV}}$ measurement location such that $\mathbf{G_{MP}}/\mathbf{H_{MY}}$ no longer describes a driving-point impedance (see de la Rochefoucauld *et al.*, 2008 for a detailed discussion of this and other

possibilities) and (b) a change in the primary mode of stapes motion that would contribute significant transverse components to the measured $\mathbf{V_S}$. Nevertheless, the appearance of the $|\mathbf{Z_C}|$ increase and $\angle\mathbf{Z_C}$ decrease above 35 kHz in both our and some previous $\mathbf{Z_C}$ measurements by different methods suggests that there is in fact an increase in $\mathbf{Z_C}$ magnitude and reactance at high frequencies.

The flatness of $|\mathbf{G_{MP}}|$ with frequency has been cited as an indication that ME sound transmission is constant across frequency (Overstreet and Ruggero, 2002; Ruggero and Temchin, 2002). In fact, the flatness could also arise from an increase in $|\mathbf{Z_C}|$ at high frequencies such that a given stapes velocity produces a higher $|\mathbf{P_{SV}}|$ or, conversely, a constant $|\mathbf{G_{MP}}|$ results from lower $|\mathbf{H_{MY}}|$. Our $\mathbf{Z_C}$ computations suggest that the constant $|\mathbf{G_{MP}}|$ is due to an increase in $|\mathbf{Z_C}|$ and is not indicative of constant cochlear input at high frequencies.

E. Contribution of middle-ear transmission to the limits of the audiometric range

The acoustic power entering the cochlea Π_C for a given sound pressure at the umbo can be computed from $\mathbf{H_{MY}}$, $\mathbf{Z_C}$, and the stapes footplate area A_{fp} by

$$\Pi_C = \tfrac{1}{2}|\mathbf{U_S}|^2\,\mathrm{Re}\{\mathbf{Z_C}\} = \tfrac{1}{2}|(\mathbf{H_{MY}}\cdot\mathbf{P_U})A_{\mathrm{fp}}|^2\,\mathrm{Re}\{\mathbf{Z_C}\} \qquad (3)$$

(Rosowski *et al.*, 1986). Equation (3) can be rearranged to yield the umbo sound pressure $\mathbf{P_{U,th}}$ necessary to provide a given constant level of sound power into the cochlea across frequency. If we assume that the auditory threshold is a cochlear isopower curve (as suggested by several authors, e.g., Khanna and Tonndorf, 1969; Khanna and Sherrick, 1981; Rosowski *et al.*, 1986; Rosowski, 1991a, 1991b) or an isovelocity curve across frequency, $\mathbf{P_{U,th}}$ provides an estimate of the audiogram with closed-field stimulus.

Figure 15 plots the sound pressure at the umbo necessary to provide a baseline level of acoustic input to the cochlea. The black curve is $\mathbf{P_{U,th}}$ that produces a cochlear isovelocity input of 10 nm/s across frequency (which corresponds to a cochlear volume velocity input of 6×10^{-15} $\mathrm{m^3/s}$), and the gray curve is $\mathbf{P_{U,th}}$ that produces a cochlear isopower input of 1.5×10^{-18} W across frequency.[14] These values were chosen to match (by eye) the most sensitive portion of the gerbil free-field audiogram (dashed line and squares; Ryan, 1976). Because $\mathrm{Re}\{\mathbf{Z_C}\}$ is negative at some frequencies above 43 kHz (Fig. 14), we show $\mathbf{P_{U,th}}$ for constant Π_C only at those frequencies where $\mathrm{Re}\{\mathbf{Z_C}\}$ is positive, and for comparison, we also show $\mathbf{P_{U,th}}$ for Π_C computed assuming that $\mathrm{Re}\{\mathbf{Z_C}\}=|\mathbf{Z_C}|$ (gray dashed line). The spectral shape of the audiogram is matched remarkably well from 1 kHz to above 40 kHz by the isopower curve and to above 50 kHz by the isovelocity curve. At low frequencies [below 1 kHz, Fig. 15(a)], the isopower curve is a better audiogram predictor than the isovelocity curve. At intermediate frequencies, where $\mathbf{Z_C}$ is constant in magnitude and resistive, $\mathbf{P_{U,th}}$ for constant Π_C and $\mathbf{P_{U,th}}$ for constant $\mathbf{V_S}$ are similar. As frequency increases above 50 kHz [Fig. 15(b)], the isovelocity curve flattens while the audiogram continues upward. To the extent that $\mathbf{P_U}$ is a good estimate of the free-field sound pressure used to measure the audiogram, the match between the audiogram and $\mathbf{P_{U,th}}$ for constant sound power (0.2–40 kHz) or $\mathbf{V_S}$ input (1–40 kHz) supports the idea that the audiogram is determined by a constant level of cochlear input.

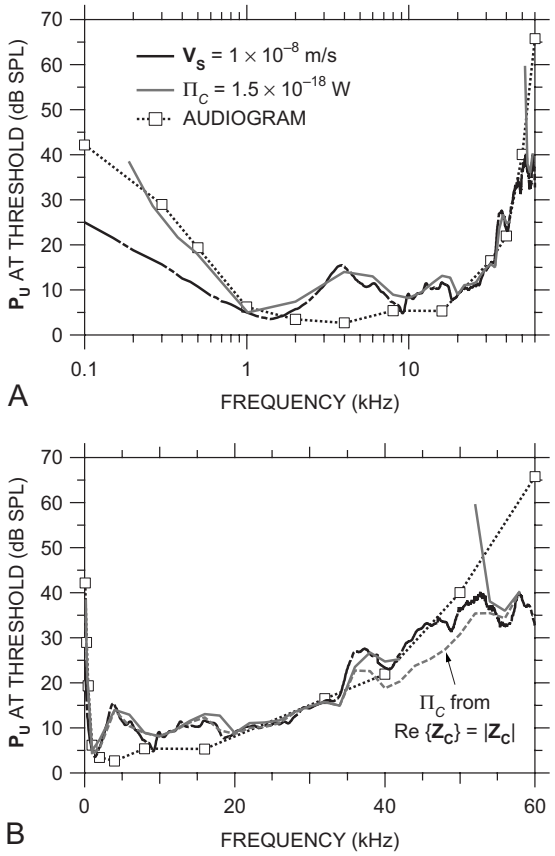

FIG. 15. Sound pressure at the umbo required to produce a constant level of cochlear input across frequency. Shown are $\mathbf{P_{U,th}}$ that produces a constant stapes velocity of 10 nm/s (equivalent to a constant stapes volume velocity of 6×10^{-15} $\mathrm{m^3/s}$) (black line) and $\mathbf{P_{U,th}}$ that provides a constant cochlear sound power input Π_C of 1.5×10^{-18} W (solid gray line, only at frequencies where $\mathrm{Re}\{\mathbf{Z_C}\}$ is positive). Also shown is $\mathbf{P_{U,th}}$ for $\Pi_C=1.5\times10^{-18}$ W computed by assuming that $\mathbf{Z_C}$ is purely resistive (dashed gray line). The mean gerbil audiogram (Ryan, 1976) is shown by the dotted line and squares. (a) Logarithmic frequency scale; (b) linear frequency scale.

The conclusions above, drawn from mean $\mathbf{H_{MY}}$ and $\mathbf{Z_C}$ data, are of course affected by potential high-frequency errors and the variance in $\mathbf{H_{MY}}$ and $\mathbf{Z_C}$, but we believe that the influence of these factors is relatively small. The negative real part of $\mathbf{Z_C}$ between 43 and 52 kHz (as $\angle\mathbf{Z_C}$ cycles; see Fig. 14) implies that power is injected into the cochlea at these frequencies from some other source or that there are errors in $\mathbf{V_S}$ measurements in this frequency range. The $\mathbf{P_{U,th}}$ for constant Π_C computed from $\mathrm{Re}\{\mathbf{Z_C}\}=|\mathbf{Z_C}|$ [assuming $\angle\mathbf{Z_C}=0$; gray dashed line in Fig. 15(b)] is therefore a lower bound on $\mathbf{P_{U,th}}$; if $\mathbf{Z_C}$ becomes reactive at high frequencies (see previous section), $\mathrm{Re}\{\mathbf{Z_C}\}<|\mathbf{Z_C}|$, and the $\mathbf{P_{U,th}}$ for constant cochlear power input is somewhat higher. The variance in $\mathbf{H_{MY}}$ can be expected to cause about a 6 dB s.d. in Π_C. Because the variance in $\mathbf{Z_C}$ is due mostly to variance in $|\mathbf{Z_C}|$ and because the $|\mathbf{Z_C}|$ variance is primarily a variance in sensitivity (see Sec. IV D above), the variance in cochlear input power is primarily in the magnitude and not in the frequency

dependence. Hence, the $|\mathbf{Z_C}|$ variance could cause the baseline power level to be different for different ears, but the spectral shape would be similar.

As mentioned above, the isopower curve in Fig. 15 relates cochlear input power to sound pressure near the TM; yet the audiogram was measured in the free field. The only data of which we are aware that relate gerbil $\mathbf{P_{EC}}$ to free-field sound pressure P_{FF} are free-field-to-eardrum transfer functions (FETFs) measured from several directions by Maki and Furukawa (2005, Fig. 2). Below 20 kHz, their FETFs show a direction-independent EC gain that peaks at about 20 dB near 8 kHz, but since the TM was stiffened for these measurements (thereby increasing $\mathfrak{R}_{EC}$; see Ravicz *et al.*, 2007), the EC gain in an unmodified ear is probably less. Above 20 kHz, the situation is more complicated—their EC gain is direction dependent, their FETFs vary with the measurement location in the EC, and their innermost measurement location ["3 mm," Fig. 2(i)] is still probably several millimeters away from the TM (based on the gain notch at 30 kHz; see Ravicz *et al.*, 2007); but, assuming that the highest EC gain among measurement locations at a given frequency is a good estimate of $|\mathbf{P_U}/P_{FF}|$ at that frequency (see Ravicz *et al.*, 2007), the EC gain is approximately unity from about 20 to 50 kHz, the highest frequency measured.

Two pieces of evidence suggest that the amount of free-field sound power entering the ME decreases at high frequencies: (1) The diffuse-field effective area EA_{TM}^{DF}, which is a measure of the sound power-collecting ability of the external ear and ME (Rosowski *et al.*, 1986, 1988; Rosowski, 1991a, 1991b), is approximately 25 mm^2 at 12 kHz but is limited by the ideal $EA^{DF}=\lambda^2/4\pi$ at higher frequencies (Ravicz *et al.*, 1996). Since EA^{DF} decreases as the square of frequency as frequency increases, this result suggests that the cochlear power produced by a constant diffuse-field sound pressure P_{DF} decreases more rapidly at high frequencies than does Π_C for a constant $\mathbf{P_U}$. (2) $\mathfrak{R}_{EC}$ increases from about 0.5 near 30 kHz to at least 0.8 above 55 kHz (Ravicz *et al.*, 2007). Each of these pieces of evidence suggests that the free-field sound pressure necessary for a constant cochlear input power is higher at high frequencies than the $\mathbf{P_{U,th}}$ estimated in Fig. 15.

Figure 15 shows that the high-frequency increase in auditory threshold that forms the upper audiometric limit is accompanied by a reduction in cochlear input. These results do not support the idea (Olson, 2001; Overstreet and Ruggero, 2002; Ruggero and Temchin, 2002) that ME sound transmission remains high even at high frequencies where cochlear response is low. These results support the idea that the limitations of ME transmission contribute to the limits of hearing.

V. SUMMARY AND CONCLUSIONS

We were able to measure stapes velocity independently in two laboratories over a frequency range that spans the gerbil auditory range, to higher frequencies than previously published measurements. These velocity measurements, when combined with reliable measurements of ME input P_U in the same ears to form the ME transfer admittance $\mathbf{H_{MY}}=\mathbf{V_S}/\mathbf{P_U}$, provide a broadband view of ME function.

Stapes motion is consistent with simple translational motion in the piston direction below 9 kHz, and the piston component of stapes motion is dominant up to at least 36 kHz except in a narrow range near 10 kHz. Single-point measurements from a direction within 45° of the piston direction can provide a reasonably good estimate of piston motion to at least 36 kHz.

The ME exhibits different behaviors over different frequency ranges. $\mathbf{H_{MY}}$ is compliance-dominated at low frequencies, and the ME behaves as a simple second-order resonant system below about 3 kHz. Above a peak near 10 kHz up to 30–35 kHz, ME transmission is consistent with a multiresonant network or a mechanical transmission line: $|\mathbf{H_{MY}}|$ is approximately constant and $d\angle\mathbf{H_{MY}}/df$ is consistent with a delay of 26–29 μs.

At higher frequencies (above 35 kHz), ME transmission does not remain constant at high frequencies: $|\mathbf{H_{MY}}|$ decreases steeply with frequency and $|\mathbf{H_{MY}}|$ flattens.

The high-frequency decrease in $|\mathbf{H_{MY}}|$ corresponds to an increase in cochlear input impedance.

The increase in gerbil auditory threshold at high frequencies coincides with a decrease in $|\mathbf{H_{MY}}|$ and sound power entering the cochlea. Therefore, reductions in cochlear input contribute to the rise in auditory thresholds at high frequencies.

Other peripheral mechanisms, e.g., decreases in external-ear sound power collection (Ravicz *et al.* 1996) and increases in EC power reflectance (Ravicz *et al.*, 2007), may also contribute to the rise in auditory thresholds at high frequencies.

ACKNOWLEDGMENTS

The authors thank Elizabeth Olson, Wei Dong, Ombeline de la Rochefoucauld, and Willem Decraemer for many helpful discussions, and William Peake, Melissa Wood, Kelly Brinsko, Heidi Nakajima, and the staff of the Eaton-Peabody Laboratory for greatly appreciated assistance. This work was supported by NIDCD R01-DC00194 (M.E.R. and J.J.R.) and The Royal Society and the Wellcome Trust (N.P.C.).

APPENDIX: METHOD OF COMPUTING PISTON AND TRANSVERSE STAPES MOTION FROM VELOCITY MEASUREMENTS

Estimation of stapes motion in the piston direction and transverse directions from measurements of stapes posterior crus target velocity $\mathbf{V_S}$ requires three steps: (1) Determine the velocity of the target in a coordinate system defined by the measurement setup (an "experimental" reference frame); (2) transform that velocity into a coordinate system aligned with the stapes (an "intrinsic" reference frame, see, e.g., Decraemer *et al.*, 1994, 2007); and (3) estimate the velocity of the entire stapes from velocity measured at one point (the target). Different methods of estimation were used at MEEI and Bristol. In both cases, the origin of the experimental reference frame was at the posterior crus target, and target

velocity was measured along the $-z'$ axis. The x' axis was approximately anterior-posterior, and the y' axis was approximately transverse.

At Bristol, $\mathbf{V_S}$ was measured repeatedly from a baseline direction $\mathbf{V}_{\mathbf{S},z'}$ and also from four to five different directions relatively similar to the baseline direction. These seven to eight measurements were used to compute the velocity of the posterior crus target in directions transverse to the baseline direction in the experimental reference frame (x',y',z') $\mathbf{V}_{\mathbf{S},x'}$ and $\mathbf{V}_{\mathbf{S},y'}$ by

$$\mathbf{V_{S'}} = \begin{Bmatrix} \mathbf{V_{Spc},}x' \\ \mathbf{V_{Spc},}y' \\ \mathbf{V_{Spc},}z' \end{Bmatrix} = [\mathbf{D}]^{-1} \begin{Bmatrix} m_1 \\ m_2 \\ \cdots \\ m_n \end{Bmatrix}, \tag{A1}$$

where the elements of $\mathbf{D}$ $(d_{1x}, d_{1y}, d_{1z}, d_{2x}, \ldots, d_{nx}, d_{ny}, d_{nz})$ describe rotations L and T from the baseline direction that define the directions of the measurements $\mathbf{M} = \{m_1, m_2, \ldots, m_n\}$ in the experimental reference plane. A minimum of three measurements are necessary; for the Bristol experiments, $n=7-8$ (as mentioned above), and Eq. (A1) describes an overdetermined system. A singular value decomposition technique (see, e.g., Decraemer *et al.*, 1994) was used to minimize errors in solving for $\mathbf{V}_{\mathbf{S},x'}$, $\mathbf{V}_{\mathbf{S},y'}$, and $\mathbf{V}_{\mathbf{S},z'}$:

$$\mathrm{Re}\{\mathbf{V_{S'}}\} = [(\mathbf{D}^T\mathbf{D})(\mathbf{D}^T\,\mathrm{Re}\{\mathbf{M}\})]^{-1} \tag{A2a}$$

and

$$\mathrm{Im}\{\mathbf{V_{S'}}\} = [(\mathbf{D}^T\mathbf{D})(\mathbf{D}^T\,\mathrm{Im}\{\mathbf{M}\})]^{-1}. \tag{A2b}$$

The velocities computed above in the experimental reference frame were then converted to velocities in the intrinsic reference frame (x,y,z). The origin of the intrinsic reference frame is at the center of the stapes footplate; the x axis is the long footplate axis (approximately anterior-posterior), the y axis is in the piston direction (inward – a left-hand coordinate system was used for left ears), and the z axis is the short footplate axis (approximately superior-inferior). First, rotations were applied about the three experimental axes: $+45°$ about the $+x'$ axis, $+15°$ about the $+y'$ axis (for right ears; $-15°$ for left ears), and $-10°$ about the $+z'$ axis, in that order. These manipulations produced the velocity of the posterior crus target in the piston direction $\mathbf{V}_{\mathbf{S},y}$ and transverse directions $\mathbf{V}_{\mathbf{S},x}$ and $\mathbf{V}_{\mathbf{S},z}$.

The piston velocity of the posterior crus target was assumed to be indicative of the piston velocity of the stapes footplate: We assume that the stapes moves as a rigid body and that the y components of motion at the posterior crus due to rotations about the x and z axes are negligible. Then the transformation of target velocity to stapes footplate involves only a simple translation of the origin from the target to the center of the stapes footplate. Because translations of the origin do not affect translational velocities, $\hat{\mathbf{V}}_{\mathbf{S},y} = \mathbf{V}_{\mathbf{S},y}$.

Estimates of transverse motion were performed at MEEI in a different way because velocity was measured from only two directions and there are insufficient data to compute the components of $\mathbf{V_S}$ in all directions. This technique is insensitive to motion out of the plane defined by the two measurement directions. The two measurements were used to compute the motion of the posterior crus target in the direction in the plane closest to piston motion and in the perpendicular direction in the plane. Target velocity was transformed to stapes footplate velocity as described above.

[1]The gerbil auditory threshold is 60 dB above its most sensitive value by 60 kHz (see Ryan, 1976).

[2]Note that $\mathbf{H_{MY}}$ has units of a specific acoustic admittance.

[3]The reduction in $\mathbf{V_S}$ with the probe tube within 0.5 mm of the umbo may be due to shadowing of the location of effective ME input by the probe tube: λ at 60 Hz (~6 mm) is only about four times the diameter of the probe tube, and sound might not diffract completely around the probe tube tip when the distance between it and the TM is small.

[4]$p(0) < 0.05$ as evaluated by Student's t test.

[5]The logarithmic mean is frequently used with data that span a wide range. An advantage is that the variance is symmetric about the mean when plotted on a logarithmic scale.

[6]The data sets in panels (A) and (B) are slightly different: the mean $\mathbf{H_{MY}}$ in panel (A) includes some measurements in which $\mathbf{V_S}$ was above the noise floor at low frequencies but not high; the mean $\mathbf{H_{MY}}$ in panel (B) includes some measurements in which $\mathbf{V_S}$ was above the noise floor at high frequencies but not low. Factors that influenced $\mathbf{V_S}$ signal-to-noise ratio include the seal around the probe tube in the EC (which affected low-frequency stimulus levels) and the strength of the laser signal reflected from the target (which affected noise levels, especially at high frequencies: lower signal strength produced higher noise).

[7]Note that this $|\mathbf{H_{MY}}|$ peak is unaffected by the notch in $|\mathbf{P_U}/\mathbf{P_{EC}}|$ near 10 kHz (Fig. 3).

[8]The product of displacement and frequency is equivalent to velocity. We chose to describe the figure in terms of displacement to make it easier to grasp intuitively.

[9]Forces are exerted on the stapes head by the incus and resisted by the stapedius muscle and tendon, inertial forces at the stapes center of gravity, and the annular ligament at the footplate edges. Neglecting reaction forces from the stapedius muscle and tendon and inertial forces, any forces applied along a line that does not include both the stapes head and the stapes centroid (coincident with the center of gravity for a uniform mass distribution), i.e., different from the piston direction, must cause a rocking moment.

[10]In that study, velocity phase accumulated an extra cycle at the magnitude notch near 3 kHz.

[11]A transmission line can be modeled as an infinite sum of discrete matched compliant and inertial elements below its cutoff frequency (a ladder-network delay line, see e.g., Magnusson *et al.*, 2001). A multiresonant network with distributed resonant frequencies can therefore be considered a discretized, truncated, and not-so-well-matched transmission line.

[12]Data generously provided by Elizabeth Olson.

[13]As suggested by Elizabeth Olson.

[14]This threshold value for Π_C is consistent with the estimate of power entering the ME $\Pi_T = 5 \times 10^{-17}$ W by Ravicz *et al.* (1992): It is expected that some power would be lost in the ME and, as mentioned above, our method of measuring stapes motion might underestimate $|\mathbf{V_S}|$ and hence Π_C by about a factor of 2. This threshold value for Π_C is also consistent with estimates for other species (Rosowski *et al.*, 1986).

Allen, J. B. (**1986**). "Measurement of eardrum acoustic impedance," in *Peripheral Auditory Mechanisms*, edited by J. B. Allen, J. L. Hall, A. Hubbard, S. T. Neely, and A. Tubis (Springer-Verlag, New York), pp. 44–51.

von Békésy, G. (**1960**). *Experiments in Hearing*, edited by E. G. Wever (McGraw-Hill, New York).

Chien, W., Ravicz, M. E., Merchant, S. N., and Rosowski, J. J. (**2006**). "The effect of methodological differences in the measurement of stapes motion in live and cadaver ears," Audiol. Neuro-Otol. **11**, 183–197.

Cooper, N. P. (**1999**). "An improved heterodyne laser interferometer for use in studies of cochlear mechanics," J. Neurosci. Methods **88**, 93–102.

Cooper, N. P., and Rhode, W. S. (**1992**). "Basilar membrane mechanics in the hook region of cat and guinea-pig cochleae: Sharp tuning and nonlinearity in the absence of baseline position shifts," Hear. Res. **63**, 163–190.

Decraemer, W. F. S., Khanna, S. M., and Dirckx, J. J. J. (**2006a**). "Estimation of stapes piston motion from uniaxial interferometer measurements along observation directions at an angle with the piston axis is prone to

substantial errors," in *Vibration Measurements by Laser Techniques: Advances and Applications*, edited by E. P. Tomasini (SPIE, Bellingham, WA), Vol. **6345**, Paper No. 63450C.
Decraemer, W. F., Khanna, S. M., and Funnell, W. R. J. (**1990**). "Heterodyne interferometer measurements of the frequency response of the manubrium tip in cat," Hear. Res. **47**, 205–218.
Decraemer, W. F., Khanna, S. M., and Funnell, W. R. J. (**1994**). "A method for determining three-dimensional vibration in the ear," Hear. Res. **77**, 19–37.
Decraemer, W. F., Khanna, S. M., and Funnell, W. R. J. (**2000**). "Measurement and modeling of the three-dimensional vibration of the stapes in cat," in *Recent Developments in Auditory Mechanics*, edited by H. Wada, T. Takasaka, K. Ikeda, K. Ohyama, and T. Koike (World Scientific, Singapore), pp. 36–43.
Decraemer, W. F., de la Rochefoucauld, O., Dong, W., Khanna, S. M., Dirckx, J. J. J., and Olson, E. S. (**2007**). "Scala vestibuli pressure and three-dimensional stapes velocity measured in direct succession in gerbil," J. Acoust. Soc. Am. **121**, 2774–2791.
Decraemer, W. F., de la Rochefoucauld, O., Dong, W., Khanna, S. M., Dirckx, J. J. J., and Olson, E. S., and (**2006b**). "Do non-piston components contribute to scala vestibuli pressure behind the footplate in gerbil?," in *Middle Ear Mechanics in Research and Otology*, edited by A. Huber and A. Eiber (World Scientific, Singapore), pp. 116–122.
Dong, W., and Olson, E. S. (**2005**). "Two-tone distortion in intracochlear pressure," J. Acoust. Soc. Am. **117**, 2999–3015.
Dong, W., and Olson, E. S. (**2006**). "Middle ear forward and reverse transmission in gerbil," J. Neurophysiol. **95**, 2951–2961.
Guinan, J. J., Jr., and Peake, W. T. (**1967**). "Middle-ear characteristics of anesthetized cats," J. Acoust. Soc. Am. **41**, 1237–1261.
Hemilä, S., Nummela, S., and Reuter, T. (**1995**). "What middle ear parameters tell about impedance matching and high frequency hearing," Hear. Res. **85**, 31–44.
Johnstone, B. M., and Sellick, P. M. (**1972**). "The peripheral auditory apparatus," Q. Rev. Biophys. **5**, 1–57.
Khanna, S., and Sherrick, C. (**1981**). "The comparative sensitivity of selected receptor systems," in *The Vestibular System: Function and Morphology*, edited by T. Gualtierotti (Springer-Verlag, New York), pp. 337–348.
Khanna, S. M., and Tonndorf, J. (**1969**). "Middle ear power transfer," Arch. Klin. Exp. Ohren Nasen Kehlkopfheilkd **193**, 78–88.
Lay, D. M. (**1972**). "The anatomy, physiology, functional significance and evolution of specialized hearing organs of gerbilline rodents," J. Morphol. **138**, 41–120.
Lighthill, J. (**1981**). "Energy flow in the cochlea," J. Fluid Mech. **106**, 149–213.
Lynch, T. J., III (**1981**). "Signal processing by the cat middle ear: Admittance and transmission, measurements and models," Ph.D. thesis, Massachusetts Institute of Technology.
Lynch, T. J., III, Nedzelnitsky, V., and Peake, W. T. (**1982**). "Input impedance of the cochlea in cat," J. Acoust. Soc. Am. **72**, 108–130.
Magnusson, P. C., Alexander, G. C., Tripathi, V. K., and Weisshaar, A. (**2001**). *Transmission Lines and Wave Propagation*, 4th ed. (CRC, Boca Raton).
Maki, K., and Furukawa, S. (**2005**). "Acoustical cues for sound localization by the Mongolian gerbil, *Meriones unguiculatus*," J. Acoust. Soc. Am. **118**, 872–886.
Merchant, S. N., Ravicz, M. E., and Rosowski, J. J. (**1996**). "Acoustic input impedance of the stapes and cochlea in human temporal bones," Hear. Res. **97**, 30–45.
Olson, E. S. (**1998**). "Observing middle and inner ear mechanics with novel intracochlear pressure sensors," J. Acoust. Soc. Am. **103**, 3445–3463.
Olson, E. S. (**2001**). "Intracochlear pressure measurements related to cochlear tuning," J. Acoust. Soc. Am. **110**, 349–367.
Olson, E. S., and Cooper, N. P. (**2000**). "Stapes motion and scala vestibuli pressure in gerbil," Abstracts of the 23rd Midwinter Meeting of the Association for Research in Otolaryngology, Abstract No. 399.
Oppenheim, A. V., and Schafer, R. W. (**1989**). *Discrete-Time Signal Processing* (Prentice-Hall, Englewood Cliffs, NJ).
Overstreet, E. H., and Ruggero, M. A. (**2002**). "Development of wide-band middle ear transmission in the Mongolian gerbil," J. Acoust. Soc. Am. **111**, 261–270.
Puria, S., and Allen, J. B. (**1998**). "Measurements and model of the cat middle ear: Evidence of tympanic membrane delay," J. Acoust. Soc. Am. **104**, 3463–3481.
Ravicz, M. E., Olson, E. S., and Rosowski, J. J. (**2007**). "Sound pressure distribution and power flow within the gerbil ear canal from 100 Hz to 80 kHz," J. Acoust. Soc. Am. **122**, 2154–2173.
Ravicz, M. E., and Rosowski, J. J. (**2004**). "High-frequency sound transmission through the gerbil middle ear," Abstracts of the 27th Midwinter Meeting of the Association for Research in Otolaryngology, Abstract No. 817.
Ravicz, M. E., Rosowski, J. J., and Voigt, H. F. (**1992**). "Sound-power collection by the auditory periphery of the mongolian gerbil Meriones unguiculatus. I. Middle-ear input impedance," J. Acoust. Soc. Am. **92**, 157–177.
Ravicz, M. E., Rosowski, J. J., and Voigt, H. F. (**1996**). "Sound-power collection by the auditory periphery of the mongolian gerbil Meriones unguiculatus. II. External-ear radiation impedance and power collection," J. Acoust. Soc. Am. **99**, 3044–3063.
de la Rochefoucauld, O., Decraemer, W. F., Khanna, S. M., and Olson, E. S. (**2008**). "Simultaneous measurements of stapes motion and intracochlear pressure in gerbil from 0.5–50 kHz," J. Assoc. Res. Otolaryngol. **9**, 161–177.
Rosowski, J. J. (**1991a**). "The effects of external- and middle-ear filtering on auditory threshold and noise-induced hearing loss," J. Acoust. Soc. Am. **90**, 124–135.
Rosowski, J. J. (**1991b**). "Erratum: The effects of external- and middle-ear filtering on auditory threshold and noise-induced hearing loss," J. Acoust. Soc. Am. **90**, 3373.
Rosowski, J. J. (**1994**). "Outer and middle ear," in *The Springer Series in Auditory Research, Volume IV: Comparative Mammalian Hearing* (Springer-Verlag, New York), pp. 172–247.
Rosowski, J. J., Carney, L. H., Lynch, T. J., III, and Peake, W. T. (**1986**). "The effectiveness of external and middle ears in coupling acoustic power into the cochlea," in *Peripheral Auditory Mechanisms*, edited by J. B. Allen, J. L. Hall, A. Hubbard, S. T. Neely, and A. Tubis (Springer-Verlag, New York), pp. 3–12.
Rosowski, J. J., Carney, L. H., and Peake, W. T. (**1988**). "The radiation impedance of the external ear of cat: Measurements and applications," J. Acoust. Soc. Am. **84**, 1695–1708.
Rosowski, J. J., Ravicz, M. E., Teoh, S. W., and Flandermeyer, D. (**1999**). "Measurements of middle-ear function in the Mongolian gerbil, a specialized mammalian ear," Audiol. Neuro-Otol. **4**, 129–136.
Ruggero, M. A., and Temchin, A. N. (**2002**). "The roles of the external, middle, and inner ears in determining the bandwidth of hearing," Proc. Natl. Acad. Sci. U.S.A. **99**, 13206–13210.
Ryan, A. (**1976**). "Hearing sensitivity of the mongolian gerbil, Meriones unguiculatis," J. Acoust. Soc. Am. **59**, 1222–1226.
Teoh, S. W., Flandermeyer, D. T., and Rosowski, J. J. (**1997**). "Effects of pars flaccida on sound conduction in ears of Mongolian gerbil: Acoustic and anatomical measurements," Hear. Res. **106**, 39–65.
Wilson, J. P., and Bruns, V. (**1983**). "Middle-ear mechanics in the CF-bat *Rhinolophus ferrumequinum*," Hear. Res. **10**, 1–13.
Zwislocki, J. J. (**1962**). "Analysis of the middle-ear function. Part I. Input impedance," J. Acoust. Soc. Am. **34**, 1514–1523.

Testing coherent reflection in chinchilla: Auditory-nerve responses predict stimulus-frequency emissions

Christopher A. Shera[a)]
Eaton-Peabody Laboratory of Auditory Physiology, Massachusetts Eye and Ear Infirmary, 243 Charles Street, Boston, Massachusetts 02114 and Department of Otology and Laryngology, Harvard Medical School, Boston, Massachusetts 02115, USA

Arnold Tubis
Department of Physics, Purdue University, West Lafayette, Indiana 47907 and Institute for Nonlinear Science, University of California, San Diego, La Jolla, California 92093, USA

Carrick L. Talmadge
National Center for Physical Acoustics, University of Mississippi, University, Mississippi 38677, USA

(Received 3 December 2007; revised 7 April 2008; accepted 8 April 2008)

Coherent-reflection theory explains the generation of stimulus-frequency and transient-evoked otoacoustic emissions by showing how they emerge from the coherent "backscattering" of forward-traveling waves by mechanical irregularities in the cochlear partition. Recent published measurements of stimulus-frequency otoacoustic emissions (SFOAEs) and estimates of near-threshold basilar-membrane (BM) responses derived from Wiener-kernel analysis of auditory-nerve responses allow for comprehensive tests of the theory in chinchilla. Model predictions are based on (1) an approximate analytic expression for the SFOAE signal in terms of the BM traveling wave and its complex wave number, (2) an inversion procedure that derives the wave number from BM traveling waves, and (3) estimates of BM traveling waves obtained from the Wiener-kernel data and local scaling assumptions. At frequencies above 4 kHz, predicted median SFOAE phase-gradient delays and the general shapes of SFOAE magnitude-versus-frequency curves are in excellent agreement with the measurements. At frequencies below 4 kHz, both the magnitude and the phase of chinchilla SFOAEs show strong evidence of interference between short- and long-latency components. Approximate unmixing of these components, and association of the long-latency component with the predicted SFOAE, yields close agreement throughout the cochlea. Possible candidates for the short-latency SFOAE component, including wave-fixed distortion, are considered. Both empirical and predicted delay ratios (long-latency SFOAE delay/BM delay) are significantly less than 2 but greater than 1. Although these delay ratios contradict models in which SFOAE generators couple primarily into cochlear compression waves, they are consistent with the notion that forward and reverse energy propagation in the cochlea occurs predominantly by means of traveling pressure-difference waves. The compelling overall agreement between measured and predicted delays suggests that the coherent-reflection model captures the dominant mechanisms responsible for the generation of reflection-source otoacoustic emissions.
 [DOI: 10.1121/1.2917805]

PACS number(s): 43.64.Jb, 43.64.Bt, 43.64.Kc [BLM] Pages: 381–395

I. INTRODUCTION

Most cochlear models represent the material properties of the cochlear partition by smooth and continuous functions of position. For example, to match trends in physiological data relating characteristic frequency to position, model parameters are varied so that the stiffness of the basilar membrane (BM) decreases exponentially from base to apex. But although continuity and smoothness can be realized in mathematics, the cochlea is a biological device assembled from discrete cellular components, each subject to developmental noise and other morphological aberrations (e.g., Finch and Kirkwood, 2000). Standard assumptions about smoothness certainly simplify the model equations, but real cochleae must be mechanically irregular.

How does mechanical irregularity affect cochlear model responses to sound? Simulations and analysis based on the application of Newton's laws have answered this question in active cochlear models: The major functional consequence of modest mechanical irregularity in the organ of Corti is the production of long-latency evoked and spontaneous otoacoustic emissions (e.g., Zweig and Shera, 1995; Talmadge *et al.*, 1998). When irregularities are introduced into the mechanics, model cochleae emit sound (or its computational equivalent); when irregularities are absent, the same models remain silent.

Biological cochleae are both intrinsically irregular (e.g., Engström *et al.*, 1966; Bredberg, 1968; Wright, 1984;

[a)]Author to whom correspondence should be addressed. Electronic mail: shera@epl.meei.harvard.edu.

Lonsbury-Martin *et al.*, 1988) and, as implied by the model analysis, also emit sound (e.g., Kemp, 1978). Buttressed by this empirical correlation, the theory of coherent-reflection filtering explains the generation of reflection-source otoacoustic emissions (OAEs) by analogy with the scattering processes that occur in cochlear models containing mechanical irregularity. In particular, the theory describes the coherent "backscattering" of cochlear traveling waves by mechanical irregularities distributed along the organ of Corti. When combined with a description of sound transmission and reflection by the middle ear, the theory provides a comprehensive account of spontaneous and reflection-source otoacoustic emissions as well as the microstructure of the hearing threshold (e.g., Shera and Zweig, 1993b; Zweig and Shera, 1995; Talmadge *et al.*, 1998, 2000).

A. Standard cochlear-model assumptions

A number of important assumptions underlie the cochlear models in which the principles and predictions of coherent reflection have been most thoroughly elaborated. These model assumptions are not statements about the mechanisms of coherent reflection—coherent reflection is an emergent consequence of the physics, not a hypothetical process whose characteristics are chosen at the outset and then explicitly incorporated into the model definition. For example, the statement that "one of the fundamental premises of the [coherent-reflection theory is that]…SFOAEs originate at the sites where the BM traveling waves reach their peaks" (Siegel *et al.*, 2005) puts the logical cart before the horse. Localization of the strongest scattering to the peak region of the traveling wave is not a built-in assumption of the model but a consequence of the physics; the statement is a conclusion, not a premise.

Rather than prescribing the details of stimulus reemission, the model assumptions all involve basic statements about how the cochlea works. Although some model assumptions are almost entirely innocuous and merely simplify the analysis (e.g., the incompressibility of the cochlear fluids), other assumptions have important functional implications and ultimately help determine the characteristics of the emissions produced by the model. This latter group comprises the three principal assumptions or approximations common to most current models of cochlear mechanics (reviewed in de Boer, 1996):

(1) The motion of the cochlear partition is driven primarily by forces that either originate locally or have been communicated from more distant locations through the scalae fluid pressure. In other words, the mechanics of the cochlear partition are well described by "point-admittance" functions that do not involve significant longitudinal coupling within the organ of Corti or tectorial membrane.
(2) The forces produced by outer hair cells couple primarily into the slow-traveling transverse pressure-difference waves that drive the motion of the cochlear partition (e.g., Voss *et al.*, 1996) rather than into longitudinal compression waves that travel at the speed of sound in a manner largely uninfluenced by mechanically tuned structures such as the organ of Corti (reviewed in Shera *et al.*, 2007).
(3) The hydrodynamics of cochlear fluid motion are well approximated by representing the tapered spiral geometry of the scalae using a rectangular box in which traveling waves transition from long-wave behavior in the tail region to short-wave behavior near the peak.

Although these standard assumptions have been employed in models that reproduce measurements of basilar-membrane motion, they—like the conventional assumption of smoothness—may not be entirely correct. Indeed, one of the three (2) has been questioned on the grounds that OAE phase gradients interpreted as roundtrip travel times appear too short to involve reverse propagation via slow pressure-difference waves (Ren, 2004; Ren *et al.*, 2006; Ruggero, 2004; Siegel *et al.*, 2005). Instead, OAE delays were taken to confirm the suggestion (Wilson, 1980) that the intracochlear forces giving rise to OAEs couple primarily if not exclusively into fast compression waves (for informal discussion, see Allen, 2003, 2006).

The studies contradicting assumption (2) base their conclusions on comparisons between otoacoustic phase gradients measured in the ear canal and mechanical delays measured on the BM or estimated from auditory-nerve responses. The specific hypotheses explored derive from conceptual models of OAE generation and/or from approximate theoretical formulas (e.g., OAE delay $\cong 2\times$ BM delay) obtained using assumptions untested in the species employed. Although the results are suggestive, compelling tests of the assumptions and approximations underlying coherent reflection require more rigorous comparisons between model predictions and experiment. The fundamental character and near ubiquity of the assumptions under scrutiny would endow any definitive conclusions with broad significance, not only for interpreting otoacoustic emissions, where the issues appear especially salient, but also for understanding the most basic operation of the cochlea.

In this paper, we test coherent-reflection theory in chinchilla using the standard model assumptions enumerated above. In particular, we compare measured stimulus-frequency otoacoustic emissions (SFOAEs) (Siegel *et al.*, 2005) with model predictions derived specifically for the chinchilla by analyzing measurements of auditory-nerve Wiener kernels (Recio-Spinoso *et al.*, 2005; Temchin *et al.*, 2005). Our strategy allows more rigorous and comprehensive tests of coherent-reflection theory than have previously been possible (e.g., Shera and Guinan, 2003; Cooper and Shera, 2004; Siegel *et al.*, 2005).[1]

II. COHERENT REFLECTION IN STANDARD COCHLEAR MODELS

The theory of coherent-reflection filtering derives from an analysis of cochlear models based on Newton's laws. For simplicity, we restrict attention to stimulus intensities in the near-threshold linear regime for which relative amplitudes of stimulus-frequency and transient-evoked OAEs are largest. In the standard cochlear model illustrated in . 1, the uncoiled

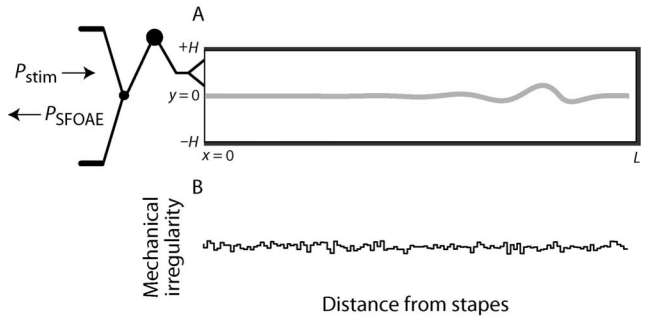

FIG. 1. Sagittal space-time slice through the symmetric two-dimensional box model of height H. The middle and external ears are represented by using balls and sticks. The cochlear partition is shown vibrating in response to a pure tone stimulus (P_{stim}) applied in the ear canal. Micromechanical irregularities (bottom panel) arising from the discrete cellular architecture of the organ of Corti appear superposed on the smooth secular variation of mechanical characteristics from base to apex. Analysis of the model equations shows that irregularities in any mechanical parameter (e.g., the effective damping) give rise to reverse-traveling waves that return to the ear canal as sound (P_{SFOAE}).

cochlea appears as a rectangular box filled with incompressible, inviscid fluid and subdivided by a flexible membrane representing the cochlear partition. Linearized equations of fluid dynamics describe the motion of the fluid and its interaction with the membrane and the boundaries of the box, including the stapes and round window. We describe the mechanics of the partition by an equivalent point admittance that characterizes the transverse motion of the organ of Corti induced by a pressure difference across its surface. The admittance includes contributions from the active forces involved in cochlear amplification. Irregularities are represented as perturbations in the mechanics of the partition.

A. Predicting stimulus-frequency emissions

In previous papers, we solved cochlear model equations to determine the effects of mechanical irregularities on model responses (e.g., Zweig and Shera, 1995; Talmadge *et al.*, 1998; Shera *et al.*, 2005a). The solutions indicate that when stimuli are applied in the ear canal, model cochleae generate reverse-traveling waves that subsequently appear in the ear canal as sound (e.g., as SFOAEs when the stimuli are single tones). For example, . 2 shows the SFOAEs produced by a typical cochlear model supplemented with random mechanical irregularities. As the simulation demonstrates, the model reproduces the major qualitative features of measured SFOAEs: a rapidly rotating phase exhibiting occasional inflections and a slowly varying amplitude punctuated by sharp notches. By employing different spatial patterns of mechanical irregularities in the simulation, one can reproduce the intersubject variability seen in measured SFOAEs.

1. An approximate analytic formula

To facilitate comparisons between theory and experiment, we derived an approximate analytic expression for the SFOAE produced by the model (Shera *et al.*, 2005a). By using perturbation theory to solve what amounts to a "scattering problem," we found that the SFOAE pressure $P_{SFOAE}(f)$ can be written in the form

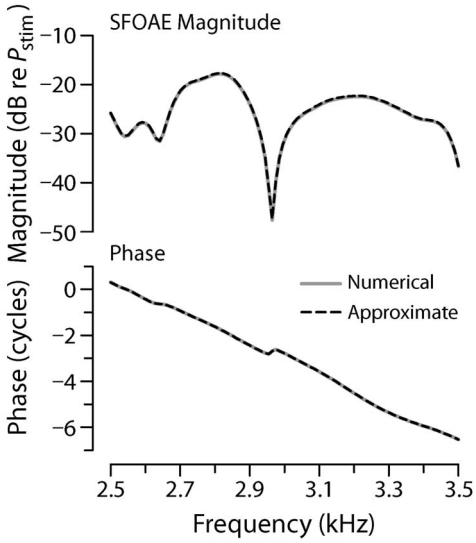

FIG. 2. Simulated SFOAEs. The figure shows the magnitude and phase of $P_{SFOAE}(f)$ computed by using a two-dimensional model of cochlear mechanics supplemented with micromechanical irregularities (for details, see Shera *et al.*, 2005a, Appendix D). Computations performed by using two different methods yield almost identical results. The solid gray line shows the SFOAEs computed by using numerical finite-difference algorithms; the dashed line uses the approximate perturbative expression given by Eq. (1). For simplicity, all calculations assume unity roundtrip middle-ear transmission gain and a stapes reflection coefficient of zero. [Adapted from Fig. 10 of Shera *et al.* (2005a).]

$$P_{SFOAE}(f) \sim P_{stim} G_{ME}(f) \int_0^L \epsilon(x,f) \mathcal{W}^2(x,f) dx, \tag{1}$$

where the $\sim$ indicates approximate proportionality,[2] P_{stim} is the ear-canal stimulus pressure, $G_{ME}(f)$ characterizes roundtrip middle-ear transmission,[3] and the integral is proportional to the cochlear reflectance, which is defined as the ratio of the outgoing to the ingoing pressure wave at the stapes. The integral sums wavelets scattered by irregularities located throughout the cochlea. In the integrand, the dimensionless function $\epsilon(x,f)$ characterizes the mechanical perturbations. Contributions from different locations are weighted by the function $\mathcal{W}^2(x,f)$, which describes both BM-fluid coupling and roundtrip wave propagation between the stapes and the site of scattering at cochlear position x. When written in a form convenient for future analysis, the weighting function is given by

$$\mathcal{W}^2(x,f) = \alpha(x,f) V_{BM}^2(x,f)/k^2(x,f), \tag{2}$$

where $V_{BM}(x,f)$ is the BM velocity normalized by the stapes velocity, $k(x,f)$ is the complex wave number of the traveling wave, and $\alpha(x,f)$ is a dimensionless hydrodynamic factor whose value is well approximated by the expression

$$\alpha(x,f) \cong \frac{k(x,f)H}{\tanh[k(x,f)H]}, \tag{3}$$

where H is the scala height (Duifhuis, 1988; Shera *et al.*, 2005a). In terms of the wave number, the perturbations $\epsilon(x,f)$ are given by $\epsilon \equiv \Delta k^2/k^2$, where the irregularities Δk^2 vanish in a hypothetical smooth cochlea. The mechanisms encapsulated in Eq. (1) for $P_{SFOAE}(f)$ are those of wave scattering: Just as light scatters as it propagates through a me-

dium of variable refractive index, so cochlear traveling waves partially reflect when they encounter irregularities in the partition mechanics.

Figure 2 establishes the validity of our semianalytic formula for $P_{\mathrm{SFOAE}}(f)$ [Eq. (1)] by comparing it with the "exact" numerical result computed by solving Laplace's equation using finite-difference algorithms (Shera *et al.*, 2005a); the two solutions are indistinguishable on the scale of the figure. By providing knowledge of functional dependencies not available from numerical simulations, the semianalytic approximation proves crucial for subsequent comparisons between theory and experiment.

III. TAILORING PREDICTIONS TO CHINCHILLA

To compare model predictions with SFOAEs measured in chinchilla (e.g., Siegel *et al.*, 2005), we need to evaluate Eq. (1) for $P_{\mathrm{SFOAE}}(f)$ using parameters appropriate to the species. The most important quantities to be determined are those defining the weighting function $\mathcal{W}^2(x,f)$ given by Eq. (2). In particular, we need to know the BM velocity response $V_{\mathrm{BM}}(x,f)$ and the complex wave number $k(x,f)$. The scalae height appearing in approximation (3) for $\alpha(x,f)$ can be obtained from anatomical measurements (Salt, 2001).

A. Estimating the traveling wave

By applying Wiener-kernel analysis to auditory-nerve fiber (ANF) responses to noise, Ruggero *et al.* were able to obtain estimates of BM mechanical transfer functions, both magnitude and phase, at characteristic frequencies (CFs) throughout the chinchilla cochlea (Recio-Spinoso *et al.*, 2005; Temchin *et al.*, 2005). As an example, the thin black line in Fig. 3(A) shows the function $V_{\mathrm{BM}}(x_o,f)$ obtained from a fiber innervating the base [$\mathrm{CF}(x_o)\cong 9$ kHz]. The transfer function is plotted as a function of the "scaling variable," $\nu(x,f)$, defined by (Shera, 2007)

$$\nu(x,f) \equiv \frac{f+\mathrm{CF}_1}{\mathrm{CF}(x)+\mathrm{CF}_1}, \tag{4}$$

where the constant CF_1 represents the approximate characteristic frequency at which the cochlear map morphs from exponential to more linear behavior in the apex. In the chinchilla, $\mathrm{CF}_1\cong 140$ Hz (Eldredge *et al.*, 1981; Greenwood, 1990). At fixed position, the scaling variable $\nu(x,f)$ represents a modified normalized frequency that reduces to the conventional form $f/\mathrm{CF}(x)$ at frequencies roughly two or more octaves above CF_1. At fixed frequency, equal intervals of $\ln \nu$ represent constant distances along the BM.

By regarding $V_{\mathrm{BM}}(x,f)$ primarily as a function of the single variable $\nu(x,f)$ rather than of the two variables x and f independently, we formalize the local scaling symmetry (Zweig, 1976) manifest by basilar-membrane transfer functions (Rhode, 1971; Gummer *et al.*, 1987) and neural tuning curves (e.g., Kiang and Moxon, 1974; Liberman, 1978). As illustrated by the snapshot of the traveling wave shown in Fig. 3(B), local scaling allows one to reinterpret the frequency response $V_{\mathrm{BM}}(x_o,f)$ measured at location x_o as an estimate of the spatial response (traveling wave) $V_{\mathrm{BM}}(x,f_o)$ at frequency f_o; both are given by the function $V_{\mathrm{BM}}(\nu)$. The

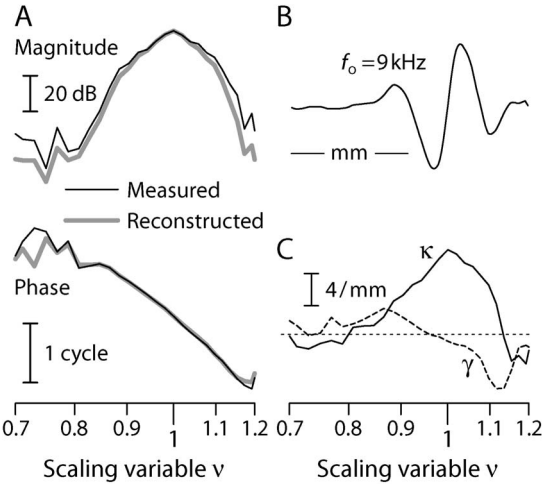

FIG. 3. Empirical estimation, inversion, and reconstruction of the BM velocity response in chinchilla. Panel (A): Thin black lines show the magnitude and phase of the ANF Wiener-kernel estimate of $V_{\mathrm{BM}}(x_o,f)$ at the cochlear location x_o tuned to approximately 9 kHz (Recio-Spinoso *et al.*, 2005). The scaling variable $\nu(x,f)$ increases along the logarithmic abscissa. Thick gray lines show the function V_{BM} reconstructed from the derived wave number [see panel (C), with $k=\kappa+i\gamma$] using the WKB approximation (for details, see Shera, 2007). Panel (B): Snapshot of the 9 kHz wave whose envelope and phase are shown in panel (A). The traveling wave was obtained by reinterpreting the abscissa as a spatial axis at fixed frequency. The scale bar represents a distance of 1 mm (Eldredge *et al.*, 1981; Greenwood, 1990). Panel (C): Solid and dashed lines show propagation and gain functions (κ and γ, respectively) obtained from V_{BM} in panel (A) using the wave number inversion formula [Eq. (5)]. For reference, thin dashes mark the zero line. [Adapted from Figs. 2, 4, and 5 of Shera (2007).]

local scaling approximation is most accurate in the region about the peak of the response [i.e., for x near x_o and for f near $\mathrm{CF}(x_o)$]. By converting transfer functions to traveling waves, local scaling permits computation of the spatial integral appearing in Eq. (1) for $P_{\mathrm{SFOAE}}(f)$.

B. Finding the complex wave number

We obtained the complex wave number of the traveling wave from the Wiener-kernel estimates of $V_{\mathrm{BM}}(x,f)$ by using the wave number inversion formula derived previously (Shera *et al.*, 2005a; Shera, 2007),

$$k^2(x,f) = -V_{\mathrm{BM}}(x,f) \Big/ \int_x^L dx' \int_{x'}^L V_{\mathrm{BM}}(x'',f)dx''. \tag{5}$$

The real and imaginary parts of k, known as propagation and gain functions, are denoted as κ and γ, respectively. Figure 3(C) shows the values of $\kappa(\nu)$ and $\gamma(\nu)$ derived from the example Wiener-kernel estimate of $V_{\mathrm{BM}}(\nu)$ shown in panel (A). The spatial integrals were performed by using local scaling.

The properties of the propagation and gain functions obtained from the chinchilla Wiener kernels are described and interpreted elsewhere (Shera, 2007). Here, we illustrate our procedure for validating the inversion procedure by using the derived wave number to reconstruct the BM velocity response. The thick gray line in Fig. 3(A) shows the function $V_{\mathrm{BM}}(\nu)$ obtained from the wave number in panel (C) by using the Wentzel–Kramers–Brillouin (WKB) formula (Shera *et al.*, 2005a).[4] The agreement with the original measure-

ments (thin black line) confirms that the propagation and gain functions obtained from Eq. (5) provide a valid representation of the complex wave number of the traveling wave.

As detailed elsewhere (Shera, 2007), we applied the inversion and reconstruction procedure outlined above to each of the 137 near-threshold Wiener-kernel BM click responses used to assemble the recently published map of near-CF BM group delays (see Fig. 13 of Temchin *et al.*, 2005). Successful reconstructions were obtained for more than 60% of the responses, representing CFs throughout the cochlea.[5] We restrict further attention to results derived by using these validated responses.

C. Modeling the perturbations

Evaluating the scattering integral in Eq. (1) for $P_{\mathrm{SFOAE}}(f)$ requires knowledge of the form and spatial distribution of any micromechanical irregularities. Although estimates of the weighting function $\mathcal{W}^2(x,f)$ and wave number $k(x,f)$ can be obtained for particular cochleae (e.g., by using the Wiener kernels), we have, as yet, no independent means of estimating the corresponding perturbations, $\epsilon(x,f) \equiv \Delta k^2/k^2 \cong 2\Delta k/k$. Although spatial irregularity presumably occurs in all mechanical parameters, it seems physiologically natural to associate the dominant contribution with irregularity in the active forces responsible for traveling-wave amplification. We therefore take $\Delta k = r(x)\gamma(x,f)$, where the "roughness" $r(x)$ characterizes the spatial pattern of irregularity and $\gamma(x,f)$ is the traveling-wave gain function (Shera, 2007), whose value can be obtained from the wave number ($\gamma \equiv \mathrm{Im}\, k$). In the short-wave region near the wave peak, irregularities in the gain function γ are equivalent to irregularities in the real part of the BM admittance.

Since the roughness $r(x)$ remains unknown, we make no attempt to predict SFOAEs in individual ears. Instead, we compute their statistical behavior (in particular, the distribution of SFOAE phase-gradient delays[6]) across an ensemble of hypothetical ears, each having the same $\mathcal{W}^2$ (i.e., the same BM velocity response and wave number) but different realizations of the roughness $r(x)$. Lacking evidence for more ordered behavior, we also assume that $r(x)$ varies randomly with position within an ear, displaying the same statistical features at all locations. The roughness used in the calculations therefore manifests no long-range correlations. Indeed, we assume that the gain function changes randomly and discontinuously from hair cell to hair cell. However, we obtain equivalent results with much smoother patterns so long as the roughness $r(x)$ contains spatial frequencies within the passband of the "spatial-frequency filter" that arises through the dynamical action of the traveling wave (see Zweig and Shera, 1995, Figs. 6 and 10).

D. Accounting for middle-ear transmission

For our purposes here, the factor $G_{\mathrm{ME}}(f)$ describing middle-ear transmission can safely be ignored. Although the roundtrip pressure gain ($|G_{\mathrm{ME}}|$) helps determine absolute emission levels, we cannot confidently predict SFOAE magnitudes for other reasons (e.g., we do not know the size of the irregularities, and the ANF Wiener kernels provide only a relative measure of tuning). Although the middle ear introduces a delay (characterized by the phase of G_{ME}), middle-ear delay appears negligible compared to cochlear delay in chinchilla (Ruggero *et al.*, 1990; Songer and Rosowski, 2007) and, in any case, is already accounted for by the Wiener-kernel transfer functions,[7] which were referenced to pressure at the eardrum (Recio-Spinoso *et al.*, 2005).

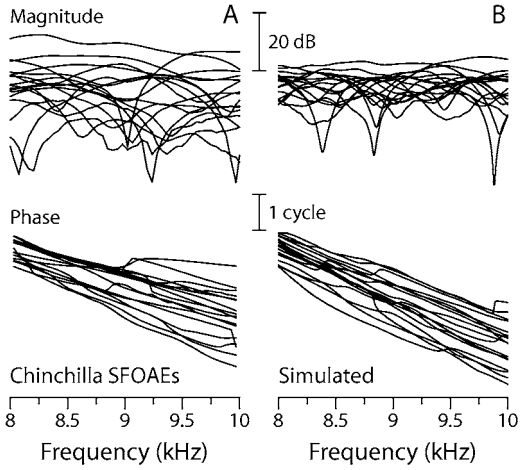

FIG. 4. Measured and simulated chinchilla SFOAEs. Panel (A) shows measured SFOAE magnitudes and phases from 17 chinchillas reported by Siegel *et al.* (2005). Stimulus probe levels were 30 dB SPL. Panel (B) shows simulated SFOAEs computed by using Eq. (1) for $P_{\mathrm{SFOAE}}(f)$ with parameters derived for the particular chinchilla whose ANF-derived BM velocity response and wave number are shown in Fig. 3. The model curves were computed by using irregularity functions consisting of 17 different samples of Gaussian spatial noise [rms value of $r(x)=0.01$]. Both measured and simulated SFOAEs are shown in a frequency range near the Wiener-kernel CF (≅9 kHz).

IV. COMPARING MEASURED AND PREDICTED SFOAEs

A. Qualitative comparison of SFOAE magnitude and phase

Figure 4 compares chinchilla SFOAE magnitude and phase (Siegel *et al.*, 2005) with model predictions computed from Eq. (1) using the example Wiener-kernel estimate of $V_{\mathrm{BM}}(x,f)$ and derived wave number $k(x,f)$ shown in Fig. 3. Both measured and computed SFOAEs span the frequency range of 8–10 kHz near the Wiener-kernel CF. The measured curves represent SFOAEs from 17 different chinchillas; the model curves show predictions for a single chinchilla (one Wiener kernel) using 17 different roughness functions $r(x)$. Each of the 17 functions $r(x)$ represents a different sample of Gaussian spatial noise (zero mean and constant variance) corresponding to rms fractional irregularities of 1%.

The simulated SFOAEs reproduce the major features of the measurements, including their noodling magnitudes and rapidly rotating phases. Although the measurements manifest a larger range of overall emission levels than the model, recall that all 17 simulations derive from the same Wiener-kernel transfer function; consequently, they do not include interanimal differences in mechanical gain that presumably contribute variability to the measured emissions. Further-

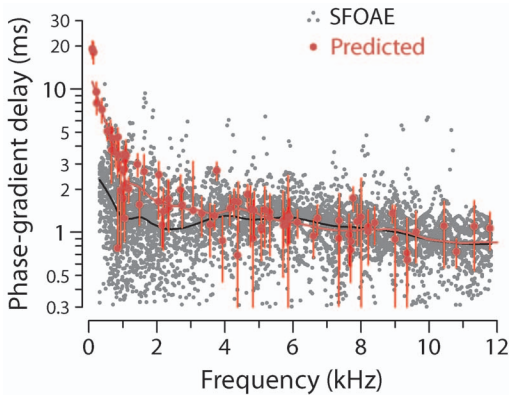

FIG. 5. (Color) Measured and predicted SFOAE phase-gradient delays. Gray dots show SFOAE delays vs frequency measured in 17 chinchillas at probe levels of 30 dB SPL (Siegel *et al.*, 2005, Fig. 4). Red dots show predictions $\hat{\tau}_{SFOAE}$ obtained by using Eq. (1) for $P_{SFOAE}(f)$ with parameters derived for chinchilla using each of the 87 successfully reconstructed Wiener kernels (Recio-Spinoso *et al.*, 2005; Shera, 2007). Model values for each Wiener kernel represent the median near-CF phase gradient computed by using 300 different roughness functions (Gaussian spatial noise). Error bars show the interquartile ranges. Loess trend lines are shown in black and red.

more, because the model roughness functions are all drawn from the same Gaussian distribution, their statistical features (e.g., rms value) are almost certainly more uniform than those of their biological counterparts. As for the phase, measured and predicted phase-gradient delays are similar; the mean delay obtained using the example Wiener kernel from Fig. 3 (1.4 ms) falls within the interquartile range of the 17 measurements. Undulations in emission magnitude (e.g., the occasional deep notches) correlate with wobbles in the phase, as expected from constraints imposed by causality (Sisto *et al.*, 2007).

Because intra- and interanimal variations in middle-ear transmission and cochlear gain have considerable effects on OAE amplitude but are difficult to control for using these data, we focus our attention here on comparisons involving emission phase, specifically the SFOAE phase-gradient delay.

B. Preliminary comparison of delays throughout the cochlea

Figure 5 compares measured and predicted SFOAE delays at frequencies below 12 kHz, the upper limit for the SFOAE measurements. The gray dots form a scatterplot of the delays from all 17 chinchillas (Siegel *et al.*, 2005). The red dots are median delays $\hat{\tau}_{SFOAE}$ computed using each of the 87 successfully reconstructed Wiener kernels; the error bars span the interquartile range, a robust measure of the spread. For each Wiener kernel, the predicted median SFOAE delay and spread are based on 300 simulations, each employing a different random roughness function and each performed by evaluating Eq. (1) at 21 frequencies straddling the CF. The corresponding phase-gradient delays were then computed by calculating the median slope of the unwrapped emission phase. Predicted mean, median, and modal delays were all essentially indistinguishable.

The distributions of measured and predicted delays overlap in the base of the cochlea ($f > 4$ kHz). At lower frequencies, however, the trend lines separate and SFOAE delays are substantially shorter than predicted by the model. At all frequencies, both measured and predicted delays manifest considerable scatter. The scatter in the predicted median delays arises from variations in mechanical tuning (e.g., bandwidths and delays), as captured by the ANF-derived Wiener kernels. Coherent-reflection theory predicts that on top of any scatter traceable to tuning, SFOAEs exhibit additional variability due to the micromechanical irregularity responsible for producing reverse-traveling waves. The error bars on the median model delays, which vary considerably from Wiener kernel to Wiener kernel, measure the variability originating in this way.

C. Complications from SFOAE source mixing

The mixed messages emerging from the comparisons in Fig. 5—compelling agreement in the base and clear disagreement in the apex—counsel taking a more careful look at the low-frequency behavior. Examination of the measured SFOAE magnitudes (Figs. 3 and 4 of Siegel *et al.*, 2005) raises a potential complication: uncontrolled mixing of SFOAE components arising from different source mechanisms (e.g., Shera and Guinan, 1999; Talmadge *et al.*, 2000; Schairer *et al.*, 2003).

In the base of the chinchilla cochlea, the sharp notches characteristic of SFOAE magnitude spectra are typically spaced irregularly and appear separated by two to four or more cycles of phase variation. Human SFOAEs manifest a similar pattern (cf. Shera and Guinan, 1999, Fig. 9), at least above 1 kHz. According to coherent-reflection theory, widely and irregularly spaced spectral notches arise from chance spatial fluctuations in the perturbations that scatter the wave. At irregularly spaced frequencies, wavelets scattered from the many different perturbations within the scattering region happen to combine nearly out of phase with one another, causing near cancellation of the net reflected wave (see Fig. 2; see also Fig. 11 of Zweig and Shera, 1995). At frequencies below 4 kHz, however, the pattern of chinchilla SFOAE notches is rather different (see Fig. 6). Unlike the notches at higher frequencies, the notches below 4 kHz appear more evenly spaced, occurring at intervals corresponding to approximately one cycle of phase rotation.

The more regular pattern of notches below 4 kHz provides strong evidence for interference between two SFOAE components with similar amplitudes but different phase-gradient delays. When the two emission components combine, they beat against each other as the stimulus frequency is varied, producing notches spaced at intervals of about one cycle of relative phase. Quasiperiodic interference notches of this sort are predicted by nonlinear models of SFOAE generation, where they result from near cancellation between reflection-source components with a steep phase slope and induced distortion components with a shallower slope (e.g., Talmadge *et al.*, 2000). A similar interference between

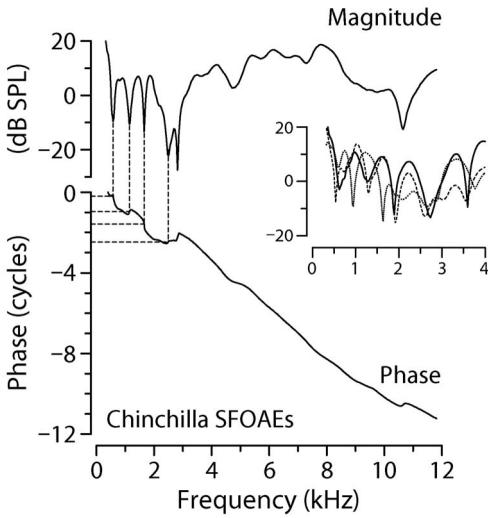

FIG. 6. SFOAE interference notches at low frequencies. Adapted from Fig. 3 of Siegel *et al.* (2005), the figure shows representative chinchilla SFOAEs (30 dB SPL probe). The solid lines in the main panel show SFOAE magnitude and phase vs frequency. The thin dashed lines connecting the top and bottom panels demonstrate that below 4 kHz, magnitude notches generally occur at intervals corresponding to about one cycle rotation of the phase. The inset shows three additional examples of magnitude notches, zooming in on the region below 4 kHz.

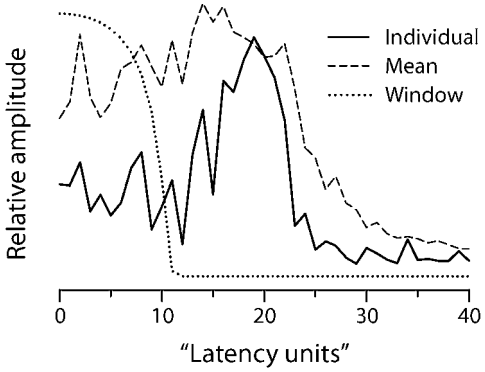

FIG. 7. Chinchilla SFOAEs in the latency domain. The solid line shows the latency-domain representation of the SFOAEs for an individual chinchilla; the dashed line shows the mean of all 17 latency functions. Latency functions are the magnitudes of the discrete Fourier transforms of the SFOAE data obtained after compensating for BM dispersion by applying the quasi-power-law transformation described in the text. The conjugate Fourier variable, shown in latency units (lu) along the abscissa, has no simple physical interpretation. The dotted line shows the matched unmixing window (a 10th-order recursive exponential with a cutoff of 10 lu) used to separate putative short- and long-latency SFOAE components.

reflection- and distortion-source components generates distortion-product OAE microstructure (e.g., Kalluri and Shera, 2001).

D. SFOAE unmixing

We test for the existence of multiple SFOAE components by trying to separate them using signal-processing procedures previously applied to unmix distortion- and reflection-source components of DPOAEs (Kalluri and Shera, 2001; Knight and Kemp, 2001). Similar methods were previously applied to separate the stimulus from the emission during the measurement of SFOAEs (Shera and Zweig, 1993a; Kalluri and Shera, 2007a). The time-windowing method we employ derives from the correspondence between phase slope in the frequency domain and signal latency in the time domain (e.g., Papoulis, 1962). If the regular pattern of SFOAE notches occurs due to interference between two emission components with different phase slopes, then Fourier analysis should reveal two components with different latencies. Complete or partial separation of the two SFOAE components can then be achieved by using appropriate time windows.

To compensate for cochlear frequency dispersion, which smears out emission components in time, rendering them more difficult to separate by windowing, we perform the Fourier analysis with respect to a transformed frequency coordinate. The transformation we employ derives from the empirical place map of chinchilla near-CF BM group delays (τ_{BMGD} in the notation of Temchin *et al.* 2005), as estimated from the ANF Wiener kernels (Recio-Spinoso *et al.*, 2005). Before computing the discrete Fourier transform, we interpolate the SFOAE measurements to frequencies spaced at intervals inversely proportional to $\tau_{\mathrm{BMGD}}(f)$, where $\tau_{\mathrm{BMGD}}(f) = a + b(f/[\mathrm{kHz}])^c$ with parameters $\{a,b,c\} = \{0.496\ \mathrm{ms}, 1.863\ \mathrm{ms}, -0.771\}$ (Temchin *et al.*, 2005; Siegel *et al.*, 2005). By compensating for BM dispersion, the procedure yields sharper more well-defined peaks in the Fourier-conjugate "latency" domain. Previous studies used similar analysis procedures based on a log-frequency coordinate (Zweig and Shera, 1995; Knight and Kemp, 2000; Kalluri and Shera, 2001).

Figure 7 shows the latency-domain representation of the SFOAEs from an individual chinchilla, as well as the mean SFOAE latency function obtained by averaging the results computed from all 17 chinchillas reported by Siegel *et al.* (2005). Because of the quasi-power-law transformation applied before the Fourier analysis, the conjugate "latency units" (lu) along the abscissa have no simple physical interpretation.[8] The peak centered near 18 lu represents the presumed long-latency component of the SFOAE; the short-latency component comprises all emission energy with latency below about 10 lu. We unmixed the SFOAE measurements for each chinchilla into components using the recursive exponential window (Shera and Zweig, 1993a; Kalluri and Shera, 2001) shown with the dotted line. Window durations in the range 10 ± 3 lu yield quantitatively similar components.

Figure 8 shows the results of unmixing the chinchilla SFOAEs into short- and long-latency components. Gray rectangles at the two extremes of the analyzed frequency range identify intervals where end effects associated with the windowing operation render the unmixed components unreliable (Kalluri and Shera, 2001). As expected, the two components have very different phase gradients. The short-latency component has a phase-gradient delay averaged across frequency of roughly 0.3 ms; the mean delay of the long-latency component is about four times longer. Since the two components have different phase gradients, their relative phase rotates with frequency. Summing the two components therefore produces alternating constructive and destructive interference.

The interference pattern produced by the rotating phase

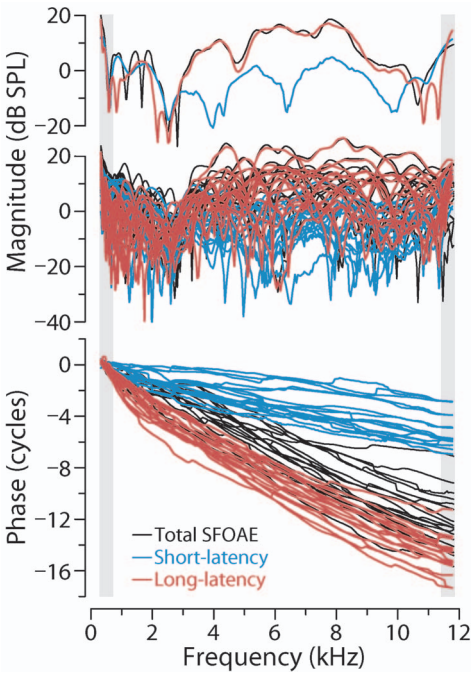

FIG. 8. (Color) Unmixed short- and long-latency SFOAE components. Top and bottom sections show the magnitude and phase of the short-latency (blue) and long-latency (red) components unmixed from the total SFOAEs (black) by time windowing. The topmost panel shows magnitude results for the example highlighted in Fig. 6. Unmixing artifacts at the highest and lowest frequencies render the components unreliable in the intervals indicated by the tall gray rectangles. The total SFOAE data were measured by Siegel *et al.* (2005).

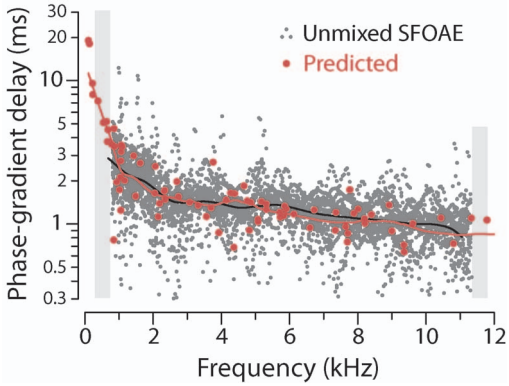

FIG. 9. (Color) Unmixed and predicted SFOAE phase-gradient delays. Gray dots show delays computed from the long-latency SFOAE components shown in Fig. 8. Red dots show predicted delays reproduced from Fig. 5 (error bars have been omitted for clarity). Gray rectangles mask delay data contaminated by unmixing artifacts. Loess trend lines appear in black and red.

depends on the component magnitudes. Figure 8 shows that the relative magnitude of the two components undergoes an abrupt transition near 4 kHz. At frequencies above 4 kHz, the long-latency component dominates the total emission, and the median level difference between the components exceeds 10 dB. Below 4 kHz, however, the median levels of the two components are nearly equal; on average, the short-latency component is about 1 dB larger than the long-latency component. In the low-frequency region, the similarity in component magnitudes, combined with the rotation of their relative phase, produces near cancellation at regular intervals. The two unmixed components therefore have properties consistent with the quasiperiodic interference notches observed below 4 kHz (and with their absence at higher frequencies). Although definitive conclusions require independent evidence for multiple SFOAE components, the unmixing analysis strongly suggests that chinchilla SFOAEs are indeed mixtures produced by multiple mechanisms, at least below 4 kHz.

E. Comparison of unmixed delays

When implemented in a linear cochlear model, the coherent-reflection mechanism generates only the long-latency reflection-source component of SFOAEs. Figure 9 compares model-predicted phase-gradient delays with those computed from the long-latency SFOAE components shown in Fig. 8. The unmixing procedure preserves the close agreement between theory and experiment in the base while substantially improving the agreement in the apex. Unfortunately, unmixing artifacts contaminate the empirical delays at the very lowest frequencies, where the discrepancy evident in Fig. 5 is largest. (Gray rectangles mask empirical delays subject to artifacts.) Nevertheless, wherever the comparison is meaningful, the agreement is striking. In particular, the model predictions capture both the magnitude and the frequency dependence of SFOAE delay.

V. DISCUSSION

A wealth of newly published data in chinchilla (Recio-Spinoso *et al.*, 2005; Temchin *et al.*, 2005; Siegel *et al.*, 2005) has enabled rigorous and comprehensive tests of the theory of coherent-reflection filtering. Although conceptually straightforward, the comparison between theory and experiment faced significant obstacles. On the theoretical side, meaningful quantitative comparisons with chinchilla SFOAEs require model predictions derived specifically for the species. By using inverse methods to derive parameters from data, we obtained model predictions that, within the framework of the assumptions, involve essentially no adjustable parameters. For this, three aspects of our approach proved critical: (1) The approximate analytic formula for $P_{\mathrm{SFOAE}}(f)$ [Eq. (1)] revealed how SFOAEs depend on the BM traveling wave and its complex wave number; (2) The wave number inversion formula [Eq. (5)] allowed estimation of $k(x,f)$ from measurements of $V_{\mathrm{BM}}(x,f)$; and (3) The Wiener-kernel transfer functions provided indirect measurements of $V_{\mathrm{BM}}(x,f)$ at locations throughout the chinchilla cochlea and at intensities roughly comparable to those used to evoke the SFOAEs. Our strategy successfully reproduces the characteristic features of chinchilla SFOAEs, including their rapidly rotating phase and a slowly varying magnitude spectrum interrupted at irregular intervals by deep notches.

On the experimental side, the apparent mixing of SFOAE components produced by different mechanisms intervened to complicate more quantitative comparisons, especially in the apical half of the cochlea, where chinchilla SFOAEs show strong evidence for interference between two components with different phase-gradient delays. Since con-

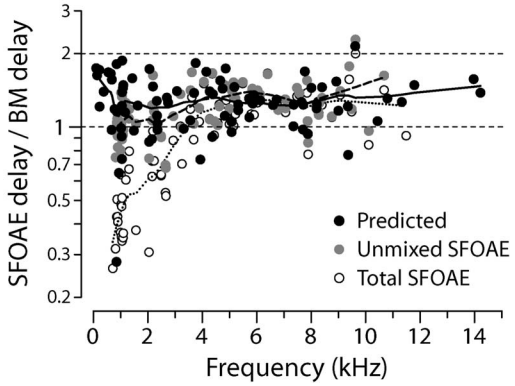

FIG. 10. Empirical and predicted delay ratios. Black dots give predicted delay ratios $\hat{\tau}_{\mathrm{SFOAE}}/\hat{\tau}_{\mathrm{BM}}$ computed by using Eq. (1) tailored to chinchilla using the ANF Wiener kernels. Gray and white dots give empirical delay ratios computed using values of $\hat{\tau}_{\mathrm{SFOAE}}$ obtained from the unmixed and total SFOAE measurements (Siegel *et al.*, 2005), respectively. BM delays were estimated from the Wiener-kernel data (Recio-Spinoso *et al.*, 2005; Temchin *et al.*, 2005).

tamination by multiple OAE components confounds straightforward comparisons between theory and experiment, we used signal-processing techniques to "unmix" the measured SFOAEs. Although definitive characterization of SFOAE components requires independent corroboration, the unmixing analysis revealed emission components with the properties necessary to reproduce the interference pattern evident in the total SFOAE. As a result, we were able to compare model predictions with both the total SFOAEs and with their putative reflection-source components. Model comparisons with the total SFOAEs yield strong agreement in the base but substantial discrepancies below 4 kHz, where the relative magnitude of the short-latency component is greatest. Unmixing the SFOAEs preserves the model's success in the base while significantly improving the agreement in the apex.

A. Relationship between SFOAE and BM delay

Our conclusions about the viability of the coherent-reflection model contrast with those of Siegel *et al.* (2005), who tested the relation $\hat{\tau}_{\mathrm{SFOAE}} \cong 2 \times$ BM delay and found it wanting. Figure 10 demonstrates, however, that the tested relationship between SFOAE and BM delays provides only an approximate statement of the model predictions in chinchilla. The black dots show predicted delay ratios $\hat{\tau}_{\mathrm{SFOAE}}/\hat{\tau}_{\mathrm{BM}}$ computed using the Wiener-kernel data. (The diacritical hat on the predicted τ_{SFOAE} denotes its median value; the hat on τ_{BM} indicates the Wiener-kernel delay near CF.[9]) The model generally predicts chinchilla delay ratios significantly less than 2 throughout the cochlea. Collapsing the predictions across frequency yields a mean delay ratio of 1.3 ± 0.3 standard deviation. Although delay ratios appear to increase at both the highest and lowest frequencies, the data are too sparse to provide much confidence in the trend.

For comparison with the model predictions, Fig. 10 also shows empirical ratios estimated by combining the measured SFOAE and Wiener-kernel data. The empirical ratio $\hat{\tau}_{\mathrm{SFOAE}}/\hat{\tau}_{\mathrm{BM}}$ was computed for each successfully reconstructed Wiener kernel by finding the median SFOAE phase-gradient delay (across all 17 chinchillas in the study of Siegel *et al.*) measured at frequencies within $\pm 2\%$ of the fiber's CF. Gray dots show ratios computed using the unmixed long-latency component; open circles show the ratios computed using the total SFOAEs. Statistical tests corroborate conclusions evident from the trend lines (see also Figs. 5 and 9). At frequencies above 4 kHz, all three distributions (predicted, unmixed, and total) are statistically indistinguishable (Kolmogorov–Smirnov test), confirming the close agreement between the theoretical and empirical ratios in the base of the cochlea. Below 4 kHz, the ratios computed using the total SFOAEs stand out from the other two (Kolmogorov–Smirnov test, $p < 0.001$), which are again statistically identical by the same test. Irrespective of its ultimate legitimacy, the unmixing procedure has at least substantially improved the agreement between theory and experiment in the apex.

The empirical delay ratios estimated from the chinchilla SFOAE and ANF data appear broadly consistent with, albeit somewhat smaller than, previous estimates obtained from the base of the cochlea in several species. In cat and guinea pig, Shera and Guinan (2003) report ratios of 1.7 ± 0.2 and 1.6 ± 0.3, respectively, values obtained by combining otoacoustic and mechanical data across studies. Direct mechanical and otoacoustic measurements in the same animals (ten guinea pigs and one chinchilla) gave a mean delay ratio of 1.8 ± 0.2 (Cooper and Shera, 2004).

B. Interpretation in terms of traveling-wave delay

If coherent reflection involves roundtrip wave propagation, why are predicted delay ratios less than two? Why, in other words, is the intuitive formula SFOAE delay $\cong 2 \times$ BM delay only approximate? To answer this question, we use the coherent-reflection model to derive a formula for $\hat{\tau}_{\mathrm{SFOAE}}$ that reveals the origin of SFOAE delays in cochlear mechanics. To anticipate, we find that SFOAE delay corresponds to the roundtrip delay experienced by pressure-difference waves rather than BM traveling waves. These two waves, the transpartition pressure and the BM velocity, have different phase-gradient delays because they are related by a complex function of frequency, the BM admittance, whose phase varies appreciably near the wave peak.

Analysis of the integral in Eq. (1) for $P_{\mathrm{SFOAE}}(f)$ using the saddle-point approximation (e.g., Bender and Orszag, 1978) shows that its contribution to the emission phase-gradient delay is largely determined by the phase slope of the integrand ($\mathcal{I}$) evaluated near its magnitude peak (Zweig and Shera, 1995, Appendix D; Shera *et al.*, 2005). Since the integrand $\mathcal{I} \equiv \epsilon \mathcal{W}^2$, the median emission delay has the approximate value

$$\hat{\tau}_{\mathrm{SFOAE}} \cong \hat{\tau}_{\mathcal{I}} = \hat{\tau}_{\epsilon} + \hat{\tau}_{\mathcal{W}^2}, \tag{6}$$

where, for example,

$$\hat{\tau}_{\mathcal{W}^2} \equiv -\partial_{\omega} \arg \mathcal{W}^2|_{\max|\mathcal{I}|}, \tag{7}$$

and the notation ∂_{ω} is shorthand for $\partial/\partial\omega$. The diacritical hat on τ_{SFOAE} denotes its median value and otherwise indicates evaluation at max $|\mathcal{I}|$. The delay τ_{ϵ} represents the phase-gradient delay associated with the smooth (nonstochastic)

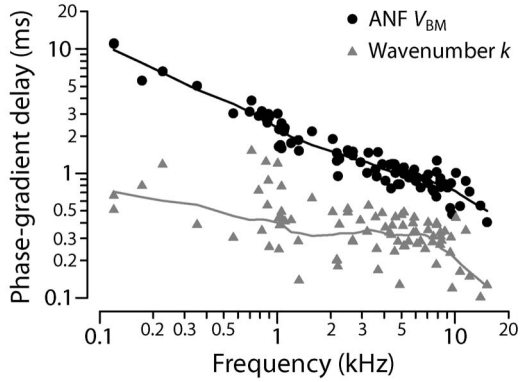

FIG. 11. BM and wave number delays. The black dots show values of the near-CF BM phase-gradient delay ($\hat{\tau}_{BM}$) computed from the Wiener-kernel estimates of $V_{BM}(x,f)$. The gray triangles show corresponding values of $\hat{\tau}_k$ computed from the same Wiener kernels. Loess trend lines are shown to guide the eyes.

component of the perturbations. Equation (6) accurately predicts $\hat{\tau}_{SFOAE}$ in both one- and two-dimensional active cochlear models (cf. Fig. 12 of Shera *et al.*, 2005a).

Approximation (6) for $\hat{\tau}_{SFOAE}$ can be expressed by using quantities determined by the Wiener-kernel measurements. We begin by examining the forms of ϵ and $\mathcal{W}^2$ appearing in the integrand. Recall that we took $\epsilon(x,f) \cong 2\Delta k/k$ with $\Delta k = r(x)\gamma(x,f)$, where $\gamma(x,f)$ is the gain function. Because Δk is real, it makes no contribution to the phase of ϵ. Hence, $\tau_\epsilon \cong -\tau_k$, where $\hat{\tau}_k$ is the phase-gradient delay of the wave number ($\tau_k \equiv -\partial_\omega \arg k$); τ_k enters with a minus sign because k resides in the denominator ($\arg k^{-1} = -\arg k$). Equation (2) for $\mathcal{W}^2$ simplifies in the short-wave regime near the wave peak. In the short-wave limit, $\alpha \to kH$ so that $\mathcal{W}^2 \equiv \alpha V_{BM}^2/k^2 \cong HV_{BM}^2/k$. Hence $\hat{\tau}_{\mathcal{W}^2} \cong 2\hat{\tau}_{BM} - \hat{\tau}_k$, where the factor of 2 comes from the exponent on V_{BM}, and τ_k again enters with a minus sign.

Combining the expressions for $\hat{\tau}_\epsilon$ and $\hat{\tau}_{\mathcal{W}^2}$ yields the approximation

$$\hat{\tau}_{SFOAE} \cong 2(\hat{\tau}_{BM} - \hat{\tau}_k). \tag{8}$$

Estimates of $\hat{\tau}_{BM}$ and $\hat{\tau}_k$ needed to evaluate Eq. (8) can be obtained by using the Wiener-kernel data. Figure 11 plots values of $\hat{\tau}_{BM}$ and $\hat{\tau}_k$ calculated from the ANF data and the derived wave numbers.[10] Figure 12 goes on to demonstrate that Eq. (8) for $\hat{\tau}_{SFOAE}$, based on the short-wave and saddle-point approximations, reproduces the model results shown in Figs. 5 and 9, which were obtained by evaluating Eq. (1) for $P_{SFOAE}(f)$ numerically. Although the saddle-point formula slightly overestimates $\hat{\tau}_{SFOAE}$ at CFs below 4 kHz [Fig. 12(B)], the approximation appears quite respectable overall; it therefore provides a useful basis for interpreting the model predictions.

The empirical values in Fig. 11 indicate that $\hat{\tau}_k$ is *positive* ($\hat{\tau}_k > 0$). The sign of $\hat{\tau}_k$, anticipated on theoretical grounds (Shera, 2001; Shera *et al.*, 2005a), reflects the nature of cochlear amplification. In particular, the sign follows from the observation that near the peak of the traveling wave, the propagation function is positive ($\kappa > 0$) and the gain function γ goes through a negative-going zero crossing (Shera, 2007).[11] Because $\hat{\tau}_k$ is positive, the predicted delay ratio is

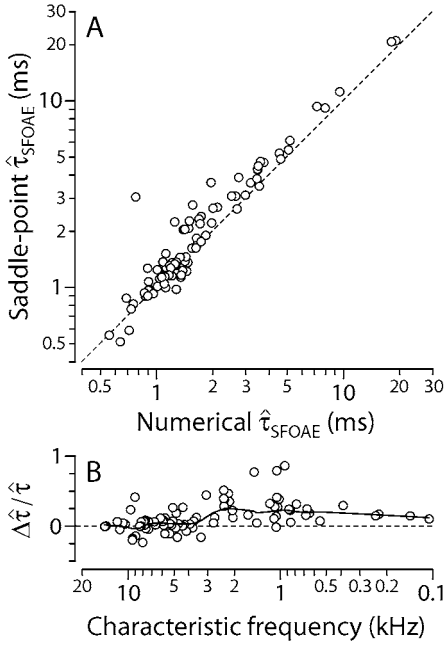

FIG. 12. Numerical and approximate SFOAE delays. The scatterplot in panel (A) shows the correlation between median SFOAE phase-gradient delays computed by using the saddle-point approximation [Eq. (8)] and values of $\hat{\tau}_{SFOAE}$ reproduced from Figs. 5 and 9 [obtained by using Eq. (1) for $P_{SFOAE}(f)$]. Each circle represents the results from an individual Wiener kernel. Short dashes show the line $y=x$. The scatterplot in panel (B) shows the fractional deviation $(\hat{\tau}_{approx} - \hat{\tau}_{numeric})/\hat{\tau}_{numeric}$ vs CF, which decreases along the abscissa. Short dashes mark the zero line and a loess trend guides the eyes. Generally quite accurate in the base of the cochlea, the saddle-point approximation overestimates the delay by roughly 10%–20% in the apex (CF < 4 kHz). Overall, the approximation provides a useful framework for interpreting the model predictions.

generally *less* than 2,

$$\hat{\tau}_{SFOAE}/\hat{\tau}_{BM} \cong 2(1 - \hat{\tau}_k/\hat{\tau}_{BM}) < 2. \tag{9}$$

Since $\hat{\tau}_k$ is perhaps 10%–20% of $\hat{\tau}_{BM}$, the approximation $\hat{\tau}_{SFOAE} \cong 2\tau_{BM}$ is valid to within $2 \times (10\text{–}20)\%$. Since the ratio $\hat{\tau}_k/\hat{\tau}_{BM}$ decreases at lower frequencies, the model delay ratio increases slightly in the apex of the cochlea (see Fig. 10).

Approximation (8) can be interpreted physically by noting that V_{BM} is given by the product of the transpartition pressure P_0 and the BM admittance: $V_{BM} = P_0 Y_{BM}$. In the short-wave regime near the peak, the relation $Y_{BM} \sim k^2/\alpha$ (Shera *et al.*, 2005a) becomes $Y_{BM} \sim k$. Evaluating the delays gives $\hat{\tau}_{BM} \cong \hat{\tau}_p + \hat{\tau}_k$, where τ_p is the phase-gradient delay of the transpartition pressure. Thus, $\hat{\tau}_p \cong \hat{\tau}_{BM} - \hat{\tau}_k$; the pressure delay is just the difference between the curves in Fig. 11. Rewriting Eq. (8) in terms of $\hat{\tau}_p$ gives

$$\hat{\tau}_{SFOAE} \cong 2\hat{\tau}_p. \tag{10}$$

In other words, the model predicts that SFOAE delay is approximately twice the *pressure* delay. Figure 13 illustrates this result with predictions obtained from individual Wiener kernels. Although the factor of 2 in Eq. (10) depends on the value of τ_ϵ (i.e., on the form of the irregularities that scatter the wave), it is consistent with the notion that energy propagation in the cochlea, both on the way in and on the way out, occurs not by means of waves on the BM but by means of

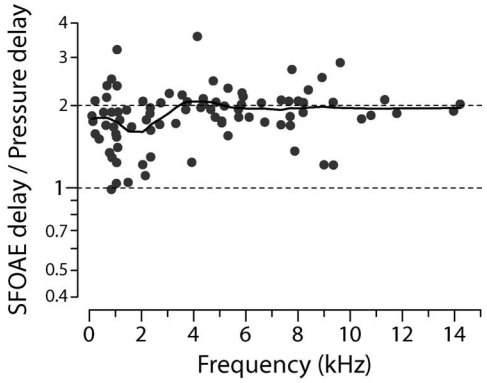

FIG. 13. Predicted pressure delay ratios. The black dots and trend line give predicted delay ratios $\hat{\tau}_{\mathrm{SFOAE}}/\hat{\tau}_p$ computed from Eq. (1) using parameters derived from the chinchilla ANF Wiener kernals. Transpartition pressures were estimated from the Wiener kernels using the formula $P_0=V_{\mathrm{BM}}/Y_{\mathrm{BM}}$ with $Y_{\mathrm{BM}}\sim k^2/\alpha$ (Shera, 2007).

traveling pressure-difference waves. Because the BM velocity and the transpartition pressure are related by a complex function of frequency—the BM admittance—the two kinds of waves have slightly different phase-gradient delays (with $\hat{\tau}_p<\hat{\tau}_{\mathrm{BM}}$ in an active cochlea).

1. Implications for compression-wave models

Although empirical delay ratios significantly greater than 1 but less than 2 agree with the predictions of the coherent-reflection model, they contradict suggestions that OAEs propagate back to the stapes primarily via fast compression (sound) waves (Ren, 2004; Ren *et al.*, 2006; Ruggero, 2004; Siegel *et al.*, 2005). Both heuristic models of fast-wave propagation (e.g., Ren, 2004) as well as more physically based models of fast-wave SFOAE generation (Shera *et al.*, 2005b) predict unmixed delay ratios less than 1. Specifically, for the same types of irregularities employed here, they predict the value $1-\hat{\tau}_k/\hat{\tau}_{\mathrm{BM}}<1$. This discrepancy between empirical delay ratios and fast-wave model predictions suggests that the forces involved in the production of long-latency OAEs couple primarily into transverse pressure-difference waves rather than into longitudinal compression waves. This conclusion is consistent with the results of "Allen–Fahey" and related experiments, which provide compelling independent evidence against the predominance of compression-wave OAEs in mammalian cochlear mechanics (Shera *et al.*, 2007).

C. Prediction of a short-latency component

The mixing of emission components produced by different mechanisms can systematically distort measured phase-gradient delays (e.g., Talmadge *et al.*, 2000). Depending on the relative amplitude of the components, the phase-gradient delay of the mixture falls somewhere between the delays of the components considered separately. Because the coherent-reflection model discussed here involves but a single mechanism—scattering from pre-existing perturbations—removing contributions from other mechanisms is logically necessary for any meaningful comparison between model predictions and experiment. By applying these ideas, we find that the discrepancy between measured and predicted delays apparent at low frequencies in Fig. 5 can be substantially reduced, perhaps even eliminated, by postulating the existence of and removing from the data a "contaminating" short-latency emission component presumed to arise by other means. [As discussed below, the coherent-reflection framework applied to a *nonlinear* cochlear model (Talmadge *et al.*, 2000) yields a natural candidate for the short-latency component.]

Skeptics might object that unmixing renders the resulting agreement essentially vacuous—the procedure merely alters the data to match the theory. The criticism, however, is unwarranted for two reasons. First, nothing guarantees at the outset that simple unmixing will yield agreement between the measured and predicted delays at any frequency, let alone over the *entire* frequency range (e.g., that it will preserve the already outstanding agreement in the base), and yet it does so. Second, the procedure not only reconciles theory and experiment in the apex, it does so constructively by making what amounts to a testable prediction. In particular, our analysis implies that consistency between the model and the data at low frequencies requires the existence of a previously unrecognized short-latency SFOAE component whose relative amplitude is largest in the apical turns of the cochlea.

Prompted by these considerations, and encouraged by the model's success in the base of the cochlea to take its predictions seriously throughout,[12] we looked more closely at the low-frequency measurements. The examination corroborated predictions by revealing that at frequencies below 4 kHz, chinchilla SFOAEs show strong evidence for interference between two components with different phase-gradient delays (see Fig. 6). Thus, both the unmixing analysis and the measured fine-structure interference patterns strongly suggest that multiple emission mechanisms are at work in the apex. Our finding that the long-latency component matches the model predictions suggests that one of the mechanisms is linear coherent reflection. For the moment, the origin of the short-latency component remains unknown, and independent evidence of its existence is obviously needed. Verification of its existence and properties would provide powerful support for the overall modeling framework.

1. Candidates for the short-latency component

The short-latency SFOAE component could arise by one (or more) of many means. The component's eponymous and shallow phase gradient immediately suggests an origin via induced (wave-fixed) sources, such as nonlinear distortion (e.g., Shera and Guinan, 1999). Indeed, wave-fixed sources provide a natural explanation for the paradox invoked by Siegel *et al.* (2005): That OAE phase-gradient delays can be substantially shorter than one-way stimulus propagation delays to the region of reverse-wave generation near the wave peak. If the cochlea were perfectly scaling symmetric, and middle-ear transmission instantaneous, wave-fixed sources would yield an emission with constant phase (i.e., zero phase-gradient delay). However, in the real ear, both violations of scaling, most salient in the apex (e.g., Kiang and Moxon, 1974; Liberman, 1978; Shera and Guinan, 2003; van

der Heijden and Joris, 2006), and finite middle-ear delays (e.g., Dong and Olson, 2006) can produce small but nonzero phase-gradient delays at least qualitatively similar to those apparent in Fig. 9.

Helpfully, the coherent-reflection framework itself provides what may be the most natural candidate for the short-latency component: wave-fixed emissions that arise by scattering off wave-induced perturbations created by nonlinearities in the mechanics [i.e., the process dubbed "nonlinear reflection" (Talmadge *et al.*, 2000)]. Although the present analysis employed linear cochlear models, the actual cochlea is nonlinear, even at the relatively low levels used for the SFOAE measurements. Adding both mechanical irregularity and nonlinearity to active models produces a mixture of wave- and place-fixed SFOAEs qualitatively similar to that seen here and in other studies (Talmadge *et al.*, 2000; Goodman *et al.*, 2003; Schairer *et al.*, 2003). In addition, simple compression-wave models predict that OAEs generated by coupling into fast waves (e.g., via volume-velocity sources in the organ of Corti) are also essentially wave fixed (Shera *et al.*, 2005b) and could, in principle, be contributing to the short-latency component.

The short-latency component could also comprise emission components that arise from the tail region of the cochlear traveling wave rather than the peak. Because the wavelength of the traveling wave is generally longer in the tail region, even place-fixed mechanisms acting in this region could produce emissions with relatively shallow phase gradients. Although their interpretation is not unequivocal (Shera *et al.*, 2004), suppression experiments suggest that contributions from the tail of the traveling wave may, in fact, be significant in chinchilla (Siegel *et al.*, 2003, 2004).

Alternatively, the appearance of a significant short-latency SFOAE component in the apex could simply be an artifact of the measurement method, which relies on nonlinear interactions between the probe and the suppressor to extract the emission. If the form and/or frequency dependence of cochlear nonlinearities differ markedly between the base and the apex (e.g., Khanna and Hao, 1999; Cooper and Dong, 2003), then the suppression method may not always reliably extract the principal emission evoked by the probe (cf. Kalluri and Shera, 2007a). As an extreme example, suppose that the mechanics in the apex were completely linear and exhibited no two-tone suppression. Then, even if the apex were to generate strong reflection-source OAEs, suppression and other "nonlinear" methods would be unable to measure them. Hence, if low-frequency OAEs were actually recorded by using these methods, then the measured emissions could only have originated from more basal (nonlinear) regions of the cochlea (i.e., from regions corresponding to the tail of the traveling wave). As a result, the measured phase-gradient delays would be correspondingly reduced. In the actual ear, the suppression method may extract a mix of emissions from tip and tail regions of the traveling wave whose relative amplitudes vary with CF, depending on the form of cochlear mechanical nonlinearities.

Finally, and most speculatively, the short-latency component may arise through the involvement of nontraditional modes of energy propagation in the cochlea. If the relative magnitude of the short-latency component is any guide, these modes presumably play a more important role in the mechanics of the apex than in the base. Evidence for multiple modes of motion in this CF region can be found in ANF click responses (Lin and Guinan, 2004; Guinan *et al.*, 2005) and in tuning curves, which have multilobed tips and group delays that change abruptly at the seams (e.g., Pfeiffer and Molnar, 1970; Kiang, 1984; van der Heijden and Joris, 2003).

D. An apical-basal transition

Independent of the status of the coherent-reflection model or of the existence or identity of any short-latency emission component, our analysis suggests that the chinchilla cochlea undergoes a transition between more "apical-like" and more "basal-like" behavior near the 4 kHz place. In Fig. 10, for example, empirical delay ratios $\hat{\tau}_{\mathrm{SFOAE}}/\hat{\tau}_{\mathrm{BM}}$ computed from the total SFOAEs change slope rather abruptly near 4 kHz; they increase with frequency below 4 kHz but remain almost constant above. The appearance of this midfrequency transition is due almost entirely to a change in the frequency dependence of $\hat{\tau}_{\mathrm{SFOAE}}$ rather than of $\hat{\tau}_{\mathrm{BM}}$. Interestingly, a similar midfrequency bend in $\hat{\tau}_{\mathrm{SFOAE}}$ occurs in other mammals, including cats, guinea pigs, and humans (Shera and Guinan, 2003). In chinchilla, the unmixing analysis suggests that the transition reflects a change in the composition of the total SFOAE: Whereas at frequencies above 4 kHz, chinchilla SFOAEs consist primarily of a single long-latency reflection-source component, at frequencies below 4 kHz, the emissions contain both short- and long-latency components in more equal proportions.

Interestingly, the 4 kHz location of the apical-basal transition in chinchilla SFOAEs corresponds closely with the CF region in which several properties of traveling-wave propagation and gain functions undergo quantitative changes (Shera, 2007). For example, the maximum value of the gain function $\gamma(x,f)$ is generally smaller, and the spatial extent of the amplification region substantially larger, at CFs below 3–4 kHz than at CFs above (see Figs. 12–14 of Shera, 2007). In cat, the otoacoustic transition frequency corresponds approximately with the CF at which ANF tuning curves change from the classic tip/tail form characteristic of high-CF fibers to the more complex multilobed shapes found in the apex (Liberman, 1978; Liberman and Kiang, 1978). Both the significance of these apical-basal transitions and the intriguing correlations between otoacoustic delays and cochlear physiology require further study.

E. Experimental and theoretical caveats

Notwithstanding the compelling agreement evident in Figs. 9 and 10, our comparison between theory and experiment requires important qualification. Necessary caveats generally fall into two partially overlapping and nonexclusive categories: limitations of the experimental data and uncertainties in the theoretical assumptions.

Wiggle room on the experimental side arises from:.

(1) The different populations of chinchillas used for the ANF and SFOAE measurements. Comparisons done using data from the same individuals would control for possible systematic differences between the groups (e.g., the nature and extent of cochlear damage due to the surgical and measurement procedures). In addition, measurements on the same subjects would presumably reveal correlations between the otoacoustic and auditory-nerve data that now appear as random scatter, reducing the power of the comparison.
(2) The different stimuli used for the otoacoustic and neural data (pure tones for the SFOAEs, wideband noise for the Wiener kernels). Due to suppression and other effects, systematic differences between responses to narrow- and wideband stimuli are expected in nonlinear systems. For example, although both data sets were measured at low intensities, the different stimulus bandwidths make it difficult if not impossible to match effective stimulus levels (cf. Kalluri and Shera, 2007b).
(3) Possible systematic differences between ANF-derived and true BM mechanical transfer functions. Although Wiener-kernel responses corrected for synaptic and neural transmission delays resemble BM mechanical measurements made at corresponding locations and intensities (Temchin *et al.*, 2005), the Wiener-kernel measurements characterize cochlear tuning as seen from the auditory nerve. They therefore presumably include contributions from internal motions of the organ of Corti or tectorial membrane visible to the inner hair cell but less prominent in the motion of the BM (e.g., Guinan *et al.*, 2005; Nowotny and Gummer, 2006; Karavitaki and Mountain, 2007; Ghaffari *et al.*, 2007). Whether (or how) these internal motions play a role in OAE generation remains unclear [cf. assumption (1) in Sec. I A].
(4) The uncertain legitimacy of the unmixing analysis. Although the evidence for a contaminating short-latency SFOAE component produced by other mechanisms seems compelling, corroborating data are needed to fully justify our procedures. The current analysis, although not entirely circular, appears at least disconcertingly spiral. If multiple SFOAE components do exist, perhaps they can be separated by using procedures that do not introduce unwanted artifacts at the edges; the unmixing artifact is especially unhelpful at the lowest frequencies, where discrepancies between theory and experiment appear largest. We note, however, that even if the unmixing analysis is entirely discarded, agreement between theory and experiment remains strong in the base (Fig. 5).
(5) Possible biases introduced by the suppression method for measuring SFOAEs, as discussed in Sec. V C.

On the theoretical side, the list of caveats includes:

(1) Possible inaccuracy of the wave number inversion procedure. Although we limited our analysis to Wiener kernels and wave numbers validated by successful reconstruction, the inversion procedure is nevertheless approximate and depends on assumptions (e.g., local scaling) with the potential to produce systematic errors in the predicted SFOAEs. The local scaling approximation is also employed when evaluating Eq. (1) for $P_{\mathrm{SFOAE}}(f)$, where it serves to convert BM transfer functions into traveling waves. Any bias due to the local scaling approximation is expected to be largest in the apical half of the cochlea, where deviations from scaling are most pronounced.
(2) Possible misrepresentation of the mechanical irregularities. Since the phase-gradient delay associated with the irregularities (τ_ϵ) contributes to $\hat{\tau}_{\mathrm{SFOAE}}$ [Eq. (6)], the form of the perturbations affects the predicted SFOAE delay. We took the dominant perturbations Δk to reside in the traveling-wave gain function, with the consequence that $\hat{\tau}_\epsilon \cong -\hat{\tau}_k$. Although we regard these perturbations as physiologically natural—and other choices, such as placing the irregularities in the propagation function κ, produce identical results—the actual perturbations remain unknown and may even vary systematically along the cochlea. Currently, the strongest evidence supporting our approach may simply be the compelling overall agreement that results (i.e., it works). Because systematic discrepancies between measured and predicted phase-gradient delays can be introduced by appropriate adjustment of perturbation phases, the choice of perturbations is the closest thing to a free adjustable parameter in the model.
(3) Deviations from one or more of the three principal assumptions about cochlear mechanics outlined in Sec. I A. For example, conventional models assume that the mechanics of the partition are well described by point-admittance functions coupled together primarily by means of scalae fluid pressures. However, if spatial "feed-forward" or "feed-backward" forces play a significant role in cochlear amplification or if the normal operation of the cochlea involves additional modes of motion and/or energy transport, then the analysis leading to Eq. (1) for $P_{\mathrm{SFOAE}}(f)$ becomes, at best, only approximate. In addition, the derivation assumes the simplified geometry of the two-dimensional box model. Therefore, even though our analysis encompasses both long- and short-wave behaviors, the predictions of Eq. (1) may deviate systematically from predictions that incorporate more realistic three-dimensional motions of both fluid and tissue.

Without minimizing the possible significance of these experimental and theoretical caveats, we note that the many ways that the model implemented here might seriously have failed—but evidently did not—strongly suggests that the coherent-reflection model captures at least the dominant mechanisms responsible for the generation of reflection-source otoacoustic emissions.

ACKNOWLEDGMENTS

We thank Mario Ruggero, Jonathan Siegel, and Andrei Temchin for generously sharing their data and for many provocative discussions. We also thank Christopher Bergevin, Paul Fahey, John Guinan, Jeffery Lichtenhan, and Elizabeth Olson for valuable comments on the manuscript. This work

was supported by Grant No. R01 DC003687 (CAS) from the NIDCD, National Institutes of Health.

[1]Preliminary accounts of this work have been presented elsewhere (Shera *et al.*, 2006).

[2]To simplify the formula, we have suppressed slowly varying "constants" and nonessential geometric factors (e.g., the area of the oval window) that make negligible contributions to the model predictions tested here. In addition, Eq. (1) assumes only first-order scattering or, equivalently, that contributions from multiple internal reflection are small enough to be neglected.

[3]Footnote 4 of Shera (2003) provides more information about $G_{\mathrm{ME}}(f)$ (there denoted G_{mert}) and its determination from a two-port description of the middle ear (e.g., Puria, 2003; Voss and Shera, 2004; Songer and Rosowski, 2007).

[4]The WKB formula is $V_{\mathrm{BM}}(x,f) \propto k^{3/2}(x,f)\exp[-i\int_0^x k(x',f)dx']$, where the proportionality factor depends on frequency (e.g., Shera, 2007). The same formula applies in response-matched one- and two-dimensional models [see Appendix A of Shera *et al.* (2005) for further discussion].

[5]Unsuccessful reconstructions often contained anomalous spikes within the peak region. Similar problems can occur when inverting model responses if the boundary conditions assumed by the inversion formula are not well satisfied.

[6]The SFOAE phase-gradient delay is defined by $\tau_{\mathrm{SFOAE}} \equiv -\partial_\omega \arg P_{\mathrm{SFOAE}}$, where P_{SFOAE} is the measured (or computed) SFOAE and ∂_ω is shorthand for $\partial/\partial\omega$.

[7]Technically, the measured Wiener kernels only include forward middle-ear delay. But if forward and reverse middle-ear delay are similar (e.g., Voss and Shera, 2004; Dong and Olson, 2006), then the factor of 2 coming from the exponent of $V_{\mathrm{BM}}^2(x,f)$ in Eq. (2) for $\mathcal{W}^2(x,f)$ accounts for reverse transmission as well.

[8]If the transformation were logarithmic (i.e., if $\{a,b,c\}=\{0,1,-1\}$), then the abscissa would represent the latency measured in periods of the stimulus frequency (Kalluri and Shera, 2001).

[9]More precisely, $\hat{\tau}_{\mathrm{BM}}$ is the phase-gradient delay of V_{BM} evaluated at $\max|\mathcal{I}|$, where $\mathcal{I}$ is the integrand in Eq. (1). In chinchilla, the location $\max|\mathcal{I}|$ is, on average, slightly basal to $\max|V_{\mathrm{BM}}|$.

[10]Below 10 kHz, the trend line for $\hat{\tau}_{\mathrm{BM}}$ in Fig. 11 agrees well with the formula of Temchin *et al.* (2005) used during the unmixing procedure to compensate for cochlear delays (see Sec. IV D). At higher frequencies, the formula of Temchin *et al.* overestimates the trend by 0.1–0.2 ms.

[11]More precisely, if $\arg k = \mathrm{atan}(\gamma/\kappa)$, then $\partial_x \arg k \cong (\kappa/|k|^2)\partial_x\gamma$, where we have assumed that $\gamma\partial_x\kappa \cong 0$ because $\gamma(\hat{x}) \cong 0$ (i.e., because of the zero crossing in γ near the peak at $\hat{x}$). Scaling implies that spatial derivatives at fixed frequency have the same sign as frequency derivatives at fixed position ($\partial_x/\partial_\omega > 0$). Thus, if $\kappa > 0$ and $\partial_x\gamma < 0$ near the peak, then $\hat{\tau}_k = -\partial_\omega \arg k > 0$. The foregoing proof was adapted from footnote 10 of Shera *et al.* (2005a).

[12]Often, Weinberg (1993) writes, "our mistake is not that we take our theories too seriously, but that we do not take them seriously enough."

Allen, J. B. (**2003**). "Moderated discussion session," *Biophysics of the Cochlea: From Molecules to Models*, edited by A. W. Gummer (World Scientific, Singapore), pp. 563–592.

Allen, J. B. (**2006**). "Moderated discussion session," *Auditory Mechanisms: Processes and Models*, edited by A. L. Nuttall, T. Ren, P. Gillespie, K. Grosh, and E. de Boer (World Scientific, Singapore), pp. 521–543.

Bender, C. M., and Orszag, S. A. (**1978**). *Advanced Mathematical Methods for Scientists and Engineers* (McGraw-Hill, New York).

Bredberg, G. (**1968**). "Cellular patterns and nerve supply of the human organ of Corti," Acta Oto-Laryngol., Suppl. **236**, 1–135.

Cooper, N. P., and Dong, W. (**2003**). "Baseline position shifts and mechanical compression in the apical turns of the cochlea," *Biophysics of the Cochlea: From Molecules to Models*, edited by A. W. Gummer (World Scientific, Singapore), pp. 261–270.

Cooper, N. P., and Shera, C. A. (**2004**). "Backward traveling waves in the cochlea? Comparing basilar-membrane vibrations and otoacoustic emissions from individual guinea-pig ears," Assoc. Res. Otolaryngol. Abstr. **27**, 1008.

de Boer, E. (**1996**). "Mechanics of the cochlea: Modeling efforts," *The Cochlea*, edited by P. Dallos, A. N. Popper, and R. R. Fay (Springer-Verlag, New York), pp. 258–317.

Dong, W., and Olson, E. S. (**2006**). "Middle ear forward and reverse transmission in gerbil," J. Neurophysiol. **95**, 2951–2961.

Duifhuis, H. (**1988**). "Cochlear macromechanics," *Auditory Function: Neurological Bases for Hearing*, edited by G. M. Edelman, W. E. Gall, and W. M. Cowan (Wiley, New York), pp. 189–212.

Eldredge, D. H., Miller, J. D., and Bohne, B. A. (**1981**). "A frequency-position map for the chinchilla cochlea," J. Acoust. Soc. Am. **69**, 1091–1095.

Engström, H., Ades, H. W., and Andersson, A. (**1966**). *Structural Pattern of the Organ of Corti* (Williams and Wilkins, Baltimore).

Finch, C. E., and Kirkwood, T. B. L. (**2000**). *Chance, Development, and Aging* (Oxford University Press, New York).

Ghaffari, R., Aranyosi, A. J., and Freeman, D. M. (**2007**). "Longitudinally propagating traveling waves of the mammalian tectorial membrane," Proc. Natl. Acad. Sci. U.S.A. **104**, 16510–16515.

Goodman, S. S., Withnell, R. H., and Shera, C. A. (**2003**). "The origin of SFOAE microstructure in the guinea pig," Hear. Res. **183**, 1–17.

Greenwood, D. D. (**1990**). "A cochlear frequency-position function for several species—29 years later," J. Acoust. Soc. Am. **87**, 2592–2605.

Guinan, J. J., Lin, T., and Cheng, H. (**2005**). "Medial-olivocochlear-efferent inhibition of the first peak of auditory-nerve responses: Evidence for a new motion within the cochlea," J. Acoust. Soc. Am. **118**, 2421–2433.

Gummer, A. W., Smolders, J. W. T., and Klinke, R. (**1987**). "Basilar membrane motion in the pigeon measured with the Mössbauer technique," Hear. Res. **29**, 63–92.

Kalluri, R., and Shera, C. A. (**2001**). "Distortion-product source unmixing: A test of the two-mechanism model for DPOAE generation," J. Acoust. Soc. Am. **109**, 622–637.

Kalluri, R., and Shera, C. A. (**2007a**). "Comparing stimulus-frequency otoacoustic emissions measured by compression, suppression, and spectral smoothing," J. Acoust. Soc. Am. **122**, 3562–3575.

Kalluri, R., and Shera, C. A. (**2007b**). "Near equivalence of human click-evoked and stimulus-frequency otoacoustic emissions," J. Acoust. Soc. Am. **121**, 2097–2110.

Karavitaki, K. D., and Mountain, D. C. (**2007**). "Evidence for outer hair cell driven oscillatory fluid flow in the tunnel of Corti," Biophys. J. **92**, 3284–3293.

Kemp, D. T. (**1978**). "Stimulated acoustic emissions from within the human auditory system," J. Acoust. Soc. Am. **64**, 1386–1391.

Khanna, S. M., and Hao, L. F. (**1999**). "Reticular lamina vibrations in the apical turn of a living guinea pig cochlea," Hear. Res. **132**, 15–33.

Kiang, N. Y. S. (**1984**). "Peripheral neural processing of auditory information," *Handbook of Physiology, Section 1: The Nervous System (Sensory Processes)*, edited by I. Darian-Smith (American Physiological Society, Bethesda), Vol. 3, pp. 639–674.

Kiang, N. Y. S., and Moxon, E. C. (**1974**). "Tails of tuning curves of auditory-nerve fibers," J. Acoust. Soc. Am. **55**, 620–630.

Knight, R. D., and Kemp, D. T. (**2000**). "Indications of different distortion product otoacoustic emission mechanisms from a detailed f_1, f_2 area study," J. Acoust. Soc. Am. **107**, 457–473.

Knight, R. D., and Kemp, D. T. (**2001**). "Wave and place fixed DPOAE maps of the human ear," J. Acoust. Soc. Am. **109**, 1513–1525.

Liberman, M. C. (**1978**). "Auditory-nerve response from cats raised in a low-noise chamber," J. Acoust. Soc. Am. **63**, 442–455.

Liberman, M. C., and Kiang, N. Y. S. (**1978**). "Acoustic trauma in cats: Cochlear pathology and auditory-nerve activity," Acta Oto-Laryngol., Suppl. **358**, 1–63.

Lin, T., and Guinan, J. J. (**2004**). "Time-frequency analysis of auditory-nerve-fiber and basilar-membrane click responses reveal glide irregularities and non-characteristic-frequency skirts," J. Acoust. Soc. Am. **116**, 405–416.

Lonsbury-Martin, B. L., Martin, G. K., Probst, R., and Coats, A. C. (**1988**). "Spontaneous otoacoustic emissions in the nonhuman primate. II. Cochlear anatomy," Hear. Res. **33**, 69–94.

Nowotny, M., and Gummer, A. W. (**2006**). "Nanomechanics of the subtectorial space caused by electromechanics of cochlear outer hair cells," Proc. Natl. Acad. Sci. U.S.A. **103**, 2120–2125.

Papoulis, A. (**1962**). *The Fourier Integral and its Applications* (McGraw-Hill, New York).

Pfeiffer, R. R., and Molnar, C. E. (**1970**). "Cochlear nerve fiber discharge patterns: Relationship to the cochlear microphonic," Science **167**, 1614–1616.

Puria, S. (**2003**). "Measurements of human middle ear forward and reverse acoustics: Implications for otoacoustic emissions," J. Acoust. Soc. Am. **113**, 2773–2789.

Recio-Spinoso, A., Temchin, A. N., van Dijk, P., Fan, Y.-H., and Ruggero, M. A. (**2005**). "Wiener-kernel analysis of responses to noise of chinchilla," J. Neurophysiol. **93**, 3615–3634.
Ren, T. (**2004**). "Reverse propagation of sound in the gerbil cochlea," Nat. Neurosci. **7**, 333–334.
Ren, T., He, W., Scott, M., and Nuttall, A. L. (**2006**). "Group delay of acoustic emissions in the ear," J. Neurophysiol. **96**, 2785–2791.
Rhode, W. S. (**1971**). "Observations of the vibration of the basilar membrane in squirrel monkeys using the Mössbauer technique," J. Acoust. Soc. Am. **49**, 1218–1231.
Ruggero, M. A. (**2004**). "Comparison of group delays of $2f_1-f_2$ distortion product otoacoustic emissions and cochlear travel times," ARLO **5**, 143–147.
Ruggero, M. A., Rich, N. C., Robles, L., and Shivapuja, B. G. (**1990**). "Middle-ear response in the chinchilla and its relationship to mechanics at the base of the cochlea," J. Acoust. Soc. Am. **87**, 1612–1629.
Salt, A. N. (**2001**). Cochlear fluids simulator v1.6h, http://oto.wustl.edu/cochlea/model Last viewed 12/01/07.
Schairer, K. S., Fitzpatrick, D., and Keefe, D. H. (**2003**). "Input-output functions for stimulus-frequency otoacoustic emissions in normal-hearing adult ears," J. Acoust. Soc. Am. **114**, 944–966.
Shera, C. A. (**2001**). "Intensity-invariance of fine time structure in basilar-membrane click responses: Implications for cochlear mechanics," J. Acoust. Soc. Am. **110**, 332–348.
Shera, C. A. (**2003**). "Mammalian spontaneous otoacoustic emissions are amplitude-stabilized cochlear standing waves," J. Acoust. Soc. Am. **114**, 244–262.
Shera, C. A. (**2007**). "Laser amplification with a twist: Traveling-wave propagation and gain functions from throughout the cochlea," J. Acoust. Soc. Am. **122**, 2738–2758.
Shera, C. A., and Guinan, J. J. (**1999**). "Evoked otoacoustic emissions arise by two fundamentally different mechanisms: A taxonomy for mammalian OAEs," J. Acoust. Soc. Am. **105**, 782–798.
Shera, C. A., and Guinan, J. J. (**2003**). "Stimulus-frequency-emission group delay: A test of coherent reflection filtering and a window on cochlear tuning," J. Acoust. Soc. Am. **113**, 2762–2772.
Shera, C. A., Tubis, A., and Talmadge, C. L. (**2005a**). "Coherent reflection in a two-dimensional cochlea: Short-wave versus long-wave scattering in the generation of reflection-source otoacoustic emissions," J. Acoust. Soc. Am. **118**, 287–313.
Shera, C. A., Tubis, A., and Talmadge, C. L. (**2005b**). "Coherent-reflection models of reflection-source OAEs with and without slow transverse retrograde waves," Assoc. Res. Otolaryngol. Abstr. **28**, 657.
Shera, C. A., Tubis, A., and Talmadge, C. L. (**2006**). "Delays of SFOAEs and cochlear vibrations support the theory of coherent reflection filtering," Assoc. Res. Otolaryngol. Abstr. **29**, 52.
Shera, C. A., Tubis, A., Talmadge, C. L., de Boer, E., Fahey, P. F., and Guinan, J. J. (**2007**). "Allen–Fahey and related experiments support the predominance of cochlear slow-wave otoacoustic emissions," J. Acoust. Soc. Am. **121**, 1564–1575.
Shera, C. A., Tubis, A., Talmadge, C. L., and Guinan, J. J. (**2004**). "The dual effect of 'suppressor' tones on stimulus-frequency otoacoustic emissions," Assoc. Res. Otolaryngol. Abstr. **27**, 538.
Shera, C. A., and Zweig, G. (**1993a**). "Noninvasive measurement of the cochlear traveling-wave ratio," J. Acoust. Soc. Am. **93**, 3333–3352.
Shera, C. A., and Zweig, G. (**1993b**). "Order from chaos: Resolving the paradox of periodicity in evoked otoacoustic emission," *Biophysics of Hair Cell Sensory Systems*, edited by H. Duifhuis, J. W. Horst, P. van Dijk, and S. M. van Netten (World Scientific, Singapore), pp. 54–63.
Siegel, J. H., Cerka, A. J., Recio-Spinoso, A., Temchin, A. N., van Dijk, P., and Ruggero, M. A. (**2005**). "Delays of stimulus-frequency otoacoustic emissions and cochlear vibrations contradict the theory of coherent reflection filtering," J. Acoust. Soc. Am. **118**, 2434–2443.
Siegel, J. H., Cerka, A. J., Temchin, A. N., and Ruggero, M. A. (**2004**). "Similar two-tone suppression patterns in SFOAEs and the cochlear microphonics indicate comparable spatial summation of underlying generators," Assoc. Res. Otolaryngol. Abstr. **27**, 539.
Siegel, J. H., Temchin, A. N., and Ruggero, M. A. (**2003**). "Empirical estimates of the spatial origin of stimulus-frequency otoacoustic emissions," Assoc. Res. Otolaryngol. Abstr. **26**, 679.
Sisto, R., Moleti, A., and Shera, C. A. (**2007**). "Cochlear reflectivity in transmission-line models and otoacoustic emission characteristic time delays," J. Acoust. Soc. Am. **122**, 3554–3561.
Songer, J. E., and Rosowski, J. J. (**2007**). "Transmission matrix analysis of the chinchilla middle ear," J. Acoust. Soc. Am. **122**, 932–942.
Talmadge, C. L., Tubis, A., Long, G. R., and Piskorski, P. (**1998**). "Modeling otoacoustic emission and hearing threshold fine structures," J. Acoust. Soc. Am. **104**, 1517–1543.
Talmadge, C. L., Tubis, A., Long, G. R., and Tong, C. (**2000**). "Modeling the combined effects of basilar membrane nonlinearity and roughness on stimulus frequency otoacoustic emission fine structure," J. Acoust. Soc. Am. **108**, 2911–2932.
Temchin, A. N., Recio-Spinoso, A., van Dijk, P., and Ruggero, M. A. (**2005**). "Wiener kernels of chinchilla auditory-nerve fibers: Verification using responses to tones, clicks, and noise and comparison with basilar-membrane vibrations," J. Neurophysiol. **93**, 3635–3648.
van der Heijden, M., and Joris, P. X. (**2003**). "Cochlear phase and amplitude retrieved from the auditory nerve at arbitrary frequencies," J. Neurosci. **23**, 9194–9198.
van der Heijden, M., and Joris, P. X. (**2006**). "Panoramic measurements of the apex of the cochlea," J. Neurosci. **26**, 11462–11473.
Voss, S. E., Rosowski, J. J., and Peake, W. T. (**1996**). "Is the pressure difference between the oval and round window the effective stimulus for the cochlea?" J. Acoust. Soc. Am. **100**, 1602–1616.
Voss, S. E., and Shera, C. A. (**2004**). "Simultaneous measurement of middle-ear input impedance and forward/reverse transmission in cat," J. Acoust. Soc. Am. **116**, 2187–2198.
Weinberg, S. (**1993**). *The First Three Minutes*, revised ed. (Perseus Books, New York).
Wilson, J. P. (**1980**). "Model for cochlear echoes and tinnitus based on an observed electrical correlate," Hear. Res. **2**, 527–532.
Wright, A. A. (**1984**). "Dimensions of the cochlear stereocilia in man and in guinea pig," Hear. Res. **13**, 89–98.
Zweig, G. (**1976**). "Basilar membrane motion," *Cold Spring Harbor Symposia on Quantitative Biology, 1975* (Cold Spring Harbor Laboratory, Cold Spring Harbor), Vol. XL, pp. 619–633.
Zweig, G., and Shera, C. A. (**1995**). "The origin of periodicity in the spectrum of evoked otoacoustic emissions," J. Acoust. Soc. Am. **98**, 2018–2047.

Fast volumetric integral-equation solver for acoustic wave propagation through inhomogeneous media

E. Bleszynski,[a] M. Bleszynski,[b] and T. Jaroszewicz[c]
Monopole Research, 739 Calle Sequoia, Thousand Oaks, California 91360

(Received 7 November 2007; revised 16 April 2008; accepted 17 April 2008)

Elements are described of a volumetric integral-equation-based algorithm applicable to accurate large-scale simulations of scattering and propagation of sound waves through inhomogeneous media. The considered algorithm makes possible simulations involving realistic geometries characterized by highly subwavelength details, large density contrasts, and described in terms of several million unknowns. The algorithm achieves its competitive performance, characterized by $\mathcal{O}(N \log N)$ solution complexity and $\mathcal{O}(N)$ memory requirements, where N is the number of unknowns, through a fast and nonlossy fast Fourier transform based matrix compression technique, the adaptive integral method, previously developed for solving large-scale electromagnetic problems. Because of its ability of handling large problems with complex geometries, the developed solver may constitute an efficient and high fidelity numerical simulation tool for calculating acoustic field distributions in anatomically realistic models, e.g., in investigating acoustic energy transfer to the inner ear via nonairborne pathways in the human head. Examples of calculations of acoustic field distribution in a human head, which require solving linear systems of equations involving several million unknowns, are presented. © *2008 Acoustical Society of America.*
[DOI: 10.1121/1.2924203]

PACS number(s): 43.66.Ba, 43.58.Ta, 43.64.Wn [TDM] Pages: 396–408

I. INTRODUCTION

There is a considerable interest in developing reliable and computationally efficient solution methods for solving the elastic/acoustic wave propagation through complex media. Possible applications include simulations of interactions with biological tissues and numerical analysis of noise propagation through the human body, in particular, through the human head.

It is a well established fact that integral-equation formulations provide the most accurate solutions to wave problems. They require, however, solving dense systems of linear equations. Traditional methods of solving such systems (e.g., through matrix inversion) are characterized by the computational complexity and memory requirements of the order of N^3. Here, N is the number of unknowns, or a number of volume elements, necessary to resolve acoustic wave variations as well as geometrical details of the object. For complex, anatomically realistic models, N can easily become of the order of millions. Hence, despite their reliability and accuracy, the conventional integral-equation-based methods become computationally prohibitively intensive to provide solutions for realistic problems of interest.

During the past decade, a significant progress has been made in the development of *fast* frequency- and time-domain integral-equation solvers and, as a result, the ability of accurate and fast numerical simulations of wave propagation and scattering in complex media has dramatically improved. Matrix compression techniques, such as the adaptive integral method (AIM),[1,2] the fast multiple method (FMM),[3] the precorrected fast Fourier transform (FFT) method,[4] and the sparse-matrix canonical grid method (SMCG),[5] have been developed. They allow solving large linear sets of equations with dense matrices utilizing storage and execution times characteristic of problems involving sparse linear systems. The physical idea behind such methods is that evaluation of interactions at large distances requires less resolution than at small distances. Consequently, the computational complexity and memory requirements of the compression methods scale approximately *linearly* with the number of unknowns N.

In this paper, we discuss adaptation of the FFT based AIM matrix compression method,[1,2] initially developed in the context of electromagnetics, to solving large-scale volumetric integral-equation problems in acoustics. In the AIM approach, the original basis functions are expanded into sets of auxiliary, far-field equivalent, point sources located on nodes of a regular Cartesian grid. As the result, the far-field part of the interaction matrix becomes a Toeplitz matrix (or, more precisely, a product of a Toeplitz and sparse transformation matrices). The Toeplitz property allows computation of the matrix-vector product by means of FFTs with the $N \log N$ solution complexity. The near-field part of the interaction matrix is, by construction, sparse. Hence, its contribution to the solution complexity is of the order of $\mathcal{O}(N)$. The approach is briefly described in Sec. V.

In comparison to other methods, we find the AIM fast solution scheme particularly suitable for solving acoustics problems. Its main advantage is that it can be applied to a wide frequency range—from tens of hertz to tens of kilohertz—with only a minor modification of the matrix compression scheme from the low- to high-frequency mode (as discussed in Sec. V A). In the FMM approach, entirely

[a]Electronic mail: elizabeth@monopoleresearch.com.
[b]Electronic mail: marek@monopoleresearch.com.
[c]Electronic mail: tomek@monopoleresearch.com.

 0001-4966/2008/124(1)/396/13/$23.00

different algorithms have to be used for low and high frequencies. The precorrected FFT method is less efficient than AIM at higher frequencies. Finally, for the considered applications, the cost of the SMCG method is significantly higher due to the necessity of computing a number of derivatives of the Green function.

We consider problems characterized by a constant density and a variable compressibility, as well as problems characterized by a variable density and very large density contrasts (such as scattering on a dense object in air).

We also note that from the point of view of the properties of integral equations, the latter type of problems may exhibit features associated with potential ill conditioning. In a separate publication,[6] we address these difficulties and present a solution.

II. INTEGRAL EQUATIONS IN ACOUSTICS

Volumetric integral equations for the pressure field—known generally as the Lippmann–Schwinger (LS) equations—can be derived from the partial-differential equations of acoustics split into two terms: one describing wave propagation in the background medium (in our case, air) and the other wave interaction with the scatterer (here, e.g., the human body), occupying a bounded spatial region (domain) Ω. The compressibility and density of the scatterer are denoted by $\kappa(\mathbf{r})$ and $\rho(\mathbf{r})$, while the corresponding parameters of the background medium are κ_0 and ρ_0. For biological tissues in air, we have

$$\frac{\rho}{\rho_0} \sim 10^3, \quad \frac{\kappa}{\kappa_0} \sim 10^{-4}. \tag{1}$$

The resulting LS equation[7] for the total pressure field $p(\mathbf{r})$ is

$$p^{(\mathrm{inc})}(\mathbf{r}) = p(\mathbf{r}) + \int_{\bar{\Omega}} d^3r' \left\{ k^2 g(\mathbf{r}-\mathbf{r}') \left(1 - \frac{\kappa(\mathbf{r}')}{\kappa_0}\right) p(\mathbf{r}') - [\nabla_{\mathbf{r}'} g(\mathbf{r}-\mathbf{r}')] \cdot \left(1 - \frac{\rho_0}{\rho(\mathbf{r}')}\right) \nabla_{\mathbf{r}'} p(\mathbf{r}') \right\}, \tag{2}$$

where $k = \sqrt{\kappa_0 \rho_0}\omega$ is the wave number in the background medium, g is the Green function of the Helmholtz equation,

$$g(\mathbf{r}) = \frac{e^{ik|\mathbf{r}|}}{4\pi|\mathbf{r}|}, \tag{3}$$

and $p^{(\mathrm{inc})}$ is the incident wave, satisfying the equations in the absence of the scatterer; $\bar{\Omega}$ denotes here the region Ω with its boundary. In our frequency-domain equations, we assume the $\exp(-i\omega t)$ time dependence of the fields. More specific regularity assumptions under which Eq. (2) is valid are given in Ref. 8, which also discusses existence and uniqueness of the solution.

III. DISCRETIZATION OF INTEGRAL EQUATIONS IN ACOUSTICS

Upon Galerkin discretization with a set of (real) scalar basis functions ϕ_α, $\alpha = 1, \ldots, N$, Eq. (2) becomes the matrix equation

$$Ax = b. \tag{4}$$

Here, the vector x consists of the expansion coefficients of the solution

$$p(\mathbf{r}) = \sum_{\alpha=1}^{N} x_\alpha \phi_\alpha(\mathbf{r}). \tag{5}$$

In the following, we refer to the coefficients x_α as the method of moments (MoM) unknowns. Further, b is the projection of the incident wave on the basis functions,

$$b_\alpha = \int_\Omega d^3r \phi_\alpha(\mathbf{r}) p^{(\mathrm{inc})}(\mathbf{r}), \tag{6}$$

and the elements of the complex stiffness matrix[9] are

$$A_{\alpha\beta} = \int d^3r \phi_\alpha(\mathbf{r}) \phi_\beta(\mathbf{r}) \tag{7a}$$

$$+ k^2 \int d^3r_1 d^3r_2 \phi_\alpha(\mathbf{r}_1) g(\mathbf{r}_1 - \mathbf{r}_2) \left(1 - \frac{\kappa(\mathbf{r}_2)}{\kappa_0}\right) \phi_\beta(\mathbf{r}_2) \tag{7b}$$

$$- \int d^3r_1 d^3r_2 [\nabla_{\mathbf{r}_1} \phi_\alpha(\mathbf{r}_1)] g(\mathbf{r}_1 - \mathbf{r}_2) \times \left(1 - \frac{\rho_0}{\rho(\mathbf{r}_2)}\right) [\nabla_{\mathbf{r}_2} \phi_\beta(\mathbf{r}_2)], \tag{7c}$$

$$= \int d^3r \phi_\alpha(\mathbf{r}) \frac{\rho_0}{\rho(\mathbf{r})} \phi_\beta(\mathbf{r}) \tag{7d}$$

$$+ k^2 \int d^3r_1 d^3r_2 \phi_\alpha(\mathbf{r}_1) g(\mathbf{r}_1 - \mathbf{r}_2) \times \left(\frac{\rho_0}{\rho(\mathbf{r}_2)} - \frac{\kappa(\mathbf{r}_2)}{\kappa_0}\right) \phi_\beta(\mathbf{r}_2) \tag{7e}$$

$$- \int d^3r_1 d^3r_2 [\nabla_{\mathbf{r}_1} \phi_\alpha(\mathbf{r}_1)] g(\mathbf{r}_1 - \mathbf{r}_2) \times \left(\nabla_{\mathbf{r}_2} \frac{\rho_0}{\rho(\mathbf{r}_2)}\right) \phi_\beta(\mathbf{r}_2), \tag{7f}$$

$$\equiv A^R_{\alpha\beta} + A^M_{\alpha\beta} + A^D_{\alpha\beta}. \tag{7g}$$

In the following, the terms A^R, A^M, and A^D [given by Eqs. (7d)–(7f)] are referred to as the *material, monopole*, and *dipole* contributions.

Equivalence of the two alternative expressions given in Eq. (7) can be checked by integrating by parts and using the definition of the Green function g. However, the individual terms in these expressions have quite different properties.

(1) The nearly diagonal term (7a) is independent of the material properties, while term (7d) [denoted by $A^R_{\alpha\beta}$ in Eq. (7g)] does depend on the density. In our problems [Eq. (1)], $\rho_0/\rho \sim 10^{-3}$; hence, $A^R_{\alpha\beta}$ is small.
(2) For a large distance R between the supports of the basis functions ϕ_α and ϕ_β, both terms (7b) and (7e) behave as $1/R$; hence, they can be interpreted as due to monopole-

monopole (MM) couplings. However, for the materials of interest [Eq. (1)], term (7e) [denoted by $A^M_{\alpha\beta}$ in Eq. (7g)] is much smaller than (7b).

(3) Depending on whether the scatterer density $\rho(\mathbf{r})$ is constant or variable over the support of ϕ_β, term (7c) behaves at large distances as $1/R^3$ or $1/R^2$, i.e., it can be interpreted as a dipole-dipole (DD) or dipole-monopole (DM) coupling. Term (7f) [denoted by $A^D_{\alpha\beta}$ in Eq. (7g)], on the other hand, is nonzero only for variable $\rho(\mathbf{r})$, and then it represents only a dipole-monopole (DM) coupling.

In other words, the DD and DM couplings of term (7c) are converted into the MM and DM couplings of terms (7d)–(7f). Generally speaking, the individual terms (7a)–(7c) tend to be large. Therefore, in order to ensure sufficient accuracy after cancellations, their numerical evaluation requires a very high precision. On the other hand, these cancellations are already incorporated in terms (7d)–(7f); hence, the latter expressions are numerically clearly preferable.

Matrix elements of Eq. (7a)–(7g) have another important property pertaining to the case of a high density scatterer immersed in a medium of low density. In such a problem, dominant contributions to the dipole term $A^D_{\alpha\beta}$ come from the coupling of all elements α to the "surface" elements β, i.e., to the elements overlapping the boundary $\partial\Omega$ of the scatterer [on which the discontinuity of $\rho(\mathbf{r})$ is large]. In fact, the dipole matrix elements $A^D_{\alpha\beta}$ are the only $\mathcal{O}(1)$ terms remaining in the limit $\rho/\rho_0 \to \infty$, $\kappa/\kappa_0 \to 0$; in other words, the columns of the matrix corresponding to surface elements are much larger than the remaining columns. The latter implies a potential difficulty—ill conditioning of the stiffness matrix. However, as we discuss in a separate paper,[6] the difficulty can be remedied and actually turned into an advantage by separating the surface and "volume" parts of the problem.

We note that, in practice, material parameters are extracted from Computed Axial Tomography (CAT) or Nuclear Magnetic Resonance (NMR) scans and assumed constant on the individual tetrahedra of the mesh. In such cases, $\rho(\mathbf{r})$ will be discontinuous across faces of many interior tetrahedra. However, those discontinuities will be much smaller than the discontinuity on the exterior boundary of the object. With typical parameters (ρ/ρ_0 in the range from 1000 to 2000), we have

$$\left|\mathrm{disc}\frac{\rho_0}{\rho(\mathbf{r})}\right|_{\partial\Omega} \sim 1 - \frac{1}{1000} \simeq 1, \tag{8a}$$

on the exterior boundary, and

$$\left|\mathrm{disc}\frac{\rho_0}{\rho(\mathbf{r})}\right|_{\bar{\Omega}\setminus\partial\Omega} \sim \left|\frac{1}{1000} - \frac{1}{2000}\right| \simeq 5\times 10^{-4}, \tag{8b}$$

inside the object. Hence, $|A^D_{\alpha\beta}(\text{surface})| \gg |A^D_{\alpha\beta}(\text{interior})|$.

In view of the anticipated applications to anatomical models, we assume in the following (in the computational complexity estimates and in the numerical examples) approximately uniform discretizations. We briefly comment, in Sec. VIII, on problems characterized by nonuniform discretizations.

IV. DISCRETIZATION WITH PIECEWISE CONSTANT BASIS FUNCTIONS

One of the simplest choices of the basis functions in Eq. (5) are constant functions ϕ_α (of value, say, 1) supported on tetrahedra t_α. We also assume that the material parameters $\rho(\mathbf{r})$ and $\kappa(\mathbf{r})$ are constant within individual tetrahedra. The matrix component A^R is then diagonal, and its elements (7d) are proportional to the volumes of the tetrahedra. The matrix elements (7e) are given by integrals over the volumes of the tetrahedra, and the matrix elements (7f) are expressed as sums of integrals over the faces of the tetrahedra since gradients of the basis functions are proportional to delta functions supported on the tetrahedron boundaries. Explicit expressions are

$$A^R_{\alpha\beta} = \delta_{\alpha\beta} v_\alpha \frac{\rho_0}{\rho_\alpha}, \tag{9a}$$

$$A^M_{\alpha\beta} = k^2 \int_{t_\alpha} d^3r_1 \int_{t_\beta} d^3r_2 g(\mathbf{r}_1 - \mathbf{r}_2)\left(\frac{\rho_0}{\rho_\beta} - \frac{\kappa_\beta}{\kappa_0}\right), \tag{9b}$$

and

$$A^D_{\alpha\beta} = \int_{\partial t_\alpha} d^2r_1 \int_{\partial t_\beta} d^2r_2 g(\mathbf{r}_1 - \mathbf{r}_2)\hat{\mathbf{n}}_\alpha(\mathbf{r}_1)\cdot\hat{\mathbf{n}}_\beta(\mathbf{r}_2)\Lambda(\mathbf{r}_2)$$
$$\equiv \sum_{f_\alpha \in \partial t_\alpha} \sum_{f_\beta \in \partial t_\beta} \hat{\mathbf{n}}_{f_\alpha}\cdot\hat{\mathbf{n}}_{f_\beta}\Lambda_{f_\beta}\int_{f_\alpha} d^2r_1 \int_{f_\beta} d^2r_2 g(\mathbf{r}_1 - \mathbf{r}_2). \tag{9c}$$

In these expressions, v_α is the volume of the tetrahedron t_α, κ_α, and ρ_α denote values of the compressibility and density parameters on the tetrahedron t_α, $\hat{\mathbf{n}}_\alpha(\mathbf{r})$ is the outer unit normal to the tetrahedron t_α boundary at the point $\mathbf{r}$, f_α is a face of the tetrahedron, and $\hat{\mathbf{n}}_{f_\alpha}$ is the outward-oriented normal to that face. Finally, $\Lambda_{f_\alpha} \equiv \Lambda(\mathbf{r})$ for $\mathbf{r} \in f_\alpha$ is the difference of the values of the function $\rho_0/\rho(\mathbf{r})$ on the positive and negative sides of the face f_α (as defined by the normal $\hat{\mathbf{n}}_{f_\alpha}$), additionally multiplied by the factor $\frac{1}{2}$ for interior faces, i.e., for $f_\alpha \subset \partial\Omega$. The sums over faces in Eq. (9c) arise because gradients of the basis functions are proportional to delta functions on the tetrahedron boundaries; actually, we were also able to convert volume integrals in Eq. (9b) to nonsingular surface integrals. The factor $\frac{1}{2}$ mentioned above is due to defining the piecewise constant basis functions as limits of continuous basis functions constituting a partition of unity on $\bar{\Omega}$ and having values $\frac{1}{2}$ on interior and 1 on boundary faces.

We implemented the constant basis function discretization in our code. We found that despite its simplicity, accurate solutions can be obtained even for very large problems. We present examples in Sec. VII.

V. FFT-BASED MATRIX COMPRESSION METHOD (AIM)

A. General formulation

The AIM approach relies on replacing the basis functions in Eqs. (7a)–(7g) by sets of auxiliary, far-field equivalent point sources located at nodes of a regular Cartesian grid

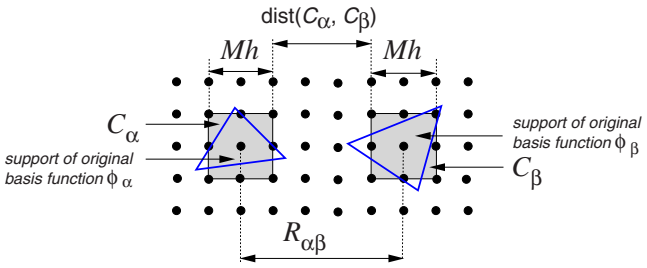

FIG. 1. (Color online) Two original basis functions supports, φ_α and φ_β, and two corresponding expansion cubes C_α and C_β. The expansion order is $M=2$, the distance between the expansion cubes is $\mathrm{dist}(C_\alpha - C_\beta)=3h$, and the distance between the centers of the expansion cubes is $R_{\alpha\beta}=5h$, where h is the Cartesian grid spacing. For the near field range $d \leqslant 3$ (where d is measured in the units of h), the two expansion cubes are in the far field.

(see Fig. 1). The far-field equivalence is understood in the sense that the two source representations, the original and the auxiliary one, generate (to the desired accuracy) the same far field. Depending on the problem, the equivalent source expansion may be applied to scalar, vector, or tensor basis functions, as well as to their derivatives. To keep the notation sufficiently general, we denote in the following by φ any of those basis functions or their components. We also note that depending on the type of the basis functions used, the index α may refer to various geometry elements: tetrahedra, their faces (triangles), or their vertices.

The compression procedure is as follows.

(1) We construct a regular Cartesian grid $\mathcal{G}$ of node spacing h, covering the scatterer $\bar{\Omega}$, and select a multipole expansion order $M=0,1,2,\ldots$ (the quadrupole expansion, $M=2$, is usually the optimal choice).
(2) Then, for each basis function φ_α, we define a cube-shaped set C_α (which we call the "expansion cube") consisting of $(M+1)^3$ Cartesian grid nodes $\mathbf{u} \in \mathcal{G}$ and covering[10] in the optimal way, according to predefined geometrical criteria, the basis function support. For example, we may require that the center $\mathbf{c}_\alpha$ of the cube C_α is located closest to the centroid of the basis function support (the center $\mathbf{c}_\alpha$ would coincide with one of grid nodes for M even and with a grid cell center for M odd).
(3) We approximate the original basis function φ_α by a set of equivalent point sources located at the nodes of the expansion cube C_α,

$$\varphi_\alpha(\mathbf{r}) \simeq \hat{\varphi}_\alpha(\mathbf{r}) = \sum_{\mathbf{u}\in C_\alpha} V_{\alpha\mathbf{u}} \delta^3(\mathbf{r}-\mathbf{u}), \tag{10}$$

where the coefficients V characterize strengths of the auxiliary sources. For low-frequency (subwavelength) problems, in which the grid spacing h is determined by the geometry resolution and can be small compared to the wavelength (say, $h \leq \lambda/10$), we determine the coefficients V so that both functions, $\varphi_\alpha(\mathbf{r})$ and $\hat{\varphi}_\alpha(\mathbf{r})$, have the same multipole moments up to the order M, i.e.,

$$\begin{aligned}
&\int d^3\boldsymbol{\rho}^{\mathbf{m}}[\varphi_\alpha(\mathbf{c}_\alpha+\boldsymbol{\rho}) - \hat{\varphi}_\alpha(\mathbf{c}_\alpha+\boldsymbol{\rho})] \\
&\equiv \int d^3\rho \rho_x^{m_x}\rho_y^{m_y}\rho_z^{m_z}[\varphi_\alpha(\mathbf{c}_\alpha+\boldsymbol{\rho}) - \hat{\varphi}_\alpha(\mathbf{c}_\alpha+\boldsymbol{\rho})] \\
&= 0 \quad \text{for } 0 \leqslant m_x, m_y, m_z \leqslant M.
\end{aligned} \tag{11}$$

Here and below, we use the multi-index notation with $\mathbf{m}=(m_x m_y m_z)$, and the multipole moments are evaluated relative to the center $\mathbf{c}_\alpha$ of the expansion cube. In order to find the set of $(M+1)^3$ coefficients V,

(a) we evaluate the set of $(M+1)^3$ multipole moments up to the order M,

$$\langle \varphi_\alpha \rangle_{\mathbf{m}}(\mathbf{c}_\alpha) = \int d^3\rho \boldsymbol{\rho}^{\mathbf{m}} \varphi_\alpha(\mathbf{c}_\alpha+\boldsymbol{\rho}) \tag{12}$$

for $0 \leqslant m_x, m_y, m_z \leqslant M$,

of the basis functions with respect to the expansion cube center $\mathbf{c}_\alpha$ (see the Appendix).

(b) we solve the set of $(M+1)^3$ equations

$$\sum_{\mathbf{u}\in C_\alpha} (\mathbf{u}-\mathbf{c}_\alpha)^{\mathbf{m}} V_{\alpha\mathbf{u}} = \langle \varphi_\alpha \rangle_{\mathbf{m}}(\mathbf{c}_\alpha) \tag{13}$$

for $0 \leqslant m_x, m_y, m_z \leqslant M$.

Equation (13) is the well-known Vandermonde system, and its closed-form solution is given, e.g., in Ref. 2. For higher frequencies, the grid spacing should be kept at about $h \leqslant \lambda/5$, and the coefficients V are preferably computed by using a least-squares approximation to the emitted far field.[11]

(4) We decompose the matrix A into the near- and far-field components. In the near-field range, we compute the matrix elements according to the original expression given by Eq. (7), while in the far-field range, we utilize the expansion (10) for the basis functions. This procedure yields the representation of the matrix elements,

$$A_{\alpha\beta} \simeq A_{\alpha\beta}^{\text{near}} + A_{\alpha\beta}^{\text{far}}, \tag{14}$$

where

$$A_{\alpha\beta}^{\text{near}} = \begin{cases} A_{\alpha\beta} - A_{\alpha\beta}^{\text{far}} & \text{for } \mathrm{dist}(C_\alpha - C_\beta) \leqslant dh \\ 0 & \text{otherwise,} \end{cases} \tag{15}$$

and

$$A_{\alpha\beta}^{\text{far}} = \sum_{\substack{\mathbf{u}\in C_\alpha, \mathbf{v}\in C_\beta \\ \mathbf{u}\neq\mathbf{v}}} V_{\alpha\mathbf{u}} g(\mathbf{u}-\mathbf{v}) V_{\mathbf{v}\beta}^T. \tag{16}$$

By construction, $A_{\alpha\beta}^{\text{near}}$ of Eq. (15) is sparse; hence, the cost of its computation and storage is *linear* in the number of unknowns.

In Eq. (15), dist $(\cdots)$ denotes the distance between the expansion cubes,

$$\mathrm{dist}(C_\alpha - C_\beta) = \min_{\mathbf{u}\in C_\alpha, \mathbf{v}\in C_\beta} \|\mathbf{u}-\mathbf{v}\|, \tag{17}$$

and the distance $\|\cdot\|$ is defined by

$$\|\mathbf{u}\| = \max\{|u_x|,|u_y|,|u_z|\}. \tag{18}$$

The integer parameter d in Eq. (15) is the *near-field range* in the units of the Cartesian grid spacing, and the parameter $\epsilon > 0$ is the *near-field tolerance*.

The maximum distance between the *centers* of two expansion cubes for which the matrix elements are calculated exactly, or the minimum distance for which the matrix elements are approximated by $A^{\text{far}}_{\alpha\beta}$, is

$$R^{\text{AIM}}_{\text{min}} = (d+M)h. \tag{19}$$

In order to avoid confusion, we refer in the following to $R^{\text{AIM}}_{\text{min}}$ as the "center-to-center" near-field range. This relation follows from the fact that due to definitions (15) and (18), the expansion cube size (Mh) has to be added to dist $(C_\alpha - C_\beta)$ in trying to determine if the two basis function supports are in the near- or in the far-field region (see also Fig. 1).

An important and numerically intensive feature of evaluating of $A^{\text{near}}_{\alpha\beta}$ [Eq. (15)] is that it requires a *subtraction* of the *far-field* matrix element $A^{\text{far}}_{\alpha\beta}$; we comment on this feature in Ref. 12. Due to the fact that the equivalent sources are located at nodes of a regular Cartesian grid, the far-field term $A^{\text{far}}_{\alpha\beta}$ of Eq. (16) is now a product of a *Toeplitz* matrix G of elements $g(\mathbf{u}-\mathbf{v})$, the sparse transformation matrix V, and its transpose V^T. The Toeplitz property allows computation of the matrix-vector product by means of FFTs, i.e., with the computational complexity of $N_{\mathcal{G}} \log N_{\mathcal{G}}$, where $N_{\mathcal{G}}$ is the number of nodes in the Cartesian grid (in practice, proportional to the number of unknowns, or tetrahedra in the geometry discretization). As the result, the solution to Eq. (4) can be obtained iteratively at the cost of $n_{\text{it}} N_{\mathcal{G}} \log N_{\mathcal{G}}$, where n_{it} is the number of iterations.

In the paragraphs above, we briefly described the formulation underlying the AIM compression technique. In Sec. VI, we give the details of the implementation of the AIM compression. We show there how the error due to the matrix compression and the computational cost of the solution depend on the compression parameters h, d, and M (the Cartesian grid spacing, the near-field range, and the multipole expansion order). We also discuss the optimal choice of these parameters, ensuring the desired accuracy and minimizing the computational cost.

B. Application of AIM compression method to integral operators in acoustics

In the case of acoustics with the discretization described in Sec. IV, we apply AIM compression to the monopole and dipole components [Eqs. (9b) and (9c)] of the stiffness matrix. In the monopole term [Eq. (9b)], we use the expansion

$$\phi_\alpha(\mathbf{r}) \simeq \hat{\phi}_\alpha(\mathbf{r}) = \sum_{\mathbf{u}\in C_\alpha} V^{(M)}_{\alpha\mathbf{u}} \delta^3(\mathbf{r}-\mathbf{u}), \tag{20}$$

for the basis functions constant on tetrahedra α. We obtain in this way the far-field approximation,

$$A^M_{\alpha\beta} \simeq k^2 \sum_{\mathbf{u},\mathbf{v}} V^{(M)}_{\alpha\mathbf{u}} g(\mathbf{u}-\mathbf{v}) V^{(M)}_{\beta\mathbf{v}} \left(\frac{\rho_0}{\rho_\beta} - \frac{\kappa_\beta}{\kappa_0}\right), \tag{21}$$

where κ_β and ρ_β are the values of compressibility and density on the tetrahedron β.

Similarly, in the dipole term [Eq. (9c)], we expand the gradient of the basis function and the product of the basis function with the gradient of the ratio of densities,

$$\nabla\phi_\alpha(\mathbf{r}) \simeq \sum_{\mathbf{u}\in C_\alpha} \mathbf{V}^{(D)}_{\alpha\mathbf{u}} \delta^3(\mathbf{r}-\mathbf{u}) \tag{22a}$$

and

$$\left(\nabla\frac{\rho_0}{\rho(\mathbf{r})}\right)\phi_\alpha(\mathbf{r}) \simeq \sum_{\mathbf{u}\in C_\alpha} \mathbf{V}^{(D\Lambda)}_{\alpha\mathbf{u}} \delta^3(\mathbf{r}-\mathbf{u}). \tag{22b}$$

The vector-valued expansion coefficients $\mathbf{V}^{(D)}$ and $\mathbf{V}^{(D\Lambda)}$ are given by

$$\mathbf{V}^{(D)}_{\alpha\mathbf{u}} = \sum_{f_\alpha\in\partial T_\alpha} \hat{\mathbf{n}}_{f_\alpha} V_{f_\alpha\mathbf{u}} \tag{23a}$$

and

$$\mathbf{V}^{(D\Lambda)}_{\alpha\mathbf{u}} = -\sum_{f_\alpha\in\partial T_\alpha} \hat{\mathbf{n}}_{f_\alpha} \Lambda_{f_\alpha} V_{f_\alpha\mathbf{u}}. \tag{23b}$$

Here, $V_{f\mathbf{u}}$ are expansion coefficients[13] for a constant basis function supported on the triangular face f and the sums are taken over all faces of the considered tetrahedra. We note that the expansion coefficients $\mathbf{V}^{(D\Lambda)}$ depend on the discontinuities Λ [Eq. (9c)] of the ratio $\rho_0/\rho(\mathbf{r})$ across the individual faces.

We find in this way the far-field approximation to the dipole component of the stiffness matrix,

$$A^D_{\alpha\beta} \simeq -\sum_{\mathbf{u},\mathbf{v}} \mathbf{V}^{(D)}_{\alpha\mathbf{u}} g(\mathbf{u}-\mathbf{v}) \cdot \mathbf{V}^{(D\Lambda)}_{\beta\mathbf{v}}. \tag{24}$$

Equations (21) and (24) provide a compressed matrix representation in terms of scalar expansion coefficients $V^{(M)}$ and two sets of vector expansion coefficients, $\mathbf{V}^{(D)}$ and $\mathbf{V}^{(D\Lambda)}$ (hence, the total of seven components). We also note that the expansion coefficients $\mathbf{V}^{(D)}_{\alpha\mathbf{u}}$ of Eq. (23a) and (23b) represent the *gradient* $\nabla\phi_\alpha$ of the basis function ϕ_α. Therefore, the zeroth order (monopole) moment of the far-field-equivalent basis function (22a) must vanish exactly; this requires a high numerical precision in evaluating the coefficients $\mathbf{V}^{(D)}$ and the pertinent far-field expansions.

VI. FEATURES AND IMPLEMENTATION OF AIM COMPRESSION

A. Error bounds on far-field matrix elements

In this section, we provide a detailed discussion of the numerical errors resulting from using the AIM matrix compression in representing the integral-equation matrix elements. Errors associated with numerical implementation of the integral-equation solver can be grouped into two types:

(1) errors introduced by discretizing the integral equation itself, in particular, constructing the stiffness matrix, and

(2) errors introduced by compressing the discretized representation of the stiffness matrix.

We note that the AIM algorithm under consideration here is used exclusively in constructing a compressed representation of the far-field part of the stiffness matrix; it does not approximate or modify the near field matrix elements. For this reason, we do not address here the general issue of the errors of above-mentioned first type, which are associated with constructing a discrete representation of an integral equation, but we limit our discussion to estimating the errors representing the differences between the integral-equation kernel matrix elements in the far field region, calculated with and without the compression.

The error estimate for matrix elements of the far-field component of the matrix A can be obtained by comparing the original matrix element,

$$A_{\alpha\beta} = \int d^3r_1 d^3r_2 \varphi_\alpha(\mathbf{r}_1) g(\mathbf{r}_1 - \mathbf{r}_2) \varphi_\beta(\mathbf{r}_2), \tag{25}$$

with the one obtained by replacing the original basis functions, φ_α, by the auxiliary ones, $\hat{\varphi}_\alpha$,

$$A^{\text{far}}_{\alpha\beta} = \int d^3r_1 d^3r_2 \hat{\varphi}_\alpha(\mathbf{r}_1) g(\mathbf{r}_1 - \mathbf{r}_2) \hat{\varphi}_\beta(\mathbf{r}_2). \tag{26}$$

The error in the matrix element is then

$$\delta A_{\alpha\beta} = A_{\alpha\beta} - A^{\text{far}}_{\alpha\beta}. \tag{27}$$

In order to estimate $\delta A_{\alpha\beta}$, we write

$$g(\mathbf{r}_1 - \mathbf{r}_2) \equiv g(\mathbf{c}_\alpha - \mathbf{c}_\beta + \mathbf{r}' - \mathbf{r}'') \equiv g(\mathbf{R}_{\alpha\beta} + \mathbf{r}' - \mathbf{r}''), \tag{28}$$

where $\mathbf{c}_\alpha$ and $\mathbf{c}_\beta$ are the centers of the expansion cubes C_α and C_β associated with the basis functions φ_α and φ_β, and $\mathbf{R}_{\alpha\beta} = \mathbf{c}_\alpha - \mathbf{c}_\beta$ is the distance between the centers of two expansion cubes.

We then expand the integrand of Eq. (27) in the Taylor series in $\mathbf{r}'$ and $\mathbf{r}''$; this expansion yields moments of the basis functions. More precisely, we write the absolute value of the argument of the Green function, $|\mathbf{R}_{\alpha\beta} + \mathbf{r}' - \mathbf{r}''| \equiv |\mathbf{R} + \boldsymbol{\rho}|$ as $R[1 - f(\mathbf{R}, \boldsymbol{\rho})]$, where $f(\mathbf{R}, \rho)$ is a power series in ρ/R, starting with the first power. We then expand the Green function as

$$g(\mathbf{R} + \boldsymbol{\rho}) = g(\mathbf{R}) \frac{e^{-ikRf(\mathbf{R},\boldsymbol{\rho})}}{1 - f(\mathbf{R}, \boldsymbol{\rho})} \equiv g(\mathbf{R}) \sum_{m=0}^{\infty} f^m(\mathbf{R}, \mathbf{r}' - \mathbf{r}'') \sum_{l=0}^{m} \frac{(-ikR)^l}{l!}. \tag{29}$$

Since, by construction, φ_α and $\hat{\varphi}_\alpha$ have identical first M multipole moments [Eq. (13)], the lowest nonvanishing moments of $\hat{\varphi}_\alpha(\mathbf{c}_\alpha + \mathbf{r}') - \varphi_\alpha(\mathbf{c}_\alpha + \mathbf{r}')$ and $\hat{\varphi}_\beta(\mathbf{c}_\beta + \mathbf{r}'') - \varphi_\beta(\mathbf{c}_\beta + \mathbf{r}'')$ [and thus the lowest order contributions to the integral (27)] come from the term $m = M+1$ and are proportional to $(\max\{a, Mh\}/R)^{M+1}$. The reason why $\max\{a, Mh\}$ appears in this expression is that the multipole moments of basis functions are evaluated relative to the expansion cube centers $\mathbf{c}_\alpha$ and $\mathbf{c}_\beta$ and, if the basis function supports a are small relative to the cube size, they may be located at distances up to about Mh from the cube center. Finally, therefore, the relative error in the matrix element is given by

$$\frac{\delta A_{\alpha\beta}}{A_{\alpha\beta}} \sim \left(\frac{\max\{a, Mh\}}{R_{\alpha\beta}} \right)^{M+1} \sum_{l=0}^{M+1} \frac{(-ikR_{\alpha\beta})^l}{l!}. \tag{30}$$

We observe that in low-frequency problems ($kR_{\alpha\beta} \ll 1$), the sum in Eq. (30) is approximately unity, and the error behaves as $(\max\{a, Mh\}/R_{\alpha\beta})^{M+1}$. On the other hand, for high frequencies (or distances $R_{\alpha\beta}$ large compared to the wavelength), the sum is dominated by its last term, and the error becomes proportional to $(k \max\{a, Mh\})^{M+1}$ and independent of the separation between the basis function supports. This is the result given in Ref. 2. Another consequence of the error estimate (30) is that the accuracy no longer improves when the grid spacing h becomes smaller than about a/M, i.e., when the expansion cube is smaller than the basis function support.

While Eq. (30) exhibits the error dependence on the relevant parameters, the coefficient in that estimate depends on the specifics of the problem, mostly through higher order moments of the basis functions. Although some bounds on these moments can be obtained,[2] it is more expedient to resort to numerical data.

In Fig. 2, we plot a typical distribution of relative errors in matrix elements for scalar piecewise constant basis functions, computed for the expansion order $M = 2$ and for several grid spacings h. The results show that a far-field accuracy of 1% or better can be ensured, for the expansion order $M = 2$, by taking

$$R^{\text{AIM}}_{\min} \geq 4h, \quad \text{i.e., } d \geq 2, \tag{31}$$

for grid spacings in the range $a/2 \leq h \leq 2a$, where a is the size of the basis function support (the errors are only weakly dependent on the ratio h/a). Analysis of the results also shows that using expansion orders $M > 2$ does not provide overall advantages, unless accuracy better than 1% is re-

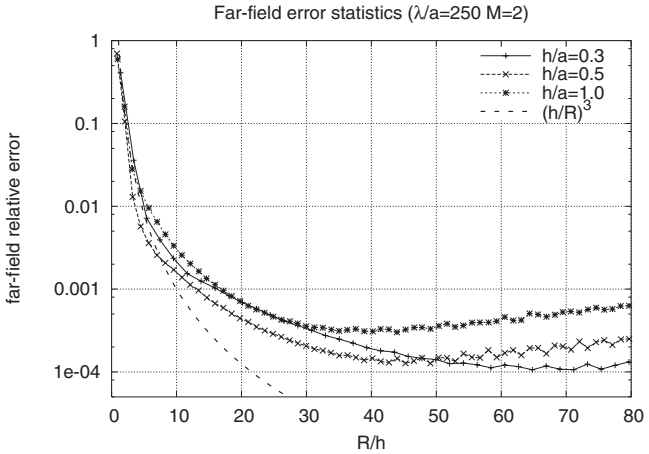

FIG. 2. Relative errors in the matrix elements $A^{\text{far}}_{\alpha\beta}$ for piecewise constant basis functions, computed for the expansion order $M = 2$ and several values of h/a, where h is the Cartesian grid spacing and a is the size of the basis function support. The error is plotted as a function of the distance $R \equiv R_{\alpha\beta}$ between the centers of the expansion cubes, measured in the grid spacing units. The dashed line shows the slope of the error curve, as predicted by Eq. (30) for low frequencies.

quired; in such cases, since the error for $M>2$ falls off more rapidly at larger distances, a relatively small increase of the range may be sufficient. However, one has to realize that an increase in the near-field range causes a rapid increase in the near-field computation cost [terms $\sim(d+M)^3$ in Eqs. (46) and (48)].

B. Fast matrix-vector multiplication in AIM algorithm

In the matrix-vector product,

$$y = Ax \quad \text{or} \quad y_\alpha = \sum_{\beta=1}^{N} A_{\alpha\beta} x_\beta, \tag{32}$$

the near-field contribution is evaluated by utilizing a sparse representation of the near-field matrix. The far-field part of the matrix-vector product is, according to Eq. (16),

$$y_\alpha^{\text{far}} = \sum_{\beta=1}^{N} \sum_{\mathbf{u},\mathbf{v}\in\mathcal{G}} V_{\alpha\mathbf{u}} g(\mathbf{u}-\mathbf{v}) V_{\mathbf{v}\beta}^T x_\beta, \tag{33}$$

where the sums are taken over all Cartesian grid nodes $\mathbf{u}$ and $\mathbf{v}$.

Equivalently, the matrix-vector multiplication (33) can be executed as the sequence of three steps,

$$\text{(A)} \quad \hat{x}_\mathbf{v} = \sum_{\beta=1}^{N} V_{\mathbf{v}\beta}^T x_\beta \quad \text{for all } \mathbf{v} \in \mathcal{G}, \tag{34a}$$

$$\text{(B)} \quad \hat{y}_\mathbf{u} = \sum_{\substack{\mathbf{v}\in\mathcal{G} \\ \mathbf{v}\neq\mathbf{u}}} g(\mathbf{u}-\mathbf{v}) \hat{x}_\mathbf{v} \quad \text{for all } \mathbf{u} \in \mathcal{G}, \tag{34b}$$

$$\text{(C)} \quad y_\alpha^{\text{far}} = \sum_{\mathbf{u}\in\mathcal{G}} V_{\alpha\mathbf{u}} \hat{y}_\mathbf{u} \quad \text{for } \alpha = 1,2,\ldots,N. \tag{34c}$$

For simplicity of notation, we suppressed in Eqs. (33) and (34) the indices numbering the components of the coefficients V and of vectors $\hat{x}$ and $\hat{y}$. According to Eqs. (21) and (24), vectors $\hat{x}$ and $\hat{y}$ (defined on the Cartesian grid) have four such components, corresponding to the pressure and the three components of its gradient.

The convolution over the Cartesian grid nodes in Eq. (34b) is implemented by means of the FFT. We evaluate the Fourier transform,

$$\tilde{y}_\mathbf{Q} = \sum_{\mathbf{u}\in\mathcal{G}} \mathcal{F}_{\mathbf{Q}u} \hat{y}_\mathbf{u}, \tag{35}$$

as a product of the Fourier transforms of the Green function and the input Cartesian vector $\hat{x}_\mathbf{v}$,

$$\text{(B1)} \quad \tilde{y}_\mathbf{Q} = \tilde{g}(\mathbf{Q}) \tilde{x}_\mathbf{Q} \quad \text{for } \mathbf{Q} \in \tilde{\mathcal{G}}, \tag{36a}$$

where

$$\text{(B2)} \quad \tilde{g}(\mathbf{Q}) = \sum_{\mathbf{v}\in\mathcal{G}} \mathcal{F}_{\mathbf{Q}\mathbf{v}} g(\mathbf{v}) \quad \text{for } \mathbf{Q} \in \tilde{\mathcal{G}}, \tag{36b}$$

and

$$\text{(B3)} \quad \tilde{x}_\mathbf{Q} = \sum_{\mathbf{v}\in\mathcal{G}} \mathcal{F}_{\mathbf{Q}\mathbf{v}} \hat{x}_\mathbf{v} \quad \text{for } \mathbf{Q} \in \tilde{\mathcal{G}}. \tag{36c}$$

Here, the matrix $\mathcal{F}$ represents the discrete Fourier transform and $\tilde{\mathcal{G}}$ is the conjugate Cartesian grid.

Subsequently, we take the inverse Fourier transform of the product,

$$\text{(B4)} \quad \hat{y}_\mathbf{u} = \sum_{\mathbf{Q}\in\tilde{\mathcal{G}}} \mathcal{F}_{\mathbf{u}\mathbf{Q}}^{-1} \tilde{y}_\mathbf{Q} \quad \text{for } \mathbf{u} \in \mathcal{G}. \tag{36d}$$

We note that the FFT of the Green function in step (B1) has to be computed and stored only once.

We also stress that evaluation of the convolution (34b) by means of FFTs does not introduce any additional numerical errors and is exact (to the machine precision), due to the fact that the data on the Cartesian grid are padded with zeros to twice the physical grid size, and thus no aliasing errors arise.

C. Estimates of algorithm computational complexity and storage

The computational complexity estimates we present here apply to the serial implementation of the volumetric AIM algorithm. The estimates are only meant as approximate guidelines; the actual performance of the algorithm will depend on the specific geometry and its discretization.

For the purpose of our estimates, we consider a regularly shaped volumetric scatterer of volume V, uniformly discretized with tetrahedra of size (edge length) a, and covered by a rectangular Cartesian $\mathcal{G}$ grid of spacing h. The total number of unknowns is then

$$N \simeq c_V \frac{V}{a^3}, \tag{37}$$

where, e.g., for a rectangular scatterer (and regular tetrahedra) $c_V \simeq 8.5$, and the number of Cartesian grid nodes covering the scatterer is

$$N_\mathcal{G} \simeq \frac{V}{h^3}. \tag{38}$$

In the following, we denote the average number of Cartesian grid nodes per unknown by

$$n_\mathcal{G} = N_\mathcal{G}/N \sim (a/h)^3. \tag{39}$$

The AIM algorithm is specifically designed for solving large problems, for which iterative methods are preferred. The central element of these methods is the matrix-vector multiplication. We start with presenting estimates for the computational complexity of the near- and far-field components of matrix-vector multiplication algorithms.

1. Near-field matrix-vector multiplication cost

According to Eq. (19), the AIM near-field volume of a given basis function is a cube of side length $2(d+M)h$, containing on the average $N/N_\mathcal{G}$ unknowns per grid cell. It follows that the total number of near-field matrix elements is

$$\mathcal{N}[A^{\text{near}}] = 2N[2(d+M)]^3 N/N_{\mathcal{G}} = 16(d+M)^3 \frac{N^2}{N_{\mathcal{G}}}. \quad (40)$$

We do not assume here matrix symmetry, and the additional prefactor 2 arises from the two matrix components, A^M and A^D [Eqs. (21) and (24)], being computed. Consequently, the near-field matrix-vector multiplication requires

$$\text{Nop}[A^{\text{near}}x] = 32(d+M)^3 \frac{N^2}{N_{\mathcal{G}}} \quad (41)$$

complex (multiplications and additions, hence the additional factor of 2) operations.

2. Far-field matrix-vector multiplication cost

Conversion of the set of MoM unknowns to the Cartesian vector in step (A) [Eq. (34a)] involves $(M+1)^3$ grid points in an expansion cube for each unknown and four components of the Cartesian vector $\hat{x}$ [cf. the comment following Eq. (34)]; the same applies to the inverse operation (C) of Eq. (34c). The number of operations is thus

$$\text{Nop}[\text{step (A)}] = \text{Nop}[\text{step (C)}] = 4 \times 2(M+1)^3 N. \quad (42)$$

(The additional factor of 2 comes, as before, from the complex multiplication and addition constituting one operation in the matrix-vector multiplication.)

In the FFT-based implementation of step (B), i.e., steps (B3) and (B4) of ?Eqs. (36a)–(36d), the numbers of operations are

$$\text{Nop}[\text{step (B3)}] = \text{Nop}[\text{step (B4)}] = 4\tfrac{5}{2} 8N_{\mathcal{G}} \log_2(8N_{\mathcal{G}})$$
$$= 80 N_{\mathcal{G}} \log_2(8N_{\mathcal{G}}), \quad (43)$$

where the factor 8 comes from the zero padding of the Cartesian vectors and where we assumed the FFT complexity as for the radix-2 algorithm, i.e., $\frac{5}{2} n \log_2 n$ for a vector of length n, and the prefactor 4 is again due to the four components of the Cartesian vectors.

Step (B2), which has to be carried out only once, belongs to the compressed matrix setup, and we do not count it as a part of matrix-vector multiplication.

Finally, step (B1) of Eq. (36a)—multiplication of Cartesian vectors—requires

$$\text{Nop}[\text{step (B1)}] = 4 \times 8N_{\mathcal{G}} \quad (44)$$

operations, where the factors are due to the four Cartesian vector components and to FFT padding. The total numbers of operations in the far-field computation [steps (A), (B), and (C)] is thus

$$\text{Nop}[A^{\text{far}}x] = 16(M+1)^3 N + 32[1 + 5 \log_2(8N_{\mathcal{G}})]N_{\mathcal{G}}. \quad (45)$$

3. Total matrix-vector multiplication cost

By collecting contributions of Eqs. (41) and (45), we can find the total computational complexity of matrix-vector multiplication in AIM. It is convenient to express it as the number of operations per unknown,

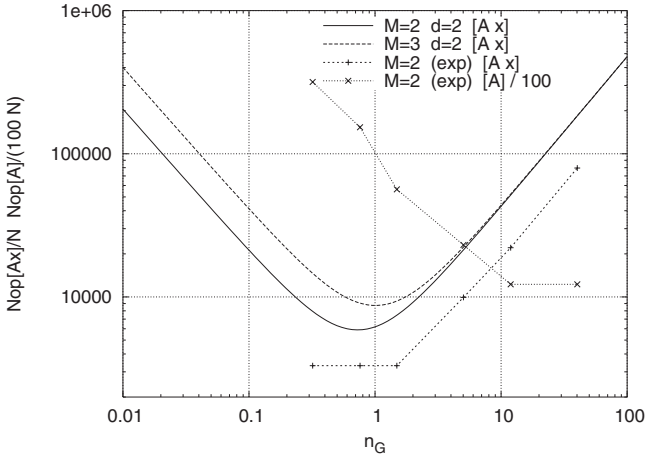

FIG. 3. The matrix-vector multiplication and matrix fill cost per unknown plotted as a function of $n_{\mathcal{G}}=N_{\mathcal{G}}/N$ in the doubly logarithmic scale. The theoretical estimates are given for $N=10^6$. The "experimental" points are taken from actual computations; in the case of the matrix fill cost, they are renormalized by the factor 1/100.

$$\frac{1}{N}\text{Nop}[Ax] = 32(d+M)^3 \frac{1}{n_{\mathcal{G}}} + 16(M+1)^3 + 32[16 + 5 \log_2(Nn_{\mathcal{G}})]n, \quad (46)$$

where $n_{\mathcal{G}}$, the number of Cartesian grid nodes per unknown, was defined in Eq. (39).

For completeness, we note that in our estimates, we neglected the (insignificant) contribution of the nearly diagonal "material" matrix A^R of Eq. (7d) and (9a).

4. Computational complexity in matrix fill

The computational cost of stiffness matrix evaluation also contains terms proportional to $n_{\mathcal{G}}^{-1}$, $n_{\mathcal{G}}^0$, and $n_{\mathcal{G}}^1$. The first term is due to the near-field contribution and the other two to the far-field contribution. However, coefficients of these terms strongly depend on the details of the algorithm implementation (such as, e.g., numerical quadratures). For this reason, we simply plot (in Fig. 3) the numbers of operations (per unknown),

$$\frac{1}{N}\text{Nop}[A], \quad (47)$$

obtained from a set numerical experiments described in Sec. VII C. In this figure, we renormalized the numbers of operations by the factor 1/100 in order to allow comparison of the curves. (In fact, the renormalized values give a direct comparison of the matrix construction cost and the iterative solution with 100 iterations.) We note that the curve representing the matrix fill cost is significantly shifted to the right relative to the other curves, which indicates that it is dominated by the near-field contribution $\sim 1/n_{\mathcal{G}}$.

5. Storage

Storage per unknown (measured in complex numbers) required for the AIM-compressed matrix is obtained in close analogy to the complexity estimate (46):

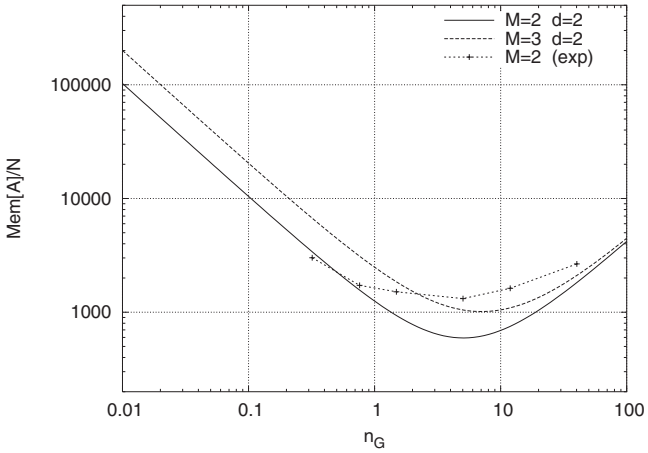

FIG. 4. The matrix storage per unknown in the AIM algorithm plotted as a function of $n_{\mathcal{G}}=N_{\mathcal{G}}/N$ in the doubly logarithmic scale. The "experimental" points are taken from actual computations.

$$\frac{1}{N}\mathrm{Mem}[A] = 16(d+M)^3\frac{1}{n_{\mathcal{G}}} + 7(M+1)^3 + 40n_{\mathcal{G}}. \qquad (48)$$

The first term is due to the near-field matrix, the second to the expansion coefficients V (we recall that seven components of the these coefficients are stored), and the third is responsible for the storage of the Cartesian representation of the Green function and the solution vector (pressure and the three components of its gradient). The factors in the coefficient in that term $(40=5\times 8)$ are due to the scalar Green function and the four vector components of the solution (factor 5) and the FFT padding (factor 8). In these estimates, as in the complexity analysis, we neglected the contribution of the nearly diagonal material matrix.

6. Optimization of compression parameters

In Figs. 3 and 4, we plot estimates of computational costs and memory requirements (per unknown) [Eqs. (46)–(48)] in a rather wide range of the parameter $n_{\mathcal{G}}=N_{\mathcal{G}}/N$. Since the theoretical predictions of Eqs. (46) and (48) are based on specific assumptions about the geometry and its discretization, they are not expected to agree precisely with the "experimental" points derived from a set of actual computations using our implementation of the algorithm. However, the trends in the theoretical estimates and the actual data are similar.

(1) The matrix fill cost and matrix storage favor larger values of $n_{\mathcal{G}}$, hence smaller Cartesian grid spacing.
(2) Minimization of the matrix-vector multiplication cost favors smaller $n_{\mathcal{G}}$ values (and thus larger grid spacing).

Although the algorithm performance will, in general, depend on the geometry and its discretization, the above results suggest that the overall optimal value of the parameter $n_{\mathcal{G}}$ should be chosen in the range from about 1 to 10, and the lowest computational costs are achieved for the multipole expansion order $M=2$ (see the error analysis of Sec. VI A). Thus, the optimal compression parameters (for which the far-field error does not exceed 1%) are approximately

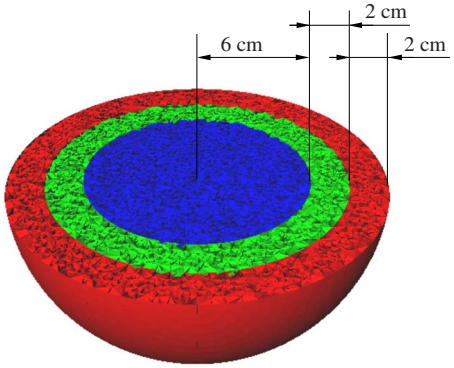

FIG. 5. (Color online) A tetrahedral mesh with about 630 000 tetrahedra used in the computations for the layered sphere.

$$h \simeq \tfrac{1}{2}a, \quad M=2, \quad d=2. \qquad (49)$$

The value $h\simeq a/2$ of the grid spacing corresponds, roughly, to $n_{\mathcal{G}}\simeq 1$ since, for a regular discretization, $N\simeq 8.5V/a^3$, if a is the edge length of the tetrahedron. The value $d=2$ corresponds to the center-to-center near-field range $R_{\min}^{\mathrm{AIM}}$ [Eq. (19)] of just four grid spacings.

VII. NUMERICAL RESULTS

We present below several numerical results illustrating the applicability, accuracy, and performance of our formulation. We note that in variable density problems involving large parameter contrasts (biological tissues in air), we used a modified integral-equation formulation equivalent to the one described here, but yielding a numerically better behaved solution. This approach results in a two-stage solution procedure, in which we first solve the surface problem with a hard object surface, and then a volumetric problem for the wave propagation inside the object. The details of this solution technique will be described in a separate publication.

In all the numerical examples, we used the minimum-residual iterative solution method of Ref. 14, which guarantees a monotonically decreasing residual norm and, in our experience, is more reliable than alternative methods. Since the numbers of iterations was relatively small (below 50 for the relative residual norm of 10^{-4}), we did not use any restarting procedures.

A. Constant density

Our constant-density problem is a three-layer sphere with an outer radius of 10 cm. The inner spherical layers have radii of 8 and 6 cm (Fig. 5). The density of the sphere is the same as the surrounding medium, and the refraction indices n of the layers, starting with the outermost one, are 0.20, 0.05, and 0.20. The sphere is excited by a plane wave of wavelength $\lambda=20$ cm.

We have generated for this problem a tetrahedral mesh with the total number of tetrahedra (unknowns) of about 630 000, corresponding to the average tetrahedron edge length of about 4 mm. Since the frequency is relatively low and the solution (pressure distribution) in the object is smooth, a coarser discretization would have been sufficient. However, in applications to anatomically realistic biological

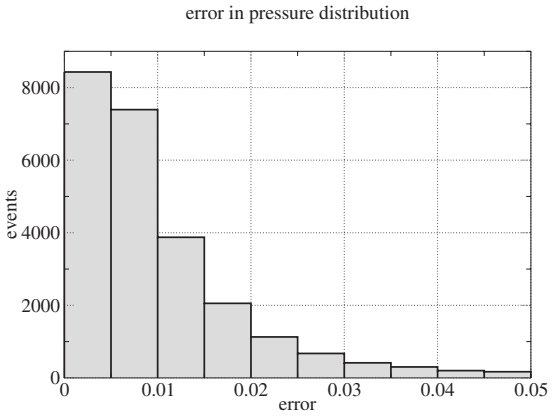

FIG. 6. Histogram of the error in the pressure distribution (relative to the maximum pressure) on a plane intersecting the sphere.

models, discretization density would be driven not by the wavelength but rather by the geometrical details of the model and inhomogeneity of the material parameters; for example, typical NMR scan data would provide resolution of about 2 mm or less. Therefore, we wanted to show that our numerical solution procedure is capable of handling resolutions of this order.

Figure 6 displays the histogram of the relative error in the pressure based on about 25 000 pressure values computed on the plane parallel to the incident wave vector and passing through the center of the sphere. The error is defined as $|p(\mathbf{r})-p_{\text{exact}}(\mathbf{r})|/|p_{\text{exact}}|_{\max}$, where p_{exact} is the analytic solution result. The histogram, generated with 0.5% bins, shows that the median error is below 1%.

B. Variable density

Any problem involving scattering on acoustic objects in air must necessarily involve large ratios of densities. In particular, ratios of density of a biological tissue (or water) to that of air are above 1000, while the refraction indices remain moderate.

1. Computations for a layered sphere with a channel

As the first example, we present results for the pressure distribution in a layered sphere with a cylindrical channel—a very simple model of a human head with an ear canal. The outer shell parameters were chosen to represent the bone of the relative density $\rho/\rho_0=1780$ and relative compressibility $\kappa/\kappa_0=8.6\times10^{-5}$, corresponding to $n\simeq0.39$. In the interior of the sphere, we take the parameters of water, $\rho/\rho_0=833$, $\kappa/\kappa_0=6.3\times10^{-5}$, and $n\simeq0.23$, which also reproduce approximately propagation of pressure waves in the brain tissue. The outer radius of the sphere is 10 cm and the inner radius is 9 cm. We constructed a tetrahedral mesh with the tetrahedron sizes of about 4 mm; hence, the thickness of the shell is about three times the tetrahedron size. The object is discretized (Fig. 7) with about $N=763\,000$ tetrahedra and excited by a plane wave of wavelength $\lambda=60$ cm (i.e., of frequency $f\simeq573$ Hz).

In this problem, a fine discretization is justified by the presence of sharp edges and corners in the geometry. Although the spatial resolution could have been coarser in the

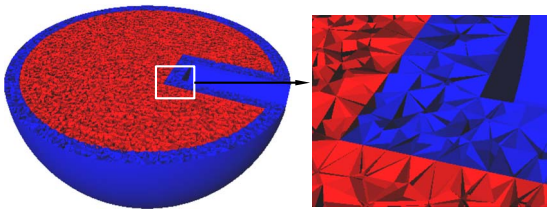

FIG. 7. (Color online) Discretization of the layered sphere with a channel, with $N=763\,000$ tetrahedra.

object interior, we have chosen a uniformly dense discretization for two reasons: (1) Large differences in the sizes of tetrahedra tend to impair the problem conditioning and may cause deterioration of the iterative solution convergence. (2) The computational cost of the solution is determined mostly by the density of the Cartesian grid used in the compression, which has to be adjusted to the finest discretization in the problem. Therefore, a solution with a locally coarsened discretization would not be much cheaper than a solution with a uniformly dense discretization, and it might encounter convergence problems. We further discuss nonuniform discretizations in Sec. VIII.

Figure 8 shows distribution of the absolute value of the pressure $|p(\mathbf{r})|$ on a plane passing through the sphere center. The above solution was obtained with the solver partly parallelized for shared-memory platforms and run on an SGI Origin 3900 system. The total computation time on eight processors was about 100 min and the maximum required memory was about 5 Gbytes.

2. Computations for a head model

As an example of a more realistic geometry, we considered a human head model discretized with about $N=1\,090\,000$ tetrahedra (Fig. 9).

We took the same material parameters and the same incident wave frequency as in the previous sphere problem (i.e., $\rho/\rho_0=10^3$, $\kappa/\kappa_0=10^{-4}$, $n\simeq0.316$, $\lambda=60$ cm, and $f\simeq573$ Hz). At this frequency, the average tetrahedron size is about $\lambda/200$.

Figure 10 shows the distribution of the absolute value of the pressure $|p(\mathbf{r})|$ in the axial plane for the indicated direction of the incident wave. As before, the solution was ob-

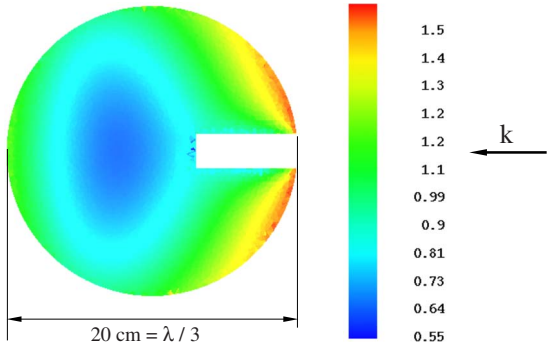

FIG. 8. (Color online) Distribution of the absolute value of the pressure $|p(\mathbf{r})|$ on a plane parallel to the channel axis and passing through the object center, computed with the discretization of Fig. 7.

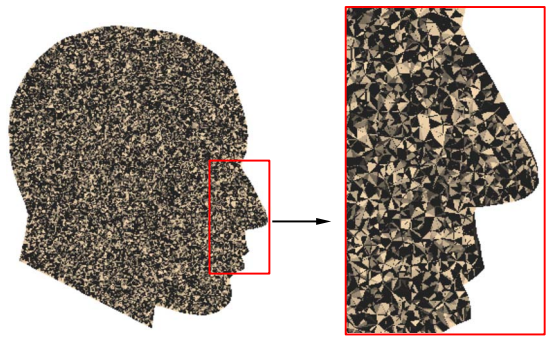

FIG. 9. (Color online) The human head model discretized with about $N = 1\,090\,000$ tetrahedra shown in the sagittal plane cut.

tained by means of the two-stage scheme. Convergence of the solutions was similar to that in the sphere problem.

C. Scaling of the fast solver performance

To establish the scaling performance of our algorithm and its implementation, we carried out computations for a set of problems involving spheres of various sizes, discretized with unstructured tetrahedral meshes. Computation times and memory, for our code run on a single AMD 64 bit processor, are shown in Fig. 11 and in Table I up to the required storage of about 4 Gbytes. For larger problems, solution on single-processor systems becomes impractical, and we utilize a shared-memory (MP) version of the code, as mentioned in Sec. VII.

In order to compare the results of Table I with the estimates of Secs. VI C and VI C 6, we converted the matrix-vector multiplication times from Table I to numbers of operations per unknown and plotted them as points in Fig. 11. Similarly, we converted the storage sizes taken from Table I to the number of stored complex numbers per unknown. Some of these numbers are plotted as "experimental points" in Fig. 4.

We note here that we should not expect a precise agreement between the "theoretical" curves and "experimental" points in Figs. 3 and 4. While the predictions for the numbers of operations and storage were based on idealized assumptions about the geometry (a perfectly uniform discretization and the object completely filling the volume of the Cartesian grid—Sec. VI C), the geometries used in our computations occupied a smaller fraction of the Cartesian grid volume and

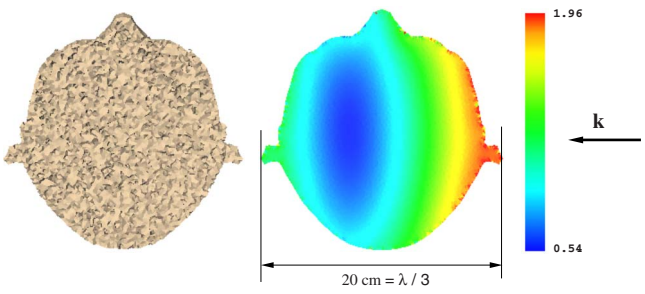

FIG. 10. (Color online) Distribution of the absolute value of the pressure $|p(\mathbf{r})|$ in the axial plane, for the head model of Fig. 9. The computation was done for $N = 1\,090\,000$ unknowns with the two-stage solution scheme. A section of the tetrahedral mesh is shown to indicate the spatial resolution.

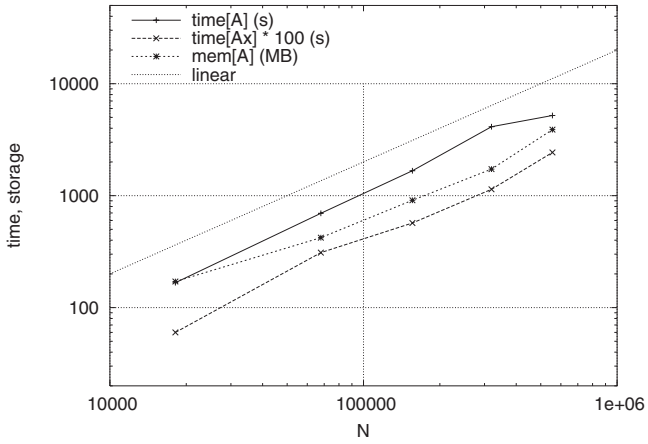

FIG. 11. Scaling of the AIM algorithm performance in the simulation of acoustic wave propagation through spheres of various sizes. The matrix-vector multiplication time is multiplied by the factor of 100. The dotted line indicates linear scaling.

their discretizations were somewhat less uniform. In the following, we discuss features of our approach for highly nonuniform discretizations.

VIII. EFFECTS OF NONUNIFORM DISCRETIZATION

In our computational complexity estimates and in the examples, we were assuming approximately uniform geometry discretizations, which would be the case in anatomical models derived from CAT or NMR scans. We now briefly comment on how computational cost estimates and the optimal compression parameters would change in the case of nonuniform discretization.

We consider a problem in which the sizes a_α of basis function supports vary in a sizable range, but continuously in space, such as in the case of graded meshes. We also assume a low-frequency regime, i.e.,

$$\frac{a}{M} < h < \frac{\lambda}{6} \tag{50}$$

(in view of the error estimate (30), there is no point in reducing the Cartesian grid spacing h below a/M). Under such conditions, the required near-field range is still a fixed multiple of the grid spacing h, as in Eq. (31). Therefore, the matrix-vector multiplication computational cost, as a function of h, is then given approximately by

TABLE I. Scaling of the AIM algorithm performance.

N	grid size	$T[A]$ (s)	$T[Ax]$ (s)	Mem$[A]$ (MB)
18 115	45^3	167	0.6	171
67 889	64^3	695	3.1	421
155 885	90^3	1670	5.7	910
319 665	108^3	4128	11.4	1726
555 933	180^3	5202	24.3	3890

$$\mathrm{Nop}(h) = C_{\mathrm{near}} \sum_{\alpha=1}^{N} \left(\frac{h}{a_\alpha}\right)^3 + C_{\mathrm{far}} \left(\frac{L}{h}\right)^3 \equiv C_{\mathrm{near}} \frac{h^3}{\langle a \rangle^3} + C_{\mathrm{far}} \frac{L^3}{h^3}, \tag{51}$$

where L is the linear object size. The first term in Eq. (51) is due to the near field and, for each basis function α, it is proportional to the number of other basis functions in the near-field range; the second term is the far-field computation cost, proportional to the total number of Cartesian grid points. The coefficients C_{near} and C_{far} depend on the geometry and its discretization but are independent of h.

The minimal computational cost is attained at

$$h_{\min} = \left(\frac{C_{\mathrm{far}} L^3 \langle a \rangle^3}{C_{\mathrm{near}}}\right)^{1/6} \tag{52}$$

and is given by

$$\mathrm{Nop}(h_{\min}) = 2\left(C_{\mathrm{near}} C_{\mathrm{far}} \frac{L^3}{\langle a \rangle^3}\right)^{1/2} \equiv (C_{\mathrm{near}} C_{\mathrm{far}} L^3)^{1/2} \left(\sum_{\alpha=1}^{N} \frac{1}{a_\alpha^3}\right)^{1/2}. \tag{53}$$

The important feature of Eq. (53) is that the sum (the last factor) is dominated by the basis functions of the smallest supports. Therefore, increasing support sizes for a small fraction of moderate size basis functions has a relatively small effect on the computational cost.

IX. SUMMARY

We described the formulation, implementation, and performance of the FFT-based matrix compression and fast solution scheme (AIM) for volumetric acoustics integral equations in inhomogeneous media. The considered method, whose complexity scales as $\mathcal{O}(N \log N)$ with the number of unknowns N, provides a very efficient approach (in terms of memory and execution time) to a variety of large-scale numerical simulations of acoustic wave propagation in inhomogeneous media, including materials with large contrasts of density and compressibility. We have demonstrated the method effectiveness on some representative numerical simulations of acoustic field distributions inside a human head. The numerical simulations we considered can be carried out on modern computers in typical times ranging from several minutes to about 2–3 h. We intend to extend our approach to an analogous FFT-based matrix compression method in the context of the complete elastodynamic wave equation, including both pressure and shear waves.

ACKNOWLEDGMENTS

We wish to acknowledge the support of Air Force Office for Scientific Research under the Contract No. FA9550-06-C-0034.

APPENDIX: MULTIPOLE MOMENTS OF PIECEWISE CONSTANT BASIS FUNCTIONS SUPPORTED ON TETRAHEDRA

The multipole moments, a scalar basis function ϕ_α, relative to a point $\mathbf{c}$ are [cf. Eq. (22a) and (22b)]

$$\langle \phi_\alpha \rangle_{\mathbf{m}}(\mathbf{c}) \equiv \langle \phi_\alpha \rangle_{m_x,m_y,m_z}(\mathbf{c}) = \int d^3 r (\mathbf{r}-\mathbf{c})^{\mathbf{m}} \phi_\alpha(\mathbf{r}) \equiv \int dx dy dz (x-c_x)^{m_x} (y-c_y)^{m_y} (z-c_z)^{m_z} \phi_\alpha(\mathbf{r}), \tag{A1}$$

where we use the multi-index notation as in Sec. V A.

For a piecewise constant basis function supported on tetrahedron, the integral of Eq. (A1) is most conveniently evaluated in terms of barycentric coordinates defined as

$$\mathbf{r} = \mathbf{v}_4 + \xi_1 \mathbf{u}_1 + \xi_2 \mathbf{u}_2 + \xi_3 \mathbf{u}_3, \quad \xi_j \geqslant 0, \quad \xi_1 + \xi_2 + \xi_3 \leqslant 1, \tag{A2}$$

where $\mathbf{v}_i$ are the tetrahedron vertices and $\mathbf{u}_j \equiv \mathbf{v}_j - \mathbf{v}_4$, for $j = 1,2,3$. The Jacobian of the transformation is $|\partial \mathbf{r}/\partial \boldsymbol{\xi}| = 6V$, where V is the volume of the tetrahedron. We have then

$$\langle \phi_\alpha \rangle_{\mathbf{m}}(\mathbf{v}_4) = 6V \int_{T_0} d^3\xi (\xi_1 u_{1x} + \xi_2 u_{2x} + \xi_3 u_{3x})^{m_x} (\xi_1 u_{1y} + \xi_2 u_{2y} + \xi_3 u_{3y})^{m_y} (\xi_1 u_{1z} + \xi_2 u_{2z} + \xi_3 u_{3z})^{m_z}, \tag{A3}$$

where T_0 is the unit tetrahedron defined by the inequalities in Eq. (A2).

By using the basic integral

$$\int_{T_0} d^3\xi \xi_1^{p_1} \xi_2^{p_2} \xi_3^{p_3} = \frac{p_1! p_2! p_3!}{(p_1+p_2+p_3+3)!}, \tag{A4}$$

we find

$$\langle \phi_\alpha \rangle_{\mathbf{m}}(\mathbf{v}_4) = 6V \sum_{\substack{p_{jx},p_{jy},p_{jz} \geqslant 0 \\ p_{1x}+p_{2x}+p_{3x}=m_x \\ p_{1y}+p_{2y}+p_{3y}=m_y \\ p_{1z}+p_{2z}+p_{3z}=m_z}} \frac{p_1! p_2! p_3!}{(m_x+m_y+m_z+3)!} \times \frac{m_x!}{p_{1x}! p_{2x}! p_{3x}!} \frac{m_y!}{p_{1y}! p_{2y}! p_{3y}!} \frac{m_z!}{p_{1z}! p_{2z}! p_{3z}!} \times u_{1x}^{p_{1x}} u_{2x}^{p_{2x}} u_{3x}^{p_{3x}} u_{1y}^{p_{1y}} u_{2y}^{p_{2y}} u_{3y}^{p_{3y}} u_{1z}^{p_{1z}} u_{2z}^{p_{2z}} u_{3z}^{p_{3z}}, \tag{A5}$$

with $p_j \equiv p_{jx}+p_{jy}+p_{jz}$ (we note that $p_1+p_2+p_3 = m_x+m_y+m_z$).

We note that in order to evaluate the multipole moments relative to another point $\mathbf{a}$ (where $\mathbf{a}$ can be, e.g., the center of an expansion cube), we can use the translation formula

$$\langle \phi_\alpha \rangle_{\mathbf{m}}(\mathbf{a}) = \sum_{p_x=0}^{m_x} \sum_{p_y=0}^{m_y} \sum_{p_z=0}^{m_z} \binom{m_x}{p_x} \binom{m_y}{p_y} \binom{m_z}{p_z} \times (c_x-a_x)^{m_x-p_x} (c_y-a_y)^{m_y-p_y} (c_z-a_z)^{m_z-p_z} \langle \phi_\alpha \rangle_{\mathbf{p}}(\mathbf{c}). \tag{A6}$$

[1]E. Bleszynski, M. Bleszynski, and T. Jaroszewicz, "A fast integral equation solver for electromagnetic scattering problems," Proceedings of the 1994 IEEE AP-S International Symposium, Seattle, WA, 20–24 June 1994, pp. 416–419.
[2]E. Bleszynski, M. Bleszynski, and T. Jaroszewicz, "AIM: Adaptive integral method for solving large-scale electromagnetic scattering and radiation problems," Radio Sci. **31**, 1225–1251 (1996).
[3]R. Coifman, V. Rokhlin, and S. Wandzura, "The fast multipole method for the wave equation: A pedestrian prescription," IEEE Antennas Propag. Mag. **35**, 7–12 (1993).
[4]J. R. Phillips and J. K. White, "Efficient capacitance computation of 3d structures using generalized pre-corrected FFT methods," Proceedings of the Third Topical Meeting on Electric Performance of Electronic Packaging, Monterey, CA, 2–4 November, 1994, pp. 253–256.
[5]C. H. Chan and L. Tsang, "A sparse-matrix canonical grid method for scattering by many scatterers," Microwave Opt. Technol. Lett. **8**, 114–118 (1995).
[6]E. Bleszynski, M. Bleszynski, and T. Jaroszewicz, "A fast integral equation algorithm for large scale simulation of acoustics field propagation in biological tissues," Proceedings of the 19th International Congress on Acoustics, Madrid, Spain, 2007, pp. 156.
[7]P. M. Morse and K. U. Ingard, *Theoretical Acoustics* (McGraw-Hill, New York, 1968).
[8]P. A. Martin, "Acoustic scattering by inhomogeneous obstacles," SIAM J. Appl. Math. **64**, 297–308 (2003).
[9]It would be more correct to refer to A as the sum of the mass and the stiffness matrices; we call it a stiffness matrix for shortness.
[10]We have to require here that Mh is larger than the diameter of the basis function support.
[11]E. Bleszynski, M. Bleszynski, and T. Jaroszewicz, "Least-squares based far-field expansion in the adaptive integral method (AIM)," Proceedings of the 13th Annual Review of Progress in Applied Computational Electromagnetics, Monterey, CA, 17–21 March 1997, pp. 944–950.
[12]It would be preferable to construct the far-field component of the matrix, $A^{\text{far}}_{\alpha\beta}$, such that it would automatically vanish for all pairs of basis functions φ_α and φ_β in the near-field range [i.e., satisfying the condition $\text{dist}(C_\alpha - C_\beta) \leqslant dh$]. If this were possible, subtraction of the far-field term in Eq. (15) could be avoided, and the cost of the near-field matrix component would be significantly reduced. However, the only way of modifying Eq. (16) is to modify the *translationally invariant* Green function g; this procedure is implicit in Eq. (16), where the condition $\mathbf{u} \neq \mathbf{v}$ is equivalent to setting $g(\mathbf{0})=0$. One could try to enforce vanishing of $A^{\text{far}}_{\alpha\beta}$ in the near-field range by setting $g(\mathbf{u})=0$ for $\mathbf{u} \in \mathcal{Z}$, where $\mathcal{Z}$ is some set of nodes (e.g., defined by $\|\mathbf{u}\| < D$ for some range D). With this modification, we would have $A^{\text{far}}_{\alpha\beta}=0$ if $\mathbf{u}-\mathbf{v} \in \mathcal{Z}$ for *all* $\mathbf{u} \in C_\alpha$ and *all* $\mathbf{v} \in C_\beta$. At the other extreme, if $\mathbf{u}-\mathbf{v} \in \mathcal{Z}$ for all $\mathbf{u} \in C_\alpha$ and all $\mathbf{v} \in C_\beta$, the matrix element $A^{\text{far}}_{\alpha\beta}$ would be computed with the original Green function g. However (except for very special geometries and for a trivial case of the monopole expansion, $M=0$, in which the sets C_α and C_β consist of single points), there will always exist basis functions for which $\mathbf{u}-\mathbf{v} \in \mathcal{Z}$ for some, but not all nodes $\mathbf{u} \in C_\alpha$ and $\mathbf{v} \in C_\beta$ and in such cases the matrix element $A^{\text{far}}_{\alpha\beta}$ will be simply evaluated incorrectly.
[13]These coefficients can be obtained as in the Appendix, but in two rather than three dimensions.
[14]Y. Saad and M. H. Schultz, "GMRES: A generalized minimal residual algorithm for solving nonsymmetric linear systems," SIAM (Soc. Ind. Appl. Math.) J. Sci. Stat. Comput. **7**, 856–869 (1986).

Psychophysical assessment of the level-dependent representation of high-frequency spectral notches in the peripheral auditory system

Ana Alves-Pinto[a] and Enrique A. Lopez-Poveda
Unidad de Audición Computacional y Psicoacústica, Instituto de Neurociencias de Castilla y León, Universidad de Salamanca, Avenida Alfonso X "El Sabio" s/n, 37007 Salamanca, Spain

(Received 4 June 2007; revised 14 April 2008; accepted 14 April 2008)

To discriminate between broadband noises with and without a high-frequency spectral notch is more difficult at 70–80 dB sound pressure level than at lower or higher levels [Alves-Pinto, A. and Lopez-Poveda, E. A. (2005). "Detection of high-frequency spectral notches as a function of level," J. Acoust. Soc. Am. **118**, 2458–2469]. One possible explanation is that the notch is less clearly represented internally at 70–80 dB SPL than at any other level. To test this hypothesis, forward-masking patterns were measured for flat-spectrum and notched noise maskers for masker levels of 50, 70, 80, and 90 dB SPL. Masking patterns were measured in two conditions: (1) fixing the masker-probe time interval at 2 ms and (2) varying the interval to achieve similar masked thresholds for different masker levels. The depth of the spectral notch remained approximately constant in the fixed-interval masking patterns and gradually decreased with increasing masker level in the variable-interval masking patterns. This difference probably reflects the effects of peripheral compression. These results are inconsistent with the nonmonotonic level-dependent performance in spectral discrimination. Assuming that a forward-masking pattern is a reasonable psychoacoustical correlate of the auditory-nerve rate-profile representation of the stimulus spectrum, these results undermine the common view that high-frequency spectral notches must be encoded in the rate-profile of auditory-nerve fibers. © *2008 Acoustical Society of America.*
[DOI: 10.1121/1.2920957]

PACS number(s): 43.66.Ba, 43.66.Dc, 43.66.Fe [RLF] Pages: 409–421

I. INTRODUCTION

The interference of sound waves within the pinna generates notches in the sound high-frequency spectrum (>6 kHz) (Shaw and Teranishi, 1968; Shaw, 1974; Lopez-Poveda and Meddis, 1996) that provide important information on the location of the sound source (reviewed by Carlile *et al.*, 2005). The usefulness of these notches as sound localization cues must depend on the quality of their representation in the peripheral auditory system, and in particular, at the auditory nerve (AN). The common notion (reviewed by Lopez-Poveda, 2005) is that spectral features beyond the cutoff frequency of phase locking (~4 kHz) (Palmer and Russell, 1986) must be represented in the AN by means of a rate-place code (Rice *et al.*, 1995; Lopez-Poveda, 1996). The quality of this representation is believed to gradually deteriorate with increasing sound level due to the broadening of the frequency response of AN fibers (Rose *et al.*, 1971) and to the saturation of their discharge rate (Liberman, 1978). The deterioration of this internal representation should impair the perception of these notches at high sound levels. However, discriminating between broadband noises with and without high-frequency spectral notches is, for most listeners, more difficult at around 70–80 dB sound pressure level (SPL) than at lower or higher levels (Alves-Pinto and Lopez-Poveda, 2005). This paradoxical result suggests either that the internal rate-place representations vary differently with level for human and lower mammals or that the quality of the rate-place representation of the spectral notch is not the only factor that determines performance on the spectral discrimination task. The present report describes a psychophysical study aimed at the following: (1) estimating the quality of the internal representation of a high-frequency spectral notch at increasing sound levels and (2) testing to what extent the quality of this representation is consistent with the noise-discrimination results described above.

The quality of the internal representation of the spectral notch was behaviorally estimated by comparing the masking patterns of forward noise maskers such as those used by Alves-Pinto and Lopez-Poveda (2005) in their spectral discrimination task. A masking pattern (or masked audiogram) is a graphical representation of the detection thresholds of masked probe tones of different frequencies as a function of probe frequency. Psychophysical forward masking is thought to reflect (to a large extent) the incomplete recovery of AN fibers from previous stimulation and/or the persistence of neural (post-AN) activity (Oxenham, 2001; Meddis and O'Mard, 2005). Whatever the case is, the detection of a low-level tonal probe is likely to depend on the discharge rate evoked by the probe in AN fibers with characteristic frequencies (CFs) approximately equal to the probe frequency. When preceded by a masker sound, this rate almost certainly

[a]Author to whom correspondence should be addressed. Present address: MRC Institute of Hearing Research, University Park, Nottingham NG7 2RD, United Kingdom. Electronic mail: ana@ihr.mrc.ac.uk.

depends on the discharge rate evoked on those same fibers by the masker (Harris and Dallos, 1979; Meddis and O'Mard, 2005). Furthermore, masker-probe interactions (e.g., suppression, distortion, or beating effects), which could potentially affect the detection of the probe, are minimized by presenting the probe after the masker. Therefore, the masking pattern of a forward masker possibly provides the best psychoacoustical correlate of the internal representation of the spectrum of the masker. Hence, it is reasonable to hypothesize that if discriminating between a flat-spectrum and a notched noise were more difficult at midlevels because the internal representations of the two spectra were more alike at those levels, then the masking patterns of the same stimuli should also be less distinguishable at those same levels.

Two sets of experiments were carried out on the same group of listeners to test the above hypothesis. The first set (experiment I) measured the threshold notch depth for discriminating between a flat-spectrum and a notched noise at increasing stimulus levels. The second set (experiments II and III) consisted of measuring the masking patterns of the two broadband noises used in the first set of experiments at different noise levels. The correlation between the results of the two sets of experiments provided the basis for testing the above hypothesis. It will be shown that the gradual deterioration in spectral discrimination with increasing level up to 70–80 dB SPL (Alves-Pinto and Lopez-Poveda, 2005) is consistent with a deterioration of the quality of the spectral-notch representation in the masking patterns. By contrast, the improvement in spectral discrimination above 80 dB SPL is *not* accompanied by an improvement in the quality of the representation of the spectral notch in the masking pattern.

The implications of these results in terms of the physiological mechanisms underlying the neural coding of high-frequency spectral notches will be discussed. It will be argued that the discrimination of high-frequency spectral features is unlikely to rely solely on comparisons of the representations of stimuli spectra in the rate profile of AN fibers, at least above 80 dB SPL. Other possible cues to discrimination at high levels will also be discussed.

II. EXPERIMENT I: DISCRIMINATION BETWEEN FLAT-SPECTRUM AND NOTCHED NOISES

The experiment was identical to the main experiment of Alves-Pinto and Lopez-Poveda (2005). It consisted of measuring the threshold notch depth for discriminating between a flat-spectrum broadband noise and a similar noise with a high-frequency rectangular spectral notch (Fig. 1) at increasing stimulus levels.

A. Methods

1. Stimuli

Stimuli consisted of bursts (total duration of 220 ms, including 10 ms cosine-squared rise/fall ramps) of random broadband (20–16 000 Hz) noise with either a flat spectrum or with a rectangular spectral notch (bandwidt of 2 kHz) centered at 8 kHz (Fig. 1). The noises were generated as described in the work of Alves-Pinto and Lopez-Poveda (2005). The reduced energy in the notch frequency band would have made the overall level of the notched noise slightly lower than that of the flat-spectrum noise. To prevent this level difference to be used as a cue for discrimination, the *overall* levels of the two noises were made equal by reducing the spectrum level of the flat-spectrum noise with respect to that of the notched noise. The reduction required for any given notch depth was always less than 0.58 dB and was determined as described by Alves-Pinto and Lopez-Poveda (2005). Level roving could have been alternatively used to prevent the use of overall level difference as a discrimination cue (Alves-Pinto and Lopez-Poveda, 2005). The level-equalization method was chosen instead because the resulting noises resembled more closely the noise maskers used to measure the masking patterns (experiments II and III).

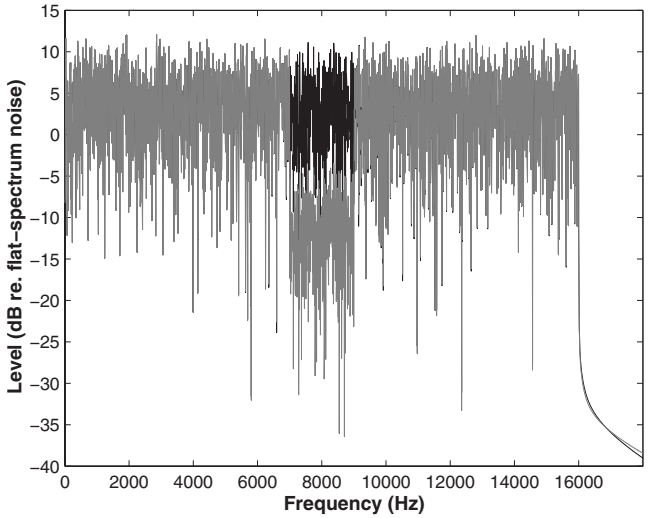

FIG. 1. Spectra of the flat-spectrum (dark trace) and notched (light trace) noises. The spectral notch was centered at 8000 Hz and its bandwidth was 2000 Hz. The notch illustrated had a depth of 15 dB relative to the spectrum level outside the notch band.

2. Procedure

The procedure was identical to that of Alves-Pinto and Lopez-Poveda (2005). Two flat-spectrum and one notched noise bursts were played in random order to the listener, who was instructed to identify the odd one out. The interstimulus period was 500 ms. A two-down, one-up adaptive procedure with feedback was employed to estimate the notch depth that produced 70.7% correct responses (Levitt, 1971). The initial notch depth was fixed at 20 dB below the reference spectrum level of the noise. The notch depth decreased or increased by 6 dB for the first six reversals and by 1 dB thereafter. Each block of trials consisted of 16 reversals and the threshold was estimated as the mean of the notch depths for the last ten reversals. When the corresponding standard deviation exceeded 6 dB, the measurement was discarded and a new threshold estimate was attempted. The thresholds reported correspond to the *geometric* mean of at least three valid measurements (see the work of Alves-Pinto and Lopez-Poveda, 2005 for details). Notch depths at threshold were measured for overall levels from 40 to 90 dB SPL, in 10-dB steps, and for an additional level of 95 dB SPL.

Listeners were tested individually in a double-wall sound attenuating chamber. Stimuli were generated digitally (24 bit, sampling rate of 48.8 kHz) with a TDT™ psychoacoustics workstation (system 3) and delivered via Etymotic™ ER2 earphones. The SPLs reported below correspond to calibrated values. The SPL reading of a sound level meter with its microphone coupled to a Zwislocki occluded ear simulator was 100 dB SPL for a 1 kHz pure tone with an amplitude of 2.3 V_{rms}.

3. Listeners

Seven volunteers (six women and one man, aged 22–35 years) participated in this experiment, all of whom had hearing thresholds within 20 dB re. ANSI 3.6-1996 (specifications for audiometers) at the audiometric frequencies (250–8000 Hz). All listeners were given at least one training session in the task before data collection. Listener S1 was one of the authors (A.A.P.).

B. Results and discussion

Figure 2 illustrates the threshold notch depth as a function of noise overall level. Each panel illustrates the results for a different listener. Error bars illustrate one standard error of the geometric mean. Triangles illustrate absolute thresholds for the flat-spectrum noise.

For most of the listeners, the threshold notch depth varied non-monotonically with level: it gradually increased with increasing level up to 70–80 dB SPL and then decreased with further increases in level. These results indicate that discrimination was more difficult at 70–80 dB SPL than at higher or lower levels. The nonmonotonic trend was less clear for S4 and S5. For S4, the threshold notch depth was still the highest at 70 dB SPL. In the case of S5, the threshold notch depth remained approximately constant above 60 dB SPL. Overall, these results were consistent with the nonmonotonic functions reported by Alves-Pinto and Lopez-Poveda (2005).

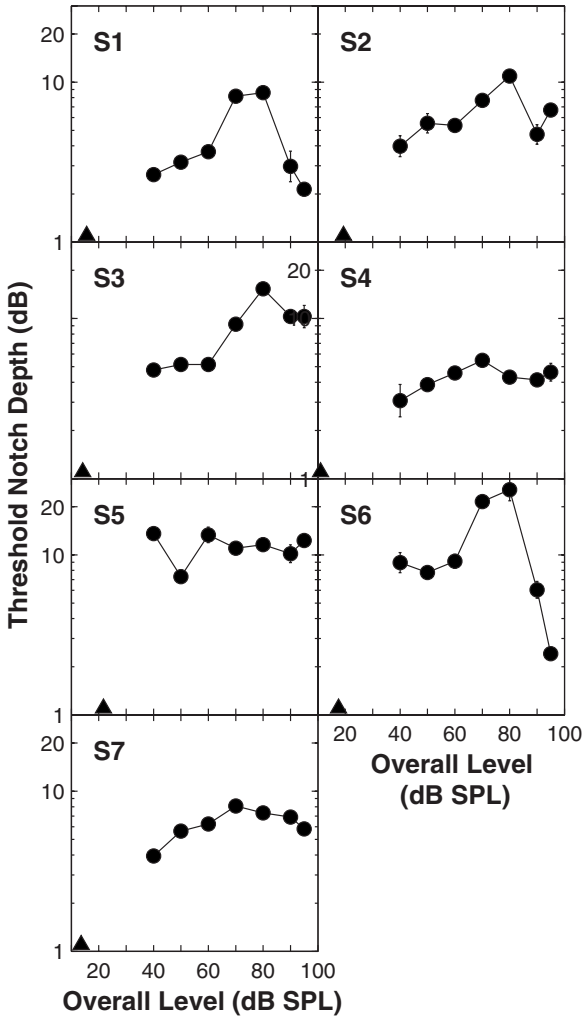

FIG. 2. Threshold notch depths for discriminating between a flat-spectrum noise and a notched noise plotted as a function of the stimulus overall level. Notches were centered at 8000 Hz and had a bandwidth of 2000 Hz. Each panel illustrates data for a single listener as indicated in the upper-left corner of each panel. Each data point corresponds to the geometric mean of at least three measurements. Error bars illustrate one standard error of the geometric mean. Shaded triangles indicate the listener's absolute hearing threshold for the flat-spectrum noise.

III. EXPERIMENT II: MASKING PATTERNS OF FLAT-SPECTRUM AND NOTCHED NOISES WITH A FIXED MASKER-PROBE TIME INTERVAL

A. Aim and rationale

The aim was to measure the forward-masking patterns of the flat-spectrum and notched noises used in experiment I for the same group of listeners. As argued in the Introduction, forward-masking patterns provide the best psychophysical estimate of the internal representation of the masker spectrum. Therefore, the overall difference between the internal representations of the flat-spectrum and the notched noise spectra can be inferred from the difference of their corresponding masking patterns. This method of estimating the internal representation of the spectral notch is based on the following two assumptions: (1) the decay of forward masking is independent of frequency and (2) the decay of forward masking is independent of probe level, at least over the range of probe levels considered in the present study. The first of these two assumptions is supported by other studies (e.g., Lopez-Poveda and Alves-Pinto, 2008). The second assumption relates to the effect of compression on forward masking and will be discussed in Sec. V. Masking patterns were measured for different masker levels to assess the effect of level on the quality of the internal representation of the masker spectrum.

B. Methods

1. Procedure

The thresholds for detecting probe tones of different frequencies in the presence of a forward noise masker were measured by using a two-interval two-alternative forced-choice adaptive paradigm. In one of the intervals, the masker was presented alone; in the other interval, the masker was followed by a brief probe tone. The two intervals were presented in random order (with an interstimulus period of 500 ms) to the listener, who was instructed to identify the interval containing the probe. Feedback was immediately

given to the listener after his/her response. The initial probe level was set so that the probe was perfectly audible at the beginning of a trial, and a two-down, one-up adaptive procedure was used to estimate the probe level corresponding to 70.7% correct responses in the psychometric function (Levitt, 1971). The level of the probe was decreased or increased in 6 dB for the first two reversals and 2 dB thereafter. The measurement ended after twelve reversals, and the threshold was estimated as the arithmetic mean of the probe level for the last ten reversals. When the corresponding standard deviation exceeded 6 dB, the measurement was discarded and a new estimate was obtained. At least three thresholds were measured in this way and their mean was taken as the true threshold. When the standard deviation of those three estimates exceeded 3 dB, an additional estimate was measured and included in the mean.

Masking patterns were obtained by measuring the detection thresholds of 15 tonal probes of different frequencies (see the following text). Each experimental session consisted of measuring the thresholds for one group of 15 probe tones. Listeners were given a short (~5–10 min) resting period in the middle of each session to reduce fatigue. The absolute thresholds for the probes (i.e., without the masker) were also measured by using the same procedure. Listeners were tested in the same sound booth and with the same equipment as previously described for experiment I. The calibration procedure was also the same.

2. Stimuli

To measure a masking pattern consisted of measuring the masked detection threshold for tonal probes of the following frequencies: 5, 6, 6.5, 6.75, 7, 7.25, 7.5, 8, 8.5, 9, 9.25, 9.5, 9.75, 10, and 11 kHz. The probes had a total duration of 10 ms, including 5 ms onset/offset cosine-squared ramps, and no steady-state portion. Masking patterns were measured for two broadband (20–16 000 Hz) random-noise maskers with different spectra: one was flat and one was similar to the former except that it contained a rectangular notch centered at 8 kHz, with a bandwidth of 2 kHz and a fixed depth of 15 dB (Fig. 1). These noise signals were similar to those used in experiment I and were generated as described by Alves-Pinto and Lopez-Poveda (2005). The overall level of the notched noise masker was 0.56 dB lower than that of the flat-spectrum noise because it had less energy in the notch frequency band. Unlike in experiment I, this level difference was not compensated for and so the two maskers had identical spectral levels outside the notch band. Maskers had a total duration of 110 ms, including 5 ms onset/offset cosine-squared ramps. Masking patterns were measured for masker overall levels of 50, 70, 80, and 90 dB SPL. The masker-probe time interval (defined from masker offset to probe onset) was fixed at 2 ms for all masker levels.

3. Listeners

Five of the seven listeners who participated in experiment I took part in this experiment. They were given at least one training session on the task before data collection.

C. Results

Figure 3 illustrates the masking patterns for the flat-spectrum (open circles) and notched noises (filled circles) for different listeners at different masker levels. Each row corresponds to a different listener. Each column corresponds to a different masker level, as indicated at the top. Squares in the first column illustrate probe absolute thresholds. Error bars represent one standard error of the mean. Vertical dotted lines depict the notch frequency band.

For all listeners, masked thresholds increased as the masker level increased. Masked thresholds were also always higher than the probe absolute thresholds which confirm that there was a masking effect.

The masking patterns were not flat even when the spectrum of the masker was flat and their shape significantly varied across listeners. Nonetheless, for all listeners, the two masking patterns differed more clearly for probe frequencies around the notch frequency band, with masked thresholds for the notched noise masking pattern being clearly lower than those for the flat-spectrum masking pattern. Masked thresholds for probes outside the notch band were very similar for the two maskers. Although the notch was, in general, more evident in the masking patterns at 50 dB SPL, it was also clearly present for higher masker levels.

The effect of level on the relative shape of the masking patterns can be better seen by analyzing the difference masking pattern, that is, by analyzing the difference between the masked probe thresholds for the two maskers (notch-flat) as a function of probe frequency (Fig. 4). This form of analysis eliminates the dependence of the masked thresholds (hence, of the masking patterns) on the individual frequency sensitivity of the listeners. Furthermore, it minimizes the influence that different rates of decay across frequencies could have on the shape of the masking patterns.

Each row of Fig. 4 illustrates the difference masking patterns for a different listener and the bottom row illustrates the mean across the five listeners. Each column corresponds to a different masker level. Error bars in the bottom row represent one standard error of the mean across listeners. Error bars in the other rows represent one standard error of the mean difference. Dotted lines indicate the difference between the spectra of the two maskers. For most listeners, the spectral notch was visible in the mean difference masking patterns at all masker levels (bottom row of Fig. 4). It is also noteworthy that standard errors increased with increasing masker level. Furthermore, the notch became wider and its tip slightly shifted toward higher frequencies. The latter is consistent with the upward spread of masking (reviewed by Moore, 2005).

D. Discussion

Assuming that a forward-masking pattern is the best psychophysical correlate of the AN rate profile of the spectrum of the masker, then the physiological studies would suggest that the spectral notch would be less clearly represented at higher than at lower levels (see the Introduction). The clear presence of the spectral notch in the difference masking patterns of most listeners at high levels did not sup-

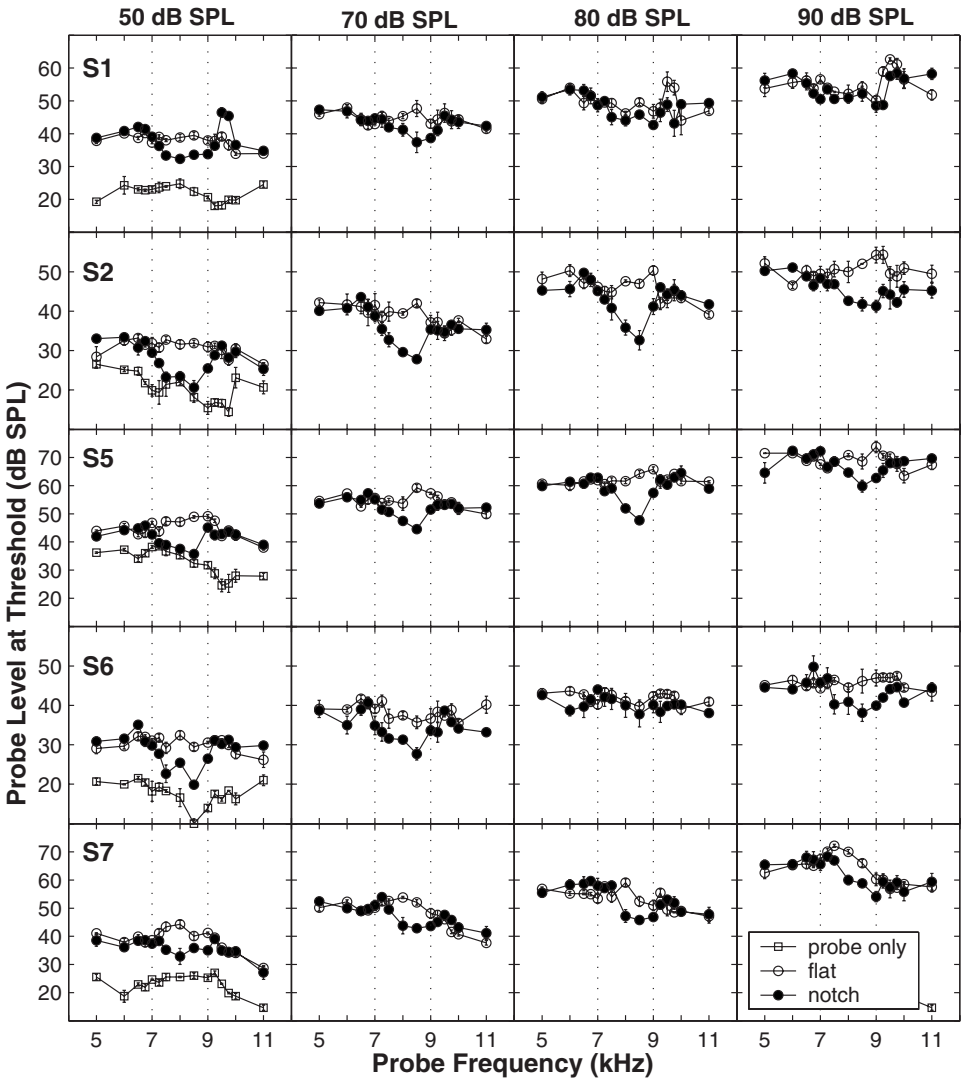

FIG. 3. Masking patterns for the flat-spectrum (open circles) and notched (filled circles) noise forward maskers for a fixed masker-probe interval of 2 ms across masker levels. Each panel illustrates the results for a different listener (rows) and level (columns). Masker levels are indicated at the top of each column. The squares in the first column represent the absolute detection thresholds for probes, i.e., the thresholds in the absence of the masker. Error bars represent one standard error of the mean. Dotted lines illustrate the boundaries of the spectral notch in the notched noise stimulus.

port this expectation (Fig. 4). Further, these masking patterns provide no explanation for the pattern of thresholds with increasing level in the discrimination task of experiment I. Given these inconsistencies, the possibility that the forward-masking patterns measured in this experiment do not capture level dependences that actually exist in the neural representation must be considered. It should be noted that probe thresholds increased with increasing masker level because the probe delay was fixed across masker levels (Fig. 3). As a result, high-level probes would have been subjected to the same processes that might have affected the quality of the neural representation of the masker spectrum. Hence, variations in probe threshold at high levels could be exaggerated (Figs. 3 and 4); they could result from changes not only in the internal representation of the masker but also of the probe.

The effects of peripheral auditory compression serve to illustrate this important point. In forward masking, it is commonly assumed that neural activity recovers exponentially after the masker offset (Harris and Dallos, 1979; Meddis and O'Mard, 2005) and that probe detection in the presence of a forward masker occurs when the response to the probe is as large as when the probe is presented alone (Harris and Dallos, 1979; but see the works of Relkin and Turner, 1988 and Meddis and O'Mard 2005). An alternative interpretation would be that the masker excitation decays exponentially with time and that probe detection occurs when the internal probe excitation just exceeds the residual masker excitation (Oxenham and Moore, 1994; Oxenham, 2001; Plack and Oxenham, 1998). Whatever the interpretation is, evidence exists that the time constants of recovery (or decay) are level independent over a wide range of levels (Plack and Oxenham, 1998; Harris and Dallos, 1979; Meddis and O'Mard, 2005). Hence, when the same masker-probe time intervals are used for all masker levels, probe detection thresholds will increase with increasing masker level. In addition, at levels of compression, the effects on the internal excitations of stimuli should be similar for the masker and the probe. As a result, the potential detrimental effects of peripheral compression on the internal representation of the masker spectrum would not be revealed in its corresponding masking pattern. Figure 5 illustrates this point. The right panel of Fig. 5(a) illustrates a hypothetical peripheral input/output (I/O) function (in log-log scale) with a linear segment (slope of 1 dB/dB) at low levels and a compressed segment at high levels (slope <1 dB/dB). The thick dark lines on the abscissa illustrate the notch depth (in decibels) for a low- and a high-level masker, respectively. Both of them have the same width to

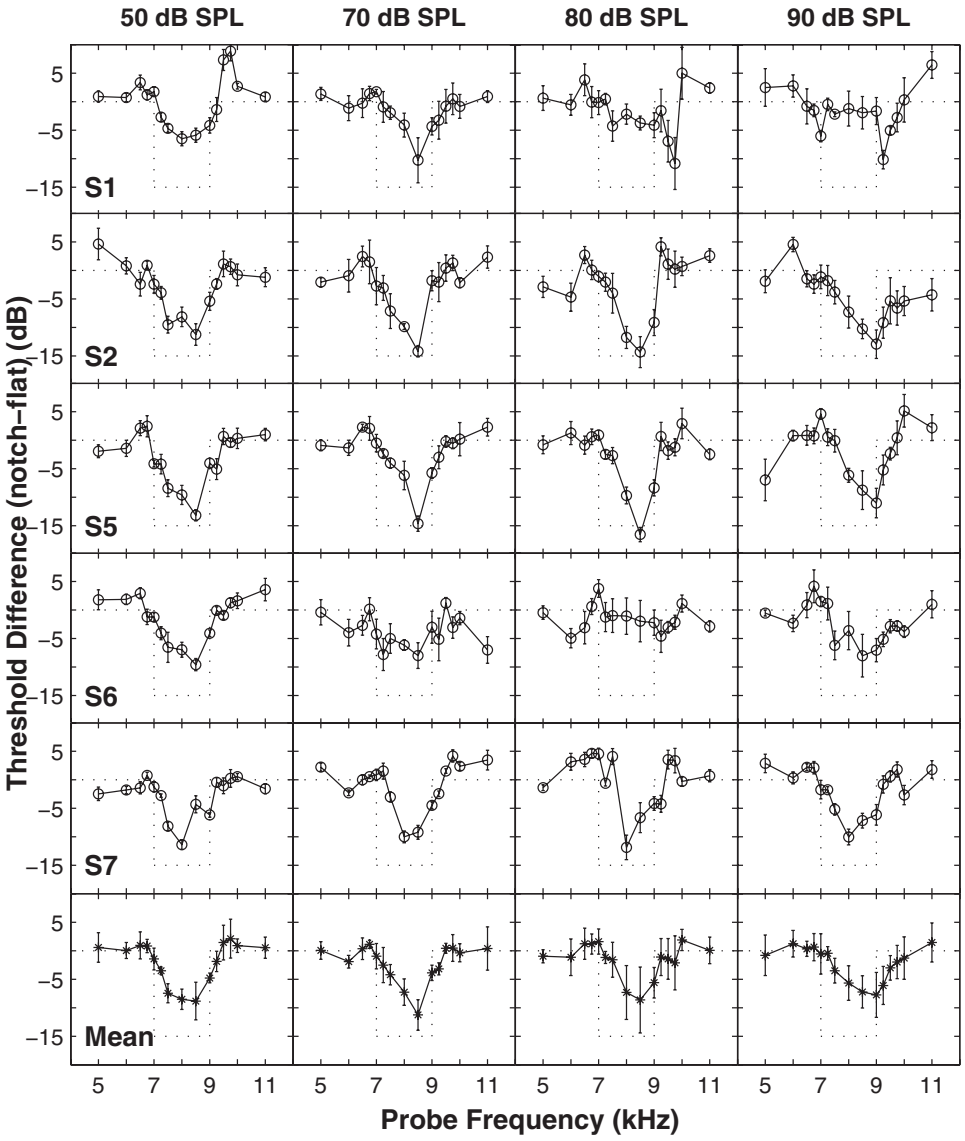

FIG. 4. The difference between the masking patterns for the flat-spectrum and notched noise maskers (notch-flat) for a fixed masker-probe time interval of 2 ms across masker levels. Each column illustrates the results for a different masker level (as indicated at the top). Each row contains the results for a different listener. Error bars represent one standard error of the mean difference. The bottom row illustrates the mean difference across listeners and the error bars illustrate one standard error of the mean. The dotted lines illustrate the difference between the spectra of the two noise maskers.

illustrate that the same notch depth is used for the two masker levels. The thick dark lines on the ordinate illustrate the corresponding internal representations of the notch (depth) for the two masker levels; i.e., the excitation at the output of the nonlinearity. Because of compression, the notch is shallower for the high-level masker than for the low-level masker in this representation.

The left panel of Fig. 5(a) is a hypothetical illustration of how the internal representation of the masker (notch) decays in time after its offset. This is based on the view that forward masking reflects persistence of neural activity, but its inverse could be interpreted as the time course of recovery from the internal masker effect. Evidence exists that this decay is exponential with two time constants (Oxenham and Moore, 1994; Plack and Oxenham, 1998). For simplicity, however, we illustrate here the case when the excitation exponentially decays in time with a single time constant, hence, the linear decay in a lin-log scale (note that time increases linearly to the left). Clearly, in this simplified model, the internal representation of the notch (depth) hardly changes in time. Assume now that masked (probe) threshold occurs when the probe excitation equals the residual masker excitation and that the masker-probe time interval is fixed at 2 ms for both masker levels, as shown in Fig. 5(a). From the excitation at time of 2 ms (vertical gray lines in the left panel), one can work backwards through the I/O function to estimate the range of (input) probe levels corresponding to the internal notch representations for the low- and the high-level maskers. The results are illustrated by the horizontal thick gray lines next to the abscissa in the right panel. Note that probe thresholds are much higher for the high-level masker than for the low-level masker. However, the range of probe levels (the width of the gray lines) is the same despite the internal representation of the notch being considerably worse (shallower) for the high-level masker. This would explain why the spectral notch was equally well represented in the masking patterns for different masker levels when the masker-probe time interval was fixed (Figs. 3 and 4). It also suggests that fixing the time interval may not be the most appropriate method to reveal the true representation of the masker spectrum at different masker levels.

Changes in the internal representation of the masker spectrum should, however, become apparent by considering different masker-probe time intervals for different masker

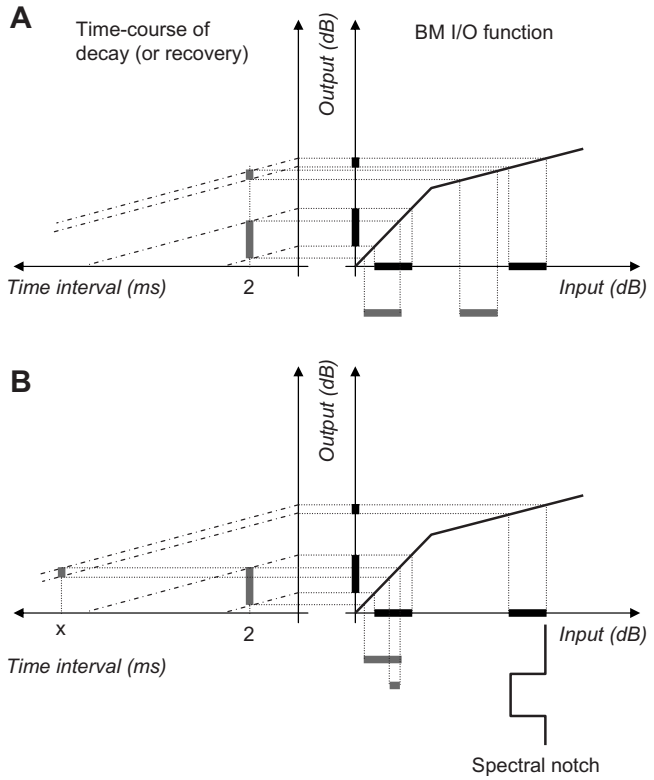

FIG. 5. Schematic explanation of the rationale of the method used to assess the internal representation of the spectral notch at different levels. (A) Representation for fixed a masker-probe time interval. The right plot illustrates a hypothetical peripheral input/output function with a linear segment at low levels (slope of 1 dB/dB) and a compressive segment at high levels (slope of <1 dB/dB). The thick dark lines on the abscissa represent the spectral notch and the width of the lines is proportional to the notch depth. The left panel illustrates a hypothetical internal representation of the spectral notch, the height of the thick gray lines being proportional to notch depth. Also illustrated is the exponential decay of the internal excitation along time, which is illustrated in a lin-log scale (see text for details). The internal representation of the notch is shallower at high levels as a result of compression. The thick gray lines on the abscissa of the right panel illustrate the range of probe levels corresponding to the internal representations of the notch for two level maskers. These were calculated by working backwards through the I/O function from the notch internal representation at time of 2 ms (vertical thick gray lines). (B) The same as in (A) but considering different masker-probe time intervals for different masker levels. Here, a longer masker-probe time interval is used for the higher-level masker, so that the resulting probe thresholds are comparable for the two masker levels. In this case, the range of probe levels (width of the horizontal gray lines) reflect the actual notch depth as internally represented (see text for details).

levels. Figure 5(b) illustrates how the internal representation of the notch (vertical dark thick lines) becomes clearly represented in the range of probe levels (i.e., in the width of the horizontal gray lines) by considering a longer masker-probe time interval for the higher-level masker. The intervals would need to be chosen such that the masked (input) probe thresholds remain approximately constant across masker levels. In this case masked probe thresholds are approximately the same for the two masker levels. Thus, any changes in the masking patterns may be mainly attributed to changes in the internal representation of the spectrum of the masker alone. The following section reports on an experiment aimed at measuring the masking patterns based on this principle.

IV. EXPERIMENT III: MASKING PATTERNS OF FLAT-SPECTRUM AND NOTCHED NOISES WITH VARIABLE MASKER-PROBE TIME INTERVAL

A. Aim and rationale

This experiment was similar to experiment II except that different masker-probe time intervals were used for different masker levels. The intervals were individually chosen for each listener such that masked probe thresholds remained approximately constant for the masker levels tested. Based on the rationale explained in the preceding section, the assumption was that the resulting masking patterns constitute the best possible psychophysical estimate of the internal representation of the masker spectrum at different levels.

B. Methods

1. Procedure and stimuli

The procedure and stimuli were similar to the ones used in experiment II except that, in this case, a 2 ms masker-probe time interval was used for the 50 dB SPL masker only, and longer masker-probe intervals were used for higher masker levels as necessary. The intervals were adjusted such that the masked threshold of an 8 kHz probe was approximately constant across masker levels. An 8 kHz tone was used because it was at the center of the notch frequency band. The actual intervals were determined as follows. The masked threshold for the 8 kHz probe tone was measured for the flat-spectrum noise masker for several masker-probe intervals, typically 2, 10, 20, and 30 ms. The flat-spectrum noise masker was used because it was the standard stimulus in experiment I. The resulting masking decay functions (shown in Fig. 6) were then fitted with either a first- or second-order polynomial (continuous lines in Fig. 6) depending on the number of points measured and the fit error. The fitted polynomial was then used to predict the masker-probe intervals that, for each masker level, gave a masked threshold for the 8 kHz probe approximately equal to the one observed for the 50 dB SPL masker. The predicted value was then experimentally confirmed (by measuring the masked probe threshold for the predicted time interval) and, if necessary, adjusted. This occurred, for example, for listener S3 at 80 and 90 dB SPL, for whom masked-probe thresholds varied ~6 dB across measures. In other words, the actual masker-probe intervals used (shown in Table I) differed slightly from fit predictions.

2. Listeners

Four listeners participated in this experiment (S1, S2, S3, and S4). Two of them (S1 and S2) participated also in experiment II. S3 and S4 were given at least one training session on the task before data collection.

C. Results

Figures 7 and 8 illustrate the masking patterns and the difference masking patterns, respectively, as in Figs. 3 and 4. Note first that for any given listener, masked thresholds were similar across masker levels as was intended (Fig. 7). Fur-

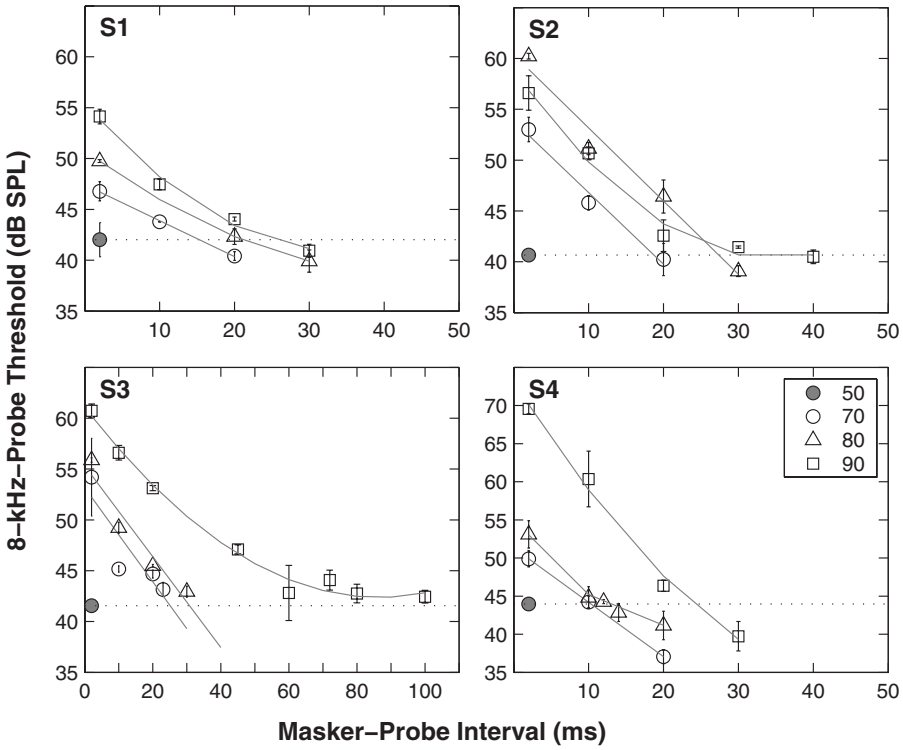

FIG. 6. Detection thresholds of an 8 kHz probe tone masked by a forward flat-spectrum-noise masker as a function of the masker-probe time interval. Each panel illustrates results for a different listener. Different symbols illustrate results for different masker levels, according to the inset in the lower-right panel. Error bars represent one standard error of the mean. The horizontal dotted line indicates the masked probe threshold for a masker level of 50 dB SPL and a masker-probe time interval of 2 ms. Continuous lines illustrate first- or second-order polynomial fits to the experimental functions.

ther, they were always higher than the probe absolute thresholds, which confirms that there was a masking effect.

As in the fixed masker-probe time interval condition (Fig. 3), the masking patterns were not flat. The notch was particularly evident in the masking pattern of the 50 dB SPL masker (Fig. 7). It was less obvious but still visible at 70 dB SPL, especially for listeners S2 and S4, and at 80 dB SPL for listener S4. At 90 dB SPL, the notch was barely visible in the masking pattern for all listeners. The difference masking patterns (Fig. 8) confirmed all these observations.

Peaks as high as 5 dB occurred at the notch edges in the difference masking patterns at 50 dB SPL for listeners S2, S3, and S4 (Fig. 8). These peaks are likely to occur as a result of cochlear suppression effects (Poon and Brugge, 1993).

D. Discussion

The forward-masking patterns of flat-spectrum and notched noises were measured for different masker levels, with different masker-probe time intervals set at different masker levels. The objective was to obtain a more realistic estimate of the internal representation of the notch at different masker levels.

Clearly, the effect of increasing masker level on the notch internal representation was very different for the fixed- and the variable-interval conditions (compare the bottom rows of Figs. 4 and 8). The notch was less clearly represented at high levels in the variable-interval condition (i.e., when the masked probe thresholds remained constant across masker levels) (Fig. 8) than in the fixed-interval condition (i.e., when masked probe thresholds increased with increasing masker levels) (Fig. 4).

Kidd and Feth (1981) reported that forward-masking patterns broadened as the masker-probe interval increased from 5 to 40 ms. This broadening would be consistent with a deterioration of the masker spectral features as represented in the masking pattern. It would also be consistent with the present results. In their study, however, the level of the (tonal) masker was fixed across masker-probe time intervals. As a result, probe thresholds decreased with increasing masker-probe time interval and, therefore, the changes in their masking patterns must have reflected changes in the internal excitation of the *probe*. In the present study, however, the masker-probe interval was precisely varied to maintain probe levels similar across masker levels (and time intervals).

The masking patterns of the flat-spectrum noise were not flat (as also reported in experiment II) and for some listeners, masked thresholds decreased with increasing frequency (e.g., S3 in Figs. 3 and 7). This may seem to be inconsistent with early studies that measured masked audiograms by using white noise as maskers and that reported a gradual increase in thresholds with increasing probe frequency (e.g., Reed and Bilger, 1973). Those early observations can be reasonably

TABLE I. Individual masker-probe time intervals (ms) used to measure the masking pattern for each of the four masker levels tested. The individual thresholds for the 8 kHz probe in the absence of masker are also shown.

Listener	8 kHz probe threshold (dB SPL)	Masker-probe time intervals (ms) for different masker levels (dB SPL)			
		50	70	80	90
S1	22.52	2	16	19	23
S2	27.61	2	19	27	34
S3	28.57	2	23	37	100
S4	19.50	2	11	12	24

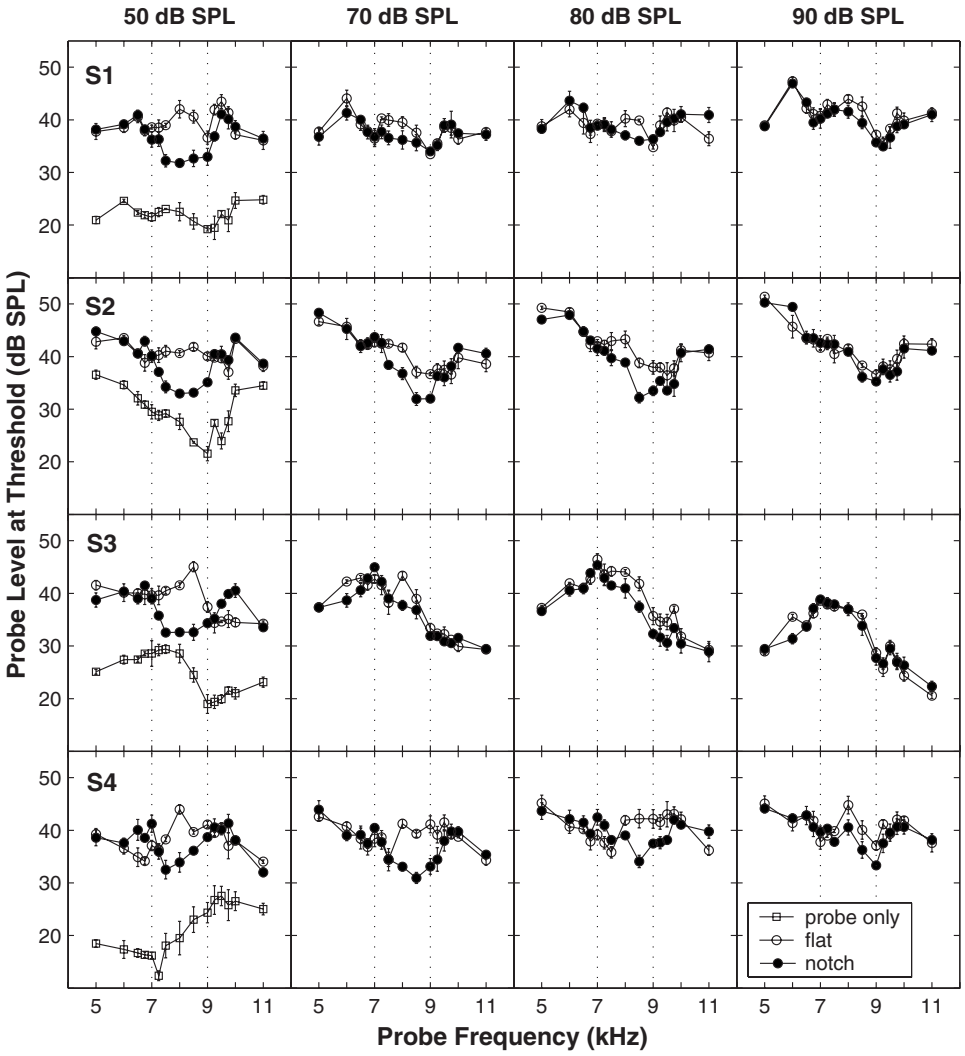

FIG. 7. The same as Fig. 3 but for a variable masker-probe time interval. The interval was varied to maintain the probe thresholds approximately constant across masker levels (see Fig. 6).

well accounted for in terms of the increasing bandwidth of auditory filters with increasing their center frequencies (Fletcher, 1940). In other words, the masking power of white noise is proportional to the width of the auditory filter centered at the probe frequency. It should be noted, however, that in the present study, the masker was not a white noise. Instead, its spectrum extended only up to 16 kHz. The lack of masking energy above that frequency could have reduced its masking power for probe frequencies close to 16 kHz. This may have facilitated the detection of higher-frequency probe tones (closer to 16 kHz) relative to that of lower-frequency tones. Furthermore, the individual listener's sensitivity to different frequencies might have also contributed to the shape of the masking pattern.

Whatever the reason is, the individual factors that determined the shapes of the masking patterns for the flat-spectrum masker will also have determined the masking pattern for the notched noise maskers. Such factors will have cancelled out in the *difference* masking patterns. Therefore, the idiosyncrasies in the shapes of the masking patterns do not compromise the conclusions on the internal representation of the spectral notch at different levels based on the difference masking pattern (bottom rows of Figs. 4 and 8).

The masked thresholds of listener S3 in the variable time interval condition (Fig. 7) were slightly lower for the 90 dB SPL masker than for the lower masker levels. Even so, the notch was already less clearly represented at 80 dB SPL and, therefore, also in this case, it can be concluded that the internal representation of the spectral notch deteriorates with increasing level. The results of this listener at 90 dB SPL should, nevertheless, be considered with reservation.

The shapes of the masking patterns may have also been influenced by off-frequency listening (Moore, 2005). Off-frequency listening, however, does not compromise the conclusion that the internal representation of high-frequency spectral notches gradually deteriorates as the stimulus level increases. One reason is that the amount (and effects) of off-frequency listening would have been approximately similar for the two noise maskers and, hence, would have cancelled out in the difference masking patterns. Second, masked thresholds were similar across masker levels and, hence, any off-frequency listening effects would have been comparable across masker levels.

A similar earlier study (Moore and Glasberg, 1983) investigated the effect of level on the quality of the internal representation of vowel formants by measuring the masking patterns of synthetic vowels in forward masking for overall levels of 50, 70, and 90 dB SPL. The masker was one of two synthetic vowels (/æ/ and /i/), both with a fundamental frequency of 100 Hz. Probe tones were immediately presented

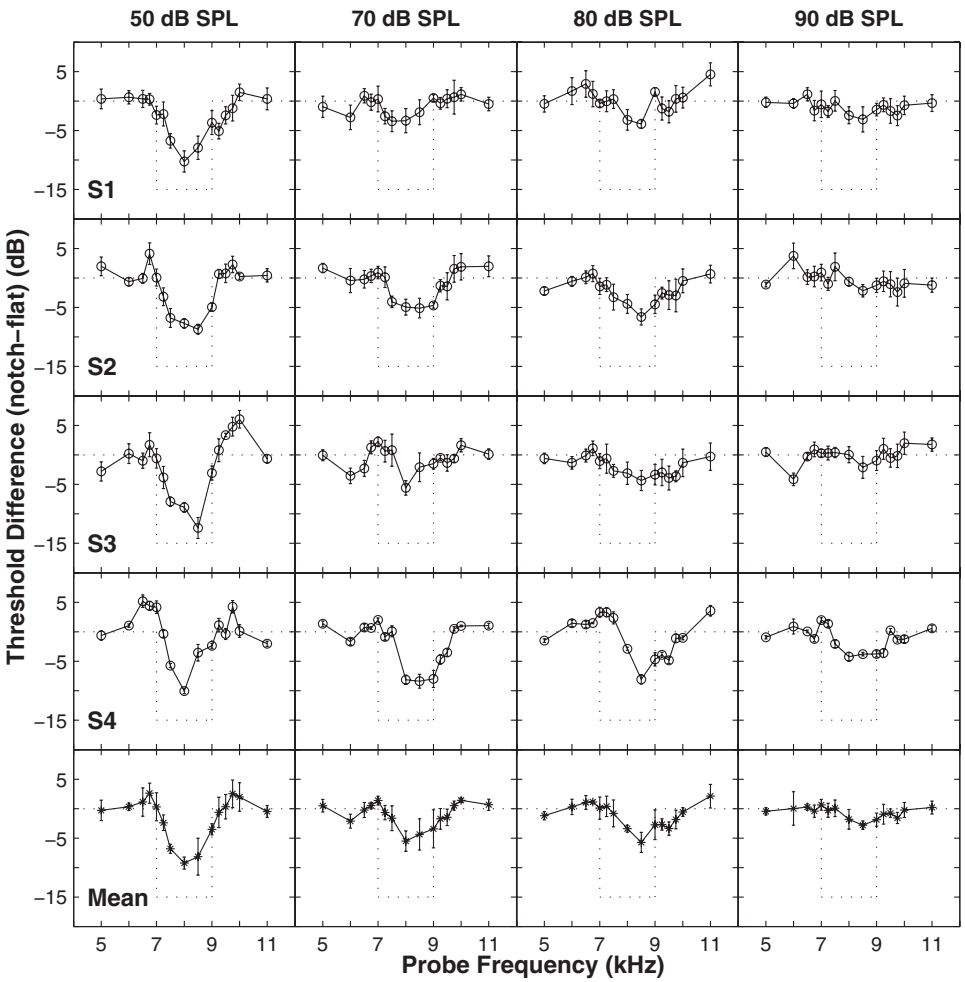

FIG. 8. The same as Fig. 4 but for a variable masker-probe time interval across masker levels.

after the maskers and their detection thresholds were measured as a function of probe frequency. Probe thresholds were expressed as the level of a broadband noise masker that would give a similar probe detection threshold. The authors concluded that the "representation of the formant structure was impaired only slightly at high masker levels" (p. 909). This conclusion is in agreement with the results reported here for the fixed masker-probe time interval condition (bottom row of Fig. 4) but not with those for the variable-interval condition (bottom row of Fig. 8). Moore and Glasberg (1983) used a fixed masker-probe time interval and, for the reasons described before, it is possible that any negative effect of level due to peripheral auditory compression was not revealed in their results. The transformation used to express probe thresholds was intended to compensate for the fact that the increase in probe thresholds was not equal to the increase in masker level. However, the compensation for the effects of compression may not have been sufficient. If probe detection had been affected by compression, the broadband noise level that corresponded to probe threshold may have also been affected by compression, even though the spectrum level of the broadband noise was much lower than the level of the probe tone.

Another possible reason for the apparent contradiction between the conclusion of Moore and Glasberg (1983) and the present results is that the spectral features considered in the two studies extended to very different frequency ranges: vowel formants were below 3.5 kHz, while the present notch extended from 7 to 9 kHz. The near-threshold bandwidth of AN fibers depends on the CF of the fiber; the higher the CF is, the wider the bandwidth is (Evans, 1975). Therefore, for broadband stimuli, the effective level driving an AN fiber is proportional to its bandwidth. As a result, a broadband stimulus that drives low-CF AN fibers below saturation might drive high-CF AN fibers at saturation. At high levels, this effect would be much stronger for high-CF units than for low-CF units, as their bandwidth increases substantially more with increasing level than that of low-CF units (Rose *et al.*, 1971). This might explain why the negative effect of increasing masker level was less obvious in the vowel masking patterns of Moore and Glasberg (1983) than in the present ones.

The results of experiments II and III, combined, are qualitatively consistent with the idea that peripheral compression contributes to a deterioration of the internal representation of the spectral notch at high levels. As previously explained, the masking patterns for the variable-interval condition probably provide a more realistic account of the quality of the internal representation of the spectral notch at different levels. For this reason, in the following section, the analysis and discussion of the results of the spectral discrimination task are based on the masking patterns for variable masker-probe time interval.

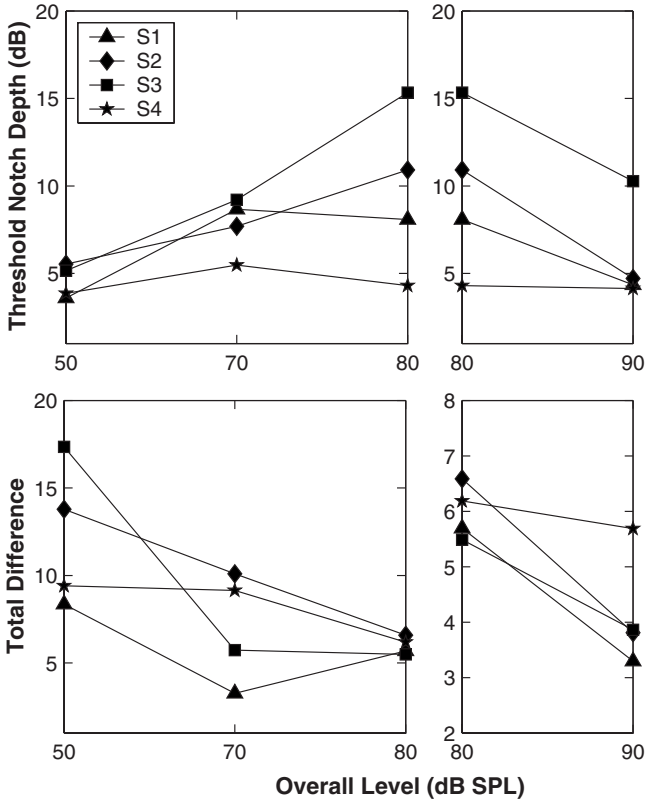

FIG. 9. The effect of increasing level on the threshold notch depths for discriminating between flat-spectrum and notched noise stimuli (upper panels, adapted from Fig. 2 for listeners S1–S4) and on the total difference between the masking patterns of flat-spectrum and notched noise maskers for variable masker-probe time intervals (lower panels, adapted from Fig. 8). Different symbols illustrate the results for different listeners. The left and right panels illustrate the results over two different level ranges: 50–80 (left) and 80–90 dB SPL (right).

V. CORRELATION BETWEEN THE RESULTS OF EXPERIMENTS I AND III

The masking patterns measured in experiment III are assumed to provide the best estimate of the internal representation of the flat-spectrum and notched noises used in the discrimination task of experiment I. These are assumed to be closely related to the excitation pattern representation of the spectra of the two noises in the peripheral auditory system, possibly in the AN (see Introduction). Therefore, the hypothesis that the discrimination is based on the comparison of the AN excitation pattern representations of the two noises was tested by correlating the shapes of the threshold notch depths versus level functions of experiment I with the total difference between the two masking patterns of experiment III. The latter was calculated as the square root of the sum (across frequencies) of the squared difference masking patterns (Fig. 8). This measure is akin to the Euclidean distance between the masked probe thresholds for the two maskers.

The lower panels of Fig. 9 illustrate the total difference between the masking patterns as a function of masker level. Different symbols illustrate the results for different listeners (results are shown only for the four listeners, S1–S4, for whom masking patterns were measured with variable masker-probe time intervals). For comparison, the upper panels of Fig. 9 show the discrimination threshold notch depths at the same four levels (adapted from Fig. 2). The results of both experiments are plotted separately for two level ranges: 50–80 (left panels) and 80–90 dB SPL (right panels). This facilitates the visual comparison of the results below and above 80 dB SPL, the level at which the trend in discrimination performance changed (from increasing to decreasing) with increasing level.

Discrimination threshold notch depths increased with increasing level from 50 to 80 dB SPL, while the total masking-pattern difference decreased over the same level range. In other words, discriminating between flat-spectrum and notched noise stimuli became more difficult as the level increased from 50 to 80 dB SPL and this is consistent with the masking patterns of the two stimuli becoming gradually more similar with increasing masker level over the same range. Strikingly, the total difference between the masking patterns continued to decrease as the level increased from 80 to 90 dB SPL and yet discrimination *improved* (or remained approximately constant for S4). Thus, above 80 dB SPL, the increasing similarity between the masking patterns does not correlate with the improvement on the discrimination task.

VI. GENERAL DISCUSSION

The aim of this study was to behaviorally investigate to what extent discriminating between broadband noise stimuli with and without *high*-frequency spectral notches relies on the comparison of the internal (supposedly AN) representation of the spectra of the two noises. The approach consisted of comparing the results of the spectral discrimination task with the shapes of the forward-masking patterns of the corresponding two noises. The forward-masking patterns were assumed to provide the best psychophysical correlate of the internal excitation patterns of the masker at the auditory periphery. The hypothesis was that if high-frequency spectral discrimination relied on comparisons of the internal representation of the spectra of the two noises, then the more similar the masking patterns are, the worse listeners should perform in the discrimination task. The results suggested that this hypothesis holds true below but not above 80 dB SPL (Fig. 9).

Assuming that a forward-masking pattern is a reasonable approximation of the AN rate-profile representation of the stimulus spectrum (see Introduction), then the deterioration of the internal representation of the spectral notch with increasing level would be consistent with the notion that the rate-profile representation of spectral features deteriorates with increasing stimulus level. This deterioration would be due to the broadening of the frequency response and to the saturation of the response of AN fibers (Rice *et al.*, 1995; Lopez-Poveda, 1996). However, rate profiles and masking patterns are different measures. Despite precautions have been taken to maximize the correspondence between the two (e.g., by using forward masking and by ensuring that the probe level was approximately constant for all masker levels), the correspondence may not be straightforward.

Indeed, the quality of the notch representation in the present masking patterns varies with level in a way consis-

tent with most, but not all, studies on the AN rate-profile representation of high-frequency spectral notches. Physiological (Rice *et al.*, 1995) and simulation (Lopez-Poveda, 1996) studies have shown that the AN rate-profile representation of high-frequency spectral notches gradually deteriorates with increasing level, which is consistent with the trend in the present making patterns for the variable-interval condition. This trend is also consistent with the quality of the level-dependent representation of the spectral notch in the simulated excitation pattern of inner hair cells (Lopez-Poveda *et al.*, 2008). By contrast, a related physiological study (Alves-Pinto, 2007; Lopez-Poveda *et al.*, 2007) suggests that the spectral notch is *better* represented in guinea-pig AN rate profiles at around 70–80 dB SPL than at lower and higher levels, which appears to be inconsistent with the trend suggested by the present masking patterns as well as with the results of the spectral discrimination task (Fig. 2). The reason for this inconsistency is unclear. Maybe a mismatch exists in the SPL calibration between the physiological and psychophysical studies. It is also possible that the masking patterns were measured for a range of levels insufficient to reveal any improvement in the representation of the spectral notch. Alternatively, the discrepancy might relate to differences in signal processing between the guinea-pig and human peripheral auditory systems. In any case, it is important to bear in mind that forward masking is not only the result of a poststimulatory reduction in AN activity and/or the persistence of neural activity but also of efferent inhibitory processes (see the work of Meddis and O'Mard, 2005 for a brief review on the topic).

Assuming that masking patterns reflect the AN rate-place representation of the spectra of the two noises, the present results suggest that discriminating between the two noises is unlikely to rely on comparing the rate-profile representations of their spectra, at least above 80 dB SPL. This undermines the conjecture of Alves-Pinto and Lopez-Poveda (2005) that the improvement in performance above 80 dB SPL could reflect an improvement in the quality of the representation of the spectral notch in the rate profile. This would occur as a result of the notch being essentially encoded by low-spontaneous–rate fibers, which have higher thresholds and wider dynamic ranges (Evans and Palmer, 1980; Sachs and Abbas, 1974). If this had been the case, the notch would have been more clearly observed in the difference masking patterns at high levels.

If the quality of the representation of high-frequency spectral notches in the excitation pattern gradually deteriorates with increasing level, what explains the improvement in spectral discrimination above 80 dB SPL (Fig. 2)? One possibility is that it is based on temporal information. It is possible that above 80 dB SPL, when the rate-place representation of the different spectra becomes statistically indistinct, the information carried in the discharge *times* of AN fibers evoked by the different spectra may become more relevant to discrimination. This is supported by a related computational modeling study on the representation of spectral notches at the level of the inner hair cells (IHCs) (Lopez-Poveda *et al.*, 2008). The simulations show that the quality of the IHC excitation pattern representation of the spectral notch decreases as sound level increases (consistent with the present masking patterns for the variable-interval condition). By contrast, when the frequency information of the receptor potential waveforms is considered, the quality of the IHC representation of the spectral notch improves above 80 dB SPL (consistent with what occurs in the spectral discrimination task). According to the model, the improvement could be possibly related to IHC nonlinearities. The plausibility of this mechanism would require almost certainly that AN responses be phase locked to the IHC receptor potential waveforms for frequencies much higher than the conventionally accepted limit for phase locking (around 4 kHz according to Palmer and Russell, 1986). On the other hand, recent studies have shown that although the number of AN spikes phase locked to the stimulus waveform rapidly rolls off with increasing frequency, statistically significant phase locking may still occur for stimulus frequencies as high as 14 kHz (Recio-Spinoso *et al.*, 2005). Therefore, the proposed mechanism is at least plausible.

The conjecture that some form of temporal code may mediate the discrimination of high frequencies *when rate cues are not available* is original as far as it refers to *aperiodic*, high-frequency stimuli. A similar conjecture was put forward long ago by Sachs and Young (1979) and Young and Sachs (1979) based on the representation of vowel spectra in the discharge pattern of the AN. It has also been suggested based on a computational model of the limits of human auditory perception for single tones (Heinz *et al.*, 2001). It is also consistent with the results of a recent modeling study (Holmberg *et al.*, 2007) according to which rate-place codes do not explain the good performance of human listeners in speech recognition at high speech levels, particularly in the presence of background noise. Speech recognition accuracy in their model improved, however, when the rate-place code information was combined with temporal information.

Another alternative explanation for the improvement in spectral discrimination at high levels could be that it reflects the activation of acoustic reflexes. The medial olivocochlear reflex activates at high level and its effect is to shift the dynamic range of AN fibers toward higher levels (Guinan, 2006). Therefore, one might think that the improvement in spectral discrimination above 80 dB SPL [Fig. 2, Alves-Pinto and Lopez-Poveda (2005)] relates to the activation of this reflex (Winslow and Sachs, 1987; Pickles, 1988). This, however, is unlikely. If it had been the case, it would have almost certainly led to a clearer representation of the spectral notch in the masking patterns above 80 dB SPL and this was not the case (Figs. 3 and 7).

One final remark: the conclusions of this study would have been markedly different if the masking patterns had been measured only with a fixed masker-probe time delay for all masker levels, as is commonly the case. The differences between the masking patterns obtained with fixed and variable masker-probe intervals demonstrate (1) the importance of choosing the correct psychophysical method to infer the internal representation of the spectrum of a sound and (2) the extent to which this representation can be affected by peripheral compression.

VII. CONCLUSIONS

The shape of the masking patterns of broadband noise forward maskers with and without a high-frequency spectral notch becomes gradually more similar as the overall level of the masker increases (at least when measures are taken for masked probe thresholds to remain constant across masker levels). This suggests that the AN rate-place representation of high-frequency spectral notches gradually deteriorates with increasing level. The result is consistent with the increased difficulty in discriminating between flat-spectrum and notched noise stimuli for stimulus levels increasing between 50 and 80 dB SPL but not with the improvement observed for further level increases above 80 dB SPL. This suggests that a form of representation other than rate place (possibly temporal) is likely to mediate high-frequency spectral discrimination, at least above 80 dB SPL.

ACKNOWLEDGMENTS

We thank Christopher J. Plack for his suggestion to vary the masker-probe interval and Ray Meddis for his comments on the results presented here. We are grateful to Richard L. Freyman and three anonymous reviewers for their comments on an earlier version of this paper. We also thank K. T. Nakamoto for helping with the english and writing style. This work was supported by Spanish FIS (Nos. PI02/0343 and G03/203), MEC (Nos. CIT-390000-2005-4 and BFU2006-07536), and IMSERSO (No. 131/06).

Alves-Pinto, A. (**2007**). "Psychophysical and physiological assessment of the representation of high-frequency spectral notches in the auditory nerve," Ph.D. thesis, University of Salamanca, Salamanca, Spain.

Alves-Pinto, A., and Lopez-Poveda, E. A. (**2005**). "Detection of high-frequency spectral notches as a function of level," J. Acoust. Soc. Am. **118**, 2458–2469.

Carlile, S., Martin, R., and McAnally, K. (**2005**). "Spectral information in sound localization," Int. Rev. Neurobiol. **70**, 399–434.

Evans, E. F. (**1975**). "Cochlear nerve and cochlear nucleus," in *Handbook of Sensory Physiology*, edited by W. D. Keidel and W. D. Neff (Springer, Berlin), pp. 1–108.

Evans, E. F., and Palmer, A. R. (**1980**). "Relationship between the dynamic range of cochlear nerve fibers and their spontaneous activity," Exp. Brain Res. **40**, 115–118.

Fletcher, H. (**1940**). "Auditory Patterns," Rev. Mod. Phys. **12**, 47–65.

Guinan J. J., Jr. (**2006**). "Olivocochlear efferents: anatomy, physiology, function, and the measurement of efferent effects in humans," Ear Hear. **27**, 589–607.

Harris, D. M., and Dallos, P. (**1979**). "Forward masking of auditory nerve fiber responses," J. Neurophysiol. **42**, 1083–1107.

Heinz, M. G., Colburn, H. S., and Carney, L. H. (**2001**). "Evaluating auditory performance limits: I. One-parameter discrimination using a computational model for the auditory nerve," Neural Comput. **13**, 2273–2316.

Holmberg, M., Gelbart, D., and Hemmert, W. (**2007**). "Speech encoding in a model of peripheral auditory processing: Quantitative assessment by means of automatic speech recognition," Speech Commun. **49**, 917–932.

Kidd, G., Jr., and Feth, L. L. (**1981**). "Patterns of residual masking," Hear. Res. **5**, 49–67.

Levitt, H. (**1971**). "Transformed up-down methods in psychoacoustics," J. Acoust. Soc. Am. **49**, 467–477.

Liberman, M. C. (**1978**). "Auditory-nerve response from cats raised in a low-noise chamber," J. Acoust. Soc. Am. **63**, 442–455.

Lopez-Poveda, E. A. (**2005**). "Spectral processing by the peripheral auditory system: facts ad models," Int. Rev. Neurobiol. **70**, 7–48.

Lopez-Poveda, E. A. (**1996**). "The physical origin and physiological coding of pinna-based spectral cues," Ph.D. thesis, Loughborough University, Leicestershire, United Kingdom.

Lopez-Poveda, E. A., and Alves-Pinto, A. (**2008**). "A variant temporal-masking curve method for inferring peripheral auditory compression," J. Acoust. Soc. Am. **123**, 1544–1554.

Lopez-Poveda, E. A., Alves-Pinto, A., and Palmer, A. R. (**2007**). "Psychophysical and physiological assessment of high-frequency spectral notches in the auditory nerve." in *Hearing, From Sensory Processing to Perception*, edited by B. Kollmeier, G. Klump, U. Hohmann, M. Langemann, S. Mauermann, S. Uppenkamp, and J. Verhey (Springer-Verlag, Heidelberg), pp. 51–59.

Lopez-Poveda, E. A., Alves-Pinto, A., Palmer, A. R., and Eustaquio-Martin, A. (**2008**). "Rate vs. time representation of the high-frequency spectral notches in the peripheral auditory system: A computational modelling study," Neurocomputing **71**, 693–703.

Lopez-Poveda, E. A., and Meddis, R. (**1996**). "A physical model of sound diffraction and reflections in the human concha," J. Acoust. Soc. Am. **100**, 3248–3259.

Meddis, R., and O'Mard, L. P. O. (**2005**). "A computer model of the auditory-nerve response to forward-masking stimuli," J. Acoust. Soc. Am. **117**, 3787–3798.

Moore, B. C. J. (**2005**). "Basic psychophysics of human spectral processing," Int. Rev. Neurobiol. **70**, 49–86.

Moore, B. C. J., and Glasberg, B. R. (**1983**). "Masking patterns for synthetic vowels in simultaneous and forward masking," J. Acoust. Soc. Am. **73**, 906–917.

Oxenham, A. J. (**2001**). "Forward masking: Adaptation or integration?," J. Acoust. Soc. Am. **109**, 732–741.

Oxenham, A. J., and Moore, B. C. J. (**1994**). "Modelling the additivity of nonsimultaneous masking," J. Acoust. Soc. Am. **80**, 105–118.

Palmer, A. R., and Russell, I. J. (**1986**). "Phase-locking in the cochlear nerve of the guinea-pig and its relation to the receptor potential of inner hair-cells," Hear. Res. **24**, 1–15.

Pickles, J. O. (**1988**). *An Introduction to the Physiology of Hearing* (Academic, New York).

Plack, C. J., and Oxenham, A. J. (**1998**). "Basilar membrane nonlinearity and the growth of forward masking," J. Acoust. Soc. Am. **103**, 1598–1608.

Poon, P. W. F., and Brugge, J. F. (**1993**). "Sensitivity of auditory nerve fibers to spectral notches," J. Neurophysiol. **70**, 655–666.

Recio-Spinoso, A., Temchin, A. N., van Dijk, P., Fan, Y. H., and Ruggero, M. A. (**2005**). "Wiener-kernel analysis of responses to noise of chinchilla auditory-nerve fibers," J. Neurophysiol. **93**, 3615–3634.

Reed, C. M., and Bilger, R. C. (**1973**). "A comparative study of S-No and E-N-o," J. Acoust. Soc. Am. **53**, 1039–1044.

Relkin, E. M., and Turner, C. W. (**1988**). "A re-examination of forward masking in the auditory nerve," J. Acoust. Soc. Am. **84**, 584–591.

Rice, J. J., Young, E. D., and Spirou, G. A. (**1995**). "Auditory-nerve encoding of pinna-based spectral cues: Rate representation of high-frequency stimuli," J. Acoust. Soc. Am. **97**, 1764–1776.

Rose, J. E., Gross, N. B., Geisler, C. D., and Hind, J. E. (**1971**). "Some effects of stimulus intensity on response of auditory-nerve fibers in the squirrel monkey," J. Neurophysiol. **34**, 685–699.

Sachs, M. B., and Abbas, P. J. (**1974**). "Rate versus level functions for auditory-nerve fibers in cats: tone-burst stimuli," J. Acoust. Soc. Am. **56**, 1835–1847.

Sachs, M. B., and Young, E. D. (**1979**). "Encoding of steady-state vowels in the auditory nerve: Representation in terms of discharge rate," J. Acoust. Soc. Am. **66**, 470–479.

Shaw, E. A. G. (**1974**). "Transformation of sound pressure level from free field to eardrum in horizontal plane," J. Acoust. Soc. Am. **56**, 1848–1861.

Shaw, E. A. G., and Teranishi, R. (**1968**). "Sound pressure generated in an external-ear replica and real human ears by a nearby point source," J. Acoust. Soc. Am. **44**, 240–249.

Winslow, R. L., and Sachs, M. B. (**1987**). "Effect of electrical-stimulation of the crossed olivocochlear bundle on auditory-nerve response to tones in noise," J. Neurophysiol. **57**, 1002–1021.

Young, E. D., and Sachs, M. B. (**1979**). "Representation of steady-state vowels in the temporal aspects of the discharge patterns of populations of auditory-nerve fibers," J. Acoust. Soc. Am. **66**, 1381–1403.

A computational model of human auditory signal processing and perception

Morten L. Jepsen
Centre for Applied Hearing Research, Acoustic Technology, Department of Electrical Engineering, Technical University of Denmark, DK-2800 Kgs. Lyngby, Denmark

Stephan D. Ewert
Medizinische Physik, Carl von Ossietzky Universität Oldenburg, D-26111 Oldenburg, Germany

Torsten Dau[a)]
Centre for Applied Hearing Research, Acoustic Technology, Department of Electrical Engineering, Technical University of Denmark, DK-2800 Kgs. Lyngby, Denmark

(Received 2 August 2007; revised 31 March 2008; accepted 17 April 2008)

A model of computational auditory signal-processing and perception that accounts for various aspects of simultaneous and nonsimultaneous masking in human listeners is presented. The model is based on the modulation filterbank model described by Dau *et al.* [J. Acoust. Soc. Am. **102**, 2892 (1997)] but includes major changes at the peripheral and more central stages of processing. The model contains outer- and middle-ear transformations, a nonlinear basilar-membrane processing stage, a hair-cell transduction stage, a squaring expansion, an adaptation stage, a 150-Hz lowpass modulation filter, a bandpass modulation filterbank, a constant-variance internal noise, and an optimal detector stage. The model was evaluated in experimental conditions that reflect, to a different degree, effects of compression as well as spectral and temporal resolution in auditory processing. The experiments include intensity discrimination with pure tones and broadband noise, tone-in-noise detection, spectral masking with narrow-band signals and maskers, forward masking with tone signals and tone or noise maskers, and amplitude-modulation detection with narrow- and wideband noise carriers. The model can account for most of the key properties of the data and is more powerful than the original model. The model might be useful as a front end in technical applications. © *2008 Acoustical Society of America.* [DOI: 10.1121/1.2924135]

PACS number(s): 43.66.Ba, 43.66.Dc, 43.66.Fe [BCM] Pages: 422–438

I. INTRODUCTION

There are at least two reasons why auditory processing models are constructed: to represent the results from a variety of experiments within one framework and to explain the functioning of the system. Specifically, processing models help generate hypotheses that can be explicitly stated and quantitatively tested for complex systems. Models of auditory processing may be roughly classified into biophysical, physiological, mathematical (or statistical), and perceptual models depending on which aspects of processing are considered. Most of the models can be broadly referred to as functional models, that is, they simulate the experimentally observed input-output behavior of the auditory system without explicitly modeling the precise internal biophysical mechanisms involved.

The present study deals with the modeling of perceptual masking phenomena, focusing on effects of intensity discrimination and spectral and temporal masking. Explaining basic auditory masking phenomena in terms of physiological mechanisms has a long tradition. There have been systematic attempts at predicting psychophysical performance limits from the activity of auditory nerve (AN) fibers (e.g., Siebert, 1965, 1970; Heinz *et al.*, 2001a, 2001b, Colburn *et al.*, 2003), combining analytical and computational population models of the AN with statistical decision theory. A general result has been that those models that make optimal use of all available information from the AN (e.g., average rate, synchrony, and nonlinear phase information) typically predict performance that is one to two orders of magnitude better than human performance, while the trends often match well human performance.

Other types of auditory masking models are to a lesser extent inspired by neurophysiological findings and make certain simplifying assumptions about the auditory processing stages. Such an "effective" modeling strategy does not allow conclusions about the details of signal processing at a neuronal level. On the other hand, if the effective model accounts for a variety of data, this suggests certain general processing principles. These, in turn, may motivate the search for neural circuits in corresponding physiological studies. Models of temporal processing typically consist of an initial stage of bandpass filtering, reflecting a simplified action of basilar-membrane (BM) filtering. Each filter is followed by a nonlinear device. In recent models, the nonlinear device typically includes two processes, half-wave rectification and a compressive nonlinearity, resembling the compressive input-output function on the BM (e.g., Ruggero and Rich, 1991; Oxenham and Moore, 1994; Oxenham *et al.*,

[a)]Author to whom correspondence should be addressed. Electronic mail: tda@elektro.dtu.dk

 0001-4966/2008/124(1)/422/17/$23.00

1997; Plack and Oxenham, 1998; Plack *et al.*, 2002). The output is fed to a smoothing device implemented as a low-pass filter (Viemeister, 1979) or a sliding temporal integrator (e.g., Moore *et al.*, 1988). This is followed by a decision device, typically modeled as the signal-to-noise ratio. Forward and backward masking have been accounted for in terms of the build-up and decay processes at the output of the sliding temporal integrator. The same model structure has also been suggested to account for other phenomena associated with temporal resolution, such as gap detection and modulation detection (e.g., Viemeister, 1979).

An alternative way of describing forward masking is in terms of neural adaptation (e.g., Jesteadt *et al.*, 1982; Nelson and Swain, 1996; Oxenham, 2001; Meddis and O'Mard, 2005). A few processing models include adaptation and account for several aspects of forward masking (e.g., Dau *et al.*, 1996a, 1996b; Buchholz and Mourjoloulus, 2004a, 2004b; Meddis and O'Mard, 2005). It appears that the two types of models, temporal integration and adaptation, can lead to similar results even though they seem conceptually different (Oxenham, 2001; Ewert *et al.*, 2007).

Dau *et al.* (1996a) proposed a model to account for various aspects of simultaneous and nonsimultaneous masking using one framework. The model includes a linear, one-dimensional transmission-line model to simulate BM filtering (Strube, 1985), an inner-hair-cell transduction stage, an adaptation stage (Püschel, 1988), and an 8-Hz modulation lowpass filter, corresponding to an integration time constant of 20 ms. The adaptation stage in that model is realized by a chain of five simple nonlinear circuits, or feedback loops (Püschel, 1988; Dau *et al.*, 1996a). An internal noise is added to the output of the preprocessing that limits the resolution of the model. Finally, an optimal detector is attached that acts as a matched-filtering process. An important general feature of the model of Dau *et al.* (1996a) is that, once it is calibrated using a simple intensity discrimination task to adjust its internal-noise variance, it is able to quantitatively predict data from other psychoacoustic experiments without further fitting. Part of this flexibility is caused by the use of the matched filter in the decision process. The optimal detector automatically "adapts" to the current task and is based on the cross correlation of a template, a suprathreshold representation of the signal to be detected in a given task, with the internal signal representation at the actual signal level.

In a subsequent modeling study (Dau *et al.*, 1997a, 1997b), the gammatone filterbank model of Patterson *et al.* (1995) was used instead of Strube's transmission-line implementation because its algorithm is more efficient and the bandwidths matched estimates of auditory-filter bandwidths more closely. The modulation lowpass filter was replaced by a modulation filterbank, which enables the model to reflect the auditory system's high sensitivity to fluctuating sounds and to account for amplitude-modulation (AM) detection and masking data (e.g., Bacon and Grantham, 1989; Houtgast, 1989; Dau *et al.*, 1997a; Verhey *et al.*, 1999; Piechowiak *et al.*, 2007). The modulation filterbank realizes a limited-resolution decomposition of the temporal modulations and was inspired by neurophysiological findings in the auditory brainstem (e.g., Langner and Schreiner, 1988; Palmer, 1995). The parameters of the filterbank were fitted to perceptual modulation masking data and are not directly related to the parameters from physiological models that describe the transformation from a temporal neural code into a rate-based representation of AM in the auditory brainstem (Langner, 1981; Hewitt and Meddis, 1994; Nelson and Carney, 2004; Dicke *et al.*, 2007).

The preprocessing of the model described by Dau *et al.* (1996a, 1997a) has been used in a variety of applications, e.g., for assessing speech quality (Hansen and Kollmeier, 1999, 2000), for predicting speech intelligibility (Holube and Kollmeier, 1996), as a front-end for automatic speech recognition (Tchorz and Kollmeier, 1999), for objective assessment of audio quality (Huber and Kollmeier, 2006), and for signal-processing distortion (Plasberg and Kleijn, 2007). The model has also been extended to predict binaural signal detection (Breebaart *et al.*, 2001a, 2001b, 2001c) and across-channel monaural processing (Piechowiak *et al.*, 2007).

However, despite some success with the model of Dau *et al.* (1997a), there are major conceptual limitations of the approach. One of these is that the model does not account for nonlinearities associated with BM processing since it uses the (linear) gammatone filterbank (Patterson *et al.*, 1995). Thus, for example, the model must fail in conditions which reflect level-dependent frequency selectivity, such as in spectral masking patterns. Also, even though the model includes effects of adaptation which account for certain aspects of forward masking, it must fail in those conditions that directly reflect the nonlinear transformation on the BM. This, in turn, implies that the model will not be able to account for consequences of sensorineural hearing impairment for signal detection since a realistic cochlear representation of the stimuli in the normal system is missing as a reference.

Implementing a nonlinear BM processing stage in the framework of the model is a major issue since the interaction with the successive static and dynamic processing stages can strongly affect the internal representation of the stimuli at the output of the preprocessing depending on the particular experimental condition. For example, how does the level-dependent cochlear compression affect the results in conditions of intensity discrimination? To what extent are the dynamic properties of the adaptation stage affected by the fast-acting cochlear compression? What is the influence of the compressive peripheral processing on the transformation of modulations in the model? In more general terms, the question is whether a modified model that includes a realistic (but more complex) cochlear stage can *extend* the predictive power of the original model. If this cannot be achieved, major conceptual changes of the modeling approach would most likely be required.

In an earlier study (Derleth *et al.*, 2001), it was suggested how the model of Dau *et al.* (1997a, 1997b), referred to in the following as the "original model," could be modified to include fast-acting compression, as found in BM processing. Different implementations of fast-acting compression were tested either through modifications of the adaptation stage or by using modified, level-dependent gammatone filters (Carney, 1993). Derleth *et al.* (2001) found that the temporal-adaptive properties of the model were

strongly affected in all implementations of fast-acting compression; their modified model thus failed in conditions of forward masking. It was concluded that, in the given framework, the model would only be able to account for the data when an expansion stage after BM compression was assumed (which would then partly compensate for cochlear compression). However, corresponding explicit predictions were not generated in their study.

Several models of cochlear processing have been developed recently (e.g., Heinz *et al.*, 2001b; Meddis *et al.*, 2001; Zhang *et al.*, 2001; Bruce *et al.*, 2003; Irino and Patterson, 2006) which differ in the way that they account for the nonlinearities in the peripheral transduction process. In the present study, the dual-resonance nonlinear (DRNL) filterbank described by Meddis *et al.* (2001) was used as the peripheral BM filtering stage in the model—instead of the gammatone filterbank. In principle, any of the above cochlear models could instead have been integrated in the present modeling framework. The DRNL was chosen since it represents a computationally efficient and relatively simple functional model of peripheral processing. It can account for several important properties of BM processing, such as frequency- and level-dependent compression and auditory filter shape in animals (Meddis *et al.*, 2001). The DRNL structure and parameters were adopted to develop a human cochlear filterbank model by Lopez-Poveda and Meddis (2001) on the basis of pulsation-threshold data.

In addition to the changes at the BM level, several other substantial changes in the processing stages of the original model were made. The motivation was to incorporate findings from other successful modeling studies in the present framework. Models of human outer- and middle-ear transformations were included in the current model, none of which were considered in the original model. An expansion stage, realized as a squaring device, was assumed after BM processing, as in the temporal-window model (Plack and Oxenham, 1998; Plack *et al.*, 2002). Also, certain aspects of modulation processing were modified in the processing, motivated by recent studies on modulation detection and masking (Ewert and Dau, 2000; Kohlrausch *et al.*, 2000). The general structure of the original perception model, however, was kept the same.

The model developed in this study, referred to as the computational auditory signal-processing and perception (CASP) model in the following, was evaluated using a set of critical experiments, including intensity discrimination using tones and broadband noise, tone-in-noise detection as a function of the tone duration, spectral masking patterns with tone and narrow-band-noise signals and maskers, forward masking with noise and tone maskers, and AM detection with wide- and narrow-band-noise carriers. The experimental data from these conditions can only be accounted for if the compressive characteristics and the spectral and temporal properties of auditory processing are modeled appropriately.

Section II specifies the processing stages of the CASP model. Section III describes the experimental methods, the stimuli in the different conditions, and the parameters used in the simulations. Section IV focuses on the results of the experiments and the corresponding simulations. The main outcomes of the study and perspectives for further modeling investigations are discussed in Sec. V.

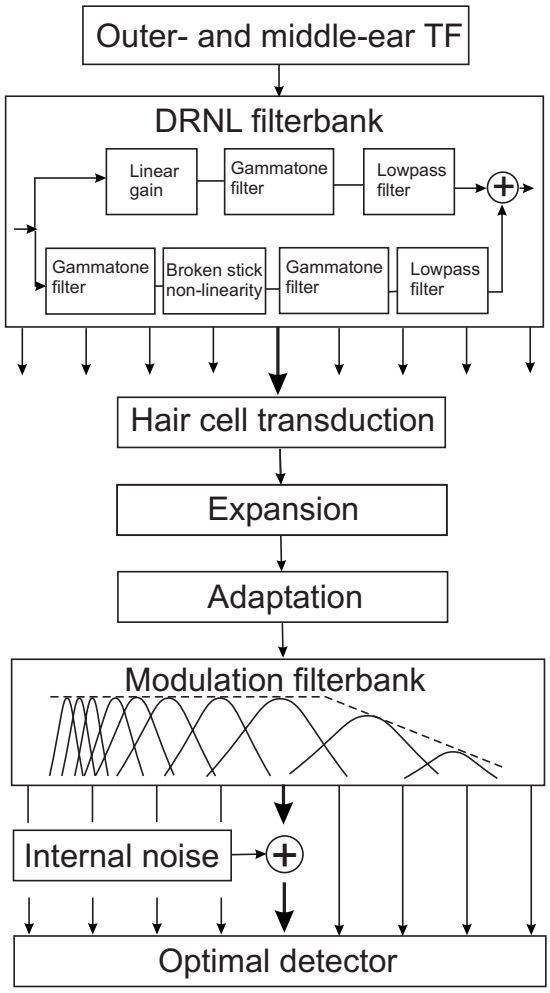

FIG. 1. Block diagram of the model structure. See text for a description of each stage.

II. DESCRIPTION OF THE MODEL

A. Overall structure

Figure 1 shows the structure of the CASP model.[1] The first stages represent the transformations through the outer and the middle ear, which were not considered by Dau *et al.* (1997a, 1997b). A major change to the original model was the implementation of the DRNL filterbank. The hair-cell transduction, i.e., the transformation from mechanical vibrations of the BM into inner-hair-cell receptor potentials, and the adaptation stage are the same as in the original model. However, a squaring expansion was introduced in the model after hair-cell transduction, reflecting the square-law behavior of rate-versus-level functions of the neural response in the AN (Yates *et al.*, 1990; Muller *et al.*, 1991). In terms of envelope processing, a first-order 150-Hz lowpass filter was introduced in the processing prior to the modulation bandpass filtering. This was done in order to limit sensitivity to fast envelope fluctuations, as observed in AM detection experiments with tonal carriers (Ewert and Dau, 2000; Kohl-

rausch *et al.*, 2000). The transfer functions of the modulation filters and the optimal detector are the same as used in the original model. The details of the processing stages are presented below (Sec. II B).

B. Processing stages in the model

1. Outer- and middle-ear transformations

The input to the model is a digital signal, where an amplitude of 1 corresponds to a maximum sound pressure level (SPL) of 100 dB. The amplitudes of the signal are scaled to be represented in pascals prior to the outer-ear filtering. The first stage of the auditory processing is the transformation through the outer and middle ears. As in the study of Lopez-Poveda and Meddis (2001), these transfer functions were realized by two linear-phase finite impulse response filters. The outer-ear filter was a headphone-to-eardrum transfer function for a specific pair of headphones (Pralong and Carlile, 1996). It was assumed that the headphone brand only has a minor influence as long as circumaural, open and diffuse-field equalized, quality headphones are considered, as was done in the present study. The middle-ear filter was derived from human cadaver data (Goode *et al.*, 1994) and simulates the mechanical impedance change from the outer ear to the middle ear. The outer- and middle-ear transfer functions correspond to those described by Lopez-Poveda and Meddis (2001, their Fig. 2). The combined function has a symmetric bandpass characteristic with a maximum at about 800 Hz and slopes of 20 dB/decade. The output of this stage is assumed to represent the peak velocity of vibration at the stapes as a function of frequency.

2. The DRNL filterbank

Meddis *et al.* (2001) developed an algorithm to mimic the complex nonlinear BM response behavior of physiological chinchilla and guinea pig observations. This algorithm includes two parallel bandpass processing paths, a linear one and a compressive nonlinear one, and its output represents the sum of the outputs of the two paths. The complete unit has been called the DRNL filter. The structure of the DRNL filter is illustrated in Fig. 1. The linear path consists of a linear gain function, a gammatone bandpass filter, and a lowpass filter. The nonlinear path consists of a gammatone filter, a compressive function which applies an instantaneous broken-stick nonlinearity, another gammatone filter, and, finally, a lowpass filter. The output of the linear path dominates the sum at high signal levels (above 70–80 dB SPL). The nonlinear path behaves linearly at low signal levels (below 30–40 dB SPL) and is compressive at medium levels (40–70 dB SPL). In the study of Meddis *et al.* (2001), the model parameters were fitted to physiological data so that the model accounted for a range of phenomena, including isovelocity contours, input-output functions, phase responses, two-tone suppression, impulse responses, and distortion products. In a subsequent study, the DRNL filterbank was modified in order to simulate the properties of the *human* cochlea (Lopez-Poveda and Meddis, 2001) by fitting the model parameters to psychophysical pulsation-threshold data (Plack and Oxenham, 2000). These data have been assumed

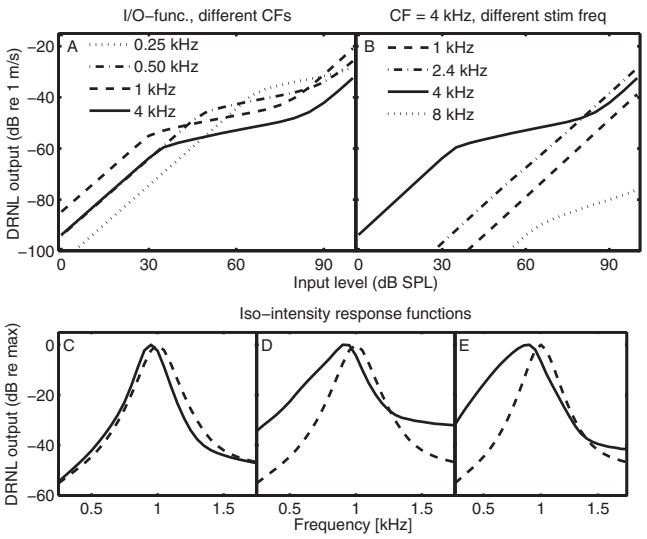

FIG. 2. Properties of the DRNL filterbank. Panel A shows the I/O functions for on-frequency stimulation at different CFs. Panel B shows the I/O functions for the filter with CF=4 kHz for tones with frequencies of 1, 2.4, 4, and 8 kHz. The solid curves in panels C, D, and E show the normalized magnitude transfer functions of the DRNL filter tuned to 1 kHz for input levels of 30, 60, and 90 dB SPL, respectively. The dashed curves indicate the transfer function of the corresponding fourth-order gammatone filter.

to estimate the amount of peripheral compression in human cochlear processing. The parameters of their model were estimated for different signal frequencies and Lopez-Poveda and Meddis (2001) suggested how to derive the parameters for a complete filterbank.

The CASP model includes the digital time-domain implementation of the DRNL filterbank described by Lopez-Poveda and Meddis (2001). However, slight changes in some of the parameters were made. The amount of compression was adjusted to stay constant above 1.5 kHz, whereas it was assumed to increase continuously in the original parameter set. This modification is consistent with recent findings of Lopez-Poveda *et al.* (2003) and Rosengard *et al.* (2005), where a constant amount of compression was estimated at signal frequencies of 2 and 4 kHz based on forward-masking experiments. A table containing the parameters that were modified is given in the Appendix. For implementation details, the reader is referred to Lopez-Poveda and Meddis (2001).

Some of the key properties of the implemented DRNL filter are reflected in the input/output (I/O) functions at different characteristic frequencies (CFs). Figure 2(A) shows I/O functions of the filters at 0.25, 0.5, 1, and 4 kHz. The 0.25 kHz function (dotted curve) is linear up to an input level of 60 dB SPL and becomes compressive at the highest levels. With increasing CFs, the level at which compression begins to occur decreases. It is well known that the compressive characteristics of the BM are most prominent near CF (0.2–0.5 dB/dB), at least for CFs above about 1 kHz, whereas the response is close to linear (0.8–1.0 dB/dB) for stimulation at frequencies well below CF (e.g., Ruggero *et al.*, 1997). Figure 2(B) shows the I/O functions for the filter centered at 4 kHz in response to tones with several input frequencies (1, 2.4, 4, 8 kHz). It can be seen that the largest response is generally produced by on-frequency

stimulation (4 kHz). The I/O functions for stimulation frequencies below CF are linear. The response to a tone with a frequency of one octave above CF (8 kHz) is compressive (dotted curve) but at a very low level.

Associated with the compressive transformation for on-frequency stimulation and the less compressive (close to linear) response to off-frequency stimulation is the level-dependent magnitude transfer function of the filter. The transfer function (normalized to the maximal tip gain) for the DRNL filter tuned to 1 kHz (solid curves) is shown for input levels of 30 dB SPL (panel C), 60 dB SPL (panel D), and 90 dB SPL (panel E). For comparison, the dashed curves indicate the transfer function of the fourth-order gammatone filter at the same CF. At the lowest level, 30 dB SPL, the transfer function of the DRNL is very similar to that of the gammatone filter. The bandwidth of the DRNL filter increases with level and the filter becomes increasingly asymmetric. With increasing level, the best frequency, i.e., the stimulus frequency that produces the strongest response, shifts toward lower frequencies, similar to physiological data from animals at higher frequencies (e.g., Ruggero *et al.*, 1997). Behavioral data from Moore and Glasberg (2003) indicated that this shift may not occur at the 1-kHz site in humans. Nevertheless, the implementation as suggested by Lopez-Poveda and Meddis (2001) was kept in the present study. The output of the DRNL filterbank is a multi-channel representation, simulating the temporal output activity in various frequency channels. Each channel is processed independently in the following stages. The separation of center frequencies in the filterbank is one equivalent rectangular bandwidth, representing a measure of the critical bandwidth of the auditory filters as defined by Glasberg and Moore (1990).

3. Mechanical-to-neural transduction and adaptation

The hair-cell transduction stage in the model roughly simulates the transformation of the mechanical BM oscillations into receptor potentials. As in the original model, this transformation is modeled by half-wave rectification followed by a first-order lowpass filter (Schroeder and Hall, 1974) with a cutoff frequency of 1 kHz. The lowpass filtering preserves the temporal fine structure of the signal at low frequencies and extracts the envelope of the signal at high frequencies (Palmer and Russell, 1986). The output is then transformed into an intensity like representation by applying a squaring expansion. This step is motivated by physiological findings of Yates *et al.* (1990) and Muller *et al.* (1991) which provided evidence for a square-law behavior of rate-versus-level functions of AN fibers near the AN threshold (in guinea pigs).

The output of the squaring device serves as the input to the adaptation stage of the model which simulates adaptive properties of the auditory periphery. Adaptation refers to dynamic changes in the gain of the system in response to changes in input level. Adaptation has been found physiologically at the level of the AN (e.g., Smith, 1977; Westermann and Smith, 1984). In the present model, the effect of adaptation is realized by a chain of five simple nonlinear circuits, or feedback loops, with different time constants as described by Püschel (1988) and Dau *et al.* (1996a, 1997a). Each circuit consists of a lowpass filter and a division operation. The lowpass filtered output is fed back to the denominator of the devisor element. For a stationary input signal, each loop realizes a square-root compression. Such a single loop was first suggested by Siebert (1968) as a phenomenological model of AN adaptation. The output of the series of five loops approaches a logarithmic compression for stationary input signals. For input variations that are rapid compared to the time constants of the lowpass filters, the transformation through the adaptation loops is more linear, leading to an enhancement in fast temporal variations or onsets and offsets at the output of the adaptation loops. The time constants, ranging between 5 and 500 ms, were chosen to account for perceptual forward-masking data (Dau *et al.*, 1996a). In response to signal onsets, the output of the adaptation loops is characterized by a pronounced overshoot. In the study by Dau *et al.* (1997a), this overshoot was limited, such that the maximum ratio of the onset response amplitude and steady-state response amplitude was 10. This version of the adaptation stage was also used in the CASP model.

4. Modulation processing

The output of the adaptation stage is processed by a first-order lowpass filter with a cutoff frequency at 150 Hz. This filter simulates a decreasing sensitivity to sinusoidal modulation as a function of modulation frequency (Ewert and Dau, 2000; Kohlrausch *et al.*, 2000). The lowpass filter is followed by a modulation filterbank. The highest modulation filter center frequencies in the filterbank are limited to one-quarter of the center frequency of the peripheral channel driving the filterbank and maximally to 1000 Hz, motivated by results from physiological recordings of Langner and Schreiner (1988) and Langner (1992). The lowest modulation filter is a second-order lowpass filter with a cutoff frequency of 2.5 Hz. The modulation filters tuned to 5 and 10 Hz have a constant bandwidth of 5 Hz. For modulation frequencies at and above 10 Hz, the modulation filter CFs are logarithmically scaled and the filters have a constant Q value of 2. The magnitude transfer functions of the filters overlap at their −3 dB points. As in the original model, the modulation filters are complex frequency-shifted first-order lowpass filters. These filters have a complex valued output and either the absolute value of the output or the real part can be considered. For the filters centered above 10 Hz, the absolute value is considered. This is comparable to the Hilbert envelope of the bandpass filtered output and only conveys information about the presence of modulation energy in the respective modulation band, i.e., the modulation phase information is strongly reduced. This is in line with the observation of decreasing monaural phase discrimination sensitivity for modulation frequencies above about 10 Hz (Dau *et al.*, 1996a; Thompson and Dau, 2008). For modulation filters centered at and below 10 Hz, the real part of the filter output is considered. In contrast to the original model, the output of modulation filters above 10 Hz was attenuated by a factor of $\sqrt{2}$, so that the rms value at the output is the same as for the low-frequency channels in response to a sinusoidal AM input signal of the same modulation depth.

5. The decision device

In order to simulate limited resolution, a Gaussian-distributed internal noise is added to each channel at the output of the modulation filterbank. The variance of the internal noise was the same for all peripheral channels and was adjusted so that the model predictions followed Weber's law in an intensity discrimination task. Specifically, predictions were fitted to intensity discrimination data of a 1 kHz pure tone at 60 dB SPL and of broadband noise at medium SPLs (see also Sec. IV A). The representation of the stimuli after the addition of the internal noise is referred to as the "internal representation." The decision device is realized as an optimal detector, as in the original model. Within the model, it is assumed that the subject is able to create a "template" of the signal to be detected. This template is calculated as the normalized difference between the internal representation of the masker plus a suprathreshold signal representation and that of the masker alone. The template is a three-dimensional pattern, with axes time, frequency, and modulation frequency. During the simulation procedure, the internal representation of the masker alone is calculated and subtracted from the internal representation in each interval of a given trial. Thus, in the signal interval, the difference contains the signal, embedded in internal noise, while the reference interval(s) contain internal noise only. For stochastic stimuli, the reference and signal intervals are affected both by internal noise and by the external variability of the stimuli. The (non-normalized) cross-correlation coefficient between the template and the difference representations is calculated, and a decision is made on the basis of the cross-correlation values obtained in the different intervals. The interval that produces the largest value is assumed to be the signal interval. This corresponds to a matched-filtering process (e.g., Green and Swets, 1966) and is described in more detail by Dau *et al.* (1996a).

III. EXPERIMENTAL METHOD

The experimental method, stimulus details, and simulation parameters are described below. In the present study, data were collected for tone-in-noise detection and forward masking, while the data on intensity discrimination, spectral masking, and modulation detection were taken from the literature (Houtsma *et al.*, 1980; Moore *et al.*, 1998; Dau *et al.*, 1997a; Viemeister, 1979).

A. Subjects

Four normal-hearing listeners, aged between 24 and 28 years, participated in the experiments. They had pure-tone thresholds of 10 dB hearing level or better for frequencies between 0.25 and 8 kHz. One subject was the first author and had experience with psychoacoustic experiments. The other three subjects had no prior experience in listening tests. These three subjects were paid for their participation on an hourly basis and received 30 min training sessions before each new experiment. There were no systematic improvements in thresholds during the course of the experiments. Measurement sessions ranged from 30 to 45 min depending of the subject's ability to focus on the task. In all measurements, each subject completed at least three runs for each condition.

B. Apparatus and procedure

All stimuli were generated and presented using the AFC-Toolbox for MATLAB (Mathworks), developed at the University of Oldenburg, Germany, and the Technical University of Denmark. The sampling rate was 44.1 kHz and signals were presented through a personal computer with a high-end, 24 bit sound card (RME DIGI 96/8 PAD) and headphones (Sennheiser HD-580). The listeners were seated in a double-walled, sound insulated booth with a computer monitor, which displayed instructions and gave visual feedback.

A three-interval, three-alternative forced choice paradigm was used in conjunction with an adaptive 1-up-2-down tracking rule. This tracked the point on the psychometric function corresponding to 70.7% correct. The initial step size was 4 dB. After each second reversal, the step size was halved until a minimum step size of 0.5 dB was reached. The threshold was calculated as the average of the level at six reversals at the minimum step size. The computer monitor displayed a response box with three buttons for the stimulus intervals in a trial. The subject was asked to indicate the interval containing the signal. During stimulus presentation, the buttons in the response box were successively highlighted synchroneously with the appropriate interval. The subject responded via the keyboard and received immediate feedback on whether the response was correct or not.

C. Stimuli

1. Intensity discrimination of pure tones and broadband noise

The data on intensity discrimination of a 1 kHz tone and broadband noise were taken from Houtsma *et al.* (1980). The just noticeable level difference was measured as a function of the standard (or reference) level of the tone or noise, which was 20, 30, 40, 50, 60, or 70 dB SPL. The duration of the tone was 800 ms, including 125-ms onset and offset raised-cosine ramps. The noise had a duration of 500 ms, including 50-ms raised-cosine ramps.

2. Tone-in-noise simultaneous masking

Detection thresholds of a 2-kHz signal in the presence of a noise masker were measured for signal durations from 5 to 200 ms, including 2.5-ms raised-cosine ramps. The masker was a Gaussian noise that was band limited to a frequency range from 0.02 to 5 kHz. The masker was presented at a level of 65 dB SPL and had a duration of 500 ms including 10-ms raised-cosine ramps. The signal was temporally centered in the masker.

3. Spectral masking with narrow-band signals and maskers

The data from this experiment were taken from Moore *et al.* (1998). The signal and the masker were either a tone or an 80-Hz wide Gaussian noise. All four signal-masker combinations were considered: tone signal and tone masker (TT),

tone signal and noise masker (TN), noise signal and tone masker (NT), and noise signal and noise masker (NN). In the TT condition, a 90° phase shift between the signal and masker was chosen, while the other conditions used random onset phases of the tone. The masker was centered at 1 kHz, and the signal frequencies were 0.25, 0.5, 0.9, 1.0, 1.1, 2.0, 3.0, and 4.0 kHz. The signal and the masker were presented simultaneously. Both had a duration of 220 ms including 10-ms raised-cosine ramps. Here, only the masker levels of 45 and 85 dB SPLs were considered, whereas the original study also used a level of 65 dB SPL.

4. Forward masking with noise and tone maskers

In the first forward-masking experiment, the masker was a broadband Gaussian noise, band limited to the range from 0.02 to 8 kHz. The steady-state masker duration was 200 ms and 2-ms raised-cosine ramps were applied. Three masker levels were used: 40, 60, and 80 dB SPLs. The signal was a 4-kHz tone. It had a duration of 10 ms and a Hanning window was applied over the entire signal duration. Thresholds were obtained for temporal separations between the masker offset and the signal onset of −20 to 150 ms. For separations between −20 and −10 ms, the signal was presented completely in the masker, i.e., these conditions reflected simultaneous masking.

The second experiment involved forward masking with pure-tone maskers. The stimuli were similar to those used by Oxenham and Plack (2000). Two conditions were used: in the on-frequency condition, the signal and the masker were presented at 4 kHz. In the off-frequency condition, the signal frequency remained at 4 kHz, whereas the masker frequency was 2.4 kHz. The signal was the same as in the first experiment. The signal and the masker had random onset phases in both conditions. The signal level at masked threshold was obtained for several masker levels. In the on-frequency condition, the masker was presented at levels from 30 to 80 dB SPL in 10-dB steps. For the off-frequency condition, the masker was presented at 60, 70, 80, and 85 dB SPLs. The separation between the masker offset and signal onset was either 0 or 30 ms.

5. Modulation detection

The data for the modulation detection experiments were taken from Dau *et al.* (1997a) for the narrowband-noise carriers and from Viemeister (1979) for the broadband-noise carriers. For the narrowband carriers, a band limited Gaussian noise, centered at 5 kHz, was used as the carrier. The carrier bandwidths were 3, 31, or 314 Hz. The carrier level was 65 dB SPL. The overall duration of the stimuli was 1 s, windowed with 200-ms raised-cosine ramps. Sinusoidal amplitude modulation (SAM) with a frequency in the range from 3 to 100 Hz was applied to the carrier. The duration of the signal modulation was equal to that of the carrier. In the case of the 314-Hz wide carrier, the modulated stimuli were limited to the original (carrier) bandwidth to avoid spectral cues. To eliminate potential level cues, all stimuli were adjusted to have equal power (for details, see Dau *et al.*, 1997a).

For the broadband-noise carrier, a Gaussian noise with a frequency range from 1 to 6000 Hz was used. The carrier was presented at a level of 77 dB SPL and had a duration of 800 ms. The signal modulation had the same duration and the stimulus was gated with 150-ms raised-cosine ramps, resulting in a 500-ms steady-state portion. Sinusoidal signal modulation, ranging from 4 to 1000 Hz, was imposed on the carrier. There was no level compensation, i.e., the overall level of the modulated stimuli varied slightly depending on the imposed modulation depth.

D. Simulation parameters

The model was calibrated by adjusting the variance of the internal noise so that the model predictions satisfied Weber's law for the intensity discrimination task from Sec. III C 1. When setting up the simulations, the frequency range of the relevant peripheral channels and the suprathreshold signal level for the generation of the template need to be specified. The range of channels was chosen such that potential effects of off-frequency listening were included in the simulations. The on-frequency channel may not always represent the channel with the best signal-to-noise ratio, particularly in the present model where the best frequency of the nonlinear peripheral channels depends on the stimulus level.

The following frequency ranges and suprathreshold signal levels were used in the simulations: For intensity discrimination with tones, the peripheral channels from one octave below to one octave above the signal frequency (1 kHz) were considered. For the broadband noise, all peripheral channels centered from 0.1 to 8 kHz were used. For both experiments, the signal level for the template was chosen to be 5 dB above the standard level. For tone-in-noise masking, the channels from one octave below to one octave above the 2-kHz signal frequency were considered. The signal level for the template was set to 75 dB SPL which is about 10 dB higher than the highest expected masked threshold in the data. For the spectral masking experiments, the channels from half an octave below to one octave above the signal frequency were considered. For the forward-masking experiment with a broadband-noise masker and a 4 kHz signal, the channels from 3.6 to 5 kHz were used. The signal level for the template was chosen to be 10 dB above the masker level. For the forward-masking experiments with pure-tone maskers, only the channel tuned to the signal frequency (4 kHz) was used and the template level was 10 dB above the masker level. In the modulation detection experiment with narrow-band carriers centered at 5 kHz, the channel at 5 kHz was considered as in the study of Dau *et al.* (1997a) in order to directly compare to the results with the original simulations. For this experiment, the simulations showed a standard deviation that was larger than that in the data. To reduce the standard deviation, simulated thresholds were averages of 20 runs instead of only 3 runs as for all other simulations. For the broadband-noise carrier condition, the channels from 0.1 to 8 kHz were used. In both cases, the modulation depth for the template was chosen to be −6 dB.

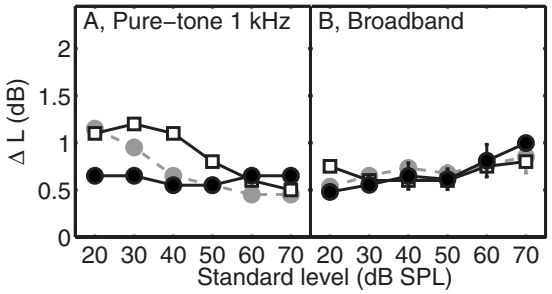

FIG. 3. Intensity discrimination thresholds for a 1-kHz tone (left panel) and broadband noise (right panel) as a function of the standard level. Model predictions (closed symbols) are shown along with measured data (open symbols) taken from Houtsma *et al.* (1980). The gray symbols represent simulations obtained with the model of Dau *et al.* (1997a).

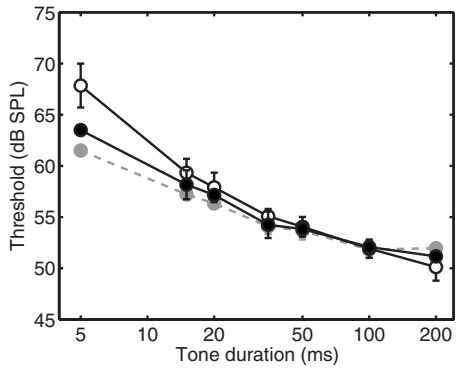

FIG. 4. Results from the tone-in-noise masking experiment with a broadband-noise masker at 65 dB SPL. The signal was a 2-kHz pure tone. The open circles show the mean detection thresholds for the four subjects as a function of signal duration. The error bars indicate one standard deviation. The closed circles indicate the predicted thresholds for the CASP model (black) and the original model (gray).

IV. RESULTS

In this section, measured data are compared to simulations. The data are represented by open symbols while simulations are shown as filled symbols. For comparison, gray symbols indicate simulations obtained with the original model. Differences between the predictions of the two models are discussed in more detail in Sec. V.

A. Intensity discrimination

For pure-tone and broadband-noise stimuli, the smallest detectable change in intensity, ΔI, is, to a first approximation, a constant fraction of the standard intensity I of the stimulus (e.g., Miller, 1947). This is referred to as Weber's law. As in many other studies, intensity differences are described in the following as just noticeable differences (JNDs) in level, ΔL.

The broadband-noise JND at medium levels (from 30 to 60 dB) was used to calibrate the model, i.e., to adjust the variance in the internal noise in the model. In the original model, the combination of the logarithmic compression of the stationary parts of the stimuli, realized in the adaptation loops, and the constant-variance internal noise produced a constant Weber fraction (for noise) throughout the entire level range.

Figure 3 shows the JNDs for the 1-kHz tone (panel A) and for broadband noise (panel (B)). The simulations (filled circles) are shown together with average data (open squares) taken from Houtsma *et al.* (1980). For the pure tone, the simulated JND is about 0.5 dB for all standard levels considered here. For the levels from 20 to 40 dB SPL, the simulated JNDs lie about 0.5 dB below the data. At higher standard levels, the simulations agree well with the data. The simulation does not reflect the near miss to Weber's law observed in the measured data, i.e., the decrease in threshold with increasing the standard level. This is discussed in detail in Sec. V A. The original model (gray symbols) accounts well for the data at 20 dB SPL and above 50 dB SPL, while the JND for 40 dB SPL lies 0.5 dB below the measured JND.

The measured JNDs for broadband noise (panel (B)) are about 0.6 dB for levels from 30 to 50 dB SPL. There is a slight increase at the lowest and the highest levels in the data, resulting in a JND of about 0.8 dB. The simulations agree very well with the data for levels from 30 to 60 dB SPL. For the lowest level (20 dB SPL), the simulated JND lies 0.3 dB below the measured JND, while it is about 0.2 dB above the measured value at the highest level. The simulations obtained with the original model show essentially the same results.

B. Tone-in-noise simultaneous masking

Figure 4 shows the average thresholds of the four listeners from the present study for tone-in-noise masking (open circles). The error bars indicate ± one standard deviation across subjects, which is typically less than 1 dB but amounts to about 2 dB for the shortest signal duration of 5 ms. For signal durations in the range from 5 to 20 ms, the threshold decreases by about 4–5 dB per doubling of signal duration, while the decrease is about 3 dB per doubling for durations above 20 ms. The data are consistent with results from earlier studies on signal integration in tone-in-noise masking (e.g., Dau *et al.*, 1996b; Oxenham *et al.*, 1997; Oxenham, 1998).

The simulations (filled circles) show a constant decay of 3 dB per doubling of signal duration. This agrees nicely with the measured data for durations at and above 15 ms. At signal durations of 200 ms and above (not shown), the simulations are consistent with the prediction of a threshold of 48 dB obtained with the classical power spectrum model of masking (Patterson and Moore, 1986), assuming a threshold criterion of 1.5 dB increase in power (due to the addition of the signal to the noise) in the passband of the 2 kHz gammatone filter. For the shortest signal duration of 5 ms, the CASP model underestimates the measured threshold by 4 dB. This results from the 3 dB per doubling decay in the simulations observed also for the short durations (5–20 ms) while the data show a somewhat larger slope in this region. The simulations with the original model (gray symbols) show similar results[2] as the CASP model.

The actual integration of signal information in the model is realized in the optimal detector. The matched-filtering process implies that a variable time constant is available that is matched to the signal duration. The integration of the cross correlator in the detector is similar to the classic notion of

temporal integration, but no fixed integration time constant is necessary for long-term integration. It is the temporal extension of the template which automatically determines the weighting of the stimuli across time. This concept is effectively close to the "multiple-looks" strategy discussed by Viemeister and Wakefield (1991). Time constants that are related to the "hard-wired" part of signal processing within the model represent a lower limit in temporal acuity. The modulation filterbank represents a set of time constants that are, however, too short to account for the long-term integration data. Thus, it is the decision device that inherently accounts for the long effective time constants observed in the present experiment. The result of the decision process depends critically on the properties of the internal representation of the stimuli which forms the input to the detector. The combination of peripheral processing, adaptation, modulation filtering, and decision making, assumed in the present model, leads to good agreement of the predictions with the data in this experimental condition.

C. Spectral masking patterns with narrowband signals and maskers

Masking patterns represent the amount of masking of a signal as a function of signal frequency in the presence of a masker with fixed frequency and level. The shapes of these masking patterns are influenced by several factors, such as occurrence of combination tones or harmonics produced by the peripheral nonlinearities, and by beating cues (Moore and Glasberg, 1987; van der Heijden and Kohlrausch, 1995). Additionally, the width and shape of the masking patterns are level dependent as a consequence of the level-dependent auditory filters. Moore *et al.* (1998) measured masking patterns using pure tones and narrowband noises as signals and pure tones and narrowband noises as maskers for masker levels of 45, 65, and 85 dB SPL. They found that temporal fluctuations (beats) had a strong influence on the measured masking patterns for sinusoidal maskers for masker-signal frequency separations up to a few hundred hertz. The data also indicated some influence of beats for the conditions with narrowband-noise maskers. The simulations obtained with the present model are compared here to the data of Moore *et al.* (1998) and with simulations of Derleth and Dau (2000) using the original model.

The open symbols in Fig. 5 show the mean data of Moore *et al.* (1998). The four panels show the results for conditions TT, TN, NT, and NN. The masking patterns for masker levels of 45 and 85 dB SPL are indicated by squares and circles, respectively. The ordinate represents masking, defined as the difference between the masked threshold and the absolute threshold at each signal frequency. The masking patterns generally show a maximum at the masker frequency. The amount of masking generally decreases with increasing spectral separation between the signal and the masker. For the TT condition, the peak in the masking patterns is particularly pronounced, since beating between the signal and the masker for frequency separations of a few hundred hertz provides a very effective detection cue in this condition (e.g., Moore *et al.*, 1998). The 45 dB SPL masker produces a symmetric pattern in all conditions, whereas the pattern for the 85 dB SPL masker is asymmetric with a considerable broadening on the high-frequency side.

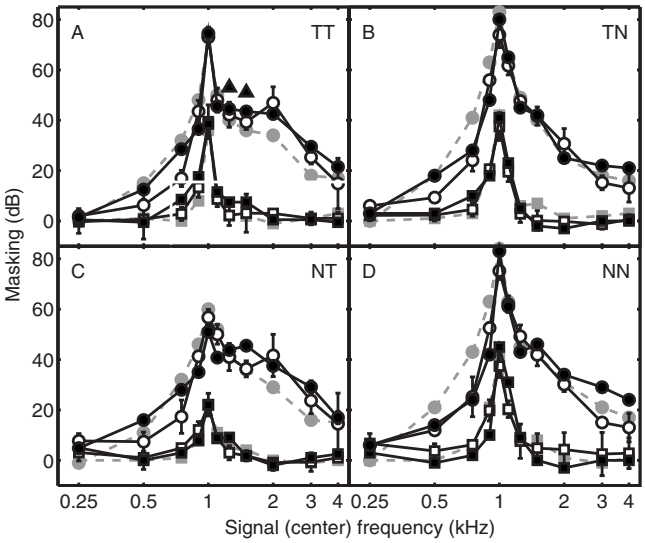

FIG. 5. Spectral masking patterns for the four stimulus conditions. Masking is the difference between the masked and the absolute threshold. The masker was centered at 1 kHz. The squares and circles indicate masker levels of 45 and 85 dB SPL, respectively. The open symbols indicate the measured data (Moore *et al.*, 1998). The closed symbols indicate the simulated patterns. Panel A represents the TT condition. The upward triangles indicate predicted masking where the modulation filters were limited to have a maximum center frequency of 130 Hz. Panels B, C, and D show the patterns in the TN, NT, and NN conditions, respectively. The gray symbols indicate predictions from Derleth and Dau (2000).

The filled symbols in Fig. 5 show the model predictions. In the TT condition, the predictions agree well with the experimental data, except for the signal frequencies of 500 and 750 Hz for the 85 dB SPL masker, where the amount of masking is overestimated. The simulations at this masker level otherwise show the asymmetry found in the measured masking pattern, which in the model is a direct consequence of the level-dependent BM filter shapes. The gray symbols plot the simulated pattern from Derleth and Dau (2000). Using level-invariant, linear gammatone filters, these predictions underestimate the amount of masking at high signal frequencies.

The two filled upward-pointing triangles in panel A indicate simulations that were obtained considering only the first eight modulation filters (with center frequencies ranging up to 130 Hz), while neglecting activity in the remaining modulation filters tuned to modulation rates above 130 Hz. These predictions exceed measured thresholds by up to 15 dB. Within the model, the reason for this deviation from the data is that the beats between the signal and the masker at rates of 150–200 Hz are not represented and cannot contribute to signal detection. Thus, in the framework of the present model, the inclusion of higher-frequency modulation filters between 130 and 250 Hz is crucial to account for the tone-on-tone masking pattern.

The masking patterns for condition TN are shown in panel B. For signal frequencies close to the masker frequency, they are broader than for the TT condition. The sharp peak at 2 kHz that occurred for the tonal masker is not

present for the noise masker. This is also the case in the simulated pattern since the beating cue for small masker-signal frequency separations is less pronounced than in the case of the tonal masker. On the low-frequency side of the masker, the predictions of the CASP model are considerably better than those obtained by Derleth and Dau (2000), where masking was overestimated by up to 18 dB. Thus, as expected, in this condition where energy cues play the most important role, the shapes of the level-dependent BM filters are mainly responsible for the good agreement between the data and the simulations.

Panel C shows the results for condition NT. When the signal and masker are centered at the same frequency, the amount of masking is about 20 dB lower than for the TN and TT conditions. This asymmetry of masking has been reported previously and explained by temporal envelope fluctuations introduced by the noise signal (e.g., Hellman, 1972; Hall, 1997; Moore *et al.*, 1998; Gockel *et al.*, 2002; Verhey, 2002). The simulated patterns agree very well with the data, except for signal (center) frequencies of 500 and 750 Hz at the high masker level, where masking is overestimated by about 10 dB. Again, the agreement between simulations and data is better for the current model than for the original model which assumed linear BM filters.

Finally, the masking patterns for the NN condition are shown in panel D. The results are similar to those for the TN condition. The simulations agree very well with the measured patterns, except for the signal center frequencies of 3 and 4 kHz, where the masking is overestimated by about 11 dB for the 85 dB masker. The simulations using the original model (Derleth and Dau, 2000, Fig. 4) showed a considerable overestimation of the masking on the low-frequency side of the masker (up to about 20 dB).

In summary, the masking patterns simulated with the CASP model agree well with the measured data in the four masking conditions. For the 45 dB masker, the predictions were similar to those obtained by Derleth and Dau (2000). For the 85 dB masker, however, the simulations were clearly improved as a consequence of the more realistic simulation of level-dependent cochlear frequency selectivity. However, it is the combination of audio-frequency selectivity and the sensitivity to temporal cues, such as beating between the signal and the masker, that is crucial for a successful simulation of masking patterns.

D. Forward masking with noise and on- versus off-frequency tone maskers

The forward-masking experiments of the present study were conducted to test the ability of the CASP model to account for data that have been explained in terms of nonlinear cochlear processing. Figure 6 shows the mean masked thresholds for the four subjects (open symbols) for three masker levels (40, 60, 80 dB SPL) as a function of the offset-onset interval between the masker and the signal. The error bars indicate ± one standard deviation. The mean absolute threshold of the subjects for the brief signal was 12 dB SPL and is indicated in Fig. 6 by the gray horizontal lines. In the simultaneous-masking conditions, represented by the negative offset-onset intervals, the masked thresholds lie slightly

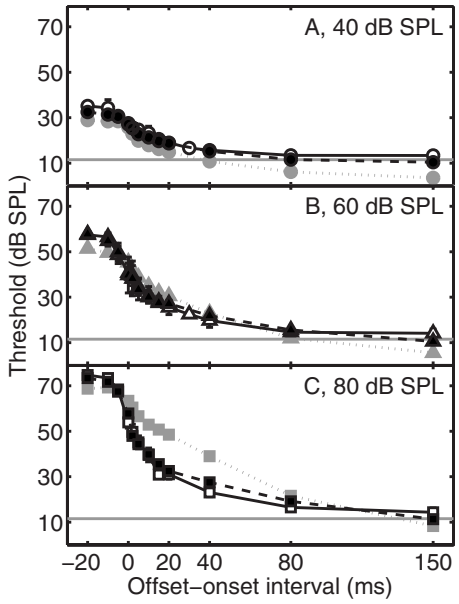

FIG. 6. Forward-masking thresholds obtained with a 10-ms, 4-kHz pure-tone signal and a broadband-noise masker. Results for masker levels of 40, 60, and 80 dB SPLs are indicated in panels A, B, and C, respectively. The open symbols represent the mean data from four subjects, while the closed symbols represent predicted thresholds. Predictions of the original model are given in gray. The abscissa represents the time interval between the masker offset and the signal onset. The horizontal gray lines indicate the absolute threshold of the signal.

below the level of the masker. As expected, the thresholds decrease rapidly for short delays and more slowly for larger delays. At a masker-signal separation of 150 ms, the three forward-masking curves converge near the absolute threshold of the signal.

The simulated forward-masking curves are indicated by the filled symbols in Fig. 6. The model accounts quantitatively for the measured thresholds for all three masker levels. The simulations obtained with the original model (gray symbols) show clear deviations from the data, with a decrease that is too shallow in the 0–40 ms region of the forward-masking curve for the highest masker level (panel C). In the CASP model, peripheral compression influences the thresholds in this region, since the signal level falls in the compressive region around 50 dB SPL. Large changes in the input level are thus required to produce small changes in the internal representation of the signal, resulting in a faster decay of forward masking.

Oxenham and Plack (2000) presented data that demonstrated the role of level-dependent BM processing in forward masking. Similar experiments, using on- and off-frequency pure-tone maskers in forward masking, were conducted here. The hypothesis was that growth of masking (GOM) functions in forward masking should depend on whether the masker and/or the signal level fall within the compressive region of the BM input-output function. If the masker and the signal levels both fall in the compressive region, which is typically the case for very short masker-signal separations, and if the compression slope is assumed to be constant, the signal level at threshold should change linearly with changing masker level by about 1 dB/dB. On the other hand, for larger masker-signal separations, the masker level may fall in

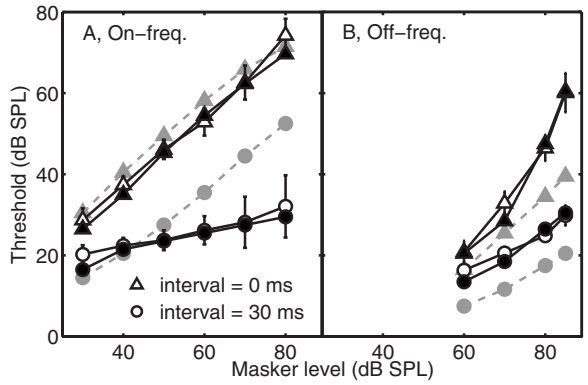

FIG. 7. Panel A shows the GOM curves obtained in the forward-masking experiment, where a 10-ms, 4-kHz pure-tone signal was masked by an on-frequency forward masker. The triangles and circles represent thresholds when the masker-signal interval was 0 and 30 ms, respectively. The open symbols show the mean data of four subjects. The black and gray symbols show simulated thresholds using the CASP and the original model, respectively. In panel B, GOM curves for an off-frequency masker at 2.4 kHz are shown using the same symbols and notation as for panel A.

the compressive region while the signal level falls in the linear region of the BM input-output function. In this case, a given change in masker level will produce a smaller change of the signal level at threshold, leading to a shallower slope of the GOM function. For off-frequency stimulation with a masker frequency well below the signal frequency, the BM response at the signal frequency is assumed to be linear at all levels. The slope of the curves should therefore be roughly independent of the masker-signal interval for off-frequency stimulation. The data presented by Oxenham and Plack (2000) provided evidence for such behavior of the GOM functions by using on- and off-frequency pure-tone maskers.

Figure 7 shows the GOM functions from the second forward-masking experiment of the present study, averaged across the four subjects. Panels A and B show the results for the on- and off-frequency conditions, respectively. Thresholds corresponding to masker-signal intervals of 0 and 30 ms are indicated by triangles and circles, respectively. In the on-frequency condition, the measured slope of the GOM function is close to unity (≈0.9 dB/dB) for the 0 ms interval. For the masker-signal interval of 30 ms, the slope of the GOM function is shallower (≈0.25 dB/dB). This was expected since the signal and masker can be assumed to be processed in different level regions of the BM input-output function. The data agree with the results of Oxenham and Plack (2000) in terms of the slopes of the GOM functions (0.82 dB/dB for the 0 ms interval and 0.29 dB/dB for the 30 ms interval).

The corresponding simulated GOM functions (filled symbols) for both masker-signal intervals are very close to the measured data. This supports the hypothesis that the nonlinear BM stage can account for the different shapes for different intervals. Since the BM stage in the original model processes sound linearly, the slopes of the predicted GOM functions (gray symbols) are similar for the two masker-signal intervals. The failure of the original model to correctly predict the GOM slope for the 30 ms interval was also observed in the first forward-masking experiment for the 30 ms interval for the 80 dB masker from the previous experiment [Fig. 6, Panel C].

For the off-frequency masker, the slope of the GOM function for the 0-ms interval is about 1.2 dB/dB, while it is 0.5 dB/dB for the 30-ms interval. These data are not consistent with the hypothesis that the GOM function for off-frequency stimulation should be independent of the interval. The variability in the average data is very low, with a standard deviation of only 1–2 dB. The data also differ from the average data of Oxenham and Plack (2000, their Fig. 3). They found GOM functions in this condition with a mean slope close to unity for all masker-signal separations. However, there was substantial variability in slope across subjects; some showed a clearly compressive GOM function while other subjects showed a linear or slightly expansive GOM function.

The initial hypothesis was that both the signal and the masker were processed linearly in the off-frequency condition. However, this is not always the case: the signal level can be above 30–40 dB and thus fall in the compressive region of the BM I/O function, while the off-frequency masker is still processed linearly. Such a situation would lead to a GOM function with a slope greater than 1, a trend which is observed in the data in panel B for the 0 ms separation, at least for the two highest masker levels. The data of Oxenham and Plack (2000) for the same interval support this idea, but this was not explicitly discussed in their study.

The simulations for the off-frequency condition closely follow the measured data. The CASP model predicts a GOM function with a slope below 1 for the 30 ms interval, as observed in the data. This is caused by the adaptation stage, which compresses the long-duration off-frequency masker slightly more than the short-duration signal. This slight compression can also be seen in the simulations obtained with the original model (gray circles). For the 0-ms interval, some of the signal thresholds lie in the compressive part (>30 dB SPL) of the BM I/O function (see also Fig. 2A). As a consequence, the GOM function has a slope above 1, since the masker is still processed linearly. The corresponding simulations obtained with the original model show a function which is essentially parallel to the 30 ms function. This model thus fails to account for the different slopes for the two masker-signal intervals.

E. Modulation detection with noise carriers of different bandwidths

In the following, AM detection with random noise carriers of different bandwidths is considered. Figure 8 shows the average data (open symbols) from Dau *et al.* (1997a) for carrier bandwidths of 3, 31, and 314 Hz. Panel (D) shows the "classical" temporal modulation transfer function (TMTF) using a broadband-noise carrier, taken from Viemeister (1979, open symbols). The modulation depth at threshold, in decibels ($20 \log m$), is plotted as a function of the modulation frequency.

The simulations (closed symbols) for the 3-Hz wide carrier account for the main characteristics of the data. The

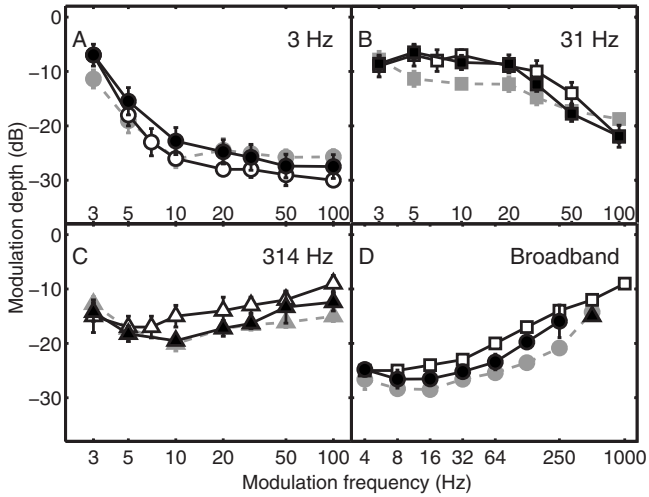

FIG. 8. TMTFs for SAM imposed on noise carriers with different bandwidths. In panels A, B, and C, the measured data of Dau *et al.* (1997a) are indicated as open symbols for carrier bandwidths of 3, 31, and 314 Hz, respectively. Panel D shows measured data from Viemeister (1979) as open symbols. The black filled symbols represent the simulated TMTFs obtained with the present model. The gray symbols indicate the simulations obtained with the original model. The black triangle indicates the predicted threshold for the 500 Hz modulation frequency when no limiting 150 Hz modulation lowpass filter was used.

simulated TMTF shows a slightly shallower threshold decrease with increasing signal modulation frequency than the measured function. For the 31-Hz wide carrier, the simulated TMTF follows the highpass characteristic observed in the data; only at 50 Hz is the measured threshold underestimated by 3–4 dB. For the 314-Hz wide carrier, the simulated thresholds roughly follow the shape of the measured TMTF, but predicted thresholds are typically 1–3 dB below the data. The agreement of the simulations with the data is slightly worse for the original model than for the present model, except for the 3 Hz bandwidth, where the agreement is similar.

Finally, the broadband TMTF (panel D) shows a lowpass characteristic with a cut-off frequency of about 64 Hz. Thresholds are generally lower than for the 314-Hz wide carrier, which is a consequence of the lower envelope power spectrum density resulting from intrinsic fluctuations in the carrier. Since the envelope spectrum of the carrier extends to the carrier bandwidth, the power density in the envelope spectrum is lower (given that the overall level of the carriers is similar in these two conditions) and stretches over a broader frequency region in the case of the broadband-noise carrier. If the model was based on a broad "predetection" filter instead of a peripheral filterbank, the distribution of power in the envelope spectrum would directly relate to the lower thresholds in the broadband condition. In the model, however, the auditory filters limit the bandwidths of the internal signals and thus the frequency range of their envelope spectra. The lower thresholds obtained with the broadband carriers result from across-frequency integration of modulation information in the model, as shown by Ewert and Dau (2000). The predicted and measured TMTFs have similar shapes for frequencies up to 250 Hz, but the simulated TMTF (closed symbols) lies 1–3 dB below the data. At 500 and 1000 Hz, the modulation is undetectable for the model (even at a modulation depth of 0 dB) and no predicted threshold is shown. This is related to the modulation lowpass filter, which reduces the sensitivity to modulation frequencies above 150 Hz. The filled triangle indicates the simulated threshold for 500 Hz when the limiting lowpass filter was left out. In this case, the result is close to the measured threshold and also similar to the simulated threshold obtained with the original model. However, both the CASP model and the original model fail to predict the measured threshold for the 1000 Hz modulation frequency. It is possible that other cues contribute to detection at these high modulation rates which are not reflected in the modulation filterbank of the present model, such as pitch (e.g., Burns and Viemeister, 1981; Fitzgerald and Wright, 2005).

V. DISCUSSION

In this section, the effects of the modifications introduced in the CASP model and their interaction with the remaining processing stages are considered. The limitations of the present modeling approach are discussed and potentials for further model investigations addressed.

A. Role of nonlinear cochlear processing in auditory masking

The original model (Dau *et al.*, 1997a) is quite successful when predicting simultaneous and nonsimultaneous discriminations and masking data, even though the model's linear processing at the BM level is not realistic. The study of Derleth *et al.* (2001) demonstrated fundamental problems when trying to implement BM nonlinearity in a straightforward way in the model: when the gammatone filterbank was replaced by a nonlinear cochlear stage, the model could not account for forward masking since the temporal-adaptive properties were substantially affected. One might argue that the assumed processing in the model, particularly the processing in the adaptation stage, is inappropriate since it leads to successful predictions only when combined with a linear BM simulation. However, the simulations obtained with the CASP model demonstrate that forward masking actually can be accounted for including the adaptation stage. One of the reasons for this result is the squaring device that simulates the expansive transformation from inner-hair-cell potentials into AN rate functions. The expansion reduces the amount of (instantaneous) compression introduced by the compressive BM stage while the overall compression in the CASP model is kept level dependent, which is different from the original model. A squaring stage was also included by Plack *et al.* (2002) in their temporal-window model and was crucial for the success of their model when describing forward masking.

In several of the experimental conditions considered here, the CASP model produced very similar predictions to the original model. In the level discrimination task, the predicted JND in level depends on the overall steady-state compression in the model, which is dominated by the logarithmic compression in the adaptation stage. This leads to a roughly constant discrimination threshold in the model independent of level (see Fig. 3). The level-dependent compression real-

ized in the cochlear processing does not affect the model predictions for broadband noise. For pure tones, the present model predicts slightly lower JNDs than the original model for the lowest standard levels of 20 and 30 dB SPLs.

The original model correctly describes Weber's law within each channel, consistent with intensity discrimination data in notched noise (Viemeister, 1983). With increasing spread of activity into different auditory channels in the multi-channel simulation shown here (Fig. 3, gray symbols), the original model predicts the near miss to Weber's law. The CASP model can no longer predict Weber's law within an individual channel as a consequence of the BM compression at midlevels. An analysis of the model's behavior revealed that, when only a single peripheral channel (centered at the signal frequency) was considered, the pure-tone JNDs were elevated in the midlevel region (50–70 dB SPL) by 0.3–0.4 dB to a maximum of about 1 dB. If a channel tuned to a higher center frequency was analyzed, for which the tone fell in the region of linear processing, the JNDs were level independent. When using an auditory filterbank (as in the simulations shown in Fig. 3), the level-independent JND contributions from the off-frequency channels produce essentially a constant JND across levels, thus minimizing the effect of on-frequency peripheral compression. Thus, the combination of information across frequency leads here to the prediction of Weber's law but does not account for the near miss to Weber's law. This result is consistent with simulations by Heinz *et al.* (2001b) when considering only AN firing rate information (average discharge counts) and disregarding nonlinear phase information. AN fibers with CFs above and below the tone frequency have phase responses that change with level (e.g., Ruggero *et al.*, 1997) and thus contribute information. In their modeling framework, Heinz *et al.* (2001b) showed that the inclusion of nonlinear phase information (at low and moderate CFs where phase information is available) as well as rate-based information can account for the near miss to Weber's law by using an across-frequency coincidence mechanism evaluating this information. Thus, it appears that lack of such an evaluation of nonlinear phase effects across CFs is responsible for the inability of the CASP model to account for the near miss to Weber's law.

The predicted detection of AM is not affected by the amount of cochlear compression in the CASP model, consistent with earlier results of Ewert and Dau (2000) for broadband TMTFs. Since both signal modulation and inherent carrier modulations are compressed in the same way, the signal-to-noise ratio (at the output of the modulation filters) does not change. This is also consistent with the observation that sensorineural hearing-impaired listeners often show about the same sensitivity to modulation independent of the amount of hearing loss (e.g., Bacon and Viemeister, 1985; Formby, 1987; Bacon and Gleitman, 1992) at least for narrow-band noise carriers and for broadband-noise carriers as long as the hearing loss is relatively flat. Accordingly, the characteristics of the spectral masking patterns (as in Fig. 5) that are associated with temporal envelope (beating) cues do not strongly depend on peripheral compression, i.e., the simulations obtained with the present model are very similar to earlier simulations using the gammatone filterbank. For example, the sharp tuning of the masking pattern for the tone signal and the tone masker and the asymmetry of masking effect for tone-on-noise versus noise-on-tone masking can be accounted for by both models.

However, cochlear nonlinear processing *does* play a crucial role in the other conditions considered in the present study. For the spectral masking patterns obtained with the high masker level (85 dB SPL), the effect of upward spread of masking is accounted for by the level-dependent frequency selectivity in the BM stage, which was not implemented in the original model. In the forward-masking conditions, where the signal and the masker were processed in different regions of the BM input-output function, the results obtained with the CASP model showed much better agreement with the data than the original model. Specifically, in the conditions with an on-frequency tone masker, the measured slopes of the GOM function strongly depend on the masker-signal interval, an effect explained by cochlear compression (Oxenham and Plack, 2000). In the forward-masking condition with the broadband-noise masker, the present model was able to account for the data for all masker levels. In contrast, the original model overestimated forward masking by 15–20 dB for masker-signal intervals of 10–40 ms at the highest masker level (80 dB SPL). These deviations are directly related to the deviations observed in the GOM functions for the tonal masker.

Ewert *et al.* (2007) compared forward-masking simulations from an earlier version of the CASP model to predictions from the temporal-window model (e.g., Oxenham and Moore, 1994; Oxenham, 2001). They investigated whether forward masking was better explained by the concept of neural persistence or temporal integration, as reflected in the temporal-window model, or by the concept of neural adaptation, as reflected in the CASP model. Ewert *et al.* (2007) showed that the two models produce essentially equivalent results and argued that the temporal-window model can be considered a simplified model of adaptation. The reason for the similarity of the two models is that the signal-to-noise ratio based decision criterion at the output of the temporal-window model acts in a way that corresponds to the division process in the adaptation stage of the present model. The remaining difference is that the CASP model includes adaptation effects of the signal itself since the model contains a feedback mechanism in the adaptation loops. In contrast, the temporal-window model only mimics adaptation effects caused by the masker which are modeled using a feed-forward mechanism (Ewert *et al.*, 2007).

B. Effects of other changes in the processing on the overall model performance

The signal transformation through the outer and middle ear was not considered and absolute sensitivity as a function of frequency was only approximated in the original model. In the current model, an outer-ear and a middle-ear transfer functions were implemented. In the experiments considered here, the effect of the absolute threshold was only observed in the forward-masking condition at the largest masker-signal intervals.

The 150-Hz modulation lowpass filter was included in the CASP model to simulate the auditory system's limited sensitivity to high-frequency envelope fluctuations. The filter was chosen based on the results of studies on modulation detection with tonal carriers where performance was limited by internal noise rather than any external statistics of the stimuli. The model accounts well for the broadband-noise TMTF for AM frequencies up to 250 Hz (see Fig. 8). However, the 150-Hz lowpass filter caused predicted thresholds to be too high for high-rate modulations. Additional model predictions for a 500 Hz modulation rate without the 150-Hz filter were very close to those obtained with the original model and the experimental data. This suggests that the slope of the 150 Hz lowpass filter (6 dB/octave) might be too steep. A shallower slope of 3–4 dB/octave would most likely not affect other simulations in the present study substantially while it would still be in line with the modulation detection data for pure-tone carriers of Kohlrausch *et al.* (2000). However, it is also possible that other cues, such as pitch, contribute to the detection of high-frequency modulations. It has been shown that SAM of broadband noise allows melody recognition, even though the pitch strength is weak (e.g., Burns and Viemeister, 1981; Fitzgerald and Wright, 2005). The model does not contain any pitch detection mechanism and is therefore not able to account for potential effects of pitch on AM detection. There might be an additional process responsible for the detection of temporal envelope pitch and (fine-structure) periodicity pitch (Stein *et al.*, 2005). Such a process might already be effective at modulation rates above the lower limit of pitch (of about 30 Hz) but particularly at high modulation rates (above about 200 Hz) which are not represented or are strongly attenuated in the internal representation of the stimuli in the CASP model.

Another modification of the original model was that the center frequencies of the modulation filters were restricted to one-quarter of the center frequency of the corresponding peripheral channel but never exceeded 1 kHz. In the spectral masking experiment of the present study, with a masker centered at 1 kHz, the simulations showed very good agreement with the data, suggesting that beating cues up to about 250 Hz can contribute to signal detection, at least in the high-level masker condition. However, it is difficult to determine the upper limit of the "existence region" of modulation filters since the sidebands are typically either spectrally resolved by the auditory filters (for tonal carriers) or the modulation depth required for detection is very large (for broadband-noise carriers) such that there is not enough dynamic range available to accurately estimate any meaningful modulation filter characteristic (Ewert and Dau, 2000; Ewert *et al.*, 2002). The combination of the first-order 150 Hz modulation lowpass filter (that provides the "absolute" threshold for AM detection) and the modulation bandpass filtering (over a modulation frequency range that scales with the carrier or "audio" frequency) appears to be successful in various experimental conditions.

C. Limitations of the model

Several studies of modulation depth discrimination (e.g., Wakefield and Viemeister, 1990; Lee and Bacon, 1997; Ewert and Dau, 2004) showed that Weber's law holds for most modulation depths, i.e., the JND of AM depth is proportional to the reference modulation depth. A modified internal-noise source would be required in the model to account for these data (Ewert and Dau, 2004). Such a noise could be modeled either by a multiplicative internal noise at the output of the modulation filters or by a logarithmic compression of the rms output of the modulation filter (see Ewert and Dau, 2004). Neither the original model nor the CASP model can predict Weber's law in this task since a level-independent fixed-variance internal noise is assumed. As described earlier, both models do account for Weber's law in intensity discrimination since the preprocessing realizes a logarithmic compression for stationary signals (due to the adaptation stage). However, the AM depth for input fluctuations with rates higher than 2 Hz (which are represented in the modulation bandpass filters) is transformed almost linearly by the adaptation stage. Thus, the CASP model fails in these conditions. This might be improved by including an additional nonlinearity in the modulation domain. Such a modification was considered to be beyond the scope of the present study.

Shamma and co-workers (e.g., Chi *et al.*, 1999; Elhilali *et al.*, 2003) described a model that is conceptually similar to the CASP model but includes an additional "dimension" in the signal analysis. They suggested a spectrotemporal analysis of the envelope, motivated by neurophysiological findings in the auditory cortex (Schreiner and Calhoun, 1995; de Charms *et al.*, 1998). In their model, a "spectral" modulation filterbank was combined with the temporal modulation analysis, resulting in two-dimensional spectrotemporal filters. Thus, in contrast to the implementation presented here, their model contains joint (and inseparable) spectro-temporal modulations. In conditions where both temporal and spectral features of the input are manipulated, the two models respond differently. The model of Shamma and co-workers has been utilized to account for spectrotemporal modulation transfer functions for the assessment of speech intelligibility (Chi *et al.*, 1999; Elhilali *et al.*, 2003), the prediction of musical timbre (Ru and Shamma, 1997), and the perception of certain complex sounds (Carlyon and Shamma, 2003). The CASP model is sensitive to spectral envelope modulation which is reflected as a variation in the energy (considered at the output of the modulation lowpass filter) as a function of the audio-frequency (peripheral) channel. For temporal modulation frequencies below 10 Hz, where the phase of the envelope is preserved, the present model could thus use spectrotemporal modulations as a detection cue. The main difference to the model of Chi *et al.* (1999), however, is that the CASP model does not include joint spectrotemporal channels. It is not clear to the authors of the present study to what extent detection or masking experiments can assess the existence of joint spectrotemporal modulation filters. The assumption of the CASP model that (temporal) modulations are processed independently at the output of each auditory

filter implies that across-channel modulation processing cannot be accounted for. This reflects a limitation of the CASP model.

D. Perspectives

Recently, comodulation masking release (CMR) has been modeled using an equalization-cancellation (EC) mechanism for the processing of activity across audio frequencies (Piechowiak *et al.*, 2007). The EC process was assumed to take place at the output of the modulation filterbank for each audio-frequency channel. In that model, linear BM filtering was assumed. The model developed in the present study will allow a quantitative investigation of the effects of nonlinear BM processing, specifically the influence of level-dependent frequency selectivity, compression, and suppression, on CMR. The model might be valuable when simulating the numerous experimental data that have been described in the literature and might, in particular, help in interpreting the role of within- versus across-channel contributions to CMR.

Another challenge will be to extend the model to binaural processing. The model of Breebaart *et al.* (2001a, 2001b, 2001c) accounted for certain effects of binaural signal detection, while their monaural preprocessing was based on the model of Dau *et al.* (1996a), i.e., without BM nonlinearity and without the assumption of a modulation filterbank. Effects of BM compression (Breebaart *et al.*, 2001a, 2001b, 2001c) and the role of modulation frequency selectivity (Thompson and Dau, 2008) in binaural detection have been discussed but not yet considered in a common modeling framework.

An important perspective of the CASP model is the modeling of hearing loss and its consequences for perception. This may be possible because the model now includes realistic cochlear compression and level-dependent cochlear tuning. Cochlear hearing loss is often associated with lost or reduced compression (Moore, 1995). Lopez-Poveda and Meddis (2001) suggested how to reduce the amount of compression in the DRNL to simulate loss of outer hair cells for moderate and severe hearing loss. This could be used in the present modeling framework as a basis for predicting the outcome of a large variety of psychoacoustic tasks in (sensorineural) hearing-impaired listeners.

VI. SUMMARY

The CASP model was developed, representing a major modification in the original modulation filterbank model of Dau *et al.* (1997a). The CASP model includes an outer- and a middle-ear transformation and a nonlinear cochlear filtering stage, the DRNL, that replaces the linear gammatone filterbank used in the original model. A squaring expansion was included before the adaptation stage and a modulation lowpass filter at 150 Hz was used prior to the modulation bandpass filterbank. The adaptation stage, the main parameters of the modulation filterbank, and the optimal detector were the same as in the original model.

Model simulations were compared to data for intensity discrimination with tones and broadband noise, tone-in-noise detection as a function of tone duration, spectral masking with tonal and narrow-band-noise signals and maskers, forward masking with tone signals and (on- and off-frequency) noise and tone maskers, and AM detection using narrow-band and wideband noise carriers.

The model was shown to account well for most aspects of the data. In some cases (intensity discrimination, signal integration in noise, AM detection), the simulation results were similar to those for the original model. In other cases (forward masking with noise and tone maskers, spectral masking at high masker levels), the CASP model showed much better agreement with the data than the original model, mainly as a consequence of the level-dependent compression and frequency selectivity in the cochlear processing.

TABLE I. The left column shows the original values of the DRNL filterbank parameters which were changed in the present study to reduce the filter bandwidths and the amount of compression at BFs higher than 1.5 kHz. The right column shows the values used in the CASP model.

	Original		Present	
Parameter	p_0	m	p_0	m
BW_{lin}	0.037 28	0.785 63	0.037 28	0.75
BW_{nlin}	−0.031 93	0.774 26	−0.031 93	0.77
$LP_{lin\ cutoff}$	−0.067 62	1.016 73	−0.067 62	1.01
$a_{CF>1.5\ kHz}$	1.402 98	0.819 16	4.004 71	0.00
$b_{CF>1.5\ kHz}$	1.619 12	−0.818 67	−0.980 15	0.00

ACKNOWLEDGMENTS

This work was supported by the Danish Research Foundation, the Danish Graduate school SNAK ("Sense organs, neural networks, behavior, and communication"), the Oticon Foundation, and the Deutsche Forschungsgemeinschaft (DFG, SFB/TRR 31). The authors would like to thank Brian C. J. Moore and two anonymous reviewers for their very helpful and supportive comments.

APPENDIX: DRNL PARAMETERS OF THE MODEL

The parameters of the human DRNL filterbank used in the CASP model were slightly different from those by Lopez-Poveda and Meddis (2001, Table III, average response). Table I shows the original parameters (Lopez-Poveda and Meddis, 2001, left column) and the parameters used here (right column). They were calculated from regression-line coefficients of the form $\log_{10}(\text{parameter}) = p_0 + m \log_{10}(\text{BF})$, where BF is expressed in Hz. Parameters a and b are the same as the original for BFs below 1.5 kHz. For larger BFs, they are set to be constant to reduce the amount of compression. The original value of the compression exponent c was 0.25 and is unchanged. The amount of compression is not determined by c alone, but by a combination of parameters a, b, and c as a consequence of the parallel processing structure of the DRNL algorithm.

[1]MATLAB implementations of the model stages are available under the name "Computational Auditory Signal-processing and Perception (CASP) model" on our laboratory's website: http://www.dtu.dk/centre/cahr/

downloads.aspx. Implementations of stages from earlier papers are also included, e.g., Dau *et al.* (1996a, 1997a).

[2]The same condition was earlier tested using the model described by Dau *et al.* (1996a). The model produced a much too shallow decay of the threshold function with increasing signal duration. This was mainly caused by the excessive overshoot produced by the adaptation stage in response to the signal onset, such that information from the steady-state portion of the signal hardly contributed to the detection of the signal. The onset response of the adaptation stage was therefore limited in the study of Dau *et al.* (1997a) in order to obtain a more realistic ratio of onset and steady-state amplitude.

Bacon, S. P., and Gleitman, R. M. (**1992**). "Modulation detection in subjects with relatively flat hearing losses," J. Speech Hear. Res. **35**, 642–653.

Bacon, S. P., and Grantham, D. W. (**1989**). "Modulation masking: Effects of modulation frequency, depth and phase," J. Acoust. Soc. Am. **85**, 2575–2580.

Bacon, S. P., and Viemeister, N. F. (**1985**). "Temporal modulation transfer functions in normal-hearing and hearing-impaired listeners," Audiology **24**, 117–134.

Breebaart, J., van de Par, S., and Kohlrausch, A. (**2001a**). "Binaural processing model based on contralateral inhibition. I. Model structure," J. Acoust. Soc. Am. **110**, 1074–1088.

Breebaart, J., van de Par, S., and Kohlrausch, A. (**2001b**). "Binaural processing model based on contralateral inhibition. II. Dependence on spectral parameters," J. Acoust. Soc. Am. **110**, 1089–1104.

Breebaart, J., van de Par, S., and Kohlrausch, A. (**2001c**). "Binaural processing model based on contralateral inhibition. III. Dependence on temporal parameter," J. Acoust. Soc. Am. **110**, 1105–1117.

Bruce, I. C., Sachs, M. B., and Young, E. D. (**2003**). "An auditory-periphery model of the effects of acoustic trauma on auditory nerve responses," J. Acoust. Soc. Am. **113**, 369–388.

Buchholz, J. M., and Mourjoloulus, J. (**2004a**). "A computational auditory masking model based on signal dependent compression. I. Model description and performance analysis," Acust. Acta Acust. **5**, 873–886.

Buchholz, J. M., and Mourjoloulus, J. (**2004b**). "A computational auditory masking model based on signal dependent compression. II. Model simulations and analytical approximations," Acust. Acta Acust. **5**, 887–900.

Burns, E. M., and Viemeister, N. F. (**1981**). "Played-again SAM: Further observations on the pitch of amplitude-modulated noise," J. Acoust. Soc. Am. **70**, 1655–1660.

Carlyon, R. P., and Shamma, S. (**2003**). "An account of monaural phase sensitivity," J. Acoust. Soc. Am. **114**, 333–348.

Carney, L. H. (**1993**). "A model for the responses of low-frequency auditory-nerve fibers in cat," J. Acoust. Soc. Am. **93**, 401–417.

Chi, T., Gao, Y., Guyton, M. C., Ru, P., and Shamma, S. (**1999**). "Spectro-temporal modulation transfer functions and speech intelligibility," J. Acoust. Soc. Am. **106**, 2719–2732.

Colburn, H. S., Carney, L. H., and Heinz, M. G. (**2003**). "Quantifying the information in auditory-nerve responses for level discrimination," J. Assoc. Res. Otolaryngol. **4**, 294–311.

Dau, T., Püschel, D., and Kohlrausch, A. (**1996a**). "A quantitative model of the effective signal processing in the auditory system. I. Model structure," J. Acoust. Soc. Am. **99**, 3615–3622.

Dau, T., Püschel, D., and Kohlrausch, A. (**1996b**). "A quantitative model of the effective signal processing in the auditory system. II. Simulations and measurements," J. Acoust. Soc. Am. **99**, 3623–3631.

Dau, T., Kollmeier, B., and Kohlrausch, A. (**1997a**). "Modeling auditory processing of amplitude modulation. I. Detection and masking with narrow-band carriers," J. Acoust. Soc. Am. **102**, 2892–2905.

Dau, T., Kollmeier, B., and Kohlrausch, A. (**1997b**). "Modeling auditory processing of amplitude modulation. II. Spectral and temporal integration," J. Acoust. Soc. Am. **102**, 2906–2919.

de Charms, R. C., Blake, D. T., and Merzenich, M. M. (**1998**). "Optimizing sound features for cortical neurons," Science **280**, 1439–1443.

Derleth, R. P., and Dau, T. (**2000**). "On the role of envelope fluctuation processing in spectral masking," J. Acoust. Soc. Am. **108**, 285–296.

Derleth, R. P., Dau, T., and Kollmeier, B. (**2001**). "Modeling temporal and compressive properties of the normal and impaired auditory system," Hear. Res. **159**, 132–149.

Dicke, U., Ewert, S. D., Dau, T., and Kollmeier, B. (**2007**). "A neural circuit transforming temporal periodicity information into a rate-based representation in the mammalian auditory system," J. Acoust. Soc. Am. **121**, 310–326.

Elhilali, M., Chi, T., and Shamma, S. (**2003**). "A spectro-temporal modulation index (STMI) for assessment of speech intelligibility," Speech Commun. **41**, 331–348.

Ewert, S. D., and Dau, T. (**2000**). "Characterizing frequency selectivity for envelope fluctuations," J. Acoust. Soc. Am. **108**, 1181–1196.

Ewert, S. D., and Dau, T. (**2004**). "External and internal limitations in amplitude-modulation processing," J. Acoust. Soc. Am. **116**, 478–490.

Ewert, S. D., Verhey, J. L., and Dau, T. (**2002**). "Spectro-temporal processing in the envelope-frequency domain," J. Acoust. Soc. Am. **112**, 2921–2931.

Ewert, S. D., Hau, O., and Dau, T. (**2007**). "Forward masking: Temporal integration or adaptation?," in *Hearing—From Sensory Processing to Perception*, edited by B. Kollmeier, G. Klump, V. Hohmann, U. Langemann, M. Mauermann, S. Uppenkamp, and J. Verhey (Springer-Verlag, Berlin), pp. 165–174.

Fitzgerald, M. B., and Wright, B. A. (**2005**). "A perceptual learning investigation of the pitch elicited by amplitude-modulated noise," J. Acoust. Soc. Am. **118**, 3794–3803.

Formby, C. C. (**1987**). "Modulation threshold functions for chronically impaired Ménière patients," Audiology **26**, 89–102.

Glasberg, B. R., and Moore, B. C. J. (**1990**). "Derivation of auditory filter shapes from notched-noise data," Hear. Res. **47**, 103–138.

Gockel, H., Moore, B. C. J., and Patterson, R. D. (**2002**). "Asymmetry of masking between complex tones and noise: The role of temporal structure and peripheral compression," J. Acoust. Soc. Am. **111**, 2759–2770.

Goode, R. L., Killion, M. L., Nakamura, K., and Nishihara, S. (**1994**). "New knowledge about the function of the human middle ear: Development of an improved analogue model," Am. J. Otol. **15**, 145–154.

Green, D. M., and Swets, J. (**1966**). *Signal Detection Theory and Psychophysics* (Wiley, New York).

Hall, J. L. (**1997**). "Asymmetry of masking revisited: Generalization of masker and probe bandwidth," J. Acoust. Soc. Am. **101**, 1023–1033.

Hansen, M., and Kollmeier, B. (**1999**). "Continuous assessment of time-varying speech quality," J. Acoust. Soc. Am. **106**, 2888–2899.

Hansen, M., and Kollmeier, B. (**2000**). "Objective modeling of speech quality with a psychoacoustically validated auditory model," J. Audio Eng. Soc. **48**, 395–409.

Heinz, M. G., Colburn, H. S., and Carney, L. H. (**2001a**). "Evaluating auditory performance limits: I. One-parameter discrimination using a computational model for the auditory nerve," Neural Comput. **13**, 2273–2316.

Heinz, M. G., Colburn, H. S., and Carney, L. H. (**2001b**). "Rate and timing cues associated with the cochlear amplifier: Level discrimination based on monaural cross-frequency coincidence detection," J. Acoust. Soc. Am. **100**, 2065–2084.

Hellman, R. P. (**1972**). "Asymmetry of masking between noise and tone," Percept. Psychophys. **11**, 241–246.

Hewitt, M. J., and Meddis, R. (**1994**). "A computer model of amplitude-modulation sensitivity of single units in the inferior colliculus," J. Acoust. Soc. Am. **95**, 2145–2159.

Holube, I., and Kollmeier, B. (**1996**). "Speech intelligibility prediction in hearing-impaired listeners based on a psychoacoustically motivated perception model," J. Acoust. Soc. Am. **100**, 1703–1716.

Houtgast, T. (**1989**). "Frequency selectivity in amplitude-modulation detection," J. Acoust. Soc. Am. **85**, 1676–1680.

Houtsma, A. J. M., Durlach, N. I., and Braida, L. D. (**1980**). "Intensity perception. XI. Experimental results on the relation of intensity resolution to loudness matching," J. Acoust. Soc. Am. **68**, 807–813.

Huber, R., and Kollmeier, B. (**2006**). "PEMO-Q—a new method for objective audio quality assessment using a model of auditory perception," IEEE Trans. Audio, Speech, Lang. Process. **14**, 1902–1911.

Irino, T., and Patterson, R. D. (**2006**). "Dynamic, compressive Gammachirp Auditory Filterbank for Perceptual Signal Processing," International Conference on Acoustics, Speech and Signal Processing, Proc. IEEE **5**, 133–136.

Jesteadt, W., Bacon, S. P., and Lehman, J. R. (**1982**). "Forward masking as a function of frequency, masker level, and signal delay," J. Acoust. Soc. Am. **71**, 950–962.

Kohlrausch, A., Fassel, R., and Dau, T. (**2000**). "The influence of carrier level and frequency on modulation and beat-detection thresholds for sinusoidal carriers," J. Acoust. Soc. Am. **108**, 723–734.

Langner, G. (**1981**). "Neuronal mechanisms for pitch analysis in the time domain," Exp. Brain Res. **44**, 450–454.

Langner, G. (**1992**). "Periodicity coding in the auditory system," Hear. Res. **60**, 115–142.

Langner, G., and Schreiner, C. (**1988**). "Periodicity coding in the inferior colliculus of the cat. I. Neuronal mechanism," J. Neurophysiol. **60**, 1799–1822.
Lee, J., and Bacon, S. P. (**1997**). "Amplitude modulation depth discrimination of a sinusoidal carrier: Effect of stimulus duration," J. Acoust. Soc. Am. **101**, 3688–3693.
Lopez-Poveda, E. A., and Meddis, R. (**2001**). "A human nonlinear cochlear filterbank," J. Acoust. Soc. Am. **110**, 3107–3118.
Lopez-Poveda, E. A., Plack, C. J., and Meddis, R. (**2003**). "Cochlear nonlinearity between 500 and 8000 Hz in listeners with normal hearing," J. Acoust. Soc. Am. **113**, 951–960.
Meddis, R., and O'Mard, L. P. (**2005**). "A computer model of the auditory-nerve response to forward-masking stimuli," J. Acoust. Soc. Am. **117**, 3787–3798.
Meddis, R., O'Mard, L. P., and Lopez-Poveda, E. A. (**2001**). "A computational algorithm for computing nonlinear auditory frequency selectivity," J. Acoust. Soc. Am. **109**, 2852–2861.
Miller, G. A. (**1947**). "Sensitivity to changes in the intensity of white noise and its relation to masking and loudness," J. Acoust. Soc. Am. **19**, 609–619.
Moore, B. C. J. (**1995**). *Perceptual Consequences of Cochlear Damage* (Oxford University Press, New York).
Moore, B. C. J., Alcantara, J. I., and Dau, T. (**1998**). "Masking patterns for sinusoidal and narrow-band noise maskers," J. Acoust. Soc. Am. **104**, 1023–1038.
Moore, B. C. J., and Glasberg, B. R. (**1987**). "Factors affecting thresholds for sinusoidal signals in narrow-band maskers with fluctuating envelopes," J. Acoust. Soc. Am. **82**, 69–79.
Moore, B. C. J., and Glasberg, B. R. (**2003**). "Behavioural measurement of level-dependent shifts in the vibration pattern on the basilar membrane at 1 and 2 kHz," Hear. Res. **175**, 66–74.
Moore, B. C. J., Glasberg, B. R., Plack, C. J., and Biswas, A. K. (**1988**). "The shape of the ear's temporal window," J. Acoust. Soc. Am. **83**, 1102–1116.
Muller, M., Robertson, D., and Yates, G. K. (**1991**). "Rate-versus-level functions of primary auditory nerve fibres: Evidence for square law behaviour of all fibre categories in the guinea pig," Hear. Res. **55**, 50–56.
Nelson, D. A., and Swain, A. (**1996**). "Temporal resolution within the upper accessory excitation of a masker," Acust. Acta Acust. **82**, 328–334.
Nelson, P. C., and Carney, L. H. (**2004**). "A phenomenological model of peripheral and central neural responses to amplitude-modulated tones," J. Acoust. Soc. Am. **116**, 2173–2186.
Oxenham, A. J. (**1998**). "Temporal integration at 6 kHz as a function of masker bandwidth," J. Acoust. Soc. Am. **103**, 1033–1042.
Oxenham, A. J. (**2001**). "Forward masking: Adaptation or integration?," J. Acoust. Soc. Am. **109**, 732–741.
Oxenham, A. J., and Moore, B. C. J. (**1994**). "Modeling the additivity of nonsimultaneous masking," Hear. Res. **80**, 105–118.
Oxenham, A. J., Moore, B. C. J., and Vickers, D. A. (**1997**). "Short-term temporal integration: Evidence for the influence of peripheral compression," J. Acoust. Soc. Am. **101**, 3676–3687.
Oxenham, A. J., and Plack, C. J. (**2000**). "Effects of masker frequency and duration in forward masking: Further evidence for the influence of peripheral nonlinearity," Hear. Res. **150**, 258–266.
Palmer, A. R. (**1995**). "Neural signal processing," in *Hearing*, edited by B. C. J. Moore (Academic, New York).
Palmer, A. R., and Russell, I. J. (**1986**). "Phase locking in the cochlear nerve of the guinea-pig and its relation to the receptor potential of inner hair-cells," Hear. Res. **24**, 1–15.
Patterson, R. D., Allerhand, M. H., and Giguere, C. (**1995**). "Time-domain modeling of peripheral auditory processing: A modular architecture and a software platform," J. Acoust. Soc. Am. **98**, 1890–1894.
Patterson, R. D., and Moore, B. C. J. (**1986**). "Auditory filters and excitation patterns as representations of frequency resolution," in Frequency Selectivity in Hearing (Academic Press, London).
Piechowiak, T., Ewert, S. D., and Dau, T. (**2007**). "Modeling comodulation masking release using an equalization-cancellation mechanism," J. Acoust. Soc. Am. **121**, 2111–2126.
Plack, C. J., and Oxenham, A. J. (**1998**). "Basilar-membrane nonlinearity and the growth of forward masking," J. Acoust. Soc. Am. **103**, 1598–1608.
Plack, C. J., and Oxenham, A. J. (**2000**). "Basilar-membrane nonlinearity estimated by pulsation threshold," J. Acoust. Soc. Am. **107**, 501–507.
Plack, C. J., Oxenham, A. J., and Drga, V. (**2002**). "Linear and nonlinear processes in temporal masking," Acust. Acta Acust. **88**, 348–358.
Plasberg, J. H., and Kleijn, W. B. (**2007**). "The sensitivity matrix: Using advanced auditory models in speech and audio processing," IEEE Trans. Audio, Speech, Lang. Process. **15**, 310–319.
Pralong, D., and Carlile, S. (**1996**). "The role of individualized headphone calibration for the generation of high fidelity virtual auditory space," J. Acoust. Soc. Am. **100**, 3785–3793.
Püschel, D. (**1988**). "Prinzipien der zeitlichen Analyse beim Hören," (Principles of Temporal Processing in Hearing), Ph.D. thesis, University of Göttingen.
Rosengard, P. S., Oxenham, A. J., and Braida, L. D. (**2005**). "Comparing different estimates of cochlear compression in listeners with normal and impaired hearing," J. Acoust. Soc. Am. **117**, 3028–3041.
Ru, P., and Shamma, S. A. (**1997**). "Representation of musical timbre in the auditory cortex," J. New Music Res. **26**, 154–169.
Ruggero, M. A., and Rich, N. C. (**1991**). "Furosemide alters organ of corti mechanics: Evidence for feedback of outer haircells upon the basilar membrane," J. Neurosci. **11**, 1057–1067.
Ruggero, M. A., Rich, N. C., Recio, A., Narayan, S. S., and Robles, L. (**1997**). "Basilar-membrane responses to tones at the base of the chinchilla cochlea," J. Acoust. Soc. Am. **101**, 2151–2163.
Schreiner, C. E., and Calhoun, B. (**1995**). "Spectral envelope coding in cat primary auditory cortex: Properties of ripple transfer functions," Aud. Neurosci. **1**, 39–61.
Schroeder, M. R., and Hall, J. L. (**1974**). "Model for mechanical to neural transduction in the auditory receptor," J. Acoust. Soc. Am. **55**, 1055–1060.
Siebert, W. M. (**1965**). "Some implications of the stochastic behavior of primary auditory neurons," Kybernetik **2**, 206–215.
Siebert, W. M. (**1968**). MIT Research Laboratory of Electronics Quarterly Report No. 88.
Siebert, W. M. (**1970**). "Frequency discrimination in the auditory system: Place or periodicity mechanism," Proc. IEEE **58**, 723–730.
Smith, R. L. (**1977**). "Short-term adaptation in single auditory-nerve fibers: Some post-stimulatory effects," J. Neurophysiol. **49**, 1098–1112.
Stein, A., Ewert, D. S., and Wiegrebe, L. (**2005**). "Perceptual interaction between carrier periodicity and amplitude modulation in broadband stimuli: A comparison of the autocorrelation and modulation-filterbank model," J. Acoust. Soc. Am. **118**, 2470–2481.
Strube, H. W. (**1985**). "Computationally efficient basilar-membrane model," Acustica **58**, 207–214.
Tchorz, J., and Kollmeier, B. (**1999**). "A model of auditory perception as front end for automatic speech recognition," J. Acoust. Soc. Am. **106**, 2040–2050.
Thompson, E., and Dau, T. (**2008**). "Binaural processing of modulated interaural level differences," J. Acoust. Soc. Am. **123**, 1017–1029.
van der Heijden, M., and Kohlrausch, A. (**1995**). "The role of envelope fluctuations in spectral masking," J. Acoust. Soc. Am. **97**, 1800–1807.
Verhey, J. L. (**2002**). "Modeling the influence of inherent envelope fluctuations in simultaneous masking experiments," J. Acoust. Soc. Am. **111**, 1018–1025.
Verhey, J. L., Dau, T., and Kollmeier, B. (**1999**). "Within-channel cues in comodulation masking release (CMR): Experiments and model predictions using a modulation-filterbank model," J. Acoust. Soc. Am. **106**, 2733–2745.
Viemeister, N., and Wakefield, G. (**1991**). "Temporal integration and multiple looks," J. Acoust. Soc. Am. **90**, 858–865.
Viemeister, N. F. (**1979**). "Temporal modulation transfer functions based upon modulation thresholds," J. Acoust. Soc. Am. **66**, 1364–1380.
Viemeister, N. F. (**1983**). "Auditory intensity discrimination at high frequencies in the presence of noise," Science **221**, 1206–1208.
Wakefield, G. H., and Viemeister, N. F. (**1990**). "Discrimination of modulation depth of sinusoidal amplitude modulation (SAM) noise," J. Acoust. Soc. Am. **88**, 1367–1373.
Westermann, L. A., and Smith, R. L. (**1984**). "Rapid and short-term adaptation in auditory nerve responses," Hear. Res. **15**, 249–260.
Yates, G. K., Winter, I. M., and Robertson, D. (**1990**). "Basilar membrane nonlinearity determines auditory nerve rate-intensity functions and cochlear dynamic range," Hear. Res. **45**, 203–220.
Zhang, X., Heinz, M. G., Bruce, I. C., and Carney, L. H. (**2001**). "A phenomenological model for the responses of auditory-nerve fibers. I. Nonlinear tuning with compression and suppression," J. Acoust. Soc. Am. **109**, 648–670.

The extent to which a position-based explanation accounts for binaural release from informational masking[a)]

Frederick J. Gallun,[b)] Nathaniel I. Durlach, H. Steven Colburn,
Barbara G. Shinn-Cunningham, Virginia Best, Christine R. Mason, and Gerald Kidd, Jr.
Hearing Research Center, Boston University, 635 Commonwealth Avenue, Boston, Massachusetts 02215

(Received 17 December 2007; revised 14 April 2008; accepted 15 April 2008)

Detection was measured for a 500 Hz tone masked by noise (an "energetic" masker) or sets of ten randomly drawn tones (an "informational" masker). Presenting the maskers diotically and the target tone with a variety of interaural differences (interaural amplitude ratios and/or interaural time delays) resulted in reduced detection thresholds relative to when the target was presented diotically ("binaural release from masking"). Thresholds observed when time and amplitude differences applied to the target were "reinforcing" (favored the same ear, resulting in a lateralized position for the target) were not significantly different from thresholds obtained when differences were "opposing" (favored opposite ears, resulting in a centered position for the target). This irrelevance of differences in the perceived location of the target is a classic result for energetic maskers but had not previously been shown for informational maskers. However, this parallellism between the patterns of binaural release for energetic and informational maskers was not accompanied by high correlations between the patterns for individual listeners, supporting the idea that the mechanisms for binaural release from energetic and informational masking are fundamentally different.
 [DOI: 10.1121/1.2924127]

PACS number(s): 43.66.Ba, 43.66.Dc, 43.66.Nm [RLF] Pages: 439–449

I. INTRODUCTION

A. Informational and energetic masking

The term masking, as it is used in this study, refers to a decrease in the detectability of a target in the presence of an interferer. In "energetic" masking (EM), the interference can be associated with overlap of the target and the interferer acoustic energy or neural activity at a given place of excitation (i.e., the basilar membrane). In "informational" masking (IM), the overlap of excitation between the target and the masker at the auditory periphery is negligible, and the interference is assumed to take place more centrally in the auditory pathway. Obviously, these are two extreme examples and the reality is that the same masker can cause both EM and IM. Because the experiments described here were designed to examine the degree to which the same mechanisms can explain binaural release from these two quite different types of masking, artificial stimuli were constructed that would allow the two types of masking to be examined largely in isolation. It should be noted at the outset, however, that the results reported here may not generalize to masking in which the reduction in performance concerns the discriminability, intelligibility, or identifiability of the target, and the target is supra-threshold. In those cases, the tasks of the listener are different from the detection task described here. For this reason, the mechanisms underlying binaural release from masking may be different as well. Nonetheless, in the interest of starting with the most fundamental case and moving to more complex situations in a systematic manner, this study is concerned with detection in a two-interval forced-choice detection task.

When the listener's task is to detect the presence of a tone of a given frequency, the amount of EM can be estimated by the use of a model (such as estimating the energy passed by filters with widths set to the critical bandwidths specified by Moore and Glasberg, 1983), but the degree of IM is harder to determine. In the majority of cases, the presence of IM is indicated by a rise in threshold or a decrease in performance across two situations for which the EM is the same or even reduced. Durlach *et al.* (2003a) suggested that the two main sources of IM appear to be the target-masker similarity and stimulus uncertainty. One way of describing these situations is that a target that should be clearly audible is in some way confused with the masker or the masker distracts the listener from the target, resulting in the perception of no target or the misapprehension that the masker is the target. For this reason, the energetic model is insufficient to predict performance in the IM conditions. Furthermore, the amount of individual variability tends to be much greater for IM. This aspect of IM has been modeled through the addition of a filter width parameter and an internal noise parameter, both of which vary across listeners (e.g., Lutfi, 1993; Oh and Lutfi 1998; Durlach *et al.*, 2005). Despite the success of such modeling, there is much that is not yet understood about IM. For example, Richards and Tang (2006)

[a)] Portions of this research were presented at the 2007 Midwinter Meeting of the Association for Research in Otolaryngology.

[b)] Present address: National Center for Rehabilitative Auditory Research, Portland VA Medical Center, 3710 SW US Veterans Hospital Road (NCRAR), Portland, Oregon 97239. Tel.: 503-220-8262. Electronic mail: frederick.gallun@va.gov.

reported modeling results that relied upon negative frequency weightings, which is incompatible with a filter-based energetic model.

B. Binaural hearing

The goal of this study was to examine whether the differences between EM and IM include different patterns of binaural release from masking. This issue has been raised by recent demonstrations of binaural release from IM (e.g., Neff, 1995; Kidd *et al.*, 1994; Arbogast *et al.*, 2002; Durlach *et al.*, 2003b; Gallun *et al.*, 2005; Best *et al.*, 2005) that have at times been characterized as resulting from perceptual separation of the target and the masker, an idea that has been out of favor in the literature on binaural unmasking for energetic maskers for over 40 years (Colburn and Durlach, 1965). One situation that has been particularly well studied involves the introduction of spatial differences between a target and a competing masker colocated in front of the listener due to the presentation of an identical copy of the masker from a second location before or after a slight delay (e.g., Freyman *et al.*, 1999; Brungart *et al.*, 2005; Rakerd *et al.*, 2006). Due to the precedence effect, the situation with a leading copy results in a shift of the perceived location of the masker toward the source position of that leading copy. Interestingly, substantial release from IM (but not EM) was found in nearly all situations in which the masker is presented from two locations with a delay, whether the spatially displaced copy leads or lags. Both Brungart *et al.* (2005) and Rakerd *et al.* (2006) even found that the release due to temporal onset discrepancies was not completely abolished until a delay of 64 ms. Based on these results, listeners seem to be able to use position differences based on the precedence effect out to very long delays. It is worth considering, however, that these long delays may result in "diffuse" or "widened" percepts that could also result in a release from IM by producing a quality difference that would counteract the perceptual similarity of the target and the masker. It is not clear, however, whether these sorts of "image width" percepts are as relevant in the real or simulated free field as they are with highly constrained stimuli presented under headphones.

Regardless of the presentation method, classic work on binaural hearing (e.g., Rayleigh, 1875; Stevens and Newman, 1936; Sandel *et al.*, 1955) emphasized the relationship between perceived location and differences in the time it takes for stimuli to arrive at the two ears [interaural differences in time, (ITDs)] and in the amplitudes of these stimuli at the two ears [interaural differences in level, (ILDs)]. Consequently, when Hirsh (1948) discovered that interaural differences applied to a tone could improve its detection in noise presented diotically (identically at the two ears) over headphones, the initial explanations focused on differences in perceived location. Specifically, Hirsh (1948) argued that phenomenologically, it seems to the listener that this binaural masking level difference (BMLD) occurs because the tone and the noise are perceived in different locations inside the head (i.e., the decision variable is based on differences in the intracranial positions of the masker and the tonal signal). This has been referred to as the "position variable" explanation. One difficulty is that the greatest BMLD occurs for a tone reversed in phase at the two ears, while the clearest lateralization difference between the target and the masker is for a tone presented monaurally (Webster, 1951). Similarly, when a monaural target and a diotic masker are presented together near threshold, the listener can detect the target but not identify the ear to which it is presented. In order to address such concerns, Webster (1951) argued that since the filtering of the critical band allows the masking noise to be treated as a slowly varying sinusoid, it is possible to account for the differences between the monaural and phase-reversed conditions by postulating that at some points in time, there will exist a time difference at the two ears that is based on the phase of the summed components of the target and masker and that will depend on the interaural phase relations of the target. This modifies the position variable explanation so that the decision is based on the perceived (fluctuating) location of the combined target and masker rather than the difference in the perceived locations of each.

Extending this approach, Jeffress *et al.* (1956) used a vector summation method to analyze the effects of adding a tone with interaural time differences to various noises and argued that the perception underlying the BMLD is not one of a tone in one location and a noise in another, but rather of a change in either the level or the location of the noise due to the addition of the tone. Using this "vector model," Jeffress *et al.* (1956) was able to account for much of the available data on the BMLD, with the exception that it does not account for BMLDs that arise from ILDs introduced into the combined stimulus. In order to address this issue, Hafter *et al.* (Hafter *et al.*, 1969; Hafter and Carrier, 1970; Hafter, 1971; Hafter *et al.*, 1973) introduced the "lateralization" model, which includes the effects of ILDs and which predicts effects of differences in time and level that vary depending on whether or not the differences are "reinforced" (both result in lateralization to the same side) or "opposed" (each alone would result in lateralization to opposite sides). The decision variable in this model is based on integrating the absolute values of the interaural differences rather than on the mean lateral position. Consequently, a noise masker results in a situation where the cue to the presence of the target is the spread of interaural-difference values, which should be greater for reinforced rather than opposed interaural differences. Hafter and Carrier (1970) reported results consistent with this explanation using masking stimuli that were tones rather than noises. This difference in masker may be quite important since a tonal masker results in fixed interaural differences, while a noise masker (with nonzero bandwidth) results in fluctuating interaural differences. Because humans are quite sensitive to fluctuations in interaural differences (Zurek and Durlach, 1987; Goupell and Hartmann, 2006, 2007a, 2007b), it is possible that when the masker is a noise, there is a cue available that is not present when the masker is a tone.

An additional complication associated with comparing opposing and reinforcing interaural differences is that when opposing time and level differences are presented over headphones, the perceived intracranial image is quite different from that obtained with a diotic version of the same stimulus.

As Hafter and Carrier (1972) demonstrated, there is no combination of ILD and ITD that results in a perception that cannot be distinguished from a diotic percept. In addition, the level difference needed to "cancel" a given time difference can vary substantially across listeners. Nonetheless, the data of Hafter and Carrier (1972) give us good reason to believe that the perceived location of a stimulus with opposing ITD and ILD values should be quite different from the perceived location with reinforcing cues. Consequently, any differences in the BMLD that occur for opposing and reinforcing cues would suggest that the perceived location (or some other interaction of time and level cues) may play a role in the formation of the BMLD. Alternatively, those situations in which opposing and reinforcing cues produce similar BMLDs provide evidence that either (1) each cue is processed independently or (2) the task is based on a cue (such as fluctuations in interaural differences) that is independent of the perceived location.

A substantively different approach to the BMLD was proposed by Durlach (1960, 1963, 1972) in his formulation of the equalization and cancellation (EC) model of binaural release from masking. The EC model postulates that the stimuli at the two ears are first processed by independent banks of bandpass filters and then passed to an EC mechanism that equalizes the levels of the maskers at the two ears. Subsequently, the total signal at one ear is subtracted from the total signal at the other ear (in the case where the masker is identical at the two ears, the only operation is the subtraction). It is the output of this EC process that serves as the signal to be detected. In the case where the output is below the level of the internal noise, the system is assumed to make its decision based on an independent monaural pathway. One substantial difference between the predictions of the EC model and the lateralization model lies in the effect of introducing time and level differences that are either reinforcing or opposing. Since the EC decision is based entirely on differences in the signals at the two ears, calculated independently, the model predicts that performance for signals in which the interaural differences are reinforcing should be identical to performance for signals in which the differences are opposing. In a test of this prediction, Colburn and Durlach (1965) reported results that conform precisely to the predictions of the EC model (replotted in Fig. 2). Whether the proper explanation is based on the combined lateralization of the target and masker or the result of an EC operation, this pattern of results has been taken as strong evidence against differences in the perceived locations of the target and the masker as an explanation for binaural release from masking. In defense of the lateralization model, however, Hafter (1971) pointed out that while the *average* perceived locations differ for opposing and reinforcing ITDs and ILDs, the instantaneous values are constantly varying for a noise masker but are fixed for a tonal masker. Because the lateralization model acts not on the average location but on the instantaneous location, Hafter (1971) argued that the data obtained with noise maskers are in agreement both with the lateralization model and with the EC model. Hafter (1971) also argued that this explains why the results of Hafter and Carrier (1970), with a tonal masker, differ from those of Colburn and Durlach (1965), with a noise masker. This point was reinforced by Domnitz and Colburn (1976), who demonstrated that all of the models described above predict dependence on the target parameters. Furthermore, all of the proposed models turn out to rely upon sensitivity to fluctuating interaural differences.

Recent results showing binaural release with informational maskers (Kidd *et al.*, 1994; Neff, 1995; Freyman *et al.*, 1999; Arbogast *et al.*, 2002; Durlach *et al.*, 2003b; Gallun *et al.*, 2005; Best *et al.*, 2005; Rakerd *et al.*, 2006) have rekindled the idea that in some situations, listeners may indeed use perceived differences in spatial location (or possibly image "width" or "diffuseness") to distinguish the target from the masker. While this may seem surprising given the results described above for EM, it is possible that the results of Colburn and Durlach (1965) do not apply to informational maskers since the mechanism of masking is not simply (or primarily) the overlap of energy in a critical band. As a result, the target and the masker may often be heard as distinct auditory objects in distinct locations in conditions where IM is the dominant form of interference. This interpretation is especially likely for situations involving actual or simulated free-field presentation, which result in a much wider range of possible perceived locations. Consequently, the mechanism of release could indeed rely upon an enhancement in the individual distinctiveness of the target and the informational masker through differences in the perceived location or other spatial attributes. This kind of formulation of the perceptual process is very different from simply detecting differences between intervals containing only the masker and those containing an object made of up of the target plus the masker. In particular, the cue proposed above for EM (fluctuating interaural differences) was specifically associated with the combined target and masker stimulus. If such fluctuations were heard as a broadening of image width, for example, there is no reason to believe that this would help distinguish the target from the masker. Because there are two issues to be examined here, binaural release for informational maskers and the role of target-masker distinctiveness, it seemed appropriate to begin with the simplest case and proceed to the more complex cases. As the simplest IM case is the detection of a tone in multitone maskers, this was chosen as a starting point. If this condition behaves like the EM condition, then it is reasonable to examine more complex conditions, while if it does not, then the two types of masking may indeed differ at a very fundamental level.

To begin to address this issue, listeners were presented with stimuli that strongly resemble those used by Colburn and Durlach (1965) but differ in that a substantial aspect of the masking is due to the target-masker similarity (and/or uncertainty about the masker frequencies) rather than energy falling in the critical band containing the target. Once baseline performance was established for informational and energetic maskers presented diotically over headphones, interaural differences were applied to the targets. Release from masking was measured for ITD alone, ILD alone, reinforcing ITD and ILD, and opposing ITD and ILD for both types of masker. While the results for both stimulus types showed the same pattern found by Colburn and Durlach (1965), the re-

lationships between the amounts of release obtained by individual listeners for the two masker types raise doubts about whether they truly share a common mechanism that is based on interaural differences rather than on perceived location.

II. METHODS

A. Listeners

Seven female listeners between the ages of 20 and 25 with audiometrically normal hearing were paid for their participation. L4 had considerable prior experience with psychophysical listening but very little with stimuli of this sort. None of the others had experience listening in psychoacoustical experiments. All were graduate students at Boston University in hearing-related disciplines (primarily speech and language pathology).

B. Stimuli

The target to be detected was a 250 ms, 500 Hz tone with 10 ms raised-cosine onsets and offsets. Noise maskers were generated digitally by creating a frequency vector with values spaced at 1 Hz intervals between 100 and 1000 Hz and associating each frequency value with a randomly chosen amplitude and phase value, drawn from rectangular distributions (thus resulting in random but not Gaussian noise). Signals were then converted to the time domain and normalized so that, after attenuation, the overall rms level was 60 dB sound pressure level (SPL) (spectrum level of 31.5 dB SPL). Multitone maskers were generated digitally by choosing from a linear distribution of ten frequencies that fell between 100 and 400 Hz and between 600 and 1000 Hz (leaving a 200 Hz wide "protected region" between 400 and 600 Hz). Each masker frequency was then associated with a random phase value drawn from a rectangular distribution and with an amplitude that was randomly varied within ± 5 dB of an arbitrary starting amplitude, also from a rectangular distribution (in decibels). Ten new multitone masker frequencies were chosen randomly before each interval of each trial, always maintaining the 200 Hz protected region. Time-domain conversion and amplitude normalization assured that, after attenuation, the overall rms level of the multitone masker was 70 dB SPL. The maskers, like the targets, were 250 ms in duration with 10 ms raised-cosine-onsets and offsets. The difference in the rms levels of the noise and multitone maskers was initially the result of a programming error but fortuitously led to similar diotic target thresholds for both maskers.

ILD values were introduced into the target by reducing the level at the left or right ear by either 6 dB ("smaller differences") or 12 dB ("larger differences"). ITD values were introduced by shifting the wave form by either 300 μs, which is equivalent to a phase delay of 54° (smaller differences) or 600 μs, which is equivalent to a phase delay of 108° (larger differences). The target and masker envelopes were applied after the phase shifts, ensuring that the onsets and offsets were synchronized, regardless of interaural differences applied to the wave forms. This removed an onset cue that would be present in a natural situation but ensured that any BMLD arises only because of ongoing binaural information.

C. Procedures

After time-domain conversion and normalization, stimuli were sent to Tucker-Davis Technology (TDT System II) 16 bit digital-to-analog converters running at a rate of 50 kHz and then low-pass filtered at 7.5 kHz. The target and masker levels at the two ears were controlled separately with a set of four PA4 computer-controlled attenuators and were appropriately combined before being presented through matched and calibrated TDH-50 earphones. Listeners were seated in individual double-walled Industrial Acoustics Company, Inc. (IAC) booths and made responses on a handheld response pad equipped with a screen providing instructions and feedback.

Trials consisted of three intervals, the first of which was a cue and either the second or the third of which contained the target. The cue consisted of the target to be detected, presented at the level at which it would be added to the masker and in the interaural configuration in which it would appear. New maskers were generated on each trial and different maskers were presented on the second and third intervals. For the multitone maskers, each masked interval contained a new, randomly drawn selection of ten frequencies. Indicators on the response pad marked the timing of the intervals and listeners reported whether the target had occurred in the second or the third interval.

The target level was varied adaptively, starting at 60 dB SPL at the more intense ear (or at both ears when no ILD was present) and then choosing successive levels using 2-down/1-up adaptive tracking (Levitt, 1971), which estimates the target level that results in 70.7% correct detections. The target level was changed by 4 dB for the first four reversals and then 2 dB for an additional ten reversals. Threshold estimates were based on the target levels obtained in the final ten reversals.

D. Conditions

Two masker conditions, noise (EM) and multitone (IM), were crossed with five interaural configurations of the target: (1) ITD alone, (2) ILD alone, (3) "reinforcing" ITDs and ILDs (left ear advanced in phase and higher in level), (4) "opposing" ITDs and ILDs (right ear advanced in phase; left ear higher in level), and (5) diotic. The masker was always presented diotically. Pilot testing with a localization procedure confirmed that in the opposing condition, an increase in level of 6 dB at the left ear and an advance of 300 μs in time at the right ear produced a percept roughly localized in the center of the head. Similar effects were obtained with an ILD of 12 dB and an ITD of 600 μs. In order to allow comparisons with the work of Colburn and Durlach (1965), all five interaural configurations (including, for symmetry, the diotic) were presented with both the larger and smaller differences.

All listeners participated in four repetitions of each unique interaural configuration condition (eight repetitions of the diotic) for each masker type, presented in blocks of the

five interaural configurations arranged in a random order. Each block consisted of either the noise or the multitone masker and either larger or smaller interaural differences. This resulted in average thresholds based on 40 reversals of the adaptive tracks for each masker type for each of the binaural conditions at each size of differences. Because the diotic conditions for the larger and smaller differences were identical, they were combined for analysis, allowing the base line measures of EM and IM to be more accurately measured (80 reversals rather than 40).

E. Calculation of the binaural masking level difference

Colburn and Durlach (1965) defined the BMLD as the ratio of the diotic threshold to the maximum of the levels at the two ears (at threshold) for a given "binaural" condition, expressed in decibels. Thus, the calculation simply involves subtracting the higher of the threshold target levels at the two ears in a given binaural condition (for example, 39 dB) from the threshold target level in the diotic condition (for example, 45 dB). Thus, in this example, the BMLD is 6 dB. For conditions where the BMLD is due entirely to the ITD, this is not problematic. For the ILD conditions, however, this may be a conservative estimate of the BMLD due to the fact that the loudness of a tone presented monaurally is less than that of the same tone presented binaurally (reviewed by Durlach and Colburn, 1978).

Consider the situation where a 12 dB ILD has been introduced by reducing the target level at the right ear by 12 dB but keeping the target level at the left ear the same. If the threshold at the ear with the higher level is unchanged, then the BMLD is 0 dB according to this calculation. If, on the other hand, the threshold is considered to be the level from which one ear is raised by 6 dB and the other lowered by 6 dB, then the BMLD is 6 dB. In addition, if the cue the listener is using is in some way related to the loudness of the target, then the calculation based on the maximum of the levels at the two ears fails to take into account that the listener has now detected a softer target in the ILD condition than in the diotic condition. Presumably, this ability reflects a binaural processing advantage, but the BMLD calculation shows none.

On the other hand, the BMLD is intended to reflect the improvement obtained with two ears relative to performance with a single ear, for which it makes sense to examine changes in the level at the ear with the maximum target level. Using the maximum value calculation both allows comparisons with the results of previous studies and ensures that there is no *overestimation* of binaural release from masking simply due to the method of calculating the differences. If the listener in the 12 dB ILD condition made responses based only on the signal at the left ear (which has the most intense target), then the results would be identical for all of the various binaural conditions. A measure based on differences between the most intense target levels presented would give the correct answer in that case, whereas a measure based on any other level would lead to overestimates of the BMLD.

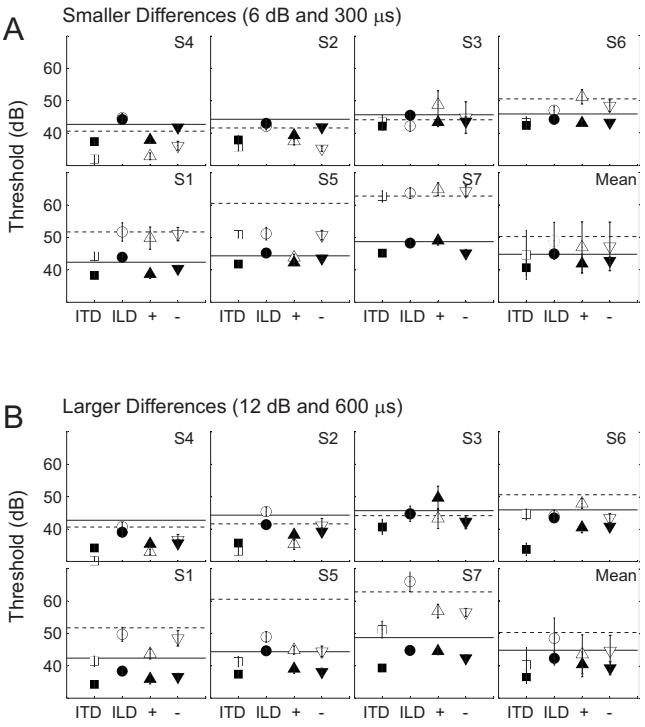

FIG. 1. Threshold level of the 500 Hz tonal target (at the ear with the more intense signal when a level difference was imposed) for all seven listeners across the 18 conditions. Diotic thresholds for the noise maskers are shown with solid lines and diotic thresholds for the multitone maskers are shown with dashed lines. Listeners are ordered by multitone thresholds. In each panel, the filled symbols correspond to the thresholds for the noise maskers and the open symbols correspond to the thresholds for the multitone maskers. The squares represent thresholds for ITD alone, the circles represent ILD alone, the triangles indicate reinforcing ITD and ILD (+), and the inverted triangles indicate opposing ITD and ILD (−). The upper panel contains the thresholds for the smaller binaural differences (6 dB and 300 μs) while the lower panel contains thresholds for the larger binaural differences (12 dB and 600 μs). Error bars represent the critical interval (± two standard errors of the mean).

For the purposes of comparing the reinforcing and opposing conditions and comparing the noise masker with the multitone masker, this issue is irrelevant. In addition, there is no reason, given current models of the BMLD, to question this calculation as it gives the appropriate predictions for the EM cases. It is worth pointing out, however, that if one assumes that the target and masker are heard as distinct auditory objects with independently perceived locations, then the role of binaural loudness may become more important than the relative influence of ITD and ILD on fluctuations of interaural differences calculated on the basis of the combined target and masker. In such a case, the current method of calculating the BMLD would potentially underestimate the amount of release obtained by the introduction of ILDs.

III. RESULTS

Figure 1 shows the individual target levels at threshold for the noise and multitone maskers. Diotic thresholds are shown by horizontal lines (solid for noise maskers and dashed for multitone maskers) and the listener panels are ordered by the level of the multitone thresholds. The upper panels (A) show the thresholds obtained with the smaller

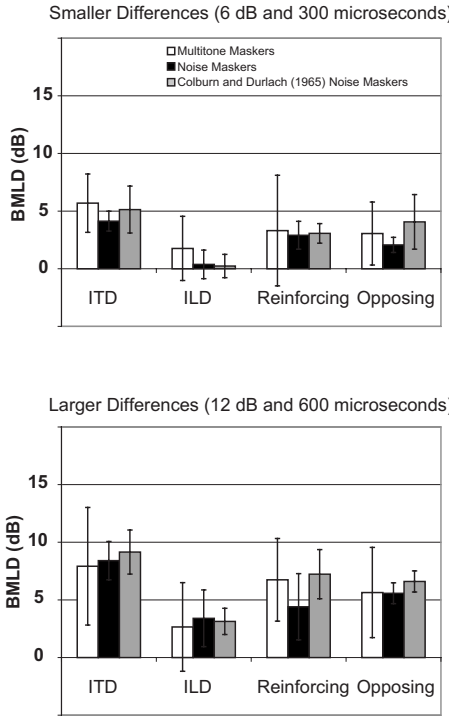

FIG. 2. Average BMLDs (differences between diotic thresholds and binaural thresholds) for four binaural conditions for smaller (upper panel) and larger (lower panel) binaural differences. Results for the noise maskers used in the current study (black bars) are plotted alongside the results reported by Colburn and Durlach (1965) for similar noise maskers (gray bars) and the results for the multitone maskers used in the current study (white bars). The error bars represent the critical interval (± two standard errors of the mean) based on seven listeners.

binaural differences (6 dB and 300 μs), while the lower panels (B) show the thresholds obtained with the larger binaural differences (12 dB and 600 μs). As can be seen, the variability across listeners is much greater for the multitone than for the noise maskers. This is true both for the diotic thresholds and for the amount of release caused by the various interaural differences.

Figure 2 shows the average BMLD values obtained in this experiment plotted alongside the results of Colburn and Durlach (1965). It should be noted that although Colburn and Durlach (1965) used phase shifts of 45° and 90° (250 and 500 μs), the ILDs used were the same. In addition, the frequency distribution of the noise stimuli used in this experiment was closely matched to theirs, even though their noise was analog and Gaussian and thus their amplitude and phase values were Rayleigh and uniform, respectively, rather than both uniform in distribution. The thresholds obtained in the current experiment, and on which the BMLDs are based, appear in Table I. A three-way repeated measures analysis of variance performed on the four BMLD conditions (entered as differences between diotic and binaural thresholds) from the current experiment across the two masker types at both sizes of interaural differences found a significant main effect of interaural configuration ($F_{3,18}=6.19, p<0.01$), a significant main effect of the size of the binaural differences ($F_{1,6}=21.88, p<0.01$), but no significant effect of masker type ($F_{1,6}=0.154, p=0.708$) and no significant interactions (F values all less than 1.1, p values all greater than 0.35). Planned paired-sample t tests found no differences between BMLDs for the opposing and reinforcing interaural differences for either masker type at either size of the differences.

TABLE I. Listener thresholds for the detection of a 500 Hz target tone in the presence of diotic noise or multitone maskers. See text for details on how smaller and larger interaural differences were applied to the target.

	Noise Masker									
	Smaller differences (6 dB, 300 μs)					Larger differences (12 dB, 600 μs)				
Listener	Diotic	ITD	ILD	Reinforcing	Opposing	Diotic	ITD	ILD	Reinforcing	Opposing
1	42.4	38.3	43.9	38.7	40.4	42.4	34.3	38.4	35.9	36.6
2	44.3	37.9	43.0	39.4	41.9	44.3	35.7	41.4	38.2	39.2
3	45.7	42.2	45.5	43.4	43.6	45.7	40.6	44.7	49.6	42.3
4	42.7	37.4	44.2	37.8	41.8	42.7	34.2	39.0	35.4	35.6
5	44.3	41.8	45.2	42.3	43.6	44.3	37.4	44.6	39.1	38.1
6	45.9	42.4	44.3	43.1	43.3	45.9	33.7	43.4	40.5	40.8
7	48.7	45.2	48.3	49.0	45.1	48.7	39.4	44.8	44.5	42.4
Mean	44.8	40.7	44.9	41.9	42.8	44.8	36.4	42.3	40.4	39.3
	Multitone Masker									
	Smaller differences (6 dB, 300 μs)					Larger differences (12 dB, 600 μs)				
1	51.7	44.2	51.7	49.8	51.1	51.7	41.4	49.7	43.7	48.5
2	41.6	35.8	42.1	37.5	35.2	41.6	33.2	45.4	35.4	41.1
3	44.1	43.4	42.2	48.8	44.8	44.1	40.8	44.7	43.3	42.1
4	40.6	32.0	44.8	32.9	36.1	40.6	30.2	40.7	32.9	36.7
5	60.6	50.9	51.2	43.8	50.7	60.6	41.3	48.9	44.9	44.4
6	50.6	43.3	47.1	51.2	48.5	50.6	44.5	44.1	47.9	43.4
7	62.8	62.7	63.7	64.9	64.3	62.8	51.2	66.0	56.9	56.5
Mean	50.3	44.6	48.9	47.0	47.2	50.3	40.4	48.5	43.5	44.6

The BMLD values were also analyzed by performing two correlational analyses. In each case, each pair of values entered corresponded to the BMLDs for an individual listener in the same interaural condition. The first analysis correlated release from the noise masker with release from the multitone masker and was performed separately for larger and smaller interaural differences. The second analysis correlated release based on larger differences with release based on smaller differences and was performed separately for the noise and multitone maskers. The logic behind the first analysis was that perhaps, the nonsignificant effects of masker type were due to variability across listeners. The second analysis was done to determine whether or not the correlational analysis had sufficient power to show a significant difference where one was thought to exist.

The correlation between the BMLDs for the noise and multitone maskers for the smaller differences was nonsignificant ($r=0.221$) as was also the case for the larger differences ($r=0.223$). On the other hand, significant correlations ($p<0.01$) were found between the BMLDs obtained with larger and smaller differences for both the noise masker ($r=0.559$) and for the multitone masker ($r=0.767$). Adding listener as a covariate had the effect of increasing the correlations slightly, but the level of significance did not change. These patterns of correlation show that while individual listeners were likely to have similar patterns of BMLDs across larger and smaller interaural differences for a given masker type, the pattern for each individual was not necessarily similar across masker types.

IV. DISCUSSION

These results cause difficulties for a purely position-based account of binaural release from IM because there was not even a trend toward greater BMLDs for reinforcing interaural differences as compared with opposing differences. The similarity between the patterns of masking release obtained with noise maskers and with multitone maskers suggests a common mechanism, but the low correlations for the individual listeners argues against such a conclusion. It might be argued that the variability in the data was simply so great that a true correlation was not able to be observed, but the high correlation for the smaller and larger differences suggests that this is probably not the case.

Due to the large individual differences, it could be the case that the results for the listeners who showed very little IM are fundamentally different from those who experienced larger amounts of IM. In particular, it might be reasonable to conclude that for L2, L3, and L4, for whom the multitone maskers were less effective than were the noise maskers (see Fig. 1), the majority of the masking was energetic rather than informational. On the basis of whether or not the multitone threshold exceeded the noise threshold, two groups can be created, with L2, L3, and L4 falling in the "LowIM" group and L1, L5, L6, and L7 falling in the "HighIM" group. On this basis, one could hypothesize that the LowIM listeners were actually using a mechanism of release for the multitone maskers that was more similar to that employed for the noise maskers than for the HighIM group. A test of this hypothesis would be to examine the correlation between the release for multitone and noise maskers separately for the two groups of listeners.

For the HighIM group, the correlation between the release for the noise and multitone maskers [plotted in Fig. 3, panel (A)] was slightly negative and failed to reach significance for either smaller or larger binaural differences [$r=-0.031$, $p=0.9$ for smaller differences (triangles); $r=-0.207$, $p=0.44$ for larger differences (diamonds)]. For the LowIM group, the correlations between the release for the noise and multitone maskers [plotted in Fig. 3, panel (B)] was significant for both sizes of differences [$r=0.659$, $p<0.05$ for smaller differences (triangles); $r=0.704$, $p<0.05$ for larger differences (diamonds)]. These results clearly show that the two groups were performing quite differently. Moreover, the significant correlation between noise and multitone maskers for the LowIM group supports the hypothesis that the dominant form of masking for the LowIM group was EM for both noise and multitone maskers. In contrast, the HighIM group had thresholds that were elevated in the presence of the multitone masker due to IM, and these thresholds were uncorrelated with their performance in the EM-dominated task.

It is still possible to argue that the low correlations for the HighIM group simply reflect higher variability for those listeners. This is not supported, however, by the fact the correlations between smaller and larger differences [plotted in Fig. 3, panels (C) and (D)] were significant for the multitone maskers for both groups ($r=0.802$, $p<0.01$ for HighIM [circles, panel (C)]; $r=0.711$, $p<0.05$ for LowIM [circles, panel (D)]), but only the HighIM group reached a significant correlation for the noise maskers ($r=0.721$, $p<0.01$ for HighIM [squares, panel (C)]; $r=0.538$, $p=0.07$ for LowIM [squares, panel (D)]). In short, these correlations suggest that while the two groups were performing consistently within a masker type, only the LowIM group was performing in the same way for the two masker types. Thus, correlational analysis supports the idea that the LowIM group used a mechanism related to release from EM for both masker types, but that the HighIM group changed strategies or mechanisms in response to the change in masker type. The Appendix describes a potential strategy based on widening and narrowing of the effective auditory filter that could account for this pattern of results.

A central question of this study was whether there was a significant difference in the release obtained with opposing and reinforcing binaural differences. The fact that the amount of release was not significantly different argues against a position-based explanation. However, it should be noted that while the trading ratio chosen (50 μs/dB) resulted in a roughly centered percept for one of the listeners, the results of Hafter and Carrier (1972) suggest caution in concluding that such a percept was present for all listeners, especially given the changes in overall level that were occurring over the course of the adaptive tracks. While it is unlikely that these differences in perceived location would have resulted in percepts identical to those obtained with reinforcing cues, it could certainly have led to greater variability. A similar

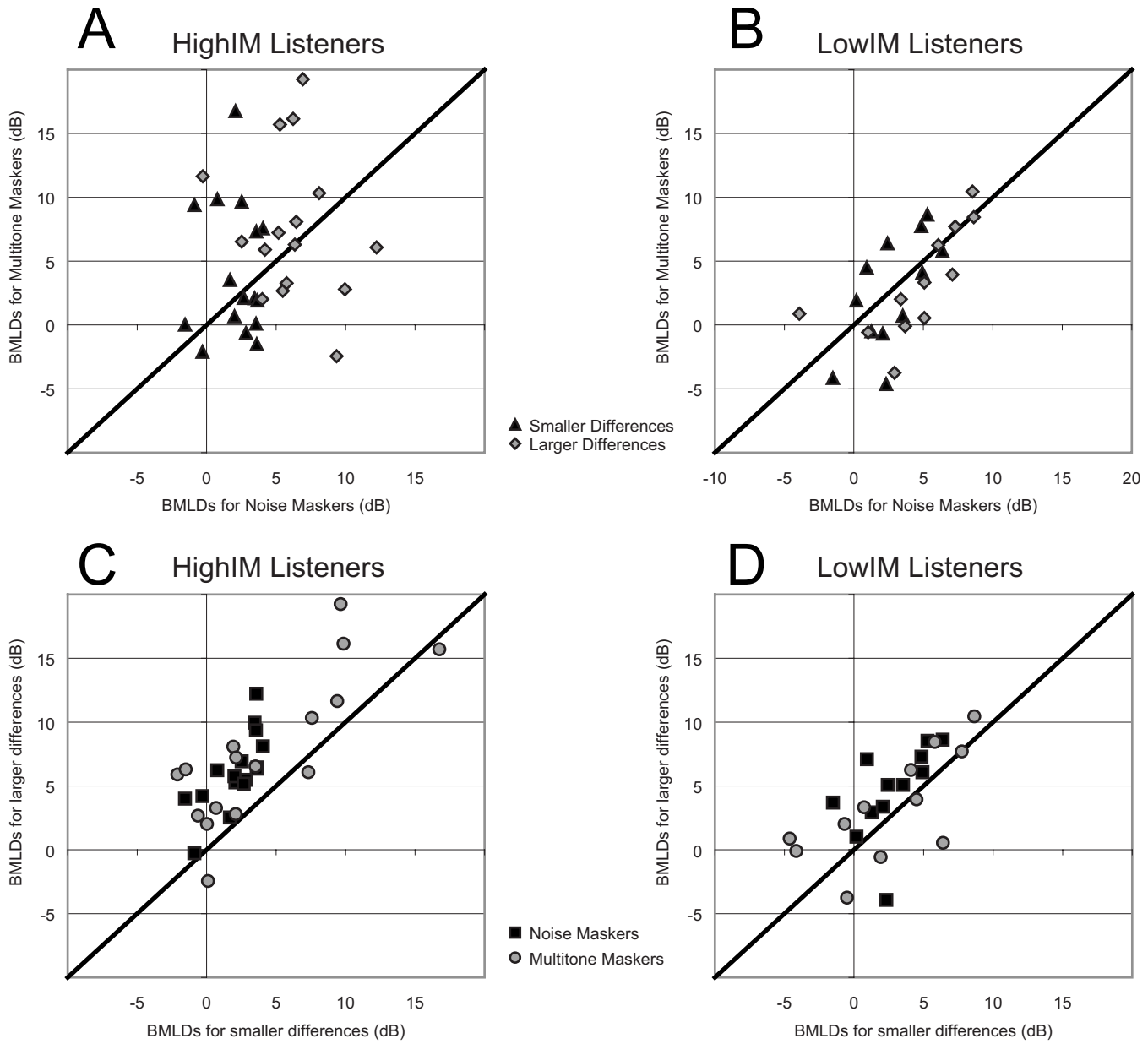

FIG. 3. BMLD values for HighIM listeners [L1, L5, L6, and L7; panels (A) and (C)] and LowIM listeners [L2, L3, and L4; panels (B) and (D)] plotted as a function of masker type and size of the binaural differences. Note that the same data appear in both the upper and lower panels.

concern could be raised regarding the fact that when the target is presented near detection threshold, it is possible that the attenuated ear is rendered inaudible, especially for 12 dB ILDs. Such inaudibility would transform both the opposing and reinforcing cues into a monaural target. The evidence against this argument comes from the fact that a similar inaudibility should have occurred for the ILD-alone condition. Since thresholds were uniformly 2–3 dB higher for the ILD-alone condition both with 6 and 12 dB ILDs, it is unlikely that ITD did not contribute.

On the other hand, variation in perceived location could have led to similar release for opposing and reinforcing cues simply due to the fact that the amount of release from IM seems to be fairly similar across a broad range of perceived locations. In this case, the nonsignificant differences between opposing and reinforcing cues for the EM and IM stimuli may give the appearance of relying upon a common mechanism when they in fact do not. Nonetheless, it is reasonable to conclude from these data that the additional perceived difference in location provided by reinforcing cues was not sufficiently informative to provide additional release.

An alternative explanation for the lack of a significant difference between the opposing and reinforcing cues is that a true difference was obscured due to averaging together the results for the two groups of listeners. In particular, it might be the case that the LowIM group would show no difference for the multitone and noise maskers, given that they performed these tasks in the same way that listeners perform typical BMLD tasks, which show no differences between opposed and reinforced differences. However, the HighIM group might show a difference for the multitone but not the noise maskers. This was not supported by the data. A series of paired *t* tests showed no significant differences between

performance on opposing and reinforcing differences ($p > 0.05$ in all cases) for either group for either masker type at either size of differences.

It is interesting to note that there was a tendency for HighIM listeners to show larger BMLDs for larger binaural differences compared to smaller differences. As the difference between LowIM and HighIM listeners on this measure [compare panels (C) and (D) of Fig. 3] was on the edge of significance for both the noise maskers ($p=0.048$) and for the multitone maskers ($p=0.052$), further testing would be necessary to determine whether or not this tendency is consistent and what it may suggest about the mechanisms contributing to binaural unmasking.

What, then, are the possible strategies that could have produced these data? There is no evidence that those listeners who experienced substantial IM had uniformly greater release from IM (or EM) or that those listeners were more sensitive to reinforcing than opposing interaural differences. Consequently, there is no evidence that any of the listeners in any of the conditions were using differences in the lateral positions of the target and the masker to detect the target. These results parallel those of Colburn and Durlach (1965) and show exactly the pattern of data that would be predicted by the EC model. What is still unclear, however, is why the individual patterns of release, which are not significantly different for the larger and smaller differences, differ for the two types of maskers (at least for the HighIM group). Could it be the case that release from EM was due to an EC operation for all listeners, but that the HighIM listeners were using a different spatial cue, such as diffuseness or perceived width, to obtain release from IM? As mentioned above and described in the Appendix, it is possible to account for the differences in performance between the HighIM and LowIM groups by postulating that the HighIM group listened through effectively wider auditory filters in the diotic multitone condition and that introducing interaural differences allowed that group to narrow their effective filters into the range used by the other listeners. Since the LowIM group did not appreciably widen their filters in response to the multitone maskers, it would be reasonable to hypothesize that they simply used the same mechanism of binaural release for the noise and multitone maskers.

Future work will need to address the potential differences between a waveform-based method (such as an EC mechanism, a correlation mechanism, or an interaural-difference mechanism) and a cue based on spatial percepts such as image width or diffuseness rather than mean lateral position. One direction that might be useful for making such a distinction is to investigate IM and EM for identification and discrimination tasks, where the presence of a spatial difference would not be sufficient to indicate the correct response. One particularly relevant example of this is the case of speech maskers overlapping speech targets, such as was studied by Edmonds and Culling (2005). Unfortunately, the situation studied by Edmonds and Culling (2005) involved two very easily segregated speech tokens, as evidenced by the nearly 20 dB improvement in diotic threshold when the masker was speech rather than noise. This suggests that the majority of the masking occurring was energetic, which may account for the similarity between the masking release for the two masker types and the lack of significant difference between the opposing and reinforcing ITD and ILD cues.

A further complication associated with extrapolating from the results presented here to IM with speech is based on evidence that spatial cues may exert their effects only after the initial grouping has occurred (Darwin and Hukin, 1999). It is possible that the irrelevance of spatial position for release from IM applies only to the simultaneous grouping of target and masker components that happens during the initial presentation of new sound objects. In this scenario, because targets and maskers evolve over time, the auditory system may be able to recruit additional mechanisms of release. By moving in a systematic manner from IM obtained with brief, simultaneously presented stimuli through IM using longer stimuli that evolve over time and finally to speech stimuli, it will be possible to determine more fully the range of mechanisms of release and the stimulus characteristics that allow each to be used.

EM and IM can both be reduced by the presence of interaural differences in the target and/or the masking stimuli. For EM, there is little reason to believe that this reduction is due to an enhancement in the perceived differences in location for the target and the masker, since reinforcing and opposing differences in interaural time and level are equally effective. The results presented here suggest that the same may be true for IM with synchronously presented tonal targets and multitone maskers. On the other hand, it is not clear from the data presented here that similar patterns of binaural release should be taken to imply similar underlying mechanisms of release for EM and IM.

ACKNOWLEDGMENTS

This work was supported by the Department of Veterans Affairs, Veterans Health Administration, Rehabilitation Research and Development Service though Associate Investigator Award No. C4855H to Frederick Gallun at the National Center for Rehabilitative Auditory Research as well as NIH-NIDCD Grant Nos. DC00100, DC04545, DC04663, and F32 DC006526 as well as AFOSR Award No. FA9550-05-1-2005. The authors are extremely grateful to Antje Ihlefeld for lending her auditory system and insights, to Jackie Stachel and Deborah Corliss for help with data collection, and of course to our listeners.

APPENDIX: POWER SPECTRUM MODEL OF MASKING RELEASE

It has been shown (Lutfi, 1993; Oh and Lutfi, 1998; Durlach *et al.*, 2005) that much of the variability across subjects and across conditions in IM tasks involving detection of tonal signals in multitone maskers can be captured by a simple model in which listeners vary the effective width of their auditory filter. While this approach seems to be lacking sufficient free parameters to effectively model such a complex phenomenon as IM, it stands as essentially the only quantitative approach that has been proposed. Accordingly, it is appropriate to determine the extent to which the data in this study can be similarly captured. This modeling exercise

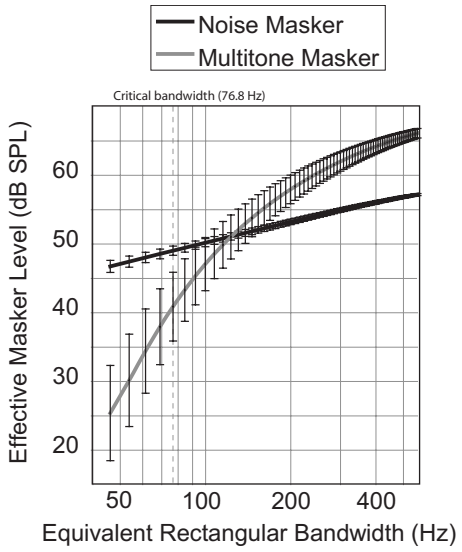

FIG. 4. Results of simulations in which 100 randomly generated noise maskers and multitone maskers were passed through filters of the type specified by Moore and Glasberg (1983). The mean effective masker level is plotted for each masker type across a range of equivalent rectangular bandwidths. Error bars indicate ±1 standard deviation across the 100 randomly generated maskers. At the limit, the functions would reach their broadband levels of 60 (noise) and 70 (multitone) dB SPL.

starts by estimating the amount of energy falling in the critical-band filter centered on the target tone and then determining the changes in that filter width that would be necessary to produce the thresholds obtained in the experiment for the various listeners.

Using the same software that generated the experimental stimuli, 100 maskers of each type were generated and filtered with a range of filter widths. Figure 4 shows the effective masker level calculated for a range of filter widths and for both masker types. The mean energy through the critical band centered on the 500 Hz target frequency, which Moore and Glasberg (1983) estimated at 76.8 Hz, is marked by the dashed line. In accordance with the fact that the noise band included energy in the region between 400 and 600 Hz while the multitone maskers did not, the average energy falling in the critical band was greater for the noise (49 dB SPL) than for the multitone masker (39.8 dB).

If all of the masking the listeners experienced was due to the masker energy falling within the critical band centered on the target, thresholds should be roughly 9 dB higher for the noise masker than for the multitone case, which was not observed for any of the listeners. As can be seen in Fig. 1 (the values also appear in Table I), the differences between the diotic thresholds for the two masker types go in the direction predicted by the energy simulation for three of the listeners, with more masking for the noise than the multitone maskers, but the greatest difference is only 2 dB. One explanation for this difference is that the listeners who are adversely affected by the multitone masker are simply widening their *effective* auditory filters in response to the variability in the stimuli, an idea suggested by Lutfi (1993) and by Durlach *et al.* (2005).

In order to ask how wide the effective filters would have to be to account for the diotic thresholds entirely on the basis of energy falling in the filter, it is useful to assume that the listeners were all using a critical-bandwidth filter in the noise masker condition. This assumption is supported by previous data (Neff *et al.*, 1993; Oxenham *et al.*, 2003), showing that performance in an IM condition is unrelated to threshold or auditory filter shape as measured in an EM condition. The predicted values lie between −6.6 dB (for L1) and −0.3 dB (for L7), which corresponds fairly well to the values McFadden (1966) and Weir *et al.* (1977) obtained using similar stimuli (although their values were reported using different units).

Assuming that the target-to-masker energy ratio at threshold is the same in the multitone masker condition and in the noise masker condition, an estimate was made of the filter width that matched the effective target-to-masker ratio (TMR) for the two conditions for each listener. For those listeners with the lowest multitone thresholds (L2, L3, and L4), the differences in thresholds were −2.7, −1.6, and −2.1 dB, respectively, which lead to estimated effective filter widths of 95, 100, and 98 Hz in the multitone masker condition. So, even though the threshold was lower than that for the noise, the filter estimate was still almost 150% of that of the critical band (76.8 Hz). For L6, L1, L7, and L5, the respective differences in threshold were 4.7, 9.4, 14.4, and 16.2 dB. These values lead to equivalent filters of 145, 207, 360, and 475 Hz wide. While this is a very large range, it is similar to that reported by Durlach *et al.* (2005), who found widths that ranged between 87 and 444 Hz for a similar multitone masking condition.

This single parameter fails to describe the full extent of the release from masking generated by introducing interaural differences, however. The noise masker, being broadband, results in small changes in effective masker energy with changes in filter bandwidth, thus requiring a "subcritical" bandwidth to account for BMLDs. Because reductions in the effective bandwidth to 38 Hz would only account for changes of about 4 dB, capturing the entire range of threshold values requires effective filters 7 Hz wide in order to explain BMLDs of 11.5 dB. Since none of the current models of the BMLD (reviewed in the Introduction) are based on a narrowing of the critical band (indeed, estimates of binaural filters are usually wider than monaural filters), there is little reason to favor a band-narrowing hypothesis over the traditional binaural mechanisms.

For the multitone maskers, the band-narrowing hypothesis is more plausible, especially if it is assumed that the threshold differences between the masker types reflect a widening of the effective auditory filter. If one postulates that interaural differences reduce uncertainty and allow listeners to focus their effective filter more appropriately, then the lower limit on effective filter width is simply the width of the critical band. For L2, L3, and L4, the maximum change in threshold that can be explained by reducing the bandwidth is about 6 dB, but the BMLDs for those listeners include several values as high as 8 dB and one value of 10.4 dB. For the remaining listeners, the maximum BMLDs are greater (up to 19.3 dB for L5), but the band-narrowing model can still account for most of their results since the effective bandwidths for the diotic condition are so wide. Perhaps, then, filter wid-

ening and narrowing account for the performance of the HighIM listeners (L1, L5, L6, and L7) but not the LowIM listeners. This is consistent with the correlational analysis reported in Sec. IV, where it appears that the LowIM group was using the same mechanism for both masker types, but the HighIM group was not.

This analysis provides support for the hypothesis that at least some listeners were widening and narrowing the bandwidths of their effective filters in response to the maskers presented and the interaural differences imposed on the target. Given that Durlach *et al.* (2005) were able to capture much of their data with a band-widening analysis and that the CoRE model of Lutfi (1993) and Oh and Lutfi, (1998) also contains the concept of an effective auditory filter of variable bandwidth, such an approach is certainly worth considering.

Arbogast, T. L., Mason, C. R., and Kidd, G., Jr. (**2002**). "The effect of spatial separation on informational and energetic masking of speech," J. Acoust. Soc. Am. **112**, 2086–2098

Best, V., Ozmeral, E., Gallun, F. J., Sen, K., and Shinn-Cunningham, B. G. (**2005**). "Spatial unmasking of birdsong in human listeners: Energetic and informational factors," J. Acoust. Soc. Am. **118**, 3766–3773.

Brungart, D. S., Simpson, B. D., and Freyman, R. L. (**2005**). "Precedence-based speech segregation in a virtual auditory environment," J. Acoust. Soc. Am. **118**, 3241–3251.

Colburn, H. S., and Durlach, N. I. (**1965**). "Time-intensity relations in binaural unmasking," J. Acoust. Soc. Am. **38**, 93–103.

Colburn, H. S., and Durlach, N. I. (**1978**). "Models of binaural interaction," in *Handbook of Perception*, edited by E. C. Carterette and M. P. Friedman (Academic, New York).

Darwin, C. J., and Hukin, R. W. (**1999**). "Auditory objects of attention: The role of interaural time differences," J. Exp. Psychol. **25**, 617–629.

Domnitz, R. H., and Colburn, H. S. (**1976**). "Analysis of binaural detection models for dependence on interaural target parameters," J. Acoust. Soc. Am. **59**, 598–601.

Durlach, N. I. (**1960**). "Note on the equalization and cancellation theory of binaural masking level differences," J. Acoust. Soc. Am. **32**, 1075–1076.

Durlach, N. I. (**1963**). "Equalization and cancellation theory of binaural masking-level differences," J. Acoust. Soc. Am. **35**, 1206–1218.

Durlach, N. I. (**1972**). "Binaural signal detection: Equalization and cancellation theory," in *Foundations of Modern Auditory Theory*, edited by J. V. Tobias (Academic, New York).

Durlach, N. I., and Colburn, H. S. (**1978**). "Binaural phenomena," in *Handbook of Perception*, edited by E. C. Carterette and M. P. Friedman (Academic, New York).

Durlach, N. I., Mason, C. R., Gallun, F. J., Shinn-Cunningham, B., Colburn, H. S., and Kidd, G., Jr. (**2005**). "Informational masking for simultaneous nonspeech stimuli: Psychometric functions for fixed and randomly mixed maskers," J. Acoust. Soc. Am. **118**, 2482–2497.

Durlach, N. I., Mason, C. R., Kidd, Jr., G., Arbogast, T. L., Colburn, H. S., and Shinn-Cunningham, B. G. (**2003a**). "Note on informational masking," J. Acoust. Soc. Am. **113**, 2984–2987.

Durlach, N. I., Mason, C. R., Shinn-Cunningham, B. G., Arbogast, T. L., Colburn, H. S., and Kidd, G., Jr. (**2003b**). "Informational masking: Counteracting the effects of stimulus uncertainty by decreasing target-masker similarity," J. Acoust. Soc. Am. **114**, 368–379.

Edmonds, B. A., and Culling, J. F. (**2005**). "The role of head-related time and level cues in the unmasking of speech in noise and competing speech," Acta. Acust. Acust. **91**, 546–553.

Freyman, R. L., Helfer, K. S., McCall, D. D., and Clifton, R. K. (**1999**). "The role of perceived spatial separation in the unmasking of speech," J. Acoust. Soc. Am. **106**, 3578–3588.

Gallun, F. J., Mason, C. R., and Kidd, G. Jr. (**2005**). "Binaural release from informational masking in a speech identification task," J. Acoust. Soc. Am. **118**, 1614–1625.

Goupell, M. J., and Hartmann, W. M. (**2006**). "Interaural fluctuations and the detection of interaural incoherence: Bandwidth effects," J. Acoust. Soc. Am. **119**, 3971–3986.

Goupell, M. J., and Hartmann, W. M. (**2007a**). "Interaural fluctuations and the detection of interaural incoherence. II. Brief duration noises," J. Acoust. Soc. Am. **121**, 2127–2136.

Goupell, M. J., and Hartmann, W. M. (**2007b**). "Interaural fluctuations and the detection of interaural incoherence. III. Narrowband experiments and binaural models," J. Acoust. Soc. Am. **122**, 1029–1045.

Hafter, E. R. (**1971**). "Quantitative evaluation of a lateralization model of masking-level differences," J. Acoust. Soc. Am. **55**, 1116–1122.

Hafter, E. R., Bourbon, W. T., Blocker, A. S., and Tucker, A. (**1969**). "A direct comparison between lateralization and detection under conditions of antiphasic masking," J. Acoust. Soc. Am. **46**, 1452–1457.

Hafter, E. R., and Carrier, S. C. (**1970**). "Masking-level differences obtained with a pulsed tonal masker," J. Acoust. Soc. Am. **47**, 1041–1047.

Hafter, E. R., and Carrier, S. C. (**1972**). "Binaural interaction in low-frequency stimuli: The inability to trade time and intensity completely," J. Acoust. Soc. Am. **51**, 1852–1862.

Hafter, E. R., Carrier, S. C., and Stephan, F. K. (**1973**). "Direct comparison of lateralization and the MLD for monaural signals in gated noise," J. Acoust. Soc. Am. **53**, 1553–1559.

Hirsh, I. J. (**1948**). "The influence of interaural phase on interaural summation and inhibition," J. Acoust. Soc. Am. **20**, 536–544.

Jeffress, L. A., Blodgett, H. C., Sandel, T. T., and Wood, C. L. III (**1956**). "Masking of tonal signals," J. Acoust. Soc. Am. **38**, 416–426.

Kidd, G., Jr., Mason, C. R., Deliwala, P. S., Woods, W. S., and Colburn, H. S. (**1994**). "Reducing informational masking by sound segregation," J. Acoust. Soc. Am. **95**, 3475–3480.

Levitt, H. (**1971**). "Transformed up-down methods in psychoacoustics," J. Acoust. Soc. Am. **49**, 467–477.

Lutfi, R. (**1993**). "A model of auditory pattern-analysis based on component-relative-entropy," J. Acoust. Soc. Am. **94**, 748–758.

McFadden, D. (**1966**). "Masking level differences with continuous and with burst masking noise," J. Acoust. Soc. Am. **40**, 1414–1419.

Moore, B. C. J., and Glasberg, B. R. (**1983**). "Suggested formulae for calculating critical bands and excitation patterns," J. Acoust. Soc. Am. **74**, 750–753.

Neff, D. L. (**1995**). "Signal properties that reduce masking by simultaneous, random-frequency maskers," J. Acoust. Soc. Am. **98**, 1909–1920.

Neff, D. L., Dethlefs, T. M., and Jesteadt, W. (**1993**). "Informational masking for multicomponent maskers with spectral gaps," J. Acoust. Soc. Am. **94**, 3112–3126.

Oh, E. L., and Lutfi, R. A. (**1998**). "Nonmonotonicity of informational masking," J. Acoust. Soc. Am. **104**, 3489–3499.

Oxenham, A., Fligor, B. J., Mason, C. R., and Kidd, G., Jr. (**2003**). "Informational masking and musical training," J. Acoust. Soc. Am. **114**, 1543–1549.

Rakerd, B., Aaronson, N. L., and Hartmann, W. M. (**2006**). "Release from speech-on-speech masking by adding a delayed masker at a different location," J. Acoust. Soc. Am. **119**, 1597–1605.

Rayleigh, J. W. S. (**1875**). "On our perception of the direction of a source of sound," Proceedings of the Musical Association, Second Session, pp. 75–84.

Richards, V. M., and Tang, Z. (**2006**). "Estimates of effective frequency selectivity based on the detection of a tone added to complex maskers," J. Acoust. Soc. Am. **119**, 1574–1584.

Sandel, T. T., Teas, D. C., Fedderson, W. E., and Jeffress, L. A. (**1955**). "Localization of a sound from single and paired sources," J. Acoust. Soc. Am. **27**, 842–852.

Stevens, S. S., and Newman, E. B. (**1934**). "The localization of pure tones," Proc. Natl. Acad. Sci. U.S.A. **20**, 593–596.

Webster, F. A. (**1951**). "The Influence of Interaural Phase on Masked Thresholds I. The Role of Interaural Time-Deviation," J. Acoust. Soc. Am. **23**, 452–462.

Wier, C. C., Green, D. M., Hafter, E. R., and Burkhardt, S. (**1977**). "Detection of a tone burst in continuous- and gated-noise maskers; defects of signal frequency, duration, and masker level," J. Acoust. Soc. Am. **61**, 1298–1300.

Zurek, P. M., and Durlach, N. I. (**1987**). "Masker-bandwidth dependence in homophasic and antiphasic tone detection," J. Acoust. Soc. Am. **81**, 459–464.

On the minimum audible difference in direct-to-reverberant energy ratio[a)]

Erik Larsen,[b)] Nandini Iyer,[c)] Charissa R. Lansing, and Albert S. Feng
Beckman Institute for Advanced Science and Technology, University of Illinois at Urbana-Champaign, Urbana, Illinois 61801

(Received 30 March 2006; revised 17 April 2008; accepted 5 May 2008)

The goals of this study were to measure sensitivity to the direct-to-reverberant energy ratio (D/R) across a wide range of D/R values and to gain insight into which cues are used in the discrimination process. The main finding is that changes in D/R are discriminated primarily based on spectral cues. Temporal cues may be used but only when spectral cues are diminished or not available, while sensitivity to interaural cross-correlation is too low to be useful in any of the conditions tested. These findings are based on an acoustic analysis of these variables and the results of two psychophysical experiments. The first experiment employs wideband noise with two values for onset and offset times to determine the D/R just-noticeable difference at −10, 0, 10, and 20 dB D/R. This yielded substantially higher sensitivity to D/R at 0 and 10 dB D/R (2–3 dB) than has been reported previously, while sensitivity is much lower at −10 and 20 dB D/R. The second experiment consists of three parts where specific cues to D/R are reduced or removed, which enabled the specified rank ordering of the cues. The acoustic analysis and psychophysical experiments also provide an explanation for the "auditory horizon effect."
 [DOI: 10.1121/1.2936368]

PACS number(s): 43.66.Ba, 43.66.Qp [AK] Pages: 450–461

I. INTRODUCTION

Reverberation has a significant influence on speech communication, sound localization, and auditory perception in general. Although speech understanding is degraded in highly reverberant environments (Nábělek and Dagenais, 1986; Nábělek, 1988), musical listening can be enhanced if the amount of reverberation is appropriate for the type of music, which is often reflected in the design of listening spaces (Blesser, 2001).

Reverberation facilitates distance judgments because in the absence of sound reflections, distance is confounded with intensity at the ear, and thus it is nearly impossible to assess how far away a sound source is unless the listener has *a priori* knowledge of sound power. For unfamiliar sounds in anechoic environments, distance judgments typically converge to a default value (Coleman, 1962), which has been termed the *specific distance tendency* (see also Gogel, 1961; Mershon and King, 1975), irrespective of the actual sound source distance, although learning does occur and judgments tend to improve over time. For familiar sounds such as speech, anechoic distance localization is possible due to intensity cues, but these can be unreliable or ambiguous (Philbeck and Mershon, 2002).

In reflective environments, acoustic cues having a one-to-one relationship with distance and which are not confounded with source characteristics are available, in particular, the "direct-to-reverberant energy ratio" or D/R (von Békésy, 1938; Mershon and King, 1975; Mershon *et al.*, 1989; Nielsen, 1993; Bronkhorst and Houtgast, 1999).[1] In a typical listening room, the direct sound field energy decays proportionally to (logarithmic) distance, while the reverberant sound field has approximately equal energy irrespective of distance. Thus, D/R can, in principle, be used to estimate the distance of a sound source. In anechoic environments, cues to distance are available for nearby sources, within approximately 1 m from the head (Brungart and Rabinowitz, 1999; Brungart *et al.*, 1999; Brungart, 1999; Shinn-Cunningham, 2000), but we do not further consider this special case.

In this study, we investigate the proficiency with which listeners discriminate signals with different D/R at various reference D/R levels. We also present an acoustic analysis of the properties of the reverberant sound field as a function of D/R, which can be used as a starting point for a more complete modeling effort. The goal of the psychophysical and acoustical analyses is to improve our understanding of perception of D/R, and thus distance perception in enclosed spaces.

Although listeners are sensitive to changes in D/R, it is not clear that this is based on an actual perception of D/R or on some other parameter that covaries with D/R. If listeners in fact do assign some D/R-equivalent measure to sounds, most prior work has assumed that this is achieved by a tem-

[a)] Portions of this work were presented in "On temporal vs. frequency-based discrimination of direct-to-reverberant energy ratio," 146th Conference of the Acoustical Society of America, Austin, TX, November 2003, and "An evaluation of two frequency-based mechanisms for direct-to-reverberant energy ratio discrimination," 147th Conference of the Acoustical Society of America, New York, NY, May 2004.

[b)] Present address: Harvard-MIT Division of Health Sciences and Technology, Speech and Hearing Bioscience and Technology, Cambridge, MA. Electronic mail: elarsen@alum.mit.edu

[c)] Currently with General Dynamics Advanced Information Systems. Electronic mail: nandini.iyer@wpafb.af.mil

poral integration method, and a model exists (Bronkhorst and Houtgast, 1999). If this hypothesis is correct, then variation in the onset time of sounds should affect the ability to discriminate changes in D/R, but most studies (Santarelli *et al.*, 2000; Bronkhorst, 2001; Zahorik, 2002a, 2002c) have found that the effect of temporal modulation (as measured by signal onset/offset time) on identification or discrimination of D/R is at most minor. Other variables, such as interaural cross-correlation (IACC), spectral variance (frequency-by-frequency variation in power spectrum), and spectral envelope, may be more important. In Sec. II, we will analyze how these variables covary with D/R to investigate their potential roles in D/R perception. This analysis reveals that spectral and binaural cues offer alternative explanations for listeners' sensitivity to D/R. In Sec. IV, we present further evidence for this by showing degradation in sensitivity to D/R when removing certain acoustic features of signals that otherwise leave D/R, as calculated from its acoustic definition, unchanged.

Two previous studies aimed to find the just-noticeable difference (JND) for D/R. Reichardt and Schmidt (1966) used classical music (presented in an anechoic chamber with four loudspeakers and a yes/no procedure) with adjustable D/R to establish the JND at various reference D/R values, holding the overall sound level constant, to develop a scale of "spatial impression" ("Räumlichkeit"). This scale ranged from fully anechoic to highly reverberant. Based on the obtained JNDs, they found 14 discernible steps in the range $(-23,23)$ dB D/R. The JND versus D/R value had a U shape, with a minimum of 2 dB at 0 dB D/R and rising to about 20 dB at ± 20 dB D/R. Zahorik (2002c) used virtual acoustics to assess the JND at 0, 10, and 20 dB D/R (roving the overall intensity level of signals) in a 2AFC procedure. He found roughly constant JNDs of 5–6 dB at these D/R for four different signal types (two noise signals, a speech syllable, and an impulse) and for both medial and lateral sources. Zahorik attributed the large discrepancy between the results of his and Reichardt and Schmidt's study mainly to the fact that Reichardt and Schmidt held the overall level of the stimuli constant, thus allowing listeners to focus on changes in the reverberant (or direct) energy level to discriminate the signals as D/R was manipulated.

In this paper, we start by analyzing ear-canal signals as a function of D/R, uncovering how room acoustics affects these signals. Applying this analysis to D/R discrimination, we find that the general properties of reverberant sound fields in enclosed spaces create well-defined physical/acoustical constraints. We hypothesize that these constraints will be reflected in behaviorally obtained discrimination thresholds; if applied to distance perception, they provide a natural explanation for the "auditory horizon effect" (see, e.g., Bronkhorst and Houtgast, 1999). We complement the acoustic analysis with behavioral discrimination data over a broad range of D/R values in a manner similar to Zahorik (2002c) but extended to negative D/R and also for "impoverished" signals. The first experiment, described in Sec. III, was conducted to establish base line D/R JNDs at −10, 0, 10, and 20 dB D/R for signals with two different onset times. In the second experiment (Sec. IV), the signals presented to listeners were modified to selectively remove potential D/R cues. Experiment 2a employs monaural listening (removing binaural cues); experiment 2b removes most spectral cues by band limiting the signals, while experiment 2c further reduces spectral cues by roving the frequency region of the narrow band signals. The JNDs for these impoverished signals, compared to the JNDs of experiment 1, can indicate the relative contribution of specific acoustic cues to discrimination of D/R.

II. ACOUSTIC ANALYSIS

External changes in a sound field correlate to changes in internal (psychological) variables. Thus, the internal processes can be probed by manipulating the external signals and linking the two with a quantitative model, as originally outlined by Fechner (1912). To properly discuss how the external environment influences perceptual processes, e.g., in the case of D/R perception, we need to briefly consider such a quantitative model. Following the approach and notation from Allen and Neely (1997), the JND for the external variable (we use the D/R JND $\Delta\nu$) is proportional to the JND for the internal variable ($\Delta\psi$). The proportionality factor depends on the functional relationship between external and internal variables ($d\psi/d\varphi$) and the physical relationship between the external variable and the quantity that is being manipulated, which is D/R (ν) in our case. The exact relationship is

$$\Delta\nu = \Delta\psi\left(\frac{d\psi}{d\varphi}\frac{d\varphi}{d\nu}\right)^{-1}. \tag{1}$$

We will propose various physical variables φ_i (e.g., interaural correlation or spectrum) that have the potential for being useful in D/R discrimination, and we compute their dependence on D/R $[\varphi_i(\nu)]$. This will allow us to compute $d\varphi_i/d\nu$ in Eq. (1) but not the other components, $\Delta\psi$ or $d\psi/d\varphi$. In the remainder, we will refer to this as modeling the effect of the *physical relationship* between D/R and the acoustic variables. This stands in contrast to analyzing the effect of *perceptual sensitivities* on the JND, which, though equally important, is beyond the scope of this work.

A complication arises in a listening task (e.g., D/R perception) where redundant cues are available. When multiple cues can be used at once, these could be combined to improve discrimination performance, leading to smaller JNDs than would be obtained if any cue was used in isolation (Lutfi and Wang, 1999; Ernst *et al.*, 2000; Ernst and Banks, 2002; Hillis *et al.*, 2004). Such an approach requires quantitative knowledge about the contribution of the various cues; in Sec. IV, we selectively remove potential cues to qualitatively assess their individual contribution for D/R discrimination without considering how they interrelate.

A. Interaural cross-correlation

Reverberation introduces binaural cues by altering the sound attributes at the two ears differentially. IACC (ϱ) is a powerful binaural cue (Blauert, 1984), and sensitivity to changes in IACC can be high: the JND $\Delta\varrho$ at $\varrho=1$ is about 0.02–0.04 but increases strongly as ϱ decreases (Pollack and

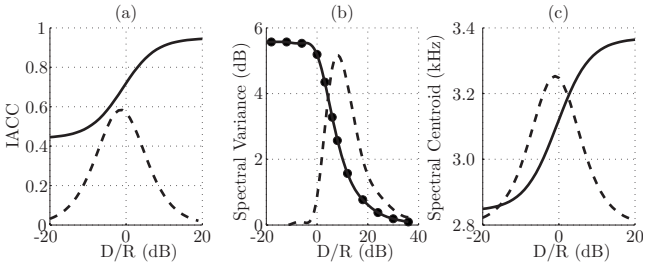

FIG. 1. Dependence of acoustic variables on D/R. Panel (a): Relation between D/R and IACC, calculated from experimental signals. Panel (b): Relation between D/R and variance of the power spectrum, adapted from Jetzt (1979). Panel (c): Relation between D/R and spectral centroid (or spectral CoG), calculated from experimental signals. In all panels, the solid line indicates the dependence of the acoustic variable on D/R, while the dashed line indicates the (arbitrarily) scaled derivative. In all cases, the acoustic variables change monotonically as a function of D/R but asymptote at large positive and negative D/R.

Trittipoe, 1959; Gabriel and Colburn, 1981; Boehnke *et al.*, 2002). Because reverberation decorrelates signals at the ears (Blauert, 1984), IACC decreases as D/R decreases, making it a potential cue for D/R.

IACC is calculated as

$$\varrho(\tau) = \frac{\overline{x_1(t)x_2(t-\tau)}}{\sqrt{\overline{x_1^2(t)}\ \overline{x_2^2(t)}}}, \tag{2}$$

where $x_1(t)$ and $x_2(t)$ are signals at the left and right ears, respectively, and τ is a time delay ($\overline{x_1}$ indicates the expected value of x_1). Applying Eq. (2) to ear signals measured in the room that was used to obtain experimental data for experiments 1 and 2 (described later) yields the relationship between IACC and D/R as shown in panel (a) of Fig. 1 (solid line); the scaled derivative of the IACC is also shown (dashed line). The maximum rate of change in IACC appears to occur at about 0 dB D/R, and otherwise, the rate of change is approximately symmetrical around this value. Equation (1) shows that the contribution of the physical relationship of D/R and IACC minimizes the JND around D/R values of 0 dB and to enlarge it at increasingly negative or positive D/R.

B. Spectral variance

Changes in sound spectrum produce salient perceptual cues (for a review, see Green, 1988). There are at least two different kinds of spectral changes that occur when a sound source moves away from a receiver or, equivalently, when D/R decreases. In this and the following section, we will analyze these two effects. Here we discuss changes in the fine structure of the spectrum, by which we mean the frequency-to-frequency variations in the magnitude spectrum that occur as a result of the interference of reflected sound waves. Prior studies have indicated that people are sensitive to such fine-structure changes (Green, 1988; Berkley and Allen, 1993). In a multitonal background, sensitivity to changes in the amplitude of a single component seems to be highest when the overall amplitude variability is small (Kidd *et al.*, 1986).

Jetzt (1979) showed that the variance (σ^2) of the spectral response between two locations in a room is exclusively determined by D/R, as reproduced in panel (b) of Fig. 1.[2] The dots are data as given by Jetzt in his Table I, and the solid line is a cubic spline interpolation of those data; the dashed trace is the scaled derivative of σ^2 as a function of D/R. The derivative has a maximum at about 8 dB D/R and is large only at positive D/R values. Thus, according to Eq. (1), the contribution of the physical relationship between D/R and spectral variance is to provide cues at moderately large positive D/R values, peaking at about 8 dB D/R.

C. Spectral envelope

A second kind of spectral change that occurs when D/R changes is the spectral envelope (sometimes also referred to as the "spectral shape"). Spectral envelope changes are thought to influence distance perception because empirical findings show that low-pass filtered signals are judged to be further away as the cut-off frequency decreases; the effect has been attributed to the relatively larger absorption of high sound frequencies in air, which creates progressive low-pass filtering as the source distance increases (Coleman, 1968; Butler *et al.*, 1980; Little *et al.*, 1992; Zahorik, 2002a, 2002c). However, the reduction in high-frequency content necessary to yield such increases in source distance is always much greater than that produced by air absorption alone. A different explanation is based on the fact that most materials commonly used in rooms absorb more high- than low-frequency energy, such that each reflected sound wave will be low-pass filtered. As the reverberant sound field consists of waves that have been reflected numerous times, the spectral envelope of the reverberant sound field will be shifted toward lower frequencies relative to the direct sound (see also Nielsen, 1993).

To remain consistent with the other acoustic parameters under consideration, we analyze spectral envelope changes with a one-parameter model.[3] To capture perceived changes in sound timbre as a function of D/R, we use the spectral centroid, or spectral center of gravity (CoG), χ, according to

$$\chi = \frac{\Sigma_{i=2}^{N} f_i X_i}{\Sigma_{i=2}^{N} X_i}, \tag{3}$$

where X_i is the ith component of the discrete power spectrum of the signal x, and the summation includes all N frequency components f_i up to the Nyquist frequency, except dc (hence the summation starts at index value 2). As explained above, the reverberant sound field has less high-frequency energy than the direct sound field, which means that CoG decreases as the relative content of reverberation is larger, i.e., as D/R decreases.

Aside from its dependence on D/R, the spectral envelope depends on the characteristics of the source signal also. For the signals that were used in experiment 1 (Sec. III), we obtain the CoG $\chi(\nu)$ as shown in panel (c) of Fig. 1 (solid line), as well as its derivative (dashed line). The maximum rate of change in CoG occurs at about 0 dB D/R and is otherwise approximately symmetrical around this value, becoming near zero at large positive and negative values. Thus, the physical relationship between D/R and the spectral envelope acts to minimize the JND around 0 dB D/R [cf. Eq. (1)].

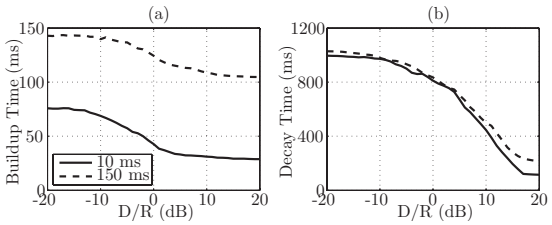

FIG. 2. Dependence of temporal cues on D/R. Panel (a): Relation between D/R and sound buildup time, calculated from experimental signals, using broadband noise with onset times of 10 and 150 ms. Panel (b): Relation between D/R and sound decay time, calculated from experimental signals, using the same two source signal types. Both sound buildup and decay times vary monotonically with D/R but asymptote at large positive and negative D/R. Buildup time varies mainly at negative D/R, while decay time varies mainly at positive D/R.

D. Temporal integration

At large positive D/R values, buildup and decay of sounds at the ear canal will closely match the onset and offset times of the sound source,[4] while at large negative D/R values, the room's reflections may alter these patterns. In most practical cases, the response time of the room, as parametrized by reverberation time (Sabine, 1962; Kuttruff, 1991), is longer than the onset/offset time of typical source signals, e.g., speech. Thus, as D/R decreases, sound buildup and decay are expected to become more sluggish, possibly providing cues to D/R.

We compute the buildup and decay of the signals used in experiment 1 by integrating the squared signal amplitude over time based on the Schroeder (1965) method for calculating reverberation time (for decay time analysis, we integrate backward in time starting at the end of the signal). We express buildup (decay) time as the period required for the signal to increase (decrease) by 60 dB at the start (end) of the signal by using straight portions of the energy buildup (decay) curves. The results of this analysis for broadband noise signals with fast (10 ms) and slow (150 ms) onset/offset times, as used in experiment 1, are shown in Fig. 2. There is a strong dependence on D/R (the derivatives of these curves are quite noisy and thus omitted).

Panel (a) of Fig. 2 shows buildup time versus D/R for the 10 and 150 ms onset time signals. These curves appear similar except for a vertical offset, i.e., changes in buildup time as a function of D/R are similar for both signals. However, for purposes of discriminating differences in buildup time, relative changes may be more relevant (Kewley-Port and Pisoni, 1984), in which case, the fast-onset signal should provide the strongest temporal discrimination cues. Panel (b) shows decay time versus D/R for both signals, and the results appear very similar, at least for D/R values up to about 5 dB, after which changes in the slow-offset signal become more gradual. Thus, potential mechanisms employing decay time to discriminate D/R should work equally well for fast- or slow-offset signals, except at relatively large D/R values, where fast-offset signals may provide stronger cues.

Another feature of these curves is that most of the change in buildup time occurs at moderately negative D/R values, between about −10 and 0 dB, especially for the fast-onset signal. In contrast, most of the change in decay time occurs at positive D/R values, between about 0 and 15 dB, for both types of signals. This may indicate that temporally based D/R discrimination mechanisms may rely primarily on differences in either buildup or decay time depending on the D/R regime.

E. Acoustic analysis: Discussion

We have analyzed the dependence of four acoustic variables on D/R: IACC, spectral variance, spectral envelope, and buildup/decay time. We have shown that these variables have a monotonic relationship with D/R, and prior studies have shown that listeners are sensitive to variations in these variables. We therefore hypothesize that discrimination of D/R can make use of any or all of these cues.

Our quantitative models of these cues are without doubt significant simplifications of how the auditory system could assess differences between signals at various D/R values. For example, spectral envelope changes are more complicated then can be captured by a single parameter such as the spectral CoG. However, these simple single-parameter approximations do capture the important fact that physical changes in ear-canal signals asymptote at large positive and negative D/R values. More sophisticated analyses would refine these results, but we do not expect that they would alter this basic fact. Also note that the particular details of the equations we used to analyze acoustic changes are somewhat arbitrary; therefore numerical values in Figs. 1 and 2 should be taken with a grain of salt and are most useful to make *relative* comparisons between D/R values or between signal types.

Equation (1) shows that the D/R JND depends on (i) the physical relationship between D/R and the acoustic variable, (ii) the transformation of the acoustic (physical) to psychological variable, and (iii) the internal sensitivity to that psychological variable. We have only considered aspect (i), such that our conclusions are limited in scope. Specifically, our analysis suggests the following:

(1) Acoustic variables change as a function of D/R only within a limited range, loosely defined as moderately valued positive and negative D/R.
(2) There are D/R regions where none of the three variables we studied changes (except in an asymptotic sense). Equation (1) predicts that as these regions are approached, the D/R JND increases and eventually becomes very large.

A corollary is that D/R discrimination is possible within a limited range of D/R values only. Our analysis does *not* suggest any of the following:

(1) At what value(s) of D/R the D/R JND is smallest (discrimination is best). This requires knowledge about how sensitivity to the underlying variables changes with D/R.
(2) The exact extent of the region in which D/R discrimination is possible. The acoustic analysis merely implies that this region is limited in extent.[5]
(3) A rank ordering of the acoustic variables in terms of contribution for D/R discrimination. This requires knowledge regarding the internal sensitivity to each of the underlying variables.

We can test these suggestions derived from the acoustic analysis by measuring D/R JNDs over a large range of D/R

values. The prediction is that at the edges of the measured region, D/R JNDs will increase. Although we do not know *a priori* how large of a D/R region is sufficient, we choose −10 to 20 dB D/R in experiment 1. From Figs. 1 and 2, we can see that at least the values of the physical variables start to asymptote at the edges of this region, such that we might expect to see some variation in D/R JND.

Many experiments on auditory distance perception yield a compressive function of perceived versus actual distance; the restricted range of perceived distances is commonly known as the "auditory horizon" effect (Bronkhorst and Houtgast, 1999; Zahorik, 2002a). This effect is consistent with our acoustic analysis. The fact that relevant acoustic properties of the perceived sound signal (IACC, spectral and temporal cues) remain essentially constant once the sound source moves to distances well beyond critical distance (large negative D/R) is an unavoidable property of room acoustics and is responsible for the auditory horizon effect. Sources well beyond the critical distance should be judged to be closer than they actually are because the signal reaching the listener's ears is very similar to the signal of a closer sound source, which explains the compression of perceived distances.[6]

III. EXPERIMENT 1: DISCRIMINATION ABILITY AS A FUNCTION OF DIRECT-TO-REVERBERANT ENERGY RATIO

The goal of experiment 1 was to assess the JND for D/R at various D/R values (−10, 0, 10, and 20 dB) and to mimic the experiments by Zahorik (2002c), although some details were different (described in Sec. III B). One major difference with Zahorik's study is that we also determine the JND at a negative D/R value. According to the analysis of Sec. II, JNDs should increase at sufficiently large positive and negative D/R. Thus this experiment also investigated the extent to which this prediction could be observed in behavioral performance.

A. Methods

1. Subjects

Eight listeners (four female, four male; age 19–36 years) participated in the experiment. All listeners had audiometric thresholds below 20 dB hearing level between 250 and 8000 Hz, prior experience in psychoacoustic experiments, and participated in daily 1 h sessions for a period of 2 weeks. Two of the authors participated as subjects. The experiment was performed both at the University of Illinois at Urbana-Champaign and at Wright-Patterson Air Force Base; four subjects were tested at each location. Since no systematic differences in mean thresholds were found between the two groups, the data from the two laboratories will be combined for subsequent analysis.

2. Stimuli

Virtual sound source technique. Two types of anechoic source signals (sample rate of 20 kHz) were convolved with Binaural room impulse response (BRIRs) measured in an auditorium to create the virtual sources that were used in the experiment. The signals were as follows:

(1) Wideband (white) noise (WBN) of 300 ms duration, including 150 ms raised cosine onset and offset (i.e., no steady-state portion). The bandwidth of this signal was limited only by the bandwidth of the acoustic response of the auditorium and the measurement system (100–10 000 Hz).
(2) WBN of 300 ms duration, including 10 ms raised cosine onset and offset.

The auditorium was a rectangular-shaped room of approximately 1000 m^3 with a shallow sloping seating area. Reverberation time T_{60} measured in the auditorium was 0.78 s (average of 0.5 and 1 kHz octave bands). To analyze the variation in D/R in the auditorium, BRIRs at several source-to-receiver distances were measured, and the corresponding D/R values were computed. The D/R decayed at a rate of approximately 4.7 dB per doubling of distance.

A power amplifier (ADCOM GFA-535II) and loudspeaker (Analog and Digital Systems L200e) were used to play maximum length sequences (Rife and Vanderkooy, 1989) of order 14 at 20 kHz (duration: 0.82 s). The loudspeaker was positioned at a distance of 4.0 m from the recording location, in the seating area of the auditorium, at 0° azimuth (straight ahead). Recording was achieved with a KEMAR and ER-1 microphones (coupled to Zwislocki ear simulators) and preamplifiers (Knowles), placed on the center of a raised stage in the front of the auditorium. The KEMAR was positioned such that there were no obstructions between it and the loudspeaker. Data were acquired by a DAQPad-6052E (National Instruments), interfaced with a laptop computer, used for signal generation and storage through custom MATLAB (The Mathworks) software and MATLAB's data acquisition toolbox. Note that the use of nonindividualized BRIRs is not expected to affect perception of D/R, as shown previously by Zahorik (2002b, 2002c). We know of no specific study that has investigated potential issues of using KEMAR for distance perception, but it appears unlikely that discrimination of D/R would be problematic with room signals recorded through KEMAR.

The measured BRIRs were manipulated in postprocessing such that any desired D/R could be obtained. The two anechoic source signals were then convolved with all manipulated BRIRs to obtain the test stimuli. Signals were stored on file in 16 bit wav format.

Direct-to-reverberant energy ratio manipulation. The measured BRIR at 4.0 m source distance was used in all subsequent signal generation procedures. It was used to construct BRIRs with any desired D/R value by scaling the direct sound portion (defined by a window of 3 ms length after direct sound onset) with an appropriate amount; these modified BRIRS were convolved with the anechoic source signals to synthesize signals used in the experiment. Although D/R manipulation can also be done by scaling the reverberant portion of the BRIR, we chose to scale the direct sound as this corresponds more closely to the physical situation in a room, where direct sound decays with increasing source distance and the reverberant level remains more or less constant. Thus, all manipulated BRIRs had the same reverberant energy level (before the level rove, see the next section).

3. Procedure

A 2I 2AFC procedure was used to determine the D/R JND. In order to assess differences in JND as a function of D/R, each signal type was used at four D/R values of 20, 10, 0, and −10 dB (order counterbalanced between subjects); these were the reference signals. The 20 dB D/R condition was only tested at the Wright-Patterson Air Force site, i.e., only with four instead of eight subjects. In each presentation trial, the reference and target signals were presented in random order, with an interstimulus interval of 500 ms. At each reference, the two signal types (10 and 150 ms) were tested in random order.

At the beginning of each block of trials, the target signal had a D/R that was 10 dB higher than the reference signal. Listeners had to identify the most reverberant sounding signal (lowest D/R), i.e., the reference signal. The adaptive variable was the D/R of the target signal (the reference signal D/R never changed within a block of trials). An adaptive step size was used, initially set to 4 dB, decreased to 2 dB after two reversals, and set to the final value of 1 dB after another two reversals. Thresholds estimated the 79.4% point on the psychometric function (probability level $p_1=0.794$) using a three-down, one-up adaptive procedure (Levitt, 1971). Signals were presented in blocks of 60 trials. Thresholds per block were obtained by averaging the D/R difference between the target and reference signals for the final ten reversals or at all reversals if fewer than ten occurred in a particular block (as was the case for approximately 10% of all blocks). All listeners practiced for at least four blocks per condition before data were collected. Following the practice sessions, data collection continued until thresholds were stable across six consecutive blocks of trials. The JND for each listener per condition was then obtained as the average threshold value obtained for the last six blocks.

Because our method of creating D/R changes leads to changes in signal level, listeners could potentially discriminate D/R using level cues. To control for this confound, the overall level of the signals was roved by $R=20$ dB, and listeners were specifically instructed to ignore the loudness of the signals. Thus, for each interval, the signal level was chosen as the nominal level plus an offset randomly chosen from a uniform distribution in the range −10 to +10 dB. The nominal presentation level was adjusted by each individual to a comfortable listening level while also ensuring sufficient audibility at 10 dB below the nominal level. The level rove ensures that detection of changes based only on signal level will lead to a threshold C that is at least

$$C = R[1 - \sqrt{2(1 - p_1)}], \tag{4}$$

as shown by Green (1988). If thresholds are lower, discrimination must have been based on other cues, in our case D/R. In this equation, p_1 is the probability level tracked, which is 0.79 in our case. With $R=20$ dB, this yields $C=7.15$ dB.

Theoretically available level cues were mediated by direct and/or overall (direct and reverberant) sound because D/R was manipulated by changing direct sound while holding reverberation constant. This method of signal manipulation means that a specific change in the D/R value is created by the exact same change in the direct sound level. Changes in overall level are always smaller, as can be shown theoretically,[7] as well as empirically by computing the overall level as a function of D/R by using the experimental signals (results not shown). It is undisputed that listeners could use the overall level of signals within trials for discrimination, but whether direct level can be extracted from the total signal and used as a discrimination cue is not certain. Until it is known whether the direct level can be a useful cue, it appears prudent to assume that it is because this leads to more stringent rejection criteria. In conclusion, as long as obtained thresholds are well below 7.15 dB at any D/R reference, use of level cues can be excluded, and thresholds are reliable indicators of D/R discrimination performance. In practice, we consider thresholds reliable if the mean is at least one standard deviation below the 7.15 dB ceiling imposed by the level rove.

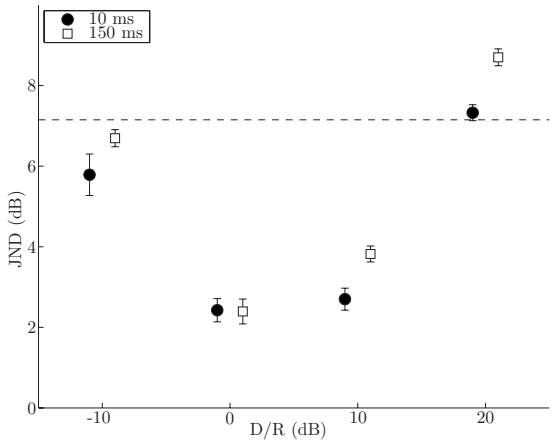

FIG. 3. Mean D/R discrimination thresholds from experiment 1 at −10, 0, 10, and 20 dB D/R; error bars indicate standard error. Filled symbols indicate fast-onset noise; open symbols indicate slow-onset noise. The dashed line at 7.15 dB indicates the lowest threshold that could be obtained if subjects used level cues only instead of D/R.

Listeners were seated in a sound-attenuating room and listened binaurally through headphones (Sennheiser HDA 200). Signal presentation was accompanied by visual displays (box outlines) on a computer monitor and listeners were required to respond to each trial by pressing the appropriate response box using a mouse (corresponding to the listening intervals) on the computer monitor. After the response was given, the box outline corresponding to the correct listening interval was highlighted to provide visual feedback regarding the correct response.

B. Results and discussion

Mean thresholds and standard errors are shown in Fig. 3 for both the fast- and slow-onset noise signals. The dashed line at 7.15 dB indicates the threshold that would be obtained if listeners had employed level cues alone instead of D/R [see Eq. (4)]. Averaged thresholds (with standard error in parentheses) for the noise signal with 150 ms onset were 6.7 (0.2), 2.4 (0.3), 3.8 (0.2), and 8.7 (0.2) dB for reference D/R of −10, 0, 10, and 20 dB, respectively. Similarly, the average thresholds for the noise signal with 10 ms onset were 5.8 (0.5), 2.4 (0.3), 2.7 (0.3), and 7.3 (0.2) dB for the same ref-

erence D/R values. These JNDs correspond to changes in the overall level of about 1, 1.5, 3, and 8 dB at −10, 0, 10, and 20 dB D/R references. The threshold at 20 dB D/R is thus likely contaminated by the overall level cues, as overall level changes exceed the 7.15 dB ceiling. If direct level cues, which vary by exactly the same amount as D/R does, are also available to the listener, the threshold at −10 dB D/R reference is also unreliable because it is less than one standard deviation below ceiling (in both conditions). Thus, for both −10 and +20 dB D/R, the thresholds we found cannot be taken as reliable indicators of the JND at those D/R. Nonetheless, it is clear that whatever the true JNDs at −10 and 20 dB D/R are, they are significantly greater than the JNDs at 0 and 10 dB D/R by at least 4 dB.

Considering for the moment that only the data at 0 and 10 dB D/R are reliable, a two-way repeated-measure analysis of variance (ANOVA) with D/R (0 and 10 dB D/R) and signal type as factors was performed. This yielded a significant main effect of signal type ($F_{(1,7)}=10.56$, $p=0.01$) and D/R ($F_{(1,7)}=22.24$, $p=0.002$). The interaction effect of D/R and signal type was also significant ($F_{(1,7)}=26.76$, $p=0.001$) due to the tendency for thresholds to increase when D/R increased from 0 to 10 dB in the slow-onset noise condition (by 1.4 dB) but not in the fast-onset noise condition (by 0.3 dB, which was not significant). Prior studies generally indicate that sound onset time has no, or at most a minor effect, on D/R discrimination and distance perception (Santarelli *et al.*, 2000; Bronkhorst, 2001; Zahorik, 2002a, 2002c). These views may need to be re-examined in view of the present results, as we did find a modest yet statistically significant effect of onset time on D/R discrimination thresholds.

At positive D/R values, sound decay time provides more powerful acoustic cues than sound buildup time (which is nearly constant in that regime) according to the analysis in Sec. II D. This may imply that at the reference of 10 dB D/R, where the JND for the slow-offset signal is larger than that for the fast-offset signal, it is more difficult for listeners to use variations in the decay time of slower- versus faster-offset sounds to discriminate D/R. At 0 dB D/R, no such difference in JND exists between the signal types. It is possible that at this particular D/R value, other cues are more powerful, rendering temporal aspects of sounds less important.

Comparison to prior studies. The obtained JNDs at 0 and 10 dB D/R are in good agreement with the data from Reichardt and Schmidt (1966) but are lower than those reported by Zahorik (2002c) (JNDs at −10 and 20 dB are quite high by Reichardt and Schmidt's results as well, but it is difficult to make quantitative comparisons as our JNDs are at or near ceiling at those D/R values). This is somewhat surprising, given that our signals and methods were more similar to those used by Zahorik (2002c). Zahorik previously pointed out that low JND estimates in the study by Reichardt and Schmidt (1966) might be the result of the methods and procedures used in that study, which did not effectively control for level confounds. Nonetheless, the results of Reichardt and Schmidt (1966) are partially supported by our data: our methods were similar to Zahorik's and involved controlling for level confounds (confirmed by our JNDs being well below the 7.15 dB threshold level at 0 and 10 dB D/R), but we still found similarly low JNDs as Reichardt and Schmidt.

Comparing our data with those of Zahorik (2002c), who measured JNDs at 0, 10, and 20 dB D/R (using methods and signals that were broadly similar to ours), we note that at 0 and 10 dB D/R, our JNDs are lower: 2.5–3.5 dB versus 5–6 dB. Differences in experimental procedure or signals used (similar but different rooms, KEMAR versus individualized BRIRs, 20 versus 40 kHz sample frequency, manipulating direct versus reverberant level to vary D/R) make a direct comparison difficult, although differences of nearly 4 dB are considerable and cannot be easily ignored. Zahorik manipulated the reverberant level of his signals to vary D/R, so it is possible that cues from the reverberant sound level had some effect on the obtained JNDs (similar to possible confounds from the direct sound level in our study at −10 and 20 dB D/R). Zahorik showed that changes in overall level were too small to account for his results, but he did not discuss the issue of the reverberant level cue.

A more qualitative and perhaps more important difference is that our JNDs steadily increase at reference D/R values of 0 to 10 to 20 dB D/R (JNDs: 2.5 to 3.3 to 8 dB), while Zahorik's JNDs remain constant at 5–6 dB over the entire range of D/R values. It is remarkable that discrimination performance could stay constant over a 20 dB range of D/R values, considering our acoustic analysis, which indicates that acoustic variables change rapidly around 0 dB D/R but are nearly constant at 20 dB D/R. Although D/R discrimination likely makes use of redundant cues, all cues that we have been able to consider become weak at large D/R values, so that increases in JND appear unavoidable. As our results differ both quantitatively and qualitatively from Zahorik's, it would appear necessary in future studies to further replicate this style of experiment to gain more insight into the importance of experimental parameters on D/R JNDs.

Comparison to acoustic analysis. In Sec. II E, we predicted on the basis of our acoustic analysis that if a sufficiently large range of D/R was sampled, one would find an increase in JND at the edges (due to the fact that acoustic variables are nearly constant in those regions). Our results presented here appear to mirror these predictions, in that we find a large increase in JNDs at −10 and 20 dB relative to JNDs at 0 and 10 dB. The increase is at least 4–5 dB but possibly more because JNDs at −10 and 20 dB were near or at the ceiling level. Some of this increase could also be explained by a decrease in sensitivity to the variables that are being discriminated, but this would be an independent additive effect. Our theoretical explanation for the auditory horizon effect (Sec. III E) then also appears to find support in the experimentally obtained D/R JNDs presented here.

Implications for distance perception. D/R JNDs of about 2.4 dB at 0 dB D/R means that JNDs for distance perception are about 25% for sources near the critical distance.[8] At about 1/3 of the critical distance (10 dB D/R, JNDs of 2.7–3.8 dB), distance JNDs are 25%–35%, while at 1/10 of the critical distance (20 dB D/R, JNDs at least 7 dB), they

are at least 55% (unless this is within 1 m of the head, in which case binaural cues can be used to maintain errors to within 30%–40%, Brungart *et al.*, 1999). For sources at three times the critical distance (−10 dB D/R, JNDs of 5.8 dB versus at least 7 dB for the fast- versus slow-onset signal), distance JNDs are 35% versus at least 55% for the fast- versus slow-onset signal. All these distance JNDs are with respect to changes that bring the source *closer* to the listener, as the D/R JNDs were measured for *positive* changes in D/R. JNDs in the opposite direction may be different.

The transformed distance JNDs of 25%–35% (valid for reference distances of about 30%–100% of the critical distance) are somewhat better than the estimated distance JNDs reported by Zahorik (2002c), which used data from Zahorik (2002a): these were around 50% of the reference distance (changes in source distance also *toward* the listener). The difference can be directly attributed to the lower D/R JNDs we obtained.

IV. EXPERIMENT 2: DISCRIMINATION ABILITY FOR IMPOVERISHED SIGNALS

The aim of experiment 2 is to reduce or remove each of the three previously discussed cues for D/R from the test signals (IACC, spectral variance, and spectral envelope). It is hoped that by observing the effect of these signal manipulations on the JND, we will gain insight into the relative importance of each cue for D/R discrimination. Binaural cues will be removed in experiment 2a, while experiment 2b will remove a large portion of both spectral variance and spectral envelope cues. Finally, experiment 2c will remove the remaining spectral envelope cues.

A. Methods

1. Subjects

The same listeners participated as in experiment 1; sessions were 1 h daily for a period of 2 weeks. One-half of the subject group ran experiment 2 before experiment 1 to control for practice effects.

2. Stimuli

Experiment 2a. Experiment 2a presented signals to the listeners monaurally (right ear only). This removes all binaural cues, including IACC (Sec. II A). The level of the signal at the right ear was raised by 3 dB relative to the level of the signals used in experiment 1 to preserve the overall intensity of the sound. The signals were otherwise identical to those used in experiment 1.

Experiment 2b. Experiment 2b presented signals dichotically but with reduced spectral cues. This was achieved by filtering the signals into narrow frequency bands, three Equivalent rectangular bandwidth (ERB) wide, around center frequencies of 500 Hz and 3 kHz. Here and in experiment 2c, only the fast-onset (10 ms) noise signal was used, convolved with appropriately manipulated BRIRs.

The reduction in independent spectral samples in the signals used in experiment 2b relative to those of experiment 1 significantly increases the uncertainty with which the variance of the power spectrum may be estimated. As this uncertainty increases, the usefulness of the spectral variance cue for D/R discrimination is reduced. Spectral envelope cues are also reduced by bandwidth reduction because variations in spectral centroid/CoG are diminished. We analyze the reduction in both spectral cues more fully in Sec. IV B. Temporal cues (sound buildup and decay) were not greatly altered for the signals and D/R regime we used (data not shown) and were similar for the 500 Hz and 3 kHz center frequency signals.

Experiment 2c. For experiment 2c, similar signals as in experiment 2b were used (dichotic presentation) but with the spectral envelope cues completely removed. This was achieved by roving the center frequency of the three ERB-wide narrow band signals by one ERB unit at both center frequencies (500 Hz and 3 kHz). By ensuring that the frequency rove was larger than the variation in the spectral CoG as a function of D/R, this effectively removed the spectral envelope cues. Note that the spectral envelope cues are already significantly reduced for narrow band versus wideband signals; the frequency rove removes the remaining spectral envelope cues. Spectral variance cues should not be affected by the frequency rove.

The low-frequency signal had a center frequency roved in the range of 500–582 Hz, while the high-frequency signal had a center frequency roved in the range of 3000–3367 Hz. The center frequency that was used for each stimulus was determined randomly out of a sample of ten center frequencies distributed uniformly between the lower and upper limits for each frequency range.

3. Procedure

Thresholds were determined using a 4I 2AFC procedure; the first and last interval always contained the target signal, which was also present in either the second or third interval, and varied randomly. The random 20 dB level rove was applied to each signal in the four intervals. In experiment 2c, all four signals were randomly roved in the center frequency by 1 ERBu. Listeners were instructed to indicate whether the reference signal (most reverberant signal) was present in either the second or third interval.

Thresholds were not collected at −10 or 20 dB D/R as the JNDs found at those D/R in experiment 1 were already at or above the ceiling level of 7.15 dB. In experiment 2a, thresholds were collected at 0 and 10 dB D/R, while in experiments 2b and 2c, thresholds were only collected at 0 dB D/R. This value was chosen because experiment 1 found lowest thresholds at that value, and it thus allows a potentially large increase in JND of the impoverished signals used in experiment 2 (before the threshold level of 7.15 dB is approached). All other procedures were identical to those reported in experiment 1.

B. Results and discussion

1. Experiment 2a: Monaural thresholds

Results from Experiment 2a are shown in Fig. 4. The subject-averaged monaural thresholds (standard error in parentheses) for the slow-onset noise were 2.9 (0.3) and 3.8 (0.2) dB for reference D/R of 0 and 10 dB, respectively. Av-

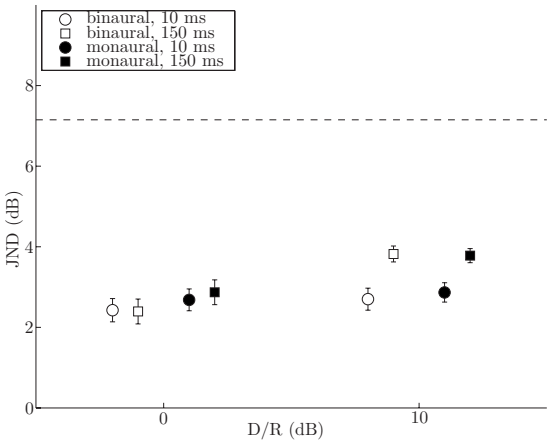

FIG. 4. Mean D/R discrimination thresholds for experiment 2a (monaural, right ear only) at 0 and 10 dB D/R, indicated by filled symbols. Open symbols are thresholds from experiment 1 (binaural) in the same conditions and are included for comparison; error bars indicate standard error. Circles indicate fast-onset noise signal; squares indicate slow-onset noise signal. The dashed line at 7.15 dB indicates the lowest threshold that could be obtained if subjects used level cues only instead of D/R.

erage JNDs for the fast-onset noise were 2.7 (0.3) and 2.9 (0.2) dB for the 0 and 10 dB reference D/R, respectively. All thresholds are more than one standard deviation below the ceiling of 7.15 dB and can be assumed reliable indicators of the D/R JND. The data from experiment 1 (0 and 10 dB D/R only) were combined with those from experiment 2a and submitted to a within-subject three-factor ANOVA, with listening mode (binaural versus monaural), reference D/R (0 and 10 dB), and signal type (noise with slow or fast on-off time) as factors. There was a significant main effect of signal type ($F_{(1,7)}=16.45$, $p=0.01$) and D/R ($F_{(1,7)}=15.31$, $p=0.01$). The two-way interaction of signal type and D/R was also significant ($F_{(1,7)}=7.09$, $p=0.04$) due to the tendency for thresholds in the slow-onset noise condition to increase as D/R increased from 0 to 10 dB (by 1.2 dB) but not for the fast-onset noise (0.3 dB, not significant). None of the other two-way (D/R and listening mode, signal type and listening mode) or the three-way interactions were significant ($p \geqslant 0.05$). As in experiment 1, the effect of onset time on JNDs was not expected based on prior studies (Santarelli *et al.*, 2000; Bronkhorst, 2001; Zahorik, 2002a, 2002c), although the effect is quite small (average over all conditions is 0.8 dB). These results show that monaural listening does not lead to statistically different discrimination thresholds as compared to binaural listening at reference D/R of 0 and 10 dB and for both signal types. If a difference does exist, the 95% confidence interval is −0.2 to 0.7 dB (subtracting monaural mean from binaural mean thresholds, pooled over D/R and signal types).

To interpret these findings with respect to our acoustic analysis in Sec. II, we make use of the study of Pollack and Trittipoe (1959), who reported psychometric functions for IACC discrimination at various reference values by using 1 s broadband noise stimuli (we used 300 ms broadband noise convolved with the auditorium impulse response). In the current study, IACC values are about 0.7 at 0 dB D/R and 0.9 at 10 dB D/R (see Fig. 1). In the study by Pollack and Trittipoe (1959), reference IACC values of 0.7 and 0.9 yielded JNDs of 0.2 and 0.07, respectively. If these IACC JNDs are extrapolated to the current study, it would appear that if listeners utilized IACC as a cue to D/R discrimination, it should have yielded D/R JNDs of approximately 10 dB at a reference D/R of 0 dB (see Fig. 1). Instead, in experiment 1, average JNDs were in the 2–3 dB range at 0 dB D/R. Near the reference D/R of 10 dB, the IACC function saturates at 0.95, and thus the requisite value (i.e., 0.97) cannot be obtained. Seemingly, listeners did not use IACC as a discrimination cue in experiment 1, and hence, thresholds remained unchanged in experiment 2a, when IACC cues were removed. At D/R values outside of the range 0–10 dB, it is not likely that IACC is an important cue; above 10 dB, IACC changes are too small to be discriminable, while below 0 dB, IACC is in the range 0.5–0.7, where discrimination is very poor and would lead to very large (>10 dB) discrimination thresholds for D/R.

Even though binaural cues are not powerful enough to be useful in D/R discrimination in ordinary circumstances, this does not imply that distance perception (for which D/R is thought to be an important cue) is equally effective via monaural or binaural listening. One line of evidence was provided by Bronkhorst (2001), who performed distance judgment experiments with manipulated BRIRs that had a range of IACC values. He showed that distance perception was progressively impaired as IACC approached unity, as distance judgments converged to small values. Based on panel (a) of Fig. 1 we might anticipate such a result, as IACC≈1 corresponds to large D/R values (implying small source-receiver distance). Although changes in D/R may be discriminated equally well for monaural as binaural listening, monaural stimuli do not evoke natural distance percepts, and the results we report here cannot be linked directly to tasks involving identification of auditory distance.

2. Experiments 2b and 2c: Narrow band thresholds with fixed and roving centers frequency

Mean thresholds from experiments 2b and 2c are shown in Fig. 5, together with those of experiment 1 for the same signal at 0 dB D/R. Note that all data were collected at 0 dB D/R by using only the fast-onset noise. Average thresholds and standard errors (in parentheses) obtained by listeners for the fixed center frequency conditions were 3.6 (0.2) and 4.2 (0.2) dB for center frequencies of 500 and 3000 Hz, respectively. The thresholds for the roved center frequency condition at 500 and 3000 Hz were 4.9 (0.4) and 6.2 (0.4) dB, respectively. The frequency-roved threshold at 3 kHz may be contaminated by direct sound level cues, as it is less than one standard deviations below the ceiling level of 7.15 dB; the other thresholds are all reliable D/R JNDs by our criterion. Similar to experiment 2a, the data obtained in the fixed center frequency condition were compared to those obtained in experiment 1 (0 dB D/R, fast-onset noise, wideband signal). To investigate the effect of spectral content (wideband, low-frequency narrow band, or high-frequency narrow band), the data were submitted to three paired-sample *t* tests (wideband versus low-frequency narrow band, wideband versus high-frequency narrow band, and low-frequency versus high-frequency narrow band) with the Bonferroni correction for

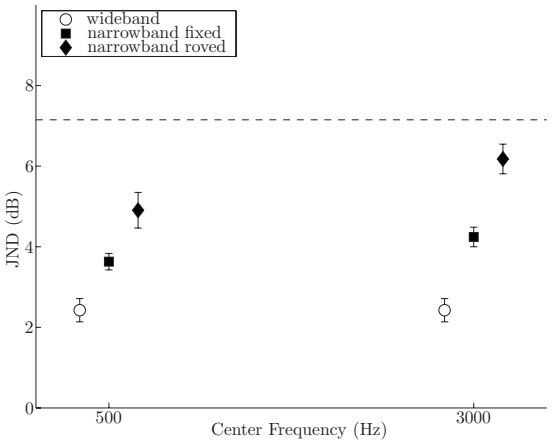

FIG. 5. D/R discrimination thresholds for the narrow band noise signals (10 ms onset/offset) used in experiments 2b and 2c at 0 dB D/R at center frequencies of 500 Hz and 3 kHz (bandwidth: 3 ERB), indicated by filled symbols. Open symbols are thresholds from experiment 1 (WBN) in the same condition, included for comparison. Squares indicate narrow band signals with a fixed center frequency; lozenges indicate narrow band signals with roved center frequency; error bars indicate the standard error. The dashed line at 7.15 dB indicates the lowest threshold that could be obtained if subjects used level cues only instead of D/R.

multiple comparisons. The difference in the mean JNDs between the wideband and both narrow band signals was statistically significant: with the low-frequency narrow band signal, the mean difference was 1.2 dB ($t_{14}=3.4$, $p=0.0043$), and with the high-frequency narrow band signal, the mean difference was 1.8 dB ($t_{14}=4.8$, $p<10^{-3}$). The mean JNDs for the two narrow band signals were not significantly different. As this experiment was designed to investigate the contribution of spectral cues for D/R discrimination, we may conclude that at 0 dB D/R, for fast-onset (10 ms) noise signals, these are important for D/R discrimination.

In order to compare the effect of roving the center frequency, a within-subject ANOVA was conducted with center frequency (500 or 3000 Hz) and spectral envelope (fixed versus roved) as main factors. The analysis revealed a significant main effect of center frequency ($F_{(1,7)}=55.81$, $p<0.01$) and a main effect of spectral envelope ($F_{(1,7)}=17.45$, $p<0.01$). The JNDs for the high-frequency signals were on average 0.9 dB higher than those for the low-frequency signals and the JNDs in the roved conditions were on average 1.6 dB higher than in the fixed conditions. The interaction between the frequency and roving condition was not significant.

To assess the effect of bandwidth reduction on spectral variance cues, it is relevant to consider the number of independent samples of the power spectrum that are available to the brain. This number is limited by the resolving power (frequency selectivity) of the cochlea, such that the number of independent samples in a given frequency band is given by the number of "nonoverlapping" auditory filters in this band, which can be computed by counting how many ERB wide the band is. Experiment 1 used signals with energy in the frequency range of 100–10000 Hz, corresponding to a bandwidth of 32 ERB, whereas experiments 2b and 2c used signals of 3 ERB wide. Thus, spectral variance estimates had available 32 versus 3 independent samples for the wideband versus the narrow band signals. This reduces the effectiveness of the spectral variance cue by an estimated factor[9] of 7.

To assess the effect of bandwidth reduction on spectral envelope cues, we calculated the spectral CoG as a function of D/R and expressed the slope as a percentage change in CoG per decibel increase in D/R. For the WBN signals from experiment 1, the peak slope value occurs around 0 dB D/R [cf. panel (c), Fig. 1] and equals 1%/dB. For the narrow band signals, the peak value also occurs around 0 dB D/R, but its value is reduced by a factor of about 6–9. For the 500 Hz signal, it is 0.11%/dB, while for the 3 kHz signal, it is about 0.17%/dB. Comparing the two narrow band signals, the low-frequency signal has slightly smaller CoG changes with D/R relative to the high-frequency signal (0.11%/dB versus 0.17%/dB), but according to Wier *et al.* (1977), discrimination of the relative changes in frequency is slightly better at 500 Hz versus 3 kHz ($\Delta F/F=0.17$ versus 0.23, respectively). Data pooled from experiments 2b and 2c indicated that JNDs for the high-frequency narrow band signals were significantly higher than the low-frequency JNDs, although the effect is small (mean difference: 0.9 dB). This seems to indicate that although physical changes in spectral envelope (as measured by CoG) are greater for the high-frequency signal, better sensitivity to spectral changes [as measured by pure tone Frequency difference limen (FDLs) relative to the reference frequency] at low frequencies leads to better discrimination performance for the low-frequency narrow band signal. However, given the limited modeling and psychophysical data used, this latter conclusion should be regarded as tentative.

Experiment 2c used the same narrow band signals, but with roved center frequencies, which prevented listeners from relying on changes in spectral envelope, thereby completely removing this cue. This was accompanied by a statistically significant increase in JNDs with respect to the fixed center frequency condition of experiment 2b (mean increase: 1.6 dB). Remaining cues to D/R are IACC, spectral variance, or temporal cues. As discussed with respect to experiment 2a, the obtained JNDs in experiment 2c are too low to be mediated by IACC. Spectral variance and temporal cues were not altered with respect to experiment 2b, so the increase in JND seems to be explained by the complete removal of spectral envelope cues.

The mean difference in JNDs from experiment 2c (narrow band, roved center frequency) and experiment 1 (broadband, 0 dB D/R, fast-onset noise) is 3.1 dB. Because binaural cues were found to be too weak to mediate discrimination in any of our experimental conditions and the signals in experiment 2c had most if not all spectral cues removed, we hypothesize that discrimination in experiment 2c relied primarily on temporal cues (differences in buildup or decay of sound as a function of D/R), which then appear to be relatively weak cues to D/R (mediating JNDs of 5–6 dB). Discrimination in experiment 2b (narrow band, fixed center frequency) probably did *not* primarily use temporal cues because these cues should have been equally effective in experiments 2b and 2c, but thresholds increased by 1.6 dB in experiment 2c versus 2b. Thus, the reason that prior studies have failed in finding strong effects of onset/offset time on

D/R discrimination and distance perception (Santarelli *et al.*, 2000; Bronkhorst, 2001; Zahorik, 2002a, 2002c) may be that in ordinary circumstances, spectral cues are more powerful (at least around 0 dB D/R), so that temporal characteristics are less important. Temporal cues would be important in such tasks when the spectral cues are less powerful or not available.

V. SUMMARY

We have proposed that D/R discrimination is based on discrimination of several underlying acoustic cues: specifically, we considered IACC, spectral variance, spectral envelope, and buildup/decay time. This proposition is based on the fact that these variables have a monotonic relationship with D/R and have a rapid rate in change around specific D/R values (Figs. 1 and 2). We have considered only the acoustic aspects of these cues as they occur in a typical auditorium, without modeling perceptual sensitivity. Our main finding was that each of these acoustic cues varied over a limited range of D/R values only, and that at large negative and positive D/R, the acoustic variables were constant. This implies that D/R discrimination, as based on these variables, becomes poor at large negative and positive D/Rs.

We measured D/R JNDs at D/R values of −10, 0, 10, and 20 dB for noise signals in "ordinary" (full-cue) and at 0 and +10 dB in reduced-cue conditions. We found the following:

- D/R JNDs for WBN signals are 2–3 dB at 0 and +10 dB D/R and at least 6–8 dB at −10 and 20 dB (experiment 1). The increase in JND at these last two D/R values is consistent with the prediction based on our acoustic analysis.
- Contrary to most prior studies, we found an effect of onset/offset time on D/R JNDs in that fast-onset/offset (10 ms) signals maintain the same JND at 0 and 10 dB D/R, while slow-onset/offset (150 ms) signals show a JND increase of about 1 dB in this range. This may indicate that even in "full-cue" conditions, temporal mechanisms are used to some extent in discriminating D/R.
- D/R discrimination does *not* rely on binaural cues such as IACC because changes in D/R corresponding to a JND produce subthreshold changes in IACC (IACC data from Pollack and Trittipoe, 1959). This was confirmed by experiment 2a, which showed that monaurally obtained JNDs are not statistically different from binaurally obtained JNDs at 0 and 10 dB D/R.
- Large reductions in frequency bandwidth lead to statistically significant increases (mean increase: 1.5 dB) in D/R JND at a reference D/R of 0 dB. The effect of bandwidth reduction is to strongly reduce both spectral variance and spectral envelope cues without affecting temporal cues. Therefore, spectral cues are important for obtaining low D/R JNDs in ordinary conditions.
- Complete elimination of spectral envelope cues by roving the center frequency of narrow band signals leads to a further significant increase in JND at a reference D/R of 0 dB (mean increase: 1.6 dB). For frequency-roved, narrow band signals, temporal cues appear to be the main mechanism listeners use to discriminate D/R. The obtained thresholds are 5–6 dB, i.e., 3 dB higher than those that are obtained when spectral cues are available.
- Narrow band noise signals (3 ERB) elicit larger JNDs at high frequencies versus low frequencies (3 kHz versus 500 Hz, mean difference: 0.9 dB), which may be due to greater sensitivity to changes in frequency at 500 Hz versus 3 kHz.

The smallest JNDs we report in full cue conditions (about 2–3 dB) are considerably smaller than previously established JNDs (about 5–6 dB) in what appear to be broadly similar conditions (Zahorik, 2002c).

Our acoustic analysis reveals the auditory horizon effect, i.e., the tendency to underestimate source distance for far sources (beyond critical distance). Acoustic variables thought to provide cues to D/R do not change appreciably beyond the critical distance, also consistent with the fact that we obtained large D/R JNDs at large negative D/R values.

ACKNOWLEDGMENTS

Research was supported by grants from the NIDCD of the National Institutes of Health (R21DC-04840), the Beckman Institute, the Charles M. Goodenberger Fund, and Phonak AG. Jont Allen and Bill Hartmann pointed out the spectral variance and interaural cross-correlation as potential cues to D/R. The authors thank the members of the Intelligent Hearing Aid group at the University of Illinois at Urbana-Champaign for comments on the original version of this manuscript. Associate Editor Armin Kohlrausch and three reviewers contributed many insightful comments that improved the quality of the final manuscript.

[1]By using $h(t)$ to indicate the impulse response between two locations in an enclosure, D/R can be computed as

$$\mathrm{D/R} \equiv 10 \log \frac{\int_0^T h^2(\tau) d\tau}{\int_T^\infty h^2(\tau) d\tau},$$

where T is chosen such that it separates the direct sound from all reflections in the impulse response (typically $T \approx 2-3$ ms).

[2]The source signal itself may also have spectral variations, but in general, these will be uncorrelated to the room response and therefore have no effect on the change in spectral variance as a function of D/R.

[3]A more comprehensive model for spectral envelope that is also perceptually relevant is the Intensity Weighted Average of Instantaneous Frequency (IWAIF) model, described by Anantharaman *et al.* (1993).

[4]To avoid confusion, we use the terms "onset" and "offset" times to describe the temporal characteristics of the sound source; "buildup" and "decay" times will be used for the ear-canal signals.

[5]In this regard, it is "unfortunate" that the greatest physical changes in all variables we analyzed occur in roughly the same D/R range. This might limit the benefit that could be obtained from the availability of redundant cues. A counterexample where redundant cues operate in different physical regimes is in sound localization, where interaural time versus level differences are most useful in different frequency regions.

[6]A similar argument for large positive D/R values implies that sources well within the critical distance should also be judged closer to it than they in fact are; thus the perceived distance would *overestimate* the actual distance. It is true that near sources are indeed usually judged to be further away than they actually are (e.g., Zahorik, 2002c).

[7]Overall level L_O equals the logarithm of the sum of the direct and reverberant *intensities* (not level), i.e.,

$$L_O = 10 \log_{10}(10^{L_D/10} + 10^{L_R/10}),$$

using L_D and L_R for direct and reverberant levels in decibel sound pressure level. It is easily verified that by holding L_R constant, a change ΔL_D will lead to $\Delta L_O < \Delta L_D$.

[8]The dependence of D/R on source distance is caused by the fact that the energy in the direct sound decays with distance, while the energy of reverberation is approximately constant throughout the entire room (Kuttruff, 1991). Conservation of energy implies that direct sound level decreases by 6 dB for every doubling of the distance d_{rs} between the source and receiver. Therefore, D/R decreases by 6 dB for every distance doubling, and we can write

$$\mathrm{D/R} = -6\log_2\left(\frac{d_{rs}}{r_c}\right) = 20\log\left(\frac{r_c}{d_{rs}}\right),$$

where r_c is the "critical distance" of the room, defined as the distance where D/R equals 0 dB (equal energy in direct and reverberant sounds).

[9]The variance of a sound power spectrum can be estimated as a stochastic variable, the *sample spectral variance*. With N independent spectral samples x_i, we define the sample spectral variance s^2 as

$$s^2 = \frac{1}{N}\sum_{i=1}^{N}(x_i - m)^2,$$

using m for the sample mean (which has to be estimated first). Assuming for simplicity that the x_i are normally distributed, then $\mathrm{var}(s^2)$, the variance of the sample variance, is (Kenney and Keeping, 1951)

$$\mathrm{var}(s^2) = \frac{N-1}{N^2}2\sigma^4,$$

using σ^2 for the population spectral variance, which is estimated by s^2. For wideband signals (experiments 1 and 2a) $N \approx 32$, $\mathrm{var}(s^2) = 0.061\ \sigma^4$; the narrow band signals (experiments 2b and 2c) were designed to have $N = 3$, and thus $\mathrm{var}(s^2) = 0.44\sigma^4$, an increase by a factor of about 7. The effectiveness of a cue is inversely proportional to its variance, so this bandwidth reduction should diminish the effectiveness of spectral variance cues by approximately a factor of 7.

Allen, J., and Neely, S. (**1997**). "Modeling the relation between the intensity just-noticeable difference and loudness for pure tones and wideband noise," J. Acoust. Soc. Am. **102**, 3628–3646.

Anantharaman, J., Krishnamurthy, A., and Feth, L. (**1993**). "Intensity-weighted average of instantaneous frequency as a model for frequency discrimination," J. Acoust. Soc. Am. **94**, 723–729.

Berkley, D., and Allen, J. (**1993**). in *Acoustical Factors Affecting Hearing Aid Performance*, 2nd ed., edited by Studebaker and Hochberg (Allyn and Bacon, Boston, MA), Chap. 1.

Blauert, J. (**1984**). *Spatial Hearing: The Psychophysics of Human Sound Localization*, 2nd ed. (MIT Press, Cambridge, MA).

Blesser, B. (**2001**). "An interdisciplinary synthesis of reverberation viewpoints," J. Audio Eng. Soc. **49**, 867–903.

Boehnke, S., Hall, S., and Marquardt, T. (**2002**). "Detection of static and dynamic changes in interaural correlation," J. Acoust. Soc. Am. **112**, 1617–1626.

Bronkhorst, A. (**2001**). "Effects of stimulus properties on auditory distance perception in rooms," in *Proceedings of the 12th ISH: Physiological and Psychological Bases of Auditory Function* (Shaker, Maastricht, The Netherlands).

Bronkhorst, A., and Houtgast, T. (**1999**). "Auditory distance perception in rooms," Nature (London) **397**, 517–520.

Brungart, D. (**1999**). "Auditory localization of nearby sources. III. Stimulus effects," J. Acoust. Soc. Am. **106**, 3598–3602.

Brungart, D., Durlach, N., and Rabinowitz, W. (**1999**). "Auditory localization of nearby sources. II. Localization of a broadband source," J. Acoust. Soc. Am. **106**, 1956–1968.

Brungart, D., and Rabinowitz, W. (**1999**). "Auditory localization of nearby sources: Head-related transfer functions," J. Acoust. Soc. Am. **106**, 1465–1479.

Butler, R., Levy, E., and Neff, W. (**1980**). "Apparent distance of sounds recorded in echoic and anechoic chambers," J. Exp. Psychol. Hum. Percept. Perform. **6**, 745–750.

Coleman, P. (**1962**). "Failure to localize the source distance of an unfamiliar sound," J. Acoust. Soc. Am. **34**, 345–346.

Coleman, P. (**1968**). "Dual role of frequency spectrum in determination of auditory distance," J. Acoust. Soc. Am. **44**, 631–632.

Ernst, M., and Banks, M. (**2002**). "Humans integrate visual and haptic information in a statistically optimal fashion," Nature (London) **415**, 429–433.

Ernst, M., Banks, M., and Bülthoff, H. (**2000**). "Touch can change visual slant perception," Nat. Neurosci. **3**, 69–73.

Fechner, G. (**1912**). *Elements of Psychophysics* (Houghton Mifflin, Boston, MA).

Gabriel, K., and Colburn, H. (**1981**). "Interaural correlation discrimination. I. Bandwidth and level dependence," J. Acoust. Soc. Am. **69**, 1394–1401.

Gogel, W. (**1961**). "Convergence as a cue to absolute distance," J. Psychol. **52**, 287–301.

Green, D. (**1988**). *Profile Analysis: Auditory Intensity Discrimination* (Oxford University Press, New York, NY).

Hillis, J., Watt, S., Landy, M., and Banks, M. (**2004**). "Slant from texture and disparity cues: Optimal cue combination," J. Vision **4**, 967–992.

Jetzt, J. (**1979**). "Critical distance measurements of rooms from the sound energy spectral response," J. Acoust. Soc. Am. **65**, 1204–1211.

Kenney, J., and Keeping, E. (**1951**). *Mathematics of Statistics*, 2nd ed. (Van Nostrand, New York, NY), pt. 2, pp. 164.

Kewley-Port, D., and Pisoni, D. (**1984**). "Identification and discrimination of rise time: Is it categorical or noncategorical?," J. Acoust. Soc. Am. **75**, 1168–1176.

Kidd, G., Mason, C., and Green, D. (**1986**). "Auditory profile analysis of irregular sound spectra," J. Acoust. Soc. Am. **79**, 1045–1053.

Kuttruff, H. (**1991**). *Room Acoustics*, 3rd ed. (Elsevier, London).

Levitt, H. (**1971**). "Transformed up-down methods in psychoacoustics," J. Acoust. Soc. Am. **49**, 467–477.

Little, A., Mershon, D., and Cox, P. (**1992**). "Spectral content as a cue to perceived auditory distance," Perception **21**, 405–416.

Mershon, D., Ballenger, W., Little, A., McMurtry, P., and Buchanan, J. (**1989**). "Effects of room reflectance and background noise on perceived auditory distance," Perception **18**, 403–416.

Mershon, D., and King, E. (**1975**). "Intensity and reverberation as factors in the auditory perception of egocentric distance," Percept. Psychophys. **18**, 409–415.

Nábělek, A. (**1988**). "Identification of vowels in quiet, noise, and reverberation: Relationships with age and hearing loss," J. Acoust. Soc. Am. **84**, 476–484.

Nábělek, A., and Dagenais, P. (**1986**). "Vowel errors in noise and in reverberation by hearing-impaired listeners," J. Acoust. Soc. Am. **80**, 741–748.

Nielsen, S. (**1993**). "Auditory distance perception in different rooms," J. Audio Eng. Soc. **41**, 755–770.

Philbeck, J., and Mershon, D. (**2002**). "Knowlegde about typical source output influences perceived auditory distance (L)," J. Acoust. Soc. Am. **111**, 1980–1983.

Pollack, I., and Trittipoe, W. (**1959**). "Binaural listening and interaural cross correlation," J. Acoust. Soc. Am. **31**, 1250–1252.

Reichardt, W., and Schmidt, W. (**1966**). "Die hörbaren Stufen des Raumeindruckes bei Musik (The audible steps of spatial impression in music performances)," Acustica **17**, 175–179.

Rife, D., and Vanderkooy, J. (**1989**). "Transfer-function measurement with maximum-length sequences," J. Audio Eng. Soc. **37**, 419–443.

Sabine, W. (**1962**). *Collected Papers on Acoustics*, Dover ed. (Peninsula, Los Altos Hills, CA).

Santarelli, S., Kopčo, N., and Shinn-Cunningham, B. (**2000**). "Distance judgements of nearby sources in a reverberant room: Effect of stimulus envelope," J. Acoust. Soc. Am. **107**, 2822.

Schroeder, M. (**1965**). "New method for measuring reverberation time," J. Acoust. Soc. Am. **37**, 409–412.

Shinn-Cunningham, B. (**2000**). "Distance cues for virtual auditory space," *Proceedings of the First IEEE Pacific-Rim Conference on Multimedia* (IEEE, New York).

von Békésy, G. (**1938**). "Über die Enstehung der Entfernungsempfindung beim Hören (On the origin of distance perception in hearing)," Akust. Z. **3**, 21–31.

Wier, C., Jesteadt, W., and Green, D. (**1977**). "Frequency discrimination as a function of frequency and sensation level," J. Acoust. Soc. Am. **61**, 178–184.

Zahorik, P. (**2002a**). "Assessing auditory distance perception using virtual acoustics," J. Acoust. Soc. Am. **111**, 1832–1846.

Zahorik, P. (**2002b**). "Auditory display of sound source distance," In *Proceedings of the International Conference Auditory Display*, Kyoto, Japan.

Zahorik, P. (**2002c**). "Direct-to-reverberant energy ratio sensitivity," J. Acoust. Soc. Am. **112**, 2110–2117.

Temporal order discrimination of tonal sequences by younger and older adults: The role of duration and rate[a)]

Mini N. Shrivastav[b)]
Department of Communication Sciences and Disorders, 336 Dauer Hall, University of Florida, Gainesville, Florida 32611

Larry E. Humes and Lacy Aylsworth
Department of Speech and Hearing Sciences, Indiana University, 200 South Jordan Avenue, Bloomington, Indiana 47405

(Received 18 December 2007; revised 20 March 2008; accepted 28 April 2008)

The effect of tone duration and presentation rate on the discrimination of the temporal order of the middle two tones of a four-tone sequence was investigated in young normal-hearing (YNH) and older hearing-impaired (OHI) listeners. The frequencies and presentation level of the tone sequences were selected to minimize the effect of hearing loss on the performance of the OHI listeners. Tone durations varied from 20 to 400 ms and presentation rates from 2.5 to 25 tones/s. Two experiments were conducted with anisochronous (nonuniform duration and rate across entire sequence) and isochronous (uniform rate and duration) sequences, respectively. For the YNH listeners, performance for both isochronous and anisochronous sequences was determined primarily by presentation rate such that performance decreased at rates faster than 5 tones/s. For anisochronous tone sequences alone, the effects of rate were more pronounced at short tone durations. For the OHI listeners, both presentation rate and tone duration had an impact on performance for both isochronous and anisochronous sequences such that performance decreased as rate increased above 5 tones/s or duration decreased below 40 ms. Temporal masking was offered as an explanation for the interaction of short durations and fast rates on temporal order discrimination for the anisochronous sequences. © *2008 Acoustical Society of America.* [DOI: 10.1121/1.2932089]

PACS number(s): 43.66.Mk, 43.66.Sr [MW] Pages: 462–471

I. INTRODUCTION

It is well documented that hearing acuity worsens with advancing age (e.g., CHABA, 1988). Along with elevated hearing thresholds, older listeners also seem to have difficulty with suprathreshold auditory processing tasks. For example, older hearing-impaired listeners seem to consistently perform worse than young normal-hearing adults on a variety of tasks on the TBAC (Test of Basic Auditory Capabilities) (Watson *et al.*, 1982; Humes and Christopherson, 1991; Humes *et al.*, 1994; Humes, 2002). The TBAC is comprised of individual subtests that each tests one aspect of suprathreshold auditory discrimination ability. One such subtest is the temporal order subtest, in which the listener discriminates the order of the two middle tones in a four-tone sequence. It has been consistently shown, based on studies measuring the reliability of the various subtests of the TBAC (Christopherson and Humes, 1992) and those involving factor analyses on young normal-hearing (YNH) listeners (Watson *et al.*, 1982; Surprenant and Watson 2001) and older hearing-impaired (OHI) listeners (Humes *et al.*, 1994), that older listeners perform worse than younger adults on the temporal order subtest of the TBAC. Based on the fact that the tonal sequences in the temporal order subtest are comprised of low- and midfrequency tones, and that these studies ensured full audibility of the sequences for all listeners, the poor performance of the older listeners is not likely attributable to hearing loss.

It is possible that this difference in performance between the two groups might be related to the nature of the tonal sequences themselves. Figure 1 provides a schematic representation of the tonal sequences used in the temporal order subtest. The top two panels (A and B) of this figure depict four-tone sequences from the temporal order subtest. The first and last tones of each sequence are 625 Hz tones, while the two middle tones are 550 and 710 Hz, with one of two possible orders (550 Hz followed by 710 Hz or 710 Hz followed by 550 Hz). Discrimination is tested using a three-interval two-alternative forced choice procedure, in which the standard was always presented first. The task of the listener is to determine which of the two comparison intervals that follow differ from the standard in terms of the order of the two middle tones.

Test difficulty across the 48 trials of the subtest is manipulated by varying the duration of the two middle tones (in log steps over a range of 20–200 ms) with a fixed and brief interstimulus interval (ISI) of 2 ms throughout. Note that along with the change in duration of the two middle tones from short (more difficult, panel A of Fig. 1) to long (less difficult, panel B of Fig. 1), this method also concurrently impacts the overall rate of presentation from fast (panel A) to

[a)]Portions of this work were presented at the 145th meeting of the Acoustical Society of America, Nashville, Tennessee, 2003, and at the Aging and Speech Communication: An International and Interdisciplinary Research Conference, Bloomington, Indiana, 2005.

[b)]Electronic mail: mnarendr@csd.ufl.edu

 0001-4966/2008/124(1)/462/10/$23.00

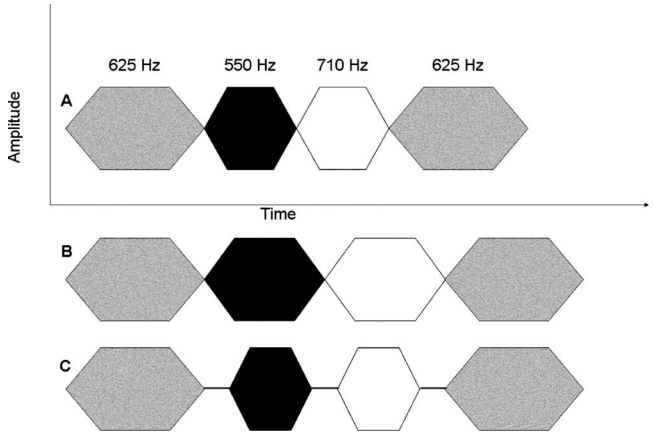

FIG. 1. Schematic illustration of anisochronous four-tone sequences used in the Test of Basic Auditory Capabilities (TBAC) to measure temporal order discrimination. Panels A and B represent sequences with different durations of the two middle tones as well as the overall rate. Panels B and C represent sequences with different durations of the two middle tones but with the same overall rate. Finally, panels A and C represent sequences with the same duration of the two middle tones, but with different overall rate. Note that for Experiment I, duration and rate changes apply only to the two middle tones, while for Experiment II, these changes apply to all four tones.

slow (panel B). Hence, when older listeners perform worse than young listeners on this task, it is not clear whether this is due to the shorter duration of the stimuli or due to the faster rates of presentation. When the duration of the individual components is reduced (as in panel A), errors may result due to insufficient processing time. For example, Newman and Spitzer (1983), based on the results of a backward masking paradigm, suggested that older listeners might require prolonged auditory processing times for stimuli when compared to younger listeners. On the other hand, a faster rate of presentation might be more challenging for older adults due to a generalized age-related slowing of speed of processing. For example, Fitzgibbons and Gordon-Salant (2004) measured auditory discrimination of the overall temporal pattern of spectrally and temporally complex tonal sequences in younger and older listeners. They found that older listeners performed worse than the younger listeners, with the age-related differences being highest at faster presentation rates. However, other studies such as Trainor and Trehub (1989) found that age-related differences in performance on temporal order discrimination tasks were obtained independent of the presentation rate used. Similar results were obtained by Fitzgibbons *et al.* (2006) for a temporal order recognition task for tonal sequences in which the sequence rate and duration were independently manipulated. They found that temporal order recognition was determined primarily by sequence rate and not by tonal duration. However, age-related differences were not limited to the faster sequence rates; rather, they were observed for all values of sequence rate tested. Hence, it appears that the decline in temporal processing abilities cannot be attributable entirely to reduced speed of processing.

Another explanation for poorer performance of listeners at higher presentation rates might be because of increased susceptibility to temporal masking of the two middle tones by the first and last tones in the sequence. Similar explanations have been presented for age-related differences in frequency discrimination tasks (Raz *et al.*, 1990). It is impossible to determine the independent effects of duration and presentation rate using the tonal sequences of the original temporal order subtest of the TBAC. However, one could sort this out by combining various durations with various ISIs to produce various rates of presentation. One such manipulation is illustrated in panel C of Fig. 1. Note that the tonal sequence shown in panel C has the same presentation rate (in units of tones/s) as that shown in panel B, but has the same tonal duration (for the two middle tones) as the sequence shown in panel A. If the performance on this task is governed by the duration of the two middle tones, then listeners should perform similarly for stimuli shown in panels A and C. On the other hand, if it is the overall presentation rate that determines performance, then stimuli shown in panels B and C should elicit similar performance. Finally, if both duration and presentation rate affect performance, listeners should perform the worst for the stimuli shown in panel A, compared to those in panels B and C. The experiments described here attempted to determine the independent effects of presentation rate and duration by manipulating duration and presentation rate in the manner just described. Two experiments were conducted because of the anisochronous or nonuniform nature of the four-tone sequence used in the temporal order discrimination task of the TBAC. As shown in Fig. 1, note that only duration of the two middle tones varies from trial to trial on this task, while that of the first and last tones remains constant (at 100 ms). This means that the duration of the first and last tones could be either greater or smaller than that of the two middle tones. Hence, the presentation rate in this condition is not uniform across the entire sequence, sometimes speeding up in the middle of the sequence and sometimes slowing down. As a result, a second experiment using isochronous four-tone sequences (same duration and ISI for all four tones in the sequence) was conducted with different participants to better examine the roles of presentation rate and stimulus duration in a temporal order discrimination task. In all other aspects, the tonal sequences used in the second experiment were similar to those used in the first experiment. The details of the two experiments are described below.

EXPERIMENT I: ANISOCHRONOUS TONE SEQUENCES METHODS

II. METHODS

A. Participants

There were 21 YNH listeners and 18 OHI listeners participated in this experiment. Of these, ten YNH and six OHI were recruited and tested at Indiana University, Bloomington, while 11 YNH and 12 OHI listeners were recruited and tested at the University of Florida, Gainesville. The testing procedures were exactly the same for all participants. The 21 YNH listeners included 20 females and one male and ranged in age from 19 to 25 years. None of them had a history of hearing loss. All the YNH listeners had pure-tone air-conduction thresholds less than 20 dB hearing level (HL) for

TABLE I. Age and air-conduction hearing thresholds in dB HL reference ANSI (1996) for the test ear for the 18 OHI participants in Experiment I. NR indicates no response at audiometric limits.

		Air conduction hearing thresholds (dB HL)						
Sub. No.	Age (Years)	250 (Hz)	500 (Hz)	1000 (Hz)	2000 (Hz)	4000 (Hz)	8000 (Hz)	Test ear
1	77	35	35	25	50	55	45	R
2	81	35	35	45	55	70	80	L
3	85	25	20	15	40	70	70	L
4	69	45	50	45	50	60	95	L
5	77	30	35	40	65	70	70	R
6	80	40	30	40	45	60	75	R
7	72	10	20	30	35	60	70	L
8	83	5	5	15	45	55	55	R
9	75	10	10	10	25	50	75	R
10	71	15	15	30	50	60	65	R
11	77	20	35	25	60	65	60	R
12	72	25	25	20	35	70	NR	L
13	76	20	30	45	40	70	NR	R
14	77	20	25	30	65	65	55	L
15	74	15	15	35	40	55	55	L
16	75	10	20	35	60	80	80	L
17	79	15	20	35	60	80	80	L
18	77	10	25	10	50	60	70	L
Mean	76.5	21.4	25	30	46.9	63.1	67.8	

frequencies ranging from 250 to 8000 Hz. OHI listeners were recruited from the patient database of the Speech and Hearing Clinic at Indiana University, Bloomington and from the community in Gainesville, Florida. This group of listeners included ten males and eight females, ranging in age from 69 to 85 years ($M=76.5$ yr). All the listeners in the OHI group had sensorineural hearing loss with thresholds ranging from normal at the low frequencies to profound at the highest frequency (8000 Hz) tested. Their ages and hearing thresholds in the test ear are presented in Table I.

B. Stimuli

The stimuli were four-tone sinusoidal sequences that were patterned after those of the temporal order subtest of the TBAC. The first and last tones of the sequences were 625 Hz sinusoids, and the two middle components were 550 and 710 Hz sinusoids. All the tones had 10-ms-long onset and offset ramps, created using a Blackman window. The order of the two middle components was varied randomly. Thus, a given sequence could have one of the two orders: 625-550-710-625 or 625-710-550-625. These sequences were generated with 21 combinations of duration and ISI to give five different rates of presentation. The rate of presentation, duration, and ISI values ranged from 2.5 to 25 tones/s, 20 to 400 ms, and 0 to 380 ms, respectively. These values were chosen such that a wide range of durations and ISIs could be tested, while including those that are encompassed by the TBAC temporal order discrimination task. In addition, the ranges selected for each of these temporal parameters encompass those commonly observed in speech. The specific values and combinations of stimulus duration, ISI, and rate parameters are presented in Table II. It should be noted that these values apply only to the middle two tones in the anisochronous sequences and the ISIs surrounding them. The leading and trailing tones were always fixed in duration at 100 ms, as in the TBAC task. Although the specification of tone durations and ISI in Table II are not

TABLE II. Rates of presentation and combinations of duration and ISI that were used for the tonal sequences. These stimulus parameters apply to the middle two tones (and the adjacent ISIs) of the sequences in Experiment I and to the entire four-tone sequence in Experiment II.

Rate (tones/s)	Duration (ms)	ISI (ms)
25	20	20
	40	0
20	20	30
	40	10
10	20	80
	40	60
	80	20
5	20	180
	40	160
	80	120
	120	80
	160	40
	180	20
	200	0
2.5	20	380
	40	360
	80	320
	160	240
	200	200
	320	80
	400	0

impacted by the presence of these fixed duration leading and trailing tones, the rate of presentation for the entire four-tone sequence is affected. Hence, for this experiment, the rates reported in Table II apply only to the middle two tones of the sequence.

The stimuli consisted of these sequences presented in a modified two-alternative forced choice format. The first four-tone sequence was the standard, against which the second and third four-tone sequences were compared. The second and third four-tone sequences differed in the order of the two middle tones of the sequence. For each combination of duration and ISI, the task of the listener was to discriminate the order of the four-tone sequences by indicating which of the two comparison tone sequences differed from the standard tone sequence. The standard stimulus and the order of the two comparison stimuli were randomized from trial to trial. The participants at the two locations (Indiana University and the University of Florida) were tested with different versions of the recordings that varied only in this randomization. All other testing procedures were exactly the same.

The stimuli were generated using the mathematical platform MATLAB (The Mathworks, Inc.) on a Dell Optiplex GXI computer. The sequences were then recorded directly from the computer to digital audio tapes. The stimuli were presented in blocks of 50 trials, with the duration-ISI combination maintained within each block. The order of presentation of the 21 duration-rate combinations was varied randomly across listeners.

All testing was done with the participant seated comfortably in a double-walled sound-treated booth. The recorded stimuli on DAT were presented to the listeners through an audiometer, and all testing was conducted monaurally using ER-3A insert earphones. In young normal listeners, maximum scores on the TBAC are achieved at presentation levels of at least 65–75 dB sound pressure level (SPL) (Christopherson and Humes, 1992). In the present study, the stimuli were presented at 85 dB SPL as measured in an HA-2 2 cm^3 coupler. This level was high enough for all stimuli to be audible to the hearing-impaired listeners, while not being uncomfortably loud for the YNH listeners. The presentation levels for the signals were set using a continuous 625 Hz calibration tone matched to the peak level of the tones in the stimulus sequences. All but three of the YNH listeners were tested in the right ear, while the older listeners were tested in their better ear. Insert earphones were also worn in the non-test ear. All testing was carried out individually and participants were paid for their participation.

C. Procedure

The testing was carried out in two sessions, each around 120 min in length. Prior to testing, the participants' air-conduction hearing thresholds were measured while they were seated in a double-walled sound-treated booth. The participants were then given written instructions as follows.

"You will hear three sound sequences: a standard sequence, followed by two test sequences. On the response sheet, the standard sequence is labeled as "S," and the two test sequences are labeled "T1" and "T2." One of the two test sequences T1 *or* T2 is different from the standard sequence S. Your task is to listen to the three sequences, and mark (X) the test sequence (T1 or T2) that is *different* from the standard S. The S on the response sheet is just to remind you that you will always hear the standard sound sequence first. Only mark T1 or T2 as your answer.

You will be given a practice version of the task consisting of eight trials. If you want to listen to further practice trials after this, you will be given a chance to do so. Some of the differences in sound sequences will be easier to hear, while others will be more difficult. Do not get discouraged, as some of the trials are designed to be more difficult. In case you are not sure of your responses, please guess, but make sure you respond for every trial."

The participants were then presented with eight practice trials. The practice trials included various duration-ISI combinations so as to familiarize the listeners with the range of stimuli used in the actual test. The same set of eight practice trials, in the same order, was presented to all listeners. Listeners marked their responses on the provided response sheets. Unlike the actual test, feedback was provided after each response for the practice trials. The test sequences were presented after the completion of the practice trials, and the participants had indicated that they were comfortable with the task. The tape was paused briefly after the first 25 trials in every block to verify that the participant was on the correct trial number. At the end of the 21 test conditions (Table II), each listener had completed a total of 1050 (21×50) trials. Frequent breaks were given throughout the test sessions as needed.

III. RESULTS AND DISCUSSION

One of the 18 older participants (number 7, Table I) could not complete three of the test conditions (20-20, 20-30, 20-80, where the two values represent tone duration and ISI, respectively) because of the high level of difficulty of these conditions. Note that these conditions fall under the fastest presentation rates of 25, 20, and 10 tones/s, respectively, and that of these three rates, the slowest (10 tones/s) was included in all subsequent analyses (see below). Hence, the analyses described in the following sections included all 21 YNH and only 17 of the 18 OHI listeners.

Figure 2 provides the mean percent-correct scores for the 21 YNH listeners (top panel) and the 17 OHI listeners (bottom panel). Performance is plotted as a function of duration+ISI (lower *x*-axis label) or presentation rate (top *x*-axis label) for the middle two tones of the sequence. The parameter for the plots in both panels is the stimulus duration. As was noted previously, given the anisochronous nature of the four-tone sequences used in this experiment, these definitions (duration+ISI and rate) apply only to the middle two tones of the sequence. In general, both groups show substantial increases in performance as rate decreases from 20 to 5 tones/s, and then slight or no increase in performance with further reductions in presentation rate below 5 tones/s (or a duration+ISI value of 200 ms). Further, this pattern holds regardless of tone duration, although the over-

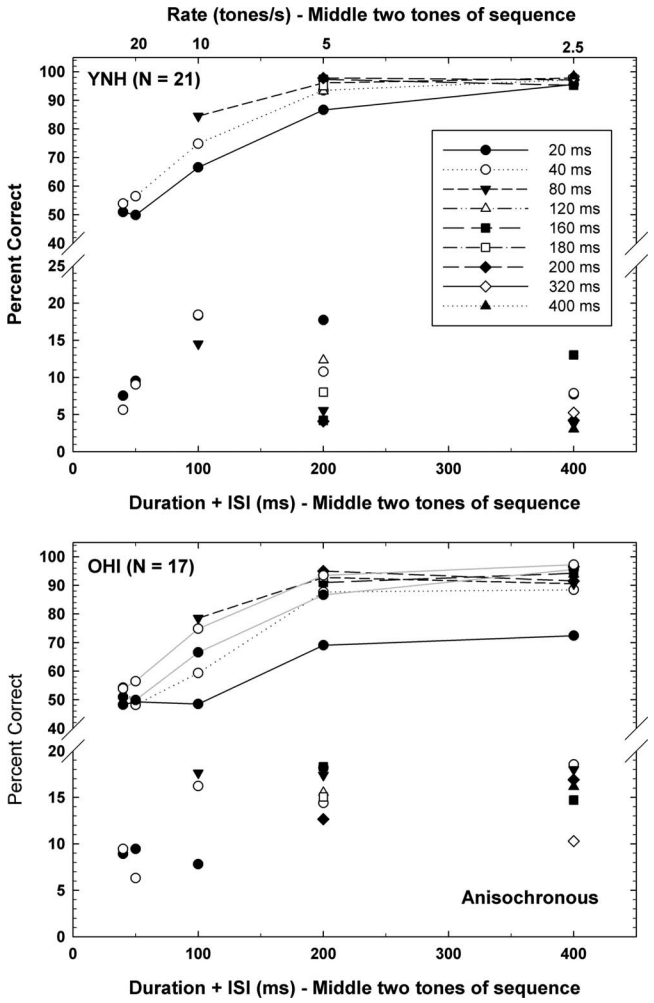

FIG. 2. Mean percent-correct performance from Experiment I (anisochronous sequences) for young normal-hearing (YNH) listeners (top) and elderly hearing-impaired (OHI) listeners (bottom). The parameter is the duration of the middle two tones of the four-tone sequence. The solid gray lines in the bottom panel represent the data for the YNH listeners from the top panel for tone durations of 20 and 40 ms. Standard deviations for each stimulus parameter are shown by using the unconnected symbols at the bottom of the graph.

all performance level appears to vary for the shorter durations (20 and 40 ms) with lower levels of performance achieved for these durations.

The data for tone durations of 20, 40, and 80 ms and presentation rates of 10, 5, and 2.5 tones/s were selected for subsequent statistical analysis. Percent-correct scores were arcsine transformed (Studebaker, 1985) to stabilize the error variance prior to analysis. Independent-samples t-tests with adjustment for multiple comparisons revealed no significant effects of test ear within the OHI group. Hence, data were combined across test ear for both OHI and YNH listeners. Data across testing sites (Indiana University and the University of Florida) were combined for each listener group as independent-samples t-tests revealed no significant differences between the two sites. The data for all nine stimulus conditions were found to be normally distributed (Kolmogorov–Smirnov Z, $p>0.01$). As a result, the general linear model (GLM) was used to examine the within-subject effects of presentation rate and tone duration and the between-subject effect of listener group. The following effects were found to be statistically significant ($p<0.01$): presentation rate [$F(2,72)=86.9$]; duration [$F(2,72)=60.1$]; and the rate x duration interaction [$F(4,144)=5.0$]. The main effect of group [$F(1,36)=11.1$] and the two-way interaction of duration x group [$F(2,72)=10.4$] were also significant ($p<0.01$).

Based on the results of these analyses, additional follow-up analyses were performed. First, two additional GLM analyses were conducted to examine the effects of presentation rate and stimulus duration within each group separately. For the YNH listeners, presentation rate [$p<0.01$; $F(2,40)=60.7$] and duration [$p<0.01$; $F(2,40)=18.7$] both had significant effects on temporal order discrimination. The interaction of rate and duration was also significant [$p<0.01$; $F(4,80)=4.5$]. Subsequent analysis of the estimated marginal means for pairwise comparisons of rate using t-tests with the Bonferroni adjustment for multiple comparisons revealed that the performance for the rate of 10 tones/s was significantly ($p<0.01$) worse than that for the 5 and 2.5 tones/s rates, and that performance for the 5 tones/s rate was significantly ($p<0.05$) worse than that for the 2.5 tones/s rate. Similar analysis for pairwise comparisons of duration revealed that the YNH listeners performed significantly worse for the 20 ms duration than for the two longer durations (40 and 80 ms), but that the performances for the two longer durations were not significantly different from each other.

For the OHI listeners, the analysis revealed significant ($p<0.01$) main effects of presentation rate [$F(2,32)=31.3$] and duration [$F(2,32)=36.7$] and a significant ($p<0.05$) interaction between these two variables [$F(4,64)=2.6$]. Subsequent examination of the estimated marginal means for all pairwise comparisons of presentation rate using t-tests with the Bonferroni adjustment for multiple comparisons revealed that the performance for the rate of 10 tones/s was significantly lower ($p<0.01$) than that of the two slower rates included in this analysis (5 and 2.5 tones/s). There was no significant difference between performances for the two slower rates. Similar *post hoc* analysis for stimulus duration revealed that the performance for the 80 ms duration was significantly better ($p<0.01$) than that for the two shorter durations (20 and 40 ms), and that the performance for the 20 ms duration was significantly poorer ($p<0.01$) than that for the 40 ms duration.

Finally, nine independent-samples t-tests with adjustment for multiple comparisons, one for each combination of the three presentation rates and three stimulus durations, were conducted to examine the effects of listener group. Two of these between-group differences were found to be significant ($p<0.006$). The OHI group performed worse than the YNH group for the 20 ms durations at the presentation rates of 10, 5, and 2.5 tones/s. None of the other differences were significant.

Why might stimulus duration interact with presentation rate, especially at the highest presentation rates? To answer this question, let us consider the temporal structure of the anisochronous four-tone sequence when the middle two tones are 20 ms in duration [see panels A and B of Fig. 1].

TABLE III. Age and air-conduction hearing thresholds in dB HL reference ANSI (1996) for the test ear for the ten OHI participants in Experiment II. NR indicates no response at audiometric limits.

		Air conduction hearing thresholds (dB HL)						
Sub. No.	Age (Years)	250 (Hz)	500 (Hz)	1000 (Hz)	2000 (Hz)	4000 (Hz)	8000 (Hz)	Test ear
1	79	20	25	55	65	70	80	R
2	70	20	30	40	60	55	60	L
3	87	20	25	40	60	55	60	L
4	80	30	25	10	45	70	60	L
5	69	25	20	20	30	60	70	R
6	81	30	35	35	45	65	75	L
7	67	15	15	20	60	60	70	R
8	68	25	30	25	25	35	80	R
9	82	25	40	45	60	75	NR	R
10	78	35	40	60	70	85	85	L
Mean	76.1	24.5	28.5	31	52.0	63.0	71.1	

Recall that the leading and trailing tones in each anisochronous sequence were each fixed in duration at 100 ms. For the 20 ms tone duration and the fastest presentation rate of 25 tones/s, the ISI was 20 ms. As a result, the middle two tones are within 80 ms of both the end of the leading tone and the beginning of the trailing tone. Thus, both tones likely are subject to forward masking from the 100 ms leading tone and backward masking from the 100 ms trailing tone in each sequence. Kelly and Watson (1986) have demonstrated previously that the presence of a leading tone, trailing tone, or both, degrades temporal order discrimination for the middle tones of tonal sequences. As the rate of presentation is decreased, however, the temporal masking effects from the leading and trailing tones should also decrease. Further, temporal masking of the two middle tones will also decrease as the duration of the middle tones increases, possibly due both to a decrease in temporal masking for tones of longer duration and to the consequent lengthening of the interval between the offset of the leading tone and onset of the trailing tone associated with increases in the duration of the middle tones.

The data for the 40 ms tone duration are consistent with this temporal masking explanation in that performance for this duration only differs significantly from the longer durations at the faster rates of presentation (>5 tones/s). Note, however, that the data for the 20 ms duration are significantly lower than those for other durations at *all* rates of presentation, including the slowest rate studied (2.5 tones/s). At the slowest rate, the time interval between offset of the leading tone and the second tone in the sequence is 380 ms. This same interval exists between the two middle tones and between the end of the third tone and the onset of the trailing tone. This ISI is well beyond one at which temporal masking effects can be expected. For the 20 ms duration, therefore, there is an effect on performance that must be attributable to the short duration itself and not to potential masking effects from the surrounding tones. Since the tones were well above detection threshold, even when taking temporal integration of signal energy into account, the 20 ms tones were clearly audible to all listeners. However, it may be that a duration of 20 ms is insufficient to allow for the development of a clear pitch percept that is sufficient to enable the listener to distinguish the order of the two middle tones or that the long ISI (e.g., 380 ms at 2.5 tones/s) is too long for retention of that percept through the sequence to enable comparison to subsequent sequences.

For a given short signal duration, temporal masking is known to decrease as the duration of the masker decreases (e.g., Kidd and Feth, 1982), at least for detection thresholds. In order to determine if results of Experiment I could be attributed at least partly to temporal masking, a subsequent experiment was then conducted that involved the use of isochronous tone sequences. Unlike the anisochronous sequences shown in Fig. 1, in these sequences, short-duration middle tones were surrounded by equally short leading and trailing tones, which would reduce the temporal masking of the middle two tones by the leading and trailing tones of the four-tone sequences. The details of Experiment II are described below.

EXPERIMENT II: ISOCHRONOUS TONE SEQUENCE

IV. METHODS

A. Participants

Ten YNH listeners and ten OHI listeners were recruited as listeners for the experiment. All listeners were recruited and tested at Indiana University, Bloomington, and none of them had participated in the first experiment. The YNH listeners were graduate students and included two males and eight females. They ranged in age from 22 to 35 years, and none of them had any history of hearing disorders. All had audiometric thresholds less than 20 dB HL for a range of frequencies from 250 to 8000 Hz. The OHI listeners were recruited from the patient database of the Speech and Hearing Clinic at Indiana University, Bloomington, and included six males and four females, ranging in age from 67 to 87 years (M=76.1 yr, SD=7.0 yr). All the listeners in the OHI group had mild to profound sensorineural hearing loss in both ears. Their ages and hearing thresholds in the test ear are presented in Table III.

B. Stimuli and procedures

The materials and apparatus used in this experiment were identical to those in Experiment I except that isochronous four-tone sequences were used throughout. The combinations of presentation rate, duration, and ISI parameters outlined previously in Table II now apply to the entire four-tone sequence, rather than to just the middle two tones of the sequence as in the first experiment. Other than this, all aspects of the equipment and procedures for Experiment II were identical to that of the Experiment I.

V. RESULTS AND DISCUSSION

One of the older participants could not complete four of the test conditions (20-20, 20-30, 40-0, and 40-10, where the two values represent tone duration and ISI, respectively) because of the high level of difficulty of these conditions. Note that all these conditions fall under the fastest presentation rates of 25 and 20 tones/s, which were not included in subsequent data analyses (see below). Hence, the analyses described in the following sections included all ten YNH and ten OHI listeners.

Figure 3 provides the mean percent-correct scores for the YNH listeners (top panel) and the OHI listeners (bottom panel). Performance is plotted as a function of duration +ISI (lower x-axis label) or presentation rate (top x-axis label). In general, both groups show substantial increases in performance as rate decreases from 20 to 5 tones/s, and then a slight or no increase in performance with further reductions in presentation rate below 5 tones/s (or a duration+ISI value of 200 ms). As with the anisochronous patterns in the previous experiment, this general pattern holds regardless of tone duration (the parameter for the plots in both panels). Further, for the YNH listeners (top panel), the overall performance level does not vary much with tone duration, whereas it does appear to vary with duration for the OHI listeners (bottom panel).

Only the data for tone durations of 20, 40, and 80 ms and presentation rates of 10, 5, and 2.5 tones/s were selected for subsequent statistical analyses since the rest of the duration values (120, 200, 320, and 400 ms) were only tested at the slowest presentation rates of 5 and 2.5 tones/s). Percent-correct scores were arcsine transformed to stabilize the error variance prior to analysis. Independent-sample t-tests with adjustment for multiple comparisons revealed no significant effects of test ear within the OHI group. Hence, data were combined across each of these variables for both OHI and YNH listeners. The data for all nine stimulus conditions were found to be normally distributed (Kolmogorov–Smirnov Z, $p>0.01$) for both groups of listeners. As a result, the GLM was used to examine the within-subject effects of presentation rate and tone duration and the between-subject effect of listener group. The main effects of rate of presentation, duration, and group were all found to be significant statistically [$p<0.01$; $F(2,36)=26.4$, $F(2,36)=8.2$, $F(1,18)=9.0$, respectively]. Among the possible interactions, only the two two-way interactions with group were found to be significant [rate x group, $F(2,36)=4.1$, $p=0.025$; duration x group, $F(2,36)=4.7$, $p=0.015$].

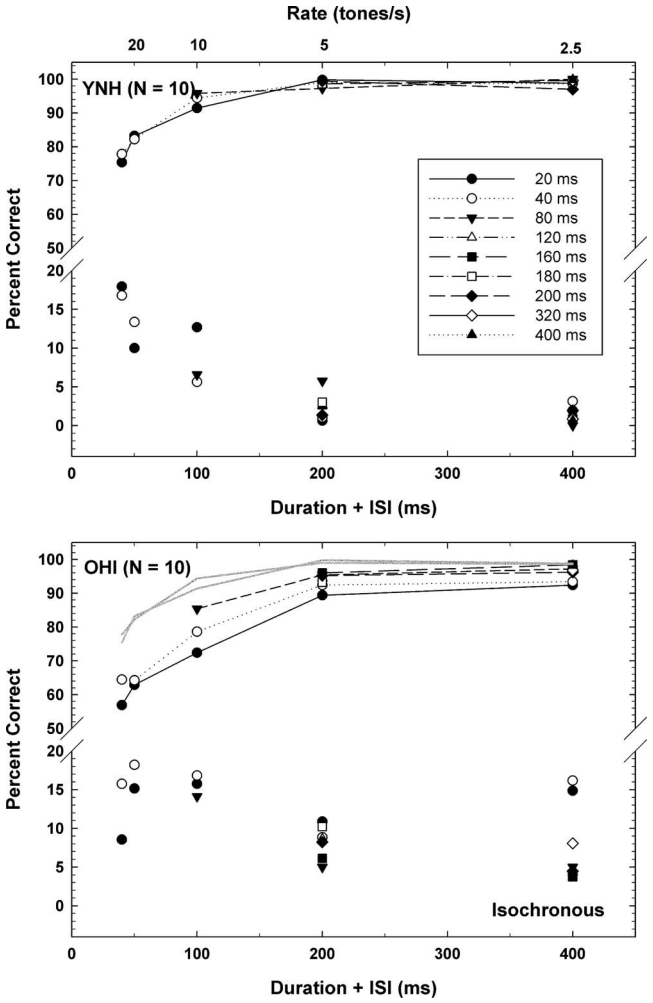

FIG. 3. Mean percent-correct performance from Experiment II (isochronous sequences) for YNH listeners (top) and OHI listeners (bottom). The parameter is the duration of the tones comprising the four-tone sequence. The solid gray lines in the bottom panel represent the data for the YNH listeners from the top panel for tone durations of 20 and 40 ms. Standard deviations for each stimulus parameter are shown by using the unconnected symbols at the bottom of the graph.

Based on the results of these analyses, additional follow-up analyses were performed. First, two additional GLM analyses were conducted to examine the effects of presentation rate and stimulus duration within each group separately. For the YNH listeners, presentation rate [$p<0.01$; $F(2,18)=6.8$] and duration [$p<0.05$; $F(2,18)=3.8$] both had significant effects on temporal order discrimination. However, subsequent analysis of the estimated marginal means for pairwise comparisons of rate and duration using t-tests with the Bonferroni adjustment for multiple comparisons revealed no significant effects. This is entirely consistent with the visual impression of the data in the top panel of Fig. 3. Note that this figure includes many additional data points not included in the statistical analysis. For these listeners, it appears that the rate alone mediates performance on this temporal order discrimination task with sizable declines in performance when the presentation rate exceeds 10 tones/s. Note that these higher presentation rates (20 and 25 tones/s) were not included in the statistical analyses described here. For the OHI listeners, the analysis revealed

significant ($p<0.01$) main effects of presentation rate [$F(2,18)=20.2$] and duration [$F(2,18)=6.8$] and no interaction between these two variables [$F(4,36)=0.7$]. Subsequent examination of the estimated marginal means for all pairwise comparisons of presentation rate using t-tests with the Bonferroni adjustment for multiple comparisons revealed that performance for the rate of 10 tones/s was significantly lower ($p<0.01$) than that of the two slower rates included in this analysis (5 and 2.5 tones/s). Similar *post hoc* analysis for stimulus duration revealed that the performance for 80 ms was significantly better ($p<0.05$) than that for the 20 ms duration, but not from that for the 40 ms duration. There was no difference between performances for the 20 and 40 ms durations. Thus, the performance of the OHI listeners begins to decrease significantly when either the presentation rate exceeds 5 tones/s or tone duration decreases below 40 ms.

Finally, the effect of listener group on performance was determined by conducting nine independent-sample t-tests with adjustment for multiple comparisons, one for each combination of the three presentation rates and three stimulus durations. Only two of the nine between-group differences were found to be significant ($p<0.006$). The OHI group performed worse than the YNH group for the 20 ms duration at the two highest presentation rates examined in these analyses (10 and 5 tones/s). There were no significant differences between groups for longer stimulus durations (i.e., 40 and 80 ms) or slower presentation rates (i.e., 2.5 tones/s).

VI. GENERAL DISCUSSION

Some previous studies have reported that females perform worse than males in temporal order judgment tasks (Wittmann and Szelag, 2003), while others (e.g., van Kesteren and Wiersinga-Post, 2007) have reported no effect of gender on these tasks. In both experiments in the present study, the younger group that was dominated by females performed better than the older group of listeners that was more gender balanced. Further, within the older group, independent-sample t-tests with adjustment for multiple comparisons revealed no significant effects of gender. Hence, in the present study, it appears that gender did not have a significant effect on performance.

The results of these two experiments suggest that the mechanisms underlying temporal order discrimination for isochronous tone sequences (Experiment I) differ from those underlying the discrimination of anisochronous tone sequences (Experiment II), especially for YNH listeners. For this group of listeners, presentation rate alone appeared to underlie performance for isochronous sequences, whereas both presentation rate and stimulus duration affected performance for anisochronous sequences. In particular, for the YNH listeners and the anisochronous patterns, performance was worse for stimulus durations less than 80 ms and high presentation rates (>5 tones/s). As discussed with regard to the results from Experiment I, this combination of conditions could result in substantial forward and backward masking of the brief middle tones by the longer leading and trailing tones of the sequence. When the leading and trailing tones were equivalent in duration to the middle two tones of the sequence (Experiment I), the forward and backward masking effects were likely reduced and only presentation rate appeared to underlie performance. For the OHI group, however, stimulus duration was an important factor underlying performance in both experiments. These listeners performed worse for the 20 ms tone duration in Experiment I even for large temporal separations between the tones in the sequence, including temporal separations far exceeding those relevant for forward or backward masking (i.e., 380 ms). Even in Experiment II, which minimized the temporal masking of the middle two tones by the leading and trailing tones of the sequence, the OHI listeners showed significant effects of stimulus duration for durations less than 40 ms. Thus, for the OHI listeners, both presentation rate and stimulus duration have an impact on performance in these temporal order discrimination tasks such that performance decreases substantially as rate increases above 5 tones/s and tone duration decreases below 40 ms. These results are different from those reported by Fitzgibbons *et al.* (2006), who found that for uniform three-tone sequences (in which the presentation rate remained the same throughout the entire sequence), only presentation rate seemed to affect performance for both younger and older listeners. Also, the age-related differences observed in that study were obtained for even the slowest presentation rate (2 tones/s) and were not limited to the fastest rates as in the present study. These differences are likely related to the nature of the listeners' tasks in the two experiments; Fitzgibbons *et al.* (2006) used a temporal order recognition paradigm involving labeling, a task with increased processing demands (Fitzgibbons and Gordon-Salant, 1998) when compared to the discrimination task used in the present experiment.

It is possible that some of these age-related differences might be related to differences between the younger and older listeners in learning the task. The present study did not incorporate feedback and training, and it is possible that given sufficient training, the performance of the older adults would have improved. It would be interesting to see if the age-related differences observed in the present study would diminish or disappear with sufficient training.

Figure 4 shows the mean results for the YNH (top) and OHI (bottom) listeners from Experiments I and II for the three shortest tone durations examined (20, 40, and 80 ms). From this figure it is apparent that for both groups, the largest changes in performance from the isochronous to anisochronous tone sequences occurred for the shortest durations (20 and 40 ms) and the fastest presentation rates (>5 tones/s). Again, this pattern of performance change is generally consistent with an increase in temporal-masking effects from the isochronous to the anisochronous sequences. The duration of the leading and trailing tones (100 ms) in the anisochronous sequences was greater than in the isochronous sequences, especially for the fast presentation rates (>5 tones/s) and short tone durations (<80 ms). Since forward masking decreases with decrease in masker (leading/trailing tone) duration (e.g., Kidd and Feth, 1982), one would expect performance to be better for the isochronous (less forward masking) sequences than the anisochronous sequences, espe-

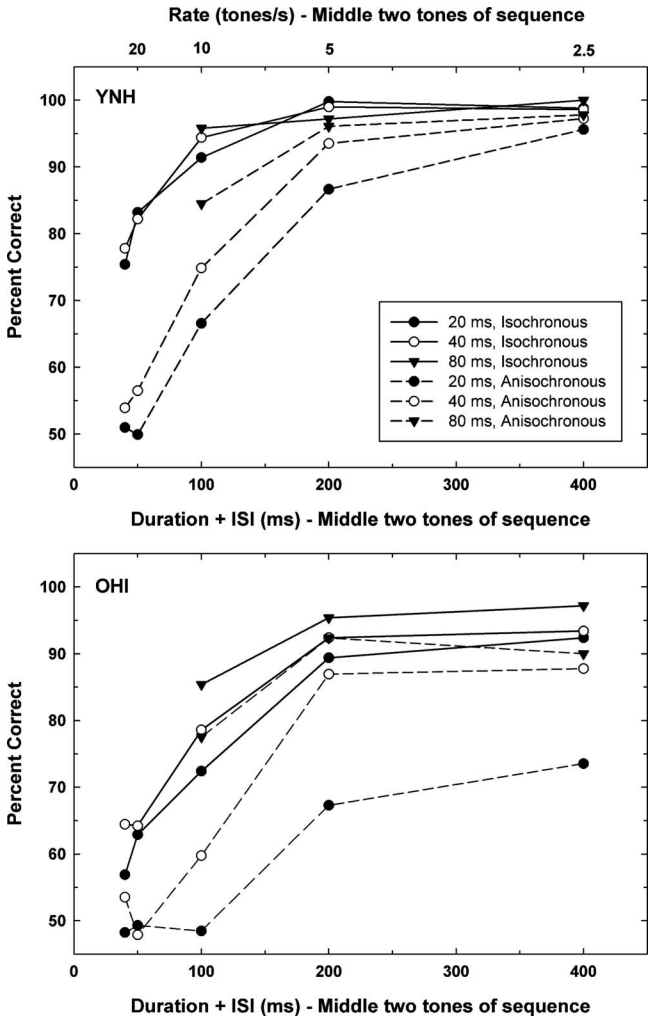

FIG. 4. Mean percent-correct performance from Experiments I and II combined for YNH listeners (top) and OHI listeners (bottom). The parameter is the duration of the middle two tones comprising the anisochronous four-tone sequence and all four tones comprising the isochronous sequence.

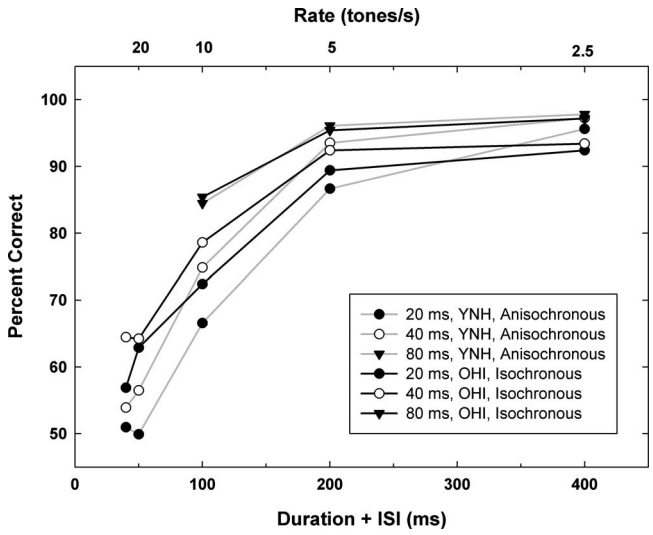

FIG. 5. A comparison of the results from the YNH listeners for the anisochronous tone sequences (filled symbols and dashed lines) to the comparable data from the OHI listeners for the isochronous sequences (unfilled symbols and solid lines). The parameter is the duration of the middle two tones comprising the anisochronous four-tone sequence and all four tones comprising the isochronous sequence.

cially for this combination of rates (>5 tones/s) and tone durations (<80 ms). As noted, such a pattern is clearly apparent in the data for the YNH listeners in the top panel of Fig. 4. It is somewhat less clear, however, that this is also the case for the data from the OHI listeners in the bottom panel. There is a trend in the same direction, but the two sets of data are not as clearly separated as in the top panel of this figure. Interestingly, Kidd *et al.* (1984) reported that pure-tone forward masking was greater in hearing-impaired listeners, but was also much less dependent on masker duration than in normal-hearing listeners. Thus, if one can extrapolate from forward masking detection experiments to forward masking discrimination experiments, this finding would suggest that the change from anisochronous to isochronous tonal sequences would have a lesser impact on the data from the OHI participants in this study than was observed for the YNH participants.

One of the striking features in the data in Fig. 4 results from a comparison of the performance of the YNH listeners for the anisochronous patterns to that of the OHI listeners for the isochronous patterns. Visualization of this comparison has been facilitated by plotting these two sets of data from Fig. 4 together in Fig. 5. If increased temporal masking from the leading and trailing tones of the sequences mediates the difference in performance between the anisochronous and isochronous tone sequences for the YNH listeners, then the comparison in Fig. 5 would indicate that the YNH listener with increased temporal masking might be a reasonable model for the performance of OHI listeners on this task. The use of masking, including temporal masking, as a simulation of the effects of sensorineural hearing loss on a variety of psychoacoustic tasks has been suggested previously (e.g., Humes *et al.*, 1988; Humes and Jesteadt, 1991). However, given the stimulus levels used, the frequencies of the tones, the audiograms of the OHI listeners, and the results of prior studies with simulated hearing loss using simultaneous masking (e.g., Humes and Christopherson, 1991), temporal masking might be more effectively simulating the effects of aging or the combined effects of aging and hearing impairment, rather than the effects of hearing loss alone. That is, audibility differences alone are unlikely to underlie the observed differences in performance between the YNH and OHI listeners. Forward masking has been linked to neural adaptation mechanisms in the auditory nerve (e.g., Smith, 1979) or more central mechanisms of persistence (e.g., Oxenham, 2001). It is also possible that aging results in greater adaptation or persistence, a phenomenon that can be simulated in YNH listeners via forward masking. The mechanisms underlying backward masking appear to be centrally located, and age-related changes have been observed in backward masking paradigms involving the detection of (e.g., Gehr and Sommers, 1999), discrimination (e.g., Raz *et al.*, 1990) and recognition (e.g., Newman and Spitzer, 1983) of auditory stimuli. Further research is required, however, to substantiate the use of some form of temporal masking as a model for age-related decline in auditory performance.

VII. SUMMARY

The following is a summary of the main findings of the study.

(1) For the YNH listeners, performance for the isochoronous sequences was affected primarily by presentation rate, while that for the anisochronous sequences was affected by both rate and stimulus duration.
(2) For the OHI listeners, both presentation rate and stimulus duration affected performance for both isochronous and anisochronous sequences.
(3) For both groups of listeners, performance was better for the isochronous sequences, especially for conditions in which short durations were combined with fast presentation rates. This was attributed to an increase in temporal masking (of the two middle tones of the sequence by the leading and trailing tones) for the anisochronous sequences when compared to the isochronous sequences.

ACKNOWLEDGMENTS

This work was funded, in part, by NIA R01 AG08293 awarded to the second author.

CHABA (**1988**). "Speech understanding and aging. Working Group on Speech Understanding and Aging. Committee on Hearing, Bioacoustics, and Biomechanics, Commission on Behavioral and Social Sciences and Education, National Research Council," J. Acoust. Soc. Am. **83**, 859–895.
Christopherson, L. A., and Humes, L. E. (**1992**). "Some psychometric properties of the Test of Basic Auditory Capabilities (TBAC)," J. Speech Hear. Res. **35**, 929–935.
Fitzgibbons, P. J., and Gordon-Salant, S. (**1998**). "Auditory temporal order perception in younger and older adults," J. Speech Lang. Hear. Res. **41**, 1052–1060.
Fitzgibbons, P. J., and Gordon-Salant, S. (**2004**). "Age effects on discrimination of timing in auditory sequences," J. Acoust. Soc. Am. **116**, 1126–1134.
Fitzgibbons, P. J., Gordon-Salant, S., and Friedman, S. A. (**2006**). "Effects of age and sequence presentation rate on temporal order recognition," J. Acoust. Soc. Am. **120**, 991–999.
Gehr, S. E., and Sommers, M. B. (**1999**). "Age differences in backward masking," J. Acoust. Soc. Am. **106**, 2793–2799.
Humes, L. E. (**2002**). "Factors underlying the speech-recognition performance of elderly hearing-aid wearers," J. Acoust. Soc. Am. **112**, 1112–1132.
Humes, L. E., and Christopherson, L. (**1991**). "Speech identification difficulties of hearing-impaired elderly persons: the contributions of auditory processing deficits," J. Speech Hear. Res. **34**, 686–693.
Humes, L. E., Espinoza-Varas, B., and Watson, C. S. (**1988**). "Modeling sensorineural hearing loss. I. Model and retrospective evaluation," J. Acoust. Soc. Am. **83**, 188–202.
Humes, L. E., and Jesteadt, W. (**1991**). "Models of the effects of threshold on loudness growth and summation," J. Acoust. Soc. Am. **90**, 1933–1943.
Humes, L. E., Watson, B. U., Christensen, L. A., Cokely, C. G., Halling, D. C., and Lee, L. (**1994**). "Factors associated with individual differences in clinical measures of speech recognition among the elderly," J. Speech Hear. Res. **37**, 465–474.
Kelly, W. J., and Watson, C. S. (**1986**). "Stimulus-based limitations on the discrimination between different temporal orders of tones," J. Acoust. Soc. Am. **79**, 1934–1938.
Kidd, G., Jr., and Feth, L. L. (**1982**). "Effects of masker duration in pure-tone forward masking," J. Acoust. Soc. Am. **72**, 1384–1386.
Kidd, G., Jr., Mason, C. R., and Feth, L. L. (**1984**). "Temporal integration of forward masking in listeners having sensorineural hearing loss," J. Acoust. Soc. Am. **75**, 937–944.
van Kesteren, M. T. R., and Wiersinga-Post, J. E. C. (**2007**). "Auditory temporal-order thresholds show no gender differences," Rest. Neur. and Neuroscience **25**, 119–122.
Newman, C. W., and Spitzer, J. B. (**1983**). "Prolonged auditory processing time in elderly: Evidence from a backward recognition-masking paradigm," Audiology **22**, 241–252.
Oxenham, A. J. (**2001**). "Forward masking: Adaptation or integration?" J. Acoust. Soc. Am. **109**, 732–741.
Raz, N., Millman, D., and Moberg, P. J. (**1990**). "Mechanism of age-related differences in frequency discrimination with backward masking: Speed of processing or stimulus persistence?" Psychol. Aging **5**, 475–481.
Smith, R. L. (**1979**). "Adaptation, saturation, and physiological masking in single auditory-nerve fibers," J. Acoust. Soc. Am. **65**, 166–178.
Studebaker, G. A. (**1985**). "A rationalized arcsine transform," J. Speech Hear. Res. **28**, 455–462.
Surprenant, A. M., and Watson, C. S. (**2001**). "Individual differences in the processing of speech and nonspeech sounds by normal-hearing listeners," J. Acoust. Soc. Am. **110**, 2085–2095.
Trainor, L. J., and Trehub, S. E. (**1989**). "Aging and auditory temporal sequencing: Ordering the elements of repeating tone patterns," Percept. Psychophys. **45**, 417–426.
Watson, C. S., Jensen, J. K., Foyle, D. C., Leek, M. R., and Goldgar, D. E. (**1982**). "Performance of 146 normal adult listeners on a battery of auditory discrimination tests," J. Acoust. Soc. Am. **71**, S73.
Wittmann, M., and Szelag, E. (**2003**). "Sex differences in perception of temporal order," Percept. Mot. Skills **96**, 105–112.

An acoustic analysis of laughter produced by congenitally deaf and normally hearing college students[a)]

Maja M. Makagon[b)]
Department of Psychology, Cornell University, 211 Uris Hall, Ithaca, New York 14853

E. Sumie Funayama
Department of Psychology, Gallaudet University, S235 Hall Memorial Building, 800 Florida Ave. NE, Washington, D.C. 20009

Michael J. Owren
Department of Psychology, Georgia State University, P.O. Box 5010, Atlanta, Georgia 30302-5010

(Received 9 December 2006; revised 24 April 2008; accepted 28 April 2008)

Relatively few empirical data are available concerning the role of auditory experience in nonverbal human vocal behavior, such as laughter production. This study compared the acoustic properties of laughter in 19 congenitally, bilaterally, and profoundly deaf college students and in 23 normally hearing control participants. Analyses focused on degree of voicing, mouth position, air-flow direction, temporal features, relative amplitude, fundamental frequency, and formant frequencies. Results showed that laughter produced by the deaf participants was fundamentally similar to that produced by the normally hearing individuals, which in turn was consistent with previously reported findings. Finding comparable acoustic properties in the sounds produced by deaf and hearing vocalizers confirms the presumption that laughter is importantly grounded in human biology, and that auditory experience with this vocalization is not necessary for it to emerge in species-typical form. Some differences were found between the laughter of deaf and hearing groups; the most important being that the deaf participants produced lower-amplitude and longer-duration laughs. These discrepancies are likely due to a combination of the physiological and social factors that routinely affect profoundly deaf individuals, including low overall rates of vocal fold use and pressure from the hearing world to suppress spontaneous vocalizations.
 [DOI: 10.1121/1.2932088]

PACS number(s): 43.66.Sr, 43.70.Gr [CHS] Pages: 472–483

I. INTRODUCTION

A. Laughter and auditory experience

Laughter is a nonverbal mode of communication that occurs on its own as well as in the context of spoken language. It is believed to be common to all humans (Darwin, 1872; Provine and Fischer, 1989; Provine and Yong, 1991), and has been described as being both innate and universal (Hirson, 1995; Provine, 2000). Laughter has been shown to occur in a variety of cultures (e.g., India: Savithri, 2000; Norway: Svebak, 1975; Papua New Guinea: Eibl-Eibesfeldt, 1989; Tanzania: (Rankin and Philip, 1963); United States: Bachorowski, *et al.*, 2001), and to be produced across ages and genders (infants and children: Grammer and Eibl-Eibesfeldt, 1990; Hall and Allin, 1897; Mowrer, 1994; Nwokah, *et al.*, 1993; Sroufe and Wunsch, 1972; adults: Bachorowski *et al.*, 2001; Hall and Allin, 1897; LaPointe *et al.*, 1990).

Recognizable laughter has furthermore been reported in case studies of individual children that were either deaf or both deaf and blind (Black, 1984; Eibl-Eibesfeldt, 1989), as well in seven infants with profound hearing loss, whose vocal production was compared to that of normally hearing individuals in the first 12 months of life (Scheiner *et al.*, 2002; 2004). These developmental results thus provide clear evidence that direct auditory experience with laughter by others is not necessary for the emergence of these sounds. Provine and Emmorey (2006) have provided evidence of basic similarities between laughter in deaf and hearing adults as well, reporting both that the former produced normal-seeming laugh sounds, and that these vocalizations occurred predominantly during pauses and at phrase boundaries occurring in sign-language production. This last finding provides a parallel to Provine's (1993) report that laughter "punctuates" rather than interrupting speech flow in normally hearing talkers. However, only Scheiner *et al.* (2002; 2004) reported acoustic analyses in this earlier work, and their limited sample size did not allow detailed comparison of laugh acoustics in the impaired and normally hearing groups. Inferences about possible effects of experience on finer-grained aspects of vocal acoustics were also hindered by the fact that each of the impaired infants received a hearing aid during the course of the study.

While these reports indicate that auditory (and visual)

[a)]Portions of this work were presented at the Human Behavior and Evolution Society conference, Austin, Texas, June 2005, and the American Society of Primatologists conference, Portland, Oregon, August 2005.

[b)]Author to whom correspondence should be addressed. Present address: Animal Behavior Graduate Group, University of California, Davis, California, 95616, USA. Electronic mail: mmmakagon@ucdavis.edu

 0001-4966/2008/124(1)/472/12/$23.00

experience is not necessary for the emergence of normative laughter, there is also evidence to suggest that social learning can influence the acoustic structure of these sounds. For example, LaPointe *et al.* (1990) noted differences in several measures of laughter in 20- versus 70-year-old adults, including number of laughs, laugh rate, and pitch-related characteristics (see also Apte, 1985). Less direct evidence includes the observation that laughter shows significant acoustic variability both within and among adult vocalizers (Bachorowski *et al.*, 2001; Hall and Allin, 1897). Although age, gender, and individual differences in both vocal-tract physiology and sense of humor are likely to be important contributors (LaPointe *et al.*, 1990; Mowrer *et al.*, 1987; Nwokah *et al.*, 1993), finding this kind of variability also raises the possibility of social or other learning.

On the one hand, then, laughter is considered to be innate, in the limited sense that direct auditory experience with laughter is not necessary to its emergence in recognizable form. On the other hand, relatively few directly relevant acoustical data are as yet available, for instance, from adult humans who have had little or no opportunity to experience laugh sounds. The current work approached this problem by identifying college-age adults with maximally diminished auditory capabilities and comparing their laughter to that produced by peers with normal hearing. Although the two groups are for simplicity referred to as differing in "auditory experience," lack of aural input is probably only one of a number of ways in which the hearing-impaired individuals tested here differed from the control participants. As a result of not hearing their own vocalizations, for instance, these deaf laughers would also have had less opportunity to acquire experience-guided control over concomitant respiratory functions, as well as laryngeal, oral, and other vocal-tract musculature.

B. Basic acoustic properties of laughter

The goal of the study was thus to examine the laughter produced by deaf vocalizers, comparing its acoustic features to laughter from normally hearing individuals. The laugh-elicitation procedures and acoustics measures used were drawn from previous work, relying most heavily on Bachorowski *et al.*'s (2001) study of 97 normally hearing male and female college students. While finding a high degree of acoustic variability both within and among the individual vocalizers (see also Edmonson, 1987), Bachorowski *et al.* also provided quantitative evidence concerning stable features such as a basic distinction between voiced and unvoiced laughters (see also Grammer and Eibl-Eibesfeldt, 1990). The former is laughter based on vowel-like, somewhat melodic sounds produced through regular, synchronized vocal-fold vibrations in the larynx. The latter, in contrast, is laughter based on noisy sounds in which the vocal folds either do not vibrate or vibrate in an irregular, desynchronized fashion. Although laughter has been argued to consist primarily of stereotyped bouts of vowel-like bursts (e.g., Provine and Yong, 1991; but see Kipper and Todt, 2003), Bachorowski *et al.* found that their participants produced a higher proportion of unvoiced or mixed laughs than the voiced variety.

Other findings included that the basic vocal-fold vibration rate fundamental frequency F_0 in voiced laughs was approximately twice that of comparable voiced sounds in spoken language and that neither voiced nor unvoiced laughter showed distinct vowel qualities, such as "ha-ha," "hee-hee," or "ho-ho." Differentiated vowel sounds are largely produced through flexible positioning of the tongue, mandible, and lips to change the resonance characteristics, or formants, of the vocal-tract cavities above the larynx. Bachorowski *et al.* reported little acoustic evidence of these kinds of articulation effects, specifically in finding some variability in the first formant ($F1$), very little in the second ($F2$), and that both formants fell predominantly in the middle of their respective ranges as observed in speech sounds. The conclusion was therefore that laughter is typically characterized by a neutral, "schwa-like" vowel quality, and is likely produced without consistently patterned repositioning of articulatory structures.

C. Nonauditory influences on laughter in deaf vocalizers

Several factors that could alter the laughter of deaf relative to normally hearing participants were also identified. For example, other aspects of vocal production by the deaf have been found to be different than in hearing individuals, including slow, monotone speech with a breathy or harsh quality (e.g., Leder and Spitzer, 1993; Okalidou and Harris, 1999; Osberger and Levitt, 1979; Osberger and McGarr, 1983). These kinds of differences are arguably expected given that normative speech development is heavily dependent both on auditory experience and on social modeling. Some researchers have also highlighted the possibility of deficient laryngeal and oral muscle control in the deaf (LaPointe *et al.*, 1990; Okalidou and Harris, 1999). Such deficiencies could contribute to the slower, elongated vowels reported for deaf speech (Bakkum *et al.*, 1995; Okalidou and Harris, 1999) and might also affect laugh production. Rhythm has also been found to be affected, for example, in phoneme and syllable timing (Rothman, 1976).

Differences in laughter produced by deaf and hearing participants could also occur as a result of individuals in the two groups responding differently to the stimulus material used to elicit laughter. Hearing-impaired persons who use sign language as a primary form of communication share a culture that can be significantly different from that of normally hearing peers, including aspects of humor (e.g., Padden and Humphries, 1990; Ladd, 2003). If so, discrepancies in laugh acoustics could occur as a result of differences in the degree or valence of emotional reactions during experimental elicitation of laughter. Finally, deaf individuals report experiencing social pressure to suppress spontaneous vocalizations, as these can be uncomfortably loud for the hearing (Leder and Spitzer, 1993). In the current work, such tendencies were anticipated to potentially decrease the amount of laughter occurring, increasing the tendency to muffle laugh-

ter sounds, for example, by keeping the mouth closed and arguably producing more laughter that might normally be associated with low-arousal, emotional responses even when vocalizers were experiencing more intense reactions.

While each of these factors could potentially contribute to differences between laughter in deaf and hearing individuals, the documented variability of laugh sounds both within and among individual vocalizers (e.g., Bachorowski *et al.*, 2001) could have the opposite effect. Specifically, given the sample-size limitations inherent to targeting a group as small as congenitally and profoundly deaf college students, a high degree of variability could obscure differences that do exist in laugh sounds occurring in the respective underlying populations. Results of the acoustic analyses will be considered in light of each of these factors, all of which are concluded to likely play some role in the outcomes.

D. The current study

The laughter samples analyzed in the current work were collected from hearing-impaired college students attending Gallaudet University (Washington, D.C.), and from normally hearing students at Cornell University (Ithaca, NY). Laughter was recorded from participants using headworn microphones as these individuals watched a series of comic movie clips. As the goal for the hearing-impaired sample was to identify individuals with the least possible exposure to laugh sounds, screening was quite restrictive. Although Gallaudet is the "first and still only university for deaf and hard of hearing people in the world" (http://www.gallaudet.edu/x251.xml), the restrictiveness of the selection criteria still strongly limited sample size for hearing-impaired participants. Specifically, these individuals were required to have congenital and bilateral hearing loss that placed them in the most severely compromised, "profoundly deaf," category of auditory impairment. Results nonetheless produced telling evidence that characteristic laughter occurs in humans in the virtual absence of auditory experience.

II. METHODS

A. Subjects

Eight female and five male students enrolled at Gallaudet University (GU) and six female and six male students enrolled at Cornell University (CU) were recruited for this study. GU students were recruited with fliers posted on campus, while CU participants were recruited through an experiment-participation website. The recruits were instructed to come to a laboratory on their respective campuses accompanied by a same-sex friend and were tested in pairs. Total initial participation was thus 26 GU and 24 CU students.

All participants were screened for fluency in written English, good or corrected-to-good vision, and the absence of respiratory ailments. GU and CU students reported American sign language (ASL) and English to be their primary or native languages, respectively. GU participants were also asked to report their age at diagnosis of deafness, severity and type of deafness, and history of hearing-aid use. All participants were tested, but only those who met the criteria of being diagnosed in infancy with bilateral and profound deafness were included in the study (with one exception). Profound deafness was defined as a hearing loss of over 90 dB, which corresponds to an inability to understand speech with or without amplification (hearing aids), and an awareness only of vibration rather than of sound. One male GU participant who was congenitally, bilaterally, and severely deaf was also included. Severe deafness was defined as a 71–90 dB loss, which translates to an inability to understand speech without amplification. At this level of deafness, speech can be understood only through a combination of speech-reading and auditory support. This severely deaf participant had never used hearing aids or other auditory facilitation, and his experience with sound was therefore deemed comparable to that of profoundly deaf individuals who did have a history of hearing-aid use.

Recordings from seven GU students were excluded from analysis due to recent hearing-aid use (less then 6 years before), failure to meet the hearing-loss criteria, or because they did not laugh during the session. CU participants were screened for self-reported normal audition, and constituted the hearing group for this study. Data from one CU female were discarded due to poor recording quality. In the end, 19 GU (12 profoundly deaf females, six profoundly deaf males, and one severely deaf male) and 23 CU participants constituted the deaf and hearing groups, respectively.

B. Materials and procedures

1. Stimuli

Eight short movie clips compiled on a digital video disk (DVD) using Mac OSX iMovie and iDVD software were used as stimuli (see Table I). Half of the clips were meant to be funny and were chosen from comedy movies for their laugh-inducing potential. The rest were taken from dramas or science-fantasy films and were meant to be emotion inducing but not humorous. The latter were included in the DVD in order to make the cover story as plausible as possible. Specifically, participants were told that the study was testing the effect of emotion on respiration, and that audiorecording was being used to document each person's breathing for later analysis. In order to appeal to both deaf and hearing students, the clips emphasized physically based action with minimal reliance on dialog. However, all clips did include English-language subtitles. Deaf students viewed the movie clips without sound, while hearing students viewed the clips at a preset, low volume.

2. Apparatus

Participants were seated in heavy-duty, metal and cloth picnic chairs oriented toward a 20 in. color television. Participant vocalizations were recorded using a Special Projects head-worn microphone, with the microphone arm running parallel to the cheek, and the tip positioned 1 in. from the left corner of the mouth. All other recording equipment was located in an adjacent control room. The microphone signal was routed through a Whirlwind SP1×3 microphone splitter, and the two resulting signals were recorded on the left and right channels of a Marantz CDR300, professional-grade

TABLE I. Movie clips used as stimuli listed by movie title, clip description, and clip duration. Clips are labeled as either humorous (h) or nonhumorous (nh), and are listed in order of presentation during the session.

Movie title	Clip description		Dur (s)
Robin Hood: Men in Tights	Robin Hood returns to Locksley only to find his castle is being repossessed	(h)	195
Harry Potter and the Sorcerer's Stone	Harry and Ron battle a troll that has cornered Hermione in the girl's bathroom	(nh)	207
Grumpy Old Men	Max and John engage in a war of pranks	(h)	150
The Trouble with Mr. Bean	Mr. Bean goes to the dentist	(h)	207
Ocean's Eleven	The Ocean's 11 team attempts to blow up a casino vault door	(nh)	255
The Naked Gun	Detective Nordberg has a series of mishaps as he attempts to stop a cocaine deal	(h)	135
Reign of Fire	Young Quinn watches as his mother accidentally wakes a dragon	(nh)	144
Cast Away	Chuck is spotted by a ship while floating in the ocean on a homebuilt raft	(nh)	287

compact disk (CD) recorder. To ensure high-quality recording of laughs produced at any amplitude, the two channels were set at different, standardized recording levels. Recording levels were set prior to each session based on a constant-amplitude, 700 Hz tone produced by a Shure AT15 tone generator with an Audio-Technica AT8202 in-line attenuator set at −10 dB. Recordings were made by using a 44.1 kHz sampling rate and archived on CDs. The movie-clip DVD was played on a Apex AD-660 DVD player, also located in the control room. Acoustic data were first processed using PRAAT acoustics software (Boersma, 2001), and then analyzed with ESPS/WAVES+5.3 ("XWAVES;" Entropic Research Laboratory). Statistical analysis was conducted using the NCSS 2000 (Jerry Hintze, Kaysville, UT) and SAS 9.2 (SAS Institute, Cary, NC) statistics packages.

3. Testing procedure

Participants came to the laboratory in same-sex, friend pairs under the impression that they would be involved in a study investigating a possible link between emotion and breathing. The participants were seated next to each other and told that their only task was to sit back, relax, and watch a series of movie clips as their breath sounds were recorded. The cover story specifically did not mention laughter, thereby helping to ensure that any laugh sounds produced would be spontaneous and natural. Each participant was then asked to complete a short demographic and screening questionnaire, as well as to read and sign a consent form authorizing both audio-recording and subsequent use of audio recorded data. Participants were fitted with head-worn microphones, reminded that their only task was to relax and watch the movie clips, and left in the testing room. Once testing was completed, participants were debriefed as to the true nature of the study and read and signed a complete, more detailed consent form. Only one pair was tested during a given session.

4. Laugh selection and acoustic analysis

Following Bachorowski *et al.* (2001), laughter was defined relatively inclusively as being any perceptible vocal event that an ordinary person would characterize as a laugh sound. Two research assistants extracted laughter from the recordings, in each case comparing recording quality on the left and right channels and selecting the better of the two. Analysis was subsequently restricted to sounds that both assistants identified as laughter. Segments containing vocalizations that directly preceded, directly followed, or overlapped a laughter bout were excluded, as speech has been shown to alter the acoustic properties of laughter (Nwokah *et al.*, 1999).

Again following Bachorowski *et al.* (2001), each laughter file was labeled at the bout and burst levels based on spectrographic representations (illustrated in Fig. 1). A bout was defined as one entire laughter episode, and a burst as a discrete sound (note, syllable, or call) occurring within that episode. Onset and offset times for bouts and bursts were marked with cursor-based labels by one of the two research assistants. Each burst was then labeled as being produced with an "open," "closed," or "mixed" mouth position, with either egressive or ingressive air flow. These determinations were made acoustically, for example, based on the presence or absence of the audible characteristics of nostril air flow for closed-mouth unvoiced sounds and the muffled quality associated with closed-mouth voiced sounds (also following Bachorowski *et al.*, 2001). The mixed-mouth designation was used for bursts in which the laugher alternated between open and closed mouth positions. Sounds that could be produced

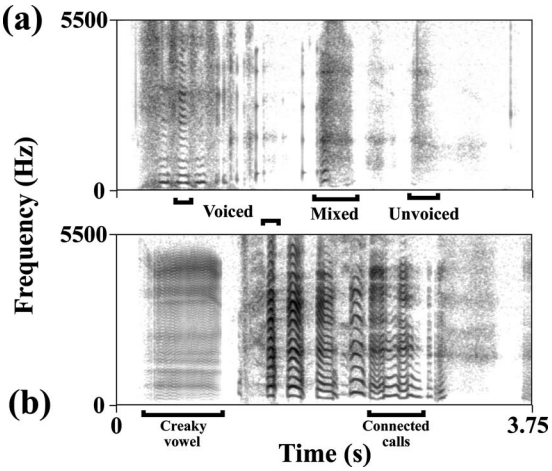

FIG. 1. Narrow band spectrograms of laugh bouts produced (a) by a normally hearing female and (b) by a deaf female. Brackets mark examples of individual bursts classified as either voiced, a mix of voiced and unvoiced, or unvoiced. Spectrograms were created using a 11.025 kHz sampling rate and 0.03 s Gaussian analysis window.

TABLE II. Definitions (and unit labels) of the acoustic measures used.

Analysis level	Measure	Definition
Bout (a laughter episode or series)	Duration	Time between bout onset and offset (s)
Burst (a continuous, discrete sound within a bout)	Duration	Time between burst onset and offset (s)
	Fundamental frequency (F_0)	Lowest-frequency harmonic in a quasiperiodic waveform (Hz)
	Formant frequency ($F1, F2$)	Center frequency of the two lowest formants, where a formant is a resonance of the vocal tract (Hz)
	Percentage voicing (% voicing)	Percentage of analysis frames in a burst from which an F_0 value could be extracted using the xwaves software pitch-extraction algorithm (%)
	Raw amplitude	Mean root-mean-square (rms) value computed over the entire burst (dB)
	Relative amplitude	A normalized amplitude value derived by subtracting a burst's raw rms (dB) amplitude from the rms (dB) value of a constant amplitude, 700 Hz calibration tone recorded on the same channel of the audio recorder using identical input settings

through either open or closed mouth positions were considered ambiguous and were not assigned labels for this analysis.

All duration and classification labels were reviewed before conducting further analyses. We performed further reliability checks approximately 24 months after the first classification based on blind relabeling of a randomly selected sample of 10% of the analyzed bouts (as in Bachorowski *et al.*, 2001). Correlating outcomes for duration (reflecting placement of onset and offset labels) showed this measure to be highly reliable (Pearson's $r=0.999$). Percent agreement (88%) and high reliability (Cohen's *kappa*, calculated in SAS) was also found for mouth position ($\kappa=0.69$). Agreement in labeling air flow direction was lower (64.6%), and reliability was requisitely more modest ($\kappa=0.42$).

Audio files were downsampled to 11.025 kHz prior to making acoustic measurements. Custom-written scripts operating based on onset and offset labels were used to automatically or semiautomatically extract bout durations, interburst durations, "raw" amplitudes, as well as F_0- and formant-related measures at the burst level. All acoustic measures are listed and defined in Table II. Relative burst amplitudes were then calculated as a ratio of absolute amplitude over the duration of the burst to the amplitude of the 700 Hz calibration tone recorded on the corresponding channel at the beginning of the session. Percentage-voicing outcomes were based on an automatic F_0 extraction routine native in the XWAVES program and were used to classify each bout and burst as unvoiced, mixed, or voiced [see Fig. 1(a)]. An unvoiced sound was one containing 25% or less voicing, mixed sounds contained between 25% and 75% voicing, and voiced sounds had 75% or more voicing. Percentage-voicing values of bursts within each bout were used to compute mean percentage voicing at the bout level. Formant frequencies were extracted for all bursts produced by deaf laughers with sufficient voicing to allow this analysis and from a representative sample of bursts produced by hearing laughers. Formant measurement procedures followed those outlined in Bachorowski *et al.* (2001) and were based on formant-peak locations in linear predictive coding spectra (ten coefficients, 40 ms Hamming analysis window, autocorrelation method) overlaid on fast Fourier transform (FFT) spectra (40 ms, Hanning analysis window) that were computed over the same waveform segment (see also Owren and Bernacki, 1998).

Statistical comparisons relied primarily on repeated-measure ANOVAs using participant identity as the subjects factor, gender as a within-group factor, and hearing status as a between-group factor. Variance distribution analyses were also conducted for all measures, in order to ensure that group differences were not traceable to any one individual. Statistical comparisons at the bout level focused on voicing classification, percentage-voicing, duration, and burst-type composition. At the burst level, comparisons included mouth position, air-flow direction, and voicing classifications, as well as duration, interburst interval, and relative amplitude.

III. RESULTS

A. Bout-level outcomes

A total of 278 laughter bouts produced by deaf participants and 734 laughter bouts produced by hearing participants were analyzed. Table III provides descriptive statistics for bout-level analyses, shown by hearing status and gender. For bouts from deaf laughers, 78.4% were classified as unvoiced, 16.9% as mixed, and 4.7% as voiced. Similarly, 71.3% of bouts from hearing laughers were unvoiced, 25.7% were mixed, and 3.0% were voiced. The number of bouts of each type did not vary by hearing status or gender nor were there significant effects of these factors on mean percentage voicing per bout. However, not all participants produced laughter bouts in all three voicing categories.

Duration analysis revealed that laughter bouts from deaf participants ($M=2.03$ s, SD=2.51) were significantly longer than laughter bouts from hearing participants ($M=1.50$ s, SD=1.50), $F(1,1011)=5.06$, $p=0.03$. This difference was also evident in separate analyses of unvoiced bouts, $F(1,740)=6.39$, $p=0.016$, but not mixed bouts, $F(1,235)=0.03$, $p=0.86$, or voiced bouts, $F(1,34)=5.30$, $p=0.61$. No significant differences were found in bout duration by gender.

B. Burst-level outcomes

Descriptive statistics for 1296 total bursts from the deaf group and 3461 total bursts from the hearing group are shown in Table IV. A clear majority of bursts were unvoiced (86.7% and 68.3% for laughter from deaf and hearing par-

TABLE III. Means and standard deviations (in parentheses) of measures used for bout-level analyses. Data are separated according to hearing status (deaf vs hearing) and gender (male vs female).

	Deaf males (n=7)			Hearing males (n=12)		
Total bouts (n)	91			372		
Bursts per bout (n)	5.84 (6.95)			1.57 (1.64)		
Percentage voicing (%)	15.14 (29.11)			19.05 (25.48)		
Bout type	Unvoiced	Mixed	Voiced	Unvoiced	Mixed	Voiced
Percentage by type (%)	80.22	9.89	9.89	69.89	25.81	4.30
Duration (s)	2.32 (0.34)	2.15 (1.20)	1.53 (0.62)	1.46 (1.50)	2.02 (2.00)	0.66 (0.36)
	Deaf females (n=12)			Hearing females (n=11)		
Total bouts (n)	187			362		
Bursts per bout (n)	1.92 (0.18)			1.42 (1.32)		
Percentage voicing (%)	14.21 (21.98)			14.64 (20.35)		
Bout type	Unvoiced	Mixed	Voiced	Unvoiced	Mixed	Voiced
Percentage by type (%)	77.54	20.32	2.14	72.65	25.69	1.66
Duration (s)	1.94 (2.55)	2.10 (0.34)	1.47 (1.23)	1.27 (1.27)	1.89 (1.35)	0.65 (0.82)

ticipants, respectively), a smaller proportion were mixed (7.1% and 20.8%), and many fewer were voiced (6.3% and 11.0%). Deaf laughers produced a significantly higher proportion of unvoiced bursts, $F(1,4757)=5.34$, $p=0.03$, and fewer mixed bursts, $F(1,4757)=11.14$, $p=0.002$, than did hearing laughers. Gender had no effect on the proportion of each type, either for unvoiced, mixed, or voiced bursts. All participants produced unvoiced bursts, 16 of 18 deaf and 22 of 23 hearing participants produced mixed bursts, and 9 deaf and 22 hearing participants produced voiced bursts. Individuals who did not produce mixed bursts also produced no voiced bursts.

Overall, duration of bursts did not differ between the deaf ($M=0.37$ s, SD=0.74) and hearing groups ($M=0.25$ s, SD=0.49), nor was there a gender effect. However, these outcomes were influenced by the large proportion of unvoiced laughs recorded. When analyzed by category, duration of unvoiced bursts did not differ between groups, but deaf laughers produced both longer voiced, $F(1,459)=6.40$, $p=0.018$, and mixed bursts, $F(1,811)=10.10$, $p=0.003$. Interburst intervals were also longer in laughter from the deaf group ($M=0.24$ s, SD=0.51) than in laughter from the hearing group ($M=0.16$ s, SD=0.25), $F(1,3731)=10.85$, $p=0.002$. However, this outcome held only for intervals that followed unvoiced bursts, $F(1,2610)=14.05$, $p=0.001$. The rate of laughter production (i.e., number of bursts per seconds) varied by hearing status, $F(1,1062)=14.27$, $p<0.001$, with mean rates of 2.7 and 3.8 bursts/s produced by deaf and hearing laughers, respectively. However, laughter rate did not differ by gender.

The mean relative amplitude of bursts produced by deaf participants ($M=0.60$ dB, SD=0.16) was significantly lower than that of hearing participants ($M=0.74$ dB, SD=0.21), $F(1,4755)=20.37$, $p<0.001$. No gender differences were found on this measure. Mean relative amplitudes were significantly lower in laughter produced by deaf participants than in hearing participants in the case of unvoiced bursts, $F(1,3485)=22.62$, $p<0.0001$, and voiced bursts, $F(1,457)=4.77$, $p=0.038$ bursts, but not for mixed bursts.

TABLE IV. Means and standard deviations (in parentheses) of measures used for burst-level analyses. Data are separated according to hearing status (deaf vs hearing) and gender (male vs female).

	Deaf males (n=7)			Hearing males (n=12)		
Total bursts (n)	531			1730		
Duration (s)	0.21 (0.23)			0.22 (0.17)		
Burst type	Unvoiced	Mixed	Voiced	Unvoiced	Mixed	Voiced
Percentage by type (%)	85.31	5.02	9.60	66.47	21.27	12.26
Duration (s)	0.19 (0.22)	0.28 (0.19)	0.31 (0.28)	0.23 (0.18)	0.21 (0.14)	0.16 (0.16)
%Voicing	0.49 (2.76)	46.45 (13.36)	95.40 (5.80)	2.36 (6.10)	47.22 (15.93)	90.97 (8.17)
	Deaf females (n=12)			Hearing females (n=11)		
Total bursts (n)	765			1731		
Duration (s)	0.27 (0.24)			0.18 (0.20)		
Burst type	Unvoiced	Mixed	Voiced	Unvoiced	Mixed	Voiced
Percentage by type (%)	87.58	8.50	3.92	70.02	20.34	9.64
Duration (s)	0.27 (0.20)	0.29 (0.20)	0.39 (0.69)	0.20 (0.16)	0.16 (0.11)	0.14 (0.43)
%Voicing	1.22 (4.28)	45.88 (15.72)	91.55 (7.81)	1.47 (4.92)	49.39 (15.10)	90.40 (8.21)

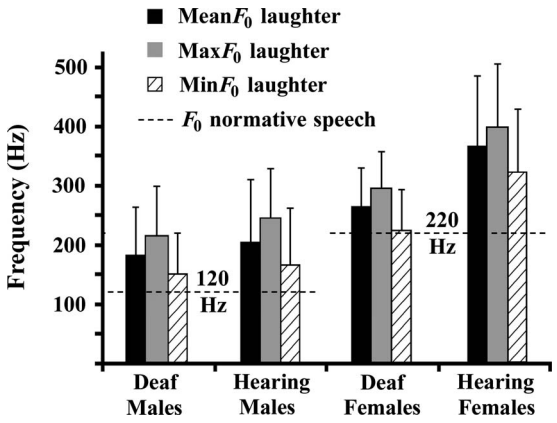

FIG. 2. Means and standard deviations are shown for the meanF_0, maxF_0, and minF_0 measures for laughter from deaf and normally hearing males and females. These results can be compared to approximate, normative F_0 values of 120 and 220 Hz, respectively, for male and female speech (e.g., Baken and Orlikoff, 1999).

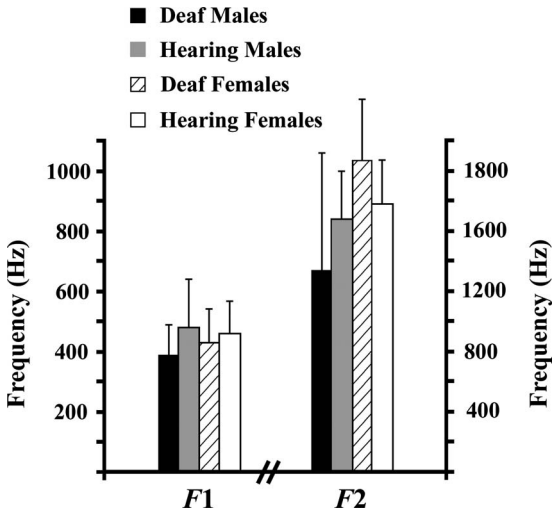

FIG. 3. Mean frequency values of $F1$ and $F2$ for all analyzable bursts from deaf males, hearing males, deaf females, and hearing females.

Laughers from each group were judged to produce bursts with open, closed, and mixed mouth positions, as well as both egressively and ingressively. For deaf laughers, 41.2% of bursts were produced with an open mouth, 56.2% with a closed mouth, and only 0.002% with a mixed mouth position. Mouth position was not acoustically evident in the remaining 2.6% of bursts from these individuals. Hearing laughers produced 33.0% open-mouth bursts, 64.4% closed-mouth bursts, 2.5% mixed-mouth bursts, and 8% were unidentifiable. The majority of bursts were deemed to show egressive air flow, including 67.3% of bursts from deaf laughers and 72.7% from hearing laughers. However, a substantial proportion of bursts was judged to be ingressive, including 22.1% from the deaf group and 17.0% from the hearing group. Most of the bursts judged to be ingressive were also unvoiced (approximately 86.3% for the deaf group and 75.3% for the hearing group). It was not possible to gauge air-flow direction from the acoustic evidence for 10.6% of the bursts from deaf laughers and 10.3% of the bursts from hearing laughers.

C. F_0 and formant outcomes

F_0 measurements were extracted from voiced parts of bursts containing over 1% voicing. Because the majority of bursts recorded were unvoiced, inclusion of bursts with less then 25% voicing served to increase the sample size. The resulting sample consisted of 108 bursts by deaf males (including 30 bursts with less then 25% voicing), 767 bursts by hearing males (including 248 bursts with less then 25% voicing), 175 bursts by deaf females (including 80 bursts with less then 25% voicing), and 647 bursts by hearing females (including 128 bursts with less then 25% voicing). Figure 2 shows means and standard deviations for mean (meanF_0), minimum (minF_0), and maximum (maxF_0) F_0 outcomes in relation to typical values for male and female speech as reported in the scientific literature.

Not surprisingly, bursts produced by males (M =200.4 Hz, SD=82.9) showed significantly lower overall meanF_0 values than did bursts produced by females (M =340.6 Hz, SD=112.6), $F(1,1619)=21.13$, $p<0.0001$. However, meanF_0 values were also significantly lower in laughter produced by deaf (M=228.2 Hz, SD=82.2) versus hearing (M=275.2 Hz, SD=125.1) participants, $F(1,1619)=6.51$, $p=0.015$. While there was no difference in meanF_0 between deaf males (M=179.8 Hz, SD=81.7) and hearing males (M=203 Hz, SD=82.8), values from deaf females (M=258.5, SD=66.6) were significantly below those of hearing females (M=360.4 Hz, SD=112.5), $F(1,780)=9.46$, $p<0.006$.

Results of analyses of maxF_0 and minF_0 values paralleled the findings for meanF_0. While F_0 values were somewhat lower in deaf males (maxF_0: M=213.7 Hz, SD=91.4; minF_0: M=150.0 Hz, SD=76.2) than in hearing males (maxF_0; M=244.2 Hz, SD=107.3; minF_0: M=164.8, SD =69.2), these differences were not statistically significant. Nonetheless, F_0 values were clearly lower in deaf females (maxF_0: M=294.6 Hz, SD=69.3; minF_0: M=223.5 Hz, SD =76.2) than in hearing females (maxF_0: M=395.4 Hz, SD =122.29; minF_0 M=319.9 Hz, SD=108.2). Statistical comparisons revealed that these differences were significant both for maxF_0, $F(1,780)=9.30$, $p=0.007$, and for minF_0, $F(1,780)=7.87$, $p<0.011$.

Formant-frequency measurements proved to be more problematic, producing a significantly smaller sample. The difficulties were traceable particularly to the relatively low amplitude of laughter produced by deaf participants. Low signal-to-noise ratios ruled out analysis of formants in unvoiced bursts, as well as eliminating a number of the voiced bursts in this modestly sized sample. Analyzing all bursts with 1% or more voicing yielded values for 69 bursts from five deaf males, 95 bursts from 15 hearing males, 80 bursts from 13 deaf females, and 36 bursts from six hearing females. Mean frequencies of the first ($F1$) and second ($F2$) formants were computed separately for each participant, with resulting grand means shown in Fig. 3. Statistical comparisons revealed no significant differences by hearing status or gender for either $F1$ or $F2$. While there was no indication of a difference between deaf and hearing males or between deaf

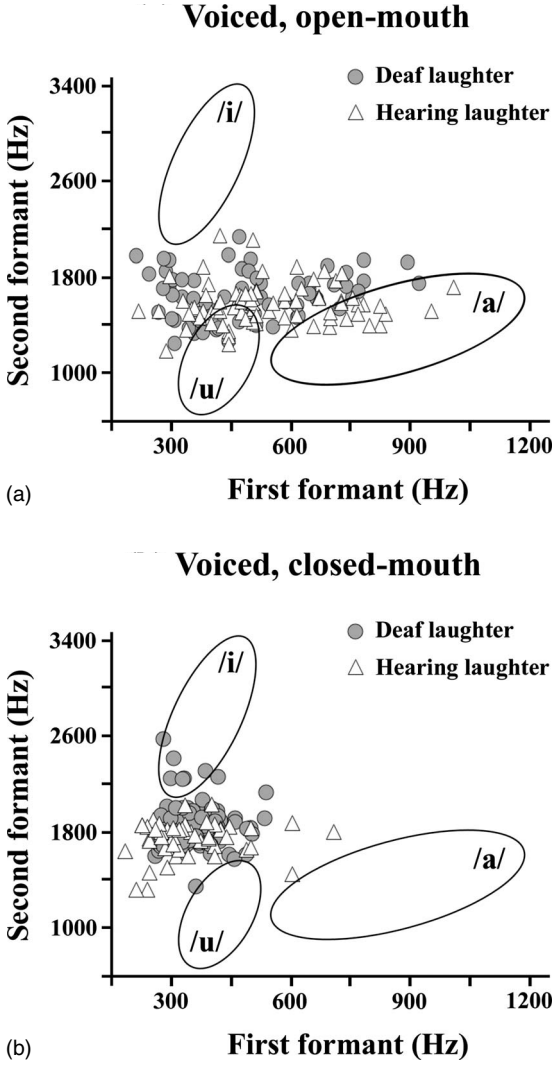

FIG. 4. Mean frequency values of $F1$ and $F2$ for individual bursts from deaf and hearing laughers producing (a) open-mouthed laughs and (b) closed-mouthed laughs with over 1% voicing. Ellipses mark the approximate boundaries of vowel-space variation in normally hearing talkers of American English (after Hillenbrand *et al.*, 1995).

and hearing females, the absence of an overall gender difference likely reflects the small sample sizes and large variances associated with some of these values.

More importantly, mean formant frequencies for these voiced laughter segments fell close to the expected $F1$ and $F2$ values for schwa sounds, which for males are approximately 500 and 1500 Hz, respectively, and approximately 590 and 1775 Hz for females. Individual voiced segments clustered around the center of American-English vowel space, as illustrated in [Fig. 4]. This figure shows open—[Fig. 4(a)] and closed-mouth (Figure 4(b)) bursts separately, plotted by $F1$ and $F2$ values. Superimposed ellipses redrawn from Hillenbrand *et al.* (1995) illustrate the range of variation associated with adult-male vowels /a/, /i/, and /u/, which form the approximate boundaries of the vowel space (female values are somewhat higher). The observations of greatest interest are that the large majority of laugh sounds are centrally located, and that the variation that does occur is largely in $F1$ frequency. While these $F1$ values can fall outside the typical schwa range, contrasts in vowel-quality are considered to reflect the relationship between $F2$ and $F1$ frequencies, with both formants showing a wide range of values (e.g., Ladefoged, 2006).

IV. DISCUSSION

This study provides an acoustic characterization of laughter produced by congenitally and profoundly deaf college students and normally hearing control participants. Overall, the results were similar to those previously reported for normally hearing adults (Bachorowski *et al.*, 2001; Mowrer *et al.*, 1987; Vettin and Todt, 2004). For example, both groups showed a high degree of acoustic variability, elevated mean F_0's, and formant values that were consistent with neutral, unarticulated vocal-tract positions. Some differences were also found, however, for instance associated with temporal, F_0, amplitude, and percentage-voicing measures. The following sections elaborate on these findings and discuss their implications for laughter in deaf vocalizers. The overall conclusion is that auditory experience, whether with sounds produced by others or by the vocalizers themselves, is not necessary for laughter to emerge in deaf individuals.

A. Laughter in deaf and hearing participants

1. Similarities

Acoustic variability. Previous acoustic analyses have indicated that laughter is highly variable at both bout and burst levels, including degree of voicing (Bachorowski *et al.*, 2001), mouth position (Bachorowski *et al.*, 2001), air-flow direction (Bachorowski *et al.*, 2001; Nwokah *et al.*, 1999), and both temporal and F_0 characteristics (Bachorowski *et al.*, 2001; Mowrer *et al.*, 1987). The laugh sounds recorded here were similarly variable, both replicating the earlier findings and extending those results to deaf laughers.

For example, both deaf and hearing participants produced bursts that could range from fully unvoiced to fully voiced. Some individuals in both groups produced bursts that were primarily of one type or another, while others produced sounds from all three categories. However, there was no reason to conclude that participants were limited in the degree of voicing they could potentially produce in their bursts. Most bouts and bursts produced by both deaf and hearing participants were unvoiced, a smaller number were mixed, and relatively few were purely voiced. This is the same order observed by Bachorowski *et al.* in their larger sample of normally hearing laughers, although higher proportions of voiced bouts and bursts were found in that study.

Similarly, bursts in both the deaf and hearing groups could be produced with open, closed, or mixed mouth positions and with either egressive or ingressive airflow. Mouth-position findings were similar to those reported by Bachorowski *et al.* (2001), although reliability was not quite as high in the current work as in this previous report. However, both studies have found most of the laughs being produced with the mouth closed, a significant number being produced with the mouth open, and only a few showing a mixed mouth position. Both deaf and hearing laughers scored here were found to not only produce a majority of egressive sounds, but also showed a nontrivial rate of ingressive sounds. This find-

ing contrasts with some earlier studies arguing that ingressive laugh sounds are extremely rare (e.g., Provine and Yong, 1991) and may also be the first case in which air-flow direction has actually been coded and quantified. This outcome should also be interpreted cautiously, however, as reliability was lower than desired for this measure, and the validity of the judgments made could not be assessed. The outcomes are included mainly as an additional point of comparison for the hearing and deaf participants, as well as to highlight the need to specifically investigate this dimension of laughter production in the future work.

Laughter in both groups was also characterized by significant temporal variability at each level of analysis. At the bout level, laughter in deaf participants lasted a minimum of 0.08 s and a maximum of 24.6 s. Laughter bouts in hearing participants were as short as 0.04 s and as long as 12.4 s. At the burst level, laughs ranged from 0.004 to 3.06 s for deaf laughers and from 0.002 to 4.02 s for hearing laughers. Considerable variation was also present in temporal factors such as bout and burst durations, with interburst intervals being greater in both laugh samples than in previous reports (cf. Bachorowski *et al.*, 2001; Mowrer *et al.*, 1987). These discrepancies may at least partly reflect inter- and intraindividual differences in intensity of response to the particular stimuli used in the various studies (Mowrer, 1994).

In the current work, mean laugh-production rates for hearing participants (3.82 bursts/s) were somewhat lower than those reported by Bachorowski *et al.* (2001) (4.37 bursts/s), but nonetheless higher than reported rates of speech (3.26 syllables/s) (Venkatagiri, 1999). Mean rates were lower among deaf laughers (2.82 bursts/s), perhaps reflecting that vocal production rates are generally slower among deaf than among hearing vocalizers (Leder and Spitzer, 1993; Okalidou and Harris, 1999; Osberger and Levitt, 1979; Osberger and McGarr, 1983). Possible reasons for these findings are discussed below.

F_0 *measures*. Several previous studies (e.g., Bachorowski *et al.*, 2001; Provine and Yong, 1991; Vettin and Todt, 2004) have found the mean F_0 of laughter in hearing individuals to be much higher than the reported mean F_0 of normative speech. In fact, large F_0 range has been described as a defining characteristic of laughter (Mowrer *et al.*, 1987). Laughter from deaf vocalizers was also characterized by large F_0 ranges. At the burst level, mean F_0 values for laughter produced by deaf females spanned 456.7 Hz. Similarly, mean F_0 values for laugh bouts produced by deaf males spanned 460.9 Hz. However, ranges of mean F_0 values were even greater among hearing laughers, being 742.4 Hz for female bursts and 550.0 Hz for male bursts.

In line with these characteristically large F_0 ranges, mean F_0's in laughter have been reported to be more than a doubling of comparable values in speech (Mowrer *et al.*, 1987). In the current study, mean F_0's were elevated in both deaf and hearing groups (see Fig. 2), although they were not twice as high as prototypical values from normative speech (e.g., 120 and 220 Hz for males and females, respectively; Baken and Orlikoff, 1999). Mean F_0 values in the speech of deaf individuals are thought to be similar to that of hearing talkers, but also vary significantly by individual talker (e.g., Lane *et al.*, 1997). Finding more or less comparable F_0 values in the laughter of deaf and hearing males, but lower F_0's in the laughter of deaf versus hearing females is therefore somewhat difficult to interpret. Taken at face value, the outcomes could indicate that laughter in deaf females does not show the same degree of F_0 increase as found in hearing females or in males overall. On the other hand, the observed difference could reflect chance effects of a high degree of individual variation, that deaf females were less engaged by the stimulus material used for laugh induction, or were showing a greater degree of damping or inhibition of their vocal responses to that material (see below).

Lack of articulation. Although the evidence is indirect, acoustic results for laughter from both deaf and hearing groups indicate an overall lack of supralaryngeal articulatory effects. For example, plotting the formants extracted from voiced laughs in $F1$-$F2$ vowel space (see Fig. 4) reveals close clustering of $F2$ values for both open- and closed-mouth versions. However, while $F1$ frequencies from closed-mouth laughter are similarly clustered, there is a greater variation in open-mouth $F1$ values. In vowel production, which has been extensively studied by using both direct and indirect methods, $F2$ frequency primarily reflects the front-to-back location of a vocal-tract constriction created by the tongue, whereas $F1$ frequency is largely determined by mouth-opening size and overall tongue height (e.g., Rosner and Pickering, 1994). Extending those principles to laughter, the overall location and the relative homogeneity in $F2$ values within the vowel space are consistent with an unconstricted vocal tract and concomitant schwalike auditory quality for both open- and closed-mouth versions.

These vowel-production principles can also make sense of finding that mouth position is critical for $F1$. On the one hand, keeping the mouth closed implies a raised jaw and little or no variation in tongue height or mouth opening [Fig. 4(b)]. $F1$ values should thus be relatively invariant for each individual laugher, and to a lesser degree, across individuals. On the other hand, lowering the jaw and parting the lips creates the possibility of significant variation in both tongue height and mouth-opening size. Given that each of these parameters can be expected to vary both within and among individual laughers, the heterogeneity observed for $F1$ values in open-mouth laughter [Fig. 4(a)] is also understandable. Overall, these outcomes are consistent with Bachorowski *et al.*'s (2001) formant-related findings for laughter from normally hearing vocalizers (see Fig. 6 in that article), and inconsistent with attributing a range of vowel qualities to these sounds (e.g., Provine, 2000; Provine and Yong, 1991).

2. Differences

Despite the overall similarity in acoustic properties of laughter shown by deaf and hearing participants, some differences were also found. These particularly included aspects of duration, amplitude, percentage voicing, and F_0. In several cases, those differences may be traceable to deficiencies in laryngeal and oral muscle control resulting from the relatively low rates of vocalization occurring in profoundly deaf individuals. Although our deaf participants' use of speech was not specifically investigated, all lived in a deaf commu-

nity in which ASL is the primary form of language communication, and all reported ASL rather than spoken English to be their primary, native language.

Researchers investigating vocal production in deaf talkers have suggested that laryngeal and oral deficiencies can affect the temporal characteristics of their speech (LaPointe *et al.*, 1990; Okalidou and Harris, 1999). Since speech and laughter utilize the same physical apparatus (Nwokah *et al.*, 1999), vocal anatomy in the deaf participants tested here may have been affected by similar constraints. One possible example emerging in the results was the longer interburst intervals found in deaf laughers, which could conceivably be analogous to interphonemic and intersyllabic temporal distortions found in deaf talkers (Rothman, 1976). However, this phenomenon only occurred following unvoiced bursts, suggesting that the two phenomena are not directly related.

A more likely parallel was revealed in finding that deaf laughers produced longer-duration voiced bursts than did hearing laughers. Figure 1(b) shows two potentially relevant examples, the first being a sustained, creaky vowel sound occurring before the laugh begins (which was not scored as a laugh). This event is a likely analog to an unvoiced exhalation or inhalation that hearing vocalizers can routinely produce just before laughter onset, but with this deaf female's vocal folds becoming engaged and vibrating somewhat irregularly. Later in the same bout, voiced bursts that would likely be separated in a hearing person's laughter are connected by ongoing, and arguably artifactual, phonation. Here again, it appears that voicing is occurring at points where the vocal folds would have become disengaged in a hearing person. These phenomena may thus be mechanistically related to the slower, elongated vowels reported for deaf speech (Bakkum *et al.*, 1995; Okalidou and Harris, 1999).

While a number of studies have reported that the mean speaking F_0 of deaf individuals does not differ from that of hearing talkers (e.g., Waldstein, 1990), others have found F_0 values to be higher in the former (e.g., Leder and Spitzer, 1993). These conflicting results may reflect the higher individual variability noted earlier for deaf talkers, who, for instance, show greater variability in their experience with speech (Lane *et al.*, 1997). Current results showed the converse, namely, that the range of mean F_0 values was smaller among deaf than among hearing laughers, differences of almost 200 and 100 Hz for females and males, respectively. The next section considers a likely cause, namely, that more purely social factors may have influenced the vocal behavior of deaf participants during testing.

Another possibility to consider is that laughter has been shown to occur in the context of language communication in both deaf signers and hearing talkers (e.g., Provine and Emmorey, 2006; Provine and Yong, 1991). While any signing that may have been produced by deaf participants in the current work would not have affected recovery of laugh sounds, that was not the case for the talking that sometimes occurred in hearing participants. For the latter, laugh sounds occurring in the context of speech were specifically excluded from analysis, which may have served to inflate the differences observed between deaf and hearing laughers on measures such as proportion of unvoiced versus voiced laughter, and F_0 values. However, the proportions of voiced laughter documented for normally hearing listeners at both bout and burst levels remained below those reported by Bachorowski *et al.* (2001), which argues against the possibility that any such effects had a major influence on current outcomes. Nonetheless, the safest conclusion may be that the results reflect a conservative estimate of the degree of similarity documented between laughs from deaf and hearing participants.

B. Social factors

While temporal aspects of the laughter recorded from deaf vocalizers may have been affected by more organic factors, group differences in relative amplitude, percentage voicing, and F_0 may also reflect that deaf participants were reacting less strongly than hearing participants to the humorous stimuli being presented (Mowrer *et al.*, 1987). In other words, the material may not have been sufficiently funny to the deaf participants to elicit as much spontaneous laughter as shown by hearing individuals.

Another possibility is that the deaf participants may have been actively inhibiting their vocal responses. While amplitudes of infant vocalizations are reported not to differ for deaf and hearing babies (Oller *et al.*, 1985), deaf adults report being actively concerned about inadvertently vocalizing too loudly and that they feel social pressure to avoid doing so (Leder and Spitzer, 1993). In addition, being unable to monitor their own production, many deaf individuals are self-conscious about the quality of their utterances and vocalizations, fearing that they may sound "funny" (Higgins, 1980, p. 94). In the current situation, this kind of social conditioning may have produced vocal suppression among the deaf participants. If so, likely effects would include not only lower-amplitude laughter, but also less voicing, and lower F_0 values in bouts and bursts in which phonation did occur. Although only one of the deaf participants explicitly reported self-consciousness and concern in the testing situation, the participants may have been under-reporting such feelings or exhibiting unconsciously controlled vocal suppression.

Emotional "contagion" could also have played a role in either one or both of the testing situations. Previous research has shown that laughter occurs much more frequently in social than in solitary settings (Provine and Fischer, 1989), and that friends, in particular are likely to trigger laughter in one another by laughing (Smoski and Bachorowski, 2003a; 2003b). Participants were tested in pairs specifically to encourage the occurrence of laughter and also targeted same-sex friends as the dyads most likely to produce laughter under these sorts of laboratory circumstances (Owren and Bachorowski, 2003). Taking this approach thus introduced the possibility that some of the laughter might be catalyzed by the social nature of the situation rather than reflecting positive responses to the humor *per se*. In the deaf participants, the trigger could be seeing the testing partner laughing, while in the hearing participants, both the sight and the sound of laughter could be involved. It is at this point impossible to know whether deaf or hearing participants would be most affected, although it seems likely that contagion resulting from visual stimulation would be less than that from

the combination of visual and auditory effects. If so, this difference could also have contributed to the deaf individuals experiencing less intense responses to the material presented than did hearing participants.

V. CONCLUSIONS

Overall, results of this study confirm that the occurrence of human laughter in fundamentally species-typical form does not depend on vocalizers having significant exposure either to laugh sounds or to other auditory input. Given the level of hearing impairment shown by our deaf participants, the sounds of their own laughter could also not be expected to provide sufficient auditory feedback to influence or tune the respiratory and vocal musculature involved in the production process. Acoustic analysis revealed that both deaf and hearing participants produced laughter, showing a number of critical features described by Mowrer *et al.* (1987) and Bachorowski *et al.* (2001). For example, neither group produced laughter that could be considered stereotyped (cf., Provine and Yong, 1991), instead exhibiting significant acoustic variability in these sounds. Furthermore, both kinds of participants produced unvoiced, mixed, and voiced laughter, with each group making these sounds with the mouth either open or closed. Both deaf and hearing vocalizers also produced more unvoiced than voiced laughter, and when voiced laughter did occur, the F_0 values involved were significantly higher than expected in normative speech. Finally, neither group showed evidence of significant supralaryngeal articulation effects.

The study thus produced firm support for the characterization of laughter as a biologically grounded behavior, although providing only indirect evidence concerning the nature of the mechanism involved. Provine and Yong (1991) and Provine (2000) have likened laughter to the fixed- or stereotyped-action patterns proposed by ethologists to underlie behavior in many nonhuman species (see Eibl-Eibesfeldt, 1989). The current results are broadly compatible with that characterization, but also contradictory in confirming previous evidence of a high degree of acoustic variability in the behavior. This degree of variability would not be expected from an action-pattern-like control system, whose hallmark should instead be a marked degree of stereotypy. The variability observed here is furthermore not attributable to the overall absence of auditory experience in the deaf participants, given similar findings for hearing participants and in other studies (Bachorowski *et al.*, 2001; Mowrer *et al.*, 1987). Conversely, in light of the current results, the variability is also not attributable to auditory learning effects among the hearing.

The acoustic differences that were found between laughter in deaf and hearing participants appear more likely to be traceable to the effects of deafness on vocal-fold response properties and other aspects of vocal production (LaPointe *et al.*, 1990; Okalidou and Harris, 1999) than to lack of auditory experience with laugh sounds. Social effects, such as suppression of spontaneous vocalization, are also likely to have influenced the sounds produced by the deaf participants. It will therefore be critical to address the issue of comfort level for deaf vocalizers during future recording work, which would be expected to yield laughs with significantly higher amplitudes and percentage-voicing scores. This problem dovetails with an issue that has not yet been adequately addressed for any nonverbal vocalization, namely, how overall arousal level affects acoustic realization of various sound types. An underlying assumption in the current work has been that greater response intensities produce higher-amplitude laughter, as well as a higher probability of voiced, rather than unvoiced, bursts and bouts. While intuitively plausible based on everyday experience, specific empirical testing is strongly needed.

Similarly, while the focus of this study was the acoustic properties of laughter, there is an evidence that specific social contexts can affect these sounds. Vettin and Todt (2004) have, for instance, proposed that laughter produced during social conversation is acoustically different from laugh vocalizations that are more specifically associated with humor and elicited under laboratory conditions. These differences are presumed not to be traceable to relative differences in vocalizer arousal level, an issue that remains to be examined in this circumstance as well. A further complication is that, paralleling effects with smiling, normally hearing humans are believed to be able to produce both spontaneous and more volitional versions of laughter (e.g., Keltner and Bonanno, 1997). In other words, in the course of acquiring volitional control over vocal production during infancy and early childhood (see Owren and Goldstein, 2008). developing humans are also likely to gain the ability to routinely produce simulated laugh sounds at appropriate moments in the furtherance of social motivations and goals. While likely a routine component of effective social interaction, volitional laughter is probably very difficult to separate empirically from truly spontaneous versions. Working with hearing-impaired laughers arguably provides a means of doing just that, specifically in cases where lack of auditory feedback and significant practice in volitional control of vocal production may rule out the occurrence of volitional laugh sounds.

Understanding the biological origins and normative features of human laughter thus requires disentangling a number of issues, including the nature of the human biological endowment underlying normative laughter, the role of physiological factors such as vocal-fold response and vocal-tract motor control, the impact of social proscriptions concerning vocal production, the influence of vocalizer arousal and emotional state, and the degree of spontaneity versus volitional control in a given instance of laughter production. The current study, which significantly strengthens the case for laughter as a biologically grounded, universal human behavior, may also prove helpful in eventually addressing these issues. While the work is only a first step in many ways, it nonetheless illustrates that laughter can be recorded from deaf vocalizers under controlled circumstances, and then fruitfully compared to sounds produced by normally hearing control participants. Refining and expanding the techniques involved may make this overall approach a potent tool in the larger endeavor of achieving a scientific understanding of human laughter.

ACKNOWLEDGMENTS

This work was supported in part by NIMH Prime Award No. 1 R01 MH65317-01A2, Subaward No. 8402-15235-X, by the Center for Behavioral Neuroscience, STC Program of the National Science Foundation under Agreement No. IBN-9876754, and by a grant from the Field of Psychology Graduate Student Research Award Fund at Cornell University to M.M.M. We thank Raylene Lotz, our project assistant at Gallaudet University, as well as Amy Chu, Danielle Inwald, Douglas Markant, and Maria Boresjsza-Wysocka, our project assistants at Cornell University. John Anderson, Erik Patel, three anonymous reviewers, and Christine Shadle provided valuable comments on earlier versions of this article.

Apte, M. L. (**1985**). *Humor and Laughter: An Anthropological Approach* (Cornell University, Ithaca).

Bachorowski, J.-A., Smoski, M. J., and Owren, M. J. (**2001**). "The acoustic features of human laughter," J. Acoust. Soc. Am. **110**, 1581–1597.

Baken, R. J., and Orlikoff, R. F. (**1999**). *Clinical Measurement of Speech and Voice* (Singular, New York).

Bakkum, M. J., Plomp, R., and Pols, L. C. W. (**1995**). "Objective analysis versus subjective assessment of vowels pronounced by deaf and normal-hearing children," J. Acoust. Soc. Am. **98**, 755–762.

Black, D. W. (**1984**). "Laughter," J. Am. Med. Assoc. **252**, 2995–2998.

Boersma, P. P. G. (**2001**). "Praat, a system for doing phonetics by computer," Glot Int. **5**, 341–345.

Darwin, C. (**1872**). *The Expression of Emotion in Man and Animals* (Murray, London).

Eibl-Eibesfeldt, I. (**1989**). *Human Ethology* (Aldine Transaction, New York).

Edmonson, M. S. (**1987**). "Notes on laughter," Anthro. Ling. **29**, 23–33.

Grammer, K., and Eibl-Eibesfeldt, I. (**1990**). "The ritualization of laughter," *Naturlichkeit der Sprache und der Kultur: Acta Colloquii*, edited by W. Koch (Bochum, Brockmeyer), pp. 192–214.

Hall, G. S., and Allin, A. (**1897**). "The psychology of tickling, laughing, and the comic," Am. J. Psychol. **9**, 1–41.

Higgins, P. C. (**1980**). *Outsiders in a Hearing World: A Sociology of Deafness* (Sage, Beverly Hills).

Hillenbrand, J., Getty, L. A., Clark, M. J., and Wheeler, K. (**1995**). "Acoustic characteristics of American English vowels," J. Acoust. Soc. Am. **97**, 3099–3111.

Hirson, A. (**1995**). "Human laughter—a forensic phonetic perspective," *Studies in Forensic Phonetics*, edited by A. Braun and J.-P. Kosten (Wissenshaftlicher Verlag, Trier), pp. 77–86.

Keltner, D., and Bonanno, G. A. (**1997**). "A study of laughter and dissociation: Distinct correlates of laughter and smiling during bereavement," J. Pers Soc. Psychol. **73**, 687–702.

Kipper, S., and Todt, D. (**2003**). "The role of rhythm and pitch in the evaluation of human laughter," J. Nonverb. Beh. **27**, 255–272.

Ladd, P. (**2003**). *Understanding Deaf Culture. In Search of Deafhood* (Multilingual Matters, Toronto).

Ladefoged, P. (**2006**). *A Course in Phonetics* (Thomson Wadsworth, New York), 5th ed.

Lane, H., Wozniak, J., Matthies, M., Svirsky, M., Perkell, J., O'Connell, M., and Manzella, J. (**1997**). "Changes in sound pressure and fundamental frequency contours following change in hearing status," J. Acoust. Soc. Am. **101**, 2244–2252.

LaPointe, L. L., Mowrer, D. M., and Case, J. L. (**1990**). "A comparative acoustic analysis of the laugh responses of 20 and 70 year old males," Int. J. Aging Human Behav. **31**, 1–9.

Leder, S. B., and Spitzer, J. B. (**1993**). "Speaking fundamental frequency, intensity, and rate of adventitiously profoundly hearing-impaired adult women," J. Acoust. Soc. Am. **93**, 2146–2151.

Mowrer, D. E. (**1994**). "A case study of perceptual and acoustic features of an infant's first laugh utterances," Humour **7**, 139–155.

Mowrer, D. E., LaPointe, L. L., and Case, J. (**1987**). "Analysis of five acoustic correlates of laughter," J. Nonverb. Beh. **11**, 191–200.

Nwokah, E. E., Hsu, H.-C., Davies, P., and Fogel, A. (**1999**). "The integration of laughter and speech in vocal communication: A dynamic systems perspective," J. Speech Lang. Hear. Res. **42**, 880–894.

Nwokah, E. E., Davies, P., Islam, A., Hsu, H.-C., and Fogel, A. (**1993**). "Vocal affect in three-year-olds: A quantitative acoustic analysis of child laughter," J. Acoust. Soc. Am. **94**, 3076–3090.

Okalidou, A., and Harris, K. S. (**1999**). "A comparison of intergestural patterns in deaf and hearing adult speakers: Implications from an acoustic analysis of disyllables," J. Acoust. Soc. Am. **106**, 394–410.

Oller, D. K., Eilers, R. E., Bull, D. H., and Carney, A. E. "Prespeech vocalizations of a deaf infant: A comparison with normal metaphonological development," J. Speech Lang. Hear. Res. **28**, 47–63.

Osberger, M. J., and Levitt, H. (**1979**). "The effect of timing errors on the intelligibility of deaf children's speech," J. Acoust. Soc. Am. **66**, 1316–1324.

Osberger, M. J., and McGarr, N. S. (**1983**). "Speech production characteristics of the hearing," *Speech and Language: Advances in Basic Research and Practice* edited by N. Lass (Academic, New York), pp. 221–283.

Owren, M. J., and Bachorowski, J.-A. (**2003**). "Reconsidering the evolution of nonlinguistic communication: The case of laughter," J. Nonverb. Behav. **27**, 183–200.

Owren, M. J., and Bernacki, R. H. (**1998**). "Applying linear predictive coding (LPC) to frequency-spectrum analysis of animal acoustic signals," *Animal Acoustic Communication: Sound Analysis and Research Methods*, edited by S. L. Hopp, M. J. Owren, and C. S. Evans (Springer-Verlag, Berlin), pp. 129–161.

Owren, M. J., and Goldstein, M. H., (**2008**). "The babbling-scaffold hypothesis: Subcortical primate-like circuitry helps teach the human cortex how to talk," *Evolution of Communicative Flexibility: Complexity, Creativity, and Adaptability in Human and Animal Communication*, edited by D. K. Oller, and U. Griebel (MIT, Cambridge), pp. 169–192.

Padden, C. A., and Humphries, T. L. (**1990**). *Deaf in America: Voices from a Culture* (Harvard University, Cambridge).

Provine, R. R. (**1993**). "Laughter punctuates speech: Linguistic, social, and gender contexts of laughter," Ethology **95**, 291–298.

Provine, R. R. (**2000**). *Laughter: A Scientific Investigation* (Viking, New York).

Provine, R. R., and Emmorey, K. (**2006**). "Laughter among deaf signers," J. Deaf Stud. Deaf Educ. **11**, 403–409.

Provine, R. R., and Fischer, K. R. (**1989**). "Laughing, smiling, and talking: Relation to sleeping and social context in humans," Ethology **83**, 295–305.

Provine, R. R., and Yong, Y. L. (**1991**). "Laughter: A stereotyped human vocalization," Ethology **89**, 115–124.

Rankin, A. M., and Philip, P. J. (**1963**). "An epidemic of laughing in the Bukoba district of Tanganyika," Cent Afr. J. Med. **12**, 167–170.

Rosner, B. S., and Pickering, J. B. (**1994**). *Vowel Perception and Production* (Oxford University, Cambridge).

Rothman, H. B. (**1976**). "A spectrographic investigation of consonant-vowel transitions in the speech of deaf adults," J. Phonetics **4**, 129–136.

Savithri, S. R. (**2000**). "Acoustics of laughter," J. Acoust. Soc. India **28**, 233–238.

Scheiner, E., Hammerschmidt, K., Jürgens, U., and Zwirner, P. (**2002**). "Acoustic analyses of developmental changes and emotional expression in the preverbal vocalizations of infants," J. Voice **16**, 509–529.

Scheiner, E., Hammerschmidt, K., Jürgens, U., and Zwirner, P. (**2004**). "The influence of hearing impairment on preverbal emotional vocalizations of infants," Folia. Phoniatr. Logop. **56**, 27–40.

Smoski, M. J., and Bachorowski, J.-A. (**2003a**). "Antiphonal laughter in developing friendships." Ann. N.Y. Acad. Sci. **1000**, 300–303.

Smoski, M. J., and Bachorowski, J.-A. (**2003b**). "Antiphonal laughter between friends and strangers." Cogn. Emot. **17**, 327–340.

Sroufe, L. A., and Wunsch, J. P. (**1972**). "The development of laughter in the first year of life," Child Dev. **43**, 1326–1344.

Svebak, S. (**1975**). "Respiratory patterns as predictors of laughter," Psychophysiology **12**, 62–65.

Venkatagiri, H. S. (**1999**). "Clinical measurements of rate of reading and discourse in young adults," J. Fluency Disorders **24**, 209–226.

Vettin, J., and Todt, D. (**2004**). "Laughter in conversation: Features of occurrence and acoustic structure," J. Nonverb. Behav. **28**, 93–115.

Waldstein, R. S. (**1990**). "Effects of postlingual deafness on speech production: Implications for the role of auditory feedback," J. Acoust. Soc. Am. **88**, 2099–2114.

The effect of multimicrophone noise reduction systems on sound source localization by users of binaural hearing aids

Tim Van den Bogaert[a)]
ExpORL, K.U.Leuven, O & N 2-Herestraat 49 bus 721, B-3000 Leuven, Belgium

Simon Doclo[b)]
ESAT-SCD, K.U.Leuven, Kasteelpark Arenberg 10, B-3001 Leuven, Belgium

Jan Wouters
ExpORL, K.U.Leuven, O & N 2-Herestraat 49 bus 721, B-3000 Leuven, Belgium

Marc Moonen
ESAT-SCD, K.U.Leuven, Kasteelpark Arenberg 10, B-3001 Leuven, Belgium

(Received 27 July 2007; revised 22 April 2008; accepted 24 April 2008)

This paper evaluates the influence of three multimicrophone noise reduction algorithms on the ability to localize sound sources. Two recently developed noise reduction techniques for binaural hearing aids were evaluated, namely, the binaural multichannel Wiener filter (MWF) and the binaural multichannel Wiener filter with partial noise estimate (MWF-N), together with a dual-monaural adaptive directional microphone (ADM), which is a widely used noise reduction approach in commercial hearing aids. The influence of the different algorithms on perceived sound source localization and their noise reduction performance was evaluated. It is shown that noise reduction algorithms can have a large influence on localization and that (a) the ADM only preserves localization in the forward direction over azimuths where limited or no noise reduction is obtained; (b) the MWF preserves localization of the target speech component but may distort localization of the noise component. The latter is dependent on signal-to-noise ratio and masking effects; (c) the MWF-N enables correct localization of both the speech and the noise components; (d) the statistical Wiener filter approach introduces a better combination of sound source localization and noise reduction performance than the ADM approach. © *2008 Acoustical Society of America.*
[DOI: 10.1121/1.2931962]

PACS number(s): 43.66.Ts, 43.66.Pn, 43.60.Fg, 43.66.Qp [BCM] Pages: 484–497

I. INTRODUCTION

Noise reduction algorithms in hearing aids are important for hearing-impaired persons to improve speech intelligibility in background noise. Multimicrophone noise reduction systems are able to exploit spatial in addition to spectral information and are hence typically preferred to single-microphone systems (Welker *et al.*, 1997; Lotter, 2004). However, the multimicrophone, typically adaptive, noise reduction algorithms currently used in hearing aids are designed to optimize the signal-to-noise ratio (SNR) in a monaural way and not to preserve binaural or interaural cues. Therefore, hearing aid users often localize sounds better when switching off the adaptive directional noise reduction in their hearing aids (Keidser *et al.*, 2006; Van den Bogaert *et al.*, 2006). This puts the hearing aid user at a disadvantage. In certain situations, such as traffic, incorrect localization of sounds may even endanger the user. In addition, interaural localization cues and spatial awareness are important for speech segregation in noisy environments due to spatial release from masking (Bronkhorst and Plomp, 1988; 1989). Changing from a bilateral, i.e., a dual-monaural, hearing aid configuration, to a binaural noise reduction algorithm, i.e., generating an output signal for both ears by using all available microphone signals, may enhance the amount of noise reduction and may increase the ability to control the adaptive processes to preserve the interaural cues between left and right hearing aids. An important limitation of most noise reduction array systems studied thus far is that they are designed to produce a single, i.e., a monaural, output. Extending these to a binaural output is not trivial.

Recently, several techniques to combine binaural noise reduction and preservation of spatial awareness have been studied. The first class of techniques is based on computational auditory scene analysis. Wittkop and Hohman (2003) proposed a method in which the incoming signal is split into different frequency bands. The estimated binaural properties, e.g., the coherence, of each frequency band are compared to the expected properties of the signal component (typically it is assumed that the signal component arrives from the frontal area with interaural time differences (ITDs) and interaural level differences (ILDs) close to 0 μs and 0 dB). This comparison determines whether these frequencies should be enhanced or attenuated. By applying identical gains at the left and the right hearing aids, interaural cues are preserved.

a)Electronic mail: tim.vandenbogaert@med.kuleuven.be
b)Presently at NXP Semiconductors, Interleuvenlaan 80 (C034), 3001 Leuven, Belgium.

However, the noise reduction performance of these methods is relatively limited and typically spectral enhancement problems such as "musical noise" occur.

The second class of techniques is based on fixed or adaptive beamforming. In the studies of Desloge *et al.* (1997), Welker *et al.* (1997), and Zurek and Greenberg (2000), fixed and adaptive multimicrophone beamforming systems were studied, designed to optimize their directional response and to faithfully preserve the interaural cues. In Desloge *et al.* (1997), six different fixed beamforming systems were tested and compared to a reference system which consisted of two independent cardioid microphones. Two of these systems used all microphone inputs from both hearing aids to calculate the output. The first system was a fixed processing scheme designed to limit the amount of ITD distortion at the output to 40 μs. The second system used a low/high pass filtering system and performed a fixed noise reduction on the higher frequencies ($f>800$ Hz) of the signal. The frequency band below 800 Hz remained unprocessed. This approach is inspired by the observation that the ITD information, which is mainly useful at low frequencies, is a dominant localization cue compared to the ILD information, present at the higher frequencies (Wightman and Kistler, 1992). Tests were performed with speech arriving from the front in a diffuse noise source scenario. Both systems showed a significant SNR gain of 2.7–4.4 dB in comparison to the reference system. In general, both systems provided the subjects with moderate localization capabilities using a test setup with a resolution of 30°.

In Welker *et al.* (1997), the low/high pass scheme described above was used in an adaptive noise reduction algorithm with two microphones, one at each ear. The high-frequency part ($f>f_c$) of the signal was now processed in an adaptive way. The algorithm was evaluated by normal hearing subjects. It was shown that f_c determined a trade-off between noise reduction and localization performance. An optimal setting of $f_c=500$ Hz was proposed which led to an effective noise reduction of 3 dB and a localization accuracy of 70%. Tests of Zurek and Greenberg (2000), with hearing-impaired subjects and $f_c=1000$ Hz, showed a SNR improvement of 2 dB when using the same algorithm.

The third class of techniques are based on blind source separation (BSS). Very recently, Aichner *et al.* (2007) proposed two methods for incorporating interaural cue preservation in BSS. The first method is based on using adaptive filters as a postprocessing stage after BSS. These filters remove the noise components, estimated by the BSS, from the reference microphone. By doing this at both sides of the head, the interaural cues of the speech component are preserved. Due to the fact that not all noise can be removed from the reference signal, it was claimed that the interaural cues of the remaining noise component are also preserved. The second method is based on constraining the BSS filters themselves, thereby avoiding distortion of the separated signals produced by the BSS. However, localization results were described very briefly using a quality rating on the output of the algorithm, and so far no results have been published on the source separation performance of these methods.

The last class, on which this paper will focus, is based on multichannel Wiener filtering (MWF). Recently, Doclo and Moonen (2002) mathematically described a MWF approach performing noise reduction in hearing aids. This approach, unlike an adaptive directional microphone (ADM), is based on using second-order statistics of the speech and the noise components to estimate the speech component in a noisy (reference) microphone signal. In Doclo *et al.* (2006), it was mathematically proven that a binaural version of the MWF generates filters which, in theory, perfectly preserve the interaural cues of the speech component but change the interaural cues of the noise component into those of the speech component. To optimally benefit from spatial release from masking and to optimize spatial awareness of the hearing aid user, it would be beneficial to also preserve the interaural cues of the noise component. Hence, two extensions of the MWF have been proposed. In the first extension, proposed by Klasen *et al.* (2006), an estimate of the interaural transfer function (ITF) was introduced into the cost function which was used to calculate the Wiener filters. This enabled putting more or less emphasis on preserving the interaural cues at the cost of some loss of noise reduction. However, if the ITF extension is emphasized too strongly, the interaural cues of the speech component will be distorted into those of the noise component. A perceptual validation of the MWF-ITF by Van den Bogaert *et al.* (2007) in a low reverberant environment showed that an optimal parameter setting could be found which improved localization performance compared to a binaural MWF without a large loss in noise reduction performance. However, this ITF extension is only valid for single noise source scenarios. The second extension is a MWF with partial noise estimate (MWF-N), first described by Klasen *et al.* (2007), which aims at eliminating only part of the noise component. The remaining, unprocessed, part of the noise signal then restores the spatial cues of the noise component of the signal at the output of the algorithm. This is similar to the work of Noble *et al.* (1998) and Byrne *et al.* (1998), in which improvements in localization were found when using open instead of closed earmolds. The open earmolds enabled the usage of the direct, unprocessed, sound at frequencies with low hearing loss to improve localization performance. In Klasen *et al.* (2007), the MWF and MWF-N approaches were compared to the approach of Welker *et al.* (1997), described earlier. This was done using objective performance measures based on anechoic data for a single noise source, fixed at 90°. To quantify localization performance, an ITD-error measure was defined, being the difference in ITD between the input and the output of the algorithms. ITD was calculated as the delay generating the maximum value in the cross correlation between the left and right ear signals. A maximum noise reduction of 27 dB was obtained and simulations showed that the ITD error of the speech component was close to zero for the MWF and the MWF-N. It was also shown that for the MWF, the ITD error of the noise component could exceed 500 μs. For the MWF-N, this error dropped below 50 μs. The work of Klasen *et al.* (2007) summarized the possible benefits and trade-offs of the MWF and the MWF-N compared to the approach of Welker *et al.* (1997). However, it remains hard to predict real-life perfor-

mance, since an anechoic environment was used and since the ITD error measure, used to predict localization performance, is based on a very simple localization model.

The main purpose of this paper was to study the effect of noise reduction algorithms on the ability to localize sound sources when hearing aid users wear a hearing aid at both sides of the head. It evaluates two recently described binaural noise reduction algorithms, namely, the MWF and the MWF-N, as well as a widely used noise reduction approach, namely, an ADM. An unprocessed condition was used as a reference. The evaluation was performed in a room with a realistic reverberation time ($T60=0.61$ s) at two different SNRs, mainly using perceptual evaluations with normal hearing subjects. The focus of the manuscript is on localization performance in the horizontal plane, for which the ITD and ILD are the main cues (Hartmann, 1999; Blauert, 1997). Since the manuscript evaluates noise reduction algorithms, noise reduction data will also be presented.

The main research questions answered in this study are the following. (a) What is the influence of a commonly used noise reduction algorithm, namely, an ADM in a dual-monaural hearing aid configuration on the ability to localize sound sources in a realistic environment? (b) What is the influence of the binaural MWF in a binaural hearing aid configuration on the ability to localize sound sources? (c) Does the MWF-N improve localization performance in comparison to the MWF? (d) How do the MWF and MWF-N perform in terms of combining noise reduction and localization performance in comparison to the ADM configuration?

II. ALGORITHMS

A. ADM

An ADM is a commonly used noise reduction technique for hearing aids (Luo *et al.*, 2002; Maj *et al.*, 2004). Unlike the MWF-based algorithms, the ADM is based on the assumption that the target signal arrives from the frontal direction and that jammer signals arrive from the back hemisphere. The ADM uses the physical differences in time of arrival between the microphones to improve the SNR by steering a null in the direction of the jammer signals. The ADM uses the microphones of one hearing aid at a given ear and consists of two stages. The first stage generates two software directional microphone signals corresponding to front- and back-oriented cardioid patterns. In the second stage, these signals are combined by an adaptive, frequency dependent, scalar β that minimizes the energy arriving from the back hemisphere at the output of the algorithm. Typically, the value of β is constrained between 0 and 0.5 to avoid distortion in the frontal hemisphere.

B. Binaural MWF

In general, the goal of a Wiener filter is to filter out noise corrupting a desired signal. Using the second-order statistical properties of the desired signal and the noise, the optimal filter or Wiener filter can be calculated. It generates an output signal which approaches the desired signal as closely as possible in a mean-square error (MSE) sense. It is based on minimizing a cost function corresponding to the difference between the desired signal (the speech component which has to be estimated) and the output of the filter. In contrast with a single channel approach, a MWF uses multiple input signals to compute a set of filters generating this output signal. See Haykin (2002) for an overview on Wiener filtering.

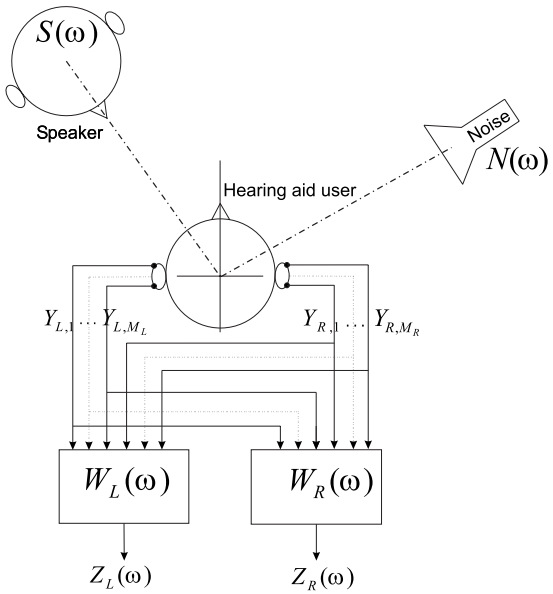

FIG. 1. Layout of a binaural noise reduction system.

Consider the binaural hearing aid configuration in Fig. 1, where the left and the right hearing aids have a microphone array consisting of, respectively, M_L and M_R microphones. The mth microphone signal $Y_{L,m}(\omega)$ of the left ear can be written in the frequency domain as

$$Y_{L,m}(\omega) = X_{L,m}(\omega) + V_{L,m}(\omega), \quad m = 1 \cdots M_L, \tag{1}$$

where $X_{L,m}(\omega)$ and $V_{L,m}(\omega)$ represent the speech and the noise components at the mth microphone input of the left hearing aid. $Y_{R,m}$, $X_{R,m}(\omega)$, and $V_{R,m}(\omega)$ are defined similarly for the right hearing aid. Assuming a link between the two hearing aids, microphone signals from a given ear (M_I) and contralateral ear (M_C) can be used to generate an output signal for each of the two hearing aids. The total number of microphones used at each ear is defined as $M=M_I+M_C$.[1] For the left and right ears, the M-dimensional input signal vectors $\mathbf{Y}_L$ and $\mathbf{Y}_R$ can be written as

$$\mathbf{Y}_L(\omega) = [Y_{L,1}(\omega), \ldots, Y_{L,M_I}(\omega), \quad Y_{R,1}(\omega), \ldots, Y_{R,M_C}(\omega)]^T, \tag{2}$$

$$\mathbf{Y}_R(\omega) = [Y_{L,1}(\omega), \ldots, Y_{L,M_C}(\omega), \quad Y_{R,1}(\omega), \ldots, Y_{R,M_I}(\omega)]^T, \tag{3}$$

with ^{T} the transpose operator. The vectors defining the speech component and the noise component, e.g., for the left ear $\mathbf{X}_L(\omega)$ and $\mathbf{V}_L(\omega)$, are defined in a similar way to the signal vectors. The filters which combine the microphone signals to optimally estimate the speech component are calculated using a Wiener filter procedure and are defined as $\mathbf{W}_L(\omega)$ and $\mathbf{W}_R(\omega)$ for the left and the right hearing aids, respectively. The output signals for the left and the right ears are equal to

$$\mathbf{Z}_L(\omega) = \mathbf{W}_L^H(\omega)\mathbf{Y}_L(\omega), \quad \mathbf{Z}_R(\omega) = \mathbf{W}_R^H(\omega)\mathbf{Y}_R(\omega), \tag{4}$$

with $\mathbf{W}_L(\omega)$ and $\mathbf{W}_R(\omega)$ M-dimensional complex vectors and ^{H} the Hermitian transpose operator. The $2M$-dimensional stacked weight vector $\mathbf{W}(\omega)$ is defined as

$$\mathbf{W}(\omega) = \begin{bmatrix} \mathbf{W}_L(\omega) \\ \mathbf{W}_R(\omega) \end{bmatrix}. \tag{5}$$

For conciseness, we will omit the frequency-domain variable ω in the remainder of the paper.

The binaural MWF produces a minimum MSE estimate of the speech component for each hearing aid. The MSE cost function J_{MSE} which should be minimized to calculate the filters $\mathbf{W}_L$ estimating the unknown speech component in the front microphone of the left hearing aid, i.e., $X_{L,1}$ from Eq. (1), and the filters $\mathbf{W}_R$ estimating the unknown speech component in the front microphone of the right hearing aid, i.e., $X_{R,1}$, equals

$$J_{\mathrm{MSE}}(\mathbf{W}) = \mathcal{E}\left\{\left\|\begin{bmatrix} X_{L,1} - \mathbf{W}_L^H\mathbf{Y}_L \\ X_{R,1} - \mathbf{W}_R^H\mathbf{Y}_R \end{bmatrix}\right\|^2\right\}, \tag{6}$$

with $\mathcal{E}$ the expected value operator. Minimizing $J_{\mathrm{MSE}}(\mathbf{W})$ leads to the optimal filters $\mathbf{W}$ producing the best minimum MSE estimate of the speech component $\mathbf{X}$ present in the reference microphones.

This cost function was, for a monaural hearing aid configuration, extended by Doclo and Moonen (2002) and Spriet *et al.* (2004) by using Eq. (1) and introducing an extra trade-off parameter μ. To enable a trade-off between speech distortion and noise reduction, they introduced the monaural speech distortion weighted MWF (SDW-MWF), which minimizes the weighted sum of the residual noise energy and the speech distortion energy. The binaural SDW-MWF cost function equals

$$J_{\mathrm{MWF}}(\mathbf{W}) = \mathcal{E}\left\{\left\|\begin{bmatrix} X_{L,1} - \mathbf{W}_L^H\mathbf{X}_L \\ X_{R,1} - \mathbf{W}_R^H\mathbf{X}_R \end{bmatrix}\right\|^2 + \mu\left\|\begin{bmatrix} \mathbf{W}_L^H\mathbf{V}_L \\ \mathbf{W}_R^H\mathbf{V}_R \end{bmatrix}\right\|^2\right\}, \tag{7}$$

where the first term represents speech distortion and the second term represents the residual noise. Note that when the trade-off parameter μ is set to 1, the SDW-MWF cost function (7) reduces to cost function (6). In the remainder of the paper the SDW-MWF algorithm will be used and evaluated. For conciseness the SDW-MWF algorithm will be referred to as MWF.

The Wiener filter solution minimizing the cost function $J_{\mathrm{MWF}}(\mathbf{W})$ equals

$$\mathbf{W}_{\mathrm{MWF}} = \begin{bmatrix} \mathbf{R}_{x,L} + \mu\mathbf{R}_{v,L} & 0_M \\ 0_M & \mathbf{R}_{x,R} + \mu\mathbf{R}_{v,R} \end{bmatrix}^{-1}\begin{bmatrix} \mathbf{R}_{x,L}e_L \\ \mathbf{R}_{x,R}e_R \end{bmatrix}, \tag{8}$$

with e_L and e_R being vectors with one element equal to 1 and the other elements equal to zero, defining the reference microphones used at both hearing aids, i.e., in the case of the front omnidirectional microphone $e_L(1)=1$ and $e_R(1)=1$. $\mathbf{R}_x$ and $\mathbf{R}_v$, which are at present still unknown, are defined as the $M\times M$-dimensional speech and noise correlation matrices, containing the autocorrelations and cross correlations (or the statistical information) of, respectively, the speech and noise components $\mathbf{X}$ and $\mathbf{V}$ over the different input channels, e.g., $\mathbf{R}_{x,L}=\mathcal{E}\{\mathbf{X}_L\mathbf{X}_L^H\}$. To find $\mathbf{W}_{\mathrm{MWF}}$ using Eq. (8), a voice activity detector is used to discriminate between "speech and noise periods" and "noise only periods." The noise correlation matrix $\mathbf{R}_v$ can be calculated during the noise only periods. By assuming a sufficient stationary noise signal, the speech correlation matrix $\mathbf{R}_x$ can be estimated during speech and noise periods by subtracting $\mathbf{R}_v$ from the correlation matrix $\mathbf{R}_y$ for the noisy signal Y. By using these correlation matrices, the filters $\mathbf{W}$ can be found [see Eq. (8)].

Since the binaural MWF is designed to produce two outputs, $Z_L(\omega)$ and $Z_R(\omega)$, respectively, estimating the speech components at the front omnidirectional microphones of the left and the right hearing aids, the interaural cues of the speech component are inherently preserved.

C. Binaural MWF-N

The rationale of the MWF-N is not to completely remove the noise component from the microphone signals but to remove only part of the noise component. The interaural cues of the unprocessed part can then be used to correctly localize the noise component. The MWF-N corresponds to estimating the desired speech component summed with a scaled version of the noise component (Klasen *et al.*, 2007). Consequently, Eq. (6) changes into

$$J_{\mathrm{MSE}\eta}(\mathbf{W}) = \mathcal{E}\left\{\left\|\begin{bmatrix} X_{L,1} + \eta V_{L,1} - \mathbf{W}_L^H\mathbf{Y}_L \\ X_{R,1} + \eta V_{R,1} - \mathbf{W}_R^H\mathbf{Y}_R \end{bmatrix}\right\|^2\right\}, \tag{9}$$

with η between 0 and 1. By using a small η more emphasis is put on noise reduction and less emphasis is put on preserving the interaural cues of the noise component. When $\eta=0$, the MWF-N reduces to the standard MWF. Similar to the MWF, a trade-off parameter can be introduced by weighting the amount of speech distortion with the residual noise energy in the partial noise estimate. In other words, the amount of speech distortion is limited at the cost of noise reduction on part $(1-\eta)$ of the noise signal. The cost function then becomes

$$J_{\mathrm{MWF}\eta}(\mathbf{W}) = \mathcal{E}\left\{\left\|\begin{bmatrix} X_{L,1} - \mathbf{W}_L^H\mathbf{X}_L \\ X_{R,1} - \mathbf{W}_R^H\mathbf{X}_R \end{bmatrix}\right\|^2 + \eta\left\|\begin{bmatrix} \eta V_{L,1} - \mathbf{W}_L^H\mathbf{V}_L \\ \eta V_{R,1} - \mathbf{W}_R^H\mathbf{V}_R \end{bmatrix}\right\|^2\right\}. \tag{10}$$

A simple relationship holds between the filter output of the MWF and the MWF-N,

$$Z_{\mathrm{MWF}_\eta L}(\eta,\mu) = \eta Y_{L,1} + (1-\eta)Z_{\mathrm{MWF},L}(\mu), \tag{11}$$

$$Z_{\mathrm{MWF}_\eta R}(\eta,\mu) = \eta Y_{R,1} + (1-\eta)Z_{\mathrm{MWF},R}(\mu). \tag{12}$$

In other words, the MWF-N solution is obtained by adding a portion of the unprocessed signals of the reference microphones (ηY) to the original MWF solution. This can be used to restore the spatial cues of the noise component in the processed signal. A similar theory is demonstrated in the work of Noble *et al.* (1998) and Byrne *et al.* (1998), in which localization performance was improved by using open instead of closed earmolds by dual-monaural hearing aid users.

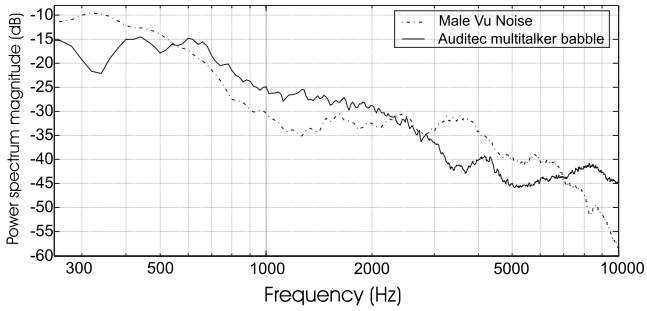

FIG. 2. Average power spectrum of the speech weighted noise signal (VU material) and the multitalker babble (Auditec). The overall SNR was 0 dB A.

Obviously, it is expected that noise reduction performance will decrease when increasing η.

III. LOCALIZATION PERFORMANCE

A. Test setup

Experiments were carried out in a reverberant room with dimensions $5.20 \times 4.50 \times 3.10$ m^3 (length $\times$ width $\times$ height) and a reverberation time $T60$, averaged over one/third octave frequencies from 100 to 8000 Hz, of 0.61 ± 0.08 s. Subjects were located at 1.90 m from the right wall and 2.05 m from the front wall. Stimuli were generated off line (see Sec. III B) and presented through headphones (Sennheiser HD650) using an RME Hamerfall DSPII soundcard. Subjects were placed inside an array of 13 Fostex 6301B single-cone speakers. The speakers were located in the frontal horizontal plane at angles ranging from −90° to +90° relative to the subject with a spacing of 15°. The speakers were placed at a distance of 1 m from the subject and were labeled 1–13. Since the stimuli were presented through headphones, loudspeakers were used only for visualization purposes. The task was to identify the loudspeaker where the target sound was heard.

B. Stimuli

The algorithms were evaluated using a steady speech weighted noise signal from the VU test material (Versfeld *et al.*, 2000) arriving from angle x° as speech component (S). A multitalker babble (Auditec) was used as the jammer sound (N) arriving from angle y°, defining the spatial scenario S_xN_y. The spectra of the speech and noise source are depicted in Fig. 2. Three different spatial scenarios were evaluated: S_0N_{60}, $S_{90}N_{-90}$, and $S_{45}N_{-45}$.

To generate the input signals for all algorithms, stimuli were convolved with the appropriate impulse responses measured between the loudspeakers of the loudspeaker array and the microphones on two behind the ear (BTE) hearing aids worn by a Cortex MK2 manikin. The manikin was placed at the position of the test subjects. The BTE devices were two dual-microphone shells with direct microphone outputs from two omnidirectional microphones on each hearing aid. The intermicrophone distance was approximately 1 cm.

Three different noise reduction algorithms were evaluated. The first two algorithms were the binaural MWF with partial noise estimate using $\eta=0.2$ (MWF-$N_{0.2}$) and the standard binaural MWF, which corresponds to the MWF-N with $\eta=0$. Both of these algorithms were implemented using for each ear two omnidirectional microphones present at that ear and the front microphone of the contralateral hearing aid to generate an output for the given hearing aid. Simulations suggested that $\mu=5$ was an appropriate value for the trade-off parameter in Eqs. (7) and (10). The third algorithm was an ADM. The ADM configuration is a commonly used dual-monaural configuration which used for each ear both microphone signals of the given hearing aid to generate the output signal for that particular hearing aid. When testing performance in the unprocessed condition (unproc), the front omnidirectional microphone signals from the left and right hearing aids were presented to the subject. The outputs of all algorithms were calculated off line. ADM and MWF filters were trained on the specific spatial scenario and were fixed after convergence. For the MWF, a perfect voice activity detector was used to calculate the filters. Pilot testing suggested that the MWF filters behaved differently at different SNRs. Therefore, stimuli were generated at two different input SNRs (0 and −12 dB A), with the input SNR being calculated in the absence of the head.

C. Protocol

In the first test condition (S,N), the speech and the noise components were filtered by the fixed filters and presented separately to the subjects. By presenting the two components separately, interactions between components were avoided (masking effects, localizing two sounds is different from localizing one sound source). In the second condition (S+N) the speech and noise components were presented simultaneously and the subject was asked to localize both components. This resembled a steady-state real-life situation.

Subjects were instructed to keep their head fixed and pointed toward the 0° direction during stimulus playback and were supervised by the test leader. The task was to identify the loudspeaker where the target sound was perceived. Although only the locations of −90°, −45°, 0°, 45°, 60°, and 90° were used to generate the stimuli, subjects were free to use all given loudspeaker positions in the frontal horizontal hemisphere (−90° to +90° in steps of 15°) to identify where the sound was perceived. Tests were restricted to the frontal hemisphere to avoid front-back confusions which would complicate the analysis of the results and which are more related to spectral cues than to interaural cues. None of the subjects experienced major problems with this restriction. Subjects were clearly instructed that the test could be unbalanced. The five subjects were all normal hearing subjects working in the Department of Exp.ORL and were used to performing listening tests.

Pilot testing showed that the presented stimuli might sound diffuse or even arriving from two different angles instead of one clear direction. Therefore, subjects were asked to give comments on how the sound was perceived using the following classification: the sound arrives from a point source with one clear direction in space (point), the sound arrives from a wider area (wide), the sound arrives from everywhere (diffuse), or more than one sound source is per-

ceived (dual). If they perceived multiple components at different locations, subjects were asked to report both locations and to report to which direction they would look when hearing this stimulus. This direction was then used as the response to the presented stimulus. Only for the condition S+N were the subjects explicitly asked to report two angles of arrival, one for the speech and one for the noise component.

The two different sound conditions (S,N and S+N) were presented in different test sessions with the angle of arrival, input SNR, and type of algorithm randomized throughout the test. Each stimulus was repeated three times, and an overall roving level of 6 dB was used (ranging from 0 to −6 dB). The presented stimuli were equalized in dB A level by adjusting the sound level, averaged over the left and right channels, to the same level for all generated stimuli. The stimuli were then presented at a comfortable level chosen by the subject. Because the task was quite hard, the subject had the possibility to repeat the same stimulus over and over again until a clear answer could be given to the test leader, who entered all responses and comments. The test leader had no information on the location of the stimulus nor the type of algorithm that was used and no feedback was given to the subjects. Typically one session took somewhat more than 1 h and several hours elapsed between different sessions. If fatigue or low concentration were observed, breaks were taken during the test.

D. Performance measures

Different error measures have been used in previous localization studies (Noble and Byrne, 1990; Lorenzi *et al.*, 1999; Van Hoesel *et al.*, 2002). Two commonly used error measures are the root-mean-square (rms) error and the mean absolute error (MAE). We focused on the MAE which is defined as

$$\mathrm{MAE}(^\circ) = \frac{\sum_{i=1}^{n} |(\text{stimulus azimuth} - \text{response azimuth})|}{n}, \tag{13}$$

with n the number of presented stimuli. For the MAE, all errors are weighted equally, while for the rms error, large errors have a larger impact than small errors. The smallest nonzero error a subject could make for one stimulus equaled 5° MAE (one error of 15° made during the three repetitions of the stimulus, $n=3$). In Sec. III E, the statistical analysis will show that this resolution was sufficient to illustrate effects of, and large differences between, the algorithms in the different spatial scenarios, which was the goal of this study.

E. Results and analysis

First the data and analysis for the condition S,N are presented, followed by the data and analysis for the condition S+N. All statistical analysis was done using SPSS 15.0. For conciseness, the term factorial repeated-measure ANOVA is abbreviated by ANOVA and pairwise comparisons discussed throughout the document were always Bonferroni corrected for multiple comparisons.

1. Condition S,N

Localization data for the condition with the speech and the noise component presented separately to the listener are given in Table I. Table I indicates where the stimulus was perceived by each subject, averaged over the three stimulus repetitions, together with the minimum, maximum, and averaged MAE values across subjects.

To compare the different algorithms, an ANOVA was carried out on the recorded MAE data. The factor algorithms (ADM, MWF, MWF-$N_{0.2}$), target (speech or noise component), SNRs (0 and −12 dB), and angles (S_0N_{60}, $S_{90}N_{-90}$, $S_{45}N_{-45}$) were used. As expected, many interactions were found between these factors, e.g., algorithm*target $p=0.004$. To disentangle these interactions, separate ANOVAs were carried out for the speech and noise components.

Speech component. An interaction was found between the factor angle and algorithm ($p=0.019$, $F=14.647$). Hence, separate ANOVAs were carried out for each spatial scenario.

For S_0N_{60} and $S_{45}N_{-45}$ no main effects were found ($p=0.470$ and $p=1.000$, respectively for the factor algorithm). For the scenario $S_{90}N_{-90}$, a main effect of the factor algorithm was found ($p=0.009$, $F=22.359$). Pairwise comparisons showed significantly lower performance for the ADM than for the MWF (difference averaged over the two SNRs =58° MAE, $p=0.039$) and the MWF-$N_{0.2}$ (difference averaged over the two SNRs=65° MAE, $p=0.019$). Table I shows that, for scenario $S_{90}N_{-90}$, none of the subjects was capable of localizing the speech component correctly when using the ADM, and sounds were most commonly localized around 0° (four out of five subjects). The MWF-$N_{0.2}$ scheme just failed to give significantly better performance than the MWF scheme (difference of 7° MAE, $p=0.057$).

When comparing the algorithms with the unprocessed condition, no main effects were found for scenarios S_0N_{60} and $S_{45}N_{-45}$ ($p>0.252$). For the scenario $S_{90}N_{-90}$, a main effect was found ($p=0.008$). Pairwise comparisons showed that only the ADM performed significantly more poorly than the unprocessed condition (a difference of 67° MAE, $p=0.038$, for SNR=0 dB and a difference of 65° MAE, $p=0.035$, for SNR=−12 dB).

Table II shows the percentage of reports of a clear directional sound image during the subjective classification of the stimuli. For the speech component, the combination of ADM and $S_{90}N_{-90}$ led to severely degraded performance compared to all other combinations. Interestingly, these stimuli were often perceived as being diffuse (53% for 0 dB and 60% for −12 dB). Subjects reported that, when perceiving a diffuse sound, 0° was often picked as the direction from where the sound was heard, since it is the neutral position in the middle of the sound array. Therefore, these 0° responses should be interpreted carefully.

Noise component. Due to an interaction with SNR ($p=0.050$), separate ANOVAs were carried out for each SNR. Since the speech and noise components were presented separately and since the presentation level for both components was calibrated to a comfortable level, the obtained results for the unprocessed stimuli are independent of SNR. Therefore, the data for the unprocessed condition were incorporated in the ANOVA for each SNR.

TABLE I. Response location (deg), averaged over three repetitions, together with the average, minimum, and maximum MAE across subjects for the three different spatial scenarios (S_0N_{60}, $S_{90}N_{-90}$, and $S_{45}N_{-45}$), and the different processing schemes (unprocessed, ADM, MWF, and MWF-$N_{0.2}$) at two different SNRs (0 and −12 dB). The speech and the noise sources were presented separately through headphones (S,N). The rows labeled "effect" show whether a significant difference from the unprocessed condition was found. *P*-values of pairwise comparisons are shown. If no main effects were found the term "nm" is used.

S_0N_{60}	S_0							N_{60}						
	unproc	ADM		MWF		MWF-$N_{0.2}$		unproc	ADM		MWF		MWF-$N_{0.2}$	
		SNR0	SNR-12	SNR0	SNR-12	SNR0	SNR-12		SNR0	SNR-12	SNR0	SNR-12	SNR0	SNR-12
T	0	0	−5	−15	0	−15	0	90	90	75	0	50	0	85
J	0	0	0	0	0	0	0	90	90	90	0	90	80	90
H	0	0	0	−5	0	0	0	65	60	70	0	45	35	65
L	−5	−5	−5	−15	−10	−15	−10	90	80	85	−5	45	75	85
O	0	20	25	5	35	−0	0	85	80	90	10	80	65	80
Loc (av)	−1	3	3	−6	5	−8	−2	84	80	82	1	62	51	81
MAE (av)	1	5	7	8	9	8	2	24	20	22	59	28	25	21
Min-max MAE	0-5	0-20	0-25	0-15	0-35	0-15	0-10	5-30	0-30	10-30	50-65	20-35	5-60	5-30
Effect		nm	nm	nm	nm	nm	nm		$p=0.687$	nm	$p=0.027$	nm	$p=1.000$	nm
$S_{90}N_{-90}$	S_{90}							N_{-90}						
	unproc	ADM		MWF		MWF-$N_{0.2}$		unproc	ADM		MWF		MWF-$N_{0.2}$	
		SNR0	SNR-12	SNR0	SNR-12	SNR0	SNR-12		SNR0	SNR-12	SNR0	SNR-12	SNR0	SNR-12
T	90	0	0	85	80	85	90	−80	−15	0	80	−55	−90	−85
J	90	0	0	90	80	90	90	−90	0	0	45	−90	−90	−90
H	70	20	15	65	55	70	75	−85	−75	−60	−25	−75	−80	−90
L	80	0	15	80	75	85	75	−70	−35	−35	80	−60	−75	−80
O	75	50	50	70	55	70	75	−75	−20	−10	80	55	30	−65
Average	81	14	16	78	69	80	81	−80	−29	−21	52	−45	−61	−82
MAE (av)	9	76	74	12	21	10	9	10	61	69	142	45	29	8
Min-max MAE	0-20	40-90	40-90	0-25	10-35	0-20	0-15	0-20	15-90	30-90	65-170	0-145	0-120	0-25
Effect		$p=0.038$	$p=0.035$	$p=0.423$	$p=0.056$	$p=1.000$	$p=1.000$		$p=0.687$	nm	$p=0.027$	nm	$p=1.000$	nm
$S_{45}N_{-45}$	S_{45}							N_{-45}						
	unproc	ADM		MWF		MWF-$N_{0.2}$		unproc	ADM		MWF		MWF-$N_{0.2}$	
		SNR0	SNR-12	SNR0	SNR-12	SNR0	SNR-12		SNR0	SNR-12	SNR0	SNR-12	SNR0	SNR-12
T	50	60	50	80	65	65	80	−50	−60	−85	75	−90	−70	−75
J	60	90	90	90	45	90	50	−45	−90	−90	75	−70	−75	−90
H	45	40	30	45	45	45	45	−75	−70	−70	−50	−75	−70	−75
L	75	70	50	75	75	85	60	−60	−45	−50	−25	−50	−60	−60
O	75	70	75	70	75	75	70	−80	−60	−75	80	75	25	−65
Average	61	66	59	72	61	72	61	−62	−65	−74	31	−42	−50	−73
MAE (av)	16	23	20	27	16	27	16	17	20	29	78	45	37	28
Min-max MAE	0-30	5-45	5-45	0-45	0-30	0-45	0-35	0-35	0-45	5-45	5-125	5-120	15-90	15-45
Effect		nm	nm	nm	nm	nm	nm		$p=0.687$	nm	$p=0.027$	nm	$p=1.000$	nm

TABLE II. Percentage of stimuli perceptually classified as being a sound arriving from a point source with one clear direction in space, averaged over five subjects, for the three different spatial scenarios and the different processing schemes. The speech and the noise sources were presented separately through headphones (S,N). In the conditions in which most sounds were not categorized as arriving from one clear direction, the percentage of diffuse sounds (di), dual sounds (du), or very broad source (br) is added.

	Level (dB)	Unproc	ADM	MWF	MWF-$N_{0.2}$		Level (dB)	Unproc	ADM	MWF	MWF-$N_{0.2}$
S_0	0	67	87	93	100	N_{60}	0	89	80	80+7du	27+53du
	−12		53	87	93		−12		93	47+40du	67+27du
S_{90}	0	75	13+53di	100	100	N_{-90}	0	89	7+27di+40br	27+73du	7+93du
	−12		27+60di	60	100		−12		53+20di+20br	7+87du	13+87du
S_{45}	0	58	87	100	100	N_{-45}	0	89	93	20+67du	7+87du
	−12		87	87	73		−12		100	27+67du	13+80du

For SNR=0 dB, a main effect of algorithm was observed ($p=0.012$). Pairwise comparisons showed significantly lower performance for the MWF than for all other strategies (versus unprocessed $p=0.027$, versus ADM $p=0.017$, versus MWF-$N_{0.2}$ $p=0.049$). This can also be observed in Table I, which shows that the noise component at the output of the MWF was generally localized at the same location as the speech component. No significant differences were found between the unprocessed condition, the ADM, and the MWF-$N_{0.2}$ ($p \geqslant 0.687$). For SNR=−12 dB, no interactions or main effects were found (angle*algorithm $p=0.115$, angle $p=0.443$, algorithm $p=0.156$), implying that all algorithms, including the MWF, performed equally well at this SNR.

Interestingly, no interaction was found at either SNR between the factor algorithm and angle, although the results in Table I suggest that the ADM distorted the localization of the noise component in the scenario $S_{90}N_{-90}$ (which was also observed when analyzing the data of the speech component). Table I shows that only one out of five subjects, subject H, localized the noise component with the ADM equally well as in the unprocessed condition.

The subjective classification, shown in Table II, showed a clear drop in performance for almost all spatial scenarios for the MWF and the MWF-$N_{0.2}$ compared to the unprocessed condition. This was quite surprising for the MWF-$N_{0.2}$ and the MWF at SNR=−12 dB since their MAE values were relatively modest in these conditions and not statistically different from those for the unprocessed condition. Interestingly, the outputs of these algorithms were often classified as being a "dual sound." Averaged over the three spatial scenarios, there were 49% and 65% of such cases for the MWF and 78% and 65% of such cases for the MWF-$N_{0.2}$ at 0 and −12 dB, respectively. When dual sounds were reported, the sound was perceived as having two components, each arriving from a different angle. Subjects reported that one part arrived approximately from the position of the original noise component, whereas the other part arrived from around the position of the speech component. When using the MWF at a SNR of 0 dB, the sound arriving from the original noise position was typically described as being softer, lower in frequency and less distorted than the other part. For the SNR=−12 dB condition, the part arriving from the original noise position was reported as being louder than the distorted part arriving from the speech position.

2. Condition S+N

Whereas in the first experiment the goal was to gain understanding of how the filtering operations perceptually affect the localization cues, the second experiment was more related to real-life performance. In this experiment, speech and noise components were presented simultaneously which resembled more a steady-state real-life listening situation. Subjects were asked to localize both the speech and noise components. Table III shows the individual data indicating where the stimuli were perceived, averaged over three repetitions, together with the minimal, maximal, and averaged MAE values for the tested subjects.

In most conditions no differences were found between the data for condition S+N and condition S,N, leading to the same differences between algorithms as discussed for condition S,N. This was assessed for the unprocessed data, the ADM data, the MWF-$N_{0.2}$ data, and for the speech component data of the MWF by an ANOVA on all MAE data (S,N and S+N). For the noise component data of the MWF, a significant effect of the factor stimulus presentation (S,N versus S+N) was found for the 0 dB data ($p=0.006$) but not for the −12 dB data ($p=0.233$). An ANOVA comparing the 0 dB data of condition S+N demonstrated, in contrast with the S,N data, no significant difference between the MWF and all other conditions (factor algorithm, $p=0.322$). The data in Table III show that, for both SNRs, the performance of the MWF approaches that for the unprocessed condition for the noise component for all three spatial scenarios. The 0 dB data of the MWF contrast with the results obtained when speech and noise components were presented separately (Table I).

F. Discussion of reference condition

Since the unprocessed condition was used as a reference condition in the Results and analysis section, a short discussion of the results for this condition is in order. For the condition S,N, the average localization responses in the unprocessed condition were relatively accurate (Table I), with average MAE values between 1° and 24°, depending on the spatial scenario. Although localization was not perfect, these values are in reasonable agreement with those found by Van den Bogaert *et al.* (2006) who used similar procedures and stimuli in their tests. In their study, when testing subjects using their own ears to localize a broadband stimulus, the MAE, averaged over all angles, was about 8°, with large errors, up to 30°, occurring at the sides of the head. Poorer performance was expected here, since localization experiments were done using headphones and since the unprocessed stimuli were generated using signals at the front omnidirectional microphone of both hearing aids. Therefore, the signals could have sounded somewhat unnatural with slightly different ITDs and ILDs than normally occurring at the eardrums and with no relevant information about height and no externalization (pinnae effect). However, this condition was taken as the reference since an evaluation was made of the influence of noise reduction algorithms for hearing aids on the localization of sound sources. Since the allowed responses were limited to the frontal hemisphere, localization at the sides of the head might have been slightly biased toward the front. However, this was true for all conditions and does not explain the differences found between algorithms.

For the unprocessed condition, a similar localization performance was observed in conditions S,N and S+N. Since the data presented here were limited to only three repetitions for each spatial scenario with a limited number of subjects, one should be careful about generalizing this observation. Other researchers have demonstrated that localizing one sound source can be affected by the absence or presence of other sound signals (Lorenzi *et al.*, 1999).

TABLE III. Response location (deg), averaged over three repetitions, together with average, minimum, and maximum MAE data over the different subjects for the three different spatial scenarios (S_0N_{60}, $S_{90}N_{-90}$, and $S_{45}N_{-45}$), and the different processing schemes (unprocessed, ADM, MWF, and MWF-$N_{0.2}$) at two different SNRs (0 and −12 dB). The speech and the noise sources were presented simultaneously through headphones (S+N).

S_0N_{60}	S_0							N_{60}						
	unproc	ADM		MWF		MWF-$N_{0.2}$		unproc	ADM		MWF		MWF-$N_{0.2}$	
		SNR0	SNR-12	SNR0	SNR-12	SNR0	SNR-12		SNR0	SNR-12	SNR0	SNR-12	SNR0	SNR-12
T	−10	0	−40	−10	−20	−5	−10	90	90	90	80	75	90	70
J	0	0	−25	0	0	0	0	90	90	90	80	75	90	90
H	0	0	0	0	0	0	−5	75	75	75	75	75	80	70
L	−15	−10	−15	−15	−15	−15	−20	90	90	80	90	90	85	90
O	0	50	−5	0	−5	0	−20	70	85	85	85	75	85	70
Average (°)	−5	8	−17	−5	−8	−4	−11	83	86	84	82	78	86	78
MAE av (°)	5	12	17	5	8	4	11	23	26	24	22	18	26	18
Min-max MAE	0-15	0-50	0-40	0-15	0-20	0-15	0-20	10-30	15-30	15-30	15-30	15-30	20-30	10-30
$S_{90}N_{-90}$	S_{90}							N_{-90}						
	unproc	ADM		MWF		MWF-$N_{0.2}$		unproc	ADM		MWF		MWF-$N_{0.2}$	
		SNR0	SNR-12	SNR0	SNR-12	SNR0	SNR-12		SNR0	SNR-12	SNR0	SNR-12	SNR0	SNR-12
T	75	0	−60	90	90	85	70	−60	−60	0	−75	−65	−85	−70
J	90	15	75	90	85	90	90	−90	−70	−80	−85	−85	−90	−90
H	65	20	20	65	55	75	45	−85	−60	−65	−65	−75	−75	−90
L	90	−5	85	90	80	90	75	−75	−55	−25	−65	−60	−70	−80
O	70	50	75	85	60	75	65	−90	−70	−35	−65	−40	−60	−60
Average (°)	78	16	39	84	74	83	69	−80	−63	−41	−71	−65	−76	−78
MAE av (°)	8	74	51	6	16	7	21	10	27	49	19	25	14	12
Min-max MAE	0-25	40-95	5-150	0-25	0-35	0-15	0-45	0-30	20-35	10-90	5-25	5-50	0-30	0-30
$S_{45}N_{-45}$	S_{45}							N_{-45}						
	unproc	ADM		MWF		MWF-$N_{0.2}$		unproc	ADM		MWF		MWF-$N_{0.2}$	
		SNR0	SNR-12	SNR0	SNR-12	SNR0	SNR-12		SNR0	SNR-12	SNR0	SNR-12	SNR0	SNR-12
T	75	75	55	75	80	60	75	−80	−60	−60	−90	−60	−90	−75
J	85	70	90	90	90	90	90	−80	−90	−80	−80	−65	−90	−90
H	45	45	45	45	45	40	50	−60	−60	−70	−75	−50	−70	−80
L	80	75	90	75	65	70	80	−65	−45	−45	−65	−55	−65	−60
O	85	90	80	75	70	75	80	−65	−60	−75	5	−10	−50	−40
Average (°)	74	71	72	72	70	67	75	−70	−63	−66	−61	−48	−73	−69
MAE av (°)	29	26	27	27	25	24	30	25	20	21	36	19	30	26
Min-max MAE	0-40	0-45	0-45	0-45	0-45	5-45	5-45	15-35	0-45	0-35	20-50	5-45	15-45	5-45

IV. NOISE REDUCTION PERFORMANCE

Besides the evaluation of the localization performance of the noise reduction algorithms, which was the main focus of this study, all tested algorithms were evaluated with respect to the suppression of noise, since a trade-off may exist between localization and noise reduction performance. The noise reduction performance of the different algorithms was measured using two out of the three spatial scenarios presented earlier.

A. Test setup

Speech reception thresholds (SRTs) were measured using an adaptive test procedure (Plomp and Mimpen, 1979). The level of the speech signals was adjusted to determine the 50% speech recognition level, i.e., the SRT. The VU sentences were used as speech material (Versfeld *et al.*, 2000) and a multitalker babble, the same as the one used in the localization experiment, was used as jammer signal. The performance of the three algorithms was evaluated for spatial scenarios S_0N_{60} and $S_{90}N_{-90}$. Tests were performed in a sound attenuating booth. Stimuli were presented under headphones (TDH-39) using a RME Hamerfall DSPII soundcard and a Tucker Davis HB7 headphone driver. The setup was calibrated so that the sound pressure level of the noise signal averaged over the left and right ears was constant and equal to 65 dB A. The level of the speech signal was adjusted with a step size of 2 dB during the adaptive procedure. The group of five normal hearing subjects tested in the localization experiment was expanded to nine normal hearing subjects, since the noise reduction data of five normal hearing subjects only showed close to significant trends.

B. Results and analysis

Table IV shows the individual SRT values (decibel SNR) of the nine normal hearing subjects for the unprocessed condition, together with the SRT gain obtained using the different noise reduction algorithms ($=SRT_{algo}-SRT_{unproc}$). To compare performance between algorithms, Bonferroni corrected pairwise comparisons were performed on the SRT data for each spatial scenario.

TABLE IV. SRT data, in decibel SNR, for the unprocessed condition, and SRT gain, of the different noise reduction algorithms relative to the unprocessed condition. Nine normal hearing subjects were tested using three different noise reduction algorithms in the spatial scenarios S_0N_{60} and $S_{90}N_{-90}$. A lower SNR score and a higher gain are better. The row labeled effect shows whether a significant difference with the unprocessed condition was observed.

	SRT (decibel SNR)	Noise reduction gain		(decibel SRT)
	unproc	MWF*	MWF-$N^*_{0.2}$	ADM*
		S_0N_{60}		
T	−5,4	6,0	2,8	2,8
J	−5,4	2,0	2,4	1,6
H	−9,8	1,6	0,0	−0,4
L	−8,2	4,4	2,8	2,0
O	−6,6	2,8	2,0	0,0
N	−5,4	4,0	2,8	2,0
A	−6,2	3,2	3.2	2.4
B	−4,2	4,4	5,6	2,4
TB	−3,8	6,4	4,8	5,6
Average		3,9	2,9	2,0
Stdev		1,6	1,6	1,7
Effect		$p=0.001$	$p=0.003$	$p=0.045$
		$S_{90}N_{-90}$		
T	−6,6	4,0	2,8	−2,8
J	−8,2	0,4	4,0	−4,0
H	−11,4	2,0	1,6	−5,2
L	−12,6	−1,6	0,4	−4,8
O	−8,6	1,2	2,0	−4,4
N	−9,0	−0,8	0,0	−2,4
A	−9,8	0,0	2,4	−6,0
B	−7,4	0,0	1,6	−5,6
TB	−9,0	−1,6	1,6	−4,4
Average		0,4	1,8	−4,4
Stdev		1,8	1,2	1,2
Effect		$p=1.000$	$p=0.011$	$p<0.001$

For the scenario S_0N_{60}, all three noise reduction algorithms gave a significant gain in SRT. The gains were 2.0 dB for the ADM ($p=0.045$), 3.9 dB for the MWF ($p=0.001$), and 2.9 dB for the MWF-$N_{0.2}$ ($p=0.003$). The MWF significantly outperformed the ADM by 1.2 dB ($p=0.003$). No significant difference was observed between the MWF and the MWF-$N_{0.2}$ ($p=0.392$), although six out of nine subjects performed more poorly with the MWF-$N_{0.2}$.

For the scenario $S_{90}N_{-90}$, a significant loss of 4.4 dB in SNR of the ADM was found ($p<0.001$). Moreover, the ADM performed significantly more poorly than all other algorithms (all comparisons $p<0.001$). The MWF gave no clear advantage over the unprocessed condition, with an average gain of 0.4 dB ($p=1.000$). The MWF-$N_{0.2}$ was the only algorithm that gave a significant SRT gain with an average gain of 1.8 dB ($p=0.011$). No significant difference was observed between the MWF and the MWF-$N_{0.2}$ ($p=0.166$), although seven out of nine subjects showed better performance with the MWF-$N_{0.2}$ than with the MWF.

V. DISCUSSION

Four research questions were raised related to the combined goals of improving speech perception in noise while preserving sound source localization using multimicrophone noise reduction algorithms. The results and analyses from the previous sections are used to answer these questions.

A. The influence of a dual-monaural ADM on the localization of sound sources

As a reference noise reduction algorithm for evaluating two recently introduced MWF-based noise reduction strategies for hearing aids, an ADM was used. Such a system is commonly implemented in current hearing aids to enhance speech perception in noise. In Secs. III E 1 and III E 2 it was observed that localization performance using the ADM was comparable to that for the unprocessed condition for spatial scenarios S_0N_{60} and $S_{45}N_{-45}$. However, a large degradation was found for scenario $S_{90}N_{-90}$ (Tables I and III), which was statistically verified for the speech component (Sec. III E 1). Perceptual evaluation showed that in spatial scenario $S_{90}N_{-90}$, the signals generated by the ADM were often described as being diffuse with no directional information present in the signal. Neither the perceptual data nor the statistical analysis showed a significant impact of SNR on localization performance.

The negative impact of adaptive and fixed directional microphones on localization performance was also observed in the work of Van den Bogaert *et al.* (2006) and Keidser *et al.* (2006). In Van den Bogaert *et al.* (2006), hearing-impaired users showed a significant decrease in localization performance when using their ADM systems compared to using omnidirectional microphones. This was observed when localizing a broadband stimulus in a noisy environment with the noise sources positioned at ±90°. A separate analysis showed that this was due to localization errors made when stimuli were presented from the sides, between ±60° and ±90°, of the head. When testing the ADM in silence with a broadband stimulus, no significant decrease in localization performance was observed. Keidser *et al.* (2006) tested the influence of multichannel wide dynamic range compression (WDRC), single channel noise reduction and directional microphones on localization performance. They observed that directional microphone settings had the largest influence on localization performance. The aspect of different directional microphone characteristics for the left and right hearing aids was assessed, using an omnidirectional pattern in both hearing aids as a reference condition. Combining a cardioid pattern at one ear with a figure-8 pattern at the other ear produced the largest decrease in localization performance. It was suggested that this could be an extreme hearing aid setting when using an ADM at both sides of the head.

In hearing aids, an ADM is typically constrained to avoid noise reduction and distortion of signals arriving from the front. For the scenarios S_0N_{60} and $S_{45}N_{-45}$, both the speech and the noise source were within or close to this area. Therefore, the interaural cues of the speech and noise components remained unchanged. However, due to this constraint, noise reduction will typically be limited in these areas. This was illustrated by the limited noise reduction performance of the ADM scheme in scenario S_0N_{60} (Sec. IV B, Table IV). Outside this area, sounds are suppressed. Therefore, both speech and noise sources were suppressed in

the spatial scenario $S_{90}N_{-90}$ which led to the negative noise reduction performance (−4.4 dB) of the ADM.

Van den Bogaert *et al.* (2005) showed that distortion of ITD cues was proportional to the amount of noise reduction for a fixed and an ADM. This explains the drop in localization accuracy for scenario $S_{90}N_{-90}$ compared to the other spatial scenarios and compared to the unprocessed condition (Sec. III E 1). This is also illustrated by the work of Keidser *et al.* (2006), in which ITD and ILD measurements on directional microphones showed large ITD and ILD distortion at angles around 90° and much lower distortion between +50° and −50°.

Localization performance for the ADM was independent of SNR (Secs. III E 1 and III E 2). This can be explained by the fact that the ADM is based on exploiting physical differences in time of arrival between the microphones in the hearing aid, which are independent of SNR. Since the coherence between microphone signals was used to attenuate the strongest source in the back hemisphere, the most coherent part of the noise signal was removed. This would explain the classification of the output as sounding "diffuse."

B. The influence of the binaural MWF on the localization of sound sources

Doclo *et al.* (2006) mathematically proven that a binaural version of the MWF perfectly preserves the interaural cues of the speech component but changes the cues of the noise component into those of the speech component. This was also observed in ITD-error simulations, used to predict localization performance in the work of Klasen *et al.* (2007). As a consequence, large localization errors of the noise component were expected in the subjective evaluation discussed in this manuscript. These errors were indeed observed and statistically confirmed for the SNR=0 dB condition when the filtered speech and noise component were presented separately to the subjects (S,N). However, they were not observed when SNR=−12 dB (Sec. III E 1) nor when the speech and noise sources were presented simultaneously (S+N) (Sec. III E 2).

This can be explained using the subjective classification in Table II. Despite the good localization performance for the SNR=−12 dB condition, Table II suggests a decrease in sound quality for both SNRs. Subjects reported that the noise component at the output of the MWF sounded as if it was produced by sound sources at two different positions, one at the original noise position which sounded relatively clear and one at the speech position which sounded more distorted. In the SNR=−12 dB condition, subjects preferred the sound arriving from the original noise location, often resulting in a correct localization of the noise component. In the SNR=0 dB condition, subjects preferred the sound arriving from the original speech location. However, individual subjects did not follow this general trend, e.g., for spatial scenarios $S_{90}N_{-90}$ and $S_{45}N_{-45}$, subject O preferred the sound arriving from the original speech location when using a MWF at a SNR=−12 dB. This demonstrates that the variability between subjects in the MWF conditions can be explained by the dual-sound phenomenon.

The reason for the dual sounds can be found in the filter generation of the MWF. Since the speech correlation matrix is estimated as $\mathbf{R}_x=\mathbf{R}_y-\mathbf{R}_n$ (Sec. II B), where $\mathbf{R}_y$ and $\mathbf{R}_n$ were computed during different time periods, this estimate will be poor at a low SNR. Hence, in the frequency region with high SNR (in our case between 3000 and 5500 Hz, see Fig. 2), a good estimate was obtained, such that the interaural cues of the noise component were changed into those of the speech component, as illustrated by Fig. 3. On the other hand, in the frequency region with low SNR (in our case between 500 and 3000 Hz, see Fig. 2), a poor estimate was obtained, such that the output contained interaural cues corresponding to the original position of the noise source. Because of these different behaviors for different frequency regions, a dual sound was created. For the low overall SNR, i.e., SNR=−12 dB, a large proportion of the noise component contained the interaural cues of the original noise angle, which resulted in a correct localization of the noise component (Table I).

Figure 3 shows the cross-correlation function and the ILD between the left and right ear signals of the unprocessed speech and noise components and of the noise component processed by the MWF and the MWF-N. These are given for the spatial scenario $S_{90}N_{-90}$ at SNR=−12 and 0 dB. The ILDs were calculated using third-order butterworth filters with cutoff frequencies based on the Bark scale (Zwicker, 1961). The cross-correlation functions, used to interpret ITD information, were calculated for the low-pass filtered left and right ear signals and were normalized to a maximum value of 1 for identical signals. A cutoff frequency of 1000 Hz was used, since the most relevant ITD information for the human auditory system is present at frequencies below 1000 Hz, e.g., Hartmann (1999). The ITD is approximated by the delay for which the cross-correlation function reaches its maximum.

For SNR=0 dB, the ITD of the MWF noise component was shifted toward the ITD of the original speech component. Also, the amplitude of the cross correlation, the amount of coherence between the left and right signals, and the width of the curve totally agree with the curve for the original speech component. Also, the ILDs of the MWF processed noise component were shifted toward those of the speech component for SNR=0 dB, except for a small region around 1000 Hz, which could be due to the low input SNR in this region (Fig. 2).

For SNR=−12 dB, the cross-correlation function of the processed noise component was shifted toward that for the speech component. However, a second peak was present around −500 μs. Also the curve was somewhat more flat than the curve for SNR=0 dB, meaning that the ITD information was less coherent than for the SNR=0 dB condition. The ILD plots show that only ILDs for frequencies between 3000 and 5500 Hz (the region with a high input SNR) were shifted toward the ILDs for the unprocessed speech component. These observations, especially at SNR=−12 dB, illustrate the dual-sound phenomenon and explain the improved localization performance when using the MWF at SNR=−12 dB compared to SNR=0 dB.

The dual-sound phenomenon also explains the good lo-

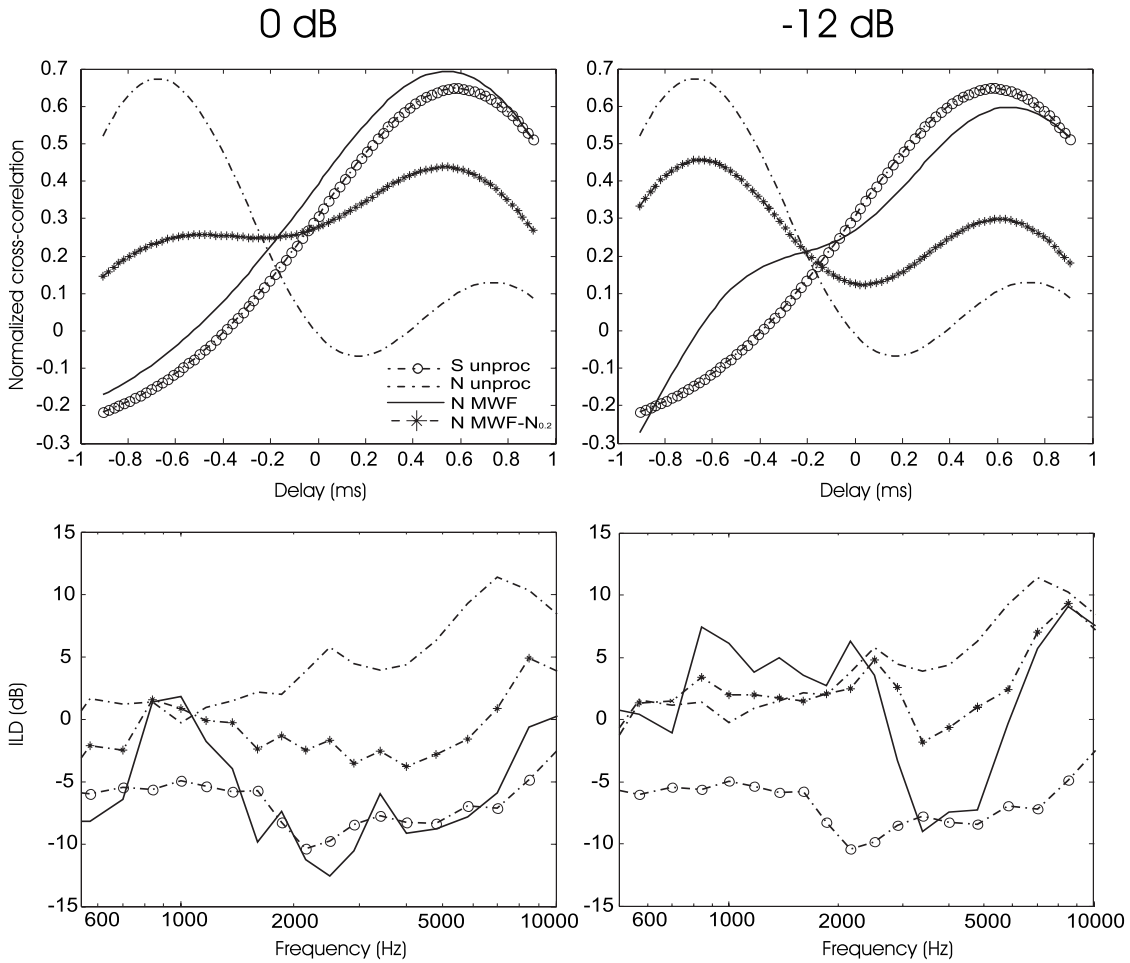

FIG. 3. ILD and cross-correlation functions between the left and right ear signals for the unprocessed speech and unprocessed noise components together with the MWF and MWF-$N_{0.2}$ processed noise components. This is shown for spatial scenario $S_{90}N_{-90}$. ILDs were calculated using a critical band analysis (bark bands).

calization performance when the speech and noise sources were played simultaneously (S+N). In this condition, the speech component masked parts of the frequency spectrum of the noise component at the output of the algorithm. The noise component was masked mostly in frequency regions with a good noise reduction performance. This is exactly the region where the interaural cues of the noise component were shifted toward the interaural cues of the speech component. When the sounds were played simultaneously, the part of the noise component with the incorrect cues was masked by the speech component. Due to this masking, the noise source could be correctly localized when using the MWF.

The significant effect of SNR and presentation format (S,N or S+N) illustrates that testing algorithms on localization performance in laboratory conditions is not straightforward and results should be interpreted carefully when generalizing to real world situations. Both presentation formats (S,N and S+N) could be relevant to real-life situations. Speech and noise presented simultaneously could be relevant to situations with converged filters and speech and noise sources playing continuously. Presenting speech and noise component separately could be relevant for the gaps present in the speech or noise components, e.g., when pauses are present in sentences.

C. The improvement in localization performance for MWF-N relative to MWF

Klasen *et al.* (2007) showed that the ITD error of the noise component generated by the MWF could be decreased by extending this algorithm to the MWF-N. It was suggested that this could result in improved localization performance. The perceptual relevance of the MWF-N was proven in Sec. III E. Large improvements were observed for all spatial scenarios when the speech and noise components were presented separately (S,N) for an input SNR=0 dB. In the other conditions, less or no room for improvement was available due to the reasons explained in the evaluation of the MWF (masking, errors in estimating the speech correlation matrix at low SNR). Hence, no statistical evidence of improvement was found for these conditions. However, nonsignificant trends were sometimes observed and a subset of the data, i.e., the data for the noise component at S+N at both SNRs in the spatial scenario $S_{90}N_{-90}$ did show significantly better performance for the MWF-N than for the MWF. Although the MWF-$N_{0.2}$ improved localization performance of the MWF to that for the unprocessed condition, a difference in perceptual evaluation remained. When presenting speech and noise components separately, the output signals of the MWF-$N_{0.2}$ were still described as arriving from two different directions

(Table II). Adding more of the unprocessed signal (e.g., MWF-$N_{0.3}$) would probably improve the sound quality but would further decrease noise reduction performance.

Figure 3 illustrates the interaural information present in the MWF and MWF-N processed noise components. When comparing the MWF curves with those for the MWF-N, it is observed that the distorted ILD and ITD cues at the output of the MWF were corrected toward the values for the unprocessed condition when using the MWF-$N_{0.2}$. This is true for both SNR=−12 and SNR=0 dB. Still, both the cross correlation and ILD graphs illustrate that not all cues were corrected. The cross-correlation curves for the signals at the output of the MWF-N still show a local maximum around the peak generated by the original speech component and the ILD cues for some frequency regions remain close to the ILD cues for the original speech component. This was observed more for SNR=0 dB than for SNR=−12 dB, since the MWF introduced larger distortions at high SNRs, meaning that a larger correction factor η was needed in this condition. This is consistent with the dual-sound phenomenon which was observed, despite the good localization performance, when using the MWF-N in the S,N condition.

D. Overall comparison of the ADM, MWF, and MWF-N

For the spatial scenario S_0N_{60}, Table IV shows that both the binaural MWF and the binaural MWF-N outperformed the dual-monaural ADM in terms of noise reduction. This is logical since the MWF is not constrained to suppressing sound sources only in the rear hemisphere. No significant difference in speech perception was found between the MWF and MWF-N. This occured despite the introduction of the unprocessed component in the MWF-N scheme [Eqs. (11) and (12)]. In scenario S_0N_{60}, the ADM perfectly preserved localization performance for both the speech and noise components, since almost no processing was done on the speech and noise components. The MWF preserved the ability to localize the speech component but not always the ability to localize the noise component, especially when speech and noise sources were presented separately at a high SNR (Table I). The MWF-N seems to enable the user to localize both the speech and the noise sources correctly at the cost of some noise reduction, e.g., 1.0 dB compared to the MWF (Sec. IV B).

For the spatial scenario $S_{90}N_{-90}$, the ADM gave a large drop in noise reduction performance, since it is designed to remove sounds not arriving from the front. Therefore, in scenario $S_{90}N_{-90}$ both the speech and the noise components were suppressed. The processing of these signals was accompanied by a large drop in localization performance (Tables I and III) which was discussed in Sec. V A. Again, the MWF outperformed the ADM in terms of noise reduction but not in terms of localization of the noise component at high SNRs (see Table I, Sec. V B). The MWF-$N_{0.2}$ seems to enable the user to combine correct sound source localization (Table I) with good noise reduction performance (see Table IV). Interestingly, the MWF-$N_{0.2}$, which adds an unprocessed component to the MWF output, outperformed the MWF in terms of noise reduction in this spatial scenario (Table IV). This might be explained by the improved localization performance when using the MWF-$N_{0.2}$ compared to the MWF (Sec. III E 1), which might have led to better speech segregation due to spatial unmasking.

VI. CONCLUSIONS

In this paper, four research questions were addressed which are related to the influence of noise reduction techniques for hearing aids on the localization of sound sources. First, the localization performance of normal hearing subjects was quantified using a dual-monaural noise reduction system, namely, an ADM which is commonly used in current high-end hearing aids. The ADM led to a significant drop in localization performance when sounds were presented from outside the frontal direction. As second and third research questions, two newly proposed binaural noise reduction algorithms were evaluated in terms of localization performance. The binaural MWF led to good localization performance for the speech component. The noise component on the other hand could be perceived as arriving from the location of the speech component when the speech and noise components were presented separately to the subjects. However, localization performance when using the MWF was in many cases better than expected due to errors in the estimation of the speech correlation matrix and due to masking effects when the speech and noise components were presented simultaneously. Results for the binaural MWF-N showed that, by adding part of the unprocessed signal (η =0.2) to the output of the MWF, localization of the noise component improved. Hence, no significant difference in localization performance was found in all scenarios when comparing the MWF-N to the unprocessed condition for both the speech and the noise components. Fourth, the combination of noise reduction and localization performance was studied, leading to the conclusion that the dual-monaural ADM configuration was not able to provide both good localization of the speech and the noise components and good noise reduction performance. On the other hand, the MWF-N enables correct sound localization of both the speech and the noise components, together with good noise reduction performance. Both MWF and MWF-N were based on a statistical Wiener filter approach. This is different from the ADM, which used the physical delay between microphones to improve the SNR. We suggest that MWF-based, binaural noise reduction techniques might introduce a better combination of sound source localization and noise reduction performance compared to a traditional ADM.

The full data set consisted of many conditions: two different ways of presenting stimuli, three spatial scenarios, four different algorithms, and two SNRs. Therefore, the subset of data for each condition became relatively small and due to this limitation, small differences between algorithms may have been undetected. However, even these limited subsets of data were sufficient to illustrate effects of, and differences between, noise reduction algorithms. Moreover, it was shown that interpreting results of localization experiments with noise reduction systems is not straightforward since these results are dependent on spatial scenario, SNR, and

masking effects. Further research, involving larger data sets for each condition, might reveal smaller differences between algorithms.

ACKNOWLEDGMENTS

T.V.d.B was funded by a Ph.D. grant of the Institute for the Promotion of Innovation through Science and Technology in Flanders (IWT-Vlaanderen). This research was partly carried out in the framework of the K.U.Leuven Concerted Research Action GOA-AMBioRICS. The authors would like to thank Steffen Fieuws of the Biostatistical center of the K.U.Leuven. The authors would also like to thank both reviewers and Brian Moore for their detailed comments, which significantly improved the manuscript.

[1]Typically M_I equals the number of microphones on the hearing aid at a given ear (for the left hearing aid: $M_I=M_L$). M_C can be constrained due to power or bandwidth limitations of the binaural link (for the left hearing aid: $M_C \leqslant M_R$). In theory M_I and M_C can be different for the left and the right hearing aids. For reasons of clarity, we assume this is not the case.

Aichner, R., Buchner, H., Zourub, M., and Kellerman, W. (**2007**). "Multichannel source separation preserving spatial information," in *Proceedings IEEE International Conference on Acoustics, Speech and Signal Processing (ICASSP)*, pp. I5–I8.

Blauert, J. (**1997**). *Spatial Hearing: The Psychophysics of Human Sound Localization*, revised ed. (The MIT Press, Cambridge).

Bronkhorst, A. W., and Plomp, R. (**1988**). "The effect of head-induced interaural time and level differences on speech intelligibility in noise," J. Acoust. Soc. Am. **83**, 1508–1516.

Bronkhorst, A. W., and Plomp, R. (**1989**). "Binaural speech intelligibility in noise for hearing impaired listeners," J. Acoust. Soc. Am. **86**, 1374–1383.

Byrne, D., Sinclair, S., and Noble, W. (**1998**). "Open earmold fittings for improving aided auditory localization for sensorineural hearing losses with good high-frequency hearing," Ear Hear. **19**, 62–71.

Desloge, J. G., Rabinowitz, W. M., and Zurek, P. M. (**1997**). "Microphone-array hearing aids with binaural output part I: Fixed processing systems," IEEE Trans. Speech Audio Process. **5**, 529–542.

Doclo, S., Klasen, T. J., Van den Bogaert, T., Wouters, J., and Moonen, M. (**2006**). "Theoretical analysis of binaural cue preservation using multichannel Wiener filtering and interaural transfer functions," in *Proceedings International Workshop on Acoustic Echo and Noise Control (IWAENC)*, Paris, France, pp. 1–4.

Doclo, S., and Moonen, M. (**2002**). "GSVD-based optimal filtering for single and multi-microphone speech enhancement," IEEE Trans. Signal Process. **50**, 2230–2244.

Hartmann, W. M. (**1999**). "How we localize sound," Phys. Today **52**(11), 24–29.

Haykin, S. (**2002**). *Adaptive Filter Theory*, 4th ed. (Prentice Hall, New Jersey), Chap. 2, pp. 94–135.

Keidser, G., Rohrseitz, K., Dillon, H., Hamacher, V., Carter, L., Rass, U., and Convery, E. (**2006**). "The effect of multi-channel wide dynamic range compression, noise reduction, and the directional microphone on horizontal localization performance in hearing aid wearers," Int. J. Audiol. **45**, 563–579.

Klasen, T. J., Doclo, S., Van den Bogaert, T., Moonen, M., and Wouters, J. (**2006**). "Binaural multi-channel Wiener filtering for hearing aids: preserving interaural time and level differences," in *Proceedings IEEE International Conference on Acoustics, Speech and Signal Processing (ICASSP)*, Toulouse, France.

Klasen, T. J., Van den Bogaert, T., Moonen, M., and Wouters, J. (**2007**). "Binaural noise reduction algorithms for hearing aids that preserve interaural time delay cues," IEEE Trans. Signal Process. **55**, 1579–1585.

Lorenzi, C. S., Gatehouse, S., and Lever, C. (**1999**). "Sound localization in noise in normal hearing listeners," J. Acoust. Soc. Am. **105**, 1810–1820.

Lotter, T. (**2004**), "Single and multimicrophone speech enhancement for hearing aids," Ph.D. thesis, RWTH Aachen.

Luo, F. L., Yang, J., Pavlovic, C., and Nehorai, A. (**2002**). "Adaptive null-forming scheme in digital hearing aids," IEEE Trans. Signal Process. **50**, 1583–1590.

Maj, J. B., Wouters, J., and Moonen, M. (**2004**). "Noise reduction results of an adaptive filtering technique for dual microphone behind the ear hearing aids," Ear Hear. **25**, 215–229.

Noble, W., and Byrne, D. (**1990**). "A comparison of different binaural hearing aid systems for sound localization in the horizontal and vertical planes," Br. J. Audiol. **24**, 335–346.

Noble, W., Sinclair, S., and Byrne, D. (**1998**). "Improvements in aided sound localization with open earmolds: observations in people with high-frequency hearing loss," J. Am. Acad. Audiol **9**, 25–34.

Plomp, R., and Mimpen, A. R. (**1979**). "Improving the reliability of testing the speech reception threshold for sentences," Audiology **18**, 43–52.

Spriet, A., Moonen, M., and Wouters, J. (**2004**). "Spatially pre-processed speech distortion weighted multi-channel Wiener filtering for noise reduction," Signal Process. **84**, 2367–2387.

Van den Bogaert, T., Doclo, S., Moonen, M., and Wouters, J. (**2007**). "Binaural cue preservation for hearing aids using an interaural transfer function multichannel Wiener filter," in *Proceedings IEEE International Conference on Acoustics, Speech and Signal Processing (ICASSP)*, Vol. IV, pp. 565–568.

Van den Bogaert, T., Klasen, T. J., Moonen, M., and Wouters, J. (**2005**). "Distortion of interaural time cues by directional noise reduction systems in modern digital hearing aids," in *Proceedings IEEE Workshop on Applications of Signal Processing to Audio and Acoustics (WASPAA)*, New Paltz, NY, pp. 57–60.

Van den Bogaert, T., Klasen, T. J., Van Deun, L., Wouters, J., and Moonen, M. (**2006**). "Localization with bilateral hearing aids: without is better than with," J. Acoust. Soc. Am. **119**, 515–526.

Van Hoesel, R., Ramsden, R., and O'Driscoll, M. (**2002**). "Sound direction identification, interaural time delay discrimination, and speech intelligibility advantages in noise for a bilateral cochlear implant user," Ear Hear. **23**, 137–149.

Versfeld, N. J., Daalder, L., Festen, J. M., and Houtgast, T. (**2000**). "Method for the selection of sentence materials for efficient measurement of the speech reception threshold," J. Acoust. Soc. Am. **107**, 1671–1684.

Welker, D. P., Greenberg, J. E., Desloge, J. G., and Zurek, P. M. (**1997**). "Microphone-array hearing aids with binaural output part II: A two-microphone adaptive system," IEEE Trans. Speech Audio Process. **5**, 543–551.

Wightman, F. L., and Kistler, D. J. (**1992**). "The dominant role of low-frequency interaural time differences in sound localization," J. Acoust. Soc. Am. **91**, 1648–1661.

Wittkop, T., and Hohman, V. (**2003**). "Strategy selective noise reduction for binaural digital hearing aids," Speech Commun. **39**, 111–138.

Zurek, P. M., and Greenberg, J. E. (**2000**). "Two-microphone adaptive array hearing aids with monaural and binaural outputs," in *Proceedings of the Ninth IEEE DSP Workshop*, Hunt, TX.

Zwicker, E. (**1961**). "Subdivision of the audible frequency range into critical bands," J. Acoust. Soc. Am. **33**, 248–249.

A new sound coding strategy for suppressing noise in cochlear implants

Yi Hu and Philipos C. Loizou[a)]
Department of Electrical Engineering, University of Texas at Dallas, Richardson, Texas 75083-0688

(Received 15 August 2007; revised 10 April 2008; accepted 16 April 2008)

In the *n-of-m* strategy, the signal is processed through *m* bandpass filters from which only the *n* maximum envelope amplitudes are selected for stimulation. While this maximum selection criterion, adopted in the advanced combination encoder strategy, works well in quiet, it can be problematic in noise as it is sensitive to the spectral composition of the input signal and does not account for situations in which the masker completely dominates the target. A new selection criterion is proposed based on the signal-to-noise ratio (SNR) of individual channels. The new criterion selects target-dominated (SNR $\geq$ 0 dB) channels and discards masker-dominated (SNR $<$ 0 dB) channels. Experiment 1 assessed cochlear implant users' performance with the proposed strategy assuming that the channel SNRs are known. Results indicated that the proposed strategy can restore speech intelligibility to the level attained in quiet independent of the type of masker (babble or continuous noise) and SNR level (0–10 dB) used. Results from experiment 2 showed that a 25% error rate can be tolerated in channel selection without compromising speech intelligibility. Overall, the findings from the present study suggest that the SNR criterion is an effective selection criterion for *n-of-m* strategies with the potential of restoring speech intelligibility.
 [DOI: 10.1121/1.2924131]

PACS number(s): 43.66.Ts, 43.66.Sr [RYL] Pages: 498–509

I. INTRODUCTION

Current cochlear implant manufacturers offer several speech coding strategies to users (see review by Loizou, 2006). The Cochlear Corporation, for instance, offers the advanced combination encoder (ACE) strategy and the continuous interleaved sampling (CIS) strategy (Vandali *et al.*, 2000). Both ACE and CIS strategies are based on channel vocoder principles dating back to Dudley's VODER in the 1940s (Dudley, 1939; Peterson and Cooper, 1957). Signal is decomposed into a small number of bands (16–22) via the fast Fourier transform or a bank of bandpass filters, and the envelopes are extracted from each band. The envelopes are used to modulate biphasic pulses which are in turn sent to the electrodes for stimulation. The number of envelopes (and number of electrode sites) selected for stimulation at each cycle differs between the CIS and ACE strategies. In the ACE strategy, only a subset *n* (n=8–10) out of 22 envelopes is selected and used for stimulation at each cycle and all 22 electrode sites are utilized for stimulation. In the CIS strategy, a fixed number (8–10) of envelopes are computed, and only the corresponding electrode sites (8–10) are used for stimulation. Several studies (Kim *et al.*, 2000; Kiefer *et al.*, 2001; Skinner *et al.*, 2002a, 2002b) have shown that most Nucleus-24 users prefer the ACE over the CIS strategy[1] and in most conditions perform as well or slightly better on speech recognition tasks (Kiefer *et al.*, 2001; Skinner *et al.*, 2002b). The ACE strategy belongs to the general category of *n-of-m* strategies, which select (based on an appropriate criterion) *n* envelopes out of a total of *m* ($n<m$) envelopes for stimulation, where *m* is typically set to the number of electrodes available.

The selection criterion used in the ACE strategy is the maximum amplitude. More specifically, 8–12 maximum envelope amplitudes are typically selected out of 22 envelopes for stimulation in each cycle.[2] Provided the signal is preemphasized for proper spectral equalization (needed to compensate for the inherent low-pass nature of the speech spectrum), the maximum selection works well as it captures the perceptually relevant features of speech such as the formant peaks. In most cases, the maximum selection criterion performs spectral peak selection. Alternative selection criteria were proposed by Noguiera *et al.* (2005) based on a psychoacoustic model currently adopted in audio compression standards (MP3). In their proposed scheme, the amplitudes which are farthest away from the estimated masking thresholds are retained. The idea is that amplitudes falling below the masking threshold would not be audible and should therefore be discarded. The new strategy was tested on sentence recognition tasks in speech-shaped noise (SSN) at 15 dB signal-to-noise ratio (SNR) and compared to ACE. A large improvement over ACE was noted when four channels were retained in each cycle, but no significant difference was found when eight channels were retained.

The maximum selection criterion adopted in the ACE strategy works well in quiet as cochlear implant (CI) users fitted with the ACE strategy have been found to perform as well or slightly better than when fitted with the CIS strategy (Kiefer *et al.*, 2001; Skinner *et al.*, 2002b). In the study by Skinner *et al.* (2002b), 6 of the 12 subjects tested had significantly higher CUNY sentence scores with the ACE strategy than with the CIS strategy. Group mean scores on CUNY sentence recognition were 62.4% with the ACE strat-

a)Author to whom correspondence should be addressed. Tel.: (972)883-4617. FAX: (972) 883-2710. Electronic mail: loizou@utdallas.edu.

egy and 56.8% with the CIS strategy. The ACE strategy offers the added advantage of prolonged battery life since not all electrodes need to be stimulated at a given instant. In noise, however, this criterion could be problematic for several reasons. First, the selected amplitudes could include information from the masker-dominated channels, thereby confusing the listeners as to which is the target and which is the masker. Second, the selection is done all the time for all segments of speech, including the low-energy segments where noise will most likely dominate and mask the target signal. Third, the maximum criterion may be influenced by the spectral distribution (e.g., spectral tilt) of the target and/or masker. If, for instance, the masker has high-frequency dominance, then the selection will be biased toward the high-frequency channels in that the high-frequency channels will be selected more often than the low-frequency channels. Clearly, a better selection criterion needs to be used to compensate for the above shortcomings of ACE in noise.

In the present study, we propose the use of channel-specific SNR as the criterion for selecting envelope amplitudes. More specifically, we propose to select a channel if its corresponding SNR is larger than or equal to 0 dB and discard channels whose SNR is smaller than 0 dB. The idea is that channels with low SNR, i.e., SNR <0 dB, are heavily masked by noise and therefore contribute little, if any, information about the speech signal. As such, those channels should be discarded. On the other hand, target-dominated channels (i.e., SNR $\geqslant 0$ dB) should be retained as they contain reliable information about the target. The proposed approach is partly motivated by the articulation index (AI) theory (French and Steinberg, 1947) and partly by intelligibility studies utilizing the ideal binary mask (IdBM) (e.g., Roman *et al.*, 2003; Brungart *et al.*, 2006; Li and Loizou, 2008). The AI model predicts speech intelligibility based on the proportion of time the speech signal exceeds the masked threshold (Kryter, 1962; ANSI, 1997). Hence, just like the AI model, the new SNR selection criterion assumes that the contribution of each channel to speech intelligibility depends on the SNR of that channel. As such, it is hypothesized that the SNR-based selection criterion will improve speech intelligibility.

A number of studies with normal-hearing listeners recently demonstrated high gains in intelligibility in noise with the IdBM technique (e.g., Roman *et al.*, 2003; Brungart *et al.*, 2006; Anzalone *et al.*, 2006; Li and Loizou, 2007, 2008). The IdBM takes values of 0 and 1, and is constructed by comparing the local SNR in each time-frequency (T-F) unit against a threshold (e.g., 0 dB). It is commonly applied to the T-F representation of a mixture signal and eliminates portions of a signal (those assigned to a "0" value) while allowing others (those assigned to a "1" value) to pass through intact. When the IdBM is applied to a finite number of channels, as in cochlear implants, it would retain the channels with a mask value of 1 (i.e., SNR $\geqslant 0$ dB) and discard the channels with a mask value of 0 (i.e., SNR <0 dB). Hence, the SNR selection criterion proposed in the present study is similar to the IdBM technique in many respects.

In the first experiment, we make the assumption that the true SNR of each channel is known at any given instance and assess performance of the proposed SNR selection criterion under ideal conditions. The results from this study will tell us about the full potential of using SNR as the new selection criterion and whether efforts need to be invested in finding ways to estimate the SNR accurately. It is not the intention of this study to compare the performance of ACE against CIS, as this has been done by others (Kiefer *et al.*, 2001; Skinner *et al.*, 2002b). Rather, the objective is to assess whether the new criterion, based on SNR, can restore speech intelligibility to the level attained in quiet as predicted by IdBM studies (Brungart *et al.*, 2006). One of the primary differences between prior IdBM studies and the present study (aside from the subjects used, normal-hearing versus cochlear implant users) is the number of channels used to process the stimuli. A total of 128 channels were used to synthesize the stimuli by Brungart *et al.*, (2006), while in the present study, only 16 channels of stimulation are available. Hence, it is not clear whether the intelligibility benefit seen in noise with the IdBM technique by normal-hearing listeners will carry through to cochlear implant users who only receive a limited amount of spectral information. The first experiment investigates the latter question. In a real system, signal processing techniques can be used to estimate the SNR (e.g., Ephraim and Malah, 1984; Hu *et al.*, 2007; Loizou, 2007, Chap. 7.3.3). Hence, in the second experiment, we assess the impact on intelligibility of the errors that can potentially be introduced when the SNR is estimated via an algorithm. The latter experiment addresses the real-world implementation of the proposed technique and will inform us about the required accuracy of SNR estimation algorithms.

II. EXPERIMENT 1: EVALUATION OF SNR CHANNEL SELECTION CRITERION

A. Subjects and material

A total of six postlingually deafened Clarion CII implant users participated in this experiment. All subjects had at least four years of experience with their implant device. Biographical data for all subjects are presented in Table I. IEEE sentences (IEEE subcommittee, 1969) corrupted in multitalker babble (MB) (ten female and ten male talkers) and continuous speech-shaped noise (SSN) were used in the test. The IEEE sentences were produced by a male speaker and were recorded in our laboratory in a double-walled sound-attenuating booth. These recordings are available from Loizou (2007). The babble recording was taken from the AUDITEC CD (St. Louis, MO). The continuous (steady-state) noise had the same long-term spectrum as the test sentences in the IEEE corpus.

B. Signal processing

The block diagram of the proposed speech coding algorithm is shown in Fig. 1. The mixture signal is first bandpass filtered into 16 channels and the envelopes are extracted in each channel using full-wave rectification and low-pass filtering (200 Hz, sixth-order Butterworth). The frequency spacing of the 16 channels is distributed logarithmically

TABLE I. Biographical data for the subjects tested.

Subject	Gender	Age (yr)	Duration of deafness prior to implantation (yr)	CI use (yr)	Number of active electrodes	Stimulation rate (pulses/s)	Etiology
S1	Female	60	2	4	15	2841	Medication
S2	Male	42	1	4	15	1420	Hydrops/Menier's syndrome
S3	Female	47	>10	5	16	2841	Unknown
S4	Male	70	3	5	16	2841	Unknown
S5	Female	62	<1	4	16	1420	Medication
S6	Female	53	2	4	16	2841	Unknown

across a 300 Hz–5.5 kHz bandwidth. In parallel, the true SNR values of the envelopes in each channel are determined by processing independently the masker and target signals via the same 16 bandpass filters and extracting the corresponding envelopes. The SNR computation process (shown at the bottom of Fig. 1) yields a total of 16 SNR values (1 for each channel) in each stimulation cycle (the SNR of channel i at time instant t is defined as $\mathrm{SNR}_i(t) = 10\log_{10}[x_i^2(t)/n_i^2(t)]$, where $x_i(t)$ is the envelope of the target signal and $n_i(t)$ is the envelope of the masker signal. Of the 16 mixture envelopes, only the mixture envelopes with SNR $\geqslant 0$ dB are retained while the envelopes with SNR <0 dB are discarded. The number of channels selected in each stimulation cycle (corresponding to a stimulation rate of 2841 pulses/s for most of our subjects) varies from 0 (i.e., none are selected) to 16 (i.e., all are selected). The selected mixture envelopes are finally smoothed with a low-pass filter (200 Hz) and log compressed to the subject's electrical dynamic range. The latter low-pass filter is used to ensure that the envelopes are smoothed and are free of any abrupt amplitude changes that may be introduced by the dynamic selection process.[3]

The SNR threshold used in the present study in the amplitude selection was 0 dB. This was a reasonable and intuitive criterion, as the objective was to retain the target-dominated channels and discard the masker-dominated channels. This threshold (0 dB) has been found to work well in prior studies utilizing the IdBM (Wang, 2005; Brungart *et al.*, 2006; Li and Loizou, 2008). The intelligibility study by Brungart *et al.* (2006) with normal-hearing listeners, for instance, showed that near perfect word identification scores can be achieved not only with a SNR threshold of 0 dB but with other SNR thresholds between −12 and 0 dB. Thus, we cannot exclude the possibility that other SNR thresholds can be used for cochlear implant users (and perhaps work equally well) and these thresholds might even vary across different subjects.

The above algorithm was implemented off-line in MATLAB and the stimuli were presented directly (via the auxiliary input jack) to CI users via the Clarion research interface platform. As the above algorithm was motivated by IdBM studies, we will be referring to it as the IdBM strategy.

C. Procedure

The listening task involved sentence recognition in noise. Subjects were tested in four different noise conditions: 5 and 10 dB SNRs in babble and 0 and 5 dB SNRs in SSN. Lower SNR levels were chosen for the SSN conditions to avoid ceiling effects as the pilot data showed that most subjects performed very well at 10 dB SNR. Two sentence lists (ten sentences/list) were used for each condition. The sen-

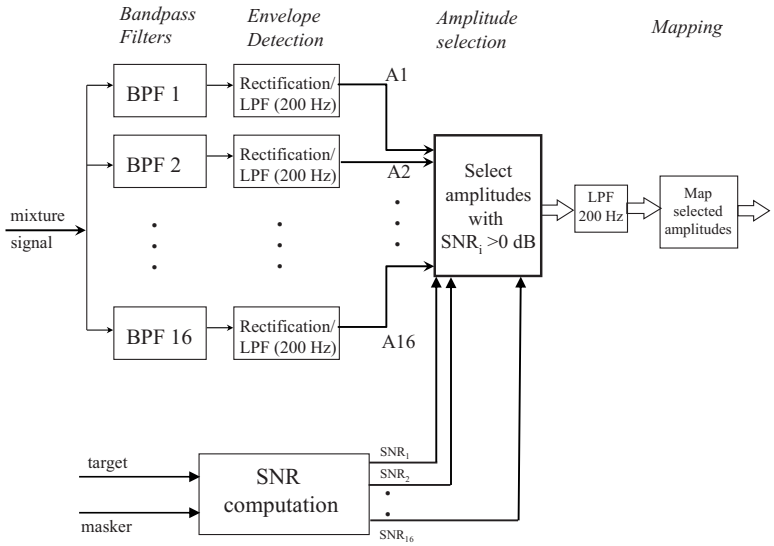

FIG. 1. Block diagram of the proposed coding strategy (IdBM).

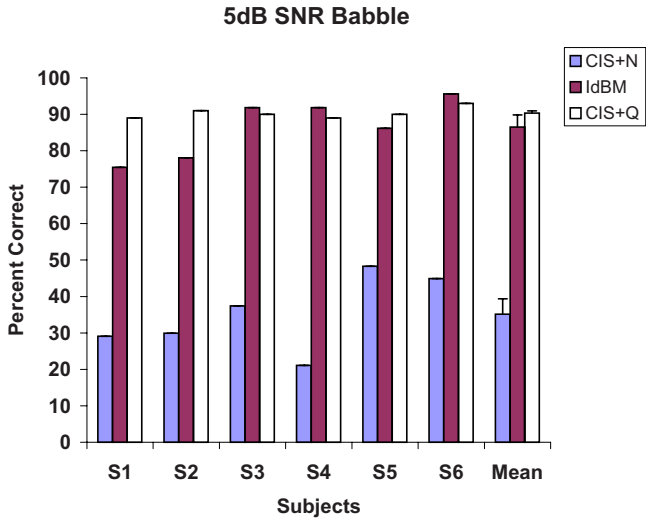

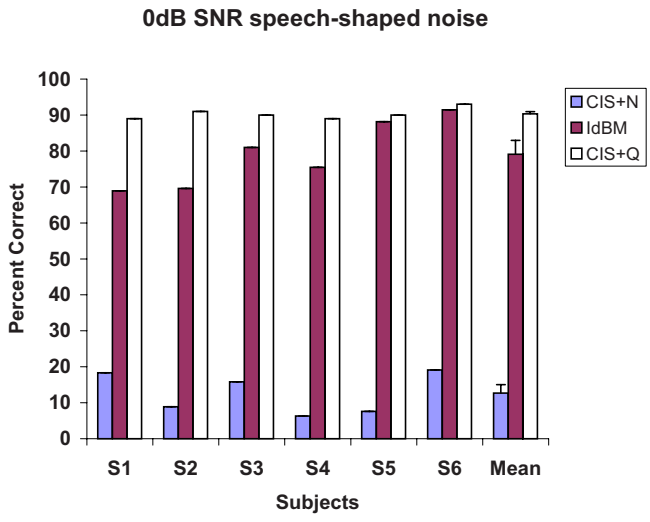

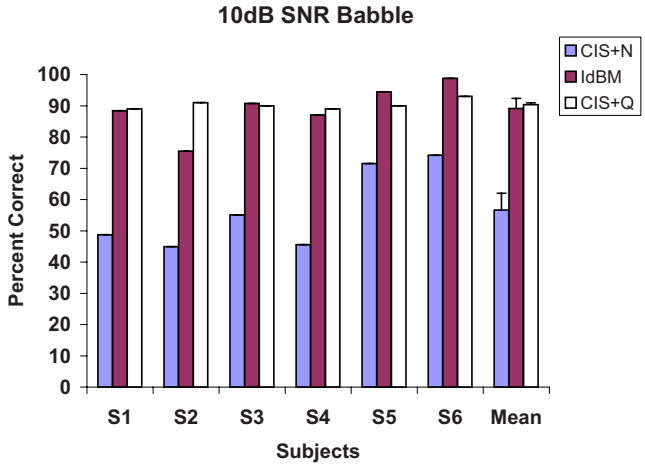

FIG. 2. (Color online) Percentage of correct scores of individual subjects, obtained with IdBM for recognition of sentences presented with MB at 5 and 10 dB SNRs. Scores obtained with the subject's everyday processor in quiet (CIS+Q) and in babble (CIS+N) are also shown for comparative purposes. The error bars indicate standard errors of the mean.

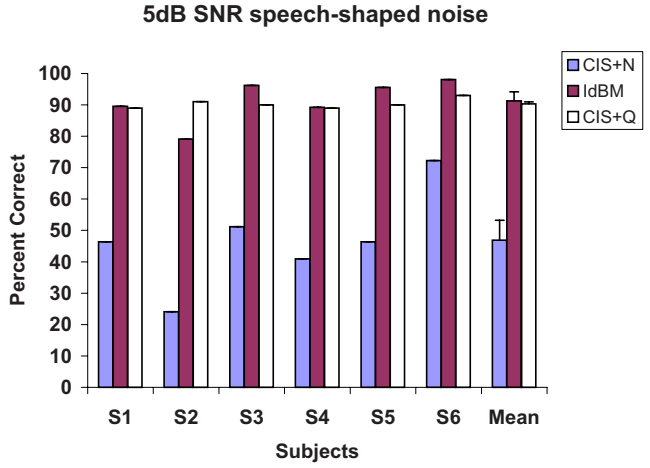

FIG. 3. (Color online) Percentage of correct scores of individual subjects, obtained with IdBM for recognition of sentences presented with SSN at 0 and 5 dB SNRs. Scores obtained with the subject's everyday processor in quiet (CIS+Q) and in noise (CIS+N) are also shown for comparative purposes. The error bars indicate standard errors of the mean.

tences were processed off-line in MATLAB by the proposed algorithm and presented directly (via the auxiliary input jack) to the subjects using the Clarion CII research platform at a comfortable level. For comparative purposes, subjects were also presented with unprocessed noisy sentences using the experimental processor. More specifically, the noisy sentences were processed via our own CIS implementation that utilized the same filters, same stimulation parameters (e.g., pulse width, stimulation rate, etc.), and same compression functions used in the IdBM strategy. Subjects were also presented with sentences in quiet. Sentences were presented to the listeners in blocks, with 20 sentences/block per condition. Different sets of sentences were used in each condition. Subjects were instructed to write down the words they heard, and no feedback was given to them during testing. The presentation order of the processed and control (unprocessed sentences in quiet and in noise) conditions was randomized for each subject.

D. Results and discussions

The sentences were scored by the percentage of the words identified correctly, where all words in a sentence were scored. Figure 2 shows the individual scores for all subjects for the multitalker babble (5 and 10 dB SNR) conditions and Fig. 3 shows the individual subject scores for the SSN (0 and 5 dB SNR) conditions. The scores obtained in quiet are also shown for comparison.

A separate statistical analysis was run for each masker condition. Two-way analysis of variance (ANOVA) (with repeated measures) was run to assess the effect of the noise level (quiet, 5 dB SNR, 10 dB SNR), effect of the processing (CIS versus IdBM), and possible interaction between the two. For the babble conditions, ANOVA indicated a highly significant effect of processing ($F[1,5]=142.5$, $p<0.0005$), significant effect of the noise level ($F[2,10]=51.5$, $p<0.0005$), and significant interaction ($F[2,10]=99.1$, $p<0.0005$). For the SSN conditions, ANOVA indicated a highly significant effect of processing ($F[1,5]=419.4$, $p<0.0005$), significant effect of noise level ($F[2,10]=105.7$, $p<0.0005$), and significant interaction ($F[2,10]=93.6$, $p<0.0005$).

Post hoc tests were run, according to Fisher's least significant difference (LSD) test, to assess differences between

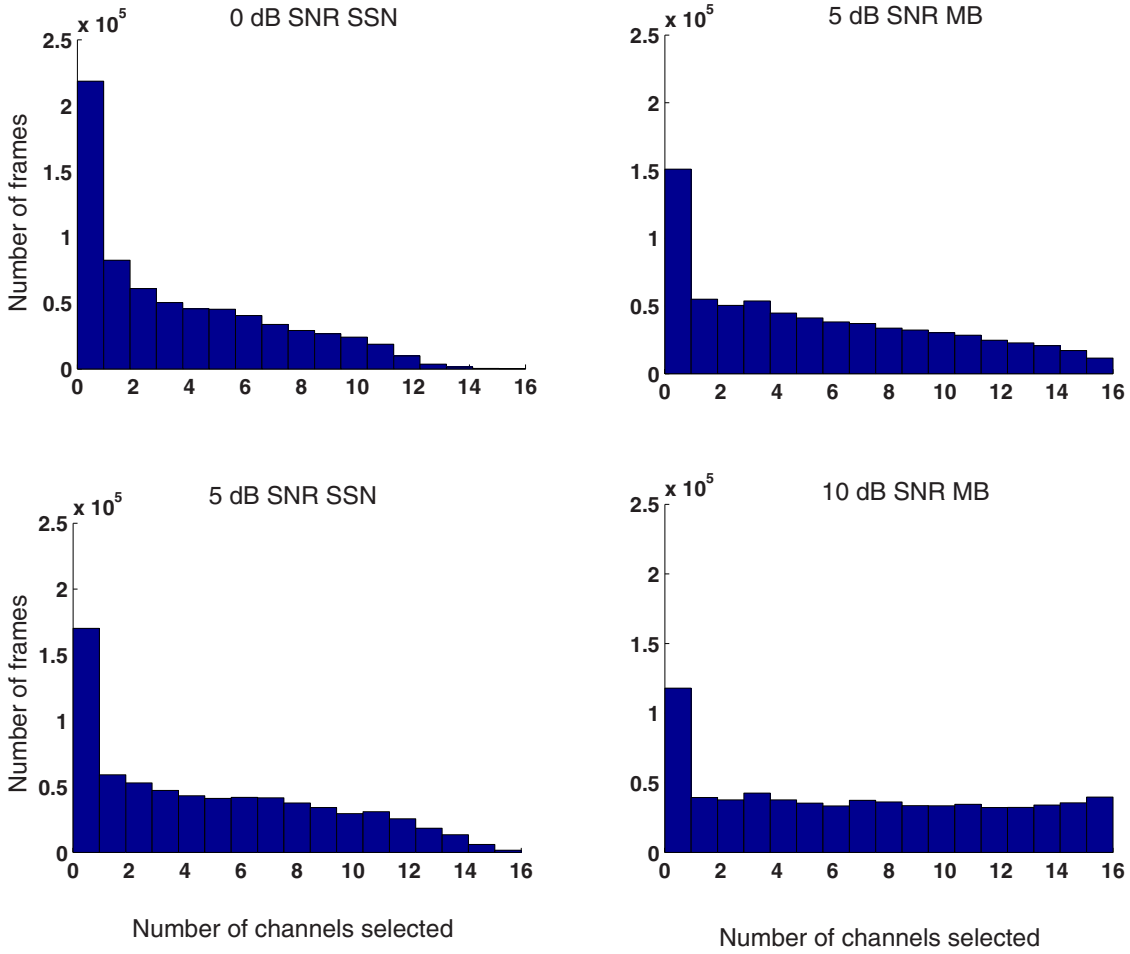

FIG. 4. (Color online) Histograms of the number of channels selected in each cycle by the IdBM strategy. The histograms were computed using a total of 20 IEEE sentences (~1 min of data) processed in the various conditions using MB and SSN as maskers.

scores obtained in noise with the proposed algorithm (IdBM) and scores obtained in quiet with the subject's daily strategy (CIS). Results indicated nonsignificant differences ($p > 0.3$) between scores obtained in noise with IdBM and scores obtained in quiet in nearly all conditions. The scores obtained with IdBM in 0 dB SNR SSN were significantly ($p = 0.009$) lower than the scores obtained in quiet. Nevertheless, the improvement over the unprocessed condition was quite dramatic, nearly 70 percentage points. The difference between scores obtained with IdBM and the scores obtained in noise with the subject's daily strategy (CIS) was highly significant ($p < 0.005$) in all conditions. Previous studies (Kiefer *et al.*, 2001; Skinner *et al.*, 2002b) have shown that ACE performs as well or better (by at most 10 percentage points) than CIS on various speech recognition tasks (some variability in the subject's scores and ACE versus CIS preferences was noted). Pilot data [4] collected with one subject indicated a similar outcome. Hence, we speculate that IdBM will perform significantly better than ACE in noise.

As shown in Figs. 2 and 3, the improvement obtained with IdBM over the subject's daily strategy was quite substantial and highly significant. The improvement was largest (nearly 70 percentage points) in 0 dB SSN as it improved consistently the subjects' scores from 10%–20% correct (base line noise condition) to 70%–90% correct. In nearly all conditions, the IdBM strategy restored speech intelligibility to the level obtained in quiet independent of the type of masker used (babble or steady noise) or input SNR level. The large improvements in intelligibility are consistent with those reported in IdBM studies (e.g., Brungart *et al.*, 2006), although in those studies, the signal was decomposed into 128 channels using fourth-order gammatone filters. The binary mask was applied in those studies to a fine T-F representation of the signal, whereas in the present study, it was applied to a rather coarse time-frequency representation (16 channels). Yet, the intelligibility gain was equally large.

Unlike the ACE strategy which selects the same number of channels (8–12 maximum) in each stimulation cycle based on the maximum criterion, the proposed IdBM strategy selects a different number of channels in each cycle depending on the SNR of each channel. In fact, IdBM may select as few as 0 or as many as 16 channels in each cycle for stimulation. To gain a better understanding of how many channels, on the average, are selected by IdBM or, equivalently, how many electrodes (on the average) are stimulated, we computed histograms of the number of channels selected in each cycle. The histograms were computed by using a total of 20 IEEE sentences processed in four noise conditions (two in MB and two in SSN). The four histograms are shown in Fig. 4 for the various SNR levels tested. As shown in Fig. 4, the most frequent number of channels selected was zero. In SSN, no channel was selected 25%–31% of the time, and in MB, no

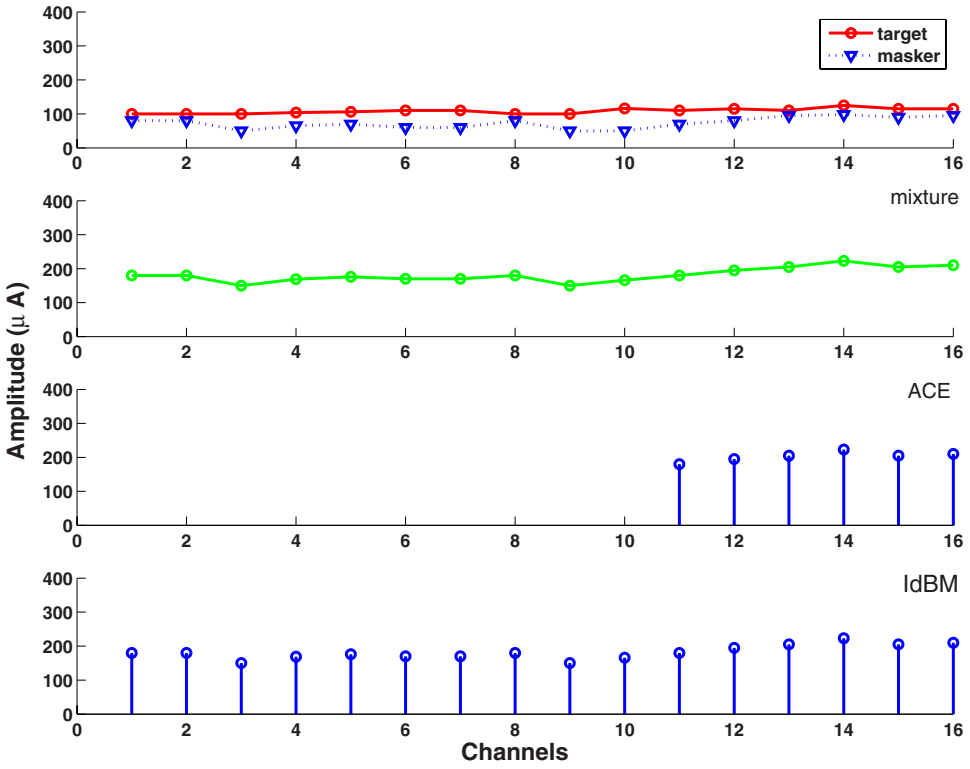

FIG. 5. (Color online) Example illustrating the selection process by ACE and IdBM strategies for a frame in which the target and mixture spectra are flat. The top panel shows the target and masker envelope amplitudes (in μAs) and the second panel from the top shows the mixture envelopes. The bottom two panels show the amplitudes selected by ACE and IdBM, respectively.

channel was selected 17%–21% of the time. This reflects the fact that low-energy speech segments (e.g., fricatives, stops, stop closures) occur quite often in fluent speech. These low-energy segments are easily and more frequently masked by background interference (compared to the high-energy voiced segments) yielding in turn a large number of occurrences of channels with SNR$<$0 dB. The distribution of the number of channels selected was skewed toward the low numbers for low SNR levels and became uniform for higher SNR levels. This reflects perhaps the fact that as the input global SNR level decreases, fewer channels with SNR $>$0 dB are available. The average number of channels selected (excluding zero) was five to six for the SSN conditions (0 and 5 dB SNRs) and seven to eight for the MB conditions (5 and 10 dB SNRs). The probability, however, of selecting a specific number of channels was roughly equal, indicating the flexibility of the SNR selection criterion in accommodating different target/masker scenarios and different spectral distributions of the input signal.

Two major factors influence the channel selection process and those include the spectral distribution of the target and the underlying SNR in each channel. Both factors are accommodated by the SNR selection criterion but not by the maximum selection criterion. Figures 5 and 6 show two examples in which the SNR criterion offers an advantage over the maximum criterion in selecting channels in the presence of background interference. Consider the example in Fig. 5 wherein the target (and mixture) spectrum is flat (e.g., fricative /f/) and the channel SNRs are positive. The IdBM strategy will select all channels, while the ACE strategy will only select a subset of the channels, i.e., the largest in amplitude. In this example, the ACE-selected channels might be perceived by listeners as belonging to a consonant with a rising-tilt spectrum or a spectrum with high-frequency dominance (e.g., /sh/, /s/, /t/). Hence, the maximum selection approach (ACE) might potentially create perceptual confusion between flat-spectra consonants (e.g., /f/, /th/, /v/) and rising-tilt or high-frequency spectra consonants (e.g., /s/, /t/, /d/). Consider a different scenario in Fig. 6, in which the target is completely masked by background interference, as it often occurs, for instance, during stop closures or weak speech segments. The IdBM strategy will not select any channel (i.e., no electrical stimulation will be provided) due to the negative SNR of all channels, whereas the ACE strategy will select a subset (the largest) of the channels independent of the underlying SNR. Providing no stimulation during stop closures or during low-energy segments in which the masker dominates is important for two reasons. First, it can, at least in principle, reduce masker-target confusions, particularly when the masker(s) is a competing voice(s) and happens to be present during speech-absent regions. In practice, an accurate algorithm would be required that would signify when the target is stronger than the masker (more on this in Sec. III D). Second, it can enhance access to voicing cues and reduce voicing and/or manner errors. As demonstrated in Fig. 4, the latter scenario happens quite often and the IdBM strategy can offer a significant advantage over the ACE strategy in target segregation. In brief, the IdBM strategy is more robust than ACE in terms of accommodating the spectral composition of the target and the underlying SNR. It is interesting to note that the SPEAK strategy (the predecessor of the ACE strategy), which was used in the Spectra 22 processor (Seligman and McDermott, 1995), selected five to ten channels depending on the spectral composition of the input signal, with an average number of six maxima. The SPEAK strategy, however, made no consideration for the underlying SNR of each channel and is no longer used in the latest Nucleus-24 speech processor (Freedom).

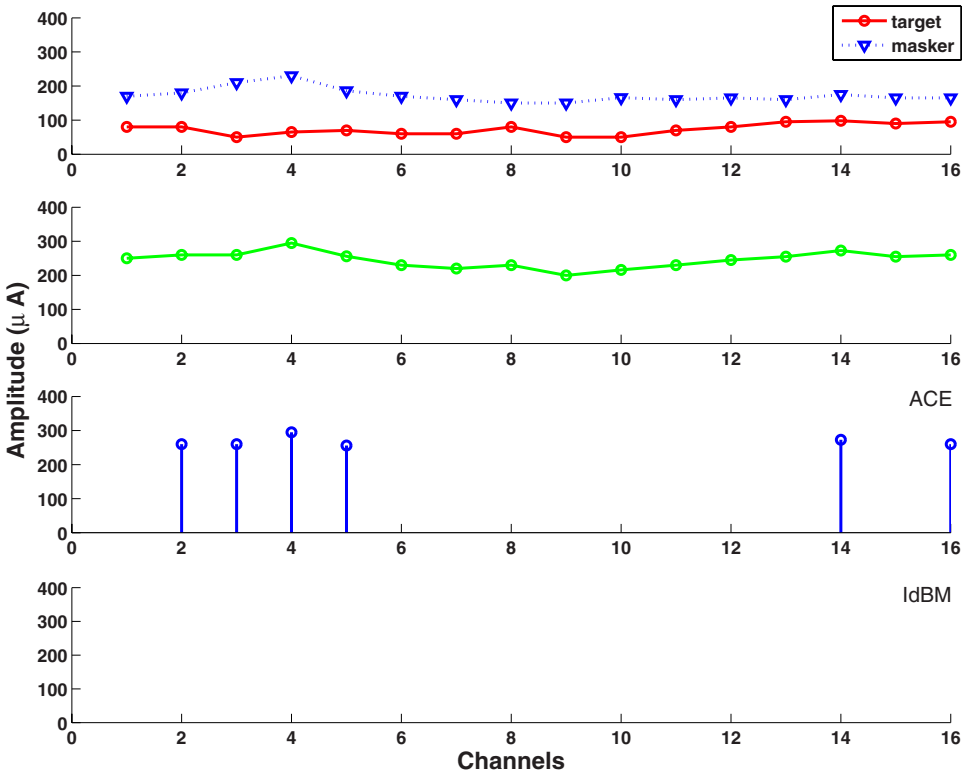

FIG. 6. (Color online) Example illustrating the selection process by ACE and IdBM strategies for a frame in which the masker dominates the target. The top panel shows the target and masker envelope amplitudes (in μAs) and the second panel from the top shows the mixture envelopes. The bottom two panels show the amplitudes selected by ACE and IdBM, respectively.

In fairness, it should be pointed out that there exist scenarios in which the maximum and SNR selection criteria select roughly the same channels (see example in Fig. 7). In voiced segments, for instance, where spectral peaks (e.g., formants) are often present, the maximum and SNR criteria will select roughly the same channels. Channels near the spectral peaks will likely have a high SNR (relative to the channels near the valleys) and will therefore be selected by both ACE and IdBM strategies. We therefore suspect that the partial agreement in channel selection between ACE and IdBM (more on this in experiment 2) occurs during voiced speech segments.

The SNR threshold used in the present study in the amplitude selection was 0 dB. Negative SNR thresholds might be used as well, as we acknowledge the possibility that masker-dominated channels could also contribute, to some

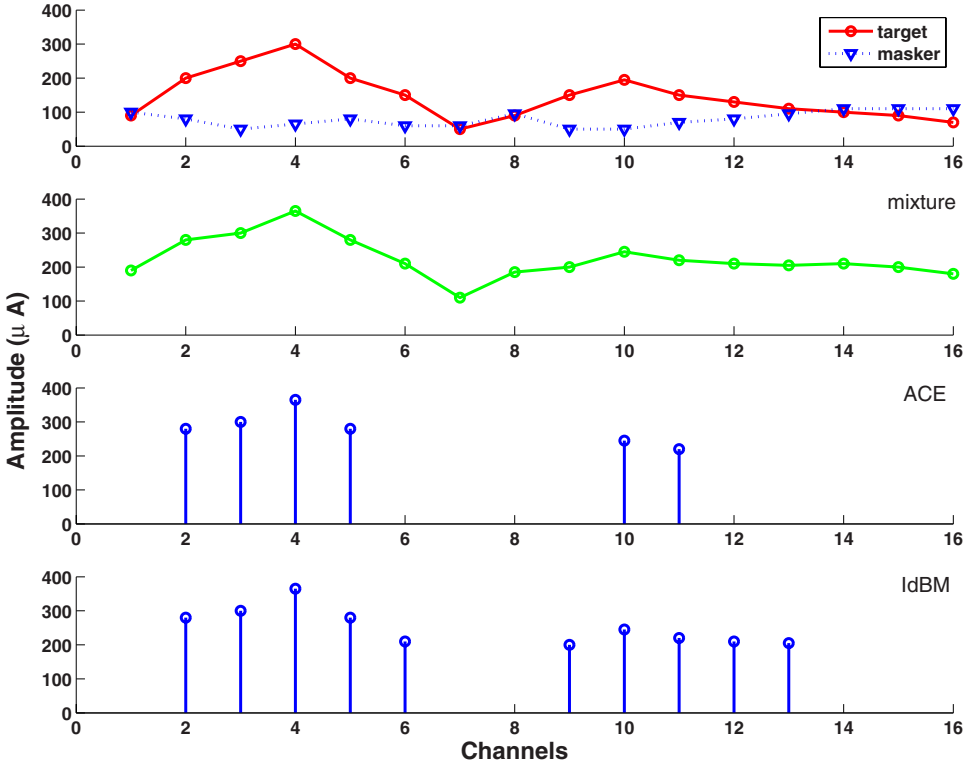

FIG. 7. (Color online) Example illustrating the selection process by ACE and IdBM strategies for a segment extracted from a vowel. The top panel shows the target and masker envelope amplitudes and the second panel from the top shows the mixture envelopes. The bottom two panels show the amplitudes selected by ACE and IdBM, respectively.

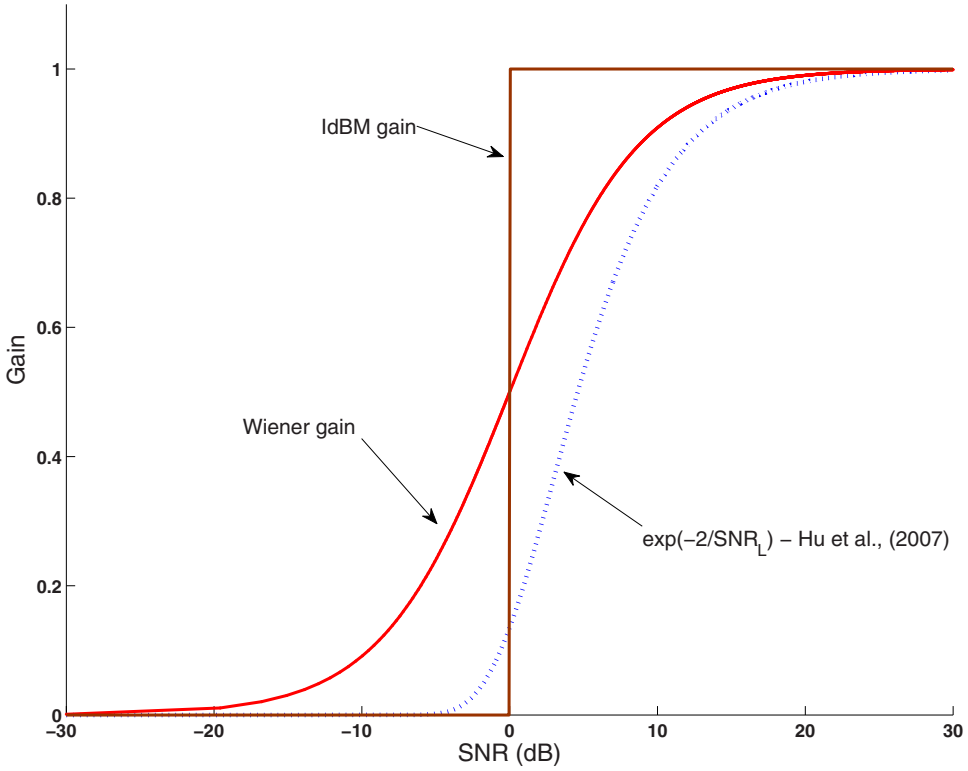

FIG. 8. (Color online) Plots of various gain functions that can be applied to mixture envelopes for noise suppression. The proposed IdBM strategy uses a binary function. The gain function used to Hu *et al.* (2007) was of the form $g(\mathrm{SNR}_L)=\exp(-2/\mathrm{SNR}_L)$, where SNR_L is the estimated SNR expressed in linear units. The Wiener gain function is superimposed for comparison and is given by the expression $g(\mathrm{SNR}_L)=\mathrm{SNR}_L/(\mathrm{SNR}_L+1)$.

extent, to intelligibility. In fact, Brungart *et al.* (2006) observed a plateau in performance (near 100% correct) for a range of SNR thresholds (−12 to 0 dB) smaller than 0 dB. Hence, we cannot exclude the possibility that other values (smaller than 0 dB) of SNR threshold might prove to be as effective as the 0 dB threshold.

The proposed *n-of-m* algorithm (IdBM) based on the SNR selection criterion can be viewed as a general algorithm that encompasses characteristics from both the ACE and CIS algorithms. When the SNR is sufficiently high (as, for instance, in quiet environments), $n=m$ (i.e., all channels will be selected) most of the time and the IdBM algorithm will operate like the CIS strategy. When n is fixed (for all cycles) to, say, $n=8$, then IdBM will operate similar to the ACE algorithm. In normal operation, the IdBM algorithm will be operating somewhere between the CIS and ACE algorithms. More precisely, in noisy environments, the value of n will not remain fixed but will change dynamically in each cycle depending on the number of channels that have positive SNR values.

The IdBM algorithm belongs to the general class of noise-reduction algorithms which apply a weight or a gain (typically in the range of 0–1) to the mixture envelopes (e.g., James *et al.*, 2002; Loizou, 2006; Hu *et al.*, 2007). The gain function of the IdBM algorithm is binary and takes the value of 0 if the channel SNR is negative and the value of 1 otherwise (see Fig. 8). Most noise-reduction algorithms utilize gain functions which provide a smooth transition from gain values near 0 (applied at extremely low SNR levels) to values of 1 (applied at high SNR values). Figure 8 provides two such examples. The Wiener gain function (known to be the optimal gain function in the mean-square error sense, see Loizou, 2007, Chap. 6) is plotted in Fig. 8 along with the sigmoidal-shaped function used by Hu *et al.* (2007). The implication of using sigmoidal-shaped functions, such as those shown in Figure 8, is that within a narrow range of SNR levels (which in turn depend on the steepness of the sigmoidal function), the envelopes (presumed to be masker dominant) will be heavily attenuated rather than zeroed out, as done in the IdBM algorithm when the SNR is negative. It remains to be seen whether such attenuation if applied to target-dominant envelopes will introduce any type of noise/speech distortion that is perceptible by the CI users. The findings by Hu *et al.* (2007) seem to suggest otherwise, but further experiments are warranted to investigate this possibility.

The binary function (see Fig. 8) used in the IdBM algorithm suggests turning off channels with SNR below threshold (0 dB, in this study) while keeping channels with SNR above threshold. In a realistic scenario, this might not be desirable as that will completely eliminate all environmental sounds, some of which (e.g., sirens, fire alarms, etc.) may be vitally important to the listener. One way to rectify this is to make the transition in the weighting function from 0 to 1 smooth rather than abrupt. This can be achieved by using a sigmoidal-shaped weighting function, such as the Wiener gain function shown in Fig. 8. Such a weighting function would provide environmental awareness, since the envelopes with SNR <0 dB would be attenuated rather than set to zero.

III. EXPERIMENT 2: EFFECT OF SNR ESTIMATION ERRORS ON SPEECH INTELLIGIBILITY

In the previous experiment, we assumed access to the true SNR value of each channel. In practice, however, the SNR of each channel needs to be estimated from the mixture

envelopes. Algorithms (e.g., Hu and Wang, 2004; Hu *et al.*, 2007) can be used in a practical system to estimate the SNR in each channel. Such algorithms will likely result in errors in estimating the SNR, as we lack access to the masker signal and, consequently, will make errors in selecting the right channels. In the present experiment, we assess the perceptual effect of SNR estimation errors on speech intelligibility. At issue is how accurate do SNR estimation algorithms need to be without compromising the intelligibility gain observed in experiment 1.

A. Subjects and material

Five of the six CI users who participated in experiment 1 also participated in the present experiment (subject S1 was not available for testing). The same speech material (IEEE Subcommittee, 1969) was used as in experiment 1. Different sentence lists were used for the new conditions.

B. Signal Processing

The stimuli were processed with the same method as described in experiment 1. We randomly selected a fixed number of channels in each cycle and reversed the decisions made using the true SNR values so as to model the errors that might be introduced when the channel SNRs are computed via an algorithm. That is, channels that were originally selected according to the ideal SNR criterion (i.e., SNR ≥ 0 dB) were now discarded. Similarly, channels that were originally discarded (i.e., SNR < 0 dB) were now retained. We varied the number of channels with erroneous decision from 2 to 12 (2, 4, 8, and 12) channels. In the 4-channel error condition, for instance, a total of 4 (out of 16) channels were wrongly discarded or selected in each cycle.

C. Procedure

The procedure was identical to that used in experiment 1. Subjects were tested with a total of 16 conditions (=4 channel errors $\times$ 2 maskers $\times$ 2 SNR levels). Two lists of sentences (i.e., 20 sentences) were used per condition, and none of the lists was repeated across conditions. The order of the test conditions was randomized for each subject.

The errors in channel selection were introduced off-line in MATLAB and presented directly (via the auxiliary input jack) to the CI users via the Clarion research interface platform.

D. Results and discussions

The sentences were scored in terms of percentage of words identified correctly (all words were scored). The top panel in Fig. 9 shows the mean percentage correct scores obtained in MB and the bottom panel of Fig. 9 shows the mean scores obtained in SSN, both as a function of the number of channels with errors. The mean scores obtained in experiment 1 for the five subjects tested are also shown and indicated as "0 number of channels with errors" for comparative purposes. A repeated-measure ANOVA with the main factors of SNR and number of channels with error was applied to the babble conditions. A significant effect of the

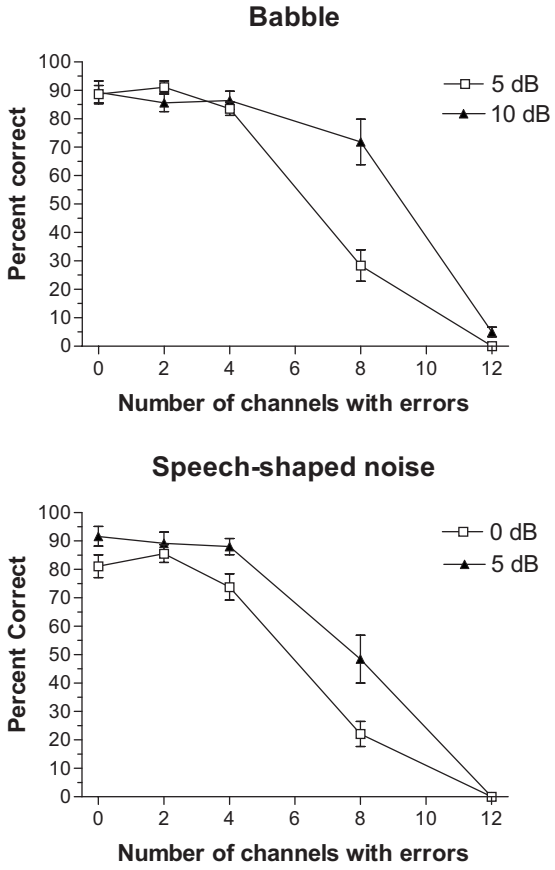

FIG. 9. Percentage of correct scores, averaged across subjects and shown as a function of the number of channels (out of 16) introduced with errors. The top panel shows the scores obtained in multitalker babble and the bottom panel shows the scores obtained in SSN. The error bars indicate standard errors of the mean.

SNR level ($F[1,4]=41.6$, $p=0.003$), significant effect of the number of channels with errors ($F[3,12]=230.7$, $p<0.0005$), and significant interaction ($F[3,12]=170.3$, $p<0.0005$) were observed. Two-way ANOVA (with repeated measures) applied to the speech-shaped conditions indicated significant effect of the SNR level ($F[1,4]=49.8$, $p=0.002$), significant effect of the number of channels with errors ($F[3,12]=222.2$, $p<0.0005$), and significant interaction ($F[3,12]=11.8$, $p=0.001$).

As shown in Fig. 9, performance remained high even when four channels were wrongly selected (or discarded). *Post hoc* tests (Fisher's LSD) confirmed that performance obtained with four wrongly selected (or discarded) channels was not statistically different ($p>0.05$) from the ideal performance obtained when no errors were introduced in the channel selection (Figs. 2 and 3). This was found to be true for both maskers and all SNR levels. In brief, the SNR selection algorithm (IdBM) presented in experiment 1 can tolerate up to a 25% (4 channels in error out of a total of 16 channels) error rate without compromising performance. With the exception of one condition (10 dB SNR babble), performance drops substantially (Fig. 9) for error rates higher than 25%.

The above findings raised the following question: How close is the maximum selection criterion used in ACE to the SNR criterion used in IdBM? This question led us to com-

TABLE II. Percentage of correct agreement between the channels selected by ACE and the channels selected by IdBM in different background conditions.

	SNR			
Masker type	0 dB	5 dB	5 dB	10 dB
SSN	60.7%	60.0%		
MB			57.4%	55.0%

pare the set of channels selected by ACE to those selected by IdBM. To that end, we processed 20 sentences through our implementation of the ACE and examined the agreement between the number of channels selected by ACE with those obtained by IdBM. To keep the proportion of channels (8/22=36%) selected by the commercial ACE strategy the same, we implemented a 6-of-16 strategy. For each stimulation cycle, we compared the six maximum channels selected by ACE with those selected by IdBM, and considered the selection decision correct if both ACE and IdBM selected or discarded the same channels. The results are tabulated in Table II for both masker types and all SNR levels tested. As shown in Table II, ACE makes the same decisions as IdBM (with regards to channel selection) 55%–60% of the time. The corresponding error rate is 40%, which falls short of the error rate needed to restore speech intelligibility (Fig. 9).

In the present experiment, we made no distinction between the two types of error that can potentially be introduced due to inaccuracies in SNR estimation. The first type of error occurs when a channel that should be discarded (because SNR$<$0 dB) is retained, and the second type of error occurs when a channel that should be retained (because SNR$>$0 dB) is discarded. From signal detection theory, we can say that the first type of error is similar to type I error (false alarm) and the second type of error is similar to type II error [5] (miss). The type I error will likely introduce more noise distortion or more target-masker confusion, as channels that would otherwise be discarded (presumably belonging to the masker or dominated by the masker) would now be retained. The type II error will likely introduce target speech distortion, as it will discard channels that are dominated by the target signal and should therefore be retained. The perceptual effect of these two types of errors introduced is likely different (e.g., Li and Loizou, 2008). Further experiments are thus needed to assess the effect of these two types of errors on speech intelligibility by CI users.

The present study, as well as others with normal-hearing listeners (e.g., Brungart *et al.*, 2006; Li and Loizou, 2007, 2008), have demonstrated the full potential of using the SNR selection criterion to improve (and in some cases restore) intelligibility of speech in multitalker or other noisy environments. Algorithms capable of estimating the SNR accurately can therefore yield significant gains in intelligibility. A number of techniques have been proposed in the computational auditory scene analysis (CASA) literature (see review by Wang and Brown, 2006) for estimating the IdBM and include methods based on pitch continuity information (Hu and Wang, 2004; Roman and Wang, 2006) and sound-localization cues (Roman *et al.*, 2003). Most of the CASA techniques proposed thus far are based on elaborate auditory models and make extensive use of grouping principles (e.g., pitch continuity, onset detection) to segregate the target from the mixture. Alternatively, the IdBM, or equivalently the SNR, can be estimated using simpler signal processing algorithms that compute the SNR in each channel from the mixture envelopes based on estimates of the masker spectrum and past estimates of the enhanced (noise-suppressed) spectrum (e.g., Hu *et al.*, 2007, Loizou, 2007, Chap. 7.3.3). Several such algorithms do exist and are commonly used in speech enhancement applications to improve the quality of degraded speech (see review by Loizou, 2007). To assess how accurate such algorithms are, we processed 20 IEEE sentences embedded in 5 and 10 dB SNR babbles (20 talkers) via two conventional noise-reduction algorithms, which we found in a previous study to preserve intelligibility (Hu and Loizou, 2007a), and computed the hits and false-alarm rates [6] of the SNR estimation algorithms (see Table III). We also processed the mixtures via the SNR estimation algorithm that was used by Hu *et al.* (2007) and tested with cochlear implant users. Overall, the percentage of errors (type I and II) made by the two algorithms, namely, the Wiener (Scalart and Filho, 1996) and the minimum mean-square error (MMSE) algorithms (Ephraim and Malah, 1984), were quite high (see Table III), thus providing a plausible explanation as to why current noise-reduction algorithms do not improve speech intelligibility for normal-hearing listeners (Hu and Loizou, 2007a), although they improve speech quality (Hu and Loizou, 2007b). In contrast, the SNR estimation algorithm used by Hu *et al.* (2007) was relatively more accurate (smaller percentage of type II errors) than the other two algorithms (MMSE and Wiener) accounting for the moderate intelligibility improvement reported by Hu *et al.* (2007) by CI users. The data shown in Table III were computed using sentences corrupted in MB, and required an algorithm for tracking the background noise (needed for the estimation of the SNR). While several noise-estimation algorithms exist (see Loizou, 2007, Chap. 9) that perform reasonably well for stationary (and continuous) noise, no algorithms currently exist that would track accurately a single competing talker. Better noise-tracking algorithms are thus needed for tackling the situation in which the target speech signal is embedded in single competing talker(s). Estimates of the masker (competing talker) spectra would be needed for accurate estimation of the instantaneous SNR in such listening situations. Hence, further research is warranted in developing algorithms capable of estimating more accurately the IdBM in various noise background conditions.

IV. CONCLUSIONS

A new channel selection criterion was proposed for *n-of-m* type of coding strategies based on the SNR values of individual channels. The new SNR criterion can be used in lieu of the maximum selection criterion presently used by the commercially available ACE strategy in the Nucleus-24 cochlear implant system. The new strategy (IdBM) requires access to accurate values of the SNR in each channel. Re-

TABLE III. Average performance, in terms of hits and false-alarm rates (Ref. 6), of three SNR estimation algorithms that were used to compute the binary mask.

Global SNR	Noise-reduction algorithm	Hits (%)	False alarm (%)
5 dB	Wiener (Scalart and Filho, 1996)	26.72	20.67
	MMSE (Ephraim and Malah, 1984)	23.25	15.53
	Hu *et al.* (2007)	53.19	17.41
10 dB	Wiener (Scalart and Filho, 1996)	28.66	18.46
	MMSE (Ephraim and Malah, 1984)	25.55	14.01
	Hu *et al.* (2007)	58.76	18.38

sults from experiment 1 indicated that if such SNR values are available, then the proposed strategy (IdBM) can restore speech intelligibility to the level attained in quiet independent of the type of masker or SNR level (0–10 dB) used. Results in experiment 2 showed that IdBM can tolerate up to a 25% error rate in channel selection without compromising speech intelligibility. Overall, the outcomes from the present study suggest that the SNR criterion has proven to be a good and effective channel selection criterion with the potential of restoring speech intelligibility. Thus, much effort needs to be invested in developing signal processing algorithms capable of estimating accurately the SNR of individual channels from the mixture envelopes.

ACKNOWLEDGMENTS

This research was supported by Grant Nos. R01 DC007527 and R03 DC008887 from the National Institute of Deafness and other Communication Disorders, NIH. The authors would like to thank the three anonymous reviewers for the valuable suggestions and comments they provided.

[1]Aside from the method used to select the envelopes, the ACE and CIS strategies implemented on the Nucleus-24 device differ in the number of electrodes stimulated. In the study by Skinner *et al.* (2002b), for instance, only 12 electrodes were stimulated in the CIS strategy, and 8 (out of 20) electrodes were stimulated in the ACE strategy. The selected (and activated) electrodes in the ACE strategy vary from cycle to cycle depending on the location of the eight maximum amplitudes, whereas in the CIS strategy, the same set of electrodes is activated for all cycles.

[2]The duration of each cycle depends largely on the stimulation rate, which might in turn vary depending on the device. The ACE strategy, for instance, operates at a higher rate compared to the SPEAK strategy.

[3]Anecdotally, subjects did not report any quality degradation in the processed speech stimuli due to the dynamic selection process of the IdBM strategy.

[4]Pilot data were collected with one subject (S2) to assess whether ACE performs better than CIS in noise. More specifically, we assessed the performance of our own implementation of a 6-of-15 strategy (ACE) on speech recognition in noise. The subject was tested on a different day with a different set of IEEE sentences following the same experimental protocol described in experiment 1. Mean percentage correct scores in the 5 and 10 dB SNR babble conditions were 21.2%. Mean percentage correct scores in the 0 and 5 dB SNR SSN were 14.3%. Comparing these scores with the scores obtained with the CIS strategy (see Figs. 2 and 3), we note that the difference in scores is small (six to eight percentage points). While we cannot assess statistical significance, it is noteworthy to mention that the small differences (six to eight percentage points) in score between CIS and ACE are consistent with those reported by Skinner *et al.* (2002b).

[5]Type I error (also called *false alarm*) is produced when deciding hypothesis H_1 (signal is present) when H_0 is true (signal is absent). Type II error (also called *miss*) is produced when deciding H_0 when H_1 is true (Kay, 1998).

[6]The estimated SNR of each T-F unit was compared against a threshold (0 dB), and T-F units with positive SNR were classified as target-dominated T-F units and units with negative SNR were classified as masker-dominated units. The binary mask pattern estimated using the MMSE and Wiener algorithms was compared against the (true) IdBM pattern. The noise power spectrum, needed in the computation of the SNR, was computed using the algorithm proposed by Rangachari and Loizou (2006). Errors were computed in each frame by comparing the true decision made by the idBM with the decision made by the SNR estimation algorithm for each T-F unit. The hits (=1-type II errors) and false-alarm (type I error) rates were averaged across 20 IEEE sentences and are reported in Table III. It should be noted that the data in Table III were computed using a SNR threshold of 0 dB in order to be consistent with the data collected with cochlear implant users in experiment 1. Use of a smaller SNR threshold (−5 dB) yielded higher hit rates (~40%), however, at the expense of increasing the false-alarm rates to near 30%. Similarly, increasing the SNR threshold to +5 dB yielded lower false-alarm rates (<10%) but decreased the hit rate to 17%.

ANSI (**1997**). "Methods for calculation of the speech intelligibility index," ANSI S3.5-1997, American National Standards Institute, New York.

Anzalone, M., Calandruccio, L., Doherty, K., and Carney, L. (**2006**). "Determination of the potential benefit of time-frequency gain manipulation," Ear Hear. **27**, 480–492.

Brungart, D., Chang, P., Simpson, B., and Wang, D. (**2006**). "Isolating the energetic component of speech-on-speech masking with ideal time-frequency segregation," J. Acoust. Soc. Am. **120**, 4007–4018.

Dudley, H. (**1939**). "Remaking speech," J. Acoust. Soc. Am. **11**, 1969–1977.

Ephraim, Y., and Malah, D. (**1984**). "Speech enhancement using a minimum mean-square error short-time spectral amplitude estimator," IEEE Trans. Acoust., Speech, Signal Process. **32**, 1109–1121.

French, N. R., and Steinberg, J. D. (**1947**). "Factors governing the intelligibility of speech sounds," J. Acoust. Soc. Am. **19**, 90–119.

Hu, G., and Wang, D. (**2004**). "Monaural speech segregation based on pitch tracking and amplitude modulation," IEEE Trans. Neural Netw. **15**, 1135–1150.

Hu, Y., and Loizou, P. (**2007a**). "A comparative intelligibility study of single-microphone noise reduction algorithms," J. Acoust. Soc. Am. **122**, 1777–1786.

Hu, Y., and Loizou, P. (**2007b**). "Subjective comparison and evaluation of speech enhancement algorithms," Speech Commun. **49**, 588–601.

Hu, Y., Loizou, P., Li, N., and Kasturi, K. (**2007**). "Use of a sigmoidal-shaped function for noise attenuation in cochlear implants," J. Acoust. Soc. Am. **122**, EL128–EL134.

IEEE Subcommittee (**1969**). "IEEE recommended practice for speech quality measurements," IEEE Trans. Audio Electroacoust. **AU-17**, 225–246.

James, C., Blamey, P., Martin, L., Swanson, B., Just, Y., and Macfarlane, D. (**2002**). "Adaptive dynamic range optimization for cochlear implants: A preliminary study," Ear Hear. **23**, 49S–58S.

Kay, S. (**1998**). *Fundamentals of Statistical Signal Processing: Detection Theory* (Prentice-Hall, Upper Saddle River, NJ).

Kiefer, J., Hohl, S., Sturzebecher, E., Pfennigdorff, T., and Gstoettner, W. (**2001**). "Comparison of speech recognition with different speech coding strategies (SPEAK, CIS, and ACE) and their relationship to telemetric measures of compound action potentials in the nucleus CI 24M cochlear implant system," Audiology **40**, 32–42.

Kim, H., Shim, Y. J., Chung, M. H., and Lee, Y. H. (**2000**). "Benefit of ACE compared to CIS and SPEAK coding strategies," Adv. Oto-Rhino-Laryngol. **57**, 408–411.

Kryter, K. D. (**1962**). "Validation of the articulation index," J. Acoust. Soc. Am. **34**, 1698–1702.

Li, N., and Loizou, P. (**2007**). "Factors influencing glimpsing of speech in noise," J. Acoust. Soc. Am. **122**, 1165–1172.

Li, N., and Loizou, P. (**2008**). "Factors influencing intelligibility of ideal binary-masked speech: Implications for noise reduction," J. Acoust. Soc. Am. **123**, 2287–2294.

Loizou, P. (**2006**). "Speech processing in vocoder-centric cochlear implants," Adv. Oto-Rhino-Laryngol. **64**, 109–143.

Loizou, P. (**2007**). *Speech Enhancement: Theory and Practice* (CRC, Boca Raton, FL).

Noguiera, W., Buchner, A., Lenarz, T., and Edler, B. (**2005**). "A psychoacoustic 'nofm'-type speech coding strategy for cochlear implants," EUR-

ASIP J. Appl. Signal Process. **18**, 3044–3059.
Peterson, G., and Cooper, F. (**1957**). "Peakpicker: A bandwidth compression device," J. Acoust. Soc. Am. **29**, 777.
Rangachari, S., and Loizou, P. (**2006**). "A noise estimation algorithm for highly nonstationary environments," Speech Commun. **28**, 220–231.
Roman, N., and Wang, D. (**2006**). "Pitch-based monaural segregation of reverberant speech," J. Acoust. Soc. Am. **120**, 458–469.
Roman, N., Wang, D., and Brown, G. (**2003**). "Speech segregation based on sound localization," J. Acoust. Soc. Am. **114**, 2236–2252.
Scalart, P., and Filho, J. (**1996**). "Speech enhancement based on a priori signal to noise estimation," Proceedings of the IEEE International Conference on Acoustics, Speech, and Signal Processing, pp. 629–632.
Seligman, P., and McDermott, H. (**1995**). "Architecture of the Spectra 22 speech processor," Ann. Otol. Rhinol. Laryngol. **104**, 139–141.
Skinner, M., Arndt, P., and Staller, S. (**2002a**). "Nucleus 24 advanced encoder conversion study: Performance versus preference," Ear Hear. **23**, 2S–17S.
Skinner, M., Holden, L. K., Whitford, L. A., Plant, K. L., Psarros, C., and Holden, T. A. (**2002b**). "Speech recognition with the nucleus 24 SPEAK, ACE, and CIS speech coding strategies in newly implanted adults," Ear Hear. **23**, 207–223.
Vandali, A. E., Whitford, L. A., Plant, K. L., and Clark, G. M. (**2000**). "Speech perception as a function of electrical stimulation rate using the Nucleus 24 cochlear implant system," Ear Hear. **21**, 608–624.
Wang, D. (**2005**). "On ideal binary mask as the computational goal of auditory scene analysis," *Speech Separation by Humans and Machines*, edited by P. Divenyi (Kluwer Academic, Dordrecht), pp. 181–187.
Wang, D., and Brown, G. (**2006**). *Computational Auditory Analysis* (Wiley, New York).

Using impedance measurements to detect and quantify the effect of air leaks on the attenuation of earplugs

Viggo Henriksen[a)]
Acoustics Research Center, Department of Electronics and Telecommunications, Norwegian University of Science and Technology, NO-7491 Trondheim, Norway

(Received 26 June 2007; revised 19 April 2008; accepted 30 April 2008)

The impedance of a simple artificial ear occluded with an earplug and bypassed with narrow air leaks was measured along with the attenuation of sound through the air leaks. A lumped element model is suggested for the simple occluded artificial ear with an air leak. The suggested model was adapted to the impedance measurements and the attenuation was predicted from the model. The attenuation predictions were compared to the attenuation measurements and were found to be within $[-3.5, +3]$ dB of the measured attenuation over the frequency range of 50–1000 Hz and an attenuation range of −2–38 dB. The average difference between the measured and predicted attenuation for four different leaks in the frequency range of 50–1000 Hz was −0.7 dB, indicating a very slight underestimation of the attenuation.
 [DOI: 10.1121/1.2932092]

PACS number(s): 43.66.Vt, 43.50.Hg [KA] Pages: 510–522

I. INTRODUCTION

Impedance measurements in the ear canal have been carried out for many years (Zwislocki, 1957a, 1957b; Allen, 1985; Keefe *et al.*, 1992; Voss and Allen 1994), and the main objectives have been to learn how the ear works and to check the physical state of individual ears. Air leaks around the measurement probe have been considered to be an unwanted artifact and measures have been taken to try to avoid such leaks. Amongst those measures are the uses of foam earplugs around the tip of the impedance probe or some sort of grease to seal leaks. For hearing protectors, air leaks are considered to be a considerable problem (Nixon, 1979) and can lead to a serious degradation of the attenuation of the protectors. Generally, earmuffs are more prone to air leaks than earplugs because the area that the muffs are supposed to seal against is often uneven and covered by hair. Growth of beard and the use of eyeglasses are two other factors that make it difficult to avoid air leaks when using earmuffs. This leads to the fact that earmuffs generally have a lower attenuation at low frequencies than earplugs. On the other hand, it turns out that earplugs can be difficult to insert optimally for untrained users and their potentially higher attenuation at low frequency diminishes. Again, one of the most critical factors to get the optimum attenuation for earplugs is to avoid air leaks at the interface between the earplug and the ear canal wall.

The question that arises is whether it is possible to detect the presence of an air leak along an earplug through some kind of measurement in the ear canal. One could always measure the attenuation of the earplug directly, but this would imply the presence of an external sound source capable of delivering a high sound pressure level (SPL) across a broad frequency range. The approach suggested here is to measure the impedance in the ear canal behind the inserted earplug and try to relate that to the attenuation of the earplug. The trend toward new hearing protectors including electronics and transducers indicate that this approach might be feasible from a purely technical standpoint. To test the approach under controlled conditions, an idealized, well controlled, artificial ear canal is used where controlled leaks are introduced along an earplug.

The main idea that is tested in this work is whether it is possible to detect an air leak into an artificial ear occluded by an earplug using impedance measurements on the inside of the earplug. It is also hypothesized that it is possible to use the impedance measurements and a model for the impedance of narrow tubes to predict what effect an air leak will have on the sound attenuation of an earplug.

In this work, the headset of an in the ear active hearing protector is used as an impedance probe. As a first step, the variability in the calibration of the impedance probe is tested. Furthermore, impedance measurements in a simplified artificial ear canal are performed with both rigid- and soft-walled narrow air leaks introduced along the earplug of the hearing protector. A model for the impedance of the artificial ear with narrow air leaks is introduced. The parameters of this model are adapted to the impedance measurements, and based on the adapted model, the attenuation of sound from outside the occluded artificial ear to the inside is estimated. Measurements of the attenuation in the artificial ear are also performed and compared to the estimates.

The structure of the paper is as follows. Section II presents the model of an earplug with a leak and its corresponding analog circuits. The relationship between impedances and attenuation is introduced. Expressions for rigid-walled narrow tubes are introduced and the modeling of soft-walled narrow tubes is discussed. In Sec. III, the measurement techniques are described for the impedance measurements and the related calibration procedure, as well as for the attenuation measurements. A parameter fitting procedure, by which the model parameters are adapted to the model, is described.

[a)]Also at SINTEF, Information and Communication Technology, Trondheim, Norway; electronic mail: viggo.henriksen@sintef.no

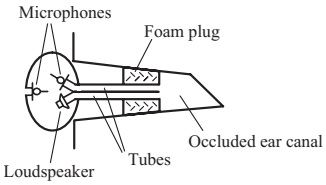

FIG. 1. Illustration of the earplug of the QUIETPRO™ headset in an ear canal.

Section IV describes two measurement series. In a first series, the variability of the impedance measurements is studied, whereas a second series includes both impedance and attenuation measurements for identical conditions. Results of these measurements are presented in Sec. V. A discussion of the results is given in Sec. VI and conclusions are drawn in Sec. VII.

II. THEORY

A. The impedance probe

Throughout this study, the headset of an in the ear active hearing protector has been used as an impedance probe. The hearing protector was the QUIETPRO™ (NACRE), which can be seen in the conceptual drawing in Fig. 1 and in the picture in Fig. 2.

The QUIETPRO™ headset consists of two earplugs, one earplug per ear. Each earplug consists of two pieces: one ear piece containing a set of transducers and one disposable foam earplug that is inserted into the ear canal. As can be seen in Fig. 1, the ear piece contains three transducers per ear: one microphone on the outside of each ear piece as well as one microphone and one loudspeaker on the inside of each ear piece. Two tubes running through the disposable foam earplug connect the two transducers on the inside of the ear piece with the ear canal cavity. The foam earplug with its tubes forms one replaceable unit that is supposed to be used a limited number of times due to hygienic reasons and to avoid deterioration of its attenuation properties. A Thevenin equivalent circuit for the earplug and for the impedance that is measured is shown in Fig. 3. The transducers can effectively be described in terms of a Thevenin generator p_{th} and a Thevenin source impedance Z_{th}. The impedance to be measured is denoted as Z_{meas} and the sound pressure inside the occlude ear canal is p_1. As will be described in Sec. III, a series of calibration measurements is required prior to the measurement of the unknown impedance, Z_{meas}, in order to find the values of p_{th} and Z_{th}.

FIG. 2. Picture of the earplug of the QUIETPRO™ headset (ear piece and foam earplug).

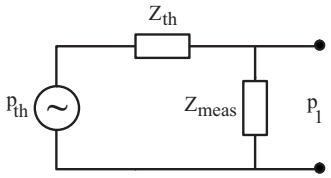

FIG. 3. Thevenin equivalent circuit for the impedance measurement setup.

B. Model of impedance and attenuation

An equivalent circuit model for an artificial ear with an air leak along the foam earplug is shown in Fig. 4. In this case, the pressure source is an assumed sound pressure outside the hearing protector.

The impedance Z_{leak} is the impedance of the air leak, including its radiation impedance at both ends, and Z_{AE} is the impedance of the artificial ear. The attenuation of sound from outside the ear canal to the inside is then found as

$$A = \frac{p_{inside}}{p_{outside}} = \frac{Z_{AE}}{Z_{AE} + Z_{leak}}. \quad (1)$$

Zwislocki (1957a) used this equation in the estimation of the impedance at the tympanic membrane of humans. He developed a procedure where he measured the attenuation for earplugs with known leaks in a known cavity and in an ear canal. These measurements were then combined to find the unknown impedance of the ear.

As mentioned earlier, the objective in this paper is to estimate the attenuation of an earplug with an air leak by using impedance measurements inside an artificial ear canal occluded by the earplug. The measured impedance is assumed to consist of the impedance of the leak in parallel to the impedance of the artificial ear, as seen in Fig. 5.

By adapting such a model to the measured impedance, the unknown impedances of the leak and the artificial ear can be found and an estimate for the attenuation can be calculated according to Eq. (1). The parameters of these two impedances are described in the following sections.

The model described above is a lumped element type of model, where each of the impedances describes a physical part of the modeled system. Such a model can only be correct as long as the wavelengths are somewhat longer than the largest dimensions in the physical part of the system described by the impedance. In other words, the model will be correct for low frequencies where the pressure variations, within each physical part described by a single impedance, are small. With the largest physical dimensions in the physical system at approximately 2.1 cm, the model should be correct at least up to 4 kHz.

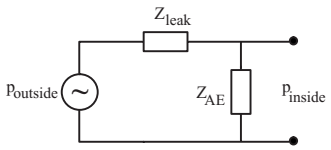

FIG. 4. Equivalent circuit for an artificial ear with an introduced air leak.

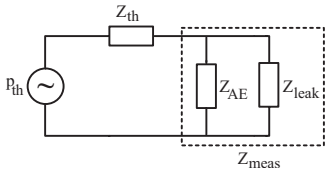

FIG. 5. Equivalent circuit model for an artificial ear with an air leak connected to the earplug.

C. Impedance of narrow air leaks

The acoustic impedance Z_{leak} of an air leak with a circular cross section of radius a and length d, which is considerably shorter than the wavelength, is given by Rschevkin (1963) and can be written as

$$Z_{\text{leak}} = j\frac{\omega\rho_0 d}{\pi a^2}\left(1 - \frac{2}{s\sqrt{-j}}\frac{J_1(s\sqrt{-j})}{J_0(s\sqrt{-j})}\right)^{-1}, \tag{2}$$

$$s = a\sqrt{\frac{\omega\rho_0}{\mu}}. \tag{3}$$

Here, ρ_0 is the density of air, μ is the viscosity coefficient of air, and J_1 and J_0 are Bessel functions of the first kind. For low frequencies, approximately $s<2$, the following approximation applies:

$$Z_{\text{leak}} = \frac{8\mu d}{\pi a^4} + j\frac{4}{3}\frac{\omega\rho_0 d}{\pi a^2}. \tag{4}$$

This expression shows that for low frequencies or narrow air leaks, the real part of the impedance is frequency independent. A related approximation is also given by Beranek (1954) for high frequencies where the real part of the impedance varies with the square root of the frequency.

Equations (2)–(4) for the impedance of air leaks are based on the assumption that the particle velocity along the leak is zero at the wall of the leak. For an air leak along a foam earplug in a real ear canal, this assumption might not be correct, but to which extent this influences the impedance of the air leak is not known. Therefore, as a first approximation, such "soft-walled" narrow tubes are here modeled as rigid-walled.

In addition to the acoustic impedance of the leak itself, radiation impedances at both ends of the leak will also affect the total impedance of the leak. Due to the small radii of the leaks used here, the radiation impedances will, however, contribute very little to the total impedance of the leaks. Still, for completeness, it should be included. Beranek (1954) gave expressions for the radiation impedances for both a plane piston at the end of a long tube and in an infinite baffle. For the measurement setups used in the work presented here, the radiation impedances of the leaks are probably somewhere in between that of a piston in a long tube and in an infinite baffle. The impedance of a piston in an infinite baffle, given as

$$Z_{\text{rad}} = \frac{0.159\omega^2\rho_0}{c} + j\frac{0.270\rho_0\omega}{a}, \tag{5}$$

is used as the radiation impedance for the leaks throughout this paper and is added to the impedance in Eq. (2) twice,[1] once for each end of the leak, to get the total impedance of air leaks. Here, c represents the speed of sound.

D. Simple artificial ear

A simple artificial ear can be made from a closed cavity of suitable physical dimensions. The acoustic impedance for a closed cavity is stiffness controlled at low frequencies were no standing waves exist. Therefore, the impedance of such an artificial ear is similar to that of a real ear in the low frequency range where no resonances or standing waves exist.

An aluminum tube with length of 29 mm and internal diameter of 7.7 mm was used as a simplified artificial ear in the measurements presented in the following sections. The tube was closed at one end with a rigid termination and open at the other end where the earplug was inserted. The foam earplug was inserted 5 to 13 mm into the open end of the tube. The acoustic impedance of the artificial ear is given as

$$Z[k] = Z_c[k]\coth(\Gamma[k]L) \tag{6}$$

by Keefe *et al.* (1992) for the discrete frequencies k and lengths L. With the propagation wave number Γ and the characteristic impedance Z_c given by Keefe (1984), the expression for the impedance of the calibration tubes includes viscothermal losses.

Such an artificial ear was used because its impedance is well known. The length was chosen such that the impedance was close to the impedance of the Brüel & Kjær type 4157 ear simulator at low frequencies. Both these artificial ears are stiffness controlled at low frequencies where the resonators of the ear simulator and the standing waves in the chosen artificial ear have no effect. Below about 1 kHz, the two are very similar and the difference in magnitude mainly depends on the insertion depth for the foam earplug in the artificial ear. Even though it is not of great importance for the work presented here, a consequence of this similarity is that the presented attenuation values should be close to what would be achieved in a real ear with the same air leaks.

III. METHODS

A. Impedance measurement method

1. General

The impedance measurements are based on the method suggested by Keefe *et al.* (1992), which is very similar to the method suggested by Allen (1985). Before the impedance, Z_{meas}, can be measured, the source characteristics of the earplug transducers, the Thevenin pressure p_{th}, and impedance Z_{th}, (see Fig. 3) must be determined. They are found using the calibration procedure described in Sec. III A 2. Once this is done, a pressure response p_1 measured across the impedance under measurement is sufficient to calculate the impedance as

$$Z_{\text{meas}}[k] = Z_{\text{th}}[k]/[p_{\text{th}}[k]/p_1[k] - 1], \tag{7}$$

where k is the discrete frequency number. The pressure response p_1 is the measured response from the ear piece loudspeaker to the microphone on the inside of the ear piece.

2. Calibration

The calibration can be done by measuring the pressure response in a set of known calibration impedances. Since one needs to find two complex quantities, Z_{th} and p_{th}, it would in theory be sufficient with two calibration impedances. However, in order to get a more robust estimate of Z_{th} and p_{th}, six different calibration impedances have been used in this study. This leads to an overdetermined system of six equations and only two unknowns. A least mean square method suggested by Keefe *et al.* (1992) is used to find Z_{th} and p_{th}. In this study, the calibration impedances were six aluminum tubes with diameter of 7.7 mm, which were terminated with a rigid wall. All the tubes had different lengths: 21, 29, 39, 48, 59, and 69 mm from the opening to the rigid termination. The foam earplugs were inserted so that their outer ends were flush with the outer end of the calibration tubes. Due to the different lengths of the leaks, foam earplugs of different lengths were used. Thus, the depth of the insertion varied between 5 and 13 mm. This reduced the length of the calibration impedances accordingly. The acoustic impedance of the calibration impedances is given by Eq. (6).

The lengths of the calibration impedances must be determined with high accuracy to get good estimates of Z_{th} and p_{th}. Here, this was done in three stages. First, the lengths of the tubes, with the approximate length of the foam earplug subtracted, were suggested as first estimates. Then, these estimates, together with the responses measured for the calibration impedances, were used to refine the estimates. This was done by inspecting the dips in the responses caused by reflections against the rigid terminations. The frequency of the dip, which is lowest in frequency, has a wavelength that corresponds approximately to four times the length between the inner end of the foam earplug and the hard termination of the calibration impedance. By finding this frequency for each of the calibration impedances, improved estimates for the physical lengths of the calibration impedances could be found. Last but not least, these estimates were fed to the least mean square algorithm that found the lengths L_i, $i=1,\ldots,6$, which best fitted the measurements. Here, the initial length values fed to the algorithm were crucial in order to get good estimates of Z_{th} and p_{th}, i.e., to get accurate calibrations. The lengths were then used to calculate the six calibration impedances using Eq. (6) and in turn Z_{th} and p_{th} in the following manner:

$$\begin{pmatrix} p_{\text{th}} \\ Z_{\text{th}} \end{pmatrix} = \left(\frac{1}{\Delta}\right) \begin{pmatrix} \sum_{i=1}^{6} |p_i|^2 \sum_{i=1}^{6} Z_i^* p_i \\ \sum_{i=1}^{6} Z_i p_i^* \sum_{i=1}^{6} |Z_i|^2 \end{pmatrix} \times \begin{pmatrix} \sum_{i=1}^{6} p_i |Z_i|^2 \\ -\sum_{i=1}^{6} Z_i |p_i|^2 \end{pmatrix}, \tag{8}$$

$$\Delta = \sum_{i=1}^{6} |Z_i|^2 \sum_{i=1}^{6} |p_i|^2 - \left| \sum_{i=1}^{6} Z_i^* p_i \right|^2 .$$

The Thevenin parameters, p_{th} and Z_{th}, then characterized the earplug and could be used to calculate a measured impedance from a measured pressure response p_1 using Eq. (7).

3. Impulse response measurements

The impedance was derived from sound pressure transfer functions. Here, impulse responses were measured using a log-swept sine signal, as implemented in the WINMLS software. The sweep range was from 16 Hz to 24 kHz. A Lynx L22 sound card, using a sampling frequency of 48 kHz, was connected to the QUIETPRO™ headset through custom made electronic amplifier circuits optimizing the signal levels between the sound card and the ear piece transducers. The swept signal was sent from the sound card to the ear piece loudspeaker and, simultaneously, the signal from the inner microphone was sampled at the input of the sound card. For the rigid-walled air leaks (see Sec. IV B 1), a 1 s long sine sweep was repeated 32 times to get an adequate signal to noise ratio (SNR) at low frequencies. Because of the temporary nature of the soft-walled air leaks, as described in Sec. IV B 1, those measurements had to be done quickly and a single run of a 0.5 s long sine sweep was found to give the best results. The main problem for the shorter measurements was the SNR at low frequencies where some accuracy was lost. During the calibration procedure, the longer measurement time was used in order to maximize the SNR whenever possible. The impulse responses were truncated at 1 and 100 ms prior to their conversion to the frequency domain using a fast fourier transform. In the truncation process, the samples for times shorter than 1 ms and longer than 100 ms were removed, leaving 99 ms long impulse responses for the further processing. The motivation for the truncation was to increase the SNR by removing the parts of the impulse responses where the signal was attenuated to a level below the noise floor of the measurement system. After the conversion to the frequency domain, the frequency responses were interpolated to 511 frequencies linearly distributed from 16 Hz to 8 kHz. A short circuit measurement between the output and input of the sound card was used to remove the influence of the computer based measurement system and the sound card. This was done by dividing all the measured frequency responses by the frequency response from the short circuit measurement. The rest of the system (amplifier circuits and ear piece) was implicitly calibrated in the calibration procedure described in Sec. III A 2.

Keefe *et al.* (1992) suggested that the microphone tube should be extended at least 3 mm past the flush surface of the foam earplug. This is to minimize the contribution of evanescent mode coupling between the flow source (i.e., the loudspeaker tube) and the microphone tube. Such a protrusion is not part of the original design of the QUIETPRO™ foam earplug. A modification was attempted, but this leads to problems when inserting the foam earplug deeply into real ear canals. Since the method developed here is expected to be used in real ears, at a later stage, the tests in the artificial

ear were done with the unmodified plug as well. Test measurements of known impedances using foam earplugs without modification did show some minor deviations, both in the impedance magnitude and phase, when they were compared to theoretical results. These deviations might be attributed to evanescent modes, but the deviations were situated close to the maxima and minima of the impedance modulus and might also be due to other measurement errors. It has been shown (Brass and Locke, 1997) that by placing the opening of the microphone and loudspeaker tubes, as shown in Fig. 1, errors of maximum 3 dB can be obtained when measuring the input impedance of ears. The error will be greatest at the minimum of the impedance, which is typically at about 6 kHz, but below 4 kHz, the error will typically be below 0.5 dB. For the artificial ear used in this work, the impedance minimum occurred at a lower frequency around 3 kHz, but given that the errors are not larger than suggested by Brass and Locke (1997), this source of error should not be too big a problem below the first impedance minimum. The maximum SPL inside the artificial ear, which was used for the measurements, was approximately 90 dB re 20 μPa during the impedance measurements. Using the same output level in a real ear would lead to approximately the same maximum SPL in the real ear. Given the measurement time of less than 1 min, this level should not be harmful to a person's hearing. The stapedius reflex is considered to set in at approximately 90–95 dB for sinusoidal stimulus (Sanborn, 1998). For impedance measurements in real ears, a slight decrease in the output level should therefore be considered.

B. Attenuation measurements

1. General

The attenuation of sound through the introduced air leaks of the foam earplug was measured as the difference in sound pressure outside and inside the artificial ear when the earplug was inserted along with the leak. The outer and inner microphones of the QUIETPRO™ ear piece were used to measure these two sound pressures when a high sound pressure was applied outside the ear piece. Due to the differences between the rigid-walled and soft-walled leaks, different measurement techniques had to be applied for the two leak types. For the rigid-walled leaks, a slow but accurate measurement technique was applied. For the soft-walled leaks, a faster measurement technique had to be used, so a technique with a good compromise between accuracy and speed was chosen.

2. Rigid-walled air leaks

For the rigid-walled air leaks, the artificial ear, which is described in more detail in Sec. II D, with the earplug inserted was placed inside an Interacoustics test chamber model TBS25. Sound was introduced into the test chamber through the internal loudspeaker of the chamber. A Rohde & Schwarz Audio Analyzer UPL was used to generate a sine sweep and measure the amplitude transfer function, in decibels, between the outer and inner microphone of the ear piece.

Before the attenuation measurements were performed, responses for the calibration of the microphones were measured. This calibration was repeated each time the foam earplug was changed.[2] The calibration measurements were done by placing the earplug inside the test chamber where it was assumed that the outer and inner microphones were exposed to close to identical sound pressures within the frequency range used. The amplitude transfer function between the two microphones was then measured using the same technique as for the attenuation measurements. The calibration of the attenuation measurements was performed afterward in MATLAB using the measured responses. The calibration was performed in the frequency domain where the amplitude transfer function (in decibels) between the two microphones, which was measured when the two microphones were subjected to the same sound field, was subtracted from the attenuation measurements.

3. Soft-walled air leaks

The measurement of the attenuation for the soft-walled air leaks required a very fast measurement technique. In the same way as for the impedance measurements, the attenuation for the soft-walled leaks was measured using the WINMLS software.[3] The output from the sound card was sent to a PA speaker system which gave a high SPL in the room where the measurements were performed. The soft-walled air leaks could not be measured inside the test chamber because the measurements had to be done quickly after the removal of the metal tube that created the air leak along the foam earplug. The artificial ear with the earplug inserted was therefore attached to a microphone stand in the sound field of the PA system.

The microphone responses used for the calibration of the attenuation measurements on the soft-walled leaks were also measured using the WINMLS software. As for the attenuation measurements, the earplug was placed in the sound field of the PA system where it was assumed that the outer and inner microphones were exposed to close to identical sound pressures within the frequency range used.

Some postprocessing of the attenuation measurements for the soft-walled leaks was performed in MATLAB. From the two impulse responses that resulted from WINMLS,[4] the transfer function between the two microphones was calculated using the MATLAB function TFESTIMATE. The two impulse responses were used as the input to the function TFESTIMATE, and the function calculated the transfer function between the two microphones using the cross power spectral density from the two impulse responses. In order to get the best compromise between frequency resolution and SNR, separate transfer functions were calculated for the low and high frequencies. These two transfer functions were later combined to one wideband transfer function. Both the low and high frequency transfer functions were calculated using the function TFESTIMATE and the two impulse responses as described above. For the low frequency transfer function, approximately 85-ms-long sequences from the two impulse responses were used in the calculation of the transfer function. For the high frequency transfer function, the sequences from the impulse responses used in the transfer function cal-

culations were approximately 11 ms long. While the longer sequences used for the low frequency transfer function led to a higher frequency resolution at the low frequencies, the shorter sequences used for the high frequency transfer function led to an increased SNR at the high frequencies that would have been compromised by the use of longer sequences from the impulse responses. The low and high frequency transfer functions were combined using the low frequency transfer function up to 300 Hz and the high frequency transfer function up from 300 Hz. The resulting wideband transfer function was then interpolated to get an even frequency resolution across the used frequency range. The calibration responses, which were measured assuming similar sound pressures at the two microphones, were treated in the exact same way as the attenuation measurements described above. The calibration was then performed by dividing the transfer function from the attenuation measurement by the transfer function from the calibration measurement. Finally, a sliding window smoothing was performed using a 1/3 octave band window to get a smoother transfer function magnitude. An unwanted artifact of this smoothing is that it will give a slight change in the slope of continuously sloping curves, but since the objective is to compare measured and estimated attenuation, it was still used. When the model-based estimate of the attenuation was compared to the measurements at a later stage, the same smoothing was performed on the attenuation estimate to remove the errors introduced by this smoothing.

C. Model fitting to the measured data

An equivalent circuit model for the impedance measured in the artificial ear with an introduced leak consists of the impedance of the air leak, including the radiation impedance, in parallel to the impedance of the artificial ear, which was given in Fig. 5. The unknown parameters are the radius of the leak and the length and area of the tube used as an artificial ear

These parameters were adapted to the impedance measurements using the MATLAB function FMINSEARCH with the error function EIMP calculated as

$$\mathrm{EIMP} = \sum_{N} |Z_{\mathrm{meas}}[k] - Z_{\mathrm{model}}[k]|^2. \tag{9}$$

Here, the sum is performed across the N discrete frequencies represented by the number k. In the adaptation, 383 discrete frequency points, linearly distributed between 30 and 6000 Hz, were used. In the adaptation process, the MATLAB function tries to find the values of the free parameters of the model, which minimize the error function EIMP. When the optimal values for the free parameters in the model were found, the attenuation was calculated using Eqs. (2), (3), (5), (6), and (1).

IV. EXPERIMENTS

A. Experiment series I: Test of variability of impedance measurements

A series of measurements was performed to test the variability in the calibration of the earplug. Five repetitions of the six-tube calibration of the earplug, using the same foam earplug, were made according to the method described in Sec. III A 2. After all five repetitions, the impedance of a test tube similar to the calibration tubes, but with a length of 33 mm from the rigid termination to the open end, was measured. For each of the five calibrations, the Thevenin pressure and impedance were calculated and used to estimate the impedance from the measurement in the test tube. Thereby, five "candidates" of impedance values were computed for the single measurement. The acoustic length of the test tube was estimated from the zero crossing of the phase of the measured impedance. Based on this, the impedance for a tube with a rigid termination was calculated from Eq. (6) and compared to the measured impedance.

Variations in the Thevenin parameters for the five repeated calibrations can mean one of two things: either the calibration method is unstable due to noisy measurements or some other factor, or the earplug system actually changes between or during the calibration runs. If the calibration method is not stable, the measured impedances will most likely be erroneous. Changes in the earplug system can also lead to erroneous measured impedances, but depending on the nature of the changes, care can be taken to minimize the changes and thereby the variations in the calibration. Due to the possibility of changes in the earplug system during the five calibration repetitions, the last calibration run, which is closest in time to the impedance measurement in the test tube, is most likely to give the most representative Thevenin parameters for the impedance measurement.

The test of the variability described here includes 31 insertions of the earplug. Such handling of the earplug system can lead to changes in the earplug system, with the possibility of changes in the Thevenin parameters that are used for calculation of the measured impedances. Experiment series II, described in Sec. IV B, also includes several insertions, and the variability test is therefore important to see if consistent measurements can be expected.

B. Experiment series II: Impedance and attenuation measurements

1. Air leaks

The validity of the model in Fig. 4 was evaluated by measuring the impedance and attenuation for a few different types of controlled air leaks. A single metal tube was placed along the foam earplug to simulate an air leak. Two tubes of different lengths and internal diameters were tested. This case, called "rigid-walled air leaks," gives a well defined air leak but might not be a good approximation for real air leaks between a foam earplug and the ear canal wall. In order to simulate a slightly more realistic leak, a "soft-walled air leak" case was used too. To introduce air leaks with softer walls but with known dimensions, at least to an extent, metal tubes were placed along the foam earplug and then removed quickly before measurements were performed, as soon as possible thereafter. This removal left a temporary impression in the foam earplug, which gave an air leak at the interface between the foam earplug and the metal wall of the artificial ear canal. For a real air leak in a real ear, the metal wall of

TABLE I. Physical dimensions of introduced air leaks.

	Tube 1, length/radius (mm)	Tube 2, length/radius (mm)
Rigid-walled	20/0.21–0.23	8/0.13–0.15
Soft-walled	12/0.26	7/0.21

the artificial ear would be replaced by the soft tissue in the ear canal, so an exact replica was not achieved, but major effects due to the soft walls in the air leak should be noticeable. Two different dimensions were also tested for the soft-walled air leaks.

Due to the properties of the foam earplugs used in the QUIETIPRO™ headset, the foam earplugs fitted nicely around the metal tubes that were inserted along their interface to the artificial ear canal wall. For the test of the rigid-walled tubes, compliant putty was placed around the outer opening of the leak tubes to avoid any additional leaks. The use of putty lead to smaller variations between measurements on different insertions of the same tube but did not remove additional leaks entirely. When the metal tubes were removed to simulate soft-walled air leaks, the size of the leaks changed rapidly which made it important to make quick measurements. It was therefore deemed necessary to make both impedance and attenuation measurements with the same time length and to start the measurements equally long after the removal of the tubes.

In Table I, the physical dimensions of the different air leaks are given. The lengths of the leaks are rounded to the nearest millimeter. For the rigid-walled leaks, the lengths are those of the metal tubes used, and for the soft-walled leaks, the lengths correspond to the lengths of the foam earplugs. The outer diameters of the metal tubes were found using a micrometer and rounded to the nearest 1/100 mm. From this, the radius of the soft-walled tubes were estimated as half the diameter of the metal tubes used to make the imprint. The inner radius of the rigid-walled leaks was estimated from their outer diameter using a high resolution digital photograph. The uncertainty of the radii is indicated by the ranges of values.

2. Impedance and attenuation measurement protocol

A series of ten insertions and measurements was performed for each leak to average out some of the variations between different insertions. The measurement protocol that was used for the impedance and attenuation measurements was as follows.

Rigid-walled air leaks:

(1) Calibrate earplug as impedance probe according to Sec. III A 2.
(2) Insert earplug in artificial ear along with the metal tube simulating air leak. Place putty around leak.
(3) Leave foam earplug to swell for at least 1 min.
(4) Measure impedance according to Sec. III A.
(5) Measure attenuation according to Sec. III B 2.
(6) Repeat steps (2)–(5) until ten insertions and measurements have been performed.

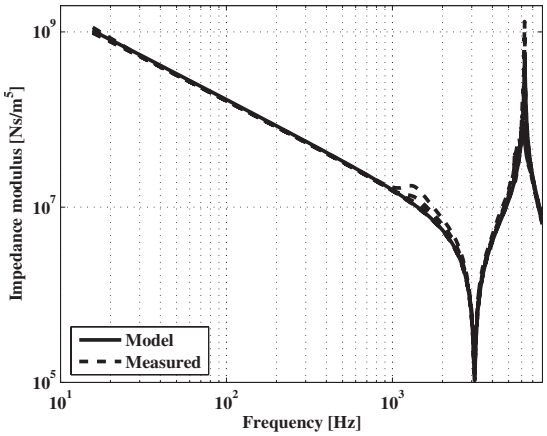

FIG. 6. Measured impedance magnitude of test tube as determined from five repetitions of the impedance calibration along with theoretical model.

Soft-walled air leaks:

(1) Calibrate earplug as impedance probe according to Sec. III A 2.
(2) Insert earplug in artificial ear along with the metal tube, which makes imprint simulating air leak.
(3) Leave foam earplug to swell for at least 1 min.
(4) Remove the metal tube quickly and measure the impedance according to Sec. III A.
(5) Insert earplug in artificial ear along with the metal tube, which makes imprint simulating air leak.
(6) Leave foam earplug to swell for at least 1 min.
(7) Remove the metal tube quickly and measure the attenuation according to Sec. III B 3.
(8) Repeat steps (2)–(7) until ten measurements of both impedance and attenuation have been performed.[5]

V. RESULTS

A. Experiment series I

Figures 6 and 7 show the results from the study of the variability in the calibration of the earplug. The figures show the impedance modulus and phase, respectively, for the measurement in a test tube with a rigid termination along with theoretical results from Eq. (6). For the theoretical calcula-

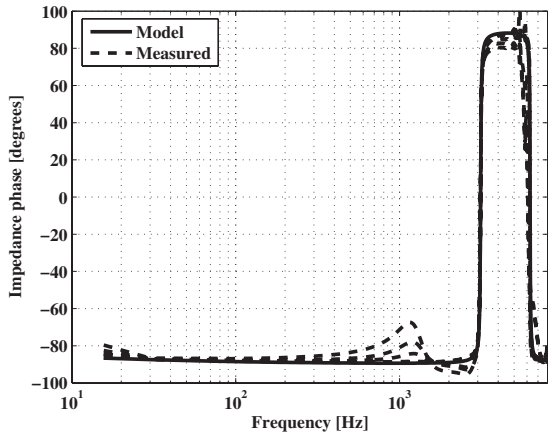

FIG. 7. Measured impedance phase of test tube as determined from five repetitions of the impedance calibration along with theoretical model.

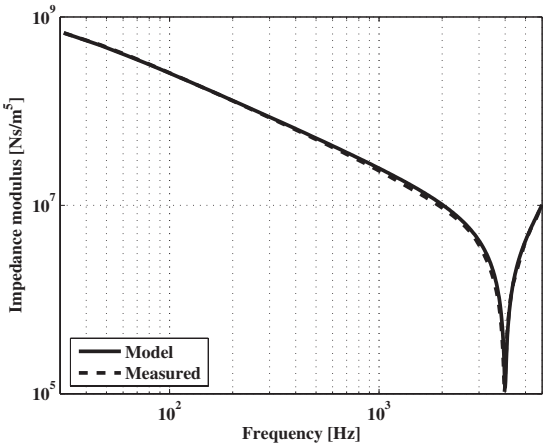

FIG. 8. Measured impedance magnitude and adapted model for a rigid-walled air leak.

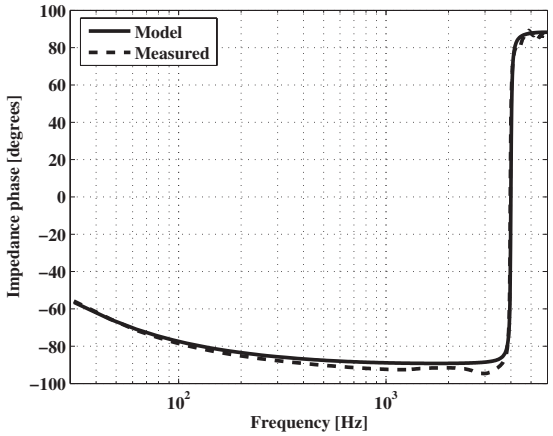

FIG. 9. Measured impedance phase and adapted model for a rigid-walled air leak.

tions, the length is chosen such that the dip and peak in the impedance modulus coincide with those of the measured results. There are five versions of the measured impedance, one calculated from each of the five calibrations of the earplug.

The differences between the five calibrations are very small at the lower frequencies. At higher frequencies, however, there are some ranges where the differences are larger. For frequencies close to the sharp dip and peak in the impedance modulus, the differences are quite large. There is also a broader range of frequencies, approximately between 800 and 3000 Hz, where differences are clearly visible. This is especially pronounced at approximately 1400 Hz where the response of the loudspeaker peaks before it starts to roll off due to the tube in front of it. In this range, the differences decrease from the first to the last calibration run, with the difference for the two last ones being no larger than it is at the lower frequencies. This is also the general trend at all frequencies, and the difference between the impedance modulus from the two latest calibrations and the theoretical result only exceeds 5% below 20 Hz and close to the dip and peak. For the phase, the difference only exceeds 5% close to the dip and peak for the two latest calibration runs, but the other calibration runs give higher differences also at other frequencies. These results indicate that for maximum accuracy, the calibration should ideally be done as close in time as possible to the actual impedance measurements and with as few as possible insertions.

B. Experiment series II

Figures 8 and 9 show one example of measured impedance modulus and phase, along with the results from the adapted model, for the artificial ear with a small rigid-walled air leak. This example is from the measurements of the narrowest air leak, which was physically estimated to have a radius between 0.13 and 0.15 mm (see Table I). The fit of the model is quite good with the largest deviation being for the phase in the frequency range of 500–3500 Hz. In part of this range, the measured phase goes slightly below −90°. This means that the real part of the impedance is negative, which is not possible for a dissipative system. The artificial ear used in this experiment is assumed to be a passive system and the model suggested for it is a passive system. The fact that the measured impedance has a negative real part implies that our model for the artificial ear is wrong or that there is a measurement error. It is most likely that it is the impedance measurement that is slightly erroneous. The measurement error is most likely due to errors in the calibration of the earplug or that some changes in the earplug between calibration and measurement have made the calibration invalid. If the negative real part of the impedance is due to measurement errors, it might be said that the model in this case is robust against the measurement errors since it will not adapt to the erroneous measurements but rather represents a physically plausible result.

The average leak radii from the model adaptations for the four different leaks are given in Table II along with the standard deviations. These values can be compared to the physically measured ones in Table I.

The shortest foam earplug used in the impedance and attenuation measurements, which was approximately 5 mm long, gave an attenuation of at least 40 dB in the frequency range of 50–1000 Hz in the artificial ear, when no leaks were introduced. In some cases, there were indications of additional leaks that were not completely sealed by the putty placed around the introduced rigid-walled leaks. These indications were found from the variation in the attenuation measurements, especially above 400 Hz for the widest rigid-walled leak. An additional test later showed that sealing this rigid-walled leak with putty sometimes leads to less attenuation than assumed, despite the fact that the putty was placed around the rigid-walled leak and that there were no apparent

TABLE II. Radius of introduced air leaks from the model adaptation (average values and standard deviations based on ten insertions of earplug and leak).

Leak type		Tube, 1, radius (mm)	Tube, 2, radius (mm)
Rigid-walled	AVG	0.208	0.131
	STD	0.010	0.003
Soft-walled	AVG	0.268	0.218
	STD	0.011	0.006

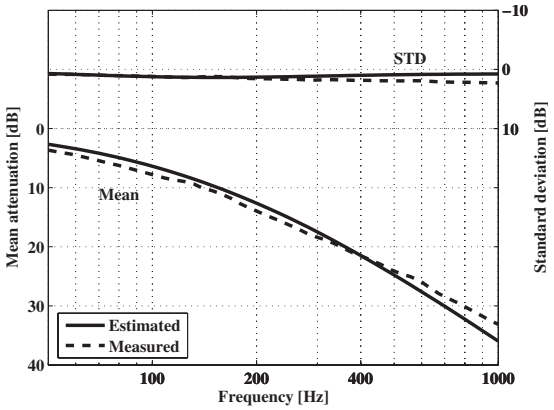

FIG. 10. Measured and estimated attenuation, mean, and standard deviation into artificial ear with a rigid-walled leak of radius 0.208 mm (acoustically estimated) and length 20 mm.

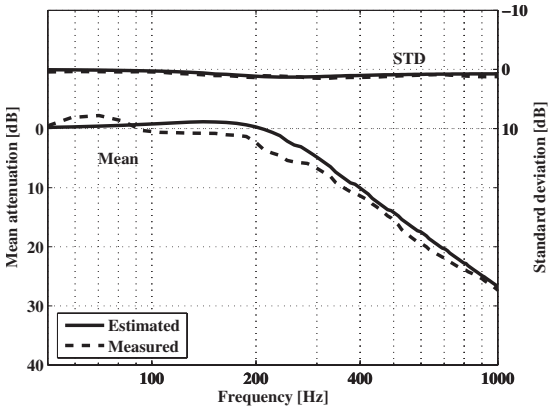

FIG. 12. Measured and estimated attenuation, mean, and standard deviation into artificial ear with a soft-walled leak of radius 0.268 mm (acoustically estimated) and length 12 mm.

leaks in the putty. A minor rearrangement of the putty could in such cases lead to a significant increase in the attenuation.

Figures 10–13 show the measured and estimated attenuation into the artificial ear with the four different types of air leaks given in Tables I and II. The estimates of the attenuation are calculated according to Eq. (1), where the values for Z_{leak} and Z_{AE} are found from the adaptation of the model, as described in Sec. III C. Shown in the figures are the mean and standard deviation based on the ten measurements that were performed for each leak. The frequency range is limited to 50–1000 Hz due to a lack of accuracy in the attenuation measurements outside this range.

The differences in attenuation for the different air leaks are mainly caused by the different dimensions of the air leaks. In general, short and wide leaks give the lowest attenuation values and an increase in the length or a decrease in the radius increases the attenuation, as expected. In Figs. 11 and 12, the measured attenuation curves show some frequency regions with increased deviations from the estimated attenuation. In Fig. 11, the deviations are most noticeable between 100 and 200 Hz. In Fig. 12, the deviations are most noticeable between 50 and 90 Hz and between 200 and 300 Hz. These increased deviations are probably not due to noise since the measured curves are averaged over ten repetitions but rather due to some unknown irregularity in the measurement setup.

Figure 14 shows the difference between the measured and estimated attenuation for the four different leaks calculated from the mean curves in Figs. 10–13. As shown in the figure, positive values imply that the model overestimates the attenuation while negative values imply that the model underestimates the attenuation. The general trend is for the model to underestimate the measured attenuation. The rigid-walled leak with inner radius of 0.208 mm is the leak that overestimates the attenuation the most. For frequencies below 400 Hz, the model underestimates the attenuation for this leak, but for frequencies above 400 Hz, there is an overestimation that increases with frequency. This increasing overestimation is probably due to inadequate sealing around the introduced air leak, which gives rise to an additional air leak and thereby a reduced attenuation, which is visible only at the higher frequencies. In the adaptation of the model to the impedance measurements, the total leak will be interpreted as one air leak. Since there seems to be at least one extra air leak with different geometries and dimensions, this will most likely give slightly incorrect results from the model.

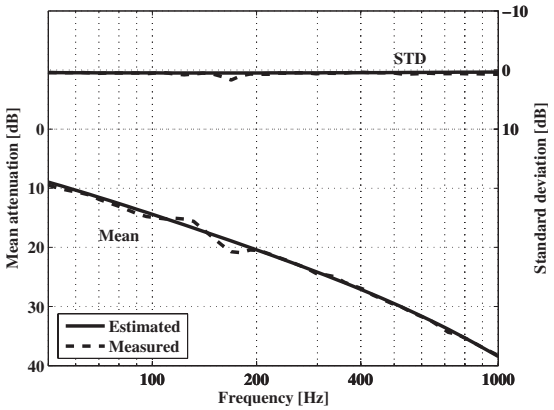

FIG. 11. Measured and estimated attenuation, mean, and standard deviation into artificial ear with a rigid-walled leak of radius 0.131 mm (acoustically estimated) and length 8 mm.

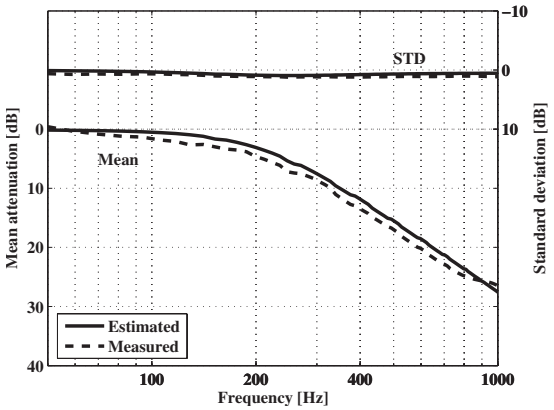

FIG. 13. Measured and estimated attenuation, mean, and standard deviation into artificial ear with a soft-walled leak of radius 0.218 mm (acoustically estimated) and length 7 mm.

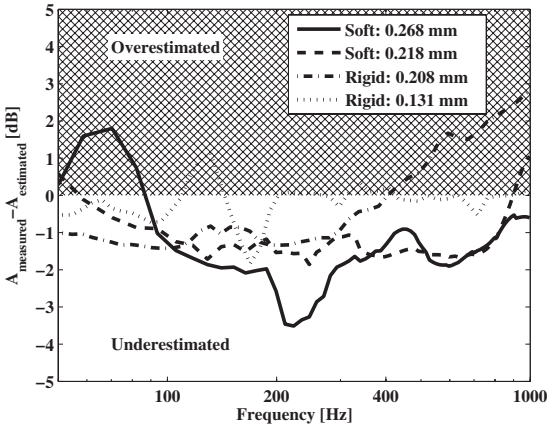

FIG. 14. Difference between measured and estimated attenuation for the four different air leaks. Calculated from the mean curves in Figs. 10–13.

The mean and standard deviations, calculated across frequency, of the difference between measured and estimated attenuation for the four different leaks are shown in Table III. The maximum and minimum difference values are also shown as well as the mean for all the four leaks. The maximum and minimum values are taken from the curves in Fig. 14, which shows the average difference for ten repeated insertions of the earplug and leaks.

The narrowest leak gives the lowest mean and standard deviation for the difference between measured and estimated attenuation. A similar mean value is achieved for the other rigid-walled leak, which has an inner radius of 0.208 mm, but this leak has the highest standard deviation of all the leaks. Both the soft-walled leaks give both a high mean and standard deviation for the difference between the measured and estimated attenuation.

VI. DISCUSSION

A. Experiment series I

As stated earlier (Sec. V A), the largest differences between the calibrations of the earplug occur close to the dip and peak in the impedance modulus. These differences are likely to be smaller in systems with a less rigid termination, such as real ears, where the dips and peaks will be less pronounced.

The differences around 1400 Hz were most likely due to a movement of the replaceable foam earplug, which changed the length of the transducer tubes slightly. This in turn affected the Thevenin parameters of the earplug and the changes were accentuated at frequencies where the transducer systems are slightly resonant. Therefore, it is important to avoid any changes in the earplug system between calibration and impedance measurements. The results also show that the impedance measurement fit the theoretical model quite well in the frequency range from 30 to 6000 Hz if care is taken not to change the earplug system after calibration. The sensitivity of the calibration to changes in the earplug system implies that for use in real ears, a new calibration should be made before each time the earplug is to be inserted in an ear. It might, however, be possible to make the design of the earplug system such that the variations in the Thevenin parameters are small enough that a sufficient accuracy in the impedance measurements is assured. Depending on the application of the impedance measurements, it might also be possible that sufficient accuracy is achieved with a single calibration using a representative foam earplug. The results from Figs. 6 and 7 show that the accuracy below 1 kHz is very similar for the five calibration repetitions, and this similarity indicates that if a limited frequency range is used, the calibration may not need to be as accurate.

B. Experiment series II

1. Impedance adaptation example

For a dissipative system, the real part of the impedance should be positive or, equivalently, the phase should stay within $\pm 90°$. This means that the impedance measurement in the example shown in Figs. 8 and 9 is most likely erroneous in the frequency range of 500–3500 Hz. It is likely that the error, which amounts to approximately 6° in the phase at its maximum, is due to errors in the calibration or that there has been a change in the earplug system after the calibration, which makes the Thevenin parameters partly erroneous. In other words, the example once again shows how important it is to avoid changes in the earplug system between calibration and measurement.

The model for the impedance of the artificial ear with an air leak might be said to be robust against the measurement errors shown in the example above since it will not adapt to

TABLE III. Mean differences between measured and calculated attenuation for the four different leaks. The means are calculated across frequency. Also shown are the standard deviations, total mean for all four leaks, and maximum and minimum differences for the four leaks.

Leak type	Inner radius (mm)	Mean of difference across frequencies and leaks (dB)	Difference across frequencies			
			Mean (dB)	STD (dB)	Maximum (dB)	Minimum (dB)
Rigid-walled	0.208	−0.7	−0.3	1.3	2.8	−1.4
	0.131		−0.2	0.5	1.1	−1.8
Soft-walled	0.268		−1.4	0.9	1.8	−3.5
	0.218		−1.1	0.8	1.1	−1.9

the erroneous measurements. The model, which represents a dissipative system, instead gives a result that is probably more physically correct in the frequency range where the measured impedance has a negative real part.

2. Leak detection

Given the results from the impedance measurements, it is clear that air leaks with dimensions within the ranges tested are clearly detectable. It was, however, not tested how small an air leak must be in order to be undetectable, but looking at the impedance phases in Figs. 7 and 9, which show a no leak case and a leak of radius between 0.13 and 0.15 mm, it can be seen that the difference in the impedance phase for the two cases is quite significant. Narrower leaks would lead to a smaller difference in the impedance phase, but it seems clear that significantly narrower leaks should be discernable from the no leak case. The limiting factor will, of course, be the accuracy with which the impedance is measured.

Keefe *et al.* (2000) found that the presence of leaks around the impedance probe led to inaccurate measurements when measuring the impedance in infant's ears. They reported measured impedances with and without leaks and suggested a method to detect leaks. Their method was based on the observation of properties in the measured impedances, which are significantly different in adults and neonates. The method might therefore be less sensitive toward the detection of leaks in impedance measurements in adults, but might still work if the leaks are large enough.

3. Measured and estimated attenuation results

As seen in Figs. 10–13, the estimates of the attenuation compare very well with the measured attenuation. There are, however, some tendencies that need to be assessed.

As can be seen in Fig. 14, there seems to be a tendency for the model to underestimate the attenuation. This underestimation implies that there is a biased error affecting the results. The three main sources of error are the following:

(1) measurement errors,
(2) inaccuracies in the adaptation of the model to the measured impedances, and
(3) inaccurate model.

Both the attenuation and impedance measurements might be affected by measurement errors. For the attenuation measurements, the most obvious errors are inadequate SNR at the microphone inside the artificial ear and errors in the calibration of the microphone responses. A low SNR at the microphone inside the artificial ear would have lead to erroneously low attenuation measurements, which is, however, the opposite of what is observed. The calibration of the microphone responses was done each time the replaceable foam tip of the earplug was changed. These repeated calibrations make it less likely that the calibration of the microphone responses for the attenuation measurements should be a source of biased errors.

The results from measurement series I imply that the impedance measurements are accurate in the frequency range from 30 to 6000 Hz, as long as care is taken not to change the earplug between calibration and measurement. The errors in the impedance measurements in measurement series I that were attributed to changes in the earplug were mainly at the higher frequencies. It is likely that any impedance measurement errors that could lead to the underestimation of the attenuation observed here would occur at the lower frequencies where the leak contributes the most to the measured impedance. Impedance measurement errors are therefore not likely either to be the main contributor to the underestimation of the attenuation. The need for accurate impedance measurements should, however, be kept in mind. As an example, it can be mentioned that an error in the estimated radius, for the narrowest rigid-walled leak, of 0.01 mm would lead to a maximum error of approximately 9° in the total impedance phase. The corresponding error in the estimated attenuation would be almost 3 dB.

In the fitting of the model to the measured impedances, the choice of fitting algorithm and number and distribution of the frequencies, at which the impedance measurements are sampled, can affect the results to a great extent. The example of the fitting of the model to an impedance measurement, shown in Sec. V B, shows a typical fit. At the lower frequencies, where the influence of the leak impedance is most pronounced, the fit is almost perfect. It is therefore no reason to suspect that the technique used to fit the model to the impedance measurements should lead to the observed underestimation of the attenuation.

The good fit of the model to the impedance measurements also implies that the model impedance represent the measured impedances quite well. Whether or not the model gives an accurate description of all parts of the physical system is, on the other hand, not certain. It is possible that there are parts of the physical system that are not described explicitly by the model, but that blend seamlessly into the total impedance when the whole system is observed from the point of the impedance measurement. For instance, there might be some unknown resistive component, not part of the leak itself, that leads to a seemingly different leak geometry when the model is fitted to an impedance measurement. Such a "missing part" in the model is, however, not too likely since the system with the leak and the artificial ear is quite simple and well known. The most likely error, leading to the observed underestimation of the attenuation, is an inaccurate part of the model. Since the model is adapted to actual impedance measurements on the same system as the attenuation measurements are performed, a constant deviation between the model and the physical system is likely to be largely compensated for. Nonlinearities due to high SPLs and/or velocities might, however, lead to changes between the impedance and attenuation measurements. Such nonlinearities are described by Mechel and Vér (1992) and Sivian (1935). It has not been assessed here whether or not the SPLs or particle velocities in the leaks were high enough to introduce the nonlinearities described by Mechel and Vér or Sivian.

The slightly higher standard deviations, seen in Table III, for the difference between measured and estimated attenuation for the soft-walled leaks are probably caused by two factors. First of all, the measurements on the soft-walled

leaks were performed a lot quicker than the measurements on the rigid-walled leaks. This was done to get consistent leaks after the removal of the metal tubes that made the imprinted leaks in the foam earplug. The shorter measurement times lead to a decrease in the accuracy in both the impedance and attenuation measurements when compared to those made on the rigid-walled leaks. The other factor likely to contribute to the higher standard deviations for the soft-walled leaks is their less consistent leak geometry. Even though additional unwanted leaks might have occurred during the measurements on the rigid-walled leaks, it is likely that the rigid-walled leaks had a more consistent geometry than the soft-walled leaks.

The higher means for the difference between measured and estimated attenuation achieved for the soft-walled leaks indicate that the modeling was less successful than for the rigid-walled leaks. This is most likely due to the difference in properties of the soft-walled leaks compared to the rigid-walled leaks. As mentioned above, the geometry of the soft-walled leaks, both in terms of size and shape, were likely to be less consistent than that of the rigid-walled leaks. In addition, the softer walls of the soft-walled leaks may have affected the impedance of those leaks, making the models used to represent them less accurate.

C. Estimates of leak radii

A comparison of the estimated leak radii in Tables I and II show that there is a very good correspondence between the physical and acoustical estimates. A more accurate analysis of the differences will not be given since the estimates of the physical dimensions have somewhat large uncertainties. Besides, the main objective in this work has been to find acoustic estimates of the radii, which together with the model give a good description of the acoustic behavior of the air leaks. The fairly small standard deviation in the predicted leak radii for the soft-walled air leaks indicates that the method used to introduce such leaks has been successful.

VII. CONCLUSION

Two main ideas have been tested in this work. First of all, it was tested whether or not impedance measurements in an artificial ear canal could be used to detect the presence of air leaks along a foam earplug. The results from the impedance measurements show that air leaks with significantly narrower radius than the air leaks tested should be clearly detectable. The major limiting factor for the detection of narrow leaks will be the accuracy of the impedance measurements.

Second, it was tested if it is possible to use the impedance measurements and a model for the impedance of narrow tubes to quantify the effect that an air leak will have on the sound attenuation of a foam earplug. The results shown in Figs. 10–13 indicate that the effect an air leak will have on the attenuation of foam earplugs is well described by the impedance measurements and the model set forward in Sec. II B. The estimated attenuation was within $[-3.5, +3]$ dB of the measured attenuation over the frequency range of 50–1000 Hz and attenuation range of −2–38 dB. The mean difference between the measured and estimated attenuation for all the four leaks in this frequency range was −0.7 dB, indicating a slight underestimation of the attenuation.

From the discussion above, in Sec. VI B 3, it can be concluded that the most likely reason for the observed difference between the measured and estimated attenuation is a small inaccuracy in the used model for the system with a leak and an artificial ear. There might be some unknown missing part in the model or, more likely, the model for the leaks might be slightly inaccurate for the conditions used in the measurements. A separate investigation of the behavior of the used leaks, at the SPLs and particle velocities experienced in the measurements, would hopefully show any nonlinearity in their behavior.

The method tested here seems promising when it comes to detecting and quantifying the effect of air leaks in foam earplugs into an artificial ear. A natural question is whether the method is feasible for real ears. The greatest challenge in this case would probably be to find a model that describes the ear in a sufficient way without being too complicated. Another question that arises is whether or not the model for air leaks is sufficient to describe the physical air leaks that sometimes arise during the use of earplugs. If positive answers could be found for these questions, one could incorporate a self-test into earplugs including the necessary transducers and processing capabilities. This self-test could be activated after the insertion of the earplugs to verify the effectiveness of the protection provided by the earplugs. It is also possible that this method could be used for the detection of leaks in earmuffs.

ACKNOWLEDGMENTS

This work was supported by the Research Council of Norway through the "Acoustic Research Centre" project. The author would like to thank Peter Svensson for his invaluable advices and support, and NACRE for supplying the disposable foam earplugs and QUIETPRO™ headset used in the experiments.

[1]Beranek (1954) gave a correction factor for the reactance term of the impedance at the rear side of a loudspeaker diaphragm mounted in a box. This correction factor was found to be insignificant for the leak radii used here and was therefore omitted.

[2]For one of the four leaks tested, the foam earplug was changed after half of the measurements had been performed. For the other three leaks, the foam earplug was only changed when the type of leak was changed. A total of five foam earplugs were therefore used during the measurements on the leaks. The change of foam earplug was done because the handling of the earplug introduces contamination, which changes the properties of the foam. In addition some of the measurements dictated the use of foam earplugs of different lengths.

[3]The length of the sine sweep in WINMLS was 0.5 s for the soft-walled air leaks, which was the same as the measurement length for the impedance.

[4]The two impulse responses were (1) from the sound card through the PA system to the inner microphone and (2) from the sound card through the PA system to the outer microphone.

[5]For one of the series of measurements of soft-walled tubes, the foam earplug was replaced half ways through the series. The impedance probe was then recalibrated before the measurements continued.

Allen, J. B. (**1985**). "Measurement of eardrum acoustic impedance," in *Peripheral Auditory Mechanisms*, edited by J. Allen, J. Hall, A. Hubbard, S. Neely, and A. Tubis (Springer-Verlag, New York, NY).

Beranek, L. L. (**1954**). *Acoustics* (McGraw-Hill, New York, NY), Chap. 5, pp. 124–135.
Brass, D., and Locke, A. (**1997**) "The effect of the evanescent wave upon acoustic measurements in the human ear canal," J. Acoust. Soc. Am. **101**, 2164–2175.
Keefe, D. H. (**1984**). "Acoustical wave propagation in cylindrical ducts: Transmission line parameter approximations for isothermal and nonisothermal boundary conditions," J. Acoust. Soc. Am. **75**, 58–62.
Keefe, D. H., Ling, R., and Bulen, J. C. (**1992**). "Method to measure acoustic impedance and reflection coefficient," J. Acoust. Soc. Am. **91**, 470–485.
Keefe, D. H., Folsom, R. C., Gorga, M. P., Vohr, B. R., Bulen, J. C., and Norton, S. J. (**2000**). "Identification of neonatal hearing impairment: Ear-canal measurements of acoustic admittance and reflectance in neonates," Ear Hear. **21**, 443–461.
Mechel, F. P., and Vér, I. L. (**1992**). "Sound-absorbing materials and sound absorbers," in *Noise and Vibration Control Engineering: Principles and Applications*, edited by L. L. Beranek and I. L. Vér (Wiley, New York, NY), Chap. 8, pp. 236–238.
Nixon, C. W. (**1979**). "Hearing protective devices: Ear protectors," in *Handbook of Noise Control*, 2nd ed., edited by C. M. Harris (McGraw-Hill, New York, NY), Chap. 12, pp. 8–10.
Rschevkin, S. N. (**1963**). *A Course of Lectures on the Theory of Sound* (Pergamon, Oxford), Chap. 7, pp. 228–233.
Sanborn, P. E. (**1998**). "Predicting hearing aid response in real ears," J. Acoust. Soc. Am. **103**, 3407–3417.
Sivian, L. J. (**1935**). "Acoustic impedance of small orifices," J. Acoust. Soc. Am. **7**, 94–101.
Voss, S. E., and Allen, J. B. (**1994**). "Measurement of acoustic impedance and reflectance in the human ear canal," J. Acoust. Soc. Am. **95**, 372–384.
Zwislocki, J. (**1957a**). "Some measurements of the impedance at the eardrum," J. Acoust. Soc. Am. **29**, 349–356.
Zwislocki, J. (**1957b**). "Some impedance measurements on normal and pathological ears," J. Acoust. Soc. Am. **29**, 1312–1317.

On the application of the lattice Boltzmann method to the investigation of glottal flow

Bogdan R. Kucinschi[a] and Abdollah A. Afjeh
Mechanical, Industrial and Manufacturing Engineering Department, University of Toledo, Ohio 43606

Ronald C. Scherer[b]
Department of Communication Disorders, Bowling Green State University, Ohio 43403

(Received 7 September 2007; revised 8 April 2008; accepted 17 April 2008)

The production of voice is directly related to the vibration of the vocal folds, which is generated by the interaction between the glottal flow and the tissue of the vocal folds. In the current study, the aerodynamics of the symmetric glottis is investigated numerically for a number of static configurations. The numerical investigation is based on the lattice Boltzmann method (LBM), which is an alternative approach within computational fluid dynamics. Compared to the traditional Navier–Stokes computational fluid dynamics methods, the LBM is relatively easy to implement and can deal with complex geometries without requiring a dedicated grid generator. The multiple relaxation time model was used to improve the numerical stability. The results obtained with LBM were compared to the results provided by a traditional Navier–Stokes solver and experimental data. It was shown that LBM results are satisfactory for all the investigated cases.
 [DOI: 10.1121/1.2924137]

PACS number(s): 43.70.Bk, 43.70.Aj [BHS] Pages: 523–534

I. INTRODUCTION

The production of voice is related to the quasiperiodic motion of the vocal folds, which is primarily a fluid-structure interaction process. This process is determined by both the biomechanical characteristics of the vocal fold tissue[1] and aerodynamic pressures.[2] It is accepted that the normal phonation involves a symmetrical motion of the vocal folds, where the motion of one vocal fold mirrors the motion of the other.[3,4] The symmetry of the glottal motion permits simplifications of the theoretical and empirical models used for the study of phonation. There are, however, situations when the glottis is asymmetric (oblique), associated with either normal or pathological conditions.[5–8] The study of the glottal flow and the resulting glottal wall pressures is important since it constitutes the driving force of the glottal vibration. Although the motion of the vocal folds is complex, a number of simplifications can be used to reduce the complexity of the models, as will be shown in Sec. II.

The present work deals with the numerical prediction of the flow through different static symmetrical configurations of the glottis. The approach proposed here is to use a relatively new computational method, namely, the lattice Boltzmann method (LBM). In the last two decades, LBM has emerged as a viable computational fluid dynamics technique. Compared to the Navier–Stokes solvers, the LBM presents the advantage of simplicity of computational algorithms, which are also suitable for parallelization. Also, it can handle efficiently complex geometric configurations, a necessary condition for the analysis of the glottal flow. Traditionally, the numerical simulations of glottal flow are based on solving the Navier–Stokes equations for both static[8–10] and moving-wall[11–13] models.

Recently, the LBM solvers have become serious competitors to conventional Navier–Stokes solvers[14] for a wide diversity of flows, including compressible and thermal flows.[15,16] Also, progress was recently made toward aeroacoustic simulations based on LBM.[17,18]

According to the authors' knowledge, the LBM method has not been used for the study of the glottal flow. The unsteady compressible nature of LBM makes this method potentially attractive for the investigation of phonatory acoustics. Although in the present work only static configurations were considered, the LBM method can be applied to moving boundaries.[19–21] The LBM appears particularly convenient for the flow within a moving glottis since it does not use a deforming mesh, while the Navier–Stokes solvers require the deformation or regeneration of the computational cells (a challenging process for glottal geometries[13]).

II. LARYNGEAL GEOMETRY

The actual human glottis is a three-dimensional airway with two primary portions. The membranous, or anterior, glottis extends from the vocal processes of the arytenoid cartilages to the anterior commissure, while the posterior, or cartilaginous, glottis extends from the vocal processes to the posterior mucosal wall between the two arytenoid cartilages.[22] The present study focuses on the membranous glottis, where the normal coronal configuration during phonation alternates between converging and diverging shapes, during the glottal opening and closing.[3] This change of shape is generated by the wall pressures, the morphological structure of the vocal folds, and the dynamics of the fluid-structure interaction process. The anterior-posterior shape of

[a]Electronic mail: bkucinsc@eng.utoledo.edu
[b]Electronic mail: ronalds@bgsu.edu

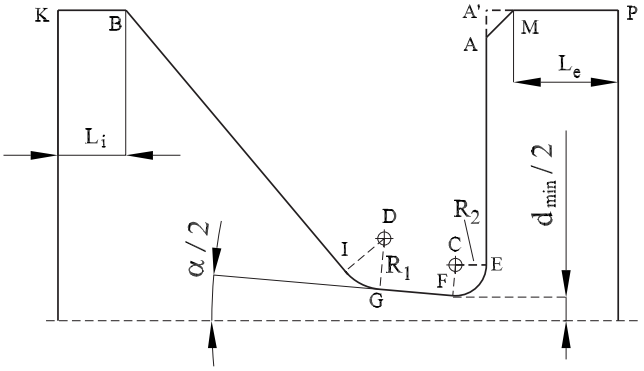

FIG. 1. The geometrical configuration of the larynx model.

the membranous glottis is not uniform during phonation, such that the glottis opens wider near the middle and tapers toward the anterior and posterior ends. Although phonation involves three-dimensional moving configurations, much simpler, two-dimensional static empirical models are commonly used for pressure measurements. The two-dimensional character of the flow is obtained by typically allowing for a uniform anterior-posterior dimension. The use of static models is justified by the so-called *quasisteady approximation*, which states that the flow physics for a certain static configuration satisfactorily approximates the flow physics in an identical configuration when the vocal folds are moving with the relatively low speeds typical for phonation. A number of studies have reasonably shown the validity of this assumption.[13,23]

The static, symmetric laryngeal configurations analyzed in the present study are based on the two-dimensional geometry of the experimental model M5, reported by Scherer and co-workers.[8,10] This is a simplified Plexiglas model of the larynx with linear dimensions 7.5 times larger than an average normal male larynx. The larger dimensions of the model have permitted the installation of pressure taps in the midsection of model folds for accurate wall pressure measurements. The vocal folds are replaceable, such that various glottal configurations (i.e., convergent, uniform, or divergent, with different minimum glottal openings) can be obtained.

Three representative configurations have been investigated: convergent ($\alpha=-10°$), uniform ($\alpha=0°$), and divergent ($\alpha=+10°$) for a glottal opening ("diameter") $d_{\min}$ of 0.04 cm. Figure 1 presents the glottal profile corresponding to the convergent geometry. The details for each configuration are shown in Table I. The x axis coincides with the glottal axis, and its origin corresponds to the abscissa of point D. The length of the inlet region L_i and exit region L_e are the same for all cases, having values of 0.2 and 0.1 cm, respectively. They have been chosen in order to decrease the computational effort, while providing a uniform flow at the inlet and a satisfactory pressure recovery downstream of the vocal folds. The use of inlet and exit regions shorter than the actual length of trachea and vocal tract, respectively, is a simplification which does not affect the predicted pressures.[8,9,13]

There is a small difference between the configurations studied in the present paper and the M5 model. For reasons related to the application of the lattice Boltzmann method, the rectangular region in M5 around point A' in Fig. 1 was trimmed with the 45° linear segment $A-M$. The purpose was to avoid singular nodes in the lattice, as will be explained in Sec. III B 1. Since the experiments showed that the pressures in this region are approximately uniform and equal to the downstream pressure, this profile alteration does not introduce significant differences in the pressure distribution.

III. METHODS

The flow through the glottal configurations presented in Sec. II was investigated computationally, using both the lattice Boltzmann method and a Navier–Stokes solver (FLUENT 6.3). The numerical results were compared against the empirical data obtained with the experimental model M5. Some of these results have been reported.[8,10,24]

A. The lattice Boltzmann method

Traditional computational fluid dynamics (CFD) methods solve the Navier–Stokes equations in order to directly determine the pressure and velocity (i.e., macroscopic variables) in the fluid. In contrast, the Boltzmann equation governs a particle distribution function $f(\mathbf{x},\mathbf{v},t)$, which depends on space $\mathbf{x}$, particle velocity $\mathbf{v}$, and time t such that

TABLE I. Geometric characteristics of the laryngeal model (all values are given in centimeters). The minimum glottal diameter is $d_{\min}=0.04$ cm for all cases.

	Convergent 10°		Uniform		Divergent 10°	
	X	*Y*	*X*	*Y*	*X*	*Y*
A	0.3000	0.7800	0.3000	0.7800	0.3000	0.7800
B	−0.7592	0.8600	−0.7750	0.8600	−0.7750	0.8600
C	0.2092	0.1108	0.2013	0.1187	0.1920	0.1446
D	0.0000	0.1885	0.0000	0.1700	0.0000	0.1700
E	0.3000	0.1108	0.3000	0.1187	0.3000	0.1446
F	0.2013	0.0203	0.2013	0.0200	0.2014	0.0370
G	0.0131	0.0391	0.0000	0.0200	0.0131	0.0206
I	−0.1059	0.0823	−0.1149	0.0736	−0.1149	0.0736
R_1	0.15		0.15		0.15	
R_2	0.0908		0.0987		0.108	

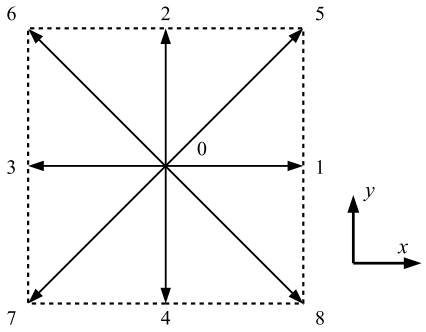

FIG. 2. The two-dimensional, nine-velocity lattice.

$$\frac{\partial f}{\partial t} + \mathbf{v} \cdot \nabla f = Q(f,f), \tag{1}$$

where Q is a collision operator. It has been shown that in the limit of a small Knudsen number, the Navier–Stokes equations can be recovered from the Boltzmann equation if the Chapman–Enskog expansion is used.[25] It is assumed that the solution of the Boltzmann equation can be expressed in the form of an infinite series,

$$f = f^{(0)} + f^{(1)} + f^{(2)} + \cdots, \tag{2}$$

where the lowest order term, $f^{(0)}$, is the equilibrium distribution function, corresponding to the Maxwell–Boltzmann distribution. If only the first two terms, $f^{(0)}$ and $f^{(1)}$, are taken into account in Eq. (2), the Navier–Stokes equations are obtained. The collision operator Q in Eq. (1) has a complex form, but it can be simplified by using the Bhatnagar–Gross–Krook (BGK) approximation,[26]

$$Q(f,f) = -\frac{1}{\lambda}(f - f^{(0)}), \tag{3}$$

where λ is the relaxation time due to collision. The relationship between the macroscopic quantities (density ρ and momentum density $\rho\mathbf{u}$) and the distribution function f is given by[27]

$$\rho = \int f(\mathbf{x},\mathbf{v},t)d\mathbf{v}, \quad \rho\mathbf{u} = \int \mathbf{v} f(\mathbf{x},\mathbf{v},t)d\mathbf{v}. \tag{4}$$

The velocity space can be discretized into a finite set of velocities, $\mathbf{v}_i$, whose directions define a lattice (e.g., Wolf-Gladrow[28]). The corresponding distribution functions become $f_i(\mathbf{x},t) \equiv f(\mathbf{x},\mathbf{v}_i,t)$. The corresponding discrete Boltzmann equation can be written as

$$\frac{\partial f_i}{\partial t} + \mathbf{v}_i \cdot \nabla f_i = -\frac{1}{\lambda}(f_i - f_i^{(0)}). \tag{5}$$

In the present paper, a two-dimensional square lattice with nine-velocity directions (Fig. 2) is used. The discrete velocities are expressed in terms of the lattice directions, $\mathbf{v}_i = c\mathbf{e}_i$, where c is the lattice speed, $c = \delta_x/\delta_t$. Here, δ_x and δ_t are the lattice space and time steps, respectively, and the lattice directions are indicated by

$$\mathbf{e}_i = \begin{cases} (0,0), & i = 0 \\ \left(\cos\left(\frac{\pi}{2}(i-1)\right), \sin\left(\frac{\pi}{2}(i-1)\right)\right), & i = 1,2,3,4 \\ \sqrt{2}\left(\cos\left(\frac{\pi}{2}\left(i-\frac{9}{2}\right)\right), \sin\left(\frac{\pi}{2}\left(i-\frac{9}{2}\right)\right)\right), & i = 5,6,7,8. \end{cases} \tag{6}$$

This model[29] is commonly referred to as D2Q9. There are only three distinct values of speed in the lattice: 0 ("rest particle") and c and $c\sqrt{2}$ on the rectangular and oblique directions, respectively. The method deals with individualized particles that travel between two lattice nodes during one time step, such that it has a Lagrangian character.

1. The lattice Boltzmann–BGK (LBGK) equation

The discrete Boltzmann equation can be discretized such that the LBGK equation is obtained,[27,28]

$$f_i(\mathbf{x} + c\mathbf{e}_i\delta_t, t + \delta_t) - f_i(\mathbf{x},t) = -\omega[f_i(\mathbf{x},t) - f_i^{(0)}(\mathbf{x},t)], \tag{7}$$

where $\omega = 1/\tau$ is a relaxation parameter corresponding to the dimensionless collision time, $\tau = \lambda/\delta_t$. Although this discretization is of first order, it has been shown[30] that at low Mach numbers, the method is second-order accurate in both space and time due to its Lagrangian nature if a suitable relationship between the dimensionless collision time and kinematic viscosity [Eq. (15)] is used. The equilibrium part of the distribution function for the nine-velocity model is given in terms of macroscopic quantities (i.e., density and velocity),

$$f_i^{(0)} = w_i\rho\left[1 + 3\frac{\mathbf{e}_i \cdot \mathbf{u}}{c} + \frac{9}{2}\frac{(\mathbf{e}_i \cdot \mathbf{u})^2}{c^2} - \frac{3}{2}\left(\frac{\mathbf{u}}{c}\right)^2\right]. \tag{8}$$

The weights w_i depend on the lattice direction,

$$w_i = \begin{cases} \frac{4}{9}, & i = 0 \\ \frac{1}{9}, & i = 1,2,3,4 \\ \frac{1}{36}, & i = 5,6,7,8. \end{cases} \tag{9}$$

The LBGK equation can be regarded as containing two steps: a local collision relaxation step, followed by a propagation on the direction i of the lattice (also referred to as "streaming step"). Equation (7) can thus be written as

$$f_i^+(\mathbf{x},t) = (1-\omega)f_i(\mathbf{x},t) + \omega f_i^{(0)}(\mathbf{x},t),$$

$$f_i(\mathbf{x} + c\mathbf{e}_i\delta_t, t + \delta_t) = f_i^+(\mathbf{x},t), \tag{10}$$

where the first equation constitutes the collision step (the "+" subscript refer to the postcollision value of the distribution function), while the second equation describes the propagation. The collision process is strictly local since it involves only f_i at the current site. The relationship between the lattice speed c and the speed of sound c_s is particular for each type of lattice. For the square lattice used in the present work, it has been shown[28] that $c_s^2 = c^2/3$.

It is customary in the literature dedicated to LBM to use dimensionless notations, such that the (dimensionless) space

and time step, as well as the lattice speed c, become equal to unity. The propagation part of Eq. (10) may thus be written as

$$f_i(\mathbf{x}+\mathbf{e}_i,t+1)=f_i^+(\mathbf{x},t). \tag{11}$$

The fluid density and velocity are obtained from the distribution function by applying the discrete form of Eq. (4),

$$\rho=\sum_i f_i,$$

$$\rho\mathbf{u}=\sum_i c\mathbf{e}_i f_i. \tag{12}$$

For low velocity flows, characterized by a low Mach number, the density variations are small. If the density is expressed as $\rho=\rho_0+\delta\rho$, the density fluctuations should be of the order $O(M^2)$ as the $M\ll 1$. By neglecting the terms of the equilibrium density functions that involve higher order dependency on M, He and Luo[31] have proposed an *incompressible* LBM model [sometimes referred to as ID2Q9 (Ref. 32)] characterized by

$$f_i^{(0)}=w_i\left\{\rho+\rho_0\left[3\frac{\mathbf{e}_i\cdot\mathbf{u}}{c}+\frac{9}{2}\frac{(\mathbf{e}_i\cdot\mathbf{u})^2}{c^2}-\frac{3}{2}\left(\frac{\mathbf{u}}{c}\right)^2\right]\right\}. \tag{13}$$

He and Luo recommend that $M<0.15$ in numerical simulations. The model is not truly incompressible, and the pressure is related to the density by $\delta p=c_s^2\delta\rho$. The incompressible Navier–Stokes equations are recovered from the incompressible lattice Boltzmann model by using the Chapman–Enskog procedure,

$$\frac{1}{c_s^2}\frac{\partial P}{\partial t}+\nabla\cdot\mathbf{u}=0,$$

$$\frac{\partial\mathbf{u}}{\partial t}+\mathbf{u}\cdot\nabla\mathbf{u}=-\nabla P+\nu\nabla^2\mathbf{u}, \tag{14}$$

where $P=c_s^2\rho/\rho_0$ is the normalized pressure. The kinematic viscosity ν depends on the dimensionless collision time, as well as on the space and time steps,

$$\nu=\frac{(2\tau-1)}{6}\frac{\delta_x^2}{\delta_t}. \tag{15}$$

In the case of the incompressible model, the fluid density and velocity are calculated as

$$\rho=\sum_i f_i,$$

$$\rho_0\mathbf{u}=\sum_i c\mathbf{e}_i f_i. \tag{16}$$

2. The multiple relaxation time (MRT) model

The dimensionless collision time τ is always greater than 0.5, but numerical instabilities may occur for the classic LBGK method for values very close to 0.5. Small values of τ are typically obtained for practical grids if the fluid presents a small kinematic viscosity (as in the case of air). Two approaches can be used to address this problem. One approach (proposed by Guo *et al.*[33]) consists of improving the discretization of the Boltzmann equation, regarded as a partial differential equation. This has the effect of introducing an artificial viscosity at the cost of significantly increasing the complexity of the implementation (a three-node stencil is required for the propagation step, instead of the classic two-node stencil). The second approach recognizes that the limitations of LBGK stem from the single-relaxation time. A generalized lattice Boltzmann equation based on multiple relaxation times has been proposed by d'Humières,[34] where the collision is performed in moment space rather than in discrete velocity space. Lallemand and Luo[35] have investigated the stability of the modified method (as well as its dispersion and dissipation) and found it superior to the classic method due to the separation of the relaxation of the kinetic modes. This MRT model will be briefly outlined as follows, by contrast with the classic model which is sometimes referred to as the single-relaxation time (SRT) model.[15,36] The distribution functions can be written as a vector in the $\mathbb{R}^9$ vector space,

$$\{f\}=\{f_i|i=0,1,\ldots,8\}. \tag{17}$$

A new set of variables corresponding to the moments of $\{f\}$ can be defined, and a vector $\{\Xi\}$ can constructed in the $\mathbb{R}^9$ vector space,

$$\{\Xi\}=(\rho,e,\varepsilon,j_x,q_x,j_y,q_y,p_{xx},p_{xy})^T, \tag{18}$$

where e is the energy, ε is related to the square of the energy, j_x and j_y are momentum densities, q_x and q_y correspond to the energy flux, while p_{xx} and p_{xy} correspond to the components of the viscous stress tensor. A transformation matrix,

$$[M]=\begin{bmatrix}
1 & 1 & 1 & 1 & 1 & 1 & 1 & 1 & 1\\
-4 & -1 & -1 & -1 & -1 & 2 & 2 & 2 & 2\\
4 & -2 & -2 & -2 & -2 & 1 & 1 & 1 & 1\\
0 & 1 & 0 & -1 & 0 & 1 & -1 & -1 & 1\\
0 & -2 & 0 & 2 & 0 & 1 & -1 & -1 & 1\\
0 & 0 & 1 & 0 & -1 & 1 & 1 & -1 & -1\\
0 & 0 & -2 & 0 & 2 & 1 & 1 & -1 & -1\\
0 & 1 & -1 & 1 & -1 & 0 & 0 & 0 & 0\\
0 & 0 & 0 & 0 & 0 & 1 & -1 & 1 & -1
\end{bmatrix}, \tag{19}$$

exists such that

$$\{\Xi\}=[M]\{f\}. \tag{20}$$

The collision in the MRT model is similar in form with that for SRT [see Eq. (10)], but with different relaxation parameters, s_k,

$$\Xi_k^+=\Xi_k-s_k(\Xi_k-\Xi_k^{(0)}), \tag{21}$$

with $k=0,\ldots,8$. Indeed, if the distribution function is taken as a vector in the $\mathbb{R}^9$ vector space, then Eq. (7) becomes

$$\{f(\mathbf{x}+\mathbf{e}_i,t+1)\}=\{f(\mathbf{x},t)\}-[\Omega](\{f(\mathbf{x},t)\}-\{f^{(0)}(\mathbf{x},t)\}), \tag{22}$$

where $[\Omega]$ is a 9×9 diagonal relaxation matrix for the D2Q9 lattice,

$$[\Omega]=\mathrm{diag}(\omega,\omega,\ldots,\omega).$$

In the case of the MRT model, the collision is executed in moment space while the propagation is still executed in discrete velocity space. The transformation between the velocity space and the moment space is contained in the relationship

$$\{f(\mathbf{x}+\mathbf{e}_i,t+1)\}=\{f(\mathbf{x},t)\}-[\Omega_{\mathrm{MRT}}](\{f(\mathbf{x},t)\}-\{f^{(0)}(\mathbf{x},t)\}), \tag{23}$$

where $[\Omega_{\mathrm{MRT}}]=[M]^{-1}[S][M]$ and $[S]$ is the diagonal relaxation matrix in the moment space,

$$[S]=\mathrm{diag}(s_0,s_1,s_2,s_3,s_4,s_5,s_6,s_7,s_8). \tag{24}$$

The conserved quantities (i.e., the quantities that are not changed by the collision process) in the athermal MRT model are the density ρ and the linear momentum $\boldsymbol{j}=(j_x,j_y)$, corresponding to the parameters with indices 0, 3, and 5, respectively, in Eq. (24). Thus, $s_0=s_3=s_5=0$. It can be shown that $s_7=s_8=\omega=1/\tau$. The rest of the parameters can be determined based on an analysis of the modes of the linearized lattice Boltzmann equation, as indicated by Lallemand and Luo.[35] In the computational code used for the present work, the values indicated by Yu[36] were used, i.e., $s_1=s_2=s_4=s_6=1.2$. The evolution equation of the MRT model can be written as

$$\{f(\mathbf{x}+\mathbf{e}_i,t+1)\}=\{f(\mathbf{x},t)\}-[M]^{-1}[S](\{\Xi\}-\{\Xi^{(0)}\}). \tag{25}$$

For computational efficiency,[37] the equilibrium values $\{\Xi^{(0)}\}$ are calculated explicitly in the moment space based on Eq. (20). Thus, $\Xi_1^{(0)}=-2\rho+3\rho_0(u^2+v^2)$, $\Xi_2^{(0)}=\rho-3\rho_0(u^2+v^2)$, $\Xi_4^{(0)}=-\rho u$, $\Xi_6^{(0)}=-\rho v$, $\Xi_7^{(0)}=-\rho(u^2-v^2)$, and $\Xi_8^{(0)}=-\rho uv$, where ρ_0 is taken as unity. The computational speed is substantially improved by replacing the matrix multiplications with explicit programing. The MRT model increases the computational effort[35,37] by about 10%–20%. The collision locality is not altered, while the propagation requires only the closest neighboring node.

B. Boundary and initial conditions

1. Wall boundary conditions

When solving the Navier–Stokes equations, a solid wall is specified by imposing no-slip boundary conditions for velocity $\mathbf{u}$ at the macroscopic level. For LBM, there is no corresponding physical boundary condition[38] for f. Traditionally, the so-called "bounce-back" condition is used at the walls, which was inherited from the lattice-gas cellular automata.[28] It can be intuitively interpreted as the backscattering of a particle initially traveling along the direction $\mathbf{e}_i$ on the opposite direction, $\mathbf{e}_{-i}=-\mathbf{e}_i$, after encountering a wall. It was shown that the bounce-back boundary conditions may yield second-order accurate results[38] for straight walls. Several methods have been proposed for curved walls.[19,38,39]

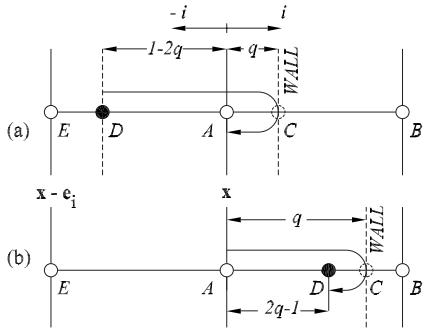

FIG. 3. Illustration of the linear BFL wall boundary conditions.

In the present work, the interpolation method due to Bouzidi *et al.*[19] was applied. This method (referred to henceforth as "BFL") assumes that the wall passes in between two lattice nodes. It is superior in terms of stability to other methods based on extrapolation and can be applied for both fixed and moving boundaries.[20] The BFL method has been recently used for the investigation of flow through constricted vascular tubes.[40] The concept behind BFL is that during a time step, the distribution is propagated over one lattice space step even when it is backscattered by the presence of a wall. The method will be summarized below for the case of linear interpolation. The location of the wall in between lattice nodes is specified as the fraction of the link in the fluid,

$$0\le q=|\mathbf{x}_C-\mathbf{x}_A|/|\mathbf{x}_B-\mathbf{x}_A|\le 1,$$

where B is a solid node. For the case $q\leqslant\frac{1}{2}$ [see Fig. 3(a)], the distribution f_{-i} at node A at time $t+1$ is equal (due to propagation) to the postcollision distribution f_i at the virtual node D at time t,

$$f_{-i}(\mathbf{x}_A,t+1)=f_{-i}^{+}(\mathbf{x}_D,t).$$

The latter can be calculated by interpolation based on the values of f_i at nodes A and E,

$$f_{-i}(\mathbf{x}_D,t)=(1-2q)f_i^{+}(\mathbf{x}_E,t)+2qf_i^{+}(\mathbf{x}_A,t).$$

Thus, one can write in lattice coordinates,

$$f_{-i}(\mathbf{x},t+1)=(1-2q)f_i^{+}(\mathbf{x}-\mathbf{e}_i,t)+2qf_i^{+}(\mathbf{x},t),\quad q\le\tfrac{1}{2}. \tag{26}$$

It can be observed that a classic bounce-back condition is recovered if $q=\frac{1}{2}$,

$$f_{-i}(\mathbf{x},t+1)=f_i^{+}(\mathbf{x},t). \tag{27}$$

For $q>\frac{1}{2}$, the value of f_{-i} at node A at time $t+1$ is obtained by linear interpolation between the values at nodes E and D [see Fig. 3(b)],

$$f_{-i}(\mathbf{x}_A,t+1)=\frac{(2q-1)f_{-i}(\mathbf{x}_E,t+1)+f_{-i}(\mathbf{x}_D,t+1)}{2q}. \tag{28}$$

Due to the propagation process,

$$f_{-i}(\mathbf{x}_E,t+1)=f_{-i}^{+}(\mathbf{x}_A,t)$$

and

$$f_{-i}(\mathbf{x}_D, t+1) = f_i^+(\mathbf{x}_A, t).$$

By using the lattice coordinates, one can write

$$f_{-i}(\mathbf{x}, t+1) = \frac{2q-1}{2q} f_{-i}^+(\mathbf{x}, t) + \frac{1}{2q} f_i^+(\mathbf{x}, t), \quad q > 1/2. \tag{29}$$

It can be noted that two nodes adjacent to the wall are necessary for BFL with linear interpolation. A more accurate, quadratic interpolation can be used.[19] In the present study, the BFL scheme with quadratic interpolation was observed to be less stable than its linear counterpart. A generalization of the BFL boundary conditions was found by Ginzburg and d'Humières based on rigorous kinetic considerations. These conditions, referred to as "multireflection" (MR) boundary conditions, provide third order kinetically accurate results.[21] Although the MR conditions were not systematically tested in the present work, some preliminary simulations resulted in numerical oscillations.

It is assumed that a wall is bordered by a sufficiently large number of fluid nodes, which signifies that the fluid is a continuous medium. In case a fluid node is located in a "corner" (such as point A' in Fig. 1), there is a single node in between two solid boundaries in one lattice direction. In order to avoid this situation, the linear segment $A-M$ was defined. For the particular investigated problem, this alteration introduces negligible modifications in the solution.

2. Pressure boundary conditions

In the case of the laryngeal flow, it is convenient to use pressure boundary conditions for both inlet and outlet since the transglottal pressure drop is typically known. It is desirable to use numerical schemes for the boundary conditions that provide both accuracy and stability. Chen *et al.*[30] have proposed a second-order extrapolation scheme for the distribution functions at the boundaries. The extrapolation can have a negative impact on the numerical stability. Guo *et al.*[41] proposed a method based on the extrapolation of only the nonequilibrium part of the distribution functions. This method is second-order accurate, while presenting superior numerical stability. Henceforth, the nonequilibrium extrapolation method for pressure boundary conditions will be outlined for completeness. A distribution function f_i can be decomposed into its equilibrium and nonequilibrium parts, consistent with Eq. (2),

$$f = f^{(0)} + f^{(\mathrm{NE})}. \tag{30}$$

Hence, the collision equation from Eq. (10) can be rewritten for a boundary node O as

$$f_i^+(O,t) = f_i^{(0)}(O,t) + (1-\omega) f_i^{(\mathrm{NE})}(O,t), \tag{31}$$

with $\omega = 1/\tau$. Let B be the neighbor node of O in the first layer of fluid immediately adjacent to the boundary. The nonequilibrium part of f can be approximated as

$$f_i^{(\mathrm{NE})}(O,t) \approx f_i^{(\mathrm{NE})}(B,t) = f_i(B,t) - f_i^{(0)}(B,t). \tag{32}$$

The equilibrium part in O is approximated as

$$f_i^{(0)}(O,t) \approx \tilde{f}_i^{(0)}(O,t) = \mathrm{function}(p(O,t), \mathbf{u}(B,t)), \tag{33}$$

where $p(O,t) = p_{\mathrm{BC}}$ is the pressure on the boundary. The boundary pressure p_{BC} is related to the density on the boundary, such that the following expression is obtained:

$$\tilde{f}_i^{(0)} = w_i \left(\frac{p_{BC}}{c_s^2} + \rho_0 \mathcal{F}_i \right), \tag{34}$$

where

$$\mathcal{F}_i = 3\frac{\mathbf{e}_i \cdot \mathbf{u}(B,t)}{c} + \frac{9}{2}\frac{[\mathbf{e}_i \cdot \mathbf{u}(B,t)]^2}{c^2} - \frac{3}{2}\left[\frac{\mathbf{u}(B,t)}{c}\right]^2.$$

Here, the incompressible model of He and Luo[31] was used for Eq. (33). The same approach was reported by Huang *et al.*[40] Guo *et al.*[41] have used a modified form of the incompressible model developed by the same team.[42]

In the context of the MRT model, the pressure boundary conditions can be cast in a particular form. The relationship stated in Eq. (20) applies to the corresponding nonequilibrium parts,

$$\{\Xi^{(\mathrm{NE})}(B,t)\} = [M]\{f^{(\mathrm{NE})}(B,t)\}, \tag{35}$$

with

$$\{\Xi^{(\mathrm{NE})}(B,t)\} = \{\Xi(B,t)\} - \{\Xi^{(0)}(B,t)\}.$$

A relation similar to Eq. (31) can also be written for the moment vector on the boundary,

$$\Xi_k^+(O,t) = \Xi_k^{(0)}(O,t) + (1-s_k)\Xi_k^{(\mathrm{NE})}(O,t), \tag{36}$$

where it was assumed that $\Xi_k^{(\mathrm{NE})}(O,t) \approx \Xi_k^{(\mathrm{NE})}(B,t)$. It can now be seen that the following relation in the discrete velocity space can be written:

$$\{f^+(O,t)\} = \{\tilde{f}^{(0)}(O,t)\} + [M]^{-1}[D][M]\{f^{(\mathrm{NE})}(B,t)\}, \tag{37}$$

where $[D] = [I] - [S]$, $[I]$ is the unit matrix in $\mathbb{R}^9$, and $[S]$ is the diagonal relaxation matrix [see Eq. (24)]. Although similar in form with the boundary condition due to Guo *et al.*,[41] this modified boundary condition incorporates the MRT concept and was observed to lead to an improved numerical stability.

3. Initial condition

An initial condition is necessary because the LBM is intrinsically an unsteady method. In the case of glottal flow, the steady-state solution is sought, and a convenient initial condition corresponds to the no-flow state. The distribution functions f_i are initialized with their corresponding equilibrium parts, $f_i^{(0)}$, calculated with Eq. (8) or (13) for the null velocity distribution and average density,

$$f_i^{(0)}(\mathbf{x}, t = t_0) = w_i \rho_0. \tag{38}$$

This choice is also convenient because it is incorrect to use the equilibrium values as initial values for f_i when the initial velocity field is not zero.[43]

TABLE II. Characteristics of the computational lattices used for the three configurations (convergent 10°, uniform and divergent 10°, and minimum diameter d_{min}=0.04 cm) for a speed of sound c_s=330 m/s.

Case	Grid N_d	Space step δ_x (10^{-5} m)	Time step δ_t (10^{-8} s)	Collision time τ (−)	Envelope grid N_X	Envelope grid N_Y	Envelope grid Total nodes	Fluid grid Fluid nodes	Fluid grid Wall nodes
Convergent 10°	12	3.077	5.383	0.502 559	467	561	261 987	136 047	2026
	24	1.600	2.799	0.504 921	899	1077	968 223	504 075	3898
Uniform	12	3.077	5.383	0.502 559	472	561	264 792	135 526	2026
	24	1.600	2.799	0.504 921	909	1077	978 993	503 103	3918
Divergent 10°	12	3.077	5.383	0.502 559	472	561	264 792	136 294	2036
	24	1.600	2.799	0.504 921	909	1077	978 993	505 969	3918

C. Particularities of the LBM implementation

The kinematic viscosity ν is connected to the dimensionless collision time τ, the speed of sound c_s, and the spatial and time steps δ_x and δ_t through Eq. (15) and the relationship between the speed of sound and the lattice speed c. If the space step is chosen, the time step and the dimensionless collision time are determined as

$$\delta_t = \frac{1}{\sqrt{3}}\frac{\delta_x}{c_s},$$

$$\tau = \frac{1}{2}\left(1 + 6\nu\frac{\delta_t}{\delta_x^2}\right). \tag{39}$$

As mentioned above, the numerical stability of the method is affected for values of the dimensionless collision time τ very close to 0.5. It can be observed that for a given value of ν, the space step has to be decreased in order to increase τ. For a fluid with a small kinematic viscosity (as air), the grid may become very fine, while the time step becomes very small. It can be verified that for a low kinematic viscosity, the grid size may become prohibitive if sufficiently large values of the dimensionless collision time are to be maintained. The MRT model is more stable such that reasonably sized grids can be used. However, numerical instabilities may occur during the start-up phase of the simulations if the actual (small) value of τ is used. It was found convenient to start calculations with a larger value, τ_s, of the dimensionless collision time (e.g., 0.75) and to decrease it progressively. Physically, this is equivalent to using a more viscous fluid during the start up. A parabolic variation of τ for the start-up phase was implemented,

$$\tau = \begin{cases} (\tau_s - \tau)(t/T_p)[(t/T_p) - 2] + \tau_s, & t \le T_p \\ \tau, & t > T_p, \end{cases} \tag{40}$$

where T_p is an arbitrary amount of time, sufficient to avoid instabilities. Since the steady-state results are of interest, the actual value of T_p does not affect the computational outcome. However, it has a significant influence on the total computational effort, such that it is desirable to use a value as small as possible, which is found by trial and error. A steady-state simulation was considered converged when the maximum error over the fluid nodes satisfies the criterion

$$\max_j \frac{\|\mathbf{u}(\mathbf{x}_j, t+1) - \mathbf{u}(\mathbf{x}_j, t)\|}{\|\mathbf{u}(\mathbf{x}_j, t+1)\|} \le \epsilon, \tag{41}$$

where ϵ was set to 10^{-6}.

A LBM code traditionally uses a rectangular grid composed of $N_X \times N_Y$ nodes on the two Cartesian axes. In the case of the glottis geometry, such a rectangular "envelope" grid contains a large number of nodes that are located outside the flow domain. The amount of unused memory is quite large because nine double-precision variables (i.e., f_i, $i=0,\ldots,8$) are stored at each node. A different approach was taken in the current implementation: only one Boolean variable is stored at each node of the envelope grid, indicating whether the node is located within the flow domain. A data structure was created such that memory is allocated for the functions f_i only at the fluid nodes. Another data structure was subsequently created for the fluid nodes adjacent to a wall ("wall nodes," whose links intersect a wall in at least one direction). The economy in terms of memory and computational time for the investigated geometries is significant because the number of nodes in the envelope grid is much larger than that actually needed for the computational domain (see Table II).

D. Finite volume Navier–Stokes solver

The general-purpose commercial CFD package FLUENT was chosen in order to provide a basis of comparison for the LBM results. FLUENT is a finite volume Navier–Stokes solver and was previously utilized for the study of the glottal flow in both fixed[8,10] and moving[13] glottal configurations. It has been shown to provide reliable results for glottal wall pressures and flow rates.

The two-dimensional, unsteady implicit version of the solver with simple pressure-velocity coupling was used for the present study. Second-order schemes were selected in FLUENT for both momentum and pressure. The unsteady solver was necessary since the convergence could not be obtained with the steady solver due to numerical oscillations at the outlet pressure boundary condition. A no-flow initial condition was considered. The simulations were carried out with a time step of 10^{-5} s until a steady incompressible laminar solution was obtained for each investigated case. The solutions were considered converged when all the reported

residuals were less than 10^{-5}. Based on symmetry, only half of the flow domain was considered in the simulations. The computational domain was discretized with quadratic cells. Unstructured mesh grids were used, with higher density in the minimum opening region. The minimum grid spacing δ_L, corresponds to the minimum glottal diameter. For the reported results, δ_L was of the order of 5×10^{-6} m (see Table VI). Different meshes were tested in order to verify that grid-independent results were obtained. A comparison between various meshes used during the tests is not presented here in order to avoid lengthening the presentation.

IV. RESULTS AND DISCUSSIONS

The values of fluid (air) properties considered in the computational simulations are as follows: density ρ_0, 1.2 kg/m^3, dynamic viscosity μ, 1.8×10^{-5} kg/m/s (with the resulting kinematic viscosity ν, 1.5×10^{-5} m^2/s), and speed of sound c_s, 330 m/s. Three transglottal pressures have been used in this study, 3, 5, and 10 cm H_2O, corresponding to 294.3, 490.5, and 981 Pa, respectively. For the LBM simulations, it was found convenient to define the grid as a function of the number of lattice units N_d necessary to cover the minimum glottal diameter $d_{\min}$, such that $\delta_x \approx d_{\min}/N_d$. The space step is slightly modified by the code such that the straight inlet and outlet parts of the model glottal geometry are allowed to pass at half-distance in between two lattice nodes (leading to a link fraction $q=\frac{1}{2}$).

Grids of different densities were used for performing the LBM simulations. For each geometry, the coarser grid was characterized by a number of intervals across the minimum diameter $N_d=12$, while for the finer grid, 24 intervals were used. The properties of the two grids are shown in Table II. Preliminary tests of the LBM code using different grid densities ($N_d=12$, 24, and 36) have shown that $N_d=24$ provide a good accuracy, together with a reasonable computational time. This also helped confirm the grid independence for the LBM simulations. The LBM grid encompasses the whole flow domain (not just half-domain, as for the FLUENT grids). One can observe in Table II that the values of the dimensionless collision time τ are close to the stability limit of 0.5 for the LBGK method. The test simulations performed with the LBGK method have lead to numerical oscillations, such that no useful set of results could be obtained. However, the MRT model presented in Sec. III A 2, together with the pressure boundary conditions of Sec. III B 2 and appropriate wall boundary conditions, has lead to stable simulations. It was observed that the wall boundary conditions have a significant influence on the stability of the numerical simulations. The linear BFL conditions lead to stable solutions for all cases. When the quadratic BFL conditions were used, bounded numerical oscillations were observed for kinematic viscosities corresponding to values of the dimensionless collision time τ generally less than 0.55 (as shown in Sec. III C, the simulations have been started with a larger value of τ, which was decreased progressively). The actual value of the dimensionless collision time for which oscillations start to occur appears to be particular to a specific geometry and transglottal pressure. It was observed that the instabilities first occur at those nodes adjacent to boundaries where the link fractions q (in any direction) present values very close to either 0 or 1. Such values are difficult to avoid for a relatively complex geometry (e.g., when arcs are intersected by the lattice links). More investigations on the applicability of the quadratic BFL conditions and the multireflection conditions[21] for the glottal flow are in progress.

The bounce-back wall boundary conditions can be enforced by imposing $q=0.5$ at all nodes adjacent to a wall (even when it does not reflect the correct wall configuration). This condition was initially implemented in the LBM code (mainly for its simplicity) but was shown to provide unsatisfactory results in terms of accuracy and even stability. This is not surprising, as the asymptotic analysis of Junk and Yang[44] has shown that for any actual value of the parameter q other than 0.5, the simple bounce-back conditions lead to a solution of the lattice Boltzmann equation, which is not a correct solution of the incompressible Navier–Stokes equations.

For the reasons stated above, the results presented in this section were obtained by using the linear BFL wall boundary conditions. Since low values of the Mach number were expected, the incompressible form of the equilibrium distribution functions [see Eq. (13)] has been implemented in the computational code. As will be shown below, the results have confirmed this assumption.

The LBM simulations predict a symmetric flow through the glottis, which is due to the symmetry of geometry and boundary conditions. The assumption of the flow symmetry was made *a priori* in the CFD code FLUENT by choosing to solve only half of the flow domain. During the numerical experimentations with FLUENT, it was observed that if the

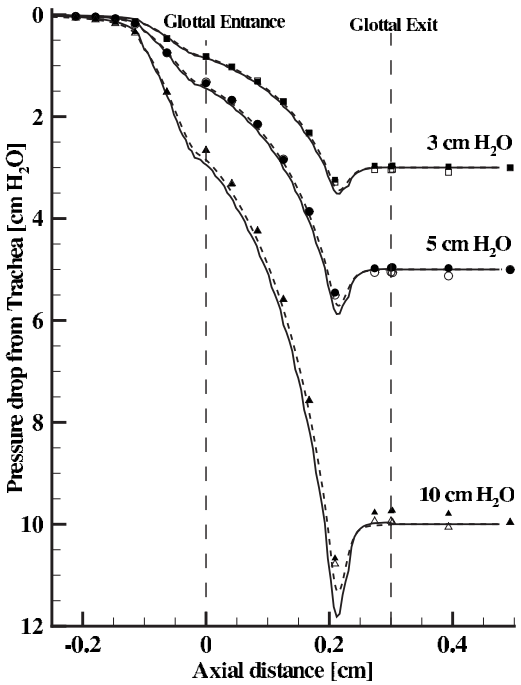

FIG. 4. Glottal wall pressures for the convergent 10°, $d_{\min}=0.04$ cm case. The LBM results are represented with solid line, while the FLUENT results are shown with dashed line. The experimental data are represented with empty symbols for the FW and filled symbols for the NFW.

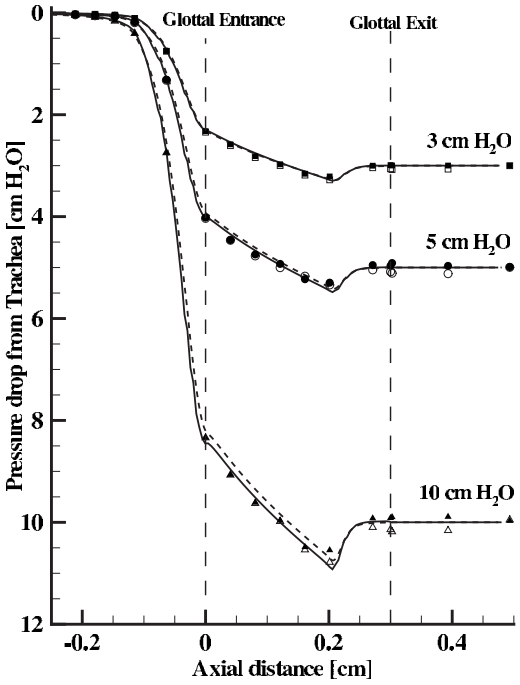

FIG. 5. Glottal wall pressures for the uniform, d_{min}=0.04 cm case. The LBM results are represented with solid line, while FLUENT results are shown with dashed line. The experimental data are represented with empty symbols for FW and filled symbols for NFW.

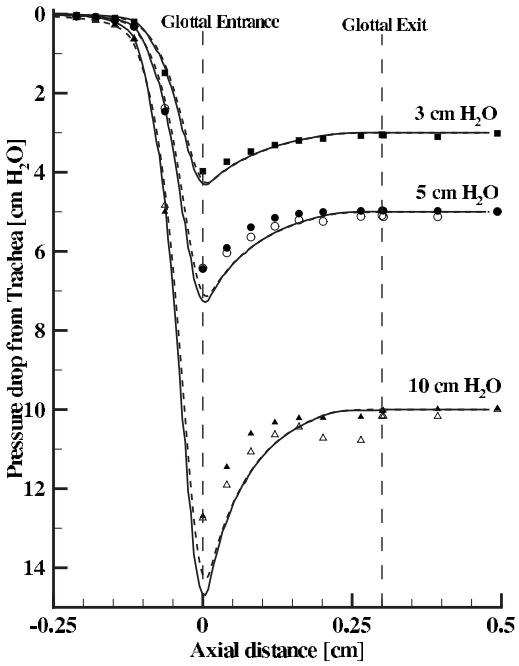

FIG. 6. Glottal wall pressures for the divergent 10°, d_{min}=0.04 cm case. The LBM results are represented with solid line, while FLUENT results are shown with dashed line. The experimental data are represented with empty symbols for FW and filled symbols for NFW.

whole flow domain is considered, the jet emerging from the glottis has a tendency to deviate (skew) from the direction of the glottal axis because of numerical reasons. Experimental observations[8,10] have shown that the glottal jet does indeed skew because of the flow conditions downstream of the vocal folds (e.g., the length of the downstream tunnel in M5). The asymmetry of the jet allows the definition of a "flow wall" (FW), toward which the flow is deviated, and a "nonflow wall"(NFW) on the other side. The measured wall pressures are slightly different, such that the NFW pressures are higher than those on the FW.

Figure 4 shows the glottal wall pressures for the convergent 10° geometry. It was convenient to represent the wall pressures as the pressure drop from the trachea (modeled by the inlet of the computational domain). The LBM results correspond to a grid density N_d=24 and are represented by solid lines. The FLUENT results are shown as dashed lines. The pressures measured on the NFW are represented by filled squares, circles, and triangles for transglottal pressures of 3, 5, and 10 cm H_2O, respectively. The FW are represented by similar but unfilled symbols. The glottal entrance is conventionally defined as the axial location corresponding to point D (i.e., X=0), while the glottal exit corresponds to the vertical segment $A-E$ in Fig. 1. The decrease in the cross-sectional area upstream of the glottal entrance accelerates the flow and causes the pressure to drop, and the minimum pressure (equivalent to the largest pressure drop) is obtained at the location of the minimum glottal diameter. The LBM pressures are generally in satisfactory agreement with the experimental data, as well as with the FLUENT results. Compared to the FLUENT results, the LBM has slightly overpredicted the value of the maximum pressure drop for 10 cm H_2O. The concept of grid independence has been separately verified for FLUENT, such that quasi-identical results are obtained (at the expense of computational time) if finer grids are used.

The wall pressures for the uniform configurations are presented in Fig. 5. The largest pressure drop is obtained for a location slightly downstream to point F (defined in Fig. 1 and Table I), where the glottal cross-sectional area starts to increase. The pressure recovery takes place up to the glottal exit. For all transglottal pressures, the largest pressure drop is less than that for the convergent configurations because the uniform geometry provides less flow acceleration and the viscous effects are more pronounced because of the longer

TABLE III. Glottal flow rate (in cm^3/s) for trans glottal pressures of 3, 5, and 10 cm H_2O: comparison between LBM results (for a grid density N_d=24), FLUENT solver results (NS), and experimental data (E) for a minimum glottal diameter d_{min}=0.04 cm.

	Convergent, 10°			Uniform			Divergent, 10°		
	LBM	NS	E	LBM	NS	E	LBM	NS	E
3	93.1	92.7	87.1	77.8	78.8	80.7	107.7	107.6	97.1
5	123.1	122.1	113.6	104.3	104.1	106.4	141.9	141.5	126.4
10	178.7	176.5	166.8	154.5	153.8	161.3	205.1	203.4	185.2

TABLE IV. Reynolds and Mach numbers based on LBM data for transglottal pressures of 3, 5, and 10 cm H_2O (minimum glottal diameter d_{min}=0.04 cm).

	Convergent 10°		Uniform		Divergent 10°	
	Re	M	Re	M	Re	M
3	620	0.071	604	0.069	693	0.079
5	800	0.091	787	0.089	899	0.102
10	1134	0.129	1115	0.127	1280	0.146

throat zone of small diameter. A good match between the numerical and experimental wall pressures can be observed for all three pressures due to the small asymmetry of the exit jet. The asymmetry increases with the transglottal pressure and is visible for 10 cm H_2O toward the glottal exit. The LBM appears to provide a slightly better approximation than FLUENT with regard to the experiment data. The LBM results were reported for a grid density N_d=24.

For the divergent 10° configurations, the wall pressures are shown in Fig. 6. As for the other cases, a grid density N_d=24 was used to obtain the plotted LBM results. The flow asymmetry in the experimental data is visible starting from 5 cm H_2O. For each transglottal pressure, the largest pressure drop is obtained at the glottal entrance (i.e., X=0). The maximum pressure drop for a divergent case is larger than the one obtained for the corresponding convergent or uniform case. The numerical results are in good agreement with the experimental data for 3 cm H_2O when the flow is symmetric. The separation points are located axially in the vicinity of X=0 (immediately upstream of point G), where the glottal diameter reaches its minimum for a divergent geometry. For larger pressures, the separation points on the two sides are not symmetric due to flow instability[10] and unequal pressures will occur on the two glottal walls. Since in the simulations a symmetric flow was assumed, larger differences between the numerical results and empirical data occur once the flow asymmetry becomes significant. Given the imprecise method of establishing the flow asymmetry, the comparisons between the two sets of computational predictions and the experimental data were generally reasonable. The LBM and FLUENT predictions agree well with each other for the lower pressure cases, while LBM tends to yield slightly larger values of the maximum pressure drop (possibly due to the linear BFL conditions).

The plots for all transglottal pressures show that in some instances, the LBM curves are less smooth than those provided by FLUENT. The explanation is that the wall pressures were reported at the fluid nodes closest to the wall (wall nodes, for which at least one link intersects the wall). This approximation leads to a small inaccuracy for the value and location of the reported pressure.

A good agreement between the LBM and FLUENT was observed for the glottal flow rate, as shown in Table III. In the calculation of the flow rate, a value of 1.2 cm was used for the anterior-posterior dimension, as in the experimental model M5. The difference between the predicted and experimental flow rates is explained by the flow asymmetry in M5. For instance, the asymmetry is evident for a divergent 10° geometry and a transglottal pressure of 5 cm H_2O, while the flow rate differs by 15.3 cm^3/s, corresponding to a relative error ε_r=12%. However, for the uniform configuration at 5 cm H_2O, presenting a good flow symmetry, the difference is 2.2 cm^3/s (i.e., ε_r=2%).

The values of both Reynolds and Mach number (calculated as $M=u_{max}/c_s$, where u_{max} is the maximum speed) for the investigated cases are listed in Table IV. One can observe that the highest value of the Mach number is 0.146, which justifies the use of the incompressible model of He and Luo.[31] Simulations at larger values of Mach number are possible for higher values of the transglottal pressures if the unaltered form [Eq. (8)] of the equilibrium distribution functions is used. The Reynolds number was calculated based on

TABLE V. Computational time for lattice Boltzmann simulations. The code was compiled with the GNU C compiler.

	Grid		CPU time (h) Δp (cm H_2O)		
	N_d	Fluid nodes	3	5	10
Convergent 10°	12	136 047	2.9	5.2	11.5
	24	504 075	27.9	29.1	36.7
Uniform	12	135 526	2.6	6.8	6.9
	24	503 103	28.5	29.0	34.8
Divergent 10°	12	136 294	5.3	5.8	6.9
	24	505 969	34.8	39.1	46.4

TABLE VI. Minimum grid spacing δ_L, local Courant number, and CPU time for FLUENT simulations.

	Grid		CPU time (h) Δp (cm H_2O)			Courant Δp (cm H_2O)		
	Cells	δ_L (10^{-6} m)	3	5	10	3	5	10
Convergent 10°	194 212	4.8	3.0	2.6	2.2	106	141	205
Uniform	209 736	5.1	3.7	3.4	2.8	69	93	136
Divergent 10°	178 088	5.0	3.8	3.4	3.2	101	132	188

the minimum glottal diameter, $\mathrm{Re}=u_{\max}d_{\min}/\nu$. The values of Reynolds number are also low for all cases, being less than 1300.

The computational time was evaluated by using a 3.2 GHz Pentium 4 machine. The current LBM implementation is costlier when compared to FLUENT. Table V presents the computational time for the LBM code, which requires a regularly spaced lattice characterized by a typically small space step, δ_x (see Table II). In contrast, FLUENT simulations are performed for only half of the flow domain and make use of grids designed such that coarser grids are sufficient in the regions with smaller gradients. One important computational aspect is that for LBM, the Courant number is limited to 1 because $\delta_x=\delta_t$ (in dimensionless notation) and the lattice speed is $c=\delta_x/\delta_t$. This involves a slow convergence for steady-state problems.[15] The no-flow initial solution also contributed to a relatively long simulation time (see Sec. III C). The FLUENT simulations (see Table VI) were performed by using an unsteady implicit solver, which allowed for large values of the local Courant number. The speed of the LBM code can be improved by using locally refined grids[39,45] and multigrid techniques.[46] There also exist algorithms for implementing LBM on arbitrary, nonuniform grids, where the nodal values of the distribution functions are estimated by interpolation.[47,48]

The current study was limited to one value of the minimal glottal diameter (i.e., 0.04 cm). However, the investigated configurations are representative of the actual geometry of the glottis, which assumed successively convergent, uniform, and divergent postures.[49,50] Although not presented here, numerical experiments for a glottal diameter of 0.08 cm suggest that LBM can be used for a wider range of glottal configurations.

V. CONCLUSIONS

A numerical method based on the solution of the lattice Boltzmann equation was proposed for the investigation of glottal flow. In the present work, the glottal flow was investigated by using LBM with the MRT model, for which suitable pressure boundary conditions were defined. Three representative static glottal configurations were studied by using this method, corresponding to different shapes of the vocal folds during phonation. The results were validated by comparison with experimental data, as well as with the results obtained with a Navier–Stokes CFD package (FLUENT). Both the glottal wall pressures and flow rates were generally in good agreement with the experimental data and the FLUENT results.

The present work was motivated by the fact that the LBM presents a number of advantages for the investigation of glottal flow. The local character of the interparticle collisions implies that most of the computational work takes place in the grid nodes, while the propagation involves only data shift to the neighbor node. For this reason, the LBM is easy to implement and is well suited for parallel computing.[14,48,51] The simple topology of the LBM lattices ensures the convenient handling of large grids. Another aspect of particular interest for glottal flows is the treatment of moving boundaries,[19,20] which from an implementation viewpoint requires only modifications in the formulation of f at the wall. Also, the inherent transient and weakly compressible character of the LBM shows potential for approaching the laryngeal acoustics.

The in-house LBM implementation used for the present work was less efficient than the Navier–Stokes solver, primarily because of the classical uniform lattice that leads to a dense computational grid. Further work envisages the implementation of algorithms that would allow to use nonuniform grids. Also, the case of moving vocal folds will be investigated, which will also permit the study of the fluid-structure interaction in the glottis.

ACKNOWLEDGMENTS

This research was supported in part by the NIH Grant No. 2R56DC003577-10A1.

[1] K. Ishizaka and J. L. Flanagan, "Synthesis of voiced sounds from a two-mass model of the vocal cords," Bell Syst. Tech. J. **51**, 1233–1268 (1972).
[2] K. Ishizaka and M. Matsudaira, "Fluid mechanical considerations of vocal cord vibration," in *SCRL Monograph* (Speech Communications Research Laboratory, Santa Barbara, 1972), Vol. 8.
[3] M. Hirano, *Clinical Examination of Voice* (Springer-Verlag, New York, 1981).
[4] I. R. Titze, *Principles of Voice Production* (Prentice-Hall, Englewood Cliffs, NJ, 1994).
[5] J. G. Svec and H. K. Schutte, "Videokymography: High-speed line scanning of vocal fold vibration," J. Voice **10**, 201–205 (1996).
[6] J. G. Svec, H. K. Schutte, and F. Sram, "Variability of vibration of normal vocal folds as seen in videokymography," in *Communication and Its Disorders: A Science In Progress*, Proceedings 24th Congress International Association of Logopedics and Phoniatrics, edited by P. H. Dejonckere and H. F. M. Peters (Nijmegan University Press, Amsterdam, 1999), Vol. 1, pp. 122–125.
[7] J. G. Svec, F. Sram, and H. K. Schutte, "Videokymography: A new high-speed method for the examination of vocal-fold vibrations," Otorinolaryngologie a foniatrie **48**(3), 155–162 (1999).
[8] R. C. Scherer, D. Shinwari, K. J. DeWitt, C. Zhang, B. R. Kucinschi, and A. A. Afjeh, "Intraglottal pressure profiles for a symmetric and oblique glottis with a divergence angle of 10 degrees," J. Acoust. Soc. Am. **109**, 1616–1630 (2001).
[9] C. G. Guo and R. C. Scherer, "Finite element simulation of the glottal flow

and pressure," J. Acoust. Soc. Am. **94**, 688–700 (1993).
[10]D. Shinwari, R. C. Scherer, K. J. DeWitt, and A. A. Afjeh, "Flow visualization and pressure distributions in a model of the glottis with a symmetric and oblique divergent angle of 10 degrees," J. Acoust. Soc. Am. **113**, 487–497 (2003).
[11]F. Alipour, C. Fan, and R. C. Scherer, "A numerical simulation of laryngeal flow in a forced-oscillation glottal model," Comput. Speech Lang. **10**, 75–93 (1996).
[12]S. L. Thomson, L. Mongeau, and S. H. Frankel, "Aerodynamic transfer of energy to the vocal folds," J. Acoust. Soc. Am. **118**, 1689–1700 (2005).
[13]B. Kucinschi, R. C. Scherer, K. J. DeWitt, and T. Ng, "An experimental analysis of the pressures and flows within a driven mechanical model of phonation," J. Acoust. Soc. Am. **119**, 3011–3021 (2006).
[14]S. Succi, *The Lattice Boltzmann Equation for Fluid Dynamics and Beyond* (Oxford University Press, New York, 2001).
[15]D. Yu, R. Mei, L.-S. Luo, and W. Shyy, "Viscous flow computations with the method of lattice Boltzmann equation," Prog. Aerosp. Sci. **38**, 329–367 (2003).
[16]G. Yan, Y. Chen, and S. Hu, "Simple lattice Boltzmann model for simulating flows with shock wave," Phys. Rev. E **59**, 454–459 (1999).
[17]X. M. Li, R. C. K. Leung, and R. M. C. So, "One-step aeroacoustics simulation using lattice Boltzmann method," AIAA J. **44**, 78–89 (2006).
[18]E. W. S. Kam, R. M. C. So, and R. C. K. Leung, "Lattice Boltzmann method simulation of aeroacoustics and nonreflecting boundary conditions," AIAA J. **45**, 1703–1712 (2007).
[19]M. Bouzidi, M. Firdaouss, and P. Lallemand, "Momentum transfer of a Boltzmann-lattice fluid with boundaries," Phys. Fluids **13**, 3452–3459 (2001).
[20]P. Lallemand and L.-S. Luo, "Lattice Boltzmann method for moving boundaries," J. Comput. Phys. **184**, 406–421 (2003).
[21]I. Ginzburg and D. d'Humières, "Multireflection boundary conditions for lattice Boltzmann models," Phys. Rev. E **68**, 066614 (2003).
[22]M. Hirano, K. Kiyokawa, and S. Kuria, "Laryngeal muscles and glottis shaping," in *Vocal Physiology: Voice Production, Mechanism and Functions*, edited by O. Fujimura (Raven, New York, 1988), Vol. **49–65**.
[23]Z. Zhang, L. Mongeau, and S. H. Frankel, "Experimental verification of the quasi-steady approximation for aerodynamic sound generation by pulsating jets in tubes," J. Acoust. Soc. Am. **112**, 1652–1663 (2002).
[24]R. C. Scherer, D. Shinwari, K. J. DeWitt, C. Zhang, B. R. Kucinschi, and A. A. Afjeh, "Intraglottal pressure distributions for a symmetric and oblique glottis with a uniform duct," J. Acoust. Soc. Am. **112**, 1253–1256 (2002).
[25]S. Chapman and T. G. Cowling, *The Mathematical Theory of Non-Uniform Gases* (Cambridge University Press, Cambridge, 1960).
[26]P. Bhatnagar, E. P. Gross, and M. K. Krook, "A model for collision processes in gases. I. Small amplitude processes in charged and neutral one-component systems," Phys. Rev. **94**, 511–525 (1954).
[27]X. He and L. S. Luo, "Theory of the lattice Boltzmann method: From the Boltzmann equation to the lattice Boltzmann equation," Phys. Rev. E **56**, 6811–6817 (1997).
[28]D. Wolf-Gladrow, *Lattice-Gas Cellular Automata and Lattice Boltzmann Models* (Springer-Verlag, Berlin, 2000).
[29]Q. H. Qian, D. d'Humières, and P. Lallemand, "Lattice BGK models for Navier-Stokes equation," Europhys. Lett. **17**, 479–484 (1992).
[30]S. Chen, D. Martinez, and R. Mei, "On boundary conditions in lattice Boltzmann methods," Phys. Fluids **8**, 2527–2536 (1996).
[31]X. He and L. S. Luo, "Lattice Boltzmann model for the incompressible Navier-Stokes equation," J. Stat. Phys. **88**, 927–944 (1997).
[32]Z. Guo, C. Zheng, and B. Shi, "An extrapolation method for boundary conditions in lattice Boltzmann method," Phys. Fluids **14**, 2007–2010 (2002).
[33]Z. Guo, C. Zheng, and T. S. Zhao, "A Lattice BGK scheme with general propagation," J. Sci. Comput. **16**, 569–585 (2001).
[34]D. d'Humières, "Generalized lattice-Boltzmann equations," in *Rarefied Gas Dynamics: Theory and Simulations, Progress in Astronautics and Aeronautics*, edited by B. D. Shizgal and D. P. Weaver (AIAA, Washington, DC, 1992), Vol. 159, pp. 450–458.
[35]P. Lallemand and L.-S. Luo, "Theory of the lattice Boltzmann method: Dispersion, dissipation, isotropy, Galilean invariance, and stability," Phys. Rev. E **61**, 6546–6582 (2000).
[36]D. Yu, Ph.D. thesis, University of Florida, 2002.
[37]D. d'Humières, I. Ginzburg, M. Krafczyk, P. Lallemand, and L.-S. Luo, "Multiple-relaxation-time lattice Boltzmann models in three dimensions," Philos. Trans. R. Soc. London, Ser. A **360**, 437–451 (2002).
[38]R. Mei, L. S. Luo, and W. Shyy, "An accurate curved boundary treatment in the lattice Boltzmann method," J. Comput. Phys. **155**, 307–330 (1999).
[39]O. Filippova and D. Hänel, "Grid refinement for lattice-BGK models," J. Comput. Phys. **147**, 219–228 (1998).
[40]H. Huang, T. S. Lee, and C. Shu, "Lattice-BGK simulation of steady flow through vascular tubes with double constrictions," Int. J. Numer. Methods Heat Fluid Flow **16**, 185–203 (2006).
[41]Z. Guo, C. Zheng, and B. Shi, "Non-equilibrium extrapolation method for velocity and pressure boundary conditions in the lattice Boltzmann method," Chin. Phys. **11**, 366–374 (2002).
[42]Z. Guo, B. Shi, and N. Wang, "Lattice BGK model for incompressible Navier-Stokes equation," J. Comput. Phys. **165**, 288–306 (2000).
[43]P. A. Skordos, "Initial and boundary conditions for the lattice Boltzmann method," Phys. Rev. E **48**, 4823–4842 (1993).
[44]M. Junk and Z. Yang, "Asymptotic analysis of Lattice Boltzmann boundary conditions," J. Stat. Phys. **121**, 3–35 (2005).
[45]J. Tölke, S. Freudiger, and M. Krafczyk, "An adaptive scheme using hierarchical grids for lattice Boltzmann multi-phase flow simulations," Comput. Fluids **35**, 820–830 (2006).
[46]J. Tölke, M. Krafczyk, and E. Rank, "A multigrid-solver for the discrete Boltzmann equation," J. Stat. Phys. **107**, 573–591 (2002).
[47]X. He, L. S. Luo, and M. Dembo, "Some progress in lattice Boltzmann method. Part I. Nonuniform mesh grids," J. Comput. Phys. **129**, 357–363 (1996).
[48]C. S. Sunder, G. Baskar, V. Babu, and D. Strenski, "A detailed performance analysis of the interpolation supplemented lattice Boltzmann method on the cray T3E and cray X1," Int. J. High Perform. Comput. Appl. **20**, 557–570 (2006).
[49]M. Hirano, "Structure and vibratory behavior of the vocal folds," in *Dynamic Aspects of Speech Production*, edited by M. Sawashima and F. Cooper (University of Tokyo, Tokyo, 1977), pp. 13–27.
[50]K. N. Stevens and D. H. Klatt, "Current models of sound sources for speech," in *Ventilatory and Phonatory Control Systems*, edited by B. Wyke (Oxford University Press, New York, 1974), pp. 279–292.
[51]M. Krafczyk, "Lattice-Boltzmann Methods: From basics to fluid-structure interaction," Course on Advanced Computational Methods for Fluid-Structure Interaction, Ibiza, Spain, 3–7 May 2006.

Theoretical simulation and experimental validation of inverse quasi-one-dimensional steady and unsteady glottal flow models

Julien Cisonni,[a] Annemie Van Hirtum, and Xavier Pelorson
Department of Speech and Cognition, GIPSA-Laboratory, UMR CNRS 5216, Grenoble Universities, 961 rue de la Houille Blanche, BP 46, 38402 Saint Martin d'Heres, France

Jan Willems
Department of Applied Phusics, Gas Dynamic and Aero-acoustics, Eindhoven University of Technology, P.O. Box 513, CC 2.24, 5600 MB, Eindhoven, The Netherlands

(Received 30 October 2007; revised 23 April 2008; accepted 23 April 2008)

In physical modeling of phonation, the pressure drop along the glottal constriction is classically assessed with the glottal geometry and the subglottal pressure as known input parameters. Application of physical modeling to study phonation abnormalities and pathologies requires input parameters related to *in vivo* measurable quantities commonly corresponding to the physical model output parameters. Therefore, the current research presents the inversion of some popular simplified flow models in order to estimate the subglottal pressure, the glottal constriction area, or the separation coefficient inherent to the simplified flow modeling for steady and unsteady flow conditions. The inverse models are firstly validated against direct simulations and secondly against *in vitro* measurements performed for different configurations of rigid vocal fold replicas mounted in a suitable experimental setup. The influence of the pressure corrections related to viscosity and flow unsteadiness on the flow modeling is quantified. The inversion of one-dimensional glottal flow models including the major viscous effects can predict the main flow quantities with respect to the *in vitro* measurements. However, the inverse model accuracy is strongly dependent on the pertinence of the direct flow modeling. The choice of the separation coefficient is preponderant to obtain pressure predictions relevant to the experimental data.
 [DOI: 10.1121/1.2931959]

PACS number(s): 43.70.Bk, 43.70.Jt [BHS] Pages: 535–545

I. INTRODUCTION

Physical modeling of phonation or voiced sound production intends to predict the vocal folds oscillatory behavior in terms of relevant physical and physiological quantities. Physical modeling is, in particular, interesting for the study of irregular phonation patterns or vocal folds dysfunction due to pathology (Kreiman and Gerratt, 2005; Mergell *et al.*, 2000; Wong *et al.*, 1991; Wurzbacher *et al.*, 2006; Zhang and Jiang, 2004). Despite the development of clinical *in vivo* measurement techniques, the observation and quantification of phonation in either normal or disordered conditions remains a difficult task often depending on invasive or indirect measurement methods (Cranen and Boves, 1988; Hertegard and Gauffin, 1995; Qiu and Schutte, 2006; Sundberg *et al.*, 1999; Svec *et al.*, 2007). Consequently, the subglottal pressure and the glottal aperture, which are the main input parameters for standard physical phonation models, are difficult to be obtained directly from *in vivo* measurements. The influence of the input parameter set on the model outcome is often assessed following an analysis-by-synthesis approach and is further compared to *in vivo* measured quantities (Drioli, 2005; Sciamarella and d'Alessandro, 2004; Wurzbacher *et al.*, 2006). Therefore, the interest of inverting classical physical phonation models is multiple and could, besides a purely scientific interest, lead to the development of noninvasive measurement techniques. At long term, inverse physical models might be validated on *in vivo* data and eventually be applied in pathological conditions or in favor of advanced voice synthesis. Moreover, in a clinical context, inverse models allow one to account for subject-dependent data. Most of the studies considering inversion of phonation models deal with inverse filtering techniques in order to estimate the glottal volume flow rate from which quantitative parameters describing the glottal source can be derived (Alku *et al.*, 1998; Frohlich *et al.*, 2001; Pelorson, 2001; Price, 1989; Rothenberg and Zahorian, 1977; Shadle *et al.*, 1999). Although inverse filtering is successful for phonation quantification purposes, it is limited to a parametrized voice source description in terms of the estimated volume flow rate. Since inverse filtering does not rely on a physical flow model and often adopts the source-filter model (Fant, 1960) neglecting glottal-supraglottal interaction, it is unable to account for the fluid-structure interaction between the vocal fold tissue and the glottal airflow during phonation. Inverting physical phonation models is interesting to obtain biomechanical data and flow properties relevant to the phonation mechanism. A first attempt to tune the parameters of a physical low dimensional glottal model to the volume flow rate obtained from inverse filtering following an analysis-by-

[a]Electronic mail: julien.cisonni@gipsa-lab.inpg.fr

synthesis approach is presented in Drioli (2005). Considering the inversion of biomechanical models, an encouraging result is presented for arteries where tissue characteristics are deduced from blood flow measurements (Lagrée, 2000). The current research explores the inversion of simplified quasi-one-dimensional flow models widely applied in classical direct phonation models (Lous *et al.*, 1998; Pelorson *et al.*, 1994; Ruty *et al.*, 2007). The aimed models are derived from Bernoulli's one-dimensional flow equation corrected for viscous effects and flow unsteadiness. The use of simplified flow theories in order to estimate the important phonation quantities, as phonation onset threshold pressure and oscillation frequency, obtained in an *in vitro* context is discussed in Ruty *et al.* (2007) and Van Hirtum *et al.* (2007). At first, direct flow models are outlined and inverse models are formulated. Then, theoretical simulations are presented in order to validate the inverse flow model outcome against the direct model input. Next, inverse flow models are validated on experimental *in vitro* data obtained with rigid glottal replicas for different glottal constriction shapes and flow conditions. The inverse modeling performance is discussed with respect to the accuracy of the direct modeling.

II. DIRECT AND INVERSE FLOW MODELS

Low-order physical phonation models exploit simplified flow models to describe the glottal airflow and the resulting pressure forces exerted on the vocal fold tissue. The underlying assumptions necessary to use simplified flow models are briefly outlined in Sec. II A. Next, direct simplified flow models are formulated in Sec. II B and inverse flow models are described in Sec. II C.

A. Assumptions and nondimensional numbers

The flow models described in Ruty *et al.* (2007) account for severe assumptions on the flow behavior through the glottal constriction. The assumptions are motivated by a nondimensional analysis of the governing *Navier–Stokes* equations while accounting for typical values of physiological geometrical and flow characteristics in case of normal phonation by a male adult (Deverge *et al.*, 2003; Pelorson *et al.*, 1994; Ruty *et al.*, 2007; Vilain *et al.*, 2004). The main nondimensional numbers considered are the geometrical aspect ratio $r_{l_g}=h_g/l_g$, *Mach* number $M=v/c_0$, *Reynolds* number $\mathrm{Re}=vh/\nu$, and *Strouhal* number $\mathrm{Sr}=fL/v$, where h_g denotes the minimum aperture, l_g is a typical width normal to the flow direction and to the constriction, v is a characteristic flow velocity, $c_0=350$ m/s is the speed of sound, h is a typical dimension, $\nu=1.5\times10^{-5}$ m^2/s is the kinematic air viscosity, L is the constriction length in the flow direction, and f is a characteristic frequency. Typical physiological values for glottal flow during voice production yields the following order of magnitudes for the nondimensional numbers: $r_{l_g}\sim O(10^{-1})$, $M^2\sim O(10^{-4})$, $\mathrm{Re}=v_g h_g/\nu\sim O(10^3)$, $\mathrm{Sr}\sim O(10^{-2})$ with v_g as the flow velocity at the minimum aperture. These typical values allow one to assume the flow as one dimensional, incompressible, laminar and quasisteady. The glottal area, $A(x)=l_g h(x)$, normal to the flow direction x, is assumed to be rectangular with fixed width l_g and glottal height $h(x)$ which only varies along the flow direction, as shown in Fig. 1. Although viscous effects can be negligible for the main flow, viscosity is expected to be important near the walls and the resulting effects are discussed in Sec. II B 1.

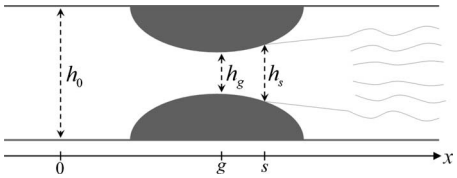

FIG. 1. Schematic representation of the glottal geometry. The x dimension indicates the flow direction. 0, g, and s indicate the positions of the origin, minimum aperture, and flow separation along the channel. The corresponding heights are indicated.

B. Direct simplified flow models

1. Direct flow models description

Under the assumptions of one-dimensional, laminar, fully inviscid, steady and incompressible flow, the one-dimensional *Bernoulli's equation* can be used to estimate the pressure distribution along the glottal constriction, where $\rho=1.2$ kg/m^3 indicates the mean air density. Therefore, the pressure difference $\Delta P_B(a,b,t)=p_a(t)-p_b(t)$ between two positions, a and b, along the constriction in the x dimension yields with $a<b$

$$\Delta P_B(a,b,t)=\frac{1}{2}\rho\frac{\Phi^2}{l_g^2}\left(\frac{1}{h_b(t)^2}-\frac{1}{h_a(t)^2}\right) \tag{1}$$

for a rectangular glottal geometry with area $A(x,t)=l_g h(x,t)$. The quantities $h_a(t)$ and $h_b(t)$ correspond to the constriction heights at positions a and b in the flow direction, while $\Phi(t)=v(x,t)A(x,t)=v(x,t)h(x,t)l_g=\mathrm{const}$ denotes the volume flow rate which is assumed to be constant along the constriction.

In order to predict a pressure drop across the constriction and hence to be useful, Eq. (1) needs to be corrected to account for the flow separation and jet formation in the diverging part of the constriction downstream of the minimum aperture $h_g(t)$ (Pelorson *et al.*, 1994). The turbulent jet formation downstream of the separation point is due to very strong viscous pressure losses and thus cannot be predicted by the Bernoulli law (Alipour and Scherer, 2006; Grandchamp *et al.*, 2007). In literature, the area associated with flow separation $A_s(t)$ is empirically *ad hoc* chosen as 1.1, 1.2, or 1.3 times the minimum glottal constriction area $A_g(t)$, i.e., $A_s(t)=c_s A_g(t)$ with $c_s=A_s(t)/A_g(t)\geqslant 1$ the *ad hoc* separation coefficient (Deverge *et al.*, 2003; Hofmans *et al.*, 2003; Lucero, 1999; Pelorson *et al.*, 1994). Accounting for a rectangular glottal area, the separation criterion becomes $c_s=h_s(t)/h_g(t)\geqslant 1$. The separation position and corresponding height $h_s(t)$ are indicated with s and $h_s(t)$, respectively, in Fig. 1. Consequently, Eq. (1) only holds down to the separation point and, therefore, c_s is an important parameter in the flow model. The pressure in the constriction after the separation point is considered to be equal to the downstream pressure. In addition to the occurrence of flow separation, the

preceding assumption of inviscid flow is also not valid for low Reynolds numbers. This is the case for small constriction heights where viscous effects cannot be neglected (Blevins, 1992; Kundu, 1990). To account for the pressure drop induced by viscous friction along the walls, an additional *Poiseuille* term $\Delta P_P(a,b,t)$ can be added to the Bernoulli term (1)

$$\Delta P_P(a,b,t) = 12\mu \frac{\Phi}{l_g} \int_a^b \frac{dx}{h(x)^3}, \tag{2}$$

where μ is the dynamic viscosity of the fluid and again $a < b$. The *Poiseuille* term $\Delta P_P(a,b,t)$ assumes a nonuniform parabolic two-dimensional velocity profile and therefore presents a viscosity related correction to the one-dimensionality assumed in Eq. (1). Although several *in vitro* experimental studies confirm the quasisteady approximation made in Eq. (1) (Deverge *et al.*, 2003; Hofmans *et al.*, 2003; Vilain *et al.*, 2004; Zhang *et al.*, 2002), pressure differences induced by flow unsteadiness due to the fluctuations of $h(x,t)$, related to wall movements and/or $p_0(t)$ in time, are important for high frequency variations and/or vocal folds wall vibrations involving collision or glottal closure (Deverge *et al.*, 2003; Vilain *et al.*, 2004). The additional pressure loss $\Delta P_U(a,b,t)$ due to the resulting unsteadiness in the volume airflow $\Phi(t)$ is expressed as

$$\Delta P_U(a,b,t) = \frac{\rho}{l_g} \int_a^b \frac{d}{dt}\left(\frac{\Phi(t)}{h(x,t)}\right) dx. \tag{3}$$

2. Direct flow models, input and output

From the pressure terms outlined in Sec. II B 1, several classical direct flow models can be considered. The physical variables defining their input and output, and the inherent model parameters are pointed out. For all direct flow models, the pressure upstream of the constriction is the main driving control parameter. This pressure is labeled $p_0(t)$ in correspondence with the 0 position indicated in Fig. 1. The downstream pressure at flow separation and beyond is assumed to be equal to the atmospheric pressure p_{atm} which corresponds to zero since all pressures are expressed relatively to p_{atm}, i.e., $p_s(t)=0$ Pa. The flow separation position $x=s$ is determined by the value of the separation coefficient c_s. Since the flow separation position determines the flow model outcome to a large extent, the coefficient c_s is an important inherent model parameter. Other known inherent model parameters are the required physical constants μ, ρ, and the glottal width l_g. The constriction geometry, which is characterized by the channel height $h(x,t)$ illustrated in Fig. 1, is assumed to be known. The pressure distribution along the constriction, i.e., $p(x,t)$ with $0 \leqslant x \leqslant s$, is estimated from the pressure difference $\Delta P(0,x,t)=p_0(t)-p(x,t)$ which can be defined by the addition of the pressure terms (1)–(3). Thus, four direct flow models based on the pressure term combinations presented in Table I are under consideration: steady Bernoulli model (BS-d), steady Poiseuille model (PS-d), unsteady Bernoulli model (BU-d), and unsteady Poiseuille model (PU-d).

For each of the four flow models, the input parameters are the set $(p_0(t),h(x,t),c_s(t))$, where $p_0(t)$ and $h(x,t)$ characterize the physical problem and $c_s(t)$ is a parameter inherent to the chosen modeling approach. The direct flow model output $(p(x,t),\Phi(t))$ is obtained in two steps. First, the volume flow rate $\Phi(t)$ is estimated from the total pressure difference across the constriction $\Delta P(0,s,t)$. Next, the pressure profile $p(x,t)$ along the constriction is obtained from the upstream pressure $p_0(t)$ and the retrieved $\Phi(t)$ value.

TABLE I. Pressure terms used in the four direct flow models.

Flow model	ΔP_B	ΔP_P	ΔP_U
BS-d	x		
PS-d	x	x	
BU-d	x		x
PU-d	x	x	x

C. Inverse simplified flow models

In this section, inverse flow models derived from each of the four direct flow models detailed in Sec. II B 2 are formulated. The assumptions discussed in Secs. II A and II B 1 extend naturally to the proposed inverse models. Therefore, the estimation of the physical quantities obtained with the proposed inverse flow models are *a priori* subjected to the same limitations as their direct counterparts. Further approximations might be introduced due to the applied inversion strategies outlined in Sec. II C 2. The inverse model variables and parameters are discussed in the following section.

1. Inverse flow models, input and output

The pressure distribution $p(x,t)$ is the main output quantity of the direct flow models. In the presented inverse flow models, the role of direct flow model input and output variables are interchanged. The pressure at the minimum constriction height $p_g(t)$ is therefore considered as the known input quantity of the inverse models. From the direct flow models previously described, three different cases of inverse problems are defined. Firstly, the upstream pressure $p_0(t)$ is the unknown quantity (inverse model 1). Secondly, the minimum constriction height $h_g(t)$ is searched (inverse model 2). Thirdly, the flow separation coefficient c_s is estimated (inverse model 3). Each of the four direct models outlined in Sec. II B 2 can be exploited to resolve the three inversion problems in order to retrieve the quantities of interest, as shown in Table II.

The interest of the first inversion problem, i.e., to retrieve the upstream pressure $p_0(t)$, is obvious since it is the main driving parameter of the direct phonation flow models determining the total pressure difference across the glottal

TABLE II. Input and output variables of the three inverse problems.

	Input	Output
Direct model (-d)	$p_0(t)$, $h_g(t)$, $c_s(t)$	$p_g(t)$, $\Phi(t)$
Inverse problem 1 (-inv1)	$p_g(t)$, $h_g(t)$, $c_s(t)$	$p_0(t)$, $\Phi(t)$
Inverse problem 2 (-inv2)	$p_0(t)$, $p_g(t)$, $c_s(t)$	$h_g(t)$, $\Phi(t)$
Inverse problem 3 (-inv3)	$p_0(t)$, $h_g(t)$, $p_g(t)$	$c_s(t)$, $\Phi(t)$

constriction. In human phonation p_0 corresponds to the subglottal pressure which is, as outlined in the introduction, very hard to retrieve from *in vivo* measurements. The glottal constriction geometry $h(x,t)$ is also a main known input parameter in direct flow modeling. Assuming a known geometrical shape for the constriction, the geometry is fully characterized by the minimum constriction height $h_g(t)$. Therefore, the second inversion problem consists in estimating $h_g(t)$. Although c_s is not a physical quantity, this parameter allows to account for major physical phenomena, i.e., flow separation and jet formation. Since the value of c_s acts to a large extent on the accuracy of the direct flow models, it is quite an issue in the literature (Alipour and Scherer, 2004; Deverge *et al.*, 2003; Hofmans *et al.*, 2003; Lucero, 1999; Pelorson *et al.*, 1994) and the third inverse problem consists in estimating this parameter. The resulting inverse models and the related inversion strategies are discussed in the next section.

2. Inverse flow models description and inversion strategies

The applied inversion strategies are adapted with respect to the direct quasi-one-dimensional flow model under consideration. In the following, the quantities estimated by the models are designated by $\hat{p}_g(t)$, $\hat{p}_0(t)$, $\hat{h}_g(t)$, $\hat{c}_s(t)$, and $\hat{\Phi}(t)$.

a. Inverse steady Bernoulli model. Inversion of the steady Bernoulli model (BS-d) given by Eq. (1) is easily obtained analytically. Firstly, the upstream pressure $\hat{p}_0(t)$ is retrieved as

$$\hat{p}_0(p_g(t),h(x,t),c_s(t),t) = p_g(t)\frac{c_s^2(t)h_g^2(t) - h_0^2}{h_0^2(c_s^2(t)-1)}. \quad (4)$$

Secondly, the minimum constriction height $\hat{h}_g(t)$ becomes

$$\hat{h}_g(p_g(t),p_0(t),c_s(t),t) = \frac{h_0}{c_s(t)}\sqrt{1+\frac{p_0(t)}{p_g(t)}(c_s^2(t)-1)}. \quad (5)$$

Thirdly, the separation coefficient $\hat{c}_s \geqslant 1$ is given as

$$\hat{c}_s(p_g(t),p_0(t),h_g(t)) = h_0\sqrt{\frac{p_0(t)-p_g(t)}{p_0(t)h_0^2 - p_g(t)h_g^2(t)}}. \quad (6)$$

Applying the assumption $h_0 \gg h_g$, the expression for $\hat{c}_s$ simplifies to

$$\hat{c}_s(t) \approx \sqrt{1-\frac{p_g(t)}{p_0(t)}} \Rightarrow \frac{p_g(t)}{p_0(t)} \approx 1-\hat{c}_s^2(t), \quad (7)$$

which illustrates that the parameter c_s determines the importance of the pressure drop at the minimum constriction height relatively to the upstream pressure p_0. Equation (7) also indicates that the steady Bernoulli model can only predict $\hat{p}_g \leqslant 0$ since $p_0 \geqslant 0$ and $c_s \geqslant 1$.

b. Inverse steady Poiseuille model. Inversion of the steady Poiseuille model (PS-d) defined by the sum of pressure terms (1) and (2) can not be achieved analytically. Therefore, a numerical iterative method is applied in order to invert the model (Kelley, 1995). This way, each of the three inversion problems becomes a classical minimization problem. By considering $\hat{p}_g(t)$ as a function of $p_0(t)$, $h_g(t)$, and $c_s(t)$, i.e., $\hat{p}_g(t)=f(p_0(t),h_g(t),c_s(t))$, the three inversion problems can be rewritten as the solution of the following three minimization problems:

$$\|p_g(t) - f(\hat{p}_0(t),h_g(t),c_s(t))\|^2 < \epsilon, \quad (8)$$

$$\|p_g(t) - f(p_0(t),\hat{h}_g(t),c_s(t))\|^2 < \epsilon, \quad (9)$$

$$\|p_g(t) - f(p_0(t),h_g(t),\hat{c}_s(t))\|^2 < \epsilon, \quad (10)$$

where ϵ denotes the tolerance of the convergence process. The minimization problem is solved with the *Newton algorithm*. The inversion process of the steady Poiseuille model can be repeated for each time instant independently or applied to a whole signal in order to obtain the searched quantity at all time instants. The position of the separation point $x=s$ and, consequently, the constriction height at separation h_s depends on the minimum constriction height h_g and the separation coefficient c_s due to the separation criterion $h_s = c_s h_g$. Therefore, the position of the separation point varies during the convergence process of minimization problems (9) and (10). The moving separation point introduces numerical discontinuities in the minimization function when a spatial discretization of the geometry is used. This is avoided by approximating the integral in Eq. (2) with a *Gauss–Chebychev* quadrature (Kincaid and Cheney, 1996)

c. Inverse unsteady Bernoulli model. The three inversion problems for the unsteady Bernoulli model (BU-d) defined by the sum of the pressure terms (1) and (3) are solved following the same approach as for the PS-d model, i.e., using numerical iterative methods. As for the steady Poiseuille model, the spatial discretization of the geometry is again avoided by approximating the integral in Eq. (3) with a Gauss–Chebychev quadrature. Contrary to the steady models, the inversion process is applied to an entire time range in order to reduce the error propagation on the inverted values, since due to Eq. (3), the predictions at instant $t=i$ are dependent on the predictions at previous instants $t<i$.

d. Inverse unsteady Poiseuille model. The strategy used for the inversion of the unsteady Poiseuille model (PU-d) is similar to the approach outlined for the inversion of the unsteady Bernoulli model.

III. THEORETICAL STUDY AND DISCUSSION

The accuracy of the inverse models with respect to theoretical simulations of the corresponding direct models is discussed in this section. The outcome of the direct models is used as the input of the inverse models in order to reestimate the original input variables of the direct models. The influence of the pressure terms, which are expressed in Eqs. (1)–(3), on the simulated results is discussed. The glottal geometry is approximated by the varying channel height $h(x)$ between two half circles with 1 cm radius, depicted in Fig. 5(d) and the upstream channel height of $h_0=23.6$ mm. The importance of the flow model parameter c_s related to flow separation in the diverging downstream part of the constriction can be assessed.

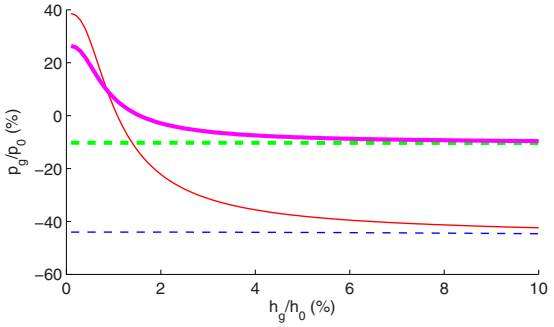

FIG. 2. (Color online) Theoretical simulations for steady flow conditions with a round constriction and upstream pressure $p_0=100$ Pa. Ratio between the pressure at the minimum constriction height and the upstream pressure p_g/p_0 as function of the ratio between the minimum constriction height and the upstream height h_g/h_0 for BS-d model with $c_s=1.05$ (thick dashed line) and $c_s=1.2$ (thin dashed line) and for PS-d model with $c_s=1.05$ (thick solid line) and $c_s=1.2$ (thin solid line).

A. Steady flow conditions

Steady flow conditions allow one to study the importance of the Poiseuille pressure term (2) on the model predictions compared to the Bernoulli pressure term (1).

1. Steady Bernoulli model

The normalized pressure at the minimum constriction height, p_g/p_0, predicted by the direct steady Bernoulli model (BS-d) is quantitatively illustrated in Fig. 2. For a fixed upstream pressure $p_0=100$ Pa, the minimum constriction height is decreased from 10% down to 0% of the upstream channel height and two separation coefficients, $c_s=1.05$ and $c_s=1.2$, are considered. In accordance with Eq. (7) the pressure drop p_g obtained from the steady Bernoulli model is fully determined by the choice of the separation coefficient c_s. Regardless of the minimum height h_g, the pressure ratio p_g/p_0 yields respectively −10% and −44% for c_s set to 1.05 and 1.2. This way, the separation coefficient c_s determines the position of flow separation through the *ad hoc* relation $h_s=c_s h_g$, the magnitude of the pressure drop as well as the spatial range in which the glottal flow exerts pressure forces on the surrounding walls. In addition, increasing c_s increases the estimated volume flow rate Φ. Since the three inverse models (BS-inv1, BS-inv2, and BS-inv3) outlined in Sec. II C 2 a are analytically derived from the direct model (BS-d), the estimated inverse model outcomes $\hat{p}_0$, $\hat{h}_g$, or $\hat{c}_s$ match the direct model input parameters exactly.

2. Steady Poiseuille model

The addition of the Poiseuille term (2) in the flow model has a major effect on the pressure predictions for small minimum apertures (Ruty *et al.*, 2007), as illustrated in Fig. 2. The discrepancy between BS-d and PS-d predictions of $\hat{p}_g$ increases as the ratio h_g/h_0 decreases. Moreover, the contribution of the Poiseuille term results in positive $\hat{p}_g$ estimates for $h_g/h_0 \leqslant 2\%$. The separation coefficient c_s is again a significant parameter for PS-d since increasing c_s increases the magnitude of the viscous contribution. In general, viscous effects should not be neglected for small apertures, i.e., for $h_g/h_0 < 10\%$ ratios. By accounting for viscous effects, the flow circulation is assumed to be more difficult so that the volume flow rate predicted by PS-d is slightly below the BS-d estimation. Moreover, even if the volume flow rates predicted by both models are very close, their relative difference increases as the constriction height decreases. Inversion of PS-d is obtained numerically, following the minimization procedure outlined in Sec. II C 2 b. The inverse model accuracy and the required number of iterations rely on the convergence parameter ϵ in Eqs. (8)–(10). The choice of ϵ relies on a trade-off between the precision of the inverse model results and the required computation time. By setting $\epsilon=10^{-8}$ in PS-inv1, PS-inv2, and PS-inv3, the error introduced by the inversion process becomes negligible and the convergence can be obtained within 20 iterations regardless of the searched variable.

B. Unsteady flow conditions

Variations in time of the upstream pressure $p_0(t)$ and/or the minimum constriction height $h_g(t)$ can affect the flow characteristics. Introducing time dependency in the direct and inverse flow model descriptions allows one to account for flow effects due to unsteadiness. As mentioned in Secs. II A and II B 1, the glottal flow is assumed to be quasisteady during normal phonation since typically $\mathrm{Sr}=10^{-2}$ holds (Zhang *et al.*, 2002). During singing, abnormal phonation or in case of vocal fold pathologies, the glottal flow might be characterized by a greater Strouhal number. This can result from an increase in the fundamental frequency f or the vocal folds length L so that unsteadiness effects can become important. Moreover, unsteadiness effects are known to be important during glottal closure (Deverge *et al.*, 2003). In Secs. III B 1 and III B 2, the unsteady Bernoulli and Poiseuille models are considered. The reported validation passes the limits of the physical values encountered during *in vivo* phonation in order to fully validate the inversion process. Due to unsteadiness, the occurrence of flow separation and jet formation is known to depend on the Reynolds number and the Strouhal number (Sobey, 1983). Classical phonation models assume a constant flow separation coefficient. In the following, the separation coefficient $c_s(t)$ is assumed to be able to vary in time.

1. Unsteady Bernoulli

The discrepancies between $\hat{p}_g(t)$ and $\hat{\Phi}(t)$ predictions obtained with BS-d and BU-d are illustrated in Fig. 3. The simulations are obtained for the round constriction shape depicted in Fig. 5(d). The input signals $p_0(t)$, $h_g(t)$, and $c_s(t)$ are varying in time with frequencies of 300, 500, and 100 Hz, respectively. These frequencies are chosen arbitrarily different in order that effects related to each parameter can be individually identified in the output waveforms. The input signals cannot be compared to those observed *in vivo*. The variation of $h_g(t)$ corresponds to $\mathrm{Sr}\approx 0.3$ so that unsteadiness has a visible influence on the models predictions. Comparing $\hat{p}_g(t)$ signals, it can be observed that the BS-d estimation is fully determined by $c_s(t)$ contrary to the BU-d estimation which presents amplitude variations due to the dependency on $h_g(t)$ expressed in Eq. (3). Thus, BU-d predicts a greater

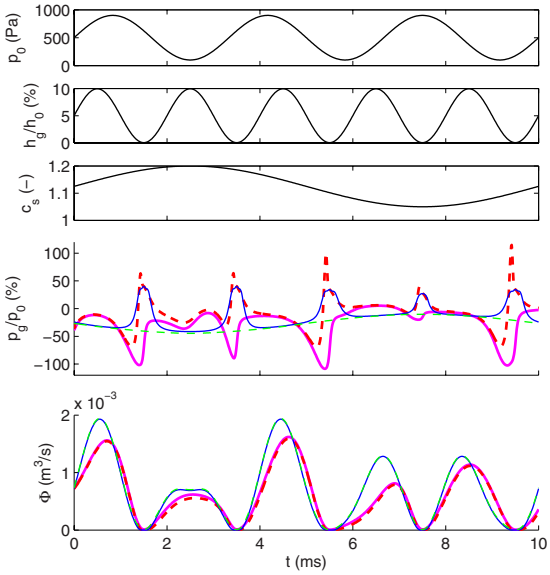

FIG. 3. (Color online) Theoretical simulations for unsteady flow conditions with a round constriction. (Three top figures) Input signals of the upstream pressure p_0, the ratio between the minimum constriction height and the upstream height h_g/h_0 and the separation coefficient c_s. (Middle) Simulated signals of the ratio between the pressure at the minimum constriction height and the upstream pressure p_g/p_0. (Bottom) Simulated signals of volume flow rate Φ. Frequency of h_g vibration is 500 Hz corresponding to Sr ≈ 0.3. Output signals are simulated by BS-d (thin dashed line), PS-d (thin solid line), BU-d (thick solid line) and PU-d (thick dashed line).

pressure drop at the minimum constriction height during the constriction closure. On the contrary, the pressure drop predicted by BU-d when the constriction is more widely open is less important than the one predicted by BS-d. The addition of Eq. (3) in the direct modeling introduces magnitude and phase differences between the volume flow rate signals generated by BS-d and BU-d, as shown in Fig. 3. Inversion of BU-d is obtained numerically as outlined in Sec. II C 2 c. The approximations introduced by the convergence process in the estimated signals $\hat{p}_0(t)$, $\hat{h}_g(t)$, and $\hat{c}_s(t)$ can be considered as negligible, as discussed in Sec. III A 2. However, despite the application of the inversion process to an entire signal, the error propagation in time can lead to inaccurate estimations at the end of the signal.

2. Unsteady Poiseuille

In PU-d, two additional pressure terms are in competition for the prediction of the flow characteristics. In Fig. 3, it can be seen that the $\hat{p}_g(t)$ signals generated by BU-d and PU-d are similar when the constriction is open. However, when the constriction is closing, viscous effects become predominant so that the $\hat{p}_g(t)$ predicted by PU-d is closer to the prediction of PS-d. Besides, viscous effects seems to be emphasized by the unsteady flow conditions since the maximum pressure peaks observed for PU-d at the constriction closure instant are higher than those observed for PS-d whereas BU-d predicts negative pressures. Concerning the volume flow rate predictions, the Poiseuille pressure term (2) has a minor influence. Thus, in Fig. 3, the $\hat{\Phi}(t)$ signals predicted by BS-d and PS-d are quasisuperposed. As noticed in Sec. III B 1, the addition of Eq. (3) in the direct modeling introduces magnitude and phase differences between the $\hat{\Phi}(t)$ signals predicted by steady and unsteady models so that the BU-d and PU-d predictions are also quasisuperposed. The considerations about the inversion of BU-d made in Sec. III B 1 hold for the inversion of PU-d.

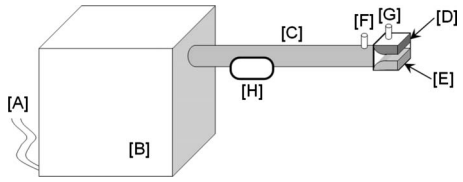

FIG. 4. Schematic representation of the experimental setup: [A] air supply, [B] pressure tank, [C] upstream pipe, [D,E] rigid vocal fold replica, [F,G] pressure taps, and [H] volume flow rate meter.

IV. *IN VITRO* VALIDATION AND DISCUSSION

The high accuracy of the inverse flow models, described in Sec. II C with respect to data obtained by simulations with the corresponding direct flow models, is pointed out in the previous Sec. III. This section assesses the validation of the inverse flow models against *in vitro* experimental data. The validity of the inverse flow models for real world flow data is likely to depend on the accuracy of the direct flow models. Therefore, the *in vitro* validation of the inverse steady and unsteady flow models, presented in, respectively, Secs. IV A and IV B, is inspired on the *in vitro* validation of flow models with glottal constriction rigid replicas reported in *a.o.* Deverge *et al.* (2003); Hofmans *et al.* (2003); Pelorson *et al.* (1994); Ruty *et al.* (2007); Van Hirtum *et al.* (2007); Vilain *et al.* (2004).

A. Steady flow conditions

The inverse model validation for steady flow conditions aims to quantify the influence of taking into account the viscosity and of the choice of the separation coefficient on the inverse model performance.

1. Setup for steady flow measurements

The experimental setup is schematically depicted in Fig. 4. Steady flow is provided by a valve controlled air supply [A] connected to a pressure tank of 0.75 m^3 [B] enabling to impose an airflow through the rigid vocal fold replica [D,E]. An upstream pipe [C] of 95 cm is used to prevent from turbulent flow at the replica position. Pressure transducers (Endevco 8507C or Kulite XCS-093) are positioned in pressure taps upstream of the replica [F] and at the minimum constriction height of the constriction [G] allowing to measure the upstream pressure p_0 and the pressure at the minimum constriction height p_g. The volume flow rate Φ is measured (TSI 4000) upstream of the constriction [H]. The *in vitro* constriction is formed by two vocal fold metal replicas in a fixed position. The minimum constriction height h_g between the two rigid vocal folds can be changed by means of two adjustment screws. Different minimum constriction heights are studied: $h_g = 0.2$ mm, $h_g = 0.5$ mm, and $h_g = 1.0$ mm. Two different constriction shapes depicted in Fig. 5 are considered, (a) uniform (with a rounded entrance) and

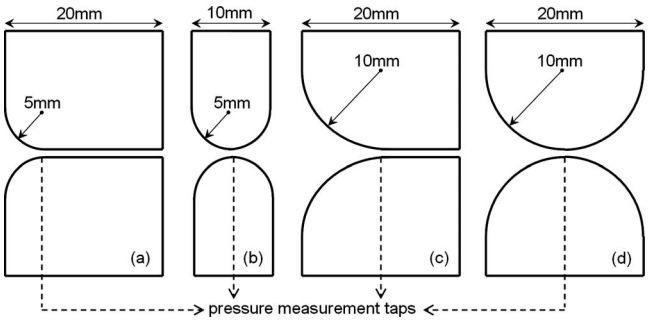

FIG. 5. Geometries of the rigid vocal fold replicas. Uniform (a) and round (b) constriction for steady flow measurements. Uniform (c) and round (d) constriction for unsteady flow measurements.

(b) round, in order to favor either the study of viscous wall effects or flow separation.

2. Uniform Constriction

A uniform channel is particularly interesting to evaluate the flow modeling with respect to viscous wall effects without interference of the flow separation position. For a uniform constriction, flow separation always occurs at the constriction end so that $h_g=h_s$. This implies that $c_s=1$ so that c_s is no further considered in this section. Therefore, two inversion problems are maintained in order to retrieve respectively the upstream pressure $\hat{p}_0$ (-inv1) and the minimum constriction height $\hat{h}_g$ (-inv2). Measurements of p_0, p_g, and Φ are presented in Fig. 6. The upstream pressure p_0 covers the

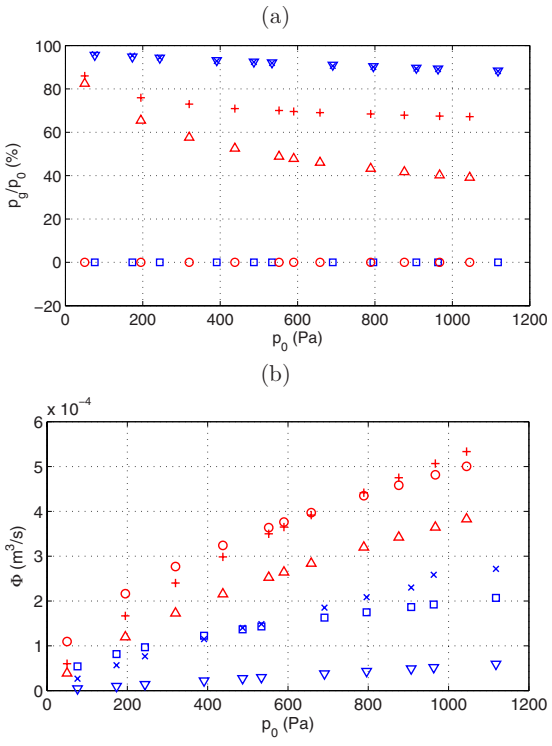

FIG. 6. (Color online) (a) Ratio between pressure at the minimum constriction height and upstream pressure p_g/p_0 and (b) volume flow rate Φ as function of the upstream pressure p_0 measured for steady flow conditions with the uniform constriction, for the minimum constriction heights h_g =0.2 mm (×) and h_g=0.5 mm (+). The corresponding predictions of the *Bernoulli* (□, ○) and Poiseuille (▽, △) models are shown.

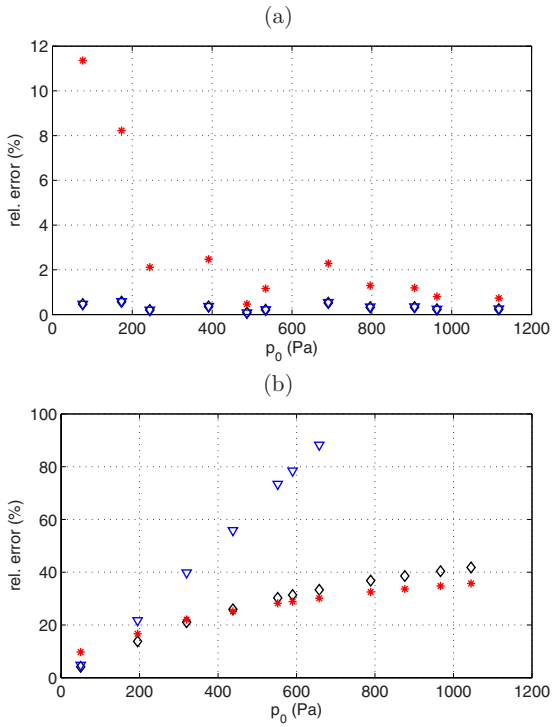

FIG. 7. (Color online) Relative errors of the steady Poiseuille models predictions compared to the steady experimental measurements performed with the uniform constriction for (a) h_g=0.2 mm and (b) h_g=0.5 mm: pressure at the minimum constriction p_g (PS-d, ◇), upstream pressure p_0 (PS-inv1, ▽) and minimum constriction height h_g (PS-inv2, ∗).

range of interest from 100 up to 1000 Pa and h_g is set to 0.2 and 0.5 mm. Predictions of $\hat{p}_g$ and $\hat{\Phi}$ given by BS-d and PS-d are shown. Following Eq. (7), BS-d predicts $\hat{p}_g$ to be equal to the downstream pressure, i.e., $\hat{p}_g=p_s=0$, regardless of p_0 and h_g. Therefore, BS-inv1 and BS-inv2 are not applicable and are not further illustrated in this section. It can be observed from Fig. 6(a) that PS-d predicts the measured pressure data with 1% for h_g=0.2 mm. In this case, the gap between the vocal fold replicas is very narrow compared to the upstream height ($h_g/h_0 \leqslant 10\%$), which indicates that viscous effects are predominant in the pressure determination and allow one to explain the very accurate pressure predictions of PS-d. For h_g=0.5 mm, the prediction error increases from 10% to 40% for p_0 increasing from 100 to 1000 Pa. In this case, viscous effects are less important and their approximation by the Poiseuille pressure term (2) does not allow to obtain accurate pressure predictions compared to *in vitro* measurements. Concerning the volume flow rate, Fig. 6(b) shows that BS-d predicts the measured data more accurately than PS-d for h_g=0.2 mm and h_g=0.5 mm. For the inverse modeling, Fig. 7 presents the relative errors between the measurements and the predictions made by PS-d, PS-inv1, and PS-inv2. This figure illustrates, in a quantitative way, the link between the predictions errors of the direct and inverse models. For h_g=0.2 mm [Fig. 7(a)], PS-inv1 predicts the measured upstream pressure p_0 within 1%, which is similar to the PS-d predictions accuracy. On the other hand, the inverse estimation of h_g with PS-inv2 appears to be more sensitive to the error made with PS-d since an error of 1% for $\hat{p}_g$ can yield up to an error of 10% for $\hat{h}_g$, in particular, for low

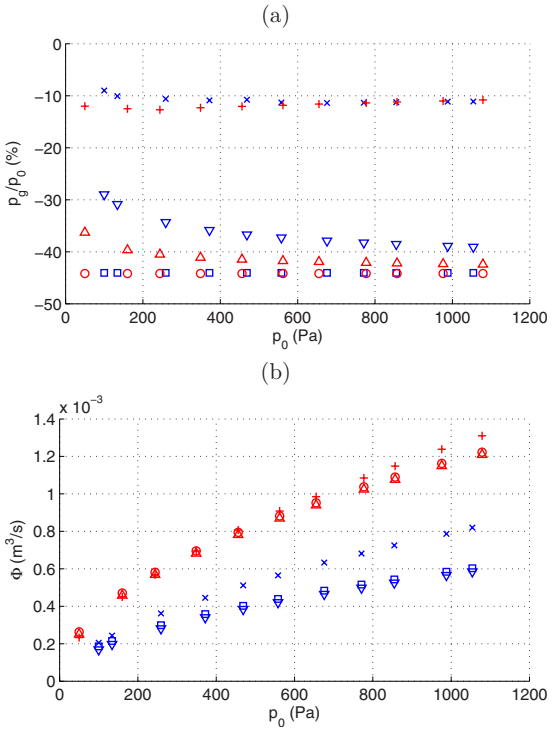

FIG. 8. (Color online) (a) Ratio between pressure at the minimum constriction height and upstream pressure p_g/p_0 and (b) volume flow rate Φ as function of the upstream pressure p_0 measured for steady flow conditions with the round constriction, for the minimum constriction heights h_g =0.5 mm (×) and h_g=1.0 mm (+). The corresponding predictions of the Bernoulli (□, ○) and Poiseuille (▽, △) models using c_s=1.2 are shown.

Reynolds numbers corresponding to low upstream pressures. For h_g=0.5 mm [Fig. 7(b)], it can be noticed that the inverse model error rates are proportional to the error rate of the direct model. In this case, the inverted upstream pressure $\hat{p}_0$ is largely overestimated and the corresponding error reaches more than 100%. The error rate of the PS-inv2 predictions is similar to the one observed for PS-d predictions. Thus, steady Poiseuille models predictions become less accurate as the experimental minimum constriction height and the upstream pressure increase.

3. Round constriction

The influence of the flow separation coefficient can be studied with a round constriction geometry since flow separation occurs in the diverging downstream part. In the quasi-one-dimensional models under study, the flow separation position is determined by the choice of the flow separation coefficient c_s. In order to limit the influence of viscous wall effects, the minimum constriction heights of h_g=0.5 mm and h_g=1.0 mm are experimentally assessed. The BS-d and PS-d predictions of the pressure $\hat{p}_g$ and the volume flow rate $\hat{\Phi}$ computed with c_s=1.2 are presented in Fig. 8 as well as the *in vitro* measurements. The value c_s=1.2 is commonly found in literature. Therefore, $h_s=c_s h_g$ yields 0.6 and 1.2 mm, respectively. As for the uniform constriction, the PS-d predictions are closer to the experimental pressure data, as shown in Fig. 8(a), even if both direct models overestimate (by a factor of 3–4) the pressure drop at the minimum constriction height. Likewise, the volume flow rate predictions given by

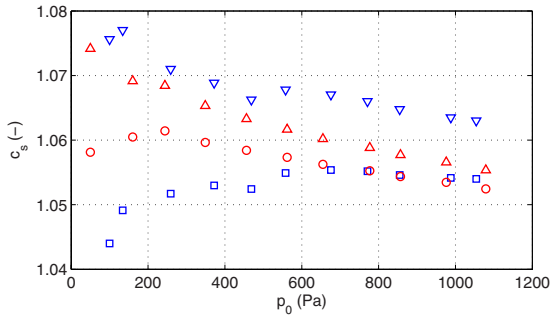

FIG. 9. (Color online) Estimation of the separation coefficient c_s from experimental measurements performed with the round constriction for h_g =0.5 mm and h_g=1.0 mm with the inverse Bernoulli (□, ○) and Poiseuille (▽, △) models.

BS-d are closer to the experimental measurements than the predictions given by PS-d. However, the difference between the BS-d and PS-d predictions decreases with increasing h_g. Regarding the pressure determination, the model's accuracy appears to depend mainly on the choice of c_s since the measured pressure ratios p_g/p_0 are about −10% and corresponds to a smaller separation coefficient. This is illustrated in Fig. 9, where Bs-inv3 and PS-inv3 are applied in order to estimate the separation coefficient $\hat{c}_s$ which best fits the experimental data for both assessed minimum apertures. The separation coefficient estimations are clearly smaller than 1.2 and moreover are found to vary as function of the Reynolds number (Sobey, 1983). Therefore, from Fig. 9, the mean value c_s=1.06 seems to be more adapted to the experimental conditions. Figure 10 shows the predictions $\hat{p}_g$ (a) and $\hat{\Phi}$ (b) given by BS-d and PS-d using this value of c_s. Thus, the model's accuracy is improved for the estimation of p_g, but the change in c_s increases the discrepancy between the estimated and measured flow rates.

B. Unsteady flow conditions

The unsteady Bernoulli and Poiseuille models include the unsteadiness pressure term (3). In this section, the inverse model's validity is tested against *in vitro* measurements performed on the setup outlined in Sec. IV B 1 for unsteady flow conditions. The results obtained for respectively uniform and round replicas are discussed in Secs. IV B 2 and IV B 3 illustrating both the steady and unsteady model's predictions.

1. Setup for unsteady flow measurements

The experimental setup used to perform steady flow measurements is maintained to perform unsteady flow measurements. The setup is schematically depicted in Fig. 4 and is described in Sec. IV A 1. The unsteady flow conditions are obtained thanks to a moving rigid constriction replica previously used and described in Deverge *et al.* (2003); Vilain *et al.* (2004). Flow variations are generated by the driven movement of one of the rigid vocal fold replicas ([E] in Fig. 4). The frequencies f under consideration are included between 3 and 30 Hz, corresponding to Strouhal numbers in the range of 10^{-3}–10^{-2}. The resulting time varying constriction height $h_g(t)$ is measured by means of an optical sensor

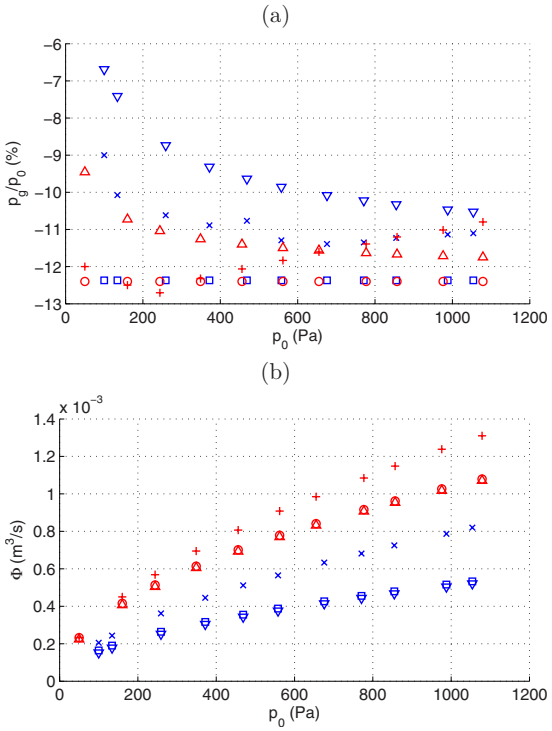

FIG. 10. (Color online) (a) Ratio between pressure at the minimum constriction height and upstream pressure p_g/p_0 and (b) volume flow rate Φ as function of the upstream pressure p_0 measured for steady flow conditions with the round constriction, for the minimum constriction heights h_g =0.5 mm (×) and h_g=1.0 mm (+). The corresponding predictions of the Bernoulli (□, ○) and Poiseuille (▽, △) models using c_s=1.06 are shown.

(OPB700). Two different constriction shapes depicted in Fig. 5 are considered: (c) uniform (with a rounded entrance) and (d) round.

2. Uniform constriction

As for steady flow conditions, a uniform constriction is assessed in order to rule out the influence of the choice of the separation coefficient on the model outcome since in this case, c_s=1. Therefore, the direct and inverse Bernoulli and Poiseuille models are validated with respect to unsteadiness. Three periods of measured and modeled signals obtained for a driving frequency of 25 Hz are shown in Fig. 11. It can be observed that direct Bernoulli models, BS-d and BU-d, are unable to predict the measured $p_g(t)$ so that the corresponding inverse models are not considered in the following. Besides, for the Strouhal number under consideration, Sr $\approx 10^{-2}$, unsteadiness has a minor impact on the pressure determination so that the $\hat{p}_g(t)$ signals given by steady and unsteady models appear quasisuperposed in Fig. 11. Thus, both direct Poiseuille models, PS-d and PU-d, predict the experimental pressure $p_g(t)$ within 20%. These two models provide a good approximation of the timing and the amplitude of the $p_g(t)$ signal. Therefore, PS-inv2 and PU-inv2 also give accurate results estimating the imposed minimum constriction height $h_g(t)$ with a mean error less than 15%. On the contrary, it can be observed that PS-inv1 and PU-inv1 are not able to estimate correctly the input upstream pressure $p_0(t)$. Indeed, the maximum error can reach 100% even if the mean error is less than 40%.

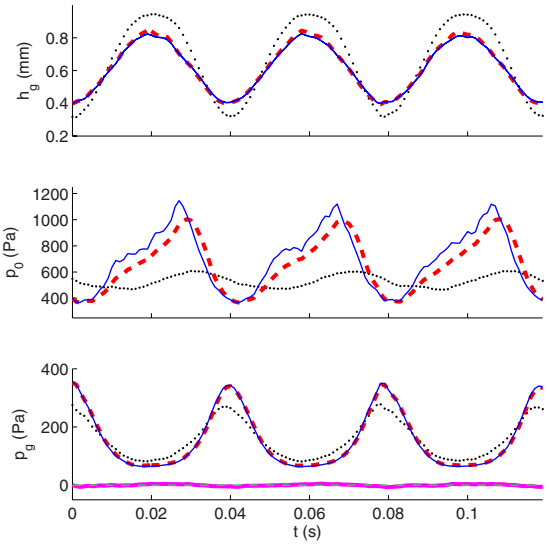

FIG. 11. (Color online) Measurements (●) and models predictions for the uniform vocal folds vibrating at 25 Hz ($S \approx 10^{-2}$): (top) minimum constriction height h_g, (middle) upstream pressure p_0 and (bottom) pressure at the minimum constriction height p_g. Predictions are given by the steady Bernoulli (thin dashed line), steady Poiseuille (thin solid line), unsteady Bernoulli (thick solid line) and unsteady Poiseuille (thick dashed line) models.

3. Round constriction

Figure 12 shows three periods of the measured and predicted signals for a round constriction vibrating at 25 Hz. The model signals presented in this figure are computed using c_s=1.2. As for the uniform constriction, direct flow modeling is significantly improved when viscous effects are taken into account. This can be observed from both the timing and the order of magnitude of $\hat{p}_g(t)$ predicted by PS-d and PU-d. Nevertheless, the overall accuracy of the direct Poiseuille models is low since the pressure drop is largely

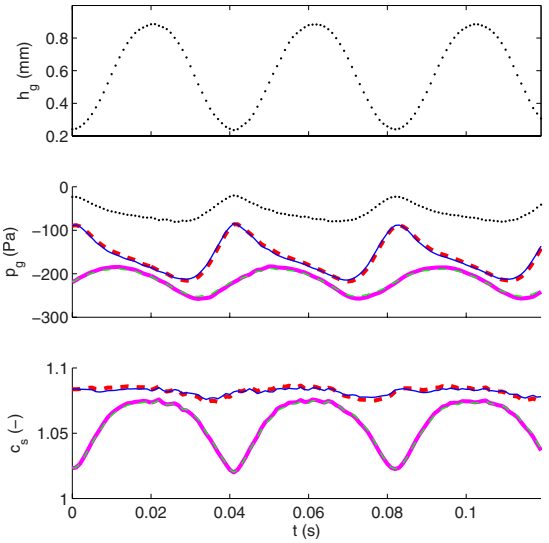

FIG. 12. (Color online) Measurements (●) and models predictions for the round vocal folds vibrating at 25 Hz ($S \approx 10^{-2}$): (top) minimum constriction height h_g, (middle) pressure at the minimum constriction height p_g (computed with c_s=1.2) and (bottom) inverted separation coefficient c_s. Predictions are given by the steady Bernoulli (thin dashed line), steady Poiseuille (thin solid line), unsteady Bernoulli (thick solid line) and unsteady Poiseuille (thick dashed line) models.

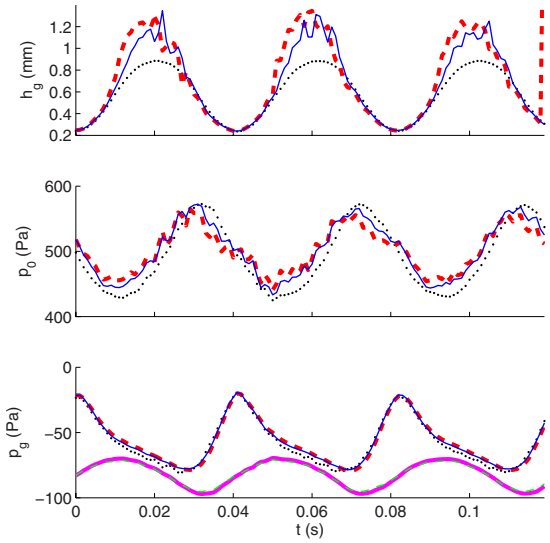

FIG. 13. (Color online) Measurements (●) and models predictions for the round vocal folds vibrating at 25 Hz ($Sr \approx 10^{-2}$): (top) minimum constriction height h_g, (middle) upstream pressure p_0 and (bottom) pressure at the minimum constriction height p_g. Predictions are computed with $c_s = 1.08$ and given by the steady Bernoulli (thin dashed line), steady Poiseuille (thin solid line), unsteady Bernoulli (thick solid line) and unsteady Poiseuille (thick dashed line) models.

overestimated, resulting in a mean error exceeding 100%. Previously, the severe impact of the choice of the separation coefficent c_s on the predictions accuracy is extensively shown. Therefore, the separation coefficient is estimated from the measured data with the inverse models (-inv3). The estimated $\hat{c}_s$ is illustrated at the bottom of Fig. 12. PS-inv3 and PU-inv3 yield $c_s \approx 1.08$, whereas for BS-inv3 and BU-inv3, $\hat{c}_s$ varies between 1.02 and 1.07. Due to the poor qualitative accuracy of BS-d and BU-d and the inconsistent values of $\hat{c}_s$ given by BS-inv3 and BU-inv3, the value of $c_s = 1.08$ obtained from PS-inv3 and PU-inv3 is used to re-estimate the direct and inverse models. The results are presented in Fig. 13 and show that the accuracy of the four direct models is largely improved. Since BS-d and BU-d are still unable to qualitatively predict $p_g(t)$, only the inverse Poiseuille models are considered to assess $\hat{p}_0(t)$ and $\hat{h}_g(t)$. As the PS-d and PU-d signals are very accurate predicting the measured $p_g(t)$ signal within 5%, the mean error of the PS-inv1 and PU-inv1 predictions is about 5% when c_s is set to 1.08. In this case, the mean error noticed for PS-inv2 and PU-inv2 is about 30%. This increased mean error is indeed due to a severe overestimation (greater than 50%) of the minimum constriction height when this one is large. The error amplification relative to direct Poiseuille models occurs when the viscosity related correction is the least effective, which shows the inaccuracy of the inviscid Bernoulli modeling. As for the uniform constriction, the steady model predictions match the unsteady model predictions to a fair extent in accordance with the low Strouhal number under consideration, $Sr \approx 10^{-2}$.

V. CONCLUSION

Inverse models derived from quasi-one-dimensional flow models commonly applied in simplified physical phonation models are formulated in order to retrieve the main physical variable and model parameters, i.e., the upstream pressure, the minimum constriction height, or the flow separation coefficient. The accuracy of the inverse models is validated firstly against theoretical simulations obtained with the corresponding direct models and secondly against *in vitro* experimental data. The proposed inverse models allow to retrieve quasiexactly the original direct model input with a minimum of computational effort. Moreover, the severe influence of flow separation, viscosity, and unsteadiness due to wall movement on the model predictions is pointed out for, respectively, a divergent round constriction shape, small apertures, and high Strouhal numbers. *In vitro* experimental validation in steady and unsteady flow conditions is achieved on rigid vocal folds replicas with uniform and round constriction shapes in order to study the impact of viscosity and flow separation on the inverse model performance. It appears that both viscosity and the flow separation position determine the relevance of the inverse quasi-one-dimensional models. A mean prediction accuracy of 20% for the searched physical variables can be achieved for a divergent round constriction shape when the flow modeling includes a viscosity related correction and uses a suitable separation coefficient. Remark that the necessity of a corrective term related to viscosity outlines the limitations of the one-dimensional inviscid Bernoulli model. Moreover, the prediction errors increase when the contribution of the viscosity related term to the pressure determination is less important. The performance of the inverse models is seen to reflect the accuracy of the direct models. Therefore, it seems interesting, on the one hand, to include the sensitivity to the input variables errors in the minimization problem and, on the other hand, to use more advanced flow models in order to validate the value of the separation coefficient. Indeed, this parameter is often chosen as a constant but this study confirms that it depends on the Reynolds number so that it should be adapted in accordance with the aimed range of flow conditions relvant to phonation.

ACKNOWLEDGMENTS

This work has been supported by a Ph.D. grant from the French Ministry of Education and Research. The authors wish to thank A. Hirschberg, Technical University of Eindhoven, The Netherlands, for kindly providing the moving rigid vocal fold replicas, D. Blanc and D. Rey, Département Automatique, GIPSA-Laboratory, France, for their help in building the experimental setup, and the anonymous reviewers for their helpful comments.

Alipour, F., and Scherer, R. (**2004**). "Flow separation in a computational oscillating vocal fold model," J. Acoust. Soc. Am. **116**, 1710–1719.
Alipour, F., and Scherer, R. (**2006**). "Characterizing glottal jet turbulence," J. Acoust. Soc. Am. **119**, 1063–1073.
Alku, P., Vilkman, E., and Laukkanen, A. (**1998**). "Estimation of amplitude features of the glottal flow by inverse filtering speech pressure signals," Speech Commun. **24**, 123–132.
Blevins, R. (**1992**). *Applied Fluid Dynamics Handbook* (Krieger, Melbourne, FL).
Cranen, B., and Boves, L. (**1988**). "On the measurement of glottal flow," J. Acoust. Soc. Am. **84**, 888–900.
Deverge, M., Pelorson, X., Vilain, C., Lagree, P., Chentouf, F., Willems, J.,

and Hirschberg, A. (**2003**). "Influence of collision on the flow through in-vitro rigid models of the vocal folds," J. Acoust. Soc. Am. **114**, 1–9.
Drioli, C. (**2005**). "A flow waveform-matched low-dimensional glottal model based on physical knowledge," J. Acoust. Soc. Am. **117**, 3184–3195.
Fant, G. (**1960**). *The Acoustic Theory of Speech Production* (Mouton de Gruyter, Berlin).
Frohlich, M., Michaelis, D., and Strube, H. (**2001**). "SIM-simultaneous inverse filtering and matching of a glottal flow model for acoustic speech signals," J. Acoust. Soc. Am. **110**, 479–488.
Grandchamp, X., Van Hirtum, A., and Pelorson, X. (**2007**). "Experimental validation of simplified free jet turbulence models applied to the vocal tract," *Proceedings of the 19th International Conference on Acoustics*, Madrid, Spain, p. 6.
Hertegard, S., and Gauffin, J. (**1995**). "Glottal area and vibratory patterns studied with simultaneous stroboscopy, flow glottography, and electroglottography," J. Speech Hear. Res. **38**, 85–100.
Hofmans, G., Groot, G., Ranucci, M., Graziani, G., and Hirschberg, A. (**2003**). "Unsteady flow through *in vitro* models of the glottis," J. Acoust. Soc. Am. **113**, 1658–1675.
Kelley, C. (**1995**). *Iterative Methods for Linear and Nonlinear Equations* (Society for Industrial and Applied Mathematics, Philadelphia, PA).
Kincaid, D., and Cheney, W. (**1996**). *Numerical Analysis* (Brooks-Cole, Pacific Grove, CA).
Kreiman, J., and Gerratt, B. (**2005**). "Perception of aperiodicity in pathological voice," J. Acoust. Soc. Am. **117**, 2201–2211.
Kundu, P. (**1990**). *Fluid Mechanics* (Academic, London).
Lagrée, P. (**2000**). "An inverse technique to deduce the elasticity of a large artery," Eur. Phys. J.: Appl. Phys. **9**, 153–163.
Lous, N., Hofmans, G., Veldhuis, N., and Hirschberg, A. (**1998**). "A symmetrical two-mass vocal-fold model coupled to vocal tract and trachea, with application to prosthesis design," Acta Acust. **84**, 1135–1150.
Lucero, J. (**1999**). "A theoretical study of the hystheresis phenomenon at vocal fold oscillation onset-offset," J. Acoust. Soc. Am. **105**, 423–431.
Mergell, P., Herzel, H., and Titze, I. (**2000**). "Irregular vocal-fold vibration, high-speed observation and modeling," J. Acoust. Soc. Am. **108**, 2996–3001.
Pelorson, X. (**2001**). "On the meaning and accuracy of the pressure-flow technique to determine constriction areas within the vocal tract," Speech Commun. **35**, 179–190.
Pelorson, X., Hirschberg, A., Van Hasselt, R., Wijnands, A., and Auregan, Y. (**1994**). "Theoretical and experimental study of quasisteady-flow separation within the glottis during phonation application to a modified two-mass model," J. Acoust. Soc. Am. **96**, 3416–3431.
Price, P. (**1989**). "Male and female voice source characteristics: inverse filtering results," Speech Commun. **8**, 261–277.
Qiu, Q., and Schutte, H. (**2006**). "A new generation videokymography for routine clinical vocal fold examination," Laryngoscope **116**, 1824–1828.
Rothenberg, M., and Zahorian, S. (**1977**). "Nonlinear inverse filtering techniques for estimating the glottal-area waveform," J. Acoust. Soc. Am. **61**, 1063–1071.
Ruty, N., Pelorson, X., Van Hirtum, A., Lopez, I., and Hirschberg, A. (**2007**). "An *in vitro* setup to test the relevance and the accuracy of low-order vocal folds models," J. Acoust. Soc. Am. **121**, 479–490.
Sciamarella, D., and d'Alessandro, C. (**2004**). "On the acoustic sensitivity of a symmetrical two-mass model of the vocal folds to the variation of control parameters," Acta Acust. **90**, 746–761.
Shadle, C. H., Barney, A., and Davies, P. O. A. L. (**1999**). "Fluid flow in a dynamic mechanical model of the vocal folds and tract. ii. implications for speech production studies," J. Acoust. Soc. Am. **105**, 456–466.
Sobey, I. (**1983**). "The occurrence of separation in oscillatory flow," J. Fluid Mech. **134**, 247–257.
Sundberg, J., Anderson, M., and Hultqvist, C. (**1999**). "Effects of subglottal pressure variation on professional baritone singers voice sources," J. Acoust. Soc. Am. **105**, 1965–1971.
Svec, J., Sram, F., and Schutte, H. (**2007**). "Videokymography in voice disorders: what to look for?," Ann. Otol. Rhinol. Laryngol. **116**, 172–180.
Van Hirtum, A., Cisonni, J., Ruty, N., Pelorson, X., Lopez, I., and van Uittert, F. (**2007**). "Experimental validation of some issues in lip and vocal fold physical models," Acta Acust. **93**, 314–323.
Vilain, C., Pelorson, X., Fraysse, C., Deverge, M., Hirschberg, A., and Willems, J. (**2004**). "Experimental validation of a quasi-steady theory for the flow through the glottis," J. Sound Vib. **276**, 475–490.
Wong, D., Ito, M., and Cox, N. (**1991**). "Observation of perturbations in a lumped-element model of the vocal folds with application to some pathological case," J. Acoust. Soc. Am. **89**, 383–394.
Wurzbacher, T., Schwarz, R., Dollinger, M., Hoppe, U., Eysholdt, U., and Lohscheller, J. (**2006**). "Model-based classification of nonstationary vocal fold vibrations," J. Acoust. Soc. Am. **120**, 1012–1027.
Zhang, Y., and Jiang, J. (**2004**). "Chaotic vibrations of a vocal fold model with a unilateral polyp," J. Acoust. Soc. Am. **115**, 1266–1269.
Zhang, Z., Mongeau, L., and Frankel, S. (**2002**). "Experimental verification of the quasisteady approximation for aerodynamic sound generation by pulsating jets in tubes," J. Acoust. Soc. Am. **112**, 1652–1663.

Relation between perceived voice register and flow glottogram parameters in males

Gláucia Laís Salomão[a)]
Applied Linguistic and Language Studies Program, Pontifical Catholic University, R. Monte Alegre, 984, Corredor Cardoso de Almeida, Perdizes, 05014-001 São Paulo, Brazil

Johan Sundberg[b)]
Department of Speech, Music and Hearing, School of Computer Science and Communication, Royal Institute of Technology, Lindstedtsvägen 24, SE-100 44 Stockholm, Sweden

(Received 3 September 2007; revised 8 April 2008; accepted 17 April 2008)

The perception of modal and falsetto registers was analyzed in a material consisting of a total of 104 vowel sounds sung by 13 choir singers, 52 sung in modal register, and 52 in falsetto register. These vowel sounds were classified by 16 expert listeners in a forced choice test and the number of votes for modal was compared to the voice source parameters: (1) closed quotient (Q_{closed}), (2) level difference between the two lowest source spectrum partials ($H1-H2$), (3) AC amplitude, (4) maximum flow declination rate (MFDR), and (5) normalized amplitude quotient (NAQ, AC amplitude/MFDR* fundamental frequency). Tones with a high value of Q_{closed} and low values of $H1-H2$ and of NAQ were typically associated with high number of votes for modal register, and vice versa, Q_{closed} showing the strongest correlation. Some singer subjects produced tones that could not be classified as either falsetto or modal register, suggesting that classification of registers is not always feasible. © *2008 Acoustical Society of America.* [DOI: 10.1121/1.2924146]

PACS number(s): 43.70.Gr, 43.71.Bp [BHS] Pages: 546–551

I. INTRODUCTION

Vocal registers are an important aspect of singing. The term register has been used for perceptually distinct regions of vocal quality that can be maintained over some ranges of pitch and loudness.[1] Voices occasionally "break" and this phenomenon can be attributed to a sudden register change. In some voices, this break can be less apparent than in others. Some singers are trained to perform a seamless transition from one register to the other. Other singing styles differently regard the register transition. For example, voluntary jumps between modal and falsetto are artistically exploited in yodeling and certain types of contemporary popular music.

Vocal registers are also an important aspect of speech. Wide fundamental frequency (F_0) sweeps may sometimes be produced with register changes for expressive purposes. On the other hand, involuntary register changes or breaks can be an important symptom of certain voice pathologies.

Many investigations have been devoted to the understanding of the mechanical and physiological properties of vocal registers. It is generally agreed that register is a phenomenon affiliated with the voice source and that it is associated with the vibrational characteristics of the vocal folds. According to authors,[1–5] the vocal folds are thicker and vibrate with a greater mass in modal register, while in the falsetto, they are thinner and more stretched. Yet, data on voice source characteristics of registers are still rare.

Several authors have also discussed the acoustic correlates of different registers (e.g., Refs. 6–10). Most of the investigations have been limited to differences in the overall spectrum slope, a voice source property that has later been found to be strongly influenced by subglottal pressure and hence vocal loudness. Nevertheless, tones sung in modal register typically present stronger overtones, while the tones sung in falsetto register tend to have a voice source fundamental of greater amplitude.[11] In particular, the level difference between the first and second partial ($H1-H2$) is relevant and has been frequently used in descriptions of voice source characteristics.[12–15] For instance, Sundberg and Högset[16] found higher ($H1-H2$) values in the falsetto register as compared to the modal register.

The perceptual aspects of voice sounds are of primary interest, particularly in singing. Moreover, perceptual aspects of voice play a prominent role in definitions of vocal registers. Hence, the relationships between voice source characteristics and perception of register seem relevant. Analyses of such relationships have been rare in the literature.

Register investigations have often focused on register contrasts, comparing tones produced in one register to tones produced by the same subject in a different register. However, registers do not necessarily differ very clearly. Indeed, classically trained singers mostly eliminate or conceal register contrasts.

Thus, register differences may sometimes be quite difficult to perceive, and voice source differences between registers are sometimes quite small. Therefore, the purpose of this study was to compare the perception of modal and falsetto register with voice source properties. 16 experts classified

[a)]Electronic mail: gsalomao@csc.kth.se and glaucia.salomao@gmail.com; Tel.: +55(11)3670-8501/3670-8374; FAX: +55(11) 3670-8503.
[b)]Electronic mail: pjohan@speech.kth.se; Tel.: +46(0)8-7907873; FAX: +46(0)8-7907854.

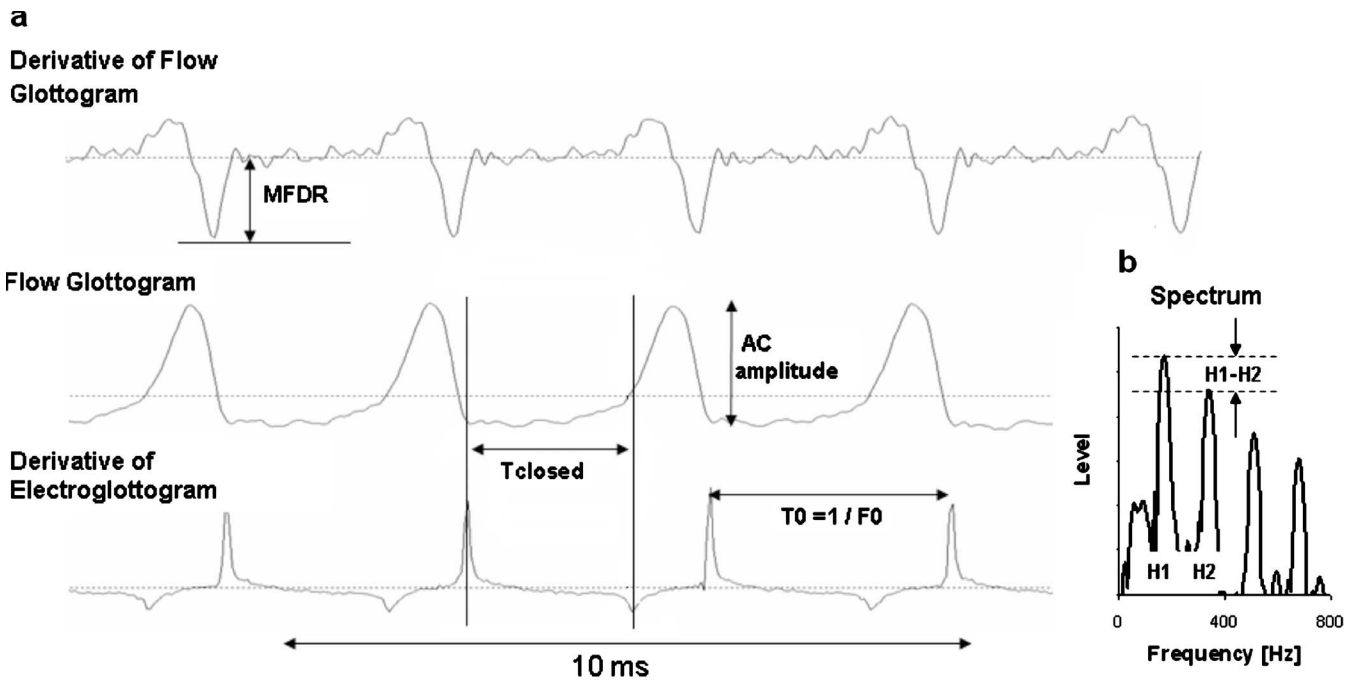

FIG. 1. Acoustical voice source measurements measured in (a) the flow glottogram, its first derivative and the dEGG signals, and in (b) in the spectrum, by means of Soundswell signal workstation program.

the tones analyzed in the previous study as modal or falsetto, and their classification was compared to the voice source properties observed.

II. METHODS

A. Recording procedures and acoustical analyses

13 males volunteered as subjects. All were members of the semiprofessional State Choir in Sao Paulo, which frequently performs together with the Sao Paulo State Orchestra. All had formally trained voices and none reported any voice problems at the time of the experiment. Each singer was asked to sing two *chromatic scales* on the vowel /a/ in a comfortable pitch range and at comfortable vocal loudness. The subjects were instructed to sing an ascending scale in modal register, extending it as far as possible. Correspondingly, they were asked to sing a descending scale in falsetto register, starting at the highest possible pitch and extending it as far as possible. No instructions were given as to what type of falsetto register they should use.[17].

The recordings were made in a sound treated booth, using a headset microphone (Audio Technica ATM75) at a distance of 17 cm. Also recorded was an electroglottograph (EGG) signal (Glottal Enterprises EG2). The signals were recorded on separate tracks of a DAT recorder (Soundcraft 328 XD).

The recordings were digitized and stored as sound files in the wav format. In these recordings were selected four adjacent pitches from the pitch range where the two registers overlapped, however, avoiding tones close to the limits of the modal and falsetto registers. These overlapping pitches substantially varied between the subjects, the lowest being G3 (in one single subject) and the highest was B4. In most cases, the lowest pitch fell within the range of C4–G4.

For each subject and pitch, a section from near the middle of the tone sung in modal and falsetto register was selected for inverse filtering. The filtering was performed by means of the custom-made DECAP program. It was set to display the waveforms and spectra of the input as well as the inverse filtered signal and also to display the derivative of the EGG (dEGG) signal, delayed by a time interval corresponding to the travel time of sound for a distance equal to the sum of vocal tract length and the microphone distance. This time interval varied between 0.9 and 1 ms.

For tuning the inverse filters, a ripple-free closed phase and a smooth source spectrum envelope, void of local minima, were used as the main criteria, see Fig. 1. As an additional criterion was used the synchronization between the moments at which the maximum flow declination rate (MFDR) occurred and the discontinuity of the dEGG waveform that reflected vocal fold contact, see Fig. 1. The filter settings were checked by synthesis by using the custom-made MADDE voice synthesis computer program. This program allows control of F_0 and six formant frequencies and bandwidths and also of the frequency and amplitude of the vibrato. The filter settings were accepted only if they generated a vowel quality similar to that produced by the subject. In addition, the consistency of the formant data used for the inverse filtering was checked. Thus, for each subject's falsetto and modal register productions, the formant frequencies used in the inverse filtering were compared. In cases where the values unsystematically varied between adjacent tones, attempts were made to revise the filter settings. The identification of the closed phase was greatly facilitated by the dEGG signal; its main positive peak should be synchronized with the trailing end of the flow pulse and the negative peak with the end of the closed phase. The dEGG showed a major positive peak, also in the falsetto tones, and mostly also a

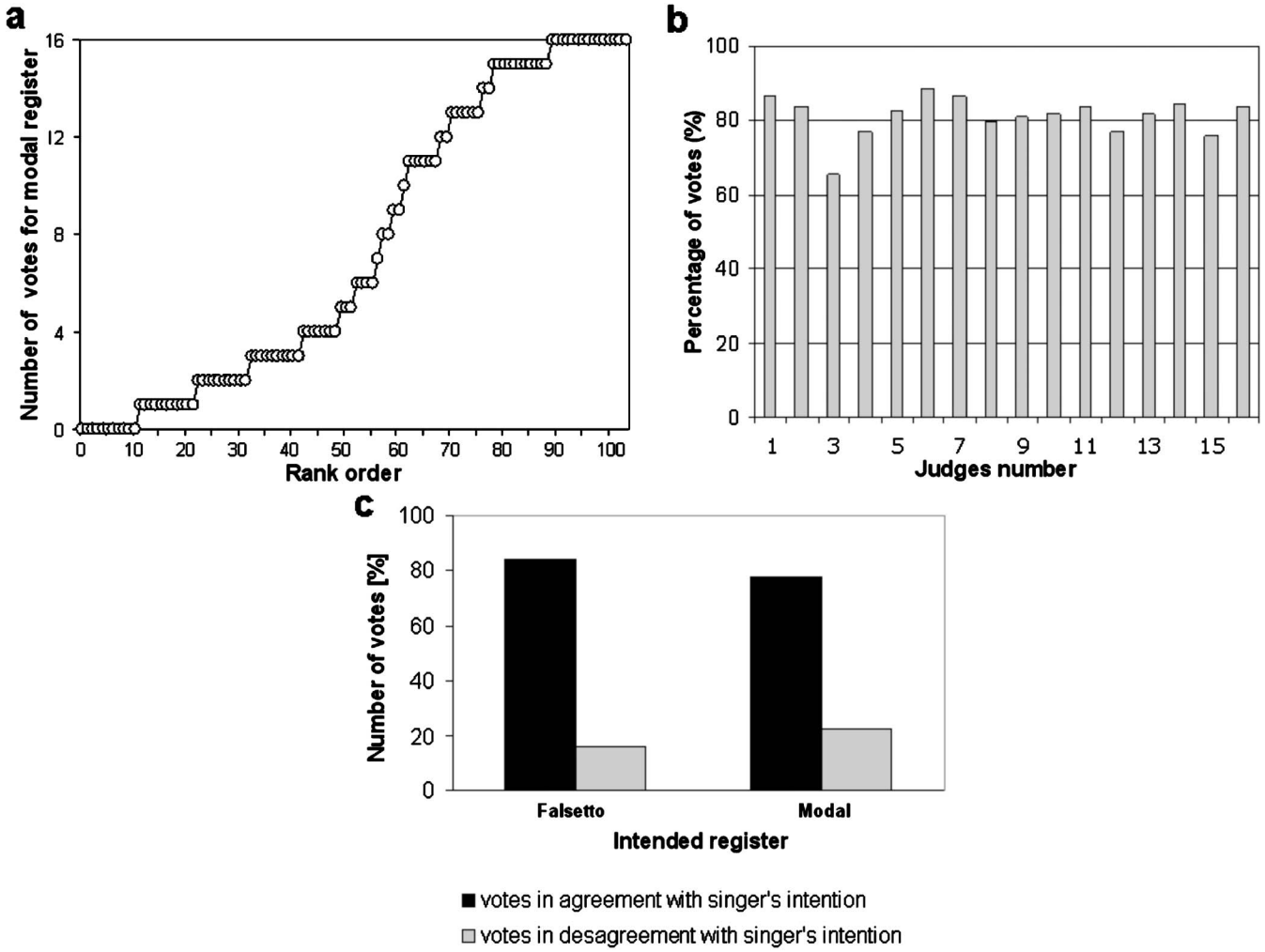

FIG. 2. [(a)–(c)] Upper left panel: Number of votes given for modal register, rank ordered according to this number. Upper right panel: Percentage of votes, given by each judge, that were in accordance with the register intended by the singer. Lower panel: Agreement (black columns) and disagreement (gray columns) between the listeners' classifications and the singers' intentions with regard to register.

much less conspicuous negative peak, corresponding to the sudden decrease of the vocal contact at the opening of the glottis.

Analyses of the flow glottograms obtained were carried out by using the various modules in the Soundswell Signal Workstation (Hitech Development, Stockholm, Sweden). The following parameters, illustrated in Fig. 1, were measured in the flow glottogram, in its first derivative and in the dEGG signals: (1) period length (T_0); (2) duration of the closed phase (Tcl); (3) peak-to-peak amplitude, i.e., the amplitude for the alternating current signal (henceforth ac amplitude); (4) MFDR.

Also, the closed quotient (Q_{closed}), defined as the ratio T_{cl}/t_0, the normalized amplitude quotient (NAQ), defined as NAQ=ac amplitude/T_0MFDR,[18] and the level difference between the two lowest partials in the spectrum of the flow glottogram ($H1-H2$) was determined.

B. Perceptual evaluation

The 104 tones selected from the original recordings mentioned above (13 singers × 4 tones × 2 registers) were copied in random order onto a compact disk by means of custom-made software which also inserted a pause of 3 s between stimuli. The program also provided a list of the stimulus order.

The 104 stimuli were evaluated by a panel of 16 voice experts. Of these, one was a professional hard rock singer with extensive experience as a teacher of singing, and one was a female classically trained singer. These subjects individually listened to the test stimuli over head phones. The remaining 14 judges were students of a course in the theory of the singing voice, where vocal registers had been a main topic. They simultaneously listened to the stimuli at a comfortable listening level over loudspeakers in a classroom. They were asked not to interact with each other during the test.

The subjects were asked to decide if the stimulus they heard was produced in modal or in falsetto register. They were given sheets containing a table with numbered lines for the 104 stimuli and two columns, one for modal and one for falsetto register votes. The subjects thus put a marking in the corresponding column just after each stimulus had been presented. The complete test took about 10 min.

TABLE I. Pearson correlations between flow glottogram parameters, observed for the 104 flow glottograms analyzed.

	Q_{cl}	$H1-H2$	NAQ	ac amp	MFDR
Q_{cl}	1	−0.810[a]	−0.861[a]	0.245[b]	0.651[a]
$H1-H2$	−0.810[a]	1	0.878[a]	−0.317[a]	−0.666[a]
NAQ	−0.861[a]	0.878[a]	1	−0.172	−0.614[a]
AC amp	0.245[b]	−0.317[a]	−0.172	1	0.766[b]
MFDR	0.651[a]	−0.666[a]	−0.614[a]	0.766[a]	1

[a]Correlation is significant at the 0.01 level (two tailed).
[b]Correlation is significant at the 0.05 level (two tailed).

III. RESULTS

A. Perceptual evaluation

Figure 2(a) shows the number of votes for modal for each of the stimuli. In the graph, the stimuli were rank ordered according to this same number of votes for modal. Thus, the stimulus that collected the highest number of votes for modal appears at the right end of the x-axis. In the figure, 16 votes means that all 16 listeners agreed that the tone was sung in modal and zero implies that they agreed that the tone was not sung in modal, i.e., they agreed that it was sung in falsetto. The figure shows 16 votes in 15 cases and 0 votes in 11 cases, i.e., a total of 26 cases of complete agreement. In 21 additional cases, all listeners except one agreed on the classification. In other words, the listeners were in almost perfect agreement with respect to register classification in almost half of the cases. This suggests some degree of consistency, since lack of consistency would be incompatible with complete agreement for several stimuli.

In most cases, the listeners' classification also agreed with the register intended by the singers. This is illustrated in Fig. 2(b), showing the percentage of cases where the different judges' votes were in agreement with the intention of the singer. The graph shows that all judges except 5 (judge numbers 3, 4, 8, 12, and 15) classified the tones in accordance with the singers' intentions in 80% of the cases or more.

Finally, the examples of modal and falsetto appeared as almost equally easy to identify. Figure 2(c) shows that of the 52 examples of falsetto register more than 80% was classified in accordance with the singers' intentions, and of the 52 examples of modal register almost 80% was classified in accordance with the singers' intentions. Thus, most of the 104 tones were perceived as representative examples of the respective registers. Pitch did not seem a factor of relevance to the classification.

B. Relationships between classification and acoustic data

A correlation analysis was carried out between the classification obtained from the listening test on the one hand, and each of the flow glottogram parameters that we analyzed in our previous investigation, on the other hand. Table I shows the correlations between the flow glottogram parameters analyzed. Each parameter is significantly correlated with most parameters, except the ac amplitude.

Figures 3(a)–3(c) show the relationship between the classification data and each of the Q_{closed}, $H1-H2$, and NAQ parameters. Tones with a high value of Q_{closed} and low values of $H1-H2$ and of NAQ were typically associated with high number of votes for modal register, and vice versa. The Q_{closed} parameter showed the strongest correlation.

A stepwise multiple regression analysis was carried out of the relationships between the number of votes for modal register and the various flow glottogram parameters. The results, listed in Tables II and III, and illustrated in Fig. 4, revealed that the Q_{closed} was the strongest predictor of the number of modal votes, followed by $H1-H2$, MFDR, and ac amplitude. NAQ, on the other hand, failed to appear as predictor in this analysis. This was probably caused by the strong correlation between NAQ and both Q_{closed} and $H1-H2$, see Table I. As can be seen in Fig. 3(a), NAQ was indeed the parameter that showed the strongest correlation with the number of votes for modal ($r=0.830$).

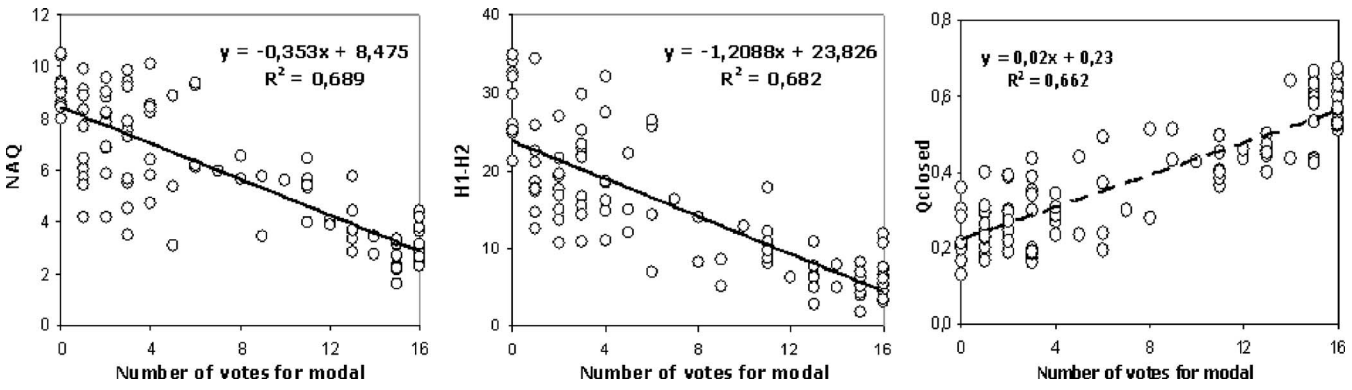

FIG. 3. [(a)–(c)] Q_{closed}, $H1-H2$, and NAQ as functions of the number of votes for modal register.

TABLE II. Predictive variables of the number of votes for modal and their statistic significance according to the SSPS analysis. Dependent variable: votes.

Model		Unstandardized coefficients		Standardized coefficients		
		B	Std. error	Beta	*t*	Sig.
1	(Constant)	−5.779	0.820		−7.044	0.000
	Q_{cl}	35.029	2.014	0.865	17.394	0.000
2	(Constant)	2.411	1.890		1.276	0.205
	Q_{cl}	23.104	3.122	0.570	7.401	0.000
	$H1-H2$	−0.249	0.053	−0.364	−4.718	0.000
3	(Constant)	1.108	1.881		0.589	0.557
	Q_{cl}	20.820	3.119	0.514	6.676	0.000
	$H1-H2$	−0.201	0.054	−0.294	−3.746	0.000
	MFDR	23.820	8.297	0.174	2.871	0.005
4	(Constant)	2.718	1.857		1.463	0.147
	Q_{cl}	16.895	3.200	0.417	5.281	0.000
	$H1-H2$	−0.186	0.051	−0.272	−3.621	0.000
	MFDR	60.981	13.705	0.445	4.449	0.000
	AC amp	−3.001	0.904	−0.253	−3.320	0.001

IV. DISCUSSION

The listeners' classifications mostly, but not always, agreed with the registers intended by the singers. The cases of disagreement could result from poor skill in voice control, as well as from skill in concealing the timbral differences between the registers. Also, three of the singers claimed that they were unfamiliar with the phenomenon of vocal registers. Of these, two produced tones that about half of the listeners classified as modal and half as falsetto. As we regarded, a great variation in stimulus properties as an advantage for the test, the tones sung by these three singers were all included in the listening test.

The ac amplitude showed a weak relationship with register. This was somewhat surprising since the ac amplitude is typically higher in falsetto than in modal register. However, ac amplitude is affected also by subglottal pressure, a higher pressure producing greater ac amplitude, other things being equal. Although no attempt was made to estimate subglottal pressure in the present investigation, it seems likely that the singers typically used higher subglottal pressures in modal than in falsetto. Another factor affecting the ac amplitude is the glottal adduction. If the glottal adduction is greater in modal than in falsetto, as suggested by the NAQ values,[19] it is possible that the effect of a higher subglottal pressure is counteracted by a firmer adduction in modal. A third factor of possible relevance is the vocal fold length that is greater in falsetto;[1–5] long vocal folds generate a greater glottal area than short vocal folds, other things being equal. It would be worthwhile to examine in more detail the relationship between the ac amplitude and register taking also subglottal pressure and its relation with loudness into account.

TABLE III. Summary of stepwise multiple regression analysis of the relationships between the various flow glottogram parameters and the number of votes for modal register; *r* refers to the correlation. The standard error of the estimate is dependent on the number of judges.

Model	*r*	Adjusted *R* square	Standard error of the estimate
Q_{closed}	0.865	0.745	3.063
Q_{closed}, $H1-H2$	0.891	0.789	2.786
Q_{closed}, $H1-H2$, MFDR	0.900	0.803	2.692
Q_{closed}, $H1-H2$, MFDR, AC amp.	0.910	0.821	2.566

According to Titze,[1] the operational definition of a register must depend on supporting perceptual evidence. The listening test showed that our singers produced a number of tones that were not unanimously classified. In about 20% of the cases, nearly half of the judges came up with different classifications. Thus, some voices produced tones that could not be unanimously classified as either falsetto or modal register, confirming the observation that registers classification is not always feasible (Titze, 1994). Rather, in some voices, there seems to be a continuous transition between these registers. In any event, our results appear to challenge the idea that modal and falsetto registers are necessarily associated with clear timbral differences. And indeed, accepting Titze's finding mentioned above, we would conclude that some singers eliminate the distinction between modal and falsetto registers; lack of perceptual evidence of timbral differences implies lack of register differences.

In view of this result, it is tempting to ask whether registers exist in all voices. We have found that the modal and falsetto registers tend to differ with respect to several flow glottogram parameters. A singer is likely to have learned to continuously vary each of these flow glottogram parameters, e.g., for expressive purposes. If this is correct, singers should also be able to eliminate timbral differences between registers by a gradual rather than an abrupt change of these parameters.

V. CONCLUSIONS

Our results show that (1) the tones with a high value of Q_{closed} and MFDR and with low values of $H1-H2$ and NAQ were typically associated with high number of votes for

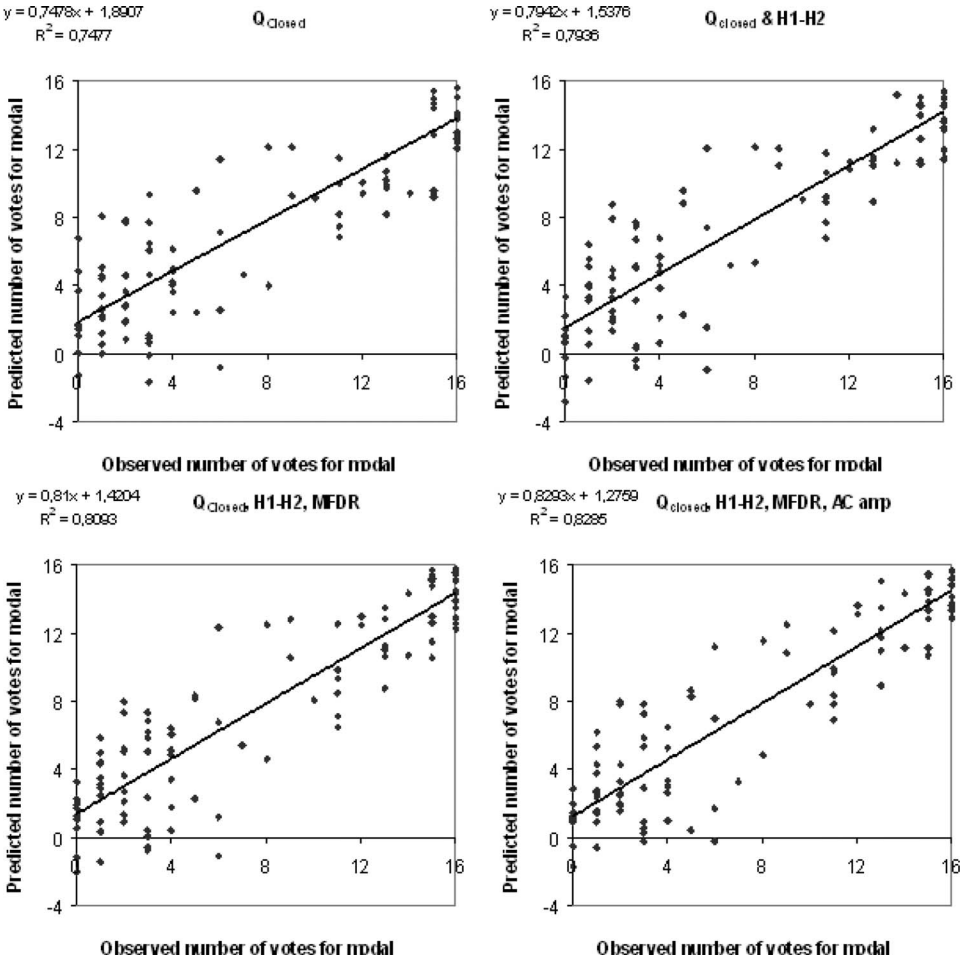

FIG. 4. Results of attempts to use flow glottogram parameters for predicting the number of votes for modal register in the listening test. The predictions were based on the stepwise multiple regression analysis. The parameters used for the predictions are listed at the top of each panel.

modal register, and vice versa; (2) the Q_{closed} and $H1-H2$ parameters presented the strongest correlation with the results of the classification test; and (3) some tones were not unanimously classified, neither as modal nor as falsetto, suggesting that classification of registers is sometimes quite difficult.

ACKNOWLEDGMENTS

The custom-made MADDE, DECAP, and GLUE softwares were written by Svante Granqvist, KTH, Sweden. The authors would like to thank the voice experts for their gentle participation in this investigation. This research, financially supported by the Brazilian Ministry of Education (Coordenação de Aperfeiçoamento de Pessoal de Ensino Superior—CAPES), was carried out during the first author's stay at the Department for Speech, Music and Hearing at KTH Stockholm, Sweden.

[1]I. Titze, *Principles of Voice Production* (Prentice-Hall, Englewood Cliffs, NJ, 1994), Chap. 10, pp. 252–278.
[2]J. W. van den Berg, "Mechanisms of the larynx and the laryngeal vibrations," in *Manual of Phonetics*, edited by B. Malberg (North-Holland, Amsterdam, 1968), pp. 278–308.
[3]M. Hirano, "Morphological structure of the vocal cord as a vibrator and its variations," Folia Phoniatr Logop **26**, 89–94 (1974).
[4]H. Hollien, "On vocal registers," J. Phonetics **2**, 125–143 (1994).
[5]I. Hiroto, "Introductory remarks," *Vocal Fold Physiology* (University of Tokyo Press, Tokyo, 1981), pp. 3–9.
[6]J. W. Large, "Towards an integrated physiologic-acoustic theory of vocal registers," The National Association of Teachers of Singing **29**, 18–40 (1972).
[7]J. W. Large, S. Iwata, and H. von Leden, "The male operatic head register versus falsetto," Folia Phoniatr Logop **24**, 19–29 (1972).
[8]R. H. Colton, "Spectral characteristics of the modal and falsetto registers," Folia Phoniatr. **24**, 337–344 (1972).
[9]R. H. Colton, "Some acoustic parameters related to the perception of modal-falsetto voice quality," Folia Phoniatr. **25**, 302–311 (1973).
[10]D. G. Miller and H. K. Schutte, "Toward a definition of male 'head' register, passagio, and 'cover' in western operatic singing," Folia Phoniatr Logop **46**, 157–170 (1994).
[11]J. Sundberg, "The source spectrum in professional singing," Folia Phoniatr. **25**, 71–90 (1973).
[12]B. Hammarberg, B. Fritzell, J. Gauffin, J. Sundberg, and L. Wedin, "Perceptual and acoustics correlates of abnormal voice qualities," Acta Oto-Laryngol. **90**, 441–451 (1980).
[13]D. H. Klatt and L. C. Klatt, "Analysis, synthesis, and perception of voice quality variations among females and male talkers," J. Acoust. Soc. Am. **87**, 820–857 (1990).
[14]H. M. Hanson and K. N. Stevens, "Subglottal resonances in female speakers and their effect on vowel spectra," Proceedings of the Eighth International Congress of Phonetic Sciences, Stockholm, Sweden, Vol. **3**, pp. 182–185 (1995).
[15]H. M. Hanson, "Glottal characteristics of female speakers: acoustic correlates," J. Acoust. Soc. Am. **101**, 466–481 (1997).
[16]J. Sundberg and C. Högset, "Voice source differences between falsetto and modal registers in counter tenors, tenors and baritones," Logoped. Phoniatr. Vocol. **26**, 26–36 (2001).
[17]H. J. Rubin and C. C. Hirt, "The falsetto: A high speed cinematographic study," Laryngoscope **70**, 1305–1324 (1960).
[18]P. Alku, T. Bäckström, and E. Vilkman, "Normalized amplitude quotient for parameterization of the glottal flow," J. Acoust. Soc. Am. **112**, 701–710 (2002).
[19]P. Alku, M. Airas, E. Björkner, and J. Sundberg, "An amplitude quotient based method to analyze changes in the shape of the glottal pulse in the regulation of vocal intensity," J. Acoust. Soc. Am. **120**, 1052–1062 (2006).

Multiple routes to the perceptual learning of speech

Jeremy L. Loebach[a] and Tessa Bent[b]
Speech Research Laboratory, Department of Psychological and Brain Sciences, Indiana University, Bloomington, Indiana 47405 and DeVault Otologic Research Laboratory, Department of Otolaryngology-Head and Neck Surgery, Indiana University School of Medicine, Indianapolis, Indiana 46202

David B. Pisoni[c]
Speech Research Laboratory, Department of Psychological and Brain Sciences, Indiana University, Bloomington, Indiana 47405 and DeVault Otologic Research Laboratory, Department of Otolaryngology-Head and Neck Surgery, Indiana University School of Medicine, Indianapolis, Indiana 46202

(Received 21 August 2007; revised 6 April 2008; accepted 18 April 2008)

A listener's ability to utilize indexical information in the speech signal can enhance their performance on a variety of speech perception tasks. It is unclear, however, whether such information plays a similar role for spectrally reduced speech signals, such as those experienced by individuals with cochlear implants. The present study compared the effects of training on linguistic and indexical tasks when adapting to cochlear implant simulations. Listening to sentences processed with an eight-channel sinewave vocoder, three separate groups of subjects were trained on a transcription task (transcription), a talker identification task (talker ID), or a gender identification task (gender ID). Pre- to posttest comparisons demonstrated that training produced significant improvement for all groups. Moreover, subjects from the talker ID and transcription training groups performed similarly at posttest and generalization, and significantly better than the subjects from the gender ID training group. These results suggest that training on an indexical task that requires high levels of controlled attention can provide equivalent benefits to training on a linguistic task. When listeners selectively focus their attention on the extralinguistic information in the speech signal, they still extract linguistic information, the degree to which they do so, however, appears to be task dependent. © *2008 Acoustical Society of America.* [DOI: 10.1121/1.2931948]

PACS number(s): 43.71.Bp, 43.71.Es, 43.66.Ts, 43.66.Lj [MSS] Pages: 552–561

I. INTRODUCTION

The acoustic speech stream contains two different sources of information: linguistic information, which carries the meaning of the utterances and indexical information, which specifies the characteristics of the speaker's voice (such as gender, age and dialect, Abercrombie, 1967; Ladefoged and Broadbent, 1957). How these two types of information interact during speech perception is still poorly understood. Does the listener encode linguistic and indexical information in independent streams via different perceptual mechanisms or are they encoded and processed together? The present study addressed this question by investigating how selectively focusing the listener's attention on linguistic or indexical information during training affects the perceptual learning of spectrally degraded speech. Using sentences that had been processed by a cochlear implant (CI) simulator, we investigated how different types of training affected perceptual learning and generalization to new sentences and sentences under more severely spectrally degraded conditions. We found that the amount of controlled attention required during the training task modulated the relative strength of perceptual learning. Training on talker identification, an indexical task that required a higher degree of attentional control and focus on the acoustic information in the signal, was just as effective as transcription training and both tasks elicited more robust generalization than training on gender identification.

A. Indexical information and cochlear implants

Research with CI users has focused almost exclusively on speech perception, leaving the perception of other types of information carried in the acoustic signal (e.g., indexical information) unexplored. For linguistic tasks, acoustic simulations of cochlear implants have provided a useful tool for determining what acoustic information is necessary for accurate speech perception (Shannon *et al.*, 1995). Designed to simulate different numbers of active electrodes in the intracochlear array, these simulations have demonstrated that successful speech perception is largely dependent on the number of acoustic channels (Shannon *et al.*, 1995). In quiet, normal hearing (NH) subjects reach asymptote with about eight channels (Dorman *et al.*, 1997), although more channels are needed when listening in noise (Dorman *et al.*, 1998). NH subjects listening to six-channel simulations perform similarly to CI users (Dorman and Loizou, 1998). Although limited spectral information is sufficient for high levels of consonant, vowel, and sentence perception, acoustic signals containing complex spectra, such as music, may require well over 30 channels to be perceived accurately (Shannon *et al.*, 2004; Shannon, 2005).

[a]Author to whom correspondence should be addressed; electronic mail: jeremyloebach@gmail.com
[b]Electronic mail: tbent@indiana.edu
[c]Electronic mail: pisoni@indiana.edu

 0001-4966/2008/124(1)/552/10/$23.00

Compared to perception of linguistic information in the speech signal, considerably less is known about the perception of indexical information in both CI users and NH subjects listening to CI simulations. Cleary and Pisoni (2002) demonstrated that prelingually deafened pediatric CI users have more difficulty discriminating talkers based on their voices than do NH children. Deaf children with cochlear implants, who could discriminate between talkers, performed comparably to NH children, but all CI users required much larger pitch differences between talkers than NH controls in order to successfully distinguish talkers (see also Cleary *et al.*, 2005). Moreover, the ability to discriminate talkers was found to be significantly correlated with several different speech perception outcome measures, indicating that the acoustic information necessary for talker discrimination is closely coupled with the information used in speech perception and spoken word recognition (Cleary *et al.*, 2005).

Compared to talker discrimination, the identification of a talker's gender is easier for both NH subjects listening to eight-channel CI simulations and CI users (Fu *et al.*, 2004). Both groups of listeners may be relying on the pitch of the fundamental frequency to classify speaker gender (Fu *et al.*, 2005). For NH subjects, the performance on gender identification tasks depends on the method of synthesis. While speech perception accuracy does not differ for noise and sinewave vocoders (Dorman *et al.*, 1997), gender discrimination is more accurate and requires fewer spectral channels for sinewave than noise vocoders (Gonzales and Oliver, 2005). Given that sinewave vocoders may encode temporal information with higher fidelity (Gonzales and Oliver, 2005), it is possible that subjects are utilizing temporal cues to discriminate the fundamental frequency.

The explicit identification of speakers by their voice alone may require more spectral detail compared to talker or gender discrimination, and subjects may be using different perceptual processes for linguistic as compared to indexical tasks (Vongphoe and Zeng, 2005). When presented with vowels produced by ten different talkers, CI users and NH subjects listening to eight-channel simulations performed equally well on vowel identification but CI users performed significantly more poorly when identifying the speakers by voice alone (Vongphoe and Zeng, 2005). When considered on a talker-by-talker basis, however, the primary source of errors in talker identification was between talkers with higher pitch voices (adult females, girls, and boys) (Vongphoe and Zeng, 2005). When boys and girls were excluded, the CI users resembled the normal hearing subjects listening to eight-channel simulations, just as they did in the vowel identification task. This alternative interpretation suggests that both linguistic and indexical tasks may rely on similar perceptual processing strategies, but when the ranges of vocal pitch overlap substantially, CI users may not be receiving sufficient spectral information to reliably identify talkers. This possibility, however, has not been experimentally addressed.

B. Perceptual learning in linguistic and indexical tasks

Understanding the perceptual interactions between indexical and linguistic properties of speech is important for a number of reasons. A talker's specific realizations of acoustic-phonetic parameters will ultimately determine their speech intelligibility (Bond and Moore, 1994; Bradlow *et al.*, 1996; Cox *et al.*, 1987; Hood and Poole, 1980), and adult listeners are constantly adjusting their internal categories to accommodate new talkers (e.g., Eisner and McQueen, 2005). Such perceptual learning, which can be defined as long-term changes in the perceptual system based on sensory experiences that influences future behaviors and responses (Goldstone, 1998; Fahle and Poggio, 2002), may play a central role in adaptation to novel talkers and speaking styles. Moreover, familiarity with a talker's voice has been shown to provide a significant benefit when listening to speech in noise (Nygaard *et al.*, 1994; Nygaard and Pisoni, 1998), indicating interactions between the linguistic and indexical channels of information, and suggesting that they may indeed be encoded in the same stream.

Perceptual learning of speech can be both talker independent and talker dependent. When a listener is explicitly trained to classify an ambiguous sound in a real word, category boundaries for other words containing the sound will be adjusted to accommodate the new pronunciation by that particular talker (Eisner and McQueen, 2005). Moreover, if the manipulated stimuli have a greater degree of potential generalizabillity (e.g., a voicing distinction for alveolars that could apply to bilabials and velars as well), perceptual learning will be robust and occur independent of talker (Kraljic and Samuel, 2006). Talker-independent perceptual learning has also been shown to be beneficial for listeners with extensive experience listening to synthetic speech produced by rule (Schwab *et al.*, 1985; Greenspan *et al.*, 1988), time-compressed speech (Dupoux and Green, 1997), foreign accented speech (Bradlow and Bent, 2008; Clarke and Garrett, 2004; Weil, 2001), and noise-vocoded speech (Davis *et al.*, 2005). Critically, the benefits of perceptual learning extend to new talkers and new speech signals created using the same types of signal degradation.

Training can have large effects on the perceptual learning of CI simulated speech. The types of tasks and stimulus materials used during training have been shown to affect post-training gains and generalization. Robust generalization and transfer of perceptual learning to novel meaningful sentences has been demonstrated for individual phonemes (Fu *et al.*, 2005), words (Loebach and Pisoni, 2008), meaningful and anomalous sentences (Burkholder, 2005; Davis *et al.*, 2005; Loebach and Pisoni, 2008), and environmental sounds (Loebach and Pisoni, 2008). Although previous research has examined the perception of indexical information in CI simulated speech, it is unknown whether training on talker identification will generalize to word or sentence recognition under conditions of severe spectral degradation, as has been shown for naturally produced speech (Nygaard and Pisoni, 1998).

C. The present study

Understanding whether indexical and linguistic tasks differentially affect perceptual learning will help to elucidate whether these sources of information are encoded in the same stream and utilize similar perceptual mechanisms for processing. Moreover, understanding how linguistic and indexical channels of information interact in speech perception may provide novel insights into possible training methodologies for new CI users. The present study compared how training on linguistic and indexical tasks affected listeners' ability to accurately perceive words in sentences. Using sentences processed with an eight-channel sinewave vocoder, NH subjects were trained to identify either the gender or identity of six talkers or transcribe their speech. Pre- to post-training comparisons of transcription accuracy scores assessed the effectiveness of training. Given the results of the previous studies, we hypothesized that subjects trained on talker identification would perform better than those who were trained on gender identification due to increased attentional demands required during training. Moreover, we predicted that training on talker identification would match or exceed the performance of subjects trained using a conventional sentence transcription task because of the controlled attention required to learn to identify the talkers from severely degraded stimuli.

II. METHODS

A. Subjects

Seventy-eight young adults participated in the study (60 female, 18 male; mean age, 21 years). All subjects were native speakers of American English and reported having normal hearing at the time of testing. Subjects were recruited from the Indiana University community and received monetary compensation ($10/session) or course credit (1 credit/session) for their participation. Of the 78 subjects tested, 6 were excluded from the final data analysis (2 failed to return for the generalization session, 1 failed to return in a timely manner, and 3 due to program malfunctions).

B. Stimuli

Stimuli consisted of 124 meaningful [76 high predictability (HP) and 48 low predictability (LP)] and 48 anomalous (AS) speech in noise test (SPIN) sentences (Kalikow *et al.* 1977; Clopper and Pisoni, 2006). SPIN sentences are balanced for phoneme occurrence in English and contain between five and eight words, the last of which is the keyword to be identified. The final word in the HP sentences is constrained by the preceding semantic context (e.g., "A bicycle has two *wheels*."), whereas in the LP sentences the preceding context is uninformative (e.g., "The old man talked about the *lungs*."). The AS sentences retained the format of their meaningful counterparts, except that all words in the sentence are semantically unrelated, resulting in a sentence that preserves proper syntactic structure but is semantically anomalous. (e.g., "The round lion held a *flood*.") A passage of connected speech (Rainbow Passage; Fairbanks, 1940) was used for the familiarization portion of the experiment. Wav files of the materials were obtained from the Nationwide Speech Corpus (Clopper and Pisoni, 2006). Materials were produced by six speakers (three male, three female) from the midland dialect.

C. Synthesis

All stimuli were processed using Tiger CIS to simulate an eight-channel cochlear implant using the CIS processing strategy. Stimulus processing involved two phases: an analysis phase, which used band pass filters to divide the signal into eight nonlinearly spaced channels (between 200 and 7000 Hz, 24 dB/octave slope) and a low pass filter to derive the amplitude envelope from each channel (400 Hz, 24 dB/octave slope); and a synthesis phase, which replaced the frequency content of each channel with a sinusoid that was modulated with its matched amplitude envelope. All training, familiarization, and testing materials were processed with the eight-channel vocoder unless otherwise noted: a subset of the materials to be used in the generalization phase were processed with four and six channels to further reduce the amount of information in the signal. All stimuli were saved as 16-bit Windows PCM wav files (22 kHz sampling rate) and normalized to 65 dB rms (LEVEL v2.0.3) (Tice and Carrell, 1998) to ensure that all stimuli were of equal intensity and to eliminate any peak clipping.

D. Procedures

All methods and materials were approved by the Human Subjects Committee and Institutional Review Board at Indiana University Bloomington. For data collection, a custom script was written for PsyScript and implemented on four Apple PowerMac G4 computers that were equipped with 15-in.-color liquid crystal display (LCD) monitors. Audio signals were presented over Beyer Dynamic DT-100 headphones and were calibrated with a voltmeter to a 1000 Hz tone at 70 dB v SPL. Sound intensity was fixed within PsyScript in order to guarantee consistent sound presentation across subjects. Multiple booths in the testing room accommodated up to four subjects at the same time. Each trial was preceded by a 1000 ms silent interval, followed by a fixation cross presented at the center of the screen for 500 ms to alert the subject to the upcoming trial. The subject was prompted to record their response after stimulus offset. For the transcription trials, a dialog box was presented on the screen signaling subjects to type in what they heard. For talker identification, subjects clicked on the one box (out of six) that contained the name of the talker that produced the sentence. For gender identification, subjects clicked on a box labeled "female" or "male." There were no time limits for responding and subjects pressed a button to advance to the next trial. Subjects performed at their own pace and were allowed to rest between blocks as needed. Each experimental session lasted approximately 40–60 min.

1. Training

Training took place over two sessions. The tasks and materials varied across blocks but the same block structure was used for all groups. All stimuli were randomized within each block. Session 1 began with a pretest to establish a

TABLE I. Tasks and stimulus materials in the pretest, familiarization, and training blocks of session 1. Feedback was only provided in the training blocks

Pretest	Familiarization	Training (feedback)
Transcribe: 30 LP sentences 30 AS sentences	Passively listen: Rainbow passage	Transcribe ID talker ID gender: 150 HP sentences

baseline level of performance before training (see Table I) and expose subjects to the processing condition in order to provide an unbiased assessment of training efficacy. In the pretest blocks, subjects transcribed 30 unique spectrally degraded LP sentences, followed by 30 unique spectrally degraded AS sentences. In these blocks, the subjects simply transcribed the sentences and received no feedback.

During the familiarization phase, subjects passively listened to spectrally degraded versions of the Rainbow passage produced by each of the six talkers in order to become familiar with the voices and synthesis condition and teach them the appropriate labels that would be used during training. During familiarization, subjects in the talker ID group were presented with the passage paired with the name of the talker who produced it (Jeff, Max, Todd, Beth, Kim, or Sue). Subjects were told that they would be asked to identify the talkers by name and they should listen carefully for any information that would help them learn to recognize the talkers' voice. Subjects in the gender ID group heard the same passages, but these were paired with the appropriate gender label (male or female) for each talker. These subjects were told that they would be asked to identify the gender of the talkers, and they should listen carefully for any information that would help them learn to recognize each talker's gender. Finally, subjects in the transcription group heard each passage presented along with the name of the talker who produced it. However, they were told that they would be asked to transcribe sentences produced by each talker and they should listen carefully in order to better understand the degraded signals.

The three training blocks in session 1 consisted of 150 spectrally degraded HP sentences (the same 25 sentences produced by each talker). During training, subjects were presented with a sentence and asked to make a response appropriate for their training group. All subjects were provided with feedback regardless of the accuracy of their responses. Subjects in the talker ID group identified the talker by clicking one of six buttons on the computer screen labeled with the talkers' names. After the subject recorded his/her response, a red circle appeared around the name of the correct talker as feedback. Subjects in the gender ID group responded by clicking one of two buttons on the computer screen that contained the appropriate gender label. After the subject recorded his/her response, a red circle appeared around the correct gender of the talker as feedback. Subjects in the transcription training group were asked to type what they thought the talker said. They received the correct transcription of the sentence as feedback.

Session 2 (Table II) was completed within 3 days of session 1 and began with a repetition of the familiarization phase in which subjects again heard the Rainbow Passage produced by each talker. The purpose of this block was to refamiliarize the listener with the voices and labels, since at least 24 h had passed since the first training session. Two training blocks followed, consisting of 90 HP sentences (15 sentences produced by each talker). Again, subjects received feedback regardless of their response.

Transfer of training to novel materials that were more spectrally degraded than the training materials was then assessed, and subjects were asked to transcribe 36 new HP sentences that were more severely spectrally degraded than the stimuli that the subjects heard during training (18 four-channels, 18 six channels). Generalization of training was tested in the following two blocks, and subjects were asked to transcribe 18 novel LP sentences and 18 novel AS sentences. Following generalization, two posttest blocks assessed the relative gains in performance due to training. Subjects transcribed 12 AS sentences and 12 LP sentences selected from the pretest blocks. We chose to conduct the posttest last in order to more accurately assess the benefits from training. In particular, we wanted to rule out the influence of procedural learning, which could distort the posttest performance (since subjects in the talker or gender ID groups had less experience with the sentence transcription task).

2. Analysis and scoring

Keyword accuracy scores were based on the final word in each sentence. Common misspellings and homophones were counted as correct responses. However, words with added or deleted morphemes were counted as incorrect. Perceptual learning during training was assessed by comparing performance across the five training blocks. Pre- to posttest comparisons provided an assessment of the gains from training across the three training groups. Comparison of performance at pre- and posttest to performance on new materials provided an assessment of generalization of training to novel

TABLE II. Tasks and stimulus materials in the refamiliarization, training, generalization, and posttest blocks of session 2. Feedback was only provided in the training blocks.

Familiarization	Training (feedback)	Generalization: Novel materials	Transfer: More degraded	Posttest
Passively listen: Rainbow passage	Transcribe ID talker ID gender: 90 HP sentences	Transcribe: 18 LP sentences 18 AS sentence	Transcribe: 18 HP (four-band SVS) 18 HP (six-band SVS) sentences	Transcribe: 12 AS sentences 12 LP sentences (from pretest)

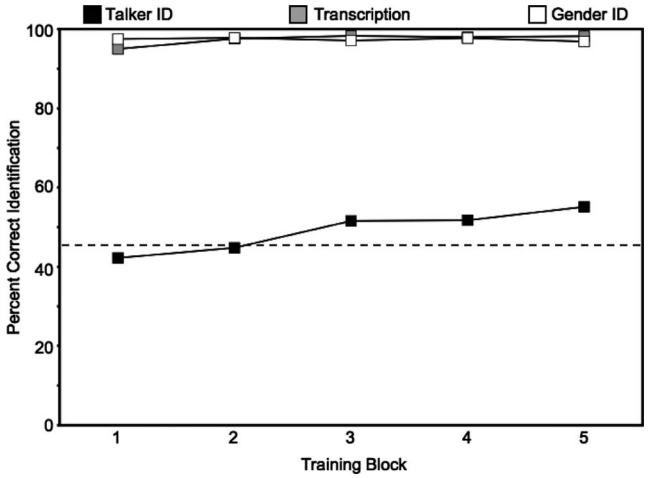

FIG. 1. Perceptual learning across the five training blocks. The dashed horizontal line indicates the level of performance that subjects must exceed in order to be considered significantly different from chance in the talker identification condition. Subjects trained to transcribe the sentences (Transcription) appear as gray squares, subjects trained to identify the gender of the talker (Gender ID) appear as white squares, and subjects trained to identify the talkers by their voices (Talker ID) appear as black squares.

stimuli. Generalization was said to have occurred if performance was significantly higher than the pretest scores and greater than or equal to posttest scores. Comparisons of the performance on the four- and six-channel stimuli provided an assessment of how well training transferred to more severely degraded stimuli.

III. RESULTS

A. Perceptual learning during training

Accuracy on the training tasks varied by training group (Fig. 1). Subjects in the gender ID and transcription training groups performed near ceiling, whereas subjects in the talker ID group performed just above chance.

Subjects in the transcription training group performed extremely well across all five training blocks, starting at 95% in block 1 and ending at 98% in block 5. A univariate analysis of variance (ANOVA) revealed a significant main effect of block $[F(4,190)=6.441,\ p<0.001]$, indicating that subjects showed an improvement across training blocks. *Post hoc* Bonferroni tests revealed that subject performance in block 1 was significantly lower than performance in all other blocks (all $p<0.009$), which did not differ from one another (all $p>0.88$). A trend toward a main effect for talker gender was observed $[F(1,190)=3.156,\ p=0.077]$, with female speech being transcribed more accurately than male speech.

Subjects' accuracy in the gender ID training condition was also extremely high across all five training blocks. Subjects' ability to identify the gender of the talkers was at ceiling (>95%) in all training blocks. The main effects for block $[F(4,190)=.228,\ p=0.922]$ and talker gender $[F(1,190)=1.324,\ p=0.251]$ were not observed, indicating that subject performance did not vary across blocks and was equal for male and female talkers.

The performance of the talker ID group was considerably more variable across subjects. Since intergender confusions (identifying male talkers as female, or female talkers as male) were rare (<2%), a more conservative level of chance was used (33.3% rather than 16.7%). According to the binomial probability distribution, performance must exceed 44.5% correct to be significantly greater than chance. Most subjects ($n=26$) were able to identify talkers at a level greater than chance beginning in block 2 and showed continued improvement as training progressed (block 1: 42.2%, block 2: 44.8%, block 3: 51.6%, block 4: 51.7%, and block 5: 55.1%). A subset of talkers ($n=5$) could never identify talkers at a level greater than chance and their data were analyzed separately. A univariate ANOVA revealed a significant main effect of block $[F(4,250)=9.428,\ p<0.001]$ with subject performance improving significantly between blocks 1 and 5 ($p<0.001$). A significant main effect of talker gender was also observed $[F(1,250)=39.509,\ p<0.001]$. Subjects identified female talkers (54%) more accurately than male talkers (44%).

B. Performance after training

1. Pretest, posttest, and generalization

An *omnibus* repeated measures analysis of variance was conducted on the data across the three experimental phases (pretest, posttest and generalization) using training condition (transcription, talker ID, and gender ID) as between subjects variables and sentence type (meaningful versus anomalous) and speaker gender (male versus female) as within subjects factors. A highly significant main effect of training was observed $[F(2,252)=10.918,\ p<0.001]$, indicating that subjects' performance was influenced by the type of training that they experienced. *Post hoc* Bonferroni tests revealed that subjects trained in the talker ID task performed as well as subjects trained in the transcription task ($p=1.00$) and both groups performed significantly better than subjects in the gender ID training task (both $p\leqslant 0.001$). The effect of sentence type was not significant $[F(1,252)=2.962,\ p=0.086]$. Performance did not differ between anomalous and meaningful sentences. A significant main effect of talker gender was observed $[F(1,252)=53.276,\ p<0.001]$. Subjects performed better on sentences produced by female talkers than on sentences produced by male talkers. None of the two-way and three-way interactions reached statistical significance (all $p>0.05$).

Using the findings from the *omnibus* ANOVA as motivation, individual univariate ANOVAs were then conducted on the data in each individual experimental phase to explore these effects in more detail (Fig. 2). For the pretest data, a significant main effect of training was observed $[F(2,252)=4.38,\ p=0.013]$, indicating differences across the three groups before training began. *Post hoc* Bonferroni tests revealed that subjects in the transcription group ($M=55.7\%$, SD=12.3) performed as well as subjects in the talker ID group ($M=51.9$, SD=14.7, $p=0.069$) and significantly better than subjects in the gender ID group ($M=50.7$, SD=13.2, $p=0.016$). However, subjects in the talker ID and gender ID groups did not differ from one another at pretest ($p=1.00$). A significant main effect of sentence type was also observed $[F(1,252)=45.880,\ p<0.001]$. On average, subjects performed better on the anomalous sentences ($M=57.4$, SD

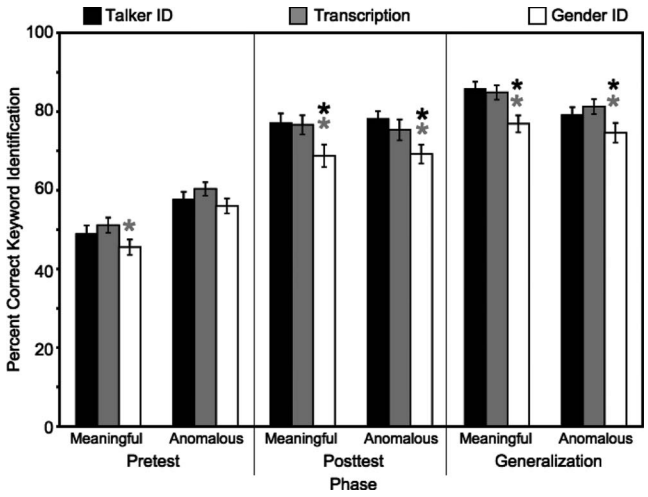

FIG. 2. Percent correct keyword identification scores for subjects trained on talker identification (talker ID), gender identification (gender ID), and sentence transcription (Transcription) on the pre-, post-, and generalization tests. Asterisks appearing over a bar indicate significant differences in performance between that group and another group (indicated by color).

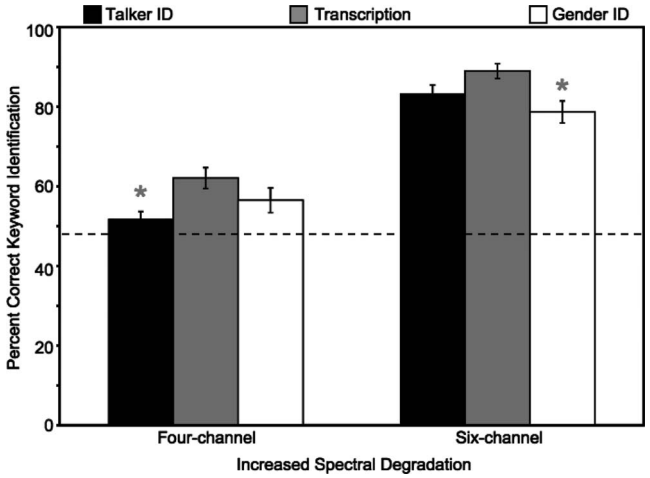

FIG. 3. Percent correct keyword identification scores for subjects trained on talker identification (talker ID), gender identification (gender ID), and sentence transcription (transcription) on the more severe spectral degradation condition. Colored asterisks appearing over a bar indicate significant differences in performance between that group and another group.

=12.0) than meaningful sentences ($M=48$, SD=13.6). Presumably, this effect is driven by the fact that all subjects received meaningful sentences first and that the better performance on the anomalous sentences (9%) is likely attributable to rapid adaptation to the processing conditions (Davis *et al.*, 2005). A significant main effect of talker gender was also observed [$F(1,252)=59.06$, $p<0.001$]. Subjects performed better on materials produced by female talkers ($M=58.2$, SD=12.7) than by male talkers ($M=47.2$, SD=12.3). None of the interactions were statistically significant, except for the two-way interaction between sentence type and talker gender [$F(1,252)=10.437$, $p<0.001$]. This effect may reflect the general performance differences on meaningful and anomalous sentences, since subjects always performed better on female talkers as compared to male talkers.

Given the main effect of training on the pretest data, comparisons of performance across groups on the posttest data must control for pretest scores (to ensure that the performance at posttest is not merely a factor of better performance at pretest). A univariate ANOVA was conducted on the posttest data specifying pretest scores as a covariate. A significant main effect was observed for pretest scores [$F(1,251)=28.441$, $p<0.001$], confirming that pretest scores differed across groups and indicating that the performance at pretest influenced performance at posttest. Despite the effect of the covariate, a significant main effect of training was still observed for the posttest scores [$F(2,251)=5.305$, $p=0.005$], indicating that training differentially affected performance at posttest (Fig. 2). *Post hoc* Bonferroni tests revealed that subjects in the transcription group ($M=76$, SD=16.9) performed as well as subjects in the talker ID group ($M=76.4$, SD=15.5, $p=1.00$), and that both groups performed significantly better than subjects in the gender ID group ($M=68.9$, SD=16.7, both $p<0.01$). The main effect of sentence type was not statistically significant [$F(1,252)=0.130$, $p=0.719$]. On average, subjects performed equally well on anomalous sentences ($M=74.5$, SD=15.3) and meaningful sentences ($M=73.6$, SD=17.3). A significant main effect of talker gender was observed [$F(1,252)=15.715$, $p<0.001$]. Subjects performed better on materials produced by female talkers ($M=78.2$, SD=15.6) as compared to male talkers ($M=69.9$, SD=16.1). None of the interactions were statistically significant, except for the two-way interaction between sentence training and talker gender [$F(2,252)=4.548$, $p=0.011$]. This effect may reflect the general performance differences provided by training, since across all three training groups, subjects always performed better on female talkers as compared to male talkers.

A univariate ANOVA on the generalization data also revealed a significant main effect of Training [$F(2,252)=8.53$, $p<0.001$], indicating that training differentially affected performance during generalization to novel materials (Fig. 2). *Post hoc* Bonferroni tests revealed that subjects in the talker ID group ($M=82.4$, SD=13.6) performed as well as subjects in the transcription group ($M=82.9$, SD=12, $p=1.00$), and both groups performed significantly better than subjects in the gender ID group ($M=75.6$, SD=14.7, both $p<0.001$). A significant main effect of sentence type was also observed [$F(1,252)=6.718$, $p=0.01$], indicating that subjects performed better on the meaningful sentences ($M=82.6$, SD=12.3) than anomalous sentences ($M=78.3$, SD=14.1). A significant main effect of talker gender was also observed [$F(1,252)=19.96$, $p<0.001$], indicating that subjects performed better on female talkers ($M=84$, SD=13.5) than male talkers ($M=76.9$, SD=13.4). None of the interactions were significant.

2. Transfer of training to increased spectral degradation

Subjects showed a graded response to stimuli that were more severely spectrally degraded (Fig. 3). Overall, subjects were more accurate at transcribing sentences in the six-channel processing condition (transcription: 83.1%; gender ID: 78.6%; talker ID: 88.9%) than sentences in the four-channel processing condition (transcription: 51.7%; gender

ID: 56.4%; talker ID: 61.9%). Comparison of the performance on the four-channel processed sentences across the training groups using a univariate ANOVA revealed a significant main effect of training [$F(2,126)=4.44$, $p=0.014$]. Subjects in the transcription training group performed significantly better than subjects in the talker ID group ($p=0.01$) but did not differ from talkers in the gender ID group ($p=0.399$). Subjects in the talker ID training group performed similarly to subjects in the gender ID group ($p=0.359$). The main effect of talker gender was not significant [$F(1,126)=.933$, $p=0.336$]. Comparison of the performance on the six-band stimuli across the training groups also revealed significant main effect of training [$F(2,126)=4.702$, $p=0.001$]. Subjects in the transcription group performed as well as subjects in the talker ID group ($p=0.465$), but significantly better than subjects in the gender ID group ($p=0.008$). Subjects in the gender ID group performed as well as subjects in the talker ID group ($p=0.213$). A significant main effect of talker gender was observed [$F(1,126)=8.273$, $p=0.005$], and subjects were significantly more accurate at transcribing the speech of female talkers than male talkers.

C. Talker ID training subgroups

An additional finding of the present study emerged when we first assessed the subject performance on the talker ID training task. As noted earlier, most ($n=26$) subjects could be trained to successfully identify talkers at a level greater than chance (44.3%). However, a small subset of subjects were unable to identify talkers at a level greater than chance. Unlike the "good" learners, these "poor" learners ($n=5$) were never able to identify talkers at a level greater than chance in any of the training blocks (1=30.8%, 2=35.4%, 3=36.3%, 4=34.7%, and 5=32.9%), as indicated by a univariate ANOVA [$F(4,40)=0.05$, $p=0.628$]. Furthermore, subjects who could not identify the talkers at a level exceeding chance performed significantly more poorly on the transcription tasks than the subjects who were able to learn the talker identification task. A series of one-way ANOVAs revealed that performance did not differ at pretest for either meaningful ($p=0.105$) or anomalous sentences ($p=0.310$). After training, however, a significant main effect of group was observed for all materials (all $p<0.003$), indicating that although subjects performed the same at pretest, their performance increased at a different rate depending on how well they performed in the training task. These findings are not likely to be caused by inattention or laziness since the transcription errors they made were phonologically related to the target words and response omissions were no more prevalent than in the good learning group. Rather it appears that the ability to detect and utilize acoustic information important for the indexical training task is related to the ability to extract acoustic information important for recognizing the linguistic content of utterances (see Cleary and Pisoni, 2002; Cleary *et al.*, 2005).

IV. DISCUSSION

The present study assessed whether training tasks that have different attentional requirements produce equivalent levels of perceptual learning, generalization, and transfer to new materials and tasks. Although all three types of training produced significant pre- to posttest gains in performance, talker ID and sentence transcription training appeared to provide the largest and most robust improvements (Fig. 2). Generalization to new stimulus materials was equivalent for the talker ID and transcription training groups, both of whom performed significantly better than the subjects trained on gender ID (Fig. 2). Generalization to materials that were more spectrally degraded showed a mixed pattern of results (Fig. 3). For stimuli that were more spectrally degraded (four and six channel), subjects trained on sentence transcription performed best, subjects trained on gender ID performed worst, and subjects trained on talker ID displayed an intermediate level of performance.

Two main conclusions can be drawn from these data. First, training on explicit indexical tasks can yield equivalent levels of perceptual learning and transfer compared to training using traditional transcription tasks if task demands are high enough to require sustained attention and deeper processing. Evidence for this conclusion comes from the across training group comparisons of posttest and generalization scores for subjects in the talker ID group who performed similarly to the subjects in the transcription training group and significantly better than the subjects in the gender ID training group (Fig. 2). Compared to gender ID training (in which subjects were at ceiling in the first training block), talker ID training is a more difficult task under CI simulations, requiring high levels of controlled attention and deeper processing. The gains observed from training on indexical tasks also suggest that when a listener is exposed to a speech signal that is meaningful in their native language they cannot help interpreting it in a linguistically significant manner. Although subjects' controlled attention in the talker and gender ID tasks was not directed toward the linguistic information in the signal, they still processed the linguistic content of the sentences automatically [similar to the effects seen in the well known Stroop effect (Stroop, 1935)]. The degree to which they did so appears to be mediated by the specific training task they were asked to carry out.

Second, the benefits of training may be determined by whether the subject can successfully access the acoustic information in the speech signal and the depth of perceptual processing required to succeed in the training task. Subjects in the talker ID group, who had to make fine acoustic-phonetic distinctions among voices and hence process the signal more deeply, performed significantly better than subjects in the gender ID group. Moreover, the poor performing subjects from the talker ID group who could not learn to identify the talkers at a level greater than chance performed significantly worse on sentence transcription than subjects who could. Taken together, these findings suggest that the access and attention to fine acoustic-phonetic details learned during talker ID training may enhance a listener's ability to extract linguistic information from the speech signal (see also, Nygaard *et al.*, 1994).

A. Transfer of indexical training to linguistic tasks: Interactions of transfer appropriate processing and levels of processing

The findings of the present study suggest that perceptual learning of spectrally degraded speech can be facilitated by processes used to carry out indexical tasks even though the specific tasks that subjects perform at training and testing are fundamentally different. The transfer appropriate processing (TAP) theory of learning and memory predicts that performance will be maximized when the task used during testing is the same as the task used during training (e.g., Morris *et al.*, 1977; Roediger *et al.*, 1989). Under the TAP framework, it would be expected that subjects in the transcription training group would receive the largest benefit from training, since the task they carried out during training (sentence transcription) was the same task that they were asked to carry out at posttest and generalization. This expectation was only partially supported. Although subjects in the transcription group performed best overall, their performance was equivalent to the subjects trained on talker ID (except for the four-channel generalization test), suggesting that a factor other than TAP influenced performance, particularly for subjects in the talker ID group.

The levels of processing (LoP) approach to learning and memory suggests that tasks that require deeper analysis and processing will yield better long term recall (Craik and Lockhart, 1972). Talker identification under a CI simulation is considerably more difficult than for natural speech. The acoustic information that specifies the voice of the talker in the unprocessed signal appears to be significantly degraded when processed through a CI speech processor, requiring more controlled attention and deeper processing. Gender identification is much easier, suggesting that the acoustic information needed to successfully identify the gender of a talker is relatively well preserved (e.g., Gonzales and Oliver, 2005). Therefore, the task demands placed on a listener are significantly higher in a talker ID task than those in a gender ID task (which requires only shallow processing). Thus, under the LoP framework, subjects in the talker ID training condition should be expected to perform better than the subjects in the gender ID group, since the latter requires considerably more detailed acoustic analysis and hence deeper processing. This expectation was supported.

The effects of TAP and LoP during training are particularly relevant to our understanding of perceptual learning in speech. The data from the present study suggest that explicit indexical training tasks can produce robust transfer to linguistic tasks despite the predictions under the TAP framework. If the training task is difficult enough to require sustained controlled attention and deep processing, transfer will be equivalent to that produced by conventional linguistic training tasks. The differences in performance between the talker ID and gender ID training conditions support this hypothesis. We chose to use a longer training period (2 days and over 240 sentences) in order to get a more accurate and stable estimation of perceptual learning due to training. Subjects in the gender ID training group performed near ceiling from the first training block, suggesting that their task was easier and required shallower processing. Subjects in the talker ID training group, however, performed more poorly, only improving above chance at the end of the second training block, and still showing evidence of improvement in the fifth and final training blocks. The task demands placed on these subjects required deeper processing, further indicating that differences in controlled attention across training conditions differentially affects perceptual learning.

These data also suggest that training tasks in which subjects have room for improvement should produce better (and more robust) perceptual learning since the subjects are constantly being challenged to improve their performance (Bjork, 1994). Subjects in the transcription and gender ID training groups performed at ceiling in the first block of training and did not have the opportunity to improve their performance. This ceiling effect may have been a result of the ease of the binary decision for the subjects in the gender ID task, or by the fact that each of the high predictability sentences was repeated six times in each block (once by each talker), creating a familiarity effect for subjects in the transcription training group. Subjects in the talker ID training group were given a much more difficult task and showed significant improvement across training blocks. Thus, the differences in performance across the training groups at posttest and generalization may be influenced not only by the demands of the training task but also by the potential room for improvement on the tasks. Greater gains in performance may have been observed for subjects in the transcription and gender ID training groups if the tasks afforded greater opportunity for improvement. Both of these tasks could be made more difficult by utilizing male and female talkers that have closer fundamental frequencies, making the gender identification task more difficult, and by using lower predictability sentences that are not repeated, making the transcription task more difficult. Overall, optimal training tasks should require more controlled attention and deeper processing but also allow substantial room for improvement.

One possible concern with the present research is the evaluation of the gains from training, and whether these are true training effects or simple exposure effects (since subjects in the gender ID and transcription were at ceiling during training). Although subjects in all training groups showed a significant pre-to posttest improvement, the amount of improvement that one would expect from merely being exposed to the materials in the absence of feedback is unknown particularly for indexical tasks. If these were simple exposure effects, however, we would expect posttest scores to be equal across all training groups (since all subjects were exposed to the same materials). This was not the case as subjects in the talker ID and transcription training groups improved their performance significantly more than subjects in the gender ID training group, indicating that these differences in performance cannot be attributed to simple exposure effects. Moreover, the gender ID task provided an internal control condition since discrimination of speaker gender is an easy task using vocoded speech, requiring shallower processing and less controlled attention. Since gains obtained from training were significantly higher for subjects in the transcription and talker ID groups than subjects in the gender ID group, we can infer differential enhancement of perceptual learning by

explicit indexical training tasks and do not need to consider a separate control group who was merely exposed to the materials. Additionally, previous research suggests that subjects improve by roughly 10% over time for sentence transcription tasks without any feedback (Davis *et al.*, 2005). Subjects in the present study exceeded this figure, improving on average 20%, indicating that pre-/posttest improvement was well above what would be expected from mere exposure alone.

B. Access to the acoustic information in the signal

An additional finding in this study was the correlation between the ability to learn to identify talkers by voice and performance in the sentence transcription tasks. Although the vast majority of subjects (84%) could learn to identify the talkers at a level greater than chance, those who could not performed significantly worse in the posttest, generalization, and transfer blocks. When considered together, the findings from the present study suggest that it is not the mere exposure to a talker or a synthesis condition that is responsible for the gains observed after training, but rather the ability to access and utilize the acoustic information required to recognize the talkers by voice. Understanding why some listeners perform poorly on talker identification despite training will require further study.

Previous research has shown that subjects, who can successfully learn to explicitly identify novel talkers by voice, display higher word identification accuracy scores in noise when compared to subjects, who could not learn to identify talkers by voice (Nygaard *et al.*, 1994). The findings of the present study replicate these earlier findings using spectrally degraded vocoded speech, suggesting that the ability to successfully encode and retain talker-specific acoustic information in memory affects perceptual learning of degraded speech. Other research has shown that pediatric CI users who could accurately discriminate talkers by voice had higher word identification scores as compared to children who could not (Cleary *et al.*, 2005). The findings of the present study replicate these findings in normal hearing subjects listening to CI simulations. When considered together, these data provide additional converging evidence for the interaction of lexical and indexical information in speech perception, and suggest that the two streams may indeed be encoded and processed together (Pisoni, 1997).

Although indexical information was traditionally thought to be encoded separately from linguistic information (see Abercrombie, 1967; Halle, 1985), the two streams of information interact at a fundamental perceptual level. Speech perception has been viewed as a talker independent process, where the listener must "normalize" the acoustic information across talkers in order to extract the context-free symbolic linguistic content from the signal (see Pisoni, 1997 for a review). While listeners do adjust internal linguistic categories to accommodate new talkers (Eisner and McQueen, 2005; Kraljic and Samuel, 2006), such indexical information does not appear to be lost or discarded following linguistic interpretation (Nygaard *et al.*, 1994, Nygaard and Pisoni, 1998). The present set of results suggest that the earliest stages of speech perception may be episodic and highly context-dependent in nature, with the listener encoding detailed indexical information along with the linguistic information and retaining both types of information well after the original sensory trace has decayed (Pisoni, 1997; Goldinger, 1998). These findings suggest that indexical and linguistic information are encoded in the same stream and interact bidirectionally to influence perception. The degree to which such indexical information is utilized, however, appears to depend on the task, listener, and specific stimulus materials.

C. Behavioral and clinical implications

The findings from the present study suggest the existence of multiple routes to the perceptual learning of speech. Although previous training studies utilize traditional methods of training that exclusively focus the listener's attention on the abstract symbolic linguistic content encoded in the speech signal (e.g., Fu *et al.*, 2005b), other routes to perceptual leaning can yield equivalent outcomes and benefits. The crucial factor seems to be the amount of controlled attention that is required of the subject and the depth of perceptual processing required to succeed in the training task. Indexical processing tasks that require significant amounts of controlled attention and deep processing (e.g., talker identification) can be just as effective as tasks that rely exclusively on explicit attention to the linguistic content of the message. This finding has important implications for training and rehabilitation paradigms for hearing impaired listeners who receive cochlear implants and hearing aids. The benefit obtained in the present study suggests that a variety of tasks and stimulus materials could be utilized effectively to maximize perceptual learning after cochlear implantation, thereby increasing outcome and benefit. Explicit training and instruction on how to distinguish and identify individual voices may provide the CI user with a more stable foundation for voice recognition that can generalize to new talkers in novel listening environments (such as voice tracking in noise). Additionally, including a wide variety of stimulus materials and challenging perceptual tasks may promote interest in training and reduce boredom and fatigue.

Although the overall goal of cochlear implantation has been to restore receptive auditory capacity for speech, there are many other nonlinguistic aspects to hearing on which a CI user could experience benefit. Sound localization, the detection and identification of ecologically significant environmental sounds, and the enjoyment of music are all aspects of normal hearing that have not been fully explored in CI users. Because all of these tasks require attention to nonlinguistic acoustic information, a greater variety in training tasks and materials may yield robust outcomes across multiple domains, many of which may also produce additional gains in speech perception and spoken language processing. If the goal of cochlear implantation is to provide the user with access to the acoustic world, perceptual learning and training paradigms for cochlear implant users should not be limited exclusively to conventional linguistic tasks that rely on word recognition and linguistic interpretation of the speech signal.

ACKNOWLEDGMENTS

This work was supported by NIH-NIDCD Training Grant No. T32-DC00012 and NIH-NIDCD Research Grant No. R01-DC00011. The authors would like to thank Althea Bauernschmidt and Larry Phillips for their assistance in data collection.

Abercrombie, D. (**1967**). *Elements of General Phonetics* (Aldine, Chicago).

Bond, Z. S., and Moore, T. J. (**1994**). "A note on the acoustic-phonetic characteristics of inadvertently clear speech," Speech Commun. **14**, pp. 325–337.

Bradlow, A. R., and Bent, T. (**2008**). "Perceptual adaptation to non-native speech," Cognition **107**, 707–729.

Bradlow, A. R., Torretta, G. M., and Pisoni, D. B. (**1996**). "Intelligibility of normal speech I: Global and fine-grained acoustic-phonetic talker characteristics," Speech Commun. **20**, 255–272.

Bjork, R. A. (**1994**). "Memory and metamemory considerations in the training of human beings," in *Metacognition: Knowing about Knowing*, edited by J. Metcalfe and A. Shimamura (MIT, Cambridge), pp. 185–205.

Burkholder, R. A. (**2005**). "Perceptual learning of speech processed through an acoustic simulation of a cochlear implant," Ph.D. thesis Indiana University.

Clarke, C. M., and Garrett, M. F. (**2004**). "Rapid adaptation to foreign-accented English," J. Acoust. Soc. Am. **116**, 3647–3658.

Cleary, M., and Pisoni, D. B. (**2002**). "Talker discrimination by prelingually deaf children with cochlear implants: Preliminary results," Ann. Otol. Rhinol. Laryngol. Suppl. **111**, 113–118.

Cleary, M., Pisoni, D. B., and Kirk, K. I. (**2005**). "Influence of voice similarity on talker discrimination in children with normal hearing and children with cochlear implants," J. Speech Lang. Hear. Res. **48**, 204–223.

Clopper, C. G., and Pisoni, D. B. (**2006**). "The Nationwide Speech Project: A new corpus of American English dialects," Speech Commun. **48**, 633–644.

Craik, F. I. M., and Lockhart, R. S. (**1972**). "Levels of processing: A framework for memory research," J. Verbal Learn. Verbal Behav. **11**, 671–684.

Cox, R. M., Alexander, G. C., and Gilmore, C. (**1987**). "Development of the connected speech test (CST)," Ear Hear. **8**, 119–126.

Davis, M. H., Johnsrude, I. S., Hervais-Adelman, A., Taylor, K., and McGettigan, C. (**2005**). "Lexical information drives perceptual learning of distorted speech: Evidence from the comprehension of noise-vocoded sentences," J. Exp. Psychol. Gen. **134**, 222–241.

Dorman, M., and Loizou, P. (**1998**). "The identification of consonants and vowels by cochlear implants patients using a 6-channel CIS processor and by normal hearing listeners using simulations of processors with two to nine channels," Ear Hear. **19**, 162–166.

Dorman, M. F., Loizou, P. C., and Rainey, D. (**1997**). "Simulating the effect of cochlear-implant electrode insertion depth on speech understanding," J. Acoust. Soc. Am. **102**, 2993–2996.

Dorman, M., Loizou, P., Fitzke, J., and Tu, Z. (**1998**). "The recognition of sentences in noise by normal hearing listeners using simulations of cochlear implant signal processors with 6-20 channels," J. Acoust. Soc. Am. **104**, 3583–3585.

Dupoux, E., and Green, K. P. (**1997**). "Perceptual adjustment to highly compressed speech: Effects of talker and rate changes," J. Exp. Psychol. Hum. Percept. Perform. **23**, 914–927.

Eisner, F., and McQueen, J. M. (**2005**). "The specificity of perceptual learning in speech processing," Percept. Psychophys. **67**, 224–238.

Fairbanks, G. (**1940**). *Voice and Articulation Drillbook* (Harper and Row, New York).

Fahle, M., and Poggio, T. (**2002**). *Perceptual Learning* (MIT Press, Cambridge).

Fu, Q-J., Chinchilla, S., and Galvin, J. J. (**2004**). "The role of spectral and temporal cues on voice gender discrimination by normal-hearing listeners and cochlear implant users," J. Assoc. Res. Otolaryngol. **5**, 253–260.

Fu, Q-J., Chinchilla, S., Nogaki, G., and Galvin, J. J. (**2005a**). "Voice gender identification by cochlear implant users: The role of spectral and temporal resolution," J. Acoust. Soc. Am. **118**, 1711–1718.

Fu, Q-J., Galvin, J. J., Wang, X., and Nogaki, G. (**2005b**). "Moderate auditory training can improve speech performance of adult cochlear implant patients," ARLO **6**, 106–111.

Goldinger, S. D. (**1998**). "Echoes of echoes? An episodic theory of lexical access," Psychol. Rev. **105**, 251–279.

Goldstone, R. L. (**1998**). "Perceptual learning," Annu. Rev. Psychol. **49**, 585–612.

Gonzales, J., and Oliver, J. C. (**2005**). "Gender and speaker identification as a function of the number of channels in spectrally reduced speech," J. Acoust. Soc. Am. **118**, 461–470.

Greenspan, S. L., Nusbaum, H. C., and Pisoni, D. B. (**1988**). "Perceptual learning of synthetic speech produced by rule," J. Exp. Psychol. Learn. Mem. Cogn. **14**, 421–433.

Halle, M. (**1985**). "Speculation about the representation of words in memory," in *Phonetic Linguistics*, edited by V. Fromkin (Academic, New York), pp. 101–114.

Hood, J. D., and Poole, J. P. (**1980**). "Influence of the speaker and other factors affecting speech intelligibility," Audiology **19**, 434–55.

Kalikow, D. N., Stevens, K. N., and Elliot, L. L. (**1977**). "Development of a test of speech intelligibility in noise using sentence materials with controlled word predictability," J. Acoust. Soc. Am. **61**, 1337–1351.

Kraljic, T., and Samuel, A. S. (**2006**). "Generalization in perceptual learning for speech," Psychon. Bull. Rev. **13**, 262–268.

Ladefoged, P., and Broadbent, D. E. (**1957**). "Information conveyed by vowels," J. Acoust. Soc. Am. **29**(1), 98–104.

Loebach, J. L., and Pisoni, D. B. (**2008**). "Perceptual learning of spectrally degraded speech and environmental sounds," J. Acoust. Soc. Am. **123**, 1126–1139.

Morris, C. D., Bransford, J. D., and Franks, J. J. (**1977**). "Levels of processing versus transfer appropriate processing," J. Verbal Learn. Verbal Behav. **16**, 519–533.

Nygaard, L. C., Sommers, M. S., and Pisoni, D. B. (**1994**). "Speech perception as a talker-contingent process," Psychol. Sci. **5**, 42–46.

Nygaard, L. C., and Pisoni, D. B. (**1998**). "Talker-specific learning in speech perception," Percept. Psychophys. **60**, 355–376.

Pisoni, D. B. (**1997**). "Some thoughts on 'normalization' in speech perception," in *Talker variability in speech processing*, edited by K. Johnson and J. W. Mullennix (Academic, San Diego), 9–32.

Roediger, H. L., Weldon, M. S., and Challis, B. H. (**1989**). "Explaining dissociations between implicit and explicit measures of retention: A processing account," in *Varieties of Memory and Consciousness: Essays in honor of Endel Tulving*, edited by H. L. Roediger and F. I. M. Craik (Hillsdale, Erlbaum), pp. 3–41.

Schwab, E. C., Nusbaum, H. C., and Pisoni, D. B. (**1985**). "Some effects of training on the perception of synthetic speech," Hum. Factors **27**, 395–408.

Shannon, R. V. (**2005**). "Speech and music have different requirements for spectral resolution," Int. Rev. Neurobiol. **70**, 121–134.

Shannon, R. V., Fu, Q.-J., and Galvin, J. (**2004**). "The number of spectral channels required for speech recognition depends on the difficulty of the listening situation," Acta Oto-Laryngol., Suppl. **552**, 1–5.

Shannon, R. V., Zeng, F.-G., Kamath, V., Wygonski, J., and Ekelid, M. (**1995**). "Speech recognition with primarily temporal cues," Science **270**, 303–304.

Stroop, J. R. (**1935**). "Studies of interference in serial verbal reactions," J. Exp. Psychol. **18**, 643–662.

Tice, R., and Carrell, T. (**1998**). LEVEL 16 V2.0.3, University of Nebraska, Lincoln, NE.

Vongphoe, M., and Zeng, F. G. (**2005**). "Speaker recognition with temporal cues in acoustic and electric hearing," J. Acoust. Soc. Am. **118**, 1055–1061.

Weil, S. A. (**2001**). "Foreign accented speech: Adaptation and generalization," Master's thesis, Ohio State University.

http://www.tigerspeech.com

Speech identification based on temporal fine structure cues

Stanley Sheft[a)]
Parmly Hearing Institute, Loyola University Chicago, 6525 North Sheridan Road, Chicago, Illinois 60626

Marine Ardoint and Christian Lorenzi
Laboratoire de Psychologie de la Perception (CNRS - Université Paris 5 Descartes), DEC, Ecole Normale Supérieure, 29 rue d'Ulm, 75005 Paris, France GDR CNRS 2967 GRAEC

(Received 1 June 2007; revised 9 April 2008; accepted 9 April 2008)

The contribution of temporal fine structure (TFS) cues to consonant identification was assessed in normal-hearing listeners with two speech-processing schemes designed to remove temporal envelope (*E*) cues. Stimuli were processed vowel-consonant-vowel speech tokens. Derived from the analytic signal, carrier signals were extracted from the output of a bank of analysis filters. The "PM" and "FM" processing schemes estimated a phase- and frequency-modulation function, respectively, of each carrier signal and applied them to a sinusoidal carrier at the analysis-filter center frequency. In the FM scheme, processed signals were further restricted to the analysis-filter bandwidth. A third scheme retaining only *E* cues from each band was used for comparison. Stimuli processed with the PM and FM schemes were found to be highly intelligible (50–80% correct identification) over a variety of experimental conditions designed to affect the putative reconstruction of *E* cues subsequent to peripheral auditory filtering. Analysis of confusions between consonants showed that the contribution of TFS cues was greater for place than manner of articulation, whereas the converse was observed for *E* cues. Taken together, these results indicate that TFS cues convey important phonetic information that is not solely a consequence of *E* reconstruction.
 [DOI: 10.1121/1.2918540]

PACS number(s): 43.71.Gv, 43.71.Es, 43.66.Mk [KWG] Pages: 562–575

I. INTRODUCTION

Following the pioneering work of Flanagan (Flanagan and Golden, 1966; Flanagan, 1980), subsequent studies of speech intelligibility have investigated the role of two temporal features of filtered speech: Fluctuations in the envelope (*E*, the relatively slow modulations in amplitude over time), and fluctuations in the temporal fine structure [TFS, the rapid oscillations with average rate close to the center frequency (CF) of the band, or in other words, the "carrier" signal]. To assess the contribution of each temporal feature to intelligibility, speech stimuli were split into an array of contiguous frequency bands (also called analysis bands) and processed to remove either *E* or TFS cues from each band, assuming that *E* and TFS are independent components of the narrowband signal. Across studies, high levels of speech intelligibility have been obtained in quiet from normal-hearing listeners on the basis of either *E* cues (e.g., Drullman, 1995; Shannon *et al.*, 1995; Smith *et al.*, 2002; Zeng *et al.*, 2004; Xu *et al.*, 2005) or TFS cues (Gilbert and Lorenzi, 2006; Lorenzi *et al.*, 2006; Gilbert *et al.*, 2007) alone.

The results obtained with "TFS speech" (i.e., speech processed to retain only TFS information) may appear surprising because it is generally considered that, at least for nontonal languages, *E* cues carry most of the information required for speech identification in quiet (e.g., Flanagan, 1980; Shannon *et al.*, 1995; Smith *et al.*, 2002), with TFS primarily conveying pitch cues which enhance segregation of the speech signal from background sounds (e.g., Qin and Oxenham, 2003, 2006; Nelson *et al.* 2003; Stickney *et al.*, 2005; Füllgrabe *et al.*, 2006). However, the descriptive analysis of the temporal information in speech by Rosen (1992) and the intelligibility of sine-wave speech tokens (e.g., Remez *et al.*, 1981, Remez and Rubin, 1990) both suggest that TFS cues play a role in linguistic contrasts. Further work is therefore needed to assess the extent to which TFS cues *alone* can convey useful linguistic information in addition to pitch.

In recent studies investigating the intelligibility of TFS speech, processing of the narrowband speech signals, that is, the outputs of the analysis filterbank, was based upon the Hilbert transform (e.g, Smith *et al.*, 2002; Xu and Pfingst, 2003; Gilbert and Lorenzi, 2006; Lorenzi *et al.*, 2006). In each subband, the Hilbert TFS was derived as $\cos[\phi(t)]$ where $\phi(t)$ corresponds to instantaneous phase, that is, the angle of the analytic signal. The Hilbert *E*, which was obtained by taking the magnitude of the analytic signal, was discarded and TFS-speech stimuli were obtained by summing all TFS subband signals. However, potential artifacts may have influenced results. Ghitza (2001) demonstrated that despite filtering or removal, *E* cues are reconstructed at the output of peripheral auditory filters and may therefore be used by listeners. Involvement of *E* reconstruction in speech identification has been empirically confirmed using either sentences (Zeng *et al.*, 2004) or vowel-consonant-vowel (VCV) stimuli (Gilbert and Lorenzi, 2006). In these studies, TFS speech signals were passed through a bank of gammachirp auditory filters (Irino and Patterson, 1997). Envelopes reconstructed from gammachirp-filter output were then

[a)]Author to whom correspondence should be addressed. Electronic mail: ssheft@luc.edu

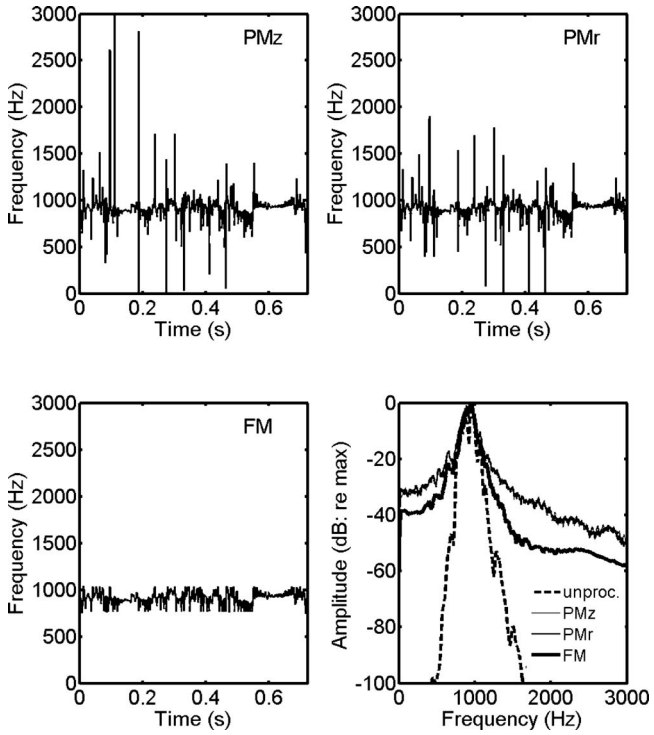

FIG. 1. For a narrowband /a s a/ speech signal, instantaneous-frequency functions with processing algorithm indicated in the upper right-hand corner of the panel, and long-term magnitude spectra (bottom-right panel). Analysis used a 0.4-octave-wide, third-order zero-phase Butterworth filter centered at 900 Hz. Magnitude spectra: Unprocessed speech (dashed line), PMz speech (continuous thin line), PMr speech (continuous line), and FM speech (continuous heavy line). Magnitude spectra were smoothed for clarity of presentation. In large part the two PM magnitude spectra overlap.

used to amplitude-modulate either noise bands or pure tones associated with the CF of the auditory filters. In agreement with Ghitza's (2001) predictions, the processed-speech stimuli were intelligible with 40–60% mean correct identification.

Several processes may contribute to this artifact originating from the use of the Hilbert transform. Ghitza (2001) pointed out that *E* reconstruction occurs because—contrary to previous assumption—the envelope and instantaneous-phase functions of band-limited signals are not independent processes (see also Papoulis, 1983). As a consequence, any manipulation of *E* will affect TFS, and *vice versa*. In addition, Gilbert and Lorenzi (2006) noted that *E* reconstruction is subsequent to processing which converts frequency modulation (FM) to amplitude modulation (AM). More precisely, the differential attenuation of auditory filtering converts the frequency excursions of TFS into dynamic variations in excitation level (that is, into *E* fluctuations). Finally, and this is a consequence of the first point, TFS subband signals extracted via the Hilbert transform typically have a greater bandwidth than the original subband signals (see Fig. 1). This results from the fact that the Hilbert *E* is not band limited. The Hilbert TFS therefore contains a wideband structure of "cancellation terms" that match and cancel the wideband content of the Hilbert *E* (Schimmel and Altas, 2005).

It follows from the above arguments that the fidelity of *E* reconstruction should be influenced by at least three factors. The first factor is the coherence between the extracted TFS and *E* signals. Because *E* and the instantaneous phase are related, any manipulation of the extracted narrowband TFS signals resulting in an improper match with the original *E* should affect the fidelity of *E* reconstruction (Schimmel and Altas, 2005). One way to achieve this kind of mismatch to reduce the fidelity of *E* reconstruction is to filter the extracted TFS signals using an all-pass filter with a random phase response. The second factor relates to effects of both analysis- and auditory-filter bandwidths. The fidelity of *E* reconstruction increases with analysis-filter bandwidth but decreases with auditory-filter bandwidth. However, the effects of changing the two bandwidths are not related by simple inversion. If the ratio of bandwidths is fixed, the fidelity of *E* reconstruction increases as auditory-filter bandwidth decreases. Gilbert and Lorenzi (2006) systematically investigated the influence of filter bandwidths on the intelligibility of TFS speech. Though results indicated that increasing the frequency resolution of the analysis filterbank did not completely abolish *E* reconstruction, the reconstructed *E* cues did not play a major role in consonant identification once the analysis bandwidth was narrower than four times the bandwidth of a normal auditory filter. The third factor is the bandwidth of the processed TFS signals. Restriction of frequency excursions to within the analysis-filter bandwidth should limit the extent of FM-to-AM conversion to degrade the fidelity of *E* reconstruction.

The goal of the present study was to extend the initial work of Zeng *et al.* (2004) and Gilbert and Lorenzi (2006). Conditions measured the ability of listeners to identify speech using stimulus configurations intended to vary the fidelity of *E* reconstruction. All speech-processing algorithms derived the analytic signals from the output of a bank of 0.4-octave-wide (i.e., ~2 ERB wide) analysis filters. Based on the complex envelope, one scheme estimated a phase-modulation (PM) function from the output of each analysis filter, while another derived a FM function. In both cases, the modulators were applied to a sinusoidal carrier at the analysis-filter CF. Though using a different processing sequence, the "PMz" implementation of the PM scheme was mathematically identical to the one previously used by Gilbert and Lorenzi (2006) and Lorenzi *et al.* (2006). A second PM implementation, "PMr," was obtained by simply randomizing the starting phase of the sinusoidal carriers in order to alter the match between *E* and TFS to degrade the fidelity of *E* reconstruction. Though similar, randomization of carrier starting phase is not equivalent to the procedure of Drennan *et al.* (2007) in which a random time-varying component is added to the PM function. Along with affecting the fidelity of *E* reconstruction, addition of a random component to the phase function influences the cross-spectral relationships among modulators, while carrier randomization in the PMz algorithm does not.

The FM algorithm was based on representation of the narrowband speech signals in terms of AM and FM functions (Loughlin and Tacer, 1996; Zeng *et al.*, 2004; Nie *et al.*, 2005; Stickney *et al.*, 2005). In this case, TFS cues corresponded explicitly to the complex pattern of FM extracted within each speech band. One advantage of this algorithm is

that it allows for restrictions on the range of FM variations in the TFS-speech signals. In the current implementation, deviations in instantaneous frequency were restricted to the analysis-filter bandwidth. A final scheme (*E*) designed to retain only *E* cues from each band was also used for comparison.

Spectral consequences of TFS extraction are illustrated in Fig. 1 for the speech VCV /a s a/. TFS signals were extracted from the output of an analysis filter centered at 900 Hz.[1] The instantaneous-frequency function (IFF)—the time rate of change of instantaneous phase—of PMz, PMr, and FM signals are shown in separate panels, with long-term spectra in the bottom right panel. For the PMz signal, the extent of IFF deviation is significantly broader than the analysis-filter passband (776–1024 Hz), and the bandwidth of the long-term magnitude spectrum is broader than that of the unprocessed VCV token. The spikes of the IFF relate to carrier phase reversals in envelope troughs of the original signal, indicating large influence of stimulus gaps on the extent of *E* reconstruction. Compared to PMz, PMr, and more notably FM signals exhibit smaller excursions in instantaneous frequency. This reduction in extent of IFF excursion with the FM scheme results in narrowing of the long-term spectral flanks when compared to the two PM schemes in the bottom-right panel. The spikes of the IFF can elicit an impulse response from auditory filters, with decay of this response coded as envelope. The contribution of reconstructed *E* cues to TFS-speech intelligibility should therefore be reduced with the PMr scheme, and even more so with the FM algorithm, when compared to the effect of PMz processing in which the IFF spikes are most prominent.

For each processing scheme (PMz, PMr, FM, and *E*), the intelligibility of VCV stimuli was evaluated in quiet at a comfortable listening level in seven young, normal-hearing listeners who received a moderate amount of training. Additional experiments investigated further the contribution of putatively reconstructed *E* cues to TFS-speech identification by (i) removing low-frequency analysis bands, (ii) increasing the frequency resolution of the analysis filterbank, and (iii) decreasing stimulus presentation level. Since these stimulus manipulations affect the second factor discussed above (namely, effects of analysis- and auditory-filter bandwidths), the fidelity of *E* reconstruction varied across conditions. In each experiment, identification data are considered in terms of quantitative estimates of the fidelity of *E* reconstruction at the output of a bank of gammatone auditory filters.

II. EXPERIMENTS

A. Method

1. Speech material

One set of 48 VCV stimuli was recorded. Speech stimuli consisted of three exemplars of 16-/aCa/ utterances (C = /p, t, k, b, d, g, f, s, ʃ, m, n, r, l, v, z, ʒ/) read by a French female speaker in quiet (mean VCV duration = 648 ms; standard deviation = 46 ms). The fundamental frequency of the female voice was estimated as 216 Hz using the YIN algorithm (de Cheveigné and Kawahara, 2002). Each signal was digitized via a 16 bit analog-to-digital converter at a 44.1 kHz sampling rate.

2. Speech processing

The original speech signals were processed with two different TFS algorithms referred to as PM and FM. A third scheme (*E*) retained only envelope rather than fine-structure modulation. Across algorithms, each VCV signal was initially bandpass filtered using third-order zero-phase Butterworth filters. The filterbank consisted of 16-0.4-octave-wide contiguous frequency or analysis bands spanning the range of 80–8020 Hz [see Gilbert and Lorenzi (2006) for additional details concerning analysis-filter characteristics].

PM conditions. To estimate the phase modulation of each analysis band, the corresponding analytic signal was shifted to baseband through use of the complex envelope. Specifically, the PM function was estimated as the angle of the product of the analytic signal and a complex exponential such that

$$\Phi_k(t) = \text{angle}\{x_{+,k}(t)\exp[-j\omega_k(t) + \theta_k]\} \quad (1)$$

with $x_{+,k}(t)$ the analytic signal of the kth analysis band, and ω_k and θ_k the angular frequency and phase, respectively, of the sinusoidal carrier used in TFS construction. As shown in Eq. (2), the subband TFS signal was generated by modulating the carrier with the derived PM function.

$$TFS_k(t) = \cos[\omega_k(t) + \Phi_k(t) + \theta_k]. \quad (2)$$

Used previously by Sheft and Yost (2001), this approach to PM estimation is similar to the approach of Schimmel and Altas (2005) for determination of the subband envelope.

In all conditions, the carrier frequency was equal to analysis-band CF. In the first implementation of the PM algorithm (PMz), θ_k was set to zero so that processing effect matched the one of Gilbert and Lorenzi (2006) and Lorenzi *et al.* (2006). In the second implementation (PMr), θ_k was selected randomly between 0 and 2π in order to degrade the relationship between the original *E* and TFS within each band. To compensate for the reduction in amplitude caused by *E* removal, TFS_k was multiplied by the root-mean-square (rms) power of the bandpass-filtered VCV. The "power-weighted" TFS signals were finally summed over all analysis bands and presented as such to the listeners.

A consequence of this weighting was that long-term spectral cues were preserved in the processed speech stimuli. The contribution of residual spectral cues to VCV identification was investigated in a pilot experiment using a 16-band analysis filterbank. For each intact VCV token, rms power was initially computed in each frequency band, and used to weight the power of a sinusoid at the band CF; both *E* and TFS cues were therefore removed. Stimuli were presented for identification to naive and experienced normal-hearing listeners. Identification performance of all listeners was at chance level, indicating that long-term spectral cues did not contribute to intelligibility in the experimental conditions of the present study.

FM condition. FM estimation for each analysis band was based on the time derivative of the unwrapped instantaneous-phase function $\phi(t)$, shifted to baseband as the deviation from subband CF. In this case,

$$FM_k(t) = [\phi_k'(t)/(2\pi)] - \mathrm{CF} \quad (3)$$

with CF given in Hz. Deviations in instantaneous frequency were restricted to not exceed the analysis-filter bandwidth (defined by filter 3-dB down points). This restriction was intended to alter *E* reconstruction at the output of auditory filters. The (restricted) *FM* function was then integrated to obtain a time-dependent phase function, $\Phi_k(t)$. As in the PM schemes, the subband TFS signal was generated according to Eq. (2) by modulating the carrier with the function $\Phi_k(t)$. This algorithm for estimating FM functions is similar to the scheme used by Zeng and colleagues (e.g., Zeng *et al.*, 2005; Nie *et al.*, 2005; Stickney *et al.*, 2005).

Simulations based on correlation estimates (see below) indicated that *E* reconstruction at the output of gammatone auditory filters is not significantly affected by carrier starting phase (θ_k). Similar to the PMr scheme, θ_k was therefore chosen randomly between 0 and 2π. TFS_k was multiplied by the rms power of the bandpass filtered VCV, with the processed stimulus the sum over all analysis bands of the weighted subband signals.

E condition. In each analysis band, temporal envelopes were extracted as the magnitude of the analytic signal and lowpass filtered at 64 Hz using a third-order zero-phase Butterworth filter. These envelopes were used to amplitude-modulate sinusoidal carriers at frequencies corresponding to the CFs of the analysis filters with carrier starting phase randomized.

3. Quantification of E reconstruction

In each experimental condition, the TFS speech signals were passed through a bank of 32 gammatone auditory filters, each 1 ERB wide (Patterson *et al.*, 1987) with CFs uniformly spaced along an ERB scale ranging from 123 to 7743 Hz. Level-dependent implementations of filtering used the formula proposed by Glasberg and Moore (1990). In each band, the temporal envelopes were extracted using the Hilbert transform and lowpass filtered at 64 Hz with a first-order zero-phase Butterworth filter. In this case, first- rather than third-order filtering was used to better approximate the temporal modulation transfer function obtained with wideband-noise carriers (Viemeister, 1979).

For each VCV utterance, mean correlation estimates were computed between the envelopes of the original VCV stimulus and the TFS signals, both derived from gammatone-filterbank output. The correlation estimates were averaged, in terms of Fisher's *z* values, across the 48 VCV utterances. A high correlation estimate indicates a close resemblance between the original *E* and the one reconstructed at the output of auditory filters. Three types of correlation estimates were considered: (i) the correlation coefficient, as used by Gilbert and Lorenzi (2006), (ii) a depth-dependent correlation estimate, and (iii) a level-dependent correlation estimate.

Insensitive to both the carrier level in each subband and the modulation depth of reconstructed *E* cues, the correlation coefficient may overestimate *E* reconstruction. To introduce these sensitivities into measures of envelope correlation, correlation coefficients were weighted to derive separate depth- and level-dependent estimates. In both cases, weighting functions were based on envelope cross-spectral power across gammatone-filterbank channels. If ac coupled, envelope cross-spectral power varies in the same linear manner for overall level and depth, independent of cross correlation. For depth-dependent estimates, channel outputs were normalized to a constant overall level for each stimulus. Following normalization, the cross-spectral power of the ac-coupled envelopes of the original and processed speech tokens was determined for each channel. The correlation coefficients determined for each channel were then scaled by the relative cross-spectral power associated with that channel. With the exception of manner of normalization, a similar approach was used to derive a level-dependent measure. In this case, channel outputs were normalized to result in a constant *ratio* of envelope ac-rms to dc-level while retaining original differences in overall level among channel outputs.

4. Procedure

All stimuli were generated using a 16-bit digital-to-analog converter at a 44.1-kHz sampling rate, and delivered monaurally to the right ear of Sennheiser HD 212 Pro headphones. The rms values of the stimuli were equalized for an average level of 80 dB(A). Listeners were tested individually in a double-walled soundproof booth. In a typical experimental session, a complete set of the 48 VCV utterances corresponding to a given experimental condition was presented at random. Each listener was instructed to identify the presented consonant. The 16 possible choices were presented on the computer monitor, and the listener entered their response with the computer mouse. Feedback was not provided. Percent-correct identification was calculated and a confusion matrix was built from the responses to the 48 VCV utterances. Reception of the phonetic features of voicing, manner of articulation (occlusive versus constrictive), place of articulation, and nasality was determined by means of information-transmission analysis (Miller and Nicely, 1955) on the individual confusion matrices (see Table I for the assignment of consonant features in French).

In the first experiment, all listeners participated in ten sessions for each of the following conditions: (1) unprocessed speech, (2) PMz TFS speech, (3) PMr TFS speech, and (4) FM TFS speech. Forty-eight-trial blocks for each of the four conditions were interleaved with the order of presentation randomized across listeners. All listeners participated in four sessions in the *E*-speech condition upon completion of the 40 TFS-speech sessions.

5. Listeners

Data were collected from seven normal-hearing listeners. Their ages ranged from 21 to 32 years (mean age: 24 years; standard deviation: four years); all were native French speakers. The same listeners participated in experiments 1 through 4, except for one listener would did not run in experiment 4. In accordance with the Helsinki declaration (2004), all listeners were fully informed about the goal of the present study and provided written consent before their participation.

TABLE I. Phonetic features of the 16 French consonants used in this study (Martin 1996).

Consonant	Voicing	Manner	Place	Nasality
/p/	unvoiced	occlusive	front	non nasal
/t/	unvoiced	occlusive	middle	non nasal
/k/	unvoiced	occlusive	back	non nasal
/b/	voiced	occlusive	front	non nasal
/d/	voiced	occlusive	middle	non nasal
/g/	voiced	occlusive	back	non nasal
/f/	unvoiced	constrictive	front	non nasal
/s/	unvoiced	constrictive	middle	non nasal
/ʃ/	unvoiced	constrictive	back	non nasal
/v/	voiced	constrictive	front	non nasal
/z/	voiced	constrictive	middle	non nasal
/ʒ/	voiced	constrictive	back	non nasal
/l/	voiced	constrictive	middle	non nasal
/r/	voiced	constrictive	back	non nasal
/m/	voiced	occlusive	front	nasal
/n/	voiced	occlusive	middle	nasal

B. Results

1. Experiment 1: Basic comparison between processing schemes

The fidelity of *E* reconstruction was first estimated for the conditions of experiment 1 [16-band analysis filterbank, 80 dB(A) level]. This experimental condition is labeled 16B in subsequent references. Results obtained with the three correlation algorithms described in Sec. II A are presented in separate panels of Fig. 2. As a function of gammatone-filter CF, the dependent variable is the correlation between envelopes of the original and TFS-processed stimuli, with processing scheme the parameter. The number in parentheses below each panel title is the mean correlation across gammatone-filter channels estimating *E* fidelity in the *E* condition. Numbers between parentheses in the figure legends correspond to the mean correlation estimate in the respective TFS condition. Overall, the three estimates of *E* reconstruction in the TFS conditions are relatively low ($r<0.4$) in most auditory channels, except for the low-frequency channels encompassing the fundamental frequency of the talker's voice. When compared to results from the *E* condition shown in each panel title, TFS correlation estimates drop by a factor that ranges from roughly 4.5 to 13.6. Note that much lower estimates of *E* reconstruction are observed with correlation algorithms dependent on either carrier level or envelope depth. To the extent that subband audibility and modulation depth are important, contingent correlations suggest limited utility of reconstructed *E* cues.

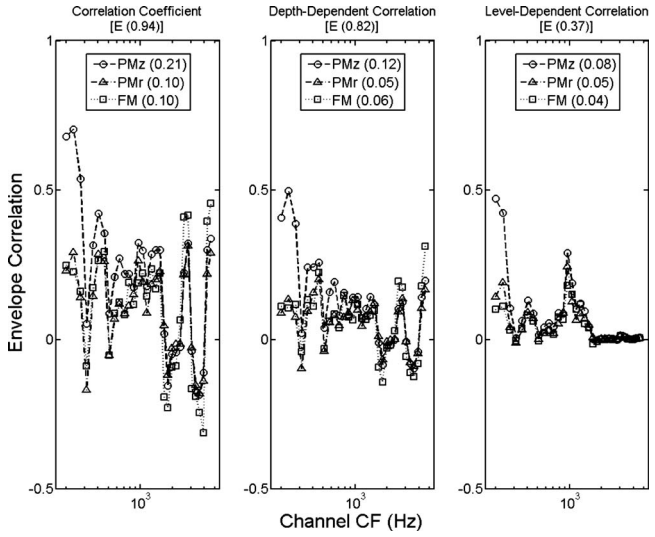

FIG. 2. Assessment of envelope reconstruction in condition 16B. Mean correlation estimates between the original speech envelopes and the envelopes of the stimuli in the PMz (circles), PMr (triangles), and FM (squares) conditions are shown a function of gammatone-filter CF. Left panel: correlation coefficient; middle panel: depth-dependent correlation estimate; right panel: level-dependent correlation estimate. The number in parentheses below each panel title is the mean correlation across gammatone-filter channels estimating *E* fidelity in the *E* condition. In each figure legend, numbers between parentheses correspond to the mean correlation estimate across filter channels in the respective TFS condition.

Across auditory channels, the three correlation estimates are generally similar for the three processing schemes, except for the lowest channels where correlation is substantially smaller, and similar, for the PMr and FM schemes compared to PMz. Overall, correlation data indicate that (i) poor reconstruction of *E* cues occurs in most auditory channels except for the lowest ones, and (ii) randomizing the starting phase of the sinusoidal carriers (as in the PMr scheme) and restricting excursions in instantaneous frequency to the passband of analysis filters (as in the FM scheme) affect mostly, and to the same extent, *E* reconstruction in the lowest auditory channels. Finally, since analysis filters were zero phase, correlation results are not appreciably altered with change in approach from use of the correlation coefficient to the maximum value of the cross-correlation function, that is, with consideration of values other than those obtained at an analysis lag of zero.

The top left panel of Fig. 3 shows mean identification scores averaged across listeners as a function of session number in the 16B conditions. The parameter is speech-processing scheme. The remaining four panels of Fig. 3 show mean percent of information received for each phonetic feature with feature indicated at the top of the panel. Mean

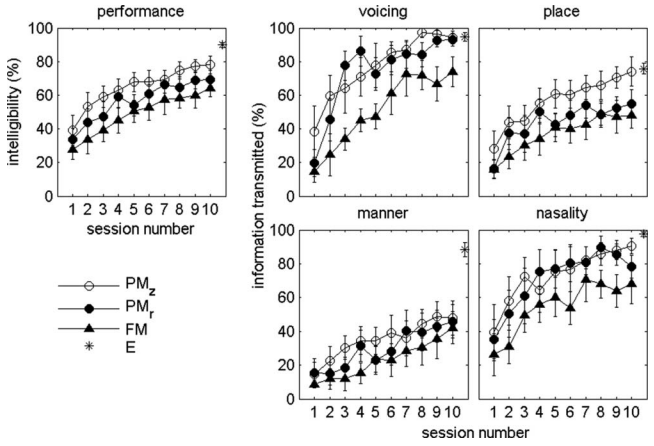

FIG. 3. Mean identification performance (left panel) and percent of information received for each phonetic feature (middle and right panels) as a function of session number for the 16-band PMz (open circles), PMr (filled circles), and FM (filled triangles) TFS-speech conditions. Mean performance averaged across four repeated session in the 16-band E-speech condition is indicated with stars on the right side of each panel. Error bars represent one standard error of the mean. A score of 6.25% corresponds to chance identification performance.

identification scores for unprocessed speech (not shown) were 100% correct for each session. All listeners showed little effect of training on the identification of speech stimuli in the 16-band *E*-speech condition. For the *E* condition, identification scores and percent of information received for each phonetic feature were therefore averaged across the four repeated sessions, with results indicated on the right side of each figure panel. With 16 possible consonants across the 48 VCV stimuli, 6.25% correct represents chance performance in measures of overall intelligibility.

Figure 3 shows that identification scores improved regularly with training for each TFS-speech condition. Error bars reveal important between-listener differences during training sessions, consistent with previous studies (e.g., Lorenzi *et al.*, 2006). However, high levels of consonant identification were globally achieved at the end of the ten repeated sessions. For individual listeners, mean scores computed across the two best sessions varied between 50 and 90% correct. Across listeners, performance was generally best in the PMz condition with 80% correct identification based on the two best sessions, and poorest in the FM condition in which the mean identification score was 65% correct. An intermediate level of performance (70% correct) was achieved in the PMr condition. This ordering of results with performance better in the PMz than PMr and FM conditions is roughly consistent with the ordering of mean correlation values in the analyses shown in Fig. 2. In the PMz and PMr conditions, mean listener scores correspond to nearly stable performance, but a trend observable in Fig. 3 suggests that intelligibility in the FM condition may have continued to improve with additional training.

Data from the PMz condition approximate the 87% correct reported by Lorenzi *et al.* (2006) from similar conditions. It is noteworthy that similar training effects were observed in the current work with the alternative TFS-processing schemes of PMr and FM. The current results also showed that with much less training (four repeated sessions only), the highest mean identification score was obtained for *E* speech (90%), consistent with results from previous studies comparing the intelligibility of *E* and TFS speech processed through a 16-band analysis filterbank (Lorenzi *et al.*, 2006; Gilbert *et al.*, 2007).

Two repeated-measures analyses of variance (ANOVA) with factor processing condition confirmed these observations. Percent-correct identification scores averaged across the two best sessions were transformed into rationalized arcsine units prior to statistical analysis. The first analysis compared the *E* condition to the average of the TFS ones, and revealed a significant effect of processing scheme [$F_{(1,6)}=13.28$, $p=0.01$]. The second analysis was more detailed and involved all four processing schemes (*E*, PMz, PMr, and FM) without averaging across TFS results. As in the first analysis, the main effect of processing scheme was significant [$F_{(3,18)}=10.79$, $p<0.001$]. *Post-hoc* analyses (Tukey HSD) indicated that identification scores for *E* speech were significantly greater than those measured for PMr and FM ($p<0.005$), but did not differ from those measured with PMz speech ($p=0.1$). Identification scores for PMz speech were significantly greater than those obtained with FM speech ($p<0.05$), but did not differ from the PMr-speech results ($p=0.3$). Identification scores for PMr and FM speech also did not differ ($p=0.67$).

The results of information-transmission analyses revealed that for each TFS-speech condition, the amount of information received for voicing, manner, place, and nasality improved with training. Different patterns of information reception were observed across speech-processing conditions at the end of training sessions. For the PMz, PMr, and FM conditions, greatest information was received for voicing and nasality, less information for place of articulation, and least for manner. For most phonetic features, greatest information was generally received in the PMz condition, and least with the FM scheme. As with the TFS-speech conditions, greatest information was also received for voicing and nasality in the *E* condition. However, less information was received for manner, and least information for place in the *E* condition, opposite the ordering obtained with TFS speech for these two features. Thus, TFS-and *E*-coding schemes differed in the ranking of phonetic information transmitted regarding the occlusive-constrictive and front-middle-back distinctions.

These observations are consistent with the results of two repeated-measures ANOVAs conducted on percent-information-received calculated across the two best sessions. The first analyses included percent-information-received for the *E* and for the mean of the three TFS conditions. Analysis showed significant main effects of factors processing scheme [$F_{(1,6)}=14.27$, $p<0.01$] and phonetic feature [$F_{(3,18)}=19.90$, $p<0.0001$], along with a significant interaction [$F_{(3,18)}=3.93$, $p<0.05$]. To obtain a more detailed view of the interaction between processing scheme and phonetic feature, the second analysis was performed without averaging across TFS conditions. As in the first analysis, there was a significant main effect of processing scheme [$F_{(3,18)}=10.39$, $p<0.001$], phonetic feature [$F_{(3,18)}=23.4$, $p<0.00001$], and a significant interaction [$F_{(9,54)}=3.10$, $p<0.005$]. *Post-hoc*

analyses (Tukey HSD) indicated that for each TFS-processing scheme (PMz, PMr, and FM), reception of voicing and nasality did not differ significantly ($p \sim 1$). The same was true for reception of place and manner ($p=0.5-0.9$). Reception of voicing and nasality was significantly greater than reception of place ($p<0.01$) and manner ($p<0.01$), except for the FM condition where they did not differ from reception of place ($p \sim 0.1$). For each phonetic feature, reception of information did not significantly vary with TFS-processing scheme ($p=0.8-1.0$), except for voicing and nasality where significantly greater information was received in the PMz then FM condition ($p<0.05$). Additional Tukey-HSD tests indicated that for the *E* condition, reception of voicing, nasality, and manner did not differ ($p=0.4-1.0$); reception of voicing and nasality were significantly greater than reception of place ($p<0.05$), but reception of place and manner did not differ ($p=0.59$).

The high levels of intelligibility (>65% correct) obtained with the TFS-processing schemes contrasts with the large drop in mean correlation-based estimates of *E* fidelity shown in Fig. 2, especially in terms of depth- and level-dependent correlation estimates. Indicating poor mean fidelity of *E* reconstruction, this comparison suggests at best a limited basis for TFS-speech recognition. Manipulations—via the use of different TFS-processing schemes—of the extent of *E* reconstruction at the output of auditory filters had clear but relatively modest effects on the intelligibility of TFS speech: (i) for the PM algorithms, randomizing the starting phase of the sinusoidal carriers did not significantly affect speech intelligibility, and (ii) restricting the excursion of instantaneous frequency within the analysis-filter passband affected the reception of voicing and nasality with the FM scheme, but left reception of place and manner unchanged. Moreover, high levels of information reception (>70%) were observed for voicing and nasality despite the reduction of reconstructed *E* cues across all forms of TFS speech. Finally, analysis of information transmission suggested that different phonetic information regarding manner was received with TFS versus *E* speech. This difference between TFS and *E* speech is in line with the fact that a number of specific *E* features such as transients, silent gaps, overall duration, and rise time can signal manner of articulation, especially the distinction between plosives and fricatives (e.g., Rosen, 1992).

Taken together, results indicate that identification of TFS speech does not rely solely on reconstructed *E* cues. Results also emphasize the notion that TFS and *E* speech do not convey the same acoustic/phonetic cues.

2. Experiment 2: Effect of removing low-frequency analysis bands

The correlation data of Fig. 2 show that for the present stimuli, potential *E* reconstruction is greatest in auditory channels centered below about 340 Hz, especially with the PMz scheme. Two factors contribute to this result. First, the low-frequency region encompasses the region of the fundamental frequency (216 Hz) of the female voice used in the current experiments. The second aspect relates to the fact that the fidelity of *E* reconstruction is inversely related to cochlear-filter bandwidth. Greater reconstruction of *E* cues is therefore expected in the low-frequency region where auditory filters are narrower.

Estimates of weighting or importance functions that indicate contribution to speech perception by CF of analysis band are not uniform. While the function of French and Steinberg (1947) has an initial highpass slope which reduces contribution from the low frequencies (and would thereby minimize anticipated effect of the stimulus manipulation of experiment 2), the 1980 Speech Transmission Index (STI) of Steeneken and Houtgast [see Steeneken and Houtgast (1999)] is relatively flat [for discussion of these differences, see Humes *et al.* (1986)]. Subsequent work by Steeneken and Houtgast (2002) did show a highpass segment when evaluating errors within a phoneme class. Effect of spectral content on within-class error is anticipated in the work of Miller and Nicely (1955). In that work, the contrast between results obtained with either lowpass or highpass filtering of stimuli showed greater predictability of error in the lowpass conditions. Miller and Nicely attributed the result to greater redundancy of speech information in the lowpass conditions. A similar emphasis on low-frequency content was reported by Turner *et al.* (1998) who measured weighting functions in broadband conditions. Turner and his co-workers interpreted their result as indicating a facilitative contribution to speech perception of redundant low-frequency content. In that demonstrations of cross-spectral utilization of redundancy are most often based on modulation [e.g., comodulation masking release, and see Sheft (2008)], and that modulation processing is the basis of the algorithms of the present work, a basis for the stimulus manipulation of experiment 2 is seen in past studies.

The goal of the second experiment was to assess the contribution of low-frequency analysis bands to TFS-speech intelligibility. In the second experiment (termed HF, for "High Frequency"), the VCV stimuli of experiment 1 were processed using the PMz, PMr, and FM schemes, but with the lowest five analysis filters centered below 340 Hz removed from the synthesis process. In the "unprocessed-speech" condition, the original VCV stimuli were simply passed through the analysis filterbank with the lowest five filters omitted in signal synthesis. Listeners were tested over four repeated sessions for each HF TFS-speech condition, and just once for the unprocessed HF speech. The three HF TFS-speech conditions were interleaved with order of presentation randomized across listeners. The apparatus, procedure, and presentation level were identical to those used in experiment 1.

In Fig. 4, bars corresponding to the HF condition show the mean identification scores and percent of information received for each phonetic feature calculated across listeners and sessions. Consistent with previous work (e.g., French and Steinberg, 1947), the mean identification score for unprocessed HF speech was 100% correct. For comparison, mean data from the two best sessions of experiment 1 (labeled 16B) are shown on the left of each panel. For each speech-processing condition, similar results were obtained in the 16B and HF conditions. Removing information in the low audio-frequency range (<340 Hz) encompassing the re-

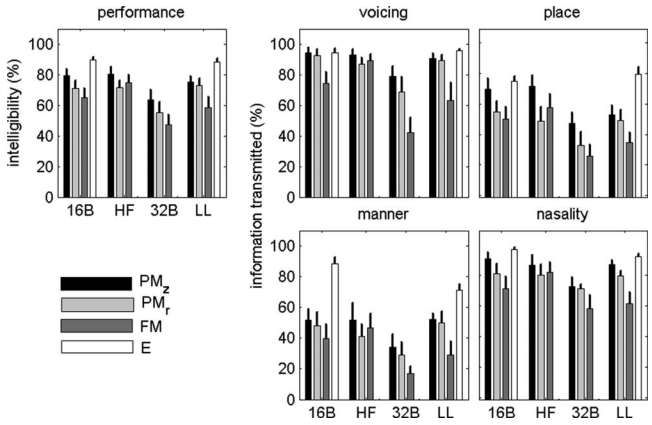

FIG. 4. Mean identification performance (left panel) and percent of information received for each phonetic feature (middle and right panels) calculated in each speech-processing condition: PMz (black bars), PMr (light gray bars), FM (dark gray bars), *E* (open bars). In each panel, data are from the 16B [16-band analysis filterbank, 80 dB(A)], HF [16-band analysis filterbank with the five lowest bands removed, 80 dB(A)], 32B [32-band analysis filterbank, 80 dB(A)], and LL [16-band analysis filterbank, 45 dB(A)] conditions. Error bars represent one standard error of the mean.

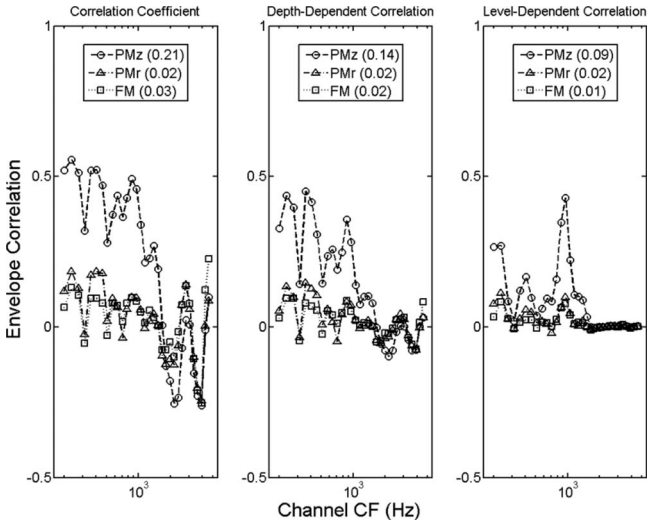

FIG. 5. For experiment 3, assessment of envelope reconstruction in condition 32B. Stimuli were processed with a 32-band analysis filterbank. Except for the omission of the mean correlation estimates for the *E* condition which was not run in experiment 3, otherwise as in Fig. 2.

gion of the stimulus fundamental frequency did not significantly affect identification scores or phonetic-feature reception, as shown by two repeated-measures ANOVAs and *post-hoc* tests.[2] These results demonstrate that *E* cues potentially reconstructed in the low audio-frequency range where auditory filters are narrowest do not contribute to the intelligibility of TFS speech.

3. Experiment 3: Effect of increasing analysis-filterbank frequency resolution

Results shown in Fig. 2 indicate that the reconstruction of *E* cues at the output of most auditory filters is not abolished with an analysis-filter bandwidth of roughly 2 ERB. Additional simulations were run to assess the effect of increasing analysis-filter resolution on *E* reconstruction. Analysis-filterbank parameters increased the number of channels from 16 to 32 while reducing filter bandwidth in half to approximately 1 ERB. Results of correlation analysis are presented in Fig. 5. Compared to the 16-channel results (see Fig. 2), correlation estimates from the 32-band condition (termed 32B) decrease markedly in most auditory channels with the PMr and FM algorithms. For the PMz scheme, correlation estimates are either unaffected or elevated in auditory channels tuned between roughly 300 and 1000 Hz. The increase in correlation observed for the PMz scheme is not dependent on the specific values of the gammatone-filter CFs.

The goal of the third experiment was to assess the effect of adjusting the bandwidths of the analysis filterbank to approximate normal auditory frequency resolution. In the 32B condition, the VCV stimuli were processed with the PMz, PMr, and FM schemes, using a 32-band analysis filterbank. In the unprocessed-speech condition, the original VCV stimuli were unaltered. Since previous studies indicate that consonant recognition asymptotes with 16-band resolution (e.g., Shannon *et al.*, 1995; Xu *et al.*, 2005), the *E* condition was not included. Listeners were tested over four repeated sessions for each 32B TFS-speech condition, and just once with unprocessed speech. The four 32B conditions were interleaved with order of presentation randomized across listeners. Apparatus, procedure, and presentation level were identical to those described in experiment 1.

In Fig. 4, bars corresponding to the 32B condition show the mean identification scores and percent of information received for each phonetic feature calculated in each TFS-speech condition. The mean identification score for unprocessed speech was 100% correct. Compared to the 16B results, consonant identification dropped by roughly 20 percentage points in every 32B condition. The greatest change in reception of phonetic information was for voicing and place in the PMr and FM conditions. It is, however, important to note that identification scores and reception of nasality remained greater than 50% in all conditions. These observations were confirmed by two repeated-measures ANOVAs and *post-hoc* analysis.[2]

Results indicate that increasing analysis-filterbank resolution to approach normal auditory resolution degrades the intelligibility of TFS speech with *all* TFS processing schemes. Although predicted on theoretical grounds, this finding is only partially consistent with the correlation data reported in Fig. 5. *E* reconstruction at the output of auditory filters is notably degraded by the increase in analysis-filter resolution for PMr and FM speech, and left unchanged (and sometimes elevated) with PMz speech. Moreover, despite correlation estimates close to zero with either the PMr or FM scheme, speech identification scores were greater than 50%. Thus, the discrepancy between correlation analysis and psychophysical data provide additional evidence that TFS-speech intelligibility is not reliant on reconstructed *E* cues. The degradation in TFS-speech intelligibility in the 32B condition remains to be explained. One possibility is that increasing frequency resolution to 32 bands not only affects the fidelity of *E* reconstruction, but also disrupts the trans-

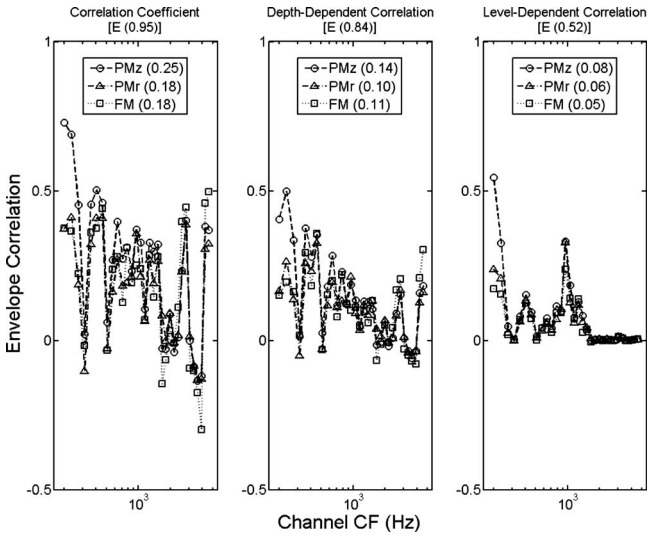

FIG. 6. For experiment 4, assessment of envelope reconstruction in condition LL. Stimulus level was 45 dB SPL, otherwise as in Fig. 2.

mission of TFS cues *per se*. This hypothesis is explored in Sec. III.

4. Experiment 4: Effect of decreasing stimulus level

Experiments 1–3 were run with stimuli presented at 80 dB(A). A number of physiological (e.g., Rhode, 1971; Robles *et al.*, 1986) and psychophysical studies (e.g., Glasberg and Moore, 2000; Rosen and Stock, 1992; Hicks and Bacon, 1999; Bernstein and Oxenham, 2006) indicate that frequency selectivity improves at low levels, at least for frequencies of 1 kHz and above. As a consequence, reducing stimulus presentation level to about 40–45 dB sound pressure level (SPL) should enhance the fidelity of *E* reconstruction for TFS speech. This predicted effect of auditory-filter resolution is opposite the one associated with analysis-filter resolution, explored in experiment 3.

Predictions concerning the effect of auditory-filter bandwidth were obtained by comparing *E* reconstruction at the output of gammatone filters for 80 and 45 dB SPL presentation levels. Results obtained at 45 dB SPL are shown in Fig. 6. For this analysis, gammatone-filter bandwidth was narrowed by a factor of 1.5 to simulate the effect of level reduction on auditory frequency resolution (Glasberg and Moore, 2000). Overall, the correlation data indicate that *E* reconstruction increases with reduction in level. The predicted changes in *E* reconstruction are rather modest. However, these changes are consistent across auditory channels and TFS-processing schemes.

The goal of the fourth experiment was to assess the effect of decreasing stimulus level on TFS-speech intelligibility. In this final experimental condition (labeled LL, for "Low Level"), the same VCV stimuli were processed using the PMz, PMr, FM, and *E* schemes described above, using the 16-band analysis filterbank. In the unprocessed-speech condition, the original VCV stimuli were unaltered. Listeners were tested over four repeated sessions for each of the four LL TFS-speech conditions and with *E* speech; data were collected from only one session with unprocessed LL speech. The TFS- and *E*-speech conditions were interleaved with order of presentation randomized across listeners. The apparatus, procedure, and presentation level were identical to those described in experiment 1, except that stimuli were presented at an average level across listeners of 45 dB SPL. This level was initially determined individually as the minimum presentation level yielding both 100% identification with unprocessed speech and an *E*-speech identification score similar to the one obtained at 80 dB(A). This lower level varied across the six listeners between 40 and 49 dB(A).

In Fig. 4, bars corresponding to the LL condition show the mean identification scores and percent of information received for each phonetic feature in each speech-processing condition (PMz, PMr, FM, and *E*). As indicated above, the mean identification score across listeners obtained for unprocessed LL speech was 100% correct. Identification scores were not significantly affected by reduction in presentation level in any of the processed-speech conditions.[3] In principle, decreasing stimulus level could affect performance for reasons unrelated to the fidelity of *E* reconstruction. However, the absence of a significant level effect on mean performance with *E* speech argues against involvement of such factors counteracting potential level effects on *E* reconstruction in the TFS conditions. In contrast to mean performance, information received for all phonetic features was significantly affected by level. Compared to results from experiments 1–3, the maximum decrease in information received due to the reduction in level was observed for place reception in the PMz-speech condition, and manner reception in the *E*-speech condition.

Results show that when expressed in terms of identification performance, TFS and *E* speech are relatively robust to change in level (and therefore audibility). The data also indicate that moderate modifications in auditory-filter bandwidth due to change in level, and that subsequent changes in *E* reconstruction, especially in the high-frequency region where level effects on frequency resolution are greater, do not affect TFS-speech intelligibility. This result indicates that changes in audibility and frequency resolution are an unlikely basis of the deficits in TFS intelligibility reported by Lorenzi *et al.* (2006) for listeners with mild-to-moderate cochlear hearing loss.

III. DISCUSSION

The goal of the present research was to evaluate the contribution of subband TFS cues to consonant identification in experimental conditions intended to reduce the reconstruction of *E* cues, an artifact resulting from the use of the Hilbert transform to extract TFS. Overall, results indicated that all factors manipulated in order to alter the fidelity of *E* reconstruction had little to no effect on TFS-speech intelligibility. Decreasing the bandwidth of analysis filters to approach normal auditory resolution and restricting the bandwidth of the processed TFS signal to the analysis-filter bandwidth in the FM scheme had greater effects on TFS-speech intelligibility than randomizing the starting phase of the subband TFS signals in the PMr scheme. Nevertheless, moderate to high levels of consonant identification and

TABLE II. The mean envelope correlation between outputs of adjacent gammatone-filterbank channels. Each column is for a different processing scheme, and each row for a separate experimental condition with 16B, 32B, and LL referring to conditions from experiments 1, 3, and 4, respectively.

	E	PMz	PMr	FM
16B	0.99	0.67	0.68	0.60
32B	[a]	0.72	0.70	0.67
LL	0.99	0.38	0.41	0.28

[a]The *E* processing scheme was not used in experiment 3.

phonetic-information reception were achieved despite such stimulus manipulations. In addition, two manipulations intended to assess the contribution of low- and high-frequency regions to *E* reconstruction (removal of frequency information in the F0 region and change in presentation level, respectively) left TFS-speech intelligibility relatively unchanged. Finally, in certain experimental conditions (e.g., condition 32B), predictions based on *E* reconstruction were not compatible with PMz-speech identification data. Taken together, results suggest that the intelligibility of TFS consonants is not dependent on reconstruction of envelope cues by auditory filtering.

Signal analysis has so far only considered local or within-channel characteristics to estimate the fidelity of *E* reconstruction in the TFS-speech conditions. Crouzet and Ainsworth (2001) measured the between-channel envelope correlations of natural speech, finding high inter-channel correlations, especially between adjacent channels. Crouzet and Ainsworth argued that these correlations in natural speech aid consonant recognition. Importance of cross-channel correlation was recognized by Steeneken and Houtgast (1999) who incorporated a redundancy correction into their STI algorithm. To further explore the distinction between *E* and reconstructed *E*, adjacent-channel envelope correlations were calculated for the stimuli of experiments 1,3, and 4 with results shown in Table II. Each table entry is the mean envelope correlation between outputs of adjacent gammatone-filterbank channels. As in the other correlation calculations, correlation estimates were averaged in terms of Fischer's *z* values across the 48 VCV utterances. Comparison of results obtained in the *E* conditions to those from the three TFS-speech conditions (PMz, PMr, and FM) indicates large drops in adjacent-channel envelope correlations if based on *E* reconstruction, most notably in the low-level conditions of experiment 4. Thus, not only is there a loss of local or within-channel fidelity with *E* reconstruction (i.e., the results of Figs. 2 and 6), there is also a loss of a more global or cross-channel fidelity implicated in speech perception.

Signal analysis also so far has been based on a single processing structure utilizing a gammatone filterbank. To evaluate the effect of model parameters, all simulations were rerun using three additional model structures. In the first, the approach of Oxenham and Moore (1997) was added to the gammatone model to incorporate the effect of basilar membrane compression. The remaining two additional model structures used gammachirp filters (Irino and Patterson, 2006), with one the static and the other the dynamic realization. Across all conditions, effects of model structure on measured correlations were relatively small, with consistently the largest effect of model type obtained in the PMz conditions. PMz results from all model structures are shown in Table III. Compared to the initial gammatone results, the largest effect of model modification on the fidelity of *E* reconstruction was obtained with the dynamic gammachirp filterbank. With fidelity of *E* reconstruction dependent on filter passband characteristics (see Sec. I) and the dynamic model temporally modifying these characteristics, some effect on *E* reconstruction is anticipated. However, the largest effects, those from the PMz conditions, are still relatively small and do not alter the interpretation of insufficient basis by *E* reconstruction to fully account for listener performance.

On first pass, the result of relatively small effect of model structure may seem surprising, especially in light of other work indicating larger effects [e.g., Stone and Moore (2007)]. However, the contrast of result is due to analysis structure. For example, Stone and Moore evaluated the effect of compression by comparing the original to the processed stimuli. In the present work, the central question is the effect of stimulus signal processing (i.e., the PMz, PMr, and FM algorithms) as estimated at some level of the auditory system. To answer this question, comparisons involve stimuli that have undergone processing through the same auditory-model structure. In other words, the analysis is not directly

TABLE III. For the PMz processing scheme, mean correlation estimates across simulated auditory filterbank channels assessing fidelity of *E* reconstruction. Each column is for a different model structure (see text for additional details). Each row is for a separate combination of experimental condition (16B, 32B, and LL referring to conditions from experiments 1, 3, and 4, respectively) and correlation metric. The values from the first column are also shown in the figure legends of Fig. 2.

	Gammatone	Compressive Gammatone	Static Gammachirp	Dynamic Gammachirp
16B Correlation Coefficient	0.21	0.23	0.24	0.34
16B Depth-Dependent Correlation	0.12	0.12	0.13	0.16
16B Level-Dependent Correlation	0.08	0.08	0.10	0.11
32B Correlation Coefficient	0.21	0.22	0.23	0.32
32B Depth-Dependent Correlation	0.14	0.14	0.14	0.15
32B Level-Dependent Correlation	0.09	0.09	0.10	0.11
LL Correlation Coefficient	0.25	0.26	0.24	0.27
LL Depth-Dependent Correlation	0.14	0.14	0.13	0.14
LL Level-Dependent Correlation	0.08	0.08	0.10	0.11

evaluating the effects of various model structures, but rather determining if use of various accepted model structures leads to differences in effect of speech-processing scheme.

The decrease in TFS-speech intelligibility with increase in number of analysis-filterbank channels from 16 to 32 is not accounted for by degradation in reconstructed *E* cues. Specifically, correlation analyses from experiment 3 predicted an effect of TFS-processing scheme not obtained in the subject data. Also, performance levels in the PMr and FM conditions were higher than would be anticipated with a correlation of reconstructed *E* of close to zero.

Alternative to involvement of *E* reconstruction, increasing frequency resolution may disrupt the transmission of TFS cues. Figure 1 illustrates that IFF spikes are one characteristic of the fine structure of filtered speech signals; increasing analysis-band frequency resolution progressively distorts this aspect of TFS speech. More generally, any attempt to alter the fidelity of *E* reconstruction should, in turn, affect the fidelity of TFS transmission because *E* and TFS are related. This hypothesis was explored by assessing the fidelity of TFS transmission. An approach similar to the one used to assess *E* reconstruction was applied to quantify the fidelity of TFS transmission. Unprocessed speech signals and TFS speech generated using the PMz, PMr, and FM schemes were passed separately through the bank of 32 gammatone auditory filters described above. Using the FM-processing scheme, TFS signals were extracted from the output of each gammatone filter. FM functions were restricted in order to keep deviations in instantaneous frequency within a 1 ERB passband. Flanagan and Golden (1966) observed similar effects on intelligibility when lowpass filtering the *E* and FM functions of vocoded speech. Consequently, FM functions were lowpass filtered at 64 Hz, using the same filtering applied in the estimation of *E* reconstruction. For each VCV utterance, mean correlation coefficients were computed between the FM functions of the unprocessed VCV stimuli and the corresponding TFS signals. Two types of correlation estimates were considered: (i) the correlation coefficient, and (ii) a level-dependent correlation estimate. A high correlation estimate indicates a close resemblance between the original TFS and that of the processed stimuli at the output of auditory filters.

Results are shown in Figs. 7 and 8 for stimuli generated with 16- and 32-band analysis filterbanks, respectively. Overall, the fidelity of TFS transmission (as estimated by both correlation indexes) is notably degraded across most auditory channels when the frequency resolution of the analysis filterbank is increased from 16 to 32 bands. This reveals that *E* reconstruction is not the only factor affected by change in the analysis filterbank. Additional simulations were therefore run to assess the fidelity of TFS transmission in the other experimental conditions. To relate listener performance to signal analysis, mean identification scores are plotted in Fig. 9 as a function of the fidelity of *E* reconstruction (top panels) and TFS transmission (bottom panels) for each experimental condition (16B, HF, 32B, LL) and TFS-speech processing scheme (PMz, PMr, FM). The variance in identification scores accounted for by each correlation estimate (R^2) is much greater for TFS fidelity (e.g., 69% of variance with the

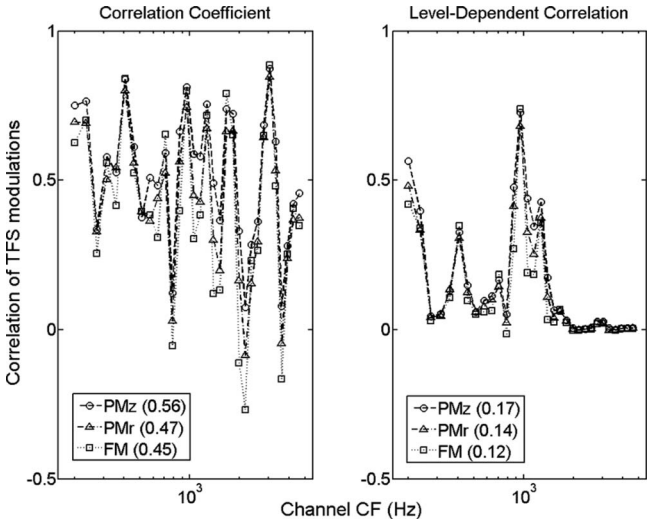

FIG. 7. Assessment of fidelity of TFS transmission in condition 16B. Mean correlation estimates computed between the TFS of the original and processed speech stimuli in the PMz (open circles), PMr (open triangles), and FM (open squares) conditions are shown a function of gammatone-filter CF. Left panel: correlation coefficient; right panel: level-dependent correlation estimate. In each figure legend, numbers between parentheses correspond to the mean correlation estimate computed across gammatone-filter channels.

level-dependent correlation estimate) than for *E* reconstruction (e.g., 35% of variance with the level-dependent estimate). To evaluate the significance of the five regressions of Fig. 9, separate ANOVAs were performed on the data of each panel. Level of significance was reduced from 0.05 to 0.01 to correct error rate for the use of five analyses based on the same listener data. Results confirmed that regressions were only significant for fidelity of TFS transmission (the bottom panels of Fig. 9) and not for the fidelity of *E* reconstruction (the top panels). For TFS results based on the correlation coefficient, analysis had $F_{(1,10)}=11.43$, $p=0.007$, and for the level-dependent results, $F_{(1,10)}=22.15$, $p=0.001$. Simulations thus confirm that altering the fidelity of *E* reconstruction also affects the fidelity of TFS transmission. More importantly,

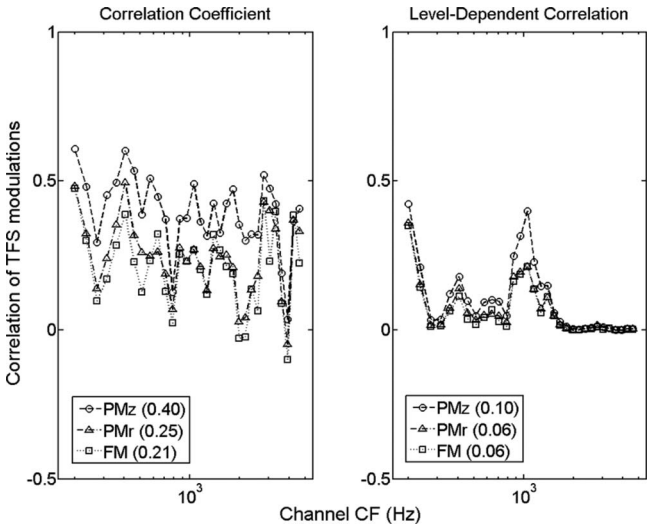

FIG. 8. Assessment of fidelity of TFS transmission in condition 32B. Stimuli were processed with a 32-band analysis filterbank, otherwise as in Fig. 7.

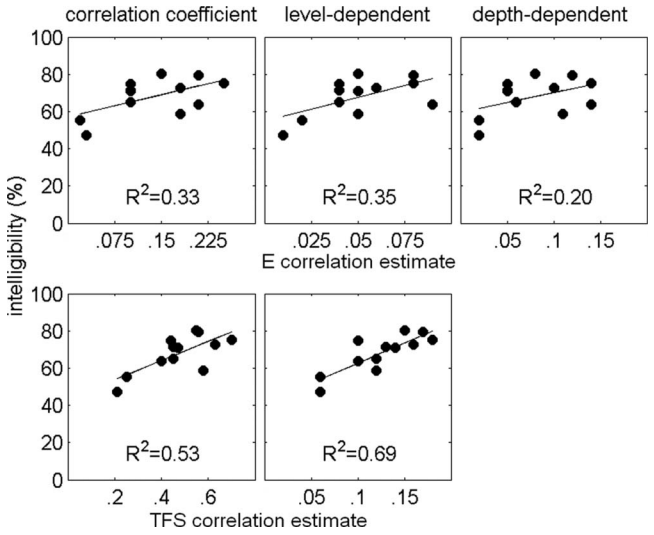

FIG. 9. Mean identification scores across listeners as a function of fidelity of *E* reconstruction (top panels) and TFS transmission (bottom panels). Each panel corresponds to a given correlation estimate. In each panel, individual symbols correspond to a given experimental condition (16B, HF, 32B, LL) and TFS-speech processing scheme (PMz, PMr, FM). Variance of identification scores accounted for by each correlation estimate (R^2) is shown in each panel.

they support the interpretation that variation in the fidelity of TFS transmissions was a stronger determinant of listener performance in the present study than was the extent of *E* reconstruction.

Despite significance of regression, low absolute values of correlation in the TFS conditions, especially in the level-dependent case, call for further comment. In general, significance of regression indicates capturing of trend despite approximation of metric. By definition, correlation averages across stimulus duration to diminish contribution of local distinctive features. As noted in the Introduction, spikes of the IFF, a local distinctive feature, are a significant contributor to *E* reconstruction. IFF spikes may also represent a significant feature in terms of fine structure, with perceptual validity established in the report of Jeffress (1968). For speech stimuli, spiking of the IFF is not simply an artifact, but rather an intrinsic stimulus aspect coding envelope troughs, onsets, offsets, and rapid phase transitions due to articulation. As such, they may convey relevant information for speech perception. Current work is evaluating the contributions of specific features of TFS to speech perception with the intention that results may allow for refinement of analysis metrics.

In a seminal study describing the temporal information present in speech, Rosen (1992) suggested that *E* cues signaled mainly segmental cues to manner and voicing, whereas TFS contributed primarily to segmental cues to place, and to a smaller extent voicing and nasality. The results of the present work are consistent with the outcome of Rosen's analysis, except that the contribution of TFS cues was greater for voicing than place. Nasality was shown to be extremely well transmitted by both *E* and TFS cues, presumably because all nasals are voiced in French. The association between manner and voicing features permits signaling of manner information by voicing patterns (cf. Rosen, 1992). The current findings also establish that TFS and E cues do not signal segmental cues in identical ways, especially in the case of manner and place. Overall, the differences in feature-transmission scores between TFS and *E* speech demonstrate that two kinds of information can be extracted from the analytic signal. Thought *E* reconstruction at the output of cochlear channels cannot be fully eliminated from the processing of TFS signals, results from the present work support the interpretation that *E* and TFS cues can make separate and distinct contributions to speech perception.

IV. CONCLUSIONS

Taken together, the results indicate that:

(1) Moderate to high levels of consonant identification can be obtained on the basis of speech fine-structure cues extracted using two different speech-processing techniques with either 16 or 32 analysis-frequency bands. Moreover, compared to temporal envelope cues, fine-structure conveys different phonetic information regarding manner and place of articulation. These data support the results of two recent studies conducted by Lorenzi *et al.* (2006) and Gilbert *et al.* (2007) suggesting that temporal fine-structure cues carry specific information useful for speech identification.
(2) Consistent with the results of Gilbert and Lorenzi (2006), envelope cues reconstructed at the output of auditory filters do not contribute substantially to consonant identification when 1- or 2-ERB-wide analysis filters are used. A signal-processing technique which extracts the FM-speech patterns within each analysis band and restricts deviations in instantaneous frequency within the analysis-filter bandwidth minimizes the contribution of such reconstructed envelope cues. However, correlation analysis indicates that such a scheme also degrades TFS speech cues.
(3) The identification of consonants on the basis of speech fine-structure cues is robust to variation in stimulus level and auditory frequency resolution. This suggests that the large deficits in TFS-speech intelligibility previously reported for listeners with mild-to-moderate cochlear hearing loss are unlikely due to changes in audibility and frequency selectivity.

Allowing for measurement of speech perception based on temporal fine-structure cues in normal-hearing and hearing-impaired listeners, results from the present procedures may help in the design of prosthetic devices. In addition, the correlation analysis suggests a role for quantitative measures of the fidelity of TFS transmission in device assessment.

ACKNOWLEDGMENTS

This research was supported by NIDCD Grant No. DC005423 to S. S., a MENRT/Paris Descartes grant to M. A., and a research fellowship from the Parmly Hearing Institute of Loyola University Chicago to C.L. This research was also supported by the GDR CNRS 2967 GRAEC. The authors thank C. Micheyl, A. Oxenham, and N. Viemeister for valuable discussions on the results of this study.

[1]The analysis filter was a third-order zero-phase Butterworth filter. The filter CF (900 Hz) was chosen to encompass formant transitions of the unprocessed vowel signal. The low and high 3-dB-cutoff frequencies of the analysis filter were 766 and 1024 Hz, respectively. In the current example, the starting phase of the PMr sinusoidal carrier was 90°, contrasting with the 0° of the PMz scheme.

[2]Two repeated-measures ANOVAs were conducted on the data collected across the seven listeners of experiments 1, 2, and 3. The first ANOVA was conducted on identification scores transformed into rationalized arcsine units prior to statistical analysis with factors experimental condition (three levels: 16B, HF, and 32B) and processing scheme (three levels: PMz, PMr, and FM). The second ANOVA was conducted on arcsine-transformed percent-information-received with factors experimental condition (three levels), processing scheme (three levels), and phonetic feature (four levels: voicing, nasality, manner, and place). The first ANOVA showed significant main effects of experimental condition [$F_{(2,12)}=20.41$, $p<0.0005$] and processing scheme [$F_{(2,12)}=21.18$, $p<0.0005$], without significant interaction between factors [$F_{(4,24)}=2.68$, $p=0.06$]. *Post-hoc* analyses (Tukey HSD) indicated that identification scores differed significantly between the 16B and 32B conditions only ($p<0.005$). The second ANOVA showed significant main effects of experimental condition [$F_{(2,12)}=18.77$, $p<0.0005$], processing scheme [$F_{(2,12)}=46.70$, $p<0.0001$], and phonetic feature [$F_{(3,18)}=30.07$, $p<0.0001$]; all interactions between factors were significant at the 0.05 level except for interaction between factors experimental condition and phonetic feature, and the triple interaction between factors experimental condition, scheme, and phonetic feature. Interaction between factors experimental condition and scheme restricted to the 16B and 32B conditions was also significant [$F_{(4,24)}=5.46$, $p<0.005$].

[3]Two repeated-measures ANOVAs were conducted on the data collected across the six common listeners of experiments 1 and 4. The first ANOVA was conducted on identification scores with factors experimental condition (two levels: 16B and LL) and processing scheme (four levels: PMz, PMr, FM, and E). The second ANOVA was conducted on percent-information-received with factors experimental condition (two levels), processing scheme (four levels), and phonetic feature (four 1evels). The first ANOVA showed that the main effect of experimental condition (i.e., stimulus level) on identification scores was not significant [$F_{(1,5)}=1.21$; $p=0.32$]. The main effect of processing scheme was significant [$F_{(3,15)}=13.41$, $p<0.001$], but the interaction between factors experimental condition and scheme was not [$F_{(3,15)}=1.25$, $p=0.33$]. The second ANOVA showed significant main effects of experimental condition [$F_{(1,5)}=9.14$, $p<0.05$], phonetic feature [$F_{(3,15)}=40.87$, $p<0.0001$], and scheme [$F_{(3,15)}=18.79$, $p<0.0001$]. The interactions between factors experimental condition and processing scheme [$F_{(3,15)}=0.23$, $p=0.87$] and between factors experimental condition and phonetic feature [$F_{(3,15)}=1.06$, $p=0.39$] were not significant. As in the l6B condition alone, the interaction between factors processing scheme and phonetic feature was significant [$F_{(9,45)}=3.02$, $p<0.01$]. This pattern of results was the same across experimental conditions because the interaction between factors experimental condition, processing scheme, and phonetic feature was not significant [$F_{(9,45)}=1.57$, $p=0.15$].

Bernstein, J. G. W., and Oxenham, A. J. (**2006**). "The relationship between frequency selectivity and pitch discrimination: Effects of stimulus level," J. Acoust. Soc. Am. **120**, 3916–3928.

Crouzet, O., and Ainsworth, W. A. (**2001**). "On the various influences of envelope information on the perception of speech in adverse conditions: An analysis of between-channel envelope correlation," in *Workshop on Consistent and Reliable Cues for Sound Analysis* (Aalborg, Denmark).

de Cheveigné, A., and Kawahara, H. (**2002**). "YIN, a fundamental frequency estimator for speech and music," J. Acoust. Soc. Am. **111**, 1917–1930.

Drennan, W. R., Won, J. H., Dasika, V. K., and Rubenstein, J. T. (**2007**). "Effects of temporal fine structure on the lateralization of speech and on speech understanding in noise," J. Assoc. Res. Otolaryngol. **8**, 373–383.

Drullman, R. (**1995**). "Temporal envelope and fine structure cues for speech intelligibility," J. Acoust. Soc. Am. **97**, 585–592.

Flanagan, J. L. (**1980**). "Parametric coding of speech spectra," J. Acoust. Soc. Am. **68**, 412–419.

Flanagan, J. L., and Golden, R. M. (**1966**). "Phase vocoder," Bell Syst. Tech. J. **45**, 1493–1509.

French, N. R., and Steinberg, J. C. (**1947**). "Factors governing the intelligibility of speech sounds," J. Acoust. Soc. Am. **19**, 90–119.

Füllgrabe, C., Berthommier, F., and Lorenzi, C. (**2006**). "Masking release for consonant features in temporally fluctuating background noise," Hear. Res. **211**, 74–84.

Ghitza, O. (**2001**). "On the upper cutoff frequency of the auditory critical-band envelope detectors in the context of speech perception," J. Acoust. Soc. Am. **110**, 1628–1640.

Gilbert, G., and Lorenzi, C. (**2006**). "The ability of listeners to use recovered envelope cues from speech fine structure," J. Acoust. Soc. Am. **119**, 2438–2444.

Gilbert, G., Bergeras, I., Voillery, D., and Lorenzi, C. (**2007**). "Effects of periodic interruptions on the intelligibility of speech based on temporal fine-structure or envelope cues," J. Acoust. Soc. Am. **122**, 1336–1339.

Glasberg, B. R., and Moore, B. C. J. (**1990**). "Derivation of auditory filter shapes from notched-noise data," Hear. Res. **47**, 103–138.

Glasberg, B. R., and Moore, B. C. J. (**2000**). "Frequency selectivity as a function of level and frequency measured with uniformly exciting notched noise," J. Acoust. Soc. Am. **108**, 2318–2328.

Hicks, M. L., and Bacon, S. P. (**1999**). "Psychophysical measures of auditory nonlinearities as a function of frequency in individuals with normal hearing," J. Acoust. Soc. Am. **105**, 326–338.

Humes, L. E., Dirks, D. D., Bell, T. S., Ahlstrom, C., and Kincaid, G. E. (**1986**). "Application of the articulation index and the speech transmission index to the recognition of speech by normal-hearing and hearing-impaired listeners," J. Speech Hear. Res. **29**, 447–462.

Irino, T., and Patterson, R. D. (**1997**). "A time domain, level dependent auditory filter: The gammachirp," J. Acoust. Soc. Am. **101**, 412–419.

Irino, T., and Patterson, R. D. (**2006**). "A dynamic compressive gammachirp auditory filterbank," IEEE Trans. Audio, Speech, Lang. Process. **14**, 2222–2232.

Jeffress, L. A. (**1968**). "Beating sinusoids and pitch changes," J. Acoust. Soc. Am. **43**, 1464.

Lorenzi, C., Gilbert, G., Carn, H., Garnier, S., and Moore, B. C. J. (**2006**). "Speech perception problems of the hearing impaired reflect inability to use temporal fine structure," Proc. Natl. Acad. Sci. U.S.A. **103**, 18866–18869.

Loughlin, P. J., and Tacer, B. (**1996**). "On the amplitude and frequency decomposition of signals," J. Acoust. Soc. Am. **100**, 1594–1601.

Martin, P. (**1996**). *Éléments de phonétique, avec application au français (Elements of Phonetics, with Application to French)* (Les Presses de l'Universite Laval, Sainte-Foy).

Miller, G. A., and Nicely, P. E. (**1955**). "Analysis of perceptual confusions among some English consonants," J. Acoust. Soc. Am. **27**, 338–352.

Nelson, P. B., Jin, S., Carney, A. E., and Nelson, D. A. (**2003**). "Understanding speech in modulated interference: Cochlear implant users and normal-hearing listeners," J. Acoust. Soc. Am. **113**, 961–968.

Nie, K., Stickney, G., and Zeng, F.-G. (**2005**). "Encoding frequency modulation to improve cochlear implant performance in noise," IEEE Trans. Biomed. Eng. **52**, 64–73.

Oxenham, A. J., and Moore, B. C. J. (**1997**). "Modeling the effects of peripheral nonlinearity in listeners with normal and impaired hearing," in *Modeling Sensorineural Hearing Loss*, edited by W. Jesteadt (Erlbaum, Mahwah, N.J.), pp. 273–288.

Papoulis, A. (**1983**). "Random modulation: A review," IEEE Trans. Acoust., Speech, Signal Process. **31**, 96–105.

Patterson, R. D., Nimmo-Smith, I., Holdsworth, J., and Rice, P. (**1987**). "An efficient auditory filterbank based on the gammatone function," in *Paper Presented at a Meeting of the IOC Speech Group on Auditory Modeling at RSRE*, Malvern, England, December 14–15.

Qin, M. K., and Oxenham, A. J. (**2003**). "Effects of simulated cochlear-implant processing on speech reception in fluctuating maskers," J. Acoust. Soc. Am. **114**, 446–454.

Qin, M. K., and Oxenham, A. J. (**2006**). "Effects of introducing unprocessed low-frequency information on the reception of envelope-vocoder processed speech," J. Acoust. Soc. Am. **119**, 2417–2426.

Remez, R. E., Rubin, P. E., Pisoni, D. B., and Carrell, T. D. (**1981**). "Speech perception without traditional speech cues," Science **212**, 947–949.

Remez, R. E., and Rubin, P. E. (**1990**). "On the perception of speech from time-varying acoustic information: Contributions of amplitude variations," Percept. Psychophys. **48**, 313–325.

Rhode, W. S. (**1971**). "Observations of the vibration of the basilar membrane in squirrel monkeys using the Mössbauer technique," J. Acoust. Soc. Am. **49**, 1218–1231.

Robles, L., Ruggero, M. A., and Rich, N. C. (**1986**). "Basilar membrane mechanics at the base of the chinchilla cochlea. I. Input-output functions,

tuning curves and phase responses," J. Neurophysiol. **41**, 692–704.
Rosen, S. (**1992**). "Temporal information in speech: acoustic, auditory and linguistic aspects," Philos. Trans. R. Soc. London, Ser. B **336**, 367–373.
Rosen, S., and Stock, D. (**1992**). "Auditory filter bandwidths as a function of level at low frequencies (125-1 kHz)," J. Acoust. Soc. Am. **92**, 773–781.
Schimmel, M., and Altas, L. E. (**2005**). "Coherent envelope detection for modulation filtering of speech," *IEEE Trans. Acoust., Speech, Signal Process.*, Philadelphia, PA, pp. 221–224.
Shannon, R., Zeng, F.-G., Kamath, V., Wygonski, J., and Ekelid, M. (**1995**). "Speech recognition with primarily temporal cues," Science **270**, 303–304.
Sheft, S. (**2008**). "Envelope processing and sound-source perception," in *Auditory Perception of Sound Sources*, edited by W. A. Yost, A. N. Popper, and R. R. Fay (Springer, New York), pp. 233–280.
Sheft, S., and Yost, W. A. (**2001**). "Auditory abilities of experienced signal analysts," AFRL Prog. Rep. No. 1, contract SPO700-98-D-4002.
Smith, Z. M., Delgutte, B., and Oxenham, A. J. (**2002**). "Chimaeric sounds reveal dichotomies in auditory perception," Nature (London) **416**, 87–90.
Steeneken, H. J. M., and Houtgast, T. (**1999**). "Mutual dependence of the octave-band weights in predicting speech intelligibility," Speech Commun. **28**, 109–123.
Steeneken, H. J. M., and Houtgast, T. (**2002**). "Phoneme group specific octave-band weights in predicting speech intelligibility," Speech Commun. **38**, 399–411.
Stickney, G. S., Nie, K., and Zeng, F.-G. (**2005**). "Contribution of frequency modulation to speech recognition in noise," J. Acoust. Soc. Am. **118**, 2412–2420.
Stone, M. A., and Moore, B. C. J. (**2007**). "Quantifying the effects of fast-acting compression on the envelope of speech," J. Acoust. Soc. Am. **121**, 1654–1664.
Turner, C. W., Kwon, B. J., Tanaka, C., Knapp, J., Hubbartt, J. L., and Doherty, K. A. (**1998**). "Frequency-weighting functions for broadband speech as estimated by a correlational method," J. Acoust. Soc. Am. **104**, 1580–1585.
Viemeister, N. F. (**1979**). "Temporal modulation transfer functions based upon modulation thresholds," J. Acoust. Soc. Am. **66**, 1364–1380.
Xu, L., and Pfingst, B. E. (**2003**). "Relative importance of temporal envelope and fine structure in lexical-tone perception," J. Acoust. Soc. Am. **114**, 3024–3027.
Xu, L., Thompson, C. S., and Pfingst, B. E. (**2005**). "Relative contribution of spectral and temporal cues for phoneme recognition," J. Acoust. Soc. Am. **117**, 3255–3267.
Zeng, F. G., Nie, K., Liu, S., Stickney, G., Del Rio, E., Kong, Y. Y., and Chen, H. (**2004**). "On the dichotomy in auditory perception between temporal envelope and fine structure cues," J. Acoust. Soc. Am. **116**, 1351–1354.
Zeng, F. G., Nie, K., Stickney, G. S., Kong, Y. Y., Vongphoe, M., Bhargave, A., Wei, C., and Cao, K. (**2005**). "Speech recognition with amplitude and frequency modulations," Proc. Natl. Acad. Sci. U.S.A. **102**, 2293–2298.

Acoustic and perceptual similarity of Japanese and American English vowels[a)]

Kanae Nishi[b)] and Winifred Strange
Ph.D. Program in Speech and Hearing Sciences, City University of New York—Graduate School and University Center, New York, New York 10016

Reiko Akahane-Yamada and Rieko Kubo
Cognitive Information Science Laboratory, Advanced Telecommunications Research Institute International and ATR Learning Technology Corporation, Kyoto 619-0288, Japan

Sonja A. Trent-Brown[c)]
Department of Psychology, University of South Florida, Tampa, Florida 33620

(Received 2 March 2007; revised 31 March 2008; accepted 19 April 2008)

Acoustic and perceptual similarities between Japanese and American English (AE) vowels were investigated in two studies. In study 1, a series of discriminant analyses were performed to determine acoustic similarities between Japanese and AE vowels, each spoken by four native male speakers using F1, F2, and vocalic duration as input parameters. In study 2, the Japanese vowels were presented to native AE listeners in a perceptual assimilation task, in which the listeners categorized each Japanese vowel token as most similar to an AE category and rated its goodness as an exemplar of the chosen AE category. Results showed that the majority of AE listeners assimilated all Japanese vowels into long AE categories, apparently ignoring temporal differences between 1- and 2-mora Japanese vowels. In addition, not all perceptual assimilation patterns reflected context-specific spectral similarity patterns established by discriminant analysis. It was hypothesized that this incongruity between acoustic and perceptual similarity may be due to differences in distributional characteristics of native and non-native vowel categories that affect the listeners' perceptual judgments. © *2008 Acoustical Society of America.* [DOI: 10.1121/1.2931949]

PACS number(s): 43.71.Hw, 43.70.Kv, 43.71.Es, 43.70.Fq [MSS] Pages: 576–588

I. INTRODUCTION

Studies of cross-language speech perception have documented that the ease with which listeners can perceive specific contrasts among speech sounds is shaped by their linguistic environment during the early years of life (e.g., Best *et al.*, 1988; Werker and Tees, 1984). Such early language-specific shaping in speech perception leads to great difficulty in learning a new phonological system as adults.

In order to explain the complex processes involved in cross-language speech perception and to predict difficulty in both perception and production experienced by adult second language (L2) learners, several models have been proposed. Among those, of particular interest here are the perceptual assimilation model (PAM) by Best (1995) and the speech learning model (SLM) by Flege (1995). Both PAM and SLM propose somewhat similar mechanisms in which learners' native phonological system acts as a sieve in processing non-native phones. Both claim that the similarity between phonetic inventories of the learners' native language (L1) and that of the L2 influences perception. In addition, both models suggest that differences in the phonetic realization (gestural and acoustic-phonetic details) of the "same" phonological segments in the two languages must be taken into consideration in establishing cross-language similarities, as well as the token variability within similar phonetic categories in the two languages—whether due to speaking styles, consonantal/prosodic contexts, or individual speakers.

Thus far, numerous studies of vowels have attempted to provide evidence for PAM and SLM, but the majority has focused on how listeners from an L1 with fewer vowel categories assimilate vowels from larger L2 inventories that include vowels that do not occur as distinctive categories in the L1. The present study examined perceptual assimilation of L2 vowels from a small inventory by listeners whose L1 included more vowels differing in "quality" (spectral characteristics), but for whom vowel length was not phonologically contrastive, namely, perception of Japanese vowels by American English (AE) listeners.

The subsequent four sections present the two models in more detail, briefly describe the vowel systems of AE and Japanese, provide summaries of previous studies that examined Japanese listeners' perception of AE vowels (Strange *et al.*, 1998; 2001) and AE listeners' use of vowel duration in perceptual assimilation of German vowels, and present the design and the research questions for the present study.

[a)]Portions of this work were presented in "Perceptual assimilation of Japanese vowels by American English listeners: effects of speaking style," at the 136th meeting of the Acoustical Society of America, Norfolk, VA, October 1998.

[b)]Present address: Boys Town National Research Hospital, 555 North 30th Street, Omaha, NE 68131; electronic mail: nishik@boystown.org
[c)]Present address: Psychology Department, Hope College, 35 E. 12th Street, Holland, MI 49423.

 0001-4966/2008/124(1)/576/13/$23.00

A. Perceptual assimilation model and speech learning model

PAM (Best, 1995) has its basis in the direct realist view of speech perception and hypothesizes that listeners directly perceive articulatory gestures from information specifying those gestures in the speech signal. It predicts *relative* difficulty in perceiving distinctions between non-native phones in terms of *perceptual assimilation* to and *category goodness* of the contrasting L2 phones with respect to L1 categories. According to PAM, if contrasting L2 phones are perceptually assimilated to two different L1 categories (two-category pattern), their discrimination should be excellent. However, if they are assimilated to a single L1 category as equally good (or poor) instances (single-category pattern), they are predicted to be very difficult to discriminate. On the other hand, if two L2 phones are assimilated to a single L1 category but are judged to differ in their "fit" to that category (category goodness pattern), their discrimination will be more accurate than single-category pairs but not as good as for two-category pairs. If both phones are perceived as speech sounds but cannot be assimilated consistently to any L1 category (uncategorizable), their discrimination will vary depending on their phonetic similarity to each other and perceptual similarity to the closest L1 categories. Finally, there can be cases where one L2 phone falls into an L1 category and the other falls outside the L1 phonological space (categorizable-uncategorizable pattern). In such a case, PAM predicts their discrimination to be very good.[1]

Although much of Flege and colleagues' work has focused on the accentedness of L2 productions by inexperienced and experienced L2 learners, his SLM (Flege, 1995) also considers the effects of cross-language phonetic similarities in predicting relative difficulties in learning both to perceive and produce L2 phonetic categories. SLM hypothesizes that L2 learners initially perceptually assimilate L2 phones into their L1 phonological space along a continuum from "identical" through "similar" to "new" (*equivalence classification*) based on L2 phones' phonetic similarities to L1 categories. If an L2 phone is "identical" to an L1 category, L1 patterns continue to be used, resulting in relatively little difficulty in perception and production. At the other extreme, if an L2 phone is phonetically "new" (very different from any L1 category), it will not be perceptually assimilated to any L1 category and eventually a new category will be created that guides both perception and production of the L2 phone. Therefore, perception and production will be relatively accurate for "new" L2 phones after some experience with the L2. However, if an L2 phone is phonetically "similar" to an L1 category, it will continue to be assimilated as a member of that L1 category. According to SLM, this pattern may lead to persistent perception and production difficulties because even though there may be a mismatch between L1 and L2 phones, learners continue to use their L1 category in perception and production. If two L2 phones are assimilated as "identical" or "similar" to a single L1 category, discrimination is predicted to be difficult, just as for PAM.

Studies have shown that the relative difficulty that late L2 learners have in discriminating L2 consonant and vowel contrasts varies considerably due to the phonetic context (i.e., allophonic variation) and token variability contributed by speakers, speaking rate, and speaking style differences (cf. Schmidt, 1996 for consonants; Gottfried, 1984 for vowels). This causes difficulties even for contrasts that may be distinctive in both languages but differ in phonetic detail across languages (cf. Pruitt *et al.*, 2006, for perception of Hindi [d-t] and [d^h-t^h] by AE listeners and Japanese listeners; Rochet, 1995, for perception of French vowels [i-y-u] by AE listeners and Brazilian Portuguese listeners). However, the majority of these reports are based on assimilation of more L2 categories into fewer L1 categories ("many-into-few" assimilation), and at present, it is not known whether PAM or SLM can account for the cases where learners are required to assimilate fewer L2 categories into a more differentiated L1 phonological inventory ("few-into-many" assimilation).

B. Japanese and American English vowel inventories

According to traditional phonological descriptions of Japanese and AE vowel inventories, the two languages differ markedly in their use of *quality* (tongue, lip, and jaw positions) and *quantity* (duration of vocalic gestures) to differentiate vowels. Japanese has a "sparse" system with five distinctive vowel qualities [i, e, a, o, ɯ] which form five long (2-mora)-short (1-mora) pairs (Homma, 1992; Ladefoged, 1993; Shibatani, 1990). These vowels vary in height (three levels) and backness (front versus back). Thus, vowel quantity or duration is phonologically contrastive, and phonetically, long-short pairs are reported to be very similar in spectral structure (Hirata and Tsukada, 2004). (Hereafter, the Japanese vowels will be transcribed as short [i, e, a, o, ɯ] and long [ii, ee, aa, oo, ɯɯ].) Only the midback vowels [o, oo], are rounded, and all vowels are monophthongal. In addition, the central and back vowels have distinctive palatalized forms [^{j}a(a), ^{j}o(o), ^{j}ɯ(ɯ)] in the majority of consonantal contexts.

In contrast to Japanese, AE has a relatively "dense" vowel system, described as including 10-11 spectrally distinctive, nonrhotic vowels [iː, ɪ, eᴵ, ɛ, æː, ɑː, ʌ, ɔː, oᵁ, ʊ, uː] that vary in height (five levels) and backness (front versus back), one rhotic vowel [ɝ], and three true diphthongs [aɪ, ɔɪ, aʊ]. The mid, low to high, back vowels [ɔː, oᵁ, ʊ, uː] are rounded, and [uː] can be palatalized in limited phonetic contexts (e.g., [^{j}u] in "view, pew, cue") and is allophonically fronted in coronal contexts (Hillenbrand *et al.*, 1995; Strange *et al.*, 2007). Although to a lesser extent than the true diphthongs, the mid, front [eᴵ] and mid, back [oᵁ] are diphthongized in slow speech and open syllable contexts, and several others of the so-called monophthongs show "vowel-inherent spectral change" in some contexts and some dialects (Hillenbrand *et al.*, 1995; Nearey, 1989; Stack *et al.*, 2006). In many dialects of AE, the distinction between [ɑː, ɔː] has been neutralized to a low, slightly rounded [ɒː]. Finally, while vowel length is not considered phonologically distinctive in AE, phonetically, "intrinsic duration" of AE vowels varies systematically (Peterson and Lehiste, 1960), with seven long vowels [iː, eᴵ, æː, ɑː, ɔː, oᵁ, uː] and four short vowels [ɪ, ɛ, ʌ, ʊ]. Vocalic duration also varies allophonically

as a function of the voicing of the following consonant, the syllable structure, and other phonetic and phonotactic variables (Klatt, 1976; Ladefoged, 1993).

C. Previous cross-language vowel perception studies

Although they differ in detail, both PAM and SLM hypothesize that L2 learners' perception and production error patterns can be predicted from the *phonetic* similarity between L1 and L2 phones because they posit that L2 learners initially attempt to perceptually assimilate L2 phones to L1 categories. However, it is important to establish phonetic similarity, independent of discrimination difficulties in order to make these claims noncircular. In some studies, Best and her colleagues describe phonetic similarity in terms of gestural features (degree and place of constriction by the tongue, lip postures, velar gestures), using rather abstract definitions of gestural characteristics (e.g., Best *et al.*, 2001). In many of Flege's studies of vowels, acoustic-phonetic similarity has been established through comparisons of formant frequencies in an F1/F2 space (e.g., Fox *et al.*, 1995; Flege *et al.*, 1999). Best, Flege, and other researchers working within these theoretical frameworks have also employed techniques that *directly* assess cross-language perceptual similarity of L2 phones, using either informal L1 transcriptions by nonnative listeners or a cross-language identification or so-called perceptual assimilation task (see Strange, 2007 for a detailed description of these techniques). In our laboratory, listeners perform a perceptual assimilation task in which they are asked to label (using familiar key words) multiple tokens of each L2 vowel as most similar to (underlying representations of) particular L1 vowel categories, and to rate their "category goodness" as exemplars of the L1 category they chose on a Likert scale (e.g., 1=very foreign sounding; 7=very native sounding). This technique has been successfully used in previous studies that investigated perceptual assimilation of larger L2 vowel inventories by listeners with smaller L1 vowel inventories (Strange *et al.*, 1998; 2001; 2004; 2005), but has never been used to assess assimilation of L2 vowels by listeners from L1s with more vowels. The following is a summary of those previous assimilation studies.

Strange *et al.* (1998) examined the influence of speaking style and speakers (i.e., [hVb(ə)] syllables produced in lists [citation condition] versus spoken in continuous speech [sentence condition]) on the assimilation of 11 AE vowels [iː, ɪ, eᴵ, ɛ, æː, ɑː, ʌ, ɔː, oᵾ, ʊ, uː] by Japanese listeners living in Japan at the time of testing. Acoustic analysis showed that the duration ratios between long and short AE vowels were the same for both conditions (1.3), but the absolute durations of vowels in sentences were somewhat longer than those in citation form. The results of perceptual assimilation tests showed that none of the 11 AE vowels were assimilated extremely consistently (i.e., with >90% consistency within and across listeners) into a single Japanese category in either condition. Japanese listeners assimilated short AE vowels in both conditions primarily into 1-mora Japanese vowels (94% in citation versus 83% in sentence), whereas the proportion of long AE vowels assimilated to 2-mora Japanese vowels was twice as great in sentence (85%) condition as in citation condition (42%). This indicated that Japanese listeners were highly attuned to vowel duration when they were given a prosodic context in which to judge the (small) relative duration differences. As for spectral assimilation patterns, consistent patterns were observed for four vowels [iː, ɑː, ʊ, uː] in both conditions. Six vowels [ɪ, eᴵ, ɛ, æː, oᵾ, ɔː] were assimilated primarily to two Japanese spectral categories, but patterns changed between citation and sentence conditions for the first five vowels, reflecting the influence of speaking style. Finally, [ʌ] was assimilated to more than two Japanese categories, suggesting its "uncategorizable" status.

In Strange *et al.* (2001), only sentence materials were used but vowels were produced in six consonantal contexts [b-b, b-p, d-d, d-t, g-g, g-k]. Similar to Strange *et al.* (1998), none of the 11 AE vowels were consistently assimilated into a single Japanese category, with the pattern varying with context and/or speaker for six vowels. Assimilation of long AE vowels to 2-mora Japanese categories also varied with speakers and contexts. More AE vowels were assimilated to 2-mora categories when followed by voiced consonants, indicating that Japanese listeners attributed (lengthened) vocalic duration to the vowels rather than to the consonants.

Strange *et al.* (2004; 2005) explored AE listeners' assimilation of North German (NG) vowels. NG has 14 vowel qualities that form seven spectrally adjacent long-short pairs. However, the spectral overlap between the long-short pairs is less marked than for Japanese, and the duration differences between spectrally similar long-short vowels (1.9 in citation, 1.5 in sentence materials) are smaller than for Japanese but greater than for AE. Results of perceptual assimilation tests showed that AE listeners categorized the 14 NG vowels primarily according to their spectral similarity to AE vowels, and largely ignored vowel duration differences.

D. The present study

The present study is part of a series investigating the influence of token variability on cross-language vowel perception. Thus far, as described above, we have investigated many-into-few assimilation patterns by systematically manipulating sources of variation (e.g., speaking style and consonantal context). The present study is the first of few-into-many assimilation studies and focused on the influence of speaking style. Other factors, such as consonantal context, speaking rate, and prosodic context, are left for future studies.

As in Strange *et al.* (1998), the effects of token variability were investigated using two utterance forms (i.e., citation and sentence) produced by multiple speakers, while phonetic context was held constant ([hVb(a)]). This specific consonantal context was chosen because in Japanese and AE, both [h] and [b] have minimal coarticulatory influence on the spectral characteristics of the vocalic nucleus. Thus, the vowels in these materials should reflect their "canonical" spectral structure that, in turn, specifies their "articulatory targets." In addition, the CVCV disyllables are phonotactically appropriate in both languages, and the consonants are very similar. The acoustic measurements of Japanese vowels are considered of archival value because no study has compared the

distributional characteristics of Japanese and American vowels in comparable materials, even though averages of spectral and duration measures for Japanese vowels have been reported (e.g., Han, 1962; Homma, 1981; Keating and Huffman, 1984; Hirata and Tsukada, 2004). While the AE corpus was partially described in our previous studies (Strange *et al.*, 1998; 2004), the Japanese corpus has not been described in any published studies.

Based on the phonetic and phonological differences between AE and Japanese vowel inventories described above, it was predicted that most of the Japanese vowels would spectrally overlap one or more AE vowels. Because AE has twice as many spectral categories as Japanese, the SLM would predict that all Japanese vowels should be assimilated into some AE category as "identical" or "similar" and none as "new" with relatively high category goodness ratings. PAM would predict that uncategorizable or categorizable-uncategorizable patterns should not be observed, but other patterns may occur as a function of token variability within a particular Japanese category as manifested as the difference in category goodness ratings.

II. ACOUSTIC SIMILARITY OF JAPANESE AND AE VOWELS

This section reports the results of both within-language and cross-language acoustic comparisons. Linear discriminant analysis (cf. Klecka, 1980) was chosen as the quantitative method because its conceptual framework resembles the perceptual assimilation processes. Discriminant analysis is a multidimensional correlational technique that establishes classification rules to maximally distinguish two or more predefined nominal categories from one another (i.e., vowel categories). The classification rules are specified by linear combinations of input variables (i.e., acoustic measures, such as formant frequencies and vowel duration) with weights for each variable determined to maximize separation of categories using the values for center of gravity of each category and within-category dispersion in the input set. By applying the classification rule established for the input set, membership of tokens in the input set can be re-evaluated (posterior classification technique), and the amount of overlap between categories can be quantified in terms of incorrect classification of tokens. It is also possible to classify a new set of data (test set) using the previously established classification rules.

In the present study, three types of discriminant analysis were performed. First, by performing analysis with and without vowel duration as a variable, the contribution of spectral and duration cues in distinguishing vowel categories were evaluated for each language (within-language, within-condition analyses). Second, by using the classification rules for the citation materials, the extent of changes in acoustic structure across speaking styles in each language was characterized (within-language, cross-condition analyses). Lastly, using the classification rules for the AE materials in each speaking style, similarity between the spectral characteristics of Japanese and AE vowels were evaluated for citation and sentence conditions separately (cross-language analyses).

A. Method

1. Speakers and stimulus materials

Four adult Japanese males (speakers 1–4; 32–39 yr old) served as speakers. All were native speakers of Tokyo dialect and resided in Japan all of their lives. All had at least eight years of English language education beginning in the seventh grade, but in the Japanese school system, little emphasis was placed on the spoken language. They had no training in phonetics and spoke very little English in their daily life. They reported no hearing or speech problems.

Stimuli were five long/short pairs of Japanese vowels [ii/i, ee/e, a/a, oo/o, ɯɯ/ɯ]. These vowels were embedded in a nonsense [hVba] disyllable and recorded in two speaking styles. First, these disyllables were read singly in lists (citation form), each preceded by an identifying number and a pause, and spoken in falling intonation. Second, each [hVba] disyllable was embedded in a carrier sentence (sentence form), *Kore wa* [hVba] *desu ne* [koɾewa#h_ba#des(ɯ)ne], which translates to "This is [hVba], isn't it?" Each speaker produced four randomized lists of 10 vowels for each form. Only the last three readings were used as stimuli. When problems with fluency or voice quality were detected, the token from the first reading was used as a replacement. Thus, a total of 240 tokens (10 vowels × 3 repetitions × 2 forms × 4 speakers) were included in the final analysis.

All tokens were recorded in an anechoic sound chamber at ATR Human Information Processing Research Laboratories in Kyoto, Japan, using a condenser microphone (SONY ECM77-77s) connected to a DAT recorder (SONY PCM-2500A, B). Each speaker sat approximately 22 cm from the microphone. Speakers read stimuli from randomized lists with identification numbers preceding each token. Speakers were instructed to read at their natural rate without exaggerating the target nonsense syllables. Recorded lists were digitally transferred to Audio Interchange File Formant (AIFF) files and down-sampled from 48 to 22.05 kHz, using a Power Macintosh 8100/100 computer and SOUNDEDIT16 (Version 1.0.1, Macromedia). AIFF files for individual tokens for analysis and perceptual testing were created from the down-sampled files by deleting the identification numbers.

The AE corpus was produced and analyzed using similar techniques, except that they were recorded in a sound booth at University of South Florida (USF). Four male speakers of general American English dialect each recorded four tokens for each of 11 vowels in the two speaking styles; three tokens were retained for analysis. Further details of the stimulus preparation for the AE stimuli are reported elsewhere (Strange *et al.*, 1998).

2. Acoustic analysis

Acoustic analysis was performed using a custom-designed spectral and temporal analysis interface in SOUNDSCOPE/16 1.44 (PPC)™ speech analysis software (Copyright 1992 GW Instruments, Somerville, MA 02143). First, the vocalic duration of the target vowel was determined by locating the beginning and ending of the target vowel using

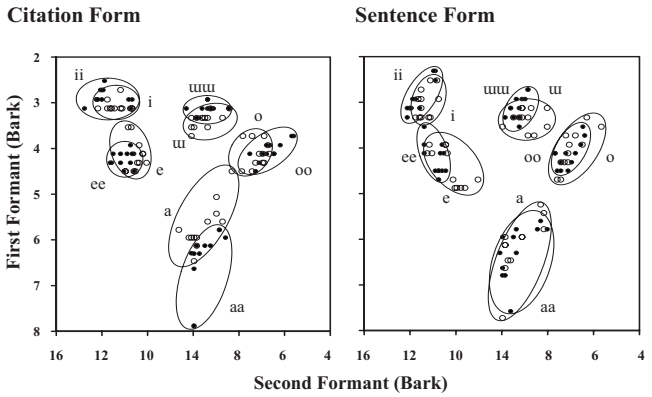

FIG. 1. Formant 1/formant 2 (bark) plots for ten Japanese vowels produced by four male speakers in [hVba] contexts in citation form (left panel) and sentence form (right panel): 12 tokens per vowel. Filled circles are for 2-mora vowels; open circles are for 1-mora vowels.

both the spectrographic and waveform representations of the stimuli. The vowel onset was the first pitch period after the preceding voiceless segment [h], and the vowel offset was determined as the reduction of the waveform amplitude and the cessation of higher formants in the spectrogram indicating the start of the [b] closure; vocalic duration was calculated as the difference between these two time points. The first three formants (F1, F2, and F3, respectively) were measured at the 25%, 50%, and 75% temporal points of the vocalic duration. Only the measurements from the 50% point (midsyllable) are used in the discriminant analyses (average values for each vowels are reported in Appendix). Linear predictive coding (LPC) spectra (14-pole, 1024-point) were computed over approximately three pitch periods (a 25 ms-Hamming window) around the 50% point. When the cross-check with the spectrographic representation indicated the LPC estimate of a formant reflected merged, spurious, or missed formants, the formant frequency was manually estimated from the wideband fast Fourier transfer (FFT) representation of the windowed portion. In very few cases where wideband FFT also failed, a narrowband FFT was used.

B. Results

1. Within-language comparisons: Within and across speaking styles

Figure 1 presents the target formant frequency data (F1/F2 bark values at vowel midpoint) for the 120 tokens of Japanese vowels produced in citation form (left panel), and the 120 tokens produced in sentence form (right panel). Ellipses surround all 12 tokens of each vowel (4 speakers $\times 3$ tokens); tokens of the long vowels are represented by filled circles, the short vowels are represented by open circles. As Fig. 1 shows, across the five long/short Japanese vowel pairs, there was little spectral overlap in either speaking style, despite considerable acoustic variability within and across speakers. Deviant tokens were found for low vowels: for [a], one each in the citation (by speaker 1) and in the sentence conditions (by speaker 2); for [aa], two in the citation condition and one in the sentence condition (both by speaker 2). However, since these tokens (and all others) were readily identified by a native Japanese listener as the intended vowels, they were considered extreme cases of token variability and were not eliminated from the analysis. Long/short pairs of the same vowel quality overlapped considerably, especially for the sentence materials. Thus, as predicted, duration appears to play an important role in separating these contrasting vowel categories.

TABLE I. Percent correct classification of within-form and cross-form discriminant analyses based on spectral parameters alone (F1/F2 in bark values) shown in the left column, and spectral parameters plus vocalic duration shown in the right column.

	F1/F2 (%)	F1/F2+Duration (%)
Japanese Corpora		
Citation Form	77	98
Sentence Form	65	100
Sentence→Citation	62	98
American English Corpora		
Citation form	85	91
Sentence form	86	95
Sentence→Citation	78	89

The duration ratios of Japanese long to short vowels (L/S ratios) averaged 2.9 for both speaking styles (ranged from 2.6 to 3.4 for each of five vowel pairs; see Appendix for detail). That is, long vowels in both forms were, on average, three times as long as short vowels. Note that these L/S ratios for Japanese vowels are greater than those for the German vowels reported in Strange *et al.* (2004) (average L/S ratio=1.9 for citation form, 1.5 for sentence form). As previously reported, average L/S ratios for AE vowels were markedly smaller compared to Japanese vowels (1.3 for both citation and sentence forms).

In order to statistically evaluate the above observations and to quantify the spectral overlap among vowels and the contribution of duration in further differentiating vowel categories, two series of discriminant analyses were performed for each language corpus. The first analysis used spectral parameters alone (F1 and F2),[2] and the second analysis used spectral parameters plus vocalic duration as input variables. In these analyses, "correct classification" was defined as the posterior classification of each token as the speaker-intended vowel category. For the formant values, as in the previous studies (Strange *et al.*, 2004; 2005; 2007) only the measurements at vowel midpoint were entered. Table I presents the results for the Japanese citation and sentence forms (also depicted in Fig. 1) and for the comparable AE corpus. For both languages, the values in the first two rows represent the within-condition differentiation of vowels in the relevant input sets. The third row shows the results of cross-condition analyses (citation as input set, sentence as test set).

As these overall correct classification rates indicate, the ten Japanese vowels were not well differentiated by spectral parameters alone, especially for the sentence materials. However, almost all of the misclassifications were within long/short vowel pairs (25 out of 28 cases for citation form and 41 out of 42 cases for sentence form). Therefore, when vowel duration was included as a parameter, classification improved to almost perfect. Thus, the Japanese five spectral

categories are well differentiated even when variability due to speaker differences was included in the corpus, and with the use of duration, those five spectral categories are further separated into ten distinctive vowel categories.

For the comparable analyses for AE vowels, spectral differentiation (F1/F2 Bark values alone) of the 11 vowels was somewhat better than for Japanese vowels, reflecting the fact that phonetically long and short AE vowels differ spectrally. As reported in Strange *et al.* (2004) study, many of the misclassifications of AE tokens included confusions between spectrally adjacent pairs [iː/eᴵ, eᴵ/ɪ, eᴵ/ɛ, æː/ɛ, ɑː/ʌ, ɔː/oᵚ, oᵚ/ʊ, uː/ʊ] and between [ɑː] and [ɔ]. When duration was included as an input variable, correct classification rates for both forms improved but to lesser degrees than for Japanese.

The next series of analyses was performed to quantify cross-condition similarity. When sentence materials were classified using parameter weights and centers of gravities established for citation materials (F1/F2 Bark values), only 62% of Japanese vowels were correctly classified. However, when both spectral and temporal parameters were included, only two tokens were misclassified as vowels of the same temporal categories ([ee] as [ii] and [ɯ] as [o]). Note that the absolute duration of vowels in sentences were, on average, 15% shorter than those in citation form. These results indicate that the spectral differences among the five vowel categories are maintained across speaking styles, and that despite the changes in vowel duration between the two speaking styles, the temporal differences between the 1- and 2-mora Japanese vowels are still large enough to differentiate the ten categories.

As for the cross-condition analysis for the AE vowels, it was predicted that the inclusion of duration in the analysis should help differentiate the 11 AE vowels in sentence form but to a lesser degree than in Japanese because there was less spectral overlap among AE vowels in each speaking style. As predicted, the cross-condition analysis revealed that the rate of correct classifications improved by 11% when duration was included, but 15 cases remained misclassified. These 15 cases include the following: six cases of long/short confusions (number of misclassified tokens): [ɪ] as [eᴵ] (1), [ɛ] as [æː] (1), [ʌ] as [aː] (1), [oᵚ] as [ʊ] (1), [uː] as [ʊ] (2); eight long/long confusions: [eᴵ] as [iː] (2), [ɑː] as [ɔː] (4), between [ɔː] and [oᵚ] (2); and one short/short confusion: [ʊ] as [ʌ].

2. Cross-language spectral similarity

Additional discriminant analyses were performed in which the spectral parameters for the 11 AE vowels served as the input set, and those for the ten Japanese vowels served as the test set. That is, these analyses determined the spectral similarity of Japanese vowels to AE vowels using the classification rules established for AE vowel categories. Separate analyses were performed for the two speaking styles. Figure 2 displays the F1/F2 Bark plots of Japanese and AE vowels. Distributions of vowels in the two languages are indicated by the ellipses (solid for Japanese and dashed for AE) that surround all 12 tokens of each vowel. Individual Japanese tokens are represented by filled circles; for clarity, individual AE tokens are not shown. Panels on the left are for citation materials, and the panels on the right are for sentence materials. The two top panels are for long Japanese vowels, and the two bottom panels are for short Japanese vowels. The same dashed ellipses for the 11 AE vowels in each form are shown in the background. As can be seen, most Japanese mid and short, low vowels were higher (lower F1 values) on average[3] and revealed greater within-category variability than the comparable AE vowels while the front and back, high vowels were spectrally quite similar across languages.

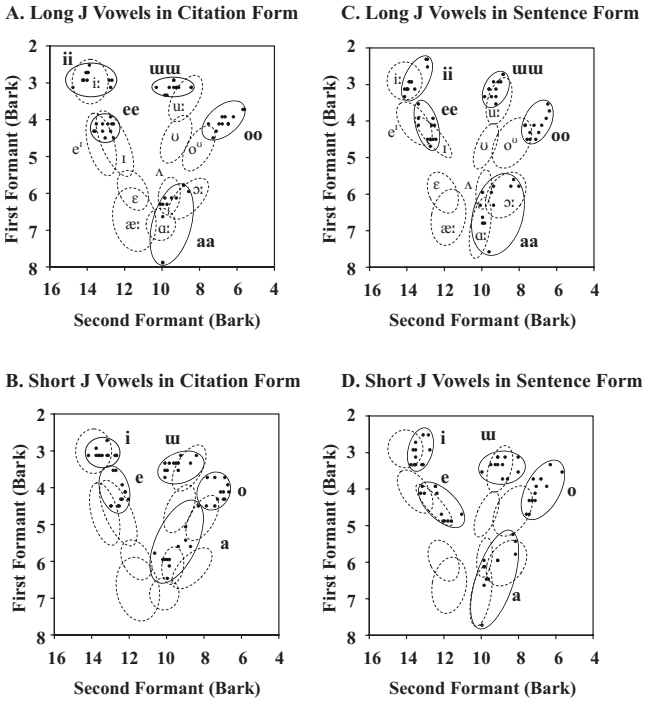

FIG. 2. Formant 1/formant 2 (bark) plots for 2-mora (upper panels) and 1-mora Japanese vowels (lower panels) produced by four male speakers in [hVba] in citation form (left panels) and sentence form (right panels) superimposed on 11 AE vowels (dotted ellipses). Solid ellipses encircle all 12 tokens of a Japanese vowel; individual AE tokens are not plotted.

In the cross-language discriminant analysis for the citation materials, the citation AE vowel corpus was used as the input set (F1/F2 Bark values as input parameters); then all tokens of the Japanese citation corpus were classified using the rules established for these AE categories. The results are summarized in Table II, where Japanese vowels are grouped in terms of the duration (1-mora and 2-mora) and tongue height (high, mid, low), as shown in the first column. The third and fourth columns display the modal AE vowels and the number of Japanese vowel tokens (max=12) classified as most similar to the respective AE category. In order to make acoustic classification consistent with the dialect profile of the listeners who performed the perceptual assimilation task in study 2, and to make results comparable between studies, Japanese tokens classified into AE [ɑː] or [ɔː] were pooled ([ɑː-ɔː]). The last two columns show the classification of the remaining tokens.

For the citation materials, 52 out of 60 tokens of 2-mora vowels were classified as spectrally comparable long AE vowels [iː, eᴵ, ɑː-ɔː, oᵚ, uː]. Some tokens of mid, front [ee] and low [aa] were spectrally similar to short AE categories ([ɪ] and [ʌ], respectively). In contrast, only 21 out of 60 tokens of 1-mora vowels were classified as spectrally com-

TABLE II. Acoustic similarity (F1/F2 in Bark values) of Japanese and American English (AE) vowles: hVb(a) syllables produced in citation.

		Modal classification		Other categories	
	Japanese. vowel	AE vowel	No. of tokens	AE vowel	No. of tokens
2-mora					
High	ii	iː	12		
	ɯɯ	uː	12		
Mid	ee	eᴵ	7	ɪ	5
	oo	oᵘ	12		
Low	aa	ɑː–ɔː	9	ʌ	3
1-mora					
High	i	iː	12		
	ɯ	uː	9	ʊ	3
Mid	e	ɪ	8	eᴵ	2
				iː	1
				ʊ	1
	o	oᵘ	9	uː	3
Low	a	ʌ	7	ɑː–ɔː	2
				ɛ	1
				oᵘ	1
				ʊ	1

parable short AE vowels [ɪ, ɛ, ʌ, ʊ], suggesting that they are spectrally more similar to AE long vowels. The classification of Japanese 1-mora mid, front and low vowels was to two or more AE spectrally adjacent vowels, indicating that they are intermediate among several AE categories.

Table III presents the results of the discriminant analysis (F1/F2 Bark values) with the AE sentence materials as the input set and the Japanese sentence materials as the test set. The results resembled those for the citation materials: 47 out of 60 tokens of 2-mora Japanese vowels were classified into spectrally comparable long AE vowels, whereas only 12 out of 60 tokens of 1-mora vowels were classified as spectrally comparable short AE vowels. Similar to citation form, high Japanese vowels [ii, i, ɯɯ, ɯ] were consistently classified as spectrally similar to long AE high vowels [iː, uː], while the mid, front [ee, e] and low vowels [aa, a] were classified as most similar to two or more AE categories. The mid, back vowel [o] in this form was more consistently classified as AE [oᵘ].

TABLE III. Acoustic similarity (F1/F2 in Bark values) of Japanese and American English (AE) vowles: hVb(a) syllables produced in citation.

		Modal classification		Other categories	
	Japanese vowel	AE vowel	No. of tokens	AE vowel	No. of tokens
2-mora					
High	ii	iː	12		
	ɯɯ	uː	12		
Mid	ee	ɪ	9	eᴵ	3
	oo	oᵘ	12		
Low	aa	ɑː–ɔː	8	ʌ	4
1-mora					
High	i	iː	10	eᴵ	2
	ɯ	uː	12		
Mid	e	ɪ	8	eᴵ	3
				ʊ	1
	o	oᵘ	12		
Low	a	ɑː–ɔː	8	ʌ	3
				oᵘ	1

C. Discussion

The results of acoustic comparisons between Japanese and AE vowels suggested the following.

(1) Regardless of speaking styles, Japanese vowels were consistently classified into five nonoverlapping spectral categories. These five spectral categories were further differentiated into short (1-mora) and long (2-mora) vowels by vowel duration. Altogether, classification was almost perfect for all ten vowel categories when F1, F2 values at vowel midpoint and vowel duration were included in the analysis.
(2) AE vowels produced in both speaking styles were differentiated by mid-syllable formant frequencies fairly well, and some vowel pairs were further differentiated by vocalic duration. However, overall correct classification was not as good as for the Japanese vowels, indicative of a more crowded vowel space.
(3) Within-language cross-condition discriminant analyses revealed that both AE and Japanese vowels produced in sentences share similar spectral and temporal characteristics to the citation material in this phonetic context, indicating that despite the effects of speaking style, the acoustic distinctions among vowel categories are maintained for both Japanese and AE.
(4) Cross-language discriminant analyses using only the spectral parameters indicated that Japanese high vowels [ii, i], [ɯɯ, ɯ], and mid, back vowels [oo, o] in both forms were spectrally similar to AE long vowels [iː], [uː] and [oᵘ], respectively, while the mid, front and low Japanese vowels in both speaking styles were found spectrally more intermediate between two or more AE categories. The Japanese 1-mora vowels [e, a] in citation form were especially variable with respect to their spectral similarity to AE vowels.

In the next section, the results from the perceptual assimilation experiment are presented and discussed in relation to the acoustic comparisons between Japanese and AE vowels presented in this section.

III. PERCEPTUAL ASSIMILATION OF JAPANESE VOWELS BY AE LISTENERS

A listening experiment was performed using the Japanese corpus analyzed in Sec. II. Native AE speakers with no experience with the Japanese language served as listeners and performed a perceptual assimilation task that involved two judgments: categorization of Japanese vowels using AE vowel category labels and rating the category goodness of the Japanese vowels as exemplars of the chosen AE vowel categories. Based on the results of the acoustic analyses, it was predicted that perceptual assimilation of Japanese high

vowels [ii, i], [ɯɯ, ɯ], and mid, back vowels [oo, o] would not be affected by speaking style and would be perceived as good exemplars of AE long vowels [iː], [uː], and [oʊ] unless AE listeners detected and responded on the basis of the considerable temporal differences between the 1- and 2-mora pairs. In comparison, perceptual assimilation of Japanese [e, ee] and [a, aa] was predicted to be less consistent (and possibly with poorer category goodness ratings) within and across listeners, reflecting the fact that spectrally, these vowels straddled more than one AE category. In addition, the effects of speaking style were expected to be observed for [ee, e, aa, a].

A. Method

1. Listeners

Twelve undergraduate students (two males and ten females, mean age=26.2 yr old) at USF served as the listeners for extra credit points. They were recruited either from introductory phonetics or phonology courses offered in the Department of Communication Sciences and Disorders. Some of them had had at least one semester of phonetics by the time of testing. All were fluent only in American English, and none of them had lived in a foreign country for an extended length of time. All reported that they had normal hearing. Among these listeners, ten had lived in Florida more than ten years, and two had lived in the northeastern United States more than ten years. Four additional listeners were tested but their data were excluded either because they failed to return for the second day of testing or because they were bilinguals.

2. Stimulus materials

Stimulus materials were the 240 tokens of ten Japanese vowels (10 vowels×4 speakers×2 utterance forms×3 repetitions) acoustically analyzed in study 1

3. Apparatus and instruments

All listening sessions including familiarization were provided individually in a sound booth in the Speech Perception Laboratory of USF. Stimuli were presented through headphones (STAX SR LAMBDA semi-panoramic sound electrostatic ear speaker). The listeners adjusted the sound volume for their comfort. For all sessions, stimulus presentation was controlled by a HYPERCARD 2.2 stack on a Macintosh Quadra 660AV computer with a 14 in. screen. The HYPERCARD stack used for the listening test had two components. The first component was for categorization and displayed 11 buttons labeled with Phonetic symbols (IPA) for 11 AE vowels [iː, ɪ, eᴵ, ɛ, æː, ɑː, ʌ, ɔː, oᵘ, ʊ, uː] and keywords in [hVd] context (heed, hid, hayed, head, had, hod, hud, hawed, hoed, hood, who'd, respectively). The second component appeared after the listener categorized a stimulus vowel and displayed a seven-point Likert scale (1=foreign, 7=English) on which the listeners judged the category goodness of the stimulus vowel in the chosen AE category.

4. Procedures

A repeated-measure design was employed in which each listener was presented all tokens from all four speakers in both utterance forms. All listeners were tested on two days: one for citation materials and the other for sentence materials. The order was counterbalanced across listeners.

a. Familiarization Before testing on day 1, all listeners completed an informed consent form and a language background questionnaire. Then, a brief tutorial on the IPA and two task familiarization sessions were given. The tutorial for the IPA provided a brief description of relationship between IPA for the 11 AE vowels and their sounds using the 11 [hVd] keywords. A HYPERCARD stack provided audio and text explanations.

Task familiarization had two parts: categorization-only and categorization and category goodness judgment. Stimuli for the categorization only familiarization were [həC_1VC_2] disyllables, where C_1-C_2 combinations were [b-d, b-t, d-d, d-t, g-d, g-t] and the V was one of the 11 AE vowels. These disyllables were embedded in a carrier sentence, "I hear the sound of [*h*əC_1VC_2] some more." The fifth author recorded 11 vowels in at least one of the C_1-C_2 context, and an additional 44 tokens were recorded by a male native speaker of AE who was not the speaker for the AE stimuli used in study 1. In the categorization-only part, these 55 tokens were presented in four blocks. The first block presented 11 tokens from the female speaker, the next two blocks presented 11 tokens from the male speaker randomly selected from his 44 tokens, and the last block presented the remaining 22 tokens from the male speaker. The listeners were asked to indicate which of the 11 AE vowels they heard by clicking on one of the response buttons on the screen. Feedback was provided by the computer program after each categorization response. When a response was incorrect, the experimenter sitting beside the listener provided explanations why the response was incorrect.

In the second part, familiarization for the category goodness judgment was given using 56 German sentence-form tokens randomly chosen from a total of 560 tokens (14 vowels×4 speakers in 5 consonantal contexts) used in Strange *et al.* (2005) study. A short task description was provided by a HYPERCARD stack and the listeners practiced on the German tokens using the same interface as the testing. In each trial, the listeners were asked to categorize a German vowel in terms of the 11 AE categories, and then indicate its category goodness in the chosen AE category on the seven-point Likert scale (1=foreign, 7=English). No feedback was provided in this part.

b. Test Each listener was tested on two days. On day 1, a testing session was given following the task familiarization. On day 2, the listeners were given only the testing session, which followed the same procedure as testing on day 1. Half of the listeners heard citation materials on day 1 and sentence materials on day 2; presentation order was reversed for the remaining listeners.

In a testing session, stimuli were blocked by speaker, and a total of four blocks of 120 trials (10 vowels×3 tokens×4 repetitions) were presented for a speaking style. Block order was counterbalanced across the listeners. An opportunity for a short break was provided after the second block. In each trial, the same stimulus was presented twice; after the first presentation of a stimulus, the listeners categorized the Japanese vowel by choosing one of the 11

TABLE IV. Perceptual assimilation patterns: Categorization responses, expressed as percentages of total responses summed over speakers and listeners for citation-form (A) and sentence-form (B) materials. Bold =modal perceptual classification; boxed=modal acoustic classification.

		AE response categories									
		iː	ɪ	eᴵ	ɛ	æː	ɑː–ɔː	ʌ	oᵁ	ʊ	uː
(A) Citation											
2-mora											
	ii	**99**	1								
	ee		2	**94**	5						
	aa					2	**89**	9			
	oo						1		**99**		1
	ɯɯ							1	2	5	**92**
1-mora											
	i	**95**	4		1						
	e		16	**76**	8						
	a					3	**57**	39			
	o							1	**95**	1	2
	ɯ							3	1	5	**91**
(B) Sentence											
2-mora											
	ii	**99**									
	ee		1	**97**	2						
	aa					1	**96**	3			
	oo								**98**		1
	ɯɯ								2	2	**96**
1-mora											
	i	**98**	2								
	e	1	23	**48**	28						
	a					2	**77**	21			
	o								**95**		4
	ɯ							2	1	7	**89**

AE responses, then the same stimulus was presented again, and the listener rated its category goodness to the chosen AE category on a seven-point Likert scale (1=foreign, 7 =English). The listeners were allowed to change their categorization response before making a rating response but were discouraged from doing so. A new trial began after the rating response was completed; thus, testing was listener paced.

No specific instruction was given in familiarization or test regarding the use of vowel duration, number of spectral categories in Japanese, or differences between AE and Japanese vowel inventories since the focus of the current study was to examine how naïve L2 listeners classify foreign speech sounds using L1 categories.

B. Results and discussion

First, for the category goodness responses, medians of ratings across all the listeners were obtained for all AE categories that received more than 10% out of 576 total responses for a Japanese vowel. As predicted from the results of the acoustic comparisons, this analysis yielded higher overall median ratings (6) for [ii, i], [ɯɯ, ɯ], [oo, o] in both conditions and [ee] in sentence condition, and slightly lower median ratings (5) for [e, aa, a] in both conditions and [ee] in citation condition.

To analyze the categorization results, each listener's responses were transferred to a spreadsheet and confusion matrices were constructed for (1) individual speakers, (2) individual listeners, and (3) two speaking styles. Examination of these matrices revealed some differences among listeners for some vowels (not associated with dialect) and between speaking styles.

Table IV presents the group data in which categorization responses were pooled across the speakers, repetitions, and listeners. In order for the results to be consistent with the majority of listeners' dialect profile, AE response categories [ɑː] and [ɔː] were pooled as [ɑː-ɔː] in this analysis.[4] The top part (A) of the table displays the categorization for citation materials, and the bottom part (B) presents the results for sentence materials. The first column lists the Japanese vowels grouped by the temporal categories (2-mora or 1-mora). The cells in columns 2–11 present percentages of responses. Numbers in boldface indicate the modal perceptual responses for each Japanese vowel; boxed entries indicate the spectrally most similar AE vowels for each Japanese vowel determined by the cross-language discriminant analyses presented in Sec. II.

As predicted from the results of acoustic comparisons, the majority of Japanese vowels were assimilated to long AE vowels. All five 2-mora vowels [ii, ee, aa, oo, ɯɯ] were consistently assimilated to long AE counterparts [iː, eᴵ, ɑː-ɔː, oᵁ, uː] respectively (overall percentages from 89% to 99%), and both high and the mid, back 1-mora vowels [i, ɯ, o] in

both speaking styles were also assimilated to AE long categories [iː, uː, oʊ], respectively (overall percentages from 89% to 98%). These patterns were consistent with their spectral similarity to AE categories, except for [ee] in sentence context. This suggests that AE listeners disregarded the temporal differences between these 1- and 2-mora Japanese vowels and perceived them as equally good exemplars of long AE vowels.

By contrast, the assimilation patterns for the other Japanese vowels were not straightforward. First, contrary to prediction from acoustical similarity, Japanese 2-mora [ee] did not show any influence of speaking style and was perceived as most similar to AE [eɪ] in both conditions. Even though some tokens of citation-form [ee] were determined spectrally to be most similar to AE [ɪ] (5 out of 12 tokens, see Table II), the influence of token variability was not observed in its assimilation pattern (94% to [eɪ]). As for sentence form [ee], 9 out of 12 tokens were spectrally similar to AE [ɪ] (see Table III), but AE listeners were not influenced by token variability or spectral similarity, and almost unanimously assimilated it to AE [eɪ]. However, for sentence-form [ee], the average vocalic duration was 140 ms, which was closer to that of AE [eɪ] (132 ms) than [ɪ] (94 ms). Therefore, although AE listeners ignored vowel duration for [ii, i, ɯɯ, ɯ, oo, o], temporal similarity may have contributed to AE listeners' perceptual assimilation of Japanese [ee].

As expected, perceptual assimilation patterns for 1-mora [a] and [e] in both forms included more than one AE category. The modal responses were long AE vowels ([ɑː-ɔː] and [eɪ], respectively), but relatively large proportions of other responses were given ([ʌ] for [a] and [ɪ, ɛ] for [e]). As indicated in Table IV, these perceptual assimilation patterns were not entirely predictable from spectral similarity comparisons. Even when vocalic duration was considered, unlike sentence-form [ee], these assimilation patterns suggest the influence of other factors.

In order to account for the less consistent overall assimilation patterns observed for [e] and [a] in both speaking styles, further examination was performed to discover whether these patterns were due to individual differences across AE listeners or to within-listener inconsistency. The results revealed that a few listeners consistently made nonmodal responses for these vowels and their responses can be classified into either spectra-based or duration-based categorizations. Spectra-based patterns were found for citation-form [e] and [a]: responses from three listeners (2, 3, 11) consisted of 83% of [ɪ] responses for citation [e]. Similarly, for citation-form [a], 52% of [ʌ] responses were made by three listeners (1, 4, 10). Although sentence-form [a] was spectrally most similar to AE [ɑː-ɔː], three listeners (1, 2, 10) perceived this vowel as most similar to AE short vowel [ʌ], suggesting the influence of duration. The response pattern for sentence [e] can be considered partially spectra-based. Six listeners made 68% of the nonmodal responses ([ɪ] or [ɛ]).[5] Of these nonmodal responses, one listener (1) responded with AE [ɪ] and [ɛ] equally often (44%); two listeners (2, 3) made [ɪ] responses most often, whereas [ɛ] was the modal response for the three remaining listeners (8, 10, 11). The [ɪ] response was consistent with the spectral and possibly temporal similarity to 1-mora [e]; other listeners may have chosen [ɛ] because 1-mora [e] (53 ms) was temporally more similar to [ɛ] (98 ms) than [eɪ] (132 ms). Still, it is not clear as to why the majority of listeners responded with spectrally and temporally less similar AE vowels in perceptually assimilating these Japanese vowels.

IV. GENERAL DISCUSSION

In the present study, the similarity of Japanese vowels to the AE vowel system was examined through acoustic comparisons and perceptual assimilation tasks, using stimulus materials produced by four male speakers from each language. Consonantal context was held constant and CV and VC coarticulatory effects were considered minimal, but the target vowels were produced in citation form and in a carrier sentence to examine the influence of token variability associated with speaking style as well as individual speakers.

Results of the acoustic analysis (Sec. II) showed that Japanese has five distinctive spectral vowel categories that were further separated into five long-short pairs. In contrast, although the 11 AE categories were differentiated fairly well by spectral measures, the inclusion of stimulus duration improved classification only slightly. Token variability due to speaking style was small for both Japanese and AE. Cross-language acoustic comparisons using only spectral measures (F1 and F2 at vowel midpoint) indicated that Japanese vowels [ii, i, ɯɯ, ɯ, oo, o] in both speaking styles were most similar to long AE vowels [iː, uː, oʊ], respectively, whereas classification of [ee, e, aa, a] straddled more than one AE category. Thus, it was predicted that if AE listeners rely primarily on the spectral cues, the perceptual assimilation patterns should reflect these acoustic similarity patterns, with highly consistent categorization of long and short [ii/i, oo/o, ɯɯ/ɯ], but less consistent assimilation of long and short [ee/e, aa/a].

Perceptual assimilation results revealed that the five 2-mora Japanese vowels [ii, ee, aa, oo, ɯɯ] produced in both speaking styles were consistently assimilated to comparable long AE vowels [iː, eɪ, ɑː-ɔː, oʊ, uː], respectively. Therefore, according to SLM (Flege, 1995), Japanese 2-mora vowels can be considered perceptually identical or highly similar to AE long vowels. On the other hand, the Japanese 1-mora vowels showed more varied patterns. The high vowels [i, ɯ] and mid, back vowel [o] were consistently assimilated to AE vowels [iː, uː, oʊ], respectively. This is in accordance with the results of spectral comparisons, and suggests that AE listeners perceived these Japanese vowels as identical or highly similar to their spectrally most similar AE *long* vowels and disregarded their shorter duration. Considering that their 2-mora counterparts [ii, ɯɯ, oo] were also assimilated to these same AE categories, the assimilation patterns of these long/short Japanese pairs can be considered examples of a "single-category pattern" in PAM (Best, 1995).

As for the remaining 1-mora vowels [e, a], the responses from a few listeners were accounted for by cross-language acoustic similarity (spectral, temporal, or both). On the other hand, the remaining AE listeners assimilated these Japanese

vowels into the same AE categories [eɪ, ɑː-ɔː] as for their 2-mora counterparts and as equally good exemplars, suggesting a "single-category" assimilation pattern. Unlike the minority responses, these responses could not be explained by cross-language acoustic similarity patterns.

Then what would explain these majority responses? Recall that the perceptual task used in the present study has been used successfully to assess assimilation of many L2 vowels by listeners from L1s with smaller vowel inventories (Strange *et al.*, 1998; 2001; 2004; 2005). In those studies, cross-language discriminant analyses predicted perceptual assimilation patterns well for most, but not all non-native vowels that had counterparts in the L1. However, for some "new" vowels, such as the front rounded vowels of German that are not distinctive in AE, context-specific spectral similarity did *not* predict perceptual similarity patterns by naïve AE listeners. Since all five Japanese vowel qualities can be considered to be present in AE, it was hypothesized in the present study that the same perceptual assimilation task should effectively reveal perceptual similarity patterns based primarily on cross-language spectral similarity. The present results suggested otherwise in some cases. For these failures, at least two explanations can be offered. One concerns the method of acoustic comparison, and the other is associated with the assumptions of the perceptual task.

As Hillenbrand *et al.* (1995) and others have shown in AE, formant trajectories for many spectrally adjacent short/long vowel pairs tend to be in the opposite directions in the vowel space, with the lax vowels (including long [æ]) moving toward more central positions, while tense vowels move toward peripheral positions in vowel space. These formant movements have been shown to affect vowel perception by AE listeners (cf. Nearey and Assmann, 1986; Nearey, 1989; Strange *et al.*, 1983). Therefore, even though both long and short Japanese vowels tend to be monophthongal, if they are spectrally similar to AE [eɪ, ɑː-ɔː] at some time point other than the vocalic midpoint, AE listeners' perceptual assimilation might be influenced by such similarity. Furthermore, as PAM hypothesizes, if listeners perceive articulatory gestures in the acoustic signal, similarity in the formant trajectories may explain the perceptual results. In order to test this hypothesis, Japanese 1-mora vowels [e] and [a] were subjected to a series of cross-language discriminant analyses using F1 and F2 values at three time points, namely, 25%, 50%, and 75% points of vowel duration. Separate analyses were performed for each speaking style using four combinations of three time points: 25% only, 75% only, 25%+75%, and 25%+50%+75%. Results showed that none of the four combinations yielded different results from those reported in Tables II and III. Therefore, although there might be some other subtle cues that have influenced perceptual assimilation, it was deemed reasonable to exclude inadequacy or insufficiency of the present acoustic comparison in failing to predict perceptual assimilation patterns for these vowels.

Turning to the second hypothesis, considering that both [e] and [a] were assimilated primarily to AE categories [eɪ, ɑː-ɔː] that are closer to the periphery in the vowel space than the spectrally more similar [ɪ, ʌ] are (see Fig. 2), the present results suggest the possible existence of other mechanisms that are not currently included in PAM or SLM. For example, although it was not intended to make such a claim, the present results resemble the "peripherality bias" that Polka and Bohn (2003) suggested to account for asymmetries in infant vowel discrimination. They summarized the results of their own studies and others and showed that the asymmetries in vowel perception by infants exhibit a bias for better discrimination in the category change paradigm when the stimuli changed from a more central to a more peripheral vowel (e.g., [ʊ] to [o], [ɛ] to [æ], [y] to [u], etc.). They concluded that this bias toward peripheral vowels may have an important role as perceptual anchors for language acquisition. Assuming this bias is present into adulthood and guides non-native speech learning, the present results for Japanese 1-mora vowels, including [e, a] might be explained by this perceptual bias toward more peripheral vowels as follows. Judging from the acoustic similarity and the observed perceptual assimilation patterns, it can be hypothesized that AE listeners compared the incoming 1-mora Japanese vowels against both long and short AE vowels, but due to their lack of attunement to duration cues and the peripherality bias, AE listeners chose more peripheral vowels as most similar to the Japanese vowels.[6]

Finally, the present study compared Japanese and AE vowels produced in relatively uncoarticulated [hVb] context in both citation and sentence conditions. More research is underway that compares how cross-language acoustic and perceptual similarities may vary when vowels are coarticulated in different consonantal contexts, and at different speaking rates and in different prosodic environments. Research on AE listeners' perceptual assimilation of North German and Parisian French vowels (Strange *et al.*, 2005) suggests that perceptual assimilation patterns often reflect context-*independent* patterns of acoustic similarity. For instance, AE listeners assimilate front, rounded vowels to back AE vowels, rather than to front, unrounded AE vowels, even in contexts in which back AE vowels are *not* fronted. However, since back AE vowels are fronted in coronal consonantal contexts (whereas front, unrounded AE vowels are never backed) (Strange *et al.*, 2007), front, rounded vowels can be considered allophonic variations of back AE vowels by AE listeners. In citation-form utterances, AE listeners were able to indicate that these front "allophones" were inappropriate in noncoronal contexts by rating them as poor exemplars of AE back vowels. However, in sentence condition, front, rounded vowels were considered "good" instances of back AE vowels even when surrounded by labial consonants. Thus, while context-specific spectral similarity did not predict assimilation of front, rounded vowels in noncoronal contexts, context-*independent* spectral similarity relationships did. Further research on acoustic and perceptual similarity of Japanese and AE vowels is needed to determine whether context-independent spectral similarity patterns might account for perceptual assimilation of Japanese [e, a], as well as the remaining 1-mora vowels.

V. CONCLUSIONS

The present study set out to test whether the perceptual task used in previous studies was also useful in assessing perceptual similarity of non-native vowels from a small vowel inventory by listeners from a relatively large vowel inventory. As in previous studies, the results showed that cross-language acoustic similarity may not always accurately predict perceptual assimilation of non-native vowels. Thus, direct assessments of perceptual similarity relationships will be better predictors of discrimination difficulties by L2 learners according to PAM and SLM. It was hypothesized that the inconsistency between acoustic and perceptual similarity results may suggest the existence of comparison processes that are influenced by listeners' knowledge about the distributional characteristics of phonetic segments in their native language. Under some stimulus and task conditions, the listeners may be able to compare phonetically detailed aspects of non-native segments, while in others, they may resort to a phonological level of analysis in making cross-language similarity judgments. Further research is needed to investigate under what conditions AE listeners may be able to utilize the large duration differences in Japanese 1-mora and 2-mora vowels when making perceptual similarity judgments and when attempting to differentiate these phonologically contrastive vowel pairs. In general, the findings of the present studies, as well as previous experiments on AE listeners' perceptual assimilation of German vowels suggest that vocalic duration differences are often ignored in relating non-native vowels to native categories.

ACKNOWLEDGMENTS

This research has been supported by NIDCD under Grant No. DC00323 to W. Strange and JSPS under Grant No. 17202012 to R. Akahane-Yamada. The authors are grateful to Katherine Bielec, Mary Carroll, Robin Rodriguez, and David Thornton for their support with HYPERCARD stack programming, subject running, and data analysis.

APPENDIX: AVERAGE FORMANT FREQUENCIES AND DURATIONS OF JAPANESE AND AMERICAN ENGLISH VOWELS

J	F1	F2	F3	Duration	AE	F1	F2	F3	Duration
				Citation form					
ii	295	2243	3123	138	iː	312	2307	2917	100
ee	443	1982	2563	154	eᴵ	472	2062	2660	122
aa	709	1175	2343	165	ɑː	753	1250	2596	109
					ɔː	678	1062	2678	132
oo	423	732	2416	154	oᵘ	500	909	2643	112
ɯɯ	322	1139	2288	146	uː	348	995	2374	104
					æː	730	1568	2519	123
i	317	2077	3027	51	ɪ	486	1785	2573	86
e	437	1785	2430	57	ɛ	633	1588	2553	91
a	615	1182	2289	53	ʌ	635	1189	2619	89
o	430	805	2375	54					
ɯ	349	1171	2302	47	ʊ	489	1148	2472	93
				long/short ratio=2.9					long/short ratio=1.3
				Sentence form					
ii	299	2189	3198	116	iː	303	2336	2961	108
ee	445	1925	2638	140	eᴵ	423	2175	2722	132
aa	687	1146	2337	138	ɑː	754	1234	2609	125
					ɔː	660	1056	2571	152
oo	434	796	2400	127	oᵘ	479	933	2571	126
ɯɯ	319	1128	2361	128	uː	342	1064	2422	115
					æː	714	1645	2456	147
i	312	2076	3115	37	ɪ	461	1826	2634	94
e	464	1770	2407	53	ɛ	627	1657	2544	98
a	672	1134	2288	49	ʌ	631	1232	2619	98
o	423	776	2345	47					
ɯ	348	1069	2343	38	ʊ	495	1202	2492	107
				long/short ratio=2.9					long/short ratio=1.3

[1]In addition to these cases of assimilation of speech sounds to L1 categories, PAM includes a case of categorization of L2 sounds to nonspeech categories (i.e., nonassimilable) where discrimination can range from good to very good, based on the psychoacoustic salience of the acoustic patterns.

[2]The preliminary analyses for Japanese vowels did not reveal considerable differences between two-formant vs three-formant analyses. Therefore, all discriminant analyses were performed using only F1 and F2 values.

[3]The lower F1 for Japanese mid and low vowels were deemed cross-language differences rather than differences in vocal tract sizes between the two speaker groups based on the acoustic similarity between Japanese [ii] and AE [iː].

[4]According to Labov *et al.* (2006), differentiation between [ɑː, ɔː] by AE speakers in Tampa area is variable overall, although they are produced distinctively before [n] and [t].

[5]In some dialects in American English, [ɪ] and [ɛ] may be merged (Labov *et al.*, 2006). However, the dialectal profiles of these listeners indicate no such relationship with their response patterns.

[6]It should be pointed out that the present study is considerably different from the studies with infants in methodological aspects. Using synthetic stimuli, Johnson *et al.* (1993) found that phonetic targets for native vowels are similar to the hyperarticulated forms, but the existence of a peripherality bias for speaker-produced stimuli by adult listeners has not yet been confirmed in any published study.

Best, C. T. (**1995**). "A direct realist view of cross-language speech perception," in *Speech Perception and Linguistic Experience: Issues in Cross-Language Research*, edited by W. Strange (York Press, Timonium, MD), pp. 171–204.

Best, C. T., McRoberts, G. W., and Goodell, E. (**2001**). "Discrimination of non-native consonant contrasts varying in perceptual assimilation to the listener's native phonological system," J. Acoust. Soc. Am. **109**, 775–794.

Best, C. T., McRoberts, G. W., and Sithole, N. N. (**1988**). "The phonological basis of perceptual loss for non-native contrasts: Maintenance of discrimination among Zulu clicks by English-speaking adults and infants," J. Exp. Psychol. Hum. Percept. Perform. **14**, 345–360.

Flege, J. E. (**1995**). "Second language speech learning: Theory, findings, and problems," in *Speech Perception and Linguistic Experience: Issues in Cross-Language Research*, edited by W. Strange (York Press, Timonium, MD), pp. 233–277.

Flege, J. E., MacKay, I. R. A., and Meador, D. (**1999**). "Native Italian speakers' perception and production of English vowels," J. Acoust. Soc. Am. **106**, 2973–2987.

Fox, R. A., Flege, J. E., and Munro, M. J. (**1995**). "The perception of English and Spanish vowels by native English and Spanish listeners: A multidimensional scaling analysis," J. Acoust. Soc. Am. **97**, 2540–2551.

Gottfried, T. L. (**1984**). "Effects of consonant context on the perception of

French vowels," J. Phonetics **12**, 91–114.
Han, M. S. (**1962**). *Japanese Phonology: An Analysis Based upon Sound Spectrograms* (Kenkyusha, Tokyo).
Hillenbrand, J., Getty, L. A., Clark, M. J., and Wheeler, K. (**1995**). "Acoustic characteristics of American English vowels," J. Acoust. Soc. Am. **97**, 3099–3111.
Hirata, Y., and Tsukada, K. (**2004**). "The effects of speaking rate and vowel length on formant movements in Japanese," in *Proceedings of the 2003 Texas Linguistics Society Conference*, edited by A. Agwuele, W. Warren, and S.-H. Park (Cascadilla Proceedings Project, Somerville, CA), pp. 73–85.
Homma, Y. (**1981**). "Durational relationships between Japanese stops and vowels," J. Phonetics **9**, 273–281.
Homma, Y. (**1992**). *Acoustic Phonetics in English and Japanese* (Yamaguchi-shoten, Tokyo).
Johnson, K., Flemming, E., and Wright, R. (**1993**). "The hyperspace effect: Phonetic targets are hyporarticulated," Language **69**, 505–528.
Keating, P. A., and Huffman, M. K. (**1984**). "Vowel variation in Jpaanese," Phonetica **41**, 191–207.
Klatt, D. H. (**1976**). "Linguistic uses of segmental duration in English: Acoustic and perceptual evidence," J. Acoust. Soc. Am. **59**, 1208–1221.
Klecka, W. R. (**1980**). *Discriminant Analysis*, (Sage, Newbury Park, CA).
Labov, W., Ash, S., and Boberg, C. (**2006**). *Atlas of North American English: Phonology and Phonetics* (Mouton de Gruyer, Berlin).
Ladefoged, P. (**1993**). *A Course in Phonetics*, 3rd ed. (Harcourt Brace, Orlando, FL).
Nearey, T. M. (**1989**). "Static, dynamic, and relational properties in vowel perception," J. Acoust. Soc. Am. **85**, 2088–2113.
Nearey, T. M., and Assmann, P. F. (**1986**). "Modeling the role of inherent spectral change in vowel identification," J. Acoust. Soc. Am. **80**, 1297–1308.
Peterson, G. E., and Lehiste, I. (**1960**). "Duration of syllable nuclei in English," J. Acoust. Soc. Am. **32**, 693–703.
Polka, L., and Bohn, O.-S. (**2003**). "Asymmetries in vowel perception," Speech Commun. **41**, 221–231.
Pruitt, J. S., Jenkins, J. J., and Strange, W. (**2006**). "Training the perception of Hindi dental and retroflex stops by native speakers of American English and Japanese," J. Acoust. Soc. Am. **119**, 1684–1696.
Rochet, B. L. (**1995**). "Perception and production of second-language speech sounds by adults," in *Speech Perception and Linguistic Experience: Issues in Cross-Language Research*, edited by W. Strange (York Press, Timonium, MD), pp. 379–410.
Schmidt, A. M. (**1996**). "Cross-language identification of consonants. Part 1. Korean perception of English," J. Acoust. Soc. Am. **99**, 3201–3221.
Shibatani, M. (**1990**). *The Languages of Japan* (Cambridge University Press, New York).
Stack, J. W., Strange, W., Jenkins, J. J., Clarke, III, W. D., and Trent, S. A. (**2006**). "Perceptual invariance of coarticulated vowels over variations in speaking style," J. Acoust. Soc. Am. **119**, 2394–2405.
Strange, W. (**2007**). "Cross-language phonetic similarity of vowels: Theoretical and methodological issues," in *Language Experience in Second Language Speech Learning: In Honor of James Emile Flege*, edited by O.-S. Bohn and M. J. Munro (John Benjamins, Amsterdam), pp. 35–55.
Strange, W., Akahane-Yamada, R., Kubo, R., Trent, S. A., and Nishi, K. (**2001**). "Effects of consonantal context on perceptual assimilation of American English vowels by Japanese listeners," J. Acoust. Soc. Am. **109**, 1691–1704.
Strange, W., Akahane-Yamada, R., Kubo, R., Trent, S. A., Nishi, K., and Jenkins, J. J. (**1998**). "Perceptual assimilation of American English vowels by Japanese listeners," J. Phonetics **26**, 311–344.
Strange, W., Bohn, O.-S., Nishi, K., and Trent, S. A. (**2005**). "Contextual variation in the acoustic and perceptual similarity of North German and American English vowels," J. Acoust. Soc. Am. **118**, 1751–1762.
Strange, W., Bohn, O.-S., Trent, S. A., and Nishi, K. (**2004**). "Acoustic and perceptual similarity of North German and American English vowels," J. Acoust. Soc. Am. **115**, 1791–1807.
Strange, W., Jenkins, J. J., and Johnson, T. L. (**1983**). "Dynamic specification of coarticulated vowels," J. Acoust. Soc. Am. **74**, 695–705.
Strange, W., Weber, A., Levy, E., Shafiro, V., Hisagi, M., and Nishi, K. (**2007**). "Acoustic variability of German, French, and American vowels: Phonetic context effects," J. Acoust. Soc. Am. **122**, 1111–1129.
Werker, J. F., and Tees, R. C. (**1984**). "Cross-language speech perception: Evidence for perceptual reorganization during the first year of life," Infant Behav. Dev. **7**, 49–63.

Pitch circularity from tones comprising full harmonic series

Diana Deutsch,[a] Kevin Dooley, and Trevor Henthorn
Department of Psychology, University of California, San Diego, La Jolla, California 92093

(Received 23 January 2008; revised 22 April 2008; accepted 23 April 2008)

This paper describes an algorithm for producing pitch circularity using tones that each comprise a full harmonic series, and reports an experiment that demonstrates such circularity. Banks of 12 tones (i.e., scales) were created, with ***F***0 varying in semitone steps. For each scale, as ***F***0 descended, the amplitudes of the odd-numbered harmonics were reduced relative to the even-numbered ones by 3.5 dB for each semitone step. In consequence, the tone with the lowest ***F***0 was heard as though displaced up an octave. In an experiment employing two such scales, all possible ordered tone pairs from each scale were presented, making 132 ordered tone pairs for each scale. Sixteen subjects judged for each tone pair whether the second tone was higher or lower than the first. The data derived from these pairwise comparisons were subjected to Kruskal's nonmetric multidimensional scaling, and excellent circularities were obtained. Individual differences in the subjects' judgments were also explored. The findings support the argument that musical pitch should be characterized as varying along two dimensions: the monotonic dimension of pitch height and the circular dimension of pitch class. © *2008 Acoustical Society of America.* [DOI: 10.1121/1.2931957]

PACS number(s): 43.75.Bc, 43.75.Cd [NHF] Pages: 589–597

I. INTRODUCTION

The American National Standards Institute defines pitch as varying along a single monotonic continuum, specifically as "that attribute of auditory sensation in terms of which sounds may be ordered on a scale extending from high to low" (ANSI, 1973). However, musicians have long acknowledged that there is a strong perceptual similarity between tones that stand in octave relation. From a musical standpoint, therefore, pitch is regarded as varying along two dimensions: the monotonic dimension of *pitch height* refers to the position of a tone along a continuum from high to low, and the circular dimension of *pitch class* (or *tone chroma*) refers to the position of a tone within the octave (see, for example, Meyer, 1904; Ruckmick, 1929; Bachem, 1948; Shepard, 1964, 1965, 1982; Pickler, 1966; Risset, 1969; Deutsch, 1969, 1973; 1999; Deutsch *et al.* 1987; Burns and Ward, 1982; Patterson, 1986; Ueda and Ohgushi, 1987; Warren *et al.*, 2003). In the Western musical scale, a note is represented first by a letter name, which refers to its position within the octave, and then by a number, which refers to the octave in which it is placed. For example, the symbols E_2, E_3, and E_4 refer to notes of the same pitch class that are placed in different octaves, and the symbols D_3, $G\#_3$, and A_3 refer to notes of different pitch classes that are placed in the same octave. Given these considerations, musical pitch is often described in terms of a helix which completes one full turn per octave (Fig. 1), so that tones that are separated by octaves are depicted as in close spatial proximity (see, for example, Shepard, 1964, 1965, 1982; Burns and Ward, 1982; Ueda and Ohgushi, 1987; Warren *et al.*, 2003).

In a seminal experiment, Shepard (1964) showed that the monotonic and circular dimensions of pitch can be decoupled experimentally. He employed a bank of tones that each consisted of ten partials which were separated by octaves. The amplitudes of the partials were scaled by a fixed, bell-shaped spectral envelope, so that those in the middle of the musical range were highest, while the others fell off gradually in both directions along a log frequency continuum. Such tones were heard as well defined in terms of pitch class, but ambiguously in terms of pitch height. Listeners were presented with ordered pairs of such tones, and they judged for each pair whether it formed an ascending or a descending pattern. When the tones within a pair were separated by a short distance along the pitch class circle, judgments of relative height were determined entirely by proximity. As the distance between the tones along the circle increased, the tendency to follow by proximity decreased, so that when the tones were separated by a half-octave, averaging across pitch classes, ascending and descending judgments occurred equally often.

Using such a bank of tones, Shepard produced an intriguing demonstration. When the pitch class circle was repeatedly traversed in clockwise steps, the impression was created of a scale that ascended endlessly in pitch. When the circle was traversed in counterclockwise steps, the scale appeared to descend endlessly instead. Risset (1969) generated some remarkable variants of this illusion using gliding tones, so giving rise impressions of endlessly ascending and descending glides. Additional work has been carried out demonstrating the importance of proximity in making judgments of relative height for octave-related complexes (see, for example, Ueda and Ohgushi, 1987; Allik *et al.*, 1989; Deutsch, 1991). Further work has shown that pitch circularities can be produced by tones whose components stand in intervals other than the octave (Burns, 1981, Nakajima *et al.*, 1988).

If pitch circularity were confined to tone complexes such as these, its implications could be considered limited on both theoretical and practical grounds. However, if such circularity could also be achieved with a bank of tones that each

[a]Electronic mail: ddeutsch@ucsd.edu

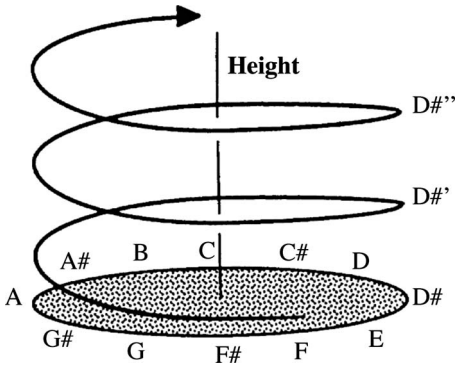

FIG. 1. The pitch helix. Musical pitch is here depicted as varying both along a monotonic dimension of height and also along a circular dimension of pitch class. The helix completes one full turn per octave, so that tones standing in octave relation are in close spatial proximity, as shown by *D*, *D′*, and *D″* in the figure.

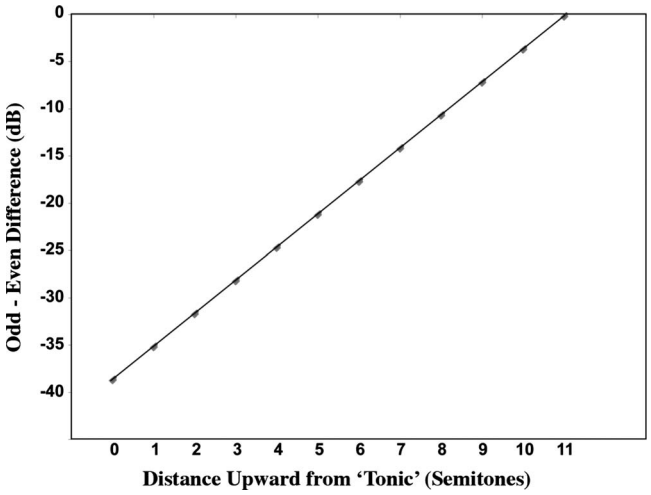

FIG. 2. Relative amplitudes of the odd and even harmonics of the tones employed in the experiment as a function of their positions along the scale. The amplitudes of the odd harmonics relative to the even ones decreased in 3.5 dB steps as their upward distance from the "tonic" decreased in semitone steps (see text for details).

comprised a full harmonic series, then its implications would be broadened, both theoretically and also for musical practice. The present study was carried out in an attempt to achieve such circularity.

Benade (1976) pointed out that a good flute player can smoothly vary the strengths of the odd harmonics of a sustained tone relative to the even ones. Suppose, then, that he begins with the note A_4 ($\boldsymbol{F}0=440$ Hz) with significant amounts of the first six harmonics; this will be heard as well-defined in terms of both pitch class and octave. If the performer then alters his manner of blowing so as to progressively weaken the odd harmonics relative to the even ones, the listener will come to realize, at some point, that he is now hearing a tone at A_5 ($\boldsymbol{F}0=880$ Hz)—exactly an octave higher. However, the transition from the lower to the higher octave will appear quite smooth. This informal observation indicates that the perceived height of a tone consisting of adjacent harmonics might be made to vary in a continuous fashion within the octave, while its pitch class remained constant. Returning to the helical model, one can surmise that to produce differences in pitch height, one need not necessarily travel along a helical path (though the latter analogy still applies to sine waves and to most instrument tones), but can also traverse a straight path along the surface of a cylinder; for example through *D#*, *D#′*, and *D#″* in Fig. 1.

Patterson *et al.* (1993) carried out an experiment to investigate this possibility. They generated a bank of tones, each of which consisted of the first 28 harmonics, with $\boldsymbol{F}0$s ranging from 31.25 to 1000 Hz. For each tone, the amplitudes of the odd harmonics relative to the even ones were reduced by 9, 18, or 27 dB, and subjects judged the octave in which each tone was placed. Averaging across subjects, at a 27 dB attenuation of the odd harmonics, the tones were judged to be roughly an octave higher, and at 9 and 18 dB attenuations, their perceived heights were judged to be roughly 29% and 77% between the lower and higher octaves. In a further study, Warren *et al.* (2003) presented three subjects with a standard tone and a test tone in which the odd harmonics were attenuated more than those of the standard. The tones were all at $\boldsymbol{F}0=80$ Hz, with harmonics up to 4 kHz, and subjects judged on each trial which of the two presented tones was higher in pitch. Reliable judgments of differences in pitch height were made at around 2 dB attenuation of the odd harmonics.

Given that the pitch of a harmonic complex tone can vary smoothly in height while remaining in the same pitch class, one can theoretically produce circular banks of tones by manipulating the relative amplitudes of the odd and even harmonics. One begins with a bank of 12 tones, each of which consists of the first six components of a harmonic series, and with $\boldsymbol{F}0$s ranging in semitone steps over an octave. For the tone with the highest $\boldsymbol{F}0$, the odd and even harmonics are identical in amplitude. Then for the tone with $\boldsymbol{F}0$ a semitone lower, the amplitudes of the odd harmonics are reduced relative to the even ones, thus raising the perceived height of this tone. Then for the tone with $\boldsymbol{F}0$ another semitone lower, the amplitudes of the odd harmonics are reduced further, thus raising the perceived height of this tone to a greater extent. One then moves down the octave in this fashion until, for the lowest $\boldsymbol{F}0$, the odd harmonics no longer contribute to perceived height. The tone with the lowest $\boldsymbol{F}0$ is therefore heard as displaced up an octave, and so as higher in pitch than the tone with the highest $\boldsymbol{F}0$. In this way, pitch circularity is achieved.[1]

II. METHOD

A. Stimulus patterns and procedure

Two banks of tones were created, which we shall refer to as *scales*. Each scale consisted of 12 tones, and each tone comprised the first six components of a harmonic series. For convenience, we shall refer to the tone with the lowest $\boldsymbol{F}0$ as the *tonic* of the scale. For the first scale, the tonic was A_4 (440 Hz), and for the second scale it was $F\#_4$ (370 Hz). For both scales, as $\boldsymbol{F}0$ moved down in semitone steps, the amplitudes of the odd harmonics relative to the even ones decreased by 3.5 dB (see Fig. 2). Specifically, for the tone with the highest $\boldsymbol{F}0$ (tone 11 in the figure) the odd and even har-

monics were equal in amplitude. For the tone with *F*0 a semitone lower (tone 10 in the figure), the odd harmonics were 3.5 dB lower than the even ones. For the tone with *F*0 a semitone lower (tone 9 in the figure), the odd harmonics were 7.0 dB lower than the even ones. Thus for the tone with lowest *F*0 (tone 0 in the figure) the odd harmonics were 38.5 dB lower than the even ones.

To achieve the above pattern of relationship for harmonic pairs 1 and 2, and harmonic pairs 3 and 4, the even harmonics were consistently high in amplitude, while the odd harmonics decreased in amplitude as the scale descended. To achieve the same pattern of relationship for harmonic pairs 5 and 6, harmonic 5 was consistently low in amplitude while harmonic 6 increased in amplitude as the scale descended (see Fig. 3). To reduce the overall amplitude differences between the tone complexes, these were adjusted slightly, leading to the pattern of amplitude relationships for the different harmonics shown in Table I. The tones were 500 ms in duration with 5 ms rise and fall times and were generated with harmonics in sine phase at a sample rate of 44.1 kHz.

For each scale, 132 ordered tone pairs were created, such that each pitch class was followed once by every other pitch class. On each trial a tone pair was presented, and the subjects judged whether it formed an ascending or a descending pattern. For each scale, the tone pairs were presented in 11 blocks of 12. Each pitch class served as the first tone of a pair once in each block, and no pitch class occurred in two successive tone pairs within a block. Other than this, the tone pairs were presented in haphazard order. The tones within a pair followed each other without pause. There were 4 s intervals between pairs within a block, and 1 min intervals between blocks. The subjects were tested in two sessions, one with the scale generated under the A_4 tonic and the other generated under the $F\#_4$ tonic. The order of presentation of the two scales was strictly counterbalanced across subjects. In addition, two subjects served in six extra sessions, and so made judgments on each scale four times altogether.

B. Instrumentation

The tones were generated on a G5 computer, using the software package PD,[2] and were recorded onto a compact disk. The compact disks were played on a Denon DCD-815 compact disk player, the output of which was passed through a Mackie CR 1604-VLZ mixer, then through a Powerplay HA 4000 headphone distribution amplifier, and presented to subjects diotically in soundproof booths via Sennheiser HD 25 SP headphones at a level of roughly 70 dB sound pressure level (SPL).

C. Subjects

Sixteen students at UCSD served as subjects in the experiment. These were 5 male and 11 female, with an average age of 24.4 years (range 20–30 years), and an average of 8.3 years of musical training (range 0–20 years). They comprised 13 right handers and 3 non-right-handers, as determined by the handedness questionnaire of Varney and Benton (1975).[3] The subjects were selected on the basis of having normal hearing as determined by audiometry, and making no more than 2 errors on a pretest in which they judged whether 120 pairs of sine wave tones formed ascending or descending patterns. In the pretest, the tones were 500 ms in duration, and there were no gaps between tones within a pair. The tones within pairs were separated by 2, 4, 6, 8, or 10 semitones, in either the upward or the downward direction.

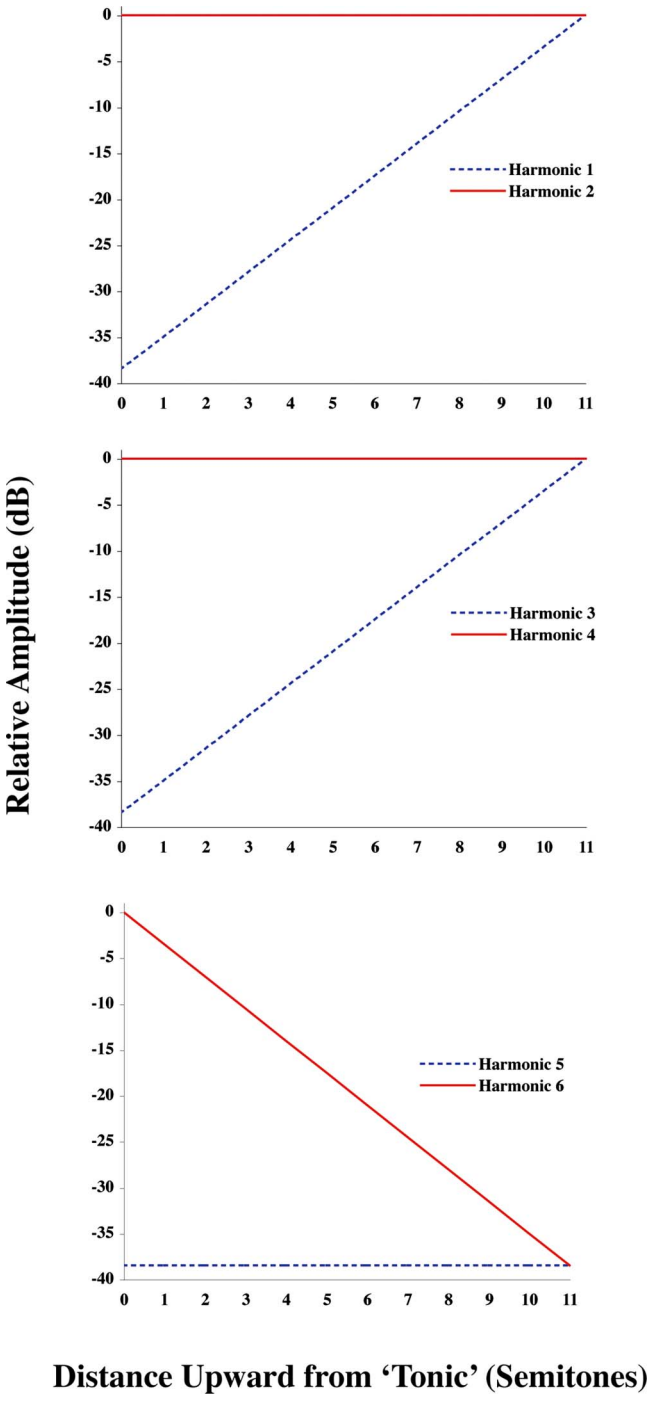

FIG. 3. (Color online) Progression of the relative amplitudes of harmonics 1 and 2, harmonics 3 and 4, and harmonics 5 and 6 as *F*0 moves upward from the "tonic."

TABLE I. Relative amplitudes (in dB) of the harmonics of the 12 tones comprising each circular scale. The distance upward along the scale is given in semitones.[a] For one scale, harmonic 1 of the tonic was 440 Hz (corresponding to A_4), and for the other scale, harmonic 1 of the tonic was 370 Hz (corresponding to $F\#_4$).

Distance upward along scale (semitones)	Harmonic number					
	1	2	3	4	5	6
0 ("tonic")	−40.5	−2	−40.5	−2	−40.5	−2
1	−36	−1	−36	−1	−39.5	−4.5
2	−31.5	0	−31.5	0	−38.5	−7
3	−28	0	−28	0	−38.5	−10.5
4	−24.5	0	−24.5	0	−38.5	−14
5	−21	0	−21	0	−38.5	−17.5
6	−17.5	0	−17.5	0	−38.5	−21
7	−14	0	−14	0	−38.5	−24.5
8	−10.5	0	−10.5	0	−38.5	−28
9	−8	−1	−8	−1	−39.5	−32.5
10	−5.5	−2	−5.5	−2	−40.5	−37
11	−3	−3	−3	−3	−41.5	−41.5

[a]It was later discovered that due to a typographical error, harmonic 5 of tone 9 was set at −39.9 dB rather than −39.5 dB. However, further testing revealed no perceptual effect resulting from this 0.4 dB amplitude discrepancy

III. RESULTS

A. Overall findings

Figure 4 shows the percentages of judgments based on pitch class proximity, as a function of semitone separation between the tones within a pair. The data are shown for the A_4 and $F\#_4$ scales separately, in each case averaged over all tone pairs and over all subjects. As can be seen, when the tones within a pair were separated by a small distance along the pitch class circle, judgments tended overwhelmingly to be based on proximity. This tendency was reduced with increasing distance between the tones along the pitch class circle, yet remained high even at the largest value of semitone separation between the tones.

A 5×2 within-subject analysis of variance (ANOVA) was performed, with value of semitone separation along the pitch class circle (1–5) and scale ($F\#_4$, A_4) as factors. (The value of 6 semitones was omitted from the analysis since at this value the same distance between the tones along the pitch class circle is traversed in either direction, so that proximity cannot be used as a cue.) The overall effect of semitone separation was highly significant [$F(4,60)=69.05$, $p<0.001$]. The overall effect of scale was nonsignificant ($F<1$), and the interaction between value of semitone separation and scale was nonsignificant [$F(4,60)=2.335$, $p>0.05$]. Pairwise comparisons revealed highly significant differences between all values of semitone separation: 1 vs 2 semitones, $p<0.02$; 2 vs 3 semitones, $p<0.001$; 3 vs 4 semitones, $p<0.001$; 4 vs 5 semitones, $p<0.001$.

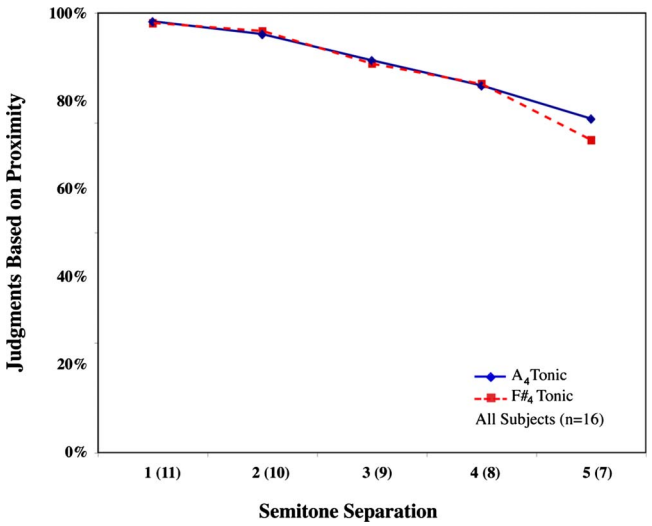

FIG. 4. (Color online) Percentages of judgments based on pitch class proximity as a function of semitone separation along the pitch class circle between the tones within a pair. The data are shown for the A_4 and $F\#_4$ scales separately, averaged across all subjects.

To determine the extent to which pitch circularity was achieved, the data were subjected to Kruskal's nonmetric multidimensional scaling, using ALSCAL (see Borg and Groenen, 2005). Figure 5 shows, for the $F\#_4$ and A_4 scales separately, the MDS solutions derived from the results pooled from all subjects, and it can be seen that excellent circularities were obtained from both scales. Figure 6 shows the stimulus configurations derived from each of the two subjects who were tested four times on both the $F\#_4$ and A_4 scales, and it can be seen that excellent circularities were obtained here also.

We can then ask whether violations of proximity, though uncommon, were related to the positions of the tones along the scale. To this end we plotted, for the $F\#_4$ and A_4 scales separately, the percentages of judgments that a tone was heard as the higher or lower of a pair, when this judgment was in violation of proximity. Figure 7 shows the results pooled from all subjects. As can be seen, an orderly, though small, tendency emerged under both scales to judge tones as higher with increasing upward position along the scale.

A 12×2 within-subject ANOVA was performed, with position along the scale (0–11) and scale ($F\#_4$, A_4) as factors. The overall effect of position along the scale was highly significant [$F(11,165)=5.715$, $p<0.001$]. The overall effect

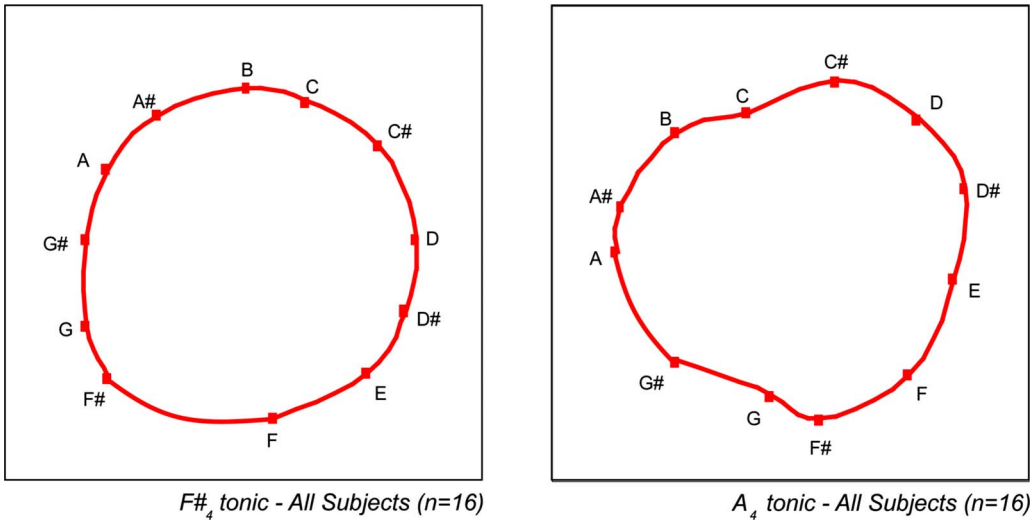

FIG. 5. (Color online) Multidimensional scaling solutions derived from the pooled data from all subjects, for tones produced under the scales based on the $F\#_4$ and A_4 tonics separately. For the $F\#_4$ tonic, stress $-1=0.0111$; $R^2=0.9991$. For the A_4 tonic, stress $-1=0.0113$; $R^2=0.9990$.

of scale was nonsignificant ($F=1$). The interaction between scale and position along the scale was marginally significant [$F(11,165)=1.898$, $p=0.043$], indicating a marginal influence of overall spectral region on the behavior of the circularity effect.

B. Individual differences

Although all subjects overwhelmingly judged the relative heights of the tones on the basis of proximity at small values of semitone separation, individual differences in judgment appeared at larger values. Since the tones were so configured that their spectral density necessarily increased with increasing position along the scale, it was hypothesized that some subjects might have been influenced by this cue. To examine this possibility, we divided the subjects into two groups on the basis of their judgments at the tritone, where proximity could not have been involved in their judgments. We found that, taking the data from both scales, six of the subjects based at least 21 of the 24 possible judgments at the tritone on this principle: they judged tones as higher when they were in higher positions along the scale, and as lower when they were in lower positions. These we designated as sp ("spectral") subjects. For the remaining ten subjects, judgments were scattered in haphazard fashion as a function of position along the scale; these we designated as pc ("pitch class") subjects. The six sp subjects comprised five right handers and one non-right-hander, two male and four female, with an average age of 24.5 years (range 23–26 years) and an average of 7.8 years of musical training (range 2–14 years). The 10 pc subjects comprised eight right handers and two non-right-handers, three male and seven female, with an average age of 24.4 years (range 20–30 years) and 8.6 years of musical training (range 0–20 years).

Figure 8 displays the tendency to base judgments on proximity as a function of semitone separation along the pitch class circle between the tones within a pair, for the pc and sp subjects separately, and for the $F\#_4$ and A_4 scales separately. As can be seen, for both scales, the pc subjects showed a remarkably strong tendency to follow by proximity, even at the largest value of semitone separation between the tones within a pair. However, the sp subjects tended less to follow by proximity as the values of semitone separation between the tones increased.

Given these apparent differences between the two subgroups, statistical analyses were carried out taking the pc and sp subjects separately. Where value of semitone separation was concerned, 5×2 within-subject ANOVAs were performed, with value of semitone separation (1–5) and scale ($F\#_4$, A_4) as factors. Taking the pc subjects alone, the overall effect of semitone separation was highly significant [$F(4,36)=30.99$, $p<0.001$], the overall effect of scale was nonsignificant ($F<1$), and the interaction between value of semitone separation and scale was also nonsignificant [$F(4,36)=2.09$, $p>0.05$]. Taking the sp subjects alone, the overall effect of value of semitone separation was significant [$F(4,20)=210.34$, $p<0.001$], the overall effect of scale was nonsignificant ($F<1$), and the interaction between the value of semitone separation and scale was also nonsignificant [$F(4,20)=2.37$, $p>0.05$].

Figure 9 displays the percentages of judgments that a tone was the higher or lower of a pair when these judgments were in violation of proximity, as a function of the position of the tone along the scale, for the pc and sp subjects separately, and for the A_4 and $F\#_4$ scales separately. As can be seen, for both scales, the sp subjects showed an increasing tendency to judge the tone as higher with increasing position along the scale; however, this was not true of the pc subjects.

To evaluate the statistical significance of these factors, 12×2 within-subject ANOVAs were performed, with position along the scale (0–11) and scale ($F\#_4$,A_4) as factors. For the pc subjects alone, the overall effect of position along the scale was nonsignificant ($F<1$), the overall effect of scale was nonsignificant ($F<1$), and the interaction between position along the scale and scale was marginally significant [$F(11,99)=2.01$; $p<0.05$], indicating for these subjects a marginal influence of overall spectral region on the behavior of the circularity effect. Taking the sp subjects alone, the overall effect of scale was nonsignificant ($F=1$), the overall

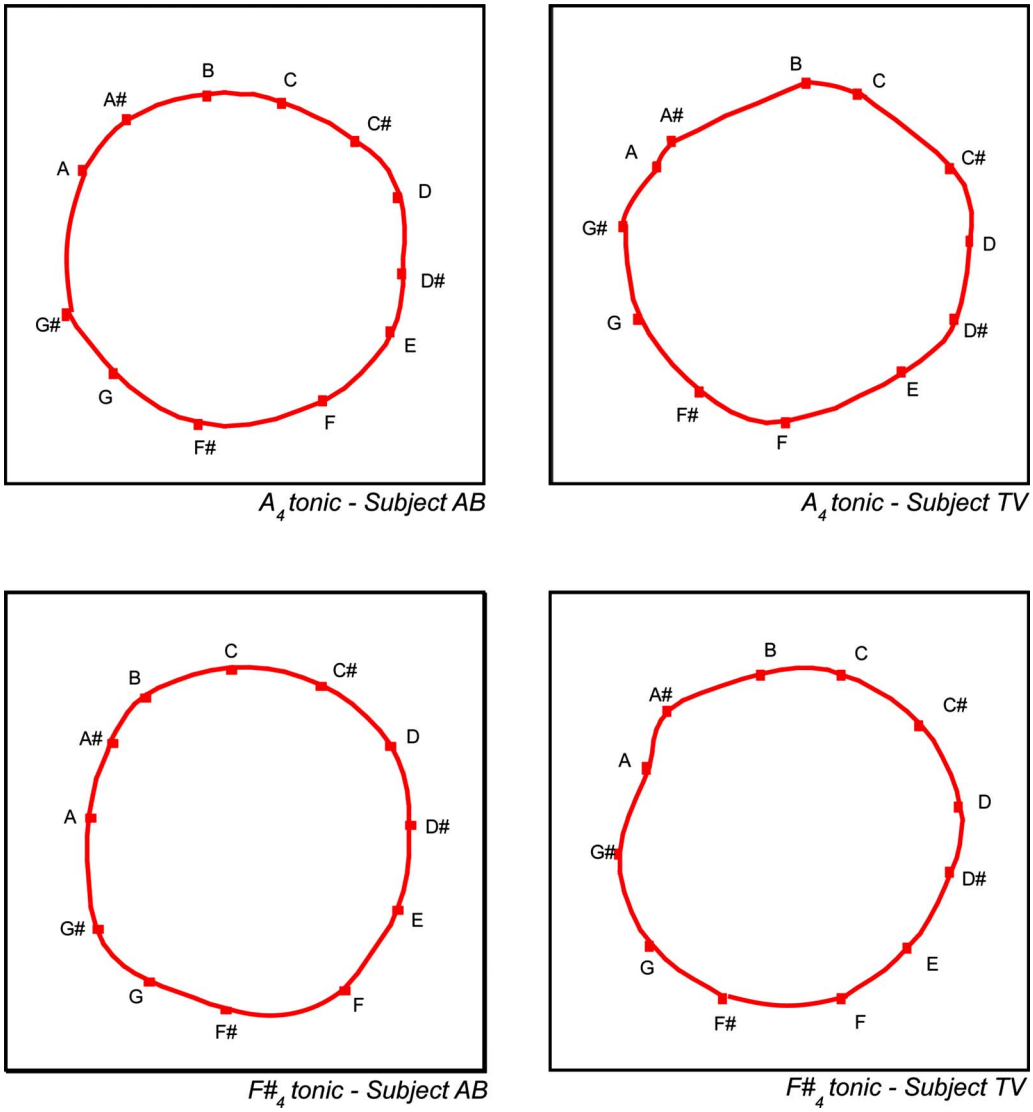

FIG. 6. (Color online) Multidimensional scaling solutions derived from the data from two subjects individually, for tones produced under the scales based on the $F\#_4$ and A_4 tonics separately. Subject AB: for the A_4 tonic, stress $-1=0.0099$; $R^2=0.9992$; for the $F\#_4$ tonic, stress $-1=0.0108$; $R^2=0.9991$. Subject TV: for the A_4 tonic, stress $-1=0.0211$; $R^2=0.9967$; for the $F\#_4$ tonic, stress $-1=0.0083$; $R^2=0.9995$.

effect of position along the scale was highly significant [$F(11,55)=29.14$, $p<0.001$], and the interaction between scale and position along the scale was nonsignificant [$F(11,55)=1.63$, $p>0.05$].

Despite these differences between the pc and sp subjects, the judgments of both subgroups were more consistent with a two-dimensional solution than a one-dimensional one. For judgments of the pc subjects on the A_4 scale, the one-dimensional solution yielded stress$-1=0.3506$ ($R^2=0.5885$), whereas the two-dimensional solution yielded stress$-1=0.0076$, ($R^2=0.9996$); on the $F\#_4$ scale, the one-dimensional solution yielded stress$-1=0.3691$ ($R^2=0.5487$), whereas the two-dimensional solution yielded stress$-1=0.0123$ ($R^2=0.9988$). For judgments of the sp subjects on the A_4 scale, the one-dimensional solution yielded stress$-1=0.1515$ ($R^2=0.9240$), whereas the two-dimensional solution yielded stress$-1=0.0191$ ($R^2=0.9979$); on the $F\#_4$ scale, the one-dimensional solution

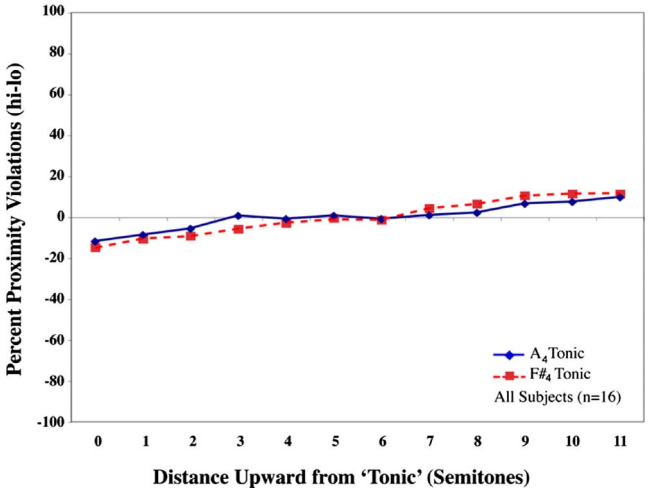

FIG. 7. (Color online) Percentages of judgments that a tone was the higher or lower of a pair, when these judgments were in violation of proximity, plotted as a function of the position of the tone along the scale. The data are shown for the A_4 and $F\#_4$ scales separately, averaged across all subjects.

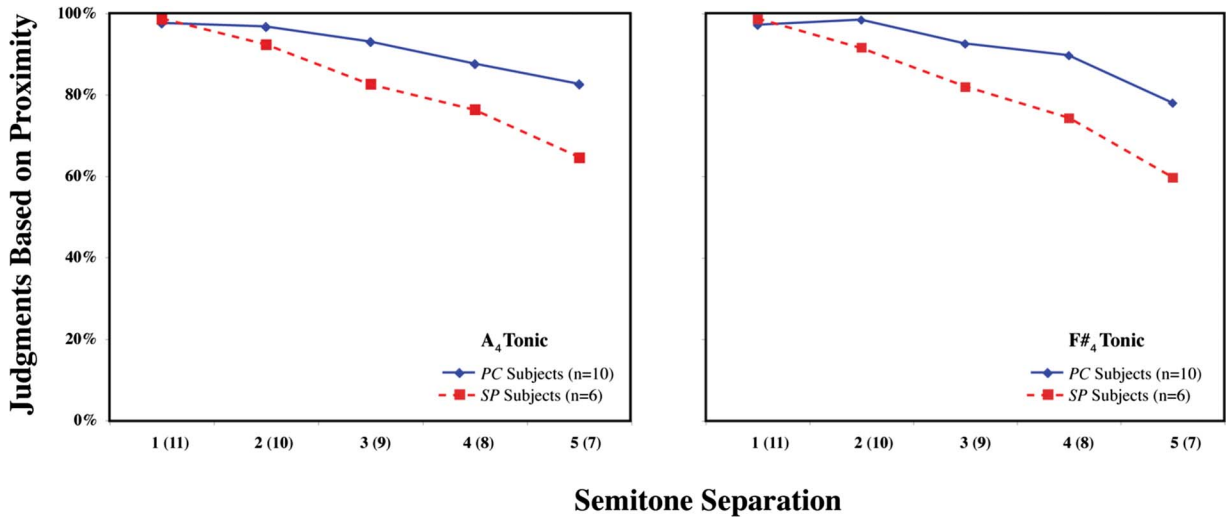

FIG. 8. (Color online) Percentages of judgments based on pitch class proximity as a function of semitone separation along the pitch class circle between the tones within a pair. The data are shown for the A_4 and $F\#_4$ scales separately and for the pc and sp subjects separately.

yielded stress$-1=0.1660$ ($R^2=0.9081$), whereas the two-dimensional solution yielded stress$-1=0.0107$ ($R^2=0.9993$).

IV. DISCUSSION

The findings obtained in the present study demonstrate that pitch circularity is not confined to octave-related (or equal-interval) complexes, but can also occur with sequences of tones that each comprise a full harmonic series. The circular component of pitch can therefore be decoupled experimentally from the height component, even for tones that are similar in spectral composition to those produced in the natural environment.

Normann *et al.* (2001), using a different algorithm, created banks of harmonic complex tones which were rendered ambiguous with respect to height by the addition of subharmonic partials. When subjects were asked to judge the relative heights of such tones, their judgments reflected considerable ambiguity. From statistical analyses of these judgments, the authors concluded that at least 39% of the subjects showed perceptions that were significantly indicative of a circular component of pitch.

We now enquire into the neural substrates of the monotonic and circular components of pitch. Warren *et al.* (2003) used functional magnetic resonance imaging (fMRI) to study patterns of brain activation in response to tone sequences of two types. In the first type, the harmonic components of the tones were at equal amplitude while ***F***0 varied, so that here pitch class and pitch height varied together. In the second type, pitch class was held constant but the relative amplitudes of the odd and even harmonics were varied, so that differences in pitch height alone were produced. The first type of sequence gave rise to activation specifically in a region anterior to primary auditory cortex, whereas the second type produced activation specifically in a region posterior to primary auditory cortex. Given these findings, we can hypothesize that the circularity obtained in the present study might have been due to activation in the anterior region identified by Warren *et al.* However, the signals in the present

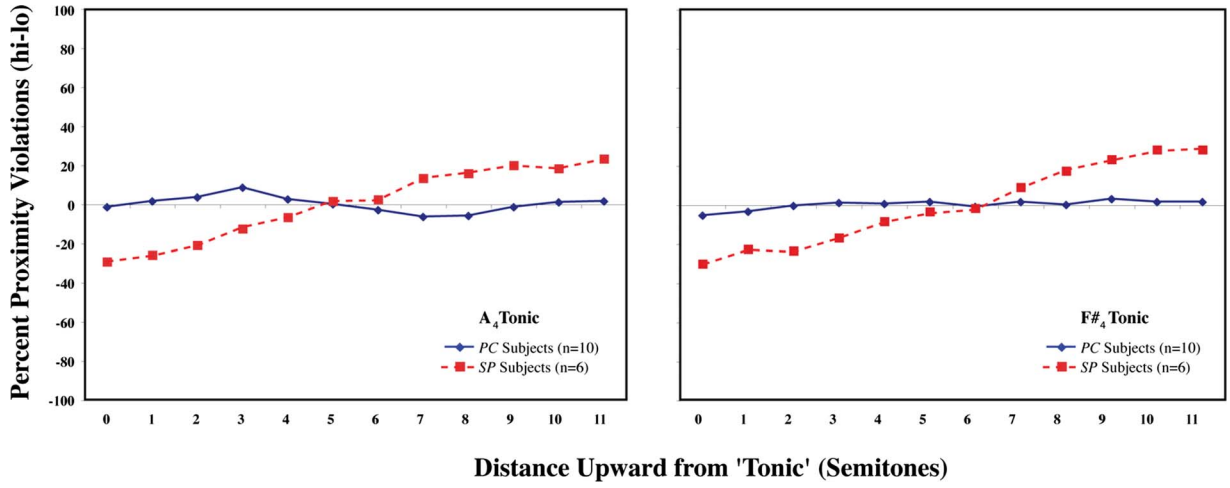

FIG. 9. (Color online) Percentages of judgments that a tone was the higher or lower of a pair, when these judgments were in violation of proximity, plotted as a function of the position of the tone along the scale. The data are shown for the A_4 and $F\#_4$ scales separately and for the pc and sp subjects separately.

study were produced by co-varying both ***F***0 and the relative amplitudes of the odd and even harmonics, so that both the regions identified by Warren *et al.* might have been involved in the effects described here. At a different level, evidence has recently been provided in the gerbil that the ventral nucleus of the lateral lemniscus is organized as a neuronal pitch helix, with pitches organized helically from top to bottom, with one octave for each turn of the helix (Langner, 2005). This finding places the lateral lemniscus as a possible source of pitch circularity.

We now turn to the basis of the individual differences in the strength of the circularity effects obtained here, i.e., between the pc and the sp subjects. Smoorenberg (1970) created successive pairs of tones, with each tone consisting of two adjacent harmonics of a missing fundamental. Either ***F***0 fell while the spectral region of the harmonics rose, or ***F***0 rose while the spectral region of the harmonics fell. Subjects judged for each pair of tones whether it rose or fell in pitch. Considerable individual differences were found in the tendency for judgments to be based on missing ***F***0 as opposed to spectral region. Houtsma and Flourens (1991) elaborated on this paradigm, and confirmed the presence of pronounced individual differences in making such judgments. Laguitton *et al.* (1998) employed a similar paradigm, but with two, three, or four adjacent harmonics. They found that left handers tended more than right handers to base their judgments on spectral region rather than ***F***0. Schneider *et al.* (2005) presented right-handed musicians with a similar task and found that those subjects who tended to base their judgments on spectral region showed a pronounced rightward, rather than leftward, asymmetry of the grey matter volume within the pitch-sensitive lateral Heschl's gyrus. Given this body of evidence, we may hypothesize that the individual differences found in the present paradigm could reflect similar differences in brain organization, with those subjects who were more sensitive to position of the tone along the scale (i.e., sp subjects) corresponding to those who based their judgments on spectrum in the earlier experiments. No effect of handedness was found in our study; however, the number of subjects tested was too small to assess handedness differences convincingly.

It should be noted that the results obtained here, as those obtained previously with octave-related complexes (Shepard, 1964; Risset, 1969; Ueda and Ohgushi, 1987; Allik *et al.*, 1989; Deutsch, 1991) and other equal-interval complexes (Burns, 1981; Nakajima *et al.*, 1988), reflected a strong influence of the principle of proximity in making judgments of relative pitch: tone pairs were heard as ascending or descending depending on which was the most proximal direction along the pitch class circle. Pitch proximity has been shown to be a powerful organizing principle in other contexts also, such as in the scale illusion (Deutsch, 1975), stream segregation for rapid sequences of single tones (Bregman, 1990; Bregman and Campbell, 1971; Dowling, 1973; Van Noorden, 1975), and short term memory for pitch (Deutsch, 1978).

At a more cognitive level, it has been shown that when a listener attributes a key to a musical passage, he or she invokes a complex set of similarity relationships between the 12 pitch classes, so that 3–5 dimensions of pitch have been proposed at this higher level of abstraction (see, in particular, Shepard, 1982; Krumhansl, 1990; and Lerdahl, 2001 for detailed discussions).

Finally, using the algorithm described here, we have generated demonstrations of endlessly ascending and descending scales and glides.[4] These circular demonstrations are analogous to those produced by Shepard and by Risset using octave-related complexes (see, for example, Houtsma *et al.*, 1987). The present findings also lead to the conjecture that by using the present algorithm for determining the relative amplitudes of the odd and even harmonics, one might be able to create banks of tones that are perceptually similar to those produced by natural instruments but that nevertheless exhibit pitch circularity. Such tones could then be made to vary in infinitely small steps along the dimensions both of pitch height and of pitch class; this could prove useful in the development of algorithms for new music.

ACKNOWLEDGMENTS

We are grateful to Joshua M. Deutsch, Monica Sweet, Heather Flowe, and Grace Leslie, and two anonymous reviewers for their helpful comments.

[1]In an earlier experiment, Deutsch and coworkers implemented this basic idea but employed a different set of parameters than those used in the present study (Deutsch, Dooley, Dubnov, Henthorn, and Wurden, paper presented at the 150th Meeting of the Acoustical Society of America, Minneapolis, October 2005). However, in this earlier experiment, the tones were low pass filtered and the effects of the resultant phase shifting were unknown.

[2]This software package was created by Miller Puckette, and is available for download at http://crca.ucsd.edu/~msp/software.html (date last viewed 4/22/08).

[3]Those subjects who scored 8–10 "rights" on the handedness questionnaire were designated as right handers; the remainder were designated as non-right-handers.

[4]Demonstrations of pitch circularity produced by sequences of tones generated in accordance with the present algorithm are available on request.

Allik, J., Dzhafarov, E. N., Houstma, A. J. M., Ross, J., and Versfeld, N. J. (**1989**). "Pitch motion with random chord sequences," Percept. Psychophys. **46**, 513–527.

American National Standards Institute (ANSI) (**1973**). *American National Psychoacoustical Terminology* (American National Institute Standards, New York).

Bachem, A. (**1948**). "Note on Neu's review of the literature on absolute pitch," Psychol. Bull. **45**, 161–162.

Benade, A. H. (**1976**). *Fundamentals of Musical Acoustics* (Oxford University Press, Oxford).

Borg, I., and Groenen, P. J. F. (**2005**). *Modern Multidimensional Scaling: Theory and Applications*, 2nd ed. (Springer, New York).

Bregman, A. S., and Campbell, J. (**1971**). "Primary auditory stream segregation and perception of order in rapid sequences of tones," J. Exp. Psychol. **89**, 244–249.

Bregman, A. S. (**1990**). *Auditory Scene Analysis: The Perceptual Organization of Sound* (MIT, Cambridge, MA).

Burns, E. (**1981**). "Circularity in relative pitch judgments for inharmonic complex tones: The Shepard demonstration revisited, again," Percept. Psychophys. **30**, 467–472.

Burns, E. M., and Ward, W. D. (**1982**). "Intervals, scales, and tuning," in *The Psychology of Music*, 1st ed., edited by D. Deutsch (Academic, New York), pp. 241–270.

Deutsch, D. (**1969**). "Music recognition," Psychol. Rev. **76**, 300–307.

Deutsch, D. (**1973**). "Octave generalization of specific interference effects in memory for tonal pitch," Percept. Psychophys. **13**, 271–275.

Deutsch, D. (**1975**). "Two-channel listening to musical scales," J. Acoust.

Soc. Am. **57**, 1156–1160.
Deutsch, D. (**1978**). "Delayed pitch comparisons and the principle of proximity," Percept. Psychophys. **23**, 227–230.
Deutsch, D., Kuyper, W. L., and Fisher, Y. (**1987**). "The tritone paradox: Its presence and form of distribution in a general population," Music Percept. **5**, 79–92.
Deutsch, D. (**1991**). "Pitch proximity in the grouping of simultaneous tones," Music Percept. **9**, 185–198.
Deutsch, D. (**1999**). "Processing of pitch combinations," in *The Psychology of Music*, 2nd ed., edited by D. Deutsch (Academic, New York), pp. 349–412.
Dowling, W. J. (**1973**). "The perception of interleaved melodies," Cogn. Psychol. **5**, 322–337.
Houtsma, A. J. M., and Fleurens, J. F. M. (**1991**). "Analytic and synthetic pitch of two-tone complexes," J. Acoust. Soc. Am. **90**, 1674–1676.
Houtsma, A. J. M., Rossing, T. D., and Wagenaars, W. M. (**1987**). *Auditory Demonstrations*, (compact disc) (Acoustical Society of America, Melville, NY).
Krumhansl, C. L. (**1990**). *Cognitive Foundations of Musical Pitch* (Oxford University Press, Oxford).
Laguitton, V., Demany, L., Semal, C., and Liegeois-Chauvel, C. (**1998**). "Pitch perception: A difference between right- and left-handed listeners," Neuropsychologia **3**, 201–207.
Langner, G. (**2005**). "Neuronal mechanisms underlying the perception of pitch and harmony," Ann. N.Y. Acad. Sci. **1060**, 50–52.
Lerdahl, F. (**2001**). *Tonal Pitch Space* (Oxford University Press, Oxford).
Meyer, M. (**1904**). "On the attributes of the sensations," Psychol. Rev. **11**, 83–103.
Nakajima, Y., Tsumura, T., Matsuura, S., Minami, H., and Teranishi, R. (**1988**). "Dynamic pitch perception for complex tones derived from major triads," Music Percept. **6**, 1–20.
Normann, I., Purwins, H., and Obermayer, K. (**2001**). "Spectrum of pitch differences models the perception of octave ambiguous tones," in Proceedings of the International Computer Music Conference, Havana, edited by A. Schloss, R. Dannenberg, and P. Driessen International Computer Music Association, San Francisco, pp. 274–276.
Patterson, R. D. (**1986**). "Spiral detection of periodicity and the spiral form of musical scales," Psychol. Mus. **14**, 44–61.
Patterson, R. D., Milroy, R., and Allerhand, M. (**1993**). "What is the octave of a harmonically rich note?" Contemp. Mus. Rev. **9**, 69–81.
Pickler, A. G. (**1966**). "Logarithmic frequency systems," J. Acoust. Soc. Am. **39**, 1102–1110.
Risset, J. C. (**1969**). "Pitch control and pitch paradoxes demonstrated with computer-synthesized sounds," J. Acoust. Soc. Am. **46**, 88(A).
Ruckmick, C. A. (**1929**). "A new classification of tonal qualities," Psychol. Rev. **36**, 172–180.
Schneider, P., Sluming, V., Roberts, N., Scherg, M., Goebel, R., Specht, H. J., Dosch, H. G., Bleek, S., Stippich, C., and Rupp, A. (**2005**). "Structural and functional asymmetry of lateral Heschl's gyrus reflects pitch perception preference," Nat. Neurosci. **8**, 1241–1247.
Shepard, R. N. (**1964**). "Circularity in judgments of relative pitch," J. Acoust. Soc. Am. **36**, 2345–2353.
Shepard, R. N. (**1965**). "Approximation to uniform gradients of generalization by monotone transformations of scale," in *Stimulus Generalization*, edited by D. L. Mostofsky (Stanford University Press, Stanford, CA).
Shepard, R. N. (**1982**). "Structural representations of musical pitch," in *The Psychology of Music*, 1st ed., edited by D. Deutsch (Academic, New York), pp. 343–390.
Smoorenberg, G. F. (**1970**). "Pitch perception of two-frequency stimuli," J. Acoust. Soc. Am. **48**, 924–942.
Ueda, K., and Ohgushi, K. (**1987**). "Perceptual components of pitch: Spatial representation using multidimensional scaling technique," J. Acoust. Soc. Am. **82**, 1193–1200.
Varney, N. R., and Benton, A. L. (**1975**). "Tactile perception of direction in relation to handedness and familial handedness," Neuropsychologia **13**, 449–454.
Van Noorden, L. P. A. S. (**1975**). Ph.D. thesis, Technische Hogeschoel Eindhoven, The Netherlands.
Warren, J. D., Uppenkamp, S., Patterson, R. D., and Griffiths, T. D. (**2003**). "Separating pitch chroma and pitch height in the human brain," Proc. Natl. Acad. Sci. U.S.A. **100**, 10038–10042.

Affect cues in vocalizations of the bat, *Megaderma lyra*, during agonistic interactions

Anna Bastian and Sabine Schmidt[a)]
Institute of Zoology, University of Veterinary Medicine Hanover, Bünteweg 17, 30559 Hanover, Germany

(Received 3 July 2007; revised 26 March 2008; accepted 15 April 2008)

Some features of emotional prosody in human speech may be traced back to affect cues in mammalian vocalizations. The present study addresses the question whether affect intensity, as expressed by the intensity of behavioral displays, is encoded in vocal cues, i.e., changes in the structure of associated calls, in bats, a group evolutionarily remote from primates. A frame-by-frame video analysis of 109 dyadic agonistic interactions recorded in approach situations was performed to categorize displays into two intensity levels based on a cost-benefit estimate. *M. lyra* showed graded visual displays accompanied by specific calls and response calls of the second bat. A sound analysis revealed systematic changes of call sequence parameters with display level. At the high intensity level, total call duration, number of syllables within a call, and the number of calls within a sequence were increased, while intervals between call syllables were decreased for both call types. In addition, the latency of the response call was shorter, and its main syllable–type durations and fundamental frequency were increased. These systematic changes of vocal parameters with affect intensity correspond to prosodic changes in human speech, suggesting that emotion-related acoustic cues are a common feature of vocal communication in mammals.
 [DOI: 10.1121/1.2924123]

PACS number(s): 43.80.Ka [JAS] Pages: 598–608

I. INTRODUCTION

Prosodic cues in human speech allow a listener to evaluate the emotional state of a speaker even if they do not speak the same language (e.g., Banse and Scherer, 1996; Scherer *et al.*, 2001) and belong to different cultures (Scherer, 2000, Scherer *et al.*, 2001; Thompson and Balkwill, 2006). The cues are prelinguistic properties also present in human affect vocalizations, e.g., infant cries (Christensson *et al.*, 1995; Michelsson *et al.*, 1996; Soltis, 2004; Bellieni *et al.*, 2004), and may thus have originated from affect cues in mammalian vocalizations. Darwin (1872) postulated a biological origin of emotional expressions in humans. The present study addresses the question whether the emotional state is expressed by vocal cues in bats, which are estimated to have split from other mammalian orders between 55 (Novacek, 1985; Koopman, 1994) and 95×10^6 (Eizirik *et al.*, 2001; Madsen *et al.*, 2001; Murphy *et al.*, 2001) years ago. This long separation makes them an interesting outgroup for a comparison to primates and humans.

Bats are highly mobile and adapted to a life in the dark due to their ability to echolocate and the coevolution of a hypertrophied auditory system (see Neuweiler, 2000). The highly developed auditory system is an ideal prerequisite for acoustic communication. Moreover, bats are an especially promising order to study affect cues in vocalizations as a number of species lives in complex societies characterized by individualized relationships (see Kulzer, 2005) and diverse interactions, for which complex communication signals are needed. Acoustic signals are ideally suited to govern these interactions, as a variety of elements can be combined to higher order structures, such as calls, phrases, and songs. In parallel, they have the potential to transmit different types of information. In fact, bats use communication calls which are hierarchically organized (e.g., Leippert, 1994; Behr and von Helversen, 2004; Ma *et al.*, 2006), context specific (e.g., Barclay and Thomas, 1979; Barclay *et al.*, 1979; Behr and von Helversen, 2004; Davidson and Wilkinson, 2004; Leippert, 1994; Pfalzer and Kusch, 2003; Schmidt, 2005; Wilkinson and Boughman, 1998), and carry population—(e.g., Dörrie *et al.*, 2001; Esser and Schubert, 1998; Russo and Jones, 1999), group- (e.g., Boughman, 1997; Wilkinson and Boughman, 1998; Scherrer and Wilkinson, 1993), or individual-specific (e.g., Balcombe, 1990; Brown, 1976; Gelfand and McCracken, 1986; Leippert *et al.*, 2000) signatures.

However, affect cues in bat communication calls have not been systematically analyzed, so far. On the one hand, this may be due to the difficulty to objectively determine the internal state of a bat behaving in a natural social setting and to associate it with call structure. To account for this problem, we assumed that a more pronounced display has higher costs and is therefore shown in situations of higher relevance to the individual (for a discussion of cost-benefit estimates, see Capp and Searcy, 1991; Enquist, 1985; Grafen, 1990; Zahavi, 1975; 1977), so that the internal state can be inferred from the intensity of the behavioral display. On the other hand, a well-defined paradigm is needed, in which the behavior can be independently classified of the vocalization to be studied for affect cues. We chose an agonistic approach context in the bat, *M. lyra*, as our paradigm. *M. lyra* is a species living in partial sexual segregation (Goymann *et al.* 2000) sharing day roots with a few up to a few hundred individuals (Bates and Harrison, 1997). At night, stable,

a)Author to whom correspondence should be addressed; Electronic mail: sabine.schmidt@tiho-hannover.de.

long-term groups of a few individuals from different day roots regularly interact at specific night roosts. These groups are characterized by individualized social bonds (Leippert, *et al.*, 2000). Anecdotal evidence has been provided for agonistic interactions which were expressed by a variable set of visual displays regularly accompanied by a broadband social call, termed aggression call (Goymann, 1995; Goymann *et al.*, 2000; Leippert *et al.*, 2000). In addition, a vocal response to the aggression call has been postulated based on the fact that a second call type frequently overlapped with the aggression call (Grube, 2003; and own observations); however, neither this interrelation nor the functional significance of the respective call types has been systematically studied so far.

As our guiding hypothesis, we assume that bats express their emotional state by vocal cues. We predict systematic changes in call structure for situations of different affect intensity. We tested this hypothesis for calls emitted in the agonistic approach context by recording captive, free-flying bats kept in small groups. Group size and composition corresponded to that of groups typically encountered at night roosts. We classified video sequences of spontaneously interacting bat dyads in the agonistic approach context as low, or high, intensity level interactions and analyzed the synchronously recorded calls. Our results are discussed with respect to the relationship between call structure and function and to shared emotion-related parameters in affect cues across different mammalian orders and humans.

II. METHODS

A. Animals and recording conditions

Subjects were adult individuals of *M. lyra* originating from Sri Lanka, equipped with necklaces carrying a letter code for identification. Animals were kept in three flight rooms (14.7, 5.3, and 5.3 m^2) of the Institute of Zoology, University of Veterinary Medicine Hanover, Germany, at a temperature of 25–28 °C and a relative humidity above 65%. Rooms were dimly illuminated by two 15 W white-light bulbs; during recordings, an additional 15 W red-light bulb was used. Animals had *ad libitum* access to water supplemented with vitamins (Multibionta, Merck Selbstmedikation GmbH, Darmstadt, Germany) or minerals (Basica, Klopfer GmbH, Germany) and were fed with mealworms enriched with Lupo San Biomineral (Luposan GmbH & Co. KG, Langenhahn, Germany) once a day; occasionally, this diet was supplemented by mice and grasshoppers.

Groups in each room consisted of an adult male and a different number of adult females. We collected data in two of the flight rooms (14.7 and 5.3 m^2), in which we kept six and three individuals, respectively. In addition, the male of the third room was occasionally brought into the other groups when the resident male was temporarily absent for other behavioral observations. We analyzed the data from nine individuals as one bat died during data acquisition, so that not enough agonistic interactions involving this bat could be recorded. Data acquisition started after an initial habituation period to the experimental setup of eight days and took place on seventy days from 8th of April until 13th of September 2005 and 26th until 29th of June 2006. Recording sessions lasted between 60 and 120 min and randomly started at different times of the day to cover the activity period of the bats.

B. Experimental setup

During recording sessions, the behavior of the bats was continuously video taped by a camcorder (DCR-HC 85E, Sony Corp., Japan) with an activated "night-shot function." To record the ultrasound communication calls, we connected the high frequency output of a bat detector (S25, Ultra Sound Advice, London, UK) via a control/filter unit (Pettersson F2000, Pettersson Elektronik AB, Uppsala, Sweden) and a high-speed A/D-card (PCM DAS 16/330, Measurement Computing Corp., USA; sampling rate of 250 kHz) to a laptop. The ultrasound Advice microphone had a flat frequeny response of ±5 dB for frequencies above 8 kHz and sharply declined below this frequency (see Schmidt *et al.*, 2000). Recordings were made with BATSOUND PRO (Version 3.31, Pettersson Elektronik AB, Uppsala, Sweden) by using a circular buffer with a storage time of 10 or 20 s (a continuous recording of ultrasound is not feasible due to file size limitations). Thus, the recording could be stopped after vocalizations had occurred in an agonistic interaction, audible at the bat detector. The bat detector microphone and the camcorder were aligned on the same tripod so that they were always directed toward the focal interaction together. A low frequency beep signal was recorded on the audio track of the camcorder at the end of the episode to synchronize the behavioral display with call recordings. In each room, the video and audio equipment was positioned at the same spot in all recording sessions.

C. Video and sound analyses

We studied dyadic agonistic interactions in the approach context by conducting a frame-by-frame video analysis combined with a multiparametrical sound analysis. The approach context comprised situations in which a bat was landing next to or even on a hanging conspecific, was attempting to land, but gave up, or was landing at the perch of the conspecific which flew off. Also, a bat may have walked toward a conspecific, passed by during take off, or headed in full flight for a perched conspecific so that a collision was imminent. In all these situations, a moving bat approached a stationary bat. This may—but need not—result in an agonistic interaction characterized by an aggressive display. To classify each agonistic interaction, we discriminated two intensity levels by rating the effort of the display based on a cost-benefit estimate. A slight pulling up of body and/or wings, mouth opening, or baring the teeth were assigned to the low intensity level, termed low intensity level interaction. More pronounced displays, i.e., biting, wing clasping, flapping, or spreading, bending forward to, or attacking the conspecific with opened mouth were assigned to the high intensity level, termed high intensity level interaction.

Video sequences with agonistic interactions were fed to the laptop via an IEEE 1394-connection and edited by using PINNACLE STUDIO SE (Version 8.4.17, Pinnacle Systems Inc.,

Mountain View, CA). Frame-by-frame analysis with a resolution of 25 frames/s was carried out with the software INTERACT (Version 32, Mangold Software and Consulting GmbH, Germany).

An agonistic interaction was analyzed if the following criteria were met: the display was completely visible, at least one social call was uttered by the bat showing the visual display used by us for classification, and both the sender and receiver of a call could be identified on the video. Two agonistic interactions were considered as independent if the second approach followed the first one after an interval of more than 5 s.

The aggression and response calls uttered during agonistic interactions were analyzed with BATSOUND PRO (Version 3.31, Pettersson Elektronik AB, Uppsala, Sweden) by using a Fast Fourier Transform size of 512 samples and a Hanning window for spectrograms. Throughout this study, we use the term call for a functional unit of vocalizations which is typically emitted in a given behavioral situation and may consist of elements of different or similar structure which are arranged in a typical fashion. A syllable is defined as a discrete call element surrounded by periods of silence (see Koodsma, 1977; Doupe and Kuhl, 1999; Ma *et al.*, 2006). We determined a set of time, frequency, and shape parameters and counted calls and elements (see Table I).

D. Statistical analysis

For descriptive statistics medians and interquartiles are given (STATISTICA Version 6.1, StatSoft Inc., Tulsa, OK); global level of significance was $p = < 0.05$ for all tests.

A multiple χ^2-test (Zöfel, 1988, p. 184) was performed to test whether the intensity level of agonistic interactions depended on the specific approach context situations. An individual based comparison of these situations was not feasible due to the large number of interactions needed for such an analysis.

Call analysis, however, was based on median values of each individual for each call parameter and each intensity level. An individual was included in the analysis if we obtained at least four calls per level and call type. We tested both call types for level specific differences by using Wilcoxon-matched-pair tests (STATISTICA Version 6.1, StatSoft Inc., Tulsa, OK). To account for multiple comparisons in the Wilcoxon-matched-pair tests, we calculated the binomial transgression probability to obtain the number of significant results observed by chance (see Bortz *et al.*, 2000, p. 50; GNU OCTAVE Version 2.1.73, John W. Eaton, University of Wisconsin, Milwaukee, WI).

As a descriptive multivariate method to reveal similarities across calls, we performed a cluster analysis (with *z*-transformed data, a city-block Manhattan distance and Ward's method) based on independent call parameters (see column "In anal." in Table I), followed by a post-hoc comparison to the behavioral display, i.e., the individual and/or intensity level grouping.

To reveal potential individual-specific differences in aggression and response call parameters for a given intensity level, we conducted a one-way Kruskal–Wallis ANOVA (SPSS Version 15.0, SPSS Inc., Chicago, IL).

An independent discriminant function analysis (SPSS Version 15.0, SPSS Inc., Chicago, IL; individuals as grouping variable, call parameters as predictor variables, "leave-one-out" method for cross validation) was calculated for call parameters if $p = < 0.05$ in the Kruskal–Wallis ANOVA.

III. RESULTS

We obtained 109 sequences of dyadic agonistic interactions in the approach context, 45 sequences with low intensity level interactions, and 64 sequences with high intensity level interactions. All nine individuals took part in agonistic interactions with different partners. In all seven approach context situations, we observed interactions of both intensity levels. However, number per level significantly differed for the seven situations (multiple χ^2-test, $\chi^2 = 34.269$, $df = 6$, $p < 0.0001$, see Table II). When a bat landed on a conspecific, low intensity agonistic interactions were significantly less frequent than expected; if the approaching bat walked toward a conspecific, low intensity agonistic interactions were significantly more frequent and high intensity agonistic interactions were significantly less frequent than expected (see Table II). This suggests that the distance between the two interacting individuals and the approach speed may affect the intensity of the display.

Apart from echolocation calls, the bats used exclusively two social call types during the agonistic interactions in the approach context (see Fig. 1): aggression calls which were uttered first and response calls of the other bat which followed in most interactions. While in most situations, the bat being approached emitted the aggression calls, the moving bat uttered them in situations where it headed for a perched bat so that a collision was imminent or landed at the perch of a bat which immediately flew off. In all situations, the distance between the opponents was larger after the interaction than during the approach.

A. Aggression calls

In the 109 agonistic interaction sequences, six bats emitted 116 aggression calls, 47 in low intensity level interactions [median call number per bat: 8.0 (7.0–9.0)], and 69 in high intensity level interactions [11.5 (10.0–13.0)]. Senders were all females which, however, directed their calls toward both, males and females. Aggression calls consisted of two components: chevron-shaped syllables and clicks (see Fig. 1). Both components may occur on their own; if both were present, chevron-shaped syllables either preceded or followed the clicks. Descriptive statistics for the aggression calls of six individuals are summarized in Table III.

Clicks (see Fig. 1; inserts c) emitted in series with a high repetition rate were characteristic syllable types of aggression calls; they were present in 92 of 116 calls. A comparison of click parameters between the two intensity levels based on median level specific calls of each individual revealed significant differences: while the duration of a single click was independent of interaction intensity level, the click series duration and the interclick interval decreased, and the number

TABLE I. Description of the parameter set measured for aggression and response calls. Call and element counts as well as shape parameters were determined in the sonagram; time parameters were measured in the oscillogram and spectral parameters in the power spectrum. Independent parameters used for cluster, one-way ANOVA, and discriminant function analyses are marked with an "X."

Call type	Parameter	Description	In anal.
Aggression call	No calls	Number of calls per interaction; two calls were treated as separate, if the interval between two calls was above 3 s	X
	Ck_{on} (ms)	Duration from click onset to maximum positive amplitude	X
	Dur call (ms)	Total call duration	
	No chevs	Number of chevron-shaped syllables	
	Dur chevs (ms)	Duration of chevron-shaped syllables	
	Dur cks (ms)	Click series duration	
	No ck	Median number of clicks	X
	Dur ck (ms)	Median click duration	X
	Ck Int (ms)	Median inter click interval	X
	Max F (kHz)	Highest frequency of the aggression call, defined as the frequency at which the response curve slope in the power spectrum rose to 1/3 of the peak to noise floor level difference above noise floor	X
	Min F (kHz)	Lowest frequency of the aggression call, defined as the frequency at which the response curve slope in the power spectrum rose to 1/3 of the peak to noise floor level difference above noise floor	X
Response call	Occ	Occurrence of response call after the aggression call	
	Lat (ms)	Latency of response call onset after aggression call onset	X
	Dur call (ms)	Total call duration	
	No sy	Total number of syllables	
	No msy	Number of complex frequency modulated syllables	X
	Dur msy (ms)	Median duration of the complex frequency modulated syllables	X
	msy int (ms)	Median interval between the complex frequency modulated syllables	X
	F_0 msy (kHz)	Median peak frequency of the fundamental of the complex frequency modulated syllables	X
	Int msy-usy (ms)	Interval between the final complex frequency modulated syllable and the first u-shaped syllable	X
	No. usy	Number of u-shaped syllables	X
	Dur usy (ms)	Median duration of the u-shaped syllables	X
	usy int (ms)	Median interval between the u-shaped syllables	X
	F_0 usy (kHz)	Median peak frequency of the fundamental of the first three u-shaped syllables	X
	$\Delta L_{H1\text{-}H2}$ (dB)	Median difference of amplitude level between fundamental and second harmonic of the first three u-shaped syllables	X
	$\Delta L_{H2\text{-}H3}$ (dB)	Median difference of amplitude level between second and third harmonic of the first three u-shaped syllables	X

of clicks increased in high intensity level interactions (see Table III). As a consequence, the click repetition rate was higher in high intensity level interactions.

Chevron-shaped syllables (see Fig. 1, inserts v) were predominantly uttered in high intensity level interactions: while chevron-shaped syllables were present in only six of 47 aggression calls emitted in low intensity level interactions, they occurred in 62 of 69 calls emitted in high intensity level interactions. Additionally, the 24 aggression calls which consisted only of chevron-shaped syllables were exclusively emitted in high intensity level interactions. The number of chevron-shaped syllables was significantly increased for median calls of each individual in high intensity level interactions (see Table III). Thus, the presence of chevron-shaped syllables caused the significantly higher total call duration in high intensity level interactions. Moreover, the bats emitted a significantly higher number of aggression calls in high intensity level interactions, which emphasizes the importance of vocalizations to express the intensity of an agonistic interaction.

TABLE II. Absolute number of agonistic interactions at the two intensity levels (low level and high level) for the seven situations within the approach context. The number per situation significantly differed between the intensity levels (multiple χ^2-test, $\chi^2=34.269$, $df=6$, $p<0.0001$). Local χ^2 values are given in parentheses; significant cells are marked by asterisks.

Situation	Low level	High level
Landing on conspecific	2 (5.13)*	19 (3.61)
Landing next to conspecific	12 (1.28)	9 (0.90)
Landing with conspecific take-off	2 (2.47)	12 (1.74)
Attempted landing	7 (<0.001)	10 (<0.001)
Walking to conspecific	12 (8.20)*	1 (5.76)*
Imminent collision	3 (1.04)	10 (0.73)
Take-off	7 (1.20)	3 (1.40)

In addition, we performed a cluster analysis to look for pattern formation in aggression calls. A *post hoc* comparison to the behavioral display revealed that the two main clusters comprised predominantly calls emitted during high (88.4%) and low (76.6%) intensity level agonistic interactions, respectively [see dotted line in Fig. 2(a)]. This suggests that the high, and low, intensity level of an agonistic interaction as rated by the visual display is reliably expressed by aggression call structure.

In contrast, a *post hoc* comparison did not disclose distinct clusters per individual, which reflects the lack of interindividual differences in the parameter set describing the aggression calls. In fact, when comparing the call parameters between the six individuals, we found no interindividual differences at both intensity levels (Kruskal–Wallis ANOVA, $H_5=>11.07$, $p>0.05$ for all parameters).

B. Response calls

In total, 114 response calls were emitted by nine bats [median call number per bat 5.0 (5.0–5.0) in low intensity level interactions and 7.0 (6.0–9.0) in high intensity level interactions]. Females as well as males addressed in agonistic interactions reacted with response calls. In two low intensity level interactions, a female did not react to an aggression call with a response call, which explains the difference in the total number of analyzed aggression and response calls.

Response calls consisted of distinct syllable types, namely, complex frequency modulated syllables, u-shaped syllables, and downward frequency modulated syllables emitted in a strict sequential order. While a series of u-shaped syllables (see Fig. 1; insert u) was always followed by a series of downward frequency modulated syllables and both types were never absent in the response calls, complex frequency modulated syllables (see Fig. 1; high level b) preceded the u-shaped syllables in 12 calls. Descriptive statistics for the median response calls of nine individuals are summarized in Table IV.

Significant agonistic interaction intensity level related differences in call structure were found for seven parameters (see Table IV). For median calls of each individual in high intensity level interactions, the total number of syllables, the number of complex frequency modulated syllables, and the number of the u-shaped syllables were significantly increased compared to low intensity level interactions. Complex frequency modulated syllables were uttered in only three of 45 low intensity level interactions calls, however, in 14 of 69 high intensity level interactions calls. Moreover,

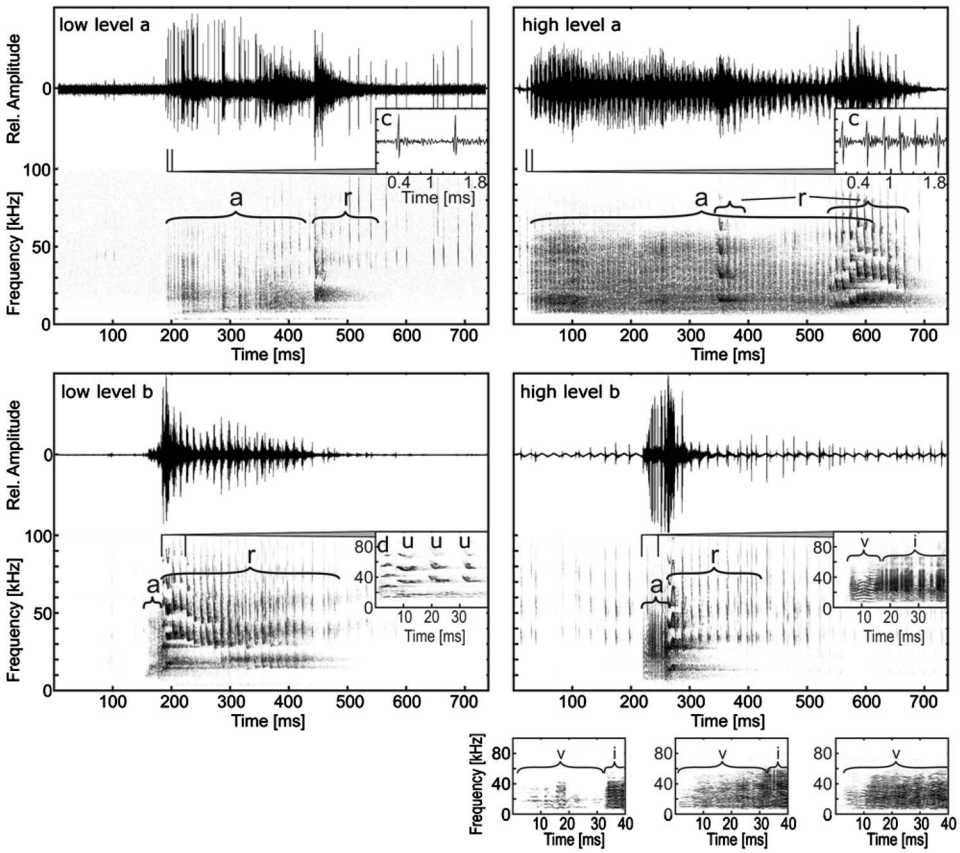

FIG. 1. Examples of calls uttered in four dyadic agonistic interactions. Two of low intensity level (low level a and low level b) and two of high intensity level (high level a and high level b). Oscillograms and sonagrams of the complete aggression call (a) and response call (r) of an interaction are given. Calls not marked by a or r are echolocation calls. The inserts represent examples of the respective syllables in more detail. For aggression call clicks emitted during low and high intensity level interactions, see oscillogram inserts c. Sonagram inserts represent chevron-shaped syllables (v) and clicks (i) of the aggression call and u-shaped syllables (u) and downward frequency modulated syllables (d) of the response calls. The three inserts below represent additional examples of aggression call sonagrams.

TABLE III. Results of the aggression call analysis (N=6 bats) for the 11 call parameters (for abbreviations, see Table I). The medians and interquartiles of median parameter values per bat are presented irrespective of the level of the agonistic interaction (Grand median) and for the two interaction levels (low level and high level). If values for a given parameter were not available for all bats, as is the case for some call components in low level interactions, the respective cell is marked with "···." The last column (Comparison) gives the results of the level comparison (Wilcoxon-matched-pair test), if applicable. Asterisks indicate significant differences taking transgression probability (Bortz *et al.*, 2000, p. 50) into account; upward and downward arrows indicate whether the parameter values increased or decreased with the intensity of the agonistic interaction.

Parameter	Grand median	Low level	High level	Comparison
No calls	1.50 (1.00-2.00)	1.00 (1.00-1.00)	3.00 (2.00-5.00)	*↑
Ck_{on} (ms)	0.065 (0.06-0.07)	0.07 (0.06-0.07)	0.06 (0.06-0.07)	n.s.
Dur call (ms)	122.30 (100.70-174.50)	66.90 (56.90-87.90)	208.50 (176.80-250.70)	*↑
Dur cks (ms)	59.64 (58.30-63.90)	66.90 (56.90-78.40)	55.90 (0.00-72.10)	*↓
No ck	27.25 (26.00-41.00)	26.00 (22.00-33.00)	74.00 (0.00-88.00)	*↑
Dur ck (ms)	0.30 (0.30-0.40)	0.35 (0.30-0.40)	0.30 (0.20-0.40)	n.s.
Int ck (ms)	0.93 (0.80-1.05)	2.60 (1.20-4.90)	0.60 (0.40-0.80)	*↓
Fmax cks (kHz)	48.20 (44.90-49.60)	48.20 (45.70-49.60)	48.20 (44.80-49.60)	n.s.
Fmin cks (kHz)	9.67 (9.50-9.90)	9.80 (9.50-10.40)	9.57 (9.30-10.30)	n.s.
Dur chev (ms)	88.83 (16.80-110.90)	···	145.40 (111.10-215.90)	No comparison
No chev	0.00 (0.00-0.00)	0.00 (0.00-0.00)	1.00 (0.00-1.00)	*↑

although the median interval between the u-shaped syllables decreased, the total call duration was significantly higher for median calls of each individual emitted during high intensity level agonistic interactions. In addition, the median fundamental frequency of the u-shaped syllables was significantly increased in these interactions. The response call followed the aggression call with a significantly shorter latency in high intensity agonistic interactions.

The *post hoc* comparison of the results of a cluster analysis with the behavioral display reflected individual as well as agonistic interaction intensity level differences [see Fig. 2(b)]. In contrast to aggression call analysis, the response calls emitted during low and high intensity level interactions were not divided by two distinct subclusters. However, we found two distinct clusters per individual which contained calls emitted during interactions of the same intensity level, respectively, in the *post hoc* analysis. The above pattern suggests that the response calls may serve to assess the intensity of an agonistic interaction only if the individuals know each other. A Kruskal–Wallis ANOVA revealed significant differences between individuals in response calls at both intensity levels for all parameters (SPSS Version 15.0, SPSS Inc., Chicago, IL). The discriminant function analysis showed a 100% correct classification (cross validated 100%) for all cases at both intensity levels (Fig. 3).

IV. DISCUSSION

The present study revealed that *M. lyra* uses two social call types of distinct structure in agonistic interactions resulting from approach situations: aggression calls and response calls. While we found no indications for individual signatures in the parameter set describing the aggression calls, they were obvious for the parameters of the response calls. The intensity of the agonistic interaction was reflected in call sequence parameters of both call types. Total call duration, number of syllable types within one call, and number of calls were increased, whereas the intervals between call syllables were decreased during the higher intensity level agonistic interactions in aggression as well as response calls. In addition, the latency of the response call was shorter, and the duration and fundamental frequency of its main syllable type, i.e., the u-shaped syllables, were increased during higher intensity agonistic interactions. This suggests that the responding bat had perceived, and reacted to, the affect intensity coded in the visual display and/or the aggression call of the first bat, indicating a communication of affect intensity. Our data provide thus an evidence for affect cues in bat acoustic communication, coding for the intensity of the agonistic interaction across call types.

In the following, we first discuss the relationship between the structure and the potential function of aggression versus response calls. Then, we compare to what extent the parameter changes in the two call types correspond to parameter changes occurring in social calls of other mammals in approach contexts of different intensities, and to prosodic cues expressing different intensity levels of anger and fear in human speech. This may help to reveal shared emotion-related parameters across mammals separated for a long time

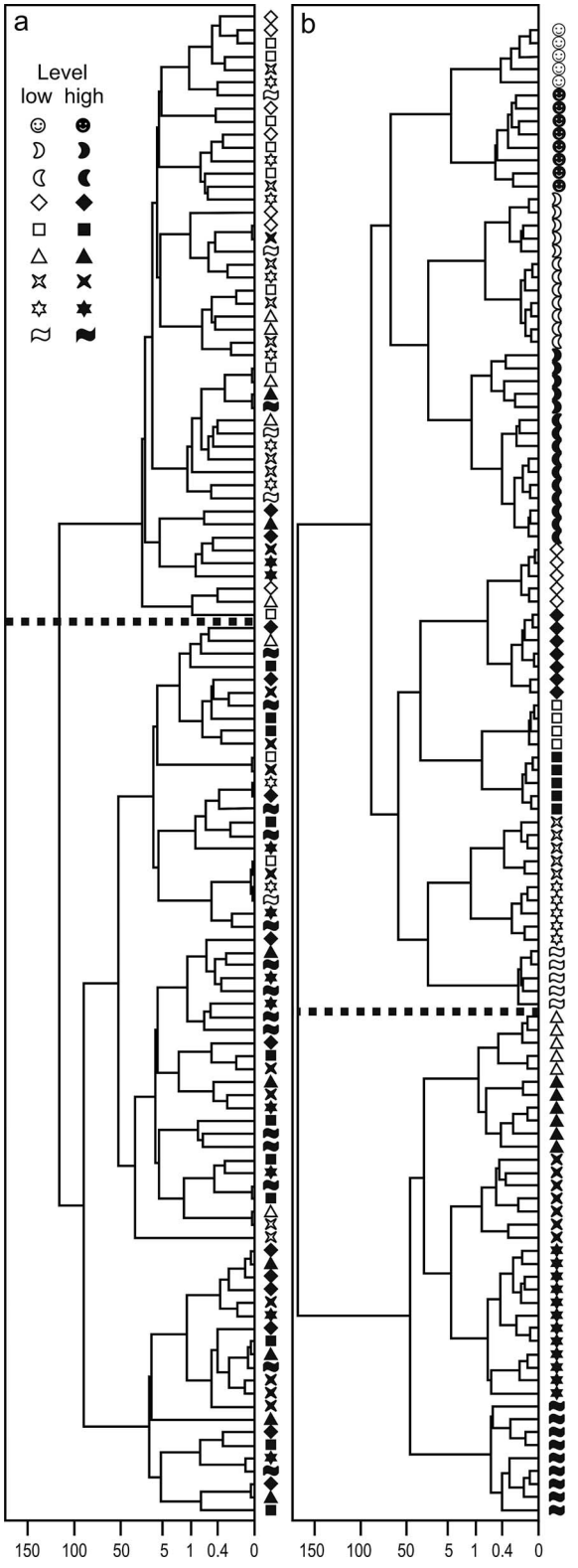

FIG. 2. Tree diagrams for aggression and response calls resulting from a cluster analysis by using Ward's method and Manhattan city-block distance. Panel a: tree diagram for aggression calls using seven parameters (see Table I, $N=6$ bats, $n=116$ calls). Panel b: tree diagram for response calls using 12 parameters (see Table I, $N=9$ bats, $n=114$ calls). The dotted lines indicate the respective two-cluster partition. Different symbols represent calls of different individuals; open symbols mark calls emitted during low intensity level interactions; filled symbols those emitted during high intensity level interactions.

in mammalian radiation. Shared emotion-related parameters may have developed from a common origin in evolution and thus constitute homologous traits, as first postulated by Darwin (1872). On the other hand, a convergent evolution of shared emotion-related parameters may have resulted from similar selection pressures, as discussed in the final paragraph of the discussion.

The two call types used by *M. lyra* during agonistic interactions in the approach context markedly differ in their acoustic properties, with noisy, broadband components prevalent in the aggression calls and harmonically structured syllables in the response calls. The aggression calls are typical for agonistic encounters between bats: indeed, the use of noisy, broadband sounds in agonistic encounters has been reported from numerous bat species belonging to different families (see Barclay *et al.*, 1979; Clement *et al.*, 2006; Davidson and Wilkinson, 2004; Fenton, 1985; Goymann *et al.*, 2000; Leippert *et al.*, 2000; Pfalzer and Kusch, 2003; Porter, 1979). Interactions in which aggression calls were followed by tonal response calls have not yet been systematically studied in other bats. Based on the motivation-structural (MS) rules (Morton, 1977), predicting the use of more harsh and low frequency sounds by hostile and more tonal sounds of higher frequency by frightened, appeasing or friendly animals, we may hypothesize that the response calls may serve to appease the aggressor.

The aggression calls in *M. lyra* are characterized by a sharp onset, clicklike energy pulses and rapid amplitude variations in the click series leading to harsh, noisy frequency spectra, and chevron-shaped syllables, which were more frequent in higher intensity agonistic interactions. An increase of call components reflecting nonlinear processes has been shown for roars of red deer stags (Reby *et al.*, 2005) responding to large, compared to small, opponents. Nonlinear processes during phonation are created by irregular vibrations of the vocal folds (Wilden *et al.*, 1998). Future studies concentrating on the chevron-shaped syllables in our study may reveal whether they similarly reflect nonlinear processes at high intensity level interactions. According to the functional concept of communication developed by Owren and Rendall (2001), *M. lyra* aggression calls are then typical stimuli shaped to alter attention, arousal, and affect in listeners by directly accessing low-level brain stem mechanisms.

In contrast, the response calls consist of multiharmonic components with distinct frequency contours and are thus ideal carriers of filter properties as suggested by source-filter theory (Fant, 1960; Fitch and Hauser, 1995; Riede *et al.*, 2005; Vannoni, 2007). Indeed, amplitude level differences between the harmonics were highly effective to separate individuals. As the individual morphology of the vocal tract in combination with the source energy determines call structure, it is not surprising that the frequency parameters of the response calls also contributed to individual distinctiveness. In addition, call sequence parameters, e.g., the temporal patterning in the stereotyped sequence of u-shaped syllables, were decisive for caller identity. Although identity cueing may be more prone to errors when based on temporal patterns rather than filter-related voice characteristics, which

TABLE IV. Results of the response call analysis (N=9 bats) for 14 parameters; for further explanations, see Table III.

Parameter	Grand median	low level	High level	Comparison
Lat (ms)	44.20 (34.70-49.8)	89.10 (63.80-94.20)	40.50 (33.8-40.7)	*↓
Dur call (ms)	150.70 (142.10-219.15)	99.80 (89.20-102.40)	202.40 (178.70-248.30)	*↑
No sy	19.00 (16.00-23.00)	13.00 (11.00-19.00)	24.00 (18.00-28.00)	*↑
No msy	1.00 (1.00-1.00)	0.00 (0.00-0.00)	1.00 (1.00-2.00)	*↑
Dur msy (ms)	3.80 (3.10-5.10)	···	3.90 (3.80-5.10)	No comparison
Int msy (ms)	10.50 (5.80-10.70)	···	2.70 (0.00-10.50)	No comparison
F_0 msy (kHz)	15.80 (13.90-16.90)	···	15.70 (13.70-16.70)	No comparison
Int msy-usy (ms)	9.70 (7.4-10.2)	···	5.20 (2.10-6.20)	No comparison
No usy	11.50 (8.00-18.00)	9.00 (7.00-11.00)	17.00 (11.00-20.00)	*↑
Dur usy (ms)	3.20 (2.65-4.30)	3.90 (2.70-4.30)	3.50 (3.10-4.70)	n.s.
Int usy (ms)	5.35 (3.47-6.10)	6.50 (4.90-7.70)	4.80 (3.60-6.10)	*↓
F_0 usy (kHz)	18.20 (17.60-19.20)	17.40 (17.30-18.40)	18.60 (17.80-19.80)	*↑
$\Delta L_{H1\text{-}H2}$ (dB)	−10.32 (−13.5-1.1)	−10.45 (−27.5-1.2)	−10.2 (−13.0-0.9)	n.s.
$\Delta L_{H2\text{-}H3}$ (dB)	7.6 (3.7-8.7)	7.75 (4.5-8.7)	7.4 (3.7-8.5)	n.s.

cue identity across call types (e.g., Reby *et al.*, 2006), temporal patterns as identity cues have been reported before for primate loud calls (e.g., Mitani and Stuht, 1998).

Other than harsh vocalizations directly addressing low-level alarm systems in listeners, voiced calls shaped by vocal tract properties such as the response call may serve to induce a learned affect in order to modulate the behavior of the listener (see Owren and Rendall, 2001). Once call structure is connected with affective states and decision making, subcortical structures may mediate the response behavior. In this scenario, pronounced identity cues, which increase call variability, are essential to control the individualized relationships between group members.

This may be the reason why MS rules are valid for aggression calls of a vast number of mammalian species, but are unable to account as convincingly for other contexts, even if fearful and friendly contexts are separately considered as suggested by August and Anderson (1987). An emotion concept taking individualized contexts into account is needed to cope with this high variability in call structures.

A central issue arising from the above discussion is that *M. lyra* may convey emotions in two different ways: by using a context-specific call type which is also reflecting the type of emotion of the sender and can be classified by MS rules, and by varying the structure within a given call type, to express the intensity of the situation.

A coding of affect intensity in call structure for agonistic approach contexts has been reported for other socially living mammals. For example, rumble structure of subdominant females depended on the distance to the dominant female in African elephants (Soltis *et al.*, 2005); at close distance, i.e., in a high intensity situation, cepstral coefficients were lower, indicating a lower tonality and unstable pitch in the rumbles, whereas their fundamental frequency remained unchanged. Female tree shrews, when experimentally confronted with sexually interested unfamiliar males, uttered squeaks with a higher intersyllable repetition rate and a higher fundamental frequency if the male came closer, i.e., in the higher intensity situation (Schehka *et al.*, 2007). Baboon grunts emitted by females approaching a mother and her young infant in order to get hold of the baby significantly differed depending on the distance from which the caller was approaching and the time passed since the last interaction between the two parties (Rendall, 2003). Here, an approaching female who had not recently interacted with the mother-infant pair is supposed to be more excited. In this high intensity situation, the number of calls and call duration were increased, while intercall intervals decreased. Moreover, grunt hoarseness and fundamental frequency were increased, its fundamental frequency contour was steeper, and its second formant frequency lower. Thus, although the above animal models belong to mammalian orders taxonomically remote from each other and bats, and although the analyzed parameter sets differed between studies, all parameter coding for affect intensity in the aggression and response calls of *M. lyra* were—if studied—also salient parameters in the other models. This suggests that these parameters function as wide-spread affect cues.

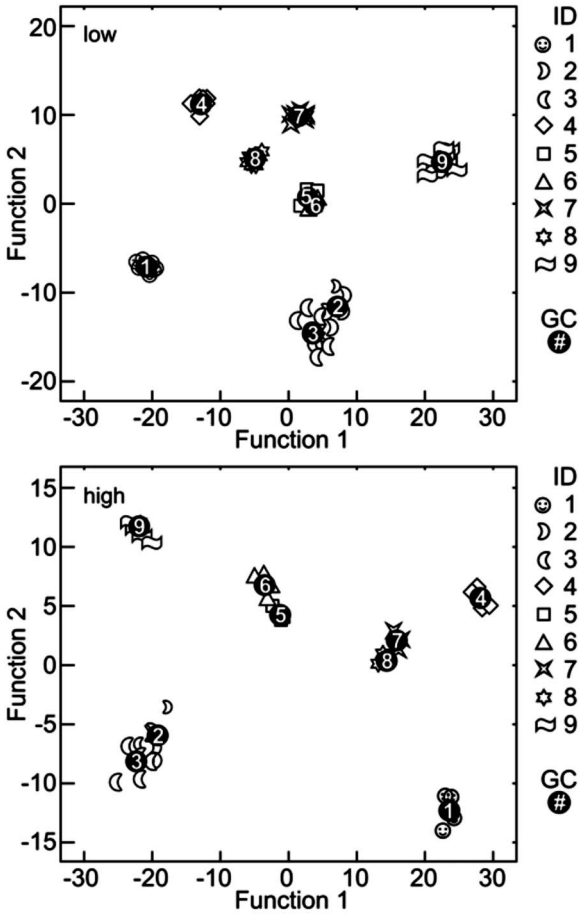

FIG. 3. Scatterplots resulting from a discriminant function analysis on response calls of low intensity level interactions ("low") and high intensity level interactions ("high"), respectively. Individual centroids (GC) and scatterplots of discriminant scores for calls on the first two discriminant functions are shown; different symbols represent calls of different individuals.

When we expand the comparison to affect intensity coding in other agonistic contexts (e.g., Gouzoules *et al.*, 1998; Reby *et al.*, 2005; Siebert and Parr, 2003), or totally different contexts, e.g., alarm (e.g., Blumstein and Armitage, 1997; Fichtel and Hammerschmidt, 2002; Warkentin *et al.*, 2001) or food announcement contexts (e.g., Elowson *et al.*, 1991), we see that the repetition rate and/or fundamental frequency shifts are wide-spread cues correlated with arousal changes in nonhuman mammals.

In humans, anger and fear are emotions characteristically occurring during agonistic interactions. For these emotions, Scherer (1986) predicted parameter differences in human speech for low and high arousal states, termed cold and hot angers and anxiety and fear. Compared to emotionally neutral speech, he expected an increase in measures associated with fundamental frequency and in speech rate as prosodic cues for hot anger and fear. Several studies have confirmed these predictions for some, but not all, fundamental frequency measures and speech rate (e.g., Bachorowski, 1999; Baenziger and Scherer, 2005; Johnstone and Scherer, 1999; Murray and Arnott, 1993; Paeschke, 2003).

Thus, certain prosodic cues discriminating between anger and fear of different intensities correspond to affect cues occurring in agonistic interactions of mammals, and vocal repetition rate and fundamental frequency measures expressing emotion acoustically may represent arousal across nonhuman mammals and humans. This shows that corresponding vocal affect cues are produced by lineages of mammals separated for up to about 100×10^6 years (see Kumar and Hedges, 1998; Murphy *et al.*, 2001; Eizirik *et al.*, 2001; Koopmann, 1994).

Two scenarios may account for the use of shared emotion-related parameters. Typical mammal societies characterized by individualized relationships and diverse interactions require complex communication signals. For these signals, similar selection pressures may apply to guarantee an optimal transmission in specific interaction contexts and, thus, drive convergent evolution in species with comparable social structure. Alternatively, if affect cues as precursors of emotional prosody emerged early and were conserved based on a common physiology in mammalian evolution, they may have been a factor driving the evolution of typical mammal societies. In this scenario, a phylogenetic tree based on transition stages of prosodic cues may be expected which correlates with a tree based on independent characters. Then, it remains a challenge to investigate to what extent mammals from different lineages, e.g., primates versus bats, can perceive and exploit emotion-related cues in acoustic communication.

ACKNOWLEDGMENTS

The behavioral observations reported in this study did not require an animal experimentation approval. Permission to keep and breed *M. lyra* in fulfillment of Sec. 11 Abs.1, S.1, No. 1 Tiersch G has been given to the Institut fuer Zoologie der Tieraerztlichen Hochschule Hannover by the Ordnungsamt, Landeshauptstadt Hannover, Gewerbe—und Veterinaerabteilung, dated 24 March 2003. We would like to thank the Department of Wildlife Conservation, Colombo, Sri Lanka for granting the export license for the bats and our cooperation partner Dr. W. B. Yapa, University of Colombo, Sri Lanka, for logistic support. We thank E. Zimmermann, M. B. Fenton, and M. J. Owren for critical comments on an earlier version of the manuscript and R. Bruening for technical support with the figures. This study was supported by a grant from the German Research Foundation, Schm 879/6, to S. S.

August, P. V., and Anderson, J. G. T. (**1987**). "Mammal sounds and motivation-structural rules: a test of the hypothesis," J. Mammal. **68**, 1–9.
Bachorowski, J. (**1999**). "Vocal expression and perception of emotion," Curr. Dir. Psychol. Sci. **8**, 53–57.
Balcombe, J. P. (**1990**). "Vocal recognition of pups by mother Mexican free-tailed bats: Do pups recognize their mothers?," Anim. Behav. **39**, 980–986.
Banse, R., and Scherer, K. R. (**1996**). "Acoustic profiles in vocal emotion expression," J. Pers Soc. Psychol. **70**, 614–636.
Barclay, R. M. R., and Thomas, D. W. (**1979**). "Copulation call of the bat *Myotis lucifugus*: a discrete situation-specific communication signal," J. Mammal. **60**, 632–634.
Barclay, R. M. R., Fenton, B. M., and Thomas, D. W. (**1979**). "Social behavior of the little brown bat, *Myotis lucifugus* II vocal communication," Behav. Ecol. Sociobiol. **6**, 137–146.
Bates, P. J. J., and Harrison, D. L. (**1997**). *Bats of the Indian Subcontinent* (Harrison Zoological Museum, Kent).
Behr, O., and von Helversen, O. (**2004**). "Bat serenades-complex courtship

songs of the sac-winged bat (*Saccopterix bilineata*)," Behav. Ecol. Sociobiol. **56**, 106–115.
Bellieni, C. V., Sisto, R., Cordelli, D. M., and Buoncore, G. (**2004**). "Cry features reflect pain intensity in term newborns: An alarm threshold," Pediatr. Res. **55**, 142–146.
Blumstein, K. B., and Armitage, D. T. (**1997**). "Alarm calling in yellow-bellied marmots: I. The meaning of situationally variable alarm calls," Anim. Behav. **53**, 143–171.
Bortz, G. J., Lienert, G. A., and Boehnke, K. (**2000**). *Verteilungsfreie Methoden in der Biostatistik (Non-parametric methods in biostatistics)* (Springer, Berlin).
Boughman, J. W. (**1997**). "Greater spear-nosed bats give group distinctive calls," Behav. Ecol. Sociobiol. **40**, 61–70.
Brown, P. (**1976**). "Vocal communication in the pallid bat, *Antrozous pallidus*," Z. Tierpsychol **41**, 34–54.
Baenziger, T., and Scherer, K. R. (**2005**). "The role of intonation in emotional expressions," Speech Commun. **46**, 252–267.
Capp, M. S., and Searcy, W. A. (**1991**). "Acoustical communication of aggressive intentions by territorial male bobolinks," Behav. Ecol. Sociobiol. **2**, 319–326.
Christensson, K., Cabrera, T., Christensson, E., Uvnaes-Moberg, K., and Winberg, J. (**1995**). "Separation distress call in the human neonate in the absence of maternal body contact," Acta Paediatr. **84**, 468–473.
Clement, M. J., Gupta, P., Dietz, N., and Kanwal, J. S. (**2006**). in *Behavior and Neurodynamics for Auditory Communication*, edited by J. S. Kanwal and G. Ehret (Cambridge University Press, Cambridge), pp. 57–82.
Darwin, C. (**1872**). *The Expression of the Emotions in Man and Animals* (John Murray, London).
Davidson, S. M., and Wilkinson, G. S. (**2004**). "Function of male song in the greater white-lined bat, *Saccopteryx bilineata*," Anim. Behav. **67**, 883–891.
Doerrie, M., Schmidt, S., Suba, M., and Sripathi, K. (**2001**). "Contact calls of the bat, Megaderma lyra: a comparison between an Indian and Sri Lankan population," Zoology **104**, 5.
Doupe, A. J., and Kuhl, P. K. (**1999**). "Bird song and human speech. Common themes and mechanisms," Annu. Rev. Neurosci. **22**, 567–631.
Eizirik, E., Murphy, W. J., and O'Brien, S. J. (**2001**). "Molecular dating and biogeography of the early placental mammal radiation," J. Hered. **92**, 212–219.
Elowson, A. M., Tannenbaum, P. L., and Snowdon, C. T. (**1991**). "Food-associated calls correlate with food preferences in cotton-top tamarins," Anim. Behav. **42**, 931–937.
Esser, K.-H., and Schubert, J. (**1998**). "Vocal dialects in the lesser spear-nosed bat *Phyllostomus discolor*," Naturwiss. **85**, 347–349.
Enquist, M. (**1985**). "Communication during aggressive interactions with particular reference to variation in choice of behaviour," Anim. Behav. **33**, 1152–1161.
Fant, G. (**1960**). *Acoustic Theory of Speech Production with Calculations Based on X-ray Studies of Russian Articulations. Description and Analysis of Contemporary Standard Russian*, (T. Mouton, The Hague).
Fenton, M. B. (**1985**). in *Animal Communication*, edited by J. Umiler-Sebeok, and T. A. Sebeok (Indiana University Press, Bloomington), pp. 63–158.
Fichtel, C., and Hammerschmidt, K. (**2002**). "Responses of redfronted lemurs to experimentally modified alarm calls: evidence for urgency-based changes in call structure," Ethology **108**, 763–777.
Fitch, J., and Hauser, H. (**1995**). "Vocal production in nonhuman primates: acoustics, physiology, and function contraints on "honest" advertisement," Am. J. Primatol **37**, 191–219.
Gelfand, D. L., and McCracken, G. F. (**1986**). "Individual variation in the isolation calls of Mexican free-tailed bat pups (*Tadarida brasiliensis mexicana*)," Anim. Behav. **34**, 1078–1186.
Gouzoules, H., Gouzoules, S., and Tomaszycki, M. (**1998**). "Agonistic screams and the classification of dominance relationships: are monkeys fuzzy logicians?," Anim. Behav. **55**, 51–60.
Goymann, W. (**1995**). "Indian false vampires, *Megaderma lyra*: a field approach on social behaviour and organization," Diploma thesis, Institute of Zoology, Ludwig-Maximilians-Universitaet Munich.
Goymann, W., Leippert, D., and Hofer, H. (**2000**). "Sexual segregation, roosting, and social behaviour in a free-ranging colony of Indian false vampires (*Megaderma lyra*)," Mamm. Biol. **65**, 138–148.
Grafen, A. (**1990**). "Biological signals as handicaps," J. Theor. Biol. **144**, 517–546.
Grube, C. (**2003**). "Dokumentation von Elementen des akustischen Sozialverhaltens beim Indischen Falschen Vampir" ("Elements of the acoustical social behavior in the Indian false vampire bat"), Diploma thesis, Institute of Zoology, University of Veterinary Medicine Hanover.
Johnstone, T., and Scherer, K. J. (**1999**). "The effects of emotions on voice quality," Proceedings of the XIV International Congress on Phonetic Sciences, pp. 2029–2032.
Koodsma, D. E. (**1977**). "Correlates of Song Organization Among North American Wrens," Am. Nat. **111**, 995–1008.
Koopman, K. F. (**1994**). *Chiroptera: Vol. 1: Systematik (Chiroptera: Vol. 1: Systematics)* (Walter de Gruyter, Berlin).
Kumar, S., and Hedges, S. B. (**1998**). "A molecular timescale for vertebrate evolution," Nature (London) **392**, 917–920.
Kulzer, E. (**2005**). *Chiroptera: Vol. 3: Biologie (Chiroptera: Vol. 3: Biology)* (Walter de Gruyter, Berlin).
Leippert, D. (**1994**). "Social behavior on the wing in the false vampire, *Megaderma lyra*," Ethology **98**, 111–127.
Leippert, D., Goymann, W., Hofer, H., Marimuthu, G., and Balasingh, J. (**2000**). "Between-litter siblicide in captive Indian false vampire bats (*Megaderma lyra*)," J. Zool. **251**, 537–540.
Ma, J., Kobayasi, K., Zhang, S., and Metzner, W. (**2006**). "Vocal communication in adult greater horseshoe bats, *Rhinolophus ferrumequinum*," J. Comp. Physiol. [A] **192**, 535–550.
Madsen, O., Scally, M., Douady, C. J., Kao, D. J., DeBry, R. W., Adkins, R., Amrine, H. M., Stanhope, M. J., de Jong, W. W., and Springer, M. S. (**2001**). "Parallel adaptive radiations in two major clades of placental mammals," Nature (London) **409**, 610–614.
Michelsson, K., Christensson, K., Rothgänger, H., and Winberg, J. (**1996**). "Crying in separated and non-separated newborns: sound spectrographic analysis," Acta Paediatr. **85**, 471–475.
Mitani, J. C., and Stuht, J. (**1998**). "The evolution of non-human primate loud calls: acoustic adaptions for long distance transmission," Primates **39**, 171–182.
Morton, E. S. (**1977**). "On the occurrence and significance of motivation-structural rules in some bird and mammal sounds," Am. Nat. **111**, 855–869.
Murphy, W. J., Eizirik, E., Johnson, W. E., Zhang, Y. P., Ryder, O. A., and O'Brien, S. J. (**2001**). "Molecular phylogenetics and the origins of placental mammals," Nature (London) **409**, 614–616.
Murray, I. R., and Arnott, J. L. (**1993**). "Toward the simulation of emotion in synthetic speech: A review of the literature on human vocal emotion," J. Acoust. Soc. Am. **93**, 1097–1108.
Neuweiler, G. (**2000**). *The Biology of Bats* (Oxford University Press, New York).
Novacek, M. J. (**1985**). "Evidence for echolocation in the oldest known bats," Nature (London) **315**, 140–141.
Owren, D., and Rendall, D. (**2001**). "Sound on the rebound: bringing form and function back to the forefront in understanding nonhuman primate vocal signaling," Evol. Anthropol. **10**, 58–71.
Paeschke, A. (**2003**). *Prosodische Analyse emotionaler Sprechweise (Prosodic analysis of emotional speech)* (Logos, Berlin).
Pfalzer, G., and Kusch, J. (**2003**). "Structure and variability of bat social calls: implications for specificity and individual recognition," J. Zool. **261**, 21–33.
Porter, F. L. (**1979**). "Social behavior in the leaf-nosed bat, *Carollia perspicillata*," Z. Tierpsychol **50**, 1–8.
Reby, D., André-Obrecht, R., Galinier, A., Farinas, J., and Cargnelutti, B. (**2006**). "Cepstral coefficients and hidden Markov models reveal idiosyncratic voice characteristics in red deer (*Cervus elaphus*) stags," J. Acoust. Soc. Am. **120**, 4080–4089.
Reby, D., McComb, K., Cargnelutti, B., Darwin, C., Fitch, W. T., and Clutton-Brock, T. (**2005**). "Red deer stags use formants as assessment cues during intrasexual agonistic interactions," Proc. R. Soc. London, Ser. B **272**, 941–947.
Rendall, D. (**2003**). "Acoustic correlates of caller identity and affect intensity in the vowel-like grunt vocalizations of baboons," J. Acoust. Soc. Am. **113**, 3390–3402.
Riede, T., Bronson, E., Hatzikirou, H., and Zuberbuehler, K. (**2005**). "Vocal production mechanisms in a non-human primate: morphological data and a model," J. Hum. Evol. **48**, 85–96.
Russo, D., and Jones, G. (**1999**). "The social calls of Kuhl's pipistelles *Pipistrellus kuhlii* (Kuhl, 1819): Structure and variation," J. Zool. **249**, 476–481.
Schehka, S., Esser, K.-H., and Zimmermann, E. (**2007**). "Acoustical expression of arousal in conflict situations in tree shrews (*Tupaia belangeri*)," J.

Comp. Physiol. **193**, 845–852.
Scherer, K. R. (**2000**). "A cross cultural investigation of emotion inferences from voice and speech: implications for speech technology," Proceedings of the Sixth International Conference on Spoken Language Processing, Beijing Vol. **2**, pp. 379–382.
Scherer, K. R. (**1986**). "Vocal affect expression: a review and a modal for future research," Psychol. Bull. **99**, 143–165.
Scherer, K. R., Banse, R., and Wallbott, H. G. (**2001**). "Emotion inferences from vocal expression correlate across languages and cultures," J. Cross Cult. Psychol. **32**, 76–92.
Scherrer, J. A., and Wilkinson, G. S. (**1993**). "Evening bat isolation calls provide evidence for heritable sigantures," Anim. Behav. **46**, 847–860.
Schmidt, S. (**2005**). "Understanding wildlife: behavioural ecology and acoustic communication in a Sri Lankan bat, *Megaderma lyra*," Sci. Sri Lanka **6**, 17–19.
Schmidt, S., Hanke, S., and Pillat, J. (**2000**). "The role of echolocation in the hunting of terrestrial prey-new evidence for an under-estimated strategy in the gleaning bat, *Megaderma lyra*," J. Comp. Physiol. **186**, 975–988.
Siebert, E. R., and Parr, L. A. (**2003**). "A structural and contextual analysis of chimpanzee screams," Ann. N.Y. Acad. Sci. **1000**, 104–109.
Soltis, J. (**2004**). "The signal functions of early infant crying," Behav. Brain Sci. **27**, 443–458.
Soltis, J., Leong, K., and Savage, A. (**2005**). "African elephant vocal communication II: rumble variation reflects the individual identity and emotional state of callers," Anim. Behav. **70**, 589–599.
Thompson, W. F., and Balkwill, L. L. (**2006**). "Decoding speech prosody in five languages," Semiotica **158**, 407–424.
Vannoni, A. G. (**2007**). "Individual acoustic variation in fallow deer (*Dama dama*) common and harsh groans: a source-filter theory perspective," Ethology **113**, 223–234.
Warkentin, K. J., Keeley, A. T. H., and Hare, J. F. (**2001**). "Repetitive calls of juvenile Richardson's ground squirrels (*Spermophilus richardsonii*) communicate response urgency," Can. J. Zool. **79**, 569–573.
Wilden, H., Herzel, H., Peters, G., and Tembrock, G. (**1998**). "Subharmonics, biphonation, and deterministic chaos in mammal vocalization," Int. J. Anim. Sound and Rec. **9**, 171–196.
Wilkinson, G. S., and Boughman, J. W. (**1998**). "Social calls coordinate foraging in greater spear-nosed bats," Anim. Behav. **55**, 337–350.
Zahavi, A. (**1975**). "Mate selection-a selection for a handicap," J. Theor. Biol. **53**, 205–214.
Zahavi, A. (**1977**). "The cost of honesty (further remarks on the handicap principle)," J. Theor. Biol. **67**, 603–605.
Zoefel, P. (**1988**). *Statistik in der Praxis (Applied statistics)* (Gustav Fischer, Stuttgart).

Classification of Risso's and Pacific white-sided dolphins using spectral properties of echolocation clicks

Melissa S. Soldevilla,[a] E. Elizabeth Henderson, Gregory S. Campbell, Sean M. Wiggins, and John A. Hildebrand
Scripps Institution of Oceanography, University of California, San Diego, 9500 Gilman Drive 0205, La Jolla, California 92093-0205

Marie A. Roch
Department of Computer Science, San Diego State University, 5500 Campanile Drive, San Diego, California 92182-7720

(Received 28 August 2007; revised 23 April 2008; accepted 24 April 2008)

The spectral and temporal properties of echolocation clicks and the use of clicks for species classification are investigated for five species of free-ranging dolphins found offshore of southern California: short-beaked common (*Delphinus delphis*), long-beaked common (*D. capensis*), Risso's (*Grampus griseus*), Pacific white-sided (*Lagenorhynchus obliquidens*), and bottlenose (*Tursiops truncatus*) dolphins. Spectral properties are compared among the five species and unique spectral peak and notch patterns are described for two species. The spectral peak mean values from Pacific white-sided dolphin clicks are 22.2, 26.6, 33.7, and 37.3 kHz and from Risso's dolphins are 22.4, 25.5, 30.5, and 38.8 kHz. The spectral notch mean values from Pacific white-sided dolphin clicks are 19.0, 24.5, and 29.7 kHz and from Risso's dolphins are 19.6, 27.7, and 35.9 kHz. Analysis of variance analyses indicate that spectral peaks and notches within the frequency band 24–35 kHz are distinct between the two species and exhibit low variation within each species. *Post hoc* tests divide Pacific white-sided dolphin recordings into two distinct subsets containing different click types, which are hypothesized to represent the different populations that occur within the region. Bottlenose and common dolphin clicks do not show consistent patterns of spectral peaks or notches within the frequency band examined (1–100 kHz). © *2008 Acoustical Society of America.*
[DOI: 10.1121/1.2932059]

PACS number(s): 43.80.Ka [WWA] Pages: 609–624

I. INTRODUCTION

Accurate classification of recorded calls to species is needed for passive acoustic monitoring of wild cetaceans. Passive acoustic monitoring is increasingly being used for towed hydrophone line transect surveys (Barlow and Taylor, 2005) and for remote, long-term monitoring of populations using autonomous instruments (Mellinger *et al.*, 2004; Sirovic *et al.*, 2004; Oleson *et al.*, 2007; Verfuss *et al.*, 2007). Recent technological advances allow long-term recordings to reach higher bandwidths (Wiggins and Hildebrand, 2007), which prompts research into use of higher frequency calls for species classification. Odontocete species regularly emit high frequency clicks and burst-pulsed calls, in addition to lower frequency whistles (Richardson *et al.*, 1995) and usage of these call types varies with behavioral state, geographic location, and geometric spacing of conspecifics (Jones and Sayigh, 2002; Lammers *et al.*, 2003; Nowacek, 2005). Advances have been made in classifying delphinid whistles to species (Oswald *et al.*, 2003; Oswald *et al.*, 2004), but little work has focused on classifying delphinid burst pulses and clicks to species (Roch *et al.*, 2007), particularly at frequencies greater than 24 kHz. While the clicks of porpoises, sperm whales, and beaked whales are easily distinguishable from delphinid clicks based on time duration, interclick interval and peak frequency characteristics (Goold and Jones, 1995; Kamminga *et al.*, 1996; Madsen *et al.*, 2005; Zimmer *et al.*, 2005), delphinid clicks thus far have remained unclassifiable at the species level.

Most echolocation click research to date has focused on the performance of sonar systems and only a few studies look for species-specific characteristics. Kamminga *et al.* (1996) showed that four species of porpoises can be distinguished at the subfamily level by time duration and dominant frequency of their clicks. Akamatsu *et al.* (1998) compared peak frequency and duration characteristics of finless porpoise (*Neophocaena phocaenoides*), baiji (*Lipotes vexillifer*), and bottlenose dolphins (*Tursiops truncatus*) and found that finless porpoise can be distinguished from the two dolphins, but show overlap in duration and frequency between the two dolphin species with a tendency toward lower frequencies from baiji and higher frequencies from bottlenose dolphins. Nakamura and Akamatsu (2003) compared clicks from six captive odontocete species and found that harbor porpoise (*Phocoena phocoena*) and false killer whale (*Pseudorca crassidens*) clicks are distinguishable from four species of dolphin clicks based on click duration and peak frequency. The clicks of baiji, short-beaked common (*Delphinus delphis*), bottlenose, and Pacific white-sided (*Lagenorhynchus obliquidens*) dolphins cannot be distinguished from each

[a]Electronic mail: msoldevilla@ucsd.edu

TABLE I. Published click characteristics of common, Risso's, Pacific white-sided and bottlenose dolphins.

	Delphinus spp.	*G. griseus*		*L. obliquidens*	*T. truncatus*	
Recording situation	Captive[a,b]	Free ranging[c]	Captive[d,e]	Captive[a,f,g]	Free ranging[h]	Captive[d]
Duration (μs)	50–250	30–75	40–100	25–100	10–20	50–80
ICI (ms)	⋯	⋯	⋯	⋯	0–400+	⋯
Source level (dB re 1 μPa at 1 m)	145–170	202–222	170–215	170	⋯	228
Peak frequencies (kHz)	23–67	40–110	30–105	50–80 100–120	40–140	110–130
−3 dB bandwidth (kHz)	⋯	15–85	30–84	9.5–36	⋯	⋯
−10 dB bandwidth (kHz)	⋯	20–125	100	⋯	⋯	⋯
Centroid frequencies (kHz)	⋯	60–90	50–80	⋯	⋯	⋯
rms bandwidth (kHz)	⋯	20–30	25	⋯	⋯	⋯

[a]Fish and Turl (1976).
[b]Evans (1973).
[c]Madsen *et al.* (2004).
[d]Au (1993).
[e]Philips *et al.* (2003).
[f]Fahner *et al.* (2003).
[g]Nakamura and Akamatsu (2003).
[h]Akamatsu *et al.* (1998).

other with these characteristics (Nakamura and Akamatsu, 2003). To our knowledge, distinct species-specific differences have not been documented within delphinid clicks.

As a result of the focus on dolphin sonar system performance, most research effort has been directed at understanding clicks produced on axis. However, on-axis clicks may not accurately represent the full ensemble of clicks that will be acquired during passive acoustic monitoring of free-range odontocetes. Au *et al.* (1978) demonstrated significant distortion in the waveshape and spectral content of clicks as a function of beam angle. They established that off-axis click durations are longer, typically due to multipaths of the initial click pulse, and suggested that the multipaths are due to reflections within the head, from the external environment, or a combination of the two. Internal reflections are dependent on anatomy and may contain additional information; however, thus far, no study has examined whether the distorted spectra from off-axis clicks contain a species-specific signature. Clicks recorded during passive acoustic monitoring surveys will come from animals of unknown acoustic orientation; therefore, detailed spectral descriptions of all recorded clicks are needed for wild dolphins, regardless of orientation.

Five species of dolphins are commonly observed in the waters offshore of southern California. Short-beaked common and long-beaked common (*D. capensis*) dolphins are small dolphins (160–210 and 190–240 cm, respectively) (Heyning and Perrin, 1994), typically sighted in offshore tropical and temperate waters in schools of hundreds to thousands of individuals (Evans, 1974; Polacheck, 1987; Selzer and Payne, 1988; Gaskin, 1992; Gowans and Whitehead, 1995). They were only recently recognized as separate species (Heyning and Perrin, 1994). Pacific white-sided dolphins are small dolphins (230–250 cm) (Walker *et al.*, 1986) endemic to cold temperate North Pacific waters (Leatherwood *et al.*, 1984; Green *et al.*, 1992) and are observed in schools ranging between 10 and 1000 individuals (Leatherwood *et al.*, 1984). The offshore population of bottlenose dolphins consists of medium-sized dolphins (290–310 cm) (Perrin and Reilly, 1984) that are typically sighted in medium-sized groups (1–30) (Shane, 1994) throughout tropical and temperate waters (Forney and Barlow, 1998). Risso's dolphins (*Grampus griseus*) are larger dolphins (400 cm) typically found in medium-sized groups (10–50) in tropical and temperate waters (Leatherwood *et al.*, 1980; Kruse *et al.*, 1999). Click feature measurements have been published for free-ranging Risso's and bottlenose dolphins and for captive Pacific white-sided, common, Risso's, and bottlenose dolphins (Table I).

This study describes echolocation clicks for five species of dolphins from the southern California region. This is the first study to describe recordings from free-ranging short-beaked common, long-beaked common, and Pacific white-sided dolphins. We describe the spectral content of echolocation clicks with emphasis on spectral peaks and notches and show that two species of dolphins have a unique peak and notch structure. We quantify the intra- and interspecific frequency variations of these peaks and establish that they represent invariant and distinctive features as required for species specificity (Emlen, 1972; Nelson, 1989), thereby demonstrating their value for species classification in passive acoustic monitoring. Finally, we examine long-term autonomous recordings and quantify the number of click bouts that exhibit the described spectral patterns.

II. MATERIALS AND METHODS

A. Study area and survey platforms

Our study area encompassed the region offshore of southern California extending from 32°42′ N, 117°10′ W along the coast to 35°5′ N, 120°47′ W and offshore to 29°51′ N, 123°35′ W and 33°23′ N, 124°19′ W (Fig. 1). Recordings were obtained in the southern California neritic and pelagic waters between November 2004 and April 2007 (Fig. 1). Data were analyzed from multiple surveys: California Cooperative of Oceanic Fisheries Investigations (CalCOFI) oceanographic surveys, San Clemente Island (SCI)

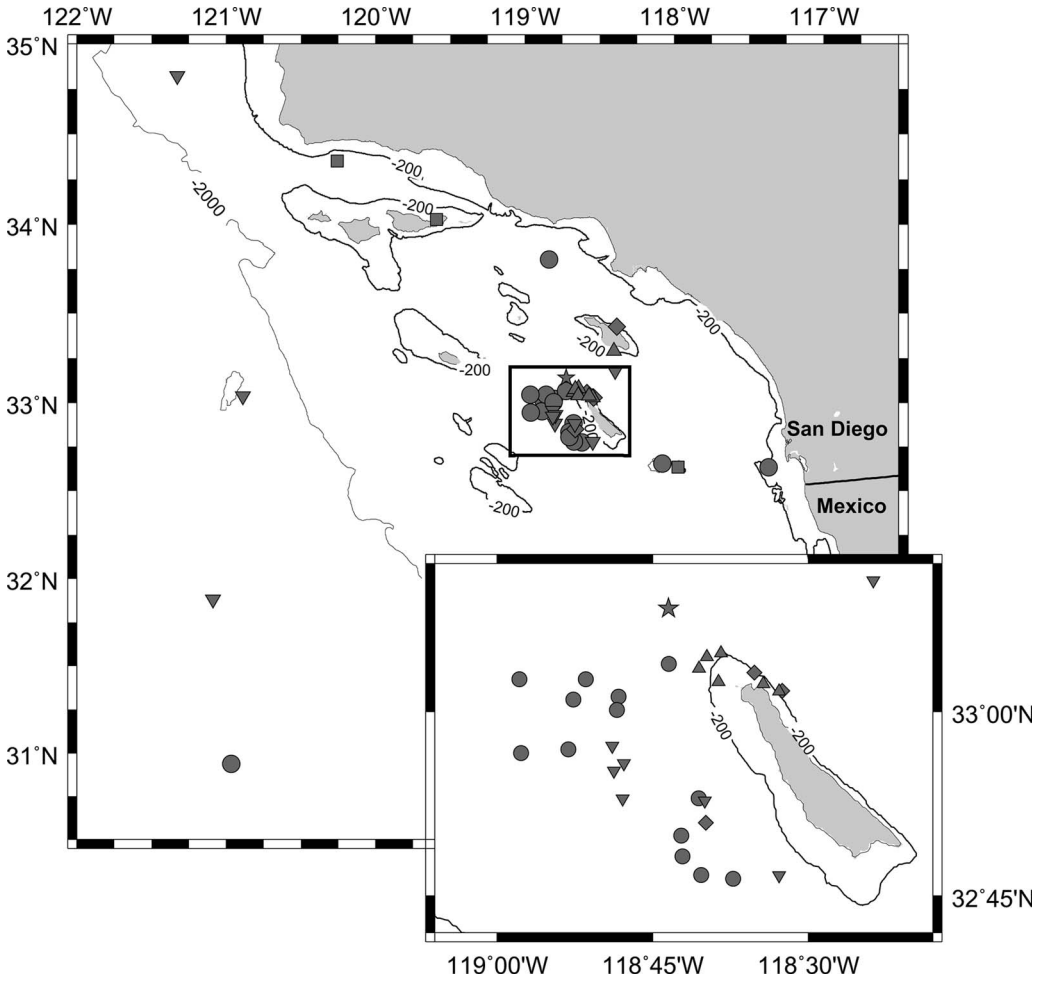

FIG. 1. Map of study area and delphinid recording locations offshore of southern California. Coastline, −200 m, and −2000 m bathymetric contours are represented. The inset expands the cluster of recordings from San Clemente Island area. This cluster represents increased effort, not increased presence. (★) FLIP location represents multiple sightings from Table V. (●) *Delphinus delphis*, (■) *Delphinus capensis*, (♦) *Grampus griseus*, (▼) *Lagenorhynchus obliquidens*, and (▲) *Tursiops truncatus*.

small boat operations, Scripps Institution of Oceanography (SIO) instrumentation servicing cruises on the R/V Robert Gordon Sproul, and Floating Instrument Platform (FLIP, Fisher and Spiess, 1963) moored observations (see Table II for survey and instrumentation details).

The durations of dolphin school recordings obtained from the four studies varied due to differing survey goals. Recording sessions from CalCOFI surveys were typically of short duration because the ship could not deviate from its course to spend time with detected animals. During SIO instrumentation surveys and SCI field operations, the vessel was held stationary as animals swam past and recordings lasted as long as the animals stayed near the boat. Continuous acoustic recordings were obtained from the moored research platform FLIP, resulting in recording sessions that last the duration that animals were audible at the FLIP hydro-

TABLE II. Survey and instrumentation information. Frequency response and gain of the acoustic instruments are described in detail in the text. Surveys conducted from stationary or drifting platforms are indicated by a blank field under tow distance. Abbreviations: CC: CalCOFI oceanographic survey; SC: southern California instrumentation survey; SCI: San Clemente Island survey; FLIP: FLIP moored observations.

Cruise name	Dates	Platform	Tow distance (m)	Hydrophone depth (m)	Hydrophone type	Circuit board	A/D converter
CC0411	Nov 2004	RV Roger Revelle	···	30	ITC 1042	R100-A	MOTU 896HD
CC0604	Apr 2006	RV New Horizon	270	15–20	SRD HS150	R100-C	MOTU 896HD
SC03	May 2006	RV Gordon Sproul	270	15–20	SRD HS150	R100-C	MOTU 896HD
SCI0608	Aug 2006	RHIB	···	10–30	SRD HS150	R300	Fostex FR2
					ITC 1042	R300	Fostex FR2
FLIP0610	Oct 2006	FLIP	···	30	SRD HS150	R300	MOTU 896HD
SCI0704	Apr 2007	RHIB	···	10–30	SRD HS150	R300	Fostex FR2

phone array. Data from these recordings were used only when the animals were within 1 km of FLIP, as determined by visual observations.

Experienced marine mammal visual observers conducted the visual observation component of this project. Marine mammal detections and species identifications were made by a set number of observers using handheld binoculars, supplemented with 25× binoculars on some platforms. Sighting information included location of group or animal, initial distance and angle from research vessel, group size, presence of calves, and general behavior. Additionally, weather and sea state data were recorded to account for missed animals due to poor sighting conditions. Acoustic recordings from all surveys were used only for schools that were determined to be single species. If an additional species was detected within 3 km, or if this could not be determined due to sea states greater than Beaufort 3, the recording was not used. Following the whistle study of Oswald *et al.* (2003), we consider 3 km a conservative distance for species identification of clicks. Published studies indicate that whistles and echolocation clicks are not detectable beyond about 1 km (Richardson *et al.*, 1995; Philpott *et al.*, 2007), while we find that they are rarely audible beyond 3 km. Differentiation between short-beaked and long-beaked common dolphins is challenging in certain areas off California. In this study, data were used only when the visual identification by species was unambiguous.

B. Acoustic sensors and digitization

The acoustic sensors used on the different surveys consist of a variety of hydrophone and preamplifier configurations (Table II). Two types of omnidirectional, spherical hydrophones were used: ITC 1042 hydrophones (International Transducer Corp., Santa Barbara, CA) and HS150 hydrophones (Sonar Research & Development Ltd., Beverley, UK). These hydrophones exhibit a flat frequency response (±3 dB) from 1 to 100 kHz. The hydrophones were connected to one of the three custom-built preamplifier and bandpass filter electronic circuit boards: R100A, R100C, and R300. The circuit boards were designed to whiten the ambient ocean noise, which results in a nonlinear frequency response that provides greater gain at higher frequencies where ambient noise levels are lower and sound attenuation is higher. The response increased 20 dB in amplitude from 10 kHz to peak at 90 kHz. The differing frequency responses of the various systems were compensated for during analysis using spectral means subtraction, as described in Sec. II C. Hydrophones and circuit boards were suspended in 2.5–5-cm-diam oil-filled hoses to provide good acoustic coupling to the seawater. Towed hydrophone arrays were weighted with 9 kg of lead wire wrapped around the tow cable ahead of the hydrophone assembly so that the array was towed between 10 and 30 m depth.

The analog signals from the hydrophone circuit boards were converted digitally and recorded with one of the two systems: MOTU audio interface and recording software or a Fostex recorder. The MOTU 896HD firewire audio interface (Mark of the Unicorn, Cambridge, MA) is capable of sampling eight channels at 192 kHz with 24 bit samples. Each channel therefore had a Nyquist frequency of 96 kHz. Gain on the MOTU is adjustable with trim knob controllers and has a light emitting diode readout of the signal amplitude. The knobs were adjusted to minimize clipping while maximizing signal strength and settings were noted. Signals were recorded directly to a computer hard-disk drive using the sound analysis and recording software Ishmael (Mellinger, 2001), with the instrumentation gain set to either −80 or −100 dB. The MOTU/Ishmael system has a flat frequency response (±0.05 dB) from 1 to 90 kHz. The Fostex FR2 field memory recorder (Fostex America, Foster Electric, USA, Inc., Gardena, CA) is capable of sampling two channels at 192 kHz with 24 bit samples, yielding a Nyquist frequency of 96 kHz, and has a flat frequency response (±3 dB) from 20 to 80 kHz. Signals were recorded directly to an 8 Gbyte Compact Flash memory card (Transcend Information, Inc., Los Angeles, CA). The recordings were subsequently downloaded onto hard-disk drives.

C. Signal analysis

Signal analysis was performed with customized routines using MATLAB (Mathworks, Natick, MA). Start and end times of clicks were automatically located using a two-step approach. In the first step, a click detection algorithm was implemented on all acoustic data to locate potential click candidates in the frequency domain. Spectra were calculated on 5.33 ms of data using a 1024-point fast fourier transform (FFT) with 50% overlap and a Hann window. Spectral means subtraction was performed on each spectrum by subtracting the mean of the spectral vectors of the surrounding 3 s of data. Individual spectra were selected as click candidates if a minimum percentage of frequency bins exceeded a minimum threshold within the bandwidth range of interest. Values for minimum percentage, threshold, and bandwidth were set as 12.5%, 13 dB, and 15–95 kHz, respectively. For each click candidate, start and end times were defined to be 7.5 ms before and after the click to provide noise for use in spectral means subtraction in the second step. Overlapping click candidates were merged. These automatic detections were subsequently scanned by a trained analyst and false detections and burst-pulse calls were removed. Clicks within burst-pulse calls may exhibit species specificity; however, their analysis is beyond the scope of this study.

In the second step, a finer resolution click detection algorithm was implemented on the data output from step 1 to search for the start and end points of each click in the time domain. To remove any noise caused by water flow around the towed hydrophone, the signal was high-pass filtered with the −3 dB point at 3 kHz using a finite impulse response filter. The Teager energy operator (Kaiser, 1990), a measure which provides nearly instantaneous energy tracking by using only three consecutive signal samples, was calculated for the clicks obtained in the first step. The Teager energy operator of a discrete time signal is defined as

$$\Psi[x(n)] = x^2(n) - x(n+1)x(n-1), \quad (1)$$

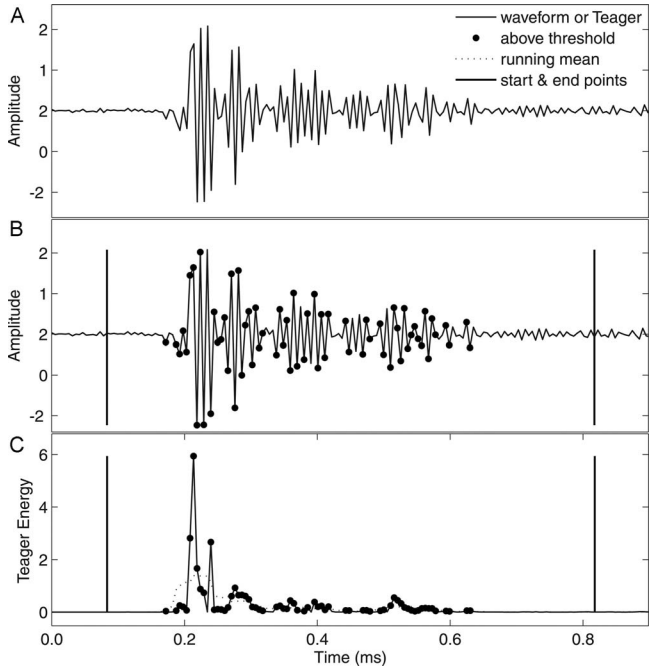

FIG. 2. Example wave form and corresponding Teager energy of a Pacific white-sided dolphin click. Note the reverberations present in the wave form. (A) The click wave form, (B) the click wave form with denotations of click end points and data points above Teager energy noise floor threshold, (C) the Teager energy of the wave form, the running mean of the Teager energy, denotations of click end points, and data points above the noise floor threshold. The solid vertical bars represent the time range of the complete click peak.

where n denotes the sample number. Kandia and Stylaniou (2006) demonstrated the utility of the Teager energy operator for detection of sperm whale regular and creak clicks. For each click, a noise floor was defined at the 40th percentile of energy, based on empirical analysis of the data. All points whose Teager energy was 100 times greater than the noise floor were tagged and grouped as belonging to a single click if they were less than 500 μs apart. If multiple clicks were present, clicks were ranked by maximum Teager energy and the strongest clicks were selected such that one click was chosen per 15 ms of data. Methods for determining the start and end points of symmetric on-axis click wave forms have been developed (Au, 1993); however, clicks obtained from random axis orientations may have distorted asymmetric wave forms, which include reverberations caused by reflections within the head, from the external environment or both (Au *et al.*, 1978) and therefore require a different analysis technique. To obtain the complete click including reverberations, a ten-point running mean of the Teager energy was calculated and start and end points were determined as the first and last points that were three times greater than the noise floor (Fig. 2).

The spectral characteristics of clicks were quantified for the 1.33 ms of data following the start of each click by calculating a 256-point FFT with a Hann window. Noise spectra were calculated from the remaining data, excluding extraneous clicks, and were averaged within each recording session. Spectral means subtraction was performed on each click spectrum by subtracting the mean noise spectrum from the corresponding recording session. Spectral magnitudes were normalized between 0 and 1, and the means and standard deviations of the normalized click spectra were calculated for each species. Additionally, concatenated spectrograms were created of all clicks analyzed for each species.

D. Click selection and statistical analysis

The original data lack the independence required for statistical analysis because click trains represent multiple clicks from one individual and an individual likely produces multiple click trains over a recording session. To reduce over-representation of an individual's clicks, a two stage process was established to limit the number of clicks and click trains analyzed from each recording session. Click trains were randomly selected from each recording session until either all trains were selected or the number of selected trains was twice the estimated group size. From each sampled click train, a single click was selected at random. Click trains were defined as clicks that were separated by less than 0.5 s; overlapping click trains, although likely to have been produced by different individuals, were grouped as a single train to reduce over-representation.

To examine spectral peak and notch structure and its variability in the frequency domain across clicks, the frequency value of consistent spectral peaks and notches was quantified for clicks of each species. Variability exists among clicks, such that the frequency value of the peaks and notches may vary, the peak or notch may not exist at all, and additional peaks and notches that are not consistent across clicks may exist. To establish and select consistent peaks and notches for statistical analysis while avoiding circularity, clicks were randomly divided into two equal groups, denoted the training and testing data. Training data clicks were used to establish expected frequency ranges for consistent peaks and notches across clicks of a given species. Testing data clicks were used for statistical comparison among species, such that the values of peaks and notches found within the established frequency ranges were quantified and analyzed. Details of the analysis of clicks from the training and testing data follow.

Using the training data clicks to establish the frequency ranges of consistent peaks and notches, a first-order regression-based peak and notch selection algorithm was implemented on the normalized click spectra. To avoid selecting minor peaks or notches, the spectra were smoothed using a five-point window and a threshold was set such that the peak or notch was required to deviate by at least 2 dB. The number of peaks and notches selected per click spectra varied, ranging between 0 and 20 and averaging 8. A histogram was generated from the frequency values of all selected peaks or notches combined across all training data clicks for each species. The histogram was calculated such that each bin was 750 Hz wide to correspond with the FFT frequency resolution. Peak and notch selections existed at all frequencies resulting in "background noise" in the histogram from which consistent peak and notch frequencies needed to be distinguished. To estimate the background noise in each histogram, peaks and notches from each click were randomly reassigned frequency values and a noise estimate histogram was generated. Actual counts of frequency values were com-

pared to estimated background noise counts using a one-tailed z-test (alpha 0.5) (Zar, 1999) for each species. Peak and notch frequency values were established as consistent if they met three conditions: (1) actual counts were significantly greater than estimated noise counts, (2) the frequency value was greater than 15 kHz (to exclude overlapping whistles), and (3) at least one adjacent frequency value was also consistent. A set of Gaussians is fitted to the peak and notch histograms of each species using Gaussian mixture models (Huang *et al.*, 2001). Frequency means and ranges are established from the mean (μ) and standard deviations ($\pm\sigma$) of the dominant Gaussian for each consistent peak or notch.

Using testing data clicks to examine differences in frequency values of peaks and notches among species, peaks and notches were statistically analyzed if they fell within the frequency ranges established using the training data. Peaks and notches from testing data clicks were selected using the peak/notch selection algorithm described above. If any peaks or notches fell within the established frequency ranges, a minimum of one per range was chosen, keeping the peak or notch that was nearest to the mean established from the training data. To examine variability in peak and notch frequencies among and within species, nested analyses of variance (ANOVAs) (Zar, 1999) were performed in SPSS 11.5 (SPSS, Inc., Chicago, IL). For each consistent peak and notch, a nested ANOVA was calculated examining the main effect of species differences in frequency value and the interaction effect of recording session nested within species. Recording session was included to test for effects due to the use of different recording systems among surveys. The nested ANOVA can only determine that differences exist among multiple comparisons; therefore, *post hoc* tests were performed to determine which, if any, recording sessions were different using Tukey's method (Zar, 1999).

To determine whether the spectral properties of clicks could be useful for classifying data from passive acoustic autonomous seafloor recorders, in this case of high-frequency acoustic recording packages (HARPs) (Wiggins and Hildebrand, 2007), 1300 days of data were reviewed for the presence of unique spectral patterns. Long-term spectral averages (LTSAs) (Wiggins and Hildebrand, 2007) were created using the Welch algorithm (Welch, 1967) by coherently averaging 4000 spectra created from 1000-point, 0% overlapped, Hann-windowed data. The resulting LTSAs had resolutions of 100 Hz and 5 s in the frequency and time domains, respectively. LTSAs were manually inspected for click bouts, and bouts containing unique spectral patterns were noted. The total counts of each type of click bout are presented.

III. RESULTS

The total numbers of recording sessions per species included in this analysis were 4 from long-beaked common dolphins, 17 from short-beaked common dolphins, 6 from Risso's dolphins, 22 from Pacific white-sided dolphins, and 7 from bottlenose dolphins (Table III). School sizes ranged between 1 and 500 animals, with the two common dolphin species typically occurring in larger schools than the other three species (Table III). The total number of clicks recorded per session ranged from 3 to almost 11 000 while the total number of click trains ranged between 1 and 582 (Table III). Example wave forms and spectra are presented for each of the five species described (Fig. 3).

Concatenated spectrograms of the individual clicks and mean spectral plots of clicks for the five dolphin species investigated reveal consistent spectral characteristics for both Pacific white-sided and Risso's dolphins (Fig. 4). Alternating high and low amplitude bands are evident at certain frequencies across the clicks of these two species. These frequency bands appear consistent for the majority of clicks across multiple recording sessions as well as for various hydrophone array configurations. No such pattern is evident for long-beaked common, short-beaked common, or bottlenose dolphins (Fig. 4).

The existence of consistent spectral peaks and notches in only two of the species is reinforced when comparing actual counts of selected peaks or notches to estimated noise counts for frequency values in the training data. Only Pacific white-sided dolphin and Risso's dolphin clicks exhibit frequency values at which the counts of peaks and notches are greater than expected by chance. The remaining three species' clicks did not have significantly greater counts of peaks or notches at any frequency values (Fig. 5). Univariate Gaussian mixture models fit to the peak histograms and notch histograms (Fig. 6) from Pacific white-sided dolphin and Risso's dolphin training data clicks provide estimates of means and standard deviations for each of the consistent peaks and notches (Table IV).

For the two species with spectral peaks and notches, calculations of the percentage of clicks from the testing data that have peaks or notches within the expected frequency ranges show that these consistent peaks and notches occur in the majority of recorded clicks, with percentages ranging between 44% and 89% (Table IV). The two species share similar spectral peaks at mean frequencies 22.2 and 37.3 kHz for Pacific white-sided dolphins and 22.4 and 38.8 kHz for Risso's dolphins. Risso's dolphins have two additional spectral peaks at mean frequencies 25.5 and 30.5 kHz and spectral notches at 19.6, 27.7, and 35.9 kHz, while Pacific white-sided dolphin clicks have spectral peaks at mean frequencies 26.6 and 33.7 kHz, and notches at 19.0, 24.5, and 29.7 kHz (Table IV).

Nested ANOVA analyses indicate that some click variables are distinct both between species and among subsets of recording sessions. Five of the seven frequency peaks and notches are significantly different between Pacific white-sided and Risso's dolphins (Table V). Only the lowest frequency peak and notch are not significantly different. In addition to the distinct separation of five peaks and notches between the two species, four of those five peaks show significant differences among recording sessions within species. Tukey's *post hoc* tests of recording session differences indicate that (1) there are no significant differences among recording sessions of Risso's dolphins and (2) there are significant differences between two distinct subsets of recording sessions of Pacific white-sided dolphins (Table VI). Click peaks and notches are consistent across recording sessions within these Pacific white-sided dolphin subsets, but distinct

TABLE III. Summary of data included in click analysis. Survey platform, numbers of clicks, click trains, and school sizes are presented for each recording of each species. Each recording session represents a new school of dolphins. Abbreviations: Dc: *Delphinus capensis*; Dd: *Delphinus delphis*; Gg: *Grampus griseus*; Lo: *Lagenorhynchus obliquidens*; Tt: *Tursiops truncatus*. CC: CalCOFI oceanographic survey; SC: southern California instrumentation survey; SCI: San Clemente Island survey; FLIP: FLIP moored observations.

Species	Recording	Survey	Clicks	Click trains	School size
Dc	1	CC0411	1256	155	500
	2	CC0604	531	22	45
	3	SC03	2377	198	200
	4	FLIP0610	2338	145	45
Dd	1	CC0604	8	3	60
	2	SC03	192	52	18
	3	SC03	164	30	250
	4	SCI0608	1030	12	230
	5	SCI0608	245	12	175
	6	SCI0608	166	30	225
	7	SCI0608	636	113	320
	8	SCI0608	9	1	180
	9	SCI0608	804	75	430
	10	SCI0608	763	38	30
	11	SCI0608	475	25	85
	12	SCI0608	624	58	7
	13	SCI0608	2269	70	190
	14	SCI0608	455	13	370
	15	SCI0608	3884	48	20
	16	SCI0608	730	26	35
	17	SCI0608	361	25	320
Gg	1	SCI0608	6	1	1
	2	SCI0608	286	24	12
	3	SCI0608	190	45	12
	4	SCI0608	1194	105	40
	5	SCI0608	3	1	18
	6	FLIP0610	2564	446	10
Lo	1	CC0604	224	3	7
	2	CC0604	508	66	4
	3	CC0604	4	1	5
	4	SC03	24	2	10
	5	SCI0608	5961	262	12
	6	SCI0704	333	92	13
	7	SCI0704	1317	145	8
	8	SCI0704	95	26	13
	9	SCI0704	127	18	22
	10	SCI0704	197	17	25
	11	FLIP0610	1409	208	25
	12	FLIP0610	5503	543	50
	13	FLIP0610	3463	358	15
	14	FLIP0610	4761	431	20
	15	FLIP0610	7085	582	20
	16	FLIP0610	916	111	17
	17	FLIP0610	171	56	50
	18	FLIP0610	2688	491	25
	19	FLIP0610	2099	364	40
	20	FLIP0610	10843	544	75
	21	FLIP0610	1075	110	8
	22	FLIP0610	1226	235	50
Tt	1	CC0604	897	32	30
	2	SC03	707	66	30
	3	SCI0608	501	24	18
	4	SCI0608	5959	386	60
	5	SCI0608	687	59	6
	6	SCI0704	120	16	30
	7	SCI0704	205	18	50

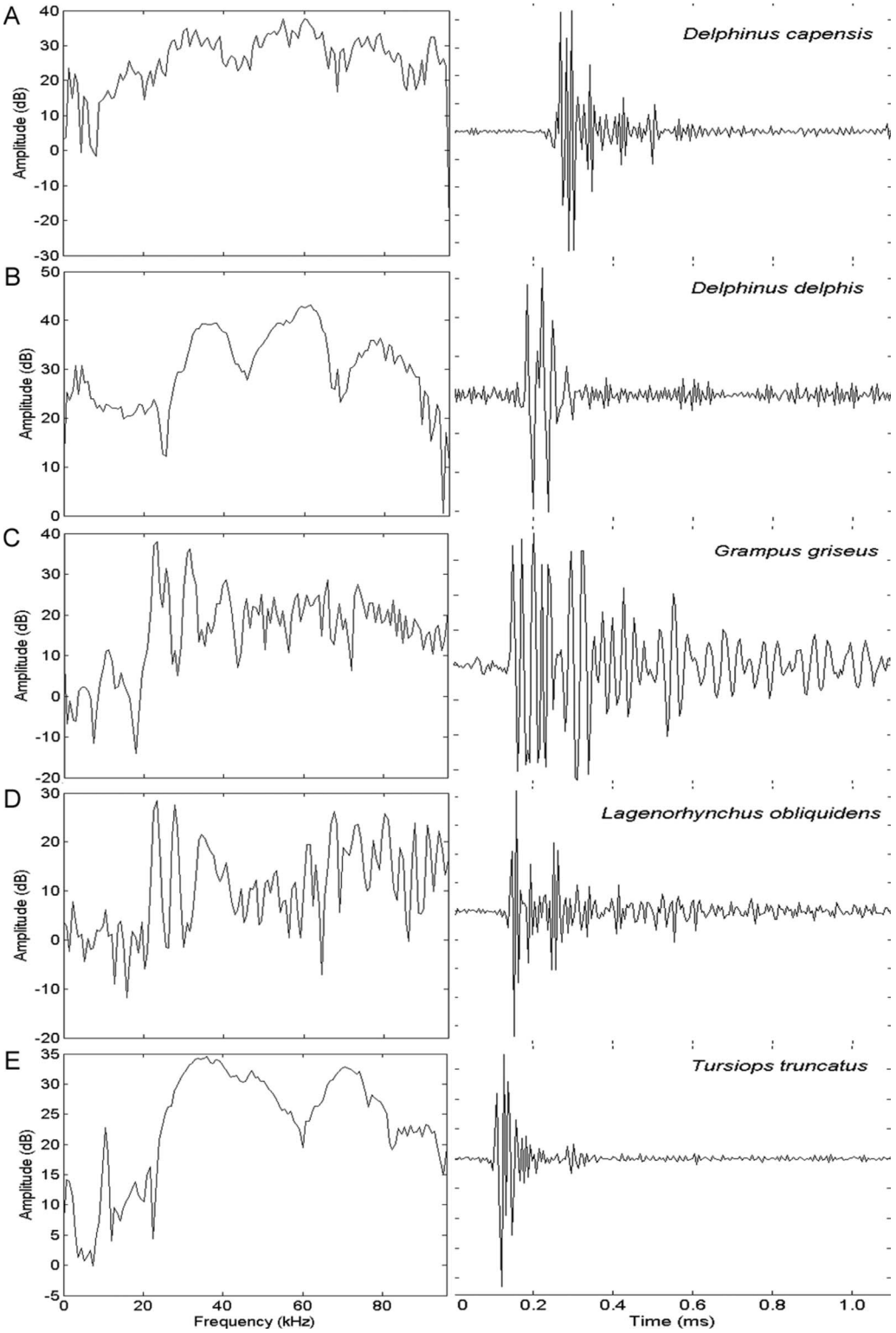

FIG. 3. Example spectra and wave forms for (A) *Delphinus capensis*, (B) *Delphinus delphis*, (C) *Grampus griseus*, (D) *Lagenorhynchus obliquidens*, and (E) *Tursiops truncatus*.

between them. Additionally, these subsets do not differ among surveys with different recording gears: subset A includes sessions from all surveys, including FLIP, while subset B only includes sessions from the FLIP survey. Only two sessions, both recorded from the FLIP survey, are not significantly different from either subset.

To obtain a clearer picture of what these two subsets of Pacific white-sided dolphin recording sessions represent, concatenated spectrograms and mean click spectra are generated for each subset (Fig. 7). The two subsets appear to represent two distinct click types in which the spectral peaks are more closely spaced in subset B. In particular, the second peak is strikingly different with mean values of 26.1 ± 0.7 and 27.4 ± 0.5 kHz for subsets A and B, respectively. Additionally, inspection of the spectra from the two recording sessions that were not significantly different from either sub-

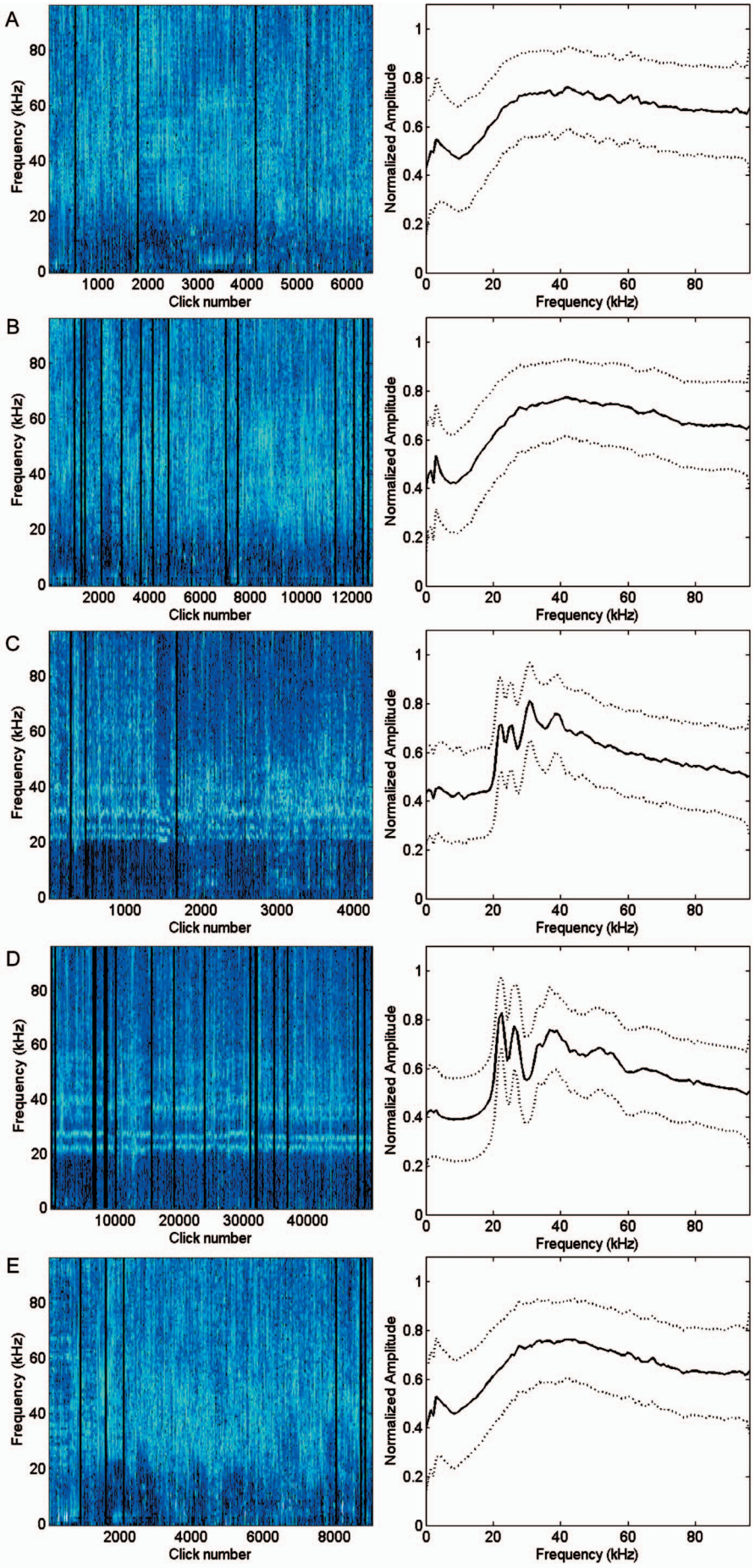

FIG. 4. Concatenated spectrograms and mean normalized spectral plots of complete clicks for each species using Hann-windowed data. (A) *Delphinus delphis*, (B) *Delphinus capensis*, (C) *Grampus griseus*, (D) *Lagenorhynchus obliquidens*, and (E) *Tursiops truncatus*. For the concatenated spectrograms, frequency is plotted on the *y*-axis. Click number, rather than continuous time, is plotted on the *x*-axis. The magnitude of the frequency content is represented by the color such that lighter blue represents greater magnitude. Alternating high and low amplitude spectral bands are apparent between 20 and 40 kHz for *G. griseus* and *L. obliquidens*. The black vertical lines in spectrograms represent breaks between recording sessions. For the mean normalized spectral plots, the solid line represents the mean and the dotted lines represent one standard deviation.

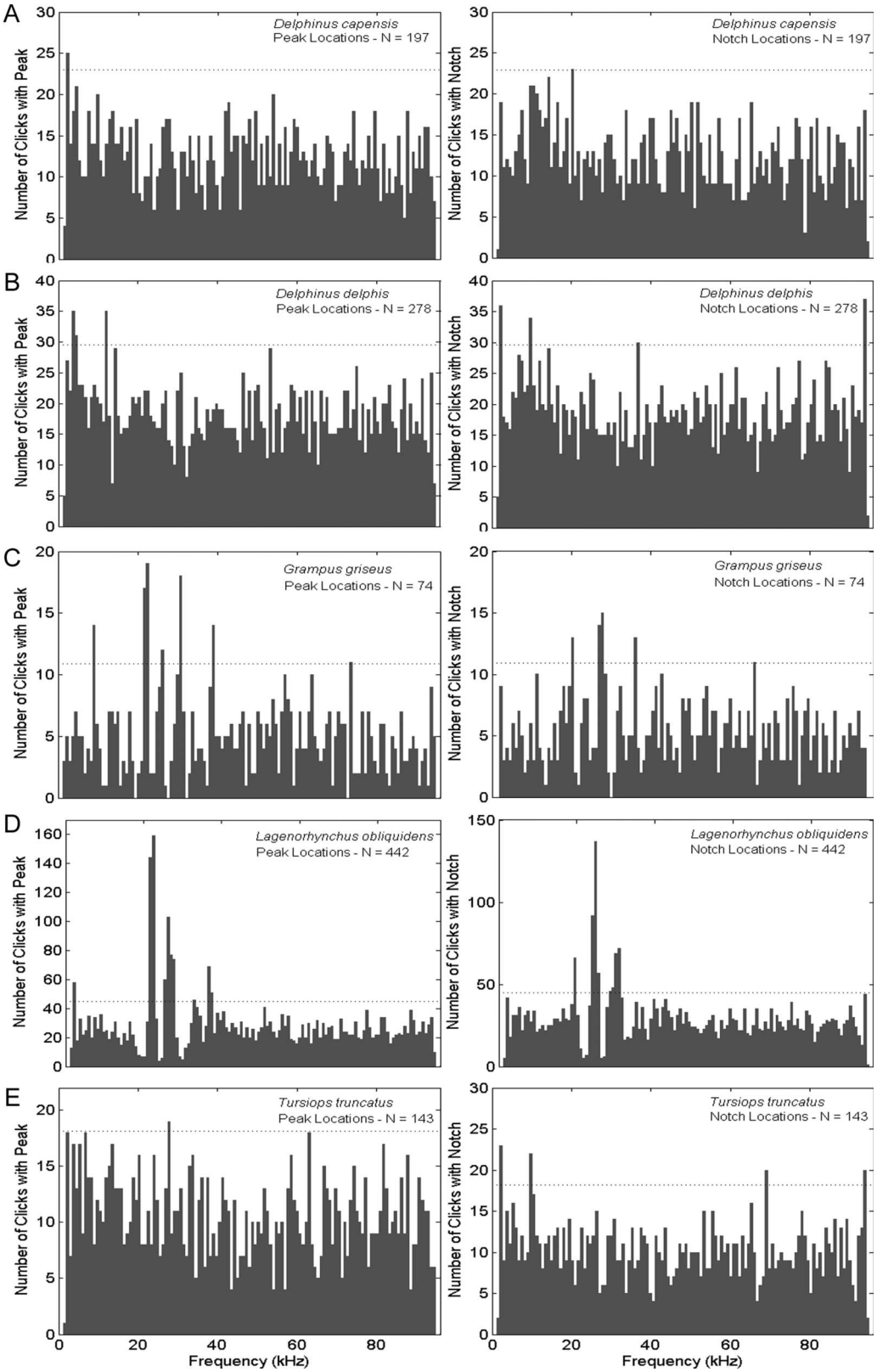

FIG. 5. Histograms of frequency values of spectral peaks (left) and notches (right) for (A) *Delphinus delphis*, (B) *Delphinus capensis*, (C) *Grampus griseus*, (D) *Lagenorhynchus obliquidens*, and (E) *Tursiops truncatus*. Each bar represents one 750 Hz FFT frequency bin. The dotted lines represent the upper boundary of estimated histogram background noise as determined from peak and notch randomization procedure. Groups of bars that rise above this line represent consistent peaks or notches that are analyzed further.

set reveals the presence of both click types rather than clicks with peaks evenly distributed between these frequencies.

Finally, an analysis of 1300 days of long-term autonomous recorder data reveals the presence of hundreds of click bouts containing the three unique spectral peak and notch patterns found for Risso's and Pacific white-sided dolphins (Fig. 8), as well as click bouts that do not contain consistent spectral peaks and notches and are therefore unidentifiable.

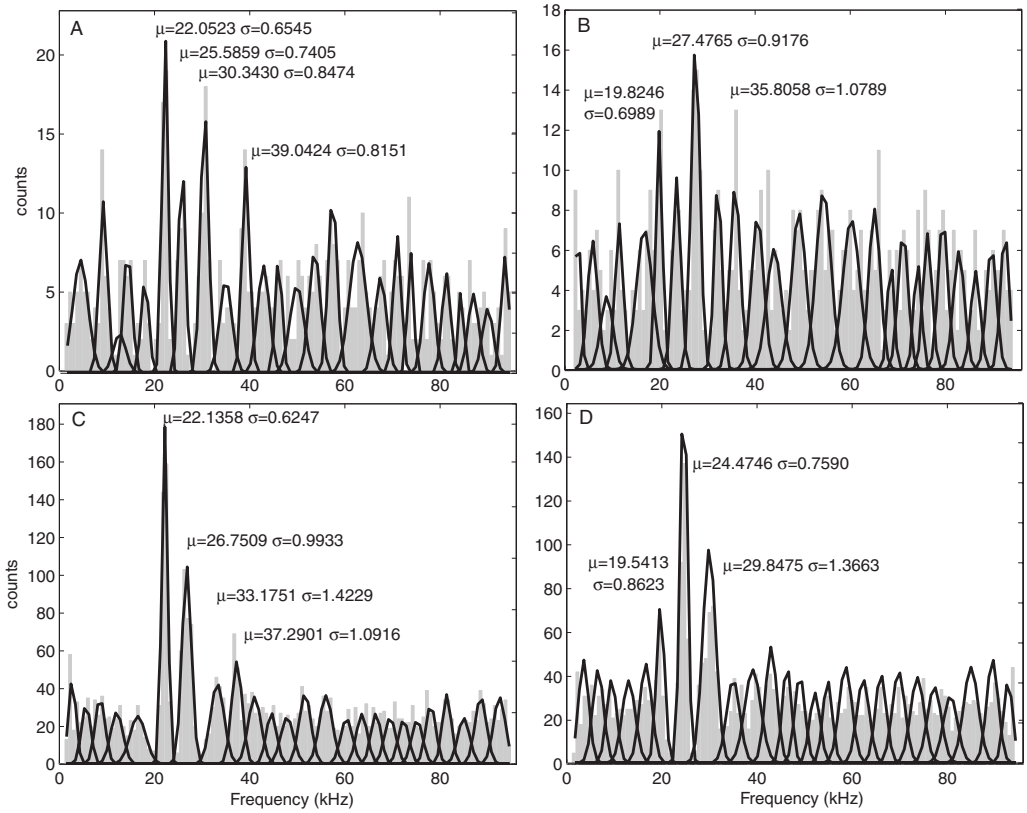

FIG. 6. Univariate Gaussian mixture model fits to spectral peak and notch histograms from the training data set for *Grampus griseus* (A) peaks and (B) notches and *Lagenorhynchus obliquidens* (C) peaks and (D) notches. Each bar represents one 750 Hz FFT frequency bin. Mean and standard deviation estimates of the Gaussian distributions of consistent peaks and notches are noted.

The total numbers of click bouts containing clicks with patterns similar to these four click types are 1769 Risso's dolphin type click bouts, 473 Pacific white-sided dolphin type A click bouts, 337 Pacific white-sided dolphin type B click bouts, and 9210 unidentifiable dolphin click bouts. Click bouts containing mixed Risso's and Pacific white-sided clicks or mixed Pacific white-sided type A and type B clicks occurred in only 14 and 10 bouts, respectively.

IV. DISCUSSION

We provide evidence for three levels of classification of echolocation clicks from wild dolphins within the southern California Bight. The first level represents the presence or absence of click spectral structure: A consistent and distinctive spectral peak and notch pattern is evident for clicks from Risso's and Pacific white-sided dolphins, while no such pattern occurs in the clicks of bottlenose and common dolphins. Therefore, clicks can be separated into two groups—those that contain consistent peaks and notches and those that do not. If this spectral structure is present, bottlenose and common dolphins can be ruled out, and the clicks can be further analyzed at the second level for species-specific differences. However, if this spectral structure is absent, no further distinction can be made until a method to classify these types of clicks is developed.

TABLE IV. Means and standard deviations of local peaks and notches for *Grampus griseus* (Gg) and *Lagenorhynchus obliquidens* (Lo). Means from training data were estimated from Gaussian mixture models. Means from testing data represent frequency variability of the value of the peak or notch used for ANOVA analyses. The percentage of total clicks containing a peak in this frequency range is also presented.

	Peak No.								Notch No.					
Training data	1		2		3		4		1		2		3	
Gg	22.1	(0.7)	25.6	(0.7)	30.3	(0.8)	39.0	(0.8)	19.8	(0.7)	27.5	(0.9)	35.8	(1.1)
Lo	22.1	(0.6)	26.7	(1.0)	33.1	(1.4)	37.3	(1.1)	19.5	(0.9)	24.5	(0.8)	29.8	(1.4)
Test data														
Gg	22.4	(0.8)	25.5	(1.0)	30.5	(1.1)	38.8	(1.1)	19.6	(1.3)	27.7	(1.1)	35.9	(1.2)
% N	72		45		82		48		46		64		54	
Lo	22.2	(0.6)	26.6	(0.9)	33.7	(1.4)	37.3	(1.4)	19.0	(1.1)	24.5	(0.9)	29.7	(1.4)
% N	89		76		45		62		51		75		66	

TABLE V. Results of nested ANOVAs testing for variation in peaks and notches between species (Pacific white-sided and Risso's dolphins) and among recordings nested within species. Significant differences are indicated by asterisks. ANOVA tests among multiple comparisons, such as among recording sessions, only indicate that significant differences exist, not which sessions were different. See text on *post hoc* analysis for further detail of the differences between recording sessions.

	Species			Recording(Species)		
	F	p		F	p	
Peak 1	0.12	0.733		1.84	0.011	
Peak 2	11.44	0.002	*	13.58	0.000	*
Peak 3	92.63	0.000	*	1.42	0.106	
Peak 4	12.21	0.001	*	2.09	0.003	*
Notch 1	2.46	0.121		1.27	0.189	
Notch 2	139.19	0.000	*	3.45	0.000	*
Notch 3	187.99	0.000	*	3.35	0.000	*

At the second level of classification, Risso's dolphins and Pacific white-sided dolphins can be distinguished to species by the frequency values of the spectral peaks and notches. In combination with the other peaks and notches, the presence of a peak or notch at 30 kHz is particularly useful for distinguishing between these two species, as 82% of Risso's dolphin clicks contain a peak while 75% of Pacific white-sided dolphin clicks contain a notch at this frequency. On the other hand, 72% and 89% of clicks from Risso's and Pacific white-sided dolphins, respectively, contain a peak at 22 kHz, which is not significantly different between the two species. If recordings are limited to a 24 kHz Nyquist frequency, as is common to digital audio tape (DAT) recorders and other systems, then only the distinction that one of these two species was present could be made, but not which one. A minimum Nyquist frequency of 40 kHz is needed to classify these clicks at the species level.

TABLE VI. Subsets of Pacific white-sided dolphin recording sessions as distinguished by Tukey's *post hoc* analyses. While different surveys used different recording gears, subset A includes recordings from all surveys, including FLIP, while subset B only includes recording sessions from FLIP. This suggests that differences between recording sessions are not a function of the differing gear used but rather represent two distinct click types produced consistently within a dolphin school as described in the text. Sessions 13 and 21, also recorded from FLIP, were not significantly different from either subset and visual inspection suggests that they contain both click types.

Subset A		Subset B	
Recording session	Survey	Recording session	Survey
1	CC0604	11	FLIP
2	CC0604	14	FLIP
4	SC03	17	FLIP
5	SCI0608	18	FLIP
6	SCI0704	19	FLIP
7	SCI0704	20	FLIP
8	SCI0704	22	FLIP
9	SCI0704		
10	SCI0704		
12	FLIP		
15	FLIP		
16	FLIP		

Finally, at the third level of classification, Pacific white-sided dolphin clicks can be separated into two click types, types A and B. In combination with the other peaks and notches, a frequency peak near either 26.1 or 27.4 kHz can distinguish these clicks as type B or A, respectively. The significance of these two click types remains unknown, but in 90% of the recording sessions in this study, one click type is prevalent per school of dolphins. Numerous interschool differences could account for the differential use of the two click types including group size, composition, behavior, or prey type. Another hypothesis is that the two click types are population specific, as supported by the presence of two genetically and morphologically distinct populations of Pacific white-sided dolphins whose distributions overlap in the southern California region (Walker *et al.*, 1986; Lux *et al.*, 1997). These populations are morphologically distinguishable by cranial measurements, in particular, the condylobasal length (Walker *et al.*, 1986), a characteristic which could influence the sound production pathway. These populations are not visually distinguishable (Walker *et al.*, 1986), making visual field identification impossible. The ability to distinguish them acoustically could offer insight into differences in the biology of each population. Recordings from other areas in the Eastern North Pacific and field studies incorporating acoustic recording with biopsy sampling could provide additional information for this question.

While several biases in data collection or analysis could account for the differentiation found among these clicks, the authors consider species and subspecies specificities to be the most viable explanation.

Potential bias 1. The use of different recording systems among the surveys included in this analysis could result in differences between click recordings. However, the consistency of the spectral characteristics within a species across surveys compared to the differences between species recorded within the same surveys strengthens the argument that these differences are related to the animals rather the recording instrumentation.

Potential bias 2. The recording of clicks from animals with unknown acoustic orientations could result in aspect-dependent spectral features due to the narrow echolocation beamwidth of dolphins [e.g., Madsen *et al.* (2004) described increasing spectral notch structure with increasing degree off axis within the clicks of Risso's dolphins]. The authors assume that clicks recorded in the wild come from random acoustic orientations since dolphins are highly mobile and typically acoustically scan their environment. Therefore, while aspect-dependent variability may exist, it does not significantly affect the frequency value of spectral peaks and notches, as the variation within species is less than that between species. It is possible that the 15%–20% of clicks that do not contain some of the peaks or notches may be due to aspect dependency. For this reason, it is important that a species or subspecies classification be based on multiple clicks.

Potential bias 3. The use of a relatively long 1.33 ms

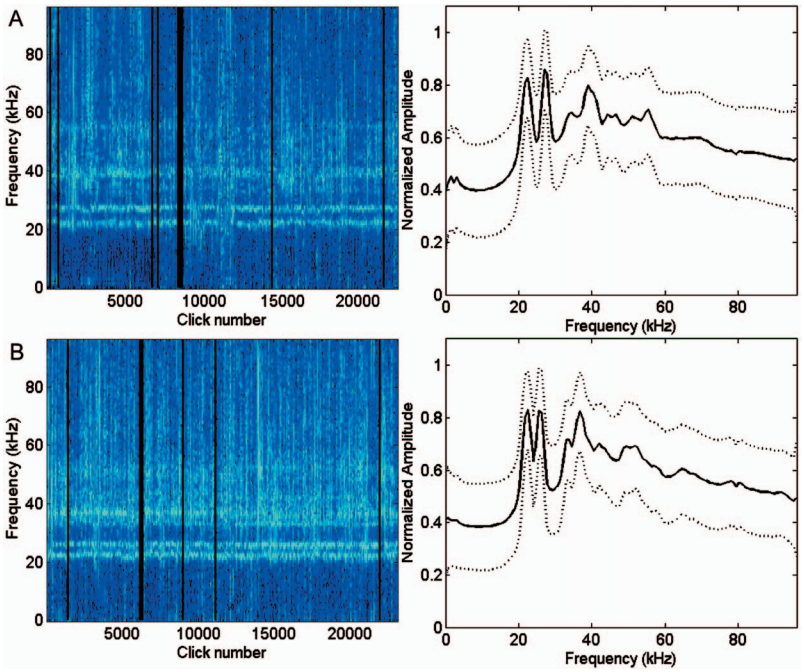

FIG. 7. Concatenated spectrograms and mean spectral plots for (A) subset A and (B) subset B of *Lagenorhynchus obliquidens* clicks using Hann-windowed data. The black vertical lines in spectrograms represent breaks between recording sessions. The consistencies of spectral peaks and notches across recording sessions of each subset are apparent, as are the distinctions between clicks from the two subsets, revealing that *Lagenorhynchus obliquidens* produce two distinct click types.

analysis window to calculate spectra could result in the inclusion of surface reflections whose effect on the spectra remains unknown and could account for the variability between the two click types recorded from Pacific white-sided dolphins. To investigate this potential bias, a subset of Pacific white-sided dolphin clicks from the FLIP survey was examined for the presence of reflections. Of 100 randomly chosen clicks, which included both click types, only 9 clicks exhibited an obvious surface reflection, while 62 clicks clearly did not have a surface reflection within the analysis window. All of these clicks contained spectral peak and notch patterns whose frequency values were not affected by the presence or absence of a reflection. Additionally, it is unlikely that surface reflections from thousands of clicks would exhibit the consistent timing necessary to result in the consistent spectral pattern that we demonstrate, given the expected variability in dolphin depths and distances.

Potential bias 4. The lack of recordings from other species that occur within the southern California Bight means clicks from autonomous recordings cannot definitively be classified to species. While those species, which have been recorded and have different spectral patterns can be excluded it is possible that an unrecorded species could have the exact same spectral pattern. While this will remain unknown until all species have been recorded during concurrent acoustic and visual surveys within this area, the probability of correctly classifying the clicks to species remains high as unrecorded species have low occurrence within this region.

An intriguing question remains as to why some species of dolphins' clicks exhibit these species-specific spectral

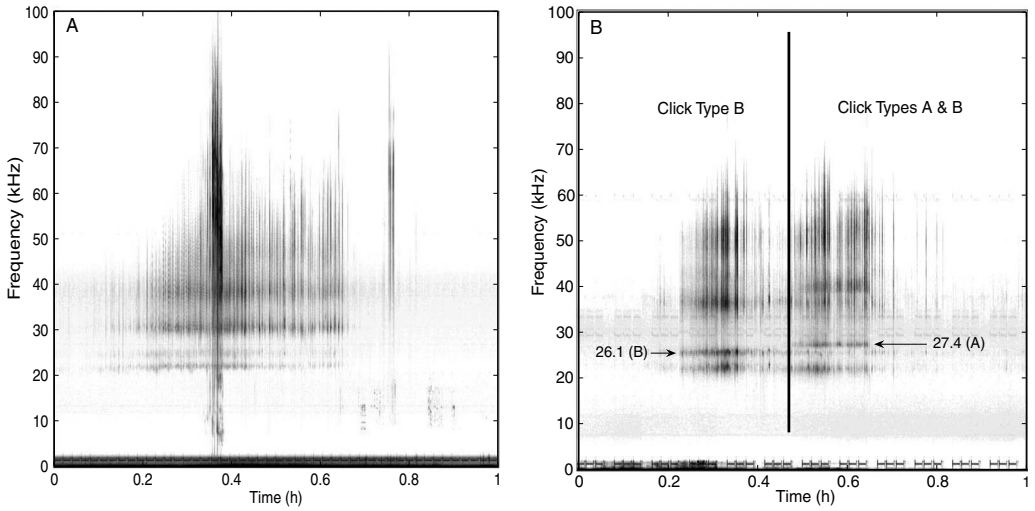

FIG. 8. LTSAs of data from seafloor HARP instruments show echolocation bouts, which exhibit similar spectral peak/notch structure to that found for (A) *Grampus griseus* and (B) *Lagenorhynchus obliquidens*, including both the 26.1 kHz (type B) and 27.4 kHz (type A) clicks. The first half hour has a group producing clicks of type B. In the second half hour, a group begins producing type A clicks while the type B clicks fade out. The vertical line represents the beginning of type A clicks. Each plot shows 1 h of data.

characteristics while others do not. Researchers in the bioacoustics field have speculated many causes for interspecific call differences including phylogenetic constraints, size constraints, morphological differences, prey preferences, niche partitioning, and environmental variability including noise conditions (Dudok van Heel, 1981; Kamminga *et al.*, 1986; Wang *et al.*, 1995; Madsen *et al.*, 2004; Oswald, 2006;). We hypothesize that the morphology of the sound production pathways, including the monkey lip dorsal bursae (MLDB) complex, the melon, airspaces, and skull, is likely to be important. There are several morphological similarities in the sound production pathways between Pacific white-sided and Risso's dolphins that are different from bottlenose and common dolphins. Pacific white-sided and Risso's dolphins have only slightly asymmetrical skulls and MLDB complexes, while bottlenose and common dolphins show strong asymmetry (Cranford *et al.*, 1996). Perhaps the minor asymmetry results in sound production organs producing clicks of similar central frequencies and amplitudes, which result in the interference pattern observed, similar to beat structure for tonal sounds made up of two similar frequencies. Additionally, Pacific white-sided and Risso's dolphins lack an extended rostrum or beak, and both species exhibit protrusions into the melon: A vertical cleft is present on the anterior surface of Risso's dolphin melon (White and Norris, 1978); and a vertical connective tissue column is present in the central melon of Pacific white-sided dolphins (Cranford *et al.*, 1996). These differences could also affect the sound production pathway potentially resulting in the click patterns described in this study.

Autonomous acoustic recording packages have been deployed throughout this region and LTSAs (Wiggins and Hildebrand, 2007) of the data reveal echolocation click bouts exhibiting the same peak and notch structure as described above (Fig. 8). The abundance of occurrences of click bouts from autonomous recordings, which contain the spectral patterns described in this study, demonstrates that these spectral patterns are distinct, repeatable, and useful for classifying Risso's and Pacific white-sided dolphin clicks during passive acoustic monitoring surveys. Ideally, an automated classification scheme could be developed to objectively classify the large amounts of acoustic data collected by these seafloor instruments. Oswald *et al.* (2007) have shown that automated methods can be used to classify dolphin whistles and a classifier, which used all call types produced by dolphins in the 5–24 kHz range, suggests that clicks can be used to automatically classify dolphin recordings (Roch *et al.*, 2007). Additionally, computer learning techniques such as those used by Roch *et al.* (2007) are often able to classify patterns that humans cannot easily distinguish such as those found in bottlenose and common dolphin clicks. Automated classifiers that incorporate higher bandwidth click data (up to 100 kHz) are currently being developed by the authors. The ability to identify dolphin clicks to species will allow researchers to investigate long-term trends in their abundance and distribution patterns using passive acoustic monitoring.

V. CONCLUSIONS

This study is the first to describe a technique for classifying dolphin recordings to species using unique spectral features of echolocation clicks. Clicks can be distinguished at three levels: (1) at the supraspecies level by the presence (Pacific white-sided and Risso's dolphins) or absence (bottlenose and common dolphins) of spectral peaks and notches, (2) at the species level by the frequency values of peaks and notches in Pacific white-sided and Risso's dolphin clicks, and (3) at the subspecies level into two distinct click types of Pacific white-sided dolphins. By extending passive acoustic monitoring equipment to higher frequencies (up to 100 kHz), some delphinid clicks can now be classified to species, which may enable researchers using passive acoustics to study their temporal and spatial distribution and abundance patterns. As the technology behind passive acoustic monitoring continues to advance, even higher frequency sampling could provide recordings from less abundant and elusive species to determine if similar spectral patterns exist. Automatic classification algorithms could be developed to objectively distinguish delphinid species by their clicks, which, along with higher sample rate recordings, may allow all delphinid species to be classified by their clicks. Furthermore, the inclusion of all call types produced by delphinids could potentially strengthen the ability to classify periods of calling to species.

ACKNOWLEDGMENTS

The authors thank the many people without whom this work would not be possible: their visual, acoustic, and small boat field personnel, Simone Baumann, Dominique Camacho, Amanda Cummins, Annie Douglas, Erin Falcone, Greg Falxa, Jennifer Funk, Chris Garsha, Lauren Hoxie, Pablo Kang, Katherine Kim, Allan Ligon, Megan McKenna, Autumn Miller, Erin Oleson, Ethan Roth, Nadia Rubio, Alexis Rudd, Greg Schorr, Michael H. Smith, Sarah Wilson, and Suzanne Yin; the cruise scientists and ship crew who have made every effort to keep their projects running smoothly; Jay Barlow, Simone Bauman, Catherine Berchok, John Calambokidis, Dave Checkley, Bruce Cornuelle, Ted Cranford, Annie Douglas, Gerald D'Spain, Jim Leichter, Megan McKenna, Lisa Munger, Erin Oleson, and three anonymous reviewers for insightful discussions and/or constructive critique of earlier versions of this manuscript; ARCS Foundation, Los Angeles chapter for supporting M.S.S. and Frank Stone and Ernie Young for supporting this work through CNO-N45. Field work was conducted under US National Marine Fisheries Service Permit No. 540-1811 issued to John Calambokidis at Cascadia Research Collective.

Akamatsu, T., Wang, D., Nakamura, K., and Wang, K. (**1998**). "Echolocation range of captive and free-ranging baiji (*Lipotes vexillifer*), finless porpoise (*Neophocaena phocaenoides*), and bottlenose dolphin (*Tursiops truncatus*)," J. Acoust. Soc. Am. **104**, 2511–2516.

Au, W. W. L. (**1993**). *The Sonar of Dolphins* (Springer-Verlag, New York).

Au, W. W. L., Floyd, R. W., and Haun, J. E. (**1978**). "Propagation of atlantic bottlenose dolphin echolocation signals," J. Acoust. Soc. Am. **64**, 411–422.

Barlow, J., and Taylor, B. L. (**2005**). "Estimates of sperm whale abundance in the northeastern temperate Pacific from a combined acoustic and visual

survey," Marine Mammal Sci. **21**, 429–445.
Cranford, T. W., Amundin, M., and Norris, K. S. (**1996**). "Functional morphology and homology in the odontocete nasal complex: Implications for sound generation," J. Morphol. **228**, 223–285.
Dudok van Heel, W. H. (**1981**). "Investigations on cetacean sonar III. A proposal for an ecological classification of odontocetes in relation with sonar," Aquat. Mamm. **8**, 65–68.
Emlen, S. T. (**1972**). "An experimental analysis of the parameters of bird song eliciting species recognition," Behaviour **41**, 130–171.
Evans, W. E. (**1973**). "Echolocation by marine delphinids and one species of freshwater dolphin," J. Acoust. Soc. Am. **54**, 191–199.
Evans, W. E. (**1974**). "Radio-telemetric studies of two species of small odontocete cetaceans," in *The Whale Problem*, edited by W. E. Schevill (Harvard University Press, Cambridge, MA), pp. 385–394.
Fahner, M., Thomas, J., Ramirez, K., and Boehm, J. (**2003**). "Acoustic properties of echolocation signals by captive Pacific white-sided dolphins (*Lagenorhynchus obliquidens*)," in *Echolocation in Bats and Dolphins*, edited by J. Thomas, C. Moss, and M. Vater (University of Chicago Press, Chicago, IL).
Fish, J. E., and Turl, C. W. (**1976**). "Acoustic source levels of four species of small whales," in Naval Undersea Center Technical Publiation, (Naval Undersea Center), , pp. 1–14.
Fisher, F. H., and Spiess, F. N. (**1963**). "Flip-floating instrument platform," J. Acoust. Soc. Am. **35**, 1633–1644.
Forney, K. A., and Barlow, J. (**1998**). "Seasonal patterns in the abundance and distribution of California cetaceans, 1991–1992," Marine Mammal Sci. **14**, 460–489.
Gaskin, D. E. (**1992**). "Status of the common dolphin, *Delphinus delphis*, in Canada," Can. Field Nat. **106**, 55–63.
Goold, J. C., and Jones, S. E. (**1995**). "Time and frequency-domain characteristics of sperm whale clicks," J. Acoust. Soc. Am. **98**, 1279–1291.
Gowans, S., and Whitehead, H. (**1995**). "Distribution and habitat partitioning by small odontocetes in the gully, a submarine-canyon on the Scotian-shelf," Can. J. Zool. **73**, 1599–1608.
Green, G., Brueggeman, J. J., Grotefendt, R. A., Bowlby, C. E., Bonnell, M. L., and K, C., Balcomb, I. (**1992**). "Cetacean distribution and abundance off Oregon and Washington. Ch. 1," in *Oregon and Washington Marine Mammal and Seabird Surveys. OCS Study 91–0093. Final Report Prepared for Pacific OCS Region, Minerals 120 Management Service* (U. S. Department of the Interior, Los Angeles, CA).
Heyning, J. E., and Perrin, W. F. (**1994**). "Evidence for two species of common dolphins (Genus *Delphinus*) from the eastern North Pacific," *Contributions in Science* (Natural History Museum, L. A. County, CA), pp. 1–35.
Huang, X., Acero, A., and Hon, H. W. (**2001**). *Spoken Language Processing* (Prentice-Hall, Upper Saddle River, NJ).
Jones, G. J., and Sayigh, L. S. (**2002**). "Geographic variation in rates of vocal production of free-ranging bottlenose dolphins," Marine Mammal Sci. **18**, 374–393.
Kaiser, J. F. (**1990**). "On a simple algorithm to calculate the "Energy" of a signal," Proceedings of IEEE ICASSP, Albuquerque, NM, pp. 381–384.
Kamminga, C., Cohen Stuart, A., and Silber, G. K. (**1996**). "Investigations on cetacean sonar XI: Intrinsic comparison of the wave shapes of some members of the *Phocoenidae* family," Aquat. Mamm. **22**, 45–55.
Kamminga, C., Kataoka, T., and Engelsma, F. J. (**1986**). "Underwater sounds of *Neophocaena phocaenoides* of the Japanese coastal population," Aquat. Mamm. **12**, 52–60.
Kandia, V., and Stylianou, Y. (**2006**). "Detection of sperm whale clicks based on the Teager-Kaiser energy operator," Appl. Acoust. **67**, 1144–1163.
Kruse, S., Caldwell, D. K., and Caldwell, M. C. (**1999**). "Risso's dolphin *Grampus griseus* (G. Cuvier, 1812)," in *Handbook of Marine Mammals*, edited by S. H. Ridgway and R. Harrison (Academic, Cambridge, MA,), pp. 183–212.
Lammers, M. O., Au, W. W. L., and Herzing, D. L. (**2003**). "The broadband social acoustic signaling behavior of spinner and spotted dolphins," J. Acoust. Soc. Am. **114**, 1629–1639.
Leatherwood, S., Perrin, W. F., Kirby, V. L., Hubbs, C. L., and Dahlheim, M. (**1980**). "Distribution and movements of Risso's dolphin, *Grampus griseus*, in the eastern North Pacific," Fish B-Noaa **77**, 951–963.
Leatherwood, S., Reeves, R. R., Bowles, A. E., Stewart, B. S., and Goodrich, K. R. (**1984**). "Distribution, seasonal movements, and abundance of Pacific white-sided dolphins in the eastern North Pacific," Sci. Rep. Whales Res. Inst. **35**, 129–157.
Lux, C. A., Costa, A. S., and Dizon, A. E. (**1997**). "Mitochondrial DNA population structure of the Pacific white-sided dolphin," Rep. Int. Whal. Comm. **47**, 645–652.
Madsen, P. T., Carder, D. A., Bedholm, K., and Ridgway, S. H. (**2005**). "Porpoise clicks from a sperm whale nose–Convergent evolution of 130 kHz pulses in toothed whale sonars?," Bioacoustics **15**, 195–206.
Madsen, P. T., Kerr, I., and Payne, R. (**2004**). "Echolocation clicks of two free-ranging, oceanic delphinids with different food preferences: False killer whales *Pseudorca crassidens* and Risso's dolphins *Grampus griseus*," J. Exp. Biol. **207**, 1811–1823.
Mellinger, D. K., "Ishmael 1.0 user's guide," NOAA Technical Report No. OAR-PMEL-120, NOAA Pacific Marine Environmental Laboratory, Seattle, WA, **2001**.
Mellinger, D. K., Stafford, K. M., and Fox, C. G. (**2004**). "Seasonal occurrence of sperm whale (*Physeter macrocephalus*) sounds in the Gulf of Alaska, 1999–2001," Marine Mammal Sci. **20**, 48–62.
Nakamura, K., and Akamatsu, T. (**2003**). "Comparison of click characteristics among Odontocete species," in *Echolocation in Bats and Dolphins*, edited by J. Thomas, C. Moss, and M. Vater (University of Chicago Press, Chicago, IL).
Nelson, D. A. (**1989**). "The importance of invariant and distinctive features in species recognition of bird song," Condor **91**, 120–130.
Nowacek, D. P. (**2005**). "Acoustic ecology of foraging bottlenose dolphins (*Tursiops truncatus*), habitat-specific use of three sound types," Marine Mammal Sci. **21**, 587–602.
Oleson, E. M., Wiggins, S. M., and Hildebrand, J. A. (**2007**). "Temporal separation of blue whale call types on a southern California feeding ground," Anim. Behav. **74**, 881–894.
Oswald, J. N. (**2006**). "An examination of the whistling behavior of small odontocetes and the development of methods for species identification of delphinid whistles," Ph.D. dissertation, University of California, San Diego, La Jolla, CA.
Oswald, J. N., Barlow, J., and Norris, T. F. (**2003**). "Acoustic identification of nine delphinid species in the eastern tropical Pacific Ocean," Marine Mammal Sci. **19**, 20–37.
Oswald, J. N., Rankin, S., and Barlow, J. (**2004**). "The effect of recording and analysis bandwidth on acoustic identification of delphinid species," J. Acoust. Soc. Am. **116**, 3178–3185.
Oswald, J. N., Rankin, S., Barlow, J., and Lammers, M. O. (**2007**). "A tool for real-time acoustic species identification of delphinid whistles," J. Acoust. Soc. Am. **122**, 587–595.
Perrin, W. F., and Reilly, S. B. (**1984**). "Reproductive parameters of dolphins and small whales of the family Delphinidae," Rep. Int. Whal. Comm. **6**, 97–133.
Philips, J. D., Nachtigall, P. E., Au, W. W. L., Pawloski, J. L., and Roitblat, H. L. (**2003**). "Echolocation in the Risso's dolphin, *Grampus griseus*," J. Acoust. Soc. Am. **113**, 605–616.
Philpott, E., Englund, A., Ingram, S., and Rogan, E. (**2007**). "Using T-PODs to investigate the echolocation of coastal bottlenose dolphins," J. Mar. Biol. Assoc. U.K. **87**, 11–17.
Polacheck, T. (**1987**). "Relative abundance, distribution and inter-specific relationship of Cetacean schools in the Eastern Tropical Pacific," Marine Mammal Sci. **3**, 54–77.
Richardson, W., Greene, C. J., Malme, C., and Thomson, D. (**1995**). *Marine Mammals and Noise* (Academic, San Diego, CA).
Roch, M. A., Soldevilla, M. S., Burtenshaw, J. C., Henderson, E. E., and Hildebrand, J. A. (**2007**). "Gaussian mixture model classification of odontocetes in the southern California Bight and the Gulf of California," J. Acoust. Soc. Am. **121**, 1737–1748.
Selzer, L. A., and Payne, P. M. (**1988**). "The distribution of white-sided (*Lagenorhynchus acutus*) and common dolphins (*Delphinus delphis*) vs environmental features of the continental-shelf of the Northeastern United States," Marine Mammal Sci. **4**, 141–153.
Shane, S. H. (**1994**). "Occurrence and habitat use of marine mammals at Santa Catalina Island, California from 1983–91," Bulletin of the southern California Academy of Sciences **93**, 13–29.
Sirovic, A., Hildebrand, J. A., Wiggins, S. M., McDonald, M. A., Moore, S. E., and Thiele, D. (**2004**). "Seasonality of blue and fin whale calls and the influence of sea lee in the Western Antarctic Peninsula," Deep-Sea Res., Part II **51**, 2327–2344.
Verfuss, U. K., Honnef, C. G., Meding, A., Dahne, M., Mundry, R., and Benke, H. (**2007**). "Geographical and seasonal variation of harbour porpoise (*Phocoena phocoena*) presence in the German Baltic Sea revealed by passive acoustic monitoring," J. Mar. Biol. Assoc. U.K. **87**, 165–176.

Walker, W. A., Leatherwood, S., Goodrick, K. R., Perrin, W. F., and Stroud, R. K. (**1986**). "Geographic variation and biology of the Pacific white-sided dolphin, *Lagenorhynchus obliquidens*, in the north-eastern Pacific," in *Research on Dolphins*, edited by M. M. Bryden and R. Harrison (Clarendon, Oxford), pp. 441–465.

Wang, D., Wursig, B., and Evans, W. (**1995**). "Comparisons of whistles among seven odontocete species," in *Sensory Systems of Aquatic Mammals*, edited by R. A. Kastelein, J. A. Thomas, and P. E. Nachtigall (De Spil, Woerden), pp. 299–323.

Welch, P. D. (**1967**). "The use of fast Fourier transform for the estimation of power spectra: A method based on time averaging over short, modified periodograms," IEEE Trans. Audio Electroacoust. **AU-15**, 70–73.

White Jr., M. J., and Norris, J., (**1978**). "A report on the *Grampus griseus* of Japan," *Hubbs/Sea World Technical Report* (Hubbs Sea World Institute, San Diego, CA), pp. 78–113.

Wiggins, S. M., and Hildebrand, J. A. (**2007**). "High-frequency acoustic recording package (HARP) for broad-band, long-term marine mammal monitoring," in *International Symposium on Underwater Technology 2007 and International Workshop on Scientific Use of Submarine Cables & Related Technologies 2007* (Institute of Electrical and Electronics Engineers, Tokyo, Japan), pp. 551–557.

Zar, J. H. (**1999**). *Biostatistical Analysis* (Prentice-Hall, Upper Saddle River, NJ).

Zimmer, W. M. X., Johnson, M. P., Madsen, P. T., and Tyack, P. L. (**2005**). "Echolocation clicks of free-ranging Cuvier's beaked whales (*Ziphius cavirostris*)," J. Acoust. Soc. Am. **117**, 3919–3927.

Comodulation masking release in bottlenose dolphins (*Tursiops truncatus*)

Brian K. Branstetter[a] and James J. Finneran
U.S. Navy Marine Mammal Program, Space and Naval Warfare Systems Center, San Diego, Code 71510, 53560 Hull St., San Diego, California 92152

(Received 11 December 2007; revised 2 April 2008; accepted 10 April 2008)

The acoustic environment of the bottlenose dolphin often consists of noise where energy across frequency regions is coherently modulated in time (e.g., ambient noise from snapping shrimp). However, most masking studies with dolphins have employed random Gaussian noise for estimating patterns of masked thresholds. The current study demonstrates a pattern of masking where temporally fluctuating comodulated noise produces lower masked thresholds (up to a 17 dB difference) compared to Gaussian noise of the same spectral density level. Noise possessing wide bandwidths, low temporal modulation rates, and across-frequency temporal envelope coherency resulted in lower masked thresholds, a phenomenon known as comodulation masking release. The results are consistent with a model where dolphins compare temporal envelope information across auditory filters to aid in signal detection. Furthermore, results suggest conventional models of masking derived from experiments using random Gaussian noise may not generalize well to environmental noise that dolphins actually encounter.
 [DOI: 10.1121/1.2918545]

PACS number(s): 43.80.Ka, 43.66.Dc, 43.66.Fe [WWA] Pages: 625–633

I. INTRODUCTION

Sound travels efficiently in marine environments resulting in a complex auditory scene generated from multiple sources. These sounds can be defined as noise if they interfere with an animal's ability to utilize (i.e., detect, classify, localize) biologically relevant acoustic signals (Richardson *et al.*, 1995). Noise sources include weather (wind, waves, precipitation), seismic, biological, as well as human generated sound. Most marine mammal experiments designed to investigate signal detection in the presence of noise maskers have utilized pure tone maskers (Johnson, 1971) or random Gaussian noise (i.e., instantaneous amplitude is randomly sampled from a Gaussian distribution) that is broadband or band limited (Johnson, 1968; Au, 1990; Au and Moore, 1990; Finneran *et al.*, 2002). These studies have focused on signal detection as a function of the frequency content and sound pressure level (SPL) of the maskers. A finding that has been replicated across many mammalian species is that masking typically occurs only when the frequency of the signal and masker are similar. In a classic masking study with human listeners (Fletcher, 1940), a band of noise with a flat spectral density level was centered on the frequency of a tonal signal. Thresholds for the masked signal increased as the bandwidth of the masker increased, but only to a certain bandwidth. Additional noise beyond this "critical bandwidth" no longer contributed to the masking of the signal. This pattern of masking has commonly been described using the power spectrum model (PSM) of masking (Moore, 1993). The assumptions of the model are as follows: (1) when a listener attempts to detect a tone in the presence of a masker, the listener will use an auditory bandpass filter centered around the frequency of the signal, (2) the amount of masking is proportional to the amount of spectral components that fall within the filter (i.e., the noise power within the filter), and (3) the signal and masker can be represented by their long-term spectra.

The PSM has been used to describe a wide range of masking experiments including critical band (Fletcher, 1940; Au and Moore, 1990), critical ratio (Fletcher, 1940; Au and Moore, 1990), and notched noise (Patterson, 1976; Finneran *et al.*, 2002) masking paradigms. However, the PSM does not generalize well to non-Gaussian noise that fluctuates over time, primarily because short-term amplitude fluctuations (temporal peaks and valleys) are ignored by the model (see the Appendix section for a brief discussion on experimental results that are inconsistent with the PSM). For example, Hall *et al.* (1984) demonstrated that broadband noise multiplied by low-pass noise resulted in a masking stimulus with a fluctuating temporal envelope. The noise stimulus was termed "comodulated" noise since the temporal envelopes across frequency regions were coherently modulated. Increasing the bandwidth of comodulated noise stimuli beyond a critical band resulted in a systematic threshold reduction, a result in direct conflict with the PSM of masking. This threshold reduction relative to Gaussian masker thresholds has been termed comodulation masking release or CMR (Hall *et al.*, 1984). Explanations for the result vary, but include a "dip-listening" strategy (Buus, 1985), a single envelope model where the power spectrum from a wideband leaky integrator is evaluated (Berg, 1996), a multiple-cues model (Hall and Grose, 1988), and an across-channel envelope correlation mechanism (Hall *et al.*, 1984; Richards, 1987; McFadden, 1988). The latter model suggests the auditory system compares temporal envelopes between an audi-

[a]Author to whom correspondence should be addressed. Electronic mail: branstet@hawaii.edu

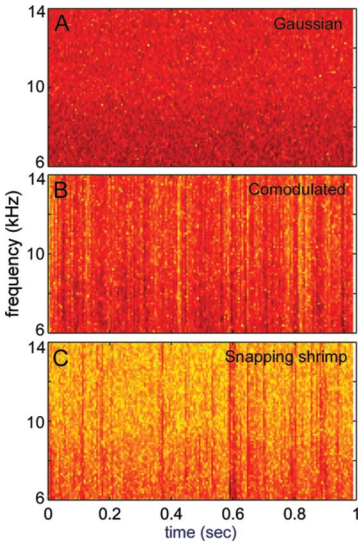

FIG. 1. (Color online) Spectrograms from Gaussian (A) and comodulated (B) noise maskers used in experiment I, as well as a spectrogram of the ambient noise (snapping shrimp) recorded from the dolphin's testing pen in San Diego Bay (C). Both snapping shrimp and CM noise are comodulated, as evident by the temporal fluctuations (vertical lines) across frequency regions. Recordings were made with a B&K 8105 hydrophone, B&K 2635 charge amp, Stanford Research SR560 filter (1–30 kHz) prior to digitization at 44.1 kHz sampling rate.

tory filter centered on the signal and flanking auditory filters (Hall *et al.*, 1984; McFadden, 1988). The addition of a sinusoidal signal to comodulated noise decreases the modulation depth in the signal channel, thus reducing the envelope correlation between the signal channel and flanking channel outputs.

Natural noise sources are often comodulated (Nelken *et al.*, 1999). Klump and Nieder (2001) hypothesized that in complex auditory scenes, noise sources that are comodulated will be perceptually grouped together, thus improving segregation of a comodulated noise source from a nongrouped signal. This proposed CMR adaptation has been demonstrated in several animals including songbirds (Klump and Nieder, 2001), chinchillas (Mott *et al.*, 1990), cats (Nelken *et al.*, 2001), gerbils (Klump *et al.*, 2001), and guinea pigs (Pressnitzer *et al.*, 2001). CMR has not been previously demonstrated in a dolphin (or any marine mammal), although noise sources in marine environments are likely to be comodulated. For example, a major source of marine noise in coastal regions is snapping shrimp (Lammers *et al.*, 2006). Snapping shrimp produce broadband transient clicks with peak-to-peak source levels often exceeding 180 dB re: 1 μPa (p-p) (Au and Banks, 1998). Thousands of snapping shrimp can inhabit a small area resulting in temporally fluctuating ambient noise where the spectro-temporal pattern is much more similar to comodulated noise than Gaussian noise (Fig. 1).

Having likely evolved in the presence of coherently modulated natural noise, the dolphin's auditory system may be well equipped for detecting signals masked by temporally fluctuating noise. Because dolphin's are acoustic specialist that rely heavily on sound for survival [for a review see Au (1993) and Nachtigall *et al.* (2000)], and the effects of noise on their well being has been a growing concern (Richardson *et al.*, 1995) an investigation of CMR with dolphin listeners is warranted. The current study tests if dolphin listeners will demonstrate CMR within a series of masker manipulations. Experiment I investigates the effect of the bandwidth of comodulated and Gaussian maskers on signal thresholds. Experiment II investigates the effects of amplitude modulation rate of comodulated maskers on signal thresholds, and experiment III tests the hypothesis that across-frequency envelope coherence is required for CMR.

II. METHODS

A. Participants

Two male bottlenose dolphins (BOB, age 28; HEP, age 42) with extensive experience with behavioral hearing tests participated in the study. Both dolphins had normal hearing at the frequencies tested, but significant high-frequency hearing loss above approximately 40 kHz as determined via auditory evoked potential testing (see Houser and Finneran, 2006). The subjects were housed in 9×9 m–9×18 m netted enclosures (pens) located in San Diego Bay, California. The study followed a protocol approved by the Institutional Animal Care and Use Committee of the Biosciences Division, Space and Naval Warfare Systems Center, San Diego, and all applicable U.S. Department of Defense guidelines for the care of laboratory animals.

B. Stimuli

1. Signals

Sinusoidal signals were digitally generated (606.1 kHz update rate, 12 bit resolution) and converted to analog with a National Instruments PCI-MIO-16E-1 multifunction board. Signals were then filtered (Stanford Research SR560; 1 kHz–30 kHz), attenuated (Tucker Davis PA5), and amplified (BGW Performance Series 4) to drive an ITC 1001 piezoelectric transducer. Signal levels were calibrated before and after each experimental session by measuring the SPL with a B&K 8105 transducer located where the midpoint between the dolphin's ears would be situated during the experiment. Calibration signals were amplified (B&K 2635 charge amp), filtered (Stanford Research SR560; 1–30 kHz) and analog to digital (A/D) converted with a National Instruments PCI-MIO-16E-1 multifunction board, at a sampling rate of 606.1 kHz. Specific details of signal frequency and amplitude are provided below for each different experiment. The signal transducer was located directly in front of the dolphin, at the same depth (1.37 m) as the dolphin, at a distance of 1.3 m.

2. Noise

Each noise stimulus was digitally synthesized (Cool Edit Pro) and saved to hard drive as a 3 min 16 bit WAV file. A digital correction filter was applied to each noise file to compensate for the transmission response of the ITC 1001 projector, resulting in flat spectrum levels (see Fig. 2). Noise files were looped and played continuously (SimgaTel C-major Audio sound card) at an update rate of 44.1 kHz, filtered (1–150 kHz, Krohn-Hite 3C series module), attenu-

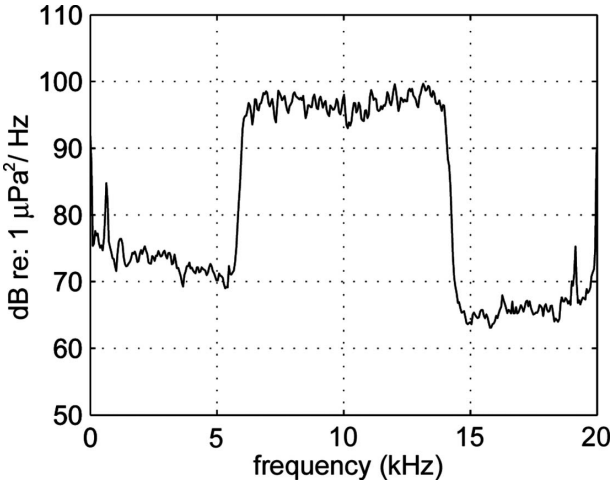

FIG. 2. Sound pressure spectral density of a noise stimulus (random Gaussian noise; 6–14 kHz, sampling rate=50 kHz) recorded from a 1.5 s catch trial during experiment I. The noise spectrum was calculated by windowed averaging with the following parameters: 1024 point Hanning window, 512 point overlap, and a fast Fourier transform length of 1024 points.

ated (Tucker Davis PA5), amplified (BGW Performance Series 4) and presented with an ITC 1001 piezoelectric transducer. Noise levels were calibrated before and after each experimental session by measuring the noise spectral density integrated over a 15 s sample, within the frequency band of each specific noise stimulus. Details of specific noise parameters are presented below within each experimental section. The noise transducer (separate from the signal transducer) was located at a distance of 0.53 m directly forward and at the same depth as the dolphin.

C. General procedure

Experimental sessions took place in a testing pen (5 $\times$9 m) adjacent to the dolphins' home pens. The ambient noise in the testing pen was dominated by snapping shrimp with an average pressure spectral density level between 67 and 83 dB re: 1 μPa^2/Hz over the frequency range of stimuli tested in this study (6–14 kHz). Testing required the dolphin to dive and position himself on an underwater "bite plate" station (polyvinyle chloride construction, depth=1.37 m) fixed to the side of the testing pen. During each dive the dolphin was presented with multiple trials, where the number of trials per dive was selected from a variable ratio schedule within a range between 2 and 15 trials. Figure 3 illustrates the time line and a spectrogram (recorded during a trial) representing stimuli presentation and the dolphin's response during a typical trial. A light positioned approximately 45° above the dolphin, at a distance of 0.5 m (aimed directly at the bite plate) was turned on at the onset of each trial and remained on for 1.5 s to signify a trial was occurring. A test tone or a catch trial (no tone) was presented 500 ms after the onset of the light and continued for 500 ms. The dolphins were trained to produce an unambiguous phonation (i.e., a loud sound clearly audible to an experimenter listening with a pair of headphones) if a tone signal was present or remain quiet if no signal was present. The dolphin's response window began 50 ms after the onset of the tone (or catch trial)

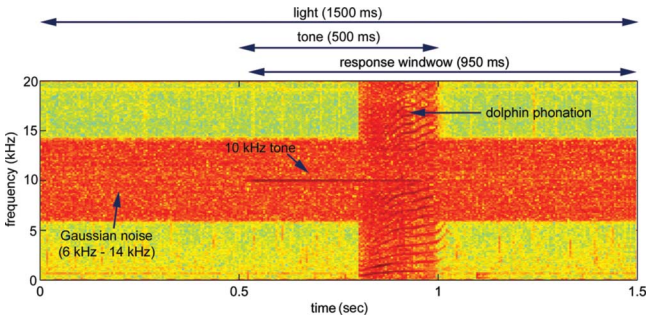

FIG. 3. (Color online) Schematic and spectrogram of a single "tone" trial from experiment I with an 8-kHz-wide Gaussian masker. Each trial began with the onset of the light, followed 500 ms later with either a tone (as in this case) or a catch trial. The response window began 50 ms after the onset of the tone and lasted for the remaining 950 ms of the trial. The dolphin's phonation response is visible about 270 ms after the onset of the tone, indicating a correct response.

and lasted 950 ms (until the light turned off). Any phonation that occurred outside of the response window, or to a catch trial, was considered a false alarm. The multiple trial paradigm and whistle response procedure have been extensively employed and allows multiple trials to be rapidly and efficiently conducted (Schlundt *et al.*, 2000; Finneran *et al.*, 2005; Finneran and Houser, 2006; Schlundt *et al.*, 2006). Tone trials and catch trials were presented in pseudo-random order (Gellerman, 1933) where 50% of the trials were "signals present" and the other 50% were "signal absent" catch trials. No more than three tone trials or three catch trials were presented consecutively.

A buzzer (secondary reinforcement) marked the end of each dive and cued the dolphin to return to the trainer's station to receive a fish reward and social reinforcement. The dolphin was differentially reinforced by being awarded one fish for every correct "hit" and one fish for every correct "rejection" accumulated during the dive. False alarms and misses were not reinforced and the dolphin received no feedback when they occurred. The inter-trial interval varied between 2.8 and 3.2 s while the inter-dive interval (IDI) varied according to the dolphin's dive time to allow him to catch his breath and eat his fish. IDIs were typically between 20 and 60 s.

Signal level was adjusted by a one-down, one-up, adaptive staircase procedure yielding thresholds at 50% correct (Levitt, 1971). Initial signal level was 10–20 dB above the dolphin's estimated threshold for each condition. An initial step size of 5 dB was implemented and after the first reversal (miss) was reduced to a 2 dB step size for the remaining trials. Trials were conducted until a minimum of 11 reversals were completed and the signal level appeared asymptotic (generally within a 4 dB range) for at least ten reversals. Thresholds were calculated by averaging the last ten reversals. The first reversal (associated with the 5 dB step size) was always omitted in the threshold estimate.

When transitioning between noise conditions, a silent interval of a few seconds resulted when the experimenter switched noise files. During this time the dolphin was typically at the trainer's station engaged in simple behaviors

(e.g., getting his belly rubbed). The dolphin showed no behavioral indicators that the noise transition might affect his performance.

Each trial was digitally recorded to confirm the responses of the dolphin (see Fig. 3). Trials were recorded with a B&K 8105 piezoelectric transducer (positioned approximately 30 cm to the left of the bite plate), amplified (B&K 2635 charge amp), filtered (Stanford Research SR560; 1–30 kHz) and A/D converted with a National Instruments PCI-MIO-16E-1 multifunction board, at a sampling rate of 50 kHz.

III. EXPERIMENT I. TONE DETECTION IN BAND LIMITED, COMODULATED, AND UNCOMODULATED NOISE

This experiment tested the dolphin's ability to detect a tone masked by either random Gaussian noise (uncomodulated noise) or random Gaussian noise that was multiplied by low-pass noise (comodulated noise). Noise bandwidth was adjusted to determine its effects on signal detection. For uncomodulated (UC) noise, a threshold increase as a function of bandwidth was expected for bandwidths less than the dolphin's critical bandwidth. Noise bandwidths beyond the critical bandwidth were expected to produce asymptotic thresholds consistent with the PSM of masking (Fletcher, 1940; Au and Moore, 1990; Moore, 1993). For comodulated (CM) noise, a threshold increase for bandwidths less than a critical bandwidth was expected. However, for CM noise, we expected to see a threshold reduction or "masking release" as the noise bandwidth increased beyond the critical band (Hall *et al.*, 1984).

A. Stimuli and procedure

The signal was a 500 ms, 10 kHz pure tone with 50 ms linear onset-offset ramps. The signal frequency was chosen because bottlenose dolphins typically produce communication signals near this frequency (Caldwell and Caldwell, 1979; Smolker and Pepper, 1999; Janik, 2000; McCowan and Reiss, 2001). CM noise was produced by digitally low-pass filtering Gaussian noise with a 32nd order Butterworth filter with a frequency cutoff of 100 Hz (Cool Edit Pro). The low-pass noise was then digitally multiplied (MATLAB 6.0) by a separate sample of Gaussian noise to produce CM noise. Both UC and CM noise were digitally bandpass filtered (32 order, Butterworth filter; Cool Edit Pro). Noise bandwidths were 0.25, 0.5, 1, 2, 4, and 8 kHz. Each noise stimulus was generated with unique Gaussian noise for both carriers and low-pass modulators resulting in a unique fine structure and temporal envelop for each stimulus. Finally, each noise stimulus was filtered with a correction filter to compensate for the transmitting response of the ITC 1001 transducer. The noise spectral density level was 95 dB re: 1 $\mu Pa^2/Hz$. Thresholds for UC and CM maskers were estimated for each bandwidth in a counterbalanced format. The participant for this experiment was BOB.

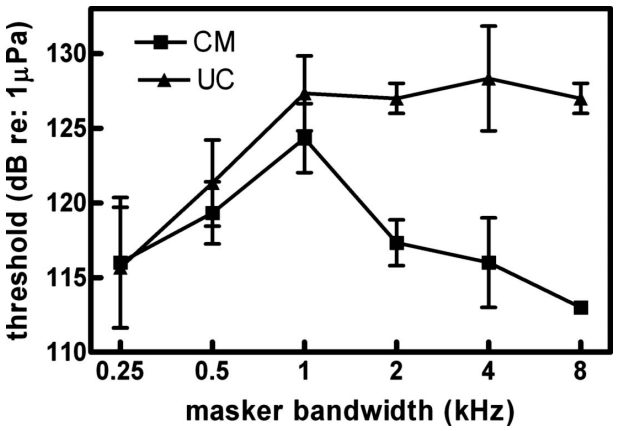

FIG. 4. Masking patterns for comodulated (CM) and uncomodulated noise (UC). The UC masking pattern shows a clear break point at around 1 kHz which is consistent with the power spectrum model of masking. The CM masking pattern shows a release from masking that occurs for bandwidth greater than 1 kHz. Error bars represent the standard deviation with an $n=3$.

B. Results and discussion

Figure 4 illustrates thresholds for UC and CM noise as a function of masker bandwidth. Each data point represents the average of three thresholds. False alarm (FA) rates were low suggesting the dolphin employed a relatively conservative decision criterion. In the UC condition the FA rate was 2.7% within the 250 Hz condition. No other false alarms were committed in the UC condition. For the CM condition, FA rates were 3.7% and 8.6% for 250 and 500 Hz maskers, respectively. FAs were not committed in any other CM condition.

The threshold pattern for UC maskers is in good agreement with the PSM of masking. Thresholds increased as the bandwidth increased and reached an asymptote at a bandwidth of about 1 kHz. A breakpoint was calculated by fitting the last four thresholds with a horizontal line (slope=0), and the first three thresholds with a straight line (variable slope) using a logarithmic scale for masker bandwidth frequency, resulting in a breakpoint (where the two lines intersect) or critical bandwidth of 1020 Hz. The corresponding Q value (Q=center frequency/bandwidth) was 9.8.

The pattern of masking for the CM noise is in good agreement with Hall *et al.* (1984). For bandwidths less than a critical bandwidth, the pattern of masking is similar between UC and CM noise, with the latter having slightly lower thresholds. However, for bandwidths greater than a critical band, thresholds for CM noise decrease. More noise results in less masking.

Assuming a 1-kHz-wide auditory filter is centered on the 10 kHz signal, the addition of CM noise in flanking filters clearly reduces the masking effect of the noise. These results are consistent with a model where envelope correlation is compared across frequency channels (Hall *et al.*, 1984; Yost and Sheft, 1989) rather than models where the signal is evaluated within a channel (Fletcher, 1940; Patterson, 1976). However, the bandwidth of the masking stimulus is not the only variable that may contribute to CMR. The temporal structure of the masker was the primary difference

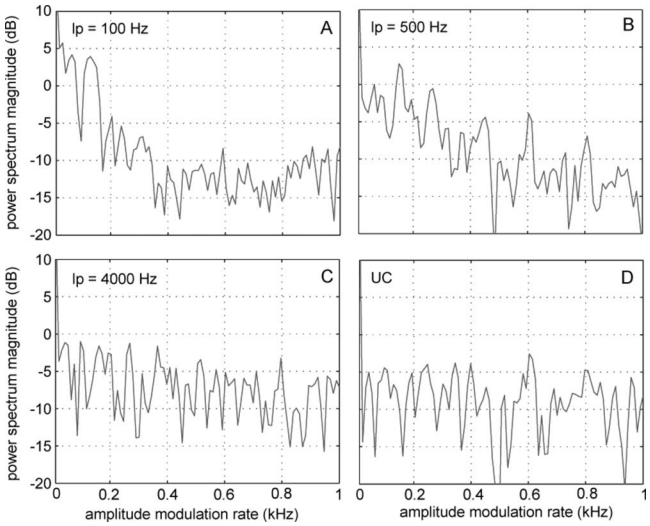

FIG. 5. Amplitude modulation (AM) rates for four representative noise conditions from experiment II. AM rates were estimated by calculating the power spectrum of Hilbert envelopes. Panel A displays AM rates dominated by low frequencies associated with the 100 Hz low-pass (lp) cutoff. Modulation rates for panels B and C are associated with the multiplied noise with low-pass cutoffs of 500 and 4000 Hz, respectively. As the low-pass cutoff frequency becomes larger, the distribution of AM rates becomes flatter until it closely resembles the Gaussian noise from the UC condition in Panel D.

between UC and CM noise. Experiment II investigated the effect of the temporal structure on CMR by holding the masking bandwidth constant and systematically changing the bandwidth of the low-pass multiplier.

IV. EXPERIMENT II. TONE DETECTION IN MULTIPLIED NOISE AS A FUNCTION OF LOW-PASS CUTOFF FREQUENCY

When Gaussian noise is multiplied by low-pass noise, the result is amplitude modulated noise whose modulation rates will be partially determined by the bandwidth of the low-pass noise. Figure 5 displays power spectra (4096 points, 44.1 kHz sampling rate) of the Hilbert envelopes from different noise conditions (1 s clips) used in experiment II. The Hilbert envelope, $H_E(t)$, can be defined as

$$H_E(t) = \sqrt{f^2(t) + h^2(t)}, \quad (1)$$

where $h(t)$ is the Hilbert transform of the original signal $f(t)$. By examining the power spectrum of the Hilbert envelope, modulation rates for each noise stimulus can be evaluated. Figure 5(D) illustrates that modulation rates associated with Gaussian noise tend to be relatively flat across the frequency spectrum shown. However, for Gaussian noise multiplied by low-pass noise [Figs. 5(A)–5(C)] modulation rates and low-pass cutoff frequencies of the multiplier are directly related. Since the low-pass noise serves to amplitude modulate the broadband Gaussian noise, we will refer to the former as the modulator. Most CMR studies have used low-frequency modulators (Hall *et al.*, 1984; Hall *et al.*, 1990; Klump and Nieder, 2001). In this study, the effect of modulation rate of comodulated noise on signal detection is investigated by manipulating the low-pass cutoff frequency of the modulator. Since the envelope structures of CM and UC noise become more similar with increased CM modulation rate [Figs. 5(A) and 5(B)], a threshold increase as a function of the modulator bandwidth was predicted.

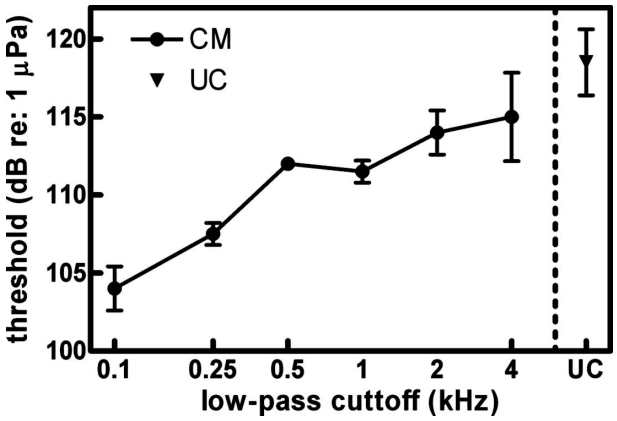

FIG. 6. Masking patterns from experiment II. Masked thresholds increase as a function of the modulator bandwidth. CM data points represent comodulated noise and UC represents Gaussian noise that was not multiplied by a modulator. Error bars represent the standard deviation with an $n=2$.

A. Stimuli and procedure

The signal was a 500 ms linear frequency sweep centered at 10 kHz with start and stop frequencies of 9.5 and 10.5 kHz. Onset / offset ramps of 50 ms were applied to reduce spectral splatter. This signal was selected because it was already in use for another experiment the dolphin (HEP) was currently participating in, and is consistent with the frequency content of dolphin social signals (McCowan and Reiss, 2001). Thresholds for pure tone and FM sweeps with 10% bandwidth have been shown to be nearly identical in a previous experiment (Finneran and Schlundt, 2007).

CM maskers were generated by multiplying low-pass noise with broadband Gaussian noise. Low-pass noise was digitally filtered (32nd order Butterworth filter; Cool Edit Pro) with frequency cutoffs of 100, 250, 500, 1000, 2000, and 4000 Hz. As in Experiment I, low-pass noise was then multiplied by broadband Gaussian noise, bandpass filtered (6–14 kHz for all noise stimuli), and spectrum levels corrected for the ITC1001 transmission response to produce a flat spectrum. A UC condition (control condition) was included that was also bandpass filtered and level corrected as the multiplied noise. The spectral density level for all noise stimuli was 90 dB re: 1 μPa^2/Hz. Noise conditions were presented in a counterbalanced format. The participant for this experiment was HEP.

B. Results and discussion

Figure 6 illustrates thresholds as a function of modulator cutoff frequency. Each data point represents the average of two thresholds. The average false alarm rate within each session was 5.2%. There was no linear trend between FAs and the low-pass cutoff that may have biased the data ($F=0.17$, $p=0.68$, $y=0.0003x+4.56$). Thresholds increased as the modulator cutoff frequency increased with the UC noise condition producing the highest threshold. One explanation for these data is that lower modulation rates in comodulated noise produce longer peaks and valleys in the temporal en-

velope. The dolphin could potentially listen "in the valleys" for the signal where less masking may occur. However, this explanation does not take into account the band widening masking release effect found in experiment I. A more comprehensive explanation for these results is that at higher modulation rates, temporal information will tend to degrade or "smear" due to the low-pass nature of the dolphin's temporal resolution (Moore *et al.*, 1984; Dolphin *et al.*, 1995; Branstetter *et al.*, 2007). Across-channel comparisons based on increasingly degraded envelope information will result in increasingly degraded signal detection. A more detailed description of this model is given in Sec. VI.

V. EXPERIMENT III. TONE DETECTION IN COMODULATED, DEVIANT, AND GAUSSIAN NOISE

Experiments I and II suggest that at least two conditions contribute to CMR in dolphins: (1) the CMR effect is greatest when noise bandwidth exceeds a critical band and (2) low AM rates contribute to a greater CMR effect. Because release from masking is greatest when the noise bandwidth exceeds a critical band (centered on the signal), an across-channel envelope comparison scheme (Hall *et al.*, 1984) seems plausible. However, this assumption has not been directly tested with a dolphin listener. One method of testing this is to mask a signal with modulated noise that is not coherent across frequency channels. A band of noise centered on the signal (on-signal band), and a second band of noise centered at a distal frequency location (flanking band), each with the same modulation rates, but different temporal envelope structures, would meet this requirement. If broadband and amplitude modulation are the only two requirements for CMR there should be no difference in thresholds if the two noise bands are coherently modulated (CM) or modulated but are noncoherent. However, if across channel envelope coherence is required, a threshold increase in a noncoherent condition is expected.

A. Stimuli and procedure

The signal was the same 10 kHz tone used in experiment I. Three noise conditions were generated:

(1) For the first condition, broadband Gaussian noise was bandpass filtered (9–11 kHz) with the same method used in the previous experiments. This band was centered on the 10 kHz signal and is termed the "on-signal band." A second band of noise was generated by bandpass filtering (6 to 8 kHz) a different sample of Gaussian noise and is referred to as the "flanking band." The two bands were digitally added together (MATLAB 6.0) and a compensation filter applied (for ITC 1001 transmitter response). This stimulus is termed uncomodulated (UC) because the noise bands are not modulated and serves as a control condition.
(2) The noise stimuli for the second condition were generated in an identical manner as the UC stimuli except the on-signal band and flanking band were multiplied by the same low-pass (0–100 Hz) Gaussian noise prior to bandpass filtering. The result is that the noise bands are comodulated and is thus termed the comodulated (CM) condition.
(3) The third noise condition was generated in an identical manner as the UC stimulus except the signal band and the flanking band are multiplied by two separate low-pass Gaussian noise samples (0–100 Hz) prior to bandpass filtering. The result is two noise bands with the same modulation rates but noncoherent temporal envelopes. The term for this noise type is "deviant" (DEV) keeping with the terminology used in Hall *et al.* (1990) who performed a similar experiment with human listeners.

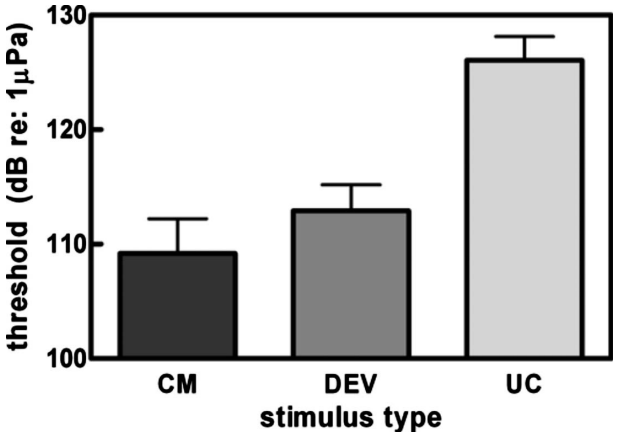

FIG. 7. Thresholds from experiment III for the comodulated (CM) condition, the deviant (DEV) condition, and the uncomodulated (UC) condition. Error bars represent the standard deviation with an $n=20$.

The spectral density level for all noise stimuli was 90 dB re: 1 $\mu Pa^2/Hz$. Noise conditions were presented in a counterbalanced format. The participant for this experiment was BOB.

B. Results

Figure 7 displays thresholds for comodulated (CM), deviant (DEV), and Gaussian noise maskers (UC). Each data point represents the average from a total of 20 reversals from two experimental sessions (errors bars represent standard deviations). No false alarms were committed during this experiment. Each reversal was considered a score for statistical tests to preserve the variance associated with each mean. A repeated measures analysis of variance ($F=286.8$, $P<0.0001$), followed by a subsequent Tukey's multiple comparison test indicate there was a significant difference between all possible threshold pairings ($p<0.001$). The threshold pattern is consistent with human data (Hall *et al.*, 1990), where the deviant noise condition produces a disruption of the CMR effect. This disruption (difference between the CM and DEV means) suggests the dolphin auditory system likely compares envelope information between the on-signal band and the flanking band. Although the DEV condition has identical across-channel modulation rates, across-channel envelopes are not correlated. A signal detection mechanism that performs across-channel correlation will thus be ineffective. However, the threshold difference between the DEV and CM

condition is small for the dolphin compared to humans. One explanation is that the on-signal masking band is wider than a critical band allowing across-channel comparison within the on-signal band and, as a result, a noticeable CMR effect is observed even in the DEV condition.

VI. GENERAL DISCUSSION

A. Bandwidth

When the bandwidth of Gaussian noise (UC) maskers increased, tonal thresholds from experiment I were consistent with the PSM of masking. Only noise within a limited bandwidth or critical band contributed to the masking of the signal. The current results for UC maskers are in good agreement with previous critical band measurements from Au and Moore, 1990, however, a direct comparison cannot be made since critical bands have not been previously measured at 10 kHz.

For CM noise maskers, when the bandwidth of the masker was less than a critical band, the pattern of masking was similar to UC maskers where thresholds increased with bandwidth. However, when the bandwidth exceeded a critical band, a substantial CMR effect was demonstrated. The addition of noise beyond a critical band leads to a decrease in detection thresholds, a result inconsistent with the PSM of masking. Remarkably, thresholds were comparable for an 8-kHz-wide CM masker (mean threshold=113 dB re 1 μPa) and a 250-Hz-wide CM masker (mean threshold=116 dB re 1 μPa). Additionally, a 14 dB threshold difference was demonstrated between CM and UC noise within the 8 kHz bandwidth condition.

B. Modulation rate and auditory mechanisms

The multiplied noise in experiment II resulted in random temporal fluctuations where the modulation rate was partially determined by the low-pass frequency cutoff. Thresholds were lowest for low modulation rates and increased systematically as a function of the low-pass cutoff. This effect may be related to the temporal resolution of the dolphin in two ways.

(1) If the dolphin is listening for the signal in the temporal gaps (i.e., within valley listening), lower modulation rates translate into longer temporal gaps, and less masking. As the modulation rate increases, the temporal gaps become smaller and more of the signal is masked. However, listening in the valleys cannot sufficiently explain the band widening CMR effect. In experiment I, comodulated noise with a bandwidth less than a critical band produced thresholds only slightly lower than Gaussian noise, despite having sufficiently long temporal gaps produced by a 100 Hz low-pass modulator. This suggests within valley listening plays a role, albeit a minor one in CMR for the dolphin. An additional mechanism is required which brings us to the second point.
(2) If the dolphin compares temporal envelopes across widely spaced auditory filters (minimal or no overlap), the comparisons will be degraded if the envelopes are unresolved due to a decreasing temporal resolution at higher modulation rates. Such a mechanism is consistent with results from both experiments I and II.

Further support for an across-channel comparison model comes from the outcome of experiment III. The PSM would predict equal thresholds for all three noise conditions because they all have identical spectral profiles. This of course was not the case. In the CM condition with comodulated envelopes between the on-signal band and the flanking band, the threshold was 17 dB lower compared to the UC condition. In the DEV condition, the spectral profile and modulation rate are identical to the CM condition. However, the DEV on-signal band and flanking bands have uncorrelated envelopes. The flanking band is unlikely to provide information about the presence or absence of a signal because it is not correlated with the on-signal band. Only temporal information within the 2 kHz on-signal band can be used for across channel comparison because it is wider than a critical band.

C. Implications for masking in the ocean

The pattern of masking derived from critical band or critical ratio measurements is often cited and used to extrapolate the effects of masking noise on marine mammals (for a review see Richardson *et al.*, 1995). However, the PSM of masking may not generalize well to all sounds that marine mammals encounter. Environmental sounds tend to be highly structured with complex amplitude fluctuations that extend across frequency regions (Nelken *et al.*, 1999). For example, Fig. 1 displays spectrograms from Gaussian (A) and comodulated (B) noise maskers used in experiment I, as well as a spectrogram of the ambient noise (snapping shrimp) recorded from the dolphin's testing pen in San Diego Bay (C). Both the comodulated noise and the snapping shrimp display similar vertical lines that represent amplitude fluctuations over the frequency region displayed. Ambient noise generated by snapping shrimp appears to be comodulated and may produce a pattern of masking congruent with the current findings but inconsistent with the PSM.

The PSM is also ill suited for describing a variety of other masking scenarios dolphins are likely to encounter. Odontocete hearing is highly directional (Au and Moore, 2001; Klishin *et al.*, 2000; Kastelein *et al.*, 2005; Branstetter and Mercado III, 2006) which results in a directional release from masking. Dolphins are highly mobile (Benoit-Bird and Au, 2003; Corkeron and Martin, 2004), traversing relatively large distances through complex sound fields that lack uniformity (Richardson *et al.*, 1995; Mercado and Frazer, 1999). Noise levels and their spectral profile can vary widely over short distances due to complex propagation effects (Richardson *et al.*, 1995). Masking patterns using auditory scenes similar to what dolphins actually encounter should be investigated if more accurate models of noise masking are to be developed.

ACKNOWLEDGMENTS

We would like to thank Linda Green, Eric Robinson, and Megan Tormey, for animal training, and Randall Dear, Caro-

line Schlundt, and Dorian Houser, for helpful suggestions and technical support. We would also like to thank two anonymous reviewers for suggestions on an earlier draft. Financial support was provided by the Office of Naval Research. The first author was supported by a National Research Council Postdoctoral Fellowship.

APPENDIX: A BRIEF CRITIQUE OF THE PSM OF MASKING

Two fundamental axioms of the PSM of masking are: (1) masking is restricted to spectral components within a hypothetical bandpass filter centered on a signal and (2) detecting a signal in noise is accomplished by an energy detector at the output of the theoretical filter. The signal-plus-noise interval will have greater energy than the noise alone interval.

The first axiom proves inadequate when complex maskers are used instead of steady-state Gaussian maskers. As previously discussed, CMR studies (Hall *et al.*, 1984; Hall *et al.*, 1990) have clearly demonstrated that comodulated noise wider than a critical bandwidth clearly influences detection thresholds. Auditory profile analysis paradigms (Green, 1993) have also demonstrated that tone detection can be significantly influenced by spectral components well beyond a critical band. Often, an increase in the number of tonal masker components beyond a critical band results in a lowering of thresholds (Green, 1992). Modulation detection interference (Yost and Sheft, 1989) provides another example of across-critical band masking. In this experiment, the ability to detect amplitude modulation of a probe tone will be impeded by the addition of a flanking pure tone, provided the flanking tone and AM rate of the probe tone were of the same frequency and similar phase. Thresholds increased 10–15 dB (in the presence of the masker) even though the probe and flanking frequencies were separated by several critical bands.

Kidd *et al.* (1989) demonstrated that in the absence of level cues, masking patterns in a band-widening study were almost identical to Fletcher's (1940) classic masking patterns, a result not easily explained by the energy-detection scheme the PSM assumes. Level cues were degraded by randomly adjusting stimulus amplitude within a 30 dB range (roving-level procedure) on each presentation, in a two-interval forced-choice task. Because the level of the noise interval will sometimes be greater than the level of the noise-plus-signal interval, comparing overall level (or the output of an energy detector) between intervals cannot serve as a reliable indicator for the presence of a signal. Level-invariant alternatives to the PSM propose that the spectral profile is compared across intervals (Berg and Green, 1990; Green and Berg, 1991) for stimuli exceeding the width of an auditory filter. However, stimuli less than a filter bandwidth are difficult for a multi-channel model to accommodate. Berg (2004) proposed a temporal model where the power spectrum of the temporal envelope was extracted from a single wideband filter and compared between the noise and noise-plus-signal intervals. Simulations for both narrow and wideband stimuli provide reasonable fits to empirical data (Kidd et al., 1989). Other researchers have proposed hybrid models employing several cues simultaneously (Kidd *et al.*, 1993; Richards and Nekrich, 1993).

Although the above studies call into question the validity of the PSM when applied to human listeners, similar evidence for dolphin listeners is lacking primarily due to the small number of similar experiments completed to date. Due to the sparse amount of evidence against the PSM with dolphin listeners (at the time of publication), the PSM model is presented with full knowledge that rejection of the model may become necessary when evidence against the model becomes available.

Au, W. W. L. (**1990**). "Target detection in noise by echolocating dolphins," in *Sensory Abilities of Cetaceans: Laboratory and Field Evidence*, J. A. Thomas, and R. A. Kastelein (Plenum, New York), pp. 203–216.
Au, W. W. L. (**1993**). *The Sonar of Dolphins* (Springer-Verlag, New York).
Au, W. W. L., and Banks, K. (**1998**). "The acoustics of the snapping shrimp *Synalpheus parneomeris* in Kaneohe Bay" J. Acoust. Soc. Am. **103**, 41–47.
Au, W. W. L., and Moore, P. W. B. (**1984**). "Receiving beam patterns and directivity indices of the Atlantic bottlenosed dolphin (*Tursiops truncatus*)," J. Acoust. Soc. Am. **75**, 255–262.
Au, W. W. L., and Moore, P. W. B. (**1990**). "Critical ratio and critical bandwidth for the Atlantic bottlenose dolphin," J. Acoust. Soc. Am. **88**, 1635–1638.
Benoit-Bird, K. J., and Au, W. W. L. (**2003**). "Prey dynamics affect foraging by a pelagic predator (*Stenella longirostris*) over a range of spatial and temporal scales," Behav. Ecol. Sociobiol. **53**, 364–373.
Berg, B. G. (**1996**). "On the relationship between comodulation masking release and temporal modulation transfer functions," J. Acoust. Soc. Am. **100**, 1013–1023.
Berg, B. G. (**2004**). "A temporal model of level-invariant, Tone-in-noise detection," Psychol. Rev. **111**, 914–930.
Berg, B. G., and Green, D. M. (**1990**). "Spectral weights in profile listening," J. Acoust. Soc. Am. **88**, 758–766.
Branstetter, B., and Mercado III, E. (**2006**). "Sound localization by cetaceans," Int. J. Comp. Psychol. **19**, 26–61.
Branstetter, B. K., Mercado III, E., and Au, W. W. L. (**2007**). "Representing multiple discrimination cues in a computational model of the bottlenose dolphin auditory system," J. Acoust. Soc. Am. **122**, 2459–2468.
Buus, S. (**1985**). "Release from masking caused by envelope fluctuations," J. Acoust. Soc. Am. **78**, 1958–1965.
Caldwell, M. C., and Caldwell, D. K. (**1979**). "The whistle of the Atlantic bottlenosed dolphin (*Tursiops truncatus*) - Ontogeny," in *Behavior of Marine Animals*, edited by H. E. Winn, and B. L. Olla (Plenum, New York), pp. 369–401.
Corkeron, P. J., and Martin, A. R. (**2004**). "Ranging and diving behaviour of two 'offshore' bottlenose dolphins, Tursiops sp., off eastern Australia," J. Mar. Biol. Assoc. U.K. **84**, 465–468.
Dolphin, W. F., Au, W. W., Nachtigall, P. E., and Pawloski, J. (**1995**). "Modulation rate transfer functions to low-frequency carriers in three species of cetaceans," J. Comp. Physiol., A **177**, 235–245.
Finneran, J. J., Carder, D. A., Schlundt, C. E., and Ridgway, S. H. (**2005**). "Temporary threshold shift (TTS) in bottlenose dolphins (*Tursiops truncatus*) exposed to mid-frequency tones," J. Acoust. Soc. Am. **118**, 2696–2705.
Finneran, J. J., and Houser, D. S. (**2006**). "Comparison of in-air evoked potential and underwater behavioral hearing thresholds in four bottlenose dolphins (*Tursiops truncatus*)," J. Acoust. Soc. Am. **119**, 3181–3192.
Finneran, J. J., and Schlundt, C. E. (**2007**). "Underwater sound pressure variation and bottlenose dolphin (*Tursiops truncatus*) hearing thresholds in a small pool," J. Acoust. Soc. Am. **122**, 606–614.
Finneran, J. J., Schlundt, C. E., Carder, D. A., and Ridgway, S. H. (**2002**). "Auditory filter shapes for the bottlenose dolphin (*Tursiops truncatus*) and the white whale (*Delphinapterus leucas*) derived with notched noise," J. Acoust. Soc. Am. **112**, 322–328.
Fletcher, H. (**1940**). "Auditory patterns," Rev. Mod. Phys. **12**, 47–65.
Gellerman, L. W. (**1933**). "Chance orders of alternating stimuli in visual discrimination experiments," J. Gen. Psychol. **42**, 206–208.
Green, D. M. (**1992**). "The number of components in profile analysis tasks,"

J. Acoust. Soc. Am. **91**, 1616–1623.
Green, D. M. (**1993**). *Auditory Intensity Discrimination* (Springer-Verlag, Berlin).
Green, D. M., and Berg, B. G. (**1991**). "Spectral weights and the profile bowl," Q. J. Exp. Psychol. A **43**, 449–458.
Hall, J. W., and Grose, J. H. (**1988**). "Comodulation masking release: Evidence for multiple cues," J. Acoust. Soc. Am. **84**, 1669–1675.
Hall, J. W., Grose, J. H., and Haggard, M. P. (**1990**). "Effects of flanking band proximity, number, and modulation pattern on comodulation masking release," J. Acoust. Soc. Am. **87**, 269–283.
Hall, J. W., Haggard, M. P., and Fernandes, M. A. (**1984**). "Detection in noise by spectro-temporal pattern analysis," J. Acoust. Soc. Am. **76**, 50–56.
Houser, D. S., and Finneran, J. J. (**2006**). "Variation in the hearing sensitivity of a dolphin population obtained through the use of evoked potential audiometry," J. Acoust. Soc. Am. **120**, 4090–4099.
Janik, V. M. (**2000**). "Whistle matching in wild bottlenose dolphins (*Tursiops truncatus*)," Science **289**, 1355–1357.
Johnson, C. S. (**1968**). "Masked tonal thresholds in the bottlenosed porpoise," J. Acoust. Soc. Am. **44**, 965–967.
Johnson, C. S. (**1971**). "Auditory masking of one pure tone by another in the bottlenosed porpoise," J. Acoust. Soc. Am. **49**, 1317–1318.
Kastelein, R. A., Janssen, M., Verboom, W. C., and Haan, D. d. (**2005**). "Receiving beam patterns in the horizontal plane of a harbor porpoise (*Phocoena phocoena*)," J. Acoust. Soc. Am. **118**, 1172–1179.
Kidd, G. J., Uchanski, R. M., Mason, C. R., and Deliwala, P. S. (**1993**). "Discriminability of narrow-band sounds in the absence of level cues," J. Acoust. Soc. Am. **93**, 1028–1037.
Klishin, V. O., Popov, V. V., and Supin, A. Y. (**2000**). "Hearing capabilities of a beluga whale, *Delphinapterus leucas*," Epidemiol. Bull. **26**, 212–228.
Klump, G. M., Kittel, M., and Wagner, E. (**2001**). "Comodulation masking release in the Mongolian gerbil," in *Twenty-Fourth Midwinter Research Meeting of the Association for Research in Otolaryngology*, St. Petersburg, FL.
Klump, G. M., and Nieder, A. (**2001**). "Release from masking in fluctuating background noise in a songbird's auditory for brain," NeuroReport **12**, 1825–1829.
Lammers, M. O., Stieb, S., Au, W. W. L., Mooney, T. A., Brainard, R. E., and Wong, K. K. (**2006**). "Temporal, geographic, and density variations in the acoustic activity of snapping shrimp (A)," J. Acoust. Soc. Am. **120**, 3013.
Levitt, H. (**1971**). "Transformed up-down methods in psyhcoacoustics," J. Acoust. Soc. Am. **49**, 467–477.
McCowan, B., and Reiss, D. (**2001**). "The fallacy of 'signature whistles' in bottlenose dolphins: A comparative perspective of 'signature information' in animal vocalizations," Anim. Behav. **62**, 1151–1162.
McFadden, D. (**1988**). "Comodulation masking release: Effects of varying the level, duration, and time delay of the cue band," J. Acoust. Soc. Am. **80**, 1658–1672.
Mercado, E., and Frazer, L. N. (**1999**). "Environmental constraints on sound transmission by humpback whales," J. Acoust. Soc. Am. **106**, 3004–3016.
Moore, B. C. J. (**1993**). "Frequency analysis and pitch perception," in *Human Psychophysics*, edited by W. A. Yost, A. N. Popper, and R. R. Fay (Springer-Verlag, New York), pp. 56–115.
Moore, P. W. B., Hall, R. W., Friedl, W. A., and Nachtigall, P. E. (**1984**). "The critical interval in dolphin echolocation: What is it?," J. Acoust. Soc. Am. **76**, 314–317.
Mott, J. B., McDonald, L. P., and Sinex, D. G. (**1990**). "Neural correlates of psychophysical release from masking," J. Acoust. Soc. Am. **88**, 2682–2691.
Nachtigall, P. E., Lemonds, D. W., and Roitblat, H. L. (**2000**). "Psychoacoustic studies of dolphin and whale hearing," in *Hearing by Whales and Dolphins*, edited by W. W. L. Au, A. N. Popper, and R. R. Fay (Springer, New York), pp. 330–363.
Nelken, I., Jacobson, G., Ahdut, L., and Ulanovsky N. (**2001**). "Neural Correlates of Co-modulation Masking Release in Auditory Cortex of Cats," in Houtsma AJM, Kohlrausch A, Prijs VF and Schoonhoven R., eds. *Physiological and Psychophysical Bases of Auditory Function*, pp. 282–289, Shaker Publishing BV, Maastricht, The Netherlands.
Nelken, I., Rotman, Y., and Bar Yosef O., (**1999**). "Response of auditory-cortex neurons to structural features of natural sounds," Nature (London) **397**, 154–157.
Patterson, R. D. (**1976**). "Auditory filter shapes derived with noise stimuli," J. Acoust. Soc. Am. **59**, 640–654.
Pressnitzer, D., Meddis, R., and Winter, I. M. (**2001**). "Physiological correlates of comodulation masking release in the mammalian ventral cochlear nucleus," J. Neurosci. **21**, 6377–6386.
Richards, V. M. (**1987**). "Monaural envelope correlation perception," J. Acoust. Soc. Am. **82**, 1621–1630.
Richards, V. M., and Nekrich, R. D. (**1993**). "The incorporation of level and level-invariant cues for the detection of a tone added to noise," J. Acoust. Soc. Am. **94**, 2560–2574.
Richardson, W. J., Greene, C. R., Jr., Malme, C. I., and Thomson, D. H. (**1995**). *Marine Mammals and Noise* (Academic Press, New York).
Schlundt, C. E., Dear, R. L., Carder, D. A., and Finneran, J. J. (**2006**). "Growth and recovery of temporary threshold shifts in a dolphin exposed to mid-frequency tones with durations up to 128 s," J. Acoust. Soc. Am. **120**, 3227(A).
Schlundt, C. E., Finneran, J. J., Carder, D. A., and Ridgway, S. H. (**2000**). "Temporary shift in masked hearing thresholds of bottlenose dolphins, *Tursiops truncatus*, and white whales, *Delphinapterus leucas*, after exposure to intense tones," J. Acoust. Soc. Am. **107**, 3496–3508.
Smolker, R., and Pepper, J. W. (**1999**). "Whistle convergence among allied male bottlenose dolphins (Delphinidae, *Tursiops* sp.)," Ethology **105**, 595–617.
Yost, W. A., and Sheft, S. (**1989**). "Across-critical-band processing of amplitude modulated tones," J. Acoust. Soc. Am. **85**, 848–857.

Mammalian laryngseal air sacs add variability to the vocal tract impedance: Physical and computational modeling

Tobias Riede[a)]
Japan Advanced Institute of Science and Technology, 1-1 Asahidai, Nomi-shi, Ishikawa 923-1292, Japan; National Center for Voice and Speech, 1101 13th Street, Denver, Colorado 80204; and Department of Biology, University of Colorado at Denver and Health Sciences, Denver, Colorado 80204

Isao T. Tokuda[b)]
Japan Advanced Institute of Science and Technology, 1-1 Asahidai, Nomi-shi, Ishikawa 923-1292, Japan

Jacob B. Munger and Scott L. Thomson
Department of Mechanical Engineering, Brigham Young University, Provo, Utah 84602

(Received 31 October 2007; revised 17 March 2008; accepted 15 April 2008)

Cavities branching off the main vocal tract are ubiquitous in nonhumans. Mammalian air sacs exist in human relatives, including all four great apes, but only a substantially reduced version exists in humans. The present paper focuses on acoustical functions of the air sacs. The hypotheses are investigated on whether the air sacs affect amplitude of utterances and/or position of formants. A multilayer synthetic model of the vocal folds coupled with a vocal tract model was utilized. As an air sac model, four configurations were considered: open and closed uniform tube-like side branches, a rigid cavity, and an inflatable cavity. Results suggest that some air sac configurations can enhance the sound level. Furthermore, an air sac model introduces one or more additional resonance frequencies, shifting formants of the main vocal tract to some extent but not as strongly as previously suggested. In addition, dynamic range of vocalization can be extended by the air sacs. A new finding is also an increased variability of the vocal tract impedance, leading to strong nonlinear source-filter interaction effects. The experiments demonstrated that air-sac-like structures can destabilize the sound source. The results were validated by a transmission line computational model. © *2008 Acoustical Society of America.* [DOI: 10.1121/1.2924125]

PACS number(s): 43.80.Ka, 43.70.Aj, 43.70.Bk, 43.25.Ba [JAS] Pages: 634–647

I. INTRODUCTION

Study on vocal tract shape and vocal fold anatomy is indispensable for understanding the acoustic property of sounds used in vocal communications. Many aspects of nonhuman anatomy are, however, poorly understood in terms of their acoustic functions. Cavities branching off or extending from the supraglottal vocal tract are ubiquitous in mammalian species. Some of those are inflatable, for example, huge *air sac* in siamang (*Symphalangus syndactylus*) (Hill and Booth, 1957; Starck and Schneider, 1960; Schneider, 1964) or in reindeer (*Rangifer tarandus*) (Frey *et al.*, 2007). Some cavities are non-inflatable because they are surrounded partially or completely by the cartilaginous or bony material, for instance, the *Bulla hyoidea* in howler monkeys (*Alouatta spec.*) (Starck and Schneider, 1960) or the human nasal cavity. Apart from the nasal cavity, only relatively small lateral laryngeal ventricles exist in humans. It is possible that major air sacs were lost during human evolution since they exist in all four great apes, the closest relatives to the human. Only one similar voluminous anatomical structure is sometimes found in humans, the *laryngocele*, which is an extension of the lateral laryngeal ventricles. It is, however, considered as pathology.

The physiological functions of mammalian air sacs or bulla-like extensions and the reason for their absence in humans are a subject of much speculation. Hereafter, for simplicity, we use the term "air sac" to refer to both inflatable air sac and non-inflatable bulla-like extension, unless stated otherwise. We investigate possible acoustic functions of air sacs on the basis of physical model experiments as well as computational simulations. Two hypotheses on acoustic roles of the air sacs are examined in the present study. The first hypothesis is that air sacs help to optimize sound radiation by improving sound transfer through the vocal tract. This will be tested by comparing the sound emissions from physical vocal tract models with and without an air sac. The second hypothesis states that air sacs affect the position of formants. This will be tested by comparing the spectral characteristics of the sound output from the vocal tract models with and without an air sac.

The mammalian voice apparatus is mainly composed of vocal folds, which work as a sound source generator, and a vocal tract, which works as an acoustic filter. The vocal tract consists of oral and pharyngeal cavities, parts of a laryngeal cavity, and sometimes a nasal cavity (Fant, 1960). An important feature of the vocal folds is their multilayered structure (Hirano and Kakita, 1985). Mammalian vocal folds generally

[a)]Electronic mail: triede@ncvs2.org
[b)]Electronic mail: isao@jaist.ac.jp

 0001-4966/2008/124(1)/634/14/$23.00

TABLE I. Overview of four different anatomical designs of air sacs and bulla reviewed by Bartels (1905), Starck and Schneider (1960), and Hayama (1970). Further references on species-specific anatomy can be found in those three sources. A fifth design with lateral air sacs extending from the ventricles [like in (A)] with the addition of a cranial medial air sac [like in (B)] is described in detail in Hayama (1970).

(A) *Saccus laryngeus lateralis*: Each of two air sacs extends from the lateral laryngeal ventricles (*Ventriculus larynges*). It exists, for instance, in *Pongo, Gorilla*, *Pan troglotydes*, and *Cebus albifrons*. In *Symphalangus syndactulus*, the two lateral laryngeal ventricles merge ventrally from the larynx to a single expandable cavity. *Alouatta spec* has lateral air sacs in addition to a median *Bulla hyoidea*.	(B) *Saccus laryngeus medianus superior* (upper or cranial medial air sac or subhyoid sac): This is connected to the laryngeal cavity via a small short tube (*Ductus pneumaticus*). The tube enters the laryngeal cavity between the upper (rostral) edge of the thyroid cartilage and the caudoventral edge of the epiglottis. The cavity is located ventrally in a singular structure. It exists, for instance, in *Lagothrix*, and *Cercopithecus*. In Alouatta, the extension is embedded into a bulla-like enlarged hyoid bone making the *Bulla hyoidea*.
(C) *Saccus laryngeus medianus* inferior (lower or caudal medial air sac, also *Saccus intercartilagineus anterior*): This opens into the laryngeal cavity at or below the level of the vocal folds and exists, for instance, in *Leontocebus rosalia*, *Callithrix jacchus*	(D) *Saccus laryngotrachealis posterior* (dorsal air sac): This extends from the laryngeal cavity between the caudal edge of the cricoid cartilage and the first tracheal ring. It exists, for instance, in *Indri indri* and *Lemur variegata*.

consist of at least two layers: a relatively loose superficial "cover" layer and a muscular "body" layer (Hirano and Kakita, 1985). The human vocal folds also have a ligament between the cover and body layers. In some species, this ligament is not very prominent (Kurita *et al.*, 1983; Riede and Titze, 2008), although the situation is unknown for most species. Functionally, most of the vocal fold vibrations occur in the cover layer because of its high degree of compliance. The vibrations are regarded as a result of the energy transfer from the glottal airflow to the vocal fold motion (Titze, 1988). To study laryngeal aerodynamics as well as vocal fold vibrations, physical models have been developed that synthesize the flow-induced vibrations of the human vocal folds (Titze *et al.*, 1995; Chan *et al.*, 1997; Chan and Titze, 2006; Thomson *et al.*, 2005; Zhang *et al.*, 2006a; 2006b; Neubauer *et al.*, 2007). Physical models have also been constructed to simulate the vocal tract to study open questions regarding vocal tract acoustics, such as nonlinear interaction between the vocal tract and the sound source (Chan and Titze, 2006; Zhang *et al.*, 2006b), acoustic role of the piriform fossa in humans (Dang and Honda, 1997), and acoustic effect of different degrees of beak opening in birds (Fletcher and Tarnopolsky, 1999). In the present study, a modified version of the physical model of the vocal folds, which has been repeatedly examined by preceding studies (e.g., Thomson *et al.*, 2005; Zhang *et al.*, 2006a; 2006b; Neubauer *et al.*, 2007), is attached to a physical model of the vocal tract that includes the air sac. Both inflatable and non-inflatable configurations of the air sac cavity are considered. We test the hypotheses that either of these structures can help amplify sound or affect vocal tract resonances. In addition to the physical model of the vocal folds, we exploit a sweep tone generator as the sound source to determine the acoustical transfer function of the vocal tract model.

The purpose of this study is not only to determine the transfer function of the vocal tract but also to consider source-filter interactions. The sound source in the larynx and the acoustic filter in the vocal tract can interact either linearly or nonlinearly (Titze, 2008). In the case of linear coupling, the vocal source signal is produced independently of the acoustic pressures in the vocal tract. Laryngeal airflow is formed by transglottal pressure and flow pulses that mirror the time-varying glottal area. In contrast, in the case of nonlinear coupling, acoustic pressure in the vocal tract contributes to the vocal source signal production. In this case, sound radiation is affected not only by vocal tract acoustics but also by the sound source at the glottis. It is likely that the nonlinear source-filter interaction is important since specific exercises in humans have revealed that high-amplitude vocalizations are more often associated with signs of severe interaction (Titze *et al.*, 2008). The air sacs can affect the sound radiation in two ways: one is to modify the acoustical property of the vocal tract filter and the other is to change the efficiency of the energy transfer at the glottis. Our primary interest is whether the air sacs can optimize the sound radiation in either of these two ways.

The present paper is organized as follows. In Sec. II, the anatomical structures of air sacs that vary among species are reviewed to introduce the basic designs of air sacs. In Sec. III, the experimental setup, including the details of the physical models that simulate the vocal folds, vocal tracts, and air sacs, is described. A computational model is also outlined here. In Sec. IV, experimental results are reported. The final section is devoted to conclusions and discussions of the present study.

II. AIR SAC MORPHOLOGY, INFLATION, AND EXPERIMENTATION

Table I summarizes basic designs of air sacs and bulla and their positions relative to the vocal folds known from the existing studies (Bartels, 1905; Starck and Schneider, 1960; Hayama, 1970). In our experiments, we investigate two basic designs: an inflatable air sac and a non-inflatable bulla-like

cavity, both of which branch off from the supraglottal vocal tract. In the case of bulla, the cavity size is always kept constant during the phonation, which must occur with open mouth or nose. In contrast, the inflatable air sacs are not supported by a skeletal frame, but they have a flexible wall composed of high amounts of elastic and collagen fibers and, to some extent, muscle fibers. Air sac walls thus contain both passive and active components that facilitate collapse. The air sac, which is connected to the rest of the vocal tract cavity via a tube-like structure (either pairwise lateral ventricles or the single *ductus pneumaticus*), expands up to a certain size, ranging from a few milliliters up to several liters in large apes (Starck and Schneider, 1960; Nishimura *et al.*, 2007) and in muskox and reindeer (Frey *et al.*, 2006, 2007). For inflation, the oral and nasal cavities are closed and the animal impels air into the air sac (in a *Valsalva-like* maneuver).

The critical point of modeling the air sac seems to be whether phonation occurs with an open or a closed mouth. With an open mouth, the air sac might serve as some sort of a side branch. With a closed mouth, however, vocalization occurs with air flowing into the air sac, and sound is emitted through the soft air sac wall and skin, which serves as the main filter. In the siamang (*Symphalangus syndactylus*), two lateral ventricles merge ventrally from the larynx into a single large air sac at a ventral neck position. Anatomical measurements in an adult female siamang cadaver (provided by Dr. Nishimura at the Japan Primate Research Institute) revealed that the lateral ventricles have an inner diameter of 1–1.5 cm and a length of approximately 4 cm; these merge ventrally into the air sac, which can maximally expand to approximately 800–1000 ml. During the boom call production of siamangs, inflation of the air sac has been reported to be accompanied by closed lips or nares (Haimoff, 1981, Tembrock, 1974). When the lips are open, the air follows the least resistance and is expelled from the mouth and possibly from the nose. The air sac deflates accordingly. It should be noted that there exists some speculation that air sacs can inflate even with open lips. For instance, entrance to the air sac can be closed by some mechanism, which keeps the air sac inflated by separating it from the vocal tract (Schön-Ybarra, 1995). Another speculation is that exhalation pressure during open-mouth phonation alone is able to inflate the air sac (Frey *et al.*, 2007). These hypotheses are, however, not a subject of this study and have to await further investigations.

Little experimentation has been performed on the acoustic roles of the air sacs. Gautier (1971) conducted a fistulation surgery of the singular, ventrally located air sac in one male DeBrazza's monkey (*Cercopithecus neglectus*). Gautier observed an effect on the amplitude of higher harmonics but not on the location of any formant. Hilloowala and Lass (1978) also reported no effect on formant positions in rhesus monkeys (*Macaca mulatta*), which also possess a singular ventrally located air sac (Schneider, 1964). They surgically removed the air sac (without detailed description of the surgical procedure) in three males and found very similar frequency values before and after surgery. Although their report is somewhat confused with the terms "fundamental frequency" and "formant frequencies" (see Table I in Hilloowala and Lass, 1978), it is most likely that they report formant frequencies since their frequency values resemble the formant values reported for rhesus monkeys by Rendall *et al.* (1998).

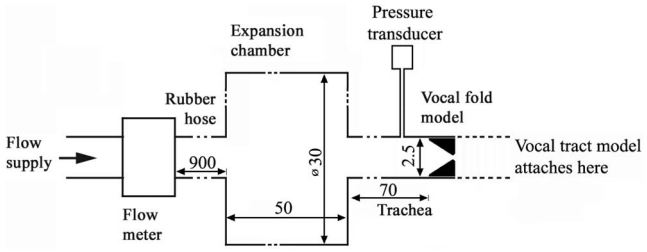

FIG. 1. Schematic of the subglottal parts of the experimental apparatus (numbers indicate distance in cm).

III. METHODS

Our experimental system is composed of a sophisticated, repeatedly tested vocal fold model, a simplified vocal tract model, and measurement devices (see Fig. 1). Details of each component are described sequentially in the following subsections.

A. Physical model of the sound source

A physical replica of the vocal fold system was constructed by using a silicone model of the vocal folds. The silicone model was a two-layer representation of the body-cover vocal fold layers. To simulate this body-cover composition, an earlier fabrication process for making one-layer (homogeneous) vocal fold models (Thomson *et al.*, 2005) was modified to include two layers. The procedure is illustrated in Fig. 2 and is as follows. Two three-dimensional computer-aided design (CAD) models were generated by using the commercial package PRO/ENGINEER. These two CAD models allowed the body and the cover to be made in series. For the first model geometry (model "A"), the dimensions of Scherer *et al.*, (2001) were used to define the vocal fold cover profile. The cross section was uniform in the dorsoventral direction. A base and two positioning guides were added to the vocal fold model to ensure proper orientation and cover thickness during fabrication. A second model (model "B") was generated by removing 2 mm of material from the vocal fold surface of model A. Rigid acrylonitrile butadiene styrene (ABS) physical models were made from the computer models using a Dimension™ rapid prototyping printer. Negative molds were made from these positive ABS models by using a two-part addition-cure silicon rubber (Smooth-Sil™ 950; this and other model-making materials referenced below are manufactured by Smooth-On Inc., Easton, PA, USA).

The two-layer vocal fold models were created by using a three-part addition-cure silicone compound (Ecoflex 0030), mixed with varying ratios of Ecoflex 0030 part A:Ecoflex 0030 part B:silicone thinner. The modulus of the cured silicone could be adjusted by varying the amount of thinner used. A ratio of 1:1:2 with a cured modulus of approximately 10 kPa was used for the body, and a ratio of 1:1:5 with a

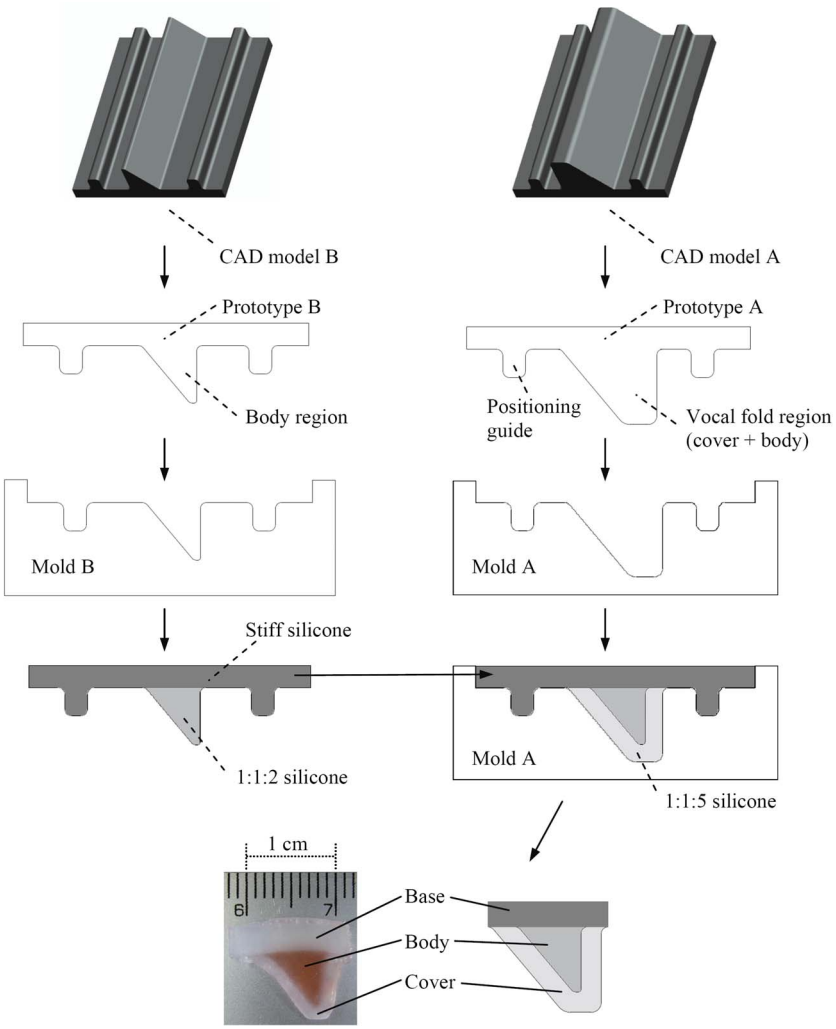

FIG. 2. (Color online) Schematic of the two-layer vocal fold fabrication process, including computer model generation, rapid prototyping, and casting of the different layers. Shown at lower left is an image of the cross section of the vocal fold model.

cured modulus of approximately 2 kPa was used for the cover. Modulus data were obtained by mounting cylindrical specimens (0.8 cm diameter and 6 cm long) of the given ratios in a tensile testing machine (Instron 3342) and strained at a rate of 1000 mm/min to 40% strain. Both ratios yielded materials with nearly linear stress-strain curves.

To fabricate the vocal folds, the body of the vocal fold model was created first. Mold B was sprayed with Universal Mold Release, and the 1:1:2 silicone mixture was poured into the mold so the liquid just filled the body area, leaving the base and guide volumes unfilled. After the body cured (~6 h), a very stiff silicone mixture (Dragon Skin) was poured into the mold to fill in the base and guides and allowed to cure for 2 h. The stiffness of the base was deemed to be sufficiently high so as to not vibrate with the vocal folds. A second mold release agent (Ease Release 800) was then sprayed into mold A. The 1:1:5 silicone mixture was poured into mold A. The silicone model cast using mold B was inserted into mold A. The cover was allowed to cure for 24 h and the entire model was removed from mold A. The portion of the base not directly under the vocal fold model was removed, and the model was then cut into two 1.7 cm lengths (for two symmetric vocal folds).

The dorsoventral and lateral surfaces of the model were attached to a 1.2 cm thick acrylic orifice plate using a liquid polyurethane adhesive (Pro Bond®, Elmer's Products, Inc.). Two such components were fastened together to form a single orifice plate, representing a full laryngeal configuration. The separation distance between the support plates was variable. The medial surface of the two folds was positioned to be in contact so that the glottis was closed when no airflow was applied. A uniform polyvinylchloride (PVC) tracheal tube (2.5 cm inner diameter) was connected upstream to an expansion chamber to simulate the subglottal system (Fig. 1).

A sweep tone experiment was conducted to stimulate the vocal tract models using an alternative sound source. To generate a well controlled sound, a horn driver (P-15F, UNIPEX) was utilized. The vocal tract models, which will be explained in detail in the following subsection, were attached to the horn driver. The sweep tone signals (pure tones whose frequency changes continuously from low to high frequency) were designed with the COOLEDIT 2000 software (Syntrillium Soft. Corp.).

B. Physical models of the vocal tract

The vocal tract models were made of PVC tubes. Four main configurations were designed as follows.

(1) As a reference configuration to study the effect of the air

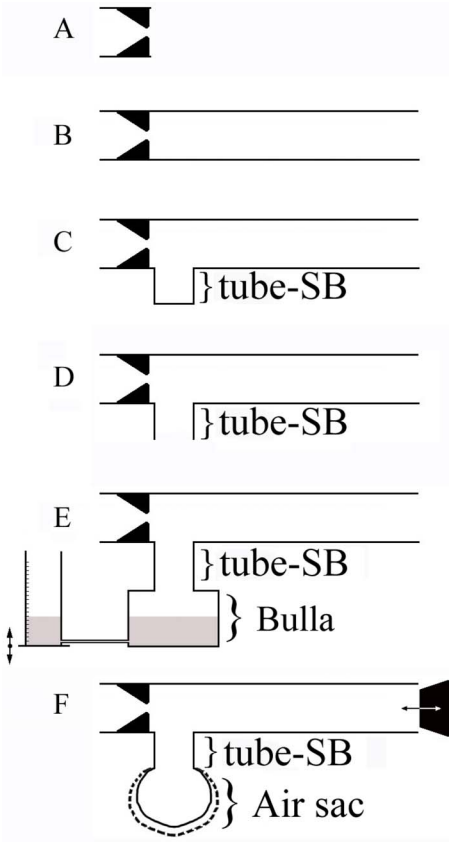

FIG. 3. (Color online) Schematic illustrations of the physical model configurations. Whereas no vocal tract is attached to the vocal fold physical model in (A) the following vocal tract models are attached to the vocal fold model in (B)–(F). (B) Single uniform tube as main vocal tract. (C) Main vocal tract with closed uniform tube side branch ("tube-SB"). (D) Main vocal tract with open tube-SB. (E) Main vocal tract with tube-SB and rigid cavity of variable volume ("bulla"). The volume is regulated by the water cavity level. (F) Main vocal tract with tube-SB and inflatable air sac ("air sac"). The inflation is regulated by "closing the mouth," i.e., inserting a plug to close the aperture of the vocal tract as if the lips are closed.

sac models, cases with no vocal tract (Fig. 3(A)) and with a main uniform tube vocal tract [25 mm inner diameter, 200 mm long; Fig. 3(B)] were considered. Note that in the situation without a vocal tract, there is no tube extending from the vocal folds.

(2) A tube-like side branch (hereafter "tube-SB") was attached to the main vocal tract [Figs. 3(C) and 3(D)]. The inner diameter was varied to examine its effect on the produced sound. Anatomically, this tube-SB may correspond to the connecting tube between the main vocal tract and a large actual air sac [lateral ventricle or *Ductus pneumaticus*; Table I(B)] or a very small air sac system alone. Both open and closed situations were considered. Acoustical measurements of the tube-SB are of particular importance for understanding the exclusive effect of the air sac models, which are attached to the vocal tract through the tube-SB.

(3) A non-inflatable bulla-like cavity was attached to the main vocal tract through the tube-SB [Fig. 3(E)]. Such a configuration exists, for example, in howler monkeys (subfamily *Alouattinae*). As a rigid non-inflatable cavity, a PVC cube ($100\times100\times100$ mm^2) was used. Variable water levels in the cavity, controlled through an outlet (3 mm) located at the lowest point of the cavity, enabled the investigation of different cavity volumes.

(4) An inflatable air sac was attached to the main vocal tract through the tube-SB [Fig. 3(F)]. Such a configuration exists, for example, in siamangs (*Symphalangus syndactylus*) and reindeers (*Rangifer tarandus*) (Frey *et al.*, 2007). An inflatable air sac was simulated by using a urinary bladder from a pig (*Sus scrofa f. domestica*) or a cow (*Bos taurus*). The bladder wall has similar wall characteristics as real air sacs. Namely, the wall contains high amounts of elastic and collagen fibers, which can be repeatedly stretched to its maximal size, i.e., few times larger than its relaxed state, without causing any damage (Ogura, 1915). Two situations were considered: closed mouth and open mouth, simulated by repeatedly opening and closing the open end (corresponding to the "mouth") of the main vocal tract with a plug. After inserting the plug, the sound persisted until the air sac model was inflated up to its maximum size.

Wall characteristics of the vocal tract model affect the formant bandwidth. A nonyielding wall (such as PVC) narrows the bandwidth and therefore might affect the overall sound pressure level. However, we are interested in the relative measurements and hence believe that the data can be compared in a fair manner. We expect the sound wave reflection on the water surface to be similar to that of the PVC surface.

C. Experimental setup

Vocal fold vibration is affected by resonances of the subglottal system (Titze and Story, 1997). A tracheal resonance (in particular, the negative reactance) in the vicinity of the fundamental frequency lowers the vocal fold efficiency (Titze, 2008), which is undesirable since a stable vocal source signal is needed here. Therefore, the length of the trachea tube was chosen based on the recommendations provided for a similar vocal fold system (Zhang *et al.*, 2006a). The vocal fold model was installed at the end of a 70 cm long PVC tube that models the trachea. An expansion chamber (inner cross-sectional diameter: 30 cm: length, 50 cm) was connected to the air flow supply through a 9 m long rubber hose so as to reduce possible flow noise from the air supply. This chamber served to simulate the change in cross-sectional area from the lungs to the primary bronchi (Ishizaka *et al.*, 1976). This design is quite similar to that tested in Zhang *et al.* (2006a), in which an ideal open-ended termination of the tracheal tube for frequencies above approximately 50 Hz was realized.

The sound generated from the physical model was recorded by using an omnidirectional microphone (Bruel and Kjær, type 4192; Nexus conditioning amplifier), located 20 cm from the sound source or from the vocal tract opening. The sound pressure level (SPL) was measured by a sound level meter (Bruel and Kjær, type 2250).

The subglottal pressure in the tracheal tube was monitored by using a pressure transducer (Differential pressure transducer, PDS 70GA, Kyowa, Japan) with a signal condi-

tioner (CDV 700A, Kyowa, Japan). The pressure transducer tube was mounted flush with the inner wall of the tracheal tube, 2 cm upstream of the vocal fold plates.

The volumetric flow rate through the glottis was measured by using a precision mass-flow meter (CMQ-V, Yamatake Corp., Japan) at the setup inlet. During the experiments, the flow rate was increased from zero to a certain maximum value in discrete increments. At each step, after the flow rate was changed, measurement was delayed for an interval of about 4–5 s in order to allow for flow field stabilization

All three signals were recorded as WAV files (16 bit resolution, 44 kHz sampling rate) on a digital recorder (R4 Edirol, Yamaha, Japan) or alternatively with a fast Fourier transform (FFT) analyzer (DL 750, Scopecorder, Yokogawa, Japan). Experiments were conducted in a sound attenuated room with controlled climate (22 °C, 75% humidity).

D. Computational simulation

In order to validate the experiments, acoustical characteristics of the physical model of the vocal tract were estimated by using the transmission line model (Flanagan, 1972; Sondhi and Schroeter, 1987). In this model, the vocal tract is represented by a series connection of many uniform tubes. Assuming plane-wave propagation, the input-output relationship of the pressure and the volume velocity at each tube is described in terms of a four terminal network. Acoustical characteristics of the vocal tract are obtained by computing the transmission characteristics of the cascaded connection of such lumped elements. This approach can be applied to estimate the transfer function of the vocal tract even in the presence of a side branch (Sondhi and Schroeter, 1987; Dang and Honda, 1996). As acoustic impedance parameters, standard values that assume a static wall condition were utilized (Flanagan, 1972). Radiation impedance at the open end of the vocal tract was determined according to Causse *et al.* (1984).

Configuration of the transmission line was constructed in accordance with the basic design of the physical model of the vocal tract including the air sac. A uniform tube was divided into a cascade connection of 1000 lumped elements. In order to match the first formant frequency, a corrected value of 19.8 cm was used as the length of the main vocal tract. All other parameters such as the length of the tube-SB, the tube diameter, and the cavity size were adopted from the original values of the physical model.

IV. RESULTS

A. Reference measurements

First, phonation threshold pressure (PTP), fundamental frequency (F0), and SPL values of the vocal fold physical model were measured without any vocal tract [Fig. 3(A)]. These measurements will serve as a reference to study the effect of different vocal tract configurations examined in the following experiments. PTP represents the minimum subglottal pressure required to initiate and sustain the vocal fold oscillations. Functionally, it provides an index for the vocal effort. PTP data are given in Table II.

TABLE II. Phonation threshold pressure (PTP) and flow rate at voice onset point for different vocal tract (VT) physical models. Values are averaged over three trial measures; the standard deviations in all cases are less than 0.5%. For uniform tube side branches (tube-SBs), two measurements are given: one for a closed side branch and the other for an open side branch.

VT model	PTP (cm H_2O	Flow rate (ml/s)
No VT	5.749	241
20 cm uniform tube	5.427	183
SB0.8ID closed/open tube-SB	5.734/5.646	216/216
SB1.3ID closed/open tube-SB	5.646/5.354	225/216
SB1.6ID closed/open tube-SB	5.719/5.383	233/216
SB1.3ID 1000 ml cavity	5.456	216
SB1.3ID 600 ml cavity	5.734	133
SB1.3ID 200 ml cavity	5.486	150

F0 of the vocal fold model ranged from 105 to 113 Hz for subglottal pressures between 6 and 20 cm H_2O. Stiffness and length of the vocal folds, which are considered as major causes to change F0, were kept constant. Figure 4 demonstrates the relationship between subglottal pressure and flow rate. The pressure-flow relationship is expected to be quadratic for an orifice with yielding walls, as is the case with the vocal folds (Alipour and Scherer, 1997).

The SPL ranged between 48 dBA (at PTP) and 69 dBA for subglottal pressures between 6 and 20 cm H_2O [Fig. 5(a)]. Next, as a basic design for all vocal tract models, only the main vocal tract model [Fig. 3(B)] was attached to the vocal fold model. Compared to the no vocal tract measurement, the main vocal tract model lowered PTP (Table II) and increased SPL for varied subglottal pressure [Fig. 5(a)]. Together with the no vocal tract measurement, this basic design is also utilized as a reference to study the relative effect of various air sac models added to the main vocal tract.

B. Side branch modeled as a uniform tube

In the case of a closed tube-SB connected to the main vocal tract [Fig. 3(C)], the SPL was further increased, where the tube-SB with an inner diameter of 0.4 or 0.8 cm provided the maximum SPL [Fig. 5(b)]. The closed tube-SB also low-

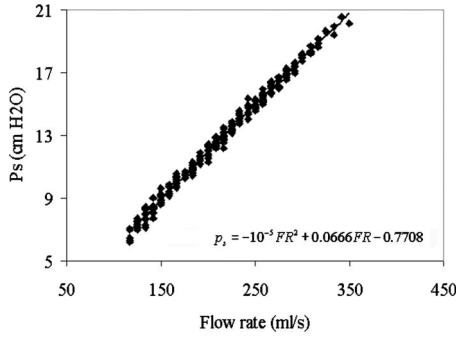

FIG. 4. Subglottal pressure–flow rate relationship of the vocal fold physical model during phonation. Data for the physical model with no vocal tract, data with a 20 cm uniform tube as the vocal tract, and data with all other tested vocal tract models are combined. Note that the pressure-flow rate relationship is identical for different vocal tracts.

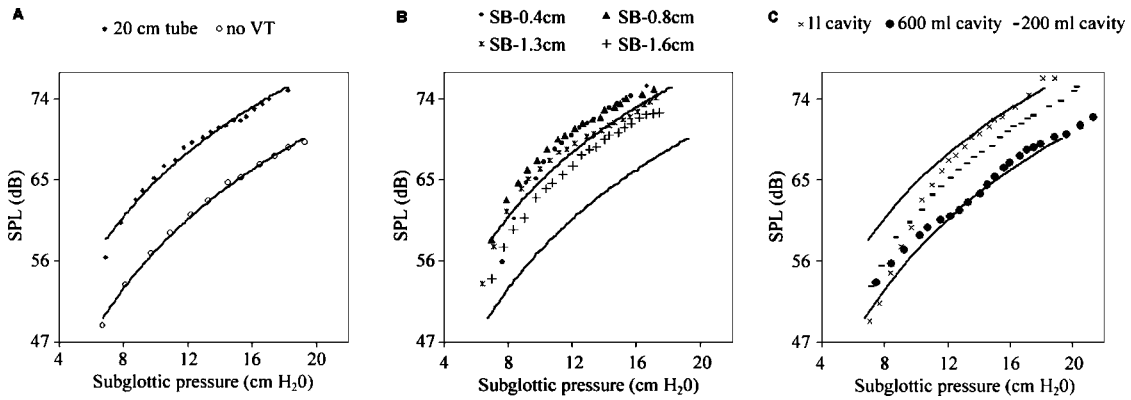

FIG. 5. Sound pressure level (SPL)—subglottal pressure relationship of the vocal fold physical model during phonation. (A) Without and with a 20 cm long tube as a vocal tract. (B) 20 cm long tube with tube-SB. Side branch is closed and mouth is open. Three side branches were tested; each has 5 cm length with different inner diameters (inner diameters, IDs: 0.4, 0.8, 1.3, and 1.6 cm). (C) 20 cm long tube with tube-SB. A rigid cavity of variable size is added to the SB tube. Results for three cavity sizes are shown (cavity sizes: 1.0, 0.6, and 0.2 l). The same trendlines as in Fig. 5(a) are drawn (lower line: physical model without vocal tract; upper line: 20 cm uniform tube vocal tract).

ered PTP below that of the basic design (Table II). The open tube-SB also showed PTP lower than the reference values (Table II).

Addition of these side branches introduces a pole/zero pair to the spectrum and consequently moves the neighboring formants (Table II). Among the four formants, the first formant is affected most strongly (12%–20%) (Table III). Depending on whether the tube-SB is closed or open, the additional pole/zero pair of a 5 cm tube-SB is located differently, at approximately 1.8 kHz for closed tube-SB and at approximately 3.6 kHz for open tube-SB (Fig. 6). Obviously, position of the pole/zero pair behaves as a quarter-wavelength resonator ($c/4L$, where c is the sound speed and L is the tube length) when the tube-SB is closed and as a half-wavelength resonator ($c/2L$) when the tube-SB is open.

To investigate whether the inner diameter of the tube-SB provides any limit on vocalization, we measured the relationship between the subglottal pressure and SPL for the open tube-SB models under the condition that the mouth was closed. The inner diameter of the side branch was varied (0.4, 0.8, 1.3, and 1.6 cm). Phonation with a side branch model with an inner diameter of 0.8 cm was possible only with a very high flow rate. No phonation was possible when the inner diameter was smaller than 0.8 cm. The results imply that there exists a minimum inner diameter required to maintain vocal fold vibrations, below which vocal fold vibration cannot be achieved (or at least demands an excessively high subglottal pressure). This may be because the increased flow resistance associated with the small tube-SB opening creates a high supraglottal pressure and thus makes the pressure difference between the subglottal and supraglottal systems insufficient for sustained vocal fold oscillation.

C. Non-inflatable bulla-like cavity

For the case of a rigid cavity attached to the main vocal tract, dependence of SPL on cavity size was studied [Fig.

TABLE III. Resonant frequencies obtained from measurements of different vocal tract (VT) models with closed and open side branches (SB: side branch; no SB: 20 cm long tube without side branch; cSB: closed side branch; oSB: open side branch; SB-0.8: side branch with inner diameter of 0.8 cm). The nth resonant frequency is denoted as Fn. The term "pole" stands for an additional resonant frequency introduced by a side branch or cavity. Values in parentheses show deviations in percentage from the resonant frequencies of the 20 cm long tube without a side branch.

VT model	pole (Hz)	F1 (Hz)	F2 (Hz)	pole (Hz)	F3 (Hz)	F4 (Hz)
No SB		380	1170		1990	2560
cSB-0.4		320 (−15.7)	1250 (+6.8)	1640	1890 (−5)	2460 (−3.9)
cSB-0.6		300 (−21)	1250 (+6.8)	1630	1890 (−5)	2450 (−4.3)
cSB-0.8		290 (−23.7)	1140 (−2.5)	1620	1820 (−8.5)	2400 (−6.3)
cSB-1.3		300 (−21)	1160 (−1)	1630	1880 (−5.5)	2500 (−2.3)
cSB-1.6		290 (−23.7)	1115 (−4.7)	1650	1900 (−4.5)	2500 (−2.3)
oSB-0.4		310 (−18.7)	1230 (+5.1)		1875 (−5.8)	2465 (−3.7)
oSB-0.6		320 (−15.8)	1260 (+7.7)		1890 (−5)	2465 (−3.7)
oSB-0.8		370 (−2.6)	1220 (+4.3)		1820 (−3.7)	2410 (−5.8)
oSB-1.3		380 (0)	1270 (+8.5)		1900 (−4.5)	2410 (−5.8)
oSB-1.6		380 (0)	1260 (+7.7)		1890 (−5)	2410 (−5.8)
cav 100 ml	115	660 (+73.7)	1320 (+12.8)		2110 (+11.6)	3030 (+18.3)
cav 500 ml	78	650 (+71)	1310 (+12)		2110 (+11.6)	3030 (+18.3)

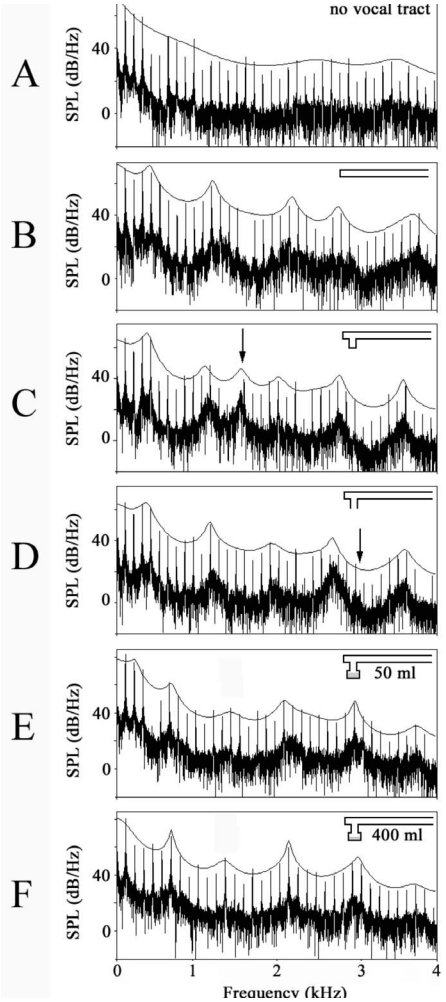

FIG. 6. Spectra and linear predictive coding (LPC) envelopes for different physical models. The vocal tract model is schematized in the top right corner of each spectrum. (A) No vocal tract [as in Fig. 3(A)], (B) uniform tube vocal tract [as in Fig. 3(B)], (C) uniform tube vocal tract with closed side branch [as in Fig. 3(C)] (arrow indicates additional pole), (D) uniform tube vocal tract with closed side branch [as in Fig. 3(D)], (E) uniform tube vocal tract with rigid cavity (50 ml volume) [as in Fig. 3(E)], (F) uniform tube vocal tract with large rigid cavity (400 ml volume) [as in Fig. 3(E)]. Note that the additional zero in the vocal tract with the open side branch overlaps with the fourth formant [arrow in panel (D)].

5(c)]. Compared to the 600 ml cavity, the 200 ml cavity gives higher SPL values, which can even exceed those of the basic design for high subglottic pressures.

It should be noted that Figs. 5(a)–5(c) reveal an interesting effect of the tube-SB as well as of the rigid cavity. Namely, the slope of the SPL-subglottal pressure relationship becomes much steeper compared to the reference measurement or the basic design. For instance, increasing the subglottic pressure from 8 to 16 cm H_2O caused an increase in SPL by 12 dB (from 54 to 66 dB) for the reference measurement [Fig. 5(a)]; a comparable amount of increase in SPL was also observed for the basic design (from 60 to 73 dB). However, in the case of the attachment of a tube-SB [Fig. 5(b), 1.3 cm diameter] or a 1 l rigid cavity [Fig. 5(c)], the same increase in subglottic pressure (from 8 to 16 cm H_2O) resulted in an increase in SPL of 20 dB (from 53 to 73 dB). This implies that within the same range of subglottic pressure, dynamic range of the sound emission can be widened by introducing the side branch or the rigid cavity.

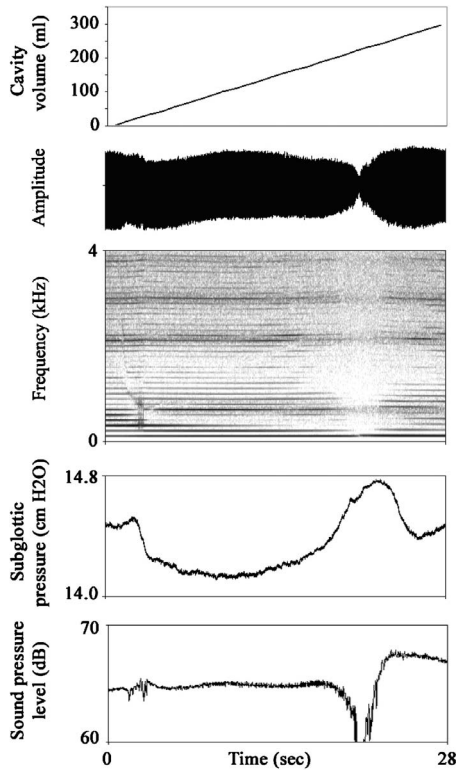

FIG. 7. Experiment with a continuous change in rigid cavity volume attached to the main vocal tract. During the experiment, the cavity was gradually filled with water. Note the aphonic regime when the resonant frequency crossed F0. Phonation started again slowly after the resonance moved beyond from F0. The SPL reached a higher level after the crossing.

To study the dependence of SPL on the rigid cavity volume in more detail, another experiment was conducted in which the cavity size was gradually changed from 0 to 300 ml (Fig. 7). At a cavity size of approximately 210 ml, the physical model ceased to vibrate. The corresponding PTP was too high to measure at this point (Fig. 8). This phenomenon is due the following nonlinear source-filter interaction. The pole/zero pair introduced by the rigid cavity depends on the cavity size (Table III). A small cavity introduces a pole/zero pair around 150 Hz. As the cavity size is increased (from 0 to 350 ml in Fig. 7), the pole/zero pair decreases and eventually crosses the fundamental frequency of the vocal fold model (F0=110 Hz) at a cavity volume of

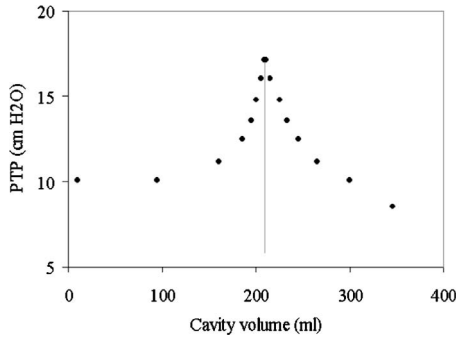

FIG. 8. Dependence of phonation threshold pressure (PTP) on the volume of the rigid cavity attached to the main vocal tract.

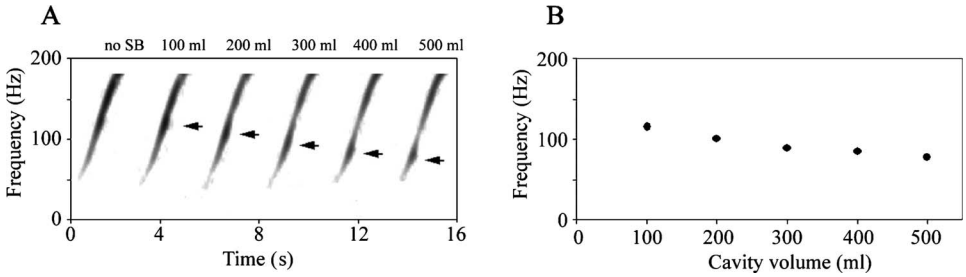

FIG. 9. (A) Spectrograms of the vocal tract model stimulated by sweep tones ranging from 90 to 150 Hz. As indicated above each spectrogram, the cavity volume was changed from 0 to 500 ml. The arrows indicate the location of a pole (vocal tract resonance peak) introduced by the cavity; "no SB" stands for no side branch. (B) Pole-cavity size relationship. For each sweeptone, an averaged FFT was calculated. The pole shows up as a peak in the FFT spectrum.

approximately 210 ml. The interaction between the sound source and the vocal tract becomes very strong and inhibits the model vibrations. Once the pole/zero pair passes away from the fundamental frequency, the source-tract interaction weakens and the vocal folds resume oscillation. The interaction effect is different on both sides of this phonation stop. The SPL was higher after the phonation stop, implying that phonation is facilitated when F0 is larger than the pole/zero pair. Before and after the phonation stop, the subglottal pressure changed by approximately 1 cm H_2O. F0 also changed from 110 to 120 Hz.

To locate a precise value of the pole/zero pair and to study its dependence on the cavity size, the transfer function of the vocal tract model was determined by a sweep tone experiment (Fig. 9). In this experiment, the vocal tract model was stimulated by a horn driver with a variable frequency ranging from 90 to 150 Hz. The cavity size was changed from 0 to 500 ml with an increment of 100 ml. The spectral analysis of the output sound shows that the pole/zero location is lowered as the cavity size is increased (Fig. 9). This is in good agreement with the computational simulation (see Sec. IV E below).

D. Inflatable air sac

To study an inflatable air sac added to the side branch [Fig. 3(F)], two distinct situations were considered: closed mouth (plug inserted) and open mouth (plug not inserted). For a given air flow rate (for instance, 34 l/min), the SPL measured with a closed mouth was approximately 59 dB for the pig urinary bladder (approximately 500 ml maximum inflation, approximately 10 cm diameter) and 68 dB for the cow urinary bladder (approximately 5 l maximum inflation, approximately 20 cm diameter).

After the plug was released from the mouth, the air sac was deflated. Gravity of the air sac, recoiling properties of the elastic tissue, and the air exiting through the open mouth caused a complete collapse. Partial inflation of the air sac, which is sometimes observed *in vivo*, was not simulated in the present experiment.

Spectral analysis of the sound emitted from the inflating air sac model indicates one major resonance in the area of 250 Hz [Fig. 10(a), bottom]. Higher harmonics are diminished. This is in good agreement with the siamang boom call, which has a major peak at the fundamental frequency between 200 and 300 Hz and only weak energy at higher harmonics [Fig. 10(b), bottom].

As shown in Figure 10(b), parts of the siamang song are characterized by a stereotypic repetition of the boom calls (arrow 2) and the scream calls (arrow 1). The fundamental frequency jumps from approximately 250 Hz in the boom call to approximately 800 Hz in the scream call. In the physical model, a relatively small shift in the fundamental frequency (up to 15 Hz) was observed when the closed mouth was quickly opened. This sudden mouth opening induces a situation with high glottal flow and high transglottal pressure, which is known to cause F0 changes in human voice (Hsiao *et al.*, 1994). Since our physical model has rather a small F0 variability (presumably primarily due to the linear stress-strain material response), the observed F0 jump was not as large as the real siamang vocalization.

The deflation process was very interesting. Using a large cow bladder, the deflation lasted for about 5–10 s. During this deflation process, the spectral characteristics of the voice initially resembled those of an open tube-SB and then later those of a closed tube-SB. This can be confirmed in the sweep tone data shown in Fig. 11. During deflation, the pole/zero pairs (arrow 2) are located at the same positions as the open tube-SB ($nc/2L$, where n is an integer). In the collapsed configuration, the pole/zero pairs (arrows 3 and 4) are located at the same positions as the closed tube-SB [$(2n-1)c/4L$]. In addition, we found in some cases a zero frequency in the range between 100 and 200 Hz. This is very similar to the pole/zero location of the non-inflatable cavity (see Sec. IV C). In contrast to the non-inflatable cavity, we never observed a phonation stop during the experiment.

We note that the vocal fold physical model was worn out rather quickly during this experiment. It is speculated that the repeated crossing of the zero frequency through F0 caused a higher stress in the vocal fold model and hence accelerated structural deterioration.

E. Computational simulation

To examine the acoustical characteristics of the physical model of the vocal tract, computational simulations were carried out to estimate the transfer functions for various configurations of the vocal tract. Figure 12 compares the transfer function of the main vocal tract (basic design) with that of the vocal tract with open or closed side branch. The open

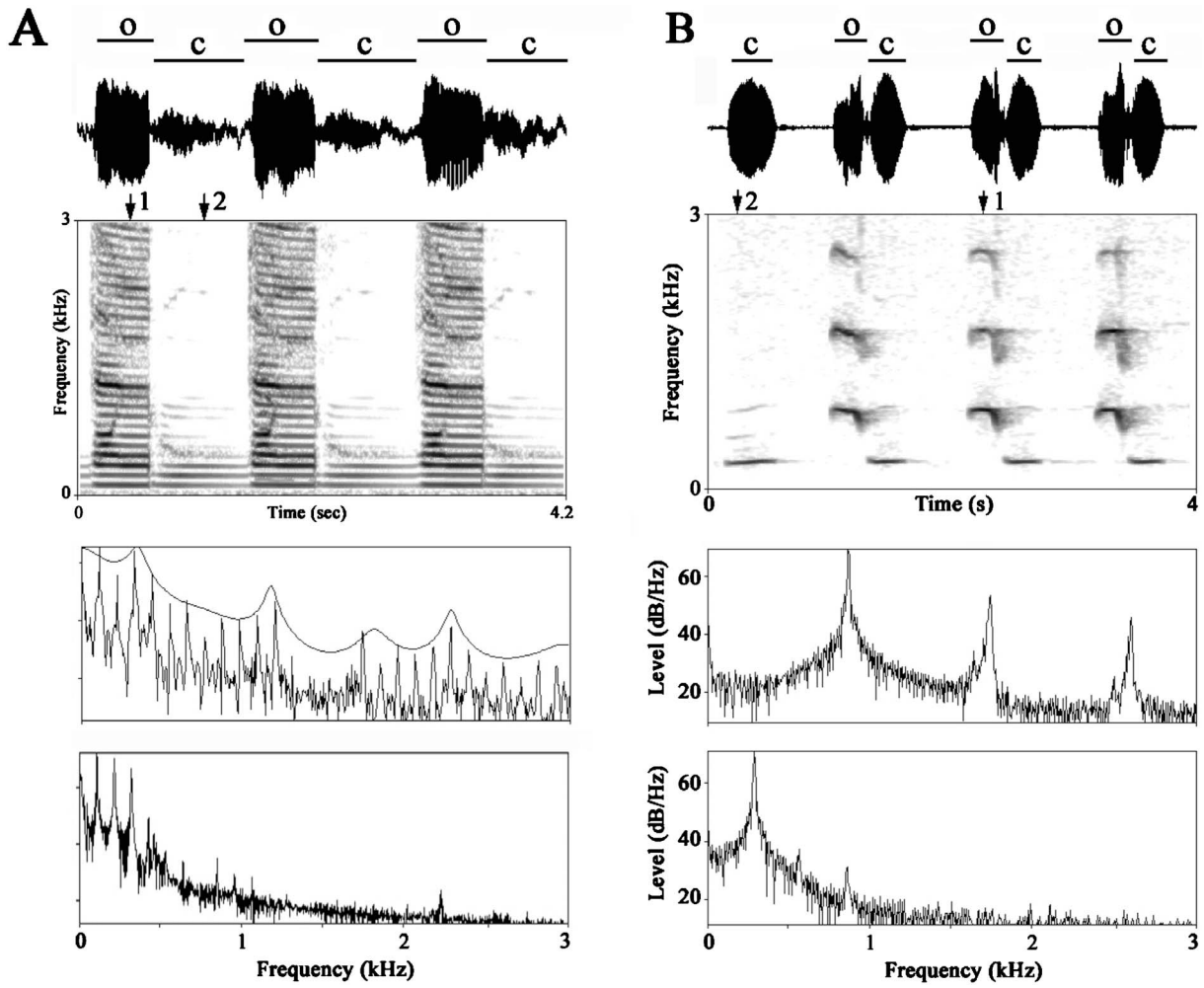

FIG. 10. Sound wave form (top panels), its spectrogram (second panels), and two spectra (third and fourth panels) from vocal fold physical model with inflatable bladder cavity (A) and from a siamang vocalization (B). Spectra are calculated from 50 ms segments indicated with arrows "1" and "2." Note that the formant structure of the open-mouth vocalization with a collapsed air sac [vocal tract model as schematized in Fig. 3(F)] resembles that of the closed side branch [see Fig. 6(c)]. "o"—open mouth or tube; "c"—closed mouth or tube.

side branch produced a pole/zero pair at approximately 3.6 kHz, whereas the closed side branch produced a pole-zero pair at approximately 1.8 kHz. The neighboring formants were moved accordingly. These results are in good agreement with the experiments summarized in Table III.

The transfer functions were also computed for the vocal tract with a rigid cavity [Fig. 13(a)]. The rigid cavity produced a pole/zero pair around 150 Hz. Location of this pair is sensitive to the cavity volume, where the dependence of the pole/zero frequencies on the cavity size is drawn in Fig. 13(b). Again, this agrees quite well with the experimental curve shown in Fig. 9. The computational model also identifies an additional pole/zero pair in the midfrequency range [Fig. 13(a)]. This pair at around 3.6 kHz might be related to the one computed for the open side branch in Fig. 12.

The experimentally obtained PTP curve shown in Fig. 8 can also be predicted by the computational model. Titze (1988) determined theoretically that PTP is dependent not only on the vocal fold parameters but also on the vocal tract input impedance. Since the input impedance corresponds to the acoustic load imposed on the vocal source, higher input impedance of the vocal tract requires a higher subglottic pressure to induce vocal fold oscillations. In Fig. 14, input impedance was drawn for the vocal tract with variable cavity size. Assuming that the input comes from the vocal source, the input impedance was computed by the convolution of the transfer function of the vocal tract with the power spectrum of the sound source signal measured from the vocal fold model (without any vocal tract). Although the computed input impedance has a peak at approximately 300 ml, which is somewhat different from the experiment, the qualitative structure of the experimental curve of Fig. 8, including the asymmetry between the left and right sides of the peak, is well reproduced by the computational model. One of the reasons for the inconsistency may be the bidirectional source-tract interaction, which is not considered in the present computation but which exists in the real experiment. The obtained peak frequency can be utilized to predict the phonation stop induced by the strong source-tract interaction of Fig. 7.

V. DISCUSSIONS

Experiments and computer simulations were carried out to investigate the questions on whether mammalian air sacs

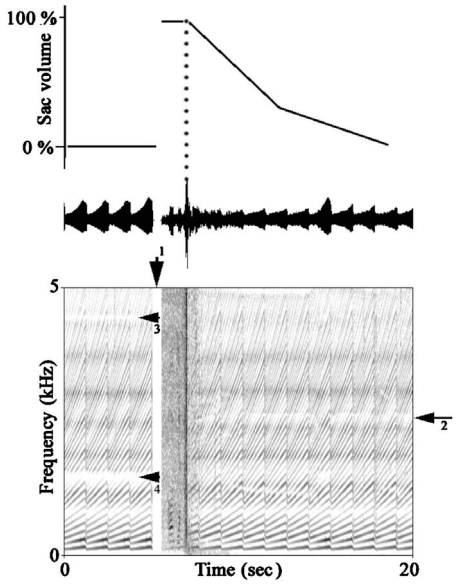

FIG. 11. Spectrogram of sweep tone (90–150 Hz) transmitted through a 20 cm tube vocal tract system with an inflatable air sac. Two situations are examined; first, a completely collapsed sac, up to about 5 s (arrow 1); second, continual deflation from air sac volume of about 5 l to complete deflation (from arrow 1 to end of sound). Arrow 2 indicates the location of zero frequency around 2500 Hz (which corresponds to zero frequency produced by the open side branch of 5 cm length). Arrows 3 and 4 indicate locations of zero frequency at about 1500 and 4500 Hz (which correspond to zero frequency produced by the closed side branch of 5 cm length). Note that during the deflation process (approximately between 9 and 14 s), another zero-like structure appears at approximately 1400 Hz, decreasing to 1300 Hz.

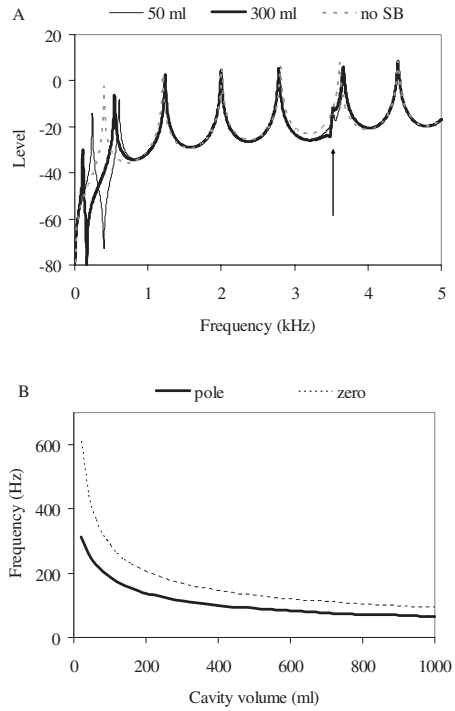

FIG. 13. (A) Transfer functions obtained by the computational model that simulates two rigid cavities (50 and 300 ml volume). Note that the first formant is affected by the pole/zero pair located in the low frequency range. The uniform tube that connects the main vocal tract and the rigid cavity introduces another pole/zero pair around 3.6 kHz (arrow), which resembles that of an open side branch. (B) Dependence of the pole/zero location on the cavity volume of the rigid cavity attached to the main vocal tract.

or bulla-like cavities affect formant position and/or SPL. Four vocal tract configurations were investigated: (1) a uniform tube-like main vocal tract without any attachment, (2) a vocal tract with open or closed uniform tube-SB, (3) a vocal tract with a tube-SB plus a rigid cavity air sac, and (4) a vocal tract with a tube-SB plus an inflatable air sac.

A uniform tube shapes the sound source signal in an expected way, i.e., formants at uneven multiples of $c/4L$ are present [Fig. 6(b)]. The 5 cm long tube-SB introduced a pole/zero pair in the midfrequency range (1.5–4.0 kHz, the exact position depends on whether the side branch is open or closed or on the length or the inner diameter of the side branch) (Dang and Honda, 1997; Dang *et al.*, 1994, 1998). As a consequence, all neighboring formants were shifted somewhat, where the first formant was most strongly shifted up to 25% [Figs. 6(c) and 6(d)]. The second and higher resonances were changed by not more than 10%.

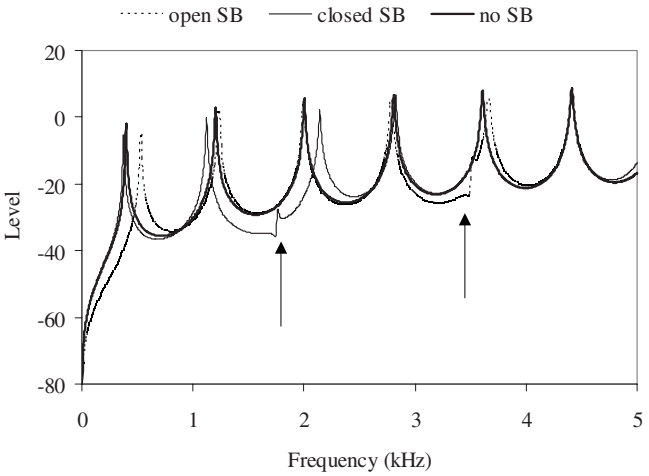

FIG. 12. Transfer functions obtained by the computational model that simulates the vocal tract without a side branch and the vocal tract with an open or a closed uniform side branch. Depending on whether the side branch is closed or open, an additional pole/zero pair of a 5 cm uniform side branch is located differently, at approximately 1.8 kHz for closed side branch (left arrow) and at approximately 3.6 kHz for open side branch (right arrow). The position of the pole/zero pair behaves according to a quarter-wavelength resonator when the side branch is closed and to a half-wavelength resonator when the side branch is open.

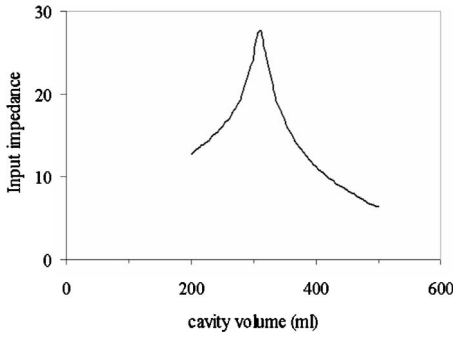

FIG. 14. Dependence of the input impedance of the vocal tract with a rigid cavity on the cavity volume. As an input signal to the vocal tract, reference sound measurement from the vocal fold physical model without a vocal tract is utilized. Since the input impedance is one of the key parameters that determine the PTP, the curve can be compared to the curve in Fig. 9.

A rigid cavity added to the tube-SB, which models the bulla hyoidea most prominent in *Allouatinae*, added a pole/zero pair in the range between 80 and 150 Hz. Again, the neighboring formants were shifted somewhat, where the first formant was shifted by up to 70% [Figs. 6(e) and 6(f)]. Finally, the inflatable air sac model added to a tube-SB was studied. In the case of a closed mouth, the air sac represents the main vocal tract, which gives rise to one major resonance below 400 Hz. On the other hand, if the mouth is open, the spectral characteristics depend on the degree of air sac inflation, which resembles either a rigid cavity or a closed side branch.

All air sac models mentioned above also have an effect on the SPL. Because of the nonlinear source-tract interaction, dependence of the SPL on the air sac configuration is hard to be systematically understood. Nevertheless, our experimental study showed that compared to the basic vocal tract configuration having no side branch, certain air sac configurations can enhance the SPL, for example, the closed tube-SB with inner diameter less than 1 cm and the rigid cavity of relatively small volume.

The present experiments also showed that the tube-SB and the rigid cavity models can widen the dynamic range of the sound emission within the same subglottal pressure range [Figs. 5 and 7]. Such physiological configurations would extend the vocal efficiency not only at higher pressures that make the sound louder but also at lower pressures. The lower levels are useful for "private" talk, in which the sender wishes to exclude unwanted listeners (eavesdroppers). To keep the voice "intelligible" in such private talk, the sound source must maintain its stable oscillations even at lower pressure levels.

A. Inflatable air sac cavity

Our inflatable air sac model suggests the presence of a single resonant frequency when the mouth is closed. Since there is no sound radiation from the mouth, the phonation occurs presumably through the air sac and skin walls. According to our experiment, when small air sac models (pig urinary bladder) were utilized, the closed mouth configuration gave a lower SPL than that of the open mouth. When large air sac models (cow urinary bladder) were utilized, the SPL values were comparable between the open and closed mouth configurations. The latter case is similar to siamang calls, which exhibit similar amplitude between scream call and boom call.

In siamang boom call, F0 is located around 250 Hz, which is close to the air sac resonance. Higher harmonics are mostly filtered out but can be observed sometimes [Fig. 10(b), bottom panel]. This F0 matching with the resonant frequency implies more efficient transmission of the sound energy than a mistuned system like our model, in which F0 (110 Hz) is more than an octave below the resonance (approximately 250 Hz) of the air sac [Fig. 10(a), bottom panel].

Phonation with closed oral and nasal cavities and into inflatable cavities has also been discussed in other contexts. For instance, ring doves (*Streptopelia risoria*) vocalize with a closed beak. They expel the air and phonate into an inflatable esophagus during their coo-call production (Riede *et al.*, 2004). The inflated esophagus of the dove is likely to act as an amplifier as well as a bandpass filter (Fletcher *et al.*, 2004). A modeling study based on the Helmholtz resonator clarified that the resonant frequency of the inflated cavity is determined mainly by the wall characteristics of the cavity and it is rather insensitive to the cavity size (Fletcher *et al.*, 2004). This enables the F0-resonance matching for a variable cavity size. Applying this idea to our inflatable cavity, we speculate that the air sac resonance is mainly determined by the wall characteristics of the bladder used in the experiment.

A large group of nonhuman primates with small air sac cavities (100 ml and less) remains to be discussed. Phonation into such a small cavity with a closed mouth situation probably plays no role, since the capacity of the air impelled into the sac is limited. Moreover, the connecting tube to those air sacs is relatively narrow ("less" than 10 mm in diameter) (Starck and Schneider, 1960). This narrow tube connection is likely to be insufficient to produce vocalizations with a closed mouth, as our side branch experiments with small inner diameter suggest. On the other hand, when the mouth is open, our closed tube-SB experiments demonstrate that there can be a positive effect of the narrow tube-SB on the SPL. These structures can thus help raise the SPL above that of the basic vocal tract configuration. This kind of sound amplification can be expected if we may regard the small air sacs as a closed tube-SB. A quarter-wavelength resonance should be detected in the spectrum.

B. Formant deviation

It seems unlikely that an air sac (either inflatable or noninflatable) alone is able to explain the severe formant deviations observed in nonhuman vocalizations. Our noninflatable air sac models changed the first formant by up to 72%, the second formant by up to 20%, and the higher formants less. In Diana monkey alarm calls, however, the first and second formants are deviated from those of the uniform vocal tract by 23% and 60%, respectively (Riede *et al.*, 2005). The severe deviation observed in the second formant seems unlikely to be produced by the air sac. Although the air sacs have been suggested to be the main reason for this effect (Lieberman, 2006), discontinuities in the nonhuman vocal tract are more likely to be the candidate (Riede *et al.*, 2006).

C. Nonlinear source-filter interaction and the efficiency of the sound source

The physical model of the vocal folds experienced lower PTP and increased SPL after the main vocal tract was added. The vocal tract models with side branches or rigid cavities also lowered PTP. Certain side branch models can decrease PTP even below that of the basic vocal tract configuration. This phenomenon is due to the nonlinear source-filter interaction as explained by theoretical studies, which state that PTP decreases as the inertive impedance of the vocal tract increases (Titze, 2004a, 2004b) and which have been confirmed in other physical model experiments (Chan and Titze,

2006). Given a similar basic design of the vocal fold source and the vocal tract filter, it is reasonable to assume the nonlinear source-filter characteristics also in nonhuman mammals, just as in humans performing specific vocal exercises (Titze *et al.*, 2008).

Of particular interest is the region where F0 and vocal tract resonance (pole/zero pair) are in close proximity. Near this region, the vocal tract impedance is quite variable and may produce dramatic changes in the source-filter interaction. This has been most impressively demonstrated here by the low frequency pole/zero pair introduced by the cavity. As the cavity resonance crosses F0, the interaction becomes so strong that the vocal folds stop vibrating. The experimental results suggest that the effect of the source-filter interaction is asymmetric about both sides of the filter resonance. For instance, SPL was higher when F0 was on the right side of the resonance than when it was on the left side (Fig. 7). This suggests that a perfect matching between vocal tract resonance and F0 is not as desirable, as previously considered (e.g., Riede *et al.*, 2006), but F0 slightly off the resonance is more beneficial for energy feedback to the sound source (Titze, 2008).

Another positive effect on SPL was found in the experiments, possibly due to the additional pole/zero pair that shifted the other formants in such a way that the fundamental frequency was located in a more beneficial range of the vocal tract impedance. More efficient energy feedback from the vocal tract to the sound source can make the sound overall louder. This provides another possibility of increasing the sound level, besides the optimal radiation theory.

In general, nonlinear source-filter interaction can be induced by various resonant frequencies, which are not necessarily due to the air sacs. However, compared to a simple situation of a vocal tract having no air sacs, the presence of the air sac gives rise to additional pole/zero pairs that may produce more areas of enhanced source production as well as more areas of source instabilities.

Howler monkeys (*Allouatinae*) are the most prominent examples with a large *Bulla hyoidea* (Starck and Schneider, 1960; Schön-Ybarra, 1995). It is interesting to note that howler monkey vocalization is characterized by a source spectrum with many bifurcations (Whitehead, 1995). Our preliminary investigation of those vocal utterances (unpublished data) suggests that source instabilities occur more often in the howler monkeys than, for instance, in Japanese macaques or chimpanzees which have an inflatable cavity (Riede *et al.*, 1997, 2004b, 2007) or in dogs and cats which possess no air sacs (Riede *et al.*, 1997, 2000).

D. Advantages and disadvantages of possessing an air sac for vocal communication

To summarize our discussions, we have recognized two acoustic effects of the air sacs. First, the air sac can increase the dynamic range of the sound emission within a given subglottic pressure range, both at the upper and lower limits. Second, vocal variability can be increased in the following three ways. (A) In the case of inflatable air sacs, open and closed mouth situations enable a switch between different radiation and filtering mechanisms. (B) In the case of noninflatable air sacs, they extend the frequency range, in which voice instability and nonlinear phenomena are induced by source-tract coupling. This provides additional vocal variability. (C) The formants of the main vocal tract are shifted by a pole/zero pair introduced by air sac. Our experiments suggest that such formant shifts are most prominent on the first formant and less on the higher formants.

The latter point leads to the question of why humans do not possess any major extensions of the vocal tract. All four great apes do possess air sacs, but not humans. Obviously, humans developed a much more convenient way to alter formants, i.e., speech articulation through varying cross-sectional vocal tract area. For predominantly close-range communications, such as human speech, of particular importance are neither loudness nor vocal variability but a stable sound source and well articulated formants. In human speech, the fundamental frequency ranges between 100 and 300 Hz (average male F0, 110 Hz; average female F0, 220 Hz). Among normal phonations of various vowels, the ones which possess the first formant closest to F0 are English vowels /i/ (first formant, 300–400 Hz) and /u/ (first formant, 280–350 Hz). The first formants in both cases are still far away from F0 in both sexes. If a pole/zero pair close to the F0 range was created by an air sac, this would interfere with F0 and could cause more voice instabilities in human voice. In this sense, the absence of air sacs in humans may be essential for maintaining a stable sound source.

ACKNOWLEDGMENTS

T.R. was supported by a short-term Postdoctoral Fellowship for North American and European Researchers by the Japan Society for the Promotion of Science (JSPS) (PE06030) and by a Postdoctoral fellowship by the "Deutsche Akademie der Naturforscher Leopoldina" (BMBF-LPD 9901/8-127). I.T.T. was supported by SCOPE (071705001) of Ministry of Internal Affairs and Communications (MIC), Japan. J.B.M. and S.L.T. were supported in part by NIH Grant No. NIDCD R01 DC05788. For technical support, we thank Dr. Ishikawa. For many helpful discussions, we are grateful to Professor Dang and Dr. Fujita.

Alipour, F., and Scherer, R. C. (**1997**). "Effects of oscillation of a mechanical hemilarynx model on mean transglottal pressures and flows," J. Acoust. Soc. Am. **110**, 1562–1569.

Bartels, P. (**1905**). "Über die Nebenräume der Kehlkopfhöhle," Z. Morphol. Anthropol. **8**, 11–61.

Causse, R., Kergomard, J., and Lurton, X. (**1984**). "Input impedance of brass musical instruments," J. Acoust. Soc. Am. **75**, 241–254.

Chan, R. W., Titze, I. R., and Titze, M. R. (**1997**). "Further studies of phonation threshold pressure in a physical model of the vocal fold mucosa," J. Acoust. Soc. Am. **101**, 3722–3727.

Chan, R. W., and Titze, I. R. (**2006**). "Dependence of phonation threshold pressure on vocal tract acoustics and vocal fold tissue mechanics," J. Acoust. Soc. Am. **119**, 2351–2362.

Dang, J., Honda, K., and Suzuki, H. (**1994**). "Morphological and acoustical analysis of the nasal and paranasal cavities," J. Acoust. Soc. Am. **96**, 2088–2100.

Dang, J., and Honda, K. (**1996**). "Acoustic characteristic of the human paranasal sinuses derived from transmission characteristic measurement and morphological observation," J. Acoust. Soc. Am. **100**, 3374–3383.

Dang, J., and Honda, K. (**1997**). "Acoustic characteristics of the piriform fossain models and humans," J. Acoust. Soc. Am. **101**, 456–465.

Dang, J., Shadle, C. H., Kawanishi, Y., Honda, K., and Suzuki, H. (**1998**).

"An experimental study of the open end correction coefficient for side branches within an acoustic tube," J. Acoust. Soc. Am. **104**, 1075–1084.
Fant, G. (**1960**). "Acoustic Theory of Speech Production," 2nd ed. (Mouton, The Hague, The Netherlands).
Flanagan, J. L. (**1972**). *Speech Analysis, Synthesis and Perception* (Springer, Berlin).
Fletcher, N. H., and Tarnopolsky, A. (**1999**). "Acoustics of the avian vocal tract," J. Acoust. Soc. Am. **105**, 35–49.
Fletcher, N., Riede, T., Beckers, G. J. L., and Suthers, R. A. (**2004**). "Vocal tract filtering and the 'coo' of doves," J. Acoust. Soc. Am. **116**, 3750–3756.
Frey, R., Gebler, A., and Fritsch, G. (**2006**). "Arctic roars—laryngeal anatomy and vocalization of the muskox (*Ovibus moschatus* Zimmermann, 1780, Bovidae)," J. Zool. **268**, 433–448.
Frey, R., Gebler, A., Fritsch, G., Nygren, K., and Weissengruber, G. E. (**2007**). "Nordic rattle—the hoarse phonation and the inflatable laryngeal air sac of reindeer (*Rangifer tarandus*)," J. Anat. **210**, 131–159.
Gautier, J. P. (**1971**). "Etude morphologique et fonctionnelle des annexes extra-laryngées des cercopithecinae; liason avec les cris d'espacement," Biol. Gabon. **7**, 229–267.
Haimoff, E. H. (**1981**). "Video analysis of Siamang (*Hylobates syndactylus*) songs," Behaviour **76**, 128–151.
Hayama, S. (**1970**). "The Saccus larynges in Primates," Journal of the Anthropological Society of Nippon. **78**, 274–298.
Hill, W. C. O. and Booth, A. H. (**1957**). "Voice and Larynx in African and Asian Colobidae," J. Bombay Natural His. Soc. **54**, 309–321.
Hillowala, R. A., and Lass, N. J. (**1978**). "Spectrographic analysis of air sac resonance in rhesus monkeys," Am. J. Phys. Anthropol. **49**, 129–132.
Hirano, M., and Kakita, Y. (**1985**). "Cover-body theory of vocal fold vibration," in *Speech Science: Physiological Aspects*, edited by R. Daniloff (College-Hill, San Diego, CA), pp 1–46.
Hsiao, T., Solomon, N. P., Luschei, E. S., Titze, I. R., Kang, L., Fu, T., and Hsu, M. (**1994**). "Effect of subglottic pressure on fundamental frequency of the canine larynx with active muscle tensions," Ann. Otol. Rhinol. Laryngol. **103**, 817–821.
Kurita, S., Nagata, K., and Hirano, M. (**1983**). "A. comparative study of the layer structure of the vocal fold," in *Vocal Fold Physiology: Contemporary Research and Clinical Issues*, edited by D. M. Bless and J. H. Abbs (College-Hill, San Diego), pp. 3–21.
Ishizaka, K., Matsudaira, M., and Kaneko, T. (**1976**). "Input acoustic-impedance measurement of the subglottal system," J. Acoust. Soc. Am. **60**, 190–197.
Lieberman, P. (**2006**). "Limits on tongue deformation—Diana monkey formants and the impossible vocal tract shapes proposed by Riede *et al.* (2005)," J. Hum. Evol. **50**, 219–221.
Neubauer, J., Zhang, Z., Miraghaie, R., and Berry, D. A. (**2007**). "Coherent structures of the near field flow in a self-oscillating physical model of the vocal folds," J. Acoust. Soc. Am. **121**, 1102–1118.
Nishimura, T., Mikami, A., Suzuki, J., and Matsuzawa, T. (**2007**). "Development of the laryngeal air sac in chimpanzees," International Journal of Primatology **28**, 483–492.
Ogura, Y. (**1915**). "Beitraege zur Kenntnis des Kehlsackes des Rentieres," J. Coll. Agr. Tohoku Imp. University, Sapporo **6**, 151–155.
Rendall, D., Owren, M. J., and Rodman, P. S. (**1998**). "The role of vocal tract filtering in identity cueing in rhesus monkey (*Macaca mulatta*) vocalizations," J. Acoust. Soc. Am. **103**, 602–614.
Riede, T., Herzel, H., Mehwald, D., Seidner, W., Trumler, E., Böhme, G., and Tembrock, G. (**2000**). "Nonlinear phenomena and their anatomical basis in the natural howling of a female dog-wolf breed," J. Acoust. Soc. Am. **108**, 1435–1442.
Riede, T., Arcadi, A. C., and Owren, M. (**2004b**). "Nonlinear acoustics in pant hoots of common chimpanzees (*Pan troglodytes*): Frequency jumps, subharmonics, biphonation, and deterministic chaos," Am. J. Primatol **64**, 277–291.
Riede, T. and Titze, I. R. (**2008**). "Vocal fold elasticity of the Rocky Mountain elk (*Cervus elaphus nelsoni*) — producing high fundamental frequency vocalization with a very long vocal fold," J. Exp. Biol. (in press).
Riede, T., Arcadi, A. C., and Owren, M. J. (**2007**). "Nonlinear acoustics in pant hoots and screams of common chimpanzees (*Pan troglodytes*). Vocalizing at the edge," J. Acoust. Soc. Am. **121**, 1758–1767.
Riede, T., Beckers, G. J. L., Blevins, W., and Suthers, R. A. (**2004**). "Inflation of the esophagus and vocal tract filtering in ring doves," J. Exp. Biol. **207**, 4025–4036.
Riede, T., Bronson, E., Hatzikirou, H., and Zuberbühler, K. (**2005**). "Vocal production mechanisms in a non-human primate: Morphological data and a model," J. Hum. Evol. **48**, 85–96.
Riede, T., Bronson, E., Hatzikirou, H., and Zuberbühler, K. (**2006**). "Multiple discontinuities in nonhuman vocal tracts—A response to Lieberman (2006)," J. Hum. Evol. **50**, 222–225.
Riede, T., Suthers, R. A., Fletcher, N., and Blevins, W. (**2006**). "Songbirds tune their vocal tract to the fundamental frequency of their song," Proc. Natl. Acad. Sci. U.S.A. **103**, 5543–5548.
Riede, T., Wilden, I., and Tembrock, G. (**1997**). "Subharmonics, biphonations, and frequency jumps-common components of mammalian vocalization or indicators for disorders?" Z. Säugetierkunde (Suppl. II) **62**, 198–203.
Scherer, R. C., Shinwari, D., DeWitt, K. J., Zhang, C., Kucinschi, B. R., and Afjeh, A. A. (**2001**). "Intraglottal pressure profiles for a symmetric and oblique glottis with a divergence angle," J. Acoust. Soc. Am. **109**, 1616–1630.
Schneider, R. (**1964**). "Der Larynx der Säugetiere (The larynx of mammals)," Handbuch der Zoologie **5**, 1–128.
Schön-Ybarra, M. (**1995**). "A comparative approach to the non-human primate vocal tract: Implications for sound production," in *Current Topics in Primate Vocal Communication*, edited by E. Zimmermann, J. D. Newman, and U. Juergens (Plenum, New York), pp. 185–198.
Sohndi, M. M., and Schroeter, J. (**1987**). "A hybrid time-frequency domain articulatory speech synthesizer," IEEE Trans. Acoust., Speech, Signal Process. **35**, 955–967.
Starck, D., and Schneider, R. (**1960**). "Respirationsorgane, Larynx," Primatologia **3**, 423–587.
Tembrock, G. (**1974**). "Sound production in *Hylobathes and Symphalangus*," in *Gibbon and Siamang*, edited by D. Rumbaugh (Karger, Basel), Vol. **3**, pp. 176–205.
Thomson, S. L., Mongeau, L., and Frankel, S. H. (**2005**). "Aerodynamic transfer of energy to the vocal folds," J. Acoust. Soc. Am. **118**, 1689–1700.
Titze, I. R. (**1988**). "The physics of small-amplitude oscillation of the vocal folds," J. Acoust. Soc. Am. **83**, 1536–1552.
Titze, I. R., and Story, B. H. (**1997**). "Acoustic interaction of the voice source with the lower vocal tract," J. Acoust. Soc. Am. **101**, 2234–2243.
Titze, I. R., Schmidt, S. S., and Titze, M. R. (**1995**). "Phonation threshold pressure in a physical model of the vocal fold mucosa," J. Acoust. Soc. Am. **97**, 3080–3084.
Titze, I. R. (**2004a**). "A theoretical study of F0-F1 interaction with application to resonant speaking and singing voice," J. Voice **18**, 292–298.
Titze, I. R. (**2004b**). "Theory of glottal airflow and source-filter interaction in speaking and singing," Acta Acust. **90**, 641–648.
Titze, I. R. (**2008**). "Nonlinear source-filter coupling in phonation: Theory," J. Acoust. Soc. Am. **123**, 2733–2749.
Titze, I. R., Riede, T., and Popollo, P. (**2008**). "Nonlinear source-filter coupling in phonation: Vocal exercises," J. Acoust. Soc. Am. **123**, 1902–1915.
Whitehead, J. M. (**1995**). "Vox Alouattinae: A preliminary survey of the acoustic characteristics of long-distance calls of howling monkeys," Int J. Primatol. **16**, 121–144.
Zhang, Z., Neubauer, J., and Berry, D. A. (**2006a**). "The influence of subglottal acoustics on laboratory models of phonation," J. Acoust. Soc. Am. **120**, 1558–1569.
Zhang, Z., Neubauer, J., and Berry, D. A. (**2006b**). "Aerodynamically and acoustically driven modes of vibration in a physical model of the vocal folds," J. Acoust. Soc. Am. **120**, 2841–2849.

Forward masking as a mechanism of automatic gain control in odontocete biosonar: A psychophysical study

Alexander Ya. Supin[a)]
Institute of Ecology and Evolution of the Russian Academy of Sciences, 33 Leninsky Prospect, 119071 Moscow, Russia

Paul E. Nachtigall[a)] and Marlee Breese[a)]
Marine Mammal Research Program, Hawaii Institute of Marine Biology, University of Hawaii, P.O. Box 1106, Kailua, Hawaii 96734, USA

(Received 9 January 2008; revised 28 March 2008; accepted 10 April 2008)

In a false killer whale *Pseudorca crassidens*, echo perception thresholds were measured using a go/no-go psychophysical paradigm and one-up-one-down staircase procedure. Computer controlled echoes were electronically synthesized pulses that were played back through a transducer and triggered by whale emitted biosonar pulses. The echo amplitudes were proportional to biosonar pulse amplitudes; echo levels were specified in terms of the attenuation of the echo sound pressure level near the animal's head relative to the source level of the biosonar pulses. With increasing echo delay, the thresholds (echo attenuation factor) decreased from −49.3 dB at 2 ms to −79.5 dB at 16 ms, with a regression slope of −9.5 dB per delay doubling (−31.5 dB per delay decade). At the longer delays, the threshold remained nearly constant around −80.4 dB. Levels of emitted pulses slightly increased with delay prolongation (threshold decrease), with a regression slope of 3.2 dB per delay doubling (10.7 dB per delay decade). The echo threshold dependence on delay is interpreted as a release from forward masking by the preceding emitted pulse. This release may compensate for the echo level decrease with distance, thus keeping the echo sensation level for the animal near constant within a certain distance range. © *2008 Acoustical Society of America.*
[DOI: 10.1121/1.2918544]

PACS number(s): 43.80.Lb [WWA] Pages: 648–656

I. INTRODUCTION

The biosonar of odontocetes (toothed whales, dolphins, and porpoises) possesses a number of unique abilities concerning detection and discrimination of objects. It has been the subject of detailed investigations over the past few decades (see Nachtigall and Moore, 1988; Au, 1993; Thomas *et al.*, 2004 for reviews). Nevertheless, many basic mechanisms underlying biosonar functions remain unexplored. One of the intriguing problems of the biosonar functioning is the avoidance of masking of faint perceived echoes by the much more intense emitted biosonar pulses. When an animal echolocates, it hears both the echo and its own emitted intense acoustic pulse. When a target is small and distant, the echo is much fainter than the outgoing pulse. Due to high sound velocity in water, the delay between the emitted pulse and echo may be as short as a few milliseconds. Normally, in these conditions, one would expect strong forward masking of the faint echo by preceding loud outgoing pulse. However, successful performance of the biosonar of odontocetes indicates that this sort of masking, if it exists, does not prevent the normal perception and analysis of the echo.

Another challenging problem concerning the biosonar of odontocetes is the problem of automatic gain control (AGC) mechanisms. The biosonar operates with echo levels varying by many tens of dB because of variation of target strengths and distances. Therefore, performance of the biosonar requires its receiving part (the auditory system) be capable of analyzing echoes under these widely varying intensities. This capability requires either a kind of AGC which keeps the response of the auditory system to the echo rather constant, or a capability of the auditory system to analyze the echo signals over a wide variety of neuronal response levels.

It is not completely known yet how the odontocete's auditory system solves these problems. One way to keep the echo level within a reasonable range is to vary the level of the outgoing signal. Experiments on animals in the wild have shown that dolphins and whales may vary the intensity of their echolocation pulses according to the distance to the target, roughly at a rate of 20 dB per distance decade (Rasmussen *et al.*, 2002; Au and Benoit-Bird, 2003; Au and Herzing, 2003; Au and Würsig, 2004). To some extent, this may compensate for the echo attenuation with distance. However, this mechanism can hardly solve the whole AGC problem because the variation of emitted pulse intensities does not influence the echo-to-transmission ratio. If this ratio is very low (because of the low target strength and/or large distance), the echo may well be masked by the much more intense preceding emitted pulse.

One of the mechanisms that serves to avoid or diminish the self-masking effect is the concentration of acoustic energy into the emitted outgoing echolocation beam directed to a target and a damping the emitted acoustic energy reaching

[a)]Author to whom correspondence should be addressed. Electronic mail: alex_supin@mail.ru.

the animal's ears. The role of the skull and melon as concentrators of emitted sounds in front of the head has been shown in a number of investigations (Cranford, 2000; Ketten, 2000) along with the presence of sound-muffling structures inside of the head, in particular, air-filled peribullar and pterygoid sinuses.

Another mechanism serving for the avoidance of self-masking in odontocete biosonar is the high temporal resolution of the auditory system. This was demonstrated in a number of psychophysical (Moore *et al.*, 1984; Nachtigall *et al.*, 2000; Helweg *et al.*, 2003) and physiological (evoked response) investigations (Supin and Popov, 1995a, 1995b; Dolphin *et al.*, 1995; Popov and Supin, 1997; Popov *et al.*, 2001; Supin *et al.*, 2001; Supin and Popov, 2004; Mooney *et al.*, 2006). The high temporal resolution of the auditory system may allow the echo to be partially or completely released from forward masking as soon as a few milliseconds or tens of milliseconds after the emitted pulse.

If the forward self-masking does exist, is it nothing but a process negatively influencing biosonar performance, a process that should be compensated by a number of mechanisms? There are some data in favor of a different point of view. Recording brain stem evoked potentials during natural echolocation has shown that the response to the echo remained almost constant with variation of target distance, although the intensity of transmitted echolocation pulses varied only slightly (Supin *et al.* 2004, 2005). These data indicate that AGC in the odontocete biosonar involves a variation of the sensitivity of the auditory system. It was first supposed that the echo response was kept constant because of its delay-dependent releasing from forward masking by the previous louder transmitted pulse. Indeed, with the target distance increase, the echo delay increases proportionally, which may result in release from masking by the preceding emitted pulse. At the same time, the echo intensity decreases with distance. These two opposite processes may compensate one another: with target distance increase, the echo intensity decreases, making the response smaller, but the echo delay increases and the response releases from masking, thus becoming larger. As a result, the echo response remains almost constant. Thus, according to the hypothesis, instead of negative influence on the biosonar performance, the forward masking of the echo by preceding emitted pulse may play a role in AGC making neuronal responses to echoes invariant of the distance to the target.

For either confirmation or negation of this hypothesis, it is important to know the rate of delay-dependent release from masking in the animal's auditory system. In conditions of *external* double-pulse stimulation (not natural echolocation), it has been shown that the rate of this release is 30–40 dB per delay decade in bottlenose dolphins (Popov and Supin, 1990) or 25–30 dB per delay decade in a false killer whale (Supin *et al.*, 2007). The double-pulse stimulation may be considered as simulating the interaction between the emitted pulse and the echo: the first (conditioning) pulse in the pair simulates the emitted pulse and the second (test) pulse simulates the echo. The rates of release from masking found in those experiments were rather close to the rate of echo attenuation with distance which is from 20 to 40 dB per distance decade, depending on the target size. This is an argument in favor of the hypothesis.

However, the data obtained in conditions of external stimulation cannot serve as an ultimate confirmation of the hypothesis. The rate of release from masking depends on the relation of intensities and frequency bands of the two pulses (Popov *et al.*, 2001). Therefore, one cannot be sure that the rate of release from masking is the very same under conditions of external stimulation and in conditions of natural echolocation. Measurement of the rate of release from masking in conditions closer to real echolocation would be a much more trustworthy confirmation of the hypothesis. The goal of the present study was a psychophysical examination of the excitability recovery of the auditory system of a whale after each emitted sonar pulse.

To approach this task in the present study, we used the technique of electronic (phantom) echo elaborated earlier (Aubauer and Au, 1998). Using this technique, instead of a real physical target, the echo is produced by an electronically playing back of an acoustic pulse that is triggered by the emitted biosonar pulse. This technique allows a flexible variation of all parameters of the echo, thus allowing a wide variety of measurements. Using this approach, we measured the thresholds of electronic echo detection as a function of the delay between the emitted biosonar pulse and echo in a false killer whale.

II. METHODS

A. Subject and experimental conditions

The experiments were carried out in facilities of the Hawaii Institute of Marine Biology, Marine Mammal Research Program. The subject was Kina, a false killer whale *Pseudorca crassidens*, an experienced approximately 30-year-old female kept in a wire-net enclosure in Kaneohe Bay, Hawaii. It was the same animal that was used in previous evoked-potential studies of echolocation (Supin *et al.* 2004, 2005, 2007). The animal was trained to echolocate and to recognize both real targets and electronic echoes, and to report the echo presence or absence using a go/no-go reporting paradigm.

The experimental facilities were laid out as follows (Fig. 1). The experimental enclosure was constructed of a floating pen frame (1), 8×10 m in size, supported by floats and bearing an enclosing wire net. This enclosure (the animal section) linked to a target section – another floating frame (2), 6×8 m in size that served as a platform for mounting targets or transducers and did not bear net. In the net divider separating these two sections, there was an opening bounded by a hoop (3), 55 cm in diameter that served as a hoop station for the animal. In front of the hoop, a hydrophone (4) was positioned 1 m from the animal's blowhole to record the echolocation pulses. At a distance of 2 m, a transducer (5) was positioned to play back electronic echoes. The hoop station (3), the hydrophone (4), and the transducer (5) were in a longitudinal straight line; altogether at a depth of 80 cm. In front of the animal, there was a movable baffle (6). When pulled up, this baffle screened the hydrophone and play-back transducer from the animal positioned in the hoop station; when it was lowered down, it opened the space in front of

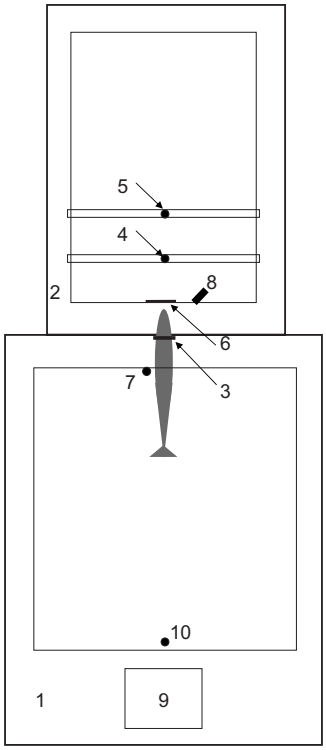

FIG. 1. Experimental design. 1 – experimental pen, 2 – transducer-holding frame, 3 – hoop station, 4 – receiving hydrophone, 5 – playing-back transducer, 6 – baffle, 7 – response ball, 8 – video camera, 9 – shack, 10 – start-position ball.

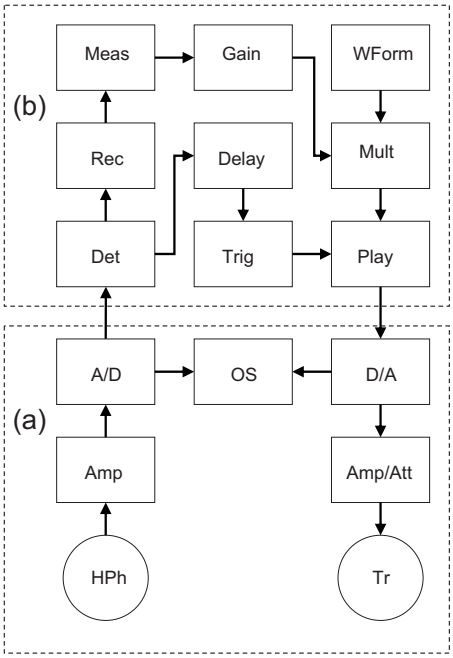

FIG. 2. Instrumentation and data processing. (a) – hardware, (b) – software. *HPh* – hydrophone, *AMP* – hydrophone amplifier, *A/D* – analog-to-digital converter, *Det* – sonar pulse detection, *Rec* – sonar pulse waveform recording, *Meas* – sonar pulse amplitude measurements, *Gain* – echo level control, *WForm* – echo waveform, *Mult* – multiplication, *Delay* – delay control, *Trig* – echo triggering, *Play* – echo playing back, *D/A* – digital-to-analog converter, *Amp/Att* – output amplifier/attenuator, *Tr* – playing transducer, *OS* – oscilloscope.

the animal. Near the hoop station, a response ball (7) was mounted above the water surface serving as an echo-present response indicator. The animal's position in the stationing hoop was monitored through an underwater video camera (8). The electronic equipment, operator, and trainer were housed in a shack (9) with a window facing the pen. A ball (10) mounted in water under the shack window marked the start position for the animal.

B. Experimental procedure

Threshold measurements were carried out using the standard go/no-go experimental paradigm with staircase variation of echo level. Each measurement session consisted of a total of 50 trials of two types: 25 echo-present and 25 echo-absent trials alternated pseudo-randomly (not more than three echo-present or three echo-absent trials in a row). Each trial contained steps as follows.

(i) The trainer called the animal to the start position (10 in Fig. 1). (ii) The animal was sent to a hoop station with a beep signal. During the animal's positioning, the baffle (6) screened the space in front of the hoop station from the animal. (iii) As soon as the animal took the position in the hoop station, the baffle was lowered down for 3 s, thus opening the space in front of the animal allowing echolocation to occur on the target area. Immediately after that, the animal emitted a train of echolocation clicks, as a rule, 20–50 clicks in a train. (iv) In echo-present trials, the playing-back program was turned on before the animal took the position in the hoop; the animal was required to signal echo detection by leaving the hoop and touching the signal ball (7) then coming to the start position (10) for fish reward (a go response); the playing-back program was turned off as soon as the animal left the hoop. In the echo-absent trails, the animal was required to wait in the hoop for 6 s, then it was signaled to leave the hoop and come for fish reward (a no-go response). Errors (misses of the signal in echo-present trials or false alarms in echo-absent trials) were not rewarded.

From trial to trial, the echo level varied by a one-up-one-down staircase procedure. The session began from an echo level well above the anticipated threshold (the warming-up part of the session). From trial to trial, the echo level varied according to the animal's response in the preceding echo-present trial. If the animal detected the echo, the echo level in the next echo-present trial decreased one step down. If the animal missed the echo, the echo level in the next trial increased one step up. The steps were 5 dB in the warming-up part of the session, until the first miss. After that, the steps were 2.5 dB (the measurement part of the session). Responses in echo-absent trials did not influence the echo level in target-present trials. The threshold was calculated as the mean of all reversal points (maxima and minima) of the staircase succession. The last one or two trials were again well above the threshold to make sure of ending the session with rewards (the cooling-down part of the session).

C. Instrumentation and data processing

The experimental equipment was designed as shown in Fig. 2. The emitted sonar pulses were picked-up by a hydrophone (*HPh* in Fig. 2) B&K 8102 with the flat frequency response up to 170 kHz. The picked-up signals were ampli-

fied by 20–40 dB within a frequency range of 5–100 kHz by a custom made amplifier (*Amp* in Fig. 2) based on a chip AD820 (Analog Devices). The amplified signal was led to an analog-to-digital converter (*A*/*D* in Fig. 2) of a data acquisition card NI DAQ-6062 (National Instruments). The digitizing was done at a sampling rate of 512 kHz. The digitized signal was processed by a standard personal computer. The processing included: (i) a sonar click was detected when the signal exceeded a preadjusted threshold level (*Det* in Fig. 2); (ii) the click waveform within a 100 μs window was acquired and stored in computer memory for further off-line analysis (*Rec* in Fig. 2); (iii) peak-to-peak amplitude of the stored click was measured (*Meas* in Fig. 2); (iv) a presynthesized echo waveform (*WForm* in Fig. 2) was multiplied (*Mult* in Fig. 2) by the amplitude value of the picked-up click and by a proportionality factor (*Gain* in Fig. 2); therefore, the amplitude of the synthesized signal was proportional to amplitude of the picked-up sonar click. The proportionality factor was controlled by the operator to vary the level of electronic echo from trial to trial. The obtained signal was played back (*Play* in Fig. 2). The playing was triggered by the instant of the sonar click picking up (*Trig* in Fig. 2) with a controlled delay (*Delay* in Fig. 2). The played-back digital signal was digital-to-analog converted (*D*/*A* in Fig. 2) by the same acquisition card NI DAQ-6062, amplified and attenuated (*Amp/Att* in Fig. 2), and played through an ITC-1032 (International Transducer Corporation) transducer (*Tr* in Fig. 2). This cycle of data processing was repeated automatically at each picked-up sonar click. Both input and output signals were monitored by an oscilloscope Tektronix TDS1002 (*OS* in Fig. 2). Data processing was controlled by a custom-made program ("virtual instrument") designed on the base of LabVIEW software (National Instruments).

The data processing (recording the click waveform, measuring its amplitude, synthesizing the played-back echo waveform) required some time; up to 3–3.5 ms. This resulted in an important limitation of available echo delays. Together with the acoustic delay of 2 ms (sound propagation for 1 m from the animal to the receiving hydrophone plus 2 m from the playing transducer to the animal), the minimal available echo delay could not be less than 5–5.5 ms if the echo were triggered by the same sonar pulse used to calculate echo parameters. To avoid this limitation, the data processing was programmed in such a way that each emitted sonar pulse triggered playing-back the echo waveform computed using the amplitude value of not the current but the *previous* pulse; after triggering, the program computed the signal to be triggered by the next sonar pulse, etc. (see signal ways in Fig. 2). The very first pulse of train did not trigger an echo. With this organization of the program, triggering was possible as soon as a few microseconds after the sonar pulse detection, i.e., with virtually zero delay. Together with the acoustic delay, the low limit of echo delays became 2 ms. This solution was based on an assumption that during a sonar click train the amplitude of the clicks varies rather gradually, not by big jumps from high to low amplitude or vice versa. If so, the error resulting from computation based on previous instead of current sonar pulse would not be large. The validity of this assumption is discussed below based on the biosonar click statistical results.

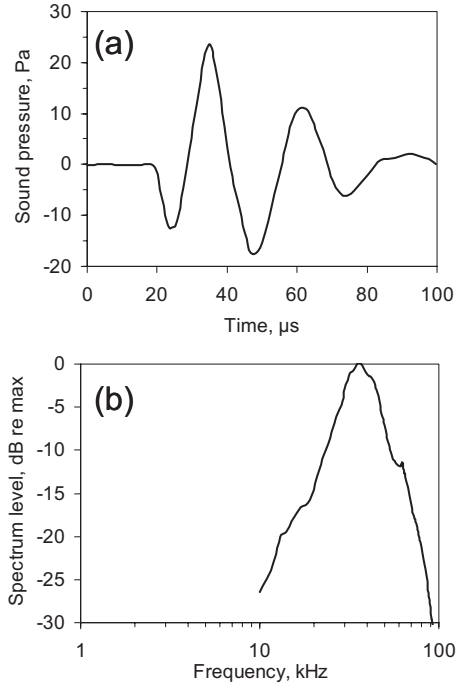

FIG. 3. Echo pulse (150 dB re 1 μPa peak/peak) waveform (a) and frequency spectrum (b).

D. Echo pulse features

Waveform, spectrum, and level of the played-back echo were monitored in the absence of the animal by positioning a receiving hydrophone (B&K8103) in the center of the hoop station.

The presynthesized echo waveform was such that after transferring through the transducer, the waveform and spectrum of the acoustic pulse were close to those of typical emitted biosonar pulses (see below). The resulting waveform (a) and frequency spectrum (b) of the acoustic echo pulse (150 dB re 1 μPa p/p) are presented in Fig. 3. The echo pulse had a spectrum peak at 35 kHz with decay down to −20 dB at 75 kHz at the high-frequency branch and 12 kHz at the low-frequency branch.

The level of the echo signal was not directly controlled by the operator. It was proportional to the amplitude of emitted sonar pulses, thus imitating an important feature of the real echo. Instead of level, the *attenuation* of the echo signal relative to the emitted sonar pulse was controlled and used to specify the echo intensity. This attenuation was calculated as a dB difference between the echo level next to the animal's head and the source level (i.e., level at 1 m distance from the head) of the emitted sonar pulse. With the instrumentation designed as described above, the echo attenuation was determined by (i) the transduction factor of the receiving hydrophone (*HPh* in Fig. 2), (ii) the transduction factor of the playing-back transducer (*Tr* in Fig. 2), (iii) the distance from the animal's head to the hydrophone, (iv) the distance from the playing-back transducer to the head, (v) the gain of the hydrophone amplifier (*Amp* in Fig. 2), (vi) the gain of the

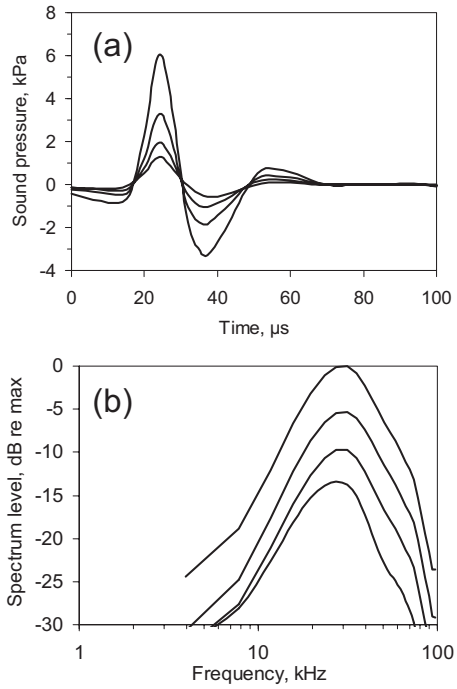

FIG. 4. Emitted sonar pulses of various levels (from lower to higher magnitudes: 185 ± 2.5, 190 ± 2.5, 195 ± 2.5, and 200 ± 2.5 dB re 1 μPa peak/peak) waveforms (a) and their spectra (from lower to higher, respectively) (b).

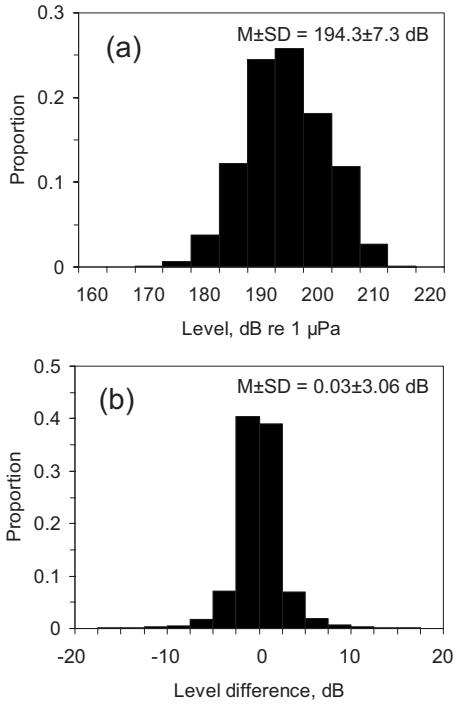

FIG. 5. Emitted sonar pulse statistics. (a) Distribution of pulse levels. (b) Distribution of level difference between successive pulses. Means (*M*) and standard deviations (*SD*) are indicated.

output amplifier-attenuator (*Amp/Att* I, Fig. 2), and (vii) the digital multiplication factor (*Gain* in Fig. 2). A variation of last three [(v)–(vii)] parameters allowed a variation of the echo attenuation within a wide range.

III. RESULTS

A. Emitted sonar clicks parameters and statistics

During the echo threshold measurements, 46 990 waveforms of emitted sonar clicks were collected and subjected to off-line analysis. Representative click waveforms of the most typical levels, from 185 ± 2.5 to 200 ± 2.5 dB re 1 μPa peak/peak, are presented in Fig. 4(a), each as an average of 200 examples. The clicks of all levels consisted of two main waves, a larger compression and smaller rarefaction wave, each lasting 15–20 μs. The frequency spectrum of these waveforms had a peak at 27–32 kHz and fell down to −20 dB at 80–88 kHz at the high-frequency branch and 5–7 kHz at the low-frequency branch.

A statistical distribution of click levels is presented in Fig. 5(a). The overall range of click levels was from 175 to 210 dB re 1 μPa peak/peak, however the most frequent (50.3% of all population) were clicks of 190–195 dB levels. Clicks of levels from 185 to 205 dB constituted 92.5% of the total population.

Because of methodological restrictions (see Sec. II), it was very important to find out how large the level differences between successive sonar clicks were. For that, the level difference between each click and the next click was calculated. The result of statistical analysis of 45 613 click pairs is presented in Fig. 5(b). In some number of cases, the difference reached from −15 dB (a preceding click was of lower level than the following one) to +15 dB (a preceding click was of higher level than the following one). However, such cases were very rare. For the majority of the clicks (79.4%) the difference between clicks was within a limit of ±2.5 dB, and for 93.4% the difference was within a limit of ±5 dB. This result shows that during each click train, the levels of the overwhelming majority of clicks varied gradually, with minor level differences between successive clicks.

B. Measurement session statistics

Thirty measurement sessions were completed, however three sessions were rejected because they contained a large proportion of false alarms (see below). Thus, results of 27 sessions were used to find the echo attenuation thresholds. In each of the sessions, the echo attenuation threshold was measured for one echo delay.

A typical time course of the measurement sessions is illustrated in Fig. 6 where the threshold measurement procedure is illustrated at two echo delays: 2.8 ms (a) and 11.2 ms (b). Both of these examples demonstrate variation of the echo attenuation according to the staircase procedure. The initial fraction of the session (15 trials in the both examples) was the warming-up part where echo levels were well above the threshold, so the echoes were detected in all these trials, and therefore the echo level decreased from trial to trial. The fraction after the first miss [17th trial in Fig. 6(a) and 18th trial in Fig. 6(b)] was the measurement part that lasted until the 48th trial in both of the examples. In this part, the echoes were detected in some echo-present trials and were missed in other trials; accordingly, the echo attenuation fluctuated up and down by 2.5 dB steps. The last two trials were the cooling-down part.

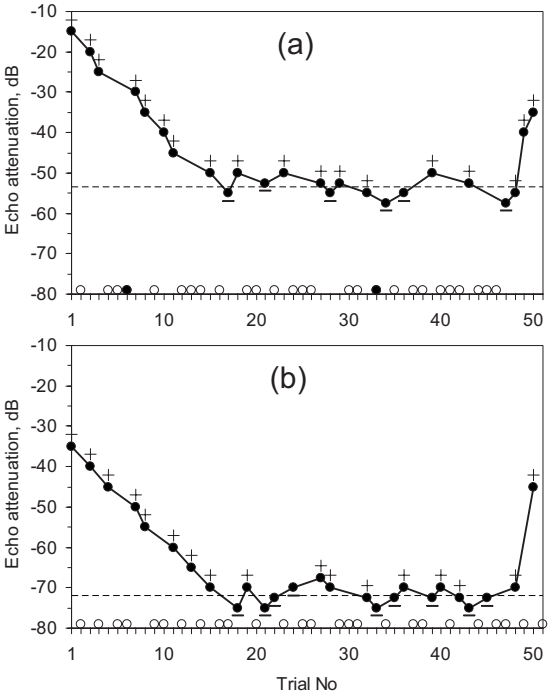

FIG. 6. Examples of measurement sessions: Echo attenuation varied by staircase rule as a function of trial number. "+" – hits, "–" – misses in echo-present trials. At the bottom of panels, echo-absent trials are marked, open dots – correct rejections, filled dots – false alarms. (a) – echo delay 2.8 ms, (b) – echo delay 11.2 ms.

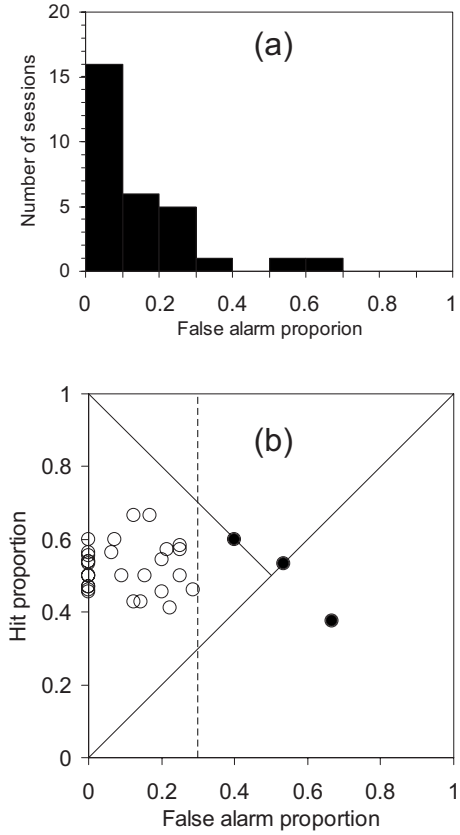

FIG. 7. Hit/false alarm statistics. (a) Distribution of sessions by false-alarm proportion. (b) ROC presentation of hit/false alarm ratios. Open and filled dots—sessions with false-alarm proportion below and above 0.3, respectively.

The presented examples demonstrate a substantial difference between thresholds found at different echo delays. At the longer delay (11.2 ms) the threshold (−72 dB) was much lower than at the shorter (2.8 ms) delay (−53.5 dB).

The echo-absent trials, constituting a half of all trials in each session, revealed an obvious bias to the no-go response. It manifested itself as a small proportion of false alarms. In the examples presented in Fig. 6, the animal committed only two false alarms in session (a) and no false alarms in session (b). The overall statistics of hits and false alarms in all sessions are presented in Fig. 7. In 27 of 30 sessions, the false alarm proportion did not exceed 30% [Fig. 7(a)]. These 27 sessions were selected for data processing and threshold calculation. The remaining three sessions with higher proportions of false alarms were excluded from analysis.

In order to reveal the bias of the animal's behavior, the hit/false alarm proportions were displayed in the receiver operation characteristic (ROC) format [Fig. 7(b)]. This presentation shows:

(i) In all the sessions, the hit proportions were from 0.4 to 0.6, i.e., close to the theoretical value of 0.5 characteristic of the one-up-one-down staircase procedure.
(ii) In all nonrejected sessions, the hit/false alarm ratios were well above the line of equal hit/false alarm proportions [the diagonal (0, 0)–(1, 1)], thus indicating that majority of go responses in echo-present trials were predominantly real hits and not a result of random guess.
(iii) In all nonrejected sessions, the hit/false alarm ratios were well below the line of neutral bias [the diagonal (0, 1)–(0.5, 0.5)], thus indicated a substantial bias to conservative no-go responses.

C. Echo attenuation threshold as a function of echo delay

Using the measurement design described above, echo thresholds (in terms of attenuation relative to the emitted pulse source level) were measured at nine echo delays: 2, 2.8, 4, 5.6, 8, 11.2, 16, 22.5, and 32 ms ($\sqrt{2}$ steps). At each of the delays, measurements were repeated three times (a total of 27 sessions analyzed). All of the obtained thresholds are presented in Fig. 8(a). In spite of a substantial data scatter, the results revealed an obvious trend: the longer the delay, the lower the echo threshold.

To characterize this trend quantitatively, the threshold estimates obtained for each of the delays were averaged. The averaged thresholds composed a function which could be segregated into two segments [Fig. 8(b)]: an oblique segment from 2 to 16 ms and a nearly flat one from 16 to 32 ms. Within the oblique segment, the mean echo threshold decreased from −49.3 dB at 2 ms to −79.5 dB at 16 ms. Being plotted on a logarithmic delay scale, this segment could be satisfactorily ($r^2=0.98$) approximated by a straight regression line. The slope (with standard error) of this line was -9.5 ± 0.6 dB per delay doubling, or -31.5 ± 2.1 dB per delay decade.

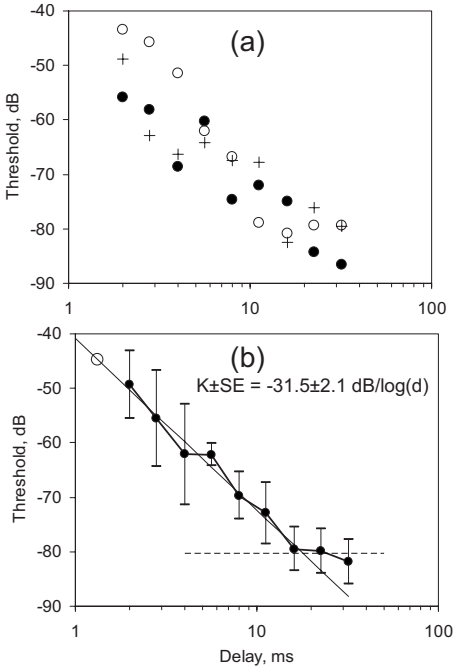

FIG. 8. Echo attenuation threshold dependence on echo delay. (a) Original data; for each of the delays, results of three measurement sessions are designated by different symbols. (b) Averaged data (means and standard deviations); oblique straight line—regression line for a segment from 2 to 16 ms, horizontal dashed line—mean level for a segment from 16 to 32 ms. Regression factor (K) and its standard error (SE) are indicated. The open circle symbol indicates the predicted target strength threshold.

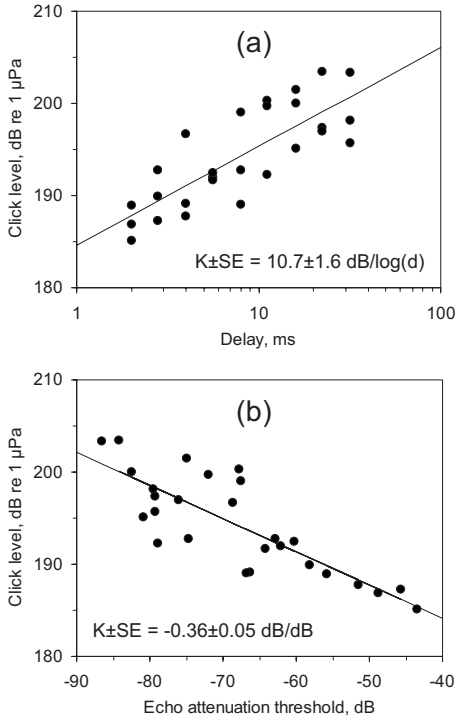

FIG. 9. Emitted click level (averaged for each of sessions over trials with near-threshold echo attenuation) dependence on echo delay (a) and echo attenuation threshold (b). Straight lines—regression lines. Regression factors (K) and standard errors (SE) are indicated.

Within the flat segment, thresholds varied to a lesser extent: from −79.5 dB at 16 ms to −81.8 dB at 32 ms. The mean level of this segment was −80.4 dB.

D. Emitted sonar click level as a function of echo attenuation threshold

In order to find out whether the emitted sonar click level varied according to echo delay, the mean click levels were calculated in measurement parts of each session, i.e., for the trials where the echo attenuation fluctuated around the threshold. The result of calculation is presented in Fig. 9 which plots the mean click levels in 27 sessions as a function of echo delay (a) and as a function of echo attenuation thresholds found in the sessions (b). The results showed a trend. The longer the delay and, respectively, the lower the threshold, the higher mean level of emitted clicks. Despite the data scatter, both presentations of the trend could be approximated by straight regression lines ($r^2=0.64$ for the function of echo delay logarithm and $r^2=0.67$ for the function of echo attenuation threshold). The slope of these regression lines were 3.2 dB per delay doubling (10.7 dB per delay decade) and −0.36 dB/dB, respectively.

IV. DISCUSSION

A. Validity of the one-up-one-down staircase procedure

Before discussing the results, the validity of the measurement procedure should be estimated. The staircase measurement procedure could have been conducted in a variety of versions. If the stimulus level is rising up after each stimulus miss, then the procedure brings the stimulus level to a value providing a probability p of signal detection of around $\sqrt[n]{0.5}$, where n is the number of signal detections required before lowering down the stimulus level. We chose a one-up-one-down procedure. With the use of this version ($n=1$), the probability of signal detection is around 0.5. In the absence of the response bias, this probability could be achieved without real signal detection, just by random choice. Therefore, in conditions of zero bias (e.g., with the use of the two-alternative forced choice procedure providing the zero bias by definition), either the one-up-two-down ($n=2$, $p=0.71$) or one-up-three-down ($n=3$, $p=0.79$) procedures can be used.

However, if the 0.5 probability of correct responses is provided by random choice, the false alarm probability should be approximately the same, around 0.5. The false-alarm proportion markedly less than 0.5 is a manifestation of a bias to no-go responses. In this situation, the 0.5 probability of signal detection could not be achieved by random choice, and it can be adopted as the threshold criterion.

The results of ROC analysis presented above (see Fig. 7) demonstrated that in our experiments, the subject really featured a significant conservative bias to no-go responses. In all sessions used for threshold evaluation, the false alarm proportion was below 0.3, and in a many sessions it was zero. In all the analyzed sessions, the hit/false alarm ratio was well above the level of random choice and in the area of no-go bias. Therefore, the one-up-one-down procedure and the threshold criterion of $p=0.5$ used in this study were adequate to the subject's behavior.

B. Validity of the echo level computation

As mentioned above (see Sec. II), technical limitations did not allow us to compute the level of shortly delayed echoes based on the amplitude of the very same emitted sonar click that triggered the echo. Instead, we used an echo waveform computed based on the level of the preceding sonar click. We adopted this procedure relying on the assumption that the click generating apparatus of the animal was not likely to change the level greatly from click to click when the clicks follow rapidly one after the other. The statistical analysis of click levels confirmed this assumption. For the overwhelming majority of sonar clicks, the level difference between successive clicks did not exceed ± 2.5 dB, and in only very few cases this difference exceeded ± 5 dB (see Fig. 5). This means that for the majority of clicks, the error resulting from the substitution of the current click level by the previous click level only rarely exceeded a few dB. In general, the systematic error should be even less than a few dB because both positive and negative differences between successive clicks were almost equally frequent (the mean of 0.03 dB), therefore, to a certain degree, compensating one another. In comparison with the range of systematic threshold variation depending on echo delay (around 30 dB, see Fig. 8), this error may be neglected.

C. Echo attenuation threshold dependence on echo delay. Implications to the AGC problem

The main result of the measurements described herein is the obvious dependence of echo attenuation threshold on echo delay: the longer the delay, the lower the threshold. In our opinion, the most logical explanation of this effect is forward masking of echoes by the preceding emitted sonar pulse which was heard by the animal before each echo. It means that the echo thresholds found at rather short delays (up to 16 ms) were actually forward masked, not absolute thresholds, and that threshold decrease with delay prolongation revealed a release from this masking.

This interpretation allows one to make some predictions about how the sensation level of the echo depends on the distance of a real target during echolocation. The real echo attenuation depends on distance with a rate from 6 dB per distance doubling (20 dB per distance decade) for a large target reflecting the sonar beam as a flat mirror to 12 dB per distance doubling (40 dB per distance decade) for a small (less then the sonar pulse wavelength) target. Suppose that for a certain target, the echo attenuation rate is intermediate between these two extremes, say 9 dB per distance doubling (30 dB per distance decade). This is the very same rate that is characteristic of echo threshold-vs-delay dependence (see Fig. 8). Since the distance and delay are directly proportional, this should result in a constant *sensation level* (the difference between the level and threshold) of the echo, independent of distance. This effect is very likely an effective mechanism of AGC, as was hypothesized earlier (Kick and Simmons, 1984: Popov and Supin, 1990; Supin *et al.*, 2007).

It seems little probable that this mechanism *exactly* compensates for the echo attenuation with distance. As pointed out above, the rate of echo attenuation with distance may be different for different targets, as well as the rate of echo release from masking may differ in different subjects. But it seems very probable that this mechanism *at least partially* (maybe, to a large extent) compensates for the echo attenuation with distance.

The forward-masking AGC mechanism may be effective only within a limited range of distances and echo delays. When the delay is large enough to reduce the masked echo perception threshold down to a level of the absolute threshold (a complete release of masking), any further increase of the delay cannot further reduce the threshold. This prediction was also confirmed by the data presented above. When the delay reached 16 ms and the attenuation threshold reached around -80 dB, a further increase of the delay (22.5 and 32 ms) little influenced the threshold. In measurement sessions with echo delays of 22.5 and 32 ms and thresholds around -80 dB, the animal produced clicks of around 200 dB re 1 μPa (see Fig. 9). Thus, in terms of sound pressure level, the echo perception threshold was around 120 dB re 1 μPa. This is the very same threshold that was found earlier for the same subject and the same pulse waveform in conditions of external stimulation (Supin *et al.*, 2007). Independently of being this threshold absolute or influenced by the background noise, it dictates the minimal detectable echo level.

One more prediction originating from the data presented above concerns the target strength threshold. Assuming that the echo sensation level is (within a certain range of conditions) independent of distance, this level should depend on the target strength. The data allow an estimate of the threshold target strength. For that, the found threshold-vs-delay dependence should be extrapolated to a delay corresponding to the target distance of 1 m. At that distance, the echo attenuation is quantitatively equal to the target strength. At the 1 m distance, i.e., 2 m double way of sound and sound velocity of 1500 m/s, the delay is 1.33 ms. Extrapolation of the regression line in Fig. 8(b) to this value results in an attenuation of -44.7 dB. It means that targets of lower strength cannot be detected independently of the emitted click level and distance, because the echo is always below the masked threshold. This prediction fits the real conditions of echolocation. For example, the target strength of a moderate-size fish was estimated as -20 to -35 dB (Benoit-Bird and Au, 2003).

Again it should be stressed that *quantitatively* this conclusion is valid only for the particular conditions. If the rate of echo attenuation with distance is not the very same as the rate of releasing from masking, the threshold target strength may be distance dependent to a certain extent.

These psychophysical data do not provide any information concerning the physiological nature of the forward masking in the whale biosonar. Similar data obtained in bats were interpreted as a manifestation of the stapedial reflex (Kick and Simmons, 1984). It should be noted, however, that in conditions of external double-click stimulation, the forward masking appeared at inter-click intervals beginning from 0.1 to 0.2 ms. The stapedial reflex can hardly be activated so quickly, so the masking was explained by occlusion of the afferent volleys in the auditory pathways (Supin and

Popov, 1995b; Popov *et al.*, 2001; Supin *et al.*, 2007). Further neurophysiological investigations are necessary to reveal the contribution of different mechanisms to the forward masking in biosonars.

D. Contribution of forward masking and variation of emitted click level to AGC

Apart from decrease of the masked threshold, the level of the emitted pulse slightly increased with increasing the echo delay in our experiments. On average, the dependence was as little as 3.2 dB per delay doubling (10.7 dB per delay decade). This is markedly less then the lowest theoretical echo attenuation with distance (6 dB per distance doubling or 20 dB per distance decade). This strategy of minor variation of emitted click level seems quite reasonable within the distance and delay range where the forward masking functions. Within this range, the possibility of echo perception is dictated more by echo attenuation relative to the emitted pulse than by the absolute echo level. Increasing the emitted pulse level proportionally increases both the masker (the self-heard emitted pulse) and the masked signal (the echo), therefore the sensation level of the echo relative to the masked threshold should remain unchanged.

However, a variation of the emitted click level may well be much more effective at long target distances and long echo delays resulting in complete release from forward masking. In this case, the possibility of perceiving the echo depends on its sound pressure level, and a sufficient level of emitted pulses may be necessary to produce an echo above the absolute threshold unhampered by forward masking.

Thus, both the forward masking and a variation of the emitted sonar click level may be effective in maintaining the optimal sensation level of the echo, but the predominant distance (therefore delay) ranges to the target are different for these two processes.

ACKNOWLEDGMENTS

The authors gratefully acknowledge funding from the U.S. Office of Naval Research Grant No. N0001415-1-0738 and the Russian Ministry of Science and Education Grant No. NSh-157.2008.4. This is contribution 1311 from the Hawaii Institute of Marine Biology. The whale work was completed under a Marine Mammal Permit issued to Paul E. Nachtigall from the NMFS office of Protected Species with protocols approved by the University of Hawaii Animal Care and Utilization Committee.

Au, W. W. L. (**1993**). *The Sonar of Dolphins* (Springer-Verlag, New York).

Au, W. W. L., and Benoit-Bird, K. J. (**2003**). "Automatic gain control in the echolocation system of dolphins," Nature (London) **423**, 861–863.

Au, W. W. L., and Herzing, D. L. (**2003**). "Echolocation signals of wild Atlantic spotted dolphin (Stenella frontalis)," J. Acoust. Soc. Am. **113**, 598–604.

Au, W. W. L., and Würsig, B. (**2004**). "Echolocation signals of dusky dolphins (*Lagenorhynchus obscurus*) in Kaikoura, New Zealand," J. Acoust. Soc. Am. **115**, 2307–2313.

Aubauer, R., and Au, W. W. L. (**1998**). "Phantom echo generation: A new technique for investigating dolphin echolocation," J. Acoust. Soc. Am. **104**, 1165–1170.

Benoit-Bird, K. J., and Au, W. W. L. (**2003**). "Acoustic backscattering by Hawaiian latjanid snappers. I. Target strength and swimbladder characteristics," J. Acoust. Soc. Am. **114**, 2757–2766.

Cranford, T. W. (**2000**). "In search of impulse sound sources in odontocetes," In *Hearing by Whales and Dolphins*, edited by W. W. L. Au, A. N. Popper, and R. F. Fay (Springer, New York), pp. 109–155.

Dolphin, W. F., Au, W. W. L., and Nachtigall, P. (**1995**). "Modulation transfer function to low-frequency carriers in three species of cetaceans," J. Comp. Physiol., A **177**, 235–245.

Helweg, D. A., Moore, P. W. B., Dankewicz, L. A., Zafran, J. M., and Brill, R. L. (**2003**). "Discrimination of complex synthetic echoes by an echolocating bottlenose dolphin," J. Acoust. Soc. Am. **113**, 1138–1144.

Ketten, D. R. (**2000**). "Cetacean ears," In *Hearing by Whales and Dolphins*, edited by W. W. L. Au, A. N. Popper, and R. F. Fay (Springer, New York), pp. 43–108.

Kick, S. A., and Simmons, J. A. (**1984**). "Automatic gain control in the bat's sonar receiver and the neuroethology of echolocation," J. Neurosci. **4**(11), 2725–2737.

Mooney, T. A., Nachtigall, P. E., and Yuen, M. E. (**2006**). "Temporal resolution of the Risso's dolphin, *Grampus griseus*, auditory system," J. Comp. Physiol., A **192**, 373–380.

Moore, P. W. B., Hall, R. W., Friedl, W. A., and Nachtigall, P. E. (**1984**). "The critical interval in dolphin echolocation: What is it?" J. Acoust. Soc. Am. **76**, 314–317.

Nachtigall, P. E., Lemonds, D. W., and Roitblat, H. L. (**2000**). "Psychoacoustic studies of whale and dolphin hearing," In *Hearing by Whales and Dolphins*, edited by W. W. L. Au, A. N. Popper, and R. J. Fay (Springer, New York), pp. 330–364.

Nachtigall, P. E., and Moore, P. W. B. (**1988**). *Animal Sonar: Processes and Performance* (Plenum, New York).

Popov, V. V., and Supin, A. Ya. (**1990**). "Auditory brain stem ponses in characterization of dolphin hearing," J. Comp. Physiol., A **166**, 385–393.

Popov, V. V., and Supin, A. Ya. (**1997**). "Detection of temporal gaps in noise in dolphins: Evoked-potential study," J. Acoust. Soc. Am. **102**, 1169–1176.

Popov, V. V., Supin, A. Ya., and Klishin, V. O. (**2001**). "Auditory brainstem recovery in the dolphin as revealed by double sound pulses of different frequencies," J. Acoust. Soc. Am. **110**, 2227–2233.

Rasmussen, M. H., Miller, L. A., and Au, W. W. L. (**2002**). "Source levels of clicks from free-ranging white beaked dolphins (*Lagenorhinchus albirostris* Gray 1846) recorded in Icelandic waters," J. Acoust. Soc. Am. **111**, 1122–1125.

Supin, A. Ya., Nachtigall, P. E., Au, W. W. L., and Breese, M. (**2004**). "The interaction of outgoing echolocation pulses and echoes in the false killer whale's auditory system: Evoked-potential study," J. Acoust. Soc. Am. **115**, 3218–3225.

Supin, A. Ya., Nachtigall, P. E., Au, W. W. L., and Breese, M. (**2005**). "Invariance of evoked-potential echo-responses to target strength and distance in an echolocating false killer whale," J. Acoust. Soc. Am. **117**, 3928–3935.

Supin, A. Ya., Nachtigall, P. E., and Breese, M. (**2007**). "Evoked-potential recovery during double click stimulation in a whale: A possibility of biosonar automatic gain control," J. Acoust. Soc. Am. **121**, 618–625.

Supin, A. Ya., and Popov, V. V. (**1995a**). "Envelope-following response and modulation transfer function in the dolphin's auditory system," Hear. Res. **92**, 38–46.

Supin, A. Ya., and Popov, V. V. (**1995b**). "Temporal resolution in the dolphin's auditory system revealed by double-click evoked potential study," J. Acoust. Soc. Am. **97**, 2586–2593.

Supin, A. Ya., and Popov, V. V. (**2004**). "Temporal processing of rapidly following sounds in dolphins: Evoked-potential study," In *Echolocation in Bats and Dolphins*, edited by J. A. Thomas, C. F. Moss, and M. Vater (University of Chicago Press, Chicago), pp. 153–161.

Supin, A. Ya., Popov, V. V., and Mass, A. M. (**2001**). *The Sensory Physiology of Aquatic Mammals* (Kluwer, Boston).

Thomas, J. A., Moss, C. F., and Vater, M. (**2004**). *Echolocation in Bats and Dolphins* (University Chicago Press, Chicago).

Time-frequency analysis and modeling of the backscatter of categorized dolphin echolocation clicks for target discrimination

Mark W. Muller
Department of Mechanical Engineering, University of Hawai'i at Manoa, 2540 Dole Street, Honolulu, Hawai'i 96822-2303
and Marine Mammal Research Program, Hawai'i Institute of Marine Biology, P.O. Box 1106, Kailua, Hawai'i 96734-1106

John S. Allen III
Department of Mechanical Engineering, University of Hawai'i at Manoa, 2540 Dole Street, Honolulu, Hawai'i 96822-2303

Whitlow W. L. Au and Paul E. Nachtigall
Marine Mammal Research Program, Hawai'i Institute of Marine Biology, P.O. Box 1106, Kailua, Hawai'i 96734-1106

(Received 28 December 2007; revised 24 April 2008; accepted 25 April 2008)

A set of dolphin echolocation clicks collected from an Atlantic bottlenose dolphin in Kaneohe Bay, Hawai'i from a previous experiment is examined in terms of their time and frequency characteristics. The center frequency and rms bandwidth are calculated for the clicks and these are clustered into four classes by using a model based on the Bayesian information criterion. The echo signatures are attained from a solid, elastic homogeneous sphere for each class of clicks from an acoustic scattering model. The results from the scattering model are compared to experimental values. The joint time-frequency content of the resulting echo signals is obtained by the reduced interference distribution (RID). The RIDs are plotted and examined for each signal class for four spherical targets of different material compositions. RID correlation values are obtained for a standard target versus comparison targets by using a time-frequency correlator. The results suggest that dolphins may discriminate by auditory inspection of the time-frequency information returned by the targets. The modification of the outgoing clicks and examination of time-frequency target information may be fundamental to a dolphin's ability to identify and discriminate targets.
 [DOI: 10.1121/1.2932060]

PACS number(s): 43.80.Lb, 43.80.Ka, 43.60.Hj, 43.20.Fn [JAS] Pages: 657–666

I. INTRODUCTION

By using echolocation, an Atlantic bottlenose dolphin, *Tursiops truncatus*, can make fine distinctions in the properties or features of targets such as size, shape, and material composition (Nachtigall, 1980; Au, 1993). The results of Au *et al.* (1988) suggest that dolphins may have developed a unique way to process complex broadband transient sonar (acoustic) echoes for target discrimination. Traditionally, discrimination hypotheses have been developed by examining how dolphins may be using temporal or spectral cues in received echo signals for target discriminations. Dubrovskiy and Krasnov (1971) suggested that dolphins discriminated spherical targets with different material compositions by difference in average oscillation period of the target echo frequency spectra. Au and Hammer (1980) and Hammer and Au (1980) suggested that dolphins may use time separation pitch cues to discriminate targets. Johnson *et al.* (1988) suggested that differences in the temporal order of the echo signals allow dolphins to perform discriminations. Furthermore, Au (1993) suggested that the use of short-time-frequency analysis may be a plausible method for target discrimination. Time-frequency approaches have shown potential for the discrimination of targets of various materials (Magand, 1996; Chevret *et al.*, 1996). Time-frequency processing takes advantage of resonance features of the targets to illustrate which echo signal characteristics contain information about the material composition of a spherical target. In a similar manner that these resonance features show the identifying characteristics of each target, it has been suggested that they may also supply them to a dolphin (Gaunaurd *et al.*, 1998). The echo signal features may allow a dolphin to extract target properties by inspection without any need for computation, and it has been claimed that this may be a possible explanation of how dolphins identify targets (Gaunaurd *et al.*, 1998).

During target discrimination tasks, dolphins operate in pulse mode, meaning they emit an echolocation click and receive the echo signal from the target before sending out another click. The lag time between emitted clicks is defined by the two-way transit time of an acoustic signal emitted by the dolphin to the target and back. The extra lag time may be to allow the animal to receive and process the echo signal (Moore and Finneran, 2004). It has been shown that dolphins can make broad changes in the spectral content of the emitted signals during discrimination tasks (Moore and Pawloski, 1990). Au (1993) argued that changes in the spectral composition of biosonar signals in a pulse train do occur and dolphins can adaptively adjust their sonar pulses to maximize

the information available in the echoes. Due to these changes in the frequency content of pulse trains and the corresponding echo trains, the time-frequency distributions of all types of echolocation signals must be considered. The goal of this study is to examine and compare the time-frequency representations of echolocation signals of targets of various material compositions to investigate whether a dolphin may use differences in time-frequency distributions as cues to perform discriminations. Furthermore, we investigate how changes in the emitted clicks may be advantageous to a dolphin during discrimination tasks.

This process can be divided into four steps. First, dolphin echolocation clicks were recorded in a controlled environment in Kaneohe Bay, Oahu, Hawai'i at the pen facility of the Marine Mammal Research Program. Second, the click signals were parametrized and clustered into classes based on spectral measurements and model-based clustering. Next, click signals from each class were introduced into an acoustic scattering model to obtain the desired echo signal for a specific target. Finally, the time-frequency distributions of the resulting signals were calculated and examined. Differences in time-frequency distributions between targets were quantified by using a time-frequency correlator. The information with respect to the discrimination hypothesis suggested by Gaunaurd *et al.* (1998) and the advantages of systematically altering emitted clicks when performing discrimination tasks were examined.

II. METHODS

A. Data collection

The dolphin echolocation clicks were collected from previously described phantom echolocation experiments (Muller *et al.*, 2007). The animal used in the experiments was a 21-year-old female *Tursiops truncatus*, born in the laboratory and used in a variety of echolocation experiments (e.g., Harley *et al.*, 1997; Aubauer *et al.*, 2000; Ibsen *et al.*, 2007). The clicks were recorded by a Brüel and Kjaer 8103 hydrophone with a flat frequency response (±3 dB) up to 120 kHz. The recorded clicks were amplified and sent to a Measurement Computing Corporation PCI-DAS4020/12 analog to digital input board, which digitized the signals at a sampling rate of 1 MHz. The clicks from both successful and nonsuccessful discrimination trials were collected.

B. Signal classification

Two common parameters used to characterize underwater acoustic signals are center frequency and root mean square (rms) bandwidth (Madsen and Wahlberg, 2007). The center frequency divides the energy of the click spectrum into two equal parts, so that the energy in the upper-frequency portion of the spectrum is equal to the energy in the lower-frequency portion. Center frequency may be a better descriptor of signals with bimodal spectra, such as dolphin echolocation clicks, than peak frequency (Au *et al.*, 1995). The center frequency of a signal $s(t)$ is defined as (Au, 1993)

$$f_0 = \langle f \rangle = \frac{\int_{-\infty}^{\infty} f|S(f)|^2 df}{\int_{-\infty}^{\infty} |S(f)|^2 df} = \frac{2}{E}\int_0^{\infty} f|S(f)|^2 df, \quad (1)$$

where $S(f)$ is the Fourier transform of $s(t)$ and E is the energy density of $s(t)$ given by

$$E = \int_{-\infty}^{\infty} |s(t)|^2 df = \int_{-\infty}^{\infty} |S(f)|^2 df. \quad (2)$$

The rms bandwidth (β) of a signal $s(t)$ is the root mean square of the band, in which the signal's Fourier transform is nonzero and is given by

$$\beta^2 = \frac{\int_{-\infty}^{\infty} (f - f_0)^2 |S(f)|^2 df}{\int_{-\infty}^{\infty} |S(f)|^2 df} = \frac{\int_{-\infty}^{\infty} f^2 |S(f)|^2 df}{\int_0^{\infty} |S(f)|^2 df} - f_0^2. \quad (3)$$

These parameters are calculated for the clicks and form the basis for the classification.

Au *et al.* (1995) classified false killer whale (*Pseudorca crassidens*) clicks into four categories based on the frequency spectra and center frequencies of the collected clicks. Houser *et al.* (1999) classified Atlantic bottlenose dolphin (*Tursiops truncatus*) clicks into seven categories by using a counterpropagation network based on the spectral conformation and relative position of the −3 and −10 dB peaks of the collected clicks. These previous studies provide an estimated range of categories where the collected clicks should be clustered. Model-based clustering which incorporates the Bayesian information criterion (BIC) (Schwarz, 1978) is used to categorize the collected clicks into the optimum number of clusters. In the model-based clustering, each cluster is represented by the Gaussian model,

$$\phi_k(\mathbf{x}|\mu_k, \Sigma_k) = (2\pi)^{-p/2}|\Sigma_k|^{-1/2} \times \exp\left[-\frac{1}{2}(\mathbf{x}_i - \mu_k)^T \Sigma_k^{-1}(\mathbf{x}_i - \mu_k)\right], \quad (4)$$

where $\mathbf{x}$ represents the data, k is an integer subscript specifying a particular cluster, and μ_k are the means at which each cluster is centered. The covariances Σ_k determine the geometric features of the clusters and each covariance matrix is parametrized by eigenvalue decomposition in the form

$$\Sigma_k = \lambda_k D_k A_k D_k^T, \quad (5)$$

where D_k is the orthogonal matrix of eigenvectors, A_k is a diagonal matrix whose elements are proportional to the eigenvalues of Σ_k, and λ_k is a scalar. The BIC is the value of the maximized log likelihood for a clustering model and the dimensions of the collected data. The BIC allows comparison of different clustering models with differing parametrizations and/or differing numbers of clusters. In general, the larger the value of the BIC, the stronger the evidence for the clustering model and number of clusters (Fraley and Raftery, 2002); i.e., the BIC will provide the optimum number of classes of clicks based on the collected click data. A MATLAB program was utilized to calculate the optimum number of click clusters by using four different models.

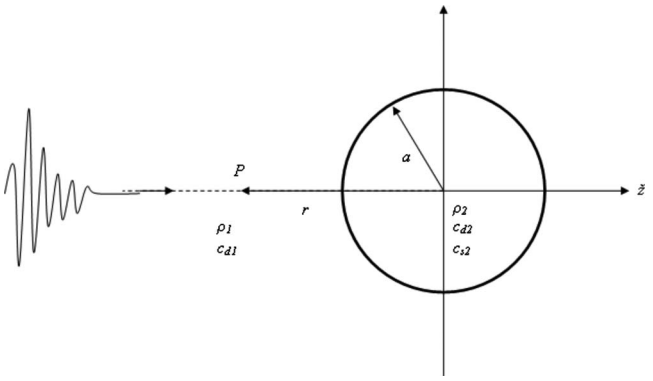

FIG. 1. Geometric setup for an echolocation click incident upon a solid, homogeneous elastic sphere.

C. Acoustic scattering model

In order to calculate the backscattered signals of interest, a model is used to obtain the echo signals of the dolphin clicks from targets of various materials. An advantage of this model is any backscattered wave form can be calculated by using any combination of dolphin echolocation click, target, and fluid medium. The algorithm is for solid, elastic homogeneous spheres in saltwater following the work of Brill *et al.* (1991). That work is extended to incorporate broadband pulses, such as dolphin echolocation clicks, and to test the robustness with an experimental comparison of backscattered spectra.

Consider a dolphin echolocation pulse incident upon an isotropic sphere, as shown in Fig. 1, where a is the radius of the sphere, ρ_1 is the density of the surrounding fluid, c_{d1} is the dilatational sound velocity of the surrounding fluid, ρ_2 is the density of the sphere, and c_{d2} and c_{s2} are the dilatational and shear sound velocities of the sphere, respectively. The far-field backscattered pressure $p_{sc}(\tau)$ at a point P at a distance r from the center of the sphere is given by (Brill *et al.*, 1991)

$$rp_{sc}(\tau) = \frac{1}{2\pi}\int_{-\infty}^{+\infty}[f_\infty(\pi,x)G(x)]e^{-ixt}dx, \tag{6}$$

where $G(x)$ is the spectrum of the incident pulse calculated by using a Fourier transform. The form function $f_\infty(\pi,x)$ describes the distribution of the scattered pressure field in a given direction in the far field as a function of frequency as given below,

$$f_\infty(\pi,x) = \sum_{n=0}^{\infty} f_n(\pi,x),$$

$$f_n(\pi,x) = \frac{a}{ix}(-1)^n(2n+1)T_n(x). \tag{7}$$

$T_n(x)$ are the determinant ratios,

TABLE I. Elastic parameters of the spheres.

Material	Density ρ (g/cc)	Dilatational velocity c_{d2} (m/s)	Shear velocity c_{s2} (m/s)
Steel	7.70	6100	5050
Brass	8.60	4700	2110
Iron	7.70	5960	3240
Lead	11.34	1960	690

$$T_n(x) = \frac{\begin{vmatrix} Red_{11} & d_{12} & d_{13} \\ Red_{21} & d_{22} & d_{23} \\ 0 & d_{32} & d_{33} \end{vmatrix}}{\begin{vmatrix} d_{11} & d_{12} & d_{13} \\ d_{21} & d_{22} & d_{23} \\ 0 & d_{32} & d_{33} \end{vmatrix}}, \tag{8}$$

for elements d_{ij}, which are combinations of the spherical Bessel functions evaluated at the sphere's surface and are given elsewhere (Brill and Gaunaurd, 1987). Echo signals are calculated for clicks incident upon steel, brass, iron, and lead spheres with elastic constants given in Table I. The density and dilatational sound velocity for the surrounding media, seawater, are estimated as $\rho = 1.12$ g/cc and $c_{d1} = 1502$ m/s, respectively.

The results obtained from the algorithm are compared to experimentally obtained results. In the frequency domain, the echo spectrum $E_t(\omega)$ can be calculated by convolution of a target transfer function $H(\omega)$ and the spectrum of any incident click $S_t(\omega)$ (Aubauer and Au, 1998),

$$E_t(\omega) = H(\omega)\cdot S_t(\omega). \tag{9}$$

The transfer function $H(\omega)$ has previously been obtained experimentally for a hollow water-filled steel sphere, a solid steel sphere, and a solid brass sphere (Aubauer *et al.*, 2000). The spectra obtained from the scattering model are compared to spectra calculated from the experimentally obtained target transfer function for clicks from each class incident upon a solid steel sphere, which was used as the standard target in previous experiments (Ibsen *et al.*, 2007; Muller *et al.*, 2007) and was used as the standard target here.

E. Time-frequency analysis

A time-frequency analysis technique, which provides simultaneous high resolution in the frequency and temporal domains, is the reduced interference distribution (RID). The RID(t,ω), with kernel $R_x(t,\tau)$, is based on a signal $s(t)$ with analytic associate $x(t)$ given by (Williams and Jeong, 1992)

$$\mathrm{RID}(t,\omega) = \int_{-\infty}^{\infty} h(\tau)R_x(t,\tau)e^{-i\omega\tau}d\tau. \tag{10}$$

The RID is in the same family as the Wigner–Ville distribution (Cohen, 1995) but with the introduction of a smoothing window $h(\tau)$. The RID diminishes cross-term interferences which are commonly observed with the Wigner–Ville distribution (WVD). The advantages of the RID over the WVD have been shown for biomedical and biological signal analysis (Williams, 1996). The RID with a Bessel smoothing win-

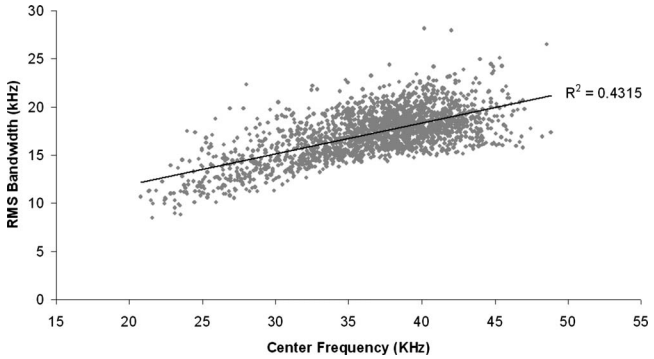

FIG. 2. Scatter plot of root-mean-square bandwidth vs center frequency of the collected clicks.

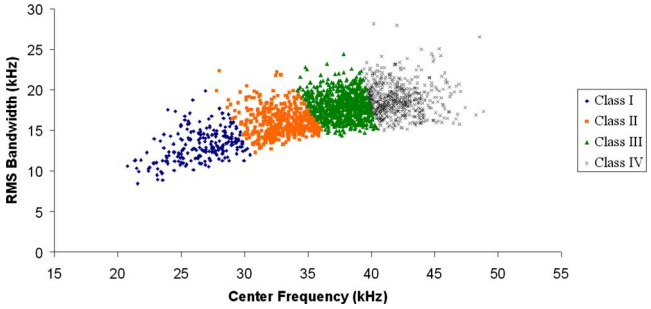

FIG. 4. (Color online) Scatter plot of the data presented in Fig. 2 clustered into four classes.

dow is applied to the echolocation signals in order to obtain high resolutions in the frequency and temporal domains simultaneously while eliminating cross-term interferences.

The features of the reduced interference distribution of the dolphin echolocation signals can be denoted as E_{ij}, where i refers to the energy in the ith frequency bin within the jth time bin. The locally optimum detector is a time-frequency correlator (Altes, 1980), which computes the quantity

$$l(e) = \sum_{i=1}^{N} \sum_{j=1}^{M} E_{ij} E_{ij}(k). \tag{11}$$

From Eq. (11), the probability $l(e)$ of misclassification between a standard echo and a comparison echo can be determined by using all the features of the signals. Boashash and Shea (1988 and 1990) used a similar time-frequency correlator for detection and classification of underwater acoustic signals. The time-frequency correlations between the standard and comparison targets for the different echo classes are reported.

III. RESULTS

Figure 2 shows the scatter plot of rms bandwidth versus center frequency of 2077 clicks. Based on the BIC, the optimum number of categories in which to group the clicks is 4 (Fig. 3). Figure 4 displays the click data clustered into the four classes. A summary of the different types of click signals is given in Table II, including the percentage of time each different click occurred, average peak-to-peak source level (sound-pressure level referenced to a distance of 1 m in front of the dolphin), center frequency, and rms bandwidth. Class I clicks are narrowband and have a single peak at low frequencies typically below 50 kHz. Class II clicks have a primary peak at low frequencies (below 50 kHz) and a secondary peak at frequencies above 50 kHz with an amplitude at a fraction of the primary peak. Class III clicks have two peaks, with approximately equal amplitudes, one below 50 kHz and one above 50 kHz. Class IV clicks are broadband and have a single peak at frequencies above 50 kHz. Representative click signals falling in the various classes are shown in Fig. 5. The four classes are similar to those reported by Au *et al.* (1995), and the source level follows the same pattern; the lowest source level corresponds to class I clicks and the highest source level corresponds to class IV clicks.

Figure 6 displays the signal wave form and respective normalized frequency spectrum for echo signals calculated by using the scattering algorithm for a click from each of the four classes, incident upon a steel sphere. Figures 7(a)–7(d) shows the comparison between echo spectra calculated from the scattering model and echo spectra calculated by using the

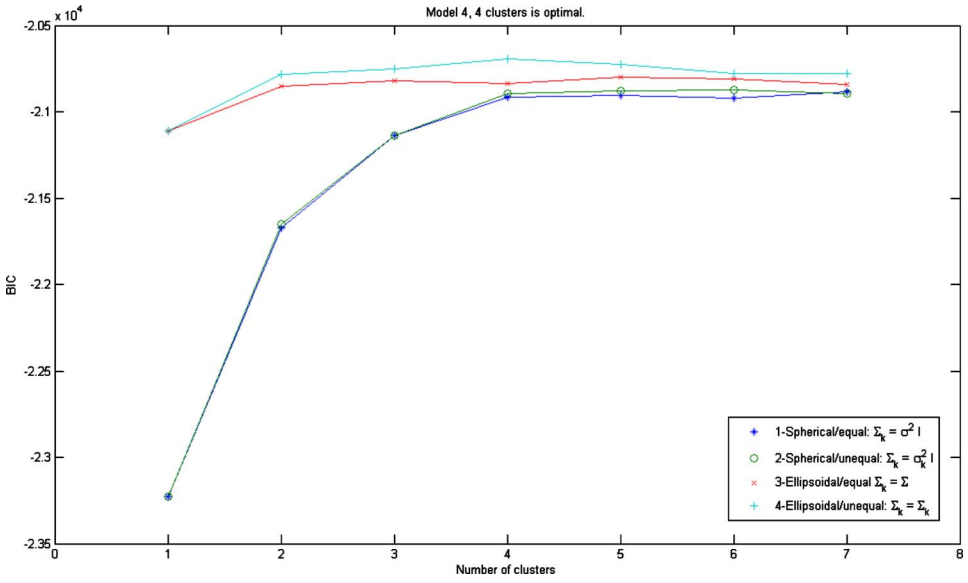

FIG. 3. (Color online) Bayesian information criterion vs number of clusters of four clustering models. The data suggest that four clusters are optimal.

TABLE II. Summary of average click signal characteristics: SL=peak-to-peak source level in dB (1 μPa), f_c=center frequency, and BW_{rms}=root-mean-square bandwidth.

Click class	%	SL (dB)	f_c (kHz)	BW_{rms} (kHz)
I	10.7	194.8 ± 5.8	26.59 ± 2.16	13.18 ± 1.94
II	22.5	196.5 ± 5.5	33.06 ± 1.71	15.99 ± 1.61
III	39.5	201.1 ± 3.9	37.00 ± 1.38	18.05 ± 1.38
IV	27.3	208.7 ± 2.8	42.15 ± 1.71	18.85 ± 1.98

experimentally obtained transfer function for each class. The correlation coefficients between the theoretical and experimental spectra for each respective class are (a) 0.9130, (b) 0.8828, (c) 0.8434, and (d) 0.9149. Figures 8–11 display plots of the RIDs of the echo signatures returned by a steel, brass, iron, and lead spheres respectively, for each of the four classes of echolocation signals. Table III shows the RID correlation values for a steel sphere versus each comparison target for each class of echolocation signal.

IV. DISCUSSION

The dolphin utilized a variety of types of echolocation clicks while performing discrimination tasks during phantom

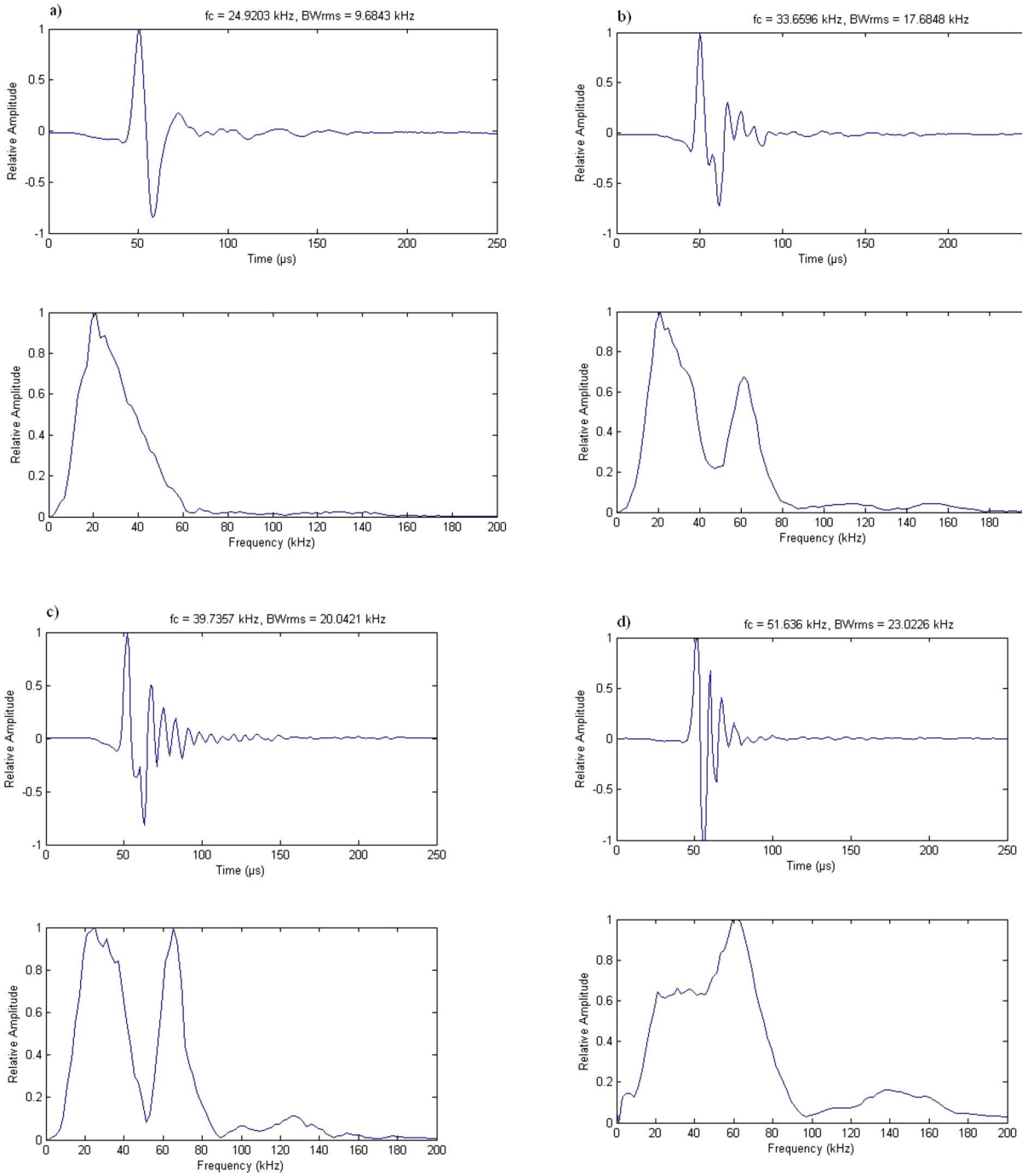

FIG. 5. (Color online) Examples of the different click types emitted by the dolphin: (a) class I, (b) class II, (c) class III, and (d) class IV. The signal wave form is shown above the respective normalized frequency spectrum. Above the wave forms are the center frequency and rms bandwidth measurements.

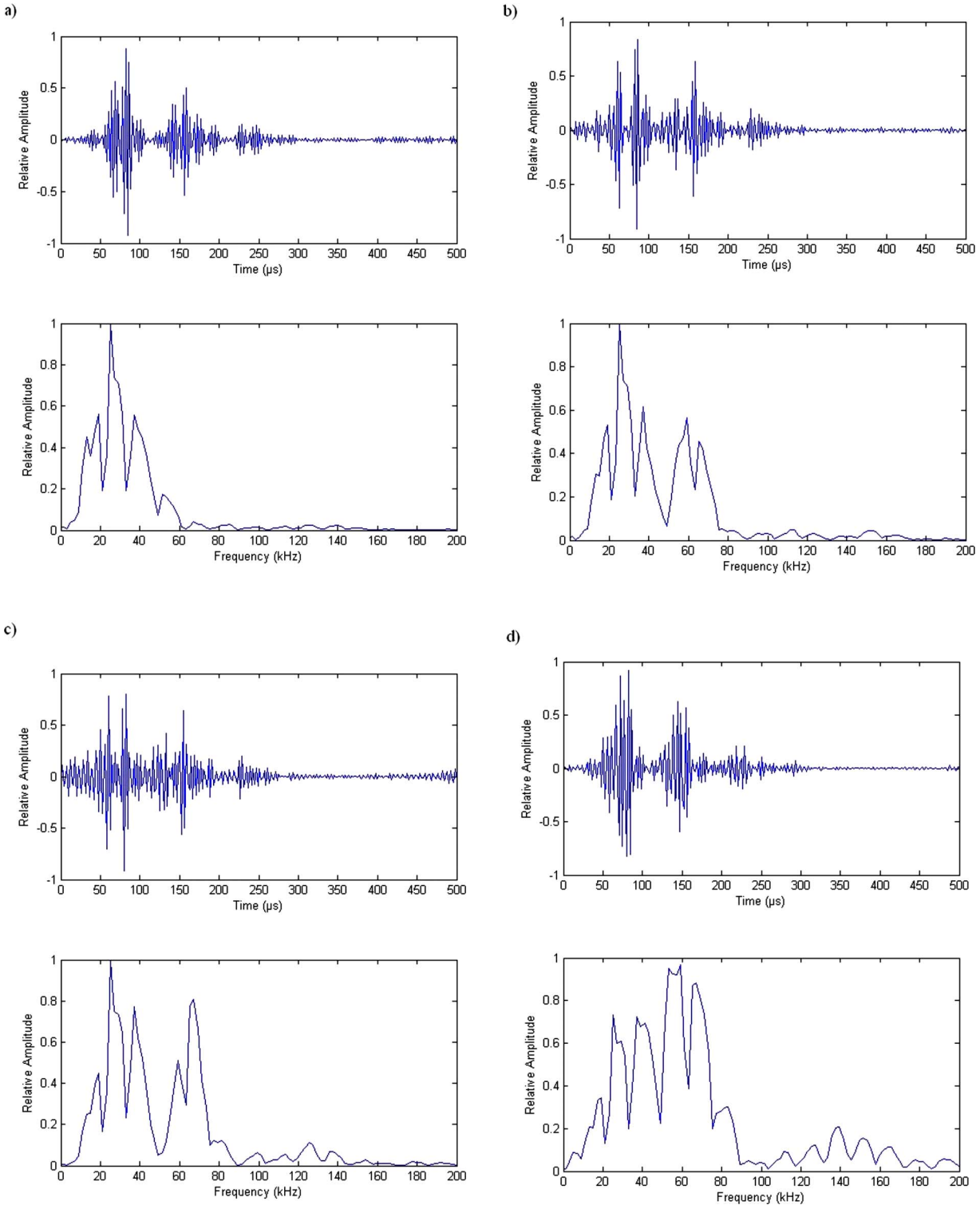

FIG. 6. (Color online) Examples of the different echo signals calculated from clicks from each of the four classes by using the scattering algorithm; (a) class I, (b) class II, (c) class III, and (d) class IV. The signal wave form is shown above the respective normalized frequency spectrum.

echolocation experiments. The echolocation clicks were categorized into four classes based on spectral measurements of the clicks and model-based clustering. Model-based clustering by using the BIC provides an alternative and a mathematical method to categorize clicks.

The acoustic scattering model produced echo signals that correlated highly with experimentally obtained echo signals. The algorithm is a model for obtaining the echo signatures and spectra for any pulse incident upon a solid, isotropic sphere. The algorithm can easily be expanded to include other targets such as solid cylinders and hollow or material-filled spheres and cylinders. The model could improve phantom echolocation experiments by eliminating the need to experimentally predetermine the transfer function for each desired target.

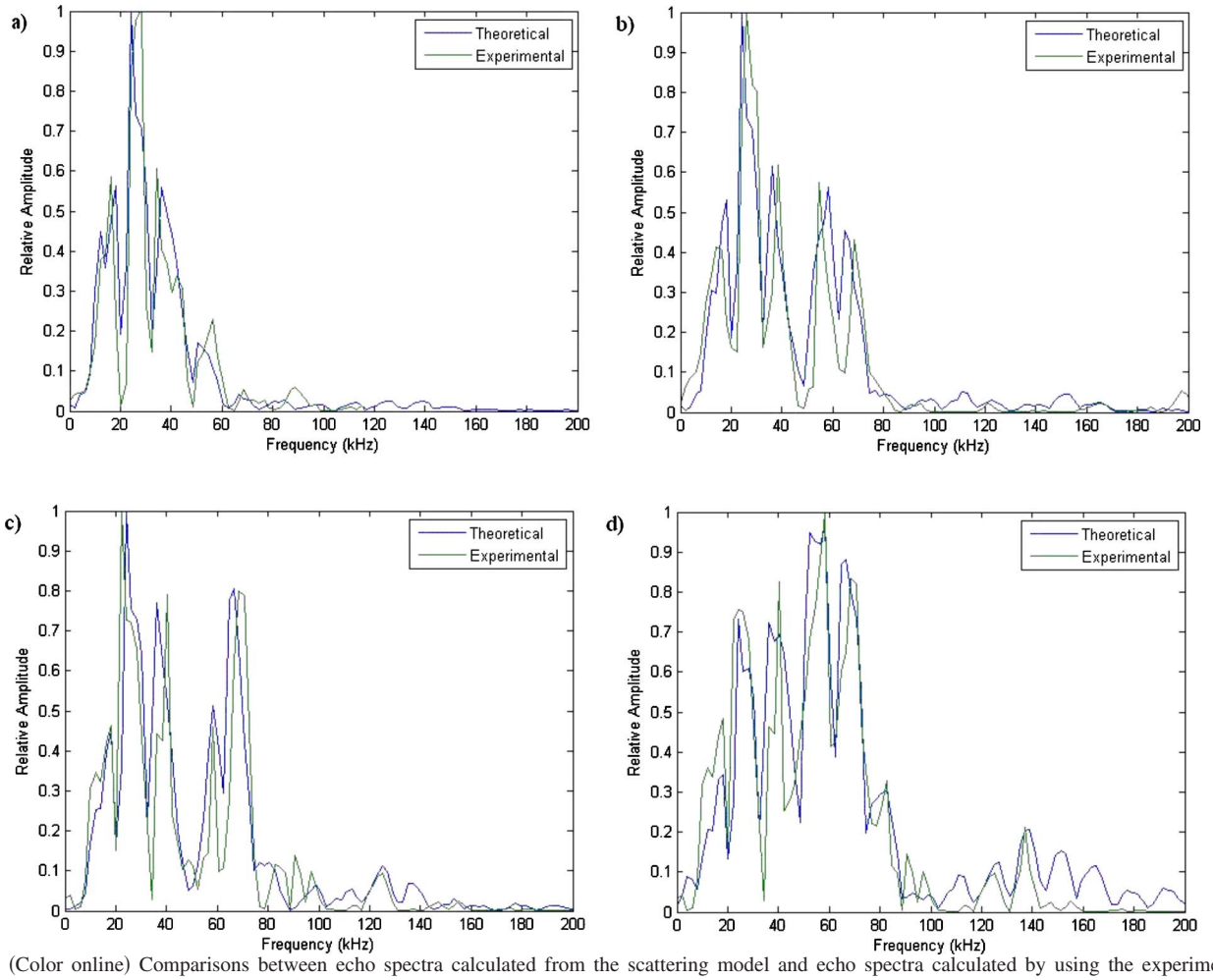

FIG. 7. (Color online) Comparisons between echo spectra calculated from the scattering model and echo spectra calculated by using the experimentally obtained transfer function for each class: (a) class I, (b) class II, (c) class III, and (d) class IV.

Since scattering of a pulse from an elastic sphere has been the subject of previous studies (Goodman and Stern, 1962; Vogt and Neubauer, 1976; Yen *et al.*, 1990), some results pertinent to the dolphin clicks are discussed. The first highlight in the time-frequency plot represents the specular reflection, the second highlight that appears later in time represents the internal reflection, and the third highlight that appears after the second highlight represents the circumferential wave (Yen *et al.*, 1990). The magnitude of the specular reflection is related to the reflectivity of the sphere due to the acoustic impedance difference with the surrounding medium. As density of the material increases, the differences in the acoustic impedances increase; the reflectivity which is proportional to the acoustic impedance increases, thus causing the intensity of the second highlight to decrease. However, it is noted in the time-frequency plots that the intensity of the secondary highlight of the brass (Fig. 9) has a greater intensity than the secondary highlight of the steel (Fig. 8), even though brass has a greater material density. This follows from the strong excitation of specific resonances of the brass sphere by the incident dolphin clicks. An examination of the form function for the brass sphere reveals that a frequency component from the clicks is nearly coincident with the second (2|1) resonance mode. The echo signals from a lead sphere (Fig. 11) reveal significant energy at higher frequencies compared to the other targets. This is due to the upper-frequency portion of the incident clicks corresponding to minima in the form function of a lead sphere, thus resulting in excitation of higher order vibratory modes.

An efficient method to discriminate targets is accomplished by analyzing the echo signatures in the joint time-frequency domain by using advanced signal processing techniques such as the reduced interference distribution. The RID plots reveal the differences between the time-frequency representations of the echo signatures of the various spherical targets which indicate that the dolphin's discriminations may be accomplished with the use of this time-frequency information. A more extensive analysis of the time-frequency representation encompassing reduction is the subject of ongoing studies. Even when the RID plots appear to be similar, such as for classes I and IV of the steel spherical target and the iron spherical target [Figs. 8(a), 8(d), 10(a), and 10(d)], examination of the relative intensity of the second and third highlights of classes III and IV [Figs. 8(b), 8(c), 10(b), and 10(c)] reveals that the RID of the steel target has a greater secondary highlight intensity than the iron sphere. The steel and iron targets can be differentiated by examining the differences in relative highlight intensities of the echo signals. This difference may be what the dolphin uses to successfully perform the discrimination, as it has been experimentally shown that dolphins can successfully discriminate between similar echo signals varying only in relative amplitudes of

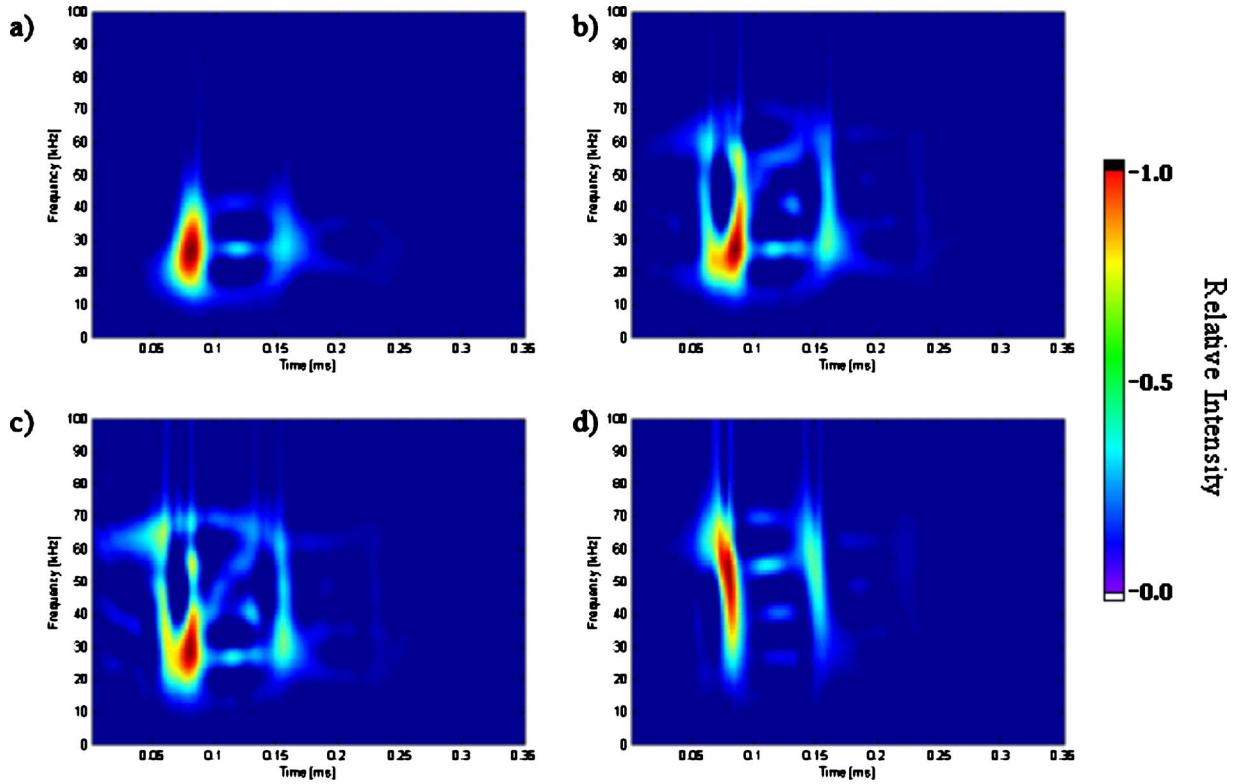

FIG. 8. (Color online) RIDs of the echo signature returned by a steel sphere for each of the four classes of clicks; (a) class I, (b) class II, (c) class III, and (d) class IV.

secondary echo highlights (Muller *et al.*, 2007). This also shows the advantages of systematically changing clicks in a click train during discrimination tasks; e.g., certain clicks return similar echoes for a standard and comparison targets while other clicks used in the same click train return different echoes for the same standard and comparison targets. This approach is one way to scientifically explain the success of dolphin discrimination performance. However, the exact

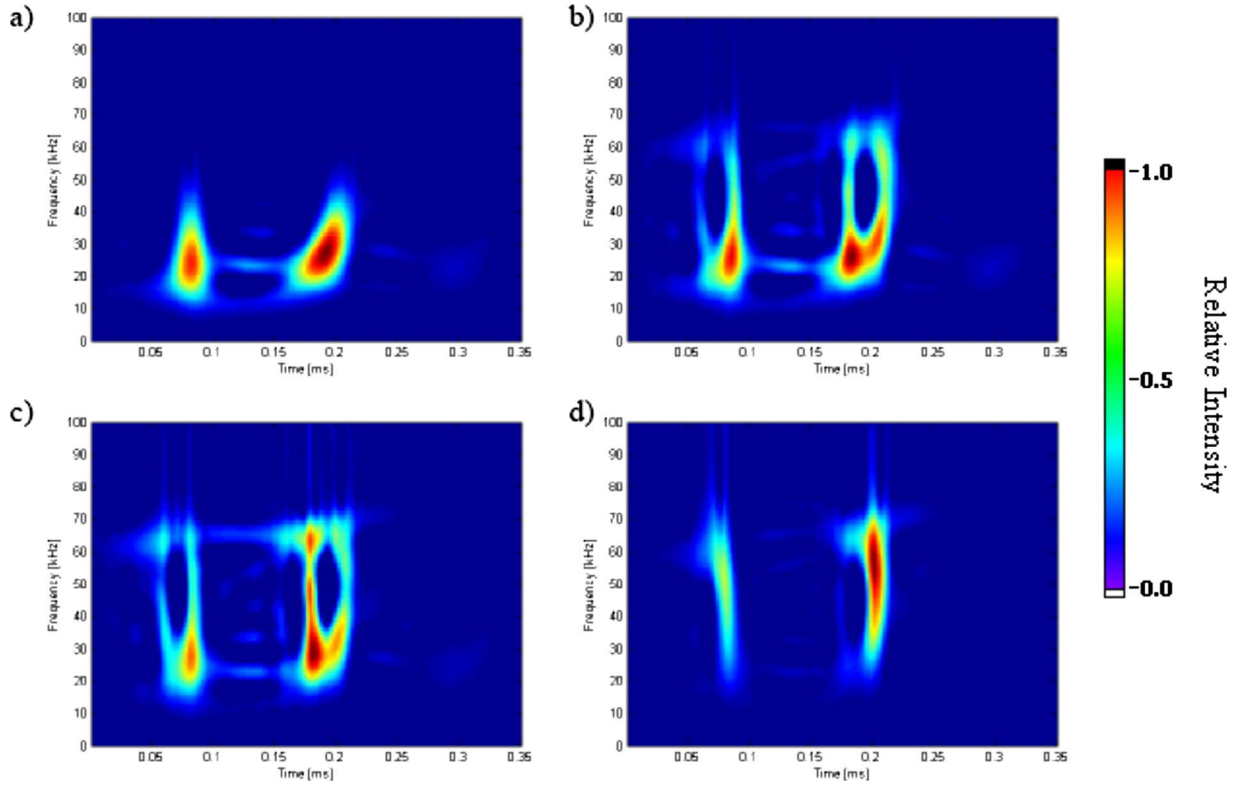

FIG. 9. (Color online) RIDs of the echo signature returned by a brass sphere for each of the four classes of clicks; (a) class I, (b) class II, (c) class III, and (d) class IV.

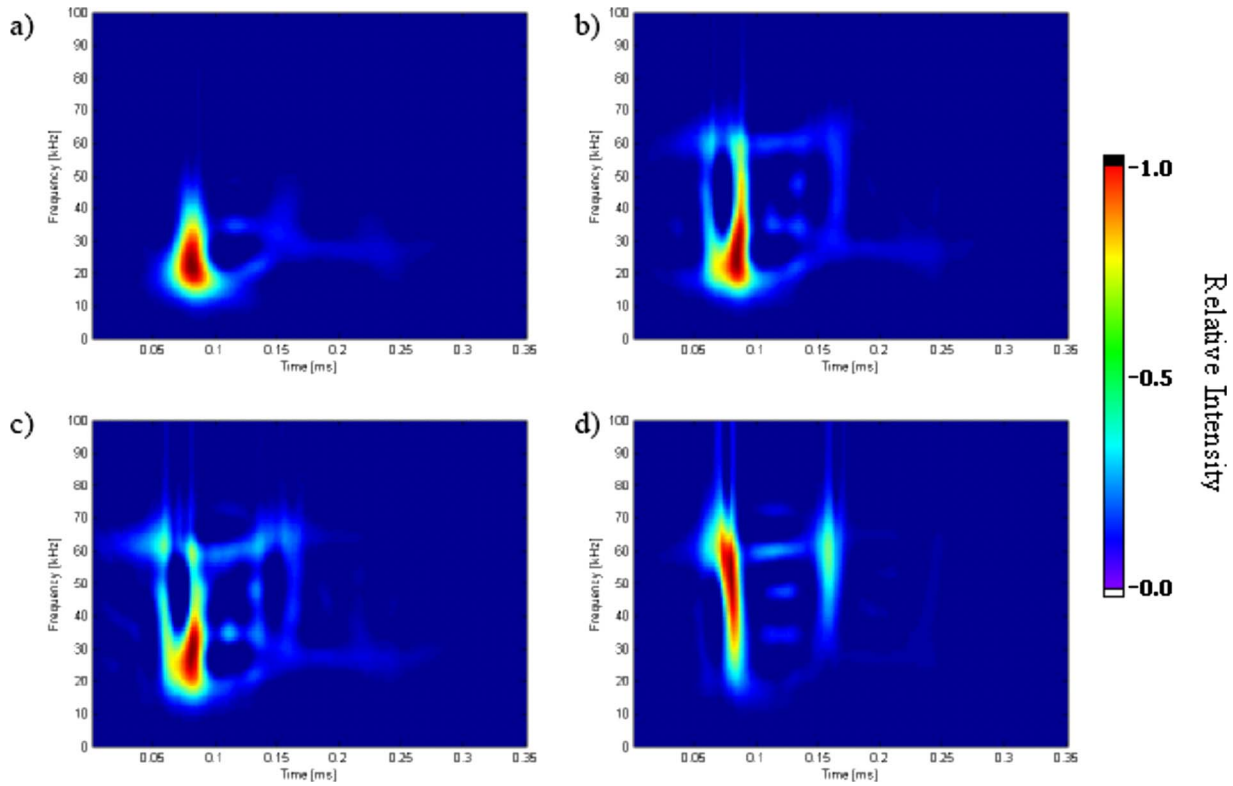

FIG. 10. (Color online) RIDs of the echo signature returned by an iron sphere for each of the four classes of clicks; (a) class I, (b) class II, (c) class III, and (d) class IV.

physiological or neuronal mechanisms that the dolphin may be using to discriminate targets are not considered here and are important for understanding dolphin sonar.

The time-frequency correlation values provide a quantitative method at examining the differences in the RIDs of the echo signals. The correlation coefficients may suggest that if

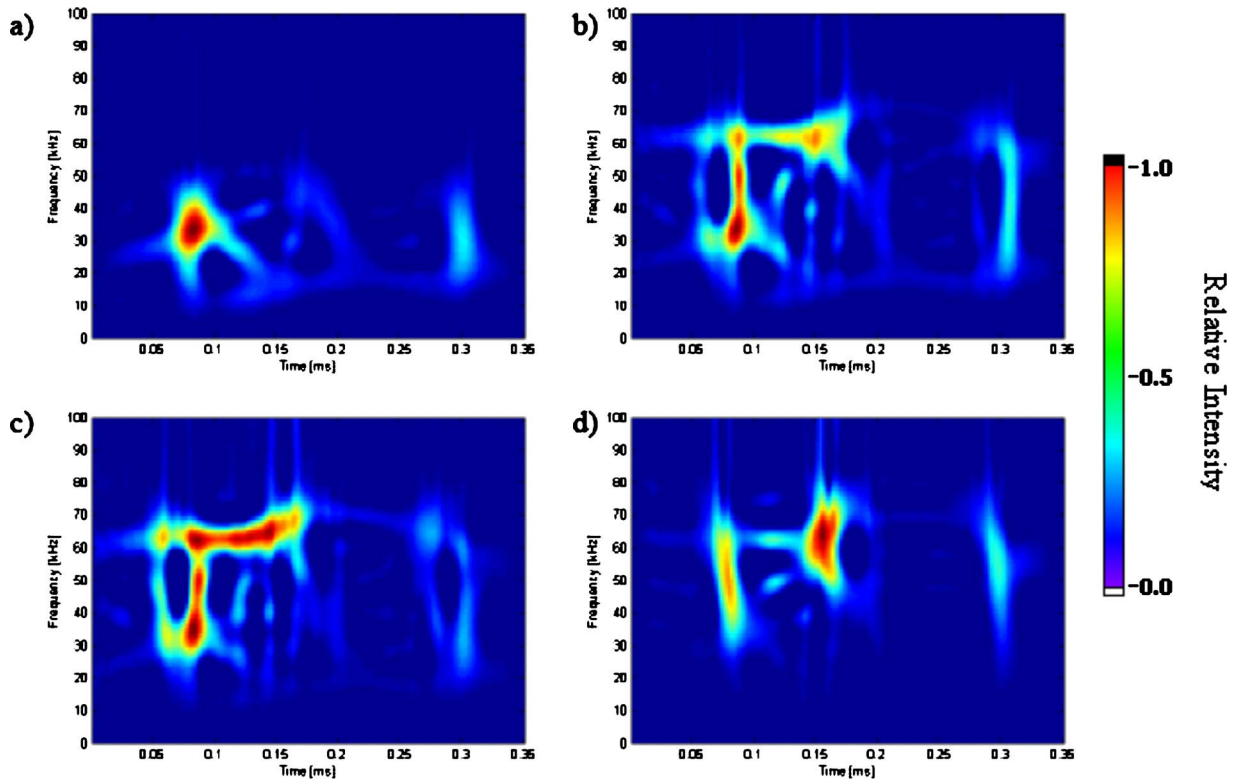

FIG. 11. (Color online) RIDs of the echo signature returned by a lead sphere for each of the four classes of clicks; (a) class I, (b) class II, (c) class III, and (d) class IV.

TABLE III. RID correlation values of the standard target (steel sphere) vs the comparison targets.

	Class I	Class II	Class III	Class IV
Steel vs brass	0.5858	0.5352	0.4789	0.4273
Steel vs iron	0.8055	0.8019	0.7566	0.7996
Steel vs lead	0.6344	0.4843	0.4785	0.4964

the dolphin is using time-frequency differences as cues for discrimination, the dolphin may use the lower frequency, narrower band class I clicks to locate a target and may be using the class IV clicks to ascertain more information about the target, as the higher frequency and broader band signals would provide more resolution. The results here support the hypothesis first suggested by Gaunaurd *et al.* (1998) that dolphins may discriminate by auditory inspection of the time-frequency information returned by the targets. Dolphins also alter their outgoing echolocation clicks to possibly provide different time-frequency information for a target which, based on the data presented here, would ultimately aid in a discrimination task (Moore, 1988). A dolphin altering outgoing clicks and using time-frequency target information may be the fundamental physical explanation of the dolphin's target identification and discrimination abilities.

ACKNOWLEDGMENTS

We thank the personnel of the Marine Mammal Research Program at the Hawai'i Institute of Marine Biology. We also thank Jason Wood for his assistance with model-based clustering. This research was approved by the University of Hawai'i Institutional Animal Care and Utilization Committee Protocol No. 93-005-13, U.S. NMFS Office of Protected Species Marine Mammal Permit No. 978-1567-02, and funded by the U.S. Office of Naval Research Grant No. N00014-05-1-0738 to P.E. Nachtigall.

Altes, R. A. (**1980**). "Models for echolocation," in *Animal Sonar Systems*, edited by R. G. Busnel and J. F. Fish (Plenum, New York), pp. 625–671.

Au, W. W. L. (**1993**). *The Sonar of Dolphins* (Springer-Verlag, New York).

Au, W. W. L., and Hammer, C. E. (**1980**). "Target recognition via echolocation by *Tursiops truncatus*," in *Animal Sonar Systems*, edited by R. G. Busnel and J. F. Fish (Plenum, New York), pp. 855–858.

Au, W. W. L., Moore, P. W. B., and Pawloski, D. A. (**1988**). "Detection of complex echoes in noise by an echolocating dolphin," J. Acoust. Soc. Am. **83**, 662–668.

Au, W. W. L., Pawloski, J. L., Nachtigall, P. E., Blonz, M., and Gisner, R. C. (**1995**). "Echolocation signals and transmission beam pattern of a false killer whale (*Pseudorca crassidens*)," J. Acoust. Soc. Am. **98**, 51–59.

Aubauer, R., and Au, W. W. L. (**1998**). "Phantom echo generation: A new technique for investigating dolphin echolocation," J. Acoust. Soc. Am. **104**, 1165–1170.

Aubauer, R., Au, W. W. L., Nachtigall, P. E., Pawloski, D. A., and DeLong, C. M. (**2000**). "Classification of electronically generated phantom targets by an Atlantic bottlenose dolphin (*Tursiops truncatus*)," J. Acoust. Soc. Am. **107**, 2750–2754.

Boashash, B., and Shea, P. (**1988**). "Time-frequency analysis applied to signaturing of underwater acoustic signals," in *IEEE Proceedings, International Conference on Acoustics, Speech, and Signal Processing*, Vol. **35**, pp. 2817–2820.

Boashash, B., and Shea, P. (**1990**). "Methodology for detection and classification of underwater acoustic signals using time-frequency analysis techniques," IEEE Trans. Acoust., Speech, Signal Process. **38**, 1829–1841.

Brill, D., and Gaunaurd, G. (**1987**). "Resonance theory of elastic waves ultrasonically scattered from an elastic sphere," J. Acoust. Soc. Am. **81**, 1–21.

Brill, D., Gaunaurd, G., Strifors, H., and Wertman, W. (**1991**). "Backscattering of sound pulses by elastic bodies underwater," Appl. Acoust. **33**, 87–107.

Chevret, P., Magand, F., and Besacier (**1996**). "Time-frequency analysis of circumferential wave energy distribution for spherical shells. Application to sonar target recognition," Appl. Signal Processing **3**, 136–142.

Cohen, L. (**1995**). *Time-Frequency Analysis* (Prentice-Hall, New York).

Dubrovskiy, N. A., and Krasnov, O. S. (**1971**). "Discrimination of elastic spheres according to material and size by the bottlenose dolphin," Tr. Akust. Inst., Moscow **17**, 9–18.

Fraley, C., and Raftery, A. E. (**2002**). "Model-based clustering, discriminant analysis, and density estimation," J. Am. Stat. Assoc. **97**, 611–631.

Gaunaurd, G. C., Brill, D., Huang, H., Moore, P. W. B., and Strifors, H. C. (**1998**). "Signal processing of the echo signatures returned by submerged shells insonified by dolphin "clicks:" Active classification," J. Acoust. Soc. Am. **103**, 1547–1557.

Goodman, R. R., and Stern, R. (**1962**). "Reflection and transmission of sound by elastic spherical shells," J. Acoust. Soc. Am. **34**, 338–344.

Hammer, C. E., and Au, W. W. L. (**1980**). "Porpoise echo-recognition: An analysis of controlling target characteristics," J. Acoust. Soc. Am. **68**, 1285–1293.

Harley, H., Roitblat, H. L., and Nachtigall, P. E. (**1997**). "Object representation in the bottlenosed dolphin (*Tursiops truncatus*): Integration of visual and echoic information," J. Exp. Psychol. Anim. Behav. Process **22**(2), 164–174.

Houser, D. S., Helweg, D. A., and Moore, P. W. (**1999**). "Classification of dolphin echolocation clicks by energy and frequency distributions," J. Acoust. Soc. Am. **106**, 1579–1585.

Ibsen, S. D., Au, W. W. L., Nachtigall, P. E., DeLong, C. M., and Breese, M. (**2007**). "Changes in signal parameters over time for an echolocating Atlantic bottlenose dolphin performing the same target discrimination task," J. Acoust. Soc. Am. **122**, 2446–2450.

Johnson, R. A., Moore, P. W. B., Stoermer, M. W., Pawloski, J. L., and Anderson, C. C. (**1988**). "Temporal order discrimination within the dolphin critical interval," in *Animal Sonar: Processes and Performance*, edited by P. E. Nachtigall and P. W. B. Moore (Plenum, New York), pp. 317–321.

Madsen, P. T., and Wahlberg, M. (**2007**). "Recording and quatification of ultrasonic echolocation clicks from free-ranging toothed whales," Deep-Sea Res., Part II **54**, 1421–1444.

Magand, F. (**1996**). "Reconnaissance de cibles par sonar actif large bande. Application a des coques de forme simple et a la classification de especes de poisons en mer," English translation "Decibel reconnaissance of broadband active sonar. Application to simple shell shapes and to the classification of fish species at sea," Ph.D. thesis, INSA Lyon, Lyon, France.

Moore, P. W. (**1988**). "Dolphin Echolocation and Audition," in *Animal Sonar, Processes and Performance*, edited by P. E. Nachtigall and P. W. B. Moore (Plenum, New York), pp. 161–168.

Moore, P. W., and Finneran, J. (**2004**). "Hearing loss and echolocation signal change in dolphins," J. Acoust. Soc. Am. **116**, 2503.

Moore, P. W. B., and Pawloski, D. (**1990**). "Investigation of the control of echolocation pulses in the dolphin (*Tursiops truncatus*)," in *Cetacean Sensory Systems: Field and Laboratory Evidences*, edited by J. A. Thomas and R. A. Kasterlein (Plenum, New York), pp. 305–316.

Muller, M. W., Au, W. W. L., Nachtigall, P. E., Allen, J. S., and Breese, M. (**2007**). "Phantom echo highlight amplitude and temporal difference resolutions of an echolocating dolphin, *Tursiops truncatus*," J. Acoust. Soc. Am. **122**, 2255–2262.

Nachtigall, P. E. (**1980**). "Odontocete Echolocation Performance on Object size, Shape, and Material," in *Animal Sonar Systems*, edited by R. G. Busnel and J. F. Fish (Plenum, New York).

Schwarz, G. (**1978**). "Estimating the dimension of a model," Ann. Stat. **6**, 461–464.

Vogt, R. H., and Neubauer, W. G. (**1976**). "Relationship between acoustic reflection and vibrational modes of elastic spheres," J. Acoust. Soc. Am. **60**, 15–22.

Williams, W. J. (**1996**). "Reduced interference distributions: biological applications and interpretations," Proc. IEEE **84**, 1264–1280.

Williams, W. J., and Jeong, J. (**1992**). *Time-Frequency Analysis*, edited by B. Boashash (Longmans, New York).

Yen, N., Dragonette, L. R., and Numrich, S. K. (**1990**). "Time-frequency analysis of acoustic scattering from elastic objects," J. Acoust. Soc. Am. **87**, 2359–2370.

Detection of targets colocalized in clutter by big brown bats (*Eptesicus fuscus*)

Sarah A. Stamper,[a] James A. Simmons, Caroline M. DeLong, and Rebecca Bragg
Department of Neuroscience, Brown University, Box GL-N, Providence, Rhode Island 02912

(Received 19 July 2007; revised 29 April 2008; accepted 30 April 2008)

Echolocating big brown bats (*Eptesicus fuscus*) frequently catch insects during aerial pursuits in open spaces, but they also capture prey swarming on vegetation, and from substrates. To evaluate perception of targets on cluttered surfaces, big brown bats were trained in a two-alternative forced-choice task to locate a target, varying in height, that was embedded partway in holes (clutter) cut in a foam surface. The holes were colocalized with the possible positions of the target at distances ranging from 25 to 35 cm. For successful perception of the target, the bat had to detect the echoes contributed by the target in the same time window that contained echoes from the clutter. Performance was assessed in terms of target reflective strength relative to clutter strength in the same time window. The bats detected the target whenever the target strength was greater than 1–2 dB above the clutter. © *2008 Acoustical Society of America.* [DOI: 10.1121/1.2932338]

PACS number(s): 43.80.Lb, 43.80.Ka, 43.66.Gf, 43.64.Bt [MCH] Pages: 667–673

I. INTRODUCTION

Big brown bats (*Eptesicus fuscus*) emit frequency-modulated (FM) sonar sounds in the 20–100 kHz band (Saillant *et al.*, 2007; Surlykke and Moss, 2000) and locate prey from echoes that return to their ears (Neuweiler, 2000). They are often observed flying in the evening in pursuit of insects, capturing prey in aerial interception maneuvers guided by echolocation (Fenton, 1995; Griffin, 1958). Video recordings made with thermal-imaging cameras document that these bats are able to successfully catch insects in flight (Simmons, 2005). However, the same infrared video recordings reveal that big brown bats can also capture beetles from vegetation and sometimes even land on the ground to seize prey (Simmons, 2005; Simmons *et al.*, 2001). Some kinds of insects taken as prey by big brown bats, such as crickets or katydids, are not commonly observed to fly at night and presumably must be taken from substrates such as the ground or vegetation (Fullard *et al.*, 2005; Kurta and Baker, 1990).

Beetles swarming in vegetation make buzzing sounds that are audible to bats (Hamr and Bailey, 1985), and crickets and katydids communicate with each other acoustically, in both cases providing bats with potential cues for passive hearing to detect and localize prey. However, when gleaning prey from clutter or substrates, the bat's actual approach and certain details of capture must be guided by some contribution from echolocation, if only to avoid collisions with vegetation or the substrate itself, and under these conditions the bats continue to emit echolocation sounds (Fullard *et al.*, 2005; Ratcliffe *et al.*, 2005; Schmidt, *et al.*, 2000). The presence of targets on surfaces or in vegetation creates a complex acoustic scene with echoes from the target and from the clutter competing to be perceived (Moss and Surlykke, 2001; Ratcliffe and Dawson, 2003). Bats that make use of sounds produced by their prey face a more tractable task than if the prey were silent, but they still have to maneuver in the clutter or approach the ground using echoes to guide their flight. For example, echoes from the ground arrive at nearly the same time as echoes from insects resting on the ground, which makes detecting the target difficult, although a grazing approach to the ground could minimize these cluttering reflections.

Insects in vegetation often are smaller than the leaves themselves so the clutter echoes are often more intense than the target, while also being located within the same time window. Among species of bats that pursue insects in aerial interception maneuvers, most species emit sounds with only one or two harmonics (Fenton, 1995). In contrast, bats that frequently hunt for prey or search for fruit in vegetation typically emit wideband FM sounds that contain three to five harmonic sweeps (Fenton, 1995; Schnitzler *et al.*, 2003; Simmons *et al.*, 1979). Big brown bats are unusual among aerial-feeding insectivorous bats in emitting sonar sounds that contain multiple harmonics, even when closing in to complete an aerial interception (Saillant *et al.*, 2007). The prevalence of harmonics in the sounds combined with the evidence that these bats take prey from surfaces raises the possibility that big brown bats capture insects in clutter more than is realized.

It is important to distinguish between the completions of aerial interceptions of flying insects close to background objects from the capture of prey that rest or swarm on leaves or the ground (Schnitzler *et al.*, 2003; see video clips in Simmons *et al.*, 2001 and Simmons, 2005). In laboratory tests, free-flying insectivorous bats (five species of *Myotis*) were able to capture insects presented at varying distances (5–50 cm) from a clutter screen that was designed to mimic the edge of vegetation (Siemers and Schnitzler, 2004). At distances of 25–50 cm, the capture success rate was almost 100%. The minimum distance from the insect to the clutter that still allowed for successful captures varied from 5 to 10 cm across species. In a similar experiment, *Eptesicus fuscus* could capture tethered insects close to a background

[a]Electronic mail: sarah_stamper@brown.edu

of clutter (artificial hanging plant) that simulated vegetation (Moss *et al.*, 2006). The bats were able to catch insects within 20–40 cm (80%–90%, respectively), but not within 10 cm (40%) of the clutter. Yet other experiments of this type with *Eptesicus nilssonii* found that, while bats cannot capture moths located below the surface of grass, their capture success increases (40%–50%) when the moths fly 50 cm or more above the grass (Rydell, 1998). Although these bats did not capture any moths at distances below 50 cm from the grass surface, they did make attempts to capture, indicating that the bats detected the presence of the insect. When echoes of the moths were measured against the grass surface, they proved to be distinguishable from their spectrograms when the insect was located as close as 10 cm below or above the surface of the grass (Jensen *et al.*, 2001). This minimum distance for acoustic detection is well below the 50 cm distance above the grass necessary for successful capture.

The aim of this study was to determine how effectively big brown bats can detect a target embedded in clutter under controlled laboratory conditions simulating an insect in vegetation. The expectation was that the bat's detection threshold would be related to the target's reflection strength in relation to the clutter, so the results were analyzed in terms of ratios of echo energy between the target and clutter.

II. METHODS

A. Subjects

Subjects were four adult male wild-caught big brown bats (*Eptesicus fuscus*) from Rhode Island. They were housed in a colony room on a reverse 12:12 light/dark cycle with a controlled temperature of 22–25 °C and 60% relative humidity. The bats were fed mealworms (*Tenebrio* larvae) and provided with vitamin-enhanced (Poly-Vi-Sol) water *ad libitum*. All subjects weighed between 14 and 15 g. Animal procedures were consistent with guidelines established by the National Institutes of Health and were approved by the Brown University Animal Care and Use Committee.

B. Psychophysical procedure

The experimental setup is shown in Fig. 1. Each bat was placed on an elevated Y-shaped platform (12 cm wide and 20 cm front to back) and trained in a two-alternative forced-choice procedure to locate, via echolocation, the presence of the target presented on either the bat's left or right. Each trial lasted 2–3 s. All trials were run double blind and in complete darkness so that one experimenter (trainer) was unaware of the target location until after the conclusion of the trial and potential visual cues were controlled. For each trial, the target was positioned and the bat's response was recorded by a second experimenter (recorder). The location of the target varied from left to right on a schedule using pseudorandom sequences (Gellermann, 1933) grouped together to make sets of 50 consecutive trials. These sets imposed the constraint that the target would not be present on the same side for more than three successive trials and that there were an equal number of left-side and right-side presentations. The bat was rewarded with a piece of a mealworm offered in plastic forceps by the trainer for each correct trial. An incorrect response was followed by a high frequency broadband sound indicating that an error had been made.

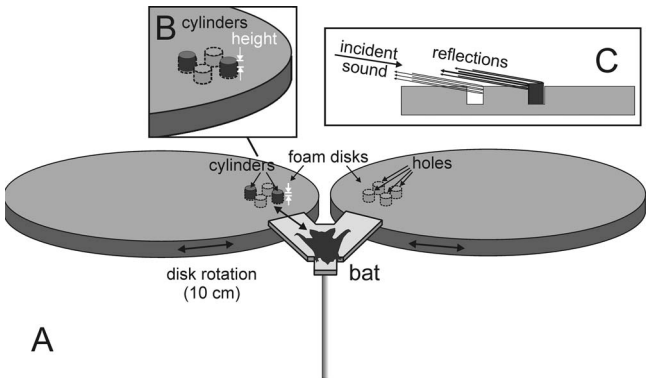

FIG. 1. (A) Diagram of the two-alternative forced-choice detection task. The bat was placed on the Y-shaped platform and trained to detect a target consisting of two small cylinders located on the right or left side. The cylinders were 5 cm apart and were embedded in holes cut into the surface of the 2.5 cm thick foam disks 90 cm in diameter. They varied in height by 12, 8, 4, or 2 mm above the surface of the foam (see inset in B). To receive food reward, the bat walked down (arrow) the side of the platform that corresponded to the target. The target's cylinders occupied two holes on the left (as indicated in B) or the right (alternated pseudorandomly), and they reflected echoes whose strength depended on the cylinders' protruding height. The other holes were empty from one trial to the next, but they generated their own reflections (inset in C) to compete with echoes from the cylinders and serve as clutter. For successful detection, the bat had to discriminate the reflections of the cylinders from these added clutter reflections. The experiment measured the bat's detection performance while the strength of the target's reflections was decreased in several steps by reducing the protruding height of the cylinders until target strength was similar to the clutter.

Trials were videotaped using a black-and-white charge coupled device (CCD) video camera (Supercircuits, Inc., Type 15-CB22-1) mounted on the ceiling to look down on the bat and the apparatus. To keep the room dark for experiments, illumination for the video recordings was provided by two infrared light emitting diode (LED) panels (Supercircuits, Inc.) mounted beside the video camera. A bat detector (Mini-3 model from Ultra Sound Advice, Ltd.) tuned to 28 kHz was located in front of the bat at a distance of 1.4 m to record its sonar broadcasts. The video signal and the audio output from the bat detector were recorded on 8 mm digital video tape using a Sony Video Walkman. During the experiments, an audible display of the bat's echolocation emissions was provided by the bat detector. For some sessions, the echolocation emissions were recorded with two ultrasonic microphones (Titley Electronics, Australia, Ltd.) at a sampling rate of 384 kHz on a digital instrumentation recorder (Sony SIR-1000W) that also recorded the video signal.

C. Target and clutter

The target to be detected consisted of two black plastic cylinders, each with a diameter of 1.6 cm, separated by 5 cm to form a dipole target. A dipole target was used because the size of the individual cylinders (1.6 cm diameter, 0.2–1.2 cm in height) approximates those of June beetles and crickets resting on a surface. Moreover, baseline information about detection and discrimination of dipoles by bats

was available from the results of new behavioral experiments (DeLong *et al.*, 2008) The dipole configuration caused echoes returning to the bat to vary slightly in amplitude and spectrum as the aspect angle was varied from one trial to the next, so that no single amplitude increment or spectral profile could be used by the bat to find the target. This variation provides more naturalistic stimuli for the detection task.

The target was presented on one of the two circular foam covered Plexiglas surfaces (90 cm in diameter and 2.5 cm thick) on the bat's left and right [Fig. 1(A)]. The target was placed into holes cut partway into the foam surface. In each (right or left) foam disk, there were four holes 1.7 cm deep and 1.7 cm in diameter, arranged in a diamond-shaped pattern with a 5 cm diagonal spacing [Fig. 1(B)]. The holes marking the four corners of the diamond were positioned as mirror images between sides. Thus, the square pattern of the holes on the left was about 90° different from the pattern on the right.

The target was inserted into two of the holes in the square pattern—always on the opposite corners of the square, so that the target had an aspect angle of about 40°–50° as a consequence of the slight trial-to-trial rotation of the disks (counterclockwise when on the left foam disk, and clockwise when on the right foam disk; see below). On any given trial, the cylinders occupied two of the holes either on the left or on the right foam disk; the remaining holes (two in the "target" side, and four on the "nontarget" side) were left to reflect echoes of the bat's sounds from their inside surfaces [see Fig. 1(C)].

The two circular foam pads were held in place on Plexiglas disks that also had a diameter of 90 cm. The Plexiglas disks under the foam could be rotated to change the location of the target relative to the bat on the Y-shaped platform. Both disks were always rotated the same distance [up to a 10 cm movement at the circumference of each disk; see arrows in Fig. 1(A)], so that the positions of the holes on both sides were at approximately the same distance from the bat on each trial. As such, the distance from the target to the bat ranged from 25 to 35 cm across trials. This span of distances prevented the bat from using a single, restricted time window to search for the target, and the resulting change in the aspect angle of the dipole prevented the bat from using a single decibel increment in amplitude or a single echo spectral shape to find the target (DeLong *et al.*, 2008).

In the experiment, the height of the target in the foam was varied so that the profile of the target protruding above the surface of the foam disk, and thus the strength of its echo, could be varied systematically. The protrusion height of the target was either +12, +8, +4, or +2 mm. These target heights were presented in descending order on successive blocks of trials. The initial training criterion was set at >90% correct performance for the first condition (+12 mm), which took 150 trials. Each subsequent condition was run for a total of 150 trials. The protrusion height of the cylinders was decreased in steps from 12 mm to 8, 4, and 2 mm. At the end of the 2 mm condition, the initial 12 mm protrusion height was repeated as a control. In all of these conditions, the empty holes were present, too, and their reflections constituted a stable component of the acoustic backscatter that comprised the proximal stimuli. Thus, the bat received echoes from the target, holes, and rest of the foam panel. The question of interest was how high the target must protrude in order to be detected.

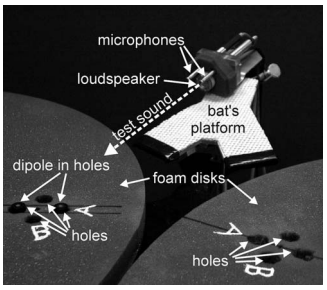

FIG. 2. Echoes from the clutter (holes) and target (dipole cylinders) were measured by projecting a 1 ms long FM signal (sweeping from 110 to 15 kHz), similar to the bat's echolocation emissions, from a 2 cm electrostatic loudspeaker and recording the echoes with two condenser microphones. To make the dipole echo measurements, the cylinders were placed in the foam holes with a specific protrusion height (12, 8, 4, or 2 mm) and the entire scene was ensonified to generate reflections.

D. Echo measurements

Figure 2 shows a photograph of the apparatus used to measure echoes from the clutter (holes) and target (dipole). A test signal consisting of a 1 ms long FM sweep (110–15 kHz) signal, similar to the bat's echolocation emissions, was projected from an electrostatic loudspeaker (LTV Model EST-2; 20 mm diameter) aimed toward the target on one of the foam disks. The returning sounds (echoes) were recorded using two Bruel & Kjaer Model 4138 ("$\frac{1}{4}$ in.") condenser microphones separated by 24 mm. The two microphones, and their placement, were used to represent the bat's two ears. The apparatus was originally constructed as part of a model of a bat's head. The test signal was generated by a Tucker-Davis Model QDA2 digital-to-analog conversion and wave form memory board running in a Pentium-III computer. This analog electrical signal was amplified and mixed with 200 V polarization using a Krohn-Hite Model 7500 power amplifier before being delivered to the loudspeaker. Overall sound pressure 10 cm in front of the loudspeaker was 100 dB SPL. Signals from the microphones were amplified by 40 dB (Bruel & Kjaer Model 5935 Microphone preamplifier/power supply), filtered to 15–100 kHz (Wavetek-Rockland Model 442 variable bandpass filter), and digitized at a sampling rate of 500 kHz and 12 bit accuracy by one of the analog-to-digital channels in a National Instruments PCI-6111e 2-channel analog-to-digital converter board.

To make the target echo measurements, the target was placed in the holes in one of the foam disks (Fig. 1). For each cylinder protrusion height (see above; 12, 8, 4, or 2 mm), the loudspeaker ensonified the target and the adjacent holes for 20 repetitions of the test signal while the signals recorded by the microphones were averaged to improve the signal-to-noise ratio. Similarly, the acoustic backscatter was measured for the holes alone and for the smooth surface of the foam disk without any holes. Echo measurements were also made for a flat target oriented perpendicular to the axis of sound

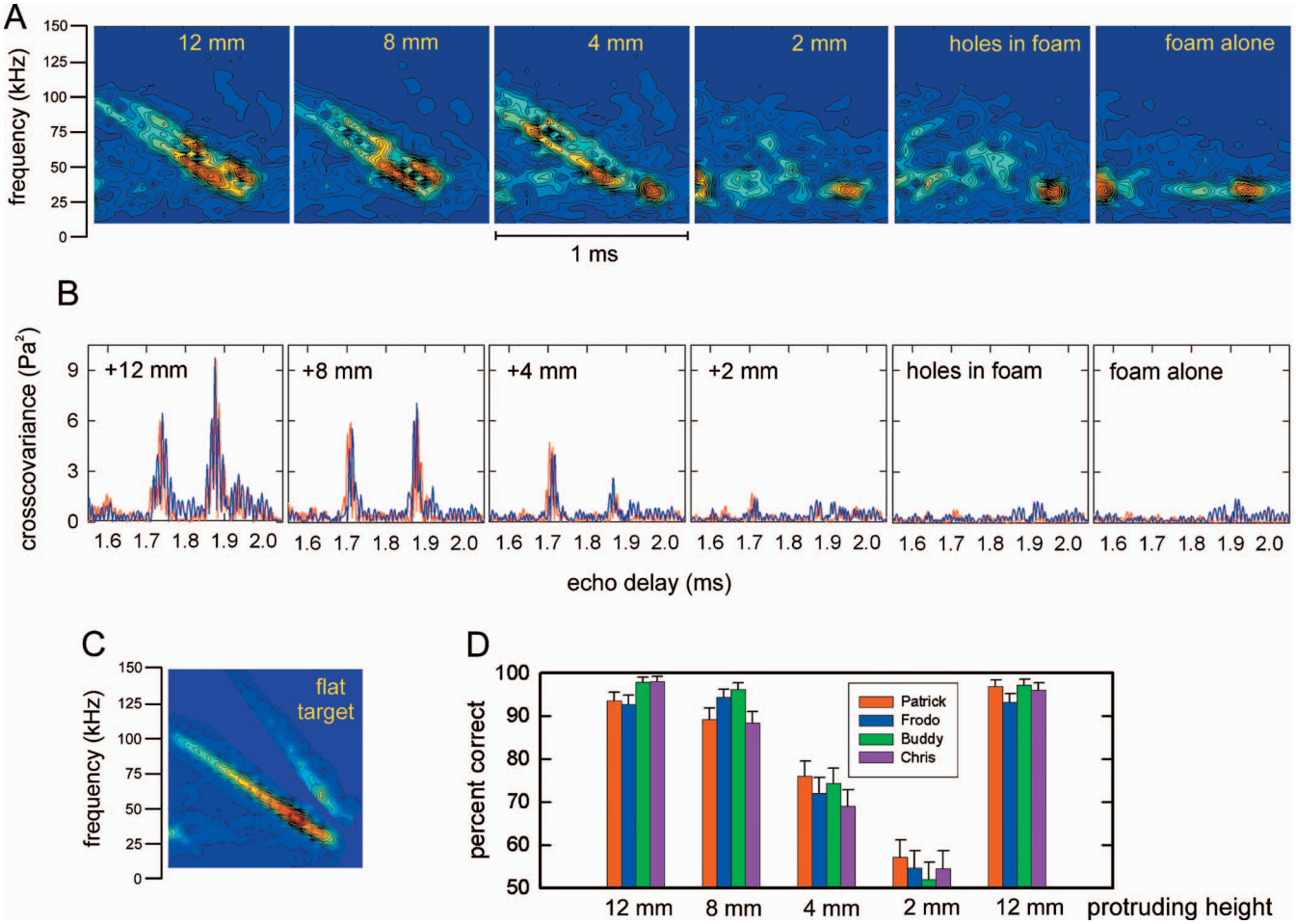

FIG. 3. (A) Spectrograms of reflections from the target at an orientation of 50° [see Fig. 1(B)] for different amounts of protrusion of the cylinders above the surface of the foam disk. The double sweeps in these spectrograms trace the separate reflections from the cylinders, which are oriented so their echoes arrive about 180 μs apart (see C for reference). (B) Output of matched filter (cross correlation receiver with full-wave-rectified plots) for the same series of reflections as in A. Red and blue curves trace outputs from left and right microphones (see Fig. 2). The twin peaks in the cross covariance curves register the separate reflections from the cylinders, while their heights have the same scale to indicate relative target strength. (C) Spectrogram for the specular reflection from a flat target oriented perpendicular to the sound from the loudspeaker (Fig. 2). The sweep pattern in C is for reference to the spectrograms in A, which show two closely spaced, overlapping sweeps from the two cylinders. The plots are labeled with the target's protrusion height (12, 8, 4, or 2 mm and empty holes). The empty holes and the blank foam surface produce acoustic scattering (clutter) across the same time window as the echoes from the target. (D) Performance (percent correct responses) of four big brown bats in detection task with different amounts of cylinder protrusion. Performance closely mirrors visibility of the FM sweeps in the spectrograms (A) or the prominence of the peaks in the cross covariance curves (B).

propagation to show the reflection from a single point target [see Fig. 3(C)]. This was used as a reference for estimating the strength of echoes reflected by the target and by the holes. Custom software written in LABVIEW and MATLAB was used to window the acoustic backscatter to a time span of 250 μs, which is the time span for echoes returning from all four holes, plus the two reflections from the dipole itself, over an equivalent distance span of 4–5 cm. This software also controlled the production of test signals by the computer boards and automatically averaged the echoes. The digital files containing the averaged echoes were processed by additional MATLAB routines to display their spectra, spectrograms, and the output of a cross correlation or matched-filter receiver operating with the wave form reflected by the flat target as a replica. Use of the flat-target echo for the correlation replica eliminated the response characteristics of the loudspeaker and the microphones from measurements made on the echoes. To represent the true relative amplitudes of the reflections across different target heights, the cross correlation outputs were expressed as cross covariance; that is, without the normalization to a maximum value of +1.0 as is used for cross correlation. When the cross covariance functions are full wave rectified, differences in the magnitudes of these functions between the flat reference target and any of the stimulus targets directly indicate relative target strength.

III. RESULTS

A. Target echoes

Recordings of reflections from the target and from the holes yielded estimates of the timing and amplitude of individual scattered signals. For the cylinders, the strongest signals were returned from their front surfaces, while for the holes, these were returned from their back surfaces [Fig. 1(C)]. These echoes are illustrated in Figs. 3(A) and 3(B). For reference, the test signal (1 ms FM sweep from 110 to 15 kHz) is represented by the spectrogram for the reflection from a flat target oriented perpendicular to the sound

path [Fig. 3(C)]. In this single, specular reflection, which is essentially the same as the incident sound, note the strong first-harmonic sweep and the much weaker second harmonic due to the distortion by the electrostatic transducer. Figure 3(A) shows the spectrograms of the reflections from cylinders with protrusion heights of 12, 8, and 4 mm. These spectrograms show the principal acoustic feature of the dipole target to be a pair of strong specular reflections, as illustrated by the two closely spaced first-harmonic FM sweeps separated by roughly 200 μs for the 12 mm target height [Fig. 3(B)]. At the 8 mm target height, the two sweeps are still prominent, while at the 4 mm target height, the second of the two sweeps appears weaker than the first sweep in the spectrogram. Additional regions of energy in the spectrograms show the reflections from the holes in the foam disks and from the foam alone. Comparison of the spectrograms for the 2 mm target height with the spectrogram for the holes alone reveals no obvious sign of the presence of the cylinders at such a low protrusion height. The pattern of reflections returned by the holes themselves is similar, indicating that the specular reflections from the front of the cylinders has declined to an insignificant level relative to the clutter. When the smooth surface of the foam disk was ensonified without the holes or the cylinders, there still is some energy in the spectrogram, indicating that some of the clutter is due not specifically to the holes but to the foam disk itself on the hard Plexiglas surface.

Figure 3(B) shows the output of a cross correlation or matched-filter receiver for the same reflections, as shown by the spectrograms in Fig. 3(A). There are two curves in each plot, one for the left microphone (red) and the other for the right microphone (blue). (Here, no special significance is attached to the use of two microphones; they were part of the echo-measuring apparatus and both their outputs are illustrated.) The curves are plots for values of cross covariance to show the amplitudes of the echoes in units that can be directly compared across different target conditions. They are the full-wave-rectified cross covariance functions of the echoes, with the reflection from the flat target used as the correlation replica. Consequently, the locations of the peaks in Fig. 3(B) directly represent delay differences between reflections, and the heights of the peaks represent relative target strength. As in the case of the spectrograms in Fig. 3(A), the cross covariance functions clearly register the locations of the two cylinders. (At an aspect angle of 40°–50°, the time separation of the reflections from the two cylinders should be about 180 μs.) For protrusion heights of 12, 8, and 4 mm, the twin peaks stand above the background returns from the holes in the foam and the foam itself, unambiguously revealing the presence of the target. However, for a cylinder protrusion height of 2 mm, the cross covariance peaks are comparable in height to the background peaks generated by the clutter, and the target's presence is only minimally registered, if at all.

Based on the hypothesis that the bat's detection of the target should depend on the relative strength of its echoes and possibly the presence of the two cylinders as a dipole, the acoustic measurements shown in Fig. 3 lead to the prediction that detection performance should be very good for protrusion heights of 12 and 8 mm, while performance should decline somewhat for a protrusion height of 4 mm and should vanish altogether for a protrusion height of 2 mm.

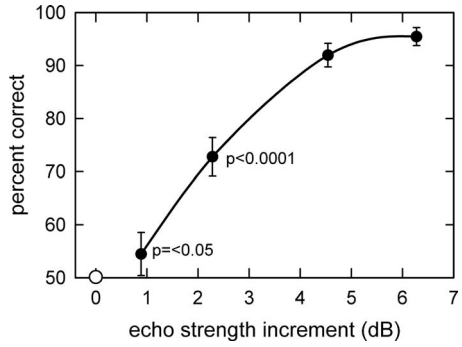

FIG. 4. Graph showing the mean performance of all four bats for different increments in target strength expressed in decibels relative to the target strength of the holes alone. Target strength is the energy reflected in a 250 μs integration-time window around each cylinder's reflection delay [see Fig. 3(B)], expressed in decibels relative to the energy reflected by the holes in the same time window. The bat's performance was significantly greater than chance ($p<0.05$) for echo increments greater than 1–2 dB.

B. Detection performance in clutter

All four bats ("Patrick," "Frodo," "Buddy," and "Chris") detected the target embedded in foam with a protrusion height of 12 mm at levels exceeding the criterion of 90% correct responses. Figure 3(D) plots the percentage of correct responses achieved by each bat to facilitate comparison to the acoustic measurements of target strength. The bats' performance varied as a function of protrusion height, with ~90% correct at heights of 12 and 8 mm, ~70%–75% correct at 4 mm, and ~55% correct at a height of 2 mm. The performance of the bats on the second presentation of the 12 mm protrusion height returned to levels better than 90% correct responses, indicating that the bats did not undergo a loss in their trained response as a consequence of exposure to the more difficult conditions of 4 and 2 mm. The behavioral results mirror changes in the strength of echoes from the target relative to the strength of the clutter echoes [Figs. 3(B) and 3(D)]. Figure 4 plots the mean performance of the bats as a function of the reflective strength of the target relative to the clutter. Relative target strength was determined by summing the energy contained in the two 250 μs time windows centered on the peak of the autocovariance function for each cylinder [Fig. 3(B)]. Then, the energy in the same two time windows for the clutter was summed in the absence of the cylinders. The ratio of target energy to clutter energy was computed for each cylinder protrusion height and expressed in decibels. The curve in Fig. 4 traces the decline in the bats' detection performance for different target conditions as the relative target strength (ratio of target energy to clutter energy in paired 250 μs windows) decreases with protrusion height. The bats' performance was greater than chance levels (50%) when the target strength increment was greater than 1–2 dB (Fig. 4).

IV. DISCUSSION

These data show that big brown bats are able to detect an insect-sized target embedded in clutter. The bat's task was to locate the target on either the left or right side, in a two-alternative forced-choice procedure, in the presence of additional reflecting structures (holes) common to both sides, which provided clutter. In psychological terms, this task could be described as either detection or discrimination; a distinction that is not important for the essential interpretation of the data. The bats' performance was graded according to the height of the cylinders protruding above the clutter, or according to the increment in echo strength, beyond that of the clutter alone, expressed in decibels. It diverged from chance when the target plus the clutter returned echoes approximately 1–2 dB greater than echoes from the clutter alone. Note that the same 250 μs time window was used for specifying the strength of the echoes for the clutter and the target plus clutter. The simplest description of the result is that the bat locates the target on the left or right by perceiving the small increment in echo strength based on target protrusion height.

In this experiment, the colocalization of the target and clutter removed the cues from the distance separation between a target and clutter present in previous field experiments (Jensen, 2001; Moss *et al.*, 2006; Rydell, 1998; Siemers and Schnitzler, 2004) that examined bats' abilities to capture prey in clutter. Because the target and clutter were colocalized, the results indicate that the bats are able to perform a task with demands similar to that of a natural situation where they are detecting insect prey (e.g., crickets and katydids) that often do not fly at night, and must be captured from substrates such as the ground or vegetation.

The trial-to-trial partial rotation of the foam disks shifted the distance from the bat on the platform to the holes and the target over a span of about 25–35 cm. As a result, echoes from the target varied in delay over a range of 1.5–2.0 ms between trials. Moreover, the delays of echoes from the target, and from the two empty holes on the same side (left or right) as the target, shifted by up to 0.5 ms relative to the echoes from the four empty holes on the other side. These movements were apart from the left-right alternations of target position. The bat could not have found the target on the left or the right just by examining whether a fixed, narrow time window contained reflections. Instead, it had to examine a broader time window because the clutter echoes and target echoes could fall anywhere within the span of delay created by trial-to-trial rotation of the disks.

The echoes from the target arrive within 300 μs of the cluttering echoes from the holes (Fig. 3). Such temporal conjunction of target and clutter echoes creates the strongest interference (Simmons *et al.*, 1989) and allows us to evaluate influence of clutter strength on detection performance without having to hypothesize a function describing the decay of clutter interference over time (important in situations where target and clutter echoes are significantly separated in time). Two earlier experiments (Masters and Jacobs, 1989; Troest and Møhl, 1986) tested detection abilities for phantom (electronically generated) targets. Because of the setups for these experiments, the bat received the target stimulus as well as competing echoes from the face of the loudspeaker used to broadcast the electronic echoes. For both experiments, the thresholds for the target stimulus were interpreted as potentially masked by echoes reflected by the loudspeaker. These loudspeaker clutter echoes arrived at delays considerably different than the test stimuli (2.9 ms earlier in Masters and Jacobs, 1989; 2.1 ms later in Troest and Møhl, 1986), and much longer than the time difference in the current experiment. Thus, the observed negative stimulus-to-clutter ratios estimated in these earlier studies might be expected because the clutter is so removed in time from the target stimuli, in which case the masking effect inherent in clutter interference would be mitigated (see Simmons *et al.*, 1989). Neither of these studies provided an explanation for how to discount the strength of the clutter when it arrives at a different time than the test echoes. In view of the relatively high echo-detection thresholds obtained in those studies compared to the audiometric sensitivity of big brown bats for either tone bursts (Koay *et al.*, 1997) or echoes (Kick, 1982), it is unclear whether those experiments actually examined the effects of clutter on echo detection.

Detection of stationary targets colocalized with clutter on a substrate, as tested here, is different from the task faced by a flying bat completing an aerial interception of prey near background objects. Previous experiments that examined aerial interception of prey by bats in the vicinity of clutter found that bats do not successfully take targets within 10–20 cm of clutter (e.g., Jensen *et al.*, 2001; Moss *et al.*, 2006; Rydell, 1998; Siemers and Schnitzler, 2004). However, it is not clear that this 10–20 cm limit of proximity for successful interception is determined by perceptual limitations of echolocation. Perhaps instead there is a reluctance of flying bats to engage targets by flying close to obstacles for mechanical reasons (Aldridge and Rautenbach, 1987; Fenton, 1995; Neuweiler, 2000; Norberg and Rayner, 1987). Because the bats and target were stationary in the present experiment, there were no issues of maneuverability to obscure the measurement of perceptual sensitivity. However, this experiment was conducted in a laboratory under favorable psychoacoustic conditions. Given the rapid motion of bats in pursuit of prey near clutter, additional perceptual limitations might prevail in the field beyond those present in our laboratory experiment.

ACKNOWLEDGMENTS

This research was funded by NIH Grant No. R01-MH069633 and ONR Grant No. N00014-04-0415.

Aldridge, H., and Rautenbach, I. L. (**1987**). "Morphology, echolocation, and resource partitioning in insectivorous bats," J. Anim. Ecol. **56**, 763–778.

DeLong, C. M., Bragg, R., and Simmons, J. A. (**2008**). "Evidence for spatial representation of object shape by echolocating bats (*Eptesicus foscus*)," J. Acoust. Soc. Am. **123**, 4582–4598.

Fenton, M. B. (**1995**). "Natural history and biosonar signals," in *Hearing by Bats*, edited by A. N. Popper and R. R. Fay (Springer-Verlag, New York), pp. 37–86.

Fullard, J. H., Ratcliffe, J. M., and Guignion, C. (**2005**). "Sensory ecology of predator-prey interactions: responses of the AN2 interneuron in the field cricket, *Teleogryllus oceanicus* to the echolocation calls of sympatric bats," J. Comp. Physiol., A **191**, 605–618.

Gellermann, L. M. (**1933**). "Chance orders of alternating stimuli in visual discrimination experiments," J. Gen. Psychol. **42**, 206–208.
Griffin, D. R. (**1958**). *Listening in the Dark* (Yale University Press, New Haven, CT/reprinted by Cornell University Press, Ithaca, NY, 1986).
Hamr, J., and Bailey, E. D. (**1985**). "Detection and discrimination of insect flight songs by big brown bats (*Eptesicus fuscus*)," Biol. Behav. **10**, 105–121.
Jensen, M. E., Miller, L. A., and Rydell, J. (**2001**). "Detection of prey in a cluttered environment by the northern bat *Eptesicus nilssonii*," J. Exp. Biol. **204**, 199–208.
Kick, S. (**1982**). "Target-detection by the echolocating bat, *Eptesicus fuscus*," J. Comp. Physiol. [A] **145**, 432–435.
Koay, G., Heffner, H. E., and Heffner, R. S. (**1997**). "Audiogram of the big brown bat (*Eptesicus fuscus*)," Hear. Res. **105**, 202–210.
Kurta, A., and Baker, R. H. (**1990**). "*Eptesicus fuscus*," Mammalian Species **356**, 1–10.
Masters, W. M., and Jacobs, S. C. (**1989**). "Target detection and range resolution by the big brown bat (*Eptesicus fuscus*) using normal and time-reversed model echoes," J. Comp. Physiol., A **166**, 65–73.
Moss, C. F., Bohn, K., Gilkenson, H., and Surlykke, A. (**2006**). "Active listening for spatial orientation in a complex auditory scene," PLoS Biol. **4**, 615–626.
Moss, C. F., and Surlykke, A. (**2001**). "Auditory scene analysis by echolocation in bats," J. Acoust. Soc. Am. **110**, 2207–2226.
Neuweiler, G. (**2000**). *The Biology of Bats* (Oxford University Press, New York).
Norberg, U. M., and Rayner, J. M. V. (**1987**). "Ecological morphology and flight in bats (Mammalia; Chiroptera): wing adaptations, flight performance, foraging strategy, and echolocation," Philos. Trans. R. Soc. London, Ser. B **316**, 335–427.
Ratcliffe, J. M., and Dawson, J. W. (**2003**). "Behavioural flexibility: the little brown bat, *Myotis lucifugus*, and the northern long ear bat, *M. septentrionalis*, both glean and hawk prey," Anim. Behav. **66**, 847–856.
Ratcliffe, J. M., Raghuram, H., Marimuthu, G., Fullard, J. H., and Fenton, M. B. (**2005**). "Hunting in unfamiliar space: echolocation in the Indian false vampire bat, *Megaderma lyra*, when gleaning prey," Behav. Ecol. Sociobiol. **58**, 157–164.
Rydell, J. (**1998**). "Bat defense in lekking ghost swifts (*Hepialus humuli*), a moth without ultrasonic hearing," Proc. R. Soc. London, Ser. B **265**, 1373–1376.
Saillant, P. A., Simmons, J. A., Bouffard, F. H., Lee, D. N., and Dear, S. P. (**2007**). "Biosonar signals impinging on the target during interception by big brown bats, *Eptesicus fuscus*," J. Acoust. Soc. Am. **121**, 3001–3010.
Schmidt, S., Hanke, S., and Pillat, J. (**2000**). "The role of echolocation in the hunting of terrestrial prey—new evidence for an underestimated strategy in the gleaning bat, *Megaderma lyra*," J. Comp. Physiol., A **186**, 975–988.
Schnitzler, H.-U., Moss, C. F., and Denzinger, A. (**2003**). "From spatial orientation to food acquisition in echolocating bats," Trends Ecol. Evol. **18**, 386–394.
Siemers, B. M., and Schnitzler, H. U. (**2004**). "Echolocation signals reflect niche differentiation in five sympatric congeneric bat species," Nature (London) **429**, 657–661.
Simmons, J. A. (**2005**). "Big brown bats and June beetles: multiple pursuit strategies in a seasonal acoustic predator-prey system," ARLO **6**, 238–242.
Simmons, J. A., Eastman, K. M., Horowitz, S. H., Farrell, M. J., and Lee, D. N. (**2001**). "Versatility of biosonar in the big brown bat, *Eptesicus fuscus*," ARLO **2**, 43–48.
Simmons, J. A., Fenton, M. B., and O'Farrell, M. J. (**1979**). "Echolocation and pursuit of prey by bats," Science **203**, 16–21.
Simmons, J. A., Freedman, E. G., Stevenson, S. B., and Chen, L. (**1989**). "Clutter interference and the integration time for echoes in the bat, Eptesicus fuscus," J. Acoust. Soc. Am. **86**, 1318–1332.
Surlykke, A., and Moss, C. F. (**2000**). "Echolocation behavior of big brown bats, *Eptesicus fuscus*, in the field and the laboratory," J. Acoust. Soc. Am. **108**, 2419–2429.
Troest, N., and Møhl, B. (**1986**). "The detection of phantom targets in noise by serotine bats; negative evidence for the coherent receiver," J. Comp. Physiol., A **159**, 559–567.

Minimizing abdominal wall damage during high-intensity focused ultrasound ablation by inducing artificial ascites

Chih-Ching Wu
Department of Mechanical Engineering, National Taiwan University, Taipei, Taiwan and Division of Medical Engineering Research, National Health Research Institute, Zhunan, Miaoli, Taiwan

Wen-Shiang Chen
Department of Physical Medicine and Rehabilitation, National Taiwan University Hospital and National Taiwan University College of Medicine, Taipei, Taiwan and Division of Medical Engineering Research, National Health Research Institute, Zhunan, Miaoli, Taiwan

Ming-Chih Ho
Department of Surgery, National Taiwan University Hospital and National Taiwan University College of Medicine, and Angiogenesis Research Center, National Taiwan University, Taipei, Taiwan and Division of Mechanics, Research Center for Applied Sciences, Academia Sinica, Taipei, Taiwan

Kai-Wen Huang
Department of Surgery, National Taiwan University Hospital, Taipei, Taiwan

Chiung-Nien Chen[a)]
Department of Surgery, National Taiwan University Hospital and National Taiwan University College of Medicine, and Angiogenesis Research Center, National Taiwan University, Taipei, Taiwan and Division of Mechanics, Research Center for Applied Sciences, Academia Sinica, Taipei, Taiwan

Jia-Yush Yen
Department of Mechanical Engineering, National Taiwan University, Taipei, Taiwan

Po-Huang Lee
Department of Surgery, National Taiwan University Hospital and National Taiwan University College of Medicine, and Angiogenesis Research Center, National Taiwan University, Taipei, Taiwan

(Received 13 July 2007; revised 4 December 2007; accepted 13 January 2008)

High-intensity focused ultrasound (HIFU) is becoming an important tool for tumor treatment [especially hepatocellular carcinoma (HCC)] in Asian countries. A HIFU system provides unique advantages of low invasiveness and absence of nonradiation. However, if the target HCC is close to the proximal surface of the liver, HIFU may overheat diaphragm, abdominal wall or skin. To avoid this complication, a method using artificial ascites in the abdominal cavity to separate the liver from the peritoneum, and to serve as a heat sink to cool overlying structures and thereby avoid inducing permanent damage was proposed. Target tissue that was 10 mm below the liver surface was ablated in 12 New Zealand white rabbits: 6 in the experimental group and 6 in the control group. Artificial ascites was established in the experimental group by injecting normal saline into the abdominal cavity until the pressure reached 150 mm H_2O. Artificial ascites not only reduced the probability and extent of thermal damage to intervening structures, but also had no adverse affect on the efficacy of HIFU ablation. © *2008 Acoustical Society of America.* [DOI: 10.1121/1.2839907]

PACS number(s): 43.80.Sh [FD] Pages: 674–679

I. INTRODUCTION

High-intensity focused ultrasound (HIFU) is a promising tool in applications such as tumor ablation, vessel destruction, and bleeding control due to its noninvasive nature and the absence of ionizing radiation.[1–7] HIFU has shown efficacy in preliminary clinical studies against solid tumors, including those of the prostate, liver, breast, kidney, bladder, pancreas, and bone.[7–11] Traditionally, most of the operable hepatocellular carcinoma (HCC) patients have to receive interventional managements including surgical resection and transarterial chemoembolization (TACE).[12] In China, HIFU ablation combined with TACE was shown to be more effective than TACE alone in the treatment of advanced-stage HCC.[13] It was also proven that HIFU appeared to be effective, safe, and feasible in the treatment of patients with HCC.[14] Patients undergoing complete HIFU ablation demonstrates conversion from presence to absence of circulating tumor-specific marker mRNA, and that HIFU would not enhance the potential risk of metastasis in patients with malignant diseases.[15]

HIFU is known to induce thermal damage in off-target tissue,[16–18] with this being especially problematic for super-

[a)]Author to whom correspondence should be addressed. Electronic mail: cnchen@ntu.edu.tw.

 0001-4966/2008/124(1)/674/6/$23.00

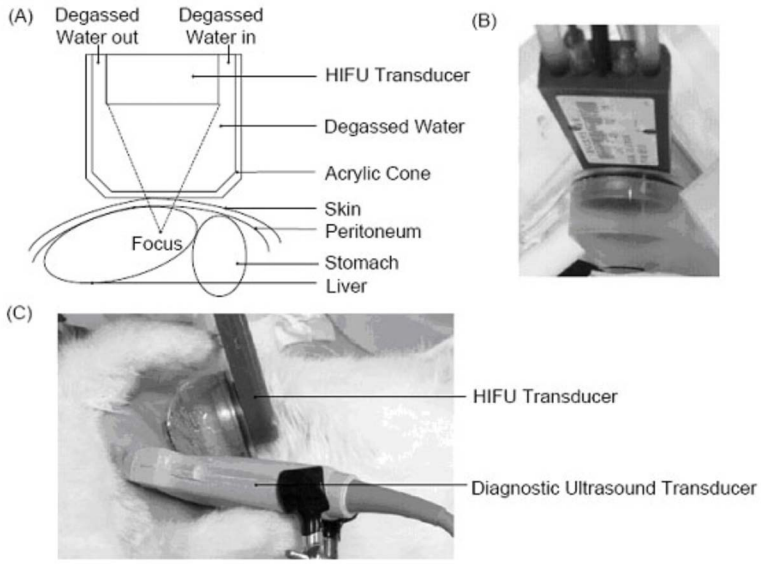

FIG. 1. (Color online) (A) Schematic diagram of the experimental setup, (B) photograph of the HIFU transducer mounted with a coupling cone, and (C) simultaneous use of the HIFU and diagnostic ultrasound transducers.

ficially situated tumors (e.g., shallow HCC), in which burn complications on overlying structures are easily induced. The use of intraperitoneal fluid injection to induce artificial ascites and thereby avoid abdominal burns has been tested in several coagulation modalities, including percutaneous radio frequency (rf) and microwave treatment of liver cancers,[19–21] but not in HIFU. The intraperitoneal injection of saline also improves the visibility of the target HCCs by separating the liver from the diaphragm, and helps to protect adjacent structures from thermal damage during ablations. Moreover, the injected saline is absorbed naturally within a few days after therapy, and no severe adverse reactions such as bleeding or seeding of tumor cells develop subsequently.[21] To extend the applications of HIFU ablations to shallow hepatic tumors and avoid burn injuries, we performed a series of experiments on the use of artificial ascites to cool the abdominal wall during HIFU ablations.

II. MATERIALS AND METHODS

A. Experimental setup

Figure 1 shows a schematic diagram of the experimental setup. A 3.5-MHz single-element focused piezoelectric transducer (Sonic Concepts, Woodinville, WA) was mounted together with a diagnostic ultrasound probe (L38, SonoSite, Bothell, WA) connecting to a portable diagnostic ultrasound device (TITAN™, SonoSite, Bothell, WA). The HIFU transducer had an aperture diameter and radius of curvature of 35 and 55 mm, respectively, and a focal depth (as measured from the exit plane of the transducer's housing rim) of 51 mm. The focal width and length (−3 dB pressure drop), as measured by a fine needle hydrophone of 0.5 mm in aperture diameter (HNR-0500, ONDA, Sunnyvale, CA) at low HIFU output (1 W electrical power), were 0.7 and 7.1 mm, respectively. The spatial-average-temporal-average intensity (I_{SATA}), calculated as the acoustic power averaged over the −3 dB cross-sectional area of the focus was 10 and 378 W/cm^2 for electrical powers of 1.5 W (for positioning) and 60 W (for ablation) in water, respectively. A transducer of high frequency and high F-number (1.57) was intentionally chosen to exacerbate the proximal heating.

The rf signal was supplied by a function generator (33120A, Agilent, Palo Alto, CA) whose output was amplified by a power amplifier (150A250, Amplifier Research, Souderton, PA). The incident and reflected powers were measured using a power meter (4421, Bird, Cleveland, OH).

B. Animal model

Twelve New Zealand white rabbits with a mean weight of 3.5 kg were used in this study. The experimental protocol was approved by the Institutional Animal Care and Use Committee at National Taiwan University College of Medicine and College of Public Health. Rabbits were anesthetized with ketamine (35 mg/kg, intramuscular injection) (Ketomin; Nang Kuang, Tainan, Taiwan) and xylazine (5 mg/kg, intramuscular injection) (Rompun; Bayer, Leverkusen, Germany). Hair was shaved and the skin cleaned with hair remover lotion (Sally Hansen, New York) so as to optimize the coupling between the skin and transducers.

For the rabbit model, most of its liver was covered by ribs. Thus, only two lesions could be produced in each rabbit. To avoid an overheating problem, one lesion was made in the right-hand side and another in the left-hand side of the upper abdomen. For all ablations, liver was treated extracorporeally without opening the rib cage. If any rib injury was found, the experiment was considered failed and the result was excluded from the final statistics.

The rabbits were divided into two groups (control and experimental) and placed in a supine position after inducing anesthesia. In each animal in the experimental group, a 14-gauge Veress needle was inserted into the abdominal cavity and normal saline was infused until the pressure reached 150 mm H_2O. A normal saline reservoir with a connecting tube to the abdominal cavity was placed 150 mm higher than the rabbit. Therefore, the saline would flow into the abdominal cavity until the abdominal pressure reached 150 mmH_2O, which separated the liver and peritoneum for a distance of

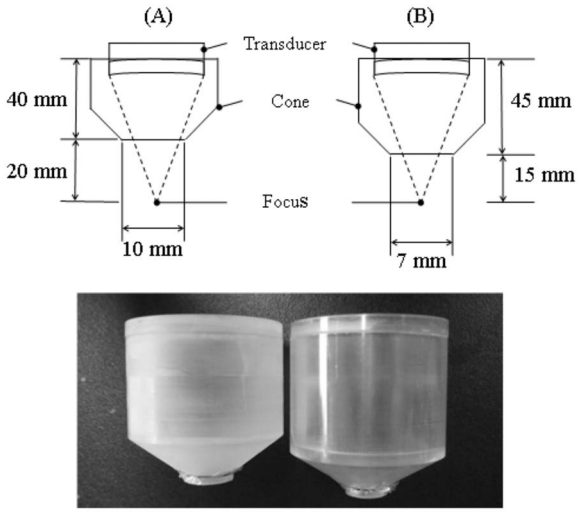

FIG. 2. Cone configuration. The distance between the exit plane of the cone and the HIFU focus was greater for the cone used in the experimental group (A) than for that used in the control group (B).

about 5 mm (Fig. 2). The abdominal wall thickness was typically 4 mm. However, if excessive pressure was applied on skin and made the skin getting concave, the artificial ascites would collapse. Therefore, a constant pressure was maintained in the abdominal cavity and thus the minor compression by either diagnostic or therapeutic ultrasound transducers would not substantially change the distribution of artificially ascites and the gap between liver surface and peritoneum. Moreover, the presence of artificial ascites did not cause any breathing difficulties in rabbits. The temperature of the injected normal saline was found to be constant at around 32 °C before, during, and after the ablation procedure, which was measured by a K-type thermocouple placed near the target liver through a 19-gauge needle. The temperature was recorded at a 0.5-s interval.

The presence of a 5-mm-thick fluid layer only in the experimental group meant that acrylic coupling cones of different heights were used in the two groups (Fig. 3). Coupling cones were filled with degassed water. The aperture of each cone was sealed with a 0.1 mm thermoplastic elastomer membrane. Commercially available ultrasound transmission gel (Other-Sonic, Pharmaceutical Innovations, NJ) was used as coupling medium between the sealing membrane and skin.

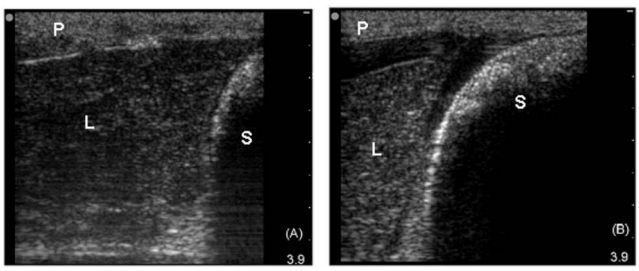

FIG. 3. Liver and peritoneum were separated by artificial ascites in the gastrohepatic space. (A) Before inducing artificial ascites, the peritoneum (P), liver (L), and stomach (S) were in close contact. (B) After inducing artificial ascites, the liver (L), stomach (S), and peritoneum (P) were clearly separated.

TABLE I. Comparison of the area of lesions induced by HIFU ablation between the control and experimental groups.

Ablation zone (mm^2)[a]	Skin[b]	Peritoneum[b]	Liver[b]
Control group	62.44 ± 28.76	45.52 ± 23.80	47.36 ± 28.21
Experimental group	4.43 ± 7.29	2.77 ± 5.19	30.55 ± 18.84
P	<0.01	<0.01	0.063

[a]Ablation zone was quantified as area of the HIFU lesion.
[b]Data are mean ± SD values (where applicable).

The distance from the focus to the exit plane of the cone was 20 and 15 mm in the experimental and control groups, respectively. In both groups the HIFU was targeted at 10 mm below the surface of the liver. (see Table I).

C. Experimental procedures

One ablation was performed on each side of the upper abdomen over the presumed position of the liver in each rabbit. Interference noise evident on ultrasound images obtained by operating the HIFU transducer at a relatively low power (1.5 W) was used to position the HIFU focus on the liver surface without inducing permanent changes. The procedure of using HIFU interference to position the focus of the HIFU on the target area is detailed elsewhere.[22] The electrical power to the HIFU transducer was then increased to 60 W for 30 s to produce lesions, after which the animal was sacrificed and the diameters of lesion on the skin, inner peritoneum, and liver surface were measured and compared between animals and groups.

D. Data analysis

After the ablated region of the liver was measured, the liver was fixed in formalin solution for microscopic examination. The liver specimens were cryosectioned at 5 μm and stained with hematoxylin and eosin. Data are presented as mean and standard deviation (SD) values. Groups were compared using Student's t-test, with $P < 0.05$ considered indicative of statistical significance.

III. RESULTS

Artificial ascites was successfully induced in the six rabbits in the experimental group. The amount of liquid needed to produce 150 mm H_2O of abdominal pressure ranged between 650 and 850 ml. Animals were sacrificed immediately after completing the HIFU ablations. The white areas of the liver shown in Fig. 4 indicate the regions of coagulation after HIFU exposure, which were either circular or nearly elliptic. Although skin and peritoneum were still damaged by HIFU in a few cases [Figs. 4(C), 4(D), and 5], their sizes were significantly smaller. Thermal damage was present in all cases in the control group [Figs. 4(A), 4(B), and 5].

Figure 6 shows microscopy images of the liver after HIFU ablation. The untreated and coagulated regions after HIFU exposure are shown in Figs. 6(B) and 6(C), respectively. Thermal damage was evident on the inner surfaces of the peritoneum and skin in four of the ablations in the experimental group, and in all ablations in the control group.

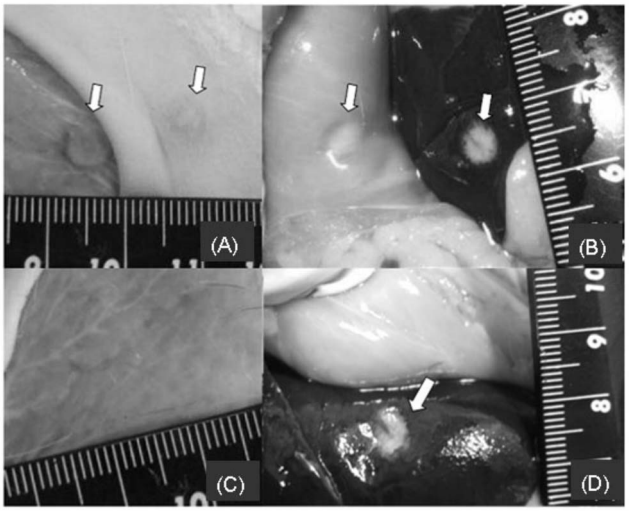

FIG. 4. (Color online) Photographs of the skin, muscle, peritoneum, and liver showing thermal damage induced by HIFU ablation (arrow). The skin and muscle layer (A) and the inner surface of the peritoneum and liver surface (B) were damaged by HIFU in the control group (no saline infusion). The skin and muscle (C) and the inner peritoneum (D) were not damaged by HIFU after infusing saline, although the liver was still damaged.

The cross-section areas of the lesions on skin in the control and experimental groups were 62.44 ± 28.76 and 4.43 ± 7.29 mm^2, respectively ($P < 0.05$), and those on inner peritoneum were 45.52 ± 23.80 and 2.77 ± 5.19 mm^2, respectively ($P < 0.05$). This indicates that the lesions on the skin and inner peritoneum were much larger in the control group than in the experimental group. Although the size of the thermal lesions on the liver surface seemed to be smaller, but it did not differ significantly compared with the control group (47.36 ± 28.21 mm^2 vs 30.55 ± 18.84 mm^2, $P = 0.063$). Figure 7(A) showed the cross section of a lesion on the surface of ablated liver. The appearance of a lesion 10 mm beneath the liver surface was shown in Fig. 7(B). Figure 7(C) was the appearance of a lesion cut along the axial direction

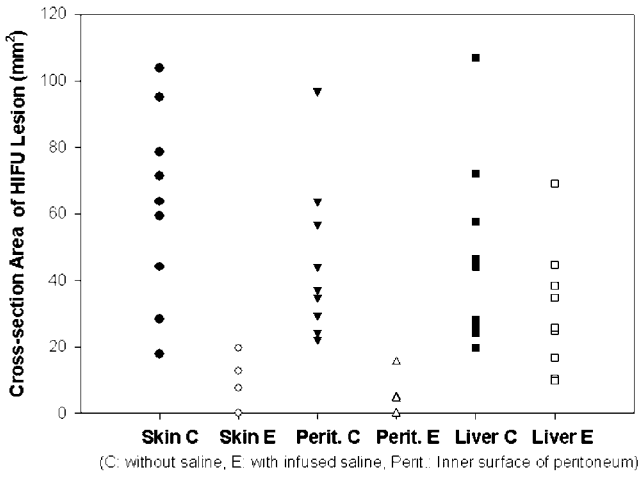

FIG. 5. Cross-section area of thermal lesions induced by HIFU exposure. The data are for 18 lesions in a total of 12 rabbits (9 lesions in each group).

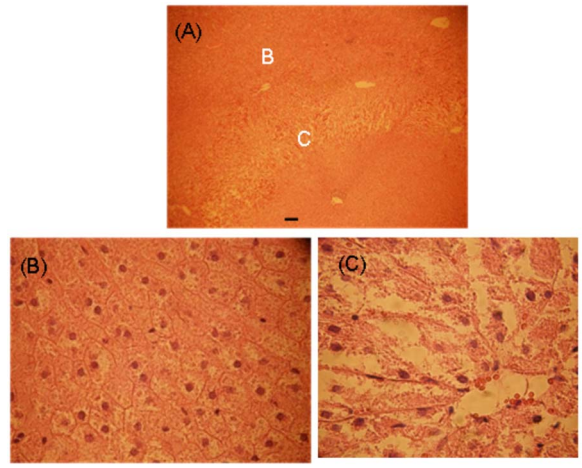

FIG. 6. (Color online) Microscopic images show liver tissue after HIFU ablation in the experimental group. In (A), locations where (B) and (C) were taken are shown [hematoxylin and eosin stain (H&E), ×40], (B) the untreated region (H&E, ×400), and (C) the coagulation necrosis region (H&E, ×400). The scale in (A) is 100 μm.

of the HIFU propagation. The cross section of a lesion 10 mm beneath the liver surface was smaller than that shown on the liver surface.

IV. DISCUSSION

The results from this study demonstrate that artificial ascites can significantly reduce the possibility and extent of thermal damage to the intervening structures when performing HIFU ablations on superficial targets in rabbit liver models. Moreover, the use of artificial ascites did not significantly reduce the diameter of lesions induced by HIFU in liver surface.

In the current study, liver was chosen as an example of using artificial ascites to reduce thermal damage of intervening structures. Rib above the liver surely would cause problems during HIFU ablation. However, artificial ascites may also be applied to other target organs in the abdominal cavity, e.g., pancreatic tumor ablation. Pancreas locates in the upper

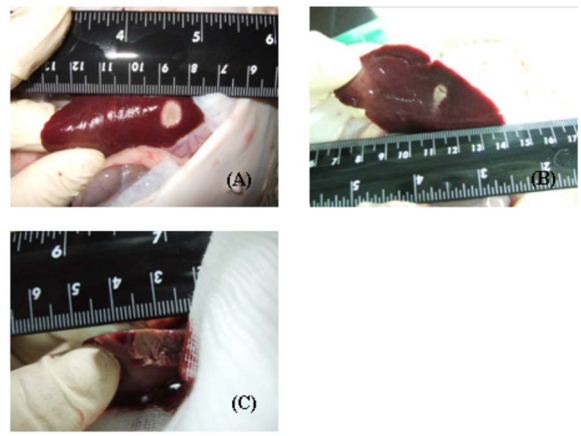

FIG. 7. (Color online) Photographs show a HIFU induced lesion in liver of the experimental group after HIFU ablation. (A) cross section of a lesion on liver surface, (B) cross section of a lesion 10 mm beneath liver surface, and (C) a lesion in liver cut along the axial direction of the HIFU propagation.

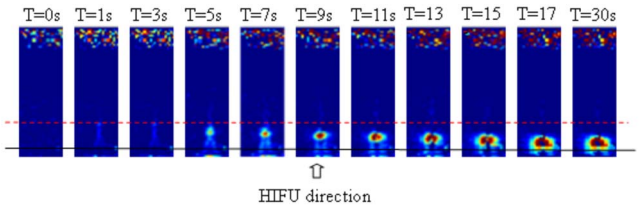

FIG. 8. (Color online) A liver ablated by HIFU at an electrical power level of 60 W. The change of temperature was monitored by MRI phase images. Dash line: focal plane and solid line: liver surface.

abdominal cavity and adequate separation between pancreas and surrounding structures such as liver, stomach, and bowel is necessary to prevent thermal complications.

In a previous study applying rf ablation to rabbit livers, artificial ascites was established by injecting 320 ml of normal saline solution to separate the liver from the diaphragm and stomach.[23] Another study using a porcine model introduced 500–1000 ml of sterile normal saline into the subphrenic space to achieve at least 1 cm of separation.[24] In our study, good separation was established once the abdominal pressure reached 150 mm H_2O, and this was maintained throughout the treatment procedure. The top-down arrangement of the HIFU transducer might result in mechanical pressure from the transducer forcing water away from the liver surface, and hence a constant-pressure setup (as used in the present study) might be a better way to ensure constant separation. In our study, the amount of liquid required to maintain this pressure ranged from 650 to 850 ml (mean, 750 ml). Using an excessive amount of normal saline caused breathing difficulties in the rabbits and resulted in the liver moving in the abdominal cavity, both affecting the precision and thus the efficiency of HIFU ablation. No adverse reactions such as bleeding, peritonitis or collateral thermal damage were found in our study or previous research using artificial ascites. The infused saline was reported to be absorbed without any treatment within a few days.[20,23]

HIFU can damage ribs when they are near the transducer focus. We found that rib damage occurred in 6 of the 24 lesions induced on the liver surface of 12 rabbits, and hence only 18 lesions (9 in each group) were included in the statistical analyses.

According to our previous study, the HIFU-induced lesions are usually tadpole-shaped with their maximally heated volumes at the head portion of the tadpole, that is, in front of the HIFU focus.[25] Probably due to vapor bubble formation, lesions shift backward with their maximally diameters locating at around 10 mm away from the HIFU focus. Therefore, we believe that the cross-section areas of lesions on liver surface may better represent the extent of tissue necrosis when the HIFU focus was 10 mm beneath the liver surface. In our recent study, we used MRI to monitor the growth of HIFU lesion in *ex-vivo* experiments. Figure 8 shows a liver ablated by HIFU at an electrical power level of 60 W. The change of its internal temperature was continuously monitored by MRI phase images. The horizontal dash line is the focal plane whereas the black horizontal line is the surface of the liver. The HIFU transducer was placed under Fig. 8. The results confirmed that the lesion simply shifted toward the HIFU transducer or liver surface, with its maximally heated region near the liver surface after 17 s of ablation.

In the control group, the thermal lesion extended from the focal region to the skin surface. In contrast, in experimental group, artificial ascites served as both a barrier and a heat sink that blocked direct heat conduction between the liver and abdominal-wall structures, thereby reducing the temperature buildup on the abdominal wall and the possibility of thermal damage.

Thermal damage was also found in the inner surface of the peritoneum and skin for four ablations in the experimental group, although these were significantly smaller than those in the control group. This might have been attributable to a reduction of the separation between the abdominal wall and liver surface due to excessive compression by the HIFU transducer during ablation.

The higher frequency (3.5 MHz) HIFU transducer was intentionally used in the current study to enhance the side effect of skin burn, and thus highlight the effect of artificial ascites in reducing the extent of thermal damage. We have also performed ablations using a lower-frequency HIFU, (1.85 MHz) on rabbit liver (electrical power of 40 W for 20 s). The skin, subcutaneous tissue, and liver were all damaged. Low frequency HIFU may still induce thermal damage when the target was superficial or when the intensity or duration of an ablation was inadequate.[16–18]

In conclusion, artificial ascites might represent an effective technique for reducing thermal damage to the skin and muscle tissue of the abdominal wall during HIFU ablation. HIFU may be a convenient method for reducing possible burn complications, especially in patients with superficial liver cancer and cirrhosis with spontaneous ascites.

ACKNOWLEDGMENTS

This research was supported by grants from the National Taiwan University Hospital (No. 95A14), National Health Research Institute (No. ME-095-PP-12), and Department of Industrial Technology, Ministry of Economic Affairs (No. 96-EC-17-A-19-S1-016).

[1]F. A. Jolesz, K. Hynynen, N. McDannold, and C. Tempany, "MR imaging-controlled focused ultrasound ablation: A noninvasive image-guided surgery," Magn. Reson Imaging Clin. N. Am. **13**, 545–560 (2005).
[2]N. A. Watkin, G. R. ter Haar, and I. Rivens, "The intensity dependence of the site of maximal energy deposition in focused ultrasound surgery," Ultrasound Med. Biol. **22**, 483–491 (1996).
[3]W. W. Roberts, "Focused ultrasound ablation of renal and prostate cancer: Current technology and future directions," Semin Urol. Oncol. **23**, 367–371 (2005).
[4]M. R. Bailey, L. N. Couret, O. A. Sapozhnikov, V. A. Khokhlova, G. ter Haar, S. Vaezy, X. Shi, R. Martin, and L. A. Crum, "Use of overpressure to assess the role of bubbles in focused ultrasound lesion shape in vitro," Ultrasound Med. Biol. **27**, 695–708 (2001).
[5]S. Vaezy, M. Andrew, P. Kaczkowski, and L. Crum, "Image-guided acoustic therapy," Annu. Rev. Biomed. Eng. **3**, 375–390 (2001).
[6]F. Wu, W. Z. Chen, J. Bai, J. Z. Zou, Z. L. Wang, H. Zhu, and Z. B. Wang, "Tumor vessel destruction resulting from high-intensity focused ultrasound in patients with solid malignancies," Ultrasound Med. Biol. **28**, 535–542 (2002).
[7]F. Wu, Z. B. Wang, W. Z. Chen, W. Wang, Y. Gui, M. Zhang, G. Zheng, Y. Zhou, G. Xu, M. Li, C. Zhang, H. Ye, and R. Feng, "Extracorporeal high intensity focused ultrasound ablation in the treatment of 1038 patients

with solid carcinomas in China: an overview," Ultrason. Sonochem. **11**, 149–154 (2004).
[8]R. O. Illing, J. E. Kennedy, F. Wu, G. R. ter Haar, A. S. Protheroe, P. J. Friend, F. V. Gleeson, D. W. Cranston, R. R. Phillips, and M. R. Middleton, "The safety and feasibility of extracorporeal high-intensity focused ultrasound (HIFU) for the treatment of liver and kidney tumours in a Western population," Br. J. Cancer **93**, 890–895 (2005).
[9]J. E. Kennedy, F. Wu, G. R. ter Haar, F. V. Gleeson, R. R. Phillips, M. R. Middleton, and D. Cranston, "High-intensity focused ultrasound for the treatment of liver tumours," Ultrasonics **42**, 931–935 (2004).
[10]T. A. Leslie and J. E. Kennedy, "High-intensity focused ultrasound principles, current uses, and potential for the future," Ultrasound Q **22**, 263–272 (2006).
[11]G. Vallancien, M. Harouni, B. Guillonneau, B. Veillon, and J. Bougaran, "Ablation of superficial bladder tumors with focused extracorporeal pyrotherapy," Urology **47**, 204–207 (1996).
[12]Y. S. Guan and Y. Liu, "Interventional treatments for hepatocellular carcinoma," Hepatobiliary Pancreat. Dis. Int. **5**, 495–500 (2006).
[13]F. Wu, Z. B. Wang, W. Z. Chen, J. Z. Zou, J. Bai, H. Zhu, K. Q. Li, C. B. Jin, F. L. Xie, and H. B. Su, "Advanced hepatocellular carcinoma: Treatment with high-intensity focused ultrasound ablation combined with transcatheter arterial embolization," Radiology **235**, 659–667 (2005).
[14]F. Wu, Z. B. Wang, W. Z. Chen, H. Zhu, J. Bai, J. Z. Zou, K. Q. Li, C. B. Jin, F. L. Xie, and H. B. Su, "Extracorporeal high intensity focused ultrasound ablation in the treatment of patients with large hepatocellular carcinoma," Surg. Oncol. **11**, 1061–1069 (2004).
[15]F. Wu, Z. B. Wang, C. B. Jin, J. P. Zhang, W. Z. Chen, J. Bai, J. Z. Zou, and H. Zhu, "Circulating tumor cells in patients with solid malignancy treated by high-intensity focused ultrasound," Ultrasound Med. Biol. **30**, 511–517 (2004).
[16]C. Chaussy and S. Thuroff, "High-intensity focused ultrasound in prostate cancer: results after 3 years," Mol. Urol. **4**, 179–182 (2000).
[17]J. Leon-Villapalos, M. Kaniorou-Larai, and P. Dziewulski, "Full thickness abdominal burn following magnetic resonance guided focused ultrasound therapy," Burns **31**, 1054–1055 (2005).
[18]S. Thuroff and C. Chaussy, "High-intensity focused ultrasound: Complications and adverse events," Mol. Urol. **4**, 183–187, 189 (2000).
[19]Y. Kondo, H. Yoshida, S. Shiina, R. Tateishi, T. Teratani, and M. Omata, "Artificial ascites technique for percutaneous radiofrequency ablation of liver cancer adjacent to the gastrointestinal tract," Br. J. Surg. **93**, 1277–1282 (2006).
[20]K. Ohmoto, M. Tsuzuki, and S. Yamamoto, "Percutaneous microwave coagulation therapy with intraperitoneal saline infusion for hepatocellular carcinoma in the hepatic dome," AJR, Am. J. Roentgenol. **172**, 65–66 (1999).
[21]K. Ohmoto and S. Yamamoto, "Percutaneous microwave coagulation therapy using artificial ascites," AJR, Am. J. Roentgenol. **176**, 817–818 (2001).
[22]C. C. Wu, C. N. Chen, M. C. Ho, W. C. Chen, and P. H. Lee, "Using the acoustic interference pattern to locate the focus of a HIFU transducer," Ultrasound Med. Biol. **34**, 137–146 (2008).
[23]Y. S. Kim, H. Rhim, and S. S. Paik, "Radiofrequency ablation of the liver in a rabbit model: Creation of artificial ascites to minimize collateral thermal injury to the diaphragm and stomach," J. Vasc. Interv. Radiol. **17**, 541–547 (2006).
[24]S. S. Raman, D. S. Lu, D. J. Vodopich, J. Sayre, and C. Lassman, "Minimizing diaphragmatic injury during radio-frequency ablation: Efficacy of subphrenic peritoneal saline injection in a porcine model," Radiology **222**, 819–823 (2002).
[25]Y. S. Tung, H. L. Liu, C. C. Wu, K. C. Ju, W. S. Chen, and W. L. Lin, "Contrast-enhanced ultrasound thermal ablation," Ultrasound Med. Biol. **32**, 1103–1110 (2006).